SCHOLARLY PUBLICATIONS

A CURRENT AWARENESS BULLETIN
OF RESEARCH OUTPUT

@DTU

(147th Edition)

MARCH 2025

BY: CENTRAL LIBRARY

DELHI TECHNOLOGICAL UNIVERSITY

(FORMERLY *DELHI COLLEGE OF ENGINEERING)*
GOVT. OF N.C.T. OF DELHI
SHAHBAD DAULATPUR, MAIN BAWANA ROAD
DELHI 110042

PREFACE

This is the **One Hundred Forty Seven** Issue of Current Awareness Bulletin started by Delhi Technological University, Central Library. The aim of the bulletin is to compile, preserve and disseminate information published by the faculty, students and alumni for mutual benefits. The bulletin also aims to propagate the intellectual contribution of Delhi Technological University (DTU) as a whole to the academia.

The bulletin contains information resources available in the internet in the form of articles, reports, presentations published in international journals, websites, etc. by the faculty and students of DTU. The publications of faculty and student which are not covered in this bulletin may be because of the reason that the full text either was not accessible or could not be searched by the search engine used by the library for this purpose.

The learned faculty and students are requested to provide their uncovered publications to the library either through email or in CD, etc. to make the bulletin more comprehensive.

This issue contains the information published during **March, 2025**. The arrangement of the contents is alphabetical. The full text of the article which is either subscribed by the university or available in the web is provided in this bulletin.

Central Library

CONTENTS

1. A Multi-cluster Security Framework for Healthcare IoT: The Synergy of Redundant Byzantine Fault Tolerance with Extensions and Coati-Based NetworK, ***3.Rohit Beniwal***, ***3.Vinod Kumar*** and ***6.Vishal Sharma***, Computer Science, DTU

2. A review on microfluidic-based electrowetting on dielectric (EWOD) in state-of-the-art adaptive electronic cooling, ***6.Amit SAHU, 3.Mohammad ZUNAID, 3.Rajesh KUMAR***, Mechanical Engg, DTU

3. Analytical modeling of fringe capacitance in opposite-doped core- shell junctionless nanowire FET, ***3.Bharti*** and ***3.Poornima Mittal***, ECE, DTU

4. A Self-Decoupled MIMO Patch Antenna System for V2X Communications, Amit Kumar***, 7.1 Sandeep*** Rana, Akhilesh, Mohan, Member, Gunjan Srivastava, Sachin Kumar and Kang Wook Kim, ECE, DTU

5. Analysing the long run relationship between CO2 emissions and Energy use of United Kingdom***, 6.Akanksha Singh*** and ***3.Nand Kumar***, Humanities, DTU

6. Advancing sentiment analysis by addressing negation handling challenge via unsupervised mathematical approach***, 6.Neha Punetha, 3.Goonjan Jain,*** A Maths, DTU

7. Blast analysis of stand alone CFST column***, 8.1 Kartikeya TIWARI , 8.1 Harsh VARDHAN, 8.1 Ayush ANAND, 6.Gaurav KUMAR, 3.Amit Kumar SRIVASTAVA***, Civil, Mechanical, DTU

8. Blast analysis of stand alone CFST column, ***8.1 Kartikeya TIWARI, 8.1 Harsh VARDHAN, 8.1 Ayush ANAND, 3. Amit Kumar SRIVASTAVA*** and ***6. Gaurav KUMAR*** Civil Engg., Mechanical Engg., DTU

9. CorrNetDroid: Android Malware Detector leveraging a Correlation-based Feature Selection for Network Traffic features, ***6.Yash Sharma*** and ***3. Anshul Arora***, Applied Mathematics, DTU

10. Comparative Assessment of Trap Charges Effect on Triple Hybrid Metal Gate Dielectric Modulated Junctionless Gate All Around Nanowire FET-Based Biosensor, Mekonnen Getnet Yirak and ***3. Rishu Chaujar***, Applied Physics, DTU

11. Comprehensive study of highly efficient Rb2AgInX6 (X = Cl, Br, I) based lead-free double perovskite solar cells, ***6.Vishal Deswal and 3.Sarita Baghel***, Applied Physics, DTU

12. Comparative Assessment of MPPT Techniques for Optimizing Photovoltaic System Efficiency, Rachna Dhir, ***3.Rachana Garg and 3.Priya Mahajan***, Electrical, DTU

13. Capturing spatiotemporal dependencies with competitive set attention for video summarization, ***7.Md Hasnat Hosen Arafat, 3.Kavinder Singh***, Computer Science, DTU

14. Comprehensive Survey on Computational Techniques for Brain Tumor Detection: Past, Present and Future, ***6.1 Priyanka Datta, 3.Rajesh Rohilla***, Ece, DTU

15. Crowdsourcing adoption in organisations: a multi-perspectiveanalysis of innovation andorganisational dynamics, Divya Mishra, and ***3.Nidhi Maheshwari***, USME, DTU

16. Deep decomposer and refiner for low-light image enhancement, ***6.Piyush Vaish 3.Anil Singh Parihar,*** Computer Science, DTU

17. Design and development of drivetrain for fully faired hybrid recumbent bicycle***,*** ***6.Siddharth GARG ,8.1 Rhythm AGGARWAL 8.Vaibhav KUMAR 3.Raghvendra GAUTAM,*** and ***8. Priyanshu SINHA***, Mechanical Electrical, DTU

18. Designing and optimization of a highly efficient and new lead-free Cs2RbGaI6 based double perovskite solar cell through SCAPS-1D and machine learning, ***6.Vishal Deswal , 3.Sarita Baghel,*** Applied Physics, DTU

19. Durrmeyer type operators linked with Boas-Buck type Polynomials, ***3. Naokant Deo*** and ***6.Sandeep Kumar***, Applied Mathematics, DTU

20. Dynamic cloud model based on decision field theory, ***6.Anjali Anjali , 3.Anjana Gupta***, Applied Mathematics, DTU

21. Deep-reinforcement-learning-based controller design for pantograph and catenary system, ***6.ROHINI SHARMA, 3.PRIYA MAHAJAN and 3.RACHANA GARG***, Electrical, DTU

22. Design and theoretical analysis of a dual-core photonic crystal fibre temperature sensor with enhanced sensitivity across an extended temperature range, ***6.Shubham Sharma, 3..Ajeet Kumar*** & Than Singh Sain, Applied Physics, DTU

23. Dynamic Response Experimental Analysis of High-Speed Rotors Equipped with Squeeze Film Dampers Under Varied Point Loading Conditions, ***6.Ratnesh Kumar Gupta*** and ***3.Ramesh Chandra Singh***, Mechanical, DTU

24. Design of an array multiplier in PFSCL style, ***6.Shikha***, Kirti Gupta, Monica Gupta, Preeti Nagrath, Bhawanand Jha, Prakhar Sharma, Mauro Zannetti, ECE, DTU

25. Dielectric Modulated InAs Pocket Heterojunction Tunnel FET for Biosensor Applications, ***6.Shashi Ranjan Upadhyaya, 3.Sumit Kale*** and ***3.Anukul Pandey***, ECE, DTU

26. Effect of nozzle shape on bubble column reactor with constant flow rate, ***6.Sachin Kumar, 3.Raj Kumar Singh*** and Bahni Ray, Mechanical Engg. DTU

27. Exploring the Transformative Impact of Blockchain, Technology on Healthcare: Security, Challenges, Benefits and Future Outlook***, 6. Anita Thakur, 3.Virender Ranga, 3.Ritu Agarwal***, IT, DTU

28. Effect of Substitutional Doping and Cu Adsorption on MoS 2 Nanowire: A Comparative DFT Study, ***6.Anurag Bhandari***, Piyush Dua, and ***3.Nitin K. Puri***, Applied Physics, DTU

29. Experimental investigation of enhanced hydrogen production from atomised water-methanol mixture in a modified plasma reformer, ***6.Neeraj Budhraja, 3.Amit Pal*** and ***3.R.S. Mishra,***Mechanical Engg., DTU

30. Examining maternal healthcare service utilization as a determinant of child health outcomes in India: Demographic and Health Survey 2019–21, ***6.Charu Tayal,*** Rajesh Sharma & ***3.Kusum Lata***, USME, DTU

31. Enhancing the durability of cast steel cylinder liners using HVOF sprayed functionally graded coatings, ***6.Prabhat Ranjan, 3.Rajesh Kumar***, R S Walia and Vinod Kumar Yadav, Computer Science, DTU

32. Field Performance Assessment of a 1.34 kW Rooftop PV plant in Delhi : Insight from two Comparative Periods, ***3.Rachna Garg, 3.Priya Mahajan***, Electrical Engg. DTU

33. High-capacity reversible data hiding in encrypted images based on difference image transfiguration, ***6.Ankur , 3.Rajeev Kumar***, Ajay K. Sharma,· Pallavi Ranjan, CSE, DTU

34. Harnessing Tc-Ls-Ga-At: a novel deep learning based hybrid approach for wind power forecasting, ***8.1 Kartik Bansal***, ***8.1 Kartik Bisht, 3.Priya Singh***, Computer Science, DTU

35. Improving software vulnerability severity prediction model performance with HDLN & FWFS: a two-stage feature selection approach,***3.Ruchika Malhotra, 6.Vidushi,*** Software Engg. DTU

36. Influence of Heat Input Variations on Tribological Performance of Bimetallic Aluminum Alloy Walls Fabricated via Cold Metal Transfer-Based Wire Arc Additive Manufacturing, ***6.Soni Kesarwani, 3.Narayana Yuvaraj, 3.Mahendra Singh Niranjan***, Mecahnical Engg., DTU

37. Integrated Advanced Oxidation Processes for Chlorophenol Degradation: Parameter Influence, Efficacy Evaluation and Toxicity Assessment with Eichhornia crassipes***, 6.Shivani Yadava,, 6.Harsh Pipila***, Sunil Kumar and ***3.Anil Kumar Haritasha***, Environmental Engg., DTU

38. Investigation on Impact of Inverter-Based Resources on Power System Using Phasor Measurement Unit, ***6.Nitisha Sudhir Darwade, 3.S. T. Nagarajan***, Electrical Engg., DTU

39. Indigenous Knowledge and Water Conservation Practices in South Africa: A Systematic Literature Review, Arvind Kumar Sahani, Garima Gupta, Subhash Anand, Vishwa Raj Sharma, Rajender Singh ,Azka Kamil , Harish Kumar 3, Alka Gagan, Vinod Kumar Mayala, Arun Pratap Mishra, Sunil Jaiswal and ***8.Jasmine Anand***, Applied Mathematics, DTU

40. Koch-curve fractal plasmonic nanoantennas on VO2 for near-field plasmonic switching, ***3.Asbah Masih*** and ***3.Yashna Sharma***, ECE, DTU

41. Micro or Meso: Do influencers influence veganism?, Sakhhi Chhabraa, Tahir A. Wanib and ***6.1 Vaishali Kaushal***, DSM, DTU

42. MXene-Integrated Composites for Biomedical Applications: Synthesis, Cancer Diagnosis, and Emerging Frontiers, ***6.Aryan Saxena, 8.1 Akshayat Tyagi***, Sushipra Vats, ***8.1 Ishita Gupta,*** Akhil Gupta, ***3. Raminder Kaur***, Saurabh Kr Tiwary, Ahmed A. Elzatahry, Maninderjeet Singh and Alamgir Karim, Applied Chemistry, DTU

43. Measuring the Impact of Infill Pattern and Infill Density on the Properties of 3D-Printed PLA via FDM, ***6.Siddharth Garg***, ***8.Aditya Singh***, and ***3.Qasim*** Murtaza, Mechanical Engg., DTU

44. Modelling and simulation of plasma-assisted 2D graphene based solar Cells, ***7.1 Shreya Vasu***, Shikha Singh and ***3.Suresh C. Sharma***, Applied Physics, DTU

45. Nanogap Sequestered Dielectric Modulated Gate Engineered Carbon Nanotube Bio-FET based Bio-Sensor,***6. Bhargavi Sharma, 3.Sonam Rewari, and 3.Yasha Hasija*** Biotechnology, ECE, DTU

46. Novel molasses-grafted poly(sodium acrylate) hydrogel: A sustainable solution for water retention and controlled dinotefuran release, 6***.Manu Nandal, 6.Vaishali Prashar, 6.Mukul Bansiwal, 8.Ishita Kapoor, 8.Tushar Kansal*** & ***3.Rajinder K. Gupta***, A Chemistry, DTU

47. Numerical analysis of various nanofluids in circular and square plate solar collector with spiral and U-bend collector pipe designs, ***6.Utkarsh Verma, 8.Shivraj Yadav, 6.Gaurav Kumar*** & ***3.Raj Kumar Singh,*** Mechanical Engg., DTU

48. Optimizing Wind Load Performance through Shape Modifications and Corner Configurations in High-Rise Buildings:A Computational Fluid Dynamics Study 6***.Sudhanshu Pandey, 8.1 Nitesh Kumar Thakur, 8.1 Paras Nath 6.Deepak Sharma*** and ***3.Ritu R***, Civil Engg., DTU

49. Photonic crystal fibres infiltrated with nitrobenzene for low peak power supercontinuum generation in NIR to MIR region, ***6.Drishti Singh Tomer & 3.Ajeet Kumar***, Applied Physics, DTU

50. Phytochemistry of Aloe vera: A Catalyst for Environment-Friendly Diverse Nanoparticles with Sustained Biomedical Benefits***, 6. S. Yadav*** , A. Khan and ***3.J. G. Sharma***, Biotech, DTU

51. Predictive Analytics of Crime Data in Social Media: A Systematic Review, Incorporating Framework, and Future Investigation Schedule***, 6.Monika, 3.Aruna Bhat***, CSE,DTU

52. Ranking of Efficient Fuzzy Portfolios by Hybrid MSBM-TOPSIS Technique, Abha Aggarwal, 3***.Anjana Gupta,*** Rajkumar Verma***, 6.1,Reenu Kumar***, Applied Mathematics, DTU

53. Realization of all optical silicon slab waveguide based universal logic gates, ***6.Yash Yadav, 3.Yogita Kalra***, Applied Physics, DTU

54. Regional disparities in social support services for vulnerable populations in France: inequalities in access and inclusion, ***6.1 Mansift Kaur*** and Neha Narula, USME, DTU

55. Secure and Efficient Routing in Fog-Enable VANETs: A Clustering-Based Approach, Anshu Devi, Ramesh Kait and ***3.Virender Ranga***, IT, DTU

56. Self-Powered Flexible Micro-Supercapacitor Based On Optimized Laser Induced Graphene Electrodes For Sustainable Energy Harvesting And Storage, Faizan T. Beigh, Vishal Singh, ***3.Bharti Singh***, And Dhiman Mallick, Applied Physics, DTU

57. The Utility of Synthetic Biology in the Treatment of Industrial Wastewaters ***8.1 Monica Joshi and 3.Jai Gopal Sharma***,Biotechnology, DTU

58. The empirical and managerial landscape of workplace spirituality: a systematic literature review of studies published in ABDC list journals, Nancy Munjal and Geeta Sachdeva, ***3.Naval Garg***, USME, DTU

59. Ultracapacitor Assisted Battery Based HESS for Electric Vehicle Considering Battery Aging, ***3.Kuldeep Singh, 3.Mukhtiar Singh, 3.Sudarshan K Valluru*** , Electrical Engg., DTU

60. Ultrasonic vibration assisted Cold Metal Transfer Direct Energy Deposition of Dissimilar SDSS2507 IN718 Alloy parts: Microstructural and Mechanical Characterization, ***6.Rajendra Prasad, 3.N. Yuvaraj and 3.Vipin***, Mechanical Engg., DTU

61. Unraveling the topological phase in Zintl semiconductors RbZn4X3 (X = P, As) through band engineering, ***6.Ramesh Kumar, 6.Rajesh Kumar***, Antik Sihi and ***3.Mukhtiyar Singh***, Applied Physics, DTU

1. *Vice Chancellor*

2. *Pro Vice Chancellor*

3. *Faculty*

4. *Teaching-cum-Research Fellow*

5. *Asst. Librarian*

6. *Research Scholar*

7. *PG Scholar*

8. *Undergraduate Student*

1.1. *Ex Vice chancellor*

2.1. *Ex Pro Vice Chancellor*

3.1. *Ex Faculty*

4.1. *Alumni*

5.1 *Others*

6.1. *Ex Research Scholar*

7.1. *Ex PG Scholar*

8.1. *Ex Undergraduate Student*

Check for updates

Transactions on Emerging Telecommunications Technologies

WILEY

RESEARCH ARTICLE

A Multi-cluster Security Framework for Healthcare IoT: The Synergy of Redundant Byzantine Fault Tolerance with Extensions and Coati-Based Network

Rohit Beniwal | Vinod Kumar | Vishal Sharma

Department of Computer Science & Engineering, Delhi Technological University, Delhi, India

Correspondence: Vishal Sharma (vishalsharma_2k20phdco506@dtu.ac.in)

Received: 6 August 2024 | **Revised:** 10 December 2024 | **Accepted:** 20 January 2025

Keywords: adaptive configuration | anomaly detection | intrusion detection | IoT networks | network security

ABSTRACT

The rapid integration of Internet of Things (IoT) devices into healthcare systems has revolutionized medical care delivery but has also introduced significant security challenges. Ensuring secure communication, privacy preservation, and system resilience in resource-constrained healthcare IoT networks is critical, given the sensitivity of the data involved and the potential for malicious attacks. This research addresses these concerns by proposing a Multi-cluster Security Framework for Healthcare IoT, designed to overcome existing limitations in security and scalability. The framework combines Redundant Byzantine Fault Tolerance with Extensions (RB-BFT X) and CoatiNet, leveraging lightweight cryptographic techniques, role-based access control, and dynamic routing algorithms. RB-BFT X enhances intra-cluster security through fault tolerance and anomaly detection, while CoatiNet optimizes inter-cluster communication using adaptive routing and self-recovery mechanisms inspired by coatis' natural behavior. Experimental results demonstrate the framework's efficacy, achieving a high detection rate of 98.20%, minimal latency, and stable throughput under various adversarial conditions. Compared to existing methods, it outperforms in maintaining network lifetime and reducing false positives, even with increased malicious activity. These findings have significant implications for enhancing the security and efficiency of healthcare IoT networks. The proposed methodology ensures robust data protection, efficient communication, and adaptability to evolving threats, contributing to safer and more reliable healthcare systems.

1 | Introduction

The Internet of Things (IoT) connects devices across various sectors, including smart homes and healthcare, offering advantages such as real-time data monitoring, streamlined operations, and enhanced user interactions [1]. However, the widespread adoption of IoT presents significant challenges, particularly in ensuring security, privacy, and resilience against cyber threats. These challenges are exacerbated by the resource limitations of IoT devices and the increased attack surface created by a large number of connected devices [2]. Traditional security approaches often fail to address these challenges effectively; for example, blockchain offers secure and transparent data management but is computationally intensive for resource-constrained IoT devices [3], while machine learning-based anomaly detection requires significant computational power that many IoT devices cannot provide [4]. Fog computing addresses latency by bringing computation closer to devices [5], and Secure Multi-Party Computation (SMPC) enables private data sharing [6], but these methods still face scalability and integration issues. These limitations highlight the need for innovative, lightweight, and adaptive security solutions tailored to the unique constraints of IoT environments [7].

© 2025 John Wiley & Sons Ltd.

Despite advances, methods like RBAC with multi-factor authentication (MFA) [8] are complex to integrate into IoT, and blockchain-based systems [9] require substantial resources. AI-based threat detection [10] performs well but demands computing power exceeding IoT capabilities. Hashing techniques [11], including SHA 2 [12] and SHA 3 [13], ensure data integrity, while Message Authentication Codes (MAC) [14] and HMAC [15] add security to data transmission. TLS [16] and DTLS [17] encrypt communication, but DTLS is optimized for unreliable datagram connections. Techniques like Diffie-Hellman Key Exchange [18] establish secure channels but face scalability and efficiency challenges [19].

Blockchain has emerged as a promising solution for IoT security by providing decentralized data management that enhances transparency and trust. References [20, 21] highlight how blockchain can be adapted to IoT needs, addressing challenges like auditability, security, and decentralization. However, these implementations often suffer from high computational and storage demands, making them less suitable for resource-constrained IoT devices. References [22, 23] integrate Explainable AI (XAI) with blockchain in cybersecurity frameworks for Zero Touch Networks (ZTN) and smart healthcare systems, showcasing improvements in transparency and trust. Despite these advances, existing frameworks face limitations in real-time adaptability and efficient handling of large-scale IoT networks, often requiring significant computational resources. References [24, 25] also propose a blockchain and deep learning-based threat detection model for Software-Defined Industrial IoT (SDIIoT), but it struggles with scalability and mitigating single points of failure. Similarly, Reference [26] introduces a security situation awareness framework for IoT software chains using machine learning and Markov game models, which effectively predicts security threats but lacks integration with lightweight cryptographic methods and dynamic routing optimization.

While current and traditional perspectives lay the foundation for developing protective measures for IoT networks, it is imperative to consider resource-limited devices. Therefore, the suggested approach outlines a new security architecture that implements robust cryptographic methods, optimal key management, and secure communication methods. The proposed framework includes two key components from their previous versions: RB-BFT X and CoatiNet. RB-BFT X refines the improved BFT [27] by overcoming the drawbacks like poor scalability and high computational cost of the improved BFT; the modifications incorporate confidentiality, integrity, and efficiency to ensure that the network satisfies security requirements. CoatiNet enhances the Coati algorithm [28] by focusing on three main areas: optimization of agents in the communication paths, continuous reallocation of data according to feedback received, and improved security frameworks to overcome the limitations of the Coati algorithm, including the inefficient communication and static handling of data in IoT networks, lower latency, better network performance, and security of the communication paths in healthcare IoT networks.

The proposed framework offers the following enhancements:

- To ensure intra-cluster security within the healthcare IoT network, a consensus layer RB-BFT X module is used, encompassing lightweight cryptography, RBAC, an anomaly detection module, and anonymization to create a unified protocol suite.
- CoatiNet for Inter-cluster and Server Communication Optimization:
  i. CoatiNet introduces a dynamic routing approach that continuously optimizes communication paths, which are designed by drawing inspiration from Coati's adaptable foraging strategies.
  ii. CoatiNet dynamically adjusts and selects the paths based on network conditions and threats through optimized routing to minimize latency.
  iii. Inspired by Coati's escape from predator strategy, the security approach, which combines the benefits of multi-layered authentication, intrusion detection, and redundancy with the backup channel, is designed.
- The performance evaluation based on accuracy, precision, recall, F1-score, latency, throughput, and intrusion detection rate metrics is done. Also, an ablation study to know the individual contributions of each component within the proposed methodology is established.

This research paper is divided into six sections as follows: Section 2 gives the literature review on the existing works related to IoT network security, Section 3 gives the system model, Section 4 gives a detailed explanation of the proposed methodology, Section 5 gives the experimental methodology and performance analysis, and the conclusion is given in Section 6.

2 | Literature Review

The literature review section outlines the work to provide IoT network security and the research gaps. Table 1 gives a summary of Section 2.

2.1 | Blockchain-Based Approaches

In a blockchain, a distributed ledger technology is implemented into one IoT network to improve device security. In 2022, Demirbaga and Aujla [29] suggested a technique that integrates the nature of blockchain technology in delivering, allowing only secure and authorized access to the query results to avoid a possible leakage of sensitive data and maintain the data's authenticity. Bodur and Yaseen [30] proposed a new approach for integrating health information exchange using a distributed document-oriented database and blockchain. By following the data categorization and consensus approaches, they always provide enhanced security measures, availability, and sharing of the information, and patients' privacy protection. However, there are limitations to adopting it, like operational complexities arising from adopting the new technology, scalability problems when there is a rise in the number of transactions, the fact that blockchain requires significant resource utilization, and legal hurdles organizations deem worthy of consideration.

2.2 | Data Security and Privacy Enhancement Approach

To contractors, several principles have been adopted in security and privacy enhancement as consideration continues to be

21613915, 2025, 3, Downloaded from https://onlinelibrary.wiley.com/doi/10.1002/ett.70098 by Delhi Technological University, Wiley Online Library on [09/03/2025]. See the Terms and Conditions (https://onlinelibrary.wiley.com/terms-and-conditions) on Wiley Online Library for rules of use; OA articles are governed by the applicable Creative Commons License

TABLE 1 | Summary of literature review.

Author name and year	Framework or tools employed	Application domain	Innovation
Kumar et al. (2024) [23]	Blockchain, Smart Contracts, Digital Twins (DTs), Self-Attention-based LSTM (SALSTM), SHAP	Cybersecurity, Zero Touch Networks (ZTN), Intrusion Detection Systems (IDS)	Integration of XAI with IDS, use of DTs for risk-free attack simulation, high accuracy in real-time threat detection.
Zhu and Deng (2022) [26]	SVM and a Markov game model	Security of IoT software chains	Simulating interactions between attackers and defenders
Kumar et al. (2023) [25]	Explainable AI (XAI), SHAP values, Blockchain, Intrusion Detection System (IDS), InterPlanetary File System (IPFS)	Consumer IoT (CIoT), Metaverse	Integration of XAI and blockchain for trust and transparency, real-time threat detection, cross-domain authentication.
Kumar et al. (2024) [22]	Blockchain, Clique Proof-of-Authority (C-PoA), Parallel Stacked LSTM (PSLSTM), Multi-Head Self-Attention (MhSA), SHAP	Smart Healthcare Systems (SHS), IoMT Cybersecurity	Integration of blockchain with XAI, novel deep learning model combining PSLSTM and MhSA, enhanced transparency and trust.
Demirbaga and Aujla (2022) [29]	Blockchain, Big data analytics tools, Zero-Knowledge Protocol (ZKP)	Healthcare (EHRs, patient data management)	Integration of blockchain and big data for data privacy, integrity, and secure access in IoT healthcare systems.
Bodur and Yaseen (2024) [30]	Document-oriented database, Blockchain, Consensus mechanisms (PoW, PoS, PoA)	Healthcare (EMRs, also banking, finance, real estate)	Secure sharing of EMRs, blockchain, and document-oriented DB for security and performance.
Guo et al. (2023) [31]	k-sums algorithm, Multi-primary node mechanism, Proxy mechanism, Dynamic reputation model	IoT environments, Smart factories, Healthcare, Smart homes	Scalable Byzantine fault-tolerant protocol, enhanced IoT device management, security, and fault tolerance.
Dhasarathan et al. (2024) [32]	Multi-Agent Systems (MAS), Deep Learning, Federated Learning	E-Healthcare, patient data privacy	Real-time privacy monitoring with MAS and deep learning.
Zhang et al. (2022) [33]	Federated Learning, Homomorphic Encryption, Secure Multi-Party Computation, Diffie-Hellman	IoT-enabled Healthcare, Skin Cancer Classification	Privacy-preserving federated learning, collusion-resistant solutions, and model training without raw data.
Yang et al. (2022) [34]	Interval type-2 fuzzy logic, GAN for trust evaluation, Codec structure	Industrial Wireless Sensor Networks, Automation	Integration of fuzzy logic and GAN for dynamic trust decision-making and resilience.
Vinitha et al. (2022) [35]	Taylor C-SSA, LEACH protocol, MATLAB simulation	Wireless Sensor Networks, Environmental monitoring, Healthcare	Optimal routing selection, energy efficiency, and security-aware routing with Taylor C-SSA.
Singh et al. (2024) [36]	SecureFlow system, Snort, SVM IDS, SDN for dynamic network management	IoT, Smart factories, Power systems, Smart communities	Hybrid knowledge-driven and data-driven approach for real-time security responses and adaptability.
Anand and Sharma (2022) [37]	Cluster Key Management, IoT Sensors, Web Interface for interaction	Precision Agriculture	Enhanced security services, improved packet delivery and reduced drops with IoT communication.

(Continues)

21613915, 2025, 3, Downloaded from https://onlinelibrary.wiley.com/doi/10.1002/ett.70098 by Delhi Technological University, Wiley Online Library on [09/03/2025]. See the Terms and Conditions (https://onlinelibrary.wiley.com/terms-and-conditions) on Wiley Online Library for rules of use; OA articles are governed by the applicable Creative Commons License

TABLE 1 | (Continued)

Author name and year	Framework or tools employed	Application domain	Innovation
Arazzi et al. (2024) [38]	Behavioral Fingerprinting, Blockchain, Distributed Consensus	IoT environments, Smart homes, Industrial IoT applications	Fully distributed trust model, blockchain integration, and anomaly detection for IoT networks.
Jeyakumar and Samraj (2024) [39]	Hybrid encryption (AES, RSA, Paillier), IoT sensors, Raspberry Pi, Cloud database	Healthcare monitoring, Remote patient monitoring	Secure communication, real-time alerts, and continuous health data monitoring.
Dhar et al. (2024) [40]	Blockchain, Quantum Key Distribution, Zero-Knowledge Proofs, Ring Signatures	IoT systems, Healthcare, Smart homes, Industrial automation	Blockchain and quantum cryptography for enhanced security, ZKPs for privacy.
Rabie et al. (2024) [41]	Certificate-less aggregate signature scheme, ECC, Distributed batch authentication	Healthcare wearable medical sensor networks	Privacy-preserving data transmission, computation cost reduction, and enhanced security.
Masood et al. (2023) [42]	Elgamal Cryptography, ECSO, Butterfly Optimization Algorithm	Healthcare (WMSNs for patient health monitoring)	Integration of cryptography and optimization for enhanced privacy and energy efficiency in WSNs.
Baucas et al. (2023) [43]	Fog-IoT architecture, Federated learning, Private blockchain	Predictive healthcare, Wearable IoT devices	Integration of federated learning and blockchain for privacy and service integrity in healthcare.
Liu et al. (2022) [44]	Blockchain, Smart Contracts, Reputation-based Consensus Mechanism	Zero-Trust IoT, Smart Vehicles, Industrial IoT systems	Decentralized IoT information sharing with fairness, privacy, and traceability mechanisms.

given to data security. One is the DCBFT protocol proposed by Guo et al. [31], which addresses efficiency, scalability, and fault tolerance in distributed systems. Kumar et al. [23] proposed a blockchain-enabled eXplainable AI (XAI) framework that combines blockchain with Parallel Stacked Long Short-Term Memory (PSLSTM) and multi-head attention to enhance cyber threat detection in smart healthcare systems. Their framework validates and secures data transmission between entities while improving explainability for decision-making.

2.2.1 | Detection Methods Using Machine Learning Techniques

Machine learning techniques play a pivotal role in IoT security. Dhasarathan et al. [32] combined deep learning with artificial bee colony optimization for anomaly detection in e-healthcare systems, achieving real-time monitoring but adding system complexity. Zhang et al. [33] utilized federated learning with homomorphic encryption for privacy-preserving detection, though high communication overhead and computational costs challenge resource-constrained IoT devices. Zhu and Deng [26] proposed a Markov game model for dynamic threat assessment, enhancing adaptability but facing computational complexity and reliance on precise data. Despite their limitations, these methods significantly improve IoT security through advanced detection and situational awareness.

Nevertheless, it is imperative to highlight that these strategies also present specific difficulties. Cryptography also has limitations due to its sophisticated nature and the expenses likely to be incurred in secure communication and employing cryptographic techniques. However, there is a reliance on third-party trust authorities, which could also potentially bring with it exposure and prevent trust from forming.

2.3 | IoT Security and Threat Detection Approach

As the use of IoT devices grows, security and chances of an attack must permanently be sealed and looked for, respectively. Based on Yang et al. [34], the authors utilized generative adversarial learning to make the detection uncertain and to enhance malicious node detection in IoT networks. The Taylor C-SSA algorithm and the trust model were suggested by Vinitha et al. [35] to improve energy efficiency and security in IoT scenarios. Singh et al. [36] proposed a two-tier IDS solution with the host status rating for holistic threat evaluation in the IoT environment. Kumar et al. [25] developed a blockchain and deep learning-based framework for securing software-defined industrial IoT (SDIIoT) environments. Their model combines blockchain-based Clique Proof-of-Authority (C-PoA) consensus mechanisms with LSTMSCAE-AGRU for anomaly detection, effectively mitigating vulnerabilities in centralized systems.

However, there are some difficulties posed by these approaches; for example, the GAN training generative adversarial networks is a very computationally intensive process. The use of security features may consume numerous resources. The decision regarding the threat may be inconclusive if there are inaccuracies in the IDS components.

21613915, 2025, 3, Downloaded from https://onlinelibrary.wiley.com/doi/10.1002/ett.70098 by Delhi Technological University, Wiley Online Library on [09/03/2025]. See the Terms and Conditions (https://onlinelibrary.wiley.com/terms-and-conditions) on Wiley Online Library for rules of use; OA articles are governed by the applicable Creative Commons License

2.4 | Security Measures in Specific Domains Approach

For domain-specific threats, situations such as precision agriculture and healthcare monitoring have been proposed to use new approaches that would suit the particular domain. Anand and Sharma [37] proposed AgroKy for adequately handling the cluster key in precision agriculture to ensure secure and reliable data transfer and reduce susceptibility to external attacks. Arazzi et al. [38] suggested using behavioral fingerprinting, distributed consensus mechanisms, and blockchain technology to enhance usability and security in multiple applications. Jeyakumar and Samraj [39] offered an outline of the solution that includes wearable sensor devices for capturing data, the cloud for storing data and encrypting the data, and the ability to monitor and process data from a remote location.

However, several difficulties may arise when addressing these new security measures, including issues in management and implementation, compatibility and integration of the new security measures, high computational needs, and complications with the existing and new rules and regulations.

2.5 | Advanced Cryptographic Techniques

Advanced cryptographic techniques are widely used to increase security and privacy within various domains. Dhar et al. [40] included blockchain and cryptographically secure quantum key distribution to increase the security of the system as well as the efficiency of the system to serve a large number of participants in the proposed system by Rabie et al. [41]; they adopted elliptic curve-based public key cryptography to afford security, privacy, and decentralization. Kumar et al. [22] integrated blockchain-enabled explainable AI mechanisms for enhancing cybersecurity decisions through validated and anonymized data exchange in IoT environments. The system employs cryptographic techniques to ensure data authenticity while maintaining lightweight operations. Some of the recent key contributions include Masood et al. [42] that proposed Elgamal cryptography, ECSO, and BO for security and real-time detection of attacks, and Baucas et al. [43] that put forward a fog-IoT, federated learning, and private blockchain for privacy and data integrity. Dhasarathan et al. [44] also have a multi-agent-based privacy metrics, deep learning, and artificial bee colony approach for further increases in privacy and real-time monitoring of patient's state for proper diagnosis and treatment. Further, the authors Liu et al. [45] put forward Blockchain-enabled Decentralized Information Exchange with features including anonymity and entity authentication. However, their approach has implementation and management challenges, increased transactions, resources needed in blockchain operations, and regulatory and compliance complications that may arise. Despite the opportunities, these techniques have some disadvantages related to the complexity of implementation, extreme resource consumption, and problems with scaling and maintenance costs, which will limit the technology's popularity. Table 1 gives the summary of the literature review.

The literature review highlights several significant gaps in the existing research on security, privacy, and efficiency within healthcare IoT and distributed systems. A major gap lies in the scalability of current fault-tolerance algorithms. Many existing methods, such as PBFT, suffer from high communication overhead, limiting their application in large-scale IoT networks, and fail to accommodate the resource constraints of IoT devices, which are typically low-power and low-memory. Additionally, there is a general lack of integrated security mechanisms that address multiple aspects such as access control, anomaly detection, and data privacy in a unified framework, leaving systems vulnerable to evolving threats. Furthermore, most existing solutions are static and do not dynamically adapt to changing network conditions or emerging security threats, which makes them inefficient for real-time IoT data. To address these gaps, the proposed methodology integrates RB-BFT X, which reduces communication complexity and utilizes lightweight cryptographic methods, making it more suitable for resource-constrained environments. It also integrates role-based access control (RBAC), behavioral anomaly detection, and data anonymization, ensuring that all security layers work together to safeguard the system. Additionally, the methodology employs CoatiNet, which uses dynamic routing algorithms to adapt to changing network conditions and threats, ensuring optimal performance and security. By combining insights from distributed systems, cryptography, and IoT security, the proposed approach aims to provide a comprehensive solution that addresses these gaps and ensures the accuracy, security, and efficiency required for modern healthcare IoT networks.

3 | System Model

As shown in Figure 1, the healthcare IoT network and its ecosystem are built based on a specific structure containing complex elements divided into several clusters based on their responsibilities essential to the system's performance. These clusters from the larger picture also consist of patients (PC_i), doctors (DC_j), receptionists (RC_k), and administrators (AC_l), and the house IoT devices that are relevant to each of them. PC_i incorporated systems include wearables in the form of health monitoring devices and medical terminals (D_{PC_i}), the operations of which are to capture and forward patient care data for further analysis and monitoring. In contrast, DC_j host devices (D_{DC_j}) provide access to patient records, diagnosis, and communication channels for health professionals. RC_k coordinate administrative work, appointment setting, and client relations through the IoT devices (D_{RC_k}), although AC_l supervise physical facilities, IoT systems and compliance with legal requirements through their devices (D_{AC_l}).

The basic structure of this network architecture is based upon a hierarchical scheme to enhance communication and management of the entire system. Main hospital servers are primarily responsible for granting patient record information and managing the network systems. Then, the Cluster Heads (CH_i, CH_j, CH_k, CH_l) are appointed to regulate communication and coordinate within the determined areas of responsibility. This design can enhance data flow, IoT security, and network expansion since different groups are hierarchical.

Data flow in the healthcare IoT network is well planned and implemented to ensure the optimized transfer of data and the information transfer is secure. Within each cluster, the

21613915, 2025, 3, Downloaded from https://onlinelibrary.wiley.com/doi/10.1002/ett.70098 by Delhi Technological University, Wiley Online Library on [09/03/2025]. See the Terms and Conditions (https://onlinelibrary.wiley.com/terms-and-conditions) on Wiley Online Library for rules of use; OA articles are governed by the applicable Creative Commons License

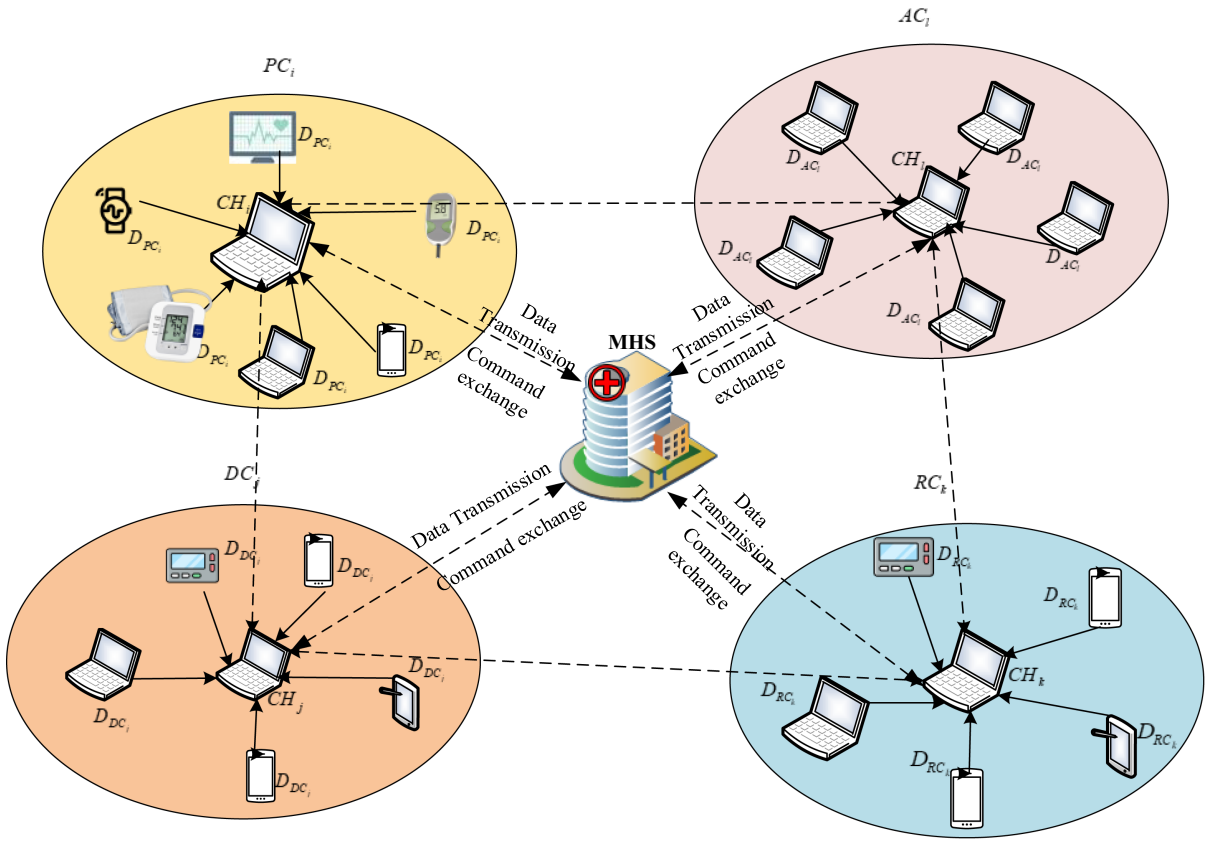

FIGURE 1 | Healthcare IoT Network System Model.

corresponding IoT devices are paired with their *CH*, which is the primary way of communication between devices of the same cluster. These *CH* serve as middlemen in conveying messages with the main hospital servers (*MHS*), where necessary, so that information flows between Clusters and servers. The communications cycle architecture of this method reduces latency as well as privacy and security barriers and allows for the easy sinking of IoT in the healthcare system.

3.1 | Attacker Model

The proposed methodology covers the following different types of threats targeting healthcare IoT networks through the attacker model.

3.1.1 | Passive Eavesdropping on Patient Clusters

A threat actor tries to eavesdrop on communication data between the IoT devices of two patients in the same cluster, and the Cluster Heads are responsible for managing several patient clusters to obtain personal medical information without modifying the original transmitted data. As a result of this process, there is a high tendency for data leakage to occur.

3.1.2 | Active Intrusion and Tampering on Doctor Clusters

The adversary actively interferes in the working process of doctor clusters, sending them malignant messages or changing the content of medical records' content to damage the information's credibility and preserve it responsibly.

3.1.3 | Insider Threats Within Receptionist Clusters

A group of insiders who have legitimate access rights represents a threat within clusters of receptionists; if they choose to take advantage of existing loopholes, they entice others to participate in the Sybil attack or sell patient information that ought to be kept confidential.

3.1.4 | Denial of Service (DoS) Attacks on Admin Clusters

Adversaries utilize DoS aimed at admin clusters to overload resources, hence leading to the deterioration of system administration and access for only those with legitimatized permissions, with additional concerns towards a worsened latency.

3.1.5 | Brute Force Attacks

Brute force attacks primarily target admin clusters, as attackers attempt to repeatedly guess authentication credentials to gain unauthorized access to administrative controls. Compromising these access points can disrupt secure communication and compromise the confidentiality of sensitive systemwide data.

21613915, 2025, 3, Downloaded from https://onlinelibrary.wiley.com/doi/10.1002/ett.70098 by Delhi Technological University, Wiley Online Library on [09/03/2025]. See the Terms and Conditions (https://onlinelibrary.wiley.com/terms-and-conditions) on Wiley Online Library for rules of use; OA articles are governed by the applicable Creative Commons License

3.1.6 | Distributed Denial of Service (DDoS) Attacks

DDoS attacks can affect all clusters, but they are particularly detrimental to admin clusters and doctor clusters. Admin clusters are critical for managing resources and overall system operations, while doctor clusters handle sensitive medical data. Overwhelming these clusters leads to widespread service interruptions, degraded performance, and inaccessibility of crucial systems.

3.1.7 | Man-In-The-Middle (MITM) Attacks

MITM attacks are most likely to target patient clusters and doctor clusters, where attackers intercept and manipulate communication between devices. This compromises the confidentiality and authenticity of personal medical data and diagnosis records, posing serious risks to patient privacy and treatment accuracy.

3.1.8 | Data Falsification Across all Clusters

Opponents interfere with the data in all the clusters and feed the target recipients with fake information. At the same time, the other relevant processes that need to be conducted for efficient healthcare management are influenced by and based on fabricated data. The danger of data leakage and contamination is amplified.

3.1.9 | Sybil Attacks Across the Network

Cyber adversaries use several fake identities/addresses to create false request or response flows, control the cluster operations, corrupt data, and cause service interruptions for healthcare systems.

3.2 | Design Goals

The design goals that seek to integrate design requirements for IoT as a concept to advance the development of a comprehensive framework that is secure, cost-effective, and compliant for healthcare IoT systems are as follows:

- *Autonomous Clustering*: Healthcare IoT systems need to be self-managing to accommodate a wide range of devices to provide quick responses to the patients as well as the efficient utilization of capabilities.
- *Secure Communication*: For the privacy of patient information and especially because of the nature of such information, the security of such communication is paramount to prevent instances of invasion of privacy and unauthorized access to such details.
- *Role-Based Access Control*: Currently, the roles played in a healthcare organization entail the usability of data at a varying degree. The Role-based access control ensures that only those individuals with the authority can access particular information, hence minimizing wrong uses as well as tampering.
- *Anomaly Detection*: The threats that healthcare networks encounter are not stagnant, which makes anomaly detection essential to the discovery of threats and possible prevention before occurring in the future and maintaining the security of the networks and their activities.
- *Data Privacy Protocols*: Privacy is a cardinal concept in all health practices worldwide when handling patients. Additional safeguards are needed to protect the privacy of the data by providing a way to ensure that patients' trust is not violated by having their information viewed or shared by people who have no business doing so.
- *Optimal Routing*: Since enhanced delivery of health care services is anchored on the shortest delivery of messages between devices and health care providers, proper routing algorithms must be in place to reduce time wastage.
- *Multi-Layered Security*: There are numerous potential dangers to Health Care IoT settings, as the sector is particularly susceptible to multiple varieties of cyber threats. Advanced measures ensure that the systems are protected from various incurrences while ensuring the delivery of healthcare to patients is not compromised.
- *Network Resilience*: Healthcare operations cannot be stopped and need to continue functioning despite the nature of the networks sharing the information. This means that the network has to be reliable to keep offering services with no compromise on patients' well-being.
- *Regulatory Compliance*: Healthcare regulatory mechanisms must be strictly adhered to because failure brings about legal consequences that infringe on the care of patients. Regulatory compliance is thus maintained by constant scrutiny and sanctioning so that laws and rules guiding the provision of health services are complied with, and trust is instilled in the sector.

4 | Proposed Secured Healthcare IoT Framework

The proposed method provides a secure healthcare IoT network through a two-stage process, as illustrated in Figure 2. The first phase ensures intra-cluster security using RB-BFT X, which groups IoT devices into role-based clusters. This phase employs lightweight cryptography to secure communication, Role-Based Access Control (RBAC) to restrict unauthorized access, and lightweight anomaly detection to identify potential threats. It begins with the initialization of IoT devices, assigning them unique IDs and locations, followed by dynamic cluster formation with the election of Cluster Heads (CHs) based on processing power and battery life. Within each cluster, secure communication is maintained while continuously monitoring device behaviors for anomalies. The second phase enhances inter-cluster and server communication using CoatiNet, inspired by coati behavior. CoatiNet incorporates dynamic routing algorithms for real-time path optimization, intrusion detection systems, redundancy protocols, and secure backup channels to ensure robust inter-cluster communication. It also provides adaptive self-recovery mechanisms that adjust to network conditions, reroute data, and reallocate resources as needed. Additionally, the methodology ensures

21613915, 2025, 3, Downloaded from https://onlinelibrary.wiley.com/doi/10.1002/ett.70098 by Delhi Technological University, Wiley Online Library on [09/03/2025]. See the Terms and Conditions (https://onlinelibrary.wiley.com/terms-and-conditions) on Wiley Online Library for rules of use; OA articles are governed by the applicable Creative Commons License

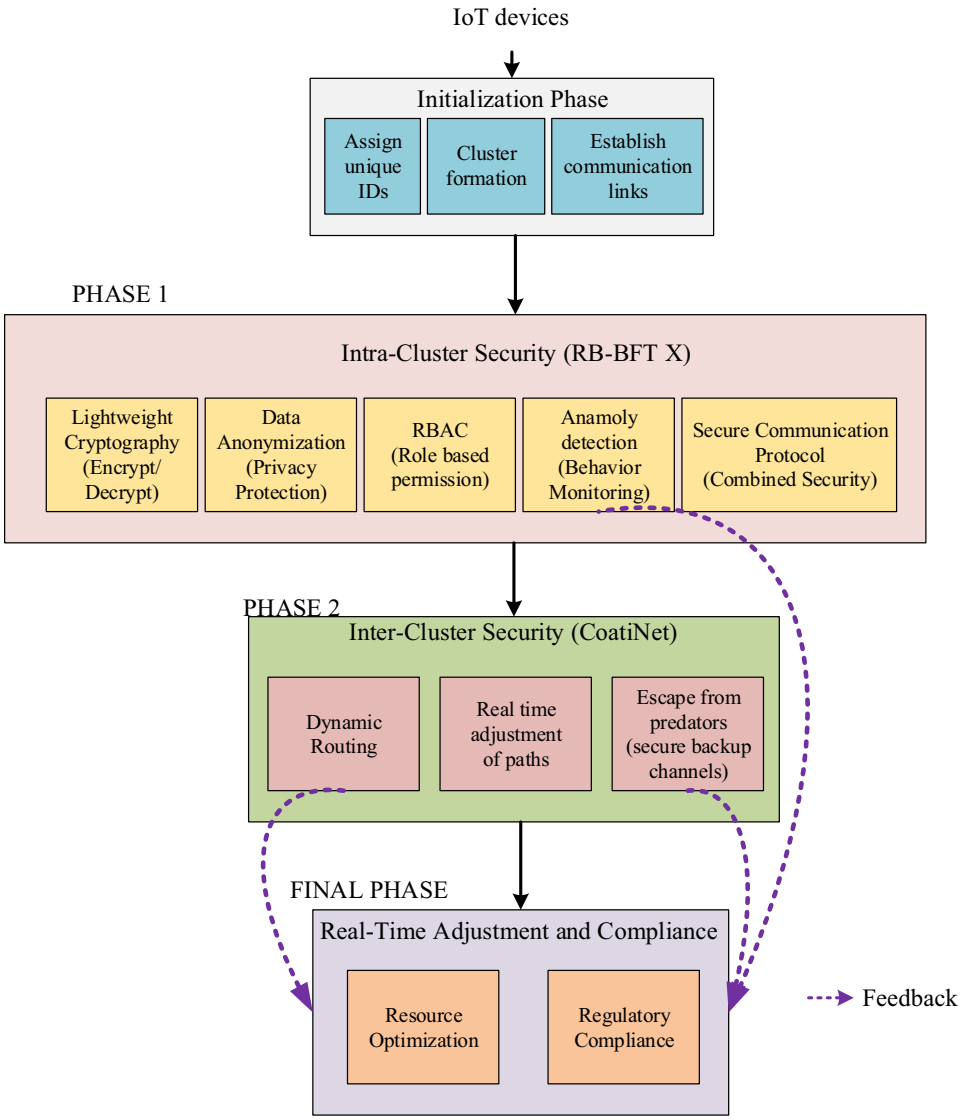

FIGURE 2 | Proposed multi-cluster security framework.

regulatory compliance by continuously monitoring operations and optimizing resource utilization. This comprehensive process flow achieves multilevel security and efficiency in handling sensitive healthcare data, addressing both intra-cluster and inter-cluster vulnerabilities effectively.

4.1 | Initialization

Starting from Phase I where the configuration of the healthcare IoT network is initiated and IoT devices and Cluster Heads are established. Initialization involves setting up the healthcare IoT network, identifying IoT devices, and configuring *CH*. Let's break down this process:

Let D be the total number of IoT devices in the network, C be the number of *CH*.

Each IoT device $d \in D$ is uniquely identified by an ID d_{id}, where $1 \leq d_{id} \leq D$ and each Cluster Head $ch \in CH$ is uniquely identified by an ID ch_{id}, where $1 \leq ch_{id} \leq C$.

Each $d \in D$ is assigned a precise physical location within the healthcare facility, denoted by coordinates (x_d, y_d) on the floor plan. This location is crucial for establishing proximity-based communication and determining the device's spatial relationship with other network entities. The network topology setup involves establishing communication links between d and ch within the healthcare facility. This setup aims to optimize communication efficiency and minimize energy consumption by organizing IoT devices into clusters based on their proximity to Cluster Heads.

Mathematically, we represent the network topology as a graph

$$G = (V, E) \tag{1}$$

where V and E are the set of vertices and edges representing d as well as ch. The connectivity between IoT devices and Cluster Heads is defined by a connectivity matrix A, where $A_{rs} = 1$ if there is a communication link between the device named d_r and Cluster Head ch_s which is related to the device d_s and $A_{rs} = 0$ otherwise. The r and s refers to the two clusters that we have assumed, d_r and d_s are the IoT devices within those clusters.

21613915, 2025, 3, Downloaded from https://onlinelibrary.wiley.com/doi/10.1002/ett.70098 by Delhi Technological University, Wiley Online Library on [09/03/2025]. See the Terms and Conditions (https://onlinelibrary.wiley.com/terms-and-conditions) on Wiley Online Library for rules of use; OA articles are governed by the applicable Creative Commons License

Once all *d* and *ch* are identified and configured, then the network topology is established, the initialization phase is complete. The network is now ready for subsequent processes.

The proposed Algorithm 1 outlines a secure multi-cluster framework for healthcare IoT networks, consisting of two key phases. In Phase 1, intra-cluster security is achieved by organizing IoT devices into role-based clusters, using lightweight cryptography, anomaly detection, and Role-Based Access Control (RBAC) to ensure secure communication and data privacy within each cluster. In Phase 2, inter-cluster communication is optimized through dynamic routing, adaptive self-recovery, and multi-layered security measures, inspired by Coati behavior, to maintain robust and efficient data transmission across clusters. The algorithm also includes real-time adjustments and backup mechanisms to respond to network disruptions and security threats, ensuring the resilience and compliance of the healthcare IoT network.

4.2 | Autonomous Cluster Formation

After the initialization step, where are identified and configured, *d* and *ch* the cluster formation process begins. This involves organizing *D* into clusters based on their roles, responsibilities and proximity to *CH*. The cluster formation process aims to optimize communication efficiency, resource utilization and management within the healthcare IoT network.

Unlike traditional methods with pre-designated *CH* s, autonomous cluster formation [45] empowers devices to elect suitable *CH* based on the trust worthiness. This election leverages an initial advertising phase where devices broadcast their capabilities, such as processing power, communication range, and battery life, to nearby devices. Each device d_r calculates a scoring function for each potential CHd_s within its communication range, denoted as $C_{candidate}$.

The score $Score(d_s)$ for each candidate $CH\ d_s$ is computed using a weighted sum of factors like processing power PP_s, battery life BL_s and centrality within the network $Centrality(d_s)$:

$$Score(d_s) = w_{pp}.PP_s + w_{BL}.BL_s + w_{Centrality}.Centrality(d_j) \quad (2)$$

where $w_{pp}, w_{BL}, w_{Centrality}$ are pre-defined weights reflecting the relative importance of each factor in *CH* selection. The device with the highest score among candidates of *CH* becomes the *CH* for that cluster:

$$CH_r = \arg\max\left(Score(d_s)\right)\ \ \forall d_s \in C_{Candidate} \quad (3)$$

where arg max is an operator that returns the argument (in this case, the device d_s) that gives the maximum value of the function $score(d_s)$. This scoring approach ensures that devices with superior processing capabilities, longer battery life and a central location within the candidate pool are more likely to be elected as CHs.

Following *CH* selection, each device d_r calculates its distance d_{rs} to nearby *CH* using a distance metric named as Euclidean distance and transmits a join request to the closest *CH*, denoted by

ALGORITHM 1 | The Proposed Secure Healthcare IoT Framework.

```
Input:
  D ← Set of IoT devices {d1, d2, ..., dn}
  CH ← Set of Cluster Heads {ch1, ch2, ..., chm}
  Parameters: Processing power (PP), Battery life (BL), Location (x, y)
  Protocols: MQTT, CoAP, HTTP
# Phase 1: Intra-Cluster Security
Initialize Network:
  For each device d ∈ D:
    Assign unique ID and physical location (x, y)
    Establish communication links with candidate CHs based on proximity
Cluster Formation:
  For each device dr ∈ D:
    For each candidate CHs ∈ CH:
      Score(chs) = wpp * PP + wbl * BL + wcentrality * Centrality(chs)
    Select CH with the highest Score(chs)
    If CH capacity is sufficient:
      Add dr to CH's member list
    Else:
      Select next highest scoring CH
Intra-Cluster Communication:
  For each communication within a cluster:
    Encrypt data using lightweight cryptography
    Monitor device behavior Xr
    If |Xr − μ| > θ * σ:
      Trigger anomaly alert and notify CH
    Apply RBAC:
      If role r has permission for operation s:
        Grant access
      Else:
        Deny access
# Phase 2: Inter-Cluster Communication
Dynamic Routing:
  For each CH pair (CHi, CHj):
    Compute latency Lij and security metric Sij
    Optimize routing table R(t):
      R(t) = argmin(Lij + Sij)
Real-Time Adjustments:
  Monitor network conditions:
    If congestion or insecure path detected:
      Identify alternate path with lower latency and higher security
      Update routing variables dynamically
Backup and Redundancy:
  For each communication path p:
    If intrusion detected (Detect(a) = 1):
      Reroute(p) = Backup(p)
    Else:
      Reroute(p) = p
Escape from Predators (Security Mechanisms):
  For each user/device u accessing resource/data d:
    If Auth(u, d) = True:
      Grant access
    Else:
      Deny access
  Monitor inter-cluster communication with IDS:
    If Detect(a) = True:
      Trigger alert and initiate response
# Network Resilience and Compliance
Adaptive Self-Recovery:
  Adjust configuration dynamically:
    C(t+1) = C(t) + α * F(t)
  Optimize resource utilization:
    Minimize ∑ |Ru − ∑ rui|
Regulatory Compliance:
  For each operation O:
    If O complies with regulations:
      Allow operation
    Else:
      Block operation
Output:
  Secure intra-cluster and inter-cluster communication
  Optimized routing, adaptive self-recovery
```


21613915, 2025, 3, Downloaded from https://onlinelibrary.wiley.com/doi/10.1002/ett.70098 by Delhi Technological University, Wiley Online Library on [09/03/2025]. See the Terms and Conditions (https://onlinelibrary.wiley.com/terms-and-conditions) on Wiley Online Library for rules of use; OA articles are governed by the applicable Creative Commons License

CH_s. The *CH* maintains a list of member devices within its communication range, represented by $Member_List_{CH_s}$.

To ensure efficient cluster formation and avoid overloading *CH*, a capacity check is implemented. The *CH* verifies if it has sufficient resources (processing power, communication bandwidth) to accommodate the joining device. If d_s falls within the communication range of CH_s and the *CH*'s capacity allows for inclusion, d_s is added to the $Member_List_{CH_s}$. This process is mathematically represented as follows:

$$Member_List_{CH_s} = Member_List_{CH_s} \cup \{d_s\} \tag{4}$$

This is achieved if $(d_{rs} \leq Communication_range_{CH_s})$and $(|Member_List_{CH_s}| < Capacity_{CH_s})$. This condition ensures that device d_r joins the cluster managed by CH_s if it is within the communication range and the cluster head has enough capacity to accommodate additional devices.

4.3 | Two-Phase Approach

The proposed methodology comprises two phases: Phase 1 focuses on safeguarding nodes to cluster head communication using RB-BFT X, ensuring secure intra-cluster operations. CoatiNet, as the second phase of the approach in Coati, focuses on optimizing inter-cluster communication, increasing the levels of latency, security, and network adaptability in healthcare IoT systems.

4.3.1 | Phase 1: Safeguarding Nodes to Cluster Head Communication

The proposed methodology employs Redundant Byzantine Fault Tolerance with Extensions (RB-BFT X) to address security challenges in healthcare IoT networks. RB-BFT X was chosen for its scalability, adaptability, and lightweight cryptographic techniques, which make it suitable for resource-constrained IoT environments. Unlike traditional fault-tolerance algorithms such as Practical Byzantine Fault Tolerance (PBFT) or Federated Byzantine Agreement (FBA), RB-BFT X incorporates features like behavioral anomaly detection, role-based access control (RBAC) and data anonymization. These features enable it to provide a comprehensive and efficient security solution tailored for dynamic and distributed healthcare IoT networks. PBFT, while robust, suffers from high communication overhead, making it less ideal for large IoT networks. Similarly, FBA is more suited for permissioned environments with pre-established trust, limiting its applicability to decentralized healthcare IoT systems. RB-BFT X addresses these limitations by enhancing scalability, reducing computational complexity, and integrating domain-specific security measures.

RB-BFT X extends the basic Byzantine Fault Tolerance algorithm by incorporating redundancy mechanisms that improve resilience against malicious or arbitrary node behaviors. Its lightweight cryptography ensures that IoT devices with limited processing power can maintain data integrity and confidentiality without significant computational overhead. The inclusion of real-time anomaly detection and dynamic adaptation makes RB-BFT X highly effective for IoT environments where security threats evolve rapidly. Let's delve into this phase 1 deeply.

4.3.1.1 | Lightweight Cryptography. RB-BFT X accomplishes this by utilizing small amounts of computation and lightweight cryptographic algorithms [46] to protect the cluster's communication links. This makes it possible to preserve private information and data authenticity in silence without overburdening contained IoT devices with computational complexity.

Let K_{pub} be the public key and K_{priv} be the private key generated for each *d* and *ch*. Encryption *E* and decryption *D* procedures may also be described as

$$c = E(m, K_{pub}) \tag{5}$$

$$m = D(c, K_{priv}) \tag{6}$$

where *m* is the plaintext message and *c* is the ciphertext.

4.3.1.2 | Data Anonymization. As for data privacy, data anonymization remains one of the key constituents of the RB-BFT X framework applied to safeguard the protection of sensitive health information exchanged periodically through IoT networks. The use of high levels of anonymity guarantees that the last acknowledged attributes of an individual shall not be subjected to identification attacks and other forms of unauthorized access. Some steps of anonymization apply randomization techniques based on clustering k-anonymity models [47], that is, grouping *K* records in clusters where it is hard to distinguish individuals from the released data. In this process, however, mathematical derivations are relevant to prove the degree of effectiveness of the particular anonymization method used. For example, let *R* be the set of the data records, and *QI* is the other part of the record, which is often called quasi-identifiers. The steps involved in this process include the partition operation, which can be done by clustering the data *R*, with each cluster $DC_1, DC_2, DC_3, DC_4 \ldots, DC_n$ providing the k-anonymity. This can be mathematically described as $\forall r, |C_i| \geq K$, where it is important to observe that every must include at least records. Furthermore, given a particular set of fields, which can be considered as sensitive in each record, the studied anonymization processes are to generalize these fields to ensure data privacy, although data usefulness is also a crucial factor. Using symbols, generalized quasi-identifiers can be denoted as *GQI*, while generalized sensitive attributes (*SA*) after anonymization are represented as *GSA* which is a constant that represents a predetermined level of sensitivity of the system for the selection of anomalies. It points to the fact that the criterion for detecting anomalies is more rigorous when the value is higher. The mathematical formulation involves defining appropriate generalization hierarchies and algorithms to balance privacy protection and data usability. By integrating such mathematical derivations into the RB-BFT X framework, robust data anonymization mechanisms can be established, ensuring secure and privacy-preserving healthcare data collection and transmission within IoT networks.

4.3.1.3 | Role-Based Access Control (RBAC). RBAC enforces access restrictions based on the specific roles of devices and users within the cluster, enhancing security and maintaining

21613915, 2025, 3, Downloaded from https://onlinelibrary.wiley.com/doi/10.1002/ett.70098 by Delhi Technological University, Wiley Online Library on [09/03/2025]. See the Terms and Conditions (https://onlinelibrary.wiley.com/terms-and-conditions) on Wiley Online Library for rules of use; OA articles are governed by the applicable Creative Commons License

the confidentiality and integrity of sensitive healthcare information. The Access Control Matrix (ACM) defines permissions for each role within the cluster.

The Access Control Matrix is represented as

$$ACM_{rs} = \begin{cases} 1 \ \ if\ roler\ \ has\ \ permission\ for\ operations \\ 0 \ \ otherwise \end{cases} \tag{7}$$

where $ACM_{rs} = 1$ if role r has permission for operation s, $ACM_{rs} = 0$ otherwise, n is the number of IoT devices and m is the number of operations.

Consider the following roles and operations:

Roles: Patient (R1), Doctor (R2), Receptionist (R3), Admin (R4).

Operations: Read Patient Data (O1), Write Patient Data (O2), Schedule Appointment (O3), Access Admin Functions (O4).

The ACM might look like this:

$$ACM = \begin{pmatrix} 1 & 0 & 0 & 0 \\ 1 & 1 & 0 & 0 \\ 0 & 0 & 1 & 0 \\ 1 & 1 & 1 & 1 \end{pmatrix} \tag{8}$$

In this matrix, Patients (R1) can only read their own data (O1); Doctors (R2) can read (O1) and write (O2) patient data; Receptionists (R3) can schedule appointments (O3); Admins (R4) have full access to all operations (O1, O2, O3, O4).

The enforcement of RBAC can be mathematically modeled as:

$$Permission\ granted = \begin{cases} 1 \ \ if\ \ ACM_{rs} = 1 \\ 0 \ \ if\ \ ACM_{rs} = 0 \end{cases} \tag{9}$$

where r is the role of the device requesting access, s is the operation or resource being requested.

4.3.1.4 | Behavioral Anomaly Detection. Behavioral anomaly detection continuously monitors the activities and behaviors of IoT devices to detect deviations that could indicate security threats. The anomaly detection is based on statistical methods.

A baseline of normal behavior is established for each type of IoT device based on historical data. This baseline is characterized by the mean (μ) and standard deviation (σ) of observed behaviors. As the IoT devices operate, their real-time behaviors (X_r) are monitored and compared against the established baseline. Any significant deviation from the norm could indicate an anomaly.

The mathematical model used for detecting anomalies is based on statistical methods. The model checks whether the observed behavior (X_r) deviates from the mean (μ) by a certain threshold (θ) times σ. The anomaly detection can be expressed as:

$$Anamoly = \begin{cases} 1 \ \ if\ \ |X_r - \mu| > \theta\sigma \\ 0 \ \ otherwise \end{cases} \tag{10}$$

where θ is a predefined threshold that determines the sensitivity of the anomaly detection system. A higher θ value implies a stricter criterion for anomaly detection.

When an anomaly is detected (i.e., when $Anamoly = 1$), the Cluster Head starts a response mechanism. This response may involve notifying the network administrators, quarantining the identified device to avoid further harm possibly in terms of damaging or corrupting other devices and subsystems within the network and carrying ahead with a series of tests to identify the root cause of the anomalous behavior.

4.3.1.5 | Secure Communication Protocols. To guarantee secure communication within the cluster, the data transmission must be confidential, integrity, and authentic; the RB-BFT X framework integrates robust secure communication protocols. The mechanisms such as cryptography, digital signatures, and hashing algorithms are essential in ensuring security when data is transferred through IoT devices and to the CH. Security, which is the basis of communicating confidentiality, employs encryption as a tool to encode data before it is transmitted. It is unreachable to anybody and is not intended, as seen in the equation. This process of transmission allows, even if the data transmitted also goes through some other taps, for the data to remain safe and secure.

The process of decrypting, which is virtually the opposite activity of encrypting, occurs at the receiving end to obtain the actual plaintext message as in the equation. To be able to decipher the message, the private key corresponding to the recipient or the developer is used to decrypt the data.

This gives rise to digital signatures, which help to ensure that the transmitted data is both authentic and of integrity. This does not only allow the receiver to ensure the information passed is accurate but also the sender's credentials. The sender then sends this message m and signs it with their private key K_{priv} to come up with a digital signature.

$$signature = sign(m, K_{priv}) \tag{11}$$

The recipient verifies the signature using the sender's public key K_{pub}. Successful verification confirms the message's authenticity and integrity, ensuring it was sent by the sender without tampering:

$$verify(signature, m, K_{pub}) \tag{12}$$

To maintain data integrity, hash functions generate fixed-size hash values from the original message. Any message alteration yields a distinct hash value, facilitating easy detection. The hash value for m is computed using a hash function H.

$$Hash = H(m) \tag{13}$$

Thus, the RB-BFT X algorithm (Algorithm 2) is chosen for its ability to address the limitations of traditional fault tolerance algorithms like Practical Byzantine Fault Tolerance (PBFT) and Federated Byzantine Agreement (FBA). PBFT's quadratic communication overhead and FBA's reliance on quorum slices hinder scalability and adaptability, especially in

21613915, 2025, 3, Downloaded from https://onlinelibrary.wiley.com/doi/10.1002/ett.70098 by Delhi Technological University, Wiley Online Library on [09/03/2025]. See the Terms and Conditions (https://onlinelibrary.wiley.com/terms-and-conditions) on Wiley Online Library for rules of use; OA articles are governed by the applicable Creative Commons License

ALGORITHM 2 | RB-BFT X.

```
Input: d: IoT devices within the cluster
CH: Cluster Head
s: Operations
r: Roles
m: Plaintext message
c: Ciphertext
Output: Secure healthcare IoT network with intra-cluster security
# Initialization
for device in d:
    Kpub[device], Kpriv[device] = generate_keys()
ACM = {}
for role in r:
    for operation in s:
        ACM[(role, operation)] = define_access_control_matrix(role, operation)
baseline_behavior = {}
for device_type in DEVICE_TYPES:
    baseline_behavior[device_type] = establish_baseline_behavior()
epsilon = define_anomaly_detection_threshold()
# Data Anonymization
R = get_dataset()
for i in range(len(CLUSTERS)):
    DC_i = CLUSTERS[i]
    partitioned_dataset = partition_dataset(R, DC_i)
    if len(partitioned_dataset) >= K:
        DC_i = partitioned_dataset
generalize_QI_and_SA(R)
# Lightweight Cryptography
c = encrypt(m, Kpub[CH])
m = decrypt(c, Kpriv[d])
# Role-Based Access Control (RBAC)
for role in r:
    for operation in s:
        if ACM[(role, operation)] == 1:
            permission_granted = 1
        else:
            permission_granted = 0
# Behavioral Anomaly Detection
for device in d:
    behavior = get_behavior(device)
    if abs(behavior - baseline_behavior[DEVICE_TYPE(device)]) > epsilon * baseline_behavior[DEVICE_TYPE(device)]:
        anomaly = 1
    else:
        anomaly = 0
# Secure Communication Protocols
signature = sign(m, Kpriv[d])
verify_signature = verify(m, signature, Kpub[d])
hash_result = hash(m)
# Response
if anomaly == 1:
    alert_administrators()
    isolate_device(d)
    initiate_diagnostics()
end if
```

resource-constrained environments like healthcare IoT systems. RB-BFT X overcomes these challenges by integrating lightweight cryptographic techniques to reduce computational overhead and role-based access control to enforce strict data policies. It also incorporates behavioral anomaly detection to identify and mitigate malicious activities in real time and employs secure communication protocols to ensure data integrity and confidentiality. These enhancements make RB-BFT X resource-efficient, scalable, and robust against adversarial attacks, providing a holistic solution for secure and reliable intra-cluster communication. This makes it an optimal choice for addressing the unique security challenges of healthcare IoT systems.

4.3.2 | Phase 2: Inter-Cluster and Server Communication Optimization Using CoatiNet

Phase 2 of the proposed methodology, known as "Inter-Cluster and Server Communication Optimization" using CoatiNet, represents a significant advancement in healthcare IoT network management.

4.3.2.1 | CoatiNet Module. Drawing inspiration from the coordinated behavior of coatis, CoatiNet introduces a dynamic, resilient, and secure communication system that addresses the unique challenges of IoT environments. Its mechanisms aim to optimize data transmission paths, improve latency, and bolster network security against potential threats while adapting to evolving conditions.

At its core, CoatiNet employs dynamic routing algorithms to optimize communication paths continuously. These algorithms adjust routes based on real-time network feedback, ensuring minimal latency and robust security. CoatiNet also integrates adaptive configuration mechanisms, enabling the system to reallocate resources and reroute data when faced with congestion or security threats. Its multi-layered security approach leverages intrusion detection systems, redundancy protocols, and secure backup channels to safeguard communication even under adversarial conditions. Furthermore, CoatiNet mimics coatis' ability to evade predators by introducing a proactive threat response mechanism, which includes path recalibration and enhanced authentication. By drawing inspiration from coati behaviors, CoatiNet introduces several advantages over traditional inter-cluster communication frameworks. Its dynamic routing algorithms prevent attackers from exploiting predictable paths, while its adaptive mechanisms enhance network resilience by redistributing resources during disruptions. The module's layered security ensures data integrity and minimizes vulnerabilities, making it particularly effective for healthcare IoT environments. Table 2 provides a conceptual mapping of coati behaviors to the key functionalities of the CoatiNet module, illustrating how the natural adaptability, cooperation, and resilience of coatis inspire its design.

4.3.2.1.1 | Encryption of Data. To prevent passive eavesdropping, all data packets transmitted between IoT devices and Cluster Heads (CHs) are encrypted using a robust encryption algorithm like AES_256 [48]. The encryption process ensures that even if an attacker intercepts the communication, they cannot access the sensitive information without the decryption key. Mathematically, for a data packet *data* and an encryption key *key*,

21613915, 2025, 3, Downloaded from https://onlinelibrary.wiley.com/doi/10.1002/ett.70098 by Delhi Technological University, Wiley Online Library on [09/03/2025]. See the Terms and Conditions (https://onlinelibrary.wiley.com/terms-and-conditions) on Wiley Online Library for rules of use; OA articles are governed by the applicable Creative Commons License

TABLE 2 | Relation between Coati behavior and CoatiNet module.

Coati characteristic	Coati behavior explanation	CoatiNet module implementation
Cooperative behavior	Coatis exhibit cooperative behavior within their groups, working together to forage, protect against predators, and care for young.	Collaborative optimization of communication paths between IoT devices and clusters, mirroring the cooperative behavior seen in coatis.
Adaptability	Coatis are highly adaptable animals, able to adjust their behavior and habitat to changing environmental conditions.	Dynamic rerouting of data and adjustment of network configurations based on real-time feedback, reflecting the adaptability of coatis to changing circumstances.
Dynamic routing	Coatis frequently change their routes while foraging to optimize food collection and avoid predators.	Employment of dynamic routing algorithms to continuously adjust communication paths between clusters, akin to the dynamic routing behavior observed in coatis.
Collaboration	Coatis collaborate within their groups to defend against predators, detect threats, and coordinate activities.	Collaboration with intrusion detection systems, authentication mechanisms, and redundancy protocols to defend against attacks and ensure uninterrupted communication, resembling the collaborative behavior seen in coatis.
Resilience	Coatis demonstrate resilience to environmental changes, adapting their behavior and strategies to survive in various conditions.	Prioritization of network resilience through redundancy mechanisms, backup channels, and adaptive configurations to withstand security breaches, network disruptions, and regulatory changes, similar to the resilience displayed by coatis in challenging environments.

the encryption function $E(data)$ is represented as:

$$c = E(data) = AES_256(data, key) \tag{14}$$

This ensures the confidentiality of the transmitted data.

4.3.2.1.2 | Dynamic Routing. Dynamic routing algorithms are employed to avoid predictable communication paths that attackers could target. These algorithms often alter the data communication paths, and antagonists can hardly track and constantly interrupt the data transfer process.

To formalize the optimization of routing in the network, consider the following variables:

N is the number of IoT devices within each cluster, M is the number of clusters in the network, $D(i, j)$ is the distance matrix of the cluster-to-cluster separation, that is, between cluster C_i and C_j, $R(t)$ is the routing table at time t which shows the current routes for data transfer.

This is a formal optimization problem that seeks to achieve a minimal total communication delay while guaranteeing the security of the links chosen as optimal. The latency L is modeled as:

$$L = \sum_{i=1}^{N} \sum_{j=1}^{M} D(i, j) \times f_{ij}(t) \tag{15}$$

where $f_{ij}(t)$ is a binary function that indicates whether data is being transmitted between clusters i and j at time t. It takes the value 1 if data transmission is occurring and 0 otherwise.

One of the main directions of the algorithm and the focus on the dynamic routing aspect of the algorithm is the process of the change of the value of the routing variables $f_{ij}(t)$ that are associated with the threats and changes in the network conditions. This updating process makes it possible to ensure that the algorithm changes as the network environment and does not constantly take the same paths because they can be the paths that the attackers can easily notice.

Dynamic Update Mechanism:

Essentially, using the probabilities of variation in these conditions and threats, the CoatiNet algorithm alters the path routing variables $f_{ij}(t)$ to reroute data through other paths. Let $f_{ij}^{*}(t)$ be the updated routing variable between clusters â and b at time t. This updated variable is established on the current network conditions together with security precaution measures.

The new routing variable can be calculated by navigating through an optimization procedure that takes into account the lowest latency while providing the best security. This optimization problem can be formulated as follows:

$$f_{ij}^{*}(t) = \arg\min\ L_{ij} + S_{ij} \tag{16}$$

where L_{ij} represents the latency along the path between clusters i and j, S_{ij} represents a security metric that quantifies the level of security along the path. This metric may include the probability of attack, presence of encryption, and so on and may relate to the issue of trust in the devices being used.

It works according to an iterative approach, which analyses numerous possible paths between clusters i and j, and then

21613915, 2025, 3, Downloaded from https://onlinelibrary.wiley.com/doi/10.1002/ett.70098 by Delhi Technological University, Wiley Online Library on [09/03/2025]. See the Terms and Conditions (https://onlinelibrary.wiley.com/terms-and-conditions) on Wiley Online Library for rules of use; OA articles are governed by the applicable Creative Commons License

chooses the path that will have least overall latency and security measure $L_{ij} + S_{ij}$.

4.3.2.1.3 | Real-Time Adjustments. The algorithm checks whether the existing path from the clusters i and j is the best one to use to deliver packets or if there is a better path to be used to reduce the time taken, or increase security. This evaluation involves considering factors such as:

- *Network Congestion*: They also said it could select another route in the event that the current one is congested or experiences high traffic turnover in order to achieve lower latency.
- *Security Threats*: It could also add additional paths between two particular computers if the current set path is considered insecure with respect to likely attacks or malicious devices.
- *Device Availability*: It takes into account the availability of devices on one or other channels or on any other possible route. This is because there is no guarantee that these particular devices are available or connected in the first place, thus keeping the data away from them where it is not needed.

In another manner, the CoatiNet algorithm considers fresh routing $f_{ij}(t)$ variables, which capture up the real-time network conditions and threats by adjusting the data transmission routes to minimize latency while ensuring the security of the healthcare IoT network.

4.3.2.1.4 | Escape From Predators. The "Escape from Predators" approach is focused on improving the protection of the healthcare IoT network by introducing effective preventive measures to protect it against different kinds of threats, including active viruses, intruders, tampering, insiders, and Denial of Service (DoS) attacks. Its components include intrusion detection system, reliable backup channels, and multi-factor authentication and authorization.

Multi-layered Authentication and Authorization:

This module provides a layered and holistic identification system of users and physical devices connecting to the IoT network. The authentication and authorization procedures provide restricted access to essential resources. The mathematical model for authentication and authorization can be illustrated as follows:

Let u represent a user or device and d represent a resource or data:

$$Auth(u,d) = \begin{cases} true & if\ u\ is authenticated for\ d \\ false & otherwise \end{cases} \tag{17}$$

Intrusion Detection System (IDS):

An IDS tracks all the traffic going through the network and determines whether there is any malicious activity or deviation from the intrusion detection policy. When the IDS discovers an intrusion, it launches alerts and responses to counter the threat as per the policy. The mathematical model for intrusion detection can be represented as follows:

Let a represent an anomaly detected by the IDS:

$$Detect(a) = \begin{cases} true & if\ a\ is \det ected \\ false & otherwise \end{cases} \tag{18}$$

Redundancy and Backup Channels:

It is expected to have multiple communication paths and redundant channels for backup communication in case of IoT network disruption. In cases of anomalous activities, the IoT network can switch to other means of passing the data between the two facilities. The mathematical representation for rerouting data can be represented as follows:

Let p represent a communication path:

$$\text{Re}route(p) = \begin{cases} B(p) & if\ Detect(a)\ is\ true \\ p & otherwise \end{cases} \tag{19}$$

This approach helps to safeguard the healthcare IoT network against various security threats by integrating authentication, intrusion detection, and redundancy measures in the system.

4.3.2.1.5 | Adapting to Change: Network Resilience and Regulatory Compliance. Adapting to change makes the healthcare IoT network resilient, uses resources effectively, and complies with the regulatory authority. This approach proposes optimizing resource utilization, adapting configurations, and regulatory compliance.

Resource Utilization Optimization (RUO):

The objective is to minimize the difference between the allocated resources (R_u) and the actual resource utilization ($\sum_{i \in A} r_{ui}$) for each resource u in the network. This is expressed as a minimization problem:

$$RUO = \min imize\ A \sum_{u \in U} \left(R_u - \sum_{i \in A} r_{ui} \right) \tag{20}$$

where U represents the set of resources, A represents the set of IoT devices or applications, R_u represents the allocated resources and r_{ui} represents the resource utilization by application i.

Adaptive Configuration:

The network configuration ($C(t)$) is adjusted at each time step based on real-time feedback ($F(t)$) and an adaptation rate (α). The new configuration at the time $t + 1$ is calculated as follows:

$$C(t+1) = C(t) + \alpha . F(t) \tag{21}$$

Regulatory Compliance:

The compliance of an operation (O) with regulatory standards ($\text{Re}g$) is determined using a compliance function. If the operation complies with the regulations, the function returns true; otherwise, it returns false:

$$Compliance(O) = \begin{cases} true & if\ O\ complies\ with\ \text{Re}g \\ false & Otherwise \end{cases} \tag{22}$$

21613915, 2025, 3, Downloaded from https://onlinelibrary.wiley.com/doi/10.1002/ett.70098 by Delhi Technological University, Wiley Online Library on [09/03/2025]. See the Terms and Conditions (https://onlinelibrary.wiley.com/terms-and-conditions) on Wiley Online Library for rules of use; OA articles are governed by the applicable Creative Commons License

By implementing these strategies, the healthcare IoT network can dynamically adapt to changing conditions, optimize resource utilization, and ensure compliance with regulatory requirements. The mathematical models provide a formal framework for achieving these objectives, allowing for efficient and effective network management. The CoatiNet algorithm is given below as Algorithm 3.

5 | Experimental Methodology and Performance Analysis

This section describes the procedure detailing the main experiments, performance measurements, and analysis before implementing the methodology to substantiate its efficacy in defending IoT networks against adversarial activities.

5.1 | Experimental Setup

The experimental setup is a practical framework within which we are to employ the proposed methodology; we strive to design it so that it would closely emulate the working conditions yet remain manageable, scientifically sound, and easily replicable. This setup would incorporate both the hardware and software systems, with Python as the preferred language of coding for the supposed methodology. For the hardware components, we use a standard computer system characterized by advanced computational power, adequate memory, and requisite networking devices, including routers and switches, to offer an actual network platform.

Python is used as the main programming language to implement the identified methodology due to its rich repository of libraries like TensorFlow and PyTorch for performing machine learning tasks. The development and testing of the methodology are carried out using PyCharm, an integrated development environment (IDE) that provides robust tools for code development, debugging, and execution. We evaluate and analyze the system perspective through performance analysis based on accuracy, precision, recall rates, time for each request (latency), and utilization of resources. After testing out a methodology, we examine the outcome to assess the effectiveness, efficiency, or otherwise of such methodology. This setup includes IoT devices and cluster heads strategically positioned with unique computational capacities, networking standards, and power supplies, as illustrated by Table 3. IoT devices have 1 GHz processors, 512 MB RAM, and battery-solar power, whereas the heads contain 2 GHz processors, 2 GB RAM, 1 TB hard disk, mains power with an available generator, and backup. These points make the proposed methodology analysis systematic, helping to capture and evaluate the effectiveness of tackling the issues of securing IoT networks.

Various malicious attacks targeting healthcare IoT networks are simulated to evaluate the system's resilience. Passive Eavesdropping is emulated using Scapy to intercept and capture packets between patient IoT devices. Active Intrusion and Tampering on doctor clusters is simulated by generating forged traffic with Scapy to manipulate medical records. Insider Threats within receptionist clusters are modeled by simulating unauthorized access with Python scripts. Denial of Service (DoS) and Distributed Denial of Service (DDoS) attacks are generated using

ALGORITHM 3 | CoatiNet.

Inputs:
- Number of IoT devices (N) within each cluster
- Number of clusters (M) in the network
- Distance between clusters Ci and Cj: D(i, j)
- Initial routing table R(t)
- Network conditions and security factors

Output:
- Secure and optimized data transmission between IoT devices and Cluster Heads
- Resilient network with adaptable configuration and regulatory compliance

Initialization:
  Initialize the routing variables: f(t)ij = 0 for all i, j
Encryption and Secure Communication:
  For each data packet to be transmitted:
  c = E_AES_256(data, key)
  Transmit the encrypted packet c between IoT devices and Cluster Heads (CHs)
Dynamic Routing Optimization:
For each time step t:
  FOR i = 1 to M DO
    FOR j = 1 to M DO
      Compute latency L_{ij} and security metric S_{ij} for the path between Ci and Cj
      f(t)*ij = arg min (L_{ij} + S_{ij})
      Update the routing table R(t) with the new routing variables f(t)*ij
    END FOR
  END FOR
Real-time Adjustments:
1. Monitor network conditions and security threats
2. **FOR** i = 1 to M DO
    FOR j = 1 to M DO
      IF network congestion OR security threats on the current path (i, j) **THEN**
        Identify alternative paths that minimize latency and maximize security
        Update the routing variables f(t)*ij accordingly
      END IF
      IF devices along the current path (i, j) are unavailable **THEN**
        Reroute the data through alternative available paths
        Update the routing variables f(t)*ij
      END IF
    END FOR
  END FOR
Escape from Predators (Security Mechanisms):
Implement multi-layered authentication and authorization:
  FOR each user/device u and resource/data d **DO**
    IF Auth(u, d) **THEN**
      Grant access
    ELSE
      Deny access
    END IF
  END FOR
Detect intrusions and anomalies using the IDS:
  IF Detect(a) **THEN**
    Trigger alerts and initiate response mechanisms
  END IF
Reroute data through redundant backup channels:
  IF Detect(a) **THEN**
    Reroute(p) = Backup(p)
  ELSE
    Reroute(p) = p
  END IF
Adapting to Change (Network Resilience and Compliance):
Optimize resource utilization:
  FOR each resource u and application i
  DO
    Minimize $|R_u - \Sigma i \in A\ r_{ui}|$
  END FOR
3. Adapt network configuration:
  C(t+1) = C(t) + α * F(t)
4. Monitor regulatory compliance:
  FOR each operation O **DO**
    IF Compliance(O) **THEN**
      Allow the operation
    ELSE
      Block the operation
    END IF
  END FOR

21613915, 2025, 3, Downloaded from https://onlinelibrary.wiley.com/doi/10.1002/ett.70098 by Delhi Technological University, Wiley Online Library on [09/03/2025]. See the Terms and Conditions (https://onlinelibrary.wiley.com/terms-and-conditions) on Wiley Online Library for rules of use; OA articles are governed by the applicable Creative Commons License

TABLE 3 | Parameter settings.

Parameter	IoT devices	Cluster heads
Physical location	(10,20), (15,25), (8,18)	(50,60), (55,65), (48,58)
Processing capabilities	CPU speed: 1 GHz, Memory: 512 MB	CPU speed: 2 GHz, Memory: 2 GB
Communication capabilities	Wi-Fi, Bluetooth, Zigbee	Wi-Fi, Bluetooth, Zigbee
Initial power level	Battery: 3000 mAh, Power source: Solar	Power source: Mains, Backup: Generator
Additional parameters	—	Storage capacity: 1 TB
Processing capabilities	CPU speed: 1 GHz, Memory: 512 MB	CPU speed: 2 GHz, Memory: 2 GB
Security features	Encryption: AES-256, Firewall: Enabled	Encryption: AES-256, Firewall: Enabled
Data retention policy	Retention Period: 30 days, Data Backup: Weekly	Retention Period: 90 days, Data Backup: Daily
Network protocol	MQTT, CoAP, HTTP	MQTT, CoAP, HTTP

Hping3 and LOIC for resource overload. Brute Force Attacks on admin clusters are simulated with custom Python scripts leveraging Paramiko. Finally, Man-in-the-Middle (MITM) attacks targeting patient and doctor clusters are carried out using Scapy for packet sniffing and injection. These simulations, developed and executed in PyCharm, provide insights into the system's vulnerability to various attacks and its ability to detect and respond to them.

5.2 | Evaluation Metrics

In the course of the experimental analysis of the presented methodology, several measures of effectiveness are used to make the evaluation. These metrics have given quantitative values so that the performance can be quantitatively measured according to the different aspects, including accuracy, precision, recall, F-score, lifetime of the network, throughput of the network, rate of detection, false positive rate, and overall system performance.

5.2.1 | Accuracy

$$\text{Accuracy} = \frac{\text{Number of correctly classified instances}}{\text{Total number of instances}} \tag{23}$$

Accuracy measures the proportion of correctly classified instances among all instances in the dataset. It provides an overall assessment of the model's correctness.

5.2.2 | Precision

$$\text{Pr ecision} = \frac{\text{True}_p}{\text{True}_p + \text{False}_p} \tag{24}$$

Precision quantifies the fraction of true positive predictions among all positive predictions made by the model, showcasing its capacity to minimize false positives.

5.2.3 | Recall (Sensitivity)

$$\text{Recall} = \frac{\text{True}_p}{\text{True}_p + \text{False}_n} \tag{25}$$

Recall evaluates the ratio of true positive predictions to all actual positive instances in the dataset, illustrating the model's capability to detect all positive instances.

5.2.4 | F-Score (F1-Score)

$$F1 = 2 \times \frac{\text{Pr ecision} \times \text{Recall}}{\text{Pr ecision} + \text{Recall}} \tag{26}$$

The F-score represents the harmonic mean of precision and recall, offering a balanced assessment of a model's performance by considering both precision and recall.

5.2.5 | Network Lifetime

Network lifetime refers to the duration for which the network remains operational before the depletion of resources or failure occurs. It is typically measured in rounds or time units.

5.2.6 | Network Throughput

Network throughput measures the rate at which data is successfully transmitted through the network. It is usually expressed in packets per second (pps) or bits per second (bps).

5.2.7 | Detection Rate

$$\text{Detection rate} = \frac{\text{Number of det ected ins tan ces}}{\text{Total number of ins tan ces}} \tag{27}$$

Detection rate measures the proportion of correctly detected instances of a specific event or condition among all instances.

5.2.8 | False Positive Rate

$$\text{False positive rate} = \frac{\text{False}_p}{\text{False}_p + \text{True}_n} \tag{28}$$

False positive rate measures the proportion of negative instances that are incorrectly classified as positive by the model.

21613915, 2025, 3, Downloaded from https://onlinelibrary.wiley.com/doi/10.1002/ett.70098 by Delhi Technological University, Wiley Online Library on [09/03/2025]. See the Terms and Conditions (https://onlinelibrary.wiley.com/terms-and-conditions) on Wiley Online Library for rules of use; OA articles are governed by the applicable Creative Commons License

These evaluation metrics collectively provide a comprehensive assessment of the proposed methodology's performance across different dimensions, facilitating informed decision making and optimization efforts.

5.3 | Experimental Analysis

In Figure 3, we compare the impact of malicious nodes on network lifetime across three methods: Federated learning [33], GALTM [34], and the proposed method. For the [33] method, network lifetime decreases from 650 rounds to 550 rounds as malicious nodes increase from 8% to 18%. Similarly, for the [34] method, the network lifespan drops from 920 rounds to 820 rounds with the same increase in malicious nodes. In contrast, the proposed method shows more resilience, with network lifetime only decreasing from 950 rounds to 870 rounds, indicating it is less affected by malicious activity.

In Figure 4, the analysis based on the effect of malicious nodes on network throughput for Federated learning [33], GALTM [34] and the proposed method is given. For Federated learning, throughput decreases from 5800 packets to 6000 packets as malicious nodes increase from 8% to 18%, indicating reduced data flow. Similarly, GALTM sees throughput drop from 19 000 packets to 17 200 packets with an increase in malicious nodes. In contrast, the proposed method maintains relatively stable throughput, ranging from 20 000 to 18 000 packets, demonstrating better resilience against malicious activity and ensuring uninterrupted data transmission.

Figure 5 shows the relationship between the detection rate and the percentage of malicious nodes for Federated learning [33], GALTM [34], and the proposed method. In the [33] method, the detection rate decreases from 90% to 88% as malicious nodes increase from 10% to 20%. Similarly, for GALTM, the detection increases from 92% to 96% as malicious nodes grow from 10% to 20%. In contrast, the proposed method shows a positive correlation, maintaining a detection rate of 94% to 97%, regardless of the increase in malicious nodes from 10% to 20%, demonstrating consistent and effective detection.

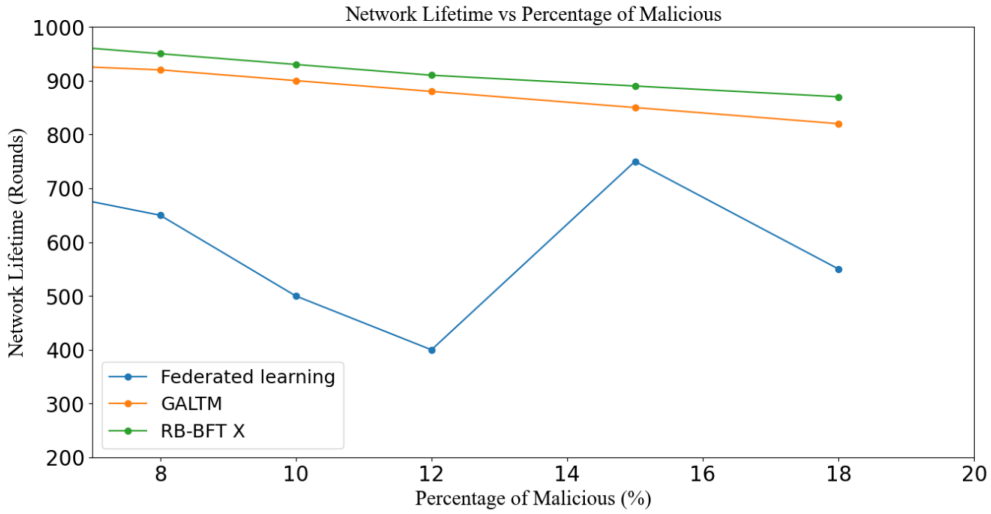

FIGURE 3 | Network lifetime versus percentage of malicious.

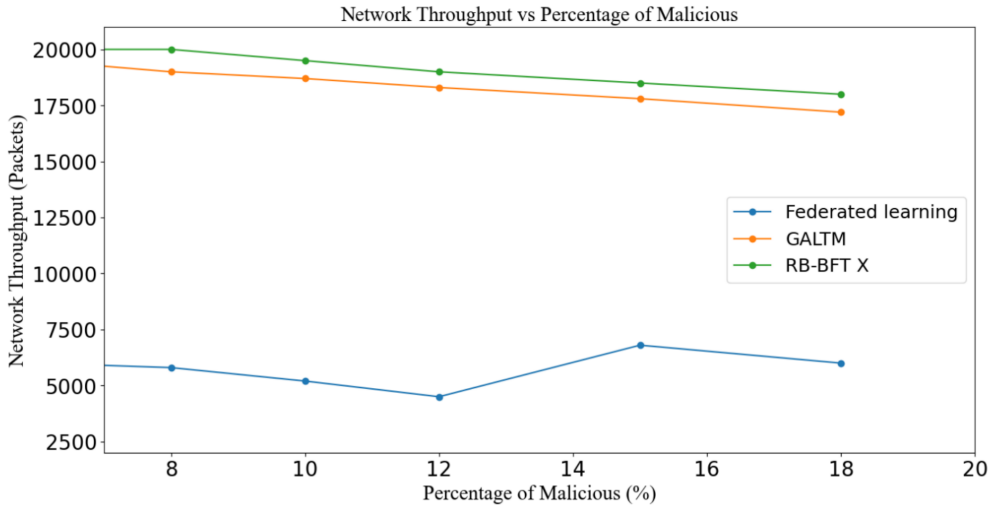

FIGURE 4 | Network throughput vs. percentage of malicioususers.

21613915, 2025, 3, Downloaded from https://onlinelibrary.wiley.com/doi/10.1002/ett.70098 by Delhi Technological University, Wiley Online Library on [09/03/2025]. See the Terms and Conditions (https://onlinelibrary.wiley.com/terms-and-conditions) on Wiley Online Library for rules of use; OA articles are governed by the applicable Creative Commons License

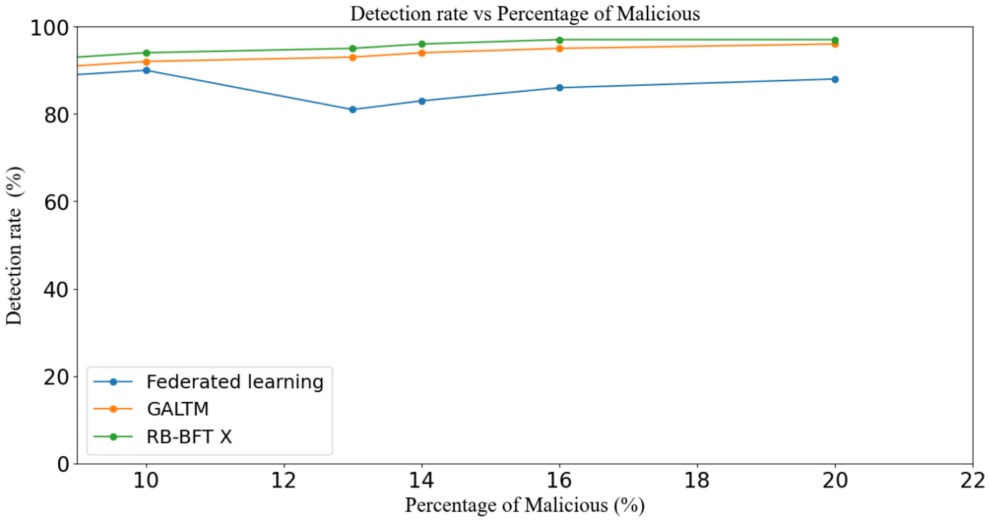

FIGURE 5 | Detection rate vs. percentage of malicious.

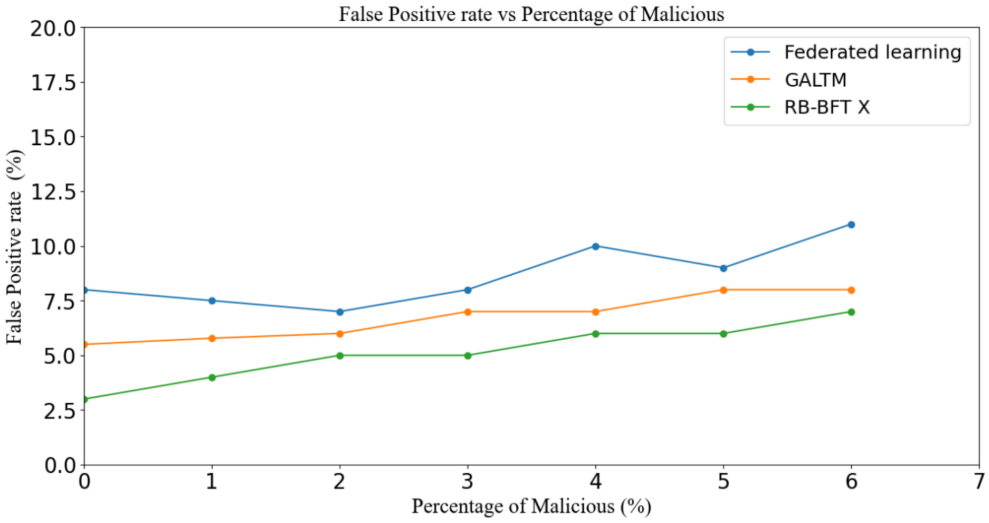

FIGURE 6 | False Positive Rate vs. Percentage of Malicious.

Figure 6 examines the impact of false positive rate (FPR) on the percentage of malicious nodes for Federated learning (FL), GALTM, and the proposed method. In the [33] method, the FPR increases from 6% to 11% as malicious nodes rise from 2% to 6%, indicating a higher misclassification rate. For the proposed method, however, the FPR remains stable between 5% and 7%, while the number of identified malicious nodes stays consistent between 2% and 6%, demonstrating the method's ability to minimize false positives while maintaining effective detection.

The comparison of various methods in Figure 7 for detecting malicious activities in a network reveals significant differences in performance across multiple metrics: accuracy, precision, recall, and F score. In terms of accuracy, the Behavioral Fingerprint method [38] has a relatively low accuracy of 78.6%. In contrast, AgroKy [37] shows a substantial improvement with 90.43%, followed closely by Fog-IOT [43] at 90.13%. RDoS-CoAP [49] further improves accuracy to 96.90%, while the proposed method excels with the highest accuracy of 98.20%.

When evaluating precision, which reflects the percentage of true positive detections among all positive detections, the Behavioral Fingerprint method achieves 79.2%, while AgroKy improves to 85.27%. Fog-IOT shows a higher precision of 90.10%, and RDoS-CoAP reaches 97.43%. The proposed method outperforms all others with a precision of 98.61%. In terms of recall, which measures the ability to detect all actual positive cases, the Behavioral Fingerprint method performs at 78.0%, while AgroKy achieves 86.31%. Fog-IOT further enhances recall to 89.95%, and RDoS-CoAP reaches 97.55%. The proposed method again outshines the others with the highest recall of 98.86%, demonstrating superior detection of all true positives.

Finally, the F score, representing the harmonic mean of precision and recall, provides a balanced performance measure. The Behavioral Fingerprint method has an F score of 76.6%, while AgroKy improves to 86.04%. Fog-IOT achieves 90.08%, and RDoS-CoAP reaches an impressive 97.31%. The proposed method leads with the highest F score of 98.70%, indicating its overall effectiveness in maintaining a balance between precision and recall.

21613915, 2025, 3, Downloaded from https://onlinelibrary.wiley.com/doi/10.1002/ett.70098 by Delhi Technological University, Wiley Online Library on [09/03/2025]. See the Terms and Conditions (https://onlinelibrary.wiley.com/terms-and-conditions) on Wiley Online Library for rules of use; OA articles are governed by the applicable Creative Commons License

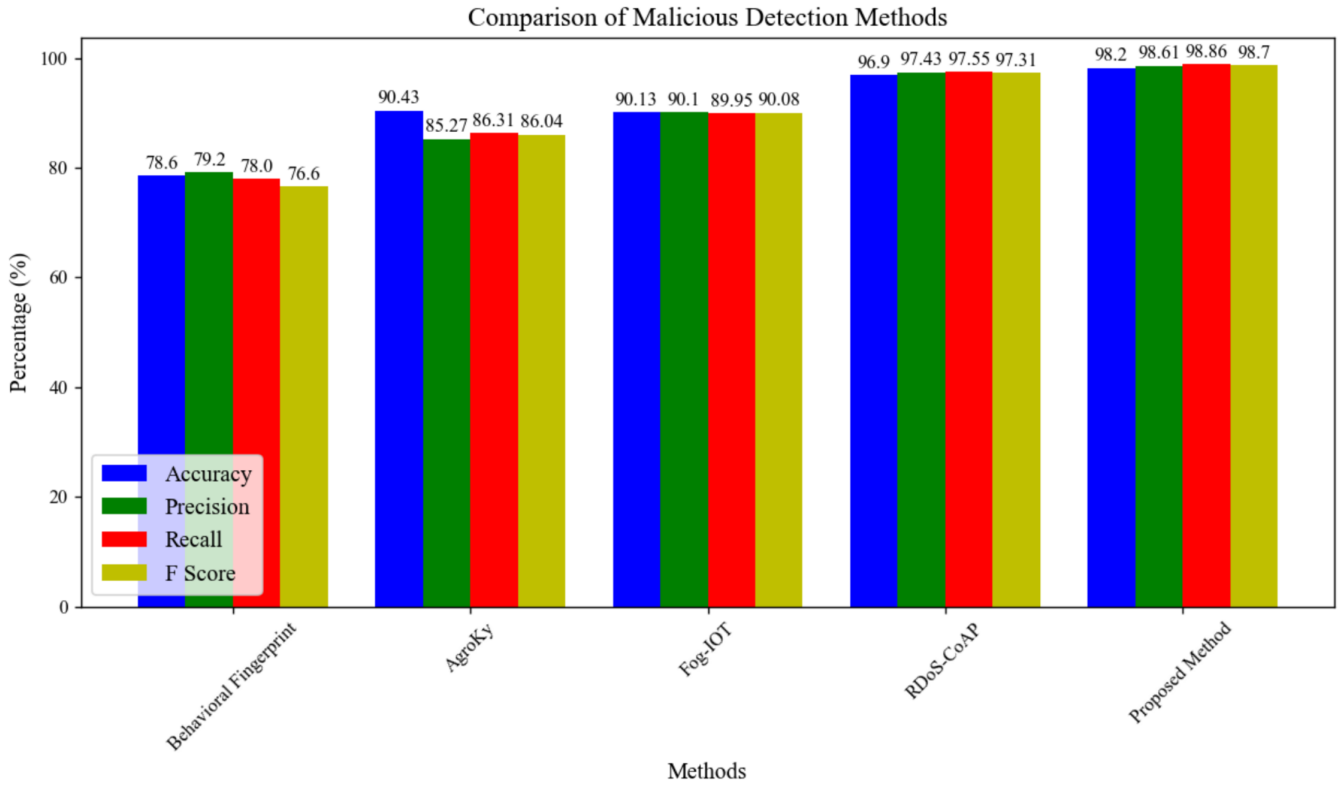

FIGURE 7 | Performance comparison analysis.

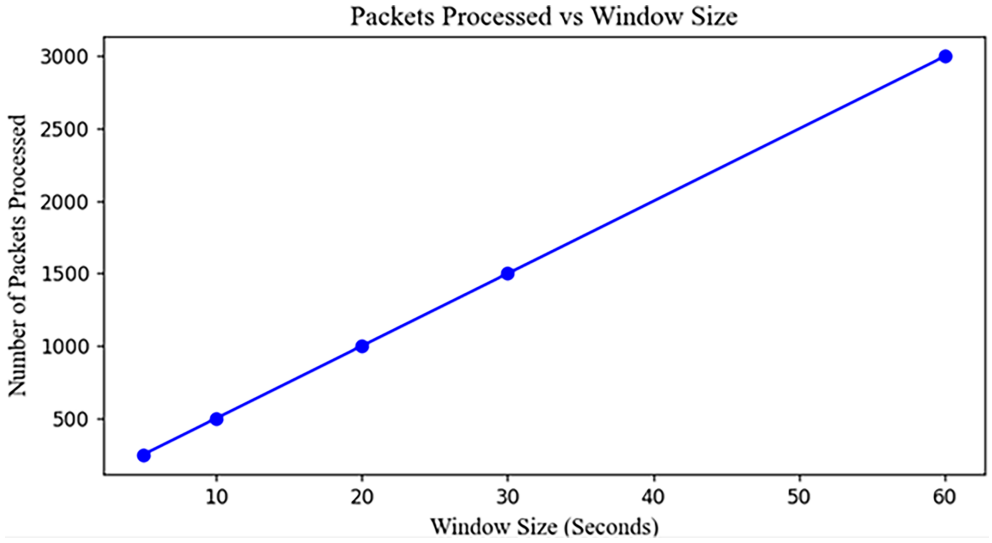

FIGURE 8 | Packets processed vs. window size.

The graph in Figure 8 illustrates the relationship between window size (in seconds) and the number of packets processed in a network system. As the window size increases, the number of packets processed also rises. With a 5-s window, 250 packets are processed, suitable for rapid, real-time analysis. Doubling the window to 10 s results in processing 490 packets, demonstrating a significant increase. From the results obtained, it can be deduced that, within the 15-s segment, the number of packets that can be processed increases to 730, which shows an improved ability to handle data. Another important fact is that increasing the window of the stream interruption to 30 s brings this number to 1450 packets, which indicates that it is possible to collect and analyze more data compared to short windows. Last but not least, when the window size is 60 s, the system processes 2900 packets, which presents its capacity to process many packets for analysis. In general, the diagram reveals that big windows enable more computations, which makes it possible to process a vast amount of information; on the other hand, possessing more complex windows is useful when performing instant analyses.

Scalability testing, as illustrated in Table 4, helps identify how a specific system performs under increased load or demand

21613915, 2025, 3, Downloaded from https://onlinelibrary.wiley.com/doi/10.1002/ett.70098 by Delhi Technological University, Wiley Online Library on [09/03/2025]. See the Terms and Conditions (https://onlinelibrary.wiley.com/terms-and-conditions) on Wiley Online Library for rules of use; OA articles are governed by the applicable Creative Commons License

TABLE 4 | Scalability evaluation.

Test scenario	No. of devices	Data traffic (packets/s/device)	Latency (ms)	Throughput (packets/sec)	CPU utilization (%)	Memory utilization (MB)	Error Rate (%)	Response time (ms)
Baseline	100	1	10	100	20	500	0.1	5
Moderate load	500	5	20	2500	40	1000	0.5	10
High load	1000	10	35	10 000	60	2000	1.0	15
Peak load	5000	50	50	250 000	80	5000	2.5	20
Extreme load	10 000	100	75	1 000 000	90	10 000	5.0	25
Low complexity	1000	10	30	10 000	55	1500	1.0	12
High complexity	1000	10	45	10 000	65	2500	1.5	18
Peak complexity	5000	50	65	250 000	85	7000	3.0	22

TABLE 5 | Method comparison.

Method	Adaptive configuration	Integrity	Privacy protection	Identity	Fairness	Authentication	Time complexity
Liu et al. [44]	No	Yes	Yes	Yes	Yes	Yes	O(n)
Bodur et al. [30]	No	Yes	Yes	Yes	No	Yes	O(n log n)
Rabie et al. [41]	No	Yes	Not mentioned	Yes	Yes	Yes	O(n^2)
Proposed	Yes	Yes	Yes	Yes	Yes	Yes	O(n)

in resources to pinpoint areas of possible congestion or drag. The following table reveals the responses for all types of systems regarding load and difficulty: standard, average, high, and complex. As the workload increases, which suggests a growing number of devices, the latencies rise, and the resource demand reaches its maximum, though throughput drops slightly. This leads to higher error rates; however, response time stays fairly constant. Also, it was observed that, depending on the complexity of the data, the resources are utilized to a different extent, where a higher complexity requires more CPU and memory. These observations allow for adding, removing, and modifying capacity, assigning resources, and enhancing systems with real-life conditions in mind.

Table 5 describes various schemes according to such parameters as adaptive to the configuration, integrity, protection of privacy data, ID authentication, fairness, authentication, and the time taken for the comparison. There is evidence of adaptive configuration regarding the proposed methodologies to achieve the required dynamics. While the proposed solution and Liu et al. [44] adopt the specification of essential security features, the scheme identified by Bodur et al. [30] needs more fairness. Rabie et al.'s [41] scheme has a notably higher time complexity, potentially impacting scalability. In contrast, the proposed methodology, along with Liu et al.'s, demonstrates linear time complexity, ensuring efficient resource utilization. Overall, the table underscores the importance of adaptability, security, and computational efficiency, positioning the proposed methodology as a promising solution for robust and scalable network systems.

5.4 | Performance Evaluation of Attack Detection

The Performance Evaluation of Attack Detection focuses on assessing the effectiveness of the proposed security framework in identifying and mitigating various malicious attacks within the healthcare IoT network. This evaluation examines key performance metrics such as Detection Rate, False Positive Rate, Latency, and Throughput to determine how well the system performs under different attack scenarios. By simulating a range of attacks, including Brute Force, DDoS, MITM, and Sybil attacks, this section provides insights into the framework's ability to maintain robust security while ensuring minimal impact on network performance.

Table 6 presents performance metrics for various malicious attack types simulated in the healthcare IoT network. The Detection Rate demonstrates the system's strong detection capabilities, with rates consistently above 95% for all attack types. Sybil attacks have the highest detection rate at 98.2%, followed by Brute Force attacks at 97.5%, and Data Tampering at 97%. The False Positive Rate remains low across all attacks, showing the system's ability to accurately distinguish between legitimate and malicious traffic, with the lowest false positive rate recorded for Sybil attacks at 1.1%, and the highest for MITM attacks at 2.5%.

In terms of Latency, DDoS and DoS attacks introduce the highest delays at 150 ms, followed by MITM attacks at 140 ms. Sybil attacks cause the least disruption with a latency of just 100 ms. As for Throughput, the system maintains high data transmission rates despite the attacks, with Sybil attacks achieving the highest throughput at 20500 packets per second (pps), followed closely by Fingerprinting attacks at 20200 pps. Brute Force and Data Tampering attacks both maintain a throughput of 19 800 pps and 19 700 pps, respectively, while MITM attacks and DDoS attacks result in slightly lower throughput at 19200 pps. These performance metrics underscore the framework's robustness in handling diverse attack scenarios, maintaining high detection rates, low false positives, and efficient network performance even under attack.

21613915, 2025, 3, Downloaded from https://onlinelibrary.wiley.com/doi/10.1002/ett.70098 by Delhi Technological University, Wiley Online Library on [09/03/2025]. See the Terms and Conditions (https://onlinelibrary.wiley.com/terms-and-conditions) on Wiley Online Library for rules of use; OA articles are governed by the applicable Creative Commons License

TABLE 6 | Performance evaluation of attack detection.

Attack type	Detection rate (%)	False positive rate (%)	Latency (ms)	Throughput (pps)
Passive Eavesdropping	96.5	1.7	110	20 200
Active intrusion	95.3	2.5	140	19 200
Insider threats	97.0	1.3	115	19 700
Denial of service (DoS)	96.8	2.1	150	18 500
Brute force	97.5	1.2	120	19 800
Distributed denial of service (DDoS)	96.8	2.1	150	18 500
Man-in-the-middle (MITM)	95.3	2.5	140	19 200
Data tampering	97.0	1.3	115	19 700
Sybil attack	98.2	1.1	100	20 500

5.5 | Ablation Study

Ablation studies, a cornerstone of research methodology, meticulously dissect the impact of individual components on system performance under various methods, illuminating crucial insights in various domains. The ablation study results are depicted in graphs, as shown in Figure 9.

5.5.1 | Method A: Proposed Model

The proposed model achieves the highest performance across all metrics with all components included. The accuracy is 98.5%, precision is 98.2%, recall is 98.8%, and F-score is 98.5%. The latency is 10 ms, throughput is 1500 packets per second, and the security metric (intrusion detection rate) is 99.2%. These results indicate the effectiveness of the integrated approach in providing robust security and high performance in the healthcare network.

5.5.2 | Method B: Without RB-BFT X

Eliminating the Redundant Byzantine Fault Tolerance with Extensions (RB-BFT X) component leads to a significant reduction in all key performance metrics. The model's accuracy declines from 98.5% to 95.0%, precision is reduced from 98.2% to 94.5%, recall is lower from 98.8% to 94.8%, and the F-score decreases from 98.5% to 94.6%. This fact demonstrates just how critical RB-BFT X is for the said model, as it ensures the targeted accuracy and precision in terms of data identification and processing. Moreover, latency specifications rise from 10 ms to 15 ms, which explains slow data transmission and throughput reduction from 1500 packets/s to 1400 packets/s, signifying poor data processing ability. The most sensitive category is security, under which the intrusion detection capability is reduced to as low as 99.2% to 96.0%. This means that RB-BFT X is necessary for the network, as it maintains its strong fault tolerance and security level.

5.5.3 | Method C: Without RBAC

Disabling of RBAC leads to a slight general degradation of performance indicators such as accuracy, which in some instances may drop from 98.5% to 96.5%, precision from 98.2% to 96.0%, recall from 98.8% to 96.2%, and the F-score from 98.5% to 96.1%. This points out that RBAC significantly improves scalability, although it is not the only factor contributing to this. The jump from 10 ms of latency up to 12 ms and the ever so slight reduction in throughput from 1500 packets/s down to 1450 packets/s indicate that RBAC plays a role in the effective administration of data from a security perspective. The impact on the security aspect has lowered significantly to a staggering 99.2%–97.5%. Finally, the practices showed that the total healthcare IoT network traffic is driven towards RBAC, which underlines its critical role in securing healthcare IoT network access.

5.5.4 | Method D: Without Behavioral Anomaly Detection

When using a model without Behavioral Anomaly Detection, it has a moderate decrease in performance compared to the first model, with accuracy from 98.5% to 97.2%, precision from 98.2% to 96.8%, recall from 98.8% to 97.1%, and the F-score from 98.5% to 96.9%. From the results, it is clear that latency rises from 10 to 11 ms and throughput drops from 1500 packets/s to 1480 packets/s, which means there is a slight delay in communication and a decline in the transmission rate. That effect is reflected in the security aspect, where the intrusion detection rate decreases from 99.2% to 97.8% of the participants, 97.8% agreed that anomaly detection effectively reduces alert fatigue and enables analysts to recognize security threats within the network.

5.5.5 | Method E: Without Coati Chase

When the Coati Chase component is removed, it positively affects the accuracy ratio negatively, thus producing a lower score of 96.8%, precision from 98.2% to 96.5%, recall from 98.8% to 96.6%, and the F-score from 98.5% to 96.5%. Latency rises from 10 to 14 ms, which shows the existence of slow communication paths, and throughput decreases from 1500 packets/s to 1420 packets/s, evidencing the relational mode of Coati Chase in data routing. The security metric is also impacted depending on the IDS type, with the ratio of detected intrusion decreasing from 99.2% to 97.3%; Coati Chase would hence contribute to ensuring the safety and reliability of the routing process within the healthcare IoT network.

21613915, 2025, 3, Downloaded from https://onlinelibrary.wiley.com/doi/10.1002/ett.70098 by Delhi Technological University, Wiley Online Library on [09/03/2025]. See the Terms and Conditions (https://onlinelibrary.wiley.com/terms-and-conditions) on Wiley Online Library for rules of use; OA articles are governed by the applicable Creative Commons License

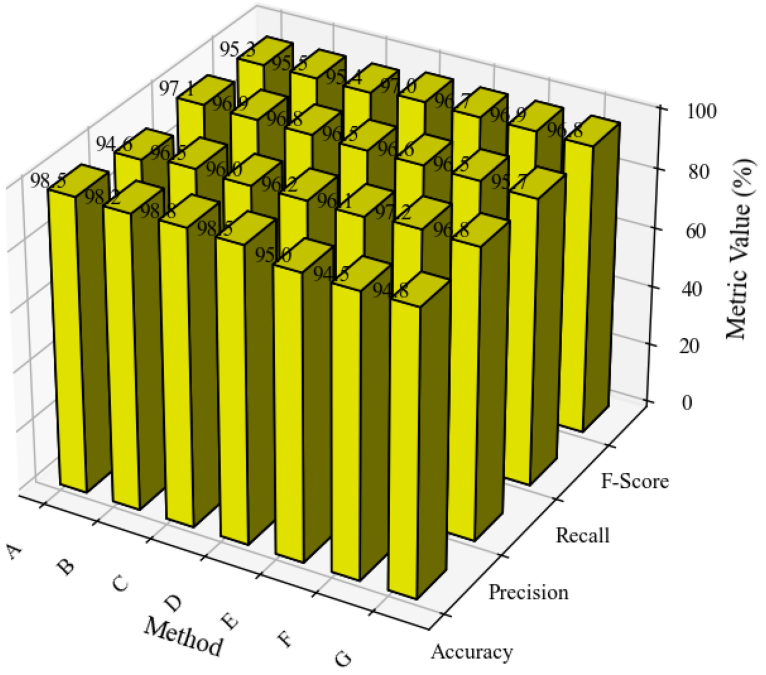

(a) Based on performance metrices

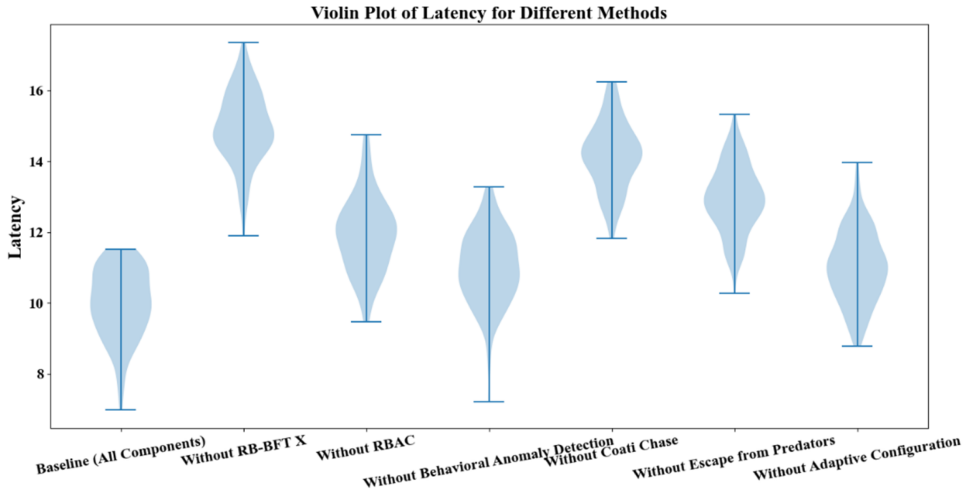

(b) Based on Latency

FIGURE 9 | Ablation results

5.5.6 | Method F: Without Escape From Predators

The conclusion that can be drawn from the figures is that the performance parameters are lower after pretraining without the Escape from Predators component, where average accuracy goes down from 98.5% to 95.7%, precision from 98.2% to 95.3%, recall from 98.8% to 95.5%, and F-score from 98.5% to 95.4%. The latency, which was at 10 ms, rises to 13 ms, and the throughput, 1500 packets per second, is reduced to 1430 packets per second, suggesting that data transmission becomes less efficient. The security impact is substantial, with the intrusion detection rate falling from 99.2% to 95.9%, highlighting its role in providing dynamic security mechanisms to protect against potential attacks.

5.5.7 | Method G: Without Adaptive Configuration

It demonstrates that when there is no Adaptive Configuration, the accuracy is lowered from 98.5% to 97.0%, precision from 98.2% to 96.7%, recall from 98.8% to 96.9%, and F-score also drops from 98.5% to 96.8%. Over the five runs, they vary the latency by going from 10 ms to 11 ms while reducing the throughput from 1500 packets/s to 1470 packets/s, suggesting that adaptive configuration helps continually optimize performance. The security metric also declines, with the intrusion detection rate dropping from 99.2% to 97.6%, underscoring the importance of adaptive configuration in ensuring the system can adapt to changes and maintain security.

21613915, 2025, 3, Downloaded from https://onlinelibrary.wiley.com/doi/10.1002/ett.70098 by Delhi Technological University, Wiley Online Library on [09/03/2025]. See the Terms and Conditions (https://onlinelibrary.wiley.com/terms-and-conditions) on Wiley Online Library for rules of use; OA articles are governed by the applicable Creative Commons License

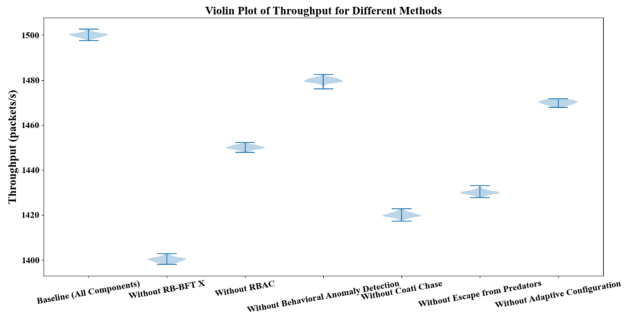

(c) Based on Throughput

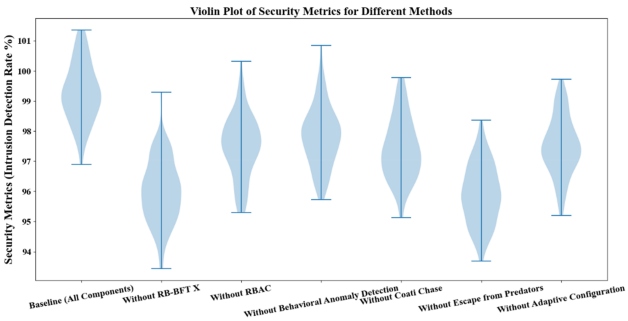

(d) Based on Security metrics

FIGURE 9 | (Continued)

6 | Discussion

The proposed Multi-cluster Security Framework for Healthcare IoT, integrating RB-BFT X and CoatiNet, effectively addresses critical challenges in healthcare IoT networks. Traditional methods for healthcare IoT security face several limitations, as evidenced by prior research. Scalability remains a major challenge, with approaches like Practical Byzantine Fault Tolerance (PBFT) and Federated Byzantine Agreement (FBA) suffering from high communication overheads and limited adaptability in large-scale IoT networks, as discussed by Singh et al. [36]. In contrast, the proposed Multi-cluster Security Framework addresses these challenges by integrating lightweight cryptographic techniques through RB-BFT X, which reduces communication complexity and enhances scalability. Resource constraints further hinder methods such as blockchain-based frameworks proposed by Demirbaga and Aujla [29] and Bodur and Yaseen [30], which require significant computational and storage resources. Similarly, Explainable AI (XAI)-driven solutions, including those by Kumar et al. [25] and Kumar et al. [22], introduce computational overhead, making them impractical for resource-constrained IoT devices. The proposed framework addresses these limitations by employing lightweight anomaly detection and efficient dynamic routing, ensuring compatibility with low-power IoT devices.

Real-time adaptability is another critical issue, as many frameworks struggle to adjust to evolving threats and network conditions dynamically. For instance, while Yang et al. [34] employ GANs for trust evaluation, their high computational requirements limit real-time applicability. Additionally, the static configurations in Zhu and Deng [26] highlight the inability to handle real-time interactions effectively. The proposed framework's CoatiNet module resolves these challenges by dynamically recalibrating communication paths and adjusting configurations in real time based on network conditions, maintaining low latency and uninterrupted communication even during high traffic or malicious activities. Data imbalance across clusters also poses a challenge, leading to bottlenecks and latency spikes, as noted in the privacy-preserving approaches by Dhasarathan et al. [32] and Zhang et al. [33]. The proposed model addresses this by incorporating dynamic workload reallocation strategies to balance data distribution and prevent resource bottlenecks. By combining RB-BFT X for intra-cluster security and CoatiNet for inter-cluster communication, the proposed framework offers a scalable, resource-efficient, and highly adaptable solution, effectively overcoming the limitations of traditional methods.

6.1 | Advantages

One of the primary strengths of the proposed methodology is its enhanced security capabilities. The framework provides multi-layered protection against common IoT threats such as passive eavesdropping, tampering, insider threats, and denial-of-service (DoS) attacks. Through lightweight cryptographic techniques and secure communication protocols, sensitive healthcare data remains well protected, even in resource-constrained environments. The RBAC mechanism further ensures access is restricted to authorized entities, reducing the risk of data breaches. Additionally, CoatiNet's dynamic routing and real-time adjustments minimize latency and sustain secure communication, even under adverse network conditions like high traffic loads or cyber threats. The framework's ability to scale efficiently and maintain performance as IoT networks grow further enhances its applicability in modern healthcare systems.

6.2 | Limitations

Despite these strengths, the framework has certain limitations. Its dependency on accurate anomaly detection poses a challenge, as insufficient or imbalanced training data may result in false positives or negatives, which can either overload the system or allow threats to bypass detection. Additionally, although CoatiNet optimizes communication paths, extreme network loads or a high percentage of malicious nodes ($>20\%$) can still lead to increased latency due to frequent rerouting and security checks. The autonomous clustering and configuration processes also require careful tuning and optimization, which may introduce complexity and delay deployment in large-scale networks. Furthermore, while the framework is designed to be scalable, its performance may diminish when scaled to extremely large networks without further optimization or the integration of external resources such as edge computing.

6.3 | Future Directions

To address these limitations and enhance the framework's capabilities, several future improvements are suggested. Incorporating advanced machine learning models, such as federated learning, can improve anomaly detection accuracy while preserving data privacy. Hybrid cryptographic approaches combining lightweight and quantum-resistant techniques can further secure the system against future threats. The integration of

21613915, 2025, 3, Downloaded from https://onlinelibrary.wiley.com/doi/10.1002/ett.70098 by Delhi Technological University, Wiley Online Library on [09/03/2025]. See the Terms and Conditions (https://onlinelibrary.wiley.com/terms-and-conditions) on Wiley Online Library for rules of use; OA articles are governed by the applicable Creative Commons License

edge computing could alleviate computational burdens on IoT devices, reducing latency and enhancing real-time performance. Advanced optimization algorithms could also be employed to improve workload distribution across clusters, addressing imbalances and ensuring consistent performance under heavy loads. Additionally, incorporating adaptive threat intelligence feeds would allow the framework to detect emerging threats and dynamically adjust its security mechanisms.

7 | Conclusion

Thus, the proposed method of securing networks in healthcare IoT is a suitable solution to the defined security threats and concerns in such a setting. It employs strong security features such as high-strength encryption (AES 256-bit), adaptive routing, and multi-factor authentication. The two core components of the system, RB-BFT X and CoatiNet, are pivotal to the overall effectiveness of the framework. RB-BFT X enhances the fault tolerance mechanisms through increased redundancy, which significantly improves key network parameters such as accuracy and the rate of intrusion detection. Its role is essential in maintaining the network's security and reliability, as the absence of RB-BFT X would result in a noticeable degradation of these parameters. On the other hand, CoatiNet provides flexibility by managing information and making real-time routing adjustments based on network conditions. Its dynamic routing capabilities outperform other algorithms by maintaining network lifetime and throughput even in the presence of malicious nodes. Moreover, the configuration capacities provided by the framework enable it to adapt seamlessly to existing regulatory and resource constraints while dynamically adjusting to changing network conditions. This adaptability ensures that the system remains resilient and efficient in healthcare IoT environments, making RB-BFT X and CoatiNet the core contributors to the architecture of the proposed methodology. Together, they form a robust foundation for addressing the unique security requirements of healthcare IoT networks.

Ethics Statement

The authors have nothing to report.

Consent

All the authors give their consent for publication willingly.

Conflicts of Interest

The authors declare no Conflicts of Interest.

Data Availability Statement

Data sharing is not applicable to this article as no new data were created or analyzed in this study.

References

1. O. Elijah, T. A. Rahman, I. Orikumhi, C. Y. Leow, and M. N. Hindia, "An Overview of Internet of Things (IoT) and Data Analytics in Agriculture: Benefits and Challenges," *IEEE Internet of Things Journal* 5, no. 5 (2018): 3758–3773.

2. K. Kimani, V. Oduol, and K. Langat, "Cyber Security Challenges for IoT-Based Smart Grid Networks," *International Journal of Critical Infrastructure Protection* 25 (2019): 36–49.

3. A. A. Hussain and F. Al-Turjman, "Artificial Intelligence and Blockchain: A Review," *Transactions on Emerging Telecommunications Technologies* 32, no. 9 (2021): e4268, https://doi.org/10.1002/ett.4268.

4. S. K. Devineni, S. Kathiriya, and A. Shende, "Machine Learning-Powered Anomaly Detection: Enhancing Data Security and Integrity," *Journal of Artificial Intelligence & Cloud Computing* 184 (2023): 2–9, https://doi.org/10.47363/JAICC/2023.

5. J. Ni, K. Zhang, X. Lin, and X. Shen, "Securing Fog Computing for Internet of Things Applications: Challenges and Solutions," *IEEE Communication Surveys and Tutorials* 20, no. 1 (2017): 601–628.

6. D. Gupta, A. Segal, A. Panda, et al., "A New Approach to Interdomain Routing Based on Secure Multi-Party Computation," in *Proceedings of the 11th ACM Workshop on Hot Topics in Networks* (Oct 29, 2012), 37–42.

7. C. Tamizhselvan, "A Novel Communication-Aware Adaptive Key Management Approach for Ensuring Security in IoT Networks," *Transactions on Emerging Telecommunications Technologies* 33, no. 11 (2022): e4605, https://doi.org/10.1002/ett.4605.

8. E. Frank, A. Luz, and H. Jonathan, Access Control and Authentication Mechanisms in Cloud Databases.

9. N. El Ioini and C. Pahl, "A Review of Distributed Ledger Technologies," in *On the Move to Meaningful Internet Systems. OTM 2018 Conferences: Confederated International Conferences: CoopIS, C&TC, and ODBASE 2018* (Proceedings, Part II 2018) (Valletta, Malta, Springer International Publishing, Cham, October 22–26, 2018), 277–288.

10. A. Yaseen, "Ai-Driven Threat Detection and Response: A Paradigm Shift in Cybersecurity," *International Journal of Information and Cybersecurity* 7, no. 12 (2023): 25–43.

11. P. Li, A. Shrivastava, J. Moore, and A. König, "Hashing Algorithms for Large-Scale Learning," *Advances in Neural Information Processing Systems* 24 (2011): 2672–2680.

12. W. Penard and T. van Werkhoven, "On the Secure Hash Algorithm Family," in *Cryptography in Context* (Wiley, 2008), 1–8.

13. M. Rao, T. Newe, and I. Grout, "Secure Hash Algorithm-3 (SHA-3) Implementation on Xilinx FPGAs, Suitable for IoT Applications," *International Journal on Smart Sensing and Intelligent Systems* 7, no. 5 (2014): 1–6.

14. S. S. Hussain, S. M. Farooq, and T. S. Ustun, "Analysis and Implementation of Message Authentication Code (MAC) Algorithms for GOOSE Message Security," *IEEE Access* 7 (2019): 80980–80984.

15. M. Bellare, "New Proofs for NMAC and HMAC: Security Without Collision Resistance," *Journal of Cryptology* 28 (2015): 844–878.

16. Z. Drias, A. Serhrouchni, and O. Vogel, "Identity-Based Cryptography (IBC) Based Key Management System (KMS) for Industrial Control Systems (ICS)," in *2017 1st Cyber Security in Networking Conference (CSNet)* (IEEE, 2017), 1–10.

17. U. Banerjee, C. Juvekar, S. H. Fuller, and A. P. Chandrakasan, "eeDTLS: Energy-Efficient Datagram Transport Layer Security for the Internet of Things," in *GLOBECOM 2017-2017 IEEE Global Communications Conference* (IEEE, 2017), 1–6.

18. R. C. Merkle, "Secure Communications Over Insecure Channels," *Communications of the ACM* 21, no. 4 (1978): 294–299, https://doi.org/10.1145/359460.359473.

19. Y. Li, S. Schäge, Z. Yang, F. Kohlar, and J. Schwenk, "On the Security of the Pre-Shared Key Ciphersuites of TLS," in *Public-Key Cryptography–PKC 2014: 17th International Conference on Practice and Theory in Public-Key Cryptography* (Proceedings 17, 2014) (Springer Berlin Heidelberg, Buenos Aires, Argentina, March 26–28, 2014), 669–684.

21613915, 2025, 3, Downloaded from https://onlinelibrary.wiley.com/doi/10.1002/ett.70098 by Delhi Technological University, Wiley Online Library on [09/03/2025]. See the Terms and Conditions (https://onlinelibrary.wiley.com/terms-and-conditions) on Wiley Online Library for rules of use; OA articles are governed by the applicable Creative Commons License

20. B. Bhushan, C. Sahoo, P. Sinha, and A. Khamparia, "Unification of Blockchain and Internet of Things (BIoT): Requirements, Working Model, Challenges and Future Directions," *Wireless Networks* 27 (2021): 55–90.

21. S. Saxena, B. Bhushan, and M. A. Ahad, "Blockchain Based Solutions to Secure IoT: Background, Integration Trends and a Way Forward," *Journal of Network and Computer Applications* 181 (2021): 103050.

22. P. Kumar, R. Kumar, M. Aloqaily, and A. N. Islam, "Explainable AI and Blockchain for Metaverse: A Security, and Privacy Perspective," *IEEE Consumer Electronics Magazine* 13, no. 3 (2023): 90–97.

23. R. Kumar, A. Aljuhani, D. Javeed, P. Kumar, S. Islam, and A. N. Islam, "Digital Twins-Enabled Zero Touch Network: A Smart Contract and Explainable AI Integrated Cybersecurity Framework," *Future Generation Computer Systems* 156 (2024): 191–205.

24. R. Kumar, P. Kumar, A. Kumar, A. A. Franklin, and A. Jolfaei, "Blockchain and Deep Learning for Cyber Threat-Hunting in Software-Defined Industrial IoT," in *2022 IEEE International Conference on Communications Workshops (ICC Workshops)* (IEEE, 2022), 776–781.

25. P. Kumar, D. Javeed, R. Kumar, and A. N. Islam, "Blockchain and Explainable AI for Enhanced Decision Making in Cyber Threat Detection," *Software: Practice and Experience* 54, no. 8 (2024): 1337–1360.

26. X. Zhu and H. Deng, "A Security Situation Awareness Approach for IoT Software Chain Based on Markov Game Model," *International Journal of Interactive Multimedia and Artificial Intelligence* 7, no. 5 (2022): 59–65.

27. F. He, W. Feng, Y. Zhang, and J. Liu, "An Improved Byzantine Fault-Tolerant Algorithm Based on Reputation Model," *Electronics* 12, no. 9 (2023): 2049.

28. M. Dehghani, Z. Montazeri, E. Trojovská, and P. Trojovský, "Coati Optimization Algorithm: A New Bio-Inspired Metaheuristic Algorithm for Solving Optimization Problems," *Knowledge-Based Systems* 259 (2023): 110011.

29. U. Demirbaga and G. S. Aujla, "MapChain: A Blockchain-Based Verifiable Healthcare Service Management in IoT-Based Big Data Ecosystem," *IEEE Transactions on Network and Service Management* 19, no. 4 (2022): 3896–3907.

30. H. Bodur and I. F. Al Yaseen, "An Improved Blockchain-Based Secure Medical Record Sharing Scheme," *Cluster Computing* 27 (2024): 7981–8000.

31. R. Guo, Z. Guo, Z. Lin, and W. Jiang, "A Hierarchical Byzantine Fault Tolerance Consensus Protocol for the Internet of Things," *High-Confidence Computing* 4, no. 3 (2023): 100196.

32. C. Dhasarathan, M. Shanmugam, M. Kumar, D. Tripathi, S. Khapre, and A. Shankar, "A Nomadic Multi-Agent Based Privacy Metrics for e-Health Care: A Deep Learning Approach," *Multimedia Tools and Applications* 83, no. 3 (2024): 7249–7272.

33. L. Zhang, J. Xu, P. Vijayakumar, P. K. Sharma, and U. Ghosh, "Homomorphic Encryption-Based Privacy-Preserving Federated Learning in Iot-Enabled Healthcare System," *IEEE Transactions on Network Science and Engineering* 10, no. 5 (2022): 2864–2880.

34. L. Yang, S. X. Yang, Y. Li, Y. Lu, and T. Guo, "Generative Adversarial Learning for Trusted and Secure Clustering in Industrial Wireless Sensor Networks," *IEEE Transactions on Industrial Electronics* 70, no. 8 (2022): 8377–8387.

35. A. Vinitha and M. S. Rukmini, "Secure and Energy Aware Multi-Hop Routing Protocol in WSN Using Taylor-Based Hybrid Optimization Algorithm," *Journal of King Saud University, Computer and Information Sciences* 34, no. 5 (2022): 1857–1868.

36. A. Singh, P. K. Chouhan, and G. S. Aujla, "SecureFlow: Knowledge and Data-Driven Ensemble for Intrusion Detection and Dynamic Rule Configuration in Software-Defined IoT Environment," *Ad Hoc Networks* 156 (2024): 103404.

37. S. Anand and A. Sharma, "AgroKy: An Approach for Enhancing Security Services in Precision Agriculture," *Measurement: Sensors* 24 (2022): 100449.

38. M. Arazzi, S. Nicolazzo, and A. Nocera, "A Novel IoT Trust Model Leveraging Fully Distributed Behavioral Fingerprinting and Secure Delegation," *Pervasive and Mobile Computing* 99 (2024): 101889.

39. M. N. Jeyakumar and J. Samraj, "Secure Medical Sensor Monitoring Framework Using Novel Hybrid Encryption Algorithm Driven by Internet of Things," *Measurement: Sensors* 33 (2024): 101122.

40. S. Dhar, A. Khare, A. D. Dwivedi, and R. Singh, "Securing IoT Devices: A Novel Approach Using Blockchain and Quantum Cryptography," *Internet of Things* 25 (2024): 101019.

41. O. B. Rabie, S. Selvarajan, T. Hasanin, G. B. Mohammed, A. M. Alshareef, and M. Uddin, "A Full Privacy-Preserving Distributed Batch-Based Certificate-Less Aggregate Signature Authentication Scheme for Healthcare Wearable Wireless Medical Sensor Networks (HWMSNs)," *International Journal of Information Security* 23, no. 1 (2024): 51–80.

42. J. A. Masood, M. Jeyaselvi, N. Senthamarai, S. Koteswari, M. Sathya, and N. K. Chakravarthy, "Privacy Preservation in Wireless Sensor Network Using Energy Efficient Multipath Routing for Healthcare Data," *Measurement: Sensors* 29 (2023): 100867.

43. M. J. Baucas, P. Spachos, and K. N. Plataniotis, "Federated Learning and Blockchain-Enabled Fog-IoT Platform for Wearables in Predictive Healthcare," *IEEE Transactions on Computational Social Systems* 10 (2023): 1732–1741.

44. Y. Liu, X. Hao, W. Ren, et al., "A Blockchain-Based Decentralized, Fair and Authenticated Information Sharing Scheme in Zero Trust Internet-Of-Things," *IEEE Transactions on Computers* 72, no. 2 (2022): 501–512.

45. R. Hyde and P. Angelov, "A Fully Autonomous Data Density Based Clustering Technique," in *2014 IEEE Symposium on Evolving and Autonomous Learning Systems (EALS)* (IEEE, 2014), 116–123.

46. M. K. Hasan, M. Shafiq, S. Islam, et al., "Lightweight Cryptographic Algorithms for Guessing Attack Protection in Complex Internet of Things Applications," *Complexity* 2, no. 2021 (2021): 1–3.

47. J. Andrew, R. J. Eunice, and J. Karthikeyan, "An Anonymization-Based Privacy-Preserving Data Collection Protocol for Digital Health Data," *Frontiers in Public Health* 11 (2023): 1125011.

48. A. Biryukov and D. Khovratovich, "Related-Key Cryptanalysis of the Full AES-192 and AES-256," in *Advances in Cryptology–ASIACRYPT 2009: 15th International Conference on the Theory and Application of Cryptology and Information Security*, Tokyo, Japan (December 6–10, 2009), Proceedings 2009; 1–18. Springer, Berlin, Heidelberg.

49. M. Al-Hawawreh, N. Moustafa, and J. Slay, "A Threat Intelligence Framework for Protecting Smart Satellite-Based Healthcare Networks," *Neural Computing and Applications* 36, no. 1 (2024): 15–35.

21613915, 2025, 3, Downloaded from https://onlinelibrary.wiley.com/doi/10.1002/ett.70098 by Delhi Technological University, Wiley Online Library on [09/03/2025]. See the Terms and Conditions (https://onlinelibrary.wiley.com/terms-and-conditions) on Wiley Online Library for rules of use; OA articles are governed by the applicable Creative Commons License

Materials Research Proceedings 49 (2025) 143-151 https://doi.org/10.21741/9781644903438-15

A review on microfluidic-based electrowetting on dielectric (EWOD) in state-of-the-art adaptive electronic cooling

Amit SAHU[1*], Mohammad ZUNAID[1], Rajesh KUMAR[1]

[1] Department of Mechanical Engineering, Delhi Technological University, Delhi, 110042, India

*amitsahu_2k21phdme506@dtu.ac.in

Keywords: Electronic Cooling, Electrowetting, Microfluidics, Surface Treatment, Micromanufacturing

Abstract. The perpetual growth of efficient computing devices, desktop computers, and power electronic systems obliges the development of effective cooling solutions capable of efficiently dissipating high heat flux and addressing hot spots at the microscales. Electrowetting (EW) cooling is compact and responds to adaptive temperature control of electronic devices. Electrowetting on dielectric (EWOD) devices are excellent for electronic cooling in Lab-on-a-Chip technology. These devices are candid, have no moving parts, and provide precise control over movement. Micro manufacturing of cooling devices enables heat transfer efficiently as compared to conventional cooling devices. This article surveys the efforts of microfluidic-based cooling devices using the electrowetting principle with single and multiple arrayed water droplet jets on hydrophobic or superhydrophobic surfaces. It discusses the suitable surface treatment methods and materials to improve the performance of electronic devices and high computing systems.

Introduction

Electronic devices and high-performance computing systems continue to demand efficient cooling systems to mitigate the adverse effects of high heat flux on performance and longevity. Conventional cooling methods are often ineffective due to surface area availability, size, and pressure drop. Prompting exploration into novel approaches such as microfluidic-based electrowetting cooling, leveraging the unique properties of superhydrophobic surfaces [1] (CA >150^{o}), and micro-manufacturing of cooling devices offers a promising avenue for enhancing heat dissipation in electronic systems [2].

Electrowetting (EW) refers to the phenomenon wherein the degree of wetting at the interface of a solid-liquid can be manipulated by applying a sufficient electrical potential gradient [3]. This process involves the redistribution of charges and dipoles at the solid-liquid interface, resulting in a change in the contact angle (CA) and manipulation of the surface tension of a droplet. As shown in Figure 1 (a) and (b), when a voltage is applied, the contact angle transitions from θ_i to θ, respectively. Lippman's equation illustrated below the contact angle (θ) changes on fluctuations of voltage applications (V), where $\boldsymbol{\varepsilon_o, \varepsilon_d, \gamma, d}$ are vacuum permittivity, dielectric constant, Free surface energy or surface tension and dielectric thickness respectively. This change occurs because opposite charges attract therefore, the presence of electrodes connecting the droplet causes the solid plate surface to draw the droplet towards it, consequently increasing wetting and decreasing the contact angle at the liquid-solid interface [4]. Usually, the surface tension of the droplet can also be altered by adding surfactants to the fluid [5]. Nevertheless, the EW technique is very novel for use in thermal management. It increases wetting on the hydrophobic surface more than that of the addition of surfactant to the droplets [6]. It also has the potential to move electrically conductive liquid metals and alloys using EWOD. These fluids usually have a much higher thermal conductivity coefficient than water or oils. Galinstan, a readily available, inexpensive, nontoxic liquid alloy with 65 times less thermal resistance of water, is suggested as a feasible coolant for adaptive EW.

Content from this work may be used under the terms of the Creative Commons Attribution 3.0 license. Any further distribution of this work must maintain attribution to the author(s) and the title of the work, journal citation and DOI. Published under license by Materials Research Forum LLC.

Materials Research Proceedings 49 (2025) 143-151 https://doi.org/10.21741/9781644903438-15

Lippman's Equation, $$\cos\theta = \cos\theta_i + \left(\frac{\varepsilon_o \cdot \varepsilon_d}{2\gamma d}\right) V^2 \quad (1)$$

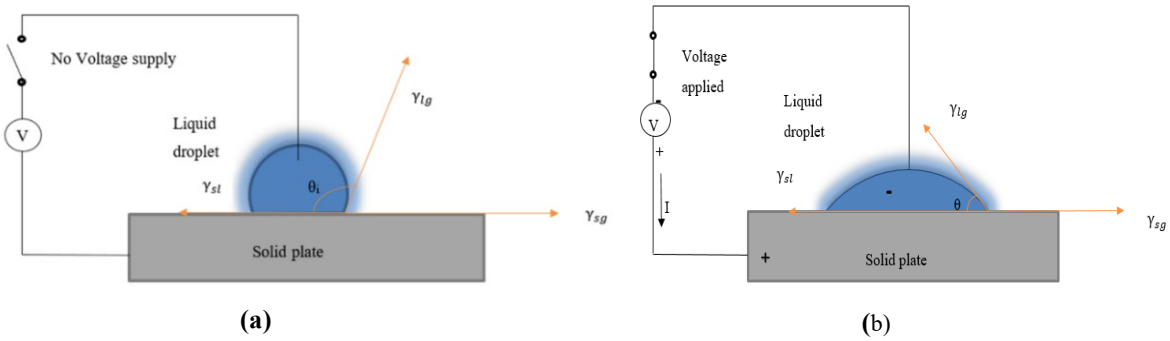

Figure 1: (a) Wetting of liquid between Solid-Liquid interface before voltage application, CA (θ_i), (b) Wetting of liquid between solid-liquid interface after application of voltage, CA (θ)

Adaptive & Non-Adaptive Cooling

The active cooling techniques are categorized as adaptive cooling. Adaptive cooling in integrated chips (ICs) controls temperature fluctuation on microchips or integrated circuits with closed-loop temperature feedback using direct or indirect sensing [7], [8]. This cooling is sensitive to temperature feedback at several IC spots and adjusts accordingly. Meanwhile, the lack of a temperature feedback system is known as non-adaptive cooling. Thus, non-adaptive systems are unable to identify hotspots or respond appropriately to them. The following ways can also be advised to control an adaptive cooling system.

- Real-time temperature sensing and feedback control
- Thermal characteristic model
- Control of chip clock frequency
- Power consumption management

Microfluidic-based EWOD

Microfluidic-based EW on dielectric (EWOD) is a hybrid digitized electronic cooling device [6], [9]. Discrete liquid droplets move on a thin layer of electrically insulating material by the electric fields, which control liquid behavior and remove heat from a surface, as shown in figure 1. Oprins et al. [10] studied the heat transfer within electrostatically actuated droplets at various velocities computationally and analytically. An external actuator or high-voltage source is required for the electric charge. This technique refers to the alteration of the wetting characteristics, usually for the surface that repels water (superhydrophobic & Hydrophobic surface), by applying an electric field normal to the flow direction. EW cooling performs admirably in both IC-level integration and adaptive digitized hotspot cooling [11]. There is no need for a continuous coolant flow. The coolant volume and the energy needed to drive the flow significantly decrease. Transporting the droplet to hot spots can result in a more consistent distribution of temperature in electronic devices [12]. Paik et al. [8] at Duke University developed an EW micro-pump that allows for the electrostatically-mediated generation and manipulation of discrete droplets [2], [4]. Furthermore, EWOD has nominal power demands and does not generate excessive heat. Also, it is distinguished by rapid switching and relatively low external voltage actuation.

Cheng & Chen [7] reported an experimental study on the novel EWOD for adaptive chip cooling with a two-dimensional patterned array of coplanar-controlled electrodes designed and programmed for hot spot cooling. They delivered one water droplet of 14 µL by the external

actuation mechanism, which quickly reduces the temperature of a hot zone by as much as 30 ^{O}C and 27 W/cm^2 flux at the chip level, while Bindiganavale et al. [11] conducted an experimental study on EWOD with 6 consecutive water droplets for adaptive hotspot cooling of the chip of flux 36 W/cm^2. Ahmad et al. [13] utilised 4 µL Di-water droplet over an electrode array prepared on the single plate EW device. Furthermore, contact line pinning and skittering of droplets over the hydrophobic electrode are examined. Park and Nam [14] also analysed the skittering of water

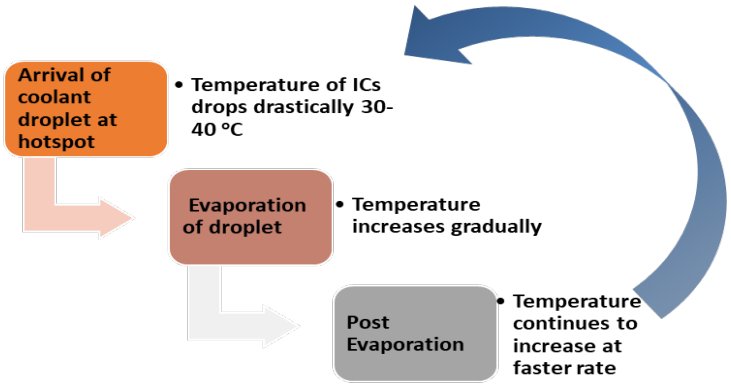

Figure 2: Sequence of hotspot cooling onset of a liquid droplet of coolant by EW

droplets over the large hydrophobic electrode surfaces, decreasing the heat transfer performance. Thus, a superhydrophilic surface is formed for a large electrode by employing an anodization process to enhance heat transfer through an EW device [15]. It promotes the dispersion of droplets, forming a thin layer of liquid over the hotspots. The droplet delivery frequency on the hydrophilic hotspot diminishes as the droplet volume increases. However, the frequency of droplet delivery should be high for the hydrophobic surfaces to reduce the maximum temperature limit at the hotspots. Moreover, the coalescence of two successive drops results in an additional cooling effect [16].

Each water droplet is experimentally stimulated across the hotspot surface whenever a liquid droplet comes into contact with a heat source, it absorbs heat, evaporates, and carries heat away from the surface. Figure 2 shows the sequence of hotspot cooling onset of liquid droplets. It is observed that there is a drastic decrease in temperature at onset and a gradual increase in temperature on evaporation of the droplets on the hot spot. Post evaporation of droplets, the temperature continues to increase at a faster rate. Each decrease and increase corresponded to one complete cycle of cooling droplets. Paik et al. [8] utilized two-dimensional patterned array electrodes for an open & closed loop system to cool hot spots with 30 & 33.3 W/cm^2 heat flux, respectively and determine the parameters that influence heat-transfer, including Droplet aspect ratio, Absolute volume of droplets, Hot-spot power density, Filler fluid mixing & concentration effect with base fluid [16].

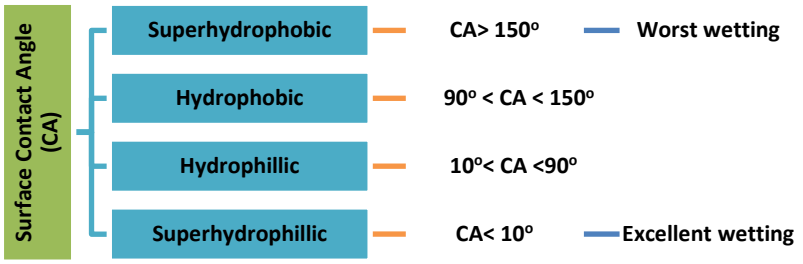

Figure 3: Surfaces with wetting characteristics without EW effect

Surface Treatment

Many techniques are used to improve heat transfer, such as surface treatment, coolant selection and enhancing surface area available for heat transfer. Surface treatment controls the surface parameters and properties, which may significantly improve heat transfer. This involves the preparation of hydrophobic/superhydrophobic surfaces (CA> 150º) [1] and fabricating a microfluidic-based chip capable of inducing water droplet formation and manipulation through EW. Hydrophilic surfaces induce high wetting, while hydrophobic surfaces induce low wetting, and superhydrophobic surfaces induce extremely low wetting, as shown in figure 3. The hydrophobic/superhydrophobic patterns in hydrophilic/superhydrophilic materials are termed biphilic surfaces, which increases the boiling heat transfer rates. The multiscale roughness of the material can cause it to become a superhydrophobic surface [17], and EW transport of the droplets over the superhydrophobic surface can significantly reduce the pressure loss than other conventional & commercial systems [15]. Chinnov et al. [18] experimentally investigated & enhanced the heat transfer efficiency of the boiling heat transfer on the biphilic surfaces.

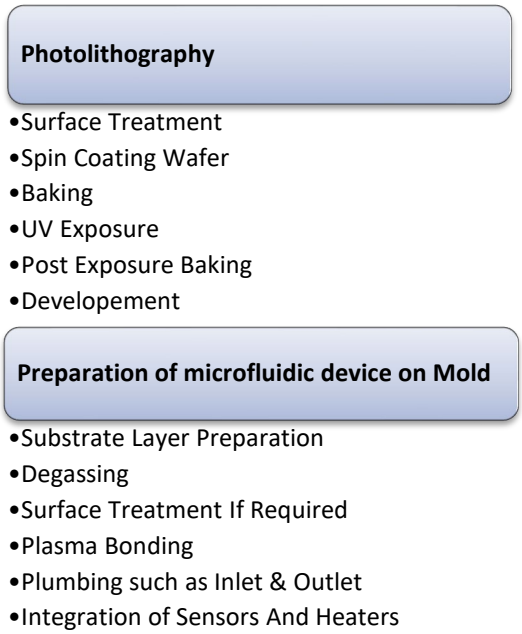

Figure 4: Process of Micro manufacturing of Microfluidics based EWOD

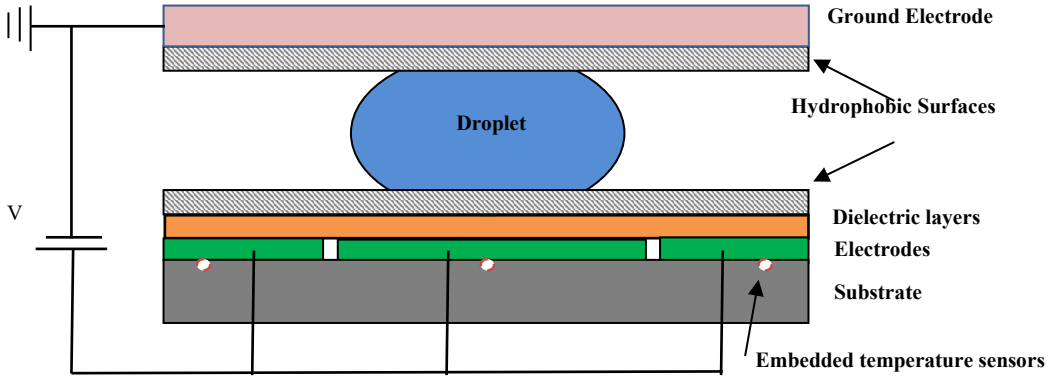

Figure 5: Arrangement of EWOD with temperature sensors to control hotspots

Microfluidic-based EWOD device necessitates two steps of manufacturing, such as Photolithography and preparation of the device on the mould, as detailed in Figure 4. The arrangement of EWOD with temperature sensors to control hotspots is shown in figure 5. Figure 5 consists of a substrate, RTD beneath an electrode layer, a dielectric layer, hydrophobic layers, a spacer for droplet movement and a top grounded electrode layer. The substrates must possess rigidity, stiffness, heat resistance, electrical insulation, and strong adhesion to metals such as SiO_2 plates and glass plates. The electrode layer should be fabricated using highly conductive materials. The use of a highly conductive electrode enables accurate control of droplet actuation on EWOD devices. Thus, electrode materials like gold, silver, and copper may be used. The dielectric layer must be manufactured using materials with a high dielectric constant, such as PDMS and Parylene C. Hydrophobic layers significantly affect droplets' surface tension and contact angles. The uppermost layer often consists of transparent, durable, and electrically conductive ITO (Indium tin oxide) glasses. This uppermost layer also functions as the grounded electrode. These Micro Electro

Mechanical Systems (MEMS) are manufactured in a specialised clean room facility. It needs special attention to curing and exposure of the device. Cleanroom facilities are designed on the federal standards (FS209E classifications) of classes as 1 for cleanest room and 100,000 for dirtiest room. The 209E cleanrooms measure the number of nanoparticles that are equal to or larger than 0.5µm in 1 cubic foot of air [19].

Hydrophobic/ superhydrophobic surface deposition depends on factors such as temperature, contact angle, and substrate material. Surfaces can be modified by following materials such as Cytonix fluoropolymer [7], Perylene C [8], Teflon [3], [8], [10-11], [20], Gold (Au) coating on CNTs textures [7], ZnO thin film [3], ZnO Nanorods (NRs) [3], ZnO bowl-like morphology, PDMS & Cytop Fluoropel coating, Ni_3S_2 Nanorod arrays [21], TiO_2/PDMS composite [22]. Wang et al. [23] fabricated a Superhydrophobic surface using Polyphenylene sulfide (PPS) & hydrophobic silica (H-SiO(2)) powder mixed in ethanol and simply sprayed on the glass substrate. ZnO NRs are widely used due to their piezoelectric, dielectric, and semiconductor properties and stable thermal, chemical and physical properties [27]. Teflon spin coating is often employed to make hydrophobic layers. The selection of surface treatment techniques depends on the temperature condition, environment, surface treatment material, thickness required, static contact angle & roll-off angle and methodology. The following advanced surface treatment methods are employed to form hydrophobic, dielectric surfaces and electrical insulation layers as shown in figure 6. Each method offers unique advantages. Thus, researchers can create surfaces in various applications by carefully selecting and optimizing the following surface treatment approaches. Table 1 illustrates materials, surface treatment methods & thickness for micro-manufacturing of dielectric, hydrophobic layers and patterning of electrodes on the substrate for the EW chip.

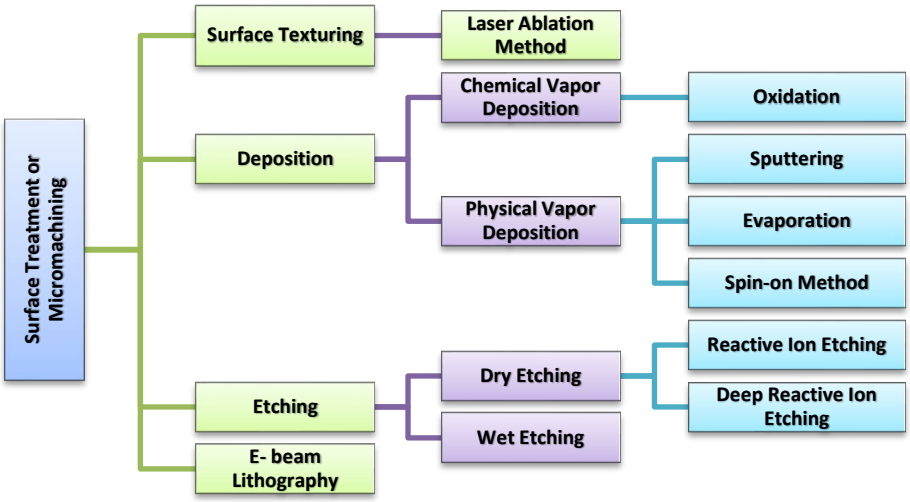

Figure 6: Advanced surface treatment methods

Surface Texturing or Micromachining: Surface texturing, also known as micromachining, is a method that entails producing small-scale patterns on a surface in order to alter its roughness and wettability. Adapting the surface texture may greatly increase the hydrophobic characteristics, resulting in higher heat transfer efficiency.

Laser Ablation Method: The laser ablation method involves the use of intense laser beams to eliminate material from a surface, resulting in the formation of accurate microstructures. This technique is highly efficient in creating customized hydrophobic surfaces that have precise patterns designed to enhance heat transfer efficiency.

***Deposition**:* Deposition methods refer to the process of spreading thin layers of materials onto a substrate to modify its surface characteristics. These approaches can encompass techniques such as sputtering, evaporation, several types of chemical vapour deposition (CVD), and the spin-on Method.

Etching: Etching uses dry and wet processes to selectively remove material from a surface to produce certain patterns and textures. These techniques can greatly modify the surface's texture and capacity to repel water, hence improving its hydrophobic characteristics.

E-beam Lithography: Electron beam lithography uses concentrated electron beams to generate highly intricate patterns on a surface. These precisely regulated hydrophobic surfaces substantially influence heat transfer efficiency.

Table 1: Materials, surface treatment methods and thickness for micro-manufacturing of dielectric, hydrophobic layers and patterning of electrodes on the substrate for EW chip

Material	**Surface type**	**Surface treatment methods**	**Thickness**	**Relevant information**	**Reference**
Cr layer	Electrode patterning	Sputtering	20 nm	For adhesion, a Cr layer is placed between the Au layer and glass substrate before electrode patterning on Au. Hydrophobic Teflon lowers droplet actuation and control voltage.	Kim et al. [3]
Au layer			90 nm		
ZnO layer	Dielectric	Atomic layer deposition	100 nm		
ZnO NRs	Dielectric Hydrophobic	Hydrothermal methods	---		
Teflon	Hydrophobic	Spin coated	20 nm		
SiO_2	Insulation	Plasma-enhanced chemical vapor Deposition (PECVD)	1.5 µm	Thermal estimations were made using fused silica wafers. Au electrodes overlapped heaters and RTDs underneath. RTD and heaters have thick SiO_2 electrical insulation. Thus, cooling efficiency rose greatly.	Cheng & Chen [7]
Si_3N_4	Dielectric	PECVD	0.25 µm		
Cytonix fluoropolymer	Hydrophobic	Spin coated	50 nm		
Gold (Au) coating on CNTs textures	Super hydrophobic	---	10 nm	CNTs on silicon micropillars to mimic the lotus effect on chip level. CNTs was further hydrophobicized by Au coated with a monolayer of 1-hexadecanethiol.	
Parylene C	Insulation	---	1 µm	Parylene C prevents electrical conduction between the electrode and droplet. Interconnected top and insulated bottom plates are hydrophobic with Teflon.	Paik et al. [8] Oprins et al. [10]
Teflon	Hydrophobic	Spin coated	---		
Indium tin oxide (ITO)	Heater & RTD patterning	Chemical wet etching	120 nm	The chip uses a glass substrate with a 165 µm thick spacer. ITO is selected due to its optical and linear thermal coefficient properties.	Bindiganavale et al. [11]
SiO_2	Insulation	PECVD	0.5 µm		
Cr layer	Electrodes patterning	E-beam evaporation/ Wet etching	100 nm		
SU8	Dielectric	Spin coated	5 µm		
Teflon	Hydrophobic	Spin coated	150 nm		
Copper foil (both side)	Coating on the clad board	Electrodeposited	17 µm	A double-sided copper-clad board is used as a substrate. Electrodes and heaters are fabricated by using chemical etching over this copper-clad board.	Ahmad et al. [13]
PDMS+ Cytop Fluoropel	Dielectric, hydrophobic	Spin coated	16 ±1 µm		
SiO_2	Insulation	PECVD	1.5 µm	The single-sided digital microfluidic (SDMF) device allows for efficient liquid manipulation on a single	Park and Nam [14]
Au layer	Glass coating	Sputter	100 nm		
Au	Electrode	---	1 µm		

Ta_2O_5	Dielectric	E-beam evaporation	120 nm	surface, while also improving thermal rejection performance through two-phase heat transfer.	
FluoroPel polymer	Hydrophobic	Spin coated	---		
Teflon	Dielectric and hydrophobic	Film or tape Coated	40 μm	The photolithography technique uses a photo-responsive dried film on a substrate. Fluorine-doped Tin Oxide (FTO) is a conductor-coated glass on the top layer of device.	Sukthang et al. [20]
FTO	Grounded electrode	---	---		
MWCNT	Hydrophilic/ Hydrophobic	CVD	---	A silicon wafer is used as a substrate. Smooth and rough multi-walled carbon nanotubes are used as the hydrophilic and hydrophobic surfaces, respectively.	Cui et al. [24]
ZnO layer	Dielectric	Electrochemical deposition	800 nm	To reach a CA of 164.8° with a contact angle hysteresis of 11.3° ($\Delta\theta = \theta_{ACA} - \theta_{RCA}$).	Zhou et al. [25]
SiO_2	Insulation	---	500 μm	The structure is created by thermally oxidizing a Si wafer. PMMA positive photoresist is used for Au electrode and Cr.	Sirbu et al. [26]
ZnO layer	Dielectric Hydrophobic	RF magnetron sputtering	400 nm		
ZnO NRs	Dielectric Hydrophobic	Liquid-phase deposition	---	ITO substrate is used for the device. At high applied voltages, large CA changes were observed.	Campbell et al. [27]
Teflon	Hydrophobic	Sputtering	---		

Future Scopes and Applications

To commercialise new efficient microelectronic devices, it must evolve as a more progressive compact heat exchanger capable of conveying more heat than conventional thermal systems. EW applications range from biotechnological microfluidics [28] to adjustable liquid lenses [29] and electronic displays (smart windows) [30]. The future scopes of the EW can be written as

- Heat transfer may increase with the exploration and preparation of novel ceramic surfaces of a superhydrophobic nature, such as lotus leaf, and the encapsulation of novel superhydrophobic nanoparticles or polymers on the surface.
- Micro-manufacturing of integrated microfluidic-based adaptive cooling chip onto the electronic substrate with the integration of electrodes, sensors and plumbing.
- Investigation of high heat flux or hotspots cooling of more than 450 W/cm^2 with the application of microfluidic-based EW cooling.
- Film boiling regimes and the possible benefits of the nanofluids may be investigated using EW cooling.

Conclusion

This study highlights the potential of microfluidic-based cooling techniques employing water droplet jets on superhydrophobic surfaces for electronic cooling applications. Integrating EW principles in Lab-on-a-Chip can greatly improve the surface area available to electronic cooling devices. It has a high heat transfer coefficient and low thermal resistance. Therefore, it can be easily integrated into small, compact devices that can handle the increasing thermal management challenges in modern electronics. It has much potential, although it is still in early development.

Reference

[1] Dash, S. U. S. M. I. T. A., Kumari, N. I. R. U., & Garimella, S. V. (2011). Characterization of ultrahydrophobic hierarchical surfaces fabricated using a single-step fabrication methodology. *Journal of Micromechanics and Microengineering*, *21*(10), 105012. https://doi.org/10.1088/0960-1317/21/10/105012

[2] Pollack, M. G., Fair, R. B., & Shenderov, A. D. (2000). Electrowetting-based actuation of liquid droplets for microfluidic applications. Applied physics letters, 77(11), 1725-1726. https://doi.org/10.1063/1.1308534

[3] Kim, J. H., Lee, J. H., Mirzaei, A., Kim, H. W., Tan, B. T., Wu, P., & Kim, S. S. (2020). Electrowetting-on-dielectric characteristics of ZnO nanorods. Scientific reports, 10(1), 14194. https://doi.org/10.1038/s41598-020-71017-7

[4] Pollack, M. G., Shenderov, A. D., & Fair, R. B. (2002). Electrowetting-based actuation of droplets for integrated microfluidics. Lab on a Chip, 2(2), 96-101. https://doi.org/10.1039/B110474H

[5] Controlling Wettability in Oil-Water systems, Bahadur research group, https://utw10954.utweb.utexas.edu/research/controlling-wettability-in-oil-water-systems.html.

[6] Baird, E., & Mohseni, K. (2008). Digitized heat transfer: a new paradigm for thermal management of compact micro systems. IEEE Transactions on Components and packaging Technologies, 31(1), 143-151. http://dx.doi.org/10.1109/TCAPT.2008.916810

[7] Cheng, J. T., & Chen, C. L. (2010). Adaptive chip cooling using electrowetting on coplanar control electrodes. Nanoscale and Microscale Thermophysical Engineering, 14(2), 63-74. http://dx.doi.org/10.1080/15567261003601771

[8] Paik, P. Y., Pamula, V. K., & Chakrabarty, K. (2008). Adaptive cooling of integrated circuits using digital microfluidics. IEEE transactions on very large scale integration (vlsi) systems, 16(4), 432-443. http://dx.doi.org/10.1109/TVLSI.2007.915434

[9] Mohseni, K., & Baird, E. S. (2007). Digitized heat transfer using electrowetting on dielectric. *Nanoscale and Microscale Thermophysical Engineering*, *11*(1-2), 99-108. http://dx.doi.org/10.1080/15567260701337555

[10] Oprins, H., Danneels, J., Van Ham, B., Vandevelde, B., & Baelmans, M. (2008). Convection heat transfer in electrostatic actuated liquid droplets for electronics cooling. *Microelectronics journal*, *39*(7), 966-974. https://doi.org/10.1016/j.mejo.2007.11.024

[11] Bindiganavale, G. S., Amaya, M., & Moon, H. (2018). Demonstration of hotspot cooling using digital microfluidic device. Journal of Micromechanics and Microengineering, 28(12), 125015. https://doi.org/10.1088/1361-6439/aae883

[12] Xu, H., Yan, R., Wang, S., & Chen, C. L. (2017). Bubble detachment assisted by electrowetting-driven interfacial wave. Physics of Fluids, 29(10). https://doi.org/10.1063/1.4996905

[13] Ahmad, I., Ranjan, A., Pathak, M., & Khan, M. K. (2022). A wettability-mediated microdroplet under electrowetting effect for hotspot cooling. IEEE Transactions on Components, Packaging and Manufacturing Technology, 12(2), 288-296. http://dx.doi.org/10.1109/TCPMT.2022.3143687

[14] Park, S. Y., & Nam, Y. (2016). Single-sided digital microfluidic (SDMF) devices for effective coolant delivery and enhanced two-phase cooling. Micromachines, 8(1), 3. https://doi.org/10.3390/mi8010003

[15] Betz, A. R., Jenkins, J., & Attinger, D. (2013). Boiling heat transfer on superhydrophilic, superhydrophobic, and superbiphilic surfaces. International Journal of Heat and Mass Transfer, 57(2), 733-741. http://dx.doi.org/10.1016/j.ijheatmasstransfer.2012.10.080

[16] Yan, Z., Jin, M., Li, Z., Zhou, G., & Shui, L. (2019). Droplet-based microfluidic thermal management methods for high performance electronic devices. Micromachines, 10(2), 89. https://doi.org/10.3390%2Fmi10020089

[17] Pontes, P., Cautela, R., Teodori, E., Moita, A. S., Georgoulas, A., & Moreira, A. L. N. M. (2020). Bubble dynamics and heat transfer on biphilic surfaces: Experiments and numerical simulation. Journal of Bionic Engineering, 17, 809-821. http://dx.doi.org/10.1007/978-981-33-4765-6_17

[18] Chinnov, E. A., Khmel, S. Y., Vladimirov, V. Y., Safonov, A. I., Semionov, V. V., Emelyanenko, K. A., & Boinovich, L. B. (2022). Boiling heat transfer enhancement on biphilic surfaces. Energies, 15(19), 7296. https://doi.org/10.3390/en15197296

[19] Federal standard for cleanroom classifications & classes; https://www.mecart-cleanrooms.com/learning-center/cleanroom-classifications-classes-1-10-100-1000-10000-and-100000-fs209e/

[20] Sukthang, K., Pengwang, E., Tuantranont, A., & Wechsatol, W. (2020, July). Rapid Fabrication of Close-Typed Electrowetting on Dielectric Devices. In *IOP Conference Series: Materials Science and Engineering* (Vol. 886, No. 1, p. 012046). IOP Publishing. http://dx.doi.org/10.1088/1757-899X/886/1/012046

[21] Yin, X., Yu, S., Hu, J., Li, H., Lv, Z., & Zhou, X. (2019). Facile fabrication of a durable Ni3S2 nanorod arrays superhydrophobic surface with self-cleaning and degradation properties. *Journal of Alloys and Compounds*, *791*, 864-873. http://dx.doi.org/10.1016/j.jallcom.2019.03.367

[22] Qing, Y., Yang, C., Sun, Y., Zheng, Y., Wang, X., Shang, Y., ... & Liu, C. (2015). Facile fabrication of superhydrophobic surfaces with corrosion resistance by nanocomposite coating of TiO2 and polydimethylsiloxane. *Colloids and Surfaces A: Physicochemical and Engineering Aspects*, *484*, 471-477. http://dx.doi.org/10.1016/j.colsurfa.2015.08.024

[23] Wang, S., Li, M., Su, B., & Lu, Q. (2010). Preparation and properties of superhydrophobic polyphenylene sulfide composite coatings. *Acta Polymerica Sinica*, *2010*(4), 449-455. http://dx.doi.org/10.3724/SP.J.1105.2010.09124

[24] Cui, W., Dong, J., Zhao, N., Liang, D., & Ma, H. (2020). Sessile Droplet Evaporation on a Structurally Heterogeneous Multiwalled Carbon Nanotube Membrane. *Journal of Thermophysics and Heat Transfer*, *34*(1), 150-153. https://doi.org/10.2514/1.T5772

[25] Zhou, J., Yang, S., Zeng, X. Y., Wu, J. H., Chen, G. P., & Huang, Y. P. (2012). Superhydrophobic ZnO for EWOD digital microfluidic device for application in micro total analysis system (μ-TAS). Journal of adhesion science and technology, 26(12-17), 2087-2098. http://dx.doi.org/10.1163/156856111X600451

[26] Sirbu, L., Ghimpu, L., Müller, R., Vodă, I., Tiginyanu, I., Ursaki, V., & Dascalu, T. (2012, October). Hydrophobic ZnO used in EWOD technology and saw devices for better bio-fluid slip at microchannel walls controlled by DC pulses. In CAS 2012 (International Semiconductor Conference) (Vol. 1, pp. 231-234). https://doi.org/10.1109/SMICND.2012.6400645

[27] Campbell, J. L., Breedon, M., Latham, K., & Kalantar-Zadeh, K. (2008). Electrowetting of superhydrophobic ZnO nanorods. Langmuir, 24(9), 5091-5098. https://doi.org/10.1021/la7030413

[28] Fair, R. B. (2007). Digital microfluidics: is a true lab-on-a-chip possible?. Microfluidics and Nanofluidics, 3, 245-281. http://dx.doi.org/10.1007/s10404-007-0161-8

[29] Krogmann, F., Shaik, R., Lasinger, L., Mönch, W., & Zappe, H. (2008). Reconfigurable liquid micro-lenses with high positioning accuracy. Sensors and Actuators A: Physical, 143(1), 129-135. http://dx.doi.org/10.1109/OMEMS.2007.4373879

[30] Zhou, K., & Heikenfeld, J. (2008). Arrayed electrowetting microwells. Applied Physics Letters, 92(11), 113515. https://doi.org/10.1063/1.2898890

This article has been accepted for publication in IEEE Access. This is the author's version which has not been fully edited and content may change prior to final publication. Citation information: DOI 10.1109/ACCESS.2025.3554151

IEEE Access
Multidisciplinary | Rapid Review | Open Access Journal

Date of publication xxxx 00, 0000, date of current version xxxx 00, 0000.

Digital Object Identifier 10.1109/ACCESS.2017.Doi Number

A Self-Decoupled MIMO Patch Antenna System for V2X Communications

Amit Kumar[1], Student Member, IEEE, Sandeep Rana[1, 2], Student Member, IEEE, Akhilesh Mohan[1]*, Member, IEEE, Gunjan Srivastava[3], Member, IEEE, Sachin Kumar[4], and Kang Wook Kim[5*]

[1]Department of Electronics and Communication Engineering, Indian Institute of Technology Roorkee, Roorkee 247667, India
[2]Department of Electronics and Communication Engineering, G. B. Pant Institute of Engineering and Technology, Pauri Garhwal 246194, India
[3]Department of Electronics and Communication Engineering, Graphic Era (Deemed to be) University, Dehradun 248002, India
[4]Department of Electronics and Communication Engineering, Galgotias College of Engineering and Technology, Greater Noida 201310, India
[5]School of Electronic and Electrical Engineering, Kyungpook National University, Daegu 41566, Republic of Korea

Corresponding author: Akhilesh Mohan (email: am@ece.iitr.ac.in); Kang Wook Kim (email: kang_kim@ee.knu.ac.kr).

ABSTRACT This article presents a new method for self-decoupling in multiple-input-multiple-output (MIMO) circular patch antenna (CPA) system. In the presented method, three shorting vias are strategically placed in the E-plane of the probe-fed CPA resonating in TM_{11} mode to create a weak-current density region on the ground plane where the adjacent antenna element can be placed. Initially, a two-element MIMO antenna system is designed, developed, and tested for vehicle-to-everything (V2X) communication in the IEEE 802.11p band. High inter-port isolation of 78 dB across the entire 5.82 to 5.98 GHz operating band is obtained. Both antenna pairs exhibit identical radiation properties, with a peak gain of 7.4 dBi. Furthermore, a 10-element MIMO antenna system is developed, showing promising results for V2X MIMO communications.

INDEX TERMS Circular patch antenna (CPA), isolation, multiple-input multiple-output (MIMO) antenna system, self-decoupling, V2X communication

I. INTRODUCTION

The growing global challenge of rising traffic fatalities and congestion can be effectively alleviated by deploying vehicle-to-everything (V2X) communication. V2X communication can enhance traffic safety by enabling vehicles to exchange real-time data with other vehicles (V2V), pedestrians (V2P), and infrastructure (V2I). The Federal Communications Commission (FCC) has allocated 5.9 GHz frequency spectrum (5.85-5.925 GHz) for V2X communications [1]. Various V2X communication entities must exchange significant data within the limited 75 MHz bandwidth. Therefore, spectrally efficient data transmission and reception techniques are required. These systems also need to address fast-fading issues caused by surrounding obstacles. Spatial multiplexing and diversity gain attributes of multiple-input-multiple-output (MIMO) systems can address these challenges by allowing multiple streams of data to be transmitted and received simultaneously and ensuring reliable communication. MIMO antenna systems are one of the promising choices for automotive applications due to their enhanced spectral efficiency, better interference mitigation, reduced channel loss, and improved signal-to-noise ratio. However, the demand for compact antenna structures in the automotive industry, where multiple antennas can be placed into a small volume, still presents a significant challenge. This underscores the urgent need for solutions to mitigate the stronger mutual coupling and performance degradation of MIMO systems.

Researchers have been exploring various methods to improve isolation in antenna systems, such as using electromagnetic bandgap structures [2], metasurfaces [3], decoupling networks [4], neutralization lines [5], resonators [6], parasitic strips [7] and combinations of these techniques. However, the use of aforementioned decoupling techniques either degrade the radiation performance or increase the overall physical footprint due to additional decoupling structures.

This work is licensed under a Creative Commons Attribution 4.0 License. For more information, see https://creativecommons.org/licenses/by/4.0/

This article has been accepted for publication in IEEE Access. This is the author's version which has not been fully edited and
content may change prior to final publication. Citation information: DOI 10.1109/ACCESS.2025.3554151

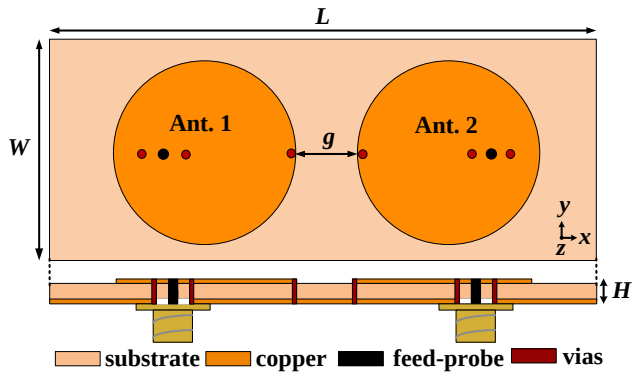

Fig. 1. Proposed self-decoupled MIMO antenna system.

In recent years, self-decoupling techniques have gained popularity for their ability to enhance inter-port isolation without the need for additional decoupling structures. These methods rely on the inherent characteristics of the antenna to achieve decoupling. For instance, in [8], a self-decoupling antenna array is designed using characteristic mode analysis of the ground plane. One antenna generates multiple parallel null-field regions on the ground plane, allowing other antennas to be positioned within these null regions. Another method in [9] involves adjusting the size of the feed strip to nullify the field generated by the feeding structure and radiating patch at a specific location on the ground plane, providing a weak-field region for the adjacent antenna element and resulting in high inter-port isolation. In [10], the transmit (T_x) antenna and the receive (R_x) antenna operate on different frequency bands. This separation helps reduce their sensitivity to signals outside their designated ranges. Both antennas use orthogonal polarizations to further minimize mutual coupling through their fields. The shorting pin in the T_x antenna is positioned in the H-plane, while the shorting pin in the R_x antenna is located in the E-plane. Due to the close proximity of the two pins, they introduce capacitive coupling between them. This coupling cancels out the inductive coupling caused by the current flowing through the antennas, resulting in nearly zero mutual impedance. By employing these three decoupling techniques, an isolation of approximately 47 dB is achieved.

Additionally, several other self-decoupling antenna structures are documented in references [11]-[19]. However, the structures reported in these references either possess good inter-port isolation over a narrower bandwidth or exhibit limited gain. On the other hand, V2X antenna systems require high gain and high inter-port isolation over the entire operating band to ensure reliable and robust communication in high vehicle density areas. These characteristics are also essential for supporting advanced V2X applications, such as autonomous driving and real-time traffic management.

This article presents a new method for antenna arrays that involves creating a region of weak surface currents on the ground plane to facilitate self-decoupling. Three shorting vias are strategically placed in the E-plane of the probe-fed circular patch antenna (CPA) resonating in TM_{11} mode to create a weak surface current region where the adjacent antenna will be placed. A high gain of 7.4 dBi, along with a high inter-port isolation of 78 dB between adjacent elements across the entire operating band of 5.82 to 5.98 GHz, is achieved by implementing the proposed self-decoupling technique. A 10-element massive MIMO antenna system is also designed and developed to further expand the proposed design approach.

The proposed MIMO antenna system includes the following features:

(i) For the first time, three shorting pins are positioned asymmetrically in the E-plane of the CPA. Despite the asymmetrical pin arrangement, CPAs operate nearly in the fundamental TM_{11} mode while facilitating self-decoupling.

(ii) To the best of the authors' knowledge, there is currently no existing planar MIMO co-linearly polarized two-port antenna system design in the literature that achieves minimum inter-port isolation of 78 dB across a fractional bandwidth of 2.7% on a compact substrate volume of $0.02\lambda_0^3$ without using circulators, hybrids or complex feed networks/multiplexing schemes. The authors have attained such high isolation solely through self-decoupling.

(iii) The proposed 10-element MIMO antenna system features an innovative and compact design with no gaps between adjacent modules. Despite the close proximity of antenna elements, the system achieves a minimum isolation of 30 dB while maintaining nearly identical radiation characteristics within the operational half-power beamwidth.

II. ANTENNA DESIGN

Fig. 1 illustrates the proposed two-element MIMO antenna system. The proposed antenna system is designed on the Rogers RO4003C substrate (ε_r = 3.55, H = 1.524 mm and tan δ = 0.0027) with a ground plane of size $L \times W$ (72 mm × 25 mm). The MIMO antenna system comprises of two probe-fed CPAs (Ant. 1 and Ant. 2), each loaded with three metallic vias (via-1, via-2, and via-3) placed in the antennas' E-plane resonating in fundamental TM_{11} mode. Both the antennas are placed closely (g = 7 mm) along the x-axis with a rotational symmetry of 180° with respect to each other.

A. ANTENNA CONFIGURATION AND WORKING MECHANISM

Fig. 2 illustrates the different design stages of the proposed MIMO antenna system. It presents the surface current distributions on the radiating patch and ground plane, along with their radiation pattern. For fair comparison, the two element MIMO antenna system at all stages of evolution is designed with the same ground plane of size $L \times W$ (72 mm ×

This work is licensed under a Creative Commons Attribution 4.0 License. For more information, see https://creativecommons.org/licenses/by/4.0/

This article has been accepted for publication in IEEE Access. This is the author's version which has not been fully edited and content may change prior to final publication. Citation information: DOI 10.1109/ACCESS.2025.3554151

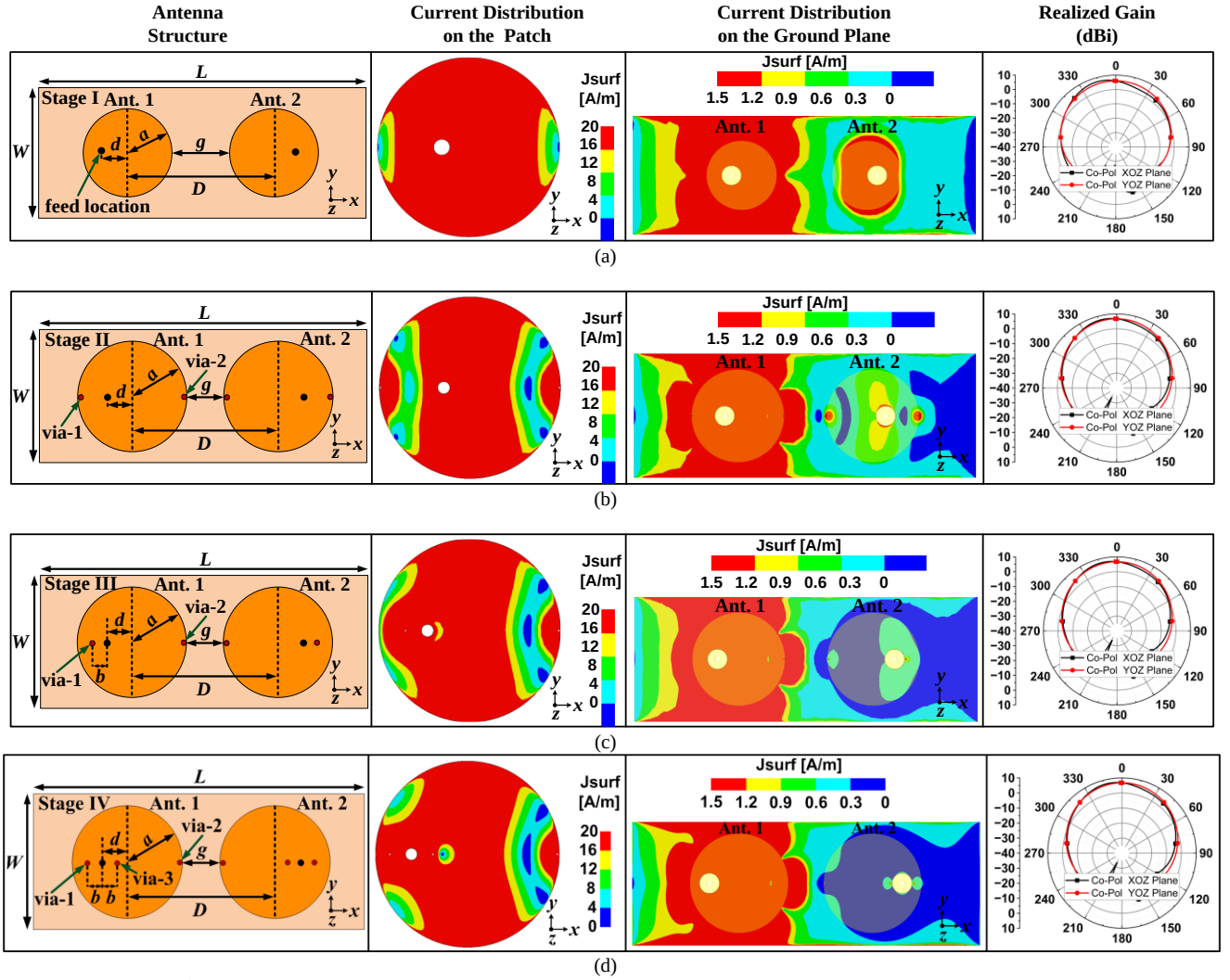

Fig. 2. Design stages of the MIMO antenna system, their corresponding surface current distribution (RMS value) on the radiating patch and the ground plane, and their realized gain at the resonant frequency (5.9 GHz) when Ant.1 is excited while Ant. 2 is terminated with 50 Ω load: (a) Stage I, (b) Stage II, (c) Stage III, and (d) Stage IV.

Table 1. Dimensions of the proposed antenna system (Unit: mm).

Parameters	*a*	*d*	*g*	*D*	*b*
Stage I	7.24	2.13	12.61	27.1	–
Stage II	9.58	2.76	7.94	27.1	–
Stage III	9.59	4.45	7.92	27.1	2.33
Stage IV	10.05	6.1	7	27.1	2.33

25 mm) and operates at the resonant frequency of 5.9 GHz. The dimensions of all design parameters are provided in Table 1 and their simulated S-parameters are given in Fig. 3. In Stage I [Fig 2 (a)], the two CPAs (Ant. 1 and Ant. 2) separated by *g* are designed to operate in TM_{11} mode with a resonant frequency of 5.9 GHz. The resonant frequency of the CPA for the TM_{11} mode is given by eq. (1) [20],

$$(f_r)_{TM_{11}} = \frac{1.8421 c_0}{2\pi a\sqrt{\varepsilon_r}} \quad (1)$$

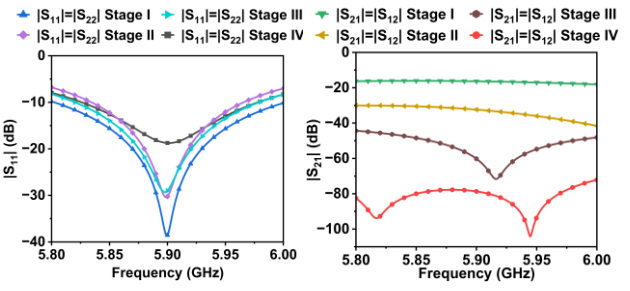

Fig. 3. S-parameters of design stages: (a) $|S_{11}|$, $|S_{22}|$, and (b) $|S_{21}|$, $|S_{12}|$.

where *a* is the radius of the CPA, ε_r is the relative dielectric constant of the substrate, and c_0 is the speed of the light in free space. The probe position for feeding the circular patch is chosen as *d* for optimum matching performance. When Ant. 1 is excited, and Ant. 2 is terminated with a 50 Ω matched load, the surface current distribution on Ant. 1 is uniform, with two nulls at the extreme ends in the E-plane of the antenna. The

This work is licensed under a Creative Commons Attribution 4.0 License. For more information, see https://creativecommons.org/licenses/by/4.0/

This article has been accepted for publication in IEEE Access. This is the author's version which has not been fully edited and
content may change prior to final publication. Citation information: DOI 10.1109/ACCESS.2025.3554151

surface current distribution exhibits strong current density near Ant. 2 on the ground plane. The ample spacing between Ant. 1 and Ant. 2 reduces the space wave and near-field coupling. However, despite this, the strong current density near Ant. 2 on the ground plane still causes enough inter-port coupling between the antennas. An inter-port isolation better than 16 dB along with a peak realized gain of 6 dBi is obtained, as depicted in Fig. 3.

In Stage II, as illustrated in Fig. 2(b), the CPAs are equipped with two shorting vias (via-1 and via-2) with a radius of 0.1 mm in the E-plane of the CPAs designed in Stage I. The additional inductance introduced by the shorting vias is parallel to the inductance of the CPA. As a result, the overall inductance of the antenna system decreases. This reduction leads to a shift in the resonant frequency of the fundamental TM_{11} mode to a higher value. To bring it back to 5.9 GHz, the radius of the patch is further increased, and the probe position is optimized for optimum matching performance. The introduction of the two shorting vias creates two additional low-impedance paths for the current to flow from the patch to the ground plane. This significantly perturbs the surface current distribution on the CPA, leading to a concentration of most of the surface current at its central regions and near the vias. The ground plane acts as the return path for the current on the patch antenna. As the current density near the vias and in the central regions of the patch increases, the current on the ground plane dynamically redistributes itself to accommodate the altered current density on the patch. This results in increased current density in the regions of the ground plane beneath the patch where there is high current density, while the surrounding areas on the ground plane experience a decrease in current density to offset this increase. Compared to Stage I, the strength of the surface current on the ground plane near Ant. 2 decreases, leading to a reduction in inter port coupling. The isolation level is better than 31 dB in the entire operating band while the obtained peak realized gain is 7.2 dBi.

In Stage III, as depicted in Fig. 2(c), via-1 is strategically positioned as close as possible to the feed probe. Due to fabrication constraints (a 4.1 mm diameter circle is etched from the ground plane to separate the central pin from the outer casing of the SMA connector), via-1 is positioned at a distance of b = 2.33 mm from the feed location. Consequently, the surface current on Ant. 1 becomes more concentrated in the central and left regions of the excited patch. The shift in the current density in the left regions of the patch leads to an increased current density in the left regions on the ground plane and induces a weaker current density on the ground plane near Ant. 2. This reduces the mutual coupling among the antennas. The isolation level is better than 48 dB at this stage.

Stage IV, which is the proposed two-element MIMO antenna system, is designed by placing another via (via-3) symmetrically to via-1 along the x-axis from the feed location. As a result, the surface current distribution on Ant. 1 shifts more toward the patch's left region along the x-axis than in the previous stage. The increased current density on the left regions of the patch further pulls the current density on the ground plane towards the left, leading to a reduction in the strength of induced surface current distribution near Ant. 2 on the ground plane. This creates a wide null-current region near Ant. 2, resulting in a drastic reduction in mutual coupling through the surface current on the ground plane. An isolation

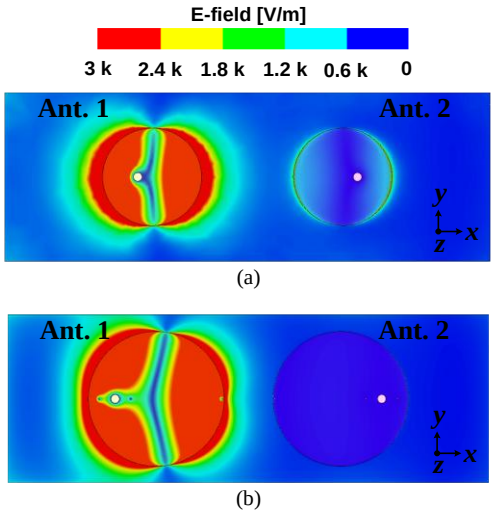

Fig. 4. E-field (RMS value) pattern at 5.9 GHz when Ant. 1 is excited while Ant. 2 is terminated with a 50 Ω load: (a) Stage I, and (b) Stage IV.

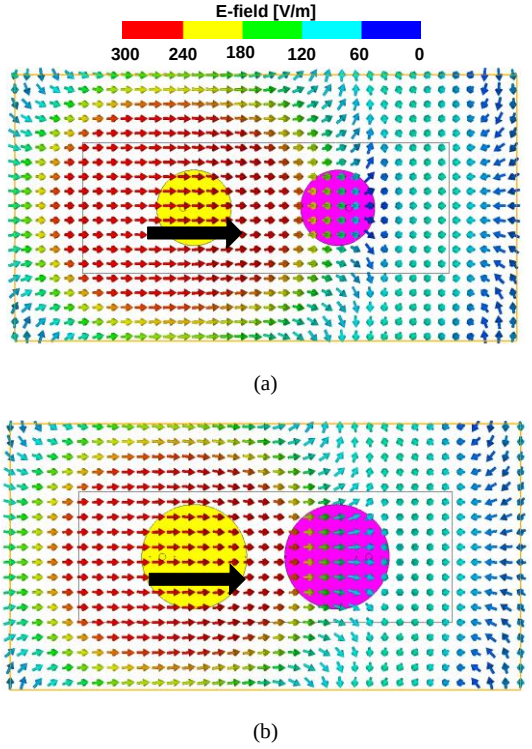

Fig. 5. E-field (vector) pattern at 5.9 GHz when Ant. 1 (left CPA along x-axis) is excited while Ant. 2 is terminated with a 50 Ω load: (a) Stage I, and (b) Stage IV.

This work is licensed under a Creative Commons Attribution 4.0 License. For more information, see https://creativecommons.org/licenses/by/4.0/

This article has been accepted for publication in IEEE Access. This is the author's version which has not been fully edited and
content may change prior to final publication. Citation information: DOI 10.1109/ACCESS.2025.3554151

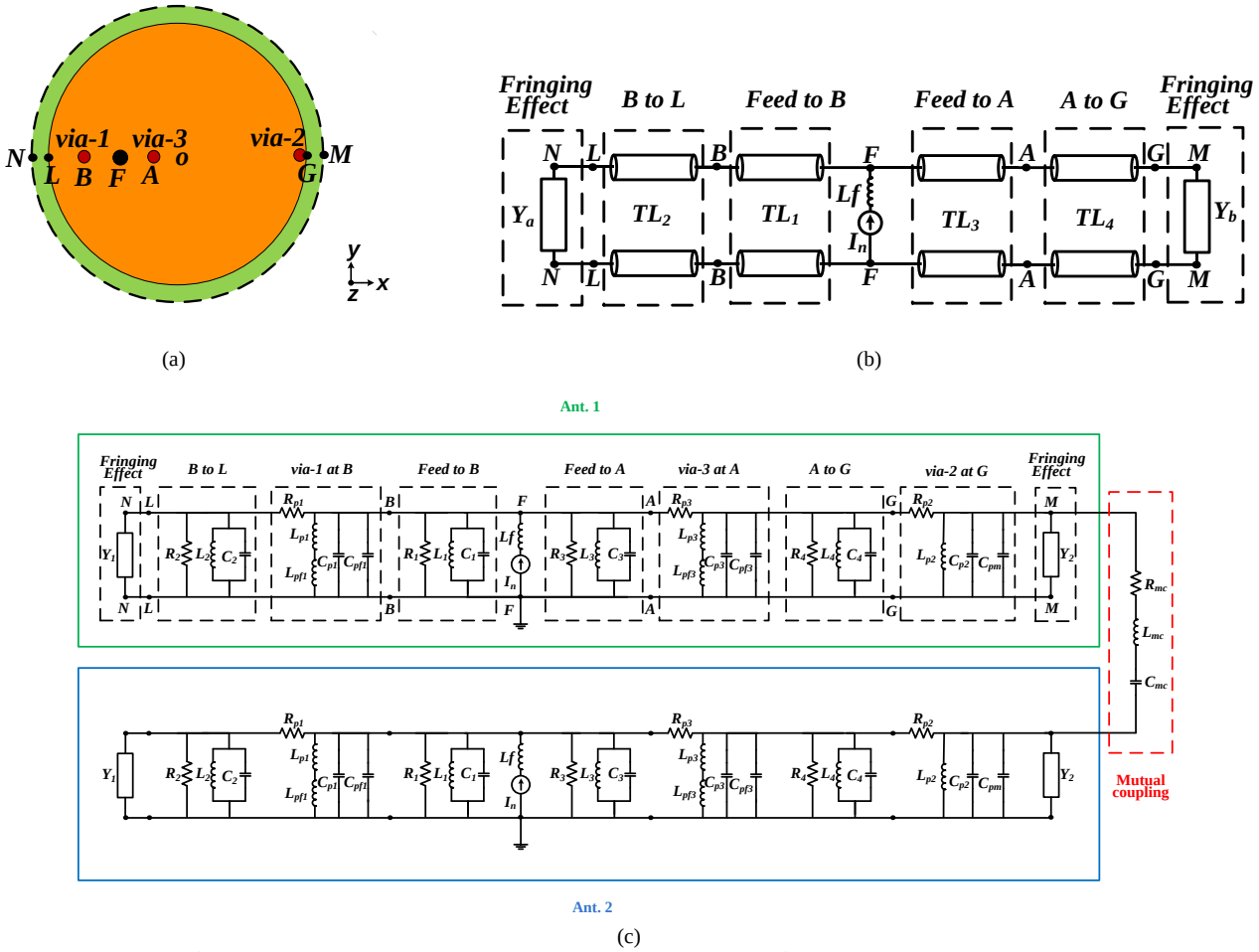

Fig. 6. (a) Unit element of the proposed MIMO antenna system, (b) Equivalent circuit model of the unit element without shorting pins, and (c) Equivalent circuit model of the proposed two-element MIMO antenna system. ($R_2 = 109\ \Omega$, $L_2 = 0.1065$ nH, $C_2 = 13.0671$ pF, $R_{p1} \approx 0\ \Omega$, $L_{p1} = 5.901$ nH, $L_{pf1} = 0.004$ nH, $C_{p1} = 0.00209$ nH, $C_{pf1} = 0.03290$ pF, $R_1 = 209.45\ \Omega$, $L_1 = 0.2506$ nH, $C_1 = 0.0509$ pF, $L_f \approx 0$, $R_3 = 92.1591\ \Omega$, $L_3 = 1.59849$ nH, $C_3 = 0.2654$ pF, $R_{p3} \approx 0\ \Omega$, $L_{p3} = 5.901$ nH, $L_{pf3} = 0.004$ nH, $C_{p3} = 0.00209$ nH, $C_{pf3} = 0.03290$ pF, $R_4 = 582.585\ \Omega$, $L_4 = 0.4169$ nH, $C_4 = 0.06903$ pF, $R_{p2} \approx 0\ \Omega$, $L_{p2} = 5.901$ nH, $C_{p2} = 0.2182$ nH, $C_{pm} = 0.55202$ pF, $R_{mc} \approx 0\ \Omega$, $L_{mc} = 2.19776$ nH, $C_{mc} = 0.000107$ pF).

level of more than 78 dB is obtained in Stage IV. Additionally, the concentrated current density in the smaller region of the patch results in more directive radiation and, thus, a higher gain can be obtained, which is also observed from the realized gain plot in Fig. 2 (gain of CPA in Stage IV is 7.5 dBi whereas for Stage I is 6 dBi).

Figs. 4(a) and (b) show the contour plots of the E-field patterns for the CPA at Stage I and Stage IV, respectively. The overall orientation and behavior of the E-field remain nearly unchanged, indicating that the CPA at Stage IV continues to operate primarily in the TM_{11} mode. Additionally, Figs. 5(a) and (b) illustrate the vector plots of the E-field patterns of the CPA at Stage I and Stage IV, respectively, in the far-field region, at a height of 18 mm above the CPA. A larger solid black arrow indicates the net direction of the E-field. The polarization in both stages is nearly the same, exhibiting linear polarization along the *x*-direction.

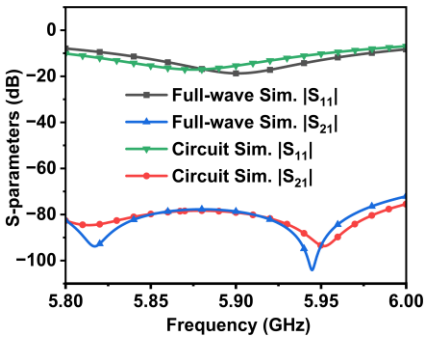

Fig. 7. Circuit model and full-wave simulations results.

B. EQUIVALENT CIRCUIT MODEL

The mathematical analysis of the proposed two-port MIMO antenna system is performed with the help of its equivalent

This work is licensed under a Creative Commons Attribution 4.0 License. For more information, see https://creativecommons.org/licenses/by/4.0/

This article has been accepted for publication in IEEE Access. This is the author's version which has not been fully edited and
content may change prior to final publication. Citation information: DOI 10.1109/ACCESS.2025.3554151

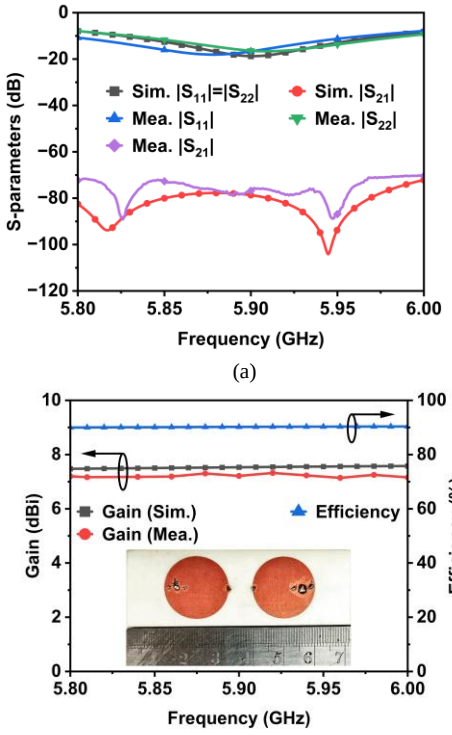

Fig. 8. Simulated and measured: (a) S-parameters, and (b) Gain of Ant. 1 with Ant. 2 terminated using 50 Ω load.

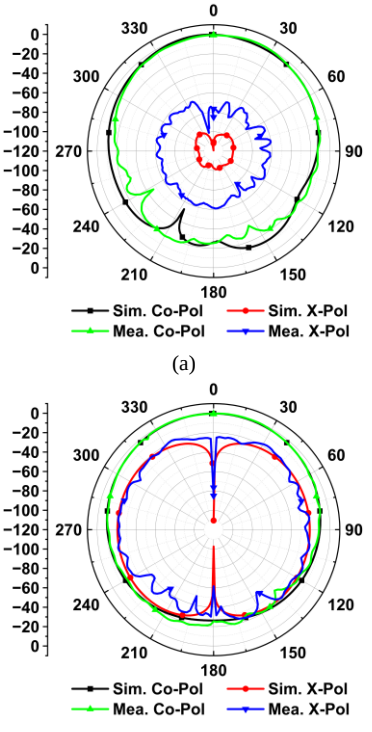

Fig. 9. Radiation patterns of Ant. 1 with Ant. 2 terminated using 50 Ω load in (a) *xoz*-plane, and (b) *yoz*-plane at the center frequency (5.9 GHz).

circuit model. The equivalent circuit model of the CPA, with symmetrically loaded shorting pins is presented in references [21] and [22].

In this section, the equivalent circuit model of the proposed two-element MIMO antenna system is developed, which incorporates three asymmetrically placed shorting pins as shown in Fig. 6. The feed point, labeled *F*, is represented as an equivalent current source in series with the feeding probe inductance, L_f. To analyze the impedance at the feed location, the CPA is divided into four transmission line sections that correspond to the current paths created by the feed-probe and the vias. The transmission line sections are distinguished by the impedance discontinuities caused by the vias, which influence their current distribution. The left branch of the circuit consists of two transmission lines: the first connects the feed to via-1, while the second extends from via-1 to the left end of the CPA. The right branch includes a third transmission line that runs from the feed to via-3, and a fourth line that reaches the right end of the CPA. Each transmission line is modeled as a parallel *RLC* circuit having impedances Z_{TLn}.

Additionally, the fringing effect at the edges is represented by the admittances Y_a and Y_b. The shorting pins at points *B*, *A*, and *G* introduce additional impedances. At location *B*, via-1 contributes an impedance Z_{p-1} having the following elements: the conductive resistance R_{p1}, the inductance L_{p1} caused by varying current flowing through it, the via-to-ground capacitance C_{p1}, as well as the additional inductance L_{pf1} and capacitance C_{pf1} resulting from the interaction between the via and the feed, as they are in close proximity. At location *A*, via-3 adds impedance Z_{p-3} with similar components: R_{p3}, L_{p3}, C_{p3}, L_{pf3}, and C_{pf3}. Finally, via-2 at location *G* adds an impedance Z_{p-2} having R_{p2}, L_{p2}, C_{p2}, and coupling capacitance C_{pm} due to coupling between via and the magnetic wall at the edge of the patch. The input impedance at the feed location, neglecting the admittance of the fringing field (as the admittance of the fringing field is low, it will not provide a strong path for current conduction), can be expressed as,

$$Z_{in} = \left(\frac{1}{Z_{TL1}+Z_{p-1}+Z_{TL2}} + \frac{1}{Z_{TL3}+Z_{p-3}+Z_{TL4}+Z_{p-2}}\right)^{-1} + j\omega L_f \quad (2)$$

The impedance of the transmission lines can be represented as,

$$Z_{TLn} = \left(\frac{1}{R_n} + \frac{1}{j\omega L_n} + j\omega C_n\right)^{-1} \quad (3)$$

The impedance of the vias can be expressed as,

$$Z_{p-1} = R_{p1} + \left(\frac{1}{j\omega L_{p1-eq}} + j\omega C_{p1-eq}\right)^{-1} \quad (4)$$

where $L_{p1-eq} = L_{p1} + L_{pf1}$, $C_{p1-eq} = C_{p1} + C_{pf1}$

Similarly,

This work is licensed under a Creative Commons Attribution 4.0 License. For more information, see https://creativecommons.org/licenses/by/4.0/

This article has been accepted for publication in IEEE Access. This is the author's version which has not been fully edited and content may change prior to final publication. Citation information: DOI 10.1109/ACCESS.2025.3554151

$$Z_{p-3} = R_{p3} + \left(\frac{1}{j\omega L_{p3-eq}} + j\omega C_{p3-eq}\right)^{-1} \quad (5)$$

where $L_{p3-eq} = L_{p3} + L_{pf3}$, $C_{p3-eq} = C_{p3} + C_{pf3}$, and

$$Z_{p-2} = R_{p2} + \left(\frac{1}{j\omega L_{p2}} + j\omega C_{p2-eq}\right)^{-1} \quad (6)$$

where $C_{p2-eq} = C_{p2} + C_{pm}$

The resonance frequency is calculated as:

$$f_r = \frac{1}{2\pi\sqrt{L_{eq}C_{eq}}} \quad (7)$$

where $L_{eq} = \left(L_1 || L_2 || L_3 || L_4 || L_{p1-eq} || L_{p3-eq} || L_{p2}\right) + L_f$ and $C_{eq} = C_1 + C_2 + C_3 + C_4 + C_{p1-eq} + C_{p3-eq} + C_{p2-eq}$.

The mutual coupling between the antennas is modeled as a series *RLC* circuit, where R_{mc} represents coupling path losses, L_{mc} denotes magnetic coupling, and C_{mc} signifies E-field coupling. The extracted values for these components are shown in caption of Fig. 6. The full-wave simulation results and circuit model results are presented in Fig. 7, which demonstrate a close alignment, showing strong consistency between them.

C. EXPERIMENTAL RESULTS

A prototype of the designed antenna system is fabricated and tested to validate the proposed self-decoupled antenna system. The S-parameters are measured using Agilent N5247A PNA-X vector network analyzer, and the radiation patterns and gain are measured in an anechoic chamber. Fig. 8(a) shows the measured and simulated S-parameters of the proposed self-decoupled antenna system, and they are in good agreement with each other. Fig. 8(b) illustrates that the simulated realized gain of the individual antenna is approximately 7.4 dBi, while the measured realized gain is approximately 7.2 dBi over the entire operating band. The measured and simulated 2-D radiation patterns are shown in Fig. 9. At the center frequency of 5.9 GHz, the simulated cross-pol of the designed antenna is 110 dB below the co-pol level, while the measured one is below 76 dB in both the *xoz* and *yoz* planes in the broadside direction.

Table 2. Comparison of the proposed antenna system with the reported two-element MIMO antenna systems.

Ref.	Decoupling Technique	f_0 (GHz)	FBW (%)	Volume (λ_0^3)	Minimum Isolation (dB)	Gain (dBi)	Efficiency (%)
[8]	Self-decoupled based on the CM of the ground plane	4	7.2	0.015	28	4.07	NA
[9]	Self-decoupled based on weak-field methods	3.5	2.8	0.031	30	7.1	NA
[11]	Self-decoupled using TM_{10} and TM_{02} modes	5.815	2.9	0.028	20	4.64	93.1
[12]	Decoupling structure composed of half-wave microstrip line and a shorting pin	3.147	1.43	0.022	18	5.5	NA
[13]	Self-decoupled through a meander-line structure for the radiating edge of the patch	4.8	2.2	0.029	15	5.2	80
[18]	Self-decoupled through mode-counteraction using TM_{10} and TM_{02} modes	4.8	0.83	0.0074	26	5.4	NA
[19]	Self-decoupled through diagonal status of resonant modes and pin-loaded microstrip line	3.3375	3.146	NA	19.8	5.8	89.75
This work	**Self-decoupled based on weak surface current on the ground plane using shorting pins**	**5.9**	**2.7**	**0.02**	**78**	**7.4**	**95**

f_0: Center frequency, λ_0: Free-space wavelength at f_0, FBW: Usable fractional bandwidth and NA: Data not available

D. COMPARISON

Table 2 compares the proposed decoupling methods with several state-of-the-art works. Some of these methods require additional decoupling structures, such as pin-loaded microstrip line [19] and half-wave shorted microstrip lines [12]. Incorporating these elements increases system complexity and expands the overall physical footprint. All the designs mentioned in the comparison table demonstrate either good inter-port isolation over a narrow bandwidth or have limited gains. In contrast, the proposed design achieves a high isolation level exceeding 78 dB solely through self-decoupling, across the entire operating band, with a fractional bandwidth of 2.7% and a realized gain of nearly 7.4 dBi. The combination of high inter-port isolation and significant gain makes the proposed design superior to other reported works.

This work is licensed under a Creative Commons Attribution 4.0 License. For more information, see https://creativecommons.org/licenses/by/4.0/

This article has been accepted for publication in IEEE Access. This is the author's version which has not been fully edited and
content may change prior to final publication. Citation information: DOI 10.1109/ACCESS.2025.3554151

E. RADIATION CHARACTERSTICS ON VEHICULAR INTEGRATION

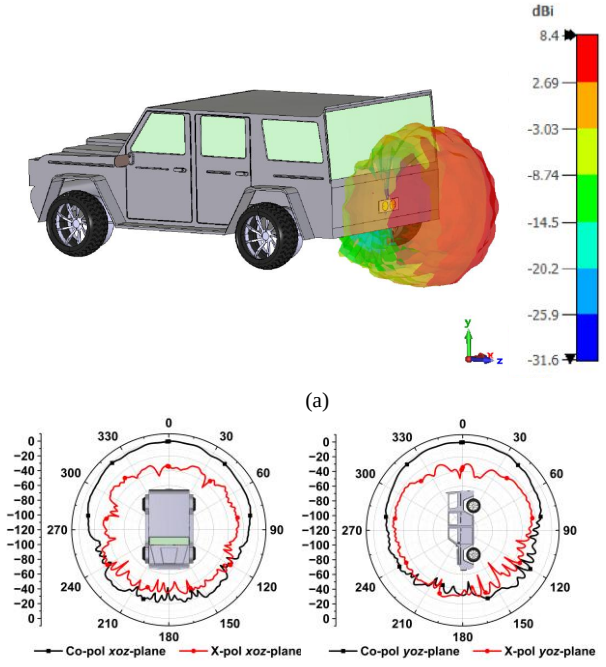

(a) (b) (c)

Fig. 10. When integrated at the rear bumper of the vehicle, (a) the 3-D realized gain, and the normalized 2-D far-field radiation patterns in the (b) *xoz*-plane, and (c) *yoz*-plane of Ant. 1 at 5.9 GHz.

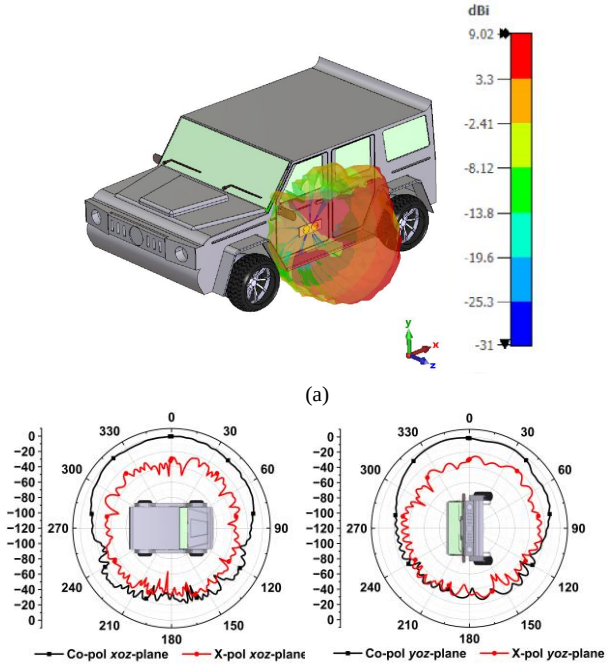

(a) (b) (c)

Fig. 12. When integrated at the side door of the vehicle, (a) the 3-D realized gain, and the normalized 2-D far-field radiation patterns in the (b) *xoz*-plane, and (c) *yoz*-plane of Ant. 1 at 5.9 GHz.

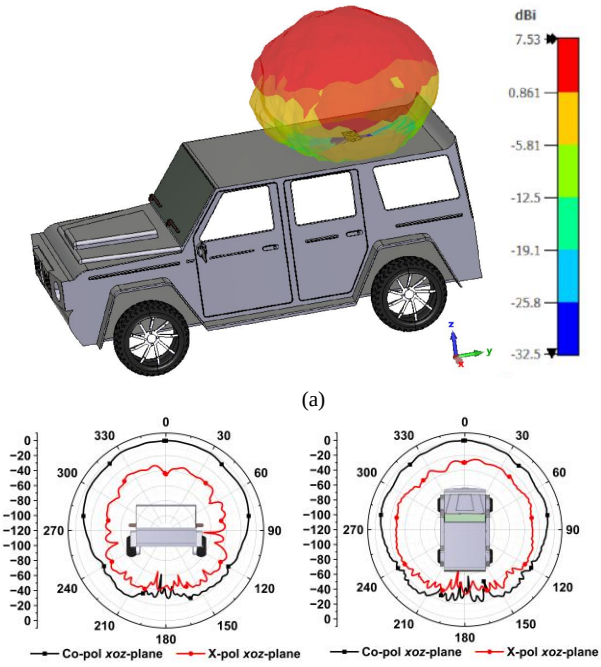

(a) (b) (c)

Fig. 11. When integrated on the roof of the vehicle, (a) the 3-D realized gain, and the normalized 2-D far-field radiation patterns in the (b) *xoz*-plane, and (c) *yoz*-plane of Ant. 1 at 5.9 GHz.

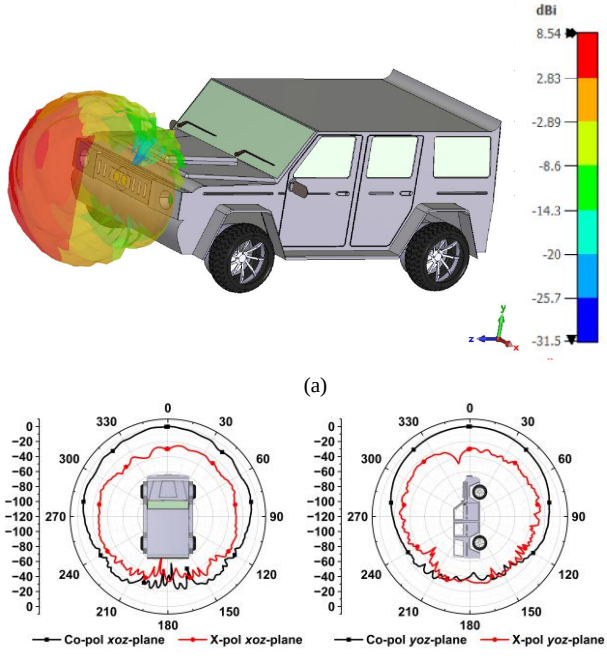

(a) (b) (c)

Fig. 13. When integrated at the front bumper of the vehicle, (a) the 3-D realized gain, and the normalized 2-D far-field radiation patterns in the (b) *xoz*-plane, and (c) *yoz*-plane of Ant. 1 at 5.9 GHz.

When a MIMO antenna system is installed in a single location, its coverage is limited. However, the coverage performance significantly improves when integrated into a distributed antenna system, forming a distributed MIMO

This work is licensed under a Creative Commons Attribution 4.0 License. For more information, see https://creativecommons.org/licenses/by/4.0/

This article has been accepted for publication in IEEE Access. This is the author's version which has not been fully edited and
content may change prior to final publication. Citation information: DOI 10.1109/ACCESS.2025.3554151

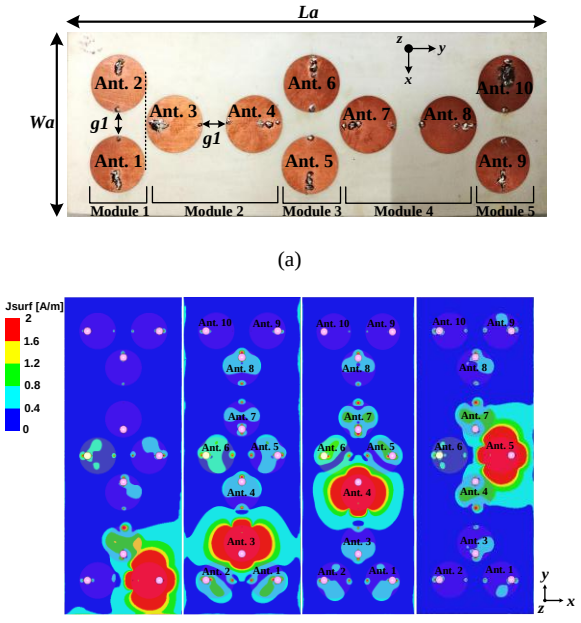

Fig. 14. (a) Proposed 10-element antenna array (Dimensions (in mm): g_1 = 7.2, L_a = 173, and W_a = 65), (b) surface current distribution (RMS value) on the ground plane on exciting antenna Ant. 1, Ant. 3, Ant. 4, and Ant. 5 (other antenna ports terminated in 50 Ω load) at 5.9 GHz.

antenna system (D-MIMO) [23]. In a D-MIMO setup, multiple MIMO antennas are strategically placed in various locations—such as on the roof, side doors, front bumper, and rear bumper. This arrangement enhances overall coverage and allows the MIMO antennas to leverage their spatial multiplexing and beamforming capabilities, which improve signal quality and reduce dead zones. By distributing the signal load and coverage, MIMO antennas in distributed antenna systems ensure consistent, high-quality connectivity, making them a superior choice for robust and reliable V2X communication.

When the antennas are installed at different locations on a vehicle, the unique surface characteristics of each location affect the radiation properties of the antennas in specific ways. The metallic components in these areas reflect and scatter the electromagnetic waves differently, resulting in varied radiation characteristics depending on their position. The radiation characteristics of the proposed MIMO antenna system are analyzed at four distinct locations on the vehicle: the roof, front bumper, rear bumper, and side door and they are depicted in Figs. 10-13. A CAD model of the vehicle is used for this study, where the vehicle body is modeled as perfect electric conductor (PEC) while other components are assigned to their respective materials. As the proposed antenna system operates in its fundamental mode, this results in relatively stable co-pol results. In contrast, the cross-pol of the designed antenna system is more affected by its position on the vehicle's surface. However, the isolation between co-pol and cross-pol consistently exceeds nearly 20 dB within the operating half-power beamwidth (HPBW). The stable co-pol

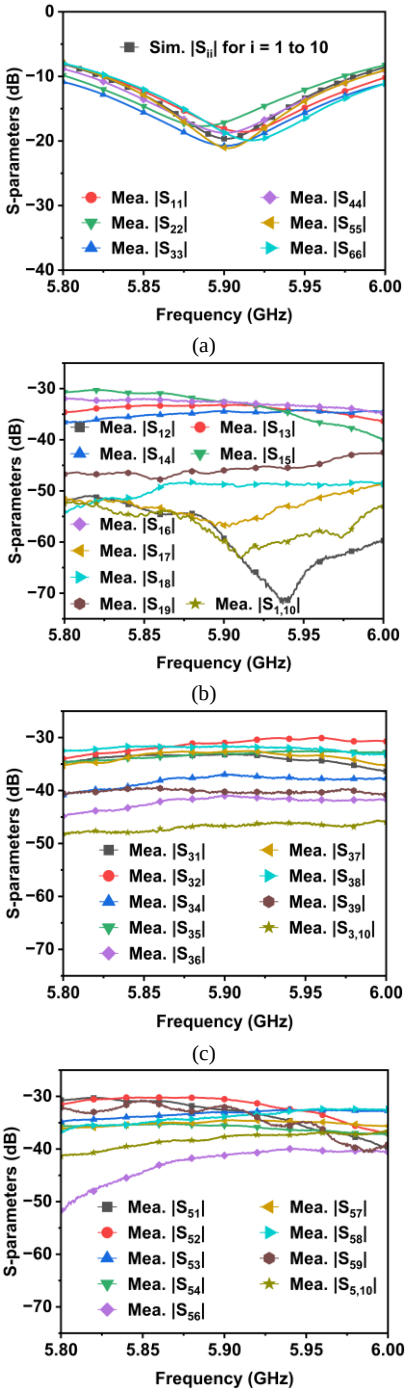

Fig. 15. (a) $|S_{ii}|$ and measured isolation of (b) Ant. 1, (c) Ant. 3, and (d) Ant. 5.

levels and high co-to-cross pol isolation at all four tested locations demonstrates the reliability of the proposed antenna system in a vehicular environment.

III. 10-ELEMENT MIMO ANTENNA SYSTEM

Higher order MIMO antenna systems offer several advantages for designing V2X communication links, such as robustness, high data rates, low latency, and high reliability for real-time

This work is licensed under a Creative Commons Attribution 4.0 License. For more information, see https://creativecommons.org/licenses/by/4.0/

This article has been accepted for publication in IEEE Access. This is the author's version which has not been fully edited and content may change prior to final publication. Citation information: DOI 10.1109/ACCESS.2025.3554151

data exchange among fast-moving vehicles. A 10-element MIMO antenna system is designed using a combination of the proposed self-decoupling technique and the polarization diversity method. However, it is possible to further increase the number of elements in the MIMO antenna system while still achieving comparable performance.

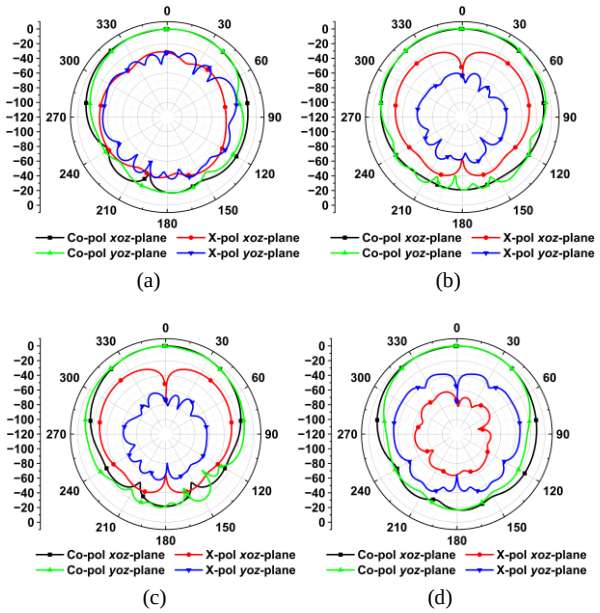

Fig. 16. Normalized 2-D far-field radiation pattern of (a) Ant. 1, (b) Ant. 3, (c) Ant. 4, and (d) Ant. 5 at 5.9 GHz.

A. ANTENNA ARRAY CONFIGURATION AND WORKING MECHANISM

The antenna array, illustrated in Fig. 14, is fabricated on the same substrate, and the optimized dimensions of the proposed antenna array are presented in the figure caption. The 10-element MIMO antenna system is designed using five self-decoupled antenna modules, with each module consisting of two self-decoupled antennas. Initially, Module 1 (comprised of Ant. 1 and Ant. 2) is positioned at the left end of the substrate. Subsequently, Module 2, a 90˚ rotated version of Module 1, is placed close to the first module. Following the same concept, Modules 3, 4, and 5 are placed. With this strategic placement of self-decoupled antenna modules, high inter-port isolation of better than 30 dB over the entire operating band is obtained. The intra-element isolation within each module is due to self-decoupling, while the polarization diversity introduces the decoupling between adjacent modules.

Table 3. Comparison of the Radiation Patterns

Parameters	Ant. 1	Ant. 3	Ant. 4	Ant. 5
Realized gain (dBi)	7.18	7.12	7.23	7.15
HPBW (deg) in *xoz*-plane	80.4	80.5	75.5	81.3
HPBW (deg) in *yoz*-plane	70.4	74.2	75.9	70.9

B. ANTENNA ARRAY PERFORMANCE

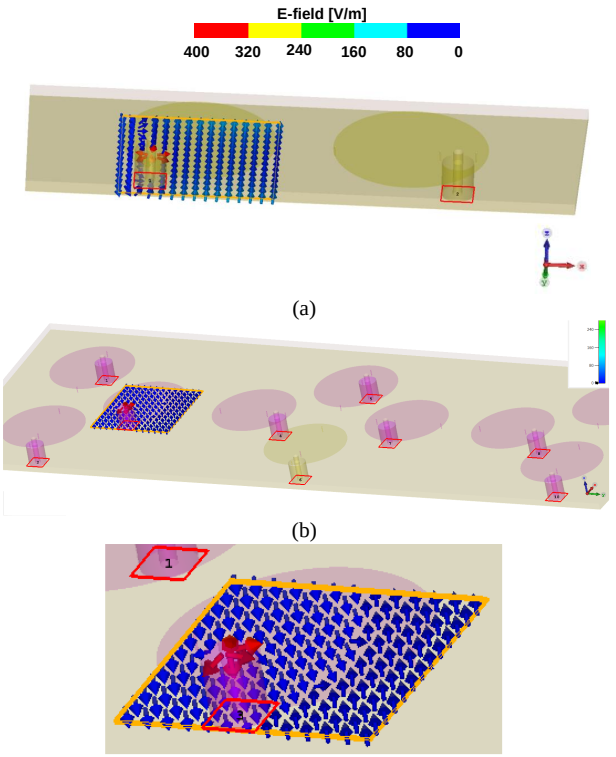

Fig. 17. E-field (vector) pattern at the back side of the radiator at 5.9 GHz when, (a) Ant.1 of proposed two-element MIMO antenna is excited, (b) Ant. 3 of 10-Element MIMO antennas is excited, and (c) Zoomed view of backside of Ant. 3 of (b).

The performance of Module 1 and Module 5 is identical. Similarly, the performance of Module 2 is comparable to that of Module 4. Additionally, the performance of Ant. 5 is similar to that of Ant. 6. Therefore, for brevity, the performances of Ant. 1, Ant. 3, Ant. 4, and Ant. 5 are presented in this article.

1) S-PARAMETERS

The simulated and measured S-parameters are given in Fig. 15. It can be observed that the inter-element isolation exceeds 30 dB throughout the entire operating band for all MIMO elements.

2) RADIATION PATTERN

Fig. 16 shows the radiation patterns of Ant. 1, Ant. 3, Ant. 4, and Ant. 5. The peak gain and HPBW for each antenna element are provided in Table 3. Notably, the co-pol measurements within the HPBW in the *xoz* and *yoz* planes are nearly identical across all antenna elements. This consistency ensures uniform signal strength throughout the coverage areas, which in turn enhances beamforming accuracy. Moreover, all antenna elements maintain co-to-cross pol isolation exceeding

This work is licensed under a Creative Commons Attribution 4.0 License. For more information, see https://creativecommons.org/licenses/by/4.0/

This article has been accepted for publication in IEEE Access. This is the author's version which has not been fully edited and
content may change prior to final publication. Citation information: DOI 10.1109/ACCESS.2025.3554151

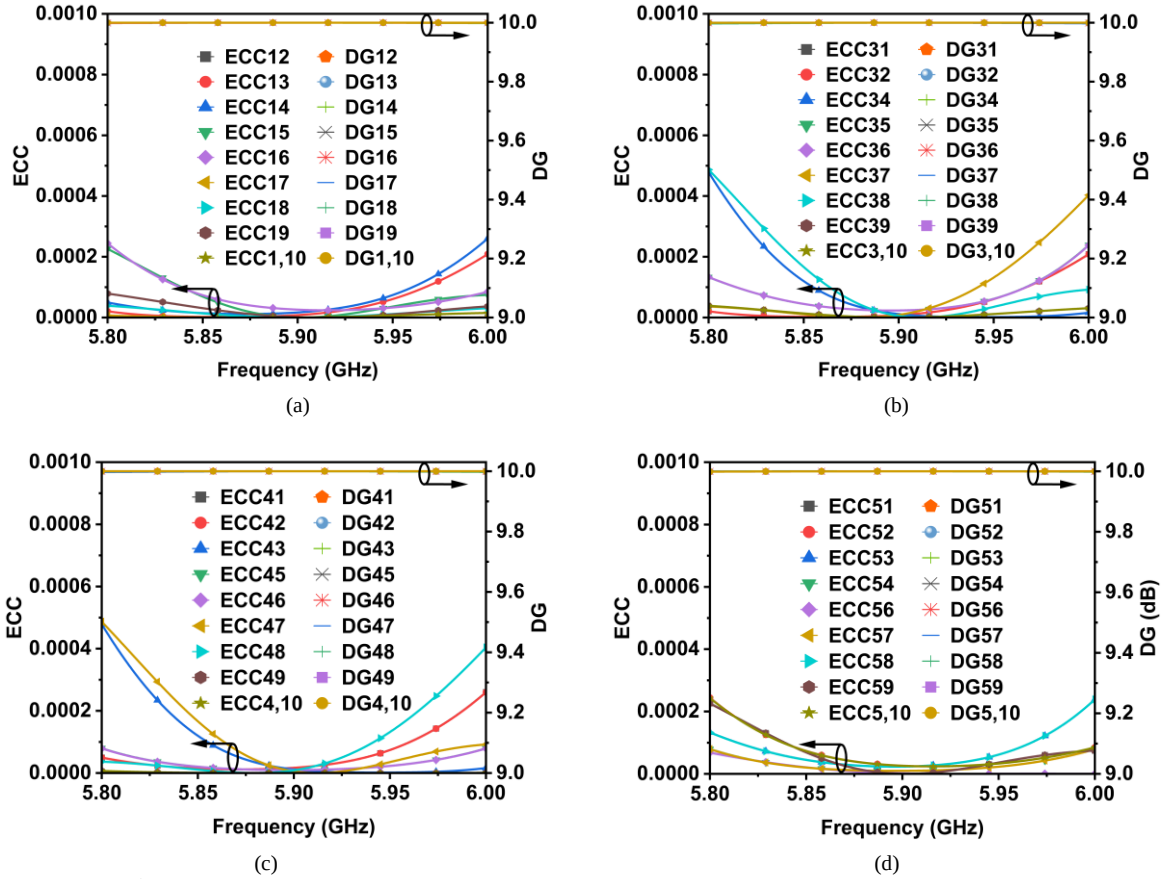

Fig. 18. ECC and DG of (a) Ant. 1, (b) Ant. 3, (c) Ant. 4, and (d) Ant. 5.

24 dB within the HPBW, minimizing interference from cross polarized signals. In the H-plane of the two-element MIMO antenna system, there is poor co-pol to cross-pol isolation in backward direction, as illustrated in Fig. 9(b). However, there is a significant improvement in co-pol to cross-pol levels on the backside of the H-plane for the 10-element MIMO antennas shown in Fig. 16. The finite ground plane causes diffraction and reflections, creating horizontal E-field components in the backward direction. Also, the higher-order modes, such as TM_{21}, are excited; these modes feature E-field components in the H-plane [24], [25]. Furthermore, the feeding probe disrupts the natural symmetry of the TM_{11} mode. These three factors contribute to an increase in undesirable horizontal E-field components in the backward direction, as shown in Fig. 17(a). As a result, the co-pol to cross-pol level in the backward direction is poor within the H-plane of the two-port MIMO antennas.

In contrast, the 10-element MIMO antenna system design has a larger ground plane than the two-element MIMO antennas. This increased ground plane size enhances the stability of the electric field near the probe, particularly in the backward direction. This improvement leads to a better vertical alignment of the E-fields, as shown in Figs. 17(b) and (c). Consequently, this adjustment results in a direct reduction of cross-polar radiation emitted in the backward direction in the H-plane of the CPA.

3) ENVELOPE CORRELATION COEFFICIENT AND DIVERSITY GAIN

Fig. 18 shows the envelope correlation coefficient (ECC) and diversity gain (DG) of the MIMO antenna elements. The ECC values are below 0.0003, indicating that the MIMO antenna elements are nearly uncorrelated. The DG remains close to the target value of 10 across the operating bandwidth. This demonstrates that the proposed MIMO antenna system can effectively utilize multiple paths to ensure high reliability in fading environments.

The performance metrics of the 10-element MIMO antenna system prove that this design is well-suited for V2X communication applications.

IV. CONCLUSION

A new method of self-decoupling in the MIMO CPA system is introduced in this article. Three shorting vias are strategically placed in the E-plane of the CPA, resonating in TM_{11} mode, to generate a weak current-density region on the ground plane where the adjacent antenna element can be positioned. Initially, a two-element MIMO antenna system is

This work is licensed under a Creative Commons Attribution 4.0 License. For more information, see https://creativecommons.org/licenses/by/4.0/

This article has been accepted for publication in IEEE Access. This is the author's version which has not been fully edited and
content may change prior to final publication. Citation information: DOI 10.1109/ACCESS.2025.3554151

designed for use in V2X communication in the 5.9 GHz band, followed by the design of a 10-element MIMO antenna system. The proposed antenna system demonstrates stable co-pol levels and high co-to-cross pol isolation in various tested locations, including the vehicle's roof, front bumper, rear bumper, and side door, within a vehicular environment. The measured results show that the proposed MIMO antenna system could be a strong candidate for applications in the V2X-ITS communication band based on IEEE 802.11p/WAVE technology [26].

ACKNOWLEDGMENT

This research was supported in part by the National Research and Development Program through the National Research Foundation of Korea (NRF) funded by the Ministry of Science and ICT (No. RS-2023-00281275), and in part by the BK21 FOUR project funded by the Ministry of Education (No. 4199990113966).

REFERENCES

[1] Federal Communications Commission. " Use of the 5.850–5.925 GHz band", United States Government, 2024. [Online]. Available: https://www.federalregister.gov/documents/2024/04/09/ 2024-07428/use-of-the-5850-5925-band.

[2] X. Tan, W. Wang, Y. Wu, Y. Liu, and A. A. Kishk, "Enhancing Isolation in Dual-Band Meander-Line Multiple Antenna by Employing Split EBG Structure," *IEEE Transactions on Antennas and Propagation*, vol. 67, no. 4, pp. 2769–2774, 2019.

[3] H. Chu, X. Pan, J. Jiang, X. Li and L. Zheng, "Adaptive and Robust Channel Estimation for IRS-Aided Millimeter-Wave Communications," *IEEE Transactions on Vehicular Technology*, vol. 73, no. 7, pp. 9411-9423, July 2024.

[4] C. Hongyun, Y. Mengyao, P. Xue and X. Ge, "Joint Active and Passive Beamforming Design for Hybrid RIS-Aided Integrated Sensing and Communication," *China Communications*, vol. 21, no. 10, pp. 1-12, Oct. 2024, doi: 10.23919/JCC.ja.2023-0213.

[5] S. Yue, S. Zeng, L. Liu, Y. C. Eldar, and B. Di, "Hybrid Near-Far Field Channel Estimation for Holographic MIMO Communications," *IEEE Transactions on Wireless Communications*, vol. 23, no. 11, pp. 15798-15813, 2024.

[6] L. Zhang, H. Kou, Y. Pang, L. Yang, X. Zhang, Z. Shang, and L. Zhang, "Design of Temperature-Pressure Sensor Based on Slot-Antenna CSRR Integrated for Applications in High-Temperature Environments," *IEEE Sensors Journal*, vol. 24, no. 17, pp. 27218-27224, 2024.

[7] S. Rana, A. Kumar, A. Mohan, B. Kumar Kanaujia and L. Matekovits, "A Planar Wideband Antenna for Full Duplex Communication With Significant Peak Gain," in IEEE Access, vol. 12, pp. 153181-153187, 2024, doi: 10.1109/ACCESS.2024.3478803.

[8] Q. X. Lai, Y. M. Pan, and S. Y. Zheng, "A Self-Decoupling Method for MIMO Antenna Array Using Characteristic Mode of Ground Plane," *IEEE Transactions on Antennas and Propagation*, vol. 71, no. 3, pp. 2126–2135, March 2023.

[9] H. Lin, Q. Chen, Y. Ji, X. Yang, J. Wang, and L. Ge, "Weak-Field-Based Self-Decoupling Patch Antennas," *IEEE Transactions on Antennas and Propagation*, vol. 68, no. 6, pp. 4208–4217, 2020.

[10] D. P. Purbey, S. Ghosal and A. De, "Shorting-Pin-Inspired Coupling Reduction in Dual-Band Dual-Polarized STAR Antenna," in IEEE Antennas and Wireless Propagation Letters, vol. 24, no. 1, pp. 43-47, Jan. 2025, doi: 10.1109/LAWP.2024.3483215.

[11] Q. X. Lai, Y. M. Pan, S. Y. Zheng, and W. J. Yang, "Mutual Coupling Reduction in MIMO Microstrip Patch Array Using TM10 and TM02 Modes," *IEEE Transactions on Antennas and Propagation*, vol. 69, no. 11, pp. 7562–7571, 2021.

[12] T. Pei, L. Zhu, J. Wang, and W. Wu, "A Low-Profile Decoupling Structure for Mutual Coupling Suppression in MIMO Patch Antenna," *IEEE Transactions on Antennas and Propagation*, vol. 69, no. 10, pp. 6145–6153, 2021.

[13] P. Kim-Thi, T. N. Van, and T. B. Thanh, "A Self-Decoupling Technique for Isolation Enhancement in Closely-Spaced MIMO Patch Antennas," *IEEE Antennas and Wireless Propagation Letters*, vol. 23, no. 6, pp. 1695–1699, 2024.

[14] J. Sui and K.-L. Wu, "Self-Curing Decoupling Technique for Two Inverted-F Antennas With Capacitive Loads," *IEEE Transactions on Antennas and Propagation*, vol. 66, no. 3, pp. 1093–1101, 2018.

[15] C. F. Ding, X. Y. Zhang, C.-D. Xue, and C.-Y.-D. Sim, "Novel Pattern- Diversity-Based Decoupling Method and Its Application to Multielement MIMO Antenna," *IEEE Transactions on Antennas and Propagation*, vol. 66, no. 10, pp. 4976–4985, 2018.

[16] X. Zhao, S. P. Yeo, and L. C. Ong, "Decoupling of Inverted-F Antennas with High-Order Modes of Ground Plane for 5G Mobile MIMO Platform," *IEEE Transactions on Antennas and Propagation*, vol. 66, no. 9, pp. 4485–4495, 2018.

[17] A. Zhao and Z. Ren, "Size Reduction of Self-Isolated MIMO Antenna System for 5G Mobile Phone Applications," *IEEE Antennas and Wireless Propagation Letters*, vol. 18, no. 1, pp. 152–156, 2019.

[18] Q. Liu, L. Zhu and W. -J. Lu, "A Simplified Design Approach and Its Application to Decoupling of 2-D MIMO Square Patch Antenna Systems," in *IEEE Antennas and Wireless Propagation Letters*, vol. 23, no. 6, pp. 1759-1763, June 2024, doi: 10.1109/LAWP.2024.3368635.

[19] H. Tran-Huy, H. N. Tuan, N. Q. Dinh, D. -N. Tran-Viet and H. -C. Park, "Multi-Element Self-Decoupled MIMO Patch Antenna With Flexible Characteristics," in *IEEE Access*, vol. 12, pp. 21569-21575, 2024, doi: 10.1109/ACCESS.2024.3362876.

[20] C. A. Balanis. Antenna Theory: Analysis and Design. Hoboken, NJ, USA:Wiley, 2016.

[21] J. -H. Ou, J. Huang, J. Liu, J. Tang and X. Y. Zhang, "High-Gain Circular Patch Antenna and Array With Introduction of Multiple Shorting Pins," in *IEEE Transactions on Antennas and Propagation*, vol. 68, no. 9, pp. 6506-6515, Sept. 2020, doi: 10.1109/TAP.2020.2983793.

[22] C. Deng, Z. Zhao and W. Yu, "Characteristic Mode Analysis of Circular Microstrip Patch Antenna and Its Application to Pattern Diversity Design," in *IEEE Access*, vol. 10, pp. 2399-2407, 2022, doi: 10.1109/ACCESS.2021.3139316.

[23] "5G Automotive Association White Paper". 5G Automotive Association, Germany, 2022. [Online] Available: https://5gaa.org/content/uploads/2022/12/5GAA_White-Paper DAS.pdf

[24] C. Kumar and D. Guha, "Nature of Cross-Polarized Radiations from Probe-Fed Circular Microstrip Antennas and Their Suppression Using Different Geometries of Defected Ground Structure (DGS)," in *IEEE Transactions on Antennas and Propagation*, vol. 60, no. 1, pp. 92-101, Jan. 2012, doi: 10.1109/TAP.2011.2167921.

[25] S. Samanta, P. S. Reddy and K. Mandal, "Cross-Polarization Suppression in Probe-Fed Circular Patch Antenna Using Two Circular Clusters of Shorting Pins," in *IEEE Transactions on Antennas and Propagation*, vol. 66, no. 6, pp. 3177-3182, June 2018, doi: 10.1109/TAP.2018.2819895.

[26] "Intelligent Transport Systems (ITS) usage". International Telecommunication Union, Geneva, Switzerland, Rep. no. ITU-R M.2445-0, 2018. [Online]. Available: https://www.itu.int/dms pub/itu-r/ opb/rep/R-REP-M.2445-2018-PDF-E.pdf.

Amit Kumar is currently pursuing his Ph.D. from Electronics and Communication Engineering (ECE) Department, Indian Institute of Technology Roorkee, India. He completed his M.Tech. in ECE Department at National Institute of Technology Warangal, India, in 2022. He has worked as research intern at Wipro, India during his M.Tech. His current areas of research include design of linear and efficient RF

This work is licensed under a Creative Commons Attribution 4.0 License. For more information, see https://creativecommons.org/licenses/by/4.0/

This article has been accepted for publication in IEEE Access. This is the author's version which has not been fully edited and
content may change prior to final publication. Citation information: DOI 10.1109/ACCESS.2025.3554151

Power amplifiers, design of microwave circuits and antennas for V2X communication. He has five publications till date.

Sandeep Rana is as an Assistant Professor at ECE Department in G. B. Pant Institute of Engineering and Technology (GBPIET), Uttarakhand, India since 2019. At present, he is on study leave to pursue his Ph.D. from the Indian Institute of Technology Roorkee, Uttarakhand, India. He received M.Tech. degree from Delhi Technological University, New Delhi, India, in 2014. He has also worked as an Assistant Professor at Graphic Era Hill University, Dehradun and Netaji Subhash Institute of Technology, New Delhi, India before joining GBPIET, Uttarakhand. He has five publications till date including two journals and three conferences. His research interests revolve around the design of microwave circuits and antennas tailored for modern wireless communication applications.

Akhilesh Mohan (Member, IEEE) received the B.Tech. degree in Electronics Engineering from Kamla Nehru Institute of Technology, Sultanpur, India, in 2002, the M.Tech. degree and Ph.D. degree in Microwave Engineering from Indian Institute of Technology Kanpur, Uttar Pradesh, India, in 2004 and 2009, respectively. From 2009 to 2010, he worked as a Scientist at Space Applications Center, Indian Space Research Organization, Ahmedabad, India. From 2010 to 2013, he was a faculty member with the Department of Electrical Engineering at Indian Institute of Technology Jodhpur, Rajasthan, India. From 2013 to 2020, he was a faculty member with the Department of Electronics and Electrical Communication Engineering at Indian Institute of Technology Kharagpur, West Bengal, India. Since 2021, he has been a faculty member with the Department of Electronics and Communication Engineering at Indian Institute of Technology Roorkee, Uttarakhand, India. Dr. Mohan has authored and co-authored more than 150 peer reviewed international journals and conference papers. His research interests include the design of microwave filters, antennas, and absorbers for wireless communication systems.

Gunjan Srivastava (Member, IEEE) received her Ph.D. degree in Microwave Engineering from the Indian Institute of Technology (Indian School of Mines), Dhanbad, India, in 2016. At present, she is working as an Associate Professor in the Department of Electronics and Communication Engineering at Graphic Era (Deemed to be) University, Dehradun, India. Earlier, she was associated with the Department of Electronics and Electrical Communication Engineering, Indian Institute of Technology Kharagpur, Kharagpur, India, as a capacity of Women Scientist. She has authored or co-authored over 25 peer-reviewed international journal and conference papers. Her main research interests are design of ultra-wideband, reconfigurable, differential, SIW, MIMO, and self-multiplexing antennas.

Sachin Kumar received the B.Tech. degree in Electronics and Communication Engineering from Uttar Pradesh Technical University, Lucknow, India, in 2009, and the M.Tech. and Ph.D. degrees in Digital Communication and RF & Microwave Engineering from Netaji Subhas University of Technology (East Campus), Delhi, India, in 2011 and 2016, respectively. He was a Post-Doctoral Research Fellow at the College of IT Engineering, Kyungpook National University, South Korea, from 2018 to 2021. He is currently working as an Associate Professor in the Department of Electronics and Communication Engineering, Galgotias College of Engineering and Technology, Greater Noida, India.

Dr. Kumar has published two books, fourteen book chapters, eight patents, one hundred and fifty research papers in SCI journals, and over fifty articles in international conferences, and his articles have been cited over 3300 times with an h-index of 31. He is an Associate Editor for the Journal *Frontiers in Antennas and Propagation* and *Franklin Open*, Academic Editor for the Journal *PLOS ONE*, Advisory Board Member for the Journal *Measurement*, Editorial Board Member for the Journal *Scientific Reports*, *Discover Electronics*, *Discover Internet of Things*, *Sensors & Transducers*, and Guest Editor for the *International Journal of Antennas and Propagation*, *Sensors*, and *Micromachines*. He is also a frequent reviewer for more than sixty scientific journals and book publishers. He has given several invited talks at prestigious institutions, and serves as the session chair, organizer, and member of the technical program committee for various national/international conferences, summits, and workshops.

His name was featured in the list of *"World's Top 2% Scientists"* in the 2023, 2022, 2021, and 2020 database released by Stanford University, USA and Elsevier. He was a recipient of the Teaching-cum-Research Fellowship from the Government of NCT of Delhi, India, and the Brain Korea 21 Plus Research Fellowship from the National Research Foundation of South Korea. He is a Fellow of the Institute of Electronics and Telecommunication Engineers, India, a Life Member of the Indian Society for Technical Education, and a Member of the Korean Institute of Electromagnetic Engineering and Science.

Kang Wook Kim received his B.S. and M.S. degrees in Electrical Engineering from Seoul National University, Korea, in 1985 and 1987, respectively. He received his Ph.D. degree in Electrical Engineering from the University of California, Los Angeles, USA, in 1996. In 1987, before pursuing his Ph.D. degree, he worked as a Researcher at the Korea Electrotechnology Research Institute. He worked as a Design Engineer in P-Com Inc., USA and Narda DBS Microwave, USA, in 1998 and 1999, respectively. In 2001, he joined Kyungpook National University, Daegu, Korea, as a Professor. He is a founder of EM-wise Communications Company Inc., Korea. His areas of research include microwave communication system and subsystems, microwave and millimeter wave components and packaging, wireless communications, broadband microwave antenna, electromagnetic interaction and numerical analysis.

This work is licensed under a Creative Commons Attribution 4.0 License. For more information, see https://creativecommons.org/licenses/by/4.0/

Social Network Analysis and Mining (2025) 15:20
https://doi.org/10.1007/s13278-025-01416-z

ORIGINAL ARTICLE

Advancing sentiment analysis by addressing negation handling challenge via unsupervised mathematical approach

Neha Punetha[1] · **Goonjan Jain**[1]

Received: 24 August 2024 / Revised: 3 October 2024 / Accepted: 6 February 2025
© The Author(s) 2025

Abstract
Sentiment analysis, a critical component of Natural Language Processing (NLP), focuses on the automatic detection and classification of emotions in text. With the vast increase in user-generated content on digital platforms, manual sentiment analysis has become impractical, necessitating advanced automated methods for efficiently processing and interpreting large-scale sentiment data. Traditional sentiment analysis techniques, which often rely on machine learning models and large pre-trained datasets, face challenges such as handling linguistic complexities like negation and adapting across different domains and languages. To address these limitations, we propose the "Evaluation based on Distance from Average Solution Optimization Technique-based Negation Handling Tagger" (EOT-NH), an innovative unsupervised sentiment classification model. The EOT-NH model incorporates multi-criteria decision-making (MCDM) principles and concepts from game theory to handle negation effectively and operate without extensive pre-training. This framework extracts key textual features—word count, context, and emotion score—while maintaining language and domain independence. Experimental evaluations demonstrate the model's competitive performance, achieving a classification accuracy of 91% on the IMDB English reviews dataset The EOT-NH model presents a robust solution for sentiment analysis, providing significant advancements in negation handling and language flexibility, making it highly applicable to dynamic, multilingual environments.

Keywords Text analysis · Negation handling · Reviews · Unsupervised approach

1 Introduction

Computational sentiment analysis plays a crucial role in detecting, extracting, and measuring human emotions and opinions from textual data. It has garnered considerable attention in the fields of humanities and social communication due to its ability to reveal underlying emotions, attitudes, and beliefs within individuals and societies. This makes sentiment analysis an invaluable resource for social and human sciences, as understanding cultural and social contexts is vital to fully grasp the emotions conveyed through various forms of communication, including written texts, speeches, and interpersonal interactions. By analyzing public opinions and emotions on social and political topics, sentiment analysis offers deep insights into how emotions and sentiments shape human behavior and societal norms (Jain et al. 2020). A key challenge in sentiment analysis research is the handling of negation, which is essential for improving the accuracy of sentiment predictions. Negation in natural language presents a complex challenge, as it reverses the meaning of phrases and alters the sentiment conveyed, often flipping positive expressions into negative ones. This poses difficulties in opinion mining within Natural Language Processing (NLP) (Li et al. 2022). Common negation words like "not" and "never" modify the meaning of sentences, such as transforming "I love this product" (positive) into "I do not love this product" (negative). Inaccurate handling of negation can lead to misclassification of sentiments (Gupta and Joshi 2021). Recent studies indicate that methods such as syntactic parsing, sentiment shifters, and machine learning algorithms can improve negation detection, leading to greater accuracy in sentiment analysis. For instance, in the sentence "I hate this product less than I used to," the phrase "less than I used to" functions as a sentiment shifter, signaling a reduction in negativity over time. Identifying these

✉ Neha Punetha
nehapunetha80@gmail.com

Goonjan Jain
goonjan_jain@hotmail.com

[1] Department of Applied Mathematics, Delhi Technological University, Delhi, India

Published online: 19 March 2025

sentiment shifters allows sentiment analysis systems to better capture emotional nuances in text. Negations like "not," "don't," and "couldn't" further underscore the complexity and importance of advanced techniques for handling negation in sentiment analysis.

- "I **do not** like this movie."
- "This food **isn't** bad."
- "I **don't** hate this book."
- "He **couldn't** be happier with his new job."

Recent developments in negation handling have the potential to greatly enhance the accuracy and reliability of sentiment analysis tools. By effectively detecting and accounting for negation in sentences, these tools can offer more precise and nuanced sentiment interpretations. This improved understanding empowers businesses and organizations to make better decisions based on a more detailed analysis of sentiment trends. The approach discussed here represents an enhancement of previously established methods, such as the NEGVOT model Ghadikolaei et al. (2014) offering a more advanced solution for handling negation in sentiment analysis.

1.1 Contribution

The key contributions of this cognitive framework are outlined below.

1. The "EDAS Optimization Technique-based Negation Handling" (EOT-NH) model offers a novel solution for sentiment analysis, effectively handling both negation-inclusive and negation-free text using MCDM principles.
2. EOT-NH model is the improved version of NEGVOT model. EOT-NH improves accuracy by 2% to 3% over NEGVOT and is designed for domain independence, making it applicable across various use cases.
3. The model introduces a mathematical optimization approach that removes the need for pre-training, enabling seamless sentiment tagging across different datasets.
4. EOT-NH is well-suited for real-time data analysis, requiring minimal adjustments and low computational resources, making it highly adaptable to dynamic environments without the need for labeled data.

1.2 Organization

The structure of the paper is organized as follows: Sect. 2 offers a comprehensive review of prior research. Section 3 outlines the preliminaries pertinent to the methodology. Section 4 evaluates the performance of the EOT-NH model for negation handling, providing a comparative analysis with previous approaches across three datasets, and validating results through statistical significance. Sections 5 and 6 summarize key findings, analyze errors, propose directions for future research, and conclude the study.

2 Related work

Various studies have explored machine learning and hybrid approaches for sentiment analysis, tackling numerous challenges in this field.

Taboada et al. (2011) lexicon-based approach integrating intensification and negation relied on manually constructed dictionaries, which may introduce biases and limitations. Additionally, the effectiveness of the method could be influenced by the comprehensiveness and accuracy of the dictionaries. Limsopatham et al. (2012) term representation for negated language in medical records considered query term dependence, but its performance may vary depending on the specific characteristics of the dataset and the nature of the queries. Xia et al. (2015) dual training algorithm for sentiment classification showed promise but may require additional computational resources and may not generalize well across diverse datasets and domains.

Xia et al. (2016) proposed a three-stage cascade approach to address the polarity shift in document-level sentiment categorization. Despite its efficacy in detecting and mitigating polarity shifts, the approach may face challenges related to scalability and adaptability across diverse datasets and linguistic contexts. Amalia et al. (2018) syntax-based rules for establishing negation scope in Indonesian improved performance with an SVM classifier. However, the effectiveness of this approach may be influenced by the complexity of the language and the quality of the dataset. Ljajić and Marovac (2019) rules for processing negation combined with lexicon-based or machine-learning approaches showed improved sentiment classification performance. However, the relative improvement may vary depending on the dataset, and the rules may not capture all nuances of negation in different languages or domains. Mao and Li (2021) introduced a gating mechanism for MTL towers, assessed in sentiment analysis and metaphor identification tasks.

However, the model's performance may vary based on dataset selection and task complexity, potentially limiting its generalizability. Singh and Paul (2021) LSTM-based deep neural network model for negation processing relied on annotated datasets, limiting its performance to the availability and quality of labeled data. Lal and Kamath (2022)

procedure for managing negations based on antonymy in WordNet focused on IMDB movie reviews. However, it may overlook subtle nuances in sentiment expression and may not generalize well to other domains. Mao et al. (2022) empirical study on prompt-based sentiment analysis and emotion identification highlighted biases in pre-trained language models. However, the generalizability of the findings may be limited by dataset selection and biases.

While these studies highlight significant contributions to sentiment analysis, they also underscore ongoing challenges, particularly related to computational requirements, scalability, and dataset dependencies. These limitations provide directions for further research to develop more efficient and adaptable sentiment analysis methods.

3 Research gap

Negation handling in sentiment analysis presents several key research gaps. Many existing approaches rely on manually constructed lexicons, which can introduce bias and limit adaptability across various languages and domains. Additionally, performance often varies significantly depending on the dataset characteristics, with current methods struggling to consistently perform well across different datasets, particularly in specialized domains or when addressing negations. Another challenge is the high computational resources required by some advanced models, which, although effective, are impractical for real-time or large-scale applications. Scalability and domain adaptation further pose issues, as many approaches find it difficult to adapt to new domains or linguistic contexts, reducing their effectiveness in diverse scenarios. Moreover, many deep learning models are heavily reliant on annotated datasets, making them less applicable in situations where labeled data is scarce or unavailable. Lastly, pre-trained language models often carry inherent biases, which can impact their generalizability and fairness, especially when handling negations in text. These gaps underscore the need for more efficient, adaptable, and scalable models to improve negation handling in sentiment analysis.

4 Methodology

In our methodology, we propose the "EDAS Optimization Technique-based Negation Handling Tagger of the Text" (EOT-NH) model. The pipeline of the proposed methodology is illustrated in Fig. 1. We calculate the context and emotion scores using the equations provided, and these scores are then supplied to the EOT-NH model to achieve the desired outcome. Section 3.1 introduces the preliminaries of the EDAS method utilized in the EOT-NH model. We have used certain notations in this manuscript like ($PCS^{\otimes}$) is the Normalized Positive Context Score, ($NCS^{\otimes}$) is the Normalized Negative Context Score and ($OCS^{\otimes}$) is the Normalized neutral context scores. Similarly there are three emotion scores i.e. ($PES^{\otimes}$) is the Normalized Positive Emotion Score, ($NES^{\otimes}$) is the Normalized Negative Emotion Score and ($OES^{\otimes}$) is the Normalized Neutral Emotion Score. *(AS_i) is the* Appraisement score and the complement of the Appraisement score *(AS_i^c).*

4.1 Proposed EDAS technique

The EDAS technique, derived from the Serbian phrase "Multi-criteria Optimization and Compromise Solution," was introduced in 1990 as a method of multi-criteria decision-making (MCDM) (Ghadikolaei et al. 2014). Developed by Serafim Opricovic, it addresses decision-making challenges involving competing and non-commensurable criteria. The technique aims to find a compromise solution that best approximates the ideal, considering all defined criteria. In MCDM problems, a finite set of discrete alternatives is evaluated across various criteria. In sentiment analysis, depicted in Fig. 1, alternatives are categorized as positive, negative, or neutral, with criteria including context and emotion. The decision-making process involves creating a decision matrix, followed by applying Algorithms 2 and 3 to determine sentiment.

4.2 Proposed model pipeline

The methodology, depicted in Fig. 1, follows a well-defined sequence of steps. First, data is collected from three different sources. The data is then thoroughly cleaned using preprocessing techniques such as tokenization, lemmatization, and the removal of stopwords to ensure it is ready for analysis. Once the data cleaning is complete, the dataset is divided into two segments using the Negex Python library: one containing statements with negations, and the other containing statements without. This segmentation enables a focused analysis of how negations impact subsequent evaluations. Finally, context and emotion scores are computed for both segments, providing detailed insights into the sentiment and contextual subtleties of the statements.The EOT-NH model is then employed to perform evaluations (ASi). resulting in two distinct cases: Case 1, for text containing negations, evaluated as (Asi^c), and Case 2, for negation-free text, evaluated as (AS_i). Subsequently, the three alternatives are ranked, with the highest-ranked alternative assigned as the tag for each review. To validate the results, a comparison is conducted between the outcomes of the EOT-NH model and the annotated dataset, ensuring alignment between model predictions and expected classifications.

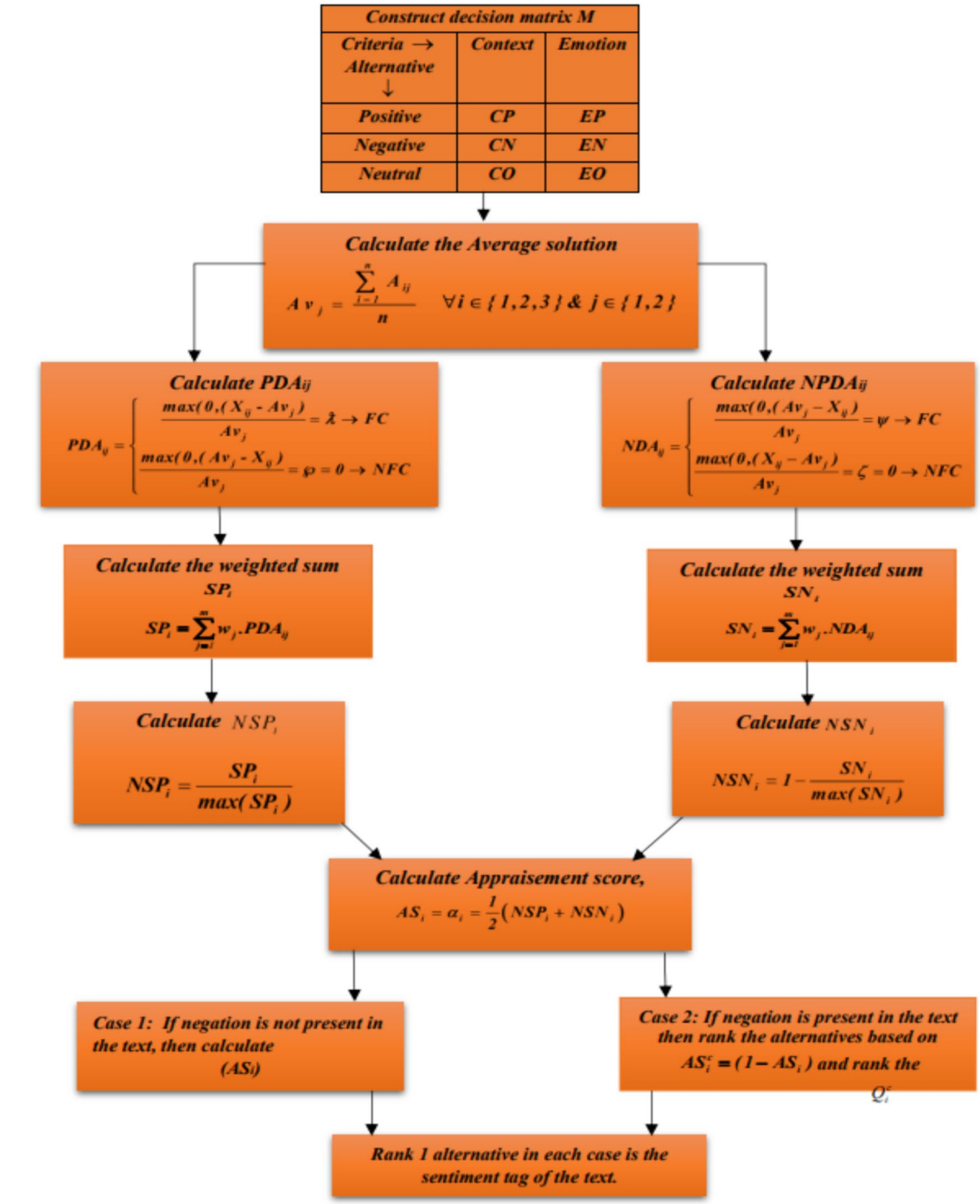

;

Fig. 1 Flowchart of the EOT-NH model

Step 1: Data Segmentation

In the initial step, we collect the dataset and process it through the Negex[1] Python library. This library aids in detecting negations within the text, allowing us to divide the dataset into two distinct parts. One part contains text segments with negations, while the other consists of text without negations.

[1] *Pip install negspacy.*

Step 2: Context Score Assessment

In this stage, we employ SentiWordNet (SWN) to compute the context score of textual comments (Esuli and Sebastiani 2006). SWN houses a comprehensive database of words categorized based on their positive or negative sentiment. From a user review, we extract the parts-of-speech (POS)-tagged content words. For each word, we refer to SWN to determine its positive and negative polarity values, thus computing the context scores of the comments. These context score values range from 0 to 1 and encompass the $(PCS^{\otimes})$, $(NCS^{\otimes})$, and $(OCS^{\otimes})$ following Algorithm 1. If certain words are not found in the SentiWordNet (SWN) lexicon, the VADER (Valence Aware Dictionary and sentiment Reasoner) Python library can be employed as an alternative to compute sentiment scores for those words. This approach ensures comprehensive sentiment analysis by complementing SWN with VADER, particularly for lexically diverse terms that may not be covered by SWN.

Table 1 MCDM components

Criteria → Alternative ↓	Context	Emotion
Positive	$(PCS^{\otimes})$	$(PES^{\otimes})$
Negative	$(NCS^{\otimes})$	$(NES^{\otimes})$
Neutral	$(OCS^{\otimes})$	$(OES^{\otimes})$

Step 3: Emotion Score Assessment

In this stage, we compute emotion scores utilizing the *text2emotion*[2] library. Emotions are classified into the categories of happiness, anger, surprise, sadness, and fear. However, in this study, the fear emotion is excluded. The emotional expressions of happiness (H), anger (A), sadness (S), and surprise (S) constitute the four elements in Eq. (5). Leveraging these four emotions, we derive the $(PES^{\otimes})$, $(NES^{\otimes})$, and $(OES^{\otimes})$ scores following Algorithm 2.

Algorithm 1 Assess the context score of the reviews

Input: *A sequence of words (W) in a review R.*

Output: $(PCS^{\otimes})$, $(NCS^{\otimes})$, *and* $(OCS^{\otimes})$ *scores.*

1: *Initialise PCS = 0 , NCS = 0 and OCS=0 for each reviews.*

2: *Obtain synsets for the word. Synsets=SentiWordNet.lookup(word).*

3: Extract positive, negative, and neutral scores for each synset

PS = synset. positiveScore
NS = synset. NegativeScore
OS=(1-(PS+NS)

4: Update Positive Context Score (PCS) and Negative Context Score (NCS)

$$PCS \leftarrow PCS + PS \text{ , } NCS \leftarrow NCS + NS \text{ and } OCS \leftarrow OCS + OS$$

5: Iterate through all synsets $(PCS^{\otimes})$, $(NCS^{\otimes})$ *and* $(OCS^{\otimes})$.

$$(PCS^{\otimes}) = \frac{PCS}{|W|} \;||\; (NCS^{\otimes}) = \frac{NCS}{|W|} \;||\; (OCS^{\otimes}) = \frac{OCS}{|W|}$$

[2] https://pypi.org/project/text2emotion/.

Algorithm 2 Assess the emotion score of the reviews

Input: *A sequence of words (W) in a review R.*
Output: *Evaluate Score* $(PES^{\otimes})$, $(NES^{\otimes})$, *and* $(OES^{\otimes})$.

1: *Load a set of emotion words and associated scores.*

$$EmotionWords \leftarrow LoadEmotionWords()$$

2: *Initialise emotion score variables H =0, A=0 ,S=0 and* S_p *=0.*

3: *Tokenize each review into words.*

4: *For all W in R, if* $W \in EmotionWords$

$$EmotionScores \leftarrow GetEmotionScores(W)$$

5: *Update emotion score variables.*

$$For\ each\ emotionScore\ variables$$
$$H \leftarrow H + emotion_score(H)$$
$$A \leftarrow A + emotion_score(A)$$
$$S \leftarrow S + emotion_score(S)$$
$$S_P \leftarrow S_P + emotion_score(S_P)$$

6: *Total emotion score E of W .*

$$E \leftarrow H + A + S + S_P$$

7: *Positive emotion score (EP) and negative emotion score (EN).*

$$EP \leftarrow H + S_P \ \| \ EN \leftarrow A + S + S_P \ \| \ EO \leftarrow \frac{H + A + S + S_P}{2}$$

8: *Evaluate* $(PES^{\otimes})$, $(NES^{\otimes})$, $(OES^{\otimes})$ *scores.*

$$(PES^{\otimes}) = \frac{EP}{E} \| (NES^{\otimes}) = \frac{EN}{E} \ \| (OES^{\otimes}) = \frac{EO}{E}$$

Step 4: Apply the EOT-NH Model

The objective of the EOT-NH model is to assign sentiment tags to text, regardless of whether it contains negations. Initially, we establish a decision matrix, as outlined in Table 1, which includes alternatives and criteria. These alternatives are categorized into positive, negative, and neutral, while the criteria consist of context and emotion, computed in Step 1. Subsequently, we compute $(\boldsymbol{AS_i})$ and $(\boldsymbol{AS_i^c})$ following Algorithm 3. The functionality of the EOT-NH model is illustrated in Fig. 1. The proposed EDAS Technique, elaborated in Algorithm 3, employs a 2×2 decision matrix similar to Table 1. Following this, the EDAS algorithms are applied to all types of text, spanning from Step 1 to Step 5, regardless of the presence of negations. If the text includes negations, we proceed through Steps 1 to 5 to rank the alternatives, with the highest-ranked alternative being designated as the final tag for the text. Conversely, if no negations are present, Step 5 triggers the ranking of alternatives. In this case, the alternative with rank 1 is chosen as the final tag. The ranking of alternatives is determined by the highest value of (AS_i^c) in the presence of negations, and by (AS_i) when negations are not present.

Table 2 Context scores evaluated using SWN

Orientation	Context score of *R2*	Rating score of *R2*	Context score of *R1*	Rating score of *R1*
Positive (P)	0.2	0.33	0.89	0.571
Negative (N)	0.8	0.5	0.21	0.143
Neutral (O)	0.1	0.17	0.11	0.43

Step 5: EDAS Technique

We follow Algorithm 1 to calculate the appraisement score, which will be taken as a payoff for the players in the game theory. There are many python[3] libraries available for MCDM technique execution. Algorithm 1 consists of two criteria. An favourable criteria (FC) is a criterion prioritized to achieve the best possible outcome. The criteria are

[3] *Pip install pymcdm.*

deemed non-favourable *(NFC)* when minimum values are desired. We looked at two factors, rating, and context, and found them to be *FC*. Given that not a single criterion meets the definition of *NFC, NFC* must be equal to zero. Subsequently, we place weights on (*W*). Considering that all of the criteria are weighted equally, $W = 0.5$ was selected. Finally, we assess the appraisement score, as displayed in Table 2. In the non-cooperative game theory, players are compensated using the appraisement scores of each review. Figure 1 represents the EOT-NH model framework for sentiment analysis of review. Where the values of AS_i are $0 \leq AS_i \leq 1$. Ranking the alternatives comes after decrementing the (*ASi*) values. The best candidate alternative is the one with the highest (*ASi*) score for text having negation. For text without negation, the deduced tag is the rank 1 of the (AS_i^c) scores.

Algorithm 3 Sentiment tagging using EDAS algorithm

Input: *Positive, negative, and neutral score of rating (RP, RN, RO) and context (CP, CN, CO).*
Output: *Appraisement score of each review.*

1: *Construct a decision matrix having 3 alternatives and 2 criteria* $\left[A_{3\times 2}\right]_{3\times 2}$.

2: *Calculate the Average solution* $Av_j = \frac{\sum_{i=1}^{n} A_{ij}}{n} \quad \forall i \in \{1,2,3\} \;\&\; j \in \{1,2\}$

3: *Calculate* PDA_{ij} *and* $NPDA_{ij}$

$$PDA_{ij} = \begin{cases} \frac{\max(0,(X_{ij} - Av_j)}{Av_j} = \lambda \rightarrow FC \\ \frac{\max(0,(Av_j - X_{ij})}{Av_j} = \wp = 0 \rightarrow NFC \end{cases}, \quad NDA_{ij} = \begin{cases} \frac{\max(0,(Av_j - X_{ij})}{Av_j} = \psi \rightarrow FC \\ \frac{\max(0,(X_{ij} - Av_j)}{Av_j} = \zeta = 0 \rightarrow NFC \end{cases}$$

4: *Calculate the weighted sum* SP_i *and* SN_i, $SP_i = \sum_{j=1}^{m} w_j . PDA_{ij}$ && $SN_i = \sum_{j=1}^{m} w_j . NDA_{ij}$

5: *Calculate* NSP_i *and* NSN_i, $NSP_i = \frac{SP_i}{\max(SP_i)}$ && $NSN_i = 1 - \frac{SN_i}{\max(SN_i)}$

6: *Calculate the Appraisement score,* $AS_i = \alpha_i = \frac{1}{2}(NSP_i + NSN_i)$

8: *Calculate the complement of the Appraisement score,* $AS_i^c = (1 - AS_i)$.

7: *The alternative with the highest rank is the tag to each text with sentiments.*

9: *If the text contains negation rank the alternatives based on step 8.*

10: *If the text content does not contain the negation, proceed to step 6.*

4.3 Numerical demonstration of the EOT-NH model

In this section, we utilized the EOT-NH model to demonstrate sentiment analysis through two illustrative examples. In Illustrative Example 1, sentiment tags were assigned to text without any negations. Similarly, in Illustrative Example 2, we illustrated the process of sentiment tagging in text containing negations. Output of example 1 and 2 is shown in Fig. 2.

4.3.1 Illustrative examples

In this section, we examine text examples that lack negations to elucidate the operational mechanics of algorithms 1, 2, and 3 within such contexts. Specifically, in Illustrative Example 1, where negations are absent, we meticulously adhere to the prescribed steps to achieve the desired outcome. Upon completing steps 2 and 3, we proceed to evaluate the context and emotion scores, as delineated in Table 2. Subsequently, we present the normalized values derived from the decision matrix, as delineated in Table 3. Additionally, Table 4 provides a detailed breakdown of the parameter values. Finally, based on the *Max(Norm(Qi))* values outlined in Table 9, we rank the alternatives. This methodical approach ensures a thorough assessment, ultimately leading to the assignment of the final tag for the

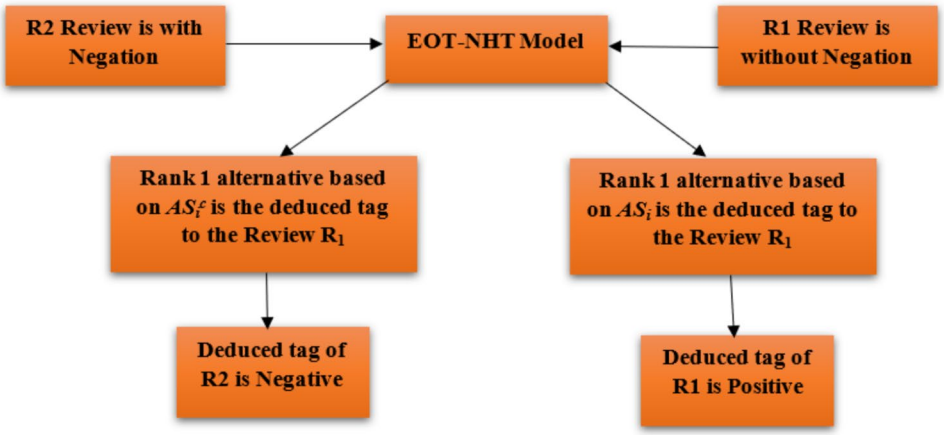

Fig. 2 Output of EOT-NH model

Table 3 Calculate the average of all the criteria

R_2			R_1		
Weightage	0.5	0.5	Weightage	0.5	0.5
	Context	Rating		Context	Rating
Positive (P)	0.2	0.33	Positive (P)	0.89	0.571
Negative (N)	0.8	0.5	Negative (N)	0.21	0.143
Neutral (O)	0.1	0.17	Neutral (O)	0.11	0.43
AV_j	0.366667	0.333333	AV_j	0.403333	0.381333

Table 4 Positive distance from average (PDA)

R_2			R_1		
Weightage	0.5	0.5	Weightage	0.5	0.5
	Context	Rating		Context	Rating
Positive (P)	0.455041	0	Positive (P)	0	0.498688
Negative (N)	0	0.515152	Negative (N)	0.478908	0
Neutral (O)	0.72752	0	Neutral (O)	0.727047	0.128609

reviews, corresponding to the alternative with the highest rank. Figure 2 shows the output of the EOT-NH model.

Illustrative Example 1: Text without Negation

R1: *"I am very satisfied with my Twizzler purchase. I shared these with others and we have all enjoyed them. I will definitely be ordering more."*
"मैं अपनी ट्विज़लर खरीद से बहुत संतुष्ट हूं। मैंने इन्हें दूसरों के साथ साझा किया और हम सभी ने इनका आनंद लिया। मैं निश्चित रूप से और अधिक ऑर्डर करूंगा।"
"main apanee tvizalar khareed se bahut sahamat hoon. mainne any lekhon ke saath saajha kiya aur ham sabhee ne isaka aanand liya. main nishchit roop se aur adhik ordar loonga."

Table 5 Negative distance from average (NDA)

R2			R1		
Weightage	0.5	0.5	Weightage	0.5	0.5
	Context	Rating		Context	Rating
Positive (P)	0.455041	0	Positive (P)	0	0
Negative (N)	0	0	Negative (N)	0.478908	0.623684
Neutral (O)	0.72752	0.484848	Neutral (O)	0.727047	0

To demonstrate the application of Algorithm 2 on texts containing negations, we utilized Illustrative Example 2, illustrate the Text with negations. After executing steps 2 and 3, we assessed the context and emotion scores, as shown in Table 5. Figure 2 visually represents the inferred tags of reviews R_1 and R_2 following all the aforementioned procedures.

Illustrative Example 2: Text with Negation

R2: *"I would never recommend having lunch in that hotel."*
"मैं कभी भी उस होटल में दोपहर का भोजन करने की अनुशंसा नहीं करूंगा।"
"main kabhee bhee us hotal mein dopahar ka bhojan karane kee anushansa nahin karoonga."

Numerical Calculation on R_1 and R_2 is shown in upcoming tables. First, we calculate the context score of English reviews using the SWN shown in Table 2.

Next, we apply the EDAS method (Algorithm 2) to these reviews. Table 3 shows the average of the three alternatives for both criteria (context and rating). Tables 4 and 5 evaluate the positive and negative distance from the average, *PDA* and *NDA*.

Next, we calculate the positive and negative distance from the average of both reviews *(R_2* and *R_1)*. Then we evaluate the weighted sum of positive, negative, and neutral distance using Algorithm 1 shown in Tables 4 and

Table 6 Weighted sum of (PDA)

R_2				R_1			
Weightage	0.5	0.5		Weightage	0.5	0.5	
	Context	Rating	SPi		Context	Rating	SPi
Positive (P)	0.22752	0	0.228	Positive (P)	0	0.249344	0.249
Negative (N)	0	0.2578	0.258	Negative (N)	0.239454	0	0.239
Neutral (O)	0.36376	0	0.364	Neutral (O)	0.363524	0.064304	0.428

Table 7 Weighted sum of (NDA)

R_2				R_1			
Weightage	0.5	0.5		Weightage	0.5	0.5	
	Context	Rating	SNi		Context	Rating	SNi
Positive (P)	0.2275	0	0.228	Positive (P)	0	0	0.000
Negative (N)	0	0	0.000	Negative (N)	0.239454	0.311842	0.551
Neutral (O)	0.3637	0.24242	0.606	Neutral (O)	0.363524	0	0.364

Table 8 Standard values of R_1 *and* R_2

	SP_i		SN_i		NSP_i		NSN_i		ASi	
	R_2	R_1	R_2	R_1	R_2	R_1	R_2	R_1	R_2	R_1
Positive *(P)*	0.23	0.249	0.23	0	0.626	0.582	0.624	1	0.625	0.791
Negative (N)	0.26	0.239	0	0.551	0.7088	0.558	1	0	0.854	0.279
Neutral (O)	0.36	0.428	0.61	0.364	1	1	0	0.339	0.500	0.670

Table 9 Appraisement score of both reviews R_1 and R_2

R_2		R_1	
	Appraisement score (AS_i)		Appraisement score (AS_i^c)
Positive (P)	0.625	Positive (P)	0.791
Negative (N)	0.854	Negative (N)	0.279
Neutral (O)	0.500	Neutral (O)	0.670

5 of both the players (R_2 *and* R_1). Tables 6 and 7 shows the weighted values of *PDA* and *NDA* for all the selected alternatives. Then standard values of NSP_i and NSN_i is evaluated in Table 8. In the end, we calculate the AS_i for all the selected alternatives, as shown in Table 9 for both the players (R_2 and R_1).

5 Result and discussion

In this section, we present a comprehensive analysis of dataset statistics across various English text domains and extend this investigation to a dataset in the Hindi language. This extension demonstrates the linguistic versatility and universality of our proposed model. We assess the robustness of the model across diverse English language domains by utilizing a comprehensive set of evaluation metrics, including accuracy, F1-score, precision, recall, and the Matthews Correlation Coefficient (MCC). These metrics were benchmarked against state-of-the-art models to establish the relative effectiveness of our approach. This consistency was critical for a reliable comparison of performance metrics. Our evaluation included both macro and micro averages for accuracy, precision, and recall, providing a holistic view of model performance at both the aggregate and individual data point levels. Additionally, we conducted a statistical significance analysis to rigorously assess the superiority of our model in comparison to existing techniques. This analysis offered critical insights into the model's ability to outperform state-of-the-art approaches, highlighting its effectiveness and potential applicability in broader contexts. In the discussion section, we also examined the error rates of various unsupervised models, offering a detailed exploration of their inherent limitations and challenges. Furthermore, we analyzed the computational complexity of our EOT-NH model, including considerations of runtime efficiency and resource requirements,

providing a clear understanding of its practicality in real-world applications.

5.1 Datasets

The proposed algorithm was executed on distinct datasets comprising English review comments (Punetha and Jain 2023a) and corresponding ratings. We also collect the data from the SemEval 2023 (Punetha and Jain 2023b) and Stanford Treebank reviews (Punetha and Jain 2023b). The statistical information of the utilized datasets is presented in Table 10.

5.2 Comparison of the text with the negation of English text

This section presents a comparative analysis of the EOT-NH model alongside four other models developed for managing negations in textual data. SentiNeg (Savanur and Sumathi 2023) model, the model by the author (Gupta and Joshi 2021), MiMuSA (Wang et al. 2023b), and NEGVOT (Punetha and Jain 2023b). Our evaluation is based on three different datasets, and the results are presented in Figs. 3, 4, and 5.

Gupta et al. employed a feature-based methodology for sentiment analysis on Twitter, with a specific focus on mitigating negations. However, their model showed significant performance deficits across various datasets. Notably, on the Amazon Product review dataset, Gupta et al.'s model lagged behind the NEGVOT model by 0.19 in terms of accuracy. Similarly, on both the SemEval2013 and Stanford review datasets, their model achieved accuracies of 0.56 and 0.48, respectively, trailing the NEGVOT model's performance. These findings consistently highlight the underperformance of Gupta et al.'s model compared to the NEGVOT model, emphasizing the latter's proficiency in negation handling within textual data.

SentiNeg, a model targeting negations at the sentence level, achieved notable accuracy, reaching 0.81 on the SemEval2013 dataset. However, it still fell short of the NEGVOT model by 0.04. Similarly, its highest MCC score on SemEval2013 was 0.68, indicating a deficit of 0.13 compared to

Table 10 Data statistics

Data set	Language	No. of reviews	Positive	Negative	Neutral
IMBD movies review[a]	English	3000	1000	1000	1000
Hotel reviews(Sarkar 2020)	Hindi	3000	1000	1000	1000
Electronic reviews (Sarkar 2020)	Hindi	3000	1000	1000	1000
SemEval 2023 reviews[b]	English	3000	1000	1000	1000
Stanford Treebank reviews[c]	English	3000	1000	1000	1000

[a]https://www.kaggle.com/datasets/lakshmi25npathi/imdb-dataset-of-50k-movie-reviews

[b]https://www.semeval.github.io/SemEval2023/tasks.html

[c]https://www.kaggle.com/datasets/atulanandjha/stanford-sentiment-treebank-v2-sst2

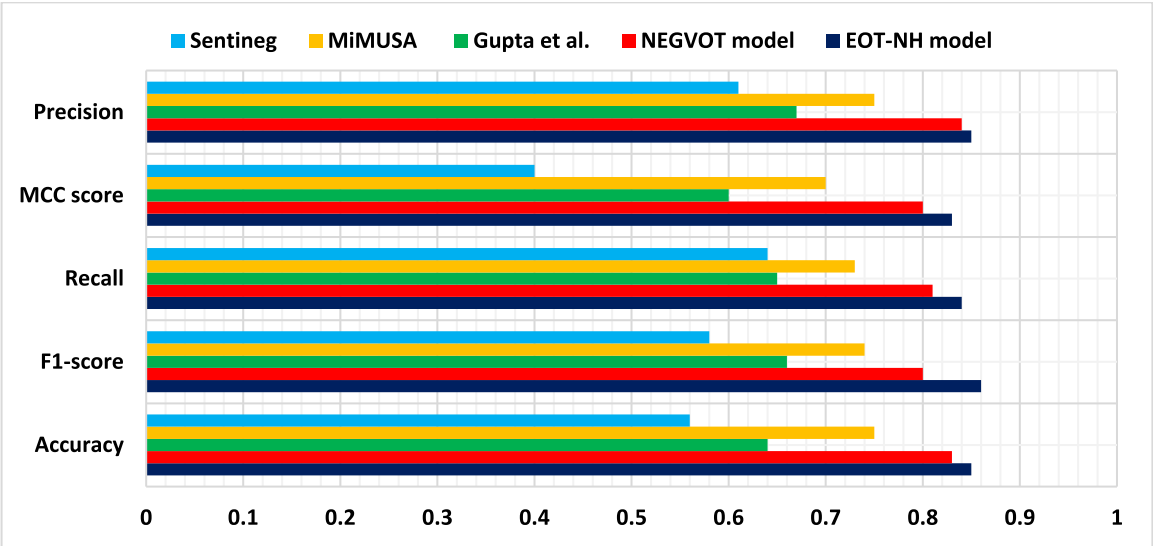

Fig. 3 Comparison of the EOT-NH model on Amazon reviews dataset

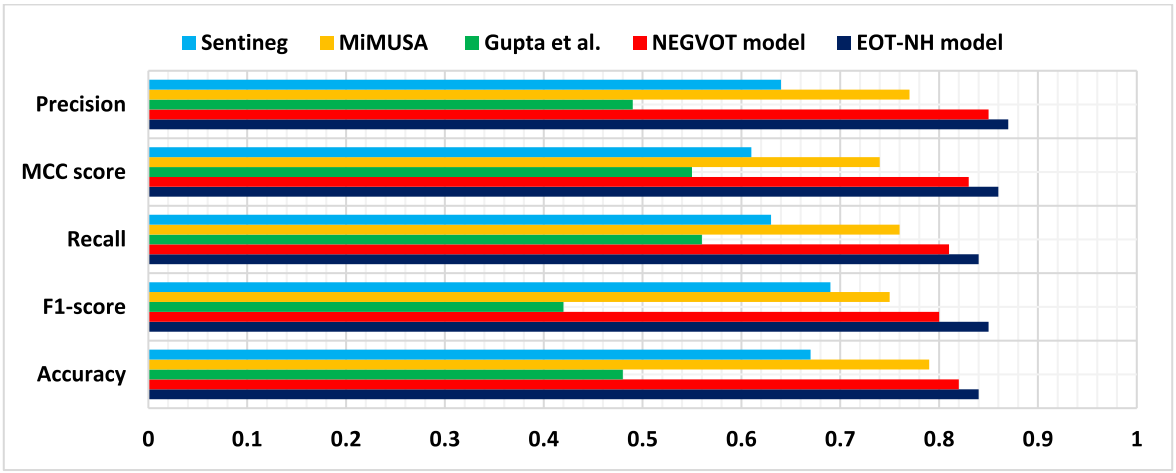

Fig. 4 Comparison of the EOT-NH model on the SemEval2023 reviews dataset

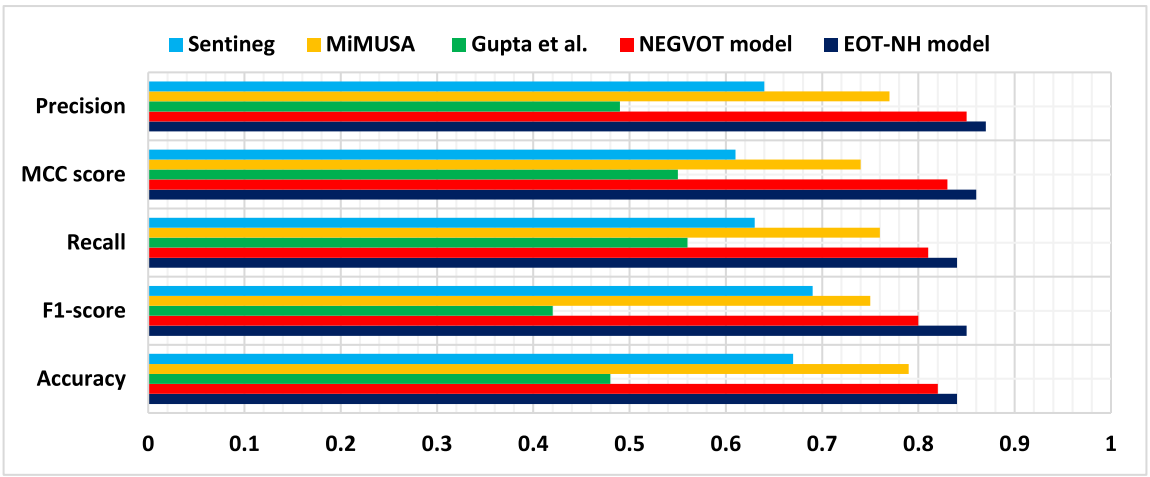

Fig. 5 Comparison of the EOT-NH model on Stanford sentiment Treebank dataset

the NEGVOT model's score. These outcomes underscore the NEGVOT model's superior efficacy in negation handling compared to SentiNeg.

The MiMuSA model aimed to address negation handling by emulating human language comprehension processes through a modular structure. While achieving a high accuracy of approximately 0.79 on the Stanford reviews dataset, MiMuSA still lagged behind the NEGVOT model by 0.03. On the SemEval2013 dataset, MiMuSA attained a precision of 0.75, trailing the NEGVOT model's precision by 0.07. Evaluation metrics consistently demonstrated lower performance for the MiMuSA model compared to the NEGVOT model, indicating the latter's superiority in negation handling within sentiment analysis tasks.

Despite the NEGVOT model's notable performance in negation handling, grounded in Multi-Criteria Decision Making (MCDM) principles, it had certain limitations. However, our current EOT-NH model represents a significant advancement, surpassing NEGVOT in terms of accuracy. The EOT-NH model achieves superior accuracy compared to existing models, reaching a peak accuracy of 87% on the SemEval dataset. Additionally, the EOT-NH model demonstrates a commendable accuracy of approximately 0.85 on Amazon reviews, with an F1-score of 0.86. These results highlight the advantages of the EOT-NH model over existing approaches in effectively handling negations within sentiment analysis tasks.

5.3 Performance evaluation on reviews of multiple domains on text without negation

In this comparative analysis, we consider four datasets comprising customer reviews from multiple domains, encompassing both English and Hindi languages. We juxtapose the

performance of the EOT-NH model against several supervised and unsupervised models.

5.3.1 Comparison on IMBD movie reviews

Vashishtha and Susan (2021) introduced an unsupervised sentiment classification system utilizing the SentiWordNet lexicon and fuzzy linguistic hedges. Their method comprehensively analyzes phrases, computes sentiment scores (senti-scores), and determines polarity by combining unigrams, bigrams, and trigrams on the same scale. Despite achieving the highest reported accuracy of 69% and an F1-score of 66%, this approach may be limited by its reliance on lexicon-based sentiment analysis, which may not capture contextual nuances effectively. In another study, SASC (Sentiment Analysis Based on Sentiment Clustering) was proposed, achieving an accuracy of 75.42% (Wang et al. 2023a). While this approach demonstrates improved performance compared to lexicon-based methods, its effectiveness may be hindered by its dependency on clustering techniques, which may struggle with complex and noisy data distributions. Additionally, a computationally efficient integrated deep learning paradigm, BERT-MultiLayered Convolutional Neural Network (B-MLCNN) (Atandoh et al. 2023), was introduced for sentiment classification. B-MLCNN treats the entire textual review as a single document and achieves an accuracy of approximately 81.2% for IMDB movie reviews. Despite its computational efficiency, B-MLCNN may face challenges in handling long textual sequences and may not effectively capture fine-grained sentiment nuances present in longer reviews. Moreover, in the BG-ST model (Punetha and Jain 2023c), an accuracy of 0.823 and an F1-score of 0.85 were reported. However, this model's applicability may be limited by its reliance on specific feature representations and its potential sensitivity to dataset characteristics, affecting its generalizability across diverse datasets. Comparatively, the EOT-NH approach outperforms existing methods in all evaluated parameters. By integrating multiple methodologies, including MCDM and game theory, EOT-NH addresses some of the limitations observed in the compared models, resulting in enhanced accuracy and robustness in sentiment analysis tasks and numeric values are given in Fig. 6.

A Z-test was conducted to compare the proportions of accurately classified reviews between two independent samples: hotel reviews and movie reviews. The hotel sample ($n1 = 1000$) had a classification accuracy of 91%, while the movie sample ($n2 = 500$) had an accuracy of 89.6%. The test was two-tailed, assessing the null hypothesis (H_0) that there is no difference between the two population proportions. The analysis showed that the null hypothesis was not rejected at the 5% significance level, indicating no statistically significant difference between the classification accuracies of the two datasets. This confirms the model's consistent performance across both samples.

6 Discussion

In this section, we analyze several aspects of this study. Initially, we conducted an ablation study to assess the impact of individual components on the overall performance. Subsequently, we delve into the significance of the study, elucidating its contributions to the existing literature and potential implications for future research. Lastly, we explore the challenges encountered during the course of the study, addressing limitations and areas for further investigation.

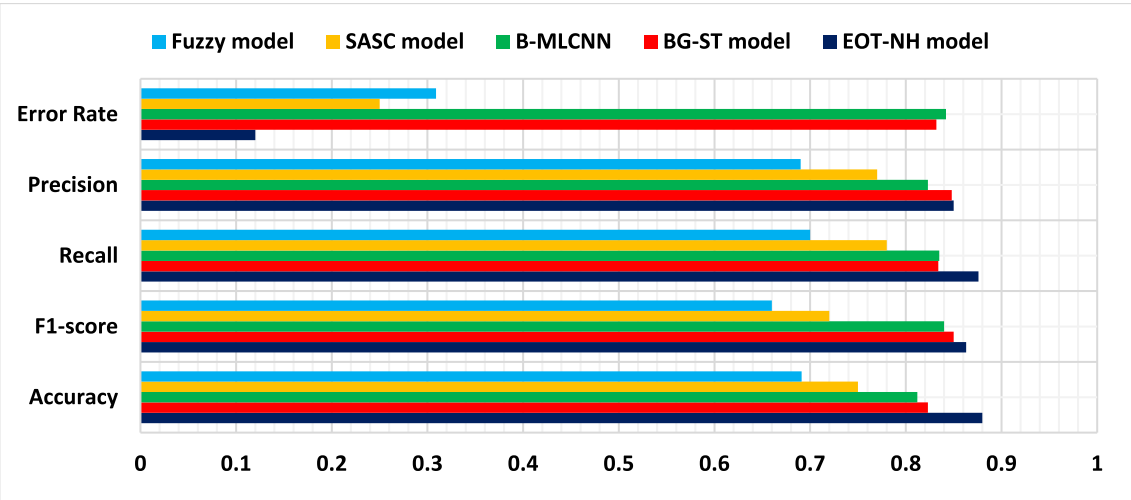

Fig. 6 Performance evaluation on IMBD movie reviews dataset

6.1 Ablation study

The ablation study offered significant insights into the operational dynamics of the proposed framework, aiding researchers in comprehending the relative significance of its various components and in refining the model for optimal performance. This subsection focuses on two critical components of the EOT-NH model, namely, the MCDM technique and the Game theory approach. Specifically, the study assesses the importance of two features within the MCDM component. This involves substituting the equivalent with alternative weighting criteria for each criterion and replacing the EDAS MCDM technique with other MCDM methods.

6.2 Weights of each criterion

The EOT-NH model comprises two integral components: an EDAS-MCDM component, and a game theory component. In our study, we investigate the impact of varying criteria weights on evaluation metrics across four distinct weighting scenarios as illustrated in Table 11. In the first scenario, all criteria are assigned equivalent weights, each set to 0.3333. This uniform distribution aims to provide a baseline comparison for subsequent weighting methods. Subsequently, in the second scenario, we employ the Criteria Importance Through Intercriteria Correlation (CRITIC) method to ascertain weights for each criterion. Following this, the Shannon entropy method is utilized in the third scenario to determine criterion weights, leveraging information theory principles to quantify uncertainty and derive optimal weight distributions. Lastly, the fourth scenario involves randomly assigning weights to the criteria. Evaluation metrics, detailed in Table 12, serve to gauge the efficacy of these weighting methodologies. Notably, the highest accuracy score of 0.91 is attained when equal weights are allocated to all criteria. Conversely, the lowest accuracy score of 0.7 is observed when random weights are applied to the criteria. An examination of the discernible patterns in various evaluation metrics underscores the significance of judiciously selecting weighting methodologies to optimize decision-making outcomes within the EOT-NH framework.

Table 11 Weighting the three different criteria

Different cases	Criteria 1 = context	Criteria 2 = emotion
Case 1: when all the criteria have equivalent weight	0.3333	0.3333
Case 2: CRITIC weighting method	0.418	0.0897
Case 3: Shannon entropy method	0.214	0.584
Case 4: random weighting method	0.512	0.236

Table 12 Performance of the EOT-NH model on different weighting criteria

	Accuracy	F1-score	Error rate	Precision
Case 1	0.91	0.87	0.2	0.9000
Case 2	0.72	0.73	0.34	0.76
Case 3	0.81	0.82	0.23	0.798
Case 4	0.700	0.712	0.698	0.721

6.3 Computational power

We take various MCDM Techniques which are parallel to the EDAS like ELECTRE, PROMETHEE (Punetha and Jain 2024), and AHP, and run the algorithm of the given framework. Table 13 shows the complexity of various MCDM Techniques. This shows that PROMETHEE, ELECTRE, and AHP require more time to run this complete framework than the EDAS method. The higher runtime observed for PROMETHEE, ELECTRE, and AHP compared to the EDAS method in the given framework can be attributed to several key factors. Firstly, these methods involve inherently complex computational procedures due to their reliance on multiple steps such as pairwise comparisons, aggregation of preferences, and computation of priority or ranking scores. In particular, PROMETHEE and ELECTRE require a lot of pairwise comparisons between options based on a lot of different criteria, which makes the computations more difficult. Additionally, AHP requires pairwise comparisons not only between alternatives but also between criteria, leading to a cubic increase in time complexity concerning the number of criteria. Lastly, the efficiency of implementation plays a crucial role, as suboptimal implementations or inefficient algorithms can further exacerbate runtime differences between these methods and the EDAS approach. Therefore, while PROMETHEE, ELECTRE, and AHP offer sophisticated decision-making capabilities, their computational complexity makes them more time-consuming to execute compared to the simpler distance-based calculations employed in the EDAS method as illustrated in Table 13.

Table 13 Computational power in various MCDM techniques

Sr. no	MCDM techniques	Time complexity	Space complexity
1	PROMETHEE	$O(n^2 \times m)$	$O(n^2 \times m)$
2	ELECTRE	$O(n^2 \times m)$	$O(n^2 \times m)$
3	AHP	$O(n^3)$	$O(n^3)$
4	EDAS	$O(n + m)$	$O(n + m)$

Table 14 Examples where the EOT-NH model failed

Sr. no	Text	Actual	Sentiment tag from EOT-NH
1	"Took longer than expected to arrive, but the quality of the product is excellent!"	Positive	Negative
2	"Had a few minor issues at first, but customer service was incredibly helpful and resolved them promptly!" 😝 😒	Negative	Positive
3	"The color was slightly off from what was shown in the pictures, but I ended up liking it even more!"	Positive	Negative
4	"The assembly instructions were unclear, but once assembled, the furniture looks fantastic!"	Positive	NULL

6.4 Challenges of the EOT-NH model

The EOT-NH model incorporates EDAS MCDM techniques. EDAS, being a multi-criteria decision-making (MCDM) technique, involves criteria and alternatives. The weight assigned to context is $w_1 = 0.6$, while the weight for emotion is $w_2 = 0.4$. For the EOT-NH model to function accurately, the essential condition is that $w_1 > w_2$. The proposed EOT-NH model fails when $w_1 = w_2 = 0.5$ and $w_1 > w_2$. Another limitation, highlighted in Table 14, includes instances where the EOT-NH model incorrectly identifies the sentiment tag. In Example 1, the text contains both positive and negative elements, with an overall positive sentiment. However, the EOT-NH model incorrectly classifies it as negative. Example 2 involves sarcasm and emojis, which the EOT-NH model fails to recognize. Example 3 contains negation and bilingual words, leading to an overall positive sentiment, but the model tags it as negative. Example 4 includes hashtags, which the EOT-NH model does not identify correctly as illustrated in Table 14.

7 Conclusion

This study introduces the innovative EOT-GT model, based on game theory, designed for sentence-level sentiment analysis in the field of Natural Language Processing. The model takes an unsupervised approach, offering a fresh perspective on sentiment analysis. Its performance is tested across English and Hindi datasets from various domains, including movie reviews, hotel reviews, electronic device reviews, and IMDB reviews. Comparative analysis shows the model's effectiveness against both unsupervised and supervised techniques. A key feature of the EOT-GT model is its ability to efficiently handle negation, making it robust across text with or without negation. Statistical cross-validation using Z-tests further demonstrates the model's strong potential for sentiment classification. Future research aims to improve the model's accuracy by integrating techniques from various lexicon resources, with a focus on challenges such as aspect-based sentiment analysis, sarcasm, irony detection, and multiclass classification. Additionally, handling multilingual datasets and refining query expansion and word sense disambiguation are areas slated for development. The EOT-GT model's promising results lay the groundwork for further advancements in NLP tasks.

Author contributions All authors contributed equally to this study.

Funding No funding was received to assist with the preparation of this manuscript.

Code availability The code generated during the current study are available from the corresponding author on reasonable request.

Dataset It will be available on reasonable request.

Declarations

Conflict of interest The authors state that they have no known competing financial interests or personal ties that could have appeared to affect the work reported in this study.

Human and animal rights No Humans or Animals were harmed in any way.

Open Access This article is licensed under a Creative Commons Attribution-NonCommercial-NoDerivatives 4.0 International License, which permits any non-commercial use, sharing, distribution and reproduction in any medium or format, as long as you give appropriate credit to the original author(s) and the source, provide a link to the Creative Commons licence, and indicate if you modified the licensed material. You do not have permission under this licence to share adapted material derived from this article or parts of it. The images or other third party material in this article are included in the article's Creative Commons licence, unless indicated otherwise in a credit line to the material. If material is not included in the article's Creative Commons licence and your intended use is not permitted by statutory regulation or exceeds the permitted use, you will need to obtain permission directly from the

copyright holder. To view a copy of this licence, visit http://creativecommons.org/licenses/by-nc-nd/4.0/.

References

Amalia R, Bijaksana MA, Darmantoro D (2018) Negation handling in sentiment classification using rule-based adapted from Indonesian language syntactic for Indonesian text in Twitter. J Phys: Conf Ser 971:012039. https://doi.org/10.1088/1742-6596/971/1/012039

Atandoh P, Zhang F, Adu-Gyamfi D et al (2023) Integrated deep learning paradigm for document-based sentiment analysis. J King Saud Univ—Comput Inf Sci 35:101578. https://doi.org/10.1016/J.JKSUCI.2023.101578

Esuli A, Sebastiani F (2006) SENTIWORDNET: A publicly available lexical resource for opinion mining. In: Proceedings of the 5th International Conference on Language Resources and Evaluation, LREC 2006, pp.417–422

Ghadikolaei AS, Esbouei SK, Antuchevičienė J (2014) Applying fuzzy MCDM for financial performance evaluation of Iranian companies. Technol Econ Dev Econ 20:274–291. https://doi.org/10.3846/20294913.2014.913274

Gupta I, Joshi N (2021) Feature-based twitter sentiment analysis with improved negation handling. IEEE Trans Comput Soc Syst 8:917–927. https://doi.org/10.1109/TCSS.2021.3069413

Jain D, Kumar A, Garg G (2020) Sarcasm detection in mash-up language using soft-attention based bi-directional LSTM and feature-rich CNN. Appl Soft Comput J 91:106198. https://doi.org/10.1016/J.ASOC.2020.106198

Lal U, Kamath P (2022) Effective negation handling approach for sentiment classification using synsets in the WordNet lexical database. In: 2022 1st International Conference on Electrical, Electronics, Information and Communication Technologies, ICEEICT 2022. https://doi.org/10.1109/ICEEICT53079.2022.9768641

Li J, Li G, Liu M et al (2022) A novel text-based framework for forecasting agricultural futures using massive online news headlines. Int J Forecast 38:35–50. https://doi.org/10.1016/J.IJFORECAST.2020.02.002

Limsopatham N, Macdonald C, McCreadie R, Ounis I (2012) Exploiting term dependence while handling negation in medical search. In: SIGIR'12—Proceedings of the International ACM SIGIR Conference on Research and Development in Information Retrieval, pp. 1065–1066. https://doi.org/10.1145/2348283.2348471

Ljajić A, Marovac U (2019) Improving sentiment analysis for twitter data by handling negation rules in the Serbian language. Comput Sci Inf Syst 16:289–311. https://doi.org/10.2298/CSIS180122013L

Mao R, Liu Q, He K et al (2022) The biases of pre-trained language models: an empirical study on prompt-based sentiment analysis and emotion detection. IEEE Trans Affect Comput. https://doi.org/10.1109/TAFFC.2022.3204972

Mao R, Li X (2021) Bridging towers of multi-task learning with a gating mechanism for aspect-based sentiment analysis and sequential metaphor identification. In: 35th AAAI Conference on Artificial Intelligence, AAAI 2021, vol. 15, pp. 13534–13542. https://doi.org/10.1609/aaai.v35i15.17596

Punetha N, Jain G (2023a) Game theory and MCDM-based unsupervised sentiment analysis of restaurant reviews. Appl Intell 53:20152–20173. https://doi.org/10.1007/s10489-023-04471-1

Punetha N, Jain G (2023b) Optimizing sentiment analysis: a cognitive approach with negation handling via mathematical modelling. Cognit Comput 16:624–640. https://doi.org/10.1007/s12559-023-10227-3

Punetha N, Jain G (2023c) Bayesian game model based unsupervised sentiment analysis of product reviews. Expert Syst Appl 214:119128. https://doi.org/10.1016/j.eswa.2022.119128

Punetha N, Jain G (2024) Recommendation framework for products using optimization algorithms. Nat Acad Sci Lett 1:1–4. https://doi.org/10.1007/S40009-024-01401-8

Sarkar K (2020) Heterogeneous classifier ensemble for sentiment analysis of Bengali and Hindi tweets. In: Sadhana—Academy Proceedings in Engineering Sciences, vol. 45. https://doi.org/10.1007/s12046-020-01424-z

Savanur SR, Sumathi R (2023) SentiNeg: algorithm to process negations at sentence level in sentiment analysis. Int J Softw Innov 11:1–27. https://doi.org/10.4018/IJSI.315741

Singh PK, Paul S (2021) Deep learning approach for negation handling in sentiment analysis. IEEE Access 9:102579–102592. https://doi.org/10.1109/ACCESS.2021.3095412

Taboada M, Brooke J, Tofiloski M et al (2011) Lexicon-based methods for sentiment analysis. Comput Linguist 37:267–307. https://doi.org/10.1162/COLI_A_00049

Vashishtha S, Susan S (2021) Highlighting keyphrases using sentiscoring and fuzzy entropy for unsupervised sentiment analysis. Exp Syst Appl 169:114323

Wang Y, Han H, He X, Zhai R (2023a) A two-stage unsupervised sentiment analysis method. Multime Tools Appl. https://doi.org/10.1007/s11042-023-14864-6

Wang Z, Hu Z, Ho SB et al (2023b) MiMuSA—mimicking human language understanding for fine-grained multi-class sentiment analysis. Neural Comput Appl. https://doi.org/10.1007/s00521-023-08576-z

Xia R, Xu F, Zong C et al (2015) Dual sentiment analysis: considering two sides of one review. IEEE Trans Knowl Data Eng 27:2120–2133. https://doi.org/10.1109/TKDE.2015.2407371

Xia R, Xu F, Yu J et al (2016) Polarity shift detection, elimination and ensemble: a three-stage model for document-level sentiment analysis. Inf Process Manage 52:36–45. https://doi.org/10.1016/J.IPM.2015.04.003

Publisher's Note Springer Nature remains neutral with regard to jurisdictional claims in published maps and institutional affiliations.

Eco. Env. & Cons. 30 (July Suppl. Issue) : 2024; pp. (S261-S266)
Copyright@ EM International
ISSN 0971–765X

DOI No.: http://doi.org/10.53550/EEC.2024.v30i04s.047

Analysing the long run relationship between CO_2 emissions and Energy use of United Kingdom

Akanksha Singh*[1] and Nand Kumar[2]

[1,2]Department of Humanities, Delhi Technological University, New Delhi 110 042, India

(Received 28 November, 2023; Accepted 17 January, 2024)

ABSTRACT

In this study, the time series data of the United Kingdom from 1965 to 2021 for energy usage, total reserves, manufacturing, GDP and total carbon emission have been examined using autoregressive distribution lag (ARDL) model. The results revealed that energy usage, manufacturing and GDP have a positive relation with CO_2 emission both in the short run and long run raising environmental concerns on the contrary only total reserves have a negative relation in the short and long run. United Kingdom increasing energy efficiency have been a top priority in the recent era, in order to achieve the target of net zero carbon emission by 2050, government need to promote policies for energy mix which would increase the usage of other renewable energy as the challenges remain for manufacturing and transportation industry because the overall emission from these sector remains largely unchanged despite advancements in fuel efficiency because the results indicates that a percentage increase in energy usage increase the CO_2 emission by 0.23% whereas 1% increase in manufacturing leads to 0.25% increase in the CO_2 emission.

Key words: *ARDL, CO2 emission, GDP, Energy mix, SDGs*

Introduction

Over time, the UK has significantly reduced its carbon dioxide (CO_2) emissions as shown in Fig. 1. Between the early 1990s and 2019, emissions had decreased by about 43%, largely as a result of a move away from coal-based energy production, improved energy efficiency, and the expansion of renewable energy sources. The energy industry has significantly reduced its emissions. This reduction was greatly aided by the closure of coal-fired power stations and their replacement with natural gas and renewable energy sources like wind and solar. A challenge has been the transportation industry. The overall emissions from this sector remained largely unchanged because of a rise in road traffic, despite advancements in fuel efficiency and the use of electric vehicles. The United Kingdom government has established challenging goals for emissions reduction. The goal is to achieve net-zero emissions by 2050, which is legally required. The UK has introduced a number of policies, including carbon pricing and subsidies for renewable energy, to achieve this.

The United Kingdom's energy mix has evolved over time, Fig. 2 shows the total energy usage of UK.

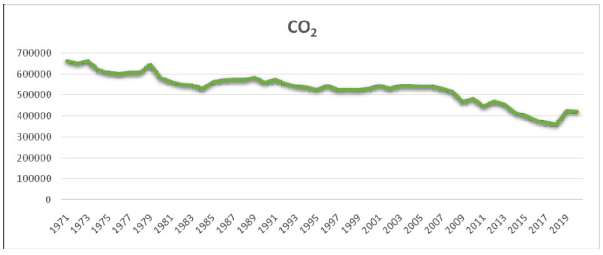

Fig. 1 CO_2 emission

While natural gas, nuclear power, and renewable energy sources have gained popularity, the amount of coal used to generate electricity has significantly decreased. The UK is now a global leader in offshore wind energy because to the significant increase of wind power in particular. In the UK, increasing energy efficiency has been a top goal. This covers metrics for building, appliance, and industrial process energy efficiency. To promote more energy-efficient housing, initiatives like the Energy Performance Certificate (EPC) have been introduced. Energy production has become more decentralized in the UK, where more homes and businesses are using solar energy and small-scale wind power to generate their own electricity. This trend to decentralized energy production has helped to cut down on transmission losses. Although there have been oscillations in energy use in the household and industrial sectors, there has been an overall trend towards increased energy efficiency. Government incentives and policies have contributed to the promotion of sustainable practices and energy efficiency.

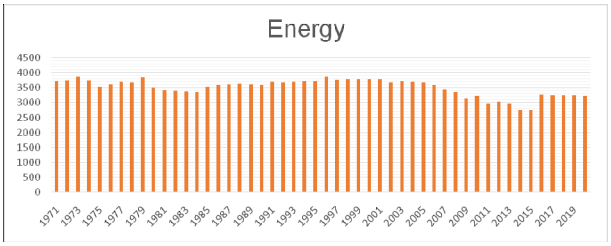

Fig. 2. Energy Usage

Emissions reduction in the transport industry is still a difficult task. It will take significant infrastructural investments to make the switch to electric vehicles and lessen reliance on fossil fuels.It will take time and effort to increase the housing stock's energy efficiency in the UK, particularly renovating older structures. In this study, we looked at the connections between CO_2 emissions, economic expansion (GDP, manufacturing value), total reserves and energy use. A multivariate model is used to investigate the causation, short and long sighted interdependence between CO_2 emission, economic growth (GDP, Manufacturing), total reserves and energy usage. The goal of the study is to identify the factors that are beneficial to environment sustainability so that we can advance in a more sustainable way.

Literature Review

A significant number of studies show that, despite the fact that economic growth does result in an increase in energy consumption, carbon emissions are not permanently reduced as a result. Some scholars use econometric models to look at the short- and long-term dynamic interactions between factors like carbon emissions, financial growth, suburbanization, and international trade in order to offer direction for the sustainable development of a region or a nation. According to the environmental Kuznets curve (EKC) theory, there is an inverse U-shaped relationship between environmental pollutants like CO_2 and GDP (Jebli *et al*., 2016; Leal and Marques, 2020; Rafiq *et al.,* 2016; Dong *et al*., 2017; Shahbaz *et al.,* 2019).

Time series data for the three major nations of the USA, France, and Japan were studied from 1965 to 2020 using the Fourier ARDL, Fourier bootstrap Toda-Yamamoto, and wavelet coherence methods. According to this analysis, France crossed the breakeven threshold in 1978, demonstrating that CO_2 levels decreased as nuclear energy use increased (Singh *et al*., 2023). The South Asian EKC hypothesis was also confirmed, demonstrating the beneficial effects of LPG use on the environment (Murshed, 2021).

GDP and CO2 emissions are inversely correlated, according to research on 31 developing countries with subpar clean energy development Aye *et al.* (2017). While few studies (Teng *et al*., 2021; Ahmed *et al*., 2019; Ahmed *et al.,* 2020; Odugbesan and Adebayo, 2020; Pablo *et al.,* 2016; Wasti *et al*., 2020) found a positive link between GDP and CO2 emissions. The most modern econometric approaches, like as ARDL, Wavelet coherence, and Fourier analysis, have been used in several research to analyse the causal relationship and unidirectional connectivity between energy, GDP, and CO_2 emissions. Yang and Zhao (2014), Adebayo *et al.,* 2020; Adebayo *et al*., 2021; Khobai and Roux (2017), Wu *et al*., 2022, Adebayo, 2020; Gao and Zhang, 2021; Faisa *et al.,* 2016, Jafari *et al*., 2015, Wang *et al*., 2019; Aydoan and Vardar, 2020; Kirikkaleli *et al*., 2020; Kirikkaleli and Adebayo. 2021.

The study found that using biofuels instead of fossil fuels reduces greenhouse gas emissions by 70%. The economic potential of biofuels was studied between 2001 and 2022 using bibliometric analysis. The research revealed that while the US, China, In-

dia, and Europe have the largest biofuel markets, many other developed and developing countries still have smaller and less developed markets for sustainable biofuels (Hasan and Coworkers, 2023).

Methodology

To test our hypothesis and accomplish our objective, we used secondary time series data that we obtained from the World Bank Development Indicators (WDI). Equation 1 was created to analyse the relationship between CO_2 emissions, GDP, energy use (EU), manufacturing value (MV), and total reserves (TR) in the context of the United Kingdom from 1965 to 2021.

$$\ln CO_2 = f(\text{lnGDP, lnEU, lnMV, lnTR}) \quad \ldots (1)$$

Here, ln is the natural log in the equation above, and Table 1 defines the variable description has definitions of the variables.

$$\Delta \ln CO2_t = a_0 + \sum_{i=1}^{n_1} a_{1i} \Delta \ln GDP_{t-i} + \sum_{i=1}^{n_1} a_{2i} \Delta \ln EU_{t-i} + \sum_{i=1}^{n2} a_{3i} \Delta MV_{t-i} + \sum_{i=1}^{n3} a_{4i} \Delta \ln TR_{t-i} + \beta_1 \ln GDP_{t-1} + \beta_2 \ln EU_{t-1} + \beta_3 \ln MV_{t-1} + \beta_4 \ln TR_{t-1} + \mu_t \ldots\ldots(2)$$

The letters a1 to a3 in the equation above reflect the short-run relationship, b1 to b3 represent the long-run relationship, and a0 the drift component. While ni is the optimal lag and t is the error term.

Variables	I(0) t-stats	I(0) p-value	I(1) t-stats	I(1) p-value

$$\Delta \ln CO2_t = \beta_0 + \sum_{i=1}^{n_1} \beta_{1i} \Delta \ln GDP_{t-i} + \sum_{i=1}^{n2} \beta_{2i} \Delta \ln EU_{t-i} + \sum_{i=1}^{n3} \beta_{3i} \Delta \ln MV_{t-i} + \sum_{i=1}^{n3} \beta_{4i} \Delta \ln TR_{t-i} + \theta ECM_{t-1} + \mu_t \ldots\ldots\ldots(3)$$

In the equation above, the letters a1 to a 4 stand for the short-run relationship, b1 to b4 for the long-run connection, and a0 for the drift element. While t is the error term and ni is the ideal lag.

Results and Discussion

The study is conducted on time series data for 57 years so ADF unit root test was applied to check the stationarity of the variables, the results indicated that the variables were stationary at first difference, ARDL model is applicable if variables are stationary at level or first difference or a mixture of both and as the variables were stationary at first difference ARDL model was well suitable for this study. The table below illustrates the results of ADF unit root test.

Table 1. ADF unit root test

CO2	-2.897	0.1713	-8.379	0.0018***
GDP	-1.591	0.78	-7.015	0.002***
EU	-2.703	0.239	-7.567	0.018***
MV	-1.488	0.822	-7.525	0.003***
TR	-2.830	0.1931	-8.618	0.0098***

***, ** &*denotes 1%, 5% & 10% significance level.

The long-term relationship between the dependent and independent variables is assessed using the Auto Regressive Distributed Lag bond (ARDL) bound test. The upper bound and lower bound are two critical variables that the test displays. The lower bound assumes that all the variables are equal, while the upper limit assumes that there is a first difference for all of them in this situation.

The null hypothesis is rejected and co-integration is shown to exist if the upper limit value is less than the F statistic. ARDL bound test is used to check the cointegration between the variables, the finding reveals that the dependent variable CO_2 and the independent variables GDP, manufacturing, energy usage and total reserves are cointegrated as the F statistic is 4.26 which is greater than 3.49 the upper bound and 2.56 the lower bound at 5% significance level. Table 2 illustrates the results of the ARDL bound test.

Table 2. ARDL bound test

Variables	F-Statistics		
F (CO_2, GDP, EU, MV, TR)	4.264781**		
Critical Value	1%	5%	10%
Lower Bound	3.26	2.56	2.2
Upper Bound	4.47	3.49	3.09

***, ** &*denotes 1%, 5% & 10% significance level.

Table 3 The results of the ARDL short run estimates are indicated in Table 4 indicating that energy usage and GDP is significant at 1% and is positively correlated with CO_2 emission, a 1% increase in the GDP will increase CO_2 by 1.12% whereas one percentage increase in energy usage will increase the CO_2 emission by 0.23% on the other hand manufacturing also has a positive relation and is significant at 10%, in all the independent variable only total reserves is negatively correlated with CO_2 emission indicating that a percentage increase in the reserves leads to 0.04 reduction in the CO_2 emission.

Table 4 displays the results of ARDL long run estimates where the results of ARDL long run esti-

Table 3. ARDL short run

Variables	Probability	t-Statistics	Coefficients
GDP	0.0001***	4.5845	1.1222
MV	0.0701*	1.8598	0.2589
EU	0.0049***	2.9732	0.2321
TR	0.0239**	-2.3450	-0.0483

***, ** &*denotes 1%, 5% & 10% significance level

mates where the results indicates that GDP, manufacturing and energy usage are significant at 1%, 10%, and 1% respectively and has a positive relationship with CO_2 emission hence it would be advisable to use more of green energy both for manufacturing process and energy use which would also impact the GDP on the other hand total reserves is significant at 5% and has a negative relation with the CO_2 emission.

Table 5 displays the results of diagnostic test Jarque-Bera normality test was employed to check whether the residual are normally distributed or not and the result reveal that the residuals are normally distributed (0.20 > 0.05). Ramsey Reset test was used to check the specification error and the result revealed that there was no specification error in the model (0.40 & gt; 0.05). Breusch-Godfery serial correlation, LM test revealed that there exist no serial correlation among the error components in the model (0.38 & gt; 0.05). Lastly the outcomes of heteroscedasticity Breusch-Pagan-Godfery test demonstrates that the data is homoscedastic.

Table 4. ARDL long run

GDP	0.0000***	4.5845	1.1222
MANUFACTURING	0.0701*	1.8598	0.2589
ENERGY	0.0049***	2.9732	0.2321
RESERVES	0.0216**	-2.3880	-0.0589

***, ** &*denotes 1%, 5% & 10% significance level

Granger causality test is used for the time series data to predict whether one variable has potential prediction impact on the other variable. The results reveals that there exist unidirectional causation between CO_2 emission-GDP, total reserves- manufacturing and CO_2 emission-reserves at 10% significance level whereas manufacturing-CO_2 and GDP-reserves have a unidirectional causuallinkage at 1% and 5% respectively. The Granger causality test results are shown in Table 6.

Table 6. Granger causality test

Direction of Causality	F-statistics	Probability
CO_2-GDP	3.16670	0.0507*
Manufacturing-CO_2	5.07605	0.0098***
GDP-reserves	3.22392	0.0482**
Reserves-manufacturing	2.89367	0.0647*
CO_2-reserves	3.02068	0.0577*

***,**&*denotes 1%, 5% & 10% significance level

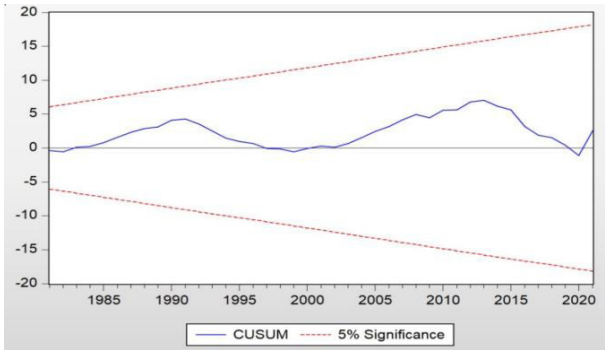

Fig. 3 CUSUM test

The stability of the model was checked by the cumulative sum of the recursive residuals stability test (CUSUM) and as the statistics were found to be between the critical bounds the model was found stable as shown in Fig. 3.

Conclusion

This study uses data from 1965 to 2021 to examine the relationships between carbon emissions, economic growth (GDP, Manufacturing, Reserves), and energy consumption of the United Kingdom. The findings reveal that energy use, GDP and manufacturing are positively related whereas total reserves have a negative relation with CO_2 emission both in the short run and long run respectively. The short

Table 5. Diagnostic tests

JB Normality Test	2.02	0.66
Ramsey RESET test	10.25	0.318
Breusch-Godfery serial Correlation	16.68	0.122
Heteroskedasticity B.P.G. test, Observed R-squared	5.46	0.325

and long run impact of GDP, energy usage and manufacturing on CO_2 emission is unfavourable that is a concern for the environment. Estimates of the linkages between economic expansion, CO_2 emissions, and energy consumption reveal that the United Kingdom has a wide range of options for establishing its energy policy toward alternative and renewable energy sources in anenvironmentally friendly and long-term manner. They could diversify their energy strategies in this direction, reducing environmental pollution while steadily and reliably increasing the energy supply over time. By supporting the development and widespread use of alternative and renewable energy technologies, it may also play a leading role in ensuring that future generations inherit a more habitable and cleaner environment.

Conflict of Interest- None

References

Adebayo, T.S., Awosusi, A.A. and Adeshola, I. 2020. Determinants of CO_2 Emissions in Emerging Markets: An Empirical Evidence from MINT Economies. *International Journal of Renewable Energy Development.* 9(3): 411-422.

Adebayo, T.S., Kirikkaleli, D., Adeshola, I., Oluwajana, D., Akinsola, G.D. and Osemeahon, O.S. 2021. Coal Consumption and Environmental Sustainability in South Africa: The role of Financial Development and Globalization. *International Journal of Renewable Energy Development.* 10(3): 527-536.

Aydo´an, B. and Vardar, G. 2020. Evaluating the role of renewable energy, economic growth and agriculture on CO2 emission in E7 countries. *International Journal of Sustainable Energy.* 39(4): 335-348.

Adebayo,T.S. 2020. Dynamic relationship between oil price and inflation in oil exporting economy: empirical evidence from wavelet coherence technique. *Energy Economics Letters.* 7(1):12–22.

Aye, G.C. and Edoja, P.E. 2017. Effect of economic growth on CO2 emission in developing countries: Evidence from a dynamic panel threshold model. *Cogent Economics & Finance.* 5(1): 1379239.

Ahmed, Z., Wang, Z. and Ali, S. 2019. Investigating the non-linear relationship between urbanization and CO 2 emissions: an empirical analysis. *Air Quality Atmosphere & Health.* 12(8): 945-953.

Ahmed, Z., Zafar, M.W. and Ali, S. 2020. Linking urbanization, human capital, and the ecological footprint in G7 countries: an empirical analysis. *Sustainable Cities and Society.* 55: 102064.

Dong, K., Sun, R. and Hochman, G. 2017. Do natural gas and renewable energy consumption lead to less CO_2 emission? Empirical evidence from a panel of BRICS countries. *Energy.* 141 (C): 1466-1478.

Faisal, Tursoy, T. And Resatoglu, N.G. 2016. Energy consumption, electricity, and GDP causality; the case of Russia, 1990-2011. *Procedia Computer Science.* 120: 671-675.

Gao, J. and Zhang, L. 2021. Does biomass energy consumption mitigate CO_2 emissions? The role of economic growth and urbanization: evidence from developing Asia. *Journal of the Asia Pacific Economy.* 26(1): 96-115.

Hasan, M., Abedin, M.Z., Amin, M.B., Nekmahmud, M. and Oláh, J. 2023. Sustainable biofuel economy: A mapping through bibliometric research. *Journal of Environmental Management.* 336: 117644.

Jafari, Y., Ismail, M.A., Othman, J. and Mawar, M.Y. 2015. Energy consumption, emissions and economic growth in Bahrain. *Chinese Journal of Population Resources and Environment.* 13(4): 297-308.

Jebli, M.B., Youssef, S.B. and Ozturk, I. 2016. Testing environmental Kuznets curve hypothesis: The role of renewable and non-renewable energy consumption and trade in OECD countries. *Ecological Indicators.* 60: 824-831.

Kirikkaleli, D., Adebayo, T.S., Khan, Z. and Ali, S. 2020. Does globalization matter for ecological footprint in Turkey? Evidence from dual adjustment approach. *Environmental Science and Pollution Research.* 28(11): 14009-14017.

Kirikkaleli, D. and Adebayo, T.S. 2021. Do renewable energy consumption and financial development matter for environmental sustainability? New global evidence. *Sustainable Development.* 29(4): 583-594.

Khobai, H. and Le Roux, P. 2017. The relationship between energy consumption, economic growth and carbon dioxide emission: The case of South Africa. *International Journal of Energy Economics and Policy.* 7(3):102-109.

Leal, P.H. and Marques, A.C. 2020. Rediscovering the EKC hypothesis for the 20 highest CO_2 emitters among OECD countries by level of globalization. *International Economics.* 164: 36-47.

Maurya, R., Gohil, N., Nixon, S., Kumar, N., Noronha, S.B., Dhali, D. and Singh, V. 2023. Rewiring of metabolic pathways in yeasts for sustainable production of biofuels. *Bioresource Technology*. 2023: 128668.

Murshed, M. 2021. LPG consumption and environmental Kuznets curve hypothesis in South Asia: a time-series ARDL analysis with multiple structural breaks. *Environmental Science and Pollution. Research*. 28(7): 8337-8372.

Odugbesan, J.A. and Adebayo, T.S. 2020. Modeling CO2 emissions in South Africa: empirical evidence from ARDL based bounds and wavelet coherence techniques. *Environmental Science and Pollution Research.* 28(8): 9377-9389.

Pablo-Romero, Maria Del, P. and Josué De Jesús, 2016. Economic Growth and Energy Consumption: The Energy-Environmental Kuznets Curve for Latin America and the Caribbean. *Renewable and Sustainable Energy Reviews.* 60:1343–50.

Rafiq, S., Salim, R. and Apergis, N. 2016. Agriculture, trade openness and emissions: an empirical analysis and policy options. *Australian Journal of Agricultural and Resource Economics.* 60(3): 348-365.

Shahbaz, M., Balsalobre-Lorente, D. and Sinha, A. 2019. Foreign direct Investment-CO2 emissions nexus in Middle East and North African countries: Importance of biomass energy consumption. *Journal of Cleaner Production.* 217: 603-614.

Singh, A., Lal, S., Kumar, N., Yadav, R. and Kumari, S. 2023. Role of nuclear energy in carbon mitigation to achieve United Nations net zero carbon emission: evidence from Fourier bootstrap Toda-Yamamoto. *Environmental Science and Pollution Research.* 30(16): 46185-46203.

Teng, J.Z., Khan, M.K., Khan, M.I., Chishti, M.Z. and Khan, M.O. 2021. Effect of foreign direct investment on CO 2 emission with the role of globalization, institutional quality with pooled mean group panel ARDL. *Environmental Science and Pollution Research.* 28(5): 5271-5282.

Wang, Z., Ahmed, Z., Zhang, B. and Wang, B. 2019. The nexus between urbanization, road infrastructure, and transport energy demand: empirical evidence from Pakistan. *Environmental Science and Pollution Research.* 26(34): 34884-34895.

Wu, L., Adebayo, T.S., Yue, X. G. and Umut, A. 2023. The role of renewable energy consumption and financial development in environmental sustainability: implications for the Nordic Countries. *International Journal of Sustainable Development & World Ecology*. 30(1): 21-36.

Wasti, S.K.A. and Zaidi, S.W. 2020. An empirical investigation between CO2 emission, energy consumption, trade liberalization and economic growth: A case of Kuwait. *Journal of Building Engineering.* 28: 101104.

Yang, Z. And Zhao, Y. 2014. Energy consumption, carbon emissions, and economic growth in India: Evidence from directed acyclic graphs. *Economic Modelling.* 38: 533–540.

Engineering Research
Express

INCLUSIVE PUBLISHING
TRUSTED SCIENCE

PURPOSE-LED
PUBLISHING™

PAPER

Analytical modeling of fringe capacitance in opposite-doped core-shell junctionless nanowire FET

To cite this article: Bharti and Poornima Mittal 2025 *Eng. Res. Express* **7** 015385

View the article online for updates and enhancements.

You may also like

- Oppositely-Doped Core-Shell Junctionless Nanowire FET: Design and Investigation
Bharti and Poornima Mittal
- Review—Recent Trends on Junction-Less Field Effect Transistors in Terms of Device Topology, Modeling, and Application
Pratikhya Raut, Umakanta Nanda and Deepak Kumar Panda
- Device design guideline for junctionless gate-all-around nanowire negative-capacitance FET with HfO_2-based ferroelectric gate stack
Yejoo Choi, Yuri Hong and Changhwan Shin

This content was downloaded from IP address 14.139.251.98 on 03/04/2025 at 05:44

Engineering Research Express

PAPER

Analytical modeling of fringe capacitance in opposite-doped core-shell junctionless nanowire FET

RECEIVED
31 October 2024

REVISED
3 March 2025

ACCEPTED FOR PUBLICATION
14 March 2025

PUBLISHED
27 March 2025

Bharti and Poornima Mittal*

Department of Electronics and Communication Engineering, Delhi Technological University, Delhi-110042, India

* Author to whom any correspondence should be addressed.

E-mail: bhartigndit@gmail.com **and** poornimamittal@dtu.ac.in

Keywords: analytical modeling, core-shell, fringe capacitance, junctionless nanowire, surface potential

Abstract

An analytical model of Oppositely Doped Core–Shell Junctionless Nanowire Field Effect Transistor (ODCS-JL-NWFET) using surface potential is proposed in this paper. The model incorporates the influence of fringe capacitance through the gate sidewall spacer on the potential distribution function. The analytical results align well with simulated outcomes across various ODCS-JL-NWFET physical parameters, such as threshold voltage, drain current, and subthreshold slope. Furthermore, the model illustrates the impact of channel length scaling on device parameters for different core thicknesses, spacer materials, and core doping concentrations. The results demonstrate that optimizing core thickness, spacer material, and core doping concentration selection can significantly reduce leakage current and subthreshold slope, offering valuable insights for designing at smaller technology nodes with low-power applications.

1. Introduction

Semiconductor technology has been a cornerstone of modern electronics, driving innovation across industries from consumer electronics to advanced computing systems. In recent years, advancements in silicon-based Complementary Metal Oxide Semiconductor (CMOS) Integrated Circuits (ICs) have significantly enhanced the integration of functionality and complexity onto a single chip. As technology progresses, the demand for more complex transistors has led to the continuous downscaling of these devices. However, this scaling down has introduced severe Short Channel Effects (SCEs) along with challenges related to ultra-sharp Source/Drain (S/D) junctions [1, 2]. To address these challenges, gate-all-around Nanowire Field Effect Transistor (NWFET) architectures have emerged as a promising solution. These architectures offer superior electrostatic control over the channel by fully surrounding it with the gate, thereby ensuring enhanced performance and scaling potential [3]. In the pursuit of better device performance, Junctionless (JL) NWFET has attracted attention as a viable alternative to conventional NWFETs. The key advantages of JL-NWFET include improved immunity to SCEs and simplified fabrication processes, attributed to the absence of junctions [4–7]. This design eliminates the need for complex thermal processing, making JL-NWFETs an attractive option for advanced semiconductor applications. However, JL-NWFETs exhibit higher OFF-state leakage current (I_{OFF}) due to heavy doping throughout the source, channel, and drain, resulting in insufficient volume depletion during the OFF-state. Additionally, they are prone to the parasitic Bipolar Junction Transistor (BJT) effect, which is caused by lateral band-to-band tunneling of electrons in the OFF-state [8].

To mitigate these issues, the core–shell (CS) structure has been proposed and explored [9–12]. In the CS structure, a core is introduced at the center of the heavily doped n-type channel of the JL-NWFET, reducing the effective channel region, now referred to as the shell region. Researchers have explored various core types-metallic [9], undoped [10], and oppositely doped [11, 12] to enhance the JL-NWFET's resistance to SCEs. The presence of a core within the channel significantly modifies the conduction characteristics of the shell region. The gate voltage can efficiently deplete the shell region in the CS architecture more effectively compared to the whole channel region in conventional JL-NWFET, leading to improved electrostatic control. The shell region

© 2025 IOP Publishing Ltd. All rights, including for text and data mining, AI training, and similar technologies, are reserved.

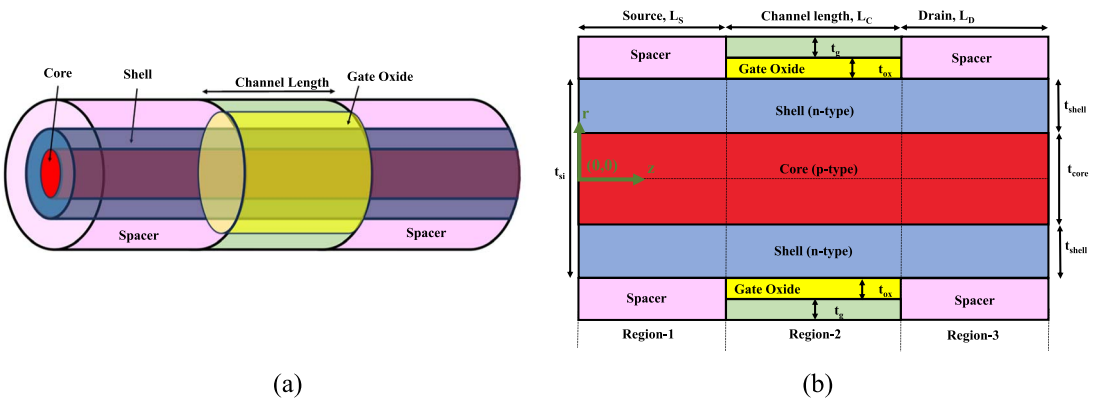

Figure 1. (a) 3-D view and (b) 2-D schematic of ODCS-JL-NWFET.

serves as the primary conduction path, indicating that carrier transport mainly occurs through the shell rather than the core. Furthermore, a highly doped core with opposite doping mitigates leakage current by promoting carrier recombination between the core and shell, resulting in volume depletion in the OFF-state. Consequently, the CS structure reduces the leakage current compared to conventional JL-NWFET. Moreover, experimental work by Lee *et al* (2015) has demonstrated the effectiveness of CS architecture in mitigating Random Dopant Fluctuations (RDFs) in JL transistors [13]. While several studies have analyzed the improved behavior of JL-NWFETs using CS architecture, there has been limited research on developing an analytical model for cylindrical CS-JL-NWFETs. Xu *et al* (2023) provided an initial analytical model for CS-JL-NWFET but did not consider the effect of fringe capacitance from the gate to S/D regions [14]. Additionally, their model derived threshold voltage and Drain Induced Barrier Lowering (DIBL) using the central potential concept, whereas the main conduction mechanism in CS-JL-NWFETs occurs in the shell region rather than in the bulk.

The fringe capacitance, which arises from the electric field at the edges of S/D junctions, must be accounted in these models. In digital circuits, it increases propagation delays by slowing signal transitions and raising RC delay, affecting the overall speed. Additionally, it contributes to dynamic power dissipation in low-power designs by influencing the charge required for node switching [15]. In analog circuits, fringe capacitance modifies the Gain-Bandwidth Product (GBW), which can degrade amplifier performance and stability. This effect is particularly critical in RF and mixed-signal designs, where small capacitance variations can lead to significant frequency response changes [16]. With the continued scaling of semiconductor technologies, NWFETs exhibit even more pronounced fringe capacitance effects due to their 3-D structures. Given the critical role of fringe capacitance in digital and analog applications, it is essential to develop accurate and straightforward models for parasitic capacitances. Previous works, such as those by Kim *et al* (2006) on Double Gate (DG) MOSFETs and by Kaushal *et al* (2021) on JL-FINFETs, have made strides in this direction [17, 18]. This paper aims to develop a physics-based analytical model for cylindrical Oppositely Doped (OD) CS-JL-NWFET that incorporates the effect of fringe capacitance. By leveraging the surface potential concept, this model seeks to enhance the understanding of the electrostatic characteristics of ODCS-JL-NWFET and provide design guidelines for their optimal performance in future integrated circuit applications.

The structure of this paper is organized as follows: section 1 provides an introduction to the study. Section 2 details the device structure and the model formulation of ODCS-JL-NWFET. Section 3 presents the verification of the derived analytical model through simulations. Finally, section 4 offers the conclusions drawn from this analysis.

2. Device structure and model formulation

The 3-D and 2-D structure of the ODCS-JL-NWFET are depicted in figures 1(a) and (b), respectively. The proposed device consists of three regions: the source extension under the spacer (region-1), the channel region under the gate oxide (region-2), and the drain extension under the spacer (region-3). The various dimensions such as channel thickness, shell thickness, core thickness, gate oxide thickness, gate electrode thickness, source extension length, channel length, and drain extension length are represented by t_{si}, t_{shell}, t_{core}, t_{ox}, t_g, L_S, L_C, and L_D, respectively.

An oppositely doped (p-type) core, with a doping concentration of $N_a = 1 \times 10^{19}\ \mathrm{cm}^{-3}$, is incorporated into the center of an n-type channel with a doping concentration of $N_d = 1 \times 10^{19}\ \mathrm{cm}^{-3}$. The shell thickness ($t_{shell} = (t_{si} - t_{core})/2$) defines the active channel region responsible for conduction [11]. Furthermore, $L_{S/D}$ denotes the

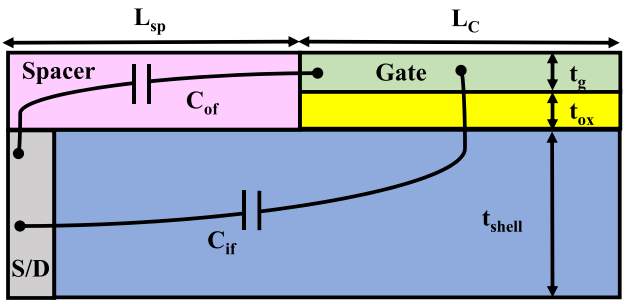

Figure 2. Depiction of outer fringe and inner fringe capacitance of ODCS-JL-NWFET.

length of the S/D extension under the spacers on both sides of the gates. It may be noted that in ODCS-JL-NWFET, $L_{sp} = L_{S/D}$, where L_{sp} is the spacer length. The HfO_2 and SiO_2 are used as the spacer material and gate oxide, respectively. This choice, as supported by previously reported work [19], optimizes the switching ratio and subthreshold slope. The SiO_2, a low-permittivity material, is used as the gate oxide to reduce capacitance and improve the switching ratio. Meanwhile, HfO_2, a high-permittivity material, is used as the spacer to help reduce I_{OFF}, thereby lowering subthreshold slope and enhancing device performance.

2.1. Surface potential modeling

Solving the 2-D Poisson's equation can determine silicon's surface electrostatic potential and electric field distribution. The electrostatic potential in the core and shell region of the channel can be expressed as follows:

$$\frac{1}{r}\frac{\partial}{\partial r}\left(r\frac{\partial}{\partial r}\psi_{core,k}(r,\,z)\right)+\frac{\partial^2\psi_{core,k}(r,\,z)}{\partial z^2}=\frac{qN_a}{\varepsilon_{si}}\;for\;0\leqslant r\leqslant\frac{t_{core}}{2},\;\;k=1,\;2,\;3 \tag{1}$$

$$\frac{1}{r}\frac{\partial}{\partial r}\left(r\frac{\partial}{\partial r}\psi_{shell,k}(r,\,z)\right)+\frac{\partial^2\psi_{shell,k}(r,\,z)}{\partial z^2}=\frac{-qN_d}{\varepsilon_{si}}\;for\;\frac{t_{core}}{2}\leqslant r\leqslant\frac{t_{si}}{2},\;\;k=1,\;2,\;3 \tag{2}$$

Here, potential distribution in core and shell region of the channel for the k^{th} region ($k = 1, 2, 3$), permittivity of silicon, acceptor concentration, electronic charge, and donor concentration are denoted as $\psi_{core}(r,z)$, $\psi_{shell}(r,z)$, ε_{si}, N_a, q, and N_d, respectively. The potential distributions along the radial direction in both the core and shell regions are described using the parabolic potential approximation [20] and are expressed as follows

$$\psi_{core,k}(r,\,z)=Y_{0k}(z)+Y_{1k}(z)r+Y_{2k}(z)r^2 \tag{3}$$

$$\psi_{shell,k}(r,\,z)=Z_{0k}(z)+Z_{1k}(z)\left(r-\frac{t_{core}}{2}\right)+Z_{2k}(z)\left(r-\frac{t_{core}}{2}\right)^2 \tag{4}$$

Using the following boundary conditions (i-iv), the arbitrary coefficients Y_{0k}, Y_{1k}, Y_{2k}, Z_{0k}, Z_{1k}, and Z_{2k} can be determined.

(i) The central potential ($\psi_{Ck}(z)$) and surface potential ($\psi_{Sk}(z)$) are as follow

$$\psi_{core,k}(0,\,z)=\psi_{Ck}(z)\;\text{and}\;\psi_{shell,k}\left(\frac{t_{si}}{2},\,z\right)=\psi_{Sk}(z) \tag{5}$$

(ii) The electric field in the center of the core region of the channel is zero by symmetry of channel potential.

$$\left.\frac{\partial\psi_{core,k}(r,\,z)}{\partial r}\right|_{r\,=\,0}=0 \tag{6}$$

(iii) The electric field at the surface is continuous.

$$\left.\frac{\partial\psi_{shell,k}(r,\,z)}{\partial r}\right|_{r=\frac{t_{si}}{2}}=\frac{C_k(V_{GS}-V_{fb}-\psi_{Sk}(z))}{\varepsilon_{si}} \tag{7}$$

Where V_{fb} signifies the flat band voltage. C_k is the capacitance per unit area for the k^{th} region and is given as

$$C_1 = C_3 = \frac{(C_{if} + C_{of})}{\pi t_{si}} \tag{8}$$

$$C_2 = \frac{\varepsilon_{ox}}{\frac{t_{si}}{2}\ln\left(1 + \frac{2t_{ox}}{t_{si}}\right)} \tag{9}$$

Here, C_1 and C_3 represent fringe capacitance per unit area, which is the combination of inner fringe capacitance per unit width (C_{if}) and outer fringe capacitance per unit width (C_{of}). Generally, C_{of} originates from both gate electrodes through the spacer dielectric, as illustrated in figure 2. Furthermore, oxide capacitance per unit area and gate oxide permittivity are represented by C_2 and ε_{ox}, respectively, in region-2. C_{if} and C_{of} are expressed as [17].

$$C_{if} = \frac{6\varepsilon_{ox}}{\pi}\ln\left(\frac{t_{ox} + t_{si}\sin\delta}{t_{ox}\cos\delta + f_{if}L_{sp}\sin\delta}\right) \tag{10}$$

$$C_{of} = \frac{2\varepsilon_{sp}}{\pi} ln\left(\frac{t_g + t_{ox}}{L_{sp}}\right) \tag{11}$$

here, f_{if}, ε_{sp}, t_g, and δ denote tuning parameter, spacer permittivity, gate electrode thickness, and plate angle, respectively.

(iv) The potentials and electric fields in the radial direction at the boundary between the core and shell regions must be continuous.

$$\psi_{core,k}\left(\frac{t_{core,k}}{2}, z\right) = \psi_{shell,k}\left(\frac{t_{core,k}}{2}, z\right) \tag{12}$$

$$\left.\frac{\partial\psi_{core,k}(r, z)}{\partial r}\right|_{r=\frac{t_{core}}{2}} = \left.\frac{\partial\psi_{shell,k}(r, z)}{\partial r}\right|_{r=\frac{t_{core}}{2}} \tag{13}$$

Using boundary conditions (i)–(iv), arbitrary coefficients in (3) and (4) are expressed as

$$Y_{0k}(z) = \psi_{Ck}(z) \tag{14}$$

$$Y_{1k}(z) = 0 \tag{15}$$

$$Y_{2k}(z) = \frac{(4\varepsilon_{si} + C_k(t_{si} - t_{core}))\psi_{Sk}(z) - 4\varepsilon_{si}\psi_{Ck}(z) - C_k(t_{si} - t_{core})(V_{GS} - V_{fb})}{\varepsilon_{si}t_{si}t_{core}} \tag{16}$$

$$Z_{0k}(z) = \frac{(4\varepsilon_{si}t_{core} + C_k t_{core}(t_{si} - t_{core}))\psi_{Sk}(z) + 4\varepsilon_{si}(t_{si} - t_{core})\psi_{Ck}(z) - C_k t_{core}(t_{si} - t_{core})(V_{GS} - V_{fb})}{4\varepsilon_{si}t_{si}} \tag{17}$$

$$Z_{1k}(z) = \frac{(4\varepsilon_{si} + C_k(t_{si} - t_{core}))\psi_{Sk}(z) - 4\varepsilon_{si}\psi_{Ck}(z) - C_k(t_{si} - t_{core})(V_{GS} - V_{fb})}{\varepsilon_{si}t_{si}} \tag{18}$$

$$Z_{2k}(z) = \frac{(-4\varepsilon_{si} - C_k(2t_{si} - t_{core}))\psi_{Sk}(z) + 4\varepsilon_{si}\psi_{Ck}(z) + C_k(2t_{si} - t_{core})(V_{GS} - V_{fb})}{\varepsilon_{si}t_{si}(t_{si} - t_{core})} \tag{19}$$

$\psi_{Ck}(z)$ can be written in terms of $\psi_{Sk}(z)$ by solving (1) and (2) simultaneously using (3) and (4) at $r = t_{core}$ and is derived as

$$\psi_{Ck}(z) = \frac{(8\varepsilon_{si} + 2C_k t_{si})\psi_{Sk}(z) - 2C_k t_{si}(V_{GS} - V_{fb}) - q(N_a + N_d)t_{core}(t_{si} - t_{core})}{8\varepsilon_{si}} \tag{20}$$

By using equations (4) and (20) to solve equation (2) at $r = t_{si}/2$, the differential equation for $\psi_{Sk}(z)$ can be represented as:

$$\frac{\partial^2\psi_{Sk}(z)}{\partial z^2} - \frac{(\psi_{Sk}(z) - W_k)}{\lambda_k{}^2} = 0 \tag{21}$$

$$\lambda_k{}^2 = \frac{\varepsilon_{si}t_{si}}{4C_k} \tag{22}$$

$$W_k = V_{GS} + \gamma_k \tag{23}$$

$$\gamma_k = \frac{qN_d t_{si} - qt_{core}(N_a + N_d)}{4C_k} - V_{fb} \tag{24}$$

where λ_k represents the scaling length of ODCS-JL-NWFET. It is interesting to note that the λ_k is the same as that of a conventional Double Gate (DG) JL-MOSFET [21] without core–shell architecture. Additionally, W_k also matches that of a standard DG-JL-MOSFET [21]. The general solution for the second-order differential equation (21) for all three regions are expressed as

$$\psi_{S1}(z) = M_1\, e^{z/\lambda_1} + N_1 e^{-z/\lambda_1} + W_1 \tag{25}$$

$$\psi_{S2}(z) = M_2\, e^{(z-L_S)/\lambda_2} + N_2 e^{-(z-L_S)/\lambda_2} + W_2 \tag{26}$$

$$\psi_{S3}(z) = M_3\, e^{(z-L_S-L_C)/\lambda_3} + N_3 e^{-(z-L_S-L_C)/\lambda_3} + W_3 \tag{27}$$

To solve arbitrary constants, the following boundary conditions are used.

(v) The surface potential in the region-1 at the source side

$$\psi_{S1}(z=0) = V_{bi} = \frac{KT}{q}\ln\left(1 + \frac{N_d}{n_i}\right) \tag{28}$$

Where V_{bi}, K, T, and n_i signify built-in potential, Boltzmann constant, thermal temperature, and intrinsic concentration, respectively.

(vi) The surface potential in the region-3 at the drain side

$$\psi_{S3}(z = L_S + L_C + L_D) = V_{bi} + V_{DS} \tag{29}$$

(vii) At the interface of regions 1–2 and 2–3, the surface potential and electric field exhibit continuity.

$$\psi_{S1}(z = L_S) = \psi_{S2}(z = L_S) \tag{30}$$

$$\psi_{S2}(z = L_S + L_C) = \psi_{S3}(z = L_S + L_C) \tag{31}$$

$$\left.\frac{\partial\psi_{S1}(z)}{\partial r}\right|_{z=L_S} = \left.\frac{\partial\psi_{S2}(z)}{\partial r}\right|_{z=L_S} \tag{32}$$

$$\left.\frac{\partial\psi_{S2}(z)}{\partial r}\right|_{z=L_S+L_C} = \left.\frac{\partial\psi_{S3}(z)}{\partial r}\right|_{z=L_S+L_C} \tag{33}$$

M_k and N_k for $k = 1, 2, 3$ are obtained by solving abovementioned boundary conditions and expressed as

$$M_1 = \left(1 + \frac{\lambda_1}{\lambda_2}\right)\left(\frac{e^{-L_S/\lambda_1}}{2}\right)M_2 + \left(1 - \frac{\lambda_1}{\lambda_2}\right)\left(\frac{e^{-L_S/\lambda_1}}{2}\right)N_2 + \left(\frac{e^{-L_S/\lambda_1}}{2}\right)(W_2 - W_1) \tag{34}$$

$$N_1 = \left(1 - \frac{\lambda_1}{\lambda_2}\right)\left(\frac{e^{L_S/\lambda_1}}{2}\right)M_2 + \left(1 + \frac{\lambda_1}{\lambda_2}\right)\left(\frac{e^{L_S/\lambda_1}}{2}\right)N_2 + \left(\frac{e^{L_S/\lambda_1}}{2}\right)(W_2 - W_1) \tag{35}$$

$$M_3 = \left(1 + \frac{\lambda_3}{\lambda_2}\right)\left(\frac{e^{L_C/\lambda_2}}{2}\right)M_2 + \left(1 - \frac{\lambda_3}{\lambda_2}\right)\left(\frac{e^{-L_C/\lambda_2}}{2}\right)N_2 + \frac{(W_2 - W_3)}{2} \tag{36}$$

$$N_3 = \left(1 - \frac{\lambda_3}{\lambda_2}\right)\left(\frac{e^{L_C/\lambda_2}}{2}\right)M_2 + \left(1 + \frac{\lambda_3}{\lambda_2}\right)\left(\frac{e^{-L_C/\lambda_2}}{2}\right)N_2 + \frac{(W_2 - W_3)}{2} \tag{37}$$

$$M_2 = \frac{(F_1 - V_{GS})A - (F_2 - V_{GS})C}{AB - CD} \tag{38}$$

$$N_2 = \frac{(F_2 - V_{GS})B - (F_1 - V_{GS})D}{AB - CD} \tag{39}$$

$$A = cosh\left(\frac{L_S}{\lambda_1}\right) + \left(\frac{\lambda_1}{\lambda_2}\right)\sinh\left(\frac{L_S}{\lambda_1}\right) \tag{40}$$

$$B = \left[cosh\left(\frac{L_D}{\lambda_3}\right) + \left(\frac{\lambda_3}{\lambda_2}\right)\sinh\left(\frac{L_D}{\lambda_1}\right)\right]e^{L_C/\lambda_2} \tag{41}$$

$$C = \left[cosh\left(\frac{L_D}{\lambda_3}\right) - \left(\frac{\lambda_3}{\lambda_2}\right)\sinh\left(\frac{L_D}{\lambda_1}\right)\right]e^{-L_C/\lambda_2} \tag{42}$$

$$D = \cosh\left(\frac{L_S}{\lambda_1}\right) - \left(\frac{\lambda_1}{\lambda_2}\right)\sinh\left(\frac{L_S}{\lambda_1}\right) \tag{43}$$

$$F_1 = V_{bi} + V_{DS} - \gamma_3 - (\gamma_2 - \gamma_3)\cosh\left(\frac{L_D}{\lambda_3}\right) \tag{44}$$

$$F_2 = V_{bi} - \gamma_1 - (\gamma_2 - \gamma_1)\cosh\left(\frac{L_S}{\lambda_1}\right) \tag{45}$$

2.2. Threshold voltage modeling

To derive the threshold voltage (V_T) for ODCS-JL-NWFET, the minimum surface potential ($\psi_{S2,min}(z)$) of the channel region (region-2) is set to zero [21]. The position of minimum surface potential (z min) is determined by differentiating equation (26) and equating the result to zero.

$$\left.\frac{d\psi_{S2}(z)}{dz}\right|_{z=z\ \min} = 0 \tag{46}$$

$$z\ \min = L_S + \frac{\lambda_2}{2}\ln\left(\frac{Z_2}{Y_2}\right) \tag{47}$$

$$\psi_{S2,\ \min}(z)|_{z=z\ \min} = 2\sqrt{Y_2 Z_2} + W_2 \tag{48}$$

By setting $\psi_{S2,min}(z)$ to zero and solving for V_{GS}, the V_T can be determined as

$$V_T = \frac{-(2\alpha_1\alpha_4 + 2\alpha_2\alpha_3 - \gamma_2) + \sqrt{(2\alpha_1\alpha_4 + 2\alpha_2\alpha_3 - \gamma_2)^2 - (4\alpha_1\alpha_2 - 1)(\alpha_2\alpha_4 - {\gamma_2}^2)}}{4\alpha_1\alpha_2 - 1} \tag{49}$$

$$\alpha_1 = \frac{AF_1 - CF_2}{AB - CD} \tag{50}$$

$$\alpha_2 = \frac{C - A}{AB - CD} \tag{51}$$

$$\alpha_3 = \frac{BF_2 - DF_1}{AB - CD} \tag{52}$$

$$\alpha_4 = \frac{D - B}{AB - CD} \tag{53}$$

2.3. Drain current and subthreshold slope modeling

The subthreshold drain current (I_{sub}) for $0 \leqslant V_{GS} < V_T$, the drain current in the linear region (I_{lin}) for $V_T \leqslant V_{GS} < V_{DS} + V_T$, and the drain current in the saturation region (I_{sat}) for $V_{DS} + V_T \leqslant V_{GS} \leqslant V_{DD}$ constitute the total drain current (I_{DS}) of ODCS-JL-NWFET. The corresponding expressions for I_{sub} [22], I_{lin} [23, 24], and I_{sat} [23, 24] are as follows

$$I_{sub} = \frac{\pi t_{si} KT\ (1 - e^{-qV_{DS}/KT})}{\int_0^{L_S}\frac{dz}{H_1(z)} + \int_{L_S}^{L_S+L_C}\frac{dz}{H_2(z)} + \int_{L_S+L_C}^{L_S+L_C+L_D}\frac{dz}{H_3(z)}} \tag{54}$$

$$H_k(z) = n_i {\mu'}_p \int_0^{t_{core}/2} e^{\left(\frac{q\psi_{core,k}(r,z)}{KT}\right)}dr + n_i {\mu'}_e \int_{t_{core}/2}^{t_{si}/2} e^{\left(\frac{q\psi_{shell,k}(r,z)}{KT}\right)}dr \tag{55}$$

$${\mu'}_p = \frac{\mu_p}{1 + \eta(V_{GS} - V_T)} \text{ and } {\mu'}_e = \frac{\mu_e}{1 + \eta(V_{GS} - V_T)} \tag{56}$$

$$I_{lin} = \sum_{k=1}^{3}\left[\frac{\beta_k\left((V_{GS} - V'_T)V_{DS} - \frac{1}{2}V_{DS}^2\right)}{L_k\left(1 - \frac{l_d}{L_k} + \frac{V_{DS}}{L_k E_C}\right)}\right] \tag{57}$$

$$I_{sat} = \sum_{k=1}^{3}\left[\frac{\beta_k(V_{GS} - V'_T)V_{DS,\ sat}}{L_k\left(1 - \frac{l_d}{L_k} + \frac{V_{DS,sat}}{L_k E_C}\right)}\right] \tag{58}$$

Here, μ_p is low field hole mobility [23], μ_e low field electron mobility [23], η is fitting parameter [23], $V'_T = V_T - DIBL$ is the effective threshold voltage [23], $\beta_k = \pi(t_{si} - t_{core}){\mu'}_e C_k + \pi t_{core}{\mu'}_p C_k$ is the process parameter,

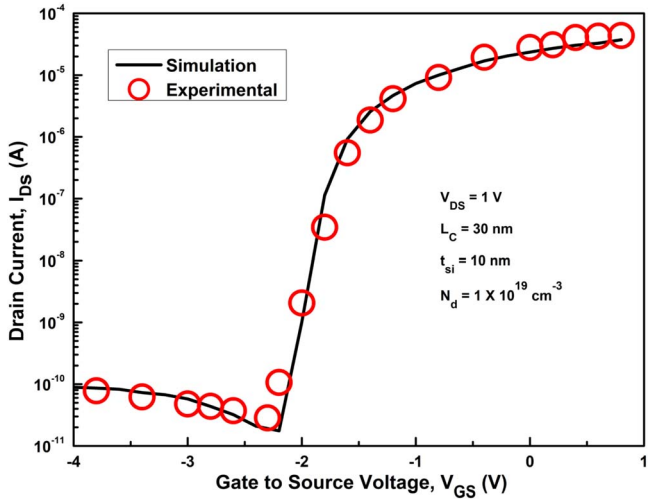

Figure 3. Transfer characteristics of simulation and experimental data for calibration.

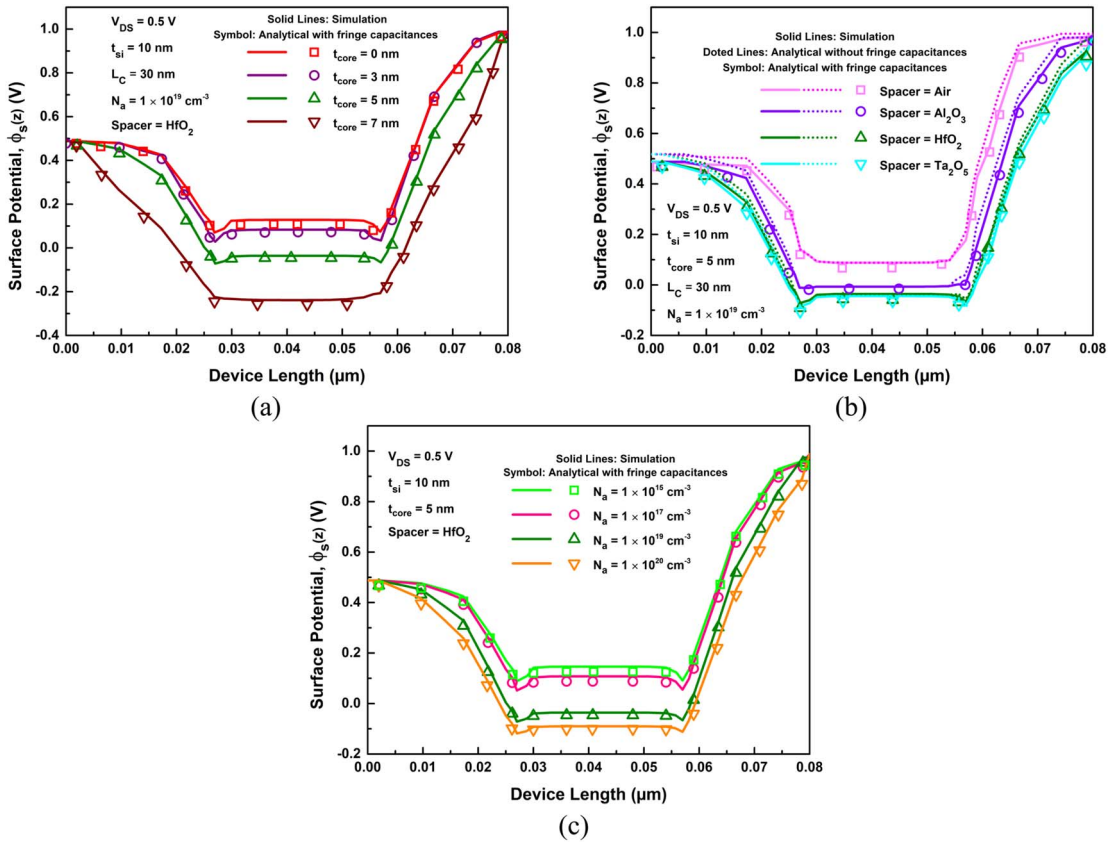

Figure 4. Surface potential ($\phi_S(z)$) profile along device length of ODCS-JL-NWFET at $V_{GS} = 0$ V for different (a) core thicknesses, (b) spacer materials with and without fringe capacitances, and (c) core doping concentrations.

$E_C = \frac{2ves}{\mu' e}$ is critical electric field at which electron velocity (v_{es}) saturates [24], l_d is the channel length modulation factor [24], and $V_{DS,sat} = \frac{V_{GS} - V_T}{1 + \frac{V_{GS} - V_T}{L_C E_C}}$ is saturation voltage [24]. Furthermore, the Subthreshold Slope (SS) is defined as the variation in V_{GS} required for every tenfold increase in I_{DS} and can be expressed as [4, 25]

$$SS = \frac{\partial V_{GS}}{\partial log_{10}(I_{DS})} \tag{59}$$

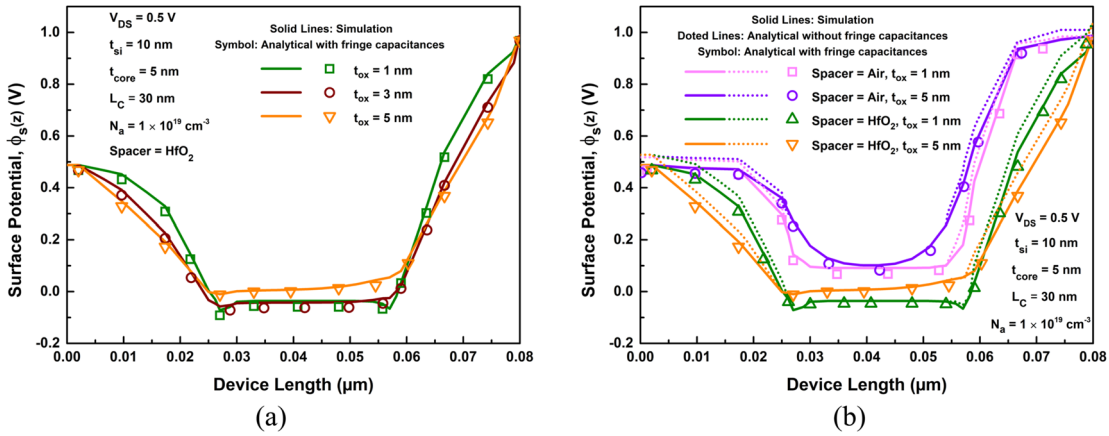

Figure 5. Surface potential ($\phi_S(z)$) profile along device length of ODCS-JL-NWFET for different (a) t_{ox} and (b) spacer materials with and without fringe capacitances and t_{ox}.

3. Results and discussion

The ATLAS 3-D device simulator from SILVACO based on TCAD [26], is used to perform device simulations. The TCAD physical models are calibrated using the experimental data from JL-NWFET [5]. Figure 3 demonstrates a comparison between the simulated and experimental transfer characteristics plots. To model the device accurately, the Boltzmann, Lombardi mobility, Shockley-Read-Hall, and Bandgap Narrowing models are applied. These models account for various factors, including Boltzmann statistics, mobility dependence on both parallel and perpendicular fields, minority carrier lifetimes, and the behavior of heavily doped regions. Additionally, the non-local BTBT model is used to capture electron tunneling effects. The Newton numerical method is employed to ensure result convergence. Thereafter calibration, the same physical models are applied to analyze ODCS-JL-NWFET.

Unless specified otherwise, the N_d is taken as 1×10^{19} cm^{-3}, $t_{ox} = 1$ nm, gate work function (ϕ_M) = 5.1 eV, $L_{sp} = L_{S/D} = 25$ nm, and $\varepsilon_{ox} = 3.9$ [19]. The developed model is first analyzed for the surface potential of ODCS-JL-NWFET with the L_C of 30 nm and t_{si} of 10 nm while varying the t_{core} from 0 to 7 nm. Different spacer materials, including air, Al_2O_3, HfO_2, and Ta_2O_5, with permittivity of 1, 9.3, 22, and 26, respectively, are also considered to analyze the effect of fringe capacitance. Furthermore, to see the effect of core doping on the performance of ODCS-JL-NWFET, the N_a has been varied from 1×10^{15} cm^{-3} to 1×10^{20} cm^{-3}. Subsequently, the impact of scaling L_C from 70 nm to 20 nm on the device parameters is evaluated. In this analysis, since the t_{si} exceeds 7 nm, quantum mechanical effects are neglected [27].

Figure 4(a) portrays the surface potential ($\phi_S(z)$) of ODCS-JL-NWFET along the device length, with t_{core} varying from 0 nm to 7 nm while maintaining HfO_2 as spacer material in OFF-state ($V_{GS} = 0$ V). The surface potential is extracted using the horizontal cut-line at 1 nm beneath the oxide-semiconductor interface during TCAD simulations. A close correlation is observed between the results from the analytical model and the TCAD simulation.

It may be noted that zero t_{core} corresponds to a conventional JL-NWFET with a gate sidewall spacer without a core–shell structure. It is observed from figure 4(a) that as t_{core} increases from 0 to 7 nm, with a fixed t_{si} of 10 nm, the minimum surface potential in the channel region (region-2) shifts downward. This implies that fewer dopants are present to shield the gate electric field's penetration into the shell region, indicating enhanced gate control over the shell region. Moreover, the expansion of the oppositely doped t_{core} suppresses the shell region, which serves as the primary conduction area, depleting it in the OFF-state, and consequently reducing leakage current. The surface potential profile of ODCS-JL-NWFET at a fixed t_{core} of 5 nm with different spacer materials, in the OFF-state, both with and without consideration of fringe capacitances in the analytical model, is shown in figure 4(b). It may be noted that air denotes the absence of spacer material, and the device corresponds to a conventional oppositely doped core–shell JL-NWFET. As observed, the analytical result with the consideration of fringe capacitances aligns well with the simulation result. The spacer having high permittivity (Al_2O_3, HfO_2, Ta_2O_5) shifts the minimum surface potential downward as compared to the air spacer. This effect can be attributed to the fact that a high-permittivity spacer enhances the fringing electric field, leading to increased depletion beyond the channel region during the OFF-state [28]. The vertical electric field experiences fewer carriers, further shifting the surface potential downward. However, it is also observed that there is no significant further reduction in surface potential when changing the spacer material from HfO_2 to Ta_2O_5. Therefore, the

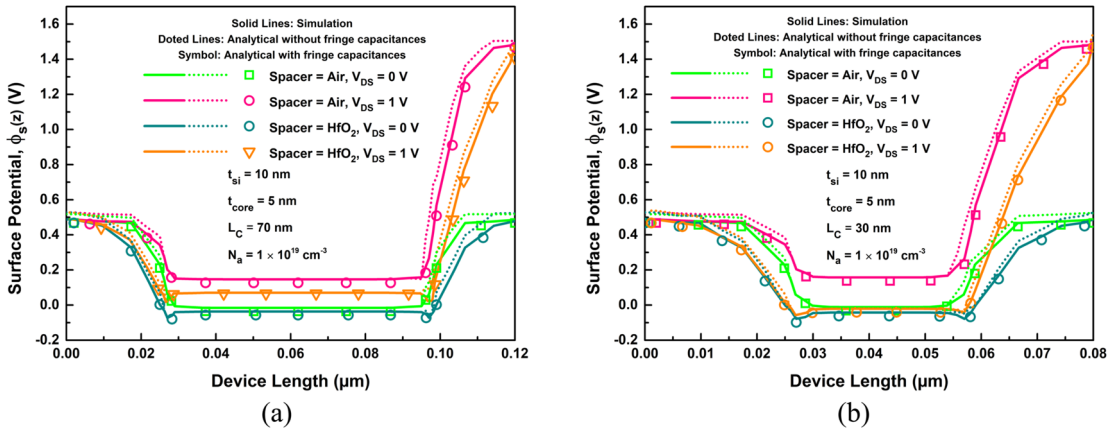

Figure 6. Surface potential ($\phi_S(z)$) profile along device length of ODCS-JL-NWFET for different spacer materials and V_{DS} at channel lengths of (a) 70 nm and (b) 30 nm with and without fringe capacitances.

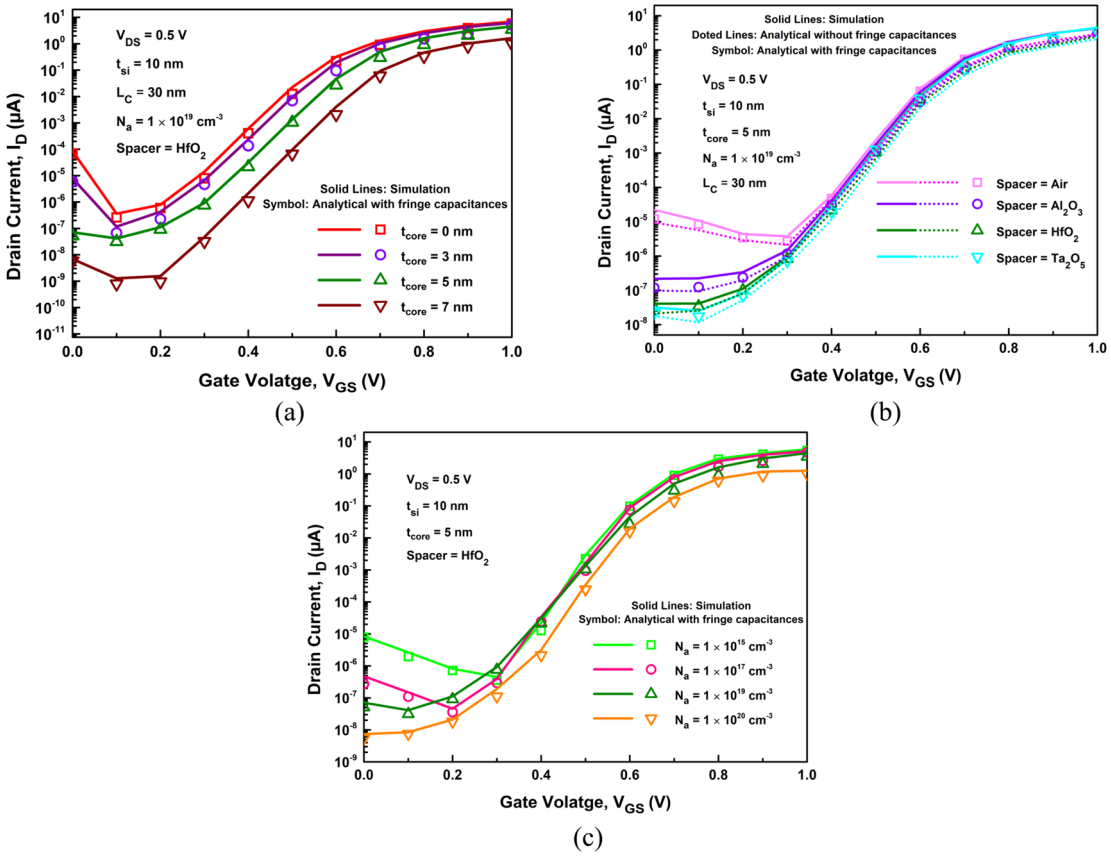

Figure 7. Transfer characteristics of ODCS-JL-NWFET for different (a) core thicknesses, (b) spacer materials with and without fringe capacitances, and (c) core doping concentrations.

choice of spacer material with a permittivity higher than HfO_2 does not result in substantial performance improvement in terms of surface potential reduction. Besides this, without considering the fringe capacitance effects in the analytical model, the surface potential increases in the S/D extension, deviating from the simulation result. This discrepancy arises because the model does not capture the increased fringing electric field due to fringe capacitance, which can shift the surface potential upward in the S/D extension to match the simulation result. Furthermore, no significant change in surface potential is observed in the channel region as fringe capacitances only affect the regions beyond the channel, primarily in the S/D extensions. The effect of different p-type core doping on the surface potential profile of ODCS-JL-NWFET by varying it from 1×10^{15} cm^{-3} to 1×10^{20} cm^{-3}, with fixed n-type shell doping of 1×10^{19} cm^{-3} in the OFF-state, is demonstrated in figure 4(c). The surface potential shifts upward with decreasing core doping as a lightly

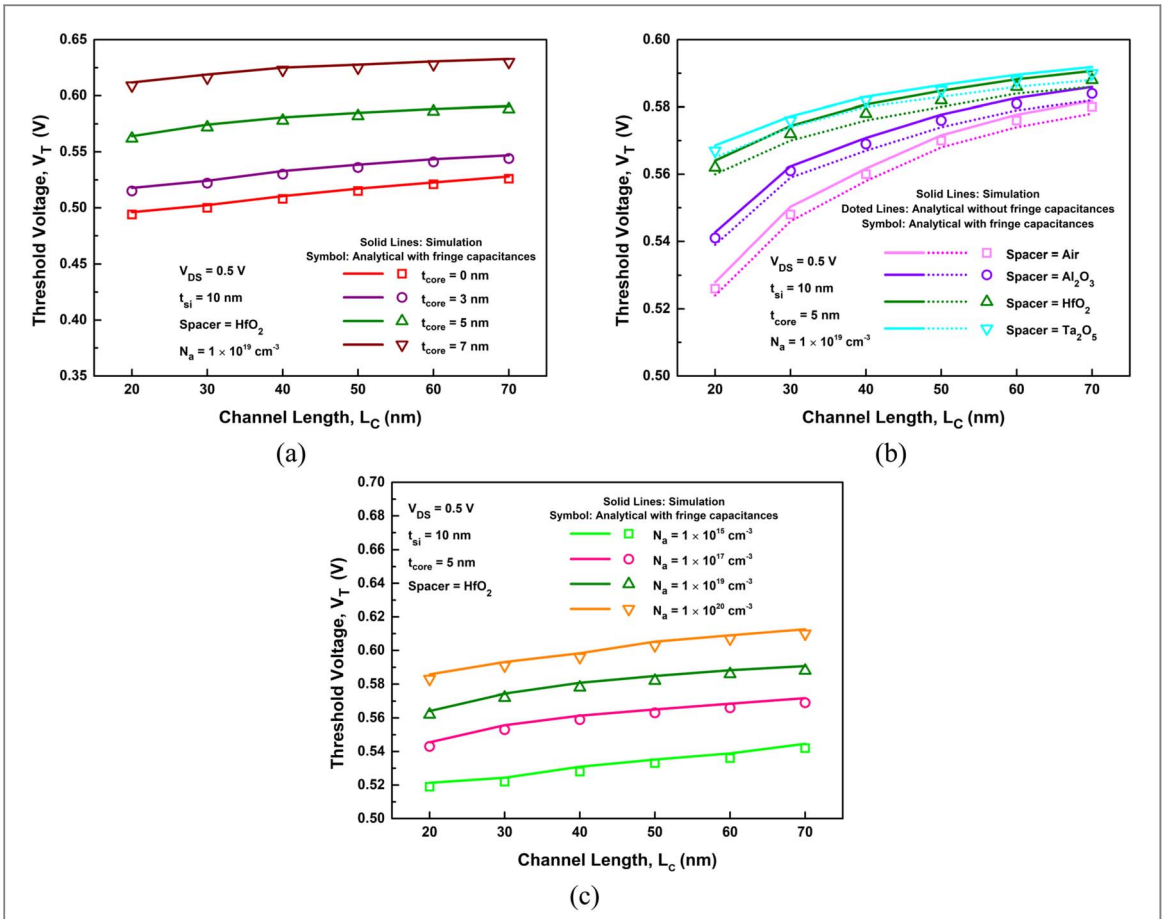

Figure 8. Effect of L_C scaling on V_T of ODCS-JL-NWFET for different (a) core thicknesses, (b) spacer materials with and without fringe capacitances, and (c) core doping concentrations.

doped core with 1×10^{15} cm^{-3} concentration may not be able to deplete the channel during OFF-state, and the vertical electric field may not shift the surface potential downward due to the presence of carriers in the shell region. Conversely, a heavily doped core with a concentration of 1×10^{20} cm^{-3} shifts the surface potential downward as it depletes the shell region more effectively.

Figure 5(a) compares the surface potential profile of ODCS-JL-NWFET for different t_{ox} at specific t_{core} (5 nm) and spacer (HfO_2) in the OFF-state. The plot indicates that as the t_{ox} increases from 1 nm to 5 nm, the surface potential shifts upwards, suggesting that the vertical electric field from the gate struggles to penetrate the thicker oxide layer, weakening the gate's control over the channel. Figure 5(b) demonstrates the surface potential profile of ODCS-JL-NWFET for different spacers and t_{ox} at fixed t_{core} in the OFF-state. The analytical model that accounts for fringe capacitances closely matches the simulation results, whereas the model without fringe capacitances shows significant deviation. This is due to the fact that the absence of fringe capacitance in the analytical model increases the surface potential in the S/D extension regions. Furthermore, it is observed that at a specific t_{ox}, the high-permittivity spacer (HfO_2) shifts the surface potential downward. This occurs because the high-permittivity spacer over the S/D extension enhances carrier depletion by increasing the fringing electric field, which leads to a downward shift in the surface potential. Although a thin t_{ox} is preferred to improve control, it can also increase leakage current. Therefore, using a high-permittivity spacer along with a thicker t_{ox} is recommended.

To understand the effect of drain bias on the scaling of L_C, the surface potential of ODCS-JL-NWFET for different V_{DS} and spacers at L_C of 70 nm and 30 nm are plotted in figures 6(a) and (b), respectively. It is evident from both figures 6(a) and (b) that when fringe capacitances are ignored, the analytical model fails to capture the enhanced depletion effect caused by the fringing electric field, leading to a higher surface potential than that is observed in the simulation results. Beside this, when V_{DS} increases from 0 V to 1 V with an air spacer, the surface potential rises upward more significantly for the shorter L_C of 30 nm (figure 6(b)) compared to the 70 nm. This suggests a greater reduction in V_T for the shorter channel, indicating that the drain bias has a more pronounced effect on shorter L_C with air spacer. Additionally, with a high permittivity spacer (HfO_2), no significant shift in the minimum surface potential is observed for a given L_C. Moreover, as the L_C is scaled from 70 nm to 30 nm with an HfO_2 spacer, the influence of drain bias on the minimum surface potential is reduced.

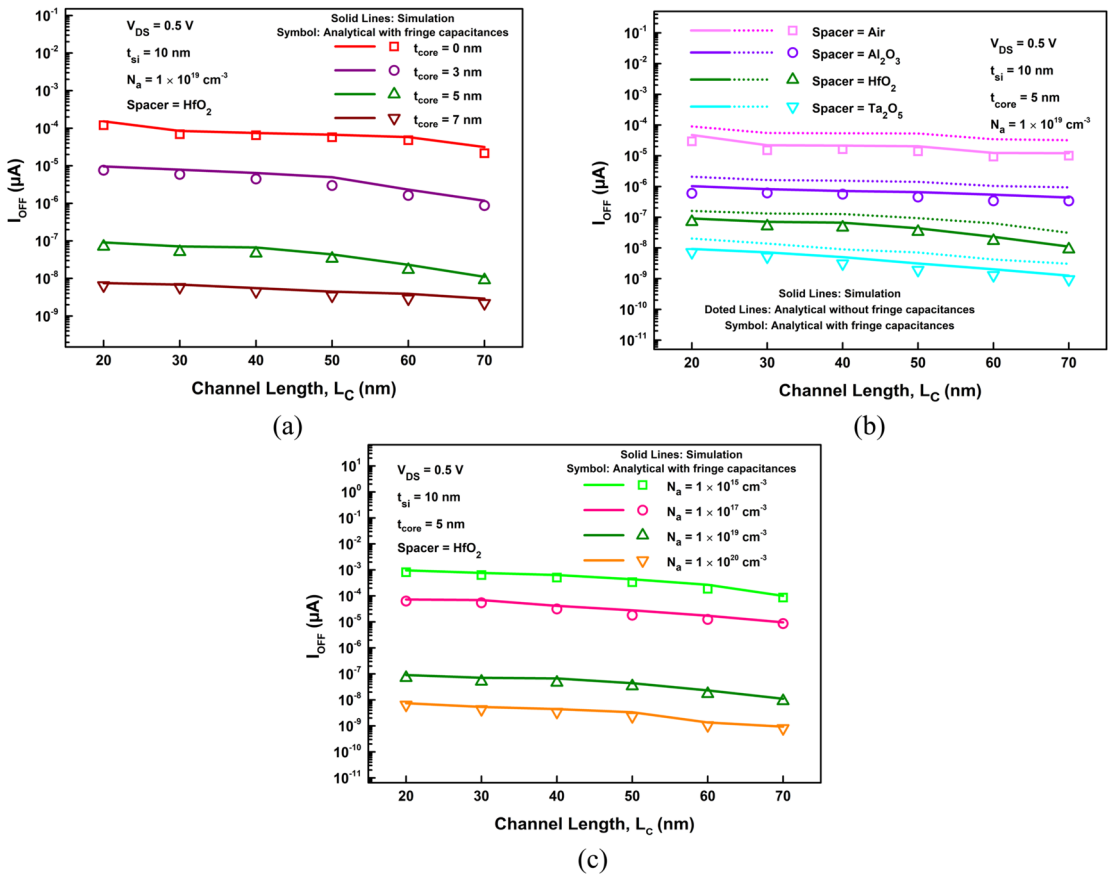

Figure 9. Effect of L_C scaling on I_{OFF} of ODCS-JL-NWFET for different (a) core thicknesses, (b) spacer materials with and without fringe capacitances, and (c) core doping concentrations.

Figures 7(a)–(c) depict the transfer characteristics of the ODCS-JL-NWFET for different core thicknesses, spacer materials, and core doping concentrations, respectively. As the t_{core} increases from 0 to 7 nm in figure 7(a), with a specific high-permittivity spacer, I_{OFF} decreases drastically by 4 orders of magnitude. This behavior is due to the fact that increasing t_{core} in the oppositely doped core aids in the depletion of carriers in the shell region during the OFF-state. Moreover, a high-permittivity spacer helps in volume depletion beyond the gate region due to an increase in the fringing electric field. However, increasing t_{core} also decreases the ON-state current (I_{ON}) at $V_{GS} = 1$ V, as the shell region, which serves as the conduction area, is reduced. The decrease in I_{ON} is more prominent when t_{core} exceeds more than half of the t_{si}. Figure 7(b) shows that when considering the fringe capacitances effect in an analytical model, a high-permittivity spacer (Ta_2O_5) reduces I_{OFF} more efficiently than a low-permittivity spacer (Al_2O_3), as a high-permittivity spacer increases gate voltage control over channel electrostatics due to the fringing electric field. Additionally, no significant decrease in I_{OFF} is observed for Ta_2O_5, therefore, HfO_2 is preferable as spacer material for ODCS-JL-NWFET. However, no significant improvement is observed in I_{ON}.

Furthermore, the analytical result without fringe capacitances increases the I_{OFF} significantly compared to the simulation result, as the model does not account for the enhanced depletion effect caused by the fringing electric field. Additionally, I_{ON} decreases due to an increase in parasitic resistances in S/D extensions without fringe capacitances consideration in analytical model. Figure 7(c) illustrates that as p-type core doping increases from 1×10^{15} cm^{-3} to 1×10^{20} cm^{-3}, I_{OFF} decreases by 3 orders of magnitude due to the effective depletion of carriers in the shell region. However, a highly doped core with a concentration of 1×10^{20} cm^{-3} degrades the I_{ON} significantly due to an increase in series resistance. The core doping of ODCS-JL-NWFET should be kept equally as the shell region because, beyond 1×10^{19} cm^{-3}, I_{ON} starts to degrade significantly. Therefore, the trade-off between I_{OFF} and I_{ON} should be carefully considered when designing the ODCS-JL-NWFET. Although increasing t_{core} decreases I_{OFF}, further increasing t_{core} beyond an optimal value does not provide additional performance benefits. This is because a larger core reduces the effective conduction area in the shell, limiting carrier transport. For t_{si} of 10 nm a t_{core} of 5 nm is preferable, as increasing t_{core} beyond this point leads to a significant degradation in I_{ON}.

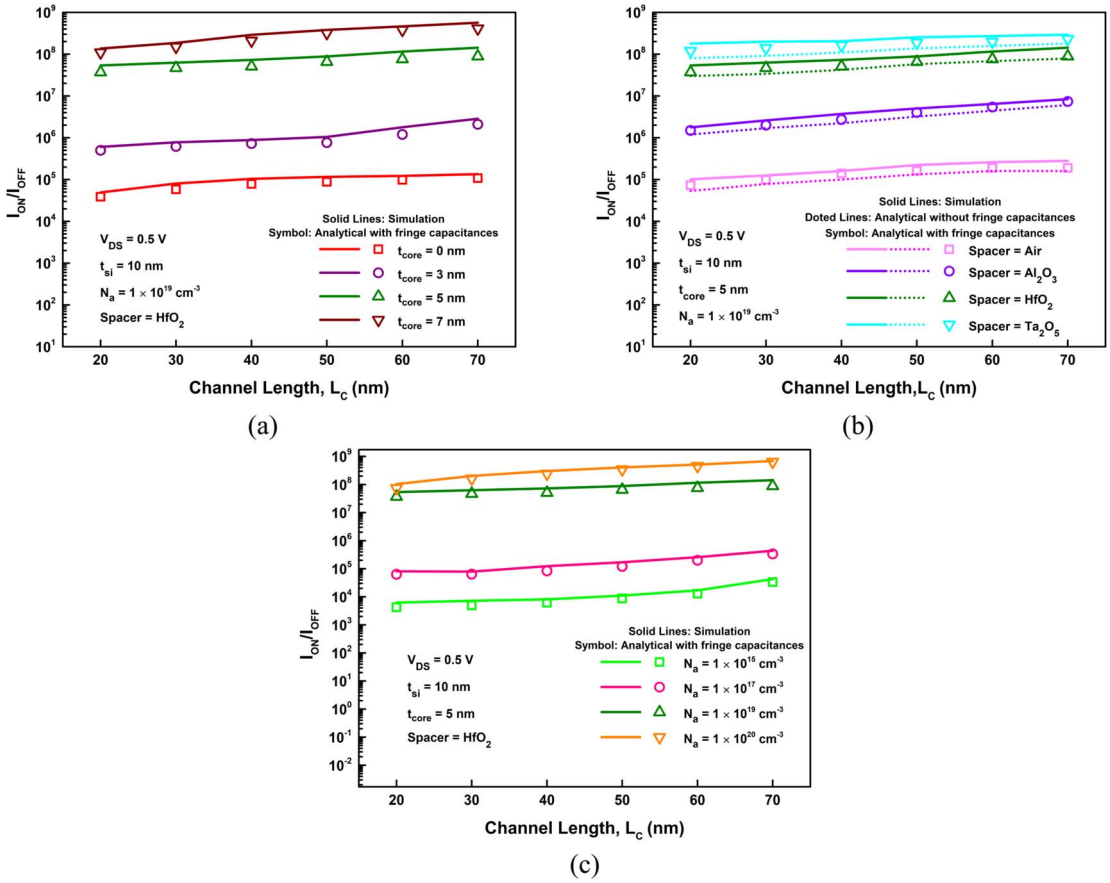

Figure 10. Effect of L_C scaling on I_{ON}/I_{OFF} ratio of ODCS-JL-NWFET for different (a) core thicknesses, (b) spacer materials with and without fringe capacitances, and (c) core doping concentrations.

To analyze the effect of L_C scaling on the characteristics of ODCS-JL-NWFET, L_C is varied from 70 nm to 20 nm. The dependence of V_T on L_C scaling is illustrated in figures 8(a)–(c) for different core thicknesses, spacer materials, and core doping concentrations, respectively. The V_T is calculated using the linear extrapolation method [19, 29, 30]. Figure 8(a) shows that at a given L_C, a wider t_{core} (7 nm) requires a higher V_T compared to a narrower t_{core} (3 nm) or no core. A thicker t_{core} depletes the channel more effectively during the OFF-state, which increases the required V_{GS} to turn the device ON, leading to a higher V_{GS}. In figure 8(b), considering fringe capacitance in the analytical model, higher permittivity spacer materials require a higher V_T, as they help to deplete S/D extension during the OFF-state. However, the improvement is less pronounced when using Ta_2O_5 compared to HfO_2 as the spacer material. On the other hand, without fringe capacitances, the analytical results decrease than the simulation as the absence of fringe capacitance weakens the coupling between the gate and the shell region, reducing the V_T. Figure 8(c) depicts that highly doped t_{core} (1×10^{20} cm^{-3}) depleted the shell region more effectively than lightly doped t_{core} (1×10^{15} cm^{-3}), resulting in increased V_T to initiate carrier conduction. In figures 8(a)–(c), V_T decreases as L_C is scaled down due to increased SCEs.

Figures 9(a)–(c) portray the effect of scaling L_C on I_{OFF} for various core thicknesses, spacer materials, and core doping concentrations, respectively. In figure 9(a), increasing t_{core} at fixed L_C reduces I_{OFF}, as discussed previously in figure 7(a). Additionally, figure 9(b) shows that by including the fringe capacitances effect in the analytical model, the spacer material with higher permittivity enhances depletion beyond the channel region and reduces I_{OFF} by suppressing unwanted carrier conduction in the OFF-state which was already discussed in figure 7(b). Additionally, without the inclusion of fringe capacitance, I_{OFF} increases due to the weaker electrostatic control. This leads to reduced depletion in the S/D extensions, allowing more I_{OFF}. Figure 9(c) illustrates that a highly doped core (1×10^{20} cm^{-3}) results in reduced I_{OFF} compared to a lightly doped core (1×10^{15} cm^{-3}) due to enhanced carrier depletion. The stronger depletion reduces carrier conduction in the OFF-state, thereby mitigating I_{OFF}. Furthermore, I_{OFF} increases as L_C decreases in figures 9(a)–(c) not by orders of magnitude but by noticeable increments due to the enhanced SCEs.

The influence of L_C scaling on the switching(I_{ON}/I_{OFF}) ratio for varying core thicknesses, spacer materials, and core doping concentrations are presented in figures 10(a)–(c), respectively. As shown in figure 10(a), a thicker t_{core} (7 nm) achieves the highest I_{ON}/I_{OFF} ratio, primarily due to a significant reduction in I_{OFF} compared

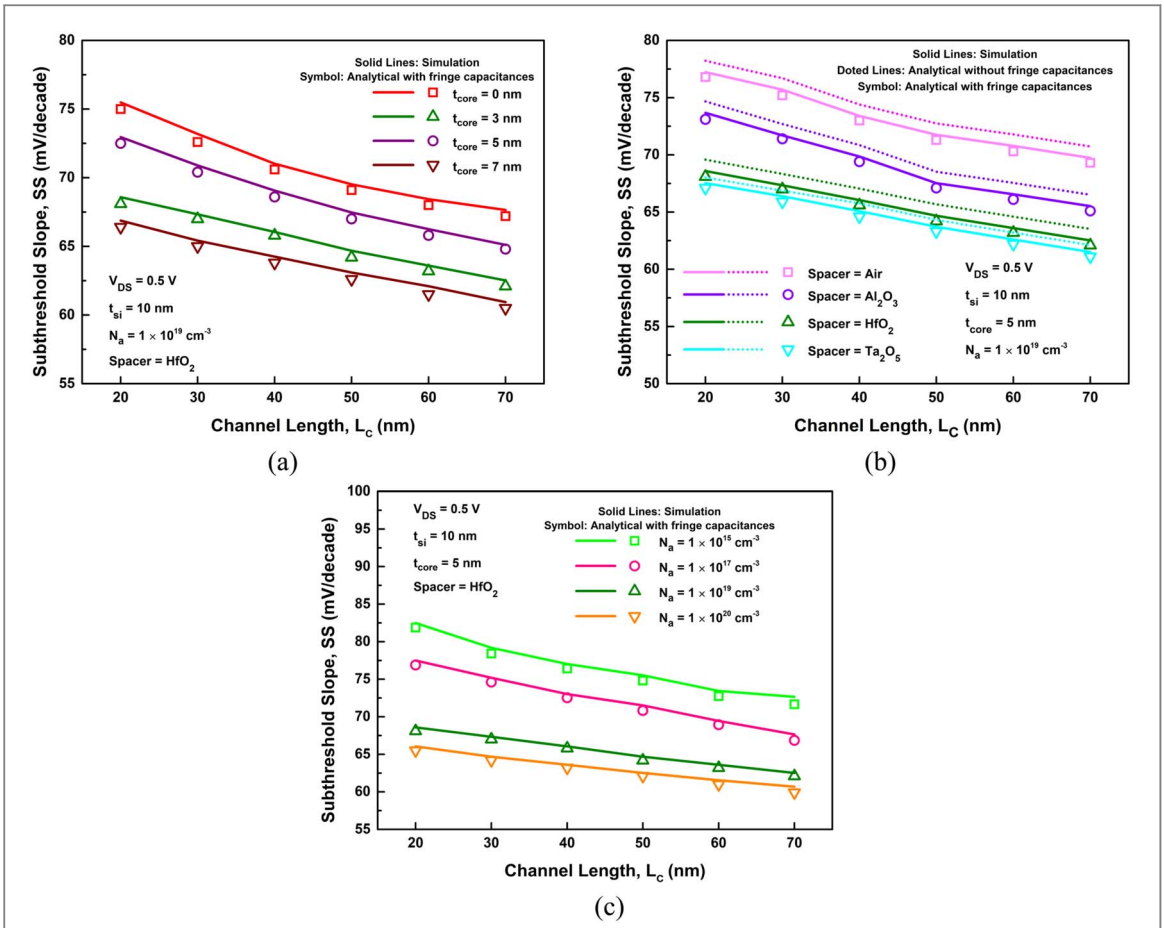

Figure 11. Effect of L_C scaling on SS of ODCS-JL-NWFET for different (a) core thicknesses, (b) spacer materials with and without fringe capacitances, and (c) core doping concentrations.

to a thinner t_{core} (3 nm) or no core. In figure 10(b), the use of a high-permittivity spacer (Ta_2O_5) results in a higher I_{ON}/I_{OFF} ratio compared to an air spacer when the inclusion of fringe capacitance is considered in the analytical model due to reduced I_{OFF}. However, the improvement in the I_{ON}/I_{OFF} ratio when switching from HfO_2 to Ta_2O_5 is relatively less. Furthermore, without fringe capacitances, I_{ON}/I_{OFF} ratio decreases than the simulation results due to an increase in I_{OFF}, as discussed in figure 9(b). Figure 10(c) demonstrates that the I_{ON}/I_{OFF} ratio increases with increasing core doping due to decreasing I_{OFF} as explained in figure 9(c). However, the enhancement in the I_{ON}/I_{OFF} ratio becomes less significant beyond a core doping concentration of 1×10^{19} cm^{-3}, making it an optimal doping level for balancing leakage suppression and ON-state performance. In figures 10(a)–(c), the I_{ON}/I_{OFF} ratio decreases with L_C scaling, not by orders of magnitude but by noticeable increments, driven by an increase in I_{OFF}. Additionally, no significant enhancement in I_{ON} is observed with L_C scaling.

Figures 11(a)–(c) compare the SS of ODCS-JL-NWFET for different core thicknesses, spacer materials, and core doping concentrations, respectively. A steep SS is desirable to efficiently switch the transistor current by minimizing subthreshold leakage, which helps reduce CMOS standby power dissipation. As shown in figure 11(a), the lowest SS is achieved with a thicker t_{core} (7 nm) due to a significant reduction in I_{OFF}, as seen in figure 9(a). Figure 11(b) indicates that considering the effect of fringe capacitance in the analytical model, a high-permittivity spacer material improves SS by depleting the S/D extension, leading to a decrease in I_{OFF}, as discussed in figure 7(b). This mitigated I_{OFF} steepens the slope of the transfer characteristics, bringing SS closer to its ideal value. Moreover, without fringe capacitances, SS increases than its simulation results due to enhanced I_{OFF} as shown in figure 9(b). Figure 11(c) illustrates that at fixed L_C, increasing core doping concentrations leads to an improved SS due to a greater extent of depletion in the shell region that mitigates I_{OFF}. The stronger depletion effect reduces the potential barrier-lowering effect caused by residual carriers, ensuring a sharper turn-on characteristic and better switching efficiency. However, SS increases with the scaling down of L_C in figures 11(a)–(c), owing to the rise in I_{OFF}, which reduces the steepness of the transfer characteristics slope.

4. Conclusion

In this paper, an analytical model of ODCS-JL-NWFET considering fringe capacitance is reported. A physics-based analytical model of the surface potential, threshold voltage, drain current, and subthreshold slope has been derived. The accuracy of the proposed model has been verified by comparing it against simulated data results obtained from a 3-D TCAD device simulator. The design guidelines derived from this analysis emphasize the optimal core thickness at half of the channel thickness, with doping equal in magnitude and opposite in type to that of the shell region. Additionally, the use of an HfO_2 spacer is recommended to effectively minimize leakage current and improve the subthreshold slope. This model offers valuable physical insights into the behavior of ODCS-JL-NWFETs and serves as a useful guideline for future research in device applications.

Ethics approval

The manuscript is not submitted to anywhere else for the publication. The submitted work is an original work and have not been published elsewhere in any form or language. The authors do not have any conflict of interest. The research does not involve any human participant and/or animal thus, informed consent in not required.

Consent for publication

All the authors understand and give their consent for the publication of the manuscript 'Analytical Modeling of Fringe Capacitance in Opposite-Doped Core–Shell Junctionless Nanowire FET' in the 'Engineering Research Express' Journal.

Competing interests

No, all the authors declare that they have no competing interests, or other interests that might be perceived to influence the results and/or discussion reported in this paper. The authors have no conflicts of interest to declare that are relevant to the content of this article.

Funding

Not Applicable.

Author's contributions

Bharti: Conceptualization, Data curation, Formal analysis, Investigation, Methodology, Validation, Writing—original draft.
Poornima Mittal: Conceptualization, Investigation, Methodology, Supervision, Visualization, Writing—review & editing.

Data availability statement

All data that support the findings of this study are included within the article (and any supplementary files).

ORCID iDs

Poornima Mittal https://orcid.org/0000-0002-9479-8628

References

[1] Riyadi M A, Suseno J E and Ismail R 2010 The future of non-planar nanoelectronics MOSFET devices: a review *J. Appl. Sci.* **10** 2136–46
[2] Ferain I, Colinge C A and Colinge J P 2011 Multigate transistors as the future of classical metal–oxide–semiconductor field-effect transistors *Nat* **479** 310–6
[3] Nagy D, Indalecio G, GarcíA-Loureiro A J, Elmessary M A, Kalna K and Seoane N 2018 FinFET versus gate-all-around nanowire FET: performance, scaling, and variability *IEEE J. Electron Devices Soc.* **6** 332–40
[4] Colinge J P *et al* 2010 Nanowire transistors without junctions *Nat. Nanotechnol.* **5** 225–9

[5] Choi S J, Moon D I, Kim S, Duarte J P and Choi Y K 2011 Sensitivity of threshold voltage to nanowire width variation in junctionless transistors *IEEE Electron Device Lett.* **32** 125–7
[6] Rajendiran P, Justeena A N, Mrabet J, Ramasamy S, Selvam P D and Nirmal D 2024 Sensitivity analysis of junctionless silicon NT-TFET and performance metrics comparison with the silicon NT-TFET *J. Nanopart. Res.* **26** 129
[7] Sharma S and Chaujar R 2022 Influence of source electrode metal work function on polar gate prompted source hole plasma in arsenide/antimonide tunneling interfaced junctionless TFET *J. Micromech. Microeng.* **32** 044004
[8] Gundapaneni S, Bajaj M, Pandey R K, Murali K V R, Ganguly S and Kottantharayil A 2012 Effect of band-to-band tunneling on junctionless transistors *IEEE Trans. Electron Dev.* **59** 1023–9
[9] Jain A K and Singha A 2021 Sub-10-nm scalability of emerging nanowire junctionless FETs using a Schottky metallic core *J. Electron. Mater.* **50** 1110–8
[10] Kumar M P V, Hu C Y, Kao K H, Lee Y J and Chao T S 2015 Impacts of the shell doping profile on the electrical characteristics of junctionless FETs *IEEE Trans. Electron Dev.* **62** 3541–6
[11] Sahay S and Kumar M J 2016 Controlling L-BTBT and volume depletion in nanowire JLFETs using core–shell architecture *IEEE Trans. Electron Dev.* **63** 3790–4
[12] Bharti and Mittal P 2024 Investigating the effect of scaling and temperature on the performance of improved junctionless nanowire FET through simulation analysis, *Phys. Scr.* **99** 086103
[13] Lee Y J *et al* 2015 High performance poly Si junctionless transistors with sub-5 nm conformally doped layers by molecular monolayer doping and microwave incorporating CO2 laser annealing for 3D stacked ICs applications *IEEE International Electron Devices Meeting (IEDM)* 2.1–2.4
[14] Xu L, Wu G, Li P and Cheng T 2023 Modeling threshold voltage and drain-induced barrier lowering effect of opposite doping core–shell channel surrounding-gate junctionless MOSFET *Microelectron. J.* **139** 105830
[15] Rodriguez S S, Tinoco J C, Martinez-Lopez A G, Alvarado J and Raskin J P 2013 Parasitic gate capacitance model for triple-gate FinFETs *IEEE Trans. Electron Dev.* **60** 3710–7
[16] Mohapatra N R, Desai M P, Narendra S G and Rao V R 2003 Modeling of parasitic capacitances in deep submicrometer conventional and high-K dielectric MOS transistors *IEEE Trans. Electron Dev.* **50** 959–66
[17] Kim S H, Fossum J G and Yang J W 2006 Modeling and significance of fringe capacitance in nonclassical CMOS devices with gate–source/drain underlap *IEEE Trans. Electron Dev.* **53** 2143–50
[18] Kaushal S and Rana A K 2021 Analytical modelling and simulation of negative capacitance junctionless FinFET considering fringing field effects *Superlattices Microstruct.* **155** 106929
[19] Bharti and Mittal P 2024 Oppositely-doped core–shell junctionless nanowire FET: design and investigation *ECS J. Solid State Sci. Technol.* **13** 013004
[20] Chiang T K 2012 A new quasi-2-D threshold voltage model for short-channel junctionless cylindrical surrounding gate (JLCSG) MOSFETs *IEEE Trans. Electron Dev.* **59** 3127–9
[21] Chiang T K 2012 A quasi-two-dimensional threshold voltage model for short-channel junctionless double-gate MOSFETs *IEEE Trans. Electron Dev.* **59** 2284–9
[22] Li C, Zhuang Y, Di S and Han R 2013 Subthreshold behavior models for nanoscale short-channel junctionless cylindrical surrounding-gate MOSFETs *IEEE Trans. Electron Dev.* **60** 3655–62
[23] Sarkhel S and Sarkar S K 2014 A comprehensive two dimensional analytical study of a nanoscale linearly graded binary metal alloy gate cylindrical junctionless MOSFET for improved short channel performance *J. Comput. Electron.* **13** 925–32
[24] Reddy G V and Kumar M J 2005 A new dual-material double-gate (DMDG) nanoscale SOI MOSFET-two-dimensional analytical modeling and simulation *IEEE Trans. Nanotechnol.* **4** 260–8
[25] Mittal P, Negi Y S and Singh R K 2016 A depth analysis for different structures of organic thin film transistors: modeling of performance limiting issues *Microelectron. Eng.* **150** 7–18
[26] 2018 Atlas User's Manual: Device Simulation Software Silvaco Inc. Santa Clara, CA, USA
[27] Mei G, Li P, Hu G, Liu R, Wang L and Tang T A 2012 Quantum mechanical effects on the threshold voltage of surrounding-gate MOSFETs *Microelectron. J.* **43** 894–7
[28] Saini G and Choudhary S 2017 Improving the subthreshold performance of junctionless transistor using spacer engineering *Microelectron. J.* **59** 55–8
[29] Ortiz-Conde A, García-Sánchez F J, Muci J, Barrios A T, Liou J J and Ho C S 2013 Revisiting MOSFET threshold voltage extraction methods *Microelectron. Reliab.* **53** 90–104
[30] Mittal P, Negi Y S and Singh R K 2015 Mapping of performance limiting issues to analyze top and bottom contact organic thin film transistors *J. Comput. Electron.* **14** 360–79

Plasmonics
https://doi.org/10.1007/s11468-025-02911-x

RESEARCH

Black Phosphorus-Based SPR Photonic Crystal Fiber Biosensor for Urinary Tract Infection Detection

Plakshi Gupta[1] · Akash Khamaru[1] · Ajeet Kumar[1]

Received: 18 February 2025 / Accepted: 18 March 2025
© The Author(s), under exclusive licence to Springer Science+Business Media, LLC, part of Springer Nature 2025

Abstract

The presented work focused on a photonic crystal fiber (PCF)-based urinary tract infection (UTI) biosensor operating on the principle of surface plasmon resonance (SPR) combined with black phosphorus (BP) layers as a plasmonic enhancer to increase the sensitivity of the sensor. There are three types of bacteria that can cause UTI: *Pseudomonas*, *Escherichia coli*, and *Enterococcus faecalis*, whose refractive indices are already available in various experimental literatures and having magnitudes 1.371, 1.388, and 1.3921, respectively. The analysis is carry forwarded by applying the finite element method (FEM)-based simulation software-COMSOL Multiphysics. The PCF structure comprises TiO_2, gold, and BP layers, forming a plasmonic layer conjugate along with square air holes running along its length. The analysis also contains the comparison of the sensor's performance with and without incorporating the BP layers, which shows that the wavelength sensitivity increases exponentially. When the sensor is composed without the BP layers, the wavelength sensitivity for different types of bacteria is 2361.11, 2924.52, and 3239.92 nm/RIU, whereas when the BP layers are placed on the top of the gold layer, the wavelength sensitivity goes as high as 5138.88, 7264.15, and 8936.69 nm/RIU. This shows an increase in the sensitivity by much more than 50%, which helps our PCF biosensor stand out as an effective alternative among other designed UTI-focused sensors.

Keywords Urinary Tract Infection · PCF Biosensor · Surface Plasmon Resonance · Black Phosphorus · Wavelength Sensitivity

Introduction

UTI (urinary tract infection) is a bacterial infection that affects kidneys, urethra, ureters, and bladders and affects more than 150 million people worldwide annually. The study of UTI varies with age, gender, abnormalities, pregnancy, anatomic, and many other factors. It mostly affects women than men due to anatomical differences in genitourinary tract [1]. According to studies, 3 to 24% of women are affected with UTI during pregnancies which leads to complications such as premature birth, anemia, chronic kidney failure, and lesser birth weight of infants. Some of the symptoms of UTIs range from pelvic pain and vomiting to severe complications like multi-organ failure or even deaths. So, timely identification and treatment of UTI is important to reduce maternal morbidity and recurrence.

UTIs can be caused by both gram-positive and gram-negative microorganisms (known as uropathogens), where *Escherichia coli* (*E. coli*) is a gram-negative bacteria. Some other bacteria leading to UTIs are *Enterococcus faecalis* (*E. faecalis*), *Pseudomonas aeruginosa*, *Klebsiella pneumoniae*, and *Staphylococcus saprophyticus* [1]. Generally, conventional methods such as urine culturing, urine microscopy, and other methods like ELISA, PCR, and biosensor detectors are used for UTI detection [2]. Urine culture is the standard method and economically friendly approach for diagnosis of uropathogens but is also time-consuming, labor-intensive, and requires growth media. To overcome these challenges, ELISA and PCR can also be used, which are rapid detection techniques but still require skilled labor and expensive equipment

✉ Ajeet Kumar
ajeetdph@dtu.ac.in

Plakshi Gupta
plakshigupta_23mscphy74@dtu.ac.in

Akash Khamaru
akashkhamaru_23phdap02@dtu.ac.in

[1] Advanced Photonics Simulation Research Laboratory, Department of Applied Physics, Delhi Technological University, Shahbad Daulatpur, Bawana Road, Delhi 110042, India

Published online: 26 March 2025

[2]. Therefore, there is a growing demand for simple, rapid, cost-effective, and highly sensitive diagnostic tools to detect UTI, which led to the development of surface plasmon resonance (SPR)-based biosensors. SPR-based biosensors measure change in refractive index depending upon the pathogen concentration in the analyte and allows the investigation of binding of molecules in real time.

Both infected and uninfected samples of urine are used with the objective of detecting as well as identifying the type of pathogen involved in UTI. The data set of uninfected urine sample with a refractive index of 1.335 is calculated, and that particular resonant point is considered as the reference point for further analysis of different pathogens. The RI of other infected samples depends upon the type of pathogen causing the urinary tract infection. The refractive index is 1.371 for *Pseudomonas*, 1.388 for *E. coli*, and 1.3921 for *E. faecalis*. The deviation from the reference point indicates the presence of specific pathogen [1, 3]. Divya et al. had proposed a dual-channel SPR-based biosensor in 2024 for detection of UTI and tuberculosis simultaneously, with a maximum wavelength sensitivity of 8235.29 nm/RIU for UTI [1].

SPR occurs at the surface of metals when an electron interacts with the light which hits the surface at a particular angle. The interaction of electrons and light is sensitive to the changes in the surrounding environment. Surface plasmons were first introduced in the 1950s by Ritchie [4]. The theory of surface plasmons was applied and an SPR configuration which was coupled with prism was introduced by Otto where plasmonic materials and prism are separated by a dielectric medium [5]. It was then updated by Kretschmann, where plasmonic materials and prism were kept in direct contact [6]. In 1980s, researchers started to use these methods for sensing purposes [7–9]. The sensing technologies that adopt SPR provide real-time analysis and are more sensitive and label-free. So, SPR sensing has vast applications in biosensing [10, 11], gas-sensing [12], chemical-sensing [13, 14] etc. The prism-based Kretschmann setup is widely being used for making the sensors, where the prism is coated with plasmonic layers like gold, silver, and TiO_2. But prism-based SPR sensor requires bulky configuration and is also not cost effective. These limitations of Kretschmann's prism-based SPR sensors opened a new path in the 1960s for optical fiber-based SPR sensors [15]. They provided better resolution and wider operating range. However, there were still some disadvantages, like they require a narrow and direct incident of light at a particular angle. To overcome these, photonic crystal fibers (PCFs) were introduced around the 2000s and were used for SPR-based detections [16].

PCFs are a type of optical fibers which contain small air holes all along its length. Such small air holes controls or provides a path to the light that moves throughout the fiber. This can be done more precisely and accurately with PCFs. Some advantages of PCFs include high birefringence, high nonlinearity, and flexible design. The advantages give rise to a lot of different applications like terahertz-based sensing [17, 18], terahertz communication [19], refractometric sensors [20, 21], pressure sensors [22], supercontinuum generation [23–25], metrology, and spectroscopy [26]. PCFs are produced in large-scale laboratories by using techniques like sol–gel casting, drilling, stacking of capillaries, and rod extrusion [27].

Combining both, SPR phenomenon and PCFs give rise to SPR-conjugated PCF sensors, which are used to detect even the small substances present in the surroundings of the sensor. It is advantageous as it has smaller size and effortless light launching, and its ability to control the evanescent field penetration has made it an effective technique for sensing. A light beam enters the PCF and penetrates to the core [28]. As the light hits plasmonic material, free electrons present there begin oscillating. A strong interaction happens when the frequency of oscillations and light matches up correctly, called resonance condition. If the refractive index of the environment or analyte changes, then this resonance condition shifts, which can be easily detected by the SPR-PCF sensor. These changes are detected by the sensor and are investigated numerically or analytically using finite element method in the COMSOL Multiphysics software. There are many types of SPR-PCF designs like U-grooved [29], metal coated [30], and D-shaped [28]. The D-shaped PCF has the advantage of easiness in fabrication as the top portion of the structure is kept flat, so the fabrication of metal layers becomes easier which effectively improves the sensitivity.

Surface plasmon polaritons (SPPs) are electromagnetic excitations of free electron densities at the intersection of metal and the fiber. So, SPP excitation is improved by the presence of a larger electron density, which is provided by the metallic thin films. These thin metallic layers are known as plasmonic materials. Plasmonic materials like gold, silver, and TiO_2 are most commonly used. Gold is known as the best plasmonic material as it is free from corrosion and oxidation and has very good chemical fixity. It shows a narrow and sharp resonance peak but has the disadvantage of poor biomolecule adsorption [31]. Silver has higher accuracy because it has excellent chemical properties and produces a sharper SPR spectrum, but it is very reactive and suffers greatly from oxidation. TiO_2, on the other hand, is used to provide adhesion between the fiber surface and the gold layer. This can also overcome the disadvantage of gold, which is poor biomolecule adsorption [32].

Recently, silicene, graphene, germanene, phosphorene, and black phosphorus (BP) are being seen to possess great plasmonic properties in the infrared and terahertz frequencies [33–36]. Silicene is a hexagonal honeycomb 2-D allotrope of silicon (Si). Germanene, just like silicene, is a 2-D honeycomb structure with small band gap material and a

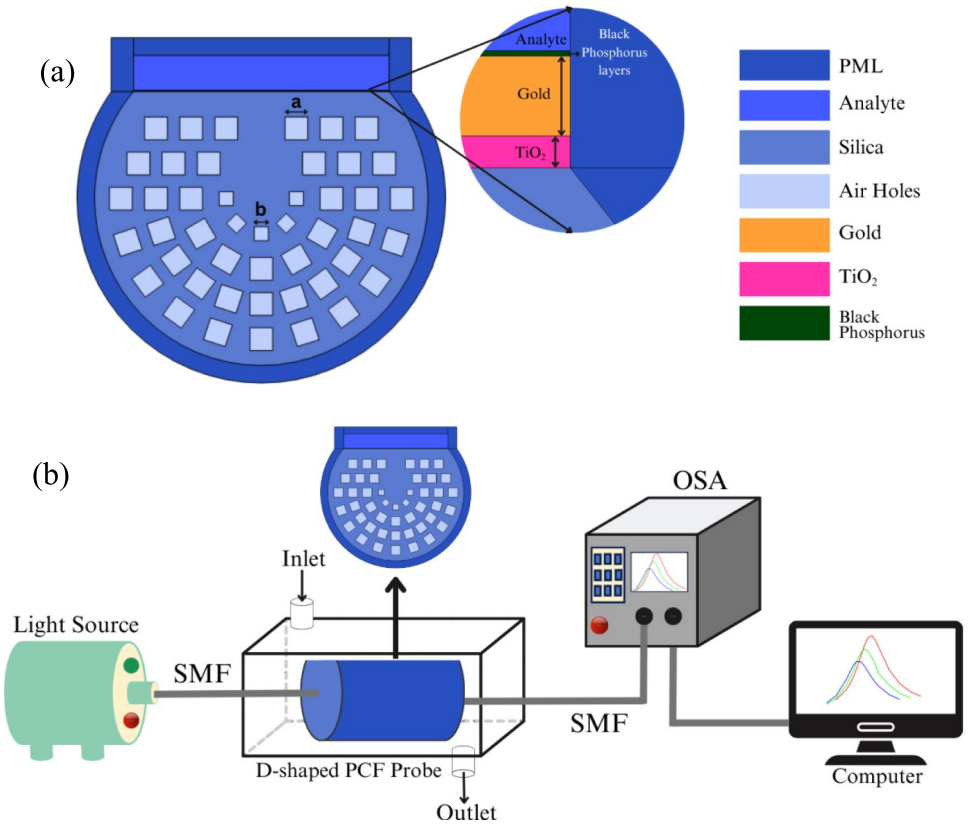

Fig. 1 **a** Designed D-shaped SPR PCF biosensor. **b** Proposed experimental setup

higher lifetime of plasmonic modes. A characteristic of phosphorene is the tunability of its band structure, which makes it useful in anisotropic plasmonic applications. Yang et al. proposed an SPR-PCF sensor with graphene as a 2-D layer and achieved the wavelength sensitivity of 2520 nm/RIU in the sensing range of 1.33–1.35 [37]; aluminum-doped zinc oxide is coated on the PCF structure by Dash et al. [38] to achieve wavelength sensitivity of 5000 nm/RIU in the sensing range of 1.32–1.34. Black phosphorus (BP) possesses a zigzagged-honeycomb structure [28]. BP has great electrical and optical properties which is attracting researchers working on plasmonics. Its properties, like direct band gap, allow it to react with light at specific wavelengths, and a smaller work function allows the electrons to jump easily between the surrounding environment and the BP layer. Higher charge mobility makes the sensor to send signals fast, resulting in rapid detection. Its ability to bind molecules tightly onto the surface of the sensor makes it very useful in biological and chemical sensing [39]. So, BP improves the sensor's ability by providing proteins, DNA, or chemical analytes an active and open site to stick to. BP is incorporated on the surface of the sensor in the form of thin layers of 0.53-nm thickness each [40]. These are some reasons that black phosphorus can be used as a plasmonic layer in biological sensors like the proposed UTI sensor.

This work proposes a TiO_2/gold/black phosphorus-layered configuration for UTI sensor with square air holes with high wavelength sensitivity. The square air holes provide higher confinement of the core light, focusing the core field only towards the plasmonic layer for effective interaction. Smaller sizes of square air holes are also used near the core, which squeezes the maximum energy of core mode to couple with the metal layers and, therefore, increases the sensitivity of the sensor [41]. Furthermore, structural parameters like the thickness of TiO_2, gold, and the number of BP layers are also optimized to achieve a higher sensitivity for the proposed UTI sensor.

Designed PCF Structure

The designed D-shaped SPR-based PCF biosensor with square air holes is displayed in Fig. 1 a with a cross-sectional and magnified view. The PCF geometry is the composition of two sizes of square air holes, situated in the cladding. The bigger square holes have side length (a) of 1.3 µm (a), and smaller ones have side length (b) of 0.8 µm, which are placed near the fiber core such that most of the light from the core is directed towards the metal layers. On the top of the flat surface of the D-shaped fiber, there is a thin layer of TiO_2 of thickness, $t_{Ti} = 16$ nm, which sticks the gold layer

on the top of it to the fiber. The thickness of the gold layer, placed above the TiO_2 layer, is $t_g = 40$ nm. It helps in the proper detection of the UTI cells from the urine sample that is made to pass through the analyte. A significant number of BP layers of thickness, $t_{BP} = 0.53$ nm each, placed above the gold layer, to enhance the sensing capability of the sensor. The BP layers stay connected due to the van der Waals forces of attractions present between them. The refractive index of the medium to be measured here is defined as bio-analyte (n_a), with analyte channel thickness, $t_a = 2$ µm, and is placed above the BP layers. To define the computational domain and get rid of the back-reflection effect, a perfectly matched layer (PML) is applied along the cylindrical geometry having width magnitude of 1 µm.

Figure 1b shows a schematic diagram of the proposed experimental setup. The coupling efficiency is first enhanced by putting a light source with a wide IR spectrum into the biosensor using a single-mode fiber (SMF). At the air-core interface, the light is incident in the biosensor and is guided into the core, through the phenomenon of modified total internal reflection (M-TIR). SPR occurs at the boundary of metal surface and the analyte. Whenever a specific molecule that is to be detected is found, the surface of the metal undergoes RI modification, which also causes alteration in the effective RI and result in wavelength shift. These changes are detected by using an optical spectrum analyzer (OSA), and connecting it to a computer system enables us to collect the data efficiently.

Methodology

The proposed structure is analyzed using the FEM-based COMSOL Multiphysics software. The PCF is composed of the pure silica material where the refractive index depends on the wavelength; therefore, Sellmeier equation is employed, which is wavelength dependent,

$$n^2(\lambda) = 1 + \frac{D_1\lambda^2}{\lambda^2 - E_1} + \frac{D_2\lambda^2}{\lambda^2 - E_2} + \frac{D_3\lambda^2}{\lambda^2 - E_3} \tag{1}$$

where λ is the wavelength of light, and $D_1 = 0.696163$, $D_2 = 0.4079426$, $D_3 = 0.8974794$, $E_1 = 0.0684043$, $E_2 = 0.1162414$, and $E_3 = 9.896161$ are constants.

The TiO_2 layer is placed above the gold layer, and it acts as an adhesive agent between the gold layer and the PCF. The refractive index of the PCF is calculated using the following formula where λ is in Å units [32]:

$$n^2 = 5.913 + \frac{0.2441}{\lambda^2 - 0.0803} \tag{2}$$

Gold metal consists of two types of electrons: free electrons and bound electrons. Drude model is used to find the dielectric constant of free electrons, and the Lorentz oscillator model is used for bound electrons. The combined model for the dielectric constant of gold metal is known as the Drude-Lorentz model [31]:

$$\varepsilon_{Au} = \varepsilon_\infty - \frac{\omega_D^2}{\omega(\omega + j\gamma_D)} - \frac{\Delta\varepsilon\Omega_L^2}{\omega^2 - \Omega_L^2 + j\Gamma_L\omega} \tag{3}$$

where $\varepsilon_\infty = 5.9673$ is the permittivity at high frequencies, occurring when electric field of light is high and an electron is not able to respond to it. $\gamma_D \sim 2\pi \times 15.92$ THz is the damping factor as the free electrons cannot move forever. $\omega_D \sim 2\pi \times 2113.6$ THz is the frequency of oscillation of the free electrons in the metal, when light strikes them. ω is the frequency of light. Similarly, $\Gamma_L \sim 2\pi \times 104.86$ THz is the damping factor for bound electrons, $\Omega_L \sim 2\pi \times 650.07$ THz is the frequency of oscillation of bound electrons, when light hits them, and $\Delta\epsilon$ is change in permittivity due to vibration of bound electrons.

The Cauchy absorbent model is used to find the refractive index of the black phosphorus layers, where λ is in nm units [42],

$$n(\lambda) = P + Q\frac{10^4}{\lambda^2} + R\frac{10^9}{\lambda^4} \tag{4}$$

$$k(\lambda) = X \times 10^{-5} + Y\frac{10^4}{\lambda^2} + Z\frac{10^9}{\lambda^4} \tag{5}$$

where $n(\lambda)$ is the real and $k(\lambda)$ is the imaginary part of the refractive index. $P = 3.57$, $Q = 6.79$, $R = 39.99$, $X = 3206$, $Y = -0.521$, and $Z = 10.26$ are constants.

Confinement loss is the amount of light that is leaked from the core region to the plasmonic metals. It is calculated using the following equations, where α_{loss} is the confinement loss in dB/cm units, λ is the wavelength, and $\mathrm{Imag}(n_{eff})$ is the imaginary part of the effective refractive index [43],

$$\alpha_{loss}(\mathrm{dB/cm}) = 8.686 \times \frac{2\pi}{\lambda} \times \mathrm{Imag}(n_{eff}) \times 10^4 \tag{6}$$

The performance of the sensor can be calculated in the two ways, that are, wavelength sensitivity (S_w) and amplitude sensitivity (S_A) [44, 45],

$$S_w(\mathrm{nm/RIU}) = \frac{\Delta\lambda_{peak}}{\Delta n_a} \tag{7}$$

where $\Delta\lambda_{peak}$ is change in the peak wavelengths for different RIs, and Δn_a is the change in RIs in the analyte.

$$S_A(\lambda) = -\frac{1}{\alpha(\lambda, n_a)}\frac{\partial\alpha(\lambda, n_a)}{\partial n_a} \tag{8}$$

where $\alpha(\lambda, n_a)$ is the loss at particular wavelength, $\partial\alpha(\lambda, n_a)$ is the difference between two loss spectra, and ∂n_a is the change in RIs in the analyte.

Fabrication Feasibility

The gold layer can be fabricated on the flat surface of the proposed D-shaped sensor by various methods like pulse laser deposition, RF sputtering, and splash technology. In pulsed laser deposition, a pulsed beam of high energy is targeted on the bulk gold, which causes ejection of the gold atoms from the bulk surface [31]. In RF sputtering technique, radio frequency energy is used to create plasma that is targeted on the bulk gold, causing the gold atoms to sputter out. Splash coating technology involves spraying or splashing liquid gold nanoparticles on the PCF's flat surface for gold layer deposition, which is then followed by a heat treatment.

The fabrication of TiO_2 can also be done using various methods such as chemical vapor deposition, sol–gel method, and atomic layer deposition [42]. But sol–gel is the most commonly used method. In this, a solution of titanium alkoxide is hydrolyzed and condensed to form a gel of TiO_2, which is then deposited on the PCF's surface and heat treated subsequently to convert it into a crystalline film.

BP layers can also be prepared by using many different methods such as mechanical peeling (most commonly used), liquid peeling, and pulsed laser precipitation. Mechanical peeling involves the peeling of thin layers of BP from the bulk crystal, physically. It involves a special type of instrument, which can be adjusted according to the thickness of BP required. In liquid peeling, a bulk piece of black phosphorus is placed in a liquid like water and then ultrasound waves are passed through it. These vibrations cause the layers to come apart and disperse into the liquid [28]. This method is used for preparation of bulk layers. Pulsed laser precipitation method requires a powerful laser to be fired at the bulk BP, and the energy from the laser breaks apart thin layers.

The square air holes can be prepared using the stack and draw method, in which the bundles of silica capillaries are traced down along the length of PCF and mingled. This technique provides mechanical stability as surface tension balances out the drawing process forces. Other than this, the square holes can also be prepared by 3-D printing method and extrusion technique. This technique allows to extract fiber by drawing from bulk glass, and any pattern like circles, squares, or rectangles can be formed. Therefore, it can be believed that the fabrication of the proposed biosensor is possible using the mentioned fabrication techniques [46].

Results and Discussions

In this section, the analysis of the proposed sensor using the COMSOL Multiphysics software are discussed, and all the combinations of structural parameters to increase the sensitivity are shown.

Electric Field Distribution and Dispersion Characteristics

There are x and y-axes electric field distribution for an SPR sensor, when the incident light beam is guided through the core. When the phase matching happens, the transfer of energy from the core to plasmonic mode occurs, and this is known as the coupling mode [28]. This transfer of energy results in the enhanced performance of the biosensor. Here, y-polarized core mode is considered because it provides the clear visibility of coupling effect as compared to the x-polarization. This happens because the plasmonic materials are placed at the top surface. Figure 2a–c show core mode, coupled mode (SPR mode), and SPP mode, respectively. Figure 2d shows the loss curve and dispersion relation for the biosensor at refractive index 1.335 in the analyte. As the resonance condition comes, the loss increases with increase in wavelength and reaches to a maximum value of 78.22 dB/cm at the wavelength of 995 nm. At the resonant point, the RI of the core and SPP mode intersects and maximum light gets coupled with plasmonic materials.

Optimization of Geometrical Parameters

For the achievement of an optimum structure, the analysis covers the investigation of the effect of the various parameters like thickness of all the plasmonic layers and different lengths of air holes. By investigating and analyzing these parameters, the biosensor's sensitivity and efficiency can be increased to detect the specific infection.

Optimization of Gold Layer

Gold is used as a plasmonic layer in the proposed SPR-PCF biosensor. The optimized thickness of gold layer is investigated by varying t_g from 35 to 45 nm in steps of 5 nm, by keeping other parameters, like $t_{Ti} = 12$ nm, $a = 1.3$ μm, and $b = 0.8$ μm, constant. The analysis with BP layers is done separately after optimizing of all other parameters. Figure 3a shows the confinement loss spectra of the structure as t_g gradually increases. The result shows that the resonant wavelength shifts towards larger wavelengths, and the confinement loss also faces decrement as the t_g increases. This can be because larger gold layer thickness can give rise to damping loss, resulting in broader peak and decreased

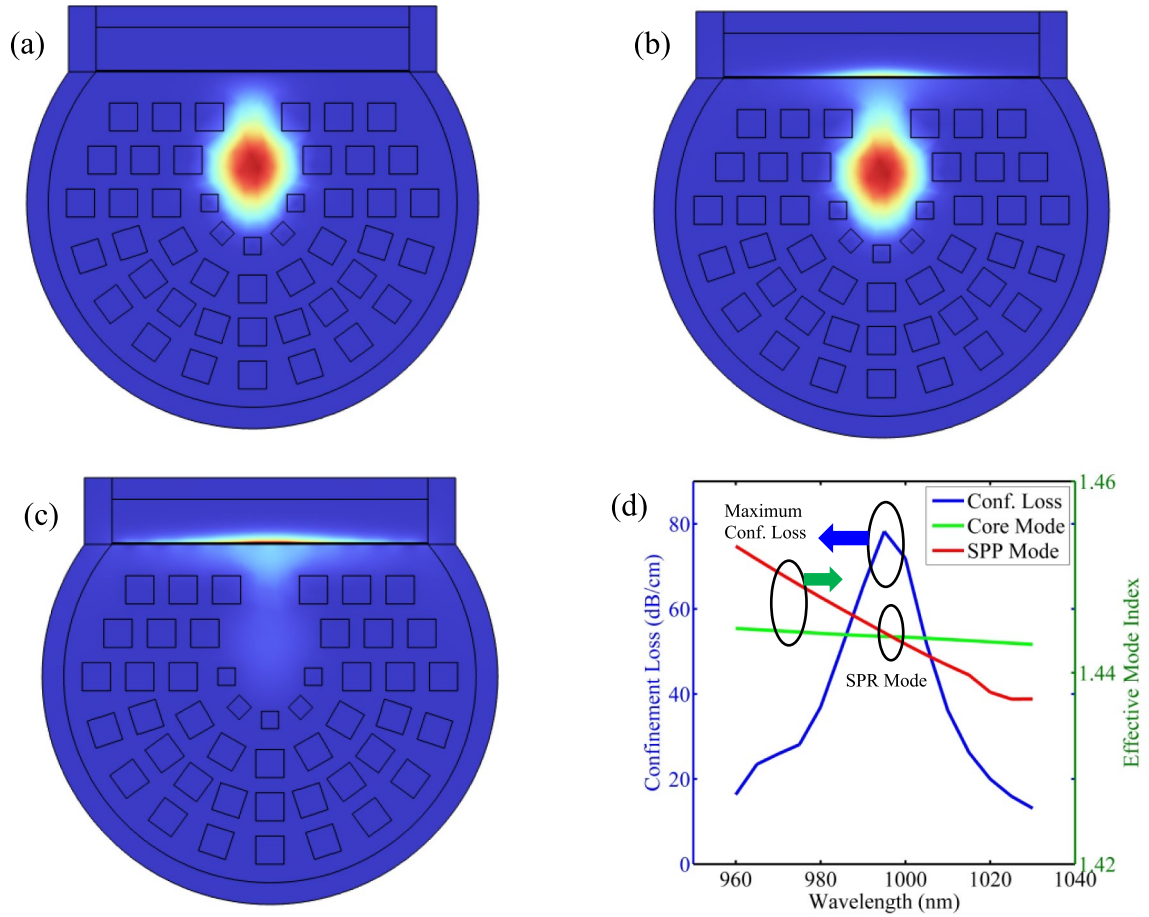

Fig. 2 **a** Core mode. **b** SPR mode. **c** SPP mode. **d** Effective mode coupling and maximum loss

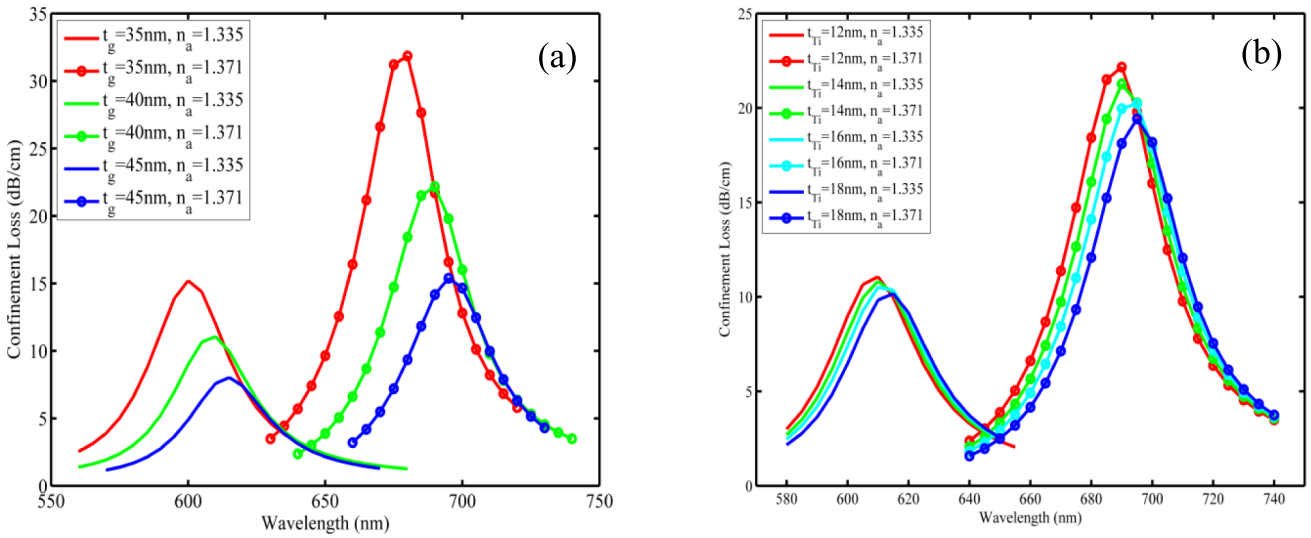

Fig. 3 Loss curves for different values of RI with variation of **a** gold layer thickness and **b** TiO_2 layer thickness

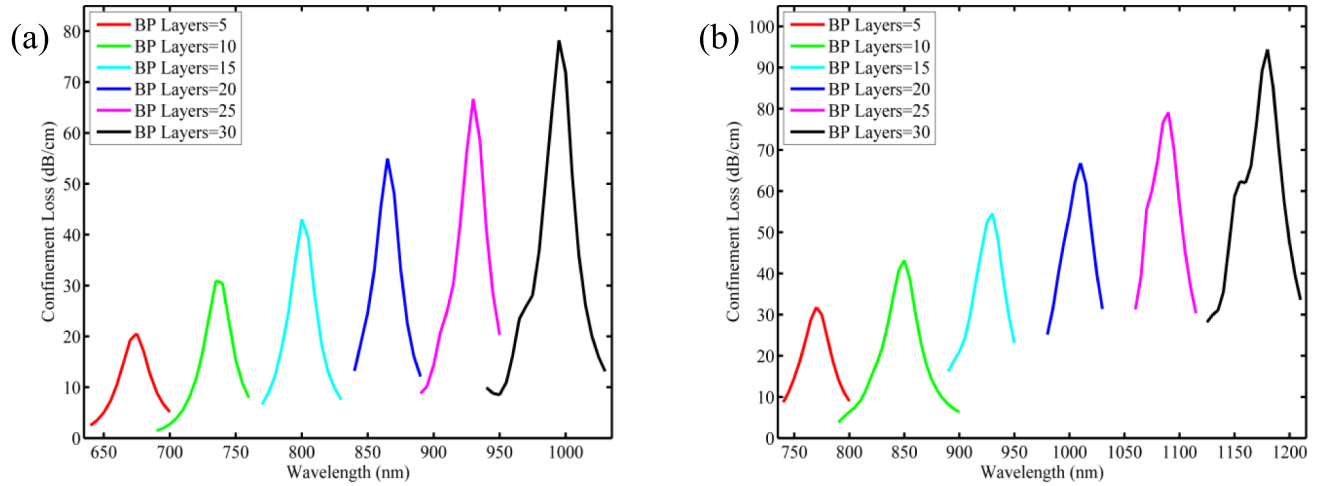

Fig. 4 Loss curves for different number of layers of black phosphorus when effective refractive index is **a** 1.335 and **b** 1.371

confinement loss. However, the sensitivity of the sensor remains the same, so 40 nm of thickness (t_g) is considered to be ideal due to moderate confinement loss.

Optimization of TiO_2 Layer

TiO_2 is mostly used as an adhesive agent between plasmonic material and the fiber structure. It can also overcome the gold's disadvantage of poor biomolecule adsorption. The confinement loss spectrum by changing the thickness of TiO_2, from 12 to 18 nm in steps of 2 nm, is shown in Fig. 3b. It is analyzed by using the optimized value of gold, i.e., 40 nm, and keeping other parameters, like $a = 1.3$ µm and $b = 0.8$ µm, constant. On increasing the metal's thickness, the confinement loss decreases because the incoming evanescent wave weakens. The corresponding sensitivity remains the same from 12 to 14-nm thickness but increases at 16 nm and then again decreases at 18 nm. So, the ideal thickness of TiO_2 is taken as 16 nm.

Optimization of Number of BP Layers

BP is used to enhance the sensitivity of the sensor and also allows the biomolecules present in the sample to bind tightly to the sensor. The optimized thickness of gold and TiO_2 layers are used, that are, $t_g = 40$ nm and $t_{Ti} = 16$ nm, respectively. The thickness of single BP layer is fixed to be 0.53 nm, but in practical research, layers of black phosphorus layers are stacked together and stay together due to the van der Waals forces of attraction. The analysis is done to find the ideal number of layers, starting from 5 to 30. The sensitivity keeps on increasing with the increment in the BP layers, and 30 layers are considered to be optimal because, beyond this layer count, the peak confinement loss magnitudes attain

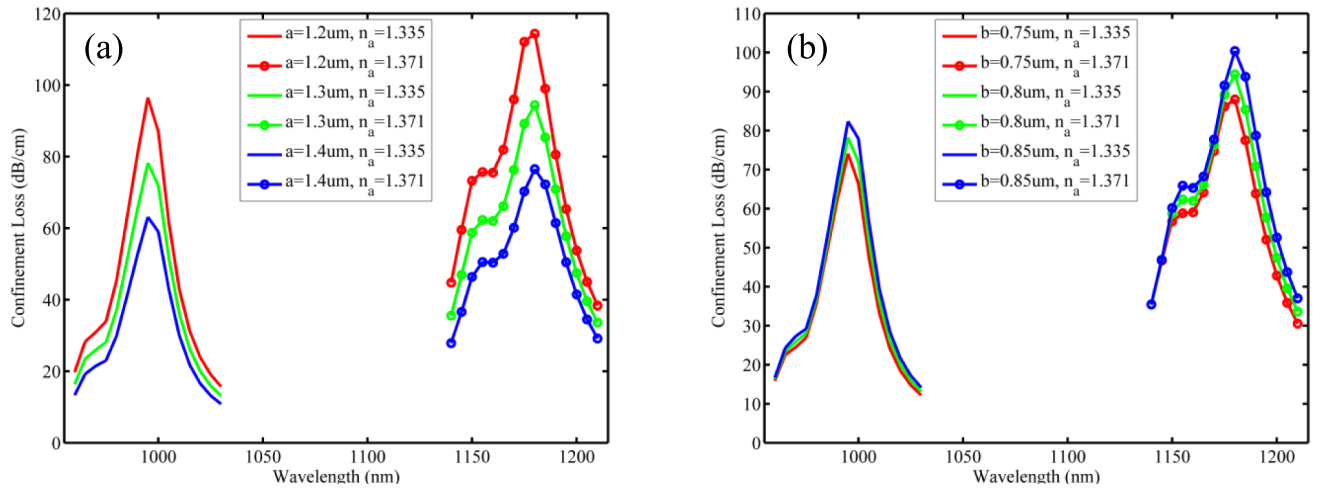

Fig. 5 Loss curves for different values of RI with variation of **a** size of bigger air hole and **b** size of smaller air hole

Table 1 Optimized structural parameters

	Thickness of gold (t_g)	Thickness of TiO_2 (t_{Ti})	Count of BP layers	Small air hole's radius (a)	Big air hole's radius (b)
Optimized parameter	40 nm	16 nm	30	0.8 μm	1.3 μm

redundancy and create ambiguity in observation of resonance mode. This is because the operating wavelength range crosses 2500 nm (silica's absorption limit) for the higher refractive index of UTI, which is 1.3921. The confinement loss spectrum for the analysis from 5 to 30 layers of BP is shown in Fig. 4.

Optimization of Square Air Holes

The sides of two types of square air holes present in the PCF structure are also optimized by using the previously optimized parameters like gold layer (40 nm), TiO_2 layer (16 nm), and 30 BP layers. The side of bigger air hole is analyzed from 1.2 to 1.4 μm in steps of 0.1 μm, and the side of smaller ones are analyzed from 0.75 to 0.85 μm in steps of 0.05 μm. The confinement loss spectrum is shown in Fig. 5a and b, and it can be concluded that the size of air holes is not affecting the sensitivity of the proposed sensor, but the confinement loss gets affected. It decreases for bigger air holes and increases for smaller ones. So, the size with moderate loss, i.e., $a = 1.3$ μm and $b = 0.8$ μm, is considered to be ideal.

The "*Optimization of* Geometrical Parameters" section shows the analysis done to optimize the structure for higher sensitivity. Table 1 shows the finally optimized parameters like gold layer, TiO_2 layer, number of BP layers, and side of

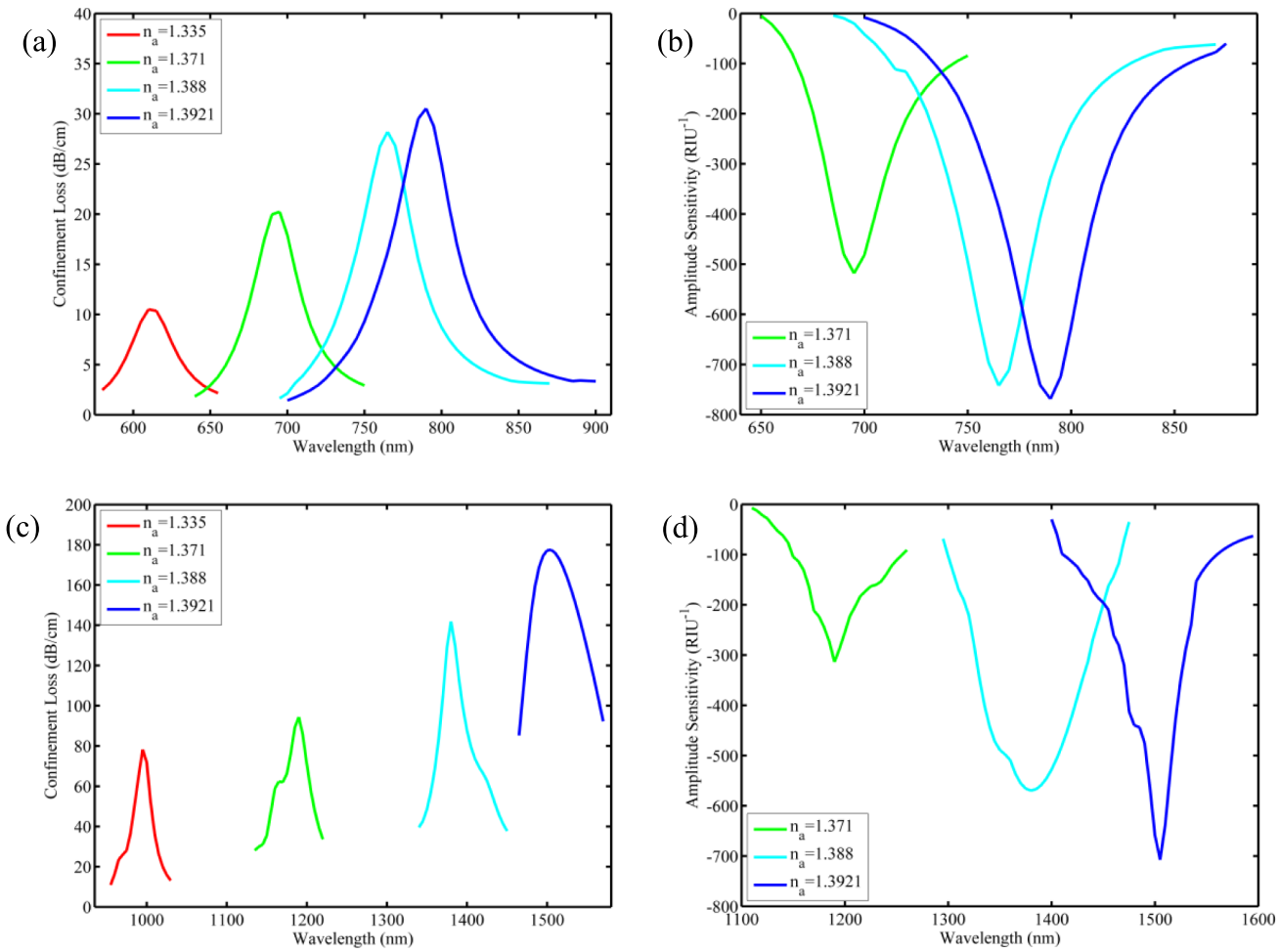

Fig. 6 Performance of proposed sensor: confinement loss **a** without BP, **c** with BP and amplitude sensitivity, **b** without BP, and **d** with BP

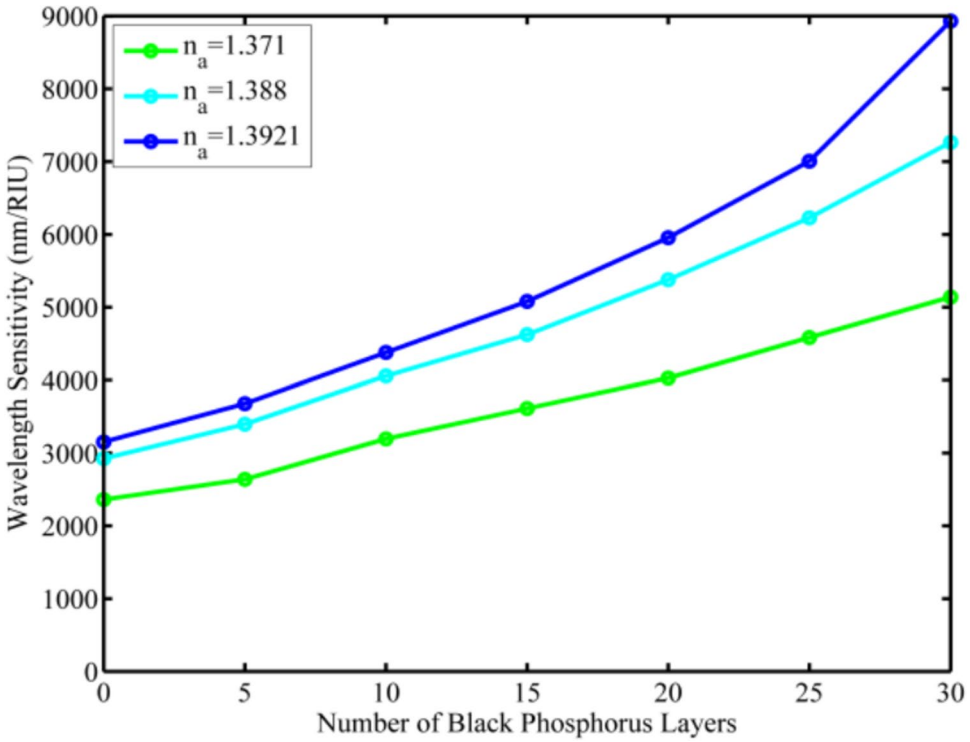

Fig. 7 Variation in sensitivity with increase in number of black phosphorus layers

square holes. They are employed for finding the final performance of the sensor, shown in the "Performance of Sensor with Optimized Parameters" section.

Performance of Sensor with Optimized Parameters

In the previous section, clear observations are made about the optimized structural parameters. To sneak at the final performance of the proposed SPR-PCF UTI sensor, the loss graphs have been plotted using the refractive index of the various bacteria of UTI. The performance of the sensor can be measured in two ways, that is by calculating wavelength and amplitude sensitivity. The main objective of this work is to make a highly sensitive UTI sensor, which is achieved using the black phosphorus layers. So, the analysis is shown without and with BP layers to get a clear observation about the effect of the BP layers and respective enhancement in the sensitivity. Figure 6a and b show wavelength and amplitude sensitivity, respectively, of the proposed structure without BP, and Fig. 6c and d show the same for the structure with BP layers. The amplitude sensitivity observes a decrement in the case of BP-gold sensor because amplitude sensitivity tells about the loss difference between two consecutive refractive indices. From the formula, we can infer that confinement loss of the detecting RI is inversely proportional to the amplitude sensitivity and the variation in the confinement loss is directly proportional to the amplitude sensitivity. In the case of only gold sensor, the peak confinement loss magnitudes are smaller, which ultimately affects and increases the amplitude sensitivity correspondingly. But in the case of BP-gold sensor, the loss curve's peak attains higher magnitude of confinement loss, which results in

Table 2 Change in wavelength and amplitude sensitivity when BP layer is added

Analyte's RI	Proposed structure without BP			Proposed structure with BP		
	Resonant wavelength (nm)	Wavelength sensitivity (nm/RIU)	Amplitude sensitivity (RIU^{-1})	Resonant wavelength (nm)	Wavelength sensitivity (nm/RIU)	Amplitude sensitivity (RIU^{-1})
1.335	610	-	-	995	-	-
1.371	695	2361.11	518.28	1190	5138.88	313.91
1.388	765	2924.52	742.15	1380	7264.15	569.63
1.3921	795	3239.92	768.67	1505	8936.69	707.31

Table 3 Sensitivity comparison for the proposed SPR-PCF sensor

Design		Coupling wavelength (nm)	RI range	Wavelength sensitivity (nm/RIU)	Amplitude sensitivity (RIU^{-1})
Graphene-based sensor [37]		590	1.33–1.35	2520	72.47
AZO-coated sensor [38]		1820	1.32–1.34	5000	167
Dual channel UTI sensor [1]	*Pseudomonas* bacteria	1640	1.371	3888.33	-
	E. coli bacteria	1780	1.388	5283.01	-
	E. faecalis bacteria	1800	1.3921	5253.94	-
Proposed UTI sensor (without BP)	*Pseudomonas* bacteria	695	1.371	2361.11	518.28
	E. coli bacteria	765	1.388	2924.52	742.15
	E. faecalis bacteria	795	1.3921	3239.92	768.67
Proposed UTI sensor (with BP)	*Pseudomonas* bacteria	1190	1.371	5138.88	313.91
	E. coli bacteria	1380	1.388	7264.15	569.63
	E. faecalis bacteria	1505	1.3921	8936.69	707.31

decrement in the amplitude sensitivity. Figure 7 shows the increase in wavelength sensitivity from 0 to 30 layers with an interval of 5 layers.

It is observed from the graphs that the wavelength sensitivity with BP layers reaches up to 5138.88 nm/RIU for *Pseudomonas*, 7264.15 nm/RIU for *E. coli*, and 8936.69 nm/RIU for *E. faecalis*. Similarly, amplitude sensitivity is 313.91 RIU^{-1}, 569.63 RIU^{-1}, and 707.31 RIU^{-1}, respectively. The performance is also tabulated in Table 2, to show the clear the difference between the sensitivities for the sensor with and without BP layers.

Tolerance of the Proposed Sensor

The fabrication techniques of the proposed sensor have already been discussed in the "Fabrication Feasibility" section. Now, to observe the tolerance of the biosensor, the structural parameters are altered by ± 5% to observe the changes in wavelength and amplitude sensitivity. When the thickness of gold layer is altered by ± 5%, i.e., when it is used as 38 nm or 42 nm instead of 40 nm, the wavelength sensitivity remains same but amplitude sensitivity changes almost by ± 20 RIU^{-1} only. When TiO_2 layer is used as 15.2 nm (− 5%) or 16.8 nm (+ 5%) instead of 16 nm, both wavelength and amplitude sensitivity do not change. And at last, when the sizes of square air holes, a and b, are varied by ± 5%, there is no change. So, it is observed that there is no major change in the sensitivity occurring, and the proposed SPR-PCF UTI sensor can be used significantly.

Table 3 shows the comparison of the proposed SPR-based PCF biosensor with previous literature works.

Conclusion

This research presents a UTI sensor, based of SPR phenomena. The UTI has three types of bacteria which affects the human body, which are *Pseudomonas*, *E. coli*, and *E. faecalis*. The structure is composed of TiO_2 and gold layers along with BP layers to increase the sensitivity of the sensor. The structure consists of square air holes of two sizes for better light confinement and effective plasmonic interaction. All these structural parameters are optimized for achieving best results from the proposed sensor. The analysis is done by taking the uninfected cell as the reference and the refractive indices of the infected cells are referred for measuring the respective sensitivity. By employing the refractive index information, highly sensitive UTI-PCF sensor is designed. The analysis is also done by comparing the structure with and without BP layers. When the sensor is operated without the BP layers, the wavelength sensitivities for different types of bacteria are 2361.11, 2924.52, and 3239.92 nm/RIU, whereas when the BP layers are incorporated, the sensitivities go as high as 5138.88, 7264.15, and 8936.69 nm/RIU. This shows that there is an increase in the sensitivities by much more that 50%, and hence, an effective UTI biosensor is designed.

Acknowledgements Plakshi Gupta, a student of Masters of Science in Physics in the Department of Applied Physics at Delhi Technological University, acknowledges for providing excellent research facilities for conducting research.

Author Contribution P.G. did the simulation and presented results and wrote the original manuscript, A. Khamaru helped in the explanation of results and helped in paper writing, A Kumar has done review & editing, Concept building, Supervision, Software, and Formal analysis.

Data Availability No datasets were generated or analysed during the current study.

Declarations

Competing Interests The authors declare no competing interests.

References

1. Divya, J., et al. "A novel dual-channel SPR-based PCF biosensor for simultaneous tuberculosis and urinary tract infection diagnosis towards SDG3." IEEE Access (2024).
2. Gür, Sinem Diken, Monireh Bakhshpour, and Adil Denizli. "Selective detection of Escherichia coli caused UTIs with surface imprinted plasmonic nanoscale sensor." Materials Science and Engineering: C 104 (2019): 109869.
3. PY Liu LK Chin W Ser TC Ayi PH Yap T Bourouina Y Leprince-Wang 2014 An optofluidic imaging system to measure the biophysical signature of single waterborne bacteria Lab Chip 14 21 4237 4243
4. Ritchie, Rufus H. "Plasma losses by fast electrons in thin films." Physical review 106.5 (1957): 874.
5. A Otto 1968 Excitation of nonradiative surface plasma waves in silver by the method of frustrated total reflection Zeitschrift für Physik A Hadrons and nuclei 216 4 398 410
6. E Kretschmann H Raether 1968 Radiative decay of non radiative surface plasmons excited by light Zeitschrift für Naturforschung A 23 12 2135 2136
7. Bo Liedberg C Nylander I Lunström 1983 Surface plasmon resonance for gas detection and biosensing Sensors and actuators 4 299 304
8. Uniyal, Arun, et al. "Numerical simulation of InP and MXene-based SPR sensor for different cancerous cells detection." Cell Biochemistry and Biophysics (2025): 1–14
9. Pal, Debashish et al. A high sensitivity refractive index based sensor for detection of acetone concentration in wastewater. Plasmonics, (2024), 1–11.
10. Uniyal, Arun, et al. "Fluorinated graphene and CNT-based surface plasmon resonance sensor for detecting the viral particles of SARS-CoV-2." Physica B: Condensed Matter 669 (2023): 415282.
11. B Karki P Sarkar G Dhiman G Srivastava M Kumar 2024 Platinum diselenide and graphene-based refractive index sensor for cancer detection Plasmonics 19 2 953 962
12. Karki, Bhishma, et al. "Tuning sensitivity of surface plasmon resonance gas sensor based on multilayer black phosphorous." Modern Physics Letters B 39.01 (2025): 2450364.
13. Karki, B., Sarkar, P., Mahmoud, K.H. et al. Detection of organic material using tungsten ditelluride based surface plasmon resonance sensor. Plasmonics (2024).
14. B Karki A Pal P Sarkar 2024 ZnO-silicon enhanced surface plasmon resonance sensor for chemical sensing SILICON 16 3861 3872
15. RC Jorgenson SS Yee 1993 A fiber-optic chemical sensor based on surface plasmon resonance Sens Actuators, B Chem 12 3 213 220
16. Skorobogatiy, Maksim, and Andrei V. Kabashin. "Photonic crystal waveguide-based surface plasmon resonance biosensor." Applied physics letters 89.14 (2006).
17. Singh, J., Khamaru, A., & Kumar, A. (2024). A refractive index based cancer cells sensor in terahertz spectrum: design and analysis. Journal of Optics, 1–9.
18. N Singh A Khamaru A Kumar 2024 Design and analysis of a rectangular core refractive index-based PCF sensor for bio-sensing application Opt Quant Electron 56 7 1133
19. G Singh S Sharma A Kumar 2024 Design and analysis of spider-web photonic crystal fiber in the terahertz regime Indian J Phys 98 8 2917 2922
20. F Meng H Wang D Fang 2022 Research on D-shape open-loop PCF temperature refractive index sensor based on SPR effect IEEE Photonics J 14 3 1 5
21. G Wang Y Lu L Duan J Yao 2020 A refractive index sensor based on PCF with ultra-wide detection range IEEE J Sel Top Quantum Electron 27 4 1 8
22. Ran, Zengling, et al. "Novel high-temperature fiber-optic pressure sensor based on etched PCF FP interferometer micromachined by a 157-nm laser." IEEE Sensors Journal 15.7 (2014): 3955–3958.
23. D Garg A Khamaru A Kumar 2024 Supercontinuum generation in Ga-Sb-S chalcogenide-based PCF using optofluidic approach Microw Opt Technol Lett 66 9 e34316
24. Khamaru, A., & Kumar, A. (2024). As38Se62 based segmented clad-graded index photonic crystal fiber for supercontinuum generation covering 3–9.5 μm with moderate peak power. Optical and Quantum Electronics, 56(7), 1246.
25. D Garg A Khamaru A Kumar 2024 Ge–As–Se–Te chalcogenide based rib-waveguide for highly coherent on-chip mid-infrared supercontinuum generation: design and analysis Opt Quant Electron 56 10 1643
26. A Benazza F Beffara JL Auguste M Olivo US Dinish G Humbert 2024 Reliable and easy-to-use SERS spectroscopy probe using a tapered opto-fluidic photonic crystal fiber Opt Express 32 3 3440 3450
27. Russell, Philip St John. "Photonic crystal fibers: basics and applications." Optical fiber telecommunications VA. Academic Press, 2008. 485–522.
28. Gupta, Plakshi, Akash Khamaru, and Ajeet Kumar. "Highly sensitive black phosphorus–layered SPR-PCF refractometric sensor." Plasmonics (2025): 1–11.
29. AMT Hoque KF Al-Tabatabaie ME Ali AM Butt SSI Mitu KK Qureshi 2023 U-grooved selectively coated and highly sensitive PCF-SPR sensor for broad range analyte RI detection IEEE Access 11 74486 74499
30. S Kumar D Kumar 2022 Sensitivity measurement based on the refractive index detection of dual-coated PCF SPR sensor Mapan 37 2 435 441
31. A Zuhayer M Abd-Elnaby SH Ahammad MM Eid V Sorathiya ANZ Rashed 2022 A gold-plated twin core d-formed photonic crystal fiber (PCF) for ultrahigh sensitive applications based on surface plasmon resonance (SPR) approach Plasmonics 17 5 2089 2101
32. U. Ramani, H. Kumar, R. Kumar, B. K. Singh, and P. C. Pandey, "Dual- core photonic crystal fiber–based plasmonic sensor for a broad range of refractive index sensing," Plasmonics, pp. 1–11, 2024
33. Yuan, Y., Yu, X., Ouyang, Q., Shao, Y., Song, J., Qu, J., & Yong, K. T. (2018). Highly anisotropic black phosphorous-graphene hybrid architecture for ultrassensitive plasmonic biosensing: theoretical insight. 2D Materials, 5(2), 025015.
34. C Vacacela Gomez M Pisarra M Gravina P Riccardi A Sindona 2017 Plasmon properties and hybridization effects in silicene Phys Rev B 95 8 085419
35. ME Dávila L Xian S Cahangirov A Rubio G Lay Le 2014 Germanene: a novel two-dimensional germanium allotrope akin to graphene and silicene New J Phys 16 9 095002

36. A Uniyal A Pal B Chauhan 2023 Long-range SPR sensor employing platinum diselenide and cytop nanolayers giving improved performance Physica B 649 414487
37. X Yang Y Lu B Liu J Yao 2017 Analysis of graphene-based photonic crystal fiber sensor using birefringence and surface plasmon resonance Plasmonics 12 489 496
38. JN Dash R Das R Jha 2018 AZO coated microchannel incorporated PCF-based SPR sensor: a numerical analysis IEEE Photonics Technol Lett 30 11 1032 1035
39. J Qiao X Kong ZX Hu F Yang W Ji 2014 High-mobility transport anisotropy and linear dichroism in few-layer black phosphorus Nat Commun 5 1 4475
40. Tong, Kai, et al. "Study on increasing measurement range and enhancing sensitivity of PCF surface-plasmon-resonance biosensor using black phosphorus." Journal of Russian Laser Research 42 (2021): 283–291.
41. Singh, Shivam, and Y. K. Prajapati. "Dual-polarized ultrahigh sensitive gold/MoS2/graphene based D-shaped PCF refractive index sensor in visible to near-IR region." Optical and Quantum Electronics 52.1 (2020): 17.
42. Lee, Seong-Yeon, and Ki-Ju Yee. "Black phosphorus phase retarder based on anisotropic refractive index dispersion." 2D Materials 9.1 (2021): 015020.
43. Khamaru, A., & Kumar, A. (2024). Highly sensitive graded index PCF-based refractometric SPR sensor offering enhanced FOM. Plasmonics, 1–13.
44. Bhuyan, A., Khamaru, A., & Kumar, A. (2024). Black phosphorus-based slotted D-shaped PCF SPR sensor for cancer detection. Plasmonics, 1–13.
45. BS, D. K., Khamaru, A., & Kumar, A. (2025). Design and analysis of twin-core side-polished SPR PCF sensor for preliminary malaria detection. Plasmonics, 1–12.
46. Upadhyay, Anurag, et al. "Analysis of proposed PCF with square air hole for revolutionary high birefringence and nonlinearity." Photonics and Nanostructures-Fundamentals and Applications 43 (2021): 100896.

Publisher's Note Springer Nature remains neutral with regard to jurisdictional claims in published maps and institutional affiliations.

Springer Nature or its licensor (e.g. a society or other partner) holds exclusive rights to this article under a publishing agreement with the author(s) or other rightsholder(s); author self-archiving of the accepted manuscript version of this article is solely governed by the terms of such publishing agreement and applicable law.

Materials Research Proceedings 49 (2025) 396-405 https://doi.org/10.21741/9781644903438-40

Blast analysis of stand alone CFST column

Kartikeya TIWARI[1,a*], Harsh VARDHAN[1,b*], Ayush ANAND[1], Gaurav KUMAR[2,c*], Amit Kumar SRIVASTAVA[1]

[1]Department of Civil Engineering, Delhi Technological University, Delhi

[2]Department of Mechanical Engineering, Delhi Technological University, Delhi

[a]kartikeyatiwari05@gmail.com, [b]harshvardhan2912@gmail.com, [c]gauravkmr716@gmail.com

Keywords: Blast Load, ANSYS, RCC Column, CFST Column, TNT

Abstract. The rise in terrorist attacks targeting various locations worldwide has underscored the importance of evaluating structures exposed to blast effects. Despite progress in the field, understanding the response of concrete-framed buildings to extreme loading conditions remains crucial before implementing any protective strategies. The majority of structures impacted by blasts or impacts were not originally designed to withstand such forces, making them particularly susceptible. Consequently, the development of new standards and guidelines for effectively countering explosive threats is a continuous effort. In this research, ANSYS was utilized to develop an in-depth finite element model of a CFST (Concrete Filled Steel Tube) Column. A three-dimensional model of a reinforced concrete column was selected for the analysis. This paper details the structural model's response to simulated blast loads and introduces two alternative designs that could inform future protection measures. The findings indicate that enhancing the design of the column significantly improves its resistance to blast impacts.

Introduction

Structures exposed to blast loads require specialized designs to ensure resilience. Critical facilities, such as government buildings, power plants, and embassies, are often at risk of terrorist attacks and must be designed to withstand such threats.[1]

Explosions generate pressure waves that impose sudden dynamic forces, leading to structural damage and casualties.[2] Accurate analysis of blast impacts requires considering high strain rates, time-dependent deformations, nonlinear material behavior, and load uncertainties. This study examines the blast responses of three column designs—RCC, Concrete-Filled Steel Tubes (CFST), and reinforced CFST—modified per mitigation guidelines. Some examples of computer programs that perform coupled analysis are LS-DYNA, ANSYS [3] and ABAQUS [4]

Literature Review

In a study on the impact of blast loading on steel columns, *Ashish K Tiwary* [5] analyzed how columns from a large building frame responded to blast loading in terms of net maximum deformation and maximum principal stress. They created an explicit dynamic ANSYS-Autodyn 3D model and conducted an implicit modal analysis to evaluate the reliability of the numerical model. Their findings indicate that column deflection is directly influenced by the stand-off distance; specifically, a smaller stand-off distance leads to greater deflection.

Y. Shi [6] proposed equations to predict the pressure and impulse on the front and back surfaces of columns with varying dimensions and shapes during blast wave interactions. These equations estimate external blast forces on standalone columns during surface explosions. Circular columns exhibit less reflection but greater diffraction compared to rectangular columns, resulting in smaller reflected waves on the front surface and larger waves on the rear. Additionally, circular columns experience shorter delays between the blast wave impacts on their front and rear surfaces, contrasting with the longer delays observed in rectangular columns.

Content from this work may be used under the terms of the Creative Commons Attribution 3.0 license. Any further distribution of this work must maintain attribution to the author(s) and the title of the work, journal citation and DOI. Published under license by Materials Research Forum LLC.

Materials Research Proceedings 49 (2025) 396-405 https://doi.org/10.21741/9781644903438-40

Ruwan Jayasooriya [7] conducted research aimed at improving the durability of concrete columns when subjected to blast impacts. Their investigation focused on assessing the blast resilience and safety of a composite column design, which consisted of an I-beam at its center encased in concrete. This composite column played a crucial role in the overall structural system. Using LS-DYNA, they developed a detailed model of the composite column to simulate its behavior accurately under blast forces. The results of their study revealed that incorporating a steel core within the column notably enhanced its structural integrity, guaranteeing that it could withstand substantial loads even following a blast incident.

H.M. Elsanadedy [8] used the LS-DYNA finite element analysis software to investigate the gradual collapse of a standard multi-storey steel-framed building in Riyadh, Saudi Arabia, caused by explosive impacts. The study examined different explosion scenarios by simulating column removal at various locations on the ground level. Findings suggested that the building could experience progressive collapse under an explosive force equivalent to a 500 kg charge, easily transportable in a small truck. To improve the building's resilience, the researchers recommended reinforcing the outer columns of the ground floor with either concrete or steel plates.

Based on the findings from the research conducted by *Ruwan Jayasooriya* [7] and *H.M. Elsanadedy* [8], it becomes clear that the impact of explosives and the location of structural components are key factors in determining how framed structures respond to blast loads, with the position of the structural elements potentially playing a more critical role.

In their study of the performance of CFST composite columns with double plate connectors, *Jayaroshna PS* [9] investigated CFST columns connected with corrugated steel plates, performed a uniaxial eccentric compression test to determine axial load bearing capacity, and then compared the results to a normal steel plate connected special shaped CFST column. According to studies, CFST columns have higher cyclic strength, ductility, and damping while costing less than a reinforced concrete column. It was discovered that the addition of concrete between the steel tubes increased overall performance.

Explosion and blast loading

An explosion occurs when energy is rapidly released in a confined area, generating a pressure or shock wave, as illustrated in Figure (1). Hot gases expand, forming a wave that moves outward at the speed of sound, reaching temperatures of 3000°C and pressures up to 300 kbar. Over time, the wave becomes more abrupt, creating a shock front with maximum overpressure, as shown in Figure (2). [5]

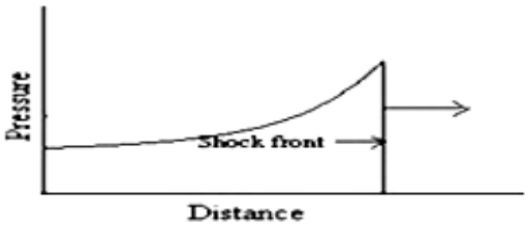

Figure 1. Variation of pressure with distance [5]

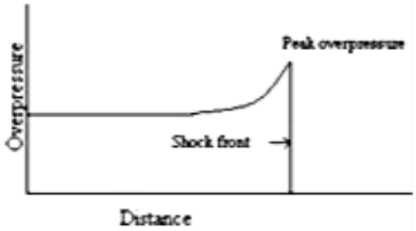

Figure 2. Formation of shock front [5]

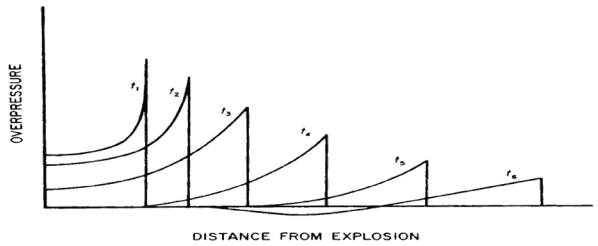

Figure 3. Variation of overpressure with distance [10]

The pressure within a shock wave decreases over time, and the pressure behind it steadily drops. At a certain distance, it falls below atmospheric pressure, creating a negative phase or suction effect. As the wave propagates, its speed nears the speed of sound. Overpressure evolution (t1-t6) is shown in Figure 3.

What effect do Blast Loads have on Buildings?

Blast loads are applied for much shorter durations compared to seismic loads, which means that the effects of material strain rate become important and need to be taken into account when evaluating how connections will perform under quick, intense blasts. Additionally, blast loads are unevenly distributed across a structure, leading to varying load strengths across the building's surface and reduced blast forces on the sides and back of the building, away from the source of the explosion.[11]

Material Properties

1. Structural Steel

Density	**7.85e-006 kg mm^-3**
Coefficient of Thermal Expansion	1.2e-005 C^-1
Specific Heat	4.34e+005 mJ kg^-1 C^-1
Thermal Conductivity	6.05e-002 W mm^-1 C^-1
Resistivity	1.7e-004 ohm mm
Compressive Yield strength	250 MPa
Ultimate Tensile Strength	460 MPa
Young's Modulus MPa	2e+005
Poisson's Ratio	0.3
Bulk Modulus MPa	1.6667e+005
Shear Modulus MPa	76923

2. Concrete 35-MPA

Density	**2.314e-006 kg mm^-3**
Specific Heat	6.54e+005 mJ kg^-1 C^-1
Shear Modulus MPa	16700
Compressive Strength fc MPa	35
Tensile Strength ft/fc	0.1
Shear Strength fs/fc	0.18

3. TNT

Density	**1.63e-006 kg mm^-3**
End Time	5.00E-03
Parameter A MPa	3.74E+05
Parameter B MPa	3747.1
C-J Detonation Velocity mm s^-1	6.93E+06
C-J Energy / unit mass mJ kg^-1	3.68E+09
C-J Pressure MPa	21000

1. Reinforced Concrete Model

The properties of the RCC column and TNT are given in Table-1. The blast pressure coming from 250x250x250mm TNT of approx. 25kg is considered from standoff distance of 2m as blast point relative to the column, The blast material is assumed to be place at 1.5m high from the ground.

Material Dimension		
Assignment	**TNT**	**CONC-35MPA**
Length X	250. mm	300. mm
Length Y	250. mm	3000. mm
Length Z	250. mm	300. mm
PROPERTIES		
Volume	1.5625e+007 mm³	2.7e+008 mm³
Mass	25.469 kg	624.78 kg

Table 1 (Properties of the RCC column and TNT)

The reinforcement bars (4) and stirrups (15) of 8mm radius are provided with clear cover between vertical reinforcement bars and concrete outer edge in the column of height 3m supported fixed at both ends. Figure (4) shows the 3D model of Reinforced concrete column in ANSYS software.

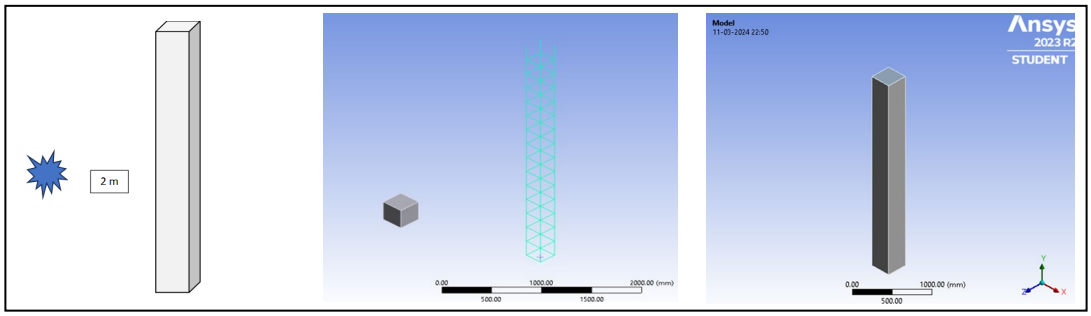

Figure 4 (3D model of Reinforced concrete column in ANSYS software)

2. Concrete-filled steel tube (CFST) model

Concrete-filled steel tube (CFST) columns are used extensively in engineering constructions including subway stations, arch bridges, and high-rise buildings because of their exceptional ductility and high strength because of a modified buckling mode and confinement effect.[12] The blast resistance of the buildings has become a factor in their design process due to the rise in terrorist bombs in recent years. When columns are subjected to blast loads, the damage they sustain may cause a partial loss of bearing capacity, which could lead to the collapse of individual columns or even the progressive collapse of the structure as a whole. [13]

MATERIAL			
Assignment	**Structural Steel**	**CONC-35MPA**	**TNT**
Length X	300. mm	290. mm	250. mm
Length Y	3000. mm	3000. mm	250. mm
Length Z	300. mm	290. mm	250. mm
PROPERTIES			
Volume	1.77e+007 mm³	2.523e+008 mm³	1.5625e+007 mm³
Mass	138.95 kg	583.82 kg	25.469 kg

Table 2 (Properties of the CFST column and TNT)

Materials Research Proceedings 49 (2025) 396-405 https://doi.org/10.21741/9781644903438-40

The properties of the CFST column and TNT are given in Table-2. Thickness of steel covering is assumed to be 5mm. Figure (5) shows the cross-sectional view of a square concrete filled tubular column.

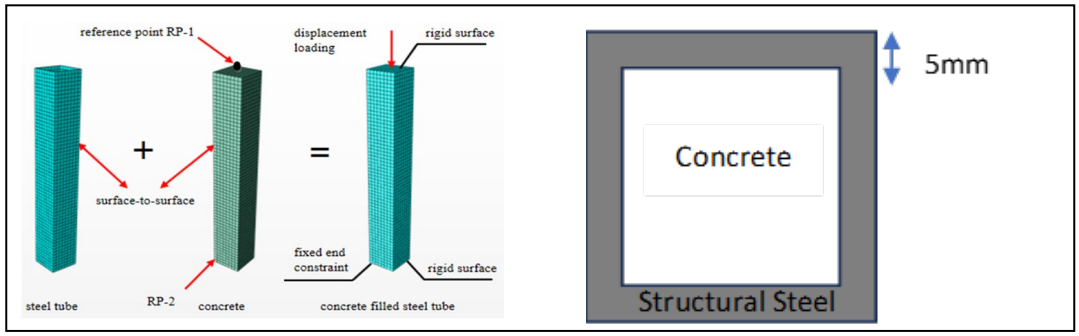

Figure 5 (a) sectional view [14] *Figure 5 (b) Cross sectional view*

3. Concrete-filled steel tube (CFST) with reinforcement model

The properties of the CFST with reinforcement column and TNT are given in Table-3. The blast pressure coming from 250x250x250mm TNT of approx. 25kg is considered from standoff distance of 2m as blast point relative to the column.

	Material		
Assignment	Structural Steel	CONC-35MPA	TNT
Length X	300. mm	290. mm	250. mm
Length Y	3000. mm	3000. mm	250. mm
Length Z	300. mm	290. mm	250. mm
	Properties		
Volume	2.25e+007 mm³	2.523e+008 mm³	1.5625e+007 mm³
Mass	176.81 kg	583.82 kg	25.469 kg

Table 3 (Properties of the CFST with reinforcement column and TNT)

The blast material is assumed to be at 1.5m hight from the ground. Thickness of outer steel covering is assumed to be 5mm. Figure (6) shows the cross-sectional view of a square concrete filled tubular column. The reinforcement bars (4) and stirrups (15) of 8mm radius are provided in the column.

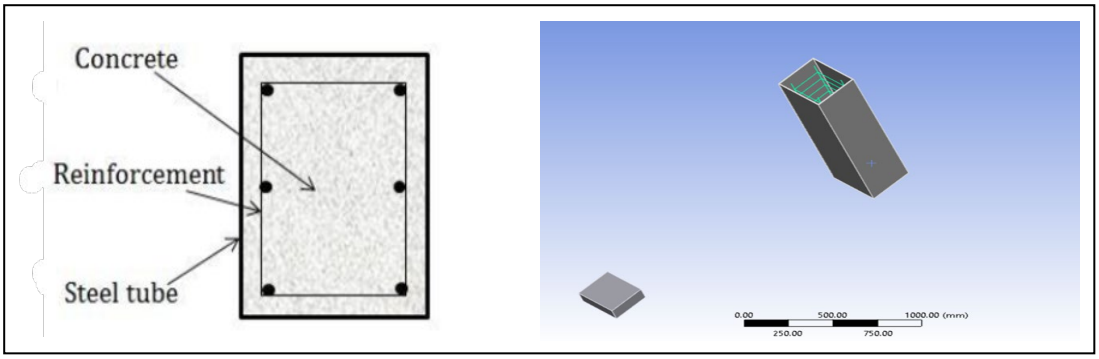

Figure 6 (Cross-sectional view of a square concrete filled tubular column)

Analysis of column for blast loading

For analysis and design ANSYS Explicit Dynamics is used, the response of the column in terms of net maximum deformation, maximum force and moment reactions is obtained for the cases given below. The results are presented in the form of plots shown in figure 7 to figure 15. It has been clearly observed that the deflection in a column is maximum at the mid span and can cause the failure of the column.

1. Maximum Deformations

Maximum deformation obtained by the RCC model is shown in figure 7, the maximum deformation by CFST model is shown in figure 8 and the maximum deformation when both RCC and CFST are combined is shown in figure 9.

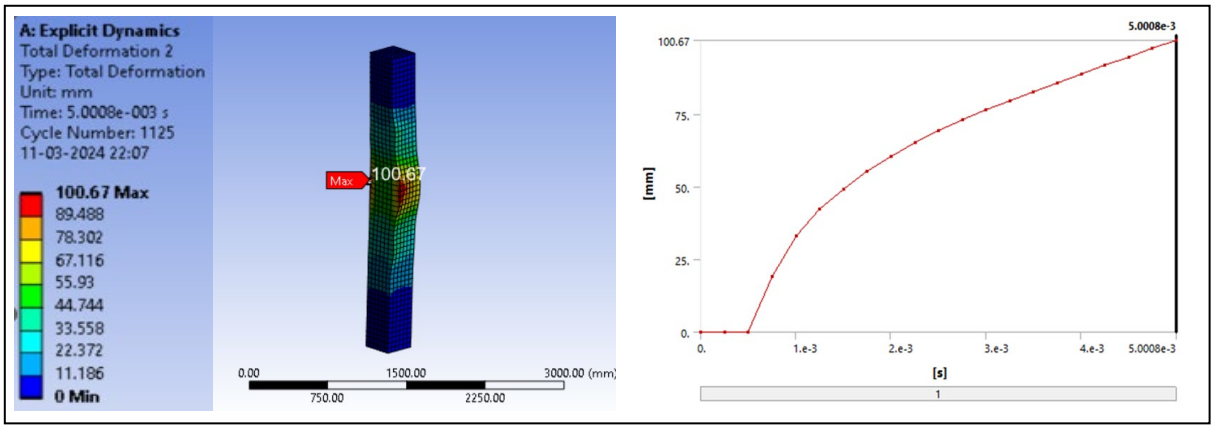

Figure 7 (Maximum deformation obtained by the RCC model)

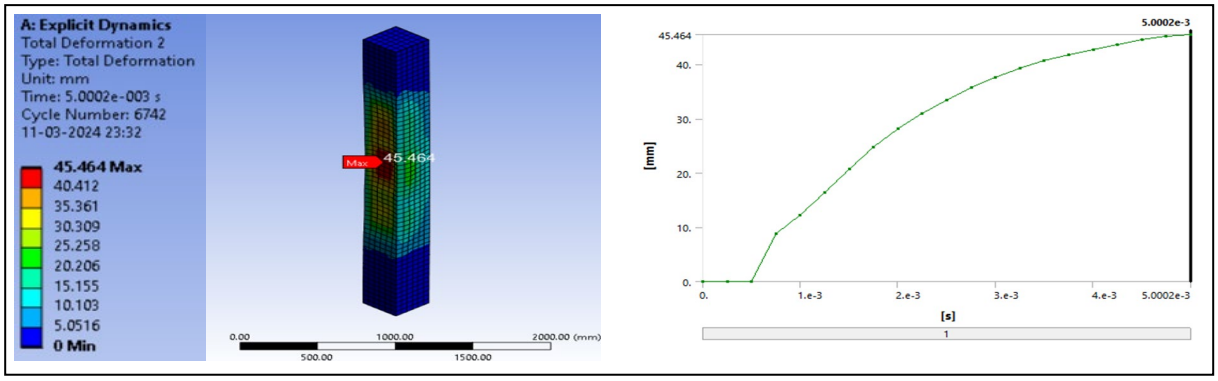

Figure 8 (Maximum deformation obtained by the CFST model)

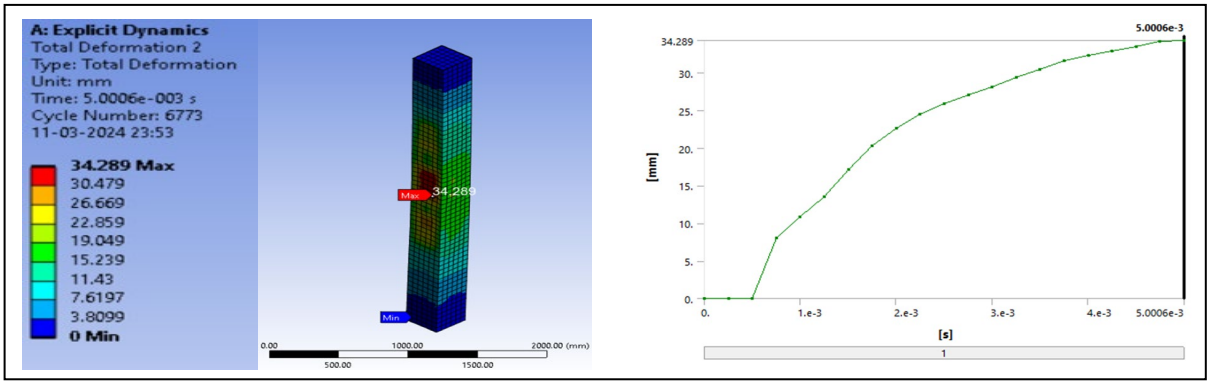

Figure 9 (Maximum deformation obtained by the CFST with reinforcement model)

2. Maximum End Reactions

Maximum end reactions obtained by the RCC model is shown in figure 10, the maximum reactions by CFST model is shown in figure 11 and the maximum reactions when both RCC and CFST are combined is shown in figure 12.

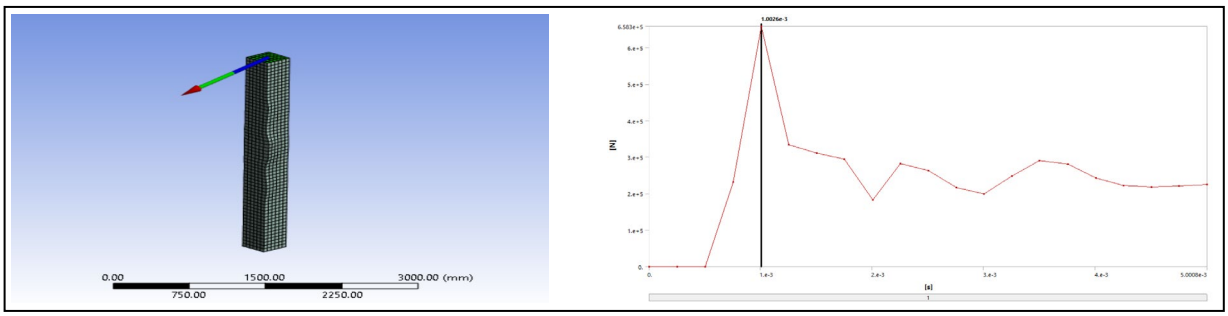

Figure 10 (Maximum end reactions obtained by RCC model)

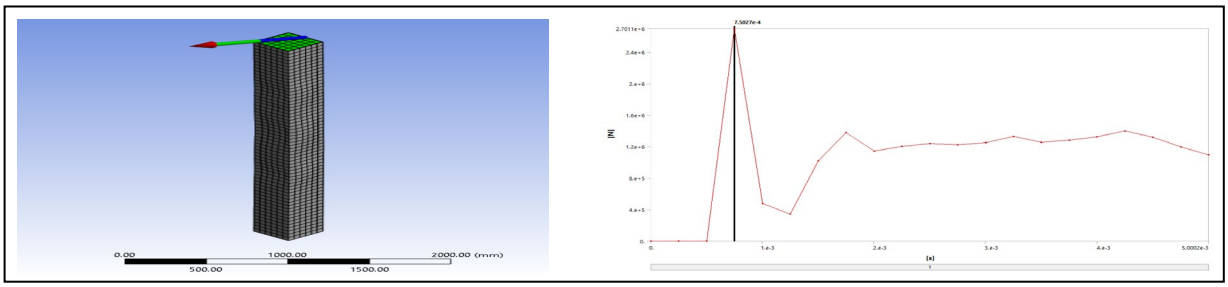

Figure 11 (Maximum end reactions obtained by CFST model)

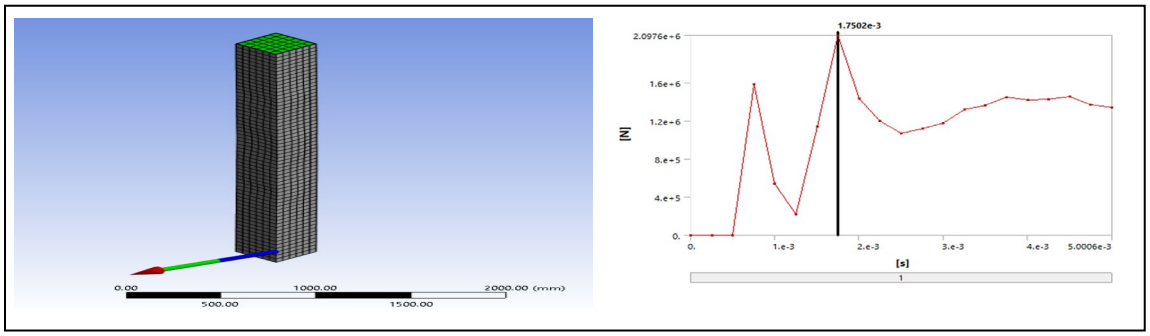

Figure 12 (Maximum end reactions obtained by CFST with reinforcement model)

3. Maximum Bending Moment

Maximum Bending moment obtained in the RCC model is shown in figure 13, the max. bending moment in CFST model is shown in figure 14 and the max. bending moment when both RCC and CFST are combined is shown in figure 15.

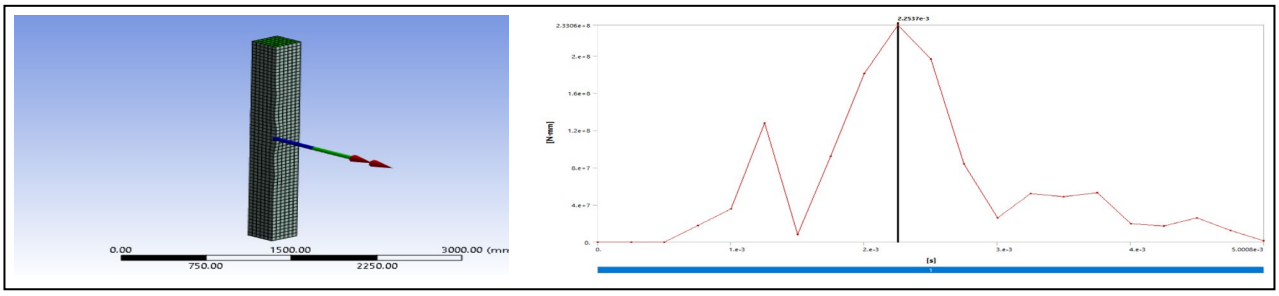

Figure 13 (Maximum Bending moment obtained in the RCC model)

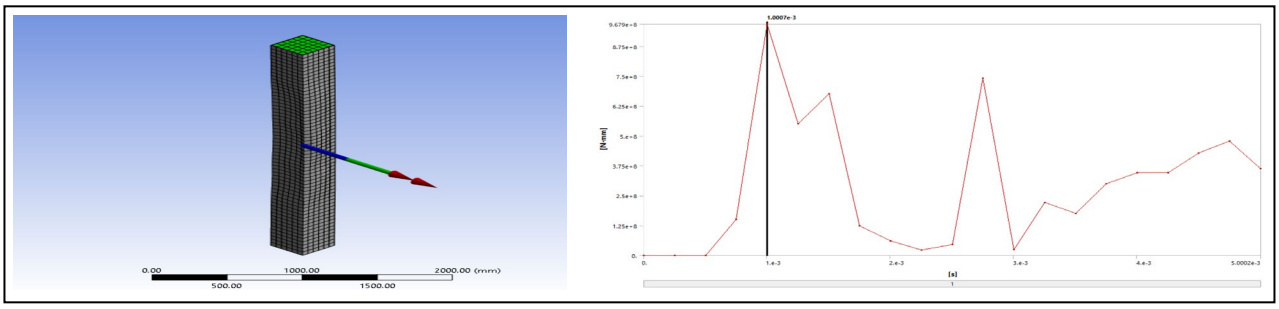

Figure 14 (Maximum Bending moment obtained in CFST model)

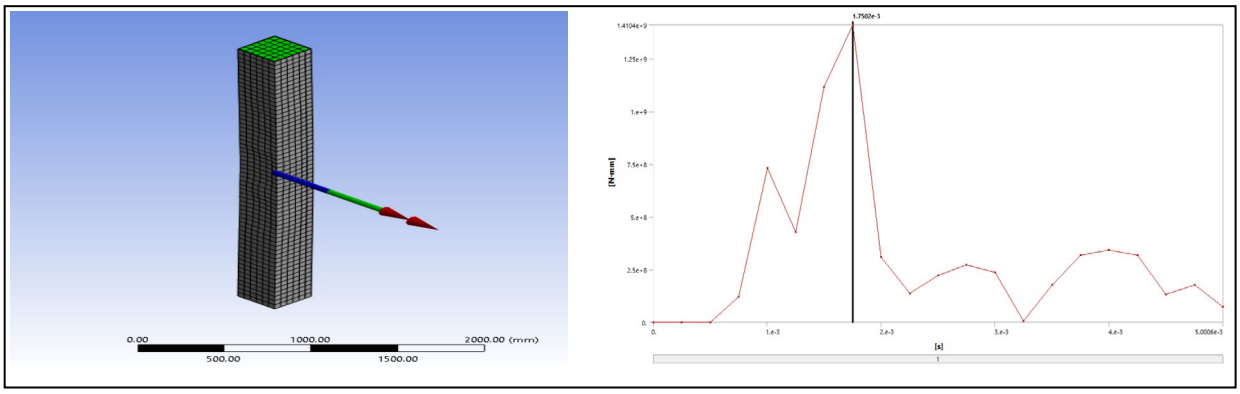

Figure 15 (Maximum Bending moment obtained in CFST with Reinforcement model)

Result & discussion

1. Comparison of maximum deformation on columns. (Table-4)

Type of Column	Max. Deformation
RCC	100.67 mm
CFST column	45.464 mm
CFST with Reinforcement	34.289 mm

Table 4 (Maximum Deformation in each column)

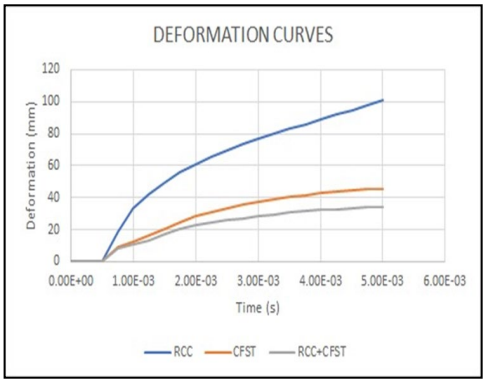

Figure 16

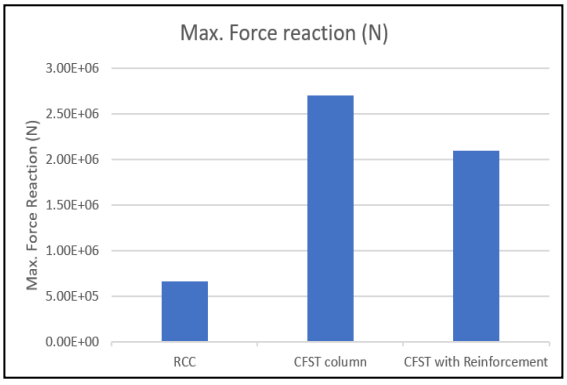

Figure 17

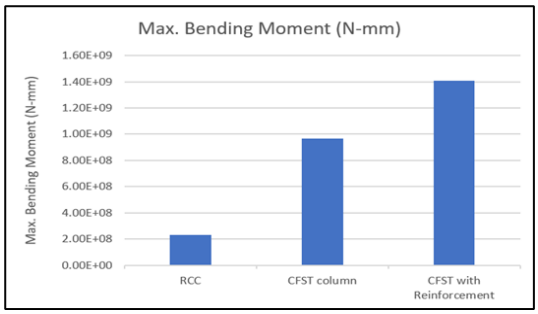

Figure 18

2. Combined maximum results obtained during analysis of the above columns on Ansys Explicit Dynamics. (Table-5)

Type of Column	Max. Deformation	Max. End reactions	Max Bending Moment
RCC	100.67 mm	6.583e+5 N	2.3306e+8
CFST column	45.464 mm	2.7011e+6 N	9.679e+8
CFST with Reinforcement	34.289 mm	2.0976e+6 N	1.4104e+9

Table 5 (Results in combined form)

Conclusion

The following are the observations and conclusions that are drawn from the study presented above:

1. Explicit dynamic analysis of the column revealed that maximum deformation of the CFST Column is 55% lesser than normal RCC Column and in case of CFST with Reinforcement it is 66% lesser than normal RCC Column. Hence, we may conclude that CFST Columns can act as game changer when it comes to showing resistance against the blast load.
2. Results also depicted that, Reaction Forces at the supports of the column increases multi-fold times (4.1 & 3.1 times) with the improvement in design, So, improvements in the Joints of column is also necessary with the improvement in the overall design.

Future Scope

- Improvements needed on the joints of both CFST & CFST with Reinforcement Columns can be further studied and analysed.
- Increased cost of columns with improved designs can also be analysed and studied.
- The work is focused only on CFST columns made of rectangular steel tubes.
- Steel tubes of different cross-sectional shape can be used.
- Material properties of the concrete filled inside the tubes can be changed.

References

[1] C. Wu and H. Hao, “Modeling of simultaneous ground shock and airblast pressure on nearby structures from surface explosions,” *Int J Impact Eng*, vol. 31, no. 6, pp. 699–717, Jul. 2005. https://doi.org/10.1016/j.ijimpeng.2004.03.002

[2] W. E. (Wilfred E. Baker, *Explosion hazards and evaluation*. Elsevier Scientific Pub. Co, 1983.

[3] “Ansys help version 15.0 ansys inc 2014 pdf”.

[4] “Abaqus Analysis User’s Guide.”

[5] A. K. Tiwari, A. Tiwary, A. K. Tiwary, A. Kumar Tiwary, and A. Kumar, "Blast Loading Effects on Steel Columns." [Online]. Available: https://www.researchgate.net/publication/355998912

[6] Y. Shi, H. Hao, and Z. X. Li, "Numerical simulation of blast wave interaction with structure columns," *Shock Waves*, vol. 17, no. 1–2, pp. 113–133, Aug. 2007. https://doi.org/10.1007/s00193-007-0099-5

[7] R. Jayasooriya, D. P. Thambiratnam, and N. J. Perera, "Blast response and safety evaluation of a composite column for use as key element in structural systems," *Eng Struct*, vol. 61, pp. 31–43, Mar. 2014. https://doi.org/10.1016/j.engstruct.2014.01.007

[8] H. M. Elsanadedy, T. H. Almusallam, Y. R. Alharbi, Y. A. Al-Salloum, and H. Abbas, "Progressive collapse potential of a typical steel building due to blast attacks," *J Constr Steel Res*, vol. 101, pp. 143–157, 2014. https://doi.org/10.1016/j.jcsr.2014.05.005

[9] "ANALYSIS OF THE PERFORMANCE OF CFST COMPOSITE COLUMNS WITH DOUBLE-PLATE CONNECTORS," 2023. [Online]. Available: www.ijcrt.org

[10] "The Effects of Nuclear Weapons - Glasstone and Dolan | Chapter III." Accessed: Mar. 23, 2024. [Online]. Available: https://www.atomicarchive.com/resources/documents/effects/glasstone-dolan/chapter3.html

[11] M. Li, Z. Zong, M. Du, Y. Pan, and X. Zhang, "Experimental investigation on the residual axial capacity of close-in blast damaged CFDST columns," *Thin-Walled Structures*, vol. 165, Aug. 2021. https://doi.org/10.1016/j.tws.2021.107976

[12] X. Zhang, H. Hao, M. Li, Z. Zong, and J. W. Bruechert, "The blast resistant performance of concrete-filled steel-tube segmental columns," *J Constr Steel Res*, vol. 168, May 2020. https://doi.org/10.1016/j.jcsr.2020.105997

[13] J. hao Zhang, B. Chen, and S. yong Jiang, "A simplified model to predict blast response of CFST columns," *J Cent South Univ*, vol. 24, no. 3, pp. 683–691, Mar. 2017. https://doi.org/10.1007/s11771-017-3469-x

[14] X. Lyu, L. Zhang, T. Zhang, B. Li, H. Li, and Y. Yu, "Prediction and analysis of ultimate bearing capacity of square cfst long column under eccentric compression after acid rain corrosion," *Materials*, vol. 14, no. 10, May 2021. https://doi.org/10.3390/ma14102568

The Visual Computer
https://doi.org/10.1007/s00371-025-03865-1

RESEARCH

Capturing spatiotemporal dependencies with competitive set attention for video summarization

Md Hasnat Hosen Arafat[1] · **Kavinder Singh**[1]

Accepted: 24 February 2025
© The Author(s), under exclusive licence to Springer-Verlag GmbH Germany, part of Springer Nature 2025

Abstract
Video summarization aims to condense long video sequences into concise and informative representations. Existing approaches often struggle to simultaneously capture temporal correlations and spatial representations, limiting their effectiveness in keyframe selection. To address these limitations, we propose the Spatiotemporal Set Attention (STSA) method, which introduces Temporal Inter-Competitive Set Attention and Spatial Intra-Competitive Set Attention. The former models long-term temporal relationships across frames, while the latter refines spatially salient regions within frames. Together, these components enable a comprehensive understanding of video content, improving the accuracy of keyframe selection. Our experiments on the TVSum and SumMe datasets demonstrate that the proposed STSA method outperforms state-of-the-art approaches, achieving higher F-scores and generating more accurate and informative summaries. The STSA model represents a significant advancement in video summarization by integrating spatiotemporal competitive attention, providing a more effective and comprehensive approach to capturing the essence of video content. The source code of the STSA and datasets (https://drive.google.com/drive/folders/1KTpftiMchP0q-pdcJ4K7HaARJloOwQA6?usp=sharing) will be available at https://github.com/ara-47/STSA.

Keywords Video summarization · Attention · Transformer · Deep learning · Spatiotemporal · Set attention

1 Introduction

In recent years, the rapid growth of multimedia content has led to a significant demand for efficient video summarization techniques, which aim to condense lengthy video sequences into short, informative summaries while preserving the most relevant information. Applications of video summarization range from video surveillance, visual analysis, sports analysis and summarization, video captioning, action generation and recognition and online video streaming platforms to content recommendation and archiving [1–4]. According to Cisco's Visual Networking Index, [1] video content is projected to account for 79% of global mobile data traffic by 2022. The exponential growth of video data necessitates an effective techniques for condensing video data into concise summaries.

Video summarization [5] aims to condense videos into shorter versions that capture essential information through keyframes or keyshots. Unlike simple compression, which reduces file size, video summarization selectively preserves significant content while discarding redundant parts. Traditional video summarization methods have predominantly relied on low-level visual features such as color histograms, or motion cues to evaluate the importance of video frames. However, these methods often struggle to capture the complexity of dynamic scenes and fail to generalize across different video domains. Furthermore, capturing the spatial and temporal dependencies [6–9] in a video plays a critical role while generating the importance of video frames. Recent advancements in deep learning, particularly the use of including LSTM [10, 11] and attention mechanisms [12–

✉ Kavinder Singh
kavinder85@gmail.com

Md Hasnat Hosen Arafat
arafatmdhasnathosen@gmail.com

[1] Machine Learning Research Laboratory, Department of Computer Science and Engineering, Delhi Technological University, Delhi, India

[1] http://media.mediapost.com/uploads/CiscoForecast.pdf.

Published online: 18 March 2025

14], have opened up new avenues for more sophisticated feature extraction and representation learning. However, these methods often focus on either temporal correlations or spatial details, neglecting the concurrent consideration. Attention-based models have addressed some limitations of LSTM-based methods but still struggle to capture inter-frame relationships [6] and intra-frame context effectively. To address these challenges, we propose a novel video summarization approach called Spatiotemporal Set Attention (STSA), which is demonstrated in Fig. 1.

In this paper, we propose a novel Spatiotemporal Set Attention (STSA) model for video summarization, which introduces an approach to capture both spatial and temporal relationships through competitive attention mechanisms. Our method integrates two key components: Temporal Inter-Competitive Set (TIS) Attention and Spatial Intra-Competitive Set (SIS) Attention, allowing for a more comprehensive understanding of video content by modeling competition between feature sets at both temporal and spatial levels to capture the spatial and temporal dependencies. Rather than focusing on simple adjacent frame relationships, TIS attention utilizes a multilayer competitive set attention mechanism that processes the entire video segment at once, enabling the model to capture long-term contextual information. This competitive dynamic ensures that the most relevant features are highlighted and refined iteratively, leading to a more accurate representation of frame importance. To complement TIS attention, we introduce the SIS attention, which explores spatial dependencies within frames by identifying salient regions. Using spatial intra-competitive set attention, SIS attention introduces competition among these salient regions, allowing the model to emphasize the most informative spatial features within each frame. By aligning temporal and spatial attention, our model achieves a richer and more nuanced representation of video content.

In summary, our contributions are as follows:

- We introduce a novel framework that integrates temporal frames into a spatiotemporal set transformer, enabling both inter- and intra-competitive set attention within video frames.
- We introduce TIS attention that captures long-range temporal correlations by enabling competition between sets of temporal features across the entire video sequence. This allows the model to prioritize frames based on their contextual relevance.
- Our model also presents SIS attention that refines temporal sets by introducing competition among salient regions within each frame. This ensures that the most informative spatial features are emphasized, improving frame-level understanding.
- Our approach iteratively aligns temporal and spatial competitive sets, refining feature representations across both dimensions. This inter- and intra-competition process captures a more holistic spatiotemporal understanding of the video.

The structure of the following paper is: Sect. 2 provides related work on approaches of video summarization. The suggested approach is described in Sect. 3. Section 4 demonstrates the results of experiments and comparisons. At last, in Sect. 5 the conclusions are provided.

2 Related work

We divided video summarization approaches into two categories, namely unsupervised approaches and supervised approaches for discussion.

2.1 Unsupervised approaches

To reduce annotation efforts, researchers developed unsupervised video summarization approaches. These methods often rely on handcrafted features for similarity analysis of frames. Early works [15, 16] developed unsupervised methods based on handcrafted features along with clustering techniques for video summarization. Other approaches, including sparse coding-based methods [17–20], aimed to extract condensed representations from handcrafted features to improve summarization performance. Generative adversarial networks (GANs) are also utilized by reformulating the original video to learn an optimal summary. Mahasseni et al. [21] introduced an adversarial-LSTM model, which performs summary generation and discrimination. Yuan et al. [22] extended this work by implementing cycle-consistent adversarial network, enhancing reciprocal information between the summarized and original videos. In addition, Jung et al. [23] incorporated variational autoencoder (VAE) into the GAN framework to capture more distinctive features for summarization. Subsequently, the use of attention mechanisms has been explored to enhance frame selection by assessing frame dependencies. Jung et al. [24] improved video summarization by using self-attention to model frame dependencies more effectively. Apostolidis et al. [25], proposed a GAN-based approach combined with an actor-critic model, framing the summarization task as a sequence generation problem. Additionally, Zhang et al. [26] developed LSTM autoencoder that tracks key object motions and employs online dictionary learning for object-focused, unsupervised summarization.

Zang et al. [27] proposed a method using reinforcement learning to enhance the quality of summaries by capturing temporal dependencies by non-local convolution network. Wang et al. [28] introduced a novel hierarchical policy approach, leveraging unsupervised rewards to address sparse reward problems and limited annotation challenges.

Gunuganti et al. [29] applied graph modeling and attention mechanisms to adversarially train an encoder for video summarization, leveraging graph relationships to improve temporal coherence and semantic capture. Another graph-based approach [30] proposed reconstructive network and contrastive graph rewards to ensure summaries retain essential content and inter-shot dependencies by employing mutual information maximization. Exploring reinforcement learning, Abbasi et al. [31] proposed a stable training and reward generation method to reconstruct masked frames and improve summary quality. Wang et al. [32] developed text-based fusion for language-guided video summarization, leveraging large language models for improved long-context understanding.

While unsupervised methods have reduced reliance on manual annotations, they still face limitations in capturing complex spatiotemporal dependencies across diverse video domains. Many approaches rely heavily on handcrafted features or specific adversarial frameworks, which can struggle to generalize across varied video content.

2.2 Supervised approaches

Supervised approaches are designed to learn the fundamental basis for video summarization from datasets containing annotated summaries [33]. Zhao et al. [34] introduced a hierarchical structure-adaptive RNN utilizing two cascaded LSTM layers: the first layer for shot segmentation and the second for predicting video summaries. Similarly, Wei et al. [35] proposed the Semantic Attended Network for Video Summarization, which includes encoder–decoder based on LSTM and frame selector that translates visual content into text descriptions, aiding in the selection of semantic segments. Ji et al. [36] introduced a model that combines a BiLSTM with attentive encoder–decoder networks to encode video frames into feature representations, using attention-based LSTMs to generate summaries. Convolutional neural networks (CNNs) are fused with the LSTM network for extraction of spatial features. Zhou et al. [37] presented two versions of summarization model containing CNN and BiLSTM, using a diversity-representativeness (DR) that calculates summaries based on diversity and representativeness. Huang et al. [38] fused CNNs and LSTM to create multi-level spatiotemporal representations, which capture frame-level importance by sequentially. Wang et al. [39] introduced a stacked model that combines LSTM and memory layers to fuse CNN-derived features, enhancing the representation of long-term dependencies between frames.

In recent developments, attention mechanisms are integrated into supervised approaches. VASNet [40] employs self-attention for keyframes identification. Liu et al. [41] proposed a hierarchical attention that uses BiLSTM along with a multi-attention mechanism to extract keyframes and generate summaries. Zhu et al. [42] introduced the Detect-to-Summarize model, which employs object recognition (anchor-free and anchor-based) methods to evaluate the importance of video frame and generate summaries, ensuring temporal consistency. Li et al. [11] proposed an approach that captures frame dependencies through pairwise temporal relations using attention techniques, enabling the generation of diverse and representative frames for the summary. Apostolidis et al. [43] enhanced frame dependency modeling by integrating absolute positional information with self-attention techniques to compute frame importance. Hsu et al. [44] introduced a video summarization architecture based on a modified vision transformer [45], which better represents inter-frame relations, leading to more effective video summarization.

Li et al. [46] developed a multimodal self-supervised framework that progressively extracts key video content using a combination of video–text semantic consistency exploration and masked frame recovery techniques. Zhang et al. [47] leveraged context representation graphs and semantic encoders for cross-modal learning, enriching temporal cues for improved summarization. Khan et al. [48] proposed vision transformer-assisted deep pyramidal refinement network for multi-scale feature refinement to improve generated summaries. Zhang et al. [49] integrated content-aware enhancement, multi-granularity encoding, and adaptive fusion to model contextual video information for precise key segment detection. Han et al. [50] introduced a novel approach to exploit motion clues from adjacent frame using multi-head attention without additional training parameters, for enhancing local–global motion representation. Yashwanth and Soni [51] proposed sequence learning networks for video summarization with key-shot selection using RNN and CNN models.

Most of the works focus on either temporal or spatial features. The unsupervised methods reduced the requirement of human-annotated data by using handcrafted rewards. Researchers employed single agent-based rewards on the temporal dependency of a single video, which may face gradient vanishing or exploitation. Further, researchers developed multimodal solutions by fusing the textual data with visual data; however, they only considered the textual–visual temporal dependencies. Moreover, they achieved sub-par performance which is achieved by other state-of-the-art works considering the visual features only.

In this paper, we introduced competitive set attention which allows the sets to compete for relevance, improving the quality of the feature representations over multiple iterations on long-range temporal correlations by enabling competition between sets of temporal features across the entire video sequence and then refining temporal sets by introducing competition among salient regions within each frame. Moreover, our method iteratively aligns temporal and spa-

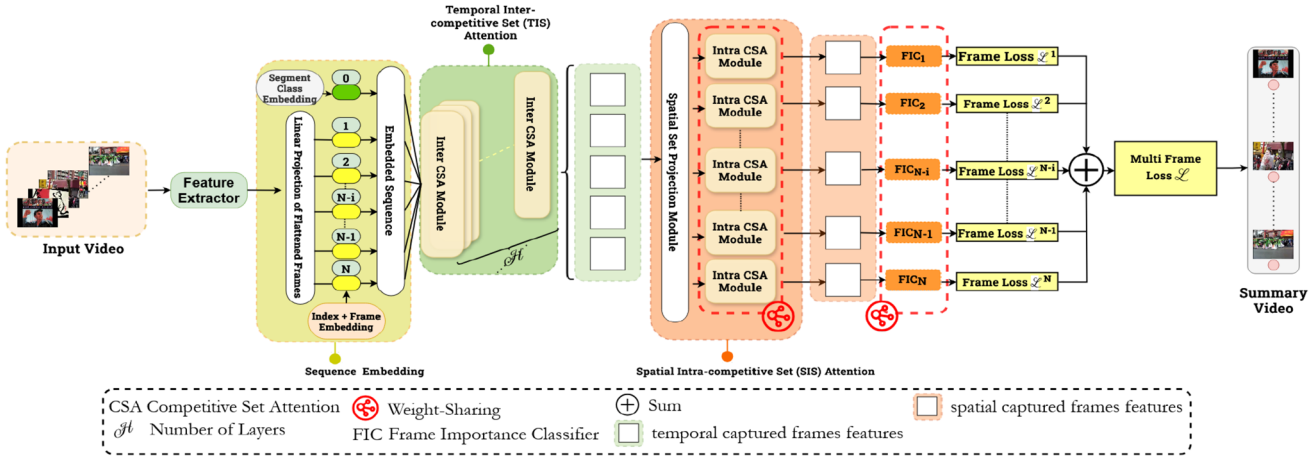

Fig. 1 The overall structures of the Spatiotemporal Set Attention for Video Summarization (STSA) for video summarization

tial competitive sets, refining feature representations across both dimensions. This inter- and intra-competition process captures a more holistic spatiotemporal understanding of the video leading to the state-of-the-art results without relying on textual data, demonstrating superior effectiveness over multimodal and single-feature methods.

3 The proposed methodology

This section introduces the Spatiotemporal Set Attention (STSA) model for video summarization. The architecture of the STSA is shown in Fig. 1 and processes a given video by first dividing it into non-overlapping segments. Each segment is fed into the STSA model. The proposed model leverages pre-trained models [45, 52, 53] to extract scene-centric features. The frame embedding is generated using the scene-centric features with a trainable projection layer. Frame embeddings for each segment are combined with segment class and index embeddings, which is passed to TIS encoder. The TIS encoder is designed to capture temporal inter-competitive set correlations between frames within each video segment. To further emphasize salient regions and learn spatial intra-competitive set attention, the SIS encoder is introduced, incorporating a spatial set projection module and aligned intra-competitive set attention. At last, the classifier layer generates the frame importance score. In the following sections, we will detail each module of the STSA model.

3.1 Feature extraction and sequence embedding

To capture scene-specific information from video frames, we employ pre-trained networks [45, 52, 53] to extract scene-centric features from each frame. Once the scene-centric features are extracted, the next step involves constructing sequence embeddings. For a video segment V, consisting of N continuous frames $\{f^i\}_{i=0}^{N}$, each frame's scene-centric features F_k^S are linearly projected to 1D features p_i^k. To encode global contextual information and enhance the model's understanding of video segment importance, we append a segment class token C_i^{class} to the flattened frame features. The combined sequence X_{V_i} is then mapped to a D-dimensional vector through a learnable frame embedding projection Fr_E. The embedding output includes both frame embeddings and the segment class token can be expressed as:

$$E_{X_{V_i}} = [c_i^{class}; p_i^1 \cdot Fr_E; p_i^2 \cdot Fr_E; \cdots p_i^k \cdot Fr_E] \quad (1)$$

To further incorporate temporal information, an index embedding $Fr_{E_{idx}}$ is added to the frame embedding sequence, producing the final sequence embedding t:

$$t = E_{X_{V_i}} + Fr_{E_{idx}} \quad (2)$$

The dimensionality of the frame embedding p_i^k is $R^{H\times W\times C}$, where H, W, and C represent the height, width, and channels of the frames. The learnable frame embedding projection Fr_E reduces the dimensionality to $R^{(H\times W\times C)\times D}$, where D is empirically selected as 768. The final sequence embedding t is then passed as the input to the TIS attention for further processing (Fig. 2).

3.2 Temporal inter-competitive set (TIS) attention

The existing attention mechanisms excel at capturing long-range dependencies, such as temporal relationships within sequences; however, they often struggle with the complex structure of videos. The extended nature of videos, combined with the challenge of understanding dynamic scene changes, limits the performance of standard attention mechanisms in

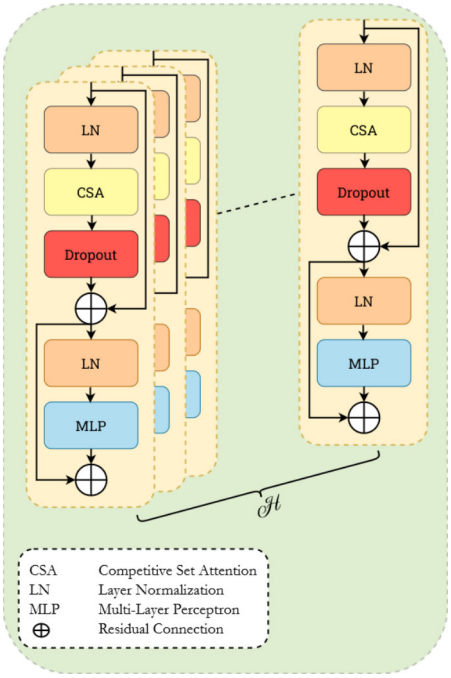

Fig. 2 The brief overview of the temporal intra-competitive set (TIS) attention encoder

video summarization tasks. To address this, we propose Temporal Inter-Competitive Set (TIS) Attention module. The core of our method lies in competitive set attention, a mechanism inspired by slot attention [54] within a modified transformer [45, 55] architecture. Unlike traditional self-attention, which treats elements independently, our competitive set attention processes frames of a video segment as competitive sets, allowing the model to capture complex inter-dependencies and relationships between frames. This results in a more accurate and meaningful segmentation of video scenes, providing a stronger global understanding of the video's context.

In place of traditional image patches used in transformer models, we process video frames directly. By treating each frame as a competitive set and learning inter-frame relationships, TIS attention effectively captures temporal dependencies across the video. To preserve temporal positional information, we introduce an index embedding mechanism inspired by the positional embedding in transformers [13, 45], which allows the model to better learn the significance of each frame within the sequence.

The proposed TIS attention module takes each frame t_i^k of a video segment V_i as input. The frame is first normalized using layer normalization $LN(\cdot)$, defined as:

$$\tilde{t_i^k} = LN(t_i^k) \tag{3}$$

The normalized frame is then passed through the H-layer competitive set attention (CSA) encoder, where each layer learns the competitive interactions between frames. The output of the k^{th} competitive set attention layer is computed as:

$$\dot{t_i^k} = CSA_{H_{Layer}}(\tilde{t_i^k}) \tag{4}$$

The competitive set attention layers process the frames through multiple stages, capturing inter-competitive set correlations, which are crucial for understanding temporal dynamics in video summarization. These layers are concatenated and projected using a learnable matrix U_T, resulting in the final competitive attention representation:

$$CSA_{H_{Layer}}(\tilde{t_i^k}) = [CSA_0(\tilde{t_i^k}), \ldots, CSA_{H-1}(\tilde{t_i^k})]U_T \tag{5}$$

where $U_T \in R^{(H \cdot D_h) \times D}$ transforms the concatenated outputs, allowing the model to learn the relationships between frames in a more global context. Through this process, the temporal inter-competitive set correlations are captured, providing a strong foundation for determining frame importance in video summarization. In TIS attention, the index embedding allows to learn the temporal ordering and significance of frames, ensuring that temporal relations between frames are captured more effectively. This mechanism replaces traditional positional embedding used in image processing transformers, making it more suitable for videos, where understanding frame transitions is crucial. The overall output of the competitive set attention, t', is computed using dropout regularization ($\mathscr{D}$) and a residual connection, described as:

$$t' = \mathscr{D}(\dot{t_i^k}) + t_i^k \tag{6}$$

This output then passes through a dense unit composed of two fully connected layers (FFN) with residual connections, further refining the temporal features:

$$t'' = FFN(\hat{t'}) + t' \tag{7}$$

This refinement step ensures that the model learns robust temporal patterns while preserving essential frame-level information (Fig. 3). In this paper, we empirically set the N = 9 and H = 4 as shown in Sect. 4.

3.3 Spatial intra-competitive set (SIS) attention

While the TIS attention module efficiently captures temporal interrelations between frames, each individual frame may contain salient regions that are crucial for meaningful summaries. To address the spatial aspect, we propose SIS attention that focuses on identifying and leveraging these spatially salient regions within each frame to determine

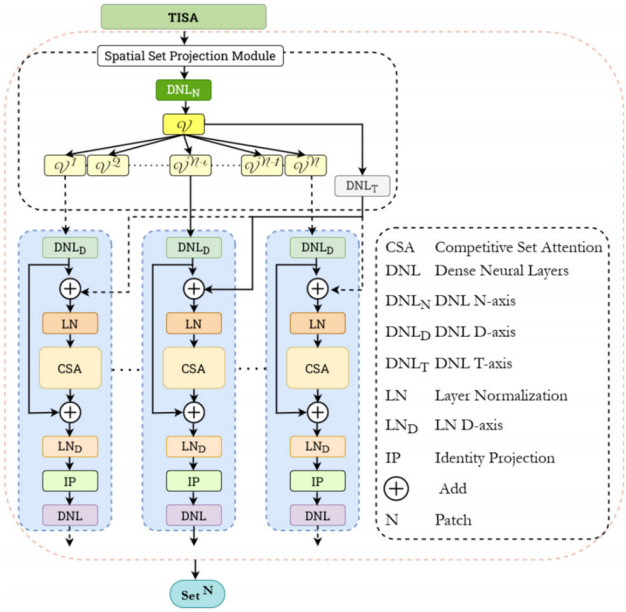

Fig. 3 The structure of the spatial intra-competitive set (SIS) attention encoder consists of the spatial set projection module (SSPM) and aligned intra-competitive set attention modules

frame importance. The spatial information, when combined with the temporal context captured by the segment class embedding, enables a more complete and holistic interpretation of the video content. SIS attention captures the intra-competitive set attention from these spatially salient regions while retaining the global contextual information learned through TIS attention. Previous approaches often focus either on temporal inter-frame relations or spatial details, but by integrating both in a competitive attention mechanism, our method provides a more comprehensive understanding of frame importance.

The SIS attention operates on the output of TIS attention, denoted as t'', which consists of temporal interrelations between frames enriched with segment class embedding. However, t'' includes both temporal frame features and segment class embedding, and thus, to focus on frame-specific spatial features, we must decompose t''. To achieve this, we remove the segment class embedding from t'', resulting in $\bar{t}$, containing only the frame embeddings. However, this decomposition alone discards the valuable global contextual information, which may cause inconsistencies across adjacent frames. To mitigate this, we introduce our trainable Spatial Set Projection (SSP) Module, which generates competitive transformer set features for each frame, effectively maintaining both the spatial and temporal context within each frame's embedding.

The SSP module applies a fully connected layer $DNL_N(\cdot)$, consisting of N neurons, to project t'' into a new feature space $\mathscr{V}$, with a dimension of $R^{N\times D}$:

$$\mathscr{V} = DNL_N(t'') \tag{8}$$

This projection ensures that the global segment class embedding is preserved within the new frame embeddings, allowing each frame to retain its global context while focusing on spatial saliency. Each encoded frame feature $\mathscr{V}^{\mathscr{N}-i}$ is passed through $DNL_D(\cdot)$ for further enhancing the frame representation:

$$x^{\mathscr{N}-i} = DNL_D(\mathscr{V}^{\mathscr{N}-i}) \tag{9}$$

To reinforce the temporal context, we used another fully connected layer $DNL_T(\cdot)$, which processes the entire sequence $\mathscr{V}$ to create a temporal integration feature. The final frame competitive transformer set feature $x_r^{\mathscr{N}-i}$ for each frame incorporates both spatial and temporal information:

$$x_r^{\mathscr{N}-i} = x^{\mathscr{N}-i} + DNL_T(\mathscr{V}) \tag{10}$$

The feature, $x_r^{\mathscr{N}-i}$, encapsulates the frame content, continuous temporal information, and global frame contextual representation, offering a powerful representation of each frame. These features are then passed to the intra-competitive set attention module, where the spatial intra-competitive attention is learned to classify frame importance.

The intra-competitive set attention mechanism is similar to that used in TIS attention but is focused on spatial features within each frame. After normalization via layer normalization (LN), the competitive set attention is applied to generate the spatial intra-competitive attention feature $Xs_r^{\mathscr{N}-i}$:

$$Xs_r^{\mathscr{N}-i} = CSA^{\mathscr{N}-i}(\hat{x_r^{\mathscr{N}-i}}) \cdot U_S \tag{11}$$

This results in the final competitive set attention feature $S^{\mathscr{N}-i}$, which integrates spatial attention across frames, allowing for effective frame importance classification.

Our method captures both local frame saliency and global temporal context through temporal and spatial intra-competitive attention mechanisms, offering a more robust solution for video summarization. The SIS attention not only preserves the global contextual frame information through its innovative projection mechanism but also effectively identifies spatially salient regions within each frame, crucial for producing human-like video summaries.

3.4 Competitive set attention

To enhance video summarization and effectively capture scene-centric features within each frame, we introduce competitive set attention mechanism. Unlike traditional attention

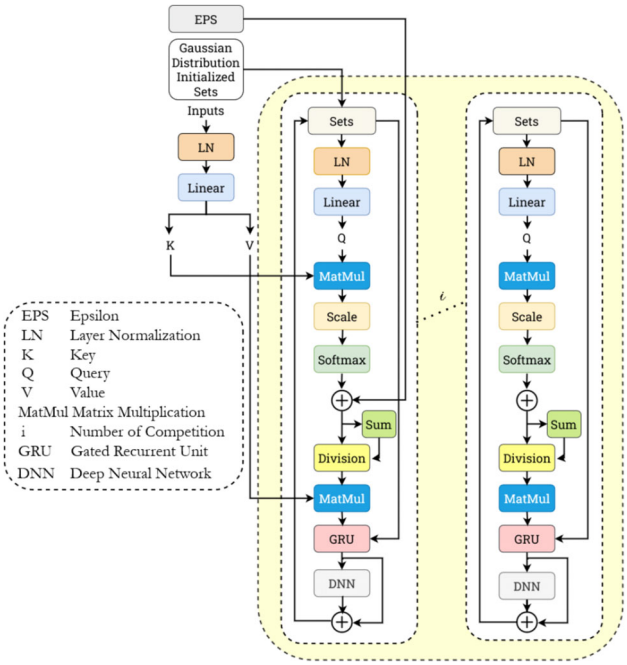

Fig. 4 The architecture of the competitive set attention (CSA) module

models that solely rely on object-centric or frame-level features, our method iteratively refines and competes between sets of features, extracting the most salient and distinct components from the video scenes. This approach allows the model to dynamically learn and update scene-specific feature representations, referred to as sets, where each set captures unique aspects of the scene in each frame.

The competitive set attention allows the sets to "compete" for relevance, improving the quality of the feature representations over multiple iterations $i = 1 \cdots T$. This mechanism ensures that different components of the input scene are represented more effectively by the attention mechanism, particularly in complex, multi-object scenes. At the start of each iteration, set representations are initialized by sampling from a standard distribution, allowing the competitive set attention to generalize to varying numbers of sets during testing, described as:

$$sets \cong \mathcal{N}(\mu, diag(\sigma)) \tag{12}$$

where $\mathcal{N}$ is a Gaussian distribution with learnable parameters μ and σ, controlling the initialization of the sets. This dynamic initialization facilitates adaptability across different video segments during test time. The competitive process then unfolds, where the sets iteratively refine their representations by attending to distinct components of the input scene. Unlike conventional attention mechanisms, which merely calculate attention weights based on a softmax function, the competitive set attention introduces an element of competition among sets using dot-product attention. This forces each set to "compete" for the most relevant part of the scene, ensuring that no important component of the input is neglected. This competitive process is governed by a softmax-based attention mechanism [56–58]:

$$attn_{i,j} = \frac{e^{M_{i,j}}}{\sum_l e^{M_{i,l}}} \tag{13}$$

where M represents the similarity between the sets and the input features. The normalization step ensures that attention coefficients sum to one, thereby ensuring that each input component is given due attention, preventing overemphasis on any single part of the scene.

To improve the stability of the attention mechanism, we utilize a weighted mean for the aggregation of input values, which is more robust compared to a simple weighted sum. This step refines the updates for the sets, leading to better generalization during training and inference:

$$W_{i,j} = \frac{attn_{i,j}}{\sum_{l=1}^{N} attn_{l,j}} \tag{14}$$

After updating the sets, we apply a gated recurrent unit (GRU) [59] to iteratively refine the set representations, allowing for a more adaptive and memory-efficient update process:

$$sets = GRU(updates, sets; \Theta) \tag{15}$$

The use of GRU as a recurrent update function allows the competitive set attention to retain crucial temporal information over multiple iterations without introducing excessive computational overhead. This method, as shown in our experimental analysis, not only captures the temporal dynamics of the video (via TIS attention) but also focuses on spatially salient regions (via SIS attention), yielding more robust video summaries.

By employing fewer parameters and focusing on salient features through competition, our model achieves faster convergence during training and enhanced performance on real-world video summarization tasks. The proposed competitive set attention architecture is illustrated in Fig. 4.

3.5 Loss and video summary generation

To generate effective video summaries, our model learns the importance of individual frames from human-created summaries using a frame importance classifier (FIC). The FIC performs binary classification to predict the importance of each frame. Given a video segment V_i, the frame loss for each frame $\mathcal{N} - i$, denoted as $\mathcal{L}^{\mathcal{N}-i}$, is defined as:

$$\mathcal{L}^{\mathcal{N}-i} = -\sum y^{\mathcal{N}-i} \log_2(\hat{y}^{\mathcal{N}-i}) \tag{16}$$

where $y^{\mathcal{N}-i}$ and $\hat{y}^{\mathcal{N}-i}$ denotes ground truth and predicted importance score (either 0 or 1), respectively. The total loss $\mathcal{L}$ is computed by summing the losses of each frame in video segment:

$$\mathcal{L} = \sum_{i=1}^{N} \mathcal{L}^{\mathcal{N}-i} \tag{17}$$

This cumulative loss allows end-to-end training of our network, facilitating the optimization of frame importance predictions across the entire video segment.

After predicting the frame importance, we generate the video summary by aggregating the frame scores into shot importance scores. As suggested in [60] and [42], we apply Kernel Temporal Segmentation (KTS) [61] to segment the video into shots. For j-th shot, importance score m_j is calculated as average of the predicted importance scores of its constituent frames:

$$m_j = \frac{1}{G_j} \sum_{k=1}^{G_j} \hat{y}^{k} \tag{18}$$

where G_j denotes the number of frames in the j-th shot, and $\hat{y}^{k}$ denotes the predicted score for k-th frame. To ensure consistency with prior works, we constrain the generated video summary to be 15% of the original video length.

The problem of importance shot selection is solved with the help of 0/1 knapsack by transforming the task suitable for it, which can be expressed as:

$$\max \sum_{j=1}^{s_h} a_j m_j \quad \text{subject to} \quad \sum_{j=1}^{s_h} a_j G_j \leq V \times 15\% \tag{19}$$

Here, s_h denotes number of shots, V denotes the total video length, and a_j denotes the selection ($a_j = 1$) or rejection ($a_j = 0$) of the j-th shot. The optimization problem is solved using dynamic programming.

4 Experimental results and analysis

4.1 Datasets

We conducted the experimentation on widely used datasets of video summarization, SumMe [62] and TVSum [63] for evaluating the performance of our STSA model. Additionally, we utilized the YouTube and OVP datasets for the augmented and transfer learning experiments. The SumMe dataset contains 25 videos covering a diverse range of topics, including sports, events, and holidays. The videos vary in length from 1 to 6 min, and each video is annotated with multiple user-generated summaries. These frame-level annotations reflect the importance of each segment, making SumMe an ideal dataset for evaluating video summarization methods. The diversity in content and user preferences adds complexity to summarization tasks. The TVSum dataset comprises of 50 videos covering a range of genres, such as how-to tutorials, documentaries, news, and user-generated content (e.g., vlogs, egocentric videos). The dataset is organized into 10 categories, each containing 5 videos. Crowd-sourced annotations provide frame-level importance scores, with 1000 annotations (20 per video) offering rich ground truth data. TVSum's diversity in both video genres and user annotations makes it particularly challenging for video summarization. We used the OVP and YouTube datasets for augmented experiments [64]. The OVP and YouTube datasets include 50 and 39 videos, respectively. The annotation of OVP and YouTube datasets is performed by 5 users. These datasets are valuable for assessing model generalizability and used in prior methods.

4.2 Implementation details

We performed our experiments on an Ubuntu system operating at Intel Xeon processor with 128GB RAM and Nvidia Titan-RTX GPU. We have implemented our approach using PyTorch. In our approach, when the last segment length is shorter than N, we extend it by repeating the last frame until the segment's length equals N. For the feature extraction, we have used a pre-trained models [45, 52, 53]. For the same-spatial resolution, all the input frames resized uniformly to the size of 224 × 224. The dimension of the scene-centric deep frames features for each frame is 512. The size of the batch is 40. Prior to the final classification layer, a dropout of 0.1 is used. For the updation of parameters of our STSA model, SGD with a momentum of 0.9 is used. The model is trained for 100 epochs. During training, cosine learning rate schedule and warm-up technique are employed to mitigate overfitting. Initially, the learning rate is 0.003 for the warm-up phase. At the 10'th epoch, the learning rate gradually increases to 0.03. Afterward, a cosine decay is applied starting from the 10th epoch.

4.3 Experimental setup and metrics

To ensure fair comparisons with existing methods, we used experimental setup as adopted by various state-of-the-art methods [12, 13, 42, 47, 49]. We evaluated the proposed method using three distinct experimental setups: canonical, augmented, and transfer. In canonical setup, each dataset is randomly split into five folds. For each experiment, training and testing data contain 80% and 20%, respectively. This process is repeated multiple times with different random

splits to ensure robust evaluation. The reported results are the average performance across all splits. In augmented experiments, we combined the SumMe and TVSum datasets with the YouTube and OVP datasets to evaluate the generalizability of our model. These additional datasets provide a diverse set of video types, allowing us to assess how well our method performs across various domains. The inclusion of multiple datasets ensures that our model is not overfitting to any specific type of video content. For transfer learning experiments, we trained our model using three datasets and evaluated it on the remaining dataset. This setting was designed to test the generalization capabilities of our model when trained on one domain and applied to another.

The evaluation of proposed model is based on comparing the generated video summaries and ground truth summaries using the harmonic mean F-score. In our experiments, we generated summaries with a duration of 15% of the original video length. The precision (P) and recall (R) are computed by analyzing the temporal overlap between generated summary (S) and ground truth summary (G). Precision quantifies the proportion of the generated summary that correctly aligns with the ground truth, whereas recall measures the extent to which the ground truth is represented within the generated summary. The equations are as follows:

$$P = \frac{duration\ of\ (G \cap S)}{duration\ of\ S} \tag{20}$$

$$R = \frac{duration\ of\ (G \cap S)}{duration\ of\ G} \tag{21}$$

Finally, the F-score is computed as:

$$F = \frac{2 \times P \times R}{(P + R)} \times 100\% \tag{22}$$

The F-score metric provides a balanced evaluation of how well the generated summary aligns with the ground truth, accounting for both the accuracy of selected segments (precision) and the coverage of important content (recall).

4.4 Ablation study

To demonstrate the effectiveness of each component of the proposed approach, we have conducted an ablation study on various components of the network. Moreover, the ablation study by utilizing backbones of different networks was conducted which shows the model stability. The proposed competitive set attention is composed of three components mainly Competitive Set Attention (CSA), Deep Residual Neural Network (RDNN), and Long Recurrent Mechanism (LRM) which introduces competition between the set to explore more context from each frame, RDNN connection, and updating the learned information with the previously learned information. Table 1 illustrates the results of the ablation study of various components of the proposed method.

Table 1 Ablation study of competitive set attention (CSA) in F-score (%)

CSA	RDNN	LRM		SumMe	TVSum
		RNN	GRU		
✗	✓	✓	✗	59.1	66.7
✗	✓	✗	✓	59.1	66.8
✓	✗	✓	✗	58.0	66.8
✓	✗	✗	✓	59.1	66.8
✓	✓	✓	✗	58.7	66.8
✓	✓	✗	✓	**59.6**	**67.3**

Bold indicates best measure for by considering values on both datasets

Table 2 Ablation study on various feature extractors

Backbone	SumMe	TVSum
ResNet-18 [52]	59.6	67.3
GoogLeNet [53]	60.4	67.9
ViT [45]	63.0	68.1

Table 3 Ablation study of input frame (N), number of sets (H), and number of competitions (i) using F-score (%)

N	H	*i*	SumMe	TVSum
9	4	3	59.1	65.9
		5	**59.6**	**67.3**
	8	3	59.1	66.7
		5	59.9	66.7
16	4	3	60.6	67.0
		5	59.9	67.0
	8	3	60.0	67.0
		5	62.1	66.8
25	4	3	60.2	66.7
		5	61.2	67.1
	8	3	57.8	66.7
		5	59.2	67.2

Bold indicates best measure for by considering values on both datasets

To show the robustness of the components in competitive set attention, we considered a normal set attention without introducing the competition during the both inter- and intra-correlations learning and used recurrent neural network (RNN) as LRM at the first row of the table, showing the stability of the proposed method which yields best results compared to the traditional methods. We have further explore another mechanism, gated recurrent unit (GRU) as LRM keeping the same components settings in the second row. On the first two row, the RDNN is also composed with LRM to learn the correlations set effectively. Furthermore, we have conducted ablation of the CSA for the both RNN and GRU as

LRM without using the RDNN. The results are shown in the 3rd and 4th rows of the table. At last, we have comprised CSA and RDNN, with the both LRM, RNN, and GRU. From the observation, the CSA and RDNN with the GRU as LRM outperform and yield best results on the both dataset SumMe and TVSum which can be seen in the last row of the table. By utilizing the introduced competition among set using CSA and LRM as update mechanism during the competition and residual network RDNN simultaneously, our proposed method shows the effectiveness in learning of the inter- and intra-competitive set attention co-relations.

Table 2 provides an ablation study that evaluates the proposed method using various backbone networks. To assess the impact of different backbone networks, we employed a pre-trained ResNet-18 [52] GoogLeNet [53], and ViT [45] which has been utilized in recent video summarization methods [13, 42, 47, 48]. As indicated by the table, ViT has achieved best performance alongside with ResNet-18 and GoogLeNet. However, during the inference with different backbones, ResNet-18 was fastest among all three backbones. We have conducted experimental inference on 20% data of SumMe and TVSum datasets for ResNet-18, GoogLeNet, and ViT. For fair comparison, we have taken same length of the videos for all three backbone network. We observed that the average time of inference taken by ResNet-18, GoogLeNet, and ViT for SumMe data was 17, 30, and 40 min, respectively. For TVSum data, the average time taken by ResNet-18, GoogLeNet, and ViT was 30, 55, and 64 min, respectively.

The proposed network contains three adaptable parameters which have a significant effect on the performance as shown in Table 3. The first key parameter in the proposed approach is N, representing the number of frames. This parameter directly influences the number of intra-competitive set attention modules within the SIS attention mechanism. The second important parameter is H, which defines the number of inter-competitive set attention modules in the TIS attention. Lastly, the parameter i controls the level of competition between sets, enhancing competition as it increases. By introducing this competitive framework, the proposed method can effectively capture more complex temporal relationships between frames, even when fewer input frames are provided. A comparative analysis of different settings for N, H, and i demonstrates the importance of each parameter, highlighting the model's robustness in achieving optimal F-score values across different combinations. Table 3 shows the comparison of various combinations of parameter settings with the F-score. The higher value of N, H, and i leads to increase in number of trainable parameters; thus, we selected values in bold as the proposed configuration.

Table 4 Quantitative performance of various methods in F-Score (%)

Methods	F1	
	SumMe	TVSum
VASNet [40]	49.7	61.4
DSNet (Based) [42]	50.2	62.1
DSNet (Free) [42]	51.2	61.9
ADSum-A [10]	45.9	64.5
ADSum-M [10]	46.1	64.3
DASP [65]	45.5	63.6
RSGN [66]	45.0	60.1
DAC [67]	47.5	59.4
MSVA [14]	53.4	61.5
SUM-GDA [11]	52.8	58.9
PGL-SUM [43]	55.6	61.0
DAN [68]	51.8	61.7
HMT [69]	44.1	60.1
RR-STG [12]	53.4	63.0
STVT [13]	55.1	67.1
DN-VSN [27]	52.0	62.8
SSPVS [46]	48.7	60.3
SSPVS+Text [46]	50.7	60.4
VSS-Net [47]	51.5	61.0
PRVLS [28]	46.3	63.0
MHGR [29]	47.6	59.0
MIMRN [30]	48.3	59.1
TR-Sum [31]	54.5	62.3
M3SUM [32]	43.6	56.9
MPFN [48]	51.9	62.5
AMFM [49]	51.8	61.0
MAS [51]	44.1	60.7
STSA-R	**59.6**	**67.3**
STSA-G	**60.4**	**67.9**
STSA-V	**63.0**	**68.1**

Bold indicates best measure for by considering values on both datasets

4.5 Quantitative results

We conducted a comparison of the proposed approach, STSA-R(STSA with ResNet-18), STSA-G(STSA with GoogLeNet), and STSA-V (STSA with ViT) against state-of-the-art approaches on both the SumMe and TVSum datasets to demonstrate the efficacy. The results of various methods, in comparison with our approach, are presented in Table 4.

All results for the contemporary methods discussed in this section are sourced directly from their respective papers for a fair comparison. As demonstrated in Table 4, the proposed method outperforms the state-of-the-art approaches on both the SumMe and TVSum datasets. The strength of our approach lies in its ability to effectively learn temporal inter-competitive set correlations and spatial intra-competitive

Table 5 Performance of various methods for canonical, augmented, and transfer settings in F-score (%)

Methods	SumMe			TVSum		
	Canonical	Augmented	Transfer	Canonical	Augmented	Transfer
DSNet (Based)	50.2	50.7	46.5	62.1	63.9	59.4
DSNet (Free)	51.2	53.3	47.6	61.9	62.2	58.0
ADSum-A	45.9	47.3	–	64.5	65.8	–
ADSum-M	46.1	47.6	–	64.3	65.7	–
DASP	45.5	47.0	–	63.6	64.5	–
RSGN	45.0	45.7	44.0	60.1	61.1	60.0
DAC	47.5	49.3	45.2	59.4	59.8	59.2
SUM-GDA	52.8	54.4	46.9	58.9	60.1	59.0
DAN	51.8	52.1	44.1	61.7	62.5	58.9
HMT	44.1	44.8	–	60.1	60.3	–
RR-STG	53.4	54.8	45.4	63.0	63.6	59.7
STVT	55.1	55.9	48.2	67.1	67.7	59.9
DN-VSN	52.0	53.2	50.6	62.8	61.8	60.9
SSPVS	48.7	50.4	45.8	60.3	61.8	57.8
SSPVS+Text	50.7	–	–	60.4	–	–
VSS-Net	51.5	52.8	48.4	61.0	61.4	58.5
PRVLS	46.3	49.7	47.6	63.0	59.2	57.0
MHGR	47.6	47	47	59.0	58.8	58.8
MIMRN	48.3	–	–	59.1	–	–
TR-Sum	54.5	–	–	62.3	–	–
M3SUM	43.6	–	–	56.9	–	–
MPFN	51.9	–	–	62.5	–	–
AMFM	51.8	52.8	46.4	61.0	60.8	58.6
MAS	44.1	–	–	60.7	–	–
STSA-R	**59.6**	**62.6**	**49.9**	**67.3**	**68.4**	**60.2**
STSA-G	**60.4**	**62.1**	**52.2**	**67.9**	**67.7**	**59.2**
STSA-V	**63.0**	**64.2**	**51.9**	**68.1**	**68.3**	**59.1**

Bold indicates best measure for by considering values on both datasets

set attention through our spatiotemporal competitive set transformer. This enables more robust frame importance classification compared to LSTM-based methods and attention mechanisms, which primarily focus on representing temporal frame information. Additionally, the combination of TIS attention with SIS attention further enhances the performance of our method. The results also demonstrate the effectiveness of the competitive set transformer structure in addressing video summarization tasks, especially when compared to methods relying on LSTM and attention mechanisms. Hence, our approach successfully learns frame importance from human-annotated summaries and achieves superior performance in video summarization on both the SumMe and TVSum datasets.

To assess the alignment between the human-annotated frame importance scores and those generated by the model, we utilized Kendall's τ and Spearman's ρ correlation coefficients, as done in [70]. In addition to these metrics, F-score values are also employed as in [13, 47, 49, 70]. Table 6 presents the quantitative comparison of the proposed method against several state-of-the-art approaches, including RSGN [66], DAC [67], DAN [68], HMT [69], STVT [13], VSS-Net [47], and AMFM [49] using Kendall's τ and Spearman's ρ correlation coefficients on the TVSum dataset.

The ranking of predicted summaries helps in computing the correlation coefficients using uniformly sampled videos as shown in previous works [13, 67, 70, 71]. For a fair comparison, we followed the same approach by sampling and ranking video summarization results according to both predicted and human-annotated frame importance scores. We averaged the ranking results across the individual human subjects to calculate the final correlation coefficients. By leveraging the TIS and SIS attention modules, our method effectively captures inter-competitive and intra-competitive set attention, allowing it to predict frame importance scores that align closely with human annotation. As a result, our approach achieves higher Kendall's τ scores and performs on

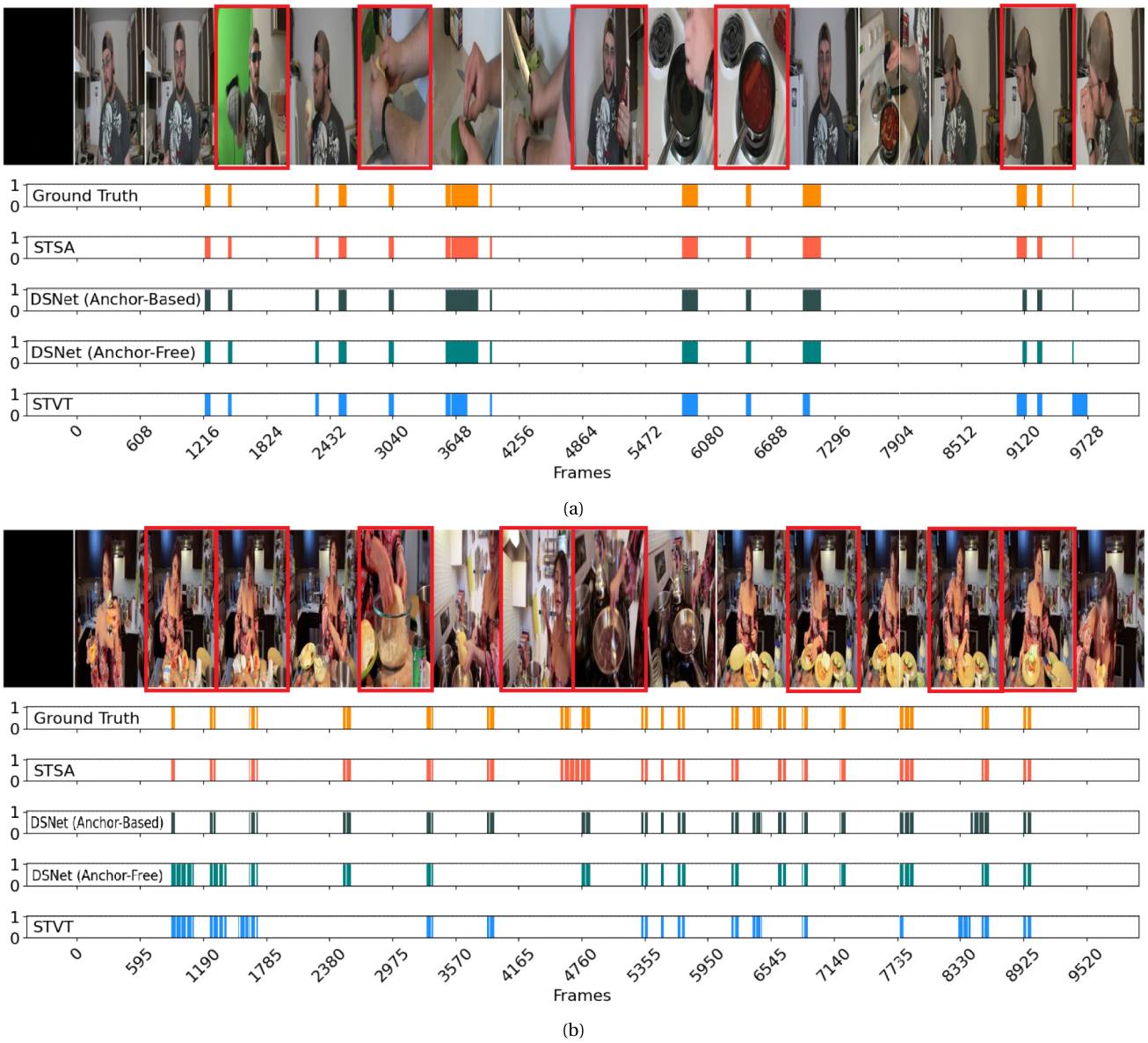

Fig. 5 The qualitative results of generated summary by STSA (proposed method), DSNet (anchor-based), DSNet (anchor-free), STVT, and ground truth

par with the state-of-the-art method [13] in terms of Spearman's ρ.

We performed augmented and transfer experiments on using YouTube and OVP datasets to assess the performance of our STSA using the setup given in [10, 13, 42, 47]. We included the OVP and YouTube datasets [64] in addition to the SumMe and TVSum datasets for the augmented experiments. Use of augmented data can help in mitigating the impact of limited training data and reducing the risk of overfitting. As demonstrated in Table 5, utilizing augmented datasets improves the performance of all contemporary methods. A few of the contemporary methods from the aforementioned performed the augmented experiments. Hence, we have only listed the contemporary methods which perform the augmented experiments. The proposed method shows a performance increase of 3% on the SumMe dataset and 1.1% on the TVSum dataset by incorporating augmented data into the training process. Moreover, in the augmented experiments, our method consistently outperforms the other contemporary methods. To introduce more rigorous testing, we performed experiments using transfer learning settings. The results, as shown in Table 5, indicate that the proposed method continues to outperform the state-of-the-art approaches. These findings highlight the method's strong ability to classify frame importance across different datasets, further proving its effectiveness.

Table 6 Kendall's and Spearman's correlation coefficients of various methods for the TVSum dataset

Methods	Kendall's τ	Spearman's ρ
RSGN [66]	0.083	0.090
DAC [67]	0.058	0.065
DAN [68]	0.071	0.099
HMT [69]	0.096	0.107
STVT [13]	0.100	0.131
SSPVS [46]	0.177	0.233
SSPVS+Text [46]	0.181	0.238
VSS-Net [47]	0.190	0.243
PRVLS [28]	0.080	0.131
MHGR [29]	0.094	0.123
TR-SUM [31]	0.092	0.122
AMFM [49]	0.179	0.233
STSA-R	**0.195**	**0.271**
STSA-G	**0.195**	**0.279**
STSA-V	**0.199**	**0.280**

Bold indicates best measure for by considering values on both datasets

4.6 Visual results

To illustrate the quality effectiveness of STSA, we present qualitative comparisons of video summaries generated by the STSA with respect to the ground truth and other state of the art such as DSNet (anchor-based), DSNet (anchor-free), and STVT. Figure 5 shows the visual results (using bar plot) of the generated summary. The bar in the plot shows that the frame is considered in the summary by the respective method, in case there is nothing in the bar plot; then frame is not selected in the generated summary.

Figure 5a shows the summary of proposed STSA, DSNet (anchor-based), DSNet (anchor-free), and STVT with the ground truth. The summary generated using considers frame falsely in summary near frame 3648 and fails to capture the frames into summary near frame number 9120 in the video. The results show that STVT fails to generate capture frames appropriately in the summary near frame number 3648 and 7296 in the video. Moreover, STVT captures extra frames in the summary near frame 9728 in the video as shown in Fig. 5a. Our proposed STSA generates an identical summary to the ground truth with missing frame in the summary and no false-positive frames in Fig. 5a.

In Fig. 5b, it can be observed from the bar plot that STVT and DSNet (anchor-free) are capturing frames into the summary which are not there in the ground truth. DSNet (anchor-based) generates better summary as compared to the other two existing methods; however, it also fails to capture the frames in the middle of the video. Further, it captures frames in summary as false positives in the end of the video. The summary generated using the proposed STSA is closer to the ground truth compared to the existing methods. However, our STSA is missing at few places in Fig. 5b.

5 Conclusion

In this paper, we introduced a novel Spatiotemporal Set Transformer (STSA) for video summarization, which effectively captures both temporal and spatial dependencies through competitive attention mechanisms. Our approach leverages the Temporal Inter-Competitive Set (TIS) attention and Spatial Intra-Competitive Set (SIS) attention modules to model long-term temporal relationships and refine spatial regions of interest within frames. Through extensive experiments on the SumMe and TVSum datasets, we demonstrated that our model outperforms state-of-the-art methods, achieving higher F-scores and generating more accurate and informative summaries. Through comprehensive experiments on the SumMe and TVSum datasets, as well as augmented and transfer learning settings, we demonstrated that the proposed method consistently outperforms state-of-the-art models. In summary, the STSA model represents a significant advancement in video summarization by integrating spatiotemporal competitive attention, providing a more effective and comprehensive approach to capturing the essence of video content.

While the proposed model shows strong performance across multiple datasets and evaluation settings, future work can explore incorporating additional contextual information, such as audio or textual metadata, to further improve summarization accuracy in more complex scenarios. Moreover, applying the STSA model to other domains, such as video surveillance or sports analysis, could reveal its broader potential in real-world applications.

Acknowledgements We would like to express our sincere gratitude to Dr. Anil Singh Parihar (Professor, Delhi Technological University, New Delhi, India) for invaluable insights, suggestions, and constructive feedback. Furthermore, we would like to thank Dr. Chun-Rong Huang (Professor, National Yang Ming Chiao Tung University, Hsinchu, Taiwan) for his support in providing the relevant files.

Funding In this study, there is no funding involved from any agency.

Data Availability No datasets were generated or analyzed during the current study.

Declarations

Conflict of interest The authors declare that they have no conflict of interest.

Humans or animals performed This article does not contain any studies involving humans or animals performed by any of the authors.

References

1. Tian, X., Wu, Z., Cao, J., Chen, S., Dong, X.: Ilidviz: An incremental learning-based visual analysis system for network anomaly detection. Virtual Reality Intell. Hardware **5**(6), 471–489 (2023)
2. Yao, J., Chen, J., Niu, L., Sheng, B.: Scene-aware human pose generation using transformer. In: Proceedings of the 31st ACM International Conference on Multimedia, MM '23, p. 2847-2855. Association for Computing Machinery, New York, NY, USA (2023). https://doi.org/10.1145/3581783.3612439
3. Chen, S., Zhong, X., Zhang, Y., Zhu, L., Li, P., Yang, X., Sheng, B.: Action-aware linguistic skeleton optimization network for non-autoregressive video captioning. ACM Trans. Multimed. Comput. Commun. Appl. (2024). https://doi.org/10.1145/3679203
4. Sheng, B., Li, P., Zhang, Y., Mao, L., Chen, C.L.P.: Greensea: Visual soccer analysis using broad learning system. IEEE Trans. Cybernetics **51**(3), 1463–1477 (2021). https://doi.org/10.1109/TCYB.2020.2988792
5. Singh Parihar, A., Pal, J., Sharma, I.: Multiview video summarization using video partitioning and clustering. J. Visual Commun. Image Representation **74**, 102991 (2021). https://doi.org/10.1016/j.jvcir.2020.102991
6. Zhu, J., Zhang, Q., Fei, L., Cai, R., Xie, Y., Sheng, B., Yang, X.: Fffn: Frame-by-frame feedback fusion network for video super-resolution. IEEE Trans. Multimed. **25**, 6821–6835 (2023). https://doi.org/10.1109/TMM.2022.3214776
7. Sheng, B., Li, P., Ali, R., Chen, C.L.P.: Improving video temporal consistency via broad learning system. IEEE Trans. Cybernetics **52**(7), 6662–6675 (2022). https://doi.org/10.1109/TCYB.2021.3079311
8. Ji, C., Chen, Y., Yang, Z.X., Wu, E.: Spatio-temporal compression for semi-supervised video object segmentation. Visual Comput. **39**(10), 4929–4942 (2023)
9. Lu, X., Quan, W., Marek, R., Zhao, H., Chen, J.X.: Siammast: Siamese motion-aware spatio-temporal network for video action recognition. Visual Comput. **40**(5), 3163–3181 (2024)
10. Ji, Z., Zhao, Y., Pang, Y., Li, X., Han, J.: Deep attentive video summarization with distribution consistency learning. IEEE Trans. Neural Networks Learn. Syst. **32**(4), 1765–1775 (2020)
11. Li, P., Ye, Q., Zhang, L., Yuan, L., Xu, X., Shao, L.: Exploring global diverse attention via pairwise temporal relation for video summarization. Pattern Recognition **111**, 107677 (2021)
12. Zhu, W., Han, Y., Lu, J., Zhou, J.: Relational reasoning over spatial-temporal graphs for video summarization. IEEE Trans. Image Process. **31**, 3017–3031 (2022)
13. Hsu, T.C., Liao, Y.S., Huang, C.R.: Video summarization with spatiotemporal vision transformer. IEEE Transactions on Image Processing (2023)
14. Ghauri, J.A., Hakimov, S., Ewerth, R.: Supervised video summarization via multiple feature sets with parallel attention. In: 2021 IEEE International Conference on Multimedia and Expo (ICME), pp. 1–6s. IEEE (2021)
15. Mundur, P., Rao, Y., Yesha, Y.: Keyframe-based video summarization using delaunay clustering. Int. J. Digital Libraries **6**, 219–232 (2006)
16. Hadi, Y., Essannouni, F., Thami, R.O.H.: Video summarization by k-medoid clustering. In: Proceedings of the 2006 ACM symposium on Applied computing, pp. 1400–1401 (2006)
17. Zhao, B., Xing, E.P.: Quasi real-time summarization for consumer videos. In: Proceedings of the IEEE conference on computer vision and pattern recognition, pp. 2513–2520 (2014)
18. Mei, S., Guan, G., Wang, Z., Wan, S., He, M., Feng, D.D.: Video summarization via minimum sparse reconstruction. Pattern Recognition **48**(2), 522–533 (2015)
19. Meng, J., Wang, S., Wang, H., Yuan, J., Tan, Y.P.: Video summarization via multi-view representative selection. In: Proceedings of the IEEE international conference on computer vision workshops, pp. 1189–1198 (2017)
20. Panda, R., Roy-Chowdhury, A.K.: Sparse modeling for topic-oriented video summarization. In: 2017 IEEE International Conference on Acoustics, Speech and Signal Processing (ICASSP), pp. 1388–1392. IEEE (2017)
21. Mahasseni, B., Lam, M., Todorovic, S.: Unsupervised video summarization with adversarial lstm networks. In: Proceedings of the IEEE conference on Computer Vision and Pattern Recognition, pp. 202–211 (2017)
22. Yuan, L., Tay, F.E., Li, P., Zhou, L., Feng, J.: Cycle-sum: Cycle-consistent adversarial lstm networks for unsupervised video summarization. In: Proceedings of the AAAI Conference on Artificial Intelligence, vol. 33, pp. 9143–9150 (2019)
23. Jung, Y., Cho, D., Kim, D., Woo, S., Kweon, I.S.: Discriminative feature learning for unsupervised video summarization. Proceed. AAAI Conf. Artif. Intell. **33**, 8537–8544 (2019)
24. Jung, Y., Cho, D., Woo, S., Kweon, I.S.: Global-and-local relative position embedding for unsupervised video summarization. In: European Conference on Computer Vision, pp. 167–183. Springer (2020)
25. Apostolidis, E., Adamantidou, E., Metsai, A.I., Mezaris, V., Patras, I.: Ac-sum-gan: Connecting actor-critic and generative adversarial networks for unsupervised video summarization. IEEE Trans. Circuits Syst. Video Technol. **31**(8), 3278–3292 (2020)
26. Zhang, Y., Liang, X., Zhang, D., Tan, M., Xing, E.P.: Unsupervised object-level video summarization with online motion auto-encoder. Pattern Recognition Lett. **130**, 376–385 (2020)
27. Zang, S.S., Yu, H., Song, Y., Zeng, R.: Unsupervised video summarization using deep non-local video summarization networks. Neurocomputing **519**, 26–35 (2023)
28. Wang, G., Wu, X., Yan, J.: Progressive reinforcement learning for video summarization. Inf. Sci. **655**, 119888 (2024)
29. Gunuganti, J., Yeh, Z.T., Wang, J.H., Norouzi, M.: Unsupervised video summarization with adversarial graph-based attention network. J. Visual Commun. Image Represent. **102**, 104200 (2024)
30. Wu, G., Song, S., Wang, X., Zhang, J.: Reconstructive network under contrastive graph rewards for video summarization. Expert Syst. Appl. **250**, 123860 (2024)
31. Abbasi, M., Hadizadeh, H., Saeedi, P.: Unsupervised video summarization via reinforcement learning and a trained evaluator. arXiv preprint arXiv:2407.04258 (2024)
32. Wang, H., Zhou, B., Zhang, Z., Du, Y., Ho, D., Wong, K.F.: M3sum: A novel unsupervised language-guided video summarization. In: ICASSP 2024-2024 IEEE International Conference on Acoustics, Speech and Signal Processing (ICASSP), pp. 4140–4144. IEEE (2024)
33. Apostolidis, E., Adamantidou, E., Metsai, A.I., Mezaris, V., Patras, I.: Video summarization using deep neural networks: A survey. Proceed. IEEE **109**(11), 1838–1863 (2021)
34. Zhao, B., Li, X., Lu, X.: Hsa-rnn: Hierarchical structure-adaptive rnn for video summarization. In: Proceedings of the IEEE conference on computer vision and pattern recognition, pp. 7405–7414 (2018)
35. Wei, H., Ni, B., Yan, Y., Yu, H., Yang, X., Yao, C.: Video summarization via semantic attended networks. In: Proceedings of the AAAI conference on artificial intelligence, vol. 32 (2018)
36. Ji, Z., Xiong, K., Pang, Y., Li, X.: Video summarization with attention-based encoder-decoder networks. IEEE Trans. Circuits Syst Video Technol. **30**(6), 1709–1717 (2019)
37. Zhou, K., Qiao, Y., Xiang, T.: Deep reinforcement learning for unsupervised video summarization with diversity-representativeness reward. In: Proceedings of the AAAI conference on artificial intelligence, vol. 32 (2018)

38. Huang, S., Li, X., Zhang, Z., Wu, F., Han, J.: User-ranking video summarization with multi-stage spatio-temporal representation. IEEE Trans. Image Process. **28**(6), 2654–2664 (2018)
39. Wang, J., Wang, W., Wang, Z., Wang, L., Feng, D., Tan, T.: Stacked memory network for video summarization. In: Proceedings of the 27th ACM international conference on multimedia, pp. 836–844 (2019)
40. Fajtl, J., Sokeh, H.S., Argyriou, V., Monekosso, D., Remagnino, P.: Summarizing videos with attention. In: Computer Vision–ACCV 2018 Workshops: 14th Asian Conference on Computer Vision, Perth, Australia, December 2–6, 2018, Revised Selected Papers 14, pp. 39–54. Springer (2019)
41. Liu, Y.T., Li, Y.J., Yang, F.E., Chen, S.F., Wang, Y.C.F.: Learning hierarchical self-attention for video summarization. In: 2019 IEEE international conference on image processing (ICIP), pp. 3377–3381. IEEE (2019)
42. Zhu, W., Lu, J., Li, J., Zhou, J.: Dsnet: A flexible detect-to-summarize network for video summarization. IEEE Trans. Image Process. **30**, 948–962 (2020)
43. Apostolidis, E., Balaouras, G., Mezaris, V., Patras, I.: Combining global and local attention with positional encoding for video summarization. In: 2021 IEEE international symposium on multimedia (ISM), pp. 226–234. IEEE (2021)
44. Hsu, T.C., Liao, Y.S., Huang, C.R.: Video summarization with frame index vision transformer. In: 2021 17th International Conference on Machine Vision and Applications (MVA), pp. 1–5. IEEE (2021)
45. Dosovitskiy, A., Beyer, L., Kolesnikov, A., Weissenborn, D., Zhai, X., Unterthiner, T., Dehghani, M., Minderer, M., Heigold, G., Gelly, S., et al.: An image is worth 16x16 words: Transformers for image recognition at scale. arXiv preprint arXiv:2010.11929 (2020)
46. Li, H., Ke, Q., Gong, M., Drummond, T.: Progressive video summarization via multimodal self-supervised learning. In: Proceedings of the IEEE/CVF winter conference on applications of computer vision, pp. 5584–5593 (2023)
47. Zhang, Y., Liu, Y., Kang, W., Tao, R.: Vss-net: visual semantic self-mining network for video summarization. IEEE Transactions on Circuits and Systems for Video Technology (2023)
48. Khan, H., Hussain, T., Khan, S.U., Khan, Z.A., Baik, S.W.: Deep multi-scale pyramidal features network for supervised video summarization. Expert Syst. Appl. **237**, 121288 (2024)
49. Zhang, Y., Liu, Y., Wu, C.: Attention-guided multi-granularity fusion model for video summarization. Expert Syst. Appl. **249**, 123568 (2024)
50. Han, T., Zhou, Q., Yu, J., Yu, Z., Zhang, J., Zhao, S.: Effective video summarization by extracting parameter-free motion attention. ACM Trans. Multimed. Comput. Commun. Appl. **20**(7), 1–20 (2024)
51. Yashwanth, K., Soni, B.: Encoder-decoder architectures based video summarization using key-shot selection model. Multimed. Tools Appl. **83**(11), 31395–31415 (2024)
52. He, K., Zhang, X., Ren, S., Sun, J.: Deep residual learning for image recognition. In: Proceedings of the IEEE conference on computer vision and pattern recognition, pp. 770–778 (2016)
53. Szegedy, C., Liu, W., Jia, Y., Sermanet, P., Reed, S., Anguelov, D., Erhan, D., Vanhoucke, V., Rabinovich, A.: Going deeper with convolutions. In: Proceedings of the IEEE conference on computer vision and pattern recognition, pp. 1–9 (2015)
54. Locatello, F., Weissenborn, D., Unterthiner, T., Mahendran, A., Heigold, G., Uszkoreit, J., Dosovitskiy, A., Kipf, T.: Object-centric learning with slot attention. Adv. Neural Inf. Process. Syst. **33**, 11525–11538 (2020)
55. Lin, X., Sun, S., Huang, W., Sheng, B., Li, P., Feng, D.D.: Eapt: Efficient attention pyramid transformer for image processing. IEEE Trans. Multimed. **25**, 50–61 (2021)
56. Bahdanau, D., Cho, K., Bengio, Y.: Neural machine translation by jointly learning to align and translate. arXiv preprint arXiv:1409.0473 (2014)
57. Luong, M.T., Pham, H., Manning, C.D.: Effective approaches to attention-based neural machine translation. arXiv preprint arXiv:1508.04025 (2015)
58. Vaswani, A., Shazeer, N., Parmar, N., Uszkoreit, J., Jones, L., Gomez, A.N., Kaiser, L.u., Polosukhin, I.: Attention is all you need. In: Advances in Neural Information Processing Systems, vol. 30. Curran Associates, Inc. (2017)
59. Cho, K., Van Merriënboer, B., Gulcehre, C., Bahdanau, D., Bougares, F., Schwenk, H., Bengio, Y.: Learning phrase representations using rnn encoder-decoder for statistical machine translation. arXiv preprint arXiv:1406.1078 (2014)
60. Zhang, K., Chao, W.L., Sha, F., Grauman, K.: Video summarization with long short-term memory. In: Computer Vision–ECCV 2016: 14th European Conference, Amsterdam, The Netherlands, October 11–14, 2016, Proceedings, Part VII 14, pp. 766–782. Springer (2016)
61. Potapov, D., Douze, M., Harchaoui, Z., Schmid, C.: Category-specific video summarization. In: Computer Vision–ECCV 2014: 13th European Conference, Zurich, Switzerland, September 6-12, 2014, Proceedings, Part VI 13, pp. 540–555. Springer (2014)
62. Gygli, M., Grabner, H., Riemenschneider, H., Van Gool, L.: Creating summaries from user videos. In: Computer Vision–ECCV 2014: 13th European Conference, Zurich, Switzerland, September 6-12, 2014, Proceedings, Part VII 13, pp. 505–520. Springer (2014)
63. Song, Y., Vallmitjana, J., Stent, A., Jaimes, A.: Tvsum: Summarizing web videos using titles. In: Proceedings of the IEEE conference on computer vision and pattern recognition, pp. 5179–5187 (2015)
64. De Avila, S.E.F., Lopes, A.P.B., da Luz, A., Jr., de Albuquerque Araújo, A.: Vsumm: A mechanism designed to produce static video summaries and a novel evaluation method. Pattern Recognition lett. **32**(1), 56–68 (2011)
65. Ji, Z., Jiao, F., Pang, Y., Shao, L.: Deep attentive and semantic preserving video summarization. Neurocomputing **405**, 200–207 (2020)
66. Zhao, B., Li, H., Lu, X., Li, X.: Reconstructive sequence-graph network for video summarization. IEEE Trans. Pattern Anal. Mach. Intell. **44**(5), 2793–2801 (2021)
67. Fu, H., Wang, H., Yang, J.: Video summarization with a dual attention capsule network. In: 2020 25th International Conference on Pattern Recognition (ICPR), pp. 446–451. IEEE (2021)
68. Liang, G., Lv, Y., Li, S., Wang, X., Zhang, Y.: Video summarization with a dual-path attentive network. Neurocomputing **467**, 1–9 (2022)
69. Zhao, B., Gong, M., Li, X.: Hierarchical multimodal transformer to summarize videos. Neurocomputing **468**, 360–369 (2022)
70. Otani, M., Nakashima, Y., Rahtu, E., Heikkila, J.: Rethinking the evaluation of video summaries. In: Proceedings of the IEEE/CVF conference on computer vision and pattern recognition, pp. 7596–7604 (2019)
71. Chen, Y., Tao, L., Wang, X., Yamasaki, T.: Weakly supervised video summarization by hierarchical reinforcement learning. In: Proceedings of the 1st ACM International Conference on Multimedia in Asia, pp. 1–6 (2019)

Publisher's Note Springer Nature remains neutral with regard to jurisdictional claims in published maps and institutional affiliations.

Springer Nature or its licensor (e.g. a society or other partner) holds exclusive rights to this article under a publishing agreement with the author(s) or other rightsholder(s); author self-archiving of the accepted manuscript version of this article is solely governed by the terms of such publishing agreement and applicable law.

Md Hasnat Hosen Arafat was born in 1999. He received the B.Tech. degree from the Department of Computer Science and Engineering, Marwadi University, India, in 2023. He is currently pursuing the master's degree in artificial intelligence with the Department of Computer Science and Engineering, Delhi Technological University, India. His research interests include video summarization and understanding.

Kavinder Singh received his B.Tech. degree in Computer Science and Engineering in 2016 from A. K. Technical University, Lucknow, India, M.Tech. degree in Information systems from Delhi Technological University, New Delhi, India in 2018. He is pursuing his Ph.D. from Delhi Technological University, New Delhi, India. He joined the Department of Computer Science and Engineering at Delhi Technological University as assistant professor in 2020. Currently, he is an assistant professor in the Department of Computer Science and Engineering at Delhi Technological University, New Delhi, India. His research interest includes image processing, object recognition, generative models, deep learning, and natural language processing.

Check for updates

Wiley
Advances in Condensed Matter Physics
Volume 2025, Article ID 3744806, 15 pages
https://doi.org/10.1155/acmp/3744806

WILEY

Research Article

Comparative Assessment of Trap Charges Effect on Triple Hybrid Metal Gate Dielectric Modulated Junctionless Gate All Around Nanowire FET-Based Biosensor

Mekonnen Getnet Yirak[1] **and Rishu Chaujar**[2]

[1]*Physics Department, Debre Tabor University, Debre Tabor, Ethiopia*
[2]*Applied Physics Department, Delhi Technological University, Delhi, India*

Correspondence should be addressed to Mekonnen Getnet Yirak; mekonnengetnet01@gmail.com

Received 7 December 2024; Accepted 1 February 2025

Academic Editor: Satya Prakash Pati

Copyright © 2025 Mekonnen Getnet Yirak and Rishu Chaujar. Advances in Condensed Matter Physics published by John Wiley & Sons Ltd. This is an open access article under the terms of the Creative Commons Attribution License, which permits use, distribution and reproduction in any medium, provided the original work is properly cited.

This work investigates how interface trap charges (ITCs) affect the performance of biosensors made from junctionless nanowire field-effect transistors (NWFETs) with triple hybrid metal gate dielectric modulated gates. The subthreshold sensitivity of double and triple metal gate silicon NWFET biosensors was investigated using the SILVACO ATLAS-TCAD simulation tool, emphasizing the impacts of positive and negative ITCs. Simulations examined the impact of uniformly immobilized biomolecules within the nanogap cavity region and evaluated key electrical characteristics, such as transconductance, switching ratio, drain current, and threshold voltage, under trap charges of $\pm 5 \times 10^{12}$ cm^{-2} at the SiO_2–silicon interface. Results showed that the triple hybrid metal gate device achieved an 184% improvement in threshold voltage shift compared to the double gate device when negative trap charges were present. The findings imply that integrating negative ITCs enhances the biosensor's performance and accuracy, emphasizing its importance in device modeling and design optimization.

Keywords: dielectric modulated; junctionless; nanowire; THM GAA JL NWFET; trap charges effect

1. Introduction

To meet the demand for smaller integrated circuits (ICs) with the same functionality and to increase the number of ICs on a single chip for more excellent device performance [1, 2], semiconductor device size has become a significant research area in recent years. Because of its constant scaling of the minimum channel length and the ensuing increase in sensitivity response, CMOS technology has emerged as a viable choice for label-free detection [3]. The feature sizes of metal–oxide–semiconductor field-effect transistors (MOSFETs) gradually decrease to increase the packing density as very large-scale integration technology advances. Because it reduces the junction electric field in the channel, increasing the channel doping in bulk MOSFETs is required for continued scaling. Furthermore, the channel region depletion widths cannot overlap the source and drain regions because of the increased doping [4]. However, mobility is reduced in the high-channel doping region due to impurity scattering [5, 6].

In contrast, short-channel effects (SCEs) significantly jeopardize continued scaling following the ITRS strategy [7]. To lower SCEs in the SOI platform, various creative architectures founded on various engineering ideas have been proposed [8]. Ionizing radiation is another issue in CMOS or MOS downscaling on electronic devices and technologies [8]. Downscaling the field-effect transistor (FET) in CMOS technology is a challenging task due to the evolution of the source/drain (S/D) junction for nanodimensional MOSFETs [9]. As a result, the combination of these impacts results in substantial reliability concerns and causes performance to degrade over a period of time [10]. To address these difficulties, bulk transistors can be replaced with devices that lack S/D junction, such as Junctionless GAA-NWFETs (nanowire FETs) [11–13] or multigate

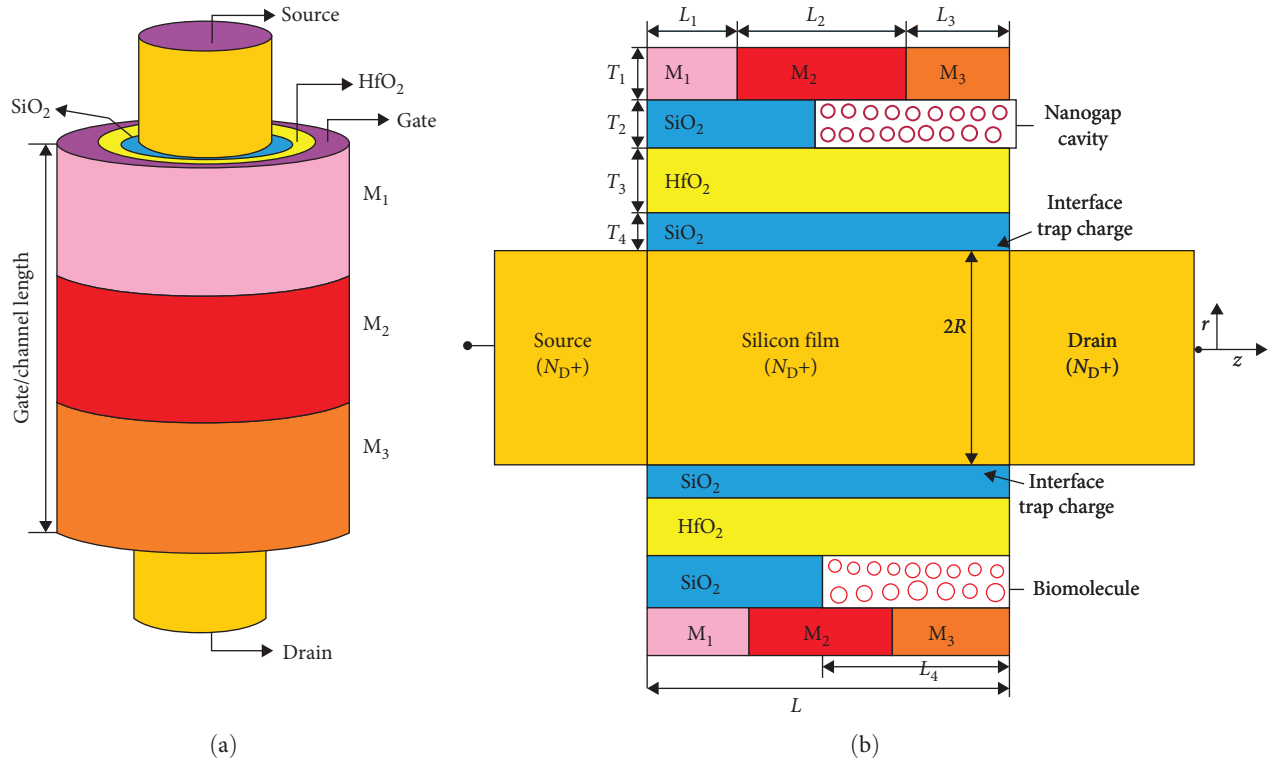

FIGURE 1: (a) The 3D schematic construction and (b) a 2D cross-sectional view with a cavity region for a triple metal gate high-k GAA-JL-NWFET.

transistors, which were proposed because of their promising device for future scaling [14]. A junctionless design makes the fabrication process more manageable by removing the necessity for p–n junctions. Instead, the gadget works by depleting carriers in an evenly doped channel. This configuration may be helpful in scalable and reproducible biosensor manufacture.

Previous research on the performance of JL-GAA NWFETs has shown that they have better label-free biomolecular detection capability and are suitable for low power sensing applications [15, 16]. To screen out certain biological disorders, for example, biological molecules including Uricase, DNA, APTES, Streptavidin, DNA, ChO_X, and biotin biomolecules are essential [17–19]. Many researchers are interested in working on NWFET-based biosensors [20] because of their ease of scalability, cost-effectiveness, label-free detection [21], compatibility with bulk CMOS [22, 23], high sensitivity [24], fruitful on-chip integration, shorter detection response time and lower fabrication cost, and low power consumption. However, with constant scaling, the quality and characteristics of the channel/gate oxide interface affect device performance and reliability [25]. The probability of creating interface traps/charges is rather considerable as IC integration density increases and device dimensions decrease, and these charges harm device performance [7]. Interface charges reduce device lifetime and efficiency and impair performance, regardless of whether they are intrinsic, process related, or operationally induced [4]. Interface trap charges (ITCs) can arise in nanoscale multigate metal oxide semiconductor FETs due to their susceptibility to impurity [26, 27]. Compared to the most advanced CMOS devices, these devices have many more faults or interface charge traps, which might affect their electrical characteristics.

In summary, this ITC can cause significant problems with device reliability and performance in scaled JL-GAA-NWFETs. Therefore, it is necessary to assess the performance degradation caused by localized charges and optimize device parameters for improved performance in sensing applications. Usually, the trap charges are located inside the dielectric material or at the contact between the dielectric and the semiconductor. Trap charges in this design can potentially change the effective threshold voltage and cause changes in the device's properties, which could compromise the accuracy of biosensing.

This work comprehensively investigates how ITCs affect the junctionless triple metal gate GAA-NWFET biosensor performance. In order to examine the impact of ITCs, several biomolecules have been immobilized in the nanogap cavity of double and triple hybrid metal gate JL-GAA-NWFETs at the same room temperature. Furthermore, the effect of localized/ITCs on device parameters such as threshold voltage, intrinsic voltage gain, transconductance, drain conductance, switching ratio, device efficiency, and tunneling current has been thoroughly investigated in relation to the density of localized interface charges (positive and negative).

2. Device Structure

Figure 1 illustrates the device architecture for n-substrate channel cylindrical junctionless high-k triple hybrid metal gate NWFET-based biosensors with ITCs. L_4 (10 nm) is the length of the nanogap cavity and silicon dioxide (SiO_2),

4042, 2025, 1, Downloaded from https://onlinelibrary.wiley.com/doi/10.1155/acmp/3744806 by Delhi Technological University, Wiley Online Library on [05/03/2025]. See the Terms and Conditions (https://onlinelibrary.wiley.com/terms-and-conditions) on Wiley Online Library for rules of use; OA articles are governed by the applicable Creative Commons License

Table 1: This table describes proposed device structural parameters.

Parameters	DG-GAA-JL-NWFET	TG-GAA-JL-NWFET
Channel length (nm)	20.00	20.00
Thickness of hafnium oxide (nm)	$HfO_2 = 1.50$ and $SiO_2 = 0.30$	$HfO_2 = 1.50$ and $SiO_2 = 0.30$
Interface oxide thickness (nm)	$SiO_2 = 1.00$	$SiO_2 = 1.00$
Length of oxide source side (nm)	$SiO_2 = 10.00$	$SiO_2 = 10.00$
Cavity length of nanogap (nm)	10.00	10.00
Thickness (drain/source) (nm)	10.00	10.00
Length (drain/source) (nm)	10.00	10.00
Nanogap cavity thickness (nm)	1.00	1.00
Silicon film diameter (nm)	10.00	10.00
Interface trap charges (ITCs)	$\pm 5 \times 10^{12}$ cm^{-2}	$\pm 5 \times 10^{12}$ cm^{-2}
Source/drain doping (N_D+)	10^{19} cm^{-3}	10^{19} cm^{-3}
Constants of dielectrics	$SiO_2 = 3.90$ and $HfO_2 = 25.00$	$SiO_2 = 3.90$ and $HfO_2 = 25.00$
Metal electrode work functions (eV)	4.86 4.50	4.96 4.86 4.50

Abbreviations: ITCs, interface trap charges; NWFET, nanowire field-effect transistor.

etching close to the source and drain end, and L (20 nm) is the channel length. L_1 (6 nm), L_2 (8 nm), and L_3 (6 nm) are the lengths of M_1, M_2, and M_3 accordingly. The diameter of the silicon film is $2R$, while the thicknesses of the metal gate, hafnium oxide, nanogap cavity, and interface (SiO_2) oxide are T_1, T_2, T_3, and T_4, respectively. A suitable region to accommodate carrier mobility between silicon film and hafnium oxide is created by the interface layer (SiO_2) between the two [28]. The gate materials denoted by M_1, M_2, and M_3 have different work functions given ($\Phi_{M1} = 4.96$, $\Phi_{M2} = 4.86$, and $\Phi_{M3} = 4.50$) respectively. While the highest work function (Φ_{M1}) near the source end regulates electron saturation velocity and doping fluctuation, the work function near the drain end (Φ_{M1}) is used for screening effects and controls high drain electric field fluctuation due to V_{DS}. The work function between the source and drain ends (Φ_{M1}) is used to modify the channel's potential profile and reduce drain-induced barrier lowering (DIBL) [26, 29]. The nanogap cavity region is used as a sensing site in which target biomolecules, like APTES, $\varepsilon = 3.57$; Biotin, $\varepsilon = 2.63$; Uricase, $\varepsilon = 1.54$; ChO_2, $\varepsilon = 3.30$; Streptaviden, $\varepsilon = 2.10$; and air, $\varepsilon = 1.0$, are introducing their dielectric constant, intergengiably [27]. Different types of ITCs (positive and negative) are given by $N_f = \pm 5 \times 10^{16}$ cm^{-2} and also without interface (neutral) charge $N_f = 0$ are simulated interchangeably to study the effects of ITCs on the proposed device biosensor performance. The damaged region induced by the interface oxide trap charges (N_f) is depicted in Figure 1b as a zigzag line toward the drain end. All the parameteries used in this device modeling are described in Table 1.

3. Device Simulation and Calibration

The Atlas-3D device simulator tool performed numerous simulations based on these structural characteristics to describe the proposed device's electrical properties. Models such as (CONMOB) concentration-dependent mobility [30] were used to investigate doping vs. mobility distribution. The carrier–carrier scattering mobility model (CCSMOB) is a model for determining carrier mobility and concentration

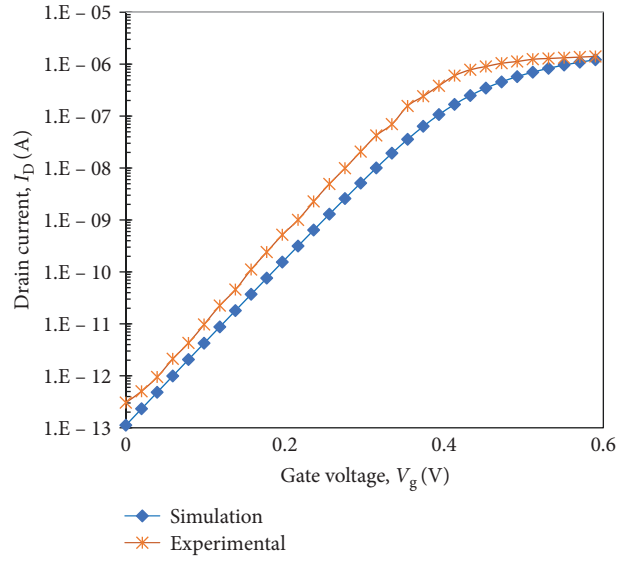

Figure 2: This figure demonstrates calibration simulation results for triple hybrid metal gate high-k GAA-JL-NWFET ($V_{DS} = 0.05$ V), with the work of [33].

[31]. Lombardi (CVT) models characterized field-dependent carrier movement in parallel and perpendicular directions [31]. This simulation excludes quantum mechanical theories since the radius of the silicon layer is more than 4 nm [11].

By considering uniformly distributed ITC ($N_f = 0$, $\pm 5 \times 10^{12}$ cm^{-2}) at the Si–SiO_2 boundary, as demonstrated in Figure 1b, its impact on device performance has been examined relative to ($N_f = 0$). In short-channel devices, ITCs close to the drain side are susceptible to a significant drain electric field [30].

We employed the models to perform device simulations for surrounding gate MOSFET [32] to TMGAA JL SiNWFET to confirm and authenticate our findings. Without considering ITC and biomolecule nanogap cavity, the simulations' use of models that closely match the simulated data and results [33] confirms their validity. As illustrated in Figure 2, our simulated data are in good agreement with the work of [33].

4042, 2025, 1, Downloaded from https://onlinelibrary.wiley.com/doi/10.1155/acmp/3744806 by Delhi Technological University, Wiley Online Library on [05/03/2025]. See the Terms and Conditions (https://onlinelibrary.wiley.com/terms-and-conditions) on Wiley Online Library for rules of use; OA articles are governed by the applicable Creative Commons License

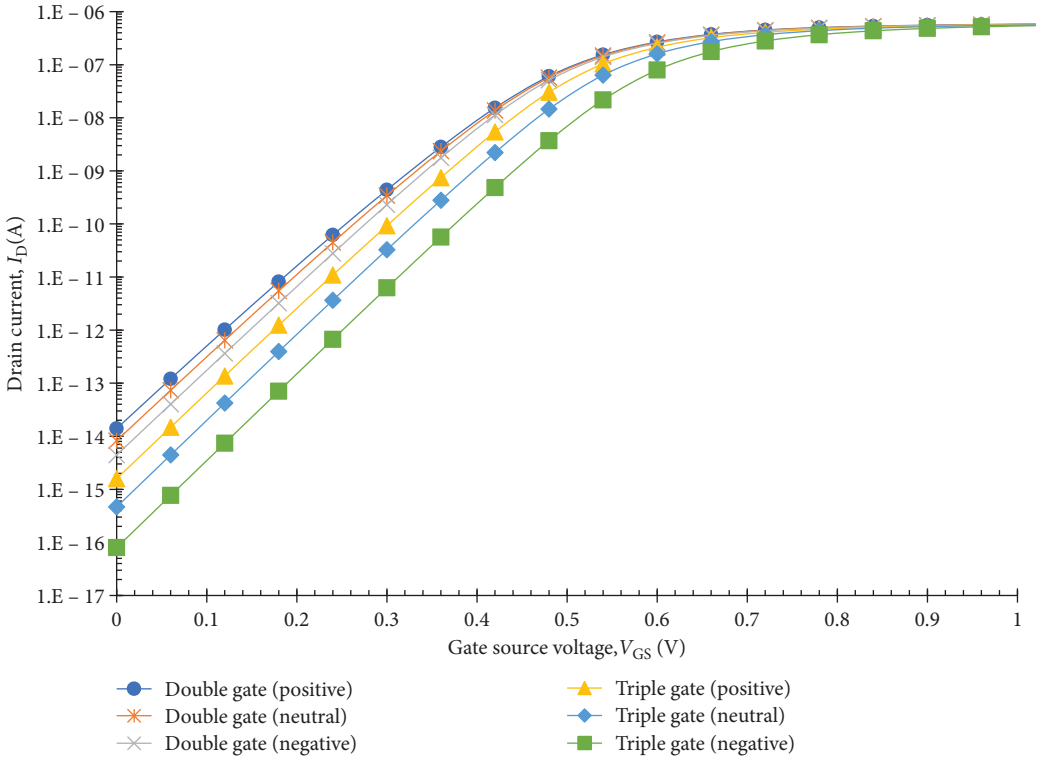

FIGURE 3: This figure describes the impact of ITCs on I_D–V_G for double and triple hybrid metal gate all around junctionless NWFET without cavity region [34], $V_{DS} = 0.05$ V and $V_{GS} = 1.0$ V. ITCs, interface trap charges; NWFET, nanowire field-effect transistor.

4. Results and Discussion

4.1. ITCs Impacts on Drain Current. Figure 3 shows the simulated results of I_D–V_G transfer characteristics on a log scale at $V_D = 0.05$ V with various ITCs for double and triple hybrid metal gates. In the presence of a negative trap charge, the graph illustrates that a triple hybrid metal gate has a smaller leakage current than a double hybrid metal gate. The highest work function (Φ_1) near the source region helps overcome electron saturation velocity and hot carrier effects via the channel by reducing the tunneling barrier [35] and enhancing carrier mobility with a negative trap charge. The nanowire structure gives a huge surface area relative to its volume, making it very sensitive to surface charges. When a biomolecule bonds to the nanowire's surface, it generates a noticeable shift in the current. Furthermore, the intermediate work function (Φ_2) reduces DIBL and parasitic resistance, improving gate controllability [36]. Since ITCs rise at the Si–SiO_2 interface, they will take an electron from an acceptor-type ITC, resulting in a stable negative ITC [7]. Similarly, the donor-type interface trap functions as a positive, confined charge [37]. These interface traps can be converted into an equivalent interface fixed charge, resulting in band bending beneath the gate [38], a rise in flat-band voltage under the damaged region, and changes in electron mobility in the channel [32]. In a triple metal gate, leakage current (I_{OFF}) results for positive and negative ITCs are 1.5×10^{-15} A and 7.97×10^{-17} A, respectively, at $V_{GS} = 0$ and $V_{DS} = 0.05$ V. The study indicates that the suggested devices are more prone to positive ITC, which causes higher tunneling current and hot carrier effects, resulting in carrier mobility loss in the channel.

4.2. Effect of ITCs on Threshold Voltage (V_{th}) and Subthreshold Swing. Trap charges can change the threshold voltage, affecting the sensor's sensitivity and baseline signal. Evaluating the effects of various metal-work functions and dielectric materials in the triple gate design on the distribution and impact of these trap charges is frequently part of a comparative analysis. Figure 4 illustrates the variation of (a) threshold voltage (V_{th}) (b) subthreshold swing at $V_{GS} = 1.0$ V and $V_{DS} = 0.05$ V with ITCs for double and triple hybrid metal gates with different trap charges. Figure 4a shows that the threshold voltage is larger for the negative interface charge than when $N_f = 0$ and the positive interface charge in both devices. Due to the smaller barrier height of a positive trap charge [7], the positive interface charge produces the highest electric field peak compared to the $N_f = 0$ and negative trap charge [10]. Higher degradation of subthreshold slope (SS) in the triple hybrid metal gate for negative ITCs is investigated due to higher electron mobility and threshold voltage than positive ITC; this enhances electrostatic gate control [39], as shown in Figure 4b compared to a double hybrid metal gate transistor.

5. Impact of Trap Charge on JL-GAA-NWFET Sensitivity

5.1. Impact of ITCs on Surface Potential-Based Sensitivity. The density of localized charges and the gate oxide capacitance both play a role in the amount of variation that occurs

4042, 2025, 1, Downloaded from https://onlinelibrary.wiley.com/doi/10.1155/acmp/3744806 by Delhi Technological University, Wiley Online Library on [05/03/2025]. See the Terms and Conditions (https://onlinelibrary.wiley.com/terms-and-conditions) on Wiley Online Library for rules of use; OA articles are governed by the applicable Creative Commons License

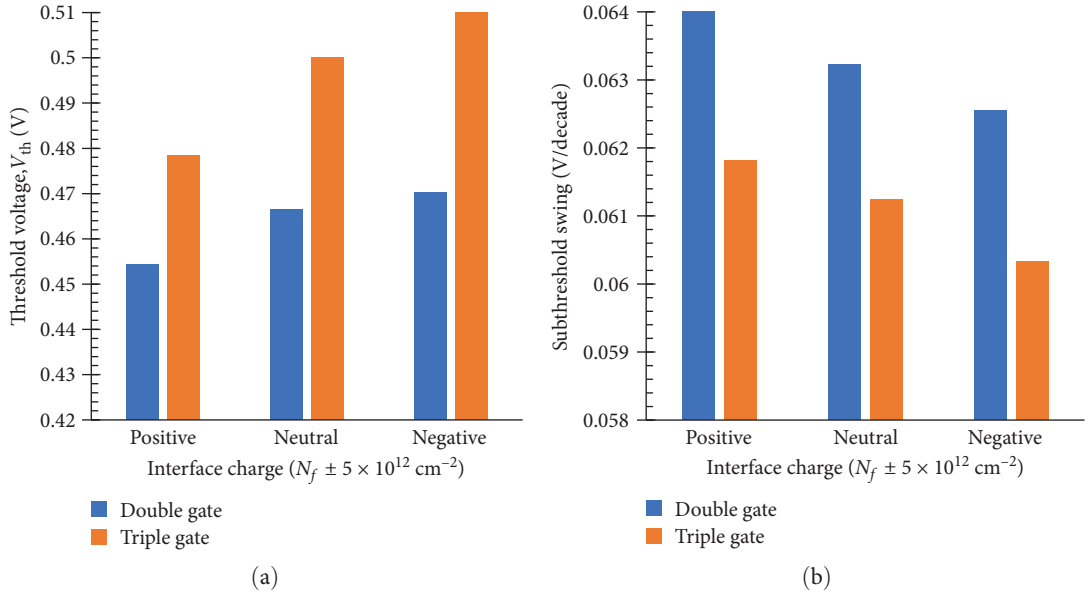

FIGURE 4: Effect of ITCs on (a) threshold voltage (V_{th}) and (b) subthreshold swing for double and triple hybrid metal GAA-JL NWFET ($V_{DS} = 0.05$ V and $V_{GS} = 1.0$ V). ITCs, interface trap charges.

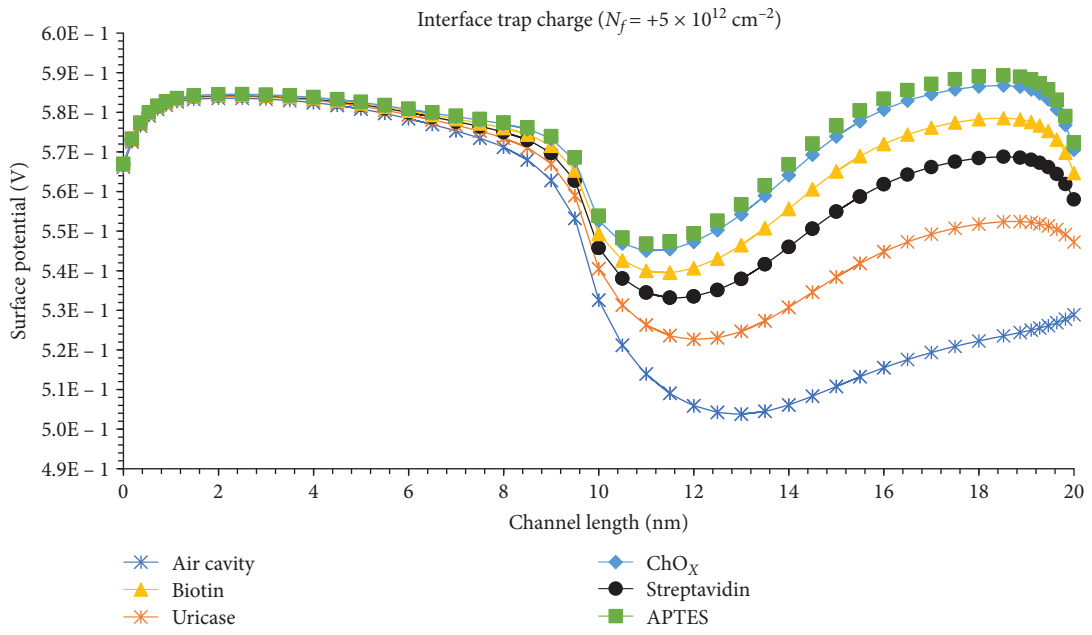

FIGURE 5: This figure describes the impact of different biomolecules on surface potential as a function of channel length in the case of negative ITC for THM-GAA-JL-NWFET ($V_{GS} = 1.0$ V and $V_{DS} = 0.05$ V). ITC, interface trap charge.

in the voltage of the flat band [8]. The junctionless channel is extremely sensitive to changes in the surface potential induced by biomolecule adsorption, which directly impacts the current across the channel, boosting the detection capabilities. The surface potential, which defines the threshold voltage fluctuation, is imperative to interpreting the proposed device's sensitivity following uniform biomolecule interaction in the targeted cavity [40]. Since a change in surface potential has an immediate and decisive impact on the device threshold voltage, DIBL, and several other electrical parameters, the change in surface potential that is caused by localized charges should be kept as low as feasible so that there is minimal deterioration [9, 23]. Figure 5 depicts the variation in the surface potential profile positively localized charges for different biomolecules in THM GAA JL NWFET architecture. It shows that surface potential increases with biomolecule dielectric constants in positively localized charges within a damaged area. This relative shift in potential is essential for determining the biosensor's sensitivity [8]. The potential profile along the channel varies in the presence of

4042, 2025, 1, Downloaded from https://onlinelibrary.wiley.com/doi/10.1155/acmp/3744806 by Delhi Technological University, Wiley Online Library on [05/03/2025]. See the Terms and Conditions (https://onlinelibrary.wiley.com/terms-and-conditions) on Wiley Online Library for rules of use; OA articles are governed by the applicable Creative Commons License

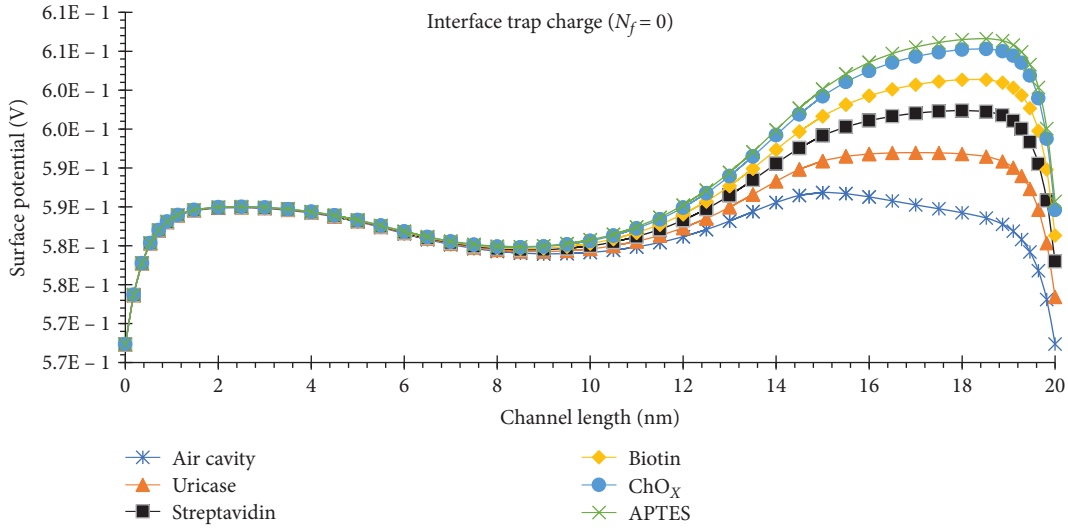

FIGURE 6: This figure describes the effect of different biomolecules on surface potential as a function of channel length without ITC for THM-GAA-JL-NWFET ($V_{GS} = 1.0$ V and $V_{DS} = 0.05$ V). ITC, interface trap charge.

biomolecules, exhibiting elevated levels at high dielectric constants. The surface potential of the channel section (drain side) where diverse biomolecules were immobilized is dictated by the dielectric constant in the nanocavity region [40]. The effective gate oxide capacitance rises as the cavity fills with diverse biomolecules ($K_{bio} > 1$) increasing the coupling between the gate and the charge carriers flowing through the channel. Negatively charged biomolecules stimulate coupling even more because they have better binding capacities than neutral biomolecules, lowering surface potential. The surface potential is decreased by a strong coupling between the gate and the channel, and this coupling grows as K_{bio} increases. Figure 5 shows this variation in surface potential along different biomolecules.

Potential variation for neutral biomolecules is depicted in Figure 6. The graph shows that the lowest surface potential rises proportionately to the dielectric constant. Near the drain side, a cavity of 10 nm is considered for biomolecule immobilization. When different biomolecules are filled uniformly in the cavity region, a higher variation in surface potential is observed, as illustrated in Figure 6. The surface potential changes on the channel's drain side, which is the section over which different biomolecules were immobilized, are determined by the dielectric constant value in the nanocavity region [34, 40]. The source side of the device has a lower surface potential since dielectric materials do not cover it. This leads us to the conclusion that the surface potential of the dielectric modulated THM-GAA-JL-NWFET varies more when the nanogap cavity's dielectric constant increases. The surface of the nanowire can absorb charges from proteins, modifying the local potential and hence modulating channel conductivity. This is especially important in biosensing applications, where sensitivity to small charge changes is required. Furthermore, the variation in surface potential can be used as a sensing metric to detect the presence of different biomolecules trapped within the nanocavity region.

Figure 7 illustrates the fluctuation in the surface potential profile along channel length for various biomolecules on the THMG GAA JL NWFET in the presence of a positively localized charge. The graph demonstrates that the lowest surface potential increases proportionally with the dielectric constant. A hollow of 10 nm in length is proposed near the drain end. The potential shifts from lower to higher when biomolecules are uniformly immobilized in the region with nanogap cavities at the drain end. Biomolecules in the nanogap cavity or vacuum gate dielectric cause variations in gate-to-channel capacitance over a greater area, resulting in changes in surface potential and subthreshold current [8]. As illustrated in Figure 7, the nanocavity region's dielectric constant value controls the channel part's surface potential (drain side), where various biomolecules are immobilized. Since dielectric materials do not shield the source side of the device, its surface potential is lower. This leads us to the conclusion that when the dielectric materials of the nanogap cavity vary, the THM-GAA-JL-NWFET's surface potential varies more. It is possible to use this change in surface potential as a sensing metric to identify different biomolecules trapped in the nanocavity area.

When there are localized charges in the damaged drain side regions, Figure 8 illustrates how the surface potential profile varies with various biomolecules. The negatively injured region exhibits the lowest surface potential compared to the undamaged region regarding negative (positive) interface localized charges [7]. Therefore, localized charges are the cause of the lowest surface potential shift. By reducing the possible channel alterations brought on by localized charges, degradation can be minimized [8]. Compared to the undamaged device, the surface potential increases or decreases due to positive and negative localized charges, as illustrated in Figure 8. The density of localized charges is directly proportional to their significance. A more significant surface potential difference is seen at the drain side for varying

4042, 2025, 1, Downloaded from https://onlinelibrary.wiley.com/doi/10.1155/acmp/3744806 by Delhi Technological University, Wiley Online Library on [05/03/2025]. See the Terms and Conditions (https://onlinelibrary.wiley.com/terms-and-conditions) on Wiley Online Library for rules of use; OA articles are governed by the applicable Creative Commons License

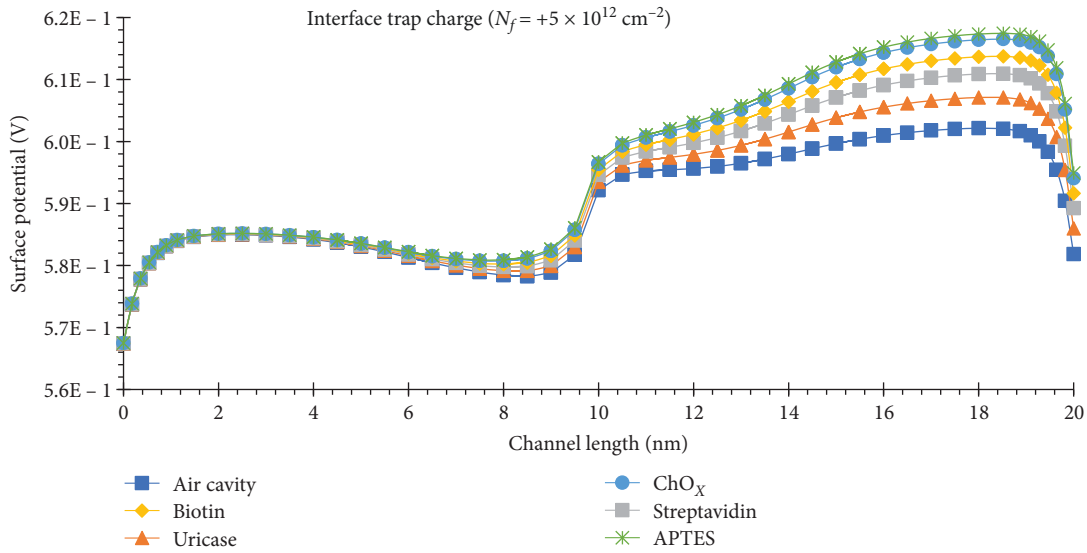

FIGURE 7: This figure describes the effect of different biomolecules on surface potential as a function of channel length in the case of positive ITC for THM-GAA-JL-NWFET ($V_{GS} = 1.0$ V and $V_{DS} = 0.05$ V). ITC, interface trap charge.

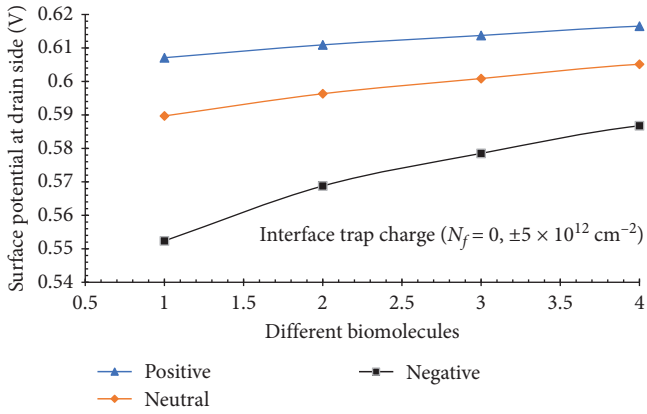

FIGURE 8: This figure describes the impact of interface trap charge on surface potential in the case of different biomolecules for THM-GAA-JL-NWFET ($V_{GS} = 1.0$ V and $V_{DS} = 0.05$ V).

biomolecule dielectric constants. The high dielectric constant in the drain side THM-GAA-JL-NWFET structure results in a weak electric field.

5.2. Impact of ITCs on Transfer Characteristics and Sensitivity. A current flows between the source and drain of a MOSFET when the gate-to-source voltage is lower than the threshold voltage. This current is referred to as subthreshold drain current, subthreshold conduction, or subthreshold leakage. Lowering the SS by adding proteins to the nanogap cavity is possible. A current flows between the source and drain of a MOSFET when the gate-to-source voltage is lower than the threshold voltage. This current is referred to as subthreshold drain current, subthreshold conduction, or subthreshold leakage. Lowering the SS by adding proteins to the nanogap cavity is possible. Figure 9 shows how various biomolecules affect the SS in the instance of TCs. When the cavity is filled with different biomolecules, the coupling between the gate and the charge carriers passing through the channel is improved ($K_{bio} > 1$). Additionally, Figure 9 illustrates how positive (negative) localized charges cause the subthreshold current to rise (fall).

5.3. Switching (I_{ON}/I_{OFF}) Ratio. For switching applications, where a high value of on-current to off-current ratio (I_{ON}/I_{OFF}) is required, the variation introduced in I_{ON}/I_{OFF} due to localized charges, which are just as crucial as subthreshold degradation. Even though the drain current rises (reduced) when positive (negative) interface localized charges are present in all regions (subthreshold, linear, and saturation), the order of change in the off-current is greater than the change in the on-current. The highest switching ratio is observed at the highest dielectric value, as clearly depicted in Figure 10. This leads to a low SS at the highest dielectric value since the effective gate oxide capacitance increases as the cavity is filled with various biomolecules ($K_{bio} > 1$), which in turn increases the coupling between the gate and the charge carriers flowing through the channel. As a result, a biosensor with a low SS will have a high degree of sensitivity. As shown in Figure 10, the density of negatively charged biomolecules is primarily responsible for the increased switching ratio.

5.4. Shifting Threshold Voltage (ΔV_{th}). Figure 11 shows how the threshold voltage sensitivity (ΔV_{th}) of the THM-GAA-JL-NWFET fluctuates with different biomolecules, which can be derived using (Equation 1). The shift in threshold voltage caused by gate oxide capacitance increases as K_{bio} value rises, as does the density of localized charge Figure 11. For example, when positive and negative localized charge densities are present compared to an undamaged device, the threshold voltage of THM-GAA-JL-NWFET is reduced by 30.40% and increased by 52.50% at the APTES biomolecule. The density of localized charges has a direct effect on threshold voltage fluctuations. This

4042, 2025, 1, Downloaded from https://onlinelibrary.wiley.com/doi/10.1155/acmp/3744806 by Delhi Technological University, Wiley Online Library on [05/03/2025]. See the Terms and Conditions (https://onlinelibrary.wiley.com/terms-and-conditions) on Wiley Online Library for rules of use; OA articles are governed by the applicable Creative Commons License

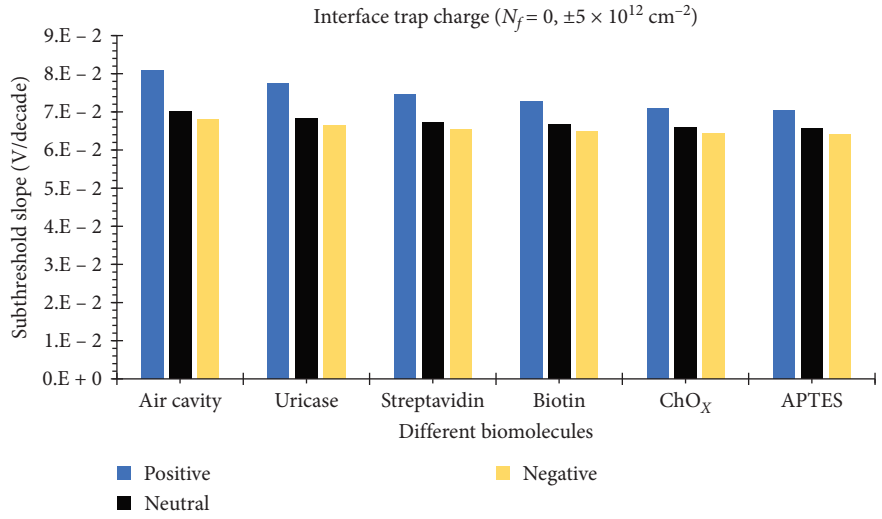

FIGURE 9: This figure describes the effect of different biomolecules on a subthreshold slope in the case of ITCs for GAA-JL-NWFET ($V_{GS} = 1.0$ V and $V_{DS} = 0.05$ V). ITCs, interface trap charges.

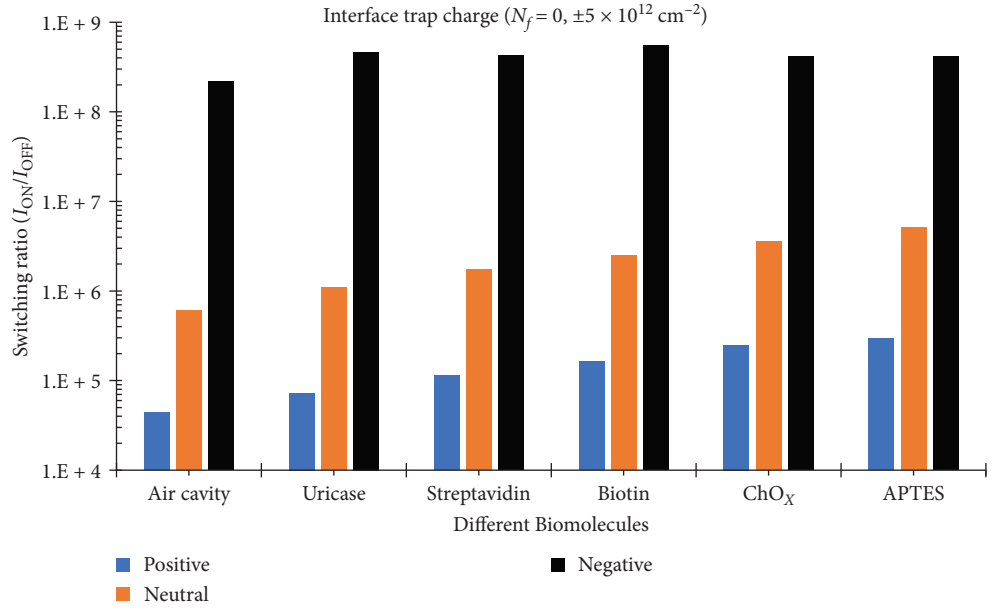

FIGURE 10: This figure describes the effect of different biomolecules on the switching ratio in the case of interface trap charges for THM-GAA-JL-NWFET ($V_{GS} = 1.0$ V and $V_{DS} = 0.05$ V).

demonstrates that as the concentration of electrically charged particles increases, so does the shift in the threshold voltage. Figure 11 shows that the rate of change in threshold voltage is greater for negatively localized charges than for positively localized charges. This is due to a significant shift in the minimum surface potential for negatively localized charges. Threshold voltage, drain current, and other MOSFET device performance measures are typically impacted by variations in the flat-band voltage brought on by positive and negative traps at the oxide-channel interface. The following equation provides the formula for determining the change in flat-band voltage:

$$\Delta V_{fb} = \frac{qN_f}{C_{OX}}, \tag{1}$$

$$C_{OX} = \frac{2\varepsilon_{OX}}{t_{Si}\ln\left(1 + \frac{2t_{OX}}{Si}\right)}, \tag{2}$$

where N_f is the interface charge density, t_{OX} is the oxide thickness, t_{Si} is the silicon film thickness, q is the charge, and ε_{OX} is the oxide's permittivity. Using Equation (3), Rahman, Shadman, and Khosru's [41] study is used to determine the MOSFET device's shifting threshold voltage (V_{th}):

4042, 2025, 1, Downloaded from https://onlinelibrary.wiley.com/doi/10.1155/acmp/3744806 by Delhi Technological University, Wiley Online Library on [05/03/2025]. See the Terms and Conditions (https://onlinelibrary.wiley.com/terms-and-conditions) on Wiley Online Library for rules of use; OA articles are governed by the applicable Creative Commons License

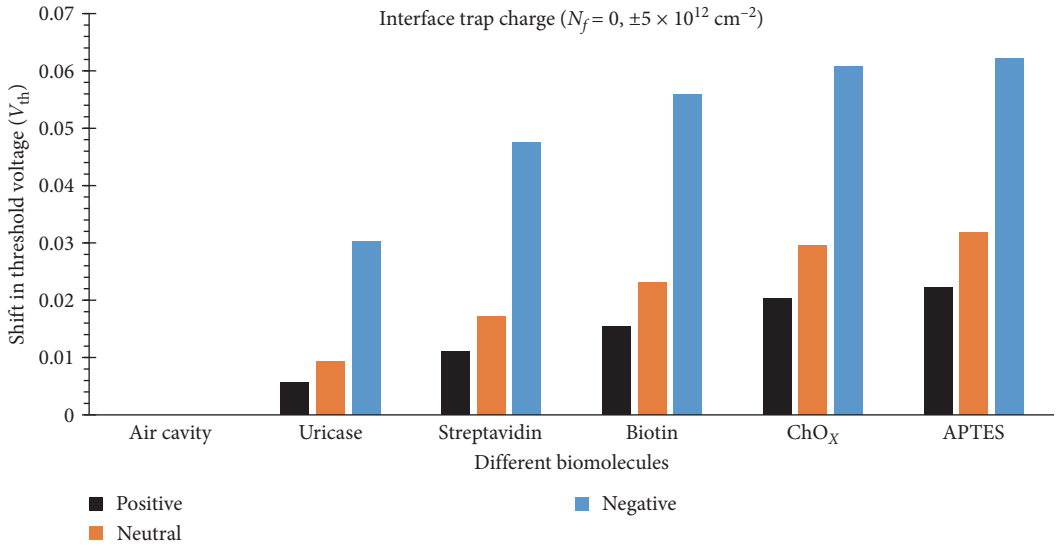

FIGURE 11: This figure describes the effect of different biomolecules on shift threshold voltage in the case of interface trap charge for hybrid metal gate all around junctionless NWFET ($V_{GS} = 1.0$ V and $V_{DS} = 0.05$ V). NWFET, nanowire field-effect transistor.

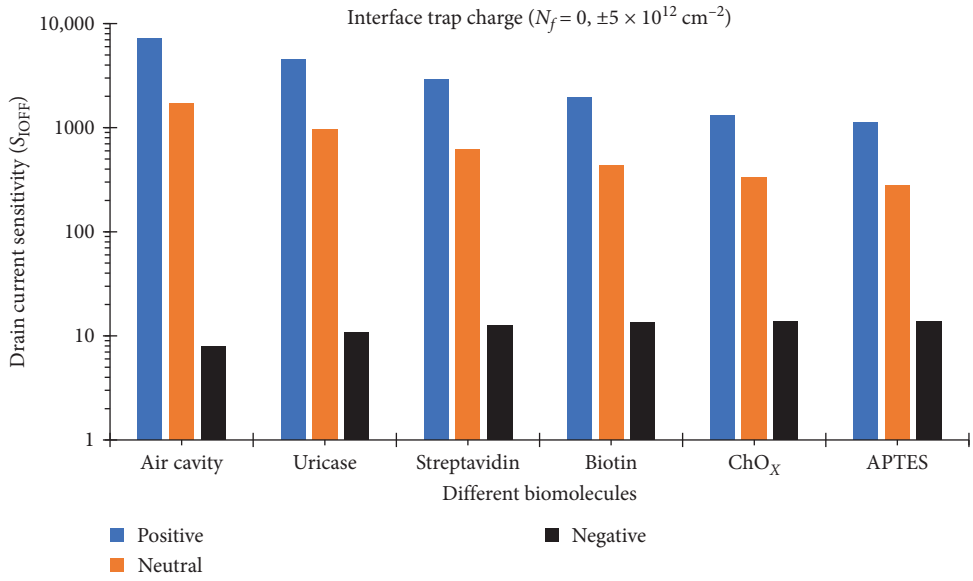

FIGURE 12: This figure describes the impact of various biomolecules on drain current sensitivity in the case of interface trap charge for triple hybrid metal GAA-JL NWFET ($V_{GS} = 1.0$ V and $V_{DS} = 0.05$ V). NWFET, nanowire field-effect transistor.

$$\Delta V_{th} = \left| V_{th(bio)} - V_{th(Air)} \right|. \quad (3)$$

5.5. Drain Current Sensitivity ($S_{I_{OFF}}$). Figure 12 depicts how localized charges affect the subthreshold drain current of the THM-GAA-JL-NWFET design. As the biomolecule dielectric constant grows, the sensitivity in the subthreshold current shift ($S_{I_{OFF}}$) decreases because the subthreshold current is inversely proportional to the gate oxide's effective dielectric constant. As K_{bio} increases, the gate gains greater control over the flow of charge carriers as the value rises and the gate oxide capacitance rises [42]. Because of the increased effective gate oxide capacitance, subthreshold current falls as the biomolecule's dielectric constant increases at a constant gate voltage. As depicted in Figure 12, negatively charged biomolecules have a greater binding capacity than positively charged and neutral biomolecules. Effects of ITCs on device sensitivity ($S_{I_{OFF}}$) or drain current sensitivity is given by Equation (4) [42]:

$$S_{I_{OFF}} = \left. \frac{I_{OFF(\text{with biomolecule})}}{I_{OFF(\text{without biomolecule})}} \right|_{V_{GS=0}}. \quad (4)$$

6. Impact of Trap Charge on JL-GAA-NWFET Analog Performance

The analog performance of THM-GAA-JL-NWFET is measured by its transconductance (g_m), drain conductance (g_d),

4042, 2025, 1, Downloaded from https://onlinelibrary.wiley.com/doi/10.1155/acmp/3744806 by Delhi Technological University, Wiley Online Library on [05/03/2025]. See the Terms and Conditions (https://onlinelibrary.wiley.com/terms-and-conditions) on Wiley Online Library for rules of use; OA articles are governed by the applicable Creative Commons License

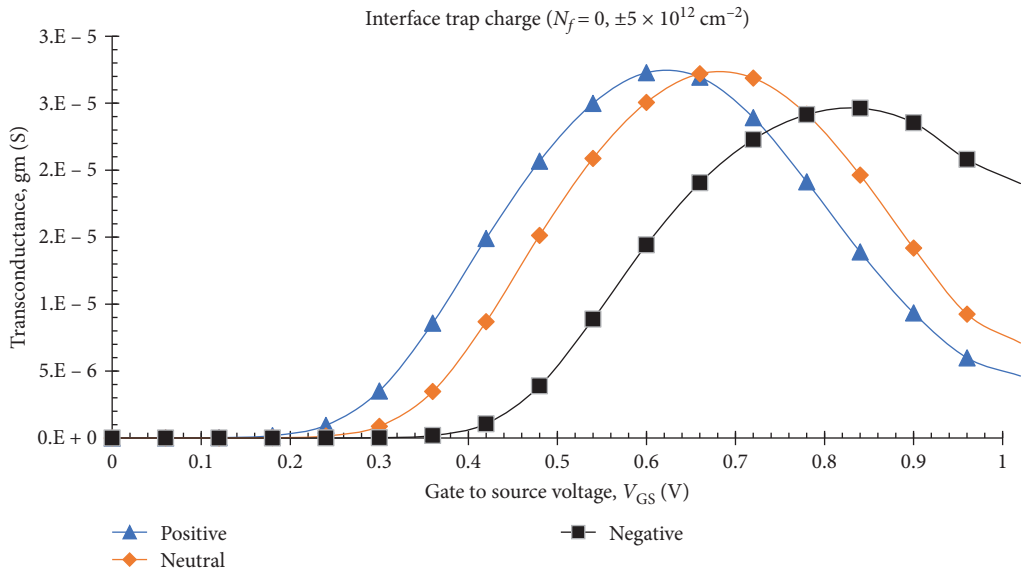

FIGURE 13: This figure describes the effect of localized trap charges on transconductance for triple hybrid metal GAA-JL NWFET ($V_{GS} = 1.0$ V and $V_{DS} = 0.6$ V). NWFET, nanowire field-effect transistor.

device efficiency, intrinsic voltage gain (A_V), and output resistance, as discussed below.

6.1. Transconductance (g_m). Transconductance evaluates the controllability of the gate over the drain current and is proportional to the transistor gain [43]. The transconductance g_m of any device determines its gain; thus, its value should be high enough to have a high gain [44]. g_m performance varies with gate voltage, with the peak value observed at low gate bias for the presence of positive and negative localized charges, as shown in Figure 13, and decreasing at high gate voltage due to mobility deterioration. Transconductance decreases due to a drop in drain current generated by localized charges. When V_{GS} is less than V_{th}, transconductance increases (decreases) due to positive (negative) fixed charges. However, if the region is highly inverted, as indicated by V_{GS} greater than V_{th}, negatively localized charges will have a stronger transconductance than positively localized charges. In the linear and subthreshold areas, the deterioration caused by localized charges is more pronounced than in the saturation zone. This is because localized charges impact band bending less when V_{GS} is larger than V_{th}. The device's transconductance at its greatest value indicates the ideal direct current bias point (Equation 5) is used to get the transconductance value:

$$g_m = \frac{\partial I_{DS}}{\partial V_{GS}} = \mu_{FE} C_i \frac{W}{L} V_D. \tag{5}$$

6.2. Drain Conductance (g_d). The change in g_d with or without ITCs as a function of gate voltage is seen in Figure 14. Drain conductance (g_d) is also used to calculate the device's intrinsic gain. g_d is relatively high in the linear area and begins to drop as drain voltages above the pinch-off voltage. In the saturation region, g_d performance is unaffected by changes in other parameters. As shown in Figure 14, the increase in output resistance is responsible for the considerable improvement in the analog performance and driving capabilities, and it also completely suppresses the drain conductance under negative trap conditions. As shown in Figure 14, output conductance drops for negative and increases for positive; it may be calculated using Equation (6) [45] at constant gate voltage (V_{GS} :).

$$g_d = \frac{\partial I_{DS}}{\partial V_{DS}}. \tag{6}$$

6.3. Intrinsic Voltage Gain (A_V). The intrinsic gain (A_V) is defined as the ratio of transconductance (g_m) to output conductance (g_d) and is calculated using Equation (7). To attain a higher A_V in analog circuit design, the g_m value should be reduced. The intrinsic benefit is maximized by increasing the value of g_d while decreasing the value of g_d. The intrinsic gain value rises due to the negative trap charges seen in Figure 15:

$$A_V = \frac{dV_{out}}{dV_{in}} = \frac{dI}{dV_g}\frac{dV_d}{dI} = g_m \frac{1}{g_d} = g_m r_o. \tag{7}$$

6.4. Device Efficiency. Device efficiency, commonly known as the transconductance generation factor, is an important metric in the design of analog circuits that assesses the effectiveness of transconductance generation and is written as (g_m/I_D) [46]. The (g_m/I_D) ratio directly measures the MOSFET's efficiency because it represents the device's amplification (g_m) divided by the energy required to achieve this amplification (I_D). It is a metric for evaluating the degree to which the gate voltage regulates the drain current [47]. In analog applications, higher g_m/I_D ratios indicate more transconductance and a more robust capability to transfer DC power into AC gain performance at a drain bias.

4042, 2025, 1, Downloaded from https://onlinelibrary.wiley.com/doi/10.1155/acmp/3744806 by Delhi Technological University, Wiley Online Library on [05/03/2025]. See the Terms and Conditions (https://onlinelibrary.wiley.com/terms-and-conditions) on Wiley Online Library for rules of use; OA articles are governed by the applicable Creative Commons License

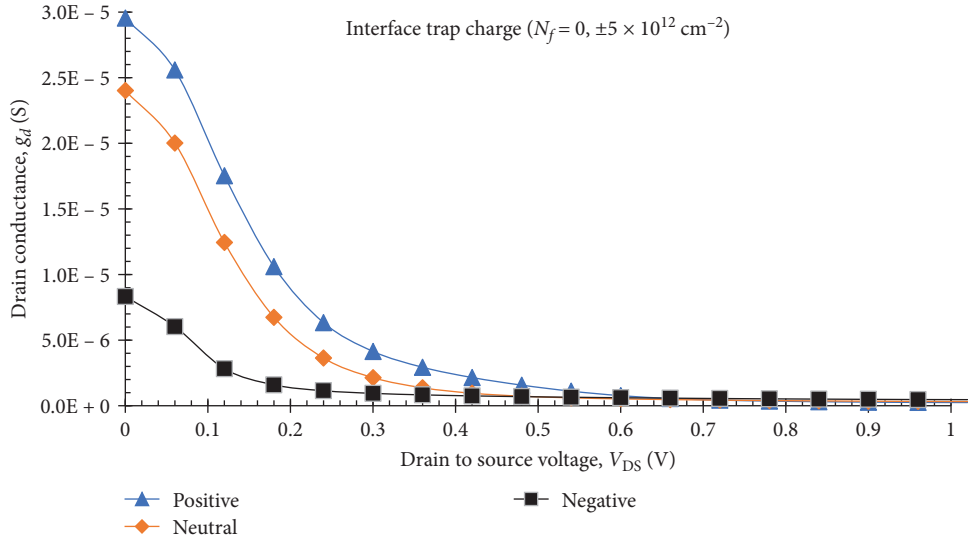

FIGURE 14: This figure describes the impact of localized trap charges on drain conductance for triple hybrid metal GAA-JL NWFET (V_{GS} = 0.6 V and V_{DS} = 1.0 V). NWFET, nanowire field-effect transistor.

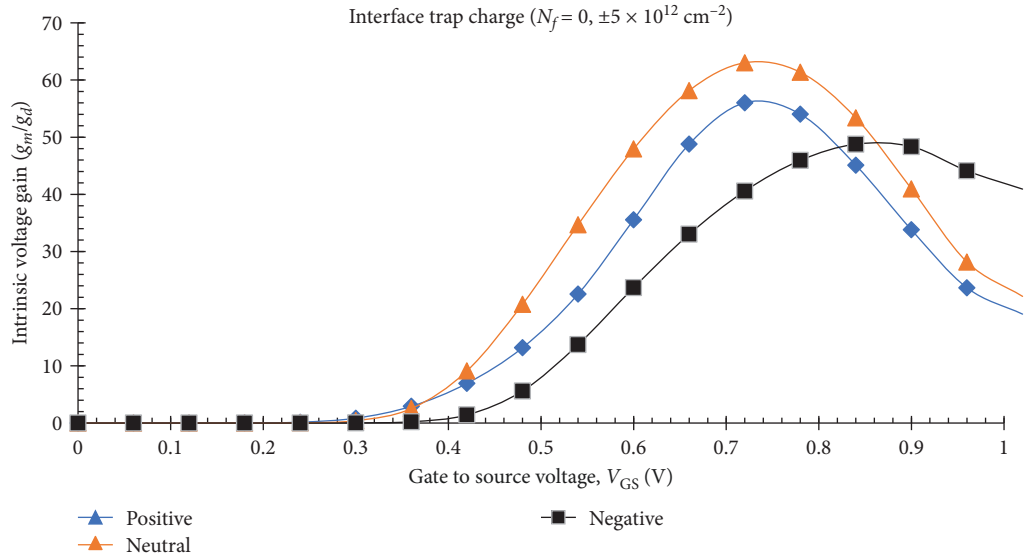

FIGURE 15: This figure describes the effect of localized trap charge on intrinsic gain for triple hybrid metal GAA-JL NWFET (V_{GS} = 0.6 V and V_{DS} = 1.0 V). NWFET, nanowire field-effect transistor.

Figure 16 shows device efficiency changes with gate voltage for THM-GAA-JL-NWFET architectures with and without traps. At a very low gate bias, the device efficiency is maximum across all variables. In contrast, in the strong inversion zone, the device efficiency rating is extremely low, suggesting that any device dissipates power. Similarly, a device with a negative (positive) fixed charge has a higher (lower) g_m/I_D than undamaged devices, as illustrated in Figure 16.

6.5. Output Resistance ($R_{out} = 1/g_d$).
One of the most crucial characteristics of an analog device is its output resistance (R_{out}) [40, 46]. The voltage gain in an analog circuit is directly proportional to R_{out}. The output resistance model is vital for excellent reliability and scalability in MOSFET. Figure 17 displays the output resistance ($1/g_d$) of the suggested device with different biomolecules in the situation of ITCs. This highlights the value of increased small-signal output resistance, as the output resistance determines the MOSFET's intrinsic gain upper limit. As shown in Figure 17, output resistance increases/decreases for negative (positive) ITC concerning the undamaged region and decreases as the biomolecule dielectric constant value increases.

Generally, ITCs have significant side effects, including a reduction in the subthreshold current due to an underlying shift in the slope of the subthreshold potential [14]. The device's subthreshold current needs to be low to switch rapidly, resulting in substantial low power consumption [46].

4042, 2025, 1, Downloaded from https://onlinelibrary.wiley.com/doi/10.1155/acmp/3744806 by Delhi Technological University, Wiley Online Library on [05/03/2025]. See the Terms and Conditions (https://onlinelibrary.wiley.com/terms-and-conditions) on Wiley Online Library for rules of use; OA articles are governed by the applicable Creative Commons License

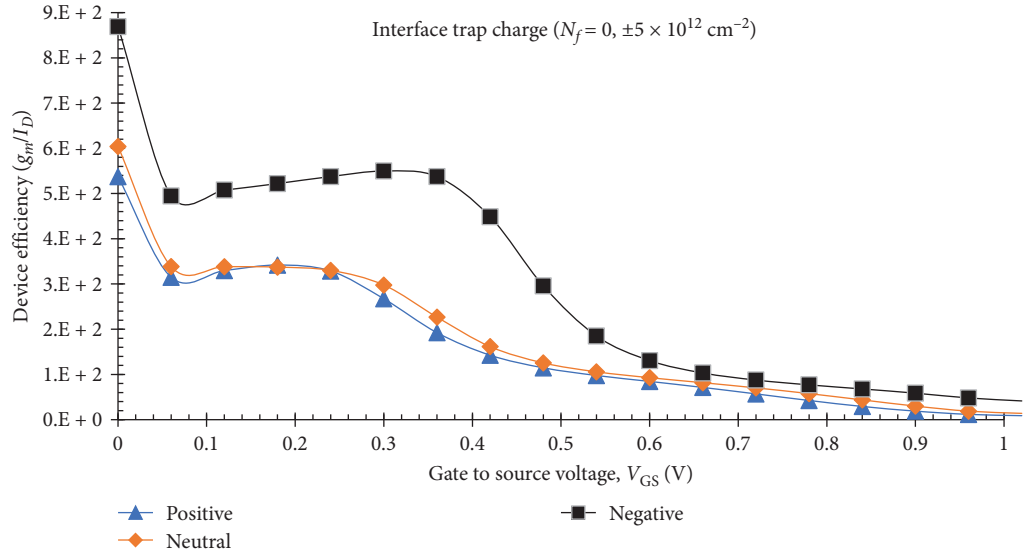

FIGURE 16: This figure describes the impact of localized trap charges on device efficiency for triple hybrid metal GAA-JL NWFET ($V_{GS} = 0.6$ V and $V_{DS} = 1.0$ V). NWFET, nanowire field-effect transistor.

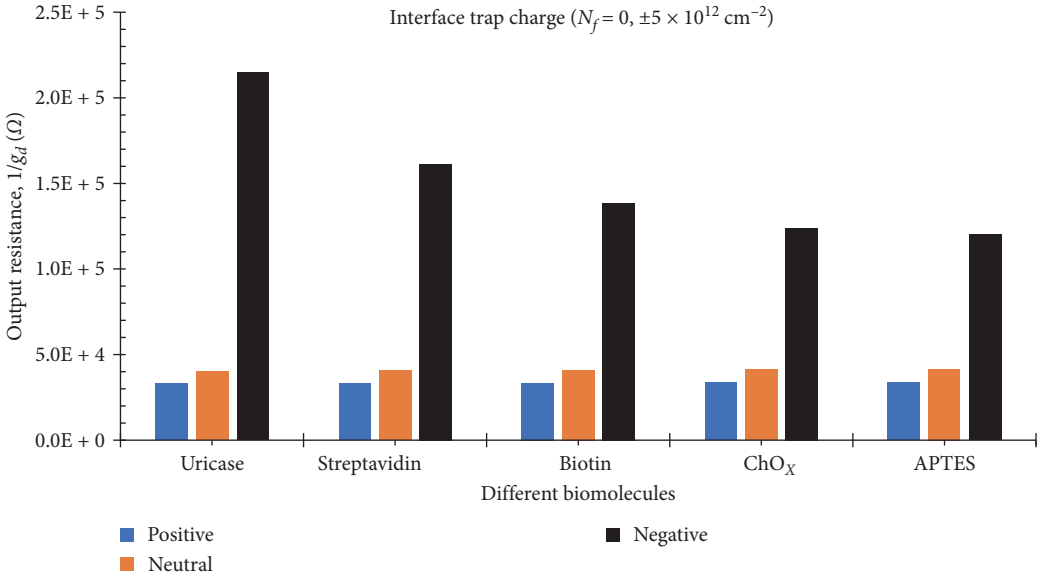

FIGURE 17: This figure describes the effect of various biomolecules on output resistance in the case of interface trap charge for triple hybrid metal GAA-JL NWFET ($V_{GS} = 1.0$ V and $V_{DS} = 0.05$ V). NWFET, nanowire field-effect transistor.

Also, immobilized biomolecules in the nanogap cavity significantly impact subthreshold current.

The effects of localized charges on drain current for three distinct biomolecules (APTES $\varepsilon = 3.57$, Biotin $\varepsilon = 2.10$, and Uricase $\varepsilon = 1.54$) are displayed in Table 2. A THM GAA-JL NWFET becomes more resilient to the SCE when the cavity's dielectric constant is raised. Therefore, a more excellent dielectric constant offers superior protection against SCEs and the degrading effects of localized charges. Thus, the value of the biomolecule's dielectric constant likewise affects the performance degradation brought on by localized charges. Table 2 summarizes the effect of localized charges on I_{OFF}, I_{ON}, and I_{ON}/I_{OFF} where negative (positive) ITCs cause the ratio to increase (decrease), the leading performance metric for digital and sensing applications.

As seen in Table 2, I_{OFF} degradation is significantly more than I_{ON} deterioration due to localized charges. In addition, biomolecules in the nanogap cavity caused subthreshold degradation. Since localized charges degrade the subthreshold characteristics of the device, they play a detrimental role when the device is to be used for switching and sensing applications.

4042, 2025, 1, Downloaded from https://onlinelibrary.wiley.com/doi/10.1155/acmp/3744806 by Delhi Technological University, Wiley Online Library on [05/03/2025]. See the Terms and Conditions (https://onlinelibrary.wiley.com/terms-and-conditions) on Wiley Online Library for rules of use; OA articles are governed by the applicable Creative Commons License

Table 2: Impact of localized charges on I_{OFF}, I_{ON}, and I_{ON}/I_{OFF} for different biomolecules (Uricase $\varepsilon = 1.54$, Biotin $\varepsilon = 2.10$, and APTES $\varepsilon = 3.57$).

ITCs	I_{OFF}			I_{ON}			I_{ON}/I_{OFF}		
	Uricase	Biotin	APTES	Uricase	Biotin	APTES	Uricase	Biotin	APTES
0	4.50E − 13	2.01E − 13	1.24E − 13	4.89E − 7	5.01E − 7	5.08E − 7	1.09E + 6	2.49E + 6	4.09E + 6
+5E12	7.11E − 12	3.12E − 12	1.79E − 12	3.99E − 7	4.42E − 7	4.59E − 7	5.61E + 4	1.41E + 5	2.56E + 5
−5E12	8.60E − 15	1.07E − 15	5.10E − 16	5.15E − 7	5.31E − 7	5.24E − 7	5.99E + 7	4.95E + 8	1.03E + 9

Abbreviation: ITCs, interface trap charges.

7. Conclusion

This study emphasizes the important role of precise device modeling in anticipating performance degradation in future nanometer-scale devices due to hot carrier effects, radiation damage, and process-induced localized charges. Significant insights into device behavior under localized charge effects were achieved by investigating the impact of ITCs on the electrical properties of innovative double and triple hybrid metal gate dielectric modulated junctionless nanowire FET (JL-NWFET) biosensors. The results reveal that localized charges at the Si–SiO_2 interface significantly impact key device properties, including threshold voltage, switching ratio, transconductance, output conductance, leakage current, intrinsic voltage gain, and SS. For instance, under negative ITCs, SS values improved to 62.6 mV/decade and 60.3 mV/decade for double and triple gate devices, respectively. Enhanced performance measures were reported in the presence of negative ITCs, such as transconductance (7.88×10^{-6} and 1.90×10^{-5}) and switching ratio (4.18×10^{6} and 4.12×10^{8}) for double and triple gate devices. Negative ITCs also reduced leakage current by 93.6%, whereas positive ITCs increased it by 1343.5%, underscoring the crucial function of charge polarity. Furthermore, the g_m/I_D ratio showed gains of 46.9% and 36.9% under negative ITCs for double and triple gate devices, respectively, showing improved efficiency under these situations.

The findings indicate that negative ITCs at the SiO_2 interface boost device performance across several electrical parameters, whereas positive ITCs lead to degradation. Additionally, the results support the potential of the proposed triple hybrid metal gate JL-NWFET as a biomarker sensor, accurately differentiating interactions between biomolecules within the nanogap cavity under negative ITCs.

Furthermore, future studies should focus on device scalability, material innovations, charge dynamics, and biosensor specificity to develop techniques to enhance the device's specificity for detecting biomolecules with various charges and concentrations.

Data Availability Statement

The authors mentioned above have all relevant data related to this study effort and will be willing to disclose them if asked to do so in the future.

Ethics Statement

The authors have reviewed all of the ethical standards and are expected to adhere to them in the future.

Conflicts of Interest

The authors declare no conflicts of interest.

Funding

This research was not supported financially.

Acknowledgments

We extend our gratitude to Debre Tabor University in Ethiopia and the Microelectronics Research Laboratory at Delhi Technological University in India for their support in this study.

References

[1] M. W. Rony, P. Bhowmik, H. R. Myler, and P. Mondol, "Short Channel Effects Suppression in a Dual-Gate Gate-All-Around Si Nanowire Junctionless NMOSFET," in *Proceedings of 9th International Conference on Electrical and Computer Engineering (ICECE)* (2016): 538–541

[2] M. G. Yirak and R. Chaujar, "Interface Trap Charge Analysis of Junctionless Triple Metal Gate High-k Gate All Around Nanowire FET-Based Biotin Biosensor for Detection of Cardiovascular Diseases," in *Microelectronics, Circuits and Systems*, (Springer, Singapore, 2021): 47–57.

[3] V. M. Generalov, O. V. Naumova, B. I. Fomin, et al., "Detection of Ebola Virus VP40 Protein Using a Nanowire SOI Biosensor, Optoelectron," *Optoelectronics, Instrumentation and Data Processing* 55, no. 6 (2019): 618–622.

[4] A. Kumar, M. M. Tripathi, and R. Chaujar, "Reliability Issues of In_2O_5Sn Gate Electrode Recessed Channel MOSFET: Impact of Interface Trap Charges and Temperature," *IEEE Transactions on Electron Devices* 65, no. 3 (2018): 860–866.

[5] X. Y. Huang, G. F. Jiao, W. Cao, et al., "Effect of Interface Traps and Oxide Charge on Drain Current Degradation in Tunneling Field-Effect Transistors," *IEEE Electron Device Letters* 31, no. 8 (2010): 779–781.

[6] R. Gautam, M. Saxena, R. S. Gupta, and M. Gupta, "Effect of Localised Charges on Nanoscale Cylindrical Surrounding Gate MOSFET: Analog Performance and Linearity Analysis," *Microelectronics Reliability* 52, no. 6 (2012): 989–994.

[7] S. K. Mohapatra, K. P. Pradhan, P. K. Sahu, G. S. Pati, and M. R. Kumar, "The Effect of Interface Trapped Charges in DMG-S-SOI MOSFET: A Perspective Study," *Advances in Natural Sciences: Nanoscience and Nanotechnology* 5, no. 4 (2014): 045015.

[8] H. Jafari, S. A. H. Feghhi, and S. Boorboor, "The Effect of Interface Trapped Charge on Threshold Voltage Shift Estimation for Gamma Irradiated MOS Device," *Radiation Measurements* 73 (2015): 69–77.

4042, 2025, 1, Downloaded from https://onlinelibrary.wiley.com/doi/10.1155/acmp/3744806 by Delhi Technological University, Wiley Online Library on [05/03/2025]. See the Terms and Conditions (https://onlinelibrary.wiley.com/terms-and-conditions) on Wiley Online Library for rules of use; OA articles are governed by the applicable Creative Commons License

[9] T. Ganguli, M. Chanda, and A. Sarkar, "Impact of Interface Trap Charges on the Performances of Junctionless MOSFET in Sub-Threshold Regime," *Computers and Electrical Engineering* 100 (2022): 107914.

[10] M. Lee, S. Palanisamy, B. H. Zhou, et al., "Ultrasensitive Electrical Detection of Follicle-Stimulating Hormone Using a Functionalized Silicon Nanowire Transistor Chemosensor," *ACS Applied Materials & Interfaces* 10, no. 42 (2018): 36120–36127.

[11] A. Chhabra, A. Kumar, and R. Chaujar, "Sub-20 Nm GaAs Junctionless FinFET for Biosensing Application," *Vacuum* 160 (2019): 467–471.

[12] T. Wang, L. Lou, and C. Lee, "A Junctionless Gate-All-Around Silicon Nanowire FET of High Linearity and Its Potential Applications," *IEEE Electron Device Letters* 34, no. 4 (2013): 478–480.

[13] Y. Pratap, M. Kumar, M. Gupta, S. Haldar, R. S. Gupta, and S. S. Deswal, "Sensitivity Investigation of Gate-All-Around Junctionless Transistor for Hydrogen Gas Detection," in *2016 IEEE International Nanoelectronics Conference (INEC)*, (Chengdu, China, 2016), 1–2.

[14] A. Rassekh, F. Jazaeri, M. Fathipour, and J. M. Sallese, "Modeling Interface Charge Traps in Junctionless FETs, Including Temperature Effects," *IEEE Transactions on Electron Devices* 66, no. 11 (2019): 4653–4659.

[15] S. L. Tripathi, R. Patel, and V. K. Agrawal, "Low Leakage Pocket Junction-Less DGTFET with Biosensing Cavity Region," *Turkish Journal of Electrical Engineering and Computer Sciences* 27, no. 4 (2019): 2466–2474.

[16] R. Chaujar and M. G. Yirak, "Effect of Trap Charges on Dielectric Modulated Triple Hybrid Metal Gate Junctionless Gate All Around Silicon Nanowire FET Based APTES Biosensor," : 1–16, nd

[17] C. Gouvea, "Biosensors for Health Applications," in *Biosensors for Health, Environment and Biosecurity*, ed. P. A. Serra, (InTech Open, 2011).

[18] Y. Wang and G. Li, "Simulation of a Silicon Nanowire FET Biosensor for Detecting Biotin/Streptavidin Binding," in *10th IEEE International Conference on Nanotechnology*, (Ilsan, Korea (South), 2010), 1036–1039.

[19] Y. Chen, R. Ren, H. Pu, et al., "Field-Effect Transistor Biosensor for Rapid Detection of Ebola Antigen," *Scientific Reports* 7, no. 1 (2017): 4.

[20] K. Kim, C. Park, T. Rim, M. Meyyappan, and J. S. Lee, "Electrical and PH Sensing Characteristics of Si Nanowire-Based Suspended FET Biosensors," in *14th IEEE International Conference on Nanotechnology (IEEE-NANO 2014)*, (Toronto, Ontario, Canada, 2014), 768–771.

[21] Z. Huang, A. Gao, S. Chen, Y. Wang, and T. Li, "Highly Sensitive Juntionless Nanowire Transistor Biosensor in Detecting Breast Tumor Marker," in *2018 IEEE SENSORS Proceedings*, (New Delhi, India, 2018), 1–4.

[22] G. Wenga, E. Jacques, A.-C. Salaün, R. Rogel, L. Pichon, and F. Geneste, "Step-Gate Polysilicon Nanowires Field Effect Transistor Compatible With CMOS Technology for Label-Free DNA Biosensor," *Biosensors and Bioelectronics* 40, no. 1 (2013): 141–146.

[23] R. Chaujar and M. G. Yirak, "Numerical Modelling for Triple Hybrid Gate Optimization Dielectric Modulated Junctionless Gate All around SiNWFET Based Uricase and ChO_X Biosensor," *Microsystem Technologies* 31, no. 1 (2025): 103–122.

[24] P. Ambhorkar, Z. Wang, H. Ko, et al., "Nanowire-Based Biosensors: From Growth to Applications," *Micromachines* 9, no. 12 (2018): 679.

[25] M. F. Transistor and Y. Taur, "ULSI Scaling Toward 10nm Gate-Lengths: Challenges and Opportunities," (2019).

[26] N. Bagga and S. Dasgupta, "Surface Potential and Drain Current Analytical Model of Gate All Around Triple Metal TFET," *IEEE Transactions on Electron Devices* 64, no. 2 (2017): 606–613.

[27] S. Singh, B. Raj, and S. K. Vishvakarma, "Analytical Modeling of Split-Gate Junction-Less Transistor for a Biosensor Application," *Sensing and Bio-Sensing Research* 18 (2018): 31–36.

[28] M. I. B. Chowdhury, M. J. Islam, M. J. Islam, M. M. Hasan, and S. U. Farwah, "Silvaco TCAD Based Analysis of Cylindrical Gate-All-Around FET Having Indium Arsenide as Channel and Aluminium Oxide as Gate Dielectrics," *Journal of Nanotechnology and its Applications in Engineering* 1 (2016): 1–12.

[29] A. Goel, S. Rewari, S. Verma, and R. S. Gupta, "Dielectric Modulated Triple Metal Gate All Around MOSFET (TMGAA) for DNA Bio-Molecule Detection," in *2018 IEEE Electron Devices Kolkata Conference (EDKCON)*, (Kolkata, India, 2019), 337–340.

[30] E. G. Ioannidis, A. Tsormpatzoglou, D. H. Tassis, C. A. Dimitriadis, G. Ghibaudo, and J. Jomaah, "Effect of Localized Interface Charge on the Threshold Voltage of Short-Channel Undoped Symmetrical Double-Gate MOSFETs," *IEEE Transactions on Electron Devices* 58, no. 2 (2011): 433–440.

[31] D. S. Software, "Atlas User's Manual," (2004).

[32] Y. S. Jean and C. Y. Wu, "The Threshold-Voltage Model of MOSFET Devices With Localized Interface Charge," *IEEE Transactions on Electron Devices* 44, no. 3 (1997): 441–447.

[33] Z. X. Chen, H. Y. Yu, N. Singh, et al., "Demonstration of Tunneling FETs Based on Highly Scalable Vertical Silicon Nanowires," *IEEE Electron Device Letters* 30, no. 7 (2009): 754–756.

[34] M. Getnet Yirak and R. Chaujar, "TCAD Analysis and Modelling of Gate-Stack Gate All around Junctionless Silicon NWFET Based Bio-Sensor for Biomedical Application," in *Proceedings of 2nd International Conference on VLSI Device, Circuit and System, VLSI DCS* (2020): 18–65

[35] W. Li, H. Liu, S. Wang, S. Chen, T. Han, and K. Yang, "Design and Investigation of Dopingless Dual-Gate Tunneling Transistor Based on Line Tunneling," *AIP Advances* 9, no. 4 (2019): 045109.

[36] M. Kumar, S. Haldar, M. Gupta, and R. S. Gupta, "Prformance Investigation of Dual Material Gate Stack Schottky-Barrier Source/Drain GAA MOSFET for Analog Applications," in *Physics of Semiconductor Devices. Environmental Science and Engineering*, eds. V. Jain and A. Verma, (Springer, Cham, 2014).

[37] A. Touhami and A. Bouhdada, "Impact of Interface Traps on Gate-Induced Drain Leakage Current in n-Type Metal Oxide Semiconductor Field Effect Transistor," *International Journal of Electronics* 92, no. 9 (2005): 539–552.

[38] N. Garg, Y. Pratap, M. Gupta, and S. Kabra, "Analysis of Interface Trap Charges of Double Gate Junctionless Nanowire Transistor (DG-JNT) for Digital Circuit Applications," in *Proceedings of International Conference, 2018 IEEE Electron Device Kolkata Conference, EDKCON* (2018): 563–567

[39] J. Yuan and J. C. S. Woo, "A Novel Split-Gate MOSFET Design Realized by a Fully Silicided Gate Process for the Improvement of Transconductance and Output Resistance," *IEEE Electron Device Letters* 26, no. 11 (2005): 829–831.

[40] M. Getnet and R. Chaujar, "Sensitivity Analysis of Biomolecule Nanocavity Immobilization in a Dielectric Modulated Triple-Hybrid Metal Gate-All-Around Junctionless NWFET Biosensor

4042, 2025, 1, Downloaded from https://onlinelibrary.wiley.com/doi/10.1155/acmp/3744806 by Delhi Technological University, Wiley Online Library on [05/03/2025]. See the Terms and Conditions (https://onlinelibrary.wiley.com/terms-and-conditions) on Wiley Online Library for rules of use; OA articles are governed by the applicable Creative Commons License

for Detecting Various Diseases," *Journal of Electronic Materials* 51, no. 5 (2022): 2236–2247.

[41] E. Rahman, A. Shadman, and Q. D. M. Khosru, "Effect of Biomolecule Position and Fill in Factor on Sensitivity of a Dielectric Modulated Double Gate Junctionless MOSFET Biosensor," *Sensing and Bio-Sensing Research* 13 (2017): 49–54.

[42] A. Das, S. Rewari, B. K. Kanaujia, et al., "Numerical Modeling of a Dielectric Modulated Surrounding-Triple-Gate Germanium-Source MOSFET (DM-STGGS-MOSFET)-Based Biosensor," *Journal of Computational Electronics* 22, no. 2 (2023): 742–759.

[43] P. Dwivedi and A. Kranti, "Applicability of Transconductance-to-Current Ratio (Gm/Ids) as a Sensing Metric for Tunnel FET Biosensors," *IEEE Sensors Journal* 17, no. 4 (2017): 1030–1036.

[44] A. Kumar, "Palladium-Based Trench Gate MOSFET for Highly Sensitive Hydrogen Gas Sensor," *Materials Science in Semiconductor Processing* 120 (2020): 105274.

[45] J. Li, H. Tsukada, T. Miyasako, et al., "High-Transconductance Indium Oxide Transistors With a Lanthanum-Zirconium Gate Oxide Characteristic of an Electrolyte," *Journal of Applied Physics* 127, no. 6 (2020): 064504.

[46] S. Kumar and D. S. Yadav, "Assessment of Interface Trap Charges on Proposed TFET for Low Power High-Frequency Application," *Silicon* 14, no. 15 (2022): 9291–9304.

[47] D. Sen, A. De, B. Goswami, S. Shee, and S. K. Sarkar, "Noise Immune Dielectric Modulated Dual Trench Transparent Gate Engineered MOSFET as a Label-Free Biosensor: Proposal and Investigation," *Journal of Computational Electronics* 20, no. 6 (2021): 2594–2603.

4042, 2025, 1, Downloaded from https://onlinelibrary.wiley.com/doi/10.1155/acmp/3744806 by Delhi Technological University, Wiley Online Library on [05/03/2025]. See the Terms and Conditions (https://onlinelibrary.wiley.com/terms-and-conditions) on Wiley Online Library for rules of use; OA articles are governed by the applicable Creative Commons License

Comparative Assessment of MPPT Techniques for Optimizing Photovoltaic System Efficiency

2025 International Conference on Sustainable Energy Technologies and Computational Intelligence (SETCOM) | 979-8-3315-2054-0/25/$31.00 ©2025 IEEE | DOI: 10.1109/SETCOM64758.2025.10932377

Rachna Dhir
Department of Electrical Engg.
J.C.BOSEUST, YMCA, Faridabad,
Haryana, India
rachna@jcboseust.ac.in

Rachana Garg
Department of Electrical Engg.
Delhi Technological University
Delhi, India
rachana16100@yahoo.co.in

Priya Mahajan
Department of Electrical Engg.
Delhi Technological University
Delhi, India
priyamahajan.eed@gmail.com

***Abstract*—The weather uncertainties and fluctuating nature of solar radiations and varying temperature results in low conversion efficiency of the PV panel thereby necessitating the extraction of maximum power from the system. To operate the system at its peak power, track of maximum power point becomes essential for any PV system. To handle the input fluctuations and inherent non-linearities of the system, an effective MPPT technique needs to be employed. In this research paper, various classical and intelligent MPPT techniques are listed, discussed and compared on various parameters. The classical Incremental Conductance algorithm, intelligent MPPT based on fuzzy logic control and ANN method is designed and tested on a PV system using MATLAB/Simulink. The PV system entails a PV array, a boost converter, MPPT control unit, and load. These methods diverge in their characteristics and their performance is evaluated on various parameters such as tracking efficiency, response time, implementation complexity, and stability under dynamic conditions. In this work, the drawbacks of the studied methods are also pointed out. Among the implemented techniques, superiority of neural network based MPPT technique is established over the classical as well Fuzzy Logic based MPPT controller for optimizing the performance of the system.**

Keywords—Artificial Neural Network, photovoltaic, Fuzzy logic control, converter, efficiency

I. INTRODUCTION

Solar technology has become increasingly efficient and cost-effective, driving rapid adoption for residential, commercial, and industrial use. Unlike other renewables that may depend on geographical constraints, solar systems can be implemented across diverse locations, from rooftops to large solar farms. This adaptability, combined with minimal environmental disruption, positions solar energy as a leading force in reducing fossil fuel reliance and fostering a sustainable energy future worldwide.

Since the worldwide demand for sustainable and renewable energy sources intensifies, solar photovoltaic (PV) systems have come out as a pivotal technology for their ability to transform sunlight into electrical energy. However, the efficiency of PV systems is inherently inconstant due to its intermittent nature of sun. Uncertain weather conditions such as radiations, temperature, and shading result into output fluctuations. To ensure that the system operate at their highest possible efficiency, it is crucial to implement Maximum Power Point Tracking (MPPT). MPPT algorithms play a central role in aggressively adjusting the operating point thereby producing the maximum power in varying environmental conditions.

A wide range of MPPT techniques has been developed across many years, each with distinct characteristics, advantages, and constraints. Conventional techniques such as (PandO), modified (PandO) and Incremental Conductance(IC) are extensively used for the simple design and easy operation[1-3].These techniques involve iterative processes that continuously perturb and adjust the working point to locate the point of maximum power. Other popular methods include Fractional Open Circuit Voltage and Fractional Short Circuit Voltage[4,5]. Among these techniques, P&O and Incremental Conductance(IC) method proves effective for accurate and efficient tracking. P & O is simple in design and simple in execution while Incremental Conductance technique causes the MPP to reach faster comparatively. However, these methods exhibit steady state oscillations and slow response under rapidly changing and partial shading conditions.

Artificial Neural Networks and Fuzzy Logic based control are two intelligent approaches for following the point of peak power in Photovoltaic systems. ANN-based MPPT utilizes a neural network model to learn and predict the optimal operating point of the PV system subjected to inputs such as irradiance and temperature. By training on historical data, ANNs can adapt to complex, non-linear behaviors in real-time, achieving efficient tracking of the peak power point under fluctuating conditions.

The FLC approach does not require precise mathematical modeling, making it robust for dynamic and unpredictable environments[6-8]. Together, these methods provide flexible and intelligent solutions for maximizing power output, with ANNs excelling in learning patterns and FLCs offering stability in uncertain operating conditions.

Maximum power point approaches based on artificial intelligence, FLC and NN based controllers have been extensively researched on and implemented on various systems [9,10]. FLC employs designing of fuzzy rule matrix and membership functions are established. The membership functions need to be constantly adjusted to obtain the desired results.

This paper puts across, a comprehensive comparative assessment of selected MPPT techniques and demonstrated their effectiveness on key performance metrics such as tracking efficiency, response time, implementation complexity, and stability by conducting simulation evaluations. The paper is organised into 4 sections : Section 2 put forth PV system topology and associated modeling. Section 3 contains design and implementation of MPPT controllers. Section 4 demonstrates simulation results followed with discussion. Section 5 provides an interpretation of the results.

979-8-3315-2054-0/25/$31.00 ©2025 IEEE

Authorized licensed use limited to: DELHI TECHNICAL UNIV. Downloaded on April 03,2025 at 04:45:12 UTC from IEEE Xplore. Restrictions apply.

II. SYSTEM TOPOLOGY

The system under study comprises of a PV array which is associated to the load via a dc-dc converter. The block diagram representation of the PV system under study is shown in Fig. 1.

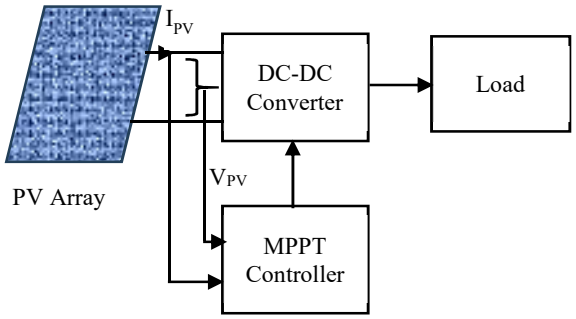

Fig. 1. Block diagram of PV system under study

While it is imperative to make the system function at its optimal point, the peak power point is tracked by employing desired controller which generates references at maximum power point.

A. Modeling of PV Cell

In Fig. 2 the PV cell is represented using one-diode model [11]. One diode model known for its simplicity, serves as a basic equivalent circuit and is commonly employed for initial approximations of solar cell behaviour. This model contains a current source and a diode, making it straightforward to analyse and comprehend. Its primary advantage is its straightforwardness, which renders it appropriate for numerous applications that require a quick estimation of a solar cell's performance.

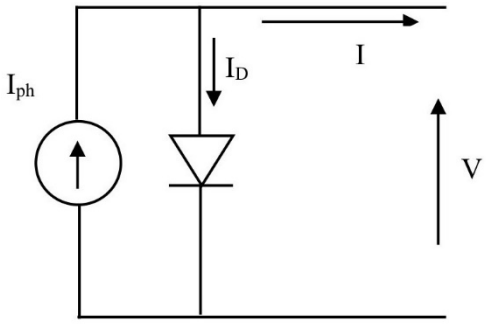

Fig. 2. Equivalent circuit of an ideal PV Cell [11]

The solar cell current can be mathematically represented as:

$$I = I_{sc} - I_0\left(e^{\frac{(V+IR_S)}{V_T z}} - 1\right) - \frac{(V+IR_S)}{R_{sh}} \quad (1)$$

Thermal Voltage, $V_T = \frac{N_S kT}{q}$

The variables in the expression are short circuit current(Isc), saturation current(I0), diode ideality factor(z), no. of series connected cells (Ns) , temperature(T), Boltzmann constant(k), q is electron charge ,series resistance is represented as Rs and the shunt resistance of the PV array represented with Rsh. Fig. 3 illustrates the P-V curve of a PV cell.

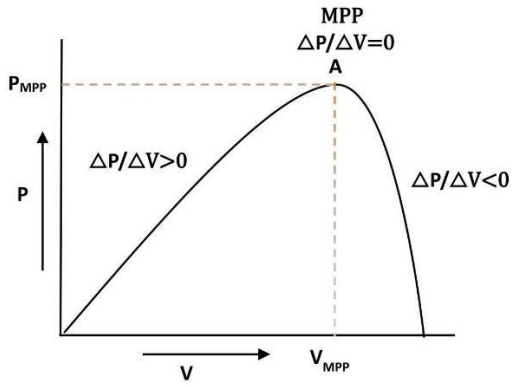

Fig. 3 Power-Voltage Curve of a PV Cell.

The Power-Voltage curve of a photovoltaic (PV) cell signifies a correspondence between the output power and the output voltage under a constant level of irradiance. It is critical in defining the performance of a solar cell, as it helps in identifying the point of maximum power (MPP). It is the optimal point where the PV cell works at its maximum best.

B. P-V and I-V Characteristics

The PV module is simulated in MATLAB Simulink. The parameter values of the module are shown in Table. 1.

TABLE. 1. SPECIFICATION OF ISOLTECH ISTH–250WH SOLAR MODULE

Sr. No	Specification	Value
1.	Total parallel strings	1
2.	Total series connected modules per string	8
3.	Power(maximum) of each module	250W
4.	Voltage at point of peak power (Vmp)	37.3V
5.	Current at point of peak power (Imp)	8.15A
6.	Voltage at open circuit (Voc)	30.7V
7.	Current at short circuit (Isc)	8.66A
8.	Temperature Constant of open circuit voltage (Voc)	-0.369%/°C
9.	Temperature Constant of short circuit current (Isc)	0.086%/°C
10.	Diode Ideality factor	1.019

The characteristic response of ISoltech ISTH–250WH Solar Module at diverse values of temperature and irradiance is illustrated in Fig. 4.

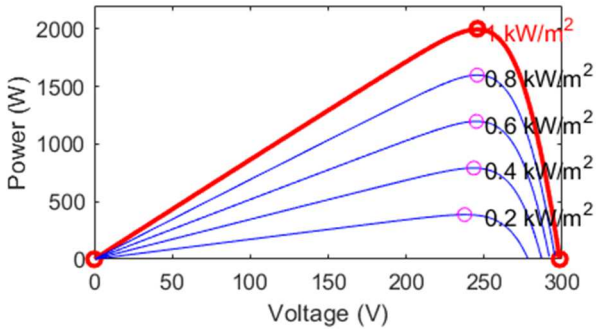

(a) P-V characteristics of the PV module at specified irradiance values

Authorized licensed use limited to: DELHI TECHNICAL UNIV. Downloaded on April 03,2025 at 04:45:12 UTC from IEEE Xplore. Restrictions apply.

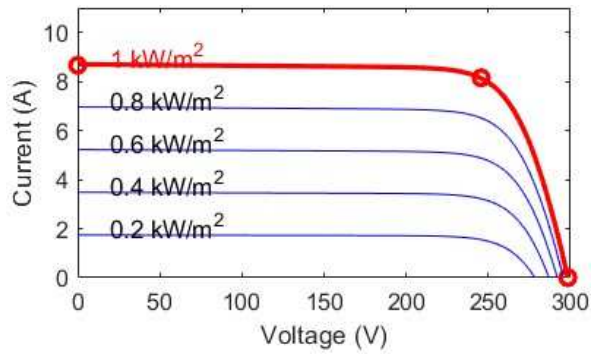

(b) I-V characteristics of the of the PV module at specified irradiance values

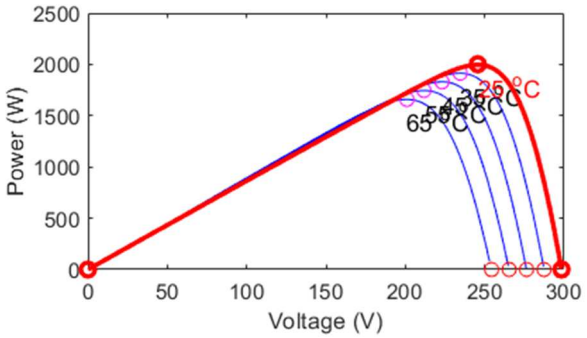

(c) P-V Characteristics of the PV array at specified temperature values

.

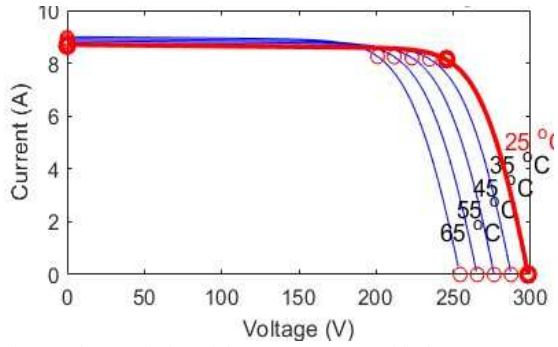

(d) I-V Characteristics of the PV array at specified temperature values.

Fig. 4. Characteristics of PV module at specified irradiance and temperature values.

III. MPPT CONTROLLERS

The Incremental Conductance method is widely used due to its simplicity and precision. ANN-based MPPT controllers use a trained neural network model to foresee the optimal operating point of the PV panels under varying environment condition. This approach allows for rapid and accurate adjustments in response to environmental changes. Fuzzy Logic Control (FLC) based MPPT leverages fuzzy logic, a form of artificial intelligence that uses membership functions and a set of predefined rules in order to design a control offering adaptability, and robustness [12].

A. Incremental Conductance

The Incremental conductance technique as illustrated in a flow chart given in Fig. 5. is based on the phenomenon that the change of the power in regard to variation in voltage is zero at the point of peak power.

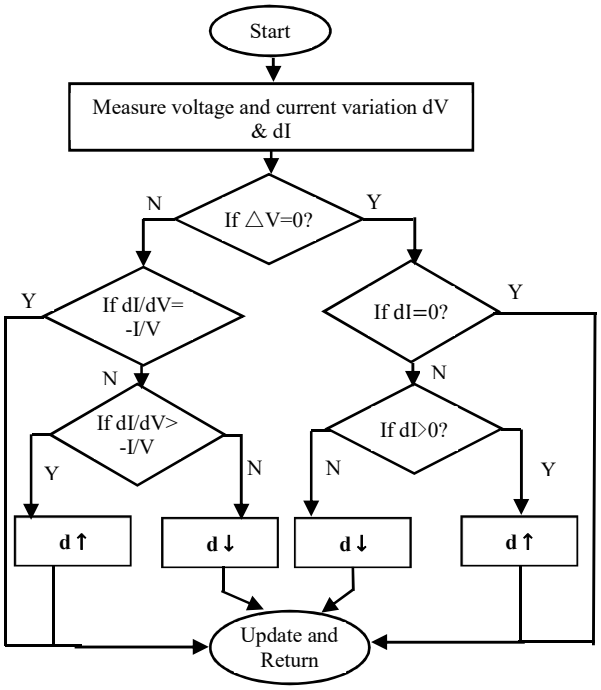

Fig. 5. Flow Chart representation of Incremental Conductance Algorithm

It continuously monitors the change in conductance (dI/dV) and compares it with the occuring conductance (I/V) of the PV array. When the power slope is zero, the system has reached the MPP. Positive slope implies that the voltage is below the MPP, and if it is negative, the voltage is above the MPP [6]. The controller adjusts the operating voltage accordingly to maintain operation at the MPP.

A. Fuzzy Logic based Controller

FLC employs a set of fuzzy rules to handle the uncertainties and non-linearities inherent in the power-voltage characteristics of solar panels.

The FLC MPPT system typically contains three main components: fuzzification, rule base, and defuzzification. In the stage of fuzzification, the inputs are converted into fuzzy variables. The rule base then processes these inputs using a set of predefined fuzzy rules relating the system behavior [13,14]. Finally, in the third and last stage i.e. defuzzification the fuzzy output results in a control action that adjusts the operating point corresponding to maximum power.

1) Controller Design

The fuzzy logic controller is designed by considering two input variables and one output. The two inputs are error(E) and change in error(△E). Whereas error is defined as change in power w.r.t. voltage. These are represented in Eqn. (2) and Eqn. (3) respectively.

$$E = \frac{dP}{dV} \tag{2}$$

$$del\ E = del\ (\frac{dP}{dV}) \tag{3}$$

where,

$$\frac{dP}{dV} = \frac{P(z) - P(z-1)}{V(z) - V(z-1)}$$

Authorized licensed use limited to: DELHI TECHNICAL UNIV. Downloaded on April 03,2025 at 04:45:12 UTC from IEEE Xplore. Restrictions apply.

The output variable is the duty cycle(D)

2) Membership Functions

In the design of fuzzy set, triangular membership functions are considered. Five membership functions were defined: Extreme low (EL), Low (L), Zero (Z), High (H) and Extreme High (EH). The membership functions are shown in Fig. 6.

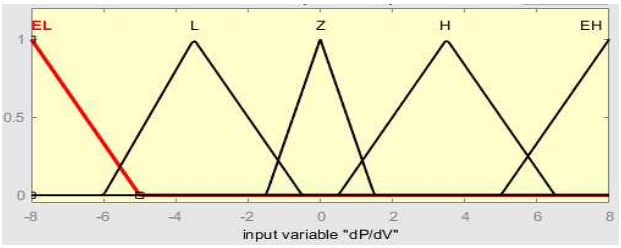

a) Input E

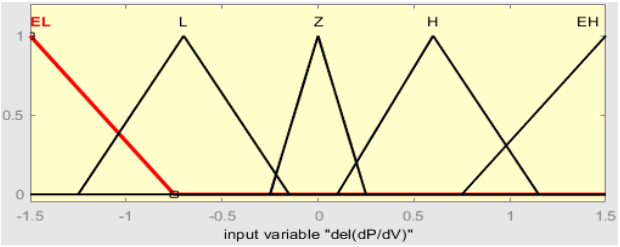

b) Input del E

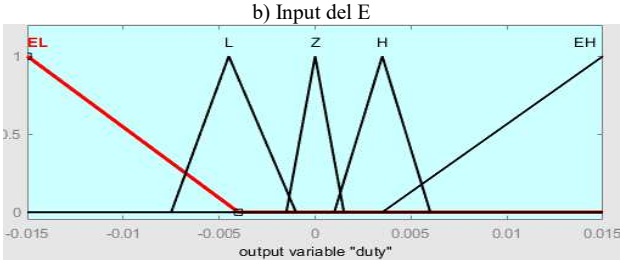

c) Output Duty Cycle D

Fig. 6. Membership functions a) Input1 : E b) Input2 : del E c) Output : duty

3) Rules

Table. 3 shows the rule set governing the fuzzy logic which are applied in the controller.

TABLE. 2. FUZZY RULES FOR ERROR AND CHANGE IN ERROR AS INPUTS [9]

E/ΔE	EL	L	Z	H	EH
EL	Z	EH	H	Z	EL
L	EH	H	Z	Z	EL
Z	EH	Z	Z	L	EL
H	EH	Z	Z	L	EL
EH	EH	L	L	EL	Z

The controller was designed using Fuzzy Logic toolbox in MATLAB and tested for various conditions.

B. Artificial Neutral Network based Controller

The PV system equipped with Neural Network based control is shown in Fig. 7. Temperature and Irradiance values are given as inputs to the control unit. Voltage at maximum power point is obtained as the output. Neural Network is further trained in order to obtain desired output.

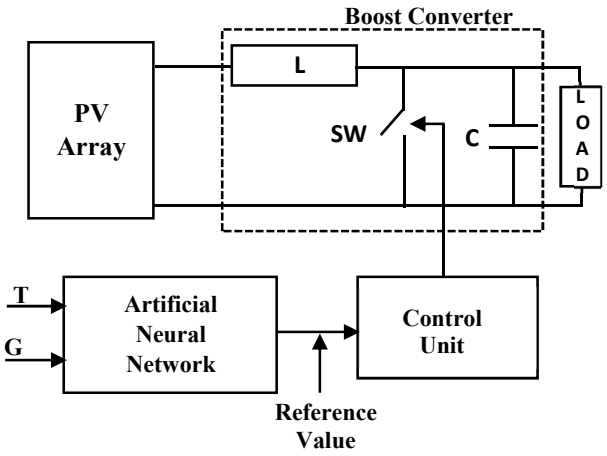

Fig. 7. PV system equipped with ANN based MPPT controller

1) Neural Network Architecture

The construction of neural network consists of three layers. The input layer receives the initial data. The immediate layer is the hidden layer where data processing occurs through neurons. The output layer generates the final result based on the data [15].

The neurons process the inputs and pass the results to the next layer. Each neuron has weights, bias and an activation function as presented in Fig 6. The weights are attuned to lessen the error. The bias is a constant value which adds up to help fit the model. The activation function determines the output of the neuron [16].

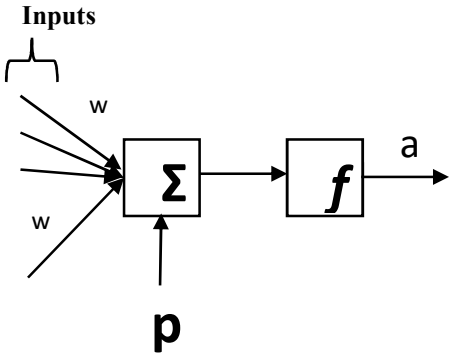

Fig. 8 Neuron Model

The neuron model [13] depicted in Fig. 8 can be represented as Eqn. (4):

$$a = f(\sum_{i=1}^{z} w_i x_i + p) \quad (4)$$

Where a=activation function
z=no. of input elements;
input element=x (i =1,2…z)
weight= w (i =1,2…z)

2) ANN Presentation

Neural Network maps the non-linearity between input and the output data. The inputs considered for the model are temperature(T) and irradiance(G)[16]. Further, it is

Authorized licensed use limited to: DELHI TECHNICAL UNIV. Downloaded on April 03,2025 at 04:45:12 UTC from IEEE Xplore. Restrictions apply.

imperative to obtain desired input and output data to train the neural network. PV model is programmed in MATLAB to obtain the desired input data.

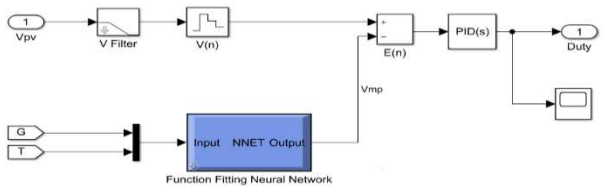

Fig. 9. Neural Network Model

The ANN illustrated in Fig. 9 encompasses hidden layer and output layer thus forming a two-layer feedforward network. The data is selected and the network trained. The network configuration as depicted in Fig. 10 is trained using Levenberg-Marquardt algorithm.

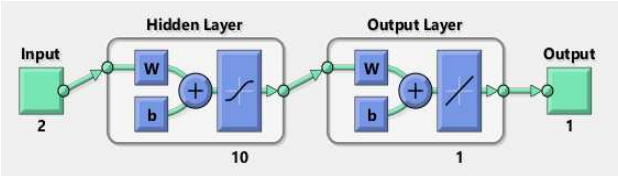

Fig. 10. Configured network

With the objective of training the neural network, one thousand samples of data corresponding to temperature, irradiance and prompted voltage of the solar panel 1Soltech ISTH-250WH is considered. Further, the data are indiscriminately divided into 70 percent, 15 percent and 15 percent. The respective fraction of data is considered for training, validation and testing.

For developing the network, number of neurons intending for the hidden layer is 10. For the purpose of training of ANN datasets, several training algorithms are mentioned in literature[17,18]. The most common are Resilient Backpropagation, Bayesian Regularisation Gradient Descent Momentum, Scaled Conjugate Gradient, Levenberg-Marquardt among others . LM algorithm is employed to train the network. The research literature establishes the supremacy of Levenberg-Marquardt algorithm because of its promptness[19].

The LM algorithm's appropriateness for MPPT is supported by the enormously low values of the gradient, Mu, and mean squared error, as depicted in Fig. 11.

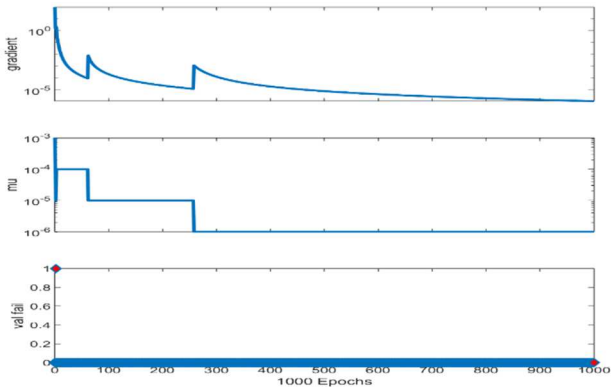

Fig. 11. Training parameters

RESULTS AND DISCUSSION

To assess the performance of the PV system, the PV array is subjected to variations in irradiance levels as shown in Fig. 12. The conventional Incremental Conductance is evaluated in comparison with ANN and Fuzzy based MPPT Controller. In this case, 2000 W PV module is considered. For the boost converter, with sampling frequency of 10 kHz, the values of L and C are 0.1164 H and 3300µF respectively. The response of the studied MPPT controllers is observed and compared and shown in Fig. 13.

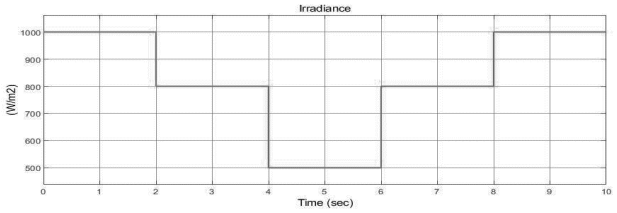

Fig. 12 Step Change in Irradiance

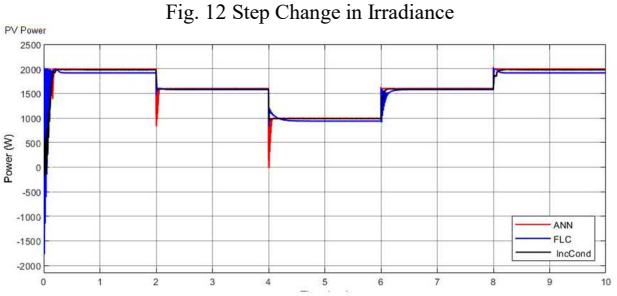

Fig. 13. Maximum power tracked under step change in irradiance values.

The Incremental Conductance algorithm based controller is precisely tracking the maximum power without any overshoot. Though it accompanies certain oscillations about the point of peak power, it responds well to the sudden change in input. Also, there is no need of parameter tuning in this technique.

On the other hand, ANN and Fuzzy based controllers have been able to minimize the oscillations while offering accuracy at the same time. The FLC based controller exhibits initial spikes and minimized oscillations around MPP. It's tracking efficiency is between (84.06-85.9%) ANN based controller has been able to accurately track the MPP without having any considerable oscillations around MPP with about 93% tracking efficiency.

As compared to the Incremental Conductance algorithm, MPPT controller designed on ANN and fuzzy logic control require parameter tuning and require memory owing to training of dataset and heavy rule base. The performance of various controllers is compared and illustrated in Table. 2.

TABLE. 2. COMPARISON OF CONTROLLERS UNDER STUDY

Performance Parameter/ Technique	**Classical Controller**	**Intelligent Controller(s)**	
	Incremental Conductance	FLC based MPPT	ANN based MPPT
Tracking Efficiency	83.24-85%	84.06-85.90%	92.68-94.7%

Authorized licensed use limited to: DELHI TECHNICAL UNIV. Downloaded on April 03,2025 at 04:45:12 UTC from IEEE Xplore. Restrictions apply.

Oscillations around MPP	High	Low	Negligible
Complexity	Simple	High	High
Memory Requirement	No	Yes	Yes
Overshoot	No	Little	No
Undershoot	Negligible	No	Moderate
Parameter tuning requirement	No	Yes	Yes

The incremental conductance can be improved by employing adaptive step size techniques. The intelligent controllers can be adaptively tuned or combined with NN technique in order to exhibit better performance, robustness, and adaptability. The NN networks can be made more robust by pretraining the network and optimizing by using multi-objective functions for better outcome.

REFERENCES

[1] Nabil Karami, Nazih Moubayed, Rachid Outbib, "General review and classification of different MPPT Techniques, Renewable and Sustainable Energy Reviews", Volume 68, Part 1, 2017, Pages 1-18, ISSN 1364-0321, https://doi.org/10.1016/j.rser.2016.09.132.

[2] Hegazy Rezk, Ahmed Fathy, Almoataz Y. Abdelaziz, A comparison of different global MPPT techniques based on meta-heuristic algorithms for photovoltaic system subjected to partial shading conditions,Renewable and Sustainable Energy Reviews, Volume 74, 2017, Pages 377-386, ISSN 1364-0321,https://doi.org/10.1016/j.rser.2017.02.051. https://www.sciencedirect.com/science/article/pii/S1364032117302708)

[3] S. Lyden, M.E. Haque, Maximum Power Point Tracking techniques for photovoltaic systems: A comprehensive review and comparative analysis, Renewable and Sustainable Energy Reviews, Volume 52, 2015, Pages 1504-1518, ISSN 1364-0321, https://doi.org/10.1016/j.rser.2015.07.172.

[4] Kasra Mohammadi, Shahaboddin Shamshirband, Chong Wen Tong, Khubaib Amjad Alam, Dalibor Petković, Potential of adaptive neuro-fuzzy system for prediction of daily global solar radiation by day of the year, Energy Conversion and Management, Volume 93, 2015, Pages 406-413, ISSN 0196-8904, https://doi.org/10.1016/j.enconman.2015.01.021.

[5] Sarvi, M., Azadian, A. A comprehensive review and classified comparison of MPPT algorithms in PV systems.Energy Syst13, 281–320 (2022). https://doi.org/10.1007/s12667-021-00427-x

[6] A. D. Martin and J. R. Vazquez, "MPPT algorithms comparison in PV systems: P&O, PI, neuro-fuzzy and backstepping controls," 2015 IEEE International Conference on Industrial Technology (ICIT), Seville, Spain, 2015, pp. 2841-2847, doi: 10.1109/ICIT.2015.7125517.

[7] Salman, S., AI, X. & WU, Z. Design of a P-&-O algorithm based MPPT charge controller for a stand-alone 200W PV system.Prot Control Mod Power Syst3, 25 (2018). https://doi.org/10.1186/s41601-018-0099-8

[8] Shang, L., Guo, H. & Zhu, W. An improved MPPT control strategy based on incremental conductance algorithm.Prot Control Mod Power Syst5, 14 (2020). https://doi.org/10.1186/s41601-020-00161-z

[9] Elobaid, L. M., Abdelsalam, A. K., & Zakzouk, E. (2015). Artificial neural network-based photovoltaic maximum power point tracking techniques: a survey. IET Renewable Power Generation, 9(8), 1043-1063. https://doi.org/10.1049/iet-rpg.2014.0359

[10] Loubna Bouselham, Mohammed Hajji, Bekkay Hajji, Hicham Bouali, A New MPPT-based ANN for Photovoltaic System under Partial Shading Conditions, Energy Procedia, Volume 111, 2017, Pages 924-933, ISSN 1876-6102, https://doi.org/10.1016/j.egypro.2017.03.255. (https://www.sciencedirect.com/science/article/pii/S1876610217302886)

[11] L. P. N. Jyothy and M. R. Sindhu, "An Artificial Neural Network based MPPT Algorithm For Solar PV System," 2018 4th International Conference on Electrical Energy Systems (ICEES), Chennai, India, 2018, pp. 375-380, doi: 10.1109/ICEES.2018.8443277.

[12] Villegas-Mier CG, Rodriguez-Resendiz J, Álvarez-Alvarado JM, Rodriguez-Resendiz H, Herrera-Navarro AM, Rodríguez-Abreo O. Artificial Neural Networks in MPPT Algorithms for Optimization of Photovoltaic Power Systems: A Review.Micromachines. 2021; 12(10):1260. https://doi.org/10.3390/mi12101260

[13] Robles Algarín C, Taborda Giraldo J, Rodríguez Álvarez O. Fuzzy Logic Based MPPT Controller for a PV System.Energies. 2017; 10(12):2036. https://doi.org/10.3390/en10122036

[14] Shiau J-K, Wei Y-C, Chen B-C. A Study on the Fuzzy-Logic-Based Solar Power MPPT Algorithms Using Different Fuzzy Input Variables.Algorithms. 2015; 8(2):100-127. https://doi.org/10.3390/a8020100

[15] S. Narendiran, S. K. Sahoo, R. Das and A. K. Sahoo, "Fuzzy logic controller based maximum power point tracking for PV system," 2016 3rd International Conference on Electrical Energy Systems (ICEES), Chennai, India, 2016, pp. 29-34, doi: 10.1109/ICEES.2016.7510590.

[16] B. Bendib, F. Krim, H. Belmili, M.F. Almi, S. Boulouma, Advanced Fuzzy MPPT Controller for a Stand-alone PV System, Energy Procedia, Volume 50,2014,Pages 383-392,ISSN 1876-6102,https://doi.org/10.1016/j.egypro.2014.06.046.

[17] Moyo, R. T., Tabakov, P. Y., and Moyo, S. (November 18, 2020). "Design and Modeling of the ANFIS-Based MPPT Controller for a Solar Photovoltaic System." ASME.J. Sol. Energy Eng. August 2021; 143(4): 041002.https://doi.org/10.1115/1.4048882

[18] R. K. Rai and O. P. Rahi, "Fuzzy Logic based Control Technique using MPPT for Solar PV System," 2022 First International Conference on Electrical, Electronics, Information and Communication Technologies (ICEEICT), Trichy, India, 2022, pp. 01-05, doi: 10.1109/ICEEICT53079.2022.9768650.

[19] Narwat, Lalit & Dhillon, Javed. (2021). Design and Operation of Fuzzy Logic Based MPPT Controller under Uncertain Condition. Journal of Physics: Conference Series. 1854. 012035. 10.1088/1742-6596/1854/1/012035.

Authorized licensed use limited to: DELHI TECHNICAL UNIV. Downloaded on April 03,2025 at 04:45:12 UTC from IEEE Xplore. Restrictions apply.

Physica Scripta

INCLUSIVE PUBLISHING TRUSTED SCIENCE

PURPOSE-LED PUBLISHING™

PAPER

Comprehensive study of highly efficient Rb_2AgInX_6 (X = Cl, Br, I) based lead-free double perovskite solar cells

To cite this article: Vishal Deswal and Sarita Baghel 2025 *Phys. Scr.* **100** 035982

View the article online for updates and enhancements.

You may also like

- Pressure effects on the opto-electronic and mechanical properties of the double perovskite $Cs_2AgInCl_6$
A A Sholagberu, W A Yahya and A A Adewale
- Tuning of band gap by anions (Cl, Br, I) of double perovskites Rb_2AgAsX_6 (Cl, Br, I) for solar cells and thermoelectric applications
Ghazanfar Nazir, Q Mahmood, M Hassan et al.
- Effect of substituting on the transition dipole moment of the double perovskite $Cs_2AgInCl_6$
Lu-lu Zhang, Jun Luo, Biao Liu et al.

This content was downloaded from IP address 14.139.251.98 on 06/03/2025 at 06:53

Physica Scripta

PAPER

Comprehensive study of highly efficient Rb_2AgInX_6 (X = Cl, Br, I) based lead-free double perovskite solar cells

Vishal Deswal and Sarita Baghel

Renewable Energy Research Laboratory, Department of Applied Physics, Delhi Technological University, Delhi, 110042, India

E-mail: vishaldeswal_23phdap01@dtu.ac.in

RECEIVED 20 September 2024

REVISED 30 December 2024

ACCEPTED FOR PUBLICATION 4 February 2025

PUBLISHED 27 February 2025

Keywords: double perovskite solar cells (DPSC), Rb_2AgInX_6, SCAPS-1D, all double perovskite tandem solar cell

Abstract

Lead-free Double Perovskite Solar Cells (DPSCs) have generated great study interest recently as a potential perovskite absorber layer, due to their cost-effectiveness, impressive stability, and superior performance. In this study, we investigated Rb_2AgInX_6(Cl, Br, I) based DPSCs using SCAPS-1D simulation software. Various properties, such as the density of states for conduction and valance bands, carrier concentration, and carrier mobility (electrons and holes), were calculated for simulation. Furthermore, we have optimized defect density, electron affinity, and thickness of absorber layers for Rb_2AgInX_6-based DPSCs. We investigated how DPSC parameters were impacted by operating temperature and then performed band gap tuning for $Rb_2AgInBr_6$-based DPSC along with their temperature stability. Tandem solar cells (TSC) have had an enormous influence on the field of photovoltaics (PV) because of their ability to effectively use a wider range of solar spectrum and reduce unwanted energy loss. In this context, we have simulated $Rb_2AgInBr_6/Rb_2AgInI_6$ based an all double perovskite tandem solar cells and optimized the same for future experimental applications. The optimized PCE of 12.14%, 26.49%, and 13.95% were obtained for Rb_2AgInX_6(X = Cl, Br, I respectively) based DPSCs. In comparison, the PCE of 38.70% was obtained for tandem structure.

1. Introduction

Perovskite materials have garnered considerable interest for their wide-ranging technological and industrial uses. Lead-based perovskites, in particular, have been extensively studied for their exceptional efficiency in photovoltaic applications. However, the adverse environmental impact of lead necessitates exploration into alternative materials. The use of 'Pb' could be replaced by applying an intricate combination of monovalent and trivalent cations, represented structurally as $A_2B'B''X_6$, where 'A' denotes a large cation (e.g., Cs^+), 'B″' and 'B′' represents either monovalent or trivalent cations, whereas 'X' denotes oxygen or halogen [1, 2]. Halide double perovskites (DPs) have emerged as a notable group of materials, drawing considerable research interest due to their remarkable optoelectronic characteristics. These include tunable bandgap, the capacity for optical absorption across a broad spectrum, outstanding photoconductivity, high carrier mobility coupled with low effective masses, extended carrier diffusion lengths, and prolonged lifetimes. Moreover, their thermoelectric properties have significantly propelled research in next-generation devices [1, 3, 4]. In this regard, numerous halide perovskites such as Cs_2BiAgI_6, $Cs_2InAgCl_6$, $Cs_2BiAgCl_6$, and $Cs_2BiAgBr_6$ have been successfully synthesized and characterized [1, 5–7]. A recent study demonstrated through simulation that $Cs_2AgInBr_6$-based Halide double perovskite solar cell (DPSC) achieved a power conversion efficiency (PCE) of 26.90%, signifying colossal potential [8].

Moreover, Kattan *et al* have investigated DPs Rb_2AgInX_6 (X = Cl, Br, I) for various solar cell applications. Authors have reported a direct band gap for these materials based on their Density Functional Theory (DFT) calculations. Hence, these materials should be further explored for solar cell applications [1].

In this study, we have studied and optimized various properties of Rb_2AgInX_6-based halide DPSCs using SCAPS-1D simulation software. Various material properties are also calculated and reported for the first time in

© 2025 IOP Publishing Ltd. All rights, including for text and data mining, AI training, and similar technologies, are reserved.

this study. Finally, a band gap tuning and temperature study suggested a suitable band gap with minimum variation in PCE over temperature. Furthermore we have also simulated an all-double perovskite tandem structure.

Recently, there has also been a focus on tandem solar cells (TSCs) to overcome the limitations of Single junction solar cells and enhancing the efficiency further [9, 10]. Tandem cells address thermalization and transmission photon loss, which primarily contribute to decreasing PCE of single-junction solar cells [9].

TSCs use the principle of distributing the illumination spectrum across many absorber layers. The absorbers are chosen based on their ability to absorb photons of different wavelengths selectively. According to the literature, a tandem arrangement consisting of two stacked cells may attain a maximum PCE of up to 42% when the bandgaps are tuned [9, 10]. In 1996, Martí *et al* proposed a theoretical statement which states that an infinite stack of connections may achieve a maximum PCE of up to 65% under the conventional AM1.5 illumination spectrum [11].

A typical two-cell stacked tandem architecture generally comprises an upper cell with a large bandgap and a bottom cell with a small bandgap. This arrangement allows for the efficient use of higher energy photons by the upper cell and lower energy photons by the bottom cell. Consequently, the upper cell decreases the amount of energy lost during transmission in the lower cell. In comparison, the lower cell decreases the amount of energy lost due to thermalization in the upper cell and makes better use of the whole spectrum of sunlight [9].

All the mentioned combinations showed substantial performance improvements in the past decade [9]. In this study, considering the suitable wide band gap of $Rb_2AgInBr_6$ (1.32 eV) and narrow bandgap of Rb_2AgInI_6 (0.46 eV), we have simulated and optimized a DP/DP ($Rb_2AgInBr_6/Rb_2AgInI_6$) tandem solar cell for better PCE.

2. Device structure and simulation methodology

We utilized the 1D Solar Cell Capacitance Simulator (SCAPS) simulation software for this simulation study. SCAPS-1D software, is primarily designed for computing semiconductor equations like continuity and Poisson's equations [12].

The Device Structure used in the simulation is (FTO/ZnSe/Rb_2AgInX_6/CBTS/Au). FTO (fluorine-doped tin oxide) is a transparent electrode within this suggested structure. Additionally, ZnSe serves as an electron transport layer (ETL) and CBTS as a hole transport layer (HTL). For simulation, the gold (Au) back contact is utilized [8, 13].

ZnSe is employed as ETL in this device configuration. This choice is motivated by the superior photostability exhibited in devices with ZnSe layers. The ZnSe layer enables greater ultraviolet (UV) light harvesting, effectively mitigating intense UV-light exposure on the perovskite film. Consequently, this helps prevent degradation associated with UV exposure, thereby contributing to enhanced photostability of the device [8, 12, 14, 15].

CBTS (Copper barium Thiostannate) is a thin film material chosen as HTL and offers enhanced light absorption capacity. Its non-centrosymmetric crystal structure, coupled with significant variation in atomic sizes within the CBTS material, provides favorable parameters for enhancing the PCE of a PSC [8, 16, 17].

The device architecture and the band alignment diagram of DPSC layers are represented in figure 1. The material parameters for CBTS, ZnSe, and FTO were obtained from previous studies and are mentioned in table 1 [8, 12, 14–17]. Some parameters for the absorber layers Rb_2AgInX_6 are taken from published literature, while others are calculated/optimized in this work. The direct bandgap values (E_g) for $Rb_2AgInCl_6$, $Rb_2AgInBr_6$, and Rb_2AgInI_6 are reported as 2.16 eV, 1.32 eV, and 0.46 eV, respectively [1]. The static dielectric values (Relative permittivity, $\varepsilon/\varepsilon 0$) for $Rb_2AgInCl_6$, $Rb_2AgInBr_6$, and Rb_2AgInI_6 are reported as 2.78, 3.24, and 4.43, respectively [1].

For $Rb_2AgInCl_6$, the effective mass of electrons (m_e^*) was reported as 0.40 times the rest mass of an electron (m_0), while the effective mass of holes (m_h^*) was found to be 1.15 times m_0. In the case of $Rb_2AgInBr_6$, m_e^* was slightly lower at 0.35 times m_0, and the m_h^* was 0.85 times m_0. Finally, for Rb_2AgInI_6, the m_e^* decreased further to 0.25 times m_0, and m_h^* was the lowest among the three materials, at 0.55 times m_0 [1].

The density of state for the valence (N_v) and conduction bands (N_c) was determined using the following equation:

$$N_{c/v} = 2\left(\frac{2\pi k_B T m_{e/h}^*}{h^2}\right)^{\frac{3}{2}} \quad (1)$$

Here, k_B represents $_{the}$ Boltzmann constant, T represents room temperature, h represents the plank's constant and $m_{e/h}^*$ effective masses of electrons/holes. The calculated values of N_C and N_V are mentioned in table 1.

Carrier mobility is an important material property necessary for semiconductor device simulation. These essential material properties can be easily computed with Boltzmann DFT software. However, since these DFT

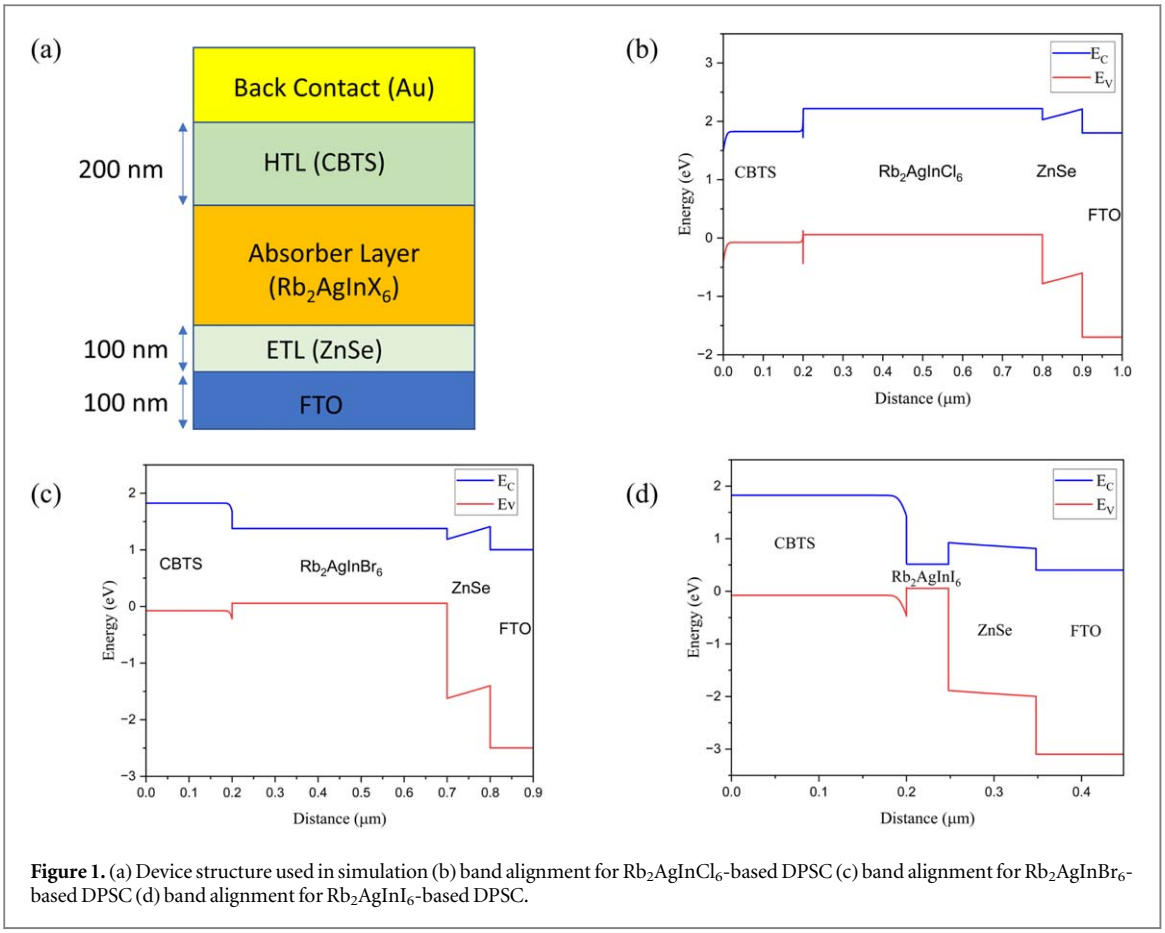

Figure 1. (a) Device structure used in simulation (b) band alignment for $Rb_2AgInCl_6$-based DPSC (c) band alignment for $Rb_2AgInBr_6$-based DPSC (d) band alignment for Rb_2AgInI_6-based DPSC.

Table 1. Various material properties used in device simulation.

Parameters	$Rb_2AgInCl_6$	$Rb_2AgInBr_6$	Rb_2AgInI_6	ZnSe	CBTS	FTO
Thickness (nm)	600	500	120	100	200	100
Band gap, E_g (eV)	2.16	1.32	0.46	2.81	1.9	3.5
Electron affinity, χ (eV)	3.9[a]	3.9[a]	4.5[a]	4.09	3.6	4.5
Dielectric permittivity, $\varepsilon/\varepsilon_0$	2.79	3.24	4.43	8.6	5.4	9.00
CB effective density of state, N_C (cm^{-3})	6.35×10^{18}[a]	5.19×10^{18}[a]	3.31×10^{18}[a]	2.2×10^{18}	2.2×10^{18}	2.2×10^{18}
VB effective density of state, N_V (cm^{-3})	3.09×10^{19}[a]	1.97×10^{19}[a]	1.02×10^{19}[a]	1.8×10^{18}	1.8×10^{19}	1×10^{19}
Electron thermal velocity, V_e ($cm\ S^{-1}$)	1×10^7	1×10^7	1×10^7	1×10^7	1×10^7	1×10^7
Hole thermal velocity, V_h ($cm\ S^{-1}$)	1×10^7	1×10^7	1×10^7	1×10^7	1×10^7	1×10^7
Electron mobility, μ_e ($cm^2\ V^{-1}\ S^{-1}$)	18.57[a]	21.93[a]	33.01[a]	400	30	2×10^3
Hole mobility, μ_h ($cm^2\ V^{-1}\ S^{-1}$)	6.46[a]	9.03[a]	15.00[a]	110	10	2×10^3
Shallow Donor density, N_D (cm^{-3})	6.41×10^{17}[a]	1.15×10^{18}[a]	2.36×10^{18}[a]	1×10^{15}	—	2×10^{19}
Shallow Acceptor density, N_A (cm^{-3})	3.08×10^{20}[a]	1.72×10^{20}[a]	8.37×10^{19}[a]	—	1×10^{18}	—
Defect density (cm^{-3})	1.3×10^{14}[a]	1.3×10^{14}[a]	1.4×10^{13}[a]	1×10^{15}	1×10^{15}	1×10^{15}
References	[1]	[1]	[1]	[8, 14]	[8, 18, 19]	[8, 20]

[a] In This Work

calculations are time-consuming, reporting all these properties in one DFT study of material is often unsuitable to researchers. We can either repeat the DFT calculations or use basic semiconductor equations to derive these properties. To get approximate values of these properties for simulation purposes.

$$\mu_{e/h} = \frac{q\tau_m}{m^*} \tag{2}$$

$$\tau = \frac{L_m}{V_{th}} \tag{3}$$

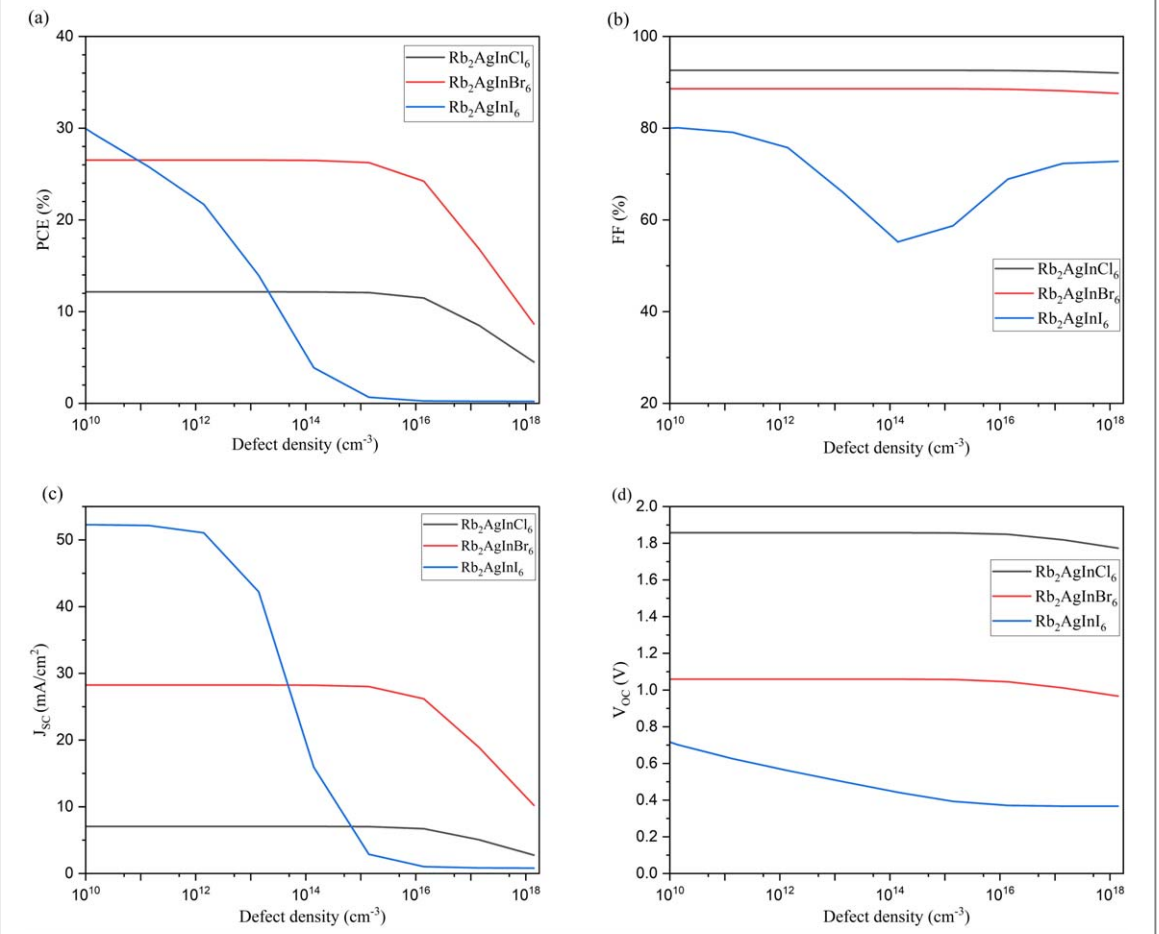

Figure 2. Variation of (a) PCE (b) FF (c) J_{SC} (d) V_{OC} with defect density for Rb_2AgInX_6-based DPSC.

Hence, mobility can be calculated as given below.

$$\mu_{e/h} = \frac{40qa}{m^*_{e/h}V_{th}} \tag{4}$$

Here, $\mu_{e/h}$ is the electron/hole mobility for the respective electron/hole effective masses ($m^*_{e/h}$). τ_m is relaxation time, and L_m is the mean free path. V_{th} is the electron/hole thermal velocity at 300 K (room temperature). The lattice constant (a_0) values are 10.55 A°, 10.90 A°, and 11.72 A° for $Rb_2AgIn(Cl/Br/I)_6$ respectively [1]. Electron and hole mobilities were calculated for Rb_2AgInX_6(X = Cl, Br, I) (mentioned in table 1).

Generally, undoped or intrinsic semiconductors have equal electron concentration (n) and hole concentration (p). However, $Rb_2AgIn(Cl/Br/I)_6$ exhibits p-type behavior owing to significant differences in their electron and hole effective masses. The hole concentrations (p) at room temperature were found to be 3.08×10^{20} cm^{-3}, 1.72×10^{20} cm^{-3}, and 8.37×10^{19} cm^{-3} for $Rb_2AgIn(Cl/Br/I)_6$, respectively [21]. Also, the relation between n and p is given by the following equation.

$$np = \sqrt{N_C N_V}\, e^{-E_g/KT} \tag{5}$$

Using this equation, the value of n can be calculated. Doping an intrinsic semiconductor changes the concentration of charge carriers, and based on the dopant used, a p-type or n-type semiconductor is formed. Since Rb_2AgInX_6 is a p-type semiconductor, Donor density (N_D) and acceptor density (N_A) can be replaced by n and p values, respectively. This ensures that the p-type behavior of the semiconductor is taken into account, and hence, solar cell parameters are closer to experimental results.

3. Results and discussion

3.1. Optimization of defect density (N_t)

We conducted batch calculations using SCAPS-1D to observe the change in characteristics of DPSCs with the defect density (N_t) change within Rb_2AgInX_6 layers. Defect density, N_t, was systematically adjusted in

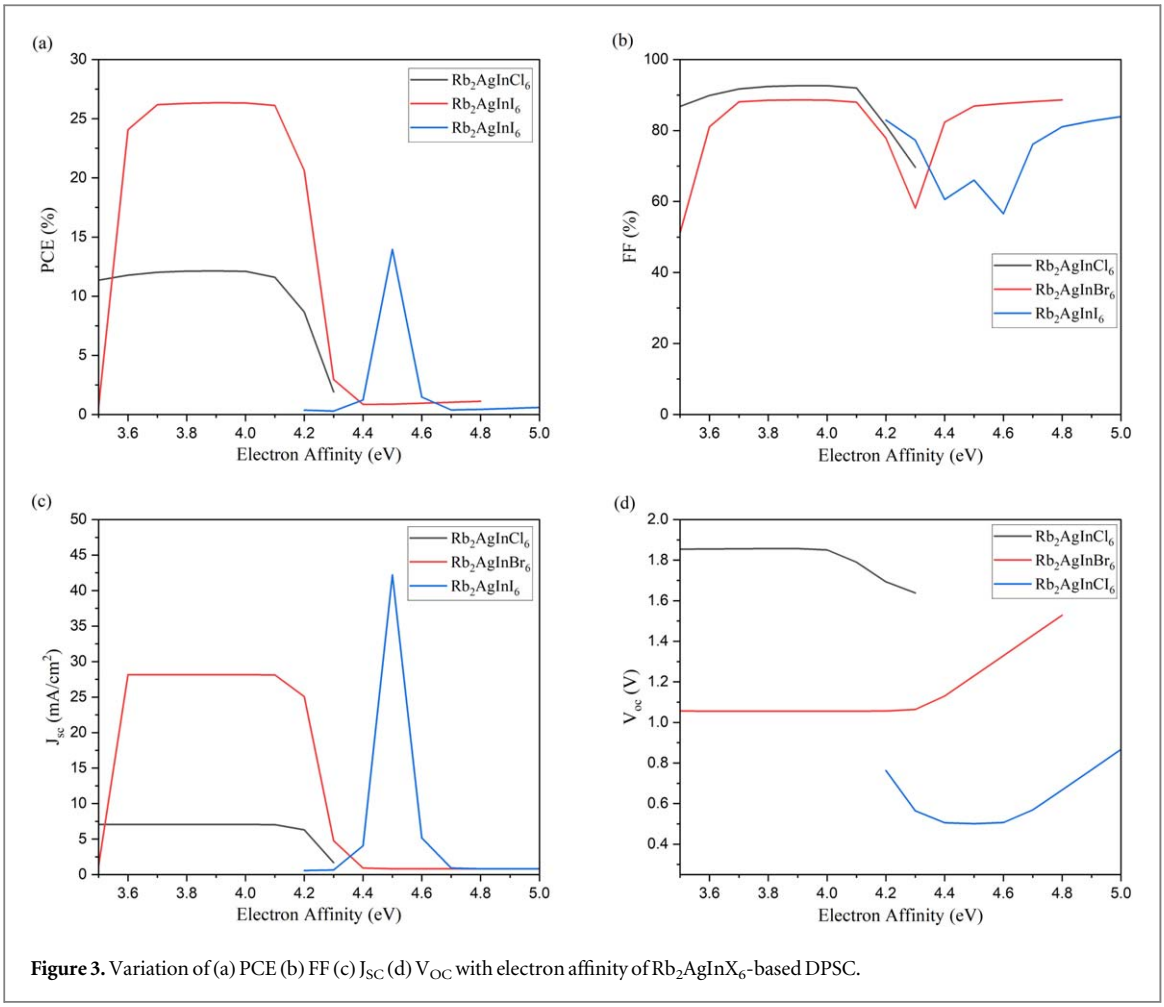

Figure 3. Variation of (a) PCE (b) FF (c) J_{SC} (d) V_{OC} with electron affinity of Rb_2AgInX_6-based DPSC.

increments of 10^1 cm^{-3} between 10^{10} cm^{-3} to 10^{18} cm^{-3}. Figure 2 displays the changes in solar cell characteristics.

Similar trends were seen for $Rb_2AgInCl_6$ and $Rb_2AgInBr_6$-based DPSCs. In both materials, no change in the PCE was seen until the N_t of 10^{11} cm^{-3} was reached. Beyond this point, the PCE experiences a slight decline, followed by a significant drop after reaching 10^{16} cm^{-3} (a drop from 11.48% at 10^{16} to 4.5% at 10^{18} for $Rb_2AgInCl_6$ and from 24.23% at 10^{16} cm^{-3} to 8.66% at 10^{18} cm^{-3} for $Rb_2AgInBr_6$). Similarly, for the short-circuit current (J_{SC}), no change is observed until defect densities of 10^{11} cm^{-3} for both $Rb_2AgInCl_6$ and $Rb_2AgInBr_6$, after which a slight decrease is observed and a drastic reduction after reaching 10^{16} cm^{-3} defect densities (a drop from 6.71 at 10^{16} to 2.76 at 10^{18} for $Rb_2AgInCl_6$ and from 26.18 at 10^{16} cm^{-3} to 10.22 at 10^{18} cm^{-3} for $Rb_2AgInBr_6$). The fill factor (FF) variation was not observed until N_t of 10^{12} cm^{-3} was reached for $Rb_2AgInCl_6$ and $Rb_2AgInBr_6$, with minimal changes afterward. The open-circuit voltage (V_{OC}) remains unchanged until defect densities of 10^{12} cm^{-3} are reached for both materials, with minor alterations afterward. Given these considerations, an optimized N_t of 1.3×10^{14} cm^{-3} is deemed suitable for further simulations of both $Rb_2AgInCl_6$ and $Rb_2AgInBr_6$-based DPSCs.

For Rb_2AgInI_6, a considerable variation in the PCE was seen, along with a rise in defect density. However, a drastic reduction occurred after reaching a N_t of 10^{13} cm^{-3} (from 11.63% at 10^{13} cm^{-3} to 4.8% at 10^{14} cm^{-3} and 0.22% at 10^{18}). There was no noticeable pattern in the FF variation. The J_{SC} did not show any change until a defect density of 10^{14} cm^{-3}; after that, it began to decrease slightly by a few decimal points. Until 10^{13}, the J_{SC} varied slightly, but after 10^{13}, a drastic decrease was observed (31.34 at 10^{13} to 17.87 at 10^{14} to 0.82 at 10^{18}). Furthermore, there was only a slight change in Voc. After thoroughly considering all factors, an optimized defect density of 1.4×10^{13} cm^{-3} will be employed for subsequent simulations of Rb_2AgInI_6-based DPSC. This decision is based on observations indicating a significant drop in DPSC parameters beyond this defect density value.

The N_t of the absorber layer is a crucial factor significantly affecting device efficiency. A high concentration of defects leads to increased recombination due to pinhole formation, a higher degradation rate of the film, reduced stability, and an overall decline in device performance [14].

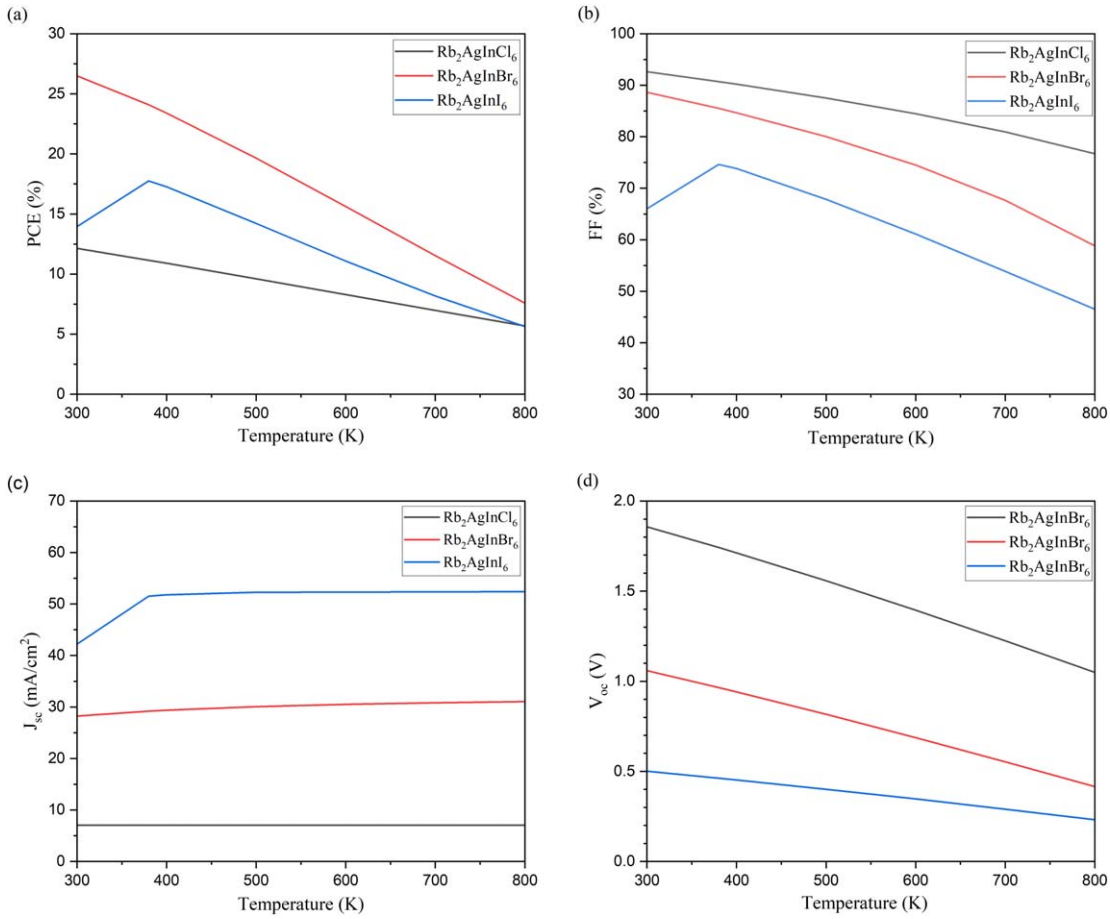

Figure 4. Variation of (a) PCE (b) FF (c) J_{SC} (d) V_{OC} with operating temperature of Rb_2AgInX_6-based DP.

3.2. Optimization of electron affinity

We conducted batch calculations using SCAPS-1D to optimize the electron affinity of the absorber layers. Every material works optimally at its particular electron affinity, making it a crucial material property. The electron affinity was adjusted between 3.5 and 5 eV in 16 steps, and device parameters were recorded

Similar trends in electron affinity variation were observed for $Rb_2AgInCl_6$ and $Rb_2AgInBr_6$. Figure 3 shows that both materials exhibit a responsive behavior within specific electron affinity ranges, with $Rb_2AgInCl_6$ active between 3.5 to 4.3 eV and $Rb_2AgInBr_6$ spanning from 3.5 to 4.8 eV. However, beyond these ranges, convergence failure is encountered. After certain electron affinities, both materials experience significant decreases in device parameters. For instance, in $Rb_2AgInCl_6$, a notable decline occurs after 4.1 eV, with the PCE dropping from 11.60% at 4.1 eV to 1.9% at 4.3 eV while in $Rb_2AgInBr_6$, a significant reduction is noted after 4.2 eV, with the PCE dropping from 20.62% at 4.2 eV to 1.12% at 4.8 eV. Similar declines beyond these critical points were observed for the J_{SC} for both materials (7.05 mA cm^{-2} at 4.1 eV to 1.68 mA cm^{-2} at 4.3 eV for $Rb_2AgInCl_6$ and 25.06 mA cm^{-2} at 4.2 eV to 0.92 mA cm^{-2} at 4.8 eV for $Rb_2AgInBr_6$). This sharp decline in device parameters accounts for the convergence failure observed beyond 4.3 eV for $Rb_2AgInCl_6$ and beyond 4.8 eV for $Rb_2AgInBr_6$. The FF for both materials increases initially up to 3.9 eV and then decreases afterward. However, for $Rb_2AgInBr_6$-based DPSC, the FF increases again from 4.4 eV onward until convergence failure, as shown in figure 4. For $Rb_2AgInCl_6$, V_{OC} saw a slight continuous decrease, while for $Rb_2AgInBr_6$, V_{OC} initially decreased slightly up to 3.9 eV but started to increase from here onwards. Optimal device parameters are achieved at an electron affinity of 3.9 eV for both materials, i.e. $Rb_2AgInCl_6$ (where a PCE of 12.14%, FF of 92.63%, J_{SC} of 7.05 mA cm^{-2}, and V_{OC} of 1.85 V were achieved) and $Rb_2AgInBr_6$ (where a PCE of 26.34%, FF of 88.61%, J_{SC} of 28.15 mA cm^{-2}, and V_{OC} of 1.05 V were achieved).

3.3. Optimization of thickness of absorber layer

The absorber layer thickness was optimized by performing batch calculations ranging from 100 nm to 1600 nm in 16 steps, and device parameters were recorded. The changes in different DPSC parameters with thickness are depicted in figure 5.

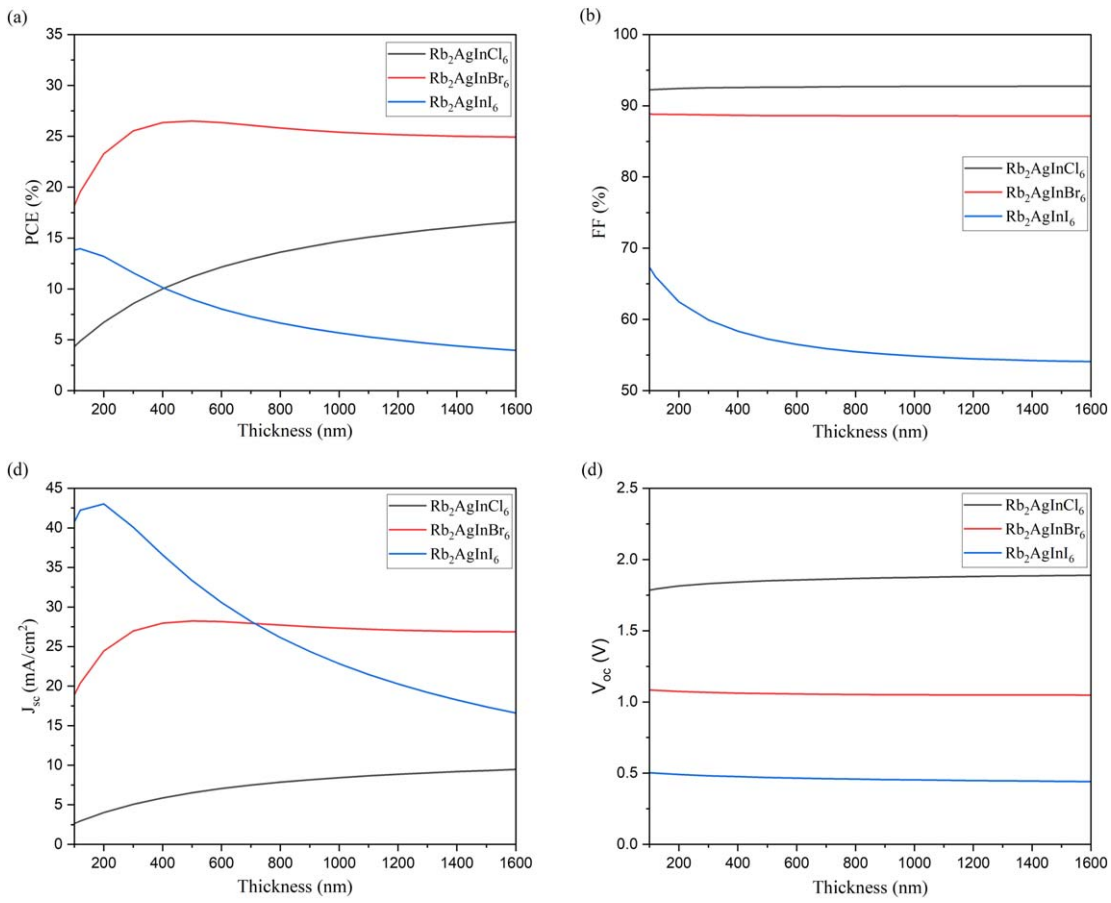

Figure 5. Variation of (a)PCE (b) FF (c) J_{SC} (d) V_{OC} with thickness of Rb_2AgInX_6-based DPSC.

For $Rb_2AgInCl_6$, a continuous increase in all device parameters was noted with the increased thickness of the absorber. However, the most significant enhancements were realized up to a thickness of 600 nm, beyond which the improvements in PCE became marginal. At the optimal thickness of 600 nm, the $Rb_2AgInCl_6$-based DPSC exhibits a PCE of 12.14%, FF of 92.63%, J_{SC} of 7.06 mA cm^{-2}, and V_{OC} of 1.86 V. Conversely, for $Rb_2AgInBr_6$, while both PCE and J_{SC} initially increased and peaked at a thickness of 500 nm, the FF and V_{OC} exhibited negligible variations, with only slight decrements observed. Consequently, the optimized thickness for the $Rb_2AgInBr_6$-based DPSC was found to be 500 nm, where it achieved a PCE of 26.49%, FF of 88.62%, J_{SC} of 28.23 mA cm^{-2}, and V_{OC} of 1.06 V.

For Rb_2AgInI_6, all device parameters exhibited a continuous decline with the rise in absorber thickness. This indicates that the optimum thickness must be in proximity of 100 nm. So, various values above and below 100 nm were considered, and finally, the optimum thickness was found at 120 nm. At this thickness, the Rb_2AgInI_6-based DPSC exhibited a PCE of 13.95%, FF of 66.01%, J_{SC} of 42.22 mA cm^{-2}, and V_{OC} of 0.50 V.

The thickness of the active layer is crucial for optimizing the PCE of PSCs. Proper selection of this thickness is essential to maximize current density and minimize reverse saturation current. In thicker absorber layers, a reduced electric field influences the recombination behavior of charge carriers, which leads to a decrease in PCE [22]. Fill factor (FF) is inversely related to the absorber's thickness, as increased thickness leads to higher series resistance and greater internal power dissipation. The open-circuit voltage (V_{OC}) decreases with increased thickness (figure 5) due to a rise in dark saturation current, which simultaneously increases charge carrier recombination [15]. Table 2 depicts the different device structures optimized and their device performance parameters.

3.4. Effect of operating temperature

In SCAPS-1D, the operating temperature of devices was varied from 300 K to 800 K, and changes in device characteristics were recorded and studied.

For $Rb_2AgInCl_6$ and $Rb_2AgInBr_6$, all device parameters decreased with an increase in temperature (figure 4). For Rb_2AgInI_6, however, the device parameters initially increased until 380 K (PCE of 17.75%, FF of 74.62%, J_{SC}

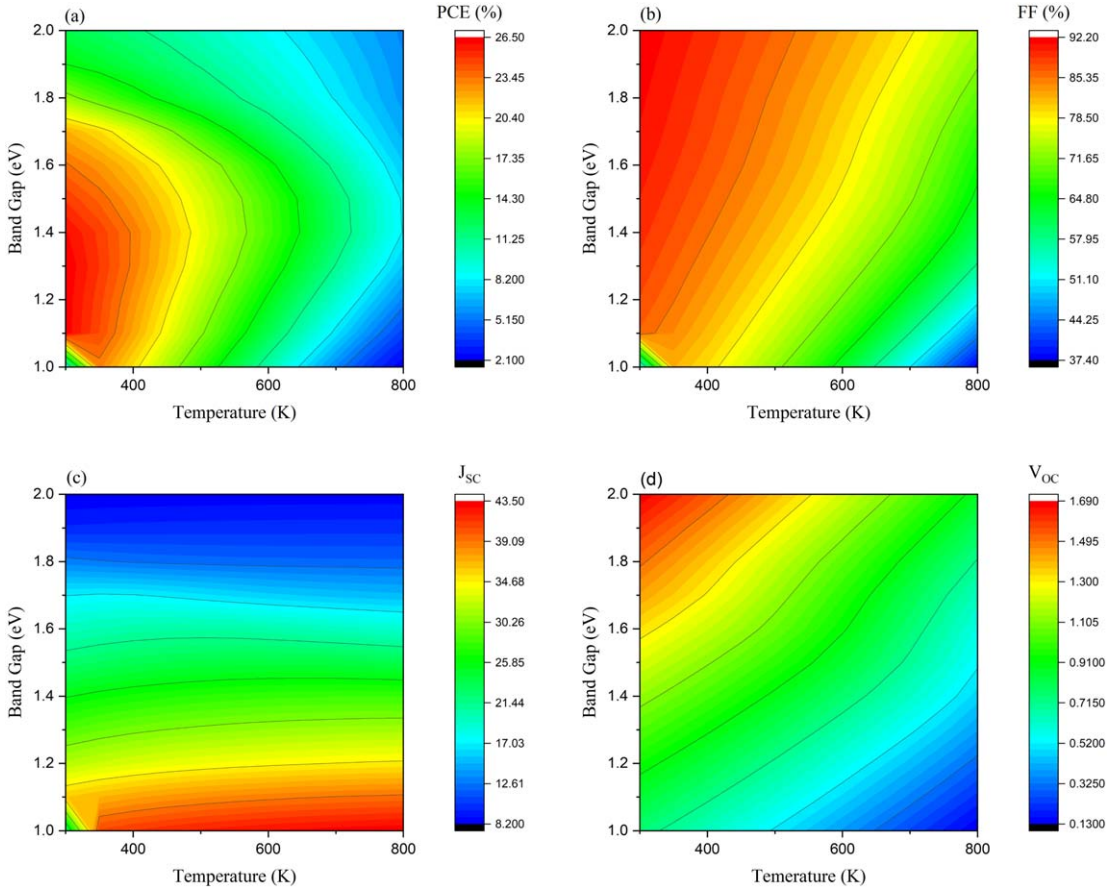

Figure 6. Contour graphs illustrating the impact of band gap and temperature on (a) PCE (b) FF (c) J_{SC} (d) V_{OC}.

Table 2. Device structure along with device performance parameters for Rb_2AgInX_6-based DPSCs.

Device structure	PCE (%)	FF (%)	J_{SC} (mA/cm^2)	V_{OC} (V)
FTO/ZnSe/$Rb_2AgInCl_6$/CBTS/Au	12.14	92.63	7.06	1.86
FTO/ZnSe/$Rb_2AgInBr_6$/CBTS/Au	26.49	88.62	28.23	1.06
FTO/ZnSe/Rb_2AgInI_6/CBTS/Au	13.95	66.01	42.22	0.50

of 51.52 mA cm^{-2}, and V_{OC} of 0.46 V), and then parameters started decreasing again. This increase in PCE can be explained by the lower bandgap of Rb_2AgInI_6, which suggests absorption in the infrared region [1, 23].

The operating temperature significantly influences the DPSC efficiency. Solar panels are usually mounted outdoors and often work at temperatures higher than 300 K. Increasing the temperature has been reported to increase structure strain and stress, leading to a rise in interfacial defects, disorder, and poor layer interconnectivity. An increase in temperature also affects the concentration and mobilities of electrons and holes, as well as the PCE of the device. A slight rise in J_{SC} is also brought on by rising temperatures, which is brought on by a reduction in the energy band gap and the formation of extra electron–hole pairs. The decrease in V_{OC} with increasing temperature might be attributed to increased series resistance, decreased carrier diffusion length, and increased interfacial defects [24–26].

3.5. Optimization of band gap along with its temperature stability

Previous studies reported that by carefully adjusting the band gap, thermodynamically stable $Cs_2AgInBr_5Cl$ may be obtained from $Cs_2AgInBr_6$ by partially replacing chlorine [8, 27]. Furthermore, it has been noted that $Cs_2AgInBr_5Cl$ and $Cs_2AgInBr_6$ have comparable optoelectronic characteristics [8, 27]. So, we optimized the band gap (E_g) and studied their temperature dependence. Contour plots were plotted to represent these variations, as shown in figure 6.

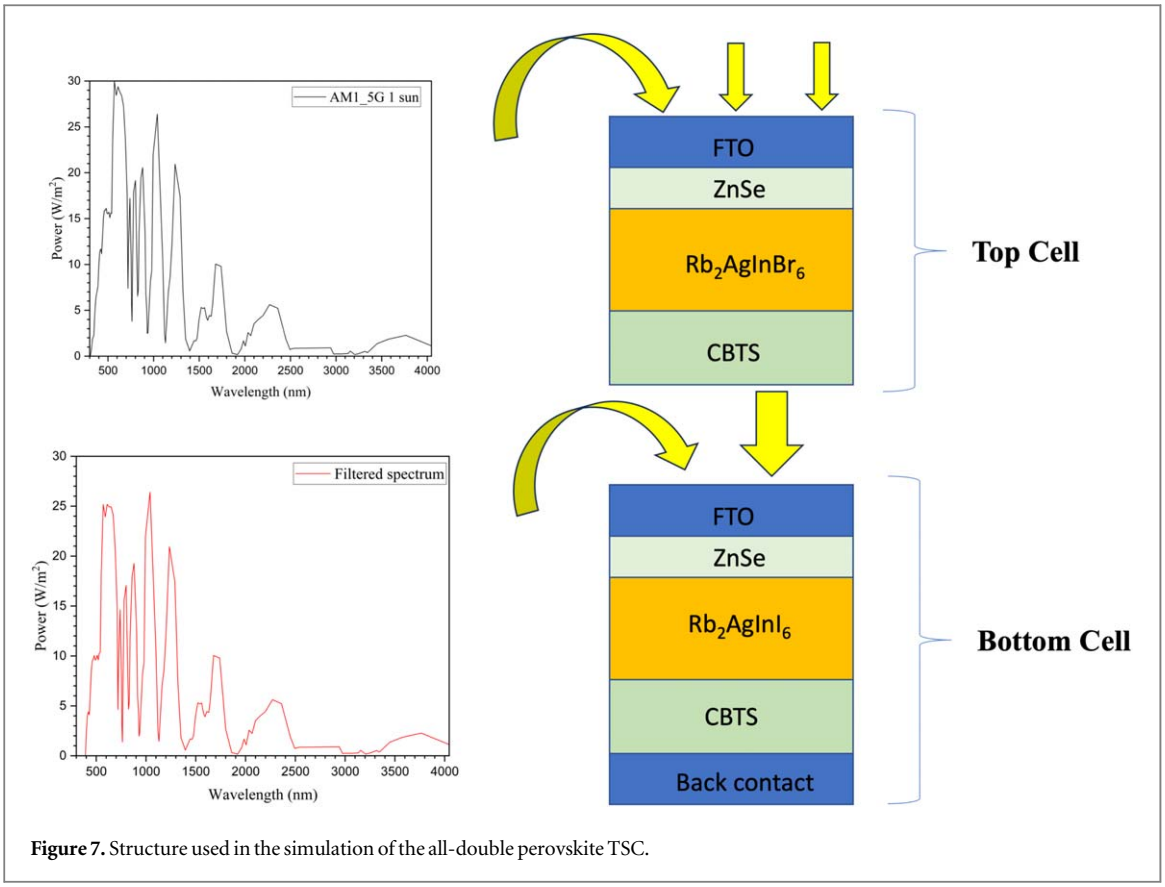

Figure 7. Structure used in the simulation of the all-double perovskite TSC.

It is observed that with an increase in band gap (E_g), the percentage drop in PCE, along with elevation in temperature (300 K to 800 K), decreases, thereby indicating more temperature stability in the device. The highest PCE is observed around E_g of 1.4 eV. Also, with an increase in E_g, the percentage rise/drop in J_{SC}, along with the elevation in temperature (300 K to 800 K), decreases in general. The slightest change in Jsc was observed at an E_g of 1.6 eV.

Also, with an increase in E_g, the percentage drop in FF, along with the elevation in temperature (300 K to 800 K), also decreases. The highest value of FF at a particular temperature is observed at 2 eV. It is also observed that the percentage drop in $V_{OC,}$ along with the elevation in temperature (300 K to 800 K), decreases with an increase in E_g. Also, at a particular temperature, the highest value of V_{OC} is observed at a band gap of 2 eV (V_{OC} continuously increases with an increase in the E_g).

Considering these variations in device parameters, a E_g of 1.4 eV is suggested for better device performance. At the same time, tuning the band gap can increase device stability without compromising significant device performance.

4. Simulation towards all double perovskite tandem solar cell

A TSC structure, with a wide band gap $Rb_2AgInBr_6$-based top cell and a lower band gap Rb_2AgInI_6-based bottom cell, is used for simulation. Two-terminal TSCs stacking two sub-cells create a reverse-biased p–n junction at their interface, limiting current flow across the device. [9, 28]. To resolve this problem, the current matching approach is used, which involves the utilization of a tunnel recombination junction (TRJ). This TRJ guarantees that there is a balanced and equal flow of current through both subcells in a TSC arrangement. Previous studies shows the influence and simulation of TRJ especially in Silicon heterojunction (SHJ) based TSC [29]. However, because of the constraints of SCAPS 1D software, simulating a tandem structure is rather complex, and such TRJ is not possible. Thus, we assume an ideal TRJ layer that does not experience any optoelectronic losses. In this scenario, we simulate the top and bottom subcells separately, each with a distinct illumination spectrum. The upper subcell is exposed to the typical AM1.5G spectrum, while the filtered spectrum obtained after transmission through the upper subcell is directed to the lower subcell. This is done to achieve the necessary current matching and, thereafter, to produce a TSC J–V curve. This is a widely used method to simulate TSCs using SCAPS-1D [9, 28, 30–32].

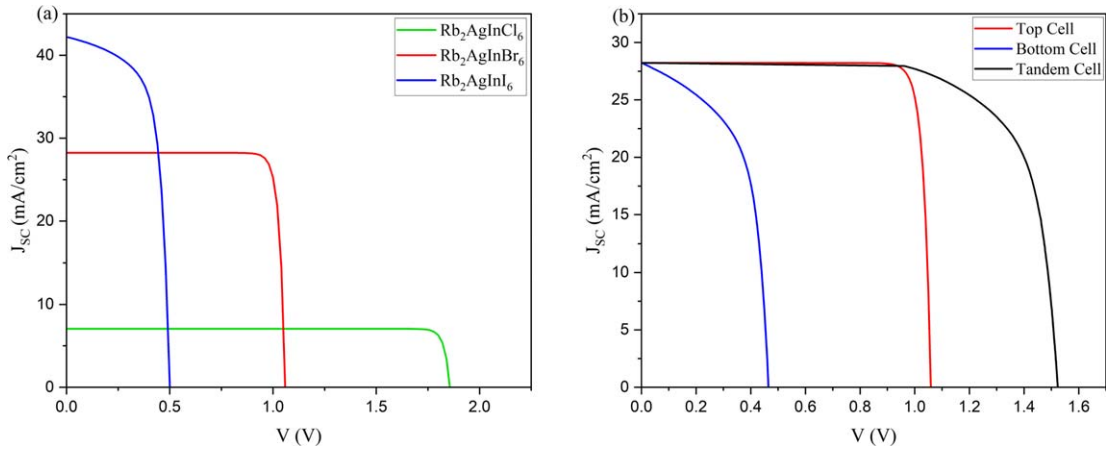

Figure 8. J versus V curves of (a) Rb_2AgInX_6-based DPSCs (b) top, bottom and tandem DPSCs.

Table 3. Device calibration to find current matching condition for optimization of Tandem solar cell.

Device	Thickness (nm)	PCE (%)	FF (%)	J_{SC} (mA/cm^2)	V_{OC} (V)
$Rb_2AgInBr_6$- Top Cell AM1.5G spectrum	500—	26.49	88.62	28.23	1.06
Rb_2AgInI_6- Bottom Cell AM1.5G spectrum	120	13.95	66.01	42.22	0.50
Optimized Rb_2AgInI_6-Bottom Cell Filtered spectrum	516	9.47	57.21	28.23	0.46
$Rb_2AgInBr_6$ /Rb_2AgInI_6-Tandem cell	500 (Top)/516 (Bottom)	38.70	71.37	28.23	1.52

$$S(\lambda) = S_0(\lambda)\exp\left(\sum_{i=1}^{4}(\alpha_{material_i}(\lambda)d_{material_i})\right) \quad (6)$$

Here, $S_o(\lambda)$ represents the standard AM1.5G spectrum, $S(\lambda)$ represents the spectrum obtained after transmission through the top cell, $\alpha(\lambda)$ is the absorption coefficient, and d is the thickness of different layers of the top cell. The material$_1$, material$_2$, material$_3$ and material$_4$ represent FTO, ZnSe, $Rb_2AgInBr_6$, and CBTS layers, respectively.

The top cell was simulated with the optimized parameters mentioned in table 1. Meanwhile, the bottom cell was simulated under the filtered spectrum obtained using (6). The proposed device structure for TSC simulation is represented in figure 7. The current matching for both cells, which is required in a 2-terminal TSC, was achieved by optimizing the thickness of the Rb_2AgInI_6-based DP bottom cell, as mentioned in table 3. After satisfying the current matching condition for both subcells, the series connection was made between the cells using SCAPS-1D to simulate the tandem solar cell. All other parameters for all layers were the same, as mentioned in table 1 earlier.

4.1. Analysis of final optimized solar cells

Figure 8 displays the J–V curves of optimized cells. The $Rb_2AgInCl_6$-based DPSC shows very high V_{OC} but a smaller J_{SC}, which results in moderate device parameters (PCE 13.95% table 2). On the other hand, Rb_2AgInI_6 shows a very high J_{SC} but a smaller V_{OC} again, resulting in a moderate device performance (PCE 12.14%, table 2). Meanwhile, $Rb_2AgInBr_6$-based DPSC shows a balanced and high JSC and V_{OC}, giving the highest performance among the Rb_2AgInX_6-based DPSCs.

Similarly, the J–V curve of TSCs showcases the reason for enhanced PCE. Due to series tandem connection, the voltage of the TSC is the cumulative sum of the voltages of top and bottom cells under current matching conditions (PCE of 38.70% table 3).

The ratio of carriers captured by the solar cell to photons incident on the cell with a certain energy is known as the Quantum Efficiency (Q.E.). The decrease in Q.E. at higher wavelengths can be explained by near-surface recombination and decreased absorption at longer wavelengths. These changes in Q.E. are depicted by the figure 9 through Q.E.-Wavelength curves for Rb_2AgInX_6 (X = Cl, Br, I) based DPSC. The Q.E. was varied from 300 nm to 900 nm and the curves shows the absorption in UV-Visible and near Infrared regions.

Table 4. Comparison with some recently reported results.

Device structure	PCE (%)	FF (%)	J_{SC} (mA/cm^2)	V_{OC} (V)	References	Type of work
FTO/ZnSe/$Cs_2AgInBr_6$/CBTS/Au	26.90	83.49	27.54	1.17	[8]	Simulation
FTO/SnO_2/$Cs_2CuBiCl_6$/Cu_2O/Au	1.87	47	4.05	0.98	[33]	Experimental
FTO/TiO_2/$Cs_2AgBiBr_6$/Spiro-OMeTAD/Au	3.48	73	5.13	0.92	[34]	Experimental
FTO/TiO_2/$Cs_2Ag_{0.95}Ga_{0.05}BiBr_6$/Spiro-OMeTAD/Au	4.52	80	6.01	0.94	[34]	Experimental
FTO/ZnSe/$Rb_2AgInCl_6$/CBTS/Au	12.14	92.63	7.06	1.86	This work	Simulation
FTO/ZnSe/Rb2AgInBr$_6$/CBTS/Au	26.49	88.62	28.23	1.06	This work	Simulation
FTO/ZnSe/Rb_2AgInI_6/CBTS/Au	13.95	66.01	42.22	0.50	This work	Simulation
Tandem Device (Top cell/Bottom cell)						
$Cs_2AgBi_{0.75}Sb_{0.25}Br_6$/silicon	37.14	88.12	19.15	2.201	[35]	Simulation
$Cs_{0.35}FA_{0.65}PbI_{1.8}Br_{1.2}$/$MA_{0.3}FA_{0.7}Pb_{0.5}Sn_{0.5}I_3$	24.80	79.4	15.04	2.02	[36]	Experimental
$Cs_2AgBiBr_6$/$Cs_4CuSb_2Cl_{12}$	28.08	87.67	12.78	2.47	[35]	Simulation
Cs_2BiAgI_6/La_2NiMnO_6	30.25	79.74	24.11	1.68	[37]	Simulation
$Rb_2AgInBr_6$/Rb_2AgInI_6	38.70	71.37	28.23	1.52	This work	Simulation

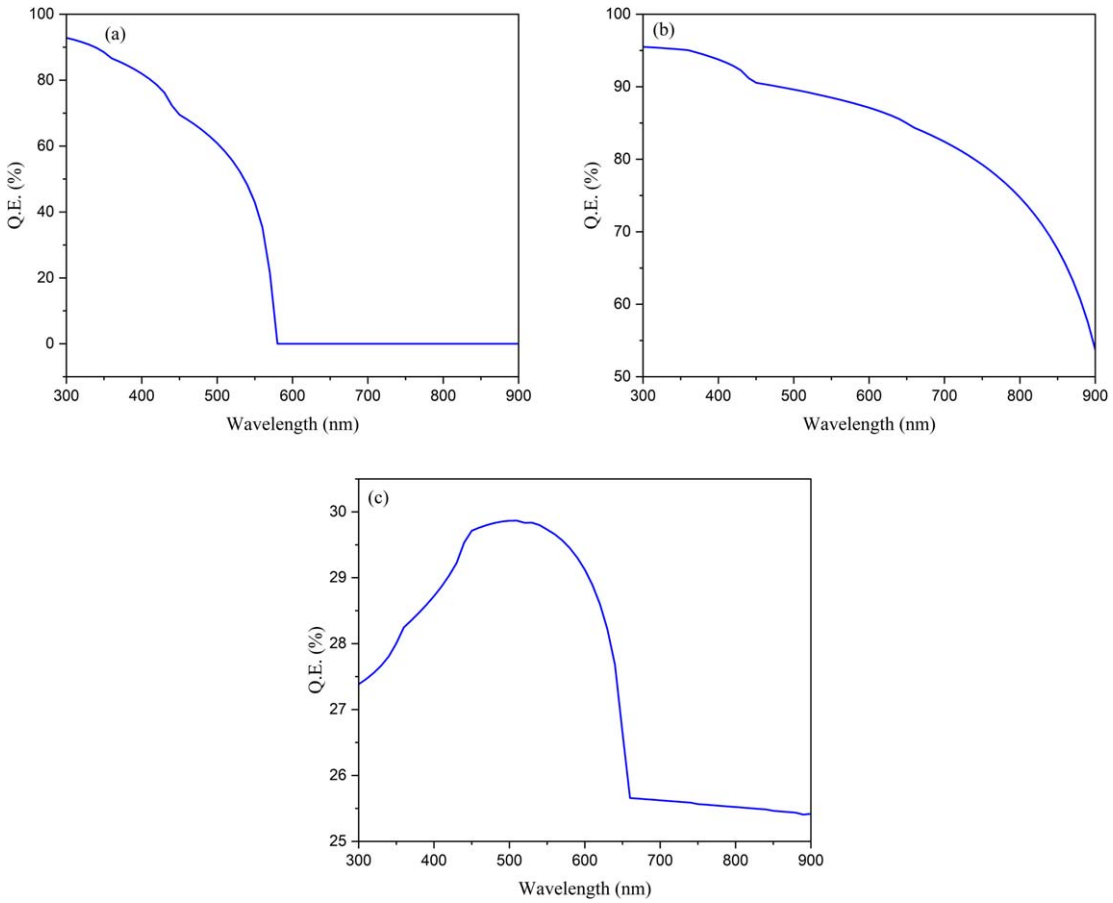

Figure 9. Q.E.-Wavelength Curve of (a)$Rb_2AgInCl_6$ (b)$Rb_2AgInBr_6$ and (c) Rb_2AgInI_6.

4.2. Comparison with recently reported results

Table 4 presents a comparison between this work and various recently reported experimental and simulated results of different photovoltaic devices, including TSCs. The performance metrics of photovoltaic devices, such as PCE, FF, J_{SC}, and V_{OC}, from this study are comparable to those found in the literature. Our findings suggest that the lead-free all-DPTSC can theoretically achieve a PCE of over 38.70%. In terms of performance, this tandem device structure emerges as a promising alternative to traditional silicon-based solar cells, providing higher efficiency, improved stability, and more cost-effective production. While 1D simulations are good for investigating material choices future work should also consider effect of cell area [38].

5. Conclusion

From this study, we can conclude that Rb_2AgInX_6(x = Cl, Br, I) is an effective DP absorber with huge potential for photovoltaic applications. In this study, we calculated some essential properties for the Rb_2AgInX_6 absorber layer for DPSC simulation, like the density of states for conduction and valance bands, carrier concentration, and carrier mobility (electrons and holes), as mentioned in table 1. In this study, we obtained optimized defect densities of 1.3×10^{14}, 1.3×10^{14}, and 1.4×10^{13} cm^{-3} for Rb_2AgInX_6 (X = Cl, Br, I respectively). The optimized electron affinities are 3.9, 3.9, and 4.5 eV for Rb_2AgInX_6 (X = Cl, Br, I, respectively). Meanwhile, optimized thickness values were obtained as 600, 500, and 120 nm for Rb_2AgInX_6 (X = Cl, Br, I, respectively). The optimized Rb_2AgInX_6(X = Cl, Br, I respectively) based DPSCs devices gave a PCE of 12.14, 26.83, and 13.95%. The effect of operating temperature was studied, and it was observed that all device parameters (PCE, J_{SC}, FF, V_{OC}) decreased with an increase in temperature for $Rb_2AgInCl_6$ and $Rb_2AgInBr_6$. However, for Rb_2AgInI_6. The device parameters initially increased until 380 K, then the parameters started decreasing again. We then optimized the band gap and studied their temperature stability. It was concluded that a band gap of 1.4 eV is suggested for enhanced device efficiency. Meanwhile, tuning band baps can increase the device's stability without compromising significant performance. In the end, we simulated an all-double perovskite TSC

with $Rb_2AgInBr_6$-based top cell and Rb_2AgInI_6-based bottom cell, which resulted in a PCE of 38.70%, which is a significant enhancement to the single junction device.

This study highlights the need to further explore the Rb_2AgInX_6-based DPSCs and all double perovskite tandem solar cells, specifically through experimental synthesis, to build on the results concluded in the simulation-based results provided in this study. Future experimental investigations may use this study's optimized and calculated parameters.

Acknowledgments

The authors thank Professor Marc Burgelman (University of Gent, Belgium) for providing SCAPS-1D software. Authors are grateful to Delhi Technological University, Delhi for funding this research.

Data availability statement

All data that support the findings of this study are included within the article (and any supplementary files).

Data availability

Data has been included in the manuscript, and further information created during or analyzed during the current study will be made available upon request.

ORCID iDs

Vishal Deswal https://orcid.org/0009-0007-8068-8966
Sarita Baghel https://orcid.org/0009-0003-2746-0453

References

[1] Kattan N A, Mahmood Q, Nazir G, Rehman A, Sfina N, Al-anazy M mana, Sofi S A, Morsi M and Amin M A 2023 Modifying electronic bandgap by halide ions substitution to investigate double perovskites Rb2AgInX6 (X = Cl, Br, I) for solar cells applications and thermoelectric characteristics *Mater Today Commun* **34** 105166
[2] Filip M R, Hillman S, Haghighirad A A, Snaith H J and Giustino F 2016 Band gaps of the lead-free halide double perovskites $Cs_2BiAgCl_6$ and $Cs_2BiAgBr_6$ from theory and experiment *J. Phys. Chem. Lett.* **7** 2579–85
[3] Al-Muhimeed T I, Aljameel A I, Mera A, Saad S, Nazir G, Albalawi H, Bouzgarrou S, Hegazy H H and Mahmood Q 2022 First principle study of optoelectronic and mechanical properties of lead-free double perovskites Cs_2SeX_6 (X = Cl, Br, I) *Journal of Taibah University for Science* **16** 155–62
[4] Zelai T, Rouf S A, Mahmood Q, Bouzgarrou S, Amin M A, Aljameel A I, Ghrib T, Hegazy H H and Mera A 2022 First-principles study of lead-free double perovskites Ga2PdX6 (X = Cl, Br, and I) for solar cells and renewable energy *Journal of Materials Research and Technology* **16** 631–9
[5] Volonakis G, Filip M R, Haghighirad A A, Sakai N, Wenger B, Snaith H J and Giustino F 2016 Lead-free halide double perovskites via heterovalent substitution of noble metals *J. Phys. Chem. Lett.* **7** 1254–9
[6] Slavney A H, Hu T, Lindenberg A M and Karunadasa H I 2016 A bismuth-halide double perovskite with long carrier recombination lifetime for photovoltaic applications *J. Am. Chem. Soc.* **138** 2138–41
[7] Volonakis G, Haghighirad A A, Milot R L, Sio W H, Filip M R, Wenger B, Johnston M B, Herz L M, Snaith H J and Giustino F 2017 $Cs_2InAgCl_6$: a new lead-free halide double perovskite with direct band gap *J. Phys. Chem. Lett.* **8** 772–8
[8] Deswal V, Kaushik S, Kundara R and Baghel S 2024 Numerical simulation of highly efficient Cs2AgInBr6-based double perovskite solar cell using SCAPS 1D *Materials Science and Engineering:* B **299** 117041
[9] Madan J, Singh K and Pandey R 2021 Comprehensive device simulation of 23.36% efficient two-terminal perovskite-PbS CQD tandem solar cell for low-cost applications *Sci. Rep.* **11** 19829
[10] Vos A D 1980 Detailed balance limit of the efficiency of tandem solar cells *J. Phys. D: Appl. Phys.* **13** 839–46
[11] Martí A and Araújo G L 1996 Limiting efficiencies for photovoltaic energy conversion in multigap systems *Sol. Energy Mater. Sol. Cells* **43** 203–22
[12] Burgelman M, Nollet P and Degrave S 2000 Modelling polycrystalline semiconductor solar cells *Thin Solid Films* **361–362** 527–32
[13] Kundara R and Baghel S 2023 Device modelling of lead free (CH3NH3)2CuX4 based perovskite solar cells using SCAPS simulation *Opt. Quantum Electron.* **55** 968
[14] Sinha N K, Ghosh D S and Khare A 2022 Role of built-in potential over ETL/perovskite interface on the performance of HTL-free perovskite solar cells *Opt Mater (Amst)* **129** 112517
[15] Sawicka-Chudy P, Starowicz Z, Wisz G, Yavorskyi R, Zapukhlyak Z, Bester M, Głowa Ł, Sibiński M and Cholewa M 2019 Simulation of TiO_2/CuO solar cells with SCAPS-1D software *Mater. Res. Express* **6** 085918
[16] Huang L *et al* 2016 Electron transport layer-free planar perovskite solar cells: further performance enhancement perspective from device simulation *Sol. Energy Mater. Sol. Cells* **157** 1038–47
[17] Menedjhi A, Bouarissa N, Saib S and Bouamama K 2021 Halide double perovskite Cs2AgInBr6 for photovoltaic's applications: optical properties and stability *Optik (Stuttg)* **243** 167198

[18] Hossain M K, Rubel M H K, Toki G F I, Alam I, Rahman M F and Bencherif H 2022 Effect of various electron and hole transport layers on the performance of $CsPbI_3$ -based perovskite solar cells: a numerical investigation in DFT, SCAPS-1D, and wxAMPS frameworks *ACS Omega* **7** 43210–30
[19] Khattak Y H, Baig F, Toura H, Beg S and Soucase B M 2019 CZTSe kesterite as an alternative hole transport layer for MASnI3 perovskite solar cells *J. Electron. Mater.* **48** 5723–33
[20] Kibbou M, Haman Z, Khossossi N, Essaoudi I, Ainane A and Ahuja R 2023 Computational insights into the superior efficiency of Cs2AgGa(Cl, Br)6 double halide perovskite solar cells *Mater. Chem. Phys.* **294** 126978
[21] Hnuna L and Pachuau Z 2023 Electronic, optical and thermoelectric properties of halide double perovskites Rb_2 $AgInX_6$ (X = Cl, Br, I) *Phys. Scr.* **98** 035814
[22] Meng X, Tang T, Zhang R, Liu K, Li W, Yang L, Song Y, Ma X, Cheng Z and Wu J 2022 Optimization of germanium-based perovskite solar cells by SCAPS simulation *Opt Mater (Amst)* **128** 112427
[23] Ibrahim, Shoukat A, Aslam F and Israr Ur Rehman M 2024 Emerging trends in low band gap perovskite solar cells: materials, device architectures, and performance optimization *Mol. Phys.* **122** e2316273
[24] Kundara R and Baghel S 2024 Predictive design of KSnI3-based perovskite solar cells using SCAPS and machine learning model *Materials Science and Engineering:* B **307** 117536
[25] Kundara R and Baghel S 2024 Performance analysis of LaFeO3 perovskite solar cells: a theoretical and experimental study *Solid State Commun.* **389** 115590
[26] Abdul Ghani I B, Khalid M, Yan H, Kashif M, Nawaz B and Wang J 2024 Boosting KSnI3-based perovskite solar cell efficiency by 22.78% through optimized charge transport and eco-friendly buffer layer *J. Mater. Sci.* **59** 14547–72
[27] Liang Y 2021 Exploring inorganic and nontoxic double perovskites Cs2AgInBr6(1−x)Cl6x from material selection to device design in material genome approach *J. Alloys Compd.* **862** 158575
[28] Burdick J and Glatfelter T 1986 Spectral response and I–V measurements of tandem amorphous-silicon alloy solar cells *Sol. Cells* **18** 301–14
[29] Madaka R, Kumar D, Singh A K, Seraj Uddin M and Kumar Rath J 2021 Tunnel recombination junction influence on the a-Si:H/SHJ tandem solar cell *Mater. Today Proc.* **39** 1970–3
[30] Kim K, Gwak J, Ahn S K, Eo Y-J, Park J H, Cho J-S, Kang M G, Song H-E and Yun J H 2017 Simulations of chalcopyrite/c-Si tandem cells using SCAPS-1D *Sol. Energy* **145** 52–8
[31] Gupta G K and Dixit A 2018 Theoretical studies of single and tandem Cu2ZnSn(S/Se)4 junction solar cells for enhanced efficiency *Opt Mater (Amst)* **82** 11–20
[32] Islam M T, Jani M R, Islam A F, Shorowordi K M, Chowdhury S, Nishat S S and Ahmed S 2021 Investigation of $CsSn_{0.5}$ $Ge_{0.5}$ I_3 -on-Si tandem solar device utilizing SCAPS simulation *IEEE Trans. Electron Devices* **68** 618–25
[33] Neelu N, Pandey N and Chakrabarti S 2023 Synthesis, structural and optical properties of lead free Cs2CuBiCl6: a potential & promising eco-friendly double perovskite for solar cell applications *Opt Mater (Amst)* **143** 114250
[34] Khan I-ul-haq, Ullah A, Mujtaba A, Almutairi B S, Shahid W, Ali A and Choi J R 2024 Bandgap reduction and efficiency enhancement in Cs_2 $AgBiBr_6$ double perovskite solar cells through gallium substitution *RSC Adv.* **14** 5440–8
[35] Kumar P and Kumar A 2024 Double perovskite tandem solar cells: design and performance investigation of the Use of CABB and CCSC as top and bottom cell absorber materials *J. Electron. Mater.* **53** 2736–52
[36] Chu Q-Q, Cheng B and Fang B 2022 Scalable and efficient all-perovskite tandem solar cells *Matter* **5** 2584–6
[37] Prasanna J L, Kumar A, M. R K, Gayathri K, Santhosh C, Aswin Kumer S V, Mohan E and Udayakumar S 2024 Enhanced efficiency of tandem perovskite solar cells utilizing Cs_2 $BiAgI_6$ and La_2 $NiMnO_6$ double perovskite absorbers with optimized charge transport layers *Int. J. Energy Res.* **2024** 3942154
[38] Fell A, Schön J, Schubert M C and Glunz S W 2017 The concept of skins for silicon solar cell modeling *Sol. Energy Mater. Sol. Cells* **173** 128–33

Archives of Computational Methods in Engineering
https://doi.org/10.1007/s11831-025-10238-3

REVIEW

Comprehensive Survey on Computational Techniques for Brain Tumor Detection: Past, Present and Future

Priyanka Datta[1,2] · **Rajesh Rohilla**[2]

Received: 2 August 2024 / Accepted: 27 January 2025
© The Author(s) under exclusive licence to International Center for Numerical Methods in Engineering (CIMNE) 2025

Abstract
Radiology also termed as the medical imaging is the medical specialty that involves the creation of images of the body parts for the purpose of diagnostics or treatment. The procedures involved therefore helps the medical professionals in diagnosing the diseases and injuries. The medical image analysis of the brain is considered as the major area of interest because of its complexity and significance and the automation of the same can be done using various tools and techniques. There are variety of image processing techniques used for the brain image analysis, to name a few are the Deep Learning, Machine Learning, hybrid models etc. There are variety of reasons such as the shape, dimension, textures and other related features due to which the analysis of the brain tumors tends to become complicated. Henceforth, this review will give a comprehensive review of the brain tumor image analysis, with the inclusion of the topics such as the fundamentals of brain tumors, brain imaging, actions involved in brain image analysis, models utilized, characteristics of brain tumor images, metrics for model evaluation and datasets of brain tumor and medical images that are available.

Keywords Brain tumor · Magnetic resonance imaging · Machine learning · Deep learning

1 Introduction

As the human brain is one of the utmost essential part of the Human's nervous system, therefore the researchers have focused a lot in carrying out the medical image analysis on brains in order to identify the neurological disorders. This analysis is being used extensively and collaboratively by the researchers in medical and technology domain to identify and assess diseases like Parkinson's disease, Alzheimer's disease and brain tumors/cancers. As per the stats, over 200,000 people die each year due to the brain cancers, that initially start as a brain tumor. Hence, it is very significant to develop the novel technologies and methods for diagnosing and treating these conditions effectively [1].

Tumors are seen as the 2nd leading cause of the death. Tumors are basically the abnormal proliferation of tissues. The non-controlled division of the cells give rise to these growths, and these are irregular in shapes and overabundance of the cells are generally the root cause for the same leading to the deviation from the normal cell life cycle formation, growth and death.

Usually, the organ or body part from which a tumor originates is used to name the tumor. The tumors that initiate from any part of the brain or the skull that also includes the bones, tissues, membranes and brain nerves are referred to as the brain tumors. The high death rate associated with these tumors—roughly 70%—highlights how seriously they can affect health outcomes. In order to effectively address the challenges presented by brain tumors, early detection and effective treatment strategies are essential [2]

Based on their precise location within the brain, brain tumors can be classified into more than 150 different types. These growths fall into one of 2 categories: benign or malignant. Examples of benign brain tumors include meningiomas, chordomas, gangliocytomas, and others. These are benign tumors that usually grow slowly and have little chance of spreading to various other body parts. Malignant brain tumors, on the other hand, are cancerous and

✉ Priyanka Datta
priyankameta.86@gmail.com

Rajesh Rohilla
rajesh@dce.ac.in

[1] G L Bajaj Institute of Technology and Management, Greater Noida, U.P., India

[2] Delhi Technological University, Delhi, India

Published online: 18 March 2025

represent a greater risk to health. Glioblastomas, medulloblastomas, and ependymomas are a few types of malignant brain tumors. These tumors have a worse prognosis and are harder to treat because of their rapid growth and ability to invade neighboring tissues. Making the distinction amongst benign and malignant brain tumors is vital for choosing the best course of action and projecting the possible outcomes for patients. Depending on the kind, location, and stage of the tumor, treatment for brain tumors may involve radiation therapy, chemotherapy, surgery [3].

The brain tumors are classified into 4 classes: Categories 1 and 2 are referred to as the "low-grade" tumors, as they tends to grow slowly and are usually benign [4]; Categories 3 and 4 are "high-grade" tumors, those are considered to be malign, also have a tendency to reoccur [5].

Category I. These tumors, like pilocytic astrocytoma, grow slowly without metastasizing, and because of their well-defined nature and low propensity for aggressive behaviour, they are frequently completely surgically removed.

Category II. These tumors, such as oligodendroglioma, grow more slowly and may eventually spread to higher grades by invading surrounding tissues. These tumors may not go away and may even get bigger.

Category III. These tumors, such as Aden squamous astrocytoma which grow more rapidly as compared to Grade II tumors and have the ability to spread to neighboring tissues. After surgery, these tumors usually need additional treatment, such as chemotherapy or radiation therapy, because surgery is frequently insufficient to treat them.

Category IV. Glioblastoma multiforme is a Grade IV tumor and is considered to be extremely aggressive and having its likeliness to be spread. The most dangerous and aggressive kind of tumors are said to be those tumors that uses blood vessels to speed up their growth [6].

To improve the Patient's probability to recover, the appropriate and the effective treatment needs to be provided and for that the brain tumors needs to be accurately detected and classified. However, due to the diverse shapes, sizes, appearances, positions, and scanning parameters of the tumors, it becomes quite a difficult task to identify the brain tumors.

There are various sophisticated as well as the conventional methods which are being used in identifying a brain tumor. To name a few, the conventional techniques such as the Leksell Gamma Knife (GK) and radioactive beams are quite efficient but have some disadvantages of being labor intensive and needs a significant human intervention. The modalities such as the Positron Emission Tomography (PET), Magnetic Resonance Imaging (MRI) and computer tomography (CT) are being used frequently for brain tumor detection. Chemical Exchange Saturation Transfer (CEST) is considered as a special technique of the MRI which promotes the possibility to image substances that are at a very low concentrations and may not be visible using the standard MRI methods. Of these modalities, MRI is a non-invasive technique that employs microwave pulses and magnetization to provide exhaustive internal body structure imaging.

The ability of the human eye to discern minute variations in intricate imaging methods is restricted. In order to help radiologists make accurate diagnoses, researchers have created Computer-Aided Diagnosis (CAD) systems. Therefore, applying machine learning (ML) is crucial to solving this problem. Although MRI images can be used to accurately identify tumor regions using traditional ML techniques, deep learning (DL) models are becoming more and more popular because of their superior performance and capacity to handle large, complex datasets and high-performance computing devices.

The remaining structure of this paper is as follows: The survey methodology used in this study is presented in Sect. 2. In Section-3, the related work is discussed. The datasets for brain tumor are examined in Sect. 4. Section 5 discussed about the brain tumor analysis and its feature extraction methods. The various methods involved in the analysis of brain tumor detection are analyzed in Sect. 6. Section 7 deliberates the performance evaluation employed in different research followed by discussion about data security and privacy in Sect. 8. Gaps and future scope are discussed in Sect. 9 and finally, the concluding remarks are addressed in Sect. 10.

2 Survey Methodology

Figure 1 describes the Workflow of this systematic literature review. The key objective of this review is to provide exhaustive information of brain tumor detection. As it is necessary to make a organized and planned review to obtain a appropriate novel research direction.

PRISMA methodology is considered to provide a guaranteed methodical exacting approach and is used extensively in brain tumor detection. PRISMA offers the improved review's structure by offering the precise instructions for choosing, locating, and assessing pertinent research. To ensure adherence to PRISMA guidelines, we followed a systematic approach throughout the review process. We define clear research questions, established rigorous selection and removal criteria and implemented a comprehensive search strategy across key databases. The PRISMA is being used due to its ability to preserve the rigour and transparency in their review process, that tends to facilitate the interpretation and validation of the study results. PRISMA [7] contributes to a thorough and trustworthy analysis of brain tumor detection techniques by mitigating bias and guaranteeing that all pertinent literature is taken into account.

There are few databases that were used in this study: IEEE Xplore, Web of Science, Academic Search, Springer,

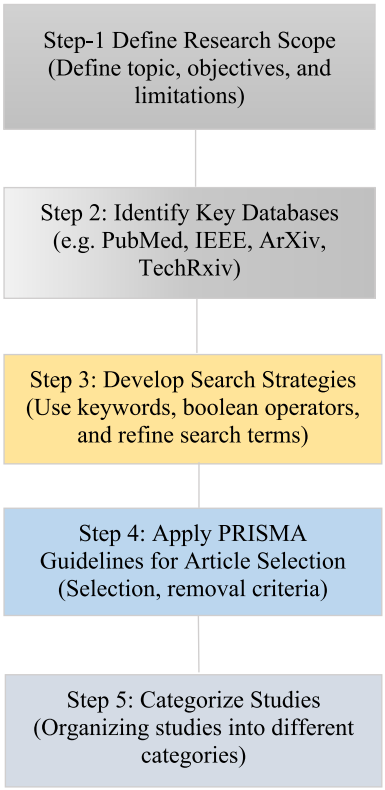

Fig.1 Workflow of the systematic literature review

SPIE Digital Library, ACM Digital Library, Elsevier, MDPI, Google Scholar, Scopus, and PubMed. In addition, searches were conducted for pertinent papers on four preprint platforms: ArXiv, TechRxiv, MedRxiv, and ChemRxiv. Additionally, a manual search was done. During the first phase, 8362 research publications were found in total.

We create specific search terms for each database to ensure we find the most relevant studies. We were looking for papers that included brain tumors. We used broad terms like "brain tumor detection", "Machine Learning", and "Deep Learning", but adapted the queries for each database. E.g. for IEEE Xplore, we emphasized "Artificial Intelligence", "Machine Learning", "Deep Learning" and "neural network" to focus on engineering field. In Pub Med, we incorporated medical terms like "brain tumor", "MRI" to target medical research, and for Web of Science, we focused on both engineering and medical research. Figure 2 shows the search criteria used for finding research articles.

Following the removal of duplicates and unnecessary articles, 1979 research articles were carefully selected for further review. On the basis of title, abstract, and introduction, 1218 of these were disqualified. After additional analysis of the remaining 651 were not included. That left 110 articles for the following stage. 22 articles were removed during the eligibility phase following a careful assessment.

The criteria to either select or remove the different research papers are given in Table 1. We use these selection criteria that focus more on recent advancements (2014–2024) in brain tumor detection, cover a range of detection methods, emphasize more on state of art DL methods, and prioritize studies with experimental data and a strong mathematical foundation. This ensures scientific precision, practical importance, and convenience for researchers familiar with English language. The diverse PRISMA stages that were adhered to in this review are depicted in Fig. 3.

To ensure research quality, we assessed all studies using Keshav's 5 Cs [8] framework, evaluating category, context, correctness, contributions and clarity. This approach enabled a thorough, structured evaluation of the relevance, transparency and quality of each study. The focus on methodological transparency helps to minimize the bias and strengthens the reliability of our findings.

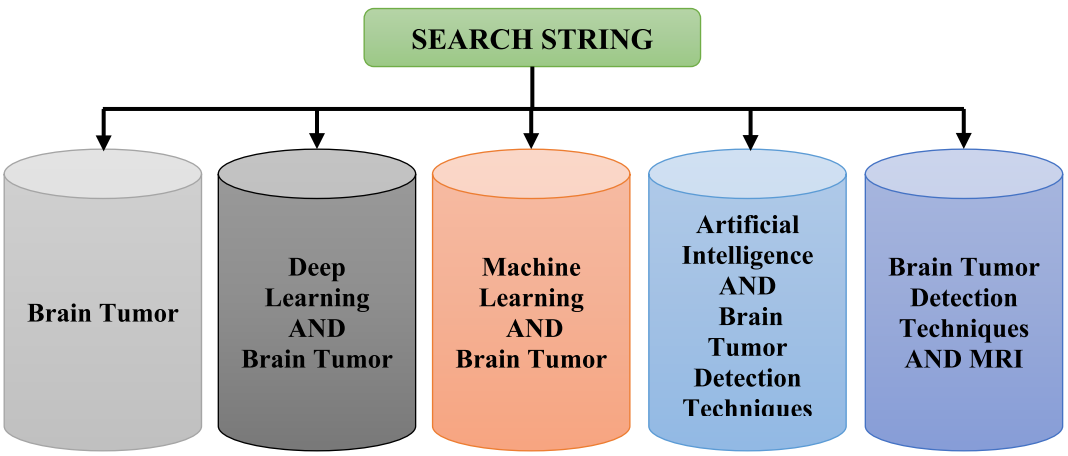

Fig.2 The search criteria used for finding research articles

2.1 Researchers—Asked Research Questions

The primary goal of this survey is to furnish a wealth of detailed information to enlighten and motivate emerging scientists in the domain of brain tumor detection. Table 2 outlines the several questionnaires pertaining to brain tumor detection that have been explored in this study. This compilation aims to aid forward-thinking scientists in grasping the foundational aspects of detecting

Table 1 Criteria for selecting and removing various research articles

S. no	Parameter	Selecting criteria	Removing criteria
1	Time Frame	Research articles that are published from 2014–2024	Research articles that are published prior to 2014
2	Analysis	Research articles encompassing various brain tumor detection	Research articles encompassing diverse cancer detection
3	Comparison	The research article focuses on DL methods utilized for brain tumor detection	The research article focuses on diverse methods used for detecting brain tumor
4	Study Selection	Research incorporating experimental findings and mathematical foundation	Research incorporating case studies and articles in languages other than English

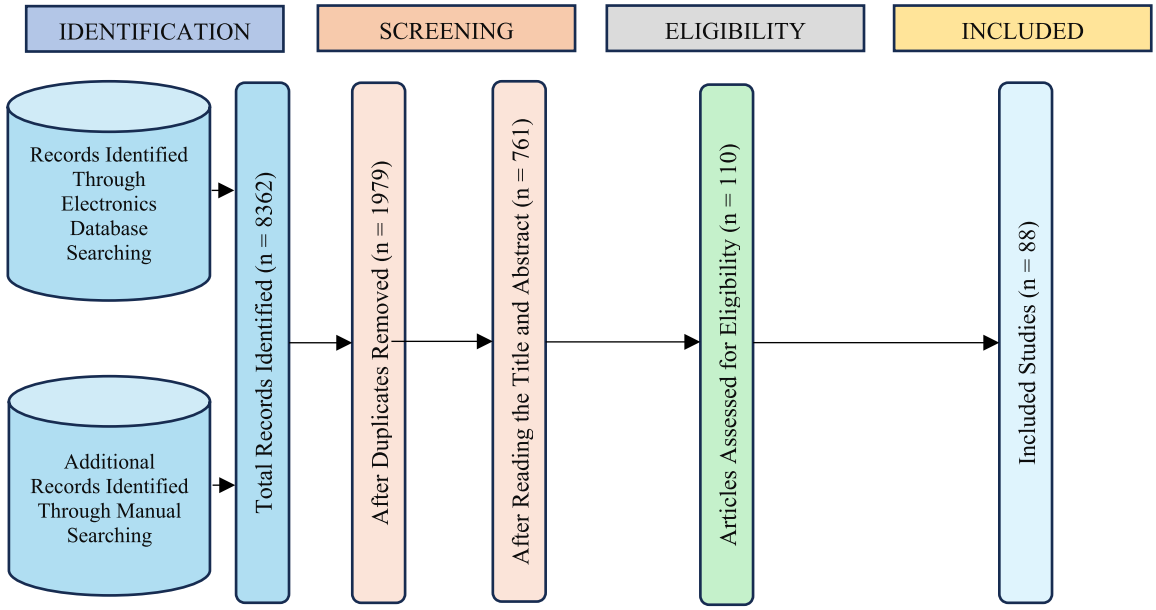

Fig.3 PRISMA flow diagram on brain tumor review strategy

Table 2 Research questions correlated to brain tumor detection

Questions	Research questions
Q1	What is a brain tumor?
Q2	Describe the detection methods for brain tumors?
Q3	What are the risk factors linked to brain tumors?
Q4	What are the various screening techniques used in detecting brain tumors?
Q5	What types of DL methods are employed in brain tumor detection?
Q6	How are DL-based brain tumor detection techniques evaluated for performance?
Q7	What challenges are associated with using DL for brain tumor detection?
Q8	What are the Future researches being conducted to explore detection of brain tumor using DL techniques?
Q9	What role does deep learning play in detecting brain tumors, and how does it differ from other approaches?

and diagnosing brain tumors, along with highlighting the unresolved challenges within the domain.

In Table 3, a checkmark (✓) showcases towards the fact that study has addressed the given research queries, while a cross (✗) showcases that it has not been addressed.

3 Related Work

There has been a no. of research that has been carried out for analyzing medical images and for studying brain tumors in the last few decades. Many studies have looked at and summarized existing works from various prospectives and time periods. In [14], there is a detailed discussion of medical image analysis utilizing the semi-supervised machine learning, multi-instance learning, and transfer learning (TL) techniques for unique organs, including references to appropriate systems. Certain survey papers, such as [15], has explored current methods relying upon DL models for the analysis of medical image, giving an outline to their problems and proposed alternatives.

Tiwari et al. [3] conducted a comprehensive review of current methodologies for brain tumor segmentation and classification in the MRIs of brain. They made analysis on 62 research papers published between 2014 and 2019. Their review includes details on MRI's and various imaging techniques related to brain, and their outcomes. It gives insights regarding the differences and gains of utilizing MRIs to derive gray matter, white matter and cerebrospinal fluid separately. Additionally, their review also focused upon the super classes and subclasses for brain tumor classifications, including a comprehensive categorization of gliomas and tumor grades depending on the severity and location within the brain.

The review includes different approaches for segmenting brain tumor images. This involves techniques like thresholding-based methods, supervised machine learning and unsupervised methods. The review additionally covers tumor classification methods, both supervised and unsupervised. The various aspects such as the technique, measurement of performance, true and false positives rates, and data sets have been summed up in a tabular format along with the textual summary from 62 articles. The review provided a comprehensive list of 19 datasets that have been utilized in previous studies on brain tumor segmentation. The authors gave references and usage frequencies for each dataset, giving a clear overview of the benchmark datasets and their availability. They highlighted that BRATS 2013 and BRATS 2015 are most frequently utilized in recent research. Moreover, the researchers presented statistical results regarding the reviewed articles country of origin, publishers, citations, publication years, datasets utilized, and methodologies deployed. They compared methods and found that Convolutional Neural Network (CNN) and Particle swarm optimization (PSO) have been dominant in most current years, with support vector machine (SVM), Fuzzy C Means (FCM), and k-means ranked 2nd from 2014 to 2019. Various performance metrices along with the appropriate equations utilized in the analysis of the brain tumors has also been explained by the authors. There are the provision of the network visualization maps for the terms and its related link to give a basic understanding of the terminologies utilized in the related articles. The authors concluded that DL and PSO methodologies are the existing and future emphasis of research in this study, and their review of most current findings on brain tumor segmentation and classification has validated this conclusion. The review paper gave a detailed overview of recent research, covering all 62 articles. It included tables and statistical analyses for easy comparison of different methods, datasets, publications, and performance metrics. Some summaries were concise because of the similarities with different works, and the paper identified the methods utilized in different studies by name. It listed benchmark datasets with their names and references. It would be helpful to incorporate additional information about the data sets, like the No. of items, data type, public availability, and ground truth availability, for selecting a suitable dataset for future researches.

A study on tumor segmentation and feature extraction techniques related to brain was carried out by Saman et al. [4]. The study discussed regarding the Magnetic Resonance Imaging systems, technology for Magnetic Resonance Imaging processing, and Magnetic Resonance Imaging sequencing, providing explanations and instances. It also detailed

Table 3 Research question recent survey related to brain tumor answered

Survey	Review year	Research questions								
		Q1	Q2	Q3	Q4	Q5	Q6	Q7	Q8	Q9
Ellah et al. [9]	2019	✓	✓	✓	✓	✓	✗	✓	✗	✓
Tandel et al. [10]	2019	✓	✗	✓	✓	✓	✗	✓	✗	✗
Nadeem et al.[11]	2020	✓	✗	✓	✗	✓	✗	✓	✓	✓
Kaifi et al. [12]	2023	✓	✗	✓	✓	✓	✓	✓	✗	✓
Younis et al. [13]	2023	✓	✗	✗	✗	✓	✓	✓	✓	✗
Proposed study	2024	✓	✓	✓	✓	✓	✓	✓	✓	✓

different levels of brain tumors, its region, symptoms, and curing methodologies. The brain tumor detection studies from past 10 years were reviewed by the paper, with a primary attention upon research from past 3 years. The authors covered the pre-processing of MRIs in detail, discussing steps such as stripping of the skulls, correction of the bias field, removal of noise, object detection, and segmentation utilizing various tools and algorithms. They provided an overview regarding the current research over segmentation of brain tumor, categorizing it into conventional methods, intensity-based methods, atlas-based methods, deformable model-based methods, as well as hybrid and deep learning methods. Authors also presented pros as well as cons of using various studies deploying these methodologies in a table format. They parallelly analyzed and reviewed the most current study related to feature derivation methodology for tumor analysis related to brain. The paper defined and described several kinds of features, inclusive of texture-based features intensity-based features and shape-based features along with their corresponding equations. Additionally, the authors discussed DL based automation feature derivation techniques.

The authors discussed the most recent emphasis on numerous CNNs and U-Nets along with their variations. Their comprehensive analysis of the features used in brain tumor segmentation was informative for understanding and comparing feature extraction and processing in comparable systems. The paper extensively referenced and mentioned over 130 research works from the past decade, contributing to the analysis of renowned methods and its performance related to the research on brain tumors. However, there were significant no. of relevant articles present in the references, many of them were not appropriately summarized, thereby making it difficult to draw conclusions based on comparison without individually reviewing the cited papers.

Certain reviews upon brain image analysis have focused on specific aspects of image processing of brains, like skull stripping. They utilized available work and data sets as the references [16, 17]. These methods were occasionally used as former or later-processing steps for analysis related to brain tumors or were connected with the studies related to the brain tumors. The datasets reviewed in this study were also utilized in the analysis method of the brain tumor. Table 4 summarizes these survey papers.

4 Dataset Used

As seen in the different research papers, researchers used number of publicly available datasets of MRI modality to test the methods suggested by them. Table5 shows list of some well-known publicly available datasets of MRI modality commonly used in the research.

5 Brain Tumor Analysis

As illustrated in Fig. 4, tasks related to analyzing brain tumors can be categorized into three primary areas: (i) detection of brain tumors versus non-tumors, (ii) segmentation of brain tumors, and (iii) classification of brain tumors. Researchers have approached these tasks using various methodologies. Different types of the brain medical images are utilized by the AI based systems as their input data.

The tumor classification task can include actions such as assessing the tumor's severity (such as benign/malignant) or identifying various tissues within the tumor (like core tumor, edema, enhancing tumor, non-enhancing tumor, etc.).

Brain tumor detection involves classifying brain MRIs as either tumor or non-tumor cases, determining whether the brain is healthy or exhibits abnormalities. A range of techniques have been deployed by the researchers that includes ML models, DL model approach and hybrid models for carrying out the classification task. [27]. This classification depends upon the datasets that comprises of healthy brain MRI's as well as those showing tumors, with labelled data used to train various models such as supervised, unsupervised, and deep learning models. These models extract distinctive features from both healthy and tumor tissues to facilitate accurate classification.

In certain studies, tumor classification is also utilized to identify specific tumor types, such as distinguishing between benign and malignant tumors, or identifying particular types of tumors [28]. However, these tasks are often not examined independently; rather it's integrated to brain tumor segmentation task. In analyzing brain MRIs, recent works have predominantly focused on utilizing deep learning models for automatic feature extraction, known as deep feature extraction. The extraction of various intensity features, shape features and texture features are some alternative approaches upon which the research has focused considerably. from MRIs. These features are either combined with the images or utilized solely as inputs for the system, leading to effective results in terms of detection and segmentation [4].

Image segmentation methods are valuable for identifying distinct regions or clusters of pixels that encompass regions of interest (ROIs), organs, or lesions within organs. This area of study forms the basis of medical image segmentation [15]. Noninvasive brain scans are being utilized into brain tumor image segmentation as explored by researchers across diverse fields. Their aim is to develop effective and precise automated systems for brain tumor segmentation, capable of segmenting tumors, classifying tumor types, and assessing severity. These systems are pivotal in detecting abnormalities promptly and facilitating timely treatment [3].

The majority of existing research is concentrated on the brain tumor image segmentation and classification

Table 4 Recent survey related to brain tumor analysis

References	Year	Approach	Technique used	Details
Al-Galal et al [2]	2021	Classification and Segmentation	Deep learning	Covering publications from 2018 to February 2020, this review provides a comprehensive overview of several topics. These include the datasets used, the deep learning methods applied, the performance metrics assessed, a detailed explanation of CNN architecture, the popular frameworks of CNNs used in medical image analysis, and the challenges faced in brain tumor analysis
Magadza et al. [18]	2021	Segmentation	Deep learning	The review provides a thorough overview of image segmentation, covering different deep learning models, architectures, datasets, performance metrics, and software tools used. It also thoroughly examines publications focusing on specific architectures, including U-Net, dual-pathway, single-pathway, ensemble, and cascaded architectures
Tiwari et al. [3]	2020	Classification segmentation	Conventional ML	Publications from 2014 to 2019 analyze brain tumor prediction using MRI, presenting insights into methods, datasets, performance metrics, and challenges of the future
Rehman et al. [17]	2020	Skull-stripping	Conventional ML and DL	An overview of datasets with visualizations, along with a review of histogram thresholding, morphology, deformable surface-based, atlas-based, region-growing, meta-heuristics, and 2D/3D CNN methods
Hesamian et al. [15]	2019	Segmentation	Deep learning	The review offers a comprehensive look at CNN architectures, covering 2D CNN, 2.5D CNN, and 3D CNN, as well as variations like FCNNs, U-Nets, CRNs, and RNNs. It also delves into different network training techniques and transfer learning methods. Additionally, the paper addresses challenges in medical imaging and proposes potential solutions to tackle these challenges effectively
Abd-Ellah et al. [9]	2019	Segmentation classification	Conventional ML and DL	A comprehensive discussion of CAD for brain MRI and datasets, including a comparative analysis of detection/classification methods, feature extraction, performance metrics, and datasets, as well as the limitations in tumor detection, classification, and segmentation
Wadhwa et al. [19]	2019	Segmentation	Conventional ML	A detailed comparison of conventional and machine learning methods, analyzing MRI modalities, time, data, abnormality types, and performance in publications on BRATS 2015 and BRATS 2013

task, as accurately delineating the tumor area from the surrounding image is critical for diagnosis. It's worth noting that only a few researchers have addressed multiple tasks simultaneously, primarily accounting for the lack of suitable datasets and the complexity associated with each task. Consequently, there's a significant future scope in developing a comprehensive and precise system capable of autonomously handling all tasks without human intervention, which remains a key objective in the realm of brain tumor image analysis.

5.1 Features Extraction Methods for Brain MRI

Brain image analysis requires the capability to extract features from brain MRIs, which are then utilized by various models and algorithms to produce outputs for analyzing brain functions. A wide array of features and models have been employed in brain image analysis studies which are outlined below:

Table 5 List of some well-known publicly available datasets of MRI modality commonly used in the research

Dataset Name	Dataset Size	Description	Link
BRATS2019 [20–22]	259 high-grade glioblastomas (HGG) and 76 low-grade gliomas (LGG) MRI volumes	Contain T1, T1-W(T1Gd), T2- W(T2), and T2-FLAIR of Glioblastoma (GBM)/HG glioma and LG glioma brain tumor	https://www.med.upenn.edu/cbica/brats2019/data.html
BRATS2020 [20–22]	55 brain slices where each slice is of dimension 240 × 240 pixels	T1, T1-weighted, post-contrast T1-weighted (T1gd), T2-weighted, and T2-flair volumes annotated as necrotic and non-enhancing tumor core (NET), enhancing tumor (ET), peritumoral edema (ED)	https://www.med.upenn.edu/cbica/brats2020/data.html
The Cancer Imaging Archive (TCIA) Publicly Accessible Repository [23]	20 Patients	DICOM Format. contain T1w (pre and post-contrast agent), FLAIR, T2w	https://www.cancerimagingarchive.net/collection/brain-tumor-progression/
Harvard Medical School Data (AANLIB) [24]	400 Patients	Contain normal and abnormal images includes cerebrovascular (stroke or "brain attack"), neoplastic (brain tumor), degenerative, and inflammatory diseases	http://www.med.harvard.edu/AANLIB/
Masoud2021 dataset [25]	7023 images	4 classes: glioma—meningioma—no tumor and pituitary	https://doi.org/10.34740/KAGGLE/DSV/2645886
Figshare dataset [26]	3064 images	Consists of 3064 T1-weighted contrast-enhanced images from 233 patients with 3 kinds of brain tumor: meningioma (708 slices), glioma (1426 slices), and pituitary tumor (930 slices)	http://dx.doi.org/10.6084/m9.figshare.1512427

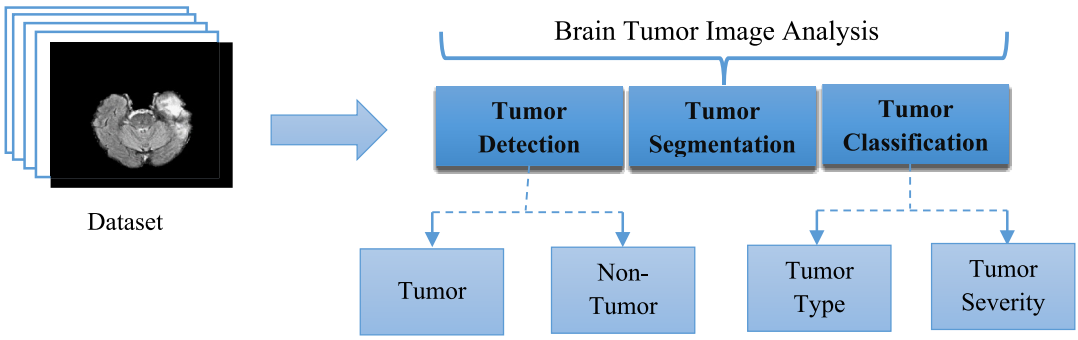

Fig.4 AI-driven system designed for tasks related to analyzing brain tumors

i. Extraction of Features: Image analysis involves the extraction of meaningful features from brain MRI's.
ii. Model Utilization: The diverse models and algorithms utilized such features subsequently to create the outputs for the tasks related to brain analysis.
iii. Features Types: Several Features are explored within the study that relates to the analysis of the brain image utilizing the aspects such as the intensity, shape, texture, frequency, and various deep learning-based features.
iv. Types of Models: The models such as inclusion of the ML algorithms and DL architectures, are employed in the study of brain image analysis in order to process the extracted features and get the valuable insights.

These model and features combinedly gives advancements in our understanding of the brain structure, functions and abnormalities, thereby fostering progress in neuroimaging research.

Brain MRI's derived features are categorized into 4 classes and is identified in [4]. The classes involve intensity-based, texture-based, shape-based, and deep learning-based features, as illustrated in Fig. 5.

5.1.1 Texture-Based Features

The collection of measurements used in image analysis for evaluation of the apparent texture of an image is referred to as the Image Texture. It provides insights into how colors or intensities are arranged within an image or a specific part of an image. Key texture-based features commonly used in analyzing brain images include gray-level co-occurrence matrix (GLCM), autocorrelation, correlation, homogeneity, energy, entropy, local binary pattern, dissimilarity, contrast, cluster shade, and prominence [29].

5.1.2 Intensity-Based Features

Derivation of the Intensity features is from the order one histogram, that encompasses 4 types of statistical measures: variance (Var), mean ($\overline{X}$), kurtosis (k) and skewness (S_k). These features are computed based on the pixel values of grayscale present within the image. Let p_i be denoted as the pixel value for a specific pixel referred to as $'i'$ lying within the grayscale image boundary. Moreover, assuming the overall pixel count is t, then the statistical mean indicates the central tendency related to image's histogram. Variance quantifies the spread or dispersion of pixel values, skewness reflects the histogram's asymmetry, and kurtosis gauges the

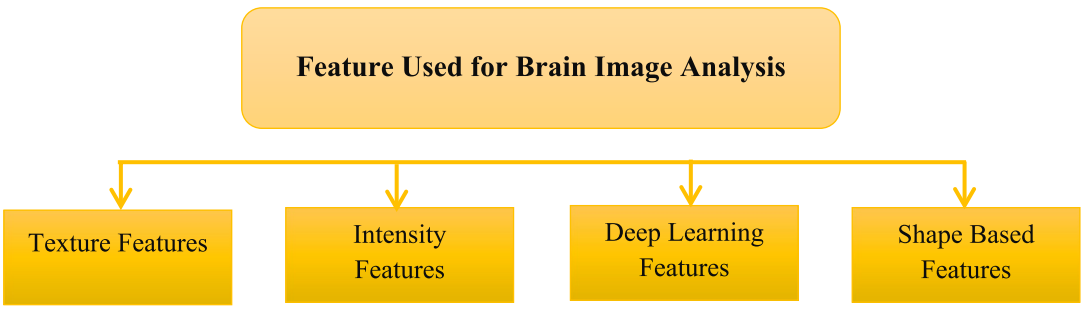

Fig.5 Types of features used in brain tumor analysis

histogram's peakedness or flatness. Eqs. 1, 2, 3, and 4 are typically employed to calculate these four features.

$$\text{Var} = \frac{1}{t}\sum_{i=1}^{t}\left(p_i - \overline{X}\right)^2 \tag{1}$$

$$\overline{X} = \frac{1}{t}\sum_{i=1}^{t} p_i \tag{2}$$

$$k = \frac{1}{t}\sum_{i=1}^{t}(p_i - \overline{X})^4 \tag{3}$$

$$S_k = \frac{1}{t}\sum_{i=1}^{t}(p_i - \overline{X})^3 \tag{4}$$

5.1.3 Features Based on Deep Learning

DL features are the combination of simple as well as the intricate features that are automatically gathered by deep learning models on each level related to CNN. As the network progresses through its layers, it discovers new features and generates feature maps. For instance, early layers might detect edges, followed by corners in subsequent layers, and progressively more complex shapes and patterns. Each layer captures increasingly detailed feature information from the input image, creating feature maps or vectors that are then processed via corresponding neural net. These features are consolidated and applied in tasks like detection related to brain tumor, segmentation, and classification.

5.1.4 Features Based on Shapes

Shape-based features describe the form of objects and include metrics such as area, volume, perimeter, convex area, polygon shape, circularity/irregularity, among others. These features can be derived from a brain MRI as part of shape-based analysis.

6 Methods

6.1 Machine Learning Techniques

Machine learning techniques, including supervised, unsupervised, and hybrid approaches, has been utilized to detect brain tumors, it's classification and segmentation. While conventional machine learning approaches and their variants keep on showing outcomes comparable to those of deep neural networks, recent research has focused primarily on deep learning methods because of their superior performance metrics.

A technique for segmenting and predicting brain tumors using adaptive SVM and modified region growing was presented by Reddy et al. [30]. To cover various methodology such as SVM, kernel clustering, fuzzy clustering, thresholding, and Convolutional Neural Network related to several medical image analysis, they summarized suggested procedures, pros and cons for the eighteen associated researches initiated in the year 2001 to year 2019.

A different model that used an Adaptive K-Nearest Neighbor classifier and Gray-Level Cooccurrence matrix (GCLM) for feature extraction achieved 98.37% accuracy and segmentation is done by probabilistic fuzzy C-means algorithm for the detection of diseased parts of the brain [31]. Moreover, an ensemble learning framework processing gradient and Gabor wavelet features performed better than other approaches with overall Dice Score scores ranging from 0.86 to 0.88 [1].

Alam et al. [32] achieved 97.5% accuracy using a hybrid approach based on template-based K means and improved fuzzy C means techniques for detection of brain tumors. A Simple Linear Iterative Clustering (SLIC)-based method utilizing Walsh Hadamard Transform (WHT) texture features for segmentation of brain tumor was proposed by Angulakshmi et al. [33], greatly enhancing performance.

In order to achieve 97.56% accuracy, Devanathan et al. [34] proposed a framework that combined bilateral filtering, artificial bee colony-based thresholding, and SVM classification. The accuracy and performance metrics of other models that used different hybrid approaches also demonstrated notable improvements.

K-means, K-Nearest Neighbour (KNN), SVM, Random Forest (RF), FCM, and artificial neural network (ANN) are among the machine learning models that show notable benefits for brain tumor analysis, despite their high computational complexity and reliance on large datasets. While clustering techniques work well for segmentation, supervised models are appropriate for detection and classification. ANN models perform well in brain tumor image analysis and are

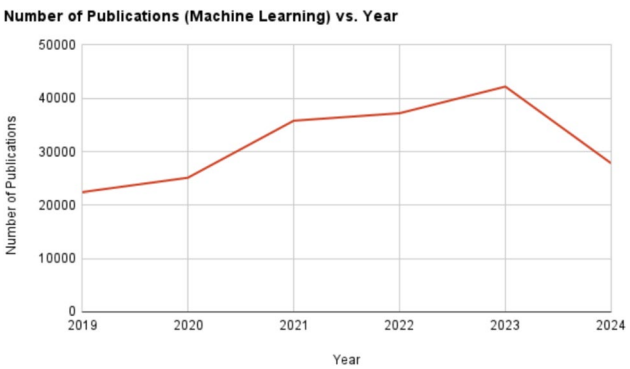

Fig.6 Last 5 years publications on machine learning based brain tumor detection

adaptable to all tasks. Figure 6 draws data from reputable publishers such as Scopus, SCI etc., and presents an overview of the growth in publications on machine learning-based brain tumor detection from 2019 to 2024. It draws attention to a growing body of research that uses sophisticated methods—like SVMs—and is frequently tested on datasets like BRATS. Important metrics are sensitivity and accuracy, and problems are computational complexity and data scarcity, which will push future research toward more complex algorithms and a wider range of datasets for better detection techniques.

6.2 Deep Learning Techniques

Deep learning is a powerful tool for analyzing brain tumors. U-Net, a specific deep learning framework, is particularly useful. It's fast and accurate because it combines shrinking and expanding sections with special filters (convolution layers) and data manipulation techniques. U-Net can find general and specific details in images, improving its results [35] While the original U-Net paper didn't go into much detail about data, some variations, like path aggregation U-Net, have improved accuracy even further. However, these variations can take longer to run because they're more complex [36].

Building upon the success of U-Net for brain tumor segmentation, researchers have proposed exciting variations. Hybrid Two-Track U-Net (HTTU-Net) utilizes dual pathways and a combined error function for improved accuracy but suffers from slow execution times [37]. Triple intersecting U-Net (TIU-Net) tackles this by combining binary and multi-class segmentation U-Nets with a specialized loss function, achieving superior performance at a higher computational cost [38]. Alternatively, Sharif et al.'s [39] method leverages pre-trained models for efficiency but faces challenges in generalizing to new datasets. These advancements highlight the ongoing effort to refine U-Net for brain tumor analysis, striving for the optimal balance between accuracy, efficiency, and generalizability.

Beyond U-Net variations, researchers are exploring entirely new deep-learning architectures. Sun et al. built a 3D Fully Convolutional Network with unique features like multi-pathway extraction and random slice processing for improved brain tumor segmentation [40]. Chen et al. [41] introduced deep convolutional symmetric neural networks (DCSNNs), which use symmetric features to boost performance while staying efficient. Zhang et al. [42] proposed ResU-Net with attention to capture details in both small and large tumors. These advancements showcase the dominance of deep learning, especially U-Net-inspired methods, in brain tumor analysis. While challenges like computational cost and data requirements persist, techniques like data augmentation and efficient architectures are paving the way for a stronger deep learning presence in medical image analysis. Figure 7 draws data from reputable publishers such as Scopus, SCI etc., and presents an overview of the growth in publications on deep learning-based brain tumor detection from 2019 to 2024.

Table 6 compares various techniques for enhancing and denoising brain MRI images. Each entry details a different study, including the publication (authors and year), datasets used, specific methods applied (e.g., filtering, transformations), and performance metrics (PSNR for noise reduction, SSIM for structural similarity). For instance, Awudong et al. [43] achieved a PSNR of 38.7532 and SSIM of 0.9781 using Variance-Stabilizing Transformation and Morphological Component Analysis, but suggest incorporating edge detection for further improvement. The table showcases the effectiveness of different techniques while acknowledging limitations like computational cost and parameter tuning,

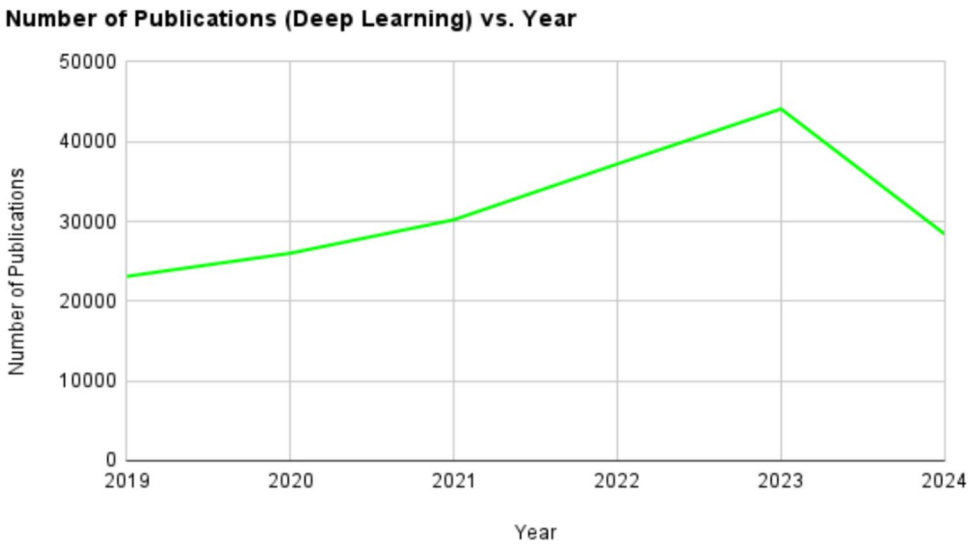

Fig.7 Last 5 years publications on deep learning based brain tumor detection

Table 6 Image Enhancement and Denoising

Reference	Year	Dataset used	Technique used	Results	Advantage(s)	Limitation(s)
Awudong et al. [43]	2024	Simulated brain database and two real clinical brain MRI datasets	variance-stabilizing transformation (VST) with Morphological Component Analysis	PSNR: 38.7532MSSIM: 0.9781	Preserve complex texture details of MRIs, provide effective denoising even when the noise distributions and intensities are unknown	Incorporating an edge detection method or the multi-modal fusion technique into the proposed denoising process can yield high-quality clinical images with improved edges and textures
Akindele et al. [44]	2023	The BrainWeb and OASIS datasets, simulated dataset	Regularized Neighborhood Pixel Similarity Wavelet Algorithm	PSNR: 46.80 SSIM: 0.9903	Features are also preserved, visually better improvement with the edges and textures being preserved	More computational complexity
Pankaj et al. [45]	2021	Both synthetic and clinical MRI datasets	Variational mode decomposition (VMD) with total variation (TV) smoothing	PSNR:34.22 SSIM: 0.55	Preserves edge and texture details	The necessity of fine-tuning parameter estimation to achieve optimal results in T1-w and PD-w images
Tian et al. [46]	2021	Both synthetic and real MRI datasets	Conditional GANs	SSIM:0.9489 Normalized MSE: 0.0167	Achieved high SSIM compared to other state of art techniques in high noise levels	Experiments are conducted with little data and lack comprehension
Tripathi et al. [47]	2020	one simulated and four real MRI datasets i.e. Synthetic data from Brainweb, Multiple Sclerosis (MS) dataset by University of Syprus, Prostate MRI dataset	CNN	PSNR: 43.18 SSIM: 0.98	Reducing the dimensions of feature maps enhances the result, Minimizes the issue of vanishing gradient using residual blocks	Need lots of computation power, network setup is cumbersome
Baselice et al. [48]	2019	Synthetic dataset from Brain web and Private MRI dataset	Kolmogorov Smirnov Non-Local Mean (KSNLM)	MSE: Gaussian noise: 0.0034 Rician Noise: 0.0036 SSIM:Guassian noise: 0.9309 Rician Noise: 0.9309	Does not need the knowledge of its statistical description as algorithm is not limited to specific noise distribution	More processing time
Jiang et al. [49]	2018	Three datasets from two public data sources of IXI dataset and Brainweb	Multi-channel Denoising CNN (DnCNN)	PSNR: 46.32 SSIM: 0.99	Achieve visually good result, removed noise but also retain details of the image, also remove noise in the background sufficiently	Performed well for specific noise level only
Biswas et al. [50]	2017	Brain MRI image	Curvelet transform combined with Wiener filter	PSNR: 50.421 MSE :0.590 SSIM:0.996	Remove gaussian noise in low and high frequency sub bands	Remove only gaussian noise
Joshi et al. [51]	2016	simulated MR images of brain	Median and Wiener filter in conjunction with the Non local means filtering technique	PSNR: 41.01 MSE: 5.18	Maintains the edges and fine structures of the image without causing significant blurring	Computation time increased

Table 6 (continued)

Reference	Year	Dataset used	Technique used	Results	Advantage(s)	Limitation(s)
Mohan et al. [52]	2015	Four images, two MRI images of human brain, CT image of pectus of hollowed chest and CT image of brain	Multistage median filtering (MMF)	PSNR: 36.0898 MSE: 15.9994 RMSE:3.9999	Improved denoising efficiency in comparison to wavelet transform	Blur the boundaries of the tissues

emphasizing the ongoing advancements in MRI image processing.

Table 7 dives into the world of brain MRI segmentation techniques, comparing their strengths and weaknesses. Each entry analyzes a different study, providing details on the publication (authors and year), the type of MRI data used (private dataset vs. public dataset like BRATS 2018), and the specific segmentation method employed (e.g., 3D CNN, cascade CNN). The table then highlights the performance using metrics like Dice Similarity Coefficient (which quantifies overlapping between segmentation and ground truth), sensitivity (ability to detect true positives), and specificity (ability to detect true negatives).

For instance, Rajendran et al. [53] achieved a remarkable F-score of 99.40% for the whole tumor and 98.29% for the tumor core using a 3D CNN on their private dataset. However, their dependence on a limited dataset restricts the generalizability of their findings. Conversely, Ranjbarzadeh et al. [54] tackled overfitting by utilizing a cascade CNN approach on the public BRATS 2018 dataset. This method attained Dice scores of 0.923 for the whole tumor and 0.9113 for the enhancing tumor, demonstrating its ability to extract various image features. However, it might struggle with segmenting very large tumors.

By showcasing these contrasting techniques, the table emphasizes the ongoing challenge of balancing computational complexity (e.g., 3D CNNs require more resources) with the requirement for substantial amounts of training data to ensure generalizability across different brain MRI scans.

Table 8 focuses on the effectiveness of various classification techniques used to analyze brain MRI images. It provides a breakdown of different studies, comparing their performance based on datasets, methodologies, and evaluation metrics. These metrics surrounds key measures such as overall accuracy, sensitivity (able to identify true positives), specificity (able to identify true negatives), and F1 Score (a balanced metric summarizing precision and recall).

A study by Zain Eldin et al. [63] marks its exceptional performance. The reason for their exceptional mark was due to the combination of CNN with a specific optimization technique (Sine–Cosine Fitness Grey Wolf Optimization) on the BRaTS 2021 dataset. This strong approach led to the yield in a near-perfect scores across all the metrics, making it to achieve 99.98% accuracy, sensitivity, specificity, and F1 score. However, the table adheres to some trade-off related to the optimization steps is significantly increasing the process time. Unlikely, some studies like Ayadi et al. [64] went for some simpler methods. Their technique employment includes Speeded Up Robust Features (DSURF) and Histogram of Oriented Gradients (HoG) in combination with the support vector machine (SVM) classifier. With the good accuracy of 90.27%, this process encompasses a very minimal computation time. The below given table encompasses

Table 7 Image segmentation

References	Year	Dataset used	technique used	Results	Advantage(s)	Limitation(s)
Rajendran et al. [53]	2023	Private MRI dataset	3D CNN	F-Score: For the whole tumor: 99.40% For tumor core:98.29%, Sensitivity: For the whole tumor: 99.39% For tumor core:98.25%	Produces much more precise and complete estimates	Small dataset
Cheng et al. [55]	2023	Three publicly available dataset	Improved version of U-Net	Hausdorff distance (HD) metric 1.82, 1.31, and 2.30 for the three datasets	Reduction of network parameters and an improved ability to capture detailed information	Only capture 2D information
Nyo et al.[56]	2022	BRATS 2015 dataset	Otsu's thresholding technique	TP: 68.7955% Accuracy:95.56`% for Level 4	Class 4 is ideal and appropriate for segmenting MRI scan	Computational cost could be high
Ding et al. [57]	2021	BRATS 2015 dataset	Two-stage GAN	Dice score: 0.85	Requires less training data	Computationally complex
Ranjbarzadeh et al. [54]	2021	BRATS 2018 dataset	Cascade CNN	Dice scores: 0.9203 (whole tumor), 0.9113 (enhancing tumor) and 0.8726 (tumor core)	Reduced computational time	Limitations when encountering large tumor volume
Zhou et al. [58]	2021	BRATS 2018	3D residual neural network	Dice scores: 0.9121 (whole tumor), 0.818 (enhancing tumor) and 0.8662 (tumor core)	Better segmentation process as well lowest computational complexity	High number of decoder parameters used. Decoder should be lightweight
Nema et al. [59]	2020	BRATS 2015 dataset and BRATS 2017 dataset	Encoder-decoder based network	Dice Similarity Coefficient (Whole): 94%	Requires less data for training	Redundancy in skip connection
Imtiaz et al. [60]	2020	BRATS 2013	Superpixel Segmentation	Specificity:0.957, Sensitivity: 0.840, PPV: 0.832, Jaccard: 0.751, Dice Score: 0.858	Quick computation time and strong resistance to rotational and scale-invariant changes	Sensitive to noise and distortions as well as extraction of redundant features
Sajid et al. [61]	2019	BRATS 2013 dataset	CNN	Dice score: 0.86, Sensitivity: 0.86 and Specificity:0.91	Data preprocessing such as bias field correction and utilizes dropout regularize to deal with the over-fitting problem	Not perform very well for LGG
Wang et al. [62]	2018	BRATS-2017 dataset	cascaded anisotropic CNN	Dice score: For enhancing tumor: 0.7859, whole tumor: 0.9050, tumor core: 0.8378	Residual connections and multi-scale predictions are utilized in these networks to enhance the segmentation performance	Require long time for training and testing

Table 8 Image classification

References	Year	dataset used	Technique used	Results	Advantage(s)	Limitation(s)
ZainEldin et al. [63]	2023	BRaTS 2021	CNN and Sine–Cosine Fitness Grey Wolf Optimization	Accuracy: 99.98% Sensitivity: 99.98% Specificity: 99.98% PPV: 99.98% NPV: 99.98% F1 score: 0.9998	Enhancement of the CNN's performance by the CNN optimization's hyperparameters to achieve higher accuracy	The extra optimization steps cause it to take long time, challenges of generalization and data diversity emerged
Atha et al. [65]	2023	Kaggle brain MRI dataset	Semi-Supervised Network	Accuracy: 94.3% Sensitivity: 92.5% Specificity: 96.5%	Improved brain MRI classification performance	not validated on a bigger dataset, unable to reveal the brain tumor's location
Ayadi et al. [64]	2022	Figshare	DSURF and HoG as feature extractor, SVM as classifier	Accuracy: 90.27%	Minimal computation time as well as can assist physicians in improving their classification results for brain cancers	Classification accuracy needs to be improved
Rao et al. [66]	2022	BRATS 2018, 2019 and 2020	Kernel based SVM	Accuracy: 99.2% (BRATS 2018), 99.36% (BRATS 2019), 99.15% (BRATS 2020)	Higher classification accuracy for timely and proper diagnosis	Only two class classification is done
Irmak et al. [67]	2021	4 publicly available datasets	CNN model for multi classification	Accuracy: 99.33% for two tumor classification, 92.66% for brain tumor type classification, 98.14% for brain tumor grade classification	CNN models can assist medical professionals in validating the initial multi class brain tumor assessment	Accuracy reduced for brain type classification
Tandel et al. [68]	2020	REMBRANDT	CNN-based DL model	Accuracy: 100% recall: 100% Precision: 100% F-score: 100% and AUC: 1 ($p < 0.0001$) for 2- class classification	AI-based transfer learning outperforms traditional machine learning methods in brain tumor classification	Incorporation of multiple MRI protocols needed
Mzoughi et al. [69]	2020	BraTS 2018 dataset	3D CNN	Accuracy: 96.49%	Deep CNN approach is used for accurate glioma tumor classification, learning local as well as global contextual information with reduced weights	In order to achieve improved performance, capsule networks (CapsNet) were not utilized in this for MRI brain tumor classification
Khan et al [70]	2020	BraTs2015, BraTs2017, BraTs2018	Transfer learning-based approach with ELM based feature selection	Accuracy (98.16%, 97.26%, and 93.40%, for the BraTs2015, BraTs2017, and BraTs2018 datasets	Extraction of features enhanced classification accuracy and decreased processing time	More classification accuracy is required
Yin et al. [71]	2020	Private dataset containing 204 brain MR images	MLP with improved whale optimization	Accuracy: 96.5%	Improved version of whale optimization algorithm is used to design an optimized system	Small dataset

Table 8 (continued)

References	Year	dataset used	Technique used	Results	Advantage(s)	Limitation(s)
Deepak et al. [72]	2019	Figshare	CNN technique for a three-class classification	Accuracy: 97.1% recall: 98.9% Precision: 98% and AUC: 0.99	Transfer learning approaches are extremely effective strategies in situations where medical images are inadequate	Samples falling under the meningioma category were incorrectly categorized, overfitting occur due to less training data

the progress made in the brain MRI accuracy with the adoption of DL and optimization techniques. However, it also emphasizes the ongoing challenges of balancing processing time and the generalizability of these models across various MRI datasets.

It is found from the literature that there is lack of annotated data due to the scarcity of data and annotation cost is high.

So, to address data scarcity, Transfer Learning (TL) is used. It involves leveraging pre-trained NN to extract relevant features from new datasets and adapting them to specific tasks. With advancement in DL, TL has been applied across various domains in computer vision, including medical imaging. In medical imaging, TL mostly involves models initially trained on non-medical image datasets, which are then fine-tuned for specific diagnostic task, including analysis of various medical image modalities. For brain tumor analysis, various TL models like VGGNet [5, 70, 73, 74], ResNet [74–76], InceptionV3 [76, 77], EfficientNet [76, 77], GoogLeNet [72, 78, 79] and AlexNet [68, 80], have proven effective, each offering unique advantage in identifying tumor patterns.

Also, synthetic data generation techniques such as Generative Adversarial Networks (GANs) and its variants [81–86], Variational encoders (VAEs) [87, 88] and diffusion models [85, 89] are used to address the problem of data insufficiency. GAN generate highly realistic and diverse synthetic images by learning the distribution of real-world data, making them useful in domains where data is limited like brain tumor. It is sometimes used for cross modality synthesis also. However, GAN can face training instability and require large balanced dataset to generate more diverse images. VAEs generate diverse samples by learning latent space representations even with scarce or noisy data. But VAE generated images tend to lack the fine details found in GAN outputs. So, some researchers use VAE with GAN [90–92] to overcome the limitations of mode collapse. Diffusion models present another promising approach and they iteratively learn to reverse noise to create realistic images and provide stable training and overcome the challenges associated with GANs. While each synthetic data improves model performance, especially in low data scenarios, real world medical data remains essential for capturing true clinical variability. Synthetic data combined with real world data can, however, offer improved model robustness and generalizability.

6.3 Hybrid Techniques

6.3.1 Image Fusion Based Models

Image fusion is a technique that combine multiple images from various sources or modalities to create a single, comprehensive image, leveraging the strength of each image,

results in images that are rich in details. This approach improves the utilization of image as well as allow clinicians to better understand image contents and can enhance patient outcome. Depending on the type of images that are fused, image fusion techniques are categorized as inter-modality fusion or intra-modality fusion. Intra-modal fusion combines images from same modality under different settings (e.g. Multiple MRIs with T1, T2, FLAIR sequence), its scope is limited to improving image quality. While inter-modal fusion integrates images from different modalities (e.g., MRI, PET, SPECT or CT) for complementary details combining structural, functional and metabolic insights which is crucial for brain tumor characterization. In research, some work is done on intra-modal fusion technique [93–96]. and some on inter-modal fusion technique [97–99].

For intra modal fusion BRATS dataset is mainly utilized. Hatamizadeh et al.[93] proposed SwinNet integrated with UNet for MRI segmentation. Zhao et al. [94] explored FCNN combined with conditional random field (CRF) for fine-grained segmentation. The problem of missing modalities is a major concern. Zhou et al. [95] proposed hybrid fusion network that integrates multiple fusion blocks and addressed missing MRI modalities by synthesizing them for enhanced analysis. Zhen et al. [96] integrated CNN and transformer, incorporating both local and global contextual features to improve segmentation accuracy.

Preethi et al.[97] used Dicrete Wavelet Transform (DWT) for PET-MRI fusion and optimal Deep Neural Network (DNN) for categorization, achieving high accuracy. Nandeesh et al. applied Principal component analysis (PCA) with curvelet transform and DWT for CT-MRI fusion improving fusion quality. Tomar et al. proposed a deep convolution generator network for CT-MRI transformation with self-attention space normalization and Dual cycle consistency loss to preserve semantic content. They also suggested self-supervised learning to reduce dependency on fully labeled data.

It is found from the literature, inter modal fusion for brain tumor analysis faces challenges like differencing in imaging, characteristics, resolution differences and information loss. Solutions are needed to ensure accurate image registration for alignment of modalities, improve resolution differences, preserves fine details and reduce information loss. To address high computational costs better optimization techniques are desirable. Additionally, better attention mechanisms and domain adaption are required for improved accuracy and overall performance.

6.3.2 Longitudinal Models

Analysis of degenerative diseases like tumor is essential using longitudinal MRI datasets as they include the data collected over multiple time points, allowing researchers to track disease progression. Liu et al.[100], a post operative MRI scan private dataset was used to evaluate a diffusion probabilistic model combined with DNN. The model achieves the DSC of 0.849 ± 0.09 and Relative Volume Difference (RVD) of 0.023 ± 0.19, demonstrating promising performance in generating high quality synthetic MRIs, segmentation and uncertainty estimates. Despite these strengths, the study face limitation, including small dataset and high computational cost.

Elazab et al. [101] employed a dataset of 18 subjects (9 private and 9 from BRATS 2014), each with 3 time points. It evaluates a 3D GAN combined with a U- Net model. The model demonstrated strong performance, achieving a DSC of 88.26% and JI of 78.97%. The study introduced an effective training strategy that enhance simultaneous model learning and incorporate a novel loss function combining L1 and dice loss. However, the approach has several limitations, including reliance on small dataset, focus on whole tumor segmentation rather than individual tumor components, the absence of shape attentive pathways in the generator and the omission of tumor shrinkage during analysis. Addressing, these limitations could further improve segmentation accuracy and the model's clinical relevance.

Pei et al. [102] evaluates the segmentation method combining Lattice Boltzmann Method (LBM) with RF classifier. The model achieves DSC of 0.82122 for complete tumor, 0.685811 for tumor core, and 0.23188 for enhancing tumor regions, with segmentation accuracy validated using ANOVA. While the approach showed promising result for tumor core tissues but require expansion but no substantial improvement for whole tumor.

Pei et al. [103] in another work, utilized the BRATS 2015 dataset to evaluate a segmentation approach combining LBM with RF classifier along with label fusion. This model demonstrates enhanced segmentation accuracy particularly for tumor core and enhanced tumor tissue but require expansion to segment other tumor associated tissues and validation on larger datasets.

The key challenge is scarcity of data because the datasets are often incomplete as patients unexpectedly drop out of the study leading to missing data across time points.

7 Performance Evaluation Metrics

For the evaluation of the performance related to the brain cancers prediction models, there are various performance metrics utilized. These performance methods are further classified into categories also referred to as prediction, segmentation and classification metrics. Figure 8 represents the performance measures classification. The comparison of deep learning and machine learning approaches in term of performance metrices is shown in Table 9. This table

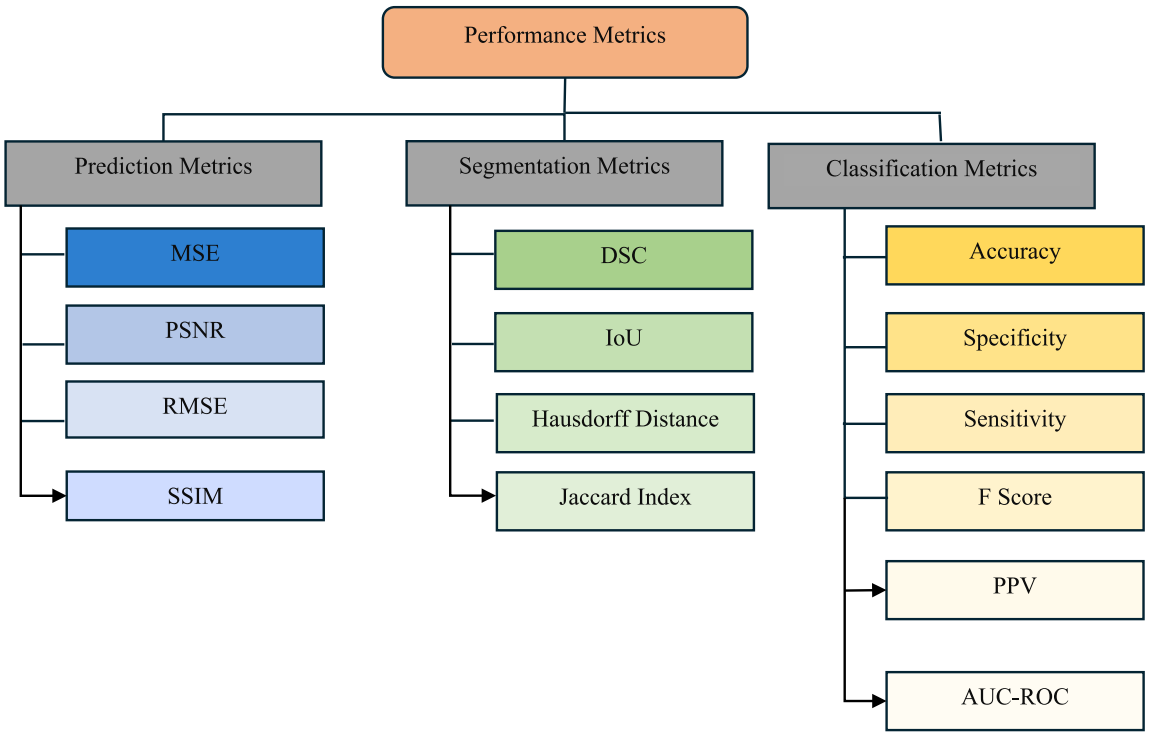

Fig.8 Classification of performance metrices

Table 9 An overview of some important evaluation metrices for bain tumor analysis

Performance Metric	References
MSE	[30, 48, 50–52, 95, 97]
PSNR	[30, 43–45, 47, 49–52, 65, 95, 97, 100]
RMSE	[52, 100]
SSIM	[30, 43–50, 95, 97, 100]
DSC	[33, 54, 57–61, 93, 94, 96, 100–103]
HD	[33, 55, 62, 93, 96]
JI	[60, 101]
Accuracy	[1, 30–32, 34, 56, 63–72]
Specificity	[30–32, 34, 60, 61, 63–65, 67, 100]
Sensitivity	[30–32, 34, 53, 60, 61, 63–67, 94]
PPV	[30, 31, 60, 63, 65–67, 72, 94]
F-Score	[31, 63, 65, 66]
AUC	[72]

displays whether the approach has employed the related performance metric or not. This classification offers a organized approach to choosing appropriate metrics for evaluating models across prediction, segmentation and classification tasks in brain tumor analysis. Each set of metrics offers specific insights pertinent to its corresponding task type, supporting robust model evaluation. In the literature performance metrics like Mean Square error (MSE), Peak Signal-to-Noise Ratio (PSNR), Root Mean Square Error (RMSE) and Structural Symmetry Index (SSIM) are mainly used for preprocessing task evaluation. For segmentation, Dice Similarity Coefficient or Dice Score (DSC), Intersection over Union (IoU), Hausdorff Distance (HD), Jaccard Index (JI) and Precision/Recall are commonly used. In classification Accuracy, Sensitivity/Recall, Specificity, Positive Predictive Value (PPV), score and Area Under ROC Curve (AUC) assess the performance of model.

8 Data Security and Privacy

Federated learning (FL) [104] offers a powerful solution for brain tumor analysis enabling institutions to collaboratively train models without sharing sensitive patient information directly. Brain imaging data, such as MRI scan is often restricted by privacy laws, making traditional data sharing approaches difficult. FL overcomes this by alloying institutions to keep data on site or share only the model updates This means that the patient information remains secure and decentralized, meeting district privacy requirement.

FL also provides access to diverse data set, a critical factor in brain tumor analysis, where tumors vary widely and are relatively rare. By training models on data from multiple sources, FL helps to create models that generalize better across different population and devices by leveraging the

various ML and DL models. The details of different detection methods are discussed in previous sections. Centralized federated learning approach is mainly used in the research [105],106, 107. Centralized federated learning approach use a central server to aggregate model updates from the distributed local servers, enabling collaborative training and maintain the data privacy. FedAvg [108–110] is another approach used for this purpose in the area of tumor detection. These approaches enhance the accuracy and reliability of tumor detection and classification and also enables the study of complex tumor cases by combining knowledge from different institutions which would be challenging with limited data from a single site.

Thus, federated learning supports high quality, privacy respecting research and have collaborative benefits in brain tumor analysis leading to improved diagnostic tools and treatment planning while it also protects patient confidentially. For these reasons, it is a promising area for researchers and deserves further exploration.

9 Gaps and Future Scope

Brain tumors being considered as a major global health concern, requirement for the development of efficient screening techniques and alternative therapies is essential to enhancing patient outcomes. Identification of any gaps or restrictions in the literature on DL based methods for brain tumor detection is quite critical aspects. addressing computational complexity, guaranteeing the generalizability of models across various populations, and requiring larger datasets to improve model training are the possible gaps that needs to be covered. Therefore, the obstacles such as overfitting and the need for significant computational resources needs to be overcome. Also, intensity inhomogeneity is a major issue with MRI images. and arises when low-frequency intensity and non-uniformity is present. While processing the images, certain characteristics are lost, which causes the tumor region to be incorrectly identified. Non-uniform region segmentation requires a lot of time, which makes Brain MRI segmentation a challenging task. MRI analysis relies significantly on image quality, which can be heavily affected by noise and distortions. This issue often caused by inappropriate imaging settings or disturbance in the transmission system. Therefore, it is essential to remove these distortions as a preprocessing step. One more issue is related to incorporation of additional features for extracting abnormalities as the processing time increases. This causes a major challenge in brain tumor image processing which is misclassification of non-tumor regions as the tumor regions. Also, the size, location, and appearance of tumors might vary. So, segmenting and classifying them is extreme challenging due to their complicated structures. Transfer Learning is promising for brain tumor analysis but has key limitations. Domain mismatch occurs as TL models are often pre-trained on non-medical images, impacting their performance. Overfitting is also a concern with small MRI datasets, and high computational demands can limit accessibility. Additionally, TL models often lack interpretability, limiting clinical adoption as it requires models that clearly explains decision making process to ensure trustworthy diagnostics. Sine–Cosine Fitness and Grey Wolf Optimization both provide significant benefit for the detection of brain tumor, like Sine–Cosine Fitness is simple and easy to implement, computationally efficient and have global search capabilities. On the other hand, Grey Wolf Optimization is robust for high-dimensional space as well as multi-objective problems. However, Sine–Cosine Fitness may struggle with complex datasets and premature convergence, while Grey Wolf Optimization may be computationally expensive.

This survey comprehends several promising future scopes for enhancing the rate of brain tumor detection using MRI scans. By putting together multi-modal imaging a more thorough diagnostic approach can be provided. Accurate and timely decision-making can be achieved by implementing these models in real-time. By examining tumor characteristics, a customized treatment plan can be developed. Moreover, image structure details can be protected and enhanced by advancements in image preprocessing such as normalization and denoising by using various advanced techniques. Advancements in image preprocessing for MRI scans can address intensity inhomogeneity and noise issues by combining adaptive normalization and deep learning based denoising along with integrating multi-modal data. This leads to more precise tumor boundaries, more reliable prediction, and can guide the denoising process to preserve both structural as well as functional characteristics of tumor. Enhanced bias field correction techniques can more effectively handle the intensity variations. These kinds of improvements would lead to more accurate segmentation and classification, ensuring better overall performance in brain tumor detection. For brain tumor, the future segmentation methods could integrate 3D models, transformers, multiscale techniques and advance imaging like Diffusion Tensor Imaging and functional MRI. Domain Adaption, AI-based boundary delineation and uncertainty quantification can enhance the accuracy, offering a more adaptable solution, improving treatment planning. To overcome the limitations associated with Sine–Cosine Fitness and Grey Wolf Optimization, they can be integrated with multi-modal data from different medical institutions as well as transfer learning models can be used, and also advancement of deep learning method can be done. These advancements can lead to more accurate and efficient models that can capable of real time processing and

better performance in complex detection tasks. Also, there is a need to explore more unused optimization techniques in the are of brain tumor analysis.

In medical image processing limitation in training data is one major drawback that can be overcome by generating synthetic data using advance AI models. Also, future research could focus on creating medical specific pre-trained models to address domain gaps. Hybrid approached that incorporate techniques like federated learning for privacy preserving adaptation should also be explored. While federated learning shows promising result in privacy preserving machine learning across institutions, its application to brain MRI image analysis remains in early stages. A multi-institutional collaborative approach using FL for MRI is still under explored. This approach could enhance robustness and generalizability of model, presenting a significant research opportunity to advance privacy concern focused collaborative machine medical imaging Also, researchers need to develop some models that work well for both complete and incomplete data. The knowledge of tumor progression can help in improving the effectiveness of treatment when talking about brain tumors, this can be achieved using longitudinal and hybrid models. After all, a more effective, accurate, and clinically feasible treatment is the goal.

10 Conclusion

This survey dives deep into the wider segments of the brain MRI analysis, meticulously giving a rich learning in segmentation and classification techniques. It gives a highlight regarding the strengths and weakness of the various approach in order to give a good help to researchers in this critical and crucial field. The dissection of the prominent techniques given in the review like 3D Convolutional Neural Networks (CNN) that encompasses the capability to learn intricate spatial relationships within MRI data. It also gives a good dive in exploring the cascade CNN's which is a method that tackles overfitting by employing a multi-stage learning process. Moreover, the survey sheds light upon the optimization techniques like Sine–Cosine Fitness Grey Wolf Optimization, which can promote the boundaries of performance by fine-tuning the hyperparameters of deep learning models.

This review also encompasses the near-perfect scores in metrics like accuracy, sensitivity (correctly identifying true positive), and specificity (correctly identifying true negatives). These advancements give a promising aspect for the early and accurate detection of the brain tumor. This review also encompasses the hurdles that needs to be addressed, reviewed and henceforth needs to be overcome such as the computational complexity in the 3D CNNs, that requires a good processing power. This work also gives a highlight regarding the risks of overfitting when being used with the limited datasets to train the models. The need for the substantial training data is also encompassed by this review in order to ensure generalizability across diverse brain MRI scans.

This survey further paves a way for the innovation in the brain tumor detection using MRI analysis by emphasizing the aspects such as striking a balance, navigation through the trade-off between computational resources needed for complex techniques and the further ability to achieve generalizable results across different datasets.

Author Contributions All authors contributed to conception and design of the study. Priyanka Datta and Rajesh Rohilla were responsible for the material preparation and analysis. Priyanka Datta wrote the manuscript, while Rajesh Rohilla handled the editing. All authors reviewed and approved the final manuscript.

Data Availability No datasets were generated or analysed during the current study.

Declarations

Conflict of interest The authors declare no competing interests.

References

1. Győrfi Á, Szilágyi L, Kovács L (2021) A fully automatic procedure for brain tumor segmentation from multi-spectral mri records using ensemble learning and atlas-based data enhancement. Appl Sci 11(2):564. https://doi.org/10.3390/app11020564
2. Al-Galal SAY, Alshaikhli IFT, Abdulrazzaq MM (2021) MRI brain tumor medical images analysis using deep learning techniques: a systematic review. Health Technol (Berl) 11(2):267–282. https://doi.org/10.1007/s12553-020-00514-6
3. Tiwari A, Srivastava S, Pant M (2020) Brain tumor segmentation and classification from magnetic resonance images: review of selected methods from 2014 to 2019. Pattern Recognit Lett 131:244–260. https://doi.org/10.1016/j.patrec.2019.11.020
4. Saman S, Jamjala Narayanan S (2019) Survey on brain tumor segmentation and feature extraction of MR images. Int J Multimed Inf Retr. https://doi.org/10.1007/s13735-018-0162-2
5. Rehman A, Naz S, Razzak MI, Akram F, Imran M (2020) 'A deep learning-based framework for automatic brain tumors classification using transfer learning', *Circuits*. Syst Signal Process 39(2):757–775. https://doi.org/10.1007/s00034-019-01246-3
6. Lundervold AS, Lundervold A (2019) An overview of deep learning in medical imaging focusing on MRI. Z Med Phys 29(2):102–127. https://doi.org/10.1016/j.zemedi.2018.11.002
7. N. P. Gupta, P. K. Malik, and B. S. Ram, (2020) A review on methods and systems for early breast cancer detection, In *2020 International Conference on Computation, Automation and Knowledge Management (ICCAKM)*, IEEE, pp. 42–46. https://doi.org/10.1109/ICCAKM46823.2020.9051554.
8. Keshav S (2007) How to read a paper. ACM SIGCOMM Comput Commun Rev 37(3):83–84. https://doi.org/10.1145/1273445.1273458
9. Abd-Ellah MK, Awad AI, Khalaf AAM, Hamed HFA (2019) A review on brain tumor diagnosis from MRI images: practical implications, key achievements, and lessons learned. Magn

Reson Imaging 61:300–318. https://doi.org/10.1016/j.mri.2019.05.028
10. Tandel GS et al (2019) A review on a deep learning perspective in brain cancer classification. Cancers (Basel) 11(1):111. https://doi.org/10.3390/cancers11010111
11. Nadeem MW et al (2020) 'Brain tumor analysis empowered with deep learning: a review taxonomy, and future challenges. Brain Sci 10(2):118. https://doi.org/10.3390/brainsci10020118
12. Kaifi R (2023) A review of recent advances in brain tumor diagnosis based on AI-based classification. Diagnostics 13(18):3007. https://doi.org/10.3390/diagnostics13183007
13. Younis A, Li Q, Khalid M, Clemence B, Adamu MJ (2023) Deep learning techniques for the classification of brain tumor: a comprehensive survey. IEEE Access 11:113050–113063. https://doi.org/10.1109/ACCESS.2023.3317796
14. Cheplygina V, de Bruijne M, Pluim JPW (2019) Not-so-supervised: a survey of semi-supervised, multi-instance, and transfer learning in medical image analysis. Med Image Anal 54:280–296. https://doi.org/10.1016/j.media.2019.03.009
15. Hesamian MH, Jia W, He X, Kennedy P (2019) Deep learning techniques for medical image segmentation: achievements and challenges. J Digit Imaging 32(4):582–596. https://doi.org/10.1007/s10278-019-00227-x
16. Fatima A, Shahid AR, Raza B, Madni TM, Janjua UI (2020) State-of-the-art traditional to the machine- and deep-learning-based skull stripping techniques, models, and algorithms. J Digit Imaging 33(6):1443–1464. https://doi.org/10.1007/s10278-020-00367-5
17. Rehman HZU, Hwang H, Lee S (2020) Conventional and deep learning methods for skull stripping in brain MRI. Appl Sci 10(5):1773. https://doi.org/10.3390/app10051773
18. Magadza T, Viriri S (2021) Deep learning for brain tumor segmentation: a survey of state-of-the-art. J Imaging 7(2):19. https://doi.org/10.3390/jimaging7020019
19. Wadhwa A, Bhardwaj A, Singh Verma V (2019) A review on brain tumor segmentation of MRI images. Magn Reson Imaging. https://doi.org/10.1016/j.mri.2019.05.043
20. Menze BH et al (2015) The multimodal brain tumor image segmentation benchmark (BRATS). IEEE Trans Med Imaging 34(10):1993–2024. https://doi.org/10.1109/TMI.2014.2377694
21. Bakas S et al (2017) Advancing the cancer genome atlas glioma MRI collections with expert segmentation labels and radiomic features. Sci Data 4(1):170117. https://doi.org/10.1038/sdata.2017.117
22. S. Bakas et al., (2018) Identifying the Best machine learning algorithms for brain tumor segmentation, progression assessment, and overall survival prediction in the BRATS challenge
23. Clark K et al (2013) The cancer imaging archive (TCIA): maintaining and operating a public information repository. J Digit Imaging 26(6):1045–1057. https://doi.org/10.1007/s10278-013-9622-7
24. Summers D (2003) Harvard whole brain atlas: www.med.harvard.edu/AANLIB/home.html. J Neurol Neurosurg Psychiatry 74(3):288–288. https://doi.org/10.1136/jnnp.74.3.288
25. 'Brain Tumor MRI Dataset | Kaggle. https://www.kaggle.com/datasets/masoudnickparvar/brain-tumor-mri-dataset
26. '"Figshare Brain Tumor Dataset | Kaggle." https://www.kaggle.com/datasets/ashkhagan/figshare-brain-tumor-dataset'.
27. C. Han et al., (2019) Infinite brain MR images: PGGAN-based data augmentation for tumor detection
28. Mohsen H, El-Dahshan E-SA, El-Horbaty E-SM, Salem A-BM (2018) Classification using deep learning neural networks for brain tumors. Futur Comput Informatics J 3(1):68–71. https://doi.org/10.1016/j.fcij.2017.12.001
29. Shapiro L, Stockman G (2001) Computer vision. Prentice-Hall, Upper Saddle River
30. Srinivasa Reddy A, Chenna Reddy P (2021) MRI brain tumor segmentation and prediction using modified region growing and adaptive SVM'. Soft Comput. https://doi.org/10.1007/s00500-020-05493-4
31. Kumar DM, Satyanarayana D, Prasad MNG (2021) MRI brain tumor detection using optimal possibilistic fuzzy C-means clustering algorithm and adaptive k-nearest neighbor classifier. J Ambient Intell Humaniz Comput 12(2):2867–2880. https://doi.org/10.1007/s12652-020-02444-7
32. Alam MS et al (2019) Automatic human brain tumor detection in MRI image using template-based K means and improved fuzzy C means clustering algorithm. Big Data Cogn Comput 3(2):27. https://doi.org/10.3390/bdcc3020027
33. Angulakshmi M, Lakshmi Priya GG (2019) Walsh hadamard transform for simple linear iterative clustering (SLIC) superpixel based spectral clustering of multimodal MRI brain tumor segmentation. IRBM 40(5):253–262. https://doi.org/10.1016/j.irbm.2019.04.005
34. B. Devanathan and K. Venkatachalapathy, (2020) An optimal multilevel thresholding based segmentation and classification model for brain tumor diagnosis, In 2020 4th International Conference on Electronics, Communication and Aerospace Technology (ICECA), IEEE, pp. 1133–1138. https://doi.org/10.1109/ICECA49313.2020.9297571.
35. O. Ronneberger, P. Fischer, and T. Brox, (2015) U-Net: convolutional networks for biomedical image segmentation, pp. 234–241, https://doi.org/10.1007/978-3-319-24574-4_28.
36. Lin F, Wu Q, Liu J, Wang D, Kong X (2021) Path aggregation U-Net model for brain tumor segmentation. Multimed Tools Appl 80(15):22951–22964. https://doi.org/10.1007/s11042-020-08795-9
37. Aboelenein NM, Songhao P, Koubaa A, Noor A, Afifi A (2020) HTTU-Net: hybrid two track u-net for automatic brain tumor segmentation. IEEE Access 8:101406–101415. https://doi.org/10.1109/ACCESS.2020.2998601
38. Zhang J, Zeng J, Qin P, Zhao L (2021) Brain tumor segmentation of multi-modality MR images via triple intersecting U-Nets. Neurocomputing 421:195–209. https://doi.org/10.1016/j.neucom.2020.09.016
39. Sharif MI, Li JP, Khan MA, Saleem MA (2020) Active deep neural network features selection for segmentation and recognition of brain tumors using MRI images. Pattern Recognit Lett 129:181–189. https://doi.org/10.1016/j.patrec.2019.11.019
40. Sun J, Peng Y, Guo Y, Li D (2021) Segmentation of the multimodal brain tumor image used the multi-pathway architecture method based on 3D FCN. Neurocomputing 423:34–45. https://doi.org/10.1016/j.neucom.2020.10.031
41. Chen H, Qin Z, Ding Y, Tian L, Qin Z (2020) Brain tumor segmentation with deep convolutional symmetric neural network. Neurocomputing 392:305–313. https://doi.org/10.1016/j.neucom.2019.01.111
42. Zhang J, Jiang Z, Dong J, Hou Y, Liu B (2020) Attention gate ResU-Net for automatic MRI brain tumor segmentation. IEEE Access 8:58533–58545. https://doi.org/10.1109/ACCESS.2020.2983075
43. Awudong B, Yakupu P, Yan J, Li Q (2024) Research and implementation of denoising algorithm for brain mris via morphological component analysis and adaptive threshold estimation. Mathematics 12(5):748. https://doi.org/10.3390/math12050748
44. Akindele RG, Yu M, Kanda PS, Owoola EO, Aribilola I (2023) Denoising of nifti (MRI) images with a regularized neighborhood pixel similarity wavelet algorithm. Sensors 23(18):7780. https://doi.org/10.3390/s23187780
45. Pankaj D (2021) A novel method for removing Rician noise from MRI based on variational mode decomposition'. Biomed

Signal Process Control 69:102737. https://doi.org/10.1016/j.bspc.2021.102737
46. Tian M, Song K (2021) Boosting magnetic resonance image denoising with generative adversarial networks. IEEE Access 9:62266–62275. https://doi.org/10.1109/ACCESS.2021.3073944
47. Tripathi PC, Bag S (2020) CNN-DMRI: a convolutional neural network for denoising of magnetic resonance images. Pattern Recognit Lett 135:57–63. https://doi.org/10.1016/j.patrec.2020.03.036
48. Baselice F, Ferraioli G, Pascazio V, Sorriso A (2019) Denoising of MR images using Kolmogorov-Smirnov distance in a non local framework. Magn Reson Imaging 57:176–193. https://doi.org/10.1016/j.mri.2018.11.022
49. Jiang D, Dou W, Vosters L, Xu X, Sun Y, Tan T (2018) Denoising of 3D magnetic resonance images with multi-channel residual learning of convolutional neural network. Jpn J Radiol 36(9):566–574. https://doi.org/10.1007/s11604-018-0758-8
50. R. Biswas, D. Purkayastha, and S. Roy, (2018) Denoising of MRI images using curvelet transform, pp. 575–583. https://doi.org/10.1007/978-981-10-4762-6_55.
51. N. Joshi, S. Jain, and A. Agarwal, (2016) An improved approach for denoising MRI using non local means filter', In 2016 2nd International Conference on Next Generation Computing Technologies (NGCT), IEEE, pp. 650–653. https://doi.org/10.1109/NGCT.2016.7877492.
52. M. R. Maneesha Mohan, C. H. Sulochana, and T. Latha, (2015) Medical image denoising using multistage directional median filter', In 2015 International Conference on Circuits, Power and Computing Technologies [ICCPCT-2015], IEEE, pp. 1–6. https://doi.org/10.1109/ICCPCT.2015.7159261.
53. Rajendran S et al (2023) Automated segmentation of brain tumor MRI images using deep learning. IEEE Access 11:64758–64768. https://doi.org/10.1109/ACCESS.2023.3288017
54. Ranjbarzadeh R, Bagherian Kasgari A, Jafarzadeh Ghoushchi S, Anari S, Naseri M, Bendechache M (2021) Brain tumor segmentation based on deep learning and an attention mechanism using MRI multi-modalities brain images. Sci Rep 11(1):10930. https://doi.org/10.1038/s41598-021-90428-8
55. Cheng D et al (2023) Brain tumor feature extraction and edge enhancement algorithm based on U-Net network. Heliyon 9(11):e22536. https://doi.org/10.1016/j.heliyon.2023.e22536
56. Nyo MT, Mebarek-Oudina F, Hlaing SS, Khan NA (2022) Otsu's thresholding technique for MRI image brain tumor segmentation. Multimed Tools Appl 81(30):43837–43849. https://doi.org/10.1007/s11042-022-13215-1
57. Ding Y et al (2021) ToStaGAN: an end-to-end two-stage generative adversarial network for brain tumor segmentation. Neurocomputing 462:141–153. https://doi.org/10.1016/j.neucom.2021.07.066
58. Zhou X, Li X, Hu K, Zhang Y, Chen Z, Gao X (2021) ERV-Net: an efficient 3D residual neural network for brain tumor segmentation. Expert Syst Appl 170:114566. https://doi.org/10.1016/j.eswa.2021.114566
59. Nema S, Dudhane A, Murala S, Naidu S (2020) RescueNet: an unpaired GAN for brain tumor segmentation. Biomed Signal Process Control 55:101641. https://doi.org/10.1016/j.bspc.2019.101641
60. Imtiaz T, Rifat S, Fattah SA, Wahid KA (2020) Automated brain tumor segmentation based on multi-planar superpixel level features extracted from 3D MR images. IEEE Access 8:25335–25349. https://doi.org/10.1109/ACCESS.2019.2961630
61. Sajid S, Hussain S, Sarwar A (2019) Brain tumor detection and segmentation in MR images using deep learning. Arab J Sci Eng 44(11):9249–9261. https://doi.org/10.1007/s13369-019-03967-8
62. G. Wang, W. Li, S. Ourselin, and T. Vercauteren, (2018) Automatic brain tumor segmentation using cascaded anisotropic convolutional neural networks, pp. 178–190. https://doi.org/10.1007/978-3-319-75238-9_16.
63. ZainEldin H et al (2022) Brain tumor detection and classification using deep learning and sine-cosine fitness grey wolf optimization. Bioengineering 10(1):18. https://doi.org/10.3390/bioengineering10010018
64. Ayadi W, Charfi I, Elhamzi W, Atri M (2022) Brain tumor classification based on hybrid approach. Vis Comput 38(1):107–117. https://doi.org/10.1007/s00371-020-02005-1
65. Atha Z, Chaki J (2023) SSBTCNet: semi-supervised brain tumor classification network. IEEE Access 11:141485–141499. https://doi.org/10.1109/ACCESS.2023.3343126
66. Rao CS, Karunakara K (2022) Efficient detection and classification of brain tumor using kernel based SVM for MRI. Multimed Tools Appl 81(5):7393–7417. https://doi.org/10.1007/s11042-021-11821-z
67. Irmak E (2021) Multi-classification of brain tumor MRI images using deep convolutional neural network with fully optimized framework. Iran J Sci Technol Trans Electr Eng 45(3):1015–1036. https://doi.org/10.1007/s40998-021-00426-9
68. Tandel GS, Balestrieri A, Jujaray T, Khanna NN, Saba L, Suri JS (2020) Multiclass magnetic resonance imaging brain tumor classification using artificial intelligence paradigm. Comput Biol Med 122:103804. https://doi.org/10.1016/j.compbiomed.2020.103804
69. Mzoughi H et al (2020) Deep multi-scale 3D convolutional neural network (CNN) for MRI gliomas brain tumor classification. J Digit Imaging 33(4):903–915. https://doi.org/10.1007/s10278-020-00347-9
70. Khan MA et al (2020) Multimodal brain tumor classification using deep learning and robust feature selection: a machine learning application for radiologists. Diagnostics 10(8):565. https://doi.org/10.3390/diagnostics10080565
71. Yin B, Wang C, Abza F (2020) New brain tumor classification method based on an improved version of whale optimization algorithm. Biomed Signal Process Control 56:101728. https://doi.org/10.1016/j.bspc.2019.101728
72. Deepak S, Ameer PM (2019) Brain tumor classification using deep CNN features via transfer learning. Comput Biol Med 111:103345. https://doi.org/10.1016/j.compbiomed.2019.103345
73. Basha NK, Ananth C, Muthukumaran K, Sudhamsu G, Mittal V, Gared F (2024) Mask region-based convolutional neural network and VGG-16 inspired brain tumor segmentation. Sci Rep 14(1):17615. https://doi.org/10.1038/s41598-024-66554-4
74. Ali S, Agrawal J (2023) Automated segmentation of brain tumour images using deep learning-based model VGG19 and ResNet 101. Multimed Tools Appl 83(11):33351–33370. https://doi.org/10.1007/s11042-023-16828-2
75. Younis A et al (2024) Abnormal brain tumors classification using ResNet50 and its comprehensive evaluation. IEEE Access 12:78843–78853. https://doi.org/10.1109/ACCESS.2024.3403902
76. Shamshad N et al (2024) Enhancing brain tumor classification by a comprehensive study on transfer learning techniques and model efficiency using mri datasets. IEEE Access 12:100407–100418. https://doi.org/10.1109/ACCESS.2024.3430109
77. İncir R, Bozkurt F (2024) Improving brain tumor classification with combined convolutional neural networks and transfer learning. Knowledge-Based Syst 299:111981. https://doi.org/10.1016/j.knosys.2024.111981
78. Rasool M et al (2022) A hybrid deep learning model for brain tumour classification. Entropy 24(6):799. https://doi.org/10.3390/e24060799

79. Matin Malakouti S, Bagher Menhaj M, Abolfazl Suratgar A (2024) Machine learning and transfer learning techniques for accurate brain tumor classification. Clin. eHealth 7:106–119. https://doi.org/10.1016/j.ceh.2024.08.001
80. Bairagi VK, Gumaste PP, Rajput SH, Chethan KS (2023) Automatic brain tumor detection using CNN transfer learning approach. Med Biol Eng Comput 61(7):1821–1836. https://doi.org/10.1007/s11517-023-02820-3
81. Li Q, Yu Z, Wang Y, Zheng H (2020) TumorGAN: a multi-modal data augmentation framework for brain tumor segmentation. Sensors 20(15):4203. https://doi.org/10.3390/s20154203
82. Sahoo S, Mishra S, Panda B, Bhoi AK, Barsocchi P (2023) An augmented modulated deep learning based intelligent predictive model for brain tumor detection using GAN ensemble. Sensors 23(15):6930. https://doi.org/10.3390/s23156930
83. Alrashedy HHN, Almansour AF, Ibrahim DM, Hammoudeh MAA (2022) BrainGAN: brain MRI image generation and classification framework Using GAN architectures and CNN models. Sensors 22(11):4297. https://doi.org/10.3390/s22114297
84. Mukherkjee D, Saha P, Kaplun D, Sinitca A, Sarkar R (2022) Brain tumor image generation using an aggregation of GAN models with style transfer. Sci Rep 12(1):9141. https://doi.org/10.1038/s41598-022-12646-y
85. Usman Akbar M, Larsson M, Blystad I, Eklund A (2024) Brain tumor segmentation using synthetic MR images—a comparison of GANs and diffusion models. Sci. Data 11(1):259. https://doi.org/10.1038/s41597-024-03073-x
86. Datta P, Rohilla R (2024) Brain tumor image pixel segmentation and detection using an aggregation of GAN models with vision transformer. Int J Imaging Syst Technol. https://doi.org/10.1002/ima.22979
87. Chatterjee S et al (2022) StRegA: unsupervised anomaly detection in brain MRIs using a compact context-encoding variational autoencoder. Comput Biol Med 149:106093. https://doi.org/10.1016/j.compbiomed.2022.106093
88. Salama WM, Shokry A (2022) A novel framework for brain tumor detection based on convolutional variational generative models. Multimed Tools Appl 81(12):16441–16454. https://doi.org/10.1007/s11042-022-12362-9
89. Dorjsembe Z, Pao H-K, Odonchimed S, Xiao F (2024) Conditional diffusion models for semantic 3D brain MRI synthesis. IEEE J Biomed Heal Informatics 28(7):4084–4093. https://doi.org/10.1109/JBHI.2024.3385504
90. Pani K, Chawla I (2024) Synthetic MRI in action: a novel framework in data augmentation strategies for robust multi-modal brain tumor segmentation. Comput Biol Med 183:109273. https://doi.org/10.1016/j.compbiomed.2024.109273
91. Ahmad B, Sun J, You Q, Palade V, Mao Z (2022) Brain tumor classification using a combination of variational autoencoders and generative adversarial networks. Biomedicines 10(2):223. https://doi.org/10.3390/biomedicines10020223
92. Han C et al (2019) Combining noise-to-image and image-to-image GANs: brain MR image augmentation for tumor detection. IEEE Access 7:156966–156977. https://doi.org/10.1109/ACCESS.2019.2947606
93. A. Hatamizadeh, V. Nath, Y. Tang, D. Yang, H. R. Roth, and D. Xu, (2022) 'Swin UNETR: swin transformers for semantic segmentation of brain tumors in MRI images, pp. 272–284. https://doi.org/10.1007/978-3-031-08999-2_22.
94. Zhao X, Wu Y, Song G, Li Z, Zhang Y, Fan Y (2018) A deep learning model integrating FCNNs and CRFs for brain tumor segmentation. Med Image Anal 43:98–111. https://doi.org/10.1016/j.media.2017.10.002
95. Zhou T, Fu H, Chen G, Shen J, Shao L (2020) Hi-Net: hybrid-fusion network for multi-modal mr image synthesis. IEEE Trans Med Imaging 39(9):2772–2781. https://doi.org/10.1109/TMI.2020.2975344
96. Zheng J, Shi F, Zhao M, Jia C, Wang C (2023) Learning intra-inter-modality complementary for brain tumor segmentation. Multimed Syst 29(6):3771–3780. https://doi.org/10.1007/s00530-023-01138-2
97. Preethi S, Aishwarya P (2021) An efficient wavelet-based image fusion for brain tumor detection and segmentation over PET and MRI image. Multimed Tools Appl 80(10):14789–14806. https://doi.org/10.1007/s11042-021-10538-3
98. M. D. Nandeesh, (2021) Multimodal image fusion using hybrid algorithms for brain tumor detection, In 2021 IEEE Mysore Sub Section International Conference (MysuruCon), IEEE, pp. 566–571. https://doi.org/10.1109/MysuruCon52639.2021.9641592.
99. Tomar D, Lortkipanidze M, Vray G, Bozorgtabar B, Thiran J-P (2021) Self-attentive spatial adaptive normalization for cross-modality domain adaptation. IEEE Trans Med Imaging 40(10):2926–2938. https://doi.org/10.1109/TMI.2021.3059265
100. Q. Liu et al., (2023) Treatment-aware diffusion probabilistic model for longitudinal MRI generation and diffuse glioma growth prediction
101. Elazab A et al (2020) GP-GAN: brain tumor growth prediction using stacked 3D generative adversarial networks from longitudinal MR Images. Neural Netw 132:321–332. https://doi.org/10.1016/j.neunet.2020.09.004
102. L. Pei, S. M. S. Reza, W. Li, C. Davatzikos, and K. M. Iftekharuddin, 'Improved brain tumor segmentation by utilizing tumor growth model in longitudinal brain MRI', S. G. Armato and N. A. Petrick, Eds., Mar. 2017, p. 101342L. https://doi.org/10.1117/12.2254034.
103. Pei L, Bakas S, Vossough A, Reza SMS, Davatzikos C, Iftekharuddin KM (2020) Longitudinal brain tumor segmentation prediction in MRI using feature and label fusion. Biomed Signal Process Control 55:101648. https://doi.org/10.1016/j.bspc.2019.101648
104. Banabilah S, Aloqaily M, Alsayed E, Malik N, Jararweh Y (2022) Federated learning review: fundamentals, enabling technologies, and future applications. Inf Process Manag 59(6):103061. https://doi.org/10.1016/j.ipm.2022.103061
105. Islam M, Reza MT, Kaosar M, Parvez MZ (2023) Effectiveness of federated learning and CNN ensemble architectures for identifying brain tumors using MRI images. Neural Process Lett 55(4):3779–3809. https://doi.org/10.1007/s11063-022-11014-1
106. Aggarwal M et al (2024) Privacy preserved collaborative transfer learning model with heterogeneous distributed data for brain tumor classification. Int J Imaging Syst Technol. https://doi.org/10.1002/ima.22994
107. W. Li et al., (2019) 'Privacy-preserving federated brain tumour segmentation', pp. 133–141. https://doi.org/10.1007/978-3-030-32692-0_16.
108. Ay Ş, Ekinci E, Garip Z (2024) A brain tumour classification on the magnetic resonance images using convolutional neural network based privacy-preserving federated learning. Int J Imaging Syst Technol. https://doi.org/10.1002/ima.23018
109. L. Zhou, M. Wang, and N. Zhou, (2024) Distributed federated learning-based deep learning model for privacy MRI brain tumor detection
110. Manthe M, Duffner S, Lartizien C (2024) Federated brain tumor segmentation: an extensive benchmark. Med Image Anal 97:103270. https://doi.org/10.1016/j.media.2024.103270

Publisher's Note Springer Nature remains neutral with regard to jurisdictional claims in published maps and institutional affiliations.

Springer Nature or its licensor (e.g. a society or other partner) holds exclusive rights to this article under a publishing agreement with the author(s) or other rightsholder(s); author self-archiving of the accepted manuscript version of this article is solely governed by the terms of such publishing agreement and applicable law.

CorrNetDroid: Android Malware Detector leveraging a Correlation-based Feature Selection for Network Traffic features

Yash Sharma and Anshul Arora

arXiv:2503.01396v1 [cs.CR] 3 Mar 2025

***Abstract*—Copious mobile operating systems exist in the market, but the Android remains the user's choice. Meanwhile, its growing popularity has also allured malware developers. Researchers have proposed various static solutions for Android malware detection. However, stealthier malware evade static analysis. This raises the need for a robust Android malware detection system capable of dealing with advanced threats and overcoming the shortcomings of static analysis. Hence, in this work, we have proposed a dynamic analysis-based Android malware detection system, *CorrNetDroid*, that works over network traffic flows. Many of the traffic features have overlapping ranges in normal and malware datasets. Therefore, we first rank the features using two statistical measures namely, *crRelevance* and *Normalized Mean Residue Similarity*, assessing feature–class and feature–feature correlations. Thereafter, we propose a novel correlation-based feature selection algorithm that deploys *NMRS* on the *crRelevance* rankings to identify the optimal feature subset for Android malware detection. The experimental results highlight that our proposed model can effectively reduce the feature set while detecting Android malware with 99.50% accuracy on considering only two network traffic features. Furthermore, our experiments demonstrate that the *NMRS*-based proposed algorithm on *crRelevance* rankings is better than other statistical tests such as chi-square, ANOVA, Mann–Whitney U test and Kruskal–Wallis test. In addition, our proposed model outperforms various state-of-the-art Android malware detection techniques in terms of detection accuracy.**

***Index Terms*—Android Security, Mobile Malware, Malware Detection, Network Traffic Features, Feature Selection**

I. Introduction

What started as a mere device for communication purposes has now become the smartphone era. We have gradually accepted smartphones as an indispensable part of our lives because of the need for communication and other daily necessities. These days, one can find an application for almost everything. Statistics depict the emergence of Android apps, as over the past 14 years, the Google Play Store has expanded significantly, increasing from 16,000 apps in 2009 to 3.553 million apps. [1]. As for the most preferred operating system, Android OS reigns at the top due to its numerous attributes. Open architecture and the availability of various feature-rich applications are just some of the merits of Android OS, and hence, Android mobile sales have grown exponentially in the past 14 years.

ysharma2098@gmail.com and anshul15arora@gmail.com.
Department of Applied Mathematics, Delhi Technological University, Delhi -110042, India

[1]https://www.bankmycell.com/blog/number-of-google-play-store-apps/)

With its increasing popularity worldwide, Android has become a victim of its own success as malware authors constantly strive to steal private information or even perpetrate advanced fraud by hiding malicious code inside applications without the user's consent. According to Kaspersky Security Network, in the first quarter of 2024, close to 10 million mobile malware incursions were blocked [2]. To address these troubling figures, researchers have suggested a range of malware detection methods in the literature. Generally, the detection approaches proposed in the literature can be classified into two categories, namely static, and dynamic. [1].

Static analysis has demonstrated significant efficiency in both feature extraction and cost-effectiveness. Examining malware without running the code itself and gathering fundamental details about an application's behavior appeared to be advantageous. However, some stealthier malware may not show their malicious behavior in static analysis, i.e., malware with advanced techniques such as code obfuscation, polymorphism, and encryption may evade static detection. Dynamic analysis, wherein applications are monitored at runtime, overcomes the shortcomings of static analysis. Therefore, in this study, we aim to develop a dynamic malware detection framework.

Stealthier malware samples establish connections with remote servers clandestinely to receive commands or to exfiltrate users' private information or device data to the server. Approximately 93% of Android malware exhibit network connectivity. Since these malware are remotely controlled, they effectively transform the mobile device into a mobile bot, presenting a significant threat to the user community.

Some dynamic Android malware detection techniques have been proposed in the literature using features such as system calls [2], cryptographic and network operation [3]. However, we chose network traffic flows to perform dynamic analysis because they provide a comprehensive and real-time view of an application's external communication. Simultaneously, features such as system calls provide limited visibility into external communications, especially if the malware disguises its activities by leveraging legitimate APIs or system calls. Moreover, anomalies may be harder to detect because some malware can mimic legitimate application behavior and alter its API or system call patterns to avoid detection. Hence we aim to analyze network traffic features for Android malware detection.

[2]https://securelist.com/it-threat-evolution-q1-2024-mobile-statistics

A. Motivation

Analyzing network traffic usage patterns is an effective way to detect malware. As a result, network traffic flows have been extensively utilized in Android malware detection. Nonetheless, there exist numerous resemblances in the traffic feature patterns between benign and malicious applications. Tables I summarizes the range of several traffic features. We extracted over nine lacs network traffic flows of the normal class and an equal number for the malware class by combining the datasets from various repositories. Additional information regarding the dataset is presented in subsequent sections. Furthermore, we extracted 16 network traffic features from the network traffic data. As seen in Table I, commonly used features, namely "Flow_Duration", "Packets_sent/received", "Bytes_sent/received" are present in overlapping ranges when observed in both normal and malware traffic.

The presence of these similar features in both datasets serves as a motivation for us to prioritize feature ranking. The aim of our proposed work is to present an efficient detection model that utilizes prioritized traffic features.

Several related studies have used the dynamic traffic features for Android malware detection. For instance, Wang et al. [4] analyzed multiple levels of network traffic features and emphasized that combining 2 levels, namely HTTP packet and TCP flow, can successfully lead to malware detection. However, they failed to consider the crucial idea of feature ranking, hence neglecting the step of feature reduction, which had the potential to enhance the quality of their results.

In several other related works, such as [5] and [6], the authors built a detection system using the best subset of features by feature ranking. More specifically, Arora and Peddoju [5] extracted 22 network traffic features. Consequently, they aimed to reduce the feature set and used information gain and chi-square test to rank the feature set. In [6], the authors tried to understand the reason behind the deviations in the application's network traffic behavior from the normal flow by observing the network traffic flows. Hence, they computed the probability scores depicting the deviation of features' behaviors from normal traffic patterns and later used the threshold approach to select the best subset of features. Nevertheless, both studies were carried out with a limited number of network traffic flows in comparison to the comprehensive dataset employed in our proposed study. More importantly, our research demonstrates superior performance as compared to both in terms of detection accuracy.

Our experiments demonstrate that our proposed *NMRS*-based detection model with *crRelevance* rankings outperforms other statistical tests such as chi-square, ANOVA, Mann–Whitney U test, Kruskal–Wallis test.

TABLE I
RANGE OF TRAFFIC FEATURES FOR MALWARE AND NORMAL MOBILE APPLICATIONS

Feature Name	Range in normal traffic	Range in malware traffic
Flow_duration	0 - 49560.3403	0 - 52122.128886
Packets_sent_per_flow	1 - 110985	1 - 48265
Packets_received_ per_flow	0 - 215014	0 - 104312
Bytes_sent	40 - 82771640	54 - 16288912
Bytes_received	0 - 1217408141	0 - 157283100

B. Research Objectives

The proposed dynamic detection approach centering the ranking of network traffic attributes gives rise to the following research questions:

1) Why is there a need to prioritize or rank network traffic features?
2) How to incorporate feature ranking while eliminating redundant features, i.e., how to rank network traffic features and select the least correlated subset?
3) How to frame a detection approach while considering both feature– class and feature– feature correlations?
4) What is the advantage(s) of feature ranking regarding detection accuracy?

Organization: In Section II, we examine some previous research in the field. This is followed by a thorough description of the proposed approach in Section III. Hereafter, we provide the results acquired using the proposed model in Section IV along with addressing certain limitations. Lastly, we wrap up the work by discussing potential areas for future research in Section V.

II. Related Work

We deliver a comprehensive analysis of existing research in Android malware detection in this section. We focus our discussion on dynamic detection models. Researchers have used dynamic features such as function call graphs, system calls [2], cryptographic and network operation [3] for Android malware detection. However, we chose network traffic flows because they provide a comprehensive and real-time view of an application's external communication, making it particularly effective in the context of Android malware detection. Simultaneously, system calls dispense limited visibility into external communications, especially if the malware disguises its activities by leveraging legitimate APIs or system calls. Besides, anomalies may be harder to detect because some malware can mimic legitimate application behavior and alter its API or system call patterns to avoid detection. Cryptographic operations focus on encryption and decryption routines but may miss the extensive context of malicious activities. Hence, we use dynamic network traffic features in this study.

In this section, we aim to discuss studies that have used TCP, HTTP, or DNS flows for Android malware detection. We divide the related work into two categories: network traffic-based analysis and traffic-based detection.

A. Network Traffic-Based Analysis

In the literature, few studies have aimed to analyze network traffic of mobile applications [7, 8]. These works did not consider malware apps. Some other techniques have analyzed the dynamic features of TCP flows, HTTP requests, and DNS queries concerning malicious Android apps. In this subsection, we review all of these techniques.

The authors in [9] analyzed the network traffic of malware samples during the first five minutes of installation and operation. They concluded that the majority of the network traffic is covered by HTTP and DNS flows. The authors in [10] analyzed the HTTP traffic generated by mobile botnets to group their families effectively. They observed statistical information related to HTTP traffic and formed malware clusters. Kumar and Sharma [11] focused on analyzing the Android Ransomware network architecture and suggested a road map for detecting such attacks. All of these studies analyzed the malware traffic and did not aim for malware detection.

B. Network Traffic-Based Detection

In the literature, several authors have focused on Android malware detection using network traffic features. This section provides a comprehensive review of all such related works proposed in the literature. We further divide this section into two subsections: network traffic-based detection with feature ranking and traffic-based detection without feature ranking.

1) Detection with Feature Ranking: First, we examine methods that have utilized any feature ranking/selection technique for Android malware detection.

Arora and Peddoju [12] proposed a hybrid detection model to combine the permissions and network traffic features extracted from Android applications. They created a hybrid feature vector and applied the FP-Growth algorithm to extract frequent patterns in combinations of permissions and network traffic features for the benign and malware datasets. In their other work [5], they extracted 22 network traffic features and further reduced the feature set with information gain and chi-square test. Upadhayay et al. [13] ranked the permissions based on their frequency in the benign and malware dataset. Next, to enhance their results, they introduced a dynamic analysis approach and coalesced the best set of network traffic features from their previous research work [5] to the newly obtained best set of permissions for malware detection.

The authors in [14] proposed an approach analyzing the text semantics of HTTP request headers with the natural language processing algorithm called N-gram. They reduced the feature set to the most influential ones by applying the statistical chi-square test. Hossain et al. [15] aimed to find a robust solution for growing ransomware attacks using network traffic features. They exploited particle swarm optimization to select only the optimal traffic characteristics and applied machine learning classifiers for malware detection. The authors in [16] devised a deep learning-based malware classification system using raw payload and CNNs. They concentrated on the raw payload of malicious network traffic, leveraging the byte data to represent related behavioral patterns of malware, and further treated the window selection algorithm's filtered (SWS) flows as documents to be processed by NLP methods.

To the best of our knowledge, no other study has assessed the ranking of dynamic attributes of TCP flows using a statistical *crRelevance* test to detect Android malware. We chose *crRelevance* for its simplicity and strong alignment with the goals of our research. Unlike other statistical tests, which often require strict assumptions such as normality of data, homogeneity of variances, and the independence of observations within mutually exclusive categories, *crRelevance* is free from these constraints. These benefits make *crRelevance* the most appropriate choice for our analysis. In this study, we proposed an *NMRS*-based feature selection algorithm with *crRelevance* rankings to detect Android malware with the most optimal attributes.

2) Detection without Feature Ranking : Within the literature, several detection mechanisms exist for detecting Android malware without any feature ranking/selection technique. This indicates that they have not given priority to the ranking of features. Within this subsection, we present a thorough review of these detection approaches.

Shabtai et al. [6] analyzed the reason behind the deviations in the application's network traffic behavior. The authors focused on the server side of the system and believed that a strong correlation exists between benign behavior patterns that can be used to detect abnormal activities. Pang et al. [17] developed an efficient and convenient network traffic collection system. The authors observed that the malware applications produced a negligible amount of network traffic data; hence, they combined imbalance algorithms with the classical machine learning algorithms for their testing methods. The authors in [4] analyzed multiple levels of traffic features and emphasized that combining two levels, namely HTTP packet and TCP flow, can be successfully employed to create a lightweight server-based malware detection model.

Mahdavifar et al. [18] emphasized the concern regarding the difficulty in accumulating well-labeled datasets and hence proposed a Deep Neural Network (DNN) based work to perform dynamic analysis for malware category classification. Liu et al. [19] suggested a Graphical Neural Network (GNN) model based on mobile network traffic with node characteristics and edge attributes. The authors in [20] focused on repackaged apps. They computed the flow similarity using the Euclidian algorithm between two sets of network traffic features.

Ullah et al. [21] proposed a multi-headed ensemble neural network by combining a convolutional neural network and gated recurrent units using the semantic features of HTTP traces and the numeric values of TCP flows. The authors in [22] employed a sequential-based deep learning (DL) model and stimulated network traffic data as a sequence of flows built upon the concept of long short-term memory. Similar to the previous work, the authors in [23] used a deep learning-based model to detect malicious Android applications but used the network traffic flows as grayscale images instead of their original numeric form.

We have highlighted the importance of ranking network traffic features for effective Android malware detection in the Introduction section. In addition, none of the above-discussed techniques applied feature ranking techniques with dynamic traffic features for mobile malware detection. In this study, we first ranked the network traffic features with *crRelevance* to find the traffic feature set with the best ability to distinguish between benign and malicious class labels. Furthermore, we proposed an *NMRS* based feature selection algorithm with *crRlevance* to identify Android malware using the most ef-

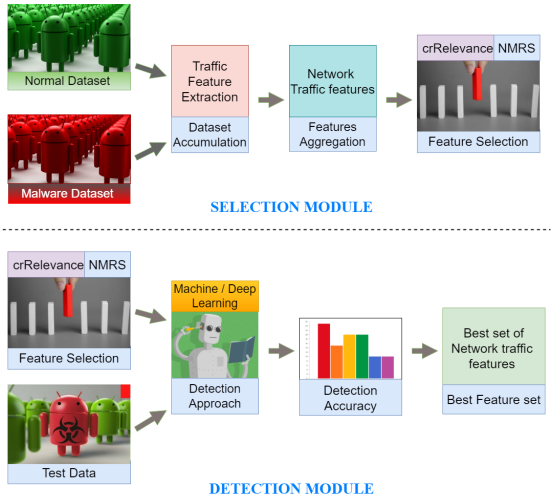

Fig. 1. CorrNetDroid System Design

fective features. We outline our proposed methodology in the following section.

III. System Design

This section delivers a comprehensive explanation of our proposed methodology. Fig. 1 provides a concise overview of our proposed model *CorrNetDroid*, which primarily consists of two modules. The first module, referred to as the *Selection Module*, involves computing network traffic features from the TCP flows of the training dataset and ranking them using a statistical measure called *crRelevance*. Such a ranking will help us grade them according to their ability to distinguish between the two class labels, normal and malware. Simultaneously, we also rank the features based on their inter-correlation score using another statistical technique called *NMRS*, which would help us eliminate the redundancy between the ranked features. In the *Detection Module*, we introduce a novel *NMRS*-based algorithm that leverages machine learning and deep learning techniques on *crRelevance* rankings to identify the optimal subset of attributes, thereby achieving higher detection accuracy. We implemented machine learning and deep learning classifiers using the Python programming language. Additionally, we utilized the Wireshark Tool to extract TCP flows from normal and malware traffic datasets. We implemented the proposed model on a desktop system featuring 8 GB of RAM, an i5-1135G7 processor, and running Windows 11 as the operating system.

The subsequent subsections provide detailed discussions on both modules of the proposed model.

SELECTION MODULE

A. Dataset Collection

To commence our research, we required a large dataset of mobile network traffic generated by benign and malicious applications. Hence, we obtained the network traffic data from the Canadian Institute for Cybersecurity (CIC). More specifically, we gathered four datasets, namely CICAndMal2017 [24], CIC-InvesAndMal2019 [25], CIC-AAGM2017 [26] and USTC-TFC2016 [27]. Combining these datasets, we gathered 9,88,280 network traffic flows each for the normal and malware apps.

TABLE II
List of Network Traffic Features

Average_packet_size **(Fi)**	Packets_sent_per_second **(Fix)**
Time_interval_between_packets_ sent **(Fii)**	Packets_received_per_ second **(Fx)**
Time_interval_between_packets_received**(Fiii)**	Packets_received_per_flow **(Fxi)**
Flow_duration **(Fiv)**	Packet_size_received **(Fxii)**
Ratio_of_incoming_to_outgoing_packets**(Fv)**	Bytes_sent **(Fxiii)**
Ratio_of_incoming_to_outgoing_ bytes **(Fvi)**	Bytes_sent_per_second **(Fxiv)**
Packet_size_sent **(Fvii)**	Bytes_received **(Fxv)**
Packets_sent_per_flow **(Fviii)**	Bytes_received_per_ second **(Fxvi)**

B. Traffic Split

Transmission Control Protocol (TCP) flows play a crucial role in ensuring reliable and efficient communication between devices on the Internet. TCP is a connection-oriented protocol that facilitates the orderly and error-checked data delivery between applications. TCP connections start off with a three-way handshake. During this process, the sender and receiver exchange SYN (synchronization) and ACK (acknowledgment) packets to set up the connection. Moreover, different operating systems and network environments support TCP. TCP connections terminate using a four-way handshake, involving FIN (finish) and ACK flags. Its ubiquity makes it suitable for diverse applications and scenarios. Hence, we aim to extract TCP flow-based network traffic features.

Table II summarizes the 16 traffic features used in our experiments. We extracted these features from the pcap flows of the benign and malware traffic. We have also highlighted the concise notation for each feature in the Table. For instance, “Fi” notation for “Average_packet_ size”, “Fiv” for “Flow_duration”, etc. In the Results section, we denote the features by their notations to facilitate comprehension and interpretation of the data.

C. Feature Selection

Several techniques exist in the literature for feature selection, however, many often overlook the correlation among features. When selecting an optimal feature subset, it is crucial to consider both feature–feature and feature-class correlations. An ideal feature subset should consist of features highly correlated with class labels while exhibiting minimal correlation with each other [28]. In contrast to many existing methods, we propose a feature selection technique that addresses both correlations: feature–feature and feature–class. We employ *crRelevance* and *NMRS* measures to achieve these correlations. In the following subsections, we discuss the working of *crRelevance* and *NMRS* measures.

1) ***crRelevance: Feature-Class Correlation****: crRelevance* is a measure used to evaluate the ability of a feature to distinguish between various class labels [29]. It yields a value within the interval of 0 to 1. The subsequent definitions establish the conceptual foundation for *crRelevance*.

Definition 1 For a feature f_k with values $\{x_1, x_2 \ldots x_n\}$ corresponding to n objects or instances in the dataset, a class range can be defined as a range $\mathrm{R} = [r_1, r_2]$ such that, $\forall x_i, x_j, r_1 \leq x_i \leq r_2, r_1 \leq x_j \leq r_2$ and $\mathrm{class}_{f_k}(x_i) = \mathrm{class}_{f_k}(x_j)$, where $\mathrm{class}_f(x)$ is the class associated with value x over feature f. In other words, a class range $\mathrm{R} = [r_1, r_2]$ over feature f is said to be associated with class A [29], if $\forall x, r_1 \leq x \leq r_2, \mathrm{class}_f(x) = A$.

Definition 2 Cardinality of a class range $\mathrm{R} = [r_1, r_2]$, denoted as $\mathrm{rcard_f(R)}$ [29] is defined as the cardinality of the set $\{x \mid x \in V, r_1 \leq x \leq r_2\}$, where V is the set of values of all the objects for feature f .

Definition 3 The class-cardinality of a class A, denoted as ccard(A) [29], is defined as the cardinality of the set $\{x \mid \mathrm{class}(x) = A\}$.

Definition 4 Core class range of class A denoted as ccrange(A), can be defined as the highest class range associated with the class A in terms of class range cardinality. A range R_i [29] associated with class A is called the core class range of A if there is no R_j in F, such that $\mathrm{rcard}(R_j) > \mathrm{rcard}(R_i)$.

Now, core range-based relevance of a class A for feature f_i, denoted by $\mathit{crRelevance}^{\mathrm{class}}_{\mathrm{f_i}}(\mathrm{A})$, is defined as follows.

$$\mathit{crRelevance}^{\mathrm{class}}_{\mathrm{f_i}}(\mathrm{A}) = \frac{\mathrm{rcard(ccrange(A))}}{\mathrm{ccard(A)}} \tag{1}$$

For a dataset D, the core class relevance of a feature $f_i \in \mathrm{F}$, denoted by *crRelevance* $(\mathrm{f_i})$ [29], can be defined as the highest *crRelevance* for a given class A_i.

$$\mathit{crRelevance}\,(f_i) = \max_{1 \leq j \leq n} \mathit{crRelevance}^{\mathrm{class}}_{f_i}\,(A_j) \tag{2}$$

In this work, we have two numerical-type continuous datasets comprising 16 features for two classes, benign and malware. We obtain the *crRelevance_normal* and *crRelevane_malware* scores for each feature after applying the above definitions to both the training datasets individually. Further, we compute the absolute difference between the *crRelevance_normal* and *crRelevane_malware* scores for each feature to identify the most distinguishing features. Higher distinguishing features will be at the top of the ranked list irrespective of their preference for either class . We would like to point out that we considered the absolute difference instead of the normal difference to avoid the accumulation of the best features on the endpoints of the ranked list rather than on the top. The features were ranked based on their scores, making sure that the feature with the highest *crRelevance score* is placed at the top, demonstrating its greater ability to differentiate across class labels.

*2) **NMRS- Feature-Feature Correlation**:* The *Normalized Mean Residue Similarity* (*NMRS*) technique ranks features according to their relevance to the output variable. However, it does not consider redundant features. In general, closely related features often produce similar results or have a similar impact on the output data. Hence, to assess if two features exhibit similar patterns, it is essential to choose a suitable similarity measure. In other words, to find the correlation between features, we use an effective method called *Normalized Mean Residue Similarity* (*NMRS*). The level of concordance [30] between feature $d_1 = (a_1, a_2, \ldots, a_n)$ with respect to another feature $d_2 = (b_1, b_2, \ldots, b_n)$ is defined by the following Equation:

$$1 - \frac{\sum_{i=1}^{n} |a_i - a_{\text{mean}} - b_i + b_{\text{mean}}|}{2 \times \max\left\{\sum_{i=1}^{n} |(a_i - a_{\text{mean}})|, \sum_{i=1}^{n} |(b_i - b_{\text{mean}})|\right\}}, \tag{3}$$

where a_{mean} is the mean of all the elements of feature d_1;

$$a_{\text{mean}} = \{a_1 + a_2 + \ldots + a_n\}/n, \tag{4}$$

and b_{mean} is the mean of all the elements of feature d_2 ;

$$b_{\text{mean}} = \{b_1 + b_2 + \ldots + b_n\}/n. \tag{5}$$

In our proposed work, because we wish to find the feature–feature correlation between all possible pairs without any relation to their classes, we concatenate the normal and malware traffic feature values. We combine the flows of both class labels for each feature and then compute the *NMRS* scores. In this way, we iteratively compute the *NMRS* score for each feature pair by considering them as d_1 and d_2 variables in the given *NMRS* equation. Pearson correlation coefficient, Spearman correlation coefficient, and Mean Squared Residue are the most commonly employed similarity/correlation measurements. Nevertheless, each of these approaches has its drawbacks. Additionally, the Pearson correlation coefficient can identify not just shifting patterns but also scaling and other patterns that are often undesirable and may involve features with a substantial disparity in their expression levels. The Spearman Rank correlation coefficient uses rank values to compute correlation, however, it is unable to identify patterns including shifting or scaling. The mean squared residue is effective in identifying changing patterns, but it cannot function in a mutual mode, hence, it cannot determine the correlation between a pair of features. Therefore, we have chosen *NMRS* as our preferred choice for the feature–feature correlation.

Using the *NMRS*-based proposed feature selection method that further uses *crRelevance* developed rankings, we answer our research question two, i.e., how to rank features in order to identify the most distinctive and least correlated features.

DETECTION MODULE

We applied several machine learning and deep learning classifiers [31] in our detection approach. Primarily, we employed nine commonly utilized classifiers, including Decision Trees, Random Forest, Bagging Classifier, Gaussian Naive Bayes, Gradient Boosting, AdaBoost, Multilayer Perceptron, Dense Neural Network, and Convolutional Neural network in our experiments. We performed all the experiments with ten-fold cross-validation. In the subsequent section, we detail the results obtained from the proposed approach.

IV. Results and Discussion

In this section, we delve into the experimental results acquired through the proposed *CorrNetDroid* model. It's important to note that we utilized separate datasets for both training and testing purposes. As elaborated in Section III.A,

we accumulated 9,88,280 TCP flows, each from the benign and malware categories, by compiling four datasets from various repositories. Of these, we use 6,94,261 flows of each category for training and the remaining 2,94,019 flows for testing. We named this as "*Testing Dataset*". In the following subsections, we initially explore the rankings derived from the two statistical measures employed in our study, namely *crRelevance* and *NMRS*. Subsequently, we delineate the detection results obtained on the *Testing Dataset*. Moreover, we conducted a comparative analysis of our proposed model with similar models designed for Android malware detection.

A. Features Ranking

We applied the statistical measure *crRelevance* separately to the benign and malware traffic features to identify the distinguishing features. As an output, the technique produces a pair of feature-class correlation scores for each feature. Furthermore, we used the sorted absolute difference between the *crRelevance*_normal and *crRelevance*_malware of features to rank them. Table **??** summarizes the network features ranked according to the absolute difference between the category scores. Table **??** highlights that the feature "Packet_size_received (Fxii)" is ranked at the top with the highest absolute difference between category scores. Similarly, the feature "Bytes_sent_per_second (Fxiv)" has the worst absolute difference and may have the worst distinguishing characteristics trait.

Our proposed feature selection and detection algorithm uses both feature–class, and feature–feature correlation, i.e., *crRelevance* and *NMRS* rankings, to identify the best subset of features. Hence, in the next step, we applied *NMRS* to all possible feature pairs (120 pairs) and ranked them in decreasing order of their correlation score. Table **??** summarizes the top 20 and bottom 20 traffic feature pairs, based on their *NMRS* correlation scores. The table can be understood as follows. The features "Average_packet_size (Fi)" and "Packet_size_received (Fxii)" have the best correlation score and thus have the best correlation between them. Similarly, the features "Time_interval_between_ packets_sent (Fii)" and "Packets_received_per_second (Fx)" have the worst correlation between them.

B. Comparison of crRelevance with other statistical tests

In this subsection, we compare the performance of our proposed model with that of some commonly used statistical tests for Android malware detection. Our proposed approach involved computing the feature– class correlation, i.e., *crRelevance* ranking, and further deploying an *NMRS*-based detection algorithm to select the best set of features that produce higher detection accuracy. Hence, to compare our model's performance, we deploy the same *NMRS*-based detection algorithm on the following statistical measures:

1) **Chi-Square** - The chi-square test evaluates the disparity between expected and observed values to assess whether the observed deviations fall within an acceptable range, and is represented by the following formula:

$$\chi_c{}^2 = \sum \frac{(O_i - E_i)^2}{E_i} \tag{6}$$

where:
c=Degrees of freedom,
O=Observed value(s), and
E=Expected value(s).

TABLE III
TRAFFIC FEATURES RANKED USING VARIOUS STATISTICAL TESTS

Chi-Square on Normal	Chi-Square on Malware	ANOVA	Mann-Whitney	Kruskal-Wallis
Fv	Fv	Fiii	Fv	Fiii
Fii	Fvi	Fiv	Fvii	Fv
Fiii	Fvii	Fvii	Fxiv	Fxii
Fvi	Fi	Fv	Fx	Fxii
Fix	Fii	Fii	Fxi	Fvi
Fx	Fxii	Fxvi	Fix	Fviii
Fvii	Fx	Fi	Fii	Fxv
Fi	Fiv	Fx	Fxiii	Fvii
Fiv	Fviii	Fviii	Fxvi	Fiv
Fxii	Fxi	Fxi	Fiv	Fxiv
Fviii	Fiii	Fxiii	Fxv	Fx
Fxi	Fix	Fvi	Fviii	Fxvi
Fxiv	Fxiii	Fxv	Fvi	Fxi
Fxvi	Fxvi	Fix	Fi	Fxiii
Fxiii	Fxv	Fxii	Fxii	Fix
Fxv	Fxiv	Fxiv	Fxiii	Fii

2) **ANOVA** - ANOVA, short for Analysis of Variance, is a statistical technique employed to examine variations between the means of different groups within a sample. It is commonly used to evaluate the null hypothesis that suggests the means of three or more groups are the same. In our case, normal and malware values of the same feature from the training dataset are taken as the two groups. The one-way ANOVA F-statistic is calculated using the following formula:

$$F = \frac{\text{Between-Group Variance (MSB)}}{\text{Within-Group Variance (MSW)}} \tag{7}$$

where:
MSB (Mean Square Between) is the variance among the group means and MSW (Mean Square Within) is the average of the variances within each group.

3) **Mann-Whitney** - The Mann-Whitney U test, alternatively referred to as the Wilcoxon rank-sum test, is a statistical method that assesses whether there is a significant difference between two independent and randomly chosen groups. The U statistic is calculated using the following formula:

$$U_1 = R_1 - \frac{n_1 \cdot (n_1 + 1)}{2} \tag{8}$$

$$U_2 = R_2 - \frac{n_2 \cdot (n_2 + 1)}{2} \tag{9}$$

where:
U_1 and U_2 are the U statistics, R_1 and R_2 are the sums of ranks and n_1 and n_2 are the sample sizes for Group 1 and Group 2, respectively.

4) **Kruskal-Wallis** - The Kruskal-Wallis test is a non-parametric test used to determine whether there are statistically significant differences between three or more

independent groups. The test assesses whether the samples originate from the same distribution or if at least one of the samples is different from the others. The formula for the test statistic is as follows :

$$H = \frac{12}{N(N+1)} \sum_{i=1}^{k} \frac{R_i^2}{n_i} - 3(N+1) \qquad (10)$$

where:
N is the total number of observations across all groups,
k is the number of groups,
R_i is the sum of ranks for group i, and
n_i is the number of observations in group i.

Table III summarizes the individual test rankings when we apply chi-square on the normal feature set and chi-square on the malware feature set along with other measures such as ANOVA, Mann–Whitney U test, and Kruskal– Wallis test. As can be seen from the table, "Ratio_of_incoming_to_ outgoing_packets (Fv)" has been ranked as the most distinguishing feature by Mann– Whitney as well as both rankings of the chi-square test, whereas, according to ANOVA and Kruskal– Wallis, the feature named "Time_interval_between_ packets_received (Fiii)" resides at the top of the table as the best feature.

For comparison, we ranked network traffic features using the four statistical tests described above and further applied our proposed *NMRS*-based algorithm on the *Testing Dataset* to determine their corresponding accuracies. Table **??** summarizes the results and it can be understood as follows. When we apply the *NMRS*-based proposed approach on chi-square rankings (on benign training dataset) and Kruskal– Wallis rankings, we achieve the highest detection accuracy of 96.22% after eliminating 14 features out of the total lot of 16 traffic features. With two features, namely "Ratio_of_incoming_to_ outgoing_packets (Fv)" and "Time_interval_between_ packets_received (Fiii)", the highest detection accuracy can be achieved. At the same time, the highest detection accuracy of 96.37% can be achieved upon considering two features, namely "Ratio_of_incoming_to_ outgoing_packets (Fv)" and "Time_interval_between_ packets_sent (Fii)" when we apply the *NMRS*-based proposed algorithm on Mann– Whitney test rankings and chi-square test rankings for malware dataset. Similarly, when we apply the *NMRS*-based proposed algorithm to ANOVA test rankings, we obtain the highest detection accuracy of 98.10% while considering two features, namely "Time_interval_between_ packets_received (Fiii)" and "Flow_Duration (Fiv)". When we apply the *NMRS*-based proposed algorithm to the *crRelevance* rankings used in our work, we obtain an accuracy of 99.5% with two features, namely "Packet_size_received (Fxii)" and "Time_interval_between_ packets_received (Fiii)". Hence, our model outperforms other similar statistical tests when we apply our proposed *NMRS* algorithm to their developed rankings.

C. Comparsion with other related works

In this subsection, we assess the performance of our proposed model with another similar work incorporating TCP flows. We do so by implementing the approach followed by the authors in [6]. Similar to the working of their proposed model, we chose Decision Table and REPTree classifiers as the base learners for the *local learning model*. We trained these classifiers with all 16 features. According to the authors, when a benign feature vector was evaluated against the models developed during the learning phase, there is a greater likelihood that the projected value would closely resemble or match the observed value. If the forecasts deviate significantly from the actual values of the relevant attributes, it indicates a higher probability that the observed vector originates from a distinct distribution. Therefore, we ranked the features in order of their probability of deviation from the pattern of benign traffic features. Table **??** summarizes the traffic features ranked in order of their deviation from normal traffic behavior. As depicted by the table, the feature "Packets_sent_per_flow (Fviii)" shows the highest probability of coming from an abnormal event. At the same time, the feature "Ratio_of_incoming_to_ outgoing_packets (Fv)" scored the lowest related to the least probability of coming from an abnormal event.

After ranking the network traffic features in order of their probability of deviation from benign traffic patterns, we proceed to find the best feature set with higher detection accuracy. Table **??** summarizes the detection results using Decision Table and RepTree classifiers as base learners. As it can be seen, upon eliminating four features out of the total set of 16 features, we managed to achieve the highest detection accuracy of 95.85% while using both Decision Table and RepTree classifiers as base learners, In other words, on considering the top 12 features, namely "Fviii, Fxv, Fxi, Fiv, Fxiii, Fix, Fxiv, Fii, Fxvi, Fiii, Fx, and Fvi", both the classifiers display the same detection accuracy of 95.85%. Whereas, with our *NMRS*-based proposed algorithm applied to *crRelevance* rankings, we could achieve a higher detection accuracy of 99.5%. Hence, we can conclude that our proposed approach outperforms this similar network traffic based Android malware detection model.

Furthermore, we evaluated our work with other resembling works of Android malware detection. Table **??** summarizes this comparison. Some studies have attempted to determine the probability of deviation from normal traffic features' patterns, whereas others have ranked the features using tests such as chi-square, information gain, and frequency ranges to select the best subset of features. As the table summarizes, our proposed model outperforms all these studies with respect to detection accuracy. Therefore, we can deduce that our suggested model surpasses numerous state-of-the-art methodologies in the existing body of knowledge for detecting Android malware.

D. Limitations

Next, we outline few limitations of the proposed methodology. The proposed model ranks TCP-based network traffic features for detection; hence, it falls under the category of dynamic analysis. The path of dynamic analysis overcomes several limitations of static analysis but also poses some barriers. Not all Android malware samples generate network traffic. It has been observed that certain types of malware

may transmit text messages discreetly in the background, without producing any noticeable network traffic. Hence, network traffic-based detection mechanisms cannot detect such samples. Dynamic analysis tools can introduce performance overhead as they monitor and analyze the execution of the program. This overhead may affect the timing and behavior of the software, potentially masking certain performance-related issues. In addition, certain mobile assaults may occur as a result of colluding apps, when harmful behavior is spread throughout multiple apps rather than being confined to a single app. Nevertheless, the current version of the proposed paradigm does not specifically address the issue of colluding apps. Hence, in our future endeavors, we intend to focus on identifying colluding applications in order to improve the detection capability of the suggested model.

V. Conclusion and Future Work

In this study, we ranked the network traffic features in order of their correlation with the class and amongst themselves using two statistical measures, namely *crRelevance* and *Normalized Mean Residue Similarity* (*NMRS*). Subsequently, we proposed a novel *NMRS*-based detection algorithm to select the best and inversely correlated features by applying various machine learning and deep learning techniques. The experimental results highlight that our proposed *NMRS*-based detection algorithm on *crRelevance* rankings can effectively reduce the feature set while detecting Android malware with 99.50% accuracy on considering two network traffic features, namely "Packet_size_received" and "Time_interval_between_ packets_received". Furthermore, our results showed that our proposed method is better than other statistical tests such as Chi-Square, ANOVA, Mann–Whitney U test and Kruskal–Wallis test. Moreover, the proposed model can detect Android malware with better accuracy than various state-of-the-art techniques. In our future work, we aim to enhance the capabilities of our model by including malware category and family classification along with the binary classification performed in this study. We also aim to integrate static features to deal with the limitations of dynamic analysis and possibly build a robust hybrid detection model.

References

[1] Y. Sharma and A. Arora, "A comprehensive review on permissions-based android malware detection," *International Journal of Information Security*, pp. 1–36, 2024.

[2] L. Singh and M. Hofmann, "Dynamic behavior analysis of android applications for malware detection," in *2017 International Conference on Intelligent Communication and Computational Techniques (ICCT)*. IEEE, 2017, pp. 1–7.

[3] P. Feng, J. Ma, C. Sun, X. Xu, and Y. Ma, "A novel dynamic android malware detection system with ensemble learning," *IEEE Access*, vol. 6, pp. 30 996–31 011, 2018.

[4] S. Wang, Z. Chen, Q. Yan, B. Yang, L. Peng, and Z. Jia, "A mobile malware detection method using behavior features in network traffic," *Journal of Network and Computer Applications*, vol. 133, pp. 15–25, 2019.

[5] A. Arora and S. K. Peddoju, "Minimizing network traffic features for android mobile malware detection," in *Proceedings of the 18th international conference on distributed computing and networking*, 2017, pp. 1–10.

[6] A. Shabtai, L. Tenenboim-Chekina, D. Mimran, L. Rokach, B. Shapira, and Y. Elovici, "Mobile malware detection through analysis of deviations in application network behavior," *Computers & Security*, vol. 43, pp. 1–18, 2014.

[7] M. Conti, L. Mancini, R. Spolaor, and N. Verde, "Analyzing android encrypted network traffic to identify user actions," *IEEE Transactions on Information Forensics and Security*, vol. 11, no. 1, pp. 114–125, 2016.

[8] G. Aceto, D. Ciuonzo, A. Montieri, and A. Pescapé, "Mobile encrypted traffic classification using deep learning: Experimental evaluation, lessons learned, and challenges," *IEEE Transactions on Network and Service Management*, vol. 16, no. 2, pp. 445–458, 2019.

[9] Z. Chen, H. Han, Q. Yan, B. Yang, L. Peng, L. Zhang, and J. Li, "A first look at android malware traffic in first few minutes," in *2015 IEEE Trustcom/BigDataSE/ISPA*, vol. 1, 2015, pp. 206–213.

[10] M. Aresu, D. Ariu, M. Ahmadi, D. Maiorca, and G. Giacinto, "Clustering android malware families by http traffic," in *2015 10th International Conference on Malicious and Unwanted Software (MALWARE)*. IEEE, 2015, pp. 128–135.

[11] A. Kumar and I. Sharma, "Understanding the behaviour of android ransomware attacks with real smartphones dataset," in *2023 International Conference for Advancement in Technology (ICONAT)*, 2023, pp. 1–5.

[12] A. Arora and S. K. Peddoju, "Ntpdroid: a hybrid android malware detector using network traffic and system permissions," in *17th IEEE international conference on trust, security and privacy in computing and communications(TrustCom/BigDataSE)*. IEEE, 2018, pp. 808–813.

[13] M. Upadhayay, A. Sharma, G. Garg, and A. Arora, "Rpndroid: android malware detection using ranked permissions and network traffic," in *2021 Fifth World Conference on Smart Trends in Systems Security and Sustainability (WorldS4)*. IEEE, 2021, pp. 19–24.

[14] S. Wang, Q. Yan, Z. Chen, B. Yang, C. Zhao, and M. Conti, "Detecting android malware leveraging text semantics of network flows," *IEEE Transactions on Information Forensics and Security*, vol. 13, no. 5, pp. 1096–1109, 2017.

[15] M. S. Hossain, N. Hasan, M. A. Samad, H. M. Shakhawat, J. Karmoker, F. Ahmed, K. F. M. N. Fuad, and K. Choi, "Android ransomware detection from traffic analysis using metaheuristic feature selection," *IEEE Access*, vol. 10, pp. 128 754–128 763, 2022.

[16] T. Lu and J. Wang, "F2dc: Android malware classification based on raw traffic and neural networks," *Computer Networks*, vol. 217, p. 109320, 2022.

[17] Y. Pang, Z. Chen, X. Li, S. Wang, C. Zhao, L. Wang, K. Ji, and Z. Li, "Finding android malware trace from highly imbalanced network traffic," in *2017 IEEE International Conference on Computational Science and*

Engineering (CSE) and IEEE International Conference on Embedded and Ubiquitous Computing (EUC), vol. 1. IEEE, 2017, pp. 588–595.

[18] S. Mahdavifar, A. F. Abdul Kadir, R. Fatemi, D. Alhadidi, and A. A. Ghorbani, "Dynamic android malware category classification using semi-supervised deep learning," in *2020 IEEE International Conference on Dependable, Autonomic and Secure Computing*, 2020, pp. 515–522.

[19] T. Liu, Z. Li, H. Long, and A. Bilal, "Nt-gnn: Network traffic graph for 5g mobile iot android malware detection," *Electronics*, vol. 12, no. 4, p. 789, 2023.

[20] M. Alshehri, "App-nts: a network traffic similarity-based framework for repacked android apps detection," *Journal of Ambient Intelligence and Humanized Computing*, vol. 13, no. 3, pp. 1537–1546, 2022.

[21] F. Ullah, S. Ullah, G. Srivastava, J. C.-W. Lin, and Y. Zhao, "Nmal-droid: Network-based android malware detection system using transfer learning and cnn-bigru ensemble," *Wireless Networks*, pp. 1–22, 2023.

[22] S. Fallah and A. J. Bidgoly, "Android malware detection using network traffic based on sequential deep learning models," *Software: Practice and Experience*, vol. 52, no. 9, pp. 1987–2004, 2022.

[23] L. Shen, J. Feng, Z. Chen, Z. Sun, D. Liang, H. Li, and Y. Wang, "Self-attention based convolutional-lstm for android malware detection using network traffics grayscale image," *Applied Intelligence*, vol. 53, no. 1, pp. 683–705, 2023.

[24] A. H. Lashkari, A. F. A. Kadir, L. Taheri, and A. A. Ghorbani, "Toward developing a systematic approach to generate benchmark android malware datasets and classification," *In the proceedings of the 52nd IEEE International Carnahan Conference on Security Technology (ICCST), Montreal, Quebec, Canada*, 2018.

[25] L. Taheri, A. F. Abdulkadir, and A. H. Lashkari, "Extensible android malware detection and family classification using network-flows and api-calls," *The IEEE (53rd) International Carnahan Conference on Security Technology, India*, 2019.

[26] A. H. Lashkari, A. F. A. Kadir, H. Gonzalez, K. F. Mbah, and A. A. Ghorbani, "Towards a network-based framework for android malware detection and characterization," in *In the proceeding of the 15th International Conference on Privacy, Security and Trust, PST, Calgary, Canada,*, 2017, pp. –.

[27] W. Wang, M. Zhu, X. Zeng, X. Ye, and Y. Sheng, "Malware traffic classification using convolutional neural network for representation learning," in *2017 International conference on information networking (ICOIN)*. IEEE, 2017, pp. 712–717.

[28] M. A. Hall, "Correlation-based feature selection for machine learning," Ph.D. dissertation, The University of Waikato, 1999.

[29] P. Borah, H. A. Ahmed, and D. K. Bhattacharyya, "A statistical feature selection technique," *Network Modeling Analysis in Health Informatics and Bioinformatics*, vol. 3, pp. 1–13, 2014.

[30] P. Mahanta, H. A. Ahmed, D. K. Bhattacharyya, and J. K. Kalita, "An effective method for network module extraction from microarray data," *BMC bioinformatics*, vol. 13, no. 13, pp. 1–11, 2012.

[31] I. H. Witten and E. Frank, "Data mining: practical machine learning tools and techniques with java implementations," *Acm Sigmod Record*, vol. 31, no. 1, pp. 76–77, 2002.

Yash Sharma is currently a doctoral student specializing in Android Security in the Department of Applied Mathematics at Delhi Technological University, Delhi, India. He holds a postgraduate degree in Mathematics from the same institution and has conducted research in Network Security as part of his academic work. He has published papers in the field of Android Security in SCIE journals, including the Journal of Network and Computer Applications (Elsevier), Multimedia Tools and Applications, International Journal of Information Security (Springer).

Anshul Arora is currently working as an Assistant Professor in the Discipline of Mathematics and Computing, Department of Applied Mathematics, Delhi Technological University Delhi, India. He has done his Ph.D. from the Department of Computer Science and Engineering, Indian Institute of Technology Roorkee, India. He has published several research papers in his field of expertise which are Mobile Security, Mobile Malware Detection, Network Traffic Analysis, and Blockchain. He is the reviewer of several renowned journals such as IEEE Transactions on Information Forensics and Security, IEEE Transactions on Computational Social Systems, Expert Systems with Applications, Computers & Security, etc.

The current issue and full text archive of this journal is available on Emerald Insight at:
https://www.emerald.com/insight/1934-8835.htm

International Journal of Organizational Analysis

Crowdsourcing adoption in organisations: a multi-perspective analysis of innovation and organisational dynamics

Divya Mishra
Vivekananda School of Business Studies,
Vivekananda Institute of Professional Studies, Delhi, India, and

Nidhi Maheshwari
University School of Management and Entrepreneurship (USME),
Delhi Technological University, Delhi, India

Received 19 November 2024
Revised 2 February2025
26 February 2025
Accepted 26 February2025

Abstract

Purpose – In response to the growing importance of crowdsourcing as a strategic tool for innovation in problem-solving, data collection and creativity, this research investigates the key dynamics influencing its adoption. Using a comprehensive framework that integrates innovation characteristics, technological readiness, organisational factors and environmental contexts, this study aims to identify and analyse critical factors that shape crowdsourcing adoption.

Design/methodology/approach – The research uses a sample of 426 senior managers from various industries in India. The data is analysed using partial least squares, a component-based approach to structural equation modelling.

Findings – The findings reveal a nuanced interplay of these factors, with relative advantage acting as a catalyst for adoption, motivated by cost reduction and perceived opportunities. Complexity serves as a notable inhibitor, emphasising challenges associated with managing diverse contributions and technical intricacies. Compatibility, technology readiness and top management support emerge as facilitators, highlighting the importance of aligning crowdsourcing initiatives with organisational structures and fostering a technologically ready and leadership-endorsed environment.

Research limitations/implications – This study enhances the understanding of crowdsourcing adoption by identifying key determinants and offering strategic insights for organisations. Future research could explore the role of decentralised structures like Distributed Autonomous Organisations and Distributed Autonomous Enterprises in adoption processes. Cross-industry and cross-cultural studies may further refine these factors, whereas policymakers can leverage these findings to foster technological readiness, streamline adoption, and align organisations with innovation strategies.

Originality/value – This study fills a crucial gap in current literature by providing a holistic framework and empirical evidence on the critical factors influencing crowdsourcing adoption. The originality lies in the integration of established theories, offering a comprehensive analysis that contributes valuable insights to both academia and practitioners in the field of organisational innovation.

Keywords Crowdsourcing adoption, Innovation dynamics, Diffusion of innovation (DOI), Technology–organisation–environment (TOE)

Paper type Research paper

1. Introduction

Today's organisations face complex challenges and rising expectations, driving them towards digital innovation to remain competitive. The dynamic nature of market shifts and

International Journal of Organizational Analysis
© Emerald Publishing Limited
1934-8835
DOI 10.1108/IJOA-11-2024-4997

the increasing demand for innovation require organisations to leverage capabilities beyond traditional approaches (Xu *et al.*, 2015; Nevo and Kotlarsky, 2020). Open innovation strategies, particularly crowdsourcing, have become critical tools in addressing organisational problems and driving innovation performance. Crowdsourcing, a subset of open innovation, involves harnessing external contributions – such as knowledge, skills or expertise – via digital platforms. This decentralised and collaborative model enables organisations to tap into diverse, distributed resources to solve complex issues (Chesbrough, 2003; Howe, 2006).

Crowdsourcing aligns with decentralisation, resource sharing and connectivity, similar to grid computing, where tasks and resources are distributed efficiently across decentralised environments (Afuah and Tucci, 2012). It provides organisations with a framework for joint activities, enhancing innovation, knowledge transfer and problem-solving across various domains. Crowdsourcing is increasingly recognised as a competitive strategy, leveraging external expertise in areas such as labour, skills and innovation. Notable applications include T-shirt designing at Threadless (Acar, 2019), micro-task execution on Amazon Mechanical Turk (Garrow *et al.*, 2020), customer idea collection at Starbucks (Johnson *et al.*, 2019) and idea generation at SAP. It offers advantages in idea generation (Schemmann *et al.*, 2016; Zhu *et al.*, 2017), problem-solving (Lee *et al.*, 2015), cost-effectiveness, information processing and adaptability (Ye and Kankanhalli, 2017).

However, crowdsourcing is not universally suitable for all organisations (Wilson *et al.*, 2017). Dependence on external expertise and information technology (IT) services introduces uncertainty, and challenges like ambiguous requirements and solver compatibility complicate adoption (Boudreau and Lakhani, 2013). Success depends on effective collaboration with external solvers to align solutions with organisational goals (Zogaj *et al.*, 2015). In addition, implicit domain knowledge requirements can hinder solver contributions, increasing organisational costs (Zhao and Zhu, 2014). This research is crucial for advancing the theoretical and practical understanding of crowdsourcing adoption, especially in decentralised environments. Although existing literature primarily examines motivations for adopting crowdsourcing, with an emphasis on resource management and cost reduction (Chou, 2021), there is limited empirical research focusing on the perspectives of the firms seeking crowdsourcing solutions (Thuan *et al.*, 2016; Qin *et al.*, 2016; Mishra and Maheshwari, 2024a). While Ye and Kankanhalli (2015) explore the role of resource and cost management in crowdsourcing adoption on the "Taskcn" platform, studies predominantly address the technical and operational aspects, with insufficient attention paid to organisational perspectives. Addressing this gap is essential for both theoretical advancements and practical implications, as a deeper understanding of the firm's perspective can aid in the development of tailored crowdsourcing strategies. Identifying key challenges and best practices can help businesses optimise crowdsourcing implementation, enhance solver engagement and mitigate risks associated with external collaboration. In addition, insights from this research can inform policymakers and industry leaders in designing supportive frameworks and technological infrastructures that enhance crowdsourcing effectiveness across different organisational settings.

To bridge these gaps, this study develops a comprehensive research framework that integrates the innovation characteristics of crowdsourcing with the technology–organisation–environment (TOE) framework, exploring the factors that shape its adoption. This framework is designed to address the decentralised and collaborative nature of crowdsourcing, highlighting its alignment with ontological principles of resource sharing and distributed problem-solving. As organisations increasingly leverage external providers

for innovation, understanding the factors influencing crowdsourcing adoption becomes critical (Benlian and Hess, 2011). The research aims to achieve two primary goals:

(1) to identify the most influential factors in the adoption of crowdsourcing from a theoretical standpoint; and

(2) to assess the readiness and capacity of organisations to adopt crowdsourcing from technological, organisational and environmental perspectives.

By integrating the Diffusion of Innovation (DOI) and Technology–Organisation–Environment (TOE) theories, this study extends the traditional TOE framework by incorporating innovation characteristics, offering a more comprehensive perspective on crowdsourcing adoption (Rogers, 2003; Tornatzky and Fleischer, 1990). This research makes a significant contribution by developing a theoretical framework that addresses gaps in the literature and aligns crowdsourcing adoption with decentralisation, resource sharing and connectivity principles (Xu *et al.*, 2015). The inclusion of innovation characteristics within the TOE framework enhances its relevance to evolving organisational needs (Chesbrough, 2003).

A key contribution of this study is its empirical focus on emerging economies, particularly India, where research on organisational crowdsourcing adoption is limited (Benlian and Hess, 2011). This focus enriches the discussions on digital transformation and open innovation (Boudreau and Lakhani, 2013). The study highlights the critical challenges and opportunities that influence decision-making in decentralised environments (Ye and Kankanhalli, 2017; Zogaj *et al.*, 2015). It also provides practical insights for managers and policymakers, offering strategic guidelines to optimise crowdsourcing strategies and drive innovation. By identifying key adoption determinants, organisations can better manage decentralised innovation (Howe, 2006; Acar, 2019). The research enhances understanding of technology adoption and organisational strategy, enabling businesses to leverage open innovation for competitive advantage (Schemmann *et al.*, 2016; Nevo and Kotlarsky, 2020). At the organisational level, the findings offer actionable guidelines to help managers and policymakers optimise crowdsourcing strategies, thus enhancing innovation performance. Identifying the key factors influencing adoption allows organisations to manage decentralised innovation more effectively, improve decision-making processes and foster greater collaboration across teams. On an individual level, the study emphasises the skills and knowledge required for employees to engage effectively in crowdsourcing initiatives. This empowerment equips individuals with the tools to adapt to new collaborative models and contribute to driving innovation within their organisations. The paper is structured as follows: Sections 2 and 3 discuss the theoretical framework and hypotheses. Section 4 details the methodology, while Section 5 presents the findings. Sections 6, 7, 8 and 9 highlight theoretical contributions, practical implications, study limitations and future research directions.

2. Background

2.1 Crowdsourcing

Crowdsourcing, a complex phenomenon, has evolved significantly since its inception (Ghezzi *et al.*, 2018; Cricelli *et al.*, 2022). In 2006, Howe introduced the term "crowdsourcing" in Wired Magazine, merging "crowd" and "outsourcing" to describe the practice of seeking expertise, performing specific tasks or engaging online communities to solve problems by involving a group of people (the crowd). In 2008, Howe categorised crowdsourcing into four types based on various application methods:

(1) crowd creation, where crowds are engaged in generating new product designs, solutions and concepts;

(2) crowd wisdom, where companies use the collective coordination, cooperation and individual cognition of the crowd to accomplish tasks;

(3) crowd labour, where crowds' intelligence is leveraged to perform simple and complex tasks; and

(4) crowdfunding, where companies seek crowd investments for specific activities (Modaresnezhad *et al.*, 2020).

Crowdsourcing has been called crowd wisdom, collaborative systems, mass cooperation and collective intelligence (Doan *et al.*, 2011) since Howe (2006) popularised the term. Other words in the literature include collective wisdom, open innovation and crowd work (Marjanovic *et al.*, 2012; Kittur *et al.*, 2013). The current research study has used the term "crowdsourcing" because it accurately describes the concept and has been frequently used (Howe, 2008; Estellés-Arolas and González-Ladrón-De-Guevara, 2012; Afuah and Tucci, 2012). As crowdsourcing has gained popularity as a new research arena, many scholars have proposed different definitions, taxonomies and frameworks for crowdsourcing.

Scholars have compared crowdsourcing to outsourcing (Howe, 2006; Saxton *et al.*, 2013), while others view it as a problem-solving approach (Afuah and Tucci, 2012). Maiolini and Naggi (2011) explored its application in business to business and small and medium-sized enterprises (SMEs). Over time, multiple definitions emerged, creating confusion (Howe, 2008; Brabham, 2008). To address this, Estellés-Arolas and González-Ladrón-De-Guevara (2012) integrated existing definitions, identifying three key elements:

(1) crowd;

(2) initiator; and

(3) process.

They defined crowdsourcing as a participatory online activity where an entity engages a diverse crowd for idea generation, problem-solving, expertise or funding. This study defines crowdsourcing as an organisational technique that uses an open call to tap into the crowd's knowledge, skills and experience. Researchers have also developed taxonomies and frameworks for crowdsourcing. Whitla (2009) identified key activities such as promotion, advertising, market research and product development. Similarly, Brabham (2013) categorised crowdsourcing by function, including knowledge discovery, distributed intelligence tasking, broadcast search and peer-vetted creative production.

With the evolution of digital platforms, the role of artificial intelligence (AI) and machine learning (ML) has expanded within crowdsourcing, optimising task allocation, assessing contributions and automating certain decision-making processes (Afuah and Tucci, 2012; Lysyakov and Viswanathan, 2023). However, concerns regarding ethics, data privacy (Alorwu *et al.*, 2022) and fair compensation (Salminen *et al.*, 2023) have also emerged as critical challenges in crowdsourcing environments (Estellés-Arolas and González-Ladrón-De-Guevara, 2012). Many platforms collect vast amounts of user data, raising privacy concerns, while ethical debates continue around fair compensation and worker rights, especially when crowdsourcing relies on unpaid or underpaid labour (Brabham, 2013). In addition, AI-driven automation is transforming crowdsourcing by improving efficiency, but it also raises concerns about transparency, bias in decision-making and the potential reduction of human involvement. These emerging areas are increasingly seen as both

challenges and opportunities in the adoption of crowdsourcing, influencing its future applications and ethical considerations.

2.2 Adoption models

Over the past few decades, researchers have sought to examine the determinants impacting the adoption of technology within organisational settings. Prominent theories such as DOI (Rogers, 2003), the technology acceptance model (TAM) (Davis, 1989), technology–organisational–environmental framework (Tornatzky and Fleischer, 1990), theory of planned behaviour, the theory of reasoned action, resource-based theory (Wade and Hulland, 2004) and social cognitive theory have been extensively used for this purpose. However, none of these individual theories offers a comprehensive explanation of the entire technology adoption process. Consequently, scholars have used various models to elucidate diverse scenarios related to technology adoption, as observed in studies by Chatterjee *et al.* (2021) and Gangwar *et al.* (2015). This research specifically delves into the influential factor affecting the adoption of crowdsourcing innovation within Indian organisations. To understand this complex phenomenon better, the study introduces a new framework. This framework combines ideas from the TOE and DOI theories and draws on insights from technology and innovation literature.

2.2.1 Diffusion of innovation theory. The Theory of Innovation Diffusion, initially formulated by Rogers (1983), is a widely used model in Information Systems (IS) research (Min *et al.*, 2021; Toufaily *et al.*, 2021; Agi and Jha, 2022). This theory delineates five crucial attributes explaining the adoption of innovation within an organisation. These attributes encompass various dimensions essential for innovation adoption within organisations. They include relative advantage, signifying the improvement an innovation brings compared to its predecessor; compatibility, indicating how well an innovation aligns with existing business processes, practices and value systems; complexity, representing the level of difficulty associated with implementing the innovation; observability, denoting the visibility of the innovation to others; and trialability, conveying the ease with which experimentation with the innovation can occur. The DOI theory concentrates on both the technological characteristics and user perceptions within an organisation. Acknowledging the complexity of organisations compared to individuals, Rogers emphasises that the innovation process is essentially a communication process using various channels within the social system.

In the context of organisational dynamics, the adoption of innovation is shaped by three fundamental factors. These factors consist of individual element, such as the attitudes of leaders towards change, as well as internal aspects related to the organisational structure, including centralisation, interconnectedness, number of employees, complexity and organisational slack. In addition, external attributes, such as the extent of system openness within the organisation, further contribute to the overall influence on innovation adoption.

2.2.2 Technology–organisation–environment framework. The technology–organisation–environment (TOE) framework, first introduced by Tornatzky and Fleischer (1990), provides a comprehensive perspective on the process of adopting innovation within organisational settings. This framework takes into account three crucial dimensions that play a substantial role in influencing innovation adoption. Within the Technology context, the TOE framework delves into both internal and external technologies that are pertinent to the organisation (Salah and Ayyash, 2024). This dimension involves an assessment of the technologies presently used by the organisation, as well as those that are potential candidates for adoption. A thorough understanding of the technological landscape empowers organisations to make well-informed decisions regarding the incorporation of new innovations.

The Organisation context dimension delves into descriptive characteristics of the firm (Malik *et al.*, 2021; Chittipaka *et al.*, 2023). This includes aspects such as organisational structure, size, managerial configuration, degree of centralisation and the availability of resources, both human and slack. In addition, it considers communication processes within the organisation, encompassing both formal and informal channels among employees. These organisational factors play a pivotal role in shaping the innovation adoption process. In the third dimension, Environment context, the TOE framework takes into account the structural aspects of the industry and the circumstances under which the organisation operates (Oliveira *et al.*, 2011; Al Hadwer *et al.*, 2021; Aligarh *et al.*, 2023). This involves an analysis of the external environment, considering factors such as industry trends, competitive forces and regulatory conditions. Understanding the broader environmental context is crucial for organisations to align their innovation adoption strategies with the prevailing conditions. By concurrently examining these three dimensions, the TOE framework provides comprehensive insights into the intricate interplay between technological, organisational and environmental factors (Tornatzky and Fleischer, 1990) that influence an organisation's decision-making regarding the adoption of technological innovations. The applicability of this framework has been instrumental in deciphering the complex dynamics of innovation adoption across diverse organisational contexts and industries, contributing significantly to the field of technology adoption research.

2.3 Related literature on crowdsourcing adoption

Crowdsourcing adoption begins with evaluating its value to organisations. Muhdi *et al.* (2011) proposed a five-step approach, starting with assessing its suitability for problem-solving, while Wexler (2011) emphasised comparing it to outsourcing and internal sourcing and persuading employees. Crowdsourcing adoption is seen as a strategic decision, requiring readiness factors such as culture, benefits, obstacles and capacity to be evaluated. A poor decision can lead to resource misuse and unforeseen challenges (Rouse, 2010; Shuai *et al.*, 2025). In addition, organisations must consider whether their operations are open to public participation (Seltzer and Mahmoudi, 2013), as the decision significantly impacts success (Muhdi *et al.*, 2011). While crowdsourcing fosters external relationships (Djelassi and Decoopman, 2013), failure can harm the organisation's brand. Mishra and Maheshwari (2024b) stress that well-planned crowdsourcing improves social linkages and innovation competence through enhanced knowledge transfer.

Interest in crowdsourcing adoption is growing, with some research focusing on aspects like task type (Ranade and Varshney, 2012) or malicious behaviour risks (Naroditskiy *et al.*, 2013). Crowdsourcing, however, requires a multidimensional evaluation (Djelassi and Decoopman, 2013; Zhao and Zhu, 2014). Afuah and Tucci (2012) identified five key factors influencing adoption:

(1) problem;
(2) knowledge;
(3) crowd;
(4) solution; and
(5) evaluator characteristics, with technology moderating their impact.

Lu *et al.* (2015) studied IT crowdsourcing and found three main adoption drivers:

(1) access to expertise;
(2) complementary resources; and

(3) bridging resource gaps, while cost reduction and risk minimisation were less critical.

Despite these findings (Afuah and Tucci, 2012; Thuan *et al.*, 2013; Lu *et al.*, 2015), two gaps remain: a lack of consensus on key adoption determinants and a focus on specific activities like micro-sourcing (Lu *et al.*, 2015), leaving the broader crowdsourcing adoption landscape unexplored.

Recent research (Bigliardi and Galati, 2016; Zahay *et al.*, 2018; Mergel, 2021) explored crowdsourcing adoption from theoretical perspectives. Bigliardi and Galati (2016) used transaction cost theory and the resource-based view to assess Italian SMEs, identifying barriers like strategic, collaboration, knowledge, financial and organisational challenges. Mergel (2021) focused on public sector adoption challenges for promoting government innovation. Most studies (Xu *et al.*, 2015; Thuan *et al.*, 2016; Love and Hirschheim, 2017; Chou, 2021; De Coninck *et al.*, 2023) assess innovation impacts or contextual factors, often using qualitative methods or secondary data. However, a gap exists in comprehensive methods that validate both direct and indirect impacts of innovation considering technological, organisational and environmental contexts. Our study addresses this by proposing an integrative research model combining innovation diffusion theory with the technology, organisation and environment context to holistically evaluate the determinants of crowdsourcing adoption.

2.4 Integrating DOI and TOE perspective for crowdsourcing adoption

Researchers have emphasised the need to integrate multiple theoretical perspectives to understand the adoption of innovative technologies (Oliveira, 2010; Wu *et al.*, 2013; Skafi, 2020). A comprehensive study context is essential for understanding organisational decisions on technology adoption. The DOI and TOE (Technology–Organisation–Environment) frameworks are widely used in IT adoption studies and are well-suited to analyse crowdsourcing adoption. The DOI framework (Rogers, 2003) focuses on innovation characteristics, such as relative advantage, complexity and compatibility, affecting adoption. However, it overlooks organisational and environmental factors. The TOE framework (Tornatzky and Fleischer, 1990) addresses this gap by considering organisational readiness and external factors that influence adoption. Integrating both frameworks offers a dual lens, encompassing innovation-specific and organisational/environmental factors, to provide a more comprehensive understanding of crowdsourcing adoption. While DOI emphasises innovation characteristics and TOE focuses on broader organisational and environmental factors, their integration enhances the analysis of complex innovations like crowdsourcing, where both internal and external factors are crucial. This dual-framework approach allows for a more holistic understanding of crowdsourcing adoption.

The extensively referenced studies were systematically categorised to discern the predominant factors scrutinised in the current body of literature on adoption studies. Following this categorisation, a meticulous examination was conducted for each identified construct, assessing its relevance to the adoption of crowdsourcing. The resulting articles that fulfilled the criteria for alignment with the proposed conceptual model are presented in Table 1. This table provides a comprehensive overview of the main categories, sub-factors and their respective sources.

Within the framework of DOI, the adoption of crowdsourcing can be analysed using three key characteristics associated with DOI innovation:

(1) relative advantage;

(2) complexity; and

(3) compatibility.

Table 1. Literature related to the theoretical framework

Context/characteristics	Factors	Sources
Innovation	Compatibility	Afuah and Tucci (2012), Saxton *et al.* (2013), Muntés-Mulero *et al.* (2013), Djelassi and Decoopman (2013), Qin *et al.* (2016)
	Complexity	Muntés-Mulero *et al.* (2013), Zahay *et al.* (2018), Evans *et al.* (2016)
	Relative advantage	Saxton *et al.* (2013), Qin *et al.* (2016), Zhao and Zhu (2014)
Technological	Technology readiness	Lynn *et al.* (2018), Fu and Chang (2016), Sadoughi *et al.* (2020)
Organisational	Support of top management	Sadoughi *et al.* (2020), Ren (2019), Ali *et al.* (2020),
	Organisational culture	Siren and Knudsen (2017). Ren (2019), Hamad *et al.* (2018), Sadoughi *et al.* (2020)
	Organisational size	Ali *et al.* (2020), Mabad *et al.* (2021), Ali *et al.* (2018)
Environmental	Technological turbulence	Johnson *et al.* (2019), Meng *et al.* (2021)
	Competitive pressure	Kohler and Chesbrough (2019), Johnson *et al.* (2019), Meng *et al.* (2021)

Source(s): Authors' analysis

These attributes are closely connected to economic benefits and perceived opportunities. However, it is important to note that trialability and observability have not been extensively studied in the context of IT innovation; hence, they are excluded from consideration in relation to crowdsourcing technology, following the established guidelines of IS research. Rogers (2003) suggested that the nature of the innovation determines the crucial type of relative advantage for adopters, which can manifest in various ways, including economic profitability or social prestige. In our specific study, we propose that crowdsourcing presents an economic advantage in terms of cost savings and opportunities. To further explore this concept, we introduce two additional variables – perceived cost reduction and perceived opportunity – as preceding factors that contribute to the relative advantage of crowdsourcing. These variables ascertain whether crowdsourcing is deemed relatively advantageous when it offers cost savings and increased opportunities.

The TOE framework emphasises the significance of the technology context in shaping the adoption of crowdsourcing within a firm. The readiness of a firm to embrace crowdsourcing is influenced by various factors inherent in the organisational context, including top management support, organisational culture and firm size. Furthermore, the environmental context, as captured by the variables of competitive pressure and technological turbulence, plays a crucial role in determining the organisation's inclination towards adopting crowdsourcing.

3. Hypotheses and conceptual model formulation

3.1 Innovation characteristics of crowdsourcing adoption

3.1.1 Relative advantage. The adoption of crowdsourcing in organisations is heavily influenced by the perceived relative advantage it offers compared to traditional methods. The concept of relative advantage, drawn from innovation theory, suggests that an innovation or approach is more likely to be adopted if it is perceived as superior to existing alternatives

(Greenhalgh *et al.*, 2004). In the context of crowdsourcing, organisations evaluate whether the method provides clear advantages such as increased innovation, cost-effectiveness and access to a broader skill set (Chung *et al.*, 2021). If organisations believe that crowdsourcing offers a relative advantage over traditional methods in terms of efficiency, speed and diversity of ideas, they are more inclined to adopt it (Thuan *et al.*, 2015). The decision hinges on the organisation's assessment of how crowdsourcing aligns with its goals, enhances competitiveness and brings about positive outcomes that outweigh any potential challenges or risks associated with external collaboration. Ultimately, the perceived relative advantage becomes a crucial factor shaping the decision-making process, driving organisations to embrace crowdsourcing as a strategic and innovative approach (Qin *et al.*, 2016). Thus, the following hypothesis is proposed:

H1. Relative advantage positively influences crowdsourcing adoption.

Perceived opportunities refer to the benefits gained from solving tasks externally through solvers, while perceived cost reduction involves savings achieved in this process. Existing literature highlights the role of attitudinal assessments in adoption intention, seen in outsourcing and IT applications at both individual and organisational levels (Featherman and Pavlou, 2003; Kim *et al.*, 2008). In internet-based applications, consumers' attitudes – considering risk, benefits and overall perception – drive adoption intention. Gewald and Dibbern (2009) found that perceived opportunities for outsourcing significantly impact adoption intentions. Studies on on-demand outsourcing emphasise how organisations' attitudes towards opportunities and costs influence adoption decisions. Based on organisational theory, our research examines how organisations' perceptions of opportunities and cost reduction impact crowdsourcing adoption, as seen in Chou (2021). Guided by the attitude–behavior framework and empirical evidence, we hypothesise that organisations' attitudinal assessments regarding the relative advantages of crowdsourcing, particularly opportunities and cost reduction, significantly shape their adoption intentions. Consequently, we hypothesise the following:

H1a. Perceived opportunities will exert a positive influence on the relative advantage of crowdsourcing.

H1b. Perceived cost reduction will exert a positive influence on the relative advantage of crowdsourcing.

3.1.2 Complexity. An innovation's perceived complexity is measured by how much effort is required to understand and implement it truly. The impact of complexity on crowdsourcing adoption decisions in organisations is a crucial consideration that weighs the benefits of external collaboration against the challenges posed by intricate project requirements (Zahay *et al.*, 2018). Complex projects, often characterised by specialised knowledge and multifaceted tasks, necessitate a careful evaluation of whether crowdsourcing is a suitable approach. Organisations must assess whether the inherent complexity of a task aligns with the capabilities of a diverse and distributed crowd (Muntés-Mulero *et al.*, 2013). While crowdsourcing offers access to a wide range of skills and expertise, the intricacy of certain projects may pose coordination challenges, quality control issues and difficulties in managing diverse contributions. Therefore, the decision to adopt crowdsourcing hinges on the organisation's ability to navigate and mitigate the complexities associated with the chosen projects. Organisations must weigh the potential benefits, such as innovation and efficiency, against the complexity of task management, ultimately determining whether crowdsourcing is a viable and effective solution for their specific operational needs

(Evans *et al.*, 2016). Therefore, it can be hypothesised that technological complexity has an inhibiting effect:

H2. Complexity will exert a negative influence on the adoption of crowdsourcing.

3.1.3 Compatibility. Compatibility measures the degree to which an innovation is perceived to be in harmony with the existing practices of potential users. Compatibility plays a pivotal role in the decision-making process regarding crowdsourcing adoption in organisations. The level of alignment between crowdsourcing and the existing organisational culture, structure and processes determines the feasibility and success of its integration (Afuah and Tucci, 2012). Organisations must evaluate whether the decentralised and collaborative nature of crowdsourcing aligns with their established workflows and communication channels. Compatibility extends to technological infrastructure as well, as the integration of crowdsourcing platforms should seamlessly complement existing systems (Saxton *et al.*, 2013; Djelassi and Decoopman, 2013). When there is a high level of compatibility, organisations are more likely to perceive crowdsourcing as a feasible and practical solution. Conversely, if the integration of crowdsourcing requires significant changes or disrupts established norms, it may face resistance or reluctance in adoption (Muntés-Mulero *et al.*, 2013). Therefore, the decision to adopt crowdsourcing hinges on the organisation's assessment of how well it fits within the current operational framework, ensuring a smooth and harmonious integration (Qin *et al.*, 2016). Therefore, technology compatibility can act as an enabler for crowdsourcing adoption in organisations. Hence, we posit the following hypothesis:

H3. Compatibility has a positive impact on the adoption of crowdsourcing.

3.2 Technology context

3.2.1 Technology readiness. The adoption of new technological innovations within organisations depends on their readiness to integrate these technologies. Technological readiness refers to an organisation's internal capability, focusing on the infrastructure and competencies that support new technologies (Oliveira and Martins, 2009). It involves not only resource availability but also the establishment of an organisational framework to support innovation, especially in crowdsourcing adoption (Schiavi and Behr, 2018). While technological resources are often the primary focus in evaluating readiness, there is a gap in literature regarding how the allocation and long-term management of these resources impact crowdsourcing success. Organisations must ensure their technological frameworks are adaptable to evolving needs (Ali and Shrestha, 2017). Ongoing allocation of resources and budgets is essential for sustaining crowdsourcing initiatives (Sadoughi *et al.*, 2020). Proper resource management, including skilled personnel and necessary infrastructure upgrades, directly influences the viability of crowdsourcing (Lynn *et al.*, 2018). Inadequate resource allocation or misalignment with long-term goals can hinder success. Therefore, the following hypothesis is proposed:

H4. Technology readiness positively relates to crowdsourcing adoption in organisations.

3.3 Organisational context

3.3.1 Support of top management. Top management support (TMS) in the context of technology adoption, as emphasised by Hsu *et al.* (2019), pertains to the extent of

commitment and resource backing provided by senior executives. Studies highlight the significance of top management's awareness of the value of embracing new technologies, such as cloud computing, in aligning organisational change processes with their expressed commitment to change. Given the complex nature of incorporating crowdsourcing, involving resource integration and process changes, senior managers play a crucial role in facilitating this transition. Numerous organisational factors influence technology adoption, with top management support consistently identified as a positive factor. In the specific context of crowdsourcing, Chou (2021) underscores the pivotal role of top management in fostering a culture of innovation. Acknowledging and encouraging executives with decision-making authority can significantly impact the successful integration of crowdsourcing, as top management's belief in the positive outcomes of crowdsourcing motivates employees to contribute ideas and develop innovative products. In essence, top management acts as a catalyst, enabling and accelerating the adoption of crowdsourcing within organisations (Djelassi and Decoopman, 2013). Thus:

H5. Top management support positively relates to crowdsourcing adoption in organisations.

3.3.2 Organisational culture. Organisational culture plays a crucial role in the successful adoption and implementation of crowdsourcing. A culture that fosters transparency, openness and experimentation is conducive to embracing crowdsourcing (von Hippel, 2005). Transparency is key during the initiation phase, as it helps communicate objectives and expectations, building trust among the crowd. Openness supports collaboration and idea exchange, especially during problem-solving and idea-generation phases, allowing diverse perspectives to contribute meaningfully (Djelassi and Decoopman, 2013). Organisations with cultures that encourage collaboration, innovative thinking and experimentation align well with crowdsourcing, enabling effective implementation and optimisation (Djelassi and Decoopman, 2013). In contrast, a resistant internal culture, such as the "not invented here" syndrome, can hinder crowdsourcing adoption by stifling collaboration and knowledge sharing (Simula and Ahola, 2014; Evans *et al.*, 2016). Cultural elements, particularly those related to technology – like user attitudes, openness to change and digital awareness – significantly impact crowdsourcing success. A culture of knowledge sharing enhances organisational expertise and optimises external contributions (Muhammed and Zaim, 2020). Moreover, a proactive attitude towards crowdsourcing and its benefits fosters an innovation-friendly environment (Scupola and Nicolajsen, 2021). Therefore, we posit the following hypothesis:

H6. The presence of a supportive organisational culture is positively correlated with the adoption of crowdsourcing within organisations.

3.3.3 Organisational size. Organisational size significantly influences crowdsourcing adoption decisions, as larger organisations can leverage greater financial and technological resources to integrate crowdsourcing as a strategic tool (Zahay *et al.*, 2018). Their expansive structures allow for flexibility and scalability, enabling them to quickly assemble diverse teams and adapt to market dynamics (Djelassi and Decoopman, 2013). In addition, larger firms have the infrastructure to manage challenges such as intellectual property, data security and workflow integration. In contrast, SMEs face challenges in crowdsourcing adoption due to financial, technical and branding limitations (Mathauer and Hofmann, 2019). However, SMEs often use crowdsourcing as a cost-effective alternative to in-house research and development (R&D), using open innovation platforms to access specialised skills and co-

create solutions (Brunswicker and Vanhaverbeke, 2015). Some SMEs may also focus on niche crowdsourcing strategies for smaller, more defined projects. Research indicates that larger firms are more likely to adopt crowdsourcing due to their capacity for risk absorption and process integration (Thuan *et al.*, 2015). However, SMEs can still benefit from crowdsourcing, especially by leveraging industry networks and digital platforms to engage external contributors. Therefore, we hypothesise that:

H7. Organisational size will exert a positive influence on the adoption of crowdsourcing.

3.4 Environment context

The Technology–Organisation–Environment (TOE) framework identifies the environmental context as a critical determinant of innovation adoption, encompassing external factors that influence organisational decisions (Tornatzky and Fleischer, 1990). In the context of crowdsourcing adoption, key environmental factors such as technological turbulence and competitive pressure play a significant role in shaping how organisations engage with external crowds. Additionally, the growing emphasis on environmental sustainability is influencing crowdsourcing strategies as organisations seek innovative solutions to address sustainability challenges.

3.4.1 Technological turbulence. Technological turbulence plays a key role in driving organisations to adopt crowdsourcing as a strategic response to rapid technological changes (Ishikawa, 2019). Crowdsourcing allows organisations to tap into external talent pools, fostering innovation and providing creative solutions to emerging challenges (Johnson *et al.*, 2019). It enables sourcing specialised knowledge needed to stay competitive in an evolving market. Beyond innovation, crowdsourcing is increasingly used to drive sustainability. Companies are leveraging crowdsourced ideas to develop cleaner technologies, optimise energy use and create sustainable production processes (Metwaly *et al.*, 2022). For example, open innovation platforms support the design of eco-friendly materials and smart energy solutions (Meng *et al.*, 2021), aligning with environmental goals and regulations. Crowdsourcing also serves as a risk mitigation strategy by distributing tasks across a diverse set of contributors, ensuring market alignment with green technologies and eco-conscious preferences (Metwaly *et al.*, 2022). Therefore, we hypothesise that:

H8. Technological turbulence positively relates to crowdsourcing adoption in organisations.

3.4.2 Competitive pressure. Competitive pressure significantly influences crowdsourcing adoption, as organisations seek to innovate, streamline operations and gain a competitive advantage (Johnson *et al.*, 2019). In competitive markets, where quick adaptation is crucial, crowdsourcing offers an efficient solution to address external challenges (Kohler and Chesbrough, 2019). It facilitates rapid execution, enabling organisations to respond swiftly to market demands (Meng *et al.*, 2021). Sustainability has become a key differentiator, with companies using crowdsourcing to co-create eco-friendly products, develop sustainable models and explore carbon reduction strategies (Ishikawa, 2019). Crowdsourcing also supports real-time consumer engagement, aligning sustainability efforts with consumer expectations and improving brand reputation (Ishikawa, 2019). In addition, crowdsourcing provides cost efficiency, risk distribution and continuous market sensing, helping organisations thrive in competitive and sustainability-focused environments (Meng *et al.*, 2021). Companies that leverage crowdsourcing for sustainability can gain an edge in areas such as circular economy initiatives, supply chain transparency and renewable energy integration (Kohler and Chesbrough, 2019). Thus, we propose the following hypothesis:

H9. Competitive pressure positively relates to crowdsourcing adoption in organisations.

Drawing from the literature discussed earlier, we present a conceptual framework rooted in DOI and TEO theories. This conceptual framework seeks to identify the determinants influencing the adoption or utilisation of crowdsourcing within organisational contexts (Figure 1).

4. Research methodology

4.1 Sampling and data collection

The study gathered data through a tailored survey targeting senior executives in R&D departments from various industries. These executives, including IS managers, business operations managers and administrators, play crucial roles in innovation strategies and R&D initiatives. Their insights are key to understanding the factors influencing crowdsourcing adoption in organisations. A purposive sampling method, recommended in quantitative research (Ebrahimi *et al.*, 2018), was used to select individuals with specific expertise and decision-making influence. The survey was distributed online via Google Forms, with communication through emails, Facebook Messenger and LinkedIn. Respondents were informed of the academic nature of the study and assured of confidentiality, with a guide

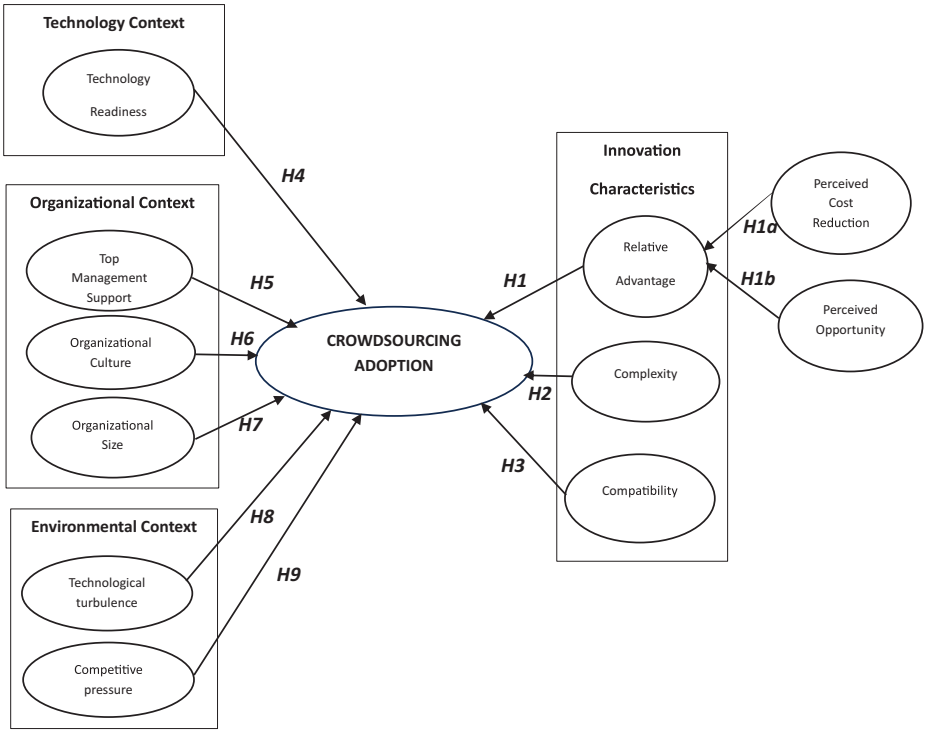

Source(s): Authors' own work

Figure 1. Theoretical framework of crowdsourcing adoption in organisations

provided to improve the response rate (Chidlow *et al.*, 2015). The survey was sent to 600 individuals, yielding 480 responses, or an 80% response rate. Following Hair *et al.* (2014), 54 incomplete or linear responses were removed. A pre-analysis sample size calculation using the "10-times rule" for partial least squares structural equation modelling (PLS-SEM) indicated a required sample size of 400 based on the model's 12 latent and 40 observed variables. With 426 responses, the sample size exceeded this requirement. Respondents were from diverse industries, including 29.3% from IT, along with education, e-commerce, manufacturing, fast-moving consumer goods and automobile sectors, providing a broad representation of crowdsourcing adoption across different organisational contexts.

As for the selection criteria of the managers, these individuals were specifically chosen for their roles in managing or influencing innovation strategies within their organisations. The study focused on managers from R&D and innovation-related departments who have substantial decision-making power and are directly involved in implementing or overseeing crowdsourcing initiatives. This targeted selection ensures that the insights gathered from the survey are highly relevant to the study's objectives. Additionally, focusing on senior managers from Indian industries allows for an in-depth understanding of crowdsourcing adoption in an emerging economy with distinct managerial structures, innovation practices and technological advancements. Among the respondents, the majority (28.17%) held positions as IS managers. Other roles included business operations managers (17.84%) and positions in administration (12.44%) as well as purchase, sales and marketing management (21.60%). This distribution of job positions is closely aligned with the study's focus on innovation and decision-making in crowdsourcing adoption. Further details about the respondents' industries, job positions and organisational sizes are presented in Table 2.

4.2 Ethical considerations

This study adhered to the highest ethical standards to ensure the protection of participants and the integrity of the data. Informed consent was obtained from all participants, ensuring they were fully aware of the study's objectives, their voluntary participation and their right to withdraw at any time without consequence. The participants were provided with clear

Table 2. Sample characteristics ($N = 426$)

Measure	Category	Frequency	%
Industry	FMCG	85	19.91
	Automobile	55	12.92
	Information technology	125	29.34
	Education	76	17.84
	Manufacturing	40	9.39
	E-commerce	45	10.56
Respondent's job position	Information system managers	120	28.17
	Other IS department managers	85	19.91
	Business operations manager	76	17.84
	Administration	53	12.44
	Other (purchase, sales, marketing)	92	21.60
Organisational size	Small	150	35.21
	Medium	225	52.81
	Large	51	11.97

Source(s): Authors' own work

information regarding the academic nature of the research and the confidentiality of their responses. To safeguard privacy, all responses were anonymised and no personal identifiers were collected. Furthermore, the data collected were securely stored and only accessible to the research team. Ethical approval was obtained from the relevant institutional review board before the commencement of data collection. The study also complied with data protection regulations, including adherence to local and international data privacy laws. By taking these steps, the study ensured that participants' rights were respected and their data remained secure throughout the research process.

4.3 Instrument development

This research was conducted through a survey, with a questionnaire formulated after an extensive review of relevant literature. The survey comprises two sections: the initial part captures general information about the organisation, including aspects such as size, the positions of respondents and the industry type. The second segment encompasses 11 independent constructs and one dependent construct, constituting a total of 40 items. A meticulous two-step pre-testing process was implemented for the items, involving pilot testing and evaluation by industrial experts and experienced academicians. All constructs and items were drawn from existing literature, and a comprehensive breakdown, including the sources for adaptation of each item, is provided in Table 3. Data collection used a Likert scale ranging from 1 to 5, where 1 indicates "strongly disagree", and 5 signifies "strongly agree". To ensure questionnaire validity, three IS industrial experts were interviewed, leading to adjustments based on their insights to enhance clarity and comprehension. Subtle adjustments were made before the conclusive data collection phase. Furthermore, to enhance measurement precision, a pilot study involving five practitioners with specialised knowledge in innovation was conducted, refining the research instruments based on their feedback.

4.4 Common method bias

To address the potential impact of common method bias (CMB) stemming from a singular survey for data collection, this study used two distinct statistical analyses. Firstly, Harman's one-factor test, as proposed by Podsakoff (2003), was executed to examine whether the items significantly loaded onto a single factor. The findings revealed the absence of a singular factor in the data.

To further evaluate the potential impact of CMB, the study used the construct-level correction approach, as recommended by Chin *et al.* (2013). This approach incorporates the measured latent marker variable (MLMV) technique, wherein unmeasured marker variables are introduced as exogenous variables that predict each endogenous variable in the model. In this study, the designated MLMV was "self-efficacy", which was assessed using five distinct items. Notably, all the significant effects observed in the model without the marker variable remained significant even in the presence of the marker variable. This suggests that no significant CMB was present in the data, indicating that the findings of this study are not affected by such bias.

5. Results and findings

The validation process for the study model involved two phases: the measurement model and the structural model. To validate the measurement model, the partial least squares (PLS) method was used, using SmartPLS 3.2.7 software and generating 5,000 bootstrap resamples to ensure robust results. PLS is particularly beneficial for handling complex models with both formative and reflective constructs, making it ideal for this study. It allows for the exploration of intricate interaction effects and provides strong predictive modelling

Table 3. Measurement items

Construct	Items	Adapted source
Perceived opportunity	PO1 – Crowdsourcing offers numerous benefits PO2 – Crowdsourcing is effective in accomplishing tasks PO3 – Crowdsourcing enhances the overall competitive edge	Benlian and Hess (2011), Ye and Kankanhalli (2015)
Perceived cost reduction	PCR1 – Crowdsourcing cuts task-solving expenses PCR2 – Crowdsourcing allows our company to economise on task execution PCR3 – Crowdsourcing offers a more cost-effective approach than alternatives such as internal task handling or engaging external solvers	Benlian and Hess (2011), Ye and Kankanhalli (2015)
Relative advantage	RA1 – Using crowdsourcing helps manage organisation operations more efficiently RA2 – Crowdsourcing makes operations better in quality RA3 – Crowdsourcing allows you to do specific tasks more quickly RA4 – Using crowdsourcing results in novel ideas and opportunities RA5 – Crowdsourcing helps boost organisation's productivity	Ifinedo (2011), Moore and Benbasat (1991), Ghobakhloo *et al.* (2011)
Complexity	CX1 – Engaging in crowdsourcing demands significant mental effort CX2 – The process of crowdsourcing can be frustrating CX3 – The utilisation of crowdsourcing is deemed too intricate for organisation operations CX4 – The skills necessary for adopting crowdsourcing are considered too complex for the organisation's employees Top of Form	Moore and Benbasat (1991), Ifinedo (2011), Thiesse *et al.* (2011)
Compatibility	CM1 – The utilisation of crowdsourcing aligns with the current IT infrastructure within my organisation CM2 – The integration of crowdsourcing aligns with the processes and operations of my organisation CM3 – The adoption of crowdsourcing aligns with our preferred work practices CM4 – The application of crowdsourcing aligns with the preferences of our clients	Sutanonpaiboon and Pearson (2008), Tripopsakul (2018)
Technology readiness	TR1 – The organisation has sufficient resources and budget allocated for adopting new technology TR2 – The organisation knows how crowdsourcing can be used to support operations TR3 – Organisations have enough internal expertise available to implement crowdsourcing TR4 – Organisations have availability of appropriate level of IT infrastructure	Ifinedo (2011), Oliveira and Martins (2010)

(*continued*)

Table 3. Continued

Construct	Items	Adapted source
Top management support	TMS1 – The top management of the organisation is supportive of implementing crowdsourcing TMS2 – The top management of organisations demonstrates robust leadership and actively participates in the process TMS3 – The top management of organisations is open to undertaking the financial and organisational risks associated with adopting crowdsourcing	Chwelos *et al.* (2001), Zhu *et al.* (2010), Shah Alam *et al.* (2011)
Organisational culture	OC1 – Organisations have positive attitude towards adopting new technologies OC2 – Organisations encourage innovative thinking OC3 – Organisations embrace external experimentation and take risks OC4 – Organisations promote collaboration and knowledge sharing	Beatty *et al.*, 2001; Soliman and Janz, 2004
Organisational size	OS1 – The total workforce size within organisations OS2 – The yearly financial volume or revenue generated by the organisation	Premkumar and Roberts (1999), Zhu *et al.* (2006), Chwelos *et al.* (2001)
Technological turbulence	TT1 – The technology landscape within the industry is evolving at a rapid pace TT2 – Significant opportunities arise in the industry due to technological shifts TT3 – Many new product ideas are now possible due to technological breakthroughs	Sethi and Iqbal (2008)
Competitive pressure	CP1 – Not adopting crowdsourcing may lead to customer loss to competitors CP2 – Crowdsourcing is crucial for strategic marketplace competitiveness CP3 – Crowdsourcing enhances our competitive advantage	Gangwar *et al.* (2015), Tripopsakul (2018)
Crowdsourcing adoption	CA1 – What is the current status of your organisation's involvement in crowdsourcing adoption? Options include: not considering at present, currently in the evaluation phase (e.g. conducting pilot studies), evaluated but not planning to adopt, evaluated and planning to adopt or already adopted crowdsourcing services, infrastructure, or platforms CA2 – If your organisation anticipates future adoption of crowdsourcing, how do you envision this happening? Choices range from not considering, a timeline of more than five years, between two and five years, between one and two years, less than one year, to already having adopted crowdsourcing services, infrastructure or platforms	Thiesse *et al.* (2011)

Source(s): Authors' own work

capabilities, ensuring accurate results even in complex research settings. In addition, PLS is well-suited for small sample sizes, making it a practical choice in this case. Despite some limitations, such as its assumptions about reflective measurement models, these do not compromise the validity of the study. PLS's focus on predictive accuracy and its ability to handle complex relationships between latent variables ensured reliable parameter estimation. The sample size in this study was adequate to mitigate overfitting concerns, further strengthening the validity of the results. In this context, PLS's strengths in handling complex models and providing robust parameter estimates make it a suitable and reliable method for validating the study's findings.

5.1 Evaluation of measurement model

The assessment conducted on the PLS-SEM encompassed two primary phases: the measurement model and the structural model. Evaluation of the measurement model focused on key aspects such as internal consistency, convergent validity and discriminant validity, adhering to the guidelines outlined by Hair *et al.* (2017). The outcomes of the analysis of the measurement model are detailed in Table 4. Cronbach's alpha values ranged from 0.819 to 0.945, indicating a robust level of internal consistency. In addition, composite reliability values were within the range of 0.849–0.961. Convergent validity was established, with average variance extracted (AVE) values exceeding 0.50. The item factor loadings, spanning from 0.866 to 0.947, further affirmed both internal consistency and convergent validity. To evaluate discriminant validity, we applied Fornell and Larcker's criterion and examined cross-loadings as suggested by Henseler *et al.* (2016). The square roots of the AVE values, presented in Table 5, surpass the respective correlation coefficients between the constructs. This observation supports the presence of discriminant validity, aligning with the criteria established by Fornell and Larcker (1981). The second criterion mandates that each indicator's loading must exceed all cross-loadings. Examination of the loading and cross-loading tables (Table 6) reveals that the loading patterns consistently exceed those of the cross-loadings.

5.2 Evaluation of structural model

After confirming the validity of the measurement model, the analysis proceeded to assess the structural model. Various indicators were scrutinised, including path coefficients (β) to gain an understanding of the significance of the relationship, determination coefficients (R^2) to gauge model variance, impact size (f^2) to evaluate the influence of the endogenous constructs and Stone-Geisser's Q^2 value to appraise the predictive relevance of the model. This assessment adhered to the guidelines outlined by Hair *et al.* (2017). The primary focus centred on the examination of path coefficients and their corresponding *t*-values to determine the significance of the relationships. The results of the hypothesis testing are summarised in Table 7.

The analysis began with path analysis on the full sample to assess the overall model fit. The goodness-of-fit (GoF) index was used to validate the model's ability to explain the empirical data, with values ranging from 0 to 1, indicating small (0.10), medium (0.25) and large (0.36) fit levels (Wetzels *et al.*, 2009). The model demonstrated a satisfactory fit with a GoF index of 0.32, indicating substantial predictive power and alignment with the empirical data. In addition, to ensure an accurate fit for PLS modelling, the standardised root mean square residual was calculated, yielding a value of 0.075. According to Hu and Bentler (1999), this is considered an acceptable fit for PLS models, with values below 0.08 generally regarded as indicating good model fit (Henseler *et al.*, 2016).

The examination of the R^2 value reveals that perceived cost reduction and perceived opportunity together explain 73.3% of the variance in crowdsourcing adoption. This

Table 4. Results of measurement model

Construct	Indicator	Item loadings >0.70	Cronbach's α (CA) >0.70	Composite reliability (CR) >0.70	Average variance extracted (AVE) >0.50
PO	PO1	0.943	0.819	0.949	0.861
	PO2	0.925			
	PO3	0.916			
PCR	PCR1	0.924	0.919	0.849	0.86
	PCR2	0.911			
	PCR3	0.948			
RA	RA1	0.916	0.941	0.955	0.809
	RA2	0.893			
	RA3	0.866			
	RA4	0.906			
	RA5	0.914			
CX	CX1	0.943	0.939	0.956	0.845
	CX2	0.922			
	CX3	0.882			
	CX4	0.928			
CM	CM1	0.914	0.931	0.951	0.828
	CM2	0.919			
	CM3	0.902			
	CM4	0.906			
TR	TR1	0.95	0.945	0.961	0.859
	TR2	0.9			
	TR3	0.926			
	TR4	0.931			
TMS	TMS1	0.927	0.89	0.932	0.819
	TMS2	0.905			
	TMS3	0.884			
OC	OC1	0.911	0.941	0.958	0.85
	OC2	0.928			
	OC3	0.934			
	OC4	0.915			
OS	OS1	0.914	0.836	0.924	0.858
	OS2	0.938			
TT	TT1	0.943	0.912	0.945	0.851
	TT2	0.883			
	TT3	0.941			
CP	CP1	0.906	0.893	0.934	0.824
	CP2	0.929			
	CP3	0.889			
CA	CA1	0.939	0.875	0.941	0.889
	CA2	0.947			

Source(s): Authors' own work

highlights their critical role in influencing organisational decisions related to adopting crowdsourcing. The path coefficient between relative advantage and crowdsourcing adoption (β = 0.445) indicates that higher levels of relative advantage led to higher levels of crowdsourcing adoption. This relationship is consistent with the expectation that organisations are more likely to adopt crowdsourcing when they perceive it as offering clear advantages. Similarly, higher levels of perceived opportunity (β = 0.326), perceived cost

Table 5. Fornell and Larcker criterion

Constructs	PO	PCR	RA	CX	CM	TR	TMS	OC	OS	TT	CP	CA
PO	*0.928*											
PCR	0.914	*0.927*										
RA	0.919	0.912	*0.899*									
CX	0.83	0.864	0.86	*0.919*								
CM	0.923	0.923	0.862	0.842	*0.91*							
TR	0.898	0.919	0.85	0.858	0.845	*0.927*						
TMS	0.873	0.913	0.864	0.828	0.824	0.917	*0.905*					
OC	0.925	0.922	0.872	0.882	0.857	0.91	0.829	*0.922*				
OS	0.909	0.925	0.851	0.878	0.86	0.917	0.901	0.85	*0.926*			
TT	0.904	0.727	0.848	0.857	0.9	0.85	0.825	0.917	0.816	*0.923*		
CP	0.922	0.921	0.856	0.918	0.754	0.916	0.897	0.921	0.739	0.916	*0.908*	
CA	0.907	0.917	0.845	0.916	0.807	0.826	0.839	0.915	0.904	0.895	0.906	*0.943*

Source(s): Authors' own work

reduction (β = 0.649), complexity (β = 0.366) and compatibility (β = 0.232) all positively influence crowdsourcing adoption, suggesting that organisations are more inclined to adopt crowdsourcing when they see it as a low-cost and compatible option. Furthermore, the higher levels of technology readiness (β = 0.110) and top management support (β = 0.287) indicate a positive impact on crowdsourcing adoption, which aligns with the notion that technological preparedness and strong leadership support are vital for successful adoption. Conversely, higher levels of organisational culture (β = −0.306), organisational size (β = −0.655) and technological turbulence (β = −0.531) have a negative impact on crowdsourcing adoption, suggesting that large organisations, those with rigid cultures and those experiencing rapid technological change may face more significant challenges in adopting crowdsourcing initiatives. In contrast, competitive pressure (β = 0.109) does not have a statistically significant effect on crowdsourcing adoption, indicating that the competitive environment alone may not drive organisations to adopt crowdsourcing practices.

A deeper exploration of the indirect effects in the model reveals that perceived cost reduction indirectly influences crowdsourcing adoption through its effect on relative advantage. The computed indirect effect (0.649 * 0.445 = 0.289) is statistically significant ($p < 0.05$), emphasising that cost reduction can enhance the perceived advantage of crowdsourcing, further encouraging adoption. Similarly, perceived opportunity has an indirect effect on crowdsourcing adoption, with statistical significance ($p < 0.05$), reinforcing the importance of both cost and opportunity perceptions in shaping adoption decisions.

The overall model explains 83.1% of the variance in crowdsourcing adoption, indicating a strong fit. The R^2 values of 0.944 for crowdsourcing adoption and 0.913 for relative advantage indicate that the model accounts for a substantial portion of the variability in these variables, supporting its validity and robustness. These findings underscore the model's effectiveness in shedding light on the determinants of crowdsourcing adoption in organisations. The evaluation of the structural model included an examination of both the coefficient of determination (R^2) and predictive relevance (Q^2), as presented in Table 8, highlighting the model's ability to explain and predict crowdsourcing adoption.

Furthermore, the analysis of effect size (f^2) allows for a deeper understanding of the individual impacts of the endogenous construct variables on crowdsourcing adoption. Compatibility has a small f^2 effect (0.013), while complexity, perceived cost reduction, relative advantage and top management support all have large effect sizes (f^2 values of 0.314,

Table 6. Item cross-loadings

Items	CA	CM	CP	CX	OC	OS	PCR	PO	RA	TMS	TR	TT
CA1	*0.939*	0.82	0.817	0.838	0.845	0.812	0.848	0.806	0.891	0.906	0.837	0.79
CA2	*0.947*	0.888	0.89	0.943	0.934	0.89	0.934	0.901	0.891	0.866	0.907	0.894
CM1	0.825	*0.914*	0.852	0.9	0.879	0.873	0.895	0.818	0.865	0.848	0.904	0.843
CM2	0.828	*0.919*	0.897	0.868	0.884	0.887	0.837	0.857	0.901	0.837	0.838	0.883
CM3	0.823	*0.902*	0.844	0.88	0.858	0.857	0.887	0.829	0.859	0.872	0.884	0.84
CM4	0.824	*0.906*	0.879	0.854	0.863	0.877	0.815	0.855	0.877	0.808	0.813	0.829
CP1	0.812	0.851	*0.906*	0.834	0.834	0.84	0.798	0.816	0.83	0.769	0.8	0.812
CP2	0.84	0.872	*0.929*	0.859	0.913	0.853	0.829	0.859	0.906	0.846	0.842	0.85
CP3	0.817	0.874	*0.889*	0.788	0.869	0.865	0.809	0.79	0.844	0.826	0.881	0.789
CX1	0.847	0.888	0.89	*0.943*	0.934	0.89	0.934	0.901	0.891	0.866	0.907	0.894
CX2	0.85	0.874	0.856	*0.922*	0.915	0.859	0.895	0.83	0.881	0.879	0.899	0.874
CX3	0.767	0.874	0.857	*0.882*	0.838	0.814	0.834	0.782	0.837	0.779	0.852	0.873
CX4	0.898	0.904	0.883	*0.928*	0.918	0.918	0.878	0.896	0.919	0.883	0.866	0.872
OC1	0.834	0.871	0.922	0.854	*0.911*	0.848	0.825	0.851	0.9	0.843	0.839	0.846
OC2	0.846	0.896	0.877	0.898	*0.928*	0.905	0.888	0.862	0.914	0.837	0.895	0.875
OC3	0.927	0.888	0.89	0.923	*0.934*	0.89	0.924	0.901	0.891	0.866	0.907	0.894
OC4	0.85	0.874	0.856	0.912	*0.915*	0.859	0.895	0.83	0.881	0.879	0.899	0.874
OS1	0.767	0.874	0.857	0.882	0.838	*0.914*	0.834	0.782	0.837	0.779	0.852	0.883
OS2	0.898	0.904	0.883	0.928	0.918	*0.938*	0.878	0.896	0.919	0.883	0.866	0.872
PCR1	0.894	0.866	0.85	0.875	0.899	0.829	*0.924*	0.901	0.891	0.853	0.865	0.86
PCR2	0.817	0.876	0.889	0.89	0.87	0.868	*0.911*	0.792	0.846	0.827	0.891	0.89
PCR3	0.92	0.884	0.853	0.918	0.907	0.877	*0.948*	0.849	0.896	0.916	0.913	0.885
PO1	0.882	0.848	0.857	0.873	0.89	0.842	0.869	*0.943*	0.885	0.856	0.854	0.828
PO2	0.829	0.871	0.862	0.88	0.877	0.851	0.876	*0.925*	0.841	0.805	0.846	0.877
PO3	0.812	0.851	0.906	0.834	0.834	0.84	0.798	*0.916*	0.83	0.769	0.8	0.812
RA1	0.83	0.884	0.844	0.864	0.844	0.872	0.831	0.819	*0.926*	0.856	0.854	0.869
RA2	0.836	0.826	0.813	0.823	0.839	0.818	0.852	0.816	*0.893*	0.805	0.84	0.796
RA3	0.79	0.846	0.785	0.852	0.833	0.824	0.855	0.77	*0.866*	0.864	0.843	0.855
RA4	0.84	0.872	0.829	0.859	0.903	0.853	0.829	0.859	*0.906*	0.846	0.842	0.85
RA5	0.847	0.897	0.878	0.898	0.928	0.905	0.888	0.864	*0.914*	0.837	0.894	0.876
TMS1	0.808	0.841	0.825	0.826	0.838	0.805	0.827	0.782	0.85	*0.927*	0.863	0.848
TMS2	0.836	0.826	0.823	0.843	0.849	0.818	0.852	0.816	0.893	*0.905*	0.84	0.796
TMS3	0.79	0.846	0.785	0.852	0.833	0.824	0.855	0.77	0.866	*0.884*	0.843	0.875
TR1	0.868	0.879	0.844	0.9	0.898	0.865	0.89	0.826	0.9	0.889	*0.95*	0.897
TR2	0.869	0.816	0.906	0.904	0.909	0.897	0.903	0.873	0.892	0.849	*0.915*	0.907
TR3	0.872	0.867	0.855	0.895	0.886	0.862	0.897	0.833	0.877	0.878	*0.926*	0.869
TR4	0.819	0.837	0.841	0.851	0.865	0.809	0.863	0.794	0.852	0.856	*0.931*	0.845
TT1	0.825	0.914	0.852	0.9	0.879	0.873	0.895	0.818	0.865	0.848	0.904	*0.943*
TT2	0.828	0.819	0.867	0.868	0.88	0.881	0.837	0.857	0.801	0.737	0.838	*0.883*
TT3	0.822	0.899	0.842	0.88	0.856	0.856	0.887	0.825	0.858	0.874	0.886	*0.941*

Source(s): Authors' own work

0.797, 0.665 and 0.742, respectively), indicating their strong influence on adoption (Table 9). Perceived opportunity has a moderate effect size (f^2 = 0.201), suggesting that while it is important, its impact is less pronounced than that of other factors. Organisational culture, organisational size, technological turbulence and competitive pressure have negligible effects, with f^2 values close to zero, pointing to their relatively minimal impact on adoption in this context.

Finally, the predictive relevance of the model was assessed using the blindfolding procedure, with Q^2 values presented in Table 10. The positive Q^2 values of 0.831 for crowdsourcing adoption and 0.733 for relative advantage confirm the model's predictive accuracy, indicating that it not only fits the observed data well but is also capable of forecasting future outcomes related to crowdsourcing adoption. These findings validate the model's robustness and its ability to capture the key determinants of crowdsourcing

Table 7. Hypotheses testing

Hypotheses	Relation	Beta	*t*-values	*p*-values
H1	RA → CA	0.445	6.285	0.000
H1a	PO → RA	0.326	6.223	0.000
H1b	PCR → RA	0.649	13.652	0.000
H2	CX → CA	0.366	12.595	0.000
H3	CM → CA	0.232	2.005	0.045
H4	TR → CA	0.110	0.181	0.001
H5	TMS → CA	0.287	6.157	0.000
H6	OC → CA	−0.306	2.942	0.003
H7	OS → CA	−0.655	7.944	0.000
H8	TT → CA	−0.531	6.053	0.000
H9	CP → CA	0.109	1.666	0.096
Indirect effect	PCR → RA → CA	0.289	5.746	0.001
	PO → RA → CA	0.145	4.344	0.003

Source(s): Authors' own work

Table 8. Coefficient of determination – R^2 values

Path relationships	R^2	Adjusted R^2
Crowdsourcing adoption (CA)	0.944	0.943
Relative advantage (RA)	0.913	0.913

Source(s): Authors' own work

Table 9. Coefficient of determination effect size – f^2 values

Constructs	Crowdsourcing adoption	Relative advantage
Compatibility	0.013	
Competitive pressure	0.001	
Complexity	0.314	
Organisational culture	0.000	
Organisational size	0.000	
Perceived cost reduction		0.797
Perceived opportunity		0.201
Relative advantage	0.665	
Top management support	0.742	
Technology readiness	0.214	
Technology turbulence	0.000	

Source(s): Authors' own work

Table 10. Predictive capacity values – Q^2

Indicators	Q^2
Crowdsourcing adoption	0.831
Relative advantage	0.733

Source(s): Authors' own work

adoption. Therefore, the comprehensive analysis not only highlights the key factors influencing crowdsourcing adoption, including perceived cost reduction, relative advantage and top management support, but also provides valuable insights into the indirect effects of cost reduction and opportunity. The strong R^2 and Q^2 values, coupled with the significant f^2 effects, underscore the importance of these variables in driving crowdsourcing adoption. These results offer practical implications for organisations seeking to enhance their adoption of crowdsourcing by emphasising cost, opportunity and managerial support while addressing barriers such as organisational size and technological turbulence.

6. Discussion

The adoption of crowdsourcing is significantly influenced by a combination of technological, organisational and environmental factors. The study reveals that seven key determinants impact the decision to adopt crowdsourcing: relative advantage, perceived cost reduction, perceived opportunity, compatibility, complexity, technology readiness and top management support. The relative advantage of crowdsourcing, which refers to its superiority over traditional methods, is a primary driver for adoption. For instance, platforms like Lego Ideas and TopCoder illustrate how crowdsourcing can enhance product quality and reduce costs compared to traditional models, supporting findings by Gangwar *et al.* (2015) and Tripopsakul (2018). Moreover, perceived cost reduction is identified as a key enabler, as organisations recognise the financial benefits of crowdsourcing through savings in labour, resources and time. Procter & Gamble's Connect + Develop program (Rajagopal and Rajagopal, 2021), which leverages external collaborators to reduce R&D costs, exemplifies this finding. In addition, perceived opportunity plays a significant role in crowdsourcing adoption, as organisations benefit from access to a wide pool of ideas and expertise. InnoCentive (Vignieri, 2021) is an example of how crowdsourcing helps organisations tap into global knowledge, thereby fostering innovation and competitive advantage.

The complexity of implementing crowdsourcing does not deter organisations, contrary to initial expectations. The study reveals that organisations are willing to adopt crowdsourcing despite its challenges. Procter and Gamble and Microsoft (Chan *et al.*, 2021), through their respective crowdsourcing initiatives, demonstrate how technological tools can mitigate the complexities of managing large external collaborations, thus enabling successful implementation. Compatibility with existing organisational structures, values and processes is another crucial factor. Crowdsourcing adoption is more likely when it aligns with organisational goals, as seen with Dell's IdeaStorm platform (Simaei *et al.*, 2023), which integrates customer suggestions into its product development seamlessly. Similarly, Microsoft's Garage program was successful due to its compatibility with the company's culture of innovation and collaboration.

Technology readiness emerges as a significant factor influencing crowdsourcing adoption, with organisations that possess robust technological infrastructure more likely to adopt crowdsourcing. General Electric's FirstBuild platform is a prime example, where technological preparedness facilitated the integration of crowdsourcing into the company's innovation processes. Achieving technological readiness, however, involves several practical intricacies, such as ensuring the availability of scalable IT infrastructure, investing in cloud-based platforms and integrating cybersecurity measures to protect crowdsourced data. It also requires continuous updates to software tools to support collaboration and idea-sharing. Furthermore, training employees to navigate these systems effectively and fostering a culture of technological adaptability are key to overcoming potential barriers. Top management support is also critical for the successful adoption of crowdsourcing. When leadership champions crowdsourcing, it signals a commitment to innovation and provides

the necessary resources for successful integration, as evidenced by Lego's management support for their Lego Ideas platform. However, organisational culture can act as a barrier to crowdsourcing adoption. Companies with hierarchical, traditional cultures may resist the decentralised and collaborative nature of crowdsourcing, a finding that aligns with Simula and Ahola's (2014) research on resistance to change.

The organisation's size plays a role in the adoption process, with larger organisations less likely to adopt crowdsourcing due to the complexity and bureaucracy inherent in their structure. Despite substantial resources, large corporations like IBM face challenges in scaling crowdsourcing initiatives across their vast organisational frameworks, as highlighted by Mathauer and Hofmann (2019). In contrast, smaller organisations may find it easier to implement crowdsourcing due to fewer hierarchical layers and more flexible decision-making processes.

From an environmental perspective, technological turbulence negatively impacts crowdsourcing adoption, as organisations in rapidly changing technological environments prioritise stability and internal innovation over external collaboration. Kodak's failure to embrace crowdsourcing during the rise of digital photography illustrates the challenges organisations face in turbulent environments. On the contrary, competitive pressure did not show a significant impact on crowdsourcing adoption. The lack of correlation suggests that organisations often prioritise internal factors such as innovation and operational efficiency over responding to external competitive pressures. LEGO's adoption of crowdsourcing through its Ideas platform illustrates this, where the decision was driven by the desire to foster creativity rather than by competitive forces, supporting Kohler and Chesbrough's (2019) assertion that the benefits of crowdsourcing extend beyond competitive concerns. Therefore, while several factors such as relative advantage, cost reduction, technology readiness and top management support facilitate crowdsourcing adoption, challenges related to organisational culture, size and environmental turbulence can hinder its integration. Organisations must carefully evaluate these factors to ensure successful implementation, balancing the benefits of crowdsourcing with the complexities inherent in its adoption.

7. Implications of research

The findings of our study hold profound significance for both practical decision-making and theoretical advancements in the realms of crowdsourcing adoption. In the following sections, we delineate the managerial and practical implications, shedding light on the actionable insights for organisational leaders and subsequently delve into the theoretical implications, elucidating the contribution of our research to the broader theoretical landscape of technology adoption and crowdsourcing.

7.1 Managerial and practical implications

This study provides valuable insights for decision-makers by identifying seven key factors influencing crowdsourcing adoption: relative advantage, cost reduction, opportunity, compatibility, complexity, technology readiness and top management support. Recognising these factors enables organisations to optimise their crowdsourcing strategies and drive innovation. Decision-makers should leverage the strategic benefits of crowdsourcing, particularly in enhancing problem-solving, productivity and innovation. For instance, InnoCentive has enabled organisations to access external expertise, leading to breakthrough solutions (Chesbrough, 2003). Perceived cost reduction and opportunity also play a vital role, as organisations seeking efficiency and resource optimisation are more inclined to integrate crowdsourcing for cost-effective access to specialised skills (Howe, 2008).

While complexity is often seen as a challenge due to issues such as managing diverse contributions and ensuring quality control, it can also serve as an enabler by fostering structured processes and technological advancements. For example, Procter & Gamble's Connect + Develop program leveraged collaboration tools to simplify workflows and enhance efficiency (Von Hippel, 2005). To mitigate potential difficulties, organisations can adopt strategies such as task simplification, structured evaluation frameworks and modern digital collaboration platforms (Brabham, 2013). Another critical aspect is compatibility, which determines how well crowdsourcing aligns with existing organisational processes and values. Starbucks' "My Starbucks Idea" platform successfully integrated customer feedback into its operations, demonstrating the importance of alignment. Start-ups, with their agile structures, often find crowdsourcing easier to integrate compared to larger enterprises.

Technology readiness is also essential, as organisations must assess their capacity to implement and support crowdsourcing initiatives with appropriate digital infrastructure. NASA's Open Innovation Program exemplifies how a strong technological foundation enhances external collaboration for problem-solving. Equally important is top management support, which plays a crucial role in fostering a collaborative culture. IBM's InnovationJam demonstrated how leadership endorsement can drive engagement and innovation (IBM, 2006). In addition, organisational culture significantly influences crowdsourcing adoption. Hierarchical structures may resist change, as seen in Toyota's initial challenges. However, Toyota's shift towards a more collaborative model highlights the importance of adaptability (Sundararajan, 2016).

Larger organisations may encounter difficulties with crowdsourcing due to rigid structures and slower decision-making processes. General Electric (GE) addressed this challenge by focusing on smaller, well-defined projects, making crowdsourcing initiatives more manageable and impactful. On the contrary, smaller, more flexible companies may find it easier to incorporate crowdsourcing due to their adaptability. The external environment also affects adoption, as technological turbulence can create uncertainty. For example, Nokia prioritised internal R&D during shifts in the mobile industry, limiting its engagement in crowdsourcing. In contrast, organisations operating in more stable environments may be more inclined to explore crowdsourcing opportunities. Interestingly, competitive pressure does not significantly drive crowdsourcing adoption. Instead, internal factors such as strategic alignment and operational efficiency play a more decisive role.

The emergence of Distributed Autonomous Organisations (DAOs) and Distributed Autonomous Enterprises (DAEs) presents new opportunities for crowdsourcing. These blockchain-based structures decentralise decision-making, offering greater transparency, reduced complexity and enhanced scalability (Tapscott and Tapscott, 2016). DAOs in decentralised finance illustrate how global collaboration can be effectively managed through blockchain, making crowdsourcing more inclusive and efficient. These findings emphasise the need for organisations to take a structured, technology-driven approach to crowdsourcing. Decision-makers must focus on strengthening internal capabilities, fostering leadership commitment and leveraging digital platforms to enhance collaboration. By strategically addressing complexity, aligning crowdsourcing with organisational goals and embracing emerging technologies, organisations can maximise the benefits of crowdsourcing to drive innovation, efficiency and sustainable growth.

7.2 Theoretical implications

This research significantly contributes to technology adoption and crowdsourcing by addressing the growing need for comprehensive approaches that integrate multiple theoretical perspectives. Recent scholarly discussions emphasise the importance of a holistic understanding, prompting researchers to combine various frameworks to more effectively explore the adoption of

innovative technologies. In response, our study integrates two key theoretical perspectives – the TOE (Technology–Organisation–Environment) framework and DOI theory – creating a robust research model that allows for a deeper understanding of crowdsourcing adoption. The TOE framework focuses on organisational and environmental factors influencing technology adoption, whereas DOI theory emphasises how innovations spread over time. By integrating both, our model offers a comprehensive view of adoption behaviours, where TOE addresses organisational readiness and external influences, and DOI highlights the role of innovation characteristics in its diffusion. This combination allows for a nuanced understanding of crowdsourcing adoption. Our study fills a gap in the literature by exploring not only direct but also indirect effects on adoption decisions, with the first empirical validation of these relationships, enhancing the theoretical landscape.

Furthermore, our research model includes reliability, validity and discriminant tests, ensuring robustness and credibility. By using a large data set, we provide a comprehensive assessment of the social, organisational and environmental factors influencing crowdsourcing adoption. This approach offers valuable insights for both academia and industry, highlighting direct and indirect determinants of adoption. Our study also paves the way for future research by incorporating DAOs and DAEs, introducing a new lens for decentralised technology adoption. These decentralised models, supported by blockchain, could disrupt traditional innovation diffusion and significantly impact organisational behaviour. To further expand the theoretical implications, future research could consider additional lenses, such as institutional theory and the resource-based view (RBV). Institutional theory could provide insights into how organisational norms, regulations and cultural forces shape crowdsourcing adoption, whereas RBV could shed light on how firms leverage their internal resources to effectively implement crowdsourcing initiatives. These perspectives would not only broaden the applicability of our findings but also inspire future investigations into the dynamic factors that drive technology adoption across different industries.

8. Limitations and future research

This study offers valuable insights into crowdsourcing adoption but has some limitations. It primarily focuses on the Indian context, which may limit the broader applicability of its findings. Future research could expand by conducting comparative studies across different countries or regions, exploring how cultural factors like uncertainty avoidance, power distance and individualism versus collectivism affect crowdsourcing adoption. These studies could provide global insights into adoption behaviours. In addition, this research mainly addresses internal factors such as organisational readiness and technology capabilities, leaving out external influences. Future studies could explore the impact of regulatory environments, public perceptions and market dynamics on crowdsourcing adoption. Understanding the role of government policies, industry regulations or societal attitudes could provide a more comprehensive view.

The study's cross-sectional design offers a snapshot of crowdsourcing adoption but does not capture the temporal dynamics. Future research could use longitudinal or experimental designs to explore causal relationships and track adoption behaviours over time. Mixed-method approaches combining quantitative and qualitative data could offer a deeper understanding of the complexities involved in decision-making. The reliance on self-reported data may introduce bias, and future studies could incorporate objective metrics or triangulate data with secondary sources like adoption rates or performance indicators.

The analysis of technological turbulence and competitive pressure could benefit from further exploration. Investigating why competitive pressure does not significantly influence adoption, considering factors like market saturation and internal innovation priorities, would be valuable. In addition, examining the impact of emerging technologies like AI and blockchain on crowdsourcing platforms would align the study with evolving technological landscapes.

Regarding theoretical advancements, while the TOE framework and DOI theory provide a strong foundation, future research could further explore how organisations can apply these frameworks to shape strategies, policies and technological investments. This would enhance the practical relevance of the study. Finally, investigating industry-specific barriers and drivers of crowdsourcing adoption could yield valuable insights. Sectors such as health care, finance and education may face unique challenges or benefits. In addition, exploring how emerging technologies like blockchain can improve transparency, security and trust in crowdsourcing could open new avenues for research. Incorporating dynamic capabilities and ecosystem perspectives could also deepen our understanding of how organisations use crowdsourcing in broader innovation strategies.

9. Conclusion

This study provides a comprehensive understanding of the key factors influencing crowdsourcing adoption by integrating the DOI theory with the Technological–Organisational–Environmental framework. The findings highlight seven critical determinants: relative advantage, perceived cost reduction, perceived opportunity, compatibility, complexity, technology readiness and top management support. While relative advantage, perceived cost reduction and perceived opportunity act as strong motivators, complexity, rather than being a barrier, emerges as an enabler, facilitating adoption by encouraging organisations to develop capabilities that align with the demands of crowdsourcing. Compatibility, technology readiness and top management support further strengthen adoption by ensuring alignment with organisational capabilities and leadership commitment.

Furthermore, the study underscores the role of organisational readiness in shaping adoption decisions. Organisations with strong technological infrastructure and proactive leadership are better positioned to integrate crowdsourcing effectively. The influence of environmental factors, such as technological turbulence and industry trends, further emphasises the need for organisations to adapt dynamically to external changes. By bridging innovation characteristics with organisational and environmental perspectives, this study contributes to both theoretical and managerial understanding of crowdsourcing adoption. The findings offer practical insights for businesses aiming to enhance digital transformation and open innovation through crowdsourcing. Future research can build on these insights by exploring longitudinal trends and cross-industry comparisons to further refine the framework and enhance its applicability in diverse organisational contexts.

References

Acar, O.A. (2019), “Motivations and solution appropriateness in crowdsourcing challenges for innovation”, *Research Policy*, Vol. 48 No. 8, p. 103716.

Afuah, A. and Tucci, C.L. (2012), “Crowdsourcing as a solution to distant search”, *Academy of Management Review*, Vol. 37 No. 3, pp. 355-375.

Agi, M.A. and Jha, A.K. (2022), “Blockchain technology in the supply chain: an integrated theoretical perspective of organizational adoption”, *International Journal of Production Economics*, Vol. 247, p. 108458.

Al Hadwer, A., Tavana, M., Gillis, D. and Rezania, D. (2021), "A systematic review of organizational factors impacting cloud-based technology adoption using technology-organization-environment framework", *Internet of Things*, Vol. 15, p. 100407.

Ali, A.X., Morris, M.R. and Wobbrock, J.O. (2018, October), "Crowdsourcing similarity judgments for agreement analysis in end-user elicitation studies", In *Proceedings of the 31st Annual ACM Symposium on User Interface Software and Technology*, pp. 177-188.

Ali, O. and Shrestha, A. (2017), "Analysis of the total cost of ownership for cloud computing technology adoption: a case study of regional municipal government sector", *Australasian Conference on Information Systems*, pp. 1-12.

Ali, O., Shrestha, A., Osmanaj, V. and Muhammed, S. (2020), "Cloud computing technology adoption: an evaluation of key factors in local governments", Information Technology and People.

Aligarh, F., Sutopo, B. and Widarjo, W. (2023), "The antecedents of cloud computing adoption and its consequences for MSMEs' performance: a model based on the Technology-organization-Environment (TOE) framework", *Cogent Business and Management*, Vol. 10 No. 2, p. 2220190.

Alorwu, A., van Berkel, N., Goncalves, J., Oppenlaender, J., López, M.B., Seetharaman, M. and Hosio, S. (2022), "Crowdsourcing sensitive data using public displays – opportunities, challenges, and considerations", *Personal and Ubiquitous Computing*, Vol. 26 No. 3, pp. 1-16.

Beatty, R.C., Shim, J.P. and Jones, M.C. (2001), "Factors influencing corporate web site adoption: a time-based assessment", *Information and Management*, Vol. 38 No. 6, pp. 337-354.

Benlian, A. and Hess, T. (2011), "Opportunities and risks of software-as-a-service: findings from a survey of IT executives", *Decision Support Systems*, Vol. 52 No. 1, pp. 232-246.

Bigliardi, B. and Galati, F. (2016), "Which factors hinder the adoption of open innovation in SMEs?", *Technology Analysis and Strategic Management*, Vol. 28 No. 8, pp. 869-885.

Boudreau, K.J. and Lakhani, K.R. (2013), "Using the crowd as an innovation partner", *Harvard Business Review*, Vol. 91 No. 4, pp. 60-69.

Brabham, D.C. (2008), "Crowdsourcing as a model for problem solving: an introduction and cases", *Convergence: The International Journal of Research into New Media Technologies*, Vol. 14 No. 1, pp. 75-90.

Brabham, D.C. (2013), "Crowdsourcing", The MIT Press eBooks, doi: 10.7551/mitpress/9693.001.0001.

Brunswicker, S. and Vanhaverbeke, W. (2015), "Open innovation in small and medium-sized enterprises (SMEs): external knowledge sourcing strategies and internal organizational facilitators", *Journal of Small Business Management*, Vol. 53 No. 4, pp. 1241-1263.

Chan, K.W., Li, S.Y., Ni, J. and Zhu, J.J. (2021), "What feedback matters? The role of experience in motivating crowdsourcing innovation", *Production and Operations Management*, Vol. 30 No. 1, pp. 103-126.

Chatterjee, S., Rana, N.P., Dwivedi, Y.K. and Baabdullah, A.M. (2021), "Understanding AI adoption in manufacturing and production firms using an integrated TAM-TOE model", *Technological Forecasting and Social Change*, Vol. 170, p. 120880.

Chesbrough, H.W. (2003), *Open Innovation: The New Imperative for Creating and Profiting from Technology*, Harvard Business Press, Boston, MA.

Chidlow, A., Ghauri, P.N., Yeniyurt, S. and Cavusgil, S.T. (2015), "Establishing rigor in mail-survey procedures in international business research", *Journal of World Business*, Vol. 50 No. 1, pp. 26-35.

Chin, W.W., Thatcher, J.B., Wright, R.T. and Steel, D. (2013), "Controlling for common method variance in PLS analysis: the measured latent marker variable approach", *New Perspectives in Partial Least Squares and Related Methods*, New York, NY, Springer, pp. 231-239.

Chittipaka, V., Kumar, S., Sivarajah, U., Bowden, J.L.H. and Baral, M.M. (2023), "Blockchain technology for supply chains operating in emerging markets: an empirical examination of

technology-organization-environment (TOE) framework", *Annals of Operations Research*, Vol. 327 No. 1, p. 46.

Chou, S.W. (2021), "Understanding crowdsourcing adoption based on IT managers' decision", *Information Technology and Management*, Vol. 22 No. 4, pp. 245-263.

Chung, T., Kim, K. and Shin, E. (2021), "Together we create value: a study of a crowdsourcing community", *Internet Research*, Vol. 31 No. 3, pp. 911-930.

Chwelos, P., Benbasat, I. and Dexter, A.S. (2001), "Empirical test of an EDI adoption model", *Information Systems Research*, Vol. 12 No. 3, pp. 304-321.

Cricelli, L., Grimaldi, M. and Vermicelli, S. (2022), "Crowdsourcing and open innovation: a systematic literature review, an integrated framework and a research agenda", *Review of Managerial Science*, Vol. 16 No. 5, pp. 1269-1310.

Davis, F.D. (1989), "Perceived usefulness, perceived ease of use, and user acceptance of information technology", *MIS Quarterly*, Vol. 13 No. 3, pp. 319-340.

De Coninck, B., Viaene, S. and Leysen, J. (2023), "Antecedents of the intention to adopt crowdsourcing for innovation in government: findings from Belgium and the Netherlands", *Government Information Quarterly*, Vol. 40 No. 1, p. 101760.

Djelassi, S. and Decoopman, I. (2013), "Customers' participation in product development through crowdsourcing : issues and implications", *Industrial Marketing Management*, Vol. 42 No. 5, pp. 683-692.

Doan, A., Ramakrishnan, R. and Halevy, A.Y. (2011), "Crowdsourcing systems on the world-wide web", *Communications of the ACM*, Vol. 54 No. 4, pp. 86-96.

Ebrahimi, P., Shafiee, B., Gholampour, A. and Yousefi, L. (2018), "Impact of organizational innovation, learning orientation and entrepreneurship on SME performance: the moderating role of market turbulence and ICT", Competitiveness in Emerging Markets: Market Dynamics in the Age of Disruptive Technologies, pp. 447-480.

Estellés-Arolas, E. and González-Ladrón-De-Guevara, F. (2012), "Towards an integrated crowdsourcing definition", *Journal of Information Science*, Vol. 38 No. 2, pp. 189-200.

Evans, R.D., Gao, J.X., Mahdikhah, S., Messaadia, M. and Baudry, D. (2016), "A review of crowdsourcing literature related to the manufacturing industry", *Journal of Advanced Management Science*, Vol. 4, pp. 224-231.

Featherman, M.S. and Pavlou, P.A. (2003), "Predicting e-services adoption: a perceived risk facets perspective", *International Journal of Human-Computer Studies*, Vol. 59 No. 4, pp. 451-474.

Fornell, C. and Larcker, D.F. (1981), "Evaluating structural equation models with unobservable variables and measurement error", *Journal of Marketing Research*, Vol. 18 No. 1, pp. 39-50.

Fu, H. and Chang, T. (2016), "An analysis of the factors affecting the adoption of cloud consumer relationship management in the machinery industry in Taiwan", *Information Development*, Vol. 32 No. 5, pp. 1741-1756.

Gangwar, H., Date, H. and Ramaswamy, R. (2015), "Understanding determinants of cloud computing adoption using an integrated TAM-TOE mode", *Journal of Enterprise Information Management*, Vol. 28 No. 1, pp. 107-130.

Garrow, L.A., Chen, Z., Ilbeigi, M. and Lurkin, V. (2020), "A new twist on the gig economy: conducting surveys on amazon mechanical turk", *Transportation*, Vol. 47 No. 1, pp. 23-42.

Gewald, H. and Dibbern, J. (2009), "Risks and benefts of business process outsourcing: a study of transaction services in the german banking industry", *Information and Management*, Vol. 46 No. 4, pp. 249-257.

Ghezzi, A., Gabelloni, D., Martini, A. and Natalicchio, A. (2018), "Crowdsourcing: a review and suggestions for future research", *International Journal of Management Reviews*, Vol. 20 No. 2, pp. 343-363.

Ghobakhloo, M., Arias-Aranda, D. and Benitez-Amado, J. (2011), "Adoption of e-commerce applications in SMEs", *Industrial Management and Data Systems*, Vol. 111 No. 8, pp. 1238-1269.

Greenhalgh, T., Robert, G., Macfarlane, F., Bate, P. and Kyriakidou, O. (2004), "Diffusion of innovations in service organizations: systematic review and recommendations", *The Milbank Quarterly*, Vol. 82 No. 4, pp. 581-629.

Hair, J.F., Hult, G.T.M., Ringle, C. and Sarstedt, M. (2014), *A Primer on Partial Least Squares Structural Equation Modeling (PLS-SEM)*, Thousand Oaks, CA: Sage Publications.

Hair, J., Hollingsworth, C.L., Randolph, A.B. and Chong, A.Y.L. (2017), "An updated and expanded assessment of PLS-SEM in information systems research", *Industrial Management and Data Systems*, Vol. 117 No. 3, pp. 442-458.

Hamad, F., Farajat, S. and Hamarsha, A. (2018), "Awareness and adoption of mobile technologies in the delivery of services in academic libraries in Jordan", *Global Knowledge, Memory and Communication*, Vol. 67 Nos 6/7, pp. 438-457.

Henseler, J., Hubona, G. and Ray, P.A. (2016), "Using PLS path modeling in new technology research: updated guidelines", *Industrial Management and Data Systems*, Vol. 116 No. 1, pp. 2-20.

Howe, J. (2006), "The rise of crowdsourcing", Wired, 14.

Howe, J. (2008), "Why the power of the crowd is driving the future of business", Crowdsourcing, pp. 1-320.

Hsu, H.Y., Liu, F.H., Tsou, H.T. and Chen, L.J. (2019), "Openness of technology adoption, top management support and service innovation: a social innovation perspective", *Journal of Business and Industrial Marketing*, Vol. 34 No. 3, pp. 575-590.

Hu, L.T. and Bentler, P.M. (1999), "Cutoff criteria for fit indexes in covariance structure analysis: conventional criteria versus new alternatives", *Structural Equation Modeling: a Multidisciplinary Journal*, Vol. 6 No. 1, pp. 1-55.

Ifinedo, P. (2011), "An empirical analysis of factors influencing internet/e-business technologies adoption by SMEs in Canada", *International Journal of Information Technology and Decision Making*, Vol. 10 No. 4, pp. 731-766.

Ishikawa, T. (2019), "Why inbound open innovation practices are driven in Japanese manufacturing firms: technological turbulence, competitive intensity", *2019 8th International Conference on Industrial Technology and Management (ICITM), IEEE*, pp. 100-104.

Johnson, J.S., Fisher, G.J. and Friend, S.B. (2019), "Crowdsourcing service innovation creativity: environmental influences and contingencies", *Journal of Marketing Theory and Practice*, Vol. 27 No. 3, pp. 251-268.

Kim, D.J., Ferrin, D.L. and Rao, H.R. (2008), "A trust-based consumer decision-making model in electronic commerce: the role of trust, perceived risk, and their antecedents", *Decision Support Systems*, Vol. 44 No. 2, pp. 544-564.

Kittur, A., Nickerson, J.V., Bernstein, M.S., Gerber, E.M., Shaw, A., Zimmerman, J., Lease, M. and Horton, J.J. (2013), "The future of crowd work", *Proceedings of the ACM Conference on Computer Supported Cooperative Work, CSCW, February*, pp. 1301-1317.

Kohler, T. and Chesbrough, H. (2019), "From collaborative community to competitive market: the quest to build a crowdsourcing platform for social innovation", *R&D Management*, Vol. 49 No. 3, pp. 356-368.

Lee, C.K., Chan, C.Y., Ho, S., Choy, K.L. and Ip, W.H. (2015), "Explore the feasibility of adopting crowdsourcing for innovative problem solving", *Industrial Management and Data Systems*, Vol. 115 No. 5, pp. 803-832.

Love, J. and Hirschheim, R. (2017), "Crowdsourcing of information systems research", *European Journal of Information Systems*, Vol. 26 No. 3, pp. 315-332.

Lu, B., Hirschheim, R. and Schwarz, A. (2015), "Examining the antecedent factors of online microsourcing", *Information Systems Frontiers*, Vol. 17 No. 3, pp. 601-617.

Lynn, T., Liang, X., Gourinovith, A., Morrison, J.P., Fox, G. and Rosati, P. (2018), "Understanding the determinants of cloud computing adoption for high performance computing", *Proceedings of the 51st HI International Conference on System Sciences*, pp. 3894-3903.

Lysyakov, M. and Viswanathan, S. (2023), "Threatened by AI: analyzing users' responses to the introduction of AI in a crowd-sourcing platform", *Information Systems Research*, Vol. 34 No. 3, pp. 1191-1210.

Mabad, T., Ali, O., Ally, M., Wamba, S. and Chen, K.C. (2021), "Making investment decisions on RFID technology: an evaluation of key adoption factors in construction firms", *IEEE Access*, Vol. 9, pp. 36937-36954.

Maiolini, R. and Naggi, R. (2011), "Crowdsourcing and SMEs: opportunities and challenges", Information Technology and Innovation Trends in Organizations, May 2011.

Malik, S., Chadhar, M., Vatanasakdakul, S. and Chetty, M. (2021), "Factors affecting the organizational adoption of blockchain technology: extending the technology–organization–environment (TOE) framework in the Australian context", *Sustainability*, Vol. 13 No. 16, p. 9404.

Marjanovic, S., Fry, C. and Chataway, J. (2012), "Crowdsourcing based business models: in search of evidence for innovation 2.0", *Science and Public Policy*, Vol. 39 No. 3, pp. 318-332.

Mathauer, M. and Hofmann, E. (2019), "Technology adoption by logistics service providers", *International Journal of Physical Distribution and Logistics Management*, Vol. 49 No. 4, pp. 416-434.

Meng, L., Qamruzzaman, M. and Adow, A.H.E. (2021), "Technological adaption and open innovation in SMEs: an strategic assessment for women-owned SMEs sustainability in Bangladesh", *Sustainability*, Vol. 13 No. 5, p. 2942.

Mergel, I. (2021), "Open innovation in the public sector: drivers and barriers for the adoption of challenge.gov", *Digital Government and Public Management*, Routledge, London and New York, pp. 94-113.

Metwaly, A., ElKattan, A. and Kaoud, M. (2022), "Toward an Egyptian managerial framework based on crowdsourcing for open innovation", *American Journal of Business*, Vol. 37 No. 1, pp. 14-33.

Min, S., So, K.K.F. and Jeong, M. (2021), "Consumer adoption of the Uber mobile application: insights from diffusion of innovation theory and technology acceptance model", *Future of Tourism Marketing*, Routledge, London and New York, pp. 2-15.

Mishra, D. and Maheshwari, N. (2024a), "Crowdsourcing a wellspring of value co-creation: an integration of social capital and organisational learning mechanisms", *Kybernetes*, Vol. 53 No. 1, pp. 424-450.

Mishra, D. and Maheshwari, N. (2024b), "Crowdsourcing-based social linkage and organizational innovation competence: knowledge transfer effectiveness and absorptive capacity as serial mediators", *Journal of Knowledge Management*, Vol. 28 No. 7, pp. 2013-2037.

Modaresnezhad, M., Iyer, L., Palvia, P. and Taras, V. (2020), "Information technology (IT) enabled crowdsourcing: a conceptual framework", *Information Processing and Management*, Vol. 57 No. 2, p. 102135.

Moore, G.C. and Benbasat, I. (1991), "Development of an instrument to measure the perceptions of adopting an information technology innovation", *Information Systems Research*, Vol. 2 No. 3, pp. 192-222.

Muhammed, S. and Zaim, H. (2020), "Peer knowledge sharing and organizational performance: the role of leadership support and knowledge management success", *Journal of Knowledge Management*, Vol. 24 No. 10.

Muhdi, L., Daiber, M., Friesike, S. and Boutellier, R. (2011), "The crowdsourcing process: an intermediary mediated idea generation approach in the early phase of innovation", *International Journal of Entrepreneurship and Innovation Management*, Vol. 14 No. 4, pp. 315-332.

Muntés-Mulero, V., Paladini, P., Manzoor, J., Gritti, A., Larriba-Pey, J.L. and Mijnhardt, F. (2013), "Crowdsourcing for industrial problems", in Nin, J. and Villatoro, D. (Eds), *Citizen in Sensor Networks*, LNCS, Berlin Heidelberg, Springer, Vol. 7685, pp. 6-18.

Naroditskiy, V., Jennings, N.R., Van Hentenryck, P. and Cebrian, M. (2013), "Crowdsourcing dilemma".

Nevo, D. and Kotlarsky, J. (2020), "Crowdsourcing as a strategic is sourcing phenomenon: critical review and insights for future research", *The Journal of Strategic Information Systems*, Vol. 29 No. 4, p. 101593.

Oliveira, F., Ramos, I. and Santos, L. (2010), "Definition of a crowdsourcing innovation service for the European SMEs", *In Current Trends in Web Engineering: 10th International Conference on Web Engineering ICWE 2010 Workshops*, Vienna, Austria, Springer, Berlin Heidelberg, July 2010, Revised Selected Papers 10, pp. 412-416.

Oliveira, F., Ramos, I. and Santos, L. (2011). *Definition of the architecture of a Crowdsourcing Innovation intermediary service for the SMEs, MCIS 2011 Proceedings.* 133.

Oliveira, T. and Martins, M.F.O. (2009), "Determinants of information technology adoption in Portugal", pp. 264-270.

Oliveira, T. and Martins, M.F. (2010), "Understanding e-business adoption across industries in european countries", *Industrial Management and Data Systems*, Vol. 110 No. 9, pp. 1337-1354.

Podsakoff, N.P. (2003), "Common method biases in behavioral research: a critical review of the literature and recommended remedies", *Journal of Applied Psychology*, Vol. 88 No. 5, pp. 10-1037.

Premkumar, G. and Roberts, M. (1999), "Adoption of new information technologies in rural small businesses", *Omega*, Vol. 27 No. 4, pp. 467-484.

Qin, S., Van der Velde, D., Chatzakis, E., McStea, T. and Smith, N. (2016), "Exploring barriers and opportunities in adopting crowdsourcing based new product development in manufacturing SMEs", *Chinese Journal of Mechanical Engineering*, Vol. 29 No. 6, pp. 1052-1066.

Rajagopal, R., (2021), "Crowd-Based business leadership and strategies", Crowd-Based Business Models: Using Collective Intelligence for Market Competitiveness, pp. 133-162.

Ranade, G. and Varshney, L.R. (2012), "To crowdsource or not to crowdsource?", Paper presented at the AAAI Workshop Human Comput. (HCOMP'12)

Ren, M. (2019), "Why technology adoption succeeds or fails: an exploration from the perspective of intra-organizational legitimacy", *The Journal of Chinese Sociology*, Vol. 6 No. 1, pp. 1-26.

Rogers, E.M. (1983), *Diffusion of Innovations*, Free Press, New York, NY.

Rogers, E.M. (2003), *Diffusion of Innovations*, 5th ed., Free Press, New York, NY.

Rouse, A.C. (2010), "A preliminary taxonomy of crowdsourcing", *ACIS 2010 Proceedings - 21st Australasian Conference on Information Systems*.

Sadoughi, F., Ali, O. and Erfannia, L. (2020), "Evaluating the factors that influence cloud technology adoption: comparative case analysis of health and non-health sectors: a systematic review", *Health Informatics Journal*, Vol. 26 No. 2.

Salah, O.H. and Ayyash, M.M. (2024), "E-commerce adoption by SMEs and its effect on marketing performance: an extended of TOE framework with ai integration, innovation culture, and customer tech-savviness", *Journal of Open Innovation: Technology, Market, and Complexity*, Vol. 10 No. 1, p. 100183.

Salminen, J., Kamel, A.M.S., Jung, S.G., Mustak, M. and Jansen, B.J. (2023), "Fair compensation of crowdsourcing work: the problem of flat rates", *Behaviour and Information Technology*, Vol. 42 No. 16, pp. 2871-2892.

Saxton, G.D., Oh, O. and Kishore, R. (2013), "Rules of crowdsourcing: models, issues, and systems of control", *Information Systems Management*, Vol. 30 No. 1, pp. 2-20.

Schemmann, B., Herrmann, A.M., Chappin, M.M. and Heimeriks, G.J. (2016), "Crowdsourcing ideas: involving ordinary users in the ideation phase of new product development", *Research Policy*, Vol. 45 No. 6, pp. 1145-1154.

Schiavi, G.S. and Behr, A. (2018), "Emerging technologies and new business frameworks: a review on disruptive business frameworks", *Innovation and Management Review*, Vol. 15 No. 4, pp. 338-355.

Scupola, A. and Nicolajsen, H.W. (2021), "Enterprise crowdsourcing and organizational culture: lessons from an engineering consultancy", *International Journal of E-Services and Mobile Applications (Applications)*, Vol. 13 No. 2, pp. 1-20.

Seltzer, E. and Mahmoudi, D. (2013), "Citizen participation, open innovation, and crowdsourcing: challenges and opportunities for planning", *Journal of Planning Literature*, Vol. 28 No. 1, pp. 3-18.

Sethi, R. and Iqbal, Z. (2008), "Stage-gate controls, learning failure, and adverse effect on novel new products", *Journal of Marketing*, Vol. 72 No. 1, pp. 118-134.

Shah Alam, S., Ali, M.Y. and Mohd. Jani, M.F. (2011), "An empirical study of factors affecting electronic commerce adoption among SMEs in Malaysia", *Journal of Business Economics and Management*, Vol. 12 No. 2, pp. 375-399.

Shuai, M., Steils, N. and Gailly, B. (2025), "Getting crowdsourcing right: aligning crowdsourcing goals and decision-making processes", *Creativity and Innovation Management*.

Simaei, A., Hirschheim, R. and Schneider, H. (2023), "Idea crowdsourcing platforms for new product development: a study of idea quality and the number of submitted ideas", *Decision Support Systems*, Vol. 175, p. 114041.

Simula, H. and Ahola, T. (2014), "A network perspective on idea and innovation crowdsourcing in industrial firms", *Industrial Marketing Management*, Vol. 43 No. 3, pp. 400-408.

Siren, A. and Knudsen, S.G. (2017), "Older adults and emerging digital service delivery: a mixed methods study on information and communications technology use, skills, and attitudes", *Journal of Aging and Social Policy*, Vol. 29 No. 1, pp. 35-50.

Skafi, M., Yunis, M.M. and Zekri, A. (2020), "Factors influencing SMEs' adoption of cloud computing services in Lebanon: an empirical analysis using TOE and contextual theory", *IEEE Access*, Vol. 8, pp. 79169-79181.

Soliman, K.S. and Janz, B.D. (2004), "An exploratory study to identify the critical factors affecting the decision to establish internet-based interorganizational information systems", *Information and Management*, Vol. 41 No. 6, pp. 697-706.

Sundararajan, A. (2016), *The Sharing Economy: The End of Employment and the Rise of Crowd-Based Capitalism*. Mit Press, 128-129.

Sutanonpaiboon, J. and Pearson, A.M. (2008), "E-commerce adoption: perceptions of managers/owners of small and medium-sized enterprises (SMEs) in Thailand", *Journal of Internet Commerce*, Vol. 5 No. 3, pp. 53-82.

Tapscott, D. and Tapscott, A. (2016), *Blockchain Revolution: How the Technology Behind Bitcoin is Changing Money, Business and the World*, Penguin.

Thiesse, F., Staake, T., Schmitt, P. and Fleisch, E. (2011), "The rise of the 'next-generation bar code': An international RFID adoption study", *Supply Chain Management: An International Journal*, Vol. 16 No. 5, pp. 328-345.

Thuan, N.H., Antunes, P. and Johnstone, D. (2013), "Factors influencing the decision to crowdsource", In *Collaboration and Technology: 19th International Conference, CRIWG 2013, Wellington, New Zealand, October 30–November 1, 2013, Proceedings 19*, Springer, Berlin Heidelberg, pp. 110-125.

Thuan, N.H., Antunes, P., Johnstone, D., Son, H.X., Hoang, N. and Xuan, H. (2015), Building an enterprise ontology of business process crowdsourcing: a design science approach. In *PACIS*, p. 112.

Thuan, N.H., Antunes, P. and Johnstone, D. (2016), "Factors influencing the decision to crowdsource: a systematic literature review", *Information Systems Frontiers*, Vol. 18 No. 1, pp. 47-68.

Tornatzky, L.G. and Fleischer, M. (1990), *The Processes of Technological Innovation*, Lexington Books, MA.

Toufaily, E., Zalan, T. and Dhaou, S.B. (2021), "A framework of blockchain technology adoption: an investigation of challenges and expected value", *Information and Management*, Vol. 58 No. 3, p. 103444.

Tripopsakul, S. (2018), "Social media adoption as a business platform: an integrated tam-toe framework", *Polish Journal of Management Studies*, Vol. 18 No. 2, pp. 350-362.

Vignieri, V. (2021), "Crowdsourcing as a mode of open innovation: exploring drivers of success of a multisided platform through system dynamics modelling", *Systems Research and Behavioral Science*, Vol. 38 No. 1, pp. 108-124.

von Hippel, E. (2005), "Democratizing innovation: the evolving phenomenon of user innovation", *Journal f□r Betriebswirtschaft*, Vol. 55 No. 1, pp. 63-78.

Wade, M. and Hulland, J. (2004), "Review: the resource-based view and information systems research: review, extension, and suggestions for future research", *Mis Q*, Vol. 28 No. 1, pp. 107-142.

Wetzels, M., Odekerken-Schröder, G. and Van Oppen, C. (2009), "Using PLS path modeling for assessing hierarchical construct models: guidelines and empirical illustration", *MIS Quarterly*, Vol. 33 No. 1, pp. 177-195.

Wexler, M.N. (2011), "Reconfiguring the sociology of the crowd: exploring crowdsourcing", *International Journal of Sociology and Social Policy*, Vol. 31 Nos 1/2, pp. 6-20.

Whitla, P. (2009), "Crowdsourcing and its application in marketing activities", *Contemporary Management Research*, Vol. 5 No. 1.

Wilson, M., Robson, K. and Botha, E. (2017), "Crowdsourcing in a time of empowered stakeholders: lessons from crowdsourcing campaigns", *Business Horizons*, Vol. 60 No. 2, pp. 247-253.

Wu, Y.U.N., Cegielski, C.G., Hazen, B.T. and Hall, D.J. (2013), "Cloud computing in support of supply chain information system infrastructure: understanding when to go to the cloud", *Journal of Supply Chain Management*, Vol. 49 No. 3, pp. 25-41.

Xu, Y., Ribeiro-Soriano, D.E. and Gonzalez-Garcia, J. (2015), "Crowdsourcing, innovation and firm performance", Management Decision.

Ye, H.J. and Kankanhalli, A. (2015), "Investigating the antecedents of organizational task crowdsourcing", *Information and Management*, Vol. 52 No. 1, pp. 98-110.

Ye, H.J. and Kankanhalli, A. (2017), "Solvers' participation in crowdsourcing platforms: examining the impacts of trust, and benefit and cost factors", *The Journal of Strategic Information Systems*, Vol. 26 No. 2, pp. 101-117.

Zahay, D., Hajli, N. and Sihi, D. (2018), "Managerial perspectives on crowdsourcing in the new product development process", *Industrial Marketing Management*, Vol. 71, pp. 41-53.

Zhao, Y. and Zhu, Q. (2014), "Evaluation on crowdsourcing research: current status and future direction", *Information Systems Frontiers*, Vol. 16 No. 3, pp. 417-434.

Zhu, J.J., Li, S.Y. and Andrews, M. (2017), "Ideator expertise and cocreator inputs in crowdsourcing-based new product development", *Journal of Product Innovation Management*, Vol. 34 No. 5, pp. 598-616.

Zhu, K., Dong, S., Xu, S.X. and Kraemer, K.L. (2006), "Innovation diffusion in global contexts: determinants of post-adoption digital transformation of European companies", *European Journal of Information Systems*, Vol. 15 No. 6, pp. 601-616.

Zhu, Y., Li, Y., Wang, W. and Chen, J. (2010), "What leads to post-implementation success of ERP? An empirical study of the Chinese retail industry", *International Journal of Information Management*, Vol. 30 No. 3, pp. 265-276.

Zogaj, S., Leicht, N., Blohm, I., Bretschneider, U. and Leimeister, J.M. (2015), "Towards successful crowdsourcing projects: evaluating the implementation of governance mechanisms", SSRN 3140601.

Further reading

Al-Momani, A.M., Mahmoud, M. and Ahmad, M.S. (2018), "Factors that influence the acceptance of internet of things services by customers of telecommunication companies in Jordan", *Journal of Organizational and End User Computing*, Vol. 30 No. 4, pp. 51-63.

Buecheler, T., Sieg, J.H., Füchslin, R.M. and Pfeifer, R. (2010), "Crowdsourcing, open innovation and collective intelligence in the scientific method: a research agenda and operational framework", The 12th International Conference on the Synthesis and Simulation of Living Systems, Odense, Denmark, 19-23 August 2010, *MIT Press*, pp. 679-686.

Chong, A.Y.L., Lin, B., Ooi, K.B. and Raman, M. (2009), "Factors affecting the adoption level of c-commerce: an empirical study", *Journal of Computer Information Systems*, Vol. 50 No. 2, pp. 13-22.

Hameed, M.A. and Arachchilage, N.A.G. (2019), "A conceptual model for the organizational adoption of information system security innovations", pp. 317-339.

Nkhoma, M. and Dang, D. (2013), "Contributing factors of cloud computing adoption: a technology-organization-environment framework approach", *International Journal of Information Systems and Engineering*, Vol. 1 No. 1, pp. 38-49.

Shahadat, M.H., Nekmahmud, M., Ebrahimi, P. and Fekete-Farkas, M. (2023), "Digital technology adoption in SMEs: what technological, environmental and organizational factors influence in emerging countries?", *Global Business Review*.

Wilson, K.B., Bhakoo, V. and Samson, D. (2018), "Crowdsourcing: a contemporary form of project management with linkages to open innovation and novel operations", *International Journal of Operations and Production Management*, Vol. 38 No. 6, pp. 1467-1494.

Corresponding author

Divya Mishra can be contacted at: divyamishra919@gmail.com

For instructions on how to order reprints of this article, please visit our website:
www.emeraldgrouppublishing.com/licensing/reprints.htm
Or contact us for further details: **permissions@emeraldinsight.com**

Signal, Image and Video Processing (2025) 19:391
https://doi.org/10.1007/s11760-025-03914-1

ORIGINAL PAPER

Deep decomposer and refiner for low-light image enhancement

Piyush Vaish[1] · **Anil Singh Parihar**[1]

Received: 15 April 2024 / Revised: 22 January 2025 / Accepted: 1 February 2025
© The Author(s), under exclusive licence to Springer-Verlag London Ltd., part of Springer Nature 2025

Abstract
Low-light imaging poses a significant challenge in various applications, including medical imaging, photography, and surveillance, due to the limited availability of illumination. The paper presents a deep decomposer and refiner for low-light image enhancement. The proposed method develops the mf-block to focus on multi-level features using variation of the receptive field. The decomposer sub-module contains down-blocks and up-blocks that leverage channel attention to process the features of mf-block for Retinex-based image decomposition. Moreover, we introduce a hybrid method for adjustment of the estimated illumination combining deep learning-based techniques with non-linear statistical methods to adjust non-uniform illumination. Additionally, we developed a refiner sub-module utilizing a similar model to reduce noise and enhance contrast in the reflectance component. The exhaustive experimentation on dataset with various low-light images demonstrates the effectiveness of our approach in significantly improving image details and reducing noise. The proposed method shows results superior to those of state-of-the-art techniques, highlighting its potential for real-world low-light imaging applications.

Keywords Image decomposition · Retinex method · Low-light image enhancement · Deep learning

1 Introduction

Low-light imaging is crucial in numerous domains [1, 5, 6], from surveillance to medical imaging. In these fields, capturing clear and detailed images under challenging lighting conditions, such as low illumination or nighttime settings, is not just desirable but often critical for effective decision-making, analysis, and understanding of visual data. However, low-light conditions impose inherent limitations on captured images, which often result in degraded visibility, reduced contrast, and increased noise levels. Thus, the development of effective techniques to enhance low-light images has become crucial, with implications for various applications where accurate image interpretation is vital.

To address the issues of low-light conditions, researchers [22–24] developed various enhancement techniques. Histogram equalization (HE) [20] has been a fundamental approach, grouping similar intensities and adjusting them based on their frequencies. Similarly, gamma correction employs a non-linear function to modulate intensity values, yet these methods often neglect the inherent properties of lightness in images, thus struggling with non-uniform illumination conditions. Alternative methods focus on image decomposition based on the Retinex theory. Early methods in Retinex theory [13] aimed to estimate reflectance as the final output often yielded over-enhanced and unnatural results. Recent efforts explored deep learning techniques [9, 38, 41] for image enhancement, albeit with limited success due to challenges in preserving naturalness, detail retention, and other complexities. Despite these advances, enhancing low-light images remains a challenging task, primarily because of the need to balance image brightness, and detail preservation in a single framework. This complexity is further compounded by the fact that Retinex-based decomposition is an ill-posed problem, meaning it is difficult to separate illumination and reflectance accurately. To address these limitations, an approach is required that can accurately decompose an image, adjust the lightness in low-illumination settings, and refine image details to ensure clarity without introducing artifacts.

In this paper, we present a deep decomposer and refiner for low-light image enhancement (DDRLIE, for easy reference). Our DDRLIE focuses on Retinex-based image decomposi-

✉ Anil Singh Parihar
parihar.anil@gmail.com

Piyush Vaish
piyush.vaish@gmail.com

[1] Machine Learning Research Laboratory, Department of Computer Science and Engineering, Delhi Technological University, Delhi, India

Published online: 10 March 2025

tion to estimate the reflectance and illumination. To enhance the lightness, an adjustment of the estimated illumination is required, and a refinement of the estimated reflectance is needed to enhance the image details and reduce noise. The proposed model contains decomposer sub-module, I-adjuster sub-module, and refiner sub-module. We propose a U-net-like architecture for decomposer sub-module with a mf-block, enabling effective focus on both local and global image features at multiple scales. The decomposition process allows for independent treatment of reflectance and illumination, leading to more accurate adjustments and enhanced image quality. Following the decomposition process, our method includes a hybrid approach for adjusting the estimated illumination named as the I-adjuster sub-module. This approach combines deep learning-based techniques with non-linear statistical method to adjust illumination variations in low-light images. By leveraging the strengths of both approaches, we achieve more accurate and robust illumination adjustment, leading to enhanced visibility and detail preservation in the final output. Furthermore, we introduce a refiner sub-module within our network architecture. This sub-module utilizes a similar deep learning model to the decomposer architecture, focusing on reducing noise and enhancing contrast in the estimated reflectance of low-light images. By refining the reflectance component separately, we can further improve image quality and ensure that important details are preserved during the enhancement process.

The major contributions of our work are:

1. We proposed a decomposer sub-module which estimates reflectance and illumination from an image simultaneously. The decomposer sub-module is a combination of multi-level feature extractor, channel attention, and focuses on impact of variation in receptive field to perform effective decomposition.
2. We proposed a new I-adjuster sub-module to perform lightness correction in the estimated illumination. The proposed I-adjuster combines the sigmoid based correction and the deep network based correction to improve the overall lightness in an image.
3. We proposed a refiner sub-module to refine the estimated reflectance. The estimated reflectance contains inherent noise, color-distortion, and others. The proposed refiner improves color and other details in the enhanced images.
4. We conduct extensive experiments to demonstrate the effectiveness and superiority of our approach compared to state-of-the-art techniques.

2 Related works

A wide variety of work is presented in the literature [26] on image enhancement that is captured under the influence of low light. In this section, we consider three categories of techniques commonly used: traditional approach [2, 20], Retinex-based approach [4, 30], and data-driven approach [28, 38–40].

Traditional histogram-based techniques aim to enhance image lightness through the manipulation of pixel intensity frequency distributions, thereby improving overall image brightness and contrast. However, traditional histogram equalization methods often suffer from over-enhancement and amplification of noise, leading to degraded image quality, particularly in low-light conditions. Parihar and Verma [20] presented an entropy-based method that optimally divides the histogram using entropy for equalization. Several algorithms [2, 15] use 2D histograms to capture local image characteristics and preserve natural features. Parihar et al. [21] leveraged fuzzy properties to develop a fuzzy difference histogram (FDH) for enhancement. While these algorithms perform well in properly illuminated regions, they often prioritize contrast enhancement over lightness improvement, leading to sub-optimal results in low-light conditions and introducing artifacts like saturation and halo effects.

Retinex-based methods provide comparably better enhancement than other methods for low-light images. Wang et al. [34] developed an innovative technique for estimating illumination in low-light images leveraging a bright-pass filter. By isolating the illumination component, the method effectively enhances the brightness and contrast of the image, leading to visually pleasing results. Fu et al. [4] incorporated a logarithmic (or traditional) variant of the Retinex to decompose reflectance and illumination to enhance low-light images. Parihar et al. [19] presented a fusion-based algorithm to estimate illumination and a simple fusion to estimate reflectance. The approach combines multiple input instances and fusion techniques to effectively separate the reflectance and illumination components, resulting in enhanced low-light images with improved visual quality. Tsai et al. [32] presented a multi-exposure fusion method that integrates contrast-limited HE, detail extraction, and homomorphic filtering to enhance contrast and detail, contributing to improved image visibility and quality. These Retinex-based models use gamma correction for illumination adjustment, which sometimes leads to inadequate enhancement.

With the progress in deep learning and its impressive results in a range of tasks [29, 31], researchers are more inclined to use data-driven approaches to tackle the issue of image quality. MSR-net [27] is developed focusing on multi-scale Retinex to apprehend the relationship among the components and the low-light images. However, both MSR-net and LLNet, introduced by Lore et al. [17], fail to fully capture the characteristics of natural low-light images, often resulting in unnatural enhancements. Wang et al. introduced GLADNet [36], a method for estimating global illumination followed by detail reconstruction to enhance low-light

images. Although GLADNet shows potential, it has a tendency to create distortions and reduce the color quality of the images it enhances. Wei et al. proposed Retinex-Net [38] that combines image decomposition, illumination adjustment, and noise reduction processes. However, Retinex-Net ignores color distortions, occasionally leading to unnatural enhancements. To overcome the constraints of earlier approaches, Zhang et al. introduced KinD [43], which offers adaptable light adjustments to address visual imperfections. However, KinD encounters challenges in enhancing fine details in very dark areas and could potentially blur authentic details when reducing noise. In contrast, Zero-DCE [7] develops a deep neural network to estimate and adjust the curve to improve the low light image. The enhancement of Zero-DCE sometimes overlooks the inherent noise in low-light images. A wide amount of low-light images without any ground truth are available which are not suitable for supervised methods. Thus, GAN-based methods are developed to use such unpaired images. EnlightenGAN [12] developed an adversarial network that can adapt to different lighting conditions utilizing the global–local discriminator. In contrast, RDGAN [33] is based on the concepts of Retinex theory. Nevertheless, techniques based on GANs frequently magnify noise and introduce different artifacts, which restricts their ability to generate enhancements that look natural. CSDGAN [18] develops a branched decoder network with adversarial training to achieve better enhancement; however, CSDGAN provides limited lightness enhancement in attempt to maintain the colors of the scene. Few attention-based approaches [39, 40] focused on local and global features to perform enhancement in low-light conditions. Rasheed and Shi [25] developed a pixel-wise estimation model to enhance low-light images using higher-order polynomials.

3 The proposed method

The proposed method uses the Retinex model to perform decomposition and estimate the respective components from the input image ($\mathbf{X}$). It estimates illumination and reflectance, which can be expressed as:

$$\mathbf{X} = \mathbf{R} \cdot \mathbf{I} \tag{1}$$

where, $\mathbf{R}$ and $\mathbf{I}$ denotes the reflectance and illumination, respectively. $\cdot$ is the element-wise multiplication. The illumination contains the lightness-related information of the scene. Reflectance contains other information about the scene related to color, texture, and many others. Ground-truth data for reflectance or illumination are not available. In the absence of ground truth for illumination and reflectance, conducting an image-to-image translation for estimation of these components is not possible. The paper presents a decomposition-oriented enhancement network that estimates reflectance and illumination to improve low-light images. The proposed method contains three sub-modules namely, decomposer, i-adjuster, and refiner. The specifics of these sub-modules are elaborated in the subsequent subsections.

3.1 Decomposer sub-module

The decomposer sub-module performs a simultaneous reflectance and illumination estimation from an image. However, decomposing an image based on the Retinex model is ill-posed without any ground-truth illumination and reflectance (or prior knowledge). We proposed a new architecture for performing low-light image enhancement using Retinex-based decomposition. Figure 1 illustrates the network architecture of the decomposer sub-module, which comprises of the mf-block, down-block, up-block, and final-block. The proposed mf-block in the decomposer sub-module performs multi-level feature extraction from an image with the aid of multiple kernels. To perform multi-level feature extraction, the proposed mf-block uses three branches with kernel sizes 3, 5, and 7. The smallest kernel size captures the local characteristics (smaller receptive field) in feature extraction. As the reflectance and illumination estimation do not contain a ground-truth instance; thus, we used a wider perspective with larger kernel sizes (larger receptive field) in feature extraction along with local neighborhood to perform simultaneous estimation. The mf-block then concatenates the output of all the convolutions with different kernel sizes and uses the 3×3 convolution to integrate the multi-level features as depicted in Fig. 2. The proposed decomposer contains three mf-blocks in the experimentation. After the multilevel feature extraction, the proposed decomposer uses multiple down-blocks to encode the image using multiple levels. The down-block integrates channel attention [10], convolutions, and max-pooling as depicted in Fig. 2. The proposed decomposer inputs the output from each down-block into the subsequent down-block and an up-block at the same level as shown in Fig. 1. To decode the encoded image, the proposed decomposer uses the same number of up-blocks. The proposed up-block uses two inputs, one from the previous up-block and the other from the down-block at same level, as illustrated in Fig. 1. The up-block first performs upsampling of the input from the previous up-block and then concatenates it with the input from the down-block; then, it uses convolution and channel attention to decode the image, as depicted in Fig. 2. The proposed decomposer contains five down-block and up-block in a hierarchical manner. At last, the decomposer sub-module uses the final-block to perform the simultaneous estimation. The final-block uses multiple convolution with leaky ReLU except the last convolution. Sigmoid as the activation helps the last convolution in the final-block in estimating the reflectance and illumina-

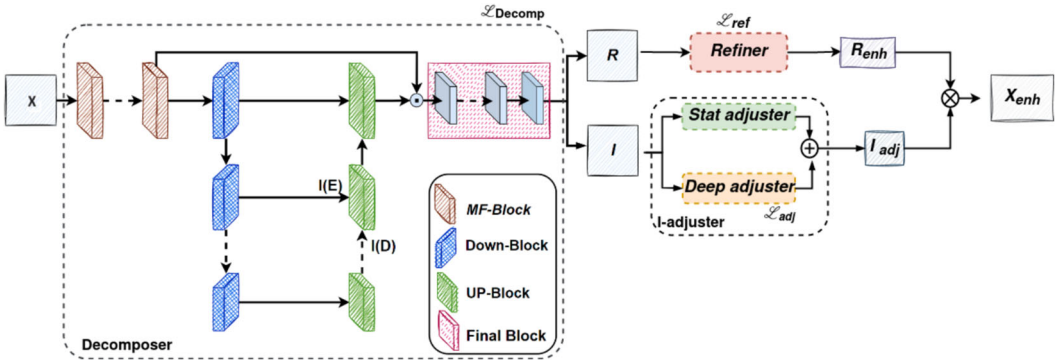

Fig. 1 Framework of proposed decomposer sub-module of DDRLIE. **I** Illumination, **R** reflectance, and **X** represents input image

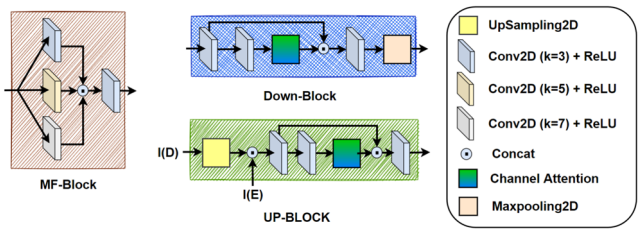

Fig. 2 Details for the architecture of mf-block, down-block and up-block for our DDRLIE

tion. The activation function in the decomposer network is a leaky ReLU function.

The loss function have a vital role for the decomposer in the absence of any ground-truth data. For an effective estimation of the components, the loss of the decomposer must consider the properties related to illumination and reflectance. Previous work [14, 43] shows that the illumination component is locally smooth, which denotes the properties of lightness, and the reflectance component contains the properties related to structure, texture and other aspects of the scene. Moreover, both components must generate the original image after performing a multiplication in element order. Thus, the constraints in the decomposer loss consider all these available properties. The loss of the decomposer ($\mathscr{L}_{Decomp}$) is represented as:

$$\mathscr{L}_{Decomp} = w_{CR}\mathscr{L}_{CR} + w_{ill}\mathscr{L}_{ill} + w_{ref}\mathscr{L}_{ref} \tag{2}$$

where $\mathscr{L}_{CR}$ denotes the content reconstruction, $\mathscr{L}_{ill}$ denotes the illumination regularity, and $\mathscr{L}_{ref}$ denotes the reflectance regularity. The content reconstruction in the loss deals with reformation of an image from the decomposed reflectance and illumination. The loss of content reconstruction is represented as:

$$\mathscr{L}_{CR} = \|\mathbf{X}_l - \tilde{\mathbf{R}}_l \cdot \tilde{\mathbf{I}}_l\|_2^2 + \|\mathbf{X}_h - \tilde{\mathbf{R}}_h \cdot \tilde{\mathbf{I}}_h\|_2^2 \tag{3}$$

where $\mathbf{X}_l$ and $\mathbf{X}_h$ denote the low-light and normal-light image. $\tilde{\mathbf{R}}_l$ and $\tilde{\mathbf{I}}_l$ denote the estimated reflectance and illumination of low-light image from decomposer sub-module, respectively. $\tilde{\mathbf{R}}_h$ and $\tilde{\mathbf{I}}_h$ denote the estimated reflectance and illumination of normal-light image from decomposer sub-module, respectively. The researchers [8, 30] discussed various properties of illumination, such as smoothing of the texture with preservation of the structure. We developed illumination regularity for the decomposer loss to perform texture smoothing while maintaining the structural details as:

$$\begin{aligned}\mathscr{L}_{ill} = {} & \|max(\mathbf{X}_l) - \tilde{\mathbf{I}}_l\|_1 + \|max(\mathbf{X}_h) - \tilde{\mathbf{I}}_h\|_1 \\ & + \left\| \frac{\nabla \tilde{\mathbf{I}}_l}{(\nabla \mathbf{J}_l + \epsilon)} \right\|_1 + \left\| \frac{\nabla \tilde{\mathbf{I}}_h}{(\nabla \mathbf{J}_h + \epsilon)} \right\|_1\end{aligned} \tag{4}$$

where $\mathbf{J}_l$ is defined as $log(max(\mathbf{R}_l))$, $\mathbf{J}_h$ is defined as $log(max(\mathbf{R}_h))$, and ϵ is a small value for the denominator limit. The additive first-order derivative for the vertical and horizontal sides is denoted as ∇. Reflectance of an image is independent of the lightness in the image. Thus, the reflectance of a scene with low-light and same scene with normal-light should be the same. Thus, we present reflectance regularity to estimate the illumination-invariant reflectance for enhancing the low-light image, which is defined as:

$$\mathscr{L}_{ref} = \|\tilde{\mathbf{R}}_l - \tilde{\mathbf{R}}_h\|_1 \tag{5}$$

where $\tilde{\mathbf{R}}_l$ and $\tilde{\mathbf{R}}_h$ represents the estimated reflectance of low-light and normal-light images, respectively. The loss maintains the consistency of reflectance as the illumination contains the properties of lightness and the influence of lightness does not affect the reflectance; thus, the reflectance of both input and ground-truth image should be the same.

The decomposer sub-module outputs an estimated reflectance and illumination from an image, which reconstruct the original image after element-wise multiplication. The estimated illumination contains major structure only with local smooth structure. Further, the estimated reflectance encompasses all texture-related and color information with almost no influence of illumination. Since, the lightness properties depends

on the illumination component. Thus, we need to perform lightness correction in the illumination component which can be achieved with the aid of proposed I-adjuster sub-module.

3.2 I-adjuster sub-module

Lightness correction is quite important in low-light image enhancement. The I-adjuster sub-module provides adaptive lightness correction to enhance low-light images using a hybrid approach. Researchers used direct amplification for lightness adjustment in a low-light image. The use of direct amplification sometimes limits the enhancement of an image. Direct amplification uses a fixed parameter to adjust the complete images. The fixed value in direct amplification works for few images however, for many of the images the fixed parameter works adversely. Direct amplification sometimes degrades the image quality rather than improving it. Further, the fixed value in direct amplification is same throughout the image which may cause problem for images with varying illumination. The images with varying lightness condition may contain few regions with normal lightness and other region with low lightness. In such images, the lightness correction should focus on the properties of estimated illumination for proper enhancement. We proposed an I-adjuster sub-module to fix the lightness in an adaptive manner. The proposed I-adjuster perform lightness correction by fusing the data-driven based illumination correction (namely, deep-adjuster) with the statistical non-linearly corrected illumination (namely, stat-adjuster) to achieve adequate adjustment in images with varying illumination. The hybrid approach uses an additive fusion process to blend the outputs of the deep-adjuster and stat-adjuster, resulting in a more nuanced and locally adaptive lightness correction.

The first unit of the proposed I-adjuster (i.e. deep-adjuster) uses data-driven network to estimate corrected illumination. The network architecture is similar to the decomposer sub-module. It generates an initial illumination map that aims to approximate the ground-truth distribution across the image. The loss function for data-driven based illumination correction can be expressed as:

$$\mathscr{L} = \|\tilde{\mathbf{R}}_l \cdot \mathbf{I}_{adj} - \mathbf{X}_h\|_2^2 + \left\| \frac{\nabla \tilde{\mathbf{I}}_l}{(\nabla \mathbf{K}_l + \epsilon)} \right\|_1 \tag{6}$$

where, $\mathbf{I}_{adj}$ denotes the adjusted illumination, and $\mathbf{K}$ denotes $\log(\tilde{\mathbf{R}})$. The deep-adjuster leverages the broad illumination patterns learned from the datasets, creating a globally consistent illumination map that is effective for general lighting conditions. However, because it focuses on global characteristics, the deep-adjuster alone may overlook local variations, which are critical for properly enhancing areas with different light intensities within the same image.

The stat-adjuster complements the deep-adjuster by providing local corrections using a non-linear transformation based on the sigmoid function. This component adjusts the illumination pixel-by-pixel, targeting darker areas for enhancement. The lightness correction of low-light region while maintaining the lightness of the regions with bright/normal light using the proposed I-adjuster can be represented as:

$$\mathbf{I}_{adj}^{s} = \tilde{\mathbf{I}}^{(1+exp^{-\tilde{\mathbf{I}}})^{-1}} \tag{7}$$

where $\mathbf{I}_{adj}^{s}$ denotes the adjusted illumination by stat-adjuster. For low-light regions, it applies a stronger scaling factor, increasing brightness significantly. In contrast, for high-light areas, this factor approaches 1, meaning these regions remain largely unaffected. Additionally, the sigmoid function ensures a smooth, continuous transition between dark and bright areas, producing a natural-looking enhancement. The non-linear response in darker areas is particularly useful because it ensures that even the most underexposed regions receive appropriate brightening, while bright regions are preserved. To integrate the outputs of the deep-adjuster and stat-adjuster, we employ additive fusion, which combines the globally estimated illumination from the deep-adjuster with the locally refined illumination from the stat-adjuster. The additive fusion allows the I-adjuster to flexibly adapt to both global and local illumination variations by blending the benefits of data-driven and statistical correction methods. The algorithm feeds the estimated reflectance to the refiner sub-module for noise removal and detail enhancement. The direct multiplication of the estimated reflectance and adjusted illumination sometimes results in noisy and unclear images. We proposed the refiner sub-module to deal with the intrinsic noise and distortions and enhance the overall image quality.

3.3 Refiner sub-module

The estimated reflectance requires to be treated for image noise, color and contrast. The refined reflectance and adjusted illumination provides the final enhanced image. Thus, refining the reflectance is also an important factor for better enhancement. Estimated reflectance may contain unclear details in regions with normal lightness, and poor colors retention. We proposed a Refiner sub-module to reduce the artifacts and improve the enhancement. The proposed Refiner uses similar deep network as the decomposition network except the use of contrast-channel attention and the last layer. It uses multi-level features to perform the final refinement to the reflectance. The multi-level feature extraction captures the broader pixel relationship and contextual information with larger receptive field. Further, the architecture of proposed refiner focuses on exploitation of contrast with the contrast-channel attention (CCA). The contrast-channel

attention estimates the contrast of feature maps while feature extraction. CCA for contrast attention [11] uses standard deviation in the proposed refiner. The proposed refiner uses global average pooling to implement standard deviation (σ_g). The standard deviation (σ_g) can be estimated as:

$$\sigma_g = \left(\frac{1}{N} \sum_{(i,j)\in\omega} (x_g^{i,j} - \mu_g)^2 \right)^{\frac{1}{2}} + \mu_g \tag{8}$$

where μ_g is the mean of feature map (x_g), and (i,j) is the position of the feature map. After the estimation of contrast, CCA performs channel down-sampling and up-sampling using the convolution operation. CCA helps in improve refinement of the image to generate the final image.

The training of the proposed refiner is performed with the aid of a multi-objective function. Our loss function focuses on contrast and details enhancement. The loss function uses depends on mean squared error and SSIM [37] loss. The computation of all losses is carried out between the refined reflectance and the reflectance of the normal-light image. Enhancing the details in the dark regions of low-light images presents a significant challenge. Thus, the proposed refiner leverages the SSIM loss for detail restoration and preservation. The SSIM loss can be expressed as:

$$\mathscr{L}_{SSIM} = 1 - SSIM(\mathbf{R}_{enh}, \mathbf{R}_{high}) \tag{9}$$

where $SSIM(\cdot,\cdot)$ denotes the structural similarity index between two items. The final combined loss for the refiner sub-module can be expressed as:

$$\mathscr{L}_{Refiner} = w_{SSIM}\mathscr{L}_{SSIM} + w_{mse}\mathscr{L}_{mse}, \tag{10}$$

where w denotes the respective weights. The empirical values of w_{SSIM} and w_{mse} are 0.5, and 0.5 respectively.

4 Experiments

4.1 Implementation set-up

Our DDRLIE method utilizes the LOL dataset [38], which consists of 500 low-light images with respective normal-light (or ground-truth). Out of all images, 485 images are utilized for training our DDRLIE, and rest 15 images are used with other images to analyse the performance. Additionally, we collected 1500 images from different sources and refined their visibility using the photo editing tool to perform training. Out of these images, 1350 images are used for training and rest 150 are used for testing. The visibility of collected images is enhanced while preserving the natural characteristics of the images. Initially, brightness and contrast adjustments were applied to improve overall clarity without altering the underlying image content. Next, noise reduction techniques are utilized to diminish graininess typical of low-light images, thus minimizing potential noise artifacts in model training. Color balance corrections were made to address color distortions, ensuring the images retained realistic hues while enhancing brightness. For training, we employed a multi-scale training strategy. We perform training on 48 and 64 as patch sizes and 12 and 8 as batch sizes, respectively, for facilitating efficient processing and optimization of the proposed decomposer sub-module. The I-adjuster sub-module refines the estimated illumination to enhance image brightness, we employ the same LOL dataset. This sub-module aids in refining the lightness of the images, complementing the decomposition process. Within the refiner sub-module, we consider patch sizes of 48, 64, and 128, and batch sizes of 24, 12, and 10. To optimize our DDRLIE, we employ the ADAM optimizer with a learning rate of $1e{-}4$, in conjunction with the standard parameters. The implementation is conducted using the TensorFlow framework, and training is performed on a computational setup comprising an NVIDIA Titan RTX GPU and an Intel Xeon CPU with 128GB RAM, ensuring efficient processing and training of the entire network. Our DDRLIE method contains around 1.7 million parameters and uses 49.4 GFLOPs to enhance 256 × 256 image. In our model, the MF-Blocks uses 32 filters in each branch. Down-Blocks and Up-Blocks include: Convolutions with 64 filters and kernel size 3×3. Final Block with five convolution layers. The last convolution layer employs sigmoid activation to normalize the output reflectance and illumination maps. The Refiner sub-module has a similar configuration.

Table 1 Ablation study

Configurations	PSNR	SSIM
Without MF-block	19.20	0.78
Without channel attention	19.66	0.79
Without contrast-channel attention	20.87	0.80
DDRLIE	21.41	0.83

PSNR and SSIM values for DDRLIE with the mentioned configuration is given below

4.2 Ablation study

This section contains the investigation related to various components used in the proposed DDRLIE method. The impact is analyzed by considering the network configuration with and without the mentioned component. The detailed analysis for enhancement using distinct configurations is demonstrated in Table 1.

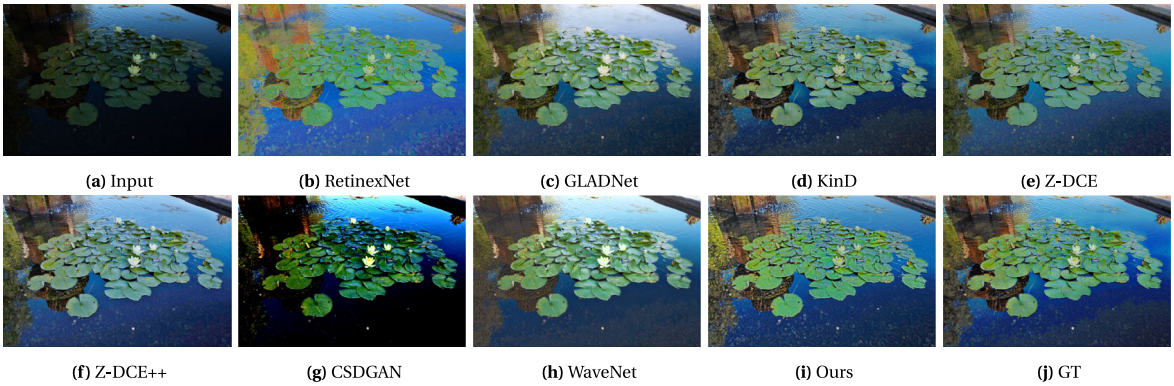

Fig. 3 Enhanced output from various methods for image "Leaves"

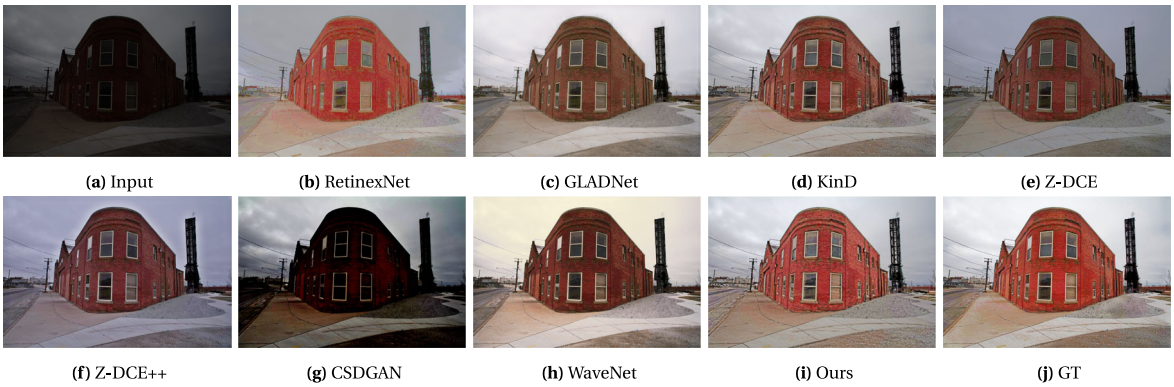

Fig. 4 Enhanced output from various methods for image "Building"

The decomposer sub-module includes the MF-block and channel attention, which are integral to DDRLIE's overall enhancement capability. The MF-block captures multi-scale features, enabling the network to handle complex illumination patterns and textures, which are common in low-light conditions. When we removed the MF-block, a notable reduction in PSNR and SSIM are observed. This decrease suggests that multi-scale feature extraction is essential for enhancing intricate details and adapting to varying light intensities within an image. Similarly, channel attention enhances the decomposer sub-module by emphasizing relevant feature channels, allowing the network to prioritize critical features while suppressing less informative ones. Without channel attention, we observed a performance drop indicating that the absence of channel-attention results in sub-optimal contrast and detail preservation. Table 1 shows the impact of each component on the overall enhancement. The contrast-channel attention (CCA) in the refiner sub-module is designed to improve the quality of estimated reflectance by selectively enhancing channels that contribute to image contrast. Removing CCA leads to a PSNR and SSIM reduction demonstrating that the absence of CCA limits the model's ability to maintain fine details and contrast, which are crucial for effective enhancement in low-light regions.

4.3 Quantitative analysis

We demonstrated the superior performance of proposed method using quantitative analysis. The quantitative measure are unable to capture all aspects in the image quality. There is no universal quantitative measure for image enhancement. We analysed the performance using two widely used quantitative measures: Peak Signal-to-Noise Ratio (PSNR), and Structural Similarity (SSIM) [37]. The SSIM measure attempts to estimate the retention of structure in the enhanced image along with the brightness of the image. SSIM uses mean and standard deviation to estimate the enhancement in the output with respect to the input. PSNR considers the difference of log of maximum signal and log of mean squared function to estimate the enhancement. These are the widely used enhancement measure in image enhancement and the quantitative analysis is shown in Table 2. The measures in Table 2 shows the mean value of SSIM and PSNR for various contemporary methods [3, 7, 16, 35, 36, 38, 42, 43], and our DDRLIE method. Bold in the table shows the best mean value for the respective measure. The Quantitative measures shows that our DDRLIE outperforms the contemporary methods. Most of the contemporary methods either fails to improve the lightness or the structural details, thus, these methods fail to

(a) Input (b) RetinexNet (c) GLADNet (d) KinD (e) Z-DCE (f) Z-DCE++ (g) CSDGAN (h) WaveNet (i) Ours (j) GT

Fig. 5 Enhanced output from various methods for image "Forest"

(a) Input (b) RetinexNet (c) GLADNet (d) KinD (e) Z-DCE (f) Z-DCE++ (g) CSDGAN (h) WaveNet (i) Ours (j) GT

Fig. 6 Enhanced output from various methods for image "Guitar"

Table 2 Quantitative metrics for performance analysis of various methods

Method	PSNR	SSIM	Params/M
RetinexNet [38]	14.16	0.57	0.8
GLADNet [36]	16.18	0.79	–
KinD [43]	15.23	0.82	8.6
Zero-DCE [7]	13.57	0.74	0.1
Zero-DCE++ [16]	13.56	0.74	–
CSDGAN [18]	18.06	0.79	–
WaveNet [3]	21.62	0.83	14.4
LLFormer [35]	19.88	0.80	24.5
EMNet [42]	20.93	0.82	–
DDRLIE	**21.41**	**0.83**	1.7

Bold values shows best result

achieve the superior value for the quantitative measure. Our DDRLIE achieves superior performance for low-light image enhancement as it enhances the lightness and various details in the scene, which helps it to achieve superior SSIM and PSNR value. To further investigate the performance of our method, we performed visual analysis in the next section.

4.4 Visual analysis

The visual analysis is given to demonstrate the superiority of our DDRLIE method. The results of RetinexNet [38], GLADNet [36], KinD [43], Zero-DCE (Z-DCE) [7], Zero-DCE++ (or Z-DCE++) [16], CSDGAN [18], WaveNet [3] and our DDRLIE are shown in Figs. 3, 4, 5 and 6. In Fig. 3, an image with various leaves is shown with enhancement using above-mentioned methods. The results of RetinexNet shows inadequate enhancement with faded colors as given in Fig. 3b. In Fig. 3c, the results of GLADNet show over enhancement in the region with proper lightness in the input image. KinD demonstrates a limited enhancement of colors with slightly limited lightness in Fig. 3d. The enhanced results of Z-DCE as given in Fig. 3e show limited contrast and color enhancement, while Z-DCE++ as given in Fig. 3f slightly improves the color balance but lacks in contrast. CSDGAN fails to provide an appropriate enhancement in Fig. 3g. The enhancement using our DDRLIE is shown in Fig. 3h. Our DDRLIE achieves superior color fidelity, enhanced contrast, and clear visibility of details. The details in the water and the leaves are clearly visible.

The input image "Building" is shown in Fig. 4 with results enhanced by other contemporary methods. The results of RetinexNet shows lightness enhancement in Fig. 4b. However, the enhanced image contains faded colors and poor contrast. The enhancement using GLADNet is shown in Fig. 4c, which shows a limited enhancement of color and other details. The results of KinD demonstrate an appropriate enhancement of lightness; however, limited enhancement is shown for the building details as shown in Fig. 4d. The results of Z-DCE and Z-DCE++ show limited enhancement of lightness. CSDGAN fails to enhance the lightness in the overall image as shown in Fig. 4g. The result of our DDRLIE is shown in Fig. 4h, which shows optimal brightness, color fidelity, and detailed visibility, effectively enhancing both structure and surrounding areas in various regions in the image.

The image "Forest" and the enhanced results using various methods is shown in Fig. 5. The results of RetinexNet is given in Fig. 5b, which shows enhancement of lightness. However, the enhanced image shows poor detail enhancement for the background and saturation of color is also evidient. GLADNet enhances the lightness; however, the color in the enhanced image seems unnatural as shown in Fig. 5d. The

enhancement using KinD [43] is shown in Fig. 5d, which enhances lightness with lesser focus on the edge details. In ZDCE [7], the limited lightness enhancement can be observed from Fig. 5e. Z-DCE++ improves the lightness with insufficient contrast as shown in Fig. 5f. CSDGAN fails to enhance the lightness as shown in Fig. 5g. Our DDRLIE achieves better lightness as compared to the other contemporary methods and the enhanced image contains better details as shown in Fig. 5g. The enhanced image of our DDRLIE contains better edges than other contemporary methods.

"Guitar" image with the enhanced results using various methods is shown in Fig. 6. RetinexNet enhaces lightness but fails to enhance the details present on the guitar as shown in Fig. 6b. The result of GLADNet as given in Fig. 6c shows enhancement of lightness but the color of the object above the guitar seems unnatural. The enhanced results of KinD and Z-DCE are shown in Fig. 6d, e respectively, contain slightly less lightness and details on the guitar. The CSDGAN enhancement shows better colors, but the lightness enhancement is poor. The enhancement of our DDRLIE is shown in Fig. 6h, which shows better lightness and color fidelity with well-defined details on guitar.

5 Conclusion

In this paper, a deep decomposer and refiner for low-light image enhancement (DDRLIE) is proposed. DDRLIE consist of three sub-modules: decomposer, i-adjuster, and refiner. Our decomposer sub-module estimates reflectance and illumination from an image using the proposed mf-block, and channel attention based up and down blocks. Followed by the estimation, the estimated illumination is adjusted based on our hybrid approach that uses data-driven and nonlinear adjustment to enhance the lightness in the image. The estimated reflectance is enhanced using the refiner sub-module to refine the noise, color and contrast in the final image. We performed an exhaustive experimentation and observed that the proposed method effectively deals with the low-light images and non-uniformly illuminated images. The enhanced of proposed method contains natural results with almost no artifacts. The enhancement shows the effective enhancement in the for region with low-light conditions. Altogether, the experimental analysis shows that the proposed method performs superior enhancement than other contemporary methods.

For future work, we aim to explore video sequences for handling illumination consistency in dynamic scenes, enabling low-light video enhancement. Additionally, we plan to investigate real-time implementations to facilitate interactive low-light enhancement in mobile and embedded systems, broadening its practical utility.

Author Contributions PV and ASP have equal contributions to the manuscript.

Funding In this research, no funding is involved from any agency.

Data Availability Data will be made available on reasonable request.

Declarations

Conflict of interest The authors declare that they have no conflict of interest.

Ethical approval Not applicable.

References

1. Aamir, M., Rahman, Z., Abro, W.A., Tahir, M., Ahmed, S.M.: An optimized architecture of image classification using convolutional neural network. Int. J. Image Graph. Signal Process. **11**(10), 30 (2019)
2. Celik, T.: Spatial entropy-based global and local image contrast enhancement. IEEE Trans. Image Process. **23**(12), 5298–5308 (2014)
3. Dang, J., Li, Z., Zhong, Y., Wang, L.: WaveNet: wave-aware image enhancement. In: Proceedings of the Pacific Conference on Computer Graphics and Applications, pp. 21–29 (2023)
4. Fu, X., Zeng, D., Huang, Y., Zhang, X.P., Ding, X.: A weighted variational model for simultaneous reflectance and illumination estimation. In: Proceedings of the IEEE Conference on Computer Vision and Pattern Recognition, pp. 2782–2790 (2016)
5. Guan, Y., Aamir, M., Hu, Z., Abro, W.A., Rahman, Z., Dayo, Z.A., Akram, S.: A region-based efficient network for accurate object detection. Traitement du Signal **38**(2) (2021)
6. Guan, Y., Aamir, M., Hu, Z., Dayo, Z.A., Rahman, Z., Abro, W.A., Soothar, P.: An object detection framework based on deep features and high-quality object locations. Traitement du Signal **38**(3) (2021)
7. Guo, C., Li, C., Guo, J., Loy, C.C., Hou, J., Kwong, S., Cong, R.: Zero-reference deep curve estimation for low-light image enhancement. In: Proceedings of the IEEE/CVF Conference on Computer Vision and Pattern Recognition, pp. 1780–1789 (2020)
8. Guo, X., Li, Y., Ling, H.: LIME: low-light image enhancement via illumination map estimation. IEEE Trans. Image Process. **26**(2), 982–993 (2016)
9. Hu, C., Xu, L., Guo, Y., Jing, X., Lu, X., Liu, P.: HSV-3S and 2D-GDA for high-saturation low-light image enhancement in night traffic monitoring. IEEE Trans. Intell. Transp. Syst. **24**(12), 15190–15206 (2023)
10. Hu, J., Shen, L., Sun, G.: Squeeze-and-excitation networks. In: 2018 IEEE/CVF Conference on Computer Vision and Pattern Recognition, pp. 7132–7141 (2018)
11. Hui, Z., Gao, X., Yang, Y., Wang, X.: Lightweight image super-resolution with information multi-distillation network. In: Proceedings of the 27th ACM International Conference on Multimedia, pp. 2024–2032 (2019)
12. Jiang, Y., Gong, X., Liu, D., Cheng, Y., Fang, C., Shen, X., Yang, J., Zhou, P., Wang, Z.: Enlightengan: deep light enhancement without paired supervision. arXiv preprint arXiv:1906.06972 (2019)
13. Jobson, D.J., Rahman, Z.U., Woodell, G.A.: A multiscale Retinex for bridging the gap between color images and the human observation of scenes. IEEE Trans. Image process. **6**(7), 965–976 (1997)
14. Land, E.H.: The Retinex theory of color vision. Sci. Am. **237**(6), 108–129 (1977)
15. Lee, C., Lee, C., Kim, C.: Contrast enhancement based on layered difference representation of 2D histograms. IEEE Trans. Image Process. **22**(12), 5372–5384 (2013)

16. Li, C., Guo, C., Loy, C.C.: Learning to enhance low-light image via zero-reference deep curve estimation. IEEE Trans. Pattern Anal. Mach. Intell. **44**, 4225–4238 (2021)
17. Lore, K.G., Akintayo, A., Sarkar, S.: LLNet: a deep autoencoder approach to natural low-light image enhancement. Pattern Recogn. **61**, 650–662 (2017)
18. Ma, L., Liu, R., Zhang, J., Fan, X., Luo, Z.: Learning deep context-sensitive decomposition for low-light image enhancement. IEEE Trans. Neural Netw. Learn. Syst. 1–15 (2021)
19. Parihar, A.S., Singh, K., Rohilla, H., Asnani, G.: Fusion-based simultaneous estimation of reflectance and illumination for low-light image enhancement. IET Image Proc. **15**, 1410–1423 (2021)
20. Parihar, A.S., Verma, O.P.: Contrast enhancement using entropy-based dynamic sub-histogram equalisation. IET Image Proc. **10**(11), 799–808 (2016)
21. Parihar, A.S., Verma, O.P., Khanna, C.: Fuzzy-contextual contrast enhancement. IEEE Trans. Image Process. **26**(4), 1810–1819 (2017)
22. Rahman, Z., Aamir, M., Ali, Z., Saudagar, A.K.J., AlTameem, A., Muhammad, K.: Efficient contrast adjustment and fusion method for underexposed images in industrial cyber-physical systems. IEEE Syst. J. **17**(4), 5085–5096 (2023)
23. Rahman, Z., Aamir, M., Pu, Y.F., Ullah, F., Dai, Q.: A smart system for low-light image enhancement with color constancy and detail manipulation in complex light environments. Symmetry **10**(12), 718 (2018)
24. Rahman, Z., Bhutto, J.A., Aamir, M., Dayo, Z.A., Guan, Y.: Exploring a radically new exponential Retinex model for multi-task environments. J. King Saud Univ. Comput. Inf. Sci. **35**(7), 101635 (2023)
25. Rasheed, M.T., Shi, D.: Pixel-wise polynomial estimation model for low-light image enhancement. KSII Trans. Internet Inf. Syst. TIIS **17**(9), 2483–2504 (2023)
26. Rasheed, M.T., Shi, D., Khan, H.: A comprehensive experiment-based review of low-light image enhancement methods and benchmarking low-light image quality assessment. Signal Process. **204**, 108821 (2023)
27. Shen, L., Yue, Z., Feng, F., Chen, Q., Liu, S., Ma, J.: MSR-Net: low-light image enhancement using deep convolutional network. arXiv preprint arXiv:1711.02488 (2017)
28. Singh, K., Parihar, A.S.: DSE-Net: deep simultaneous estimation network for low-light image enhancement. J. Vis. Commun. Image Represent. **91**, 103780 (2023)
29. Singh, K., Parihar, A.S.: Bff: bi-stream feature fusion for object detection in hazy environment. SIViP **18**(4), 3097–3107 (2024)
30. Singh, K., Parihar, A.S.: Illumination estimation for nature preserving low-light image enhancement. Vis. Comput. **40**(1), 121–136 (2024)
31. Singh, K., Parihar, A.S.: MRN-LOD: multi-exposure refinement network for low-light object detection. J. Vis. Commun. Image Represent. **99**, 104079 (2024)
32. Tsai, H.C., Lin, H.J., Leou, J.J.: Multiexposure image fusion using intensity enhancement and detail extraction. J. Vis. Commun. Image Represent. **33**, 165–178 (2015)
33. Wang, J., Tan, W., Niu, X., Yan, B.: RDGAN: Retinex decomposition based adversarial learning for low-light enhancement. In: 2019 IEEE International Conference on Multimedia and Expo (ICME), pp. 1186–1191. IEEE (2019)
34. Wang, S., Zheng, J., Hu, H.M., Li, B.: Naturalness preserved enhancement algorithm for non-uniform illumination images. IEEE Trans. Image Process. **22**(9), 3538–3548 (2013)
35. Wang, T., Zhang, K., Shen, T., Luo, W., Stenger, B., Lu, T.: Ultra-high-definition low-light image enhancement: a benchmark and transformer-based method. In: AAAI Conference on Artificial Intelligence, vol. 37, pp. 2654–2662 (2023)
36. Wang, W., Wei, C., Yang, W., Liu, J.: GLADNet: low-light enhancement network with global awareness. In: 2018 13th IEEE International Conference on Automatic Face & Gesture Recognition (FG 2018), pp. 751–755. IEEE (2018)
37. Wang, Z., Bovik, A.C., Sheikh, H.R., Simoncelli, E.P.: Image quality assessment: from error visibility to structural similarity. IEEE Trans. Image Process. **13**(4), 600–612 (2004)
38. Wei, C., Wang, W., Yang, W., Liu, J.: Deep Retinex decomposition for low-light enhancement. arXiv preprint arXiv:1808.04560 (2018)
39. Xu, L., Hu, C., Hu, Y., Jing, X., Cai, Z., Lu, X.: UPT-Flow: multi-scale transformer-guided normalizing flow for low-light image enhancement. Pattern Recognit. **158**, 111076 (2025)
40. Xu, L., Hu, C., Zhang, B., Wu, F., Cai, Z.: Swin transformer and ResNet based deep networks for low-light image enhancement. Multimedia Tools Appl. **83**(9), 26621–26642 (2024)
41. Xu, L., Hu, C., Zhu, W., Wu, F., Cai, Z., Ye, M., Lu, X.: Degrade for upgrade: learning degradation representations for real-world low-light image enhancement. Comput. Electr. Eng. **119**, 109622 (2024)
42. Ye, D., Ni, Z., Yang, W., Wang, H., Wang, S., Kwong, S.: Glow in the dark: low-light image enhancement with external memory. IEEE Trans. Multimedia **26**, 2148–2163 (2024)
43. Zhang, Y., Zhang, J., Guo, X.: Kindling the darkness: a practical low-light image enhancer. In: Proceedings of the 27th ACM International Conference on Multimedia, pp. 1632–1640 (2019)

Publisher's Note Springer Nature remains neutral with regard to jurisdictional claims in published maps and institutional affiliations.

Springer Nature or its licensor (e.g. a society or other partner) holds exclusive rights to this article under a publishing agreement with the author(s) or other rightsholder(s); author self-archiving of the accepted manuscript version of this article is solely governed by the terms of such publishing agreement and applicable law.

Sādhanā (2025)50:46
https://doi.org/10.1007/s12046-025-02692-3
© Indian Academy of Sciences

Deep-reinforcement-learning-based controller design for pantograph and catenary system

ROHINI SHARMA*, PRIYA MAHAJAN and RACHANA GARG

Electrical Department, Delhi Technological University, Rohini, New Delhi 110042, India
e-mail: rs2456sharma@gmail.com; priyamahajan.eed@gmail.com; rachana16100@yahoo.co.in

MS received 11 December 2023; revised 17 February 2024; accepted 20 October 2024

Abstract. The articulated suspension system of a pantograph and catenary system has a power collection junction, i.e., a contact network, between the pantograph and the catenary. For stable current collection and maintaining control contact force, the junction should be reliable and safe with respect to external disturbances and irregularity at the contact point, which may vary due to the speed of the train. This study proposes a novel fuzzy-based controller to control the contact force. The proposed controller, fuzzy-based fractional order proportional integral derivative (F^2OPID), uses fuzziness to evaluate control contact force. The error functions of the proposed controller are monitored by a bilateral long short-term memory network. The gains of the F^2OPID controller are evaluated using an Aquila optimizer. The system is analyzed on Matlab platform based on variations in train speed, stiffness coefficient, and length of the span. From the analysis, it has been observed that oscillation in contact force has been reduced using the proposed controller compared with other methods.

Keywords. Catenary model; Bi-LSTM; catenary; contact force; fractional orders; aquila optimization (AO).

1. Introduction

The pantograph and catenary system is a crucial part of a high-speed railway. The pantograph transmits power from the catenary to the traction system. A single locomotive has two pantographs [1] that will alternately raise and touch the contact wire. The contact wire is present as a component of the catenary and is stimulated by a traction transformer [2]. In high-speed trains, the traction transformer's power is transmitted at 25 kV to the electric locomotive [3, 4]. Arcing occurs at the contact point due to external disturbances [5, 6]. To regulate the force at the contact wire, an active tension system is used.

The stability of acquiring power for the railway system is restricted by the contact between the pantograph and the catenary system. The pan head may sustain damage or develop defects such as scratches, holes, and uneven surfaces due to the ongoing interaction between the contact wire and the pantograph [7, 8]. This disrupts the electric train's power supply. To minimize the wear on the contact wire and irregularity, it is necessary to regularly monitor the pantograph's condition [9, 10]. For monitoring, Zhang *et al* [11] used a deep convolutional neural network followed by edge detection. The contact state was recognized using the contact point; the employed neural network scheme would be used to detect the contact point based on the video record. Furthermore, to enhance the performance of condition monitoring for high-speed railway systems, Wang *et al* [12] proposed a Bayesian network. The model was analyzed on inspection data and maintenance records from Beijing to Guangzhou, China. The network checks the probabilistic correlation between various data types, which is extracted from multiple performance indicators on the catenary. From the multiple performance measures, 66.2% of false data was reduced concerning the China database.

The irregularity between the pantograph and the catenary is also due to frictional force. The interruption during power supply to the locomotive can be reduced by controlling this force. Zhu *et al* [13] used a partial state feedback control for high-speed nonlinear systems using the backstepping approach to control this force. This approach uses a closed-loop system for time-varying reference forces of a railway pantograph–catenary system. A higher-order derivative was used to measure the elasticity coefficient, whereas unmeasurable states were analyzed by an observer. The states were used again by a backstepping approach to generate a closed-loop control structure. Furthermore, using the same backstepping approach on a closed-loop control, Liu *et al* [14] presented a scheme for contact force fluctuation reduction. While using the coefficient of catenary, force control is highly disturbance free and the robustness of the model is improved. Song and Li [15] used a high-gain observer to implement an adaptive control system for a pantograph–catenary system. Without using a linearization or an approximation method, two degrees of freedom were used to couple nonlinear pantograph and catenary systems.

*For correspondence
Published online: 14 March 2025

A neural network was used to generate the adaptive control structure. When two locomotive systems are in continuous and smooth interaction, uncertainty and disturbance are taken into account in the control structure. Through simulation and theoretical research, the quality of the supply that is collected from the contact wire to the pantograph is examined. The interaction between the pantograph and the contact wire will cause the railway system to receive more supply, thus increasing its speed. Meanwhile, the environment will have an impact on this interaction, leading to arcing or appearance of outliers on the contact wire. In addition, the input signal is made worse by flaws in the pantograph surface. Therefore, by reducing the power of their interaction, the condition of the pantograph and the catenary should be checked and controlled.

To control the supply at the contact wire, a number of controllers and optimization approaches are employed. The evolutionary algorithm with a proportional integral derivative controller [16] is applied after the detection of force for the pantograph–catenary system. Vikas Soni *et al* [17] used a hybrid gray wolf optimization pattern search (Hgwo-ps) to optimize the parameter of two-degree-of-freedom proportional integral derivative (PID) controllers. The integral of time multiplied by absolute error (ITAE) is considered for a multi-area interconnected system. In addition, Laith Abualigh *et al* [18] proposed a novel population-based optimization, Aquila optimization (AO). This technique validates the optimal solution for different optimization problems based on narrow and expanded exploration to compensate for errors through filtering. The fuzzy-based classifier [19], where image data is acquired using a sensor and camera at the poles of the electric supply system, is used to determine the pantograph's health. A deep learning architecture is then used for health monitoring; in this case, data is gathered from the pantograph's current collector strip [20]. Monitoring is carried out using image processing. A fuzzy logic controller [21, 22] is also used to govern the environment's dynamic state using a streamlined pantograph–catenary system. A solid control structure design can also be used to make robust control using a degree-of-freedom-based control strategy [23]. According to this analysis, control based on two degrees of freedom performs better than control based on one degree of freedom [24].

This paper presents a control structure for the pantograph–catenary system, focusing on the interaction between the contact wire and the pantograph, which can be affected by environmental conditions, arcing, and irregularities on the pantograph surface. The control system model aims to improve locomotive performance by reducing contact force fluctuation and fast-tracking reference force under uncertainty. As uncertainty in a pantograph–catenary system is difficult to track, a rule-based decision-making scheme named fuzzy system has been used with a PID controller. The regulation of contact force is realized using a two-degree-of-freedom-based fuzzy-based fractional order proportional integral derivative (F^{2}-OPID) for a lumped mass model to achieve a trustworthy structure. The gain of F^{2}OPID is evaluated using an Aquila optimizer, and the error functions of the proposed controller are monitored using a bilateral long short-term memory (Bi-LSTM) network. A railway network model of a pantograph and catenary system is shown in figure 1.

In the present study, a control structure for a pantograph–catenary system is formulated and analyzed under various conditions of irregularity in the system.

- A mathematical model of a pantograph–catenary system is modeled based on two degrees of freedom, with the consideration of external disturbance and irregularities.
- A deep-learning-based control structure that evaluates the amount of irregular force created on the pantograph–catenary system is extracted using Bi-LSTM.
- Using the data of extracted force, a controller structure of F^{2}OPID that uses fuzziness for the evaluation of controlled contact force is proposed. A comparison of the proposed work with the existing schemes is shown in table 1.

The rest of this paper is organized as follows.

Section 2 presents mathematical modeling of the pantograph–catenary system. Section 3 discusses the design of the controller architecture to control the contact force. An analysis of the proposed system is presented in section 4, and finally, in section 5, conclusions of the study are provided.

2. Modeling of pantograph–catenary system

A two-degree-of-freedom model is used for modeling the pantograph–catenary system in real-time applications, as shown in figure 2.

Hence, the dynamic motion of the pantograph–catenary system is described as follows:

$$m_1 a_1 - k'(d_2 - d_1) - c'(v_2 - v_1) + k(t)d_1 = 0 \quad (1)$$

$$m_2 a_2 + k'(d_2 - d_1) + c'(v_2 - v_1) + c''v_2 = s + D(t) \quad (2)$$

where m_1 and m_2 represent the mass of the pantograph head and frame with damping coefficients c' and c'', respectively, as shown in table 2. k' and $k(t)$ represent the stiffness of the pantograph and the catenary, and parameters a_1, a_2, d_1, d_2, v_1, and v_2 represent acceleration, displacement and velocity of the locomotive at instance t of the pantograph–catenary system. The external disturbance faced by the system is noted as $D(t)$, which is summed up with control signal S to generate stabilized contact force concerning the speed and length of locomotive. The stiffness of the catenary is evaluated using the following equation:

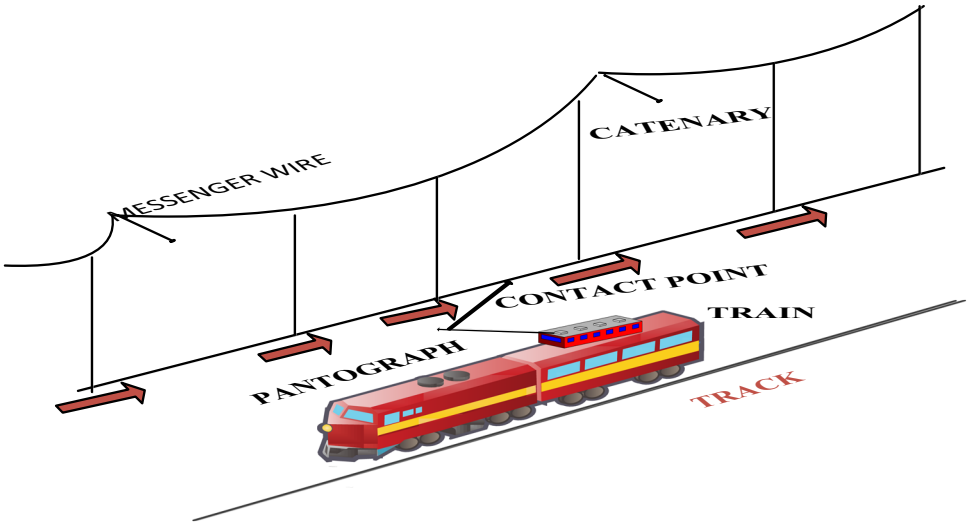

Figure 1. A typical network of catenary and railway track system.

Table 1. Comparative analysis of state-of-the-art techniques.

Technique [reference]	Pantograph–catenary model	Uncertainty	Response
Deep convolutional network [18]	Linear two-degree-of-freedom model	Not considered	Highly unstable
Bayesian network [19]	Two-degree-of-freedom model	Not considered	Poor reliability
Backstepping partial state feedback control [20]	Two-degree-of-freedom model	Not considered	The number of derivative terms increases
Backstepping controller [21]	Two-degree-of-freedom linear mass model	Not considered	Derivative term exploitation problem occurs
Adaptive controller [22]	Nonlinear two-degree-of-freedom model	Considered	Slow response
Proposed	Two-degree-of-freedom model	Considered	Fast response

$$k(t) = k_0\left(1 + \alpha\cos\left(\frac{2\pi v}{L}t\right)\right) \tag{3}$$

where α is variation in stiffness through the span, L is length of the catenary span, V is speed of the locomotive, α is coefficient of stiffness variation, and k_o is average stiffness coefficient. The state variables of the pantograph–catenary system are represented as follows:

$$\Lambda(t) = [d_1, v_1, d_2, v_2]^T. \tag{4}$$

Velocity and displacement are as follows:

$$\Lambda'(t) = A(t)\Lambda(t) + Bs(t) + D(t) \tag{5}$$

$$F_C(t) = C(t)\Lambda(t). \tag{6}$$

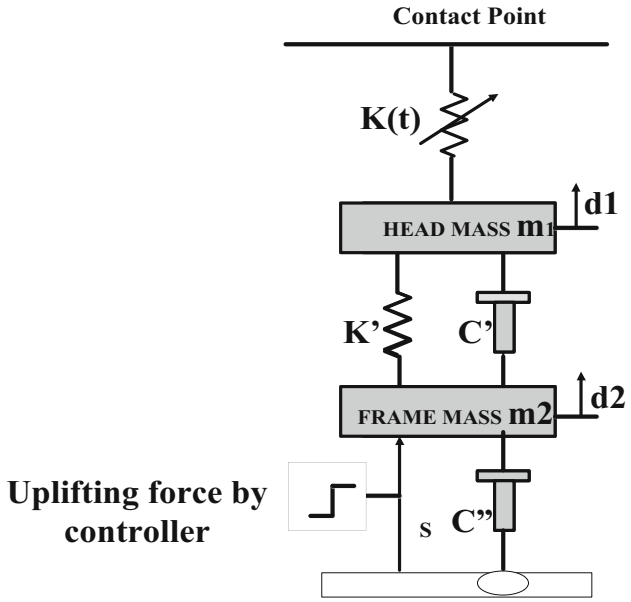

Figure 2. Lumped mass model of pantograph with two mass.

Table 2. Parameters.

Symbology	
m_1 and m_2	Pan head mass and frame mass
C′ and C″	Damping of pan head suspension and frame
K′ and K(t)	Stiffness of the pantograph and catenary
d_1 and d_2	Displacement of pan head suspension

The above equation is simplified to formulate displacement and velocity as follows:

$$A(t) = \begin{bmatrix} 0 & 1 & 0 & 0 \\ \frac{-k' + k(t)}{m_1} & \frac{-c'}{m_1} & \frac{k'}{m_1} & \frac{c'}{m_1} \\ 0 & 0 & 0 & 1 \\ \frac{k'}{m_2} & \frac{c'}{m_2} & \frac{-k'}{m_2} & \frac{-c' + c''}{m_2} \end{bmatrix} \tag{7}$$

$$B = \begin{bmatrix} 0 & 0 & 0 & \frac{1}{m_2} \end{bmatrix}^T \tag{8}$$

$$D(t) = [\,0 \quad 0 \quad 0 \quad \delta(t)\,]^T \tag{9}$$

$$C(t) = [\,k(t) \quad 0 \quad 0 \quad 0\,] \tag{10}$$

$$\Lambda'(t) = \begin{bmatrix} d_1 \\ \frac{(d_2 - d_1)(2k' - k(t)) + 2c'(v_2 - v_1)}{m_1} \\ d_2 \\ \frac{-2k'(d_2 - d_1) - 2c'(v_2 - v_1)}{m_2} \end{bmatrix} \begin{bmatrix} d_1 \\ v_1 \\ d_2 \\ v_2 \end{bmatrix} + \begin{bmatrix} 0 \\ 0 \\ 0 \\ \frac{1}{m_2} \end{bmatrix} s(t) + \begin{bmatrix} 0 \\ 0 \\ 0 \\ \delta(t) \end{bmatrix} \tag{11}$$

When simplifying the above equation, we get

$$F_C(t) = k_0(1 + \alpha\cos\left(\frac{2\pi v}{L}t\right)d_1. \tag{12}$$

Hence, to complete the state space expression, the controlled signal has to be derived with the aim of reducing the uncertainty in the generated contact force in the pantograph–catenary system.

3. Deep-learning-based controller design

The contact force on the system is originally predicted to achieve the controlled signal for uplifting force. The AO method for optimized PID settings constantly regulates this generated signal. Based on a static force at the contact site, an F^{2}OPID controller generates a control signal using this projected force. Bi-LSTM-based networks are used to forecast the observed force on the system. Mass, stiffness, and displacement in the lumped mass model are used to generate a contact force at the contact site based on the reference signal collected from the controller. The design of the proposed model is shown in figure 3.

3.1 *Bi-LSTM network*

The Bi-LSTM network cross-validates the inputs at different neurons through forward and backward passes at the hidden layer. The system uses uplifting force and controlled contact force from previous instances as input. Hence, at the hidden layer, neurons learn the status of uplifting force and controlled force by F^{2}OPID in the previous stage by backward and forward exchange of weight between them. Consider $F_C(t-1)$ and $F_u(t-1)$ as the two inputs, and the objective is to evaluate the optimal force in them by training using a reference force of 100 newtons. The processing step and output of the neural network at the hidden layer are given below.

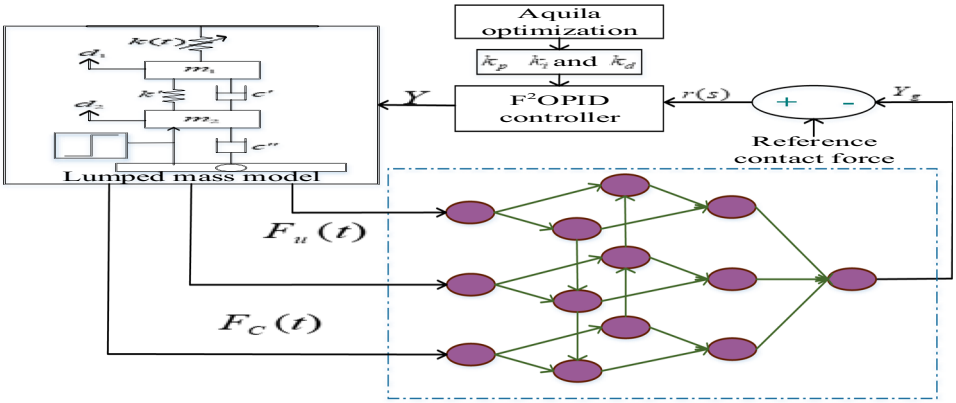

Figure 3. Architecture of Bi-LSTM F²OPID model.

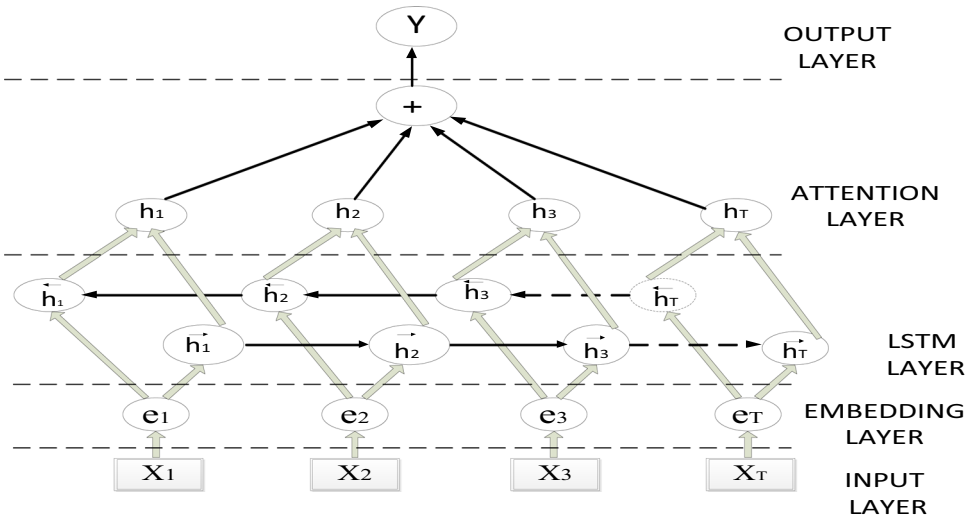

Figure 4. Bidirectional LSTM model.

$$h_c^1 = \mathrm{H}(\varpi_{ih^1} x_g + \varpi_{h^1 h^1} h_{c-1}^1 + bias_{h^1}) \tag{13}$$

$$h_c^2 = \mathrm{H}(\varpi_{ih^2} f_c + \varpi_{h^2 h^2} h_{c+1}^2 + bias_{h^2}) \tag{14}$$

$$f'_{cg} = \varpi_{h^1 f'} h_c^1 + \varpi_{h^2 f'} h_c^2 + bias_{f'} \tag{15}$$

where h_c^1 and h_c^2 are neurons at the hidden layer of forward and backward passes, *bias* indicates the bias, indicates the bias, and ϖ denotes the weight update between the input layer (i) and hidden layers (h_c^1, h_c^2). The predicted irregular force in the pantograph–catenary system of the locomotive is in figure 4

$$Y_g = conv(f'_{cg}) \tag{16}$$

3.2 *F²OPID controller*

The F²OPID model is introduced, which uses fuzziness for the evaluation of the controlled contact force. Here, the output of eq. (16) is given to the controller along with the reference force to generate controlled force on uplifting. This controller acts like a feedback control system using the controlled signal of the second iteration for error evaluation. The transfer function of the proposed controller is given as follows:

$$Z(s) = K_p r(s) + K_i r(s) * \frac{1}{s^{\lambda}} + K_d r(s) * s^{\mu} \tag{17}$$

where $r(s)$ is the error signal, k_p, k_i, and k_d are the gain of proportional, derivative, and integral terms, which are derived using AO, and the parameters λ, μ are used to represent the fractional orders of the controller, which are selected using the fuzzy system. The fractional parameters

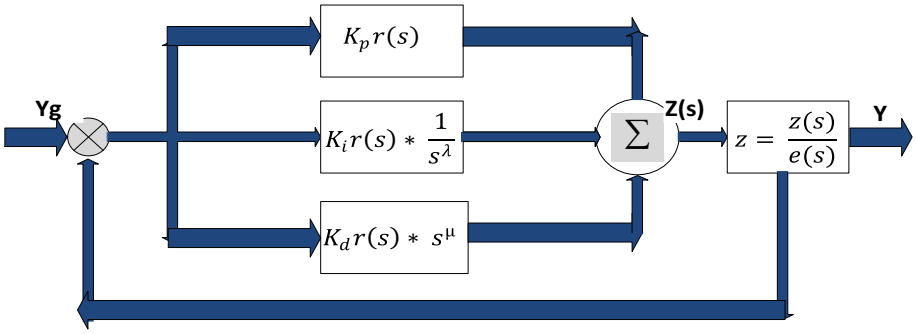

Figure 5. Architecture of the proposed controller.

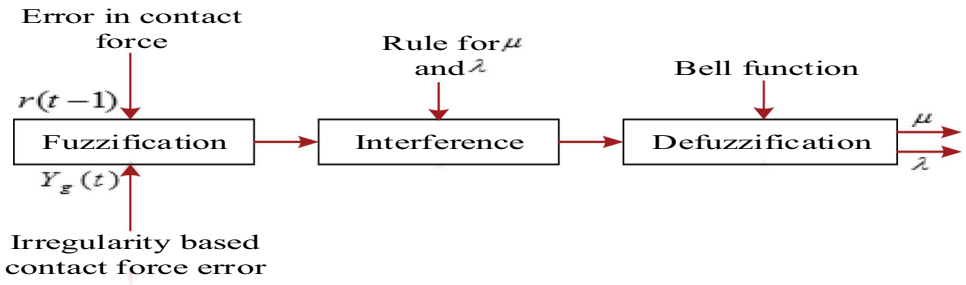

Figure 6. Fuzzification and defuzzification.

Table 3. Membership rules for obtaining μ and λ.

	Irregularity error					
	Membership rules for obtaining μ			Membership rules for obtaining λ		
Error	PS	D	PL	PS	D	PL
PS	>0	>0	0.3–0.7	>0	>0	0.3–0.7
D	>0	0.3–0.7	<1	>0	0.3–0.7	<1
PL	0.3–0.7	<1	<1	0.3–0.7	<1	<1

*PS indicates the positive small value, D indicates the desired value, and PL indicates the positive large value.

are in the range of $0<\lambda<1$ and $0<\mu<1$; they are used to improve the stability of the system. When the constraint of λ, μ violates the system, the controller acts like a traditional controller, which will improve the stability only at the negative real part or positive real part. The output of the controller over the feedback loop is as follows:

$$Z(\ddot{s}) = \frac{z(s)}{e(s)} = \left[\frac{K_p r(s) + K_i r(s) * \frac{1}{s^\lambda} + K_d r(s) * s^\mu}{s}\right]. \quad (18)$$

The diagrammatical representation of the above equation is presented in figure 5. Using fuzzy logic functions, 3x3 rules are generated for fractional orders using a bell membership function, as shown in figure 6. The rules are presented in table 3.

Furthermore, the gains are evaluated using Aquila optimizer due to the vulnerable behavior of optimization in the PID controller [25]. This inspired us to utilize it for the performance improvement of the contact force on the pantograph–catenary system.

3.3 *Aquila optimization*

The aim of the proposed technique is to obtain the optimal number of $K_p, K_i, and K_d$. The reason for using the AO algorithm is it has enhanced population diversity and

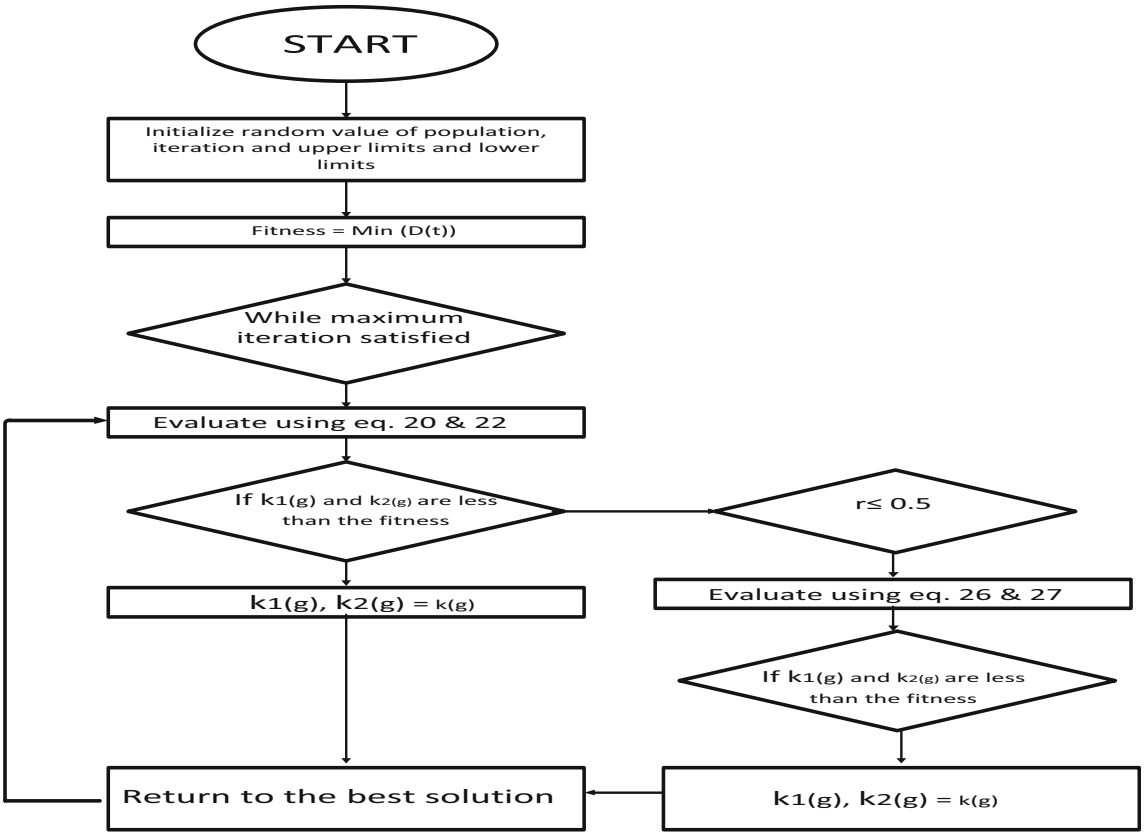

Figure 7. Flowchart of Aquila optimizer.

Table 4. Simulation settings.

Specifications and simulation settings [14]							
PAC system		Bi-LSTM		Fuzzy		Aquila optimizer	
m_1	9.1 kg	Layers	4	Total rules	9 rules per fractional term	Population size	20
m_2	17.2 kg	Hidden neurons	63	Membership	Bell function	Iteration	100
k'	7×10^3 N/m	Input neurons	101			Random number	[0, 1]
c'	130 Ns/m						
c''	30 Ns/m						
k_{cat}	1.535×10^6 N/m						
k_{pan}	8.23×10^4 N/m						

optimal selection can be realized in this method. In addition, due to the narrow and expanded position update stage, the precise value of the contact force is achieved with respect to the dynamics of the pantograph–catenary system. The proposed algorithm stimulates the AO procedure in four methods: selecting the search space by high soar with vertical stoop, exploring within a diverge search space by contour flight with short guide attack, exploiting within a converge search space by low flight with slow descent attack, and swooping by the walk and grab prey method.

Consider the population as the coefficients required. Initially, they are selected randomly with a total population of K_a. Each of the coefficients is set by upper and lower boundary limits as ub_a and lb_a where a is the dimension of the coefficients in its search space. Then, a solution set with the random coefficient r is given as follows [26]:

$$k_a = r \times (ub_a - lb_a) + lb_a \tag{19}$$

3.3.1 *Expanded exploration* The algorithm has narrow and expanded exploration for the formulation of

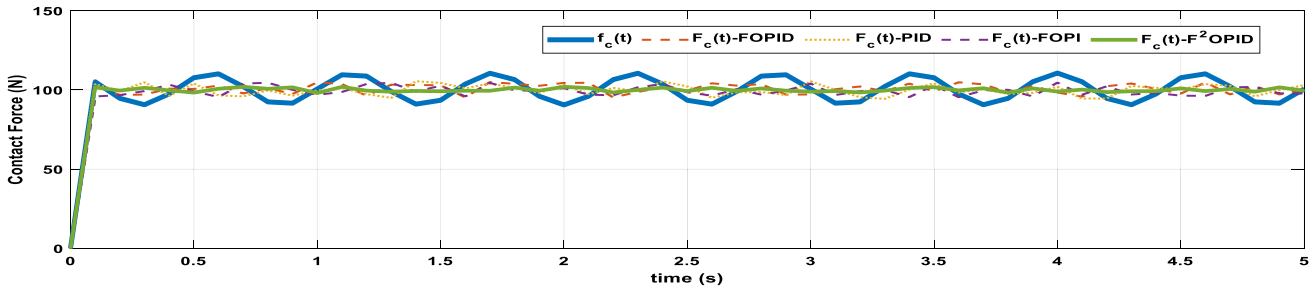

Figure 8. Contact force regulation for applied disturbance.

Table 5. Optimal parameters selected by fuzzy and Aquila optimizer.

Parameters	F^2OPID	FOPID	FOPI	PID
k_p	3.16	5	4.35	1.2
k_i	3.96	3.7	2.28	10
k_d	1.59	6.2	–	8.2
μ	0.8	0.75	0.59	1
λ	0.8	0.52	0.97	1

Table 6. Comparison of VSE and computation time (CT).

	VSE (%)	CT (s)	RMSE	ITSE
F^2OPID	92.8	18.02	1.18	0.052
FOPID	86.23	22.15	3	0.32
FOPI	79.973	32.8078	14.74	0.837
PID	79.55	22.67	3.3	0.48

proportional and integral gains. The formulation of derivative gain narrow exploration is used since it needs to compensate for errors through filtering. The updated equation in the proceeding iteration for $K_p$andK_i is as follows:

$$K_1(g+1) = K_b(g)\left(1 - \frac{g}{G}\right) + (K_l(g) - K_b(g) * r) \quad (20)$$

where $K_1(g+1)$ is the solution of the next iteration of g and iteration $K_b(g)$ is the best solution in gth iteration in a total iteration of G. $(1 - \frac{g}{G})$ helps control the expanded search through the number of iterations. A random value of a solution is $K_l(g)$, which is represented as

$$K_l(g) = \frac{1}{K}\sum_{a=1}^{K} K_a(g). \quad (21)$$

3.3.2 *Narrowed exploration* The derivative gain is obtained as

$$K_2(g+1) = K_b(g).L + K_q(g) + (u - v) * r, \quad (22)$$

where $K_2(g+1)$ is the solution of the next iteration of g, which is generated by K_2, and $K_q(g)$ is any solution between [1, K]. Here, the levy function L is used to filter the derivative gain, which is given as

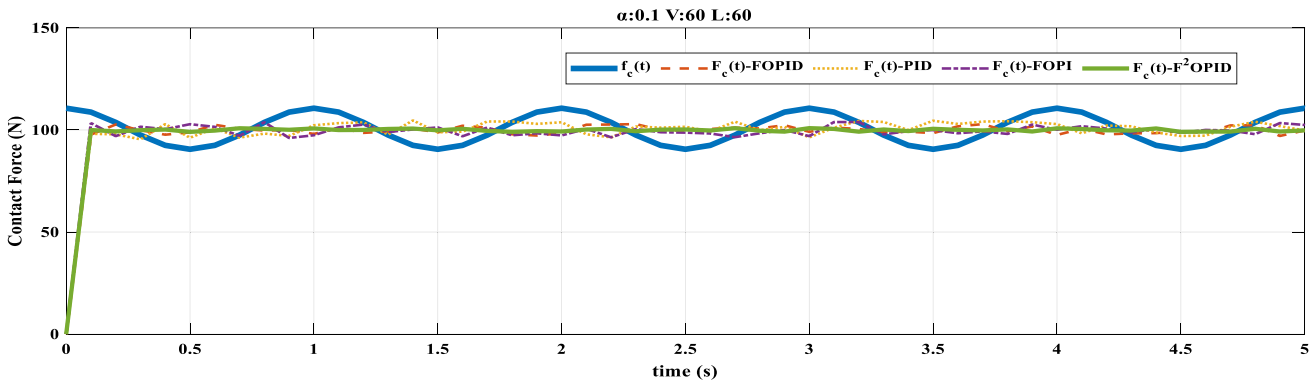

Figure 9. Contact force when $\alpha = 0.1;\ V = 60Km/hr.;\ L = 60m.$

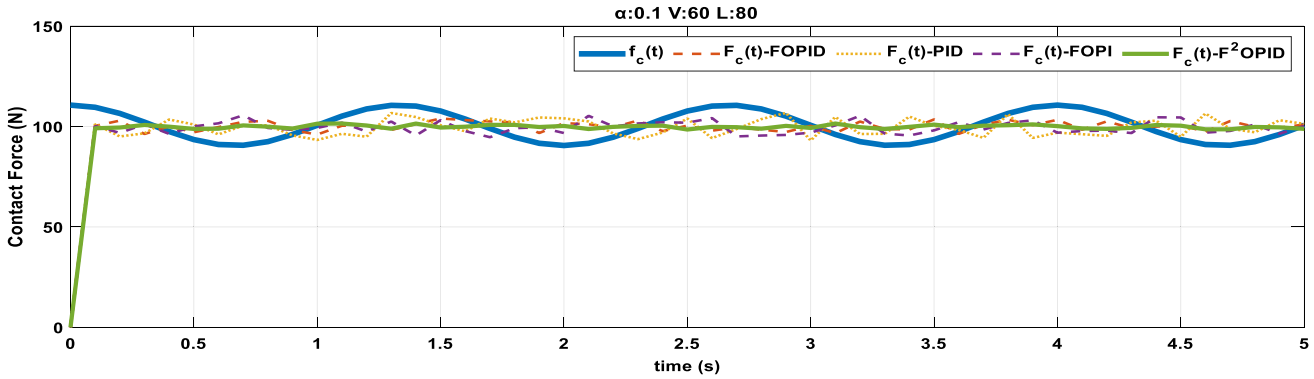

Figure 10. Contact force when $\alpha = 0.1;\ V = 60Km/hr.;\ L = 80m.$

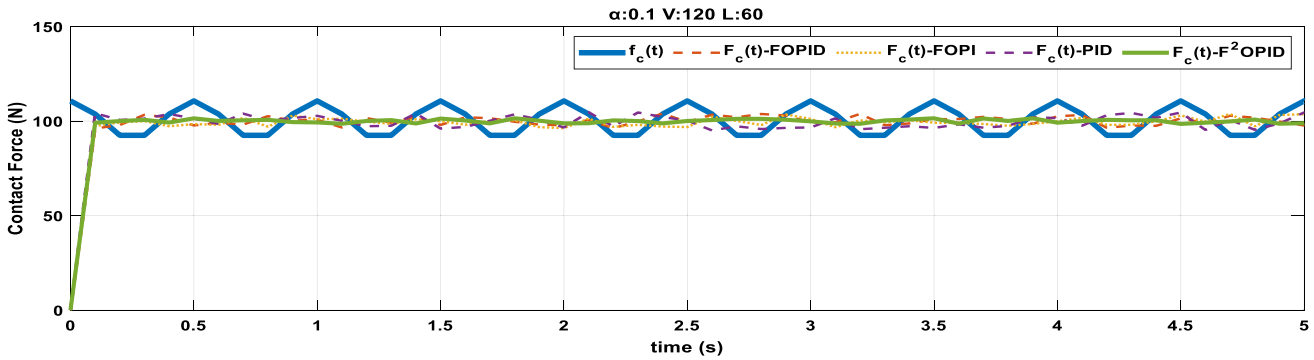

Figure 11. Contact force when $\alpha = 0.1;\ V = 120Km/hr.;\ L = 60m.$

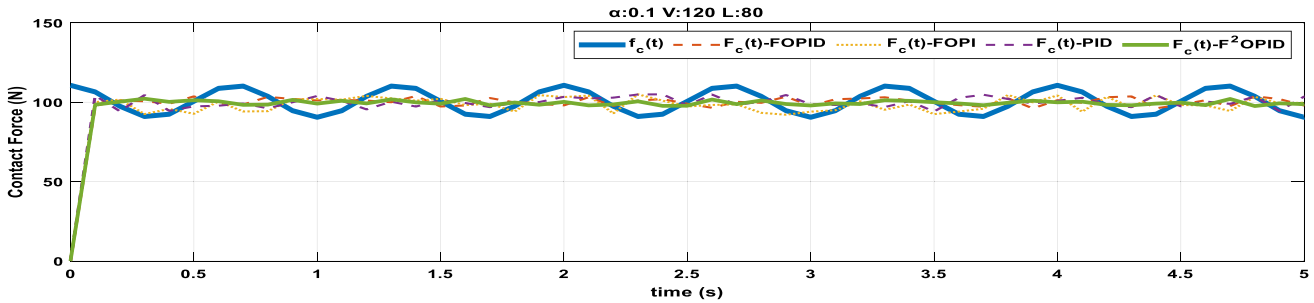

Figure 12. Contact force when $\alpha = 0.1;\ V = 120Km/hr.;\ L = 80m.$

$$L = w\left(\frac{\eta\sigma}{|\vartheta|^{\frac{1}{\theta}}}\right) \tag{23}$$

where W and θ are constants of 0.01 and 1.5, respectively, η and ϑ are random numbers between [0, 1], and the value of σ is obtained as follows:

$$\sigma = \left(\frac{\Gamma(1+\theta)\times\sin(\pi\theta/2)}{\Gamma(\frac{1+\theta}{2}).(2\hat{}(\theta-1/2))\theta}\right). \tag{24}$$

The filtering function for the derivative term is given as follows:

$$\begin{aligned} u &= r\cos(\varphi) \\ n &= r\sin(\varphi) \end{aligned}. \tag{25}$$

Both $rand\varphi$ are constant values.

3.3.3 *Expanded exploitation* In the third method, the exploration of gain parameters is updated as follows:

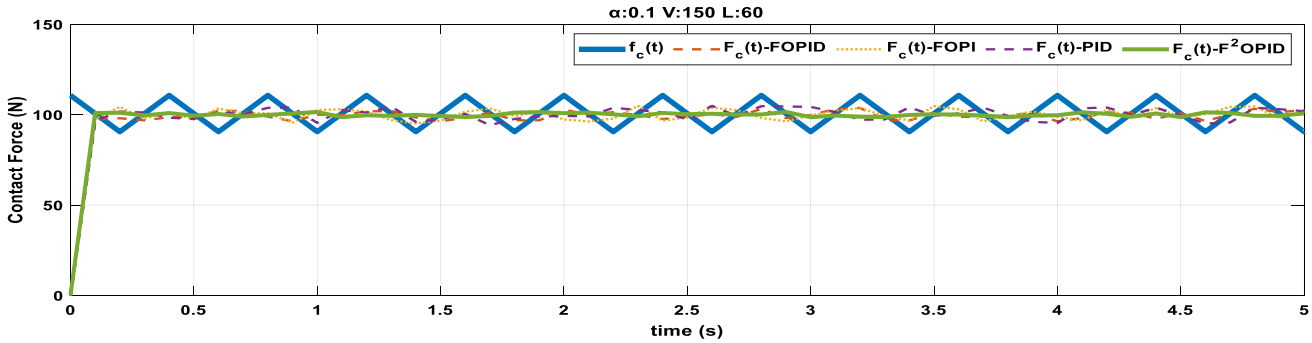

Figure 13. Contact force when $\alpha = 0.1;\ V = 150Km/hr.;\ L = 60m.$

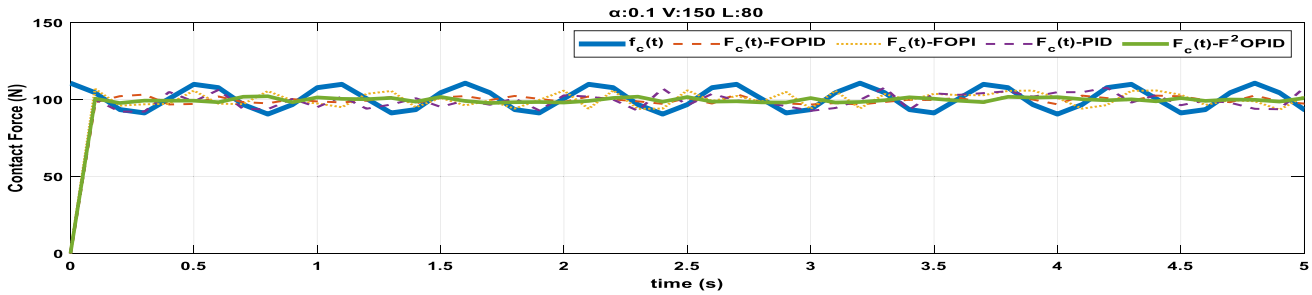

Figure 14. Contact force when $\alpha = 0.1;\ V = 150Km/hr.;\ L = 80m.$

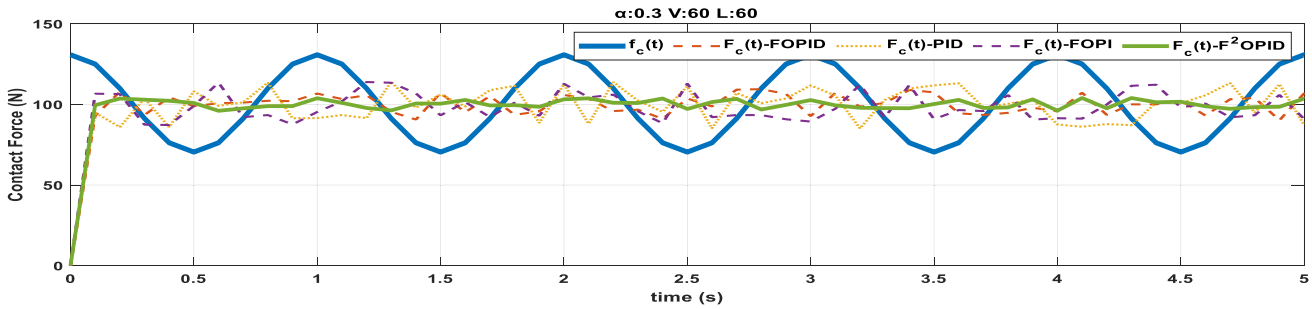

Figure 15. Contact force when $\alpha = 0.3;\ V = 60Km/hr.;\ L = 60m.$

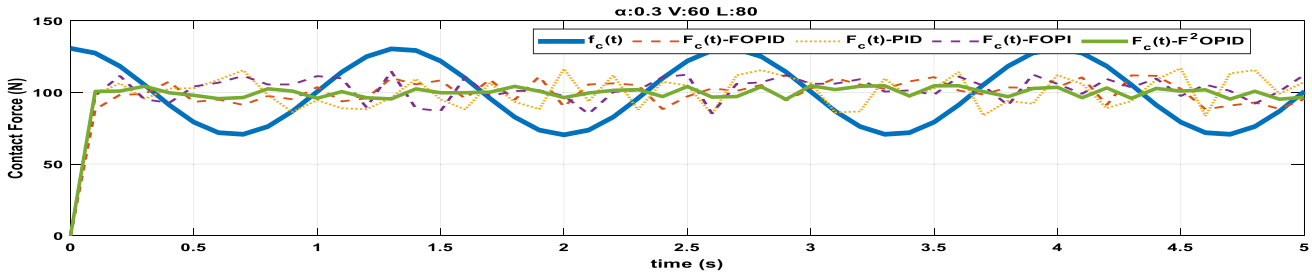

Figure 16. Contact force when $\alpha = 0.3;\ V = 60Km/hr.;\ L = 80m.$

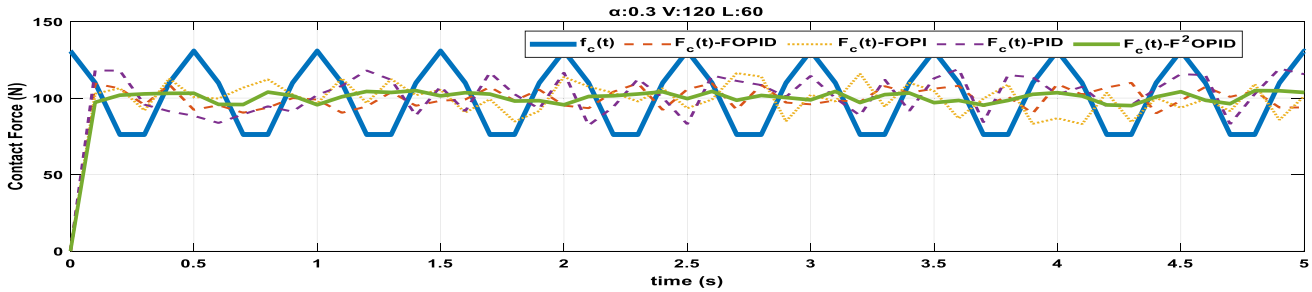

Figure 17. Contact force when $\alpha = 0.3;\ V = 120Km/hr.;\ L = 60m.$

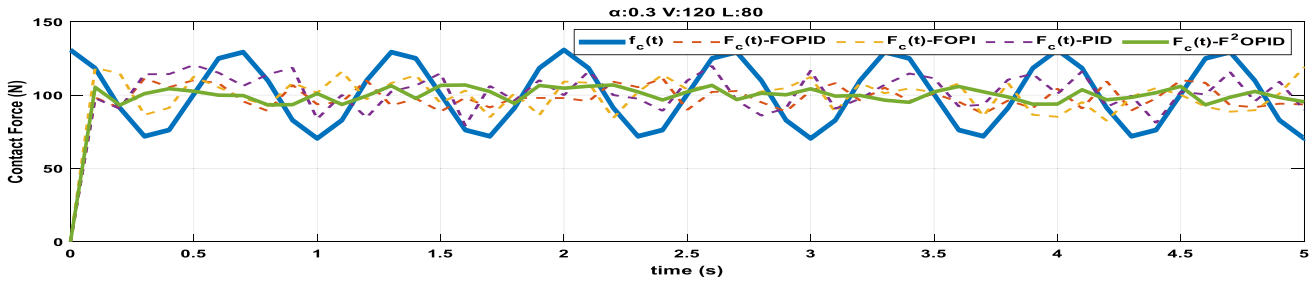

Figure 18. Contact force when $\alpha = 0.3;\ V = 120Km/hr.;\ L = 80m.$

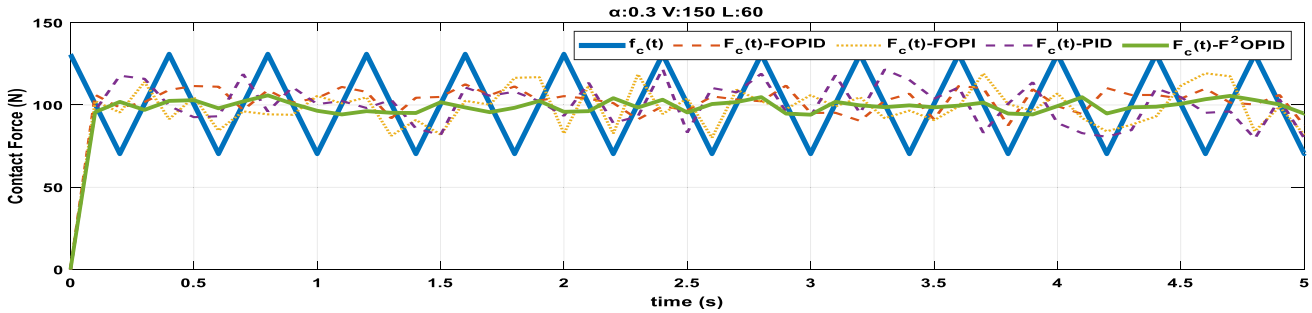

Figure 19. Contact force when $\alpha = 0.3;\ V = 150Km/hr.;\ L = 60m.$

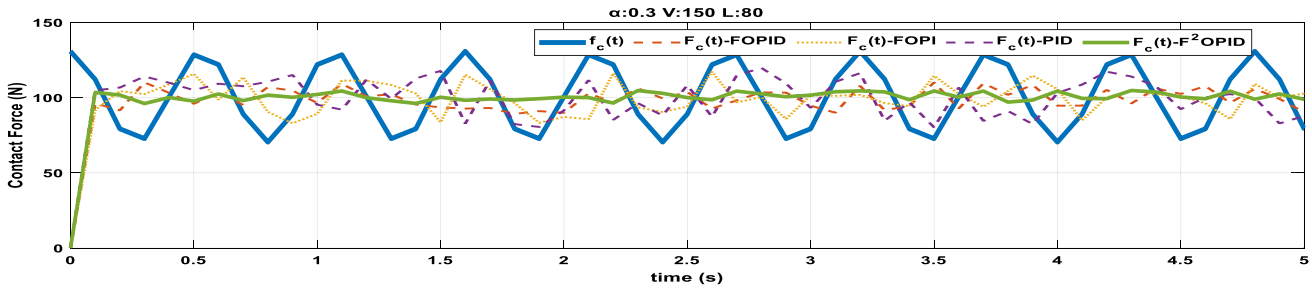

Figure 20. Contact force when $\alpha = 0.3;\ V = 150Km/hr.;\ L = 80m.$

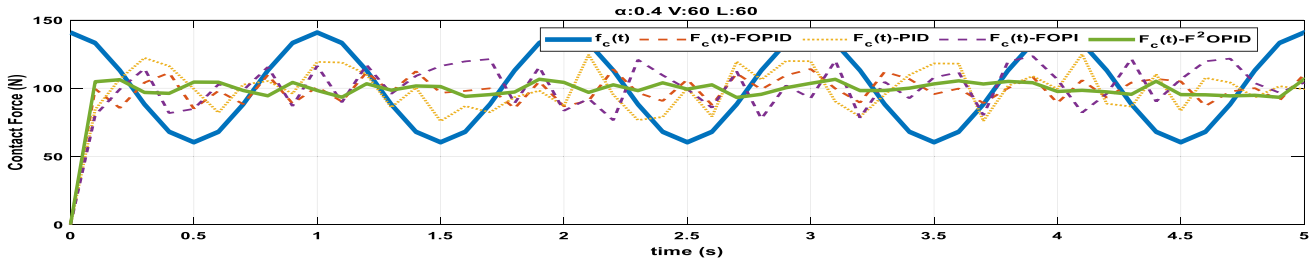

Figure 21. Contact force when $\alpha = 0.4;\ V = 60Km/hr.;\ L = 60m.$

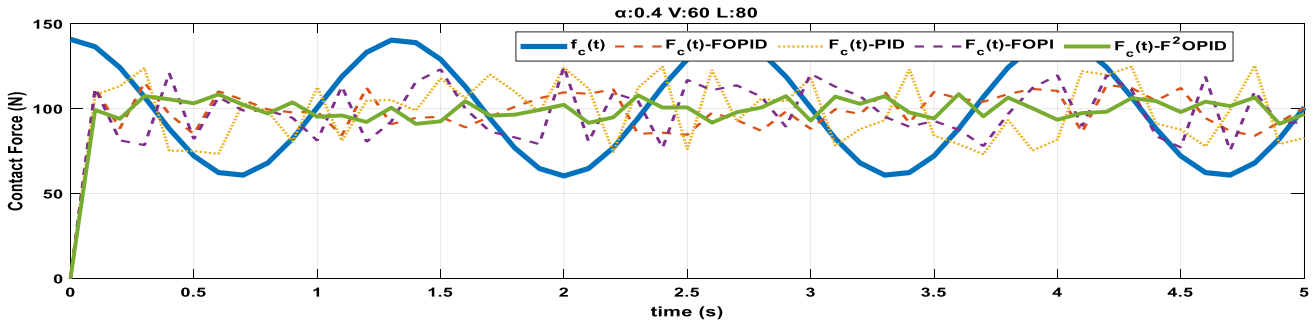

Figure 22. Contact force when $\alpha = 0.4;\ V = 60Km/hr.;\ L = 80m.$

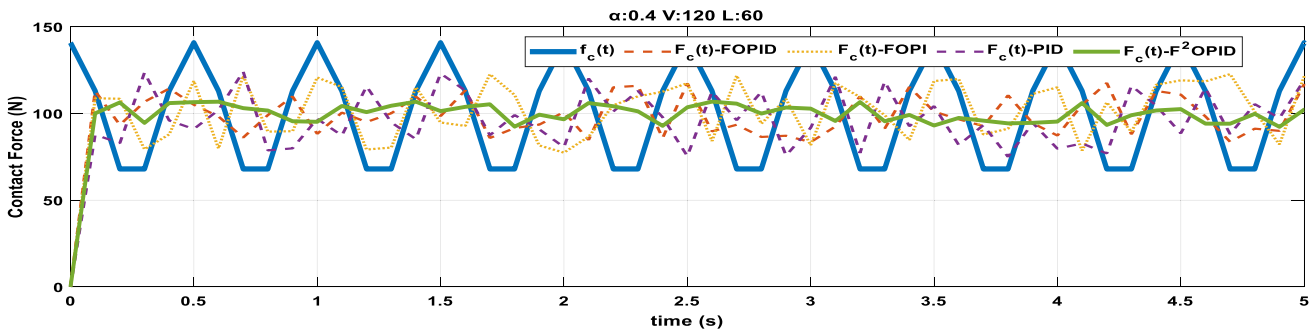

Figure 23. Contact force when $\alpha = 0.4;\ V = 120Km/hr.;\ L = 60m.$

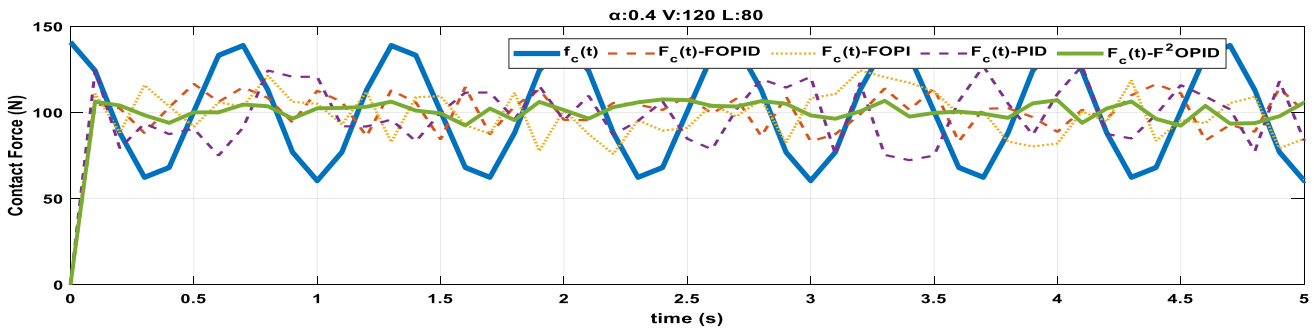

Figure 24. Contact force when $\alpha = 0.4;\ V = 120Km/hr.;\ L = 80m.$

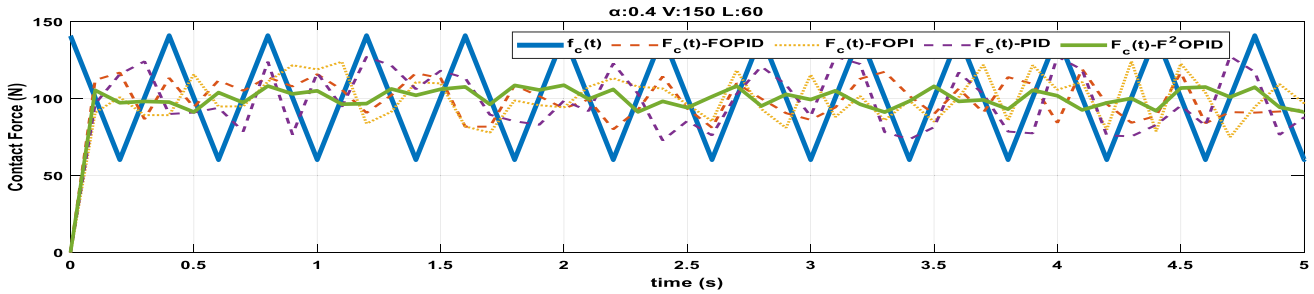

Figure 25. Contact force when $\alpha = 0.4;\ V = 150Km/hr.;\ L = 60m.$

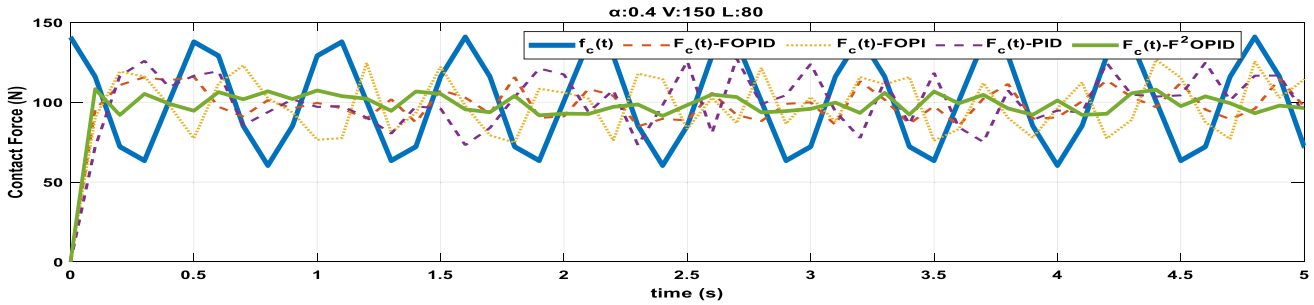

Figure 26. Contact force when $\alpha = 0.4;\ V = 150Km/hr.;\ L = 80m.$

$$K_1'(g+1) = (K_b(g) - K_l(g)) \cdot \alpha - r + ((ub_a - lb_a).r + lb_a) \times \delta \tag{26}$$

where $K_1'(g+1)$ is the solution of the next iteration of g [27].

3.3.4 *Narrowed exploitation* This method is also called the walk and grab prey method where AO attack for the last location is given as follows:

$$K_2'(g+1) = QK_b(g) - (\chi' K(g) r) - (\chi'' L) + \chi' * r \tag{27}$$

where α and δ are control parameters. Q is the quality function of the optimization: $Q = g^{\wedge}\left(\frac{2r-1}{(1-G)^2}\right)$. $\chi' = 2r - 1$ and $\chi'' = 2(1 - g/G)$ are the incremental and decremented factors [28]. The flowchart of the optimization is shown in figure 7.

4. Results and analysis

The objective of the work is to reduce oscillations in the contact force generated at the contact point of the pantograph–catenary system. The simulation is performed for varying stiffness coefficients and speeds of the train. A nominal contact force on the system is considered 100N. The simulation parameters are presented in table 4. To test the efficiency of the proposed controller, the results are obtained and compared with other methods. The supremacy of the proposed controller is established by comparing its results with those of PID, fractional order proportional integraFOPI, andand fractional order proportional integral derivative FOPID.

Figure 8 illustrates the control of the pantograph–catenary system's contact force when a significant external disturbance is present. The force is assessed for the planned FOPID, PID, and FOPI controllers. This figure shows that the proposed method achieves a high level of stability for a fuzzy system's approach to error reduction estimation. Table 5 lists the regulation's chosen ideal gain and fractional term characteristics.

When the fractional terms are equal to unity, the controller become a standard PID controller,setting the fractional Order to 0 and 1 efficetively yields to PI and PD controller respectively. The vibration suppression efficiency (VSE) for the applied disturbance is given as follows:

$$VSE = \left(1 - {}^{\theta}/_{\theta_o}\right) \cdot 100 \tag{28}$$

where θ is the amplitude of the controlled signal and θ_o is the amplitude of the observed signal at the pantograph–catenary system. Here, root mean square error (RMSE) and integral time square error (ITSE) are also evaluated to validate the regulation with and without the controller. Table 6 shows that the VSE of the proposed controller is very high in the range of 92.8%, which is higher than other controller values such as FOPID, FOPI, and PID, which reached values of 86.23%, 79.97%, and 79.55%,

Table 7. Comparison of VSE and computation time for variation in stiffness.

		$\alpha = 0.1$						$\alpha = 0.3$					
	V	60		120		150		60		120		150	
Controller	L	60	80	60	80	60	80	60	80	60	80	60	80
PID	CT(s)	35.41	35.67	35.58	38.45	36.23	38.43	34.78	36.65	35.45	36.35	36.41	34.56
	VSE (%)	80.21	79.33	79.21	79.26	79.33	79.29	78.82	79.07	83.59	81.86	77.43	77.61
	RMSE	0.18	0.21	0.19	0.18	0.18	0.22	0.24	0.31	0.33	0.32	0.34	0.34
	ITSE	0.03	0.04	0.03	0.030	0.03	0.045	0.08	0.09	0.11	0.099	0.11	0.113
FOPI	CT(s)	32.45	33.34	33.58	35.85	34.26	36.78	31.56	33.25	31.44	33.31	32.31	31.52
	VSE (%)	79.540	78.8347	79.107	78.336	79.549	79.658	77.404	75.943	79.997	81.334	78.450	75.943
	RMSE	0.175	0.2	0.1186	0.178	0.177	0.217	0.27	0.299	0.31	0.29	0.328	0.31
	ITSE	0.0252	0.0337	0.0222	0.0368	0.0296	0.0435	0.0748	0.0887	0.0838	0.093	0.104	0.0887
FOPID	CT(s)	31.16	32.45	34.85	33.2	32.18	31.2	30.2	32.45	30.78	33.8	31.48	31.34
	VSE (%)	83.53	83.41	83.49	83.55	83.53	83.45	84.09	83.95	84.08	82.62	86.94	84.21
	RMSE	0.15	0.17	0.16	0.17	0.16	0.16	0.30	0.27	0.24	0.27	0.26	0.26
	ITSE	0.02	0.024	0.02	0.025	0.02	0.02	0.05	0.07	0.057	0.07	0.068	0.065
F^2OPID	CT(s)	20.01	19.22	19.23	22.67	19.78	18.97	21.29	18.78	19.86	19.31	20.05	17.28
	VSE (%)	88.20	88.09	88.21	88.09	88.11	87.97	89.71	89.45	89.56	90.01	89.55	89.99
	RMSE	0.12	0.13	0.13	0.14	0.13	0.14	0.17	0.19	0.19	0.214	0.20	0.18
	ITSE	0.01	0.012	0.012	0.017	0.01	0.016	0.026	0.03	0.03	0.041	0.035	0.02

		$\alpha = 0.4\alpha = 0.4$					
	V	60		120		150	
Controller	L	60	80	60	80	60	80
PID	CT(s)	36.74	36.45	35.12	34.3	34.45	36.66
	VSE (%)	80.03	81.24	76.14	87.31	77.06	78.95
	RMSE	0.29	0.39	0.37	0.38	0.39	0.37
	ITSE	0.13	0.14	0.15	0.14	0.15	0.13
FOPI	CT(s)	32.53	32.00	31. 14	30.11	33.01	32.1
	VSE (%)	85.6808	77.661	82.8425	71.304	85.5124	85.680
	RMSE	0.282	0.354	0.37	0.38	0.37	0.36
	ITSE	0.1354	0.1297	0.1336	0.1165	0.1222	0.1566
FOPID	CT(s)	32.4	32.45	33.15	30.06	31.89	31.23
	VSE (%)	86.58	85.41	87.27	87.01	87.19	87.44
	RMSE	0.37	0.30	0.30	0.31	0.34	0.31
	ITSE	0.08	0.087	0.091	0.09	0.11	0.08
F^2OPID	CT(s)	21.56	19.8	22.02	19.08	20.78	20.09
	VSE (%)	92.24	92.72	94.53	98.03	93.41	91.26
	RMSE	0.21	0.24	0.22	0.22	0.236	0.23
	ITSE	0.04	0.05	0.045	0.045	0.051	0.05

Table 8. Comparison with state-of-the-art techniques for variation in stiffness coefficient.

Stiffness	Speed and length	Methods	VSE (%)	CT (s)
$\alpha = 0.3$	V=60 km/hr. L=60m	MZL [14]	82.31	22.51
		KM [14]	83.51	80.59
		F^2OPID	89.71	21.29
	V=60 km/hr. L=80m	MZL [14]	84.85	21.06
		KM [14]	85.51	81.05
		F^2OPID	89.41	18.7

respectively. Similarly, the error factor by the adopted controller is highly reduced compared with these methods.

4.1 *System performance under varying conditions*

The locomotive's speed and span length are two key factors for the stability of the smooth current collection system. Hence, these two terms are varied for the analysis of the system. The vibration level at the contact point and oscillation are observed under varying conditions.

4.1.1 *System performance for stiffness at* $\alpha = 0.1$

To check the robustness of the proposed controller, system performance is evaluated under varying velocity and span length and both. The contact force on the system is calculated for span lengths of 60 meters and 80 meters while accounting for stiffness variation of 10% and setting the speed to 60 km per hour. Figures 9 and 10 show that, despite the length of the span being extended, the force's vibration level at the contact point does not significantly alter.

It has been observed that variations in train's speed and span length result in noticeable changes in outcome for the contact force, as shown in figures 11, 12, 13 and 14. This shows the relationship between the locomotive's stiffness and speed.

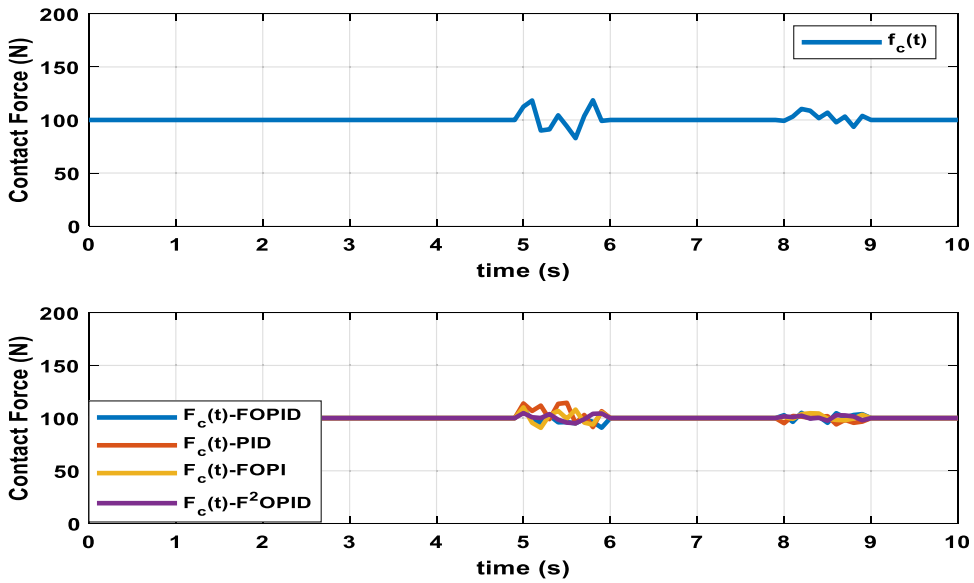

Figure 27. Contact force when speed of the locomotive is varied.

Table 9. Stability analysis for speed variation.

Controller	Rise time (s)	Settling time (s)	Steady-state error
MZL [14]	0.42	0.81	Moderate
SIFLC [15]	5.27	0.8	Moderate
Backstepping controller [21]	Nil	0.2	High
Adaptive controller [22]	0.45	1.3	High
FOPID	0.14	0.94	Low
FOPI	0.135	0.98	Low
PID	0.1	1	Low
F^{2}OPID	0.12	0.78	Nil

4.1.2 *System performance for stiffness at* $\alpha = 0.3$ The pantograph–catenary system exhibits increased levels of oscillation when the stiffness coefficient is changed, as shown in figures 15 and 16. Figures 15 and 16 show system performance when the span length changes from 60 meters to 80 meters and the stiffness coefficient is set to 30% change, with a speed of 60 km per hour.

Figures 17, 18, 19 and 20 show how the contact force at the contact point is controlled when the speed is changed to 120 km/hr and 150 km/hr, respectively, but the span length remains the same as in other situations. Compared with other scenarios, this one exhibits a larger degree of oscillation and unstable output, indicating that oscillation increases as speed increases.

4.1.3 *System performance for stiffness at* $\alpha = 0.4$ In practical addition, the pantograph–catenary system exhibits increased levels of oscillation when the stiffness coefficient is changed, as can be observed in figures 21 and 22. Figures show system performance when the span length is changed from 60 meters to 80 meters when the stiffness coefficient is set to 40% change, with a speed of 60 km per hour.

Figures 23, 24, 25 and 26 show how the contact force at the contact point is controlled when speed is changed to 120 km/hr and 150 km/hr, respectively, but the span length remains the same as in other conditions. Compared with other scenarios, this one exhibits a larger degree of oscillation and unstable output, indicating that oscillation increases as speed increases.

4.2 *Comparative analysis*

For all the above scenarios, performance measures such as VSE, RMSE, CT, and ITSE are provided in table 7. The table shows that the proposed method performs better than FOPID, FOPI, and PID.

In table 8, the proposed method is compared with Karnik–Mendel (KM) [14] and Moradi–Zirkohi–Lin (MZL) [14] methods with a stiffness variation of 60%, a speed of 60Km/hr., and span lengths of 60m and 80m. Better performance is achieved for F^2OPID with a speed of 60 Km/hr. and a length of 60m: 89.71% of VSE and 89.41 % of VSE, respectively.

4.3 *Transient analysis*

To study the transient response and settling time of the system, the speed of the train is varied at 5s and increased to 120Km/hr under transient conditions at 8s, and then, the speed is suddenly decreased to 80Km/hr. The results of the proposed F^2OPID, FOPID, FOPI, and PID controller are presented in figure 27.

The calculated and observed parameters, along with steady-state errors, are presented in table 9 for both the implemented controller and state-of-the-art controllers such as MZL [14], single-input fuzzy logic control (SIFLC) [15], backstepping controller [21], and adaptive controller [22] on a pantograph–catenary system.

From the analysis, a minimal settling time with a zero steady-state error is observed for the proposed controller. Some other methods like backstepping controller, MZL, and SIFLC have also maintained a similar settling time, but the steady-state error in these methods is high. Hence, the proposed method is better than the other methods.

5. Conclusion

A model for the control of contact force on the pantograph–catenary system of an electric train under conditions of external disturbance is presented in this study. Using a deep learning technique, the control model is built to recognize changes in contact force brought on by irregularities on the pantograph head. According to the analysis, compared with the MZL approach, the proposed model has less vibration, resulting in an increased VSE of order 89.71%. In addition, compared with other methodologies, transient analysis yielded an average settling time of 0.78s and a rise time of 0.12s with zero steady-state inaccuracy, which is the lowest among the techniques studied. Compared with the MZL approach, vibration suppression for the suggested method is insignificant when stiffness variation is extremely high.

List of symbols

F^2OPID	Fuzzy-based fractional order proportional integral derivative
Bi-LSTM	Bilateral long short-term memory network
AO	Aquila optimizer
Hgwo-ps	Hybrid gray wolf optimization pattern search
PID	Integral and derivative controllers
ITAE	Integral of time multiplied by absolute error
CT	Computation time
VSE	Vibration suppression efficiency
RMSE	Root mean square error
ITSE	Integral time square error
m_1, m_2	Pan head mass and frame mass
C′ & C″	Damping of pan head suspension and frame
K′ & K(t)	Stiffness of the pantograph and catenary
d_1, d_2	Displacement of pan head suspension
$r(s)$	Error signal
k_p	Gain of proportional term
k_i	Gain of integral term
k_d	Gain of derivative term
λ,μ	Fractional orders of the controller
α	Stiffness variation coefficient
V	Locomotive's speed

L	Span length
MZL	Moradi–Zirkohi–Lin
SIFLC	Single-input fuzzy logic control
KM	Karnik–Mendel

References

[1] Gil J, Gregori S, Tur M and Fuenmayor F J 2022 Analytical model of the pantograph–catenary dynamic interaction and comparison with numerical simulations. *Veh. Syst. Dyn.* 60(1): 132–155

[2] Zhang L, Liang S, Li X and Jia Y 2021 Modelling on novel cable traction power supply system and power distribution analysis. *IEEE Trans. Power Deliv.* 37(2): 745–754

[3] Elbelkasi M S, Badran E and Abdel-Rahman M 2020 Overview of DC and AC electric railway systems considering energy efficiency enhancement methods. *Port-Said Eng. Res. J.* 24(1): 128–140

[4] Gao S 2020 Automatic detection and monitoring system of pantograph–catenary in China's high-speed railways. *IEEE Trans. Instrum. Meas.* 70: 1–12

[5] Huang S, Yu L, Zhang F, Zhu W and Guo Q 2018 Cluster analysis based arc detection in pantograph-catenary system. *J. Adv. Transp.* 1(2018):1329265

[6] Yang Z, Xu P, Wei W, Gao G, Zhou N and Wu G 2020 Influence of the crosswind on the pantograph arcing dynamics. *IEEE Trans. Plasma Sci.* 48(8): 2822–2830

[7] Song Y, Rønnquist A, Jiang T and Nåvik P 2021 Identification of short-wavelength contact wire irregularities in electrified railway pantograph–catenary system. *Mech. Mach. Theory* 162: 104338

[8] Song Y, Liu Z, Rønnquist A, Nåvik P and Liu Z 2020 Contact wire irregularity stochastics and effect on high-speed railway pantograph–catenary interactions. *IEEE Trans. Instrum. Meas.* 69(10): 8196–8206

[9] Liu S, Wei Y, Yin Y, Feng T and Lin J 2021 Structural health monitoring method of pantograph–catenary system based on strain response inversion. *Front. Phys.* 9: 691510

[10] Song Y, Wang H and Liu Z 2021 An investigation on the current collection quality of railway pantograph-catenary systems with contact wire wear degradations. *IEEE Trans. Instrum. Meas.* 70: 1–11

[11] Zhang D, Gao S, Yu L, Kang G, Zhan D and Wei X 2019 A robust pantograph–catenary interaction condition monitoring method based on deep convolutional network. *IEEE Trans. Instrum. Meas.* 69(5): 1920–1929

[12] Wang H, Núñez A, Liu Z, Zhang D and Dollevoet R 2019 A Bayesian network approach for condition monitoring of high-speed railway catenaries. *IEEE Trans. Intell. Trans. Syst.* 21(10): 4037–4051

[13] Zhu B, Ren Z, Xie W, Guo F and Xia X 2019 Active nonlinear partial-state feedback control of contacting force for a pantograph–catenary system. *ISA Trans.* 91: 78–89

[14] Liu Z, Liu Y, Zhou N, Zou D and Tu H 2018 Backstepping controller design for pantograph-catenary system. *IOP Conference Series: Materials Science and Engineering, IOP Publishing* 428(1): 012045

[15] Song Y and Li L 2020 Robust adaptive contact force control of pantograph–catenary system: an accelerated output feedback approach. *IEEE Trans. Ind. Electron.* 68(8): 7391–7399

[16] Al-Awad N A, Abboud I K and Al-Rawi M F 2021 Genetic algorithm-PID controller for model order reduction pantographcatenary system. *Appl. Comput. Sci.* 2(2021):28–39

[17] Vikas S, Parmar G and Kumar M 2021 A hybrid grey wolf optimization and pattern search algorithm control of multi-area interconnected power system. *Int. J. Adv. Intell. Paradigms* 18(3): 265–293

[18] Abualigah L, Yousri D, Abd Elaziz M, Ewees A A, Al-Qaness M A and Gandomi A H 2022 Aquila optimizer: a novel meta-heuristic optimization algorithm. *Comput. andInd. Eng.* 1;157:107250

[19] Karaduman G and Akin E 2020 A new approach based on predictive maintenance using the fuzzy classifier in pantograph-catenary systems. *IEEE Trans. Intell. Transp. Syst.* 23(5):4236-–46

[20] Karaduman G and Akin E 2020 A deep learning based method for detecting of wear on the current collector Strips' surfaces of the pantograph in railways. *IEEE Access* 8: 183799–183812

[21] Lin T C, Sun C W, Lin Y C and Zirkohi M M 2022 Intelligent contact force regulation of pantograph–catenary based on novel type-reduction technology. *Electronics* 11(1): 132

[22] Farhan M F, Shukor N S A, Ahmad M A, Suid M H, Ghazali M R and Jusof M M 2019 A simplify fuzzy logic controller design based safe experimentation dynamics for Pantograph-Catenary system. *Indones. J. Electr. Eng. Comput. Sci.* 14(2): 903–911

[23] Song Y, Wang Z, Liu Z and Wang R 2021 A spatial coupling model to study dynamic performance of pantograph-catenary with vehicle-track excitation. *Mech. Syst. Signal Process.* 151: 107336

[24] Yu P, Liu K Z, Li X and Yokoyama M 2021 Robust control of pantograph-catenary system: comparison of 1-DOF-based and 2-DOF-based control systems. *IET Control Theory Appl.* 15(18): 2258–2270

[25] Mokrani N and Rachid A 2013 A robust control of contact force of pantograph-catenary for the high-speed train, in *2013 European Control Conference (ECC)*, IEEE, 4568–4573

[26] Mahajan S, Abualigah L, Pandit AK, Altalhi M. Hybrid Aquila optimizer with arithmetic optimization algorithm for global optimization tasks. Soft Computing. 26(10):4863–81.

[27] Zhang J, Zhang H, Song B, Xie S and Liu Z 2019 A new active control strategy for pantograph in high-speed electrified railways based on Multi-Objective robust control. *IEEE Access* 7: 173719–173730

[28] Aribowo W, Supari B S and Suprianto B 2022 Optimization of PID parameters for controlling DC motor based on the aquila optimizer algorithm. *Int. J. Power Electron. Drive Syst. (IJPEDS)* 13(1): 808–2814

Springer Nature or its licensor (e.g. a society or other partner) holds exclusive rights to this article under a publishing agreement with the author(s) or other rightsholder(s); author self-archiving of the accepted manuscript version of this article is solely governed by the terms of such publishing agreement and applicable law.

Materials Research Proceedings 49 (2025) 350-359 https://doi.org/10.21741/9781644903438-35

Design and development of drivetrain for fully faired hybrid recumbent bicycle

Siddharth GARG[1,a*], Rhythm AGGARWAL[1,b], Priyanshu SINHA[2,c], Vaibhav KUMAR[1,d], Raghvendra GAUTAM[1,e]

[1]Department of Mechanical Engineering, Delhi Technological University, Delhi 110042, India

[2]Department of Electrical Engineering, Delhi Technological University, Delhi 110042, India

[a]officialsiddharthgarg@gmail.com, [b]rhythm4901@gmail.com, [c]priyanshusinha.dtu@gmail.com, [d]vaibhav.ky.2003@gmail.com, [e]raghvendrag80@yahoo.com

Keywords: Recumbent Bicycle, Velomobile, Hybrid Drivetrain, MATLAB, HEV

Abstract. Due to the rapid consumption of fossil fuels, the effects of climate change have become very rampant in recent years. Harvesting human and electric energy in the form of hybrid electric vehicles (HEVs) is a cleaner and more economical solution to the problem of urban mobility. Fully faired recumbent bicycles, also called velomobiles, while retaining all the good features of bicycles (eco-friendly, small frontal area), also incorporate the beneficial features of cars (protection from weather and crashes, extra added stability). This study examines the three drivetrains possible for velomobiles (fully electric, fully human-powered, and hybrid, the latter of which incorporates both human and electric energy). It compares them on the parameters of maximum speed, acceleration, range, and driving power needed. The simulations were designed in MATLAB Simulink, and the results were verified by actual human testing performed under suitable conditions. The testing revealed that the hybrid drivetrain model is the most efficient to use and to satisfy all the desired benchmarks of ASME e-HPVC.

INTRODUCTION

Amidst a rapidly escalating climate crisis, the world stands at a critical juncture. Central to this environmental upheaval is the pervasive use of fossil fuels in vehicles, expelling greenhouse gases at an unprecedented rate. Therefore, governments across the globe have been pushing for more sustainable modes of transportation. One of the areas of research has been biofuels [1–4]; although they have shown promising results, none of them has been able to match hybrid electric vehicles (HEVs) [5]. The main objective of this study is to examine possible drivetrains for fully-faired recumbent bicycles. Recumbents have been in use for an extended period but have not seen any upgrade from their original design, which is one of the reasons for their loss in popularity [6]. The incorporation of a hybrid drivetrain will make it a suitable contender for urban mobility, where the distance to be travelled is small, and only one passenger space is required [7]. In this work, an electric human-powered fully faired recumbent is designed in the context of participating in the American Society of Mechanical Engineers Electric-Human Powered Vehicle Challenge (ASME e-HPVC). This study outlines the development process of three Simulink models for drivetrains, which were designed in MATLAB. They are tested on various criteria, including range, acceleration, speed and driving power. Based on the results, an actual model for vehicle testing (Fig. 1) is constructed. The simulation results are verified experimentally by members of Team Raftaar of Delhi Technological University. The main contribution of this study is the in-depth description of the design for an efficient hybrid drivetrain for recumbent bicycles using a model-based design methodology and software modelling and simulation, along with verification of the results via actual testing.

Content from this work may be used under the terms of the Creative Commons Attribution 3.0 license. Any further distribution of this work must maintain attribution to the author(s) and the title of the work, journal citation and DOI. Published under license by Materials Research Forum LLC.

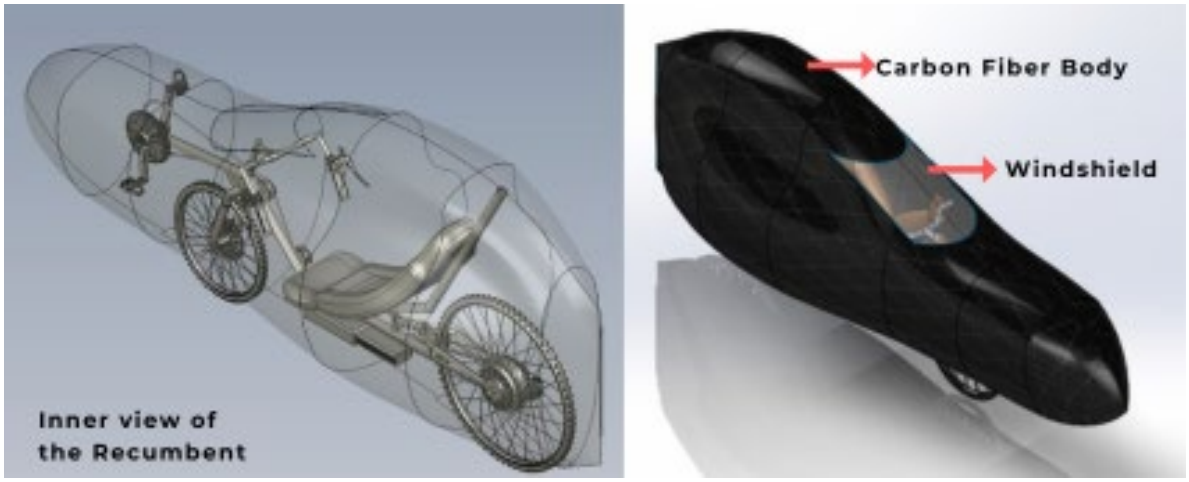

***Fig. 1**. 3D CAD model of the fully-faired hybrid recumbent bicycle used for actual testing purposes.*

EXPERIMENTAL SETUP

Simulink Modelling

MATLAB Simulink is a graphical programming environment used for modelling, simulating, and analysing dynamic systems and control algorithms. Three possible drivetrains are modelled in the software as mentioned below in Table 1.

Table 1: Input values for the Simulink model

Parameter	Value
Weight	110 kg (70 kg + 40 kg)
Coefficient of Drag	0.063
Coefficient of Rolling Resistance	0.04
Density of air	1.127 kg/m^3
Frontal Area	0.473 m^2
Input torque	variable
Aux load	0
Efficiency	1
Gear Ratio (for human powered and hybrid)	4
Radius of Tyre	0.66 m

(a) Fully Human Powered

In the Simulink model for fully human powered vehicle (Fig. 2), the required torque is taken as an input in the form of pedalling and converted into force (Eqs. 1 and 2) [8]. Aerodynamic and rolling resistance forces are then subtracted to determine the net force acting on the wheels. The net force is integrated to obtain the acceleration, which is further integrated to determine the velocity. The power is calculated by multiplying the net force and velocity. The change in distance travelled is used to calculate the crank rotation, allowing the model to determine the force applied by the rider. This force is then converted back to torque, and the cycle continues.

$$\text{Human Input Torque} = \text{Length of Crank } (L_c) \times \text{Chain Force} \times \text{Gear Ratio} \quad (1)$$

Chain Force = ½ × (cos 2(Crank Angle) + 1) × Rider's Weight (2)

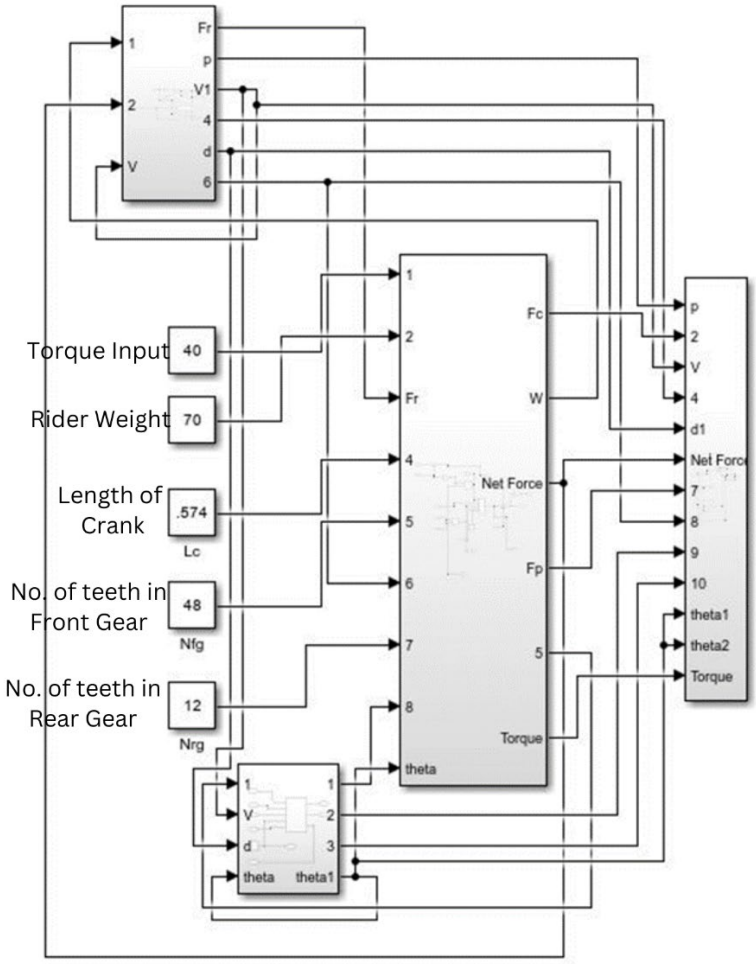

Fig. 2. Simulink model for a human powered drivetrain for the recumbent bicycle

(b) Fully Electric Powered

In this model (Fig. 3), the motor managed by a throttle provides the necessary torque (Eq. 3). To determine the values of acceleration, velocity and acceleration, the net force that remains after removing the frictional and drag losses is integrated multiple times and the values at different stages are noted (Eq. 4) [9]. Consequently, we calculated the required driving power by multiplying net effective force and vehicle speed (Eq.5) [10]. By operating it with the battery capacity, we arrived at the vehicle range (Eq.6).

Electric Input Torque = Input Force × Radius of Tyre (3)

Net Force (F) = Input Force – (Aerodynamic Drag + Rolling Resistance) (4)

Driving Power = Input Force × Velocity (V) (5)

$$\text{Range} = \frac{Battery\ Capacity \times Velocity}{(Driving\ Power + Aux\ Load) \times Output\ Efficiency} \quad (6)$$

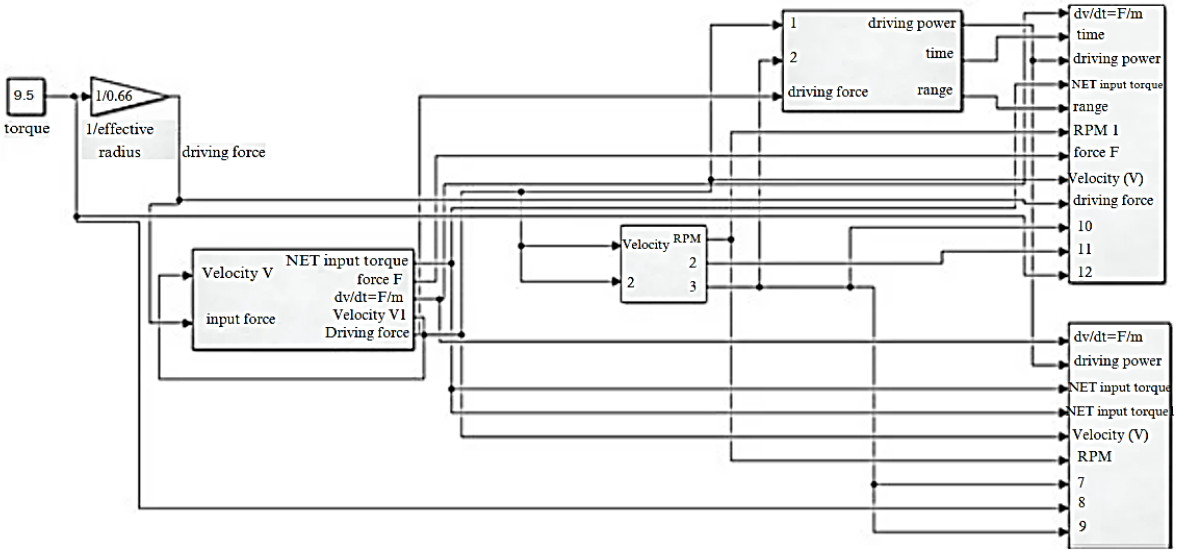

Fig. 3. Simulink model for an electric powered drivetrain for a recumbent bicycle

(c) Hybrid Drivetrain (Human and Electric Powered)

Fig. 4 presents the hybrid model proposed here, which amalgamates human-powered and motor-assisted aspects for comprehensive vehicle dynamics analysis. The system takes input torque from pedalling and transforms it into force. The net force acting on the wheels is derived by accounting for the aerodynamic and rolling resistance forces. Integration techniques are employed to ascertain acceleration and velocity, which, in turn, lead to power computation (Eq. 7) [11].

$$\text{Hybrid Input Torque} = \text{Human Input Torque} + \text{Electric Input Torque} \quad (7)$$

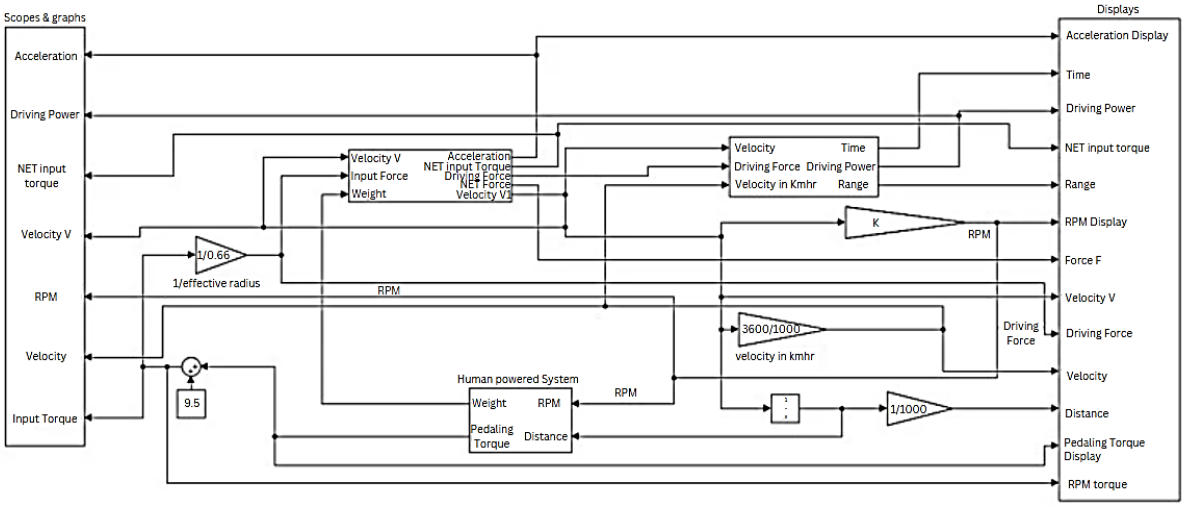

Fig. 4. Simulink model for the hybrid drivetrain (both human and electric power are used in combination) for the fully faired recumbent bicycle

Vehicle Fabrication

The vehicle under study is a 2-wheeler, rear-wheel drive recumbent bicycle, as depicted in Fig. 5. The crank set is placed in front of the vehicle. The frame of the vehicle had a wheelbase of 1.474 m and a trail of 0.05 m. The gear ratio for the sprocket and the crank is 4:1. A 48 V 500 W hub motor was used in the hub of the rear tyre. The motor was controlled by a 48V~35A motor controller and 48V 10Ah Battery. Air-dampened, short travel suspension on the rear tyre was used

Materials Research Proceedings 49 (2025) 350-359 https://doi.org/10.21741/9781644903438-35

for all-round performance [12–15]. The vehicle used 26-inch (0.66 m) rear and 20-inch (0.508 m) diameter front tyres (inflation pressure of 30 PSI). All subjects utilised the same chassis during the experiments (a carbon fibre and titanium frame of 1.8 kg). Disc brakes of 180 mm on both wheels were used. Over the seat, direct steering mechanism with a steering angle of 72° was used for precise control and to reduce weight [5,16,17]. The chassis was fully faired with a 40 kg, 12-piece carbon fibre fairing, specially manufactured using the vacuum bagging technique, additive manufacturing and brazing for custom joints [18–21].

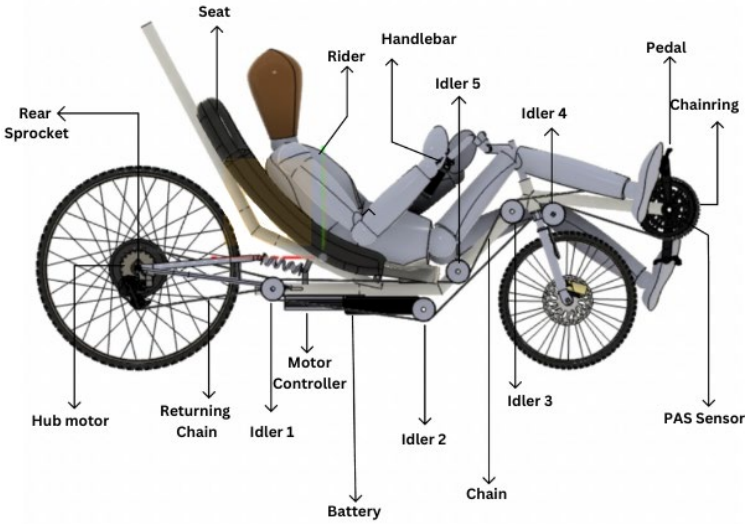

Fig. 5. Picture depicting detailed schematic of the drivetrain of recumbent bicycle

Testing Conditions

The rider was 20 years of age, had a 70 kg body mass, and was 173 cm tall. The rider was part of the research and development team and clearly understood the risks involved. Testing was carried out according to the standards set for ASME for the e-HPVC. The experiments were performed on a road with 3 km of straight stretch with no elevation. The wind speed was recorded to be 18 kmph. A Garmin cycle speedometer edge 1030 was used to measure the speed. The testing began every day at approximately 10:00 hours and were concluded at about 15:00 hours [22–24]. An eight samarium-cobalt magnet PAS sensor was mounted on the chainring to measure the intensity of the pedals. The motor controller then uses this information to supply the motor with the necessary, proportional current.

Fig. 6. Actual testing of vehicle carried out at Delhi Technological University campus by the members of Team Raftaar

RESULTS

From the above simulation, various parameters and graphs for comparison were obtained, which were then utilised while implementing our actual recumbent vehicle.

Fig. 7. Graph between the driving power and velocity for all three cases.

Fig. 7 depicts the required driving power against the vehicle's velocity graph plotted for the three powertrains: human-powered, electric, and hybrid. The graph clearly illustrates that the driving power is directly proportional to the vehicle's velocity in all three cases. Notably, the hybrid model demonstrates the highest velocity compared to the human-powered and electric models. This finding confirms that the hybrid powertrain, which combines human and electric propulsion, achieves the maximum velocity among the three configurations.

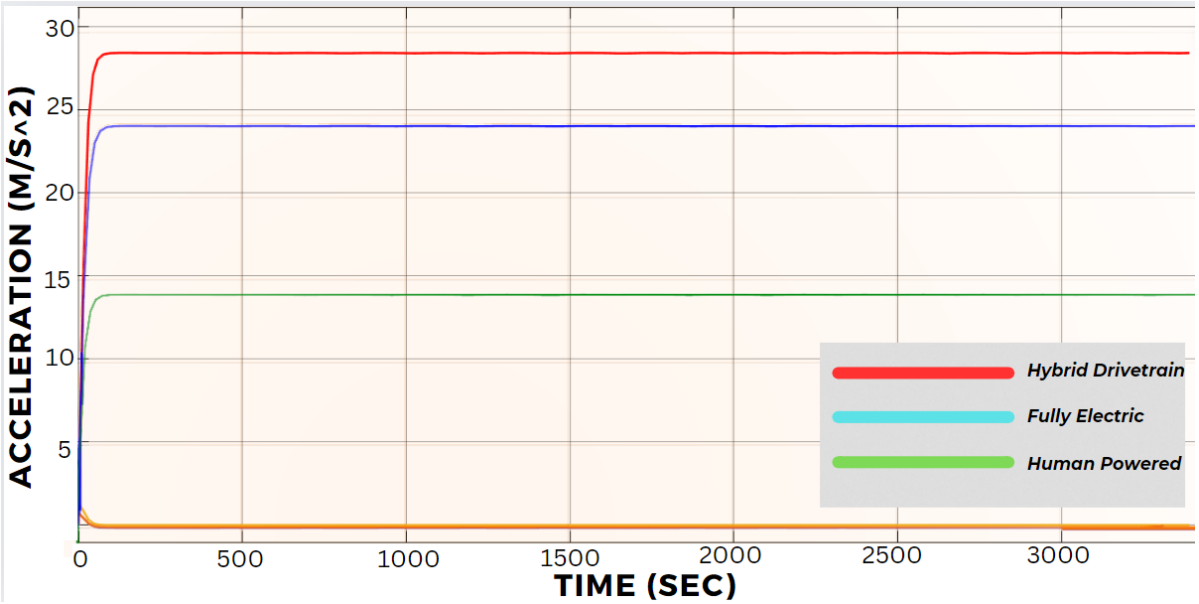

Fig. 8. Graph between time and acceleration for all three cases

The analysis of the time versus acceleration (Fig. 8) and time versus velocity (Fig. 9) graphs reveals a common trend across all models, where they exhibit an initial period where both acceleration and velocity experience changes before stabilizing. During the initial period, vehicle takes some time to gain velocity from rest, and changes in acceleration accompany this process. The acceleration is not constant during this transient phase but shows fluctuations as the vehicle accelerates and overcomes resistive forces such as friction and air drag. However, after this initial

transient period, both the acceleration and velocity reach a steady state, where they become constant. In this state, the vehicle maintains a constant acceleration, corresponding to a consistent velocity increase over time.

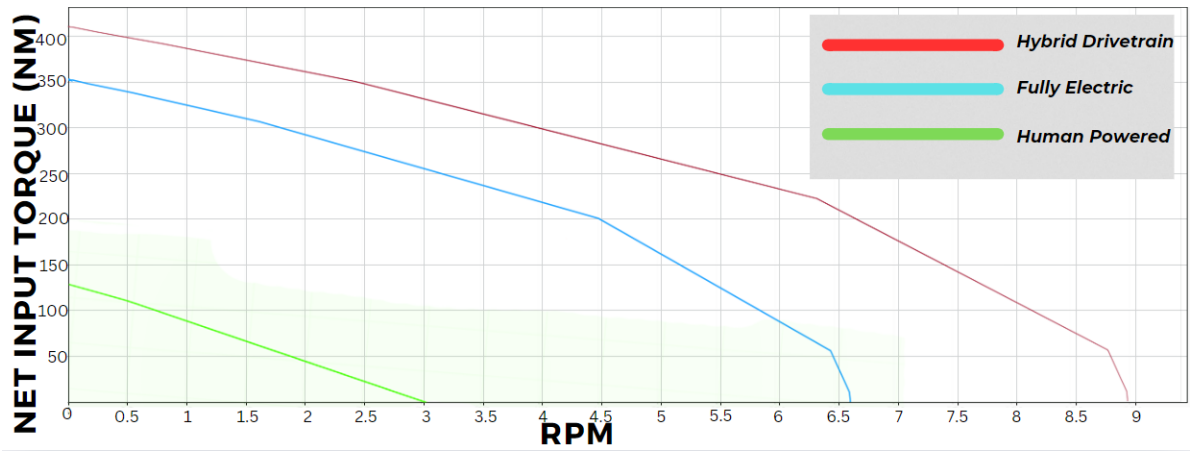

Fig. 9. Graph between the RPM and Net input torque for all three case

In Fig. 9, graph's net input torque represents the value obtained after subtracting the drag and resistance forces from the required forces. The graph exhibits an interesting pattern, where initially, at the starting rotations per minute (RPM) (which is zero), the net torque is at its maximum value, equivalent to the required torque for the given driving conditions. As the speed of the vehicle increases, the drag and resistance forces also increase, resulting in a decrease in the net torque. As the vehicle continues to accelerate, the net torque gradually approaches zero. Simultaneously, the RPM of the vehicle steadily increases as it gains speed. The graph shows how the net torque decreases as the RPM increases, indicating that the vehicle requires less torque to maintain higher RPM levels due to reduced resistive forces at higher speeds. Consistent with the previous findings, the hybrid model again has the highest RPM among the three powertrains.

The hybrid model was implemented in the vehicle based on the comprehensive analysis of the various graphs and parameters obtained from the simulations. It has demonstrated numerous advantages over human-powered and electric models regarding range, velocity, and maximum RPM. The experimental results of the actual testing data and simulated data are tabulated in Table 2.

Table 2: Comparison of the results of all the drivetrain models

Properties	**Human Powered (Simulink)**	**Electric (Simulink)**	**Hybrid (Simulink)**	**Hybrid (Experimental)**
Required Torque (Nm)	3.04	9.5	12.54 (9.5 + 3.04)	10.2
Driving Power (Watt)	39	350	559	524
Max. Velocity (km/hr)	45	88	106	97
RPM	110.5	352.72	426.42	389.84
Range (km)	-	53.29	70.15	75.25

For the results tabulated in Table 2, the required torques were set to 3.04 Nm, 9.5 Nm, and 12.54 Nm for the human-powered, electric, and hybrid Simulink models, respectively. The experimental error for all the results was under 10% (arising due to varying air resistance and friction), indicating the efficacy of the model. When analysing the hybrid model, a combination of torques from human-powered and electric models was utilised. As a result, there were improved outcomes compared to those of the electric model, specifically regarding range and velocity. Remarkably, this improvement is achieved while maintaining the same input torque and driving power from the electric motor.

CONCLUSIONS

This study systematically compared three Simulink models representing electric, human-powered, and hybrid bicycles while supplementing the analysis with a real-life experiment on the hybrid variant. The findings unequivocally demonstrate that the hybrid bicycle outperforms both electric and human-powered counterparts in key technical aspects such as range, velocity, and power. The simulations provided valuable insights into the theoretical performance of each drivetrain type, revealing the advantages and limitations of each. However, the real-life experiment on the hybrid bicycle provided empirical evidence with an error percentage metric of 8.66%, 6.26%, 8.49%, 8.58%, and 7.27% for torque, power, velocity, RPM, and range, respectively, validating the superiority of the simulations and indicating the high accuracy and reliability of the findings. Considering the results from both the simulations and the real-life experiment, the hybrid bicycle emerged as the most promising option for various applications, especially when a balance between range, velocity, and power is desired. The ability of HEVs to leverage both electric power and human input showcases a sustainable and efficient means of transportation.

ACKNOWLEDGMENT

This work was supported by Delhi Technological University, Delhi-110042, India (sanction order number DTU/DSW/2022-23/F.No.90/132)

DECLERATION

Competing Interest: The authors declare no competing interests.

Author Contribution: *All authors contributed to the study conceptualisation and vehicle fabrication.* ***S.Garg****: Manuscript writing and editing, vehicle testing.* ***R.Aggarwal****: Manuscript writing and MATLAB simulation* ***P.Sinha****: MATLAB simulation* ***V.Kumar****: Vehicle testing and CAD modelling* ***R.Gautam****: Manuscript editing and supervision. All authors read and approved the final manuscript.*

REFERENCES

[1] R. Gautam, N.A. Ansari, P. Thakur, A. Sharma, Y. Singh, Status of biofuel in India with production and performance characteristics: a review, International Journal of Ambient Energy 43 (2022) 61–77. https://doi.org/10.1080/01430750.2019.1630298

[2] D. Sikha, R. Gautam, S. Kumar, Performance And Combustion Analysis Of Diesel And Sesame Biodiesel In Small Capacity Diesel Engine, Design Engineering (2021) 4923–4938.

[3] R. Gautam, S. Kumar, Performance and combustion analysis of diesel and tallow biodiesel in CI engine, Energy Reports 6 (2020) 2785–2793. https://doi.org/https://doi.org/10.1016/j.egyr.2020.09.039

[4] S. Kumar, R. Gautam, Prospects of Factor Affecting Biodiesel Selection Strategies Based on Various Aspects: An Indian Perspective, Journal of Engineering Research (Kuwait) 10 (2022) 208–219. https://doi.org/10.36909/jer.ICAPIE.15043

[5] Y. Sharma, R. Yadav, S. Verma, M. Sehgal, R. Gautam, Study About the Future of Electric Vehicles in the Current Indian Scenario, SAE Technical Paper (2019).

[6] H. Ahmed, O.M. Qureshi, A.A. Khan, Reviving a ghost in the history of technology: The social construction of the recumbent bicycle, Soc Stud Sci 45 (2015) 130–136. https://doi.org/10.1177/0306312714560640

[7] K. Singh, N.S. Iyengar, D. Ashok, Design and Analysis of Human Powered Hybrid Vehicle, International Journal of Mechanical Engineering and Technology (IJMET 9 (2018) 594–605. https://doi.org/10.13140/RG.2.2.29245.36320

[8] P.D. Soden, B.A. Adeyefa, Forces applied to a bicycle during normal cycling, J Biomech 12 (1979) 527–541. https://doi.org/10.1016/0021-9290(79)90041-1

[9] J.B. Spicer, C.J.K. Richardson, M.J. Ehrlich, J.R. Bernstein, M. Fukuda, M. Terada, Effects of frictional loss on bicycle chain drive efficiency, Journal of Mechanical Design, Transactions of the ASME 123 (2001) 598–605. https://doi.org/10.1115/1.1412848

[10] F. Valero, F. Rubio, C. Llopis-Albert, J.I. Cuadrado, Influence of the Friction Coefficient on the Trajectory Performance for a Car-Like Robot, Math Probl Eng 2017 (2017). https://doi.org/10.1155/2017/4562647

[11] V. Sankaranarayanan, S. Ravichandran, Torque sensorless control of a human-electric hybrid bicycle, in: 2015 International Conference on Industrial Instrumentation and Control (ICIC), IEEE, 2015: pp. 806–810. https://doi.org/10.1109/IIC.2015.7150852

[12] B. Howey, B. Bilgin, A. Emadi, Design of an External-Rotor Direct Drive E-Bike Switched Reluctance Motor, IEEE Trans Veh Technol 69 (2020) 2552–2562. https://doi.org/10.1109/TVT.2020.2965943

[13] B.C. Langford, C.R. Cherry, D.R. Bassett, E.C. Fitzhugh, N. Dhakal, Comparing physical activity of pedal-assist electric bikes with walking and conventional bicycles, J Transp Health 6 (2017) 463–473. https://doi.org/10.1016/j.jth.2017.06.002

[14] J. Partyka, Comparative Analysis of the Mobility Assessment Methods for Tracked Vehicles, in: Materials Research Proceedings, Association of American Publishers, 2022: pp. 221–226. https://doi.org/10.21741/9781644902059-32

[15] E. Tournon, P. Venet, B. Barbedette, A. Lelievre, J. Aubry, A. SARI, Efficiency Comparison between Series Hybrid Bike and Traditional Bike, in: 2019 Fourteenth International Conference on Ecological Vehicles and Renewable Energies (EVER), IEEE, 2019: pp. 1–7. https://doi.org/10.1109/EVER.2019.8813618

[16] M.S.M. Sani, N.A. Nazri, S.N. Zahari, N.A.Z. Abdullah, G. Priyandoko, Dynamic Study of Bicycle Frame Structure, in: IOP Conf Ser Mater Sci Eng, Institute of Physics Publishing, 2016. https://doi.org/10.1088/1757-899X/160/1/012009

[17] N.R. Miller, D. Ross, The Design of Variable-Ratio Chain Drives for Bicycles and Ergometers—Application to a Maximum Power Bicycle Drive, Journal of Mechanical Design 102 (1980) 711–717. https://doi.org/10.1115/1.3254810

[18] S. Garg, A. Sardar, R. Srivastava, S. Verma, A.K. Madan, Variation in Tensile Strength of 3D Printed PLA Parts by Varying Infill Density and Infill Pattern, Saudi Journal of Engineering and Technology 8 (2023) 103–107. https://doi.org/10.36348/sjet.2023.v08i05.004

[19] S. Garg, Q. Murtaza, Comparative Analysis of Dip-Brazing and TIG Welding on the Properties of Al-64430 Joints, J Adhes Sci Technol (2024) 1–15. https://doi.org/10.1080/01694243.2024.2409317

[20] S. Garg, Q. Murtaza, Effect of filler paste's mixing ratio on the properties of Al-64430 dip-brazed joints, Welding in the World 68 (2024) 2459–2471. https://doi.org/10.1007/s40194-024-01772-y

[21] S. Garg, S. Bansal, Q. Murtaza, Failure investigation of an elbow pipe used in sewage water treatment facility, Materials and Corrosion 75 (2024) 1185–1192. https://doi.org/10.1002/maco.202414336

[22] M.-K. Tran, M. Akinsanya, S. Panchal, R. Fraser, M. Fowler, Design of a Hybrid Electric Vehicle Powertrain for Performance Optimization Considering Various Powertrain Components and Configurations, Vehicles 3 (2020) 20–32. https://doi.org/10.3390/vehicles3010002

[23] C. Capelli, L.P. Ardigò, F. Schena, P. Zamparo, Energy cost and mechanical efficiency of riding a human-powered recumbent bicycle, Ergonomics 51 (2008) 1565–1575. https://doi.org/10.1080/00140130802238614

[24] E. Bressel, S. Bliss, J. Cronin, A field-based approach for examining bicycle seat design effects on seat pressure and perceived stability, Appl Ergon 40 (2009) 472–476. https://doi.org/10.1016/j.apergo.2008.10.001

Journal of Modern Optics

ISSN: (Print) (Online) Journal homepage: www.tandfonline.com/journals/tmop20

Design and theoretical analysis of a dual-core photonic crystal fibre temperature sensor with enhanced sensitivity across an extended temperature range

Shubham Sharma, Ajeet Kumar & Than Singh Saini

To cite this article: Shubham Sharma, Ajeet Kumar & Than Singh Saini (20 Mar 2025): Design and theoretical analysis of a dual-core photonic crystal fibre temperature sensor with enhanced sensitivity across an extended temperature range, Journal of Modern Optics, DOI: 10.1080/09500340.2025.2481172

To link to this article: https://doi.org/10.1080/09500340.2025.2481172

Published online: 20 Mar 2025.

Submit your article to this journal

Article views: 49

View related articles

View Crossmark data

Full Terms & Conditions of access and use can be found at
https://www.tandfonline.com/action/journalInformation?journalCode=tmop20

JOURNAL OF MODERN OPTICS
https://doi.org/10.1080/09500340.2025.2481172

Taylor & Francis
Taylor & Francis Group

Check for updates

Design and theoretical analysis of a dual-core photonic crystal fibre temperature sensor with enhanced sensitivity across an extended temperature range

Shubham Sharma[a], Ajeet Kumar[a] and Than Singh Saini[b]

[a]Advanced Photonics Simulation Research Lab, Department of Applied Physics, Delhi Technological University, Delhi, India; [b]Department of Physics, National Institute of Technology Kurukshetra, Kurukshetra, India

ABSTRACT

We present a novel dual-core photonic crystal fiber (DC-PCF) temperature sensor with a unique arrangement of circular air holes, enabling ultra-high sensitivity and stability. The DC-PCF features dual solid cores separated by a ring of air holes, functioning as dual waveguides. This highly birefringent structure operates on the principle of mode coupling between the two cores. The sensor is designed for temperature measurement by connecting one core to a broadband light source and the other to an optical spectrum analyzer. Numerical analysis and simulations using the finite element method (FEM) in COMSOL Multi-physics demonstrate its effectiveness over a broad 0–1400°C range. Due to its core asymmetry, the 8 cm-long DC-PCF sensor achieves a high-temperature sensitivity of 25 pm/°C, surpassing previous designs. Its compact and robust structure makes it a promising solution for precise high-temperature measurements, with significant potential for industrial applications.

ARTICLE HISTORY
Received 28 November 2024
Accepted 12 March 2025

KEYWORDS
Dual-core photonic crystal fibre; mode coupling; PCF-based temperature sensor; relative sensitivity

1. Introduction

Photonic Crystal Fibres (PCFs) are an advanced type of optical fibre distinguished by their unique microstructured design, which offers high flexibility and adaptability in various applications, including low-loss guidance, sensing, highly nonlinear, large-mode-area, and effective single-mode operation, etc. Due to their unique properties, PCFs enable precise control over light propagation, making them ideal for environments where high sensitivity, low interference, and stable signal transmission are essential. In particular, PCFs have gained attention for temperature sensing, where traditional optical fibres face challenges such as limited polarization stability and higher loss [*1*]. PCFs have potential applications in areas such as dispersion compensation, filtering, polarization maintenance, splitting, coupling, combining, birefringence, and various sensing applications [*2*]. PCFs are characterized by their ability to confine and manipulate light using a structured arrangement of air holes within a fibre made of a single material. Such structural changes provide superior optical properties compared to traditional optical fibres, such as high birefringence, enhanced nonlinearity, tailored dispersion, and significant light confinement [*3*]. Fibre optic sensors have emerged as a strong alternative to conventional electronic sensors due to recent advancements in component cost reduction and performance enhancement [*4*–*7*]. Optical fibre sensors have evolved to surpass traditional electronic sensors in multi-sensing applications, including temperature, pressure [*8*], strain [*9*], stress [*10*], and auditory signals. Their growing significance lies in several key advantages: lightweight design, high sensitivity, cost-effectiveness, immunity to electromagnetic interference, and the ability to support multiplexed sensor networks, making them highly suitable for a wide range of applications [*4*–*7*]. Unlike conventional fibre sensors, PCF-based sensors offer improved sensitivity and performance by adjusting structural parameters. Optimizing performance can be achieved by modifying factors such as pitch, diameter, number of rings of air holes, and thickness of the plasmonic material (in the case of surface plasmon-based PCF sensors) [*11*]. These features enable PCFs to be used for a wide array of sensing applications where high precision and sensitivity are crucial. The ability of PCFs to integrate multiple sensing capabilities into a single fibre structure has sparked significant interest in the development of dual-core photonic crystal fibre (DC-PCF) sensors [*12*]. The dual-core structure causes

CONTACT Ajeet Kumar ajeetdph@dtu.ac.in Advanced Photonics Simulation Research Lab, Department of Applied Physics, Delhi Technological University, Delhi 110042, India

© 2025 Informa UK Limited, trading as Taylor & Francis Group

an asymmetry that increases birefringence, which is helpful for polarization-based sensing and communication. These sensors have been applied in various fields, such as biosensing [13], temperature sensing [14], pressure sensing, and refractive index sensing [15]. In particular, DC-PCF-based temperature sensors, which operate on the principle of the thermo-optic effect, have shown great potential due to their sensitivity to changes in temperature [16]. There are several methods available to determine the sensitivity of PCF-based temperature sensors. Common approaches include calculating sensitivity by measuring the peak shift in the transmission spectrum caused by thermal effects [17] and assessing sensitivity based on changes in the birefringence of PCFs [18]. Numerous research organizations have actively pursued the improvement of dual core-PCF's temperature sensitivity. Chaudhary et al. investigated a temperature sensor based on a twin-core photonic crystal fibre and demonstrated a temperature sensitivity of approximately 21.5 pm/^{0}C over a range of 0–1200°C [12]. S. Jegadeesan et al. studied a temperature and pressure sensor utilizing dual-core microstructure photonic crystal fibre, achieving a temperature sensitivity of approximately 20 pm/^{0}C across a range of 0–1000°C [19]. S. Revathi et al. proposed a pressure and temperature sensor based on a dual-core Photonic Quasi-crystal fibre and obtained a temperature sensitivity of about 20 pm/^{0}C over the range of 0–1000°C [20]. D. Chen et al. showed a dual-core PCF-based pressure and temperature sensor, which demonstrated a temperature sensitivity of approximately 20.7 pm/^{0}C over a range of 0–1000 °C [21]. Choudhary et al. developed a temperature sensor using a twin-core PCF, achieving a temperature sensitivity of approximately 20 pm/°C within a range of 0-1000°C [22]. Cheng et al. developed a high-sensitivity temperature sensor using a highly birefringent PCF, achieving a temperature sensitivity of approximately 8.01 nm/°C within the – 20–20°C range [18]. Jiang et al. introduced a high-sensitivity temperature sensor that uses a tapered hollow-core fibre sealed with PDMS. This sensor achieved a temperature sensitivity of approximately – 3.2321 nm/°C within the 38–48°C range [23].

This work presents the new cross-sectional design of a temperature sensor based on a DC-PCF capable of measuring temperatures up to 1400°C. When light enters the first core, it travels through the DC-PCF and couples into the second core. Currently, temperature-sensitive materials such as silica [24] and TOPAS [25], among others, are being used, with silica having shown exceptional performance in temperature sensing due to its stability and linear response to temperature changes [26]. In particular, silica is highly effective for temperature sensing because its refractive index changes predictably with temperature variations. When the temperature is applied to the DC-PCF, the refractive index of silica changes, leading to a shift in the transmission spectrum, demonstrating the impact of temperature on the sensor. To enhance the performance of the proposed PCF temperature sensor, the geometrical parameters of the PCF are optimized. The theoretical analysis reveals that our PCF-based temperature sensor operates within a range of 0–1400 °C, achieving a maximum temperature sensitivity of 25 pm/°C, making it highly suitable for high-precision temperature control. This results in the calculation of temperature sensitivity. In comparison to other temperature sensors in the literature, the proposed sensor shows stable sensitivity across a broad temperature range. Adjusting the structural parameters has achieved an optimal design for maximum sensitivity. Our design offers superior temperature sensitivity and compact size compared to other optical fibre temperature sensors. Notably, its temperature sensitivity is higher than that of previously reported sensors. This work provides a valuable reference for related experimental research and the development of high-performance PCF temperature sensors.

2. Geometry analysis

This paper examines the temperature-sensing characteristics of the proposed cross-sectional PCF design, using the full vector FEM to enhance its sensing capabilities. The finite element method is particularly effective for analyzing photonic crystal fibres with various shapes, sizes, and porosity patterns [27]. Thus, we have used this method to numerically analyze the performance of the optical fibre temperature sensor in our study**.** The proposed DC-PCF features dual-fibre cores separated by a ring of air holes. The suggested DC-PCF's structure is shown in Figure 1. In the cross-section, the symmetrical cores P and Q are aligned horizontally. These air holes enable the structure to function as dual waveguides. Regular hexagonal large air holes generally surround the cladding layer, and the diameter is d_1. We have positioned the inner air holes (d_2) and the smaller air holes (d_3) to create a dual-core fibre structure within the PCF. The central core has a diameter (d_4), and a ring of smaller circular air holes is arranged around this central diameter (d_4), forming the dual-core configuration. The middle air hole's (d_2) lattice constant is set to Λ_2, the small air hole's (d_3) lattice constant is set to Λ_3, and the lattice constant of d_1 is set to Λ_1. The purpose of these air holes is to keep the light well confined within the two cores. After simulation study, the ideal parameters are calculated as $d_1 = 2$ µm, $\Lambda_1 = 3$ µm, $d_2 = 1.6$ µm, $\Lambda_2 = 2$ µm, $d_3 = 1$ µm, $\Lambda_3 = 5.8$ µm and $d_4 =$

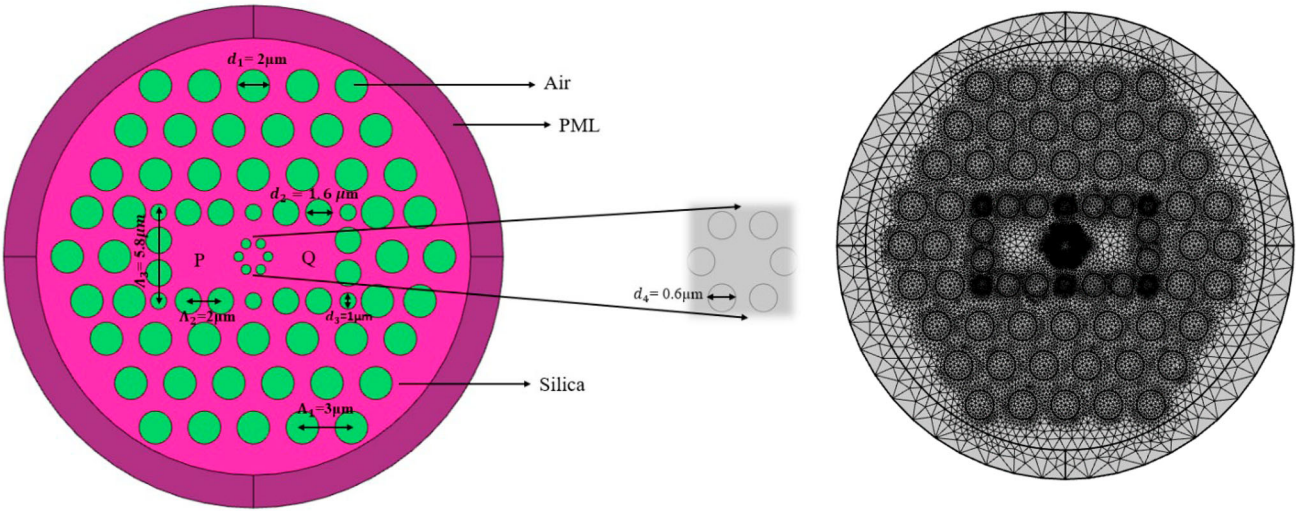

Figure 1. A cross-sectional view of the geometry structure of the dual-core PCF temperature sensor and mesh of temperature sensor.

0.6 µm. As illustrated in Figure 1, the meshing statistics for the proposed PCF design included 1,916 edge elements, 296 vertex elements, and 25,448 triangular elements. The surrounding medium's refractive index (R.I.) significantly influences the propagation of light within the core region. As a result, varying the temperature range from 0 to 1400°C leads to a noticeable shift in coupling length, transmission curve, and birefringence [28]. The material properties play a crucial role in the numerical analysis of temperature-sensing characteristics. Here, we have outlined the material models used for silica and air. Silica, which serves as the cladding material in the proposed PCF sensor, is described using the theoretical model known as the Sellmeier formula.

$$n^2_{fusedsilica}(\lambda) = 1 + \frac{P_1\lambda^2}{\lambda^2 - Q_1} + \frac{P_2\lambda^2}{\lambda^2 - Q_2} + \frac{P_3\lambda^2}{\lambda^2 - Q_3} \quad (1)$$

The symbol λ represents the operational wavelength in µm, and the Sellmeier coefficients are:$P_1 = 0.696166300$, $P_2 = 0.407942600$,$P_3 = 0.897479400$, $Q_1 = 4.67914826 \times 10^{-3}\mu m^2$, $Q_2 = 1.35120631 \times 10^{-2}\mu m^2$ and $Q_3 = 97.9340025\mu m^2$ respectively [29].

3. Schematic diagram for dual-core temperature sensor

Figure 2 shows the schematic diagram of the PCF sensor configuration. Essential instruments include an optical spectrum analyzer (OSA), temperature controller, and broadband light source. A broadband light source connected via a single-mode fibre (SMF) can be used to introduce light into fibre core P of the proposed DC-PCF. The output signal from fibre core Q can then be observed through an additional SMF using an optical spectrum analyzer. As the temperature-sensitive silica material responds to changes in temperature, its refractive index shifts, causing variations in the transmission spectrum recorded by the OSA. The transmission spectrum is displayed on a laptop connected to the OSA, while a temperature control module in the setup simulates different ambient temperatures to study these changes [30]. With temperature control, one can modify the PCF's surrounding environment temperature.

4. Results analysis

The dual fibre cores within the PCF form two waveguides, each of which is independent of the other (accompanied by a coupling mode) because of the small core-to-core length. The proposed sensor model is analyzed using COMSOL Multiphysics software, which has also been used to calculate all relevant optical properties. We have calculated the birefringence, coupling length, confinement loss**,** power transmission, and wavelength sensitivity of the sensor. Figure 3 illustrates the electric field vector and amplitude distribution for the DC-PCF in the following modes: (a) x-pol. even mode (b) x-pol. odd mode and (c) y-pol. even mode and (d) y-pol. odd mode. These super-modes are responsible for the coupling effect seen in DC-PCF. The transmission power spectrum is analyzed to evaluate the sensing performance of the proposed dual-core PCF sensor. Temperature sensing is observed at specific wavelengths by monitoring the

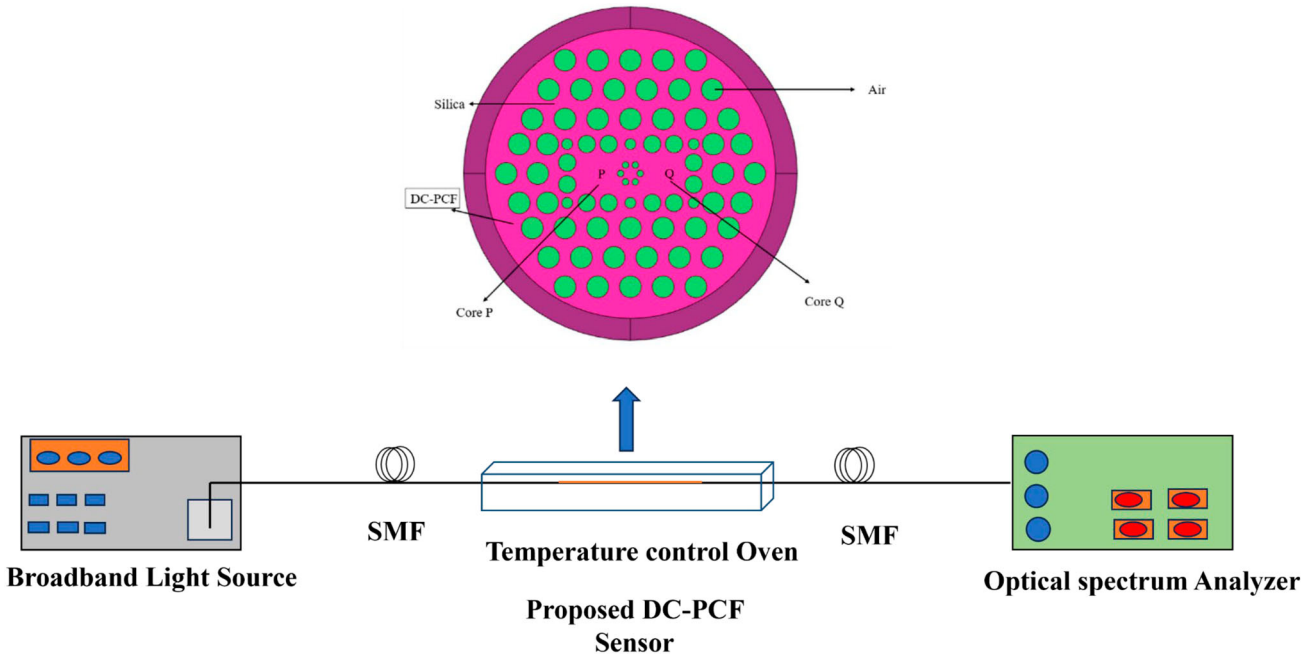

Figure 2. Schematic diagram of DC-PCF setup of the temperature sensing.

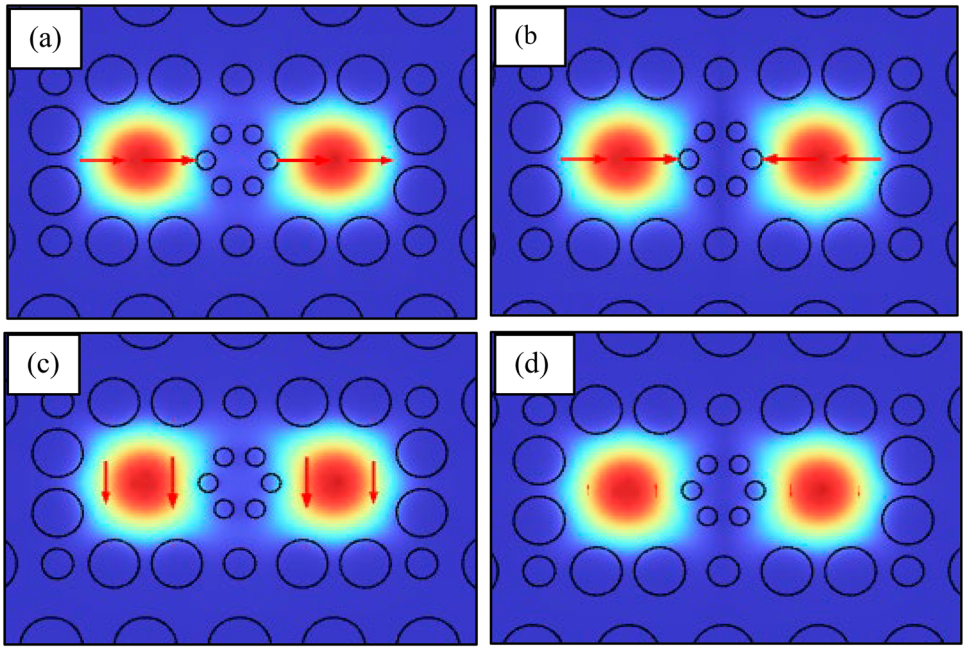

Figure 3. Electric field distribution of the DC-PCF for (a) x-pol even mode, (b) x-pol odd mode, (c) y-pol even mode, (d) y-pol odd mode

shift in the transmission power spectrum corresponding to the changes in temperature.

We had initially examined how the wavelength affects the effective mode index of the propagating mode for x-polarization over a temperature range of 0°C to 1400°C. Specifically, at a wavelength of 1.55 µm, the effective mode index for the even modes of x-polarization is 1.4237, while for the odd modes, it is 1.4238. In comparison, for y-polarization, the effective mode index for the even modes is 1.4239, and for the odd modes, it is 1.4241. Figure 4 shows that the effective mode index decreases with an increase in wavelength. It also shows the variation in n_{eff} across the even and odd modes for both x- and y-polarizations as the wavelength changes [31]. Furthermore, the effective mode index for y-polarization (even and odd mode) is higher than that for x-polarization (even and odd mode) but decreases as the temperature increases.

Figure 5 shows the variation of the effective mode index difference between the even and odd modes

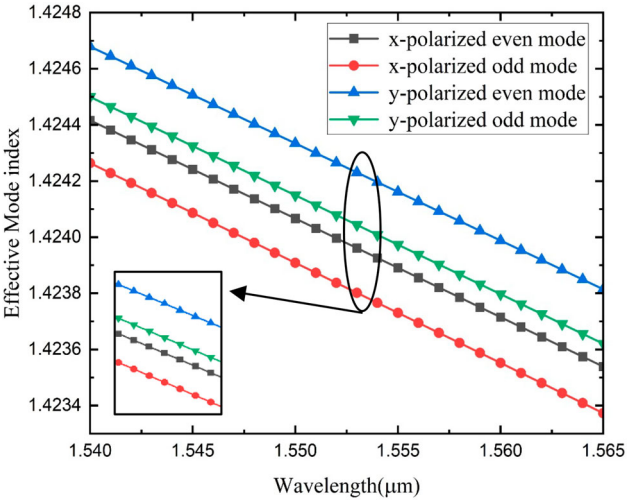

Figure 4. The change in the effective mode index (n_{eff}) as a function of wavelength.

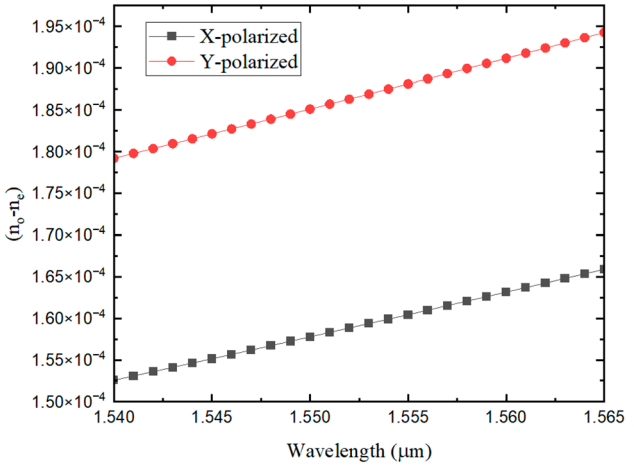

Figure 5. The change in ($n_e - n_o$) with wavelength.

($\Delta n_{eo} = |n_{even} - n_{odd}|$) for both x- and y- polarized directions. The variation in the effective mode index of x-polarized light in the proposed PCF is observed across a wavelength range of 1.540 µm to 1.565 µm. The effective mode index difference increases with increasing wavelength, but the effective mode index difference increases and shifts upward by increasing the temperature range from 0°C to 1400°C. This increase in Δn_{eo} in the dual-core DC-PCF indicates that light becomes more tightly confined within the core [12].

Birefringence is the difference in the effective mode index for different modes of x-polarization and y-polarization. This difference can be determined using a specific formula.

$$B = |Re(n_{eff}^{x}) - Re(n_{eff}^{y})| \tag{2}$$

where Re denotes the effective mode index's real component and n_{eff}^{x} and n_{eff}^{y} respectively, are the effective mode

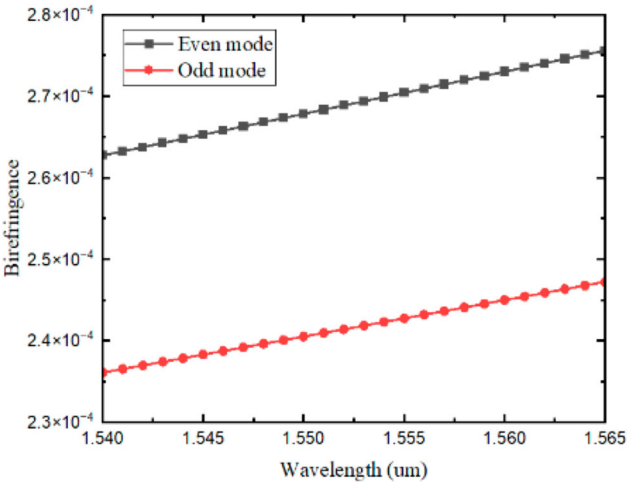

Figure 6. Birefringence variation as a function of applied wavelength.

indices in the x- and y-polarizations [32]. Figure 6 shows the relationship between birefringence and wavelength. In our design, birefringence results from the asymmetricity between the core and the air holes within the fibre cladding [33]. As wavelength increases, birefringence also rises in both x- and y-polarizations. Due to the horizontal alignment of the two fibre cores, the variation in the effective mode index is more significant in the x-polarization direction. The x- and y-polarized coupling lengths are almost equivalent when low birefringence makes light splitting difficult. Consequently, birefringence is higher in x-polarization than in y-polarization [34]. The birefringence in the proposed sensor ranges from 2.36×10^{-4} to 2.7×10^{-4}, following an upward trend. Both the sensitivity and coupling length of this design are directly connected to its birefringence. Starting at 2.36×10^{-4}, the birefringence increases linearly with increasing wavelength, reaching a maximum value of 2.7×10^{-4}.

The coupling length is the shortest distance at which light can be effectively transmitted through the core of a photonic crystal fibre (PCF). This length applies to both x- and y-polarization and can be calculated using Eq. (3) [12].

$$L_C = \frac{\pi}{|\beta_{even}^{i} - \beta_{odd}^{i}|} = \frac{\lambda}{2|n_{even}^{i} - n_{odd}^{i}|} \tag{3}$$

For each $i = x, y$ polarization, the DC-PCF's even and odd mode propagation constants are β_{even}^{i} and β_{odd}^{i}, appropriate. The terms n_{even}^{i} and n_{odd}^{i} denote the even and odd mode effective mode indices and λ denotes the wavelength [35, 36]. By applying Eq. (3) across various wavelengths, we have calculated the coupling length curves for both x- and y-polarized modes. The coupling

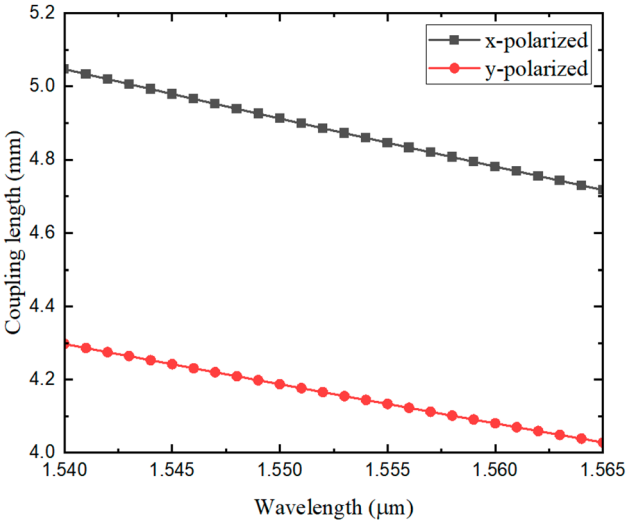

Figure 7. The coupling length changes as a function of wavelength.

length represents the distance over which power transfer occurs between two distinct fibre cores [37]. Figure 7 illustrates the relationship between coupling length and wavelength for both polarizations. It is clear that as the wavelength increases, the coupling length decreases for both modes. Consequently, the transmission spectrum peak for x-polarization shifts more sensitively, demonstrating higher sensitivity.

Confinement loss (CL) refers to the propagation loss caused by leakage and determines the light confinement ability of any PCF. A lower confinement loss indicates better confinement, which is essential for any PCF-based sensor. CL depends on the imaginary part of the effective mode index and is expressed as follows.

$$CL = \frac{20}{\ln 10}\frac{2\pi}{\lambda}\mathrm{Im}(n_{eff}) = 8.686k\mathrm{Im}[n_{eff}] \quad (4)$$

where the effective mode index's imaginary part is denoted by $Im[n_{eff}]$ and λ indicates the wavelength, and k is the propagation constant ($k = \frac{2\pi}{\lambda}$) in free space [29]. Using Eq. (4), the confinement loss (CL) of the proposed DC-PCF is calculated. For the x- and y-polarized even and odd modes, the CL at a wavelength of 1.555μm is as follows: $8.49\times10^{-08}dB/m$ for the x-polarized even mode, $9.01\times10^{-08}dB/m$ for the y-polarized even mode, $1.58\times10^{-07}dB/m$ for the x-polarized odd mode, and $1.73\times10^{-07}dB/m$ for the y-polarized odd mode.

As optical power is transmitted through the PCF, mode coupling occurs between the two fibre cores. As a result of this coupling, a transmission curve is observed at the output of the PCF, reflecting the interaction between the modes in the two cores [38]. The DC-PCF power transfer $P_{out}(\lambda)$ is calculated using Eq. (5)

$$P_{out}(\lambda) = \sin^2\left(\frac{|n_e - n_o|\pi z}{\lambda}\right) \quad (5)$$

Here, $\Delta n_{eo} = |n_e - n_o|$. In this context, z represents the distance between the cores, λ and denotes the operating wavelength. The maximum value of the transmission curve reaches unity and exhibits a sinusoidal pattern. The optical power of the proposed dual-core photonic crystal fibre (DC-PCF) comprises both x-and y-polarizations. Figure 8 shows the relationship between power transmission and wavelength. From Eq. (5), we observe that the transmission spectrum follows a sinusoidal pattern. The total transmitted optical power should be described in terms of this sinusoidal curve's peak and trough values rather than using a fixed unit. The transmission spectra of an 8 cm-long DC-PCF operating within the wavelength range of 1.506μm to 1.570μm at temperatures ranging from 0°C to 1400°C. The shifting of peaks in response to temperature increases detected over a broad range of 0–1400°C is used to determine the sensitivity of the proposed DC-PCF for temperature sensing. Figure 8 shows the peak wavelength shift ($\Delta\lambda_{peak}$) for temperature variations ranging from 0°C to 1400°C. The corresponding wavelength shifts are observed at 1.520, 1.525, 1.530, 1.535, 1.540, 1.545, 1.550, and 1.555 micrometers.

The overall sensitivity is determined by analyzing the correlation between the shifts in wavelength peaks and the corresponding variations in temperature.

$$S_\lambda(\mu mRIU^{-1}) = \frac{\Delta\lambda_{peak}}{\Delta T} \quad (6)$$

where ΔT is the overall temperature change, and $\Delta\lambda_{peak}$ denotes the complete shift in peak wavelength for temperature variation [39]. The sensitivity of the temperature sensor is determined by measuring the shift in

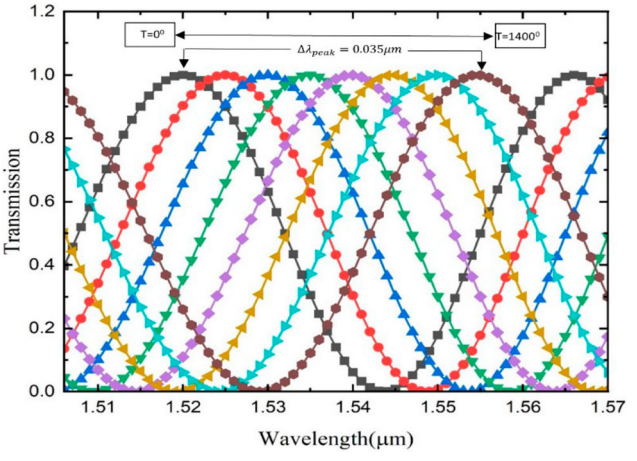

Figure 8. Transmission spectrum of an 8 cm DC-PCF as a function of applied temperature versus operating wavelength.

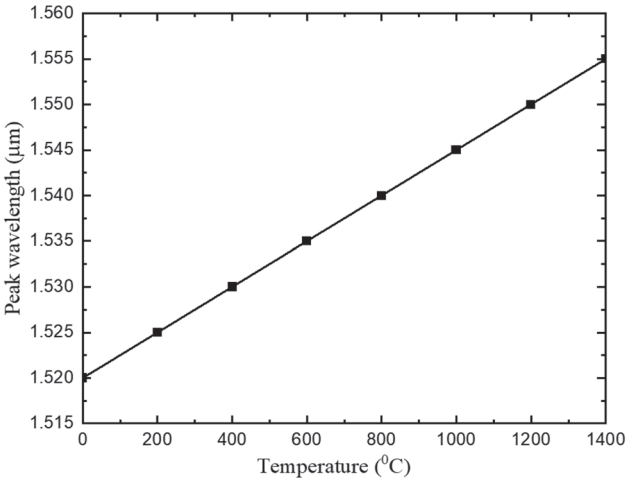

Figure 9. The correlation between the applied temperature (°C) and the peak wavelength of the transmission spectrum.

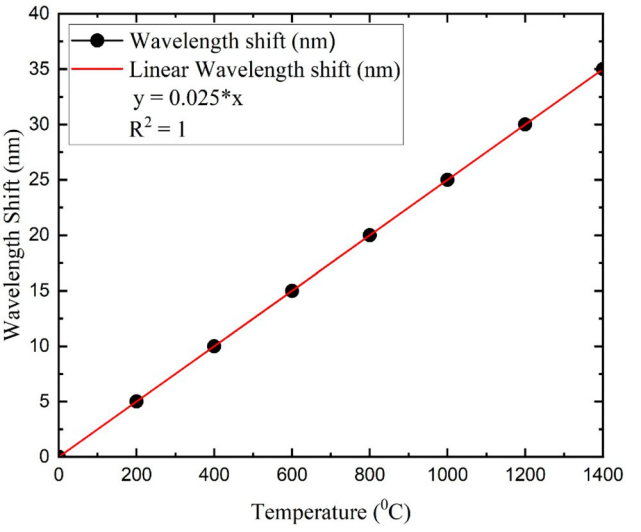

Figure 10. The numerical line fitting for an 8 cm DC – PCF over a temperature range from 0°C to 1400°C.

peak wavelength over the temperature range from 0°C to 1400°C for each value within that range. For x-polarization, this sensor achieves a sensitivity of approximately 25 pm/°C. This high sensitivity is achieved through the use of a very short coupling length, measured in the millimetre range.

When the fibre is heated, the thermo-optic effect induces a small variation in the refractive index of the DC-PCF above room temperature. Silica, as a ceramic, has absorbing applications as a filler in composites due to its nearly negligible thermal expansion. Eq. (7) is used to find the relationship between the applied temperature and refractive index [40].

$$n = n_0 + T\frac{dn}{dt} \tag{7}$$

where n_0 is the pure silica's RI at 0 degrees Celsius, the following formula is used to determine silica's thermo-optic coefficient [34].

$$\frac{dn}{dt} = 10^{-5}(1/^0C) \tag{8}$$

For the temperature range of 0–1400 °C, Figure 9 illustrates the wavelength peak shift, showing a linear increase toward higher wavelengths as the temperature rises.

Figure 10 shows the numerical fitting of wavelength shifts in the DC-PCF transmission curve under applied temperature. As the temperature rises from 0°C to 1400°C, the peak wavelength shifts to higher values, reflecting a positive slope in the linear fit of the wavelength peak [12]. For an 8 cm fibre, the dual-core PCF achieves a temperature sensitivity of 25 pm/°C.

5. Effect of diameter changes on sensitivity

Within the sensor's temperature range of 0–1400^{0}C. The power transmission graph for the DC-PCF spanning in the x-polarized mode is displayed in Figure 11. The DC-PCF has air holes with variable diameters and a length of 8 cm. Based on Figure 11, which illustrates changes within ±0.2 µm throughout a temperature sensing range of 0-1400^{0}C, the dual-core PCF may reach a temperature sensitivity of around 20 pm/^{0}C at d_1 = 1.8 µm, 25 pm/^{0}C at d_1 = 2 µm, and 21.4 pm/^{0}C at d_1 = 2.2 µm, respectively. The graph illustrates that when the diameter of the hole rings is assumed to be 1.8 µm, a red shift toward a higher wavelength is noticed, and when the diameter of the hole rings is assumed to be 2.2 µm, a blue shift toward a lower wavelength is noted. Figure 12 shows the diameter ±0.2 µm variation in the transmittance curve of DC-PCF for the x-polarized mode with varied diameters. The suggested DC-PCF obtains a sensitivity of around 20 pm/^{0}C at diameter (d_2) = 1.4 µm, 25pm/^{0}C at diameter (d_2) = 1.6 µm, and 20 pm/^{0}C at diameter (d_2) = 1.8 µm, respectively. The suggested DC-PCF sensor can reach its highest sensitivity at d_2 = 1.6 µm by adjusting the diameter. Figure 13 depicts the DC-PCF transmission curve with different fibre diameters, 0.8, 1, and 1.2 µm, respectively. The sensitivity values of around 20 pm/^{0}C at d_3 = 0.8 µm, 20.5 pm/^{0}C at d_3 = 1.2 µm, and 25 pm/^{0}C at d_3 = 1 µm can be achieved by the suggested DC-PCF and the same analysis is tabulated in Table 1. The DC-PCF sensor that has been suggested has better sensitivity at d_3 = 1 µm, according to diameter optimization [12]. Table 2 displays some previous published research work based on temperature sensing and

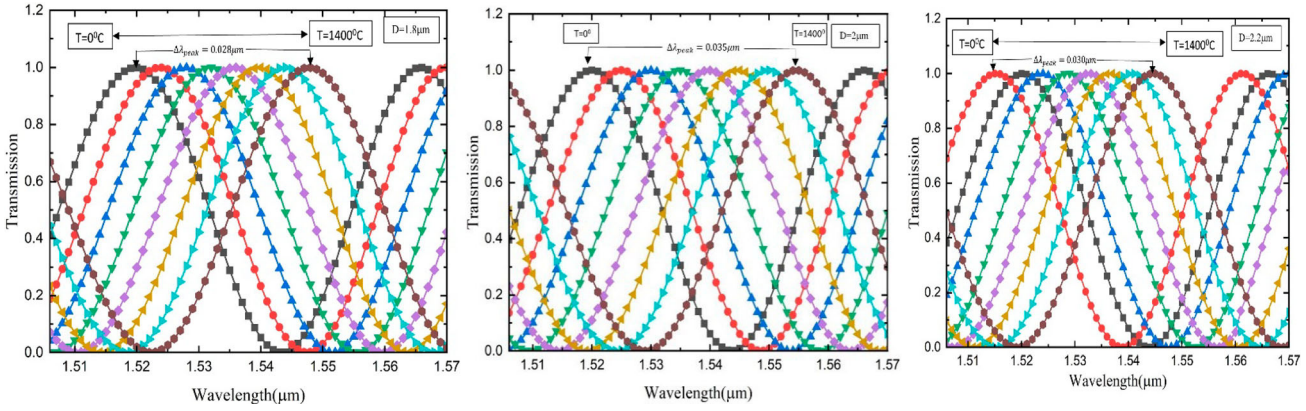

Figure 11. Shows the DC-PCF transmission curve with distinct diameters of d = 1.8 μm, d = 2 μm, and d = 2.2 μm.

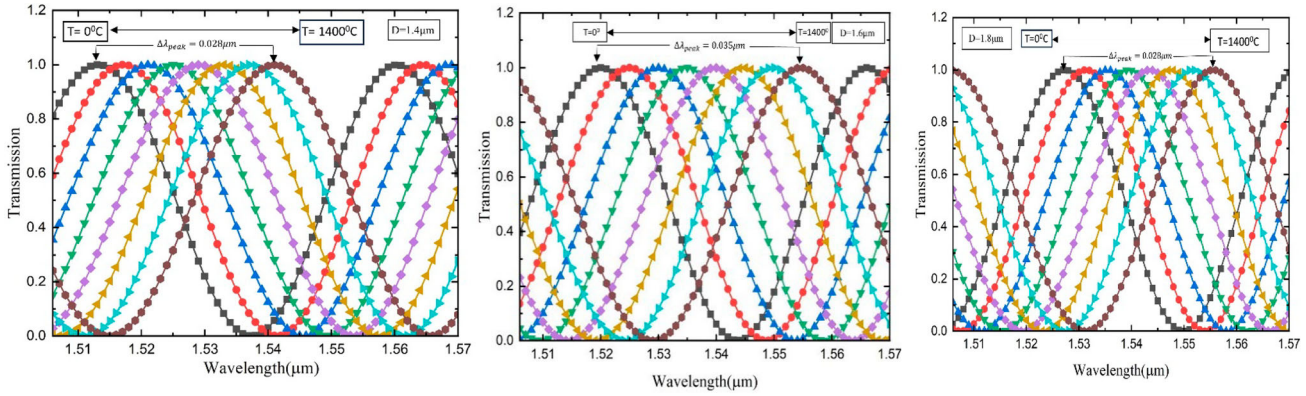

Figure 12. Shows the DC-PCF transmission curve with different diameters of d = 1.4 μm, d = 1.6 μm, and d = 1.8 μm.

also focuses on the superior performance of our proposed PCF sensor.

6. Conclusion

The proposed dual-core PCF-based, extremely sensitive temperature sensor operates effectively across a broad temperature range. We have attributed the improved sensitivity to our proposed structure's unique configuration of circular air holes. Using a silica background, various optical parameters of the proposed temperature sensor model have been examined over the temperature

Table 1. Sensitivity comparison of the suggested DC-PCF at various diameters.

d_1 (μm)	Sensitivity (pm/^{0}C)	d_2 (μm)	Sensitivity (pm/^{0}C)	d_3 (μm)	Sensitivity (pm/^{0}C)
1.8	20	1.8	20	0.8	20
2	25	1.6	25	1	25
2.2	21.4	1.4	20	1.2	20.5

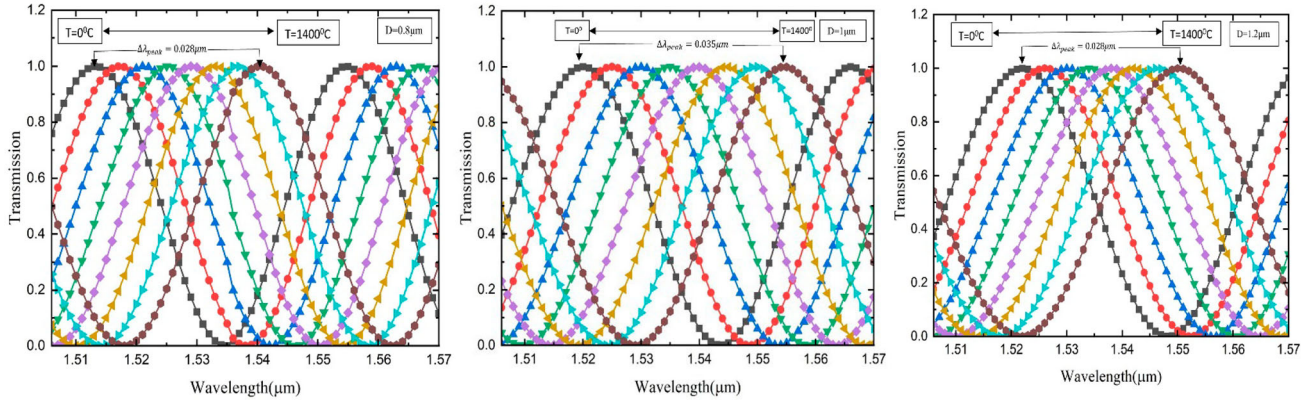

Figure 13. Shows the DC-PCF transmission curve with different diameters of d = 0.8 μm, d = 1 μm, and d = 1.2 μm.

Table 2. The performance of other PCF sensors and the suggested PCF sensor are contrasted.

Reference	PCF Structure	Sensitivity (pm/°C)	Temperature range (°C)
[20]	Dual-core photonic quasi-crystal fibre	20	0–1000
[22]	Twin core PCF	18.5	0–600
[12]	Twin core PCF	21.5	0–1200
[19]	Dual-core – PCF	20	0–1000
[21]	Dual-core – PCF	20.7	0–1000
[41]	Silica glass solid-core PCF	15.61	0–1000
Proposed PCF	Dual-core PCF	25	0–1400

range of 0^0C to 1400^0C. All numerical calculations were conducted using a FEM-based approach with COMSOL Multiphysics software. Using the thermo-optic coefficient equation, the R.I. of pure silica at different temperatures is determined. Additionally, calculating the coupling length and transmission spectrum helps to evaluate the temperature sensitivity of the proposed PCF. Temperature sensitivity of around 25 pm/^{0}C has been achieved by the proposed PCF with an 8 cm fibre length, operating across a wide temperature sensing range of 0–1400^0C. The proposed DC-PCF can be fabricated using existing PCF manufacturing techniques.

Acknowledgments

Shubham Sharma highly acknowledges the support from the Delhi Technological University, Delhi, for providing the research fellowship and necessary support to conduct this research work.

Disclosure statement

No potential conflict of interest was reported by the author(s).

References

[1] Siddik AB, Hossain S, Paul AK, et al. High sensitivity property of dual-core photonic crystal fiber temperature sensor based on surface plasmon resonance. Sens Biosensing Res. **2020**;29:100350.
[2] Liu E, Liu J. Quasiperiodic photonic crystal fiber. Chin Opt Lett. **2023**;21(6):060603.
[3] Vatani S, Biney J, Faramarzi V, et al. Advances in plasmonic photonic crystal fiber biosensors: exploring innovative materials for bioimaging and environmental monitoring. Chem Select. **2024**;9(28):e202401265.
[4] Giallorenzi TG, Bucaro JA, Dandridge A, et al. Optical fiber sensor technology. IEEE Trans Microwave Theory Tech. **1982**;30:472–511.
[5] Krohn DA, MacDougall T, Mendez A. Fiber optic sensors: fundamentals and applications. Bellingham (WA): Spie Press; 2014, 4.
[6] Udd E, Spillman WB., editors. Fiber optic sensors: an introduction for engineers and scientists. Hoboken, New Jersey: John Wiley & Sons; 2024.
[7] Fidanboylu K, Efendioglu HS. Fiber optic sensors and their applications. In 5th Int Adv Technol Symp (IATS'09). **2009**;6:2–3.
[8] Gao J, Jiang C, Li L, et al. High sensitivity temperature and gas pressure sensor based on PDMS sealed tapered hollow-core fiber. Opt Fiber Technol. **2024**;82:103634.
[9] Hou M, Wang Y, Liu S, et al. Multi-components interferometer based on partially filled dual-core photonic crystal fiber for temperature and strain sensing. IEEE Sensors J. **2016**;16(16):6192–6196.
[10] Yu X, Shum P. A novel stress and strain sensor based on triple-core photonic crystal fiber. Adv Sens Syst Appl II. **2005**;5634:571–578. SPIE.
[11] Rahman KM, Shah Alam M, Ahmed R, et al. Irregular hexagonal core-based surface plasmon resonance sensor in the near-infrared region. Results Phys. **2021**;23:103983.
[12] Chaudhary V, Singh S. Twin core photonic crystal fiber-based temperature sensor with improved sensitivity over a wide range of temperature. Opt Quantum Electron. **2023**;55(1):53.
[13] Azman MF, Mashrafi M, Haider F, et al. Polarization selective PCF-based plasmonic biosensor for multi-analyte detection. Plasmonics. **2024**: 1–10.
[14] You Q, Pan H, Zhao Z, et al. Highly sensitive wide detection range semicircular convex slot PCF temperature sensor based on surface plasmon resonance. IEEE Sensors J. **2024**.
[15] Liu J, Dong J, Liu Q, et al. High-Performance gold-nanowires-coated PCF-SPR sensor for refractive index detection. Plasmonics. **2024**: 1–10.
[16] Zhao Y, Deng Z-q, Li J. Photonic crystal fiber-based surface plasmon resonance chemical sensors. Sens Actuators, B. **2014**;202:557–567.
[17] Yan L, Wang Q, Yin B, et al. Research on simultaneous measurement of magnetic field and temperature based on petaloid photonic crystal fiber sensor. Sensors. **2023**;23(18):7940.
[18] Cheng Q, Fan S, Guan Y, et al. Enhanced sensitivity of temperature sensor by a novel birefringent photonic crystal fiber with PDMS filling. Opt Commun. **2024**;565:130697.
[19] Jegadeesan S, Dhamodaran M, Shanmugapriya SS. Numerical analysis of dual-core photonic crystal fiber-based temperature and pressure sensor for oceanic applications. Opt Appl. **2019**;2:49.
[20] Revathi S, Inabathini SR, Pal J. Pressure and temperature sensor based on a dual-core photonic quasi-crystal fiber. Optik (Stuttg). **2015**;126(22):3395–3399.
[21] Chen D, Hu G, Chen L. Pressure/temperature sensor based on a dual-core photonic crystal fiber). 2011 Asia communications and photonics conference and exhibition (ACP), IEEE, 2011, 1–10.
[22] Chaudhary VS, Kumar D, Mishra R, et al. Twin core photonic crystal fiber for temperature sensing. Mater Today Proc. **2020**;33:2289–2292.
[23] Gao J, Jiang C, Li L, et al. High sensitivity temperature and gas pressure sensor based on PDMS sealed tapered hollow-core fiber. Opt Fiber Technol. **2024**;82:103634.
[24] Singh G, Sharma S, Kumar A. Design and simulation of solid-core octagonal photonic crystal fiber for

terahertz wave propagation. Microw Opt Technol Lett. **2024**;66(5):e34173.
[25] Hossain MS, Hossen R, Al-Amin M, et al. Evaluation of THz wave transmission performance in TOPAS-based heptagonal photonic crystal fiber (He-PCF). Heliyon. **2024**;10(3.
[26] Gao S, Wei K, Yang H, et al. Design of surface plasmon resonance-based D-type double open-loop channels PCF for temperature sensing. Sensors. **2023**;23(17):7569.
[27] Fu S, Jin W, Liu L, et al. Ultrahigh sensitivity surface plasmonic resonance temperature sensor based on polydimethylsiloxane-coated photonic crystal fiber. Plasmonics. **2024**: 1–13.
[28] Wang Y, Yan X, Cheng T, et al. High sensitivity with wide detection range refractive index sensor based on dual-core photonic crystal fiber. J Opt. **2022**: 1–11.
[29] Rifat AA, Amouzad Mahdiraji G, Sua YM, et al. Highly sensitive multi-core flat fiber surface plasmon resonance refractive index sensor. Opt Express. **2016**;24(3): 2485–2495.
[30] Chaudhary V, Singh S, Chaudhary VS, et al. Design and optimization of terahertz-based d-shaped photonic crystal fiber for blood component detection. IEEE Sensors J. **2024**.
[31] Gamal Y, Younis BM, Hegazy SF, et al. Highly sensitive multi-functional plasmonic biosensor based on dual-core photonic crystal fiber. IEEE Sensors J. **2022**;22(7): 6731–6738.
[32] Liu Z, Wen J, Zhou Z, et al. A highly birefringent photonic crystal fiber with three rows of circular air holes. In Photonics. **2023**;10:527, MDPI.
[33] Garg D, Singh J, Kumar A. Design and theoretical study of rectangular photonic crystal fiber-based sensor for chemical sensing in the terahertz regime. Indian J Phys. **2024**: 1–9.
[34] Ji Y, Du Y, Dai J, et al. Dual-Core photonic crystal fiber polarization beam splitter based on a nematic liquid crystal with an ultra-short length and ultra-wide bandwidth. Electronics (Basel). **2024**;13(12):2343.
[35] Saitoh K, Sato Y, Koshiba M. Coupling characteristics of dual-core photonic crystal fiber couplers. Opt Express. **2003**;11(24):3188–3195.
[36] Wang Z, Taru T, Birks TA, et al. Coupling in dual-core photonic bandgap fibers: theory and experiment. Opt Express. **2007**;15(8):4795–4803.
[37] Pravesh R, Kumar D, Pandey BP, et al. Design and analysis of a double D-shaped dual-core PCF sensor for detecting biomolecules in the human body. IEEE Sensors J. **2024**.
[38] Russell PSJ. Photonic-crystal fibers. J Lightwave Technol. **2006**;24(12):4729–4749.
[39] Gauvreau B, Hassani A, Fehri MF, et al. Photonic bandgap fiber-based surface plasmon resonance sensors. Opt Express. **2007**;15(18):11413–11426.
[40] Rodrigues LM, Marinkovic BA. Effects of fused silica addition on thermal expansion, density, and hardness of alumix-231 based composites. Materials (Basel). **2022**;15(10):3476.
[41] Yu H, Wang Y, Ma J, et al. Fabry-Perot interferometric high-temperature sensing up to 1200 C based on a silica glass photonic crystal fiber. Sensors. **2018**;18(1): 273.

Journal of Information & Optimization Sciences
ISSN 0252-2667 (Print), ISSN 2169-0103 (Online)
Vol. 46 (2025), No. 1, pp. 53-64
DOI : 10.47974/JIOS-1851

Design of an array multiplier in PFSCL style

Shikha *
Department of Electronics and Communication Engineering
Bharati Vidyapeeth's College of Engineering
Paschim Vihar 110063
New Delhi
India

and

Department of Electronics and Communication Engineering
Delhi Technological University
Rohini 110042
Delhi
India

Kirti Gupta †
Department of Electronics and Communication Engineering
Bharati Vidyapeeth's College of Engineering
Paschim Vihar 110063
New Delhi
India

Monica Gupta ‡
Department of Electronics and Communication Engineering
Bharati Vidyapeeth's College of Engineering
Paschim Vihar 110063
New Delhi
India

* *E-mail:* **shikha.bvcoe@bharatividyapeeth.edu (Corresponding Author)**
† *E-mail:* **kirti.gupta@bharatividyapeeth.edu**
‡ *E-mail:* **monica.gupta@bharatividyapeeth.edu**

© Taru Publications

Preeti Nagrath [#]
Department of Computer Science and Engineering
Bharati Vidyapeeth's College of Engineering
Paschim Vihar 110063
New Delhi
India

Bhawanand Jha [§]
Department of Electronics and Communication Engineering
Bharati Vidyapeeth's College of Engineering
Paschim Vihar 110063
New Delhi
India

Prakhar Sharma [@]
Department of Design
4 MediaTek
U.S.A.

Mauro Zannetti [^]
Department of Industrial & Information Engineering and Economics
University of L'Aquila
I-67100 L'Aquila
Italy

Abstract

In intergreted circuit design, the current trend is to create circuits that work well for both digital and analog (mixed signal) applications. The PFSCL has been a optimum choice in these applications. This paper proposed three different architectures of 2-bit array multiplier in PFSCL style. The architecture-1 uses PFSCL NOR/OR gates, the architecture-2 uses PFSCL Fundamental cell (FC), and the last architecture-3 integrates memristors with PFSCL design circuit. All proposed architectures are simulated in LT Spice tool with 90nm PTM technology. Out of all the proposed architectures, architecture-3 observes the most efficient in all the performance parameter. The proposed architecture-3 observes maximum reduction of 39 %, 66 % in paramter like delay and power consumption respectively, additionally, offers a maximum area saving of 97 % as compared to proposed architecture-2.

Subject Classification: *94C11.*

Keywords: *Mixed-signal design, Digital circuits, PFSCL, Fundamental cell, Memristor.*

This article has been corrected with minor changes. These changes do not impact the academic content of the article.

[#] *E-mail:* **preeti.nagrath@bharatividyapeeth.edu**
[§] *E-mail:* **bhawanand.jha@bharatividyapeeth.edu**
[@] *E-mail:* **prakhar.sharma@mediatek.com**
[^] *E-mail:* **mauro.zannetti@univaq.it**

1. Introduction

Advancements in fabrication have enabled the mixing of billions of components on a solo chip, enhancing performance and reducing costs. CMOS technology remains dominant in VLSI due to its high speed and low static power consumption [1-3]. However, scaling CMOS faces challenges, such as balancing power and speed, and addressing switching noise caused by significant current during transitions. These issues drive the need for alternative design approaches to support mixed-signal IC integration.

Researchers have explored alternative logic styles, with PFSCL system have analog and digital circuits fabricated on the same substrate being a suitable choice in mixed-signal environments due to its high-speed advantages [4-8]. PFSCL gates utilize a constant current source, ensuring stable power consumption, and various PFSCL circuits like adders, serializers, and flip-flops have been proposed [9-15]. However, multiplier designs in PFSCL remain unexplored. This paper focuses on efficient 2-bit array multiplier architectures in PFSCL, which multiply two 2-bit binary numbers to produce a 4-bit output [16-17]. Three architectures are introduced: using conventional PFSCL NOR/OR gates, PFSCL fundamental cells (FC), and memristors.

The paper has five sections. The first section introduce the benefits in the chosen logic style. An overview of 2-bit array multiplier and conventional PFSCL designs is presented in Section II. Section III presents the different

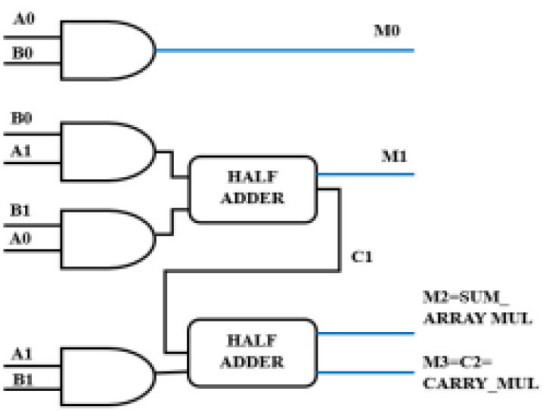

Figure 1

Block diagram of 2-bit array multiplier [16-18]

architectures of 2-bit array multiplier in PFSCL style. Following this, Section IV outlines the performance comparison and functional verification of all the proposed architectures through simulations using 90nm CMOS technology parameters. Lastly, conclusions are drawn in Section V.

2. Basic concepts

This section first briefly presents the concepts related to array multiplier. Thereafter, different schemes to realize PFSCL circuit is presented.

2.1 *Array (2-bit) Multiplier*

An array multiplier is defined in a digital circuit that performs multiplication via a grid of adders and AND gates. A 2-bit array multiplier consists of four AND gates and two half-adders, with carry values added sequentially, as shown in Fig. 1 (a) [16-18]. The whole method of a 2-bit array multiplier can be explained as: For a 2-bit array multiplier, with inputs A = A0A1 and B = B0B1, the product bits (M_3, M_2, M_1, M_0) are calculated as follows: The least significant bit (M (0)) is the result AND operation of A0 by B0. The next bit (M (1)) is obtained by first performing AND operation on (A1B0) and (B1A0). The output of these AND gates is further used for half adder operation to obtain the desired result at M1. This process is repeated for the remaining bits to complete the multiplication.

2.2 *PFSCL style*

Positive Feedback Source Coupled Logic) is a single-ended variant of Source Coupled Logic designed to enhance switching speed compared to traditional SCL implementations. A conventional PFSCL inverter, as illustrated in Fig. 2. It consists of load transistors, the pull-down network (PDN), and bias current source (I_{SS}). The PDN, implemented using transistors M_1 and M_F, is responsible for executing the logic operation. It directs the bias current (I_{SS}) through PDN branches. The PMOS transistors (MP_1) play a crucial role in converting the current into a voltage signal to produce required output. The operation of the PFSCL inverter, is described below:

For the input value (A) is low, I_{SS} flows through the M_F keeping V_{OH} ($V_{OH} = V_{DD}$). When a high A steers I_{SS} through M_1, making ($V_{OL} = V_{DD} - V_{SWING}$).

In the literature, three standard PFSCL configurations have been proposed to realize different using this style [7]. The first is the conventional PFSCL design approach which involves NOR/OR [6-7] gates, the second PFSCL design approach uses fundamental cell (FC) [15] while the third integrated memristor in PFSCL circuit design [18].

2.2.1 NOR/OR PFSCL design

The conventional PFSCL design employs only PFSCL NOR/OR gates. A generic PFSCL NOR/OR gate connects input transistors (A_1, ----A_N) in parallel and source-coupled them to a transistor M_F driven by the gate output as shown in Fig. 3 [6-7,15]. The conventional PFSCL based NOR/OR gates are used for the realization of complex logic functions which are typically built using a series of NOR/OR gates. To implement an XOR2 function, three 2-input gates are required. This PFSCL design approach can be extended to implement other complex functions, but it generally results in a high number of gate count. To improves the performance of PFSCL NOR/OR design another PFSCL design is suggested in [14].

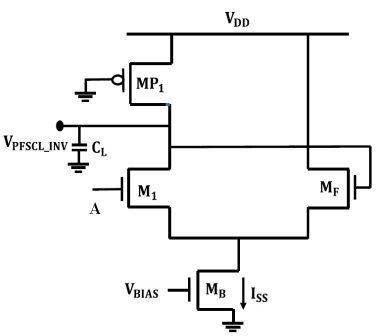

Figure 2
Conventional PFSCL Inverter [7]

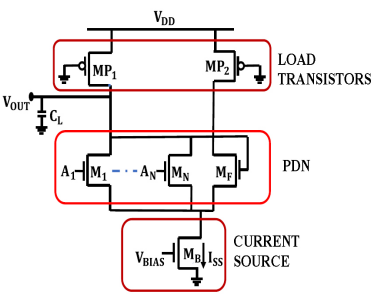

Figure 3
Gate level XOR2 gate [19]

2.2.2 PFSCL FC design

To address the problems with the PFSCL NOR/OR design, an alternative design has been suggested, which uses a FC in the PFSCL design [14,18]. A FC includes two triple-tail cells (TTCs) to implement functions involving two variables. Figure 4(a) shows the MOS-based diagram of a PFSCL FC. At a particular instance, only one TTC is active,

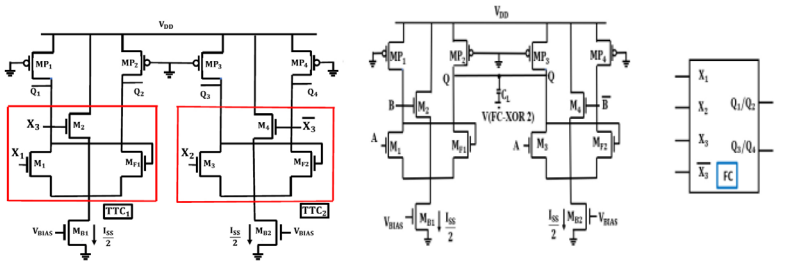

(a) (b) (c)

Figure 4

(a) Conventional Fundamental cell [13] (b) Symbol (c) FC based 2-input XOR

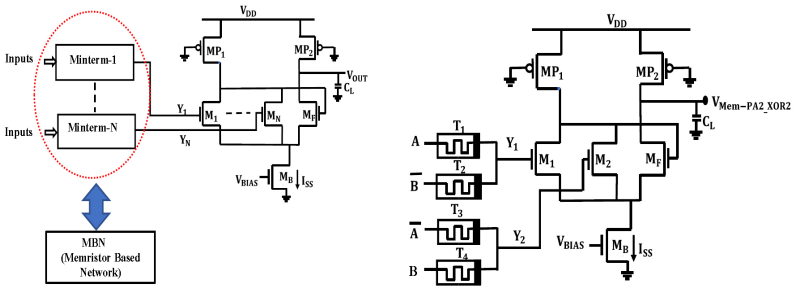

(a) (b)

Figure 5

Memristor based design (a) Mem-PA2 [18] (b) XOR2 gate

while the other is turned OFF. For example, to implement an XOR2 function, input A drives to both X_1 and X_2, and X_3 is set to B. The outputs Q_1 and Q_4 from TTC_1 and TTC_2 are combined, as shown in Fig. 4(b) with its representative is shown in Fig. 4(c)). The conventional PFSCL FC in circuit design is observed to be more efficient than conventional PFSCL NOR/OR design because it reduces the number of cascade structure for complex function realization leading to lower current sources and overall low power consumption. However, it is important to note that PFSCL FCs require larger middle transistors in the TTCs, which increases the footprint of the PFSCL design and limits its flexibility for certain applications.

2.2.3 Memristor based PFSCL design

A new approach integrates memristors with PFSCL to enhance complex function designs as compared to Memristor-CMOS hybrid integrated circuits [20]. The Mem-PA1 method uses a memristor based

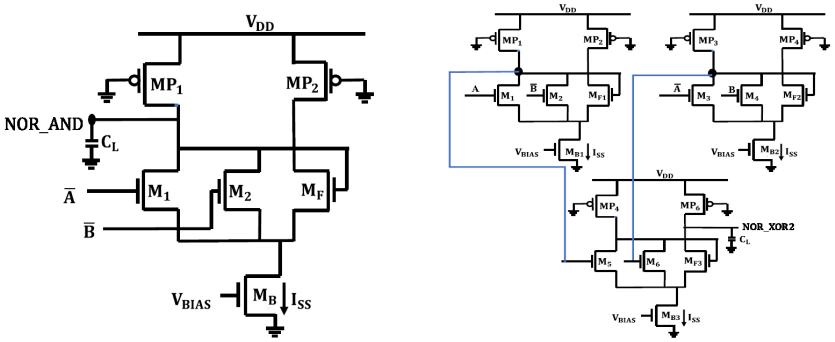

Figure 6

(a) Proposed architecture-1 (a) AND gate (b) XOR2 gate

network in PFSCL style, while Mem-PA2 involves the memristor based network with NOR/OR gates in PFSCL style. It has been found that the Mem-PA2 design performs better than Mem-PA1, So, Mem-PA2 is the preferred method for further implementation. The block diagram for Mem-PA2 is shown in Fig. 5(a) [18]. The design of Mem-PA XOR2 function is shown in Fig. 5(b).

3. Proposed architectures

In this section, three different architectures of 2-bit array multiplier are proposed in PFSCL style. To build complex functions realization, this proposed architecture-1 requires a lot of PFSCL NOR/OR gates based AND and XOR as shown in Fig. 6(a) &(b).

3.1 *Proposed architecture-1*

The first realization employs a NOR/OR PFSCL design, utilizing four AND gates and two half adders to implement the 2-bit array multiplier. The half adder consists of a PFSCL NOR/OR-based carry circuit and an XOR2 gate formed with two NOR gates and one OR gate. To build complex functions realization, this proposed architecture-1 requires a lot of PFSCL NOR/OR gates. As a result, increased propagation additionally, reduce the speed benefits of the PFSCL style. So, to improve the performance of proposed architecture -1, another architecture is proposed in next section.

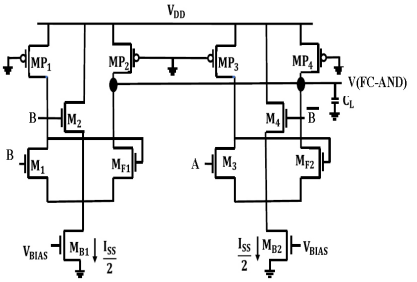

Figure 7
PFSCL FC AND gate

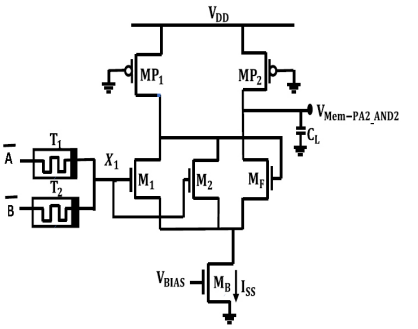

Figure 8
Mem-PA2 based AND gate

3.2 *Proposed architecture-2*

In this architecture-2 involves PFSCL fundamental cell-based design. For the implementation of AND function in PFSCL FC, connect input B to M_1, input A to M_3, and set M_3 to B and the output is obtained by combining outputs Q_2 from TTC_1 and Q_4 from TTC_2, as shown in Fig. 3(a). The same process is follows for implementation of XOR2 gate. This is more efficient than proposed architecture-1 due to reduced cascading which leads to low power consumption.

3.3 *Proposed architecture-3*

Architecture-3 utilizes the Mem-PA2 method, integrating a memristor-based network (MBN) within PFSCL NOR/OR gates for the 2-bit array multiplier. It requires fewer PFSCL gates compared to Architectures 1 and 2, minimizing gate count and area. This optimization significantly improves performance and efficiency of the PFSCL circuits. The same process is follows for implementation of AND gate as shown in Fig. 7.

4. Simulation Section

In this simulation section, the functionality of 2-bit array multiplier is verified and the performance of proposed architectures is compared in terms of in propagation delay, power, power delay product (PDP), gate count and area. All simulations environments are carried out using LT spice with 90 nm CMOS technology. The parameters involve with a voltage supply, current, load capacitance and voltage swing of 1.1V,100 μA, 50 fF,

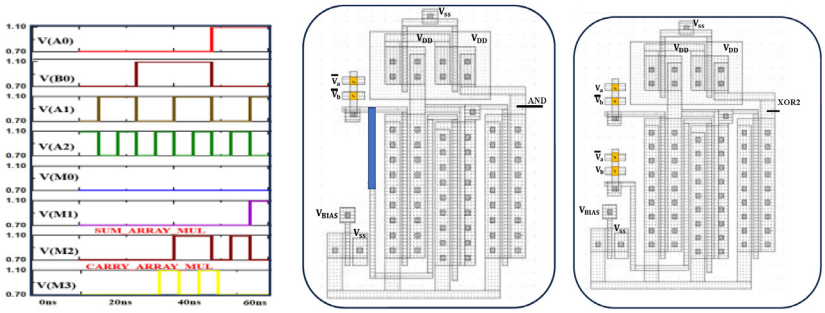

(a) (b) (c)

Figure 9

(a) Timing waveform of proposed architecture -3 for 2-bit array multiplier

Table 1

Performance comparison for a 2-bit Array

Designs / Parameter	SUM_ARRAY_MUL			CARRY_ARRAY_MUL		
	Architecture-1	Architecture-2	Architecture-3	Architecture-1	Architecture-2	Architecture-3
Propagation Delay (ps)	1970	1785	1450	1630	1785	992
Gate count	11	6	6	6	6	2
Power (μW)	1100	660	660	660	660	220
PDP (fJ)	2167	1178.1	1089	1075.8	1178.1	218.24
Area (μm^2)	751	5490	320	331	5490	132

and 400 mV respectively. Layouts are put forward for area comparison are created using Microwind.

4.1 *Function verification*

The timing waveforms of proposed architecture-3 of 2-bit array multiplier is shown Fig. 8. The simulated waveform of the 2-bit array multiplier, illustrating the inputs (A0, B0, A1, A2) and their corresponding output (M0, M1, M2, M3). The following results can be made from the obtained results:

4.2 *Performance comparison*

The proposed architecture-3 achieves a significant improvement in propagation delay, reducing it by 26% in SUM_ARRAY_MUL and 39% in CARRY_ARRAY_MUL compared to architecture-1. This enhancement results from the elimination of multiple stages present in architecture-1, which otherwise increase delay. Additionally, architecture-3 demonstrates a substantial reduction in power consumption, with decreases of 40% and 66% in SUM_ARRAY_MUL and CARRY_ARRAY_MUL, respectively, due to its lower gate and current source count. These optimizations contribute to significantly reduced power-delay product (PDP) values. Furthermore, architecture-3 offers notable area efficiency, with a reduction of 94% and 97% in the area for SUM_ARRAY_MUL and CARRY_ARRAY_MUL, respectively. The simulated results are shown in table 1. The area layouts of the AND and XOR2 gates for architecture-3 are depicted in Figures 9(b) and 9(c), while the layouts of other architectures are omitted for brevity.

5. Conclusions

The mixed-signal PFSCL design style has become a preferred option for use in applications requiring high-speed, low-power digital circuits. In this paper, we introduce three distinct 2-bit array multiplier architectures based on the PFSCL approach. Architecture-1 employs PFSCL NOR/OR gates, while architecture-2 utilizes the PFSCL Fundamental Cell (FC). The third architecture, architecture-3, integrates memristors with the PFSCL circuit design. All three architectures were simulated using the LT Spice tool with 90nm PTM technology. Among the proposed designs, architecture-3 stands out as the most efficient across all key performance metrics, offering the highest speed along with the lowest power consumption and area, making it an ideal choice for resource-constrained applications such as high-performance computing and low-power embedded systems.

References

[1] R. Sàez, M. Kayal, M. Declercq, and M. Schneider, “Digital circuit techniques for mixed analog/digital circuits applications,” in *Proc. IEEE Int. Conf. Electron., Circuits, Syst.*, Rodos, Greece, pp. 956–959 (1996).

[2] S. Kiaei, S. H. Chee, and D. Allstot, "CMOS source-coupled logic for mixed-mode VLSI," in *Proc. IEEE Int. Symp. Circuits Syst.*, New Orleans, LA, USA, pp. 1608–1611 (1990). doi: 10.1109/ISCAS.1990.112444.

[3] Andhra Pradesh, "Design and analysis of CMOS-based Op-Amp for low-power biomedical applications."

[4] M. Alioto, A. Fort, L. Pancioni, S. Rocchi, and V. Vignoli, "An approach to the design of PFSCL gates," in *Proc. Int. Symp. Circuits Syst.*, Kobe, Japan, pp. 2437–2440 (2005).

[5] M. Alioto, L. Pancioni, S. Rocchi, and V. Vignoli, "Power–delay–area–noise margin tradeoffs in positive feedback MOS current-mode logic," *IEEE Trans. Circuits Syst. I Reg. Papers*, vol. 54, no. 9, pp. 1916–1928 (2007). doi: 10.1109/TCSI.2007.904685.

[6] N. Pandey, M. Gupta, and K. Gupta, "A PFSCL-based configurable logic block," in *Proc. IEEE India Conf. (INDICON)*, New Delhi, India, pp. 1–4 (2015). doi: 10.1109/INDICON.2015.7443260.

[7] K. Gupta, N. Pandey, and M. Gupta, "Model and design of improved current mode logic gates," in *Proc. IEEE Int. Conf. Electron., Circuits, Syst.*, Singapore (2020).

[8] R. Sivaram, K. Gupta, and N. Pandey, "Power efficient architecture for positive feedback source-coupled logic," in *Proc. IEEE Emerging Trends in Industry 4.0 (ETI 4.0)*, Pune, India, pp. 1–6 (2021).

[9] K. Gupta, P. Shukla, and N. Pandey, "On the implementation of PFSCL adders," in *Proc. 2nd Int. Innovative Appl. Comput. Intell. Power, Energy, Control with Their Impact on Humanity (CIPECH)*, Ghaziabad, India, pp. 287–291 (2016). doi: 10.1109/CIPECH.2016.7918784.

[10] K. Gupta, U. Mittal, R. Baghla, P. Shukla, and N. Pandey, "On the implementation of PFSCL serializer," in *Proc. 3rd Int. Conf. Signal Process. Integrated Netw. (SPIN)*, Noida, India, pp. 436–440 (2016).

[11] R. K. Agrawal, N. Pandey, and K. Gupta, "Implementation of PFSCL razor flip-flop," in *Proc. Int. Conf. Comput. Methodologies Commun. (ICCMC)*, Erode, India, pp. 6–11 (2017).

[12] K. Gupta, U. Mittal, R. Baghla, and N. Pandey, "Implementation of PFSCL demultiplexer," in *Proc. Int. Conf. Comput. Techn. Inf. Commun. Technol. (ICCTICT)*, New Delhi, India, pp. 490–494 (2016).

[13] A. Tyagi, N. Pandey, and K. Gupta, "PFSCL-based linear feedback shift register," in *Proc. Int. Conf. Comput. Techn. Inf. Commun. Technol. (ICCTICT)*, New Delhi, India, pp. 580–585 (2016).

[14] N. Pandey and K. Gupta, "Realization of positive feedback source-coupled logic even parity generator/checker," in *Proc. 7th Int. Conf. Comput., Commun., Control Autom. (ICCUBEA)*, Pune, India, pp. 1–6 (2023).

[15] N. Pandey, K. Gupta, and M. Gupta, "An efficient triple-tail cell based PFSCL D-latch," *Microelectron. J.*, vol. 45, no. 8, pp. 1001–1007 (2014).

[16] M. Jhamb and M. Kumar, "Optimized Vedic multiplier using low-power 13T hybrid full adder," *J. Inf. Optim. Sci.*, vol. 44, no. 4, pp. 675–687 (2023).

[17] K. Gupta, N. Pandey, and M. Gupta, "A novel active shunt-peaked MCML array multiplier," *J. Multi-Discip. Eng. Technol.*, vol. 6, no. 2, pp. 1–8 (2012).

[18] S. Shikha, N. Pandey, and K. Gupta, "Memristor-based architectures for PFSCL circuit realizations," *Circuits, Syst., Signal Process.*, vol. 42, pp. 1–28 (2023).

[19] J. Rofeh, A. Sodhi, M. Payvand, M. A. Lastras-Montaño, A. Ghofrani, A. Madhavan, and L. Theogarajan, "Vertical integration of memristors onto foundry CMOS dies using wafer-scale integration," in *Proc. IEEE 65th Electron. Compon. Technol. Conf. (ECTC)*, pp. 957–962 (2015). doi: 10.1109/ECTC.2015.7159710.

[20] Q. Xia, W. Robinett, M. W. Cumbie, N. Banerjee, T. J. Cardinali, J. J. Yang, and R. S. Williams, "Memristor-CMOS hybrid integrated circuits for reconfigurable logic," *Nano Lett.*, vol. 9, no. 10, pp. 3640–3645 (2009). doi: 10.1021/nl901874j.

Received August, 2024

Inorganic Chemistry Communications 176 (2025) 114316

Contents lists available at ScienceDirect

Inorganic Chemistry Communications

journal homepage: www.elsevier.com/locate/inoche

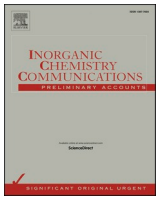

Research Article

Designing and optimization of a highly efficient and new lead-free Cs_2RbGaI_6 based double perovskite solar cell through SCAPS-1D and machine learning

Vishal Deswal, Sarita Baghel *

Renewable Energy Research Laboratory, Department of Applied Physics, Delhi Technological University, India

ARTICLE INFO

Keywords:
Machine Learning
Double Perovskite Solar Cell (DPSC)
SCAPS-1D

ABSTRACT

Lead-free double Perovskite materials have emerged as an alternative non-toxic semiconductor material for solar cell applications with exceptional performance, stability, and affordability. This work primarily focuses on designing and optimizing Cs_2RbGaI_6 based double perovskite solar cell (DPSC) through SCAPS-1D simulation and machine learning. We calculated essential material properties, like the density of states and carrier mobilities, using DFT data reported in the literature. Some other properties, like electron affinity, defect density, and absorber layer thickness, were optimized using SCAPS-1D software. The suitable Electron Transport layer and Hole transport layer were also chosen, and effect of their thickness on PCE was analyzed. This device with optimized parameters showed a PCE of 22.17 %. Machine learning helps verify scientific claims and expedites scientific discovery and research gaps. In light of the recent increase in the rapid use of machine learning in science, we also developed a machine learning model using random forest regression model with R^2 value of 1.9985. We used the model to create a SHAP summary plot to analyze the impact of thickness and defect density of absorber layer, along with device operating temperature on the PCE of DPSC. To develop this machine learning model, 1008 data points were generated through SCAPS-1D simulations.

1. Introduction

Perovskite materials have emerged as top contender to replace traditional Si-based solar cells due to their remarkable opto-electronic properties [1–5]. Majority of stable and highly efficient perovskite solar cells are based on toxic lead thereby limiting their usage [6–8]. To overcome these limitations, the scientific community has explored double perovskite materials ($A_2BB'X_6$). These double perovskite solar cells (DPSCs) offer advantages like tunable bandgap, sustainable and non-toxicity in addition to being stable and efficient thereby an excellent choice.

Recently in a DFT study, Cs_2RbGaI_6 having a band gap of 1.8 eV was reported and it shows interesting optoelectronic properties for application in photovoltaics [9]. The material requires further exploration to investigate its usage as a solar cell absorber. In this study we used some of reported material properties to calculate density of states and carrier mobilities and thereby designing an DPSC based on Cs_2RbGaI_6 and optimized and studied various properties like defect density, electron affinity, thickness of absorber layer, thickness of ETL and HTL, and operating temperature.

The growing implementation of machine learning (ML) techniques in photovoltaics design is helping to streamline the process of predicting power conversion efficiency (PCE) [10]. Compared to traditional simulation methods, which are often complex and time-intensive, ML models provide a faster, more user-friendly approach, even for individuals without deep expertise in solar research [11]. This makes them particularly valuable in photovoltaic (PV) labs.

ML techniques like, artificial neural networks (ANNs), support vector machines (SVMs), random forests (RFs), and XGBoost (XGB), have been successfully applied to datasets produced by simulators, which are readily accessible [10]. These algorithms use large datasets which contain information on input parameters, material properties, experimental variables, and target characteristic values. Their ability to detect patterns and correlations within the data allows ML models to capture insights that simulators may overlook.

Moreover, as ML models continuously learn from newly available data, they become better at predicting PCE by adapting to factors like evolving material properties, changing environmental conditions, and

* Corresponding author.
E-mail address: saritabaghel@dtu.ac.in (S. Baghel).

https://doi.org/10.1016/j.inoche.2025.114316
Received 18 December 2024; Received in revised form 5 March 2025; Accepted 9 March 2025
Available online 11 March 2025
1387-7003/© 2025 Elsevier B.V. All rights are reserved, including those for text and data mining, AI training, and similar technologies.

shifts in device architecture [12–15]. This adaptability gives ML-based models an edge over simulators in terms of computational efficiency and speed, without sacrificing accuracy. This is especially beneficial for tasks such as designing, optimizing and material screening of DPSC.

The use of ML models is becoming increasingly common for handling complex, real-time datasets, ensuring precise and reliable predictions [16]. These models, which integrate different ML algorithms, are scalable for huge datasets and robust to variations, making them a valuable asset for increasing the PCE and dependability of photovoltaic research. The use of ML for forecasting PCE, offers a more flexible, accurate, and efficient alternative to traditional simulation techniques [10].

Initially a dataset of 1008 points was generated through SCAPS-1D simulation then it was used to train machine learning model. This model is then used for creating SHAP summary analysis of thickness, defect density and device temperature on PCE of DPSC. The developed machine learning model predicts nearly same as the simulated values which is indicated by the high R^2 value.

2. Methodology

2.1. Simulation methodology

In this study we have used Solar Cell Capacitance Simulator (SCAPS) for numerical simulation of solar cell, which uses various semiconducting relations to determine solar cell characteristics.

In this study we have first made and optimized the device structure including its absorber layer, Electron transport layer (ETL) and Hole transport layer (HTL). Material properties of these transport layers were taken from previous studies. Some material properties of the absorber layer were adopted from published literature while some others like density of states and carrier mobilities were calculated and others like electron affinity, defect density and thickness were optimized in this work.

Cs_2RbGaI_6 has effective mass of electron and holes ($m^*_{e/h}$) as 0.15 m_0 and 0.29 m_0 (m_0 is rest mass of electron) respectively [9]. These values can be used to derive the the density of states for the valance (N_v) and conduction (N_c) bands using the following equation.

$$N_{c/v} = 2\left(\frac{2\pi k_B T m^*_{e/h}}{h^2}\right)^{\frac{3}{2}} \quad (1)$$

Here, k_B is the Boltzmann constant, T is room temperature, h is the plank's constant and $m^*_{e/h}$ is effective masses of electrons/holes. The determined values of N_C and N_V are mentioned in Table 1.

An essential material attribute required for the modeling of semiconductor devices is carrier mobility. With DFT software, these crucial material characteristics are easily calculated. However, presenting all these features in a single DFT analysis of a material is typically inappropriate for researchers due to the time-consuming nature of these DFT computations. To obtain these characteristics' approximate values for simulation purposes, we may either repeat the DFT computations or use fundamental semiconductor equations.

$$\mu_{e/h} = \frac{q\tau_m}{m^*} \quad (2)$$

$$\tau = \frac{L_m}{V_{th}} \quad (3)$$

Hence, mobility can be calculated as given below.

$$\mu_{e/h} = \frac{40qa}{m^*_{e/h} V_{th}} \quad (4)$$

Here, $\mu_{e/h}$ is carrier mobility for electrons/holes respectively and $m^*_{e/h}$ is their respective effective masses. τ_m is relaxation time, and L_m is the mean free path. V_{th} represents electron/hole thermal velocity at 300 K (room temperature). The lattice constant (a_0) value for Cs_2RbGaI_6 is 12.63 A^0 [9]. The calculated values of $\mu_{e/h}$ for the same is mentioned in Table 1.

Table 1
Material Properties of different layers of optimized solar cell.

Material Properties	$Cs_2RbGaI6$	ZnSe	CBTS	FTO
Thickness (nm)	600	100	200	100
E_g (eV)	1.8	2.81	1.9	3.5
χ (eV)	4*	4.09	3.6	4.5
$\varepsilon/\varepsilon_0$	3.24	8.6	5.4	9.00
N_C (1/cm^3)	1.46×10^{18}*	2.2×10^{18}	2.2×10^{18}	2.2×10^{18}
N_V (1/cm^3)	3.92×10^{18}*	1.8×10^{18}	1.8×10^{19}	1×10^{19}
V_e (cm/s)	1×10^7	1×10^7	1×10^7	1×10^7
V_h (cm/s)	1×10^7	1×10^7	1×10^7	1×10^7
μ_e (cm^2/Vs)	50.29*	400	30	2×10^3
μ_h (cm^2/Vs)	30.67*	110	10	2×10^3
N_D (1/cm^3)	_	1×10^{15}	_	2×10^{19}
N_A (1/cm^3)	_	_	1×10^{18}	_
Defect Density (1/cm^3)	1×10^{14}*	1×10^{15}	1×10^{15}	1×10^{15}
Reference	[9]	[5,17]	[5,18,19]	[5,20]

*In this work.

2.2. Developing machine learning model

After optimizing the solar cell and its various parameters to maximize efficiency, we developed a machine learning (ML) model. Among several ML models, Random Forest Regression was selected, as it produced an R^2 value close to 1. This model was initially trained on a dataset of 1008 data points, obtained through simulations by varying the thickness and defect density of the absorber layer, as well as the operating temperature of the solar cell. These variations resulted in different values of power conversion efficiency (PCE). A plot comparing the real values with the predicted values from the trained ML model was generated using Python. Additionally, we used the trained model to create a SHAP summary plot, which helped analyze the effects of various parameters on PCE and compare them. We also added a small python script which will predict the PCE of the DPSC given the three input parameters. Using this we finally compared the ML predicted PCE with that given via simulation. Fig. 2 represents the workflow representing the machine learning analysis adopted in this study.

3. Results and Discussion

3.1. Optimization of transport layers

The ETL and HTL play an important role in transfer of charges inside Photovoltaics. The ETL moves the electrons from absorber to outside circuit, while the HTL ensures effective movement of holes. Proper charge transport is crucial for avoiding recombination, which in turn helps generate more electrical current and enhances PCE of photovoltaic devices. In our study, five HTLs (Table 2) and three ETLs (Table 3) were analyzed for their impact on DPSC performance.

These specific ETL and HTL materials were selected based on their successful application in previous studies, where they significantly improved PCE and demonstrated other advantageous properties for integration into solar cells [17,19,21–32]. Table 2 and Table 3 list the simulation parameters for the HTLs and ETLs, respectively. The J-V curve and Photovoltaic parameters for different device structures are depicted in Fig. 3, Fig. 4 and Fig. 5.

Using the traditional configuration of ETL and HTL (FTO/TiO_2/Cs_2RbGaI_6/Spiro-OMeTAD/Au), the solar cell achieved a 19.51 % efficiency. Our research shows that among the three ETLs, devices with ZnSe as the ETL exhibited the highest efficiency due to its broader band gap (Fig. 1). ZnSe-based solar cells also displayed greater photostability, as ZnSe helps block UV light, thereby shielding the perovskite layer from UV-related damage [17,26,33]. Two HTLs, $MASnBr_3$ and CBTS (Copper

Table 2
Properties of different HTLs used for simulation.

Material Properties	CBTS	Spiro-OMeTAD	$MASnBr_3$	CuO	PEDOT:PSS
Thickness (nm)	200	200	200	200	200
E_g (eV)	1.9	3	2.15	1.51	1.6
χ (eV)	3.6	2.2	3.39	4.07	3.4
$\varepsilon/\varepsilon_0$	5.4	3	8.2	18.1	3
N_C ($1/cm^3$)	2.2×10^{18}	2.2×10^{18}	1×10^{20}	2.2×10^{19}	2.2×10^{18}
N_V ($1/cm^3$)	1.8×10^{19}	1.8×10^{19}	1×10^{18}	5.5×10^{20}	1.8×10^{19}
V_e (cm/s)	1×10^{7}	1×10^{7}	1×10^{7}	1×10^{7}	1×10^{7}
V_h (cm/s)	1×10^{7}	1×10^{7}	1×10^{7}	1×10^{7}	1×10^{7}
μ_e (cm^2/Vs)	30	2.1×10^{-3}	1.6	100	4.5×10^{-2}
μ_h (cm^2/Vs)	10	2.16×10^{-3}	1.6	0.1	4.5×10^{-2}
N_D ($1/cm^3$)	–	–	–	–	–
N_A ($1/cm^3$)	1×10^{18}	1×10^{18}	1×10^{18}	1×10^{18}	1×10^{18}
Defect Density ($1/cm^3$)	1×10^{15}	1×10^{15}	1×10^{15}	1×10^{15}	1×10^{15}
Reference	[19,21]	[21–24]	[25]	[21,26]	[21,27]

Table 3
Properties of Different ETLs used for simulation.

Material Properties	ZnSe	TiO_2	IGZO
Thickness (nm)	100	100	100
E_g (eV)	2.81	3.2	3.050
χ (eV)	4.09	4	4.160
$\varepsilon/\varepsilon_0$	8.6	9	10
N_C ($1/cm^3$)	2.2×10^{18}	2×10^{18}	5×10^{18}
N_V ($1/cm^3$)	1.8×10^{18}	1.8×10^{19}	5×10^{18}
V_e (cm/s)	1×10^{7}	1×10^{7}	1×10^{7}
V_h (cm/s)	1×10^{7}	1×10^{7}	1×10^{7}
μ_e (cm^2/Vs)	400	20	1.5
μ_h (cm^2/Vs)	110	10	0.1
N_D ($1/cm^3$)	1×10^{15}	9×10^{16}	1×10^{17}
N_A ($1/cm^3$)	–	–	–
Defect Density ($1/cm^3$)	1×10^{15}	1×10^{15}	1×10^{15}
Reference	[17]	[14,17,18]	[21,28,29]

Barium Thiostannate), achieved maximum efficiencies of 22.17 % and 21.86 % respectively when combined with ZnSe. Therefore, CBTS is suggested as best HTL layer for optimized results with maximum PCE. CBTS, a thin-film material, offers a tunable band gap and better absorption of light. Its non-centrosymmetric crystal structure and atomic size variations make it ideal for enhancing the PCE of solar cells [24,34].

Therefore, the device structure FTO/ZnSe/$Cs_2RbGaBr_6$/CBTS/Au was chosen to optimize absorber layer parameters such as thickness, temperature, defect density, and electron affinity. The optimized layers' simulation parameters are shown in the above tables, and the band alignment diagram and device structure for future optimization are presented in Fig. 1.

3.1.1. *Thickness optimization of ETL and HTL*

Fig. 6 shows the Contour plots depicting impact of HTL and ETL thickness variation on various DPSC parameters. With increase in thickness of HTL from 100 nm to 1600 nm less than 1 percent increase in PCE is observed. While with increase in thickness of ETL in the same range nearly 2 percent drop in PCE is observed. This observation may conclude that a thicker HTL and a thinner ETL should be preferred for better efficiency of solar cell. However, since this increase in PCE with HTL thickness is insignificant in comparison to increase in thickness therefore a moderate thickness of 200 nm for HTL is a good choice as also reported in previous literature [5]. 100 nm is chosen as optimized thickness for ETL. Lower thickness of ETL ensures larger transmittance of light to the absorber layer thereby increasing the efficiency.

3.2. *Optimization of electron affinity*

The band alignment between the HTL, absorber, and ETL plays a crucial role in controlling carrier recombination at the interfaces, which in turn affects the open-circuit voltage (V_{OC}). Adjusting the electron affinity (χ) of the absorber influences key performance metrics, such as J_{SC}, V_{OC}, fill factor (FF), and power conversion efficiency (PCE).

Fig. 7 shows the effect of Electron Affinity on various DPSC parameters. Electron affinity was varied between 3.5 eV to 4.6 eV to find an optimal value. Devices exhibit optimal performance when the electron affinity of the absorber is 4.0 eV. When χ is too low (e.g., 3.5 eV), a spike forms at the HTL/absorber interface, acting as a barrier to hole flow and increasing recombination, which results in lower V_{OC} and FF. As χ increases, this barrier decreases, leading to performance improvements. However, when χ exceeds 4.1 eV, a spike appears at the absorber/ETL interface, hindering electron flow and reducing V_{OC} and FF [35,36]. Thus, optimization of band offsets is necessary to enhance perovskite solar cell (PSC) performance.

3.3. *Defect density optimization*

To investigate how defect density affects the performance of Cs_2RbGaI_6-based solar cells, a series of simulations were run using SCAPS-1D software. Fig. 8 depicts the Effect of Defect Density on various

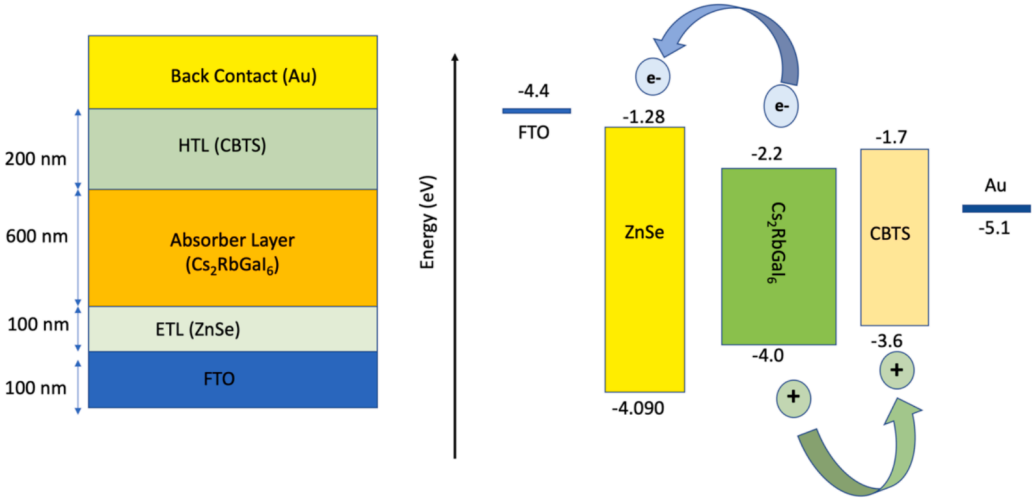

Fig. 1. Structure of DPSC and band alignment diagram of Different DPSC layers.

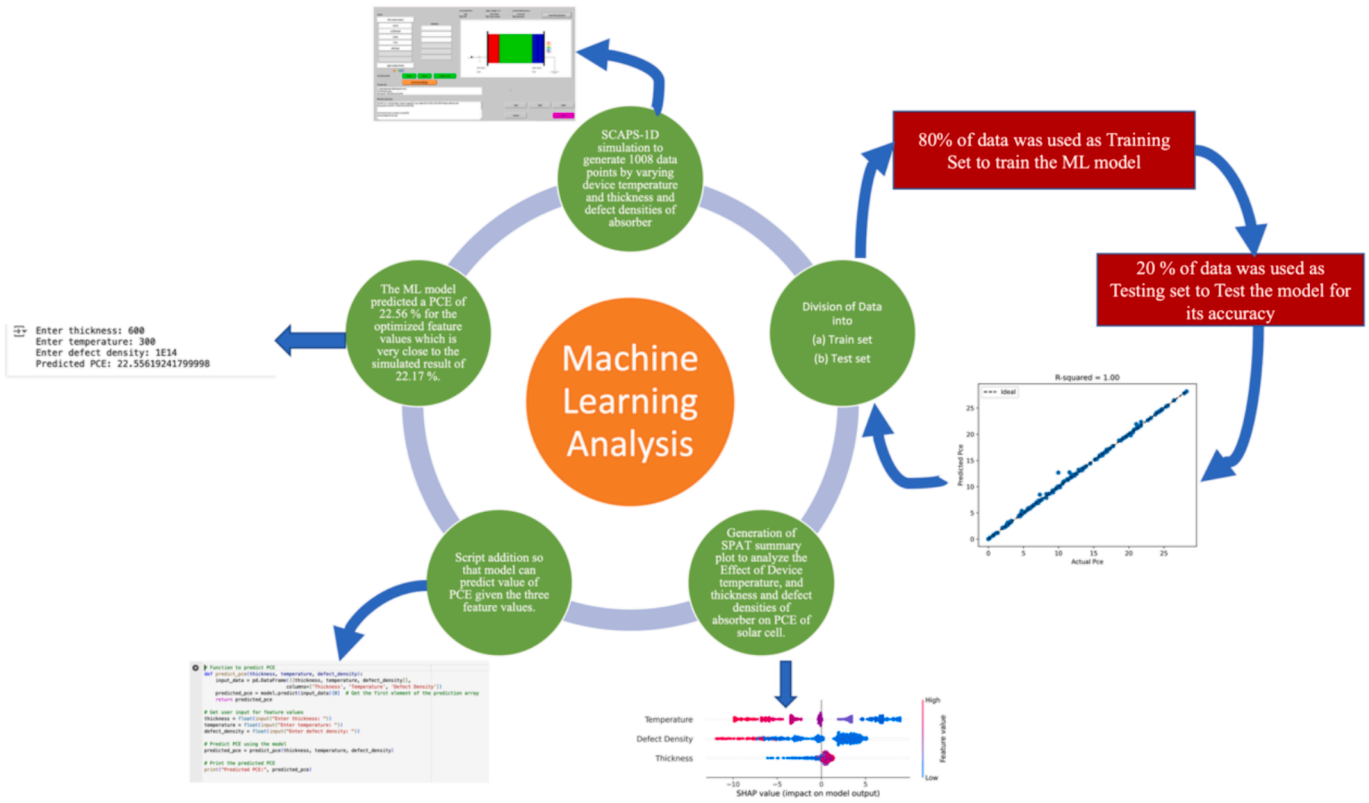

Fig. 2. Workflow of machine learning analysis.

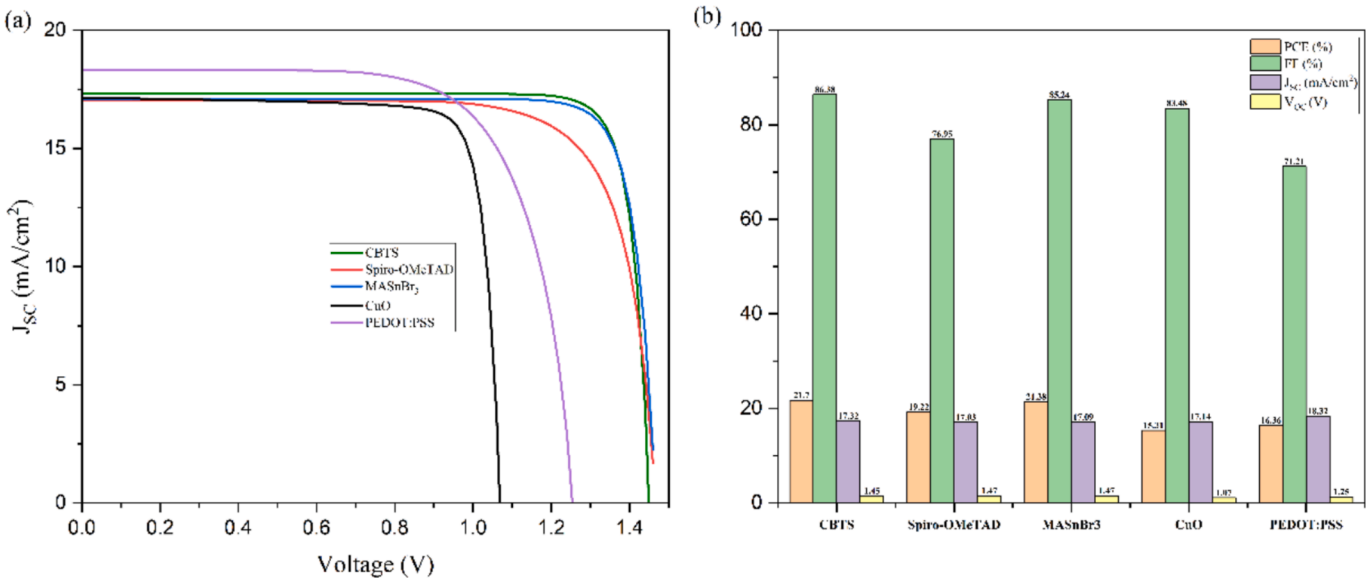

Fig. 3. (a) J-V curve of DPSC with various HTLs and IGZO as ETL (b) PCE, FF, J_{SC} and V_{OC} of DPSC with various HTLs and IGZO as ETL.

DPSC parameters. The defect density (N_t) in the absorber layer was varied in increments of 10^1 while maintaining the layer thickness at 600 nm. All other parameters for the ETL, HTL, FTO, and absorber layers were kept unchanged. The findings revealed that higher defect densities led to a reduction in solar cell efficiency. A constant PCE of 23.79 % was observed until N_t of 10^{10} cm^{-3}. After this point PCE started to decrease and a significant drop in PCE was observed above N_t of 10^{14}. A similar trend was observed in case of FF and V_{oc} as shown in Figure below. Meanwhile a significant drop in J_{sc} was observed after a N_t of 10^{16} cm^{-3}.

From these conclusions we can safely optimize the device even with high N_t of 10^{14} cm^{-3} which gives a PCE of 22.17 %.

The defect concentration in the active layer is a crucial factor in determining device efficiency. High defect levels result in increased recombination rates, leading to issues such as film degradation, formation of pinholes, and reduced stability, all of which negatively impact the performance of the device [17].

3.4. Thickness optimization

Batch simulations using SCAPS-1D were conducted to evaluate how

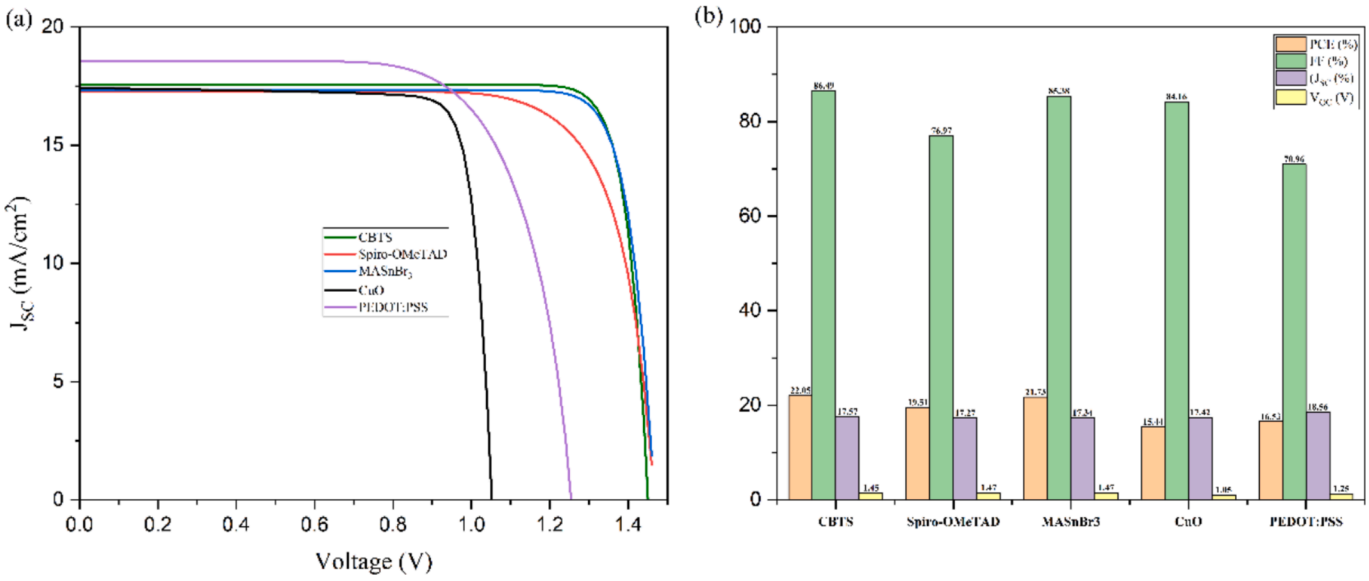

Fig. 4. (a) J-V curve of DPSC with various HTLs and TiO_2 as ETL (b) PCE, FF, J_{SC} and V_{OC} of DPSC with various HTLs and TiO_2 as ETL.

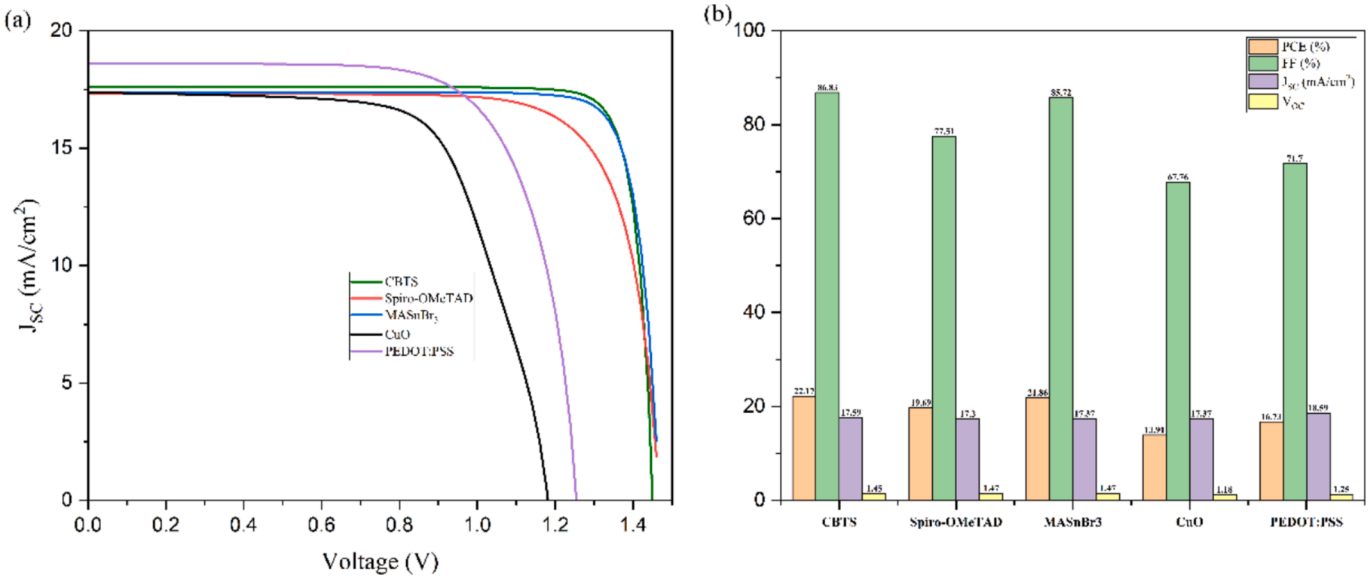

Fig. 5. (a) J-V curve of DPSC with various HTLs and ZnSe as ETL (b) PCE, FF, J_{SC} and V_{OC} of DPSC with various HTLs and ZnSe as ETL.

absorber layer thickness affects the efficiency and performance of Cs_2RbGaI_6 solar cells. Fig. 9 shows the Effect of Absorber Thickness on DPSC parameters. The thickness was varied in 100 nm steps, with defect density fixed at 10^{14} cm^{-3}, while keeping other layer parameters unchanged. As thickness increased, efficiency improved, reaching a peak of 22.72 % at 1100 nm due to better photon absorption. However, beyond 1100 nm, recombination effects caused a decline in efficiency. Fill Factor (FF) and V_{OC} showed a continuous decrease with increase in thickness although not drastically. Similarly, a continuous rise in J_{SC} was observed with increase in thickness of absorber, which also led to an increase in PCE. It was also observed that after 600 nm, further gains in PCE were minimal due to increased recombination [37]. Therefore, 600 nm was identified as the optimal thickness. Proper thickness selection is crucial for minimizing recombination and maximizing current density, as excessive thickness increases internal power loss and reduces V_{OC} and FF due to higher series resistance [26]. Optimum PCE of 22.17 was observed at the thickness of 600 nm.

3.5. Machine learning

As discussed in the methodology section, a machine learning (ML) algorithm was used to develop an ML model, trained on a dataset of 1008 data points. This model was employed to plot the real values against the values predicted by the ML model, achieving an R^2 value of 0.9985, as shown in Fig. 10. Subsequently, the trained model was used to generate a SHAP summary plot to analyze the relative effects of the absorber layer's thickness and defect density, as well as the operating temperature of solar cell, on the power conversion efficiency (PCE) as shown in Fig. 11. SHAP summary plot concludes that Thickness is the most influential factor in predicting PCE, with higher thickness generally leading to higher PCE. Defect Density has a negative effect on PCE, with higher defect density lowering PCE. Temperature has a more nuanced relationship with PCE, and its impact might depend on the values of other features.

This trained model was further instructed to calculate root mean square error (RMSE) of 0.2712.

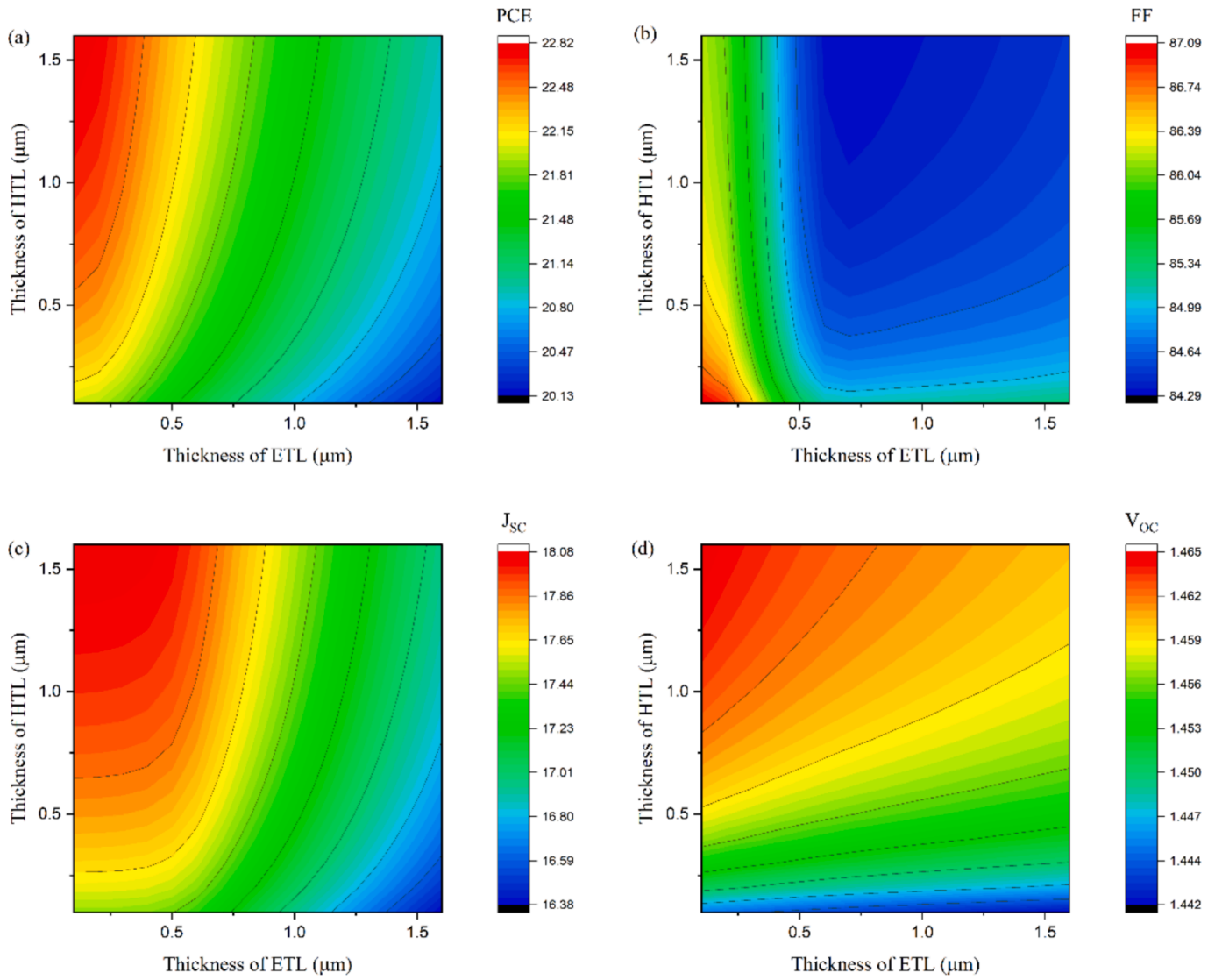

Fig. 6. Contour plots depicting impact of HTL and ETL thickness variation on (a) PCE (b) FF (c) J_{SC} and (d) V_{OC}.

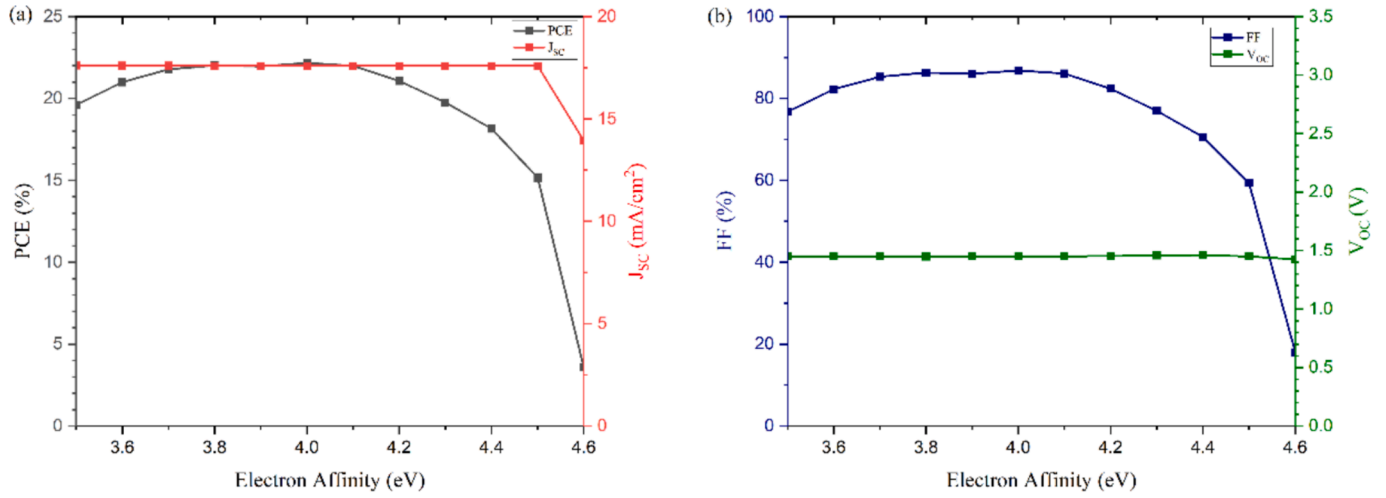

Fig. 7. Effect of Electron Affinity on (a) PCE and J_{SC} (b) FF and V_{OC} of Cs_2RbGaI_6 based DPSC.

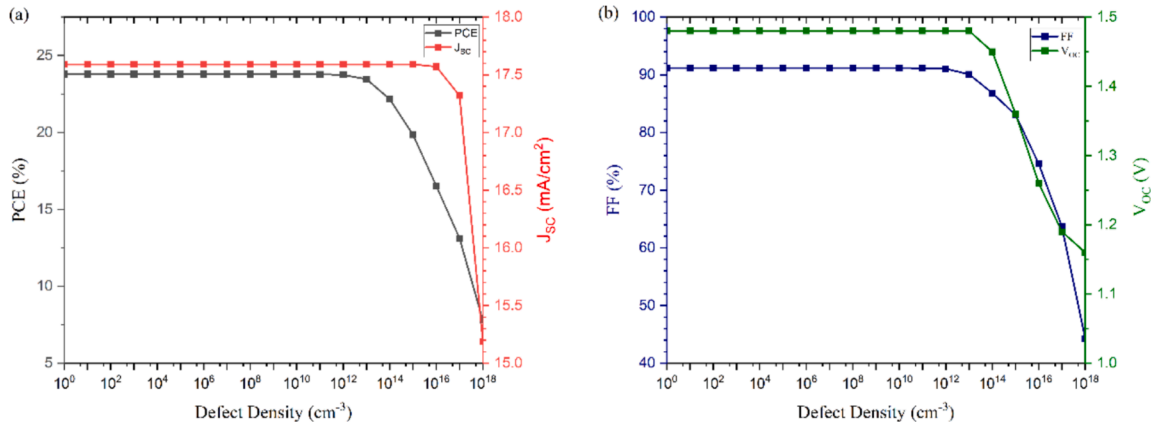

Fig. 8. Effect of Defect Density on (a) PCE and J_{SC} (b) FF and V_{OC} of Cs_2RbGaI_6 based DPSC.

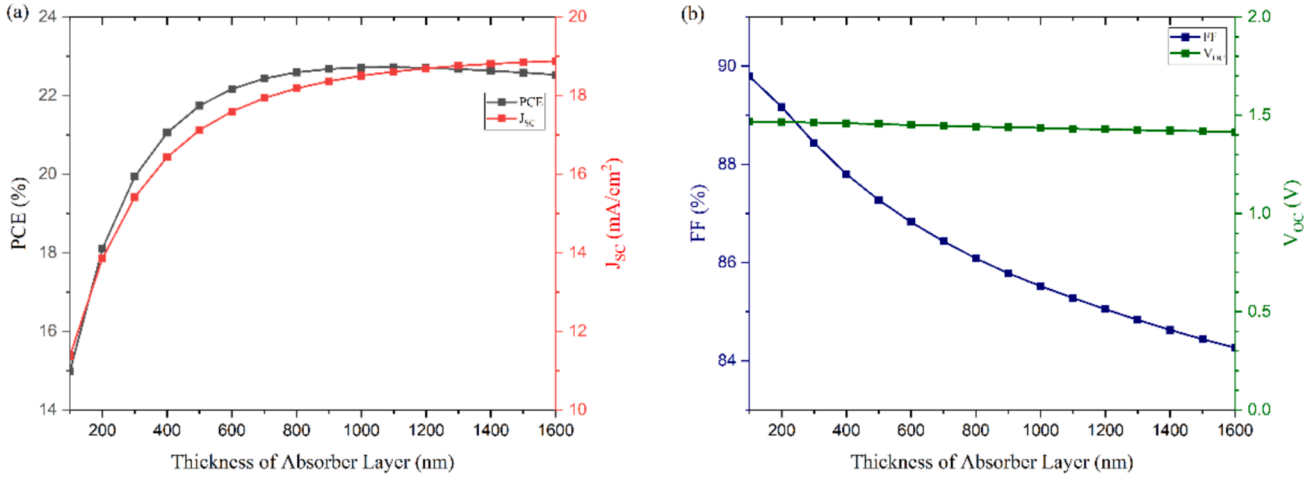

Fig. 9. Effect of Absorber Thickness on (a) PCE and J_{SC} (b) FF and V_{OC} of Cs_2RbGaI_6 based DPSC.

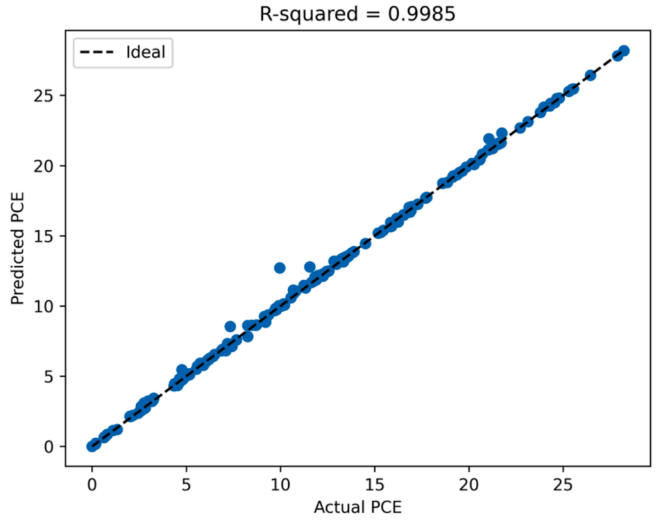

Fig. 10. Plot of PCE predicted by trained ML model with the actual PCE values obtained through simulation. ML model delived a high R^2 value of 0.9985.

Once we developed and trained the ML model its imperative that it can we used in future to predict the PCE of Cs_2RbGaI_6 based solar cell given the feature values. To achieve this a simple python script was added to our code so that when we input the feature values the ML model will predict the PCE for us. The same was tested for our SCAPS optimized DPSC, features values i.e., Thickness of 600 nm, Defect density of 10^{14} cm^{-3}, and temperature of 300 K were inserted when the prompt came when the code is run. The ML model predicted a PCE of 22.56 % which is very close to the simulated result of 22.17 %.

4. Conclusion

In this study, we comprehensively studied and optimized Cs_2RbInI_6-based lead-free double perovskite solar cells (DPSCs), concluding that it is a highly efficient material for solar cell applications. Initially, we calculated essential material properties for Cs_2RbInI_6, such as the density of states for the valence and conduction bands, as well as carrier mobilities. Additional properties, including electron affinity, defect density, and absorber layer thickness, were optimized using SCAPS-1D simulations.

We also optimized the electron transport layer (ETL) and hole transport layer (HTL), finding that ZnSe and CBTS gave the highest power conversion efficiency (PCE) as ETL and HTL, respectively, making them the recommended layers. The impact of ETL and HTL thicknesses was analyzed using contour plots, and it was concluded that a thicker HTL (200 nm) and a thinner ETL (100 nm) are ideal for achieving higher efficiency. We also studied the effect of electron affinity on device performance, identifying 4 eV as the optimal value. The impact of defect density on device performance was further analyzed, with results indicating that the cell could achieve high efficiency even at a relatively high defect density of 10^{14} cm^{-3}, chosen as the optimized value. The absorber

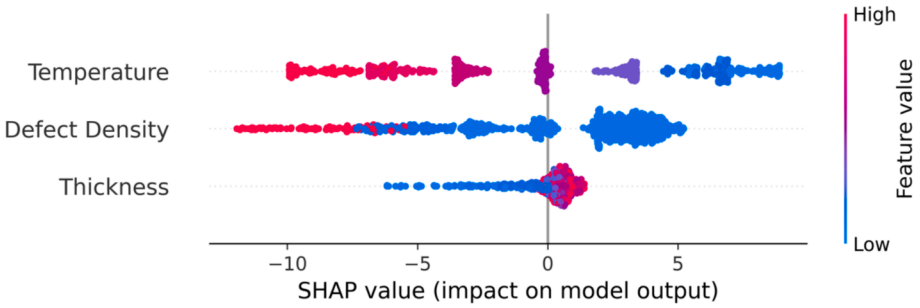

Fig. 11. SHAP summary analysis of operating Temperature of device, Defect Density of absorber layer, and Thickness of absorber layer.

layer thickness was varied between 100 nm and 1600 nm, with 600 nm selected as the ideal thickness.

Additionally, we developed a machine learning (ML) model capable of both analyzing the effect of various feature values and predicting the solar cell efficiency based on these inputs. We trained the model using 1,008 data points generated from SCAPS-1D simulations by varying the device operating temperature, absorber layer thickness, and defect density. Random forest regression was selected for the ML model, achieving an R^2 value of 0.9985, indicating a high predictive accuracy. A SHAP summary plot was used to interpret the model, showing that among the three varied features, temperature has the most significant effect on PCE, while Defect Density has a negative effect on PCE, with higher defect density lowering PCE. Additionally, temperature showed a complex relationship with PCE, indicating that its impact depends on the values of other features. Using a custom Python script, we obtained ML-predicted efficiency values for the optimized parameters from the simulations. The model predicted an optimized PCE of 22.56 %, closely matching the 22.17 % obtained from simulations.

This study underscores the potential of Cs_2RbInI_6-based solar cells, particularly for further exploration via experimental synthesis, with the findings here offering a basis for enhancing PCE during fabrication. Furthermore, it highlights the valuable role of ML in analyzing the impact of various features on solar cell performance and emphasizes the potential of ML as an efficient alternative to simulation-based methods for achieving accurate results in shorter timeframes.

CRediT authorship contribution statement

Vishal Deswal: Writing – original draft, Visualization, Methodology, Investigation, Formal analysis, Data curation, Conceptualization. **Sarita Baghel:** Writing – review & editing, Validation, Supervision, Software, Resources, Project administration, Formal analysis.

Declaration of competing interest

The authors declare that they have no known competing financial interests or personal relationships that could have appeared to influence the work reported in this paper.

Acknowledgment

The authors thank Professor Marc Burgelman (University of Gent, Belgium) for providing SCAPS-1D, software. Authors are thankful to Delhi Technological University, Delhi for funding this research.

Data availability

Data will be made available on request.

References

[1] A. Kojima, K. Teshima, Y. Shirai, T. Miyasaka, Organometal Halide Perovskites as Visible-Light Sensitizers for Photovoltaic Cells, J Am Chem Soc 131 (2009) 6050–6051, https://doi.org/10.1021/ja809598r.
[2] H.J. Snaith, Perovskites: The Emergence of a New Era for Low-Cost, High-Efficiency Solar Cells, J Phys Chem Lett 4 (2013) 3623–3630, https://doi.org/10.1021/jz4020162.
[3] N.-G. Park, Organometal Perovskite Light Absorbers Toward a 20% Efficiency Low-Cost Solid-State Mesoscopic Solar Cell, J Phys Chem Lett 4 (2013) 2423–2429, https://doi.org/10.1021/jz400892a.
[4] K.T. Butler, J.M. Frost, A. Walsh, Band alignment of the hybrid halide perovskites $CH_3NH_3PbCl_3$, $CH_3NH_3PbBr_3$ and $CH_3NH_3PbI_3$, Mater Horiz 2 (2015) 228–231, https://doi.org/10.1039/C4MH00174E.
[5] V. Deswal, S. Kaushik, R. Kundara, S. Baghel, Numerical simulation of highly efficient Cs2AgInBr6-based double perovskite solar cell using SCAPS 1-D, Mater. Sci. Eng. B 299 (2024) 117041, https://doi.org/10.1016/j.mseb.2023.117041.
[6] A. Walsh, Principles of Chemical Bonding and Band Gap Engineering in Hybrid Organic–Inorganic Halide Perovskites, J. Phys. Chem. C 119 (2015) 5755–5760, https://doi.org/10.1021/jp512420b.
[7] N.M. Ravindra, P. Ganapathy, J. Choi, Energy gap–refractive index relations in semiconductors – An overview, Infrared Phys Technol 50 (2007) 21–29, https://doi.org/10.1016/j.infrared.2006.04.001.
[8] S. Adachi, Band gaps and refractive indices of AlGaAsSb, GaInAsSb, and InPAsSb: Key properties for a variety of the 2–4-μm optoelectronic device applications, J Appl Phys 61 (1987) 4869–4876, https://doi.org/10.1063/1.338352.
[9] A. Mera, S.A. Rouf, T. Zelai, N.A. Kattan, Q. Mahmood, Study of inorganic double perovskites Cs2RbZI6 (Z = Ga, In) as energy harvesting aspirant: a DFT approach, Opt Quantum Electron 55 (2023) 918, https://doi.org/10.1007/s11082-023-05195-9.
[10] N. Shrivastav, M. Aamir Hamid, J. Madan, R. Pandey, Exploring KGeCl3 material for perovskite solar cell absorber layer through different machine learning models, Solar Energy 278 (2024) 112784, https://doi.org/10.1016/j.solener.2024.112784.
[11] O. Al-Saban, M. Alkadi, S.M.H. Qaid, A.A.A. Ahmed, S.O. Abdellatif, Machine Learning Algorithms in Photovoltaics: Evaluating Accuracy and Computational Cost Across Datasets of Different Generations, Sizes, and Complexities, J Electron Mater 53 (2024) 1530–1538, https://doi.org/10.1007/s11664-023-10897-7.
[12] N. Shrivastav, J. Madan, R. Pandey, Predicting photovoltaic efficiency in Cs-based perovskite solar cells: A comprehensive study integrating SCAPS simulation and machine learning models, Solid State Commun 380 (2024) 115437, https://doi.org/10.1016/j.ssc.2024.115437.
[13] Z. Hui, M. Wang, X. Yin, Y. Wang, Y. Yue, Machine learning for perovskite solar cell design, Comput Mater Sci 226 (2023) 112215, https://doi.org/10.1016/j.commatsci.2023.112215.
[14] F. Häse, L.M. Roch, P. Friederich, A. Aspuru-Guzik, Designing and understanding light-harvesting devices with machine learning, Nat Commun 11 (2020) 4587, https://doi.org/10.1038/s41467-020-17995-8.
[15] J. Li, B. Pradhan, S. Gaur, J. Thomas, Predictions and Strategies Learned from Machine Learning to Develop High-Performing Perovskite Solar Cells, Adv Energy Mater 9 (2019), https://doi.org/10.1002/aenm.201901891.
[16] M. Hajihosseinlou, A. Maghsoudi, R. Ghezelbash, Stacking: A novel data-driven ensemble machine learning strategy for prediction and mapping of Pb-Zn prospectivity in Varcheh district, west Iran, Expert Syst Appl 237 (2024) 121668, https://doi.org/10.1016/j.eswa.2023.121668.
[17] N.K. Sinha, D.S. Ghosh, A. Khare, Role of built-in potential over ETL/perovskite interface on the performance of HTL-free perovskite solar cells, Opt Mater (amst) 129 (2022) 112517, https://doi.org/10.1016/j.optmat.2022.112517.
[18] M.K. Hossain, M.H.K. Rubel, G.F.I. Toki, I. Alam, M.F. Rahman, H. Bencherif, Effect of Various Electron and Hole Transport Layers on the Performance of $CsPbI_3$-Based Perovskite Solar Cells: A Numerical Investigation in DFT, SCAPS-1D, and wxAMPS Frameworks, ACS Omega 7 (2022) 43210–43230, https://doi.org/10.1021/acsomega.2c05912.
[19] Y.H. Khattak, F. Baig, H. Toura, S. Beg, B.M. Soucase, CZTSe Kesterite as an Alternative Hole Transport Layer for MASnI3 Perovskite Solar Cells, J Electron Mater 48 (2019) 5723–5733, https://doi.org/10.1007/s11664-019-07374-5.
[20] M. Kibbou, Z. Haman, N. Khossossi, I. Essaoudi, A. Ainane, R. Ahuja, Computational insights into the superior efficiency of Cs2AgGa(Cl,Br)6 double

halide perovskite solar cells, Mater Chem Phys 294 (2023) 126978, https://doi.org/10.1016/j.matchemphys.2022.126978.
[21] M.K. Hossain, M.H.K. Rubel, G.F.I. Toki, I. Alam, M.F. Rahman, H. Bencherif, Effect of Various Electron and Hole Transport Layers on the Performance of CsPbI3-Based Perovskite Solar Cells: A Numerical Investigation in DFT, SCAPS-1D, and wxAMPS Frameworks, ACS Omega 7 (2022) 43210–43230, https://doi.org/10.1021/acsomega.2c05912.
[22] Y. Raoui, H. Ez-Zahraouy, N. Tahiri, O. El Bounagui, S. Ahmad, S. Kazim, Performance analysis of MAPbI3 based perovskite solar cells employing diverse charge selective contacts: Simulation study, Sol. Energy 193 (2019) 948–955, https://doi.org/10.1016/j.solener.2019.10.009.
[23] S. Abdelaziz, A. Zekry, A. Shaker, M. Abouelatta, Investigating the performance of formamidinium tin-based perovskite solar cell by SCAPS device simulation, Opt Mater (amst) 101 (2020) 109738, https://doi.org/10.1016/j.optmat.2020.109738.
[24] L. Huang, X. Sun, C. Li, R. Xu, J. Xu, Y. Du, Y. Wu, J. Ni, H. Cai, J. Li, Z. Hu, J. Zhang, Electron transport layer-free planar perovskite solar cells: Further performance enhancement perspective from device simulation, Sol. Energy Mater. Sol. Cells 157 (2016) 1038–1047, https://doi.org/10.1016/j.solmat.2016.08.025.
[25] X. Meng, T. Tang, R. Zhang, K. Liu, W. Li, L. Yang, Y. Song, X. Ma, Z. Cheng, J. Wu, Optimization of germanium-based perovskite solar cells by SCAPS simulation, Opt Mater (amst) 128 (2022), https://doi.org/10.1016/j.optmat.2022.112427.
[26] P. Sawicka-Chudy, Z. Starowicz, G. Wisz, R. Yavorskyi, Z. Zapukhlyak, M. Bester, Ł. Głowa, M. Sibiński, M. Cholewa, Simulation of TiO_2 /CuO solar cells with SCAPS-1D software, Mater Res Express 6 (2019) 085918, https://doi.org/10.1088/2053-1591/ab22aa.
[27] H. Alipour, A. Ghadimi, Optimization of lead-free perovskite solar cells in normal-structure with <math altimg="si1.svg"> <mrow> <msub> <mtext>WO</mtext> <mn>3</mn> </msub> </mrow> </math> and water-free PEDOT:PSS composite for hole transport layer by SCAPS-1D simulation, Opt Mater (Amst) 120 (2021) 111432. 10.1016/j.optmat.2021.111432.
[28] A. Hima, Enhancing of CH3NH3SnI3 based solar cell efficiency by ETL engineering, International Journal of Energetica 5 27 (2020) 10.47238/ijeca.v5i1.119.
[29] K. Deepthi Jayan, V. Sebastian, Modelling and comparative performance analysis of tin based mixed halide perovskite solar cells with <scp>IGZO</scp> and <scp>CuO</scp> as charge transport layers, Int J Energy Res 45 (2021) 16618–16632, https://doi.org/10.1002/er.6909.
[30] K.Q. Wang, Y. He, M. Zhang, J.J. Shi, W.W. Cai, Promising Lead-Free Double-Perovskite Photovoltaic Materials Cs2MM′Br6(M = Cu, Ag, and Au; M′ = Ga, In, Sb, and Bi) with an Ideal Band Gap and High Power Conversion Efficiency, J. Phys. Chem. C 125 (2021) 21160–21168, https://doi.org/10.1021/acs.jpcc.1c05699.
[31] M. Burgelman, K. Decock, S. Khelifi, A. Abass, Advanced electrical simulation of thin film solar cells, Thin Solid Films 535 (2013) 296–301, https://doi.org/10.1016/j.tsf.2012.10.032.
[32] Z. Zhang, J. Su, J. Hou, Z. Lin, Z. Hu, J. Chang, J. Zhang, Y. Hao, Potential Applications of Halide Double Perovskite Cs2AgInX6 (X = Cl, Br) in Flexible Optoelectronics: Unusual Effects of Uniaxial Strains, J Phys Chem Lett 10 (2019) 1120–1125, https://doi.org/10.1021/acs.jpclett.9b00134.
[33] M. Burgelman, P. Nollet, S. Degrave, Modelling polycrystalline semiconductor solar cells, Thin Solid Films 361–362 (2000) 527–532, https://doi.org/10.1016/S0040-6090(99)00825-1.
[34] A. Menedjhi, N. Bouarissa, S. Saib, K. Bouamama, Halide double perovskite Cs2AgInBr6 for photovoltaic's applications: Optical properties and stability, Optik (stuttg) 243 (2021), https://doi.org/10.1016/j.ijleo.2021.167198.
[35] S. Li, P. Liu, L. Pan, W. Li, S.-E. Yang, Z. Shi, H. Guo, T. Xia, S. Zhang, Y. Chen, The investigation of inverted p-i-n planar perovskite solar cells based on FASnI3 films, Sol. Energy Mater. Sol. Cells 199 (2019) 75–82, https://doi.org/10.1016/j.solmat.2019.04.023.
[36] M. Noman, M. Shahzaib, S.T. Jan, Z. Khan, M. Ismail, A.D. Khan, Optimizing band gap, electron affinity, & carrier mobility for improved performance of formamidinium lead tri-iodide perovskite solar cells, Mater. Sci. Eng. B 300 (2024) 117114, https://doi.org/10.1016/j.mseb.2023.117114.
[37] X. Meng, T. Tang, R. Zhang, K. Liu, W. Li, L. Yang, Y. Song, X. Ma, Z. Cheng, J. Wu, Optimization of germanium-based perovskite solar cells by SCAPS simulation, Opt Mater (amst) 128 (2022) 112427, https://doi.org/10.1016/j.optmat.2022.112427.

Vishal Deswal He is working on perovskite solar cell and is currently a doctoral student at Delhi Technological University (DTU), Delhi.

Sarita Baghel She is working as Assistant Professor at Delhi Technological University (DTU), Delhi. She is leading perovskite solar cells research group at Renewable Energy Research Laboratory at DTU.

ECS Journal of Solid State Science and Technology

ACCEPTED MANUSCRIPT

Dielectric Modulated InAs Pocket Heterojunction Tunnel FET for Biosensor Applications

To cite this article before publication: Shashi Ranjan Ranjan Upadhyay *et al* 2025 *ECS J. Solid State Sci. Technol.* in press
https://doi.org/10.1149/2162-8777/adc338

Manuscript version: Accepted Manuscript

Accepted Manuscript is “the version of the article accepted for publication including all changes made as a result of the peer review process, and which may also include the addition to the article by IOP Publishing of a header, an article ID, a cover sheet and/or an ‘Accepted Manuscript’ watermark, but excluding any other editing, typesetting or other changes made by IOP Publishing and/or its licensors”

This Accepted Manuscript is **© 2025 The Electrochemical Society (“ECS”). Published on behalf of ECS by IOP Publishing Limited. All rights, including for text and data mining, AI training, and similar technologies, are reserved.**.

This article can be copied and redistributed on non commercial subject and institutional repositories.

Although reasonable endeavours have been taken to obtain all necessary permissions from third parties to include their copyrighted content within this article, their full citation and copyright line may not be present in this Accepted Manuscript version. Before using any content from this article, please refer to the Version of Record on IOPscience once published for full citation and copyright details, as permissions will likely be required. All third party content is fully copyright protected, unless specifically stated otherwise in the figure caption in the Version of Record.

View the article online for updates and enhancements.

This content was downloaded from IP address 14.139.251.98 on 01/04/2025 at 05:39

Dielectric Modulated InAs Pocket Heterojunction Tunnel FET for Biosensor Applications

Journal:	*ECS Journal of Solid State Science and Technology*
Manuscript ID	JSS-105568.R1
Manuscript Type:	Research Paper
Date Submitted by the Author:	06-Mar-2025
Complete List of Authors:	Upadhyay, Shashi Ranjan; Delhi Technological University, Electronics and Communication Kale, Sumit; Delhi Technological University, Electronics and Communication Pandey, Anukul; Delhi Technological University, Electronics and Communication
Keywords:	Sensors, Semiconductors, Simulation, Modeling

SCHOLARONE™
Manuscripts

Accepted Manuscript

Dielectric Modulated InAs Pocket Heterojunction Tunnel FET for Biosensor Applications

Shashi Ranjan Upadhyay[a], Sumit Kale[a], Anukul Pandey[a]

[a]*Department of Electronics & Communication Engg., Delhi Technological University, Bawana Rd, New Delhi, 110042, Delhi, India*

Abstract

This work proposes a dielectric-modulated InAs Pocket Heterojunction Tunnel FET (HJ-TFET) for high-performance biosensing applications. The device features a cavity on the source side and an InAs pocket on the source channel junction, significantly enhancing tunneling current and device sensitivity. The study examines the influence of biomolecule dielectric constants and charge densities on the electrostatics of the device. The results indicate that an increase in the dielectric constant improves the sensitivity, while neutral, positive, or negative biomolecule charges modulate the device response, demonstrating charge-dependent sensitivity variations. Comparative analysis reveals superior performance metrics: threshold voltage sensitivity doubles, drain current sensitivity increases 66 times, and ON-OFF current ratio sensitivity improves fourfold over existing FET-based biosensors. These findings underscore the potential of the InAs pocket HJ-TFET as a robust, high-sensitivity biosensor for detecting biomolecules.

Keywords: HJ-TFET, Hetero junction, Nano-cavity, Sensitivity, Biosensor

1. Introduction

Nanosensor technology has become indispensable in a variety of sectors, including medicine, agriculture, defense, aerospace, and health monitoring, its relevance extending into everyday life. The COVID-19 pandemic underscored the critical need for advanced biosensors, particularly chip-based solutions [1, 2], highlighting their pivotal role in health monitoring and disease detection [3].

Nanoscale biosensors offer exceptional spatial resolution, enabling the detection of individual biomolecules and facilitating molecular-level biological

Accepted Manuscript
For Review Only

studies. The foundation for FET-based biosensors was laid in 1970 by P. Bergveld [4], who pioneered the use of MOS transistors for ion activity detection. Since then, these biosensors have evolved significantly, celebrated for their high sensitivity, cost-effectiveness, lightweight design, and scalability for mass production. However, challenges such as short-channel effects (SCEs), high sub-threshold swing (SS), and prolonged response times remain unresolved [5].

JFET-based biosensors face additional hurdles, requiring extensive doping, which introduces issues like random dopant fluctuations, device instability, and fabrication difficulties at the nanoscale. These limitations reduce their effectiveness for biosensing applications. Tunnel FET (TFET)-based biosensors provide a promising alternative, addressing these challenges through their compact design, CMOS-compatible fabrication processes, mass production feasibility, and label-free detection capabilities [6].

TFETs excel in high-speed, low-power sensing due to their distinct charge transport mechanism, minimal leakage current, resistance to SCEs, and lower gate voltage requirements. These characteristics offer superior speed and sensitivity compared to traditional MOSFETs [7, 14]. Furthermore, their suppressed SCEs and the ability to overcome the kT/q limit of conventional FETs enhance device performance, ensuring quicker response times and higher sensitivity for nanoscale biosensing applications [8].

Recent research in biosensors has focused on two primary biomolecule detection mechanisms: gating effects and dielectric modulation, with dielectric modulation emerging as a promising approach. For example, Narang et al. [9] explored TFET biosensors based on P-N-P-N, providing insight into electrical characteristics, although detailed sensitivity analyses remain underexplored. Similarly, N. Kannan et al. [10] demonstrated high sensitivity in impact ionization-based MOS transistor biosensors but did not address the effects of varying biomolecule concentrations. Shoorideh et al. [11] highlighted the effectiveness of FET-based biosensors in the subthreshold region, but did not investigate critical sensitivity parameters such as threshold voltage or switching ratio [12].

Advanced Tunnel FET designs, including heterostacked or vertical TFETs, have shown potential for improved performance metrics. However, these designs introduce significant manufacturing complexity, pose challenges for large-scale production and impact commercial viability [13]. Consistent device performance across large batches remains a key limitation.

To address these challenges, this work introduces a Dielectric-Modulated

Accepted Manuscript
For Review Only

Heterojunction Tunnel FET (HJ-TFET) as a novel biosensor for high-sensitivity biomolecule detection. The device incorporates a hetero-pocket at the junction of source towards the channel, which enhances the quantum tunneling of the charge carriers. This innovation achieves low power consumption alongside improved sensitivity and performance. Simulation results have been validated through calibrated graphs, and suggested fabrication methods provide a practical pathway for device realization. For different dielectric constants, the device's essential electrical parameters—such as surface potential, energy band fluctuation, electric field distribution, and transfer characteristics—are examined. The dielectric modulation in the HJ-TFET biosensor enables precise biomolecule detection, optimizing sensitivity and specificity. The study also evaluates the biosensor response to charged and neutral biomolecules, with sensitivity parameters including drain current sensitivity (S_{Id}), threshold voltage shift (ΔV_{th}), and ON-OFF current ratio sensitivity ($\Delta \frac{I_{\mathrm{ON}}}{I_{\mathrm{OFF}}}$).

2. Device Architecture and Simulation Set-up

2.1. Device Architecture

The 2D architecture of the Heterojunction TFET-based biosensor, along with its geometric descriptions, is illustrated in Fig. 1. The device features InAs hetero pockets at the source-channel junction, which significantly enhance Band-to-Band Tunneling (BTBT) [15]. The device is constructed on a 20 nm thick SiO_2 insulating layer, commonly referred to as the buried oxide layer having length of 100nm.

In Fig. 2, the fabrication process shown includes a number of crucial steps. Masking and lithography are used to define the source and drain regions, followed by their deposition [16]. The InAs hetero pockets are deposited using the Molecular Beam Epitaxy (MBE) technique [17]. A 40 nm thick layer of hafnium oxide (HfO_2) is deposited using LPCVD, and the aluminum gate is created using dry etching [18]. Subsequently, a 20 nm layer of HfO_2 is selectively removed from the source side to form nano-cavities.

To enhance the device's current-driving capability, metal electrodes are placed over the source and drain. The nano-cavities, formed by etching the dielectric, expose a 1 nm thick silicon layer to the air, facilitating the immobilization of biomolecules [19]. Various dielectric materials are incorporated into the nano-cavities on the source side to enable systematic biosensing analysis. The detailed fabrication steps for this device are outlined in Fig. 2.

Accepted Manuscript
For Review Only

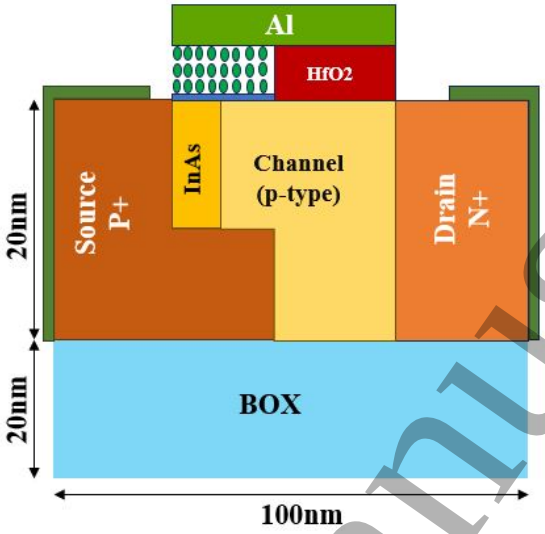

Figure 1: Structural view of the proposed device

2.2. Calibration and Simulation

The simulation assumes a dry environment for sensing applications. The doping densities in various device regions, nano-cavity area, and other simulation parameters, are summarized in Table 1. The simulations are conducted using the Silvaco TCAD simulator, incorporating a concentration-dependent mobility model, recombination model like consrh, and Fermi-Dirac statistics transport model to account for the effects of heavy doping densities [41, 42, 43].

To ensure accuracy, the simulation results are calibrated against experimental data [20]. Calibration is performed by varying the gate to source voltage (V_{gs}) from 0 to 3V while keeping the drain voltage (V_{ds}) fixed at 1V. The comparison, depicted in Fig. 3, demonstrates that the simulated results closely align with the experimental data up to approximately half of the voltage range.

For the Tunnel FET, a bandgap narrowing and bbt.nonlocal model is employed, enhancing the tunneling current and thereby improving the device's overall current-driving capability [21].

Accepted Manuscript
Review Only

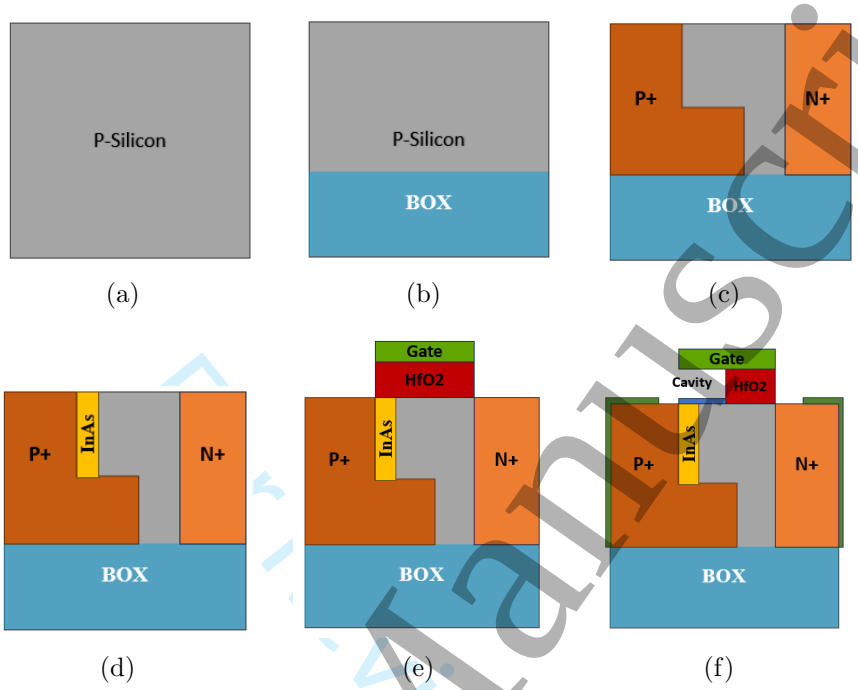

Figure 2: Steps for Fabricating the HJ-TFET Biosensor (a) P-Silicon growth, (b) BOX formation, (c) Deposition of p+ source and n+ Drain, (d) InAs doping using MBE process, (e) HfO_2 deposition, and (f) Formation of nano-cavity and metalization

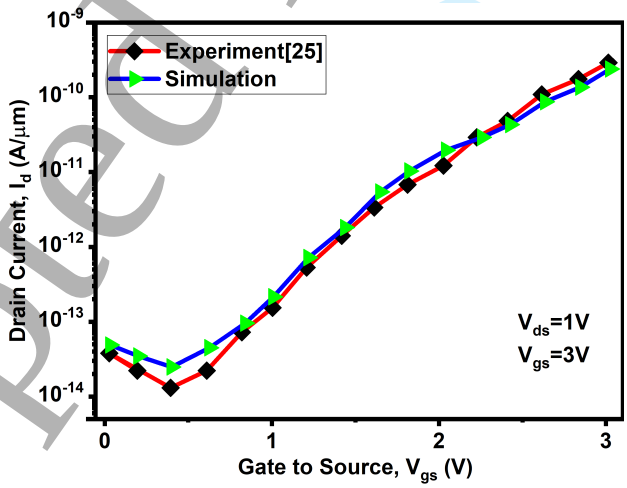

Figure 3: I_d Vs V_{gs} Calibration Graph

Accepted Manuscript

Table 1: DEVICE DESIGN PARAMETERS

Parameters	**Value**
Doping density N^+ (cm^{-3}), N_D	1×10^{18}
Doping density P^+ (cm^{-3}), N_A	1×10^{20}
Source Length (nm), L_s	30
Extended Source Length (nm), L_{ex}	20
Source Thickness (nm), L_s	20
Drain Length (nm), L_d	30
Drain Thickness (nm), T_d	20
Gate Length (nm), L_g	40
Gate Thickness (nm), T_g	5
Pocket (InAs) Length (nm), L_p	5
Pocket (InAs) Thickness (nm), T_p	10
Length of Nano-cavity (nm), L_c	20
Thickness of Nano-cavity (nm), T_c	5
Gate-Oxide Thickness (nm), T_{ox}	6
Channel Length (nm), L_{ch}	40

3. Results and Discussion

3.1. DC Characteristics

This section presents the TCAD simulation study of the Heterojunction Tunnel FET (HJ-TFET)-based biosensor device. The DC characteristics, which describe the relationship between the applied voltage and the resulting current under direct current (DC) conditions, are critical for evaluating the performance and functionality of Tunnel FET-based biosensors [22].

Key aspects of the DC characteristics are examined under the influence of various charged biomolecules. The analysis includes the electric field distribution, energy-band diagrams, tunneling rate, and I_d vs. V_{gs} characteristics. The effects of gate-oxide thickness, source-drain doping concentration, and interface trap densities on device performance are also evaluated. Variations in on-state current, sub-threshold swing and threshold voltage are analyzed to assess the device's sensitivity and detection accuracy [23].

Additionally, the study explores how biomolecule attachment modulates tunneling junction characteristics, offering insights into the device's ability to

Accepted Manuscript
For Review Only

achieve selective and sensitive biosensing. A critical performance parameter, the current ON/OFF ratio, is evaluated to determine the device's ability to distinguish between conducting (ON) and non-conducting (OFF) states. A higher ON/OFF ratio is essential for enhancing the signal-to-noise ratio, ensuring reliable and effective biosensing applications [24].

The incorporation of a PNPN structure in TFETs has been shown to enhance the drain current by modifying the electric field distribution and surface potential, thereby facilitating increased band-to-band tunnelling. This enhancement is primarily due to the introduction of a narrow, highly doped n-type pocket between the source and channel regions, which sharpens the energy band bending and increases the electric field at the source-channel junction. PNPN-based biosensor also has the advantages of high Ion, low leakage, steep SS [25].

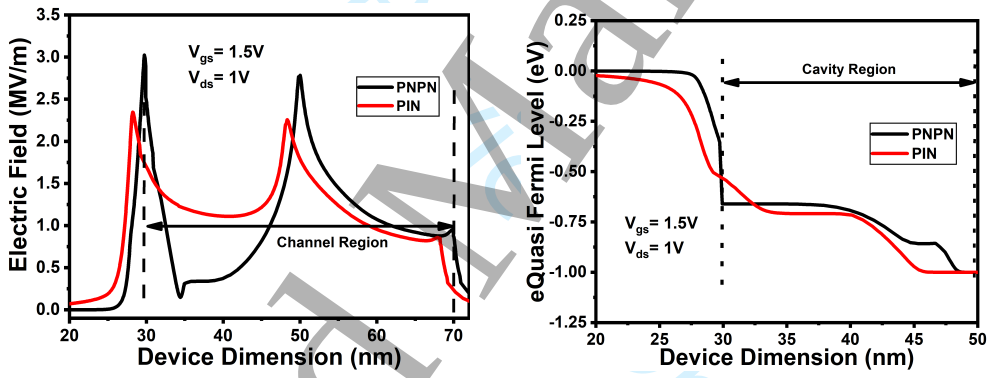

(a) (b)

Figure 4: Characteristics for p-n-p-n and p-i-n structure (a) Electric Field behavior, (b) eQuasi Fermi Level variation

In Fig. 4(a), it is showing that the we are getting the high peak lateral electric field at the p-n interface then p-i interface. That high field supports the more charge to flow that will indirectly lead to more on current. And decrease in the vertical direction electric field, which lowers the interface traps' rate of generation and increases reliability. In Fig. 4(b), quasi fermi level for electron drastically decreases at the pocket layer that has n-type of doping. Its showing that the large concentration difference which lead to high tunnelling current. But for P-i-N type, not getting the sharp changes. Another for optimal length causes the N+ pocket to begin to partially empty and

Accepted Manuscript

raises the concentration of charge between the channel and the source as it moves toward the drain side.

The extended source design in TFETs has proven to be a game-changer in addressing key performance limitations of conventional TFETs. One of its biggest advantages is the boost in the ON current (I_ON) by expanding the source region, the tunneling area increases, as InAs is a low band gap leading to stronger vertical band-to-band tunnelling and better current flow [26], as the tunneling width is very narrow and the position of the quasi-Fermi electron level at source causes the tunnelling current of 0.1 mA/μm in the proposed TFET structure as in Fig. 5(a)

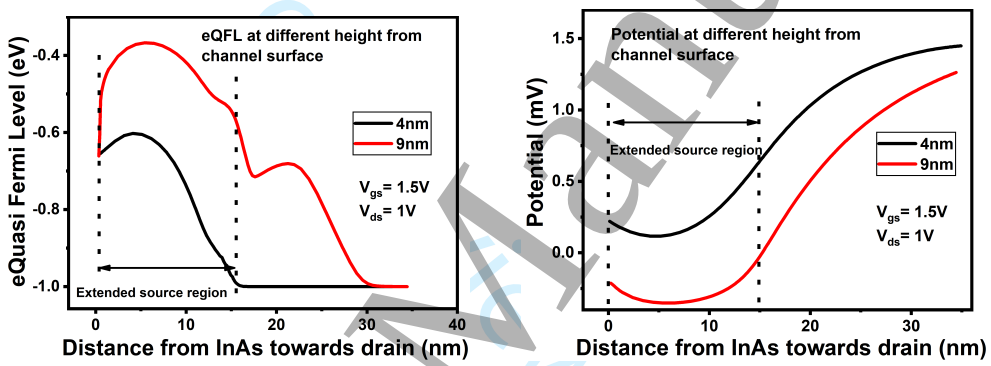

Figure 5: Characteristics for L-shape electrode (a) eQuasi Fermi Level variation, (b) Potential Energy variation , (c) Electric Field behavior

Another major issue in TFETs is ambipolar leakage, where unwanted charge carriers flow in the wrong direction, reducing efficiency. The extended source helps tackle this by modifying the energy band profile, effectively

Accepted Manuscript

suppressing leakage. Additionally, subthreshold swing (SS) performance improves with an extended source, meaning the transistor switches on and off more efficiently, consuming less power. In Fig. 5(b) show that the behavior of the potential energy across the channel at different height from the surface, its show that near the extended part of source the low potential and changing exponentially towards drain that will enable high tunneling. In Fig. 5(c) show that the behaviour of the electric field across the channel, its show that near the extended part of source getting the high electric field that will enable the high current density along the lateral direction.

Electrode Covering the open sides of the source and drain electrodes with an L-shaped in a TFET is an approach that significantly reduces trap charges and enhances the performance of biosensors. By extending the electrode in an L-shape around the source and drain, this structure helps improve charge transport, minimize recombination, and boost tunnelling efficiency, all of which are essential for high-precision biomolecule detection [27].One of the major advantages of this design is that it suppresses interface trap charges, leading to a lower subthreshold slope and making the sensor highly sensitive to even the smallest charge variations. Additionally, the L-shaped electrode improves electrostatic control, reduces leakage currents, and enhances the transistor's switching behaviour, ensuring greater stability and reliability in biosensing applications.

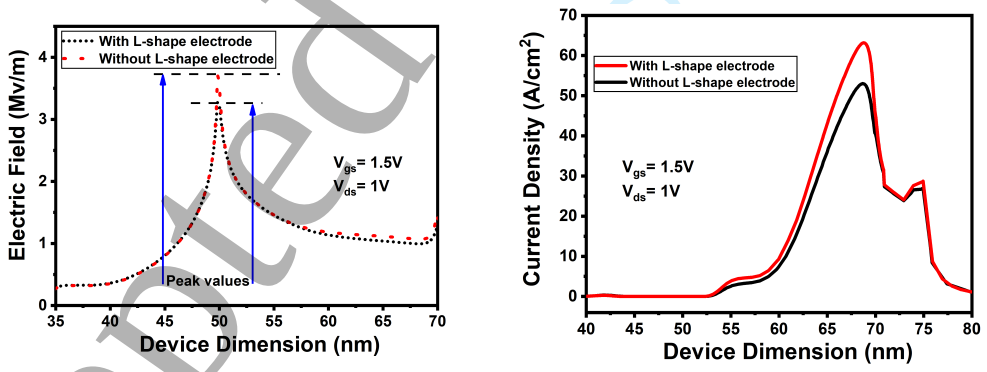

(a) (b)

Figure 6: Characteristics for L-shape electrode (a) Electric Field behavior, (b) eQuasi Fermi Level variation

In Fig. 6(a), shown that Electric field behaviour for devices with and without L-shape a electrode. At the cavity end length, obtained peak values

Accepted Manuscript

for electric filed with L-shape electrode that show that the more tunnelling happening which led to higher current in the device.In Fig. 6(b)shown that the drain current density behaviour along the channel length, with L-shape electrode getting the best current density with respect to the without L-shape electrode. Peak current density obtained at the channel-drain interface.

3.1.1. For Neutral Charge Bio-molecules (N_{bio}=0)

Figure 7 illustrates the device transfer characteristics other parameters of the HJ-TFET-based biosensor under the influence of neutral biomolecules. The simulations consider various dielectric constants (ε_k = 1, 3, 5, 8, 10, 12), where ε_k = 1 represents air, with V_{ds} and V_{gs} fixed at 1V and 1.5V, respectively.

Neutral biomolecules, lacking a net charge, do not significantly contribute to the electric field intensity. As such, they minimally affect the surface potential or the electric field value at the tunneling junction [28]. This absence of direct interaction leads to negligible alterations in the energy band structure of the semiconductor. The energy bands remain relatively flat, with minimal band bending, resulting in reduced tunneling efficiency as the energy barrier for electron tunneling remains largely unaffected.

Furthermore, neutral biomolecules do not introduce additional charge carriers into the system. Consequently, the ion current remains low or unchanged in their presence [29], limiting the biosensor's sensitivity compared to scenarios involving charged biomolecules.

The potential distribution within the device is similarly unaffected by neutral biomolecules. Since there is no change in the charge density at the interface, the potential remains stable, and the depletion region width is not significantly modified [30]. This stability results in a lack of responsiveness when detecting neutral biomolecules, as there are no substantial changes in the potential to influence the current response.

The reduced sensitivity to neutral biomolecules highlights a limitation of the HJ-TFET-based biosensor in detecting such entities. Enhancements to the device design may be necessary to improve responsiveness to neutral species, ensuring broader applicability in biosensing applications.

3.1.2. For Positive Charge Bio-molecules

Figure 8 depicts the device transfer characteristics and other parameters of the HJ-TFET-based biosensor under the influence of positively charged

Accepted Manuscript
For Review Only

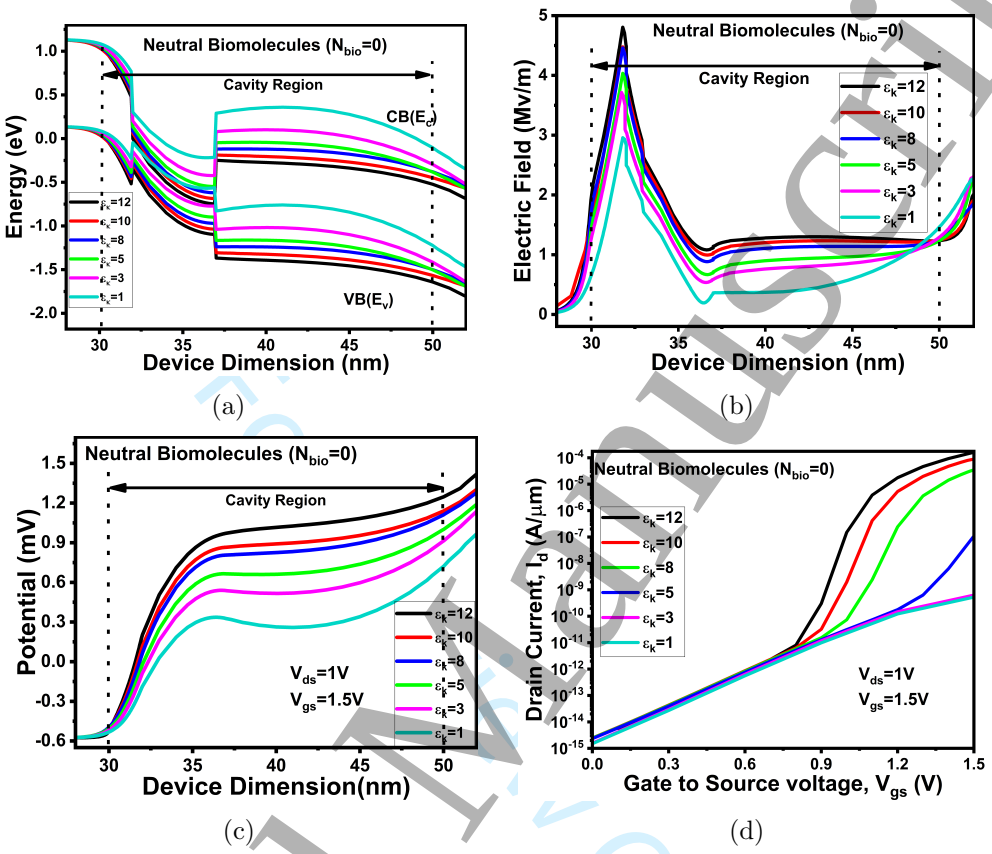

Figure 7: Device Characteristics for multiple values of permittivity ε_k=1,3,5,8,10,12 and $N_{\text{bio}} = 0(neutral)$ (a) Energy-Band Diagram (Conduction Band and Valence Band), (b) Electric Field behavior, (c) Potential variation, (d) transfer characteristics (I_d vs V_{gs})

biomolecules.As simulation observed across different dielectric constants, variations in ε_k significantly influence key parameters, with $V_{ds} = 1\text{V}$ and $V_{gs} = 1.5\text{V}$. For this analysis a positive charge concentration of $5 \times 10^{11}, \text{cm}^{-2}$ is considered.

When positively charged biomolecules are present, they increase the surface potential of the channel, enhancing the electric field near the tunneling junction. This stronger electric field facilitates electron tunneling, leading to a significant improvement in the biosensor's sensitivity. The presence of positively charged biomolecules induces an upward shift in the energy bands near the semiconductor surface, which directly impacts the tunneling current. The charge density of these biomolecules influences the degree

Accepted Manuscript

of energy band bending [31], thereby modifying the potential barrier that electrons must overcome to contribute to the current. As the concentration of positively charged biomolecules increases, the effective gate voltage rises, attracting more charge carriers into the channel. This enhances the device's overall conductivity, leading to a substantial increase in the ion current and improving the current response of the biosensor.

Additionally, the interaction of positively charged biomolecules affects the potential distribution within the device. The increased positive charge reduces the depletion region width, allowing more charge carriers to participate in conduction. These changes significantly influence the tunneling characteristics, enhancing the biosensor's performance and its ability to detect positively charged biomolecules [23].

3.1.3. For Negative Charge Bio-molecules

Figure 9 illustrates the device transfer characteristics and other parameters of the HJ-TFET-based biosensor under the influence of negatively charged biomolecules. As simulation observed across different dielectric constants, variations in ε_k significantly influence key parameters, with $V_{ds} = 1\text{V}$ and $V_{gs} = 1.5\text{V}$. The negative charge concentration analyzed is $-5 \times 10^{11}, \text{cm}^{-2}$.

Negatively charged biomolecules near the tunneling junction enhance the electric field, increasing tunneling. This results in improved sensitivity of the biosensor. The energy band diagram reveals a downward shift in energy bands near the semiconductor surface due to negatively charged biomolecules. This shift increases the tunneling width and alters the potential barrier that electrons must overcome, thereby affecting the tunneling current [32]. As the concentration of negatively charged biomolecules rises, the effective gate voltage decreases, leading to a widening of the depletion region and a reduction in ion current. Additionally, the presence of impurities introduced by negative charges limits the number of charge carriers available for conduction, further impacting the device's performance.

The interaction of negatively charged biomolecules also modifies the potential distribution within the device. This interaction increases the potential drop across the channel and reduces the effective gate voltage, which directly influences the tunneling characteristics and overall current response of the biosensor. These findings highlight the critical role of negative biomolecules in determining the HJ-TFET biosensor's performance, offering insights into optimizing device sensitivity for specific biosensing applications.

Accepted Manuscript
For Review Only

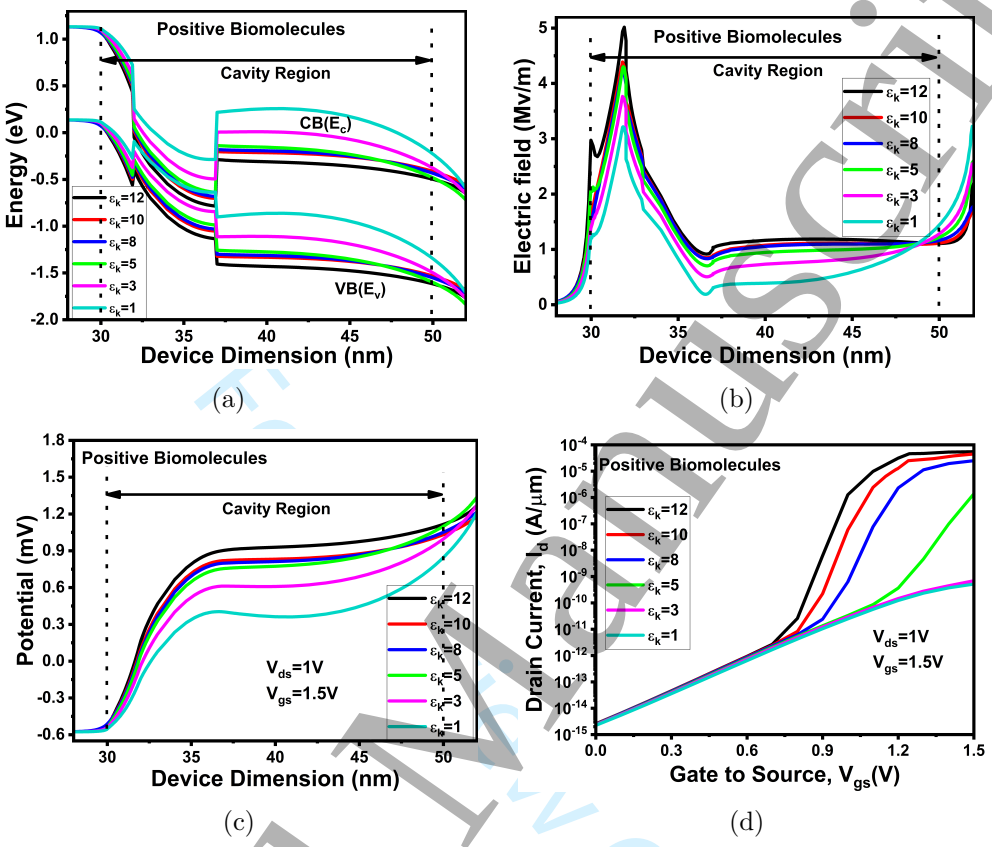

Figure 8: Device Characteristics for different values of permittivity ε_k=1,3,5,8,10,12 and $N_{\text{bio}} = 5 \times 10^{11} cm^{-2}(positive)$ (a) Energy Band Diagram(Conduction Band and Valence Band), (b) Electric Field behavior, (c) Potential variation, (d) transfer characteristics (I_d vs V_{gs})

3.2. Sensitivity Analysis

The TCAD simulation study presented in this section focuses on the dielectrically modulated HJ-TFET-based biosensor. The dielectric constants (ε_k) of proteins involved in DNA/RNA interactions exhibit significant variations depending on their structural and functional properties. Buried acids and bases within the staphylococcal nucleus typically exhibit dielectric constants in the range of 10–12. Charged amino acids show dielectric constants ranging from 11 to 25, while food proteins, such as gluten and zein, display dielectric constants between 5 and 7. These variations are critical for understanding protein-nucleic acid interactions, as they influence electrostatic

Accepted Manuscript
For Review Only

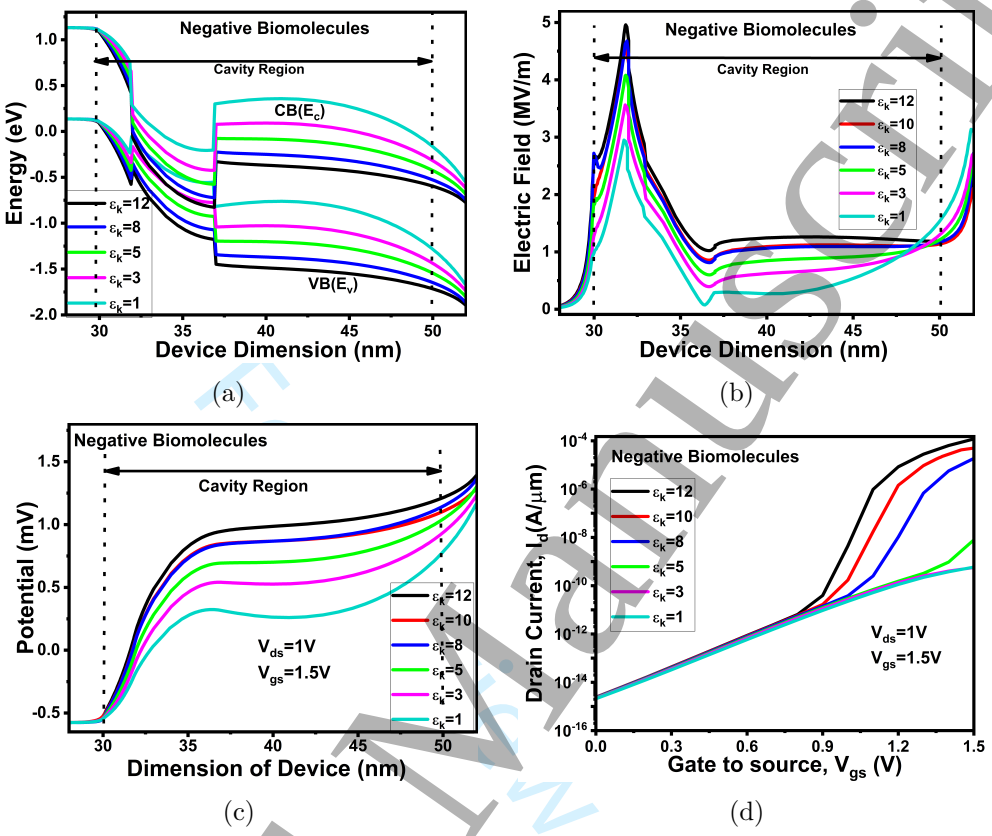

Figure 9: Device Characteristics for different values of permittivity ε_k=1,3,5,8,10,12 and $N_{\text{bio}} = -5\times10^{11} cm^{-2} (negative)$ (a) Energy Band Diagram(Conduction Band and Valence Band), (b) Electric Field behavior, (c) Potential variation, (d) transfer characteristics (I_d vs V_{gs})

forces, protein stability, and molecular folding.Adding a table 2 that lists various biomolecules that uses for simulation along with their corresponding dielectric constants.

Furthermore, lower dielectric constants correspond to tightly packed, hydrophobic regions, while higher dielectric constants are linked to charged residues and polar molecular environments [33]. Understanding these dielectric variations allows insights into biosensor sensitivity and the detection of molecular interactions.

Accepted Manuscript
For Review Only

Table 2: Various Biomolecues with corresponding Dielectric constants

Biomolecule	Dielectric Constant (K)	Charge at pH 7.0
Biotin	2.63	Slightly Negative
Gluten	5	Neutral
Zein	7	Neutral
Chlorobenzene	9	Neutral
Keratin	10	Neutral/Polar
Gelatin	12	Positive
Glutamic Acid	12	Negative

3.2.1. Sensitivity Analysis for Neutral Bio-Molecules

Figure 10 demonstrates the changes in the drain current sensitivity of the biosensor under varying dielectric constants of neutral bio-molecules. As shown in the results, an increase in the dielectric constant of neutral bio-molecules causes the effective gate voltage to drop. This leads to a reduction in the tunneling region, subsequently affecting the drain current response of the device. Additionally, the dielectric properties of these neutral bio-molecules influence the threshold voltage sensitivity (ΔV_{th}). Higher dielectric constants result in greater deviations in the threshold voltage, reflecting the biosensor's response to the presence of these molecules.

The observed shift in sensitivity can be attributed to the buildup of neutral bio-molecules altering the electric field at the tunneling junction, thereby modulating the electrostatic potential and tunneling conditions. These findings highlight that the presence and variations of neutral bio-molecules are integral to tuning the electric field distribution and improving the sensitivity of di-electrically modulated HJ-TFET biosensors.

$$\Delta\left(\frac{I_{ON/OFF}|\varepsilon_{k>1}}{I_{ON/OFF}|\varepsilon_{k=1}}\right) = \frac{I_{ON/OFF}|\varepsilon_{k>1} - I_{ON/OFF}|\varepsilon_{k=1}}{I_{ON/OFF}|\varepsilon_{k=1}} \tag{1}$$

$$\Delta V_{th|\varepsilon_k>1} = V_{th|\varepsilon_k>1} - V_{th|\varepsilon_k=1} \tag{2}$$

$$S_{I_d|\varepsilon_{k>1}} = \frac{I_d|\varepsilon_{k>1} - I_d|\varepsilon_{k=1}}{I_d|\varepsilon_{k=1}} \tag{3}$$

The sensitivity calculation equation for different parameters as eq(1) for $I_{ON/OFF}$ current sensitivity calculation similarly eq(2) for threshold voltage

Accepted Manuscript
For Review Only

sensitivity and eq(3) for the Drain current sensitivity [2]. Where $\varepsilon_{k=1}$ indicates the nano-cavity filled with air and $\varepsilon_{k>1}$ indicates the nano-cavity filled with bio-molecules.

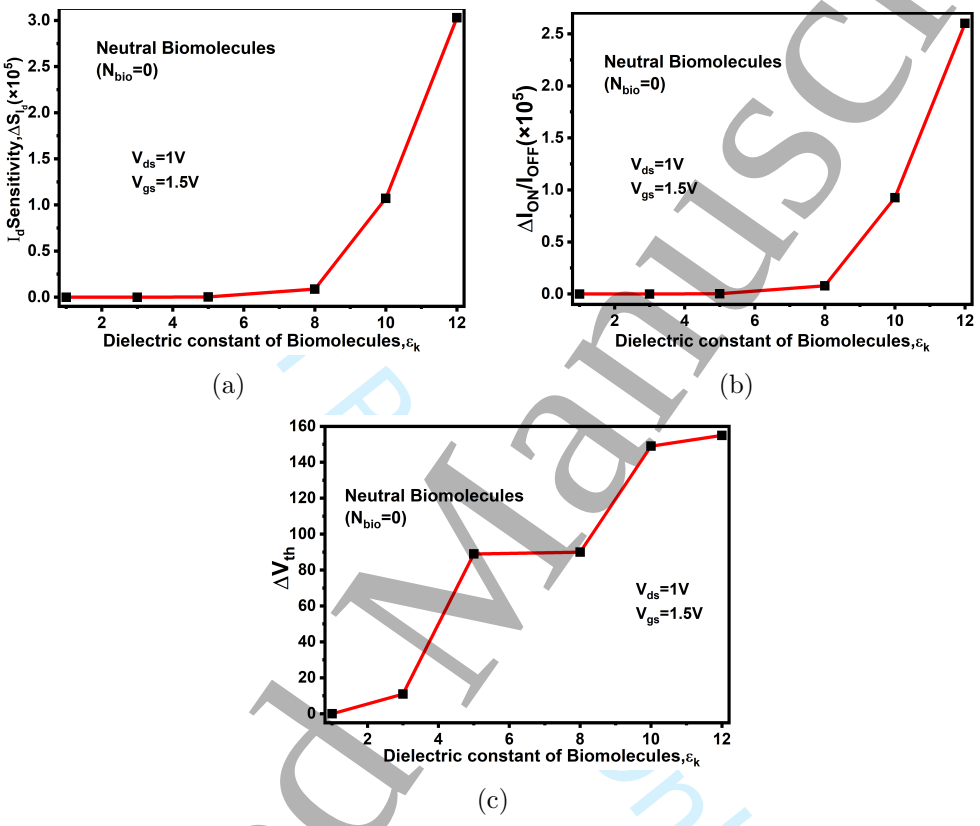

Figure 10: Sensitivity Variations (a) I_d Sensitivity vs bio-molecules(ε_k), (b) sensitivity vs bio-molecules(ε_k) , (c) Threshold Voltage sensitivity vs bio-molecules(ε_k)

Dielectric constant(ε_k) has an impact on biosensor response time as well [21]. Different concentrations of neutral bio-molecules can alter the effective dielectric environment, affecting the electric field in the vicinity of the tunnel intersection. For instance, as the concentration of neutral bio-molecules increases, the effective dielectric constant may change, impacting the sensitivity parameters.

3.2.2. Sensitivity Analysis for charged Bio-molecules

The impact on sensitivity in the presence of charged bio-molecules when varying their concentration in dielectrically modulated HJ-TFET-based biosen-

Accepted Manuscript

sors is significant as shown in Fig. 11. The different bio-molecules concentration takes for analysis are 5×10^{11}, 1×10^{12} and 5×10^{12}. The dielectric constant for this analysis is taken to 12. As the positively charged bio-molecule concentration increases, the drain current in HJ-TFET biosensors increases. More effective electron transfer from the energy's valence band (VB) to the conduction band (CB) is made possible by the enhanced electric field at the tunneling junction. The enhancement of the depletion zone by an increase in positive charge results in increased tunneling at the junction and a consequent rise in drain current flow. The threshold voltage sensitivity (ΔV_{th}) also increases because the presence of charge bio-molecules modifies the electric field and the potential barrier at the channel, resulting in a greater change in the threshold voltage as the concentration increases. When the number of negatively charged bio-molecules rises, biosensors' drain current tends to fall. This happens because negatively charged bio-molecules decrease the efficiency of the gate voltage, increasing the tunneling width and decreasing the device's drain current together [36]. The negative charges can repel carriers in the channel, further diminishing the current. The concentration of negatively charged bio-molecules also affects the threshold voltage sensitivity (ΔV_{th}). Higher concentrations can lead to a more significant deviation in the threshold voltage, as the negative charges influence the electric field and potential barrier at the channel. The ON-OFF current ratio sensitivity ($\Delta I_{ON}/I_{OFF}$) is also positively affected by the concentration of bio-molecules with a positive charge. As the concentration increases, the ON current rises significantly, leading to a higher $I_{ON} - I_{OFF}$ current ratio, This is a critical component in assessing the bio sensor's functionality.

Table 3: Sensitivity Comparison of HJ-TFET based Biosensor with the State-of-the-art Biosensors

Bio-sensors	ΔS_{I_d}	$\Delta I_{ON}/I_{OFF}$	ΔV_{th}
SG-ESTFET [34]	60×10^2	60×23^3	80 mV
DG-ESTFET [34]	45×10^2	15×10^3	74 mV
Vertical-TFET [37]	40	10	54 mV
Lateral-TFET [37]	10	10^3	66 mV
DMG JL-TFET [38]	1.08×10^{-3}	-	-
DMG-GDS-HJL-TFET [39]	4.1×10^{-4}	-	-
SiGe TFET [40]	1.08×10^{-3}	-	0.004 mV
This Work	37×10^4	26×10^4	191 mV

Accepted Manuscript
For Review Only

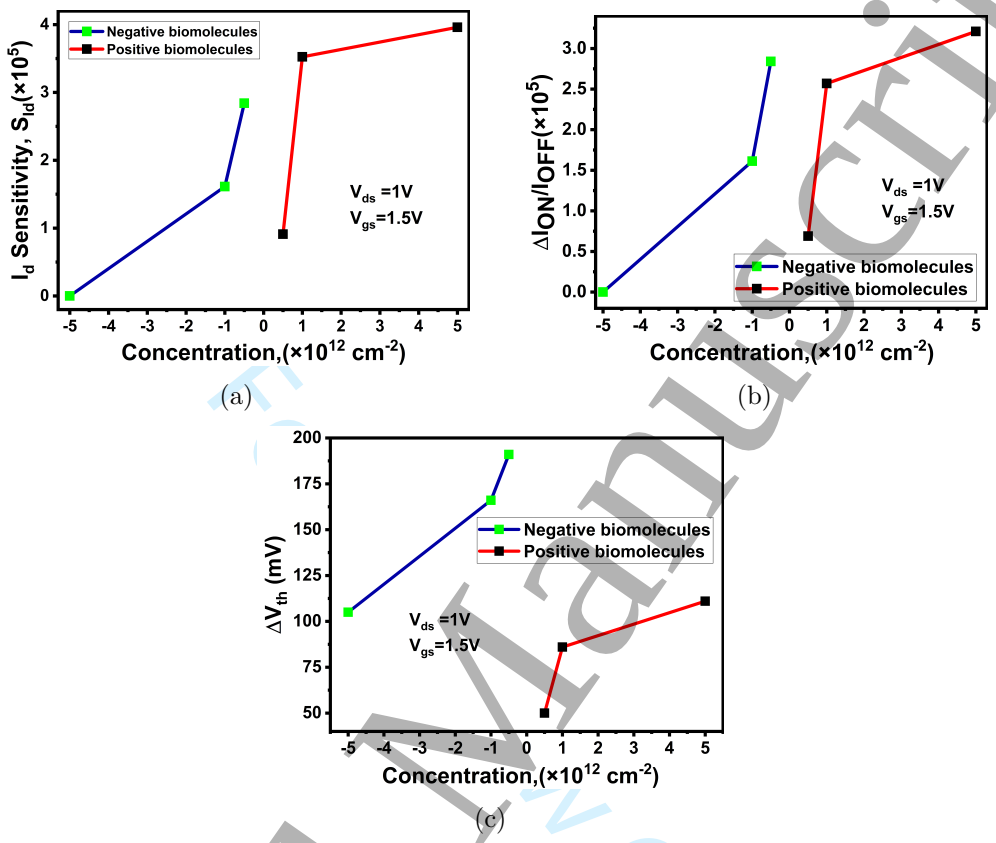

Figure 11: Sensitivity Variations (a) I_d Sensitivity $S_{(I_d)}$ vs bio-molecules(ε_k), (b) $\Delta_{I_{ON}/I_{off}}$ sensitivity vs bio-molecules(ε_k) , (c) Threshold Voltage sensitivity (ΔV_{th} vs bio-molecules(ε_k)

The dielectric constant(ε_k) affects the biosensors' sensitivity of the surrounding medium. When the concentration of the negatively charged biomolecules increases, the effective dielectric environment changes, This may affect the electric field near the device's tunneling junction. The effect of concentration on sensitivity is more pronounced at lower dielectric constants. Performance comparison with recent Bio-sensors is depicted in Table 3.

4. Conclusion

This study presents a hetero-junction Tunnel FET (HJ-TFET)-based biosensor utilizing dielectric modulation. Sensitivity analysis revealed that

Accepted Manuscript
For review only

increasing the dielectric constant (ε_k = 1,3,5,8,10,12) enhances biosensor performance. Sensitivity metrics, including threshold voltage sensitivity (ΔV_{th}), ON-OFF current ratio sensitivity ($\Delta \frac{I_{\text{ON}}}{I_{\text{OFF}}}$), and drain current sensitivity (S_{Id}), were analyzed across varying biomolecule concentrations. Positively charged bio-molecules significantly enhance sensitivity, with optimal performance achieved when the nano-cavity is fully filled. This results in threshold voltage sensitivity **doubled**, drain current sensitivity improving by **66 times**, and ON-OFF current ratio sensitivity increasing by a factor of **four**. The findings highlight that the proposed HJ-TFET-based biosensor offers high sensitivity, particularly for positively charged bio-molecules, and shows strong potential for low-power, high-performance bio-sensing applications with optimized nano-cavity filling.

References

[1] Stern, E, Klemic, JF, Routenberg, DA, Wyrembak, PN, Turner-Evans, DB, Hamilton, AD, LaVan, DA, Fahmy, TM Reed, "Label-free immunodetection with CMOS-compatible semiconducting nanowires", Nature, vol. 445, no. 7127, pp. 519-522, 2007.

[2] A. Kumar, S. Kale, A comparative analysis of cavity positions in charge plasma based tunnel FET for biosensor application. IETEJ. Res. (2023).

[3] A. Kumar, S. Kale, Dual-k reconfigurable silicon nanowire Schottky barrier transistor for biosensing application, presented at the 8thIEEE Electron Devices Technology and Manufacturing(EDTM) Conference, Bangalore, India, Mar. 3–6 (2024)

[4] P. Bergveld, "Development of an ion-sensitive solid-state device for neurophysiological measurements," IEEE Trans. Biomed. Eng., vol. BME-17, no. 1, pp. 70–71, Jan. 1970.

[5] N.N. Poojari, R.R. Singh, N. Ahmed, S. Kale, A comparative study of short gate and full gate dielectric modulated Schottky barrier TFET for biosensing application. SILICON 14(18), 12223–12233 (2022).

[6] Y. Khatami and K. Banerjee, "Steep subthreshold slope n- and p-type tunnel-FET devices for low-power and energy-efficient digital circuits," IEEE Trans. Electron Devices, vol. 56, no. 11, pp. 2752–2761, Nov. 2009.

Accepted Manuscript
For Review Only

[7] D. Sarkar and K. Banerjee, "Proposal for tunnel-field-effect-transistor as ultra-sensitive and label-free biosensors," Appl. Phys. Lett., vol. 100, no. 14, p. 143108, 2012.

[8] B. R. Raad, K. Nigam, D. Sharma, P.N. Kondekar, "Performance investigation of bandgap, gate material work function and gate dielectric engineered TFET with device reliability improvement," Superlattices and Microstruct., vol. 94, pp. 138-146, 2016.

[9] R. Narang, K. V. S. Reddy, M. Saxena, R. S. Gupta and M. Gupta, "A Dielectric-Modulated Tunnel-FET-Based Biosensor for Label-Free Detection: Analytical Modeling Study and Sensitivity Analysis," in IEEE Transactions on Electron Devices, vol. 59, no. 10, pp. 2809-2817, Oct. 2012

[10] N. Kannan and M. J. Kumar, "Charge-Modulated Underlap I-MOS Transistor as a Label-Free Biosensor: A Simulation Study," in IEEE Transactions on Electron Devices, vol. 62, no. 8, pp. 2645-2651, Aug. 2015

[11] K. Shoorideh and C. O. Chui, "On the origin of enhanced sensitivity in nanoscale FET-based biosensors," Proceedings of the National Academy of Sciences, vol. 111, no. 14, pp. 5111–5116, Mar. 2014

[12] M. G. Yirak and R. Chaujar, "TCAD analysis and modelling of gate-stack gate all around junctionless silicon NWFET based bio-sensor for biomedical application," in Proc. IEEE VLSI Device Circuit Syst., Jul. 2020, pp. 60–65.

[13] K. Vanlalawmpuia and B. Bhowmick, "Analysis of Hetero-Stacked Source TFET and Heterostructure Vertical TFET as Dielectrically Modulated Label-Free Biosensors," IEEE Sensors Journal, vol. 22, no. 1, pp. 939–947, Jan. 2022,

[14] A. Kumar and S. Kale, "Noise and Sensitivity Analysis of the Dielectric Modulated Reconfigurable SiNW-SBT for Biosensor Applications," Micro and Nanostructures, pp. 207923–207923, Jul. 2024

[15] K. Ganapathi, Y. Yoon, and S. Salahuddin, "Analysis of InAs vertical and lateral band-to-band tunneling transistors: Leveraging vertical tun-

Accepted Manuscript
For Review Only

neling for improved performance," Applied Physics Letters, vol. 97, no. 3, p. 033504, Jul. 2010

[16] A. Rasool, Shahnaz Kossar, S. Parveen, and U. Rasool, "Heterojunction Tunnel Field-Effect Transistors (TFETs) and Applications," pp. 471–479, Jan. 2024

[17] M. R. Tripathy, A. Kumar Singh, S. Chander, P. K. Singh, K. Baral and S. Jit, "Device-Level Performance Comparison of Some Pocket Engineered III-V/Si Hetero-Junction Vertical Tunnel Field Effect Transistor," 2020 5th International Conference on Devices, Circuits and Systems (ICDCS), Coimbatore, India, 2020, pp. 180-183

[18] Reza Meshkin, "An Extended-Source Tunneling-FET with Gate-Overlapped n+-Doped Pocket," Journal of Electronic Materials, vol. 52, no. 9, pp. 5980–5986, Jun. 2023

[19] Vy Anh Tran, Giang, Thu-Thao Thi Vo, Van Dat Doan, V. Vo, and Van Thuan Le, "Recent Applications and Prospects of Nanowire-Based Biosensors," Processes, vol. 11, no. 6, pp. 1739–1739, Jun. 2023

[20] F. Mayer et al., "Impact of SOI, Si1-xGexOI and GeOI substrates on CMOS compatible tunnel FET performance," in IEDM Tech. Dig.,Dec. 2008, pp. 1–5.

[21] A. Kumar, V. Thakur, S. Kumar, S. Kale, K.R Singh, "Sensitivity Investigation of Underlap Gate Cavity-Based Reconfigurable Silicon Nanowire Schottky Barrier Transistor for Biosensor Application," Silicon, Aug. 2024

[22] N. N. Reddy and D. K. Panda, "A Comprehensive Review on Tunnel Field-Effect Transistor (TFET) Based Biosensors: Recent Advances and Future Prospects on Device Structure and Sensitivity," Silicon, Aug. 2020

[23] R. Ghosh, R. P. Nelapati, P. Saha, R. Chinthaginjala, T. Kim, and K. S., "Sensitivity analysis of bi-metal stacked-gate-oxide hetero-juncture tunnel fet with Si0.6Ge0.4 source biosensor considering non-ideal factors," PLOS ONE, vol. 19, no. 6, p. e0301479, Jun. 2024

Accepted Manuscript
For Review Only

[24] I. Katsouras et al., "Controlling the on/off current ratio of ferroelectric field-effect transistors," Scientific Reports, vol. 5, no. 1, Jul. 2015

[25] D. B. Abdi, M. J. Kumar, "In-Built N+ Pocket p-n-p-n Tunnel Field-Effect Transistor," IEEE Electron Device Letters, vol. 35, no. 12, pp. 1170–1172, Dec. 2014

[26] Kaur and G. Saini, "Drain Source-Engineered Double-Gate Tunnel FET for Improved Performance," Journal of Electronic Materials, vol. 53, no. 7, pp. 3901–3913, May 2024

[27] S. K. Verma, S. Singh, G. Wadhwa, and B. Raj, "Detection of biomolecules using Charge-Plasma based gate underlap dielectric modulated doping less TFET," Transactions on Electrical and Electronic Materials, vol. 21, no. 5, pp. 528–535, Jun. 2020

[28] L Swati, J. Kaur, and A K Singh, "Performance investigation of Ge-based dielectric modulated junctionless TFET as a label-free biosensor," Applied Physics A, vol. 130, no. 2, Jan. 2024

[29] D. Singh, S. Pandey, K. Nigam, D. Sharma, D. S. Yadav, and P. Kondekar, "A Charge-plasma-based dielectric-modulated junctionless TFET for biosensor label-free detection," IEEE Trans. on Electron Devices, vol. 64, no. 1, pp. 271-278, 2017.

[30] P. Vimala,L. Krishna, S Sharma," TFET Biosensor simulation and analysis for various biomolecules," Silicon, 14(13), 7933-7938.

[31] P. Dwivedi,R. Singh, "Investigation the impact of the gate work-function and biases on the sensing metrics of TFET based biosensors." Engineering Research Express 2, no. 2 (2020): 025043.

[32] A. K. Gupta, A. Raman, and N. Kumar, "Design and investigation of a novel charge plasma-based core-shell ring-TFET: Analog and linearity analysis," IEEE Trans. Electron Devices, vol. 66, no. 8, pp. 3506–3512, Aug. 2019.

[33] L. Li, C. Li, Z. Zhang, and E. Alexov, "On the Dielectric 'Constant' of Proteins: Smooth Dielectric Function for Macromolecular Modeling and Its Implementation in DelPhi," Journal of Chemical Theory and Computation, vol. 9, no. 4, pp. 2126–2136, Mar. 2013

Accepted Manuscript
For Review Only

[34] J. Talukdar, G. Rawat and K. Mummaneni, "Dielectrically Modulated Single and Double Gate Tunnel FET Based Biosensors for Enhanced Sensitivity," in IEEE Sensors Journal, vol. 21, no. 23, pp. 26566-26573, 1 Dec.1, 2021

[35] R. Singh, A. Naugarhiya,G. P. Mishra. "Endurance Behavior of Z-Shaped Charge Plasma Tunnel FET for Biosensing Application." Journal of Circuits, Systems and Computers 33, no. 2 (2024).

[36] Chattopadhyay and A. Mallik, "Impact of a spacer dielectric and a gate overlap/underlap on the device performance of a tunnel field-effect transistor," IEEE Trans. Electron Devices, vol. 58, no. 3, pp. 677–683, Mar. 2011.

[37] S. Anand, A, Singh, S. I. Amin, and A. S. Thool, "Design and performance analysis of dielectrically modulated doping-less tunnel FET-based label free biosensor," IEEE Sensors J., vol. 19, no. 12, pp. 4369–4374,Jun. 2019

[38] V. Thakur, A. Kumar, S. Kale, Analytical modeling of space engineered reconfigurable silicon nanowire Schottky barrier transistor for biosensing applications. Micro Nanostruct. 188, 207799 (2024).

[39] H. Xie, H. Liu, S. Chen, T. Han, and S. Wang, "Electrical performance of InAs/GaAs0.1Sb0.9 heterostructure junctionless TFET with dual-material gate and Gaussian-doped source," Semicond. Sci. Technol., vol. 35, no. 9, Sep. 2020, Art. no. 095004.

[40] S. Kumar, Y. Singh, B. Singh, and P. K. Tiwari, "Simulation study of dielectric modulated dual channel trench gate TFET-based biosensor," IEEE Sensors J., vol. 20, no. 21, pp. 12565–12573, Nov. 2020

[41] V. Thakur, A. Kumar, and S. Kale, "Numerical modeling and performance analysis of underlap gate cavity integrated reconfigurable silicon nanowire Schottky barrier transistor biosensors," Applied Physics A (2024), pp.1-13.

[42] A. Kumar, and S. Kale, "Analytical Modeling of Silicon Nanowire Dielectric Modulated Schottky Barrier Reconfigurable FET (SiNW-DM SB RFET) Biosensor, ECS J. Solid State Sci. Technol. (2024):13, 113005.

Accepted Manuscript
For Review Only

[43] A. Kumar, and S. Kale, "Spacer-Engineered Reconfigurable Silicon Nanowire Schottky Barrier Transistor as a Label-Free Biosensor," Silicon (2024): 16(5), pp.2023-2036.

Accepted Manuscript
For Review Only

arXiv:2503.02243v1 [math.CA] 4 Mar 2025

Durrmeyer type operators linked with Boas-Buck type polynomials

Naokant Deo and Sandeep Kumar

Department of Mathematics, Delhi Technological University
Delhi-110042, India
naokantdeo@dce.ac.in

Department of Mathematics, Maitreyi College, University of Delhi
Delhi 110021, India
sandeepkumardps@gmail.com

Abstract

The present article intends to introduce the sequence of Baskakov-Durrmeyer type operators linked with the generating functions of Boas-Buck type polynomials. After calculating the moments, including the limiting case of central moments of the constructed sequence of operators, in the subsequent sections, we estimate the convergence rate using the Ditzian-Totik modulus of smoothness and some convergence results in Lipchitz-type space.

Keywords: Boas-Buck polynomials, Modulus of smoothness, Lipschitz-type space, Rate of Convergence.

MSC: 41A10, 41A25 and 41A30.

1 Introduction

Suppose that $\xi, \mathcal{S}, \mathcal{T}, \mathcal{U}$ and $\mathcal{V}$ are analytic functions defined on some disc $|z| < \rho$ with $\rho > 1$. Let the power series expansions of these analytic functions are

$$\xi(s) = \sum_{j=0}^{\infty} p_j s^j, \qquad \mathcal{S}(s) = \sum_{j=0}^{\infty} q_j s^j, \qquad \mathcal{T}(s) = \sum_{j=0}^{\infty} r_j s^{j+1},$$

$$\mathcal{U}(s) = \sum_{j=0}^{\infty} u_j s^{j+2}, \qquad \mathcal{V}(s) = \sum_{j=0}^{\infty} v_j s^{j+3},$$

where the coefficients of the above series representation meets with $p_j \neq 0, q_j \neq 0$ and $r_j \neq 0$. Now, according to R. Goyal [10] and E. D. Rainville [4], we have polynomials generating function $\Theta_j(x)s^j$ as:

$$\mathcal{S}(s).\xi\left(x^2\mathcal{T}(s) + x\mathcal{U}(s) + \mathcal{V}(s)\right) = \sum_{j=0}^{\infty} \Theta_j(x)s^j.$$

Using the polynomial generating function Θ_j, S. Verma and S. Sucu [14] described the following operators

$$\mathcal{B}_n(f;x) = \frac{1}{\mathcal{S}(1).\xi\left(n^2x^2\mathcal{T}(1) + nx\mathcal{U}(1) + \mathcal{V}(1)\right)} \sum_{j=0}^{\infty} \Theta_j(nx) f\left(\frac{j}{n}\right), \tag{1.1}$$

with some restrictions for the positivity like $\xi(s) \geq 0,\ \forall\ s \in \mathbb{R}$, and $\Theta_j(x) \geq 0;\ j = 0, 1, 2 \ldots$ for all $x \geq 0$ and $\mathcal{S}(1) > 0$. In the reference of convergence of the sequence (1.1) we assume that, $\mathcal{T}'(1) = 0, \mathcal{T}''(1) = 0$ and $\mathcal{U}'(1) = 1$ and apply the Korovkin-type theorem. Many authors [13], [11], [12], [5], [15], [8] and [3] discussed the convergence of the related operators. The remarkable work of [14], [7] and [1] allow us to define a sequence of Baskakov-Durrmeyer type operators linked with the generating function of Boas-Buck type polynomials under the same assumptions and restrictions.
For $\sigma > 0$, consider a class of functions $C_\sigma[0,\infty) = \{f \in C[0,\infty) : |f(s)| \leq M(1+s^\sigma)\}$, for some $M > 0$ with the norm $\|f(s)\| = \sup_{s\in[0,\infty)} \frac{|f(s)|}{1+s^\sigma}$. Now, for $f \in C_\sigma[0,\infty)$, we construct

$$\tilde{\mathcal{B}}_n(f;x) = \frac{1}{\mathcal{S}(1).\xi\left(n^2x^2\mathcal{T}(1) + nx\mathcal{U}(1) + \mathcal{V}(1)\right)} \sum_{j=0}^{\infty} \frac{\Theta_j(nx)}{B(j,n+1)} \times \int_0^\infty \frac{s^{j-1}}{(1+s)^{n+j+1}} f(s)ds, \tag{1.2}$$

where B is a beta function, defined as $B(j,n+1) = \frac{\Gamma(j)\Gamma(n+1)}{\Gamma(j+n+1)}$.
Alternatively the operators (1.2) may be written as:

$$\tilde{\mathcal{B}}_n(f;x) = \int_0^\infty \underline{\mathcal{V}}_n(x,s)(f;x)f(s)ds, \tag{1.3}$$

where

$$\underline{\mathcal{V}}_n(x,s) = \frac{1}{\mathcal{S}(1).\xi\left(n^2x^2\mathcal{T}(1) + nx\mathcal{U}(1) + \mathcal{V}(1)\right)} \sum_{j=0}^{\infty} \frac{\Theta_j(nx)}{B(j,n+1)} \frac{s^{j-1}}{(1+s)^{n+j+1}}.$$

This article intends to investigate the convergence properties of the operators (1.2). Firstly, we calculate the moments and central moments, including the limiting case of the constructed operators' and then prove the convergence using Korovkin's theorem. After making some convergence results based on the modulus of continuity, Lipchitz-type space, and weighted space, we estimates the convergence for the functions of bounded variations.

2 Some results on the operators $\mathcal{B}_n$ and $\tilde{\mathcal{B}}_n$

Lemma 2.1. *From [7], for $x \in [0,\infty)$ and $p(x) = n^2x^2\mathcal{T}(1) + nx\mathcal{U}(1) + \mathcal{V}(1)$ important results related to the operators (1.1) are follows:*

$$\begin{aligned}
\mathcal{B}_n(1;x) &= 1 \\
\mathcal{B}_n(s;x) &= \frac{\xi'(p(x))}{\xi(p(x))}x + \frac{1}{n}\left[\frac{\mathcal{S}'(1)}{\mathcal{S}(1)} + \mathcal{V}'(1)\frac{\xi'(p(x))}{\xi(p(x))}\right] \\
\mathcal{B}_n\left(s^2;x\right) &= \frac{\xi''(p(x))}{\xi(p(x))}x^2 + \left[\frac{\xi'(p(x))}{\xi(p(x))}\left(\frac{2\mathcal{S}'(1)}{\mathcal{S}(1)} + \mathcal{U}''(1) + 1\right)\right. \\
&\quad \left. + 2\mathcal{V}'(1)\frac{\xi''(p(x))}{\xi(p(x))}\right]\frac{x}{n} + \left[\frac{\mathcal{S}''(1) + \mathcal{S}'(1)}{\mathcal{S}(1)} + \left(\frac{2\mathcal{S}'(1)\mathcal{V}'(1)}{\mathcal{S}(1)}\right.\right. \\
&\quad \left.\left. + \mathcal{V}''(1) + \mathcal{V}'(1)\right)\frac{\xi'(p(x))}{\xi(p(x))} + (\mathcal{V}'(1))^2\frac{\xi''(p(x))}{\xi(p(x))}\right]\frac{1}{n^2}.
\end{aligned}$$

Lemma 2.2. *For $x \in [0,\infty)$, and with the help of Lemma 2.1, we have*

$$\begin{aligned}
\tilde{\mathcal{B}}_n(1;x) &= 1\\
\tilde{\mathcal{B}}_n(s;x) &= \frac{\xi'(p(x))}{\xi(p(x))}x + \frac{1}{n}\left(\frac{\mathcal{S}'(1)}{\mathcal{S}(1)} + \mathcal{V}'(1)\frac{\xi'(p(x))}{\xi(p(x))}\right)\\
\tilde{\mathcal{B}}_n(s^2;x) &= \frac{n}{n-1}\frac{\xi''(p(x))}{\xi(p(x))}x^2 + \frac{x}{n-1}\left[2\mathcal{V}'(1)\frac{\xi''(p(x))}{\xi(p(x))} + \left(2 + 2\frac{\mathcal{S}'(1)}{\mathcal{S}(1)}\right.\right.\\
&\quad \left.\left. + \mathcal{U}''(1)\right)\frac{\xi'(p(x))}{\xi(p(x))}\right] + \frac{1}{n(n-1)}\left[\left(\mathcal{V}''(1)\right)^2\frac{\xi''(p(x))}{\xi(p(x))}\right.\\
&\quad \left. + \left(2\frac{\mathcal{S}'(1)}{\mathcal{S}(1)}\mathcal{V}'(1) + 2\mathcal{V}'(1) + \mathcal{V}''(1)\right)\frac{\xi'(p(x))}{\xi(p(x))} + \frac{2\mathcal{S}'(1) + \mathcal{S}''(1)}{\mathcal{S}(1)}\right].
\end{aligned}$$

Proof. By simple calculations, we get

$$\tilde{\mathcal{B}}_n(s^2;x) = \frac{1}{n-1}\left[n\mathcal{B}_n(s^2;x) + \mathcal{B}_n(s;x)\right].$$

Now, by simple computations and using the Lemma 2.1, required result follows. □

Lemma 2.3. *Using Lemma 2.1 and Lemma 2.2, central moments of the operators (1.2) are given by,*

$$\begin{aligned}
\tilde{\mathcal{B}}_n((s-x);x) &= \left[\frac{\xi'(p(x))}{\xi(p(x))} - 1\right]x + \frac{1}{n}\left(\frac{\mathcal{S}'(1)}{\mathcal{S}(1)} + \mathcal{V}'(1)\frac{\xi'(p(x))}{\xi(p(x))}\right)\\
\tilde{\mathcal{B}}_n\left((s-x)^2;x\right) &= \left[\frac{n}{n-1}\frac{\xi''(p(x))}{\xi(p(x))} - 2\frac{\xi'(p(x))}{\xi(p(x))} + 1\right]x^2\\
&\quad + \left[\frac{2}{n-1}\mathcal{V}'(1)\frac{\xi''(p(x))}{\xi(p(x))} + \frac{1}{n-1}\left(2 + \mathcal{U}''(1)\right.\right.\\
&\quad \left.\left. + \frac{2\mathcal{S}'(1)}{\mathcal{S}(1)}\right)\frac{\xi'(p(x))}{\xi(p(x))} - \frac{2}{n}\left(\mathcal{V}'(1)\frac{\xi'(p(x))}{\xi(p(x))} + \frac{\mathcal{S}'(1)}{\mathcal{S}(1)}\right)\right]x\\
&\quad + \frac{1}{n(n-1)}\left[\left(\mathcal{V}'(1)\right)^2\frac{\xi''(p(x))}{\xi(p(x))} + \left(2\mathcal{V}'(1)\frac{\mathcal{S}'(1)}{\mathcal{S}(1)}\right.\right.\\
&\quad \left.\left. + 2\mathcal{V}'(1) + \mathcal{V}''(1)\right)\frac{\xi'(p(x))}{\xi(p(x))} + \frac{2\mathcal{S}'(1) + \mathcal{S}''(1)}{\mathcal{S}(1)}\right].
\end{aligned}$$

Proof. Simple computations and the Lemma 2.2, leads the required proof. □

Now, to study the convergence properties of the operators (1.2), we assume that $\lim_{t\to\infty}\frac{\xi'(t)}{\xi(t)} = 1$ and $\lim_{t\to\infty}\frac{\xi''(t)}{\xi(t)} = 1$ that are point wise valid on the analytic functions $\mathcal{S}(s), \mathcal{T}(s), \mathcal{U}(s)$ and $\mathcal{V}(s)$. Also, we assume the following considerations:

$$\lim_{n\to\infty} n\left[\frac{\xi'(p(x))}{\xi(p(x))} - 1\right] = \ell_1(x),$$

$$\lim_{n\to\infty} n\left[\frac{n}{n-1}\frac{\xi''(p(x))}{\xi(p(x))} - n\frac{\xi'(p(x))}{\xi(p(x))} + 1\right] = \ell_2(x).$$

In the next Lemma, we discuss the limiting cases of the operators (1.2), by applying the above assumptions on the Lemma 2.3.

Lemma 2.4. *For the operators (1.2), we may write:*

$$\lim_{n\to\infty} n\tilde{\mathcal{B}}_n((s-x);x) = \ell_1(x)x + \frac{\mathcal{S}'(1)}{\mathcal{S}(1)} + \mathcal{V}'(1),$$

$$\begin{aligned}\lim_{n\to\infty} n\tilde{\mathcal{B}}_n\left((s-x)^2;x\right) &= \ell_2(x)x^2 + x\left(2+\mathcal{U}''(1)\right)\\ &= \eta_1(x)(say).\end{aligned}$$

Moreover, for $n \in \mathbb{N}$ and some constant c, we have

$$\begin{aligned}\tilde{\mathcal{B}}_n\left((s-x)^2;x\right) &\leq \frac{\ell_2(x)x^2 + x\left(2+\mathcal{U}''(1)\right)}{n}\\ &\leq \frac{\ell_2(x)x^2 + cx}{n}.\end{aligned}$$

Since the limiting value $\ell_2(x)$ exists finitely, therefore for all $x \in [0,\infty)$, there exists $\mathcal{M} > 0$, such that $\ell_2(x) \leq \mathcal{M}$, taking it into the account, we may write:

$$\tilde{\mathcal{B}}_n\left((s-x)^2;x\right) \leq \frac{\mathcal{M}.x(x+1)}{n}.$$

Theorem 2.1. *For any compact subset S of $[0,\infty)$ and a continuous function f defined on $[0,\infty)$, the sequence $\tilde{\mathcal{B}}_n(f;x)_{n\geq 1}$, converges uniformly to the function f on S.*

Proof. By simple computations and using the Lemma 2.2 we see that, For $i = 0,1,2$, the sequence $\tilde{\mathcal{B}}_n\left(t^i;x\right)_{n\geq 1}$, converges uniformly on S to the function $e_i(x) = x^i$. Hence, by using Bohman-Korovkin's theorem [2], the required result follows. □

3 Key Results

Let's consider the Lipchitz-type space explained by O. Szász [9]to build the convergence of the operators (1.2) in this space. For $0 < r \leq 1, x \in (0,\infty)$ and $s \in [0,\infty)$, we have

$$Lip^*_{\mathcal{K}} := \{f \in C[0,\infty) : |f(s)-f(x)|\} \leq \mathcal{K}_f \frac{|s-x|^r}{(s+x)^{\frac{r}{2}}},$$

where the constant $\mathcal{K}_f$ depends on f. In the following theorem, we establish a relation towards the rate of convergence of the operators $\tilde{\mathcal{B}}_n(f;x)$ in the Lipchitz-type space.

Theorem 3.1. *(Point-wise convergence) Let f be a function in a Lipchitz class $Lip^*_{\mathcal{K}}$ and $r \in (0,1]$. Then,*

$$\left|\tilde{\mathcal{B}}_n(f;x) - f(x)\right| \leq \frac{\mathcal{K}}{x^{\frac{r}{2}}}\left(\tilde{\mathcal{B}}_n\left((s-x)^2;x\right)\right)^{\frac{r}{2}}.$$

Proof.

$$\left|\tilde{\mathcal{B}}_n(f;x) - f(x)\right| \leq \int_0^\infty \underline{\mathcal{V}}_n(x,s)\,|f(s)-f(x)|\,ds,$$

on applying Hölder's inequality with $p = \frac{2}{r}$ and $q = \frac{2-r}{2}$ and Lemma 2.3, we have

$$\begin{aligned}\left|\tilde{\mathcal{B}}_n(f;x) - f(x)\right| &\leq \left(\int_0^\infty \underline{\mathcal{V}}_n(x,s)\left(|f(s)-f(x)|^{\frac{2}{r}}\right)ds\right)^{\frac{r}{2}}\left(\int_0^\infty \underline{\mathcal{V}}_n(x,s)ds\right)^{\frac{2-r}{2}}\\ &\leq \left(\int_0^\infty \underline{\mathcal{V}}_n(x,s)\left(|f(s)-f(x)|^{\frac{2}{r}}\right)ds\right)^{\frac{r}{2}}\\ &\leq \mathcal{K}\left(\int_0^\infty \underline{\mathcal{V}}_n(x,s)\left(\frac{(s-x)^2}{s+x}\right)ds\right)^{\frac{r}{2}}\\ &\leq \frac{\mathcal{K}}{x^{\frac{r}{2}}}\left(\tilde{\mathcal{B}}_n\left((s-x)^2;x\right)\right)^{\frac{r}{2}}.\end{aligned}$$

□

Theorem 3.2. *Let $\mathcal{C}_B[0,\infty)$ be the class of all real-valued continuous and bounded functions and for f. Then, for $x \in [0,\infty]$ and $\delta > 0$, we have*

$$\left|\tilde{\mathcal{B}}_n(f;x)\right| \leq 2\varpi\left(f;\sqrt{\tilde{\mathcal{B}}_n\left((s-x)^2;x\right)}\right),$$

where, the modulus of continuity $\varpi(f;\delta)$ is given by

$$\varpi(f;\delta) := \sup_{|x-y|<\delta\, x,y\in[0,\infty)} \sup |f(x)-f(y)|.$$

Proof. For $f \in \mathcal{C}_B[0,\infty)$, we have

$$\begin{aligned}
\left|\tilde{\mathcal{B}}_n(f;x)-f(x)\right| &= \left|\frac{1}{\mathcal{S}(1).\xi(p(x))}\sum_{j=0}^{\infty}\frac{\Theta_j(nx)}{B(j,n+1)}\right. \\
&\quad \left.\times\int_0^{\infty}\frac{s^{j-1}}{(1+s)^{n+j+1}}(f(s)-f(x))\,ds\right| \\
&\leq \frac{1}{\mathcal{S}(1).\xi(p(x))}\sum_{j=0}^{\infty}\frac{\Theta_j(nx)}{B(j,n+1)} \\
&\quad \times\int_0^{\infty}\frac{s^{j-1}}{(1+s)^{n+j+1}}|f(s)-f(x)|\,ds \\
&\leq \frac{1}{\mathcal{S}(1).\xi(p(x))}\sum_{j=0}^{\infty}\frac{\Theta_j(nx)}{B(j,n+1)} \\
&\quad \times\int_0^{\infty}\frac{s^{j-1}}{(1+s)^{n+j+1}}\left(1+\frac{1}{\delta}|s-x|\right)\varpi(f;\delta)ds \\
&\leq \left(1+\frac{1}{\delta}\frac{1}{\mathcal{S}(1).\xi(p(x))}\sum_{j=0}^{\infty}\frac{\Theta_j(nx)}{B(j,n+1)}\right. \\
&\quad \left.\times\int_0^{\infty}\frac{s^{j-1}}{(1+s)^{n+j+1}}|s-x|\,ds\right)\varpi(f;\delta), \qquad (3.1)
\end{aligned}$$

on the account of Cauchy-Schwarz inequality and Lemma2.4, we get

$$\begin{aligned}
&\sum_{j=0}^{\infty}\frac{\Theta_j(nx)}{B(j,n+1)}\int_0^{\infty}\frac{s^{j-1}}{(1+s)^{n+j+1}}|s-x|\,ds \\
&\leq \left(\sum_{j=0}^{\infty}\frac{\Theta_j(nx)}{B(j,n+1)}\int_0^{\infty}\frac{s^{j-1}}{(1+s)^{n+j+1}}(s-x)^2\,ds\right)^{\frac{1}{2}} \\
&\quad \times\left(\sum_{j=0}^{\infty}\frac{\Theta_j(nx)}{B(j,n+1)}\int_0^{\infty}\frac{s^{j-1}}{(1+s)^{n+j+1}}ds\right)^{\frac{1}{2}}. \qquad (3.2)
\end{aligned}$$

From (3.1) and (3.2), we may write

$$\left|\tilde{\mathcal{B}}_n(f;x)-f(x)\right| \leq \left(1+\frac{1}{\delta}\left(\tilde{\mathcal{B}}_n\left((1;x)\right)^{\frac{1}{2}}\left(\tilde{\mathcal{B}}_n\left((s-x)^2;x\right)\right)^{\frac{1}{2}}\right)\varpi(f;\delta),$$

considering $\delta = \left(\tilde{\mathcal{B}}_n\left((s-x)^2;x\right)\right)^{\frac{1}{2}}$ and using the above inequality, we get the required result. □

Now, we assess the rate of convergence by using the Ditzian-Totik modulus of smoothness $\varpi_{\chi^\gamma}(f,\delta)$ and Peetre's $K-$functional $K_{\chi^\gamma}(f,\delta), 0\leq\gamma\leq 1$. For $f\in C_B[0,\infty)$ and $\chi(x)=\sqrt{x(1+x)}$, the Ditzian-Totik modulus of smoothness is explained as:

$$\varpi_{\chi^\gamma}(f,\delta)=\sup_{0\leq i\leq\delta}\sup_{x\pm\frac{i\chi^\gamma(x)}{2}\in[0,\infty)}\left|f\left(x+\frac{i\chi^\gamma(x)}{2}\right)-f\left(x-\frac{i\chi^\gamma(x)}{2}\right)\right|,$$

and the Peetre's $K-$functional is defined as:

$$K_{\chi^\gamma}(f,\delta)=\inf_{\varphi\in W_\gamma}\{\|f-\varphi\|-\delta\|\chi^\gamma\varphi'\|\},$$

where W_γ is a subspace of all real valued functions defined on $[0,\infty)$, and $\varphi\in W_\gamma$ which is locally absolutely continuous with norm $\|f^\gamma\varphi'\|\leq\infty$. In [[16], Theorem 2.1.1], there exists a constant $\mathcal{D}\geq 0$ such that

$$\mathcal{D}^{-1}\varpi_{\chi^\gamma}(f,\delta)\leq K_{\chi^\gamma}(f,\delta)\leq\mathcal{D}\varpi_{\chi^\gamma}(f,\delta). \tag{3.3}$$

Theorem 3.3. *For $f\in C_B[0,\infty)$ then, we have*

$$|\mathcal{B}_n(f;x)-f(x)|\leq\mathcal{D}\varpi_{\chi^s}\left(f;\chi^{1-\gamma}(x)\frac{1}{\sqrt{n}}\right).$$

Proof. For $\varphi\in W_\gamma$, first we write the following

$$\varphi(s)=\varphi(x)+\int_x^s\varphi'(s)ds.$$

Applying $\mathcal{B}_n(.;x)$ and using Hölder's inequality, we have

$$\begin{aligned}\left|\tilde{\mathcal{B}}_n\left(\varphi(s);x\right)-\varphi(x)\right| &\leq \tilde{\mathcal{B}}_n\left(\int_x^s|\varphi'(u)|\,du;x\right)\\ &\leq \|f^\gamma\varphi'\|\tilde{\mathcal{B}}_n\left(\left|\int_x^s\frac{du}{\chi^\gamma(u)}\right|;x\right)\\ &\leq \|f^\gamma\varphi'\|\tilde{\mathcal{B}}_n\left(|s-x|^{1-\gamma}\left|\int_x^s\frac{du}{\chi(u)}\right|^\gamma;x\right).\end{aligned} \tag{3.4}$$

Let $I=\left|\int_x^s\frac{du}{\chi(u)}\right|$, now first we simplify expression I,

$$\begin{aligned}\left|\int_x^s\frac{du}{\chi(u)}\right| &\leq \left|\int_x^s\frac{du}{\sqrt{u}}\right|\left(\frac{1}{1+x}+\frac{1}{1+s}\right)\\ &\leq 2\left|\sqrt{s}-\sqrt{x}\right|\left(\frac{1}{1+x}+\frac{1}{1+s}\right)\\ &\leq 2\frac{|s-x|}{\sqrt{s}+\sqrt{x}}\left(\frac{1}{1+x}+\frac{1}{1+s}\right).\end{aligned} \tag{3.5}$$

Now, we use the inequality $|p+q|^\gamma\leq|p|^\gamma+|q|^\gamma, 0\leq\gamma\leq 1$, then from (3.5), we get

$$\left|\int_x^s\frac{du}{\chi(u)}\right|^\gamma\leq 2^\gamma\frac{|s-x|^\gamma}{x^{\frac{\gamma}{2}}}\left(\frac{1}{(1+x)^{\frac{\gamma}{2}}}+\frac{1}{(1+s)^{\frac{\gamma}{2}}}\right). \tag{3.6}$$

From (3.4) and (3.6) and using Cauchy inequality, we get

$$\begin{aligned}\left|\tilde{\mathcal{B}}_n(\varphi(s);x)-\varphi(x)\right| &\leq \frac{2^\gamma\|\chi^\gamma\varphi'\|}{x^{\frac{\gamma}{2}}}\tilde{\mathcal{B}}_n\left(|s-x|\left(\frac{1}{(1+x)^{\frac{\gamma}{2}}}+\frac{1}{(1+s)^{\frac{\gamma}{2}}}\right);x\right)\\ &= \frac{2^\gamma\|\chi^\gamma\varphi'\|}{x^{\frac{\gamma}{2}}}\left(\frac{1}{(1+x)^{\frac{\gamma}{2}}}\left(\tilde{\mathcal{B}}_n\left((s-x)^2;x\right)\right)^{\frac{1}{2}}\right.\\ &\quad\left.+\left(\tilde{\mathcal{B}}_n\left((s-x)^2;x\right)\right)^{\frac{1}{2}}.\left(\tilde{\mathcal{B}}_n\left((1+s)^{-\gamma};x\right)\right)^{\frac{1}{2}}\right).\end{aligned} \tag{3.7}$$

From Lemma 2.2, we may write

$$\left(\tilde{\mathcal{B}}_n\left((s-x)^2;x\right)\right)^{\frac{1}{2}} \leq \sqrt{\frac{\mathcal{M}}{n}}.\chi(x), \tag{3.8}$$

where $\chi(x)=\sqrt{x(1+x)}$.
For $x\in[0,\infty)$, $\tilde{\mathcal{B}}_n\left((1+s)^{-\gamma};x\right)\to(1+x)^{-\gamma}$ as $n\to\infty$. Thus for $\varepsilon>0$, we find a number $n_0\in\mathbb{N}$ such that

$$\tilde{\mathcal{B}}_n\left((1+s)^{-\gamma};x\right)\leq(1+x)^{-\gamma}+\varepsilon, \text{ for all } n\geq n_0.$$

By choosing $\varepsilon=(1+x)^{-\gamma}$, we obtain

$$\tilde{\mathcal{B}}_n\left((1+s)^{-\gamma};x\right)\leq 2(1+x)^{-\gamma}, \text{ for all } n\geq n_0. \tag{3.9}$$

From (3.7)-(3.9), we have

$$\begin{aligned}\left|\tilde{\mathcal{B}}_n(\varphi(\lambda);x)-\varphi(x)\right| &\leq 2^{\gamma}\|\chi^{\gamma}\varphi'\|\left(\tilde{\mathcal{B}}_n\left((s-x)^2;x\right)\right)^{\frac{1}{2}}\left\{\chi^{-\gamma}(x)\right.\\ &\quad\left.+x^{-\frac{\gamma}{2}}\left(\tilde{\mathcal{B}}_n\left((1+s)^{-\gamma};x\right)\right)^{\frac{1}{2}}\right\}\\ &\leq 2^{\gamma}\|\chi^{\gamma}\varphi'\|\sqrt{\frac{\mathcal{M}}{n}}\chi(x)\left(\chi^{-\gamma}(x)+\sqrt{2}x^{-\frac{\gamma}{2}}(1+x)^{-\frac{\gamma}{2}}\right)\\ &\leq 2^{\gamma}(1+\sqrt{2})\|\chi^{\gamma}\varphi'\|\sqrt{\frac{\mathcal{M}}{n}}\chi^{1-\gamma}(x),\end{aligned} \tag{3.10}$$

now, we write

$$\begin{aligned}\left|\tilde{\mathcal{B}}_n(f(s);x)-f(x)\right| &\leq \left|\tilde{\mathcal{B}}_n\left(f(s)-\varphi(s);x\right)\right|\\ &\quad+\left|\tilde{\mathcal{B}}_n\left(\varphi(s);x\right)-\varphi(x)\right|+|\varphi(x)-f(x)|\\ &\leq 2\|f-\varphi\|+\left|\tilde{\mathcal{B}}_n\left(\varphi(s);x\right)-\varphi(x)\right|.\end{aligned} \tag{3.11}$$

From (3.10) and (3.11) and for sufficiently large n, we obtain

$$\begin{aligned}\left|\tilde{\mathcal{B}}_n\left(f(s);x\right)-f(x)\right| &\leq 2\|f-\varphi\|+2^{\gamma}\left(1+\sqrt{2}\right)\|\chi^{\gamma}\varphi'\|\sqrt{\frac{\mathcal{M}}{n}}\chi^{1-\gamma}(x)\\ &\leq \mathcal{D}\left\{\|f-\varphi\|+\frac{\chi^{1-\gamma}(x)}{\sqrt{n}}\|\chi^{\gamma}\varphi'\|\right\}\\ &\leq \mathcal{D}\varpi_{\chi^s}\left(f;\chi^{1-\gamma}(x)\frac{1}{\sqrt{n}}\right),\end{aligned} \tag{3.12}$$

where $\mathcal{D}\geq\max\{2,2^s(1+\sqrt{2})\sqrt{\mathcal{M}}\}$. From (3.12) the result is concluded. □

4 Weighted Approximation

First we define a class of functions $C_B^{x^2}[0,\infty)=\{f\in C_B[0,\infty)\text{ for each } x\in[0,\infty);|f(x)|\leq\mathcal{K}_f(1+x^2)\}$. Let $C_B^*[0,\infty)$ be a subspace of $C_B^{x^2}[0,\infty)$ consisting all the real functions existing the following limit $\lim\limits_{n\to\infty}\dfrac{|f(x)|}{1+x^2}$ and norm in the subspace $C_B^*[0,\infty)$ is defined by $\|f\|_{x^2}=\sup\limits_{x\in[0,\infty)}\dfrac{f(x)}{1+x^2}$. The weighted modulus of continuity for any $f\in C_B^*[0,\infty)$ and $\delta>0$, by [6] is explained as:

$$\vartheta(f,\delta)=\sup_{x\in[0,\infty),0<h\leq\delta}\frac{f(x+h)-f(x)}{1+(x+h)^2}, \tag{4.1}$$

where $\vartheta(f,\delta)$ holds the following properties:

1. $\vartheta(f,\delta)$ is an increasing function of δ, and $\lim_{n\to\infty}\vartheta(f,\delta)=0$.

2. For each $m\in\mathbb{N},\vartheta(f,k\delta)\leq k\vartheta(f,\delta)$ and for each $\alpha\in(0,\infty),\vartheta(f,\alpha\delta)\leq(1+\alpha)\vartheta(f,\delta)$.

Theorem 4.1. *For each real function $f\in C_B^*[0,\infty)$, we have*

$$\lim_{n\to\infty}\|\tilde{\mathcal{B}}_n(f;.)-f\|_{x^2}=0.$$

Proof. To prove this theorem, it is acceptable to verify the following conditions,

$$\lim_{n\to\infty}\|\tilde{\mathcal{B}}_n(t^r;x)-x^r\|_{x^2}=0,\ \ r=0,1,2. \tag{4.2}$$

Since $\tilde{\mathcal{B}}_n(1;x)=1$, therefore for $r=0$ holds.
Using Lemma 2.3, we have

$$\begin{aligned}\|\tilde{\mathcal{B}}_n(t;x)-x\|_{x^2} &= \sup_{x\in[0,\infty)}\frac{|\tilde{\mathcal{B}}_n(t;x)-x|}{1+x^2}\\ &\leq \left|\frac{\xi'(p(x))}{\xi(p(x))}x+\frac{1}{n}\left(\frac{\mathcal{S}'(1)}{\mathcal{S}(1)}+\mathcal{V}'(1)\frac{\xi'(p(x))}{\xi(p(x))}\right)-x\right|\\ &\quad\times\sup_{x\in[0,\infty)}\frac{1}{1+x^2}.\end{aligned}$$

As $n\to\infty$ and using $\lim_{t\to\infty}\frac{\xi'(t)}{\xi(t)}=1$ and $\lim_{t\to\infty}\frac{\xi''(t)}{\xi(t)}=1$, the required inequality of the theorem holds good for $r=1$. In the similar way by using the Lemma 2.3, we may obtain $\|\tilde{\mathcal{B}}_n(t^2;x)-x^2\|_{x^2}=0$. It follows that the theorem holds for $r=2$ as $n\to\infty$. Thus, on applying Korovkin's theorem required result follows. □

Corollary 4.1. *Let $\alpha>0$ and $f\in C_B^*[0,\infty)$, then*

$$\lim_{n\to\infty}\sup_{x\in[0,\infty)}\frac{|\tilde{\mathcal{B}}_n(f;x)-f(x)|}{(1+x^2)^{1+\alpha}}=0.$$

Proof. For any fixed $\epsilon_0>0$, we have

$$\begin{aligned}\sup_{x\in[0,\infty)}\frac{|\tilde{\mathcal{B}}_n(f;x)-f(x)|}{(1+x^2)^{1+\alpha}} &\leq \sup_{x\leq\epsilon_0}\frac{|\tilde{\mathcal{B}}_n(f;x)-f(x)|}{(1+x^2)^{1+\alpha}}+\sup_{x\geq\epsilon_0}\frac{|\tilde{\mathcal{B}}_n(f;x)-f(x)|}{(1+x^2)^{1+\alpha}}\\ &\leq \|\tilde{\mathcal{B}}_n(f;.)-f\|_{C[0,\epsilon_0]}+\|f\|_{x^2}\sup_{x\geq\epsilon_0}\frac{|\tilde{\mathcal{B}}_n\left((1+t^2);x\right)|}{(1+x^2)^{1+\alpha}}\\ &\quad+\sup_{x\geq\epsilon_0}\frac{|f(x)|}{(1+x^2)^{1+\alpha}}.\end{aligned}$$

Using theorem (4.1) and for the fixed $\epsilon_0>0$ (sufficiently large), we quickly seen that $\sup_{x\geq\epsilon_0}\frac{|\tilde{\mathcal{B}}_n\left((1+t^2);x\right)|}{(1+x^2)^{1+\alpha}}$ tends to zero as $n\to\infty$. Above fact concludes the proof. □

5 Rate of Convergence

Now we discuss the convergence rate of the operators (1.2) with a derivative of bounded variation. Let f be a continuous function taken from $DBV[0,\infty)$, which is the class of real-valued continuous functions with bounded derivative in each sub-intervals of $[0,\infty)$. It very well may be seen that, for all $f\in DBV[0,\infty)$, represented by

$$f(x)=f(c)+\int_c^x g(t)dt,\ \ x\geq c>0,$$

where $g(t)$ is a function of bounded variation on the class of finite sub-intervals of $[0,\infty)$.

Now we define an auxiliary function ψ_x by

$$\psi_x(t)=\begin{cases}\psi(t)-\psi(x^-) & \text{if } 0\le t<x\\ 0 & \text{if } t=x\\ \psi(t)-\psi(x^+) & \text{if } x<t<\infty.\end{cases}$$

Lemma 5.1. *For every $x\in(0,\infty)$ and n to be very large. Then*

1. *For $0\le y<x$, we may write*

$$\xi_n(x,y)=\int_0^y \underline{\mathcal{V}}_n(x,s)ds\le\frac{C_1\left|\eta_1(x)\right|}{(x-y)^2}.$$

2. *If $x<z<\infty$, then*

$$1-\xi_n(x,z)=\int_z^\infty \underline{\mathcal{V}}_n(x,s)ds\le\frac{C_1\left|\eta_1(x)\right|}{(z-x)^2}.$$

Proof. Using Lemma 2.3 and 2.4, for a very large n and $0\le y<x$, we have

$$\begin{aligned}\xi_n(x,y) &= \int_0^y \underline{\mathcal{V}}_n(x,s)ds\\ &\le \int_0^y \frac{(x-t)^2}{(x-y)^2}\underline{\mathcal{V}}_n(x,s)ds\\ &\le \frac{1}{(x-y)^2}\tilde{\mathcal{B}}_n((x-s)^2;x)\\ &\le \frac{C_1\left|\eta_1(x)\right|}{n(x-y)^2}.\end{aligned}$$

In the similar way we can obtain second result. □

Theorem 5.1. *(Bounded Variation) Let $f\in DBV[0,\infty)$ then for all $x\in(0,\infty)$ and a very large n, we have*

$$\begin{aligned}\left|\tilde{\mathcal{B}}_n(f;x)-f(x)\right| \le{}& \left[\left(\frac{\xi'(p(x))}{\xi(p(x))}-1\right)x+\frac{1}{n}\left(\frac{\mathcal{S}'(1)}{\mathcal{S}(1)}+\mathcal{V}'(1)\frac{\xi'(p(x))}{\xi(p(x))}\right)\right]\\ &\left|\frac{f'(x^+)+f'(x^-)}{2}\right|+\sqrt{C_1|\eta_1(x)|}\left|\frac{f'(x^+)+f'(x^-)}{2}\right|\\ &+\frac{C_1|\eta_1(x)|}{x}\sum_{j=1}^{[\sqrt{n}]}\left(\bigvee_{x-\frac{x}{j}}^{x}f'_x\right)+\frac{x}{\sqrt{n}}\left(\bigvee_{x-\frac{x}{\sqrt{n}}}^{x}f'_x\right)\\ &\times\left(4\mathcal{K}_f+\frac{(\mathcal{K}_f+|f(x)|)}{x^2}\right)C_1|\eta_1(x)|+\left|f'(x^+)\right|\\ &\times\sqrt{|C_1\eta_1(x)|}+\frac{C_1|\eta_1(x)|}{x^2}\left|f(2x)-xf'(x^+)-f(x)\right|\\ &+\frac{x}{\sqrt{n}}\left(\bigvee_{x}^{x+\frac{x}{\sqrt{n}}}f'_x\right)+\frac{C_1|\eta_1(x)|}{x}\sum_{j=1}^{[\sqrt{n}]}\left(\bigvee_{x}^{x+\frac{x}{j}}f'_x\right).\end{aligned}$$

Proof. Using the operators (1.2) and for all x lies on positive real line, we obtain

$$\begin{aligned}\tilde{\mathcal{B}}_n(f;x)-f(x) &= \int_0^\infty \tilde{\mathcal{B}}_n(x,s)(f(s)-f(x))ds\\ &= \int_0^\infty\left(\tilde{\mathcal{B}}_n(x,s)\int_x^s f(v)dv\right)ds. \qquad (5.1)\end{aligned}$$

For $f \in DBV[0,\infty)$, we have

$$\begin{aligned} f'(v) &= \frac{1}{2}(f'(x^+)+f'(x^-)) + f'_x(v) + \frac{1}{2}(f'(x^+)-f'(x^-))sgn(x) \\ &\quad +\delta_x(v)(f'(v) - \frac{1}{2}(f'(x^+)+f'(x^-)), \end{aligned} \tag{5.2}$$

where

$$\delta_x(v) = \begin{cases} 1, & v = x \\ 0, & v \neq x. \end{cases}$$

For every $x \in [0,\infty)$, using (5.2) and (1.3), we get

$$\begin{aligned} \tilde{\mathcal{B}}_n(f;x) - f(x) &= \int_0^\infty \underline{\mathcal{V}}_n(x,s)\,(f(s)-f(x))\,ds \\ &= \int_0^\infty \underline{\mathcal{V}}_n(x,s)\left(\int_s^x f'(u)du\right)ds \\ &= -\int_0^x \underline{\mathcal{V}}_n(x,s)\left(\int_s^x f'(u)du\right)ds \\ &\quad +\int_x^\infty \underline{\mathcal{V}}_n(x,s)\left(\int_s^x f'(u)du\right)ds. \end{aligned} \tag{5.3}$$

Now, we simplify the above expressions into two parts. Let

$$A_1 = \int_0^x \underline{\mathcal{V}}_n(x,s)\left(\int_s^x f'(u)du\right)ds,$$

and

$$A_2 = \int_x^\infty \underline{\mathcal{V}}_n(x,s)\left(\int_s^x f'(u)du\right)ds.$$

Since $\int_x^s \delta_x(s)ds = 0$, using (5.2), we get

$$\begin{aligned} A_1 &= \int_0^x \left\{\int_s^x \left(\frac{1}{2}(f'(x^+)+f'(x^-)) + f'_x(u)\right.\right. \\ &\quad \left.\left. +\frac{1}{2}(f'(x^+)-f'(x^-))sgn(u-x)\right)du\right\}\underline{\mathcal{V}}_n(x,s)ds \\ &= \frac{1}{2}\left(f'(x^+)+f'(x^-)\right)\int_0^x (x-s)\underline{\mathcal{V}}_n(x,s)ds \\ &\quad +\int_0^x \underline{\mathcal{V}}_n(x,s)\left(\int_s^x f'_x(u)du\right)ds \\ &\quad -\frac{1}{2}\left(f'(x^+)-f'(x^-)\right)\int_0^x (x-s)\underline{\mathcal{V}}_n(x,s)ds. \end{aligned} \tag{5.4}$$

Similarly, we may write

$$\begin{aligned} A_2 &= \frac{1}{2}\left(f'(x^+)+f'(x^-)\right)\int_x^\infty (s-x)\underline{\mathcal{V}}_n(x,s)ds \\ &\quad +\int_x^\infty \underline{\mathcal{V}}_n(x,s)\left(\int_x^s f'_x(u)du\right)ds \\ &\quad +\frac{1}{2}\left(f'(x^+)-f'(x^-)\right)\int_x^\infty (s-x)\underline{\mathcal{V}}_n(x,s)ds. \end{aligned} \tag{5.5}$$

Now, from the relations (5.3)-(5.5), we get

$$\begin{aligned}\tilde{\mathcal{B}}_n(f;x)-f(x) &= \frac{1}{2}\left(f'(x^+)+f'(x^-)\right)\int_0^\infty (s-x)\underline{\mathcal{V}}_n(x,s)ds\\ &+\frac{1}{2}\left(f'(x^+)-f'(x^-)\right)\int_0^\infty |x-s|\,\underline{\mathcal{V}}_n(x,s)ds\\ &-\int_0^x\left(\int_t^x f'_x(u)du\right)\underline{\mathcal{V}}_n(x,s)ds\\ &+\int_x^\infty\left(\int_x^t f'_x(u)du\right)\underline{\mathcal{V}}_n(x,s)ds.\end{aligned}$$

Thus,

$$\begin{aligned}\left|\tilde{\mathcal{B}}_n(f;x)-f(x)\right| &\le \left|\frac{f'(x^+)+f'(x^-)}{2}\right|\left|\tilde{\mathcal{B}}_n(s-x;x\right|\\ &+\left|\frac{f'(x^+)-f'(x^-)}{2}\right|\tilde{\mathcal{B}}_n(|s-x|\,;x)\\ &+S_n(f',x)+T_n(f',x).\end{aligned}\tag{5.6}$$

Where,

$$S_n(f',x)=\left|\int_0^x\left(\int_s^x f'_x(u)du\right)\underline{\mathcal{V}}_n(x,s)ds\right|,$$

and

$$T_n(f',x)=\left|\int_x^\infty\left(\int_x^s f'_x(u)du\right)\underline{\mathcal{V}}_n(x,s)ds\right|.$$

Now, using the Lemma 5.1, and the properties of integration, we estimate $S_n(f',x)$ and $T_n(f',x)$.

$$S_n(f',x)=\int_0^x\left(\int_s^x f'_x(u)du\right)\frac{\partial\xi_n(x,s)}{\partial s}ds=\int_0^x f'_x(s)\xi_n(x,s)ds$$

$$\begin{aligned}|S_n(f',x)|=\int_0^x |f'_x(s)|\xi_n(x,s)ds &\le \int_0^{x-\frac{x}{\sqrt{n}}}|f'_x(s)|\,\xi_n(x,s)ds\\ &+\int_{x-\frac{x}{\sqrt{n}}}^x |f'_x(s)|\,\xi_n(x,s)ds.\end{aligned}$$

Using the fact $f'_x(s)=0$, and $\xi_n(x,s)\le 1$, we may write

$$\begin{aligned}\int_{x-\frac{x}{\sqrt{n}}}^x |f'_x(s)|\,\xi_n(x,s)ds &= \int_{x-\frac{x}{\sqrt{n}}}^x |f'_x(s)-f'_x(x)|\,\xi_n(x,s)ds\\ &\le \int_{x-\frac{x}{\sqrt{n}}}^x\left(\bigvee_s^x f'_x\right)ds\le\left(\bigvee_{x-\frac{x}{\sqrt{n}}}^x f'_x\right)\int_{x-\frac{x}{\sqrt{n}}}^x ds\\ &= \frac{x}{\sqrt{n}}\left(\bigvee_{x-\frac{x}{\sqrt{n}}}^x f'_x\right).\end{aligned}\tag{5.7}$$

Taking $s = x - \frac{x}{u}$, and use the Lemma 5.1, we obtain

$$\begin{aligned}
\int_0^{x-\frac{x}{\sqrt{n}}} |f_x'(s)|\, \xi_n(x,s) ds &\leq C_1|\eta_1(x)| \int_0^{x-\frac{x}{\sqrt{n}}} \frac{|f_x'(s)|}{(x-s)^2} ds \\
&\leq C_1|\eta_1(x)| \int_0^{x-\frac{x}{\sqrt{n}}} \left(\bigvee_s^x f_x' \right) \frac{ds}{(x-s)^2} \\
&= \frac{C_1|\eta_1(x)|}{x} \int_1^{\sqrt{n}} \left(\bigvee_{x-\frac{x}{u}}^x f_x' \right) du \\
&\leq \frac{C_1|\eta_1(x)|}{x} \sum_{j=1}^{[\sqrt{n}]} \left(\bigvee_{x-\frac{x}{j}}^x f_x' \right). \qquad (5.8)
\end{aligned}$$

From (5.7) and (5.8), we get

$$|S_n(f',x)| \leq \frac{C_1|\eta_1(x)|}{x} \sum_{j=1}^{[\sqrt{n}]} \left(\bigvee_{x-\frac{x}{j}}^x f_x' \right) + \frac{x}{\sqrt{n}} \left(\bigvee_{x-\frac{x}{\sqrt{n}}}^x f_x' \right). \qquad (5.9)$$

Now, using integration by parts and Lemma 5.1, we get

$$\begin{aligned}
T_n(f',x) &\leq \left| \int_x^{2x} \left(\int_x^s f_x'(u)du \right) \frac{\partial}{\partial s} \left(1 - \xi_n(x,s)ds\right) \right| \\
&\quad + \left| \int_{2x}^{\infty} \left(\int_x^s f_x'(u)du \right) \underline{\mathcal{V}}_n(x,s)ds \right| \\
&\leq \left| \int_x^{2x} f_x'(u)du \right| |1 - \xi_n(x,2x)| + \int_x^{2x} |f_x'(s)| \left(1 - \xi_n(x,s)\right) ds \\
&\quad + \left| \int_{2x}^{\infty} \left(f(s) - f(x)\right) \underline{\mathcal{V}}_n(x,s)ds \right| \\
&\quad + |f'(x^+)| \left| \int_{2x}^{\infty} (s-x) \underline{\mathcal{V}}_n(x,s)ds \right|. \qquad (5.10)
\end{aligned}$$

Here, we simplify the following integration into two parts,

$$\begin{aligned}
\int_x^{2x} |f_x'(s)| \left(1 - \xi_n(x,s)\right) ds &= \int_x^{x+\frac{x}{\sqrt{n}}} |f_x'(s)| \left(1 - \xi_n(x,s)\right) ds \\
&\quad + \int_{x+\frac{x}{\sqrt{n}}}^{2x} |f_x'(s)| \left(1 - \xi_n(x,s)\right) ds \\
&= I_1 + I_2. \qquad (5.11)
\end{aligned}$$

Using the Lemma 5.1,

$$\begin{aligned}
I_1 &= \int_x^{x+\frac{x}{\sqrt{n}}} |f_x'(s) - f_x'(x)| \left(1 - \xi_n(x,s)\right) ds \\
&\leq \int_x^{x+\frac{x}{\sqrt{n}}} \left(\bigvee_x^{x+\frac{x}{\sqrt{n}}} f_x' \right) ds = \frac{x}{\sqrt{n}} \left(\bigvee_x^{x+\frac{x}{\sqrt{n}}} f_x' \right). \qquad (5.12)
\end{aligned}$$

Again, using the Lemma 5.1 and put $s = x + \frac{x}{u}$, we get

$$\begin{aligned} I_2 &\leq C_1|\eta_1(x)| \int_{x+\frac{x}{\sqrt{n}}}^{2x} \frac{1}{(s-x)^2} \left|f'_x(s) - f'_x(x)\right| ds \\ &\leq C_1|\eta_1(x)| \int_{x+\frac{x}{\sqrt{n}}}^{2x} \frac{1}{(s-x)^2} \left(\bigvee_x^s f'_x\right) ds \\ &\leq \frac{C_1|\eta_1(x)|}{x} \int_1^{\sqrt{n}} \left(\bigvee_x^{x+\frac{x}{u}} f'_x\right) du \\ &\leq \frac{C_1|\eta_1(x)|}{x} \sum_{j=1}^{[\sqrt{n}]} \left(\bigvee_x^{x+\frac{x}{j}} f'_x\right). \end{aligned} \tag{5.13}$$

Using (5.11)-(5.13), we get

$$\begin{aligned} \int_x^{2x} \left|f'_x(s)\right| (1 - \xi_n(x,s))\, ds &= \frac{C_1|\eta_1(x)|}{x} \sum_{j=1}^{[\sqrt{n}]} \left(\bigvee_x^{x+\frac{x}{j}} f'_x\right) \\ &\quad + \frac{x}{\sqrt{n}} \left(\bigvee_x^{x+\frac{x}{\sqrt{n}}} f'_x\right). \end{aligned} \tag{5.14}$$

Now, from (5.10) and (5.14) and the Cauchy-Schwarz inequality taking into the account, we get

$$\begin{aligned} T_n(f', x) &\leq \mathcal{K}_f \int_{2x}^{\infty} (s^2+1) \underline{\mathcal{V}}_n(x,s) ds + |f(x)| \int_{2x}^{\infty} \underline{\mathcal{V}}_n(x,s) ds \\ &\quad + \left|f'(x^+)\right| \sqrt{|C_1\eta_1(x)|} + \frac{C_1|\eta_1(x)|}{x^2} \left|f(2x) - xf'(x^+) - f(x)\right| \\ &\quad + \frac{x}{\sqrt{n}} \left(\bigvee_x^{x+\frac{x}{\sqrt{n}}} f'_x\right) + \frac{C_1|\eta_1(x)|}{x} \sum_{j=1}^{[\sqrt{n}]} \left(\bigvee_x^{x+\frac{x}{j}} f'_x\right). \end{aligned} \tag{5.15}$$

Since $x \leq s - x$, and $s \leq 2(s-x)$ when $s \geq 2x$, we have

$$\begin{aligned} &\mathcal{K}_f \int_{2x}^{\infty} (s^2+1) \underline{\mathcal{V}}_n(x,s) ds + |f(x)| \int_{2x}^{\infty} \underline{\mathcal{V}}_n(x,s) ds \\ &\quad \leq (\mathcal{K}_f + |f(x)|) \int_{2x}^{\infty} \underline{\mathcal{V}}_n(x,s) ds + 4\mathcal{K}_f \int_{2x}^{\infty} (s-x)^2 \underline{\mathcal{V}}_n(x,s) ds \\ &\leq \frac{(\mathcal{K}_f + |f(x)|)}{x^2} \int_0^{\infty} (s-x)^2 \underline{\mathcal{V}}_n(x,s) ds + 4\mathcal{K}_f \int_0^{\infty} (s-x)^2 \underline{\mathcal{V}}_n(x,s) ds \\ &\leq \left(4\mathcal{K}_f + \frac{(\mathcal{K}_f + |f(x)|)}{x^2}\right) C_1|\eta_1(x)|. \end{aligned} \tag{5.16}$$

Using (5.15) and (5.16), we have

$$\begin{aligned} T_n(f', x) &\leq \left(4\mathcal{K}_f + \frac{(\mathcal{K}_f + |f(x)|)}{x^2}\right) C_1|\eta_1(x)| + \left|f'(x^+)\right| \sqrt{|C_1\eta_1(x)|} \\ &\quad + \frac{C_1|\eta_1(x)|}{x^2} \left|f(2x) - xf'(x^+) - f(x)\right| + \frac{x}{\sqrt{n}} \left(\bigvee_x^{x+\frac{x}{\sqrt{n}}} f'_x\right) \\ &\quad + \frac{C_1|\eta_1(x)|}{x} \sum_{j=1}^{[\sqrt{n}]} \left(\bigvee_x^{x+\frac{x}{j}} f'_x\right). \end{aligned} \tag{5.17}$$

using (5.6),(5.9) and (5.17), we reach to the required result. □

6 Another extension of sequence of operators $\mathcal{B}_n(f;x)$

Here, we define the Sz'asz-type Durrmeyer variant of the operators $\mathcal{B}_n(f;x)$ under the same conditions and limitations as those outlined in the article's introduction. For $f \in C_\sigma[0,\infty)$ and $p(x) = n^2x^2\mathcal{T}(1) + nx\mathcal{U}(1) + \mathcal{V}(1)$, we have

$$\mathcal{B}_n^*(f;x) = \frac{n}{\mathcal{S}(1).\xi(p(x))} \sum_{j=0}^{\infty} \Theta_j(nx) \int_0^{\infty} e^{-ns} \frac{(ns)^j}{j!} f(s)ds.$$

In a manner similar to that described in this article, one can prove the convergence results for the operators $\mathcal{B}_n^*(f;x)$.

References

[1] Sahai, A., Prasad, G.: *On simultaneous approximation by Modified Lupas operators*, J. Approx. Theory, 45 (1985), 122-128.

[2] Gadzjiv, A.D.: *Theorems of the type of P.P. Korovkin type theorems*, Math. Zametki, 20(5) (1976), 781–786, English Translation , Math Notes 20(5-6) (1976), 996–998.

[3] Acu, A.M., Buscu, I.C., Rasa, I.: *A sequence of Appell polynomials and the associated Jakimovski-Leviatan operators,* Anal. Math. Phys.,(2021) 11:88, doi:https://doi.org/10.1007/s13324-021-00525-0.

[4] Rainville, E.D.: *Special Functions*, Macmillan, New York, USA, (1960).

[5] Gavrea, I., Rasa I.: *Remarks on some quantitative korovkin-type results*, Revue d'Analyse Numérique et de Théorie de l'Approximation, 22(2)(1993), 173-176.

[6] Yüksel, I., Ispir, N.: *Weighted approximation by a certain family of summation integral-type operators,* Comput. Math. Appl. 52(10-11) (2006), 1463-1470.

[7] Sidharth, M., Agrawal, P.N., Araci, S.: *Szász- Durrmeyer operators involving Boas-Buck polynomials of blending type,* J. Inequal. Appl. 2017(1):122, doi:https//doi.org/ 10.1186/s13660-017-1396-x.

[8] Deo, N., Kumar, S.: *Durrmeyer variant of apostal-genocchi-baskakov operators,* Quaest. Math.(2020). https://doi.org/10.2989/16073606.2020.1834000.

[9] Szász, O.: *Generalization of S. Bernstein's polynomials to the infinite interval,* J. Res. Natl. Bur. Stand. 97 (1950), 239-245.

[10] Goyal, R.: *An extension of a class of generating functions,* Ultra Sci. Phys. Sci. **15**(2003), 289-292.

[11] Boas, R.P., Buck, R.C.: *Polynomials defined by generating relations*, Amer. Math., 63, (1956), 626-632.

[12] Boas, R.P., Buck, R.C.: *Polynomial Expansion of analytic functions*, Springer Verlag, Berlin, (1958).

[13] Sucu, S., Verma, S.: *Approximation by sequence of operators involving analytic functions*, Mathematics, 7(2)(2019), 188.

[14] Verma, S., Sucu, S.: *Operators obtained by using certain generating function for approximation*, Mathematics, 10(2022), 2239.

[15] Gupta, V., Rassias, T.M.: *Moments of Linear Operators and Approximation*, (2019), Springer.

[16] Ditzian, Z., Totik, V.: *Moduli of Smoothness*, Springer, New York, 1987.

The Journal of Supercomputing (2025) 81:620
https://doi.org/10.1007/s11227-025-06989-2

Dynamic cloud model based on decision field theory

Anjali Anjali[1] · **Anjana Gupta**[1]

Accepted: 25 January 2025
© The Author(s), under exclusive licence to Springer Science+Business Media, LLC, part of Springer Nature 2025

Abstract
Real-world applications are characterized by uncertainties, with randomness and fuzziness being the significant challenges inherent in human cognition. The Cloud Model (CM) synthesizes these uncertainties, enabling the transformation between qualitative and quantitative instantiations. Integrating CM with Decision Field Theory (DFT) is essential for managing the complexities of dynamic and probabilistic decision-making. Our research introduces a novel Dynamic Cloud Model based on Decision Field Theory (DCM-DFT). It incorporates an innovative methodology for creating dynamic clouds by capturing initial uncertainty using cloud descriptors. We built a custom time series model to compute attention weights for forecasted periods, effectively managing the full spectrum of uncertainty fluctuations in a decision maker's dynamic mental state. We demonstrate DCM-DFT's practical implementation using the Lifestyle and Wellbeing real-time dataset, showcasing fluctuations in decision ranking of alternatives over time. A comparative study exhibits DCM-DFT's enhanced performance over traditional approaches, significantly improving decision-making preferences in dynamic and uncertain environments.

Keywords Cloud model · Decision field theory · Time series forecasting · Uncertainty · Decision-making

1 Introduction

In the quest for a perfect day, it is the small, seemingly insignificant decisions that often hold the most power. These daily choices, ranging from what we eat to how we manage our time, collectively shape our broader lifestyle. Micro-level decisions

✉ Anjana Gupta
anjanagupta@dce.ac.in

Anjali Anjali
anjali_2k22phdam01@dtu.ac.in

[1] Department of Applied Mathematics, Delhi Technological University, New Delhi, Delhi 110042, India

Published online: 14 March 2025

influence the subsequent hours, and the way we structure our routines during these hours determines the quality of our entire day. Consistent fluctuations in our decisions can disrupt daily routines, leading to long-term lifestyle changes. Taking care of these micro decisions can lead to a positive macro-level routine that improves our general quality of life and well-being. Making wise choices on both a micro and macro level is essential to living a healthy and satisfying life. But the process is made even more difficult by the uncertainty that surrounds these choices.

In order to navigate these uncertainties, cloud models offer a powerful tool, bridging the gap between qualitative conceptualizations and their quantitative representations. Uncertainties like unpredictability, fuzziness, incompleteness, and imprecision are frequently encountered by the human cognitive process, which is intricately linked to language and thought. Li et al. [1] introduce cloud models that offer a structured approach to handling these intricacies. To enable bidirectional cognitive transformation between the intention and expansion of concepts, cloud models use forward and backward cloud transformations (FCT and BCT) [2]. Three numerical characteristics known as cloud descriptors: Expectation (Ex), Entropy (En), and Hyperentropy (He) form the basis of the theoretical framework established by the cloud models. In order to integrate human cognition from coarser to finer, Wang et al. [2] provided a generic cloud model with normal distribution that establishes a connection between the normal cloud. Changlin Xu et al. [3–6] introduced the FCT and BCT and made an analysis of the two existing single-step BCT algorithms. This transformation algorithm reveals that the second-order normal cloud [7] and the normal distribution are both special cases of the second-order generic normal cloud. Anjali et al. [8] introduce Shannon entropy to enhance model accuracy and decision-making in cloud models, proposing the Shannon entropy-based backward cloud transformation algorithm. Chauhan et al. [9] introduced a cloud model based on multiplicative unbalanced linguistic term sets and further introduced a scale function that creates a map between the linguistic data and numerical interval values. Since the introduction of cloud models, several researchers have devoted their efforts to enhancing cloud specialized studies such as integrated cloud [10], quality assessment [11, 12], risk assessment [13–18], image segmentation [19], assessing the extent of the damage to a concrete structure after a disastrous fire [20], risk assessment of water inrush in karst tunnels [21] along with more wide-ranging applications. Liu et al. [22] studied aims to remove the bottlenecks and improve the risk assessment of failure mode and effects analysis in an uncertain environment.

Most of the widely used multi-attribute decision-making methods [23, 24] were developed for static conditions and fail to accurately capture the decision-making behaviors of individuals in dynamic and real-world settings. In such an environment, decision-makers face significant ambiguity and uncertainty. Quantifying this uncertain information in a way that mimics human thinking is essential for scientific and automated decision-making. There are a number of traditional theories that struggle to address these challenges, including prospect theory [25], random utility maximization models (RUM) [26], random regret minimization methods, multinomial logit models [27], evidence theory [28]. These theories do not explain the probabilistic nature of preferential choice and have limited predictive accuracy [29].

Human decision-making is dynamic, where choices and preferences change over time. Understanding how we navigate uncertainty in our daily lives requires a knowledge of how preferences and choices evolve over time. Busemeyer et al. [30, 31] developed decision field theory (DFT) which provides a comprehensive framework for capturing this fluidity in decision-making processes. According to DFT, decisions are not static choices, but are the result of changing internal states and external factors. Multiattribute decision field theory proposed by Diederich et al. [32] explains the stochastic and dynamic character of decision-making and explains the observed variations in choice probability. Hotaling et al. [33] propose an alternative account, decision field theory-planning, in which individuals plan future choices on the fly through repeated forward-looking mental simulations. Numerous researchers such as Ma et al. [34] have investigated human dynamic decision-making behaviors by proposing a fuzzy dynamic route choice algorithm of wargame. Saaty et al. [35] incorporated the time factor into the Analytic Hierarchy Process and the Analytic Network Process, leading to the development of the dynamic analytic hierarchy process and the dynamic network process. Busemeyer et al. [36] bridge the expanse between the neurophysiological and behavioral decision-making literatures specifically, decision field theory. Lee et al. [37] proposed extended DFT updates the subjective evaluation for the options and the attention on the attribute, where Bayesian belief network is employed to infer these updates under the dynamic environment.

Despite significant progress, existing cloud models struggle to adapt to dynamic changes in stochastic processes. As of now, there has not been an introduction of a cloud model capable of accommodating the dynamic fluctuations in randomness and fuzziness. Furthermore, DFT lacks clearly defined initial preference points for estimation. Setting all initial preferences to zero ignores valuable historical information, restricting the model's ability to incorporate prior data and accurately reflect dynamic decision-making.

Accurately measuring the distance between alternatives is essential for capturing the complexity of decision-making in multi-attribute contexts. Various methods have been employed to define the distance between alternatives in DFT applications. Roe et al. [38] suggested using "psychological" distances but ultimately opted for distances based on the relative positioning of alternatives within the multi-attribute evaluation space. Hotaling et al. [39] introduced a new parameter in the feedback matrix, which allowed distances between less competitive alternatives to increase more gradually. Berkowitsch et al. [26] developed a generalized distance function between alternatives in the multi-attribute space. Qin et al. [40] applied the Euclidean distance, representing the straight-line distance in this space. However, Euclidean distance often overlooks the different levels of importance associated with each attribute. Furthermore, traditional methods that focus primarily on the positional relationships between alternatives do not capture both the central tendency and the variability of attributes. They neglect to incorporate first and second-order uncertainty. This limitation hinders their ability to fully capture the complexity of distance measurements in decision-making scenarios. We recognize this as a limitation in the existing literature.

DFT models the process of making choices as a continuous, time-dependent accumulation of preferences, where the mental state of an individual fluctuates as they

weigh different attributes. Several studies have proposed different methods for weighting fluctuations in an individual's mental state. Dynamic problems have often been formulated as Markov decision processes, where the next system state depends on a Markov transition probability [41]. Busemeyer et al. introduced a connectionist neural network approach to decision-making while assuming that attention weights are identically and independently distributed over time according to a simple Bernoulli process, that is, attention weights shifts in an all-or-none manner from one attribute at one moment with some fixed probabilities [42]. Yang et al. [43] presented a dynamic stochastic decision-making method using time-sequence weights obtained through the technique for order preference by similarity to ideal solution, emphasizing the idea of 'stressing the present rather than the past'. However, these studies do not account for the initial weighting associated with individual data. Given the inherent randomness and fuzziness of the human mind, assigning full weight to one attribute at a time (τ) and then completely shifting that weight to another attribute at a later time ($\tau + h$) fails to capture the full spectrum of fluctuations in an individual's mental state. Further, DFT assumes abrupt shifts in attribute weights by shifting in an all-or-none manner from one attribute to another, leading to an incomplete representation of the decision-making process. The influence of previous weight preferences on future decisions is crucial, yet this is overlooked in these models. Incorporating the effect of previous weights on subsequent preferences is essential for better reflecting real-time mental state dynamics. This is identified as a gap in the existing research.

In dynamic and uncertain decision-making environments, time series analysis (TSA) provides a valuable framework for forecasting trends and evaluating dynamic weights based on historical data. This approach enables decision-makers to adjust their strategies by identifying temporal patterns, allowing for more informed and adaptive predictions of future states. These models incorporate various techniques, such as autoregressive integrated moving average (ARIMA) [44], seasonal-ARIMA exponential smoothing, and machine learning algorithms, to account for time-based dependencies. The adaptability of this approach is particularly valuable in complex environments where traditional static models fall short. Various studies [45–47] have demonstrated the applicability of TSA across different domains such as healthcare spending, epidemiological forecasting and many more. These applications underscore the versatility of TSA in supporting decision-making across various sectors.

In conclusion, throughout past research substantial progress has been made in modeling dynamic decision-making. From the introduction of cloud models and their application in handling cognitive uncertainties to the evolution of decision field theory, various frameworks have been proposed to enhance our understanding of decision behaviors. However, many significant challenges remain to be addressed, as discussed above.

To address these challenges, this study introduces a novel Dynamic Cloud Model based on Decision Field Theory (DCM-DFT), which integrates the cloud model with decision field theory to address key challenges in dynamic human decision-making under uncertainty. To the best of our knowledge, this is the first study to investigate the dynamic nature of clouds. The integration of the Cloud Model and Decision Field Theory fills the above mentioned gaps in existing research by incorporating a cognitive framework that dynamically captures continuous spectrum of fluctuations

in randomness and fuzziness in decision-making processes. This leads to a complete representation of decision-making process. Given the inherent uncertainties in decision-making at time (τ), we first generate clouds for each alternative at the initial time. We then iteratively update these clouds for the next interval ($\tau + h$) to incorporate the evolving randomness and fuzziness in decision-making behavior over time. The cloud score derived from forward and backward cloud transformation algorithms captures the alternative's associated variability and hence serves as the initial preference vector for representing uncertainty. This approach effectively addresses both the static and dynamic ambiguity present in the decision-making data. Furthermore, to accurately evaluate dynamic weights and continuously adjust them, we developed a custom time series forecasting model to assess preferences and forecast the trend for the updating time periods. We develop the cloud feedback matrix by incorporating cloud distances into the feedback matrix using cloud descriptors (Ex, En, He) to enhance the integration of the models. This effectively captures first and second-order uncertainties, facilitating better adaptation in decision-making scenarios.

The rest of the paper is structured as follows: Sect. 2 presents a brief overview of the necessary preliminaries and definitions relevant to our proposed research. In Sect. 3, we introduce the proposed methodology and the foundational elements necessary for integrating cloud models with decision field theory, followed by an exploration of dynamic weight evaluation methods through time series forecasting. Section 4 details our proposed Dynamic Cloud Model based on Decision Field Theory (DCM-DFT) algorithm, including the computation of probabilities within the DCM-DFT framework. Section 5 presents a real-life case study implementation using the Lifestyle and Wellbeing dataset. In Section 6, we provide results and a comprehensive comparative analysis of our proposed methodology against existing methods. Finally, Section 7 concludes the paper and discusses potential future directions.

Table 1 presents an overview of the common abbreviations used throughout this article.

We next summarize the key advantages and innovations of our proposed work compared with various existing research in Table 2.

2 Preliminaries

In this section, we explore the essential principles of the cloud model (CM), its corresponding algorithm, and decision field theory (DFT), along with related concepts that are crucial to our proposal.

2.1 Core principles of the cloud model and transformation algorithms

The Cloud Model is designed to represent the uncertainties inherent in vague or imprecise concepts reflecting the characteristics of human cognition. Fundamentally, the cloud model is developed to capture both the randomness and fuzziness of a concept. Randomness is derived from probability theory, while fuzziness is incorporated using fuzzy and rough set theories. The cloud model captures the understanding of concepts

Table 1 List of abbreviations and symbols utilized in the study

Abbreviation/symbol	Definition/Description	Characteristic
DFT	Decision Field Theory	Model that examines preference formation in decision-making processes within cognitive psychology.
CM	Cloud Model	A framework for describing qualitative concepts using randomness and fuzziness
Ex	Expectation	Statistical expectation of the cloud drops related to a concept within the universe.
En	Entropy	Degree of unpredictability associated with a qualitative concept.
He	Hyper-entropy	Degree of uncertainty related to entropy En
MCDM	Multi-Criteria Decision-Making	Decision-making problems based on multiple criteria
$\hat{S}(C)$	Score of Cloud	Measures the importance of cloud drops
V_τ	Valence vector at time step τ	Represents the immediate attractiveness of alternatives
W_{TSA}	Weight vector at time τ	Dynamic weights for each attribute at a given time obtained by TSA forecasting
C	Contrast matrix	Used to compare evaluations of different alternatives
$\mathbb{S}$	Cloud feedback matrix	Updates preferences based on cloud behaviors
μ	Expected valence vector	Average attractiveness of decision options
χ	Covariance matrix of valence vector	Captures variability in valence values
ξ_τ	Expected value of preference vector	Mean value of preferences at time τ
Ω_τ	Covariance matrix of preference vector	Measures uncertainty in preference values
RUM	Random Utility Model	A model used to predict choice behavior
α	Sensitivity parameter	Controls the responsiveness of the model to changes
β	Memory parameter	Reflects the retention of past preferences

Table 1 (continued)

Abbreviation/symbol	Definition/Description	Characteristic
C_i, C_j	Cloud representations	Different clouds representing concepts
s_{ij}	Elements of the cloud feedback matrix	Defines the influence of one alternative on another
$d(C_i, C_j)$	Distance between clouds C_i and C_j	Measures attribute distances between alternatives
τ	Time variable	Represents discrete time steps in decision-making
h	Time step	Represents a small increment in time
$P(\tau)$	Preference state vector at time τ	Reflects the decision-maker's current preferences
N	Sample size	Number of alternatives considered

characterized by uncertainty and randomness, facilitating the transition from qualitative interpretations to their quantitative counterparts. In the cloud model approach, the uncertainty of the concept is expressed by higher-ordered entropy aside of the expectation, entropy and hyper-entropy [1]. This approach is extensively used to capture the uncertainty inherent in the decision alternatives. We present a brief overview of the cloud model based on the work of Deyi Li and Yi Du [1, 48].

Definition 1 Let U represent a universal set defined by specific numerical values, and W denote the qualitative concept associated with U. If there exists a number $x \in U$ that randomly embodies the concept W, and the certainty degree $\mu(x) \in [0, 1]$ for W is a stochastic value tending toward stabilization, then the distribution of x over U is termed a **cloud**, and every x with the certainty degree μ is referred to as a **cloud drop** [1].

Definition 2 Let U be the universe of discourse and W be a qualitative concept over U. If $x \in U$ serves as a random realization of concept W satisfying $x \sim \mathcal{N}(Ex, En'^2)$, $En' \sim \mathcal{N}(En, He^2)$, and the certainty degree y of x belonging to concept W meets the following condition:

$$y = e^{-\frac{(x-Ex)^2}{2(En')^2}} \tag{1}$$

then the distribution of x within the universe U is known as a **normal cloud**, and each x with certainty degree is termed a **normal cloud drop** [1].

- Expectation Ex denotes the statistical mean of the cloud drops. In other words, it is the point that is most representative of the qualitative concept while quantifying the concept [1].

Table 2 A summary of key innovations and advantages of the proposed model compared with existing research

Paper	Model proposed	Integration of cloud model with decision field theory	Uncertainty handling Measurement (Dynamic)	Distance Measurement	Dynamic adaptability	Weighting mechanism
[11]	Cloud model-based Assessment Approach	No	Cloud descriptors (No)	No	Not dynamic	Static weights
[34]	Fuzzy dynamic route choice model	No	Fuzzy Logic (No)	Euclidean distance	Partially Dynamic	Predefined weights
[15]	Comprehensive Weight-Cloud Model	No	Golden-section ratio entropy (No)	No	Not dynamic	AHP weights
[9]	Multiplicative Unbalanced Interval Cloud (MUIC)	No	Cloud descriptors (No)	No	Not dynamic	N/A
[19]	Histogram Image Segmentation	No	Cloud descriptors (No)	No	Not dynamic	N/A
[8]	Shannon Entropy-based Backward Cloud Transformation (SEBCT)	No	Shannon Entropy (No)	Cloud Distance	Not dynamic	AHP weights
[33]	Decision Field Theory -Planning (DFT-P)	No	Via preference simulations (No)	No	Partially dynamic	N/A

Table 2 (continued)

Paper	Model proposed	Integration of cloud model with decision field theory	Uncertainty handling Measurement (Dynamic)	Distance Measurement	Dynamic adaptability	Weighting mechanism
[20]	Assessment method based on Game Theory-Cloud Model	No	Game theory with cloud model (No)	No	Not dynamic	Comprehensive weights
Current paper	Dynamic cloud model based on decision field theory (DCM-DFT)	Yes	Dynamic handling of fuzziness and randomness using cloud descriptors (*Ex*, *En*, *He*), (Yes)	Cloud Hamming distance	Fully dynamic via time-series-based weight adjustments and cloud updates.	Dynamic weight via time-series forecasting

N/A not available

- Entropy *En* represents the measurement of uncertainty related to the qualitative concept, illustrating the degree of dispersion among the drops. It is determined by both the randomness and the fuzziness of the concept [1].
- Hyper-entropy *He* quantifies the uncertainty associated with entropy, specifically measuring the second-order entropy.

Note 1: These three parameters, (Ex, En, He), are collectively referred to as cloud descriptors and are informally known as a cloud.

Definition 3 Score of Cloud

For a cloud drop (x, y), its contribution to concept W is assessed through the score function $S = xy$. Using the numerical characteristics and a forward normal cloud generator, n cloud drops $\langle (x_1, y_1), (x_2, y_2), \ldots, (x_n, y_n) \rangle$ can be generated. The estimated score $\hat{S}$ of cloud C is computed as follows [49]:

$$\hat{S}(C) = \frac{1}{n} \sum_{i=1}^{n} x_i y_i . \tag{2}$$

Note 2: For two clouds represented as C_1 and C_2, if $\hat{S}(C_1) \geqslant \hat{S}(C_2)$, then $C_1 \geqslant C_2$. In other words, the higher the score of a cloud, the greater the value of cloud. This relationship allows for a direct comparison of clouds based on their scores, providing a clear ranking mechanism.

2.2 Cloud transformation algorithm

The cloud model serves as a cognitive transformation framework that facilitates the uncertain transition between the intension and extension of concepts through cloud transformation algorithms [8]. This includes both forward cloud transformation and backward cloud transformation [6, 50], introduced as follows:

Algorithm 1 Forward Cloud Transformation (FCT) Algorithm [48]

1: **Input:** Cloud descriptors Ex, En, He and the count of cloud drops n.
2: **Output:** n cloud drops along with their certainty degrees.
3: Generate a random variable En_i' that follows a normal distribution with mean En and variance He^2.
4: Generate a random variable x_i that follows a normal distribution with mean Ex and variance En_i'
5: Compute the certainty degree y_i using Equation (1), which represents the likelihood that x_i belongs to concept T.
6: Repeat steps 3-5 until a total of n cloud drops are generated.

Next, Wang et al. [4, 50] introduced a Backward Cloud Transformation (BCT) algorithm that relies on sample variance and the first-order sample absolute central moment. This algorithm yields the estimates $(\hat{Ex}, \hat{En}, \hat{He})$ for (Ex, En, He) from the sample data.

Algorithm 2 Backward Cloud Transformation (BCT) Algorithm [1]

1: **Input:** Drops$(x_i), i = 1, 2, \ldots, n$.
2: **Output:** The estimates $(\hat{Ex}, \hat{En}, \hat{He})$ of (Ex, En, He).
3: Step 1: The most representative sample of the qualitative concept, known as the mathematical expectation (sample mean) Ex from the random sample (drops x_i), is given by:

$$\hat{Ex} = \bar{X} = \frac{1}{n}\sum_{i=1}^{n} x_i \tag{3}$$

4: *Step 2:* Determine the estimation of entropy $\hat{En}$ which is a measure to capture both the randomness and fuzziness of the concept, known as entropy, is expressed as:

$$\hat{En} = \sqrt{\frac{\pi}{2}} \times \frac{1}{n}\sum_{i=1}^{n} \left| x_i - \hat{Ex} \right| \tag{4}$$

5: *Step 3:* Compute the estimator $\hat{He}$ which measures the uncertainty degree of entropy, or hyperentropy, is given by:

$$\hat{He} = \sqrt{\Lambda_0^2 - \hat{En}^2}, \quad \text{where} \quad \Lambda_0^2 = \frac{1}{n-1}\sum_{i=1}^{n}(x_i - \bar{X})^2 \tag{5}$$

where Λ_0^2 is the sample variance.

Human decision-making is subject to fluctuations over time. Decision field theory, developed by Busemeyer et al. [30], provides a framework to model the decision maker's fluctuations in preferences and evaluate the alternatives using a dynamic-cognitive approach. It is a dynamic model of decision-making rather than a static model as it describes how an individual's preference evolve across time until a decision is reached. A decision is made as soon as the preference process reaches a decision criterion or threshold for any alternatives [32]. DFT does not assume decision as a fixed state of preference. It predicts how decisions change under pressure and how choice context changes preferences.

2.3 The decision field theory

Decision Field Theory (DFT) [38] models dynamic decision-making by capturing how preferences evolve over time. It is based on the idea that information is sequentially sampled and accumulated over time to make a decision [38]. The core principle of DFT is that the preference for alternatives changes dynamically based on previous states and current evaluations. The preference state vector $P(\tau)$ at time τ reflects the decision maker's current preferences. The evolution of this preference state from time τ to $\tau + h$ is governed by the following linear difference equation [51]:

$$P(\tau + h) = S \cdot P(\tau) + V(\tau + h), \tag{6}$$

where h represents an arbitrarily small step, S is the feedback matrix, and $V(\tau)$ represents the valence of alternatives at time τ. During the time intervals, the evaluation of each option is compared with others and these comparisons change the preferences

up or down depending on whether an alternative has an advantage or disadvantage of the attended attribute [38].

Components details:

- The feedback matrix $S = [s_{ij}]_{N\times N}$ captures the influence of past preferences on current states. It is defined as [38]:

$$S = [s_{ij}] = F[D(A_i, A_j)], \tag{7}$$

  where F is a decreasing function and A_i and A_j are alternatives. D measures attribute distances across alternatives and calculated using distance function between each pair of alternatives. These distances account for individual attribute values and their relative importance. It includes diagonal elements s_{ii} which reflect the memory of the previous preference state for each alternative. Off-diagonal elements s_{ij}, $i \neq j$ represent competitive interactions between alternatives, typically negative to account for lateral inhibition. A positive definite matrix S with eigenvalues less than 1 ensures system stability [52].
- The valence vector $V(\tau)$ represents the immediate attractiveness of alternatives based on current evaluations defined as [38]:

$$V(\tau) = C \cdot M \cdot W(\tau), \tag{8}$$

  where matrix M contains evaluation data for alternatives. It is an alternative vs. attribute matrix which contains decision-making information. The valence fluctuates because the decision maker's attention switches back and forth between anticipated consequences [32]. Vector $W(\tau)$ is the dynamic weight vector indicating the importance of attributes at time τ, and matrix C is the contrast matrix with elements c_{ij}, where $c_{ii} = 1$ and $c_{ij} = -1/(N-1)$ for $i \neq j$, with N being the number of alternatives. Contrast matrix is used to compare alternatives against each other.

3 Proposed methodology

This section introduces the integration of a Cloud Model with Decision Field Theory, which incorporates a unique method for implementing the initial uncertainty measurement, cloud feedback matrix and the calculation of dynamic weights.

3.1 Integration of cloud model and decision field theory

The integration of the Cloud Model (CM) and Decision Field Theory (DFT) represents an advancement in the modeling of decision-making processes under uncertainty. This integrated framework captures both the static uncertainty inherent in the decision maker's data and the dynamic nature of the decision process. This discussion explores the theoretical synergy between these two frameworks, proposing a unified approach that leverages their respective strengths to enhance the representation and analysis

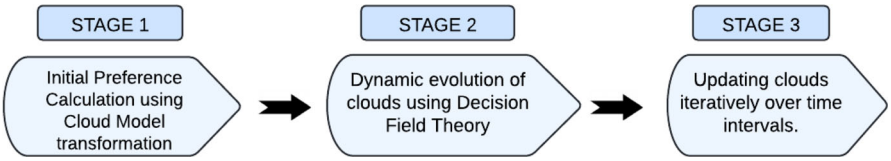

Fig. 1 Three-stage framework for dynamic cloud model based on decision field theory

of human cognition and decision dynamics. The integration of CM and DFT can be conceptualized as a three-stage process shown in Fig. 1.

Stage I: Initial Preference calculation using Cloud model transformation

The Cloud Model is employed to represent the initial uncertain preferences using its qualitative-quantitative nature by incorporating the randomness and fuzziness. This stage captures the static aspect of uncertainty, providing a detailed analysis of the initial state of the decision-maker's cognitive framework. The Cloud Model employs forward and backward cloud transformation algorithms. With the help of Backward cloud transformation, we generate cloud descriptors (Ex, En, He), which are subsequently used in forward cloud transformation to create clouds for each alternative. Next, we evaluate the cloud scores of the alternatives by utilizing the cloud score function. Further, these cloud scores were used to determine the initial preference in the decision making.

Stage II: Dynamic evolution of clouds using Decision field theory

In this stage, we showcase the dynamic nature of uncertainty through cloud generation. We generate clouds for each alternative at the initial time (τ) then utilizing the key linear difference equations of DFT to enhance dynamic behavior. This effectively incorporates the inherent dynamic uncertainties in decision-making. The initial uncertain perceptions and preferences modeled by the CM serve as inputs to the dynamic system which then evolve dynamically according to the principles of DFT. This process incorporates a cloud feedback matrix which utilizes the concept of cloud Hamming distance to evaluate distances. Dynamic weights are then continuously updated using time series forecasting methods.

Stage III: Updating clouds iteratively over time intervals

In this stage, we demonstrate the iterative updating of clouds for the next time interval ($\tau+h$). This is achieved by calculating the cloud descriptors for the next interval using the preference vector obtained from the current iteration. As a result, clouds are generated for each time step, reflecting their dynamic nature and capturing both static and dynamic uncertainties. The process continues iteratively until an external or internal stopping time is defined.

3.2 Initial uncertainty representation with CM

Integration of the Cloud Model with Decision Field Theory requires the initial preference state vector $P(\tau = 0)$, which is crucial as it signifies the starting point for the dynamic evolution of preferences. The cloud score $\hat{S}$, defined in Definition 3, is a metric used to evaluate a cloud, representing its mathematical expectation, the fuzziness

in a qualitative concept, and the higher-order uncertainty. A higher score indicates a larger and more significant cloud. We use the cloud score as the initial preference vector because it effectively addresses the static ambiguity in the decision maker's data by combining both the value of cloud drops (x_i) and their certainty degrees (y_i). This measure provides a more comprehensive representation of the overall contribution of each alternative to the concept W. By incorporating certainty degrees, the cloud score captures the variability associated with each alternative, leading to a more accurate and detailed initial preference state. In practical scenarios, decision-makers often consider both the perceived value and the confidence in their evaluations. The cloud score aligns with this empirical observation by reflecting both aspects in the initial preference vector.

3.3 Cloud feedback matrix $\mathbb{S}$

Consider the set of clouds $C_i(\mathrm{Ex}_i, \mathrm{En}_i, \mathrm{He}_i)$, $i = 1$ to N, where N is the number of alternatives. The cloud feedback matrix, denoted by $\mathbb{S}$, incorporates the cloud distance, which measures the dissimilarity between two clouds, based on (Ex, En, He) and evaluates attribute distances among alternatives. Unlike the Euclidean distance, which calculates straight-line distances between points, the cloud Hamming distance accounts for both the expected value and the degrees of variability (entropy and hyper-entropy). This characteristic allows it to more effectively capture the uncertainties present in the decision-making process. Moreover, the cloud feedback matrix considers the influence of neighboring alternatives, reflecting the lateral inhibition effects in decision-making. This implies that the preference state of a specific alternative at the current moment is influenced by its own preference state as well as those of other alternatives from the previous moment. The cloud feedback matrix is defined as follows:

$$\mathbb{S} = I - \beta \exp(-\alpha \times d(C_i, C_j)), \tag{9}$$

where α and β are sensitivity and memory parameters [52], respectively, and $d(C_i, C_j)$ represents the cloud Hamming distance[1] [53] given by :

$$d(C_i, C_j) = \sqrt{\frac{\underline{d}^2(C_i, C_j) + \bar{d}^2(C_i, C_j)}{2}} \tag{10}$$

[1] The cloud Hamming distance $d(C_a, C_b), a, b \in \mathbb{N}$ satisfies the following key properties:

- Symmetry: $d(C_a, C_b) = d(C_b, C_a)$.
- Law of Indiscernibility: $d(C_a, C_b) = 0$ if and only if $C_a = C_b$.
- Triangle Inequality: $d(C_a, C_c) \leq d(C_a, C_b) + d(C_b, C_c)$ for any clouds C_a, C_b, and C_c.
- Non-Negativity: $d(C_a, C_b) \geq 0$ for all a and b.

$$\begin{aligned}\underline{d}(C_i, C_j) &= \left| \left(\mathrm{Ex}_i - 3\sqrt{\mathrm{En}_i^2 + \mathrm{He}_i^2} \right) - \left(\mathrm{Ex}_j - 3\sqrt{\mathrm{En}_j^2 + \mathrm{He}_j^2} \right) \right| \\ \bar{d}(C_i, C_j) &= \left| \left(\mathrm{Ex}_i + 3\sqrt{\mathrm{En}_i^2 + \mathrm{He}_i^2} \right) - \left(\mathrm{Ex}_j + 3\sqrt{\mathrm{En}_j^2 + \mathrm{He}_j^2} \right) \right| \end{aligned} \tag{11}$$

The interconnections in the cloud feedback matrix are typically negative, producing competitive influences. $\mathbb{S}$ is positive definite, symmetric, and its eigenvalues are less than one to ensure system stability for appropriate values of α and β. The diagonal elements of $\mathbb{S}$ maintain the memory of the system's previous states, while the off-diagonal elements enable competitive interactions among the alternatives [38].

3.4 Dynamic weights via time series forecasting

In dynamic and uncertain decision-making environments, the ability to adjust weights in real-time is crucial for accurate forecasting and effective decision-making. Time series forecasting methods offer a robust methodology for predicting future trends by leveraging historical data. The objective is to continuously modify the weights assigned to various attributes over time, allowing the decision-making process to be more adaptive to shifting data patterns. This is achieved by identifying patterns in the time series that are self-correlated but offset in time. This facilitates a deeper understanding of the underlying time-dependent dynamics influencing decision variables.

AutoRegressive Integrated Moving Average (ARIMA) model, denoted as (p, d, q) is a time series analysis (TSA) model. The auto-regressive component p captures the influence of previous values, while the integrated component d accounts for trends in the data. The moving average component q reflects the impact of past random disturbances [44].

The TSA process using ARIMA follows these steps: As shown in Fig. 2, the workflow begins by analyzing historical time series data which undergoes Data Pre-processing, which includes important tasks like Data Cleaning and Preparation, Handling Missing Values, and Data Scaling. These steps are essential to ensure that the dataset is consistent, accurate, and ready for analysis. The next step is stationarity verification using the Augmented Dickey-Fuller (ADF) Test. If the data is non-stationary, differential computing is applied. Each decision-making parameter is modeled independently using a separate ARIMA model based on its own time-series data. This approach improves forecasting accuracy and ensures relevance in capturing the dynamics of each parameter. If the series remains non-stationary after differencing, we do not discard the weight series outright. Instead, additional transformations, such as logarithmic or power transformations, methods like seasonal decomposition or even advanced nonlinear models (e.g., machine learning methods) could be explored. We achieve stationarity after twice differencing for each of the alternatives used in our application. Although the methodology is designed to handle all scenarios and non-stationary data will not terminate the process. Instead, it is carefully transformed or modeled to ensure meaningful weight series are retained.

Once stationarity is achieved, ARIMA parameters (p, q, d) are estimated. We selected the best parameters based on methods like AIC, BIC, and error metrics like

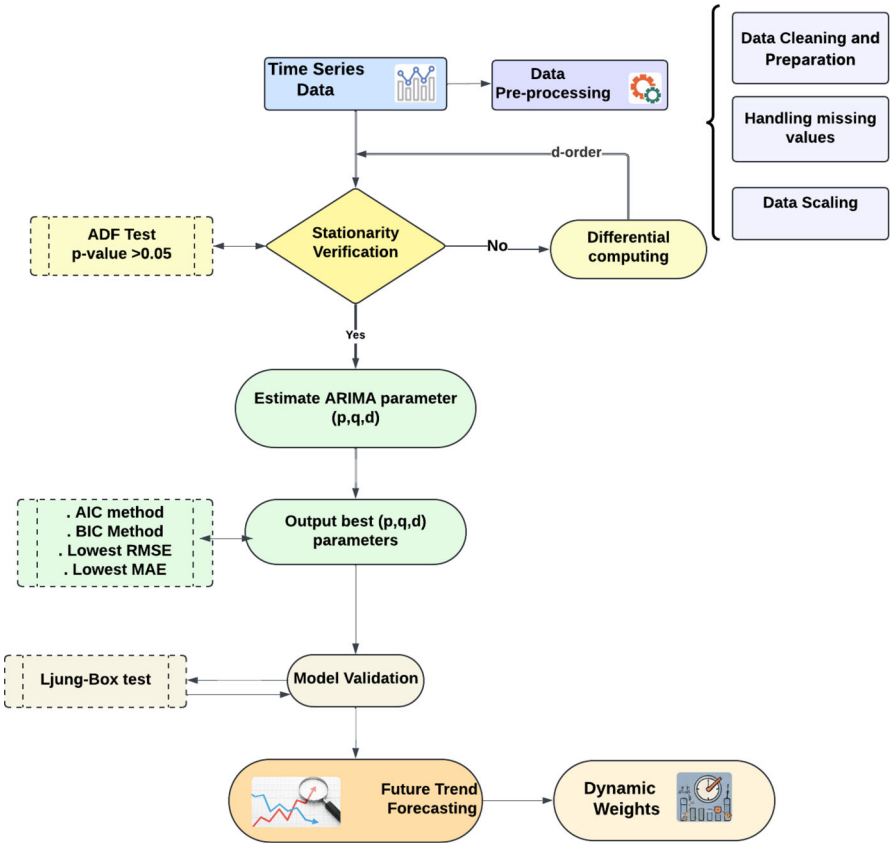

Fig. 2 Optimal ARIMA model selection algorithm

RMSE and MAE. After parameter selection, model validation is done using the Ljung-Box test. Finally, the model forecasts future trends. After forecasting the values for each attribute, dynamic weights are calculated by normalizing the forecasted values over time. This normalization ensures that the weights accurately represent the significance of each attribute based on the latest data and reflect the relative importance over time. These dynamic weights are then used to assess preferences for the coming years, allowing for more responsive and informed decision-making as the context evolves.

4 Proposed DCM-DFT algorithm

As outlined in the Section 3, the integration framework combining Cloud Model (CM) and Decision Field Theory (DFT), along with the dynamic weights derived from Time Series Analysis (TSA), serves as the foundation for the proposed algorithm. In this section, we introduce a novel approach of Dynamic Cloud Model based on Decision Field Theory (DCM-DFT) and probability computation under this framework.

4.1 Dynamic cloud model based on decision field theory (DCM-DFT)

The objective of the DCM-DFT model is to obtain a set of dynamic clouds, evaluate preferences for alternatives and compute the probabilities associated with selecting each alternative. The methodology is divided into three main stages, with detailed steps outlined below.

Input Data and data pre-processing:

The DCM-DFT process takes input as an alternative vs. attribute data matrix at a given time τ. Construct the original decision-making matrix by organizing the decision-maker's information into an alternative-attribute matrix M, where rows represent alternatives and columns represent attributes. Ensure all data entries are pre-processed (handling missing values or outliers) and normalized to ensure comparability across attributes.

Parameter Settings:

In forward cloud transformation set number of cloud drops n. Use predefined constants α, β for the cloud feedback matrix. Set an externally controlled stopping time τ threshold in order to terminate the process.

Stage 1: Evaluation of initial preference using cloud model

Let the row vector $P_\tau = [P_{1\tau}, P_{2\tau}, \cdots, P_{N\tau}]'$ represents the preference state at time τ for the set of N alternatives.

Step 1: Perform Backward Cloud Transformation (BCT).

In order to evaluate the initial preference vector $P_{\tau=0}$, we calculate cloud descriptors from the backward cloud transformation (BCT) Algorithm 2 using the following equations:

$$\begin{cases} Ex_{\tau=0} = \dfrac{1}{N}\displaystyle\sum_{i=1}^{N} x_i \\ En_{\tau=0} = \sqrt{\dfrac{\pi}{2}} \times \dfrac{1}{N}\displaystyle\sum_{i=1}^{N} |x_i - Ex_{\tau=0}| \\ \Lambda^2_{\tau=0} = \dfrac{1}{N-1}\displaystyle\sum_{i=1}^{N} (x_i - Ex_{\tau=0})^2 \\ He_{\tau=0} = \sqrt{\Lambda_0^2 - En^2_{\tau=0}} \end{cases} \tag{12}$$

where N is the number of alternatives.

Step 2: Apply Forward Cloud Transformation (FCT) Algorithm.

Using these cloud descriptors $(Ex, En, He)_{\tau=0}$ as input vectors in the Forward Cloud Transformation (FCT) Algorithm 1 which generates the m cloud drops x_i and their certainty degree y_i.

Step 3: Calculate the initial preference vector.

Calculate the scores of the obtained clouds using the formula:

$$\hat{S}(C) = \frac{1}{m} \sum_{i=1}^{m} x_i y_i. \tag{13}$$

The derived scores serve as an initial preference vector P_τ for the time $\tau = 0$. These scores provide a comprehensive representation of each alternative's contribution to the concept W. This method effectively captures all uncertainties inherent in the decision-maker's data, making it ideal for representing initial preferences.

Stage 2: Dynamic Evolution with CM-DFT

In this stage, we begin by calculating essential vectors and matrices, including the valence vector V_τ, preference vector P_τ, the contrast matrix C, and the cloud feedback matrix $\mathbb{S}$. These elements are crucial for computing the key linear difference Equation (6) of DFT.

Step 1: Calculate Key Vectors and Matrices.

Let the row vector $V_\tau = [v_{1\tau}, v_{2\tau}, \ldots, v_{N\tau}]'$ represents the valence vector at time τ, where each component $v_{i\tau}$ denotes the input valence for alternative i ($i \in 1, 2, \ldots, N$) and reflects the relative attractiveness of the alternatives at time τ, based on their expected values for a specific attribute. The general form of the valence vector is given by equation:

$$V_\tau = C \cdot M \cdot W_\tau \tag{14}$$

where the decision-maker matrix M contains evaluation information for all alternatives across different attributes.

- The weight vector $W_\tau = (w_{\tau_1}, w_{\tau_2}, \cdots, w_{\tau_N})'$ holds the relative importance assigned to each attribute of M, calculated using a time series forecasting method to generate dynamic weights. These forecasted weights are normalized so that the sum of weights for each attribute equals 1, as discussed in Section 3.
- The contrast matrix C is used to compare the weighted evaluations of different options produced by MW_τ. It facilitates the comparison of alternatives by assessing their relative performance.

Step 2: Construct the Cloud Feedback Matrix. The matrix $\mathbb{S}$, known as the cloud feedback matrix, is defined by:

$$s_{ij} = -\beta \times e^{-\alpha \sqrt{\frac{\vec{d}^2(C_i, C_j) + \bar{d}^2(C_i, C_j)}{2}}} \qquad for \;\; i \neq j \tag{15}$$

In order to calculate the distance, we utilize the hamming distance of clouds based on the 3-sigma rule as discussed in Section 3. *Step 3:* Update Preference Vector.

The dynamic behavior of the decision-maker is evaluated using the key differential equation of DFT, which evaluates the preference vector $P_{\tau+h}$ for time $\tau + h$:

$$P_{\tau+h} = \mathbb{S} \cdot P_\tau + V_{\tau+h}. \tag{16}$$

where h represents an arbitrarily small time step. Preference states can vary from positive (approach states) to negative (avoidance states), with the magnitude of each preference reflecting the degree of inclination toward either approaching or avoiding.

Stage 3: Obtaining iterative clouds for different time intervals

Expectation (Ex), entropy (En), and hyper-entropy (He) are the three numerical descriptors that characterize cloud models.

Step 1: Update Cloud Descriptors.

To obtain the cloud for the next time interval ($\tau+h$), the preference vectors calculated for that specific time step are utilized. If preference vectors are negative, max-min normalization is used to transform them. After normalization (if needed), the cloud descriptors are updated based on the preference vector at the time interval ($\tau + h$) as follows:

$$\begin{cases} Ex_{\tau+h} = Ex_{\tau} \\ En_{\tau+h} = P_{(\tau+h)} \times En_{\tau} \\ He_{\tau+h} = P_{(\tau+h)} \times He_{\tau} \end{cases} \tag{17}$$

The mathematical expectation is a fundamental statistical property of the dataset and it remains unchanged, as it represents the central tendency of the cloud drops and is not directly influenced by the preferences. In contrast, both entropy and hyper-entropy are directly affected by the preference vector, reflecting changes in uncertainty and its second-order measurement. *Step 2:* Generate New Clouds. Using the updated descriptors (Ex, En, He)$(\tau + h)$, generate the cloud for the next time step. Repeat this process iteratively for successive time intervals to model the dynamic evolution of preferences. In conclusion, this section outlines a comprehensive approach that integrates cloud models and DFT to dynamically update clouds and assess preferences over time, ensuring accurate and adaptable decision-making. Fig. 3 depicts a flow diagram illustrating the process of our proposed research model. The process begins by taking a real-time dataset from decision-makers as input and constructing an alternative vs. attribute matrix for the initial time, τ. In Stage 1, the initial preferences are evaluated using cloud model theory, resulting in cloud scores representing these preferences. These scores serve as the output of Stage 1 and are incorporated into Stage 2. Stage 2 focuses on the dynamic evolution of clouds. By employing the ARIMA method for time series forecasting, dynamic weights are derived and used to calculate the Valence vector for each time interval. As a result, Preference Vectors are generated for each time step. In Stage 3, the clouds are iteratively updated, and scores are computed for each subsequent time interval ($\tau + h$). The algorithm proceeds to determine the rank of the alternatives for each time interval, enabling dynamic behavior preference analysis to be performed comprehensively. Algorithm 3 outlines the pseudocode for the Dynamic Cloud Model based on Decision Field Theory.

Algorithm 3 Dynamic Cloud Model based on Decision Field Theory (DCM-DFT)

Input: Decision matrix M at time τ, dynamic attribute weights W_τ, number of alternatives N
Output: Dynamic clouds $(Ex_{\tau+h}, En_{\tau+h}, He_{\tau+h})$
Procedure *Stage 1: Initial Preference Evaluation Using Cloud Model*
  foreach *alternative* $i \in \{1, \cdots, N\}$ **do**
    Compute $Ex_{\tau=0}, En_{\tau=0}, He_{\tau=0}$ using BCT Algorithm 2;
  end foreach
  Use FCT Algorithm 1 to generate cloud drops x_i and certainty y_i;
  Compute initial preference vector $P_{\tau=0}$ using cloud score Equation (2);
end
Procedure *Stage 2: Dynamic Evolution with CM-DFT*
  foreach *time step* $\tau + h$ **do**
    Calculate valence vector V_τ, preference vector P_τ, contrast matrix C, cloud feedback matrix $\mathbb{S}$;
    Update preference vector: $P_{\tau+h} = S \cdot P_\tau + V_{\tau+h}$;
    where valence vector $V_{\tau+h} = C \cdot M \cdot W_{\tau+h}$ and dynamic weight vector $W_{\tau+h}$;
  end foreach
end
Procedure *Stage 3: Update Cloud Descriptors*
  foreach *time interval* $\tau + h$ **do**
    Update $Ex_{\tau+h}, En_{\tau+h}, He_{\tau+h}$ based on the preference vector $P_{\tau+h}$;
    Utilize Equation (17);
    If necessary, normalize preference vector using max-min normalization;
  end foreach
end

4.2 Probability computation under DCM-DFT framework

In this subsection, we demonstrate how to compute the likelihood of selecting a particular alternative from a given set of N alternatives within the Dynamic Cloud Model based on Decision Field Theory (DCM-DFT) framework.

The iterative expansion of Equation (16) results in the following expression for the preference vector at time τ [52]:

$$P_\tau = \sum_{k=0}^{\tau-1} \mathbb{S}^k \cdot V_{\tau-k} + \mathbb{S}^\tau \cdot P_0 \tag{18}$$

where $\mathbb{S}$ is the cloud feedback matrix and P_0 is the initial preference vector taken as scores computed by the process of cloud transformation algorithms as discussed in Stage 1 of Section 4.1.

To compute the variance for a given random variable X, we use the properties of variance operator $Var(D \cdot X) = D \cdot Var(X) \cdot D'$, where D is a constant matrix and '$'$' denotes the transpose operator. Utilizing variance property to calculate the expected valence $E[V_\tau]$ and covariance matrix $Cov[V_\tau]$, given by [52]:

$$E[V_\tau] = \mu = C \cdot M \cdot W_{TSA}, \quad Cov[V_\tau] = \chi = C \cdot M \cdot \varphi \cdot M' \cdot C' \tag{19}$$

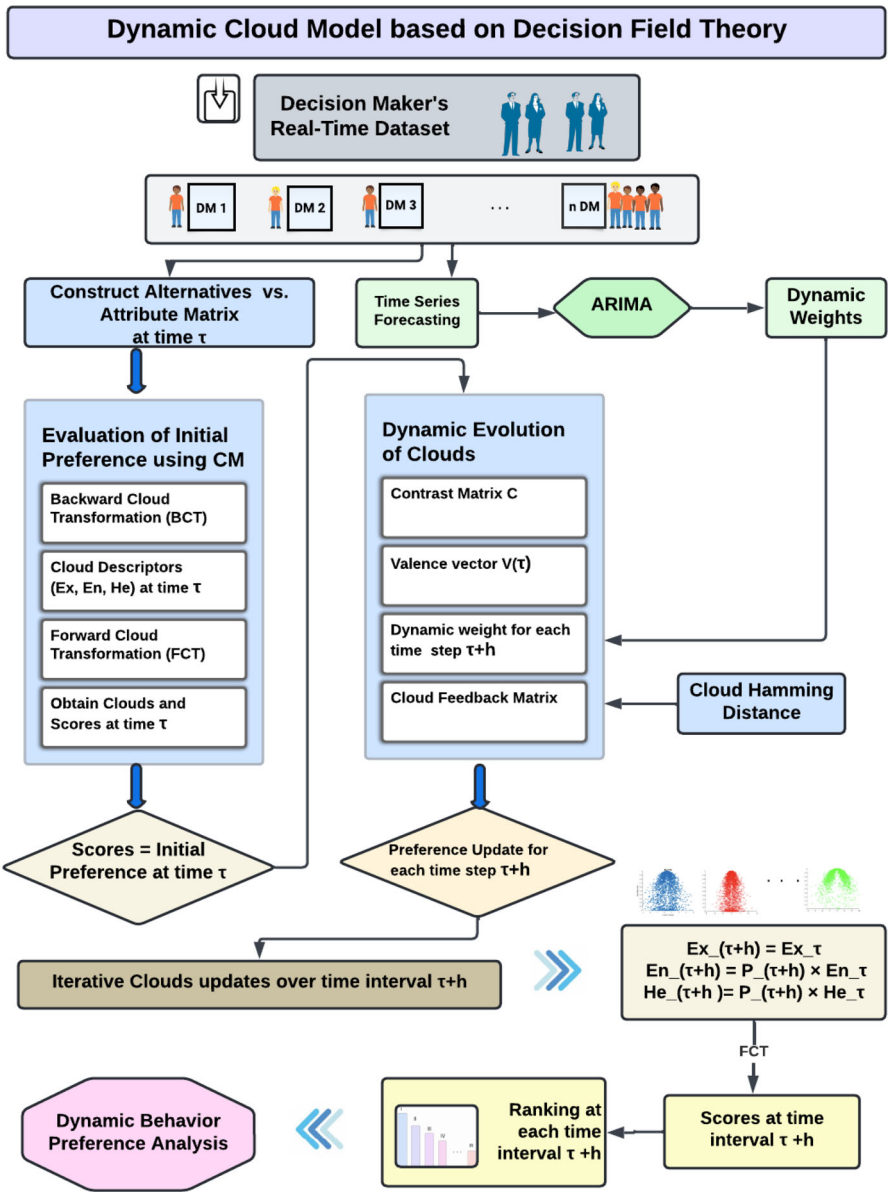

Fig. 3 Flowchart illustrating the implementation of the proposed research model

where $\varphi = Cov[W_{TSA_m}]$ and $W_{TSA_m} = [w_1, w_2, ..., w_N]'$ is the weights obtained by time series methodology as discussed in Sect. 3.4.

Now, calculate the expected value and covariance of P_τ [52]. With cloud feedback matrix $\mathbb{S}$ being a constant, $E[P^\tau]$ reduces to:

$$E[P_\tau] = \xi_\tau = \sum_{k=0}^{\tau-1} S^k \cdot \mu + \mathbb{S}^\tau \cdot P_0 = (I - \mathbb{S})^{-1}(I - \mathbb{S}^\tau) \cdot \mu + \mathbb{S}^\tau \cdot P_0 \tag{20}$$

$$Cov[P_\tau] = \Omega_\tau = Cov\left[\sum_{k=0}^{\tau-1} \mathbb{S}^k \cdot V_{\tau-k} + \mathbb{S}^\tau \cdot P_0\right] = \sum_{k=0}^{\tau-1}\left[\mathbb{S}^k \cdot \chi \cdot (\mathbb{S}^k)'\right] \tag{21}$$

After computing the expected value (ξ_τ) and the covariance matrix (Ω_τ) of the preference values at time τ, we calculate the probability of choosing one alternative from a set of N alternatives. Based on the multivariate central limit theorem [54], P_τ converges to the multivariate normal distribution. Under DCM-DFT, alternative A_i is chosen if it has a higher preference value at time τ than all other alternatives A_j for $j \neq i$. This probability is computed as:

$$\Pr\left[P_\tau[A_i] - P_\tau[A_j] > 0 \text{ for all } j \neq i\right] = \int_{X>0} \exp\left[-(X - \Gamma)'\Lambda^{-1}(X - \Gamma)/2\right] / \left(2\pi|\Lambda|^{0.5}\right) dX \tag{22}$$

where $X = \begin{bmatrix} P_\tau[A_i] - P_\tau[A_1] \\ P_\tau[A_i] - P_\tau[A_2] \\ \vdots \\ P_\tau[A_i] - P_\tau[A_{i-1}] \\ P_\tau[A_i] - P_\tau[A_{i+1}] \\ \vdots \\ P_\tau[A_i] - P_\tau[A_N] \end{bmatrix}$,

$\Gamma = L\xi_\tau$, $\Lambda = L\Omega_\tau L'$ and L is a matrix that consists of a column vector of 1's and a negative identity matrix of size $N - 1$.

5 Real-life application: a case study

Human decision-making is at the heart of establishing a healthy and productive lifestyle. In our daily routines, numerous macro-level and micro-level factors contribute to making a day perfect. Micro-level decisions collectively shape our macro-level lifestyle, with daily choices building a routine that impacts overall well-being. Therefore, small daily decisions are pivotal in forming a larger, cohesive routine that ultimately impacts our overall lifestyle. Consistent fluctuations in our decisions can disrupt our daily routines and, consequently, our long-term lifestyle. In this section, we begin by introducing the dataset used for the application in Sect. 5.1. Next, we identify trends and forecast the weights using the TSA methodology, as outlined in

Sect. 5.2. Finally, Sect. 5.3 illustrates the proposed methodology to analyze human behavior dynamics over time.

5.1 Data collection and description

The *Lifestyle and Well-being Data*[2], sourced from Kaggle, is a rich collection of 15,972 survey responses with 20 attributes that provide detailed insights into various aspects of individuals' lifestyle choices and behaviors. Table 3 provides a description of the lifestyle and wellbeing attributes, along with their original scale, linguistic descriptions, and nature of attributes. It is a real-time dataset spans from July 2015 to March 2021, giving us almost 6 years of data. The dataset contains a gender distribution where 61.72% of respondents are female and 38.28% are male. One of the core features is the work-life balance score, which serves as a comprehensive evaluation of how individuals harmonize their professional and personal lives. It assesses five key aspects of life as shown in Fig. 4: Healthy Body, which reflects fitness and healthy habits; Healthy Mind, indicating emotional well-being; Expertise, measuring personal and professional growth; Connection, evaluating social networks and exploration tendencies; and Meaning, assessing compassion and the pursuit of a fulfilling life. This dataset serves as a rich resource for understanding how everyday choices and habits contribute to overall life satisfaction and health.

Data preprocessing

The Lifestyle and Wellbeing dataset encompasses 20 attributes, including cost and benefit categories, as shown in Table 3. To assess the nature of these attributes, we employed the Delphi method [55] to gather expert opinions. The experts classified attributes like Fruits & Veggies, Weekly Meditation, Daily Steps, Sufficient Income, Time For Passion and others as benefit attributes. In contrast, attributes such as Daily Stress, Lost Vacation, and Daily Shouting are identified as cost attributes. We sorted the dataset by the AGE criterion, which includes four primary categories: 'Less than 20', '21 to 35', '36 to 50', and '51 or more'. Fig. 5 offers a visual overview of how the surveyed individuals are distributed across the specified age ranges, both in terms of percentage and actual count.

Data Scaling

Different attributes as shown in Table 3 originally vary in their scales and linguistic descriptions. To ensure consistency, we standardize these linguistic sets by converting all attributes to a uniform scale ranging from 1 to 10. This standardization is done using modified Weitendorf's Linear Normalization method [56], which adjusts each attribute's range to fit within the new scale [Min New, Max New]. The general formula used for this normalization is:

$$x_{norm} = \frac{x - \min(x)}{\max(x) - \min(x)} \times (\text{Max New} - \text{Min New}) + \text{Min New} \tag{23}$$

where x is the original value, $\min(x)$ and $\max(x)$ represents the minimum and maximum value in the original dataset, and x_{norm} is the normalized value. The normalization

[2] https://www.kaggle.com/datasets/ydalat/lifestyle-and-wellbeing-data

Table 3 Attributes of the lifestyle and wellbeing dataset

Attribute name	Abbreviation	Description	Original scale with linguistic description	Nature of criterion
Fruits & Veggies	FV	The daily intake of fruits or vegetables.	0–5, 0: Never, 5: Always	Benefit Criterion
Daily Stress	STRESS	The typical amount of stress experienced each day.	0–5, 0: No stress, 5: Very high stress	Cost Criterion
Places Visited	PV	The frequency of visiting new places.	0–10, 0: Never, 10: Very Often	Benefit Criterion
Core Circle	CC	The number of people very close to an individual.	0–10, 0: None, 10: Many People	Benefit Criterion
Supporting Others	SO	The number of people helped to achieve a better life.	0–10, 0: None, 10: Many People	Benefit Criterion
Social Network	SN	The number of people interacted with during a typical day.	0–10, 0: No interaction, 10: Many People	Benefit Criterion
Achievement	ACH	The number of remarkable achievements an individual is proud of.	0–10, 0: None, 10: Many Achievements	Benefit Criterion
Donation	DON	The frequency of donating time or money to good causes.	0–5, 0: Never, 5: Very Often	Benefit Criterion
BMI Range	BMI	The body mass index (BMI) range, indicating normal weight or overweight.	1 & 2, 1: Normal weight ($\leq$ 25), 2: Overweight ($\geq$ 25)	Neither Benefit nor Cost
To Do Completed	TODO	The effectiveness of completing weekly to-do lists.	0–10, 0: Not at all, 10: Very well	Benefit Criterion
Flow	FW	The number of hours spent in a fully immersive mental state (flow) during a day.	0–10, 0: None, 10: Many Hours	Benefit Criterion

Table 3 (continued)

Attribute name	Abbreviation	Description	Original scale with linguistic description	Nature of criterion
Daily Steps	STEPS	The number of steps (in thousands) walked daily.	1–10, 1: 1,000 Steps, 10: 10,000+ Steps per day	Benefit Criterion
Live Vision	VISION	The number of years for which an individual's life vision is very clear.	0–10, 0: Not Clear, 10: Very Clear	Benefit Criterion
Sleep Hours	SH	The typical length of sleep.	1–10, 1: Less than 4 hours, 10: 10+ Hours	Benefit Criterion
Lost Vacation	LV	The number of vacation days lost annually.	0–10, 0: None, 10: All Vacation Days	Cost Criterion
Daily Shouting	DS	The frequency of shouting or sulking at someone.	0–10, 0: Never, 10: Very Often	Cost Criterion
Sufficient Income	SI	The sufficiency of income to cover basic life expenses.	1 & 2, 1: Not Sufficient, 2: Fully Sufficient	Benefit Criterion
Personal Awards	PA	The number of recognition received in an individual's life.	0–10, 0: None, 10: Many Recognition	Benefit Criterion
Time For Passion	TFP	The number of hours spent daily on activities an individual is passionate about.	0–10, 0: None, 10: Many Hours	Benefit Criterion
Weekly Meditation	WM	The number of times in a week when an individual has the opportunity to think about themselves.	0–10, 0: No opportunities, 10: Numerous opportunities	Benefit Criterion

process ensures that all attributes are comparable and on the same scale, facilitating accurate analysis and interpretation.

Data Visualization

The primary objective of this analysis is to explore the relationship between key lifestyle factors as mentioned in Fig. 4 and their collective impact on work-life balance

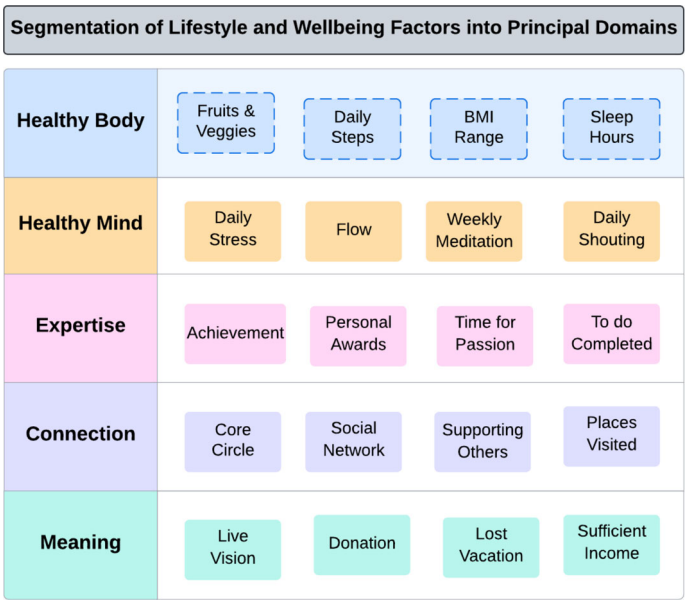

Fig. 4 Lifestyle and Wellbeing attributes

Fig. 5 Distribution of age categories

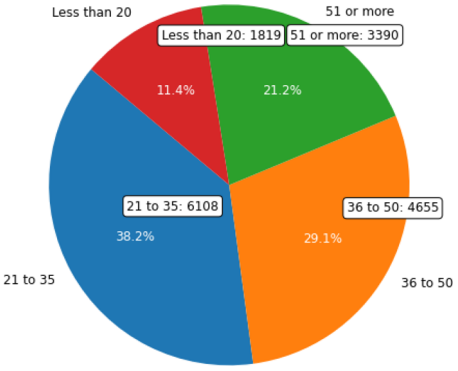

score. Heatmaps effectively visualize these relationships, using a color-coded matrix to highlight both positive and negative correlations among various variables, allowing for easy identification of patterns and trends within the data. As shown in Fig. 6, the diagonal values in the heatmap represent the correlation of each attribute with itself. Several attributes exhibit strong positive correlations. Supporting others (SO) is correlated with Donation (DON) at a value of 0.39 and with Core Circle at a value of 0.34. The highest correlation in the heatmap is between Time for Passion (TFP) and Flow (FW), with a value of 0.48. This suggests that people who dedicate time to their passions also experience a higher sense of flow in their activities. Passion-related

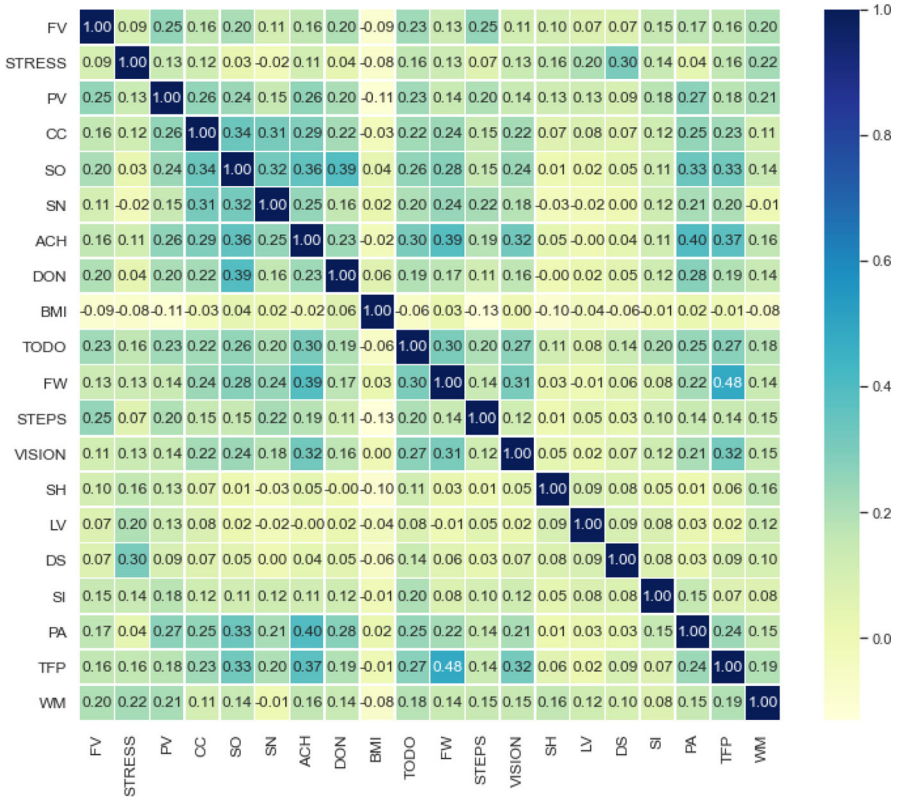

Fig. 6 Correlation Heatmap of Lifestyle Factors

activities, like Meditation and Time For Passion, correlate with Flow and Live Vision, highlighting their importance for mental wellbeing.

Figure 7 illustrates the trends in average Work-Life Balance (WLB) scores across four age groups from 2015 to 2021: Less than 20, 21 to 35, 36 to 50, and 51 or more, revealing distinct patterns within each group. Each bar indicates the average WLB score for a specific year and age group. Over the years, the scores fluctuate showcasing, the varying perceptions of work-life balance among different demographics. This highlights the importance of the WLB score in understanding how age affects individuals' experiences in balancing their professional work and personal life commitments.

5.2 Time series analysis of lifestyle and wellbeing attributes: historical trends and forecasts

In this subsection, we present a time series analysis via graph for various attributes of the Lifestyle & Wellbeing application, applying the ARIMA methodology as outlined in Sect. 3.4.

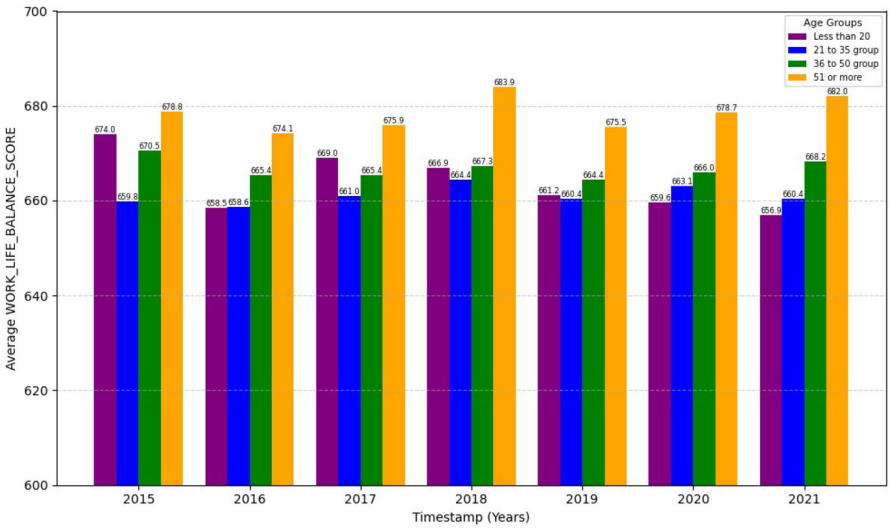

Fig. 7 Trends in Work-Life Balance Scores Across Age Groups (2015-2021)

The stationarity of the data is examined using statistical tests like the Augmented Dickey-Fuller (ADF) test [44]. If the data is stationary, no differencing is needed, and modeling can proceed. Conversely, if the data is non-stationary, differencing (d-order) is applied to stabilize the mean and eliminate trends. We made all attributes stationary by incrementing the d-order as necessary. This step is essential since the ARIMA model requires stationary time series data. The ADF test provides both the ADF statistic and p-value, with a p-value below 0.05 suggesting stationarity and a value above 0.05 indicating non-stationarity [45].

Table 4 presents the results of the stationarity test for various Lifestyle & Wellbeing attributes. The analysis reveals varied patterns among attributes, where FV, STRESS, DS, SI, PA, CC and others are stationary, indicating consistent trends over time. In contrast, attributes such as PV, BMI and others show non-stationarity, suggesting fluctuations and changing trends. This highlights that while some aspects of lifestyle remain stable, others are more dynamic and subject to variability.

We constructed the ARIMA model and determined the order of attributes using a structured approach to evaluate different combinations of parameters (p, d, q). In this study, the parameter ranges are defined with $p, q \in \{0, 8\}\}$, d set at 0, 1, and 2 to allow for up to second-order differencing. This approach generates all possible combinations of these parameters, resulting in a comprehensive set of candidate models. Each candidate model is fitted to the training dataset, and predictions are then made for the test dataset. The model's performance is assessed using key metrics: Root Mean Square Error (RMSE), Mean Absolute Error (MAE), Akaike Information Criterion (AIC) and Bayesian Information Criterion (BIC) [44]. These metrics help to determine the optimal combination of model parameters (p, d, q) and evaluate how well each model fits the data. The results are stored in a list and then sorted to identify the model with the lowest RMSE and MAE, as shown in Table 4. The best ARIMA

Table 4 Stationarity test and evaluation metrics for optimal ARIMA order obtained across various lifestyle & wellbeing attributes

Lifestyle & Well-being Attributes	Stationarity of data	ADF stats	p-Value	RMSE	MAE	AIC	BIC	Optimal ARIMA Order obtained
FV	Stationary	− 4.065	0.001	0.009	0.008	− 11.53	− 6.681	(4,0,4)
STRESS	Stationary	− 10.636	0.000	0.106	0.077	− 11.228	− 9.238	(0,2,4)
PV	Non-stationary	− 1.156	0.692	0.428	0.425	14.676	17.461	(1,1,5)
CC	Stationary	− 3.948	0.002	0.008	0.008	5.107	7.830	(2,2,6)
SO	Non-stationary	− 0.776	0.826	0.249	0.247	− 2.271	0.639	(3,0,1)
SN	Stationary	− 4.483	0.000	0.258	0.234	15.102	18.684	(6,1,2)
ACH	Non-stationary	− 1.550	0.509	0.182	0.171	− 7.08	− 3.897	(7,1,0)
DON	Non-stationary	− 0.306	0.925	0.230	0.175	18.538	23.71	(5,1,2)
BMI	Non-stationary	1.625	0.998	0.162	0.153	− 3.361	− 1.371	(4,1,0)
TODO	Non-stationary	− 0.828	0.811	0.122	0.109	− 4.176	− 0.197	(7,1,2)
FW	Non-stationary	1.340	0.997	0.190	0.148	1.17	6.342	(7,1,5)
STEPS	Non-stationary	− 1.790	0.385	0.013	0.009	0.755	2.745	(0,1,4)
VISION	Non-stationary	− 0.186	0.940	0.178	0.172	− 4.68	− 1.497	(3,1,4)
SH	Non-stationary	− 2.607	0.092	0.032	0.027	− 5.775	− 3.354	(0,2,7)
LV	Non-stationary	− 0.163	0.943	0.104	0.076	10.148	14.127	(3,1,6)
DS	Stationary	− 4.832	0.000	0.001	0.001	− 17.588	− 11.769	(4,0,6)
SI	Stationary	− 2.940	0.041	0.162	0.157	8.739	12.134	(3,0,2)
PA	Stationary	− 3.973	0.002	0.019	0.019	− 6.32	− 3.411	(3,0,1)
TFP	Non-stationary	− 1.225	0.663	0.304	0.283	− 1.892	0.098	(2,1,2)
WM	Non-stationary	0.188	0.972	0.015	0.012	− 13.717	− 12.523	(0,1,2)

order is selected based on performance metrics, ensuring an optimal balance between accuracy and complexity. This structured approach enables efficient identification of a suitable ARIMA model.

Figure 8 (Part 1 & Part 2) illustrates both the historical and forecasted values of the 20 attributes listed in Table 3 from July 2015 to December 2025 using optimal ARIMA order obtained from Table 3. The solid blue line represents the historical data, ranging from July-December 2015 to January-June 2021, highlighting fluctuations with distinct peaks and troughs. The forecasted values, indicated by the dashed red line, begin in January-June 2021 and extend to July-December 2025. The x-axis displays time periods in six-month intervals, ranging from July 2015 to December 2025, while the y-axis represents the attribute values. A vertical dotted line marks the transition between historical and forecasted data. Surrounding the forecasted values is a yellow shaded region representing the 95% confidence interval, which illustrates the uncertainty in the predictions. The interval widens over time, indicating growing unpredictability as the forecast extends further into the future. This can be shown in graphs of attributes like STEPS, LV, PV, while some attributes, like FV, SO, TODO shows relatively stable, less future uncertainty. The forecasts for attributes like BMI, ACH, FW and others demonstrate high accuracy, with minimal deviation from observed values. This indicates that the selected ARIMA model successfully captures their trends.

5.3 Implementation of proposed DCM-DFT algorithm

The objective of this subsection is to demonstrate the implementation of the proposed Dynamic Cloud Model based on the Decision Field Theory (DCM-DFT) algorithm on the Lifestyle and Wellbeing dataset. To begin, we construct a 4×20 alternative vs. attribute matrix representing the 20 attributes across four age groups. Figure 9 shows the transpose of decision matrix, utilizing the dataset spanning from 2015 to 2021. We aim to forecast the dynamic changes in preferences from January (Jan) 2021 to December (Dec) 2025 and generate dynamic clouds for the four age group's alternatives for the forecasted periods to assess the dynamic changes in behavior and uncertainty over six-month intervals. July-December 2025 is considered the externally controlled stopping criterion for the forecast.

We start by implementing the backward cloud transformation Algorithm 2 to derive cloud descriptors (*Ex*, *En*, *He*) for each age alternative. By applying Eq. (12) from Stage 1 of the proposed DCM-DFT algorithm, we obtain the cloud descriptors for the initial time $\tau = 0$ for each age group, shown as follows:

$$\begin{array}{c} \\ \mathrm{Ex}_{\tau=0} \\ \mathrm{En}_{\tau=0} \\ \mathrm{He}_{\tau=0} \end{array} \begin{array}{c} \begin{array}{cccc} \text{Less than 20} & \text{21-35 group} & \text{36-50 group} & \text{51 or more} \end{array} \\ \begin{bmatrix} 5.623 & 5.651 & 5.941 & 6.253 \\ 1.221 & 1.121 & 1.159 & 1.296 \\ 2.829 & 2.601 & 2.663 & 2.889 \end{bmatrix} \end{array} \tag{24}$$

Utilizing the cloud descriptors derived from Eq. (24) and employing the forward cloud transformation Algorithm 1, we generate the initial clouds corresponding for each age alternative, which are visually represented in Fig. 10. The x-axis is labeled as "Cloud Drops" and the y-axis as "Membership". Each plot represents the distribution of cloud

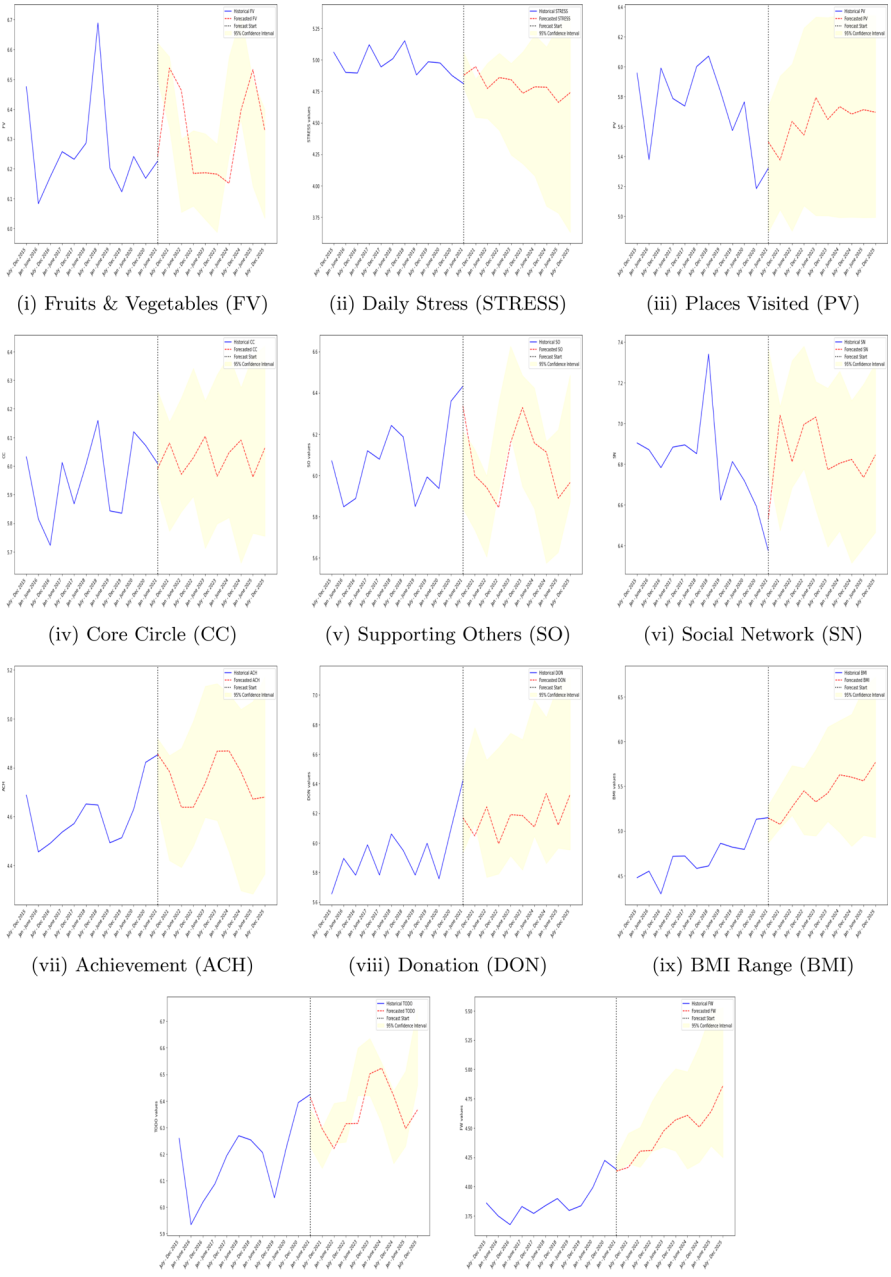

(i) Fruits & Vegetables (FV) (ii) Daily Stress (STRESS) (iii) Places Visited (PV)

(iv) Core Circle (CC) (v) Supporting Others (SO) (vi) Social Network (SN)

(vii) Achievement (ACH) (viii) Donation (DON) (ix) BMI Range (BMI)

(x) To-Do Completed (TODO) (xi) Flow (FW)

Fig. 8 Historical and Forecasted time series graphs using optimal ARIMA model for various Lifestyle & Wellbeing attributes for the time period July-Dec 2015 to July-Dec 2025 (Part 1). Historical and Forecasted time series graphs using optimal ARIMA model for various Lifestyle & Wellbeing attributes for the time period July-Dec 2015 to July-Dec 2025 (Part 2)

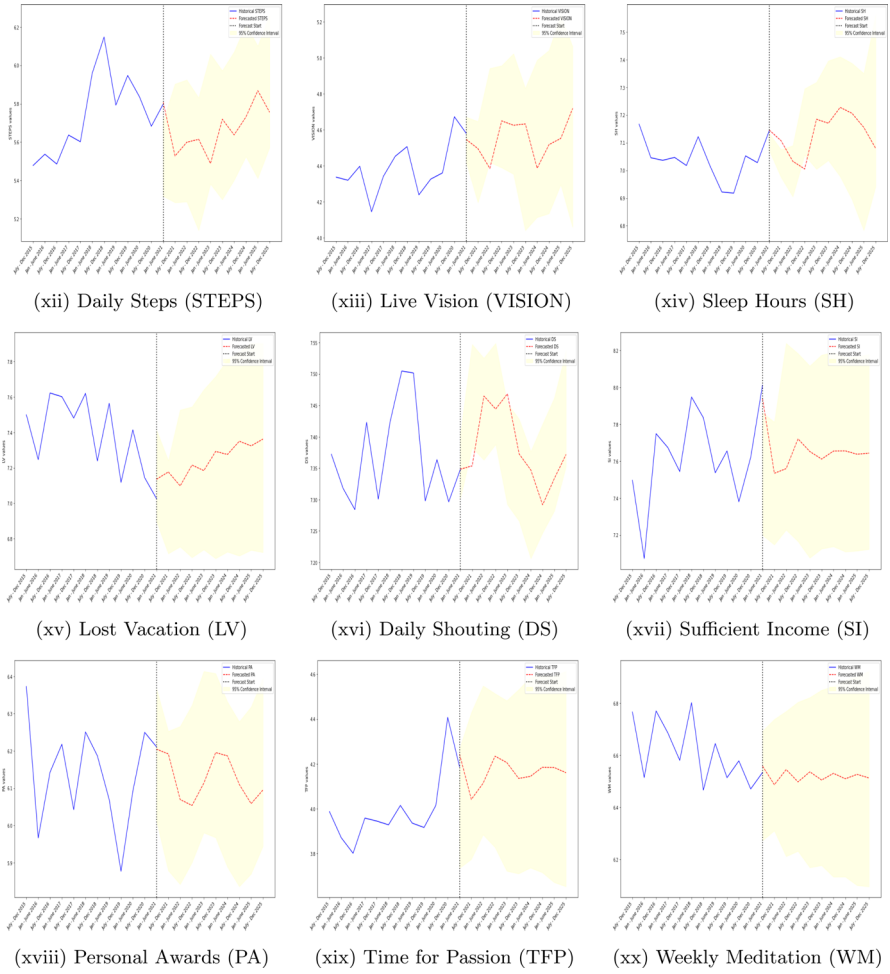

(xii) Daily Steps (STEPS) (xiii) Live Vision (VISION) (xiv) Sleep Hours (SH)

(xv) Lost Vacation (LV) (xvi) Daily Shouting (DS) (xvii) Sufficient Income (SI)

(xviii) Personal Awards (PA) (xix) Time for Passion (TFP) (xx) Weekly Meditation (WM)

Fig. 8 continued

drops within the alternatives, which corresponds to how members of each age group exhibit uncertainty under 20 lifestyle attributes. For in-depth analysis of clouds, we incorporated derived cloud descriptors into Eqs. (25), (26), and (27). These equations define the upper and lower primary membership functions, as well as the difference function, which reflects the uncertainty of a cloud $C(Ex, En, He)$, as follows [57]:

$$\begin{cases} y_{\text{upper}} = e^{-\frac{(x-Ex)^2}{2(En+3He)^2}} \\ y_{\text{lower}} = e^{-\frac{(x-Ex)^2}{2(En-3He)^2}}. \end{cases} \tag{25}$$

$$y_{\text{diff}} = y_{\text{upper}} - y_{\text{lower}} = e^{-\frac{(x-Ex)^2}{2(En+3He)^2}} - e^{-\frac{(x-Ex)^2}{2(En-3He)^2}}. \tag{26}$$

	Less than 20	21-35 group	36-50 group	51 or more
FV	5.797	5.844	6.409	7.056
STRESS	5.039	4.933	4.790	5.269
PV	5.447	5.837	5.641	5.715
CC	6.092	5.855	6.004	6.004
SO	5.201	5.609	6.453	6.768
SN	7.621	6.555	7.088	6.532
ACH	4.817	4.459	4.649	4.674
DON	4.788	5.271	6.290	7.036
BMI	3.029	4.106	5.371	5.726
TODO	5.838	5.988	6.244	6.581
FW	3.988	3.801	3.834	4.005
STEPS	5.991	5.594	5.771	5.654
VISION	4.563	4.154	4.316	4.763
SH	7.185	7.107	6.955	6.971
LV	7.204	7.270	7.402	7.694
DS	7.138	7.351	7.013	7.982
SI	6.744	6.975	7.927	8.550
PA	5.605	5.838	6.368	6.661
TFP	4.011	3.985	3.905	4.124
WM	6.360	6.477	6.383	7.296

Fig. 9 Transpose of 4×20 alternative vs. attribute matrix

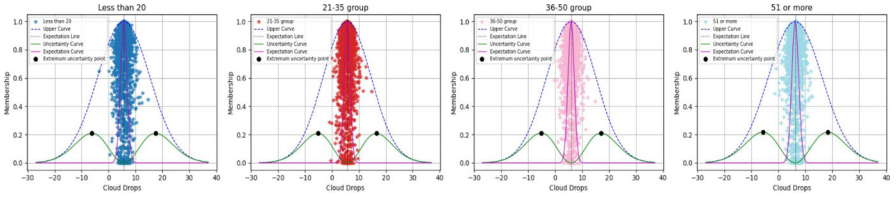

Fig. 10 Initial visual representation of Clouds corresponding to each age group's alternative

Using Eq. (26), the extremum points of uncertainty are given by:

$$x_{\text{extremum}} = Ex \pm 2\sigma_1\sigma_2\sqrt{\frac{\ln\sigma_1 - \ln\sigma_2}{\sigma_1^2 - \sigma_2^2}}, \tag{27}$$

where $\sigma_1 = |En + 3He|$ and $\sigma_2 = |En - 3He|$. As shown in Fig. 10, the visual representation comprises 1,000 cloud droplets, each assigned a specific degree of membership. This effectively highlights the relationship between uncertainty and the decision maker's confidence in a multi-criteria decision-making (MCDM) scenario. The uncertainty inherent in a decision-making alternative is represented by the green curve, while the pink curve illustrates the expectation. This demonstrates that the clouds follow a normal distribution and are characterized by a significant level of

Table 5 Cloud Score and Ranking corresponding to four age alternatives for initial time period

Alternatives	Cloud Score	Rank
Less than 20	4.352	III
21-35 group	4.292	IV
36-50 group	4.643	II
51 or more	4.781	I

uncertainty. Black dots represent the extremum uncertainty points obtained by Equation (27). There is a high degree of alignment in the areas of least uncertainty between the expected value and the two endpoints. Although, the waist is the region with the most uncertainty, showing a lower degree of confidence, resonating with human subjective knowledge.

Score Calculation

Using the scoring concept defined in Definition 2, we calculate the importance levels assigned by decision makers across the four age alternatives. A higher score indicates that a particular alternative holds more significance in the decision-making process, reflecting a greater preference or priority. The scores associated with each alternative for the cloud descriptors (Ex, En, He) are illustrated in Table 5. The ranking of the scores at this stage reveals the following order: $C_{51 \text{ or more}} > C_{36\text{-}50 \text{ group}} > C_{\text{Less than 20}} > C_{21\text{-}35 \text{ group}}$, where $C := C(Ex, En, He)$ represents the cloud. The highest score is achieved by the '51 or more' age group, while the '21-35 group' ranks lowest. This score calculation reflects the preferences of the decision maker while incorporating the inherent uncertainty in the decision-making process. These scores serve as the input preference vector for subsequent iterations.

Obtain Dynamic Clouds for the time period Jan-June 2021:

The preference vector for the period Jan-June 2021 (JJ21) is updated according to the following expression:

$$P_{\tau=JJ21} = \mathbb{S} \cdot P_{\tau=initial} + V_{\tau=JJ21} \tag{28}$$

where $V_{\tau=JJ21} = C \cdot M \cdot W_{\tau=JJ21}$, and $W_{\tau=JJ21}$ is the weight vector derived from time series forecasting for the Jan-June 2021 period. The scores indicated in Table 5 serve as the preference vector for the July- December 2020 period. The eigenvalues of the cloud feedback matrix $\mathbb{S}$ are [0.0011, 0.9635, 0.9917, 0.9996], all of which are less than unity. The sensitivity and memory parameters, α and β, derived from the dataset, fall within the ranges $\beta \in [0, 0.262]$ and $\alpha \in [0.1, 5]$. Under these conditions, matrix $\mathbb{S}$ remains positive definite, thereby ensuring the stability of the system. As a result, the updated preference vector corresponding to the four alternatives for the Jan-June 2021 period is:

$$\begin{array}{c} \text{Less than 20} \quad \text{21-35 group} \quad \text{36-50 group} \quad \text{51 or more} \\ P_{\tau=JJ21} \left[\begin{array}{cccc} -0.95654 & -0.74919 & 0.25264 & 1.47130 \end{array} \right] \end{array} \tag{29}$$

This provides a clear indication of how different age groups are valued. The age group of 51 or more years has the highest positive preference, signifying that this group is

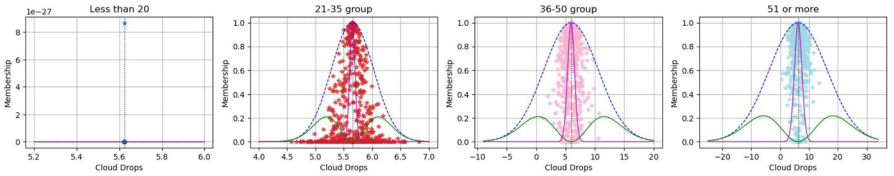

Fig. 11 Clouds corresponding to each age alternative for time period Jan-June 2021 (JJ21)

the most favored and seen as having the highest utility. In contrast, the age groups of 21-35 and Less than 20 show negative preferences which suggest that these groups are less desirable. Utilizing Equation (17) to obtain cloud descriptors as discussed in Stage 3 of the proposed DCM-DFT algorithm. The updated cloud descriptors for the Jan-June 2021 period are presented as follows:

$$\begin{array}{c} \\ \mathrm{Ex}_{\tau=JJ21} \\ \mathrm{En}_{\tau=JJ21} \\ \mathrm{He}_{\tau=JJ21} \end{array} \begin{array}{c} \begin{array}{cccc} \text{Less than 20} & \text{21-35 group} & \text{36-50 group} & \text{51 or more} \end{array} \\ \begin{bmatrix} 5.623 & 5.651 & 5.941 & 6.253 \\ 0 & 0.0994 & 0.556 & 1.296 \\ 0 & 0.2307 & 1.277 & 2.889 \end{bmatrix} \end{array} \tag{30}$$

Figure 11 provides a visual representation of the clouds corresponding to the four age categories for the Jan-June 2021 period. Clouds $C_{\text{Less than 20}}(5.623, 0, 0)$, $C_{21-35group}(5.651, 0.099, 0.230)$, $C_{36-50group}(5.941, 0.556, 1.277)$, and $C_{51ormore}(6.253, 1.296, 2.889)$, shown in Fig. 11, illustrate that the cloud for the Less than 20 age group has zero entropy and hyperentropy, while the other groups exhibit increasing levels of uncertainty and variability with age.

Upon analyzing the updated preferences, we observe the following ranking of scores as shown in Table 6 for the period Jan-June 2021.

This table indicates the relative preferences of different groups. The ranking reveals fluctuating patterns over time, indicating inconsistency in their preferences or decision-making behaviors. Initially, the 21-35 age group was the least favored as shown in Table 5, but by the period of Jan-June 2021, the 'Less than 20' group had become the least preferred. This change reflects evolving trends in decision-making and preferences across different age groups, providing valuable insights into how perceptions and priorities shift over time. The dynamic nature of this ranking underlines the importance of considering temporal changes when analyzing choices among varying alternatives.

Dynamic Cloud Generation for Forecasted Period: July-Dec 2021 to July-Dec 2025:

Table 6 Updated Score and Ranking for Jan-June 2021 period

Alternatives	Cloud Score	Rank
Less than 20	3.3005×10^{-10}	IV
21-35 group	1.5378	III
36-50 group	2.7162	II
51 or more	3.2340	I

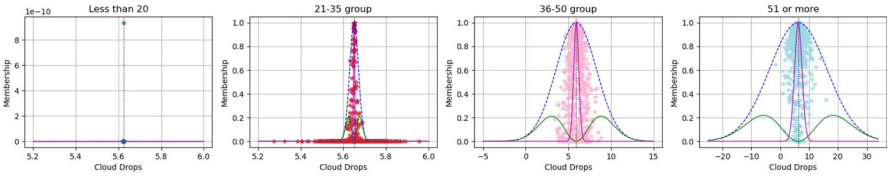

Fig. 12 Clouds corresponding to each alternative for the time period July-Dec 2021 (JD21)

We iterate the DCM-DFT algorithm over successive time periods to generate dynamic clouds. The algorithm incorporates the preference vector obtained from the previous state to determine priorities for each subsequent period and obtain updated clouds. This process continues in six-month intervals until reaching an externally controlled stopping time. Figure 12 shows the clouds for each alternative for the period July-Dec 2021, with Figs. 13, 14, 15, 16, 17, 18, 19, 20 presenting the dynamic clouds at six-month intervals up to July-Dec 2025.

Calculation of Probabilities

In order to calculate the probability of choosing a particular age group alternative over others, we apply the methodology discussed in Sect. 4.2. Using Equation (22) on the 4×20 alternative vs. attribute matrix, we derived the following probabilities:

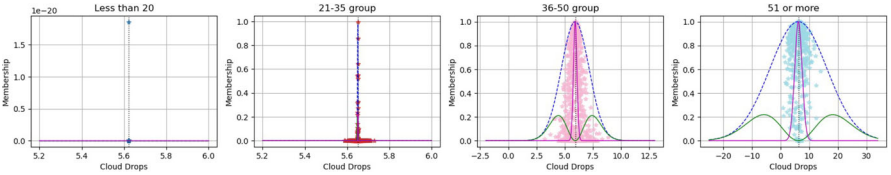

Fig. 13 Clouds corresponding to each alternative for the time period Jan-June 2022 (JJ22)

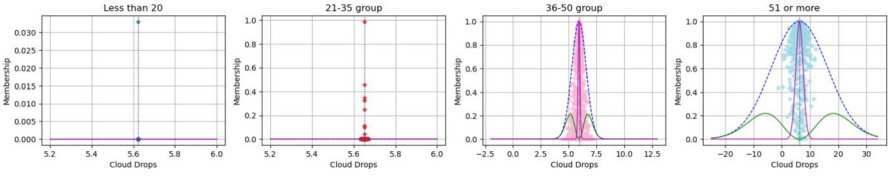

Fig. 14 Clouds corresponding to each alternative for the time period July-Dec 2022 (JD22)

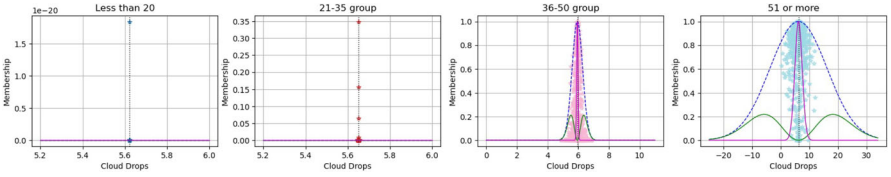

Fig. 15 Clouds corresponding to each alternative for the time period Jan-June 2023 (JJ23)

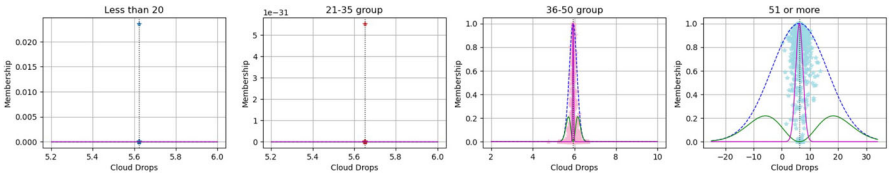

Fig. 16 Clouds corresponding to each alternative for the time period July-Dec 2023 (JD23)

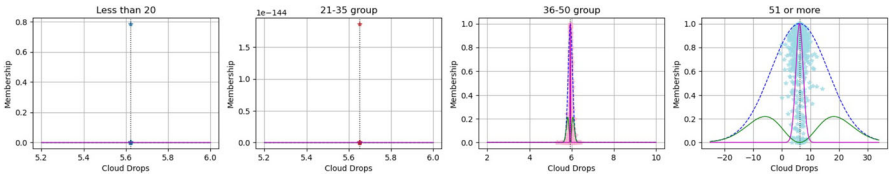

Fig. 17 Clouds corresponding to each alternative for the time period Jan-June 2024 (JJ24)

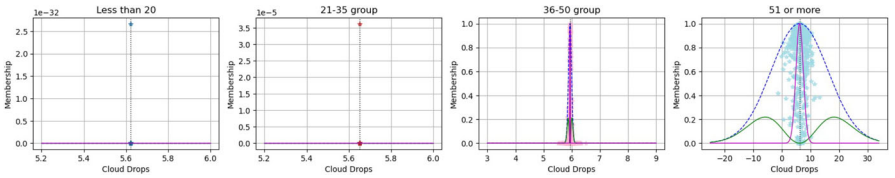

Fig. 18 Clouds corresponding to each alternative for the time period July-Dec 2024 (JD24)

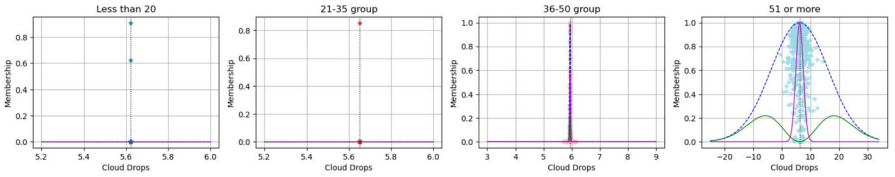

Fig. 19 Clouds corresponding to each alternative for the time period Jan-June 2025 (JJ25)

the probability of preferring the 'Less than 20' age group is 0.0119, the '21-35 group' is 1.03×10^{-06}, the '36-50 group' is 0.0023, and the '51 or more' group is 0.9851. These results indicate that the '21- 35' age group demonstrates the least confidence in maintaining a good lifestyle, while the '51 or more' group excels in both personal and professional aspects, establishing a consistent and stable lifestyle. This is reflected in their high probability of being chosen. In contrast, the '36-50' and 'Less than 20' age groups are still facing challenges in achieving a better lifestyle. Their lower focus on health and weekly meditation affects their certainty in decision-making.

The analysis of the proposed DCM-DFT model highlights the differences in decision-making among age groups. The root cause for these differences lies in behavioral psychology, inherent uncertainties, age-specific life stages, and the trends

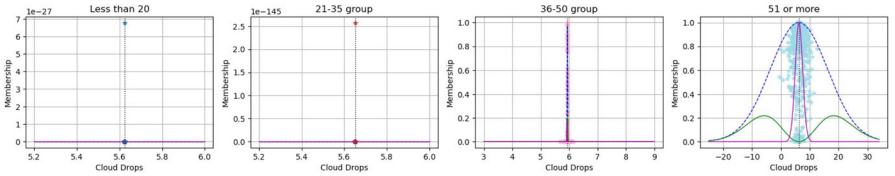

Fig. 20 Clouds corresponding to each alternative for the time period July-Dec 2025 (JD25)

observed in the dataset. Less than 20 age groups, i.e., younger individuals, exhibit higher variability in maintaining a work-life balance, which reflects the evolving nature of their priorities. In contrast, 51 or more (older groups) demonstrate more stability due to established routines and life experiences. For the 21 to 35 group, attributes such as Sufficient Income (SI) and Achievement (ACH) are more dominant, reflecting a focus on career development and financial stability. Meanwhile, the 36 to 50 group balances professional commitments with personal growth, as indicated by attributes like Supporting Others (SO) and Personal Awards (PA), resulting in moderate fluctuations in their decision-making patterns.

6 Results and discussion

This section presents the results from the implementation of the proposed DCM-DFT model and provides a discussion on the findings.

Table 7 provides an analysis of how preferences (P_τ) and valence vectors (V_τ) evolve over time for different age groups across six month intervals in the form of tuple (P_τ, V_τ). These vectors obtained by above discussed methodology represent the dynamics of each alternative's attractiveness and overall preference during each period. Table 8 outlines the cloud descriptors (Ex, En, He) alongside the computed scores and uncertainty extremum points from Equation (27) for each age group over different time periods. The table demonstrates how cloud descriptors evolve, with the *51 or more* group showing the highest consistency in scores with broader distribution ranges. Over time, the extremum points ($extre_1$ and $extre_2$) reflect the variations in uncertainty levels for each group.

As observed in Figs. 11, 12, 13, 14, 15, 16, 17, 18, 19, 20, the behavior of the clouds reveals significant differences in decision-making patterns across various age groups over time. The cloud for the age group *Less than 20* diminishes first, becoming extremely concentrated within a narrow range. This indicates that *Less than 20* age group have a lack of experience or confidence in lifestyle choices. For this age group, both $En = He = 0$, which implies the value of x becomes a constant equal to Ex. This signifies that the Less than 20 age group achieves certainty much earlier in the process compared to other age groups. The consistently increasing negative preference values and low scores as observed from Tables 7 and 8 emphasize their weakest ability to influence decisions about their way of life and general wellbeing.

Compared to the *Less than 20* group, the *21-35 group's* cloud follows a normal distribution as observed in Fig. 11, with a broader distribution of cloud drops as

Table 7 Preference and valence vectors for different time periods

Alternative	JJ21	JD21	JJ22	JD22	JJ23
Less than 20	(− 0.5531, − 0.35199)	(− 0.8929, − 0.33820)	(− 1.2327, − 0.34397)	(− 1.5687, − 0.34091)	(− 1.9038, − 0.34093)
21-35 group	(− 0.4869, − 0.30042)	(− 0.7696, − 0.29817)	(− 1.0360, − 0.29723)	(− 1.2922, − 0.29690)	(− 1.5383, − 0.29633)
36-50 group	(0.1773, 0.10680)	(0.2818, 0.10240)	(0.3945, 0.10313)	(0.5098, 0.10315)	(0.6272, 0.10313)
51 or more	(0.8892, 0.54561)	(1.3967, 0.53398)	(1.8994, 0.53807)	(2.3855, 0.53465)	(2.8581, 0.53413)
Alternative	JD23	JJ24	JD24	JJ25	JD25
Less than 20	(− 2.2411, − 0.34404)	(− 2.5804, − 0.34708)	(− 2.9195, − 0.34798)	(− 3.2545, − 0.34502)	(− 3.5912 , − 0.34783)
21− 35 group	(− 1.7757, − 0.29670)	(− 2.0042, − 0.29659)	(− − 2.2260, − 0.29847)	(− 2.4382 ,− 0.29709)	(− 2.6440 , − 0.29849)
36-50 group	(0.7482, 0.10469)	(0.8731, 0.10651)	(1.0003, 0.10703)	(1.1269 , 0.10468)	(1.2572 ,0.10675)
51 or more	(3.3204, 0.53605)	(3.7717, 0.53717)	(4.2138, 0.53942)	(4.6425 , 0.53743)	(5.0626 , 0.53958)

seen by the range of x which is [4.5, 7]. This reflects a wider range of preferences and variability in lifestyle decisions aimed at enhancing well-being and achieving a better life. For the time period Jan-June 2022, cloud for *21-35 group* spans a narrower section of the x-axis, indicating that their decision-making, though more confident, but is somewhat constrained. The cloud remains visible till maximum five iterations after which it begins to diminish. This transition suggests a less influence and ability to maintain their engagement in decision-making.

The *36-50 age* group is particularly noteworthy for its clear demonstration of the dynamic evolution in decision-making behavior compared to other groups. During the period Jan-June 2021, the *36-50 age* group's cloud, as depicted in Fig. 11, initially appears broader suggesting diverse decision-making preferences. As time progresses, from Jan-June 2021 to July-Dec 2025, the cloud gradually narrows, transitions into a bell-shaped distribution and eventually becomes more concentrated around the expectation line as depicted by Figs. 12, 13, 14, 15, 16, 17, 18, 19, 20. This change reflects a shift toward more consistent and concentrated preferences over time. Gradually, the cloud starts to diminish, i.e., decrease in both *En* and *He* is observable signaling a steady convergence toward certainty as time goes on. This highlights the age group's transition toward more confident and focused decision-making and reflects their ability to weigh both personal and professional lifestyle decisions.

The *51 or more* age group exhibits a distinctive cloud behavior in decision-making patterns. From the time period Jan-June 2021 till July-Dec 2025, the cloud sustains its form and remains visible till all the iterations, suggesting that they have more stability in choices and consistent decision-making patterns. The diminishing phenomenon is less pronounced for this age group's cloud and persistently shows a broad distribution,

reflecting a relatively higher degree of uncertainty. This is shown by extremum point $extre_1 = 18.28$ and $extre2 = -5.77$ specify that individuals within this age group accommodate a wider range of choices. Throughout, this group exhibits the highest preferences and valence values shown in Table 7, suggesting strong influence across all time periods, with high growth projected for the future.

Figure 21 illustrates the graphical representation of cloud scores and preferences according to the DCM-DFT methodology. It highlights the shifting dynamics of decision-making among four age segments, reflecting changes in attitudes over time, with July-Dec 2025 (JD25) serving as the externally controlled stopping threshold.

6.1 Advantages of DCM-DFT

Following are the various reasons in favor of using proposed Dynamic cloud model based on decision field theory:

- *Enhanced Uncertainty Representation*: Proposed DCM-DFT algorithm effectively incorporates uncertainty and randomness in decision-making processes through the cloud transformation algorithm. This allows DCM-DFT to model more realistic decision scenarios where the decision-maker's preferences and the environment are inherently uncertain.
- *Higher-Order Uncertainty*: Traditional DFT primarily addresses first-order uncertainty in preferences. DCM-DFT, with the inclusion of hyper-entropy, addresses higher-order uncertainty, providing a more better and comprehensive understanding of the decision-making process.
- *Dynamic Adaptation*: DCM-DFT allows for dynamic adaptation of preferences over time, incorporating feedback mechanisms through the cloud feedback matrix utilizing cloud hamming distance. This model effectively captures the competitive interactions between alternatives and is essential for accurately representing real-world choices, where preferences and conditions fluctuate and change randomly over time.
- *Enhanced Stability and Robustness*: The cloud model's parameters (Ex, En, He) can be adjusted to represent different levels of certainty and uncertainty, making DCM-DFT more flexible in adapting to various decision contexts. Positive definiteness of the cloud feedback matrix and less than unity magnitude of its eigenvalues guarantees the stability of the decision-making process. This enhanced stability and flexibility improves robustness for long-term decision-making models.
- *Predictive Strengths of DCM-DFT*: The proposed algorithm not only adapts to changes over time but also anticipates future behaviors based on dynamic inputs by the utilization of time series forecasting method.

6.2 Comparative analysis

Here, we provide a detailed analysis to exhibit the impact and authenticity of our proposed model. We conduct a comprehensive comparison with traditional Random

Table 8 Cloud descriptors, Scores and Extremum Points corresponding to four alternatives across time periods

Time Period	Alternative	Cloud descriptors			Score	Extremum uncertainty points	
		Ex	En	He		$extre_1$	$extre_2$
July 15-March 21	Less than 20	5.623	1.221	2.829	4.781	17.4180	− 6.1720
	21-35 group	5.651	1.121	2.601	4.643	16.4959	− 5.1939
	36-50 group	5.941	1.159	2.663	4.352	17.0406	− 5.1586
	51 or more	6.253	1.296	2.889	4.292	18.2811	− 5.7751
JJ21	Less than 20	5.6231	0.0000	0.0000	3.26×10^{-8}	–	–
	21-35 group	5.6506	0.0514	0.1194	1.1943	6.1485	5.1527
	36-50 group	5.9406	0.5870	1.3488	2.7500	11.5625	0.3187
	51 or more	6.2530	1.2964	2.8890	3.4816	18.2810	− 5.7750
JD21	Less than 20	5.6231	0.0000	0.0000	1.47×10^{-9}	–	–
	21-35 group	5.6506	0.0028	0.0064	0.3595	5.6773	5.6239
	36-50 group	5.9406	0.3011	0.6920	2.2304	8.8249	3.0563
	51 or more	6.2530	1.2964	2.8890	3.2193	18.2810	− 5.7750
JJ22	Less than 20	5.6231	0.0000	0.0000	1.63×10^{-191}	–	–
	21-35 group	5.6506	0.0002	0.0004	0.0715	5.6523	5.6489
	36-50 group	5.9406	0.1565	0.3595	1.8387	7.4390	4.4422
	51 or more	6.2530	1.2964	2.8890	3.3347	18.2810	− 5.7750
JD22	Less than 20	5.6231	0.0000	0.0000	1.47×10^{-15}	–	–
	21-35 group	5.6506	0.0000	0.0000	0.0231	–	–
	36-50 group	5.9406	0.0822	0.1889	1.3847	6.7280	5.1532
	51 or more	6.2530	1.2964	2.8890	3.4032	18.2810	− 5.7750
JJ23	Less than 20	5.6231	0.0000	0.0000	2.10×10^{-10}	–	–
	21-35 group	5.6506	0.0000	0.0000	0.0007	–	–
	36-50 group	5.9406	0.0437	0.1004	1.1208	6.3591	5.5221
	51 or more	6.2530	1.2964	2.8890	3.4210	18.2810	− 5.7750
JD23	Less than 20	5.6231	0.0000	0.0000	0.0000	–	–
	21-35 group	5.6506	0.0000	0.0000	2.72×10^{-35}	–	–
	36-50 group	5.9406	0.0235	0.0540	0.7797	6.1657	5.7155
	51 or more	6.2530	1.2964	2.8890	3.3877	18.2810	− 5.7750
JJ24	Less than 20	5.6231	0.0000	0.0000	3.30×10^{-144}	–	–
	21-35 group	5.6506	0.0000	0.0000	1.88×10^{-199}	–	–
	36-50 group	5.9406	0.0128	0.0294	0.5580	6.0631	5.8181
	51 or more	6.2530	1.2964	2.8890	3.3222	18.2810	− 5.7750
JD24	Less than 20	5.6231	0.0000	0.0000	1.68×10^{-34}	–	–

Table 8 (continued)

Time Period	Alternative	Cloud descriptors			Score	Extremum uncertainty points	
		Ex	En	He		$extre_1$	$extre_2$
	21-35 group	5.6506	0.0000	0.0000	0.0000	–	–
	36-50 group	5.9406	0.0070	0.0161	0.4514	6.0077	5.8735
	51 or more	6.2530	1.2964	2.8890	3.3774	18.2810	− 5.7750
JJ25	Less than 20	5.6231	0.0000	0.0000	1.98×10^{-5}	–	–
	21-35 group	5.6506	0.0000	0.0000	5.56×10^{-197}	–	–
	36-50 group	5.9406	0.0039	0.0089	0.3701	5.9777	5.9035
	51 or more	6.2530	1.2964	2.8890	3.4484	18.2810	− 5.7750
JD25	Less than 20	5.6231	0.0000	0.0000	3.36×10^{-9}	–	–
	21-35 group	5.6506	0.0000	0.0000	8.17×10^{-148}	–	–
	36-50 group	5.9406	0.0022	0.0050	0.2728	5.9614	5.9198
	51 or more	6.2530	1.2964	2.8890	3.2394	18.2810	− 5.7750

[1] '–' indicates that extremum uncertainty points cannot be determined since *En* and *He* are zero

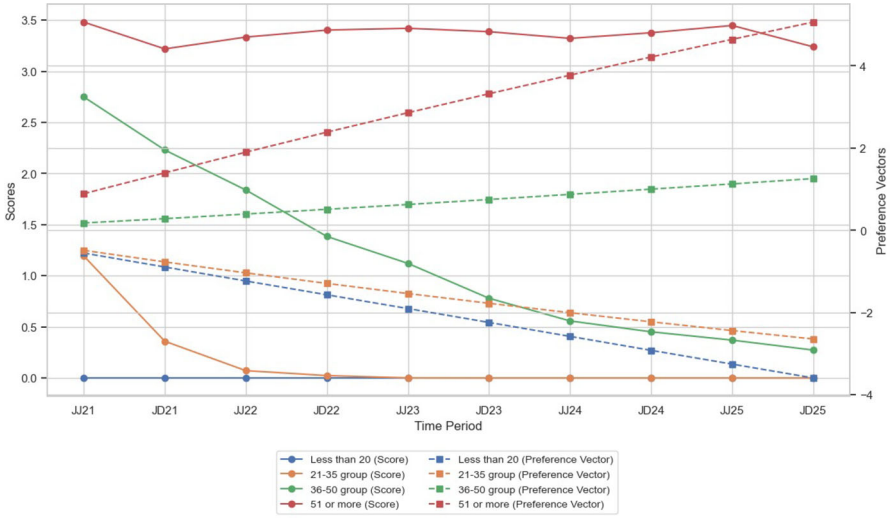

Fig. 21 Combined Graph of Cloud Scores and Preference Vectors

Utility Models (RUM) and Decision Field Theory (DFT) along with comparisons to various Multi-Criteria Decision-Making (MCDM) techniques.

Comparison with traditional RUM and DFT models:

Random Utility Models (RUM) is a subset of probabilistic choice models originally developed to address inconsistencies in observed patterns of individual behavior. RUM

serves as a framework for understanding decision-making preferences and construct utility functions based on expected utility maximization to predict decision outcomes. It is based on the hypothesis that every individual is a rational decision-maker and select alternatives based on maximizing perceived utility [27]. RUM encompasses various models such as: Multinomial Logit (MNL), Random Regret Minimization (RRM), and Single-Level Hierarchical Logit and Probit Models [27]. The MNL model focuses on calculating probabilities based on a linear utility function for the evaluation alternatives, while RRM emphasizes on minimizing potential regret by comparing the chosen option to others. In the Single-Level Hierarchical Logit model, the probabilities of choosing an alternative are determined by the logit function, which ensures that higher utility values correspond to higher choice probabilities. The logit and probit models both assume that alternatives are compared on the basis of their respective subjective utilities and that the alternatives with the highest utility are most likely chosen [26]. However, they differ in their error theories (the logit model assumes an independently and identically distributed (i.i.d.) Gumbel error, while the probit model assumes a normal distribution of errors), which lead to differences in the alternative's utilities and, consequently, their probability calculations [26].

The criteria for assessing the performance of RUM models are rooted in the different methods for estimating choice probabilities. These models adopt a static, outcome-oriented approach, focusing on predicting observable outcomes without incorporating cognitive process assumptions. Although, DFT [39] is dynamic model but fails to capture the continuous spectrum of fluctuations in randomness and fuzziness, leading to an incomplete representation of decision-making process. In contrast, the DCM-DFT model introduces a cognitive framework that dynamically captures decision-making processes by considering the interdependence of alternatives and uncertainties.

Table 9 provides a detailed comparison of rankings and probabilities for the age group alternatives based on estimated choice probabilities. The results from traditional models are compared to those of our proposed DCM-DFT model. Higher probabilities indicate more favorable choices, except for the Random Regret Minimization (RRM) model, where probabilities represent regret, and lower regret implies a more favorable alternative. The analysis of Table 9 reveals that the 51 or more age group consistently emerges as the most favorable alternative, with the highest probability in most models. The RRM probability for the 51 or more age group is observed as 0.00, signifying that choosing this alternative incurs no regret making it the most favorable.

Although the rankings produced by Decision Field Theory (DFT) and our proposed DCM-DFT model are similar, supporting the validity of our method but also the underlying approaches differ significantly. The primary distinction lies in the numerical computation of probabilities, influenced by the introduction of the cloud Hamming distance and dynamic weights obtained by the time series forecasting method. DFT focuses on capturing the dynamic evolution of decision-making preferences but does not account for higher order uncertainty and forecasted behavioral preferences shifts.

Comparison with traditional MCDM techniques:

We compare the DCM-DFT algorithm with various Multi-Criteria Decision-Making (MCDM) techniques [23, 24] such as: Technique for Order of Preference by Similarity to Ideal Solution (TOPSIS), Simple Additive Weighting (SAW), and PROMETHEE methods, as shown in Table 10. The rankings derived from each

Table 9 Ranking comparison across various RUM models and DFT

Attributes	Single-level hierarchical logit [27]		Multinomial Logit [26]		Random regret minimisation [27]	
Age group	Logit probability	Ranking	MNL probability	Ranking	RRM probability	Ranking
Less than 20	0.000	IV	0.0000	IV	0.63442	IV
21-35 group	0.00001	III	0.00001	III	0.36558	III
36-50 group	0.00193	II	0.00193	II	0.00001	II
51 or more	0.99806	I	0.99806	I	0.0000	I
Attributes	Decision field theory [38]		Probit model [27]		Our proposed method (DCM-DFT)	
Age group	Choice probability	Ranking	Probit probability	Ranking	Choice probability	Ranking
Less than 20	0.05149	II	0.08862	IV	0.01142	II
21-35 group	0.00023	IV	0.10355	III	0.0000	IV
36-50 group	0.01285	III	0.32018	II	0.00340	III
51 or more	0.93541	I	0.48765	I	0.98452	I

approach highlight the significance assigned to each alternative. Analysis of Table 10 reveals that higher scores in metrics such as Net Flow (PROMETHEE), Relative Closeness (TOPSIS), Performance Score (SAW), and DCM-DFT Score consistently correspond to higher rankings of the alternatives. The 51 or more age group ranks first across all methods, with the highest scores (DCM-DFT Score: 3.4816), indicating it is the most favorable alternative.

Conventional MCDM methods consider data static and deterministic, often failing to capture subtle variations or uncertainties in human judgment. Furthermore, weights in these methods are calculated solely on objective characteristics of the dataset, neglecting the psychological factors that shape a decision-maker's choices. Hence, MCDM techniques fall short of accurately reflecting human decision-making dynamics. In contrast, our DCM-DFT model not only tracks preference dynamics with cloud descriptors and cloud hamming distance properties but also incorporates time series forecasting to predict future preferences, offering a more robust and forward-looking decision-making framework.

The computational complexity of the proposed DCM-DFT methodology, as shown in Table 11, is broken down into three stages. Stage 1, which involves initial preference calculations and cloud drop generation, has a complexity of $\mathcal{O}(N \cdot m)$, where N represents the number of alternatives and m the number of cloud drops. Stage 2, dealing with the dynamic evolution of preferences across τ time steps, incurs a complexity of $\mathcal{O}(N^2 \cdot \tau)$. Finally, Stage 3 updates cloud descriptors with a complexity of $\mathcal{O}(N \cdot \tau)$. The overall complexity of the algorithm is $\mathcal{O}(N^2 \cdot \tau + N \cdot m)$, ensuring it remains computationally efficient even for real-time decision-making processes.

Table 10 Comparison of Rankings by MCDM techniques

Alternative	PROMETHEE [24]		TOPSIS [23]		SAW [24]		Our proposed method	
	Net flow	Ranking	Relative closeness	Ranking	Performance score	Ranking	DCM-DFT score	Ranking
Less than 20	− 0.97545	IV	0.4054	III	0.8918	IV	0.000	IV
21-35 group	− 0.86525	III	0.3778	IV	0.8936	III	1.1943	III
36-50 group	0.29555	II	0.5544	II	0.9370	II	2.7500	II
51 or more	1.54515	I	0.6041	I	0.9853	I	3.4816	I

Table 11 Computation complexity of the defined methodology

Stages	Complexity
Stage 1: Initial Preference Calculation	$\mathcal{O}(N \cdot m)$
Stage 2: Dynamic Evolution	$\mathcal{O}(N^2 \cdot \tau)$
Stage 3: Cloud Descriptor Update	$\mathcal{O}(N \cdot \tau)$
Total Complexity	$\mathcal{O}(N^2 \cdot \tau + N \cdot m)$

7 Conclusion and future work

This study presents a novel Dynamic Cloud Model based on Decision Field Theory (DCM-DFT) along with probability computation. To the best of our understanding, this is the first research exploring clouds' dynamic nature, addressing key challenges in human decision-making under uncertainty. The proposed study incorporates cloud models to capture the fuzziness and randomness inherent in cognitive processes and combines them with DFT's ability to dynamically evolve preferences over time. We introduce a cloud feedback matrix to capture competitive interactions among alternatives and represent initial uncertainty through the cloud scores derived from forward and backward cloud transformation algorithms. Furthermore, we introduce dynamic weight computation through the time series forecasting method. This integration improves decision accuracy and strengthens the decision-maker's ability to dynamically navigate uncertainties while increasing the adaptability of decision models to evolving environments. Subsequently, this methodology is applied to address a real-time decision problem for Lifestyle and Wellbeing. The dynamic behavior of clouds is observed from Jan-June 2021 to July-Dec 2025 for the four age group alternatives, evaluated across 20 lifestyle attributes.

Results deduce the dynamic nature of decision-making across different age groups, with the oldest group consistently emerging as the most influential in the decision models, while younger groups exhibit more variability in their impact. Based on the findings, it can be concluded that individuals aged *51 or more* tend to make better lifestyle choices, leading to a healthier body, mind, and a greater sense of purpose in life. This is further validated by the work-life balance score, which remains consistently highest for the 51 or more age group shown by Fig. 7. Furthermore, we conducted a comparative analysis of our proposed model against various decision-making models. The DCM-DFT model demonstrates superior applicability in complex, real-world scenarios, offering deeper insights into human behavior patterns and preferences over time. The proposed model is applicable to any real-time dataset. Additionally, we discuss the computational complexity of our proposed model. This methodology could be extended for future research to analyze cloud dynamic behavior similarity utilizing cloud similarity measurements. The combined influence of both preference intensity and time pressure can be further studied.

Although the proposed methodology is a well-defined model, it has certain limitations. Its full potential is achieved primarily when applied to real-time datasets, which may not always be readily accessible. Additionally, the integration of dynamic weight

adjustments through time-series forecasting and the use of cloud descriptors increases the computational demands compared to traditional decision-making models.

Appendix

Table 12 presents the descriptive statistics for each attribute in the Lifestyle and Well-being dataset.

Algorithm 4 outlines the pseudocode for generating dynamic clouds, assessing alternative preferences with dynamic weights from a custom ARIMA model, and calculating the likelihood of selecting one alternative over another.

Table 12 Descriptive Statistics of Lifestyle & Well-being Attributes

Lifestyle & Well-being Attributes	Count	Mean	Standard Deviation	Min	25%	50%	75%	Max
FV	15972.00	6.26	2.60	1.00	4.60	6.40	8.20	10.00
STRESS	15972.00	4.98	2.46	1.00	2.80	4.60	6.40	10.00
PV	15972.00	5.71	2.98	1.00	2.80	5.50	8.20	10.00
CC	15972.00	5.96	2.56	1.00	3.70	5.50	8.20	10.00
SO	15972.00	6.05	2.92	1.00	3.70	5.50	10.00	10.00
SN	15972.00	6.83	2.78	1.00	4.60	6.40	10.00	10.00
ACH	15972.00	4.60	2.48	1.00	2.80	3.70	6.40	10.00
DON	15972.00	5.89	3.33	1.00	2.80	6.40	10.00	10.00
BMI	15972.00	4.70	4.43	1.00	1.00	1.00	10.00	10.00
TODO	15972.00	6.17	2.36	1.00	4.60	6.40	8.20	10.00
STEPS	15972.00	5.70	2.89	1.00	3.00	5.00	8.00	10.00
VISION	15972.00	4.38	2.91	1.00	1.90	3.70	5.50	10.00
SH	15972.00	7.04	1.20	1.00	6.00	7.00	8.00	10.00
LV	15972.00	7.39	3.32	1.00	5.50	10.00	10.00	10.00
DS	15972.00	7.36	2.41	1.00	6.40	8.20	10.00	10.00
SI	15972.00	7.56	4.00	1.00	1.00	10.00	10.00	10.00
PA	15972.00	6.14	2.78	1.00	3.70	5.50	9.10	10.00
TFP	15972.00	3.99	2.46	1.00	1.90	3.70	5.50	10.00
WM	15972.00	6.61	2.71	1.00	4.60	7.30	10.00	10.00
WLB	15972.00	666.75	45.02	480.00	636.00	667.70	698.50	820.20

Algorithm 4 Dynamic Cloud Model for Analyzing Preferences under uncertainty Using Decision Field Theory

Input: Decision Making Real-time Dataset
Output: Assessment of Preferences of alternatives
Function *alternative_vs_attribute_matrix(n, data)*
  return *matrix_M*;
Procedure *Dynamic Cloud Model Based on Decision Field Theory (DCM-DFT)*
  foreach *matrix_M* **do**
    Stage 1: Evaluate Initial preference using Cloud model;
    Stage 2: Dynamic Evolution of clouds;
    Stage 3: Update Cloud descriptors;
    Follow Algorithm 3
  end foreach
  Output: Dynamic Clouds $(Ex_{\tau+h}, En_{\tau+h}, He_{\tau+h})$ with $P_{\tau+h}, V_{\tau+h}$
Function *Dynamic weights by time series model*
  Input: Processed Data
  Procedure *Stationarity Check*
    Perform ADF test on attributes;
    If p-value ≤ 0.05, data is stationary; else, non-stationary.
  Procedure *Custom ARIMA Model Fitting*
    foreach (p, d, q) *combination* **do**
      $p \leftarrow 0$ **to** 8
      $d \leftarrow 0$ **to** 2
      $q \leftarrow 0$ **to** 8
    end foreach
    Fit ARIMA(p, d, q) model and compute RMSE, MAE, AIC, BIC
    if *RMSE and MAE are lowest so far* **then**
      Update best model with current (p, d, q)
      Validate the model
    end if
    foreach *Forecasted value corresponding to each attribute* **do**
      Normalize forecasted values
    end foreach
    Output: Dynamic weights corresponding to each attribute
Function *Probability computation under DCM-DFT framework*
  Input: Cloud feedback matrix $\mathbb{S}$, Decision matrix M, Dynamic weight vector W_{TSA}, and initial preference vector $P_{\tau=0}$
  Procedure *For each time* τ
    Compute $\xi_\tau \leftarrow (I - S)^{-1} \cdot (I - S^\tau) \cdot \mu + S^\tau \cdot P_{\tau=0}$,
    where $\mu \leftarrow C \cdot M \cdot W_{TSA}$
    Compute $\Omega_\tau \leftarrow \sum_{k=0}^{\tau-1} [\mathbb{S}^k \cdot \chi \cdot (\mathbb{S}^k)']$,
    where $\chi \leftarrow C \cdot M \cdot \varphi \cdot M' \cdot C'$, $\varphi \leftarrow diag(w) - (w \cdot w')$
    foreach *Age group Alternative* **do**
      Compute $\Pr[P_\tau[A_i] - P_\tau[A_j] > 0 \text{ for all } j \neq i] \leftarrow$
      $\int_{X>0} \exp\left[-(X-\Gamma)'\Lambda^{-1}(X-\Gamma)/2\right] / \left(2\pi|\Lambda|^{0.5}\right) dX$,
      where $\Gamma \leftarrow L\xi_\tau, \Lambda \leftarrow L\Omega_\tau L'$
    end foreach
  Output: Probability of choosing one alternative over others

Author contributions A: conception, methodology, composition, editing and revision; AG: conception, methodology, formal analysis, and review.

Funding The authors indicate that they did not receive any funding from organizations for the submitted work.

Data availability The authors confirm that the data supporting the findings of this study are accessible within the article.

Declarations

Conflict of interest The authors disclose no competing interests relevant to this article's content.

Ethical approval This article does not include any research involving human participants or animals conducted by the authors.

References

1. Li D, Du Y (2007) Artificial Intelligence with Uncertainty. Chapman and Hall/CRC 1st edn., London. https://doi.org/10.1201/9781584889991
2. Wang G, Xu C, Li D (2014) Generic normal cloud model. Inf Sci 280, 1–15 https://doi.org/10.1016/j.ins.2014.04.051
3. Wang G, Xu C, Zhang Q, Wang X (2012) A multi-step backward cloud generator algorithm. Rough Sets and Current Trends in Computing: 8th International Conference, RSCTC 2012, Chengdu, China, August 17–20, 2012. Proceedings 8. Springer, Berlin, Heidelberg, pp 313–322
4. Xu C, Wang G, Zhang Q (2014) A new multi-step backward cloud transformation algorithm based on normal cloud model. Fundamenta Informaticae 133(1):55–85. https://doi.org/10.3233/FI-2014-1062
5. Xu C-L, Wang G-Y (2017) A novel cognitive transformation algorithm based on gaussian cloud model and its application in image segmentation. Numerical Algorithms 76(4):1039–1070. https://doi.org/10.1007/s11075-017-0296-y
6. Xu C, Wang G (2019) Bidirectional cognitive computing model for uncertain concepts. Cogn. Comput. 11(5):613–629. https://doi.org/10.1007/s12559-019-09666-8
7. Wang GY, Xu CL, Zhang QH, Wang XR (2013) p-order normal cloud model recursive definition and analysis of bidirectional cognitive computing. Chinese Journal of Computers 36(11):2316–2329. https://doi.org/10.3724/SP.J.1016.2013.02316
8. Anjali AG (2025) A novel shannon entropy-based backward cloud model and cloud k-means clustering. The Journal of Supercomputing 81(1):65. https://doi.org/10.1007/s11227-024-06528-5
9. Chauhan P, Gupta A, Malhotra T (2023) A novel cloud model based on multiplicative unbalanced linguistic term set. The Journal of Supercomputing 79:1–31. https://doi.org/10.1007/s11227-023-05295-z
10. Li DY, Han JW, Shi XM, Man CC (1998) Knowledge representation and discovery based on linguistic atoms. Knowledge-Based Systems 10(7):431–440. https://doi.org/10.1016/S0950-7051(98)00038-0
11. Wang D, Liu D, Ding H, Singh VP, Wang Y, Zeng X, Wu J, Wang L (2016) A cloud model-based approach for water quality assessment. Environmental Research 148:24–35. https://doi.org/10.1016/j.envres.2016.03.005
12. Wang D, Zeng D, Singh VP, Xu P, Liu D, Wang Y, Zeng X, Wu J, Wang L (2016) A multidimension cloud model-based approach for water quality assessment. Environmental Research 149:113–121. https://doi.org/10.1016/j.envres.2016.05.012
13. Song W, Zhu J, Wang H, Chang A (2020) Multistage risk assessment of direct delivery business from local oil refineries in sinopec group based on normal cloud model. International Journal of Production Research 58(18):5624–5650. https://doi.org/10.1080/00207543.2019.1656835
14. Song W, Zhu J (2019) A multistage risk decision making method for normal cloud model considering behavior characteristics. Applied Soft Computing 78:393–406. https://doi.org/10.1016/j.asoc.2019.02.033
15. Zhang W, Wu X, Lei Y, Shao J, Wang Z (2023) Risk assessment of water and sand inrush in mining under thick loose layer based on comprehensive weight-cloud model. Geofluids 2023:1–12. https://doi.org/10.1155/2023/1181284
16. Lin CJ, Zhang M, Li LP, Zhou ZQ, Liu S, Liu C, Li T (2020) Risk assessment of tunnel construction based on improved cloud model. Journal of Performance of Constructed Facilities 34(3):04020028. https://doi.org/10.1061/(ASCE)CF.1943-5509.0001421
17. Wang J-C, Liu J-Q, Wei Q, Wang P (2021) Risk assessment based on combined weighting-cloud model of tunnel construction. Tehnicki Vjesnik 28(1), 203–210 https://doi.org/10.17559/TV-20200917163330

18. Xie S, Chen Y, Dong S, Zhang G (2020) Risk assessment of an oil depot using the improved multi-sensor fusion approach based on the cloud model and the belief jensen-shannon divergence. Journal of Loss Prevention in the Process Industries 67:104214. https://doi.org/10.1016/j.jlp.2020.104214
19. Qin K, Xu K, Liu F, Li D (2011) Image segmentation based on histogram analysis utilizing the cloud model. Computers & Mathematics with Applications 62(7):2824–2833. https://doi.org/10.1016/j.camwa.2011.07.048
20. Gao Z, Ma D, Guo X, Wang W, Wang Z (2019) The comprehensive assessment method of concrete damage after disastrous fire based on game theory-normal cloud model. Mathematical Problems in Engineering, 1–14 https://doi.org/10.1155/2019/7658426
21. Wang X, Li S, Xu Z, Hu J, Pan D, Xue Y (2019) Risk assessment of water inrush in karst tunnels excavation based on normal cloud model. Bulletin of Engineering Geology and the Environment 78(5):3783–3798. https://doi.org/10.1007/s10064-018-1294-6
22. Liu J, Wang D, Lin Q, Deng M (2023) Risk assessment based on fmea combining dea and cloud model: A case application in robot-assisted rehabilitation. Expert Systems with Applications 214:119119. https://doi.org/10.1016/j.eswa.2022.119119
23. Hwang C-L, Lai Y-J, Liu T-Y (1993) A new approach for multiple objective decision making. Computers & Operations Research 20(8):889–899. https://doi.org/10.1016/0305-0548(93)90109-V
24. Hwang C-L, Yoon K (2012) Multiple Attribute Decision Making: Methods and Applications - A State-of-the-Art Survey, vol 186. Springer, Berlin
25. Song Y, Yao H, Yao S, Yu D, Shen Y (2017) Risky multicriteria group decision making based on cloud prospect theory and regret feedback. Mathematical Problems in Engineering 2017(1):9646303. https://doi.org/10.1155/2017/9646303
26. Berkowitsch N, Scheibehenne B, Rieskamp J (2013) Rigorously testing multialternative decision field theory against random utility models. Journal of Experimental Psychology: General 143(3):1331–1348. https://doi.org/10.1037/a0035159
27. Cascetta E (2009) Transportation Systems Analysis: Models and Applications vol. 29. Springer, London. https://doi.org/10.1007/978-0-387-75857-2
28. Zhou J, Liu L-F, Sun L-J, Xiao F (2019) A multi-criteria decision-making method for hesitant fuzzy linguistic term set based on the cloud model and evidence theory. Journal of Intelligent & Fuzzy Systems 36(2):1797–1808. https://doi.org/10.3233/JIFS-18051
29. Rieskamp J (2008) The probabilistic nature of preferential choice. Journal of Experimental Psychology: Learning, Memory, and Cognition 34(6):1446–1465. https://doi.org/10.1037/a0013646
30. Busemeyer JR, Townsend JT (1993) Decision field theory: a dynamic-cognitive approach to decision making in an uncertain environment. Psychological review 100(3):432–459
31. Busemeyer JR, Townsend JT (1992) Fundamental derivations from decision field theory. Mathematical Social Sciences 23(3):255–282
32. Diederich A (2003) Mdft account of decision making under time pressure. Psychonomic Bulletin & Review 10(1):157–166
33. Hotaling JM (2020) Decision field theory-planning: A cognitive model of planning on the fly in multistage decision making. Decision 7(1):20–42. https://doi.org/10.1037/dec0000113
34. Ma R, Liu S, Xu Z, Zhang Y, Ni Y (2024) Research on fuzzy dynamic route choice model and algorithm of wargame. International Journal of Machine Learning and Cybernetics, 1–18 https://doi.org/10.1007/s13042-023-02069-0
35. Saaty TL (2007) Time dependent decision-making; dynamic priorities in the ahp/anp: Generalizing from points to functions and from real to complex variables. Mathematical and Computer Modelling 46(7–8):860–891
36. Busemeyer JR, Jessup RK, Johnson JG, Townsend JT (2006) Building bridges between neural models and complex decision making behaviour. Neural Networks 19(8):1047–1058. https://doi.org/10.1016/j.neunet.2006.05.043
37. Lee S, Son Y-J, Jin J (2008) Decision field theory extensions for behavior modeling in dynamic environment using bayesian belief network. Inf Sci 178(10):2297–2314. https://doi.org/10.1016/j.ins.2008.01.009
38. Roe RM, Busemeyer JR, Townsend JT (2001) Multialternative decision field theory: A dynamic connectionst model of decision making. Psychological review 108(2):370. https://doi.org/10.1037/0033-295X.108.2.370
39. Hotaling JM, Busemeyer JR, Li J (2010) Theoretical developments in decision field theory: comment on tsetsos, usher, and chater. **117**(4), 1294–1298 https://doi.org/10.1037/a0020401

40. Qin H, Guan H, Wu Y-J (2013) Analysis of park-and-ride decision behavior based on decision field theory. Transportation Research Part F: Traffic Psychology and Behaviour 18:199–212. https://doi.org/10.1016/j.trf.2013.02.001
41. Rust J (1994) Structural estimation of markov decision processes. Handbook of Econometrics 4:3081–3143. https://doi.org/10.1016/S1573-4412(05)80020-0
42. Busemeyer JR, Johnson JG (2004) Computational models of decision making. Blackwell handbook of judgment and decision making, 133–154
43. Yang Z-l, Huang L-c (2017) Dynamic stochastic multiattribute decision-making that considers stochastic variable variance characteristics under time-sequence contingency environments. Mathematical Problems in Engineering 2017(1), 7126856 https://doi.org/10.1155/2017/7126856
44. Ho SL, Xie M (1998) The use of arima models for reliability forecasting and analysis. Computers & Industrial Engineering 35(1–2):213–216. https://doi.org/10.1016/S0360-8352(98)00066-7
45. Jain H, Patel R (2024) Analysis & forecasting of juvenile crime using variance threshold and time series algorithm. Multimedia Tools and Applications, 1–28 https://doi.org/10.1007/s11042-024-19780-x
46. Dritsakis N, Klazoglou P (2019) Time series analysis using arima models: An approach to forecasting health expenditures in usa. International Economics/Economia Internazionale 72(1):77–106
47. ArunKumar K, Kalaga DV, Kumar CMS, Chilkoor G, Kawaji M, Brenza TM (2021) Forecasting the dynamics of cumulative covid-19 cases (confirmed, recovered and deaths) for top-16 countries using statistical machine learning models: Auto-regressive integrated moving average (arima) and seasonal auto-regressive integrated moving average (sarima). Applied Soft Computing 103:107161. https://doi.org/10.1016/j.asoc.2021.107161
48. D, L, Changyu L, Wenyan G (2009) A new cognitive model: Cloud model. International Journal of Intelligent Systems 24(3), 357–375 https://doi.org/10.1002/int.20340
49. Wang J, Peng L, Zhang H, Chen X (2014) Method of multi criteria group decision making based on cloud aggregation operators with linguistic information. Inf Sci 274:177–191. https://doi.org/10.1016/j.ins.2014.02.130
50. Wang G, Xu C (2012) Cloud model-a bidirectional cognition model between concept's extension and intension. In: Hassanien, A.E., Salem, A.-B.M., Ramadan, R., Kim, T. (eds.) Advanced Machine Learning Technologies and Applications. Communications in Computer and Information Science, vol. 274, pp. 391–400. Springer, Berlin, Heidelberg. https://doi.org/10.1007/978-3-642-35326-0_39
51. Busemeyer JR, Diederich A (2002) Survey of decision field theory. Mathematical Social Sciences 43(3):345–370. https://doi.org/10.1016/S0165-4896(02)00016-1
52. Hancock TO, Hess S, Choudhury CF (2018) Decision field theory: Improvements to current methodology and comparisons with standard choice modelling techniques. Transportation Research Part B: Methodological 107:18–40
53. Liu Tao WJ-Q (2012) Uncertain linguistic multi-criteria group decision-making approach based on integrated cloud. Control and Decision 27, 1185–1190
54. Montgomery D, Runger G (2014) Applied Statistics and Probability for Engineers. John Wiley and Sons, New York, p 765
55. Brown BB (1968) Delphi process: a methodology used for the elicitation of opinions of experts
56. Weitendorf D (1976) Beitrag zur optimierung der räumlichen struktur eines gebäudes. PhD thesis, Verlag nicht ermittelbar
57. Yang X, Yan L, Zeng L (2013) How to handle uncertainties in ahp: The cloud delphi hierarchical analysis. Inf Sci 222:384–404. https://doi.org/10.1016/j.ins.2012.08.019

Publisher's Note Springer Nature remains neutral with regard to jurisdictional claims in published maps and institutional affiliations.

Springer Nature or its licensor (e.g. a society or other partner) holds exclusive rights to this article under a publishing agreement with the author(s) or other rightsholder(s); author self-archiving of the accepted manuscript version of this article is solely governed by the terms of such publishing agreement and applicable law.

Journal of Vibration Engineering & Technologies (2025) 13:249
https://doi.org/10.1007/s42417-025-01804-x

ORIGINAL PAPER

Dynamic Response Experimental Analysis of High-Speed Rotors Equipped with Squeeze Film Dampers Under Varied Point Loading Conditions

Ratnesh Kumar Gupta[1] · **Ramesh Chandra Singh**[1]

Received: 29 October 2024 / Revised: 7 March 2025 / Accepted: 11 March 2025
© Springer Nature Singapore Pte Ltd. 2025

Abstract
High-speed rotating equipment may vibrate due to variable point loads and dynamic loads, affecting reliability, performance, and safety. Squeeze film dampers are often used to reduce rotor vibration and achieve system stability (SFDs). This study aims to test SFDs for reducing high-speed rotor vibrations in circumstances with changing point loads. In the paper,the dynamic behavior of a variable-point-loaded high-speed rotor system was investigated through experiments. A comprehensive literature review establishes the theoretical underpinnings and techniques for rotor dynamics and SFD technology. The use of theoretical models aids in the setup of experiments and the interpretation of findings. A unique experimental test setup is designed to represent high-speed rotor systems with variable point loads. This testing apparatus contains movable loading mechanisms. Ten, twenty, thirty, forty, and fifty centimetres are the loads from the shaft terminal support. Three oil samples were used to collect experimental data between 2500 and 10,500 rpm. The oil pressure supplied was 5 bar for the testing. After every placement, the vibration amplitudes along the x and z axes are measured using SFD integration and precise equipment. The SFD-equipped rotor system is assessed using vibration levels under different loading conditions, both with and without the damper. According to the study, a significant factor influencing shaft vibrations is the distance between the point load and the terminal support. When loads are closer together than when they are further apart—especially when the loads are positioned longer than the main shaft—the vibration amplitude is larger in the closer loads. Rotor vibration is continuously lowered by the SFDs. SFD dampers continuously lower the rotor vibration magnitudes. The setup of the research demonstrates the effect of control on rotor parameters by SFD and oil viscosity. This illustrates how the Self-Contained Fluid Drive and oil viscosity control may affect the rotor system vibrations. Enhancement of the durability and functionality of the system has also been proposed in the research. It also offers suggestions for enhancing the system's durability and functionality.

Keywords Vibration · Squeeze film damper · High-speed Rotor · Vibration control · Oil pressure · Oil blends · Variable point load

Introduction

Effective vibration control is crucial for optimizing the performance and durability of high-speed rotating machinery. The initial models were passive dampers which used oil films between rotating and stationery components to reduce vibrations. This helped absorb energy and reduce the vibrations. This basic idea was used to the development of SFDs to improve vibration reduction. Vibrations were lessened by the hydrodynamic effect produced by a thin coating of oil. Vibrations are lessened by the lubricant pressure variation brought on by the rotor rotation. By transferring the shaft's kinetic energy to the fluid, a reduction in vibration boosts the system's stability. The SFDs of today are very complex systems that are created for specific purposes. Gas turbines and other applications have several uses for hybrid systems. Vibration control is significant for the safety of high-speed spinning equipment, making it last longer, and also

✉ Ratnesh Kumar Gupta
ratneshgpt@gmail.com

[1] Delhi Technological University, New Delhi, Delhi 110042, India

Published online: 27 March 2025

increasing work efficiency. To absorb energy and decrease the number of vibrations, early passive damping systems used oil films between rotating and stationary components. These fundamental concepts lead to the development of SFDs and a variety of advanced damping devices [1]. SFDs power machines by using the hydraulic effect in the thin layer of oil or air between a rotor and a solid surface. Moving rotors cause changes in the oil coating's pressure, which lowers sound stimulation. Moving kinetic energy from the spinning system into the fluid makes the system more stable and lowers the size of fluctuations [2]. Innovations in materials, manufacturing techniques, and computational tools have led to advancements in SFD technology [3]. Unlike its more basic cylindrical predecessors with homogeneous film thickness, today's SFDs have more complex geometries tailored to specific applications [4]. Electric motors, gas turbines, pumps, compressors, and turbochargers are just some of the applications that have prompted researchers to explore hybrid systems that combine various damping methods, combinations of tilting pads, and labyrinth seals to improve damping. Their adaptability to different work settings, load profiles, and environmental variables makes them indispensable in challenging industrial contexts [5]. SFDs are useful, but they need perfect lubricant selection, design and operating parameter optimization, and manufacturing accuracy [6]. A description of the functions, history, design, problems, and future potential of squeeze film dampers follows this introduction [7]. This study looks at these features to make SFD technology better and its use in high-speed spinning gear in many different industries. Figure 1 shows a simple picture of how a squeeze film damper is put together.

Hydrodynamic forces in a damper system arise due to the oil layer that develops between the damper bearing (the stationary part surrounding it) and the damper journal (the revolving shaft or sleeve). When the journal rotates, it drags the oil, creating a pressure gradient in the oil film. This pressure increase supports the load on the damper, producing hydrodynamic lift and reducing metal-to-metal contact. In addition to dissipating vibration energy, this decreases the strains applied to the support structure. Squeeze film dampers are widely used in turbo equipment, commercial compressors, aviation jet engines, and other applications to increase damping and rotational speed range and decrease vibration. The design for greater operating speeds and power-to-weight ratios drives lighter and more flexible rotor-bearing systems into regular use in turbo-machines. Squeeze film dampers (SFDs) are widely used in high-speed turbomachinery

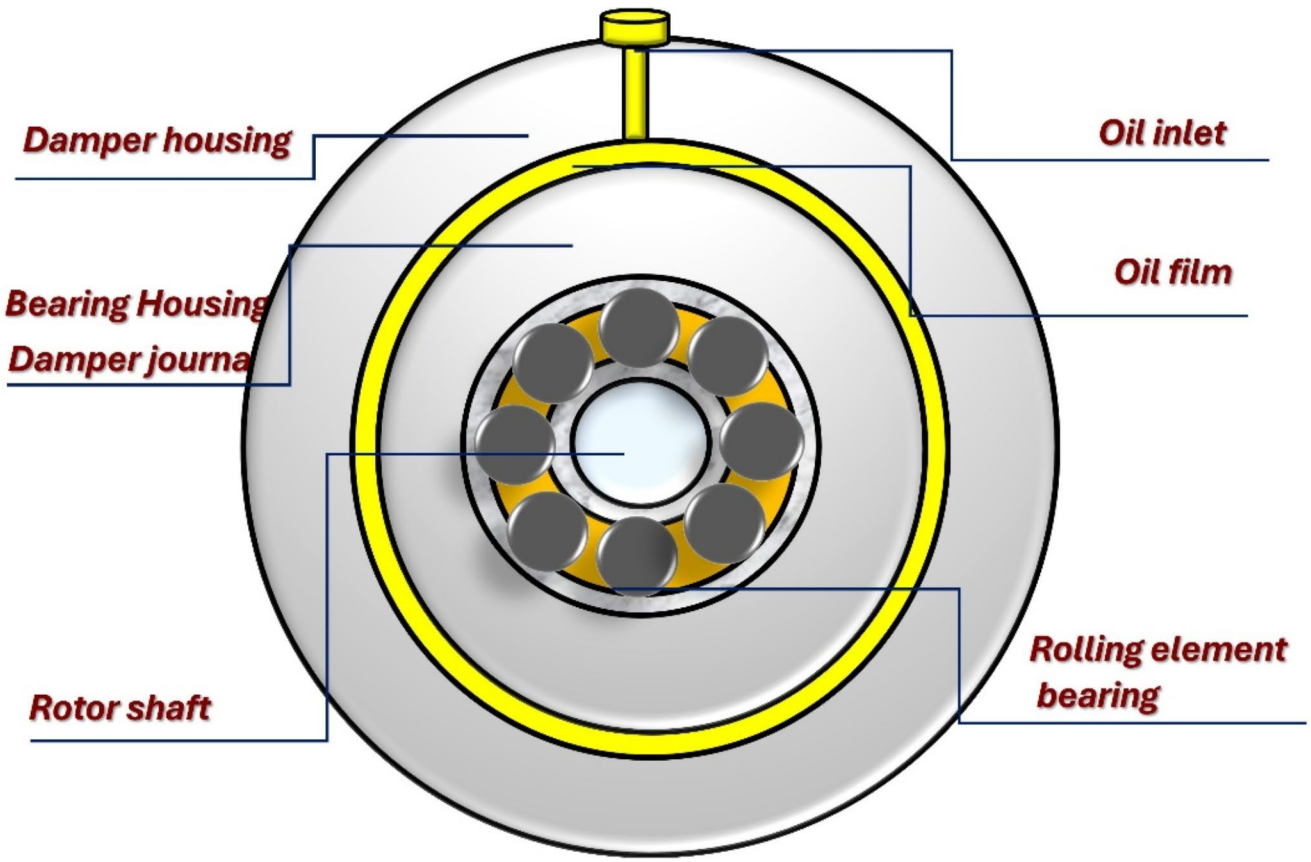

Fig. 1 Assembly of squeeze film damper

as they may lessen the rotor vibrations' amplitude and the forces applied to the structure. Furthermore, the capacity of viscous dampers to dissipate energy facilitates the dynamic stability characteristics of this rotor-bearing system [8]. Several researchers have offered several vibration control approaches aimed at increasing rotor stability and operational duration. The author created a vibration monitoring tool that captures rotor vibration measurements instantly. However, the observation gadget gave out malfunctioning signals [9]. To address the problem of blade vibration [10], A resistance damper was created based on the concept of resistive energy dissipation. However, the friction damper displayed substantial nonlinearity. We used braided metal wire dampers [11]. To reduce vibration. The shock absorber has the disadvantage of only having an impact at the critical speed. To conduct a comprehensive examination of pulsations in the exhaust pressure of a 200 MW Francis turbine [12], developed An innovative assessment approach that combines experimental model disintegration (EEMD) and entropy methods. Improvements to the process are still required to raise the accuracy of the characteristic results [13]. This study examines the link between the combined support parameters of design and provides a model of the combined support-containing rotor system. along with the vibration performance. In [14] unpressurized short SFDs were employed to assess the robustness of the response and the steady state vibrations of the basic flexible rotor using the Routh-Hurwitz criterion. In theory [15], studied SFDs with cantering components, masses distributed at midspan, and a simple flexible rotor mechanism that stabilizes [16]. The impact of fluid resistance on the efficiency of SFDs in damping motion has been investigated experimentally and theoretically in several research. Fluid resistance frequently increases the tangential component of the fluid film reaction forces, whereas a rapid strategy usually reduces the radial component [17]. A hypothetical study has been conducted on the steady-state imbalance reaction of a Jeffcott rotor based on extended SFDs that perform circular cantered orbits (CCO) due to lubrication. Lubricant inertia is shown to transform the Jeffcott rotor into a second bending mode, reducing the move loads to the supports and the likelihood of bi-stable nature and the jump occurrence. Direct numerical integration is used [13, 18, 19], The study used a basic flexible rotor with SFDs to investigate how design and operating variables affect the steady-state response, both with and without retaining springs. To investigate the impact of design and operational parameters on the constant state response, bifurcation onset speed, and broad range of nonsynchronous actions, a straightforward flexible rotor integrating SFDs in operation with and without retaining springs. A new, apparently fast computer integration method has been used to study and record the whole set of aero-engine disturbance characteristics for the rotor system with integrated support. according to [20], With the friction defect, the new model of a paired support rotor design takes into account the stator housing of the aero engine. With the rubbing defect, the creative concept of a paired support rotor system [21]. Experimental research is done on the dynamic response of a flexible ring squeeze film damper (ERSFD) rotor to axial force, oil supply, structural factors, and imbalance. the Moore friction factor calculation and the outer squeezing film's shearing action to evaluate the oil qualities of ERSFD [22]. used to assess how lubricating and damping forces from internal rotor elements affect the modal analysis of a complicated rotor system. In every previous study, the impacts were overlooked. SFD lubricant inertia on SFD parameters and specific SFD dynamics were employed, either fully or in part, utilizing the Reynolds equation and estimates (long bearing and short bearing approximations). The cooperatively supported test rig was constructed using the genuine twin rotor mechanism [23]. Utilizing the component mode synthesis approach and the finite element method, the vibration feature and reactivity of natural bending were examined and connected to both time- and frequency-domain experimental data [24]. investigates, over an extended period, the oil film characteristics and bearing capacity with different pedestal contact states. The deformation of the elastic ring affects the dynamic qualities of the ERSFD [25–28]. Direct and cross-coupled damping and inertia are expressed in terms of force coefficients. The authors of a novel multifaceted discrete reliable optimize (MODRO) method [29]. for the engineering design of structures in the face of uncertainty. The outcome proved that an algorithm is capable of producing an optimal design. The squeeze film damper has successfully employed a variety of modeling and experimental techniques, including Bond graph, Matlab, Simulink, finite element method (FEM), and other analytical techniques. Several SFDs, their input and output process characteristics, and the modeling method employed are displayed in Table 1.

After reviewing the research papers, we find the gap that the comparative study of vibration amplitude with and without squeeze film damper with respect to different oil samples still necessary. So that we will be able to understand the role of squeeze film damper in controlling the vibration amplitude of high-speed rotor shaft, with varying point loading conditions. For this analysis, this research is to conduct an in-depth investigation of the amplitude of shaft vibrations under varying point load circumstances. As part of this investigation, It will compare and contrast situations in which a squeeze film damper is not present with those in which it is present. A systematic modification of load placement is included in the experimental setup. More specifically, the load placement is varied at distances of 10,

Table 1 Lists the various kinds of SFDs and their input, and the feature extract

Authors	SFD	Input parameters	Output parameters analysis	Feature extract
[30] B.Halder et al.	SFD with stabilizer	6000 rpm speed and five oil samples	swirl balance	Newtonian lubricant that is viscoelastic
[31] A.EI. Shafei et al.	Adaptive hybrid SFD	Maximum speed: 15,000 rpm	critical speed testing for vibration, uncertainty analysis,	Adaptive control signal design possibility
[32] P.Bonello et al.	SFD with an uneven ball bearing for self-alignment	500 Hz is the frequency	Magnitude 10–2 m/N Anomalies at the x and y-axes	Large order system that is tractable and versatile
[33] Asad. A. Khalid et al.	Teflon SFD Steel SFD	3 bar of oil pressure and 6000 rpm rotor speed	Amplification of vibrations The resonance frequency Eccentricity ratio	Steel and Teflon damper compression
[34] Sergio E et al.	SFD with bubbly lubricant	Speed 6000 rpm, frequency 60 Hz, air volume friction	Dampness, Stiffness, and Inertia	Air entrainment has a significant impact on air damping inside SFD.
[8] L.San Andress et al.	Sealed SFD	Pump ring O-ring Oil pump pr. 2. Bar	reducing inertia	An O-ring has 20 times the rigidity of a piston ring.
[35] Bingbing et al.	SFD with central spring	Speed and spring stiffness	Adjust pitching, rolling displacement time, and hovering	A key factor in damping behavior is the core spring structure's stiffness.
[36] Z.Han et al.	Elastic ring SFD	Oil film thickness and oil pressure	Oil coefficients, journal whirl, eccentricity, and offset angle	When it comes to oil film characteristics, ERSFD performs better than elastic SFD.
[37] Z.Luo et al.	SFD with squirrel cage	shaft length, speed shaft diameter, damper radius, and dynamic viscosity	radius of the vibration orbit, shaft displacement at the x and y axes	Non-synchronous disc response at various speed range locations
[38] Sina Hamzen et al.	Short-length cavitated SFD	The Reynolds number squeezed 1500 rpm is the angular velocity.	size, vibration at the transient orbit radius and x and y axes	High-speed jet engines and turbines: the impacts of SFD inertia
[39] Xichen et al.	Elastic support SFD	Oil film speed, length, and shaft diameter	Typical flight factors include rising, turning, and maneuvering.	Within a specific range, the journal's swirling orbit range
[40] Yipeng et al.	Integral SFD, bearing damper	Angle, length, stress, and stiffness oil film height	Force transmitted Energy in the system	ISFED distance 59.3% transmitted force is reduced by 26.6% rotor system energy.
[41] Haobo. wang et al.	SFD for bistable vibration	Disk distance, stiffness speed, and shaft size (HPC, HPT)	Critical speed for whirl speed Damping stiffness	Examining how unbalanced mass affects rotor vibration.

20, 30, 40, and 50 centimeters from the end support of the shaft. The experimentation data was recorded for speeds 2500 to 10,500 rpm for this the three different oil samples were used. During the testing, the supply oil pressure was fixed at 5 bar. Measurements of the vibration amplitudes along the x and z axes are recorded after each placement. These measurements are taken for both the with and without squeeze film damper at each set of experiments with great care. When the load is positioned near the support, there is a perceptible rise in vibration amplitudes along both axes. The results obtained from several vibrational signal studies demonstrate this.

Conversely, a corresponding decrease in vibration amplitudes is seen when the load is moved further away from the support. In addition, when the loading point is larger than the shaft's main length, the vibration amplitudes diminish more quickly. In addition to providing insightful information on the dynamic behavior of the shaft under various load scenarios, this exhaustive analysis makes clear how the

vibrational patterns that have been discovered are affected by the use of a squeeze film damper.

Using a Squeeze Film Damper (SFD), In the second phase of the study, a squeeze film damper (SFD) was placed in place of the end support to guarantee a consistent loaded state. The main aim was to determine the amplitudes of vibration along the X and Z axes. The supply oil pressure was maintained at 5 bar while many sets of oil samples with different viscosities were utilized for the experiment.

The loading state was a reflection of the conditions that existed back when the SFD was not there. The oil supply pressure remained constant, and the point loading was constantly shifting. Throughout the investigation, the identical oil supply pressure of 5 bar was applied to a wide range of oil samples that presented varying degrees of viscosity. Because of this scientific approach, it.

An important trend was observed in the experimental data with regard to the influence of oil viscosity on vibration amplitude. As soon as the viscosity of the oil reached its ideal level, the vibration amplitude in both the X and Z axes showed a corresponding drop. The fact that this is the case suggests that there is a physical correlation between the viscosity of the oil and the amplitudes of the vibrations that are created.

With and without a squeeze film damper, an assessment of the amplitude of vibrations: Both with and without the SFD, the vibration amplitudes of each oil sample were analysed and paired. The findings made it abundantly clear that the rotor vibration amplitudes were much reduced when the SFD was used. Furthermore, the pattern seen suggested that a drop in vibration amplitude occurred simultaneously with an increase in oil viscosity up to a certain threshold. This was the case before the threshold was reached. Within the rotor system, this highlights the reciprocal influence that oil viscosity and the SFD have on the decrease of vibration occurrences.

Material and Method Without SFD

During the experimental examination, three different oil samples were used. These samples were carefully created by combining kerosene oil and crankcase oil in different amounts. The kinematic viscosities of the oil samples were measured as follows: oil sample 1 had a value of 18.449mm^2/sec, oil sample 2 had a value of 27.807 mm^2/sec, and oil sample 3 had a value of 54.666 mm^2/sec. The deliberate manipulation of oil composition and viscosity is a fundamental part of the experiments to determine how lubricant qualities affect the dynamic behavior of the system. A consistent oil pressure of 5 bar was maintained throughout the testing experiments. The system's dynamic forces were represented by a spinning load. At regular intervals, this load was varied at five different distances from the damper support. Ten, twenty, thirty, forty, and fifty centimeters were the precise distances from the end support when measured. It was a proximity sensor that was positioned five centimeters from the end support that was used to measure the vibration signals. To provide accurate data gathering and a thorough investigation of the vibratory responses of the system to a variety of loads, the positioning of the sensors was very carefully considered. Another part of the testing was a detailed investigation of the system's reaction to different rotor speeds. To provide a more accurate description, the rotor was rotated at five distinct speeds: 2500, 4500, 6500, 8500, and 10,500 revolutions per minute. An extensive number of speed settings were included in the system to provide an all-encompassing evaluation of its performance in a variety of operational scenarios. the interactions that occur between the rotor velocities, loading conditions, and oil qualities to this complex technology were analysed in depth. This leads to a fundamental comprehension of the dynamics of the system as well as the capacity of the squeeze film damper to lessen vibrations.

Experimental Test Rig Detailed Without SFD

The setup of this experiment comprises the rotor test rig that is stationary between two supports and has a shaft that is 87 centimetres in length and 2.2 centimetres in diameter. As can be seen in Fig. 2, a rotating mass that is 2.2 centimetres by 1.4 centimetres in size and weighs 550 g is carefully placed at various positions along the rotor. The use of proximity probing allows for the accurate recording of vibration amplitudes along the X and Z axes, particularly at a distance of five centimetres from the end support. After that, the spinning mass is pushed systematically to distances of 10, 20, 30, 40, and 50 centimetres from the endpoint support, and the vibration amplitudes that arise from this movement are recorded to conduct an in-depth analysis.

Description of Test Rig with SFD

The accompanying table, which is referred to as Table 2 , offers detailed documentation of the specific features that are associated with the actual testing rig, as well as the dimensions of each component that is included inside it. Through the use of tabulation, we can get the essential parameters that are necessary for a comprehensive comprehension of the experimental environment. This enables for accurate examination and interpretation of the rig's performance under several conditions.

The experimental setup, which includes the squeeze film damper (SFD), is shown visually in Figs. 3 and 4. A

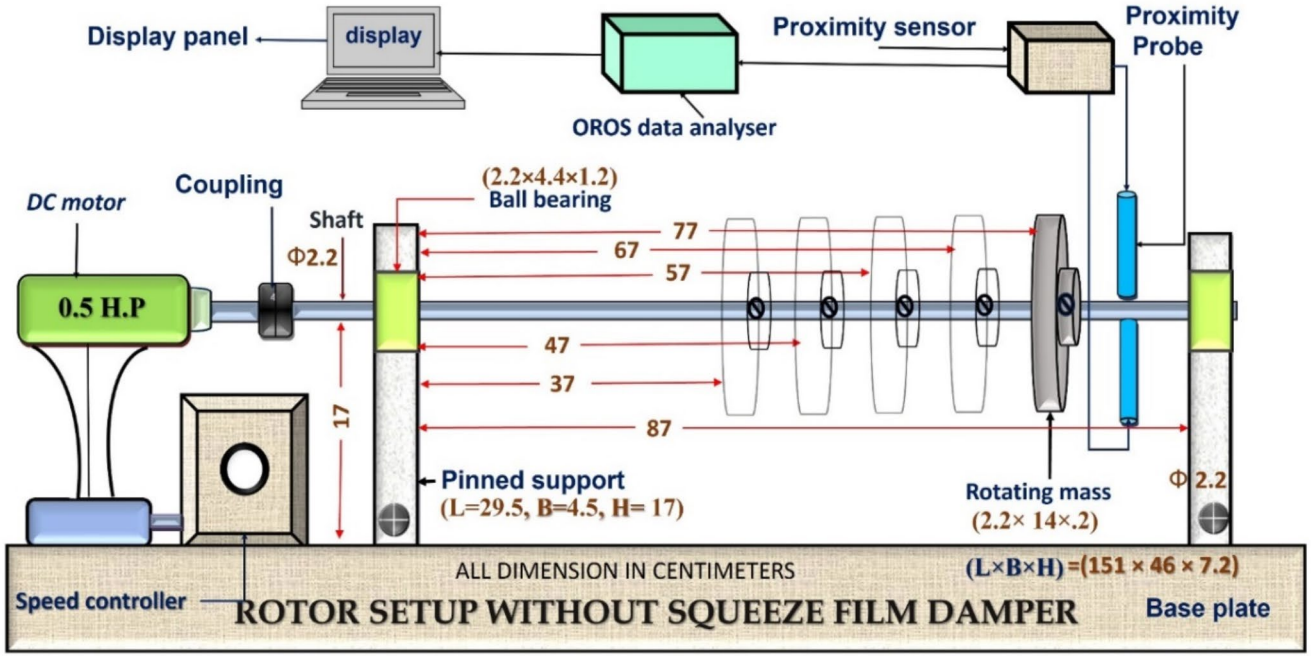

Fig. 2 Rotor bearing system without squeeze film damper

Table 2 Parameter detail of experimental set-up vibration analysis with SFD

Experimental Test Rig details	
Rotor shaft components' materials	*Mild steel*
The rotor shaft's length and diameter	*1000 mm*, *22 mm*
Distance between two supports of a rotor	*870 mm*
Damper journal Boundary dimension	*44 × 50 × 64 mm*
Damper housing Boundary dimension	*50 × 56 × 64 mm*
Length of the damper	*50 mm*
Boundary dimension of rotating mass	*22 × 140 × 20 mm*
Mass of rotating disc	*550gm*
The boundary dimension of ball bearings is utilized in squeeze film damper, type	*22 × 44 × 12 mm*, *Koyo*, *Japan*
Spacer	*4 mm*
Rotor shaft mass	*3.5 kg*
Rotor shaft Density	*7800 kg/m3*
O-ring seal material and diameter	*Rubber*, *46 mm*
Single phase DC motor 0.5 hp	*12000rpm*
Type of coupling used	*flexible Lovejoy*

schematic representation of the experimental setting is also shown in these drawings. These graphics serve as essential parts of the experimental paperwork and provide a detailed explanation of how the test rig is set up. A theoretical overview of the system is included in the schematic, which is displayed in Fig. 3. The schematic also illustrates the desired arrangement of components. Figure 4, on the other hand, provides a picture that is accurate and incorporates the actual implementation of the test rig in the real world, complete with the squeeze film damper that is included in it.

Material and Method with SFD

During the experimental examination, three different oil samples were used. These samples were carefully created by combining kerosene oil and crankcase oil in different amounts. The kinematic viscosities of the oil samples were measured as follows: oil sample 1 had a value of 18.449mm^2/sec, oil sample 2 had a value of 27.807 mm^2/sec, and oil sample 3 had a value of 54.666 mm^2/sec. The deliberate manipulation of oil composition and viscosity is a fundamental part of the experiments, to determine how lubricant qualities affect the dynamic behavior of the system.A consistent oil pressure of 5 bar was maintained throughout the testing experiments. The dynamic forces on the system were represented by a rotating load. At five distinct intervals from the damper support, this load was regularly changed. Exact measurements of 10, 20, 30, 40, and 50 cm were made from the end support. The vibration signals were measured using a proximity sensor placed at five centimeters from the end support. The sensors were thoughtfully placed to enable precise data collection and a comprehensive examination of the system's vibrational responses under varied loads. Another part of the testing was a detailed investigation of the system's reaction to different rotor speeds. Five distinct rotational speeds are applied to the rotor: 2500, 4500, 6500, 8500, and 10,500 revolutions per minute (rpm). The inclusion of a large number of speed settings makes it possible to conduct an exhaustive evaluation of the system's capability in a variety of different operating conditions. It is possible to conduct an in-depth investigation of the interactions that

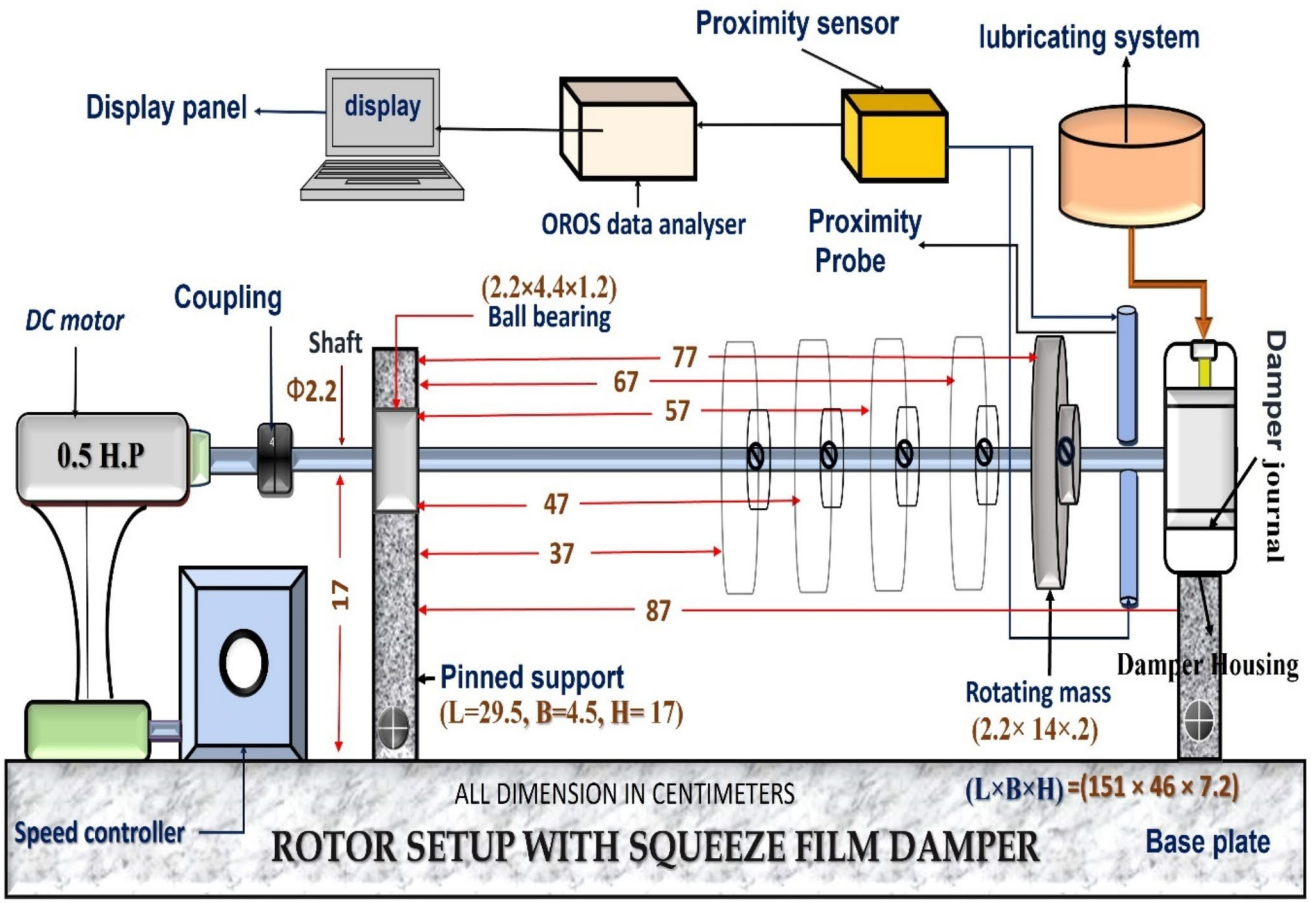

Fig. 3 Rotor bearing system with squeeze film damper

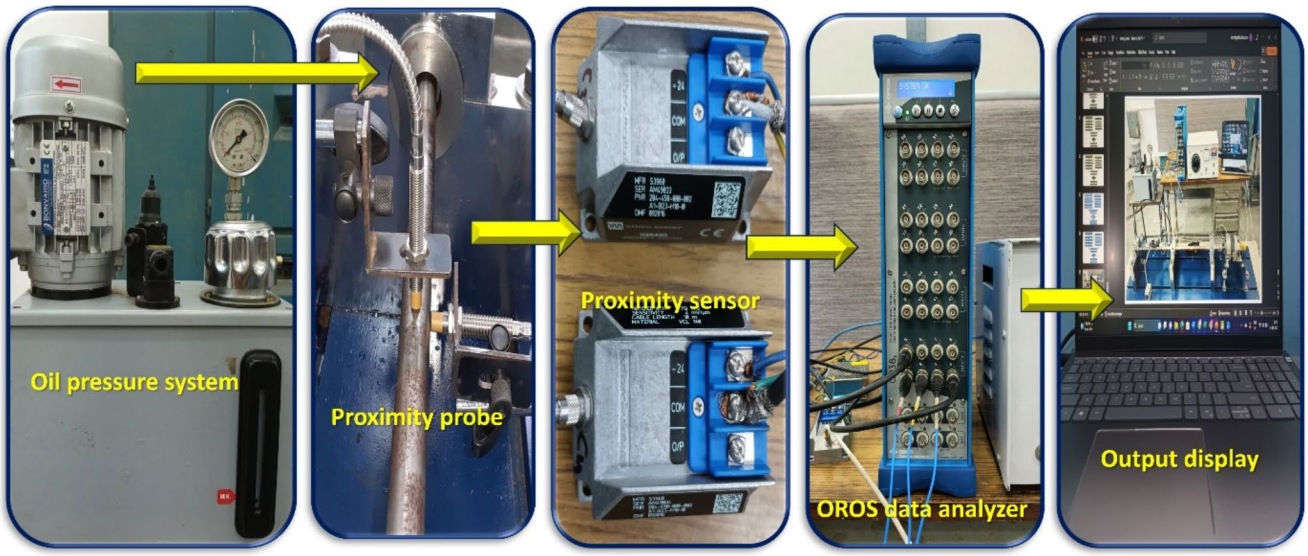

Fig. 4 Actual Rotor bearing system with squeeze film damper

Table 3 Vibration amplitude(μm) of the rotor shaft without SFD

Speed (rpm)	2500		4500		6500		8500		10,500	
Load Distance (c.m)	axis-x	axis-z	axis-x	axis-z	axis-x	axis-z	axis-x	axis-z	axis-x	axis-z
10	65.2	66.3	84.9	85.2	120.2	121.2	135.2	134.2	165.7	164.2
20	60.5	60.9	77.6	78.1	102.5	103.4	111.6	110.5	141.3	140.4
30	50.4	51.4	69.4	68.8	89.7	88.8	92.7	93.5	112.5	111.6
40	46.2	47.2	57.6	56.9	73.9	74.7	81.8	82.5	94.6	95.4
50	30.4	31.4	35.7	36.1	52.6	53.9	60.7	61.4	71.5	72.8

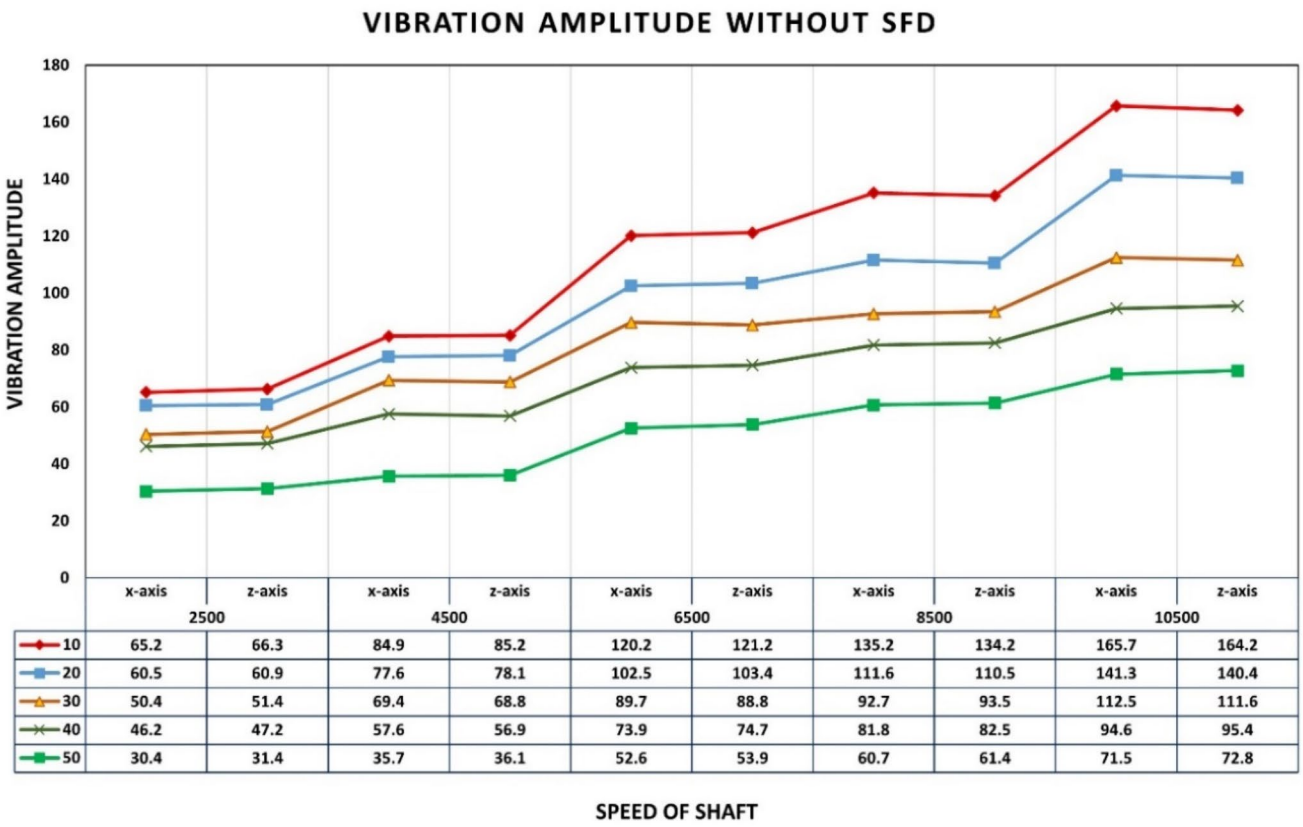

Fig. 5 Vibration amplitude of shaft at x-z axes without SFD

occur between the rotor speeds, loading conditions, and oil qualities by using this approach. This leads to a fundamental comprehension of the dynamics of the system as well as the capacity of the squeeze film damper to lessen vibrations.

Experiment Investigation Without Squeeze Film Damper

Throughout the experiment, a variety of speeds—from 2500 to 10,500 revolutions per minute (RPM)—are applied to the rotor under examination. To support a 550-gram spinning mass, loading points are positioned carefully, ranging from 10 to 50 centimeters from the end support. The vibration data are shown in Table 3, and the appropriate graphical representation is shown in Fig. 5.

A detailed analysis of the experimental data demonstrates that loading the support near the load caused the vibration amplitude to significantly rise in both directions. This behavior suggests that the system is more sensitive to loading conditions in the vicinity of the assistance. On the other hand, when the load was moved farther away from the support in a systematic manner, there was a constant decrease in the amplitude of vibration. The complex connection between the load location and the resulting vibratory response is shown by this intricate relationship.

Remarkably, a very important finding arose when the loading point surpassed the midpoint of the shaft's length. Currently, there was a noticeable and swift decrease in the magnitude of vibration. This event indicates a crucial limit in the system's behavior, indicating that once a particular distance from the support is reached, the system undergoes a

Table 4 Vibration amplitude(μm) of the rotor shaft with SFD for oil sample 1

Speed (rpm)	2500		4500		6500		8500		10,500	
Load Distance (c.m)	axis-x	axis-z	axis-x	axis-z	axis-x	axis-z	axis-x	axis-z	axis-x	axis-z
10	52.3	51.5	74.3	75.2	110.3	109.2	117.2	118.1	135.3	136.2
20	46.1	45.2	62.5	63.4	91.2	92.4	99.5	98.7	118.5	119.4
30	39.2	38.6	51.8	52.2	78.5	77.6	82.3	83.5	94.5	95.7
40	35.2	36.4	42.6	43.1	65.3	66.2	71.5	72.6	82.6	83.4
50	27.3	28.2	31.2	32.3	41.5	42.1	50.1	49.5	58.2	59.3

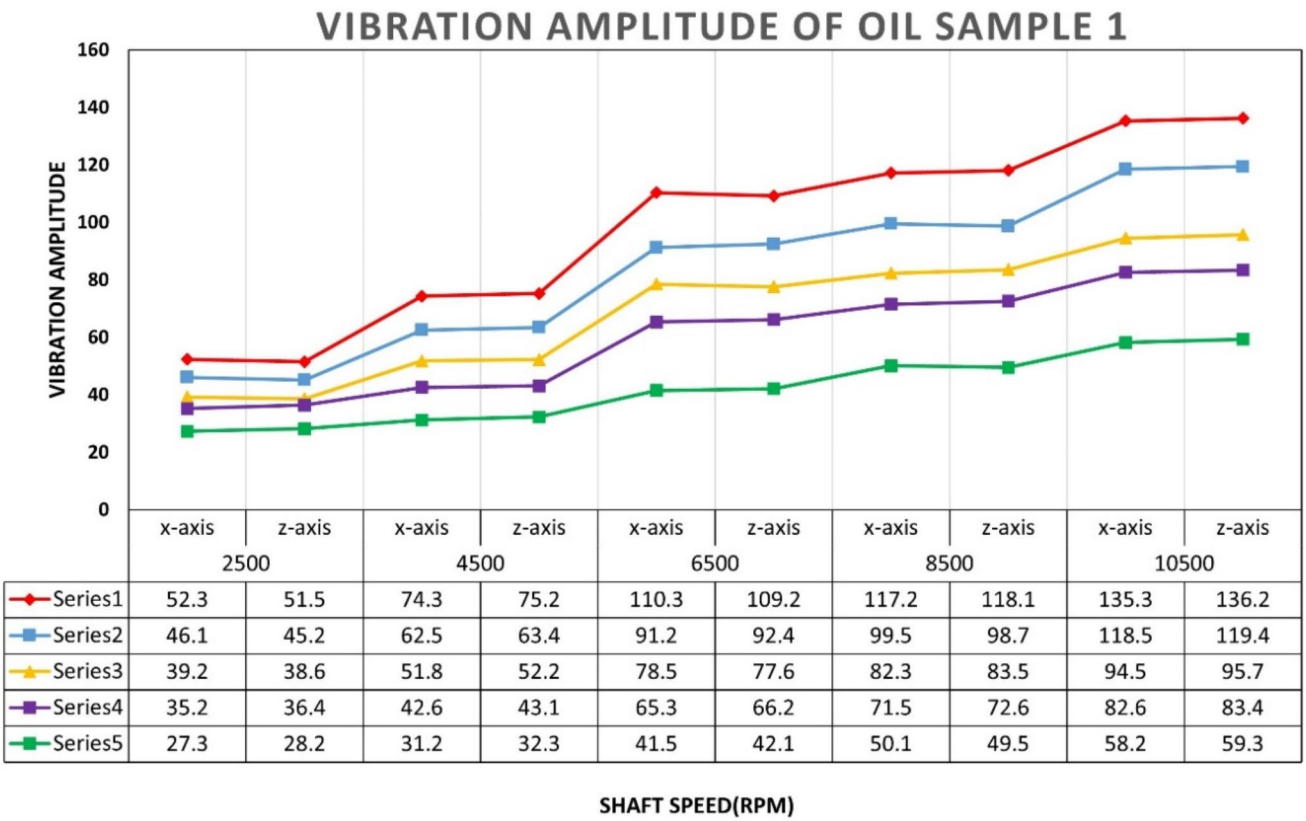

Fig. 6 Vibration amplitude without squeeze film damper oil1

stronger stabilization, perhaps because of a redistribution of forces and moments acting on the rotor. These findings are important for understanding and advancing rotor dynamics. The patterns that were found emphasize how important load placement is in shaping the system's vibrational qualities. Further investigation of these dynamics may improve prediction model accuracy and make it easier to develop methods for minimizing vibrations in spinning machinery. This might have applications in several engineering specialties.

Experimental Results and Analysis

A thorough review of the vibration amplitudes seen in the rotating shaft after the subject is methodically conditioned at various speeds is shown in Table 4. This information was meticulously compiled for a squeeze film damper operating at a fixed oil supply pressure of 5 bar. With an observed kinematic viscosity of 18.449 mm³/sec, oil sample 1 may be thoroughly analyzed. Information regarding various vibration amplitudes, speed ranges, and load points is included in the table. This makes it possible to thoroughly examine the dynamic behavior of the system using the given experimental conditions.

The detailed information provided in Fig. 6 facilitates the identification of patterns, trends, and relationships between important variables. This improves our understanding of how the vibrational responses in the squeeze film damper setup are affected by the oil viscosity, rotor speed, and load position.

Detailed information on the vibration that was shown by the spinning shaft under a range of loading circumstances

Table 5 Vibration amplitude(μm) of the rotor shaft with SFD for oil sample

Speed (rpm)	2500		4500		6500		8500		10,500	
Load Distance (c.m)	axis-x	axis-z	axis-x	axis-z	axis-x	axis-z	axis-x	axis-z	axis-x	axis-z
10	42.3	41.4	64.3	65.2	99.9	99.1	109.2	110.1	124.3	125.8
20	36.2	35.3	52.5	53.4	81.2	82.4	89.5	88.7	108.6	109.5
30	29.2	28.6	41.8	42.2	68.5	67.6	72.3	73.5	84.5	85.7
40	25.2	26.4	32.6	33.1	55.3	56.2	61.8	62.7	82.6	83.4
50	20.3	21.2	24.2	25.3	33.5	34.1	40.1	41.5	54.7	55.3

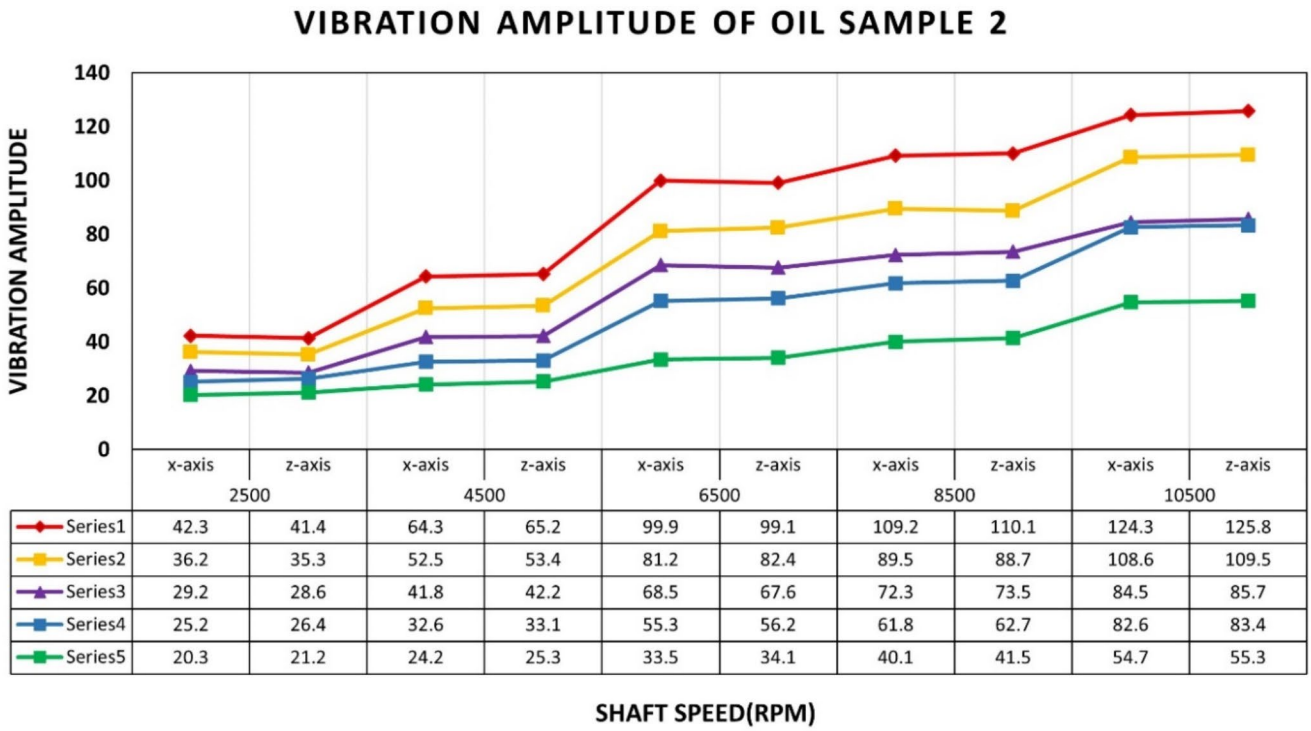

Fig. 7 Vibration in the absence of squeeze film damper oil 2

and at many different speeds is included in Table 5. The information is collected with accuracy by using a squeeze film damper that has a constant oil supply pressure of five bars. Using the findings, a comprehensive analysis is performed on oil sample 2, which stands out due to its kinematic viscosity rating of 27.807 mm3/sec. Each row in the table is a representation of the ideal arrangement of load point, speed range, and the vibration amplitude that this combination produces. The experimental conditions are provided to conduct a comprehensive investigation of the dynamic behavior of the system.

To help identify trends, patterns, and relationships between important variables, Fig. 7 provides essential insights. Our comprehension of this phenomenon may be enhanced by studying the impact of load location, rotor speed, and oil viscosity on the vibrational responses of the squeeze film damper arrangement.

There is a detailed review of the vibration amplitudes that the spinning shaft presented under various loading situations and speeds, which can be found in Table 6. To guarantee that the squeeze film damper functions with a consistent oil supply pressure of 5 bar, it is necessary to pick the available data with great consideration. The observations provide a comprehensive analysis of oil sample 3, which stands out because its kinematic viscosity is 54.666 mm3/sec. The rows of the table correspond to a different combinations of load point, speed range, and vibration amplitude. This allows for a comprehensive examination of the dynamic behavior of the system under specific experimental conditions, which is made feasible by the table's construction.

Figure 8 provides useful information that enables us to see trends, patterns, and linkages among significant elements. This increases our knowledge of how the squeeze film damper arrangement's vibrational responses are influenced by load positioning, rotor speed, and oil viscosity.

Table 6 Vibration amplitude(μm) of the rotor shaft with SFD for the oil sample 3

Speed (rpm)	2500		4500		6500		8500		10,500	
Load Distance (c.m)	axis-x	axis-z	axis-x	axis-z	axis-x	axis-z	axis-x	axis-z	axis-x	axis-z
10	32.4	31.7	54.3	55.2	87.3	88.2	97.2	98.1	115.3	116.2
20	27.1	26.2	42.5	43.4	71.3	72.7	79.5	78.7	98.9	99.8
30	20.2	21.6	34.8	35.2	58.4	57.6	62.3	63.5	74.5	75.7
40	15.2	16.4	22.6	23.1	35.5	36.8	51.5	52.6	64.6	63.4
50	11.3	10.5	15.2	16.5	21.5	22.7	30.1	29.5	38.4	37.5

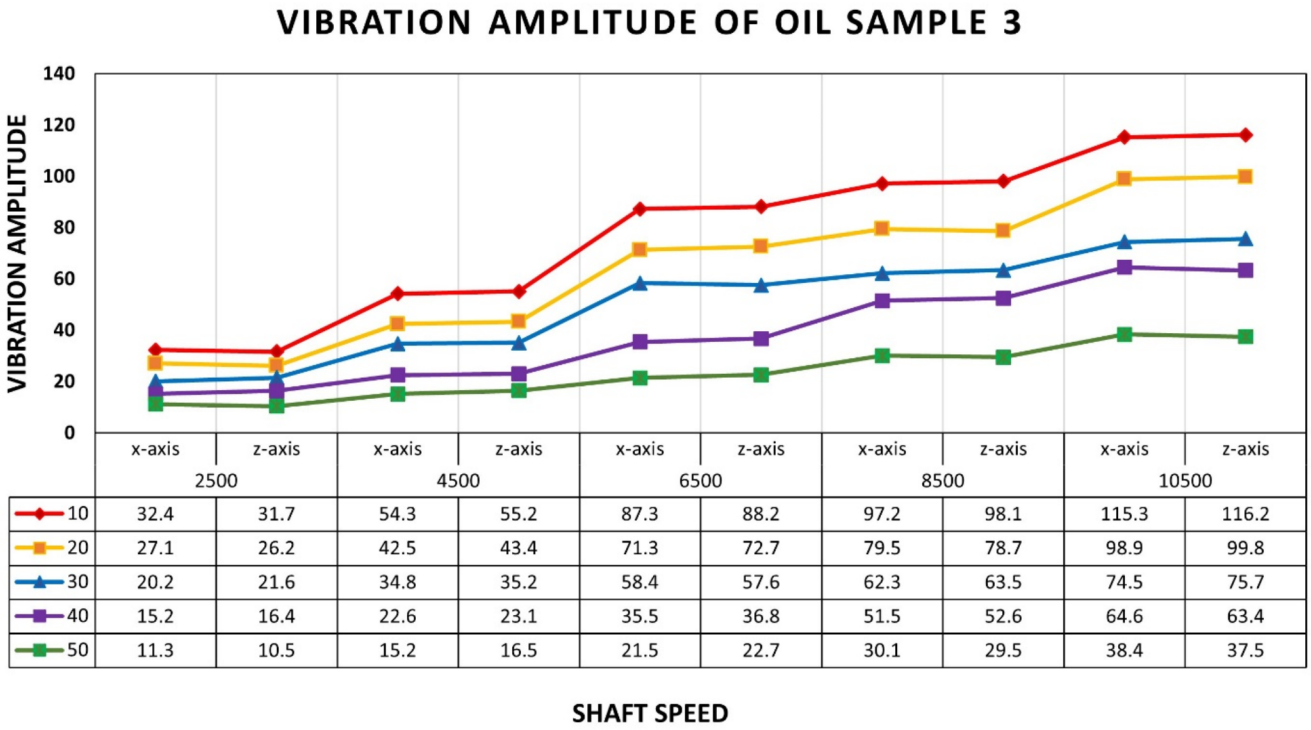

Fig. 8 Vibration amplitude of x-z axes without squeeze film damper oil 3

Experimental Findings and Discussion

Initial Phase of the Investigation

The load was placed purposefully at 10, 20, 30, 40, and 50 centimetres from the end support during the first phase of our investigation. The shaft's vibration amplitudes in the x and z axes therefore showed patterns that were easy to see. Importantly, there was a discernible increase in vibration amplitude in both axes when the load was positioned close to the support. However, the amplitude of the vibration decreases in a proportional manner whenever the weight is shifted farther away from the support. One of the most noteworthy discoveries was the rapid decrease in vibration amplitude that occurred as the loading point advanced beyond the halfway point of the shaft.

Second Phase of the Investigation

After replacing the end support with a squeeze film damper (SFD), the vibration amplitudes along X, Z axes were calculated in the second section of our experiment. As a part of the method, a large number of oil samples with a range of viscosities were analyzed. When the experiment is done with a constant load, which replicates the first setup but does not contain the SFD, exciting results are attained. This allowed for the repetition of the experiment.

Different Oil Study Samples and Viscosity Levels

The results unambiguously revealed that there is a relationship between the magnitude of the vibration and the viscosity of the oil. As the viscosity of the oil samples increased and reached an acceptable level, the vibration amplitude for both the X and Z axes decreased at a consistent rate, as shown by the findings. In systems that consist of squeeze

film dampers, it is important to give careful consideration to the selection of oil viscosity since, according to the findings of our study, this choice has a major influence on assessing the overall vibration characteristics.

The Study Compared the Squeeze Film Damper (SFD) on High-Speed Rotor Vibration Amplitudes

According to the findings of the investigations, the presence of the SFD resulted in a noticeable reduction in the amplitude of the rotor vibrations. In addition to demonstrating how effective the squeeze film damper is in reducing vibrations, the decrease was constant over a broad variety of viscosity oil samples. This provides useful information that can be used to optimize the performance of the damper when it is put into practical use.

Conclusion

This study investigates high-speed shaft vibration amplitude under point stress. investigated shaft vibration with weights at different terminal support lengths. High-speed rotating equipment applications need this study because excessive vibrations may cause structural damage, poor performance, and catastrophic collapse. Also, squeeze film dampers (SFDs) are studied for vibration reduction. Damping spinning systems using SFDs helps in the proper distribution of energy and reduction in vibrations. SFD optimization for practical applications requires understanding the effect of load circumstances on vibrations.

Important conclusions emerged after diligent inquiry and examination.

- Through analysis, it has been shown that there is a high correlation between vibration amplitudes and load placement distances. As one moves further away from the main shaft, the vibrations decrease in intensity and become more focused at the terminal support. The precise positioning of the load is essential to minimize shaft vibration.
- The presence of SFDs resulted in a considerable reduction in vibration amplitudes compared to situations without dampers. This demonstrates the efficacy of SFDs in mitigating rotor vibrations and enhancing system stability.
- The study offered valuable insight into the intricate relationship between vibration reduction and oil viscosity. The vibration amplitudes steadily decrease when the oil viscosity reaches acceptable levels. Choosing the appropriate oil viscosity is crucial for optimizing SFD (static frequency deviation) performance and controlling vibrational excursions.
- The importance of complete system optimization. When engineers limit vibrations via load placement, SFD integration, and oil viscosity selection, the high-speed shaft systems may last longer and their reliability also increases.

This study provides crucial insights into high-speed shaft dynamics under various load circumstances. Shaft flexural dampers and oil viscosity reduce vibrations. These results are crucial to enhancing engineering procedures for rotating gear reliability and performance in diverse industrial situations.

Declarations

Conflicts of interests The writers affirm that their work is devoid of any conflicts of interest.

References

1. Zapoměl J, Ferfecki P, Kozánek J (2017) Modelling of magnetorheological squeeze film dampers for vibration suppression of rigid rotors. Int J Mech Sci 127:191–197. https://doi.org/10.1016/j.ijmecsci.2016.11.009
2. Zhongliang Xie Zhongliang Xie Jian Jiao Stanislaw Wrona Stanislaw Wrona (2022) The fluid-structure interaction lubrication performances of a novel bearing: experimental and numerical study. Tribiology Int 179. https://doi.org/10.1016/j.triboint.2022.108151
3. Jiang H, Yu S, Wang S, Ding X, Jiang A (2024) Research status and development trend of cylindrical gas film seals for aeroengines, processes. 12. https://doi.org/10.3390/pr12010069
4. Jia X, Zheng Q, Jiang Y, Zhang H (2019) Leakage and rotordynamic performance of T type labyrinth seal. Aerosp Sci Technol 88:22–31. https://doi.org/10.1016/j.ast.2019.02.043
5. Kurz R, Sheya C (2006) Electric drive vs gas turbines. Turbomach Int 47:20–21
6. Cunha BZ, Daniel GB (2022) Effects of bearing lubrication conditions on rotor dynamic behavior. Proc Inst Mech Eng Part J J Eng Tribol 236:563–580. https://doi.org/10.1177/13506501211010563
7. Burrows C.R., Keogh P.S., Sahinkaya M.N. (2009) Progress towards smart rotating machinery through the use of active bearings. Proc Inst Mech Eng Part C J Mech Eng Sci 223:2849–2859. https://doi.org/10.1243/09544062JMES1487
8. San Andrés L, Koo B, Jeung S-H C. Design Engineer Sean, Experimental Force Coefficients for Two Sealed Ends Squeeze Film Dampers (Piston Rings And O-Rings): An Assessment of Their Similarities and Differences Gt2018-76224, n.d. http://proceedings.asmedigitalcollection.asme.org
9. Xu X, Lei Y, Li Z (2020) IEEE Trans Ind Electron 67:2326–2336. https://doi.org/10.1109/TIE.2019.2903774. An Incorrect Data Detection Method for Big Data Cleaning of Machinery Condition Monitoring
10. Rizvi A, Smith CW, Rajasekaran R, Evans KE (2016) Dynamics of dry friction damping in gas turbines: literature survey. JVC/

Journal Vib Control 22:296–305. https://doi.org/10.1177/1077546313513051
11. Ma Y, Liang Z, Wang H, Zhang D, Hong J (2013) Theoretical and experimental steady-state rotordynamics of an adaptive air film damper with metal rubber. J Sound Vib 332:5710–5726. https://doi.org/10.1016/j.jsv.2013.06.002
12. Wang W, Chen Q, Yan D, Geng D (2019) A novel comprehensive evaluation method of the draft tube pressure pulsation of Francis turbine based on EEMD and information entropy. Mech Syst Signal Process 116:772–786. https://doi.org/10.1016/j.ymssp.2018.07.033
13. Inayat-Hussain JI (2009) Bifurcations in the response of a flexible rotor in squeeze-film dampers with retainer springs, chaos. Solitons Fractals 39:519–532. https://doi.org/10.1016/j.chaos.2007.01.086
14. Rabinowitz MD, Hahn EJ (1977) Stability of Squeeze-Film-Damper supported flexible rotors. J Eng Gas Turbines Power 99:545–551. https://doi.org/10.1115/1.3446549
15. Cunningham RE, Fleming DP, Gunter EJ (1975) Design of a Squeeze-Film damper for a Multi-Mass flexible rotor. Am Soc Mech Eng 1383–1389
16. San Andres LA, Vance JM (1988) Effect of fluid inertia on the performance of squeeze film damper supported rotors. J Eng Gas Turbines Power 110:51–57. https://doi.org/10.1115/1.3240086
17. El-Shafei A (1991) Unbalance response of a Jeffoott rotor incorporating long squeeze film dampers. J Vib Acoust Trans ASME 113:85–94. https://doi.org/10.1115/1.2930160
18. Inayat-Hussain JI (2005) Bifurcations of a flexible rotor response in squeeze-film dampers without centering springs, chaos. Solitons Fractals 24:583–596. https://doi.org/10.1016/j.chaos.2004.09.047
19. Inayat-Hussain JI, Kanki H, Mureithi NW (2003) On the bifurcations of a rigid rotor response in squeeze-film dampers. J Fluids Struct 17:433–459. https://doi.org/10.1016/S0889-9746(02)00146-9
20. Chen G (2009) A new rotor-ball bearing-stator coupling dynamics model for whole aero-engine vibration. J Vib Acoust Trans ASME 131:0610091–0610099. https://doi.org/10.1115/1.4000475
21. Han Z, Ding Q, Zhang W (2019) Dynamical analysis of an elastic ring squeeze film damper-rotor system. Mech Mach Theory 131:406–419. https://doi.org/10.1016/j.mechmachtheory.2018.10.011
22. Chouksey M, Dutt JK, Modak SV (2012) Modal analysis of rotor-shaft system under the influence of rotor-shaft material damping and fluid film forces. Mech Mach Theory 48:81–93. https://doi.org/10.1016/j.mechmachtheory.2011.09.001
23. Shi M, Yang Y, Wang J, Deng W, Zhang D (2021) Analysis of dynamic characteristics of ring squeeze film Damper-Rotor system. https://doi.org/10.21203/rs.3.rs-966661/v1
24. Zhang W, Ding Q (2015) Elastic ring deformation and pedestal contact status analysis of elastic ring squeeze film damper. J Sound Vib 346:314–327. https://doi.org/10.1016/j.jsv.2015.02.015
25. Gehannin J, Arghir M, Bonneau O (2010) Complete squeeze-film damper analysis based on the bulk flow equations. Tribol Trans 53:84–96. https://doi.org/10.1080/10402000903226382
26. Andrés LS, Delgado A (2012) A novel bulk-flow model for improved predictions of force coefficients in grooved oil seals operating eccentrically. J Eng Gas Turbines Power 134:1–10. https://doi.org/10.1115/1.4004736
27. Hamzehlouia S, Behdinan K (2016) Squeeze film dampers executing small amplitude Circular-Centered orbits in High-Speed turbomachinery. Int J Aerosp Eng 2016. https://doi.org/10.1155/2016/5127096
28. Hamzehlouia S, Behdinan K (2017) A study of lubricant inertia effects for squeeze film dampers incorporated into high-speed turbomachinery. Lubricants 5. https://doi.org/10.3390/lubricants5040043
29. Sun G, Zhang H, Fang J, Li G, Li Q (2018) A new multi-objective discrete robust optimization algorithm for engineering design. Appl Math Model 53:602–621. https://doi.org/10.1016/j.apm.2017.08.016
30. Haldar B, Mukharjee A, Karmakar R (1990) Theoretical and Experimental Studies on Squeeze Film Stabilizers for Flexible Rotor-Bearing Systems Using Newtonian and Visooelastio Lubricants. http://www.asme.org/a
31. El-Shafei A, El-Hakim M (2000) Department, experimental investigation of adaptive control applied to HSFD supported rotors. J Eng Gas Turbines Power 122:685–692
32. Bonello P, Brennan MJ, Holmes R (2002) Non-linear modelling of rotor dynamic systems with squeeze film dampers - An efficient integrated approach. J Sound Vib 249:743–773. https://doi.org/10.1006/jsvi.2001.3911
33. Khalid AA, Albagul A, Faris W, Ismail GA (2006) An experimental study on steel and teflon squeeze film dampers. Shock Vib 13:33–40. https://doi.org/10.1155/2006/387302
34. Diaz SE, San Andrés LA (1999) A method for identification of bearing force coefficients and its application to a squeeze film damper with a bubbly lubricant. Tribol Trans 42:739–746. https://doi.org/10.1080/10402009908982277
35. Han B, Ding Q (2018) Forced responses analysis of a rotor system with squeeze film damper during flight maneuvers using finite element method. Mech Mach Theory 122:233–251. https://doi.org/10.1016/j.mechmachtheory.2018.01.004
36. Han Z, Ding Q, Zhang W (2019) Dynamical characteristic analysis of elastic ring squeeze film damper in rotor system. Mech Mach Sci Springer Sci Bus Media B V 56–71. https://doi.org/10.1007/978-3-319-99262-4_5
37. Luo Z, Wang J, Tang R, Wang D (2019) Research on vibration performance of the nonlinear combined support-flexible rotor system. Nonlinear Dyn 98:113–128. https://doi.org/10.1007/s11071-019-05176-2
38. Hamzehlouia S, Behdinan K (2021) Squeeze film dampers supporting high-speed rotors: rotordynamics. Proc Inst Mech Eng Part J J Eng Tribol 235:495–508. https://doi.org/10.1177/1350650120922082
39. Chen X, Gan X, Ren G (2020) Dynamic modeling and nonlinear analysis of a rotor system supported by squeeze film damper with variable static eccentricity under aircraft turning maneuver. J Sound Vib 485. https://doi.org/10.1016/j.jsv.2020.115551
40. Zhang Y, He L, Yang J, Zhu G, Jia X, Yan W (2021) Multi-objective optimization design of a novel integral squeeze film bearing damper. Machines 9. https://doi.org/10.3390/machines9100206
41. Wang H, Zhao Y, Luo Z, Han Q (2022) Analysis on influences of squeeze film damper on vibrations of rotor system in aeroengine. Appl Sci 12. https://doi.org/10.3390/app12020615

Publisher's Note Springer Nature remains neutral with regard to jurisdictional claims in published maps and institutional affiliations.

Springer Nature or its licensor (e.g. a society or other partner) holds exclusive rights to this article under a publishing agreement with the author(s) or other rightsholder(s); author self-archiving of the accepted manuscript version of this article is solely governed by the terms of such publishing agreement and applicable law.

Check for updates

Received: 6 September 2024 | Revised: 21 November 2024 | Accepted: 3 January 2025

DOI: 10.1002/cjce.25624

RESEARCH ARTICLE

THE CANADIAN JOURNAL OF CHEMICAL ENGINEERING

Effect of nozzle shape on bubble column reactor with constant flow rate

Sachin Kumar[1] | **Raj Kumar Singh**[1] | **Bahni Ray**[2]

[1]Department of Mechanical Engineering, Delhi Technological University, New Delhi, India

[2]Department of Mechanical Engineering, Indian Institute of Technology Delhi, New Delhi, India

Correspondence
Bahni Ray, Department of Mechanical Engineering, Indian Institute of Technology Delhi, New Delhi, India.
Email: bray@iitd.ac.in

Abstract

The present investigation is focused on the bubble formation from different shaped nozzles: straight nozzle, straight converging nozzle, straight diverging nozzle, converging nozzle, and submerged nozzle, with a constant flow rate of 0.008 m/s and static contact angle of 45°, respectively. The effective dimension of the nozzle has been taken as 2 mm radius and 3 mm height. The impact of varying nozzle shapes on changes in bubble volume and the occurrence of different pinch-off times have been observed. A maximum pinch-off time of 1.854 s on straight nozzle and minimum of 0.078 s on converge nozzle with bubble volumes 111.36 mm^3 and 62.12 mm^3 was obtained. Maximum bubble volume attained from diverging nozzle was 123.21 mm^3 with optimum pinch-off time, which is highly useful for bioreactor application.

KEYWORDS

bubble formation, bubble pinch-off, nozzle shape, volume of fluid

1 | INTRODUCTION

In the last few years, researchers have extensively focused on bubble formation and pinch-off time from submerged orifices because it has been applied in many industrial applications like refinement of chemical processing industries, sewage water, and industrial wastewater purification. It is widely used in ocean engineering and microalgae production in bioreactors and photobioreactors.[1] In wastewater treatment, bubble flow is crucial in enhancing dissolved oxygen levels, which is highly beneficial for increasing chemical kinetics in wastewater.[2,3]

Initially, the understanding of bubble behaviour in an air–water system was established through experiments conducted by Pinczewski.[4] This study evaluated the formation of gas bubbles under high injection rates and high system pressure conditions, correlating the terminal rise velocity with bubble volume. Over time, there has been an increasing focus on studying Newtonian fluid behaviour compared to non-Newtonian fluids. Deshpande et al.[5] explored the interaction between leading and trailing bubbles at various flow rates using a Newtonian fluid (water). They introduced the concept of the bubble flow rate number ($N_W = (Bo)(Fr)^{0.5}$, Bo is Bond number, and Fr is Froude number). Some researchers have focused on the forces influencing bubble formation. Pamperin and Rath[6] investigated bubble formation with normal and reduced gravity with different gas flow rates. After a significant period of time, Davidson and Schüler[7] examined bubble motion in viscous liquids, exploring various viscosities and flow rates. Alhendal et al.[8] investigated 3-D bubble formation driven by the Marangoni effect, using both experimental data and simulations with the volume-of-fluid (VOF) method to track bubbles under zero-gravity conditions. Chakraborty et al.[9] studied the coupled level set method and volume of fluid method used to simulate the bubble formation and calculated the buoyancy force effect on bubble formation under reduced gravity conditions g/g_e was in the range of $10^0, 10^{-1}$, and 10^{-2}. Simmons et al.[10] investigated single bubble formation from the mouth of the nozzle at a solid surface that was dipped in an incompressible viscous Newtonian

 © 2025 Canadian Society for Chemical Engineering.

liquid. The study employed the finite element method for simulation, which allowed for tracking the bubble interface and calculating the bubble formation time and volume for a range of orifice radii. Additionally, the Ohnesorge number $\left(Oh = \frac{\mu}{\sqrt{\rho\sigma L}}\right)$ was also calculated to analyze the bubble dynamics and its relation to the liquid's viscosity μ, surface tension σ, and density ρ. Zhang and Tan[11] developed a theoretical model to calculate the bubble volume, weeping rate, and weep point at a submerged orifice and used Oseen's modification to check the potential flow to represent the interaction between the successive bubbles.

Li et al.[12] and Yujie et al.[13] studied the VOF method using multi-orifice setup to observe and analyze the movement of bubbles. As researchers focus on the different wetting angles, Gnyloskurenko et al.,[14] Corchero et al.,[15] Gerlach et al.,[16] Das et al.,[17] Chen et al.,[18] Wang et al.,[19] Chakraborty et al.,[20] and Buwa et al.[21] studied the different wetting conditions of bubbles by using the couple level set/volume of fluid (CLSVOF) method.

Dietrich et al.[22] and Zhu et al.[23] utilized particle image velocimetry (PIV) systems to illustrate bubble formation occurring at both micro and macro scales under low gas flow rates. Their investigations overlooked the influence of gravity while accounting for the forces acting on the bubble during its growth. Liu et al.[24] and Albadawi et al.[25] explored four distinct forms of gas–liquid flow patterns, ascertaining the magnitude of the forces and observing the bubble formation pattern in a specific gas type. Kurimoto et al.,[26] Zhang et al.,[27] and Babu and Das[28] utilized high-speed video cameras to capture images of growing bubbles in both clean and contaminated systems, subsequently determining the bubble's volume, aspect ratio, and contact angle through image processing.

Researchers have also studied the bubble formation behaviour in different fluids in different flow directions and conditions. Tomar et al.[29] presented a coupled level-set (LS) and VOF method for modelling incompressible two-phase flows with surface tension. It was found that for water at near critical condition, a decrease in superheat from 15 to 10 K leads to oscillations with subharmonics influencing the time period of the ebullition cycle. Abbassi et al.[30,31] explored bubble generation in Newtonian and non-Newtonian fluids with varying viscosities using the VOF method under diverse operating conditions, encompassing wetting and non-wetting contact angle variations and higher viscosity solutions. Their findings indicated that the static contact angle did not impact the aspect ratio upon separation. Mohseni et al.[32] conducted experimental investigations into several facets of the bubble formation phenomenon, encompassing bubble size, bubbling frequency, dynamics of bubble growth, and the bubbling regime. Muilwijk and Van den Akker[33] examined experimental results regarding the bubble formation process both with and without liquid co-flow, maintaining a constant chamber Bond number range of 0.1–0.6. Boubendir et al.[34] and Huber et al.[35] investigated the nozzle effect and the behaviour of the contact line, observing variations in detachment time based on nozzle types with different wetting properties. However, Boubendir et al. used the cylindrical microtube to investigate the surface tension under varying gravitational conditions, whereas Huber et al. used different wetting conditions with different orifice materials such as stainless steel and PTFE.[34,35]

A lot of work has been done for bubble formation in submerged orifice, but the effect of orifice shape has not been explored much. Hence, the current research work is mainly focused on different nozzle shape structures and their effect on bubble volume and pinch-off time, emphasizing the different force balances involved. The static contact angle of 45° was used in each nozzle shape to determine the bubble volume and pinch-off time. The study has a major impact on the chemical industries, aeration in bioreactors, and photobioreactors.

2 | COMPUTATIONAL DOMAIN AND MATHEMATICAL MODEL

The study employs an axisymmetric domain to represent bubble formation, featuring a straight nozzle with further converging and diverging sections. As the bubble size gradually increases, multiple forces act upon the bubble. A modest flow rate of 0.008 m/s is used for the investigation. The working fluid is water at 20°C temperature. The bubble formation exhibits axisymmetry, with the origin of the (r, z) coordinate system situated at the centre of the cylinder formed by the nozzle wall. The gas flow rate through the nozzle, characterized by radius R_0, remains constant. Properties of the liquid phase, such as density ρ_l and air density denoted as $\rho_{g,}$ are considered. Surface tension between the liquid and gas phases is assumed to be constant. Additionally, the static contact angle represents the wetting angle between the solid–liquid–gas phases. The simulation involves solving two equations: continuity and Navier–Stokes equations for an incompressible Newtonian fluid, incorporating specific boundary conditions.

2.1 | Mathematical formulation

A fraction called void fraction, symbolized by F, is introduced to denote the portion of liquid within a control

1939019x, 0, Downloaded from https://onlinelibrary.wiley.com/doi/10.1002/cjce.25624 by Delhi Technological University, Wiley Online Library on [05/03/2025]. See the Terms and Conditions (https://onlinelibrary.wiley.com/terms-and-conditions) on Wiley Online Library for rules of use; OA articles are governed by the applicable Creative Commons License

volume (cell). This parameter assumes various values to facilitate the mathematical treatment of the two-phase using a VOF technique. The void fraction assumes different values, aiding in the effective mathematical handling of the two-phase phenomenon:

$$F = \begin{cases} 0 & \text{gas phase cell} \\ 1 & \text{liquid phase cell} \\ 0 < F < 1 & \text{two} - \text{phase cell} \end{cases}$$

By incorporating the void fraction, it becomes feasible to establish a unified set of governing equations for a two-phase flow system. This set of equations comprises continuity and Navier–Stokes equations tailored for incompressible Newtonian fluids. Formulated around the void fraction, these equations encompass both continuity and Navier–Stokes equations.

$$\nabla \cdot v = 0 \tag{1}$$

$$\rho(H)(\partial v|\partial t) + v\nabla v = -\nabla p + \rho(H)g + \nabla.\left[\mu(H)\left(\nabla v + (\nabla v)^T\right)\right] + f_{sv} \tag{2}$$

where v symbolizes the velocity vector, t denotes time, and p stands for pressure. Gravitational acceleration is succinctly expressed as $g = (0, -g)$. Density and dynamic viscosity are elucidated as $\rho(H)$ and $\mu(H)$.

$$\rho(F) = \rho_l(H) + \rho_g(1 - H) \tag{3}$$

$$\mu(F) = \mu_l(H) + \mu_g(1 - H) \tag{4}$$

In simulations of two-phase flows involving liquid and gas, the liquid phase is denoted by l and the gas phase by g. The surface tension force per unit volume, represented by f_{sv}, can be integrated into the momentum equation using the CSF model proposed by Brackbill et al.[36] as follows:

$$f_{sv} = \sigma\kappa(\varphi)\nabla \mathrm{H}(\varphi), \tag{5}$$

where σ denotes the surface tension coefficient, $\kappa(\varphi)$ is local mean curvature, and the Heaviside function is denoted as $H(\varphi)$, defined as follows:

$$H(\varphi) = \begin{cases} 1 & \text{if } \varphi > 0 \\ 0 & \text{otherwise} \end{cases} \tag{6}$$

The signed distance function φ is established as the distance from a specific point to the interface. Positive values denote points within the liquid region ($\varphi > 0$), while negative values signify points within the gas region ($\varphi < 0$). The contour where $\varphi = 0$ precisely delineates the interface. Accordingly, the local mean curvature can be expressed as follows:

$$\kappa = \nabla \cdot \frac{\nabla\varphi}{|\nabla\varphi|} \tag{7}$$

The passively advected void fraction, denoted as F, is expressed as follows:

$$\frac{\partial F}{\partial t} + \mathrm{v} \cdot \nabla F = 0 \tag{8}$$

Employing a coupled VOF and LS technique to track the motion of the air bubble necessitates discretizing the transport equation for the LS function, similar to Equation (8), which offers several advantages:

$$\frac{\partial \varphi}{\partial t} + \mathrm{v} \cdot \nabla \varphi = 0 \tag{9}$$

The equations are discretized following the method described by Gerlach et al.[16] They are defined on a Cartesian grid with uniform spacing and utilize a staggered arrangement for flow variables. Mass conservation is ensured by the coupled VOF and LS method, employing a discretized transport equation and calculating interface normal and curvature. Temporal integration of the continuity and momentum equations is conducted using the second-order Euler time step method. The simulations are conducted using ANSYS Fluent version 2020R1.

2.2 | Computational domain

Figure 1 illustrates the model utilized in this study, with the axisymmetric (r, z) coordinate system centre at the nozzle's mouth. The radius of the orifice is represented as R_0. Symmetry and no-slip boundary conditions are enforced at the nozzle's mouth ($r = 0$) and the corner side ($r = R$) in Figure 1, where $w = 0, u = 0$, respectively. The pressure outlet with zero-gauge pressure is considered at the outlet. Moreover, a parabolic velocity profile in the z-direction is defined as follows:

$$W(\mathrm{r}) = 2w_0\left(1 - r^2/{R_0}^2\right), \tag{10}$$

19390019x, 0, Downloaded from https://onlinelibrary.wiley.com/doi/10.1002/cjce.25624 by Delhi Technological University, Wiley Online Library on [05/03/2025]. See the Terms and Conditions (https://onlinelibrary.wiley.com/terms-and-conditions) on Wiley Online Library for rules of use; OA articles are governed by the applicable Creative Commons License

where $w_0 = \dot{Q}/\pi R_0^2$ represents the average velocity at the nozzle. Initially, the bubble height undergoes fluctuations, but its velocity profile stabilizes as it crosses the nozzle wall. The velocity field maintains no-slip boundary conditions (wall with $u = w = 0$) at the orifice plate. In this scenario, a static contact angle of $\theta = 45^\circ$ is assumed to prevent the bubble from descending below the nozzle periphery at the top surfaces. The computational model measures $20r \times 10r$, where the radius of the orifice is $r = 2$ mm, and the nozzle height is set as $1.5r$. A mesh size of 0.1 mm (Section 5) ensures sufficient resolution for capturing the bubble's contour. The time step has been set to 10^{-6} s (less than the capillary time).

Figure 2 shows different nozzle shapes taken for our study with notation described in Table 1.

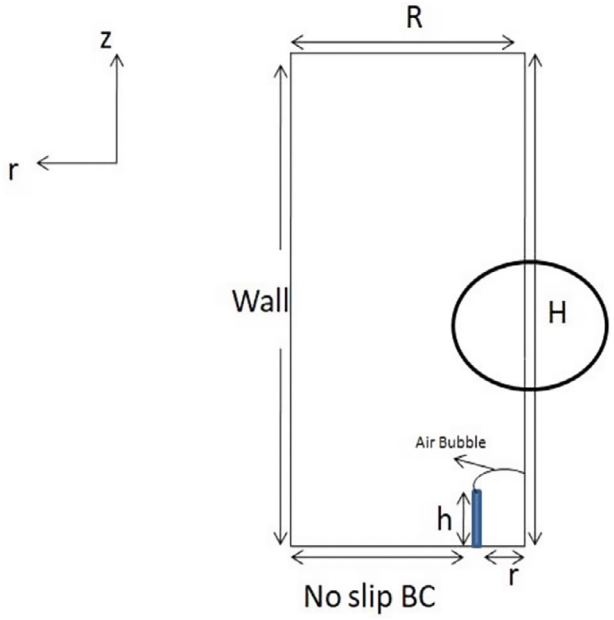

FIGURE 1 Schematic of the computational domain.

3 | VALIDATION

A grid independent test is done, and a mesh size of 0.1 mm is chosen for the simulations, since bubble volume variation from 0.35 mm to 0.1 mm is 8.9% (Table 2).

Figure 3 presents a direct comparison between the bubble shapes obtained from numerical simulations and the experimental results of Zhang and Shoji[37] for $\dot{Q} = 100$ mL/min and $D_0 = 2$ mm. The bubble shapes showed strong qualitative agreement, with excellent alignment in the total formation time, T.

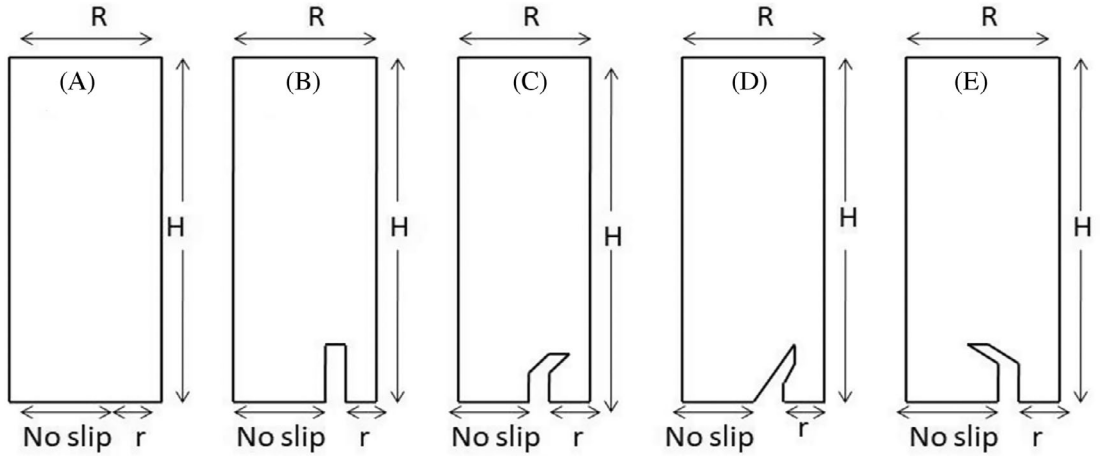

FIGURE 2 Computational domains for different nozzle shapes with constant radius 2 mm and nozzle height 3 mm. (A) Submerged nozzle; (B) straight nozzle; (C) straight converging nozzle; (D) converging nozzle; (E) straight diverging nozzle.

TABLE 1 Nozzle shape specification with different angle.

Type	Nozzle name	Angle with straight nozzle	Full ht. nozzle (mm)	Alignment of nozzle mouth with base
A	Submerged nozzle	-	0	Horizontal
B	Straight nozzle	0°	3	Horizontal
C	Straight converging nozzle	45°	3	Horizontal
D	Converging nozzle	45°	3	Vertical
E	Straight diverging nozzle	135°	3	Horizontal

19390019x, 0, Downloaded from https://onlinelibrary.wiley.com/doi/10.1002/cjce.25624 by Delhi Technological University, Wiley Online Library on [05/03/2025]. See the Terms and Conditions (https://onlinelibrary.wiley.com/terms-and-conditions) on Wiley Online Library for rules of use; OA articles are governed by the applicable Creative Commons License

4 | RESULTS AND DISCUSSION

4.1 | Effect of different nozzle shapes on bubble pressure and bubble velocity

Overall, this numerical result provides the explicit view of bubble formation with different nozzle shapes, which has important applications in various fields such as engineering and biology.[1] According to our data, the pressure exerted due to the nozzle shape has a significant role even when the nozzle height remains constant. Our study showed that the bubble formed through the diverging nozzle attained a maximum pressure difference of 1050 Pascal (Figure 4A) at a bubble apex height of 6 mm compared to other nozzle shapes. This result suggests that the diverging portion required a greater amount of momentum force (1.47×10^{-4} N in Figure 5D) to generate a hemispherical shape of the bubble at $T = 0.15$ s. Converging nozzle bubbles also acquired 1080 Pascal at 6 mm bubble apex height. The diverging and converging nozzle acquired nearly the same maximum pressure at the same height. Other nozzles do not show the peak value at 6 mm (6 mm height is near to pinch off time of bubble with given nozzle

TABLE 2 Mesh-independent study of a submerged orifice with a 2 mm orifice diameter and a static contact angle 45°.

Mesh size (mm)	Nodes	Bubble volume (mm^3)
0.5	1701	244.73
0.35	3460	134.45
0.1	40,501	122.95

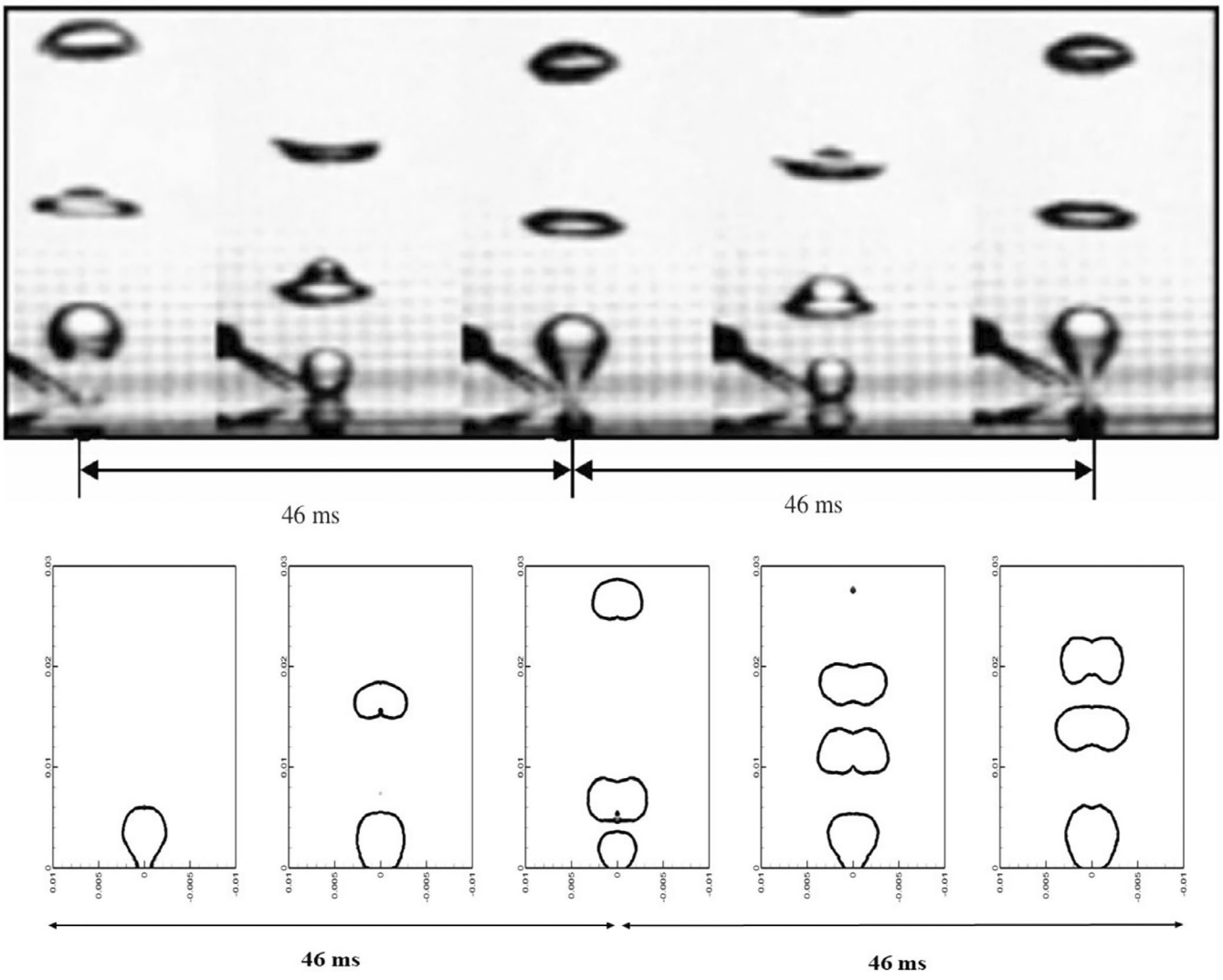

FIGURE 3 Comparison between numerically computed bubble shapes and the experiments of Zhang and Shoji,[37] $Q = 100$ mL/min, $D_0 = 2$ mm.

19390019x, 0, Downloaded from https://onlinelibrary.wiley.com/doi/10.1002/cjce.25624 by Delhi Technological University, Wiley Online Library on [05/03/2025]. See the Terms and Conditions (https://onlinelibrary.wiley.com/terms-and-conditions) on Wiley Online Library for rules of use; OA articles are governed by the applicable Creative Commons License

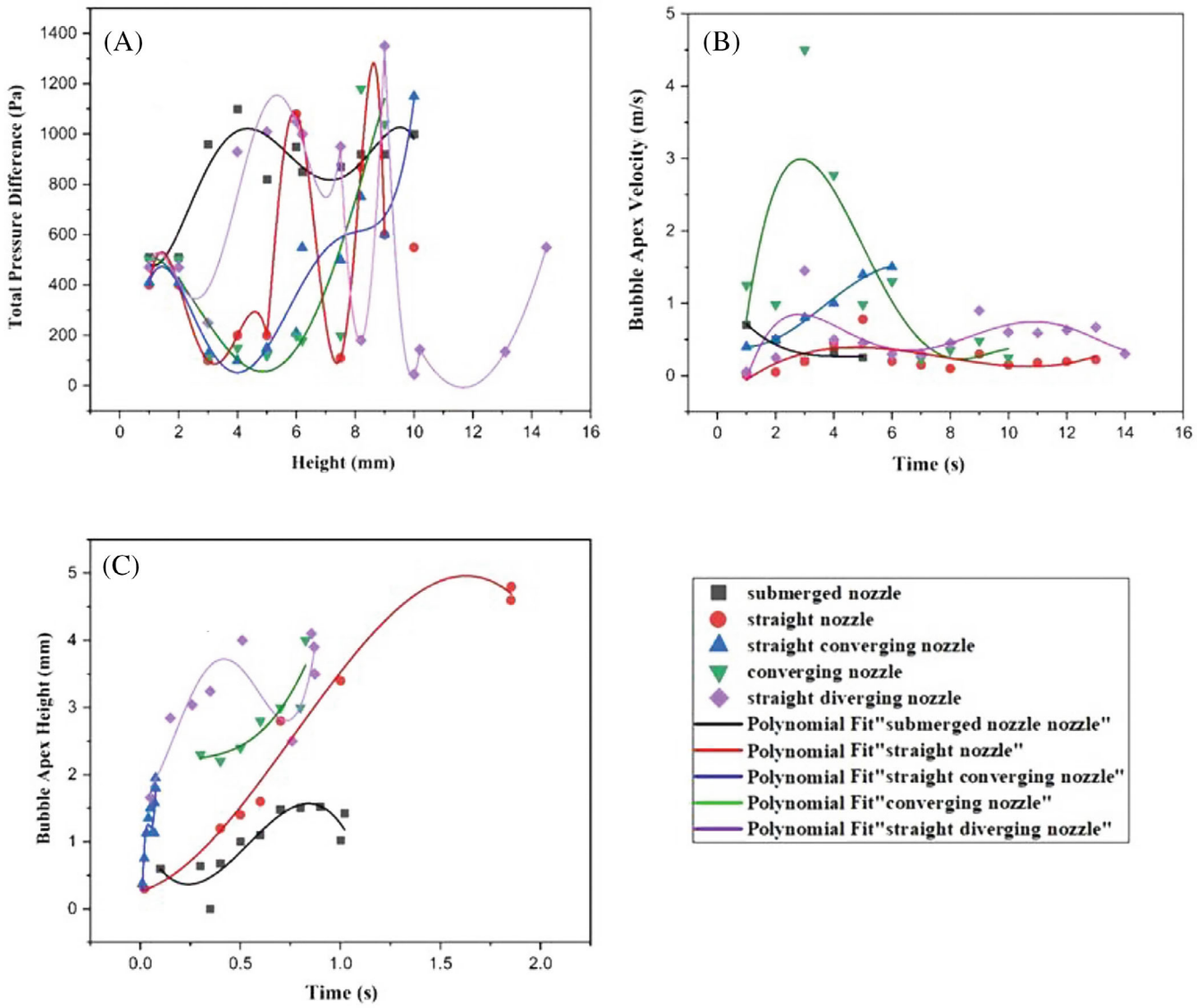

FIGURE 4 (A) Total bubble pressure inside the bubble, (B) bubble apex velocity with height, and (C) bubble apex height with time.

shape). Hence, our data predict that the pressure was maximum in converging or straight diverging nozzles due to the nozzle shape. Therefore, our study indicates that the diverging portion should necessitate more force per unit area for bubble generation. So, it has maximum bubble volume. Figure 4A–C predicted that the nozzle shape creates different apex velocities with different pressure differences, which is useful for maintaining equilibrium between forces. In the converging nozzle, bubble formation occurs in the shortest amount of time (0.826 s), indicating that within the converging section, the bubble attains its maximum velocity (4.5 m/s) at a height of 3 mm inside the nozzle, as depicted in Figure 4B. This velocity is higher when compared to other nozzle shapes. The study's findings also reveal that the apex velocity of the bubble from the converging nozzle is at its maximum. Figure 4B,C shows that bubble velocity and bubble apex height vary with different nozzle shapes. The bubble from straight nozzle attains minimum velocity and maximum bubble apex height. This showed that the upper edge of the nozzle has a great impact on the bubble detachment time. For the converging nozzle, the bubble apex velocity is maximum at 3 mm height of the nozzle. The bubble apex velocity gradually increases and then decreases for all nozzles except the submerged nozzle, where velocity is maximum initially.

The straight diverging nozzle has a similar velocity to a straight nozzle (Figure 4B). It has a maximum value compared to other nozzles, but its apex height is less than a straight nozzle (Figure 4C). Submerged nozzles have a minimum velocity with minimum apex height, which shows that the impact of submerged nozzles on bubble formation is minimal compared to other nozzles. This predicted that the mouth of the nozzle plays an important role. As per our observation

19390019c, 0, Downloaded from https://onlinelibrary.wiley.com/doi/10.1002/cjce.25624 by Delhi Technological University, Wiley Online Library on [05/03/2025]. See the Terms and Conditions (https://onlinelibrary.wiley.com/terms-and-conditions) on Wiley Online Library for rules of use; OA articles are governed by the applicable Creative Commons License

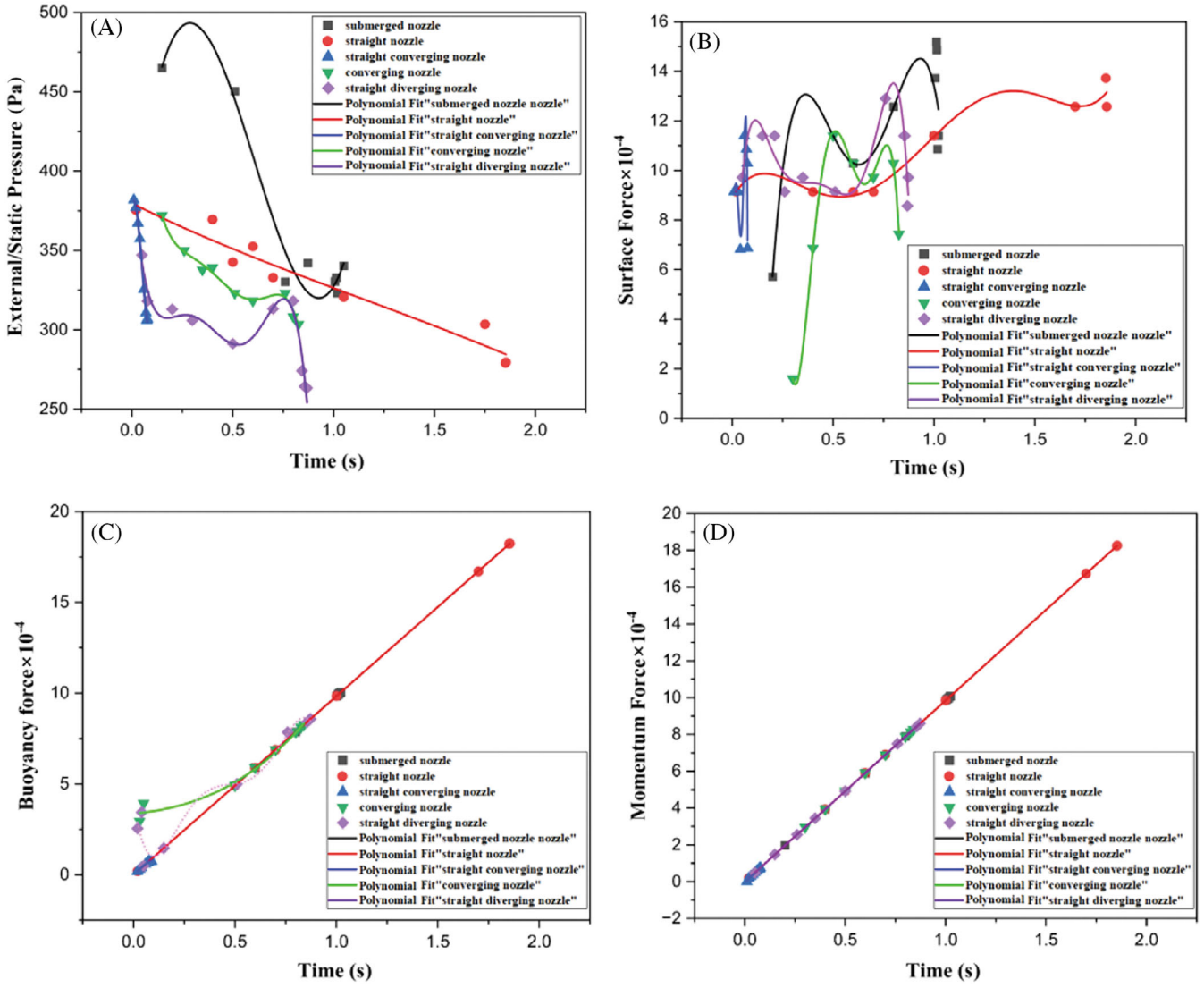

FIGURE 5 (A) Hydrostatic pressure, (B) surface force, (C) buoyancy force, and (D) momentum force.

with different nozzle shapes, straight converging nozzles have a minimum apex height of 8.65 mm with minimum pinch-off time compared to other nozzles. In different nozzle shapes, the minimum pinch-off time in a straight converging nozzle is 0.072 s, which is very beneficial for ring spargers in bioreactors or photobioreactors and many industrial applications.[1–3]

5 | EFFECT OF NOZZLE SHAPES ON DIFFERENT FORCES DURING BUBBLE FORMATION

Our simulation results revealed the interplay of several forces, including surface tension, pressure force, and buoyancy force and hydrostatic pressure force as given in Table 3. We neglect the inertia and drag forces, focusing on the bubble enlargement rather than its movement after detachment. The bubbles are considered spherical shape in all calculations.

TABLE 3 Different forces acting on the bubble.

Hydrostatic pressure force	$P = \rho_l gh$
Surface force	$\sigma = \frac{F}{L}$
Buoyancy force	$F_b = \left(\rho_l - \rho_g\right)gV$
Momentum force	$F = \rho_g A V_0^2$

Within the graph, the minimum buoyancy force (0.757×10^{-4} N in Figure 5C) is observed on a straight converging nozzle, and the surface force (10.29×10^{-4} N in Figure 5B) shows that both buoyancy force and surface

1939019x, 0, Downloaded from https://onlinelibrary.wiley.com/doi/10.1002/cjce.25624 by Delhi Technological University, Wiley Online Library on [05/03/2025]. See the Terms and Conditions (https://onlinelibrary.wiley.com/terms-and-conditions) on Wiley Online Library for rules of use; OA articles are governed by the applicable Creative Commons License

force contribute to detaching the bubble earlier as compared to other nozzle shapes. On the other hand, a straight nozzle takes maximum time to detach as compared to other nozzles, which shows that a straight nozzle has a maximum surface force of 13.72×10^{-4} N in Figure 5B with a maximum buoyancy force of 18.24×10^{-4} N in Figure 5B. The straight diverging nozzle has maximum surface force and buoyancy force, but after some time, buoyancy force gets minimized, and surface force increases to create the maximum surface area. Hence, it is observed that the straight diverging nozzle made a maximum bubble volume as compared to other nozzles, as shown in Figure 5.

The converging nozzle displays less surface force compared to the straight converging nozzle, primarily due to its nozzle shape. This is the key reason for the bubble detachment from the straight converging nozzle. The behaviour of the submerged nozzle is similar to other nozzles, as indicated in Figure 5. Except for the straight converging nozzle or straight diverging nozzle, all nozzles exhibit a linear relationship with buoyancy force. The nozzle shapes also show a linear dependency on momentum force.

The hydrostatic force acting on the bubble is influenced by the container's height. In the initial period, the submerged nozzle experiences the highest hydrostatic pressure (465 Pa in Figure 5A), highlighting the significant influence of nozzle shape on hydrostatic pressure dynamics. The hydrostatic pressure for the straight nozzle decreases as the bubble's height increases. However, it is important to note that the straight nozzle requires a substantial amount of time to reach the pinch-off point. This observation suggests that momentum force plays a crucial role in the behaviour of the straight nozzle.

Figure 5B demonstrates the interplay between internal pressure force and surface force in the context of a straight nozzle. In the case of the surface force, it attempts to reach a maximum value at around 2 s, while the hydrostatic pressure force aims to reach a minimum value around the same time. This behaviour suggests that the hydrostatic pressure is minimized, allowing the surface area of the bubble to expand maximally. This observation aligns with the fundamental principles of bubble physics, and our collected data supports this conclusion. This trend is consistent across different nozzle shapes as well. The nozzle shapes have a quantitative impact on the bubbly flow in the bioreactor application, mainly on the mass transfer coefficient (K_La) since the mass transfer coefficient is inversely proportional to the diameter of an air bubble.

6 | BUBBLE FORMATION FROM DIFFERENT NOZZLE SHAPES

6.1 | Bubble formation from a submerged nozzle

This simulation uses a submerged nozzle with a 2 mm radius and a constant flow rate of 0.008 m/s. The simulation captures the growth of a bubble over time, with results shown for different instants. The buoyancy, pressure, and surface forces acting on the bubble cause its gradual expansion (see Figure 6). Ultimately, the dominant forces of buoyancy and pressure overcome the surface tension; at that time, the bubble tends to detach.[6]

At the initial stage, the bubble rises with a constant velocity and makes an interface inside the water. As time lapses, bubble shape changes due to applied forces inside or outside the bubble interface. At $T = 1.0$ s, a trapezoidal shape bubble is formed, depicting the surface force (11.4×10^{-4} N in Figure 5B) trying to overcome internal pressure force and hydrostatic pressure force (Figure 4A).

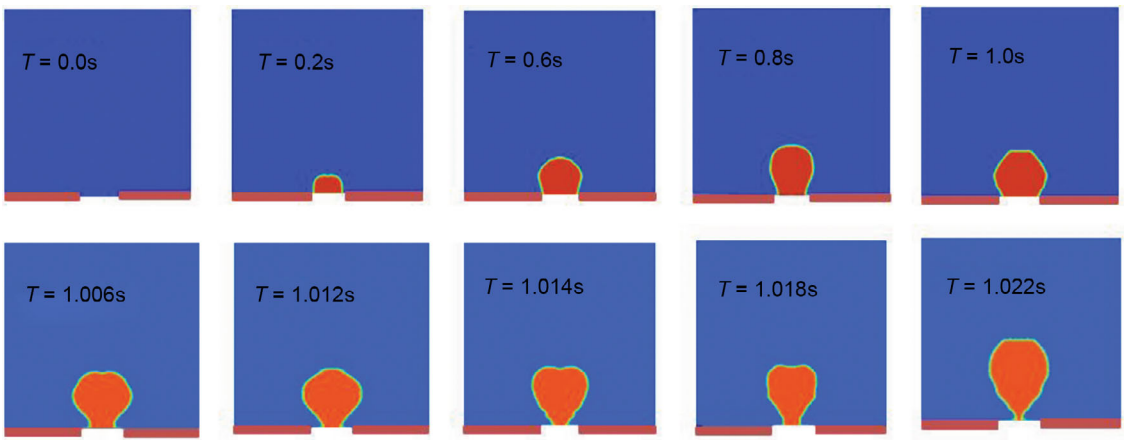

FIGURE 6 Instantaneous bubble shape from a submerged nozzle with an air flow rate of 0.008 m/s.

1939019x, 0, Downloaded from https://onlinelibrary.wiley.com/doi/10.1002/cjce.25624 by Delhi Technological University, Wiley Online Library on [05/03/2025]. See the Terms and Conditions (https://onlinelibrary.wiley.com/terms-and-conditions) on Wiley Online Library for rules of use; OA articles are governed by the applicable Creative Commons License

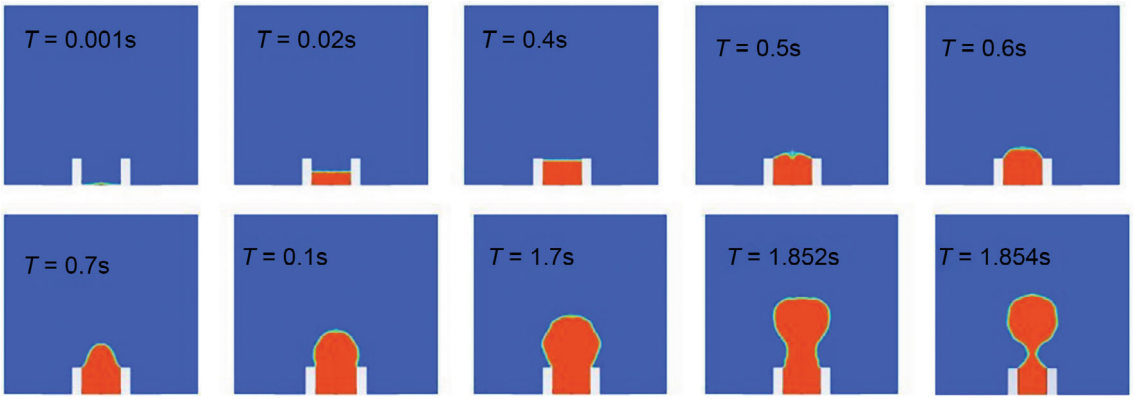

FIGURE 7 Bubble formation from straight nozzle at different time steps with air flow rate 0.008 m/s.

Up to $T = 1.012$ s, the momentum force will be increased, and the bubble shape will attain a curved shape with the start of the neck formation. At $T = 1.014$ s, the bubble shape will be like a heart shape, which predicts that the buoyancy force (9.98×10^{-4} N in Figure 5C) will be dominated by trying to pinch off the bubble. At $T = 1.022$ s, the base of the bubble takes a 'V' shape, which shows that the surface tension force tries to elongate the bubble because the momentum force (10.01×10^{-4} N in Figure 5D) dominates at that time. After that, the bubble has been pinched off.

6.2 | Bubble formation from straight nozzle

Straight nozzle bubble formation and pinch-off are shown in Figure 7. The drag force between the nozzle wall and the liquid is not considered due to the no-slip boundary condition.[38] Initially, it is observed that the injection of air into the nozzle orifice results in a slow increase in air volume due to the high pressure of the surrounding liquid and the surface force. Over time, the air–liquid interface expands and reaches the height of the nozzle wall, with small vortices forming in the liquid Figure 8. Up to 0.4 s, it has been observed that the interface is assumed to be a hemispherical shape due to the counteracting forces of internal pressure (100 Pa) and surface force above 5.717×10^{-4} N (shown in Figures 4 and 5). After that, the liquid–air interface gradually rises with time, and up to 0.5 s, the nozzle length fills with air. The hydrostatic pressure acts higher (346.2 Pa) in Figure 4A in a small region, which initiates vortices at 0.5 s. After that, the bubble tries to make a hemispherical shape and encounters the external pressure (352.45 Pa in Figure 5A) with more force. At that instant of time, the

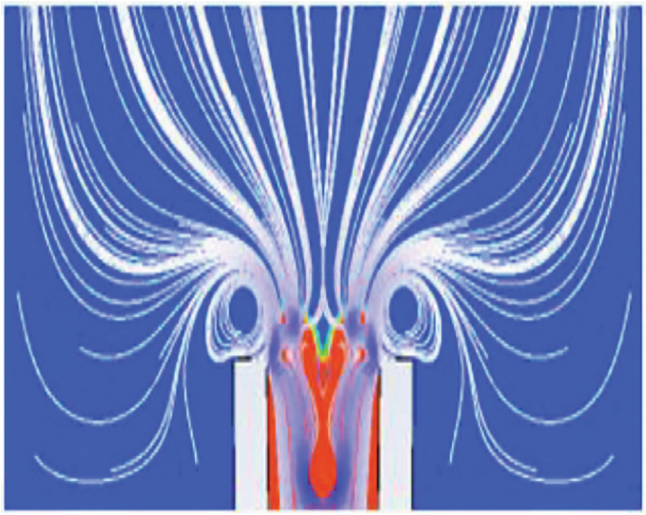

FIGURE 8 Vortex formation during the initial period of time at 0.5 s.

buoyancy force (5.9×10^{-4} N in Figure 5C), which is much higher as compared to the surface tension, causes the bubble to take on an oblate shape as shown at $t = 0.6$ s. It can be concluded that at $t = 1.7$ s onwards, the buoyancy force (16.7×10^{-4} N in Figure 5C) will be acted in an upward direction, and surface tension will be operated in reverse order, which makes the shape of a bubble-like trapezoid (Figure 5B,C). The hydrostatic bubble pressure will counteract the internal bubble pressure. Hence, the hydrostatic external pressure (279.025 Pa) in Figure 4A will get higher than the remaining force. So, the bubble tries to flatten in the upper portion instead of a spherical apex at $T = 1.852$ s. The pinch-off occurs at 1.855 s when the buoyancy force (18.22×10^{-4} N in Figure 5C) counteracts the surface tension and inertia forces.

19390019x, 0, Downloaded from https://onlinelibrary.wiley.com/doi/10.1002/cjce.25624 by Delhi Technological University, Wiley Online Library on [05/03/2025]. See the Terms and Conditions (https://onlinelibrary.wiley.com/terms-and-conditions) on Wiley Online Library for rules of use; OA articles are governed by the applicable Creative Commons License

6.3 | Bubble formation from a straight converging nozzle

In the straight converging nozzle, as the air volume inside the nozzle gradually increases, the air–liquid interface initially rises. At $t = 0.02$ s, the interface centre becomes concave and goes deeper inside Figure 9. The interface fluctuates until $t = 0.03$ s. A vortex is generated similar to the straight nozzle, and a liquid drop is entrapped inside the bubble. As the outlet portion of the nozzle gradually converges to a 1 mm radius, it helps generate a vortex and minimizes the pinch-off time. Due to the interplay between the capillary force and normal force due to the inclined wall, a water drop is formed inside the air bubble.[34] The water drop internal pressure is higher than the internal pressure of the bubble, which is the most significant point in this converged nozzle. A bubble generated from the nozzle tip is hemispherical ($t = 0.04$ s), which indicates that the bubble got into equilibrium with several forces.[27,28] After that, bubble volume increases, and the bubble pinch-off occurs at nearly 0.076 s. The water droplet mixes with the water, and the air bubble moves forward after the pinch-off.

6.4 | Bubble formation from converging nozzle

In this type of nozzle, the base of the nozzle is cylindrical, the upper portion of the nozzle is conical in shape, and the upper edge of the cone is perpendicular to the base of the nozzle, which creates the most significant role in the bubble formation. In the initial period, the air gradually increases and fills the nozzle portion against the cylinder's hydrostatic pressure.[16,23,26] After 0.2 s, the bubble takes a specific shape because the momentum force dominates (8.275×10^{-4} N in Figure 5D), acting against the surface tension. The surface tension force retains the spherical shape of the bubble up to 0.4 s. At 0.5 s, the bubble takes the heart shape due to the normal force component. At 0.6–0.7 s, a bubble's base bulges outward, showing that the surface tension force is maximum in this instant. After 0.8 s, the buoyancy force (8.26×10^{-4} N) and momentum force (8.27×10^{-4} N in Figure 5C,D) reach the maximum, and the bubble elongates due to this force. Thereafter, the bubble is detached from the nozzle and moves upward with the help of buoyancy and pinch-off pressure on the bubble (Figure 10).

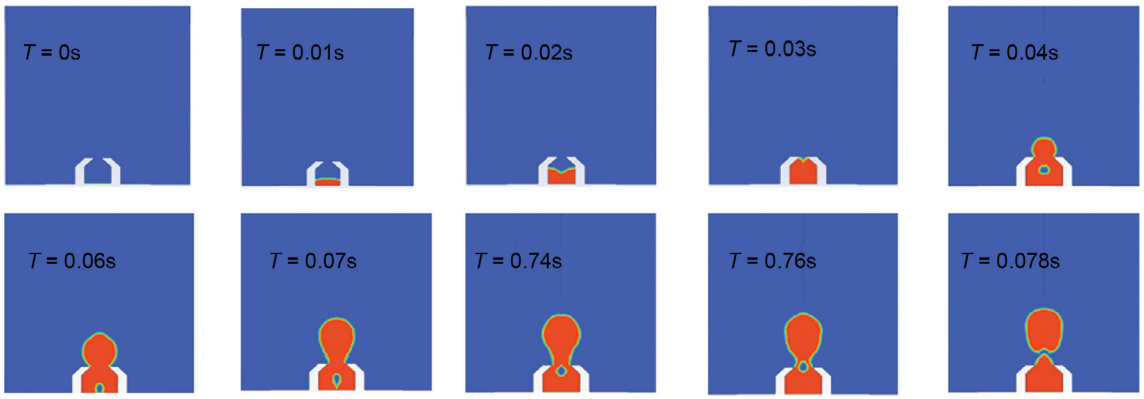

FIGURE 9 Bubble formation from the straight converging nozzle at different time steps with an airflow rate of 0.008 m/s.

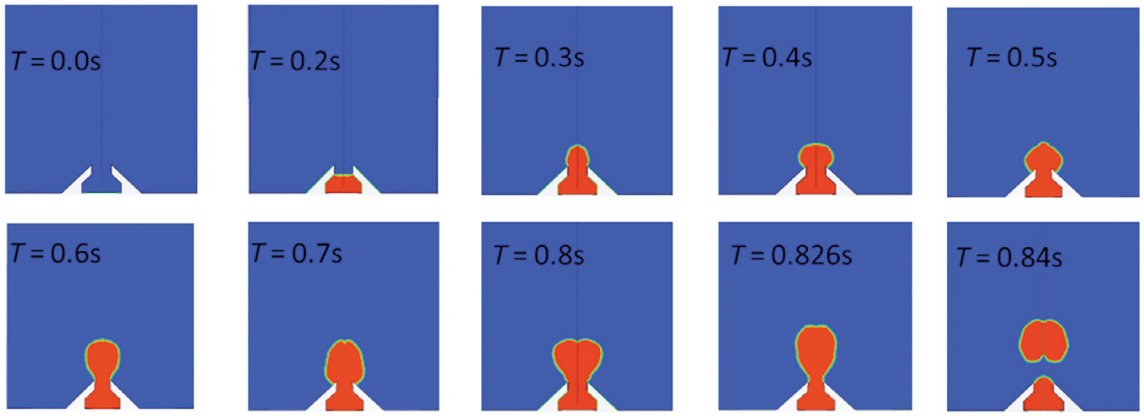

FIGURE 10 Bubble formation of converging nozzle with air flow rate 0.008 m/s.

1939019x, 0, Downloaded from https://onlinelibrary.wiley.com/doi/10.1002/cjce.25624 by Delhi Technological University, Wiley Online Library on [05/03/2025]. See the Terms and Conditions (https://onlinelibrary.wiley.com/terms-and-conditions) on Wiley Online Library for rules of use; OA articles are governed by the applicable Creative Commons License

6.5 | Bubble formation from a straight diverging nozzle

In this case, a bubble is formed using a diverging nozzle with an overall height of 3 mm, a base radius of 2 mm, and a diverging angle of 135°. The nozzle is designed to widen in the upper portion, creating a unique bubble shape[35] (Figure 11). Initially, the bubble forms a hemispherical and then inverted U-shape until $t = 0.35$ s. However, at $t = 0.51$ s, the bubble apex becomes hemispherical, and the base takes the shape of the skirt. This shape provided the information that this bubble has more volume than other nozzle shapes. The nozzle surface area exerts two components of force on the bubble—a normal force that helps create the skirt-like shape and a tangential force that provides the base of the bubble. At $t = 0.76$ s, the bubble flattens out to achieve equilibrium between the forces acting on it. Then, at $t = 0.852$ s, the air gradually increases, causing the bubble to elongate and spread at the base to maintain equilibrium between internal and hydrostatic pressure near 2.2 Pa (see Figures 4 and 5A). The bubble retains the same shape up to $t = 0.856$ s. After $t = 0.868$ s, the buoyancy force reaches its maximum (8.54×10^{-4} N) and attempts to pinch off the bubble from the nozzle.

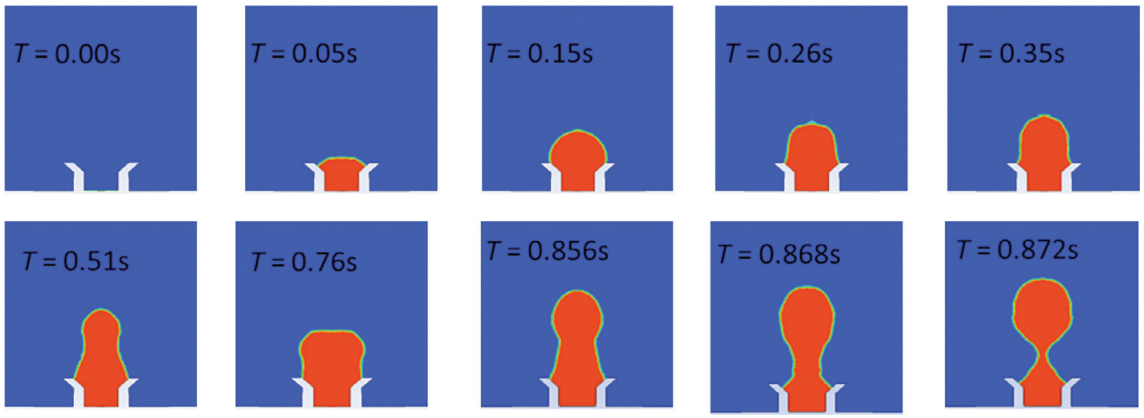

FIGURE 11 Bubble formation of the diverging nozzle with air flow rate 0.008 m/s.

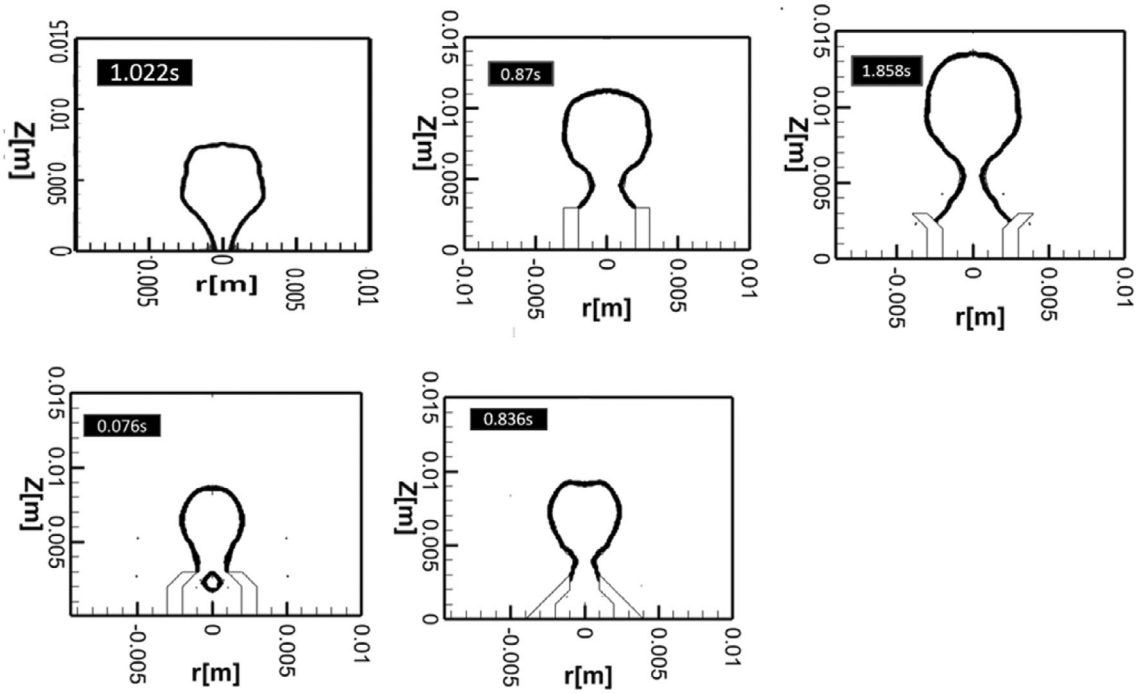

FIGURE 12 Bubble shape before pinch-off with different nozzle shapes.

1939019x, 0, Downloaded from https://onlinelibrary.wiley.com/doi/10.1002/cjce.25624 by Delhi Technological University, Wiley Online Library on [05/03/2025]. See the Terms and Conditions (https://onlinelibrary.wiley.com/terms-and-conditions) on Wiley Online Library for rules of use; OA articles are governed by the applicable Creative Commons License

TABLE 4 Different nozzle shapes with bubble volume and pinch-off time (s).

Nozzle shape	Bubble vol. (mm^3)	Pinch-off time (s)
Straight nozzle	111.36	1.858
Straight converging nozzle	62.12	0.076
Converging nozzle	49.08	0.836
Straight diverging nozzle	123.21	0.872

7 | COMPARISON OF BUBBLE FORMATION FROM DIFFERENT NOZZLE SHAPES

It is observed that the nozzle shape has a high impact on the bubble shape with a constant flow rate, as shown in Figure 12. Every nozzle shape has a different pinch-off time. The detailed specifications of different nozzle shapes with bubble volume, surface area, and pinch-off time are given in Table 4.

The maximum bubble volume is seen for the diverging nozzle, and the maximum pinch-off time is seen for the straight nozzle. The minimum pinch-off time has a straight, converging nozzle, which is a highly beneficial nozzle shape where the requirement of the small bubble with minimum time is like a waste treatment plant, bioreactor, photobioreactor, and many more applications.

Here the particular shapes have been designed since the most important factor coming into picture is when water droplet enters into the air bubble due to contact pressure force. This equation is as follows:

$$F_{CP} = \pi r_0^2 \left(P_g - P_T\right),$$

where F_{CP} is contact pressure force, P_g is gas pressure, P_T is bubble tip pressure, and r_0 is radius of orifice.

The height of the nozzle shape was considered as 3 mm because the bubble formation was not observed in every nozzle shape when the height of the nozzle shape was increased or decreased from 3 mm. As we can observe, when the height of the nozzle shape was increased beyond 3 mm, in the above equation, if P_g is smaller than P_T, then negative pressure is generated at the bubble tip (as shown in Figure S1B). This creates the tendency of the water droplet to enter into the air bubble, due to which bubble formation does not take place.

8 | CONCLUSION

This study has concluded that the bubble formation for the different shaped nozzles with constant height produces a different bubble volume at a constant static angle of 45°. The study revealed that the bubble shape also varies with the nozzle shape (nozzle mouth), demonstrating that the pinch-off time also changes. Different forces like hydrostatic force, surface tension force, momentum force, and buoyancy force are calculated, and their impact on the bubble is shown.

It is observed that the longest pinch-off time occurred with the straight nozzle, reaching 1.858 s. This duration suggests that the maximum inertia force acts on the straight nozzle at a constant height. That is why the momentum force has attained its maximum value of 18.26×10^{-4} N. The straight nozzle attained a bubble volume of 111.36 mm^3. On the other hand, the diverging nozzle had maximum volume of 123.21 mm^3 with optimum time of 0.872 s. Both nozzles have major impact on bubble column reactor. Since straight nozzle has high residence time of bubble, this suggests that the chemical reaction inside the bioreactor or column reactor will be more fruitful. In diverging nozzle, having maximum bubble volume which enhances the surface area of the bubble is good for a fast rate of reaction. Hence, it is concluded that both nozzles have their own specification depending on the utility of the reactor.

In the case of the diverging nozzle, although the bubble volume is 123.21 mm^3, the pinch-off time reaches 0.872 s. This scenario suggests that the buoyancy force or surface force is maximized in the straight nozzle. Hence, a straight nozzle does not achieve a higher volume since external pressure is higher than a diverging nozzle. The diverging nozzle region has maximum volume with less buoyancy or momentum force since it has low external pressure compared to other nozzle shapes. This predicts that the bubble volume of the diverging nozzle is maximized due to less external pressure force. The differences in bubble volume and nozzle shape have significant implications for industrial applications, highlighting the importance of nozzle selection based on specific requirements and objectives.

NOMENCLATURE

A	area of orifice (m^2)
a	acceleration of the particle (m/s^2)
ρ_l	density of liquid (kg/m^3)
ρ_g	density of gas (kg/m^3)
F	void fraction
F_b	buoyancy force (N)
f_{wns}	force per unit line acting at the contact line (N/m)
f_{sv}	surface tension force per unit volume
F_m	momentum force
F_p	pressure force
F_s	surface tension force

1939019x, 0, Downloaded from https://onlinelibrary.wiley.com/doi/10.1002/cjce.25624 by Delhi Technological University, Wiley Online Library on [05/03/2025]. See the Terms and Conditions (https://onlinelibrary.wiley.com/terms-and-conditions) on Wiley Online Library for rules of use; OA articles are governed by the applicable Creative Commons License

F_h	hydrostatic pressure
g	gravitational acceleration (m/s^2)
H	heavy side function
L	perimeter of bubble (m)
m	mass of the particle (kg)
N	Newton (unit of force)
Pa	Pascal (unit of pressure)
P	pressure
r	radial component of cylindrical polar coordinate
R	extension of computational domain in r- r-direction
R_0	orifice radius (m)
T	formation time period (s)
v	velocity vector
V_0	inlet velocity of air (m/s)
V	volume of the bubble (m^3)
z	vertical component of cylindrical polar coordinate
Z	extension of computational domain in z-direction

Greek letters

θ	angle of solid edge
κ	local mean curvature
μ	dynamic viscosity
ρ	density
σ	surface tension
$\emptyset$	level set function
φ	contact angle

AUTHOR CONTRIBUTIONS

Sachin Kumar: Writing – original draft; conceptualization; data curation; formal analysis; investigation. **Raj Kumar Singh:** Supervision; software. **Bahni Ray:** Supervision; writing – review and editing; validation.

ACKNOWLEDGEMENTS

The authors are thankful to Design Centre Lab, Department of Mechanical Engineering, Delhi technological University for providing lab facility and access to the software Ansys Fluent 2022R1. The authors did not receive any funding to conduct the current research work.

PEER REVIEW

The peer review history for this article is available at https://www.webofscience.com/api/gateway/wos/peer-review/10.1002/cjce.25624.

DATA AVAILABILITY STATEMENT

The data that support the findings of this study are available from the corresponding author upon reasonable request.

ORCID

Sachin Kumar https://orcid.org/0009-0008-4356-0223

REFERENCES

[1] Z. Yao, H. Xu, J. Li, T. Xu, *Chem. Eng. Res. Des.* **2023**, *189*, 680.
[2] Z. Liu, B. Li, F. Qi, S. C. P. Cheung, *Powder Technol.* **2017**, *319*, 139.
[3] P. Krýsa, M. Šoóš, *Int. J. Heat Mass Transfer* **2022**, *199*, 123466.
[4] W. V. Pinczewski, *Chem. Eng. Sci.* **1981**, *36*, 405.
[5] D. A. Deshpande, M. D. Deo, F. V. Hanson, A. G. Oblad, *Chem. Eng. Sci.* **1992**, *47*, 1669.
[6] O. Pamperin, H. J. Rath, *Chem. Eng. Sci.* **1995**, *50*, 3009.
[7] J. F. Davidson, B. O. G. Schüler, *Chem. Eng. Res. Des.* **1997**, *75*, S105.
[8] Y. Alhendal, A. Turan, P. Hollingsworth, *Acta Astronaut.* **2013**, *88*, 108.
[9] I. Chakraborty, B. Ray, G. Biswas, F. Durst, A. Sharma, P. S. Ghoshdastidar, *Phys. Fluids* **2009**, *21*, 6.
[10] J. A. Simmons, J. E. Sprittles, Y. D. Shikhmurzaev, *Eur. J. Mech. B/Fluids* **2015**, *53*, 24.
[11] W. Zhang, R. B. H. Tan, *Chem. Eng. Sci.* **2000**, *55*, 6243.
[12] Y. Li, G. Q. Yang, J. P. Zhang, L. S. Fan, *Powder Technol.* **2001**, *116*, 246.
[13] Z. Yujie, L. Mingyan, X. Yonggui, T. Can, *Chem. Eng. Sci.* **2012**, *73*, 55.
[14] S. V. Gnyloskurenko, A. V. Byakova, O. I. Raychenko, T. Nakamura, *Colloids Surf., A* **2003**, *218*, 73.
[15] G. Corchero, A. Medina, F. J. Higuera, *Colloids Surf., A* **2006**, *290*, 41.
[16] D. Gerlach, N. Alleborn, V. Buwa, F. Durst, *Chem. Eng. Sci.* **2007**, *62*, 2109.
[17] A. K. Das, P. K. Das, P. Saha, *Exp. Therm. Fluid Sci.* **2011**, *35*, 618.
[18] N. Chen, X. Chen, A. Delgado, *Adv. Mater. Sci. Eng.* **2020**, *2020*, 5213234.
[19] T. Wang, H. X. Li, J. F. Zhao, K. K. Guo, *Microgravity Sci. Technol.* **2019**, *31*, 279.
[20] I. Chakraborty, G. Biswas, P. S. Ghoshdastidar, *Int. J. Heat Mass Transfer* **2013**, *58*, 240.
[21] V. V. Buwa, D. Gerlach, F. Durst, E. Schlücker, *Chem. Eng. Sci.* **2007**, *62*, 7119.
[22] N. Dietrich, N. Mayoufi, S. Poncin, N. Midoux, H. Z. Li, *Chem. Eng. Sci.* **2013**, *92*, 118.
[23] X. Zhu, J. Xie, Q. Liao, R. Chen, H. Wang, *Int. J. Heat Mass Transfer* **2014**, *68*, 324.
[24] C. Liu, B. Liang, S. Tang, E. Min, *Chin. J. Chem. Eng.* **2013**, *21*, 1206.
[25] A. Albadawi, D. B. Donoghue, A. J. Robinson, D. B. Murray, Y. M. C. Delauré, *Chem. Eng. Sci.* **2013**, *90*, 77.
[26] R. Kurimoto, T. Yasuda, H. Minagawa, *Chem. Eng. Process.* **2016**, *104*, 154.
[27] J. Zhang, Y. Yu, J. Hu, *K. Cheng Je Wu Li Hsueh Pao/Journal Eng. Thermophys.* **2018**, *39*, 561.
[28] R. Babu, M. K. Das, *Chem. Eng. Sci.* **2018**, *179*, 172.
[29] G. Tomar, G. Biswas, A. Sharma, A. Agrawal, *Phys. Fluids* **2005**, *17*, 1.
[30] W. Abbassi, S. Besbes, M. El Hajem, H. Ben Aissia, J. Y. Champagne, J. Jay, *Eur. J. Mech. B/Fluids* **2017**, *65*, 284.
[31] W. Abbassi, S. Besbes, M. Elhajem, H. Ben Aissia, J. Y. Champagne, *Comput. Fluids* **2018**, *161*, 47.
[32] E. Mohseni, T. Ziegenhein, S. F. Reinecke, U. Hampel, *Chem. Eng. Sci.* **2021**, *242*, 116698.

1939019x, 0, Downloaded from https://onlinelibrary.wiley.com/doi/10.1002/cjce.25624 by Delhi Technological University, Wiley Online Library on [05/03/2025]. See the Terms and Conditions (https://onlinelibrary.wiley.com/terms-and-conditions) on Wiley Online Library for rules of use; OA articles are governed by the applicable Creative Commons License

[33] C. Muilwijk, H. E. A. Van den Akker, *Chem. Eng. Sci.* **2019**, *202*, 318.
[34] L. Boubendir, S. Chikh, L. Tadrist, *Int. J. Multiphase Flow* **2020**, *124*, 103196.
[35] M. Huber, D. Dobesch, P. Kunz, M. Hirschler, U. Nieken, *Chem. Eng. Sci.* **2016**, *152*, 151.
[36] J. Brackbill, D. Kothe, C. Zemach, *J. Comput. Phys.* **1992**, *100*, 335.
[37] L. Zhang, M. Shoji, *Chem. Eng. Sci.* **2001**, *56*, 5371.
[38] S. Kumar, R. K. Singh, B. Ray, *Biennial International Conference on Future Learning Aspects of Mechanical Engineering*, Springer Nature Singapore, Singapore **2023**, p. 213.

SUPPORTING INFORMATION

Additional supporting information can be found online in the Supporting Information section at the end of this article.

How to cite this article: S. Kumar, R. K. Singh, B. Ray, *Can. J. Chem. Eng.* **2025**, 1. https://doi.org/10.1002/cjce.25624

1939019x, 0, Downloaded from https://onlinelibrary.wiley.com/doi/10.1002/cjce.25624 by Delhi Technological University, Wiley Online Library on [05/03/2025]. See the Terms and Conditions (https://onlinelibrary.wiley.com/terms-and-conditions) on Wiley Online Library for rules of use; OA articles are governed by the applicable Creative Commons License

Check for updates

ChemistrySelect

Research Article
doi.org/10.1002/slct.202403122

Chemistry Europe
European Chemical Societies Publishing

www.chemistryselect.org

Effect of Substitutional Doping and Cu Adsorption on MoS_2Nanowire: A Comparative DFT Study

Anurag Bhandari,[a] Piyush Dua,[b] and Nitin K. Puri*[a, c]

In this study, we have investigated the effect of substitutional doped (Cu-doped MoS_2NW) and surface-adsorbed Cu atom (Cu-MoS_2NW) on the electronic properties of MoS_2 nanowire (NW) using Density Functional Theory (DFT). Our adsorption study revealed that the adsorption of the Cu atom was a chemisorption. Electron Localization Function (ELF) analysis indicates that the Cu atom formed a covalent and ionic bond with MoS_2NW upon adsorption and substitutional doping, respectively. These findings indicate that a charge transfer occurred between the Cu atom and MoS_2NW during the interaction, confirmed by the Bader charge method. Further, the work function calculation indicates that Cu-doped MoS_2NW exhibits a large negative variation in the work function, indicating enhanced electron emission capability of the Cu-doped MoS_2NW systems. All of our systems are thermodynamically stable based on our cohesive energy calculations. Overall, the DFT results suggest that Cu-doped MoS_2NW systems exhibit superior electrical conductivity, enhanced charge transfer, and larger variation in the work function compared to pristine MoS_2NW and Cu-MoS_2NW. These findings confirmed that substitutional doping is an effective way to modify the electronic properties of MoS_2NW. Therefore, Cu-doped MoS_2NW systems hold potential for applications in field emission and nanoelectronics devices.

1. Introduction

Two-dimensional (2D) materials such as graphene,[1] hexagonal boron nitride(hBN),[2] Transition metal dichalcogenides (TMDs),[3] and black phosphorene[4] have attracted considerable attention for both the theoretician and experimentalists due to their wide range of application in the various nanoelectronics and optoelectronics devices. Therefore, among the various 2D materials, MoS_2 which is a layered transition metal dichalcogenide formed by the vertical stacking of weakly coupled S-Mo-S layers has attracted considerable interest of the researchers due to their unique physical, catalytic, optical, and electronic properties they are finding their applications in the field of hydrogen evolution reaction (HER),[5] storage,[6] gas sensors,[7] catalysis, energy conversion,[8] photodetectors,[9] photocatalysis, photoelectrochemical and stretchable electronics. Contrary to graphene zero band gap limitations, MoS_2, in its bulk form, is an indirect band semiconductor with a band gap value of 1.2 eV, whereas an atomically thin layer of MoS_2 is a direct band semiconductor with a band gap value of 1.8 eV.[10] As a consequence, MoS_2 exhibits basic properties like gate control, wide band gap, high current capability, and good electrical transport. All these findings suggest that MoS_2 can serve as an alternative to graphene for the application of nanoelectronics and optoelectronics. Currently, the trend in the research is primarily focused on utilizing 2D materials to their maximum potential in various applications. However despite such advances MoS_2 also exhibit low electron mobility compared to graphene[11] which hinder their practical implementation in various nanoelectronics devices like transparent electrode etc. Therefore, there is a need to modulate the intrinsic properties of MoS_2 to make them fit for practical use. In this regard, researchers have adopted various effective methods to modulate the intrinsic properties of materials, such as defect engineering,[12] substitutional doping,[13] adatom adsorption,[14] and substrate engineering.[15] Among the various methods, it has been well proven that the adsorption of transition metal (TM) atoms onto 2D material effectively modulates the intrinsic properties of 2D materials. For example- Xu et al. studied the adsorption of various alkali metals (Li, Na), alkaline earth metals (Be, Mg), 3d TM atoms (Ti, V, Cr, Mn, Fe, Co), and precious metals (Ag, Au, Pt) onto dumbbell C_4N.[16] Their study revealed that the adsorption of the above-mentioned metals opens the zero-band gap of dumbbell C_4N, making it a promising candidate for electronic devices. Similarly, Zhang et al. studied the structural, electronic, magnetic, and optical properties of 4d TM atoms adsorbed onto blue phosphorene.[17] Their study revealed that adsorbing 4dTM onto blue phosphorene effectively modifies blue phosphorene's structural, electronic, magnetic, and optical properties. On the other side, there have been various reports regarding the adsorption of various TM atoms onto the MoS_2 monolayer for various applications. Kadioglu et al. investigated the adsorption of Au, Cu, and Au_xCu_y nanoclusters on MoS_2 monolayer for sensing CO and H_2O.[18] Their results revealed that the adsorption of Au, Cu, and AuxCuy nanoclusters onto the

[a] A. Bhandari, Prof. N. K. Puri
Department of Applied Physics, Delhi Technological University, New Delhi 110042, India
E-mail: nitinkumarpuri@dtu.ac.in

[b] Dr. P. Dua
Department of Applied Sciences, DBS Global University, Mi-122, behind Pharma City, Selakui, Central Hope Town, Dehradun, Uttarakhand 248011, India

[c] Prof. N. K. Puri
National Institute of Electronics & Information Technology (NIELIT), Patna 801106, India

© 2025 Wiley-VCH GmbH

MoS_2 monolayer enhanced the chemical activity and sensitivity towards CO and H_2O molecules. Sharma et al. investigated the catalytic activity of Cu-embedded MoS_2 monolayer for CO.[19] They found that the basal plane of the MoS_2 sheet gets activated upon substitutional doping of the Cu atom at S vacancy, which catalyzes the oxidation of CO effectively without poisoning. Rawal et al. studied the effects of defect on the catalytic activity of the 29 adatoms of Cu, Ag, and Au nanoparticles (NP) onto MoS_2 monolayer towards CO.[20] Wang et al. investigated the structural, electronic, and magnetic properties of adsorbed transition metal from Sc to Zn onto MoS_2 monolayer using DFT. They conclude that all the TM atoms got adsorbed chemically except Zn, whereas the electronic and magnetic properties of the MoS_2 monolayer can be effectively modified by adsorbing different TM atoms. Thus, TM adsorbed MoS_2 monolayer can be utilized for spintronics.[21] In another study, Li et al. emphasized that the adsorption of alkali metal, alkaline earth metals, 3d TM, noble metal, and non-metal atoms induce magnetic moments and transforms the band gap from semiconductor to metallic, semi-metallic, making them promising candidates for spintronics and electronic devices.[22] Moreover, Joseph et al. synthesized Cu-doped MoS_2 hydrothermally to analyze the effect of Cu doping on the thermoelectric properties of MoS_2.[23] Recently, Zhou et al.[24] reported a method for selectively exposing and activating the inert basal planes of 2H-MoS_2 for CO_2 hydrogenation to methanol, achieved through the physically constrained sulfidation of ultrafine MoO_2 nanocores into hollow, few layer MoS_2 spheres within a mesoporous silica framework. The spherical curvature of MoS_2 induces strain and sulfur vacancies (S_v) on the typically inactive basal planes. This increases the exposure of in-plane sulfur vacancies while minimizing the exposure of edge vacancies, significantly enhancing its catalytic performance in synthesizing CH_3OH from the hydrogenation of CO_2. In contrast, the adsorption of the Cu atom onto MoS_2 facilitated the activation of H_2, delivering a remarkable CH_3OH production rate of 6.11 $mol{\cdot}molMo^{-1}{\cdot}h^{-1}$ and a high CH_3OH selectivity of 72.5% under reaction conditions of 260 °C, 5 MPa, and 24000 $mL{\cdot}gcat^{-1}{\cdot}h^{-1}$. They conclude that the Cu/MoS_2/SiO_2 catalyst demonstrates excellent stability, maintaining its silica-encapsulated hollow core-shell structure throughout the reaction process. Wang et al. studied the electrocatalytic activity of the Cu-decorated MoS_2 monolayer paving the way for application in electronics and energy storage.[25] The above literature survey suggests that there exists a plethora of literature regarding the Cu decoration onto various MoS_2 nanostructures. However, to the best of the author's knowledge, there have been no reports regarding the effect of substitutional doping (Cu-doped MoS_2NW) and surface-adsorbed Cu atom (Cu-MoS_2NW) on the electronic properties of MoS_2 NW. This reported gap in the research motivated us to investigate the electronic properties of MoS_2 NW upon substitutional doping and surface-adsorption of Cu atom. Therefore, in this work, we have extensively investigated the effect of substitutional doping and surface-adsorption of Cu atoms onto electronic properties of MoS_2 NW using DFT. We have selected the Cu atom as a dopant for this study because it has been well proved experimentally that it has good chemistry with MoS_2.The adsorption of the Cu atom was analyzed by calculating the adsorption energy and distances. In addition, the electronic properties and conductivity of the Cu-decorated MoS_2 NW were calculated through DOS, PDOS, and work function. Further, the structure stability of the optimized Cu-decorated MoS_2 NW structures nature of the bond formation, and the charge transfer mechanism during the Cu interaction with MoS_2 NW were analyzed utilizing cohesive energy, ELF, and the Bader charge method. Finally, we have compared our calculated DFT results for both the systems.

2. Methodology

2.1. Computational Details

We have used the Linear Combination of Atomic Orbital (LCAO) calculator in the Quantum ATK[26] package to ensure accuracy while calculating the electronic properties of the various optimized structures. To approximate the nucleus and valence electrons interaction, the Fritz-Haber-Institute (FHI)[27] pseudopotential was implemented. For transition metals (TM) atoms such as Cu and Mo, the Double Zeta Polarized (DZP)[28] basis set was considered to ensure accuracy during the calculation. To consider the electron-electron interaction effectively, we have considered Generalized Gradient approximation (GGA)[29] with the predefined function Perdew Burke Ernzheof (PBE)[30] as an exchange-correlation function (XC). Further, we have selected 200 Ha (400 eV) and 10^{-6} eV as the cutoff energy and energy convergence criteria for the ground state energy calculation. According to the Monhorst-Pack grid scheme, we have implemented $1 \times 1 \times 51$ K points for calculating the density of states (DOS). For the adsorption study, MoS_2 NW was grown along the Z axis by continuously repeating the 1×1 unit cell of MoS_2 monolayer four times along the X and Y directions, resulting in 4×4 supercells. The 4×4 supercells contain 16 Mo and 32 S atoms with a vacuum layer of 10 Å was applied along the X and Y directions to prevent interactions between the adjacent periodic replicas. Equations (1) and (2) were used to determine the strength of the interaction during the adsorption of the Cu atom onto the surface of MoS_2 NW and the thermodynamic stability of the various adsorption configurations, respectively.

$$E_{ads} = E_{Total} - E_{(MoS_2)} - E_{(Cu)} \quad (1)$$

$$E_{coh} = \frac{E_{(MoS_2)} - \left[n_{Mo}E_{Mo} + n_{(S)}E_S\right]}{N} \quad (2)$$

where E_{Total} represents the total energy of the Cu adsorbed MoS_2 NW, $E_{(MoS_2)}$ represents the energy of the MoS_2 NW, $E_{(Cu)}$ represents the energy of the isolated copper atom,$E_{(s)}$represents the energy of the isolated sulfur atom, $E_{(Mo)}$ represent the energy of the isolated Mo atom, $n_{(Mo)}$, $n_{(S)}$, represents the number of Mo and S atoms, and N represents the total atoms within the system, respectively.

© 2025 Wiley-VCH GmbH

23656549, 2025, 7, Downloaded from https://chemistry-europe.onlinelibrary.wiley.com/doi/10.1002/slct.202403122 by Delhi Technological University, Wiley Online Library on [05/03/2025]. See the Terms and Conditions (https://onlinelibrary.wiley.com/terms-and-conditions) on Wiley Online Library for rules of use; OA articles are governed by the applicable Creative Commons License

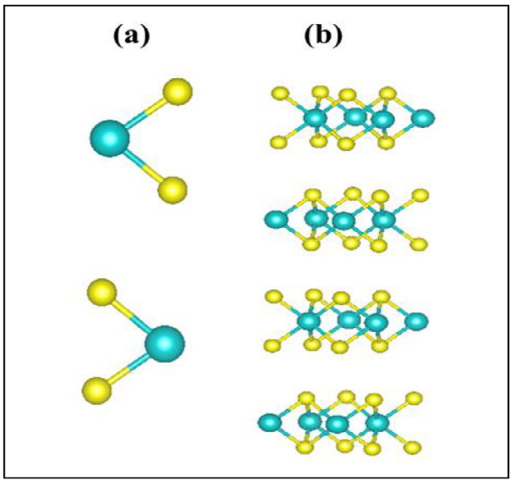

Figure 1. Optimized (a) MoS_2 monolayer and (b) MoS_2 NW structure. The atoms in yellow and cyan colors represent the S and Mo atoms, respectively.

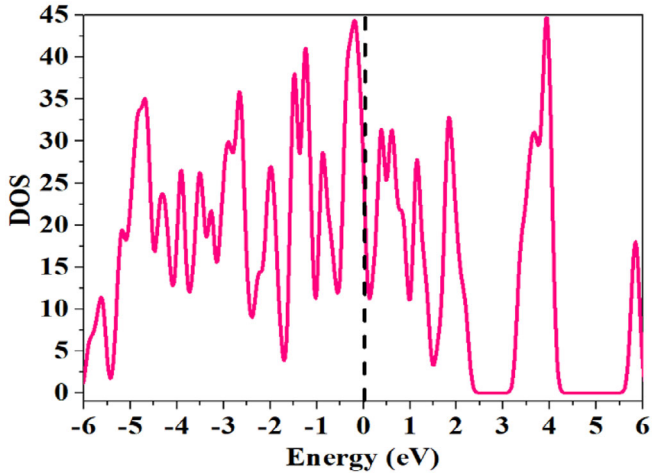

Figure 3. DOS plot for the MoS_2 NW. The black dotted line represents the fermi level set to zero for reference.

3. Results and Discussion

3.1. Structure and Electronic Properties Analysis of MoS_2 Monolayer and MoS_2 NW

To investigate the differences in the geometrical and electronic properties of the MoS_2 monolayer and MoS_2 NW. For this purpose, initially, we optimized the geometry. After optimization, the resulting optimized lattice parameters for the optimized MoS_2 monolayer were $a = 3.244$ Å and $c = 12.880$ Å with a c/a ratio of 3.97, consistent with the previous theoretical calculation.[31] Further, the band structure was plotted for the optimized MoS_2 monolayer. The resulting band structure in Figure 2a illustrates that the MoS_2 monolayer exhibits a direct band gap of about 1.56 eV, verified from the DOS plot in Figure 2b and agreed with the previously reported theoretical studies.[32] In the optimized MoS_2 NW shown in Figure 1b, each S atom is coordinated with multiple Mo atoms, resulting in a distorted octahedral arrangement of atoms within the layer, confirming the existence of 1T phase in MoS_2 NW. This type of structural arrangement of atoms within the layer facilitates high tensile strength and significant overlapping between the d orbitals of Mo atoms, facilitating a pathway for efficient electron movement, which is advantageous for the application of field effect transistor,[33] energy storage,[34] and as a catalyst in electrochemical reactions.[35] The diameter, height, and Mo—S bond length for the optimized MoS_2 NW were 7.44 Å, 20 Å, and 2.35 Å, respectively. Moreover, the resulting DOS plot in Figure 3 illustrates the existence of continuous impurity states near the Fermi

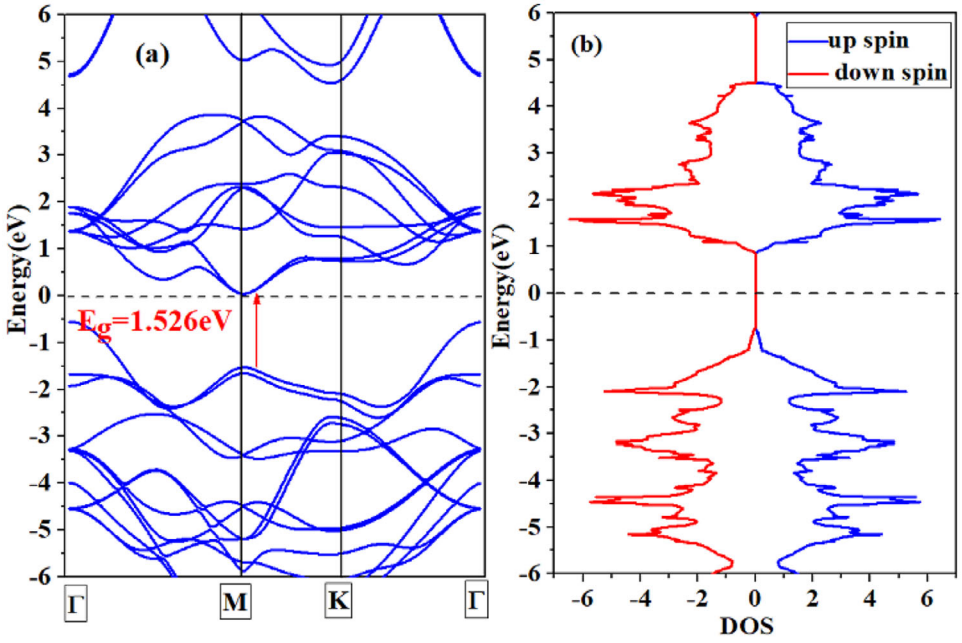

Figure 2. Plotted (a) Band structure and (b) DOS for the MoS_2 monolayer respectively.

© 2025 Wiley-VCH GmbH

23656549, 2025, 7, Downloaded from https://chemistry-europe.onlinelibrary.wiley.com/doi/10.1002/slct.202403122 by Delhi Technological University, Wiley Online Library on [05/03/2025]. See the Terms and Conditions (https://onlinelibrary.wiley.com/terms-and-conditions) on Wiley Online Library for rules of use; OA articles are governed by the applicable Creative Commons License

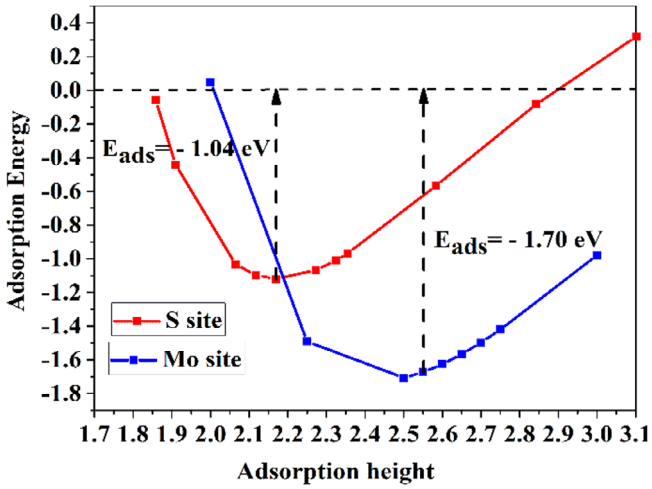

Figure 4. The plotted red and blue curves represent the variation of the adsorption energy with adsorption heights for Cu adsorbed onto MoS_2 NW at S and Mo sites, respectively.

level (E_F), reduces the band gap from 1.56 eV to zero, confirming the metallic behavior of the 1T phase of MoS_2 NW, consistent with the study performed by Seivane et al.[36] The observed transition from the semiconductor to a metallic was due to the quantum confinement effect. Hence, the complete agreement of the calculated band gap value proved the validity and reliability of our computational procedure.

3.2. Adsorption of Cu Atom Onto the MoS_2 NW

To analyze the interaction of the Cu atom with MoS_2 NW, we have considered the S site (on top of the S atom) and the Mo site (on top of the Mo atom) as the preferential adsorption sites for the Cu atom. This is because both Mo and S atoms contain vacant d and p orbitals that can readily accept electrons from the Cu atom through charge transfer during the interaction. Therefore, we have considered different orientations of the Cu atom at the Mo and S sites, as shown in 4a–s as the input geometries for the adsorption study. Further, adsorption energies were calculated using Equation (1) and reported in Table 1 for all these different adsorption configurations. From the reported value in Table 1, we found that the adsorption energies gradually decrease, attain minima, and then increase with increased adsorption heights. On plotting the adsorption energy as a function of adsorption height, the resulting curve was found to be a U-shaped curve, as shown in Figure 5. The minima of the adsorption energy curve correspond to the minimum adsorption energies and optimized adsorption height. From Figure 5, we found that the Cu atom preferred to be adsorbed at a height of 2.10 Å and 2.50 Å with the adsorption energies −1.04 eV and −1.70 eV at the S and Mo sites, respectively. It was based on energy minimization; we found that the Cu atom preferred to be adsorbed at the Mo site. Therefore, the Cu atom adsorbed at the Mo site was referred to as "Cu-MoS_2NW" and selected for the rest of the calculation. The reported negative value of the adsorption energies in Table 1 indicates that the adsorption process was exothermic, spontaneous, and energetically favourable. Additionally, the calculated sum of the corresponding atomic radii for the Cu-Mo atoms (2.73 Å) was larger than the reported adsorption height (2.50 Å) on the comparison. This indicates that covalent interaction exists between the Cu atom and MoS_2 NW during the adsorption. Hence, the calculated high adsorption energy and the existence of covalent interaction between the Cu atom and MoS_2NW suggest that the adsorption of the Cu atom onto MoS_2 NW was a chemisorption.

Table 1. The calculated adsorption energies and heights for the Cu atom adsorbed onto MoS_2 NW at Mo and S sites.

Adsorption Height (Å)[a]	Adsorption Energy(eV)[b]	Adsorption Height (Å)[c]	Adsorption Energy(eV)[d]
1.80	−0.03805	2.0	0.04943
1.85	−0.40184	2.25	−1.49111
2.0	−0.9630	2.50	−1.70622
2.05	−1.02261	2.55	−1.67339
2.10	−1.04492	2.60	−1.62624
2.20	−0.99535	2.65	−1.56628
2.25	−0.9423	2.70	−1.4974
2.28	−0.89945	2.75	−1.42075
2.50	−0.51971	3.0	−0.97992
2.75	−0.06315	–	–
3.0	0.31902	–	–

[a] Calculated adsorption height at S site.
[b] Calculated adsorption energy at S site.
[c] Calculated adsorption height at Mo site.
[d] Calculated adsorption energy at Mo site.

Table 2. Comparison of the calculated adsorption energies for the Cu-MoS_2NW with previously reported adsorption energies for TM adsorbed onto various 2D materials.

Systems	Adsorption Energy (eV)	Reference
Cu-SnO monolayer	1.342 ev	[37]
Cu-GaN monolayer	1.07 eV	[38]
Cu-hBN monolayer	0.407 eV	[39]
Cu-MoS_2 monolayer	1.307 eV	[21]
Cu-graphene monolayer	0.228 eV	[40]
Cu-MoS_2 NW	1.70 eV	Present work

3.3. Comparison of the Calculated Adsorption Energies for the Cu-MoS_2 NW

In this section, we have compared our calculated adsorption energy for the Cu-MoS_2NW with the previously reported adsorption energies for TM adsorbed onto various 2D materials by different authors. From the reported adsorption energies in Table 2, we found that the Cu atom got adsorbed onto the,SnO monolayer, GaN monolayer, hBN monolayer, MoS_2 monolayer,

© 2025 Wiley-VCH GmbH

23656549, 2025, 7, Downloaded from https://chemistry-europe.onlinelibrary.wiley.com/doi/10.1002/slct.202403122 by Delhi Technological University, Wiley Online Library on [05/03/2025]. See the Terms and Conditions (https://onlinelibrary.wiley.com/terms-and-conditions) on Wiley Online Library for rules of use; OA articles are governed by the applicable Creative Commons License

Research Article
doi.org/10.1002/slct.202403122

Chemistry Europe
European Chemical Societies Publishing

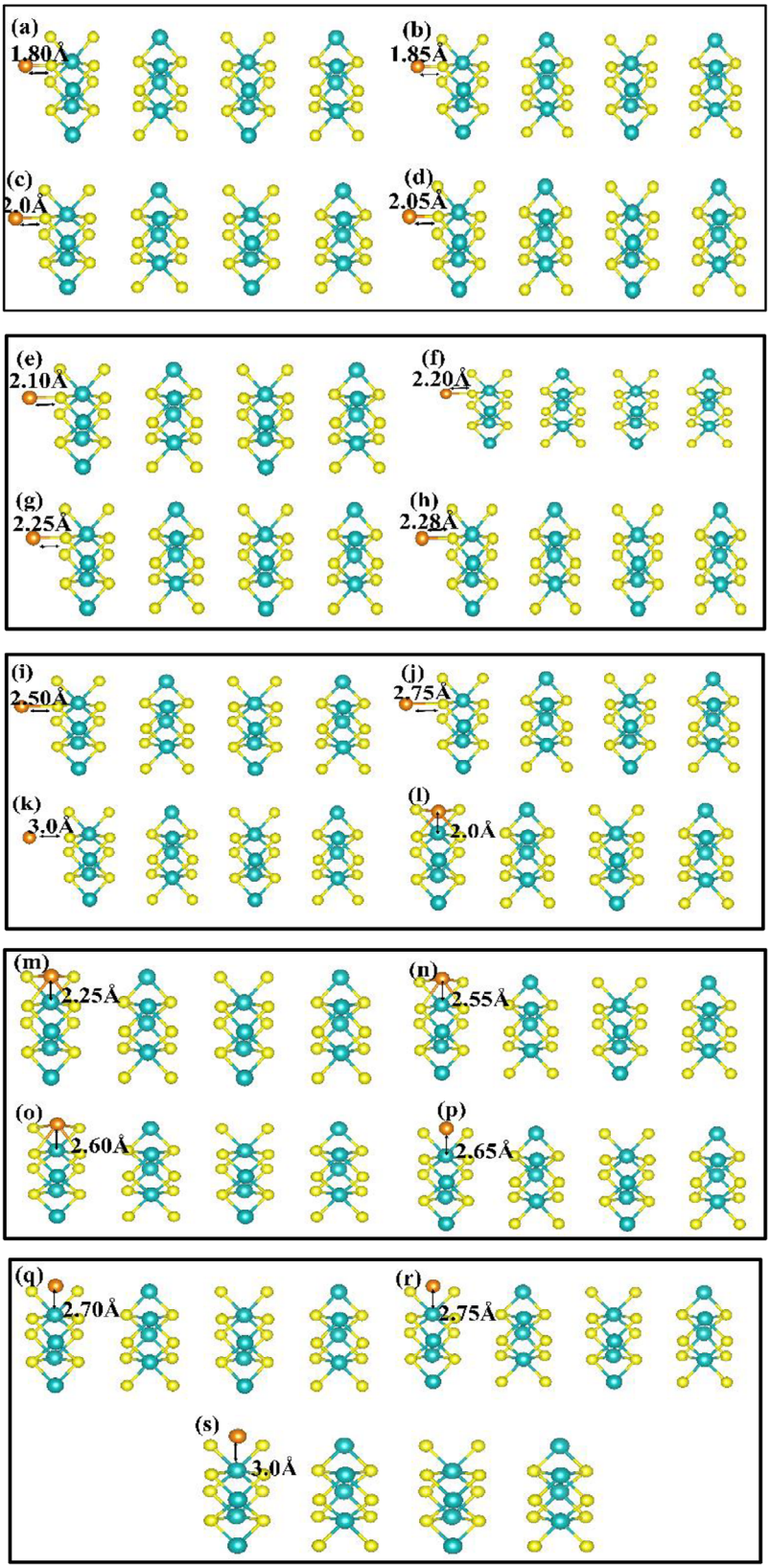

Figure 5. Top view of the different optimized adsorption configurations (a)–(k) at the S site and (l)–(s) at the Mo site, respectively.

© 2025 Wiley-VCH GmbH

23656549, 2025, 7, Downloaded from https://chemistry-europe.onlinelibrary.wiley.com/doi/10.1002/slct.202403122 by Delhi Technological University, Wiley Online Library on [05/03/2025]. See the Terms and Conditions (https://onlinelibrary.wiley.com/terms-and-conditions) on Wiley Online Library for rules of use; OA articles are governed by the applicable Creative Commons License

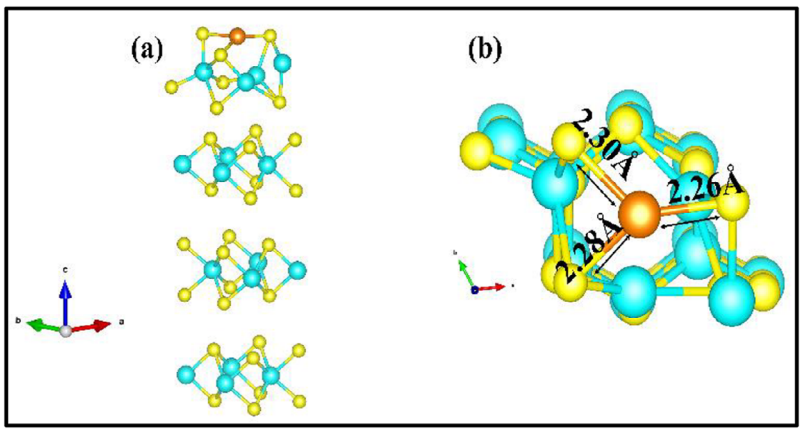

Figure 6. (a) Side view and (b) top view of the optimized Cu-doped MoS_2 NW structures.

and graphene monolayer, with adsorption energies 1.342 eV, 1.07 eV, 0.407 eV, 1.307 eV, and 1.13 eV respectively. The comparison showed that the adsorption energy for the Cu-MoS_2NW was higher than the Cu atom adsorbed onto the SnO monolayer, GaN monolayer, MoS_2 monolayer, and graphene monolayer. This indicates that MoS_2NW has a better adsorption affinity for Cu atoms than SnO monolayer, GaN monolayer, MoS_2 monolayer, and graphene monolayer.

3.4. Structure Analysis of the Cu-doped MoS_2 NW

In this section, we have analyzed the structural properties of the substitutional doped structure. For this purpose, we replaced one of the atoms of MoS_2 NW from the lattice with the Cu atom and optimized the doped structure. After optimization, we found that the doped Cu atom was displaced and occupied the interstitial sites where it bonded with the neighboring three S atoms, as shown in Figure 6. From Figure 6b, we found that the three Cu—S bond lengths in the optimized structure were found to be 2.30 Å, 2.26 Å and 2.28 Å which is shorter than the Mo—S (2.35 Å) bond length of the pristine MoS_2 NW. This indicates that the dopant atom causes the overall structure to be somewhat corrugated due to the protrusion of the Cu atom away from the surface of MoS_2 NW. Moreover, the Mo—S bond lengths in the resulting optimized structure no longer remained a fixed value and underwent variations from 2.36Å–2.63 Å. On comparison, we found that the variations in the Mo—S bond lengths upon substitutional doping were more significant than the Mo—S (2.35 Å) bond length of the pristine MoS_2 NW. This indicates that the surface of the MoS_2

NW undergoes expansion to accumulate the large atomic radius Cu atom (1.28 Å) within the lattice. These findings suggest that substitutional doping of the Cu atom causes structural distortion within the lattice. For the rest of the study, we have abbreviated the optimized substitutional doped structure as "Cu-doped MoS_2 NW". To determine the bonding strength of the Cu atom with the MoS_2 NW and the stability of the Cu-doped MoS_2 NW structures, we have calculated the binding energy (E_b) and formation energy (E_f) using Equation (3) and Equation (4) respectively.

$$E_b = E_{Cu-MoS_2+gas} - (E_V + E_{Cu}) \quad (3)$$

$$E_f = E_{Cu+MoS_2} - E_{MoS_2} - \mu_{Cu} + \mu_x \quad (4)$$

where $E_{Cu-MoS2}$, E_V, E_{Cu}, μ_{Cu}, and μ_X represents the total energies of the substitutional doped Cu atom into MoS_2 NW, total energies of the defected MoS_2 NW, total energies of the isolated Cu atom, and chemical potentials of the isolated Cu and ejected atoms from the MoS_2 NW, respectively. According to Equations (3) and (4), the binding and formation energies for the Cu-doped MoS_2 NW were −11.326 eV and −5.662 eV, respectively. The calculated high formation and binding energy suggests that the Cu atom binds strongly with the MoS_2 NW, and the Cu-doped MoS_2 NW structures are stable.

3.5. Thermodynamic Stability of the Cu-MoS_2NW and Cu-doped MoS_2NW Systems

To analyze the thermodynamic stability of the substitutionally doped and Cu-adsorbed optimized structures, we have calculated the cohesive energy/atom (E_{coh}/atom) using Equation (2)[55] And reported in Table 4. According to Equation (2), we found that the cohesive energy for the MoS_2NW, Cu-MoS_2NW, and Cu-doped MoS_2NW systems was found to be −5.22 eV/atom, −5.15 eV/atom, and -eV/atom respectively. The calculated negative value of the cohesive energy suggests that all our systems are thermodynamically stable. On comparison, we found that the increasing order of thermodynamic stability is Cu-doped MoS_2NW < Cu-MoS_2NW < MoS_2NW. The observed low cohesive energy of Cu-doped MoS_2NW and Cu-MoS_2NW systems with respect to MoS_2 NW can be attributed to the strong interaction of the Cu atom with the surface atoms, thereby reducing the interaction of the surface atoms with the bulk atom. As a consequence, it reduces the overall cohesive energy of the systems. From Table 3 and Table 4, we found that various computational studies suggest that generally, on doping the cohesive energy decreases as observed in the different 2D and 1D nanostruc-

© 2025 Wiley-VCH GmbH

23656549, 2025, 7, Downloaded from https://chemistry-europe.onlinelibrary.wiley.com/doi/10.1002/slct.202403122 by Delhi Technological University, Wiley Online Library on [05/03/2025]. See the Terms and Conditions (https://onlinelibrary.wiley.com/terms-and-conditions) on Wiley Online Library for rules of use; OA articles are governed by the applicable Creative Commons License

Table 3. Reported calculated cohesive energies for the various 2D materials from various previous computational studies.

System	Cohesive Energy (eV)	Reference
Aluminene(Planar)	−1.96 eV/atom	[41]
Aluminene(P6mmm)	−2.32 eV/atom	
Aluminene(Buckled)	−3.47 eV/atom	
Aluminene(P3m1)	−3.27 eV/atom	
Aluminene(Triangular,Pmmn)	−2.76 eV/atom	
Aluminene(Triangular,Pmmn)	−3.27 eV/atom	
Aluminene(4-layerslab, 8-Pmmn)	−3.16 eV/atom	
Gallenene (Puckered)	−2.32 eV/atom	
Indiene (Planar)	−1.81 eV/atom	
Indiene (Buckled)	−1.83 eV/atom	
Indiene (Pucker, sw)	−1.88 eV/atom	
Silicene (Buckled)	−4.57 eV/atom	[42]
Silicene (P3m1)	−3.91 eV/atom	[43]
Germanene (Buckled)	−3.24 eV/atom	[43]
Germanene (P3m1)	−2.93 eV/atom	[44]
Stanene (Buckled)	−3.31 eV/atom	[45]
Stanene (P3m1)	−2.73 eV/atom	[43]
Plumbene (Buckled)	−2.28 eV/atom	[46]
SiGe (Buckled)	−4.81 eV/atom	[47]
SiGe (P3m1)	−2.56 eV/atom	[48]
SnSi (Buckled)	−3.61 eV/atom	[49]
SnSi (P3m1)	−.2.28 eV/atom	[50]
SnGe (Buckled)	−3.79 eV/atom	[49]
SnGe(P3m1)	−2.25 eV/atom	[50]
Cu-graphene	2.490eV	[51]
α-CuC	4.99eV	[52]
β-CuC	4.97eV	
α-LiC	4.66eV	
β-LiC	4.66eV	
Cu_2Si_3	3.45eV	
Bulk MoS_2	4.95 eV/atom	[53]
MoS_2 monolayer	4.96 eV/atom	

tures like Aluminene (Planar), Aluminene(P6mmm), Aluminene (4-layers slab, 8-Pmmn), Aluminene (Triangular, Pmmn), Indiene, Cu-graphene, SnGe, SnSi, Stanene, Mo_6Se_6 NW, $Mo_6S_2Se_3$ NW, $Mo_6S_4I_2$ NW, $Mo_6S_2Se_3$ NW, $Mo_6S_2Se_3$ NW, $Mo_{12}S_{18}$ NW, and $Mo_{12}Se_{18}$NW respectively. A similar trend was observed for the MoS_2NW, Cu-MoS_2NW, and Cu-doped MoS_2 NW systems. Also, the calculated high cohesive energy suggests that MoS_2NW, Cu-doped MoS_2NW, and Cu-MoS_2 NW systems can be synthesized experimentally via high energy methods such as Chemical Vapour Deposition (CVD) and molecular beam epitaxy (MBE). This finding was consistent with the Ding et al. results that SiX and XSi_3 (where X = B, C, N, Al, and P atoms) could be synthesized via CVD and MBE methods based on cohesive energy calculations.[56]

Table 4. Reported cohesive energies for the various 1D materials along with MoS2NW, Cu-doped MoS2NW, and Cu-MoS2NW.

System	Cohesive Energy (eV)	Reference
Mo_6Se_6 NW	−4.97 eV/atom	[54]
$Mo_6S_3Se_3$ NW	−5.15 eV/atom	
$Mo_6S_4I_2$ NW	−4.93 eV/atom	
$Mo_6Se_4I_2$ NW	−4.69 eV/atom	
$Mo_6S_2Se_2I_2$ NW	−4.81 eV/atom	
$Mo_{12}S_{18}$ NW	−4.88 eV/atom	
$Mo_{12}Se_{18}$ NW	−4.57 eV/atom	
$Mo_{12}S_6I_{12}$ NW	−3.86 eV/atom	
$Mo_{12}Se_6I_{12}$ NW	−3.73 eV/atom	
$Mo_{12}Se_9I_9$ NW	−3.67 eV/atom	
MoS_2 NW	−5.22 eV/atm	Present work
Cu-doped MoS_2 NW	−3.20 eV/atom	Present work
Cu-MoS_2 NW	−5.15 eV/atom	Present work

3.6. Electron Localization Function (ELF) Analysis

We have utilized ELF as an effective tool to visualize electron density distribution, lone pairs, and bonding pairs of electrons around the interacting atom. Therefore, we have performed an ELF calculation for the Cu-MoS_2 NW and Cu-doped MoS_2 NW systems. The ELF plot shown in Figure 6 illustrates that the ELF value varies between 0 and 1, with red, blue, and green colors corresponding to the ELF value 1, 0, and 0.5, respectively. The ELF value close to 1 corresponds to a region where electrons are fully localized or have a high electron density. In contrast, the ELF values close to 0 and 0.5 correspond to areas with low electron density and partially delocalized electrons. From Figure 7a, we found a large region of high electron density around the S atoms identified by sizeable red color spherically symmetric rings with a small area of partially delocalized electrons between the Mo-S atoms identified by green spherically unsymmetrical rings. These findings suggest that covalent interaction with a partially ionic nature exists between the Mo and S atoms in the case of the Cu-MoS_2NW system. Additionally, a region of partially delocalized electrons exists between the Cu and Mo atoms, indicating that the Cu and Mo atoms mutually share transferred electrons during the interaction. This confirms that strong covalent bonding exists between the Cu and Mo atoms during the Cu adsorption, which is consistent with our adsorption study. Similarly, for the Cu-doped MoS_2 NW, we found a large spherically red color region around the S atoms rather than Cu atoms, as shown in Figure 7b. These findings suggest that electrons are strongly localized around the S atom compared to the Cu atom, indicating that the Cu atom loses electrons to the nearby S atom, thereby increasing the electron density around the S atom. All these findings confirmed that the interaction of the Cu atom with the nearby S atoms is purely electrostatic. Moreover, a green colored region exists between the Mo—S atoms, indicating that electrons are mutually shared between the Mo—S atoms, again confirming that covalent bonding exists between Mo—S atoms. Hence, our ELF result suggests that covalent and electrostatic

© 2025 Wiley-VCH GmbH

23656549, 2025, 7, Downloaded from https://chemistry-europe.onlinelibrary.wiley.com/doi/10.1002/slct.202403122 by Delhi Technological University, Wiley Online Library on [05/03/2025]. See the Terms and Conditions (https://onlinelibrary.wiley.com/terms-and-conditions) on Wiley Online Library for rules of use; OA articles are governed by the applicable Creative Commons License

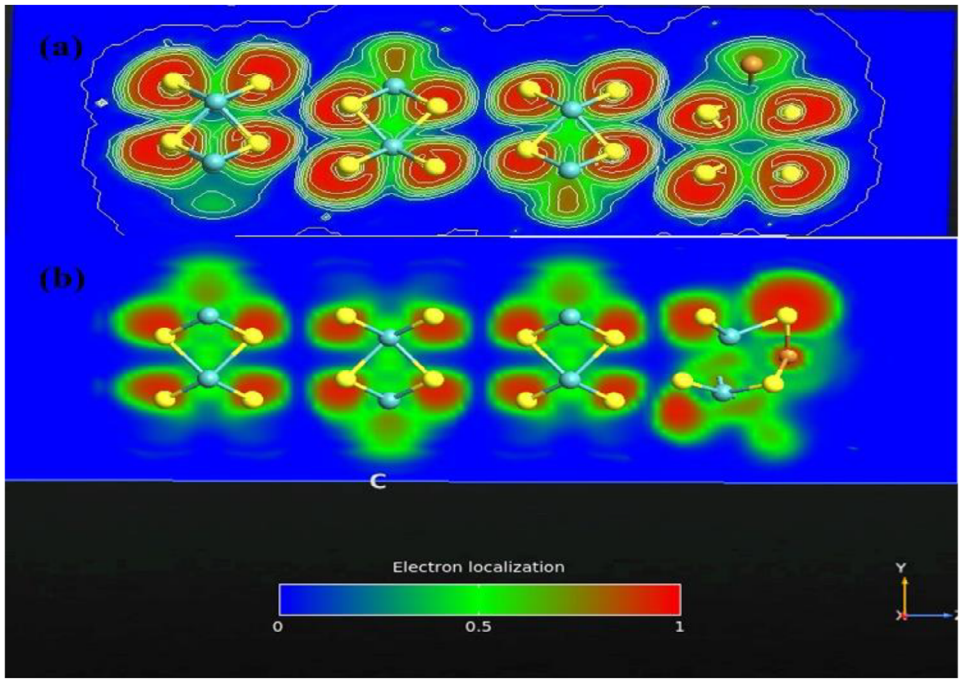

Figure 7. ELF plot for (a) Cu-MoS_2 NW system and (b) Cu-doped MoS_2 NW system, respectively. The ELF magnitude is given in a color scheme in which red, blue, and green correspond to high electron density, low electron density, and free electrons, respectively.

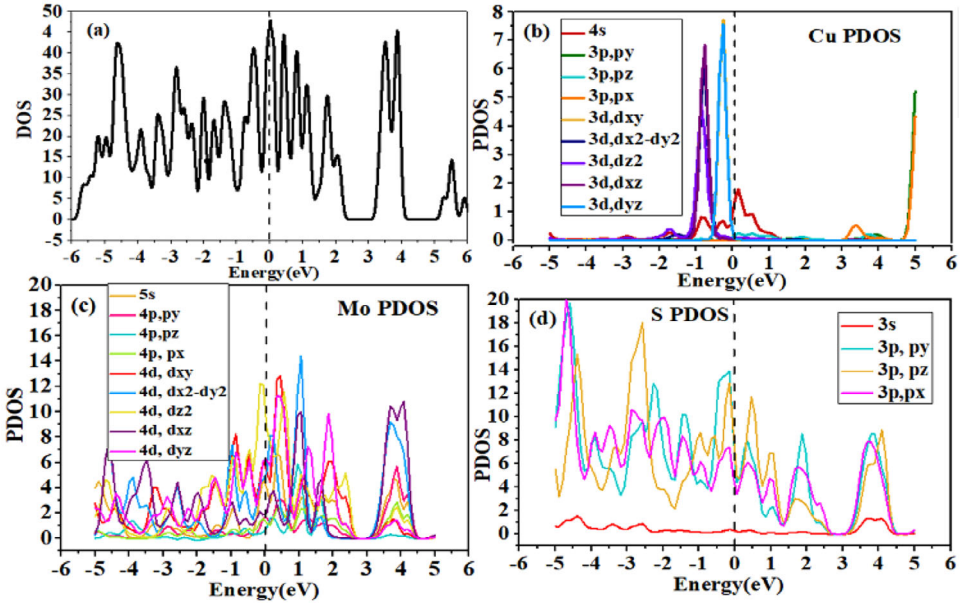

Figure 8. Calculated (a) DOS for the Cu adsorbed MoS_2 NW. PDOS for (b) Cu, (c) Mo, and (d) S atoms, respectively. The black dotted line represents the Fermi level.

interaction exists between the Cu atom and MoS_2 NW in the case of Cu-MoS_2 NW and Cu-doped MoS_2 NW systems.

3.7. Effect of Cu Adsorption on the Electronic Properties of MoS_2 NW

To analyze the effect of introducing the Cu atom as a foreign atom onto MoS_2 NW, we have calculated DOS and PDOS for the Cu- MoS_2 NW and Cu-doped MoS_2NW systems. From Figures 8a and 9a, we found that continuous impurity states exist around the Fermi level (E_F) for both systems. This indicates that the metallic nature of the MoS_2 NW remained preserved even upon substitutional doping and Cu adsorption onto MoS_2 NW. We also found an increase in the peak intensity for both systems. This indicates that charge transfer occurs during the interaction of the Cu atom with the MoS_2 NW. On comparison, we found that the peak intensity of Cu-doped MoS_2 NW was higher than that

© 2025 Wiley-VCH GmbH

23656549, 2025, 7, Downloaded from https://chemistry-europe.onlinelibrary.wiley.com/doi/10.1002/slct.202403122 by Delhi Technological University, Wiley Online Library on [05/03/2025]. See the Terms and Conditions (https://onlinelibrary.wiley.com/terms-and-conditions) on Wiley Online Library for rules of use; OA articles are governed by the applicable Creative Commons License

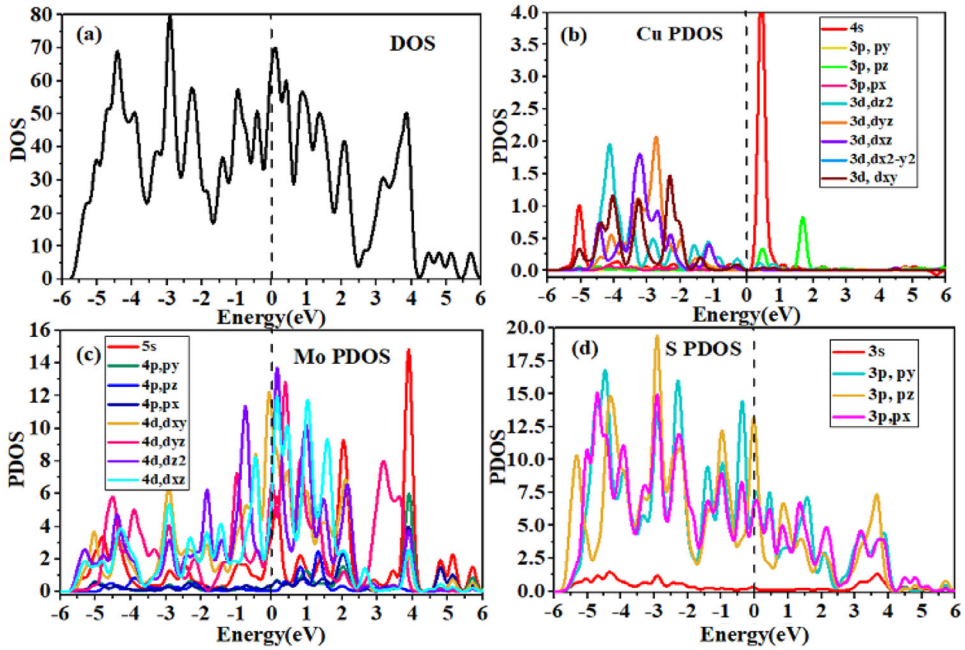

Figure 9. Calculated (a) DOS for the Cu-doped-MoS_2 NW. PDOS for (b) Cu, (c) S, and (d) Mo atoms, respectively.

of Cu-MoS_2 NW, indicating that significant charge transfer occurs in the case of Cu-doped MoS_2 NW. Significant charge transfer indicates better electrical conductivity of the Cu-doped MoS_2 NW than Cu-MoS_2 NW and pristine MoS_2 NW, making the Cu-doped MoS_2 NW a promising candidate for nanoelectronics. We also observed a shift in the Fermi level towards the conduction band, indicating that the Cu atom has an n-type doping effect. Further, PDOS was calculated to determine the contribution of the atomic orbital to the DOS. The PDOS plot in Figure 8c,d illustrates there exists multiple overlapping between the 4d(d_{xy}) and 3p(p_z)-S atomic orbitals in the energy range from −1 eV to 2 eV leading to the strong hybridization between the atomic orbitals to form molecular orbitals responsible for the formation of a covalent bond. Similarly, from Figure 8(b) and 8(c)we found that the 4s-Cu and 4d(d_{xy})-Mo atomic orbitals overlap in the energy range 0 eV–1 eV, indicating strong hybridization and charge was transferred from the 4 s orbital of Cu atom to 4d(d_{xy}) orbital of Mo atom during the interaction. In contrast, for the Cu-doped MoS_2 systems, the PDOS plot in Figure 9c,d illustrated that multiple overlapping exists between the 5s-Mo and 3p(p_z)-S atomic orbitals in the energy range from 0 eV to 1 eV, indicating strong hybridization between the atomic orbitals to form molecular orbitals involved in the formation of the strong covalent bond between them. From Figure 9b,c we found that electron transferred from the 4s-Cu atomic orbital to the 3p(p_z)-S atomic orbitals was responsible for the formation of the ionic bond between the Cu and nearby S atoms during the interaction. This type of hybridization indicates that the electronic states are not isolated but are aligned with the existing electronic states of MoS_2 NW. Consequently, these electronic states act as effective charge carriers, facilitating easy charge transfer from the Cu atom to the MoS_2 NW. These findings indicate that the Cu atom-induced electronic states are less likely to trap charge carriers for long periods, reducing the probability of acting as recombination centers. Moreover, we also noted that the contribution from the Cu atom to the DOS was considerably more significant in the Cu-doped MoS_2 NW compared to the Cu-MoS_2 NW system. This is consistent with our observation that a substantial charge was transferred from the Cu atom to MoS_2 NW in the case of Cu-doped MoS_2 NW, which is consistent with our DOS calculation. Hence, our DOS and PDOS results were in good agreement with each other.

3.8. Bader Charge and Electron Density Difference Analysis

We have performed the Bader charge method and Electron density difference for the Cu-MoS_2 NW and Cu-doped MoS_2 NW systems to analyze the charge transfer mechanism during the interaction. The positive and negative values of the Bader charge indicate charge loss and gain during the interaction. According to the Bader charge method, we found that the Cu atom loses 0.047e to the MoS_2NW in the case of Cu-MoS_2NW, whereas the surface Mo atoms lose 0.692e,1.344e,1.414e, and 1.880e to the adjacent S atoms, as shown in Figure 11a. In contrast, for the Cu-doped MoS_2 NW system, we found that the Cu atom loses 0.371e, whereas the nearby neighbouring S atoms gain −0.586e, −0.848e, and −0.745e, as shown in Figure 11b. In comparison, we found that significant charge transfer was observed from the Cu atom in the case of Cu-doped MoS_2NW. These findings validate that the Cu-doped MoS_2NW system exhibits better electrical conductivity than the Cu-MoS_2 NW system. Further, to validate our findings, we have described the charge transfer qualitatively using the electron density difference diagram for the Cu-doped MoS_2NW and Cu-MoS_2NW. The red and blue regions indicate the charge gained and loss region in Figure 10. The electron den-

© 2025 Wiley-VCH GmbH

23656549, 2025, 7, Downloaded from https://chemistry-europe.onlinelibrary.wiley.com/doi/10.1002/slct.202403122 by Delhi Technological University, Wiley Online Library on [05/03/2025]. See the Terms and Conditions (https://onlinelibrary.wiley.com/terms-and-conditions) on Wiley Online Library for rules of use; OA articles are governed by the applicable Creative Commons License

Research Article
doi.org/10.1002/slct.202403122

Chemistry Europe
European Chemical Societies Publishing

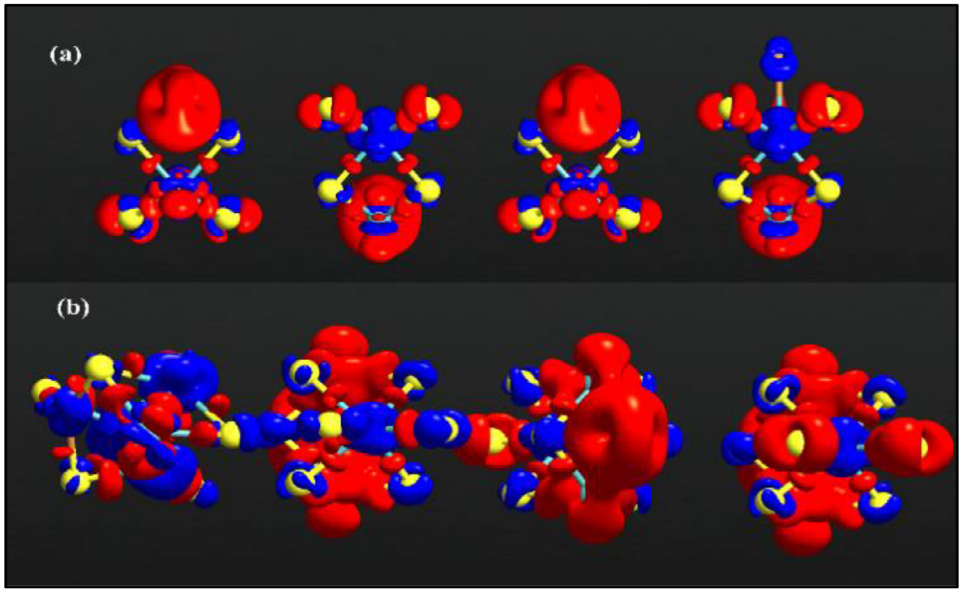

Figure 10. Electron density difference diagram for (a) Cu-MoS_2 NW and (b) Cu-doped MoS_2 NW systems. The red and blue regions indicate charge gain and charge loss regions, respectively.

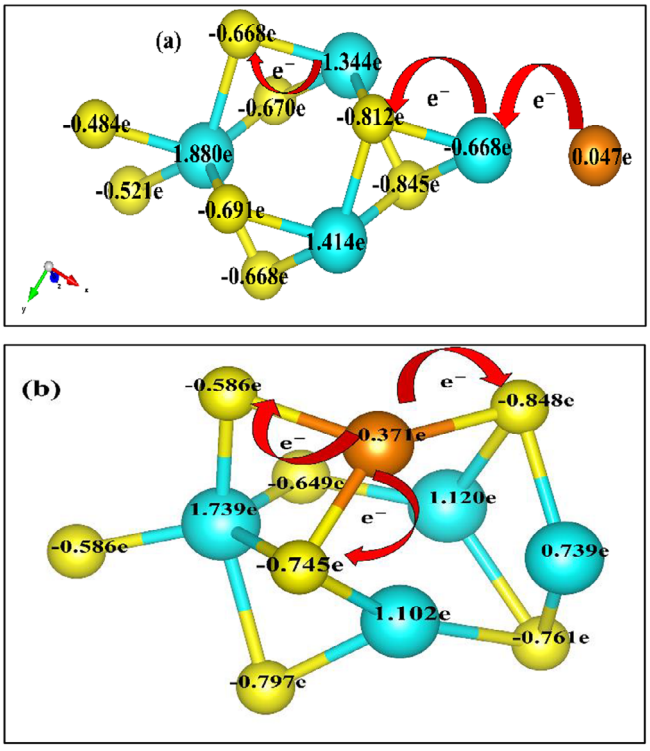

Figure 11. Calculated Bader charge distribution for the surface atoms of (a) Cu-MoS_2 NW and (b) Cu-doped MoS_2 NW, respectively. The red arrows represent the directions of electron transfer from the Cu atom to the MoS_2 NW.

sity difference diagram in Figure 10a illustrates the blue-coloured region around the Cu and Mo atoms, whereas the red-coloured region around the S atom. The red and blue region indicates that the S atom gains electrons, whereas the Mo and Cu atoms lose electrons in the case of Cu-MoS_2NW. In contrast to the Cu-doped MoS_2NW, Figure 10b illustrates a large red region around the S atom and a large blue region around the Mo and Cu atoms. Large blue and red areas indicate that a substantial charge was gained by the S atom and lost by the Mo and Cu atoms during the interaction. This again suggests that substantial charge transfer occurs from the doped Cu atom to the MoS_2 NW during the interaction. The observed charge lost and gained can be attributed to the difference in the electronegativity between the interacting atoms. According to the Pauling scale, the electronegativity of Mo(χ_{Mo}), S(χ_S), and Cu(χ_{Cu}) differ by 13.68% and 35.78% with respect to χ_{Cu}. Slight differences in the electronegativity make Cu and Mo atoms partially positive and negative. This creates a local weak electric field between the Cu and surface atoms, resulting in a weak charge transfer from the Cu atom to the MoS_2NW in the case of Cu-MoS_2NW. Consequently, valence electrons are mutually shared, confirming that the Cu atom interacts with MoS_2 NW via covalent interaction, which agrees with our ELF study. Conversely, considerable differences in the electronegativity between the S—Cu atoms make Cu and nearby S atoms electrons deficient and electrons rich species. This creates a strong electric field between the interacting S—Cu atoms, causing substantial charge transfer from the Cu atom to the nearby S atom. This is why, upon geometry optimization, the Cu atom got occupied at the interstitial sites where the Cu atom got bonded with the three S atoms to maximize the electrostatic interaction. Hence, our Bader charge analysis agrees with electron density difference results.

3.9. Effect of Cu Adsorption on the Work Function of MoS_2 NW

The work function is considered an essential parameter for nanoelectronic devices because any variation in the work function influences the charge injection capability of the material,

© 2025 Wiley-VCH GmbH

23656549, 2025, 7, Downloaded from https://chemistry-europe.onlinelibrary.wiley.com/doi/10.1002/slct.202403122 by Delhi Technological University, Wiley Online Library on [05/03/2025]. See the Terms and Conditions (https://onlinelibrary.wiley.com/terms-and-conditions) on Wiley Online Library for rules of use; OA articles are governed by the applicable Creative Commons License

thereby significantly impacting the performance of nanoelectronic devices. It is observed that the adsorption of transition metal atoms strongly influences the work function. For example-Chi et al. studied the variation in the work function of GaN NW and GaN monolayer upon the alkali metal adsorption using the first principle calculation. They reported that the work function of the GaN monolayer changes from 4.21 eV to 2.47 eV, 1.88 eV, 1.49 eV,1.29 eV, and 0.84 eV upon the adsorption of Li, Na, K, Rb, and Cs metal atoms onto GaN monolayer.[57] In contrast, they also observed that the work of the pristine GaN NW changes from 4.11 eV to 2.45 eV, 2.32 eV, 2.06 eV, 1.81 eV, and 2.38 eV upon the adsorption of Li, Na, K, Rb, and Cs metal atoms onto GaN NW.[58] In another study, Sahin et al.[59] reported that the work function of the silicene changes from 4.77 eV to 4.39 eV, 4.25 eV, 4.09 eV, 4.68 eV, 4.81 eV, 4.47 eV, 4.77 eV, 4.84 eV, 4.65 eV, 4.73 eV, 4.81 eV, 5.0 eV,4.97 eV, and 4.90 eV upon the adsorption of Li, Na, K, Be, Mg, Ca, Ti, V, Cr, Mn, Fe, Co, Mo and W onto silicene. Therefore, based on the above findings, we have also evaluated the variation in the work function of the MoS_2 NW upon substitutional doping and adsorption of the Cu atom. For this purpose For this purpose, the work function of the pristine MoS_2 NW and Cu-doped MoS_2 NW and Cu-MoS_2 NW systems was calculated using Equation (5).

$$\phi = E_{inf} - E_F \tag{5}$$

where E_{inf} and E_F represent the electrostatic potential at infinity and Fermi level energy, the electrostatic potential at infinity is assumed to be zero in the present work. Further, the variation in the work function ($\triangle\phi$) for the Cu-doped MoS_2 NW and Cu-MoS_2 NW was calculated by subtracting the work function of the Cu-doped MoS_2 NW and Cu-MoS_2 NW from that of the pristine MoS_2 NW. The computed work function values for the pristine MoS_2 NW, Cu-doped MoS_2 NW, and Cu-MoS_2 NW were found to be 4.99 eV, 3.792 eV, and 3.845 eV, respectively. These findings indicate that the value of the work function decreases and undergoes negative variation to 24% and 22.9% upon substitutional doping and adsorption of Cu atom onto MoS_2NW. A similar trend in the work function was observed by Ouma et al.[60] While studying the effect of substitutional doped and adatoms 3d TM onto the TcS_2 monolayer. The observed variation in the work function of Cu-doped MoS_2 NW and Cu-MoS_2 NW was due to the existence of a strong electric field between the substitutional doped Cu atom and MoS_2NW that facilitates redistribution of electron density around the dopant site and substantial charge transfer from the Cu atom to MoS_2NW. According to Equation (6), an exponential relationship exists between the emitted electron current densities and variation in the work function.

$$j = AT^2 e\frac{-\Delta\Phi}{K_B T} \tag{6}$$

where j is the emitted electron current densities (A/m^2), A is a Richard constant ($A/m^2\ K^2$), ϕ is the work function of the material in eV, T is the temperature in K, and K_B is the Boltzmann constant in eV/K respectively. Therefore, a significant variation in the work function of Cu-doped MoS_2NW than Cu-MoS_2NW indicates better electron emission capability of Cu-doped MoS_2NW. Hence, the work function analysis suggests that the Cu-doped MoS_2NW system can be utilized in field emission devices.

4. Conclusion

In this study, we have systematically investigated the structural and electronic properties of substitutional doping and adsorption of Cu atom onto MoS_2 NW using first principles calculation. According to the adsorption study, the Cu atom prefers to be adsorbed at the Mo site with an adsorption energy of about −1.70 eV. This results in the chemical bond formation between the Cu atom and MoS_2NW during the interaction. In contrast, substitutional doping of the Cu atom distorts the structure to accommodate the Cu atom and exhibits strong covalent bonding with the Cu atom. According to the Bader charge method, the Cu atom loses 0.047e and 0.371e to the MoS_2 NW in the case of Cu-MoS_2NW and Cu-doped MoS_2NW, respectively. Significant charge transfer leads to enhancement in the conductivity and variation in the work function. The DOS results suggest that the Cu atom induces an electronic state near the Fermi level, facilitating easy charge transfer from the Cu atom to MoS_2NW. There was also a shift in the fermi level towards CB, indicating that the Cu atom has an n-type effect on substitutional doping and adsorption. From the work function calculation, we found that the work function of the Cu-doped MoS_2 NW and Cu-MoS_2NW systems undergo 24% and 22.9% with respect to that of pristine MoS_2NW. Further from the PDOS study, we found that in case of Cu-MoS_2NW strong hybridization exists between the 4d(d_{xy})-Mo and 3p(p_z)-S atomic orbitals responsible for the formation of covalent bond whereas for the Cu- doped-MoS_2 systems, hybridization between the 4s-Cu atomic orbital to the 3p(p_z)-S atomic orbitals was responsible for the formation of the ionic bond between the Cu and nearby S atoms during the interaction. Moreover, our calculated cohesive energy suggests that the pristine MoS_2NW, Cu-MoS_2NW, and Cu-doped MoS_2NW systems are thermodynamically stable. Finally, our DFT result suggests that substitutional doping is an effective way to modulate the electronic properties of MoS_2NW as Cu-doped MoS_2 NW systems exhibit better electrical conductivity than pristine MoS_2NW and Cu-MoS_2NW due to better charge transfer and variation in the work function. Thus, the Cu-doped MoS_2NW system is a promising candidate for nanoelectronics and field emission device applications.

Acknowledgements

We greatly thank Prof. Prateek Sharma, Vice-Chancellor, Delhi Technological University, Delhi, India, for arranging the research facilities. All the authors would like to thank and gratefully acknowledge Prof. Rishu Chaujar, Prof.Ruchika Malhotra, Yash Pathak, and Kanika Sharma for their support. The Nanomaterial Research Laboratory, Department of Applied Physics, Delhi Technological University, Shahbad Daulatpur, Main Bawana Road, New Delhi,110042, supported this work.

© 2025 Wiley-VCH GmbH

23656549, 2025, 7, Downloaded from https://chemistry-europe.onlinelibrary.wiley.com/doi/10.1002/slct.202403122 by Delhi Technological University, Wiley Online Library on [05/03/2025]. See the Terms and Conditions (https://onlinelibrary.wiley.com/terms-and-conditions) on Wiley Online Library for rules of use; OA articles are governed by the applicable Creative Commons License

Conflict of Interests

The authors declare no conflict of interest.

Data Availability Statement

The data that support the findings of this study are available from the corresponding author upon reasonable request.

Keywords: Adsorption · Copper · DFT · MoS_2 · Nanowire

[1] E. Galvagno, E. Tartaglia, M. Stratigaki, C. Tossi, L. Marasco, F. Menegazzo, C. Zanardi, F. Omenetto, C. Coletti, A. Traviglia, *Adv. Funct. Mater.* **2024**, *34*, 2313301X.
[2] a) K. Sharma, N. K. Puri, B. Singh, *Anal. Bioanal. Chem.* **2024**, *416*, 4789–4805; b) K. Sharma, N. K. Puri, B. Singh, in *Hexagonal Boron Nitride*, Elsevier, **2024**, pp. 511–552; c) K. Sharma, N. K. Puri, B. Singh, *Appl. Nanosci.* **2024**, *14*, 217–230.
[3] A. Kumar, M. Kumar, *IEEE Sens. J.* **2024**, 1530-437.
[4] W. Zhang, X. Zhang, L. K. Ono, Y. Qi, H. Oughaddou, *Small* **2024**, *20*, 2303115.
[5] L. Liu, N. Liu, B. Chen, C. Dai, N. Wang, *Catalysts* **2024**, *14*, 126.
[6] Y. Zhang, R. Zhang, Y. Guo, Y. Li, K. Li, *J. Alloys Compd.* **2024**, *998*, 174916.
[7] A. Mirzaei, M. Alizadeh, H. R. Ansari, M. Moayedi, H. Safaeian, M. H. Lee, T.-U. Kim, J.-Y. Kim, H. W. Kim, S. S. Kim, *Nanotechnology* **2024**, *35*, 332002.
[8] Y. Jiao, A. M. Hafez, D. Cao, A. Mukhopadhyay, Y. Ma, H. Zhu, *Small* **2018**, *14*, 1800640.
[9] K. Kumar, D. Kaur, *Sol. Energy Mater. Sol. Cells* **2024**, *268*, 112736.
[10] T. Dutta, N. Yadav, Y. Wu, G. J. Cheng, X. Liang, S. Ramakrishna, A. Sbai, R. Gupta, A. Mondal, Z. Hongyu, A. Yadav, *Nano Mater. Sci.* **2024**, *6*, 1–23.
[11] O. Samy, S. Zeng, M. D. Birowosuto, A. El Moutaouakil, *Crystals* **2021**, *11*, 355.
[12] Z. Hu, Z. Wu, C. Han, J. He, Z. Ni, W. Chen, *Chem. Soc. Rev.* **2018**, *47*, 3100–3128.
[13] L. Loh, Z. Zhang, M. Bosman, G. Eda, *Nano. Res.* **2021**, *14*, 1668–1681.
[14] Y. Luo, C. Ren, S. Wang, S. Li, P. Zhang, J. Yu, M. Sun, Z. Sun, W. Tang, *Nanoscale Res. Lett.* **2018**, *13*, 1–9.
[15] Y. Wu, L. Wang, H. Li, Q. Dong, S. Liu, *Chin. Chem. Lett.* **2022**, *33*, 153–162.
[16] M. Xu, H. Wang, S. Sun, H. Li, X. Li, Y. Chen, Y. Ni, *Physica. Status Solidi.* **2020**, *257*, 1900205.
[17] J.-M. Zhang, J.-P. Duan, Y.-H. Huang, X.-M. Wei, *Phys. E* **2022**, *138*, 115116.
[18] Y. Kadioglu, G. Gökoğlu, O. Üzengi Aktürk, *Appl. Surf. Sci.* **2017**, *425*, 246–253.
[19] A. Sharma, A. Srivastava, M. Husain, M. S. Khan, *J. Mater. Sci.* **2018**, *53*, 9578–9588.
[20] T. B. Rawal, D. Le, T. S. Rahman, *J. Phys. Chem. C* **2017**, *121*, 7282–7293.
[21] Y. Wang, B. Wang, R. Huang, B. Gao, F. Kong, Q. Zhang, *Physica E: Low-dimensional Systems and Nanostructures* **2014**, *63*, 276–282.
[22] X. D. Li, Y. M. Fang, S. Q. Wu, Z. Z. Zhu, *AIP Advances* **2015**, *5*, 057143–0571439.
[23] D. Joseph, M. Navaneethan, R. Abinaya, S. Harish, J. Archana, S. Ponnusamy, K. Hara, Y. Hayakawa, *Appl. Surf. Sci.* **2020**, *505*, 144066.
[24] S. Zhou, W. Ma, U. Anjum, M. Kosari, S. Xi, S. M. Kozlov, H. C. Zeng, *Nat. Commun.* **2023**, *14*, 5872.
[25] Z. Wang, H. Kannan, T. Su, J. Swaminathan, S. N. Shirodkar, F. C. Robles Hernandez, H. C. Benavides, R. Vajtai, B. I. Yakobson, A. Meiyazhagan, P. M. Ajayan, *Nanoscale Advances* **2021**, *3*, 1747–1757.
[26] S. Smidstrup, T. Markussen, P. Vancraeyveld, J. Wellendorff, J. Schneider, T. Gunst, B. Verstichel, D. Stradi, P. A. Khomyakov, U. G. Vej-Hansen, *J. Phys.: Condens. Matter* **2019**, *32*, 010953–018984.
[27] V. N. Jafarova, G. S. Orudzhev, *Solid State Commun.* **2021**, *325*, 110038–111098.
[28] E. R. Davidson, D. Feller, *Chem. Rev.* **1986**, *86*, 681–696.
[29] J. P. Perdew, K. Burke, M. Ernzerhof, *Phys. Rev. Lett.* **1996**, *77*, 3865.
[30] D. C. Langreth, J. P. Perdew, *Phys. Rev. B* **1980**, *21*, 5469.
[31] J. A. Wilson, A. Yoffe, *Adv. Phys.* **1969**, *18*, 193–335.
[32] A. Kumar, P. K. Ahluwalia, *Mater. Chem. Phys.* **2012**, *135*, 755–761.
[33] B. Zong, Q. Li, X. Chen, C. Liu, L. Li, J. Ruan, S. Mao, *ACS Appl. Mater. Interfaces* **2020**, *12*, 50610–50618.
[34] Y. Yin, S. Wei, L. Zhang, Z. Guo, H. Huang, S. Sai, J. Wu, Y. Xu, Y. Liu, L. Zheng, X. Fan, X. Cui, *Chem. Res. Chin. Univ.* **2020**, *36*, 1122–1127.
[35] X. Gan, J. Zhang, J. Liu, Y. Bai, X. Su, W. Wang, Z. Cao, H. Zhao, Y. Ao, P. Wang, *ACS Appl. Nano Mater.* **2023**, *6*, 11725–11736.
[36] L. F. Seivane, H. Barron, S. Botti, M. A. Lopes Marques, Á.n. Rubio, X. López-Lozano, *J. Mater. Res.* **2013**, *28*, 240–249.
[37] K. Nie, X. C. Wang, W. B. Mi, *Appl. Surf. Sci.* **2019**, *493*, 404–410.
[38] G.-X. Chen, H.-F. Li, X. Yang, J.-Q. Wen, Q. Pang, J.-M. Zhang, *Superlattices Microstruct.* **2018**, *115*, 108–115.
[39] S. Li, M. Zhou, M. Li, G. Lu, X. Wang, F. Zheng, P. Zhang, *J. Appl. Phys.* **2018**, *123*, 095110.
[40] M. Amft, S. Lebègue, O. Eriksson, N. V. Skorodumova, *J. Phys.: Condens. Matter* **2011**, *23*, 395001.
[41] P. Hess, *Nanoscale Horiz.* **2021**, *6*, 856–892.
[42] H. M. Shodja, F. Ojaghnezhad, A. Etehadieh, M. Tabatabaei, *Mech. Mater.* **2017**, *110*, 1–15.
[43] J. C. Garcia, D. B. De Lima, L. V. C. Assali, J. F. Justo, *J. Phys. Chem. C* **2011**, *115*, 13242–13246.
[44] M. R. Arshee, S. Adnan, M. Motalab, P. Bose, *RSC Adv.* **2019**, *9*, 34437–34450.
[45] M. J. Cherukara, B. Narayanan, A. Kinaci, K. Sasikumar, S. K. Gray, M. K. Y. Chan, S. K. R. S. Sankaranarayanan, *J. Phys. Chem. Lett.* **2016**, *7*, 3752–3759 1948–7185.
[46] A. Mahmood, G. Rahman, *J. Phys.: Condens. Matter* **2020**, *32*, 205501.
[47] H. Şahin, S. Cahangirov, M. Topsakal, E. Bekaroglu, E. Akturk, R. T. Senger, S. Ciraci, *Physical Review B–Condensed Matter and Materials Physics* **2009**, *80*, 155453.
[48] P. Jamdagni, A. Kumar, A. Thakur, R. Pandey, P. K. Ahluwalia, *Mater. Res. Express* **2015**, *2*, 016301.
[49] Y. Wang, Y. Ding, *Appl. Surf. Sci.* **2016**, *382*, 1–9.
[50] M. Fadaie, N. Shahtahmassebi, M. R. Roknabad, O. Gulseren, *Comput. Mater. Sci.* **2017**, *137*, 208–214.
[51] X. Liu, C.-Z. Wang, M. Hupalo, W. C. Lu, M. C. Tringides, Y. X. Yao, K.-M. Ho, *Phys. Chem. Chem. Phys.* **2012**, *14*, 9157–9166.
[52] C. Zhu, H. Lv, X. Qu, M. Zhang, J. Wang, S. Wen, Q. Li, Y. Geng, Z. Su, X. Wu, Y. Li, Y. Ma, *J. Mater. Chem. C* **2019**, *7*, 6406–6413.
[53] S. Ahmad, S. Mukherjee, *Graphene* **2014**, *3*, 52.
[54] P. S. E. Yeo, M.-F. Ng, *Chem. Mater.* **2015**, *27*, 5878–5885.
[55] a) A. S. Ali, X. Wang, Z. Tayyab, M. A. K. Y. Shah, I. Hussain, K. A. Alibrahim, M. Tayyab, S. Rauf, *Mater. Sci. Eng., B*, **2025**, *313*, 117925; b) D. Yang, T. Ran, X. Zhai, F. Du, J. Song, C. Zhang, F. Huang, T. Fan, 21st International Conference on Electronic Packaging Technology (ICEPT), IEEE **2020**, pp. 1–4.
[56] Y. Ding, Y. Wang, *J. Phys. Chem. C* **2013**, *117*, 18266–18278.
[57] Z. Cui, X. Wang, E. Li, Y. Ding, C. Sun, M. Sun, *Nanoscale Res. Lett.* **2018**, *13*, 1–9.
[58] Z. Cui, E. Li, X. Ke, T. Zhao, Y. Yang, Y. Ding, T. Liu, Y. Qu, S. Xu, *Appl. Surf. Sci.* **2017**, *423*, 829–835.
[59] H. Sahin, F. M. Peeters, *Physical Review B—Condensed Matter and Materials Physics* **2013**, *87*, 085423.
[60] C. N. M. Ouma, K. O. Obodo, C. Parlak, G. O. Amolo, *Phys. E.* **2020**, *123*, 114165.

Manuscript received: July 1, 2024

© 2025 Wiley-VCH GmbH

23656549, 2025, 7, Downloaded from https://chemistry-europe.onlinelibrary.wiley.com/doi/10.1002/slct.202403122 by Delhi Technological University, Wiley Online Library on [05/03/2025]. See the Terms and Conditions (https://onlinelibrary.wiley.com/terms-and-conditions) on Wiley Online Library for rules of use; OA articles are governed by the applicable Creative Commons License

Physica Scripta

INCLUSIVE PUBLISHING TRUSTED SCIENCE

PURPOSE-LED PUBLISHING™

PAPER

Enhancing the durability of cast steel cylinder liners using HVOF sprayed functionally graded coatings

To cite this article: Prabhat Ranjan *et al* 2025 *Phys. Scr.* **100** 045010

View the article online for updates and enhancements.

You may also like

- Economic prospects of Steel Reinforced Functionally Graded Concrete (SRFGC) beam structures
B S Gan, S Kiryu, A Han et al.
- Capacitive deionization of NaCl from saline solution using graphene/CNTs/ZnO NPs based electrodes
Naman Arora, Fawzi Banat, G Bharath et al.
- Wall-climbing performance of gecko-inspired robot with soft feet and digits enhanced by gravity compensation
Bingcheng Wang, Zhiyuan Weng, Haoyu Wang et al.

This content was downloaded from IP address 14.139.251.98 on 01/04/2025 at 05:40

Physica Scripta

PAPER

Enhancing the durability of cast steel cylinder liners using HVOF sprayed functionally graded coatings

RECEIVED
22 September 2024

REVISED
14 February 2025

ACCEPTED FOR PUBLICATION
5 March 2025

PUBLISHED
20 March 2025

Prabhat Ranjan[1], **Rajesh Kumar**[1], **R S Walia**[2] and **Vinod Kumar Yadav**[3,*]

[1] Delhi Technological University, New Delhi, India
[2] Department of Production and Industrial Engineering, Punjab Engineering College, Chandigarh, India
[3] Department of Engineering and Technology, PSS Central Institute of Vocational Education, Bhopal (MP), India
[*] Author to whom any correspondence should be addressed.

E-mail: prabhatturbo@yahoo.com, dr.rajeshmits@gmail.com, waliaravinder@pec.edu.in and vinod.det@psscive.ac.in

Keywords: cast steel cylinder liners, corrosion resistance, functionally graded material, HVOF coatings, wear resistance

Abstract

This study investigates the performance of high-velocity oxygen fuel (HVOF) sprayed coatings on cast steel cylinder liners, specifically focusing on the Ni-Cr, WC-Co-Cr and WC-Co powder compositions to create functionally graded material (FGM) coatings. The wear resistance, evaluated using linear reciprocating tribometer, revealed that the FGM coated sample-A (designated as FGC-A) exhibits a minimal weight loss of 0.0010 g, outperforming FGM coated sample-B (FGC-B), with 0.0019 g weight loss, and FGM coated sample-C (FGC-C), with 0.0026 g weight loss. Furthermore, the results of immersion corrosion tests, in 50% H_2SO_4, indicated that FGC-A had the least corrosion weight loss of 0.47%, which is significantly better than FGC-B (1.37%) and FGC-C (1.87%). These results demonstrate that FGC-A offers superior wear and corrosion resistance compared to its counterparts. An empirical model to predict the wear loss in HVOF coatings, based on process parameters, was also developed and it was observed that optimizing the parameters such as oxygen flow, kerosene flow, stand-off distance, and feed rate play vital role in enhancing the quality of the coatings. In this study, the best settings for the process were found to be an oxygen flow of 867 m min^{-1}, a kerosene flow of 24 liters per hour, a stand-off distance of 340 mm, and a material feed rate of 86 grams per minute. These values were identified as the most effective for achieving strong and durable coatings with improved hardness and resistance to wear.

1. Introduction

The corrosion of engine component, like cylinder liners, is influenced by the accumulation of iron or aluminium (Al) and sulphur in the lubricating oil [1]. Sulphur present in the fuel initially gets oxidized to form sulphur dioxide (SO_2) during combustion. As the development phase progresses, some of the SO_2 is converted into sulphur trioxide (SO_3), which then reacts with water vapour in the gas to form sulfuric acid (H_2SO_4) vapour. When the temperature of the liner surface drops below the dew point temperature of H_2SO_4 vapour, the condensation of H_2SO_4 and water occurs, resulting in a concentrated H_2SO_4 solution. This acid solution is responsible for the corrosion observed in cast iron (CI) and steel liners that are used in the marine diesel engines [2]. Researchers in past have explored how SO_2 affects the metallic materials at high temperatures. In the temperature range of 200 to 450 °C, the CI and Al liners have shown great stability due to oxide layer formation, thermal stability, corrosion resistance to SO_2, and mechanical durability. Although SO_2 does not cause corrosion below 400 °C, when it gets incorporated into motor oils, its adverse contributions to liner deterioration become apparent. Studies conducted on SO_2 as a component of either fuels or intake air indicate that lubricants contain sulphurous acid (H_2SO_3) and H_2SO_4 are responsible for the significant corrosive wear of the liners. A subsequent study by Cordtz *et al* [3] experimentally investigated the cold corrosion wear using modified engine simulation conditions. They observed that higher water vapor concentrations in the charge gas results in increased liner wear, with sulfuric acid having a comparatively lower impact. In addition, it has also

© 2025 IOP Publishing Ltd. All rights, including for text and data mining, AI training, and similar technologies, are reserved.

been observed that although engines equipped with Exhaust Gas Recirculation (EGR) technique reduce NOx emissions, but they put their liners at risk of corrosion because they contaminate their lubricating oils with unwanted soot [4–6]. Abnormal corrosion in liners is considered an undesirable phenomenon; however, a slight and controlled corrosion rate is beneficial for maintaining adequate surface roughness. This roughness helps retain a thin lubricating oil film, which assists in local lubrication [1, 7]. Additionally, the corrosion rate is accelerated by factors such as liner temperature, engine load conditions, and charge air humidity [1, 8]. Many researchers [9–11] have focused on the application of electrochemical impedance spectroscopy (EIS) to electrochemical corrosion and static immersion properties in order to assess the corrosion resistance of coated aluminium alloys, such as marine CI liners and AlSi24, A356. In the recirculating test involving the Piston Ring Cylinder Liner (PRCL) pair, the use of emulsified biodiesel was associated with substantial wear and oil degradation. This was also corroborated by earlier studies [12] on bio-oils, which revealed their corrosive nature. Important data concerning thermal stability and volumetric changes of metal wear debris in oil exposed to high temperature corrosion can be provided through lube oil tests like Thermogravimetric Analysis, Differential Scanning Calorimetry etc. Certain coatings, such as ceramic, metallic, or polymeric types, are applied to engine components like cylinder liners to act as protective barriers against corrosive substances such as acids, salts, and humidity found in the engine environment. These coatings are crucial in preventing the harmful effects of corrosion, which can weaken the metal and reduce its lifespan. Applying high-hardness and toughened coatings helps in reducing wear, friction, and degradation, leading to sustained engine performance and efficiency over the long term due to the fact that they will provide a moving surface capable of resisting frictional force and abrasive forces that are comparatively longer than the original ones. Coatings produced using high-velocity oxygen fuel (HVOF) technology, characterized by low heat input and high kinetic energy output, offer benefits such as a dense structure and strong cohesive strength [13, 14]. These coatings are widely utilized for surface protection and the repair of industrial components, as well as for enhancing the corrosion and wear resistance of equipment, thereby extending its service life. Recently, Tungsten (WC)-based coatings, prepared through HVOF, have gained significant attention from both domestic and international researchers, who have been investigating the preparation techniques and properties of these coatings [15–17]. Tungsten-Cobalt (WC-Co) cemented carbide is an alloy material produced through the powder metallurgy process, with WC as the hard phase and Co as the bonding phase. This material is widely applied in aerospace, chemical machinery, and various other industrial sectors due to its distinct properties, including high hardness, wear resistance, compressive strength, elastic modulus, corrosion resistance, and low thermal expansion coefficient. When sprayed using HVOF, tungsten carbide composites exhibit exceptional wear resistance, enhancing the surface durability of equipment and extending its operational life. As a hard material with superior wear resistance, WC is frequently incorporated as a reinforcing phase in coatings, significantly improving the wear resistance of substrate surfaces [18–20]. The chromium (Cr) plays a crucial role in enhancing both wear resistance and corrosion resistance, when used in FGM coatings. The WC-10Co-4Cr coating, applied using optimized HVOF spraying, is known for its excellent wear and corrosion resistance and has been widely utilized in industries such as aviation, petrochemical, and ship building. It has been found that WC-10Co-4Cr exhibits outstanding oxidation resistance due to its high oxidation activation energy. The coating's high fracture toughness and hardness positively influence its fretting corrosion resistance. Additionally, WC-Co-Cr is considered an ideal material for developing dense, high-hardness coatings in applications requiring superior tribo-corrosion performance [21–24]. In line with this, $Fe_{57}Cr_{15}Mo_8P_{10}C_0B_3$ amorphous coatings were applied to 316 L stainless steel using the HVOF spraying technique.

Zhang *et al* [25] employed Taguchi's L16 orthogonal to optimize the process parameters, with oxygen flow rate as the most significant factor affecting the coating porosity. They observed that, under optimal conditions, the coatings exhibit minimal porosity, enhanced hardness, improved corrosion resistance, and superior wear performance. Their experimental validation confirmed the effectiveness of Taguchi's method in optimizing HVOF parameters, demonstrating its reliability in developing high-performance coatings for tribo-corrosion applications. A theoretical model was developed [26] to optimize HVOF parameters for WC-NiCr coatings using fine feedstock, recommending an oxygen-to-kerosene ratio of 3.3 and a shorter torch barrel to reduce decarburization. The optimized parameters produced coatings with low porosity, improved corrosion resistance, and reduced brittleness, minimizing the need for post-spray grinding. The HVOF coating process is used to enhance material longevity and surface properties by spraying molten or semi-molten powder. In the study [27], the response surface methodology (RSM) and Artificial Neural Networks (ANN) were applied to optimize powder composition for minimal porosity and maximum hardness in high-temperature environments. Analysis of 25 coatings showed that ANN provided more accurate predictions than RSM for achieving dense, high-quality coatings.

In summary, the literature review presented here collectively underscored the importance of advanced coatings, such as WC-Co-Cr and Fe-based amorphous coatings, in enhancing wear and corrosion resistance of engine liners. The use of HVOF technology, coupled with optimization techniques such as Design of

Experiments (DOE) and Taguchi's method, has shown promise in developing high-performance coatings for tribo-corrosion applications by conducting optimized number of experiments. With an emphasis on wear and corrosion resistance as well as mechanical testing, the present study methodically assesses the performance of FGM coatings produced from WC-Co-Cr, WC-Co, and Ni-Cr powders when applied to cast steel cylinder liners. The method of optimization of experiments, using Design of Experiments of the multi-layered FGM coatings, developed by our own group [28], along with its corrosion and wear characteristics, are studied in this paper on the similar concentrations. Utilizing Design of Experiments (DOE) methods, the processes were optimized by examining how different factors affects the measurement results.

In this research, a five-layered functionally graded material (FGM) coating has been developed for cylinder liner applications to overcome the limitations of conventional single- or double-layer coatings. Traditional coatings are often prone to abrupt material transitions, leading to stress concentration and delamination. In contrast, the functionally graded multi-layered design ensures a gradual transition in composition and microstructure, resulting in improved adhesion, thermal stability, and wear resistance under extreme operating conditions. The multi-layered design introduces a gradual transition in material composition and microstructure, addressing critical challenges such as stress concentration, thermal mismatch, and poor adhesion. Each layer is designed to offer specific functionalities, including increased resistance to thermal fatigue, enhanced load-bearing capacity, and improved corrosion protection, thereby contributing to an extended service life in high-performance applications. This development is especially significant for internal combustion engines operating under extreme conditions, where traditional coatings may deteriorate due to wear, thermal degradation, or inadequate bonding strength. This innovative approach demonstrates the potential of multi-layered FGM coatings for demanding applications, providing a foundation for further advancements in coating technology and performance optimization. Furthermore, the novelty of this work lies in the integration of WC-Co-Cr, WC-Co, and Ni-Cr powders to create functionally graded coatings with superior tribological and corrosion resistance. The study also employs Design of Experiments (DOE) techniques to optimize key process parameters-oxygen flow rate, kerosene flow, and stand-off distance-for enhanced coating performance. In contrast to conventional coatings, which can undergo early degradation in harsh tribological and corrosive environments, the functionally graded approach offers superior mechanical integrity and durability. This results in improved operational efficiency, lower maintenance costs, and enhanced reliability for applications in the marine, aerospace, and automotive industries, where liners are subjected to high temperatures, corrosive conditions, and varying loads. Moreover, the application of empirical modelling and advanced statistical techniques, such as ANOVA and Signal-to-Noise (S/N) ratio analysis, enables precise optimization of HVOF parameters. This approach enhances coating uniformity, reduces defects, and strengthens the reliability and reproducibility of FGM coatings for critical industrial applications.

2. Materials and methodology

In the present work, 10 mm × 10 mm × 5 mm cast steel samples were prepared for corrosion testing. Surface refinement with emery sheets of different grit sizes were used to initially prepare the material for the planned coating applications. The HVOF thermal spray method was used to apply the FGM coatings using three types of agglomerated and sintered powders. The methodology for applying Functionally Graded Material (FGM) coatings using the High-Velocity Oxygen Fuel (HVOF) thermal spray method involves several essential steps. First, agglomerated and sintered powders are selected, typically comprising materials like WC-Co, WC-Co-Cr, or Ni-Cr, that are designed to enhance the wear and corrosion resistances. Agglomerated powders are used to improve flowability and control particle size distribution during the spraying process. The surface preparation of the cast steel cylinder liners involved cleaning the substrates using solvents or alkaline cleansers to remove any impurities. The surface roughness was achieved through abrasive blasting using garnet or aluminium oxide, targeting a range of 3–6 microns. After abrasive blasting, the samples were degreased to remove any residual abrasives, ensuring a clean surface for coating application. In the HVOF method, a mixture of oxygen and fuel (kerosene) is ignited in a combustion chamber, producing a high-velocity, high-temperature flame. The powder particles are injected into this flame, rapidly heated and accelerated, then deposited onto the substrate, forming a dense coating. The nozzle-to-surface distance and flow rates are carefully controlled to achieve uniform coating application with varying material compositions, creating a gradient structure. Sintered powders are used for added strength and durability during spraying. After application, coatings undergo evaluation through surface characterization techniques, ensuring enhanced performance in harsh environments.

Figure 1 shows the layer by layer description of the FGM coatings that were deposited over the substrate. To maintain consistent coating quality, parameters such as oxygen and kerosene flow rates, nozzle-to-surface distance and carrier gas flow rate were controlled and optimized to ensure the precision. By utilizing SEM in surface characterization, a thorough analysis of the wear and corrosion resistance of the coatings was conducted.

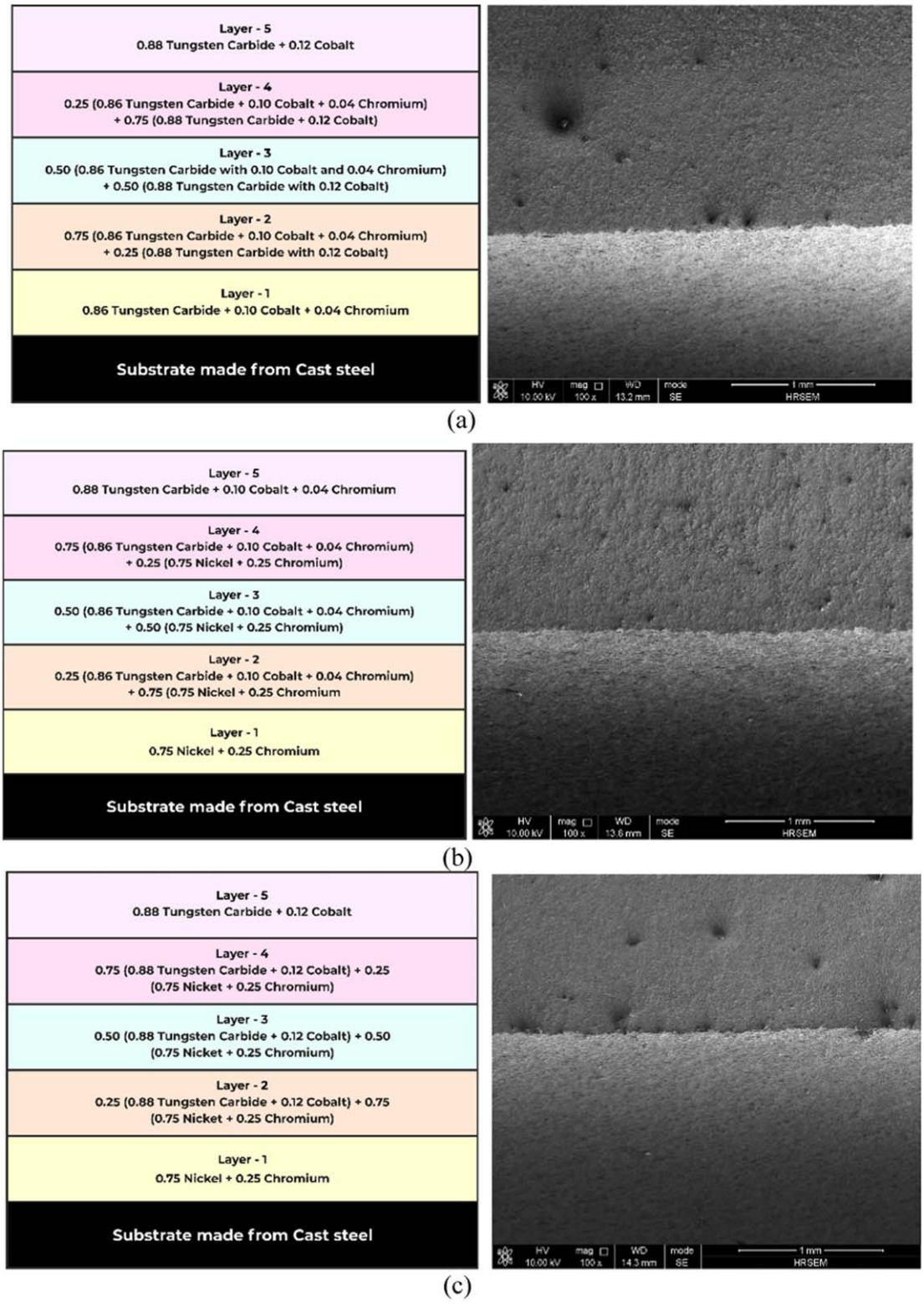

Figure 1. Detailed concentrations of the layer-wise coatings and their uniformity check using SEM images (a) FGC-A (b) FGC-B (c) FGC-C.

Wear testing was conducted using cylindrical pins coated with FGMs. For the corrosion testing, the pins were immersed in a solution of 50% sulphuric acid (H_2SO_4), and the respective weight loss measured indicated how severe the corrosion was. The purpose of these tests was to show that FGM coatings can extend the lifespan of cast iron cylinder liners in challenging environments. The use of L9 orthogonal array (a popular design in Taguchi methods) to examine the influence of major process parameters on wear resistance was carried out systematically. This method made it possible to study the principle effects of four variables with fewer experimental runs than a full factorial design.

Table 1. Process parameter and their level.

Process parameter	Level 1	Level 2	Level 3
Oxygen (m min^{-1})	863.0	865.0	867.0
Kerosene (liters $hour^{-1}$)	23.00	24.00	25.00
Stand-off distance (mm)	330.0	340.0	350.00
Feed Rate (g min^{-1})	82.00	84.00	86.00

Table 2. L9 orthogonal array.

Experiment	Oxygen (m min^{-1})	Kerosene (liters $hour^{-1}$)	Stand-Off distance (mm)	Feed rate (g min^{-1})	Wear loss (mg)	SNRA6
1	863	23	330	82	0.99	0.087296
2	863	24	340	84	0.94	0.537443
3	863	25	350	86	0.91	0.819172
4	865	23	340	86	0.93	0.630341
5	865	24	350	82	0.98	0.175478
6	865	25	330	84	0.88	1.110347
7	867	23	350	84	0.96	0.354575
8	867	24	330	86	0.84	1.514414
9	867	25	340	82	0.98	0.175478

The L9 orthogonal array allowed for nine experiments, with each factor having three levels. As a result, three samples were prepared for each experimental analysis to ensure consistent results, and the average values were used for analysis. The methodology clearly identified how each factor influenced the response variable-wear loss-while keeping the experiments manageable.

Table 1 provides an overview of the process parameters used in this study, highlighting the levels for oxygen flow rate (863, 865, 867 m min^{-1}), kerosene flow rate (23, 24, and 25 liters $hour^{-1}$), stand-off distance (330, 340, and 350 mm), and feed rate (82, 84, and 86 g min^{-1}). The wear loss (in mg) was measured as the response variable, the corresponding values of which are listed in table 2.

3. Results and discussion

This study focuses on evaluating the wear and corrosion resistance of FGM coatings made from the mixing of Ni-Cr, WC-Co-Cr and WC-Co powders on cast steel cylinder liners. By employing DOE technique, the process parameters were optimized to assess how various factors influences the characteristics of the materials.

3.1. Hardness of coating

In this study, the hardness of the coatings applied to the substrates was assessed using the Vickers Hardness Test (highly polished diamond indenter in the form of a square-based pyramid with an angle of 136° between faces) under standard operating conditions. The coating structure was divided into distinct zones i.e., Zone 1 that represents the outermost layer, while Zones 2 and 3 encompasses the inner layers and the substrate interface, respectively. Due to the homogeneity observed in SEM analyses, layers 2, 3, and 4 were grouped as Zone 2. Figure 2 illustrates the hierarchical trend in hardness across the samples. FGC-A exhibited the highest hardness, followed by FGC-B, with FGC-C having the lowest. This variation is primarily attributed to the differing concentrations of tungsten carbide (WC) relative to the metallic binder. FGC-A, with a higher WC content, demonstrated superior hardness, while FGC-B, despite a more uniform distribution, showed reduced hardness due to a softer binder material. Enhancement of the cast steel hardness using WC-Co-Cr coatings offers numerous advantages in industrial setups. Increased hardness improves wear resistance, providing protection against abrasion, corrosion, and friction-induced wear, which is critical in environments where machinery and tools are subjected to harsh operating conditions. The improved hardness also translates into greater resilience at elevated temperatures, making WC-Co-Cr coatings particularly suitable for processes like hot-forging, casting, welding, and other high-temperature applications owing to its high melting point. Moreover, the enhanced hardness boosts the overall strength of the material, reinforcing it against mechanical stresses and environmental factors, which is especially relevant in heavy machinery and equipment exposed to extreme operating conditions. These benefits collectively contribute to longer operational lifespans, greater efficiency, and reduced maintenance requirements for industrial components.

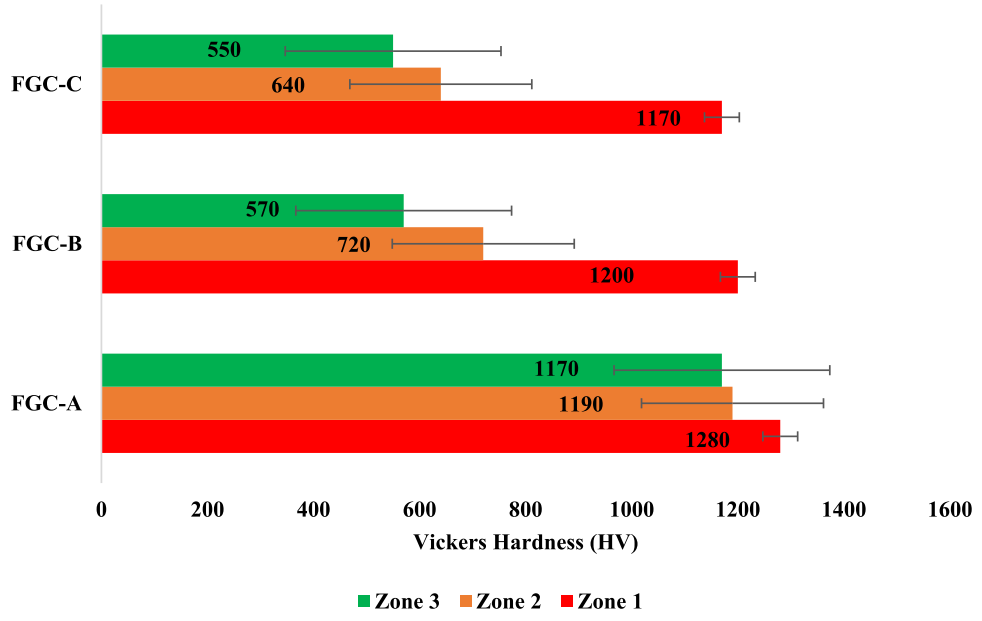

Figure 2. Zone-wise hardness of the coatings deposited over cast steel base metal.

3.2. Wear behaviour

The analysis of wear phenomena through scanning electron microscopy (SEM) provides crucial insights into the performance of Functionally Graded Coating (FGC) samples under a specified loading condition. The wear test (following ASTM G133-05 standards), conducted using a linear reciprocating tribometer, is a primary and viable technique of evaluating the wear resistance of the materials. The sliding distance was fixed as 15 mm, frequency 50 hertz, and load 20 N. When subjected to a 20 N load, the worn surfaces of FGC-A, FGC-B, and FGC-C exhibit distinct features, including small pits and grooves, primarily caused by the detachment of carbide particles. Additionally, ductile iron particles can be observed on the FGM coating surface, indicating a transfer of material from the counter fcorrdisc. The cutting wear mechanism, shown in the rectangular box, further clarifies the wear processes under these conditions. The observed differences in wear resistance between the samples can be attributed to the variations in composition, microstructure, and material properties. As evident from the weight loss data and SEM images, FGC-C exhibits the greatest wear, suggesting that its properties are less suited for applications demanding high wear resistance compared to FGC-A and FGC-B.

The wear resistance of materials is a critical property, particularly for components subjected to high mechanical stresses and abrasive environments. The results show that FGC-A, with a weight loss of 0.0010 mg, outperformed both FGC-B (0.0019 mg) and FGC-C (0.0026 mg), indicating a better resistance to wear. This difference in wear resistance can be attributed to the materials' composition and the distribution of phases within the coating. The composition of FGC-A likely includes a combination of materials that provide enhanced hardness and resilience against abrasive forces. This could explain why it exhibited minimal wear, as seen in the SEM images, which show only minor grooves on the surface. These characteristics enable FGC-A to distribute the applied stresses more effectively, reducing localized wear.

In contrast, FGC-B and FGC-C displayed progressively higher weight losses, suggesting that their compositions might not be as well-suited for resisting wear. FGC-B showed more pronounced wear patterns with debris and plastic deformation, indicating that it may be less efficient in absorbing and redistributing mechanical stresses. FGC-C, on the other hand, experienced the most severe wear, characterized by deep grooves, wear debris, and spalling. These results indicate that FGC-C might contain a phase or a composition that weakens its overall ability to handle high frictional stresses.

Microstructure plays a pivotal role in determining a material's wear resistance. In FGC coatings, the gradual variation in composition and microstructure, which typically involves transitions in hardness, contributes to superior wear resistance. The layers in FGCs can respond to mechanical stresses differently based on their individual properties, making them more resilient compared to single-layer coatings. The microstructure of FGC-A, which shows only minor grooves under SEM examination, indicates that the material is likely optimized for resisting wear. The distribution of phases within FGC-A likely leads to a more uniform stress distribution, preventing localized failure and crack propagation. On the other hand, the SEM images of FGC-B and FGC-C, showing severe wear with spalling and deeper grooves, suggest that their microstructures may not be as effective in distributing stresses. FGC-B's greater wear compared to FGC-A indicates that its microstructure might be less

cohesive or might not support load distribution as efficiently. FGC-C, with its deep grooves and spalling, appears to be experiencing significant localized material breakdown under stress, which highlights a possible weakness in its microstructure that reduces its overall wear resistance. The wear resistance of these materials is also influenced by the operational conditions they are subjected to during testing. Factors such as load, sliding distance, and abrasive type affect the wear behavior. The linear tribometer test, which simulates real-world wear conditions, likely highlighted the inherent differences in how each material responds to applied stress. FGC-A, with its minor wear patterns, suggests that it can endure harsher operational conditions without significant degradation. FGC-B and FGC-C, however, exhibited increasing severity in wear, which points to their relative inability to withstand the same stresses without experiencing significant material loss.

The wear testing results and SEM analysis provide valuable insights into the wear resistance of FGC coatings. FGC-A's optimal composition and microstructure make it the best performer among the three, exhibiting the least wear and highest resistance to mechanical stresses. FGC-B shows moderate wear, while FGC-C demonstrates the highest wear, with deep grooves and spalling. The differences in wear resistance can be attributed to variations in material composition, microstructure, and the coatings' ability to absorb and redistribute mechanical stresses. FGC coatings, in general, offer enhanced wear resistance compared to conventional single-layer coatings, making them suitable for demanding applications. However, FGC-C's performance suggests that further optimization of its composition and microstructure is required for improved wear resistance.

This test uses specific parameters like stroke length (15 mm), frequency (15 Hz), load (20 N), and time (5 min), to simulate the real-world conditions and assess material performance under sliding and reciprocating motion. The developed coatings FGC-A, FGC-B, and FGC-C were tested using this method, and weight loss was recorded to measure the wear resistance.

The worn surfaces, as analyzed through SEM, exhibit several distinct wear phenomena, including cracks, wear debris, grooves, delamination, and smear regions, which collectively illustrate the differences in the wear resistance of the FGC samples (figure 3). Cracks are observed as sharp, linear defects on the surface, originating due to localized stress concentrations during sliding. These cracks, particularly prevalent in FGC-B and FGC-C, are propagated by cyclic loading and material fatigue, eventually contributing to the initiation of surface failure. The detachment of carbide particles and fragmentation of the material during sliding interactions result in the formation of wear debris, which is scattered across the surface. This debris, functioning as third-body abrasives, exacerbates material removal and accelerates surface degradation. Grooves, identified as elongated scratches or indentations, are primarily caused by the plowing action of entrapped particles or asperities from the counter-body. The prominence of grooves, especially in FGC-C, suggests inadequate microstructural cohesion to resist abrasive forces. Delamination, visible as regions where material layers have separated, occurs due to subsurface cracks propagating parallel to the surface. This phenomenon, often exacerbated by weak interfacial bonding between the layers, contributes significantly to material loss. The presence of delamination was most pronounced in FGC-C, correlating with its higher weight loss during wear tests. Smear regions, which appear as smooth, plastically deformed areas, are formed when localized heat and pressure soften the material, causing it to flow and adhere. The transfer of ductile iron particles from the counter-disc to the coating surface, as noted in the revised manuscript, further supports the occurrence of smearing. These wear mechanisms were more severe in FGC-C, highlighting deficiencies in its composition and microstructure. In contrast, FGC-A exhibited fewer cracks, grooves, and delamination regions, indicating its superior ability to distribute applied stresses uniformly and resist mechanical and thermal stresses. This aligns with the conclusion that the integrity of the microstructure and the distribution of phases are critical in improving the wear resistance of functionally graded coatings. The causes behind these phenomena further underscore the necessity of optimizing the material's composition and processing parameters to mitigate such damage.

3.3. Corrosion behaviour

The corrosion resistance of Functionally Graded Coating (FGC) samples was evaluated by measuring the weight loss after 48 h immersion in a 50% H_2SO_4 solution (following ASTM G31-72 standards) Initial and final weights for FGC-A, FGC-B, and FGC-C were recorded to assess the extent of corrosion. The results showed varying levels of corrosion resistance among the samples.

FGC-A demonstrated the least weight loss, starting at 4.22 grams and dropping to 4.20 grams, which amounts to a loss of just 0.02 grams, or approximately 0.47%. This indicates that FGC-A has the highest corrosion resistance among the tested materials. FGC-B, on the other hand, experienced a greater weight loss. Its initial weight of 4.38 grams decreased to 4.32 grams, corresponding to a 0.06-gram reduction, or 1.37%. This shows that FGC-B is more prone to corrosion compared to FGC-A. FGC-C exhibited the most significant weight loss, starting at 4.28 grams and dropping to 4.20 grams, resulting in a weight loss of 0.08 grams, or 1.87%. This indicates that FGC-C had the poorest corrosion resistance among the three samples. Therefore, the results

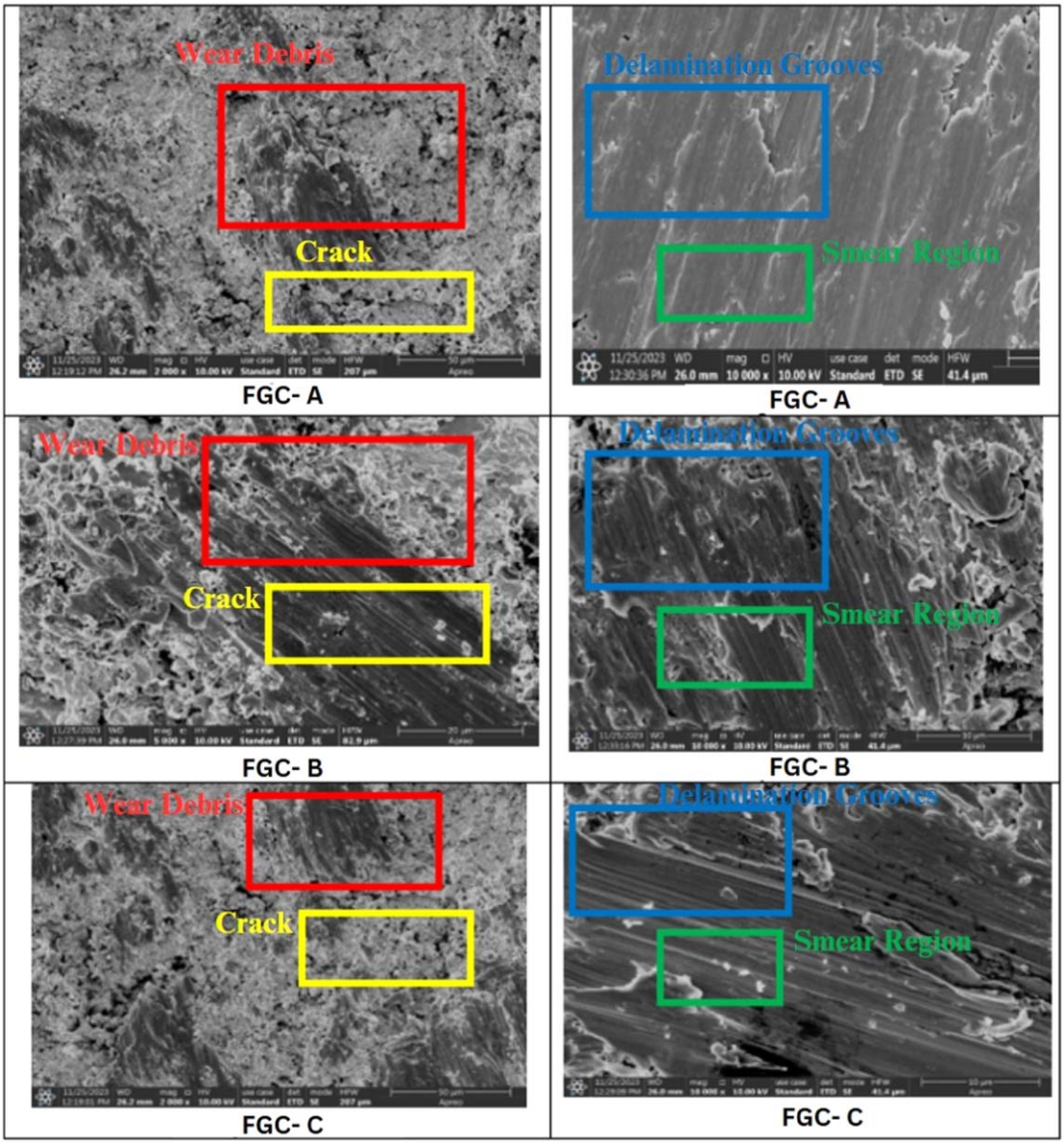

Figure 3. Worn surface images of FGCs.

clearly show that FGC-B outperformed FGC-C in corrosion resistance. The corrosion test results confirmed that FGC-A was the most corrosion-resistant sample, with the smallest percentage of weight loss (0.47%), followed by FGC-B (1.37%), and FGC-C (1.87%).

The SEM images (figure 4 and 5), taken before and after the corrosion test, illustrates the damage caused by the acidic environment. Before exposure, all three samples (FGC-A, FGC-B, and FGC-C) showed distinct surface features such as embedded particles, which were used as reference points. After the test, the surface of FGC-A shows relatively minor corrosion damage, with some localized pitting and surface roughening, consistent with its superior corrosion resistance and low weight loss. In contrast, FGC-B exhibits more pronounced corrosion, with deeper pits, cracks, and evidences of material loss. This suggests that FGC-B, though better than FGC-C, was still more susceptible to corrosion compared to FGC-A.

It can also be observed that the surface of FGC-C is severely corroded, with extensive pitting, cracking, and spalling. The higher weight loss percentage of 1.87% observed for FGC-C indicates significant degradation due to its relatively porous microstructure and weaker corrosion resistance. This increased porosity facilitates greater penetration of the corrosive medium (50% H_2SO_4 solution), accelerating the material's degradation. Additionally, the lower chromium content in FGC-C reduces its ability to form a protective oxide layer, further contributing to its susceptibility to corrosion. The SEM analysis and weight loss percentages support the conclusion that FGC-A was the most resistant to corrosion, followed by FGC-B, with FGC-C being the least resistant.

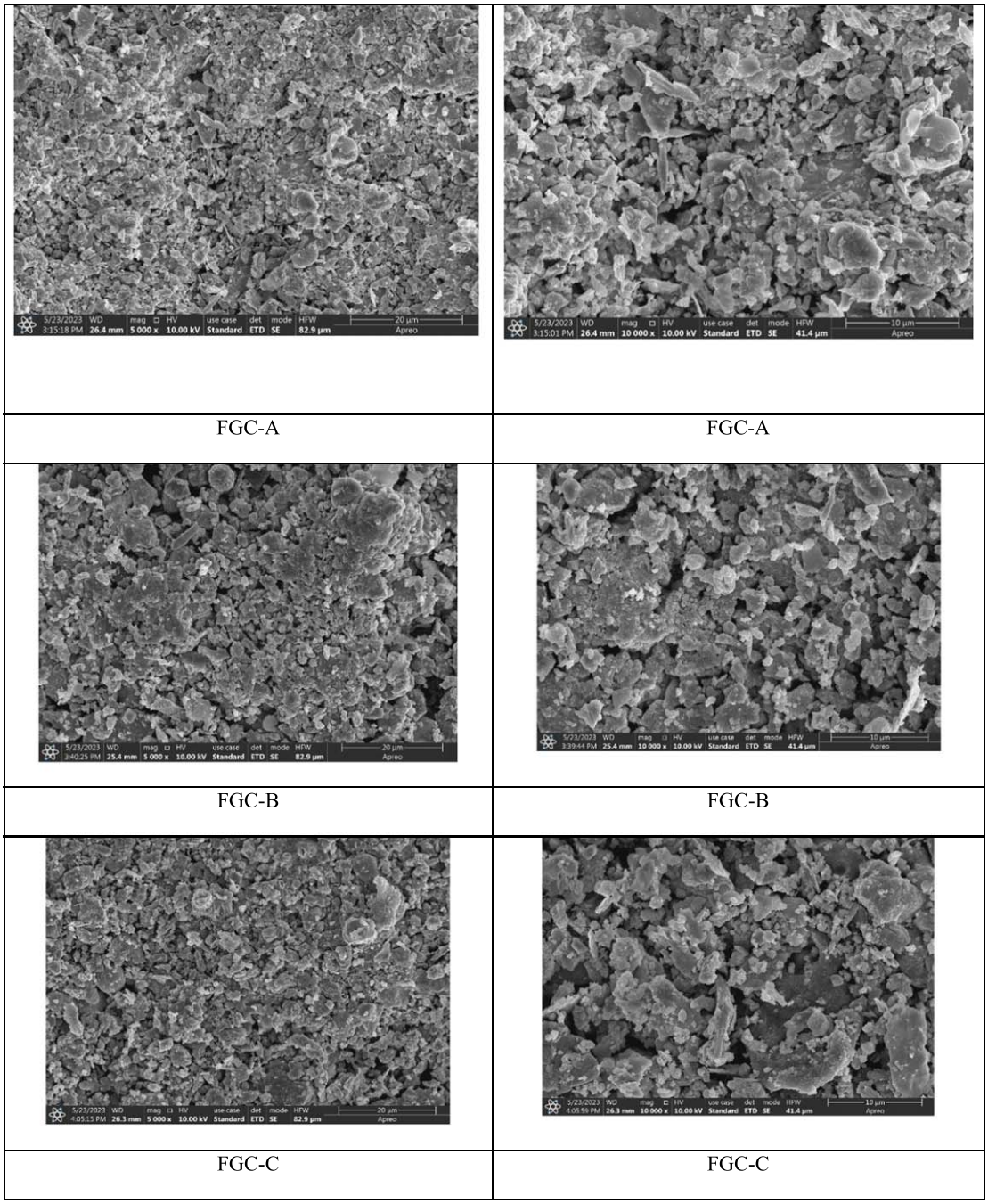

Figure 4. SEM of top surface of coating without corrosion.

3.4. Optimization of process parameters using DOE

In this study, statistical software Minitab 22 was employed to conduct an Analysis of Variance (ANOVA), which helps to determine the significance of different factors influencing wear loss. ANOVA enables to assess to what extent the parameter contributes to variations in the results, thereby identifying which factors have the most substantial impact. The Signal-to-Noise (S/N) ratio was calculated specifically for wear loss, helping to identify the optimal settings for each parameter to minimize the wear. The 'smaller is better' quality characteristic was applied in this analysis, which means that a lower wear loss is desirable. This approach allows for the identification of the process conditions that lead to improved performance and enhanced wear resistance of the coatings.

Development of empirical model and effect of process parameters

An empirical model was developed based on multi variable regression analysis. The following expression is developed to model the wear loss (Model parameters: S = 0.0244381, R-Sq. = 88.30%, R-sq. (adj.) = 76.61%, and R-sq. (pred.) = 38.40%)

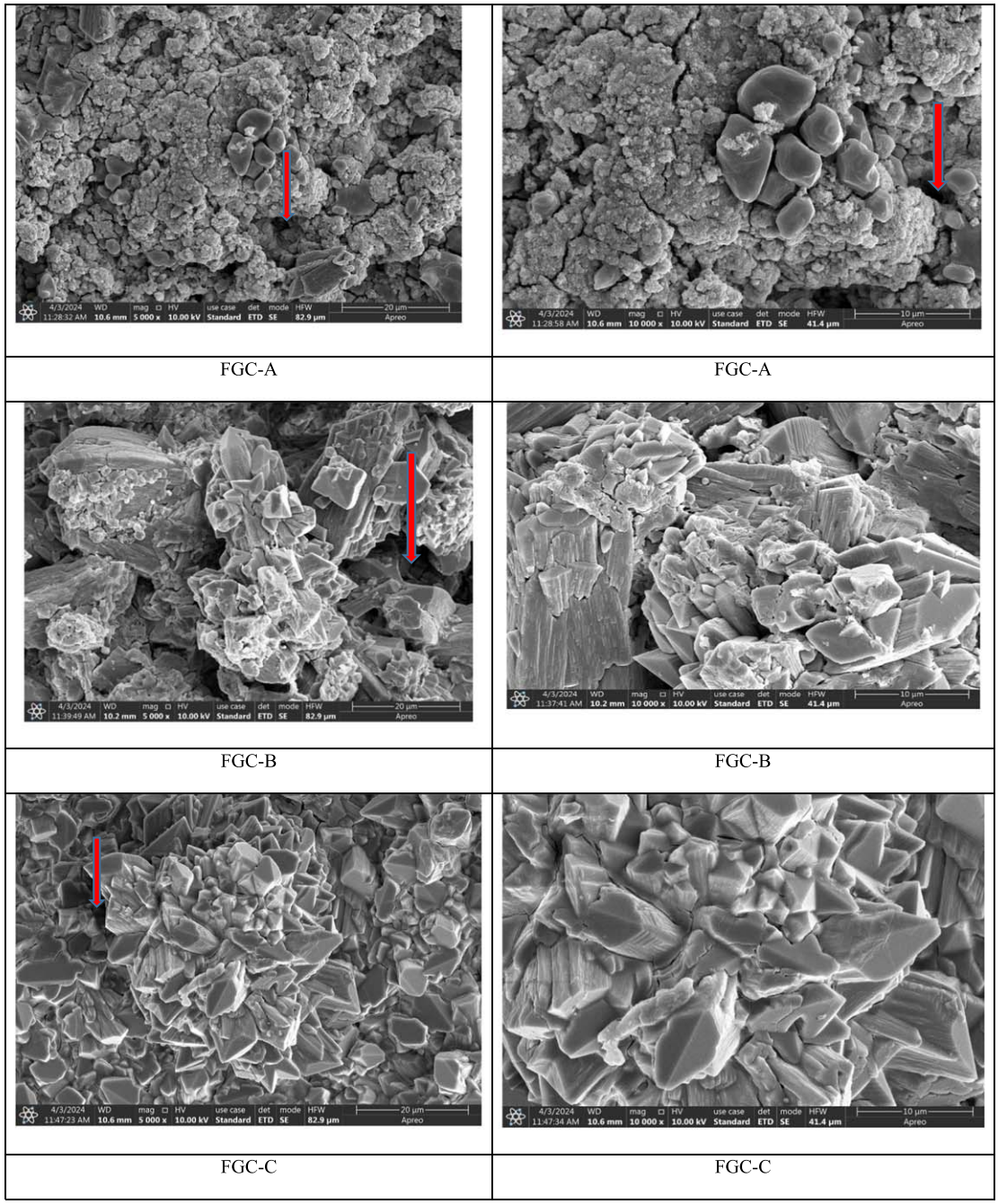

Figure 5. SEM of top surfaces of coating after corrosion.

Table 3. Analysis of variance.

Source	DF	Adj. SS	Adj. MS	F-value	P-value
Regression	4	0.01803	0.00451	7.55	0.038
Oxygen (m min^{-1})	1	0.0006	0.0006	1	0.373
Kerosene (liters per hour)	1	0.00202	0.00202	3.38	0.14
Stand-off distance (mm)	1	0.00327	0.00327	5.47	0.079
Feed rate (g min^{-1})	1	0.01215	0.01215	20.34	0.011
Error	4	0.00239	0.0006		
Total	**8**	**0.02042**			

$$\textbf{Wear loss}(\text{mg}) = 1.0344 - 0.01000\ \ \text{Oxygen}\ \ (\text{m/min}) - 0.01833\ \ \text{Kerosene}\ \ (\text{litres per hour}) + 0.02333\ \ \text{Stand} - \text{off distance}(\text{mm}) - 0.04500\ \ \text{Feed rate}(\text{g/m})$$

Table 4. Response table for signal to noise ratios.

Level	Oxygen (m min^{-1})	Kerosene (Liters per hour)	Stand-off-distance (mm)	Feed rate (g min^{-1})
1	0.4813	0.3574	0.9040	0.1461
2	0.6387	0.7424	0.4478	0.6675
3	0.6815	0.7017	0.4497	0.9880
Delta	**0.2002**	**0.3850**	**0.4563**	**0.8419**
Rank	4	3	2	1

Table 5. Response table for means.

Level	Oxygen (m min^{-1})	Kerosene (Liters per hour)	Stand-off distance (mm)	Feed rate (g min^{-1})
1	0.9467	0.9601	0.9033	0.9833
2	0.9301	0.9203	0.9502	0.9267
3	0.9267	0.9233	0.9503	0.8933
Delta	**0.020**	**0.04**	**0.0467**	**0.090**
Rank	4	3	2	1

The high value of R-sq. shows the model is adequate in the confidence interval of 95%. Table 3 shows the analysis of variance which indicate the F-value of developed model is 7.55 and p value of model is 0.038 which, is less than 0.05 indicating that the model is statistically correct and it can be utilized for the forecasting the wear loss within the range of the available experimental domain. These results highlight the importance of precise control over process parameters to achieve optimal wear resistance in HVOF coatings.

From tables 4 and 5, it can be observed that the order of influence of process parameters is Feed rate (g min^{-1}), Stand-off distance (mm), Kerosene (litres per hour) Oxygen (m min^{-1}).

Figure 6 shows the main effect plot of means and figure 7 shows the main effect plot for SN ratios. The effect of key process parameters is discussed in the preceding section.

3.4.1. Effect of oxygen

Although oxygen is considered a less influential parameter in the overall HVOF process, an increased supply of oxygen reduces the wear rate, as depicted in figure 6. This reduction occurs because sufficient oxygen ensures complete fuel combustion, which is critical for achieving optimal flame temperature and energy output in the HVOF system. When combustion finishes, the intense heat from the flame melts the feedstock particles evenly. These melted particles are then quickly shot toward the surface (substrate) at high speeds, which helps them coat the surface more effectively. As a result, a denser and more cohesive coating with fewer defects (like pores and voids) is formed. This improved coating structure enhances hardness, as well as wear resistance. Insufficient oxygen, on the other hand, leads to incomplete combustion, lower flame temperature, reduced particle melting, and diminished particle velocity, which contribute to a weaker, less wear-resistant coating. Therefore, although oxygen may not be the most dominant factor, its adequate supply is crucial for achieving high-quality coatings and reducing wear. The optimum wear rate yielded at oxygen level of 867 m min^{-1}.

3.4.2. Effect of kerosene

The supply of kerosene is a crucial factor in influencing the quality of HVOF coatings, as it directly impacts the combustion process and, consequently, the coating's wear resistance. As shown in figure 6, an initial increase in kerosene supply leads to the reduction in wear loss, up to an optimal point of 24 litres per hour. This reduction occurs because, when the fuel supply is adequately balanced with oxygen, higher flame temperatures are produced, resulting in better melting and acceleration of the feedstock particles. This, in turn, improves the coating density, strengthens bonding with the substrate, and enhances wear resistance.

However, exceeding this optimal fuel supply can result in incomplete combustion, as the oxygen available becomes insufficient to burn the excess fuel. Incomplete combustion lowers the flame temperature, reducing the melting effect and the velocity of the particles. This leads to poor adhesion of the coating and increased porosity, which in turn weakens the bonding between particles and the substrate. As a result, the coating quality degrades, and wear loss increases. Therefore, it is essential to maintain an optimal balance between kerosene and oxygen supply to ensure the highest performance of coatings in HVOF processes.

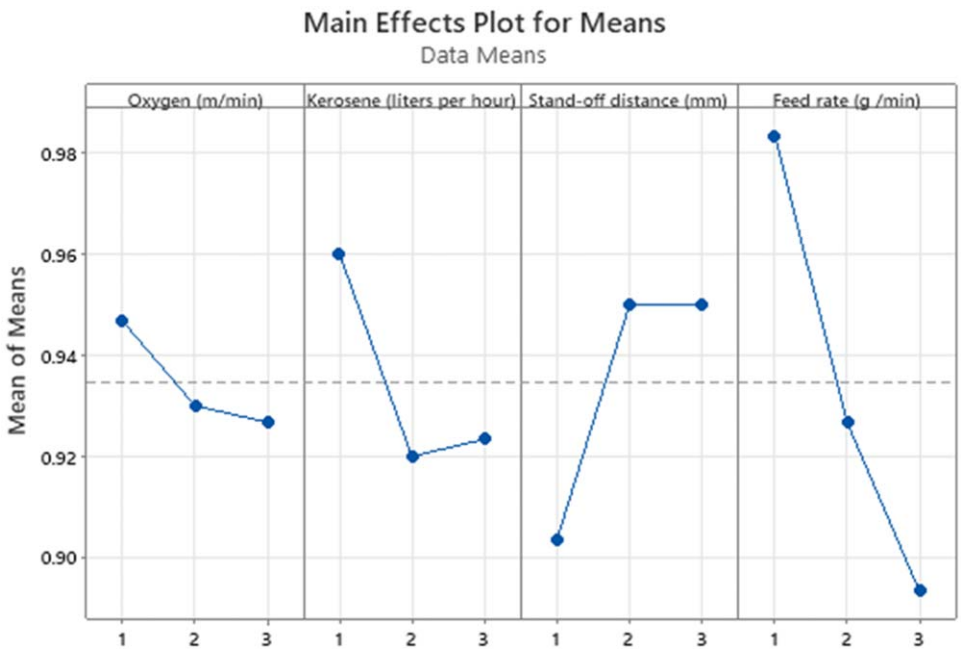

Figure 6. Main effect plots for means.

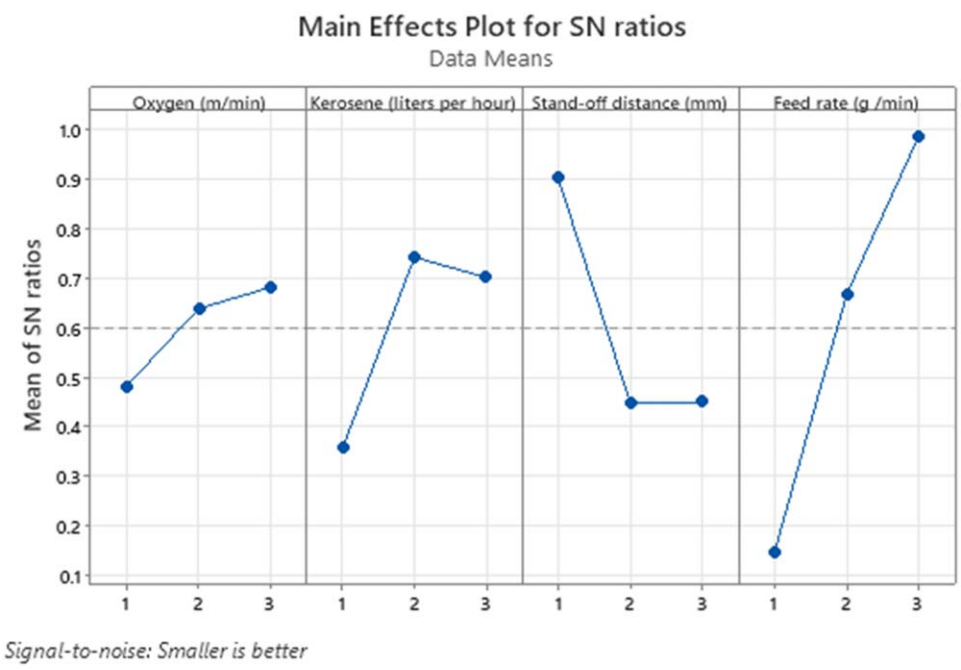

Figure 7. Main effect plot for SN ratios.

3.4.3. Effect of stand-off distance

Stand-off distance plays a significant role in the HVOF coating process as it directly influences the interaction between the flame, particles, and the substrate. As depicted in figure 6, an increase in the stand-off distance to 340 mm results in a higher wear rate. This occurs because, as the spray nozzle moves farther away from the surface (substrate), the particles slow down during their longer journey, reducing their speed by the time they reach the surface. Additionally, particles experience more cooling during this travel, leading to a reduction in their molten state upon reaching the substrate. This causes weaker bonding, increased porosity, and, consequently, a higher wear loss. However, after a certain stand-off distance, increasing the distance further has minimal impact on reducing wear loss. This is because, at greater distances, particle velocity and temperature

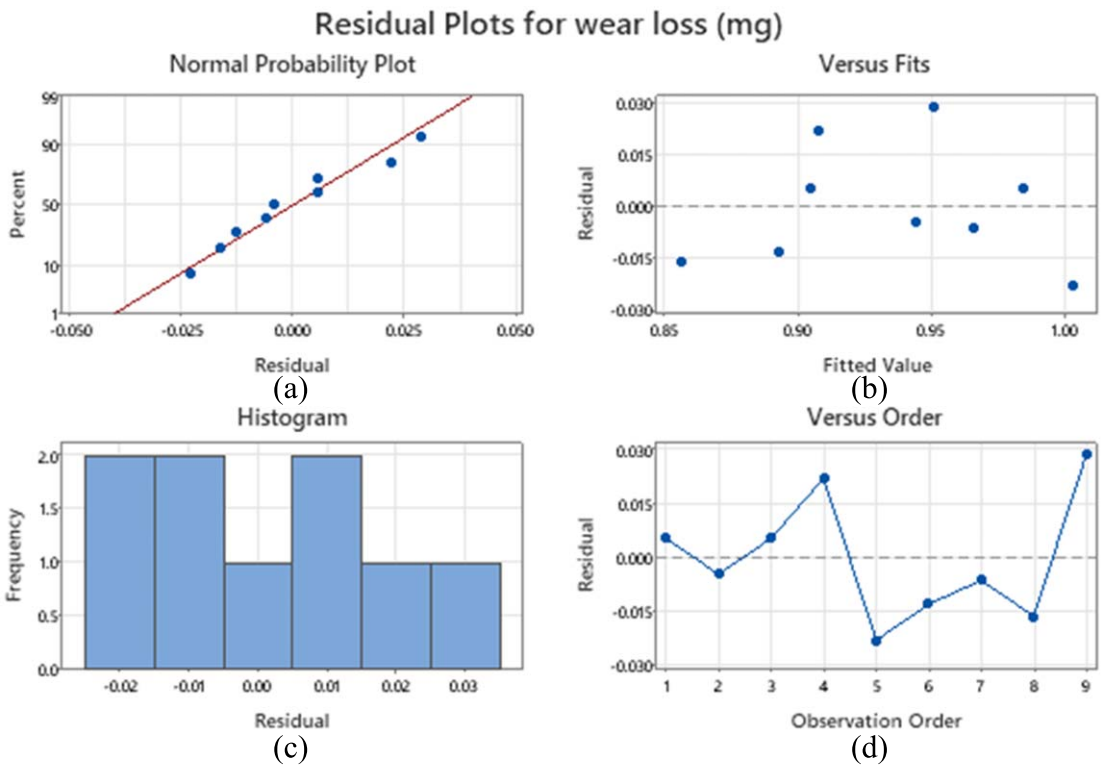

Figure 8. (a): Normal probability plot (b) residual verses fits plot (c) histogram plot and (d) residual versus order plot.

have already been decreased to a point where the cooling effect gets stabilizes. As a result, the coating properties stop deteriorating beyond a certain point, and wear loss stabilizes. In essence, the coating quality reaches a limit where further increases in stand-off distance no longer have a noticeable effect on wear loss, indicating that the performance has plateaued.

3.4.4. Effect of feed rate

The feed rate was identified as the most influential process parameter in the HVOF coating process, having a significant impact on wear loss, as indicated in figure 6. Initially, as the feed rate increases, the wear loss gets reduced. This reduction can be attributed to the higher amount of material supplied to the flame, leading to an improved coating thickness and density. The increased volume of molten particles reaching the substrate enhances the coating's integrity, reduces porosity, and strengthens the bonding, thereby improving wear resistance. However, beyond a certain threshold, further increases in feed rate results in the opposite effect, leading to higher wear loss. This reversal occurred because excessive feed rates overwhelms the thermal energy available in the HVOF process. When too much material is fed into the flame, it doesn't have enough energy to completely melt all the particles. As a result, partially melted or un melted particles were deposited onto the substrate, leading to a less cohesive coating with increased porosity and weaker bonds. This decline in coating quality diminished its wear resistance, ultimately resulting in higher wear loss. The optimal results for minimizing wear loss were achieved with an oxygen flow rate of 867 m min^{-1}, a kerosene flow rate of 24 liters per hour, a stand-off distance of 340 mm, and a feed rate of 86 g min^{-1}.

Figure 8 shows the (a) Normal probability plot (b) Residual verses fits plot (c) Histogram plot and (d) residual versus order plot. The normal probability plots show that the data points are fitted near the straight line which justifies that the data are adequate. Figure 8(a) shows that the residuals are normally distributed which are essential parameters for the regression models. It can also be observed that the points on the normal probability plot are aligning closely with the diagonal line, indicating that the residuals follow a normal distribution. Figure 8(b) depicts that residuals are randomly scattered around zero with no discernible pattern. Figure 8(c) provides a visual representation of the distribution of residuals. It can be seen that the fitted model has residuals that are symmetrically distributed around zero, which indicates a normal distribution. Figure 8(d) shows that the residuals do not exhibit any patterns in the order of data collection. From the analysis of above residual plots, it is confirmed that the regression model is adequately prepared for the given set of conditions.

Table 6. Model validation parameters.

Process parameter	Optimum level	Model value of wear (mg)	Average experimental value of wear loss (mg)
Oxygen (m min^{-1})	867	0.85 ± 0.012	0.858
Kerosene (liters $hour^{-1}$)	24		
Stand-Off Distance (mm)	340		
Feed Rate (g min^{-1})	86		

3.5. Validation of the experimental model

Confirmation tests were conducted to check the validity of the developed model. For confirmation test, five samples were fabricated at the optimum level of process parameters and their average value was compared with the model value of the wear loss. The optimized values for the process parameters were determined to be an oxygen flow rate of 867 m min^{-1}, a kerosene flow rate of 24 liters per hour, a stand-off distance of 340 mm, and a feed rate of 86 g min^{-1}. The results revealed that the model values are within the range of 95% of confidence interval as shown in table 6. Equation (1) shows the expression for the calculation of confidence interval.

$$\text{Confidence interval (CI)} = Z \times \frac{\sigma}{\sqrt{n}} \tag{1}$$

For 95% confidence interval value of $Z = 1.96$, $\sigma = 0.0137$, $n = 5$
At optimum level of process parameters, the value of average wear loss was found to be 0.858 mg.

4. Conclusions

This study evaluated the performance of Functionally Graded Material (FGM) coatings applied to cast steel cylinder liners using the High-Velocity Oxygen Fuel (HVOF) thermal spray process. The parameters of the multi-layered coatings, composed of WC-Co-Cr, WC-Co, and Ni-Cr powders, were optimized using the Design of Experiments (DOE) technique to improve their wear and corrosion resistance. The following conclusions were drawn:

1. A novel five-layered FGM coating for cylinder liners has been developed, enhancing wear and corrosion resistance, thereby highlighting its potential for high-temperature cylinder liner applications.
2. FGC-A demonstrated the highest hardness among the coatings due to its higher tungsten carbide content, which enhanced its wear resistance and made it suitable for high-temperature applications as encountered in internal combustion engines.
3. FGC-A demonstrated exceptional wear resistance, exhibiting only minimal weight loss (0.0010 mg) and negligible surface grooves. It outperformed both FGC-B and FGC-C, owing to its optimized composition and microstructure, making it particularly suitable for severe working environments. In addition, FGC-A also showed the highest corrosion resistance with a weight loss of 0.47% after immersion in a 50% H_2SO_4 solution for 48 h. This was followed by FGC-B (1.37%) and FGC-C (1.87%).
4. The study identified optimal HVOF process parameters as follows: an oxygen flow rate of 867 m min^{-1}, a kerosene flow rate of 24 liters per hour, a stand-off distance of 340 mm, and a feed rate of 86 g min^{-1}.
5. Future research on functionally graded coatings should focus on optimizing material composition through hybrid or nano-reinforced coatings to enhance wear resistance, corrosion protection, and thermal stability. Advanced techniques like plasma and cold spraying could improve adhesion, density, and performance. Long-term durability studies under real-world conditions would provide deeper insights. Expanding applications to aerospace, marine, and biomedical industries could unlock new possibilities. Machine learning and AI-driven optimization could refine coating design for superior mechanical and tribological properties. These efforts will drive continuous innovation and industrial adoption of high-performance coatings for demanding engineering applications.

Data availability statement

The data cannot be made publicly available upon publication because they contain sensitive personal information. The data that support the findings of this study are available upon reasonable request from the authors.

ORCID iDs

Prabhat Ranjan https://orcid.org/0000-0001-5758-5490

References

[1] Kjemtrup L, Cordtz R F, Meyer M and Schramm J 2017 Experimental investigation of sulfuric acid condensation and corrosion rate in motored bukh DV24 diesel engine: internal combustion engine fall technical conference (ICEF 2017) *Proc. ASME 2017 Intern. Combust. Engine Div. Fall Tech. Conf.* (https://doi.org/10.1115/ICEF2017-3652)
[2] Kjemtrup L, Cordtz R F, Jensen M V and Schramm J 2020 An experimental investigation of the corrosive influence of SO_2 relative to H2SO4 of marine engine cylinder liners *Lubr. Sci.* **32** 131–44
[3] Cordtz R F, Kjemtrup L, Jensen M V and Schramm J 2022 An experimental study of the effect of condensing water vapour on the cold corrosion wear of marine engine cylinder liners *Lubr. Sci.* **34** 103–11
[4] Naegeli D W and Marbach H W 1988 Role of sulfur oxides in wear and deposit formation in Army diesel engines. Interim report, October 1985-September 1987 *Southwest Research Inst.* (Belvoir Fuels and Lubricants Research Facility) AD-A-206054/9/XAB; BFLRF-248 Accessed: Sep. 21, 2024 https://osti.gov/biblio/5778942
[5] Schramm J, Henningsen S and Sorenson S C 1994 Modelling of corrosion of cylinder liner in diesel engines caused by sulphur in the diesel fuel *SAE International* (SAE Technical paper) 940818 (https://doi.org/10.4271/940818)
[6] Dziubak T and Dziubak S D 2022 A study on the effect of inlet air pollution on the engine component wear and operation *Energies* **15** 3
[7] Olander P, Hollman P and Jacobson S 2013 Piston ring and cylinder liner wear aggravation caused by transition to greener ship transports–Comparison of samples from test rig and field *Wear* **302** 1345–50
[8] Cordtz R, Mayer S, Eskildsen S S and Schramm J 2018 Modeling the condensation of sulfuric acid and water on the cylinder liner of a large two-stroke marine diesel engine *J. Mar. Sci. Technol.* **23** 178–87
[9] Rao X, Sheng C, Guo Z, Xu C, Dai L and Yuan C 2022 Corrosion behaviors of cylinder liner in marine diesel engine burning low sulfur fuel oil: an experimental and molecular dynamics simulation study *Tribol. Int.* **171** 107575
[10] Xie H, Cheng Y, Li S, Cao J and Cao L 2017 Wear and corrosion resistant coatings on surface of cast A356 aluminum alloy by plasma electrolytic oxidation in moderately concentrated aluminate electrolytes *Trans. Nonferrous Met. Soc. China* **27** 336–51
[11] Alves S A, Fernandez-Lopez P, Lopez-Ortega A, Fernandez X, Quintana I, San-José J T and Bayon R 2022 Enhanced tribological performance of cylinder liners made of cast aluminum alloy with high silicon content through plasma electrolytic oxidation *Surf. Coat. Technol.* **433** 128146
[12] Song R, Yu H, Song H and Hu X 2022 Effects of biomass fast pyrolysis fuel on the tribological behaviour of heavy-duty diesel engine lubricating oil *Appl. Sci.* **12** 5
[13] Chen X, Li C, Li S, Han X, Jiang H and Zhao X 2023 HVOF spray performance optimization analysis and experimental research of WC–12Co coating on Ti alloy *Met. Mater. Int.* **29** 3548–65
[14] Behera N, Medabalimi S R and Ramesh M R 2023 Elevated temperatures erosion wear behavior of HVOF sprayed WC-Co-Cr/Mo coatings on Ti6Al4V substrate *Surf. Coat. Technol.* **470** 129809
[15] Matikainen V, Bolelli G, Koivuluoto H, Sassatelli P, Lusvarghi L and Vuoristo P 2017 Sliding wear behaviour of HVOF and HVAF sprayed Cr3C2-based coatings *Wear* **388–389** 57–71
[16] García-Rodríguez S, López A J, Bonache V, Torres B and Rams J 2020 Fabrication, wear, and corrosion resistance of HVOF sprayed WC-12Co on ZE41 magnesium alloy *Coatings* **10** 5
[17] Voorwald H J C, dos Santos Vieira L F, de Oliveira Velloso V M, Fernandes M F and Cioffi M O H 2022 Investigation of HVOF-sprayed WC- and NiCr-based coatings to improve corrosion and wear performance of high-strength steel *J. Braz. Soc. Mech. Sci. Eng.* **44** 96
[18] Weicheng K, Hui S, Jiaxu G, Jie W and Yuling L 2019 Electrochemical corrosion behavior of HVOF sprayed WC–12Co coating on H13 hot work mould steel *Anti-Corros. Methods Mater.* **66** 827–34
[19] Yao J, Liu F, Wang X, Liu H, He T, Dai W, Tan L, Huang L and Liu Y 2024 Enhancing comprehensive properties of HVOF thermally sprayed WC-10Co coatings using two grain inhibitors *Surf. Coat. Technol.* **477** 130323
[20] Zhang F G 2019 Friction and wear behavior of WC/Ni cemented carbide tool material irradiated by high-intensity pulsed electron beam *Ceram. Int.* **45** 15327–33
[21] Liu Y, Liu W, Ma Y, Meng S, Liu C, Long L and Tang S 2017 A comparative study on wear and corrosion behaviour of HVOF- and HVAF-sprayed WC–10Co–4Cr coatings *Surf. Eng.* **33** 63–71
[22] Jafari M, Enayati M H, Salehi M, Nahvi S M and Park C G 2013 Comparison between oxidation kinetics of HVOF sprayed WC–12Co and WC–10Co–4Cr coatings *Int. J. Refract. Met. Hard Mater.* **41** 78–84
[23] kumar A, Sharma A and Goel S K 2016 Erosion behaviour of WC–10Co–4Cr coating on 23-8-N nitronic steel by HVOF thermal spraying *Appl. Surf. Sci.* **370** 418–26
[24] Murugan K, Ragupathy A, Balasubramanian V and Sridhar K 2014 Optimizing HVOF spray process parameters to attain minimum porosity and maximum hardness in WC–10Co–4Cr coatings *Surf. Coat. Technol.* **247** 90–102
[25] Zhang C *et al* 2024 Optimization of HVOF spraying parameters for enhanced Fe-based amorphous coatings: a taguchi approach *Intermetallics* **173** 108419
[26] Singh S, Osi A, Joshi V V, Wade S, Berndt C C, Schläfer T, Howse H and Ang A S M 2024 Development of fine WC-NiCr powder coatings by optimising HVOF spray parameters *Int. J. Refract. Met. Hard Mater.* **121** 106667
[27] Shankar R, Balasubramanian K R, Sivapirakasam S P and Ravikumar K 2021 ANN and RSM models approach for optimization of HVOF coating *Mater. Today Proc.* **46** 9201–6
[28] Ranjan P, Kumar R, Walia R S and Yadav V K 2024 Experimental and computational investigation of FGM coated cylinder liners prepared using HVOF technique *Phys. Scr.* **99** 085045

Children's Health Care

ISSN: (Print) (Online) Journal homepage: www.tandfonline.com/journals/hchc20

Examining maternal healthcare service utilization as a determinant of child health outcomes in India: Demographic and Health Survey 2019–21

Charu Tayal, Rajesh Sharma & Kusum Lata

To cite this article: Charu Tayal, Rajesh Sharma & Kusum Lata (25 Feb 2025): Examining maternal healthcare service utilization as a determinant of child health outcomes in India: Demographic and Health Survey 2019–21, Children's Health Care, DOI: 10.1080/02739615.2025.2465305

To link to this article: https://doi.org/10.1080/02739615.2025.2465305

View supplementary material

Published online: 25 Feb 2025.

Submit your article to this journal

Article views: 4

View related articles

View Crossmark data

Full Terms & Conditions of access and use can be found at
https://www.tandfonline.com/action/journalInformation?journalCode=hchc20

CHILDREN'S HEALTH CARE
https://doi.org/10.1080/02739615.2025.2465305

Taylor & Francis
Taylor & Francis Group

Check for updates

Examining maternal healthcare service utilization as a determinant of child health outcomes in India: Demographic and Health Survey 2019–21

Charu Tayal[a], Rajesh Sharma[b], and Kusum Lata[a]

[a]University School of Management and Entrepreneurship, Delhi Technological University, New Delhi, India; [b]Humanities and Social Sciences, National Institute of Technology Kurukshetra, Kurukshetra, India

ABSTRACT

In India, poor child health outcomes (CHOs) is a longstanding issue. This study examines the impact of maternal healthcare service utilization (MHCSU) on under-five CHOs, including stunting, wasting, anemia, underweight, and overweight in India, using data from the 2019–21 Indian Demographic and Health Survey. In India, a mother who consumed iron folic acid (IFA) tablets for at least 180 days [OR 0.94; 95% CI 0.9–0.99] and who received postnatal care (PNC) [OR 0.91; 95% CI 0.85–0.98] had lower odds of having an anemic child. The odds of being underweight were higher among children [OR 1.05; 95% CI 1.0–1.1] whose mothers were more than three months pregnant at the time of their first antenatal care (ANC) checkup. The skilled assistance during delivery reduced the odds of wasting [OR 0.96; 95% CI 0.92–0.99] and anemia among children. Notably, mothers who attended at least four ANC visits were more likely to have an overweight child, as each additional ANC visit has been associated with an increase in the child's weight. In summary, our results demonstrate that MHCSU has a significant impact on CHOs in India. Pertinent public health programs, increased accessibility and affordability of maternal healthcare services, greater engagement with frontline health workers, and women's empowerment can further improve CHOs in India.

Introduction

The period from birth to five years is the most crucial period for critical growth and developmental processes (Baek et al., 2022; Oumer et al., 2022). Yaya et al. (2020) contend that adequate nutrition during this period plays a vital role in a child's cognitive, physical, emotional, and social development. Poor child health outcomes (CHOs) not only harm children's physical health but also adversely impact their emotional well-being and self-esteem (Komakech et al., 2022). Furthermore, early CHOs significantly affect later-life outcomes as children who perform poorly on health indicators are more

CONTACT Rajesh Sharma rajesh.sharma@nitkkr.ac.in Humanities and Social Sciences, National Institute of Technology Kurukshetra, A328, Kurukshetra, Haryana, India
Supplemental data for this article can be accessed online at https://doi.org/10.1080/02739615.2025.2465305.
© 2025 Taylor & Francis Group, LLC

likely to have lower school achievement and earnings in adulthood than their counterparts (Alderman, 2009; McGovern et al., 2017; Moffat et al., 2022). Notably, a poor start to life has long-lasting effects on the individual's life as it can lower their productivity, reduce income-earning ability, and increase vulnerability to chronic diseases and obesity during adulthood (Popkin et al., 2020; Siddiqui et al., 2020; J. C. Wells et al., 2020; J. C. K. Wells et al., 2018; Yaya et al., 2020).

The sustainable development goal 2 "Zero hunger," aims to eradicate malnutrition by 2030, including reducing the prevalence of stunting and wasting in children aged less than five years by 2025 (UNDP, 2022). Nearly half of all deaths among children are due to malnutrition, as it makes them more vulnerable to infections, increasing the probability of dying from diseases that are preventable in nature (Paul & Saha, 2022). Numerous scholars found that child malnutrition is negatively related with a country's economic growth; hence, the objective of economic development cannot be met without addressing the issue of child malnutrition (Abu-Fatima et al., 2020; Hakizimana, 2022; Mary, 2018; Nugent et al., 2020; Seth & Jain, 2022). As per a report titled "The State of Food Security and Nutrition in the World 2022," global stunting and wasting among under-five children were 22% and 6.7% in 2020, respectively (FAO, 2022). This report further underscores that the global prevalence of obesity among children has increased, and 42% of under-five children are anemic, with no marked improvement in the last two decades (FAO, 2022). It is deeply concerning that child malnutrition remains alarmingly high in India, with under-five stunting at 35.5% and underweight at 32.1% (IIPS & ICF, 2022). Moreover, the prevalence of wasting in India, at 19.3%, stands as the highest globally, underscoring the critical need for targeted interventions (Economic Times, 2022).

CHOs are related to several factors, including the socioeconomic conditions of the mother, the weight of women during pregnancy, contaminated drinking water, hygiene, psychological counseling and family planning practices (Aneesh, 2021; Maulina et al., 2022; McGovern et al., 2017; Woldeamanuel & Tesfaye, 2019). Scarce evidence is available to contextualize mothers' crucial role in childcare practices and health status in the Indian context (Paul & Saha, 2022). Maternal health care services primarily refer to antenatal care (ANC), delivery care and postnatal care (PNC) (James et al., 2021). ANC may help in preventing malnutrition among children as it aids in the early detection and prevention of factors that may adversely affect child health (Shyam et al., 2020). Adequate nourishment during pregnancy, nutritional counseling, and emotional and psychological support may prevent infant mortality and neonatal mortality and affect the holistic development of a child (Von Hinke et al., 2022; Young et al., 2022). Delivery care may potentially ensure the presence of skilled health personnel and round-the-clock supervision during the critical period of childbirth, minimizing the risk of child mortality and morbidity

(Yoseph, 2020). PNC checkups are essential for educating mothers about warning signs, breastfeeding practices, vaccinations and hygiene, which may assist in preventing poor CHOs (Ahmadinezhad, 2022).

Over the years, only a few studies have investigated the link between ANC and CHOs in India using previous Demographic and Health Survey (DHS) data. A study conducted using data from previous India DHS data (2015–16) found that women who received no ANC checkup, had lower education, and lower family income were more likely to have stunted children (Das et al., 2022). Studies conducted in Odisha (a state in India) found similar results, where inadequate ANC checkups, poor wealth index and poor sanitary conditions contributed to poor CHOs in the form of underweight, stunting and anemia among under-five children (Chakrabarti et al., 2021; Nambiar et al., 2022). Another study analyzed Indian DHS data from previous rounds (1998-–2016) and found that an increased average number of ANC visits reduced poor CHOs (Srivastava & Upadhyay, 2020). Additionally, in Odisha, a lower number of institutional and skilled deliveries contributed to underweight among under-five children (Nambiar et al., 2022). Chakrabarti et al. (2021) found that PNC significantly lowered the odds of stunting and anemia among children. Notably, a few existing studies have provided contrary results in developing countries (Choi et al., 2022; Haby et al., 2022; Mullany et al., 2009; Shyam et al., 2020; Solans et al., 2021; Spies et al., 2022; Syeda et al., 2021; Wali et al., 2020).

Against this backdrop, the main objective of this study is to examine the impact of MHCSU on CHOs using the latest round of DHS in India, 2019–21, which is a nationally representative sample of 219,187 women aged 15–49 years, who have given live birth in the five years preceding the survey (IIPS & ICF, 2022) (Figure 1). Our empirical analyses focus on five indicators of MHCSU – ANC visits, number of days IFA tablets consumed, number of months pregnant at the time of first ANC checkup, skilled birth attendant

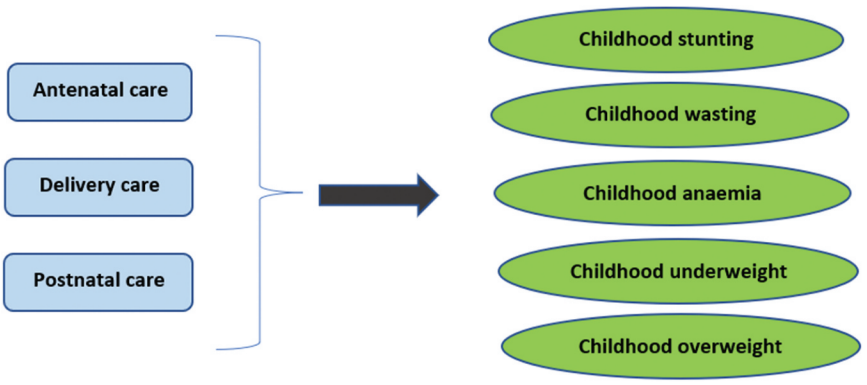

Figure 1. Association between maternal healthcare service utilization and child health outcomes.

during delivery and PNC received by mothers and five under-five CHOs – stunting, wasting, anemia, underweight and overweight. In the hypothesized model, MHCSU influences CHOs in terms of under-five stunting, wasting, anemia, underweight and overweight (Figure 1)

The main contribution of the paper is to provide empirical evidence on the association between MHCSU and CHOs using high-quality nationally representative DHS data; thereby, increasing the generalizability of our results for all children aged less than five years in India (IIPS & ICF, 2022). Second, as per DHS (2019–21) number of children who are overweight, severely wasted and anemic has increased in India compared to previous survey round; therefore, it is crucial to understand the potential influence of maternal health care on CHOs (Von Hinke et al., 2022). Third, to the best of our knowledge, this is the first study to examine comprehensively the relationship between MHCSU and CHOs using a bucket of five major child health indicators. Due to the persistent prevalence of childhood malnutrition and the dearth of supporting evidence in India on the impact of MHCSU on CHOs, this study significantly contributes to the existing literature on child health using national-level evidence. Lastly, this study aids in evidence-based policymaking toward improving CHOs in a developing country such as India.

Materials and methods

Data source

The data for this study were extracted from DHS 2019–21, known as National Family Health Survey (NFHS-5) in India. The NFHS-5 is a nationally representative dataset of Indian households conducted by the International Institute for Population Sciences (IIPS), under the stewardship of the Ministry of Health and Family Welfare (MoHFW), Government of India (IIPS & ICF, 2022). NFHS-5 covered a population-representative sample survey of 636,699 households with a response rate of 98%, 724,115 women aged 15–49 years with a response rate of 97% and 101,839 men aged 15–54 years with a response rate of 92% (IIPS & ICF, 2022). Moreover, all children aged 0–5 years in the sampled households were covered. The main aspiration of NFHS is to administer reliable datasets on health, family welfare, fertility level, maternal and child health, infant mortality and socio-economic characteristics of individuals (IIPS & ICF, 2022). This information intends to assist policymakers in evaluating India's health sector and in identifying new key areas where targeted intervention is required. The approach of two-stage stratified sampling was employed in the survey, wherein clusters were first selected using probability proportional to cluster size, followed by the systematic

selection of 22 households from the household listing in each cluster (IIPS & ICF, 2022)[1] A detailed description of the sampling procedures for the survey is available online at https://dhsprogram.com/data/available-datasets.cfm. As this study focuses on MHCSU and CHOs, the final study participants comprised 88,035 women respondents, after excluding respondents with missing responses to the selected relevant variables.

Outcome variables

To examine the impact of MHCSU on CHOs, five anthropometric indicators were considered: stunting, wasting, anemia, underweight and overweight among children under the age of five years. According to the World Health Organization (WHO), a child is categorized as stunted if the height-for-age z score of the child is two standard deviations below the median WHO child growth standards (WHO, 2023). Likewise, a child is defined as wasted if weight-for-height z score of the child is two standard deviations below the median WHO child growth standards (WHO, 2023). The child is anemic if hemoglobin level, adjusted for altitude is less than 11.0 g/dl (WHO, 2024). A child is considered underweight if weight-for-age z score of the child is two standard deviations below the median WHO child growth standards and overweight if weight-for-height z score of the child is two standard deviations above the median WHO child growth standards (WHO, 2023).

The outcome variables were dichotomized into two categories: a child is not stunted/not wasted/not anaemic/not underweight/not overweight coded as "0" and a child is stunted/wasted/anaemic/underweight/overweight coded as "1."

Explanatory variables

The selected MHCSU predictor variables included in the analysis are: ANC visits (<4ANC visits and ≥ 4 ANC visits), number of days IFA tablets consumed (<180 days and ≥180 days), number of months pregnant at the time of first ANC checkup (<4 months and ≥4 months), presence of skilled birth attendant during delivery (yes or no) and PNC received by mothers (yes or no).

Furthermore, we included several confounding variables relating to child, maternal and household characteristics. The child's characteristics included the child's gender (male/female) and birth order (firstborn, 2nd-4th, 5th or more). The maternal characteristics included maternal age at the time of childbirth[2] (13–24, 25–34, 35–49 years) and educational attainment (no

[1]Total of 30,198 Primary Sampling Units (PSUs) were selected from 707 Indian districts (IIPS & ICF, 2022). The data were adjusted to control for sampling unit, strata and sample weight..

[2]The maternal age at the time of childbirth was calculated by subtracting the child's age from the woman's current age at the time of the survey (Tayal et al., 2024). The data for women aged 15–49 years were taken from DHS (2019–21).

education, primary, secondary, or higher education). Lastly, household characteristics included the respondents' place of residence (rural/urban), the religion they belong to (Hindu, Muslim, other religions), caste (Scheduled Caste [SC], Scheduled Tribe [ST], Other Backward Class [OBC], none of them) and household wealth quintile [3] (poorest, poorer, middle, richer, and richest).

Analytical strategy

Descriptive statistics and multivariable logistic regression were employed in the study. The methodology applied to examine the impact of MHCSU on CHOs using India DHS (2019–21) is described below.

Multivariable logistic regression

The outcome variables in this study, namely, under-five stunting, wasting, anemic, underweight and overweight, were dichotomous. Therefore, multivariable logistic regression was employed to analyze the association between MHCSU and CHOs in India.

The multivariable logistic regression model can be expressed as follows.

$$\ln \frac{P_1}{1-P_1} = \alpha_1 + \beta_i X_i \tag{1}$$

In the above equation, $\ln \frac{P_1}{1-P_1}$ refers to the log (odds) of the outcome variables, whereas P_1 is the probability (likelihood) of the child being stunted, wasted, anaemic, underweight, or overweight (Cabrera, 1994). The parameter α_1 measures the log odds of outcome variables in relation to the base category, and β_i is the maximum likelihood estimator for the i^{th} control variable (Cabrera, 1994). The maximum likelihood estimation of β is interpreted as the differential logarithm of a child being stunted, wasted, anaemic, underweight and overweight, associated with covariates X, compared to the base category[4] The regression coefficients can be interpreted using estimated log odds ratio (ORs) with 95% confidence intervals (CIs). The analysis was performed using STATA version 12.0 StataCorp LP, College Station, TX, USA. Furthermore, the Hosmer-Lemeshow test was used to assess the validity of statistical models (Supplementary File; Table 1).

[3]The DHS defines the Wealth Index categories based on a household's standard of living, which is calculated using household asset ownership and characteristics. These categories include: Poorest, Poorer, Middle, Richer and Richest. The wealth index is a composite measure of a household's cumulative living standard. It is calculated using easy-to-collect data on a household's ownership of selected assets, such as televisions, bicycles, and refrigerators; materials used for housing construction; and types of water access and sanitation facilities. Additionally, the classification is based on a principal component analysis (PCA) of these assets. The assets are weighted and grouped into categories to create a composite score that represents the wealth level of the household.

[4]To investigate the effect of the number of ANC visits, number of days IFA tablets consumed, number of months pregnant at the time of first ANC checkup, the presence of skilled birth attendant during delivery and PNC received by mothers on CHOs, separate adjusted logistic regression models were employed..

Results

Descriptive statistics

Table 1 presents the socio-economic and demographic characteristics of children aged 0–5 years and mothers aged 13–49 years. The majority of children were male (53.96%) and of second to fourth birth order (59.92%). Most women belonged to the 25–34 year age category at the time of childbirth (49.25%) and had secondary educational attainment (55.48%).

Table 1. Socio-economic and demographic characteristics of a child aged 0–5 years and women aged 13–49 years who had at least one live birth in the past five years preceding the survey in India, DHS (2019–21).

Variables	Frequency	Percentage
Child Characteristics		
Child gender		
Male	47,503	53.96
Female	40,532	46.04
Childbirth order		
Firstborn (ref.)	31,530	35.82
2^{nd}- 4^{th} born	52,753	59.92
5^{th} or higher birth order	3,752	4.26
Maternal Characteristics		
Maternal age at childbirth		
13–24	40,260	45.73
25–34	43,358	49.25
35–49	4,417	5.02
Maternal education		
No education	13,902	15.79
Primary	9,721	11.04
Secondary	48,839	55.48
Higher	15,573	17.69
Household Characteristics		
Place of residence		
Urban	20,610	23.41
Rural	67,425	76.59
Religion		
Hindu	69,963	79.47
Muslim	8,982	10.20
Others	9,090	10.33
Caste		
Scheduled Caste	18,459	20.97
Scheduled Tribe	16,474	18.71
Other Backward Class	36,645	41.63
None of them	16,457	18.69
Wealth Index		
Poorest	17,504	19.88
Poorer	19,436	22.08
Middle	18,557	21.08
Richer	17,470	19.84
Richest	15,068	17.12

Source: Authors' calculations based on DHS survey data.

The DHS defines the Wealth Index as a composite measure of a household's cumulative living standard, calculated using principal component analysis (PCA) of data on household asset ownership (e.g., televisions, bicycles, refrigerators), housing materials, and access to water and sanitation, and classifies households into five categories: Poorest, Poorer, Middle, Richer, and Richest.

Table 2. Prevalence of child health outcomes and maternal health care services utilization among children aged 0–5 years and women aged 13–49 years who had at least one live birth in the past five years preceding the survey in India, DHS (2019–21).

Variables	Frequency	Percentage
Stunting		
Yes	29,849	33.91
No	58,186	66.09
Wasting		
Yes	16,194	18.39
No	71,841	81.61
Anaemia		
Yes	60,201	68.38
No	27,834	31.62
Underweight		
Yes	24,313	27.62
No	63,722	72.38
Overweight		
Yes	2,981	3.39
No	85,054	96.61
Attended at least 4 ANC visits		
Yes	58,797	66.79
No	29,238	33.21
Consumed IFA tablets for at least 180 days		
Yes	27,029	30.70
No	61,006	69.30
Number of months pregnant at the time of first ANC visit		
<4 months	68,257	77.53
≥4 months	19,778	22.47
Skilled assistance during delivery		
Yes	71,849	81.61
No	16,186	18.39
Mother's received PNC		
Yes	79,010	89.75
No	9,025	10.25

Source: Authors' calculations based on DHS survey data.

Approximately three-fourth of respondents resided in rural areas (76.59%) and identified themselves as Hindus (79.47%). Most respondents belonged to the OBC caste (41.63%) and to poorer wealth quintile households (22.08%) (Table 1). A summary of the prevalence of child health outcomes and maternal health care services utilization is presented in Table 2. It is concerning that most children (68.38%) are anemic in India. Notably, the prevalence of stunting (33.91%), wasting (18.39%), and underweight (27.62%) was high among children, raising public health concerns. Almost 3% of children were overweight. Furthermore, majority of the women (69.30%) did not consume IFA tablets for at least 180 days. Approximately 67% of women attended at least four ANC visits, while 77.53% attended the first ANC checkup in the first trimester. Additionally, 18.39% of women did not have skilled assistance during delivery, and 10.25% did not receive PNC (Table 2). Figure 2–3 (Supplementary File) illustrates the state-wise geographical variation in under-five CHOs and MHCSU among children aged 0–5 years and mothers aged 13–49 years in India.

Estimating the impact of MHCSU on under-five CHOs in India

Table 3 presents the results of the multivariate logistic regression for estimating the influence of MHCSU on CHOs in India using DHS (2019–21). A mother who consumed IFA tablets for at least 180 days had lower odds of having an anemic child [OR 0.94; 95% CI 0.9–0.99]. The odds of being underweight were higher among children [OR 1.05; 95% CI 1.0–1.1] whose mothers were more than three months pregnant at the time of the first ANC checkup. Interestingly, our study found that the mothers who attended at least four ANC visits were more likely to have an overweight child [OR 1.13; 95% CI 1.02–1.25]. The skilled assistance during delivery reduced the odds of wasting [OR 0.96; 95% CI 0.92–0.99] and anemia [OR 0.9; 95% CI 0.85–0.95] among children. Mothers who received PNC had lower odds of having an anemic child [OR 0.91; 95% CI 0.85–0.98].

Furthermore, the odds of stunting [OR 0.89; 95% CI 0.86–0.92], wasting [OR 0.93; 95% CI 0.90–0.96], and underweight [OR 0.86; 95% CI 0.83–0.89] were lower among female children. As a child's birth order increases, the odds of being stunted [OR 1.57; 95% CI 1.42–1.73] and underweight [OR 1.31; 95% CI 1.19–1.45] also increases. In contrast, with the increase in a child's birth order, the odds of being overweight decrease [OR 0.67; 95% CI 0.53–0.85]. A mother who belonged to mature age (35–49 years) at the time of childbirth had lower odds of having a stunted [OR 0.80; 95% CI 0.73–0.89] and anemic [OR 0.77; 95% CI 0.7–0.85] child. Educated mothers were less likely to have stunted [OR 0.81; 95% CI 0.77–0.85], wasted [OR 0.89; 95% CI 0.85–0.94], anemic [OR 0.84; 95% CI 0.78–0.89] and underweight [OR 0.8; 95% CI 0.76–0.84] children.

Our study found that children residing in rural areas were less likely to be stunted [OR 0.92; 95% CI 0.88–0.98], wasted [OR 0.93; 95% CI 0.89–0.97] and underweight [OR 0.89; 95% CI 0.85–0.94]. By contrast, the odds of being anemic [OR 1.07; 95% CI 1.01–1.14] were higher among children residing in rural areas. The poor performance of CHOs was prevalent among children belonging to both Hindu and Muslim communities. However, children from Muslim families were more likely to be stunted [OR 1.20; 95% CI 1.08–1.34], wasted [OR 1.67; 95% CI 1.55–1.81], anemic [OR 1.28; 95% CI 1.15–1.43] and underweight [OR 1.22; 95% CI 1.09–1.36]. The odds of stunting [OR 1.22; 95% CI 1.14–1.31], wasting [OR 1.21; 95% CI 1.14–1.28], anemia [OR 1.37; 95% CI 1.26–1.5] and underweight [OR 1.37; 95% CI 1.27–1.49] were the highest among children belonging to Scheduled Tribes. The odds of being stunted [OR 0.53; 95% CI 0.49–0.58], wasted [OR 0.61; 95% CI 0.57–0.65], anemic [OR 0.85; 95% CI 0.78–0.92] and underweight [OR 0.44; 95% CI 0.41–0.48] were the lowest among children belonging to the richest quintile. On the contrary, children from the richest households were more likely to be overweight [OR 1.38; 95% CI 1.15–1.65] in India.

Table 3. Multivariate logistic regressions for analyzing the impact of maternal health care services utilization on child health outcomes using DHS (2019–21) conducted in India.

Dependent Variable → Independent Variables↓	Stunting		Wasting		Anaemia		Underweight		Overweight	
	OR	CI (95%)	OR	CI (95%)	OR	CI (95%)	OR	CI (95%)	OR	CI (95%)
Attended 4+ ANC visits										
No (Ref.)										
Yes	0.97	(0.94–1.01)	1.02	(0.98–1.05)	0.96	(0.92–1.01)	0.98	(0.95–1.02)	1.13*	(1.02–1.25)
Number of days IFA consumed										
Less than 180 days (Ref.)										
At least 180 days	0.97	(0.93–1.01)	1	(0.96–1.03)	0.94*	(0.9–0.99)	0.98	(0.94–1.03)	1.07	(0.97–1.17)
Number of months pregnant at the time of first ANC visit										
<4 months (Ref.)										
≥4 months	1.04	(0.99–1.09)	1	(0.96–1.04)	0.95*	(0.9–1)	1.05*	(1–1.1)	0.95	(0.86–1.06)
Skilled assistance during delivery										
No (Ref.)										
Yes	1.01	(0.96–1.05)	0.96*	(0.92–0.99)	0.9*	(0.85–0.95)	0.98	(0.94–1.03)	1.08	(0.96–1.21)
Mother's received PNC										
No (Ref.)										
Yes	1.01	(0.95–1.07)	1.02	(0.97–1.07)	0.91*	(0.85–0.98)	0.98	(0.93–1.04)	0.94	(0.82–1.08)
Child gender										
Male (Ref.)										
Female	0.89*	(0.86–0.92)	0.93*	(0.9–0.96)	0.99	(0.95–1.03)	0.86*	(0.83–0.89)	0.96	(0.89–1.05)
Birth order										
First born (Ref.)										
2nd- 4th born	1.2*	(1.15–1.25)	0.98	(0.95–1.02)	0.96*	(0.91–1)	1.15*	(1.1–1.2)	0.76*	(0.69–0.84)
5th or higher birth order	1.57*	(1.42–1.73)	0.92	(0.85–1.01)	0.94	(0.84–1.05)	1.31*	(1.19–1.45)	0.67*	(0.53–0.85)
Maternal age at childbirth										
13–24 (Ref.)										
25–34	0.88*	(0.85–0.92)	1	(0.96–1.03)	0.95*	(0.91–0.99)	0.94*	(0.9–0.98)	1.13*	(1.03–1.25)
35–49	0.8*	(0.73–0.89)	1.04	(0.96–1.12)	0.77*	(0.7–0.85)	0.91	(0.83–1.01)	1.13	(0.91–1.42)
Maternal education										
No education (Ref.)										
Primary	0.94	(0.88–1)	0.9*	(0.85–0.95)	0.92*	(0.85–1)	0.94	(0.88–1)	0.86	(0.72–1.02)
Secondary	0.81*	(0.77–0.85)	0.89*	(0.85–0.94)	0.84*	(0.78–0.89)	0.8*	(0.76–0.84)	0.94	(0.81–1.08)
Higher	0.64*	(0.6–0.69)	0.83*	(0.78–0.88)	0.72*	(0.66–0.78)	0.65*	(0.61–0.71)	1.09	(0.92–1.29)
Place of residence										
Urban (Ref.)										

(*Continued*)

Table 3. (Continued).

Dependent Variable → Independent Variables↓	Stunting		Wasting		Anaemia		Underweight		Overweight	
	OR	CI (95%)	OR	CI (95%)	OR	CI (95%)	OR	CI (95%)	OR	CI (95%)
Rural	0.92*	(0.88–0.98)	0.93*	(0.89–0.97)	1.07*	(1.01–1.14)	0.89*	(0.85–0.94)	0.95	(0.84–1.06)
Religion										
Others (Ref.)										
Hindu	1.07	(0.98–1.17)	1.45*	(1.36–1.54)	1.2*	(1.1–1.31)	1.12*	(1.02–1.23)	0.88	(0.74–1.05)
Muslim	1.2*	(1.08–1.34)	1.67*	(1.55–1.81)	1.28*	(1.15–1.43)	1.22*	(1.09–1.36)	0.98	(0.79–1.21)
Caste										
None of them (Ref.)										
SC	1.25*	(1.17–1.33)	1.12*	(1.06–1.18)	1.17*	(1.1–1.25)	1.24*	(1.15–1.33)	0.92	(0.8–1.05)
ST	1.22*	(1.14–1.31)	1.21*	(1.14–1.28)	1.37*	(1.26–1.5)	1.37*	(1.27–1.49)	0.99	(0.84–1.17)
OBC	1.14*	(1.08–1.21)	1.12*	(1.07–1.17)	0.98	(0.92–1.03)	1.15*	(1.08–1.22)	0.88*	(0.78–1)
Wealth Quintile										
Poorest (Ref.)										
Poorer	0.88*	(0.83–0.93)	0.86*	(0.82–0.9)	0.95	(0.89–1.01)	0.82*	(0.78–0.87)	1.14	(0.99–1.32)
Middle	0.75*	(0.71–0.79)	0.77*	(0.73–0.81)	0.89*	(0.83–0.95)	0.66*	(0.63–0.7)	1.28	(0.97–1.5)
Richer	0.62*	(0.58–0.66)	0.72*	(0.68–0.76)	0.83*	(0.77–0.89)	0.56*	(0.52–0.59)	1.33*	(1.12–1.57)
Richest	0.53*	(0.49–0.58)	0.61*	(0.57–0.65)	0.85*	(0.78–0.92)	0.44*	(0.41–0.48)	1.38*	(1.15–1.65)

Level of significance for logistic model: * Significant at 5% level; OR, Odds ratio; CI, Confidence interval; ref.: Reference category of the variable.
Source: Authors' calculations based on DHS (2019–21) survey data

Discussion

In this paper, we examined the impact of MHCSU on CHOs in India using nationally representative DHS data (2019–21). Our study underscores several significant findings. First, the concerningly poor CHOs are prevalent in India, with 68.38% of children under the age of five being anemic. Second, under-five wasting at 18.39% is the highest in the world (Economic Times, 2022). Third, 69.30% of the female respondents did not consume IFA tablets for at least 180 days, and approximately one-third did not attend at least 4 ANC visits, reflecting suboptimal MHCSU in India.

Furthermore, in tandem with the previous studies conducted in Ethiopia (Yazew, 2022; Yazew & Daba, 2022) and Indonesia (Krisnana et al., 2020), our study found that the odds of being underweight were higher among children whose mothers were more than three months pregnant at the time of the first ANC checkup. The ANC visits during the initial months of pregnancy are imperative as they allow mothers to consult health professionals about fetal health issues (Nana et al., 2022; Alem et al., 2022). We found that consumption of IFA tablets for at least 180 days reduced the odds of anemia among children. The probable reason is that antenatal multiple micronutrient supplementations improve the child and mother's health by preventing the risk of adverse pregnancy including facial clefts, fetal death and fetal growth restriction (Krisnana et al., 2020; Sengpiel et al., 2014; Shinde et al., 2022). Notably, the mothers who attended at least four ANC visits were more likely to have an overweight child. This may seem counterintuitive, but a plausible explanation could be that adequate ANC checkups and prenatal nutritional guidance reduce the possibility of birth defects, miscarriage and malnutrition among children (Grant & Smarr, 2022). Lansdale et al. (2024) argue that each additional ANC visit leads to a 0.03 kg increase in a child's weight, based on a study in West Africa.

We found that skilled assistance during delivery reduced the odds of wasting and anemia among children. A study conducted in India using previous DHS data (2015–16) found that women who had received at least 4 ANC visits were more likely to opt for skilled assistance during delivery (M. A. Islam et al., 2024). Adequate ANC visits provide women with information on risk identification, fetal assessment, health education, immunization and nutrition guidance, leading to improved CHOs (M. A. Islam et al., 2024; Kuhnt & Vollmer, 2017). Skilled assistance during delivery effectively addresses maternal hemorrhage and sepsis by ensuring the use of sterile equipment, while also managing complications like pre-eclampsia and eclampsia (Bale et al., 2003). The skilled attendants can also administer antiretroviral therapies, provide initial care for sick and/or low-birth-weight infants, refer them for further treatment, and support early breastfeeding initiation (Bale et al., 2003).

Therefore, skilled assistance during delivery is imperative for improved CHOs. Our study found that the odds of under-five anemia were lower among children whose mothers have received PNC. PNC visits have several positive ramifications, including promoting colostrum feeding and breastfeeding practices, follow-up for premature and/or low birth weight newborns, treating potential infections or other diseases, preventing pneumonia and diarrhea, and imparting nutritional and hygiene guidance (Singh et al., 2017). McCauley et al. (2022) contend that PNC improves CHOs as mothers are informed about a child's growth, feeding and well-being. A case-control study conducted at SAT Hospital in Kerala (a state in India) found that the absence of exclusive breastfeeding led to under-five anemia among children (Anjali et al., 2019). Schemes such as Focused Antenatal Care, a client-based service in Ghana, Basic Public Health Service scheme and New Rural Cooperative Medical Scheme in China, national health insurance schemes in Tanzania and Lagos, and Safe Motherhood Initiative in Africa are associated with the improvements in the maternal health service utilization and hence similar schemes can be initiated in India (Haruna et al., 2019; Rahman et al., 2022; Rotimi-Oyedepo & Ajao, 2022; You et al., 2016; Zhao et al., 2019, 2020).

Additionally, our study also highlighted that the prevalence of stunting, wasting and being underweight was higher among male children compared to female children. A plethora of studies have confirmed similar findings (Ali et al., 2017; Khan et al., 2019; Siddiqa et al., 2022; Thurstans et al., 2022). Khan et al. (2019) vehemently argue that male children require more calories for growth and development than female children, making them more susceptible to malnutrition. Moreover, poor CHOs among male children could be explained by differences in calorie intake, physical activity behavior, and environmental factors (Saha et al., 2022). Male fetuses are more likely to experience placental insufficiency, infections and pre-term delivery (Ingemarsson, 2003; Marino et al., 2011). Notably, male children tend to spend more time playing outdoors, leading to greater energy expenditure and increased exposure to environmental risks and sources of infection (Akombi et al., 2017; Gewa & Yandell, 2011). This exposure makes male children more prone to poor CHOs. Additionally, we found that as a child's birth order increases, the odds of being stunted and underweight also increase. Compared to first-born children, those who were second-born or later generally receive inadequate breastfeeding, less attention and improper nutritional intake (Adeyemi et al., 2022). Our results align with studies conducted in East African countries and India (Das et al., 2022; Ibeji et al., 2022; Saha et al., 2022; Srivastava & Upadhyay, 2020; Tamirat et al., 2021; Woldeamanuel & Tesfaye, 2019).

In tandem with the previous studies conducted in Nigeria (Adeyemi et al., 2022; Ibeji et al., 2022), Ethiopia (Yazew & Daba, 2022), Pakistan (Asif et al., 2022) and India using DHS 2015–16 (Das et al., 2022), our study found that maternal age and education are significant determinants of childhood stunting, wasting, anemia and underweight in India. Mothers of mature age and with higher educational attainment are more likely to be informed and conscious about their child's nutrition, exhibit more health-seeking behavior, and ensure timely vaccination and proper healthcare (Adeyemi et al., 2022; Patel et al., 2019). Our study found that a child born in a rural region was more likely to be anemic, in line with a similar observation in Nigeria (Ibeji et al., 2022). The probable reasons can be a lack of access to good health care, poor sanitation and lack of awareness in the rural areas of developing countries (Hall et al., 2018; Sisay et al., 2022).

The present study also found an increased risk of poor CHOs among families belonging to the Muslim religion and scheduled tribes. Notably, children belonging to the Muslim religion and Scheduled Tribes experience the highest magnitude of poor CHOs in India. This result is similar to the results of a previous study conducted in Madhya Pradesh, India, using data from the National Family Health Survey-3 (2005–06) (Shyam et al., 2020). There is evidence that no-or-partial immunization is more common among children whose mothers belong to non-Hindu religion or backward caste (T. Islam et al., 2021; Puri et al., 2020). Moreover, in India, traditional practices, customs, dietary practices, and attitudes are often influenced by an individual's religion and caste, thereby impacting CHOs (Puri et al., 2020). We found that children belonging to the richest wealth quintile households had lower odds of being stunted, wasted, anemic and underweight. Notably, wealthier household quintiles play a significant role in reducing the likelihood of poor CHOs, with a greater magnitude of impact. This finding is in line with studies conducted in Nigeria (Adeyemi et al., 2022; Ibeji et al., 2022), Ethiopia (Woldeamanuel & Tesfaye, 2019; Yazew & Daba, 2022) and India (Das et al., 2022). On the contrary, children belonging to the richest wealth quintile were more likely to be overweight. Similar findings were observed in a previous study conducted in the Indian context (Saha et al., 2022). This is because, one the one hand, richest households have availability of high-quality nutrient supplements, more purchasing capacity and access to healthcare services which improve CHOs (Chowdhury et al., 2020; Waghmare et al., 2022). However, Fruhstorfer et al. (2016) contended that families belonging to wealthy households often adopt modern lifestyle conviniences, such as reduced physical activity, reliance on breastfeeding substitutes, and unhealthy dietary habits, which can lead to a higher propensity for overweight and obesity in children.

Implications for practice

MHCSU is crucial for improving CHOs in India. The role of frontline health workers can be expanded to provide vital support and improve MHCSU. Furthermore, policymakers should prioritize regular health education sessions, nutritional guidance and improved access to financial incentive schemes to promote MHCSU. Future research can analyze previous DHS rounds to assess temporal changes in child health outcomes in India. Additionally, further studies may examine the impact of the quality of maternal healthcare services on child health outcomes.

Limitations of the study

The results of this study must be viewed in the light of a few limitations. First, the study used cross-sectional data. Therefore, we abstain from providing causal interpretations regarding the relationship between maternal healthcare services and CHOs (Alem et al., 2022). Second, DHS data were collected retrospectively and are self-reported; thus, our findings are prone to recall bias, information bias, underreporting and social desirability bias (Alem et al., 2022; Komakech et al., 2022; Paul & Saha, 2022). Lastly, we acknowledge that due to the secondary nature of data, important variables such as women's knowledge about the timing of ANC and PNC, women's perception of the quality of MHCSU, and time of recognition of pregnancy were not included in this study (Alem et al., 2022).

Conclusion

In summary, we found that a mother who consumed IFA tablets for at least 180 days and who received PNC had lower odds of having an anemic child. It is important to note that, mothers who attended at least four ANC visits were more likely to have an overweight child. Each additional ANC visit has been associated with slight increases in child weight, likely due to improved prenatal nutrition and health outcomes. Children whose mothers had their first ANC checkup after three months had higher odds of being underweight. Furthermore, skilled assistance during delivery reduced the odds of wasting and anemia among children. Furthermore, we observed that a child's gender, birth order, maternal age, maternal education, religion, caste and household wealth profoundly influence the CHOs in India.

Towards the achievement of sustainable development goal 2 targets relating to child nutrition, policymakers should extensively focus on schemes such as Janani Suraksha Yojana, Surakshit Matritva Aashwasan and Janani Shishu Suraksha Karyakaram. These initiatives aim to promote ANC visits, increase the consumption of IFA tablets by pregnant women,

and ensure adequate availability and affordability of maternal healthcare services and nutrition. Along with this, direct and improved engagement with frontline health workers is required to achieve optimal maternal and newborn health outcomes. Furthermore, awareness generation, financial incentive schemes such as Janani Suraksha Yojana and Mahatma Gandhi National Rural Employment Guarantee Act, and ensuring women's access to quality education, microfinance, skill training, and employment opportunities are imperative. More studies, including qualitative and longitudinal research, are needed to test and compare the effectiveness, cost-effectiveness, acceptability, and sustainability of various strategies for improving the quality of maternal health care and client-provider interactions, especially for the poor and vulnerable in India.

Disclosure statement

No potential conflict of interest was reported by the author(s).

Funding

The author(s) reported there is no funding associated with the work featured in this article.

ORCID

Rajesh Sharma http://orcid.org/0000-0001-7468-1249

Ethical approval

The data used is available in public domain (http://www.measuredhs.com/) thus ethical approval was not required.

References

Abu-Fatima, O., Abbas, A. A. G., Racalbuto, V., Smith, L., & Pizzol, D. (2020). Child undernutrition in Sudan: The social and economic impact and future perspectives. *The American Journal of Tropical Medicine and Hygiene*. https://doi.org/10.4269/ajtmh.20-1251

Adeyemi, O., Toure, M., Covic, N., van den Bold, M., Nisbett, N., & Headey, D. (2022). Understanding drivers of stunting reduction in Nigeria from 2003 to 2018: A regression analysis. *Food Security*, *14*(4), 995–1011. https://doi.org/10.1007/s12571-022-01279-8

Ahmadinezhad, M. (2022). *Mothers' perceptions of the quality of postnatal care provided in health centers and the associated factors: A cross-sectional study*. Retrieved October 6, 2022, from https://ijcbnm.sums.ac.ir/article_48059.html

Akombi, B. J., Agho, K. E., Hall, J. J., Wali, N., Renzaho, A. M. N., & Merom, D. (2017). Stunting, wasting and underweight in Sub-Saharan Africa: A systematic review.

International Journal of Environmental Research and Public Health, *14*(8), 863. https://doi.org/10.3390/ijerph14080863

Alderman, H. (2009). The economic cost of a poor start to life. *Journal of Developmental Origins of Health and Disease*, *1*(1), 19–25. https://doi.org/10.1017/s2040174409990158

Alem, A. Z., Yeshaw, Y., Liyew, A. M., Tesema, G. A., Alamneh, T. S., Worku, M. G., Teshale, A. B., & Tessema, Z. T. (2022). Timely initiation of antenatal care and its associated factors among pregnant women in Sub-Saharan Africa: A multicountry analysis of demographic and health surveys. *PLOS ONE*, *17*(1), e0262411. https://doi.org/10.1371/journal.pone.0262411

Ali, Z., Saaka, M., Adams, A., Kamwininaang, S. K., & Abizari, A. (2017). The effect of maternal and child factors on stunting, wasting and underweight among preschool children in Northern Ghana. *BMC Nutrition*, *3*(1). https://doi.org/10.1186/s40795-017-0154-2

Aneesh, M. R. (2021). Quality of drinking water and sanitation in India. *Indian Journal of Human Development (Print)*, *15*(1), 138–152. https://doi.org/10.1177/09737030211003658

Anjali, T. R., Abbas, S., Elizabeth, K. E., & Leelakumari, M. (2019). Association between breastfeeding practices and anemia in children aged 6-60 months. *International Journal of Contemporary Pediatrics*, *6*(5), 2027. https://doi.org/10.18203/2349-3291.ijcp20193718

Asif, M. F., Pervaiz, Z., Afridi, J. R., Safdar, R., Abid, G., & Lassi, Z. S. (2022). Socio-economic determinants of child mortality in Pakistan and the moderating role of household's wealth index. *BMC Pediatrics*, *22*(1). https://doi.org/10.1186/s12887-021-03076-2

Baek, Y., Owen, A. J., Fisher, J., Tran, T., & Ademi, Z. (2022). Lifetime impact of being underweight or overweight/obese during childhood in Vietnam. *BMC Public Health*, *22*(1). https://doi.org/10.1186/s12889-022-13061-8

Bale, J. R., Stoll, B. J., & Lucas, A. O. (2003). The essential competencies of a skilled birth attendant. Improving birth outcomes. NCBI Bookshelf. https://www.ncbi.nlm.nih.gov/books/NBK222088/

Cabrera, A. (1994). Logistic regression analysis in higher education: An applied perspective. *Agathon Press*, *10*, 225–256.

Chakrabarti, S., Pan, A., & Singh, P. (2021). Maternal and child health benefits of the Mamata conditional cash transfer program in Odisha, India. *The Journal of Nutrition*, *151*(8), 2271–2281. https://doi.org/10.1093/jn/nxab129

Choi, M. J., Yu, J., & Choi, J. (2022). Maternal pre-pregnancy obesity and gestational diabetes mellitus increase the risk of childhood obesity. *Children*, *9*(7), 928. https://doi.org/10.3390/children9070928

Chowdhury, T. R., Chakrabarty, S., Rakib, M., Afrin, S., Saltmarsh, S., & Winn, S. (2020). Factors associated with stunting and wasting in children under 2 years in Bangladesh. *Heliyon*, *6*(9), e04849. https://doi.org/10.1016/j.heliyon.2020.e04849

Das, P., Das, T., & Roy, T. B. (2022). Stunting, a linear growth anomaly in under-five year (U5) children: A risk factors' analysis from maternal, household and individual background in Indian context. *Child Indicators Research*, *15*(3), 1025–1042. https://doi.org/10.1007/s12187-021-09898-x

The Economic Times. (2022, October 16). *India ranks 107 on 2022 global hunger index, behind Pakistan, Bangladesh and Nepal. The Economic Times*. Retrieved July 12, 2023 from, https://economictimes.indiatimes.com/news/india/mca-orders-inspection-of-byjus-books/articleshow/101677339.cms

FAO, IFAD, UNICEF, WFP, WHO. (2022). *The state of food security and nutrition in the world 2022. Repurposing food and agricultural policies to make healthy diets more affordable*. https://doi.org/10.4060/cc0639en

Fruhstorfer, B. H., Mousoulis, C., Uthman, O. A., & Robertson, W. (2016). Socio-economic status and overweight or obesity among school-age children in Sub-Saharan Africa - a systematic review. *Clinical Obesity*, *6*(1), 19–32. https://doi.org/10.1111/cob.12130

Gewa, C. A., & Yandell, N. (2011). Undernutrition among Kenyan children: Contribution of child, maternal and household factors. *Public Health Nutrition*, *15*(6), 1029–1038. https://doi.org/10.1017/s136898001100245x

Grant, A., & Smarr, B. (2022). Feasibility of continuous distal body temperature for passive, early pregnancy detection. *PLOS Digital Health*, *1*(5), e0000034. https://doi.org/10.1371/journal.pdig.0000034

Haby, K., Gyllensten, H., Hanas, R., Berg, M., & Premberg, S. (2022). A lifestyle intervention during pregnancy and its effects on child weight 2.5 years later. *Maternal and Child Health Journal*, *26*(9), 1881–1890. https://doi.org/10.1007/s10995-022-03395-5

Hakizimana, E. (2022). *How children malnutrition affect African countries GDP. The Inspirer*. http://rwandainspirer.com/2017/11/28/how-children-malnutrition-affect-african-countries-gdp/

Hall, C., Bennett, C., Crookston, B., Dearden, K., Hasan, M., Linehan, M., Syafiq, A., Torres, S., & West, J. (2018). Maternal knowledge of stunting in rural Indonesia. *International Journal of Child Health and Nutrition*, *7*(4), 139–145. https://doi.org/10.6000/1929-4247.2018.07.04.2

Haruna, U., Dandeebo, G., & Galaa, S. Z. (2019). Improving access and utilization of maternal healthcare services through focused antenatal care in rural Ghana: A qualitative study. *Advances in Public Health*, *2019*, 1–11. https://doi.org/10.1155/2019/9181758

Ibeji, J. U., Mwambi, H., & Iddrisu, A. K. (2022). Spatial variation and risk factors of malaria and anaemia among children aged 0 to 59 months: A cross-sectional study of 2010 and 2015 datasets. *Scientific Reports*, *12*(1). https://doi.org/10.1038/s41598-022-15561-4

Ingemarsson, I. (2003). Gender aspects of preterm birth. *BJOG: An International Journal of Obstetrics & Gynaecology*, *110*(s20), 34–38. https://doi.org/10.1046/j.1471-0528.2003.00022.x

International Institute for Population Sciences (IIPS) & ICF. (2022). National Family Health Survey (NFHS-5), 2019-21: India. Mumbai: IIPS.

Islam, M. A., Nahar, M. T., Siddiquee, T., Toma, A. S., Hoque, F., & Hossain, M. Z. (2024). Prevalence and determinants of utilizing skilled birth attendance during home delivery of pregnant women in India: Evidence from the Indian Demographic and Health Survey 2015-16. *PLOS ONE*, *19*(3), e0295389. https://doi.org/10.1371/journal.pone.0295389

Islam, T., Mandal, S., & Chouhan, P. (2021). Influence of socio-demographic factors on coverage of full vaccination among children aged 12-23 months: A study in Indian context (2015-2016). *Human Vaccines & Immunotherapeutics*, *17*(12), 5226–5234. https://doi.org/10.1080/21645515.2021.1977056

James, K. S., Mishra, U. S. & Pallikadavath, S. (2021). Sequential impact of components of maternal and child health care services on the continuum of care in India. *Journal of Biosocial Science*, *54*(3), 450–472. https://doi.org/10.1017/s002193202100016x

Khan, S., Zaheer, S., & Safdar, N. F. (2019). Determinants of stunting, underweight and wasting among children< 5 years of age: evidence from 2012-2013 Pakistan Demographic and Health Survey. *BMC Public Health*, *19*(1). https://doi.org/10.1186/s12889-019-6688-2

Komakech, J. J., Walters, C. N., Rakotomanana, H., Hildebrand, D. A., & Stoecker, B. J. (2022). The associations between women's empowerment measures, child growth and dietary diversity: Findings from an analysis of Demographic and Health Surveys of seven countries in Eastern Africa. *Maternal & Child Nutrition*, *18*(4). https://doi.org/10.1111/mcn.1342

Krisnana, I., Widiani, N. M., & Sulistiawati, S. (2020). Prenatal and postnatal factors related to the incidence of stunting in the coastal area Surabaya, Indonesia. *Sri Lanka Journal of Child Health*, *49*(3), 223. https://doi.org/10.4038/sljch.v49i3.9138

Kuhnt, J., & Vollmer, S. (2017). Antenatal care services and its implications for vital and health outcomes of children: Evidence from 193 surveys in 69 low-income and middle-income countries. *BMJ Open*, *7*(11), e017122. https://doi.org/10.1136/bmjopen-2017-017122

Lansdale, A. J., Bountogo, M., Sie, A., Zakane, A., Compaoré, G., Ouedraogo, T., Lebas, E., Lietman, T., & Oldenburg, C. E. (2024). Associations between antenatal care visit attendance and infant mortality and growth. *The American Journal of Tropical Medicine and Hygiene*, *110*(6), 1270–1275. https://doi.org/10.4269/ajtmh.23-0659

Marino, M., Masella, R., Bulzomi, P., Campesi, I., Malorni, W., & Franconi, F. (2011). Nutrition and human health from a sex-gender perspective. *Molecular Aspects of Medicine*, *32*(1), 1–70. https://doi.org/10.1016/j.mam.2011.02.001

Mary, S. (2018). How much does economic growth contribute to child stunting reductions? *Economies*, *6*(4), 55. https://doi.org/10.3390/economies6040055

Maulina, R., Qomaruddin, M. B., Sumarmi, S., Fahrul, A., & Haryuni, S. (2022). Antenatal depression as a stunting risk factor: A systematic review. *Open Access Macedonian Journal of Medical Sciences*, *10*(F), 234–240. https://doi.org/10.3889/oamjms.2022.8501

McCauley, H., Lowe, K., Furtado, N., Mangiaterra, V., & van den Broek, N. (2022). Essential components of postnatal care - a systematic literature review and development of signal functions to guide monitoring and evaluation. *BMC Pregnancy and Childbirth*, *22*(1). https://doi.org/10.1186/s12884-022-04752-6

McGovern, M. E., Krishna, A., Aguayo, V. M., & Subramanian, S. (2017). A review of the evidence linking child stunting to economic outcomes. *International Journal of Epidemiology*, *46*(4), 1171–1191. https://doi.org/10.1093/ije/dyx017

Moffat, R., Sayer, A., DeCook, K., Cornia, A., Linehan, M., Torres, S., Mulokozi, G., Crookston, B., Hall, C., & West, J. (2022). A national communications campaign to decrease childhood stunting in Tanzania: An analysis of the factors associated with exposure. *BMC Public Health*, *22*(1). https://doi.org/10.1186/s12889-022-12930-6

Mullany, L. C., Falle, T. Y., Thatte, N., Khatry, S. K., LeClerq, S. C., Darmstadt, G. L., Katz, J., & Tielsch, J. M. (2009). Potential role of traditional birth attendants in neonatal healthcare in Rural Southern Nepal. *Journal of Health, Population, and Nutrition*, *27*(1). https://doi.org/10.3329/jhpn.v27i1.3317

Nambiar, A., Agnihotri, S. B., Singh, A., & Arunachalam, D. (2022). Region matters: Mapping the contours of undernourishment among children in Odisha, India. *PLOS ONE*, *17*(6), e0268600. https://doi.org/10.1371/journal.pone.0268600

Nana, M., Stannard, M. T., Nelson-Piercy, C., & Williamson, C. (2022). The impact of preconception counselling on maternal and fetal outcomes in women with chronic medical conditions: A systematic review. *European Journal of Internal Medicine*, *108*, 52–59. https://doi.org/10.1016/j.ejim.2022.11.003

Nugent, R., Levin, C., Hale, J., & Hutchinson, B. (2020). Economic effects of the double burden of malnutrition. *Lancet*, *395*(10218), 156–164. https://doi.org/10.1016/s0140-6736(19)32473-0

Oumer, A., Girum, T., Fikre, Z., Bedewi, J., Nuriye, K., & Assefa, K. (2022). Stunting and underweight, but not wasting are associated with delay in child development in Southwest Ethiopia. *Pediatric Health, Medicine and Therapeutics*, *13*, 1–12. https://doi.org/10.2147/phmt.s344715

Patel, R., Gupta, A., Srivastava, S., & Bansod, D. W. (2019). Effects of sanitation practices on adverse pregnancy outcomes in India: A conducive finding from recent Indian Demographic Health Survey. *BMC Pregnancy and Childbirth*, *19*(1). https://doi.org/10.1186/s12884-019-2528-8

Paul, P., & Saha, R. (2022). Is maternal autonomy associated with a child's nutritional status? Evidence from a cross-sectional study in India. *PLOS ONE*, *17*(5), e0268126. https://doi.org/10.1371/journal.pone.0268126

Popkin, B. M., Corvalan, C., & Grummer-Strawn, L. M. (2020). Dynamics of the double burden of malnutrition and the changing nutrition reality. *Lancet*, *395*(10217), 65–74. https://doi.org/10.1016/s0140-6736(19)32497-3

Puri, P., Khan, J., Shil, A., & Ali, M. (2020). A cross-sectional study on selected child health outcomes in India: Quantifying the spatial variations and identification of the parental risk factors. *Scientific Reports*, *10*(1). https://doi.org/10.1038/s41598-020-63210-5

Rahman, M. M., Taniguchi, H., Nsashiyi, R. S., Islam, R., Mahmud, S. R., Rahman, S., Jung, J., & Khan, S. (2022). Trend and projection of skilled birth attendants and institutional delivery coverage for adolescents in 54 low- and middle-income countries, 2000-2030. *BMC Medicine*, *20*(1). https://doi.org/10.1186/s12916-022-02255-x

Rotimi-Oyedepo, V. O., & Ajao, E. O. (2022). Factors influencing the utilisation of maternal health care services among women of reproductive age in Lagos Island LGA, Lagos State. *International Journal of Nursing, Midwife and Health Related Cases*, *8*(2), 67–80. https://doi.org/10.37745/ijnmh.15/vol80n2pp6780

Saha, J., Chouhan, P., Ahmed, F., Ghosh, T., Mondal, S., Shahid, M., Fatima, S., & Tang, K. (2022). Overweight/obesity prevalence among under-five children and risk factors in India: A cross-sectional study using the national family health survey (2015-2016). *Nutrients*, *14*(17), 3621. https://doi.org/10.3390/nu14173621

Sengpiel, V., Bacelis, J., Myhre, R. W., Myking, S., Pay, A. S. D., Haugen, M., Brantsæter, A. L., Meltzer, H. M., Nilsen, R. M., Magnus, P., Vollset, S. E., Nilsson, S., & Jacobsson, B. (2014). Folic acid supplementation, dietary folate intake during pregnancy and risk for spontaneous preterm delivery: A prospective observational cohort study. *BMC Pregnancy and Childbirth*, *14*(1). https://doi.org/10.1186/s12884-014-0375-1

Seth, P., & Jain, P. (2022). *What impacts child malnutrition in India and why we need to be aware of these factors*. *The Wire*. https://thewire.in/health/what-are-the-factors-that-impact-child-malnutrition-in-india

Shinde, S., Wang, D., Yussuf, M. H., Mwanyika-Sando, M., Aboud, S., & Fawzi, W. W. (2022). Micronutrient supplementation for pregnant and lactating women to improve maternal and infant nutritional status in low- and middle-income countries: Protocol for a systematic review and meta-analysis. *JMIR Research Protocols*, *11*(8), e40134. https://doi.org/10.2196/40134

Shyam, A., Fuller, N., & Shah, P. (2020). Is child undernutrition associated with antenatal care attendance in Madhya Pradesh, India? *Journal of Family Medicine and Primary Care*, *9*(3), 1380. https://doi.org/10.4103/jfmpc.jfmpc_1041_19

Siddiqa, M., Zubair, A., Kamal, A., Ijaz, M., & Abushal, T. (2022). Prevalence and associated factors of stunting, wasting and underweight of children below five using quintile regression analysis (PDHS 2017-2018). *Scientific Reports*, *12*(1). https://doi.org/10.1038/s41598-022-24063-2

Siddiqui, F., Salam, R. A., Lassi, Z. S., & Das, J. K. (2020). The intertwined relationship between malnutrition and poverty. *Frontiers in Public Health*, *8*, 8. https://doi.org/10.3389/fpubh.2020.00453

Singh, K., Brodish, P., Chowdhury, M. E., Biswas, T. K., Kim, E. T., Godwin, C., & Moran, A. (2017). Postnatal care for newborns in Bangladesh: The importance of health-related factors and location. *Journal of Global Health*, *7*(2). https://doi.org/10.7189/jogh.07.020507

Sisay, M., Atenafu, A., Hunegnaw, M. T., & Lorato, M. M. (2022). Prevalence and factors associated with stunting and thinness among school age children in rural primary schools,

East Dembia District, Northwest Ethiopia. *BMC Nutrition*, *8*(1). https://doi.org/10.1186/s40795-022-00624-6

Solans, M., Barceló, M. A., Morales-Suárez-Varela, M., Moya, A., & Saez, M. (2021). Prenatal exposure to antibiotics and risk of childhood overweight or obesity: A systematic review and meta-analysis. *Obesity Reviews*, *23*(S1). https://doi.org/10.1111/obr.13382

Spies, M., Geyer, K., Raab, R., Brandt, S., Meyer, D., Günther, J., Hoffmann, J., & Hauner, H. (2022). Child anthropometrics and neurodevelopment at 2 and 3 years of age following an antenatal lifestyle intervention in routine care-a secondary analysis from the cluster-randomised gelis trial. *Journal of Clinical Medicine*, *11*(6), 1688. https://doi.org/10.3390/jcm11061688

Srivastava, S., & Upadhyay, A. K. (2020). A success story of reduction in childhood stunting and underweight in India: Analysis of pooled data from three rounds of Indian Demographic and Health Surveys (1998-2016). *Journal of Biosocial Science*, *54*(1), 106–123. https://doi.org/10.1017/s002193202000070x

Syeda, B., Agho, K., Wilson, L., Maheshwari, G. K., & Raza, M. Q. (2021). Relationship between breastfeeding duration and undernutrition conditions among children aged 0-3 years in Pakistan. *International Journal of Pediatrics and Adolescent Medicine*, *8*(1), 10–17. https://doi.org/10.1016/j.ijpam.2020.01.006

Tamirat, K. S., Tesema, G. A., & Tessema, Z. T. (2021). Determinants of maternal high-risk fertility behaviors and its correlation with child stunting and anemia in the East Africa region: A pooled analysis of nine East African countries. *PLOS ONE*, *16*(6), e0253736. https://doi.org/10.1371/journal.pone.0253736

Tayal, C., Sharma, R., & Lata, K. (2024). Evidence from maternal healthcare services in South Asia: Demography vs. healthcare. *International Journal of Healthcare Management*, 1–13. https://doi.org/10.1080/20479700.2024.2430877

Thurstans, S., Opondo, C., Seal, A., Wells, J. C., Khara, T., Dolan, C., Briend, A., Myatt, M., Garenne, M., Mertens, A., Sear, R., & Kerac, M. (2022). Understanding sex differences in childhood undernutrition: A narrative review. *Nutrients*, *14*(5), 948. https://doi.org/10.3390/nu14050948

UNDP. (2022). *Sustainable development goals*. Retrieved November 12, 2022. https://www.undp.org/sustainable-development-goals

Von Hinke, S., Rice, N., & Tominey, E. (2022). Mental health around pregnancy and child development from early childhood to adolescence. *Labour Economics*, *78*, 102245. https://doi.org/10.1016/j.labeco.2022.102245

Waghmare, H., Chauhan, S., & Sharma, S. K. (2022). Prevalence and determinants of nutritional status among women and children in Pakistan. *BMC Public Health*, *22*(1). https://doi.org/10.1186/s12889-022-13059-2

Wali, N., Agho, K. E., & Renzaho, A. M. (2020). Factors associated with stunting among children under 5 years in five South Asian countries (2014-2018): Analysis of demographic health surveys. *Nutrients*, *12*(12), 3875. https://doi.org/10.3390/nu12123875

Wells, J. C. K., Wibaek, R., & Poullas, M. (2018). The dual burden of malnutrition increases the risk of cesarean delivery: Evidence from India. *Frontiers in Public Health*, *6*. https://doi.org/10.3389/fpubh.2018.00292

Wells, J. C., Sawaya, A. L., Wibaek, R., Mwangome, M., Poullas, M. S., Yajnik, C. S., & Demaio, A. (2020). The double burden of malnutrition: Aetiological pathways and consequences for health. *Lancet*, *395*(10217), 75–88. https://doi.org/10.1016/s0140-6736(19)32472-9

WHO. (2023). *Malnutrition in children*. Retrieved April 22, 2024, from https://www.who.int/data/nutrition/nlis/info/malnutrition-in-children

WHO. (2024). *Anaemia*. Retrieved December 19, 2024, from https://www.who.int/data/nutrition/nlis/info/anaemia#:~:text=WHO%20defines%20anaemia%20in%20children%20aged%20under%205,to%20measure%20haemoglobin%20levels%20are%20easy%20to%20administer

Woldeamanuel, B. T., & Tesfaye, T. T. (2019). Risk factors associated with under-five stunting, wasting, and underweight based on Ethiopian demographic health survey datasets in Tigray region, Ethiopia. *Journal of Nutrition and Metabolism*, *2019*, 1–11. https://doi.org/10.1155/2019/6967170

Yaya, S., Oladimeji, O., Odusina, E. K., & Bishwajit, G. (2020). Household structure, maternal characteristics and children's stunting in Sub-Saharan Africa: Evidence from 35 countries. *International Health*, *14*(4), 381–389. https://doi.org/10.1093/inthealth/ihz105

Yazew, T. (2022). Underweight and associated factors among children under five years in North Shewa Zone, Oromia, Ethiopia: An observational community-based study. *F1000research*, *11*, 39. https://doi.org/10.12688/f1000research.55680.1

Yazew, T., & Daba, A. (2022). Associated Factors of Wasting among Infants and Young Children (IYC) in Kuyu District, Northern Oromia, Ethiopia. *Biomed Research International*, *2022*(1), 1–8. https://doi.org/10.1155/2022/9170322

Yoseph, M. (2020). *Institutional delivery services utilization and its determinant factors among women who gave birth in the past 24 months in Southwest Ethiopia - BMC Health Services Research*. BioMed Central. https://bmchealthservres.biomedcentral.com/articles/10.1186/s12913-020-05121-9

You, H., Gu, H., Ning, W., Zhou, H., & Dong, H. (2016). Comparing maternal services utilization and expense reimbursement before and after the adjustment of the new rural cooperative medical scheme policy in rural China. *PLOS ONE*, *11*(7), e0158473. https://doi.org/10.1371/journal.pone.0158473

Young, N., Bowman, A., Swedin, K., Collins, J., Blair-Stahn, N. D., Lindstedt, P. A., Troeger, C., & Flaxman, A. D. (2022). Cost-effectiveness of antenatal multiple micronutrients and balanced energy protein supplementation compared to iron and folic acid supplementation in India, Pakistan, Mali, and Tanzania: A dynamic microsimulation study. *PLOS Medicine*, *19*(2), e1003902. https://doi.org/10.1371/journal.pmed.1003902

Zhao, P., Diao, Y., You, L., Wu, S., Yang, L., & Liu, Y. (2019). The influence of basic public health service project on maternal health services: An interrupted time series study. *BMC Public Health*, *19*(1). https://doi.org/10.1186/s12889-019-7207-1

Zhao, P., Han, X., You, L., Zhao, Y., Yang, L., & Liu, Y. (2020). Maternal health services utilization and maternal mortality in China: A longitudinal study from 2009 to 2016. *BMC Pregnancy and Childbirth*, *20*(1). https://doi.org/10.1186/s12884-020-02900-4

Thermal Science and Engineering Progress 61 (2025) 103535

Contents lists available at ScienceDirect

Thermal Science and Engineering Progress

journal homepage: www.sciencedirect.com/journal/thermal-science-and-engineering-progress

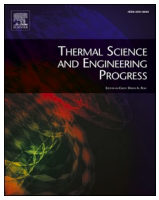

Experimental investigation of enhanced hydrogen production from atomised water-methanol mixture in a modified plasma reformer

Neeraj Budhraja *, Amit Pal, R.S. Mishra

Department of Mechanical Engineering, Delhi Technological University, Delhi 110042, India

ARTICLE INFO

Keywords:
Hydrogen Production
Modified Plasma Reformer
Ultrasonic Transducer
Hydrogen Slectivity
Methanol Conversion Percentage

ABSTRACT

Hydrogen is a clean energy carrier with a very high energy content by mass. However, about 97–98 % of H_2 production is through steam reforming, which lowers the benefits of cleaner fuel. In current work, a modified plasma reformer was used to enhance hydrogen production, and the performance parameters like feed flow rate (0.5 to 4.5 LPM), methanol concentration (0 to 35 %) and voltage (4 to 8 V) were analyzed at three different ultrasonic transducer frequencies (0.3, 1.7 and 2.4 MHz). The results showed that the higher frequency (2.4 MHz) transducer had about 8–10 % higher tendency of H_2 production rate against the other two transducers of frequencies 1.7 MHz and 0.3 MHz, respectively. The process parameters that influenced the H_2 production rate include input voltage, which showed a 14–25 % increase in the H_2 production rate from 4 kV to 7.5 kV, and beyond 7.5 kV, it declined. Similarly, the highest H_2 production rate was observed at the higher methanol concentration of 35 % and feed flow rate of 3.5 LPM. The hydrogen selectivity (HS) and methanol conversion (MCP) also calculated and found both positive and negative impacts as per the variations in influencing parameters. The highest raise in HS and MCP were observed about 30–45 % for input voltage whereas the reduction was about 30–40 % for methanol concentration. The feed flow rate showed mixed response.

1. Introduction

The commercial usage of hydrogen energy started long ago, but the production processes are still conventional [1,2]. About 97–98 % of production was from steam reforming of natural gas, and 2–3 % was from water electrolysis [3,4]. The steam reforming is an energy-consuming and pollution-31 generating process [5]. And the raw materials are mainly natural gas and coal gas, which further degrades the environment [6]. When combined with other renewable energy sources, water electrolysis is a cleaner hydrogen production process. In contrast, the hydrogen production rate for water electrolysis is very low. Hence, the industries were forced to consume hydrogen produced from conventional processes using non-renewable and polluting raw materials [7,8], which leads to over-exploitation of fossil fuels. Another hydrogen-producing method is plasma reforming, which can be a game changer in low energy consumption, eco-friendliness, and less polluting raw materials for hydrogen production [9]. The plasma generation requires electricity, which may be generated from renewable energy sources, further reducing dependence on conventional fuels during production [10].

The over-exploitation of non-renewable energy sources has created many environmental problems. A group of countries sits annually for an annual environmental issues analysis and prepares a report on the actions taken and future roadmaps. This report was published as the 'CoP Sustainability Report'. The primary objective of the CoP is "To prevent global temperature surpassing 2℃ by the end of the century and progress towards this target is reviewed each year at the event." The CoP-26 was held in Glasgow, Scotland, United Kingdom [11]. The 197 parties in the event prioritized using low-carbon alternatives of energy sources. In addition, the CoP-27 held in Sharm El-Sheikh, Egypt, focused on carbon neutrality in energy sources [12]. Meanwhile, the recently held CoP-28 in Dubai, United Arab Emirates, debated whether fossil fuel phase down or complete phase out [13]. Hence, alternative energy sources must be renewable and consume environmentally friendly raw materials such as biomass and agricultural products.

There are many such contenders for raw materials of alternative energy like biomass, biogas, biodiesel, and alcohol. In alcohols, the methanol has the highest hydrogen content, about 12.5 % w/w of hydrogen. Besides this, methanol becomes carbon–neutral when produced from biomass based raw material through fermentation process

* Corresponding author.
E-mail address: neeraj_budhraja@yahoo.com (N. Budhraja).

https://doi.org/10.1016/j.tsep.2025.103535
Received 23 December 2024; Received in revised form 17 March 2025; Accepted 21 March 2025
Available online 23 March 2025
2451-9049/© 2025 Elsevier Ltd. All rights are reserved, including those for text and data mining, AI training, and similar technologies.

and using renewable energy sources [14]. Many studies have used alcohols, mainly methanol, for hydrogen production. *Wu et al.* (2024) used methanol to produce hydrogen in a steam reforming process [15]. The best result (98 % methanol conversion) was obtained at 3600 mL/g.h gas hourly space velocity (GHSV), whereas 6000 mL/g.h GHSV showed a 100.8 mL/min reformate flow rate. In contrast, *Ranjekar* and *Yadav* (2021) analyzed the reaction mechanism and reaction pathways involved in the methanol-reforming process [16]. *Bepari et al.* (2022) discussed the catalytic effects of carbon catalysts in methanol-reforming. The result showed 46 % methanol conversion at 300℃ while 40 % methanol conversion at 250℃ and gave more than 90 % hydrogen selectivity with good stability for 42 h [17]. Hence, methanol is one of the exceptional raw material for hydrogen production.

The most widely used method for hydrogen production is methane steam reforming. However, nowadays, methanol-reforming with/ without catalysts is another process being used by researchers/scientists for hydrogen production [18,19]. *Pinzari (2023)* used nanocrystalline TiO_2 to produce hydrogen in a methanol reformer for enhanced methanol conversion. The testing was performed between 200℃ and 400℃ at 50.0 h^{-1} GHSV [20]. It was observed that TiO_2 nanocrystalline improved the methanol conversion and hydrogen production. *Jin et al. (2023)* performed methanol reforming using $NiTiO_3$ nano-catalyst and obtained a significant rise in hydrogen production [21]. The higher methanol conversion (>95 %) and about 90 % hydrogen selectivity were achieved at 550-600℃. The study also showed that methanol decomposition was dominated at low temperatures, whereas higher temperatures showed dominance in the methanol–water decomposition. *Mironova et al.* (2023) studied methanol steam reforming using a metal–carbon catalyst for hydrogen production and found good stability for continuous operation for more than 30 h [22]. *Hafeez et al.* (2020) conducted modeling of a methanol-reforming micro-reactor for hydrogen production. The computational fluid dynamics analysis showed higher methanol conversion with rising temperature, steam-to-methanol ratio, and residence time [23]. Hence, these parameters are significant for enhanced hydrogen production through methanol-reforming.

Researchers develop simulation models of the reforming process to understand the reaction pathways better. Thus, *Budhraja et al.* (2023) generated a methanol-reforming model and observed 95 % methanol conversion at 400℃. Meanwhile, the methanol-to-water ratio enhanced methanol conversion [10]. The reaction temperature significantly affected hydrogen production and showed a 10.5 % rise in hydrogen selectivity from 100℃ to 400℃ [9]. *Chen et al.* (2024) simulated an integrated methanol-reformer and used heat from a proton exchange membrane fuel cell [24]. The study conducted a systematic investigation to understand the effects of various parameters. The steam-methanol ratio and reformer temperature significantly influenced the hydrogen production. *Zhao et al.* (2023) used a hybrid methanol reformer assisted with solar energy. The system utilized solar heat and heat from proton exchange membrane fuel cells for methanol conversion [25]. Thus, the study showed the importance of temperature in the methanol-reforming process. *Wang* and *Wang* (2016) performed methanol-reforming for hydrogen production in a micro-reactor reaction chamber. An increase of 2.6 % and 5.46 % in hydrogen production rate and methanol conversion was attained at 270℃ and 0.95 h^{-1} space velocity [26].

The current study modified a plasma reformer with a magnetic electrode to generate a plasma vortex. The plasma vortex creates more plasma-feed interaction sites to enhance hydrogen production through reforming. The influencing parameters, such as input voltage, methanol concentration, and feed flow rate, were varied to understand the parameter performance. The three ultrasonic frequency transducers were installed to atomize the water-methanol mixture before sending it to the plasma reformer. The hydrogen selectivity and methanol conversion percentage were also measured to understand the influence on various parameters on hydrogen production. A hydrogen purification unit was also installed to purify the hydrogen up to 99 % purity. The experimental study will help understand the parameter performance, resulting in enhanced hydrogen production. It will aid in developing a large-scale methanol reformer for hydrogen production, and the produced hydrogen can be used for fuel cells and other commercial applications.

2. Material and method

The raw materials and the production process used were discussed, and the purification method, mathematical calculations, and analysis implemented were also proposed in this section.

2.1. Raw materials

The commercial grade methanol (ONGC/LPG/09/2015), which was 99.9 % pure and distilled water (de-ionized/ de-mineralized), was procured to prepare a water-methanol mixture at different methanol concentrations (5 %, 20 % and 35 %) to be fed into the reactor. All the chemicals were high-grade and did not require any further processing to prepare samples for plasma reformer feed. The samples contained a water-methanol mixture in different compositions. The composition of various feeds is depicted in Table 1.

2.2. Feed atomization

The water-methanol mixture cannot be fed directly to the plasma reformer/ reactor; therefore, the feed atomization was carried out. Three different ultrasonic transducers (or atomizers) with frequencies of 0.3 MHz, 1.7 MHz, and 2.4 MHz were installed for feed atomization. The ultrasonic transducers and their circuit are shown in Fig. 1. The working principle of the ultrasonic transducer depends on the sound frequency at the ultrasonic level generated by the metal diaphragm connected with the piezo-ceramic element. The ultrasonic sound waves vibrate the metal diaphragm to convert liquid feed into minute droplets with a diameter within a few nanometres (nm) range. The atomized feed was then fed into the plasma reformer for further processing. The specifications of the atomizers are depicted in Table 2.

2.3. Plasma reforming process

The process of water-methanol reforming was carried out in the plasma reformer designed and developed within the laboratory (shown in Fig. 2). The plasma reformer consists of two electrodes (one cylindrical copper-based alloy and another neodymium-based ring-type magnet) placed in a cylindrical tube of inner diameter 20 mm. A high-voltage generator was designed with a flyback transformer that generated a potential difference between 1.0 kV and 10 kV at the output terminals. The atomized feed was fed into the reformer and passed through the two electrodes. The plasma arc jumps from the Cu electrode to the magnet electrode when the distance between the two electrodes ranges from 7 mm to 13 mm. The plasma arc created a high-temperature zone that breaks down the hydrogen bond of the feed. Hence, water and methanol molecules split into species like H, CO, and O ions. These ions

Table 1
Composition of water-methanol feed.

Sample No.	Water Content (%age)	Methanol Concentration (%age)
1	100	0
2	95	5
3	90	10
4	85	15
5	80	20
6	75	25
7	70	30
8	65	35

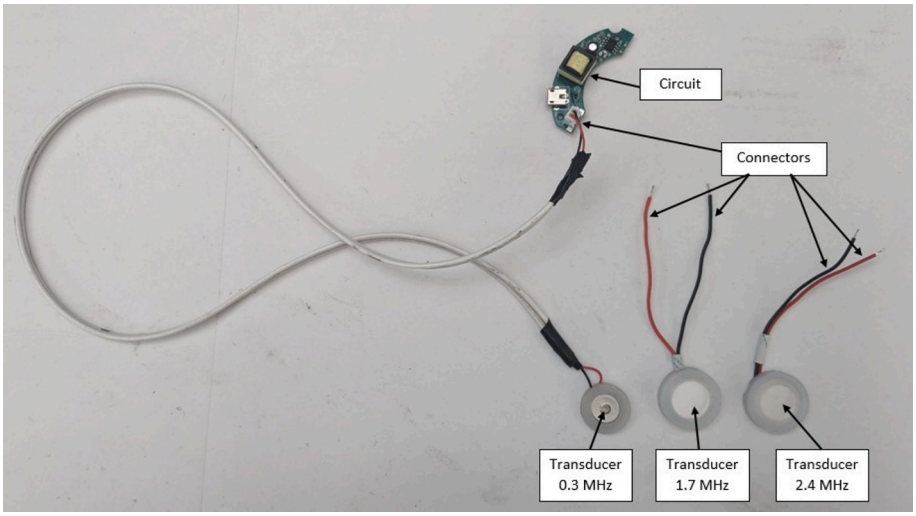

Fig. 1. Various ultrasonic transducers with circuit.

Table 2
Specifications of each atomizer.

Details	0.3 MHz	1.7 MHz	2.4 MHz
Model	SKU: 835,845	SKU: 790,464	SKU: 815,786
Resonant Frequency (MHz)	0.3 (+/- 3 kHz)	1.7 (+/- 7 kHz)	2.4 (+/- 7 kHz)
Diameter (mm)	20	20	20
Power Rating (W)	2.5	2.5	2.5
Electrostatic capacity (pF)	3000	3000	2200

recombine to form compounds like H_2, CO_2, and CO. The H_2 molecules were separated and stored in hydrogen storage bags, and tedlar bags of 1 L were used to collect samples to test the product's purity. The plasma arc vortex was formed within the plasma reformer, presented in Fig. 3.

2.4. Hydrogen purification unit

Hydrogen purification becomes very necessary to obtain pure hydrogen for applications such as fuel for fuel cells and other industrial applications. The gaseous mixture from the plasma reformer consists of gases such as H_2, N_2, CO, CO_2, etc. The hydrogen purification was performed by passing a pressurized gaseous mixture through a zeolite sieve. The void diameter of the zeolite sieve was slightly more than the kinematic diameter of hydrogen molecules; thus, the hydrogen molecules passed through the sieve, whereas other gaseous molecules, being more prominent than the void diameter, got stuck. Once the first sieve got choked from larger gaseous molecules, the other sieve began working. After purification, a small amount of hydrogen gas passes through the first sieve in the reverse direction. The choked voids get unblocked and become ready for operation after the second sieve gets choked. Therefore, the zeolite sieve's automatic ON/OFF switching performs a continuous hydrogen purification. The purified hydrogen was taken for sample testing in tedlar bags for qualitative gas chromatography analysis.

2.5. Gas chromatography

Quantitative analysis is an essential criterion for determining a product's purity level. The hydrogen purity was determined using an Agilent make Gas Chromatography (GC) attached with a Thermal Conductivity Detector (TCD) that detects the sample's thermal conductivity

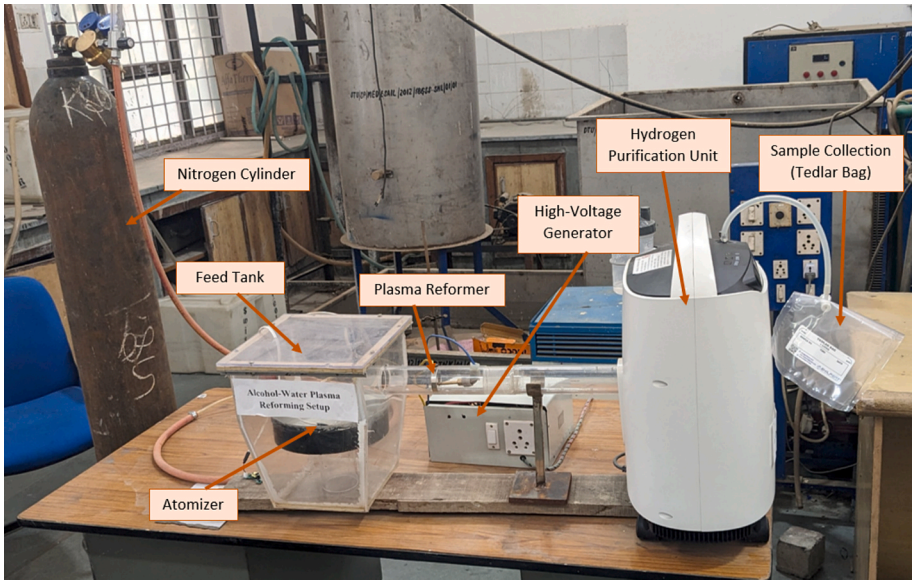

Fig. 2. Experimental setup for plasma reforming.

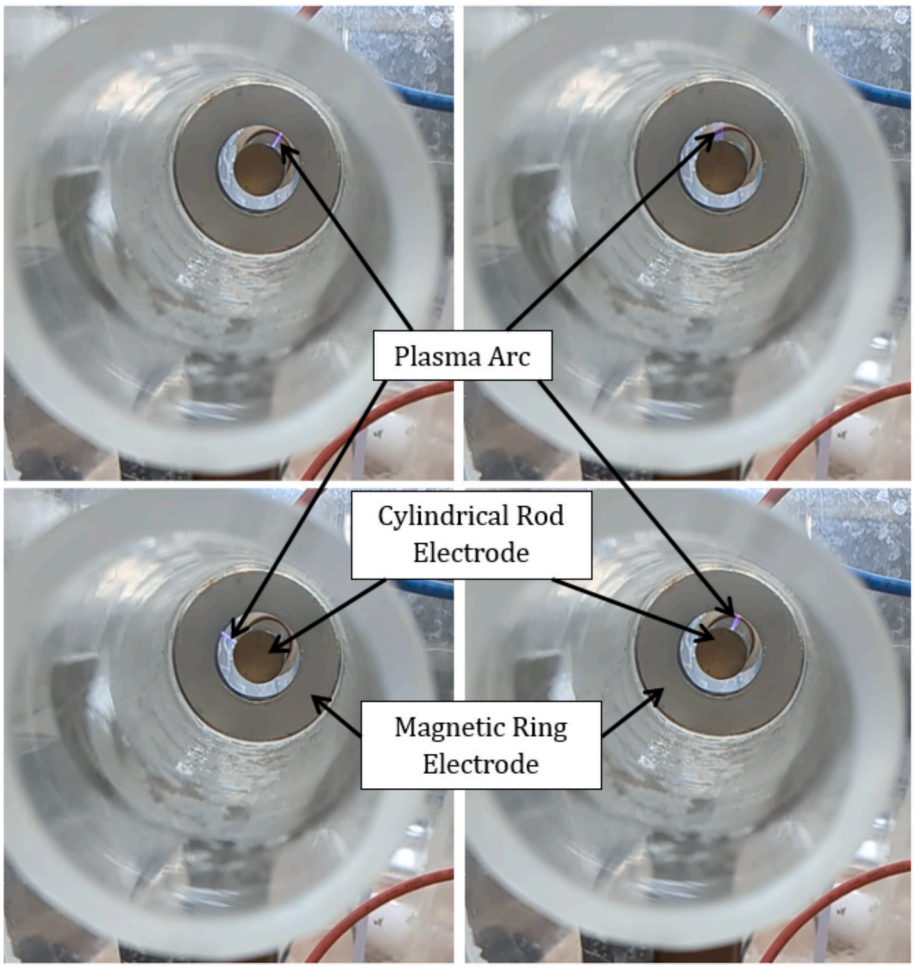

Fig. 3. Plasma arc vortex formation inside plasma reformer.

and compares it with the reference flow in carrier gas. The details of GC-TCD are represented in Table 3. The samples were collected in the Tedlar bags. The gas sample was taken from the Tedlar bag using a 1.0 mL syringe and then inserted into the GC-TCD for qualitative analysis.

2.6. Hydrogen production rate

The amount of hydrogen gas produced during the plasma reforming process was measured in hydrogen production rate, R_{H_2} (mol/day) using Eq. (1),

$$R_{H_2} = \frac{W_{H_2}}{T \times 24} \tag{1}$$

Where W_{H_2} represents the amount of hydrogen produced in mol, and T represents the total time in hours.

Table 3
Specifications of Gas chromatography.

Make	Agilent
Model	8860 GC System
Detector	Thermal conductivity detector
Column	HP-5
Carrier gas	Nitrogen
Oven temperature	50℃ (10 min.) with 10℃/min to 120℃ (5 min.)
TCD temperature	180
Sample	0.1 mL

3. Results and discussion

This section describes the results obtained during experimentation and analyses the results through discussions. The effects of various process parameters, namely input voltage, methanol concentration, and feed flow rate, were studied. The three ultrasonic transducers with ultrasonic frequencies of 0.3 MHz, 1.7 MHz, and 2.4 MHz were used to atomize the water-methanol mixture, and the effects with different parameters were observed. The results obtained were discussed separately for each parameter, taking the other two parameters constant.

3.1. Effects of input voltage

The input voltage is a significant parameter of plasma generation. A minimum and maximum input voltage is necessary for an electron to jump from one electrode to another in the air. The lower voltage will not produce enough energy for an electron jump. Meanwhile, the higher voltage will make a continuous electron jump from a single closest point between two electrodes. Hence, a specific voltage range will produce a plasma vortex due to the magnetic effect.

Fig. 4 shows the influence of the input voltage from 4.0 kV to 8.0 kV on the hydrogen production rate (mol/day). The input voltage range was maintained between 4.0 kV and 8.0 kV because the electron jump was not observed below 4.0 kV; hence, there was no plasma generation. In contrast, above 8.0 kV made a continuous electron jump from a single point, and no plasma arc vortex was generated. Therefore, the input voltage range was maintained between 4.0 and 8.0 kV. A water-methanol mixture with a 35 % methanol concentration and feed flow

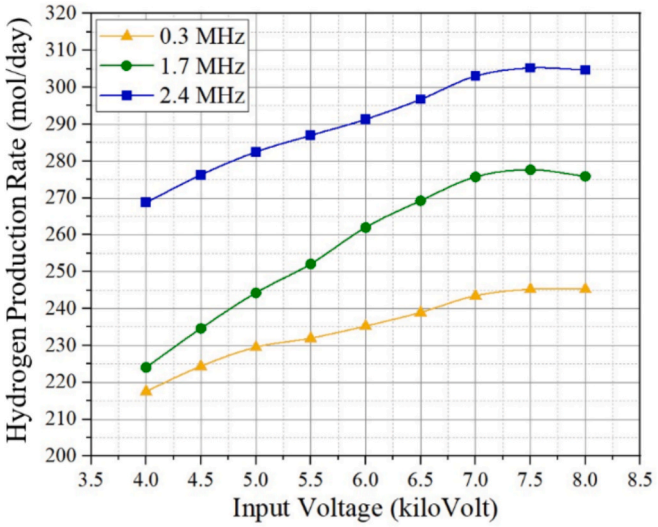

Fig. 4. Hydrogen production rate w.r.t. input voltage.

rate of 4.0 LPM was maintained.

The behaviour of three different curves for 0.3 MHz, 1.7 MHz, and 2.4 MHz ultrasonic transducer was represented in Fig. 4. The hydrogen production rate was observed between 215 mol/day and 306 mol/day. The highest hydrogen production rate was achieved with a 2.4 MHz ultrasonic transducer followed by 1.7 MHz and 0.3 MHz transducers. The curves showed that the hydrogen production rate increased with the increase of input voltage and reached the peak value at about 7.5 kV. Beyond 7.5 kV, the hydrogen production rate showed a slight decline. About a 14 % rise in hydrogen production rate was observed when input voltage was increased from 4.0 kV to 7.5 kV for a 2.4 MHz ultrasonic transducer.

The effects of input voltage on the hydrogen selectivity (HS) and methanol conversion percentage (MCP) were shown in Fig. 5(a) and (b). The HS curve showed a steeper rise with increase in input voltage. The curves further showed that the higher ultrasonic frequency has more tendency for hydrogen production than lower frequency ranges. Similarly, the MCP also had positive influence in raising hydrogen generation with respect to input voltage. The higher input voltage generated enough energy to ionize the atomized water-methanol mixture. The ionization led to the breakdown of hydrogen bonds and, thus, generated hydrogen ions that combined to form hydrogen molecules. About 32 % and 20 % raise were observed in HS and MCP from lower to peak values.

3.2. Effects of methanol concentration

The methanol concentration in the mixture affects the hydrogen yield (or hydrogen production rate) during the plasma reforming process. The higher hydrogen content in the methanol, as opposed to water molecules, produces more hydrogen when the reforming process occurs. The methanol concentration range was maintained between 0 % and 35 % during the experimentation. The lower limit (0 %) represents 100 % water and no methanol content, whereas 35 % means 65 % water and 35 % methanol content by volume. Beyond 35 % methanol concentration, it was observed that the atomized mixture caught fire and started burning within the plasma reactor. Therefore, the methanol concentration was maintained below 35 %.

Fig. 6 depicts the influence of methanol concentration on hydrogen production rate. The methanol concentration was maintained between 0 % and 35 %, and the input voltage and feed flow rate were retained at 3.5 kV and 4.0 LPM, respectively. The various curves represented the ultrasonic transducers of 0.3 MHz, 1.7 MHz, and 2.4 MHz frequencies. Fig. 6 showed that the highest hydrogen production rate was attained with a 2.4 MHz ultrasonic transducer followed by 1.7 MHz and 0.3 MHz transducers. The higher ultrasonic frequency tends to atomize liquid mixture molecules at finer droplets. The smaller the molecular droplets, the more smoothly molecular bond breakage occurs. The results showed

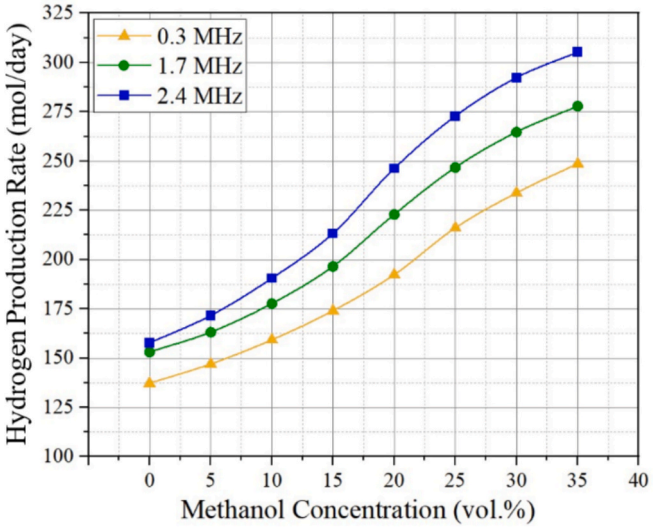

Fig. 6. Hydrogen production rate w.r.t. methanol concentration.

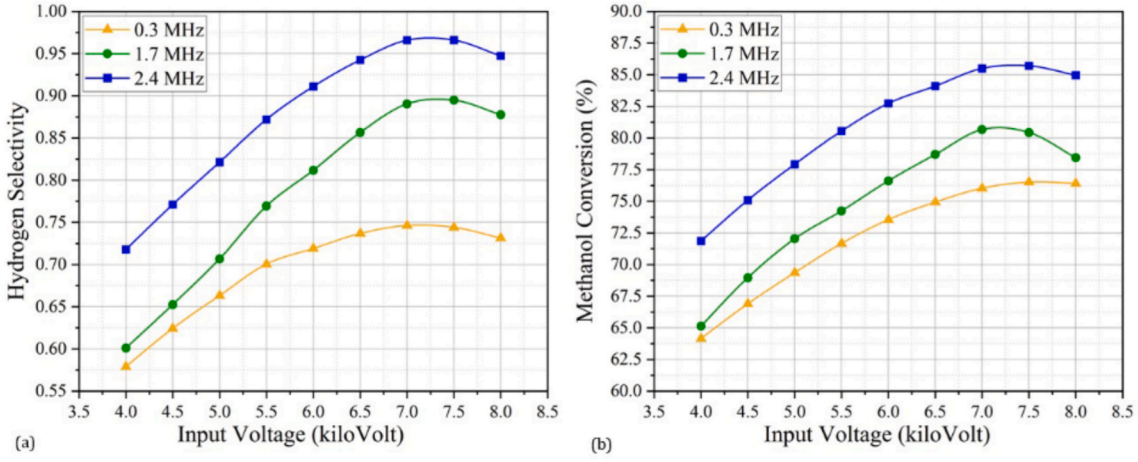

Fig. 5. Effect of input voltage on (a) Hydrogen selectivity, and (b) Methanol conversion percentage.

a 90 % rise in hydrogen production rate from 0 % to 35 % methanol concentration. A similar trend was observed for all ultrasonic transducers. Therefore, the higher methanol concentration in the water-methanol mixture gave a higher hydrogen production rate, and the highest hydrogen production rate of 306 mol/day was achieved for 35 % methanol concentration using a 2.4 MHz ultrasonic transducer at 3.5 kV input voltage and 4.0 LPM feed flow rate.

The influence of methanol concentration in volume percentage on the hydrogen selectivity (HS) and methanol conversion percentage (MCP) were represented in Fig. 7(a) and (b). The HS curve showed a decline with increase in methanol concentration. The curves further showed that the higher ultrasonic frequency has more tendency for hydrogen production than lower frequency ranges. Similarly, the MCP also decreased with methanol concentration that is due to more methanol content in feed, and thus, much of the methanol goes unreacted in higher methanol concentrations. About 42 % and 32 % reduction were observed in HS and MCP from higher to lower values when methanol concentration was increased from 5 % to 35 % by volume.

3.3. Effect of feed flow rate

The feed flow rate is the amount of raw material (of feed) fed to the reactor at a given interval of time. The feed flow rate directly impacts the production rate because the more feed available, the more the product will generate. Here, the feed flow rate considered was between 0.5 LPM and 4.5 LPM. The experiments were also performed beyond 4.5 LPM, but the hydrogen production rate declined significantly. The other parameters, like input voltage and methanol concentration, were maintained at 3.5 kV and 35 %.

The influence of feed flow rate on hydrogen production rate for different ultrasonic frequency transducers was represented in Fig. 8. The ultrasonic frequencies generated were 0.3 MHz, 1.7 MHz, and 2.4 MHz for feed atomization. The results showed a sudden rise from about 40 mol/day to 272 mol/day when the feed flow rate was increased from 0.5 LPM to 3.0 LPM for a 2.4 MHz ultrasonic transducer. It raised about 6.5 times the initial value, whereas the peak (306 mol/day) of hydrogen production rate was achieved at 3.5 LPM, and the rise was about 13 %. The hydrogen production rate declined with a further rise in the feed flow rate. Similar trends were observed for 0.3 MHz and 1.7 MHz ultrasonic transducers.

Meanwhile, the highest hydrogen production rate was obtained using a 2.4 MHz ultrasonic transducer. The higher feed availability in the reactor reduced the tendency of feed ionization, and much of the feed passed without contacting the plasma arc zone; therefore, fewer water-methanol molecules broke down to form radicals. In contrast, the lower feed flow rate reduced feed availability for reforming. Hence, the

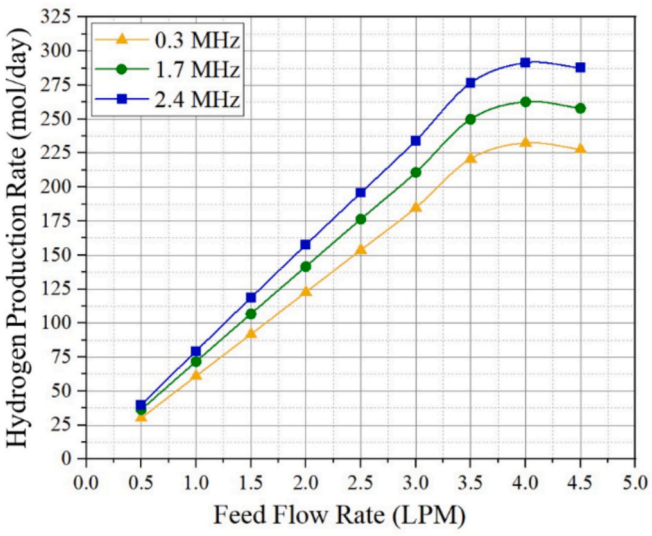

Fig. 8. Hydrogen production rate w.r.t. feed flow rate.

feed flow rate between 3.0 LPM and 4.0 LPM was considered significant for a higher hydrogen production rate at 3.5 kV input voltage and 35 % methanol concentration, respectively.

The effects of feed flow rate on the hydrogen selectivity (HS) and methanol conversion percentage (MCP) were depicted in Fig. 9 (a) and (b). Results showed that the HS curve initially inclined then declined with increase in feed flow rate. The curves further showed that the higher ultrasonic frequency has more tendency for hydrogen production than lower frequency ranges. In contrast, the MCP showed a decrease from 0.5 LPM to 3.5 LPN then a raise was observed with increase in feed flow rate. It is due to more methanol content in feed, and thus, much of the methanol goes unreacted in higher methanol concentrations. About 45 % enhancement was observed in HS from lower to peak values whereas about 14 % decline was observed in MCP from higher to lower values when feed flow rate was increased from 0.5 LPM to 3.5 LPM, respectively.

3.4. Hydrogen purification and qualitative analysis

The purity of a compound becomes an essential criterion for its application. Similarly, hydrogen applications like fuel cells for power generation demand hydrogen gas input with a purity level of about 99.9 % in proton exchange fuel cells. Hence, much research has been

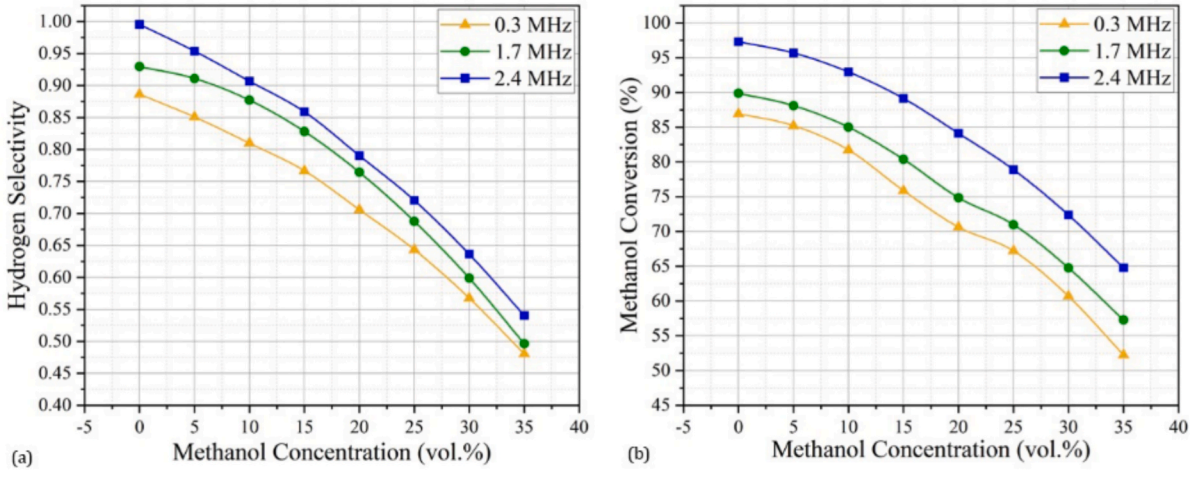

Fig. 7. Effect of methanol concentration on (a) Hydrogen selectivity, and (b) Methanol conversion percentage.

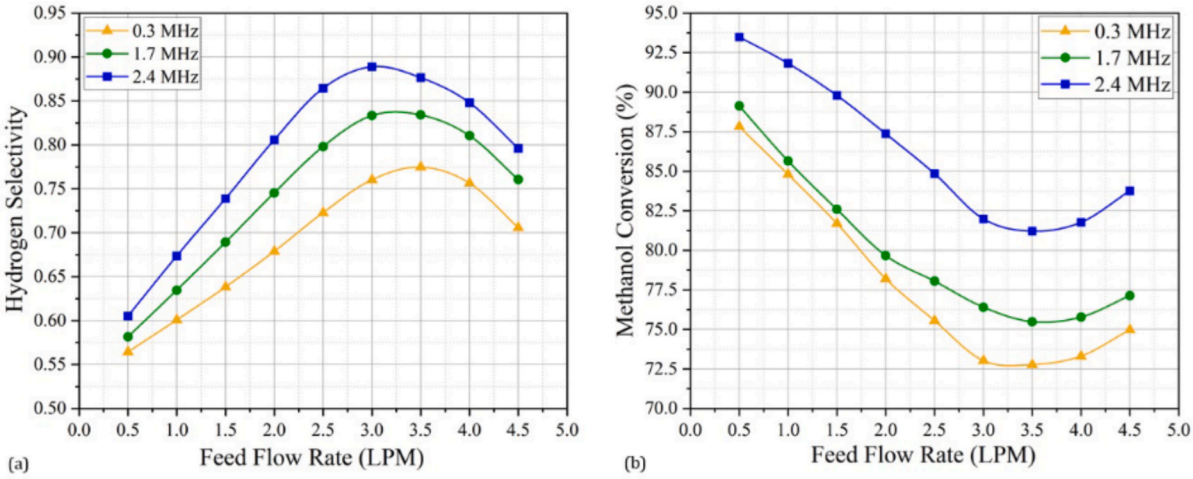

Fig. 9. Effect of feed flow rate on (a) Hydrogen selectivity, and (b) Methanol conversion percentage.

conducted to separate hydrogen from a mixture of hydrogen-rich gases. Here, a hydrogen purification unit that works on the principle of oxygen concentration was used; the composition of a gaseous mixture containing gases like hydrogen, carbon dioxide, nitrogen, and oxygen was determined using Agilent make gas chromatography (GC) having thermal conductivity detector (TCD). The chromatogram showing gas composition before purification is represented in Fig. 10. The sample in Fig. 10 was having the maximum hydrogen content and the various process parameters are at 4.0 LPM feed flow rate, 7.0 kV input voltage and 35 % methanol concentration at 2.4 MHz transducer frequency, respectively.

The oxygen concentrator-type hydrogen purification unit has a compressor that compresses the gaseous mixture from the plasma reformer. The compressed gaseous mixture was then passed through a zeolite sieve membrane with a void diameter just above the kinematic diameter of hydrogen. Thus, the hydrogen molecules passed from the zeolite sieve membrane, leaving carbon dioxide, nitrogen, and other gases with bigger molecular diameters than sieve voids. However, in the process, the oxygen molecules also pass through the sieve because of their smaller molecular diameter than sieve voids. Therefore, the raw material chamber was kept oxygen-free by air tightening and injecting nitrogen gas from a nitrogen gas cylinder, allowing the nitrogen gas to flow for about 5 min before starting the plasma reformer.

The gas composition was also measured after the gaseous mixture passed through the hydrogen purification unit. The samples were collected in tedlar bags of 1 L capacity and analyzed again in the GC-TCD. The chromatogram showing qualitative analysis was conducted in Fig. 11. The results showed that the uncleaned gaseous mixture had about 32.2 % hydrogen content. In contrast, the hydrogen content observed was 99 % when passed through the hydrogen purification unit. In contrast, a small fraction of about 1 % of oxygen was also present after purification. It was due to methanol-reforming, which contains oxygen content. The oxygen molecules may be captured using oxygen absorbers, and hydrogen gas of purity of more than 99 % may be obtained.

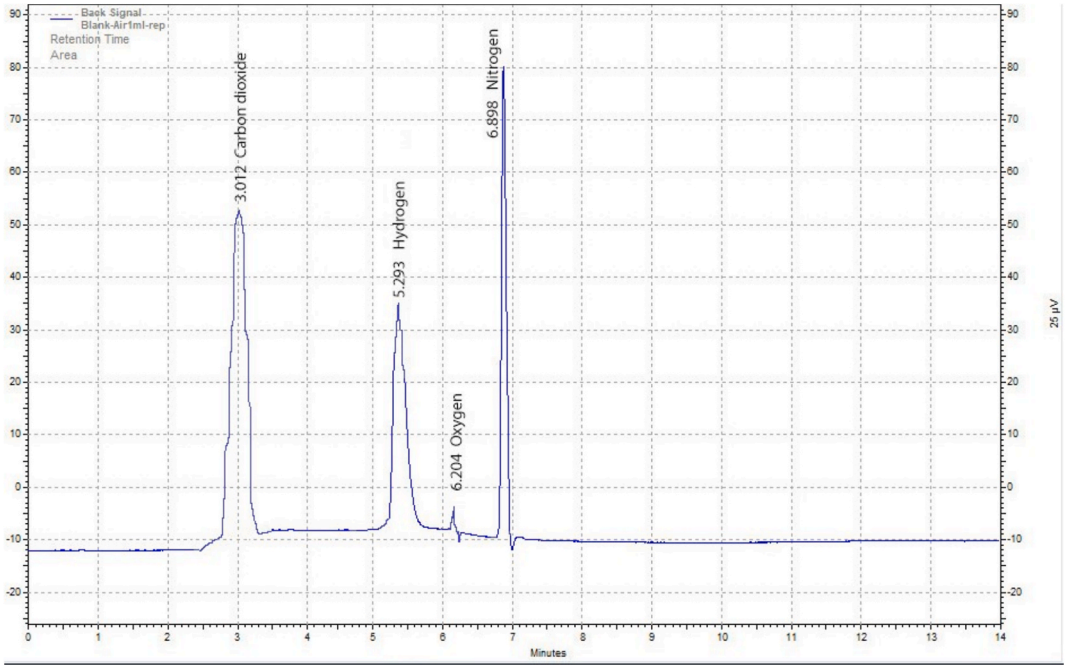

Fig. 10. Composition of the gaseous mixture.

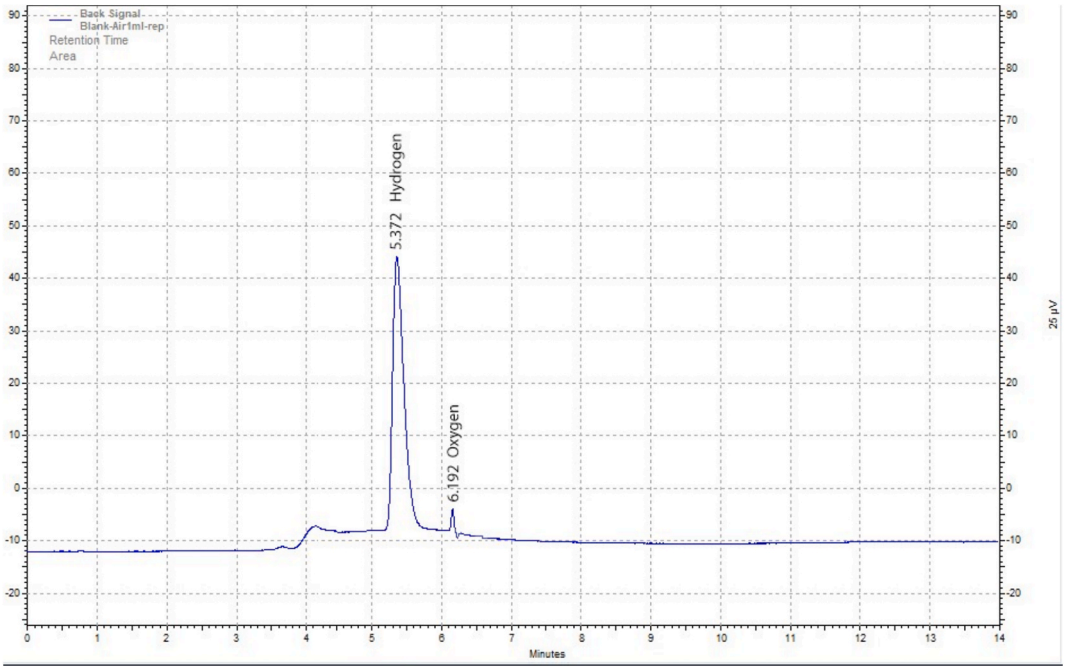

Fig. 11. The gas composition of purified gas.

4. Conclusions

The experimental investigation of enhanced hydrogen production from atomised water-methanol mixture in a modified plasma reformer was performed. The study was conducted on the influence of three operating parameters: input voltage, methanol concentration, and feed flow rate at three different ultrasonic transducer frequencies, i.e., 0.3 MHz, 1.7 MHz, and 2.4 MHz, respectively. The following outcomes were witnessed:

- The atomization of the water-methanol mixture at 2.4 MHz ultrasonic frequency showed maximum hydrogen production rate, followed by 1.7 MHz and 0.3 MHz transducers.
- The hydrogen production rate rose by about 14 %, with the input voltage rise from 4 kV to 7.5 kV. In comparison, the maximum percentage rise of about 25 % was observed at 1.7 MHz ultrasonic frequency.
- The HS and MCP also increased about 32 % and 20 % with the increase in input voltage and reached at peak value between 7 kV and 7.5 kV.
- The higher methanol concentration showed a higher hydrogen production rate and reached 306.2 mol/day hydrogen production rate using a 2.4 MHz ultrasonic transducer.
- About 42 % and 32 % reduction were observed in HS and MCP from higher to lower values when methanol concentration was increased from 5 % to 35 % by volume.
- The higher feed flow rate positively influenced the hydrogen production rate and peaked at 3.5 LPM. Beyond 3.5 LPM, the hydrogen production rate declined.
- The feed flow rate showed opposite impacts on HS and MCP. The HS enhanced from lower to peak values between 0.5 LPM and 3.5 LPM whereas about the MCP declined from higher to lower values at same feed flow rate.
- All three ultrasonic transducers observed a similar trend for methanol concentration and feed flow rate, where 2.4 MHz showed the highest hydrogen production rate, followed by 1.7 MHz and 0.3 MHz, respectively.

Therefore, the experimental investigation of the plasma reforming of the water-methanol mixture showed the potential of generating a gaseous mixture rich in hydrogen gas. Then, the hydrogen from the gaseous mixture can be extracted for various applications. The inputs in the experimental setup may be used to generate a design of experiments that will analyze the results mathematically and develop an optimal value for optimizing the hydrogen production rate. The hydrogen generated in the experiment is about 99 % purity level; therefore, it may be considered for insertion in fuel cells for power generation and other industrial applications.

CRediT authorship contribution statement

Neeraj Budhraja: Writing – original draft, Visualization, Methodology, Investigation, Formal analysis, Data curation, Conceptualization. **Amit Pal:** Writing – review & editing, Validation, Supervision, Resources, Methodology, Investigation. **R.S. Mishra:** Writing – review & editing, Supervision.

Declaration of competing interest

The authors declare that they have no known competing financial interests or personal relationships that could have appeared to influence the work reported in this paper.

Acknowledgement

The authors are thankful to the Research Lab, Department of Mechanical Engineering, Delhi Technological University, for developing a plasma reformer to conduct experiments within the lab.

Data availability

All the data used in the manuscript have been properly cited with corresponding reference.

References

[1] J. Zhao, R. Shi, Z. Li, C. Zhou, T. Zhang, How to make use of methanol in green catalytic hydrogen production? Nano Select 1 (2020) 12–29, https://doi.org/10.1002/nano.202000010.

[2] R. Zhang, C. Huang, L. Zong, K. Lu, X. Wang, J. Cai, Hydrogen Production from Methanol Steam Reforming over TiO_2 and CeO_2 Pillared Clay Supported Au Catalysts, Appl. Sci. 8 (2018) 176, https://doi.org/10.3390/app8020176.

[3] D.H. Lee, T. Kim, Plasma-catalyst hybrid methanol-steam reforming for hydrogen production, Int J Hydrogen Energy 38 (2013) 6039–6043, https://doi.org/10.1016/j.ijhydene.2012.12.132.

[4] N. Budhraja, A. Pal, R.S. Mishra, Plasma reforming for hydrogen production: Pathways, reactors and storage, Int J Hydrogen Energy 48 (2023) 2467–2482, https://doi.org/10.1016/j.ijhydene.2022.10.143.

[5] M. Tayyab, S. Mansoor, Z. Akmal, M. Khan, L. Zhou, J. Lei, et al., A binary dumbbell visible light driven photocatalyst for simultaneous hydrogen production with the selective oxidation of benzyl alcohol to benzaldehyde, J Colloid Interface Sci 665 (2024) 911–921, https://doi.org/10.1016/j.jcis.2024.03.190.

[6] M. Tayyab, Y. Liu, Z. Liu, Z. Xu, W. Yue, L. Zhou, et al., A new breakthrough in photocatalytic hydrogen evolution by amorphous and chalcogenide enriched cocatalysts, Chem. Eng. J. 455 (2023), https://doi.org/10.1016/j.cej.2022.140601.

[7] Q. Shen, Z. Cai, G. Chen, X. Zhang, S. Li, G. Yang, Optimization of the sol gel synthesis process parameters by orthogonal experiment of novel spinel oxide catalyst CuFe1.2Al0.8O4 with improved performance for methanol steam reforming, J Solgel Sci Technol 107 (2023) 490–502, https://doi.org/10.1007/s10971-023-06136-4.

[8] M.K. Awasthi, R.K. Rai, S. Behrens, S.K. Singh, Low-temperature hydrogen production from methanol over a ruthenium catalyst in water, Catal Sci Technol 11 (2021) 136–142, https://doi.org/10.1039/D0CY01470B.

[9] N. Budhraja, A. Pal, R.S. Mishra, Optimizing Methanol Reforming Parameters for Enhanced Hydrogen Selectivity in an Aspen Hysys Simulator using Response Surface Methodology, Energ. Technol. 11 (2023), https://doi.org/10.1002/ente.202300203.

[10] N. Budhraja, A. Pal, R.S. Mishra, Modeling and analysis for enhanced hydrogen production in process simulation of methanol reforming, Energy Sources Part A 45 (2023) 11553–11565, https://doi.org/10.1080/15567036.2023.2262414.

[11] COP26 SUSTAINABILITY REPORT. 2021.

[12] COP27 OFFICIAL SUSTAINABILITY REPORT. 2022.

[13] COP28 SUSTAINABILITY REPORT. 2023.

[14] Budhraja N. Pal A. Kumar A. Kumar A. Pal A. Kachhwaha S.S. Jain P.K. 2021 Springer Singapore Singapore 10.1007/978-981-15-9678-0_28 . Investigations on Ethanol as the Raw Material for Hydrogen Production, Storage, and Applications. In:.

[15] Q. Wu, Y. Wang, H. Zhou, X. Qiu, D. Mei, Measurement of reaction temperature distribution inside of methanol steam reforming microreactor using infrared thermography, Appl Therm Eng 238 (2024) 121909, https://doi.org/10.1016/j.applthermaleng.2023.121909.

[16] A.M. Ranjekar, G.D. Yadav, Steam Reforming of Methanol for Hydrogen Production: A Critical Analysis of Catalysis, Processes, and Scope, Ind Eng Chem Res 60 (2021) 89–113, https://doi.org/10.1021/acs.iecr.0c05041.

[17] S. Bepari, M. Khan, X. Li, N. Mohammad, D. Kuila, Effect of Ce and Zn on Cu-Based Mesoporous Carbon Catalyst for Methanol Steam Reforming, Top Catal 66 (2023) 375–392, https://doi.org/10.1007/s11244-022-01772-6.

[18] M. Tayyab, Y. Xie, X. Tan, M. Usman, M.C. Tang, S.S. Chen, A ternary dumbbell MoS2 tipped Zn0.1Cd0.9S nanorods visible light driven photocatalyst for simultaneous hydrogen production with organics degradation in wastewater, Chem. Eng. J. 505 (2025), https://doi.org/10.1016/j.cej.2024.159064.

[19] M. Tayyab, U.E. Kulsoom, Y. Liu, S. Mansoor, M. Khan, Z. Akmal, et al., Visible light-driven photocatalytic H_2 evolution and dye degradation by electrostatic self-assembly of CdS nanowires on Nb_2C MXene, Int J Hydrogen Energy 51 (2024) 1400–1413, https://doi.org/10.1016/j.ijhydene.2023.09.199.

[20] F. Pinzari, The effect of nanocrystalline TiO_2 on structure and catalytic activity of CuO–ZnO in combined methanol reforming, React. Kinet. Mech. Catal. 136 (2023) 367–379, https://doi.org/10.1007/s11144-023-02357-4.

[21] Q. Jin, X. Meng, P. Wu, Y. Li, M. Xu, R. Zhou, et al., Methanol steam reforming for hydrogen production over $NiTiO_3$ nanocatalyst with hierarchical porous structure, RSC Adv 13 (2023) 16342–16351, https://doi.org/10.1039/D3RA02891G.

[22] E.Y. Mironova, A.A. Payen-Lytkina, M.M. Ermilova, N.V. Orekhova, N. A. Zhilyaeva, M.N. Efimov, et al., Methanol Steam Reforming on Metal–Carbon Catalysts Having Different Carbon Supports, Inorg. Mater. 59 (2023) 729–735, https://doi.org/10.1134/S0020168523070117.

[23] S. Hafeez, E. Aristodemou, G. Manos, S.M. Al-Salem, A. Constantinou, Modelling of packed bed and coated wall microreactors for methanol steam reforming for hydrogen production, RSC Adv 10 (2020) 41680–41692, https://doi.org/10.1039/d0ra06834a.

[24] Z. Chen, B. Yin, Z. Wei, F. Dong, Coupling of high-temperature proton exchange membrane fuel cells with methanol steam reforming: Modeling and simulation for an integrated coupled for power generation system, Energy Convers Manag 301 (2024) 118044, https://doi.org/10.1016/j.enconman.2023.118044.

[25] K. Zhao, H. Kong, S. Tan, X.-G. Yang, H. Zheng, T. Yang, et al., Analysis of a hybrid system combining solar-assisted methanol reforming and fuel cell power generation, Energy Convers Manag 297 (2023) 117664, https://doi.org/10.1016/j.enconman.2023.117664.

[26] F. Wang, G. Wang, Performance and cold spot effect of methanol steam reforming for hydrogen production in micro-reactor, Int J Hydrogen Energy 41 (2016) 16835–16841, https://doi.org/10.1016/j.ijhydene.2016.07.083.

Check for updates

Transactions on Emerging Telecommunications Technologies

WILEY

SURVEY ARTICLE

Exploring the Transformative Impact of Blockchain Technology on Healthcare: Security, Challenges, Benefits, and Future Outlook

Anita Thakur | Virender Ranga | Ritu Agarwal

Delhi Technological University, Delhi, India

Correspondence: Virender Ranga (virenderranga@dtu.ac.in)

Received: 26 April 2024 | **Revised:** 26 November 2024 | **Accepted:** 14 December 2024

Funding: The authors received no specific funding for this work.

Keywords: blockchain | challenges | healthcare | security | use cases

ABSTRACT

This study aims to methodically explore the diverse applications of blockchain technology (BT) within the healthcare domain. Additionally, it seeks to analyze the inherent challenges of integrating BT into healthcare systems. Furthermore, this study elucidates blockchain's advantageous contributions to the healthcare domain. The suggested research thoroughly reviews the literature from various databases, using predetermined criteria, such as exclusion and inclusion, to identify pertinent studies. It also demonstrates the properties of blockchain and its functionality for the patient, healthcare providers, or overall healthcare infrastructure to assist the healthcare industry in a contemporary direction. The substantial advantages of BT within the medical field are notable. However, it is vital to acknowledge the security vulnerabilities by employing a blockchain-centered strategy to mitigate these challenges, allowing for the creation of a robust and streamlined system and framework. The importance of this study is that as this investigation navigates the convergence of healthcare and BT, it not only delineates the multifaceted applications of BT but also meticulously examines the associated security challenges. The findings of this study chart a course toward a technologically advanced, secure, and efficient healthcare ecosystem, improving patient outcomes and reshaping the future of healthcare delivery worldwide.

1 | Introduction

Healthcare has been an indispensable part of every living being's life. The healthcare sector regularly encounters challenges in providing and retrieving medical records, financial remuneration to healthcare providers, and insurance coverage [1]. The lack of medical records can endanger patients, as doctors may be unaware of crucial details such as current medications, history of laboratory tests, operations, surgeries, and diagnoses. Healthcare record-keeping is subject to tremendous change in developed and developing nations. This vital information is prone to threats like manipulation, deletion, and unauthorized access. To trust another party to keep our data safe could be very dangerous [2].

As per the data furnished by the Protenus breach barometer, 2020 witnessed a breach of over 50 million patient records across 905 distinct incidents, signifying a substantial 44% upsurge in hacking-related breaches. Subsequently, in 2021, approximately 40 million records were compromised, encompassing 758 recorded incidents, with an additional noteworthy 42% increase in breaches attributed to insider threats. In the year 2022, an alarming 50 million-plus records have been compromised in

© 2025 John Wiley & Sons Ltd.

905 separate incidents, and hacking-related breaches continue to exhibit a 44% increment; similarly, according to the October 2023 [3] report, the 59M+ patient records were breached in 956 incidents. Healthcare services constitute a complex ecosystem involving interactions among patients, healthcare providers, physicians, medical staff, and various infrastructure elements. Recognizing the critical significance of security and privacy within healthcare is paramount. The prevalence of security breaches poses a considerable concern. Notably, from October 2009 to December 31, 2021, the Office for Civil Rights within the Department of Health and Human Services (HHS) documented 4 419 medical data violations, each involving 500 or more records. In 2021, these violations translated into an average of 1.95 daily incidents involving compromising over 500 data records [4].

The statistics presented in the Health Insurance Portability and Accountability Act (HIPAA) report [5] indicate that instances of data breaches primarily stem from unauthorized access, theft, hacking, IT incidents, and disclosure. Furthermore, the report highlights that network servers are the prevailing location for breached protected health information. Another data protection regulatory body, the General Data Protection Regulation (GDPR), is pivotal in safeguarding personal health data. The fundamental aim of GDPR is to enhance and modernize the existing directive concerning protecting the individual records of European Union (EU) citizens. The main goal of this regulatory framework is to give citizens more control over how their data is managed. At the same time, it tries to set up strict rules about how data can be handled and used [6, 7].

The GDPR outlines a foundational set of principles that dictate the appropriate handling of personal data. These encompass the requirements of legality and transparency in dealings with data subjects. Specifically, there is a stipulation for a clearly defined purpose for data collection and constraints on subsequent data processing beyond archival purposes. Ensuring data accuracy is very important, with provisions for timely updates when necessary. Furthermore, the regulation mandates the maintenance of personal data in a format that facilitates the identification of data subjects for no longer than the duration deemed essential. Security is paramount, entailing the need to process personal data in a manner that ensures its integrity and confidentiality. Lastly, the controller bears the responsibility of not only adhering to these principles but also demonstrating compliance with the regulatory framework [7–9].

The current landscape of healthcare data management presents significant challenges. Security breaches due to hacking and unauthorized access expose sensitive patient information, while fragmented systems impede the smooth data flow between providers. This lack of control and security necessitates a more robust and secure system to ensure patient privacy and facilitate seamless data exchange within the complex healthcare ecosystem. There are some key concerns about the healthcare data:

- *Security*: The misuse of healthcare data presents a pressing concern for the healthcare sector, with costly data breaches potentially costing millions of dollars. Any malicious party with direct or indirect access to the records can sabotage data security [10].
- *Privacy/Anonymity*: Preserving data confidentiality and safeguarding patients' anonymity from external entities is paramount due to the inherent privacy concerns associated with the information. Primarily, the determination of who may access their confidential information and the extent of such access should be vested exclusively in the hands of the respective patients [11].
- *Interoperability*: Interoperability pertains to the seamless transfer and sharing of data across diverse sources. Presently, healthcare applications encounter notable challenges in establishing effective communication channels. The advent of an innovative interoperability framework serves to streamline the electronic sharing and exchange of data between EHR systems [12].
- *Access Control*: Access control ensures legitimate and controlled healthcare data access, publicly or privately. Access to the data records and permitted activities is only in the possession of the physician assigned to the patient. Patients must be fully empowered to access and share their medical data, exercising their right to control how and with whom they share such information [13].
- *Data Sharing*: Data sharing ensures that the data in transit can be secured through authentication protocols and encryption techniques, thus protecting unauthorized access, modification, or observation. As the data is scattered in multiple locations, keeping it up-to-date and having a unified view of these dispersed records is a challenging task [14].
- *Integrity*: Integrity guarantees that health data has not been changed at any phase and ensures the correctness of healthcare data that healthcare professionals gather without any fabrication or modification [15].

After performing an exhaustive literature survey, this study answers the following research questions (RQs):

- Role of BT in transforming the healthcare domain.
- How does blockchain handle the security issues of the healthcare system?
- What are the benefits and challenges of incorporating the BT in healthcare?

1.1 | Motivation and Contributions

Currently, the predominant focus of suggested surveys on blockchain in healthcare revolves around EHR and health data management. However, critical facets within the healthcare domain, such as supply chain management, remote patient monitoring, and clinical trial data management, demand a thorough examination. Through our evaluation, we assert that blockchain is a safe mechanism to promote transformation in the healthcare industry. Our research focuses not only on the application of blockchain in various healthcare areas but also delves into the security challenges emerging within the healthcare domain upon integrating blockchain. As shown in Table 1, our study contrasts with an existing analysis within a parallel domain, providing a foundational overview of BT and its diverse

21613915, 2025, 3, Downloaded from https://onlinelibrary.wiley.com/doi/10.1002/ett.70087 by Delhi Technological University, Wiley Online Library on [09/03/2025]. See the Terms and Conditions (https://onlinelibrary.wiley.com/terms-and-conditions) on Wiley Online Library for rules of use; OA articles are governed by the applicable Creative Commons License

TABLE 1 | Key comparison of our study with prior literature.

Ref.	HR	RQ	Features of BC in HC	Areas Covered in Healthcare					Security	Benefits	Challenges	HIPAA Compliance
				Health Record	CDM	RPM	SCM	PA				
1	✗	☑	☑	✓	✗	✗	✗	✗	✓	☑	✗	✗
2	✓	✗	✓	☑	✗	✓	✓	✗	✓	✗	✗	☑
8	✓	✗	✓	✓	☑	✗	✓	✗	☑	✓	✓	✓
10	✓	✗	✓	✓	✗	✗	✗	✗	✓	✓	☑	✗
16	✓	✗	✓	✓	✓	✗	✓	✗	☑	✗	✓	✗
17	✓	✗	✓	✓	✗	✗	✓	✗	✗	✓	✓	✗
18	✗	✗	☑	✓	☑	✗	☑	✗	☑	✓	✓	✗
19	✓	✓	✓	✓	✗	✗	✗	✗	✓	✗	☑	✓
20	✗	✗	✗	✓	✗	✗	✓	✗	☑	✗	✓	✗
21	✗	✓	✓	✗	✗	✗	✓	✗	☑	☑	☑	✗
22	✗	✗	✗	✗	✗	✗	✓	✗	✗	✗	✓	✗
23	✗	✗	✗	✗	✓	✗	✗	✗	☑	✗	✓	✗
24	✗	✗	✗	✓	✗	✓	✗	✗	✗	✓	✗	✗
25	✗	✗	☑	✓	✗	✗	✗	✗	✗	✓	✓	✗
26	✗	✓	✓	✓	✓	✗	✓	✗	✗	✗	✓	☑
Our study	✓	✓	✓	✓	✓	✓	✓	✓	✓	✓	✓	✓

Note: In the Table 1, the attribute's name represents the attributes: *HR*: Healthcare Requirement, *RQ*: Research Questions, *Features of BC in HC*: Features of Blockchain in Healthcare, *Security*: Security Consideration, *Benefits*: Benefits of incorporating blockchain in Healthcare, *Challenges*: Drawbacks of Incorporating Blockchain in Healthcare, *CDM*: Clinical Trial Data Management, *RPM*: Remote Patient Monitoring, *SCM*: Supply Chain Management, *PA*: Patient Autonomy, *HIPAA compliance*: Mitigating the Cause of data breach specified by HIPAA using BT, ✓: Represents the coverage of the topic, ✗: Topic is not covered, ☑: Represents the partial coverage of the topic.

applications across various healthcare fields. Our work offers key contributions, such as:

- *Extensive Analysis of Healthcare Transformation*: One of the primary contributions of our study is its focus specifically on healthcare transformation through the adoption of BT. We do not merely scratch the surface but delve into the intricacies of blockchain to revolutionize the healthcare domain. By framing pertinent research questions, our study seeks to shed light on the intricate relationship between BT and the healthcare sector.
- *Evaluation of Existing Blockchain-Adopting Healthcare Solutions*: Our study meticulously assesses the existing healthcare solutions integrated with BT. We pay particular attention to security, privacy, benefits, and challenges associated with these implementations. By critically examining these solutions, we can derive valuable lessons and insights to inform future developments in blockchain and healthcare.
- *Identification of Benefits and Challenges*: In addition to highlighting the advantages, our study also identifies and discusses the various limitations and challenges of incorporating BT into healthcare systems. This in-depth evaluation goes beyond a general understanding to provide a nuanced perspective on the specific practical hurdles that impede the capability of blockchain in healthcare. Identifying and analyzing these challenges offers valuable insights into what must be overcome to unlock its true potential in the healthcare industry.
- *Blockchain's Potential in Addressing Cause of Data Breaches mentioned HIPAA Compliance*: According to HIPAA compliance guidelines, data breaches stem from improper disposal, loss, theft, unauthorized access/disclosure, and hacking/IT incidents. Among these, theft, unauthorized access/disclosure, and hacking/IT incidents are prevalent and require targeted mitigation. This study offers insights into leveraging BT to address and mitigate these challenges.

1.2 | Roadmap

The paper unfolds in the following structure: Section 2 outlines a comprehensive overview of BT, covering its workflow, taxonomy, and evolution. Section 3 depicts the research methodology used in this study, detailing the criteria for inclusion and exclusion of research papers. Section 4 delves into the results by examining blockchain's groundbreaking possibilities in healthcare, including its benefits and challenges. Section 5 discusses and summarizes the paper with its motive, contribution, and discussion. Section 6 presents the concluding remarks of our study and suggests potential directions for future research work. Section 7 elaborates on our additional insights into this topic.

2 | Mainstream Adoption: Blockchain

Before going into more details, let's look at the blockchain's history, as shown in Figure 1. Haber and Stornetta [16] presented a data structure for joining a series of temporally ordered messages with each other at the 1990 CRYPTO conference. In 1991, they illustrated the chain of blocks secured by the cryptographic mechanism for the first-time. The fundamental concept of BT first appeared in the late 1980s and early 1990s. In 2008, S. Nakamoto [17] announced a white paper proposing a DLT known as the blockchain, which facilitates digital assets' secure and immutable transfer.

The underlying network architecture of blockchain adheres to a peer-to-peer model, distinct from server-based or centralized networks, wherein all participating nodes engage in direct coordination devoid of overarching control by any centralized authority [18]. Blockchain, at its core, constitutes a distributed

21613915, 2025, 3, Downloaded from https://onlinelibrary.wiley.com/doi/10.1002/ett.70087 by Delhi Technological University, Wiley Online Library on [09/03/2025]. See the Terms and Conditions (https://onlinelibrary.wiley.com/terms-and-conditions) on Wiley Online Library for rules of use; OA articles are governed by the applicable Creative Commons License

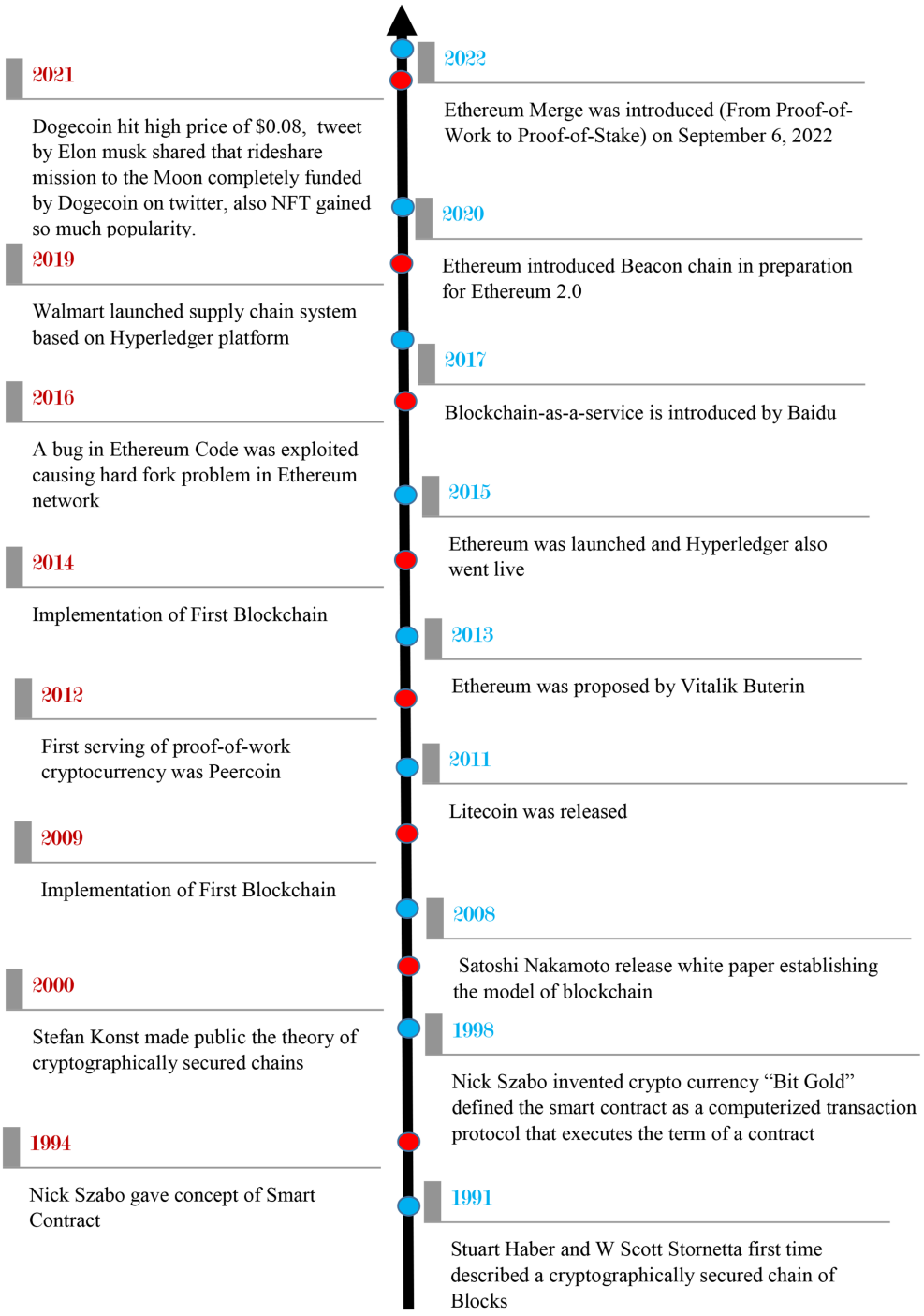

FIGURE 1 | Significant dates in the history of blockchain.

public ledger data structure that facilitates the storage and organization of data records in a decentralized way. All participants in the network hold a synchronized record of every transaction. These transactions are grouped into interconnected blocks, guaranteeing the consistency and accuracy of the data over time. In essence, blockchain embodies a chronological sequence of immutable records, where each valid block is cryptographically connected to the preceding valid block, illustrated in Figure 2.

BT facilitates the secure processing of transactions in a decentralized network, eliminating the central trusted third party [18–20]. There are different categories of blockchain:

- *Permissionless Blockchain*: Permissionless blockchains like Bitcoin and Ethereum are decentralized, providing unrestricted access for all participants to interact and contribute data. They are publicly accessible and devoid of centralized

21613915, 2025, 3, Downloaded from https://onlinelibrary.wiley.com/doi/10.1002/ett.70087 by Delhi Technological University, Wiley Online Library on [09/03/2025]. See the Terms and Conditions (https://onlinelibrary.wiley.com/terms-and-conditions) on Wiley Online Library for rules of use; OA articles are governed by the applicable Creative Commons License

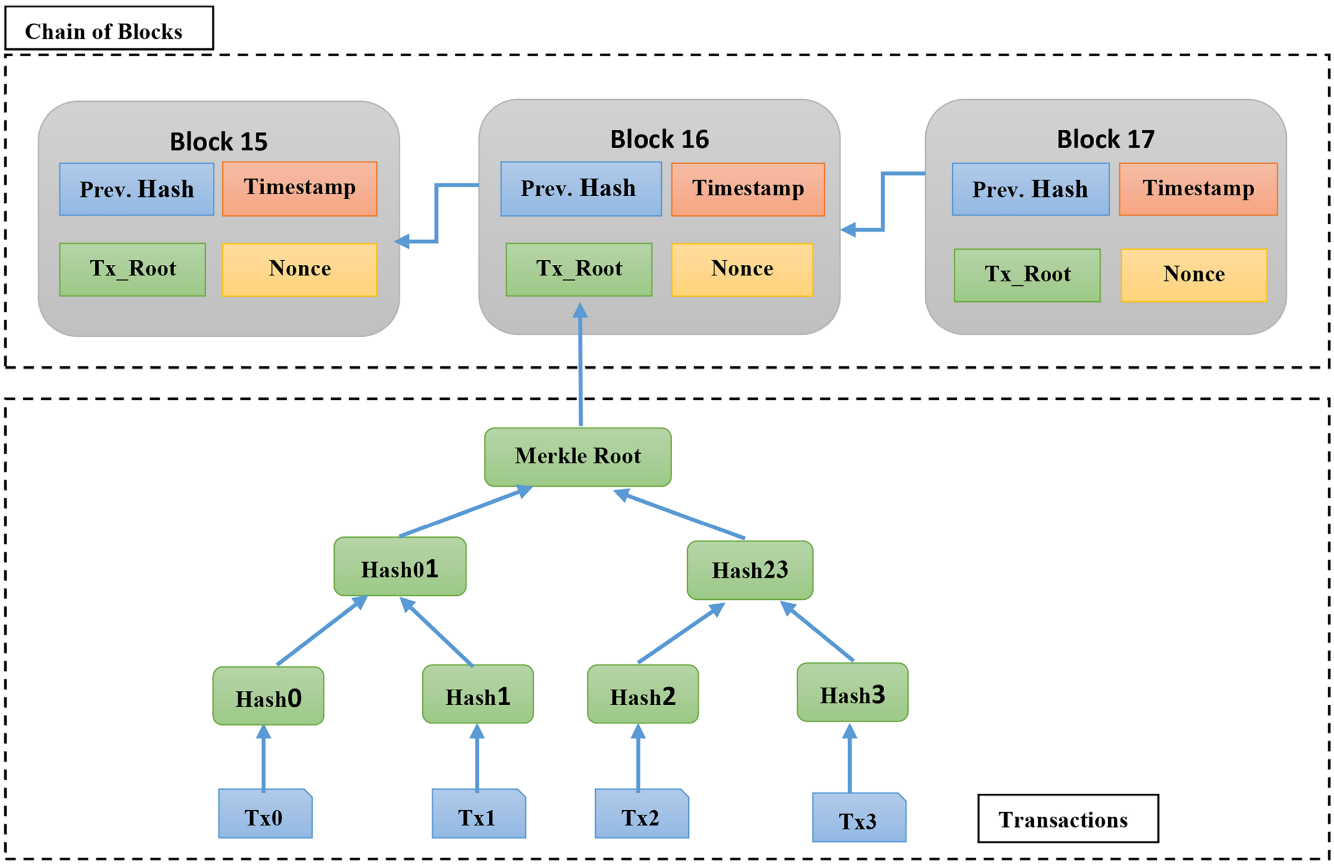

FIGURE 2 | Visualization of a blockchain's architectural layout, featuring interconnected blocks.

ownership, allowing anyone to publish blocks without the central authority's approval. Prominent examples of permissionless blockchains include Ethereum, Litecoin, and Bitcoin.

- *Permissioned Blockchain*: In permissioned blockchain [21], the user cannot freely join the network; it only authorizes a restricted set of readers and writers. A public blockchain can be configured as a permissioned blockchain, but only restricted participants can contribute to performing the transactions.
- *Private Blockchain*: is governed by an entity controlling users' participation in the network. Blockchain works well for privately owned companies or organizations with a restricted working environment. Hyperledger Fabric, Hyperledger Sawtooth, Multichain, and Corda are representative cases of private blockchains [22].
- *Public Blockchain*: does not restrict participants from reading, viewing transactions, and downloading the blockchain.

BT exhibits caution regarding particular security vulnerabilities; as a result, healthcare can face direct or indirect implications from its weaknesses. Here, the study offers a brief insight into potential attack vectors, including denial of service (DoS) attacks [23], double spending incidents [24], eclipse attacks [25], selfish mining strategies [26], block discarding [27], challenges related to rising difficulty levels [28], anonymity concerns [29], and the notorious 51% attack [30]. In a blockchain network, miners (or validators in some systems) work together to validate new blocks of transactions. This consensus process ensures that all participants agree on the ledger's state and prevents fraudulent activity. If a block fails this validation, it is promptly discarded, as depicted in Figure 3. In a blockchain network, the prevailing principle dictates that the longest chain is considered legitimate. The probability denoted as Q_z quantifies the likelihood of the attacker node outpacing the honest chain by z blocks [31–33].

$$Q_0 = 1, Lim_{z\to\infty} \quad Q_z = 0 \tag{1}$$

$$Q_z = pQ_{z+1} + qQ_{z-1}, z = 1, 2, 3, \ldots, \infty \tag{2}$$

if $p > q$,

$$A_z = Q_{z+1} - Q_z, r = q/p \tag{3}$$

from the Equation (2), we get

$$Q_z - Q_0 = \sum_{k=0}^{z-1}(Q_{k+1} - Q_k) = (1 - r^z/1 - r)A_0 \tag{4}$$

from the Equation (1), we get

$$Q_z = r^z = (q/p)^z, p > q \tag{5}$$

$$Q_z = 1, p \le q \tag{6}$$

21613915, 2025, 3, Downloaded from https://onlinelibrary.wiley.com/doi/10.1002/ett.70087 by Delhi Technological University, Wiley Online Library on [09/03/2025]. See the Terms and Conditions (https://onlinelibrary.wiley.com/terms-and-conditions) on Wiley Online Library for rules of use; OA articles are governed by the applicable Creative Commons License

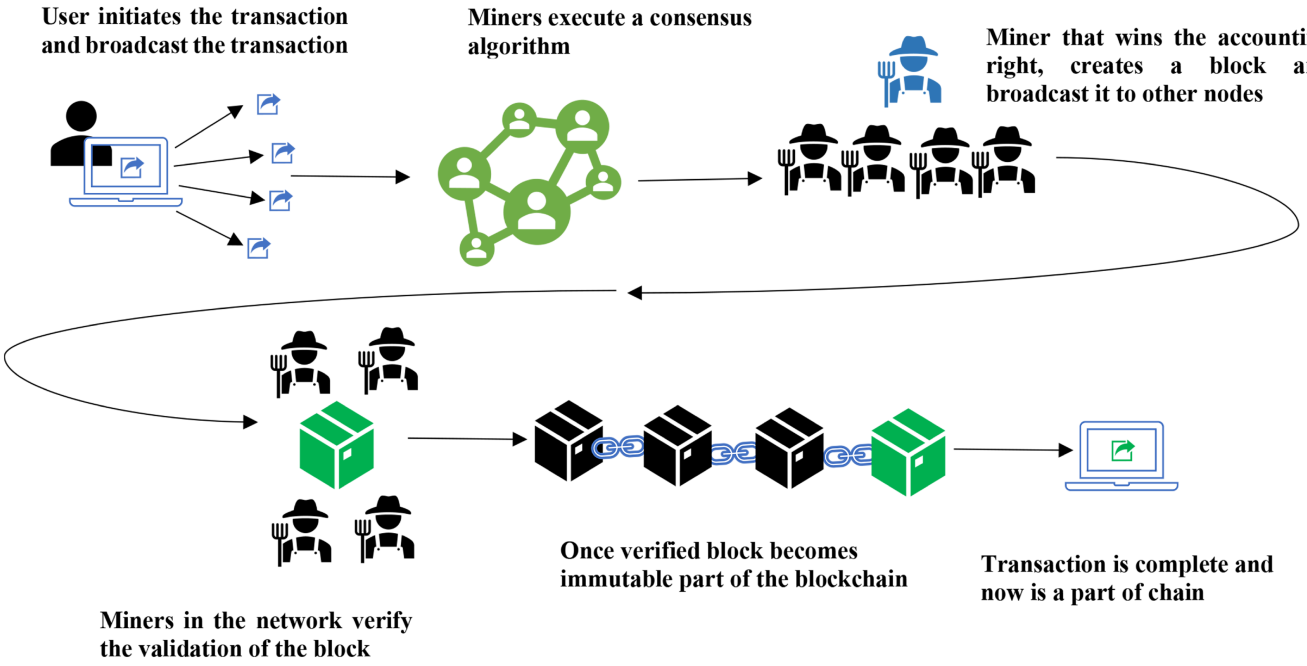

FIGURE 3 | Workflow of blockchain transactions.

we can say that

$$Q_z = \begin{cases} 1, & \text{p} \le q \\ (q/p)^z, & \text{p} > q \end{cases} \tag{7}$$

where p = probability of legitimate node mining the block; q = probability of attacker mining the new block before the legitimate node; Q_z = probability that attackers catch up with honest nodes from z blocks.

The taxonomy in Figure 4 illustrates various platforms of blockchain that can help the developer/user to develop their enterprise applications. Performance analysis incorporating measures such as latency, throughput, resource consumption, and success rate of the platform can help choose the right platform [34, 35]. A consensus mechanism is a protocol used to guarantee that all validators/nodes/contributors in a distributed network reach agreement on the current state of the network [33, 36–38]. BT also comes with various potential characteristics [39, 40] and threats [41–45].

For a blockchain network to remain operational, its participants must reach a consensus about the current state of the shared ledger and how data is packaged into blocks. In a distributed system, a consensus protocol ensures that all participating nodes agree on the same state of the system, particularly the order in which transactions occur. The consensus mechanism allows reading and updating to a certain state that guarantees the transaction's ordering and the integrity of the content across geographically distributed areas in a decentralized manner. The topology of the network agents is depicted using a directed graph $G = (V, E)$ by the formulas given below [46, 47].

V represents the Nodes $V = 1,2,3,\ldots,n$ and E represents the Edges $E \subseteq V \times V$,

$$N_i = j \in V : (i, j) \in E$$

Neighbors of agent i is represented by N_i. To solve the consensus problem and reach an agreement regarding the state of n agents with dynamics

$$\dot{x}_i(t) = u_i(t)$$

can be represented as an nth order linear system:

$$\dot{x}_i(t) = \sum_{j \in (N_i)} (x_j(t) - x_i(t)) + b_i(t), \qquad x_i(0) = z_i \in \mathbb{R}, b_i(t) = 0 \tag{8}$$

The collective dynamics of the following group of agents (8) can be written as follows:

$$\dot{x} = -Lx \tag{9}$$

L is graph Laplacian of network $L = [l_{ij}]$

$Q_z = \begin{cases} -1, & j \in N_i \\ |N_i|, & j = i \end{cases}$ Different blockchains utilize various consensus mechanisms that include proof-of-stake (PoS) [48], PoW [49], practical byzantine fault tolerance (PBFT) [50], and proof-of-authority (PoA) [51]. PoW is a consensus mechanism that specifies the proof of validity for the participant or the miner. In the PoW mechanism shown in Figure 5, all the transactions are gathered and bundled to form a block. A challenge or difficulty is set for the block, and miners in the network are believed to decipher this complex mathematical difficulty. The block is considered valid only if its reference or calculated hash does not exceed a certain threshold (b). The first miner who solves this problem gets the reward, and the verified block is then attached to the blockchain [52]. The shortcoming of PoW is that it needs a considerable amount of resources and time to figure out the solution to the complex puzzle. In PoW, most malicious nodes can

21613915, 2025, 3, Downloaded from https://onlinelibrary.wiley.com/doi/10.1002/ett.70087 by Delhi Technological University, Wiley Online Library on [09/03/2025]. See the Terms and Conditions (https://onlinelibrary.wiley.com/terms-and-conditions) on Wiley Online Library for rules of use; OA articles are governed by the applicable Creative Commons License

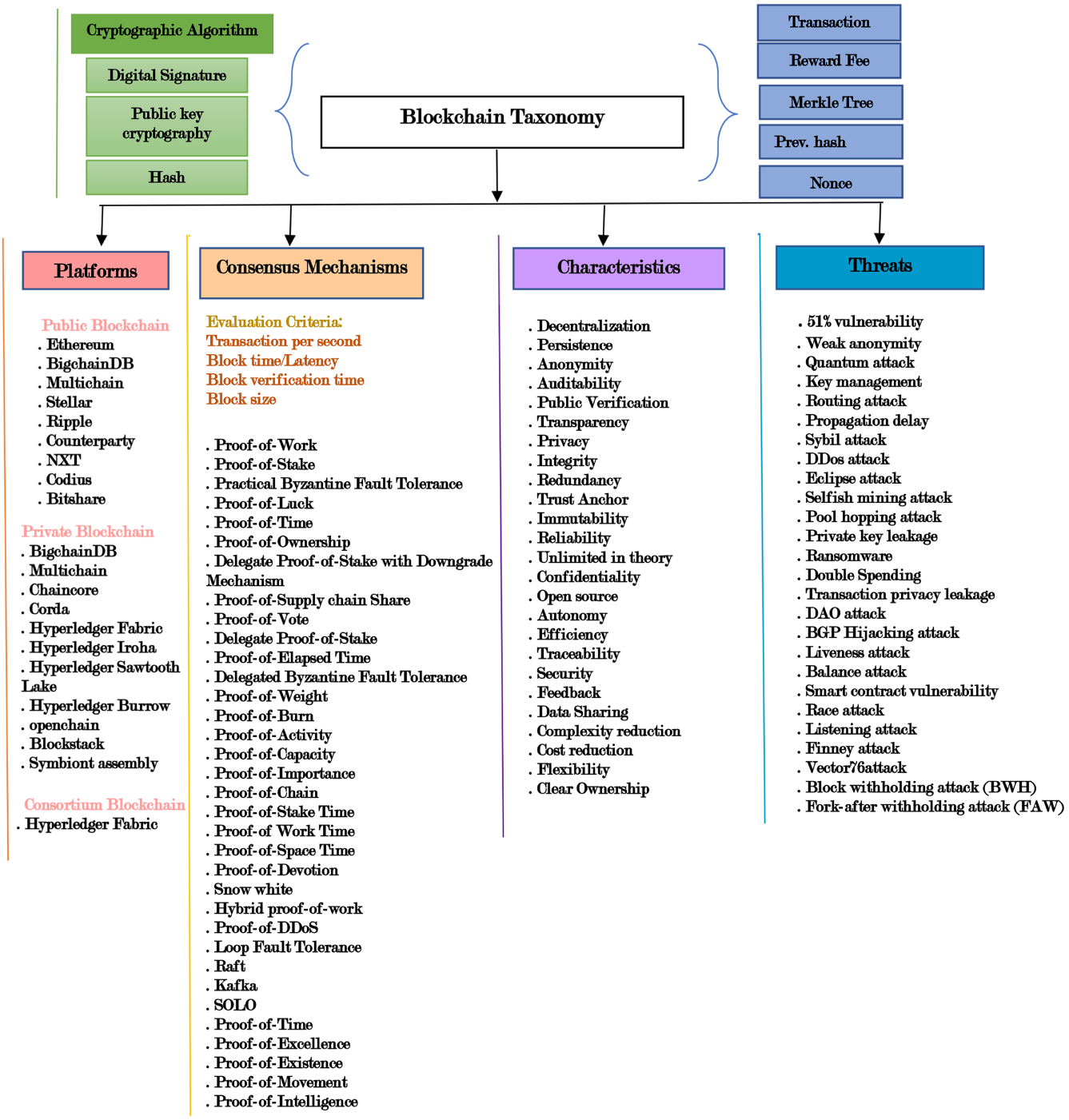

FIGURE 4 | Taxonomy of blockchain showcasing platform, consensus mechanism, characteristics, threats.

influence the network and perform a 51% attack on the network [53]. The nonce is incremented to fulfill Equation (b), and the hash is computed repeatedly until a valid block is found.

$$nonce = nonce + 1 \quad \ldots\ldots\ldots\ldots\ldots\ldots (a)$$

$$Hash(Block) \leq (V_t) \quad \ldots\ldots\ldots\ldots\ldots (b)$$

$$V_t = M/D \quad \ldots\ldots\ldots\ldots\ldots\ldots\ldots\ldots (c)$$

Hash is a hash function with a variable number range $[0, M]$. The Target value represented as V_t is a threshold determined by the mining difficulty. The calculated value of the hash has to be less than the threshold value for a proposed block to be included in the chain of the blockchain.

$$D \in [1, M]$$

is the Target difficulty. Let us find a valid block: A miner with sufficient resource availability and hardware capability performs k operations per second at k/D.

$$P\{T(k) \leq t\} = 1 - exp(-kt/D) \quad \ldots\ldots (d)$$

There are n miners in the network with the hash rate $k_1, k_2, \ldots, k_n$.

21613915, 2025, 3, Downloaded from https://onlinelibrary.wiley.com/doi/10.1002/ett.70087 by Delhi Technological University, Wiley Online Library on [09/03/2025]. See the Terms and Conditions (https://onlinelibrary.wiley.com/terms-and-conditions) on Wiley Online Library for rules of use; OA articles are governed by the applicable Creative Commons License

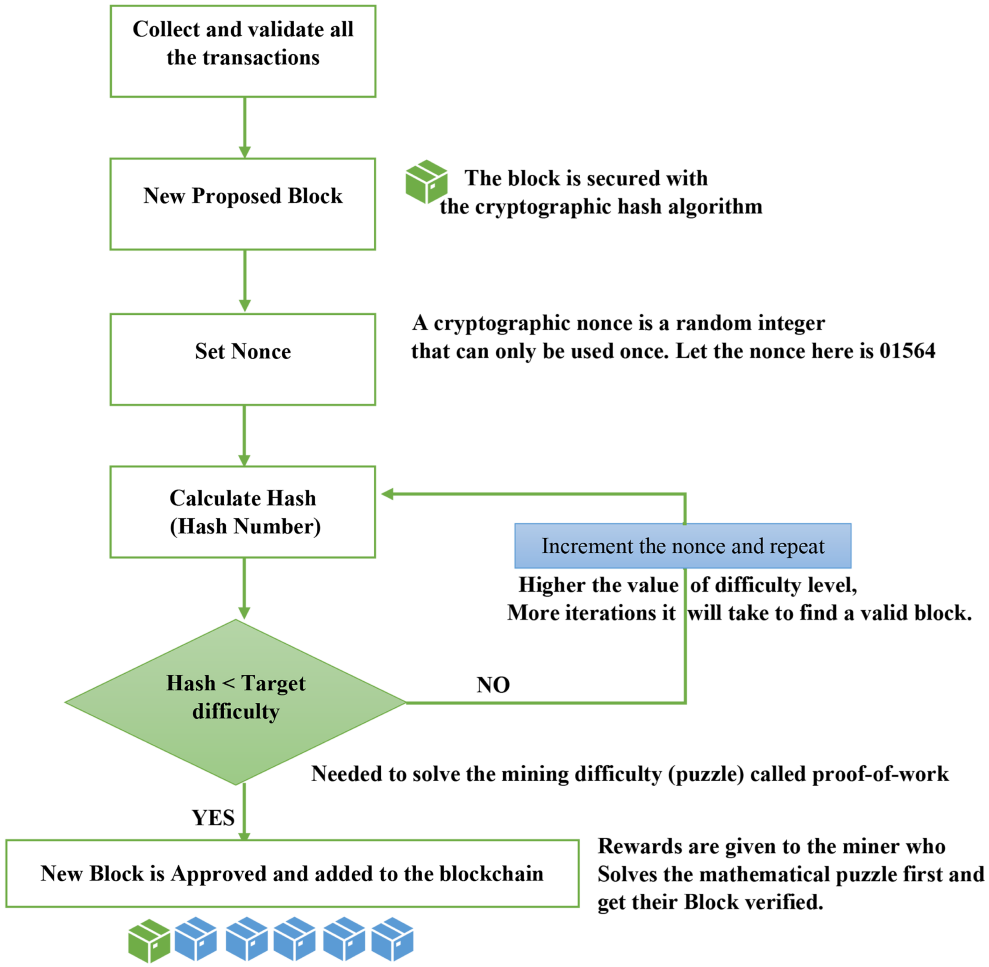

FIGURE 5 | Flow of Proof-of-Work consensus mechanism.

The time to find the valid block T equals the (e). $P\{Tdef = min(T_1, T_2, \ldots, T_n) \leq t\} = 1 - exp(-tD\sum_n^{j=1} k_i) \ldots (e)$ $P\{T = T_i\} = k_i / \sum_n^{i=1} k_j \ldots \ldots (f)$.

To keep the blockchain functioning across the geographically distributed area and to ensure security, privacy, and correctness, the shared public ledger has consensus mechanisms that are fault-tolerant and maintain the identical blockchain globally.

3 | Research Methodology

This section illustrates the methodological framework adopted for the systematic review of existing literature. The process comprised three primary stages: Planning, reviewing, and reporting. In the planning phase, clear research objectives and questions are established. Subsequently, the reviewing stage involved the selection of pertinent articles based on a well-defined selection. Finally, the findings of this research are comprehensively reported, as illustrated in Figure 6. This research analysis helps in identifying the areas where more research is required. The systematic review enables us to investigate current

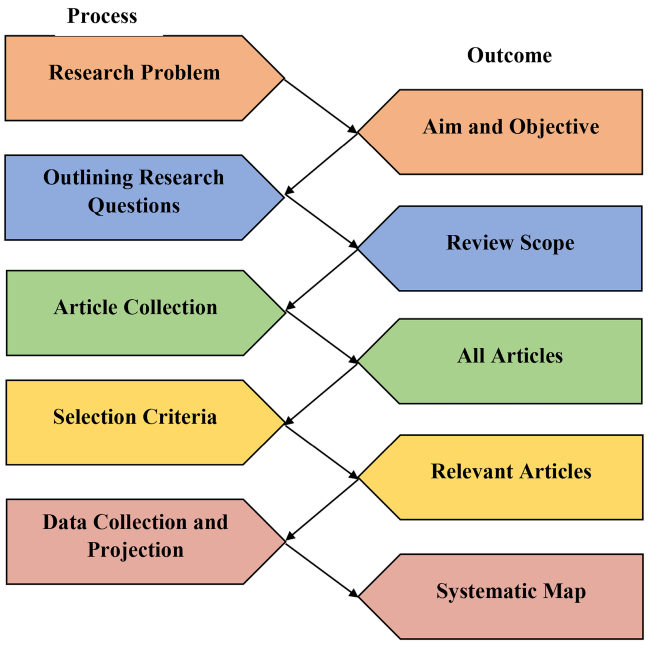

FIGURE 6 | Research methodology and mapping process.

21613915, 2025, 3, Downloaded from https://onlinelibrary.wiley.com/doi/10.1002/ett.70087 by Delhi Technological University, Wiley Online Library on [09/03/2025]. See the Terms and Conditions (https://onlinelibrary.wiley.com/terms-and-conditions) on Wiley Online Library for rules of use; OA articles are governed by the applicable Creative Commons License

trends in the technology, methods, and concepts used to create blockchain-enabled healthcare.

3.1 | Research Objectives

A central objective of this investigation is to conduct a theoretical analysis of the transformative influence of BT within the healthcare sector. This encompasses an examination of existing BT-based solutions, their approaches to addressing healthcare needs, and a comprehensive evaluation of the associated benefits and challenges. To achieve this goal, we commenced by reviewing the relevant literature on BT and its applications in healthcare, as detailed in Sections 2 and 4. The Section 4 serves as the primary focus of this research, delving into the existing solutions for healthcare. This includes a thorough examination of proposed solutions and prototypes, providing a comprehensive overview of the current landscape of BT-based healthcare innovations.

3.2 | Research Questions

This section delineates the research questions as follows:

- *RQ1: Role of BT in transforming the healthcare domain*: This research question explores how blockchain can be used precisely to refine the efficiency and efficacy of healthcare delivery, including patient autonomy, patient-doctor consultation, pharmaceutical supply chains, and hospital operations.
- *RQ2: How does blockchain handle the security issues of the healthcare system?* This research question enables us to understand the various security problems of the healthcare sector and the approaches through which BT can help resolve these issues. As discussed earlier, the healthcare system has different security requirements in securing patients' and hospital data from unauthorized access and keeping track of patient data, hospital bills, and medications.
- *RQ3: Benefits and challenges of incorporating BT in healthcare*: This research question presents the advantages and drawbacks of integrating BT into healthcare.

3.3 | Articles Collection Procedure

This exhaustive literature survey includes all the state-of-the-art studies briefly describing BT in the healthcare system from 2017 to 2024. The survey examines the studies included to elucidate the benefits and risks of including blockchain in the medical industry. Major research paper publishing platforms, including Web of Science, IEEE, Springer, Wiley Online Library, ACM digital libraries, Elsevier, and many more, are searched rigorously to conduct this study (Figure 7). The pie chart in Figure 8 shows the categorization of all 182 studies (see reference) based on sources such as journals, conferences, transactions, and others and publishers such as Springer, IEEE, arXiv, JMIR, Taylor & Francis, ACM, MDPI, Elsevier, and Wiley Online Library. This study is conducted from March 2022 to April 2024, and repeated before the paper submission to refine the research and search for new articles related to the study area.

"blockchain" AND "healthcare"

"blockchain" AND ("medical" OR "health")

"blockchain" AND "remote patient monitoring"

"blockchain" AND "clinical trial"

"blockchain" AND "patient autonomy"

"blockchain" AND "health data security"

"blockchain" AND ("healthcare" OR "PHR" OR "EHR")

"blockchain" AND ("patient health record" OR "electronic health record")

"blockchain" AND ("patient monitoring" OR "remote monitoring" OR "clinical trial")

"blockchain" AND ("supply chain management" OR "pharmaceutical supply chain" OR "drug supply chain")

3.4 | Selection Criteria

A comprehensive search is conducted across multiple scientific databases, including PubMed, IEEE Xplore, Web of Science, Scopus, Google Scholar, ScienceDirect, SpringerLink, ACM Digital Library, and Elsevier's Engineering Village to collect the research articles. This broad search strategy ensures access to high-quality research and review articles published in reputable journals across diverse disciplines. Once relevant articles are identified, they undergo a meticulous evaluation process. Using clearly defined inclusion and exclusion criteria, articles are critically assessed to ensure their relevance to the research topic, as defined in Table 2.

This rigorous filtering process helps in selecting studies that meet the standards of methodological rigor, data integrity, and scholarly contribution. The prior studies specified in languages other than English are excluded. Various criteria are applied for the refinement of the survey, such as excluding duplicate papers, papers based on titles, abstracts, conclusions, and documents that do not satisfy the requirements of the study, as illustrated in Figure 7.

3.5 | Data Collection and Projection

In this phase, the relevant articles gathered through the selection criteria were reviewed in detail to assess their contributions and methodologies, specifically in the context of blockchain applications in healthcare. Each paper was thoroughly analyzed to understand the specific approach it took in leveraging blockchain technology for healthcare-related challenges.

We examined the key contributions of the studies, focusing on how blockchain was applied to various healthcare domains such as patient data management, electronic health records (EHR), healthcare supply chains, clinical trials, patient monitoring, and

21613915, 2025, 3, Downloaded from https://onlinelibrary.wiley.com/doi/10.1002/etr.70087 by Delhi Technological University, Wiley Online Library on [09/03/2025]. See the Terms and Conditions (https://onlinelibrary.wiley.com/terms-and-conditions) on Wiley Online Library for rules of use; OA articles are governed by the applicable Creative Commons License

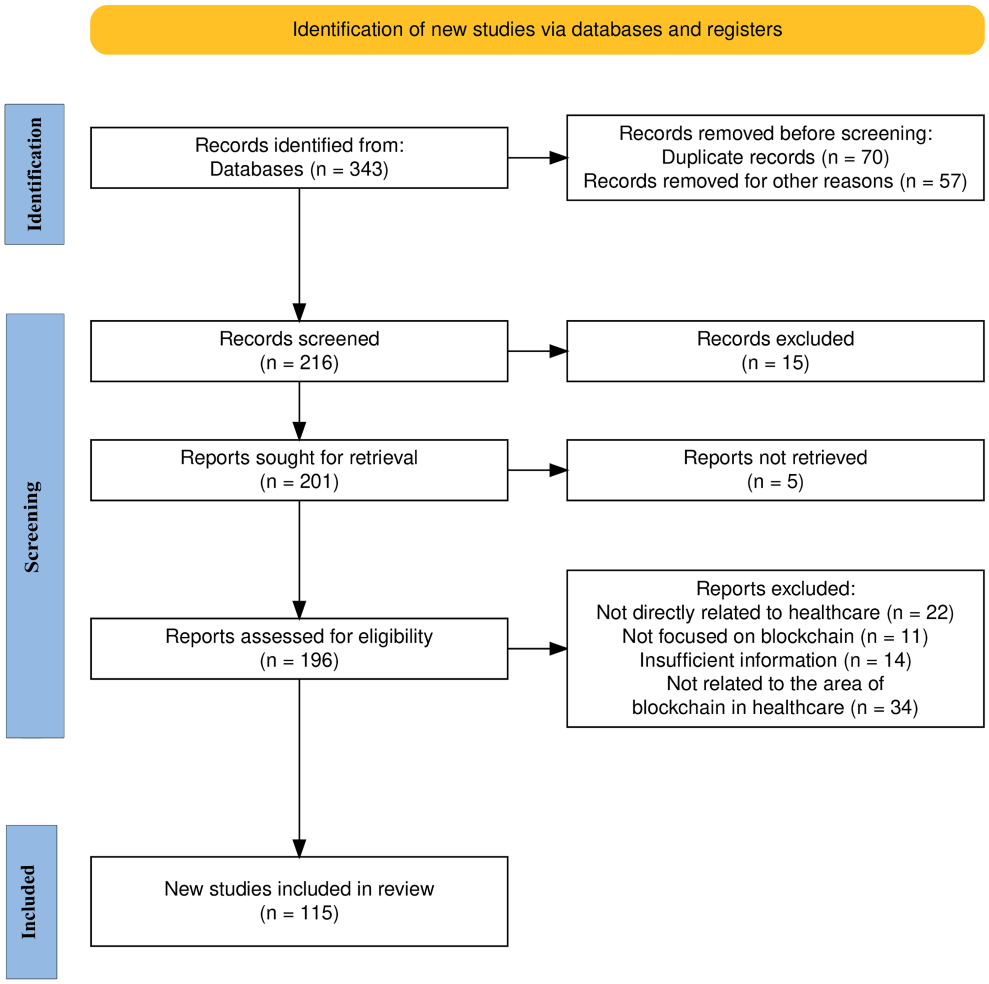

FIGURE 7 | Execution of study selection process.

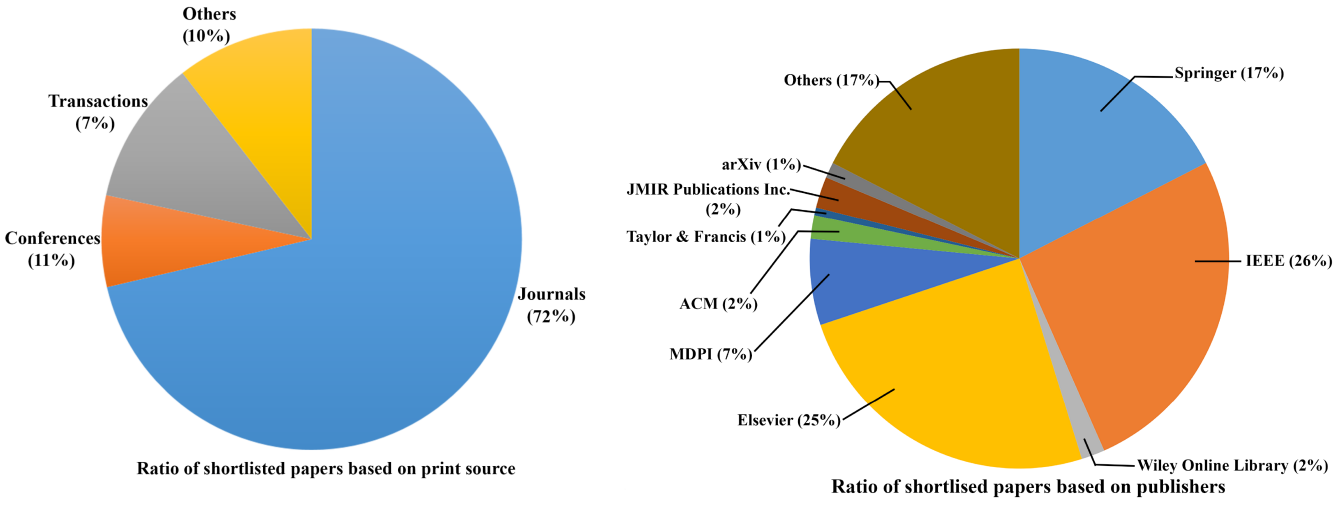

FIGURE 8 | Categorization of study based on print sources and publishers.

21613915, 2025, 3, Downloaded from https://onlinelibrary.wiley.com/doi/10.1002/ett.70087 by Delhi Technological University, Wiley Online Library on [09/03/2025]. See the Terms and Conditions (https://onlinelibrary.wiley.com/terms-and-conditions) on Wiley Online Library for rules of use; OA articles are governed by the applicable Creative Commons License

TABLE 2 | Criteria for study inclusion and exclusion.

Criteria	Eligibility criteria
Inclusion	• A study that addresses patient health records • Pharmaceutical supply chain • Benefits and challenges of blockchain • Performance analysis of blockchain-based healthcare systems • Most studies published from 2017 onward • Reports from HIPAA journal and GDPR compliance
Exclusion	• The studies that are conducted in a language other than English • Studies, not relevant to the selected domain

health data security. The review also involved a detailed analysis of the technical approaches used in these studies, including the blockchain platforms and consensus mechanisms, scalability and security measures considered, and potential for real-world implementation.

4 | Results

This section summarizes the findings related to our research questions. We analyzed 115 studies to get a comprehensive picture of the answers. We have extensively searched reputable databases to gather as much vital information as possible.

In our research paper, we have cited a total of 182 articles. Of these, 115 are full papers that are used to conduct surveys and explore answers to our research questions. The remaining 67 studies are cited primarily to provide essential background information for our work. Figure 9 represents the distribution of selected research articles on blockchain in healthcare across the years 2017 to 2024, showcasing trends in publication popularity. The research was conducted between March 2022 and April 2024; however, the data for 2024 does not represent the full year, as research and publications are still ongoing. This demonstrates the continued growth and rising popularity of blockchain in healthcare, highlighting its increasing recognition as a transformative technology for addressing key challenges in the sector. In our study, the majority of the selected articles are published in journals, which account for the highest number of publications across all focus areas. This reflects a significant preference for peer-reviewed journals as the primary medium for the dissemination of blockchain-related healthcare research. Among the areas analyzed, the health records domain has the largest representation, as shown in Figure 10. Notably, the prime focus areas of the study are patient health records, the pharmaceutical supply chain or supply chain management, clinical trial data management, and remote patient monitoring, which we have discussed in detail in RQ1.

RQ1: Role of BT in transforming the healthcare domain: In this part, we have reviewed the role of BT in the various areas of healthcare. BT provides the ease of accessing patients' health records, checking medical prescriptions, sharing secure data across providers, verifying drug provenance, securing clinical

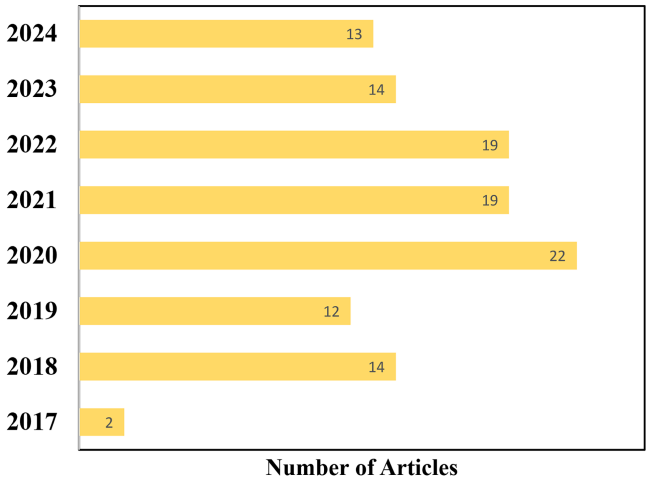

FIGURE 9 | Publication year of state-of-the-art studies.

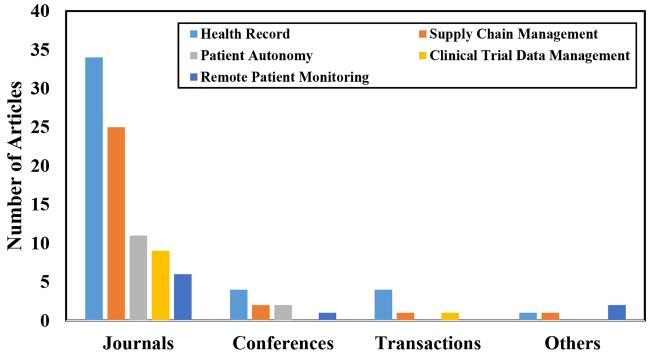

FIGURE 10 | Publication type of state-of-the-art studies.

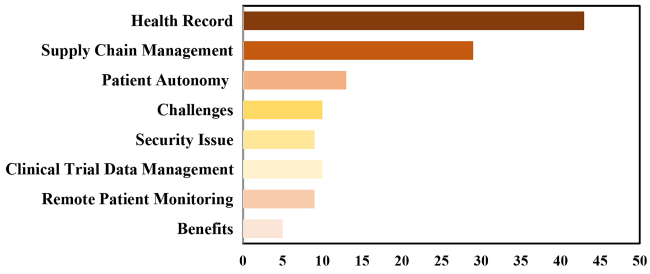

FIGURE 11 | Number of publications across key areas showing the research trend in blockchain-enabled solutions in healthcare.

trials, medical devices supply chain, revenue management, temperature-controlled supply chain, and transferring funds [54, 55].

The study categorizes key focus areas of blockchain applications in healthcare into patient health records, pharmaceutical supply chain management, clinical trial data management, and remote patient monitoring. Among these, health records and supply chain management emerged as the most extensively discussed topics, as shown in the analysis of the selected studies. Figure 11 illustrates that patient health records dominate the focus, followed closely by supply chain management. Applications such

21613915, 2025, 3, Downloaded from https://onlinelibrary.wiley.com/doi/10.1002/etr.70087 by Delhi Technological University, Wiley Online Library on [09/03/2025]. See the Terms and Conditions (https://onlinelibrary.wiley.com/terms-and-conditions) on Wiley Online Library for rules of use; OA articles are governed by the applicable Creative Commons License

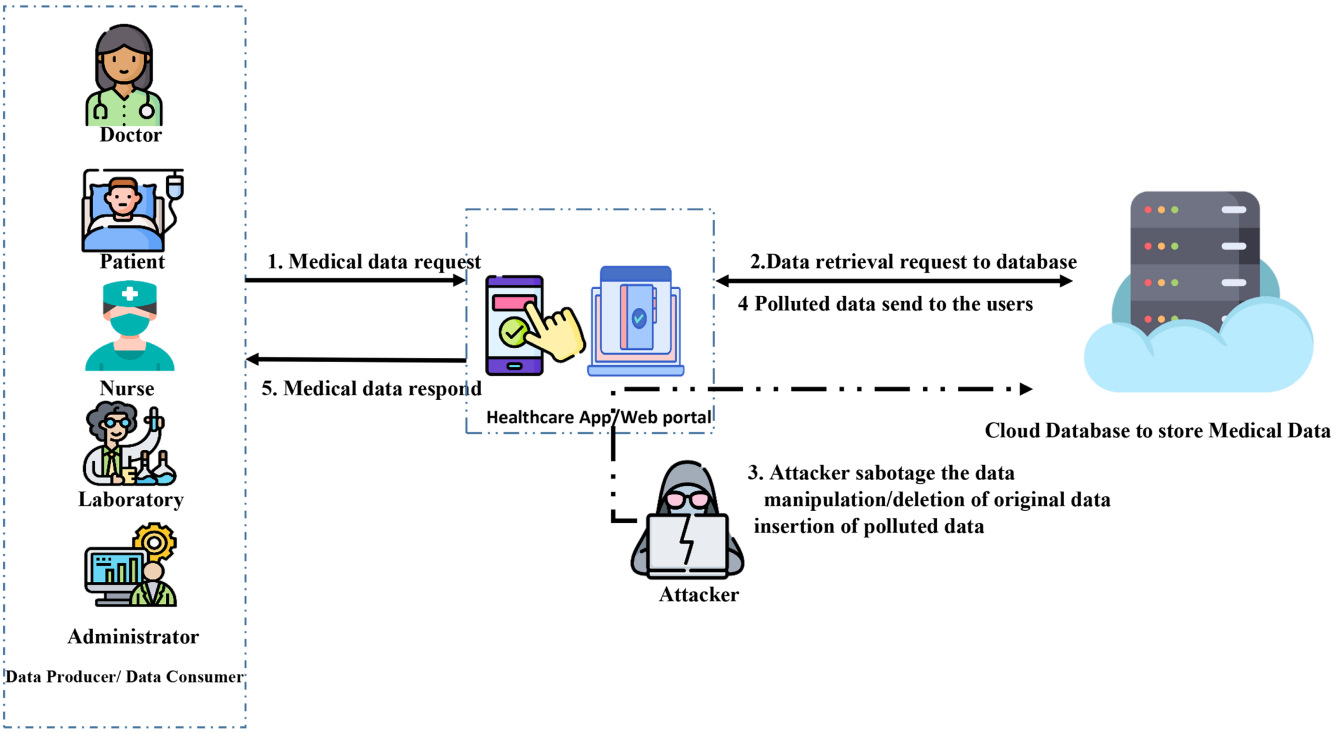

FIGURE 12 | Tampering data in a cloud-based EHR system.

as remote patient monitoring and clinical trial data management also highlight blockchain's role in advancing personalized healthcare and enhancing research integrity. Furthermore, studies on security issues and the challenges of implementing blockchain reflect the ongoing efforts to address barriers to its adoption. This demonstrates the broad potential of BT to not only secure sensitive patient data but also optimize operational efficiency across various healthcare processes.

BT has given many developed and developing countries the confidence to incorporate blockchain into the digital healthcare system and transform it. The primary concern in the healthcare system is to ensure that patient's health records are tamper-proof and accessible only to the authorities to whom they wish to show their data. BT improves security, interoperability, and overall user experience [56]. Traditionally, healthcare industries used a centralized system to manage and maintain patient records and hospital data. The centralized control over the data and the need to share the data with the doctor, laboratory, patient, administrator, and researchers is a cost-intensive and time-consuming process. Later, cloud-based EHR systems helped the hospital care to record and manage the data; they provided mobility and scalability benefits [57] as illustrated in Figure 12, but came with various barriers such as data verification, preservation, interoperability, data leakage, data manipulation, unauthorized access, and tempering the records [58, 59].

EHRs aim to deliver privacy and security to individual health documents. The HIPAA addresses these concerns through two key rules: The Privacy Rule safeguards medical records, EHRs, and PHI, while the Security Rule protects electronic personal health information from various threats. However, blockchain EHRs allow more efficient transmission of information across settings, improving data completeness, consistency, and decision support. Every transaction generated by the patient is recorded in the immutable log of the transaction, which can only be added by the digital agreement (shown in Figure 13), also known as a smart contract and consensus mechanism that provides security against tampering and malicious alteration [60]. The blockchain-based distributed mechanism ensures the append or retrieval of medical data by an authorized person and secures data accessibility between the patient and the healthcare providers [61].

The attributes of BT that must be considered when implementing it in the healthcare system include the blockchain platform, storage scheme, consensus mechanism, blockchain type, operational cost, privacy, and security of healthcare data. In light of these considerations, we have conducted an evaluation of cutting-edge blockchain solutions in various domains such as health records (Table 3), pharmaceutical, and drug supply chain management (Table 4), clinical trials (Table 5), remote patient monitoring (Table 6), and patient autonomy (Table 8). PcBEHR [62] system architecture provides controls for patients to manage and control their medical data. In PcBEHR, patients have ownership of their medical data and can give access permission to their data. The patient-controlled blockchain-enabled EHR solution utilizes the functionality of access control, privacy, and interoperability. MedRec [63] is a decentralized electronic medical record (EMR) management system that uses blockchain to record sensitive information and operations while providing confidentiality, authentication, accountability, and data sharing to crucial data. To maintain confidentiality, MedRec uses a smart contract to grant viewership rights. It gives patients complete access to their medical data from multiple providers in a single location.

21613915, 2025, 3, Downloaded from https://onlinelibrary.wiley.com/doi/10.1002/ett.70087 by Delhi Technological University, Wiley Online Library on [09/03/2025]. See the Terms and Conditions (https://onlinelibrary.wiley.com/terms-and-conditions) on Wiley Online Library for rules of use; OA articles are governed by the applicable Creative Commons License

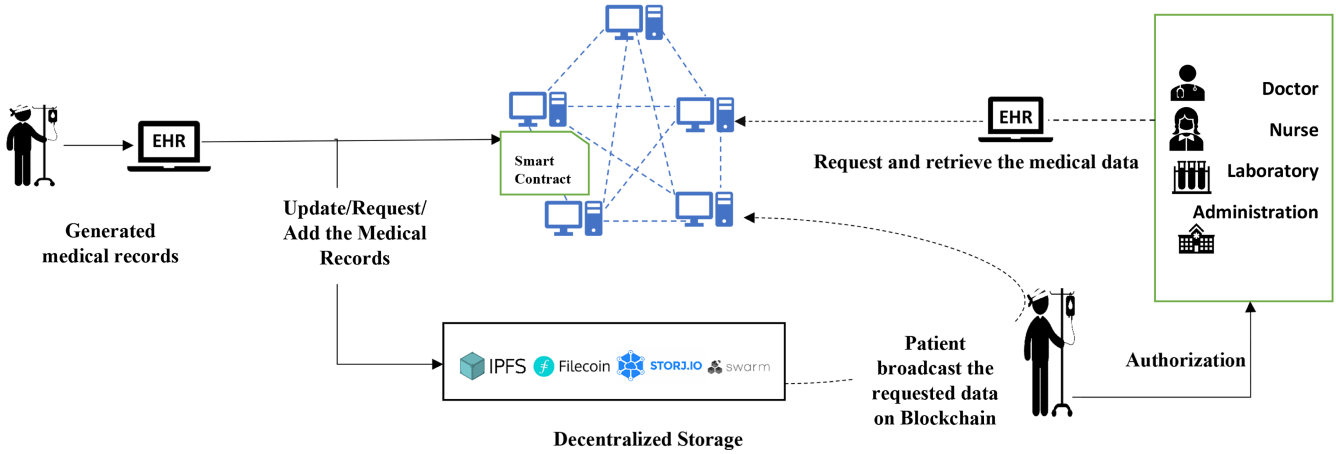

FIGURE 13 | Healthcare system based on blockchain.

In a study by Chen et al. [119], a storage scheme is developed that utilizes BT and cloud storage to manage patients' sensitive healthcare records effectively. This system ensures adequate management and secure healthcare data storage within a digital archive, with restricted access granted solely to authorized personnel. The optimal solution for data management and access control is to store every transaction's information on the blockchain. However, because of limited storage, scalability, and cost issues, medical data is recorded on cloud storage. To provide patient records with security and secrecy, Saberi et al. [120] developed a break-glass model that incorporates blockchain, attribute-based access control (ABAC), and the InterPlanetary File System (IPFS). This healthcare model offers the availability of EMRs and EHRs promptly. Blockchain logs all access requests and grants and revokes access to medical records. The purpose of the Break-Glass mechanism is that every enrolled EMR owner can provide their medical data reading permission to the health professional. In an emergency, EMR trusted parties use healthcare authorization to set new attributes on EMRs.

ACTION-EHR [77] concentrated on the mobility and accessibility of healthcare data to facilitate secure, trustable data sharing and management. This patient-centric system permits the patient to manage their health data. This system facilitates the secure aggregation and sharing of medical data. The generated health data is encrypted with a hybrid cryptosystem that utilizes the public key and symmetric-key cryptosystem, and encrypted data is added to the cloud storage. To manage the system's interoperability, the authors have employed HL7. Data sharing and information exchange are challenging parts of EHRs. Chelladurai et al. [121] offered a smart health system to exchange health/medical data that uses the modified Merkle tree to secure the immutable log and provide data accessibility, updating records, data exchange, and viewership on the blockchain. It has been established that healthcare data is vulnerable to all kinds of attacks, and there is a massive increase in the hacking of healthcare data.

BIoTHR, [122] is an IoT-based private blockchain-assisted EHR that focuses on privacy preservation and secure exchange of data by using the Blockchain and Swarm exchange technique. This swarm exchange paradigm introduces agility, flexibility, transparency, high availability, and security to the BIoTHR. The foremost reason for incorporating blockchain in healthcare is to achieve high-performance, access control, high data security, and secure data exchange. The pharmaceutical products and drugs supply chain is no exception to the need for safety, security, data provenance, and governance in the healthcare system. Traditionally, the medical supply chain faced traceability, transparency, shipment expiration, and tracking challenges. Medical data proliferation necessitates a wide range of medical products and drugs. Leveraging BT facilitates comprehensive pharmaceutical and medical supply chain oversight, enabling robust drug traceability, counterfeit detection, and improved drug monitoring. The detailed studies and performance metrics associated with this approach are further elaborated in Tables 4 and 7.

Detecting the counterfeited drug is relatively complex due to its resemblance to the original product. Blockchain enables access control for each participant via smart contracts, enabling traceability, visibility, and protection of all the activity of the individual participants [123]. Keeping track of medicine from manufacturing to end user or consumer and maintaining records of side effects caused by the medication for future reference helps the pharmaceutical industry lower drug counterfeiting [124]. Blockchain-based Medledger [125] system employs Hyperledger Fabric blockchain and smart contract (chaincode) to attain drug traceability for counterfeit drugs. The solution leverages decentralized file storage for storing private and sensitive data, providing traceability and transparency. To prevent the proliferation of counterfeit goods, a tool called PharmaCrypt [126], based on blockchain that focuses on the rapid scanning of products, is introduced that timestamps every product and maintains the record of every single transaction in the supply chain. Counterfeit products can be traced using this approach, and security and safety can be achieved. At the time of packaging, the package's bar code gets scanned, and the hash value of a specific product gets recorded on the blockchain. The product's movement through the supply chain is tracked with tamper-proof timestamps on the blockchain, allowing for comprehensive traceability and enabling the detection and elimination of counterfeit products before they reach consumers.

21613915, 2025, 3, Downloaded from https://onlinelibrary.wiley.com/doi/10.1002/ett.70087 by Delhi Technological University, Wiley Online Library on [09/03/2025]. See the Terms and Conditions (https://onlinelibrary.wiley.com/terms-and-conditions) on Wiley Online Library for rules of use; OA articles are governed by the applicable Creative Commons License

TABLE 3 | A comparative assessment of blockchain solutions for health record.

Ref.	Year	Proposed solution	BT	Domain	Benefits	Limitations	Privacy and security	Storage scheme	Performance metrics
[64]	2024	Presented an exhaustive assessment of EHRs, focusing on the preservation of privacy and emphasizing the importance of privacy, security, and confidentiality within the EHR system	Blockchain	EHR	Study examines the risks associated with EHR privacy, elucidates the distinctions between security, confidentiality and privacy, evaluates privacy-preserving solutions, and proposes potential avenues for future research to enhance EHR privacy	Limited attention is given to the BT in enhancing the security, confidentiality and privacy of EHR	…	…	…
[65]	2024	Proposed a framework named BC-UADS) provides a secure and trusted way for doctors to access a patient's EHR metadata on the blockchain for real-time applications	Proof-of-Reputation	EHR	Framework exhibits robust security measures against both passive and active attacks and also offers improved execution speed, communication, and storage cost efficiency	Scalability of the framework is not discussed	…	Blockchain	Execution Time, Storage Cost, Communication Cost
[66]	2024	Study tackles challenges in secure-cloud infrastructure for patient data by proposing a novel blockchain-based system with enhanced privacy and security through a Blockchain-Based Access Control Model	Hyperledger Fabric	Patient data	Improved scalability, privacy, availability, security and access control	No information about the performance evaluation	Symmetric key encryption	Cloud	…
[62]	2023	Paper explored how BT can address challenges in healthcare, proposing a framework to assess its suitability and introducing a secure, patient-centric blockchain system for EHRs, comparing it to existing solutions for performance and cost	Ethereum	EHR	Patient-centric approach, cost-effective and accurate	No detailed analysis on scalability, response time, security measures used to protect patient data	…	IPFS	Accuracy, Cost
[67]	2023	Proposed a secure patient-controlled healthcare system using blockchain with fine-grained access control, hidden access policies, efficient federated blockchain management, and adaptive multi-keyword retrieval for medical records	Blockchain	Medical Data	Offers reliable and safe adaptive multi-keyword search along with secure access control with hidden policies, enhancing healthcare effectiveness and medical information security	Absence of User revocation and attribute revocation	ABE	Blockchain	Storage cost, Computation cost
[68]	2022	Proposed an efficient and secure healthcare system using a blockchain network and Multi-Objective Squirrel Search Optimization Algorithm	Blockchain with MOSSOA	Medical data	Enhanced security and scalability	No detailed information about data privacy-preservation	MOSSOA	Blockchain	Throughput, Efficiency, Delay, Computational overhead, Storage cost

(Continues)

21613915, 2025, 3, Downloaded from https://onlinelibrary.wiley.com/doi/10.1002/ett.70087 by Delhi Technological University, Wiley Online Library on [09/03/2025]. See the Terms and Conditions (https://onlinelibrary.wiley.com/terms-and-conditions) on Wiley Online Library for rules of use; OA articles are governed by the applicable Creative Commons License

TABLE 3 | (Continued)

Ref.	Year	Proposed solution	BT	Domain	Benefits	Limitations	Privacy and security	Storage scheme	Performance metrics
[69]	2022	Proposed a blockchain-based PHI management system named eHealthChain for health data management	Hyperledger Fabric	PHI	Data sharing, patient-centric, improved data management	Lack of information about patients' data privacy, security policies, access control mechanisms, and interoperability	…	Blockchain	…
[70]	2022	Introduced a novel deletable consortium blockchain-based secure EHRs storage model named DS-Chain in a multi-cloud paradigm	Ethereum blockchain	EHR	Confidentiality of sensitive information, integrity, correctness, deletion of expired EHR, security, privacy	Access control, data-sharing, and interoperability have not been explored	Public/private key	Multi-cloud storage	Communication overhead, Computational overhead
[71]	2022	Presented medical blockchain for medical record data sharing and privacy preservation through cryptography design	Consortium blockchain	EHR	Integrity, authentication, anonymity, confidentiality, availability, transmission security, privacy, immutability, unforgeability	Access-control, interoperability, scalability	Public/private key	…	Execution time
[72]	2022	Proposed SEMRES- a blockchain-based medical records exchange with triple security protection that ensures the confidentiality of data	Private blockchain with PoA	EMR	Security and privacy of medical data, confidentiality, correctness	Lacks access control policies	Hybrid AES/RSA	Blockchain	…
[73]	2021	Implemented a blockchain-based healthcare system that ensures secure transaction, traceability, and transparency	Hyperledger Fabric	Medical data	Traceability, transparency	Lack of details on security policies, access control, and confidentiality are not considered	…	…	…
[74]	2021	Offered a blockchain-based security framework to provide security and privacy to patients' EHR	Public blockchain	EHR	Access control, user authorization, identity management, data privacy, availability, integrity, patient privacy-preservation	Lack of focus on security, scalability, and interoperability	RSA cryptography, Public/private key	Blockchain	…
[75]	2021	Proposed a blockchain-based EHR system to access the patient record effectively without involving third parties	Ethereum platform	EHR	Privacy, security, interoperability	Lack of discussion on access control, data integrity, and scalability	Cryptography Hash	Blockchain	Contract execution time
[76]	2020	Presented a blockchain-based patient-centric framework that guarantees the security of health records	Hyperledger Platform	EHR	Verifiability, transparency, availability	The study does not discuss security issues, interoperability, access control	…	…	Latency, Throughput, Resource consumption

(Continues)

21613915, 2025, 3, Downloaded from https://onlinelibrary.wiley.com/doi/10.1002/ett.70087 by Delhi Technological University, Wiley Online Library on [09/03/2025]. See the Terms and Conditions (https://onlinelibrary.wiley.com/terms-and-conditions) on Wiley Online Library for rules of use; OA articles are governed by the applicable Creative Commons License

TABLE 3 | (Continued)

Ref.	Year	Proposed solution	BT	Domain	Benefits	Limitations	Privacy and security	Storage scheme	Performance metrics
[77]	2020	Proposed a patient-centric system based on permissioned BT to facilitate data sharing and optimize cancer patient care management	Permissioned blockchain (Hyper-ledger Fabric)	EHR	Privacy, security, access control, well-defined data sharing, accessing, and modifying policies	Technical and regulatory issues	PKI-based asymmetric encryption, Digital Signature	AWS cloud storage + on-chain storage	…
[78]	2020	Proposed an efficient EHR based on blockchain for improving security and efficiency	Hyperledger Fabric	EHR	Permission-based EHR system with cryptography key, designed access control policy algorithm with smart contract, optimizes system performance	Lack of scalability	Symmetric key + private key	On-chain storage	Latency, Throughput, RTT, Resource consumption, Network traffic
[79]	2020	Presented a privacy-preserving EHR management solution named PREHEALTH that stores patients' records effectively and provides anonymity and unlikability	Hyperledger Fabric	EHR	Security, auditability, anonymity, privacy preservation	No detailed discussion on data sharing and access control of EHRs	…	…	Average CPU% performance
[80]	2019	The proposed MedChain is an efficient data-sharing scheme that integrates the structured P2P network, digest chain, and blockchain to overcome data-sharing issues	Private blockchain	EHR	Improved flexibility, higher efficiency, and security in data sharing, tamper-proof, attack-resistance, access revocation, access control, privacy-preserving, data stream support, non-repudiation, metadata update, and block search, storage space recycling	Data movement issue: Access to data requires patients' manual approval; automatic data sharing needs to be explored, lack of automated generation and upload of information of data streams, no proper mechanism is provided for the high storage handling issue	Elliptic curve cryp-tography, Pub-lic/private key pair	Blockchain	Responsiveness, Bandwidth, Transaction rate
[81]	2018	Presented a blockchain-based architectural framework for exchanging health data in a secure, controlled manner by integrating user-generated policies with smart contracts	Public blockchain	PHR	Data protection, privacy, controlled data exchange, data security, timed smart contract	Scalability, interoperability, performance measures such as throughput and scalability are not taken	Public/private key	Local storage	Query time, Latency, Average response time

(Continues)

21613915, 2025, 3, Downloaded from https://onlinelibrary.wiley.com/doi/10.1002/ett.70087 by Delhi Technological University, Wiley Online Library on [09/03/2025]. See the Terms and Conditions (https://onlinelibrary.wiley.com/terms-and-conditions) on Wiley Online Library for rules of use; OA articles are governed by the applicable Creative Commons License

TABLE 3 | (Continued)

Ref.	Year	Proposed solution	BT	Domain	Benefits	Limitations	Privacy and security	Storage scheme	Performance metrics
[82]	2018	Proposed PBE-DA (Pseudonym-based Encryption with Different Authorities) to protect the patient's privacy by utilizing the blockchain in the eHealth record system	Consensus blockchain	EHR	Privacy-preserving, anonymity, efficiency, security, anonymous access, checking, and updating patient data	Vulnerability measures need to be performed in medical data sharing	PBE-DA using elliptic curve cryptography	Cloud storage	Processing time
[83]	2018	Proposed utilizing the blockchain-based smart contract to manage the protected health information produced by the IoT medical sensors and provide secure automated remote patient monitoring	Consortium blockchain	PHI	Confidentiality, availability, immutability, traceability, speed, privacy, transparency	Authentication protocols should be discussed, and there is a lack of information regarding the designated EHR storage database, presumption about the security of cloud and IP	…	…	…
[84]	2018	Presented a novel architecture named FHIRChain based on blockchain for scalable and secure clinical data sharing, also demonstrated an FHIRChain-based Dapp for participant authentication	Public blockchain	EHR	Secure authentication, prevention from unauthorized data access, increased modularity, scalable data integrity, and enhanced trust	It does not address semantic interoperability, compatibility issues	Public/ private key pair	Off-chain/ on-chain storage	…
[85]	2018	Proposed a secret data-sharing model leveraging blockchain for a secure health record system with proxy re-encryption for granular access control	Private blockchain	EHR	Privacy preservation of on-chain data, authentication, consent revocation, confidentiality, the solution to the issue of limited storage	Privacy and security considerations are not fully explored, experimental evidence is not there to support the theory, scalability issue	Proxy re-encryption	Blockchain	…
[86]	2018	A secure attribute-based signature scheme (ABS) (to ensure that the patient affirms the data based on the attributes) with multiple authorities is adopted to ensure the validity and authenticity of EHRs. By utilizing the advantages of ABS with BT, patients can only access and endorse the records according to the attribute; no other confidential records or information are shown to the patient	…	EHR	Privacy-preservation for patients, unforgeability, collision resistance, multi-authority	Lack of focus on the access control and scalability issues	Attribute-based signature	…	…

(Continues)

21613915, 2025, 3, Downloaded from https://onlinelibrary.wiley.com/doi/10.1002/ett.70087 by Delhi Technological University, Wiley Online Library on [09/03/2025]. See the Terms and Conditions (https://onlinelibrary.wiley.com/terms-and-conditions) on Wiley Online Library for rules of use; OA articles are governed by the applicable Creative Commons License

TABLE 3 | (Continued)

Ref.	Year	Proposed solution	BT	Domain	Benefits	Limitations	Privacy and security	Storage scheme	Performance metrics
[87]	2018	Proposed a secure and privacy-preserving personal health information sharing scheme via consortium blockchain to improve the diagnosis in eHealth systems. PEKS achieves secure data sharing, access control, and privacy preservation	Private and consortium blockchain	PHI	Access control, safe search, data auditing, time controlled revocation, privacy preservation	Lack of focus on interoperability and scalability	Public key encryption with keyword search	Blockchain	Storage overhead, Performance overhead, Time overhead
[88]	2018	Proposed a blockchain-based information management system that handles the patients' information, allowing efficient EMRs access and EMRs retrieval	Hybrid consensus mechanism	EMR	Tamper-proof, anonymity, privacy-preservation, attack-resistance, secure data-sharing, reduced energy consumption, network congestion	Lack of information about network congestion, confidentiality issues	Symmetric cryptography, Public/private key	Local storage or cloud storage (not clearly defined)	Data flow, Latency
[89]	2018	Presented a data-preservation system based on blockchain for sensitive medical data that ensures verifiability and validity of data and privacy to users	Ethereum platform	Medical data	Data security, secure data storage, consistency of data	No detailed information about DPS notifying the user about the illegal operation	SHA256, ECC algorithm, Asymmetric key cryptography	Blockchain	Operation cost, Response time
[90]	2017	OmniPHR, a distributed model for integrated PHRs, is proposed for patients and healthcare providers to provide a unified view of health data	…	PHR	Emphasized interoperability, limited storage, and scalability issues, the safety of sensitive data and updated health records, maintaining access to health records	The model follows the specific type and location data, data outside the scope of the model is not shared, the model also deals with data entry duplication, security and privacy components need to be discussed more	Public key encryption, Digital signature	…	…
[91]	2017	Proposed a secure, trustable, permissioned blockchain framework for sharing EHRs for cancer patient care	Hyperledger Fabric with PBFT protocol	EMR	This solution can reduce the cost and record-sharing turnaround time, improved decision-making, the solution ensures security, availability, and fine access-control users' authenticity	Interoperability has not been discussed	Symmetric key encryption, Proxy re-encryption algorithm, Digital signature verification	Cloud-based storage	…

21613915, 2025, 3, Downloaded from https://onlinelibrary.wiley.com/doi/10.1002/ett.70087 by Delhi Technological University, Wiley Online Library on [09/03/2025]. See the Terms and Conditions (https://onlinelibrary.wiley.com/terms-and-conditions) on Wiley Online Library for rules of use; OA articles are governed by the applicable Creative Commons License

TABLE 4 | A comparative assessment of blockchain solutions for supply chain management in healthcare.

Ref.	Year	Technologies	Approach	Solution	Evaluations	Key contribution	Gaps
[92]	2024	Hyperledger Fabric	Framework	The study updated the digital signature method and added an enhanced hash function to enhance drug traceability	Signature time, Verification time, Throughput, Storage space	Improved hash function, enhanced digital signature algorithm edDSA, ideal for complex settings	The regulatory considerations of using a blockchain-based traceability system in the pharmaceutical sector are not covered in detail
[93]	2024	Ethereum, PoS	Framework	In order to address tracing and tracking concerns in the pharmaceutical supply chain, this study offers an architecture that blends Barcode technologies, Distributed File Storage System and Blockchain into a secure Barcode method	Time and Cost Analysis	Without the use of centralized companies or blind parties, PharmaChain 3.0 guarantees correct sharing of information, capture, and identification about drugs produced between participating entities	Does not provide a detailed analysis of the scalability of the proposed system
[94]	2024	Blockchain	Review	The study explores the application of BT to the tracking of medical resources, which is essential for detecting fake medications in the supply chain's logistical infrastructure	…	Study the safeguarding and facilitation of seamless exchange of medical records to the mitigation of counterfeit pharmaceuticals within the logistics of the supply chain	Does not address the potential challenges and barriers to implementing blockchain in healthcare
[95]	2023	Ethereum	Framework	A decentralized framework utilizing BT is proposed to enable the online distribution of pharmaceutical products, eliminating intermediaries	Transaction cost and Execution cost	Framework improves confidence and transparency in the pharmaceutical supply chain industry	Do not address how their proposed solution would handle the large volume of transactions required for such a system
[96]	2023	Ethereum, dPOW	Framework	Introduced VaccineChain is a safe vaccination supply chain that utilizes checkpoint-assisted scalable BT, with selective revocation capabilities	Communication Overhead, Computational Overhead, Throughput, Latency	VaccineChain offers a secure, scalable blockchain system for managing vaccine supply chains through dynamic authentication, tamper-proof data, and real-world validation	Unclear evaluation considering implementation challenges, regulatory hurdles, and integration with existing systems
[97]	2023	Blockchain	Review	Investigates the barriers to adopting new technology in healthcare using a framework and expert inputs, then analyzes them using two evaluation techniques	Fuzzy DEMATEL	Provides insights into the challenges that need to be addressed for successful implementation, including regulatory and legal issues, lack of awareness and understanding, and technical challenges	Inadequate attention to security and privacy concerns, such as the risk of data breaches and unauthorized access
[98]	2023	Hyperledger Fabric	Framework	Introduced a new blockchain framework named Vacledger using smart contracts on a private network to track and verify the movement of COVID-19 vaccines throughout the supply chain	Cost estimation, Algorithm complexity	Demonstrate the effectiveness of the system in managing supply chain operations securely and transparently	Not Implemented

(Continues)

21613915, 2025, 3, Downloaded from https://onlinelibrary.wiley.com/doi/10.1002/ett.70087 by Delhi Technological University, Wiley Online Library on [09/03/2025]. See the Terms and Conditions (https://onlinelibrary.wiley.com/terms-and-conditions) on Wiley Online Library for rules of use; OA articles are governed by the applicable Creative Commons License

TABLE 4 | (Continued)

Ref.	Year	Technologies	Approach	Solution	Evaluations	Key contribution	Gaps
[99]	2023	Blockchain, IoT	Review	To comprehensively examine the existing body of research pertaining to advanced technologies, with a specific focus on the utilization of IoT and blockchain in the management of smart cities and drug supply chains	...	Provides a detailed analysis of the benefits of using blockchain and IoT technologies in smart cities and drug supply management, including improved security, transparency, and efficiency	No in-depth analysis of the potential security and privacy risks associated with supply chain
[89]	2023	Hyperledger Fabric	Framework	A novel medical equipment tracking method on an alliance chain, using a combined access control model implemented as a secure smart contract for dynamic permissions	Throughput	Merges RBAC's simplified administration with ABAC's adaptability for fine-grained, dynamic permission control	Does not provide the threat model
[100]	2022	Blockchain	SLR	Performed an exhaustive analysis of existing literature, specifically examining the implementation of BT in the pharmaceutical sector	...	Explore how BT can revolutionize the pharmaceutical industry by enhancing supply chain management, and others, while also acknowledging the challenges of regulation, scalability, and interoperability	Does not provide detailed analysis of the cost-benefit trade-offs of implementing BT in the pharmaceutical industry
[101]	2022	Hyperledger Composer	Framework	Proposes a blockchain-based system for secure drug tracking throughout the supply chain, using mathematical models to optimize recall efficiency and delivery costs	Latency, Throughput	Utilizing mathematical models in both forward and backward supply chains to minimize time and cost in medicine delivery and recall processes	Does not provide a detailed analysis of the cost and time savings achieved through the proposed system
[102]	2021	Ethereum	Framework	Leverages BT with smart contracts to track drugs throughout the medical supply chain, fostering trust among participants through tamper-proof data	Gas	Using smart contracts and consensus mechanisms to guarantee data validity and implementing a real-world case study to demonstrate its effectiveness	Does not address the regulatory compliance and threat model
[103]	2021	Hyperledger Fabric, Besu	Review	Examines current challenges in tracking products within the pharmaceutical supply chain and proposes a blockchain-based solution for improved provenance, traceability, and counterfeit prevention	...	Explores two decentralized blockchain architectures, Hyperledger Fabric, and Besu, for tracking medications in the pharmaceutical supply chain, focusing on meeting critical needs such as security and traceability	Does not address the potential challenges in integrating BT with existing systems in the supply chain
[104]	2020	Hyperledger Fabric	Framework	Describes a successful implementation of a blockchain-based solution for tracking and tracing medications throughout the pharmaceutical supply chain	Accuracy	Real-time tracking and verification throughout the supply chain	Does not explicitly address how the system handles patient privacy while ensuring medication traceability
[105]	2019	Hyperledger Fabric	Framework	A Secure and transparent drug supply chain is established through on-chain drug record transactions, ultimately contributing to a smarter healthcare ecosystem	Throughput, Resource Utilization, and Latency	System securely manage drug supply chains with tamper-proof records and controlled access	Issues related to scalability, security, and privacy are not considered

21613915, 2025, 3, Downloaded from https://onlinelibrary.wiley.com/doi/10.1002/ett.70087 by Delhi Technological University, Wiley Online Library on [09/03/2025]. See the Terms and Conditions (https://onlinelibrary.wiley.com/terms-and-conditions) on Wiley Online Library for rules of use; OA articles are governed by the applicable Creative Commons License

TABLE 5 | A comparative assessment of blockchain solutions for clinical trial.

Ref.	Year	Technologies	Approach	Solution	Evaluations	Key contribution	Gaps
[106]	2023	PBFT	Framework	Explores the potential of blockchain for collaborative auditing in clinical trials, aiming to design a secure and efficient system for improved data integrity and sustainable auditing practices	Latency, Scalability, Throughput	Purposed a framework to enhanced transparency, accountability, and security in collaborative clinical trials by employing smart contracts to streamline processes and ensure tamper-proof record	Does not provides analysis of the potential risks and challenges associated with implementing BT in clinical trials, such as data privacy concerns, regulatory compliance, and the need for standardization
[107]	2022	Hyperledger Fabric	Framework	An intelligent traffic control system combining PSO-based optimization and fuzzy logic for real-time network adjustments, achieving autonomous efficiency improvements	Latency, Throughput	Leverages a combined fuzzy logic and optimization to enhance blockchain performance and enhances performance within a clinical trial service platform	Does not address the challenges related security, scalability, and regulatory compliance
[108]	2022	Ethereum, GOQuorum	Framework	Develop a secure, transparent, streamlined, and adaptable system for managing clinical trials using blockchain	Average TPS	Better monitoring and management of clinical trials, offers innovative solutions for eTMF management, reproducible data analysis, secure EDC, efficient payments, and patient recruitment with smart contracts, proven effective through case studies	High memory consumption and node crash
[109]	2022	Blockchain	Review	Utilizing BT in clinical trials	…	Extensive exploration of problems in clinical trials, and blockchain characteristics in fulfilling the requirement of clinical trials	Does not discuss any potential regulatory or legal challenges
[110]	2021	Blockchain	Review	Blockchain's unique capabilities to offer solutions to address challenges in clinical trials like accurate reporting, monitoring, data management, and patient recruitment	…	Explores the use of blockchain in clinical trials (CTs) by examining its features and benefits, categorizing existing research by CT tasks, blockchain type, and protocols, analyzing ongoing development, and identifying key implementation challenges	Does not discuss existing challenges in clinical trials
[111]	2021	Blockchain	Review	Utilization of blockchain in clinical trial	…	Extensive review on potential benefits such as security, traceability, transparency in clinical trails	Need of detailed analysis of technical, social, and organizational challenges
[112]	2020	Hyperledger Fabric	Framework	Research investigates the feasibility of blockchain-based data management for clinical trials through a breast cancer case study	…	By streamlining data management, fostering trust, and reducing regulatory hurdles, the system offers a cost-effective approach to sustainable clinical research	Needs to ensure scalability for larger studies
[84]	2019	Ethereum	Framework	FHIRChain, a blockchain framework designed for healthcare data interoperability that leverages existing smart contract-enabled blockchains	…	Study contributes to secure and efficient sharing of clinical data between healthcare providers	Semantic interoperability issues, legacy system incompatibility, lack of control over data misuse, and potential deployment costs on public blockchains

21613915, 2025, 3, Downloaded from https://onlinelibrary.wiley.com/doi/10.1002/ett.70087 by Delhi Technological University, Wiley Online Library on [09/03/2025]. See the Terms and Conditions (https://onlinelibrary.wiley.com/terms-and-conditions) on Wiley Online Library for rules of use; OA articles are governed by the applicable Creative Commons License

TABLE 6 | A comparative assessment of blockchain solutions for remote patient monitoring.

Ref.	Year	Technologies	Approach	Solution	Evaluations	Key contribution	Gaps
[113]	2024	Ethereum	Framework	Framework secures remote health monitoring for isolated patients, ensuring trustworthy connections to hospital information systems within a secure network	Transaction fee	Development of a secure remote healthcare monitoring system using BT, which provides a cost-effective solution for securely storing, transmitting, and patient essential signs	Lack of detailed information regarding integration with existing systems, scalability, interoperability, and privacy concerns, regulatory compliance, and cost-benefit analysis
[114]	2024	Blockchain	Framework	Propose a new architecture for remote patient monitoring using SDN and blockchain to improve security and data management in a 5G environment	Latency, Packet Error, Communication Overhead, Throughput, Reliability	A remote patient health monitoring system utilizes IoMT, SDN, Blockchain, and 5G technologies to control sensor networks and securely manage patient data with a focus on preserving patient privacy through a combined SDN and Blockchain approach within the 5G network	No detailed analysis on costs associated with implementing and maintaining the proposed system
[115]	2023	Blockchain	Review	In this paper, the applicability of blockchain platforms for remote patient monitoring in the context of IoT-based e-health is assessed	…	Highlights the advantages of using blockchain in enhancing security, privacy, and interoperability in remote patient monitoring systems	Does not provide the existing challenges in remote patient monitoring systems and also challenges after incorporating the blockchain
[116]	2023	Hyperledger, Fog Computing	Framework	Light-weight, Fog-enabled, Blockchain-based RPM system offers quick response times and excellent security	Consensus time, Execution time, Energy consumption	Presents an architecture for a smart and secure remote Health monitoring system that employs IoT devices for collecting patient data, fog computing for real-time response and data aggregation, and a modified blockchain structure with a local and global chain and a lightweight consensus mechanism for efficient and secure data storage and transmission	Though offering security and efficiency, this lightweight blockchain-based system might face limitations in scalability, device processing demands, and potential privacy compromises
[117]	2020	Ethereum	Framework	Presents a healthcare system leveraging blockchain with smart contracts that allow remote patient monitoring, secure data access, and reduced forgery for increased trust	Gas consumption (transaction and execution cost)	System enables secure patient and doctor enrollment, real-time health monitoring, device tracking and maintenance, and IoT device authorization, ensuring privacy and decentralization	Need of scalability, regulations, and energy consumption analysis
[83]	2018	Ethereum	Framework	System leverages blockchain's secure ledger for verifiable patient data while maintaining privacy through permissioned access and anonymous accounts	…	Safeguarding the privacy and accuracy of patient information gathered by remote monitoring devices	Lack of regulatory compliance, and scalability assessment
[118]	2018	Blockchain (PoW)	Framework	Proposed a blockchain-based protocol for data privacy and security. The authors used the PoW-based protocol GHOSTDAG to achieve high throughput and avoid security scalability issues	…	Resolve the issues related to privacy and security vulnerability, limit the scalability issues, improve high throughput and fast remote monitoring system	Lack of Interoperability, Lack of details on the storage of healthcare data

21613915, 2025, 3, Downloaded from https://onlinelibrary.wiley.com/doi/10.1002/ett.70087 by Delhi Technological University, Wiley Online Library on [09/03/2025]. See the Terms and Conditions (https://onlinelibrary.wiley.com/terms-and-conditions) on Wiley Online Library for rules of use; OA articles are governed by the applicable Creative Commons License

TABLE 7 | Solution for pharmaceutical supply chain based on BT.

Ref	Year	Solution	Blockchain type/ consensus mechanism	Storage scheme	Performance metrics
[129]	2022	ChainDrugTrac: Drug traceability	Ethereum	IPFS	None
[130]	2021	Counterfeit Medicine Penetration	Hyperledger Fabric with PBFT	On-chain	Throughput
[131]	2021	Drug traceability	Ethereum	IPFS + on-chain storage	None
[125]	2021	Blockchain Medledger: Drug traceability	Hyperledger Fabric	IPFS	Not Conducted
[104]	2020	BRUINchain: Drug tracking, tracing, and verification	Hyperledger Fabric with PBFT	Off-chain storage	None
[105]	2019	Drug supply chain integrity management	Hyperledger Fabric	Blockchain	Throughput, Latency, Resource utilization
[132]	2019	Anti-Counterfeit Medicine Management	Ethereum	IPFS	None
[133]	2018	Drugledger: Drug traceability and regulation	Permissioned	Not clear	None

BRUINchain [104], a blockchain-based system, leverages Hyperledger Fabric, blockchain application server, notification and verification services, and smart contracts to achieve drug tracing, tracking, and verification. BRUINchain scans the barcode of the drug packages, flags the expired product, detects the suspected and expired product, quarantines the counterfeit drug, and directly verifies the product with the manufacturer. BT is in the quest to make the healthcare sector a smart healthcare sector by providing the decentralization, immutability, security, and transparency to achieve secure EHR/EMR/PHI information access and exchange, efficient pharmaceutical supply-chain, secure medical insurance storage, and even efficient hospital waste management. Pham et al. [127] introduced a remote healthcare system for doctors, patients, and hospitals that takes only crucial medical data and stores it in a blockchain, reducing its size. MIStore, [128] is a medical insurance storage system that adopts BT to provide high credibility to the user. MIStore may assist the insurance company in getting information regarding patients' healthcare spending.

4.1 | Countering Healthcare Data Breaches With Blockchain

According to the HIPAA 2023 Report [134], a report by security researcher *Jeremiah Fowler* uncovered an unsecured database belonging to India's largest diagnostic center in Noida, India. This database encompassed the medical test records of over 12 million individuals, comprising comprehensive information such as the attending physician's particulars, patient names, test locations, detailed test outcomes, and other sensitive medical data. Alarmingly, this repository was openly accessible on the internet without any requisite password, raising significant concerns regarding data security and privacy breaches within the healthcare sector. A healthcare data breach is a serious incident involving unauthorized access, disclosure, or loss of sensitive patient information within a healthcare system. Unauthorized breaches in data security commonly stem from hacking incidents and unauthorized access or disclosure, frequently identified as prevailing causes leading to data breaches.

Blockchain addresses unauthorized access and disclosure issues through its inherent structure of decentralization and cryptographic security. The data stored on a blockchain is distributed across a network of computers, making it very difficult for anyone to tamper with the information without approval from the majority of participants [135].

Access control mechanisms are crucial in addressing unauthorized access and disclosure within blockchain systems. These mechanisms are enforced through smart contracts and cryptographic keys. Smart contracts define the rules and permissions governing access to specific data or actions on the blockchain. Various access control mechanisms implemented through smart contracts, such as attribute-based, role-based, and fine-grained access control, can specify who has the authority to read, write, or execute certain operations within the network. Smart contracts can encode patient consent preferences. Patients can set rules for who can access their data and under what circumstances, ensuring compliance with regulations like GDPR or HIPAA.

Smart Contract Based Access Control: Smart contracts, alternatively referred to as digital contracts, represent computer protocols specifically engineered to distribute, validate, or enact contractual agreements in an automated, data-driven fashion. In healthcare, smart contract-based access control mechanisms within a blockchain ecosystem offer significant advantages for securing sensitive patient data. These smart contracts can regulate and manage access to medical records, ensuring that only authorized individuals, such as healthcare providers or patients themselves, have permission to view or modify specific information [136].

Smart contracts can define access levels, specifying who can access certain data, under what conditions, and for what duration. For instance, a patient might grant temporary access to

21613915, 2025, 3, Downloaded from https://onlinelibrary.wiley.com/doi/10.1002/ett.70087 by Delhi Technological University, Wiley Online Library on [09/03/2025]. See the Terms and Conditions (https://onlinelibrary.wiley.com/terms-and-conditions) on Wiley Online Library for rules of use; OA articles are governed by the applicable Creative Commons License

a specialist for a limited period or allow a healthcare provider access to particular records for treatment. These contracts execute automatically, ensuring compliance with predetermined rules and eliminating the need for intermediaries [137]. Yuan et al. [138] introduced a patient-centered access control model for medical health records based on BT. This model includes smart contracts that grant patients continuous access to their patient medical health records (PMHR). When external entities or institutions seek access to these records, patients retain the autonomy to authorize or deny such requests. In cases where patients opt to share their PMHR, the institution seeking access must obtain explicit authorization from the patients. This approach aims to incentivize proactive patient sharing of medical health records, promoting greater engagement in the sharing process.

The author advocates for a robust access control framework through BT in a smart health system operating within fog computing to safeguard patients' confidentiality. Li et al. [139] proposed scheme leverages blockchain's capabilities to oversee and document users' activities via smart contracts, guaranteeing the system's transparency and dependability. All user operations are systematically logged and verified using blockchain, ensuring a secure and transparent environment for managing the smart health system.

BT has the potential to significantly enhance patient autonomy in the healthcare sector. By leveraging blockchain's decentralized and transparent nature, patients can gain greater control over their medical records, allowing them to access, manage, and share their health information securely and efficiently. This can lead to improved health outcomes, increased patient engagement, and enhanced trust in the healthcare system. Furthermore, blockchain-based systems can enable patients to make informed decisions about their care, provide consent for data sharing, and ensure that their medical records are accurate and up-to-date (Table 8). Overall, the integration of BT in healthcare has the potential to revolutionize the way patients interact with their health information, ultimately leading to greater autonomy and empowerment.

RQ2: Blockchain to handle healthcare security issues: The GDPR report provides an exposition of challenges about the potential anonymization of personal data to a degree that aligns with the stipulated anonymization standards within the GDPR. This analysis underscores two salient compliance dilemmas: GDPR presupposes the presence of a data controller, a presumption frequently inconsistent with the inherent characteristics of BT, where decentralization often prevails. The "right to be forgotten," a fundamental tenet of GDPR, poses intrinsic difficulties within an immutable ledger, as data, once recorded, cannot be readily erased. Within the framework of blockchain infrastructure, an evaluative assessment is conducted concerning certain inherent attributes. Consequently, this examination contemplates the potential for establishing controllership structures and fosters contemplation of the intricate interplay between accountability and governance [7–9].

Healthcare is a highly data-driven field that generates, distributes, archives, and accesses large volumes of data daily. Data is generated every time a patient goes to a healthcare practitioner for a medical examination or takes some tests in the laboratory, that is, CT scan, X-ray, or blood tests, and many more. The data generated in the pharmaceutical supply chain could be a list of items and their specifications. The patient's medical information is disseminated amongst the healthcare providers to oversee the patient's status and suggest therapeutic interventions. The patient's medical information is then recorded in the hospital database and can easily be accessed by the patient or doctor. Data stored in the hospital database is predisposed to all kinds of threats. An unauthorized person can vandalize the data, data can get stolen, and the privacy of the patient and secured data sharing may not be maintained [151, 152].

Under the auspices of the GDPR, explicit provisions are in place mandating the encryption of personal data during its storage and the sharing and transfer process. This mandate is incorporated in GDPR Articles; there has been discourse surrounding the potential efficacy of pseudonymization in safeguarding the privacy and security of data, positing that it may mitigate the imperative for data encryption. However, it is crucial to underscore that, within the GDPR framework, even pseudonymized data retains its classification as personal information. As such, it remains subject to the GDPR's encryption requirements, reinforcing the need for encryption as a paramount safeguarding measure [153].

While Article 9 of GDPR does provide certain exemptions for the processing of sensitive data, it is essential to mention that these exemptions necessitate a comprehensive understanding and adherence to the fundamental principles of lawful processing, as elucidated in Article 6, and the principle of data minimization. Specifically, these principles stipulate that personal data must adhere to the criteria of being "appropriate, pertinent, and restricted to what is essential with the objectives for which they are being processed," as delineated in Article 5 [7, 153]. The healthcare industry must adopt a mechanism or technology to ensure data security, integrity, and privacy [54]. BT is faithful and trustworthy in protecting the healthcare industry through a cryptographic hash function, permissioned blockchain [19], anti-tampering policies [154], consensus algorithm, immutability, replication of data, and better data storage Table 9.

Blockchain, a technology leveraging cryptography for security, safeguards the data by making it tamper-proof. The cryptographic attack attempts to reveal the encrypted data of the patient and healthcare domain and tries to forge the data. One of the substantial security threats in the healthcare industry is monitoring and eavesdropping on patients' vital information. The information may contain the patient's ID, address, location, and medical condition. Blockchain uses cryptography to provide protection and anonymity to the patient, validate the claim the participating entities make against the asset, and validate the data. Blockchain offers encryption algorithms to the data when data is added to the blockchain, which makes this encrypted data challenging for the attacker to decipher. Securing patient information and healthcare providers' identities is one of many challenges that BT can handle.

SEMRES [72] is a blockchain-based medical framework focusing on secure medical data exchange through triple encryption authentication architecture. The framework comprises three modules, i.e., combined encryption and decryption architecture (CEDA), decentralized EMR repository, and content verification.

21613915, 2025, 3, Downloaded from https://onlinelibrary.wiley.com/doi/10.1002/ett.70087 by Delhi Technological University, Wiley Online Library on [09/03/2025]. See the Terms and Conditions (https://onlinelibrary.wiley.com/terms-and-conditions) on Wiley Online Library for rules of use; OA articles are governed by the applicable Creative Commons License

TABLE 8 | A comparative assessment of blockchain solutions for patient autonomy.

Ref.	Year	Methodology	Blockchain	Autonomy aspect	Evaluations	Key contribution	Gaps
[140]	2024	Experimental	Ethereum	Consent management & Data ownership	Transaction cost and time	Proposed a blockchain-based framework for secure, transparent, and patient-centric management of EHRs, enabling the patient to have greater control over their health data	Need to analyze the overhead related to communication and storage
[141]	2024	Experimental	HLF	Access control	Computational overhead, Average latency, Throughput	Proposed a secure access control using CP-ABE blockchain-based outsourcing, enabling efficient and secure sharing of EHRs while minimizing computational overhead	Need to consider the forward/backward security and attribute-level or user-level revocation
[142]	2024	Experimental	Ethereum	Consent aware approach	Computational cost, Gas, Latency, Execution time	A secure and efficient mechanism for sharing personal information among users is proposed, leveraging BT to ensure accountability, scalability, and authenticity, while utilizing off-chain storage to reduce storage pressure	An in-depth examination of the overhead associated with storage and communication is needed. Additionally, an exploration of strategies to mitigate the risk of side-chain attacks is required
[143]	2024	Experimental	Ethereum	Access Control	File size, Execution time, Gas consumption	A blockchain-based healthcare data management system is designed to securely store and share EHRs, leveraging IPFS for scalability and incorporating smart contracts and ABE to ensure authorized access, accountability, and transparency	A thorough approach is needed to enhance performance, minimize latency, and costs, making it suitable for devices with constrained capabilities
[62]	2023	Experimental	Ethereum	Data ownership	Accuracy, Cost	Paper explores how BT can address challenges in healthcare, proposing a framework to assess its suitability and introducing a secure, patient-centric blockchain system for EHRs, comparing it to existing solutions for performance and cost	Need a detailed analysis on scalability, response time, security measures used to protect patient data
[138]	2023	Experimental	Ethereum	Access control	Encryption/ Decryption time	Introduces an advanced proxy re-encryption scheme for PMHR data and a blockchain-based access control mechanism to ensure secure and controlled access	The privacy preservation mechanisms need to be analyzed in detail
[144]	2023	Experimental	Proposed Dual-Blockchain	Access Control	Communication & Computational Overhead	Proposes a dual-blockchain framework for secure EMR sharing, incorporating a novel identity-based TAKA protocol to ensure privacy and fine-grained access control	Need a detailed analysis on storage overhead

(Continues)

21613915, 2025, 3, Downloaded from https://onlinelibrary.wiley.com/doi/10.1002/ett.70087 by Delhi Technological University, Wiley Online Library on [09/03/2025]. See the Terms and Conditions (https://onlinelibrary.wiley.com/terms-and-conditions) on Wiley Online Library for rules of use; OA articles are governed by the applicable Creative Commons License

TABLE 8 | (Continued)

Ref.	Year	Methodology	Blockchain	Autonomy aspect	Evaluations	Key contribution	Gaps
[145]	2021	Experimental	Ethereum	Supervision	Complexity and Overhead analysis	Paper provides a blockchain-based access control scheme for eHealth systems that allows medical institutions to utilize patient data legally without prior authorization while ensuring that patients maintain ownership and oversight of their data, along with an incentive mechanism to encourage data sharing	May remain a risk of misuse by third parties if access controls are not strictly monitored and enforced
[146]	2020	Implementation	Ethereum	Informed consent, Data ownership, Access control	Correctness and Cost	Introduces a decentralized architecture utilizing BT for managing patient-centered PHRs, ensuring secure, immutable, and private handling of medical information, while incorporating smart contracts, IPFS, and reliable oracles, and allowing for adaptable implementation tailored to the needs of the healthcare sector	Required to thoroughly investigate scalability, regulatory compliance, and communication costs
[147]	2020	Survey	…	Self-Sovereign identity	…	Paper provides a comprehensive review of BT's applications in self-sovereign healthcare, focusing on patient data exchange, identity, and governance challenges	Needs to address the security and privacy concerns associated with blockchain-based self-sovereign patient identity management systems
[148]	2020	Experimental	Ethereum	Information exchange	Processing time	Introduces a blockchain-based patient-centric HIE model that addresses security, privacy, data provenance, and patient control concerns by leveraging smart contracts for personalized data access	Requirement for each healthcare facility to set up a blockchain node and convert their servers into blockchain adapters, which may hinder widespread adoption, Scalability concern
[149]	2019	Experimental	Ethereum	Data sharing	Computation overhead	Presents PESchain, a patient-controlled HRs sharing system utilizing consortium blockchain to enhance secure sharing, privacy-preserving access authorization, and efficient EHR deletion processes among medical institutions	Detailed analysis of storage overhead, communication overhead and execution time is essential
[150]	2018	Review	…	Interoperability	…	Paper contributes to healthcare interoperability by proposing BT as a solution for transitioning to patient-driven data exchange while identifying associated challenges and barriers to implementation	Need to discuss any potential regulatory or legal challenges in detail

21613915, 2025, 3, Downloaded from https://onlinelibrary.wiley.com/doi/10.1002/ett.70087 by Delhi Technological University, Wiley Online Library on [09/03/2025]. See the Terms and Conditions (https://onlinelibrary.wiley.com/terms-and-conditions) on Wiley Online Library for rules of use; OA articles are governed by the applicable Creative Commons License

TABLE 9 | Blockchain to handle healthcare security issues.

Ref	Solution	Security level	$C1$	$C2$	$C3$	$C4$	$C5$	$C6$	Contributions	Gaps
[72]	SEMRES	●	×	✓	✓	×	×	✓	Triple security modules ensure secure medical data exchange, A hybrid of RSA and AES encryption mechanisms is used to encrypt medical data, Combined encryption and decryption architecture	Lack of details on the threat model, specific security threats, and computational complexity
[155]	BlockMedCare	●	✓	✓	✓	✓	✓	✓	Proxy Re-encryption cryptosystem combined with Blockchain to store hash data used Ethereum blockchain based on Proof-of-Authority	Concern related to insider threat
[156]	Chen et al.	◔	×	✓	✓	✓	✓	✓	Blockchain-based searchable encryption scheme, Symmetric encryption algorithm to encrypt health data	Need to address computational complexity
[157]	HealthBlock	◕	✓	✓	✓	✓	✓	✓	Mitigate centralized data storage vulnerabilities, Practical byzantine fault tolerance consensus algorithm	Computational overhead need to be discussed in detail
[158]	BCHealth	◕	✓	✓	✓	✓	✓	✓	Ring signature to provide anonymity to the users and ARX ciphers encryption algorithm to guarantee security and privacy to users, Improved scalability and energy efficiency with the help of proof-of-authority	Increase in data access time
[159]	CP-BDHCA	◕	×	×	✓	×	✓	✓	Secure communication between the different healthcare entities, Security against threats, Authentication using RSA and AES	Limited access control
[160]	Blockchain and quantum blind signature for secure EHR	◕	×	×	✓	×	×	✓	Quantum blind signature is used for key distribution	Can struggle with scalability, especially when dealing with large amounts of healthcare data
[161]	MedSBA	●	×	✓	✓	✓	✓	✓	Attribute-based encryption and private Blockchain ensure user privacy and fine-grain access control	Need to analyze computational complexity and scalability implications
[162]	SRHB	◓	×	✓	✓	×	×	✓	Designed a secure and robust healthcare-based blockchain with an attribute-based encryption approach to transmit healthcare data	Deals with scalability issues
[163]	BinDaaS	◓	×	✓	✓	×	✓	✓	Blockchain and deep-learning techniques for EHR records sharing, Collision attack resistance is ensured by lattice-based cryptography	Not cost-effective

Note: In the Table 9, $C1$, $C2$, …, $C6$ are the characteristics provided by the corresponding solution. $C1$: Availability $C2$: Authentication $C3$: Privacy $C4$: Integrity $C5$: Confidentiality $C6$: Security The security level shows that the solution proposed by the authors incorporates the cryptographic hash function, encryption algorithm, consensus mechanism, and permissioned or private Blockchain.

21613915, 2025, 3, Downloaded from https://onlinelibrary.wiley.com/doi/10.1002/ett.70087 by Delhi Technological University, Wiley Online Library on [09/03/2025]. See the Terms and Conditions (https://onlinelibrary.wiley.com/terms-and-conditions) on Wiley Online Library for rules of use; OA articles are governed by the applicable Creative Commons License

CEDA encrypts medical data using a hybrid mechanism of AES and RSA cryptographic algorithms, and this encrypted data is referred to as the secure encrypted medical record. A decentralized EMR repository utilizes SHA256 to generate the secure encrypted medical record (SMeR) hash value. For data decryption and secure data exchange, the data owner uses their private key to sign the block's content. This content block contains the index of SMeR in the Decentralized EMR repository (DERy), the Hash of SMeR, and Authority status. This signed block proves the data owner's authorization and can be the port of the Decentralized EMR repository. Content decryption and verification are performed following data transmission to ensure the data is correct.

A breach of the healthcare system can cause the unauthorized leak of sensitive and confidential medical data. Storing the data in centralized storage attracts malicious users and leads to cyberattacks. HealthBlock [157] is a secure blockchain-based healthcare data management system that focuses on upgrading/enhancing the privacy and security of EHRs by adopting decentralized data storage. HealthBlock provides resistance against security issues such as spoofing attacks, tampering threats, and repudiation by using fabric certificates, cryptographic functions, and fabricated digital signatures for specific tasks. In healthcare, there is a need for regular patient monitoring when it comes to severe health issues or chronic diseases.

BlockMedCare [155] is a blockchain-based healthcare system incorporating IoT and IPFS that concentrates on regular remote patient monitoring. BlockMedCare focuses on security, scalability, and processing time and assures the security element with the blockchain and proxy re-encryption cryptosystem. In the encryption techniques, both the public key and secret key are acquired by the patient ($pk_{patient}$, $sk_{patient}$)and the physician($pk_{physician}$, $sk_{physician}$). The patient encrypts the data using $pk_{patient}$ and generates Prek using pre.rekey($sk_{patient}$, $pk_{physician}$). After receiving the encrypted data, Prek Hospital re-ciphers it and sends it to the physician, where the physician decrypts the data using their secret key. The healthcare domain deals with various attacks; even the protected and encrypted data become vulnerable. An attacker in the blockchain can also forge patients' data, but they must possess high computing power and massive resources and energy to spend. Even though a 51% attack compromises the blockchain network, the key details and data storage location in the cloud can be disclosed. However, since the appropriate attribute-based encryption encrypts the data encryption key, the attacker cannot access medical information if the complex problem of Decisional modified bilinear Diffie-Hellman (DMBDH) is not solved [161].

RQ3: Benefits and Challenges of incorporating BT in healthcare: Among many blockchain applications, healthcare is one of the areas where blockchain has great potential to showcase its capabilities [8, 164]. Sharing the data and providing the availability of medical data to authenticated healthcare providers, researchers, patients, and other consumers is crucial in improving the quality of the healthcare system. BT usage scenarios in healthcare are increasing daily, providing clinical data sharing, maintaining the medical history, global data sharing, medical research, healthcare data access control, drug supply-chain management, billing, and clinical trials [165].

Remote patient monitoring, pharmaceutical supply chains, clinical trials, EHRs, and health insurance claims are the research areas focused on in the healthcare domain. Because of its decentralized approach, BT mitigates the problems in traditional systems. SCACIoMT employs BT to safeguard patients against malicious activities and vulnerabilities [166].

The main motivation for using the blockchain in healthcare or any other area is to bolster the security of the infrastructure and safeguard against unauthorized or malicious actors [167]. The blockchain provides many benefits, including secure data exchange and sharing regulation via smart contracts, synchronization management of health systems, access control, and secure data storage [168]. Providing security and privacy to health records, anonymity to patient identity, regular remote monitoring of patient data, and availability of healthcare data are a few but not limited *benefits* that can be achieved with BT.

1. Secure EHR: Security and privacy preservation are the essential benefits of the blockchain to the healthcare industry, including security to store, manage, and exchange patient medical data. Blockchain uses a smart contract that creates immutable health records, updates the records, provides secure data sharing, and provides a unified view of the scattered data [90].
   Malicious entities can sabotage these records, and to achieve resistance against manipulation, tampering attacks, and forgery attacks, a cryptographic algorithm such as pairing-based cryptography [169] is employed to protect against illegal and malicious activity. Regarding patient involvement and interaction, blockchain-based EHR grants patients increased autonomy regarding their medical records while allowing healthcare agents and other healthcare entities to update patient data in real-time.
2. Improved remote patient monitoring: In cases of urgency where the patient cannot visit the hospital but needs adequate treatment, a blockchain-based RPM is employed to improve healthcare quality. Real-time data plays the most critical and challenging part in healthcare [116]. The patient is equipped with medical or wearable devices, which collect data on water level, blood pressure, oxygen level, and many more. The collected data is given to the smart contract, which then analyzes that data as per the threshold value and triggers the alert based on the findings [83]. For instance, a smart device sends blood pressure data to an individual contract named HealthContractCaller and BloodPressureMonitor [117] for remote patient monitoring. If the blood pressure value surpasses the limits, an alert is forwarded to the patient, doctor, and health center.
3. Secure health information exchange: Data sharing and interoperability are the primary concerns in the healthcare domain, i.e., to guarantee that only approved entities can access medical records and that all the components of the healthcare system are properly communicating with each other and have no data inconsistency between a remote data provider and recipient. The technical necessities outlined in the "Shared Nationwide Interoperability Roadmap" from the Office of the National Coordinator for Health IT (ONC

21613915, 2025, 3, Downloaded from https://onlinelibrary.wiley.com/doi/10.1002/ett.70087 by Delhi Technological University, Wiley Online Library on [09/03/2025]. See the Terms and Conditions (https://onlinelibrary.wiley.com/terms-and-conditions) on Wiley Online Library for rules of use; OA articles are governed by the applicable Creative Commons License

HIT) standard show the data exchange of electronic health registration [170].

The ONC mandates that data be shared privately and securely, without unintended or unauthorized modification, while enabling the information's availability and accessibility to authorized parties. FHIRChain [84] is a blockchain-based architecture enclosing the HL7 Fast Healthcare Interoperability Resources (FHIR) paradigm for scalable shared healthcare data to meet ONC requirements. EdgeMediChain [171] leverages edge computing and blockchain to assure the scalability and security of health data exchange. The hybrid architecture comprises four layers: (a) end-user, (b) Edge pool, (c) global blockchain, and (d) off-chain storage. The global blockchain provides increased latency for block processing. To address privacy and data inconsistency issues in HIE, Zhuang et al. [148] created a patient-centric data exchange system that incorporates the special qualities of smart contracts, DLT, and blockchain.

4. Improved drug traceability and pharmaceutical supply chain: Pharmaceutical drug supply chain management is crucial in the medical industry. However, it still experiences various complexities and losses due to counterfeiters. Counterfeit drugs include medicines or drugs that have failed the quality standards and have not been approved by the regulators. Blockchain can help maintain the medicine standard and verify the authenticity of medicine/drugs from the production to the consumer [165]. To handle medication traceability, Liu et al. [172] offered an intelligent tracking and tracing solution. The architecture includes five layers of the BIoT platform, which include (a) the perception layer, (b) the off-chain layer, (c) the blockchain, (d) the application, and (e) the user layer. This blockchain architecture strictly regulates drug management to provide secure tracing and tracking, from collecting the drug data and verifying device identity and transactions to receiving feedback on drug quality. In the blockchain, decentralized off-chain storage and smart contracts guarantee product traceability in the medical supply chain [173]. A smart contract provides approval among the parties to eliminate intermediaries and allow all participating stakeholders to access the immutable, tamper-proof events logs.

5. Clinical trials: Data transparency may deter those who attempt to report only positive outcomes selectively. Furthermore, it is sometimes necessary to keep the clinical trial protocol confidential and not public to all stakeholders because it may contain research and commercial secrets. BT could guarantee that trial data is recorded in real-time. Every transaction made throughout the trial is time-stamped and stored in a blockchain that allows stakeholders to transfer consent in real-time. BT helps manage patient admission problems, data management, and data analysis in clinical trials [110]. In clinical trials, Albanese et al. [174] offered a dynamic consent management approach (SCoDES) centered on the Hyperledger blockchain to improve the method for monitoring patient consent and guaranteeing the privacy of shared data. By incorporating the features of Quorum, Zhuang et al. [108] redesigned the conventional clinical trial management system (CTMS) to create a safe, auditable, and universal CTMS. BT offers many benefits to the healthcare system, including immutability, decentralization, security, transparency, and traceability. Still, some challenges are related to identity management, scalability, interoperability, cost uncertainty, and legal and regulatory issues. These obstacles prevent users and stakeholders from globally implementing this technology.

BT inherently addresses numerous security vulnerabilities. The applications utilizing blockchain for system development may inadvertently inherit or directly manifest these vulnerabilities. These challenges are particularly pertinent in healthcare, posing the risk of exposing medical information to specific forms of insecurity. The primary objective for incorporating this section is to confront the challenges inherent in implementing healthcare solutions that utilize BT. The researcher aims to address these *difficulties* and pave the way for overcoming them, driven by a desire to surmount the hurdles posed by integrating blockchain in healthcare solutions. In addition to the issues of privacy, security, and scalability that arise when introducing blockchain into healthcare systems, other factors must be taken into account, such as the cost of operation, computation power requirements, data governance, cultural acceptance, and data disclosure willingness, as well as the lack of relevant legislation.

1. *Challenges related to data security*: BT has several specific security issues due to its architecture and implementation. Blockchain is an immutable decentralized ledger technique with a weak defense mechanism against a few particular attacks. Blockchain deals with vulnerabilities such as double spending attacks, anonymity issues, difficulty raising attacks, block withholding attacks, consensus-based attacks, selfish mining attacks, mining malware, timejack attacks, Finney attacks, race attacks, 51% attacks, and block discarding attacks. These attacks are based on consensus, P2P networks, and smart contract vulnerabilities. The concept of consensus is used to help the peers reach an agreement about a specific state in the network and form trust and reliability in a blockchain network. The solutions to these issues can be rectified by monitoring node behavior, improving consensus, and increasing hash rate [175].

2. *Privacy leakage*: The foremost requirement of the healthcare industry is to render anonymity and privacy to patients' health data and identity. Every patient is vulnerable to attacks on their personal medical information, which may reveal their identity. While BT secures data with encryption techniques and cryptographic hash functions, dispersing encrypted records throughout the network introduces potential privacy concerns. Authorized nodes can access this data, and if security measures fail, sensitive information could be exposed. These challenges make access control and privacy leakage a critical topic of concern in the blockchain, so access control should be adequately addressed. Various studies have integrated encryption techniques, multi-tier architecture, and access control mechanisms with BT to safeguard health data's user identity and privacy.

21613915, 2025, 3, Downloaded from https://onlinelibrary.wiley.com/doi/10.1002/ett.70087 by Delhi Technological University, Wiley Online Library on [09/03/2025]. See the Terms and Conditions (https://onlinelibrary.wiley.com/terms-and-conditions) on Wiley Online Library for rules of use; OA articles are governed by the applicable Creative Commons License

Healthchain [176] focuses on privacy preservation by incorporating the permission blockchain and using off-chain storage IPFS to store the EHRs. It also includes a cryptographic public key encryption algorithm to guarantee the data's integrity, privacy, and security. A hybrid privacy-preserving framework, hOCBS [177] leverages consensus mechanism and off-chain storage to ensure secure data sharing, privacy preservation, and dynamic consent management. Other popular key technologies and cryptographic solutions that serve as foundational elements for preserving privacy in blockchain are secure multi-party computation, homomorphic encryption, ring signature, zero-knowledge proof, and many more [178].

3. *Scalability*: Scalability is the major obstacle in blockchain-based solutions. Millions of people use wearable devices to keep track of their health status; private clinics, healthcare centers, insurance providers, and individual patients are generating a high volume of data. The decentralized architecture of blockchain systems can struggle to accommodate large data records, as the data is stored across a distributed network, making it difficult to have a unified view. To provide the necessary scalability, the exponential increase in medical data generation necessitates more and more node participation in networks with high storage capacity.
   The high amount of data also increases the latency and decreases the performance of the blockchain since processing this large-scale data requires significant time and computational power. The blockchain scales inadequately as the count of nodes in the network grows. Consensus protocols, including PoW and PoA, are adopted to ensure scalability. The solution adopts a well-defined consensus protocol and off-chain storage for scalability and high-performance.
   The proposed framework [179] uses IPFS off-chain storage to solve scalability issues in the blockchain-leveraging healthcare system. The patient's public key encrypts the records, and encrypted records are moved to the IPFS storage. IPFS provides security and privacy to medical data and handles the scalability issue. The user can control data access by permitting only the authorized node to access the data. BCHealth [158] adopted an improved and modified blockchain network and PoA consensus algorithm that ensures the enhanced performance and scalability of the privacy-preserving architecture. The data owner controls their data and decides who can access it.
   BlockMedCare [155] used off-chain database storage based on the IPFS system to ensure scalability. Blockchain provides flexibility in accessing and maintaining the integrity of sensitive data, so storing sensitive information on the blockchain can expose it to several severe attacks. After encrypting the patient data with a public key, the encrypted data gets transferred to IPFS storage. Blockchain does not store all data; the IPFS produces a distinct hash for every data piece and stores it on the blockchain.

4. *Interoperability*: No healthcare-specific blockchain standard ensures applications built on different blockchain platforms can talk to each other without problems. Part of the problem is that the platforms are hard to use and understand, with various smart contract features, consensus methods, and transaction strategies [180]. Interoperability enables the two blockchains to work together, but no specific standard protocol allows two blockchains to collaborate and incorporate each other. The lack of standardized interoperability between blockchains hinders seamless information exchange, restricting access to collaborative patient data for a holistic view and limiting the availability of critical healthcare information. The solution is an open protocol standardization through which different blockchain platforms can communicate [120, 121]. Cross-chain interoperability allows one or multiple blockchains to communicate with each other across platforms that may be homogeneous or heterogeneous. Existing literature predominantly focuses on EHRs managed within a single blockchain framework. However, EHRs are increasingly shared across healthcare organizations using diverse frameworks. Consequently, achieving inter-organizational EHR interoperability necessitates exploring cross-chain interoperability to facilitate effective information sharing. Various proposed solutions to address interoperability challenges primarily include sidechains, blockchain routers, and smart contract-based approaches. These technologies enable seamless communication and data exchange between different blockchain networks and frameworks, facilitating more efficient interoperability across diverse platforms [168, 180].

5. *Technical complexity and Issues*: Implementing blockchain in healthcare faces hurdles. The system might struggle to handle large amounts of data quickly, and storing all that information could be expensive. Additionally, integrating blockchain with existing healthcare infrastructures can be complex and challenging. Integrating blockchain into healthcare systems demands extensive changes, including funds, planning, expertise, and time [173]. Compatibility issues may necessitate acquiring new systems, adding to implementation costs. The lack of standardized data across diverse healthcare providers presents a hurdle to the efficient sharing and analysis of patient data [55]. Beyond the technical hurdles previously mentioned, the adoption of blockchain in healthcare necessitates a robust network infrastructure. This distributed ledger architecture relies on a network of interconnected computational nodes to collectively provide the processing power required for transaction validation and block creation. However, concerns persist regarding the unforeseen operational costs associated with their long-term maintenance [54].

6. *Difficult to use*: Integrating BT into operational frameworks poses substantial obstacles due to its complexity. Furthermore, in industries such as healthcare, physician suppliers, and insurance providers, there is still a heavy dependence on traditional approaches, hindering blockchain solutions' smooth implementation. Effectively coordinating these heterogeneous components to adopt blockchain as a revolutionary invention remains exceedingly difficult. The current intricacy of BT requires a significant level of technical expertise, including the handling of public/private cryptographic keys and adherence

21613915, 2025, 3, Downloaded from https://onlinelibrary.wiley.com/doi/10.1002/ett.70087 by Delhi Technological University, Wiley Online Library on [09/03/2025]. See the Terms and Conditions (https://onlinelibrary.wiley.com/terms-and-conditions) on Wiley Online Library for rules of use; OA articles are governed by the applicable Creative Commons License

to specified procedural protocols, thereby restricting its user-friendliness and accessibility.

7. *Computing Power Consumption*: In the blockchain, decentralized consensus methods employing verification-focused algorithms ensure the consistency and authenticity of transactions. Public blockchains extensively utilize consensus algorithms, contributing to significant energy consumption [58]. In systems like Medrec [63], individual healthcare institutions maintain their data autonomously. Data security and accessibility rely on the data custodians themselves. The system uses the PoW mechanism to achieve consensus despite the drawbacks of limited processing speeds, slow transaction confirmations, and high energy consumption.

8. *Cost*: Incorporating BT in healthcare presents several cost challenges. Initial implementation costs are substantial, encompassing expenses for software development and hardware upgrades. Ongoing operational expenses include maintenance, monitoring, and updates, alongside investments in cybersecurity and regulatory compliance [181]. Training healthcare professionals in BT adds further costs, necessitating educational programs and resources. Data migration and integration with existing systems require financial outlay, as does scaling blockchain solutions to accommodate growing data volumes [182]. Ensuring the security of patient data involves investments in encryption, access controls, and compliance measures. Managing these costs requires strategic decision-making, collaboration among stakeholders, and a clear understanding of the technology's potential and financial implications in healthcare settings [80].

9. *Latency*: Blockchain's decentralized nature ensures enhanced security and data integrity, but it also requires extensive computational resources and time to validate and record transactions across the network. This process introduces latency, particularly in healthcare, where real-time data access and processing are essential. While BT offers substantial benefits for data security and integrity in healthcare, addressing the latency challenges is critical to ensuring medical care's overall efficiency and effectiveness, particularly since it can be effectively integrated into the healthcare ecosystem. Solutions such as optimizing blockchain protocols, using hybrid models that combine blockchain with other technologies, and improving network infrastructure are essential to mitigate latency and enhance the performance of blockchain-based healthcare systems.

10. *Regulatory Concerns*: Integrating BT into healthcare faces a significant hurdle: Ensuring compliance with existing regulations and data privacy laws. For widespread adoption, collaboration between healthcare stakeholders and regulatory bodies is crucial [8, 103]. A key challenge lies in scaling blockchain systems across different regions, where legal frameworks may conflict. Government regulations and cultural nuances pose substantial barriers to implementation. Extensive stakeholder engagement and support are necessary to address these uncertainties and gain acceptance from the global healthcare community [54, 55, 167].

5 | Discussion

This study aims to thoroughly evaluate the current research on BT in healthcare and its possibilities in the future by conducting a systematic literature review. To achieve this objective, we have formulated three broad research inquiries.

RQ1 examined the transformative potential of BT within the healthcare sector. The primary objective is to assess how blockchain's inherent functionalities could satisfy the industry's critical requirements for secure data storage and exchange. The literature survey revealed a dominant focus on leveraging blockchain for data sharing, health record management, and access control mechanisms. Conversely, utilizing blockchain in other domains, including supply chain management, patient autonomy clinical trials, remote patient monitoring, audit trial management, and drug prescription management, appeared significantly less prevalent, as shown in Figure 11. This research inquiry investigates the potential of BT to empower patients with greater control over who can access their personal health information. Such a development would signify a significant increase in patient autonomy, as individuals would be granted the authority to determine who has permission to view their data. This includes enhanced data ownership, improved access control, increased transparency, enhanced security, and improved interoperability. While there are challenges such as scalability, interoperability, regulatory compliance, and technical complexity, the potential benefits of blockchain for patient autonomy are compelling.

While the disruptive nature of blockchain in healthcare is undeniable and has attracted widespread interest from healthcare providers, its real-world impact on the industry is still emerging. Theoretical concepts dominate the field; however, a few operational frameworks have limited user adoption. Nevertheless, the rapid evolution of this domain suggests that blockchain has a significant and positive influence on healthcare in the coming years. Several factors contribute to the measured adoption process, such as stakeholder digital literacy gaps and a strong preference for paper-based documentation. Despite clear advantages, widespread implementation is further hampered by patient and healthcare professional resistance to change.

The investigation undertaken by *RQ2* explored recent advancements in using blockchain to address healthcare domain security concerns. The decentralized nature of blockchain offers substantial advantages over centralized storage systems. Its cryptographic hashing and immutable data features enhance resistance against unauthorized access, tampering, and breaches. Current research in data storage explores two primary methodologies: Off-chain and on-chain storage. The primary challenge is balancing data privacy during storage and transmission while concurrently optimizing performance.

An analysis of the literature reveals that a commonly adopted approach to ensuring data integrity involves encrypting data

21613915, 2025, 3, Downloaded from https://onlinelibrary.wiley.com/doi/10.1002/ett.70087 by Delhi Technological University, Wiley Online Library on [09/03/2025]. See the Terms and Conditions (https://onlinelibrary.wiley.com/terms-and-conditions) on Wiley Online Library for rules of use; OA articles are governed by the applicable Creative Commons License

before hashing it. Additionally, a third-party system such as IPFS generates unique identifiers. Furthermore, numerous encryption techniques, including homomorphic encryption, pseudonym-based encryption, attribute-based encryption with multiple authorities, and proxy re-encryption, are being investigated to uphold privacy preservation (Table 9).

RQ3 carefully examined the benefits and challenges of adopting BT in healthcare. BT promises to transform healthcare by enhancing data security, privacy, and interoperability. While blockchain offers many benefits, its implementation in healthcare faces significant challenges. Security vulnerabilities, privacy leakage, scalability constraints, and the lack of standardized interoperability protocols are key hurdles that must be addressed. Additionally, integrating blockchain with existing healthcare infrastructure necessitates overcoming technical complexities and addressing cost concerns. Regulatory uncertainties surrounding data privacy and legal frameworks across different regions further complicate widespread adoption.

It is important to differentiate between BT's inherent benefits and flaws and the common challenges across technological advancements. For instance, interoperability and regulatory issues are not unique to blockchain implementation but rather recurring hurdles encountered when adopting any novel technology. Despite these challenges, the ongoing research and development efforts toward blockchain in healthcare are promising. Standardized protocols and interoperable frameworks are being actively explored to enable seamless data exchange across diverse blockchain platforms. Solutions leveraging off-chain storage and optimized consensus mechanisms are being developed to address scalability limitations and latency issues. Looking forward, fostering collaboration among stakeholders, including healthcare providers, researchers, policymakers, and technology developers, is crucial for overcoming the existing challenges and realizing the full potential of blockchain in healthcare.

6 | Conclusion and Future Scope

In this comprehensive survey paper, we have undertaken an exhaustive examination of the transformative capabilities of BT in the healthcare sector. This investigation has been conducted against the backdrop of the manifold challenges that currently beset the healthcare industry. It is essential to mention here that the utility of BT can be extended beyond healthcare, finding applications in diverse domains such as smart city development, financial services, and the energy sector, ensuring medical care's overall efficiency and effectiveness, particularly since BT furnishes the healthcare industry with a robust infrastructure with essential attributes, including agility, flexibility, security, and adaptability.

In the course of this study, we sought to elucidate the following salient inquiries: (a) how BT catalyzes the transformation of healthcare systems, (b) its capabilities in addressing the security concerns inherent to healthcare data, and (c) the substantial advantages and challenges encountered when integrating blockchain into healthcare operations. Notably, advanced cryptographic algorithms and anti-tampering mechanisms significantly bolster the privacy and security of medical data compared to conventional centralized data management paradigms. Furthermore, blockchain demonstrates its capacity to process voluminous data while upholding the utmost security, confidentiality, privacy, and data integrity standards.

Within the purview of this inquiry, we have explored blockchain-based solutions tailored for EHRs, secure authentication of patients and healthcare providers, pharmaceutical supply chain management, and the broader regulatory framework governing healthcare institutions. It is discernible that BT has the potential for beneficial impacts across healthcare and other sectors. However, it is important to acknowledge the associated challenges related to security vulnerabilities, scalability, interoperability, and computational resource requirements. Considering blockchain type and consensus mechanisms is imperative to mitigate privacy risks.

Furthermore, the literature reviewed underscores the importance of preserving integrity, security, confidentiality, access control, data sharing, and healthcare data privacy through blockchain's inherent capabilities, such as smart contracts, public key encryption, and decentralized autonomous authentication protocols. It is incumbent upon stakeholders to recognize the imperative of accommodating the burgeoning volume of healthcare data, which continues to grow exponentially, posing a significant storage challenge. In this context, it is recommended to carefully select an appropriate consensus protocol and adopt off-chain storage solutions as viable strategies to address the burgeoning storage demands engendered by healthcare data proliferation.

Future work may include:

- Advancing the integration of blockchain technology in healthcare by tackling challenges related to scalability, security vulnerabilities, and interoperability.
- Developing a specialized blockchain framework for healthcare that incorporates efficient access control mechanisms, optimized storage solutions, and enhanced privacy preservation techniques.
- Exploring advanced consensus protocols and hybrid approaches, such as off-chain storage, to manage the increasing volume of healthcare data more effectively.
- Creating standardized, interoperable frameworks to enable seamless data exchange across diverse blockchain platforms, fostering greater collaboration among healthcare providers, researchers, and developers.

Author Contributions

Anita Thakur: implementation, experimentation, manuscript writing, writing – original draft, conceptualization, methodology, visualization. Virender Ranga: conceptualization, methodology, writing – review and editing, supervision, investigation. Ritu Agarwal: writing – review and editing, supervision, investigation.

Acknowledgments

The authors have nothing to report.

21613915, 2025, 3, Downloaded from https://onlinelibrary.wiley.com/doi/10.1002/ett.70087 by Delhi Technological University, Wiley Online Library on [09/03/2025]. See the Terms and Conditions (https://onlinelibrary.wiley.com/terms-and-conditions) on Wiley Online Library for rules of use; OA articles are governed by the applicable Creative Commons License

Ethics Statement

The authors have nothing to report.

Consent

All authors have approved the manuscript and given their full consent for its publication.

Conflicts of Interest

The authors declare no conflicts of interest.

Data Availability Statement

The authors confirm that the data supporting the results and findings of this study are available within the article.

References

1. M. Z. A. Bhuiyan, A. Zaman, T. Wang, G. Wang, H. Tao, and M. M. Hassan, "Blockchain and Big Data to Transform the Healthcare," in *Proceedings of the International Conference on Data Processing and Applications* (Association for Computing Machinery, 2018), 62–68.

2. E. J. De Aguiar, B. S. Faiçal, B. Krishnamachari, and J. Ueyama, "A Survey of Blockchain-Based Strategies for Healthcare," *ACM Computing Surveys (CSUR)* 53, no. 2 (2020): 1–27.

3. PROTENUS, "*Breach Barometer Report*," (2023), https://www.protenus.com/breach-barometer-report/.

4. HIPAA, "*Healthcare Data Breach*," (2022), https://www.hipaajournal.com/healthcare-data-breach-statistics/.

5. HIPAA, "*Healthcare Data Breach*," (2023), https://www.hipaajournal.com/october-2023-healthcare-data-breach-report/.

6. D. Gonçalves-Ferreira, M. Sousa, G. M. Bacelar-Silva, et al., "OpenEHR and General Data Protection Regulation: Evaluation of Principles and Requirements," *JMIR Medical Informatics* 7, no. 1 (2019): e9845.

7. EU, "EU General Data Protection Regulation (GDPR): Regulation (EU) 2016/679 of the European Parliament and of the Council of 27 April 2016 on the Protection of Natural Persons With Regard to the Processing of Personal Data and on the Free Movement of Such Data, and Repealing Directive 95/46/EC (General Data Protection Regulation)," *Official Journal of the European Union* (2022), https://eur-lex.europa.eu/eli/reg/2016/679/oj.

8. M. S. Arbabi, C. Lal, N. R. Veeraragavan, D. Marijan, J. F. Nygård, and R. Vitenberg, "A Survey on Blockchain for Healthcare: Challenges, Benefits, and Future Directions," *IEEE Communications Surveys & Tutorials* 25, no. 1 (2022): 386–424.

9. A. B. Haque, A. N. Islam, S. Hyrynsalmi, B. Naqvi, and K. Smolander, "GDPR Compliant Blockchains–a Systematic Literature Review," *IEEE Access* 9 (2021): 50593–50606.

10. R. Zhang, R. Xue, and L. Liu, "Security and Privacy for Healthcare Blockchains," *IEEE Transactions on Services Computing* 15, no. 6 (2021): 3668–3686.

11. R. Khan, X. Tao, A. Anjum, et al., "θ-Sensitive K-Anonymity: An Anonymization Model for IoT Based Electronic Health Records," *Electronics* 9, no. 5 (2020): 716.

12. C. Balis, I. Tagopoulos, and K. Dimola, "Moving Towards a Blockchain-Based Healthcare Information System," in *ICIMTH* (IOS Press, 2019), 168–171.

13. S. F. Aghili, H. Mala, M. Shojafar, and P. Peris-Lopez, "LACO: Lightweight Three-Factor Authentication, Access Control and Ownership Transfer Scheme for e-Health Systems in IoT," *Future Generation Computer Systems* 96 (2019): 410–424.

14. N. Tariq, M. Asim, F. Al-Obeidat, et al., "The Security of Big Data in Fog-Enabled IoT Applications Including Blockchain: A Survey," *Sensors* 19, no. 8 (2019): 1788.

15. H. Wang, K. Li, K. Ota, and J. Shen, "Remote Data Integrity Checking and Sharing in Cloud-Based Health Internet of Things," *IEICE Transactions on Information and Systems* 99, no. 8 (2016): 1966–1973.

16. S. Haber and W. S. Stornetta, *How to Time-Stamp a Digital Document* (Springer, 1991).

17. S. Nakamoto, "*Bitcoin: A Peer-to-Peer Electronic Cash System*," (2008).

18. S. S. Sarmah, "Understanding Blockchain Technology," *Computer Science and Engineering* 8, no. 2 (2018): 23–29.

19. M. Liu, K. Wu, and J. J. Xu, "How Will Blockchain Technology Impact Auditing and Accounting: Permissionless Versus Permissioned Blockchain," *Current Issues in Auditing* 13, no. 2 (2019): A19–A29.

20. M. Niranjanamurthy, B. Nithya, and S. Jagannatha, "Analysis of Blockchain Technology: Pros, Cons and SWOT," *Cluster Computing* 22 (2019): 14743–14757.

21. A. Thakur, D. V. Ranga, and R. Agarwal, "Performance Benchmarking and Analysis of Blockchain Platforms," in *Proceedings of the International Conference on Innovative Computing & Communication (ICICC)* (Elsevier SSRN series, 2023).

22. A. Thakur, V. Ranga, and R. Agarwal, "Workload Dynamics Implications in Permissioned Blockchain Scalability and Performance," *Cluster Computing* 27 (2024): 11569–11593.

23. R. Singh, S. Tanwar, and T. P. Sharma, "Utilization of Blockchain for Mitigating the Distributed Denial of Service Attacks," *Security and Privacy* 3, no. 3 (2020): e96.

24. S. Zhang and J. H. Lee, "Double-Spending With a Sybil Attack in the Bitcoin Decentralized Network," *IEEE Transactions on Industrial Informatics* 15, no. 10 (2019): 5715–5722.

25. E. Heilman, A. Kendler, A. Zohar, and S. Goldberg, "Eclipse Attacks on {Bitcoin's}{Peer-to-Peer} Network," in *24th USENIX Security Symposium (USENIX Security 15)* (IEEE, 2015), 129–144.

26. M. Kedziora, P. Kozłowski, M. Szczepanik, and P. Jóźwiak, "Analysis of Blockchain Selfish Mining Attacks," in *Information Systems Architecture and Technology: Proceedings of 40th Anniversary International Conference on Information Systems Architecture and Technology–ISAT 2019: Part I* (Springer, 2020), 231–240.

27. D. K. Tosh, S. Shetty, X. Liang, C. A. Kamhoua, K. A. Kwiat, and L. Njilla, "Security Implications of Blockchain Cloud With Analysis of Block Withholding Attack," in *Proceeding of the 2017 17th IEEE/ACM International Symposium on Cluster, Cloud and Grid Computing (CCGRID)* (IEEE, 2017), 458–467.

28. D. Kraft, "Difficulty Control for Blockchain-Based Consensus Systems," *Peer-to-Peer Networking and Applications* 9 (2016): 397–413.

29. Y. Yu, Y. Li, J. Tian, and J. Liu, "Blockchain-Based Solutions to Security and Privacy Issues in the Internet of Things," *IEEE Wireless Communications* 25, no. 6 (2018): 12–18.

30. S. Sayeed and H. Marco-Gisbert, "Assessing Blockchain Consensus and Security Mechanisms Against the 51% Attack," *Applied Sciences* 9, no. 9 (2019): 1788.

31. C. Ye, G. Li, H. Cai, Y. Gu, and A. Fukuda, "Analysis of Security in Blockchain: Case Study in 51%-Attack Detecting," in *Proceeding of the 2018 5th International Conference on Dependable Systems and Their Applications (DSA)* (IEEE, 2018), 15–24.

32. X. Yang, Y. Chen, and X. Chen, "Effective Scheme Against 51% Attack on Proof-Of-Work Blockchain With History Weighted Information," in *Proceedings of the 2019 IEEE International Conference on Blockchain (Blockchain)* (IEEE, 2019), 261–265.

21613915, 2025, 3, Downloaded from https://onlinelibrary.wiley.com/doi/10.1002/ett.70087 by Delhi Technological University, Wiley Online Library on [09/03/2025]. See the Terms and Conditions (https://onlinelibrary.wiley.com/terms-and-conditions) on Wiley Online Library for rules of use; OA articles are governed by the applicable Creative Commons License

33. D. Mingxiao, M. Xiaofeng, Z. Zhe, W. Xiangwei, and C. Qijun, "A Review on Consensus Algorithm of Blockchain," in *Proceedings of the 2017 IEEE International Conference on Systems, Man, and Cybernetics (SMC)* (IEEE, 2017), 2567–2572.

34. S. M. Sarkintudu, H. H. Ibrahim, and A. B. Abdwahab, "Taxonomy Development of Blockchain Platforms: Information Systems Perspectives," in *AIP Conference Proceedings, 2016* (AIP Publishing, 2018).

35. S. Bouraga, "A Taxonomy of Blockchain Consensus Protocols: A Survey and Classification Framework," *Expert Systems with Applications* 168 (2021): 114384.

36. S. M. H. Bamakan, A. Motavali, and A. B. Bondarti, "A Survey of Blockchain Consensus Algorithms Performance Evaluation Criteria," *Expert Systems with Applications* 154 (2020): 113385.

37. B. Lashkari and P. Musilek, "A Comprehensive Review of Blockchain Consensus Mechanisms," *IEEE Access* 9 (2021): 43620–43652.

38. A. Baliga, "Understanding Blockchain Consensus Models," *Persistent* 4, no. 1 (2017): 14.

39. A. B. Goldstein, N. Sokolov, V. Elagin, A. V. Onufrienko, and I. A. Belozertsev, "Network Characteristics of Blockchain Technology of on Board Communication," in *Proceedings of the 2019 Systems of Signals Generating and Processing in the Field of on Board Communications* (IEEE, 2019), 1–5.

40. W. Viriyasitavat and D. Hoonsopon, "Blockchain Characteristics and Consensus in Modern Business Processes," *Journal of Industrial Information Integration* 13 (2019): 32–39.

41. J. Cheng, L. Xie, X. Tang, N. Xiong, and B. Liu, "A Survey of Security Threats and Defense on Blockchain," *Multimedia Tools and Applications* 80 (2021): 30623–30652.

42. X. Li, P. Jiang, T. Chen, X. Luo, and Q. Wen, "A Survey on the Security of Blockchain Systems," *Future Generation Computer Systems* 107 (2020): 841–853.

43. S. Soni and B. Bhushan, "A Comprehensive Survey on Blockchain: Working, Security Analysis, Privacy Threats and Potential Applications," in *Proceedings of the 2019 2nd International Conference on Intelligent Computing, Instrumentation and Control Technologies (ICICICT)*, vol. 1 (IEEE, 2019), 922–926.

44. N. Rathod and D. Motwani, "Security Threats on Blockchain and Its Countermeasures," *International Research Journal of Engineering and Technology* 5, no. 11 (2018): 1636–1642.

45. N. Anita and M. Vijayalakshmi, "Blockchain Security Attack: A Brief Survey," in *Proceedings of the 2019 10th International Conference on Computing, Communication and Networking Technologies (ICCCNT)* (IEEE, 2019), 1–6.

46. R. Olfati-Saber and R. M. Murray, "Consensus Problems in Networks of Agents With Switching Topology and Time-Delays," *IEEE Transactions on Automatic Control* 49, no. 9 (2004): 1520–1533.

47. R. Olfati-Saber, J. A. Fax, and R. M. Murray, "Consensus and Cooperation in Networked Multi-Agent Systems," *Proceedings of the IEEE* 95, no. 1 (2007): 215–233.

48. C. T. Nguyen, D. T. Hoang, D. N. Nguyen, D. Niyato, H. T. Nguyen, and E. Dutkiewicz, "Proof-Of-Stake Consensus Mechanisms for Future Blockchain Networks: Fundamentals, Applications and Opportunities," *IEEE Access* 7 (2019): 85727–85745.

49. M. Jakobsson and A. Juels, "Proofs of Work and Bread Pudding Protocols," in *Secure Information Networks: Communications and Multimedia Security IFIP TC6/TC11 Joint Working Conference on Communications and Multimedia Security (CMS'99) September 20–21, 1999* (Springer, 1999), 258–272.

50. W. Li, C. Feng, L. Zhang, H. Xu, B. Cao, and M. A. Imran, "A Scalable Multi-Layer PBFT Consensus for Blockchain," *IEEE Transactions on Parallel and Distributed Systems* 32, no. 5 (2020): 1146–1160.

51. T. A. Syed, A. Alzahrani, S. Jan, M. S. Siddiqui, A. Nadeem, and T. Alghamdi, "A Comparative Analysis of Blockchain Architecture and Its Applications: Problems and Recommendations," *IEEE Access* 7 (2019): 176838–176869.

52. O. Vashchuk and R. Shuwar, "Pros and Cons of Consensus Algorithm Proof of Stake. Difference in the Network Safety in Proof of Work and Proof of Stake," *Electronics and Information Technologies* 9, no. 9 (2018): 106–112.

53. B. Sriman, S. Ganesh Kumar, and P. Shamili, "Blockchain Technology: Consensus Protocol Proof of Work and Proof of Stake," in *Intelligent Computing and Applications: Proceedings of ICICA 2019* (Springer, 2021), 395–406.

54. M. Attaran, "Blockchain Technology in Healthcare: Challenges and Opportunities," *International Journal of Healthcare Management* 15, no. 1 (2022): 70–83.

55. K. Yaeger, M. Martini, J. Rasouli, and A. Costa, "Emerging Blockchain Technology Solutions for Modern Healthcare Infrastructure," *Journal of Scientific Innovation in Medicine* 2, no. 1 (2019): 1.

56. T. T. Kuo, H. E. Kim, and L. Ohno-Machado, "Blockchain Distributed Ledger Technologies for Biomedical and Health Care Applications," *Journal of the American Medical Informatics Association* 24, no. 6 (2017): 1211–1220.

57. N. Mekawie and K. Yehia, "Challenges of Deploying Cloud Computing in eHealth," *Procedia Computer Science* 181 (2021): 1049–1057.

58. I. Abu-Elezz, A. Hassan, A. Nazeemudeen, M. Househ, and A. Abd-Alrazaq, "The Benefits and Threats of Blockchain Technology in Healthcare: A Scoping Review," *International Journal of Medical Informatics* 142 (2020): 104246.

59. R. Sivan and Z. A. Zukarnain, "Security and Privacy in Cloud-Based e-Health System," *Symmetry* 13, no. 5 (2021): 742.

60. J. Hathaliya, P. Sharma, S. Tanwar, and R. Gupta, "Blockchain-Based Remote Patient Monitoring in Healthcare 4.0," in *Proceedings of the 2019 IEEE 9th International Conference on Advanced Computing (IACC)* (IEEE, 2019), 87–91.

61. V. Ramani, T. Kumar, A. Bracken, M. Liyanage, and M. Ylianttila, "Secure and Efficient Data Accessibility in Blockchain Based Healthcare Systems," in *Proceeding os the 2018 IEEE Global Communications Conference (GLOBECOM)* (IEEE, 2018), 206–212.

62. B. K. Rai, "PcBEHR: Patient-Controlled Blockchain Enabled Electronic Health Records for Healthcare 4.0," *Health Services and Outcomes Research Methodology* 23, no. 1 (2023): 80–102.

63. A. Ekblaw and A. Azaria, "Medrec: Medical Data Management on the Blockchain," *Viral Communications* (2016), https://viral.media.mit.edu/pub/medrec.

64. R. Nowrozy, K. Ahmed, A. Kayes, H. Wang, and T. R. McIntosh, "Privacy Preservation of Electronic Health Records in the Modern Era: A Systematic Survey," *ACM Computing Surveys* 56 (2024): 1–37.

65. P. Soni, S. H. Islam, A. K. Pal, N. Mishra, and D. Samanta, "Blockchain-Based User Authentication and Data-Sharing Framework for Healthcare Industries," *IEEE Transactions on Network Science and Engineering* 11 (2024): 3623–3628.

66. I. Masood, A. Daud, Y. Wang, A. Banjar, and R. Alharbey, "A Blockchain-Based System for Patient Data Privacy and Security," *Multimedia Tools and Applications* 83 (2024): 60443–60467.

67. J. Liu, Y. Fan, R. Sun, L. Liu, C. Wu, and S. Mumtaz, "Blockchain-Aided Privacy-Preserving Medical Data Sharing Scheme for e-Healthcare System," *IEEE Internet of Things Journal* 10 (2023): 21377–21388.

68. B. Jaishankar, S. Vishwakarma, P. Mohan, A. K. S. Pundir, I. Patel, and N. Arulkumar, "Blockchain for Securing Healthcare Data Using Squirrel

21613915, 2025, 3, Downloaded from https://onlinelibrary.wiley.com/doi/10.1002/ett.70087 by Delhi Technological University, Wiley Online Library on [09/03/2025]. See the Terms and Conditions (https://onlinelibrary.wiley.com/terms-and-conditions) on Wiley Online Library for rules of use; OA articles are governed by the applicable Creative Commons License

Search Optimization Algorithm," *Intelligent Automation & Soft Computing* 32, no. 3 (2022): 1815–1829.

69. P. Pawar, N. Parolia, S. Shinde, T. O. Edoh, and M. Singh, "eHealthChain–a Blockchain-Based Personal Health Information Management System," *Annals of Telecommunications* 77, no. 1 (2022): 33–45.

70. R. Mishra, D. Ramesh, D. R. Edla, and L. Qi, "DS-Chain: A Secure and Auditable Multi-Cloud Assisted EHR Storage Model on Efficient Deletable Blockchain," *Journal of Industrial Information Integration* 26 (2022): 100315.

71. J. S. Lee, C. J. Chew, J. Y. Liu, Y. C. Chen, and K. Y. Tsai, "Medical Blockchain: Data Sharing and Privacy Preserving of EHR Based on Smart Contract," *Journal of Information Security and Applications* 65 (2022): 103117.

72. Y. L. Lee, H. A. Lee, C. Y. Hsu, H. H. Kung, and H. W. Chiu, "SEMRES-A Triple Security Protected Blockchain Based Medical Record Exchange Structure," *Computer Methods and Programs in Biomedicine* 215 (2022): 106595.

73. A. Jain and D. S. Jat, "Implementation of Blockchain Enabled Healthcare System Using Hyperledger Fabric," in *Proceedings of the International Conference on Data Science, Machine Learning and Artificial Intelligence* (IEEE, 2021), 37–47.

74. I. Abunadi and R. L. Kumar, "BSF-EHR: Blockchain Security Framework for Electronic Health Records of Patients," *Sensors* 21, no. 8 (2021): 2865.

75. T. Fatokun, A. Nag, and S. Sharma, "Towards a Blockchain Assisted Patient Owned System for Electronic Health Records," *Electronics* 10, no. 5 (2021): 580.

76. A. P. Singh, N. R. Pradhan, A. K. Luhach, et al., "A Novel Patient-Centric Architectural Framework for Blockchain-Enabled Healthcare Applications," *IEEE Transactions on Industrial Informatics* 17, no. 8 (2020): 5779–5789.

77. A. Dubovitskaya, F. Baig, Z. Xu, et al., "ACTION-EHR: Patient-Centric Blockchain-Based Electronic Health Record Data Management for Cancer Care," *Journal of Medical Internet Research* 22, no. 8 (2020): e13598.

78. S. Tanwar, K. Parekh, and R. Evans, "Blockchain-Based Electronic Healthcare Record System for Healthcare 4.0 Applications," *Journal of Information Security and Applications* 50 (2020): 102407.

79. C. Stamatellis, P. Papadopoulos, N. Pitropakis, S. Katsikas, and W. J. Buchanan, "A Privacy-Preserving Healthcare Framework Using Hyperledger Fabric," *Sensors* 20, no. 22 (2020): 6587.

80. B. Shen, J. Guo, and Y. Yang, "MedChain: Efficient Healthcare Data Sharing via Blockchain," *Applied Sciences* 9, no. 6 (2019): 1207.

81. S. Amofa, E. B. Sifah, O. B. Kwame, et al., "A Blockchain-Based Architecture Framework for Secure Sharing of Personal Health Data," in *Proceedings of the 2018 IEEE 20th International Conference on e-Health Networking, Applications and Services (Healthcom)* (IEEE, 2018), 1–6.

82. S. Badr, I. Gomaa, and E. Abd-Elrahman, "Multi-Tier Blockchain Framework for IoT-EHRs Systems," *Procedia Computer Science* 141 (2018): 159–166.

83. K. N. Griggs, O. Ossipova, C. P. Kohlios, A. N. Baccarini, E. A. Howson, and T. Hayajneh, "Healthcare Blockchain System Using Smart Contracts for Secure Automated Remote Patient Monitoring," *Journal of Medical Systems* 42 (2018): 1–7.

84. P. Zhang, J. White, D. C. Schmidt, G. Lenz, and S. T. Rosenbloom, "FHIRChain: Applying Blockchain to Securely and Scalably Share Clinical Data," *Computational and Structural Biotechnology Journal* 16 (2018): 267–278.

85. T. T. Thwin and S. Vasupongayya, "Blockchain Based Secret-Data Sharing Model for Personal Health Record System," in *2018 5th International Conference on Advanced Informatics: Concept Theory and Applications (ICAICTA)* (IEEE, 2018), 196–201.

86. R. Guo, H. Shi, Q. Zhao, and D. Zheng, "Secure Attribute-Based Signature Scheme With Multiple Authorities for Blockchain in Electronic Health Records Systems," *IEEE Access* 6 (2018): 11676–11686.

87. A. Zhang and X. Lin, "Towards Secure and Privacy-Preserving Data Sharing in e-Health Systems via Consortium Blockchain," *Journal of Medical Systems* 42, no. 8 (2018): 140.

88. K. Fan, S. Wang, Y. Ren, H. Li, and Y. Yang, "Medblock: Efficient and Secure Medical Data Sharing via Blockchain," *Journal of Medical Systems* 42 (2018): 1–11.

89. H. Li, L. Zhu, M. Shen, F. Gao, X. Tao, and S. Liu, "Blockchain-Based Data Preservation System for Medical Data," *Journal of Medical Systems* 42 (2018): 1–13.

90. A. H. Mayer, C. A. da Costa, and R. D. Righi, "OmniPHR: A Distributed Architecture Model to Integrate Personal Health Records," *Journal of Biomedical Informatics* 71 (2017): 70–81.

91. A. Dubovitskaya, Z. Xu, S. Ryu, M. Schumacher, and F. Wang, "Secure and Trustable Electronic Medical Records Sharing Using Blockchain," in *AMIA Annual Symposium Proceedings. 2017* (American Medical Informatics Association, 2017), 650.

92. Y. Cao, S. Guan, D. Wang, and Z. Wang, "BE-AC: Reliable Blockchain-Based Anti-Counterfeiting Traceability Solution for Pharmaceutical Industry," *Cluster Computing* 27 (2024): 8119–8139.

93. A. K. Bapatla, S. P. Mohanty, and E. Kougianos, "PharmaChain 3.0: Efficient Tracking and Tracing of Drugs in Pharmaceutical Supply Chain Using Blockchain Integrated Product Serialization Mechanism," *SN Computer Science* 5, no. 1 (2024): 149.

94. X. Liu, R. Shah, A. Shandilya, M. Shah, and A. Pandya, "A Systematic Study on Integrating Blockchain in Healthcare for Electronic Health Record Management and Tacking Medical Supplies," *Journal of Cleaner Production* 447 (2024): 141371.

95. S. Abdallah and N. Nizamuddin, "Blockchain-Based Solution for Pharma Supply Chain Industry," *Computers & Industrial Engineering* 177 (2023): 108997.

96. R. Mishra, D. Ramesh, D. R. Edla, and L. Qi, "VaccineChain: A Checkpoint Assisted Scalable Blockchain Based Secure Vaccine Supply Chain With Selective Revocation," *Journal of Industrial Information Integration* 34 (2023): 100485.

97. A. K. Yadav and D. Kumar, "Blockchain Technology and Vaccine Supply Chain: Exploration and Analysis of the Adoption Barriers in the Indian Context," *International Journal of Production Economics* 255 (2023): 108716.

98. U. J. Munasinghe and M. N. Halgamuge, "Supply Chain Traceability and Counterfeit Detection of COVID-19 Vaccines Using Novel Blockchain-Based Vacledger System," *Expert Systems with Applications* 228 (2023): 120293.

99. H. Malik, T. Anees, M. Faheem, M. U. Chaudhry, A. Ali, and M. N. Asghar, "Blockchain and Internet of Things in Smart Cities and Drug Supply Management: Open Issues, Opportunities, and Future Directions," *Internet of Things* 23 (2023): 100860.

100. N. Zakari, M. Al-Razgan, A. Alsaadi, et al., "Blockchain Technology in the Pharmaceutical Industry: A Systematic Review," *PeerJ Computer Science* 8 (2022): e840.

101. D. Agrawal, S. Minocha, S. Namasudra, and A. H. Gandomi, "A Robust Drug Recall Supply Chain Management System Using Hyperledger Blockchain Ecosystem," *Computers in Biology and Medicine* 140 (2022): 105100.

102. S. K. Panda and S. C. Satapathy, "Drug Traceability and Transparency in Medical Supply Chain Using Blockchain for Easing the Process and Creating Trust Between Stakeholders and Consumers," *Personal and Ubiquitous Computing* 28 (2021): 75–91.

21613915, 2025, 3, Downloaded from https://onlinelibrary.wiley.com/doi/10.1002/ett.70087 by Delhi Technological University, Wiley Online Library on [09/03/2025]. See the Terms and Conditions (https://onlinelibrary.wiley.com/terms-and-conditions) on Wiley Online Library for rules of use; OA articles are governed by the applicable Creative Commons License

103. M. Uddin, K. Salah, R. Jayaraman, S. Pesic, and S. Ellahham, "Blockchain for Drug Traceability: Architectures and Open Challenges," *Health Informatics Journal* 27, no. 2 (2021): 14604582211011228.

104. W. Chien, d J. Jesus, B. Taylor, et al., "The Last Mile: DSCSA Solution Through Blockchain Technology: Drug Tracking, Tracing, and Verification at the Last Mile of the Pharmaceutical Supply Chain With BRUINchain," *Blockchain in Healthcare Today* 3 (2020): 30953.

105. F. Jamil, L. Hang, K. Kim, and D. Kim, "A Novel Medical Blockchain Model for Drug Supply Chain Integrity Management in a Smart Hospital," *Electronics* 8, no. 5 (2019): 505.

106. N. A. A. Abdu and Z. Wang, "Blockchain Framework for Collaborative Clinical Trials Auditing," *Wireless Personal Communications* 132, no. 1 (2023): 39–65.

107. F. Jamil, S. Ahmad, T. K. Whangbo, A. Muthanna, and D. H. Kim, "Improving Blockchain Performance in Clinical Trials Using Intelligent Optimal Transaction Traffic Control Mechanism in Smart Healthcare Applications," *Computers & Industrial Engineering* 170 (2022): 108327.

108. Y. Zhuang, L. Zhang, X. Gao, et al., "Re-Engineering a Clinical Trial Management System Using Blockchain Technology: System Design, Development, and Case Studies," *Journal of Medical Internet Research* 24, no. 6 (2022): e36774.

109. L. Hang, C. Chen, L. Zhang, and J. Yang, "Blockchain for Applications of Clinical Trials: Taxonomy, Challenges, and Future Directions," *IET Communications* 16, no. 20 (2022): 2371–2393.

110. I. A. Omar, R. Jayaraman, K. Salah, I. Yaqoob, and S. Ellahham, "Applications of Blockchain Technology in Clinical Trials: Review and Open Challenges," *Arabian Journal for Science and Engineering* 46, no. 4 (2021): 3001–3015.

111. D. Katiyar and S. Singhal, "Blockchain Technology in Management of Clinical Trials: A Review of Its Applications, Regulatory Concerns and Challenges," *Materials Today Proceedings* 47 (2021): 198–206.

112. T. Hirano, T. Motohashi, K. Okumura, et al., "Data Validation and Verification Using Blockchain in a Clinical Trial for Breast Cancer: Regulatory Sandbox," *Journal of Medical Internet Research* 22, no. 6 (2020): e18938.

113. J. Kongsen, D. Chantaradsuwan, P. Koad, M. Thu, and C. Jandaeng, "A Secure Blockchain-Enabled Remote Healthcare Monitoring System for Home Isolation," *Journal of Sensor and Actuator Networks* 13, no. 1 (2024): 13.

114. A. Rahman, M. A. H. Wadud, M. J. Islam, et al., "Internet of Medical Things and Blockchain-Enabled Patient-Centric Agent Through SDN for Remote Patient Monitoring in 5G Network," *Scientific Reports* 14, no. 1 (2024): 5297.

115. N. Badri, L. Nasraoui, and S. L. Azouz, "A Comprehensive Review of Blockchain Integration in Remote Patient Monitoring for E-Health," *International Journal of Network Management* 34, no. 2 (2024): e2254.

116. O. Cheikhrouhou, K. Mershad, F. Jamil, R. Mahmud, A. Koubaa, and S. R. Moosavi, "A Lightweight Blockchain and Fog-Enabled Secure Remote Patient Monitoring System," *Internet of Things* 22 (2023): 100691.

117. H. S. Z. Kazmi, F. Nazeer, S. Mubarak, S. Hameed, A. Basharat, and N. Javaid, "Trusted Remote Patient Monitoring Using Blockchain-Based Smart Contracts," in *Advances on Broad-Band Wireless Computing, Communication and Applications: Proceedings of the 14th International Conference on Broad-Band Wireless Computing, Communication and Applications (BWCCA-2019)*, vol. 14 (Springer, 2020), 765–776.

118. G. Srivastava, A. D. Dwivedi, and R. Singh, "*Automated Remote Patient Monitoring: Data Sharing and Privacy Using Blockchain. Arxiv Preprint ArXiv:1811.03417*," (2018).

119. Y. Chen, S. Ding, Z. Xu, H. Zheng, and S. Yang, "Blockchain-Based Medical Records Secure Storage and Medical Service Framework," *Journal of Medical Systems* 43 (2019): 1–9.

120. M. A. Saberi, M. Adda, and H. Mcheick, "Break-Glass Conceptual Model for Distributed EHR Management System Based on Blockchain, IPFS and ABAC," *Procedia Computer Science* 198 (2022): 185–192.

121. U. Chelladurai and S. Pandian, "A Novel Blockchain Based Electronic Health Record Automation System for Healthcare," *Journal of Ambient Intelligence and Humanized Computing* 13, no. 1 (2022): 693–703.

122. P. P. Ray, B. Chowhan, N. Kumar, and A. Almogren, "BIoTHR: Electronic Health Record Servicing Scheme in IoT-Blockchain Ecosystem," *IEEE Internet of Things Journal* 8, no. 13 (2021): 10857–10872.

123. A. Farouk, A. Alahmadi, S. Ghose, and A. Mashatan, "Blockchain Platform for Industrial Healthcare: Vision and Future Opportunities," *Computer Communications* 154 (2020): 223–235.

124. K. B. Adsul and S. Kosbatwar, "A Novel Approach for Traceability & Detection of Counterfeit Medicines Through Blockchain," *International Journal of Current Engineering and Technology* (2020).

125. M. Uddin, "Blockchain Medledger: Hyperledger Fabric Enabled Drug Traceability System for Counterfeit Drugs in Pharmaceutical Industry," *International Journal of Pharmaceutics* 597 (2021): 120235.

126. N. Saxena, I. Thomas, P. Gope, P. Burnap, and N. Kumar, "Pharmacrypt: Blockchain for Critical Pharmaceutical Industry to Counterfeit Drugs," *Computer* 53, no. 7 (2020): 29–44.

127. H. L. Pham, T. H. Tran, and Y. Nakashima, "A Secure Remote Healthcare System for Hospital Using Blockchain Smart Contract," in *Proceedings of the 2018 IEEE Globecom Workshops (GC Wkshps)* (IEEE, 2018), 1–6.

128. L. Zhou, L. Wang, and Y. Sun, "MIStore: A Blockchain-Based Medical Insurance Storage System," *Journal of Medical Systems* 42, no. 8 (2018): 149.

129. E. K. Kambilo, H. B. Zghal, C. G. Guegan, V. Stankovski, P. Kochovski, and D. Vodislav, "A Blockchain-Based Framework for Drug Traceability: Chaindrugtrac," in *Proceedings of the 37th ACM/SIGAPP Symposium on Applied Computing* (ACM, 2022), 1900–1907.

130. P. Pandey and R. Litoriya, "Securing e-Health Networks From Counterfeit Medicine Penetration Using Blockchain," *Wireless Personal Communications* 117 (2021): 7–25.

131. A. Musamih, K. Salah, R. Jayaraman, et al., "A Blockchain-Based Approach for Drug Traceability in Healthcare Supply Chain," *IEEE Access* 9 (2021): 9728–9743.

132. H. L. Pham, T. H. Tran, and Y. Nakashima, "Practical Anti-Counterfeit Medicine Management System Based on Blockchain Technology," in *Proceedings of the 2019 4TH Technology Innovation Management and Engineering Science International Conference (TIMES-ICON)* (IEEE, 2019), 1–5.

133. Y. Huang, J. Wu, and C. Long, "Drugledger: A Practical Blockchain System for Drug Traceability and Regulation," in *P2018 IEEE International Conference on Internet of Things (iThings) and IEEE Green Computing and Communications (GreenCom) and IEEE Cyber, Physical and Social Computing (CPSCom) and IEEE Smart Data (SmartData)* (IEEE, 2018), 1137–1144.

134. HIPAA, "*Healthcare Data Breach*," (2023), https://www.hipaajournal.com/12-million-medical-laboratory-records-exposed-online/.

135. W. Moulahi, I. Jdey, T. Moulahi, M. Alawida, and A. Alabdulatif, "A Blockchain-Based Federated Learning Mechanism for Privacy Preservation of Healthcare IoT Data," *Computers in Biology and Medicine* 167 (2023): 107630.

136. J. Li, D. Han, Z. Wu, J. Wang, K. C. Li, and A. Castiglione, "A Novel System for Medical Equipment Supply Chain Traceability Based on Alliance Chain and Attribute and Role Access Control," *Future Generation Computer Systems* 142 (2023): 195–211.

21613915, 2025, 3, Downloaded from https://onlinelibrary.wiley.com/doi/10.1002/ett.70087 by Delhi Technological University, Wiley Online Library on [09/03/2025]. See the Terms and Conditions (https://onlinelibrary.wiley.com/terms-and-conditions) on Wiley Online Library for rules of use; OA articles are governed by the applicable Creative Commons License

137. X. Wang, P. Jiang, T. Baker, T. Li, and L. Zhu, "Enabling Privacy and Leakage Resistance for Dynamic Blockchain-Based Access Control Systems," *Computer Standards & Interfaces* 84 (2023): 103690.

138. W. X. Yuan, B. Yan, W. Li, L. Y. Hao, and H. M. Yang, "Blockchain-Based Medical Health Record Access Control Scheme With Efficient Protection Mechanism and Patient Control," *Multimedia Tools and Applications* 82, no. 11 (2023): 16279–16300.

139. J. Li, D. Li, and X. Zhang, "A Secure Blockchain-Assisted Access Control Scheme for Smart Healthcare System in Fog Computing," *IEEE Internet of Things Journal* 10 (2023): 15980–15989.

140. T. Nhan, K. Upadhyay, and K. Poudel, "Towards Patient-Centric Healthcare: Leveraging Blockchain for Electronic Health Records," in *Proceedings of the 2024 Computers and People Research Conference* (ACM, 2024), 1–8.

141. P. Li, D. Zhou, H. Ma, and J. Lai, "Flexible and Secure Access Control for EHR Sharing Based on Blockchain," *Journal of Systems Architecture* 146 (2024): 103033.

142. X. Qu, Z. Yang, Z. Chen, and G. Sun, "A Consent-Aware Electronic Medical Records Sharing Method Based on Blockchain," *Computer Standards & Interfaces* 92 (2024): 103902.

143. J. Kaur, R. Rani, and N. Kalra, "Attribute-Based Access Control Scheme for Secure Storage and Sharing of EHRs Using Blockchain and IPFS," *Cluster Computing* 27, no. 1 (2024): 1047–1061.

144. G. Peng, A. Zhang, and X. Lin, "Patient-Centric Fine-Grained Access Control for Electronic Medical Record Sharing With Security via Dual-Blockchain," *IEEE Transactions on Network Science and Engineering* 10, no. 6 (2023): 3908–3921.

145. C. Gan, A. Saini, Q. Zhu, Y. Xiang, and Z. Zhang, "Blockchain-Based Access Control Scheme With Incentive Mechanism for eHealth Systems: Patient as Supervisor," *Multimedia Tools and Applications* 80 (2021): 30605–30621.

146. M. M. Madine, A. A. Battah, I. Yaqoob, et al., "Blockchain for Giving Patients Control Over Their Medical Records," *IEEE Access* 8 (2020): 193102–193115.

147. B. Houtan, A. S. Hafid, and D. Makrakis, "A Survey on Blockchain-Based Self-Sovereign Patient Identity in Healthcare," *IEEE Access* 8 (2020): 90478–90494.

148. Y. Zhuang, L. R. Sheets, Y. W. Chen, Z. Y. Shae, J. J. Tsai, and C. R. Shyu, "A Patient-Centric Health Information Exchange Framework Using Blockchain Technology," *IEEE Journal of Biomedical and Health Informatics* 24, no. 8 (2020): 2169–2176.

149. S. Jiang, H. Wu, and L. Wang, "Patients-Controlled Secure and Privacy-Preserving EHRs Sharing Scheme Based on Consortium Blockchain," in *2019 IEEE Global Communications Conference (GLOBECOM)* (IEEE, 2019), 1–6.

150. W. J. Gordon and C. Catalini, "Blockchain Technology for Healthcare: Facilitating the Transition to Patient-Driven Interoperability," *Computational and Structural Biotechnology Journal* 16 (2018): 224–230.

151. V. Merlo, G. Pio, F. Giusto, and M. Bilancia, "On the Exploitation of the Blockchain Technology in the Healthcare Sector: A Systematic Review," *Expert Systems with Applications* 213 (2023): 118897.

152. C. C. Agbo, Q. H. Mahmoud, and J. M. Eklund, "Blockchain Technology in Healthcare: A Systematic Review," in *Healthcare*, vol. 7 (MDPI, 2019), 56.

153. A. Hasselgren, P. K. Wan, M. Horn, K. Kralevska, D. Gligoroski, and A. Faxvaag, "*Gdpr Compliance for Blockchain Applications in Healthcare. Arxiv Preprint arXiv:2009.12913*," (2020).

154. M. Iqbal and R. Matulevičius, "Comparison of Blockchain-Based Solutions to Mitigate Data Tampering Security Risk," in *Business Process Management: Blockchain and Central and Eastern Europe Forum: BPM 2019 Blockchain and CEE Forum, Vienna, Austria, September 1–6, 2019*, vol. 17 (Springer, 2019), 13–28.

155. K. Azbeg, O. Ouchetto, and S. J. Andaloussi, "BlockMedCare: A Healthcare System Based on IoT, Blockchain and IPFS for Data Management Security," *Egyptian Informatics Journal* 23, no. 2 (2022): 329–343.

156. L. Chen, W. K. Lee, C. C. Chang, K. K. R. Choo, and N. Zhang, "Blockchain Based Searchable Encryption for Electronic Health Record Sharing," *Future Generation Computer Systems* 95 (2019): 420–429.

157. B. Zaabar, O. Cheikhrouhou, F. Jamil, M. Ammi, and M. Abid, "HealthBlock: A Secure Blockchain-Based Healthcare Data Management System," *Computer Networks* 200 (2021): 108500.

158. K. M. Hossein, M. E. Esmaeili, T. Dargahi, A. Khonsari, and M. Conti, "BCHealth: A Novel Blockchain-Based Privacy-Preserving Architecture for IoT Healthcare Applications," *Computer Communications* 180 (2021): 31–47.

159. H. Ghayvat, S. Pandya, P. Bhattacharya, et al., "CP-BDHCA: Blockchain-Based Confidentiality-Privacy Preserving Big Data Scheme for Healthcare Clouds and Applications," *IEEE Journal of Biomedical and Health Informatics* 26, no. 5 (2021): 1937–1948.

160. M. Bhavin, S. Tanwar, N. Sharma, S. Tyagi, and N. Kumar, "Blockchain and Quantum Blind Signature-Based Hybrid Scheme for Healthcare 5.0 Applications," *Journal of Information Security and Applications* 56 (2021): 102673.

161. S. M. Pournaghi, M. Bayat, and Y. Farjami, "MedSBA: A Novel and Secure Scheme to Share Medical Data Based on Blockchain Technology and Attribute-Based Encryption," *Journal of Ambient Intelligence and Humanized Computing* 11, no. 11 (2020): 4613–4641.

162. A. Mubarakali, "Healthcare Services Monitoring in Cloud Using Secure and Robust Healthcare-Based BLOCKCHAIN (SRHB) Approach," *Mobile Networks and Applications* 25, no. 4 (2020): 1330–1337.

163. P. Bhattacharya, S. Tanwar, U. Bodkhe, S. Tyagi, and N. Kumar, "Bindaas: Blockchain-Based Deep-Learning As-a-Service in Healthcare 4.0 Applications," *IEEE Transactions on Network Science and Engineering* 8, no. 2 (2019): 1242–1255.

164. R. W. Ahmad, K. Salah, R. Jayaraman, I. Yaqoob, S. Ellahham, and M. Omar, "The Role of Blockchain Technology in Telehealth and Telemedicine," *International Journal of Medical Informatics* 148 (2021): 104399.

165. T. Kumar, V. Ramani, I. Ahmad, A. Braeken, E. Harjula, and M. Ylianttila, "Blockchain Utilization in Healthcare: Key Requirements and Challenges," in *Proceedings of the 2018 IEEE 20th International Conference on e-Health Networking, Applications and Services (Healthcom)* (IEEE, 2018), 1–7.

166. R. Akkaoui, "Blockchain for the Management of Internet of Things Devices in the Medical Industry," *IEEE Transactions on Engineering Management* 70, no. 8 (2021): 2707–2718.

167. S. Ramzan, A. Aqdus, V. Ravi, D. Koundal, R. Amin, and M. A. Al Ghamdi, "Healthcare Applications Using Blockchain Technology: Motivations and Challenges," *IEEE Transactions on Engineering Management* 70, no. 8 (2022): 2874–2890.

168. S. Biswas, K. Sharif, F. Li, Z. Latif, S. S. Kanhere, and S. P. Mohanty, "Interoperability and Synchronization Management of Blockchain-Based Decentralized e-Health Systems," *IEEE Transactions on Engineering Management* 67, no. 4 (2020): 1363–1376.

169. G. Zhang, Z. Yang, and W. Liu, "Blockchain-Based Privacy Preserving e-Health System for Healthcare Data in Cloud," *Computer Networks* 203 (2022): 108586.

170. K. DeSalvo, *Connecting Health and Care for the Nation: A Shared Nationwide Interoperability Roadmap Draft Version 1.0* (Office of the National Coordinator for Health Information Technology, 2015).

21613915, 2025, 3, Downloaded from https://onlinelibrary.wiley.com/doi/10.1002/ett.70087 by Delhi Technological University, Wiley Online Library on [09/03/2025]. See the Terms and Conditions (https://onlinelibrary.wiley.com/terms-and-conditions) on Wiley Online Library for rules of use; OA articles are governed by the applicable Creative Commons License

171. R. Akkaoui, X. Hei, and W. Cheng, "EdgeMediChain: A Hybrid Edge Blockchain-Based Framework for Health Data Exchange," *IEEE Access* 8 (2020): 113467–113486.

172. X. Liu, A. V. Barenji, Z. Li, B. Montreuil, and G. Q. Huang, "Blockchain-Based Smart Tracking and Tracing Platform for Drug Supply Chain," *Computers & Industrial Engineering* 161 (2021): 107669.

173. L. Soltanisehat, R. Alizadeh, H. Hao, and K. K. R. Choo, "Technical, Temporal, and Spatial Research Challenges and Opportunities in Blockchain-Based Healthcare: A Systematic Literature Review," *IEEE Transactions on Engineering Management* 70, no. 1 (2020): 353–368.

174. G. Albanese, J. P. Calbimonte, M. Schumacher, and D. Calvaresi, "Dynamic Consent Management for Clinical Trials via Private Blockchain Technology," *Journal of Ambient Intelligence and Humanized Computing* 11, no. 11 (2020): 4909–4926.

175. Z. Wenhua, F. Qamar, T. A. N. Abdali, R. Hassan, S. T. A. Jafri, and Q. N. Nguyen, "Blockchain Technology: Security Issues, Healthcare Applications, Challenges and Future Trends," *Electronics* 12, no. 3 (2023): 546.

176. S. Chenthara, K. Ahmed, H. Wang, F. Whittaker, and Z. Chen, "Healthchain: A Novel Framework on Privacy Preservation of Electronic Health Records Using Blockchain Technology," *PLoS One* 15, no. 12 (2020): e0243043.

177. K. Miyachi and T. K. Mackey, "hOCBS: A Privacy-Preserving Blockchain Framework for Healthcare Data Leveraging an On-Chain and Off-Chain System Design," *Information Processing & Management* 58, no. 3 (2021): 102535.

178. J. B. Bernabe, J. L. Canovas, J. L. Hernandez-Ramos, R. T. Moreno, and A. Skarmeta, "Privacy-Preserving Solutions for Blockchain: Review and Challenges," *IEEE Access* 7 (2019): 164908–164940.

179. J. Jayabalan and N. Jeyanthi, "Scalable Blockchain Model Using Off-Chain IPFS Storage for Healthcare Data Security and Privacy," *Journal of Parallel and Distributed Computing* 164 (2022): 152–167.

180. E. R. D. Villarreal, J. García-Alonso, E. Moguel, and J. A. H. Alegría, "Blockchain for Healthcare Management Systems: A Survey on Interoperability and Security," *IEEE Access* 11 (2023): 5629–5652.

181. S. Rahmadika and K. H. Rhee, "Toward Privacy-Preserving Shared Storage in Untrusted Blockchain P2P Networks," *Wireless Communications and Mobile Computing* 2019, no. 1 (2019): 6219868.

182. N. Islam, Y. Faheem, I. U. Din, M. Talha, M. Guizani, and M. Khalil, "A Blockchain-Based Fog Computing Framework for Activity Recognition as an Application to e-Healthcare Services," *Future Generation Computer Systems* 100 (2019): 569–578.

21613915, 2025, 3, Downloaded from https://onlinelibrary.wiley.com/doi/10.1002/ett.70087 by Delhi Technological University, Wiley Online Library on [09/03/2025]. See the Terms and Conditions (https://onlinelibrary.wiley.com/terms-and-conditions) on Wiley Online Library for rules of use; OA articles are governed by the applicable Creative Commons License

2025 International Conference on Sustainable Energy Technologies and Computational Intelligence (SETCOM) | 979-8-3315-2054-0/25/$31.00 ©2025 IEEE | DOI: 10.1109/SETCOM64758.2025.10932584

Field Performance Assessment of a 1.34 kW Rooftop PV plant in Delhi : Insight from two Comparative Periods

Atul Avasthi
Electrical Engineering Department
Delhi Technological University
Delhi, India
atul_2k21phdee27@dtu.ac.in

Rachana Garg
Electrical Engineering Department
Delhi Technological University
Delhi, India
rachnagarg@dce.ac.in

Priya Mahajan
Electrical Engineering Department
Delhi Technological University
Delhi, India
priyamahajan@dtu.ac.in

***Abstract*—India's growing energy demands and focus on energy security highlight the potential of SPV plant. With abundant solar resources, the country is well-positioned to harness solar energy for sustainable development. This study evaluates the performance of a 1.34 kW SPV system at Delhi Technological University, analyzing data from February to August in 2023 and 2024. Key metrics include energy generation, performance ratio (PR), capacity factor (CF), and system efficiency.**

Results show higher energy generation, PR, and CF in 2023 due to better solar irradiation and lower temperatures, while 2024 performance declined under reduced solar irradiation and higher ambient temperatures. These findings underscore the impact of local environmental conditions on PV efficiency and highlight the need for continuous monitoring of rooftop systems in urban settings like Delhi. Insights from this study support policymakers in optimizing renewable energy integration and meeting solar capacity targets.

***Index Terms*—PV plant, PV modules, Performance ratio, Capacity factor, Plant efficiency, DTU**

I. Introduction

In the 21st century, India's foremost objective is energy security, a goal unattainable solely through conventional energy resources [1]. The scarcity of such resources and the environmental challenges pose underscore the imperative to transition towards renewable energy sources [2]. In the pursuit of the nation's energy security objectives, renewable energy is poised to assume a central role. Solar photovoltaic (PV) energy systems hold significant promise in meeting current energy demands while facilitating sustainable development [3]. Within the Indian context, solar PV conversion technology is favored over other renewable energy alternatives due to the abundance and intensity of solar radiation [4] [5]. India receives a daily solar irradiation ranging from 4–7kWh/m^2, with an annual irradiation of 1.2 to 2.3 MWh per square meter per year. The country experiences an average of 250–300 clear sunny days annually, with sunshine durations ranging from 2300 to 3200 hours per year [6] [7] [8]. Hence, SPV plants offer both individuals and industrialists the chance to produce electricity using solar energy. The Indian government has implemented numerous programs to foster the advancement of the solar sector, with the Jawaharlal Nehru National Solar Mission (JNNSM) being a significant milestone, launched in 2010 under the banner of 'Solar India', JNNSM aims to attain grid parity by the year 2023 [9]. The plan outlined the deployment of 20,000 MW of grid-connected and 2000 MW of off-grid solar power across three phases: the first phase until 2012–13, the second phase from 2013 to 2017, and the third phase from 2017 to 2022 [10]. The Government of India has targeted expanding India's renewable energy installed capacity to 500 GW by 2030 [11]. India has promised to source nearly half its energy from non-fossil fuel sources by 2030 [12].

In January 2024, the Delhi government unveiled the Delhi Solar Policy 2024, which introduces various financial incentives tailored for residential, commercial, and industrial solar consumers. The primary objective of this policy is to attain a solar capacity of 4.5 GW by March 2027. Delhi is landlocked city with limited space, roof solar PV plants are the preferred option due to lack of available land for ground mounted PV installations. In cities like Delhi roof top solar PV plants ranging from 1 kW to 3 kW are commonly installed due to space constraints and suitability of rooftop installations [13].To enhance the adoption of solar rooftop capacity and enable residential households to generate their own electricity, the Government of India approved the "PM Surya Ghar Yojana" on February 2024 [14].

It is imperative to meticulously evaluate all performance parameters of installed PV plants to inform technology selection, project development, and the viability assessment of new projects in specific locations. The primary challenge facing photovoltaic (PV) systems lies in efficiently capturing sunlight and converting it into electricity. When solar photovoltaic modules operate in real-world environments, their output characteristics deviate from standard test conditions. The output power of a solar photovoltaic (SPV) module is influenced by local climatic parameters such as temperature, wind, humidity, dust deposition, as well as geographical factors like latitude and longitude [15].

Numerous researchers have conducted studies on roof top

979-8-3315-2054-0/25/$31.00 © 2025 IEEE

Authorized licensed use limited to: DELHI TECHNICAL UNIV. Downloaded on April 03,2025 at 04:43:40 UTC from IEEE Xplore. Restrictions apply.

grid-connected solar photovoltaic (SPV) systems, ranging from kilowatt to megawatt scales, across various geographic locations to evaluate system feasibility and performance. The authors [16] carried out a simulation study of 5 kWp grid-connected solar photovoltaic power plant in Manipur was evaluated, comparing measured performance metrics with simulation results. The study found a performance ratio of 74.4% and a capacity utilization factor of 14.31%. Researchers [17] analyzed the performance of a 1.72 kWp photovoltaic (PV) system in Ireland and reported that, despite high average wind speeds, low insolation levels, and moderate ambient temperatures, the system achieved the highest yearly average PV module efficiency. [18] compared the actual and simulation performance of 3.2 kWp SPV plant at the Nelson Mandela Metropolitan University, South Africa. The results revealed that the measured annual performance ratio of 84.3% highlights the significant solar potential of the Eastern Cape region in Africa, demonstrating its suitability for solar power generation.

In a separate investigation carried out in Italy, particularly within the grounds of the University of Salento, scientists sought to explore how climatic factors influence the efficacy of a photovoltaic (PV) system installed within a specific geographical area. This PV system, totaling 960 kWp in capacity, was split into two subsections with differing tilt angles (ranging from 3 to 15 degrees) and nominal powers (353.3 kWp and 606.6 kWp). The study involved an analysis of various performance indicators, such as overall yield, standard yield, efficiency of the PV system, performance ratio (PR), and losses due to cell temperature [19] [20].

The authors [21] conducted a simulation study of a 50 MW SPV plant at Kurnool, South India. The system was monitored over one year from April 2018 to March 2019. During this time, the capacity utilization factor varied between 18.90% and 29.34%, resulting in an annual average of 24.65%. Similarly, the performance ratio ranged from 75% to 83%, with an annual average of 79.94%.

A study was carried out to evaluate how temperature fluctuations affect the performance of a 20 kWp grid-connected solar photovoltaic system throughout different seasons. The research revealed that during the summer season, as the module temperature surpassed 45°C, there was a decrease in module efficiency by 0.08% for every degree increase in temperature. In the monsoon season, as the module temperature rose to 35°C, the module efficiency decreased by 0.04% per degree rise in temperature. During the post-monsoon period, when the module temperature exceeded 38°C, the module efficiency declined by 0.06% per degree rise in temperature. However, in winters, despite the module temperature reaching 35°C, there was only a minimal reduction in efficiency, attributed to the cooling effect of the breeze and lower ambient temperatures [22] [23].

This paper aims to present the findings resulting from the field performance monitoring of a 1.34 kW rooftop photovoltaic (PV) system installed at the Electrical Engineering Department of Delhi Technological University. In this study, the data were analyzed for the periods from February 2023 to August 2023 and from February 2024 to August 2024 to assess the compatibility of PV systems for integration into buildings within Delhi. This study overviews the PV system setup and introduces various performance assessment factors based on the collected data, including yearly energy production, capacity factor, and performance ratio.

II. The Photovoltaic system

A 1.34 kW rooftop solar PV plant is installed at the Electrical Engineering Department, Delhi Technological University, Delhi. The system includes four ENVIRO PVM6-335 modules with a total area of 7.77 m² and an installed capacity of 1.34 kWp, typical for domestic setups. Each 335 Wp module, composed of mono-crystalline silicon cells, achieves an efficiency of 17.28% under standard test conditions. The modules are mounted at a fixed 30° tilt, facing south, on 1-meter-high frames, and interconnected in series-parallel configurations. A Hoymiles MI 1200 inverter, with 96.5% efficiency and 1200 W maximum AC output, integrates the generated power into the building's electrical system. Figure 1 provides a block diagram, and Table 1 details the PV module specifications.

TABLE I
PV Module/Array Specifications

Specification	
Type	Mono
Module efficiency	17.28%
Maximum power (Pmax)	335W
Maximum power voltage (Vpm)	37.9 V
Maximum power current (Ipm)	8.85 A
Open circuit voltage (Voc)	46.27 V
Short circuit current (Isc)	9.41 A
Operating range temperature	$-40\,°C$ to $+85\,°C$

TABLE II
PV Inverter Specifications

Specification	
Input	
DC power Maximum	1520 W
DC voltage Maximum	60 V
PV voltage at MPP	48 V
Output	
Nominal output voltage	230 V AC
AC power Maximum	1200 W
Max. Output current	6 A
Maximum efficiency	96.5%

The solar irradiation sensor utilized had an accuracy level of ±8% and a resolution of 1 W/m². For temperature measurements, the PV module employed a PT 100-M type sensor with an accuracy of ±0.5°C, while the ambient temperature was monitored using a JUMO PT 100 U type sensor with a similar accuracy of ±0.5°C. An anemometer, specifically a small wind transmitter, was used to measure wind speed with an accuracy of ±5%. Table 2 provides details on the hoyniles inverter specifications.

Authorized licensed use limited to: DELHI TECHNICAL UNIV. Downloaded on April 03,2025 at 04:43:40 UTC from IEEE Xplore. Restrictions apply.

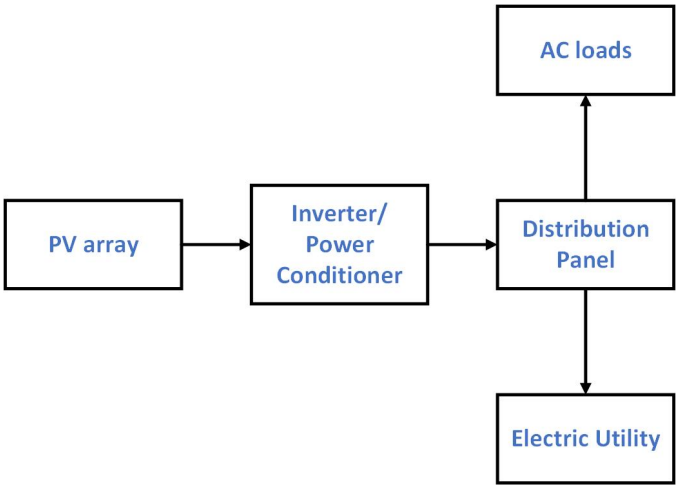

Fig. 1. Schematic representation of a grid-connected photovoltaic (PV) system

Evaluating the operational performance and reliability of a solar power plant requires a detailed examination of key operational metrics, including data acquisition and monitoring, performance ratio (PR), capacity factor (CF), and plant efficiency. These parameters are fundamental to assessing the system's efficiency and energy output, providing critical insights for optimizing the performance of photovoltaic installations. In this study, some of the aforementioned parameters were utilized to evaluate the performance of the 1.34 kW rooftop solar PV plant.

A. Data acquisition & Monitoring

The data acquisition system utilized a combination of components including a Hoymiles 1200 PV micro-inverter, Trackso, and S-miles. Trackso was employed to measure in-plane total solar radiation received by the PV modules. Furthermore, supplementary sensors for capturing ambient temperature, wind speed, and temperature of rear side of PV modules is integrated with Trackso. Both Trackso and the inverter were interconnected to the S-miles through a serial RS485 link and a Power Injector. Data recorded at 15-minute intervals within the S-miles was extracted via an SD card and subsequently imported directly into a computer for analysis.

B. Performance ratio

The performance ratio (PR) provides insight into the comprehensive impact of various losses affecting the normal power output of a PV array. These losses stem from factors such as incomplete utilization of incident solar irradiation, array temperature and inefficiencies or failures in system components. By evaluating the PR, one can gauge how closely a PV system achieves its ideal performance during real-world operation. Moreover, the PR facilitates comparisons between PV systems, irrespective of their location, tilt angle, orientation, or nominal rated power capacity. The performance ratio is mathematically defined by the following equations.

$$\text{PR} = \frac{E_{\text{AC}}}{\text{irradiation (kWh/m}^2) \times A \times \eta} \times 100 \qquad (1)$$

where E_{AC} is the total AC energy generated in kWh, A is the total area of the solar PV modules in m^2 and η is efficiency of PV module.

C. Capacity factor

The capacity factor (CF) is a metric utilized to quantify the energy output of an electric power generation system. A CF value of unity signifies that the system consistently delivers its full-rated power. It is calculated as the ratio of the actual annual energy output to the theoretical energy output if the PV system were to operate at full rated power ($P_{\text{PV, rated}}$) continuously for 24 hours a day throughout the year. The formula for calculating the capacity factor is given in Eq.2.

$$\text{CF} = \frac{Y_F}{24 \times 365} = \frac{E_{AC}}{\text{P}_{\text{PV rated}} \times 8760} = \frac{H_T \times \text{PR}}{\text{P}_{\text{PV rated}} \times 8760} \qquad (2)$$

where Y_F is final energy yield; H_{T} is the total solar irradiation or solar insolation over time (in kWh/m²).

D. Energy generation

The total daily (E_{AC_d}) and monthly (E_{AC_m}) energy generated by the PV system are obtained in Eq.3:

$$E_{AC_d} = \sum_{t=1}^{24} E_{AC} \quad \text{and} \quad E_{AC_m} = \sum_{d=1}^{N} E_{AC} \qquad (3)$$

where N is the number of days in the month.

The instantaneous energy output was determined through measurements of the energy generated by the PV system following the DC/AC inverter at 15-minute intervals.

E. Plant efficiency

Plant efficiency is the ratio of total energy output to the net input solar energy, which is called plant efficiency in Eq 4.

$$\eta_{\text{sys}} = \left(\frac{E_{\text{AC}}}{A \times H_{\text{T}}} \right) \times 100 \qquad (4)$$

E_{AC} is the AC energy output (in kWh). A is the total area of the solar modules (in m²). H_{T} is the total solar irradiation or solar insolation over time (in kWh/m²).

III. Results

Delhi Technological University (DTU) is located in North - West part of Delhi State. The solar irradiation and ambient temperature of the study location from February 2023 to August 2023 and February 2024 to August 2024 (211 days) are collected from the data acquisition system of the plant located in DTU.

A. Weather data

Figure 2 illustrates the comparison of solar irradiation and ambient temperature (in °C) from February to August for the years 2023 and 2024. Solar irradiation in 2023 is consistently higher across all months compared to 2024. In 2023, irradiation values increase from February, peak in May, and gradually decline towards August. This trend reflects the seasonal variation of solar insolation, with May typically

Authorized licensed use limited to: DELHI TECHNICAL UNIV. Downloaded on April 03,2025 at 04:43:40 UTC from IEEE Xplore. Restrictions apply.

receiving the highest irradiation due to longer daylight hours and clearer skies. Similarly, in 2024, solar irradiation follows the same seasonal pattern but remains lower throughout the observed period.

In 2023, the higher solar irradiation coincides with relatively lower ambient temperatures, creating favorable conditions for efficient photovoltaic (PV) operation. Conversely, in 2024, despite slightly reduced irradiation, the higher ambient temperatures likely further diminish PV efficiency, underscoring the importance of temperature management in PV system design.

Ambient temperatures in 2023 gradually rise from February, peak around May-June, and slightly decline by July-August, reflecting typical seasonal weather patterns. In contrast, 2024 experiences consistently higher ambient temperatures than 2023, particularly from April to June, with a more pronounced peak in May-June. This suggests the possibility of increased heatwaves or warmer weather conditions during this period. The elevated temperatures in 2024 may negatively impact solar PV performance, as high module temperatures are known to reduce efficiency.

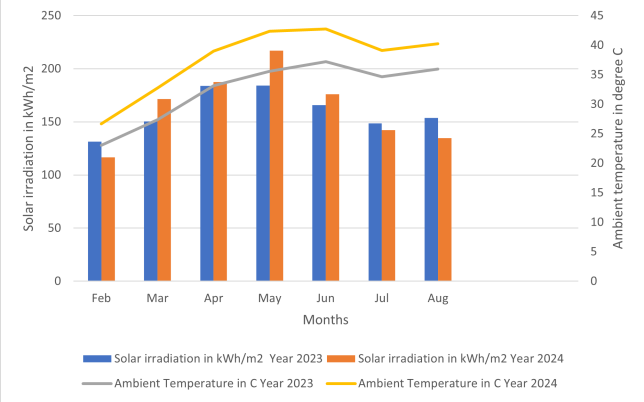

Fig. 2. Solar irradiation and ambient temperature data of experimental location

B. Energy generation

Figure 3 compares monthly energy generation (kWh) from a 1.34 kW system between 2023 and 2024. In 2024, energy production is more consistent, slightly surpassing 2023 from February to June but dipping in August. Notably, July 2024 shows a significant improvement (150 kWh) over 2023 (110 kWh), while April and August 2023 exhibit higher peaks (180–200 kWh). The trends suggest seasonal variability, with higher generation during longer daylight months. Overall, the 2024 performance indicates greater stability, though the 2023 system outperformed in peak months like April and August.

C. Perforance ratio

Figure 4 compares the monthly performance ratios (PR) for a 1.34 kW solar power plant between 2023 and 2024. Across the months from February to August, the data reveal notable variations in PR, reflecting differences in system efficiency or external conditions impacting energy output.

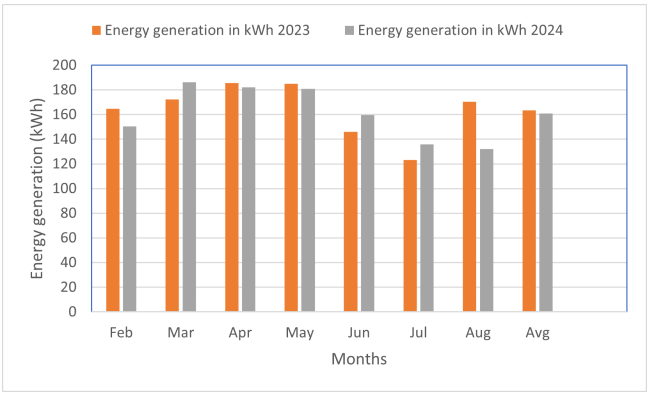

Fig. 3. Monthly energy generation by the 1.34 kW SPV plant

In February, both years exhibit high PRs, with 2023 slightly outperforming 2024. This trend continues in March, where the performance ratio in 2023 remains superior, though both years show a consistent decrease. April and May highlight a significant drop in 2024 compared to 2023, with May showing the largest performance gap. From June to August, the performance ratio in 2024 improves, closing the gap with 2023 but still generally remaining lower. However, August presents a slight exception, as both years perform similarly.

When averaging across all months, 2023 shows a higher overall PR than 2024, indicating better operational efficiency or favorable conditions for energy production during the earlier period. The fluctuation in PR across both years suggests that seasonal variations, maintenance practices, or external environmental factors might have influenced the solar plant's overall performance.

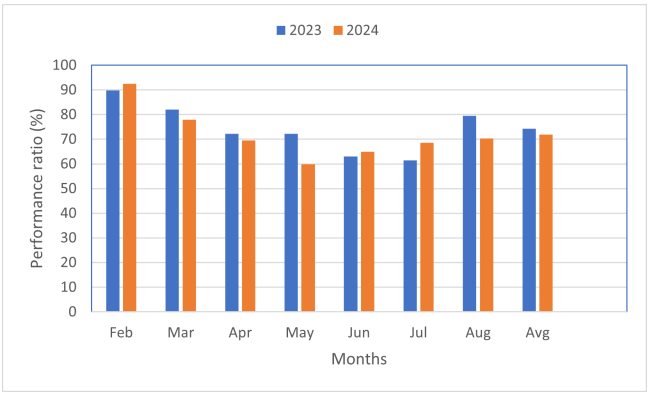

Fig. 4. Monthly performance ratio of 1.34 kW plant

D. Capacity factor

Figure 5 illustrates the capacity factor (CF) of a 1.34 kW solar power plant for the period from February to August, comparing data between 2023 and 2024. The capacity factor is generally higher in 2023 than in 2024, reflecting better system utilization or more favorable environmental conditions in the earlier year. February starts with similar CFs for both years, but from March onward, 2023 consistently outperforms

Authorized licensed use limited to: DELHI TECHNICAL UNIV. Downloaded on April 03,2025 at 04:43:40 UTC from IEEE Xplore. Restrictions apply.

TABLE III
MONTHLY COMPARISON OF SOLAR IRRADIATION, ENERGY GENERATION, CAPACITY FACTOR, PERFORMANCE RATIO, AND PLANT EFFICIENCY FOR A 1.34 KW ROOFTOP PV SYSTEM AT DTU (2023 AND 2024).

Month	Year	Solar irradiation (kWh/m^2)	Energy Generation (kWh)	Capacity Factor (%)	Performance Ratio (%)	Plant Efficiency (%)
February	2023	131.4	164.57	18.00	89.78	16.17
	2024	116.52	150.30	16.44	92.46	16.65
March	2023	150.42	172.25	17.02	82.08	14.78
	2024	171.50	186.31	18.41	77.87	14.02
April	2023	184.00	185.51	18.94	72.27	13.01
	2024	187.63	182.03	18.58	69.54	12.52
May	2023	184.07	182.83	18.06	72.20	12.82
	2024	216.90	180.94	17.88	59.79	10.77
June	2023	165.91	145.93	14.90	63.05	11.35
	2024	176.10	159.63	16.30	64.98	11.69
July	2023	143.69	123.25	12.18	61.49	11.07
	2024	142.10	135.79	13.42	68.50	12.34
August	2023	153.65	170.31	16.83	79.45	14.31
	2024	134.70	132.19	13.60	70.34	12.67

2024, with noticeable differences in May and June, where the 2023 values are particularly higher. In July and August, the trend remains, though the gap narrows in August, where the 2024 CF approaches that of 2023. On average, 2023 exhibits a higher overall capacity factor than 2024, suggesting reduced efficiency or lower solar insolation in the latter year. These trends may indicate seasonal effects or system-related factors that require further investigation for optimization of performance in 2024.

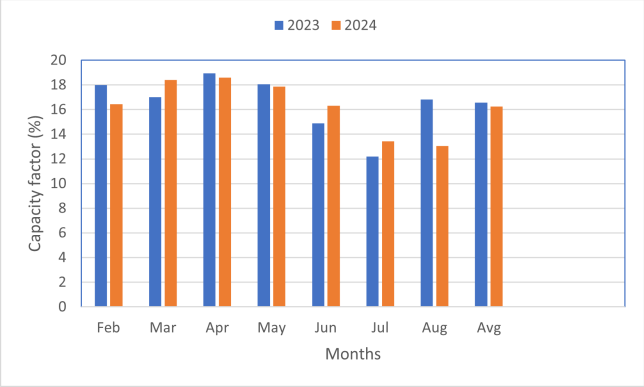

Fig. 5. Monthly capacity factor of 1.34 kW SPV plant

The major variation in the performance ratio and capacity factor of the plant mainly depends on the total energy generation of the PV plants. The performance ratio is directly correlative to the solar irradiation fall on the surface of the PV modules. On the other hand, Capacity factor of the plant depends on the running time of the plant.

E. Plant efficiency

The figure 6 compares plant efficiency (%) between 2023 and 2024 across the months from February to August and shows a slight overall decline in efficiency in 2024. While February exhibited similar high efficiency for both years, with values around 16%, there was a noticeable drop in efficiency in 2024, especially from April to June, where the plant's performance significantly lagged behind 2023. In contrast, March and July saw relatively smaller differences between the two years. The average plant efficiency across the months was higher in 2023, indicating an overall reduction in 2024's performance. This suggests that operational or external factors may have impacted the plant's efficiency more in 2024.

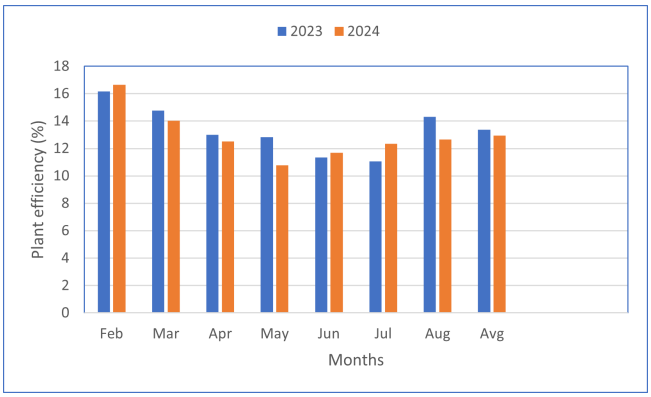

Fig. 6. Monthly plant efficiency of the 1.34 kW plant

Table III presents the comparative analysis of the different performance parameters SPV plant such as solar irradiation, energy generation, capacity factor, performance ratio, and the plant efficiency from February to August 2023 and 2024 of the 1.34 kW SPV plant. Year 2024 shows higher solar irradiation values than Year 2023 (e.g., March, April, May, June). February and August have lower irradiation in 2024 compared to 2023. Variation in solar irradiation is affected by weather patterns and cloud cover differences between years.

Energy generation correlates well with solar irradiation. Higher irradiation months (e.g., March 2024, June 2024)

Authorized licensed use limited to: DELHI TECHNICAL UNIV. Downloaded on April 03,2025 at 04:43:40 UTC from IEEE Xplore. Restrictions apply.

produce more energy than their 2023 counterparts. Despite higher irradiation, energy generation in April and May 2024 is slightly lower than in 2023 due to potential operational inefficiencies or higher clipping losses.

The capacity factor generally mirrors energy generation trends. Higher CF values are noted in 2024 for months like March, June, and July. February 2024 has a lower CF despite better PR and efficiency, reflecting reduced energy generation due to lower irradiation.

PR values in 2024 are generally lower than in 2023 for most months, except February and June, which show improvements. The drop in PR for months like March and April 2024 suggests efficiency losses due to higher temperatures and soiling.

Plant efficiency is consistently lower in 2024 for most months (notable in May, April, and March), except for February and June. Higher ambient temperatures in 2024 could have led to heat-related efficiency losses.

IV. Conclusion

This study provides a comprehensive analysis of the performance of a 1.34 kW rooftop solar photovoltaic (SPV) system installed at Delhi Technological University, with a particular focus on its energy generation, performance ratio (PR), capacity factor (CF), and plant efficiency over two distinct periods: February to August 2023 and February to August 2024. The data reveal key insights into how environmental conditions and operational factors influence the efficiency of solar PV systems within the urban context of Delhi, a city characterized by limited space for ground-mounted installations.

The findings suggest that monthly energy generation (in kWh) of a 1.34 kW system for 2023 and 2024, highlighting seasonal variations likely influenced by climatic conditions. In 2023, energy generation is notably higher in February, April, and June, while 2024 exhibits improved performance in July. Both years demonstrate a consistent trend of increased energy generation during the months from March to August. On average, the energy output in 2023 marginally exceeds that of 2024, possibly due to variations in environmental factors such as ambient temperature.

The study underscores the importance of environmental factors such as temperature, and solar irradiation in determining the performance of PV systems. The comparison between the two years provides valuable data that can guide future efforts to enhance the performance of rooftop PV systems in urban environments, offering critical insights for both policy formulation and technology deployment.

References

[1] H. G. Brauch, "Environment and security in the middle east: conceptualizing environmental, human, water, food, health and gender security," *Integrated water resources management and security in the Middle East*, pp. 121–161, 2007.

[2] X. Cheng, C. Yan, K. Ye, and K. Chen, "Enhancing resource efficiency through the utilization of the green bond market: An empirical analysis of asian economies," *Resources Policy*, vol. 89, p. 104623, 2024.

[3] N. S. M. N. Izam, Z. Itam, W. L. Sing, and A. Syamsir, "Sustainable development perspectives of solar energy technologies with focus on solar photovoltaic—a review," *Energies*, vol. 15, no. 8, p. 2790, 2022.

[4] S. Manju and N. Sagar, "Progressing towards the development of sustainable energy: A critical review on the current status, applications, developmental barriers and prospects of solar photovoltaic systems in india," *Renewable and Sustainable Energy Reviews*, vol. 70, pp. 298–313, 2017.

[5] A. Avasthi, R. Garg, and P. Mahajan, "Comparative analysis of bifacial and monofacial floating solar power plants: Performance evaluation and economic analysis," *Iranian Journal of Science and Technology, Transactions of Mechanical Engineering*, pp. 1–19, 2024.

[6] A. Sharma, P. Mahajan, and R. Garg, "Analysing the impact of various incentives on solar tariff in india," *International Journal of Sustainable Energy*, vol. 41, no. 2, pp. 126–147, 2022.

[7] S. Sambhi, H. Sharma, V. Bhadoria, P. Kumar, R. Chaurasia, G. Fotis, and V. Vita, "Technical and economic analysis of solar pv/diesel generator smart hybrid power plant using different battery storage technologies for srm ist, delhi-ncr campus," *Sustainability*, vol. 15, no. 4, p. 3666, 2023.

[8] A. Avasthi, R. Garg, and P. Mahajan, "Optimizing energy harvesting: a comprehensive analysis of tracking technologies in a 2 mwp floating solar photovoltaic system," *Electrical Engineering*, pp. 1–19, 2024.

[9] S. K. Kar, A. Sharma, and B. Roy, "Solar energy market developments in india," *Renewable and sustainable energy reviews*, vol. 62, pp. 121–133, 2016.

[10] A. Kumar, N. Patel, N. Gupta, and V. Gupta, "Photovoltaic power generation in indian prospective considering off-grid and grid-connected systems," *International Journal of Renewable Energy Research (IJRER)*, vol. 8, no. 4, pp. 1936–1950, 2018.

[11] A. K. Mathur and S. Singh, "Status of india's renewable energy commitments for the paris agreement," in *2019 International Conference on Power Generation Systems and Renewable Energy Technologies (PGSRET)*, pp. 1–5, IEEE, 2019.

[12] S. Thambi, A. Bhatacharya, and O. Fricko, "India's energy and emissions outlook: results from india energy model," 2018.

[13] O. Solar, "Solar in delhi: Potential, solar policy, and solar subsidy," 2024.

[14] G. of India, "Pm surya ghar muft bijli yojana," 2024. Accessed: 2024-11-23.

[15] P. Borah, L. Micheli, and N. Sarmah, "Analysis of soiling loss in photovoltaic modules: A review of the impact of atmospheric parameters, soil properties, and mitigation approaches," *Sustainability*, vol. 15, no. 24, p. 16669, 2023.

[16] T. S. D. Singh, B. A. Shimray, A. B. Singh, and S. N. Meitei, "Performance measurement of 5 kwp rooftop grid-connected spv system in moderate climatic region of imphal, manipur, india. energy sustain develop 73, 292–302," 2023.

[17] L. Ayompe, A. Duffy, S. McCormack, and M. Conlon, "Measured performance of a 1.72 kw rooftop grid connected photovoltaic system in ireland," *Energy conversion and management*, vol. 52, no. 2, pp. 816–825, 2011.

[18] D. Okello, E. Van Dyk, and F. Vorster, "Analysis of measured and simulated performance data of a 3.2 kwp grid-connected pv system in port elizabeth, south africa," *Energy conversion and management*, vol. 100, pp. 10–15, 2015.

[19] M. Malvoni, A. Leggieri, G. Maggiotto, P. Congedo, and M. De Giorgi, "Long term performance, losses and efficiency analysis of a 960 kwp photovoltaic system in the mediterranean climate," *Energy conversion and management*, vol. 145, pp. 169–181, 2017.

[20] H. O. Prasad, S. K. Mahanta, and S. Bojjagani, "Evaluation of particle pollution influence on loss of solar power generation between commercial and background areas in lucknow, india," *Environment, Development and Sustainability*, pp. 1–10, 2023.

[21] V. Boddapati and S. A. Daniel, "Performance analysis and investigations of grid-connected solar power park in kurnool, south india," *Energy for sustainable development*, vol. 55, pp. 161–169, 2020.

[22] M. S. Vasisht, J. Srinivasan, and S. K. Ramasesha, "Performance of solar photovoltaic installations: Effect of seasonal variations," *Solar Energy*, vol. 131, pp. 39–46, 2016.

[23] G. Anbazhagan, D. Navamani, L. Anbazhagan, S. Muthusamy, S. Pandiyan, H. Panchal, M. Ramachandran, S. C. M. Sundararajan, and K. K. Sadasivuni, "Performance investigation of 140 kw grid connected solar pv system installed in southern region of india–a detailed case study and analysis," *Energy Sources, Part A: Recovery, Utilization, and Environmental Effects*, vol. 45, no. 4, pp. 10472–10486, 2023.

Authorized licensed use limited to: DELHI TECHNICAL UNIV. Downloaded on April 03,2025 at 04:43:40 UTC from IEEE Xplore. Restrictions apply.

Int J Syst Assur Eng Manag
https://doi.org/10.1007/s13198-025-02738-z

ORIGINAL ARTICLE

Harnessing Tc-Ls-Ga-At: a novel deep learning based hybrid approach for wind power forecasting

Kartik Bansal[1] · **Kartik Bisht**[1] · **Priya Singh**[1]

Received: 13 April 2024 / Accepted: 1 March 2025
© The Author(s) under exclusive licence to The Society for Reliability Engineering, Quality and Operations Management (SREQOM), India and The Division of Operation and Maintenance, Lulea University of Technology, Sweden 2025

Abstract In recent years, the demand for renewable energy, particularly wind power, has surged as a sustainable solution to address energy needs while minimizing environmental impact. Accurate wind power forecasting is essential for grid operators, energy traders, and stakeholders to manage output fluctuations, optimize energy generation, and maintain grid stability. The use of Artificial Intelligence and Machine Learning has transformed wind power prediction by facilitating more in-depth analysis of complex data sets. Deep learning models, in particular, have shown remarkable capability in capturing intricate wind patterns, ushering in a new era in wind power forecasting. However, challenges persist due to wind's inherent variability, complex terrain influences, and reliance on meteorological models, which may introduce errors. In this study, we have proposed a novel hybrid approach incorporating TCN (Temporal Convolutional Neural Networks), Attention, LSTM (Long Short Term Memory), Gating and Dense layer mechanisms to improve wind power output prediction. Furthermore, Adam optimizer is used to boost the model performance. Our novel hybrid model, after a comprehensive comparative analysis with traditional deep learning methods, demonstrates superiority in wind power forecasting, affirming its effectiveness. This innovative approach not only advances current wind power forecasting but also lays a foundation for future research in the field.

✉ Priya Singh
priya.singh.academia@gmail.com

Kartik Bansal
kartikbn21000@gmail.com

Kartik Bisht
bishtkartik386@gmail.com

[1] Delhi Technological University, Delhi, India

Keywords Wind power · Deep learning · Time series forecasting · Hybrid approach · LSTM · Attention · Gating mechanism

1 Introduction

Wind power generation plays a pivotal role in meeting the increasing global demand for renewable energy. As a clean and abundant resource, wind energy offers significant potential for reducing carbon emissions and mitigating the effects of climate change (Gong et al. 2023). The harnessing of WP (Wind Power) relies on accurate forecasting to optimize energy production, ensure grid stability, and support effective integration into existing energy systems. Consequently, the development of robust forecasting methodologies is essential for maximizing the efficiency and reliability of wind power generation.The fundamental principle behind WPF (Wind Power Forecasting) lies in predicting the future output of wind turbines based on various meteorological parameters such as wind speed, direction, temperature, and atmospheric pressure (Ramirez-Rosado et al. 2009).

Over the years, numerous techniques and methodologies have been developed for WPF, ranging from conventional statistical models to advanced machine learning algorithms. Traditional methods, such as persistence models and numerical weather prediction models, rely on historical data and physical principles for estimating future WP output. In recent years, there has been a growing emphasis on utilizing data-driven approaches, particularly deep learning techniques (Malhotra and Singh 2023), for wind power forecasting. Promising results have been observed with deep learning models like LSTM networks and CNN (Convolutional Neural Networks) in effectively capturing temporal dependencies and spatial patterns within wind data.

Published online: 26 March 2025

Despite significant advancements in wind power forecasting techniques, challenges remain, including uncertainty in weather predictions, inaccurate sensor readings, data scarcity in certain regions, and the need for real-time adaptation to dynamic environmental conditions. Addressing these challenges requires developing more robust, adaptive, and scalable forecasting methodologies capable of meeting the evolving needs of the renewable energy sector.

The purpose of this research is to advance wind power forecasting by introducing a novel hybrid deep learning approach designed to predict wind power output 24 h into the future with greater accuracy. This approach integrates multiple deep learning techniques to leverage their combined strengths for improved forecasting performance. The effectiveness of the proposed model is assessed through comprehensive evaluation metrics, including MSE,MAE and RMSE by comparing its performance against traditional deep learning techniques using a benchmark dataset. The goal is to demonstrate significant improvements over existing methods and provide a robust solution for more reliable wind power forecasting.

In the present work we have

- Proposed a novel hybrid approach for effective Wind Power Forecasting 24 h into the future
- Evaluated the performance of the model using the metrics MSE (Mean Squared Error), MAE (Mean Absolute Error), RMSE (Root Mean Squared Error), Improvement over the baseline using a benchmark dataset
- Compared the performance of the novel approach with the traditional deep learning techniques

The proposed hybrid model combining TCN, LSTM, Attention mechanisms, Gating, and Dense layers have been widely applied in various time-series forecasting tasks, including wind power prediction. However, our work introduces a novel integration and configuration of these techniques, specifically tailored to address the unique challenges of wind power forecasting, including high variability, complex terrain influences, and meteorological model inaccuracies. Uniqueness of the Proposed Approach is clearly evident from how the hybrid model leverages a carefully designed synergy between TCN, LSTM, and Attention, enhanced with custom gating mechanisms.

The proposed hybrid model represents a novel integration of state-of-the-art deep learning techniques tailored specifically for wind power forecasting. This model uniquely combines Temporal Convolutional Networks (TCN), Long Short-Term Memory (LSTM) networks, an Attention Mechanism, and Gating mechanisms. The TCN effectively captures short-term temporal dependencies, which are critical for modeling the rapid fluctuations in wind speeds. LSTM complements this by capturing long-term dependencies, thereby addressing seasonal and diurnal variations in wind patterns. The Attention Mechanism dynamically highlights significant time steps, ensuring that the model focuses on the most impactful features of the data. Lastly, the Gating mechanism enhances the selective flow of information through the network, improving the overall efficiency and interpretability of the model. This unique combination not only mitigates limitations seen in traditional models but also establishes a robust framework for addressing the non-linearity and variability inherent in wind power data.

Rest of the paper is organized as follows: Sect. 2 discusses related work, Sect. 3 details the proposed hybrid approach, Sect. 4 presents experimental results, and Sect. 5 concludes and suggests future research directions (Basu and Campbell 2020).

2 Related work

Wind power forecasting is crucial for renewable energy management, with various methodologies and techniques developed to address its challenges. This section reviews recent literature on WPF approaches.

Deep learning methodologies have become increasingly prominent in the field of WPF. Zhang et al. proposed a Multi-layer Stacked Bidirectional LSTM (MBLSTM) with Temporal Pattern Attention mechanism for ultra-short-term forecasting (Zhang et al. 2023). As per the study conducted by Aslam et al. they introduced a dual-attention based encoder-decoder model utilizing LSTM networks, optimized through Bayesian techniques (Aslam et al. 2022). Ensemble-based approaches have shown promise in improving forecasting accuracy. Rosa de Jesús et al. developed a deep learning ensemble combining individual and hybrid models (Rosa de et al. 2020), while Gong et al. introduced a hybrid model based on a temporal convolutional network and an Informer (Gong et al. 2023). Attention mechanisms have been incorporated to enhance forecasting models. Xiong et al. proposed the AMC-LSTM model, utilizing attention mechanisms and deep learning for wind power prediction (Xiong et al. 2022).

Hybrid neural network architectures have also been explored. Tefera et al. introduced a CNN-LSTM hybrid model, outperforming benchmark models after hyperparameter tuning (Tefera et al. 2023). CNN-LSTM hybrid architecture has also been explored by San et al. in their research (San et al. 2023). Alternative approaches, such as spatio-temporal modeling and signal decomposition, have been investigated. Del Campo et al.proposed deep learning approaches for wind power forecasting, treating it as a spatio-temporal prediction problem (del Campo et al. 2023). Mujeeb et al. utilized Wavelet Packet Transform (WPT) for signal decomposition and incorporated multiple exogenous

inputs for enhanced forecasting accuracy (Mujeeb et al. 2019). A hybrid LSTM-LightGBM model has been proposed by Faruque et al. for WPF in Australia (Faruque et al. 2023).

Song et al. proposed a novel approach using TCN-LSTM and transfer learning for wind power prediction in extreme wind scenarios. By pre-training a TCN-LSTM model and fine-tuning with Sparrow Search Algorithm, they achieved improved adaptation to extreme conditions (Song et al. 2022). Hossain et al. developed a hybrid deep learning model combining GRU, LSTM, and fully connected neural networks for ultra-short-term wind power forecasting (Hossain et al. 2020). This model demonstrated effective utilization of diverse architectures to forecast wind power generation accurately (Hossain et al. 2020). Zhu et al. introduced a novel approach to short-term wind power forecasting by combining complete ensemble empirical mode decomposition with adaptive noise CEEMDAN, support vector regression, and temporal convolutional network for feature extraction, prediction, and residual refinement, respectively (Zhu et al. 2022).

The review highlights the diverse methodologies available for wind power forecasting, each offering unique advantages. This study aims to contribute novel insights, pushing the boundaries of current understanding in the field. A comparison of recent works has been done in Table 1.

3 Proposed work

The proposed model architecture is designed to address the intricate temporal dynamics of wind power data, leveraging a novel hybrid approach that integrates temporal convolutional, gating, LSTM, attention, and dense neural network components along with Adam optimizer to boost the performance of the model. The flow of the model architecture starts from the input data obtained after feature engineering, progressing through distinct layers tailored to capture different aspects of the data.

3.1 Dataset description

The SDWPF (Spatial Dynamic Wind Power Forecasting) (Zhou et al. 2024) dataset has been used for the purpose of this research. The dataset is an open source dataset and is provided by the Longyuan Power Group which is recognized as the leading wind power producer in China and Asia (Zhou et al. 2022). It contains data of 134 wind turbines from a wind farm in China over half a year (Zhou et al. 2022) and consists of more than 4,000,000 data entries across 13 distinct features which makes it a very comprehensive and rich resource for analysis. Its reputation as a standard benchmark in wind power forecasting underscores its reliability and utility. The dataset's notable strengths, including its expansive scope, diverse content, and precise measurements, make it an ideal candidate for accurate wind power forecasting models.

3.2 Assumptions

We have proposed our hybrid model taking into account the following assumptions -

Relevance of weather features: It's assumed that weather features such as wind speed, direction, temperature, humidity, etc., significantly impact wind power generation. Therefore, including these features as inputs to the model is essential for accurate forecasting

Model generalization: The model assumes that patterns learned from historical data will generalize well to unseen future data. This assumption implies that the relationships between weather features and wind power generation remain relatively consistent over time.

Stationarity of data: There's an assumption of stationarity in the data, implying that the statistical properties of the data, such as mean and variance, remain relatively constant over time. However, this assumption might be relaxed using techniques like data differencing or adaptive learning.

Homogeneity of data: It's assumed that the dataset used is homogeneous, meaning that the data is representative of the target population and does not contain significant biases or inconsistencies.

3.3 Feature engineering

Prior to model construction, Feature Engineering is essential. This process refines existing features, combines them, and addresses any inherent issues.

Delete redundant features: Upon dataset analysis, redundant features labeled Pab (pitch angle blade) were identified due to perfect correlation. To streamline the dataset, only one of these features was retained.

Transform angle features: Angle features Wdir, Ndir, and Pab were initially encoded in degrees, posing a challenge for model interpretation due to numerical discontinuity. To mitigate this, these features were transformed into their sine/cosine representations, preserving directional information.

Create time features: The features Etmp and Itmp displayed highly negative values, potentially indicating errors. Linear interpolation was employed to correct these values.

3.4 Architecture of proposed hybrid model

Input data: Step 1-2

The refined wind power data obtained after feature engineering is the initial input to our hybrid model. This data encapsulates important features, characteristics and temporal

Table 1 Comparison of recent works

Paper Reference	Overview	Method Used	Results
Ahmadi et al. (2022)	- Wind power forecasting is important for balancing supply and demand. - Federated learning-based method achieves accurate and private wind power forecasting.	Comparison between private distributed, non-private centralized, and fully private localized models	- Federated learning-based wind power forecasting achieves 87.96% accuracy. - The proposed model has 83.63% accuracy and higher generalizability.
Hanifi et al. (2022)	- ML models improve wind power forecasting accuracy. - Novel optimisation algorithm enhances LSTM model performance.	Grid search-tuned Auto-Regressive Integrated Moving Average (ARIMA) model	- The proposed optimisation algorithm improves power prediction accuracy and accelerates the optimisation process. - The algorithm results in improvements of the RMSE of 7.89%, 5.9%, and 2.65% compared to other models.
Huang et al. (2023)	- Proposed deep learning model-transformer for wind power forecasting. - Transformer showed higher accuracy and efficiency compared to LSTM.	Comparison with other deep learning models such as LSTM	- The transformer-based wind power forecasting model showed higher accuracy and efficiency compared to other deep learning models such as LSTM. - The transformer model also demonstrated good migration performance.
Lv et al. (2023)	- Hybrid model for wind speed forecasting outperforms benchmarks. - Combines VMD, GRU, and GSRCV for accurate predictions.	Variational mode decomposition (VMD) for wind speed data processing, Gated recurrent unit (GRU) for wind speed forecasting, Grid search with rolling cross-validation (GSRCV) for parameter optimization	- RMSE: 0.2047, MAE: 0.1435, MAPE: 3.77%, SMAPE: 3.74%.
Bommidi et al. (2023)	- Hybrid model for wind speed interval prediction using ICEEMDAN, ATCN, Bi-LSTM. - Outperformed comparison models by 36%, 47%, and 17%.	Wavelet decomposition, Improved Grey Wolf Optimizer, Sequence-to-sequence model with Long Short-Term Memory (LSTM)	- Proposed approach outperformed comparison models with 36%, 47%, 17% improvements. - Tested with 5-min, 10-min, and 30-min ahead wind speed interval prediction.
Chang et al. (2024)	- Mean squared error (MSE) reduced by 65.0%. - Mean absolute error (MAE) reduced by 43.8%.	- Proposed hybrid model for long-term wind power forecasting using NWP data. - Model reduces MSE and MAE by 65.0% and 43.8% compared to current state-of-the-art model.	NWP subsequence correction for wind speed, Multi-scale deep learning regression for power data mapping
Liu et al. (2022)	- LGB-GPR model improves point forecast accuracy by up to 20.0%. - LGB-GPR model improves probabilistic forecast reliability by up to 21.5%.	- Proposed hybrid model combines LGB and GPR for wind speed prediction. - Experimental results show improved accuracy and reliability compared to single GPR model.	Light Gradient Boosting Machine (LGB), Gaussian Process Regression (GPR)
Ye et al. (2020)	- WD-IGFCM-LSTMS model outperforms traditional forecasting. - Achieves continuous sequence forecasting with improved accuracy.	- Novel approach combines WD, IGFCM, and LSTMS for wind power forecasting. - Outperforms traditional models, enables continuous sequence forecasting in simulations.	Wave Division, Improved Grey Wolf Optimizer, Sequence-to-Sequence model with Long Short-Term Memory (LSTM)

patterns of wind power data, enabling the neural network to learn and extract meaningful insights for accurate forecasting (Fig. 1).

TCN with GLU: Step 3-6

The input data is first passed through a Convolutional Layer with GLU (Gated Linear Unit) activation which is a key component of Temporal Convolutional Network architecture. It has the capability to effectively capture the complex temporal dependencies in the input time series data. Through the GLU activation, the model is able to learn local patterns and relationships which are of great significance in modeling the dynamic nature of wind power generation.

Attention layer: Step 7-8

The output from the TCN with GLU layer is passed through an Attention Layer. This component dynamically assesses the relevance of each time step within the sequence, allowing the model to focus on important temporal dependencies for wind power forecasting. By highlighting significant time steps, the attention mechanism enhances the model's capability to capture intricate long-term dependencies, thereby improving overall forecasting performance.

LSTM layer: Step 9-10

The output from the Attention Layer is forwarded to the next layer, which is LSTM. LSTM layer has the ability to capture both short and long term dependencies effectively, from the input sequential data. They learn from the sequential nature of wind power data, adapting to changing patterns and trends and retaining memory over extended time intervals. Leveraging the power of LSTM enhances the capability of the model to comprehensively understand the complex relationships prevalent in wind power dynamics giving more accurate forecasts.

Dense layers with dropout and batch normalization: Step 11-17

After the LSTM layer, the model architecture incorporates Dense layers with an added functionality of Dropout along with Batch Normalization. This helps in extracting high level features from the data while reducing the chances of overfitting. Dropout functions by randomly deactivating a fraction of neurons from the network during training to prevent dependency on specific features, while Batch Normalization accelerates and stabilizes the training process by normalization of inputs to each layer. Thus, these techniques improve the model generalization and robustness.

Output: Step 18-22

Finally, Global Average Pooling is applied to transform the extracted features into lower dimension and also retain the useful information. Thus, the final wind power forecasts output are generated after utilizing the condensed features. The power forecasts provide valuable insights that support decision making in grid operation, renewable energy management, and resource allocation.

Following the model architecture definition, we incorporate and harness the power of *Adam optimizer*, a popular choice for training neural networks. Adam optimizer efficiently adjusts the parameters of the model while training in order to minimize the prediction error and improve forecasting accuracy (Kingma and Ba 2017).

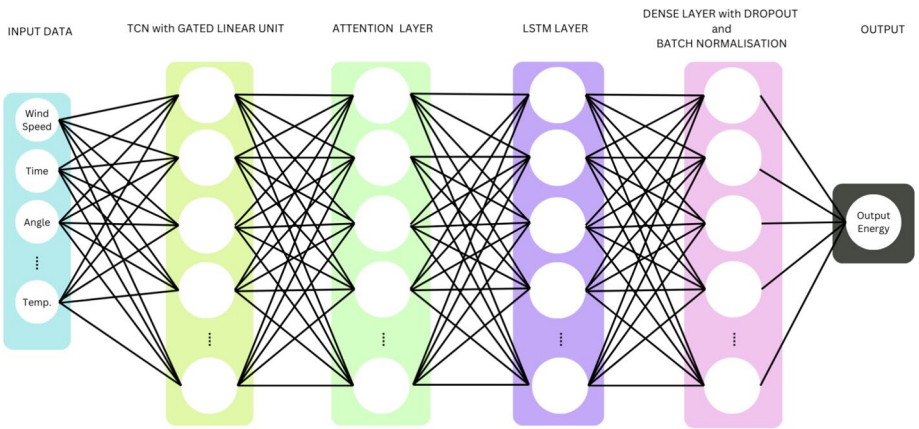

Fig. 1 Architecture Diagram of the Proposed Model

Algorithm 1 Hybrid Model for Wind Power Forecasting

Require: $num_features$: Number of input features, $days_in_past$: Number of days of historical data, TCN_WIDTH: Width of the Temporal Convolutional Network, OUT_STEPS: Number of output steps
Ensure: Forecasted wind power values
Initialize model with input shape $(days_in_past \times 24, num_features)$
Apply masking to handle variable-length sequences
Extract last $TCN_WIDTH \times 2$ time steps using a Lambda layer
Apply Conv1D layer with GLU activation:
    $conv_output \leftarrow \text{Conv1D}(128 \times 2, \text{activation} = \text{'sigmoid'}, \text{kernel_size} = TCN_WIDTH \times 2, \text{padding} = \text{'same'})(last_time_steps)$
    $gated_output \leftarrow \text{Lambda}(\lambda x : x[:, :, : 128] * x[:, :, 128 :])(conv_output)$
Apply attention mechanism:
    $attention_output \leftarrow \text{Attention}(\text{use_scale} = \text{True})([gated_output, gated_output])$
Apply LSTM layer:
    $lstm_output \leftarrow \text{LSTM}(64, \text{return_sequences} = \text{True})(attention_output)$
Apply Dense layers with Dropout and Batch Normalization:
    $dense1 \leftarrow \text{Dense}(128, \text{activation} = \text{'relu'})(lstm_output)$
    $dropout1 \leftarrow \text{Dropout}(0.2)(dense1)$
    $norm1 \leftarrow \text{BatchNormalization}()(dropout1)$
    $dense2 \leftarrow \text{Dense}(64, \text{activation} = \text{'relu'})(norm1)$
    $dropout2 \leftarrow \text{Dropout}(0.2)(dense2)$
    $norm2 \leftarrow \text{BatchNormalization}()(dropout2)$
Apply Global Average Pooling:
    $global_avg_pooling \leftarrow \text{GlobalAveragePooling1D}()(norm2)$
Generate output for forecasting:
    $output \leftarrow \text{Dense}(OUT_STEPS \times 1, \text{activation} = \text{'linear'})(global_avg_pooling)$
    $reshaped_output \leftarrow \text{Reshape}([OUT_STEPS, 1])(output)$
return $reshaped_output$

3.5 Mathematical model of the hybrid approach

To describe the hybrid model mathematically, we need to detail the operations and transformations that the input data undergoes through each layer of the model. Here's a step-by-step breakdown:

3.5.1 Input and masking

Let $\mathbf{X}$ be the input tensor of shape (N, T, F), where N is the batch size, T is the time steps (`days_in_past` ×24), and F is the number of features.

$$\mathbf{X} \in \mathbb{R}^{N \times T \times F} \tag{1}$$

After masking, the input tensor becomes:

$$\mathbf{X}_{\text{masked}} = \text{Masking}(\mathbf{X}, \text{mask}_{\text{value}} = -1.0) \tag{2}$$

3.5.2 Temporal convolutional network (TCN) with gated linear unit (GLU)

Extract the last few time steps using a lambda operation:

$$\mathbf{X}_{\text{tcn}} = \mathbf{X}_{\text{masked}}[:, -2 \cdot \text{TCN}_{\text{WIDTH}} :, :] \tag{3}$$

Apply a 1D convolution:

$$\mathbf{X}_{\text{conv}} = \sigma(\mathbf{W} * \mathbf{X}_{\text{tcn}} + \mathbf{b}) \tag{4}$$

where σ is the sigmoid activation, $\mathbf{W}$ are the convolutional weights, and $\mathbf{b}$ is the bias. This is followed by the GLU operation:

$$\mathbf{X}_{\text{glu}} = \mathbf{X}_{\text{conv}}[:, :, : 128] \odot \mathbf{X}_{\text{conv}}[:, :, 128 :] \tag{5}$$

where $\odot$ represents element-wise multiplication.

3.5.3 Attention mechanism

The attention mechanism computes a context-aware representation of the inputs:

$$\mathbf{Q} = \mathbf{X}_{\text{glu}} \tag{6}$$

$$\mathbf{K} = \mathbf{X}_{\text{glu}} \tag{7}$$

$$\mathbf{V} = \mathbf{X}_{\text{glu}} \tag{8}$$

The attention scores are computed as:

$$\mathbf{A} = \text{softmax}\left(\frac{\mathbf{Q}\mathbf{K}^T}{\sqrt{d_k}}\right) \tag{9}$$

where d_k is the dimension of the key vectors. The output of the attention mechanism is:

$$\mathbf{X}_{\text{att}} = \mathbf{A}\mathbf{V} \tag{10}$$

3.5.4 LSTM layer

The LSTM layer processes the attention output:

$$\mathbf{h}_t, \mathbf{c}_t = \text{LSTM}(\mathbf{X}_{\text{att}}, \mathbf{h}_{t-1}, \mathbf{c}_{t-1}) \tag{11}$$

where $\mathbf{h}_t$ is the hidden state and $\mathbf{c}_t$ is the cell state at time step t.

3.5.5 Dense layers with dropout and batch normalization

The LSTM output is passed through dense layers with dropout and batch normalization:

$$\mathbf{X}_{\text{dense1}} = \text{ReLU}(\mathbf{W}_1\mathbf{h}_t + \mathbf{b}_1) \tag{12}$$

$$\mathbf{X}_{\text{dropout1}} = \text{Dropout}(\mathbf{X}_{\text{dense1}}, \text{rate} = 0.2) \tag{13}$$

$$\mathbf{X}_{\text{norm1}} = \text{BatchNorm}(\mathbf{X}_{\text{dropout1}}) \tag{14}$$

$$\mathbf{X}_{\text{dense2}} = \text{ReLU}(\mathbf{W}_2\mathbf{X}_{\text{norm1}} + \mathbf{b}_2) \tag{15}$$

$$\mathbf{X}_{\text{dropout2}} = \text{Dropout}(\mathbf{X}_{\text{dense2}}, \text{rate} = 0.2) \tag{16}$$

$$\mathbf{X}_{\text{norm2}} = \text{BatchNorm}(\mathbf{X}_{\text{dropout2}}) \tag{17}$$

3.5.6 Global average pooling

The output of the second dense layer is globally averaged:

$$\mathbf{X}_{\text{gap}} = \frac{1}{T}\sum_{t=1}^{T}\mathbf{X}_{\text{norm2}}[:, t, :] \tag{18}$$

3.5.7 Output layer

The final dense layer produces the output:

$$\mathbf{y} = \mathbf{W}_3\mathbf{X}_{\text{gap}} + \mathbf{b}_3 \tag{19}$$

$$\mathbf{y}_{\text{reshaped}} = \text{Reshape}(\mathbf{y}, [\text{OUT}_{\text{STEPS}}, 1]) \tag{20}$$

3.6 Model compilation

The model is compiled using the Adam optimizer:

$$\text{Loss} = \frac{1}{N}\sum_{i=1}^{N}(\mathbf{y}_{\text{true}} - \mathbf{y}_{\text{pred}})^2 \tag{21}$$

$$\text{Optimizer} = \text{Adam}(\boldsymbol{\theta}) \tag{22}$$

3.7 Complexity analysis of the hybrid model

The total complexity of the model can be approximated by summing the complexities of each component. The dominant terms, which contribute the most to the overall complexity, are the attention mechanism and the LSTM layer. Thus, the overall complexity can be expressed as:

$$O(N \times T^2 \times F + N \times T \times H \times (H + F)) \tag{23}$$

Memory usage in the model involves storing the weights and activations for each layer. Key factors affecting memory consumption include:

- *Weights*: The size of the weight matrices in convolutional layers, LSTM layers, and dense layers.
- *Activations*: The intermediate activations at each layer, especially in the LSTM and attention layers, which need to be stored for backpropagation.

4 Results and discussions

In this study, we have proposed a novel hybrid approach for WPF. For evaluating the performance of the proposed model key metrics such as Mean Squared Error, Mean Absolute Error, Root Mean Square Error and Improvement over Random Baseline were used (Salleh et al. 2022). The model yielded impressive results, evident from the values recorded

across various metrics like MSE of 20000.64 kW, MAE of 72.88 kW, RMSE of 141.42 and 80.86 % Improvement over the random baseline. A comparative analysis was conducted to assess and prove the model's superior performance and effectiveness. We compared it with four traditional deep learning techniques: Convolutional LSTM, TCN, Attention Based LSTM, and Gated Recurrent Unit across three performance metrics MSE, MAE, Improvement over Random Baseline. The results of the comparative analysis are shown in Table 2. Our novel approach consistently outperformed the traditional techniques across all three metrics and demonstrated its effectiveness and superior predictive power in generating wind power forecasts (Table 3).

Further investigation and analysis of the result was carried out. Traditional Deep learning techniques: Convolutional LSTM, TCN, Attention Based LSTM, and Gated Recurrent Unit showed varying levels of accuracy in wind power forecasting. These techniques have limitations in certain aspects. Poor performance of Convolutional LSTM and TCN in terms of MSE and MAE is indicative of their inability to capture both short and long term dependencies effectively. Convolutional LSTM and TCN are not very efficient

Table 2 Complexity analysis of the proposed hybrid model

Layer	Operation	Complexity	Explanation
Input and masking	Masking layer	$O(N \times T \times F)$	Applies a mask to each element in the input tensor
Temporal convolutional network (TCN)	1D Convolution with dilation	$O(N \times T \times F \times K)$	1D convolution processes input features
TCN (cont.)	Gated linear unit (GLU)	$O(N \times T \times F)$	Element-wise multiplication with gating mechanism
Attention mechanism	Scaled dot-product attention	$O(N \times T^2 \times F)$	Computes dot products between query and key matrices
LSTM layer	LSTM cell	$O(N \times T \times H \times (H + F))$	Matrix multiplications for gates and cell states
Dense layers	Dense layer	$O(N \times T \times H \times D)$	Matrix multiplication between hidden state and weights
Dense layers (cont.)	Dropout	$O(N \times T \times H)$	Masks out neurons with element-wise operations
Dense layers (cont.)	Batch normalization	$O(N \times T \times H)$	Normalizes activations across the batch
Global average pooling	Global average pooling	$O(N \times T \times F)$	Computes average across time steps for each feature
Output layer	Dense layer	$O(N \times D \times O)$	Maps pooled features to the output space

Table 3 Performance comparison of the proposed hybrid model with the state-of-the-art techniques

S.No.	Technique	MSE (kW)	MAE (kW)	RMSE (kW)	Improvement over random baseline
1	Convolutional LSTM	26110.12	90.66	161.5	76.19%
2	TCN	30465.91	96.85	174.54	74.57%
3	Attention based LSTM	31350.28	89.09	177.06	76.60%
4	Gated recurrent unit	25461.67	101.95	159.57	73.23%
5	Proposed novel hybrid model	20000.64	72.88	141.42	80.86%

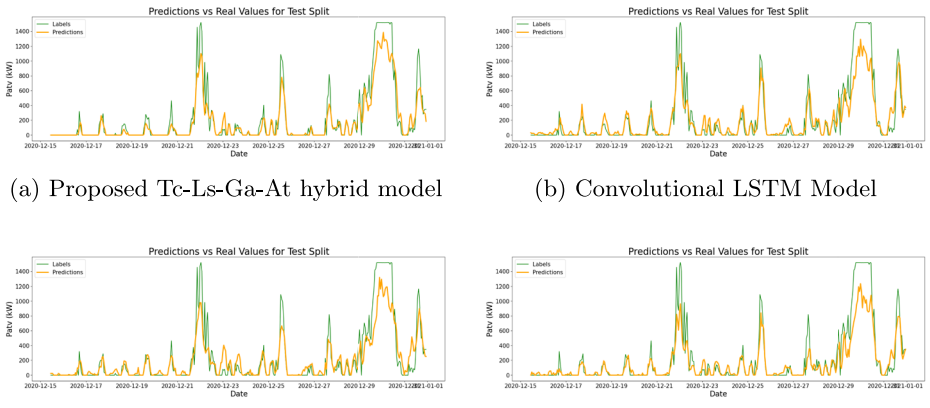

Fig. 2 Prediction performance of proposed hybrid model with the state-of-the-art techniques

(a) Proposed Tc-Ls-Ga-At hybrid model

(b) Convolutional LSTM Model

(c) TCN Model

(d) Attention-based LSTM Model

in temporal modeling, capturing complex patterns across long sequences. Moreover, these techniques are sensitive to hyperparameters and require careful tuning for achieving optimal performance. Attention Based LSTM and GRU models lacked in certain areas like extracting intricate temporal relationships or managing complex data sequences, but still showed some improvements. Therefore, it is crucial to address these limitations. In contrast, our proposed hybrid model excelled and demonstrated superior performance across all three metrics, as it harnessed and collectively utilized the power of all these individual techniques.

The hybrid model efficiently utilized the advantage of temporal convolutional technique for detection of local patterns, LSTM technique for memory retention in the network, focussing only on the relevant features through attention mechanisms, efficient sequence processing and controlling flow of information through GRU and extracting high level features through dense layers. Moreover, the hybrid approach enables the model to overcome the limitations of the individual techniques and leverage the strength of each technique to its advantage thus, resulting in better forecasting results, manifested by the substantial reduction in MSE, MAE and RMSE metrics, and increase in the Improvement over the baseline metric (Fig. 2).

Below are Output Plots depicting Predicted values vs Real Values for various Deep Learning techniques

4.1 Limitations

Though the hybrid approach demonstrates superior performance in WPF, it is important to discuss some limitations of the approach. Combining various techniques like TCN, LSTM, Attention, Gating etc increases the complexity of the model and makes it computationally more expensive. Therefore, a larger amount of processing power and memory is required. Also, due to the intricate dependencies between the layers the training time of the model is increased. Significant experimentation and research needs to be done in order to choose the optimal set of hyperparameters as hybrid models are more sensitive to it and also there is a higher risk of overfitting.

A trade-off between model complexity and performance is required to address these limitations.

5 Conclusion and future work

Our research presents a novel approach to wind power forecasting, amalgamating TCN, LSTM networks, attention mechanisms, gating mechanisms and dense layers. The efficiency of our approach has been validated through various performance metrics like MSE, MAE, RMSE and Improvement over the random baseline. The model is capable of accurately capturing both short and long term fluctuations in the wind power data by harnessing the power of each constituent technique. The proposed hybrid model intends to push the boundaries of this field by contributing to the advancements in accurately forecasting the power outputs from wind energy and efficiently managing the grid.

Future research goals can focus on the application of graph neural networks, transformers and other advanced deep learning techniques that help in improved modeling of spatial dependencies and temporal patterns in the realm of wind power forecasting (Malhotra and Singh 2023). Integration of uncertainty estimation methods, reinforcement learning algorithms for dynamic control of wind farm operations offer huge grounds for future research. Including multi-domain forecasting would enable a more holistic approach to energy management and ensure that renewable energy sources are smoothly integrated into the smart grid.

Funding No funding was received from any organization for conducting this research work.

Declarations

Conflict of interest The authors confirm that there are no known Conflict of interest and no financial interests associated with this work.

Human or animals rights None of the authors conducted any experiments with human participants or animals for this work.

Informed consent The authors confirm that no experiments were conducted with any human participant or animal for this work.

References

Ahmadi A, Talaei M, Sadipour M, Moradiamani A, Jalili M (2022) Deep federated learning-based privacy-preserving wind power forecasting. IEEE Access. https://doi.org/10.1109/ACCESS.2022.3232475

Aslam M, Nam J, Jung J (2022) An encoder-decoder model with dual-attention mechanism for wind power forecasting. In: 2022 IEEE power & energy society general meeting (PESGM). pp 01–05. https://doi.org/10.1109/PESGM48719.2022.9916813

Basu S, Campbell RH (2020) Going by the numbers: learning and modeling Covid-19 disease dynamics. medRxiv. https://doi.org/10.1101/2020.05.18.20106112

Bommidi BS, Kosana V, Teeparthi K, Madasthu S (2023) Hybrid attention-based temporal convolutional bidirectional lstm approach for wind speed interval prediction. Environ Sci Pollut Res 30(14):40018–40030. https://doi.org/10.1007/s11356-022-24641-x

Chang Y, Yang H, Chen Y, Zhou M, Yang H, Wang Y, Zhang Y (2024) A hybrid model for long-term wind power forecasting utilizing nwp subsequence correction and multi-scale deep learning regression methods. IEEE Trans Sustain Energy 15(1):263–275. https://doi.org/10.1109/TSTE.2023.3283242

del Campo R, Anguiano E, Romero Á, Dorronsoro JR (2023) Deep learning applied to wind power forecasting: a spatio-temporal approach. In: Valenzuela O, Rojas F, Herrera LJ, Pomares H, Rojas I (eds) Theory and applications of time series analysis. Springer, Cham, pp 207–219

Faruque MO, Hossain MA, Alam SMM, Islam MR, Islam MR, Guo Y (2023) A hybrid lstm-lightgbm model for precise short-term wind power forecasting. In: 2023 IEEE international conference on applied superconductivity and electromagnetic devices (ASEMD). pp 1–2 https://doi.org/10.1109/ASEMD59061.2023.10368796

Gong M, Yan C, Xu W, Zhao Z, Li W, Liu Y, Li S (2023) Short-term wind power forecasting model based on temporal convolutional network and informer. Energy 283:129171. https://doi.org/10.1016/j.energy.2023.129171

Hanifi S, Lotfian S, Zare-Behtash H, Cammarano A (2022) Offshore wind power forecasting-a new hyperparameter optimisation algorithm for deep learning models. Energies. https://doi.org/10.3390/en15196919

Hossain MA, Chakrabortty RK, Elsawah S, Ryan MJ (2020) Hybrid deep learning model for ultra-short-term wind power forecasting. In: 2020 IEEE international conference on applied superconductivity and electromagnetic devices (ASEMD). pp 1–2 https://doi.org/10.1109/ASEMD49065.2020.9276090

Huang S, Yan C, Qu Y (2023) Deep learning model-transformer based wind power forecasting approach. Front Energy Res 10:1055683. https://doi.org/10.3389/fenrg.2022.1055683

Kingma DP, Ba J (2017) Adam: a method for stochastic optimization

Liu G, Wang C, Qin H, Fu J, Shen Q (2022) A novel hybrid machine learning model for wind speed probabilistic forecasting. Energies 15(19):6942. https://doi.org/10.3390/en15196942

Lv S, Wang L, Wang S (2023) A hybrid neural network model for short-term wind speed forecasting. Energies 16(4):1841. https://doi.org/10.3390/en16041841

Malhotra R, Singh P (2023) Recent advances in deep learning models: a systematic literature review. Multimed Tools Appl 82(29):44977–45060. https://doi.org/10.1007/s11042-023-15295-z

Mujeeb S, Javaid N, Gul H, Daood N, Shabbir S, Arif A (2019) Wind power forecasting based on efficient deep convolution neural networks

Ramirez-Rosado IJ, Fernandez-Jimenez LA, Monteiro C, Sousa J, Bessa R (2009) Comparison of two new short-term wind-power forecasting systems. Renew Energy 34(7):1848–1854. https://doi.org/10.1016/j.renene.2008.11.014

Rosa de Jesús DA, Mandal P, Wu YK, Senjyu T (2020) Deep learning ensemble based new approach for very short-term wind power forecasting. In: 2020 IEEE power & energy society general meeting (PESGM). pp 1–5 https://doi.org/10.1109/PESGM41954.2020.9281473

Salleh NSM, Suliman A, Jørgensen BN (2022)Comparison of electricity usage forecasting model evaluation based on historical load dataset duration using long short-term memory architecture. In: Alfred R, Lim Y (eds) Proceedings of the 8th international conference on computational science and technology. pp 675–686. Springer, Singapore

San KM, Singh JG, Prakash N K (2023) Wind speed forecasting using hybrid model of cnn and lstm with wavelets. In: 2023 international conference in advances in power, signal, and information technology (APSIT). pp 297–301 https://doi.org/10.1109/APSIT58554.2023.10201713

Song J, Peng X, Yang Z, Wei P, Wang B, Wang Z (2022) A novel wind power prediction approach for extreme wind conditions based on tcn-lstm and transfer learning. In: 2022 IEEE/IAS industrial and commercial power system Asia (I &CPS Asia). pp 1410–1415 https://doi.org/10.1109/ICPSAsia55496.2022.9949665

Tefera E, Martínez-Ballesteros M, Troncoso A, Martínez-Álvarez, F (2023) A new hybrid cnn-lstm for wind power forecasting in Ethiopia. In: García Bringas, P, Pérez García, H, Martínez de Pisón, FJ, Martínez Álvarez, F, Troncoso Lora, A, Herrero, Á, Calvo Rolle, JL, Quintián, H, Corchado, E (eds) Hybrid artificial intelligent systems. pp 207–218. Springer, Cham

Xiong B, Lou L, Meng X, Wang X, Ma H, Wang Z (2022) Short-term wind power forecasting based on attention mechanism and deep learning. Electr Power Syst Res 206:107776. https://doi.org/10.1016/j.epsr.2022.107776

Ye L, Zhao J, Lu P, Pei M, Chen M, Wang B (2020) Combined approach for short-term wind power forecasting considering meteorological fluctuation and feature extraction. pp 1334–1343 https://doi.org/10.1109/ICPSAsia48933.2020.9208615

Zhang H, Zhu Q, Li W, Li X, Xie C, Xiang C, Fan J (2023) Ultra short term power forecasting of wind generation based on improved lstm. In: 2023 3rd power system and green energy conference (PSGEC). pp 176–180 https://doi.org/10.1109/PSGEC58411.2023.10255886

Zhou J, Lu X, Yea Xiao (2024) Sdwpf: a dataset for spatial dynamic wind power forecasting over a large turbine array. Sci Data 11:649. https://doi.org/10.1038/s41597-024-03427-5

Zhou J, Lu X, Xiao Y, Su J, Lyu J, Ma Y, Dou D (2022) Sdwpf: a dataset for spatial dynamic wind power forecasting challenge at kdd cup 2022

Zhu J, Su L, Li Y (2022) Wind power forecasting based on new hybrid model with tcn residual modification. Energy AI 10:100199. https://doi.org/10.1016/j.egyai.2022.100199

Publisher's Note Springer Nature remains neutral with regard to jurisdictional claims in published maps and institutional affiliations.

Springer Nature or its licensor (e.g. a society or other partner) holds exclusive rights to this article under a publishing agreement with the author(s) or other rightsholder(s); author self-archiving of the accepted manuscript version of this article is solely governed by the terms of such publishing agreement and applicable law.

Signal, Image and Video Processing (2025) 19:365
https://doi.org/10.1007/s11760-025-03911-4

ORIGINAL PAPER

High-capacity reversible data hiding in encrypted images based on difference image transfiguration

Ankur[1,4] · Rajeev Kumar[1] · Ajay K. Sharma[2] · Pallavi Ranjan[3]

Received: 12 September 2024 / Revised: 30 November 2024 / Accepted: 31 January 2025
© The Author(s), under exclusive licence to Springer-Verlag London Ltd., part of Springer Nature 2025

Abstract
Reversible data hiding in encrypted images (RDHEI) has garnered significant attention from researchers over the last decade, mainly due to its potential to embed secret information into encrypted images without referencing the original image. However, most state-of-the-art (SOTA) RDHEI methods do not provide optimal embedding capacity (EC) and full reversibility of the image. To bridge this gap, a novel RDHEI method based on difference image transfiguration is proposed. The method initially employs the Median edge detector to predict pixels of the image, subsequently deriving a difference image. Some of the most significant bit planes of the difference image are then cleaned in order to create a large space for embedding the secret information. Additionally, this cleaning process results into a transfigured image that enhances the visual security. However, at the same time, it also generates a weight matrix which is essentially nothing but an overhead, that must be recorded for reconstruction of the original image. To significantly reduce the overhead size, the weight matrix is first encoded using a novel location difference technique to compressible lists, and then Huffman encoding is employed. Subsequently, the transfigured image is encrypted along with the compressed overhead and the secret information is embedded in the reserved space. As a result, the method ensures high EC while preserving the complete reversibility of the image. Comparative experiments validate the efficacy of the proposed method relative to the SOTA methods.

Keywords RDHEI · Encrypted images · Media edge detector · High payload · Bit-Plane cleaning · Transfigured image

1 Introduction

In recent times, the demand for cloud storage capacity has surged dramatically, with an increasing number of users opting to store their personal data on cloud platforms. It has been the cloud storage's advantages such as usability, accessibility, cost-effectiveness, scalability, etc., over traditional storage systems, that have contributed to the usage appeal. However, complete security and privacy management is still a big concern for many users. To address this concern, data hiding appears to be one of the most viable options as it enables the embedding of secret information in a multimedia cover and the faultless extraction of the information by authorized users. Moreover, the cover can be restored to its original state upon extraction of the hidden information at the receiving end. In this specific case, the terminology "reversible data hiding" (RDH) has been used [1–3]. The aspect of reversibility makes the data hiding more pertinent to meet cloud user's security and privacy requirements. However, to provide the required level of privacy and confidentiality, the cover media is usually encoded using one of the available cryptographic methods/systems such as stream cipher, and then utilized for embedding the secret information. This form of data hiding which embeds the message in an encrypted image is generally known as RDHEI [4–35]. Therefore, RDHEI enables the information owner to hide their information behind a cover image without being aware of the image's content. In the last half decade and so, many RDHEI methods

✉ Rajeev Kumar
rajeevkumar@dtu.ac.in

Ankur
ankur_2k20phdco507@dtu.ac.in

Ajay K. Sharma
director@nitdelhi.ac.in

Pallavi Ranjan
pallavi.ranjan@murdoch.edu.au

1 Delhi Technological University Delhi, Delhi, India

2 National Institute of Technology, Delhi, India

3 Murdoch University, Dubai, UAE

4 Bennett University, Greater Noida, Uttar Pradesh, India

Published online: 06 March 2025

have been introduced with a fundamental goal of obtaining larger EC, reduced image distortion, and good information security. These methods can majorly be categorized as Vacating Room After Encryption (VRAE) and Reserving Room Before Encryption (RRBE), in purview of encoder. In VRAE methods [6–11], room for information embedding is vacated after encryption of the image. However, embedding large amounts of data poses a challenge due to the considerable increase in image entropy after encryption, leading to the destruction of spatial correlation. In contrast, RRBE [12–35] methods reserve a room for data embedding before the image encryption by pre-processing the image. Thus, spatial correlation of clear images is efficiently utilized and hence these methods are capable of embedding enormous amounts of data. In purview of decoder, the extraction of hidden information and reconstruction of the cover image can be done either jointly [6, 8, 16] or separately [7, 9, 11–15, 17–30, 33–36] based on the availability of authorization information/key at the receiving end. It has been observed that the traditional RDHEI methods achieve low EC or result in a lossy reconstruction of the original image, in other words, have a trade-off between EC and reconstructed image quality. In order to mitigate the aforementioned trade-off, this paper presents an RDHEI method based on difference image transfiguration (DIT). The proposed method aims to achieve a very high EC while ensuring errorless reconstruction of the cover image. The key contributions of this work are mentioned below:

- The proposed method employs the MED to exploit the usually prevalent high correlation among adjacent pixels of meaningful/natural images for generating an image of lower magnitude prediction values. Thus, the generated image's most significant bit (MSB) planes usually contain zeros with few exceptions, which are cleaned to reserve a contiguous and wide space for secret information embedding.
- The cleaning process also leads to a transfigured image that is notably different from the original image. At the same time, the cleaning process also generates a weight matrix which is required for the original image reconstruction. The weight matrix is first transformed into compressible lists using novel difference location techniques which are later on compressed by employing Huffman encoding, to significantly reduce their size.
- Moreover, encryption techniques are employed on the transfigured image to provide anonymized contents and in turn help in achieving enhanced visual security.
- Experimental results demonstrate that the suggested method provides a larger EC than the SOTA methods while ensuring the complete reversibility of the original image.

The remaining part of the paper is organized as follows: Section II provides a summary of related work. Next, Section III presents our proposed method. In Section IV, experimental results and analysis are presented. Lastly, Section V concludes the paper with future work recommendations.

2 Related work

In this section, RRBE based high-capacity RDHEI methods are briefly reviewed. One of the earliest RRBE based RDHEI methods was discussed by Ma et al. [18]. In this method, a room is created inside the image using histogram shifting. Here, the shifting of the first three least significant bits (LSBs) is done from one region to another region which leads to an embedding rate (ER) of up to 0.5 bits per pixel (bpp). However, this method does not guarantee a perfect reconstruction of the original image. Cao et al. [19] discussed a patch-level sparse representation-based RDHEI method by taking inspiration from traditional RDH methods for exploiting the redundancy within the image to achieve superior performance. The method exploits local structures (such as patches or regions) of the image to create a bigger room inside the image for data hiding as the adjacent pixels are usually highly correlated. The method is able to embed on average 1 *bpp* of secret information which is higher than the same of the erstwhile methods. However, the quality of reconstructed images is deteriorated as the obtained PSNR (Peak signal-to-noise ratio) is only about 40 dB to 50 dB for smooth images. To take benefits of probabilistic and homomorphic properties of the cryptosystem, Zhang et al. [20] encrypt the cover image using a public key cryptography. Next, multi-layer wet paper coding is used to embed the secret information into the LSB-planes of the encrypted image. Thus, the method achieves the ER of roughly 0.5 *bpp* with a distortion of about 40 dB. However, the method may result in failed data extraction and image recovery in case of excessive payload embedding.

To address the concern of deteriorated image quality, Yi et al. [21] discuss an RDHEI method with binary block embedding. The method introduces the usage of the MSB-planes for embedding the secret information seeing the prevalent high spatial correlation among the MSB-planes of neighboring pixels. The shift from LSB to MSB resulted in a substantial enhancement of the EC compared to previous RDHEI methods. However, the method does not guarantee optimal performance in all scenarios as it only explores the local correlation. Subsequently, Puteaux et al. [22] extended the MSB-based embedding work by introducing a prediction method to further increase the EC. The pre-processed image is encrypted and the secret message is embedded by replacing MSBs with the bits of the secret message. Thus, the total ER of the marked encrypted image can reach 1 *bpp*.

On similar lines to incorporate secret information in several MSBs and embed additional data, Mohammadi et al. [24] make use of difference predictor to calculate the difference error for all pixels from the centre pixel and embed multiple MSB. Thus, the local correlation is efficiently exploited which leads to an improvement in EC. Ankur et al. [23] extended the Puteaux et al.'s [22] by leveraging neighborhood correlation in blocks and additionally utilizing the multiple MSB for data embedding. However, the methods fails to efficiently utilize the correlation of bit-planes. For this, Yu et al. [25] propose an RDHEI method based on hierarchical embedding which is basically an extension of Mohammadi et al. [24]. The method firstly generates a hierarchical label map based on a prediction technique. Next, the label map is split into three categories based on the magnitude of PEs. The smallest and largest magnitude PEs are then used for embedding the secret information. Thus, embedding performance is somewhat improved over the SOTA high capacity RDHEI methods, but the computational cost increases.

Unlike earlier RDHEI methods, the parametric binary tree labeling (PBTL) technique [26, 27] labels predicted pixels to create additional embedding space, achieving around 1.75 bpp EC but lacking overhead compression. Different from others, Fu et al. [29] introduced a novel RDHEI method utilizing L-shaped block embedding and improved binary-block embedding to enhance the EC by fully exploiting prediction errors. Similarly, Ankur et al. [30] proposed a link-chain approach for variable-sized blocks. Despite their advantages, both methods lack adaptability in balancing the trade-off between EC and image quality.

To address the aforementioned limitation, Yin et al. [28] discuss a novel RDHEI method based multi-MSB prediction and Huffman encoding to further boost the EC. The method makes bit-wise comparison, starting from MSB towards LSB, of the original pixel value with the predicted value, instead of treating the pixel value as a single unit for comparison and compressed the error by Huffman encoding. Thus, the multi-MSB method is able to achieve ER of near about 2.58 *bpp* on average while still ensuring complete reversibility of the image.

Subsequently, the labels are encoded using fixed Huffman encoding, akin to [28], before being embedded in the encrypted image with the aid of ECC. As a result, enlarged EC is achieved. However, the method has its own limitations such as key size limitations, implementation complexity, etc., because of the adoption of ECC for image encryption Chen et al. [33] discuss an RRBE-RDHEI method that divides the image into two sets: 4 MSB and 4 LSB-plane. Since similarity between the pixels of MSB-plane is significantly high, a compression technique is employed to reduce their size and create a space for embedding. Next, LSBs are shifted to the created space on the MSB-planes side. Hence the LSB-planes are used for data embedding which yields around 2.5 *bpp* average ER. Simialrly, Liu et al. [34] proposed utilizing block-based bit-plane reallocation to enhance embedding capacity while ensuring reversibility and security. However, the method struggles with scalability across diverse datasets, requiring parameter adjustments. Yin et al. [35] introduce an RDHEI method in which bit-plane of PEs are compressed. In the method, initially the original image is uniformly partitioned into the blocks and the PEs are calculated by the median edge detector (MED). The bit planes of the PEs are rearranged by block scanning to improve the compression rate. Afterward, extended run-length encoding is employed to vacate the room which is filled by the secret information by employing multi-LSBs substitution. Thus, the average ER of more than 3 *bpp* is achieved, which is significantly higher than the SOTA methods.

After the analysis of the related work, it is clear that embedding capacity (EC) remains a significant challenge within the domain of RDHEI. Although some methods have achieved an average embedding rate (ER) of more than 3 bpp, which is considerably higher, but have not been successful in ensuring the complete reversibility as the spatial correlation of natural images has not been fully exploited. To address this limitation, this paper introduces a new RDHEI method based on difference error transfiguration. This method is capable of performing error-free data extraction and image recovery while providing high capacity. The details of the proposed method are discussed in Section III, and its performance is experimentally evaluated in Section IV.

3 Proposed method

This section introduces a novel RDHEI method based on difference image transfiguration (DIT-RDHEI). The proposed method involves four stages, as illustrated in Fig. 1. The first stage is difference image transfiguration, where the content owner generates an image with multiple cleaned MSBs. In the second stage which is image encryption, the content owner encrypts the image with an image key and embeds supporting information (SI) while reserving space for data embedding. The third stage involves data embedding, where the data hider embeds secret information in the reserved space. In the final stage, extraction and recovery, the recipient extracts the hidden data and reconstructs the original image. Thus, an effective method for secure and efficient data hiding is introduced.

3.1 Difference image transfiguration

This sub-section comprises four parts: difference image generation, multi-MSB cleaning, compressible list generation using the location difference technique (LDT), and overhead

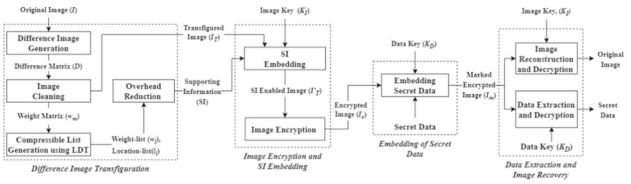

Fig. 1 Block diagram of the proposed DIT-RDHEI method

reduction. Following the generation of the difference matrix in the first part, the cleaning process yields a transfigured image and weight matrix. Subsequently, the weight matrix is compressed using the LDT, and finally, overhead is minimized and results in supporting information (SI).

3.1.1 Difference image generation

For the original image I of size $M \times N$, the pixel values are predicted to generate a predicted image (P). For prediction, firstly Median Edge Detection (MED) predictor which has successfully been used in the well-known compression standard JPEG-LS [37], is employed. The MED predictor utilizes left, upper, upper left pixels for prediction. For example: To predict the pixel located at (i, j) of image I, three pixels i.e., left (le), upper (up), upper left (ul) pixels, are used to make the prediction, where $le = I(i-1, j)$,$up = I(i, j-1)$ and $ul = I(i-1, j-1)$ respectively as per the Eq. (1).

$$P(i,j) = \begin{cases} max(le, up) & \text{if } ul \le min(le, up), \\ min(le, up) & \text{elseif } ul \ge max(le, up), \\ le + up - ul, & \text{otherwise} \end{cases} \quad (1)$$

where $P(i, j)$ denotes the predicted value of the current pixel $I(i, j)$ and values of i and j can lie in the range as follows $2 \le i \le M$ and $2 \le j \le N$, respectively.

It is to be noted that MED requires the original pixels of the first row and first column to be retained as reference pixels. In order to reduce the number of reference pixels, the first row and first column pixels except the very first pixel i.e., $I(1, 1)$, are also predicted as follows: $P(i, 1) = I(i-1, 1)$ where $2 \le i \le M$; $P(1, j) = I(1, j-1)$, where $2 \le j \le N$; and $P(1, 1) = I(1, 1)$, is used. Thus, only $I(1, 1)$, is retained as the reference pixel, which is represented as p^{ref}. Next, a difference matrix D of size $M \times N$ is generated using Eq. (2), defined as follows:

$$D(i, j) = I(i, j) - P(i, j) \quad (2)$$

where $D(i, j)$ denotes the difference between the original $I(i, j)$ and predicted $P(i, j)$ pixels located at location i,j, $1 \le i \le M$ and $1 \le j \le N$. Thus, the difference (matrix) D will have both positive and negative values in the range of $[-255...255]$, as $I(i, j)$ and $P(i, j)$ both have the pixel

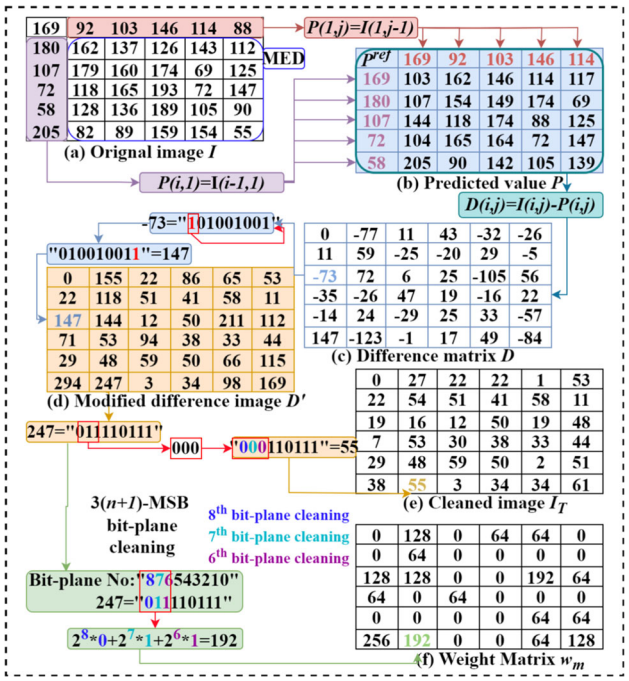

Fig. 2 An illustrative example for difference image generation and cleaning process

values in the range (0 to 255). It means total of nine bits are required to represent each value of D as one bit is exclusively required to represent sign and other 8 bit can represent the magnitude of difference. Thus, total 9 bit-planes of size $M \times N$ are needed to represent D. The sign (or 8^{th}) bit-plane of D is usually highly random or in other words has very less sparsity as both positive and negative values are equally possible, in comparison to other MSB-planes which usually have large sparsity but in decreasing order. The reason of this is the prevalent correlation among adjacent pixels of the original meaningful images.

Since the 8^{th} bit-plane is highly random as it represents the sign bit, the bit-planes are initially rearranged by doing a circular one-bit left shift as follows so that all the least sparse bit-planes can be gathered on LSB side:

$$D'(i, j) = 2 \times |D(i, j)| + \begin{cases} 1 & \text{if } D(i, j) < 0, \\ 0, & \text{otherwise} \end{cases} \quad (3)$$

where $|.|$ represents the absolute value of '.'. Thus processing, the modified difference image (D') is obtained. To clearly understand the difference image generation process, an illustrative example is presented in Fig. 2. In the example, a 6×6 image (I) is considered and the pixels are predicted using MED predictor. For the first row and first column, the pixels are predicted directly by their last pixel such that $P(1, j) = I(1, j-1)$ and $P(i, 1) = I(i-1, 1)$, as shown in the upper and left part of the image, respectively.

Thus, only the very first pixel i.e., 169, is required to be retained as the reference pixel (p^{ref}). Next, the differences are calculated for each pixel using Eq. (2) and the bit-planes of the matrix D as shown in Fig. 2c are rearranged using Eq. (3) to get the modified difference image D' as depicted in Fig. 2d.

3.1.2 Multi-MSB cleaning

The bit-plane sparsity is directly related to the embedding space or room. More specifically, the sparser the bit-plane is the bigger the embedding space will be. As seen, the sparseness is the highest at MSB-plane i.e., the modified difference image $D'_{e^{[8]}}$ which keeps on decreasing towards the LSB-planes i.e., $D'_{e^{[0]}}$. The MSB-planes of D' generally contain 0's, with few exceptions i.e., 1's because of the prevalent spatial correlation among the adjacent pixels of the original image. These exceptions can be avoided by cleaning the bit-planes so that a large room can be created for data embedding. More specifically, the 1's in the selected bit-planes are substituted by 0's to make them cleaned so that secret information can be embedded. However, a bit-plane $D'^{[k]}$ is assumed to be $Clean$ if all of its preceding bit-planes are also cleaned along with satisfying the property of cleanliness i.e., $D'^{[k]}(i, j) = '0'$ where $1 \leq i \leq M$,$1 \leq j \leq N$, which means all the bits of the bit-plane must be '0'. The cleaning process starts from the sparsest bit-plane i.e., MSB-plane (8^{th}) and continues to move towards LSB-plane of D' until Eq. (4) is true. The Eq. (4) suggests that the pure EC provided by n bit-planes is less than the same of $(n-1)$ bit-planes, or in other words, overhead in the form of SI added by n^{th} bit-plane is more than the added bits of the secret data. As a result, the n^{th} bit-plane cannot be used to boost the EC.

$$EC^{PET}(n) \leq EC^{PET}(n-1) \tag{4}$$

where $8 \geq n \geq 1$ and EC^{PET} denotes pure EC that can be computed using Eq. (5) defined as follows:

$$EC^{PET}(n) = (M \times N \times n) - L^{SI} \tag{5}$$

where L^{SI} represents the length of SI. The details about SI are described in the next sub-section 3.1.4. Thus, the value of n which represents the number of embeddable bit-planes, is determined. The value of n is dependent on the characteristics of the original image. More specifically, the higher the smoothness of the original image, the greater the value of n. Next, the aforementioned cleaning process is performed with the help of Eq. (6) for $n+1$ MSB-planes of D'.

$$I_T(i, j) = \begin{cases} D'(i, j) - 2^k & \text{if } f(D'(i, j), k) = 1, \\ D'(i, j), & \text{otherwise} \end{cases} \tag{6}$$

where $f(x, y) = \left\lfloor \frac{x \bmod 2^{y+1}}{2^y} \right\rfloor$ is a function for extracting the y^{th} LSB bit of x, 'mod' is modulo operator and k represents the bit-plane number such that $8 \geq k \geq (8-n)$. For ensuring the reversibility, these replacements (from 1's to 0's during the cleaning) are iteratively recorded by making modifications in a zero matrix namely weight (w_m) of size $M \times N$, as per the Eq. (7) defined as follows:

$$w_m(i, j) = \sum_{k=8}^{8-n} D'(i, j) \times 2^k \quad \text{if } f(D'(i, j), k) = 1 \tag{7}$$

Thus, for each replacement in the k^{th} bit-plane, weight is increased by 2^k. Hence, the values of weights in w_m can lie in range (0 to 511). To demonstrate this, the example-1 shown in Fig. 2 is further considered, where 3 MSB-planes of D' are cleaned by replacing all the 1's by 0's, to get the cleaned (or transfigured) image I_T as shown in Fig. 2e. At the same time, corresponding replacements for the cleaned bits are recorded in the weight matrix as shown in Fig. 2f, with the help of Eq. (7).

3.1.3 Compressible list generation using location difference technique

As evident from the weight matrix w_m of the example-1 and also in general, the count of '0' elements, remains high as replacements are done only for $n+1$ MSB-planes of D'. This sparsity presents an opportunity to reduce the size of w_m, which is essentially an overhead, by compressing it. However, the number of unique elements in the weight matrix w_m is limited, and they are scattered in small groups due to the correlations. If their location in the same sequence is available, the weight can be collected in a list after skipping the 0' elements. To achieve an optimal compression rate, a new technique called the Location difference technique (LDT) has been developed. This technique collects the given weights in a weight-list by utilizing their location, enabling optimal compression performance through Huffman encoding.

More specifically, the LDT first generates a location matrix (l_m) to mark the locations of replacements as well as the number of replacements, according to Eq. (8), defined as follows:

$$l_m(i, j) = \sum_{k=8}^{8-n} f(w_m(i, j), k) \tag{8}$$

Next, both the matrices w_m and l_m are uniformly partitioned into $\alpha \times \beta$ sized non-overlapping blocks, where α and β are user-defined thresholds such that $\alpha \ll N$ and $\beta \ll M$, where $\ll$ represents "significantly lesser than" sign. Now, each block of l_m is scanned in raster scan manner and groups are formed, where the location of each element is marked as

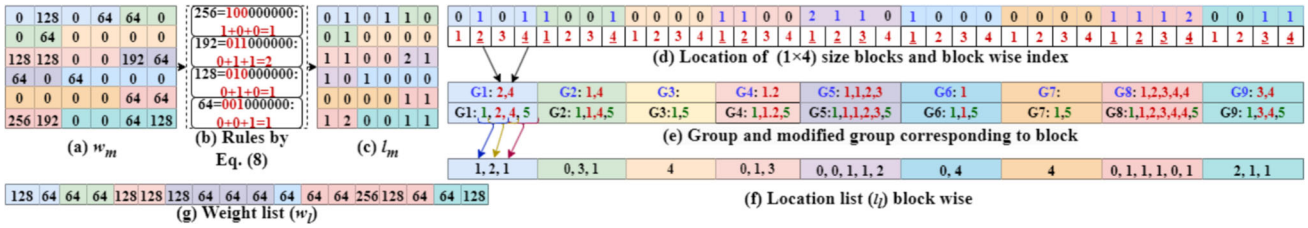

Fig. 3 An illustrative example of location difference technique

many times as its magnitude. For example: if the first element is '2', or '1' or '0' then two times '1' or one time '1' or no entry/representation in the corresponding group, is made, respectively. Subsequently, '1' and $(\alpha \times \beta) + 1$ are added as the first and the last element of each group. Now, the difference between two consecutive elements of each group is computed and all the differences are concatenated to form a list namely location list (l_l). Similarly, w_m is first divided into blocks of the same size as l_m was partitioned and then each block of w_m is also scanned in raster scan manner. Next, every element is represented in 9-bit binary representation. For every non-zero bit, its position value is added into a list namely weight list (w_l). Thus, obtained weight list (w_l) represents the magnitude of change due to replacement and the location lists (l_l) represents the corresponding location at which changes have been made in the same order. It can be observed that the image partitioning into blocks of $(\alpha \times \beta)$ helps in significantly lowering the range and enhance the frequencies of elements in the lists. As the new range of elements in the location list is (0 to $\alpha \times \beta$) which is significantly lesser than the range if no division is considered i.e., (0 to $M \times N$). Thus, the frequencies of elements (representing the difference) are significantly increased which will immensely help while employing the compression method.

To clarify the proposed process, Example 1 is extended into Example 2 to demonstrate the key steps.

The weight matrix w_m, shown in Fig. 2(e), is also utilized in Fig. 3a of Example 2. The location matrix (l_m), as shown in Fig. 3c, is generated using Eq. (8). This matrix tracks the number of '1's replaced during the cleaning process for each pixel (Fig. 3b)). The matrix is then divided into 1×4 blocks, as seen in Fig. 3(d), where $\alpha = 1$ and $\beta = 4$, yielding a total of 9 blocks: $B_1\{0,1,0,1\}$, $B_2\{1,0,0,1\}$,..., $B_9\{0,0,1,1\}$. These blocks are scanned in a raster-scan manner, as illustrated in the first row of Fig. 3e.

For each block, groups are formed based on the location matrix (l_m). For instance, for B_1, the group is $G_1\{2,4\}$, where the second and fourth positions correspond to the '1' values in B_1. Similarly, the groups for all blocks are: $G_1\{2,4\}$, $G_2\{1,4\}$, $G_3\{\}$, $G_4\{1,2\}$, $G_5\{1,1,2,3\}$, $G_6\{1\}$, $G_7\{\}$, $G_8\{1,2,3,4,4\}$, $G_9\{3,4\}$. These group formations are illustrated in Fig. 3(e).

Next, each group is adjusted so that the first element is '1' and the last element is $(\alpha \times \beta) + 1 = 5$, as shown in the second row of Fig. 3(e). The differences between consecutive elements of each group are then computed, as illustrated in Fig. 3(f), and concatenated to form the location list (l_l). The final location list is: $l_l = 1, 2, 1, 0, 3, 1, 4, 0, 1, 3, 0, 0, 1, 1, 2, 0, 4, 4, 0, 1, 1, 1, 0, 1, 2, 1, 1$.

For the generation of the weight list (w_l), the weight matrix w_m is also divided into 1×4 blocks (Fig. 3a). Each block element is then represented in 9-bit binary form, and for every non-zero bit, its position value is added to the weight list (w_l). The final weight list is: w_l = 128, 64, 64, 64, 128, 128, 128, 64, 64, 64, 64, 64, 64, 256, 128, 64, 64, 128. For composite values like 191, they are split into their component parts, i.e., 128 and 64.

3.1.4 Overhead reduction

The generated lists l_l and w_l from LDT are now compressed using Huffman encoding. Since w_l represents the bit position at which replacements (from 1's to 0's,) were done during the cleaning process, the number of distinct elements is only $n + 1$. Moreover, their frequency is also in decreasing order. More specifically, the lower magnitude elements are the most repetitive and the higher magnitude ones are the least. So, a pre-fix Huffman tree of the maximum height n with $2n + 1$ nodes can be used to provide optimal compression. As a result, the length of the Huffam codes will be $1, 2, \ldots, n$, and n bits where the most frequent and the least frequent are represented by '1'Afterward bit Huffman code. Therefore, total $n(n + 3)/2$ bits are required to represent the prefixed Huffman code. Next, w_l is turned into bit-stream (b^{wgt}) by replacing each element with its determined Huffman code, for further processing. Similarly, location-list (l_l) can also be compressed. Though l_l contains only $(\alpha \times \beta) + 1$ unique elements but their frequencies are highly random. Because of this, the Huffman tree cannot be fixed but devised based on their frequencies. Thus, Huffman code rules of $[\lceil \log_2((\alpha \times \beta)+1) \rceil \times ((\alpha \times \beta)+1) +$ length of code] are obtained, where each $\lceil \log_2((\alpha \times \beta) + 1) \rceil$ bit represents any of the code. The codes are concatenated to form a code rule bit-stream (h^l),

Finally, l_l is converted into a bit-stream (b^{loc}) by replacing each element with its Huffman code.

It is to be noted that the Huffman (or even Arithmetic) encoding can also be directly employed without first encoding with LDT, but directly encoding with these methods won't help much as the total number of toinct values in w_m are 2^{n+1}. To prove the point and show the contribution of the proposed LDT, experimental results to show the compressed size and running time for all the three encoding methods, are provided in Table 1. For the experiments, two standard test image *Lena* and *Airplane* have been considered. It is clearly visible from the Table 1 that the LDT method significantly helps in achieving the optimal compression performance with computation time.

Thus processing, different pieces of information such as number of embeddable bit-planes (n), Huffman code rules (h^l), location difference bitstream (b^{loc}), weight bitstream (b^{wgt}), reference pixel (p^{ref}), etc., have been obtained which must be recorded in a specific order so that image recovery (at the receiving end,) can be ensured. The following information is referred to as supporting information (SI), and its length is denoted by L^{SI}. SI is separated into two sections based on the need: Primary Supporting Information (PSI) and Second Supporting Information (SSI). PSI includes only n and L^{SI} of size i.e., $[6+\lceil \log_2(M \times N)\rceil]$ bits, which is necessary for data hiding, data extraction, and image reconstruction. SSI includes h^l, b^{loc}, b^{wgt} and p^{ref} which are concatenated in the specified sequence and is required for image reconstruction.

In the next stage, the content owner encrypts the obtained transfigured image with an image key while also embedding the SI and reserving space for data embedding.

3.2 Image encryption and SI embedding

In the proposed method for image encryption is done using AES-CTR, the process commences with the generation of a pseudo-random matrix (ξ) of size $M \times N$ utilizing the image key (K_I) as the seed.

Now before applying the mandatory encryption, the SI is embedded in I_T so that this information can also be encrypted. Therefore, enhanced security against the unauthorized decoding of the image can be achieved. The SI is embedded in a raster scan manner from the MSB-plane to the LSB-plane of I_T by the bit-replacement technique of Eq. (9), defined as follows.

$$I'_T(i,j)=I_T(i,j)+\begin{cases}((b^{SI}\times 2^{k-1}) & \text{if } f(I_T(i,j),k)=0,\\ ((b^{SI}-1)\times 2^{k-1}) & \text{otherwise}\end{cases} \tag{9}$$

where $k = 7, 6, \ldots, 8-n$ and b^{SI} represents to be embedded bit of SI. The first case of Eq. (9) always holds for SI embedding, as the Multi-MSB of I_T is always zero. The second case, on the other hand, addresses the issue of overflow that may occur during data embedding. Following the aforementioned embedding of SI, the mandatory encryption is performed as follows:

$$I_e(i,j) = I'_T(i,j) \oplus \xi(i,j) \tag{10}$$

where $\oplus$ denotes the bit-wise exclusive-or operation.

It is to be noted that initial $[6+\lceil \log_2(M \times N)\rceil]$ MSBs in raster scan are not encrypted by Eq. (10) because it contains PSI, which is required during data hiding.

3.3 Embedding of secret data

In this subsection, the data hider first read the Primary Supporting information (PSI) to know the number of embeddable bit-planes (n) that can hold data and the length of SI (L^{SI}) from the encrypted image (I_e), prior to data hiding. For this, the data hider extracts $[6+\lceil \log_2(M \times N)\rceil]$ bits using the function $f(I_e(i,j),k)$, by reading the image in raster scan manner where the initial 3 bits give n and the remaining $[3+\lceil \log_2(M \times N)\rceil]$ bits represent L^{SI}. Next, the secret data is encrypted using the data key (K_d) and embedded in the image I_e using a bit replacement technique or by Eq. (9) after bypassing the pixels having SI bits. The end result is a marked encrypted image (I_m).

3.4 Data extraction and image recovery

As the proposed DIT-RDHEI method supports separability property of RDHEI, all the three cases 1) the receiver possesses only the data key; 2) the receiver possesses only the image key; and 3) the receiver possesses both the keys can be considered. In any of the case, PSI is first read/extracted in the raster scan from the MSB-plane to the LSB-plane from the image I_m as done by the data hider.

Case-1: the recipient has access only to the data key K_d which means he is exclusively responsible for the data extraction. In this situation, the recipient reads the bits of all the n bit-planes like PSI extraction, by skipping the first L^{SI} bits and then decrypts the above remaining bits with K_d to obtain the lossless data.

Case-2: the recipient has access only to the image key (K_I), which means he can only reconstruct the identical image. For this, a pseudo-random matrix (ξ) of size $M \times N$ using key K_I is generated and image decryption is performed using Eq. (10) to get the decrypted image (I_d). Next, the SSI is extracted from I_d in a manner identical to the PSI extraction, where the length of SI is L^{SI}, which is already obtained from PSI. After skipping the PSI bits,

Table 1 Performance of Difference LDT, HE and AE

Supporting information ($bits$) / Computational time ($seconds$)	Compression technique		
	LDT+HE	HE	AE
Matrix w_m of Lena	219655/0.037247	321070/0.027705	231032/1.708585
Matrix w_m of Airplane	255943/0.03728	339695/0.029919	271329/ 1.965141

$\lceil \log_2((\alpha \times \beta)+1) \rceil \times ((\alpha \times \beta)+1)$ bits are obtained from the SSI, where the decimal value of each $\lceil \log_2((\alpha \times \beta)+1) \rceil$ bits sequentially represents each code length of the Huffman code rule. Following that, Huffman coding rules are extracted from the leftover SSI based on the lengths previously stated for each code.

Using the remaining SSI and the previously obtained Huffman code, $M \times N$ dimensional location matrices with initial zero values are then created. To convert the remaining bits of SI to l_m, Huffman code values are successively read from SI and after decoding substituted in a $(\alpha \times \beta)$-sized block of l_m during raster scan, with each block also being contracted during raster scan.

After updating the entire l_m blocks, prefixed Huffman codes for weight matrix are determined similarly to section 3.1.4. Following that, weight matrices (w_m) are recovered from the leftover SSI. Because the Huffman code for weight is present, the Huffman value is retrieved from the SSI and decoded. Then weights are updated in w_m for every non-zero l_m in raster scan manner

After detaching all the weights, only 8 bits are left in SSI, which reflect the reference pixel (p^{ref}). Next, the cleaned image I_T is determined from LSB planes of I_d. Then, to obtain the modified difference image (D'), n MSB-planes of the I_T are replaced by the weight matrix (w_m) and image D' is obtained. Afterwards, bit-planes rearrangement is reversed to obtained the difference matrices (D) as follows:

$$D(i,j) = \begin{cases} +\frac{D'(i,j)}{2} & \text{if} D(i,j) \bmod 2 = 0 \\ -\lfloor \frac{D'(i,j)}{2} \rfloor & \text{otherwise} \end{cases} \quad (11)$$

For the image reconstruction, reference pixel (p^{ref}) is substituted at $\bar{I}(1,1)$, first row and column is obtained by following substitution, $\bar{I}(i,1) = D(i,1) + \bar{I}(i-1,1)$ where $2 \le i \le M$, $\bar{I}(1,j) = D(1,j) - \bar{I}(1,j-1)$ where $2 \le j \le N$; and remaining pixels are predicted by MED predictor, and $\bar{I}(i,j) = D(i,j) + \bar{P}(i,j)$, where $\bar{P}(i,j)$ is the predicted value. The obtained final image is identical to the original image which indicates lossless image reconstruction and in turn proves reversibility of the DIT-RDHEI.

Case-3: if the data-hiding key K_d and the image key K_e are available with recipient then he can extract the hidden data and can also reconstruct the original image without loss by following the first case and the second case, respectively.

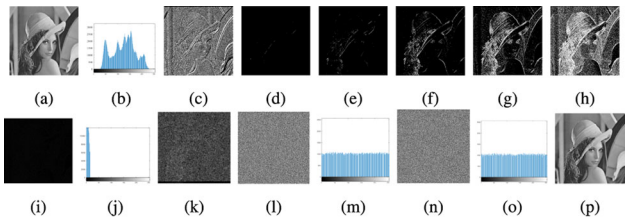

Fig. 4 Illustration of the proposed DIT-RDHEI method on image *Lena* of size 512 × 512 (**a**) I, ((**b**) Histogram of I, ((**c**) D, ((**d-h**) Binary image n =1, 2, 3, 4, and 5, ((**i**) I_T, ((**j**) Histogram of I_T ((**k**) SI enabled I'_T, ((**l**) I_e, ((**m**) Histogram of I_e, ((**n**) I_m after embedding the 828921 bits, ((**o**) Histogram of I_m and ((**p**) Reconstructed image

4 Experimental results and analysis

This section discusses the experimental results of the proposed DIT-RDHEI method and their analysis on comparison with the SOTA methods. The discussion and analysis of the experimental results have been divided into five parts detailed as follows. In the first section, a comprehensive explanation of the DIT-RDHEI using the test image *Lena* as an example is provided. The second part discusses performance analysis on different test images and datasets such as BOSSbase [38] and BOWS-2 [39]. In the third part, the security analysis of the method under consideration is done followed by the comparison of the DIT-RDHEI with the SOTA, in the penultimate part. In the last part, time complexity analysis is done.

4.1 A complete example for the DIT-RDHEI method

In this sub-section, a comprehensive illustration of the proposed DIT-RDHEI method is provided. For this, grayscale test image *Lena* of 512 × 512 pixel as depicted in Fig. 4a is considered. The histogram of the image *Lena* to show the frequency distribution of 256 levels of grayscale, is shown in Fig. 4b. Unlike previous RDHEI methods, the PBTL technique [26, 27] labels predicted pixels to enhance embedding capacity (EC), achieving over 1.75 bpp. However, it lacks overhead compression, limiting EC. Wang et al. [40] improve EC by classifying PEs and using Huffman encoding, a strategy also adopted by Su et al. [41], though both methods fail to fully exploit bit-plane correlations. The image shows that almost all of the pixels are black except very few whites, which in turn indicates the greater sparsity. However, this cleaning process results into SI mentioned in the Table 2.

As discussed above, the cleaning process is continued until Eq. (4) is true. For the image *Lena*, it has been found that for $n = 5$ the pure EC decreases as the SI is determined to be of the length 502566 bits in comparison to 219655 bits for $n = 4$. The binary images for each of the bit-planes cleaning i.e., n=2,3,4 and 5 are shown in Fig. 4e-4h to demonstrate the sparsity of each of the bit-planes. It can be clearly observed that white regions keep on increasing as the value of n increases which means sparsity keeps on decreasing. The binary image displayed in Fig. 4h showcases a notable excess of white pixels, signifying a substantial generation of overhead in terms of SI, which violates Eq. (4) due to the high overhead.

Next, after cleaning the top MSB n+1 bit-planes of the image, a transfigured image I_T is obtained as shown in Fig. 4i. The histogram of the transfigured image is shown in Fig. 4k, where it can be clearly observed that pixel values are lying only in the range of 0 to 15 as 4-MSB-planes of the difference image have already been cleaned to get this transfigured image. The transfigured image is divided into $\alpha \times \beta$ blocks. To clearly understand the effect of different block sizes with $n = 4$, experimental data which depicts the bifurcation of SI, EC, and ER for *Lena*, is presented in Table 3. It can be observed that the image's pure EC increases until the block size reached 12×12, afterwards it begins to drop.

Next, SI of 219655 bits is embedded and the resultant image as shown in Fig. 4l, is obtained. Next, the image is encrypted using stream cipher as per Eq. (11). The encrypted image and its histogram are presented in Fig. 4m and 4n, respectively, which clearly shows complete decorrelation with the original image. Afterwards, the data hider embeds the secret information i.e., 828921 bits in the encrypted image. The marked encrypted image and its histogram are depicted in Fig. 4o and 4j, respectively. Again, it is evident from the histogram that there is no correlation between the original image and the encrypted-marked image. Following this, the receiver extracts hidden data and recovers the original image based on key availability. As shown in Fig. 4p, the result is identical to Fig. 4a, proving the method's reversibility.

4.2 Performance analysis on different test image and dataset

In this sub-section, the efficacy of the proposed DIT-RDHEI method is evaluated. For performance evaluation, commonly used metrics: peak signal-to-noise ratio (PSNR) and EC in terms of ER, are adopted to test the reversibility and measure the payload capacity of the method, respectively. Firstly, six standard test images: *Lena*, *Baboon*, *Airplane*, *Jetplane* (F-16), *Tiffany* and *Man* (Male), each of size 512×512 pixels as shown in Fig. 5, from SIPI dataset [42], are considered. The experimental results are presented in Fig. 6 where

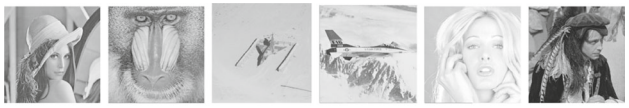

(a) Lena (b) Baboon (c) Airplane (d) Jetplane (e) Tiffany (f) Man

Fig. 5 Test images

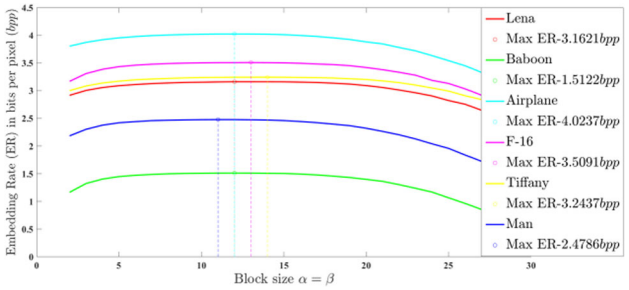

Fig. 6 Performance analysis of DIT-RDHEI method on different thresholds

EC (in *bpp*) is displayed for different block sizes considering different values for $\alpha \times \beta$. In this analysis, $\alpha = \beta$ has been considered for simplicity, in cases where the image dimensions are not perfectly divisible by the selected block size $\alpha \times \beta$, the DIT-RDHEI method adapts by treating the edge blocks as smaller-sized blocks. It is to be noted that the achieved PSNR by the DIT-RDHEI between the original and the recovered image for all the test images is positively infinite ($+\infty$), which proves that the DIT-RDHEI is a pure reversible data hiding method. Since the achieved PSNR (in all the cases) is $+\infty$ dB, the same is not shown in the figure to avoid meaning less entry. As shown in Fig. 8, a smooth image such as *Lena* provides greater ER than a complex image such as *Baboon*. It is because the number of the embeddable bit-planes in *Lena* is greater than the same in *Baboon*. In other words, the maximum ER i.e., 4.0237 is achieved in case of the smoothest image i.e., *Airplane* and in contrast, the minimum ER i.e., 1.5122 is provided by the most complex image i.e., *Baboon*. This indicates that the DIT-RDHEI method makes effective use of spatial correlation. As a result, approximately half of the bits (i.e., 4 bits) in a smother image are easily utilized for embedding while maintaining the identical image, and it is also analyzed that the EC is highest when the threshold ($\alpha \times \beta$) is in the range of 11×11 to 14×14, so it is fixed as 12×12 for further analysis.

Further, the DIT-RDHEI is evaluated in two datasets: BOSSBase and BOWS-2, both having 10,000 grayscale images with size 512×512. In Fig. 7, the experimental results for ER at $\alpha = \beta = 12$ are presented. The obtained PSNR is $+\infty$ dB, which again proves the reversibility aspect. For BOSSBase and BOWS-2, net ER is 3.7010 and 3.5784 *bpp*, with PSNR $+\infty$ dB, respectively, in the average case. The greatest ER i.e., 6.8181, 6.6604 and 5.9598 *bpp* is achieved by three images at index number 5162, 5215 and 5542 *bpp*,

Table 2 SI Bifurcation, EC and ER for different n

n	Size of h^l $(bits)$	Size of b^{loc} $(bits)$	Size of b^{wgt} $(bits)$	Size of SI $(bits)$	Pure embedding capacity $(bits)$	Embedding rate (bpp)
1	6498	2894	123	9547	252597	0.9636
2	2705	15248	1971	19956	504332	1.9239
3	2672	56258	13452	72414	714018	2.7238
4	2842	160067	56714	219655	828921	3.1621
5	5318	317119	180097	502566	808154	3.0829

Table 3 SI Bifurcation, EC and ER for $\alpha \times \beta$ with $n = 4$

$\alpha \times \beta$	Size of h^l $(bits)$	Size of b^{loc} $(bits)$	Size of b^{wgt} $(bits)$	Size of SI $(bits)$	Pure embedding capacity $(bits)$	Pure embedding rate (bpp)
2×2	29	227150	56714	283928	764648	2.9169
4×4	170	190191	56714	247107	801469	3.0574
8×8	1040	167637	56714	225423	823153	3.1401
10×10	1747	163411	56714	221904	826672	3.1535
11×11	2204	161637	56714	220587	827989	3.1585
12×12	2842	160067	56714	219655	828921	3.1621
13×13	3464	159492	56714	219702	828874	3.1619
14×14	4202	158835	56714	219783	828793	3.1616
16×16	7163	157570	56714	221479	827097	3.1551
20×20	25148	155959	56714	237853	810723	3.0927

respectively in the BOSSBase dataset. Similarly, in BOWS-2 dataset, image at index 1478, 8414 and 1559, provide the highest ER i.e., 6.3224, 5.9301 and 5.7915 *bpp* respectively. Although the ER of worst image in BOSSBase is 0.9410 *bpp* while in BOWS-2, it is 0.8439 *bpp*. This analysis proves that the DIT-RDHEI has acceptable performance and can be applied in privacy protection.

4.3 Security analysis

The proposed DIT-RDHEI method aims to provide security to both, the hidden data and the cover image. For this, the proposed RDHEI method uses two keys: an image key for cover image encryption and a data key for data encryption. The original (I), encrypted (I_e), and marked encrypted (I_m) images of *Lena* are shown in Figs. 4a, 4l, and 4n, respectively. Both I_e and I_m appear completely perplexed and noisy, ensuring the original content is non-perceivable. The histograms of I_e and I_m (Figs. 4m, 4n) are nearly uniform across intensity values, contrasting with the original *Lena* image's histogram (Fig. 4b). This confirms that DIT-RDHEI achieves strong perceptual security.

To further evaluate its performance as far as encryption is concerned, several statistical metrics such as horizontal, vertical correlation, Shannon entropy, NPCR, UACI, PSNR, and SSIM are considered. The experimental results considering the aforementioned metrics are demonstrated in Table IV, for the test image *Lena*. The correlation in I is high in all horizontal, vertical, and diagonal directions. As shown in Table IV, the correlation for the I is close to one in all directions, whereas the correlation for I_e and I_m is close to zero, indicating that the method is capable of breaking the correlation of the I. Information entropy quantifies the uncertainty in pixel intensity distribution of an encrypted image. For a grayscale image, the maximum entropy is 8. A higher Shannon entropy indicates evenly distributed pixels. As shown in Table VI, the high entropy of I_e and I_m reflects their unpredictability.

NCPR and UCID also determine the percentage of image pixel change. The NPCR of I_m is close to 100%, i.e., 99.60, indicating a high secure image, as the greater number of NPCR denotes a more mismatch. Despite the fact that the percentage value of UCID is higher, visual security is considered to be of high quality. The UCID for I_e and I_m is 73.00 and 72.95, respectively. Finally, the PSNR, and SSIM are examined for I_e and I_m to account for the greater mismatch. PSNR and SSIM are low for both images when compared to I, indicating that the images are substantially mismatched and structurally distinct from the I.

4.4 Comparison with state of art methods

To comprehensively and comparatively assessment the performance of the DIT-RDHEI method, some of the notable and recently developed high-capacity SOTA methods such as the works of Yu et al. [25], Yi et al. [26], Wu et al. [27], Yin et al. [28], Fu et al. [29], Ankur et al. [30], Gao et al. [31], Chen et

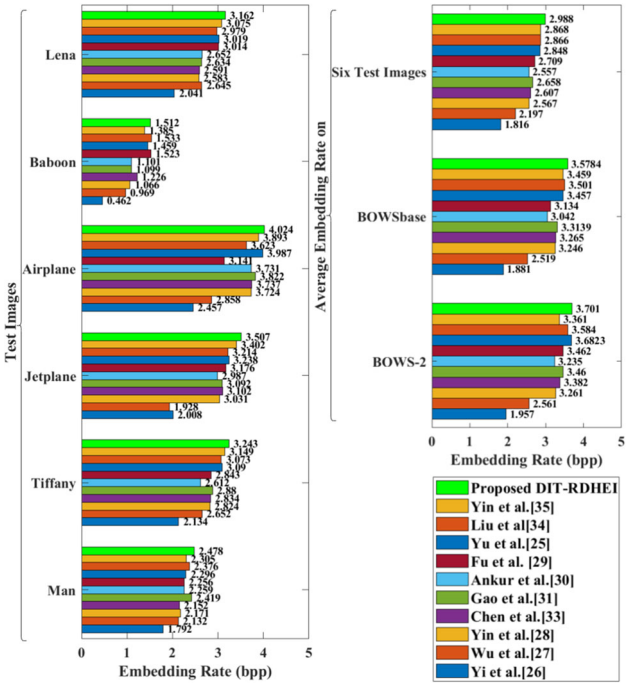

Fig. 7 Comparison of ER (*bpp*) between proposed DIT-RDHEI method and SOTA methods

al. [33], Liu et al. [34] and Yin et al. [35], have been considered. The aforementioned SOTA methods majorly belong to the RRBE-RDHEI category as RRBE-RDHEI methods usually provide higher EC than VRAE-based ones. Since the DIT-RDHEI always losslessly reconstructs the image which leads to an $+\infty$ dB PSNR with one SSIM, ER has been considered as a major performance metric for comparison with SOTA methods. To persuasively analyze the performance, the parameters for each of the aforementioned methods are tuned to get the highest ER. As evident from Fig. 6, the DIT-RDHEI achieves the highest ER for the $\alpha \times \beta$ ranging between 11×11 to 14×14. Moreover, the ER fluctuation within the aforesaid range is also negligible. et al.'s method [28].

As a result, for the maximum ER, $\alpha \times \beta$ has been considered to be 12×12 for all the comparisons.

A comprehensive comparison of the DIT-RDHEI method with leading state-of-the-art (SOTA) techniques was conducted across six test images: *Lena*, *Baboon*, *Airplane*, $F-16$, *Tiffany*, *Man*, and the average of all six images. As illustrated in Fig. 7, the DIT-RDHEI method demonstrated superior performance overall. For the *Lena* image, the method achieved an embedding rate (ER) of 3.162 bpp, surpassing all existing methods. For the *Airplane* image, which features the smoothest texture among the test set, DIT-RDHEI achieved an ER of 4.024 bpp, outperforming the 3.987 bpp achieved by the method of Yu et al. [25]. Similarly, DIT-RDHEI outperformed SOTA methods for $F-16$, *Tiffany*, and *Man* images. However, the method exhibited slightly lower performance on the highly complex *Baboon* image, which is characterized by low spatial correlation and high entropy. Despite this, the DIT-RDHEI method achieved an average ER of 2.988 bpp across the six test images, surpassing the previous best average ER of 2.868 bpp recorded by Yin et al. [35].

Further, two datasets: BOSSbase and BOWS-2 have also been considered for performance comparison of the DIT-RDHEI with the SOTA methods as shown in Fig. 7. It is indicated that the proposed technique has higher ER than any of the existing SOTA methods [25–31, 33–35] on BOSSBase and BOWS-2 datasets. It can also be observed from the Fig. 7 that any of the existing aforementioned methods except Yu et al. [25] and Liu et al. [34] for the BOSSbase and BOWS-2, does not surpass 3.5 *bpp* ER for any of the datasets. Thus, the DIT-RDHEI gains 0.0184 and 0.0774 *bpp* ER, for the BOSSbase and BOWS-2, respectively. The aforementioned extensive evaluation shows that the DIT-RDHEI completely outperforms the existing SOTA methods [25–30, 33–35].

4.5 Time complexity analysis

As discussed above, the proposed DIT-RDHEI method comprises four stages, and at each stage, at most $M \times N$ pixels and constant number of bit-planes are processed. Consequently, the worst case time complexity can be $O(M \times N)$, at each stage. Additionally, two Huffman trees are formed during the overhead processing, however, their number of nodes remains constant, resulting in a constant time complexity. Thus, the overall time complexity of the method is $O(M \times N)$.

5 Conclusion

In this paper, we proposed a new high-capacity RDHEI method based on difference image transfiguration. The proposed (DIT-RDHEI) method employed MED to generate a highly sparse difference image and transfigured the same to create a big room for embedding. Experimental results demonstrated that the proposed DIT-RDHEI method provides higher ER than the SOTA methods, while ensuring the complete reversibility of the original image. More specifically, the DIT-RDHEI provides the highest average payload of 3.5784 and 3.7010 *bpp* for BOSSbase and BOWS-2 datasets ever, respectively, while ensuring complete reversibility of the original images. Additionally, DIT-RDHEI method provides greater visual security as embedding is done in the transfigured image which is completely different than the original image. In future work, we aim to optimize overhead size by developing more effective predictors for sparse difference images. Additionally,

exploring adaptive techniques will enhance performance on complex images, addressing current challenges while broadening the method's applicability.

Data/Code availability The data/code can made available on request to the first author.

Declarations

Conflict of interest The authors declare that they have no Conflict of interest.

References

1. M. Celik, G. Sharma, A. Tekalp, and E. Saber, "Reversible data hiding," in *Proceedings. International Conference on Image Processing*, vol. 2, pp. II–II, 2002
2. Ni, Z., Shi, Y.-Q., Ansari, N., Su, W.: Reversible data hiding. IEEE Trans. Circuits Syst. Video Technol. **16**(3), 354–362 (2006)
3. Kumar, N., Kumar, R., Caldelli, R.: Local moment driven pvo based reversible data hiding. IEEE Signal Process. Lett. **28**, 1335–1339 (2021)
4. Puech, W., Chaumont, M., Strauss, O.: A reversible data hiding method for encrypted images". Security, forensics, steganography, and watermarking of multimedia contents **X6819**, 534–542 (2008)
5. Zhang, X.: Reversible data hiding in encrypted image. IEEE Signal Process. Lett. **18**(4), 255–258 (2011)
6. Hong, W., Chen, T.-S., Wu, H.-Y.: An improved reversible data hiding in encrypted images using side match. IEEE Signal Process. Lett. **19**(4), 199–202 (2012)
7. Liu, Z.-L., Pun, C.-M.: Reversible data hiding in encrypted images using chunk encryption and redundancy matrix representation. IEEE Trans. Dependable Secur. Comput. **19**(2), 1382–1394 (2022)
8. Liao, X., Shu, C.: Reversible data hiding in encrypted images based on absolute mean difference of multiple neighboring pixels. J. Vis. Commun. Image Represent. **28**, 21–27 (2015)
9. Qian, Z., Zhang, X.: Reversible data hiding in encrypted images with distributed source encoding. IEEE Trans. Circuits Syst. Video Technol. **26**(4), 636–646 (2015)
10. Liu, Z.-L., Pun, C.-M.: Reversible data-hiding in encrypted images by redundant space transfer. Inf. Sci. **433**, 188–203 (2018)
11. Ankur, R. Kumar, and A. K. Sharma, "Adaptive two-stage reversible data hiding in encrypted images using prediction error expansion," in *2023 Third International Conference on Secure Cyber Computing and Communication (ICSCCC)*, pp. 427–432, 2023
12. Di, F., Huang, F., Zhang, M., Liu, J., Yang, X.: Reversible data hiding in encrypted images with high capacity by bitplane operations and adaptive embedding. Multimed. Tools Appl. **77**, 20917–20935 (2018)
13. Xiao, D., Xiang, Y., Zheng, H., Wang, Y.: Separable reversible data hiding in encrypted image based on pixel value ordering and additive homomorphism. J. Vis. Commun. Image Represent. **45**, 1–10 (2017)
14. Ge, H., Chen, Y., Qian, Z., Wang, J.: A high capacity multi-level approach for reversible data hiding in encrypted images. IEEE Trans.Circuits Syst. Video Technol. **29**(8), 2285–2295 (2019)
15. J.-C. Chang, Y.-H. Chou, C.-H. Ni, and H.-L. Wu, "Reversible data hiding in pairwisely encrypted images," in *2016 Third International Conference on Computing Measurement Control and Sensor Network (CMCSN)*, pp. 60–63, IEEE, 2016
16. Shiu, C.-W., Chen, Y.-C., Hong, W.: Encrypted image-based reversible data hiding with public key cryptography from difference expansion. Signal Process. Image Commun. **39**, 226–233 (2015)
17. Chen, Y.-C., Shiu, C.-W., Horng, G.: Encrypted signal-based reversible data hiding with public key cryptosystem. J. Vis. Commun. Image Represent. **25**(5), 1164–1170 (2014)
18. Ma, K., Zhang, W., Zhao, X., Yu, N., Li, F.: Reversible data hiding in encrypted images by reserving room before encryption. IEEE Trans. Inf Forensics Secur. **8**(3), 553–562 (2013)
19. Cao, X., Du, L., Wei, X., Meng, D., Guo, X.: High capacity reversible data hiding in encrypted images by patch-level sparse representation. IEEE Trans. Cybern. **46**(5), 1132–1143 (2015)
20. Zhang, X., Long, J., Wang, Z., Cheng, H.: Lossless and reversible data hiding in encrypted images with public-key cryptography. IEEE Trans. Circuits Syst. Video Technol. **26**(9), 1622–1631 (2015)
21. Yi, S., Zhou, Y.: Binary-block embedding for reversible data hiding in encrypted images. Signal Process. **133**, 40–51 (2017)
22. Puteaux, P., Puech, W.: An efficient msb prediction-based method for high-capacity reversible data hiding in encrypted images. IEEE Trans. Inf. Forensics Secur. **13**(7), 1670–1681 (2018)
23. Ankur, Kumar, R., Sharma, A.K.: High capacity reversible data hiding with Contiguous space in encrypted images. Comput. Electr. Eng. **112**, 109017 (2023)
24. Mohammadi, A., Nakhkash, M., Akhaee, M.A.: A high-capacity reversible data hiding in encrypted images employing local difference predictor. IEEE Trans. Circuits Syst. Video Technol. **30**(8), 2366–2376 (2020)
25. Yu, C., Zhang, X., Zhang, X., Li, G., Tang, Z.: Reversible data hiding with hierarchical embedding for encrypted images. IEEE Trans. Circuits Syst. Video Technol. **32**(2), 451–466 (2022)
26. Yi, S., Zhou, Y.: Separable and reversible data hiding in encrypted images using parametric binary tree labeling. IEEE Trans. Multimed. **21**(1), 51–64 (2018)
27. Wu, Y., Xiang, Y., Guo, Y., Tang, J., Yin, Z.: An improved reversible data hiding in encrypted images using parametric binary tree labeling. IEEE Trans. Multimed. **22**(8), 1929–1938 (2019)
28. Yin, Z., Xiang, Y., Zhang, X.: Reversible data hiding in encrypted images based on multi-msb prediction and huffman coding. IEEE Trans. Multimed. **22**(4), 874–884 (2020)
29. Fu, Z., Chai, X., Tang, Z., He, X., Gan, Z., Cao, G.: Adaptive embedding combining lbe and ibbe for high-capacity reversible data hiding in encrypted images. Signal Process. **216**, 109299 (2024)
30. Ankur, R. Kumar., Sharma, A.K.: Link chain driven reversible data hiding in encrypted images for high payload". Signal Image Video Process. **18**(8), 5841–5856 (2024)
31. Gao, G., Zhang, L., Lin, Y., Tong, S., Yuan, C.: High-performance reversible data hiding in encrypted images with adaptive huffman code. Digit. Signal Process. **133**, 103870 (2023)
32. Ankur, R. Kumar., Sharma, A.K.: Bit-plane based reversible data hiding in encrypted images using multi-level blocking with quadtree". IEEE Trans. Multimed. **26**, 4722–4735 (2024)
33. Chen, F., Yuan, Y., He, H., Tian, M., Tai, H.-M.: Multi-msb compression based reversible data hiding scheme in encrypted images. IEEE Trans. Circuits Syst. Video Technol. **31**(3), 905–916 (2021)
34. Liu, L., Chen, C., Wu, Y., Chang, C.-C., Wang, A.: Reversible data hiding in encrypted images with block-based bit-plane reallocation". Multimed. Tools Appl. **45**, 1–22 (2024)
35. Yin, Z., Peng, Y., Xiang, Y.: Reversible data hiding in encrypted images based on pixel prediction and bit-plane compression. IEEE Trans. Dependable Secur. Comput. **19**(2), 992–1002 (2022)
36. Qin, C., Qian, X., Hong, W., Zhang, X.: An efficient coding scheme for reversible data hiding in encrypted image with redundancy transfer. Inf. Sci. **487**, 176–192 (2019)

37. Weinberger, M.J., Seroussi, G., Sapiro, G.: The loco-i lossless image compression algorithm: principles and standardization into jpeg-ls. IEEE Trans. Image Process. **9**(8), 1309–1324 (2000)
38. P. Bas, T. Filler, and T. Pevnỳ, "Break our steganographic system: the ins and outs of organizing boss," in *International workshop on information hiding*, pp. 59–70, Springer, 2011
39. P. Bas and T. Furon, "Image database of bows-2," *Accessed: Jun*, vol. 20, pp. 2016–2017, 2017
40. Wang, X., Chang, C.-C., Lin, C.-C., Chang, C.-C.: On the multi-level embedding of crypto-image reversible data hiding. J. Vis. Commun. Image Represent. **87**, 103556 (2022)
41. Su, G.-D., Chang, C.-C.: Toward high-capacity crypto-domain reversible data hiding with huffman-based lossless image coding". Vis. Comput. **39**, 1–16 (2022)
42. A. G. Weber, "The usc-sipi image database: Version 5," http://sipi.usc.edu/database/, 2006

Publisher's Note Springer Nature remains neutral with regard to jurisdictional claims in published maps and institutional affiliations.

Springer Nature or its licensor (e.g. a society or other partner) holds exclusive rights to this article under a publishing agreement with the author(s) or other rightsholder(s); author self-archiving of the accepted manuscript version of this article is solely governed by the terms of such publishing agreement and applicable law.

Software Quality Journal (2025) 33:17
https://doi.org/10.1007/s11219-025-09714-7

RESEARCH

Improving software vulnerability severity prediction model performance with HDLN & FWFS: a two-stage feature selection approach

Ruchika Malhotra[1] · **Vidushi**[1,2]

Accepted: 3 February 2025
© The Author(s), under exclusive licence to Springer Science+Business Media, LLC, part of Springer Nature 2025

Abstract
Software Vulnerability Severity Prediction (SVSP) is an evolving domain of software engineering. Ensuring the robustness and continuous operation of software systems relies heavily on the accuracy of SVSP models. However, the effectiveness of SVSP models relies heavily on the features used for training. The presence of redundant, correlated, or irrelevant features can significantly degrade model performance. To address this issue, researchers employ Feature Selection (FS) methods to streamline feature sets, reducing computational costs in model development. However, selecting appropriate FS methods and utilizing their combined strength to achieve a more efficient model remains a challenge in many existing techniques documented in the literature. In this paper, to overcome the problems associated with a large number of features, two new FS modules are proposed which have not been explored so far. The first module employs a combination of Convolutional Neural Network and Bidirectional Long Short-Term Memory, referred to as the Hybrid Deep Learning Network (HDLN) module while the second module utilizes Information Gain and Grey Wolf Optimization techniques, forming the Filter Wrapper Feature Selection (FWFS) module. The efficacy of the proposed feature selection approach is evaluated through the Area under the Curve (AUC). Upon analyzing the results, it is determined that the proposed module enhances the performance of the SVSP model. The prediction models crafted using the HDLN module exhibited the most superior performance, boasting an average AUC value of 0.88. Following closely, the FWFS module, employing Extreme Gradient Boosting as a classifier, demonstrated the second-best performance, achieving an average AUC value of 0.86.

Keywords Hybrid Feature Selection · Prediction Model · Software Vulnerability · Machine learning algorithms

✉ Vidushi
vidushi_2k18phdco23@dtu.ac.in

[1] Department of Software Engineering, Delhi Technological University, New Delhi, India

[2] School of Engineering and Technology, Vivekananda Institute of Professional Studies-Technical Campus, New Delhi, India

1 Introduction

A software vulnerability is frequently exploited by attackers to gain access to a software system (Alves et al., 2016). The degree to which a software system is vulnerable considerably affects the system's overall quality (Erturk & Akcapinar, 2015). Moreover, with large software becoming a reality, the complexity and diversity grow exponentially, and it is impossible to develop error-free software. Therefore, developing a Software Vulnerability Severity Prediction Model (SVSPM) is crucial, which takes data available on software vulnerability as input. Software vulnerability reports, software metrics, and source code can be processed and can be taken as input to SVSPM. When textual data is used as input, high-dimensional features are likely to be developed. High-dimensional data suffer from data quality problems that degrade the model's performance and increase computational cost. To mitigate these problems, various FS methods (Liu et al., 2010) can be applied. FS methods select the most relevant features (variables) from a dataset, which improves model performance by reducing overfitting and computational cost. It helps enhance the model's accuracy and efficiency by removing irrelevant or redundant data and finding the optimal subset that holds maximum information. Previous research in this field indicates that if FS methods are not applied, the prediction model's performance will be degraded (Khazaei et al., 2016; Russell et al., 2018; Wang et al., 2019). Hence, the FS is considered a vital aspect of the prediction process. The FS methods can be broadly categorized into two categories (1) Filter methods, and (2) Wrapper methods (Liu & Yu, 2005). Researchers widely use filter methods because of their simplicity and speed. The choice of the classifier technique does not bias the result of the filter methods. When a learning technique is used in the selection process for the wrapper, they are computationally more expensive but perform better than filter methods.

In the past, research has been carried out on comparing the results of different FS methods and trying to find the best one (Jeon & Kim, 2021; Russell et al., 2018; Wang et al., 2019; Yong et al., 2020). Some studies (Stuckman et al., 2017) also demonstrated either no or slight improvement in the results using FS methods. Some studies (Davari et al., 2017; Kudjo et al., 2019; Tang et al., 2020) did not opt to go in this direction and applied only preprocessing techniques. Because of the variation in datasets in practical applications, no single FS method is best suited for all the datasets. Inspired by this, this study concentrates on developing a unified module for FS to eliminate the limitations found in existing FS methods. We can assume following scenario: A software company, responsible for the security of Mozilla products, wants to predict the likelihood of vulnerabilities in its software releases. The vulnerability data they possess is large and complex, including textual descriptions of bugs and reports. Predicting severity of vulnerabilities accurately is challenging because the dataset is highly imbalanced, and many features (words, phrases, and attributes) may be irrelevant, leading to dimensionality concerns. Reducing these irrelevant features while maintaining meaningful information is crucial for efficient and accurate predictions. To achieves this, in this study, by amalgamating a variety of FS techniques into a single module. This integration aims to mitigate the weaknesses inherent in individual FS methods, thereby enhancing the overall efficacy of feature selection processes. Through this approach, the framework offers a more comprehensive solution for FS. To this end, we have developed an SVSPM which automates the process of predicting the severity of software vulnerability. This helps speed up the process of prioritizing the vulnerabilities so that more severe ones can be

fixed first. When high dimensional data act as input to SVSPM, removing the curse of dimensionality becomes important. Therefore, two new FS modules are designed for dimensionality reduction.

The first module is based on deep learning methods. In literature, it is found that deep learning methods are gaining popularity and giving good results in this field (Das et al., 2021; Failed, 2021; Sun et al., 2023, 2024). The module uses the Convolutional Neural Network (CNN) and Bidirectional Long Short-Term Memory (Bi-LSTM) and is named as Hybrid Deep Learning Network (HDLN) module. In the HDLN module, the CNN model is a kind of deep neural network that is applied to many fields such as image classification, speech recognition, and bioinformatics. Convolution, pooling, and fully connected layers make up the structure of a standard CNN. Recently, CNN has been used for Natural Language Processing (NLP) problems and has given good results (Du et al., 2017; Ghourabi et al., 2020; Rhanoui et al., 2019). CNN can extract essential features from textual data. However, it cannot interlink the present information with the past information. For this, another deep neural network model, Bi-LSTM, is used in Schuster and Paliwal (1997) which is a kind of recurrent neural network that can do data processing in two directions containing two hidden layers, thereby giving better results in NLP (Tai et al., 2015; Yin et al., 2017).

The second module uses Information Gain (IG) and Grey Wolf Optimization (GWO). It is named as Filter-Wrapper FS (FWFS) module. In the FWFS module, Information Gain is used as the term frequency-inverse document frequency, which is also used to find class labels for term-weighting, similar to FS. Among metaheuristic optimization techniques, Particle Swarm Optimization (PSO), Artificial Bee Colony (ABC), and Genetic Algorithm (GA) are popular ones that are used to find optimal features. However, it has some drawbacks, such as being trapped in local optima (Xue et al., 2016). A new optimization technique called Grey Wolf Optimizer (GWO) was created by Mirjalili et al. (2014), and it has recently received a lot of attention for addressing the problem of FS in various disciplines. It tries to copy the hunting behavior of wolves and gives much robustness compared to PSO and GA optimizers against initialization (Emary et al., 2015). On the bright side, GWO is known for its fast convergence rate and computational efficiency, particularly for small to medium-sized optimization problems. It can quickly explore the search space and converge to a solution within a reasonable amount of time, making it suitable for our problem. Moreover, GWO has shown promising performance in some real-world optimization problems. IG is a filter method and GWO is a wrapper method. Filter methods are considered to be fast whereas wrapper methods are considered to be more accurate. Therefore, IG acts as a Fast Feature Selector (FFS), and GWO acts as an Accurate Feature Selector (AFS). Combining these two in the FWFS module also combines the strengths of both aiming to eliminate the non-significant features and find an optimal subset of features for SVSP. As FS has to be applied to textual data of large dimensions, FFS is applied first and IG score is found for all the features. Features are selected according to their increasing order of IG scores. A high value of Information Gain indicates that the feature provides a significant amount of information about the target variable and is therefore valuable for prediction or classification tasks. After the selection of features via FFS, AFS is applied in order to find the optimal subset of features. As FS is a binary problem, standard GWO is converted to binary GWO (bGWO) which updates the grey wolf position vector to be binary (Emary et al., 2015).

To evaluate the performance of the SVSPM, Area under the Curve (AUC) values are used as a performance parameter across five Mozilla datasets. The values of AUC are recorded for all four levels of severity. The choice of AUC is made as it is considered

a good choice among various other parameters as it finds a balance between specificity and sensitivity values. it is also considered to be a nice option when dealing with imbalanced data problems (He & Garcia, 2009). Statistical testing is also applied to the result values obtained to find a significant difference among various experimental scenarios, judging the effectiveness of the proposed modules for FS.

The primary contributions of this study are outlined as follows:

1. This paper addresses vulnerability data presented in textual format and tackles the challenges posed to prediction models by dimensionality concerns.
2. The paper introduces two novel FS modules. The HDLN module explores the efficacy of integrating CNN and the Bi-LSTM network, while the FWFS module investigates the effectiveness of combining the metaheuristic algorithm GWO with IG.
3. Extensive testing is conducted to evaluate the functionality of the proposed strategy in terms of model performance, aiming to assess the effectiveness of the suggested FS modules.
4. Statistical analysis is employed to compare the performance of models utilizing the proposed FS modules, aiming to identify any significant differences.

In this study, the following research questions are addressed:

RQ1. How does SVSPM perform better when different FS methods are used to make the data less dimensional?

The effectiveness of various methods used for dimensionality reduction is measured on the dataset of five different products of Mozilla using AUC as a performance measure.

RQ1.1 When the HDLN module is used to lower the dimensionality of the data, what performance improvement does SVSPM experience?

With the aid of this RQ, we looked into our findings after implementing the deep learning FS methods and discovered enhancements in the SVSPM's performance when compared to the performance of the SVSPM without the FS method.

RQ1.2 When the FWFS module is used to lower the dimensionality of the data, what performance improvement does SVSPM experience?

With the aid of this RQ, we looked into our findings after implementing the filter-wrapper FS method and discovered enhancements in the SVSPM's performance when compared to the performance of the SVSPM without the FS method.

RQ2. Which module of FS among the two proposed modules gave the best results?

Addressing this RQ, the most effective method of FS is found, and a final judgment is given, stating the best method for FS.

RQ3. Whether the performance of SVSPM developed boosted significantly with the help of FS methods used to reduce the dimensionality of data?

Based on the results of the Friedman test, a significant difference in the performance of SVSPM is found.

This paper is organized as follows: Sect. 2 provides a brief review of past work. Section 3 outlines the preliminary steps required to conduct the study. The methodology for developing the proposed framework is detailed in Sect. 4. Section 5 presents the results obtained. Potential threats to validity are discussed in Sect. 6. Finally, Sect. 7 offers concluding remarks.

2 Related work

The SVSPM prediction model is primarily constructed using machine learning algorithms. To improve its performance, researchers combined feature selection (FS) techniques with particular classifiers. In the sections that follow, we will examine previous research on the development of SVSPM and delve into studies on feature selection using the hybridization of filter wrapper methods and deep learning methods.

2.1 Software vulnerability severity prediction

In this section, we have listed the latest research done on the development of SVSPM. The author in Kekül et al. (2021) proposes a machine learning framework to automate the classification of software vulnerabilities. It utilizes Natural Language Processing (NLP) techniques like bag of words, TF-IDF, and n-grams for feature extraction, and applies Naïve Bayes, decision trees, KNN, MLP, and random forest for prediction. The study evaluates the model using data from CVSS 2.0 and CVSS 3.1 and compares the effectiveness of different NLP techniques paired with various machine learning algorithms to determine the best combination for accurate vulnerability prediction.

The study (Chen et al., 2020) introduces a new approach term frequency-inverse gravity moment (TF-IGM) as an alternative to the commonly used term frequency-inverse document frequency (TF-IDF) for better weighting and identifying important terms in vulnerability descriptions. The study finds that TF-IGM outperforms the traditional TF-IDF in classifying software vulnerabilities. Additionally, the use of feature selection techniques significantly improves classification accuracy.

The study (Kudjo et al., 2020a) uses the concept of Bellwether analysis in predicting software vulnerability severity. The Bellwether analysis identifies a "lead" dataset (the bellwether) that performs well in forecasting for other similar datasets. This method can improve the accuracy of vulnerability severity predictions by leveraging transfer learning techniques.

The authors in Sharma et al. (2021) propose a method for prioritizing software vulnerabilities based solely on their descriptions. The authors eliminate the need for traditional scoring systems by using Natural Language Processing (NLP) techniques like word embeddings combined with a convolutional neural network (CNN). This approach helps categorize vulnerabilities into different severity levels, which improves efficiency in prioritization.

Recent studies focus on predicting vulnerability severity, with an emphasis on effectively handling textual data from vulnerability descriptions. Along these lines, our work also addresses the core challenge of converting textual data into meaningful feature vectors while overcoming the curse of dimensionality. To tackle this, we developed two advanced modules: the first leverages deep learning techniques, and the second utilizes evolutionary computing, providing a more efficient approach to feature selection and vulnerability prediction.

2.2 Feature selection using hybrid filter wrapper algorithm

Alomari et al. (Alomari et al., 2022) study proposes a hybrid feature selection method combining Principal Component Analysis (PCA) and the Grey Wolf Optimizer (GWO) algorithm for Arabic news article classification. This approach enhances classification

accuracy by reducing the feature space effectively. Yang et al. (Yang et al., 2024) propose a fast dual-module hybrid feature selection algorithm designed for high-dimensional data. The method integrates a filter-based module for rapid feature ranking and a wrapper-based module to refine the selected features. By combining these two approaches, the algorithm effectively reduces computational complexity while maintaining high classification accuracy. The study demonstrates the algorithm's efficiency and performance across various high-dimensional datasets, making it suitable for large-scale feature selection tasks. Robindro et al. (Robindro et al., 2024) introduce a hybrid distributed feature selection method combining Particle Swarm Optimization (PSO) with Mutual Information (MI). The MI filter ranks features, and PSO refines the selection by searching for optimal feature subsets. This approach enhances feature selection efficiency and improves classification accuracy in distributed environments. Hancer et al. (Hancer, 2024) introduce a hybrid wrapper-filter feature selection method, enhanced by an improved evolutionary algorithm and a novel initialization scheme. This approach balances computational efficiency and accuracy, accelerating the search for optimal feature subsets. The method outperforms traditional techniques in high-dimensional datasets and improves classification accuracy. Anju et al. (Anju & Judith, 2024) present a hybrid feature selection method for predicting software defects, combining both wrapper and filter approaches to enhance prediction accuracy. The method selects the most relevant features to improve model performance while reducing computational complexity. It demonstrates superior results in identifying software defects compared to traditional feature selection techniques.

2.3 Feature selection using hybrid deep learning algorithm

Jain et al. (Jain et al., 2020) present a sarcasm detection model for mash-up languages using a soft-attention-based bi-directional LSTM and a feature-rich CNN. The bi-directional LSTM captures contextual dependencies from both past and future tokens, while the CNN extracts critical features like syntactic and semantic cues. This hybrid approach significantly improves sarcasm detection in multilingual social media content. Ayetiran et al. (Ayetiran, 2022) proposes a hybrid CNN-BiLSTM model with an attention mechanism for aspect-based sentiment classification. The model captures both local features and long-range dependencies in text, while the attention mechanism enhances sentiment prediction by focusing on important words. This approach improves accuracy, particularly when applied to benchmark datasets. The paper (Thekkekara et al., 2024) presents an attention-based CNN-BiLSTM model for detecting depression in social media text. The CNN captures local patterns in text, while the BiLSTM handles long-term dependencies, and the attention mechanism highlights key depression-related words. This approach improves the accuracy of detecting depressive content in user posts on social platforms. The work in Sun and Chu (2020) presents a hybrid model combining Convolutional Neural Networks (CNN), Bidirectional Long Short-Term Memory (BiLSTM), and an attention mechanism for text sentiment analysis. CNN captures local features, while BiLSTM processes long-range dependencies, and attention enhances important feature focus. The model achieves improved accuracy in sentiment classification tasks compared to traditional methods. The effectiveness of the CNN-BiLSTM hybrid model in sentiment analysis encouraged us to adapt it to our own field of study aiming to assess its impact on the performance of the model, expecting similar improvements.

The above-stated literature depicts the success of these hybrid approaches. Nonetheless, the "No Free Lunch" (NFL) theorem in optimization (Wolpert & Macready, 1997) proves

logically that, with so many problems out in the research domain, no single optimization algorithm can solve all such problems. Relating it to our context of FS, no algorithm can find the optimal set of features for every dataset. Because of this, attempted to hybridize and improve two of the most recent and popular algorithms, GWO and WOA, to solve binary FS problems over textual data more effectively.

3 Preliminaries

In this section of the paper, various preliminaries required for this study are summarized.

3.1 Independent and dependent variables

This study aims at the severity prediction of security vulnerabilities, which is a multi-class problem. The output label or dependent variable is the severity level of vulnerabilities, which can take four values, 'low,' 'medium,' 'high,' and 'critical'. A dataset of vulnerability reports of different software is collected to make this prediction. Several fields are present in a vulnerability report, for example, CVE ID, vulnerability type, publish date, update date, access, complexity, authentication, etc. However, we used an unstructured portion of the vulnerability report for making a prediction, i.e., vulnerability description. Therefore, vulnerability description acts as an independent variable of our study.

3.2 Data collection

Vulnerability reports of five different products of Mozilla are used as datasets in this study. These are Mozilla Firefox (MF), Mozilla Seamonkey (MS), Mozilla Thunderbird (MT), Mozilla Firefox ESR (MF ESR), and Mozilla Thunderbird ESR (MT ESR). The vulnerability reports are extracted which are offered by the CVE following the CVSS framework (Zerkane et al., 2016) for scoring the severity of the vulnerability. This scoring system gives a score to vulnerability in the range of 0 to 10. According to version v3.0 of CVSS, which is the most recent version, a 'None' rating is given to vulnerabilities with a 0.0 score, a 'Low' rating is given to vulnerabilities with a score of 0.1–3.9, 'Medium' rating is given to vulnerabilities with a score of 4–6.9, 'High' rating is given to vulnerabilities with a score of 7–8.9 and 'Critical' rating is given to vulnerabilities with a score of 9–10. Table 1 below gives the dataset's details in context with severity labels. Out of all the attributes of a vulnerability report, vulnerability description is used to carry out experiments in this study as it is unstructured data. Mining unstructured data is a challenge as it is vague and may contain noise. Figure 1 gives

Table 1 Dataset Description

Dataset	Low	Medium	High	Critical
MF	164	897	296	516
MT	22	372	164	363
MS	13	291	61	333
MF ESR	10	284	175	203
MT ESR	1	69	15	131

an example of a vulnerability and all the attributes present in the vulnerability report related to that vulnerability.

3.3 Data preprocessing

Before working with the data, it needs to be pre-processed so that it becomes suitable to be given as input to the classifier using ML algorithms. In our case, we have unstructured data. This unstructured data is pre-processed using standard techniques: tokenization, stop word removal, and stemming (Vijayarani et al., 2015). In tokenization, a sequence of words is divided into individual, meaningful words termed tokens. In stop word removal, various words that do not hold any important information and act as connectors helping with framing the sentences are removed from the text. Stemming helps in reducing any word to its root form, thus reducing duplication.

3.4 Feature selection methods

3.4.1 Information gain

Among filter methods for FS, we used Information Gain (IG) in this study. It is used vividly in the literature. However, its limited use for mining vulnerability reports (Khazaei et al., 2016; Kudjo et al., 2020a; Malhotra & Vidushi, 2021) made us explore it for mining vulnerability reports.

IG (Schuster & Paliwal, 1997) just identifies the words that best clarify the desired concept. It determines the total amount of bits needed to encode any class distribution L is G (L), as seen below.

$$G(L) = -\sum_{c \in C} \frac{n(l)}{N} log_2 p(l) \tag{1}$$

$$\text{where}, N = \sum_{c \in C} n(l) \tag{2}$$

After observing an attribute, A, the number of bits needed to encode a class will be:

$$G(L|A) = -\sum_{a \in A} p(a) \sum_{l \in L} p(a) log_2(p(a)) \tag{3}$$

The attribute having the highest IG is given the highest rank as a high value of Information Gain denotes that a feature is useful for prediction since it offers important information about the target variable, which is denoted by the symbol Ai

$$Infogain(Ai) = \mathrm{G(L)} - \mathrm{G}\left(\frac{\mathrm{L}}{\mathrm{Ai}}\right) \tag{4}$$

#	CVE ID	CWE ID	# of Exploits	Vulnerability Type(s)	Publish Date	Update Date	Score	Gained Access Level	Access	Complexity	Authentication	Conf.	Integ.	Avail.
1	CVE-2021-38502			Exec Code	2021-11-03	2022-07-12	4.3	None	Remote	Medium	Not required	Partial	None	None

Thunderbird ignored the configuration to require STARTTLS security for an SMTP connection. A MITM could perform a downgrade attack to intercept transmitted messages, or could take control of the authenticated session to execute SMTP commands chosen by the MITM. If an unprotected authentication method was configured, the MITM could obtain the authentication credentials, too. This vulnerability affects Thunderbird < 91.2.

Fig. 1 Example of vulnerability report and attribute present related to a vulnerability

The higher value of IG indicates more significance of that term. Hence top N terms having the top values of IG can be selected to construct the model.

3.4.2 Grey wolf optimization

The evolutionary algorithm Grey Wolf Optimization (GWO) has recently been released. Mirjalili et al. (Mirjalili et al., 2014) have proposed it. Based on the social structure and hunting habits of grey wolves, this algorithm's foundation was created. Alpha, beta, delta, and omega are the four hierarchy levels that the GWO algorithm assigns to wolves. The alpha group represents the best option, followed by the beta group for the runner-up position, and the delta group for the third-best option. The remainder of the answers fall into the category of omega. Encircling the prey, stalking the prey, and finally attacking the prey are the three steps that make up the GWO approach. The first stage of encircling the prey can be depicted mathematically using the following equation:

$$\vec{Y}(i+1) = \vec{Y}_t(i) + \vec{P}.\vec{R} \tag{5}$$

$$\vec{R} = \left|\vec{Q}.\vec{Y}_t(i) - \vec{Y}(\mathrm{i})\right| \tag{6}$$

where $\vec{Y}$ and $\vec{Y}_t$ indicate the position of the wolf vector and the prey vector at an iteration i. Coefficients $\vec{P}$ and $\vec{Q}$ are calculated as depicted below:

$$\vec{P} = 2\vec{p}.\vec{n}_1 - \vec{p} \tag{7}$$

$$\vec{Q} = 2.\vec{n_2} \tag{8}$$

$\vec{n}_1$ and $\vec{n}_2$ are vectors that were produced at random in the range [0, 1], and $\vec{p}$ decreases linearly from 2 to 0 over iterations. In the second step or hunting, alpha signifies the best probable outcome, while beta and delta indicate potential prey locations. The best places available in the decision space are updated by Omega based on these three best options. This method of hunting is stated as follows:

$$\vec{Y}(i+1) = \frac{y_1 + y_2 + y_3}{3} \tag{9}$$

where $\vec{y_1}, \vec{y_2}, \vec{y_3}$ are the three best solutions at iteration i. These are calculated as follows:

$$\vec{y_1} = \vec{Y_\alpha} - P_1.\left(\vec{R_\alpha}\right) \tag{10}$$

$$\vec{y_2} = \vec{Y_\beta} - P_2.\left(\vec{R_\beta}\right) \tag{11}$$

$$\vec{y_3} = \vec{Y_\delta} - P_3.\left(\vec{R_\beta}\right) \tag{12}$$

and $\vec{R_\alpha}$, $\vec{R_\beta}$ and $\vec{R_\delta}$ are calculated as follows:

$$\overrightarrow{R_\alpha} = \left|\overrightarrow{Q_1}.\overrightarrow{P_\alpha}. - \vec{P}\right| \tag{13}$$

$$\overrightarrow{R_\beta} = |\overrightarrow{Q_2}.\overrightarrow{P_\beta}. - \vec{P}| \tag{14}$$

$$\overrightarrow{R_\delta} = |\overrightarrow{Q_3}.\overrightarrow{P_\delta}. - \vec{P}| \tag{15}$$

The attacking mechanism of grey wolf is expressed on the basis of vector $\vec{p}$. The range of this vector is [−p, p]. Over iterations, the value of $\vec{p}$ is lowered linearly from 2 to 0 and is denoted by:

$$\vec{p} = 2 - i.\frac{2}{MIter} \tag{16}$$

where MIter stands for the maximum iterations, and i represents iteration counter Fig. 2.

In the binary version of GWO (Mirjalili et al., 2014), to deal with binary optimization problems such as the FS problem (Firpi & Goodman, 2004), the continuous search space is converted to binary using the sigmoid transfer function using Eq. (17).

$$x_{sig} = \frac{1}{1 + e^{-x_i}}, \tag{17}$$

$$x_{binary} = \{0 if rand < x_{sig} 1 otherwise \tag{18}$$

where x_{sig} is a continuous feature value that is inputted to the sigmoid function, rand is a random number generated from the uniform distribution that belongs to [0,1], and x_{binary}, is the updated binary position.

3.5 Deep learning models

3.5.1 Basic CNN model

The CNN model is a deep neural network used in a variety of industries, including bioinformatics, image classification, and speech recognition. Layers with convolution, pooling, and fully linked connections make up the conventional CNN design. CNN has recently been employed to solve NLP issues and has produced successful outcomes (Du et al., 2017; Ghourabi et al., 2020; Rhanoui et al., 2019). Apart from that (Kim & Jeong, 2019; Li et al., 2021; Schirrmeister et al., 2017; Sharma et al., 2021) provide a strong foundation for the claim that CNNs are effective in extracting features from text making the use of the max-pooling layer. For example, through the use of max pooling with a 2×2 window and stride of 2, we efficiently reduce the size of the data, retaining only the most critical information

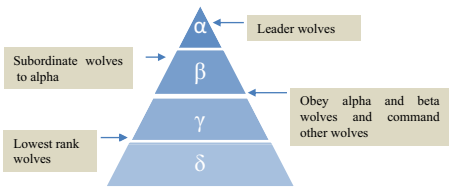

Fig. 2 Hierarchy of wolves

from the text without losing essential n-grams. This allows us to handle the large feature space typical in textual data.

For example, Let's assume we have a small grid of values representing n-gram scores like this:

[5, 1, 2, 4]
[9, 6, 3, 8]
[1, 2, 4, 0]
[7, 8, 1, 5]

After applying a 2×2 max pooling layer with a stride of 2, the result would be:

[9, 8]
[8, 5]

This reduces the overall data size by half but keeps the most important values (the maximum ones).

The polling layer of the CNN model lessens the computational complexity. The output size of one stack layer to the next is decreased by the polling approach while vital data is kept intact. The most popular polling method is known as max-polling, which places the max value element in the polling window. The output of the pooling layer is fed into and mapped to the next layers by the flattening layer. The CNN model's final layer is the fully linked layer.

3.5.2 Bidirectional-long short-term memory networks

CNN can extract important features from textual data. However, it cannot interlink the present information with the past information. While CNNs are powerful for pattern recognition tasks, they may face challenges in directly capturing temporal dependencies. Addressing this limitation often requires incorporating additional architectures or techniques designed specifically for handling sequential data. For this, another deep neural network model, Bi-LSTM can be used. Bi-LSTM (Schuster & Paliwal, 1997) is a type of LSTM model. It belongs to the category of RNN. It processes the data in both forward and backward directions of data in both directions making Bi-LSTM different from the LSTM network. BiLSTMs handle sequential data by processing the input sequence in both forward and backward directions simultaneously, allowing them to capture information from past and future contexts and model long-range dependencies effectively. This makes them well-suited for a wide range of sequential data tasks where understanding the context from both directions is important. Additionally, it has produced positive outcomes in natural language processing (Tai et al., 2015; Yin et al., 2017). This methodology has proven to be effective, particularly when analyzing documents and extensive entries. It creates a connection between the words in the document to forecast its tone.

3.6 Data balancing strategy

Most of the ML algorithms are designed on the assumption that the data over which they will be working is balanced. If applied to imbalanced data, the results often become skewed, showing biased outcomes toward the majority class (Kekül et al., 2021). As shown in Table 1, the data in this case is imbalanced, with low and high classes in the minority for all five databases, whereas medium and critical classes dominate. To address this,

data balancing techniques like oversampling and undersampling are often employed. These methods aim to improve the model's ability to handle class imbalance by either increasing the number of minority class instances or reducing the majority class.

One of the advantages of data balancing techniques is that they help improve model performance by ensuring that minority classes are better represented, thus enabling the model to capture more meaningful patterns across all classes. Balancing techniques also help to reduce bias in the model's predictions, leading to a more equitable evaluation of all classes. This is particularly important in real-world applications, where imbalanced data is common, such as in fraud detection, medical diagnosis, or rare event prediction.

However, data balancing methods come with disadvantages as well. Oversampling techniques, for example, can increase the risk of overfitting by simply duplicating minority class instances or generating synthetic ones, which may cause the model to learn noise rather than general patterns. Undersampling, on the other hand, reduces the amount of data from the majority class, which can result in a loss of valuable information and lead to poorer overall model performance. Additionally, both techniques may introduce longer training times, as oversampling increases the dataset size while undersampling reduces the diversity of the data available for learning.

In this work, SMOTE (Synthetic Minority Oversampling Technique) is employed to address the problem of data imbalance, which offers a solution by generating synthetic samples of the minority class through interpolation rather than duplication (Spelmen & Porkodi, 2018). While it mitigates some of the challenges of traditional oversampling, the broader advantages and disadvantages of data balancing techniques remain important considerations in model development.

3.7 Classification algorithms

Under this category, we concentrated on ensemble learners. It combines multiple ML algorithms to achieve good results to make a single prediction model. The main objective here is to compensate for the error caused due to one ML algorithm with the help of another ML algorithm and get a better-performing model overall (Sagi & Rokach, 2018). Ensemble classifiers often outperform individual base learners, especially in terms of predictive accuracy. By combining multiple models, ensemble classifiers can capture diverse patterns in the data, leading to more robust and accurate predictions. Their effectiveness in improving predictive accuracy and generalization performance has been well-established in both research and practice. This study used three ensemble learners: Bagging, Gradient Boosted Decision Tree (GBDT), and eXtreme Gradient Boosting (XGBoost). Bagging (bootstrap aggregation) is an independent method. Its pseudo-code can be referred from Breiman et al. (Breiman, 1996). It creates a composite classifier by combining the output of different learning algorithms into a single prediction model. On the other hand, unlike bagging, boosting the performance of the next learning technique depends on the prior ones that are developed. More details on GBDT and XGBoost can be found in Bahad and Saxena (2020).

3.8 Performance measures

The base of any performance measure is the confusion matrix. With the help of the confusion matrix, further parameters of performance measures can be calculated. In this study, the problem is not just a binary problem. It is a multiclass classification problem.

In this study, we used AUC as the performance measure to evaluate the effectiveness of our experiment conducted. AUC as a performance measure is a popular choice among researchers as it finds a balance between both specificity and sensitivity values. Additionally, AUC is insensitive to changes in the class distribution or prevalence of the positive class (He & Garcia, 2009). Overall, AUC offers a more comprehensive and robust evaluation of classifier performance compared to traditional metrics like accuracy, sensitivity, specificity, and precision, making it widely used in classification tasks. Its value ranges from 0 to 1 and is shown by a plot of the sensitivity and specificity values on the x- and y-axes, respectively. If the value of AUC is substantial and reaches 1, the prediction model is regarded as having produced accurate results. An AUC value of 1 denotes the model's perfect performance; an AUC value between 0.9 and 0.99 denotes the model's excellent performance; an AUC value between 0.8 and 0.89 denotes the model's good performance; an AUC value between 0.7 and 0.79 denotes the model's fair performance; and an AUC value below 0.7 denotes the model's subpar performance.

3.9 Statistical tests

According to the experiment, appropriate statistical tests are found to perform hypothesis testing. It is necessary to apply statistical tests as it can be misleading to derive a conclusion based on performance measures (Olson & Delen, 2008). Statistical tests are categorized as parametric and nonparametric statistical tests. Parametric statistical tests are used if the data on which it is needed to be applied follows some strict assumptions. If not, then nonparametric statistical tests are applied. The selection of statistical tests also depends on the number of data samples we deal with. Are we going to apply the test to two or more two samples that are dependent or independent of each other. The researcher finds an appropriate statistical test applicable to his study based on all these conditions. One-way ANOVA, Mann Whitney U test, Friedman test, and Wilcoxon signed-rank test are some of the statistical tests. According to our data, the widely accepted Friedman test is applicable.

4 The proposed methodology

This section outlines the methodology proposed in the paper, which focuses on dimensionality reduction and the development of a feature selection (FS) module aimed at improving model performance. The primary objective is to introduce two novel FS modules not addressed in existing literature: one based on Filter-Wrapper FS (FWFS), and the other based on a Hybrid Deep Learning Network (HDLN). To evaluate the effectiveness of the proposed modules, five additional scenarios are considered. These scenarios involve developing SVSPMs using different FS methods: one without FS, one utilizing Information Gain (IG) for FS, and another employing Grey Wolf Optimization (GWO) for FS. The rationale behind selecting IG and GWO for FS is to isolate individual components of the FWFS module and assess their impact on results. Furthermore, Convolutional Neural Network (CNN) and Bidirectional Long Short-Term Memory (Bi-LSTM) models are used for FS in two additional scenarios. These choices aim to investigate whether the combined use of CNN and Bi-LSTM, as in the HDLN module, leads to performance improvements.

4.1 Main scenario 1: HDLN module

This module integrates two neural networks, CNN and Bi-LSTM. This combination is chosen because CNN is renowned for its effectiveness in extracting features from text. Meanwhile, the Bi-LSTM network processes data in both forward and backward directions, thereby preserving the chronological order of the data. By integrating these architectures, the resulting model gains the ability to extract hierarchical representations that encompass both spatial and temporal aspects of the data. This fusion enhances the model's contextual understanding, robustness to variability, and effectiveness in capturing complex relationships. More specifically, CNN is effective in learning hierarchical representations of features from raw input data. CNNs possess the capability to automatically extract features at various levels of abstraction, effectively `performing feature selection by emphasizing the most discriminative features for the given task. However, they cannot establish connections between present and past data. Hence, adding Bi-LSTM addresses this limitation by simultaneously processing input sequences in both forward and backward directions, ensuring effective handling of sequential data. Consequently, this combined architecture proves highly suitable for a diverse range of sequential data tasks wherein understanding the context in both directions is essential.

The proposed framework comprises three sections as illustrated in Fig. 3. The number of layers and parameters employed by the HDLN module is depicted in Fig. 4. Further in the text, the structure of the HDLN module is delineated, along with a detailed description of its parameters.

Preprocessing: In this phase, raw data is preprocessed using tokenization, stop word removal, and stemming. The reduced data is then fed into the embedding layer using Word-2Vec embedding to produce an embedding matrix used as input by the convolution layer. The text is converted via Word2Vec into a vector of numerical values. The embedding matrix is composed of a sentencing matrix which may be written as:

$$S_m = \{V(W_1), V(W_2), \ldots\ldots, V(W_i)\} \tag{19}$$

where Wi is the word of the sentence, and V (W_i) is the word vector of dimension K. Maximum sequence length is 250, i.e., i is taken to be 250 here. K is the number of integers to which Word2Vec converts every word into. In this paper, the value of K is 100.

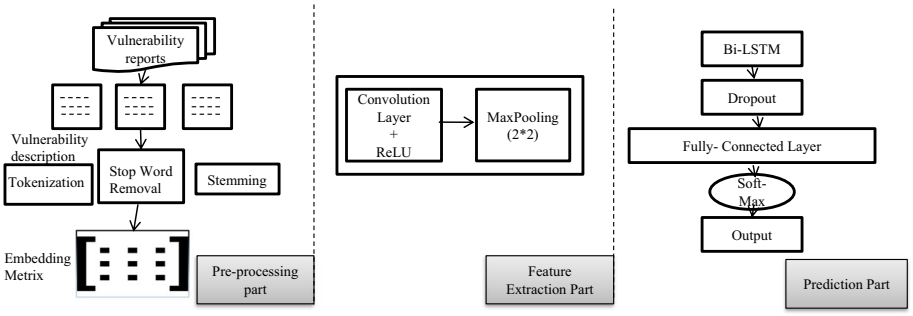

Fig. 3 Framework of HDLN module

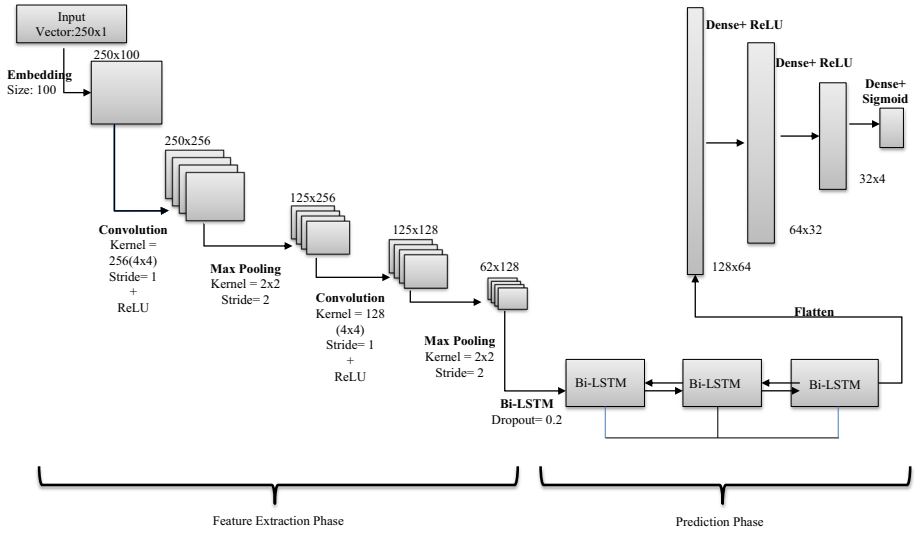

Fig. 4 Layers and parameters of NN of HDLN module

Feature Extraction based on CNN: The embedding matrix generated in the above step is taken as input. Two convolution layers and two max-pooling layers are applied alternatively in this stage. The first convolution layer contains 256 filters of dimension 4×4, and the second convolution layer contains 128 filters of dimension 4×4. Filters applied in the convolution layer also act as n-gram detectors. As the filter slides from top to bottom with a stride of 1 and passes through the whole S_m, it generates a local eigenvector set C_m as follows:

$$C_m = f(S_m * F) \tag{20}$$

where F denotes the filter and f represents the RELU activation function. It replaces negative values with zeros reducing the non-linearity of the network. The detected n-grams achieving the highest score are then passed to the max pooling layer of dimension 2x2 and stride of 2 which reduces the size of the data.

Prediction based on Bi-LSTM Network. The output generated from the max pooling layer is concatenated and acts as input to this stage. Every word in the feature set is fed into the Bi-LSTM network cell. Bi-LSTM carries slightly different hidden computations. After that dropout (0.2) layer is implemented to prevent our model from overfitting. Every current input (or neuron) in the layer of the network is connected to every input (or neuron) in the layer that comes after it using the dense layer, also referred to as the completely connected layer. This network uses two dense layers. The final layer is the Softmax layer. It is often the last layer in any neural network. To achieve the desired output, the Softmax layer uses sigmoid as an activation function to assign classes to vulnerability prediction.

Smaller filter sizes, such as 2×2, were found to be inadequate in capturing sufficient contextual information, while larger filter sizes like 5×5 or 6×6 added unnecessary complexity without yielding significant improvements in accuracy. A 4×4 filter size offered the optimal balance, effectively capturing relevant word patterns while maintaining computational efficiency (Johnson & Zhang, 2014; Kalchbrenner et al., 2014; Zhang & Wallace, 2015). Furthermore, increasing the number of filters enhances the model's ability to

capture detailed features, but it also raises the risk of overfitting and increases computational demands. A configuration of 256 filters in the first layer, to capture a wide range of initial patterns, followed by 128 filters in the second layer to refine these patterns, was found to strike the best balance between performance and computational efficiency (Johnson & Zhang, 2014; Santos & Gatti, 2014; Zhang & Wallace, 2015).

The choice of a 2×2 max-pooling size with a stride of 2 is consistent with standard CNN architectures, as it effectively reduces the spatial dimensions of the feature maps while preserving important information (LeCun et al., 1998). A dropout rate of 0.2 was selected to mitigate overfitting and ensure better generalization during training (Hochreiter, 1997). This allows the model to capture essential features while maintaining computational efficiency and preventing overfitting, ultimately improving the overall performance of the vulnerability prediction task.

4.2 Main scenario 2: FWFS module

Filter methods for feature selection (FS) are computationally inexpensive and rapid. However, they may not always yield the optimal performance for SVSPMs. On the other hand, wrapper methods can achieve better classification performance for SVSPMs but are computationally intensive and time-consuming. To leverage the benefits of both approaches, an FWFS module is proposed, which integrates filter and wrapper methods to assess the fitness of feature subsets. The proposed architecture consists of three sections, illustrated in Fig. 5 and elaborated upon below:

1. Data generation: The first step is to generate input data from the raw unstructured data available. This requires a series of sub-steps. As we have unstructured data, there is a need to preprocess this data. The traditional preprocessing steps for unstructured data are tokenization, stop word removal, and stemming. After applying all these steps, we are left with a reduced set of tokens compared with the original data set. For vectorization unigram Bag-Of -Word (BoW) model is used which works on the vocabulary of features. For example, 'Sudo before 1.9.13 does not escape control characters in sudoreplay output.' is the vulnerability description for Vulnerability 1 (V1), and 'Sudo before 1.9.13 does not escape control characters in log messages.' is the vulnerability description for Vulnerability 2 (V2). Now V1 and V2 are represented as [1 1 1 1 1 1 0 0 1 1 1 1 1] and [1 1 1 1 1 1 1 1

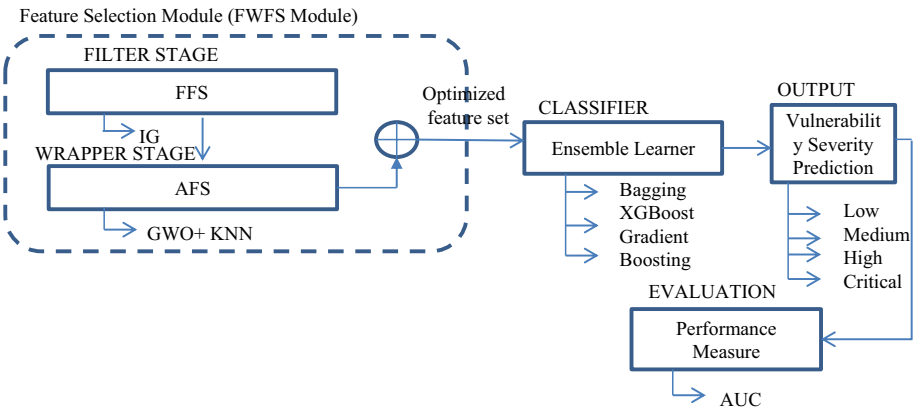

Fig. 5 Framework of FWFS module

1 0 1 0 1] respectively on the basis of vocabulary < before characters control does escape in log messages, not output sudo sudoreplay 1.9.13 > of size 13. These vectors are then weighted according to their frequency in the text using the TF-IDF approach, and feature vectors are formed. It is considered to be a powerful and easy statistical method for term weighting (Ramos, 2003; Witten et al., 2016).

2. Feature Selection: The second step focuses on reducing the number of features, known as dimensionality reduction. This term was first coined by Richard Bellman (1957). It is very important to reduce dimensionality, eliminating those words that possess no or least information from the text. The main concern of the filter part of the FWFS module is to fasten the process fitness evaluation. Therefore, the IG method, a computationally cheap method, is used to form the fitness evaluation based on the Min-Redundancy Max-Relevance (MRMR) criterion (Long & Ding, 2005) acting as an FFS. Feature vectors generated in Step 1 are used to evaluate the IG of all features using Eq. (4), and the features subset having the highest value for IG is finally selected. In the wrapper part of the FWFS module bGWO technique is used. It is a newly-proposed swarm intelligence technique analogous to the hunting and dominancy behavior of grey wolves in nature (Faris et al., 2018). This algorithm has been used to a vast number of issues in the literature. Important features are extracted through the GWO technique which acts as AFS with fitness function as minimizing the error rate of K-NN where K-NN is applied as the final classifier. As shown in Eq. (21), the following fitness function is utilized in this paper.

$$Fitness(X) = (\alpha * ErrorRate) + (1 - \alpha)\frac{N - S}{S} \tag{21}$$

where X represents the subset of features chosen by the GWO algorithm, ErrorRate represents the K-NN classifier's error rate on the training dataset, α represents a factor that balances the error rate and the size of the features chosen, N represents the total number of features in the dataset, and S represents the size of the features subset.

The selection of the most significant features (words) based on bGWO is listed below in the following steps:

1. The initial position of the wolves is generated, which is the total number of words.
2. The importance of every wolf is calculated based on a fitness function.
3. Wolfs are classified into four groups alpha, beta, delta, and omega.
4. The movement of wolves is seen toward the best wolf of the group, i.e., the alpha wolf.
5. Wolves of low worth are deleted, and the best wolfs representing nothing, but the features based on dominance and crowding distance are selected.

Every algorithm starts with the setting of parameters and initialization of the population, randomly. Table 2 outlines the parameter settings used to conduct this study. All the parameters are either chosen based on domain-specific information, as in the case of the parameters α, β, or by doing small trial simulations, or they are chosen based on what is commonly found in the literature, as in the case of the remaining parameters. Through prior studies, it is observed that the Grey Wolf Optimizer (GWO) tends to converge within a reasonable number of iterations, and setting it to 70 is sufficient to achieve convergence

Table 2 List of parameters used

Repetition of Runs	20
Number of Iterations	70
Search Agents	8
Dimension	Number of features
Search Domain	[0 1]
α	0.99
B	0.01

in many cases. Our primary goal is to compare the performance of the various feature selection problems compared to the proposed module for feature selection.

FS selects the features that boost and maximize the performance of the classifier. Binary chromosome illustration is utilized to depict the feature subset selection as depicted in Fig. 6. The chromosome's length indicates the total number of features. The value '1' suggests selecting the feature and the value '0' suggests rejecting the feature.

3. As shown in Table 1, the dataset exhibits imbalance. To address this imbalance, SMOTE, an oversampling strategy, is employed.

4. Classification: When the input data is reduced and balanced, it is fed into the classifier, and the final output is generated. Instead of using simple ML algorithms to develop a classifier, more powerful ensemble learners (Schirrmeister et al., 2017) are exploited. Among the ensemble learning techniques investigated, we have delved into Bagging and Boosting methods, including Gradient Boosting Decision Trees (GBDT) and XGBoost due to their exceptional predictive performance, robustness to overfitting, flexibility in handling diverse data types, feature importance analysis capabilities, and widespread adoption in both academia and industry. The outcomes are documented using Area Under the Curve (AUC) as a metric for performance evaluation. Following the recording of results for the primary scenarios, an additional five scenarios are executed, with subsequent recording and analysis of the results. For hypothesis testing, statistical analysis is performed to judge whether the performance of different strategies differs significantly or not. For this purpose, we need to frame a null hypothesis (Ho) and an alternate hypothesis (H1). Both are stated below.

Ho: The performance of SVSPMs developed using different FS strategies is the same and does not differ significantly.

RQ1. How does SVSPM perform better when different FS methods are used to make the data less dimensional?

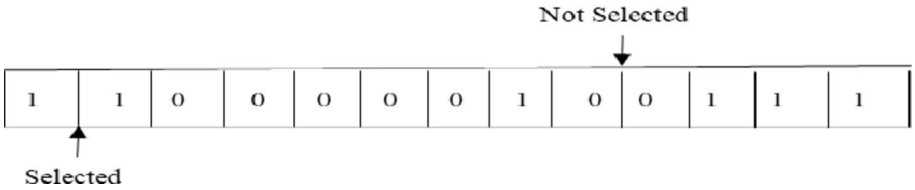

Fig. 6 Solution representation

Table 3 AUC values for Mozilla Firefox

Feature Selection	Model	Low	Medium	High	Critical	AVERAGE
Deep Learning	Bi-LSTM	0.86	0.84	0.7	0.91	0.83
	CNN	0.85	0.81	0.7	0.92	0.82
HDLN	CNN + Bi-LSTM	0.89	**0.86**	0.76	0.92	0.86
Filter Method	IG + Bagging	0.9	0.73	0.89	0.92	0.86
	IG + GB	0.94	0.77	0.89	0.91	0.88
	IG + XGB	0.93	0.77	0.88	0.92	0.88
Wrapper Method	GWO + Bagging	0.89	0.72	0.85	0.88	0.84
	GWO + GB	0.94	0.78	0.88	0.91	0.88
	GWO + XGB	0.95	0.76	0.89	0.92	0.88
FWFS	GWO + IG + Bagging	0.91	0.75	0.85	0.89	0.85
	GWO + IG + GB	0.94	0.76	0.87	0.92	0.87
	GWO + IG + XGB	**0.95**	0.78	**0.9**	**0.93**	**0.89**
No Feature Selection	Bagging	0.79	0.72	0.79	0.86	0.79
	GB	0.76	0.7	0.77	0.87	0.78
	XGB	0.79	0.72	0.82	0.89	0.81

Table 4 AUC values for Mozilla Thunderbird

Feature Selection	Model	Low	Medium	High	Critical	AVERAGE
Deep Learning	Bi-LSTM	0.92	0.78	0.83	0.95	0.87
	CNN	0.89	0.73	0.76	0.94	0.83
HDLN	CNN + Bi-LSTM	**0.95**	**0.81**	0.86	**0.95**	**0.89**
Filter Method	IG + Bagging	0.78	0.61	0.81	0.83	0.76
	IG + GB	0.86	0.68	**0.93**	0.87	0.84
	IG + XGB	0.8	0.66	0.9	0.86	0.81
Wrapper Method	GWO + Bagging	0.74	0.63	0.87	0.8	0.76
	GWO + GB	0.83	0.68	0.93	0.87	0.83
	GWO + XGB	0.83	0.66	0.9	0.87	0.82
FWFS	GWO + IG + Bagging	0.83	0.68	0.89	0.82	0.81
	GWO + IG + GB	0.81	0.69	0.88	0.85	0.81
	GWO + IG + XGB	0.85	0.7	0.9	0.88	0.83
No Feature Selection	Bagging	0.59	0.63	0.68	0.78	0.67
	GB	0.41	0.66	0.79	0.79	0.66
	XGB	0.5	0.66	0.78	0.8	0.69

The result values are recorded in Tables 3, 4, 5, 6, 7 for AUC and Tables 8, 9, 10, 11, 12 for the F1 measure. When AUC values are observed for the Mozilla Firefox vulnerability database, the highest values obtained are 0.95, 0.86, 0.90, 0.93, and 0.89 for GWO + IG + GXB, CNN + Bi-LSTM, GWO + IG + GXB, GWO + IG + GXB, GWO + IG + GXB models respectively. 0.76, 0.70, 0.70,0.86, and 0.78 are the lowest values obtained using NOFS + GB, NOFS + GB, Bi-LSTM, and CNN, NOFS + Bagging NOFS + GB. NOFS stands for No FS. The result values are in the sequence of a low,

Table 5 AUC values for Mozilla Seamonkey

Feature Selection	Model	Low	Medium	High	Critical	AVERAGE
Deep Learning	Bi-LSTM	0.86	0.81	0.72	0.92	0.83
	CNN	0.86	0.72	0.71	**0.94**	0.81
HDLN	CNN + Bi-LSTM	**0.95**	**0.82**	**0.86**	**0.94**	**0.89**
Filter Method	IG + Bagging	0.66	0.65	0.79	0.72	0.71
	IG + GB	0.78	0.71	0.82	0.81	0.78
	IG + XGB	0.73	0.68	0.8	0.8	0.75
Wrapper Method	GWO + Bagging	0.64	0.66	0.75	0.74	0.70
	GWO + GB	0.74	0.7	0.83	0.82	0.77
	GWO + XGB	0.8	0.68	0.83	0.8	0.78
FWFS	GWO + IG + Bagging	0.68	0.65	0.78	0.72	0.71
	GWO + IG + GB	0.81	0.72	0.82	0.82	0.79
	GWO + IG + XGB	0.82	0.73	0.85	0.84	0.81
No Feature Selection	Bagging	0.46	0.61	0.54	0.71	0.58
	GB	0.73	0.6	0.71	0.72	0.69
	XGB	0.63	0.61	0.74	0.71	0.67

Table 6 AUC values for Mozilla Firefox ESR

Feature Selection	Model	Low	Medium	High	Critical	AVERAGE
Deep Learning	Bi-LSTM	0.96	0.78	0.87	0.95	0.89
	CNN	0.95	**0.8**	0.81	0.9	0.87
HDLN	CNN + Bi-LSTM	**0.97**	**0.8**	**0.91**	**0.97**	**0.91**
Filter Method	IG + Bagging	0.76	0.71	0.78	0.86	0.78
	IG + GB	0.8	0.69	0.81	0.92	0.81
	IG + XGB	0.75	0.66	0.81	0.9	0.78
Wrapper Method	GWO + Bagging	0.75	0.68	0.75	0.9	0.77
	GWO + GB	0.76	0.68	0.8	0.92	0.79
	GWO + XGB	0.78	0.65	0.83	0.9	0.79
FWFS	GWO + IG + Bagging	0.73	0.73	0.84	0.83	0.78
	GWO + IG + GB	0.75	0.69	0.82	0.85	0.78
	GWO + IG + XGB	0.82	0.68	0.83	0.94	0.82
No Feature Selection	Bagging	0.71	0.66	0.75	0.9	0.76
	GB	0.72	0.65	0.79	0.9	0.77
	XGB	0.73	0.68	0.8	0.87	0.77

medium, high, and critical severity level. The fifth value is the average result of all these four severity levels. A similar analysis for the remaining four databases is documented further in the text. For Mozilla Thunderbird, 0.95, 0.81, 0.93, 0.95, 0.89 are the highest values obtained with the use of CNN + Bi-LSTM, CNN + Bi-LSTM, IG + GB, CNN + Bi-LSTM, and CNN + Bi-LSTM respectively. 0.41, 0.61, 0.68, 0.78, and 0.66 are the lowest values obtained with the use of NOFS + GB, IG + Bagging, NOFS + Bagging, NOFS + Bagging, and NOFS + GB respectively. For Mozilla Seamonkey, 0.97, 0.80, 0.91, 0.97, and 0.91 are

Table 7 AUC values for Mozilla Thunderbird ESR

Feature Selection	Model	Low	Medium	High	Critical	AVERAGE
Deep Learning	Bi-LSTM	Nan	0.83	0.76	0.85	0.81
	CNN	Nan	0.9	0.89	0.94	0.91
HDLN	CNN + Bi-LSTM	Nan	**0.9**	0.9	**0.95**	**0.92**
Filter Method	IG + Bagging	Nan	0.66	0.8	0.77	0.74
	IG + GB	Nan	0.72	0.98	0.8	0.83
	IG + XGB	Nan	0.76	**0.97**	0.83	0.85
Wrapper Method	GWO + Bagging	Nan	0.65	0.82	0.74	0.74
	GWO + GB	Nan	0.68	**0.97**	0.78	0.81
	GWO + XGB	Nan	0.77	**0.97**	0.83	0.86
FWFS	GWO + IG + Bagging	Nan	0.64	0.82	0.73	0.73
	GWO + IG + GB	Nan	0.72	**0.97**	0.8	0.83
	GWO + IG + XGB	Nan	0.76	**0.97**	0.83	0.85
No Feature Selection	Bagging	Nan	0.61	0.62	0.7	0.64
	GB	Nan	0.55	0.56	0.59	0.57
	XGB	Nan	0.62	0.79	0.69	0.70

Table 8 F1 measure for Mozilla Firefox

Feature Selection	Model	Low	Medium	High	Critical	AVERAGE
Deep Learning	Bi-LSTM	0.8	0.79	0.66	0.88	0.78
	CNN	0.81	0.77	0.65	0.86	0.77
HDLN	CNN + Bi-LSTM	0.8	**0.82**	0.72	**0.89**	0.81
Filter Method	IG + Bagging	0.85	0.69	0.83	0.88	0.81
	IG + GB	0.9	0.74	0.85	0.87	0.84
	IG + XGB	0.88	0.72	0.8	0.85	0.81
Wrapper Method	GWO + Bagging	0.84	0.68	0.82	0.81	0.79
	GWO + GB	0.78	0.71	0.79	0.8	0.77
	GWO + XGB	0.85	0,68	0.77	0.83	0.82
FWFS	GWO + IG + Bagging	0.87	0.72	0.79	0.85	0.81
	GWO + IG + GB	0.9	0.71	0.83	0.88	0.83
	GWO + IG + XGB	**0.89**	0.75	**0.85**	**0.89**	**0.85**
No Feature Selection	Bagging	0.77	0.66	0.76	0.83	0.76
	GB	0.7	0.65	0.74	0.82	0.73
	XGB	0.7	0.7	0.77	0.83	0.75

the highest values obtained using the CNN + Bi-LSTM model for all four severity levels and the average case. 0.46, 0.60, 0.54, 0.71, and 0.58 are the lowest values obtained with the use of NOFS + Bagging, NOFS + GB, NOFS + Bagging, NOFS + GB, and NOFS + Bagging respectively. For Mozilla Firefox ESR, 0.97, 0.80, 0.91, 0.97, and 0.91 are the highest values obtained using the CNN + Bi-LSTM model for all four severity levels and as well as for average cases. 0.71, 0.65, 0.75, 0.83, and 0.76 are the lowest values obtained with the use of NOFS + Bagging, NOFS + GB, NOFS + Bagging, GWO + IG + Bagging, and

Table 9 F1 measure for Mozilla Thunderbird

Feature Selection	Model	Low	Medium	High	Critical	AVERAGE
Deep Learning	Bi-LSTM	0.85	0.75	0.8	0.8	0.80
	CNN	0.86	0.68	0.71	0.88	0.78
HDLN	CNN + Bi-LSTM	**0.9**	**0.76**	0.8	**0.89**	**0.84**
Filter Method	IG + Bagging	0.71	0.6	0.77	0.79	0.72
	IG + GB	0.85	0.66	**0.89**	0.81	0.80
	IG + XGB	0.77	0.65	0.85	0.83	0.78
Wrapper Method	GWO + Bagging	0.7	0.6	0.82	0.79	0.73
	GWO + GB	0.78	0.62	0.87	0.83	0.78
	GWO + XGB	0.78	0.64	0.84	0.81	0.77
FWFS	GWO + IG + Bagging	0.79	0.64	0.83	0.77	0.76
	GWO + IG + GB	0.78	0.64	0.83	0.81	0.77
	GWO + IG + XGB	0.81	0.67	0.86	0.82	0.79
No Feature Selection	Bagging	0.55	0.6	0.61	0.77	0.63
	GB	0.4	0.62	0.77	0.74	0.63
	XGB	0.5	0.62	0.75	0.78	0.66

Table 10 F1 measure for Mozilla Seamonkey

Feature Selection	Model	Low	Medium	High	Critical	AVERAGE
Deep Learning	Bi-LSTM	0.81	0.76	0.69	**0.88**	0.79
	CNN	0.8	0.7	0.67	**0.88**	0.76
HDLN	CNN + Bi-LSTM	**0.91**	**0.78**	**0.82**	**0.88**	**0.85**
Filter Method	IG + Bagging	0.65	0.65	0.75	0.7	0.69
	IG + GB	0.73	0.66	0.78	0.79	0.74
	IG + XGB	0.68	0.66	0.78	0.77	0.72
Wrapper Method	GWO + Bagging	0.61	0.62	0.71	0.69	0.66
	GWO + GB	0.7	0.69	0.78	0.77	0.74
	GWO + XGB	0.78	0.65	0.78	0.79	0.75
FWFS	GWO + IG + Bagging	0.65	0.61	0.73	0.69	0.67
	GWO + IG + GB	0.78	0.68	0.78	0.77	0.75
	GWO + IG + XGB	0.77	0.69	0.81	0.79	0.77
No Feature Selection	Bagging	0.44	0.6	0.5	0.68	0.56
	GB	0.69	0.55	0.65	0.69	0.65
	XGB	0.6	0.58	0.71	0.67	0.64

NOFS + Bagging respectively. For Mozilla Thunderbird ESR, 0.90, 0.97, 0.95, and 0.92 are the highest values obtained using CNN + Bi-LSTM, CNN + Bi-LSTM, and CNN + Bi-LSTM for the medium and critical levels of severity. The third value is for the average case. For the high severity level, 0.97 is the highest value obtained using several models, which are IG + XGB, GWO + GB, GWO + XGB, GWO + IG + GB, and GWO + IG + XGB. 0.55, 0.56, 0.59, and 0.57 are the lowest values obtained with the use of the NOFS + GB model for all levels and as well as for the average case. For this database, we could not get

Table 11 F1 measure for Mozilla Firefox ESR

Feature Selection	Model	Low	Medium	High	Critical	AVERAGE
Deep Learning	Bi-LSTM	0.91	0.72	0.83	0.89	0.84
	CNN	0.88	0.75	0.77	0.81	0.80
HDLN	CNN + Bi-LSTM	**0.93**	**0.76**	**0.86**	**0.93**	**0.87**
Filter Method	IG + Bagging	0.71	0.66	0.73	0.83	0.73
	IG + GB	0.77	0.65	0.78	0.86	0.77
	IG + XGB	0.71	0.62	0.77	0.85	0.74
Wrapper Method	GWO + Bagging	0.71	0.63	0.71	0.85	0.73
	GWO + GB	0.73	0.62	0.76	0.87	0.75
	GWO + XGB	0.75	0.61	0.77	0.86	0.75
FWFS	GWO + IG + Bagging	0.7	0.7	0.81	0.8	0.75
	GWO + IG + GB	0.72	0.63	0.78	0.81	0.74
	GWO + IG + XGB	0.77	0.65	0.8	0.9	0.78
No Feature Selection	Bagging	0.68	0.66	0.7	0.85	0.72
	GB	0.68	0.61	0.73	0.87	0.72
	XGB	0.69	0.65	0.77	0.83	0.74

Table 12 F1 measure for Mozilla Thunderbird ESR

Feature Selection	Model	Low	Medium	High	Critical	AVERAGE
Deep Learning	Bi-LSTM	Nan	0.77	0.7	0.8	0.76
	CNN	Nan	0.81	0.8	0.79	0.80
HDLN	CNN + Bi-LSTM	Nan	**0.88**	0.84	**0.89**	**0.87**
Filter Method	IG + Bagging	Nan	0.62	0.77	0.72	0.70
	IG + GB	Nan	0.68	0.92	0.76	0.79
	IG + XGB	Nan	0.7	0.92	0.79	0.80
Wrapper Method	GWO + Bagging	Nan	0.6	0.74	0.7	0.68
	GWO + GB	Nan	0.63	0.91	0.72	0.75
	GWO + XGB	Nan	0.73	**0.93**	0.77	0.81
FWFS	GWO + IG + Bagging	Nan	0.6	0.8	0.68	0.69
	GWO + IG + GB	Nan	0.66	**0.93**	0.77	0.79
	GWO + IG + XGB	Nan	0.7	**0.93**	0.75	0.79
No Feature Selection	Bagging	Nan	0.56	0.6	0.66	0.61
	GB	Nan	0.51	0.5	0.55	0.52
	XGB	Nan	0.58	0.73	0.62	0.64

results for a low level of severity as it had very few numbers of instances under it. More or less similar patterns were seen for the values of the F1 measure.

In a nutshell, out of the total 19 best values, 14 values are given by the model using the HDLN module for FS, four values are given by the model using the FWFS module for FS, and the remaining one value which is for high severity level of Mozilla Thunderbird database is given by IG + GB. The value is 0.93. However, the second-highest value is 0.90, given by the FWFS module. If we look at average case values for all five databases,

referring to Table 13, four values are obtained by the HDLN module, and one value is obtained by the FWFS module. Similarly, if we briefly analyze the lowest values based on average case values, all five values are obtained when no FS method is applied. Therefore, referring to the above result analysis, it can be stated that our proposed models definitely helped in improving the efficiency of SVSPM. A deeper analysis of results is done in further RQs below.

RQ1.1 *When the HDLN module is used to lower the dimensionality of the data, what performance improvement does SVSPM experience?*

To address this RQ, Fig. 7. is constructed using values from Table 13. It compares the performance of the model constructed using the HDLN module with the CNN model and Bi-LSTM model. It is clearly depicted in Fig. 7. that the model using the HDLN module gave the best performance of 0.86, 0.88, 0.88, and 0.88 for Mozilla Firefox, Mozilla Thunderbird, Mozilla Seamonkey, Mozilla Firefox ESR, and Mozilla Thunderbird ESR respectively. From the Bi-LSTM model, the HDLN module gave a percentage improvement of 3.61%, 2.24%, 3.40%, 3.40%, and 2.23% for all five databases respectively. From the CNN model, the HDLN module gave a percentage improvement of 4.65%, 6.74%, 5.68%, 5.68%, and 5.68% for all five databases respectively.

This analysis demonstrates the superiority of the HDLN module in terms of overall classification performance. The module is more effective in capturing features and making accurate predictions across different Mozilla databases, particularly when compared to traditional models like CNN and Bi-LSTM. Thus, the HDLN module proves to be a highly efficient and robust solution for the task at hand.

RQ1.2 When the FWFS module is used to lower the dimensionality of the data, what performance improvement does SVSPM experience?

When Fig. 8. is analyzed it can be observed that, for all five databases, models developed without FS, irrespective of classifier used gave a poor performance (depicted by blue line in the graphs) and models developed using FWFS module gave the best performance (depicted by yellow line in the graph).

Table 13 Average result values

Feature Selection	Model	MF	MT	MS	MF ESR	MT ESR	AVERAGE
Deep Learning	Bi-LSTM	0.83	0.87	0.85	0.85	0.86	0.85
	CNN	0.82	0.83	0.83	0.83	0.83	0.83
HDLN	CNN + Bi-LSTM	0.86	**0.89**	**0.88**	**0.88**	**0.88**	**0.88**
Filter Method	IG + Bagging	0.86	0.76	0.81	0.81	0.79	0.81
	IG + GB	0.88	0.84	0.86	0.86	0.85	0.85
	IG + XGB	0.88	0.81	0.84	0.84	0.83	0.84
Wrapper Method	GWO + Bagging	0.84	0.76	0.80	0.80	0.79	0.80
	GWO + GB	0.88	0.83	0.85	0.85	0.84	0.85
	GWO + XGB	0.88	0.82	0.85	0.85	0.84	0.85
FWFS	GWO + IG + Bagging	0.85	0.81	0.83	0.83	0.82	0.83
	GWO + IG + GB	0.87	0.81	0.84	0.84	0.83	0.84
	GWO + IG + XGB	**0.89**	0.83	0.86	0.86	0.85	0.86
No Feature Selection	Bagging	0.79	0.67	0.73	0.73	0.71	0.73
	GB	0.78	0.66	0.72	0.72	0.70	0.72
	XGB	0.81	0.69	0.75	0.75	0.73	0.74

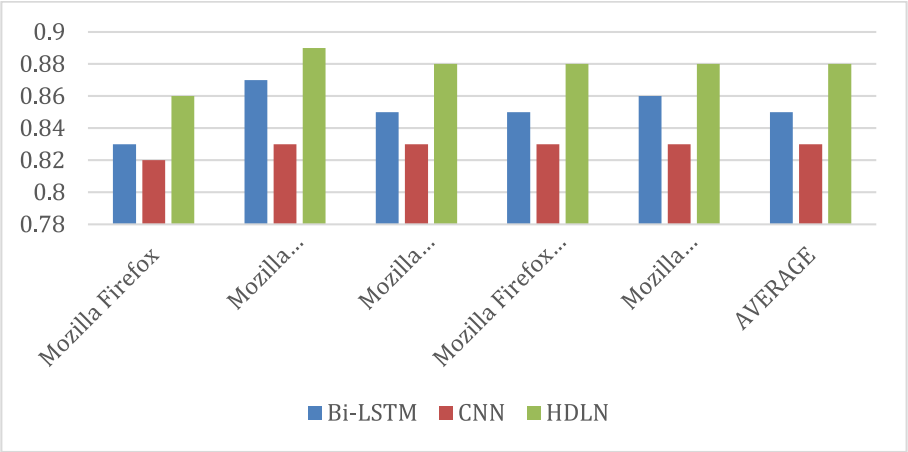

Fig. 7 AUC values comparing performance of HDLN module with CNN & BI-LSTM model

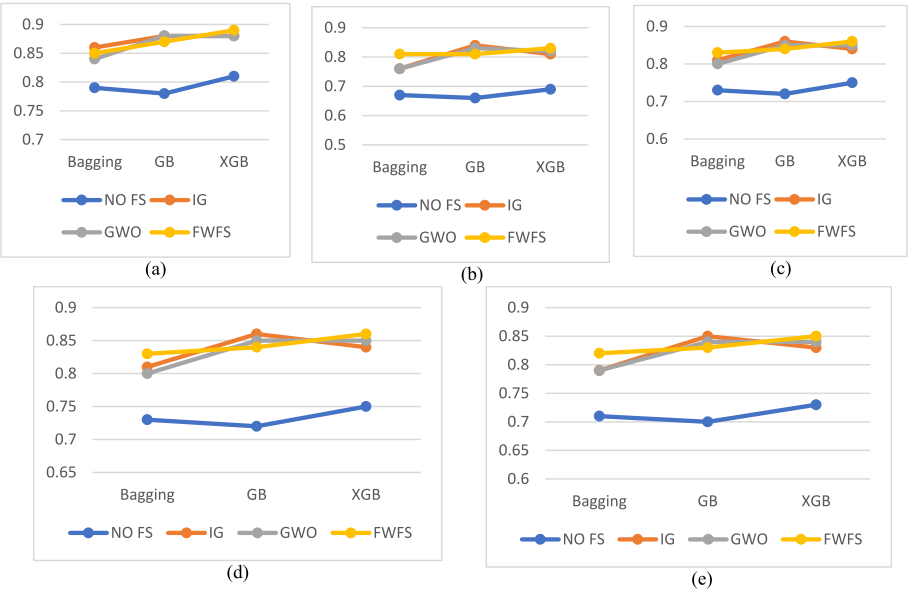

Fig. 8 AUC values comparing performance of FWFS module with No FS, IG, and GWO methods of FS for (**a**) Mozilla Firefox (**b**) Mozilla Thunderbird (**c**) Mozilla Seamonkey (**d**) Mozilla Firefox ESR (**e**) Mozilla Thunderbird ESR

The average percentage improvement of 9.58%, 18.06% and 14.86% is recorded when IG FS method is applied over bagging, GB, and XGB model. The average percentage improvement of 10.95%, 18.06% and 13.51% is recorded when GWO FS method is applied over bagging, GB, and XGB model. The average percentage improvement of 13.70%, 16.67% and 16.22% is recorded when FWFS module is applied over bagging, GB, and XGB model.

In conclusion, feature selection is crucial for enhancing model performance, and the FWFS module consistently delivers the best results across all classifiers. The FWFS module outperformed both the IG and GWO methods, demonstrating its superior ability to identify relevant features and improve classification accuracy. These findings highlight the importance of incorporating advanced FS techniques to achieve optimal model performance.

RQ2. Which module of FS among the two proposed modules gave the best results?

To address RQ2, graph of Fig. 9. is constructed based on percentage improvement in the performance of the model using HDLN module and FWFS module for FS from the model using no FS. We have one model under the HDLN module, i.e., the CNN + Bi-LSTM model, and three models under the FWFS module, i.e., GWO + IG + Bagging, GWO + IG + GB, GWO + IG + XGB. For Mozilla Firefox, GWO + IG + XGB has the highest improvement of 9.88, followed by GWO + IG + GB with 7.72.

For the other four databases, highest percentage improvement is given by CNN + Bi-LSTM model. The values are 29.35, 29.35, 18.51, and 30.95 for Mozilla Sea monkey, Mozilla Thunderbird, Mozilla Firefox ESR, and Mozilla Thunderbird ESR. GWO + IG + GB gave the second-highest improvement for the remaining four databeses. The values are 20.65, 17.95, 6.17, and 21.98 for Mozilla Sea monkey, Mozilla Thunderbird, Mozilla Firefox ESR, and Mozilla Thunderbird ESR, respectively.

Thus, it can be summarized and stated that out of five cases, the model belonging to the HDLN module gave the best results, hence HDLN module has better performance than the FWFS module. If the average result values of all five databases are further averaged, then also HDLN gave the highest result of 0.88, and the IG + GWO + XGB model of the FWFS module gave the second-highest result of 0.86. These values are recorded in Table 13.

On the other hand, this analysis highlights that, although the CNN + Bi-LSTM model offers the most robust performance improvement overall, the FWFS module, particularly when using the GWO + IG + XGB and GWO + IG + GB combinations, also provides substantial enhancements, making it a competitive alternative.

RQ3. Whether the performance of SVSPM developed boosted significantly with the help of proposed FS modules used to reduce the dimensionality of data?

To address RQ3, null and alternate hypotheses are formulated as follows:

H0: The performance of SVSPMs developed using different FS strategies is the same and does not differ significantly.

H1: The performance of SVSPMs developed using different FS strategies differs significantly.

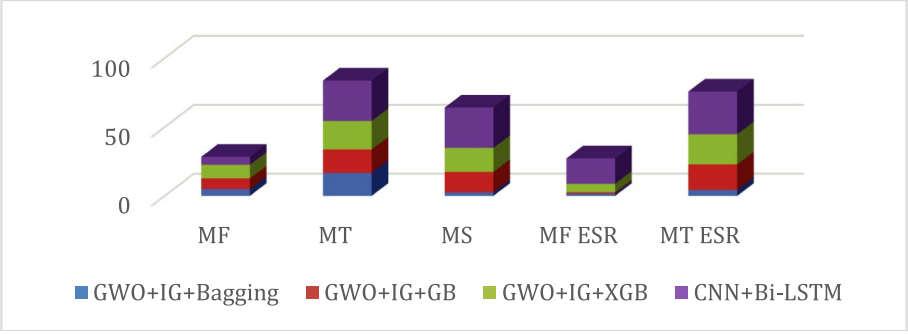

Fig. 9 Percentage improvement of HDLN module and FWFS module with model using No FS

To test the above-stated hypothesis, α is considered to be 0.05, i.e., 95% confidence level. In Table 14, the results of the Friedman test are documented. The mean rank for all four levels of severity and the average case for all models are documented databases-wise. A large value of rank obtained by a particular model indicates that that model is better.

When Friedman's test was conducted, considering all scenarios of FS on five different databases used in this study, the p-value came out to be 0.00($p < 0.05$). The p-value indicates that the results of Friedman's test are significant. It can be seen from Friedman's test result table that the best rank is achieved by the CNN-BiLSTM model of 12.88, 14.80, 14.10, and 13.60 for low, medium, critical level, and average cases. For a high level, the best rank of 12.90 was achieved by the GWO + IG + XGB model. Worst ranks are obtained for no FS.

As Friedman's test results are significant, the null hypothesis (H0) is rejected, and the alternate hypothesis (H1) is accepted. Hence, it can be stated that significant improvement is observed in the performance of SVSPM developed after applying the proposed modules for FS. HDLN module emerges as the best module to improve the performance of SVSPM, followed by GWO + IG + XGB, which comes under the FWFS module.

5 Threats to validity

Threats to the validity of our study are discussed in this section. Empirical software engineering, according to Wohlin (2007), (Johnson & Zhang, 2014), is essential to any empirical study to identify and address threats to the validity of the experimental findings. The following are some potential threats to the validity of the results.

Software vulnerabilities of five different products of Mozilla are collected, and experiments are performed on those. There is a possibility that new vulnerabilities may be reported now and are not present in the database collected by us, leading to a threat to validity. The database contains vulnerabilities in five different products of Mozilla. Therefore, the results

Table 14 Friedman's test result

Model	Mean Rank (Low)	Mean Rank (Medium)	Mean Rank (High)	Mean Rank (Critical)	Mean Rank (Average)
Bi-LSTM	11.63	13.60	5.70	12.30	11.00
CNN	10.88	13.30	4.40	12.10	10.80
CNN + Bi-LSTM	12.88	14.80	9.80	14.10	13.60
IG + Bagging	6.38	5.50	6.80	6.10	5.90
IG + GB	11.00	9.30	12.20	9.20	11.30
IG + XGB	7.13	7.30	10.30	9.10	8.60
GWO + Bagging	4.88	4.60	5.90	5.00	4.70
GWO + GB	9.38	8.60	11.00	9.20	9.40
GWO + XGB	10.88	6.80	12.20	9.50	10.90
GWO + IG + Bagging	6.63	7.10	8.80	3.70	6.30
GWO + IG + GB	9.00	9.60	10.10	7.90	8.70
GWO + IG + XGB	12.38	10.70	12.90	12.60	12.70
Bagging	1.88	2.70	2.10	2.80	1.60
GB	2.63	2.00	3.10	3.30	1.60
XGB	2.50	4.10	4.70	3.10	2.90

of this study may be generalized to the domains of Mozilla products but may differ for other domains posing a threat to external validity. The use of open-source and publicly available datasets reduces the threat to construct validity. To generalize results, the experiment is carried out by using an FS module that works in two stages, trying to handle the curse of dimensionality problem. Vulnerability description is used among so many fields available in vulnerability reports to carry out the experiment posing a threat to the validity of results. To reduce the risk of validity of the conclusion, tenfold cross-validation statistical tests are applied during the development of SVSPM. AUC performance measure is used to evaluate the effectiveness of the SVSPM developed. AUC finds a balance between both specificity and sensitivity values, reducing the threat to the validity of results.

6 Concluding remarks

As software complexity rises, achieving error-free software becomes nearly unattainable. Consequently, software testing persists even after release to uncover potential vulnerabilities. The prevalence of vulnerability data in textual format presents a challenge for prediction models due to dimensionality issues. To tackle this challenge, the study introduces two Feature Selection (FS) modules designed to alleviate dimensionality concerns and enhance the performance of prediction models. The proposed FS modules, HDLN and FWFS, employ distinct approaches: HDLN utilizes the CNN-Bi-LSTM model for SVSPM development, while FWFS employs IG + GWO for FS. To assess the efficiency of these modules' models, various alternative models are developed, including those utilizing CNN only, Bi-LSTM only, IG only, GWO only, and ensemble classifiers like Bagging, GB, and XGB. Due to dataset imbalance, SMOTE is applied as a data balancing technique. The dataset is then divided into training and testing sets using tenfold cross-validation. Evaluating the findings of SVSPM across four severity levels involves recording corresponding AUC values. Statistical tests are employed to bolster the reliability of the results. The analysis reveals that the application of FS methods significantly enhances SVSPM performance compared to models developed without FS. Among these, the HDLN module yields the most favorable results, followed by the FWFS module.

The proposed approach has significant practical applications in cybersecurity, software maintenance, and risk management. The primary goal of the developed model is to automate the process of assigning priority levels to vulnerabilities based on descriptions found in databases like CVE (Common Vulnerabilities and Exposures) or bug reports. Instead of relying on manual analysis, the model employs machine learning to extract key information from text and determine the urgency or severity of each vulnerability. This enables faster, more efficient security management. By using historical data from past vulnerabilities, the model improves the accuracy of prioritization, predicting the criticality of new vulnerabilities. Its ability to streamline feature selection enhances the accuracy and efficiency of vulnerability severity predictions, which is crucial for prioritizing security patches and mitigating high-risk vulnerabilities in large software systems. In cybersecurity, this can improve automated vulnerability management and proactive defense strategies.

This approach helps organizations allocate patching resources more effectively by focusing on high-risk vulnerabilities that could significantly impact their systems. As a result, critical vulnerabilities can be addressed first, ensuring security teams concentrate on the most pressing issues. The demonstrated improvement in predictive performance (AUC values of 0.88 and 0.86) underscores the model's practical potential in real-world scenarios.

Our research addresses the obstacles posed by high-dimensional textual data through the introduction of an effective Feature Selection (FS) module. Our future endeavors entail investigating multiple data balancing techniques, including SMOTE, ADASYN, ROS, RUS, SMOTEBoost, and EasyEnsemble, to further improve our SVSPM. Additionally, we aim to develop a specialized data balancing module tailored to meet the specific requirements of SVSPM.

Authors' contribution Ruchika Malhotra and Vidushi conceptualized the idea presented in the manuscript. Vidushi carried out the experiments and wrote the first draft of the manuscript. Ruchika Malhotra supervised the work, reviewed the draft and finalized the manuscript. Both authors read and approved the final manuscript.

Funding The author did not receive support from any organization for the submitted work.

Data availability No datasets were generated or analysed during the current study.

Declarations

Conflict of Interest The authors declare no competing interests.

References

Alomari, O. A., Elnagar, A., Afyouni, I., Shahin, I., Nassif, A. B., Hashem, I. A., & Tubishat, M. (2022). Hybrid feature selection based on principal component analysis and grey wolf optimizer algorithm for Arabic news article classification. *IEEE Access, 10*, 121816–121830.

Alves, H., Fonseca, B., Antunes, N. (2016). Software metrics and security vulnerabilities: dataset and exploratory study. In: 12th European dependable computing conference (EDCC), Gothenburg, Sweden. pp 37–44. https://doi.org/10.1109/EDCC.2016.34

Anju, A. J., & Judith, J. E. (2024). Hybrid feature selection method for predicting software defect. *Journal of Engineering and Applied Science, 71*(1), 124.

Ayetiran, E. F. (2022). Attention-based aspect sentiment classification using enhanced learning through CNN-BiLSTM networks. *Knowledge-Based Systems, 252*, 109409.

Bahad, P., Saxena, P. (2020). Study of AdaBoost and Gradient Boosting Algorithms for Predictive Analytics. In: International Conference on Intelligent Computing and Smart Communication. Algorithms for Intelligent Systems. Springer, Singapore. https://doi.org/10.1007/978-981-15-0633-8_22

Bellman, R. (1957). Dynamic programming. Princeton University press.

Breiman, L. (1996). Bagging predictors. *Machine Learning, 24*, 123–140. https://doi.org/10.1007/BF00058655

Chen, J., Kudjo, P. K., Mensah, S., Brown, S. A., & Akorfu, G. (2020). An automatic software vulnerability classification framework using term frequency-inverse gravity moment and feature selection. *Journal of Systems and Software, 167*, 110616.

Das, S. S., Serra, E., Halappanavar. M., Pothen, A., Al-Shaer, E., (2021). V2W-BERT: A framework for effective hierarchical multiclass classification of software vulnerabilities. In *IEEE 8th International Conference on Data Science and Advanced Analytics (DSAA)*, pp. 1–12. https://doi.org/10.1109/DSAA53316.2021.9564227

Davari, M., Zulkernine, M., Jaafar, F. (2017). An Automatic Software Vulnerability Classification Framework. In: International Conference on Software Security and Assurance (ICSSA), pp. 44–49. https://doi.org/10.1109/ICSSA.2017.27.

Du, J., Gui, L., Xu, R., and He. Y. (2017). A convolutional attention model for text classification. In: Proceedings of the National CCF Conference on Natural Language Processing and Chinese Computing. 183–195. https://doi.org/10.1007/978-3-319-73618–1_

Emary, E., Zawbaa, H.M., Grosan, C., Hassenian, A.E. (2015). Feature subset selection approach by grey-wolf optimization. In: Afro-European Conference for Industrial Advancement, pp. 1–13. https://doi.org/10.1007/978-3-319-13572-4_1

Erturk, E., & Akcapinar, E. (2015). A comparison of some soft computing methods for software fault prediction. *Expert syStems with Applications, 42*(4), 1872–1879. https://doi.org/10.1016/j.eswa.2014.10.025

Shahid, M.R., & Debar, H., (2021). "CVSS-BERT: Explainable Natural Language Processing to Determine the Severity of a Computer Security Vulnerability from its Description," *2021 20th IEEE International Conference on Machine Learning and Applications (ICMLA)*, Pasadena, CA, USA, pp. 1600–1607, https://doi.org/10.1109/ICMLA52953.2021.00256.

Faris, H., Aljarah, I., Al-Betar, M. A., & Mirjalili, S. (2018). Grey wolf optimizer: A review of recent variants and applications. *Neural Computing and Applications, 30*(2018), 413–435. https://doi.org/10.1007/s00521-017-3272-5

Firpi, H. A., & Goodman, E. (2004). Swarmed feature selection. In Proceedings of the 33rd applied imagery pattern recognition workshop, Washington, DC, USA. *IEEE Computer Society*, 112–118. https://doi.org/10.1109/AIPR.2004.41

Ghourabi, A., Mahmood, M. A., & Alzubi, Q. M. (2020). A hybrid CNN-LSTM model for SMS spam detection in Arabic and English messages. *Future Internet, 12*(9), 156. https://doi.org/10.3390/fi12090156

Hancer, E. (2024). An improved evolutionary wrapper-filter feature selection approach with a new initialisation scheme. *Machine Learning, 113*(8), 4977–5000.

He, H., & Garcia, E. A. (2009). Learning from Imbalanced Data. *IEEE Transactions on Knowledge and Data Engineering, 21*(9), 1263–1284. https://doi.org/10.1109/TKDE.2008.239

Hochreiter, S. (1997). *Long Short-term Memory*. Neural Computation MIT-Press.

Jain, D., Kumar, A., & Garg, G. (2020). Sarcasm detection in mash-up language using soft-attention based bi-directional LSTM and feature-rich CNN. *Applied Soft Computing, 91*, 106198.

Jeon, S., & Kim, H. K. (2021). AutoVAS: An automated vulnerability analysis system with a deep learning approach. *Computers & Security, 106*, 102308. https://doi.org/10.1016/j.cose.2021.102308

Johnson, R. and Zhang, T., (2014). Effective use of word order for text categorization with convolutional neural networks. *arXiv preprint* arXiv:1412.1058.

Kalchbrenner, N., Grefenstette, E. and Blunsom, P., (2014). A convolutional neural network for modelling sentences. *arXiv preprint* arXiv:1404.2188.

Kekül, H., Ergen, B., & Arslan, H. (2021). A multiclass hybrid approach to estimating software vulnerability vectors and severity score. *Journal of Information Security and Applications, 63*, 103028.

Khazaei, A., Ghasemzadeh, M., & Derhami, V. (2016). An automatic method for CVSS scores prediction using vulnerabilities description. *Journal of Intelligent & Fuzzy Systems, 30*(1), 89–96. https://doi.org/10.3233/IFS-151733

Kim, H., & Jeong, Y. S. (2019). Sentiment classification using convolutional neural networks. *Applied Sciences, 9*(11), 2347.

Kudjo, P. K., Chen, J., Mensah, S., Amankwah, R., & Kudjo, C. (2020a). The effect of Bellwether analysis on software vulnerability severity prediction models. *Software Quality Journal, 28*, 1413–1446.

Kudjo, P. K., Aformaley, S. B., Mensah S., Chen, J. (2019). The Significant Effect of Parameter Tuning on Software Vulnerability Prediction Models. In: IEEE 19th International Conference on Software Quality, Reliability and Security Companion (QRS-C), pp. 526–527. https://doi.org/10.1109/QRS-C.2019.00107.

LeCun, Y., Bottou, L., Bengio, Y., & Haffner, P. (1998). Gradient-based learning applied to document recognition. *Proceedings of the IEEE, 86*(11), 2278–2324.

Li, Z., Liu, F., Yang, W., Peng, S., & Zhou, J. (2021). A survey of convolutional neural networks: Analysis, applications, and prospects. *IEEE Transactions on Neural Networks and Learning Systems, 33*(12), 6999–7019.

Liu, H., Motoda, H., Setiono, R., Zhao, Z. (2010). Feature selection: an ever-evolving frontier in data mining. In *Proc. the fourth workshop on feature selection in data mining*, vol. 4, pp. 4–13.

Liu, H., & Yu, L. (2005). Toward integrating feature selection algorithms for classification and clustering. *Knowledge and Data Engineering, IEEE Transactions on, 17*(4), 491–502. https://doi.org/10.1109/TKDE.2005.66

Long, F., & Ding, C. (2005). Feature selection based on mutual information criteria of max-dependency, max-relevance, and minredundancy. *IEEE Transactions on Pattern Analysis and Machine Intelligence, 27*(8), 1226–1238. https://doi.org/10.1109/TPAMI.2005.159

Malhotra R., Vidushi (2021). Severity Prediction of Software Vulnerabilities Using Textual Data. In: International Conference on Recent Trends in Machine Learning, IoT, Smart Cities, and Applications. Advances in Intelligent Systems Computing, vol 1245. Springer, Singapore, https://doi.org/10.1007/978-981-15-7234-0_41

Mirjalili, S., Mirjalili, S. M., & Lewis, A. (2014). Grey Wolf Optimizer. *Advances in Engineering Software., 69*, 46–61. https://doi.org/10.1016/j.advengsoft.2013.12.007

Olson, D. L., & Delen, D. (2008). Performance evaluation for predictive modelling. *Advanced Data Mining Techniques,* pp. 137–147.

Ramos, J. (2003). Using TF-IDF to determine word relevance in document queries. *Proceedings of the First Instructional Conference on Machine Learning, 242*, 133–142.

Rhanoui, M., Mikram, M., Yousfi, S., & Barzali, S. (2019). A CNN-BiLSTM model for document-level sentiment analysis. *Machine Learning and Knowledge Extraction, 1*(3), 832–847. https://doi.org/10.3390/make1030048

Robindro, K., Devi, S. S., Clinton, U. B., Takhellambam, L., Singh, Y. R., & Hoque, N. (2024). Hybrid distributed feature selection using particle swarm optimization-mutual information. *Data Science and Management, 7*(1), 64–73.

Russell, R., Kim, L., Hamilton, L., Lazovich, T., Harer, J., Ozdemir, O., Ellingwood, P., McConley, M. (2018). Automated Vulnerability Detection in Source Code Using Deep Representation Learning. 757–762. https://doi.org/10.1109/ICMLA.2018.00120.

Sagi, O., & Rokach, L. (2018). Ensemble learning: A survey. *WIREs, 8*(4), e1249. https://doi.org/10.1002/widm.1249

Dos Santos, C. & Gatti, M., (2014). Deep convolutional neural networks for sentiment analysis of short texts. In *Proceedings of COLING 2014, the 25th international conference on computational linguistics: technical papers* , pp. 69–78.

Schirrmeister, R. T., Springenberg, J. T., Fiederer, L. D. J., Glasstetter, M., Eggensperger, K., Tangermann, M., Hutter, F., Burgard, W., & Ball, T. (2017). Deep learning with convolutional neural networks for EEG decoding and visualization. *Human Brain Mapping, 38*(11), 5391–5420.

Schuster, M., & Paliwal, K. K. (1997). Bidirectional recurrent neural networks. *IEEE Transactions on Signal Process, 45*, 2673–2681. https://doi.org/10.1109/78.650093

Sharma, R., Sibal, R., & Sabharwal, S. (2021). Software vulnerability prioritization using vulnerability description. *International Journal of System Assurance Engineering and Management, 12*, 58–64.

Spelmen, V. S., Porkodi, R. (2018). A Review on Handling Imbalanced Data. In: International Conference on Current Trends towards Converging Technologies (ICCTCT), 1–11, https://doi.org/10.1109/ICCTCT.2018.8551020.

Stuckman, J., Walden, J., & Scandariato, R. (2017). The Effect of Dimensionality Reduction on Software Vulnerability Prediction Models. *IEEE Transactions on Reliability, 66*(1), 17–37. https://doi.org/10.1109/TR.2016.2630503

Sun, X., Ye, Z., Bo, L., Wu, X., Wei, Y., Zhang, T., & Li, B. (2023). Automatic software vulnerability assessment by extracting vulnerability elements. *Journal of Systems and Software, 204*, 111790. https://doi.org/10.1016/j.jss.2023.111790

Sun, X., Li, L., Bo, L., Wu, X., Wei, Y., & Li, B. (2024). Automatic software vulnerability classification by extracting vulnerability triggers. *Journal of Software: Evolution and Process, 36*(2), e2508. https://doi.org/10.1002/smr.2508

Sun, F. & Chu, N., (2020). Text sentiment analysis based on CNN-BiLSTM-attention model. In *2020 International Conference on Robots & Intelligent System (ICRIS),* pp. 749–752. https://doi.org/10.1109/ICRIS52159.2020.00186

Tai, K.S., Socher, R., Manning, C.D. (2015). Improved semantic representations from tree-structured long short-term memory networks. arXiv, arXiv:1503.00075. https://doi.org/10.48550/arXiv.1503.00075

Tang, G., Meng, L., Wang, H., Ren, S., Wang, Q., Yang, L., Cao, W. (2020). A Comparative Study of Neural Network Techniques for Automatic Software Vulnerability Detection. In: International Symposium on Theoretical Aspects of Software Engineering (TASE). https://doi.org/10.1109/TASE49443.2020.00010

Thekkekara, J. P., Yongchareon, S., & Liesaputra, V. (2024). An attention-based CNN-BiLSTM model for depression detection on social media text. *Expert Systems with Applications, 249*, 123834.

Vijayarani, S., Ilamathi, J., & Nithya, S. (2015). Preprocessing Techniques for Text Mining-An Overview. *International Journal of Computer Science & Communication Networks, 5*, 7–16.

Wang, P., Zhou, Y., Sun, B., Zhang, W. 2019. Intelligent Prediction of Vulnerability Severity Level Based on Text Mining and XGBboost. In: Eleventh International Conference on Advanced Computational Intelligence (ICACI). pp. 72–77, https://doi.org/10.1109/ICACI.2019.8778469.

Witten, I. H., Frank, E., Hall, M. A., & Pal, C. J. (2016). *Data mining: Practical machine learning tools and techniques*. Morgan Kaufmann.

Wohlin, C. (2007). Empirical Software Engineering: Teaching Methods and Conducting Studies. In: Empirical Software Engineering - Dagstuhl Seminar Proceedings (LNCS 4336), pp. 135–142. https://doi.org/10.1007/978-3-540-71301-2_42

Wolpert, D. H., Macready, W. G., et al. (1997). No free lunch theorems for optimization. *IEEE Transactions on Evolutionary Computation, 1*(1), 67–82.

Xue, B., Zhang, M., Browne, W. N., & Yao, X. (2016). A survey on evolutionary computation approaches to feature selection. *IEEE Transactions on Evolutionary Computation, 20*(4), 606–626. https://doi.org/10.1109/TEVC.2015.2504420

Yang, G., He, J., Lan, X., Li, T., & Fang, W. (2024). A fast dual-module hybrid high-dimensional feature selection algorithm. *Information Sciences, 681*, 121185.

Yin, W., Kann, K., Yu, M., Schütze, H. (2017). Comparative study of CNN and RNN for natural language processing. arXiv:1702.01923. https://doi.org/10.48550/arXiv.1702.01923

Yong, F., Yongcheng, L., Cheng, H., & Liang, L. (2020). FastEmbed: Predicting vulnerability exploitation possibility based on ensemble machine learning algorithm. *PLoS ONE, 15*(2), e0228439. https://doi.org/10.1371/journal.pone.0228439

Zerkane, S., Espes, D., Parc, P. L., Cuppens, F. (2016). Vulnerability analysis of software defined networking. In: International symposium on foundations and practice of security (pp. 97–116). Springer, Cham. https://doi.org/10.1007/978-3-319-51966-1_7

Zhang, Y. and Wallace, B., (2015). A sensitivity analysis of (and practitioners' guide to) convolutional neural networks for sentence classification. *arXiv preprint* arXiv:1510.03820.

Publisher's Note Springer Nature remains neutral with regard to jurisdictional claims in published maps and institutional affiliations.

Springer Nature or its licensor (e.g. a society or other partner) holds exclusive rights to this article under a publishing agreement with the author(s) or other rightsholder(s); author self-archiving of the accepted manuscript version of this article is solely governed by the terms of such publishing agreement and applicable law.

Ruchika Malhotra is Head of Department of Software Engineering Department Delhi Technological University (formerly Delhi College of Engineering), Delhi, India. She is Associate Dean in Industrial Research and Development, Delhi Technological University. She was awarded with prestigious Raman Fellowship for pursuing Post doctoral research in Indiana University Purdue University Indianapolis USA. She received her master's and doctorate degree in software engineering from the University School of Information Technology, Guru Gobind Singh Indraprastha University, Delhi, India. She was an Assistant Professor at the University School of Information Technology, Guru Gobind Singh Indraprastha University, Delhi, India. She has received IBM Faculty Award 2013. Her h-index is 33 as reported by Google Scholar. She is reported to be in the list of world's top 2% scientists by Stanford University. She is author of book titled "Empirical Research in Software Engineering" published by CRC press and co-author of a book on Object Oriented Software Engineering published by PHI Learning. Her research interests are in software testing, improving software quality, statistical and adaptive prediction models, software metrics and the definition and validation of software metrics. She has published more than 200 research papers in international journals and conferences.

Vidushi is currently working as an Assistant Professor at Vivekananda Institute of Professional Studies and also pursuing her doctoral degree from Delhi Technological University. She completed her master's degree in Computer Science from the Jaypee Institute of Information Technology University, India. Her research interests are in software quality improvement and applications of machine learning techniques in software vulnerability prediction. She has various publications in international conferences and journals.

BILINGUAL PUBLISHING GROUP

Journal of Environmental & Earth Sciences

https://journals.bilpubgroup.com/index.php/jees

REVIEW

Indigenous Knowledge and Water Conservation Practices in South Africa: A Systematic Literature Review

Arvind Kumar Sahani [1], ***Garima Gupta*** [2], ***Subhash Anand*** [3*], ***Vishwa Raj Sharma*** [4], ***Rajender Singh*** [5], ***Azka Kamil*** [6], ***Harish Kumar*** [3], ***Alka Gagan*** [3], ***Vinod Kumar Mayala*** [7], ***Arun Pratap Mishra*** [3], ***Sunil Jaiswal*** [3], ***Jasmine Anand*** [8]

[1] *Department of African Studies, University of Delhi, Delhi 110007, India*

[2] *Department of Environment Planning, School of Planning and Architecture Delhi, Delhi 110012, India*

[3] *Department of Geography, Delhi School of Economics, University of Delhi, Delhi 110007, India*

[4] *Department of Geography, Shaheed Bhagat Singh College, University of Delhi, Delhi 110007, India*

[5] *Department of Geography, Shivaji College, University of Delhi, Delhi 110007, India*

[6] *Department of Geography, Kamala Nehru College, University of Delhi, Delhi 110007, India*

[7] *Department of Economics, Hansraj College, University of Delhi, Delhi 110007, India*

[8] *Department of Applied Mathematics, Delhi Technological University, Delhi 110042, India*

ABSTRACT

Water scarcity poses a significant challenge globally, with South Africa exemplifying the severe socio-economic and environmental impacts of limited water access. Despite advances in modern water management systems, the integration of indigenous knowledge (IK) into formal frameworks remains underutilized. This study systematically reviews the role of indigenous water conservation practices in South Africa, analyzing over 50 high-quality sources using the PRISMA methodology. The findings highlight the effectiveness of IK in addressing water scarcity through techniques such as rainwater harvesting, terracing, and wetland management, which are low-cost, environmentally sustainable, and deeply rooted in cultural practices. Indigenous methods also enhance climate resilience by enabling communities to adapt to droughts and floods through practices such as weather prediction and adaptive farming techniques. Furthermore, these

*CORRESPONDING AUTHOR:

Subhash Anand, Department of Geography, Delhi School of Economics, University of Delhi, Delhi 110007, India; Email: sanandpvs@gmail.com

ARTICLE INFO

Received: 5 December 2024 | Revised: 11 December 2024 | Accepted: 16 December 2024 | Published Online: 14 February 2025

DOI: https://doi.org/10.30564/jees.v7i2.7988

CITATION

Sahani, A.K., Gupta, G., Anand, S., et al., 2025. Indigenous Knowledge and Water Conservation Practices in South Africa: A Systematic Literature Review. Journal of Environmental & Earth Sciences. 7(2): 248–261. DOI: https://doi.org/10.30564/jees.v7i2.7988

COPYRIGHT

Copyright © 2025 by the author(s). Published by Bilingual Publishing Group. This is an open access article under the Creative Commons Attribution-NonCommercial 4.0 International (CC BY-NC 4.0) License (https://creativecommons.org/licenses/by-nc/4.0/).

practices foster social inclusivity and community empowerment, ensuring equitable water access and intergenerational knowledge transfer. The study underscores the potential of integrating IK with modern water technologies to create holistic solutions that are scalable, sustainable, and aligned with South Africa's goal of achieving water security by 2030. Policy recommendations emphasize the need for institutional support, data collection, and financial incentives to sustain and mainstream indigenous approaches. By bridging the gap between traditional and contemporary systems, this research provides a roadmap for leveraging diverse knowledge systems to address water scarcity and build resilient communities.
Keywords: Water Scarcity; Indigenous Knowledge; Water Conservation; Climate Resilience; Sustainable Water Management; South Africa

1. Introduction

1.1. Global and South African Water Scarcity: An Overview

Water scarcity is recognized as one of the most significant global challenges, affecting not only individual communities but also broader social and economic stability worldwide. The United Nations (UN) reports that approximately 2.2 billion people lack safely managed drinking water services, highlighting the extensive and urgent nature of this issue[1]. This is the situation even though the United Nations formally recognized access to safe water and sanitation as a fundamental human right in 2002. According to the United Nations, "the basic human right of access to safe and adequate drinking water is crucial to leading a life with equality and dignity," which is why water and sanitation services should be recognized as fundamental human rights[2]. Also, Goal 6 of the SDGs (Sustainable Development Goals) recognizes access to safe, affordable, and clean drinking water as a basic human right. By 2030, Sustainable Development Goal 6 aspires to "check the equitable access and effective management of clean drinking water and sanitation for all"[3]. According to the UN's 2023 Water Development Report, an estimated 80% of wastewater flows back into ecosystems untreated, contaminating water sources and posing a severe risk to human health and biodiversity, which further worsens the existing issue[4]. These issues underscore the necessity of innovative solutions and sustainable practices in water management.

South Africa exemplifies the complex dynamics of water scarcity due to recurrent droughts, socio-economic disparities, and population growth. Historical inequalities have exacerbated access issues, as disadvantaged communities, especially those in rural regions, experience limited access to clean water despite post-1994 policy changes. The UN indicates that in developing regions such as sub-Saharan Africa, up to 60% of the population remains vulnerable to water scarcity, underscoring the regional disparity in water access and quality[5]. In South Africa alone, an estimated 14 million people—mainly from historically marginalized communities—do not have direct access to safe drinking water, with droughts worsening the situation, as demonstrated by recent water crises in regions like Cape Town[6, 7]. The projected increase in water demand driven by population growth, climate change, and urbanization necessitates sustainable water management practices that consider the needs of vulnerable populations. The UN has highlighted indigenous knowledge as an essential component of resilience-building in regions susceptible to water crises, noting that local and indigenous practices provide tailored, sustainable water management techniques that support both environmental and social well-being[8]. In South Africa, integrating indigenous knowledge with formal water management systems is essential for addressing both immediate and long-term water needs, particularly in light of the country's goal to achieve water security for all by 2030[1].

1.2. The Role and Relevance of Indigenous Knowledge

Indigenous knowledge (IK) refers to the traditional knowledge systems developed by local communities over generations, reflecting their deep understanding of the environment, its cycles, and the natural resources available to them. It is a dynamic system that includes a range of practices, beliefs, and skills passed down through generations and adapted over time to changing environmental conditions[9].

IK is highly localized, as it is deeply rooted in the specific geographic, ecological, and cultural contexts of a community, often linking natural phenomena to spiritual and cultural beliefs[10]. In contrast to scientific knowledge, which tends to be more universal and analytical, indigenous knowledge is holistic and context-specific. It involves an intimate relationship between humans and their environment, where knowledge is often intertwined with cultural practices, including agriculture, medicine, and water management[11]. Indigenous/traditional knowledge systems are also founded on empirical observations, with communities relying on long-term interactions with their surroundings to make predictions and develop strategies for resource management[12].

In the context of water conservation, IK plays a crucial role, especially in arid and semi-arid regions, where water scarcity is a persistent challenge. Indigenous communities have developed techniques and technologies over centuries to sustainably manage water resources. These practices include water harvesting, soil erosion prevention, and the sustainable use of available water sources, often ensuring water security during periods of drought[13]. For instance, traditional rainwater harvesting systems, such as the use of stone channels and dams, have been instrumental in enhancing local water storage capacities[14]. The relevance of indigenous knowledge in the modern context of water conservation lies in its resilience and adaptability. Many indigenous techniques have remained effective over time, and they offer sustainable alternatives to the industrial approaches to water management, which may be resource-intensive and environmentally damaging[11]. As climate change exacerbates water scarcity, incorporating indigenous knowledge into national and local water governance can provide valuable insights into sustainable practices and foster resilience in communities facing the growing threat of droughts and water shortages[15].

1.3. Innovative Aspect of the Research

This research innovatively bridges the gap between traditional indigenous practices and contemporary water management strategies by systematically exploring how the two can synergize to enhance water conservation and resilience. By employing a robust methodology, including a systematic review of over 50 high-quality studies, this work highlights the unique strengths of indigenous practices—such as their low-cost, culturally embedded, and ecologically adaptive features—and explores ways to integrate these with modern technologies for greater efficiency. The research also pioneers an interdisciplinary approach, combining ecological, socio-cultural, and technological perspectives to propose holistic, scalable solutions that align with Sustainable Development Goals (SDGs), particularly Goal 6 on water security and equitable access.

1.4. Research Gap

Despite the recognition of water scarcity as a critical issue globally and in South Africa, there is limited systematic research on the integration of indigenous water conservation practices with modern water management systems. Existing studies primarily focus on documenting individual indigenous practices or assessing modern water technologies, often neglecting how these two approaches can complement each other to address the growing water crisis effectively. Furthermore, many studies overlook the socio-cultural dimensions of indigenous knowledge, such as its role in fostering community-based governance and resilience to climate change. Additionally, there is a lack of empirical data evaluating the long-term sustainability and scalability of these practices within the framework of South Africa's national water policies.

2. Methodology: PRISMA Screening and Selection

2.1. Systematic Review Process Using PRISMA

To systematically evaluate the role of indigenous knowledge in water conservation, this study employed the PRISMA (Preferred Reporting Items for Systematic Reviews and Meta-Analyses) framework to conduct a thorough review of existing literature. An initial pool of over 1000 articles was identified using keywords such as "indigenous water conservation practices in South Africa," and "traditional water management practices in South Africa". The articles were screened based on relevance, empirical quality, and geographical focus, eventually narrowing the selection to 47 high-quality sources for an in-depth analysis.

2.2. Inclusion and Exclusion Criteria

Articles selected for review were required to meet specific inclusion criteria: they needed to focus on indigenous practices in water conservation, include data or case studies specific to South African contexts, and be published within the last 25 years. Exclusion criteria eliminated studies without empirical data, literature lacking regional specificity, and non-peer-reviewed sources. This careful selection process ensured a robust, focused review of pertinent literature on indigenous water management[14]. A visual representation of this selection process is shown in the PRISMA flow diagram in **Figure 1**, detailing each stage of article screening and exclusion.

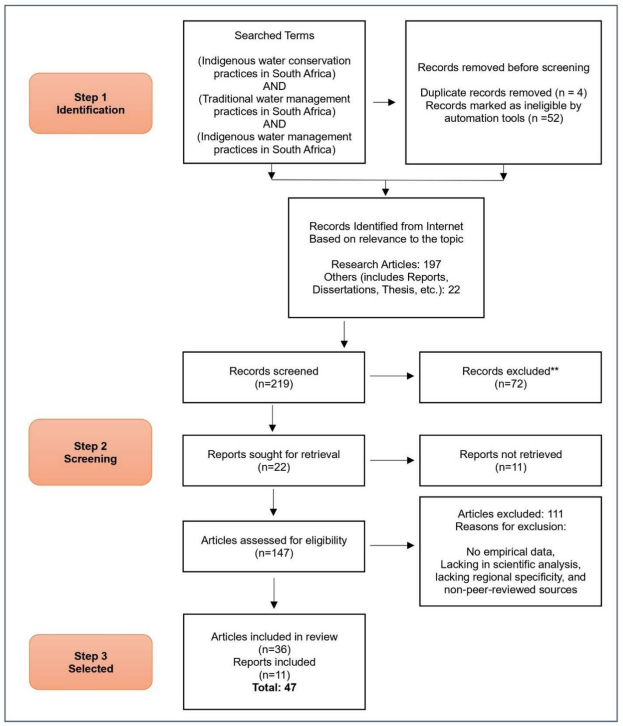

Figure 1. Overview of the screening process.

The articles included in the review were selected based on specific inclusion and exclusion criteria. To be included, the articles had to focus on indigenous knowledge (IK) and water conservation, particularly in South Africa or regions with similar contexts, and provide empirical data or case studies. Only peer-reviewed publications from the last 25 years were considered to ensure relevance and academic rigor. Excluded articles were those without empirical evidence, non-peer-reviewed sources, or those not directly related to water conservation practices. Additionally, articles that lacked geographical relevance to South Africa or similar regions were excluded, ensuring the review was region-specific and focused on the effectiveness of indigenous water management practices. These criteria helped create a focused and reliable review of IK's role in water conservation.

3. Characteristics that Distinguish Indigenous Practices from Modern Approaches

After reviewing the literature, a structured view of the factors that distinguish indigenous practices from modern ones, capturing both the social and ecological dimensions of these traditional methods, has been formulized. Water scarcity can be effectively managed, especially in arid and semi-arid regions, by using indigenous knowledge in methods of water management like rainwater harvesting, "sacred water governance" which emphasizes a spiritual connection with water—and stone-based terracing to retain water[16]. These techniques provide sustainable solutions through practices that are deeply ingrained in local cultural understanding of the environment. The **Table 1** below shows the characteristics of indigenous practices.

Indigenous Knowledge (IK) refers to the cumulative knowledge systems developed by local communities over generations through close interaction with their environment. It reflects a deep understanding of natural cycles and resource management, often rooted in specific ecological, cultural, and spiritual contexts. Unlike modern scientific methods, IK is holistic and adaptive, incorporating empirical observations and cultural traditions to address resource-related challenges. In water management, IK includes practices such as rainwater harvesting, sacred water governance, and stone-based terracing for water retention[11].

Differences between Indigenous and Modern Water Management Practices

Indigenous Knowledge (IK) in water management is rooted in traditions passed down through generations, offering time-tested, resilient practices adapted to local conditions[17]. It integrates cultural and spiritual values, with rituals and taboos emphasizing respect for nature, as seen in the Zulu community's sacred view of water, contrasting with

Table 1. Characteristics that distinguish indigenous practices from modern approaches.

Factor/Indicator	Indigenous Practices	Modern Practices	References
Historical continuity	Rooted in generations of tradition and are time-tested, developed over centuries within a specific community or region.	Modern practices are often based on recent scientific research, technological developments, and are not necessarily tied to a long history within a specific community.	[17]
Cultural and spiritual significance	Integrated with cultural beliefs, spiritual values, and often governed by taboos or rituals that create a unique relationship with the environment.	Generally, lack a cultural or spiritual dimension; are typically implemented based on functional, technical, or economic considerations rather than traditional beliefs.	[12, 14]
Local ecological knowledge	Draws on intimate knowledge of local ecosystems, weather patterns, and plant and animal behaviors, built up through generations of observation and adaptation.	Relies on scientific data, technological tools, and standardized approaches, often not specific to the local ecosystem but based on generalized scientific knowledge.	[10, 14]
Resource availability and minimal external inputs	Uses readily available natural resources like stones, clay, and native plants, minimizing reliance on external resources or industrial products.	Often requires external inputs such as industrial materials, synthetic chemicals, or advanced technology, which can be costly and may not be locally sourced.	[15, 18]
Community-based management and knowledge transmission	Managed collectively by the community, with knowledge transferred orally or through apprenticeships. Practices are embedded in community responsibility.	Often managed by centralized authorities, and knowledge is documented in formal texts or digital formats, not requiring community transmission.	[13, 15]
Adaptation to natural cycles and climate resilience	Highly adapted to local climate cycles, ensuring resilience against droughts and floods. Designed to align with natural ecological rhythms rather than productivity goals.	Modern practices focus on maximizing productivity and often rely on irrigation or other technology, which may not be ecologically sustainable in the long term.	[10, 11]
Social inclusivity and knowledge sharing	Inclusive in nature, designed for the benefit of the whole community, with knowledge-sharing frameworks that ensure widespread access and participation.	Often focused on efficiency or economic gains, sometimes leading to unequal access or benefits, and knowledge is shared through formal systems, excluding those without formal training.	[17, 18]

the technical focus of modern systems[19]. IK relies on sustainable resource use, employing locally available materials like stones and clay, avoiding the financial and environmental costs of industrial inputs often required in modern methods[18]. It emphasizes community-based management and knowledge-sharing, ensuring inclusivity and strengthening social ties, whereas modern systems are typically centralized and less accessible to marginalized groups[15]. Additionally, IK aligns with natural cycles, fostering resilience against climate extremes through practices like drought-resistant cropping, which modern approaches may overlook in their focus on productivity[14]. Finally, IK promotes equity by benefiting entire communities, ensuring inclusive participation, in contrast to the efficiency-driven and sometimes inequitable nature of modern water management systems[17].

Further, every indigenous practice (cases from the articles/report reviewed) was aligned with the formulized indicators (as mentioned below in the **Table 2**).

4. Impact of Indigenous Water Conservation Practices in South Africa

The effectiveness of indigenous water conservation techniques in South Africa is demonstrated by their ability to promote community-based governance, increase climate change resilience, and manage water resources sustainably. Indigenous water management practices in South Africa have proven to be not only effective in preserving water resources but also crucial for enhancing climate resilience, improving social inclusivity, and fostering community-based water governance. The cases of IK (mentioned below) demonstrate that these practices, which have evolved over generations, offer sustainable solutions for contemporary water challenges. By combining traditional knowledge with modern technology, South Africa can develop more holistic and resilient water management strategies to address the growing pressures of climate change and water scarcity.

Table 2. Indigenous knowledge cases aligned with indicators.

Factor/Indicator	Indigenous Practices	References
Historical continuity	1. Limpopo Province Terracing: Indigenous terracing techniques have been used for centuries to manage soil erosion and water retention. 2. Rainwater Harvesting in Karoo: This practice has been passed down through generations, using locally made containers of stones for collecting rainwater. 3. Grazing Management in Namaqualand: Traditional practices involve controlled grazing to prevent soil erosion and water depletion, based on generational knowledge.	[17]
Cultural and spiritual significance	1. Sacred Water Sites in Limpopo: Sacred water sources are protected and governed by taboos, limiting access to preserve water quality and spiritual integrity. 2. Ritualistic Water Use in Eastern Cape: Traditional rituals tied to water usage are carried out before using water for farming, which emphasizes spiritual respect for the resource. 3. Water-Related Rituals of the Zulu Community: Water is used in purification rituals, which imbue water use with spiritual meaning and align it with broader cultural practices. 4. Rainmaking Ceremonies in the Karoo: Rain dances or prayers are held to invoke rainfall, which reinforces the spiritual connection to water.	[12–14]
Local ecological knowledge	1. Karoo Weather Prediction via Local Indicators: Farmers use behavioral cues from plants and animals to predict rainfall and manage water resources. 2. Indigenous Vegetation Knowledge in KwaZulu-Natal: Knowledge of local plant species that help conserve water and maintain soil fertility. 3. Farming Practices Based on Soil and Water Knowledge in Limpopo: Knowledge of soil water retention based on soil types and their ability to conserve moisture in arid conditions. 4. Seasonal Rain Forecasting in the Eastern Cape: Indigenous farmers use the position of certain stars or birds to predict seasonal rains, ensuring optimal water management for crops. 5. Indigenous techniques for managing bush encroachment to prevent excessive water absorption by the invasive species.	[10, 12, 14, 17]
Resource availability and minimal external inputs	1. Stone-Lined Channels in Mpumalanga: Farmers use locally available stones and clay to create rainwater harvesting channels, avoiding industrial materials. 2. Clay Pits for Water Storage in Limpopo: Clay pits are dug in local areas to collect and store rainwater, using minimal external materials. 3. Bush-based Water Sources in Eastern Cape: Local communities rely on indigenous plants and bushes for water storage, minimizing the need for technology or external inputs. 4. Natural Springs in KwaZulu-Natal: Indigenous communities collect water from natural springs, ensuring sustainable usage without reliance on external inputs.	[13, 15, 17, 18, 20]
Community-based management and knowledge transmission	1. Rainwater Harvesting in Karoo: Knowledge of rainwater harvesting techniques is passed down orally through generations. 2. Mpumalanga Collective Water Management: Water conservation techniques like contour farming are managed collectively by the community. 3. Shared Water Knowledge in Limpopo: Farmers in Limpopo share their knowledge on water management strategies in regular community meetings, fostering collective responsibility. 4. Community-Based Irrigation Systems in KwaZulu-Natal: Smallholder farmers work together to manage irrigation systems, ensuring equitable water distribution.	[11, 13, 15, 17, 18]
Adaptation to natural cycles and climate resilience	1. Shifting Planting Times in KwaZulu-Natal: Farmers adjust planting times based on seasonal shifts, responding to climatic changes and conserving water. 2. Drought-Tolerant Crops in Limpopo/Karoo: Farmers select drought-tolerant crops that are well-suited to arid conditions, conserving water in times of drought. 3. Adaptation to Dryland Farming in Eastern Cape: Indigenous farmers employ adaptive techniques like mulching to maintain soil moisture during dry spells. 4. Indigenous Drought Strategies in Limpopo: Use of indigenous knowledge for managing seasonal droughts, including adjusting farming practices to avoid water depletion.	[10, 11, 14, 17]
Social inclusivity and knowledge sharing	1. Mpumalanga Collective Soil and Water Conservation: Smallholder farmers implement water conservation techniques together, ensuring equitable access to water. 2. Karoo Drought Adaptation Techniques: Knowledge of water conservation is shared through community meetings, ensuring widespread participation in drought preparedness strategies. 3. Water Use Education in Limpopo: Knowledge of water conservation methods is shared with all community members, including elders teaching younger generations. 4. Water Sharing Systems in KwaZulu-Natal: Communities share water resources, with local water sharing practices ensuring that water is accessible to all, irrespective of wealth.	[13, 15, 17, 18]

4.1. Indigenous Water Conservation Practices and Rural Water Security in South Africa

Indigenous water conservation practices have significantly enhanced water security in rural South Africa by providing sustainable and cost-effective solutions. Techniques such as rainwater harvesting and natural storage systems, including clay pits and stone-lined channels, have reduced water stress by up to 30% in areas like Limpopo and the Karoo[10]. In the Eastern Cape, these methods have increased water availability by 20–25% during droughts[20]. Practices such as sacred water site preservation, governed by cultural rituals, and traditional weather prediction further enhance sustainability and resilience to climate change[14, 16]. Moreover, collective governance of water resources promotes equitable access and strengthens community ties, improving agricultural productivity by up to 50% in regions like Limpopo[15]. These approaches are essential for rural areas with limited access to modern infrastructure.

4.2. Improved Water Security in Rural Areas

Indigenous water conservation practices such as rainwater harvesting and the construction of check dams have helped rural communities in South Africa secure their water supplies, especially in areas that lack access to formal water infrastructure. In the Karoo region, for example, indigenous farmers use techniques such as rainwater harvesting pits and small retention dams. These systems help retain and store water during the rainy season, which can be used during the dry months. Ncube in his study provides that communities using indigenous water harvesting methods reported up to 30% less water stress compared to those who depended exclusively on external water sources[10]. Similarly, in the Eastern Cape, indigenous farming communities have seen a 20–25% increase in water availability during dry periods due to the use of traditional water management methods such as rainwater storage pits[20]. Studies also mention that traditional rainwater harvesting techniques have shown to improve water availability by 30% in dry seasons, especially for households and small-scale farms in regions like Limpopo[21, 22]. Also, Mango et al. (2017) document the adoption of traditional rainwater harvesting and soil erosion control methods in the Chinyanja Triangle, which have proven effective in sustaining agricultural productivity in semi-arid regions[23]. Similarly, in the Mbhashe and Mnquma municipalities, indigenous practices like the use of traditional water pits and stone-lined reservoirs have provided sustainable solutions for household water security[24].

4.3. Indigenous Knowledge in Addressing Climate Change and Enhancing Resilience

Indigenous knowledge of local climatic patterns and ecosystems enables communities to adapt to extreme weather events, such as floods or droughts, ensuring that their water systems remain functional during these times. For instance, in KwaZulu-Natal, communities have developed systems that integrate weather prediction with water storage, ensuring they are prepared for rainfall patterns. According to Vilakazi et al., these communities have improved resilience by maintaining water availability in times of extreme drought, with some areas reporting a 40% increase in water conservation efficiency when integrating traditional methods with modern technologies[14]. Similarly, indigenous systems like the "cooling dam" method, which uses natural barriers to reduce evaporation, have enhanced the ability to manage seasonal variations in water flow, contributing to a 15% improvement in water retention in the Karoo and Limpopo province[11]. Further, Reij et al. also highlight that those indigenous practices such as terracing and agroforestry, widespread across Africa, have been pivotal in soil and water retention, enabling agricultural sustainability in arid regions[25]. In the above **Table 2**, under the ecological knowledge understanding the various types of soil and their differing capacities to hold water should be the primary focus of farming practices. Important practices include choosing crops that can withstand drought, using conservation tillage, adding organic matter, putting water harvesting techniques into practice, and using drip irrigation systems to maximize water use on clay-rich soils, which typically retain more moisture than sandy soils[26].

4.4. Preservation of Biodiversity

Many indigenous practices are aligned with the need to protect local biodiversity, which plays an essential role in water conservation. For example, the maintenance of traditional wetlands and river systems helps preserve ecosystems that regulate water flow and quality. Agholor and Nkosi

documented that communities in Limpopo province have preserved wetlands through traditional practices like controlled burning and selective harvesting of aquatic plants. These practices have helped maintain ecosystem services such as water filtration, with evidence showing a 12% increase in the quality of local water sources[19]. Indigenous knowledge plays a crucial role in managing bush encroachment, which impacts groundwater recharge. Practices such as selectively clearing water-intensive species can improve water infiltration and minimize evapotranspiration losses[26]. Aldworth et al. (2023) highlight that those areas with high woody plant density, particularly dense mopane, experience 12% greater evapotranspiration during wetter years compared to cleared areas, leading to reduced groundwater and soil water recharge; however, they don't focus on any indigenous practices[27]. Again, indigenous communities manage wetlands to recharge groundwater sources, which is critical for ensuring water availability during dry periods. This practice not only conserves water but also helps maintain biodiversity and ecosystem health. In regions like KwaZulu-Natal, wetland management by local communities has led to improved groundwater retention and a reliable water source for agriculture and domestic use[9]. This has reduced the reliance on municipal water supplies, which can be scarce or unreliable, especially in remote areas. In addition, some other studies underline the role of traditional ecological knowledge in managing invasive species, such as alien freshwater fisheries and invasive plants, which threaten local biodiversity and water resources[28, 29]. Similarly, the Venda community in the Limpopo Province of South Africa is particularly associated with the protection of sacred groves and springs. These sacred water sources, such as Lake Fundudzi and Phiphidi Waterfalls, hold profound spiritual significance for the Venda people. They are considered sacred spaces connected to ancestral spirits and are preserved through cultural taboos and rituals. These practices not only maintain the sanctity of the sites but also ensure ecological conservation by protecting the surrounding biodiversity and water quality[16].

4.5. Social and Economic Benefits

Indigenous water management practices are often rooted in collective community action and shared responsibility. This inclusivity helps ensure that the benefits of water conservation reach all members of the community, particularly vulnerable groups. The empowerment of women through involvement in water management processes has been a key feature of indigenous systems. In communities where women are integral in managing water resources, there has been a 30–40% improvement in household water access[12]. The shared knowledge transmission helps bridge generational gaps and ensures the long-term sustainability of these practices. In Limpopo, a community-based irrigation system that uses indigenous methods of water distribution has led to a 50% increase in agricultural productivity, which has in turn improved local food security and access to water[15]. Similarly, Richardson and Van Wilgen emphasize on the role of community engagement in managing invasive plants, which threaten water availability and quality. Such practices reinforce the need for community-driven approaches to safeguard both water resources and biodiversity[29]. Furthermore, Harvey and Reed emphasized community-managed water systems, particularly in regions where centralized water distribution is unreliable. These systems are often based on indigenous methods of equitable water sharing, such as the "lekgotla" system, where communities collaboratively decide on water distribution during shortages[30]. The Zulu people hold water as sacred, often associating it with ancestral spirits. Traditional practices include the protection of springs (izigodi) and rivers, viewed as spiritual entities that require ritual offerings to ensure their vitality. These rituals, often led by elders, emphasize collective responsibility in safeguarding water sources for future generations[18].

Indigenous practices often require fewer external inputs and are less reliant on expensive infrastructure. This cost-effectiveness has been especially beneficial in rural areas, where the costs of modern water management systems are prohibitive. Communities employing indigenous methods have reported significant savings compared to those who depend on costly modern water infrastructure. According to a report by WRC (Water Resource Conservation) Report communities in the Eastern Cape saved up to 40% of water management costs by utilizing traditional systems such as gravity-fed water channels and stone-lined water channels for irrigation[13]. Traditional sand dams built by local communities in the Western Cape have shown a 50% reduction in water loss compared to modern, concrete-based dam designs[11]. Postel highlighted that traditional water conservation systems, such as small-scale irrigation channels and

hand-dug wells, are more affordable and easier to maintain compared to large-scale dams and pipelines. In regions with limited financial resources, such as rural South Africa, these methods provide a practical and sustainable alternative[31]. The adoption of indigenous water conservation techniques (WCTs) should not be viewed in isolation; rather, their value lies in their contribution to broader social and economic goals such as human development, poverty alleviation, and environmental sustainability. The use of WCTs is recognized as a key strategy for ensuring sustainable agriculture, which in turn supports sustainable livelihoods, particularly in rural communities. By improving water management, these practices help foster long-term economic growth and enhance the resilience of local communities[32].

4.6. Environmental Sustainability

Indigenous water practices tend to be low-cost and environmentally friendly, relying on locally available materials such as rocks, clay, and native plants. For example, stone terraces used by farmers in Limpopo help control runoff and conserve soil moisture, enhancing crop yields and reducing soil erosion. Such methods decrease the need for expensive irrigation systems, making them accessible for low-income communities[22, 33]. Additionally, the use of natural resources minimizes ecological disruption and promotes biodiversity. Similarly, Basdew, et. al. document the integration of indigenous knowledge in KwaZulu-Natal, where communities use rotational grazing and wetland conservation to bolster water resilience. These practices have ensured sustainable resource use while preserving ecosystem health as well[34]. On the other hand, practices such as conservation tillage and agroforestry not only help in improved water retention by ensuring the long-term sustainability of water resources but also reduce soil degradation[35, 36]. Furthermore, Finn and Jackson in their study challenge the conventional environmental flow assessments, advocating for the inclusion of indigenous values to reflect the cultural significance of water bodies[37]. Such approaches align with studies that call for managing environmental flows to maintain ecological integrity[38]. Among the Xhosa, wells and springs (amanzi sources) are communally maintained and governed by indigenous laws. Elders and traditional leaders allocate water usage rights during dry seasons, ensuring fairness and preventing conflicts. These systems promote water conservation by mandating specific times and methods for drawing water, aligning with sustainable resource management principles[18, 39].

4.7. Water Conservation through Traditional Knowledge of Weather Prediction

Indigenous knowledge systems incorporate weather prediction and seasonal planning based on natural indicators. By interpreting animal behavior, plant growth, and celestial observations, communities can predict weather patterns, adjust water usage, and prepare for possible droughts. This knowledge has reduced crop failures by up to 15% in areas that depend heavily on rain-fed agriculture, as seen in case studies across the Eastern Cape[40]. The KwaZulu-Natal communities use natural indicators such as tree blooming cycles and animal behavior to predict rainfall patterns, allowing farmers to plan their planting and irrigation schedules accordingly[34]. Furthermore, Bryan et al. and Ziervogel et al. note that integrating these practices into national climate adaptation frameworks can enhance resilience to droughts and extreme weather events, which are becoming more frequent due to climate change[41, 42]. Similarly, in their study Edgar et.al. provide that in Limpopo Province the Venda and Pedi communities, have long relied on indigenous knowledge for predicting weather patterns and managing water resources. These communities, residing in regions like Thohoyandou and surrounding rural areas, used specific natural indicators such as; bird migration, flowering cycles, and animal behavior[16].

4.8. Reduction in Waterborne Disease

Proper water management and traditional filtering techniques using locally available materials, such as sand and specific plant roots, have been reported to reduce waterborne diseases. Communities utilizing such techniques in rural South Africa report fewer cases of water-related illnesses, which supports public health while providing a safe, drinkable water supply[43]. Indigenous water purification techniques, such as the use of moringa seeds and sand filtration, have reduced waterborne illnesses in communities by up to 30%, as noted by Naidoo et al. in their study[22].

4.9. Integration of Modern Technology with Indigenous Knowledge

Recent efforts have focused on combining indigenous knowledge with modern water management technologies to enhance the overall effectiveness of water conservation efforts. Alexander et al. advocate for linking indigenous and scientific knowledge to combat the adverse effects of climate change, citing the value of traditional water-sharing systems and natural resource stewardship[44]. Similarly, Muller advocated for blending these traditional practices with urban planning strategies to ensure resilience in rapidly urbanizing areas. For example, green roofs and rain gardens inspired by traditional water-harvesting designs have been integrated into urban water management plans[45]. Further, a study highlighted the successful integration of indigenous rainwater harvesting methods with modern weather forecasting systems in several South African communities. This hybrid approach resulted in a 35% increase in water conservation rates and has been widely adopted in community-driven water management programs[46]. In KwaZulu-Natal, the integration of traditional water storage techniques with digital water tracking systems has led to more efficient water management, reducing water wastage by 25%[14].

5. Discussion

5.1. Policy Implications and Recommendations

Research highlights the potential benefits of integrating indigenous water conservation practices into South Africa's national water policies to enhance water security. Integrating indigenous knowledge into South Africa's formal water management systems could bridge existing policy and infrastructure gaps. Collaborative programs between governmental agencies and indigenous communities could ensure that traditional practices are recognized and supported. Research has shown that indigenous knowledge can complement technological solutions by adding a layer of social and environmental adaptability. Recognizing and supporting these methods can empower communities and promote resilience against water scarcity[9, 22, 40, 47]. Singh et al. and Zvobgo et al. further suggest that providing financial incentives for traditional approaches, such as rainwater harvesting, could sustain these practices and reduce reliance on centralized water infrastructure[33, 34, 40]. Similarly, Briggs and Sharp underscore the need to integrate indigenous knowledge into policy-making, ensuring socio-cultural inclusivity and equitable water access[48]. The WRC Report in the year 2011 also emphasizes the need for innovative water conservation and management approaches that integrate local knowledge[49]. However, to effectively implement these interventions, policies should mandate the systematic collection of data on indigenous practices to assess their impact. This data would enable policymakers to evaluate their effectiveness and scale up successful approaches accordingly[21, 43].

5.2. Integration with Modern Water Management Practices

Research suggests that the traditional indigenous water practices should be integrated with contemporary water management frameworks in order to achieve maximized efficiency, resilience, and sustainability. If integrated thoughtfully, this combined approach can leverage the ecological sensitivity of indigenous practices with the technological advancements of modern systems. For example, indigenous rainwater harvesting and aquifer recharge methods can be enhanced through modern storage systems and distribution networks, offering a reliable water source in arid or drought-prone areas[33, 40]. Moreover, indigenous water practices emphasize the conservation and equitable distribution of water resources within communities, which aligns with contemporary goals for sustainable resource management and inclusive governance[22, 43]. This integrated approach can provide resilience against climate-induced water shortages, as both systems together offer adaptive strategies that respond to variable rainfall, groundwater levels, and ecosystem needs[9]. Furthermore, Bakker underscores the ethical dimension of water as a common resource, advocating for indigenous perspectives that prioritize collective welfare over privatization. By integrating indigenous and scientific approaches, South Africa can build robust, inclusive water management systems that address its unique socio-ecological challenges while ensuring resilience in the face of climate change[50].

5.3. Potential Challenges in Integrating Indigenous Knowledge with Modern Technology

Integrating indigenous knowledge (IK) with modern technology presents several challenges that need to be care-

fully navigated. These include cultural and epistemological differences, as IK is holistic and context-specific, while modern technology is analytical and standardized[18]. The oral, localized nature of IK also makes it difficult to document and standardize, conflicting with the formal documentation required by modern technology[15]. Additionally, the integration of IK with modern technology risks creating dependency on costly, external technologies that may not be accessible in rural communities, threatening the sustainability of IK practices. Institutional resistance to incorporating IK into policy, combined with its lack of formal recognition, can hinder its integration with modern systems[50, 51]. Furthermore, modern technologies may struggle to account for the intricate, localized understanding of climate variability embedded in IK, particularly in the face of non-linear climate impacts[52]. Lastly, the exploitation of IK without proper consent or benefit-sharing mechanisms poses risks to cultural heritage and community empowerment. However, a collaborative approach in which the modern technology respects and incorporates the IKS is required to successfully integrate both systems, leading to more context-specific and sustainable solutions for climate change and water management[53].

5.4. Major Findings

- Effectiveness of Indigenous Practices: Indigenous water conservation techniques, such as rainwater harvesting and community-based irrigation, have significantly improved water security, reducing water stress by up to 30% in rural areas with limited infrastructure.
- Contribution to Climate Resilience: Indigenous practices like weather prediction, drought-tolerant cropping, and adaptive planting schedules help communities build resilience to climate change, improving water retention and agricultural productivity during extreme weather events.
- Environmental Sustainability: These practices promote minimal ecological disruption, conserve soil and water, and protect biodiversity. Sacred water sites and the management of wetlands and invasive species contribute to ecosystem conservation.
- Social Inclusivity and Community Empowerment: Indigenous practices foster social equity by involving the entire community in water management, promoting knowledge sharing, and empowering women, thus enhancing the sustainability of water systems and social cohesion.
- Cost-Effectiveness: Indigenous methods are low-cost and require minimal external inputs, making them accessible to economically disadvantaged communities, particularly in rural South Africa.
- Integration with Modern Technology: Integrating indigenous knowledge with modern water management technologies improves efficiency and creates adaptive solutions, such as combining traditional rainwater harvesting with digital tracking systems for enhanced water conservation.

5.5. Future Research Directions

Further research is needed to systematically document indigenous water management practices across different regions. Understanding the mechanisms and ecological principles underlying these practices could enhance their adaptation to contemporary challenges, such as urbanization and climate change. Additionally, exploring indigenous perspectives on wastewater treatment and reuse could broaden sustainable water management approaches[22].

6. Conclusions

In conclusion, indigenous water conservation practices provide valuable, sustainable solutions that align with modern water management goals and address pressing environmental challenges. These practices—rooted in centuries of localized knowledge—contribute to sustainable resource use, community resilience, and environmental stewardship. As highlighted in recent studies, indigenous practices such as rainwater harvesting, aquifer recharge, and community-based water governance have shown measurable effectiveness in conserving water resources, reducing vulnerability to drought, and sustaining ecological balance. Integrating these traditional methods with modern technologies can offer a holistic approach to water management that balances innovation with respect for cultural heritage and ecological knowledge. However, there are still shortcomings in integration of IKS with the modern technology. Such integration calls for policy recognition, research support, and community involvement to ensure that indigenous knowledge remains a central, respected component of sustainable development

efforts. Embracing this synergy between indigenous and modern water practices represents a promising path toward achieving water security and resilience in South Africa and beyond, fostering sustainable development that honors and utilizes diverse knowledge systems.

Author Contributions

All the Authors contributed equally to write this article. All authors have read and approved the final manuscript.

Funding

This work received no external funding.

Institutional Review Board Statement

There is no requirement of any approval from any institution because it is "Not applicable" for studies not involving humans or animals.

Informed Consent Statement

This manuscript is based on the secondary data so it is not required any consent from anyone. Not applicable for this study.

Data Availability Statement

We are publishing our article first time in your journal and we have not created any data so it is not applicable for us.

Conflicts of Interest

There is no conflict of interest among all the authors.

References

[1] UN, 2021. The United Nations world water development report 2021: Valuing water. ISBN NO. 978-92-3-100434-6, 21 Mar 2021. Available from: https://www.unwater.org/publications/un-world-water-development-report-2021

[2] UN, 2010. UN water. Available from: https://www.unwater.org/water-facts/human-rights-water-and-sanitation (cited 22 November 2024).

[3] UNGA, 2016. The human rights to safe drinking water and sanitation: Resolution adopted by the General Assembly. Available from: https://digitallibrary.un.org/record/821067?v=pdf (cited 25 November 2024).

[4] UN, 2023. UN world water development report 2023: Partnerships and cooperation for water. ISBN No. 978-92-3-100576-3, 15 Mar 2023. Available from: https://www.unwater.org/publications/un-world-water-development-report-2023

[5] UN, 2018. Water for sustainable development 2018–2028: An international decade for action. Available from: https://www.un.org/en/events/waterdecade/ (cited 25 November 2024).

[6] Muyambo, F., Jordaan, A., Bahta, Y., 2017. The role of indigenous knowledge in drought risk reduction: A case of communal farmers in South Africa. Jàmbá: Journal of Disaster Risk Studies. 9(1), 1–6.

[7] Calverley, C., Walther, S., 2022. Drought, water management, and social equity: Analyzing Cape Town, South Africa's water crisis. Frontiers in Water. 4, 910149. DOI: https://doi.org/10.3389/frwa.2022.910149

[8] UNESCO, 2017. Local and Indigenous Knowledge Systems (LINKS). Available from: https://www.unesco.org/en/links (cited 25 November 2024).

[9] Olokesusi, F., 2006. Survey of indigenous water management and coping mechanisms in Africa: Implications for knowledge and technology policy. ATPS SPECIAL PAPER SERIES No. 25. Available from: https://atpsnet.org/wp-content/uploads/2017/05/special_paper_series_25.pdf (cited 25 November 2024).

[10] Ncube, B., 2018. Insights into indigenous knowledge strategies for coping and adapting to drought in agriculture: A Karoo scenario, South Africa. Indilinga African Journal of Indigenous Knowledge Systems. 17(1), 92–108. Available from: https://hdl.handle.net/10520/EJC-fe65c371a

[11] Budeli, A., 2021. An exploration of african indigenous knowledge methods of water conservation and management in the Limpopo Province of South Africa [Master's thesis]. Limpopo, South Africa: University of Venda. pp. 85–155.

[12] Swatuk, L., 2010. The state and water resources development through the lens of history: A South African case study. Water Alternatives. 3(3), 521–536. Available from: https://www.water-alternatives.org/index.php/allabs/114-a3-3-4/file

[13] WRC, 2009. Indigenous water harvesting and conservation practices: historical context, cases and implications. TT 392/09, April 2009. Available from: https://www.wrc.org.za/wp-content/uploads/mdocs/TT%20392-09%20Agricultural%20water%20management.pdf

[14] Vilakazi, B., Zengeni, R., Mafongoya, P., 2019. Indigenous strategies used by selected farming communities in KwaZulu Natal, South Africa, to manage soil, water,

and climate extremes and to make weather predictions. Land Degradation & Development. 30(16), 1999–2008. DOI: https://doi.org/10.1002/ldr.3395

[15] Thakur, R., Rane, A., Harris, G., et al., 2020. Government initiatives and policies for water conservation and wastewater treatment in South Africa and indigenous knowledge. In: Singh, Yulia Milshina, Kangming Tian, Deepak Gusain, João Paulo Bassin (eds.). Water Conservation and Wastewater Treatment in BRICS Nations. Elsevier: Amsterdam, Netherlands. pp. 285–293. DOI: https://doi.org/10.1016/B978-0-12-818339-7.00014-X

[16] Edgar, B., Eva, M., Lee, K., 2022. Disappearance of African indigenous knowledge of water conservation and management in Limpopo Province of South Africa: An IKS perspective. African Journal of Development Studies. 12(2), 49–73. Available from: https://hdl.handle.net/10520/ejc-aa_affrika1_v12_n2_a3

[17] Denison, J., Wotshela, L., 2012. An overview of indigenous, indigenised and contemporary water harvesting and conservation practices in South Africa. Irrigation and Drainage. 61, 7–23.

[18] Agholor, A., Nkosi, M., 2020. Sustainable water conservation practices and challenges among smallholder farmers in Enyibe Ermelo Mpumalanga Province, South Africa. Journal of Agricultural Extension. 24(2), 112–123. DOI: https://doi.org/10.4314/jae.v24i2.12

[19] Basu, M., Dasgupta, R., 2023. Exploring indigenous water knowledge, values, and practices: Insights and examples. In: Basu, M., Dasgupta, R. (eds.). Indigenous and Local Water Knowledge, Values and Practices. Springer: Singapore. pp. 1–9. DOI: https://doi.org/10.1007/978-981-19-9406-7_1

[20] Fanteso, B., Yessoufou, K., 2022. Diversity and determinants of traditional water conservation technologies in the Eastern Cape Province, South Africa. 194(3), 161. Environmental Monitoring and Assessment. 194(161), 1–14. DOI: https://doi.org/10.1007/s10661-022-09848-2

[21] Chisenga, J., 2002. Indigenous knowledge: Africa's opportunity to contribute to global information content. South African Journal of Libraries and Information Science. 68(1), 16–20. Available from: https://hdl.handle.net/10520/EJC61124

[22] Naidoo, N., Longondjo, C., Vrdoljak, M., 2013. Investigating operational indigenous knowledge of water and waste management, and establishing ways to integrate them into water services management. Report number 1941/1/13, October 2013. Available from: https://www.wrc.org.za/wp-content/uploads/mdocs/1941-1-131.pdf

[23] Mango, N., Makate, C., Tamene, L., et al., 2017. Awareness and adoption of land, soil and water conservation practices in the Chinyanja Triangle, Southern Africa. International Soil and Water Conservation Research. 5(2), 122–129. DOI: https://doi.org/10.1016/j.iswcr.2017.04.003

[24] Mapuka, F., Nel, W., Kalumba, A., 2024. Exploring household water conservation methods in rural South Africa: A case of the Mbhashe and Mnquma local municipalities. Sustainable Water Resources Management. 10(4), 145. DOI: https://doi.org/10.1007/s40899-024-01127-x

[25] Reij, C., Scoones, I., Toulmin, C., 2013. Sustaining the soil: Indigenous soil and water conservation in Africa. Routledge: London, UK. pp. 181–188 DOI: https://doi.org/10.4324/9781315070858

[26] WRC, 2023. Woody encroachment: Understanding its impact on water resources. Water Wheel, May–June 2023. pp. 8–28. Available from: https://www.wrc.org.za/wp-content/uploads/mdocs/WW%20May%20-%20June%202023_WOODY%20ENCROACHMENT.pdf

[27] Aldworth, T.A., Toucher, M.L.W., Clulow, A.D., et al., 2023. The Effect of Woody Encroachment on Evapotranspiration in a Semi-Arid Savanna. Hydrology, 10(1), 9. DOI: https://doi.org/10.3390/hydrology10010009

[28] Cambray, J.A., 2003. Impact on indigenous species biodiversity caused by the globalisation of alien recreational freshwater fisheries. Hydrobiologia. 500(1), 217–230. DOI: https://doi.org/10.1023/A:1024648719995

[29] Richardson, D., Van Wilgen, B., 2004. Invasive alien plants in South Africa: How well do we understand the ecological impacts? Working for water. South African Journal of Science. 100(1), 45–52. Available from: https://hdl.handle.net/10520/EJC96214

[30] Harvey, P., Reed, R., 2007. Community-managed water supplies in Africa: sustainable or dispensable?. Community Development journal. 42(3), 365–378. DOI: https://doi.org/10.1093/cdj/bsl001

[31] Postel, S., 2000. Entering an era of water scarcity: The challenges ahead. Ecological applications. 10(4), 941–948. DOI: https://doi.org/10.1890/1051-0761(2000)010[0941:EAEOWS]2.0.CO;2

[32] Knox, A., Meinzen-Dick, R., 1999. Property rights, collective action and technologies for natural resource management. Policy Brief no. 1, October 1998.

[33] Singh, P., Milshina, Y., Tian, K., et al., 2020. Water conservation and wastewater treatment in BRICS nations: Technologies, challenges, strategies and policies. Elsevier: Amsterdam, The Netherlands. pp. 353–363.

[34] Basdew, M., Jiri, O., Mafongoya, P., 2017. Integration of indigenous and scientific knowledge in climate adaptation in KwaZulu-Natal, South Africa. Change and Adaptation in Socio-Ecological Systems. 3(1), 56–67. DOI: https://doi.org/10.1515/cass-2017-0006

[35] Mrabet, R., 2002. Stratification of soil aggregation and organic matter under conservation tillage systems in Africa. Soil and Tillage Research. 66(2), 119–128. DOI:

https://doi.org/10.1016/S0167-1987(02)00020-X

[36] Andersson, J., D'Souza, S., 2014. From adoption claims to understanding farmers and contexts: A literature review of Conservation Agriculture (CA) adoption among smallholder farmers in southern Africa. Agriculture, Ecosystems & Environment. 187, 116–132. DOI: https://doi.org/10.1016/j.agee.2013.08.008

[37] Finn, M., Jackson, S., 2011. Protecting indigenous values in water management: A challenge to conventional environmental flow assessments. Ecosystems. 14(8), 1232–1248. DOI: https://doi.org/10.1007/s10021-011-9476-0

[38] Dyson, M., Bergkamp, G., Scanlon, J., 2003. Flow: The essentials of environmental flows. IUCN: Gland, Switzerland & Cambridge, UK. pp. 1–136.

[39] Jacob, D., Nelson, I., Izah, S., 2024. Indigenous water management strategies in the Global South. In: Izah, S.C., Ogwu, M.C., Loukas, A., et al. (Eds.). Water Crises and Sustainable Management in the Global South. Springer: Singapore. pp. 487–525. DOI: https://doi.org/10.1007/978-981-97-4966-9_16

[40] Zvobgo, L., Johnston, P., Williams, P., et al., 2022. The role of indigenous knowledge and local knowledge in water sector adaptation to climate change in Africa: A structured assessment. Sustainability Science. 17, 2077–2092. DOI: https://doi.org/10.1007/s11625-022-01118-x

[41] Bryan, E., Deressa, T., Gbetibouo, G., et al., 2009. Adaptation to climate change in Ethiopia and South Africa: options and constraints. Environmental Science & Policy. 12(4), 413–426. DOI: https://doi.org/10.1016/j.envsci.2008.11.002

[42] Ziervogel, G., New, M., van Garderen, E., et al., 2014. Climate change impacts and adaptation in South Africa. Wiley Interdisciplinary Reviews: Climate Change. 5(5), 605–620. DOI: https://doi.org/10.1002/wcc.295

[43] Prins, F., Etale, A., Ablo, A., et al., 2022. Water scarcity and alternative water sources in South Africa: Can information provision shift perceptions?. Urban Water Journal. 20(10), 1438–1449. DOI: https://doi.org/10.1080/1573062X.2022.2026984

[44] Alexander, C., Bynum, N., Johnson, E., et al., 2011. Linking indigenous and scientific knowledge of climate change. BioScience. 61(6), 477–484. DOI: https://doi.org/10.1525/bio.2011.61.6.10

[45] Muller, M., 2009. Adapting to climate change: Water management for urban resilience. In: Muller, M. (ed.). Adapting Cities to Climate Change. Routledge: London, UK. pp. 291–307. https://doi.org/10.1177/0956247807076726

[46] Viljoen, G., van der Walt, K., 2018. South Africa's water crisis-an interdisciplinary approach. Tydskrif vir Geesteswetenskappe. 58(3), 483–500.

[47] Anderson, E., Jackson, S., Tharme, R., et al., 2019. Water scarcity and alternative water sources in South Africa: can information provision shift perceptions?. Wiley Interdisciplinary Reviews: Water. 6(6), e1381. DOI: https://doi.org/10.1002/wat2.1381

[48] Briggs, J., Sharp, J., 2004. Indigenous knowledges and development: A postcolonial caution. Third World Quarterly. 25(4), 661–676. DOI: https://doi.org/10.1080/01436590410001678915

[49] Middleton, B., Bailey, A., 2011. Water resources of South Africa. Report number TT 513/11, Nov 2011. Available from: https://wrcwebsite.azurewebsites.net/wp-content/uploads/mdocs/TT%20513-11.pdf

[50] Bakker, K., 2007. The "commons" Versus the "commodity": Alter-globalization, anti-privatization, and the human right to water in the Global South. Antipode. 39(3), 430–455. DOI: https://doi.org/10.1111/j.1467-8330.2007.00534.x

[51] DWS, 2021. Strategic Report number RP83/2021, 9 March, 2021. Available from: https://www.dws.gov.za/documents/Other/Strategic%20Plan/2021/Revised2020-21To2024-2025StrategicPlan_09March2021.Rev01.pdf

[52] Madzivhandila, T.S., 2024. Integrating Indigenous Knowledge Systems (IKS) to Climate Change Adaptation in South Africa: Lessons from the "Past". South African Journal of Higher Education. 38(5), 159–168. DOI: https://doi.org/10.20853/38-5-6417

[53] Richter, B., Mathews, R., Harrison, D., et al., 2003. Ecologically sustainable water management: managing river flows for ecological integrity. Ecological Applications. 13(1), 206–224. DOI: https://doi.org/10.1890/1051-0761(2003)013[0206:ESWMMR]2.0.CO;2

Arabian Journal for Science and Engineering
https://doi.org/10.1007/s13369-025-10082-4

RESEARCH ARTICLE-MECHANICAL ENGINEERING

Influence of Heat Input Variations on Tribological Performance of Bimetallic Aluminum Alloy Walls Fabricated via Cold Metal Transfer-Based Wire Arc Additive Manufacturing

Soni Kesarwani[1] · **Narayana Yuvaraj**[1] · **Mahendra Singh Niranjan**[1]

Received: 22 October 2024 / Accepted: 19 February 2025
© King Fahd University of Petroleum & Minerals 2025

Abstract

Wire arc additive manufacturing (WAAM) provides advantages such as complex geometries and reduced waste, but its mechanical and tribological properties differ from those of traditionally manufactured parts. While aluminum alloy parts fabricated via WAAM have broad applications in industries like aerospace, automotive, and marine, they usually encounter challenges like high friction and wear. Therefore, studying the tribological behavior is essential to ensure the durability and performance of WAAM walls of aluminum alloys in such demanding environments. In this current study, the CMT-based WAAM technique was used to fabricate three bimetallic walls with ER4043 and ER5356 filler wires, employing three heat input combinations: low (223.8 J/mm and 162 J/mm), medium (236.8 J/mm and 175.2 J/mm), and high (251.7 J/mm and 186.7 J/mm).The tribological performance of each wall was assessed under varying loads (20 N, 30 N, and 40 N), followed by a detailed analysis of the walls exhibiting the lowest wear rates. The results revealed that the wall fabricated with the low heat input exhibited the minimum wear rate (0.0019 mm^3/m) under a 20 N load and the lowest coefficient of friction of 0.25 under a 40 N load, specifically in the ER5356 layer, where adhesive and delamination wear mechanisms were observed. Optical and field emission scanning electron microscopy, along with electron backscatter diffraction imaging of the wall with the minimum wear rate, showed equiaxed coarse grains in the ER4043 layer, finer grains in the ER5356 layer, and fine equiaxed grains at the interface layer. The ER5356 layer exhibited the highest hardness, being 21.86% and 6.77% greater than the interface and ER4043 layers, respectively. Additionally, the energy absorbed during impact was 25.76 J, and fractography analysis confirmed a ductile fracture mode characterized by dimples and voids.

Keywords WAAM · CMT · Bimetallic Wall · Heat input · Wear · Microstructure · Mechanical properties

1 Introduction

Aluminum alloys have gained worldwide attention during the last decade due to their lightweight and high-strength high strength, and excellent properties at high and low temperatures [1]. They also exhibit good weldability and formability, making them highly flexible materials [2]. These attributes have shown the widespread use of aluminum alloys in various fields, like aerospace, transportation, marine, and automotive industries [3]. Another way to improve the properties of aluminum parts includes the use of joining dissimilar aluminum alloy by welding [4]. This method provides an opportunity to fabricate parts with tailored properties and functions [5]. The ongoing evolution of materials aims to produce products with homogenized attributes, and metal additive manufacturing (AM) is a high-interest topic due to its capability to fuse metallic layers to form complete structures [6]. AM of metal, especially the wire arc additive manufacturing (WAAM), has revolutionized the fabrication of dissimilar aluminum alloy components, unveiling a faster, flexible, and prolonged production process that actually responds significantly to cost and time savings [7]. WAAM displays a novel and advantageous technique to an AM, mainly because of its high deposition rate, efficient material utilization, relatively low production and equipment costs, and superior flexibility and

✉ Soni Kesarwani
sonikesh0@gmail.com

Narayana Yuvaraj
yuvraj@dce.ac.in

Mahendra Singh Niranjan
mahendraiitr2002@gmail.com

[1] Department of Mechanical Engineering, Delhi Technological University, Delhi 110042, India

Published online: 06 March 2025

scalability compared to laser or electron beam-based AM processes [8, 9]. Cold metal transfer (CMT)-WAAM is more appropriate for the fabrication of aluminum alloys due to its low heat input (HI), optimized synergic lines, and lower cost of both filler materials and equipment [10]. Heat input is a critical parameter for WAAM; it directly affects the cooling rate and, consequently, the microstructure of bimetallic aluminum alloy walls [10]. Heat input not only affects grain structure and phase distribution but also affects the formation of residual stress [11]. Higher heat input leads to coarse grain structures with lower hardness, while lower heat input may increase hardness and make the material more susceptible to cracking [12]. Achieving appropriate heat input balance is crucial; excessive heat is likely to be associated with severe thermal cycles, leading to distortion and reduced dimensional accuracy, while insufficient heat can result in poor fusions, weak bondings, and porosity [12]. Therefore, controlled heat input is essential for optimizing bonding and preserving the mechanical and wear properties of each alloy layer in bimetallic WAAM components. This is especially important in industries such as aerospace, automotive, and marine, where precise properties are vital [11]. Till now, researchers have successfully manufactured various single-material aluminum alloy walls using the arc-based technique, such as the, Al–Mg alloy [11] alloy, Al-Si [12] alloy, Al-Cu [13] and Al-Li [14] alloy. Also, many researchers have attempted to form a transition between the different materials alloys by introducing an interlayer, such as AA 2319 /5B06 aluminum alloys [15], AA6060/AA5087 [16], AA7075/AA5356 [17] and Ti6Al4V/Al6.21Cu [18], etc. Some of the research has been made on bimetallic alloy/dissimilar alloy using CMT-WAAM technique like, Koli et al. [19] used the arc-based method to fabricate a single wall of 308L. Their analysis aimed to examine the impact of HI on the wear rate, and metallurgical properties of the wall. The results displayed a reduction in micro-hardness along the height of the wall. The highest wear rate (0.1254 mm^3/m) was observed under higher HI conditions at 180 N and within the initial 200 m sliding distance. Conversely, the lowest wear rate (0.02158 mm^3/m) was recorded under lower HI conditions at 120 N and between 200 to 400 m of sliding distance. Ashish et al.[20] used an arc-based technique to fabricate the wall of 316L. They analyzed the microstructure and mechanical properties at different spatial directions (0°, 90°, and 45°) and evaluated wear characteristics along the deposited wall. The conclusions indicate that the highest wear rate occurs at 30 N, while the lowest wear rate is observed at 20 N. In terms of tensile strength and hardness, samples oriented at 0° display higher ultimate tensile stress (UTS) compared to other orientations. The coefficient of friction (COF) value for the ASS samples decreases within the range of 0.541–0.568. The arc-based DED process yields a highly heterogeneous microstructure represented by distinct grain formations at different locations along the build direction. Ashish et al. [21] manufactured the wall of a multi-material alloy of SS316LSi and ER70S-6 using a twin wire arc additive manufacturing technique. The following investigations concentrated on evaluating the mechanical, microstructural, and tribological properties of the developed functionally graded material (FGM) structure. The results reveal that the as-deposited FGM displays superior wear resistance and mechanical performance in comparison with individual SS316LSi and ER70S-6 filler wires. Chakkravarthy et al.[22] manufactured the wall of Al4043 alloy through the CMT-WAAM process, using preferred orientations with torch angles of 10° and 15°. Samples built with a 15° torch angle revealed textured grains. Micro-hardness measurements displayed values of 61HV in the depositional direction and 65HV in the build direction. Among the factors concerned, it was observed that in Al4043 alloy, the sliding direction had a more significant impact on wear. Vishal et al. [23] studied the impact of microstructure evolution on mechanical, tribological, and corrosion characteristics of WAAM-fabricated SS316L walls. Results showed a microstructure featuring fine equiaxed grains near the base plate and coarse columnar grains in the upper regions. The printed components displayed improved mechanical properties, including increased micro-hardness and tensile strength, with reduced ductility than the traditionally produced steel. Tribological performance across various regions was evaluated under varied loading conditions, demonstrating improved wear resistance in the fabricated parts. Also, under flowing conditions, WAAM and wrought steel displayed slightly higher corrosion rates compared to stagnant, moderately saline conditions. Gaofeng et al. [24] employed CMT-based WAAM to fabricate wall-shaped NiTi components, changing depositing speeds. The study investigated the various properties like hardness, tensile strength, etc., and wear behavior of the produced NiTi walls. Conclusions showed that as the wall height increased, micro-hardness, ultimate tensile stress, and elongation also increased. The upper region of the wall displayed an equiaxed microstructure. Good homogeneity on wear resistance was achieved with different depositing speeds. Teng et al.[25] used the WAAM technique to fabricate a multi-material wall, including TC4 and TC11 alloys, followed by examining their microstructure, mechanical, and tribological performance. Results displayed that TC4 showed greater hardness compared to TC11. Moreover, the micro-hardness of both alloy samples exhibited a tendency to increase with deposition height. The average compression yield strength and UTS of TC11 alloy exceeded those of TC4 alloy. Additionally, the COF decreased with increasing load. Yongshi et al. [26] produced a WAAM wall using high-manganese steel and chromium coating on the deposited wall. They compared the corrosion resistance and wear performance between the deposited wall and the chromium-added wall. The results

indicated that the coated wall exhibited superior wear and corrosion resistance performance. Xiang et al. [27] study variances in microstructure, mechanical properties, and wear rate between nickel aluminum bronze (NAB) alloys fabricated through WAAM and casting. WAAM-NAB exhibits a 46% increase in bending strength and an 18% rise in tensile strength than the as-cast alloy. Also, the COF value for the WAAM wall is 56% lower than the cast alloy.

From the above existing literature, it is evident that an extensive exploration has been done on the fabrication of single and multi-material WAAM walls. Regardless, a significant research gap continues concerning the fabrication of multi-material walls of aluminum alloys, specifically utilizing the CMT-based WAAM process. This is crucial for many practical applications, as the production of bimetallic walls with two different alloys may be necessary to attain a wider range of desired properties while also potentially reducing costs [15]. Furthermore, aluminum alloys from the 4XXX and 5XXX series have not yet been explored in combination with bimetallic WAAM walls, despite their promising applications in various sectors where their tribological behavior remains largely unexplored. Also, aluminum alloy components fabricated through WAAM often encounter challenging conditions, such as high friction, contact, and sliding wear [28]. This poses a significant concern, as these components are commonly used in industries like aerospace, automotive, and marine, where such conditions are prevalent. Thereafter, tribological testing becomes necessary to comprehensively predict the performance of WAAM-fabricated aluminum alloys in these demanding environments and to ensure their durability, efficiency, and sustained performance over time [29]. Hence, this study aims to fill this gap. Additionally, heat input stands as a critical operating parameter in WAAM processes that influences the final properties of the components; its effect on the tribological performance of bimetallic WAAM walls has yet to be explored to enhance their potential for application. Therefore, the principal novelty of this work includes (1) examining how heat input affects the tribological performance of bimetallic aluminum alloy walls produced through the CMT-WAAM method and (2) investigating the microstructure, mechanical properties, and heat input's role in achieving the bimetallic wall with the minimum wear rate. Balancing heat input is necessary to optimize the wear behavior of bimetallic WAAM walls and provide their usefulness for practical applications demanding superior tribological performance. In addition, the controlled heat input and wear-resistant material lead to cost-effective production while achieving the desired mechanical properties for engine block and chassis parts.

In this study, a bimetallic CMT-WAAM wall is fabricated using ER4043 and ER5356 materials through a bidirectional deposition strategy with varying heat inputs gained by adjusting the current value. The primary objective is to evaluate the wear performance of each wall under three different loads using a pin-on-disc tribometer at various layers of the bimetallic wall: ER4043, interface, and ER5356 layers. Moreover, a thorough study has investigated the microstructure, mechanical properties, and impact test of the bimetallic wall exhibiting the minimum wear rate.

2 Experimental Procedures

2.1 Materials

In this study, a CMT machine manufactured by Fronius was used to fabricate a bimetallic wall utilizing ER5356 and ER4043 filler wires, both having 1.2 mm diameter, on an ER5083-O base plate (Dimension-150 mm × 16 mm × 8 mm) (Fig. 1). The chemical compositions of the filler wires and base plate are mentioned in Table 1. Filler wires ER4043 and ER5356 have been selected for this study because of their cost-effectiveness, wide availability, and compatibility with the WAAM process. ER4043 contains 5% silicon [12], which enhances its hardness, while ER5356 contains 5% magnesium which improves its strength and corrosion resistance [11]. Both alloys exhibit wear resistance behavior, making them ideal for marine and lightweight aerospace and automotive structures, as well as high-load components like pistons and bearings [11, 12]. However, the WAAM process may influence their wear behavior, making it essential to understand how it affects these alloy's performance in a wear intensive environment and optimize their use in these applications.

2.2 Fabrication of WAAM Walls

Three WAAM walls were fabricated using different current combinations of ER5356 and ER4043 filler wires. The current combinations were selected based on a review of previous literature [15–18], preliminary trials, and visual assessments such as bead height and thickness (Table 2). Fabrication was carried out in a controlled environment using pure Ar gas at a flow rate of 16 L/min, and a torch angle of 90° for all walls. The process began with depositing the layers of ER5356 onto the base plate, followed by the layers of ER4043 over the top of ER5356 layers, as shown in Fig. 2. To prevent delamination and ensure proper solidification, a 2-min dwell time was maintained between successive layers of the same material, while a 30-min interval was allowed between the layers of different filler materials. The other two WAAM walls were fabricated using the same method. Each fabricated WAAM wall initially measured 100 mm × 150 mm × 14 mm. Afterward, the unwanted sections were removed, and face-milling was performed to achieve a flat surface, resulting in a final dimension of 100 mm × 135 mm

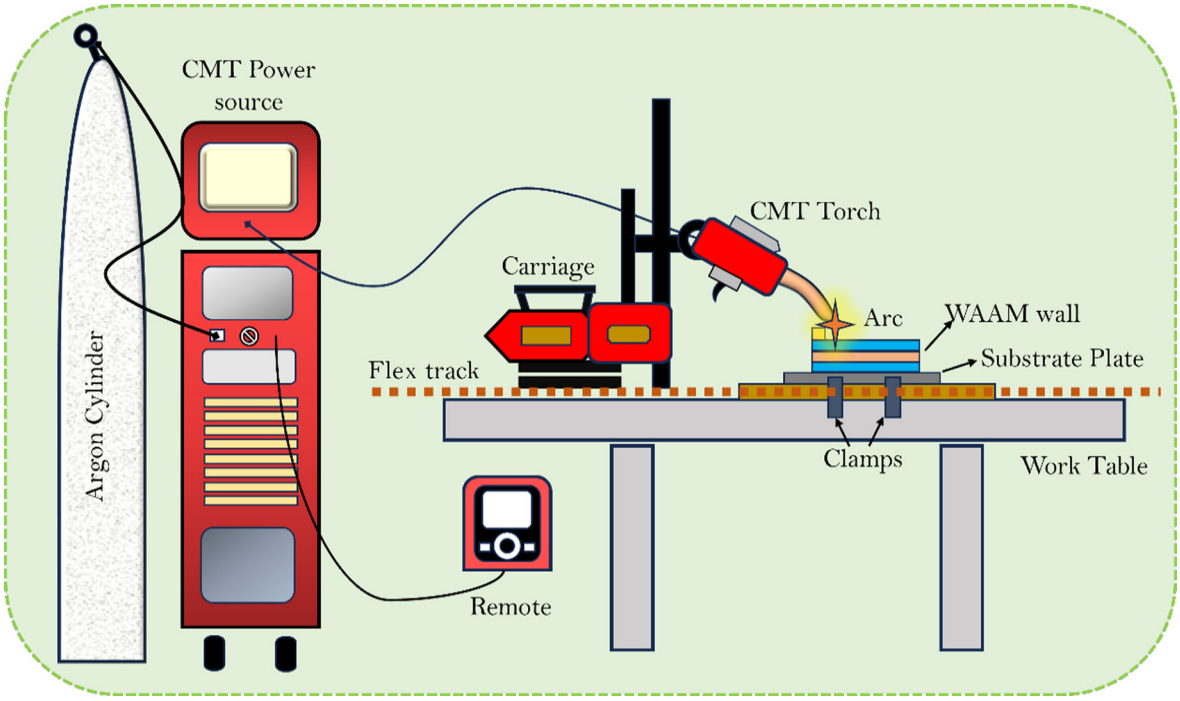

Fig. 1 CMT-WAAM lab setup

Table 1 Chemical composition of materials (in wt%)

Materials	Si	Cu	Fe	Zn	Mg	Mn	Cr	Ti	Al
ER4043	5.25	0.3	0.8	0.1	0.05	0.05	–	0.02	Bal
ER5356	0.03	0.01	0.15	0.01	4.83	0.14	0.11	0.09	Bal
ER5083	0.4	0.1	0.4	0.07	4.0	4.2	–	0.15	Bal

Table 2 Calculation of heat input for different process parameters during bidirectional deposition

S.No Unit	Filler wire	*I* (A)	*V* (V)	TS (mm/s)	Wire feed rate (m/min)	HI (J/mm)	Sample identifications
1	ER4043	90	13.5	6	6	162	A
	ER5356	115	14.6		7.8	223.8	
2	ER4043	95	13.7	6	6.3	175.2	B
	ER5356	120	14.8		8.1	236.8	
3	ER4043	100	14	6	6.6	186.7	C
	ER5356	125	15.1		8.3	251.7	

$\times$ 10 mm. Samples for various tests were then extracted from each prepared wall, as shown in Fig. 2.

Now, to calculate the heat input (HI) for each fabricated WAAM wall, Eq. (1) [28] was used-

$$\mathrm{HI} = \frac{\eta * I * V}{T S} \mathrm{J/mm} \tag{1}$$

where $I(A)$, $V(V)$ and TS(mm/s) represent the arc current, voltage and travel speed, respectively, while η denotes the arc thermal efficiency (set to 0.8) for CMT in each sample. The calculated heat input values are shown in Table 2. The HI calculation for the three walls was used to classify them into categories: low heat input wall, medium–low heat input wall, and high heat input wall. These walls were identified as Sample A, Sample B, and Sample C, respectively.

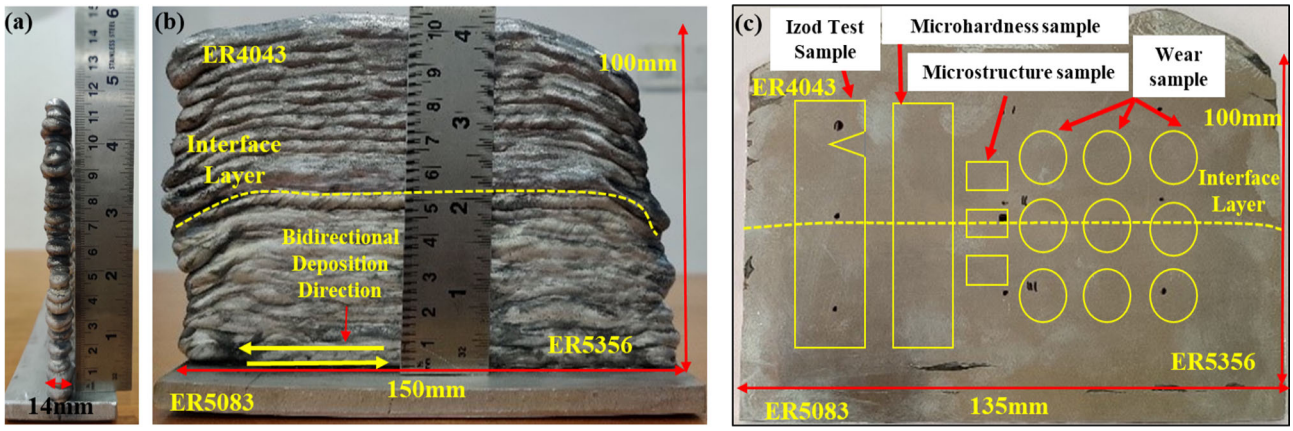

Fig. 2 Bimetallic wall: **a** side view, **b** front view, **c** specimen extracted from the milled wall

2.3 Wear Test

Wear tests were performed on samples A, B, and C at three different load levels, with the test parameters selected based on literature [22, 28, 29], which indicates that loads ranging from 10 to 40 N are commonly used in wear analysis studies of aluminum alloys. The parameters chosen for the test are mentioned in Table 3. Wear tests were performed on nine specimens from each wall sample, with three specimens extracted from three distinct zones within the same wall: the upper, bottom, and interface layers of the bimetallic wall, as shown in Fig. 3d. Cylindrical pins, each 8 mm in dia. and 10 mm in height, were machined for the wear testing. The tests were carried out at room temperature operating a pin-on-disk tester, following the ASTM G99-17 standards. Sample preparation for the test involved (i) cleaning the surface with acetone, (ii) checking surface evenness, and (iii) measuring the initial weight using an analytical balance with an accuracy of 0.01 mg. The EN24 counter disk was chosen, and the specimens were secured in a holder positioned against the rotating disk, as mentioned in Fig. 3a–c. After testing, the samples were cleaned with acetone, and wear debris was collected on butter paper. The wear rate was calculated using the volume loss method.

Table 3 Sliding wear test at dry conditions

Description	Wear test parameters
Applied normal load	20 N, 30 N and 40 N
Disc rotational speed	398 rpm
Sliding distance	1500 m
Sliding velocity	1.25 m/sec
Disc track diameters	60 mm

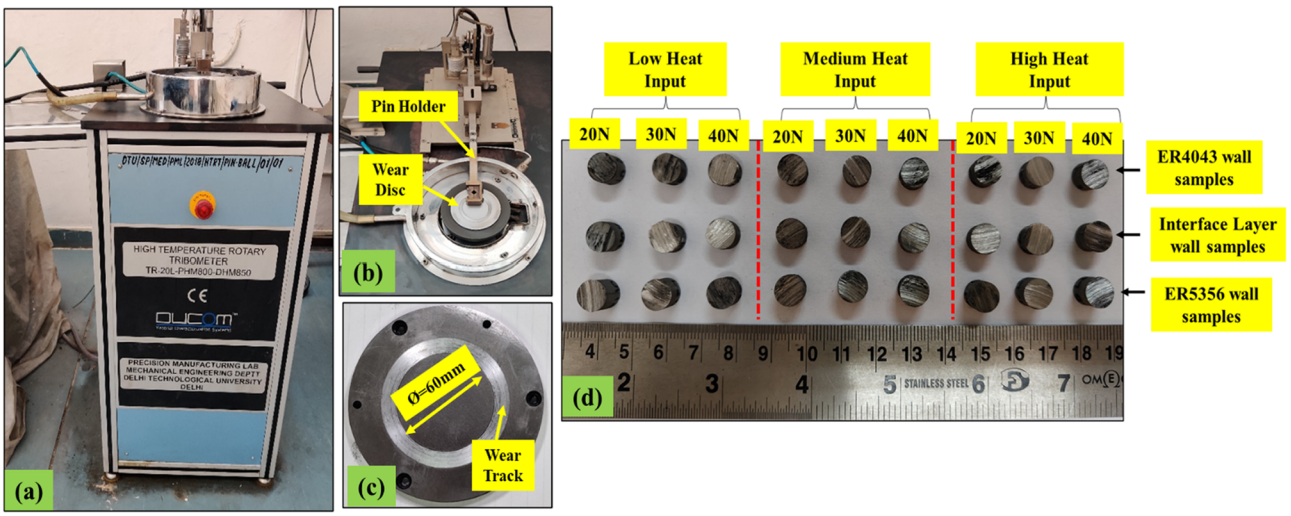

Fig. 3 **a** Setup of pin-on-disc tribometer, **b** wear pin in contact with the disc, **c** wear disc, **d** worn sample

2.4 Microstructural Analysis

After the wear test, the specimens were cut for various microstructural examinations. The samples were cold-mounted using an epoxy-hardener combination for observation under an optical microscope. The specimens underwent dry and wet polishing following mounting to achieve a mirror-like surface finish. Keller's reagent was then applied for etching. The microstructure was analyzed using an OLYMPUS optical microscope and a ZEISS Gemini 1 Sigma-500 field emission scanning electron microscope (FESEM) with an energy dispersive spectrometer (EDS). Electron backscatter diffraction (EBSD) analysis was conducted after the specimens were electrolytically etched using a solution of 10% perchloric acid and 90% methanol (14V for 10 s), and its data were analyzed using TSL-OIM software (version 7.3). A BRUKER D8 advance X-ray powder diffractometer (XRD) was used to identify the intermetallic compounds formed during the WAAM process. For post-wear analysis, the worn surface and wear debris were examined utilizing a JEOL JSM-6610 LV Scanning Electron Microscope (SEM).

2.5 Micro-hardness Test

Vickers micro-hardness tests were performed with indentations made perpendicular to the deposition direction at specific locations: the bottom, interface, and upper layers. The tests were executed on Struers Duramin-40 M1 micro-hardness tester, applying a constant load of 500g (0.5HV) with a 10 s dwell time between each indentation. The test samples were prepared as per ASTM E-92 standards. Diamond-shaped indentations were made at five different points on the cross sectional area of the low HI wall sample, as shown in Fig. 2, and then the average hardness value for each specimen was calculated.

2.6 Impact Test

Impact tests were performed employing an Izod impact testing machine, with specimens prepared as per the ASTM E23 standards having specifications illustrated in Fig. 4. The machine has a maximum impact absorption capacity of 120 foot-pounds (162.29 J) with a hammer weighing 16 kg. Before releasing the hammer, the indicator is set to zero, and the hammer lock is positioned at its highest striking point. The specimen was tested at room temperature, with the test specimens cut perpendicular to the deposition direction.

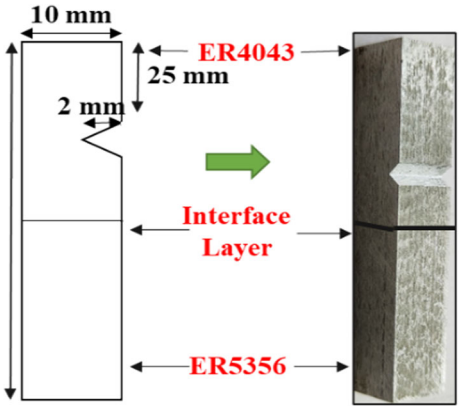

Fig. 4 Specimen dimension of Izod impact test

3 Results and Discussion

3.1 Wear Test Analysis

3.1.1 Effect of Load and Heat Input on Wear Rate

The wear rate value and the average COF value are mentioned in Table 4. Figure 5, displays that the bottom layer of the sample A wall at 20 N shows the lowest wear rate, while the upper layer of the sample C wall at 40 N shows the highest wear rate. The wear rate of specimens increases with the load across all layers: upper, interface, and bottom. Specifically, the wear rate of sample wall at 20 N, 30 N, and 40 N for the upper layer is 0.0037 mm^3/m, 0.0041 mm^3/m and 0.0047 mm^3/m, the interface layer is 0.0020 mm^3/m, 0.0028 mm^3/m and 0.0035 mm^3/m, and the bottom layer are 0.0019 mm^3/m, 0.0025 mm^3/m, and 0.0032 mm^3/m, respectively. This increasing trend is due to the higher contact pressure between the pin and the disk at greater loads, which enhances mechanical interlocking between asperities on the contacting surfaces. Additionally, frictional heating increases with higher loads, softening the material at contact points and making it more susceptible to wear. Chakkravarthy et al. [22] reached similar conclusions regarding the effect of increasing applied loads. The study also shows that the wear rate increases as HI increases. Koli et al.[19] also observed a similar trend. Higher HI transfers more energy to the material during deposition, causing grain growth and producing coarser grains. This shows more significant material removal during wear testing, especially in regions exposed to higher temperatures, such as the upper layers of the wall. Increased HI also causes more pronounced thermal gradients, exacerbating wear by promoting differential thermal expansion and contraction [30]. It has been proven that the sample C (251.7 J/mm /186.7 J/mm) wall shows a higher wear rate than the sample A and B walls. Specifically, the sample C wall at 40 N load exhibits a wear rate of 50.52% higher in

Table 4 Wear rate and average COF value of each sample

Sample	Layer position	Loads	Wear rate (mm^3/m)	COF (μ)
A	ER4043	20	0.0037	0.38
		30	0.0041	0.36
		40	0.0047	0.33
	Interface layer	20	0.0020	0.32
		30	0.0028	0.30
		40	0.0035	0.29
	ER5356	20	0.0019	0.29
		30	0.0025	0.26
		40	0.0032	0.25
B	ER4043	20	0.0064	0.52
		30	0.0073	0.50
		40	0.0081	0.47
	Interface layer	20	0.0058	0.48
		30	0.0065	0.45
		40	0.0074	0.41
	ER5356	20	0.0055	0.40
		30	0.0058	0.36
		40	0.0063	0.31
C	ER4043	20	0.0087	0.59
		30	0.0091	0.54
		40	0.0095	0.50
	Interface layer	20	0.0085	0.53
		30	0.0088	0.47
		40	0.0091	0.41
	ER5356	20	0.0077	0.45
		30	0.0079	0.40
		40	0.0081	0.36

the upper layer, 60.49% higher in the interface layer, and 48.14% higher in the bottom layer than the sample A wall. The wear rate increases from ER5356 layer to ER4043 layer because the upper layer experiences the highest temperature difference between layers, due to the continuous addition of new molten material on top of previously solidified layers. Consequently, the upper layer's material properties may differ from the interface and bottom layers due to varying cooling rates and thermal histories. Ashish et al. [21] also concluded that higher wear rates occur in the upper layer side due to the thermal gradient along the height of the wall. Therefore, selecting a wall with lower heat input, i.e., Sample A is recommended for achieving a lower wear rate in practical engineering applications.

3.1.2 Effect of Load and Heat Input on COF

The average COF values of the WAAM wall at different HIs and loads are depicted in Table 4 and Fig. 6. Also, through the analysis, it is visible that the COF value in bimetallic WAAM walls is significantly influenced by load, HI, and layer position. As the load increases, the COF tends to decrease while the wear rate increases. Specifically, the sample C wall sample at 20 N (upper layer) shows the highest COF value, which is 8.47% and 15.25% higher than at 30 N and 40 N loads, respectively. Similarly, for the sample A wall, the COF at 20 N (upper layer) is 5.26% and 13.16% higher than at 30 N and 40 N loads. Because increased load results in higher frictional heating, which can soften the material, causing it to be more susceptible to wear. This thermal effect can reduce the COF as the material deforms more easily and the frictional resistance decreases [31]. Also, COF values validate the relationship expressed by the formula: $\mu = F/N$, where μ denotes the COF, F signifies the frictional force, and N represents the applied load. This explains how the COF is inversely proportional to the normal load. Tang et al. [25], and Vedabouriswaran et al. [32] also noted that COF decreases with increasing normal loads. Further, the layer

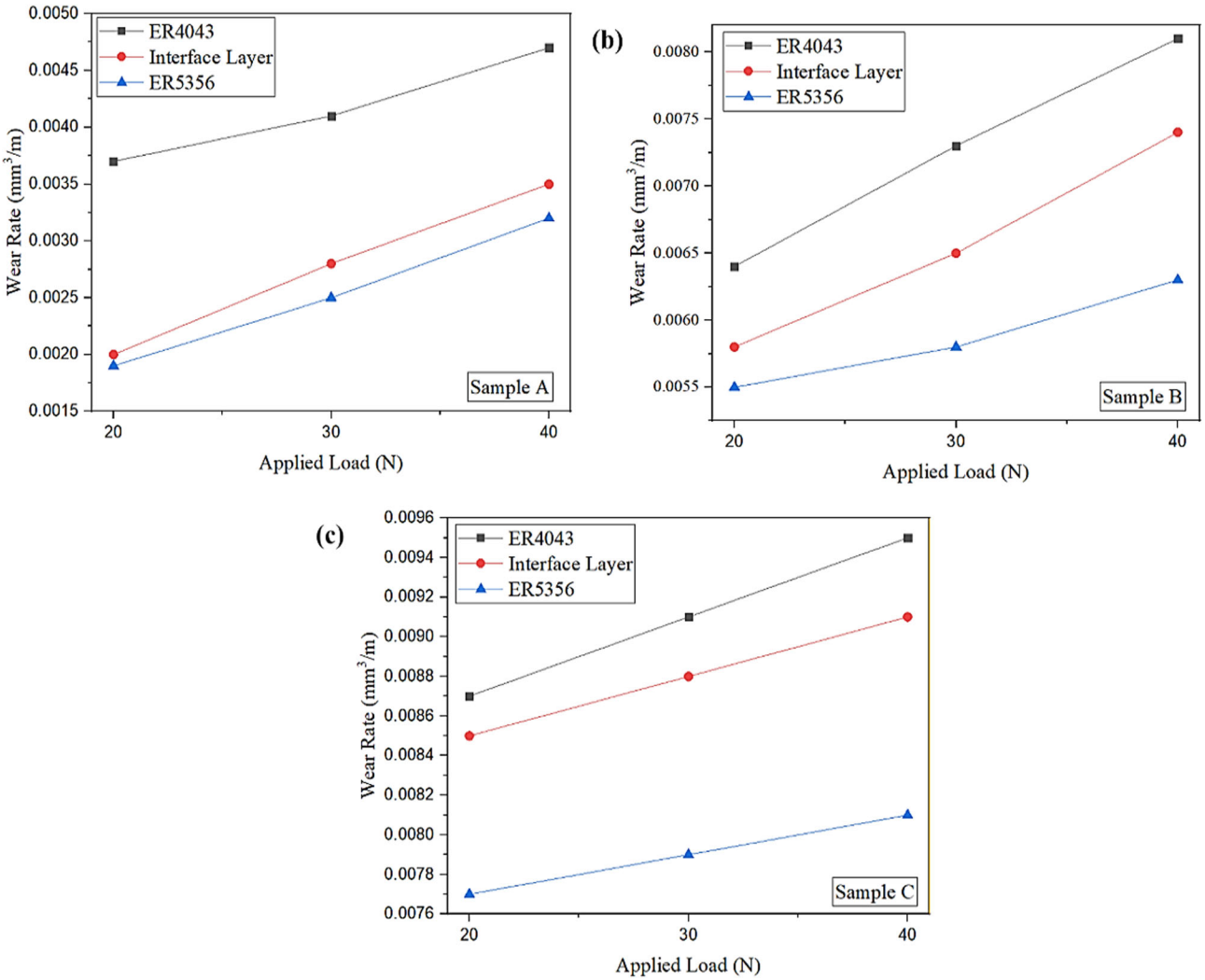

Fig. 5 Wear rate versus applied load plot for **a** Sample A, **b** Sample B, **c** Sample C

position (upper, interface, and bottom layer) within the wall significantly affects the COF. The upper layers, subjected to higher temperature gradients, exhibit higher COF and wear than the bottom and interface layers [28]. These variations emphasize the intricate interaction between thermal and mechanical factors in determining the frictional behavior of bimetallic WAAM walls [30]. HI also plays a crucial role; higher HI leads to coarser grains and increased surface roughness, elevating the COF due to mechanical interlocking and adhesion [31]. Consequently, the investigation reveals that sample A walls have a lower COF value than the sample A and B walls, making the low HI bimetallic wall more promising in terms of frictional performance.

3.1.3 Worn Surface Analysis

Figure 7 depicted the SEM images of the worn pin surfaces under a 40N load, highlighting the wear mechanisms on the wall's surface during testing. A total of nine specimens, three from each wall, were selected at the 40 N load due to their higher wear rates compared to the other load conditions across all wall samples. The HI during the WAAM process significantly impacts the wear behavior of aluminum alloys. The highest wear rate was observed in Sample C, within the ER4043 region, at a 40 N load, while the lowest wear rate occurred in Sample A, within the ER5356 region, at a 20 N load. These findings align with the SEM morphology of the worn surfaces, with Fig. 7c showing the most severe wear and Fig. 7g showing the least.

Now, in the context of WAAM walls of aluminum alloys, the primary wear mechanisms depicted after the wear test are abrasion, adhesion, and delamination, respectively. The SEM images in Fig. 7a–i reveal that all three sample surfaces underwent different wear mechanisms, and debris was identified on the worn surfaces. The SEM images of the worn pin surfaces display that abrasive wear is dominant in the ER4043

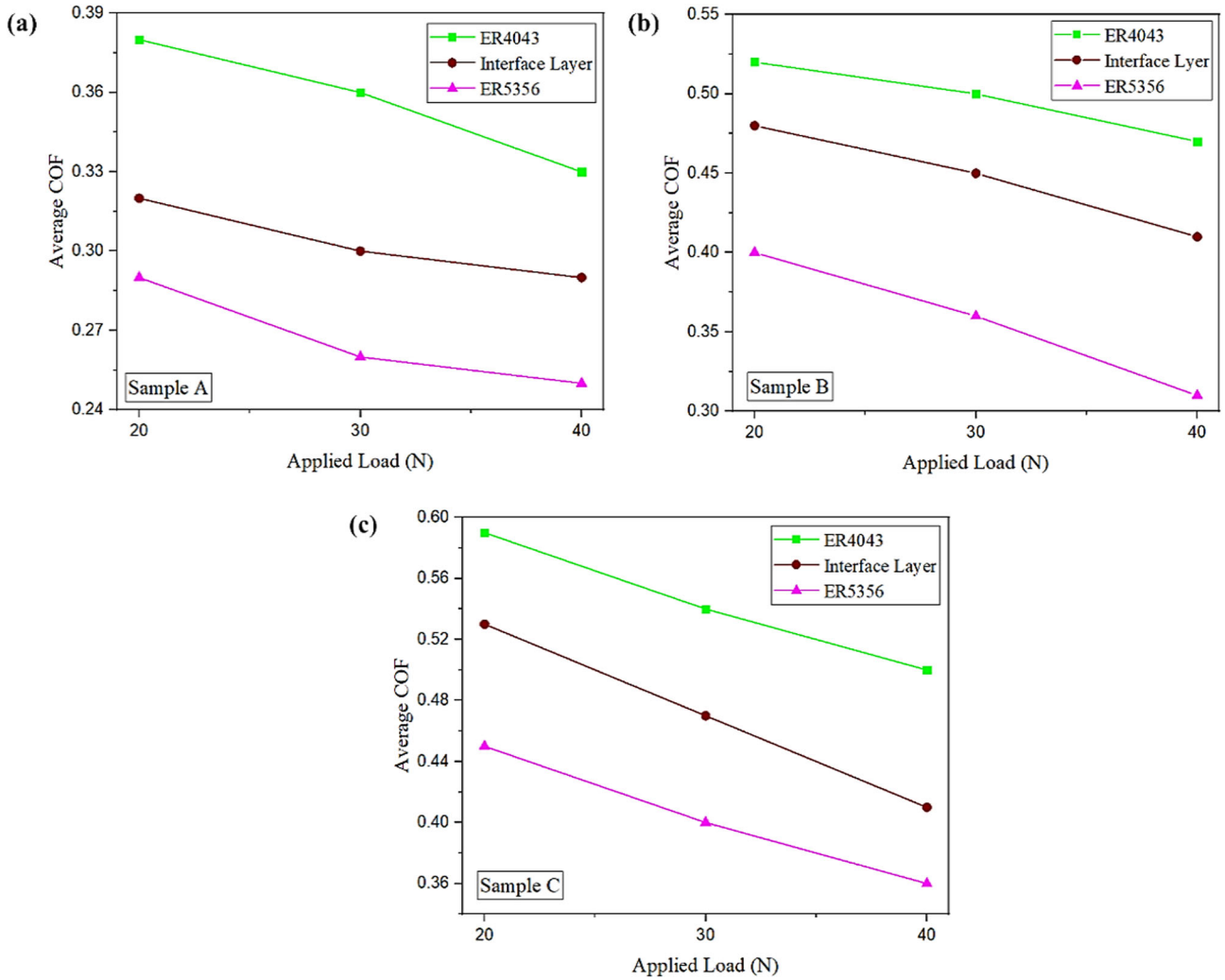

Fig. 6 COF versus applied load plot for **a** Sample A, **b** Sample B, **c** Sample C

layer due to its relatively soft nature compared to the interface and ER5356 layers. Abrasive wear involves material removal from a surface by hard particles or asperities [33]. In WAAM walls, the abrasive wear resistance is significantly influenced by the distribution of hard phases, such as intermetallic compounds, within the microstructure [34]. The ER5356 layer exhibits a smoother surface in the sample A wall than the ER4043 and interface layers. Adhesive wear arises when two surfaces slide against each other, causing material transfer from one surface to the other [35], often due to the material's inherent ductility and tendency to adhere to the counter material in aluminum alloys [36]. The test results clearly reveal that in the sample C wall, the ER4043 layer experienced more adhesive wear and debris compared to the sample A and B walls, mainly toward the ER5356 and interface layers, due to the higher temperature gradient. Despite a constant sliding distance for 40 N loads, delamination becomes observable on the worn surfaces due to the formation and removal of large wear particles from subsurface crack propagation [37]. This cycle of building and removal persists until the wear process is finished [38]. Variations in HI can affect the material's resistance to adhesive, abrasive, and delamination wear, emphasizing the importance of variation in HI during the WAAM process to improve wear performance.

3.1.4 Wear Debris

Figure 8 shows the SEM images of wear debris obtained from different regions of Sample A under a 40N load. The worn surface morphology indicates that as the load increases, the wear rate also rises, forming metallic particle debris. These particles are larger in size due to the higher load, as evident in Fig. 8a. It is evident that there is a consistent increase in the average size of detached metallic wear debris when moving from the bottom to the upper layers under a 40 N load, as clearly shown in Fig. 8a–c. This makes it more difficult for the

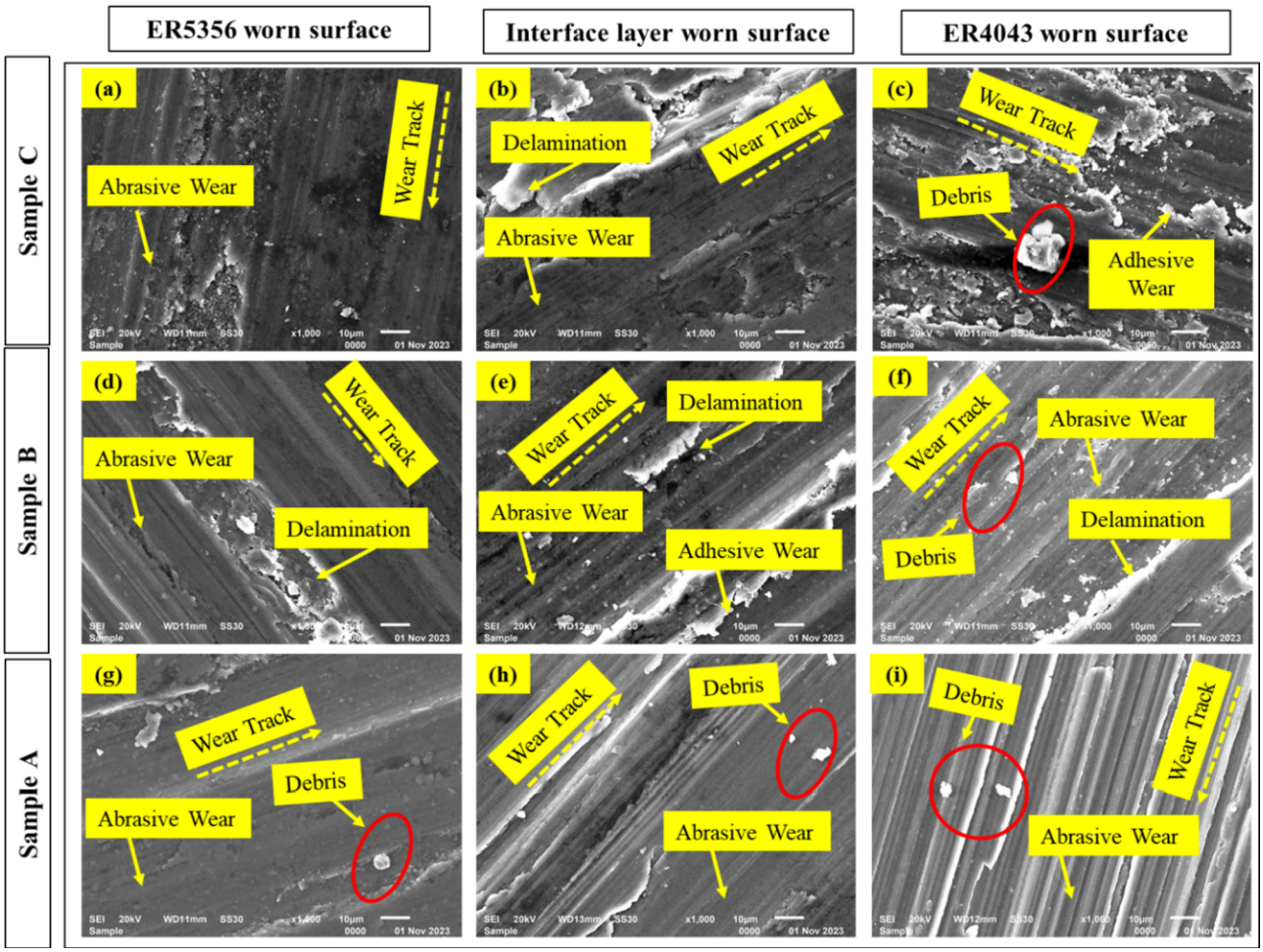

Fig.7 SEM image of the worn surface under a 40N load

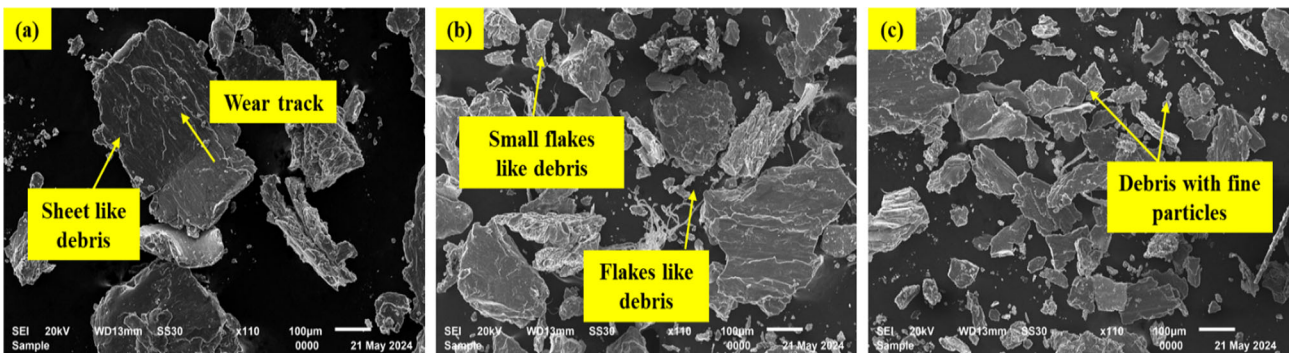

Fig. 8 Wear debris of Sample A at 40 N, (**a**) At ER4043, (**b**) At interface layer, (**c**) At ER5356

debris to fracture and form a protective layer [21]. One of the contributing factors to this difference in size is the increase in contact pressure between the pin and the disk at higher loads [35]. Higher contact pressure enhances the mechanical interlocking between the asperities of the contacting surfaces, resulting in greater material removal through abrasion and adhesion, leading to more wear debris [36].

As a result, the ER4043 layer exhibits a higher wear rate, producing larger debris compared to the bottom and interface layers. The figure also shows that the worn debris has varying shapes. These differences in the shape and size of debris can be attributed to factors such as temperature gradients, plastic deformation, strain-hardening, adhesion, and material

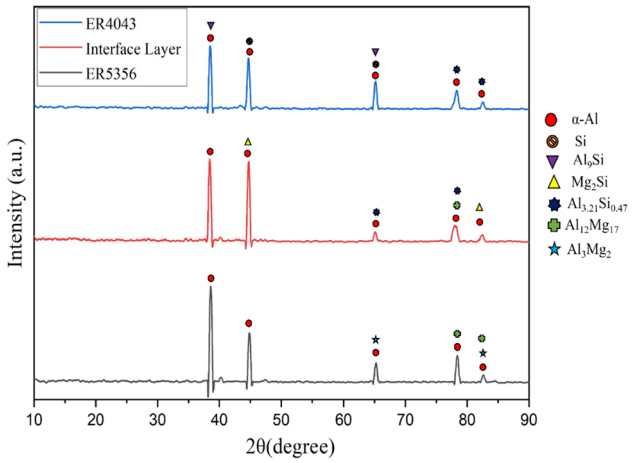

Fig.9 XRD plot of the Sample A

transfer [19], which occur during the interaction between the pin and the disk.

3.2 Analysis of WAAM Wall Having Minimum Wear Rate

3.2.1 X-Ray Diffraction (XRD) Analysis

The XRD spectrum confirms the presence of various intermetallic components within Sample A, namely α-Al, Si, Al_9Si, Mg_2Si, $Al_{3.21}Si_{0.47}$, $Al_{12}Mg_{17}$, and Al_3Mg_2 as shown in Fig. 9. The highest peak corresponds to α-Al, which is observed in the ER5356 layer compared to other interface and upper layer samples. The presence of α-Al is confirmed in all formed peaks of the ER4043, interface, and ER5356 layers. Additionally, the XRD study outlines the existence of several intermetallic compounds containing both stoichiometric (α-Al, Si, Al_9Si, Mg_2Si, $Al_{12}Mg_{17}$, and Al_3Mg_2) and non-stoichiometric ($Al_{3.21}Si_{0.47}$) compositions. In detail, α-Al, Si, Al_9Si, and $Al_{3.21}Si_{0.47}$ compounds are formed toward the upper layer, while α-Al, Mg_2Si, $Al_{3.21}Si_{0.47}$, and $Al_{12}Mg_{17}$ are formed at the interface layer, and α-Al, Si, $Al_{12}Mg_{17}$, and Al_3Mg_2 toward the ER5356 layer. Al, Si, Al_9Si, and Al_3Mg_2 formation is ascribed to reactions concerning the individual aluminum alloy filler wires [39]. Intermetallic compounds such as Mg_2Si, $Al_{3.21}Si_{0.47}$, and $Al_{12}Mg_{17}$ may have formed from reactions between the ER5356 and ER4043 filler wires.

3.2.2 Microstructure Analysis

The microstructural evaluation of the bimetallic wall in Sample A was carried out on the ER4043 layer, the interface, and the ER5356 layer, as shown in Fig. 10. Figure 10a–f illustrates the variation in optical microstructure along the height of the wall showing a strong metallurgical bond with no indication of solidification cracks at the interface layer.

In the case of the low wear rate wall (Sample A), the optical image of the sample depicts coarse equiaxed grains toward the ER4043 side, fine grains toward the ER5356 side, and fine equiaxed grains at the interface layer. The optical micrographs show a clear view of the heterogeneous

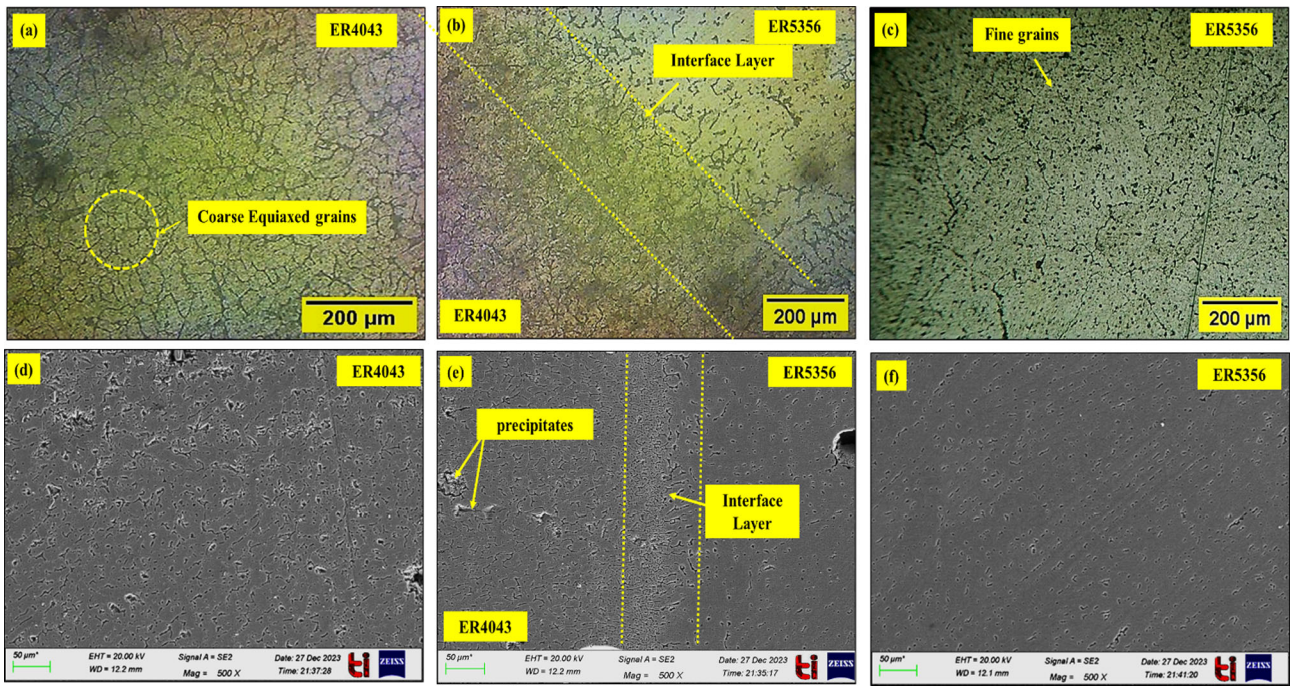

Fig. 10 Microstructural images of various regions within the wall: **a–c** optical microscopy, **d–f** FESEM

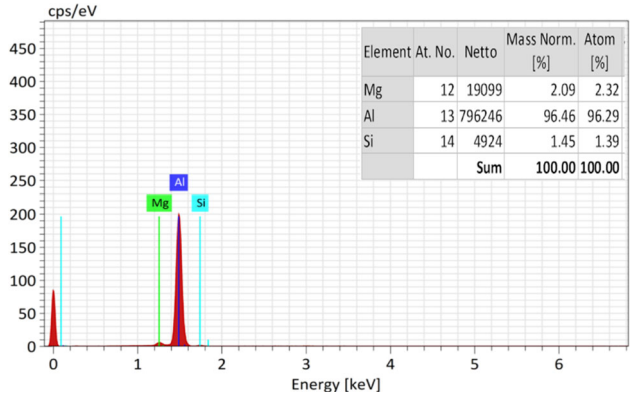

Fig.11 EDS analysis at the interface layer of the wall

microstructure present along the height of the bimetallic wall. This heterogeneity arises from the phenomenon of grain enlargement and the formation of coarse grains, which are results of the repeating thermal cycling undergone during the fabrication process, illustrated by varying cooling rates [17].FESEM analysis displayed similar patterns in all three locations, consistent with the observations from the optical micrograph. According to Fig. 11, the EDS analysis provides quantitative data on the weight percentages of silicon (Si) and magnesium (Mg) at the interface layer of Sample A. Notably, the weight percentage of Mg (2.09%) is higher than that of Si (1.45%) at this interface. This difference indicates a significant presence of magnesium relative to silicon at the interface, with the existence of Mg and Si noticed to their complete diffusion within the interface layer of both aluminum alloys. An EBSD test was conducted to analyze the grain structure developed at the interface layer of Sample A. Figure 12. displays the inverse pole figure (IPF) image of the interface, which confirms the size variation of the grain between the ER5356 interface and the ER4043 layer during cooling. The analysis indicates that the average grain size is ~ 7.7 μm in the ER5356 layer and ~ 83.28 μm in the ER4043 layer. This happens due to the upper layer cools more rapidly than the bottom and the interface layer [15]. Also, due to rapid cooling, it can show a less refined microstructure with coarser grains, which are less wear-resistant. The IPF also verifies coarse equiaxed grains on the ER4043 side, fine grains on the ER5356 side, and fine equiaxed grains at the interface layer. Grain orientations are randomly distributed, with no obvious preferred orientation. This result is compatible with the optical micrograph and FESEM analysis of the low wear rate WAAM wall.

3.2.3 Micro-hardness Analysis

Micro-hardness test results display a decreasing trend in hardness values along the height of the wall, as illustrated in Fig. 13. Average values of hardness in the upper, interface, and bottom layers are 68.07HV, 77.69HV, and 82.95HV, respectively. Therefore, the hardness value of the bottom layer increases by 21.86% and 6.77% in comparison to the upper layer and interface layer. Wang et al. [17], Ashish et al. [20] investigated the hardness at three locations and concluded that a similar trend along the height of the wall. Such variations in hardness distribution along the height of the wall are attributed to the high-temperature gradients undergone during the fabrication process [41]. This observation is further clarified by the wear test results, which show that the upper layer showed a higher wear rate than the bottom and interface layers. This can be attributed to the lower hardness values shown in the upper layer. Also, during the layer-by-layer deposition, the base plate behaves as a heat sink, promoting rapid cooling and leading to the formation of a finer-grained microstructure [15]. Therefore the combination of higher cooling rates and distinct thermal cycles

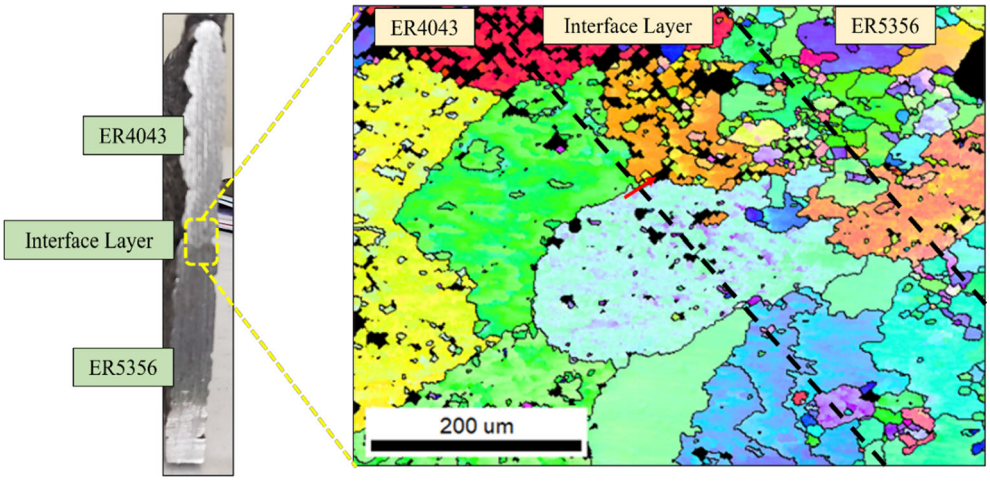

Fig.12 IPF map at the interface layer of the wall

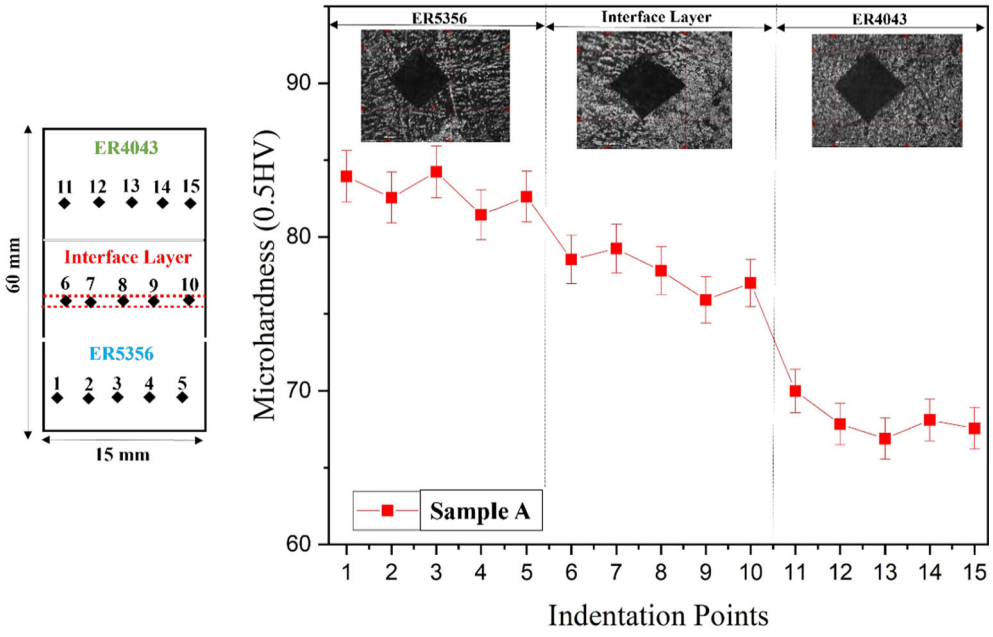

Fig.13 Micro-hardness variation in each layer of the wall

in the bottom layers results in a finer microstructure and increased hardness compared to the middle and upper layers in WAAM-fabricated aluminum alloy components [17]. Further analysis via EBSD revealed that the grain size, mainly toward the ER4043, increased that of the other two wall locations, i.e., the bottom layer and the interface layer. This result also aligns with the Hall–Petch effect, indicating an inverse relationship between the grain size and hardness value [39]. Moreover, XRD analysis showed the formation of magnesium (Mg) compounds, and also the EDS analysis confirms the presence of a weight % of Mg than Si; this is one more reason for the decreasing trend of the average hardness value along the height of the wall. Because Mg is a major contribution to hardness enhancement, it potentially helps as an additional influencing factor. Prakash et al. [40] observed that the presence of Mg_2Si and Mg significantly enhances the hardness of the fabricated wall.

3.2.4 Impact Test

The Izod impact test was carried out on the more wear-resistant bimetallic wall of Sample A. Before testing, the machine's air calibration value was 8 foot-pounds (10.85 J). During the test, the total energy recorded with the sample was 27 foot-pounds (36.61 J). Subtracting the air value, the final impact energy absorbed by the sample was estimated to be 19 foot-pounds (25.76 J). This relative impact energy suggests that Sample A exhibits good toughness, as it absorbed a substantial amount of energy before fracturing. This is consistent with the occurrence of dimples and voids observed in the fractography in Fig. 14, which are indicators of ductile fracture. Ashish et al.[20] also conducted the Izod test and concluded the similar results. The deformation behavior, illustrated by a roughly 45° fracture plane, exhibits shear stress surpassing the shear strength of the structure, leading to plastic yielding [40]. The results display a non-uniform dimple on the mentioned surface of the specimen, along with shear fibrous tearing of the material typical of ductile materials [41]. Hence, fractographic analyses confirm that the fracture is fully ductile, including a 100% shear fracture according to ASTM E23-18.

4 Conclusions

The present study employs the CMT-WAAM method to deposit the three bimetallic walls of aluminum alloys and investigate the influence of heat input on the wear behavior of each wall under three loads. It further examines the microstructure, mechanical properties, and impact resistance of the minimum wear rate WAAM wall. The findings of this study emphasize that heat input plays a vital role in affecting both the wear rate and the COF, with significant variations observed across the different layers (bottom, interface, and upper) at varying heat input levels, which demonstrates the direct influence of heat input on wear behavior. These results underline the importance of controlling heat input to optimize wear resistance. Based on the outcomes of this study, the key findings are as follows:

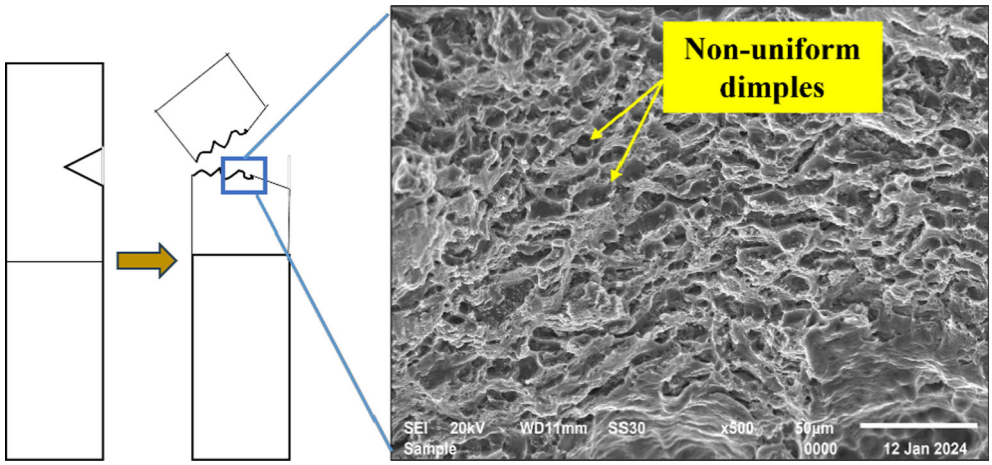

Fig.14 SEM image of the impact fracture surface

(1) Bimetallic walls of ER4043 and ER5356 filler wire have been successfully fabricated via. CMT-based WAAM technique under three distinct heat inputs (low, medium, and high).
(2) Maximum wear rate (0.0095 mm^3/m) and coefficient of friction (COF) (0.59) is observed in the upper (ER4043) layer of the wall under high heat input at 40 N and 20 N loads. While the minimum wear rate (0.0019 mm^3/m) and COF (0.25) are found in the bottom (ER5356) layer of the wall under low heat input (223.8 J/mm and 162 J/mm) at the 20 N and 40 N load. SEM analysis of worn surfaces at 40 N loads revealed adhesive and delamination wear mechanisms.
(3) XRD analysis revealed the presence of several intermetallic compounds, including α-Al, $Al_{12}Mg_{17}$, Mg_2Si, Si, Al_9Si, Al_3Mg_2, and $Al_{3.21}Si_{0.47}$, across the different layers of the bimetallic wall. These compounds exhibited varying peak intensities, particularly in the wall associated with the lowest wear rate.
4) Optical, FESEM, and EBSD images showed equiaxed coarse grains on the ER4043 side, fine grains on the ER5356 side, and fine equiaxed grains at the interface layer, with average grain size approximately 7.7 µm in the bottom layer and 83.28 µm in upper layer, and differences in Mg (2.09%) and Si (1.45%) weight percentages at the interface layer, indicated in EDS analysis.
5) The hardness values of the bottom layers increased in comparison with the interface and upper layers by 21.86% and 6.77%, respectively. This variation along the height of the wall is shown due to the thermal cycles undergone during the WAAM process.
6) The energy absorbed during the Impact test of the bimetallic wall is 25.76 J, with a ductile fracture mode confirmed d by dimples and voids.

Supplementary Information The online version contains supplementary material available at https://doi.org/10.1007/s13369-025-10082-4.

Declarations

Conflict of interest The authors declare no competing interests.

References

1. Kumar, S.A.; Pramanik, S.; Yagati, P.K.: Research progress in arc based additive manufacturing of aluminium alloys –a review. Measurement **200**, 111672 (2022). https://doi.org/10.1016/j.measurement.2022.111672
2. Nazir, A.; Gokcekaya, O.; Billah, Md.M.K.; Ertugrul, O.; Jiang, J.; Sun, J.; Hussain, S.: Multi-material additive manufacturing: a systematic review of design, properties, applications, challenges, and 3D printing of materials and cellular metamaterials. Mater. Des. **226**, 111661 (2023). https://doi.org/10.1016/j.matdes.2023.111661
3. Tawfik, M.; Nemat-Alla, M.; Dewidar, M.: Enhancing the properties of aluminium alloys fabricated using wire + arc additive manufacturing technique - a review. J. Market. Res. **13**, 754–768 (2021). https://doi.org/10.1016/j.jmrt.2021.04.076
4. Srivastava, M.; Rathee, S.; Tiwari, A.; Dongre, M.: Wire arc additive manufacturing of metals: a review on processes, materials and their behaviour. Mater. Chem. Phys. **294**, 126988 (2023). https://doi.org/10.1016/j.matchemphys.2022.126988
5. Wu, B.; Pan, Z.; Ding, D.; Cuiuri, D.; Li, H.; Xu, J.; Norrish, J.: A review of the wire arc additive manufacturing of metals: Properties, defects and quality improvement. J. Manuf. Process. **35**, 127–139 (2018). https://doi.org/10.1016/j.jmapro.2018.08.001
6. Rosli, N.A.; Alkahari, R.M.; Abdollah, B.F.M.; Maidin, S.; Ramli, R.F.; Herawan, G.S.: Review on effect of heat Input for wire arc additive manufacturing process. J. Market. Res. **11**, 2127–2145 (2021). https://doi.org/10.1016/j.jmrt.2021.02.002
7. Koli, Y.; Yuvaraj, N.; Aravindan, S., et al.: Enhancement of mechanical properties of 6061/6082 dissimilar aluminium alloys through ultrasonic-assisted cold metal transfer welding. Arab. J. Sci. Eng. **46**, 12089–12104 (2021). https://doi.org/10.1007/s13369-021-05844-9
8. Singh, P.R.; Gangi, S.S.; Kumar, S.R.: Recent advances in the manufacturing processes of functionally graded materials: a review.

Sci. Eng. Compos. Mater. **25**(2), 309–336 (2018). https://doi.org/10.1515/secm-2015-0395
9. Tomar, B.; Shiva, S.; Nath, T.: A review on wire arc additive manufacturing: processing parameters, defects, quality improvement and recent advances. Mater. Today Commun. **31**, 103739 (2022). https://doi.org/10.1016/j.mtcomm.2022.103739
10. Wang, S.; Gu, H.; Wang, W.; Li, C.; Ren, L.; Wang, Z.; Zhai, Y.; Ma, P.: The influence of heat input on the microstructure and properties of wire-arc-additive-manufactured Al-Cu-Sn alloy deposits. Metals **10**(1), 79 (2019). https://doi.org/10.3390/met10010079
11. Su, C.; Chen, X.; Gao, C.; Wang, Y.: Effect of heat input on microstructure and mechanical properties of Al-Mg alloys fabricated by WAAM. Appl. Surf. Sci. **486**, 431–440 (2019). https://doi.org/10.1016/j.apsusc.2019.04.255
12. Chen, C.; Sun, G.; Du, W.; Liu, J.; Zhang, H.: Effect of equivalent heat input on WAAM Al-Si alloy. Int. J. Mech. Sci. **238**, 107831 (2023). https://doi.org/10.1016/j.ijmecsci.2022.107831
13. Wang, Y.; Chen, X.; Konovalov, S.; Su, C.; Siddiquee, N.A.; Gangil, N.: In-situ wire-feed additive manufacturing of Cu-Al alloy by addition of silicon. Appl. Surf. Sci. **487**, 1366–1375 (2019). https://doi.org/10.1016/j.apsusc.2019.05.068
14. Zhong, H.; Qi, B.; Cong, B., et al.: Microstructure and mechanical properties of wire + arc additively manufactured 2050 Al–Li alloy wall deposits. Chin. J. Mech. Eng. **32**, 92 (2019). https://doi.org/10.1186/s10033-019-0405-z
15. Chang, T.; Fang, X.; Liu, G.; Zhang, H.; Huang, K.: Wire and arc additive manufacturing of dissimilar 2319 and 5B06 aluminum alloys. J. Mater. Sci. Technol. **124**, 65–75 (2022). https://doi.org/10.1016/j.jmst.2022.02.024
16. Hauser, T.; Reisch, R.T.; Seebauer, S.; Parasar, A.; Kamps, T.; Casati, R.; Volpp, J.; Kaplan, A.F.: Multi-material wire arc additive manufacturing of low and high alloyed aluminium alloys with in-situ material analysis. J. Manuf. Process. **69**, 378–390 (2021). https://doi.org/10.1016/j.jmapro.2021.08.005
17. Yipeng, W.; Shuo, Z.; Hong, L.; Hodúlová, E.; Zhuoxin, L.; Baoqiang, C.: Microstructure and mechanical properties of 7075/5356 aluminum alloy laminated composite fabricated by wire arc additive manufacturing. Mater. Lett. **367**, 136638 (2024). https://doi.org/10.1016/j.matlet.2024.136638
18. Xu, N.; Shen, J.; Hu, S.; Tian, Y.; Bi, J.: Bimetallic structure of Ti6Al4V and Al621Cu fabricated by cold metal transfer additive manufacturing via Nb interlayer added by TIG. Mater. Lett. **302**, 130397 (2021). https://doi.org/10.1016/j.matlet.2021.130397
19. Koli, Y.; Aravindan, S.; Rao, P.V.: Wear characteristics of wire-arc additive manufactured SS308L. ASME J Tribol **145**(3), 031706 (2023). https://doi.org/10.1115/1.4056191
20. Yadav, A.; Srivastava, M.; Jain, P.K.; Rathee, S.: Microstructure transformations and improving wear resistance of austenitic stainless steel additively fabricated by arc-based DED process. Def. Technol. (2024). https://doi.org/10.1016/j.dt.2024.02.006
21. Yadav, A.; Srivastava, M.; Jain, P.K.; Rathee, S.: Microstructure and tribological behaviour of dissimilar steel functional structure developed via arc-based DED process. Tribol. Int. **197**, 109782 (2024). https://doi.org/10.1016/j.triboint.2024.109782
22. Chakkravarthy, V.; Jerome, S.: Fabrication of preferentially oriented Al4043 alloy and its wear anisotropy. Mater. Lett. **280**, 128578 (2020). https://doi.org/10.1016/j.matlet.2020.128578
23. Kumar, V.; Dwivedi, S.; Mandal, A.; Dixit, R.A.: Experimental investigations on the microstructural evolution and their influence on mechanical, tribological and corrosion performance of wire-arc additive manufactured SS316L structure. Mater. Today Commun. **38**, 107673 (2024). https://doi.org/10.1016/j.mtcomm.2023.107673
24. Liu, G.; Zhou, S.; Lin, P.; Zong, X.; Chen, Z.; Zhang, Z.; Ren, L.: Analysis of microstructure, mechanical properties, and wear performance of NiTi alloy fabricated by cold metal transfer based wire arc additive manufacturing. J. Market. Res. **20**, 246–259 (2022). https://doi.org/10.1016/j.jmrt.2022.07.068
25. Teng, J.; Jiang, P.; Cong, Q.; Cui, X.; Nie, M.; Li, X.; Zhang, Z.: A comparison on microstructure features, compression property and wear performance of TC4 and TC11 alloys fabricated by multi-wire arc additive manufacturing. J. Market. Res. **29**, 2175–2187 (2024). https://doi.org/10.1016/j.jmrt.2024.01.256
26. Zhang, Y.; Liu, Z.; Wang, Y.; Zhai, Y.; Cui, C.; Zhang, Q.; Du, Z.; Yuan, Y.; Wang, X.: Study on the role of chromium addition on sliding wear and corrosion resistance of high-manganese steel coating fabricated by wire arc additive manufacturing. Wear **540–541**, 205242 (2024). https://doi.org/10.1016/j.wear.2024.205242
27. Cai, X.; Yang, Y.; Qiao, Y.; Wang, Z.; Zhou, J.; Xue, F.: Experimental investigation on wear resistance and corrosion behavior of nickel-aluminium bronze alloy fabricated by wire-arc additive manufacturing. J. Market. Res. **26**, 5801–5815 (2023). https://doi.org/10.1016/j.jmrt.2023.08.313
28. Hemachandra, M.; Thapliyal, S.; Mahammod, B.P., et al.: Influence of microstructural characteristics on the mechanical and wear behavior of wire arc additive manufactured and cast eutectic Al-Si alloy. SILICON **16**, 2441–2463 (2024). https://doi.org/10.1007/s12633-024-02848-6
29. Azlin, M.F.A.M.; Abdullah, A.B.; Nasir, R.M.; Rajendran, R.; Yusuf, S.Y.M.; Hussain, Z.: Wear behaviour of additive manufactured aluminium alloy ER5356. Mater. Sci. Forum **1101**, 9–16 (2023). https://doi.org/10.4028/p-9e75iv
30. Teng, J.; Jiang, P.; Cui, X.; Nie, M.; Li, X.; Liu, C.; Zhang, Z.: Revealing microstructural evolutions, mechanical properties and wear performance of wire arc additive manufacturing homogeneous and heterogeneous NiTi alloy. J. Market. Res. **27**, 1593–1610 (2023). https://doi.org/10.1016/j.jmrt.2023.10.055
31. Li, G.; Hao, S.; Gao, W., et al.: The effect of applied load and rotation speed on wear characteristics of Al-Cu-Li alloy. J. of Materi Eng Perform **31**, 5875–5885 (2022). https://doi.org/10.1007/s11665-022-06613-x
32. Vedabouriswaran, G.; Aravindan, S.: Wear characteristics of friction stir processed magnesium RZ 5 composites ASME. J. Tribol. **141**(4), 041601 (2019). https://doi.org/10.1115/1.4042039
33. Renner, P.; Jha, S.; Chen, Y.; Raut, A.; Mehta, S.G.; Liang, H.: A review on corrosion and wear of additively manufactured alloys. ASME. J. Tribol **143**(5), 050802 (2021). https://doi.org/10.1115/1.4050503
34. Dixit, T.; Prasad, K.; E.: Effect of temperature and sliding velocity on the dry sliding wear mechanisms of boron modified Ti-6Al-4V alloys. Lubricants **10**, 296 (2021). https://doi.org/10.3390/lubricantWAAM0110296
35. Harsha, A.P.; Wäsche, R.; Joyce, T.J.: Friction and wear of two polyethylenes under different tribological contact conditions. Polym. Polym. Compos. **29**(5), 393–404 (2021). https://doi.org/10.1177/0967391120920130
36. Baby, A.K.; Priyaranjan, M.; Deepak, L.K.; Rajendrakumar, P.: Tribological behaviour of hypereutectic Al-Si automotive cylinder liner material under dry sliding wear condition in severe wear regime. Proc. Inst. Mech. Eng. Part J: J. Eng. Tribol. **235**(7), 1450–1462 (2021). https://doi.org/10.1177/1350650120964616
37. Kumar, T.S.; Thankachan, T.; Shalini, S., et al.: Microstructure, hardness and wear behavior of ZrC particle reinforced AZ31 surface composites synthesized via friction stir processing. Sci. Rep. **13**, 20089 (2023). https://doi.org/10.1038/s41598-023-47381-5
38. Bharat, K.C.; Anandakrishnan, V.: Investigations on dry sliding wear behavior of a wire arc additively manufactured nickel-based superalloy. Tribol. Trans. **65**(5), 912–923 (2022). https://doi.org/10.1080/10402004.2022.2101569
39. Singh, V.; Niranjan, M.S.; Murtaza, Q.: Effect of Al-Si and Al-Mg filler wires on microstructure and mechanical properties of bead-on-plate weld on AA6061-T6 using CMT welding. Proc. Inst.

Mech. Eng. Part E: J. Process Mech. Eng. (2024). https://doi.org/10.1177/09544089241241046E

40. Seth, P.P.; Parkash, O.; Kumar, D.: Structure and mechanical behavior of in situ developed Mg2Si phase in magnesium and aluminium alloys – a review. RSC Adv. **10**(61), 37327–37345 (2020). https://doi.org/10.1039/d0ra02744h
41. Doumenc, G.; Couturier, L.; Courant, B.; Paillard, P.; Benoit, A.; Gautron, E.; Girault, B.; Pirling, T.; Cabeza, S.; Gloaguen, D.: Investigation of microstructure, hardness and residual stresses of wire and arc additive manufactured 6061 aluminium alloy. Materialia **25**, 101520 (2022). https://doi.org/10.1016/j.mtla.2022.101520
42. Waqas, A.; Xiansheng, Q.; Jiangtao, X.; Chaoran, Y.; Fan, L.: Impact toughness of components made by GMAW based additive manufacturing. Proc. Struct. Integr. **13**, 2065–2070 (2017). https://doi.org/10.1016/j.prostr.2018.12.207
43. Qin, W.A.; Xiong, X.; Zheng, J.; Wang, C.; H,: Analysis of ductile fracture obtained by charpy impact test of a steel structure created by robot-assisted GMAW-based additive manufacturing. Metals (Basel) **9**, 1208 (2019). https://doi.org/10.3390/met9111208

Springer Nature or its licensor (e.g. a society or other partner) holds exclusive rights to this article under a publishing agreement with the author(s) or other rightsholder(s); author self-archiving of the accepted manuscript version of this article is solely governed by the terms of such publishing agreement and applicable law.

ISSN 1063-455X, Journal of Water Chemistry and Technology, 2025, Vol. 47, No. 1, pp. 17–30. © Allerton Press, Inc., 2025.
Ukrainian Text © The Author(s), 2025, published in Khimiya i Tekhnologiya Vody, 2025, Vol. 47, No. 1, pp. 23–39.

PHYSICAL CHEMISTRY OF WATER TREATMENT PROCESSES

Integrated Advanced Oxidation Processes for Chlorophenol Degradation: Parameter Influence, Efficacy Evaluation, and Toxicity Assessment with *Eichhornia crassipes*

Shivani Yadav[a], *, Harsh Pipil[a, b], **, Sunil Kumar[c], and Anil Kumar Haritash[a]

[a] *Department of Environmental Engineering, Delhi Technological University, Delhi, 110042 India*

[b] *Manav Rachna Centre for Advance Water Technology and Management, Manav Rachna International Institute of Research and Studies, Faridabad, 121004 India*

[c] *Solaris Chemtech Industries, Bhuj, Gujarat, 370001 India*

**e-mail: shivaniyadav_phd2k19@dtu.ac.in*

***e-mail: harsh_phd2k19@dtu.ac.in*

Received April 26, 2024; revised September 10, 2024; accepted September 30, 2024

Abstract—This study investigated the degradation of a mixture of chlorophenol solution using various Advanced Oxidation Processes (AOPs). At different optimized conditions obtained for trichlorophenol, dichlorophenol, and monochlorophenol individually, additional optimization was performed for treating mixed chlorophenols (Mi-CPs). In photocatalysis degradation, rapid and complete removal of Mi-CPs was reported at pH 6.0, TiO_2 dose of 0.25 g/L, and H_2O_2 concentration of 10.0 mM within 270 min. In the case of photo-Fenton's process, the complete removal was observed in 12 min at pH 3.0, Fe(II) 0.5 mM, and H_2O_2 10.0 mM. Different AOPs integrated methods were also employed towards efficient removal. Solar-derived processes exhibited enhanced degradation rates. Assessment of electrical energy per unit order indicated sonication or UV-driven processes as energy-intensive processes over solar processes. For instance, solar-Fenton's process resulted in complete chlorophenol removal in 8 min, whereas solar catalysis resulted in degradation of the toxicant within 315 min, albeit slightly longer than UV-driven catalysis. Hence, solar processes can be considered as an environmentally friendly approach for treating industrial wastewater. Furthermore, the toxicity analysis conducted for treated effluent using a macrophyte reported the disruption of plant tissues and ultimately plant death, signifying the presence of chemical species obstructing the plant metabolism and growth.

Keywords: wastewater treatment, AOPs, solar energy, toxicity, sustainability

DOI: 10.3103/S1063455X25010084

INTRODUCTION

Chlorophenols are a group of organic compounds characterized by a phenolic ring substituted with chlorine atoms. These compounds are pervasive environmental contaminants arising from industrial processes, agricultural activities, and the use of chlorinated chemicals. Their occurrence in different environmental media (water, soil, and air) has raised concerns owing to their toxicity, persistence, and potential adverse effects on human health and ecosystems [1]. The compounds are resistant to biodegradation and persist in the environment for a long period of up to 28 years. They are labelled as kind of priority pollutants by US Environmental Protecting Agency (USEPA) considering their estrogenic, mutagenic and carcinogenic effects. Since they are persistent and have low biodegradability even at trace levels, the U.S. Agency for Toxic Substance and Disease Registry has classified them on the priority list of hazardous substances [2].

Chlorophenols enter the environment through various industrial activities such as wood preservation, pesticide manufacturing, and synthesis of chemicals. These are released into the environment primarily due to the manufacture and use of chlorinated solvents and disinfectants [3]. The persistence of chlorophenols in the environment also raises concerns about bioaccumulation. Failure to properly dispose of industrial waste and chlorophenol-containing effluents contributes to environmental degradation. Landfills and waste disposal sites may serve as long-term sources of chlorophenol release into the environment, contaminating the soil biome. The chloro-derivative phenols negatively impact soil quality, affecting plant growth and microbial activity. Contaminated soil may lead to reduced crop yields and pose challenges to

agricultural sustainability. The administration of chlorine-based pesticides in agriculture causes such compounds to leach into the soil and water [4]. Runoff from pesticide-addressed farms serves as the principal source of pollution in surface water bodies. Aquatic organisms are particularly vulnerable to chlorophenol contamination. Fish, algae, and other aquatic life may experience reduced reproduction, growth abnormalities, and disruption of the food chain [5].

Chlorophenols pose health risks to humans through exposure via ingestion, inhalation, or dermal contact. They are known to cause various health issues, including liver and kidney damage, disruption of the endocrine system, and have carcinogenic effects. Long-term exposure can result in chronic health problems [1]. Several treatment strategies focus on advanced oxidation processes (AOPs) to address organic contamination [6]. Photocatalytic processes, utilizing catalysts like titanium dioxide (TiO_2) activated by UV light, generate reactive oxidation species (ROS) for the degradation of chlorophenolic compounds [3, 7]. Another treatment process, Fenton's oxidation involves the use of iron catalysts and hydrogen peroxide to produce hydroxyl radicals, facilitating the oxidation of recalcitrant [8, 9].

Since chlorophenols pose a significant environmental challenge, impacting human health and ecosystems, the fundamental treatment approach, particularly through Advanced Oxidation Processes, is crucial for mitigating chlorophenol contamination. The current research aims at a comprehensive approach integrating AOPs with optimization techniques using Response Surface Methodology for efficient remediation solutions. Based on the optimized results obtained for different chlorophenolic compounds (Trichlorophenol, Di chlorophenol and monochlorophenol), the study investigated the treatment of synthetically prepared wastewater having a mixture of the above-mentioned chlorinated compound. Addressing the sustainable treatment of hazardous compounds like chlorophenols is essential for safeguarding the environment and ensuring the well-being of both human and ecological systems, the toxicity assessment of the compound was also carried out using *Eichhornia crassipes*. The ultimate goal of industrial ecology is sustainable development and water hyacinth as an unwanted nuisance on the waterways can be used as a raw material for the sustainable treatment of industrial wastewater.

EXPERIMENTAL

Chemicals

Analytical grade 2,4,6-trichlorophenol (TCP) (purity 98%), $FeSO_4 \cdot 7H_2O$, and hydrogen peroxide (30% w/v) were purchased from Thermo Fisher Scientific, whereas analytical grade 2,4-dichlorophenol (DCP), 4-chlorophenol (MCP) (98% purity), KOH and H_2SO_4 (used for pH adjustment) were obtained from Central Drug House (CDH), India. Degussa P25 nano-TiO_2 photocatalyst (NPC) (anatase to rutile ratio 80 : 20) was procured from Evonik Industries, Germany. Hydroxylammonium chloride, sodium acetate, and 1,10-phenanthroline were purchased from SRL Chemicals, India.

Experimental Setup

The photocatalytic and photo-Fenton treatment of mixed-CPs (Mi-CPs) was executed under optimized conditions as established in previous studies for individual chlorophenols (TCP, DCP and MCP) [3, 4, 7]. The removal kinetics of Mi-CPs was studied using a synthetic stock solution of 200 mL of strength 100 ppm, prepared by combining different chlorophenols in the ratio of 2 : 4 : 4 (MCP : DCP : TCP). The UV_{365} induced experiments (UV_{365} photocatalysis, sono-photocatalysis, and photo-Fenton) were conducted in a fabricated chamber having 8 UV tubes (power rating 36 W for each tube) arranged in a horizontal manner. The cumulative UV chamber source intensity, as determined by [10], was 672 W/m^2. In the case of photocatalysis, the reaction mixture comprising Mi-CPs, NPC, and H_2O_2 was UV irradiated ($\lambda = 365$ nm) with continuous magnetic stirring at 200 rpm and air sparging to ensure homogeneousness during the reaction. A 5 mL aliquot was extracted using a pre-rinsed syringe at 15 min interims followed by centrifugation at 5000 rpm for 10 min. For Fenton's and Integrated-Fenton's treatment, analysis was carried out at per-minute intervals. The experimental procedure was repeated until the residual concentration of Mi-CPs stabilized, indicating no further degradation. To ensure the precision of the analysis, all experiments were carried out in triplicates.

Analysis of Mi-CPs

The removal profile of mixed-CPs was analytically determined using a double-beam UV-Vis spectrophotometer (Lab India UV 3092 model). An absorption spectrum was generated in the wavelength range of 190 to 800 nm, and the wavelength of maximum absorption (λ_{max}) was detected at 283 nm. To establish

a quantitative relationship, a calibration graph for mixed-CPs was constructed in concentrations ranging from 10 to 100 mg/L at 10 mg/L intervals. The removal efficiency of Mi-CPs was subsequently estimated using the following equation:

$$Efficiency(\%) = \left[\frac{C_i - C_t}{C_i}\right] \times 100, \quad (1)$$

where C_i represents the preliminary concentration of Mi-CPs before treatment (100 mg/L) and C_t is the concentration of Mi-CPs at any time t after photooxidation.

Mineralization of Mi-CPs was examined via TOC Analyzer (TOC-L Shimadzu Make, Japan) to substantiate the observations over a UV-Vis spectrophotometer. Mineralization was calculated using the following expression:

$$Mineralisation(\%) = \left[\frac{TOC_i - TOC_f}{TOC_i}\right] \times 100, \quad (2)$$

where TOC_i refers to the initial TOC of Mi-CPs before treatment (100 mg/L) and TOC_f is the final TOC of Mi-CPs after treatment.

The intensity of incoming solar radiation was determined using an Apogee Pyranometer. The residual ferrous ion (Fe^{2+}) concentration and the total dissolved iron were analyzed using a spectrophotometer at 510 nm using the 1,10-phenanthroline method as mentioned in APHA Method 3500-Fe. Iodometric titration was performed to calculate the residual concentration of H_2O_2 in the solution.

The Figure of Merit is the Electrical Energy per Order

The removal rate of organic contaminants is proportionate to the rate of electrical energy use in terms of the figure of merit. Since AOPs are electric-energy-intensive processes and the use of electrical energy presents a major portion of the operating cost, the simple figure-of-merit-based electric energy consumption is essential [11]. The implementation of treatment units on a commercial scale considers various factors including economics, effluent quality goals, operation and robustness, regulations, etc. The standard figure-of-merit provides a direct link to the electrical energy or solar energy efficiency of AOPs. Since the strength of pollutant concentration is low in the current study, the electric energy per order is considered a suitable figure of merit. This is attributed to the amount of electric energy involved in lowering the concentration of pollutants by one order of magnitude in irrespective of the contaminant concentration. Electrical energy per order is the electric energy (kWh) required to treat 1 m^3 of contaminant, and it was evaluated using the following formula [11]:

$$E_{EO}^{TOC} = \frac{Pt \times 1000}{V \log\left[\frac{TOC_i}{TOC_f}\right]}, \quad (3)$$

where P is the rated power in kW; t is the time taken to degrade Mi-CPs in hours; TOC_i refers to the initial TOC of Mi-CPs before treatment (100 mg/L); and TOC_f is the final TOC of Mi-CPs after treatment.

Plant Material and Toxicity Assessment

A water hyacinth of almost similar size was collected from the pond on the university campus. The experimental design consists of three experimental cells: control, treated wastewater and untreated wastewater as depicted in Fig. 1. Five to six plants for each were placed in 20 L of medium. The experiment was conducted for 7 days, and the physiological response of plant samples was analyzed for pH, chlorophyll a, chlorophyll b and carotenoids, ascorbic acid, and proline using the standard procedure [12] at the beginning of the experiment and the end of 7 days.

RESULTS AND DISCUSSION

Photocatalysis Experiment

Photocatalytic oxidation of Mi-CPs using NPC was found to be efficient in eliminating the aforementioned organic impurity. The study emphasized the effect of process conditioning parameters like NPC dose, pH, and oxidizing agent H_2O_2 for the degradation of Mi-CPs based on the optimized conditions obtained for different chlorophenols. The optimized conditions obtained for Set-A: MCP (pH 4.0, TiO_2

Fig. 1. Experimental unit design for toxicity assessment.

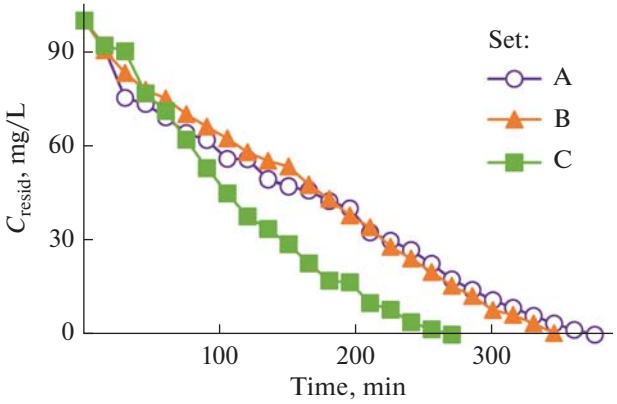

Fig. 2. The effect of process conditioning parameters for photocatalytic degradation of Mi-CPs.

dose 0.15 g/L and H_2O_2 10.0 mM); Set-B: DCP (pH 5.0, TiO_2 dose 0.2 g/L and H_2O_2 10.0 mM) and for Set-C: TCP (pH 6.0, TiO_2 dose 0.25 g/L and H_2O_2 10.0 mM) (Fig. 2). The sample suspension of 100 mg/L Mi-CPs was initially kept in dark for 30 min further followed by UV irradiation. An initial dark phase was employed to attain the adsorption/desorption equilibrium of chlorophenols with the photocatalyst (NPC). It was observed that the complete removal occurred in all the experimental runs, however, Set-C was found to be more efficient and rapid.

Effect of NPC. Considering the complex structure of the compounds, the dose for complete degradation of respective chlorophenols also increased with an increasing number of attached chlorine atoms. The optimized dose for MCP degradation was 0.15 g/L; for DCP 0.21 and 0.25 g/L in case of TCP. It can be noted from Fig. 2 that the quicker and complete degradation efficiency was attained at the NPC dose of 0.25 g/L. Although complete removal was observed in all the cases, however, the pace of reaction was faster at 0.25 g/L dose and the time taken to degrade the CP mixture solution completely was 285 min. Degradation at the maximal dose of photocatalyst is attributed to the toxicity factor associated with the chlorophenols. TCP has more chlorine atoms attached; hence it is more toxic as compared to other CPs and thus a larger amount of NPC is required for effective degradation. Moreover, because of the presence of a substantiate proportion of TCP in the reaction mixture, the lesser dose of NPC took more time to degrade. The increasing NPC amount boosts the availability of active sites, thus accelerating the adsorption process too. Enhanced binding of electron–hole pairs with water promotes the generation of hydroxyl radicals. It was also observed that the mineralization efficiency of the mixture was of the following order:

Set-C (92%) > Set-B (88%) > Set-A (85%) as compared to others. Hence, Set-C was considered as the optimized option for the degradation of a mixture of chlorophenols.

NPC comprises two phases: rutile and anatase phases. The Anatase phase demonstrates a longer period of electron–holes with lesser recombination of charge carriers. The elevated degradation rate with an increased NPC dose is because of the electron–hole pairs generated resulting in the mass transfer of electrons and holes from the interior to the surface of anatase TiO_2. Whereas the rutile TiO_2 part has a smaller band gap that generates electron–hole pairs when irradiated with low-energy photons making it advantageous for anatase TiO_2 to utilize these electron–hole pairs [13]. Thus, the synergetic effect of the rutile and anatase phases of NPC plays a crucial role in photocatalytic efficiency. The generated electron-hole pairs react either directly with the organic pollutant or with surface-bound water to produce hydroxyl radicals [4]. The increasing amount of NPC leads to an increase in the availability of active sites, thus improving the adsorption process too. Hence, the more the binding of electron–hole pairs with water, the more the production of hydroxyl radicals [7, 9]. The efficiency could be rationalized in terms of the photocatalytic activity of NPC that depends on factors such as the capability of generation of electron–hole pairs when illuminated with light having a wavelength of less than 400 nm, the inhibition of recombination of photo-generated charge pairs, and the efficiency of electron and hole pairs to transfer charge to organic contaminants adsorbed on NPC [6, 14]. The photo-generated valence band holes and conduction band electrons reduce the electron acceptor species and oxidize the electron donor species adsorbed on the catalyst surface. The hydroxyl and perhydroxyl radicals carry out the photooxidation of CPs [4].

$$TiO_2 + h\nu \rightarrow TiO_2(e^-) + TiO_2(h^+), \quad (4)$$

$$O_2 + e^- \rightarrow OH\bullet, \quad (5)$$

$$H_2O + h^+ \rightarrow OH\bullet. \quad (6)$$

Thus, the optimization of the photocatalyst dose reduces its amount and the treatment cost. Further experimentation was carried out using the NPC concentration of 0.25g /L.

Effect of pH. pH is a significant operating parameter regulating the efficiency of the treatment processes. pH determines the surface charge properties of photocatalysts, which governs the behaviour of pollutants [9]. In the present study, experiments were performed at different optimized pH conditions: 4.0, 5.0, and 6.0. The interaction and affinity between NPC and CPs are governed by pH. Variation in the working pH value affects the surface charge or isoelectric point of NPC. The ionization state of the photocatalyst surface undergoes either protonation or deprotonation depending on the employed pH (Eqs. (7) and (8), where TiOH is the primary hydrated surface functionality of TiO_2. Since the point of zero charges (p_{zc}) of TiO_2 is around 6.2, it carries a net positive charge, whereas the chloro-derivative phenol compounds have negative charges ($pK_a = 7.98$). Thus, at $pH < pH_{pzc}$, the positive charge on the photocatalyst gradually exerts an electrostatic force of attraction towards the negatively charged chlorophenolic compound (Eq. (8)) [4]. Therefore, the polar attraction intensifies the adsorption of organics over the photocatalyst surface, facilitating photocatalytic degradation.

$$Ti{-}OH + H^+ \leftrightarrow TiOH_2^+. \quad (7)$$

Conversely, in the case of $pH \geq pH_{pzc}$, TiO_2 carries a net negative charge (Eq. (8)), which hampers the adhesion of CP onto the catalyst surface.

$$TiOH + OH^- \leftrightarrow TiO^- + H_2O. \quad (8)$$

The increased density of now negatively charged catalysts and chlorophenols both exert columbic repulsion, resulting in lesser adsorption of pollutants over the surface of TiO_2. This results in a decreased rate of degradation and lesser removal efficiency. Considering the above phenomena, the optimized pH values obtained in the case of MCP, DCP and TCP were 4.0, 5.0, and 6.0, respectively. Complete degradation was observed under all the pH conditions for the Mi-CPs solution. Nevertheless, the rate of reaction was faster in the case of pH 6.0 and it was also found that the observed TOC mineralization was higher.

Effect of Oxidant Concentration. The addition of oxidant enhances the degradation of organic contaminants. The effect of hydrogen peroxide was studied at 10.0 mM. Optimization studies related to oxidant concentration in the case of MCP and DCP reported 10.0 mM as the optimized dose, thus for the degradation of Mi-CPs, 10.0 mM was used. H_2O_2 is a more efficient electron acceptor than oxygen and generates hydroxyl radicals by reacting with conduction band electrons and inhibiting the electron–hole pair

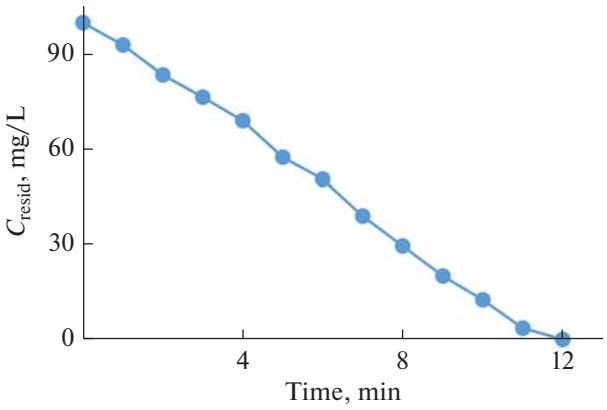

Fig. 3. Photo-Fenton degradation of Mi-CPs.

recombination. UV irradiation photolyzes H_2O_2 which generates hydroxyl radicals necessary for photo-mineralization of organic pollutants (Eq. (9)).

$$(e^-)TiO_2 + H_2O_2 \rightarrow TiO_2 + OH^{\bullet} + OH^-. \quad (9)$$

The addition of H_2O_2 along with TiO_2/UV has a synergistic effect, enhancing the efficiency of the treatment system by generating two hydroxyl radicals or producing hydrogen ions for generating perhydroxy radicals (Eqs. (10)–(12)) [6].

$$O^{2-} + H^+ \rightarrow HO_2^{\bullet}, \quad (10)$$

$$H_2O_2 \rightarrow 2HO^{\bullet}, \quad (11)$$

$$H_2O_2 \rightarrow O_2^{2-} + 2H^+. \quad (12)$$

Similar observations were also reported in other relevant studies carried out for the treatment of contaminated water using the photocatalytic treatment [15]. Thus, 10.0 mM of H_2O_2 was considered as the optimized oxidant concentration.

Photo-Fenton Experiment

Degradation of the Mixture of CPs is studied using photo-Fenton's process. Considering the optimized conditions obtained in the case of MCP (pH 3.0, Fe^{2+} 0.7 mM, and H_2O_2 10.0 mM); for DCP (pH 3.0, Fe^{2+} 0.5 mM, and H_2O_2 5.0 mM) and TCP (pH 3.0, Fe^{2+} 0.5 mM, and H_2O_2 10.0 mM), Mi-CPs solution was subjected to degradation at pH 3.0, Fe^{2+} 0.5 mM, and H_2O_2 10.0 mM (Fig. 3). The addition of H_2O_2 imparted a dark brown colour to the reaction mixture and the solution became turbid within a few seconds. As the reaction proceeded, the colour started to fade changing from dark brown to light yellow and colourless, indicating completion of the reaction and CPs were non-detectable within 12 min of the reaction time. In addition, 93% TOC mineralization was also observed.

Effect of pH. The solution pH determines the removal efficiency of organic pollutants in the photo-Fenton system. It is evident from the literature that Fenton's process works efficiently under acidic conditions (pH 3 is optimum) [10, 16]. This is attributed to the stability of Fe^{2+} and H_2O_2 which is higher at pH 3.0. At extremely acidic conditions, complex iron species and oxonion ($H_3O_2^+$) are formed, and the removal efficiency is decreased due to the scavenging behaviour of H^+-consuming hydroxyl radicals (Eq. (13)). Furthermore, a lesser solubility of ferrous ions results in formation of complex ions species and peroxonium ions, $H_3O_2^+$ (Eq. (13)) as well, probably, because of increased peroxide stability and decreased reactivity of Fe(II) [9] (Ghoneim et al., 2011).

$$H_2O_2 + H^+ \rightarrow H_3O_2^+, \quad (13)$$

$$OH\bullet + H^+ + e^- \rightarrow H_2O. \quad (14)$$

Under alkaline conditions, the solubility of Fe(III)/Fe(II) decreases, and iron precipitates as $Fe(OH)_3/Fe(OH)_2$ sludge, while H_2O_2 dissociates to form water and oxygen. This results in inactivation and inhibition of further generation of $^{\bullet}OH$ radicals [6]. Also, the electrostatic force of repulsion between CP and catalyst surface (Fe acts as a catalyst in Fenton's process) dominates under alkaline conditions reducing the dissociation of CPs. Furthermore, the dissociation constant (pK_a) for CPs lies in the range from 4.7 for PCP to 9.41 for MCP and 6.23 for TCP which suggests the ionization of polychlorophenols to begin at lower pH. Hence, in the present study, the complete degradation of CPs was observed at an optimum pH of 3.0. Moreover, under the following conditions, $2.0 > pH > 4.0$, the potential for hydroxyl radical decreases, thus decreasing the efficiency of the treatment process [3]. Hence, pH 3.0 is considered as the favourable working condition in the case of Fenton's processes.

Effect of Fe^{2+}. Iron is a significant factor determining the removal rate of the recalcitrant pollutants in the Fenton treatment [6]. In the present study, an experiment was performed at an iron concentration of 0.5 mM. The redox recycling process of Fe^{2+}/Fe^{3+} takes place in the bulk solution generating reactive oxidative species (Eq. (15)), while some ferrous ion species are generated through reactions (16) and (17).

$$Fe^{2+} + H_2O_2 + H^+ \rightarrow Fe^{3+} + {}^{\bullet}OH + H_2O, \quad (15)$$

$$Fe^{3+} + H_2O_2 \rightarrow Fe^{2+} + HOO^{\bullet} + H^+, \quad (16)$$

$$Fe^{3+} + HOO^{\bullet} \rightarrow Fe^{2+} + O_2 + H^+. \quad (17)$$

The OH radicals generated during the reaction between iron and H_2O_2, attack the π system of the aromatic phenolic ring accelerating the oxidation of CPs. The residual concentration of total dissolved iron and ferrous ions determined at the end of the reported experiment completes the consumption of ferrous ions, whereas the total dissolved iron concentration measured was 0.03 mM.

Effect of H_2O_2. The effect of H_2O_2 was studied at the optimized concentration of 10.0 mM. Peroxide acts as an electron acceptor and inhibits the recombination of electron–hole pairs thus facilitating the generation of OH radicals (Eq. (18))

$$H_2O_2 + e^-_{CB} \rightarrow OH^{\bullet} + OH^-. \quad (18)$$

Optimization of H_2O_2 is significant when H_2O_2 is present in excess amounts and acts as a scavenger leading to self-destruction of peroxide (Eq. (18)). The hydroperoxyl radicals are produced in the reaction between OH radicals and excess peroxide (Eq. (20)). The reduction potential of these hydroperoxyl radicals (1.0 V) is less than that of hydroxyl radicals (2.8 V). Thus, it is the most probable reason for a decrease in the degradation rate with an increase in H_2O_2 concentration above the optimized value.

$$2H_2O_2 \rightarrow 2H_2O + O_2, \quad (19)$$

$$OH + H_2O_2 \rightarrow H_2O + HO_2. \quad (20)$$

Besides, the residual concentration of H_2O_2 calculated at the end of the experiment was 3.5 mM indicating that only 6.5 mM of H_2O_2 was consumed during the complete oxidation of CPs.

Integrated Processes for the Degradation of Mi-CPs

Different photocatalytic and Fenton-integrated processes were employed at optimized conditions. Figure 4 depicts the removal efficiency and mineralization of different processes.

Ultrasound-assisted photocatalysis process. The sono-photocatalysis pathway involves activation of the surface of the photocatalyst, mass transfer of organic contaminants and breaking the aggregation. The sonolysis process was performed in a sonication bath at the operating frequency of 40 kHz [9]. The effect of ultrasound and photocatalysis was reflected in the treatment of Mi-CPs (Fig. 4). The process reported complete degradation of the CPs-mixture in 270 min with 95% mineralization. The synergistic integration of the increased free radical formation and enhanced catalytic activity increased the efficiency of the process. Photocatalyst enhances the bubble cavitation phenomenon causing an increased migration of reactive species into the liquid bulk region. Thus, the intensification leads to a higher concentration of free radicals as a result of ultrasound in the peroxide species [17]. Cavitation causes cleavage of H_2O_2 produced by the coupling process, increasing the generation of reactive radical species which further carries out the oxidation of the substrate and other intermediates. A higher production of OH radicals in the bubble-bulk interface enhances greater interaction with organic pollutants in the bulk-liquid medium [3]. A similar effect was also observed under the influence of solar light.

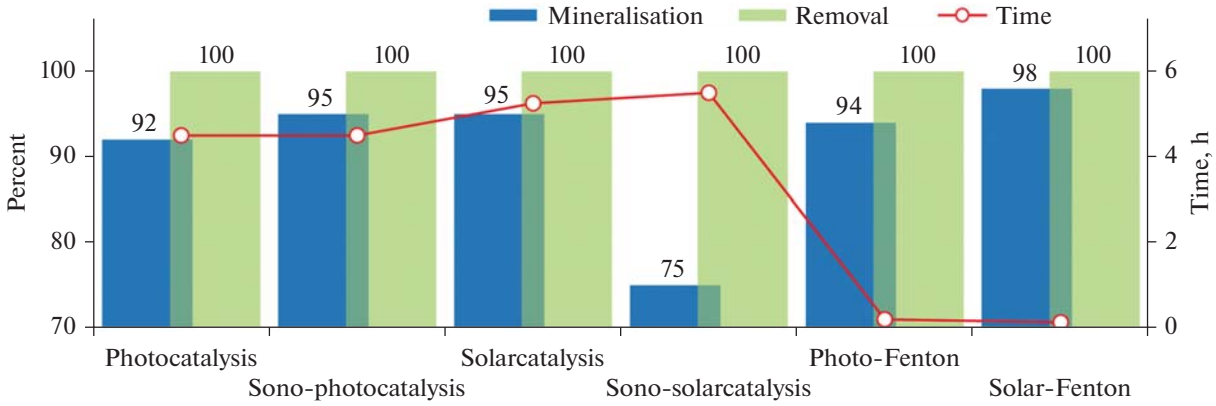

Fig. 4. Removal efficiency and mineralization per cent of different AOPs.

Solar-induced AOPs. One of the major challenges of AOPs is switching from energy-intensive processes to sustainable and renewable energy sources. Solar photochemistry plays a vital role in pollution remediation transforming the pollutants into non-toxic compounds. Since no solar spectrum modification can occur, solar energy could be harnessed to increase the efficiency of treatment systems. Solar-driven AOPs investigated in the present study have reported some promising results. Solar-assisted degradation processes were conducted in March with an average solar radiation of 760 W/m^2 within the experiment duration. The solar-Fenton reported complete degradation of organic pollutants with 98% TOC reduction within 8 min, which is comparatively faster compared to the photo-Fenton process (Fig. 4). In photocatalysis, the rate of electrons excited from the valence band to the conduction band of the photocatalyst is influenced by the intensity of light affecting the rate of photocatalytic reaction and photocatalyst activation [18]. In solar driven NPC induced catalysis, 100% removal efficiency was attained in 315 min with 95% mineralization. Moreover, solar-induced sono-photocatalytic process also reported 100% degradation although nearly 75% mineralization was there. The lesser mineralization could be conditional since the solar light (Average solar radiation 682 W/m^2 during experiment hours) might be less proficient for the ample generation of hydroxyl radicals for effectively degrading the intermediary compounds because of the fractional proportion of UV in the solar spectrum as compared to direct UV light used in photocatalysis effective for photo-activating the photocatalyst. In addition, the solar spectrum is harnessed naturally, thereby offsetting the cost of treatment against UV light.

Electrical Energy per Unit Order (E_{EO})

Since AOPs are considered as energy-intensive processes, the energy efficiency was evaluated using the figure of merit in terms of electrical energy per unit order. Table 1 describes the comparative assessment of different treatment processes and associated energy. It can be observed from Table 1 that the power consumed by UV-driven treatment processes is higher as compared to solar-derived treatment. In the case of UV-driven processes, the total power consumed is 0.3 kW, which is primarily associated with the power rating of the 8 UV tubes in the UV chamber each of the power rating of 36 W. The power of magnetic stirrer (8.5 W) and air sparger (3.5 W) also added to the cumulative power consumed in UV_{365} photocatalysis. Thus, the electrical energy consumed per unit order was found to be maximum for UV_{365} photocatalysis and ultrasound assisted photocatalysis. In the case of ultrasound-integrated process, the power associated with sonicator bath increased the consumed energy. Moreover, the ultrasound-induced photocatalysis was found to be the most energy intensive. The process resulted in no significant removal and took similar time as compared to the photocatalysis alone. The time consumed in UV_{365} photocatalysis was either more or similar to that of sono-UV_{365} photocatalysis but slightly differed in the mineralization of the compound. The electrical energy per order for photo-Fenton's process observed was less time-consuming and was terminated within a few minutes. Moreover, the concomitant power factor with the Fenton processes was much lower. Since low electrical energy order reflects the processes as most energy efficient, hence, the solar-assisted treatment units were most energy effective as the processes successfully harnessed the naturally available renewable light source for carrying out degradation.

Economic Analysis of Different AOPs. A comparative cost assessment was carried out for various treatment processes employed for degradation of Mi-CPs such as photocatalysis, sono-photocatalysis, solar-

Table 1. Comparison of different processes for the maximum time taken for degradation

Process	Conditions					
	catalyst	ultrasound, kHz	pH	H_2O_2, mM	light source	intensity, W/m^2
Photocatalysis	TiO_2 0.1 g/L	–	5.0	10.0	UV tubes 365 nm	672
Sono-photocatalysis	TiO_2 0.1 g/L	40	5.0	10.0	UV tubes 365 nm	672
Solarcatalysis	TiO_2 0.1 g/L	–	5.0	10.0	Solar	682
Sono-solarcatalysis	TiO_2 0.1 g/L	40	5.0	10.0	Solar	682
Photo-Fenton	Fe 0.7 mM	–	3.0	7.0	UV tubes 365 nm	672
Solar-Fenton	Fe 0.7 mM	–	3.0	7.0	Solar	682

Process	Max degradation efficiency, %	Time for complete/max degradation, min	Mineralization, %	Electrical energy per unit, kWh/m^3
Photocatalysis	100	285	92	6.058
Sono-photocatalysis	100	270	95	2.701
Solarcatalysis	100	315	95	0.31
Sono-solarcatalysis	100	330	75	0.58
Photo-Fenton	100	12	93	0.64
Solar-Fenton	100	08	98	0.294

catalysis, sono-solar-catalysis, photo-Fenton and solar-Fenton (Table 2). The assessment was conducted taking into account the factors such as the time of treatment, amount of chemicals and associated cost of chemicals, the total power consumed during the reaction, and the energy-efficient factor. For instance, in photocatalysis oxidation, the reaction was complete in 285 min with 100% efficiency for a 0.25 mg/L catalyst dose at pH 6.0 along with a 10.0 mM oxidant dose. The experiments were conducted in a UV chamber equipped with 8 UV tubes, each rated at 36 W for a collective power of 288 W. Additionally, the air-sparger and magnetic stirrer had power ratings of 3.5 and 8.5 W, respectively, making the cumulative power consumption of 300 W or 0.3 kWh. The cost of hydrogen peroxide used was INR 1.14/L. Accounting for the fractional loss occurred during analysis (20%), the residual photocatalyst was recovered and oven-dried at 105°C. The recovered NPC was then assessed using the following formula:

$$TiO_2\,Recovered = \frac{w_2}{w_1} \times 100, \tag{20}$$

where w_1 is the initial weight of NPC added, and w_2 is the recovered NPC weight after the experiment.

Since the cost of Degussa P25 NPC catalyst was INR 22.680/100 g, with only 20% consumed or lost, thus the cost was INR 11.34/L for 100 mg/L of synthetic wastewater. With industrial electricity cost at 8.5 INR per unit of kWh in many Indian states, the overall operational cost for the photocatalysis process was 17.00 INR or 0.21 USD. On the other hand, photo-Fenton 100% degradation was achieved within minutes and in the case of the photo-Fenton process and with a lower cost of chemical, demonstrated an overall treatment cost of 0.9 INR, significantly less than photocatalysis. Sonication-integrated processes incurred higher costs because of the additional power consumption (100 W), although sono-photocatalysis had lower operational costs as the process reported earlier complete degradation as compared to UV-photocatalysis. Due to the reduced treatment time compared to UV-photocatalysis, the operational cost of sono-photocatalysis was less than that of UV photocatalysis. Solar-driven processes, such as solar-Fenton, solar-catalysis, and sono-solar-catalysis, reported notably cost-efficient and energy-efficient results as compared to photocatalysis, promoting renewable and environmentally sustainable approaches that reduce dependence on energy-intensive treatments.

Toxicity Assessment using Eichhornia crassipes

Water hyacinth, a floating aquatic plant is one of the most productive photosynthetic plants in the world. Studies on water hyacinths show that they improve the wastewater effluent from oxidation ponds [19] and integrated treatment systems. Water hyacinth has been reported to reduce BOD and SS when

Table 2. Economic analysis of the operating cost of different AOPs used in the current study (with 85% TiO_2 recovery)

Treatment method	Energy	Time of treatment	Rate of Energy	Cost of electricity	Chemical consumed	Cost of chemical	Cost of treatment	Cost of treatment
	kWh	h	INR/kWh	INR/kWh		INR/L		USD/L
Photo-Fenton (UV_{365})	0.06	0.2	8.50	0.5	$FeSO_4 \cdot 7H_2O$ H_2O_2 (30%)**	0.115 0.8	01	0.02
Photocatalysis (UV_{365})	1.35	4.5	8.50	11	TiO_2 (P25) H_2O_2 (30%)**	11.34* 1.14	24	0.29
Sono-Photocatalysis (UV_{365})	1.76	4.5	8.50	15	TiO_2 (P25) H_2O_2 (30%)**	11.34* 1.14	27	0.33
Solar-Fenton	0.001	0.1	8.50	0.010	$FeSO_4 \cdot 7H_2O$ H_2O_2 (30%)**	0.115 0.8	01	0.01
Solar-catalysis	0.063	5.25	8.50	0.5	TiO_2 (P25) H_2O_2 (30%)**	11.34* 1.14	13	0.016
Sono-Solar-Catalysis	0.57	5.5	8.50	5	TiO_2 (P25) H_2O_2 (30%)**	11.34* 1.14	17	0.21

* 15% loss of NPC is calculated; ** w/v.

Table 3. Physiological response of water hyacinth

Particulars		Initial	After 7 days		
			Control	Treated	Untreated
pH	–	5.5	5.8	6.2	6.3
Chlorophyll a	mg/g	2.048	1.588	1.31	0.934
Chlorophyll b		0.649	0.578	0.45	0.312
Carotenoids		0.101	0.07	0.05	0.06
Ascorbic acid		0.4488	0.421	0.39	0.37
Proline		0.69	0.7699	0.8632	0.8991

used in secondary treatment of domestic wastewater [20] and textile mill effluents [21]. The plant is highly effective in absorbing and accumulating various heavy metals and this effectiveness of water hyacinth is investigated in this study for industrial wastewater treatment. The plant was used to assess the toxicity of chlorophenol-contaminated wastewater from treated as well as untreated synthetically prepared industrial effluent. The performance of the water hyacinth was evaluated by assessing the physiological response of the plant (Table 3).

Table 3 represents the physiological response of water hyacinth over 7 days, assessing the control (presumably conditions without any specific treatment), treated (post AOPs treatment), and untreated (conditions without treatment, but not under the controlled, initial conditions) groups. It can be observed from this Table that a slight shift in pH towards more alkaline conditions occurs. The concentration of photosynthetic pigments was estimated before the experiment and after 7 days. It can be observed from Table 3 that the chlorophyll content decreased significantly in both treated and untreated samples. A slight difference was observed in the case of control. The untreated sample has the most significant decrease for chlorophyll a and chlorophyll b. A similar trend was observed in carotenoid content as well. The decreased photosynthetic pigments could be attributed to the stressed conditions that plants were exposed to. To survive under the pollutant/salinity stress condition, the plants exhibit defence mechanisms or adaptations

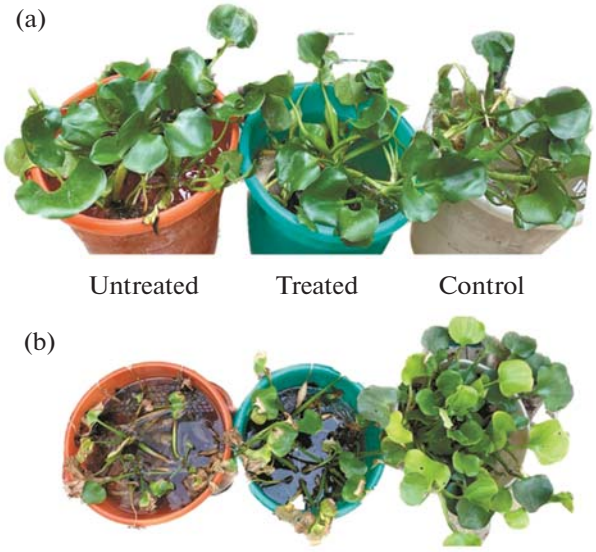

Fig. 5. Physical appearance of the plant before (a) and after 7 days (b).

which might result in reduced pigment content further decelerating the plant metabolism [22]. Stress conditions induce inactivation of antioxidant enzymes while flavonoid synthesis is up-regulated. Ascorbic acid is considered a powerful water-soluble antioxidant scavenger of ROS [23]. However, in the case of *E. crassipes* cultured in treated and untreated wastewater, the ascorbic acid content was found to be in decreasing order with not so significant change under controlled conditions. Increased stress conditions and inactivation of antioxidant enzymes could be attributed to the decline in the level of ascorbic acid. Another indicator of stress marker in plants (Proline) was found in increased levels according to estimations. In habitats with stress imparting contaminants, the plants are confronted with high levels of reactive oxygen species (ROS). Proline accumulation corresponds to the defensive mechanism to counteract oxidative stress damages such as pigment degradation. Studies have reported a similar trend in the physiological response of plants under stressed conditions [22]. In the current study, at the end of 7 days, the plants cultured in treated and untreated cells could not survive owing to the toxicity of the compound (Fig. 5). Moreover, in the case of AOPs treated wastewater, there may be a possibility of formation of by-products, which are capable enough to inhibit plant growth and disrupt the metabolism leading ultimately to the death of the plant tissues.

CONCLUSIONS

The study focused on the optimization and degradation of a mixed chlorophenol solution employing various Advanced Oxidation Processes (AOPs), including photocatalysis, solar-catalysis, sonolysis-induced photocatalytic oxidation, solar-sonophotocatalysis, photo-Fenton's, and solar-Fenton's. Notably, rapid and complete photocatalytic degradation of Mi-CPs was observed at pH 6.0, NPC dose of 0.25 g/L, and H_2O_2 concentration of 10.0 mM within the 270-min time interval. In the context of the photo-Fenton process, instantaneous removal was attained in 12 min at pH 3.0, Fe(II) concentration of 0.5 mM, and H_2O_2 concentration of 10.0 mM. Furthermore, solar-derived processes exhibited a more enhanced degradation rate, less energy-intensive and more proficient results as compared to sonication or UV-driven processes, and therefore, they could be considered as an environmentally sound approach. The solar-Fenton process achieved complete chlorophenol removal in 8 min, while solar catalysis resulted in contaminant degradation within 315 min. Although the solar-catalysis process requires slightly more time than UV-driven catalysis, it remains a viable preference for treating low-strength wastewater. Thus, the optimization and application of AOPs play a pivotal role in securing sustainable solutions for the remediation of such hazardous compounds, contributing significantly to the preservation of diverse environmental matrices. Moreover, illuminating is the imperative need for sustainability, the harnessing of natural light emerges as a judicious approach for treating industrial effluents laden with xenobiotic impurities. However, the toxicity analysis study suggested the invasive macrophyte is intolerant to oxidative stress

conditions even when cultured in treated effluent thus suggesting the need for further treatment processes of the treated wastewater. The study highlights the degradation of highly complex parent compounds. However, the possibility of formation of intermediates of chemical species cannot be ruled out, which is evident in the toxicity analysis using the macrophyte.

ABBREVIATIONS AND NOTATION

AOPs	advanced oxidation processes
CP	chlorophenol
DCP	2,4-dichlorophenol
DTU	Delhi technological university
INR	Indian rupee
MCP	4-chlorophenol
Mi-CPs	mixed chlorophenols
NPC	Degussa P25 nano-TiO_2 photocatalyst
PCP	pentachlorophenol
ROS	reactive oxidation species
SS	suspended solids
TCP	2,4,6-trichlorophenol
USEPA	US Environmental Protecting Agency

ACKNOWLEDGMENTS

The authors are grateful to the Department of Environmental Engineering at Delhi Technological University (DTU) for providing the infrastructure and the opportunity to carry out the present study.

AUTHOR CONTRIBUTION

Shivani Yadav: Conceptualization, execution, data compilation and draft writing.

Harsh Pipil: Conceptualization, execution, data compilation and draft writing.

Sunil Kumar: Conceptualization, supervision, reviewing and editing

Anil Kumar Haritash: Conceptualization, supervision, reviewing and editing.

FUNDING

This work was supported by ongoing institutional funding. No additional grants to carry out or direct this particular research were obtained.

CONFLICT OF INTEREST

The authors of this work declare that they have no conflicts of interest.

AVAILABILITY OF DATA AND MATERIALS

Necessary data has been provided along with this manuscript.

REFERENCES

1. Wei, D., Zhao, C., Khan, A., Sun, L., Ji, Y., Ai, Y., and Wang, X., Sorption mechanism and dynamic behavior of graphene oxide as an effective adsorbent for the removal of chlorophenol based environmental-hormones: A DFT and MD simulation study, *Chem. Eng. J.*, 2019, vol. 375, pp. 121964. https://doi.org/10.10167j.cej.2019.121964
2. USEPA, Edition of the Drinking Water Standards and Health Advisories, Washington, DC: EPA, 2004.
3. Yadav, S., Kumar, S., and Haritash, A.K., A comprehensive review of chlorophenols: Fate, toxicology and its treatment, *J. Environ. Manage.*, 2023, vol. 342, p. 118254. https://doi.org/10.10167j.jenvman.2023.118254
4. Pipil, H., Yadav, S., Kumar, S., and Haritash, A.K., Synergistic potency of ultrasound and solar energy towards oxidation of 2,4-dichlorophenol: A chemometrics approach, *Environ. Sci. Pollut. Res.*, 2024, vol. 31, pp. 8186–

8209.
https://doi.org/10.1007/s11356- 023-31598-y

5. Bhattacharya, T., and Chakraborty, S., Eco-restoration potential of vegetation for contaminated water bodies, in *Phytomanagement of Polluted Sites: Market Opportunities in Sustainable Phytoremediation*, Amsterdam: Elsevier, 2018.
https://doi.org/10.1016/B978-0-12-813912-7.00017-X
6. Pipil, H., Yadav, S., Chawla, H., Taneja, S., Verma, M., Singla, N., and Haritash, A.K., Comparison of TiO_2 catalysis and Fenton's treatment for rapid degradation of Remazol Red Dye in textile industry effluent, *Rend. Lincei, Sci. Fis. Nat.*, 2022, vol. 33, no. 1, pp. 105–114.
https://doi.org/10.1007/s12210-021-01040-x
7. Pipil, H., Yadav, S., Kumar, S., and Haritash, A.K., Evaluating the photocatalytic degradation efficacy of 2,4,6-trichlorophenol: Performance evaluation and influencing factors, *J. Water Clim. Change*, 2024, vol. 15, no. 3, pp. 1091–1101.
https://doi.org/10.2166/wcc.2024.483
8. Yadav, S., Pipil, H., Chawla, H., Taneja, S., Kumar, S., and Haritash, A.K., Textile industry wastewater treatment using eco-friendly techniques, in *Proc. Int. Conf. on Innovative Technologies for Clean and Sustainable Development*, Cham: Springer, 2022, pp. 63–74.
https://doi.org/10.1007/978-3-030-93936-6_6
9. Yadav, S., Kumar, S., and Haritash, A.K., Solar light and ultrasound-assisted rapid Fenton's oxidation of 2,4,6-trichlorophenol: Comparison, optimization, and mineralization, *Rend. Lincei, Sci. Fis. Nat.*, 2023, vol 34, pp. 1197–1207.
https://doi.org/10.1007/s12210-023-01192-y
10. Verma, M., and Haritash, A.K., Degradation of amoxicillin by Fenton and Fenton-integrated hybrid oxidation processes, *J. Environ. Chem. Eng.*, 2019, vol 7, no. 1, p. 102886.
https://doi.org/10.1016/jjece.2019.102886
11. Bolton, J.R., Bircher, K.G., Tumas, W., and Tolman, C.A., Figures-of-merit for the technical development and application of advanced oxidation technologies for both electric- and solar- driven systems (IUPAC Technical Report), *Pure Appl. Chem.*, 2001, vol 73, no. 4, pp. 627–637.
https://doi.org/10.1351/pac200173040627
12. Bates, L.S., Waldren, R.P., and Teare, I.D., Rapid determination of free proline for water-stress studies, *Plant Soil*, 1973, vol. 39, no. 1, pp. 205–207.
13. Bagbi, Y., Sarswat, A., Mohan, D., Pandey, A., and Solanki, P.R., Lead and chromium adsorption from water using L-cysteine functionalized magnetite (Fe_3O_4) nanoparticles, *Sci. Rep.*, 2017, vol. 7, no. 1, p. 7672,
https://doi.org/10.1038/s41598-017-03380-x
14. Verma, M., and Haritash, A.K., Photocatalytic degradation of Amoxicillin in pharmaceutical wastewater: A potential tool to manage residual antibiotics, *Environ. Technol. Innovation*, 2020, vol. 20, pp. 101072.
https://doi.org/10.1016Zj.eti.2020.101072
15. Thind, P.S., Kumari, D., and John, S., TiO_2/H_2O_2 mediated UV photocatalysis of Chlorpyrifos: Optimization of process parameters using response surface methodology, *J. Environ. Chem. Eng.*, 2018, vol. 6, no. 3, pp. 3602–3609.
https://doi.org/10.1016/jjece.2017.05.031
16. Sharma, A., Verma, M., and Haritash, A.K., Degradation of toxic azo dye (AO7) using Fenton's process, *Adv. Environ. Res.*, 2016, vol. 5, no. 3, pp. 189–200,
https://doi.org/10.12989/aer.2016.5.3.189
17. Anandan, S., Ponnusamy, V.K., and Ashokkumar, M., A review on hybrid techniques for the degradation of organic pollutants in aqueous environment, *Ultrason. Sonochem.*, 2020, vol 67, p. 105130.
https://doi.org/10.10167j.ultsonch.2020.105130
18. Ortiz, I., Rivero, M.J., and Margallo, M., Advanced oxidative and catalytic processes, in *Sustainable Water and Wastewater Processing*, Amsterdam: Elsevier, 2019, pp. 161–201.
https://doi.org/10.1016/B978- 0-12-816170-8.00006-5
19. Polprasert, C., and Khatiwade, M.R., An integrated kinetic model for water Hyacinth ponds used for wastewater treatment, *Water Res.*, 1998, vol. 32, no. 1, pp. 179–185.
https://doi.org/10.1016/S0043-1354(97)00191-7
20. Nesir, N., Potential use of water hyacinth *(E. crassipes)* for wastewater treatment in Serbia. http://www.balwois.com/balwois/administration/full-paper/ffp-623.pdf. Accessed January 13, 2024.
21. Gamage, N.S., and Yapa, P.A.J., Use of water hyacinth (*Eichhornia crassipes* (Mart.) Solms) in treatment systems for textile mill effluents. A case study, *J. Natl. Sci. Found., Sri Lanka*, 2001, vol. 29, nos. 1–2, pp. 15–18.
22. Lekshmi, P.D., Watson, A.S., and Bai, R.S., A study on the physiological and biological responses of *Eichhornia crassipes* (Mart.) Solms in relation to pollution stress, *Plant Physiol. Rep.*, 2022, vol. 27, no. 2, pp. 308–320.
https://doi.org/10.1007/s40502-022-00648-x

23. Smirnoff, N., Ascorbic acid: Metabolism and functions of a multi-facetted molecule, *Curr. Opin. Plant Biol.*, 2000, vol. 3, no. 3, pp. 229–235.

Publisher's Note. Allerton Press remains neutral with regard to jurisdictional claims in published maps and institutional affiliations.
AI tools may have been used in the translation or editing of this article.

Arabian Journal for Science and Engineering
https://doi.org/10.1007/s13369-025-10114-z

RESEARCH ARTICLE-ELECTRICAL ENGINEERING

Investigation on Impact of Inverter-Based Resources on Power System Using Phasor Measurement Unit

Nitisha Sudhir Darwade[1] · **S. T. Nagarajan**[1]

Received: 20 November 2024 / Accepted: 27 February 2025
© King Fahd University of Petroleum & Minerals 2025

Abstract
Integration of inverter-based resources (IBRs) in power system is the necessity of present power system. With IBR rapidly integrating into the grid in last few decades has raised challenges in the power system to maintain stability. There is necessity to investigate dynamic stability due to the integration of IBR to mitigate the negative impacts on the system. Motivated by the challenges of integrating IBR in power system, a comprehensive investigation on several aspects of stability has been carried out. Responses of integrating IBR on various benchmarks have been analysed in time domain with phasor measurement unit (PMU). The results of the investigation indicate indirect effect on stability by reduction in system inertia and direct effect on protection settings. To investigate the phenomenon which are of interest in few microseconds to milliseconds, EMT simulations have to be performed. Therefore, simulation studies have been carried out in real time step of 50μseconds using EMTP–RV and OPAL RT simulator with HYPERSIM environment on benchmark systems of nine-bus system, single-machine system and Kundur's two-area system with photovoltaic generator (PV).

Keywords Renewable energy source (RES) · Synchronous generator (SG) · Photovoltaic (PV) · Transmission system operators (TSO) · Inverter-based resources (IBRs) · Kinetic energy (K.E) · Phasor measurement unit (PMU)

1 Introduction

Integration of inverter-based renewable energy sources (IBRs) in power grids has led to the renewed research of stability in power systems [1]. Conventionally, stability of a power system is described as the capacity of an electric power system to revert to a state of operational equilibrium after exposure to a disturbance [2]. Broadly, the multiple forms of stability may be classified as voltage stability, frequency stability, and rotor angle stability. The frequency and rotor angle stability are strongly connected to the active power imbalance, while voltage stability is related to the reactive power imbalance in the system. The stability of the power system is also dependent on the type of disturbance in the system; for significant disturbance, it is described as transient stability, and for minor perturbations, it is defined as small signal stability [1, 2].

The conventional classification of stability is presently undergoing a revision to integrate the stability challenges produced by the integration of IBR in the system, which has been introduced as resonance and converter-driven stability. Initially, the IBRs were being incorporated into the distribution system and had no significant influence on the overall stability of the power system. However, with the integration of large IBRs in transmission networks the stability of the power system is being compromised owing to the lack of normal synchronous generator behaviour during disturbance in the system [3]. Furthermore, the integration of IBRs has a direct effect on the factors that determine the stability of the system, like inertia, fault currents, oscillatory modes of the system, and power quality concerns such as voltage flicker and distortion [4–6].

Upon literature survey, various studies have been carried out to verify the influence of IBR on power system stability. The primary factors that have been explored in the literature include frequency, rotor angle, voltage, current, distance protection, directional protection, and differential protection scheme [5, 7, 8]. Among them, the influence of IBR on inertia, power oscillations, and protection is a key source of concern about the stability of the system. Earlier, the integration of

✉ Nitisha Sudhir Darwade
nitishasudhirdarwade_2k21phdee11@dtu.ac.in

[1] Department of Electrical Engineering, Delhi Technological University, Delhi, India

Published online: 19 March 2025

IBR was thought to be the major cause of decrease in the inertia of the system owing to which stability is affected [9].

Further in the literature research, the relevance of inertia in the power system has been comprehensively defined, and the influence of IBR in the power system-related stability has been studied in reports [4, 9], The impact of IBR has been explored by altering the inertia of the generator or by incorporating IBR into the system. Researchers have evaluated the effects of decreased inertia and the effect of integration of IBR on frequency by examining different under-frequency load-shedding situations of the power systems [4]. Andreas et al. exhibit the integration of IBR in the grid in the previous several years, due to which the inertia of the power system has been decreased.

The following literature mainly dealt with the frequency fluctuation and oscillation in power systems due to reduction of inertia with the integration of IBR. Son et al. [10] derived the relationship between nadir frequency and inertia using Frequency Nadir Index (FNI). Atia and Jovica [11] replicate several IEEE standard benchmark systems by including IBR in order to demonstrate the influence of energy storage on frequency response. Andreas et al. [12] studied inter-area oscillations in case of fault by lowering the inertia of the generator in a two-area system. Liu et al. [13] examined the influence of virtual network inertia on power oscillation by producing power via several types of IBR at various locations of two-area systems. Xu et al. [14] showed the influence of decreased system inertia on primary frequency response and local area mode oscillations of small-scale systems and large-scale synthetic models. You et al. [15] examined the influence of integration of PV on inter-area mode oscillation and found that with the integration of PV in the system, oscillating frequency rises and mode shape gets modified and may develop new oscillatory modes. Zhou et al. [16] worked on low-frequency oscillations of power electronics-interfaced photovoltaic power plants. This virtual synchronous generator (VSG) has been added to inherit virtual inertia and damping to increase the stability of the system. Agrawal et al. [17] researched on the power systems to investigate primary frequency response and oscillatory modes by lowering the value of inertia and substituting SG with a wind generator. These research papers focus on multiple aspects of the impact of IBR in the power system. However, most literature considers study on the microgrids, while larger grids have not been considered. Dynamics of the system in the real power system has been neglected, and most of the simulation studies have not been considered either in real-time simulator or in practical scenarios. Also, study has not been expanded to illustrate the influence of IBR by adopting IBR alone or in combination with synchronous generators in the system.

In addition to inertia, the impact of IBR on protection has been studied further in the literature [18]. Yijing Liu et al. [19] investigated the ACTIVSg200 synthetic network to assess the influence of inertia on the critical clearing time of the fault. Chowdhury and Fischer [20] demonstrated the malfunctioning of transmission line protection in the presence of IBR in the system. Haddadi et al. [21] predicted malfunctioning of distance and differential protection methods with the incorporation of IBR in the system. Hooshyar et al. [7] studied the influence of IBR on short-circuit current and impedance followed by failures in the system. Mishra et al. [22] studied negative sequence current response in the presence of IBR and presented a strategy for distance protection. Grande et al. [23] exhibited the difference in the response of voltage and current generated by integration of IBR in the system. However, the above literature studies are deficient to validate comprehensive protection studies for hybrid systems that incorporate various renewable energy sources, conventional generating, and storage integration.

Conventionally, the study of dynamics of power systems impacted by IBRs was mostly based on local measurements. Recently, phasor measuring units (PMUs) are extensively being employed to measure and communicate voltage, current, frequency, and rate of change of frequency (ROCOF) for wide area measurement systems (WAMS). Furthermore, PMUs are capable of detecting the dynamics in power systems under steady state and transient circumstances [24]. Due to variation in inertia of power systems due to IBRs, estimating inertia is vital in the grid linked to various kinds of generating power systems, about which new research has been carried out to examine the system and its influence on the power system. Ashton et al. [25] examined frequency response by employing a phasor measuring unit (PMU) for change of inertia of the generator. Bagher and Hosien [26] determined inertia utilizing the response of frequency deviation with respect to time using PMUs. Panda et al. [27] determined distinct values of inertia constant utilizing unique responses of ROCOF gathered from PMUs of different locations. Kerdphol et al. [28] computed inertia by evaluating the frequency spectra and mode morphologies of the data collected from the PMU.

This research study proposes a systematic technique to assess the impact of inertia on stability as well as on protection and inter-area modes with PMUs. A complete simulation research has been undertaken on multiple benchmark systems considering various circumstances. Simulation investigations have been conducted out in real time employing EMTP-RV and OPAL RT real-time simulator. HYPERSIM software has been applied to simulate IEEE benchmark nine-bus system, single-machine infinite bus system and Kundur's two-area systems. The basic notion of this work derives from the influence of the system's inertia on stability and protection in a larger sense. The research study primarily focuses on the influence of inertia of the system H_{system} on frequency, bus voltage phase angle, fault current, and inter-area oscillation, which have been explored using PMU measurements.

To summarize,

- This research study examines the impact of reduced system inertia H_{system} on frequency response.
- The impact of low inertia on critical clearing time has been experimentally validated.
- Fault current for different values of power generation from IBR under different fault conditions has been investigated.
- Further, this study analyses the inter-area mode oscillation of power in the presence of IBR in the system.
- Overall, a comprehensive study on the impact of IBR interaction in power systems on major aspects of stability has been carried out.

The remaining paper has been arranged in Sects. 2, 3, 4 and 5. Section 2 covers the relationship between power system inertia, protection setting, and stability. In Sect. 3, PV farm and phasor measurement unit have been discussed briefly. In Sect. 4, three case study systems have been simulated for various scenarios to verify the effect of reducing inertia on system stability. Obtained results have been discussed in graphs and tabular form. Section 5 concludes this study.

2 Relation between Power System Inertia, Protection setting and Stability

During active power disturbance in the power system, the frequency deviates from its nominal value. Normally, the frequency of the system shall be restored by governor control setting of the generator. However, response of the governor is normally delayed by few seconds to restore the system frequency. Therefore, there is a steep change in the frequency of the system which is restricted by the release of kinetic energy from rotor masses of generator. In literature, kinetic energy of the system is represented in terms of generating capacity defined as the ratio of kinetic energy stored to the rating of generator denoted as H [29]. The mathematical representation of H can be expressed in the following subsection.

2.1 Expression of Power System Inertia

The inertia constant H of a synchronous machine is defined as the time in seconds for which the machine can supply its rated power from its stored kinetic energy in the rotor [30]. Inertia can be calculated as,

$$\boldsymbol{H} = \frac{1}{2}\frac{\boldsymbol{J}\boldsymbol{\omega}_{\boldsymbol{n}}^2}{\boldsymbol{S}_{\boldsymbol{n}}}[\mathrm{s}] \tag{1}$$

where J is the moment of inertia of a generator and turbine [kg/m^2],$\boldsymbol{\omega_n}$ is the rated mechanical angular velocity of the rotor [rad/s], and S_n is the rated apparent power of the generator [VA].

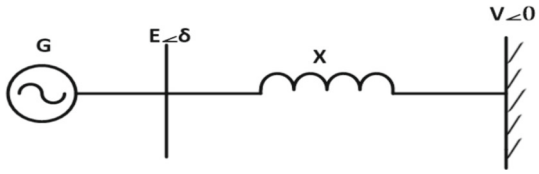

Fig. 1 Single-machine infinite bus system

The aggregate equivalent inertia $\boldsymbol{H_{sys}}$ of power system can be defined as time for which system can supply its rated power from its stored kinetic energy in the rotor. Aggregated inertia of power system can be calculated by using inertia of individual turbine generator [31]

$$\boldsymbol{H}_{\boldsymbol{sys}} = \frac{\sum_{i=1}^{N}\boldsymbol{S}_{\boldsymbol{ni}}\boldsymbol{H}_{\boldsymbol{i}}}{\boldsymbol{S}_{\boldsymbol{n,sys}}}[\mathrm{s}] \tag{2}$$

where

$$\boldsymbol{S}_{\boldsymbol{n,sys}} = \sum_{\boldsymbol{i}=1}^{\boldsymbol{N}}\boldsymbol{S}_{\boldsymbol{ni}}[\mathrm{MVA}] \tag{3}$$

S_{ni} is the rated apparent power of generator i [MVA], H_i is the inertia constant of turbine generator i [s], and i is the number of synchronous generators.

2.2 Relation of Inertia with Bus Phase Angle Difference of Voltages and Critical Clearing Time

The impact of inertia in the power system can be observed from a system shown in Fig. 1, where the power transfer through transmission line by a synchronous generator in terms of bus voltages and bus phase angle between the buses can be expressed as in Eq. (4). [32],

$$\mathrm{P} = \frac{EV}{X}Sin\delta \tag{4}$$

where δ is phase angle difference of voltage. Generator rotor angle can be considered to be the same as generator bus voltage angle if the generator stator reactance is neglected. The dynamics introduced in the system during disturbance in the system can be expressed in terms of swing Eq. (5). It can be observed that the rate of change of generator rotor angle is dependent on the inertia H of the system.

$$\frac{\mathrm{d}^2\delta}{\mathrm{dt}^2} = \frac{\pi f}{2H}(\mathrm{Pm}-\mathrm{Pe}) \tag{5}$$

The critical clearing time can be evaluated be equal area criterion (EAC) plotted in Fig. 2.

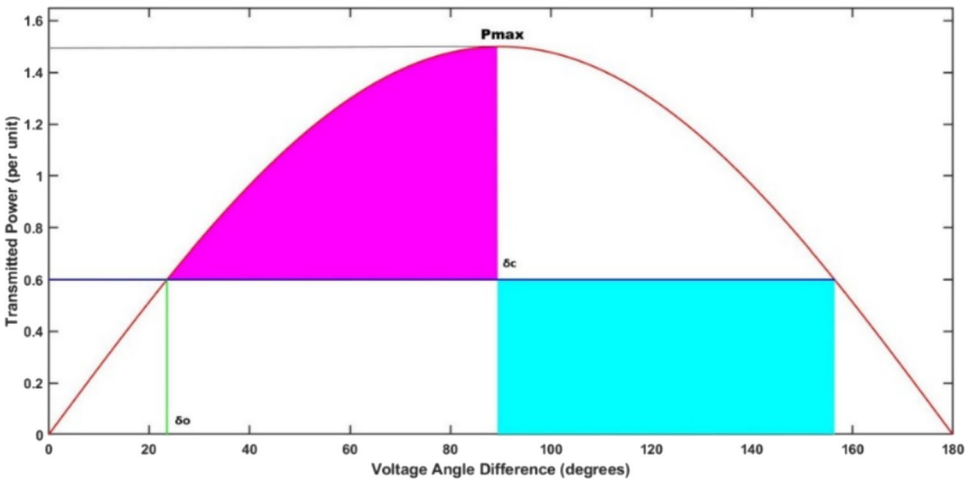

Fig. 2 EAC for three-phase fault

Critical clearing time to clear the fault can be deduced as (7) [32],

$$\mathrm{tc} = \sqrt{\frac{2H(\delta_c - \delta_0)}{\pi f_0 P_\mathrm{m}}} \tag{7}$$

where t_c = critical clearing time, H = inertia of system, δ_c = critical clearing angle, δ_0 = initial operating angle, and P_m = mechanical input power. Reduced inertia decreases critical clearing time which in turn affects the protection relay settings and stability. As the generation with IBR is largely intermittent in nature, it is inconvenient to change setting of protection relays differently for conventional synchronous generator and IBR. Thus, protection of the system is one of the major concerns with IBR [15, 18, 20, 21].

3 PV Farm Implementation and PMU

3.1 Photovoltaic Farm Implementation

PV and wind farm have a large share in IBR generation of present power systems across the world. In this study only PV farms have been integrated in simulation studies as IBR generation. In simulation studies a detailed representation of PV has been considered. Block diagram representation for PV generation system and schematic diagram for PV farm connected to grid are shown in Fig. 3a and b.

PV generating system block comprises PV array connected to an inverter through a boost converter and RL choke filter which is used to limit total harmonic distortion as shown in Fig. 3a. This complete block is connected to step up transformers via point of common coupling PCC and then through a feeder line and three-winding transformer to the grid as shown in Fig. 3b. This scheme has been developed and controlled on OPAL RT HYPERSIM and EMTP-RV real-time simulator to form a PV farm.

3.2 Phasor Measurement Unit (PMU)

Recently, phasor measurement unit (PMU) is being installed on large scale for wide area measurement systems (WAMSs) to measure electrical quantities during steady and transient state [33]. As per IEEE C37.118.1–2011, PMU gets analog signals of voltage and current and estimates phasor, positive sequence component of voltage and current, and frequency and rate of change of frequency (ROCOF). All these electrical quantities are time stamped by referring to the Universal Time Coordinate (UTC) as a standard; Global Positioning Satellite (GPS) communication is used to synchronize these time stamped data [34]. Functional block diagram of a PMU is as represented in Fig. 4.

In this study, two PMUs have been used to measure rotor angle in a single-machine infinite bus model. Bus voltage phase angle difference can be measured by utilizing Eq. (8).

$$\delta = E\angle\mathrm{PMU1} - V\angle\mathrm{PMU2} \tag{8}$$

where PMU1 is used to measure phase angle of generator side bus and PMU2 is used to measure load side bus.

4 Case Studies: Impact of Reducing Inertia on System Stability

In this section, an investigation on the impact of inertia on power systems with three case studies has been performed considering various scenarios in each case.

- Case I: The role of kinetic energy on load changes on nine-bus benchmark systems has been investigated.

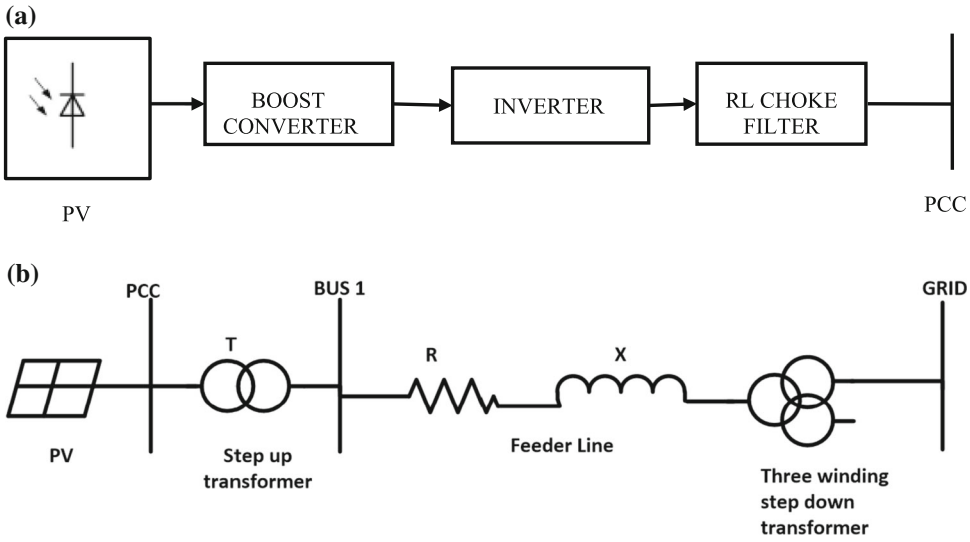

Fig. 3 **a** Block diagram of photovoltaic generation system, **b** schematic diagram for PV farm connected to grid

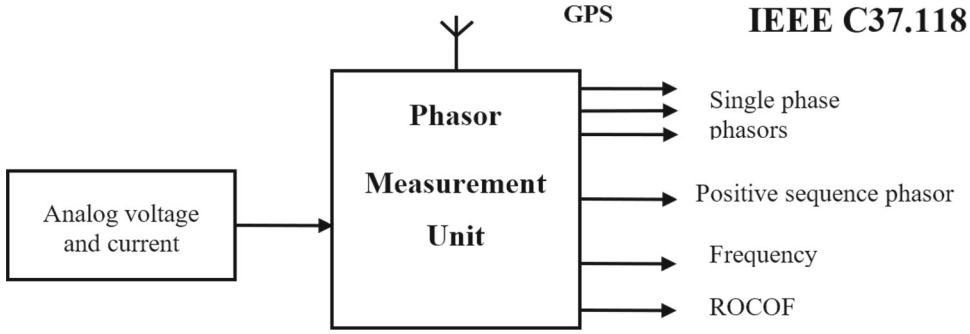

Fig. 4 Block diagram of phasor measurement unit

- Case II: The impact of inertia on fault current and rotor angle on single-machine infinite bus has been analysed.
- Case III: The impact of IBR on power oscillations in Kundur's two-area system has been studied.

4.1 CASE I: Role of Kinetic energy on Load Changes

Nine-bus benchmark system [31] shown in Fig. 5 has been simulated on OPAL–RT HYPERSIM real-time simulator. Nine-bus system consists of three synchronous generators of rating 512MVA, 270 MVA and 125MVA, respectively, connected to three transformers to make the system operate at constant voltage of 230 kV. Three loads A, B, and C placed at bus, respectively, 5, 6, and 8 consume 315 MW. Generator 1 is considered to be swing bus inertia of which is assumed to be constant at 4.112 s. Inertia of generator 2 and 3 has been varied step by step in the range of 1–9 s to study its impact on the frequency response of the system. The same phenomenon has been verified by integration of PV in the system. The time step for simulation is kept at 50μseconds, and sampling rate is 20000samples/seconds. Load flow has been performed for initialization, and simulation has been carried for 50 s. The data of the system have been considered from ref [31].

Under this case, four scenarios have been considered to analyse impact on kinetic energy in the system.

- In scenario I: Inertia of generator SG2 has been varied and frequency response has been studied.
- In scenario II: Inertia of generator SG3 has been varied and frequency response has been studied. A comparison study of frequency and time to reach nadir frequency for generators SG2 and SG3 has been performed.
- In scenario III and IV detailed PV farms have been incorporated at generator bus 2 and bus 3 to analyse and verify frequency response.

4.1.1 SCENARIO I: Inertia Variation of SG2

In this scenario, the inertia of SG1 and SG3 is considered at 4.112 s, whereas inertia constant H of SG2 has been varied from 1 to 9 s and an additional 50 MW load at bus 8 has been applied at 1 s to analyse its impact on frequency response. The frequency response of the system is plotted in Fig. 6. It can be observed that, with the increase in load

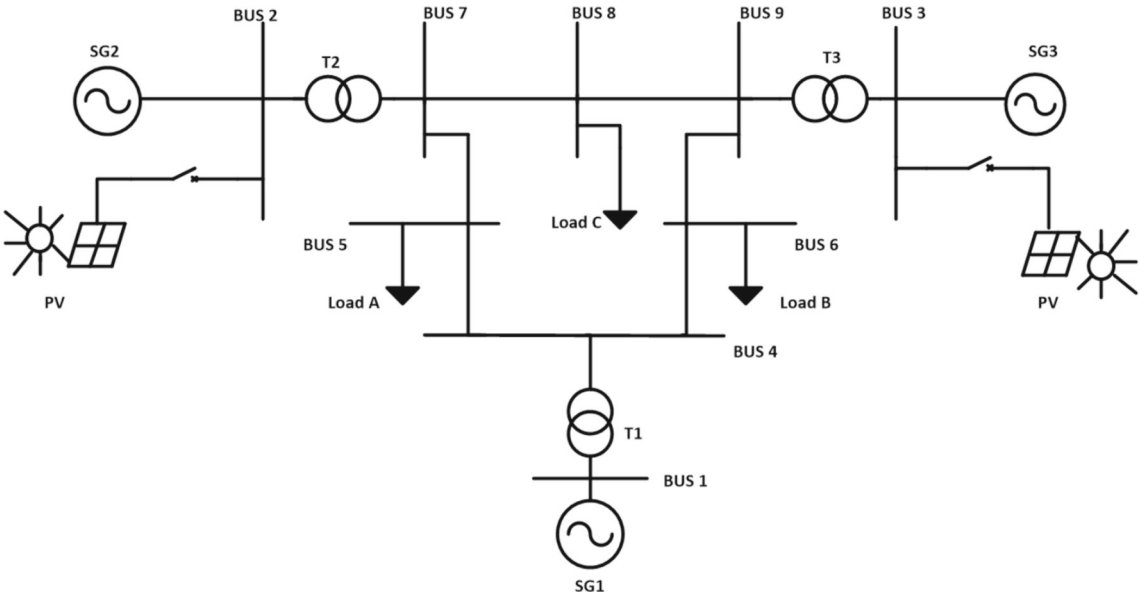

Fig. 5 Nine-bus systems

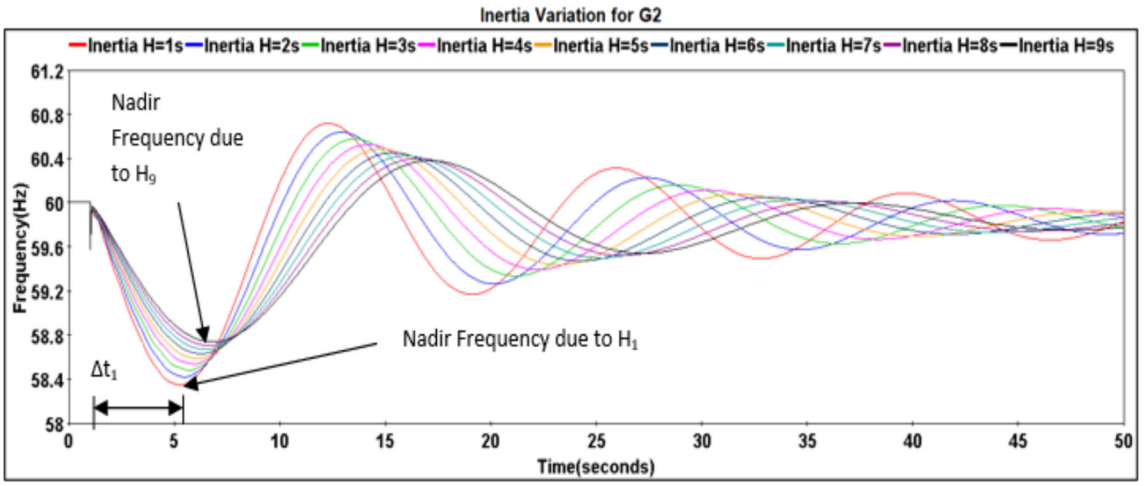

Fig. 6 Frequency plot at bus 8 with respect to time

Table 1 Nadir frequency and time to reach Nadir frequency

Sr. No	Inertia (seconds)	Scenario 1		Scenario 2	
	G2 for scenario 1 and G3 for scenario 2	Frequency Nadir (Hz)	Time to reach nadir frequency Δt (seconds)	Frequency nadir (Hz)	Time to reach nadir frequency Δt (seconds)
1	1	58.3479	4.24119	58.4653	4.62766
2	2	58.4179	4.48543	58.4930	4.74511
3	3	58.4794	4.67941	58.5170	4.86318
4	4	58.5368	4.92199	58.5403	4.98433
5	5	58.5878	5.11465	58.5628	5.02803
6	6	58.6316	5.26944	58.5856	5.05994
7	7	58.6706	5.42420	58.6069	5.13875
8	8	58.7068	5.57900	58.6276	5.17682
9	9	58.7398	5.79476	58.6472	5.21732

at 1 s, frequency drops till nadir frequency and gets recovered. However, nadir frequency changes with respect to the magnitude of inertia constant H. It is clearly observable that nadir frequency decreases at faster rate with the reduction in inertia. Results of the simulation are taken to further explain the behaviour of response from Fig. 6. Nadir frequency is the lowest point of frequency and Δt is the time to reach nadir frequency after the application of disturbance. When $H = 9$ s, frequency drops to 58.7398 Hz and $\Delta t\ 9 = 5.79476$ s, while with $H = 1$ s frequency goes to 58.3479 Hz and $\Delta t1 = 4.24119$ s. Corresponding values for complete range of H for 1 – 9 s are tabulated in Table 1.

4.1.2 SCENARIO II: Inertia Variation of SG3

Same type of disturbance as in scenario I has been applied to bus 8 at 1 s. Here, inertia of SG1 and SG2 is assumed to be constant at 4.1112 s, whereas inertia of generator SG3 is varied from 1 to 9 s. Corresponding frequency response plot of the system is observed in Fig. 7. For $H = 9$ s frequency drops to 58.6472 Hz and $\Delta t9 = 5.21732$ s, whereas for $H = 1$ s frequency decreased to 58.4653 Hz and time taken $\Delta t_1 = 4.62766$ s. Observed response data for H of 1–9 s are tabulated in Table 1. In Table 1 the second column indicates the value of inertia G2 for scenario 1 and that of G3 for scenario 2.

So, it is evident that when load increases on the system the frequency drops, but the system with higher inertia frequency decreases slowly. Nadir frequency and time to reach nadir frequency depend on inertia of the system.

4.1.3 Comparison for Scenario I and II

A comparison plot of frequency response of SG2 and SG3 for inertia variation, nadir frequency and time to reach nadir frequency is shown in Fig. 8.

For the same inertia value, the frequency responses of SG2 and SG3 are different because of the different MVA ratings of individual generators. The MVA rating of SG2 is 270 MVA, and SG3 is 125 MVA, so the effect on H_{system} by generator SG2 will be more impactful on the system than SG3. Therefore, the nadir frequency variation response is wider in the case of SG2. Hence, it can be augmented that frequency response doesn't depend only upon the inertia of an individual generator, but it responds according to the whole inertia of the system.

Table 2 represents total inertia of the system for 18 combinations in which MVA rating and inertia are constant for G1, while inertia of G2 and G3 varied one at a time; accordingly, inertia of the whole system has been calculated**.** From Table 2, when G1 = 512MVA, G2 = 270 MVA, G3 = 125 MVA, H1 = 4.112 s, H2 = 1 s, H3 = 4.112 s,

So, H1G1 = 2105.34MVA.s, H2G2 = 270, MVA.s, H3G3 = 514 MVA.s, $H_{system} = 3.1856$ s.

In a similar manner H_{system} has been estimated for the rest of combinations.

Data from Table 2 have been utilized to plot Fig. 9. Plot represents nadir frequency with respect to H_{system}, and nadir frequency decays with respect to H_{system}. So, it can be augmented that H_{system} changes not only with respect to inertia of an individual generator but with inertia of whole system. If the inertia of each individual generator is known, H_{system} can be estimated for the whole system which will be useful to prevent under-frequency load shedding (UFLS).

4.1.4 SCENARIO III: Replacement of SG2 with PV

In order to verify the observations of scenario I and scenario II, a PV farm has been implemented at bus 2. SG2 has been replaced with five small generators of equal rating and one small generator has been tripped off at a time to reduce power flow of synchronous generator and generate the same power flow in the system through PV. 50 MW load at bus 8 is added at 5 s, and its frequency response is plotted in Fig. 10. PV has been incorporated in the range of 20–80% share of SG2.

It can be analysed from Fig. 10 as the percentage of PV farm share is increased, nadir frequency decreases accordingly Δt increases and vice versa. Table 3 presents detailed study of frequency response for the given percentage share of PV with SG2. For 20% share by PV with SG2 frequency reduced to 58.3108 Hz in 5.5325 s, and with the increase in share of PV frequency decreases at faster rate.

4.1.5 SCENARIO IV: Replacement of SG3 with PV

SG3 has been replaced with five small generators of equal rating, and PV has been implemented at bus 3. 50 MW additional load has been added at bus 8 at 5 s. SG3 has been reduced percentage wise, and PV has been increased in the system in order to analyse its impact on frequency response. Frequency with respect to time for the percentage share of PV is plotted in Fig. 11.

Table 4 presents MVA rating of SG3 and PV and its response on frequency. When the percentage share of PV is 20% of total 125 MVA of SG3, frequency reduces to 59.6092 Hz in 5.28290 s as PV share increases and power supply from SG3 reduces frequency decreases at faster rate. By studying above scenarios, as load on the system increases frequency reduces but reduction in frequency is lesser with synchronous generator as compared with PV. Hence, it can be concluded that synchronous generator prevents abrupt change in frequency drop during disturbed condition and attempts to maintain frequency stability; however, with PV frequency deviates instantly. In the grid load deviates often and thus frequency stability is major concern in case of PV.

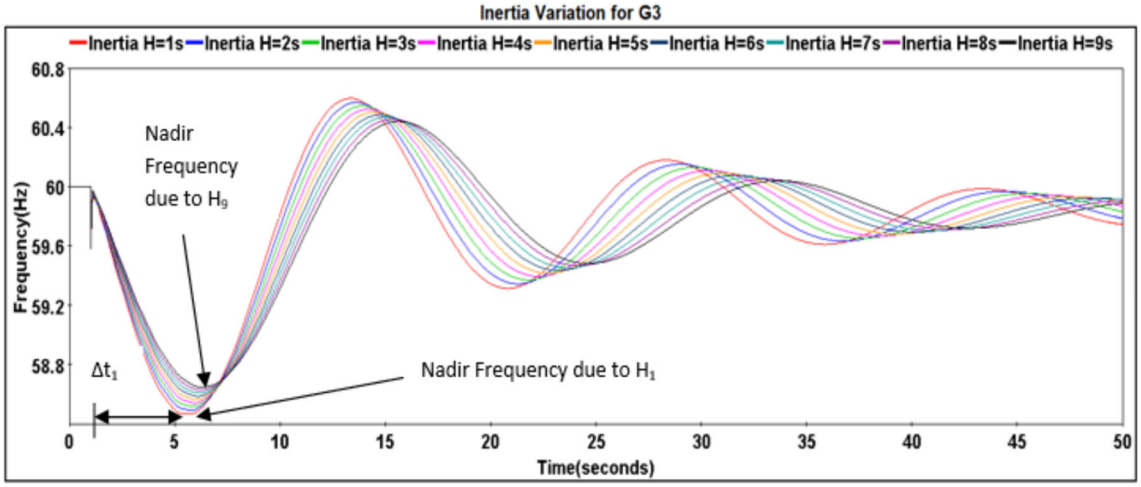

Fig. 7 Frequency plot at bus 8 with respect to time

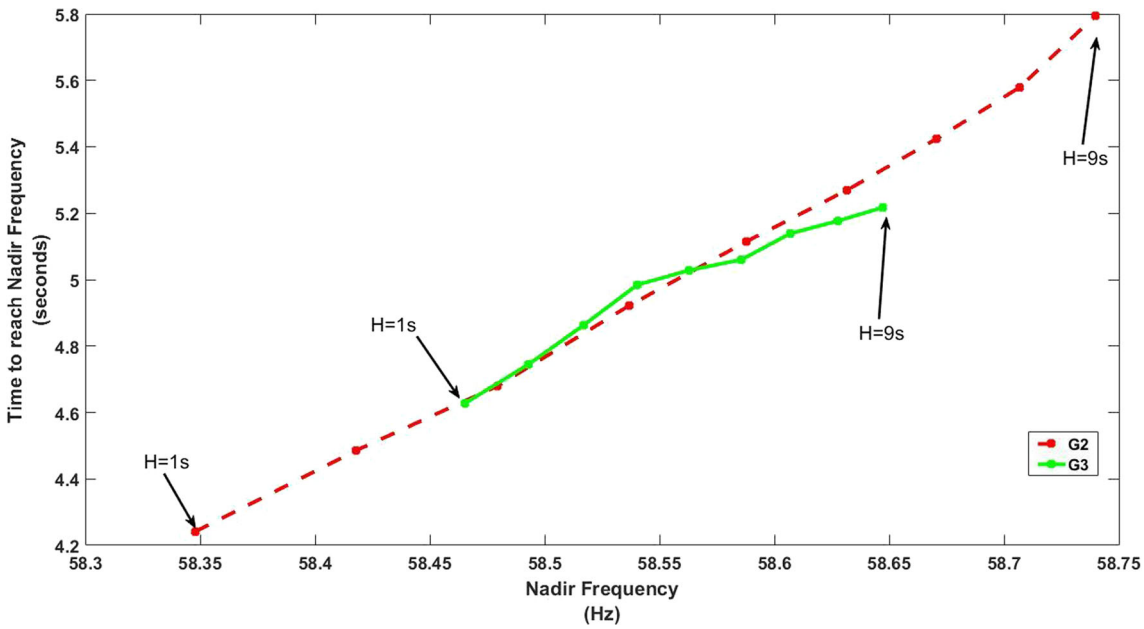

Fig. 8 Nadir frequency with respect to time for G2 & G3

Integration of IBR to power system forms more unstable and complicate power system.

4.2 CASE II: Impact of IBR on Rotor Angle Stability and Protection Relay Setting

In this case a single machine of 100 MVA feeds active power of 60 MW and reactive power 45MVAR to infinite bus through two parallel transmission lines of 100 km is shown in Fig. 12 [32]. Phasor measurement units (PMUs) have been placed across transmission lines to measure bus voltage angle. Three-phase fault (LLL) and double-phase-to-ground fault (LLG) have been considered in this case to study the impact of inertia on generator rotor angle and protection relay settings. The data of the system are given in the appendix.

Two scenarios have been considered in this case to analyse rotor angle oscillations and fault current.

Scenario I: Rotor angle oscillations has been observed after a three-phase fault with different inertia values.
Scenario II: Influence of fault current variations has been studied due to IBR on protection relay settings.

Table 2 H_{system} with variation of individual generator's inertia

Sr. No	G1 MVA	G2 MVA	G3 MVA	H_1 s	H_2 s	H_3 s	H_1G_1 MVA.s	H_2G_2 MVA.s	H_3G_3 MVA.s	H_{system}
1	512	270	125	4.112	1	4.112	2105.34	270	514	3.1856
2	512	270	125	4.112	2	4.112	2105.34	540	514	3.4823
3	512	270	125	4.112	3	4.112	2105.34	810	514	3.7810
4	512	270	125	4.112	4	4.112	2105.34	1080	514	4.0786
5	512	270	125	4.112	5	4.112	2105.34	1350	514	4.3763
6	512	270	125	4.112	6	4.112	2105.34	1620	514	4.6740
7	512	270	125	4.112	7	4.112	2105.34	1890	514	4.9717
8	512	270	125	4.112	8	4.112	2105.34	2160	514	5.2693
9	512	270	125	4.112	9	4.112	2105.34	2430	514	5.5670
10	512	270	125	4.112	4.112	1	2105.34	1110.24	125	3.6831
11	512	270	125	4.112	4.112	2	2105.34	1110.24	250	3.8209
12	512	270	125	4.112	4.112	3	2105.34	1110.24	375	3.9587
13	512	270	125	4.112	4.112	4	2105.34	1110.24	500	4.0966
14	512	270	125	4.112	4.112	5	2105.34	1110.24	625	4.2343
15	512	270	125	4.112	4.112	6	2105.34	1110.24	750	4.3722
16	512	270	125	4.112	4.112	7	2105.34	1110.24	875	4.5100
17	512	270	125	4.112	4.112	8	2105.34	1110.24	1000	4.6478
18	512	270	125	4.112	4.112	9	2105.34	1110.24	1125	4.7856

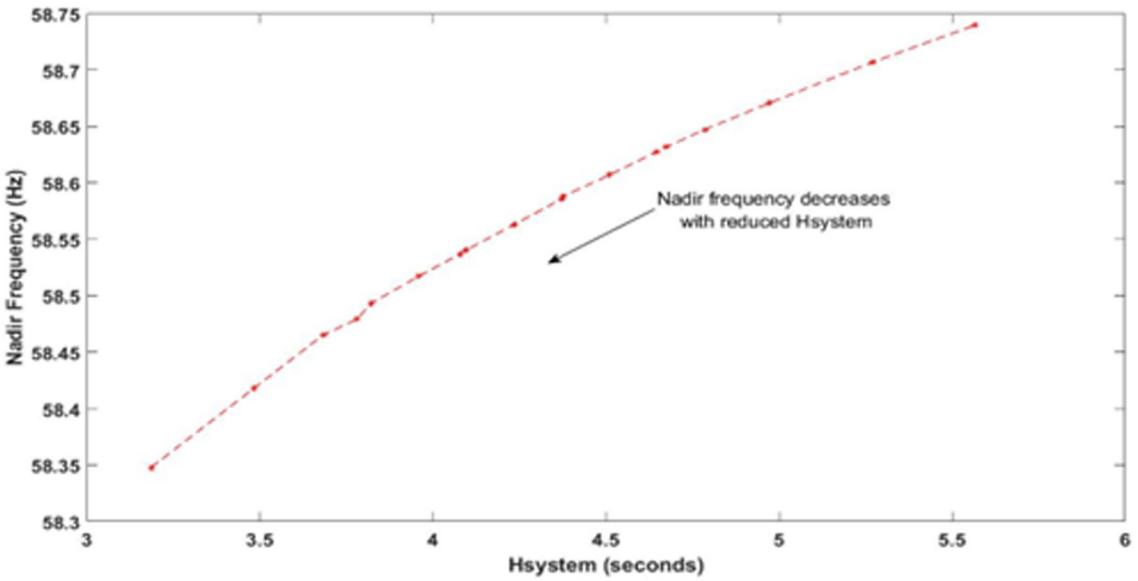

Fig. 9 Nadir frequency with respect to H_{system}

4.2.1 SCENARIO I: Effect of Inertia on Rotor Angle Stability

To analyse rotor angle behaviour with variation in inertia, this scenario has been performed. The inertia of the generator is considered as 6.112 s, and a three-phase (LLL) fault has been applied at 1 s at line 2 near bus 2. Fault is cleared after 0.39415 s with tripping of line 2. Voltage bus angle of the generator is plotted in Fig. 13. The inertia of the generator is then reduced to 3.112 s assuming a system equivalent to operating with IBR, and the bus voltage angle has been plotted in comparison with the previous case. With $H = 6.112$ s when fault occurs rotor angle oscillates and settles down after few seconds, whereas with $H = 3.112$ s rotor angle increases beyond 180° and goes out of step.

Critical clearing time is observed from Fig. 13 and calculated using Eq. (7) tabulated in Table 5. Critical clearing

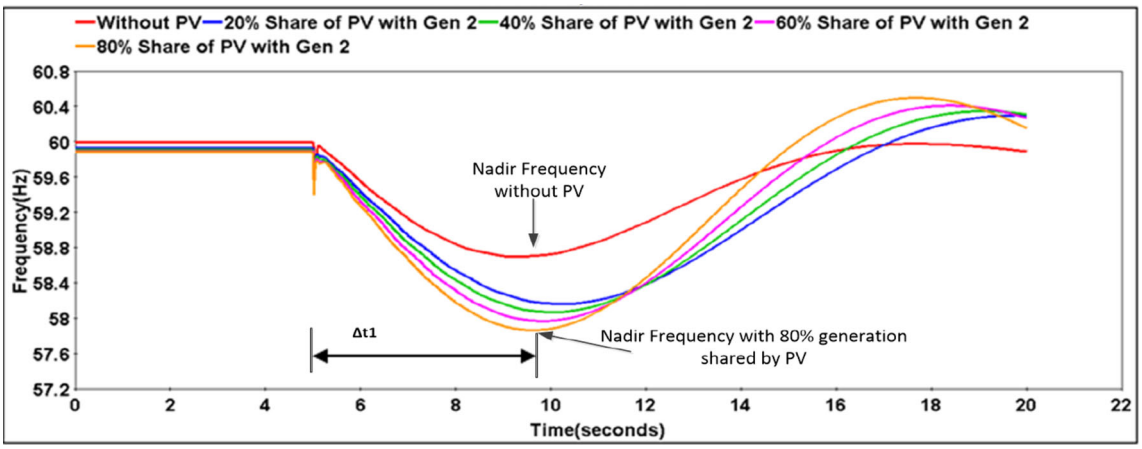

Fig. 10 PV farm connected with G2

Table 3 Nadir frequency with respect to time after implantation of PV at bus 2

Sr. no	% share of PV	MVA Rating of synchronous generator	Power of SG2 synchronous generator	MVA rating of PV	POWER of PV at bus 2	Nadir frequency (Hz)	Time to reach nadir frequency Δt (seconds)
1	20%	216MVA	130.4 MW	54MVA	32.6 MW	58.3108	5.5325
2	40%	162MVA	97.8 MW	108MVA	65.2 MW	58.3063	5.5553
3	60%	108MVA	65.2 MW	162MVA	97.8 MW	58.2994	5.5909
4	80%	54MVA	32.6 MW	216MVA	130.4 MW	58.2965	5.6027

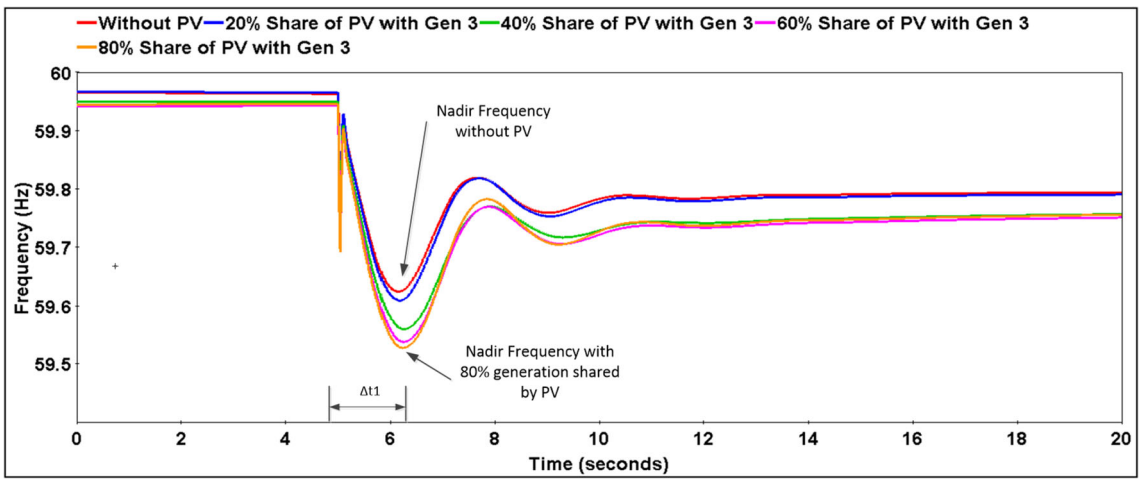

Fig. 11 PV farm connected with G3

time for a fault decreases with reduced inertia. If fault clearing time is less than critical clearing time, the rotor angle is stable, but if fault clearing time is more than critical clearing time, the rotor angle gets unstable. Thus, the change in the system's inertia could lead to an unstable condition due to the change in critical clearing time.

4.2.2 SCENARIO II: Effect of IBR on Protection Setting

To analyse the effect of IBR on relay setting, a three-phase fault (LLL) and double-phase-to-ground fault (LLG) has been applied on a single-machine infinite bus at line 2 near bus 2 at 1 s and fault cleared at 1.017 s. As shown in Fig. 14a, LLL fault is applied at 1 s, fault current starts to flow and goes beyond peak-up value and just after clearance short-circuit

Table 4 Nadir frequency with respect to time after implementation of PV at bus 3

Sr. no	% share of PV	MVA Rating of synchronous generator	Power of SG2 synchronous generator	MVA Rating of PV	POWER of PV at Bus 2	Nadir frequency	Time to reach nadir frequency Δt
1	20%	100 MVA	68 MW	25 MVA	17 MW	59.6092	5.28290
2	40%	75 MVA	51 MW	50 MVA	34 MW	59.5589	5.26425
3	60%	50 MVA	34 MW	75 MVA	51 MW	59.5372	5.24885
4	80%	25 MVA	17 MW	100 MVA	68 MW	59.5270	5.24320

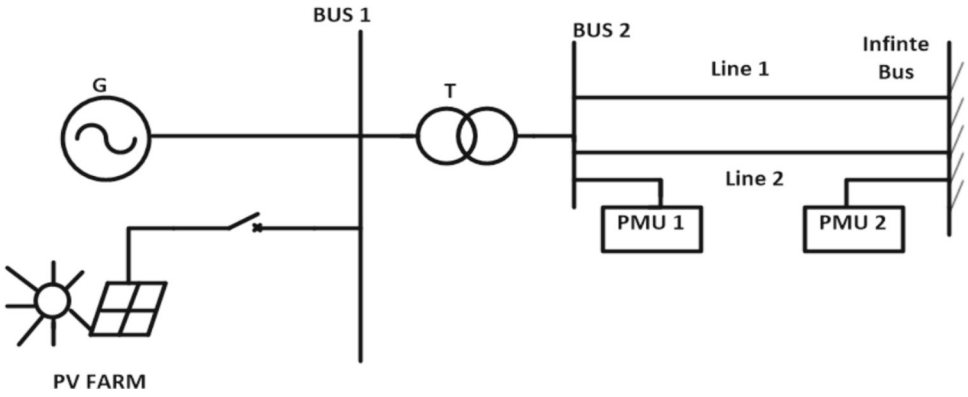

Fig. 12 Single-machine infinite bus model

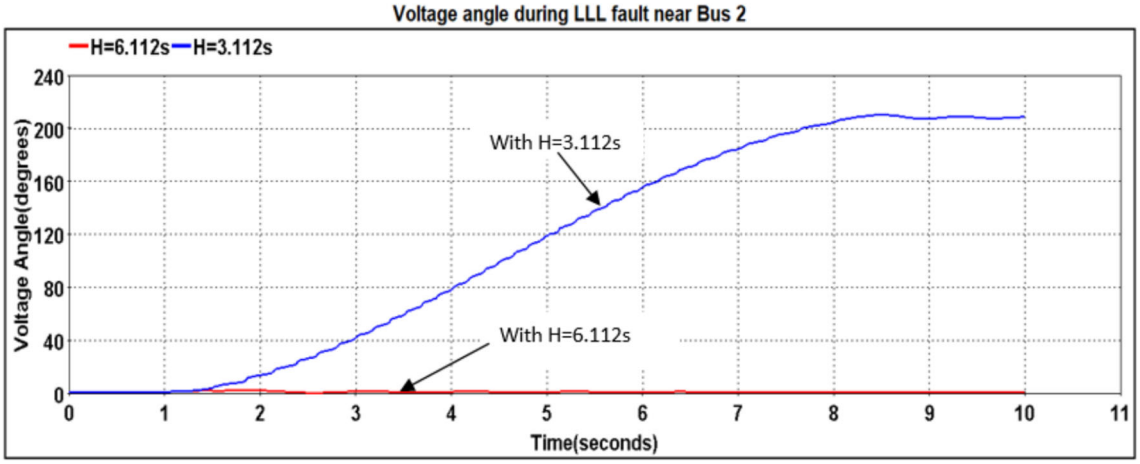

Fig. 13 Voltage angle δ during LLL fault

Table 5 Effect of inertia for a fault duration of 0.39415 s

Inertia	Critical clearing time (observed value)	Critical clearing time (calculated value)	Rotor angle
6.112 s	0.4600 s	0.347 s	Stable
3.112 s	0.3283 s	0.247 s	Unstable

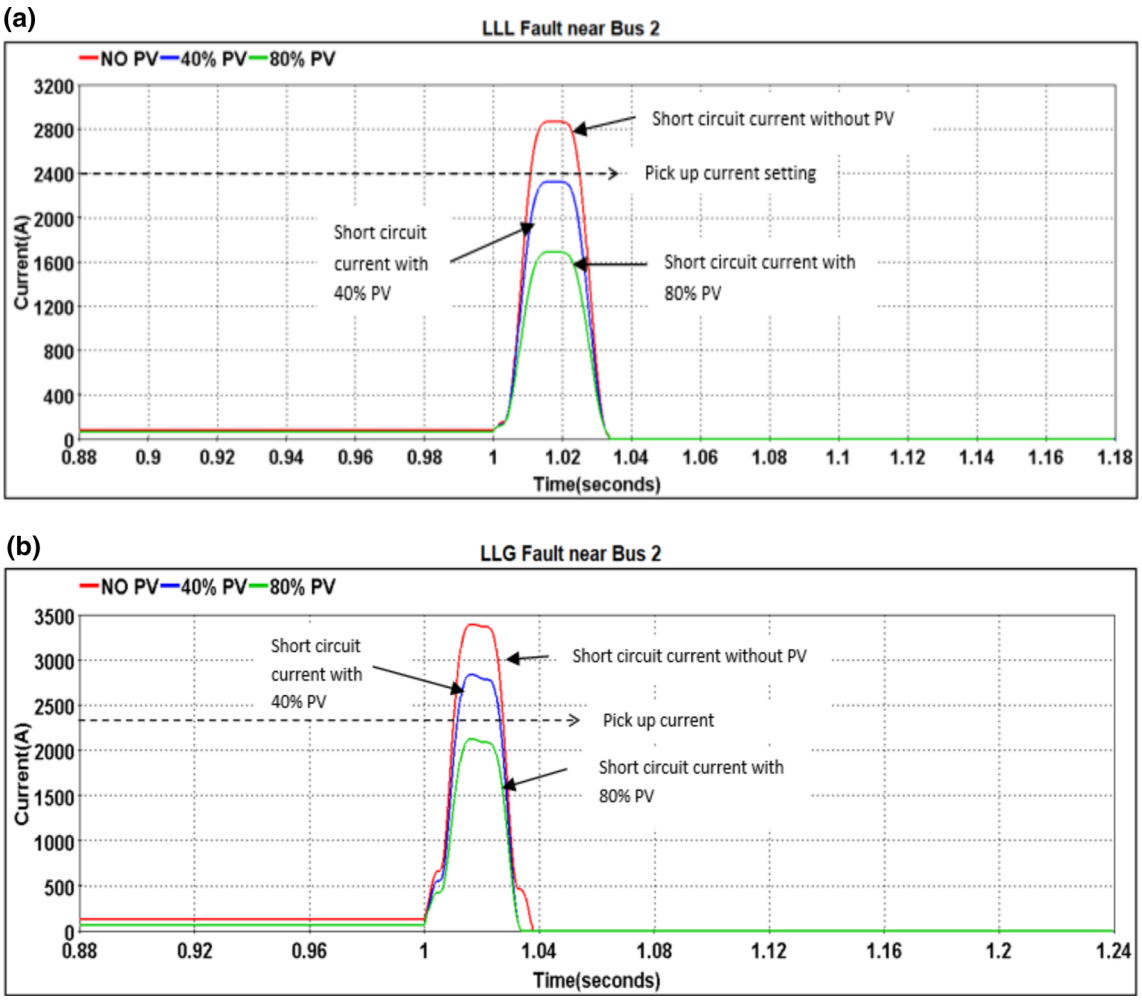

Fig. 14 **a** Response of current during LLL fault near bus 2, **b** response of current during LLG fault near bus 2

current goes to zero. However, with the integration of 40% and 80% of PV short-circuit current shall not reach pick-up current setting due to which fault may not get clear and persists in the system for long duration. From Fig. 14a it can be observed that system consists of only synchronous generator and magnitude of short-circuit current reaches 2864A. However, with 40% share of PV short-circuit current attains 2321A and with sharing of 80% short-circuit current reaches 1685A which is much lesser than short current response of conventional generators.

LLG fault is applied at line 2 near bus 2 at 1 s, and fault has been cleared at 1.017 s. As shown in Fig. 14b without PV in the system magnitude of short-circuit current reaches 3391A. However, with 40% integration of PV short-circuit current attains 2835A and with 80% integration of PV short-circuit current reaches 2118A. If pick-up current setting is 2400A as shown in Fig. 14a and b, fault current with integrating PV in the system shall not reach pick-up value of current in case of LLL fault, while in case of LLG it shall reach pick-up value with 40% but fails in case of 80% integration of PV.

By analysing above scenarios, it can be concluded that reduction of inertia affects rotor angle stability. With reduced inertia, critical clearing time reduces and thus system can get unstable before clearance of fault. Besides, integration of IBR affects amplitude of short-circuit current. As the penetration of PV increases in the grid and power sharing of synchronous generator decreases, then the magnitude of short-circuit current decreases. Resulting fault current shall not reach pick-up value of protective relay and does not get cleared, due to which the fault sustains for longer duration of time damaging the system and equipment.

4.3 CASE III: Impact of IBR on Small Signal Stability

Kundur's two-area system [31] with 75 MW PV farm as shown in Fig. 15 has been simulated in EMTP-RV real-time simulator. Results has been analysed for the effect of inertia reduction by IBR. In two-area system two modes of oscillations occur prominently: local area mode and inter-area mode of oscillation. In this study inter-area mode oscillation

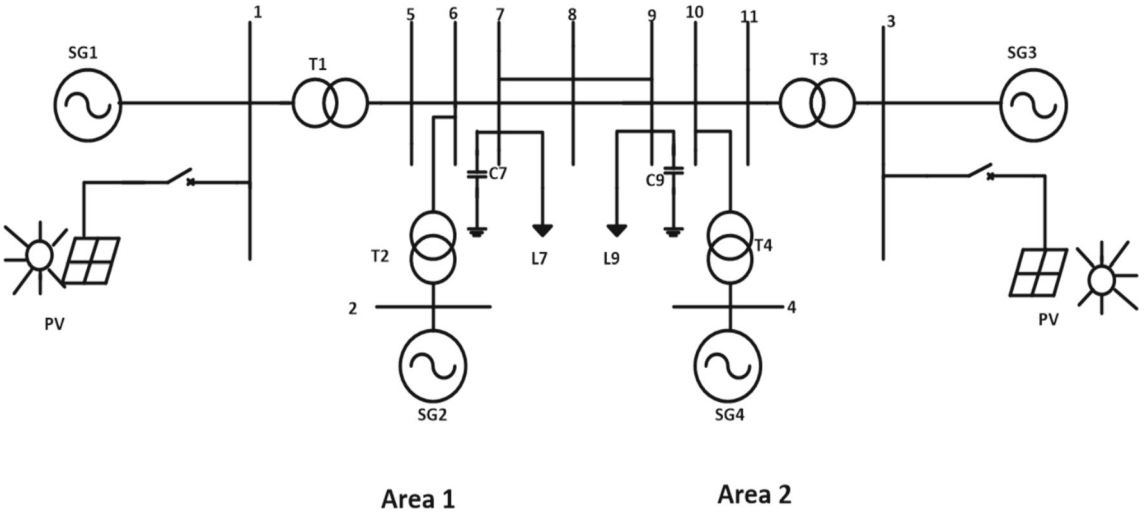

Fig. 15 Kundur's two-area system

has been observed. The system has been initialized with a transfer of 400 MW from area 1 to area 2. A three-phase-to-ground fault has been applied on a tie line near the terminal of area 1 at 3.0 s, and the fault is cleared at 3.01 s by tripping the faulted line from both the ends resulting in only one transmission line connected between the two areas.

In this case four scenarios have been studied to observe power oscillations.

- Scenario I: Without integrating PV inter-area mode oscillation has been observed.
- Scenario II: SG1 has been replaced with PV farm to observe inter-area mode oscillation.
- Scenario III: SG3 has been replaced with PV farm to observe inter-area mode oscillation.
- Scenario IV: Both SG1 and SG3 have been replaced with PV farm to observe inter-area mode oscillation

4.3.1 SCENARIO I: Without Connecting PV

Two-area system as shown in Fig. 14 has been simulated. Tie line carries 400 MW power sharing equal amount of power before fault as shown in Fig. 16. After the occurrence of fault, one line gets tripped off, then power on another line oscillates for few seconds and then it gets stabilized transmitting full amount of 400 MW power from area 1 to area 2.

4.3.2 SCENARIO II: SG1 Replaced with PV Farm

Here, SG1 has been replaced with PV in area 1, while remaining three generators supply power as previously. It has been observed that before fault both the lines carry equal amount of power as in scenario 1. After the application of fault, power increases drastically on one line; after clearance of fault one line gets tripped off, while power of another one causes unstable oscillations and leads to instability as shown in Fig. 17.

4.3.3 SCENARIO III: SG3 Replaced with PV Farm

In this scenario in area 2, G3 has been replaced with PV farm. Load in area 2 has been shared by PV; hence, tie line power shall not get affected by it causing stable power flow from area 1 to area 2 after the clearance of fault as shown in Fig. 18.

4.3.4 *SCENARIO IV:* SG1 and SG3 Replaced with PV Farm

In both the areas SG1 and SG3 are replaced by PV farm. Power of uninterrupted line oscillates after the clearance of fault leads to instability as shown in Fig. 19.

By analysing the above scenarios, it can be concluded that the tie line transmits an equal amount of power from area 1 to area 2 before the fault, even in the presence of PV, while after clearing the fault by tripping of one line another line carries full amount of power from area 1 to area 2 in the absence of PV or if PV is in area 2. When PV is in area 1, power oscillates and leads to instability [35]. With the lower inertia damping ratio gets reduced which causes more power oscillation in the tie line. The frequencies of the oscillations depend on the strength of the system and the moments of inertia of the generator rotors. Fault in area 1 causes more oscillation in area 1. Post-fault in two-area system causes inter-area oscillation due to the flow on uninterrupted line, voltage at tie line bus near area 1 being reduced which causes a reduction in load and hence generator power gets reduced. Since the torque applied to the generator rotors is constant, the torque imbalance causes the generator rotors to accelerate

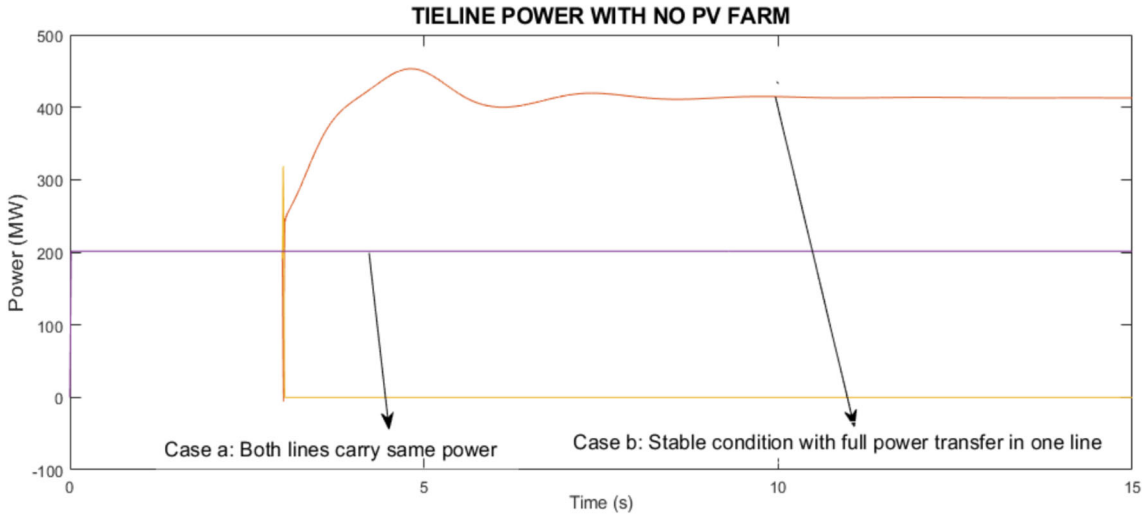

Fig. 16 Power flowing through tie line with SG

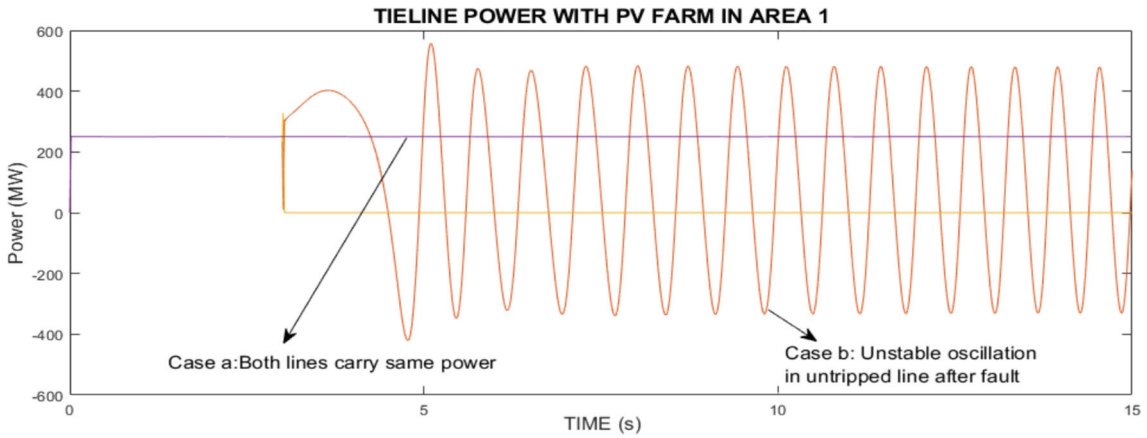

Fig.17 Power flowing through tie line with PV in area 1

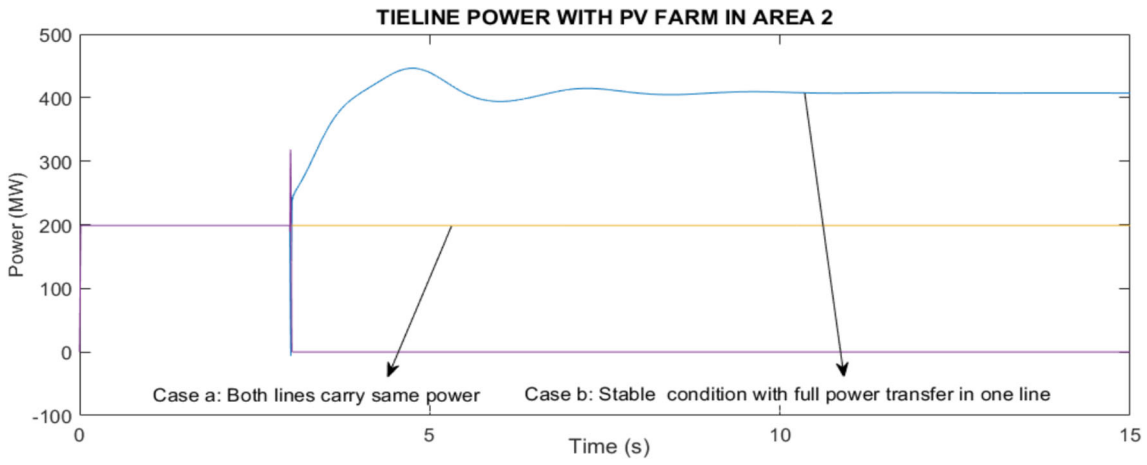

Fig. 18 Power flowing through tie line with PV in area 2

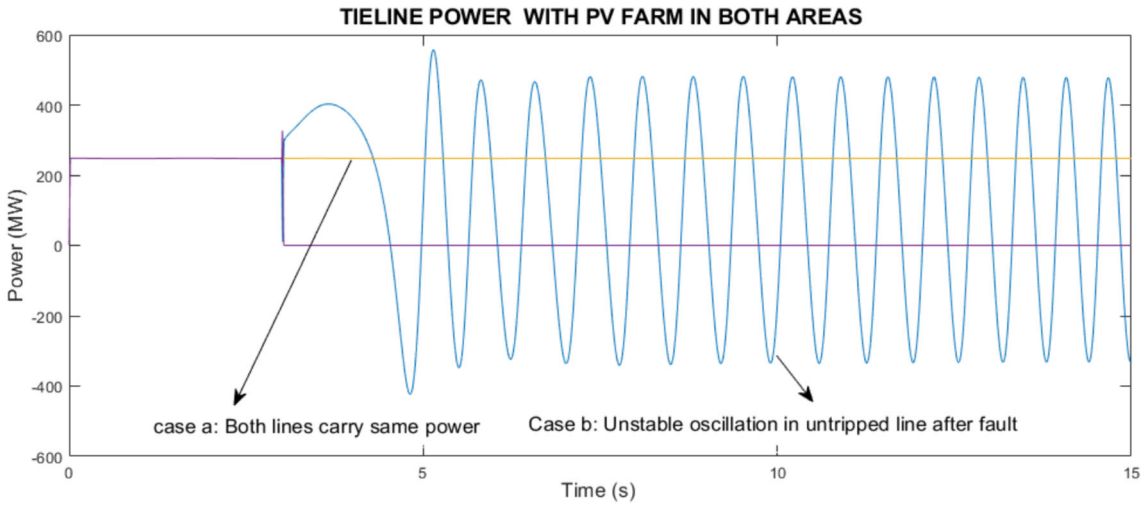

Fig. 19 Power flowing through tie line with PV in both areas

an increase in the rotor speed rendering the system stable. The absence of inertia in the system fails to increase the speed of the rotor, leading to the instability of the system.

5 Conclusion

This research presents a comprehensive analysis on impact of the IBR on power system with various benchmark models along with different types of disturbance.

It can be concluded from the analysis that:

- Integration of IBR in power system results in reduction in system inertia
- Reduction in system inertia results in a reduced frequency nadir, increasing the likelihood of false triggering of under-frequency relay.
- A decrease in system inertia reduces the critical clearing time, heightening the risk of system instability.
- Low system inertia intensifies inter-area oscillations, potentially causing instability.
- In addition to reduction in inertia, controllers in IBRs decrease short-circuit current during faults, potentially leading to maloperation of protective devices.
- Overall the conclusion of the above analysis suggests that the integration of IBR in power system decreases power system lesser stability margin.

Appendix

Synchronous generator.

MVA rating = 100 MVA.

Voltage rating = 22 kV.

Nominal power of turbine = 100 MW.

Reactive power = 45 MVAR.

X'd = 0.315.

Shaft.

$H = 6.112$ s.

Transformer.

Primary connection = star ground

Secondary connection = delta lag

Base primary winding voltage (rmsLL) = 22 kV

Base secondary winding voltage (rmsLL) = 220 kV

Base power=100 MVA

Base frequency = 50 Hz

Rm = 1.081 MΩ

Lm = 2.8663E3.

L1 = 637.00E−6H

L2 = 637.00E−6H

Three-phase pi line

Line length = 100 km

Zero seq (R0) = 0 Ω/km L0 = 10E−6 H/km C0 = 1E−9 F/km.

Positive seq (R1) = 1E−9 Ω/km L1 = 3.852E−3 H/km C1 = 1E−9 F/km.

References

1. Hatziargyriou, N., et al.: Definition and classification of power system stability - revisited and extended. IEEE Trans. Power Syst. **36**(4), 3271–3281 (2021). https://doi.org/10.1109/TPWRS.2020.3041774
2. Kundur, P., et al.: Definition and classification of power system stability. IEEE Trans. Power Syst. **19**(3), 1387–1401 (2004). https://doi.org/10.1109/TPWRS.2004.825981

3. Mitra A. P.; Sundaresh L.; Ramasubramanian D.: Stability of Inverter-Based Resource (IBR) Dominated Systems with Different Types of Local Loads
4. Power System Operation Corporation Limited in collaboration with Report on Assessment of Inertia in Indian Power System (2022)
5. Rezaei N.; Uddin M. N.: An analytical review on state-of-the-art microgrid protective relaying and coordination techniques. In IEEE Transactions on Industry Applications, vol. 57(3), pp. 2258–2273 Institute of Electrical and Electronics Engineers Inc., 01 May (2021). https://doi.org/10.1109/TIA.2021.3057308.
6. Nagpal, M.; Henville, C.: Impact of power-electronic sources on transmission line ground fault protection. IEEE Trans. Power Deliv.Deliv. **33**(1), 62–70 (2018). https://doi.org/10.1109/TPWRD.2017.2709279
7. Hooshyar, A.; Azzouz, M.A.; El-Saadany, E.F.: Distance protection of lines connected to induction generator-based wind farms during balanced faults. IEEE Trans. Sustain. Energy **5**(4), 1193–1203 (2014). https://doi.org/10.1109/TSTE.2014.2336773
8. Hooshyar, A.; Azzouz, M.A.; El-Saadany, E.F.: Distance protection of lines emanating from full-scale converter-interfaced renewable energy power plants-part I: problem statement. IEEE Trans. Power Deliv.Deliv. **30**(4), 1770–1780 (2015). https://doi.org/10.1109/TPWRD.2014.2369479
9. Denholm P.; Mai T.; Kenyon R. W.; Kroposki B.; O'malley M.: Inertia and the power grid: a guide without the spin, (2020). [Online]. Available: www.nrel.gov/publications.
10. Son, Y.; Ha, Y.; Jang, G.: Frequency Nadir estimation using the linear characteristics of frequency control in power systems. Energies **17**, 1061 (2024). https://doi.org/10.3390/en17051061
11. IEEE Power and energy society and institute of electrical and electronics engineers. In 2017 IEEE PES Innovative Smart Grid Technologies Conference Europe (ISGT-Europe): conference, proceedings, Torino, 26–29 Sept 2017
12. Ulbig A.; Borsche T.S: Andersson G; Zurich E.: Impact of Low Rotational Inertia on Power System Stability and Operation
13. Liu, C.; Cai, G.: Power-oscillation evaluation in power systems with high penetration of renewable power generation based on network virtual inertia. IET Renew. Power Gener.Gener. **13**(1), 138–145 (2019). https://doi.org/10.1049/iet-rpg.2018.5306
14. Xu T.; Jang W; Overbye T.: Location-Dependent Impacts of Resource Inertia on Power System Oscillations. [Online]. Available: http://hdl.handle.net/10125/50230
15. You, S., et al.: Impact of high PV penetration on the inter-area oscillations in the US Eastern interconnection. IEEE Access **5**, 4361–4369 (2017). https://doi.org/10.1109/ACCESS.2017.2682260
16. Zhou, X.; Cheng, S.; Wu, X.; Rao, X.: Influence of photovoltaic power plants based on VSG technology on low frequency oscillation of multi-machine power systems. IEEE Trans. Power Deliv.Deliv. **37**(6), 5376–5384 (2022). https://doi.org/10.1109/TPWRD.2022.3177042
17. Hawaii International Conference on System Sciences (2020)
18. Telukunta, V.; Pradhan, J.; Agrawal, A.; Singh, M.; Srivani, S.G.: Protection challenges under bulk penetration of renewable energy resources in power systems: a review. CSEE J. Power Energy Syst. **3**(4), 365–379 (2017). https://doi.org/10.17775/CSEEJPES.2017.00030
19. North Dakota State University. Institute of electrical and electronics engineers, and IEEE power and energy society. In 2018 North American Power Symposium (NAPS), 9–11 Sept 2018
20. Chowdhury, R.; Fischer, N.: Transmission line protection for systems with inverter-based resources - part II: solutions. IEEE Trans. Power Deliv.Deliv. **36**(4), 2426–2433 (2021). https://doi.org/10.1109/TPWRD.2020.3030168
21. Haddadi, A.; Zhao, M.; Kocar, I.; Karaagac, U.; Chan, K.W.; Farantatos, E.: Impact of inverter-based resources on negative sequence quantities-based protection elements. IEEE Trans. Power Deliv.Deliv. **36**(1), 289–298 (2021). https://doi.org/10.1109/TPWRD.2020.2978075
22. Mishra, P.; Pradhan, A.K.; Bajpai, P.: Adaptive distance relaying for distribution lines connecting inverter-interfaced solar PV plant. IEEE Trans. Industr. Electron.Industr. Electron. **68**(3), 2300–2309 (2021). https://doi.org/10.1109/TIE.2020.2975462
23. Grande L.S.A.; Arrabé R.G.; Arnaltes S.; Amenedo J.L.R.: Influence of negative-sequence control under converter-interface-based generation in distance protection relays. In Proceedings - 2023 IEEE International Conference on Environment and Electrical Engineering and 2023 IEEE Industrial and Commercial Power Systems Europe, EEEIC / I and CPS Europe 2023, Institute of Electrical and Electronics Engineers Inc., (2023). https://doi.org/10.1109/EEEIC/ICPSEurope57605.2023.10194720.
24. Agrawal P.K.; Agrawal V.K.; Rathour H.: Application of PMU-Based Information in the Indian Power System. In International Journal of Emerging Electric Power Systems, (2013)
25. Ashton, P.M.; Saunders, C.S.; Taylor, G.A.; Carter, A.M.; Bradley, M.E.: Inertia estimation of the GB power system using synchrophasor measurements. IEEE Trans. Power Syst. **30**(2), 701–709 (2015). https://doi.org/10.1109/TPWRS.2014.2333776
26. Dānishgāh-i Shīrāz and Institute of Electrical and Electronics Engineers, 2016 24th Iranian Conference on Electrical Engineering (ICEE), Shiraz University, Iran 10–12 May 2016
27. Panda, R.K.; Mohapatra, A.; Srivastava, S.C.: Online estimation of system inertia in a power network utilizing synchrophasor measurements. IEEE Trans. Power Syst. **35**(4), 3122–3132 (2020). https://doi.org/10.1109/TPWRS.2019.2958603
28. Kerdphol T.; Watanabe M.; Nishikawa R.; Tamaki T.; Mitani Y.; Determining inertia of 60 Hz Japan power system using PMUs from power loss event. In 2021 IEEE Texas Power and Energy Conference, TPEC 2021. Institute of Electrical and Electronics Engineers Inc., (2021). https://doi.org/10.1109/TPEC51183.2021.9384932.
29. Anderson P.M.; Diego S.; Fouad C.A.A.: Power system control and stability, 2 edn (2003)
30. E. Ørum et al. Future system inertia participants. [Online]. Available: www.entsoe.eu
31. Power-System-Stability-and-Control-by-Prabha-Kundur.
32. power system analysis - hadi saadat- ElCom.
33. Phadke A.G.; Thorp J.S.: Synchronized phasor measurements and their applications. In Power Electronics and Power Systems, Springer, Boston (2008). https://doi.org/10.1007/978-0-387-76537-2.
34. System Relaying Committee of the IEEE Power and Society. IEEE standard for synchrophasor measurements for power systems sponsored by the power system relaying committee IEEE power and energy society 2011
35. Klein, M.; Rogers, G.J.; Kundur, P.; Toronto, O.: A fundamental study of inter-area oscillations in power systems. IEEE Trans. Power Syst. **6**, 914–821 (1991)

Springer Nature or its licensor (e.g. a society or other partner) holds exclusive rights to this article under a publishing agreement with the author(s) or other rightsholder(s); author self-archiving of the accepted manuscript version of this article is solely governed by the terms of such publishing agreement and applicable law.

Physica Scripta

INCLUSIVE PUBLISHING TRUSTED SCIENCE
PURPOSE-LED PUBLISHING™

ACCEPTED MANUSCRIPT

Koch-curve fractal plasmonic nanoantennas on VO_2 for near-field plasmonic switching

To cite this article before publication: Asbah Masih *et al* 2025 *Phys. Scr.* in press https://doi.org/10.1088/1402-4896/adc5af

Manuscript version: Accepted Manuscript

Accepted Manuscript is "the version of the article accepted for publication including all changes made as a result of the peer review process, and which may also include the addition to the article by IOP Publishing of a header, an article ID, a cover sheet and/or an 'Accepted Manuscript' watermark, but excluding any other editing, typesetting or other changes made by IOP Publishing and/or its licensors"

This Accepted Manuscript is **© 2025 IOP Publishing Ltd. All rights, including for text and data mining, AI training, and similar technologies, are reserved.**.

During the embargo period (the 12 month period from the publication of the Version of Record of this article), the Accepted Manuscript is fully protected by copyright and cannot be reused or reposted elsewhere.

As the Version of Record of this article is going to be / has been published on a subscription basis, this Accepted Manuscript will be available for reuse under a CC BY-NC-ND 4.0 licence after the 12 month embargo period.

After the embargo period, everyone is permitted to use copy and redistribute this article for non-commercial purposes only, provided that they adhere to all the terms of the licence https://creativecommons.org/licences/by-nc-nd/4.0

Although reasonable endeavours have been taken to obtain all necessary permissions from third parties to include their copyrighted content within this article, their full citation and copyright line may not be present in this Accepted Manuscript version. Before using any content from this article, please refer to the Version of Record on IOPscience once published for full citation and copyright details, as permissions may be required. All third party content is fully copyright protected, unless specifically stated otherwise in the figure caption in the Version of Record.

View the article online for updates and enhancements.

This content was downloaded from IP address 14.139.251.98 on 03/04/2025 at 05:44

Koch-Curve Fractal Plasmonic Nanoantennas on VO_2 for Near-field Plasmonic Switching

Asbah Masih and Yashna Sharma*

Department of Electronics and Communication Engineering, Delhi Technological University, Delhi, India

*yashnasharma@dtu.ac.in

ABSTRACT

We propose a fractal plasmonic gold nanoantennas (FPNs) based on the Koch-curve fractal on top of a thin layer of vanadium dioxide (VO_2), on a SiO_2 substrate for near-field plasmonic switching. The proposed FPN on the VO_2 thin layer is based on two gold Koch-curve based fractal plasmonic nanopillar segments present next to each other with a small gap between them. The thin VO_2 layer below the FPNs is used as the phase change material for active near-field switching in this fractal plasmonic nanoantenna. The application of heat, electric field or optical radiation leads to the phase transition of the underlying VO_2 layer from its semiconductor to its metallic state, thus leading to an active switching of the field between the two segments of the Koch-curve FPNs from a low (OFF) to a high (ON) value. Exhaustive numerical analysis is carried out by employing Finite Difference Time Domain (FDTD) analysis to determine the E-field enhancement of the proposed switch with VO_2 in its semiconductor (OFF state of the switch) and metallic (ON state of the switch) phase. The intensity switching ratio (ISR) is reported as the ratio of E-field enhancement at the center of the proposed Koch-curve FPNs with VO_2 in its metallic (ON) state to that with VO_2 in its semiconducting (OFF) state. It is shown that, as the number of iterations of the Koch-curve fractal plasmonic antennas is increased, the ISR increases from ~22 for iteration 0 to ~2500 for iteration 2. In addition, spectral tunability is demonstrated by varying the geometrical specifications like the length of the proposed Koch-curve FPN. Moreover, the effect of the thickness of the Koch-curve and the thickness of the VO_2 film for different iterations of the proposed FPN based switch is systematically analysed to obtain high ISRs at the desired wavelength.

Keywords: Plasmonics, Near-field, Nanoantenna, Phase change materials, VO_2, Koch Fractal

INTRODUCTION

In the recent past, the development of plasmonic devices that are capable of demonstrating ultrafast response with an ultrasmall footprint has intrigued researchers. Plasmonics deals with the control of electromagnetic (EM) radiation at sub-wavelength scales and is based on the excitation of surface plasmon polaritons (SPPs), localized surface plasmons (LSPs) and coupled plasmon resonances in metallic nanostructures [1-3]. When incident light

Accepted Manuscript

is coupled into the collective oscillations of the conduction band electrons at the interface between a thin metallic film and a dielectric, electromagnetic waves called surface plasmon polaritons (SPPs) are generated. In contrast, when there is interaction between incident light and a metallic nanoparticle, non-propagating collective oscillations called localized surface plasmons (LSPs) are exhibited by the conduction electrons of nanoparticles. The designs and geometries of metallic nanostructures capable of supporting such plasmon resonances are often engineered to tailor the plasmon resonance wavelengths and localized electromagnetic field enhancements offered by these metallic nanostructures. These engineered nanostructures are used for numerous applications in the past like ultrasensitive sensing [4], photovoltaics [5], non-linear optics [6], data storage [7] and many others [8-13].

In addition to the above applications, it is well known that the confinement of EM fields to sub-nanometer volumes by using metallic nanostructures with funneling geometries leads to the generation of localized EM hotspots with very high values of localized EM fields [14,15]. Such engineered metallic nanostructures, called plasmonic nanoantennas, can funnel the freely propagating electromagnetic energy (far-field) to a localized sub-nanometer volume (near-field), and are capable of re-radiating it back to the free space at a high efficiency. Plasmonic nanoantennas have been used in the past for various applications like ultrasensitive sensing [16], solar energy harvesting [17], optical trapping [18], and many others [19-21]. Although many applications based on passive plasmonic nanoantennas have been proposed, the active control of nanoantenna characteristics has gained immense interest recently due to its inevitable applications such as optical modulation [22], switching [23], and reconfigurable plasmonic devices [24]. In the past, the active control of the far-field of plasmonic nanoantennas or nanostructures has been demonstrated by employing optically active materials [25], thermo-optical materials [26], phase change materials [27], thermo-responsive polymers [28], electro-optic polymers [29], liquid crystals [30], metal nanoparticles embedded in hydrogels [31], and self-tunable plasmonic materials [32]. However, in addition to actively controlling the far-field of a plasmonic nanoantenna, the active control of the near-field of a plasmonic nanoantenna is equally important due to its potential to be employed for numerous applications like SERS [33], particle tweezing [34], non-linear optics [35] and switchable lasing [36]. In the past, the active control of the near-field of a plasmonic nanoantenna has been demonstrated by Abate *et al.* [37] who demonstrated near field switching based on gold nanorod antennas on VO_2 which could reversibly transform from being plasmonic dipole nanoantennas to monopole nanoantennas as the phase of VO_2 changes. Further, Bergamini *et al.* demonstrated switching using a single gold nanoantenna on a VO_2 film under different polarizations [38]. Near field switching has also been demonstrated by Savaliya *et al.* using VO_2 dipole nanostructures on Au substrates [39], Park *et al.* using gold dipole antennas with a cavity filled with VO_2 [40] and Gupta *et al.* by employing ring-rhombus nanoantenna [41] amongst others.

In the recent past, phase change materials (PCMs) have been extensively used for active plasmonic switching due to various benefits such as potential ultrafast speeds, low power consumption and lower cost [42-44]. These phase change materials undergo collective electronic and/or structural transitions along with large variations in optical and electrical properties on exposure to external stimulants. In this paper, we use vanadium dioxide (VO_2) as the PCM to realize a plasmonic nanoantenna capable of active near-field switching. Vanadium dioxide, undergoes a phase transition from being a monoclinic insulator to a tetragonal metal

Accepted Manuscript

when thermal [45], electrical [46] or optical [47] stimulus is applied to it. The possibility of an insulator-to-metal transition in VO_2 by employing optical radiation also opens the possibility of realizing a potential ultrafast all-optical plasmonic near-field switch based on the designs proposed in this paper. VO_2 has been chosen due to its numerous advantages such as low thermal hysteresis [48] possibility of a near-room temperature transition [49], ultrafast speed [50], its capability to go through many switching cycles without getting degraded [51], and the availability of suitable fabrication methodologies for the growth of VO_2 thin films [52].

We propose plasmonic fractal nanoantennas based on the Koch-curve fractal on a VO_2 film for active plasmonic near-field switching. It must be noted that although, fractal plasmonic nanoantennas based on the Sierpinski fractal [36,53], Koch snowflake fractal [54], Cayley fractal [55], ternary tree fractal [56], Cesaro-type fractal [57] and others have been proposed in the past for applications such as photovoltaics [58], fluorescence enhancement [59] and third harmonic generation [60], the application of fractal nanoantennas for near-field switching remains relatively unexplored. We systematically show active switching of the near-field of a plasmonic nanoantenna based on the modified Koch-curve fractal geometry (See Fig. 1). The basis shape and the iterative fractalization process of the structure are based on a Koch curve fractal. The plasmonic nanoantenna is formed by placing two gold nanopillars with Koch-curve geometries in a face-to-face arrangement on a thin VO_2 layer on a SiO_2 substrate. As shown in

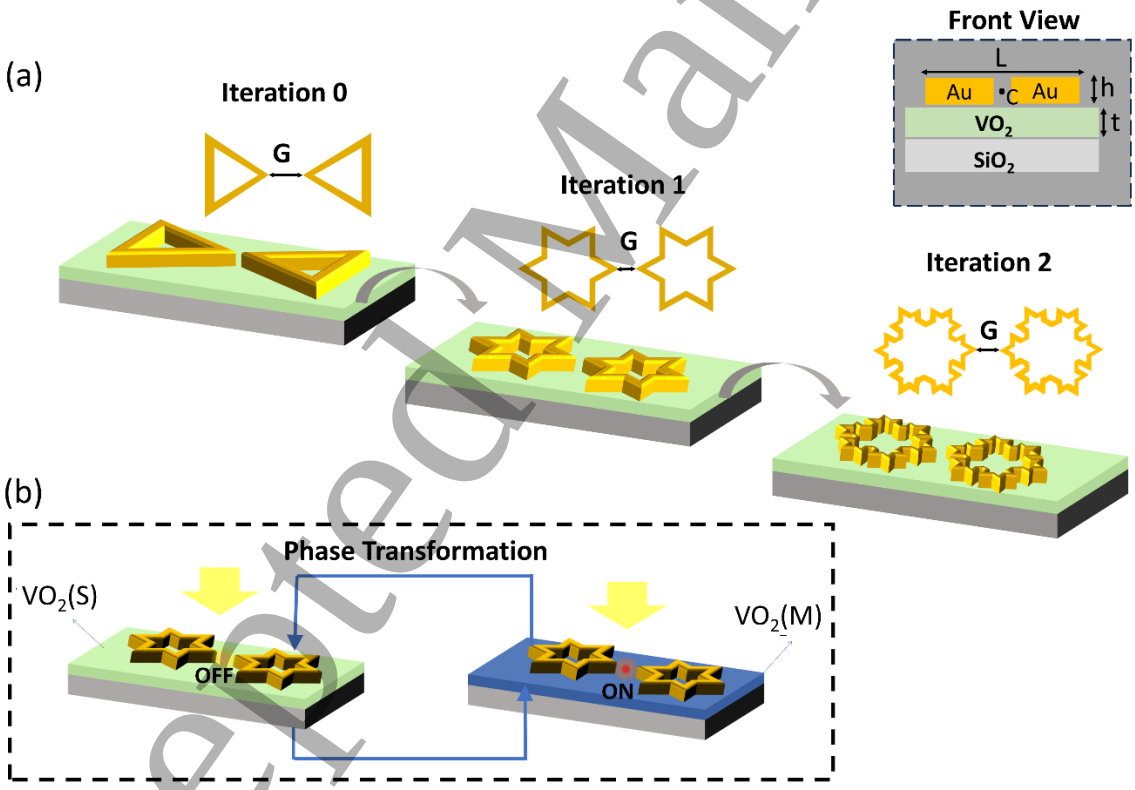

Fig. 1. (a) Schematic of the proposed Au Koch-curve fractal plasmonic nanoantenna (FPN) on VO_2 for active E-field switching showing Iteration 0, Iteration 1 and Iteration 2 of the FPN. The plasmonic nanoantenna segments have a height 'h', with the gap between two FPN segments being 'G'. The thickness of the Koch curve is taken as 'c' and the VO_2 layer is taken to be 't' nm thick. The near field intensity is measured at point C which is located at the center of the two FPN segments. (b) Near-field switching in Koch-curve fractal plasmonic nanoantenna. The VO_2 layer undergoes a transition from the semiconductor-to- metallic state on being exposed to heat, electric field or optical radiation leading to transition from the 'OFF' to the 'ON' state of the E-field at the region between the two FPN segments.

Accepted Manuscript

Fig. 1, the height of the Koch-curve nanopillars is 'h', with the thickness of the underlying VO_2 layer being 't'. The proposed Koch curve nanoantenna has a gap, G, between the two Koch-fractal pillars, with the total length of the switch being 'L' such that 'L' is the sum of the length of the two Koch-curve segments and the gap between them. The thickness of the Koch curve for the fractal plasmonic nanoantenna is taken as 'c' nm. As shown in Fig. 1, the basic shape (Iteration 0) of the Koch-curve fractal plasmonic nanoantenna is formed by starting with two equilateral triangles facing each other in a bowtie configuration. In the first iteration, each edge of the structure is equally divided into three segments, with an equilateral triangle pointing outwards in the central segment, such that the base of this new triangle is equal to the central segment. The outer curve of the resulting geometry, with the curve thickness being 'c' nm, is taken as the Iteration 0 of the nanoantenna. The higher order fractals (Iteration 2 and above) are obtained by applying this transformation iteratively. The different iterations of the Koch-curve fractal plasmonic nanoantenna (FPN) are shown in Fig. 1. It must be noted that, in this paper, we analyse the performance of the near-field switch up to Iteration 2, as the higher iterations are not amenable to fabrication owing to feature sizes less than 10 nm. In addition, we have considered all geometric structures with sharp corners to have sufficient rounding to account for fabrication related constraints in achieving sharp corners.

The performance of the suggested switch is analysed in terms of the near-field intensity switching ratio (ISR), which is the ratio of the near-field intensity in the center (point C in Fig. 1) of the two Koch-curve nanopillar antenna segments (See Fig. 1) when the switch is in its ON and OFF state, respectively. It should be noted that point C is also the vertical center of the FPNs. When VO_2 layer is in its insulator/semiconductor state, the near-field intensity at point C, is very low and denotes the OFF state of the switch. However, on exposure to heat, electric field or optical energy, the underlying VO_2 layer undergoes a semiconductor to metal transition, followed by significant changes in its optical properties. This leads to a high field enhancement at point C, thus, switching the proposed switch to its ON state. Thus, ISR is measured as $I_{(ON)}/I_{(OFF)}$ for the proposed switch. It must be noted that the performance of the proposed near-field switch in terms of the near field intensity switching ratio is better than all formerly reported values of ISR for near field plasmonic switches based on VO_2. In the past, an ISR ~7 has been achieved using gold dipole antennas with a cavity filled with VO_2 [39], and an ISR of ~80 was reported by using Au ring-rhombus nanoantenna in conjunction with VO_2 [41]. In addition, an ISR of ~900 was reported in one of our previous works based on Sierpinski-fractal plasmonic nanoantennas on VO_2 [36]. However, here, we report an ISR as high as ~ 2500 by employing the Koch-curve FPNs which has not been reported previously.

Finite difference time domain (FDTD) method has been employed to systematically analyze the near-field intensity enhancement, the intensity switching ratio and the wavelength of maximum ISR for the proposed design of the switches based on the Koch-curve fractal plasmonic nanoantennas. We have exhaustively analysed the effect of structural parameters like the length of the switch, the gap between the nanoantenna segments and the thickness of the VO_2 layer on the ISR achieved from these switches.

METHODS

We have employed an electromagnetic solver (Lumerical FDTD Solutions) by Lumerical Solutions Inc. [61] to numerically analyse the electromagnetic behaviour of the

Accepted Manuscript

Koch-curve FPN based switches. The Finite Difference Time Domain (FDTD) method transforms the continuous time Maxwell's equations into discrete-time difference equations, divides the space and time into grids, and subsequently solves for the E and H fields. After careful convergence testing, the grid size was kept to be 1 nm uniformly in the x, y and z directions. The near field reflectance spectra and the ISR for the proposed switches for different mesh sizes is shown in Supplementary Note 1 (See Supplementary Information). Linearly polarized light (polarized along the antenna axis) was incident normally on the proposed nanostructure, with the range of wavelengths from 600 nm to 2400 nm. Perfectly matched layer (PML) boundaries were employed in X-, Y- and Z- directions. The optical constants for gold and vanadium dioxide were based on the Lorentz Drude model [2], and were appropriately fitted for the operational range of wavelengths employed. The material constants for VO_2 are also shown in Supplementary Note 2 (See Supplementary Information). An exhaustive analysis of the effect of geometric specifications of the Koch-curve FPN on the ISR spectra was carried out. For the analysis, the length of the switch, L, was varied from 450 nm to 650 nm, the thickness of the VO_2 layer, t, was varied from 10 nm to 50 nm, and the gap between the nanoantenna segments was varied from 5 nm to 20 nm and the Koch-curve thickness was varied from 25 nm to 35 nm.

It must also be noted that the proposed Koch-curve FPN based switches can be fabricated by using a thin film deposition process [62] to deposit a thin film of VO_2 on a SiO_2 substrate. Subsequently, electron beam lithography or helium ion beam (HIB) milling [54,63] can be used to fabricate the proposed Koch-curve FPNs. A thin film of gold can be deposited before HIB milling (or before liftoff using EBL) using electron beam evaporation [64]. Further, for all the simulations executed in this paper, a rounding radius of 3 nm has been taken wherever sharp corners are present. This is because fractal features with sharp corners are often difficult to fabricate with the existing nanolithography tools [65].

RESULTS AND DISCUSSIONS

Finite difference time domain (FDTD) has been used to simulate and analyze the switching ability of the Koch-curve FPNs on vanadium dioxide, in terms of the intensity switching ratio (ISR). The enhancement of the E-field ($|E|/|E_0|$) and the near-field intensity ($|E|^2/|E_0|^2$) at the center of the two Koch-curve FPN segments facing each other (See Fig. 1), are exhaustively calculated for 0^{th}, 1^{st} and 2^{nd} iterations of the proposed Koch-curve FPN based switch with VO_2 in its semiconducting (OFF state of the switch) and metallic state (ON state of the switch). The ISR is calculated such that $ISR = I_{(ON)}/I_{(OFF)}$, where $I_{(ON)}$ and $I_{(OFF)}$ are the near field intensities (at the center of the two FPN segments) for the ON and OFF state of the switch, respectively. Further, an in-depth analysis of the various geometric parameters of the proposed switch such as the length of the switch, gap between the FPN segments, and the thickness of the VO_2 layer on the near-field ISR has also been carried out to analyze the switching performance of the proposed Koch-curve FPN.

Figure 2(a) exhibits the near-field intensity enhancement spectra at the center of the two Koch-curve FPN segments for iteration 0, for the cases when VO_2 is in its semiconducting and metallic state, respectively. The thickness of the VO_2 film, the gap between the FPN segments, the thickness of the Koch curve and the height of the antenna above the surface of the substrate are taken as 20 nm, 10 nm, 30 nm and 80 nm, respectively. The resultant intensity switching

Accepted Manuscript

ratio (ISR) for the iteration 0 of the Koch-curve based switch is shown on the secondary axis of Fig. 2(a). When VO_2 is in its metallic state, the highest intensity enhancement between the two FPN segments is observed at ~1835 nm. However, when VO_2 is present in its insulator state, the wavelength of highest intensity enhancement red-shifts beyond 2.5 μm along with the creation of one more plasmonic mode at ~1650 nm. This is expected as the refractive index (real part) of VO_2 increases when VO_2 changes from its metallic to its semiconducting state [66]. In addition, it should be observed that, in the wavelength region between 900 nm to 1800 nm, there is a significant differential between the near-field intensity enhancement of the switch with VO_2 (M) and VO_2 (S) such that the proposed switch can be visualized as being ON with VO_2 (M), and being OFF with VO_2 (S). As the E-field intensity enhancement is significantly off-resonance at a wavelength of 1170 nm for VO_2(S), for the iteration 0 of the proposed switch, the highest ISR of ~ 22 is seen at a wavelength of ~ 1170 nm.

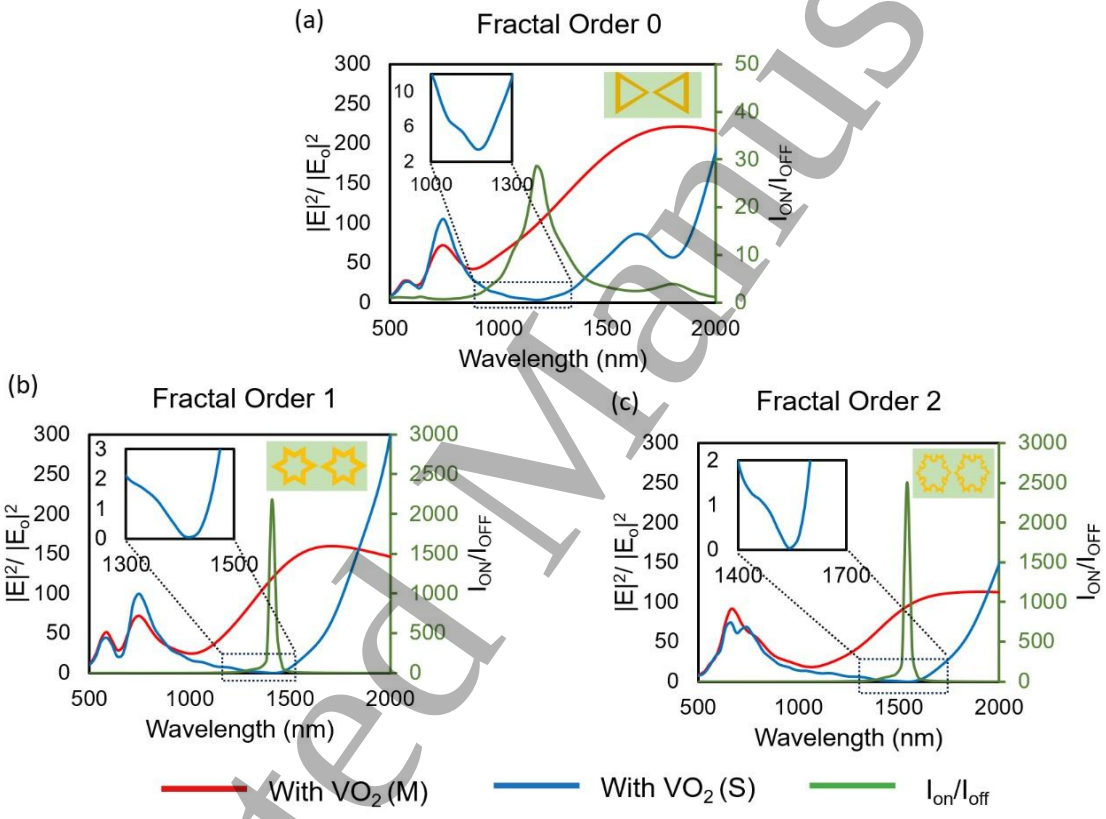

Fig. 2. E-field intensity ($|E|^2/E_0|^2$) enhancement spectra for the proposed Koch-curve FPNs, with VO_2 in the insulating and metallic state, along with the Intensity Switching Ratio (I_{ON}/I_{OFF}) shown on the secondary axis for (a) Iteration 0 (b) Iteration 1 and (c) Iteration 2. The intensity enhancement is plotted in red for VO_2(M) and in blue for VO_2 (S) on the primary axis, and the I_{ON}/I_{OFF} values are plotted for each case on the secondary axis. For these simulations, the length of the switch, L = 650 nm; height, h = 80 nm; VO_2 layer thickness, t = 20 nm; thickness of the Koch curve, c = 30 nm and gap, G = 10 nm.

Figure 2(b) exhibits the effect of varying the number of iterations of the proposed Koch-curve FPN. As the number of iterations increases from 0 to 1, the ER spectra of the switch undergoes a significant change with VO_2 (M) and VO_2 (S), respectively. It is evident that, with VO_2 (M), there is a reduced near-field enhancement due to the altered polarizability of the Koch-curve fractals with order 1. However, for VO_2 (S), along with the expected red-shift in

Accepted Manuscript

the resonance wavelength, the near-field enhancement spectrum exhibits an extraordinarily strong off-resonance around a wavelength of ~ 1410 nm (See inset of Fig. 2(b)). This leads to a 100-fold enhancement in the ISR for the iteration 1 of the Koch-curve FPN based switch. Fig. 2(b) shows that an ISR of ~ 2100 can be obtained at a wavelength of ~1410 nm with the first iteration of the Koch-curve FPN based plasmonic switch. The scattering spectra of the proposed switches with VO_2(M) and VO_2(S) are also given in Supplementary Note 3 (See Supplementary Information).

Fig. 2(c) shows the effect of increasing the number of iterations for the proposed Koch-curve fractal plasmonic nanoantenna based switches. It can be observed from the shape of the iteration 2 of the Koch-curve fractal nanoantenna that the plasmonic behaviour of this nanoantenna is expected to be significantly different as compared to the lower order fractal designs. Fig. 2(c) shows that with VO_2(M), the switch exhibits a damping in the near-field intensity at the center of the two FPNs as compared to iteration 0 and 1 of the FPN based switch. With VO_2 (S), the plasmon resonance wavelength exhibits a red-shift compared to iteration 0 and 1, along with the presence of a strong off-resonance, resembling a Fano-type dip, at a wavelength of ~1540 nm (See inset of Fig. 2(c)). This results in a high intensity switching ratio of ~ 2500 at a wavelength of ~1540 nm, which can be achieved by employing the proposed switch. Further, it should be noted that an exhaustive analysis of the values for the maximum ISR obtained with different possible positions of the vertical coordinate, C, is discussed in Supplementary Note 4 (See Supplementary Information). It was observed that the highest enhancement was obtained for the case when the value of the coordinate C = 40 nm, i.e., at the vertical center of the FPNs and thus, ISR was evaluated at this point for all simulations in this manuscript. Further, Fig. S2(a) shows the average ISR obtained by averaging the ISR over all possible vertical coordinate positions of point C. It can be clearly seen that as the fractal order of the FPNs is increased from 0 to 2, the average ISR increases from ~40 to ~1550. In addition, it should be noted that a Koch curve fractal was chosen over the solid Koch snowflake fractal as higher ISRs could be obtained upon fractalization in these switches as compared to fractalized solid Koch snowflake FPNs (See Supplementary Note 5, Supplementary Information).

Figure 3 shows the E-field enhancement ($|E|/|E_0|$) maps for the various iterations of the proposed Koch-curve FPN based switches. The E-field profiles are shown for the proposed switch for both the ON (with VO_2 (M)) and OFF state (with VO_2 (S)) of operation. Figs 3(a)-(c) exhibit the E-field profiles for iteration 0,1 and 2 of the Koch-curve FPN based switch with VO_2(M) at the wavelengths of maximum ISR, respectively. The magnified E-field profiles for all iterations clearly show that the E-field is highly localized at the center of the two nanoantenna segments with a high E-field enhancement, effectively making the switch 'ON' in this state. Figs. 3(d)-(f) show the E-field profiles for the iterations 0, 1 and 2 of the proposed switch for the case with VO_2(S). Fig. 3(d) shows that at $\lambda \approx 1170$ nm, with VO_2(S), the E-field enhancement for iteration 0 is very low as compared to the case with VO_2(M), effectively making the switch 'OFF'. In addition, Fig. 3(e) shows that, with VO_2 (S), for iteration 1

Accepted Manuscript

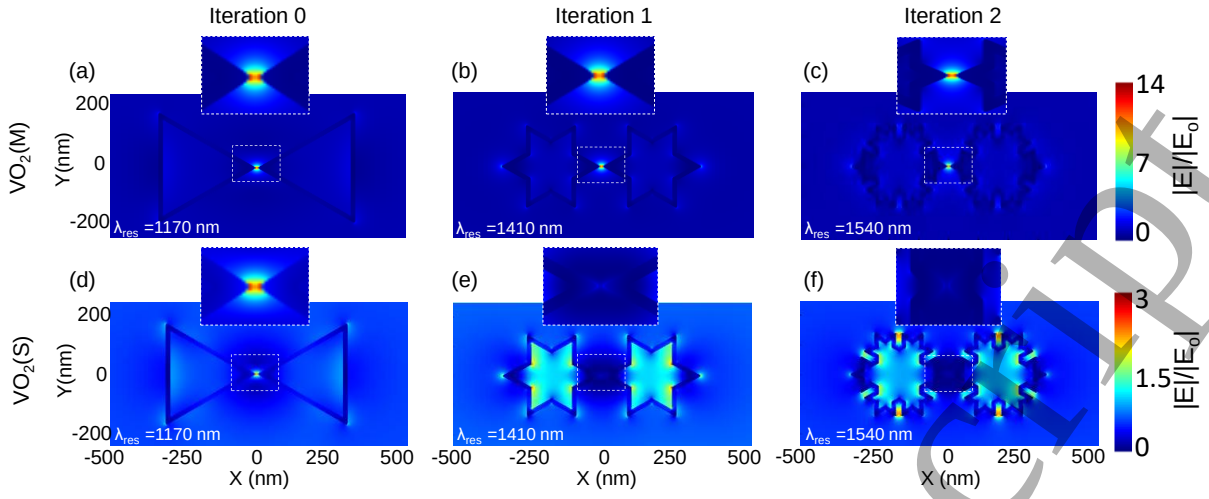

Fig. 3. E-field enhancement maps for the Koch-curve FPN based switch with VO_2(M) (ON) for (a) Iteration 0 (b) Iteration 1 and (c) Iteration 2 of the FPN. E-field enhancement maps of the Koch curve FPN with VO_2(S) (OFF) for (d) Iteration 0 (e) Iteration 1 and (f) Iteration 2 of the FPN. The E-field enhancement at the center of the FPN segments has been magnified in each case for clarity. The scale bar shows the magnitude of the E-field enhancement. The length of the switch is taken as 650 nm, the height if the FPNs is taken to be 80 nm, the VO_2 layer thickness is 20 nm, the Koch curve is taken to be 30 nm thick, and the gap, G is 10 nm.

of the FPN based switch, the E-field enhancement at the center of the FPN segments becomes even lower than the case for iteration 0, which results in an overall increase in the ISR. Further fractalization shows that, with VO_2(S), the E-field enhancement at the center of the FPN segments continues to decrease with higher fractal orders. Hence, higher fractal orders of the suggested Koch-curve based fractal result in higher intensity switching ratios.

Figure 4 shows the effect of the VO_2 layer thickness on the near-field enhancement ($|E|/|E_0|$) between the FPN segments and the ISR for the suggested switch, with VO_2 (M) and VO_2 (S). It must be noted that the effect of the thickness of the VO_2 layer is a critical parameter which can be efficiently controlled during the fabrication of such switches, and thus can be used to fine-tune the switching efficiency and the wavelength of operation of the switch. The length of the switch, the gap between the FPN segments and the Koch curve thickness are kept as 650 nm , 10 nm and 30 nm for this analysis. For iteration 0, with VO_2 in its metallic state, the color map shows the near-field enhancement spectra as a function of the thickness of the VO_2 layer. It may be noticed that two plasmonic modes with high near field enhancement, M1 (at a higher wavelength) and M2 (at a lower wavelength) , are present for the proposed nanoantenna. We speculate that this could possibly be explained by the plasmon hybridization model [67] employing which the proposed hollow cavity Koch-curve FPN can be viewed as the combination of an outer solid Koch- snowflake nanoantenna and an inner cavity Koch-snowflake nanoantenna. The interaction between the plasmons of the outer solid Koch-snowflake nanoantenna and the inner cavity Koch-snowflake nanoantenna leads to the splitting of the primary plasmonic mode of a Koch-snowflake nanoantenna into two modes (M1 and M2). Further, it may be noticed that the higher wavelength mode M1 undergoes a blue-shift,

Accepted Manuscript

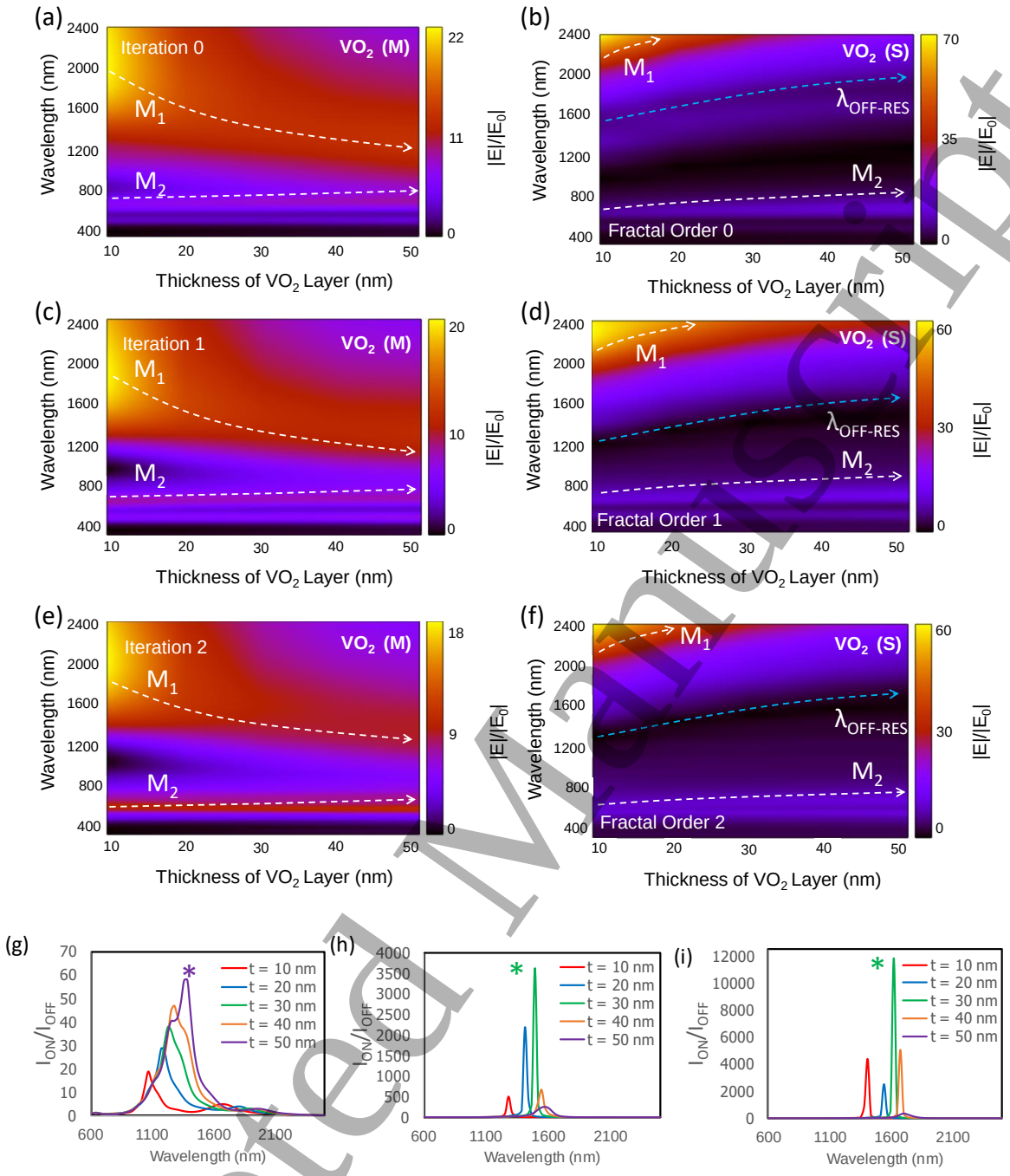

Fig. 4. Color maps showing the effect of the thickness of the VO_2 layer (t) on the E-field enhancement spectra for the proposed Koch-curve FPN based switches for (a) Iteration 0 with VO_2 (M), (b) Iteration 0 with VO_2 (S), (c) Iteration 1 with VO_2 (M), (d) Iteration 1 with VO_2 (S), (e) Iteration 2 for VO_2 (M) and (f) Iteration 2 for VO_2 (S). ISR spectra are shown for (g) Iteration 0, (h) Iteration 1, and (i) Iteration 2 of the proposed switch for different values of VO_2 thickness. The length of the switch, the thickness of the Koch curve, the gap between the FPN segments and the height of the FPN are taken as 650 nm, 30 nm, 10 nm and 80 nm, respectively. See Supplementary Note 6 (Supplementary Information) for detailed data for (a)-(f).

and the lower wavelength mode M2 exhibits a red-shift as the thickness of the VO_2 (M) layer increases. This can be understood by visualizing the 'VO_2 layer on SiO_2' as an effective medium such that the net effective dielectric constant of the effective medium is determined based on the dielectric constants of VO_2 (M) and SiO_2. As the permittivity of VO_2 (M) is negative for $\lambda > 1130$ nm, and the permittivity of SiO_2 is positive for all wavelengths [66, 68],

Accepted Manuscript

it can be deduced from the effective medium theory that the net permittivity of the 'VO_2 layer on SiO_2' substrate will decrease as thickness of VO_2 is increased for $\lambda > 1130$ nm, whereas the net permittivity will increase as VO_2 thickness is increased for $\lambda < 1130$ nm. As the plasmon resonance wavelength depends on the effective permittivity of the underlying substrate [1], the plasmonic mode M1 (at a wavelength > 1130 nm) undergoes a blue-shift, and the plasmonic mode M2 (at a wavelength < 1130 nm) undergoes a slight red-shift on increasing the thickness of the VO_2 layer. Further, it may be noticed that the magnitude of E-field enhancement decreases on increasing the VO_2 layer thickness because of the increase in the imaginary part of the net dielectric constant owing to the lossy nature of VO_2 (M).

Fig. 4(b) shows the effect of the VO_2 layer thickness on the E-field enhancement between the FPN segments with VO_2 (S). It must be noted that the mode M1 is red-shifted beyond 2400 nm in this case. However, the tail of the mode has been shown in the figure as M1. It is well known that the permittivity of VO_2 (S) is positive for all wavelengths. As the permittivity of SiO_2 is also positive, the net permittivity of the effective medium comprising of a 'VO_2 layer on SiO_2' increases as the thickness of the VO_2 layer is increased. This leads to a red-shift in both the modes (M1 and M2) with an increase in the VO_2 layer thickness. As a result, the off-resonance wavelength (shown in green) also exhibits a red-shift with an increase in the VO_2 thickness. A similar trend can be seen in Figs. 4 (c)-(d) for iteration 1, and in Figs. 4 (e)-(f) for iteration 2 of the proposed Koch-curve FPN based switch. Figs. 4(g)-(i) show the effect of the VO_2 layer thickness on the ISR for the proposed switch with iteration 0,1 and 2, respectively. With the increase in the thickness of the VO_2 layer, the wavelength of maximum ISR (λ_{max}) exhibits a red-shift spanning the favourable O-, E-, S- and C- bands of optical communication. Further, as the iterations increase from 0 to 2, there is an increase in the ISR for all values of VO_2 layer thickness. Moreover, Figs. 4 (g)-(i) show that for iteration 0, a VO_2 layer thickness of 50 nm results in the highest ISR, and for the iteration 1 and 2, a VO_2 thickness of 30 nm provides the highest ISR. Thus, it can be concluded that fractalization changes the overall EM behaviour of the switch, which results in a specific optimal value of VO_2 layer thickness for each iteration to achieve the highest ISR.

Figure 5 illustrates the effect of the length of the Koch-curve FPN based switch on the switching efficiency as a function of wavelength for iterations 0,1 and 2. For this analysis, the VO_2 layer thickness, the thickness of the Koch curve, the gap between the FPN segments and the height of the FPN are taken as 20 nm, 30 nm, 10 nm and 80 nm, respectively. Figs. 5(a) and (b) exhibit the effect of increasing the length of the switch from 450 nm to 650 nm on the near-field intensity enhancement spectra, with VO_2(M) and VO_2(S), respectively. Figs. 5(a)-(b) show the near-field intensity enhancement versus wavelength for iteration 0, where it is evident that the dominant plasmonic mode exhibits an almost linear red-shift in its plasmon resonance wavelength with both VO_2(M) and VO_2(S), as the length of the switch is increased. With VO_2(M), the plasmon resonance wavelength exhibits a red-shift from 1436 nm to 2000 nm. With VO_2(S) the plasmon resonance wavelength for the dominant mode is shifted beyond 2500 nm and hence cannot be visualized. However, Fig. 5(b) shows that the off resonant wavelengths red-shifts from 1064 nm to 1170 nm. This red-shift on increasing the length of the switch is

Accepted Manuscript

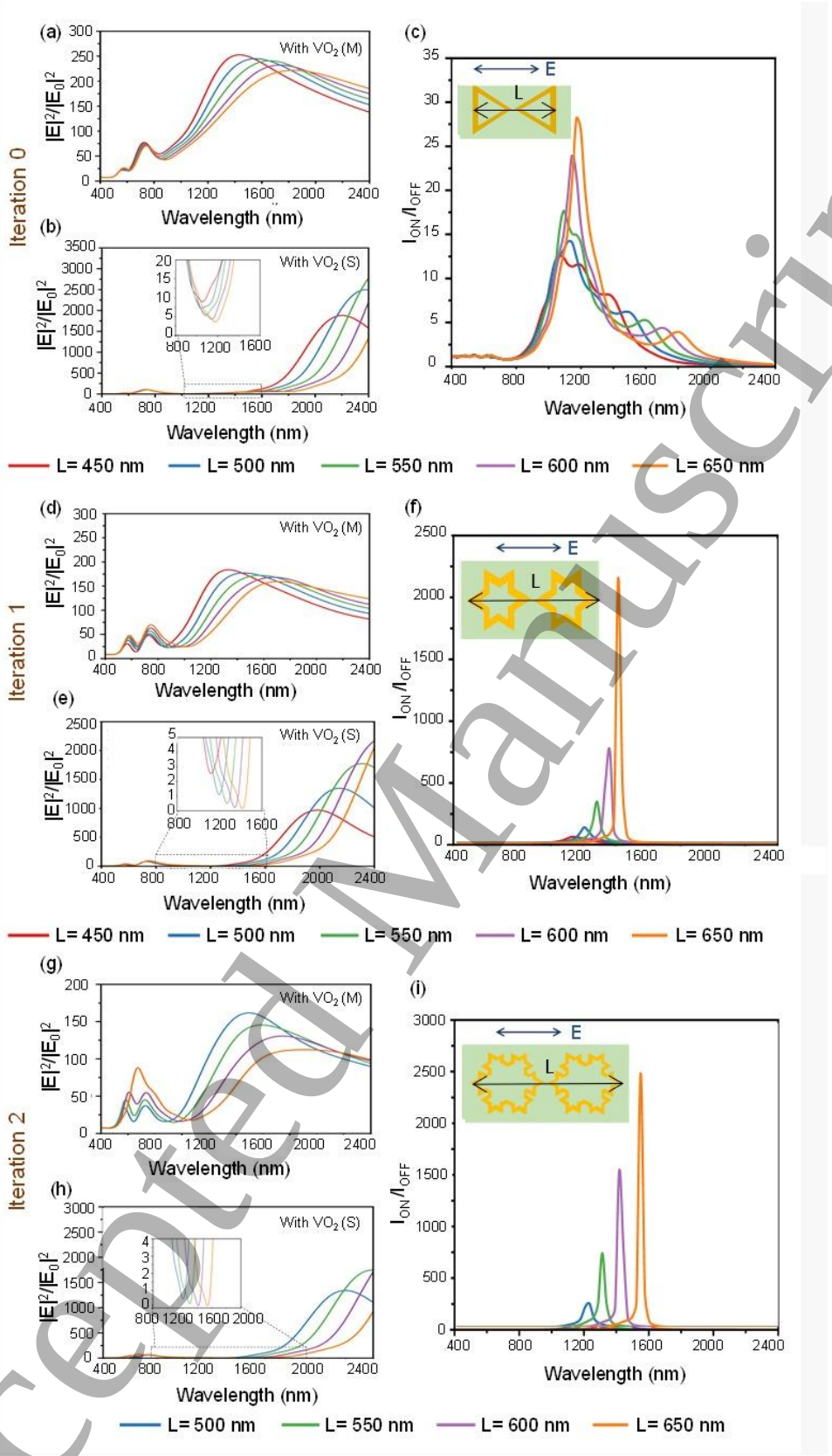

Fig. 5. Effect of the length of Koch-curve FPN segments, 'L', on the near-field intensity enhancement ($|E|^2/|E_0|^2$) as a function of wavelength for iteration 0 of the FPN with (a) VO_2 (M) and (b) VO_2(S), and on the (c) ISR as a function of wavelength; on the near-field intensity enhancement as a function of wavelength for iteration 1 of the FPN with (d) VO_2 (M) and (e) VO_2 (S), and on the (f) ISR as a function of wavelength; and on the near-field intensity enhancement ($|E|^2/|E_0|^2$) as a function of wavelength for iteration 2 of the FPN with (f) VO_2 (M) and (g)

Accepted Manuscript

VO_2 (S), and on the (h) ISR as a function of wavelength. The thickness of the VO_2 layer, the thickness of the Koch curve, the gap between the FPN segments and the height of the FPN are taken as 20 nm, 30 nm, 10 nm and 80 nm, respectively.

expected as a variation in the length leads to a variation in the dipolar polarizability of the nanostructure, leading to the red-shift . Fig. 5 (c) shows the ISR versus wavelength for iteration 0 of the Koch-curve FPN when the length, L, is varied from 450 nm to 650 nm. The λ_{max} can be varied from 1064 nm to 1170 nm for iteration 0, along with an increase in the magnitude of maximum ISR. A similar trend can be observed through Figs. 5(d)-(e) for the near field intensity enhancement spectrum for iteration 1 of the proposed switch. Fig. 5(f) shows that for iteration 1, the λ_{max} can be varied from 1330 nm to 1729 nm by varying the length. Figs. 5(g)-(h) show the near-field intensity enhancement spectra for the iteration 2 of the proposed switches as a function of the switch length. The length of 450 nm was specifically excluded while carrying out this analysis for iteration 2, as fractalization of order 2 at this length would result in feature sizes that are not amenable to the existing fabrication methodologies. Fig. 5(i) exhibits that for iteration 2, the λ_{max} red-shifts from 1463 nm to 1915 nm with length. Hence, with iteration 1 and 2 of the proposed switch, it can be concluded that length of the FPN based switch can be varied to realize wavelength tunability over a spectral region wider than 400 nm spanning over multiple bands of the optical communication window. In addition, simulations to determine the effect of fractalization on the ISR spectra for realistic structures such as those where the two components of the FPN dimer are not identical were also carried out and are discussed in Supplementary Note 7 (See Supplementary Information). It was found that, for realistic structures where two components of the FPN dimer are not similar, although the first order fractalization results in higher ISR, fractalization to a second order may not be always advantageous, and may result in lower ISR as compared to the first order fractals.

Figure 6 exhibits the effect of the thickness of the Koch curve, c, on the ISRs for iterations 0,1 and 2 of the proposed Koch-curved FPN-based switch. The length of the FPN based switch, the height, h, the VO_2 layer thickness, t, and the gap, G, between the FPN segments were kept constant as 650 nm, 80 nm, 20 nm, and 10 nm respectively for this analysis. It can be observed from Fig. 6(a) that for iteration 0, as the thickness of the Koch curve is increased from 25 nm to 35 nm, there is a blue-shift in the λ_{max} from 1250 to 1170 nm. In accordance with the plasmon hybridization model [67], the proposed fractal plasmonic nanoantenna based on the Koch curve can possibly be visualized as a hollow cavity nanoantenna whose electromagnetic behaviour can be explained by the interaction between the plasmons of the outer solid Koch-snowflake nanoantenna and the inner cavity Koch-snowflake nanoantenna. This interaction between the outer and inner plasmons depends significantly on the thickness of the Koch-curve. As the thickness of the Koch curve increases, the interaction between the plasmons from the solid and cavity Koch-snowflakes reduces, resulting in a blue-

Accepted Manuscript

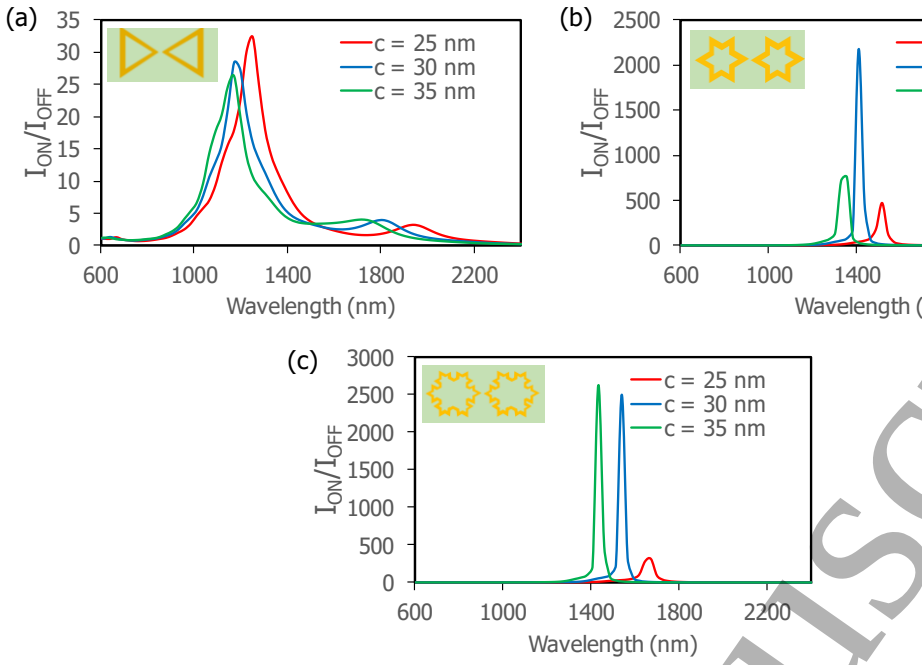

Fig. 6. Effect of the thickness of Koch curve on the ISR of the proposed Koch-curve FPN based switch for (a) iteration 0, (b) iteration 1 and (c) iteration 2 of the FPN with the values of L = 650 nm, h = 80 nm, t = 20 nm and G = 10 nm. The reflectance spectra for the switch with VO_2 (M) and VO_2 (S) for the effect of the Koch curve thickness for all iterations of the FPN are given in Supplementary Note 8.

shift of the resultant plasmonic modes, both when VO_2 is in its semiconducting or metallic state (See Supplementary Note 8) for the effect of Koch-curve thickness on the E-field intensity spectra with VO_2 (S) and VO_2 (M) for all iterations). This results in an overall blue-shift of the λ_{max} with an increase in the thickness of the Koch-curve. A similar behaviour can be seen for Figs. 6(b) and (c) where the λ_{max} for the Koch-curve FPN based switch with iterations 1 and 2 shows a significant blue-shift with increasing thickness of the Koch-curve. Further, it may be noted that as the number of iterations increases, the optimal thickness of the Koch-curve for which maximum ISR can be obtained increases from 25 nm for iteration 0 to 35 nm for iteration 2. Thus, it can be concluded that the Koch curve thickness in the proposed FPNs can also be varied to tune the ISR and the wavelength of maximum ISR.

CONCLUSIONS

Fractal plasmonic nanoantennas (FPNs) based on the Koch-curve fractal on top of a thin film of vanadium dioxide (VO_2) on a SiO_2 substrate for near-field plasmonic switching have been proposed. Finite Difference Time Domain (FDTD) simulations were used to exhaustively analyze the switching ability, i.e., the intensity switching ratio (ISR) for the different iterations of the FPN based switch. It can be concluded that as the number of iterations of the Koch-curve fractal plasmonic nanoantenna on VO_2 are increased from 0 to 2, there is a 100-fold enhancement in the near-field ISR achieved through these switches. Further, the effect of varying the length of the switch on the ISR was analyzed to demonstrate wavelength tunability over a spectral region wider than 400 nm can be achieved for the 1st and 2nd iteration of the proposed FPN based switches. Further, the ISR and the wavelength of maximum ISR can be fine-tuned by varying the VO_2 thickness of the proposed switch. Thus,

Accepted Manuscript

the proposed switches can be efficiently employed for near-field switching with a high ISR which can potentially be tuned over a large wavelength range.

ACKNOWLEDGEMENT

The authors wish to express their gratitude towards the Delhi Technological University (DTU) for their support and resources.

DECLARATION OF COMPETING INTEREST

The authors declare no competing interests.

REFERENCES

[1] Stefan A. Maier. Plasmonics: Fundamentals and Applications. Springer, New York, USA (2007). ISBN: 9780387331508. DOI: https://doi.org/10.1007/0-387-37825-1

[2] Lukas Novotny and Bert Hecht. Principles of Nano-Optics.New York: Cambridge University Press, New York, (2006). ISBN: 9780511813535. DOI: https://doi.org/10.1017/CBO9780511813535

[3] Eleonora Petryayeva and Ulrich J. Krull. "Localized surface plasmon resonance: Nanostructures, bioassays and biosensing-A review", Analytica Chimica Acta, volume 706, issue 1, pages 8-24 (2011). DOI: https://doi.org/10.1016/j.aca.2011.08.020

[4] Meihua Lin, Jingjing Wang, Guobao Zhou, Jianbang Wang, et al. "Programmable engineering of a biosensing interface with tetrahedral DNA nanostructures for ultrasensitive DNA detection.", Angewandte Chemie - International Edition, vol. 54, no. 7, pp. 2151–2155, (2015). DOI: https://doi.org/10.1002/anie.201410720

[5] Congcong Wu, Kai Wang, Munkhbayar Batmunkh, Abdulaziz S.R. Bati, et al., "Multifunctional nanostructured materials for next generation photovoltaics," Nano Energy, vol. 70, p. 104480, (2020). DOI: https://doi.org/10.1016/j.nanoen.2020.104480

[6] Falah A-H. Mutlak, Raied K Jamal, and Ala F. Ahmed. "Pulsed laser deposition of TiO2 nanostructures for verify the linear and non-linear optical characteristics.", Iraqi Journal of Science, vol. 62, no. 2, pp. 517–525, (2021). DOI: 10.24996/ijs.2021.62.2.18.

[7] M. Mansuripur, A. R. Zakharian, A. Lesuffleur, Sang-Hyun Oh, et al. "Plasmonic nano-structures for optical data storage.", Optics Express, vol. 17, issue.16, pp. 14001-14014, (2009).DOI: https://doi.org/10.1364/OE.17.014001

[8] Pathakoti, Kavitha, Manjunath Manubolu, and Huey-Min Hwang. "Nanostructures: Current uses and future applications in food science.", Journal of food and drug analysis vol. 25, no. 2, pp. 245–253, (2017). DOI: https://doi.org/10.1016/j.jfda.2017.02.004

[9] Seyed-Behnam Ghaffari, Mohammad-Hossein Sarrafzadeh, Maryam Salami and Arvin Alvandi. "A comparative study of the action mechanisms and development strategies of different ZnO-based nanostructures in antibacterial and anticancer applications.", Journal of Drug Delivery Science and Technology, vol. 91, p. 105221, (2024). DOI: https://doi.org/10.1016/j.jddst.2023.105221

Accepted Manuscript

[10] Zhiqiang Du, Canhui He, Jinhao Xin, et al. “Terahertz dynamic multichannel holograms generated by spin-multiplexing reflective metasurface", Opt. Express, vol. 32, pp. 248-259, (2024). DOI: https://doi.org/10.1364/OE.510046

[11] Kaiyu Guo, Miao Zhang, Zhiqiang Du, et al., “Terahertz spin-selective metasurface for multichannel switching of OAM”, Results in Physics, vol. 56, 107279, (2024). DOI: https://doi.org/10.1016/j.rinp.2023.107279

[12] Ruixing Nie, Canhui He, Runxuan Zhang, et al., “Vanadium dioxide-based terahertz metasurfaces for manipulating wavefronts with switchable polarization”, Optics & Laser Technology, vol. 159, 109010, (2023). DOI: https://doi.org/10.1016/j.optlastec.2022.109010.

[13] Jinhao Xin, Zhiqiang Du, Zekai Zhou, et al., “Optical reflective metasurfaces enable spin-decoupled OAM and focusing”, Physical Chemistry Chemical Physics, 25(40), 27008-27016 (2023). DOI: https://doi.org/10.1039/D3CP02321D

[14] Stephanie Dodson, Mohamed Haggui, Renaud Bachelot, Jérôme Plain, et.al. "Optimizing electromagnetic hotspots in plasmonic bowtie nanoantennae.", The journal of physical chemistry letters, vol.4, issue3 (2013). DOI: https://doi.org/10.1021/jz302018x

[15] Wei Ding, Renaud Bachelot, Sergei Kostcheev, Pascal Royer, et. al. "Surface plasmon resonances in silver Bowtie nanoantennas with varied bow angles.", Journal of Applied Physics, vol. 108, issue 12, (2010). DOI: https://doi.org/10.1063/1.3524504

[16] Li Dongxiao, Hong Zhou, Ziwei Chen, Zhihao Ren, et al. "Ultrasensitive molecular fingerprint retrieval using strongly detuned overcoupled plasmonic nanoantennas.", Advanced Materials, vol. 35, serial 32, (2023). DOI: https://doi.org/10.1002/adma.202301787

[17] Van Tran Tan, Huu-Quang Nguyen, Young-Mi Kim, Gyeongsik Ok,et. al. "Photonic–plasmonic nanostructures for solar energy utilization and emerging biosensors." Nanomaterials, vol. 10, serial 11, (2020). DOI: https://doi.org/10.3390/nano10112248

[18] Alemayehu Nana Koya, Joao Cunha, Tian-Long Guo, Andrea Toma, et. al. “Novel Plasmonic Nanocavities for Optical Trapping-Assisted Biosensing Applications”, Advanced Optical Materials,vol 8, issue 7, (2020). DOI: https://doi.org/10.1002/adom.201901481

[19] Jinxing Chen, Zuyang Ye, Fan Yang and Yadong Yin. "Plasmonic nanostructures for photothermal conversion." *Small Science*, vol. 1, issue. 2, (2021). DOI:https://doi.org/10.1002/smsc.202000055

[20] Keng-Te Lin , Han Lin and Baohua Jia. "Plasmonic nanostructures in photodetection, energy conversion and beyond" *Nanophotonics*, vol. 9, no. 10, pp. 3135-3163, (2020), https://doi.org/10.1515/nanoph-2020-0104

[21] Francisco Duarte, João Paulo N. Torres, António Baptista, and Ricardo A. Marques Lameirinhas. "Optical nanoantennas for photovoltaic applications.", Nanomaterials vol. 11, no. 2, pp. 1–25, (2021). DOI: https://doi.org/10.3390/nano11020422

[22] Martina Abb,, Pablo Albella, Javier Aizpurua, and Otto L. Muskens. "All-optical control of a single plasmonic nanoantenna–ITO hybrid." Nano letters, vol. 11, issue 6 pp. 2457-2463, (2011) DOI: https://doi.org/10.1021/nl200901w

Accepted Manuscript

[23] Wei-Shun Chang, J. Britt Lassiter, Pattanawit Swanglap, Heidar Sobhani, et al., "A plasmonic Fano switch," Nano Lett., vol. 12, pp. 4977–4982, (2012). DOI: https://doi.org/10.1021/nl302610v

[24] Jialong Peng, Hyeon-Ho Jeong, Qianqi Lin,, Sean Cormier et al. "Scalable electrochromic nanopixels using plasmonics", Sci. Adv., vol. 5, Issue 5,(2019). DOI: 10.1126/sciadv.aaw2205

[25] Takayuki Okamoto, Tomoyuki Kamiyama, and Ichirou Yamaguchi. "All-optical spatial light modulator with surface plasmon resonance," Opt. Lett., vol. 18, issue 18, pp. 1570-1572, (1993). DOI: https://doi.org/10.1364/OL.18.001570

[26] Thomas Nikolajsen, Kristjan Leosson, and Sergey I. Bozhevolnyi, "Surface Plasmon Polariton Based Modulators and Switches Operating at Telecom Wavelengths.", Appl. Phys. Lett., vol. 85, issue 24, pp. 5833-5835,(2004). DOI: https://doi.org/10.1063/1.1835997

[27] Mikhail A. Kats, Romain Blanchard, Patrice Genevet, Zheng Yang, et. al., "Thermal Tuning of Mid-Infrared Plasmonic Antenna Arrays Using a Phase Change Material.", Opt. Lett., vol. 38, issue 3, pp. 368−370, (2013). DOI: https://doi.org/10.1364/OL.38.000368

[28] Nina Jiang, Xiaolu Zhuo, and Jianfang Wang. "Active Plasmonics: Principles, Structures, and Applications", Chemical Reviews, 118 (6), 3054-3099 (2018). DOI: https://doi.org/10.1021/acs.chemrev.7b00252

[29] Arif E.Çetin, Ahmet A. Yanik, Alket Mertiri, Shyamsunder Erramilli, et. al., "Field-Effect Active Plasmonics for Ultracompact Electro-Optic Switching.", Appl. Phys. Lett., vol. 101, issue 12, (2012). DOI: https://doi.org/10.1063/1.4754139

[30] Wayne Dickson, Gregory A. Wurtz, Paul R. Evans, Robert J. Pollard, and Anatoly V. Zayats. "Electronically Controlled Surface Plasmon Dispersion and Optical Transmission through Metallic Hole Arrays Using Liquid Crystal", Nano Letters, 8, 1, 281–286 (2008). DOI: https://doi.org/10.1021/nl072613g

[31] Praveen Thoniyot, Mein Jin Tan, Anis Abdul Karim, David James Young, et.al.,"Nanoparticle–hydrogel composites: concept, design, and applications of these promising, multi-functional materials", Adv. Sci., vol. 2, issue 1-2, (2015). DOI: https://doi.org/10.1002/advs.201400010

[32] Xiaoli Wang and Bruno Palpant,"Large and Ultrafast Optical Response of a One-Dimensional Plasmonic–Photonic Cavity.", Plasmonics, vol. 8, pp. 1647-1653, (2013).DOI: 10.1007/s11468-013-9583-1

[33] Sameh Kessentini, , Dominique Barchiesi, Cristiano D'Andrea, Andrea Toma, et. al., "Gold dimer nanoantenna with slanted gap for tunable LSPR and improved SERS." The Journal of Physical Chemistry C, vol. 118, issue 6, pp. 3209-3219, (2014). DOI: https://doi.org/10.1021/jp409844y.

[34] Yatao Ren, Qin Chen, Mingjian He, Xiangzhi Zhang, et. al. "Plasmonic optical tweezers for particle manipulation: principles, methods, and applications.", ACS nano, vol.15, issue 4, pp. 6105-6128, (2021). DOI: https://doi.org/10.1021/acsnano.1c00466

[35] Hayk Harutyunyan, Giorgio Volpe, Romain Quidant, and Lukas Novotny."Enhancing the nonlinear optical response using multifrequency gold-nanowire antennas." Physical review letters, vol.108, issue 21, (2012). DOI: https://doi.org/10.1103/PhysRevLett.108.217403

Accepted Manuscript

[36] Yashna Sharma and Anuj Dhawan. "Active near-field plasmonic switches based on Sierpiński-fractal nanoantennas on VO_2 films.", Journal of Optics, vol. 24, issue 6, (2022). DOI: 10.1088/2040-8986/ac6208

[37] Yohannes Abate, Robert E. Marvel, Jed I. Ziegler, et al. "Control of plasmonic nanoantennas by reversible metal-insulator transition." Sci Rep, vol. **5**, (2015). DOI: https://doi.org/10.1038/srep13997

[38] Luca Bergamini, Bigeng Chen, Daniel Traviss, et al. "Single-nanoantenna driven nanoscale control of the VO_2 insulator to metal transition" Nanophotonics, vol. 10, no. 14, pp. 3745-3758, (2021). DOI: https://doi.org/10.1515/nanoph-2021-0250

[39] Priten B. Savaliya, Arun Thomas, Rishi Dua, and Anuj Dhawan."Tunable optical switching in the near-infrared spectral regime by employing plasmonic nanoantennas containing phase change materials", Opt. Express, vol. 25, issue 20, pp. 23755–23772, (2017). DOI: https://doi.org/10.1364/OE.25.023755

[40] Jun-Bum Park, Il-Min Lee, Seung-Yeol Lee, et. al. " Tunable subwavelength hot spot of dipole nanostructure based on VO_2 phase transition" Opt. Express, vol. 21,13, pp. 15205–15212. (2013) DOI: https://doi.org/10.1364/OE.21.015205

[41] Nitin Gupta, Priten B. Savaliya, and Anuj Dhawan. "Plasmonic nanoantennas on VO2 films for active switching of near-field intensity and radiation from nanoemitters", Opt. Express, vol. 28, issue 19, pp. 27476-27494, (2020). DOI: https://doi.org/10.1364/OE.391655

[42] Kirti Dalal and Yashna Sharma. "Plasmonic switches based on VO_2 as the phase change material", Nanotechnology, vol. 35, issue 14, (2024). DOI**:** 10.1088/1361-6528/ad1642

[43] Nikolaos Farmakidis, Nathan Youngblood, June Sang Lee, Johannes Feldmann, et. al. "Electronically reconfigurable photonic switches incorporating plasmonic structures and phase change materials" Adv. Sci., vol. 9, issue 20,(2022). DOI: https://doi.org/10.1002/advs.202200383

[44] Arun Thomas, Priten Savaliya, Kamal Kumar Anuj Dhawan, et. al. "Au nanowire- VO_2 spacer-Au film based optical switches", J. Opt. Soc. Am. B, vol. 35, issue 7, pp. 1687–97, (2018). DOI: https://doi.org/10.1364/JOSAB.35.001687

[45] Yashna Sharma, Veeranjaneya A. Tiruveedhula, John F. Muth, and Anuj Dhawan. "VO_2 based waveguide-mode plasmonic nano-gratings for optical switching", Optics Express, vol. 23, issue 5, pp. 5822-5849 (2015). DOI: https://doi.org/10.1364/OE.23.005822

[46] Brett A. Kruger, Arash Joushaghani, and Joyce K. S. Poon. "Design of electrically driven hybrid vanadium dioxide (VO_2) plasmonic switches", Optics Express, vol. 20, issue 21, pp. 23598-23609 (2012). DOI: https://doi.org/10.1364/OE.20.023598

[47] Nardeep Kumar, Armando Rúa, Jennifer Aldama, Karla Echeverría, Félix E. Fernández, and Sergiy Lysenko. "Photoinduced surface plasmon switching at VO_2/Au interface", Optics Express, vol. 26, issue 11, pp. 13773-13782 (2018). DOI: https://doi.org/10.1364/OE.26.013773

[48] Kai Liu, Sangwook Lee, Shan Yang, Olivier Delaire, and Junqiao Wu. "Recent progresses on physics and applications of vanadium dioxide", Materials Today, volume 21, issue 8, pp. 875-896 (2018). DOI: https://doi.org/10.1016/j.mattod.2018.03.029

Accepted Manuscript

[49] G. V. Jorgenson, and J. C. Lee. “Doped vanadium oxide for optical switching films”, Solar Energy Materials, volume 14, issues 3-5, pages 205-214 (1986). DOI: https://doi.org/10.1016/0165-1633(86)90047-X

[50] Sébastien Cueff, Jimmy John, Zhen Zhang, Jorge Parra, et. al.“VO_2 nanophotonics”, APL Photonics, vol. 5, issue 11, (2020). DOI: https://doi.org/10.1063/5.0028093

[51] Urvashi Solanki and Prasanta Mandal. “Phase sensitive VO_2-metal switchable plasmonic metasurface for thermal controlling of broad band near-infrared absorption”,Opt. Quantum Electron., vol. 54, (2022). DOI: https://doi.org/10.1007/s11082-022-04180-y

[52] Kirti Dalal and Yashna Sharma.“ Broadband plasmonic switches based on nanodisc-dimers with progressively increasing diameters on a plasmonic film with a VO2 spacer”, Optics Communications, vol. 530, (2023). DOI: https://doi.org/10.1016/j.optcom.2022.129121

[53] Semih Cakmakyapan, Neval A. Cinel, Atilla Ozgur Cakmak, and Ekmel Ozbay. "Validation of electromagnetic field enhancement in near-infrared through Sierpinski fractal nanoantennas." Optics express, vol.22, issue 16, pp. 19504-19512, (2014). DOI: https://doi.org/10.1364/OE.22.019504

[54] Edson P. Bellido, Gabriel D. Bernasconi, David Rossouw, Jérémy Butet, ., et al. "Self-similarity of plasmon edge modes on Koch fractal antennas." ACS nano, vol. 11, issue 11, pp. 11240-11249, (2017). DOI: https://doi.org/10.1021/acsnano.7b05554

[55] Samuel Gottheim, Hui Zhang, Alexander O. Govorov and Naomi J. Halas."Fractal nanoparticle plasmonics: The Cayley tree.", ACS nano, vol. 9, issue 3, pp. 3284-3292, (2015).DOI: https://doi.org/10.1021/acsnano.5b00412

[56] Ravi S. Hegde and E. H. Khoo. "Broadband optical response in ternary tree fractal plasmonic nanoantenna." Plasmonics, vol. 11, pp. 465-473, (2016).DOI: 10.1007/s11468-015-0059-3

[57] Ekin Aslan, Erdem Aslan, Ren Wang, Mi K. Hong, et al. "Multispectral Cesaro-type fractal plasmonic nanoantennas." ACS Photonics, vol. 3, issue 11, pp. 2102-2111 (2016). DOI: https://doi.org/10.1021/acsphotonics.6b00540

[58] Mohammad Ali Shameli and Leila Yousefi. "Absorption enhanced thin-film solar cells using fractal nano-structures.", IET Optoelectronics, vol 15, issue 5, pp. 248-253, (2021).DOI: https://doi.org/10.1049/ote2.12036

[59] Jun Dong, Hairong Zheng, Xuqiang Li, Xiaoqing Yan, Yu sun, and Zhenglong Zhang. "Surface-enhanced fluorescence from silver fractal like nanostructures decorated with silver nanoparticles." Applied Optics, vol.50, issue 31, pp. G123-G126, (2011). DOI: https://doi.org/10.1364/AO.50.00G123

[60] Anton Husakou, Song-Jin Im, Kwang-Hyon Kim, and Joachim Herrmann."High harmonic generation assisted by metal nanostructures and nanoparticles." Progress in Nonlinear Nano-Optics,pp: 251-268, (2015). DOI: https://doi.org/10.1007/978-3-319-12217-5_14

[61] FDTD: 3D Electromagnetic Simulator, Lumerical Inc. [Online]. Available: https://www.ansys.com/en-in/products/optics/fdtd

Accepted Manuscript

[62] Sergiy Lysenko, Armando Rua Felix E Fernandez, Jose A.Jimenez,et. al. "Light-induced ultrafast phase transitions in VO2 thin film.", Applied Surface Science, vol. 252, issue 15, pp. 5512-5515. (2006). DOI: 10.1016/j.apsusc.2005.12.137

[63] Lisa Seitl, Florian Laible, Simon Dickreuter, Dominik A Gollmer, et. al. "Miniaturized fractal optical nanoantennas defined by focused helium ion beam milling", Nanotechnology, vol. 31, issue 7, (2019). DOI: 10.1088/1361-6528/ab5120

[64] George Chen,and Ping Hui."Thermal conductivities of evaporated gold films on silicon and glass.", Applied physics letters, vol. 74, issue 20, pp. 2942-2944. (1999). DOI: 10.1063/1.123973

[65] Michal Horák, Kristýna Bukvišová, Vojtěch Švarc, Jiří Jaskowiec, et al. "Comparative study of plasmonic antennas fabricated by electron beam and focused ion beam lithography.", Sci Rep, vol. 8, (2018). DOI: https://doi.org/10.1038/s41598-018-28037-1

[66] Hans W. Verleur, A. S. Barker, Jr., and C. N. Berglund. "Optical Properties of VO_2 between 0.25 and 5 eV", Reviews of Modern Physics, vol.40, issue 4, 737 (1968). DOI: https://doi.org/10.1103/RevModPhys.40.737

[67] Emil Prodan, Radloff C, Naomi J Halas andP. Nordlander. "A hybridization model for the plasmon response of complex nanostructures", Science, vol. 302, issue 5644, pp. 419-422, (2003). DOI: 10.1126/science.1089171

[68] Edward D. Palik. Handbook of Optical Constants of Solids. Academic Press (1998). ISBN: 9780080556307.

Accepted Manuscript

JMEPEG
https://doi.org/10.1007/s11665-025-10837-y

©ASM International
1059-9495/$19.00

ORIGINAL RESEARCH ARTICLE

Measuring the Impact of Infill Pattern and Infill Density on the Properties of 3D-Printed PLA via FDM

Siddharth Garg, Aditya Singh, and Qasim Murtaza

Submitted: 25 June 2024 / Revised: 1 October 2024 / Accepted: 9 November 2024

In this research, 16 different infill patterns and 5 infill densities for each infill pattern (a total of 80 unique samples) were fabricated to be tested on microhardness, surface deformation and tensile tests. These samples were also simulated using finite element analysis in ANSYS for tensile tests for comparison with the experimental values. The change in values of microhardness and surface deformation across the samples was insignificant, indicating that these two parameters do not play a significant role in influencing these mechanical properties of the 3D-printed samples. The tensile strength of the samples experienced a steady increase as the infill density increased, with quarter cubic pattern demonstrating highest strength at 34.1 MPa for 100% density, while the lowest strength was recorded for lightning pattern at 10.9 MPa for 20% density. The difference between the experimental and simulated results was found to be 12%. Scanning electron microscopy was carried out to determine the reasons behind this difference, which revealed the presence of raster gap voids, partial neck growth voids and intra-bead voids, which form as melt flow and solidification characteristics of the filament are unable to sustain the ideal conditions for more than a few seconds in real life.

Keywords 3D printing, FEA, PLA, SEM, tensile

1. Introduction

Fused deposition modeling (FDM) has recently emerged as the most commonly used additive manufacturing technology because it is fast to create, easily accessible, and low in cost. In FDM, a thermoplastic filament such as PLA (polylactic acid), ABS, or PEEK is heated to a semi-liquid state and extruded into bead-shaped paths through a heating panel mounted on the print head, while it moves relative to the built tray in a predetermined manner according to the G-code input in it (Fig. 1). This deposition occurs layer by layer in 2D, where once a layer is finished, the extruder nozzle moves and starts a new layer on top of the previous one (Ref 1, 2). PLA, being a biodegradable polymer that can be easily dyed into any color, makes it the most sought-after material for rapid prototyping (Ref 3, 4). Integrating a customizable porous structure with PLA has increased the absorption capacity of printed specimens, making them more suitable for areas where parts need adequate cushioning (Ref 5). Since 3D-printed parts are lightweight, and complex geometries can also be printed using FDM, which, if made through conventional machining, can lead to material wastage and long machining times, they are extensively used in the automobile and aerospace industries (Ref 6). In addition, the ability of 3D printing to make customizable parts has also led to its usage in the food, medical and fashion industries (Ref 7).

Prajapati et al. carried out research to determine the correlation between the infill density and compression strength of PLA through ASTM D695, where they concluded that a greater infill density produced more compressive strength (Ref 9). Tanveer et al. studied the correlation between the impact strength of a specimen with its infill density and shell thickness through ASTM D256 and reported that the impact strength increased as the infill density increased and the outer layer thickness decreased (Ref 10). Cwikla et al. tested the tensile strength of samples while varying shell thickness and observed an increase in tensile strength as the shell thickness of the 3D-printed samples was increased (Ref 11). Tang et al. tested the tensile strength of PLA samples while varying the print speed and print temperature and found that the tensile strength increased as the print temperature increased from 200 to 230 °C and then decreased as the print temperature further increased to 240 °C. Similarly, it increased with increasing print speed, reaching a maximum strength at a print speed of 60 mm/min (Ref 12). Abbas et al. carried out Taguchi optimization and reported that the layer thickness has the biggest influence on the printing time of the samples, with more layer thickness resulting in less print time (Ref 13). Celebi et al. printed samples with different layer thicknesses and carried out bending tests using ASTM D790, where they found that increasing the layer thickness increased the bending strength of the specimens (Ref 14).

Previous studies carried out on the 3D printing of PLA is, although extensive, but fragmented in nature, with no comprehensive study being carried out comparing all the major infill patterns commonly used for printing specimens across major testing parameters. This research aims to provide a comprehensive analysis of all major infill patterns and infill densities available on the most commercially used slicing softwares used

Siddharth Garg, Aditya Singh, and **Qasim Murtaza**, Delhi Technological University, Delhi 110042, India. Contact e-mails: officialsiddharthgarg@gmail.com and aditya72003@gmail.com.

Published online: 19 March 2025

for printing and the impact of these two print parameters on the mechanical properties of 3D-printed specimens. Finite element analysis (FEA) has also been carried out to verify the experimental results of the tensile test and to find out the possible reasons behind the difference between the simulated and actual test results. This will help industries, as well as individuals, select the optimal infill pattern and infill density according to the properties desired by their printed part.

2. Experimental Procedure

2.1 Material

For the fabrication of the samples, a white colored Numakers PLA + 1.75 mm thickness (tolerance ± 0.3 mm) filament, imported from Virginia, USA, was utilized, which is manufactured using 100% virgin 3D850 biopolymer resin (Fig. 2a), resulting in low shrinkage and enhanced dimensional stability. XRD analysis of the filament was carried out with a Bruker D8 Advance, through which the absence of broad diffraction peaks can be observed (Fig. 2b), indicating the semi-amorphous nature of the PLA filament used (Ref 15, 16). The filament had a density of 1.24 gm/cm^3, melting temperature of 165 °C, tensile strength of 50 MPa, shore hardness of 40 D, decomposition temperature of 260 °C, and insolubility with water. To minimize the moisture content in the 3D-printed samples, the filament was stored in a vacuum bag before the fabrication of samples (Ref 17).

2.2 Sample Preparation

For the testing, 16 unique infill patterns (Archimedean Curve, Concentric, Cross, Cross 3D, Cubic-Subdivision, Cubic, Gyroid, Grid, Hilbert Curve, Lightning, Line, Octet, Tri-Hexagon, Quarter Cubic, Triangle and Zig-Zag) were chosen (Fig. 3), and five infill densities (20, 40, 60, 80 and 100%) were printed for each pattern (Fig. 4). To eliminate testing bias, five samples of each infill pattern and density (a total of 400

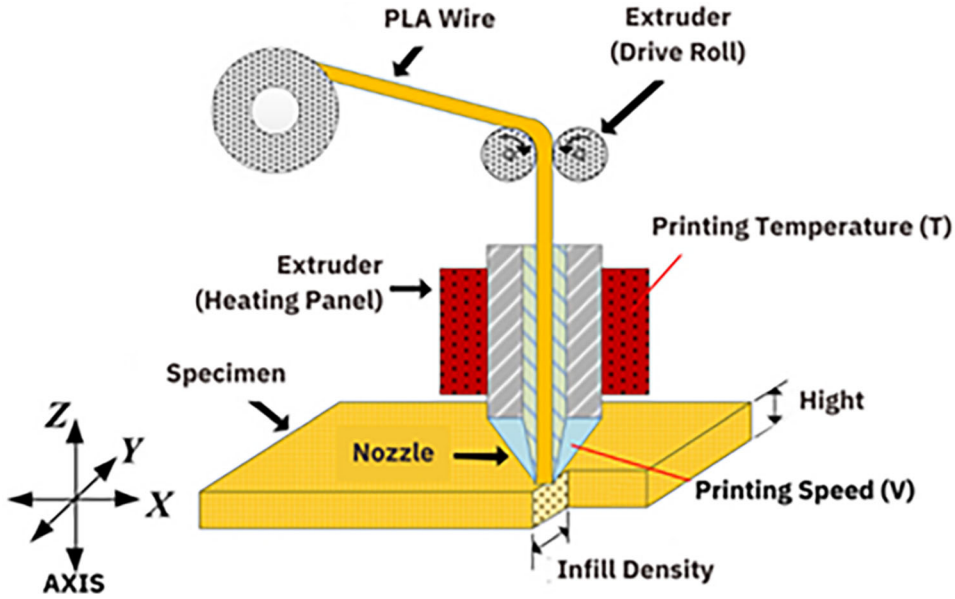

Fig. 1 FDM process for PLA. Used with permission from Y. Yang, X. Dai, B. Yang, P. Zou, F. Gao, J. Duan, and C. Wang, Optimization of Polylactic Acid 3D Printing Parameters Based on Support Vector Regression and Cuckoo Search, *Polym Eng Sci* 63(10), John Wiley and Sons Inc, 2023 (Ref 8)

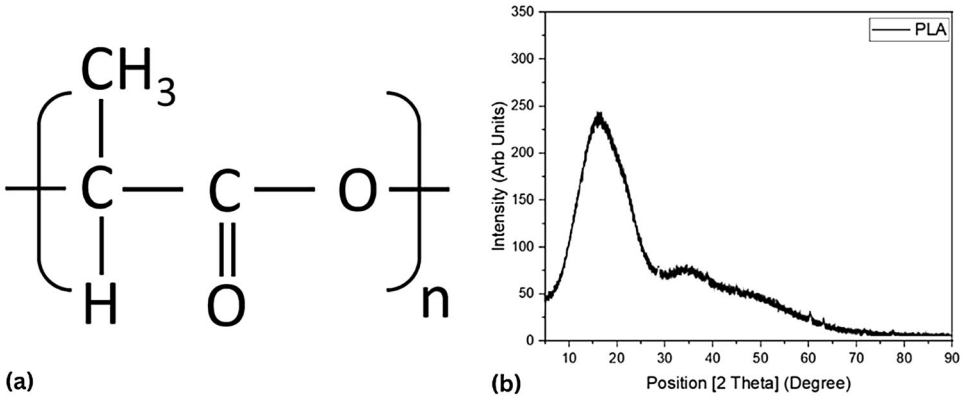

Fig. 2 (a) Chemical structure of PLA (b) XRD pattern of PLA used for 3D printing

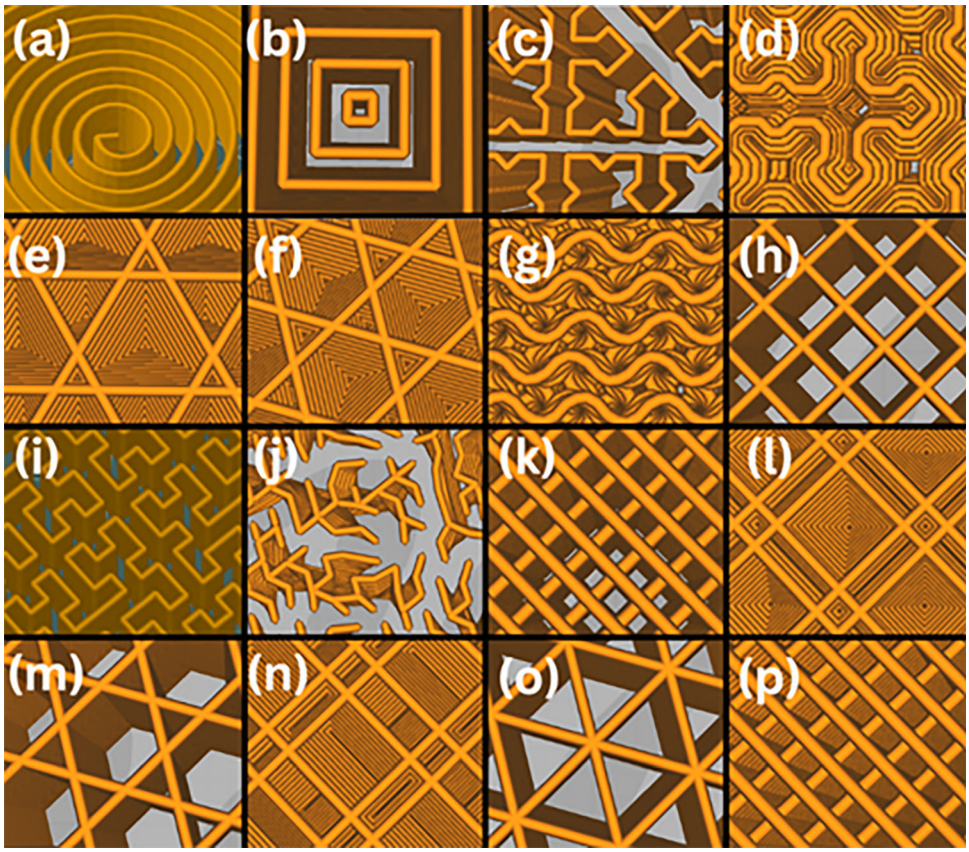

Fig. 3 3D structure of different infill patterns sliced in Ultimaker Cura and Prusa Slicer (a) Archimedean Curve (b) Concentric (c) Cross (d) Cross 3D (e) Cubic-Subdivision (f) Cubic (g) Gyroid (h) Grid (i) Hilbert Curve (j) Lightning (k) Line (l) Octet (m) Tri-Hexagon (n) Quarter Cubic (o) Triangle (p) Zig-Zag

Fig. 4 Different infill densities used for fabrication of the samples (a) 20% (b) 40% (c) 60% (d) 80% (e) 100%

samples) were printed using Creality Ender-3 3D printer (Fig. 5) with a 0.4 mm diameter nozzle and stored in vacuum bags before being taken out for testing.

The samples were first designed in SolidWorks 2022, and then, the .STL files were imported using open-source slicing softwares. Prusa Slicer 2.7.0 was chosen for Hilbert Curve and Archimedean Curve, while the remaining 14 infill patterns were sliced in Ultimaker Cura 5.3.0 (Ref 18-20). The generated G-codes were then input into the 3D printer, and the samples were fabricated along the X-axis according to the optimal print conditions given in Table 1 (Fig. 6), which have been tested and optimized for PLA in the previously carried out research works, as variation in these properties leads to variation in recorded observations for different testing parameters (Ref 21-29).

2.3 Testing Procedure

Vickers microhardness test was carried out on the samples using a Dramin-40 Struers hardness tester (Fig. 7a) according to ASTM E384, with a load of 10 g and a dwell period of 10 seconds (Ref 30-32). Five random sample points were taken for each sample to eliminate any testing bias and obtain a mean value for the sample's microhardness. FaroArm 3D scanner (Fig. 7b), with a least count of 0.01 μm, was utilized to calculate the surface roughness produced on the printed samples. The top printed surface was laid facing upwards on a flat marble floor in a room maintained at 25 °C and 35% RH, and the scanning gun was used to scan the top surface, collecting approximately 60,000 points per scan with a deviation mean of 0.03 μm (Ref 33). These points were imported to PolyWorks software and superimposed on top of the CAD model of samples designed in SolidWorks 2022 to calculate the mean deviation across the printed surface. The tensile samples were 3D printed into a dumbbell shape according to the ASTM D638 Type 1 standard, and the printed samples were tested on Tinius Olsen UTM (Fig. 7c) with a cross-head speed of 5 mm/min (Ref 34-36). For the fracto-

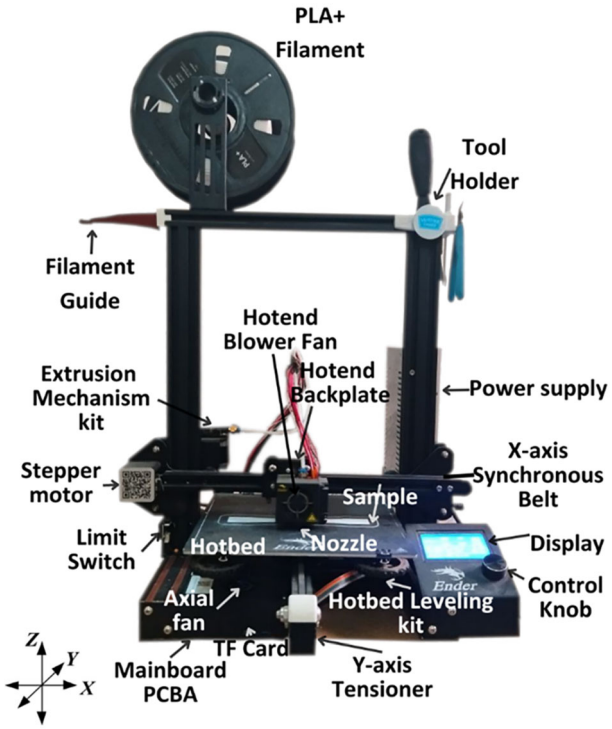

Fig. 5 Labeled image of Creality Ender-3 3D printer used to fabricate PLA samples

Table 1 Print parameters used for printing the samples

Print parameter	Value
Print temperature	225 °C
Bed temperature	60 °C
Print speed	60 mm/s
Layer height	0.12 mm
Wall line count	2
Wall thickness	0.8 mm
Base and top line count (each)	2
Base and top thickness	1 mm
Raster angle	± 45°
Built plate material	Glass

graphic analysis of the broken joint and to identify the print defects in the sample, scanning electron microscopy (SEM) analysis was carried out using Zeiss Evo 50 under high vacuum conditions, where the samples were first sputter coated with a gold-palladium coating for 45 seconds before being mounted into the vacuum chamber (Ref 37).

To simulate the tensile tests on ANSYS, the .STL files were generated from the G-codes generated for each infill pattern and density using G-code reverser. These files were subsequently imported to ANSYS 2024 R1 to be tested using explicit dynamics. For pre-processing, the samples were assigned the properties of PLA, mentioned in Table 2. For the analysis, bottom jaw of the dumbbell was fixed, and the upper jaw was assigned a displacement constraint to replicate the ASTM D638 Type−1 test carried out for the 3D-printed samples (Fig. 8). A curvature-based perturb triangle mesh was assigned an element size of 0.4 mm for proper meshing of the samples (Ref 38). An end time of 0.005 second and displacement of 20 mm were assigned to the samples, based on previous studies where fracture growth and failure were recorded within 20 mm displacement (Ref 39). The samples were analyzed for stress and strain concentration along with energy absorption.

3. Results

3.1 Microhardness

All the tests were carried out in a room maintained at 25 °C, and the standard deviation recorded was under 5% to ensure that no testing error was carried out. The Vickers microhardness recorded for all the samples ranged between 14.5 HRC and 17.9 HRC. The microhardness of the samples showed a small but gradual increase of approximately 10% as the infill density increased from 20% to 100%. This escalation can be attributed to the increase in interlayer bonding between the deposited layers as the infill density increases, which results in the decrease in air gap between the layers and an increase in the number of layers (Ref 40). For similar infill densities, the microhardness for all infill patterns was in the range of 15%, with the gyroid pattern recording the maximum hardness values while concentric pattern recorded the lowest hardness values. This deviation can be attributed to the variation in packing density for different infill patterns that have been fabricated. Overall, the deviation recorded for varying infill patterns and infill densities across all samples was under 23% (Fig. 9), which, compared to previous studies carried out to compare the variation in hardness due to changing printing speed, bed temperature and nozzle temperature, is very low, where variations up to 200% were recorded (41-43). The microhardness of a sample is highly dependent on the quality of fusion that occurs between the polymer layers while printing and its crystallinity, both of which are temperature-dependent phenomena. Since the temperature parameters were kept constant for this study, a large change in the microhardness was not recorded.

3.2 Surface Deformation

For any sample fabricated through FDM, a low surface deformation/roughness is desirable so that it can meet the desirable tolerances needed for the part to be used in an assembly. For this study, mean surface deformation, R_a, was calculated by taking the top face of the printed samples and scanning it using a FaroArm scanner and superimposing it on a CAD model using PolyWorks 2022 software (Ref 44). The recorded R_a values for all the samples fluctuated between 6.02 μm and 6.62 μm (under 10%). From these observations (Fig. 10), no consistent pattern was visible across infill patterns and infill densities, and the value for surface deformation did not seem to vary for the 3D-printed samples as these input parameters of infill pattern and density were varied. Similar findings were also reported by Dezaki et al Ref 45. The temperature difference caused during 3D printing is a principal factor that causes thermal distortion and deforms the surface (Ref 41). As the printing and cooling temperatures are varied, the rate of diffusion of PLA molecules and the time taken for them to bond with each other vary, impacting the temperature gradient and bonding between the layers (Ref 42). Hence, the main reason for the constant readings can be attributed to

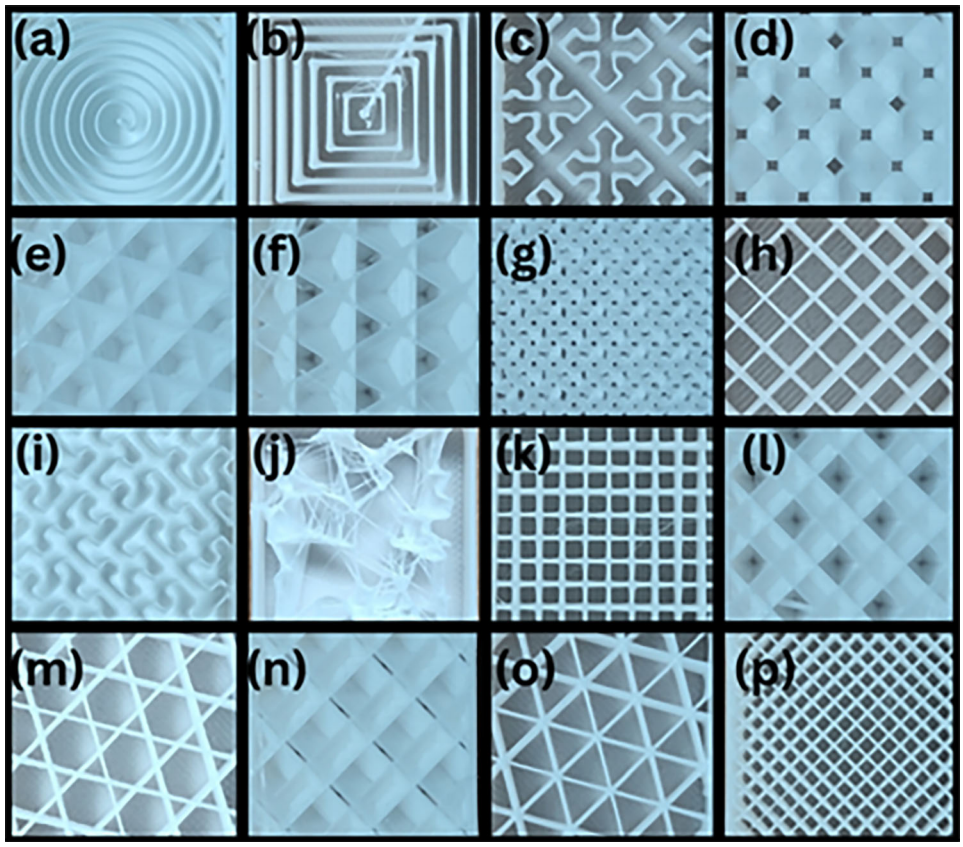

Fig. 6 3D-printed samples of PLA with different infill patterns (a) Archimedean Curve (b) Concentric (c) Cross (d) Cross 3D (e) Cubic-Subdivision (f) Cubic (g) Gyroid (h) Grid (i) Hilbert Curve (j) Lightning (k) Line (l) Octet (m) Tri-Hexagon (n) Quarter Cubic (o) Triangle (p) Zig-Zag

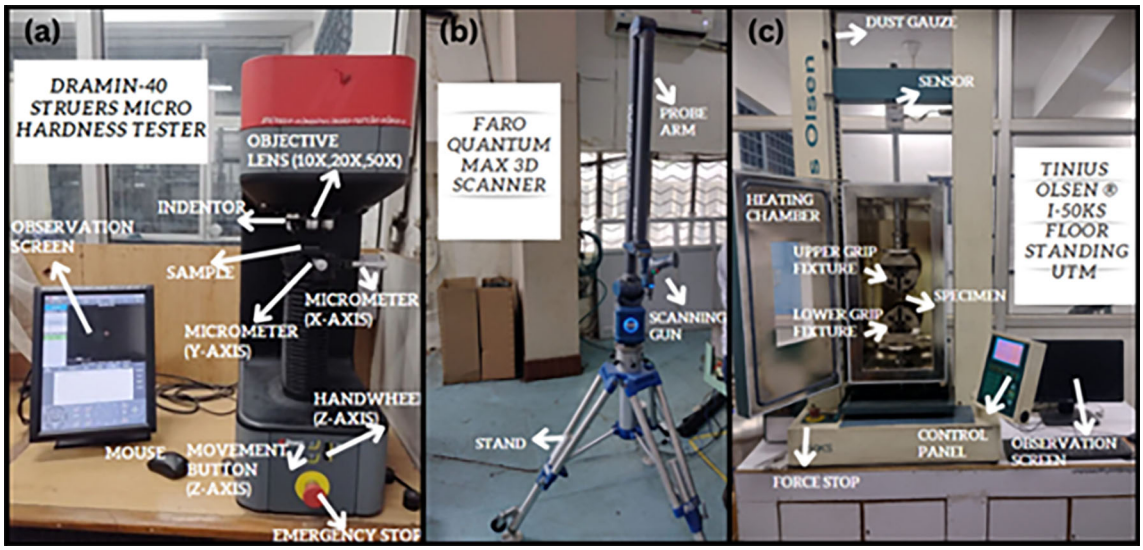

Fig. 7 Testing equipment used for (a) microhardness test (b) surface roughness test (c) tensile test

constant printing and cooling temperatures for all the printed samples, which resulted in equal warpage and delamination of the samples. This temperature dependence has also been confirmed through previous studies, where R_a values have varied to 250% as the print parameters such as nozzle and bed temperature are varied, indicating a parabolic relation between them (Ref 46-50).

3.3 Tensile Strength

Five tensile samples (Fig. 11) for each infill pattern and density were 3D printed to be tested for tensile testing. The standard deviations across all samples were under 4.5%, ensuring that no testing error had occurred. Unlike the theoretical expectation of being fully solid, the 100% infill

Table 2 Properties of PLA used for simulation in ANSYS

Properties	Value
Density	1250 kg/m^3
Coefficient of thermal expansion	1.3*10^{-4} °C^{-1}
Young's modulus	3.4*10^9 Pa
Poisson's ratio	0.35
Bulk modulus	5.2*10^9 Pa
Shear modulus	1.2*10^9 Pa
Nodes	1351296
Elements	1257040

density samples were not found to be 100% solid. This anomaly arises due to the presence of air gaps that are generated during the layer-by-layer deposition of extruded PLA (Ref 51, 52). FEA was carried out for the samples to stimulate the breaking load needed for the samples to reach the breaking point. Alharbi et al. carried out mesh sensitivity analysis and concluded that the results for stress did not vary significantly when the mesh size was varied within a suitable range, thus ensuring reliable results for all FEAs (Ref 53).

The results for the UTS recorded through actual testing, and the FEM were plotted using Origin 2024. The highest tensile strength (experimental) was recorded for Quarter Cubic pattern

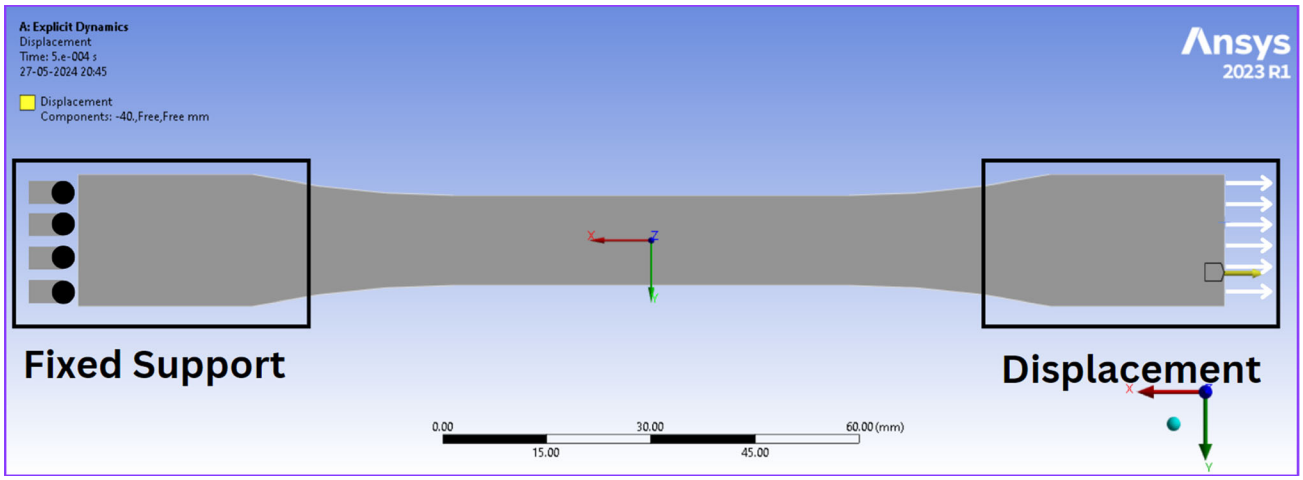

Fig. 8 Marked dumbbell sample used for analysis

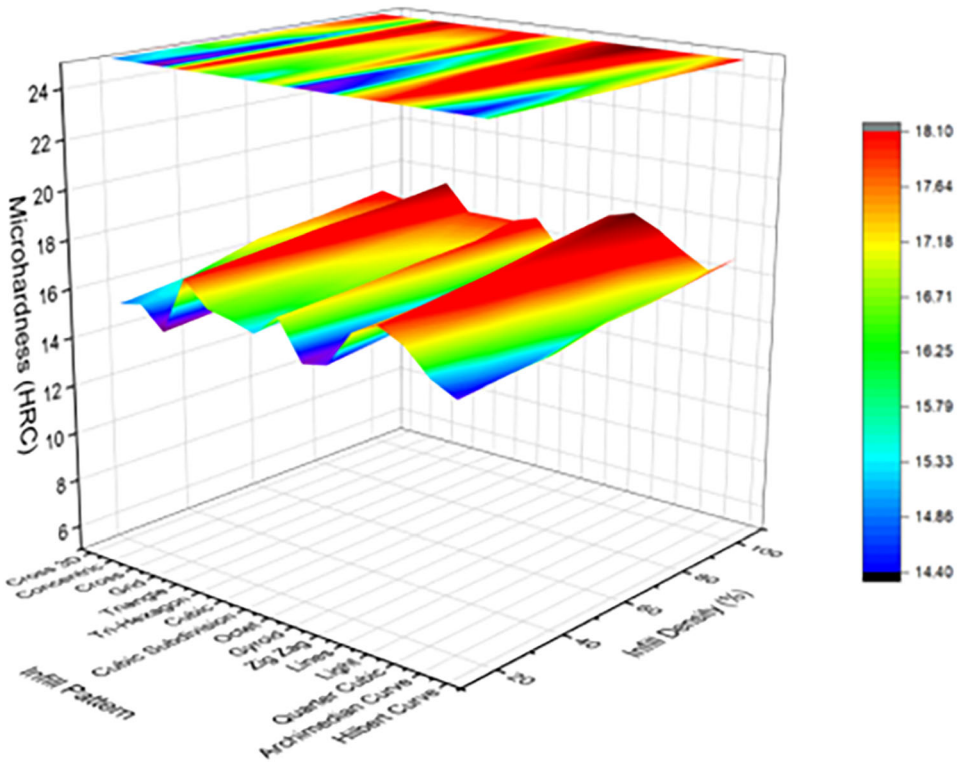

Fig. 9 Graph depicting the microhardness trend

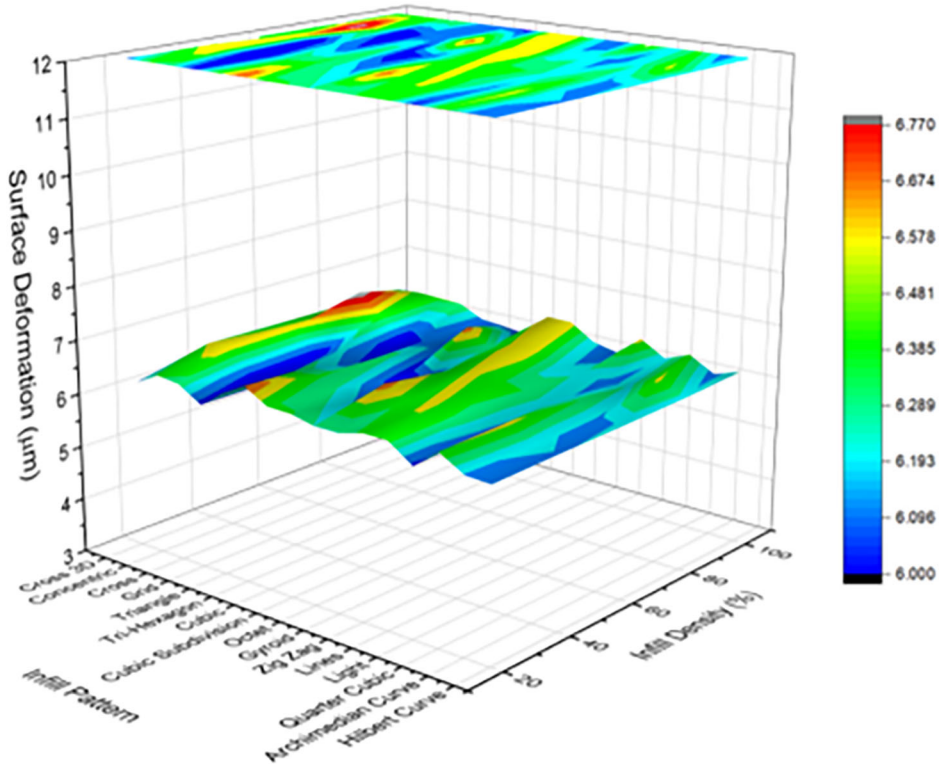

Fig. 10 Graph depicting the surface deformation recorded across the samples

(34.1 MPa for 100% density), followed by Zig-Zag pattern (33.4 MPa for 100% density), while the lowest tensile strength was recorded for Lightning pattern (10.9 MPa for 20% density) followed by Cross pattern (11.5 MPa for 20% density). These readings are consistent with previous studies carried out on PLA (Ref 19, 54-56). From the graphs (Fig. 12), a clear trend of increasing UTS as the infill density increases can be observed, with an average 85% increase in strength as the density increases from 20 to 100%. From this, one can conclude that more infill density directly results in more strength for the sample, while this relation is linear for some samples, others display sudden jumps in strength as the density is increased. This occurs due to an increase in volume fraction as the density increases, which creates a continuation in the resistant region for the mesostructure of the specimen, gradually increasing the energy-absorbing capacity of the specimen as the stresses become evenly distributed (Ref 57). The average difference between the simulated results through FEA and experimental results was recorded at 12%, which is similar to the results reported in previous studies (Ref 58, 59).

All the printed samples showed an elongation of less than 6%, indicating the brittle nature of the sample, which was consistent among all the PLA samples, irrespective of their infill pattern and density. The SEM image of the fractured area reveals a smooth and homogenous crack surface, with little plastic deformation indicating rapid crack propagation (not along the printed filament) and brittle fracture (Ref 60). From the micrograph, we can also observe that there is no debonding between layers even after failure, depicting the successful nature of the 3D print being carried out (Ref 61). In the upper region (crack nucleation site) of the failed fiber, beach markings can be observed (Fig. 13a), which depicts the resistance created during loading of the sample before it ultimately fails in a rapid

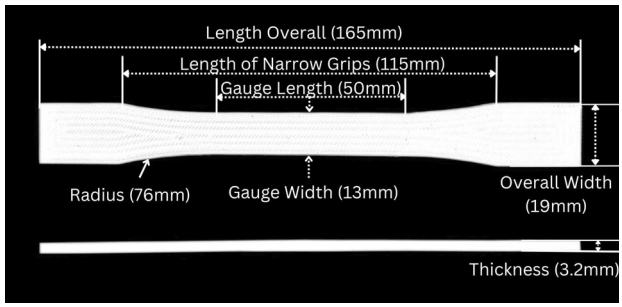

Fig. 11 Labeled tensile sample according to ASTM D638 used for testing

manner (Ref 37). Ridge marks on the fracture surface were also observed in Quarter Cubic samples, indicating high amount of energy dissipation during the failure, which is consistent with the tensile observations (Fig. 13b) (Ref 62). Along with the brittle nature of PLA, voids present in the sample also contribute to the smooth fracture surface, as they act as stress concentrators, and as the fracture occurs, the crack propagates away from these voids (Ref 63). The white edges around the fracture surface are formed due to the strain that PLA, a semi-crystalline polymer, experiences during tensile deformation of the sample as its amorphous parts start to align in the direction of the axis of strain by increasing its opaqueness (Ref 64).

Flaking was also observed in samples (Fig. 14a) indicating craze crack propagation in the samples and the sudden and brittle nature of it, which is further supported by very low density of dimple formation at the fracture surface (Fig. 14b) (Ref 63, 65). These dimples were aligned in the direction of

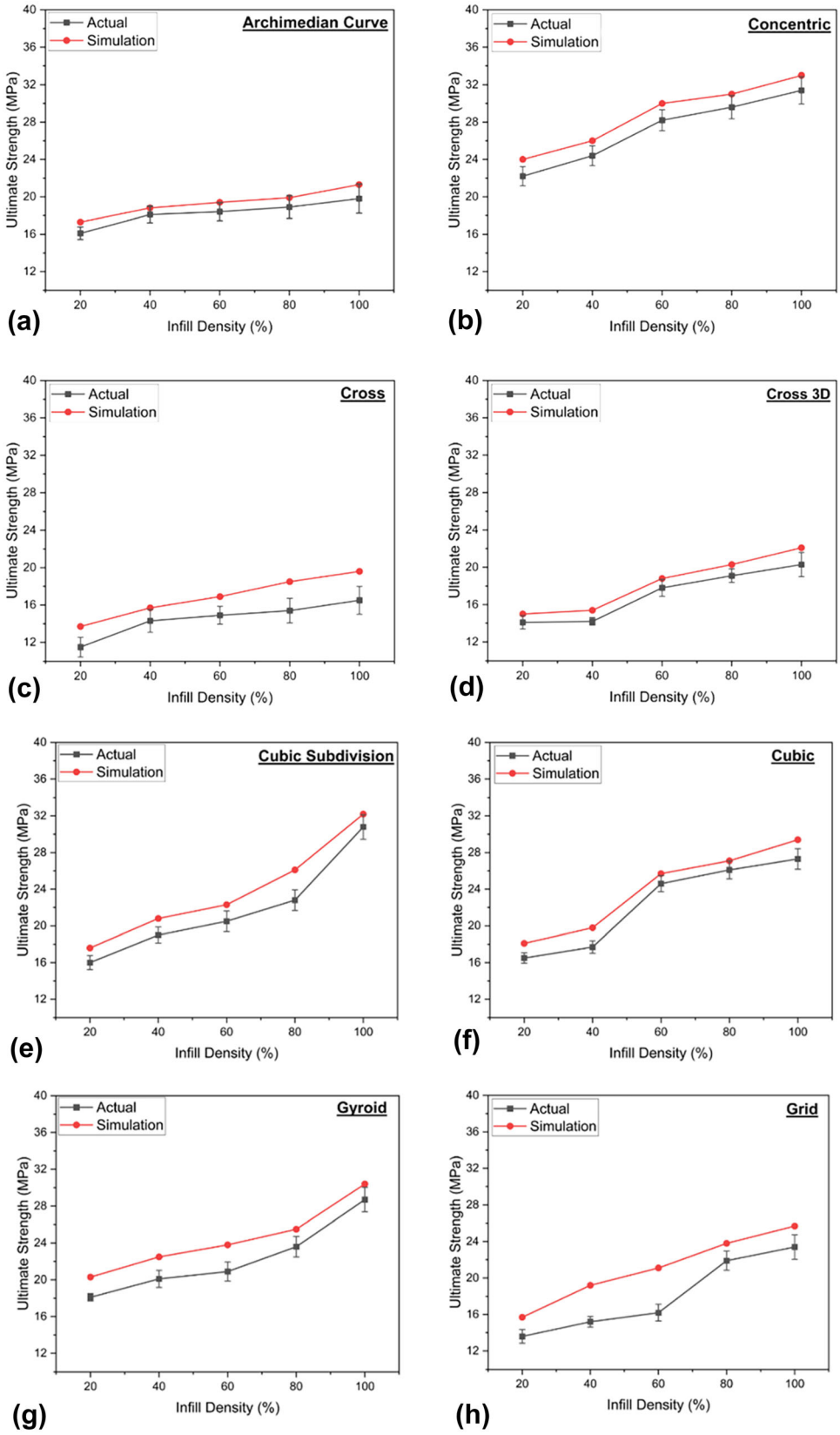

Fig. 12 Graphs depicting the recorded ultimate strength values of specimens under actual load conditions and simulated using ANSYS (a) Archimedean Curve (b) Concentric (c) Cross (d) Cross 3D (e) Cubic-Subdivision (f) Cubic (g) Gyroid (h) Grid (i) Hilbert Curve (j) Lightning (k) Line (l) Octet (m) Tri-Hexagon (n) Quarter Cubic (o) Triangle (p) Zig-Zag

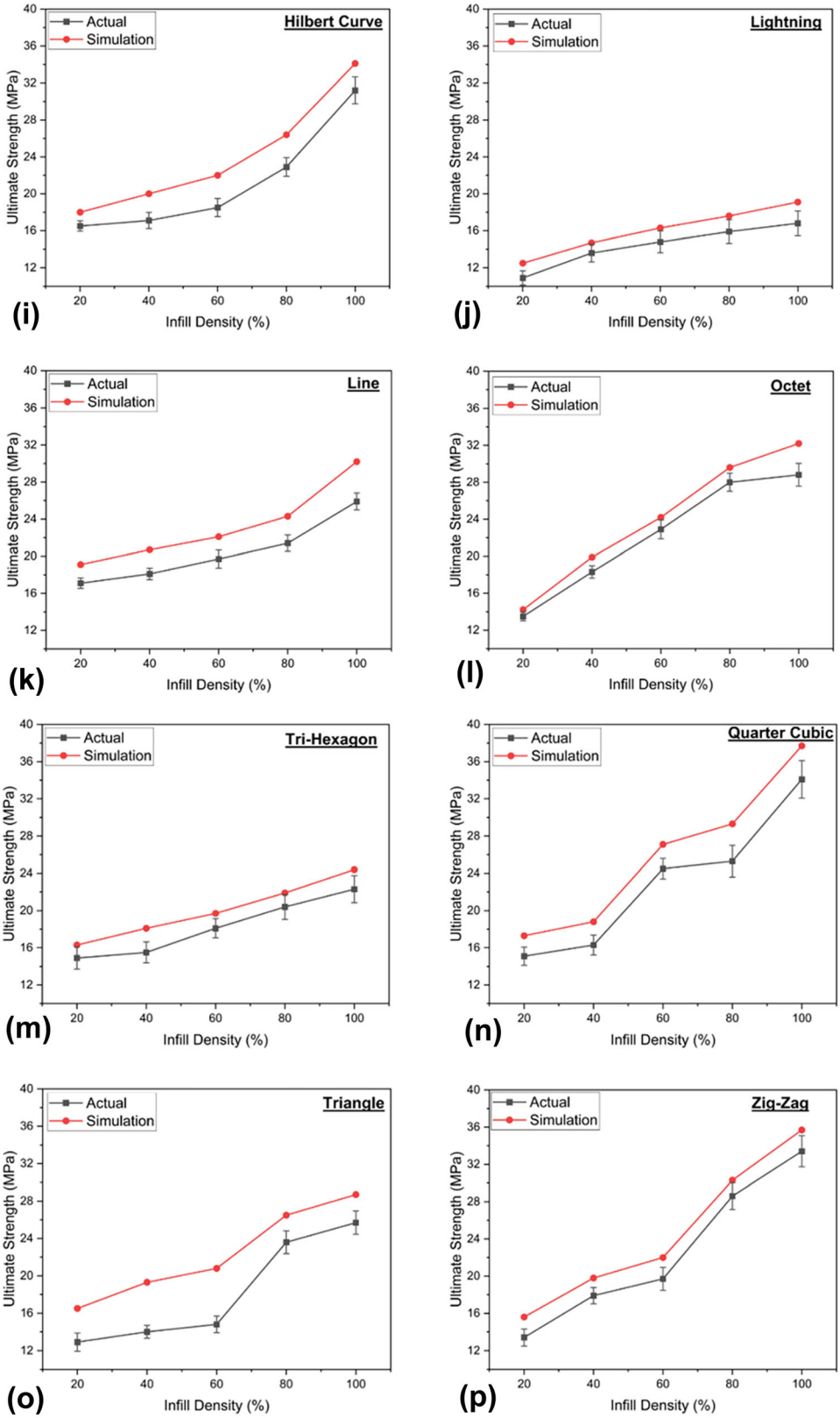

Fig. 12 continued

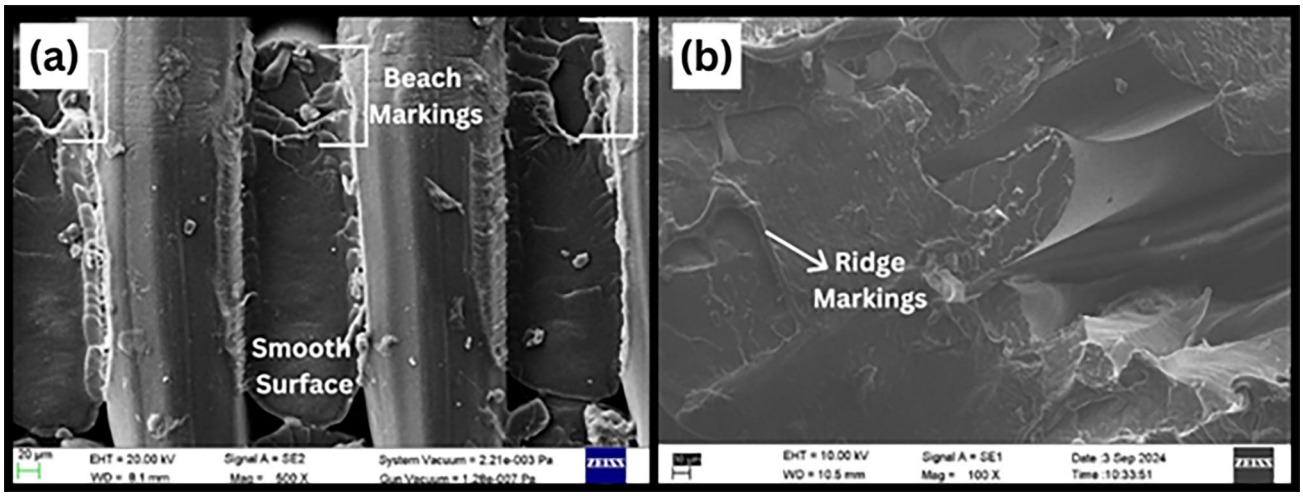

Fig. 13 Fractographic image depicting (a) smooth surface indicating brittle fracture [Grid pattern sample] (b) Ridge marks on the smooth fracture surface [Quarter Cubic pattern sample]

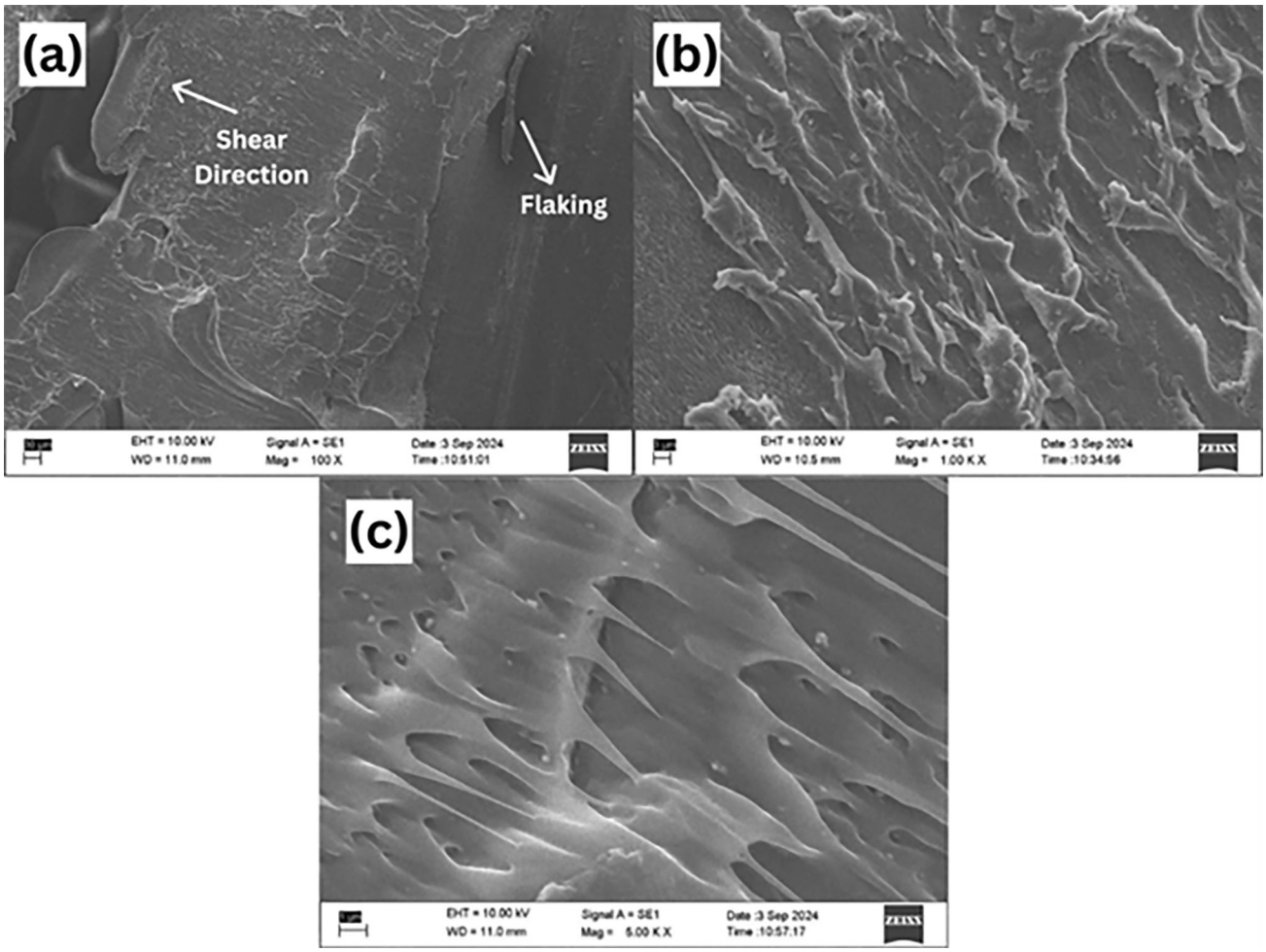

Fig. 14 SEM images for fracture surfaces (a) Depiction of shear direction [Cross 3D pattern sample] (b) Presence of dimples [Cross pattern sample] (c) Elliptical nature of dimples [Cross pattern sample]

shear for all the samples, hence showing elliptical shape (Fig. 14c).

4. Discussion

To determine the reason behind the 12% average error between the simulated and experimental results for the tensile test, SEM was carried out for a cross section of a 3D-printed sample. It revealed the presence of voids across the printed sample, namely raster gap voids, partial neck growth voids and intra-bead voids, which have degraded the properties of 3D printed samples (Ref 66). The most prominent among these were the raster gap voids, also known as air gap voids, which were consistently visible across the sample (Fig. 15). These are essentially separations between adjacent rasters/filaments. These raster gap voids were even detected in samples with 100% infill density. Apart from these, partial neck growth voids, although unevenly distributed, were also visible. Under ideal conditions, these should not form at all as 100% coalescence between two filaments should be there (similar to simulated conditions); however, in real life, it is impossible to achieve as FDM processes are unable of sustaining neck growth beyond a few seconds following the material deposition, as the layers start to solidify before coalescence can be achieved due to even material flow and incomplete filling during FDM (Ref 67). The bonding between individual filaments of the same layer and the neighboring filaments is driven by the thermal energy of semi-molten material. For proper bonding, it is essential that the interface temperature of the deposited material, once it comes in contact with the previously deposited filament, remains above the glass transition temperature prior to bonding. Thus, print parameters like print speed, print temperature, bed temperature and layer height, which affect the melt flow of filament, have been shown to demonstrate an important role in determining the bond quality between the filaments, as it needs to be consistent across the sample and any variation can lead to the formation of voids (Ref 68).

Upon further magnification, small, nearly circular pores also known as intra-bead voids were also visible inside the filament/bead (Fig. 16a). These have previously been shown to have an essential role in developing crack initiation inside the filament due to them acting as stress concentrators, as they cause non-homogenous heat dissipation within the part during manufacturing (Ref 69, 70). The formation of intra-bead voids is also driven by the melt flow and solidification characteristics of the filament, with unevenness in the parameters disturbing the flow and creating voids in it (Fig. 16b).

The presence of these voids apart from the voids present due to varying infill density is the primary reason behind the

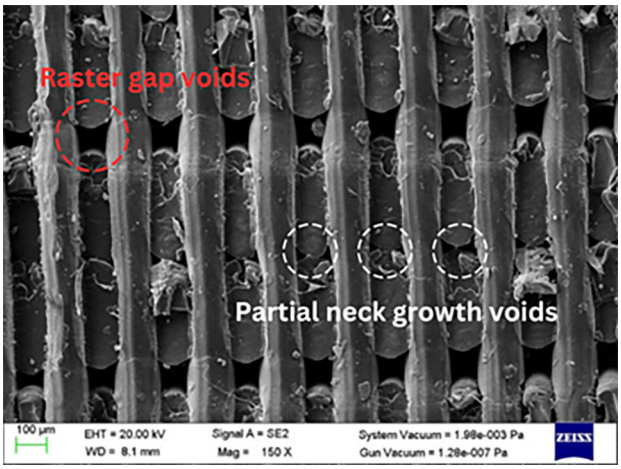

Fig. 15 Presence of voids in the printed sample [Line pattern sample]

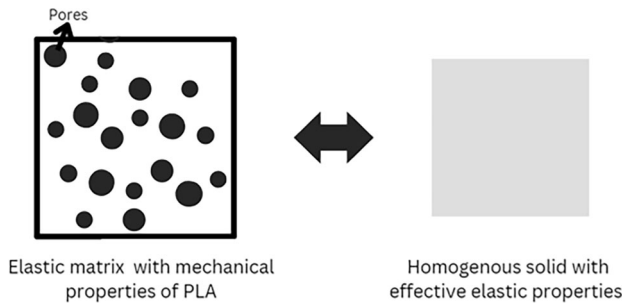

Fig. 17 Proposed model by Wang et al. for equivalent homogenous solids (RVE) used for simulation

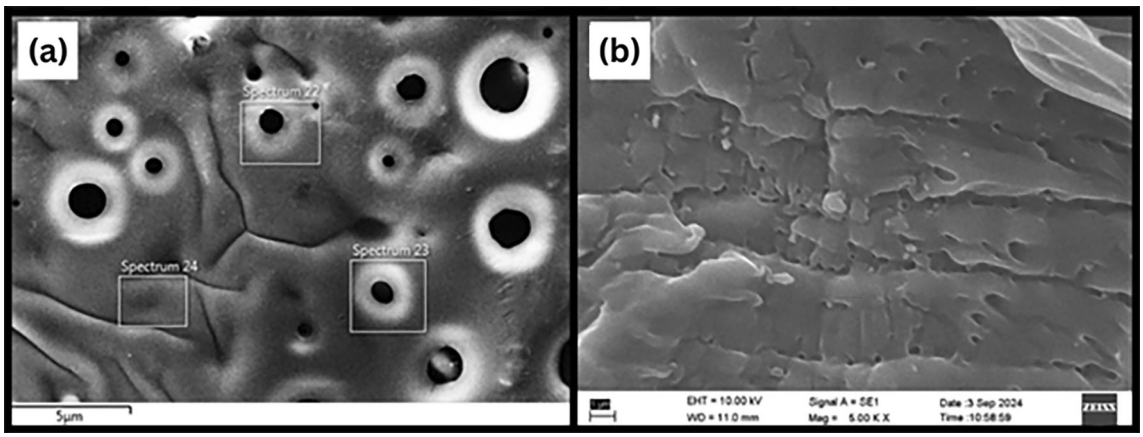

Fig. 16 (a) Formation of nearly circular pores inside the filament [Gyroid pattern sample] (b) Multiple pore formation inside each layer of PLA [Lightning pattern sample]

difference in the experimental and simulation results for the tensile test; as in ANSYS, the models assume 100% ideal conditions and the presence of no voids inside the sample, which have been shown to deteriorate the strength of 3D-printed samples. To counter this, a micromechanical model was presented by Wang et al. correlating the mechanical properties of 3D-printed PLA samples and the internal voids present in the printed samples (Ref 71). Using x-ray computed tomography (XCT), a three-dimensional detailed model of internal pores, including their size, shape and location, was generated. Micromechanical modeling was used to create a representative volume element (RVE) that predicts macroscopic mechanical properties based on quantitatively measured features of interior pores measured by XCT. (Pore structures were assumed to be spherical with varying sizes and were placed in random non-overlapping manner for simulation.) The mapped pore size distribution was used to generate the RVE (using a MATLAB script) to predict the macroscopic properties and generate a homogenous solid with an effective volume (total available volume—total volume of pores) with effective elastic properties to be then used for simulation (Fig. 17). This model resulted in lowering the difference between the actual and simulated results by up to 8%, hence generating a more effective model for simulation.

5. Conclusions

3D printing of PLA was carried out using FDM, and samples were fabricated for 16 infill patterns and 5 infill densities for each pattern (a total of 80 unique samples). The following conclusions can be drawn from the fabrication and subsequent testing of the samples-

1. A slight increase of about 10% was observed in the microhardness as the infill density increased from 20 to 100%, while for a constant infill density, it did not vary much across infill patterns (15% standard deviation across the patterns). Thus, the infill pattern and density do not seem to be important factors for microhardness, which can see variations up to 200% when the print temperature parameters are varied.
2. There was no visible pattern for surface deformation across the infill patterns and densities, where all the R_a values fluctuated between 6.02 μm and 6.62 μm (under 10% standard deviation). Thus, the infill pattern and density are also not important factors for surface deformation, which can see variations up to 250% when the print temperature parameters such as nozzle temperature and bed temperature are varied.
3. The experimental tensile strength of the samples increased as the infill density increased. The highest strength was recorded for quarter cubic pattern (34.1 MPa for 100% density), while the lowest was recorded for lightning pattern (10.9 MPa for 20% density). The average difference between the experimental and simulated results for the tensile strength was recorded at 12%.
4. The main reason behind this difference was the formation of voids, namely raster gap voids, partial neck growth voids and intra-bead voids, which form as the melt flow and solidification characteristics of the filament are unable to sustain the ideal conditions for more than a few seconds.

References

1. M.T. Birosz, D. Ledenyák, and M. Andó, Effect of FDM Infill Patterns on Mechanical Properties, *Polym Test*, 2022, **113**
2. D. Rahmatabadi, M. Khajepour, A. Bayati, K. Mirasadi, M. Amin Yousefi, A. Shegeft, I. Ghasemi, M. Baniassadi, K. Abrinia, M. Bodaghi, and M. Baghani, Advancing Sustainable Shape Memory Polymers through 4D Printing of Polylactic Acid-Polybutylene Adipate Terephthalate Blends, *Eur. Polym. J.Polym. J.*, 2024, **216**, p 113289.
3. T.A. Son, P.S. Minh, and T. Do Thanh, Effect of 3D Printing Parameters on the Tensile Strength of Products, *Key Eng. Mater. Eng. Mater.*, 2020, **863**, p 103–108. https://doi.org/10.4028/www.scientific.net/KEM.863.103
4. U.K. Komal, B.K. Kasaudhan, and I. Singh, Comparative Performance Analysis of Polylactic Acid Parts Fabricated by 3D Printing and Injection Molding, *J. Mater. Eng. Perform. Eng. Perform*, 2021, **30**(9), p 6522–6528.
5. A. Tsouknidas, M. Pantazopoulos, I. Katsoulis, D. Fasnakis, S. Maropoulos, and N. Michailidis, Impact Absorption Capacity of 3D-Printed Components Fabricated by Fused Deposition Modelling, *Mater. Des.*, 2016, **102**, p 41–44.
6. M. Qamar Tanveer, G. Mishra, S. Mishra, and R. Sharma, Effect of Infill Pattern and Infill Density on Mechanical Behaviour of FDM 3D Printed Parts- a Current Review, *Mater. Today Proc.*, 2022, **62**, p 100–108.
7. N. Shahrubudin, T.C. Lee, and R. Ramlan, An Overview on 3D Printing Technology: Technological, *Mater. Appl. Proc. Manuf.*, 2019, **35**, p 1286–1296. https://doi.org/10.1016/j.promfg.2019.06.089
8. Y. Yang, X. Dai, B. Yang, P. Zou, F. Gao, J. Duan, and C. Wang, Optimization of Polylactic Acid 3D Printing Parameters Based on Support Vector Regression and Cuckoo Search, *Polym. Eng. Sci. Eng. Sci.*, 2023, **63**(10), p 3243–3253.
9. A.R. Prajapati, S.R. Rajpurohit, N.H. Patadiya, and H.K. Dave, Analysis of Compressive Strength of 3D Printed PLA Part, *Adv. Manuf. Process. Lecture Notes Mech. Eng.*, 2021 https://doi.org/10.1007/978-981-15-9117-4_22
10. Md. Qamar Tanveer, A. Haleem, and M. Suhaib, Effect of Variable Infill Density on Mechanical Behaviour of 3-D Printed PLA Specimen: An Experimental Investigation, *SN Appl. Sci.*, 2019 https://doi.org/10.1007/s42452-019-1744-1
11. G. Ćwikła, C. Grabowik, K. Kalinowski, I. Paprocka, and P. Ociepka, The Influence of Printing Parameters on Selected Mechanical Properties of FDM/FFF 3D-Printed Parts, *IOP Conf. Ser. Mater. Sci. Eng.*, 2017, **227**(1), p 012033. https://doi.org/10.1088/1757-899X/227/1/012033
12. C. Tang, J. Liu, Y. Yang, Y. Liu, S. Jiang, and W. Hao, Effect of Process Parameters on Mechanical Properties of 3D Printed PLA Lattice Structures, *Compos. Part C: Open Access*, 2020, **3**, p 100076. https://doi.org/10.1016/j.jcomc.2020.100076
13. T. Fadhil Abbas, H. Basil Ali, and K. Kadhim Mansor, Influence of FDM Process Variables' On Tensile Strength, Weight, and Actual Printing Time When Using Abs Filament, *Int. J. Modern Manuf. Technol.*, 2022, **14**(1), p 7–13.
14. A. Çelebi, Experimental and Statistical Investigation of the Bending and Surface Roughness Properties on Three-Dimensional Printing Parts, *J. Test. Eval. Eval.*, 2022, **50**(4), p 2069–2082. https://doi.org/10.1520/JTE20210682
15. M. Kukla, I. Sieracki, W. Maliga, and J. Górecki, Compression Strength of PLA Bolts Produced via FDM, *Materials*, 2022, **15**(24), p 8740. https://doi.org/10.3390/ma15248740
16. S.-M. Lai and P.-W. Li, Effect of Thermoplastic Polyurethane-Modified Silica on Melt-Blended Poly(Lactic Acid) (PLA) Nanocomposites, *Polym. Polym. Compos.. Polym. Compos.*, 2017, **25**(8), p 583–592. https://doi.org/10.1177/096739111702500803
17. Q. Ma, M.R.M. Rejab, A.P. Kumar, H. Fu, N.M. Kumar, and J. Tang, Effect of Infill Pattern, Density and Material Type of 3D Printed Cubic

Structure under Quasi-Static Loading, *Proc. Ins. Mech. Eng. C J. Mech. Eng. Sci.*, 2021, **235**(19), p 4254–4272.
18. B. Pernet, J.K. Nagel, and H. Zhang, Compressive Strength Assessment of 3D Printing Infill Patterns, *Procedia CIRP*, 2022, **105**, p 682–687. https://doi.org/10.1016/j.procir.2022.02.114
19. A. Pandzic, D. Hodzic, and A. Milovanovic, Effect of Infill Type and Density on Tensile Properties of PLA Material for FDM Process, *Annals of DAAAM and Proceedings of the International DAAAM Symposium*, Danube Adria Association for Automation and Manufacturing, DAAAM, 2019, p 0545–0554, https://doi.org/10.2507/30th.daaam.proceedings.074
20. M. Moradi, A. Aminzadeh, D. Rahmatabadi, and A. Hakimi, Experimental Investigation on Mechanical Characterization of 3D Printed PLA Produced by Fused Deposition Modeling (FDM), *Mater. Res Exp.*, 2021, **8**(3), p 035304. https://doi.org/10.1088/2053-1591/abe8f3
21. A.A. Ansari and M. Kamil, Effect of Print Speed and Extrusion Temperature on Properties of 3D Printed PLA Using Fused Deposition Modeling Process, *Mater. Today Proc.*, 2021, **45**, p 5462–5468. https://doi.org/10.1016/j.matpr.2021.02.137
22. L. Marsavina, C. Vălean, M. Mărghitas, E. Linul, N. Razavi, F. Berto, and R. Brighenti, Effect of the Manufacturing Parameters on the Tensile and Fracture Properties of FDM 3D-Printed PLA Specimens, *Eng Fract Mech*, 2022, **274**
23. M.M. Hanon, R. Marczis, and L. Zsidai, Influence of the 3D Printing Process Settings on Tensile Strength of PLA and HT-PLA, *Period. Polytech. Mech. Eng. Budapest Univ. Technol. Econ.*, 2021, **65**(1), p 38–46.
24. H. Bakhtiari, M. Nikzad, and M. Tolouei-Rad, Influence of Three-Dimensional Printing Parameters on Compressive Properties and Surface Smoothness of Polylactic Acid Specimens, *Polymers*, 2023, **15**(18), p 3827. https://doi.org/10.3390/polym15183827
25. H. Gonabadi, Y. Chen, A. Yadav, and S. Bull, Investigation of the Effect of Raster Angle, Build Orientation, and Infill Density on the Elastic Response of 3D Printed Parts Using Finite Element Microstructural Modeling and Homogenization Techniques, *Int. J. Adv. Manuf. Technol.*, 2022, **118**(5–6), p 1485–1510. https://doi.org/10.1007/s00170-021-07940-4
26. N. Vidakis, C. David, M. Petousis, D. Sagris, N. Mountakis, and A. Moutsopoulou, The Effect of Six Key Process Control Parameters on the Surface Roughness, Dimensional Accuracy, and Porosity in Material Extrusion 3D Printing of Polylactic Acid: Prediction Models and Optimization Supported by Robust Design Analysis, *Adv. Indus. Manuf. Eng.*, 2022, **5**, p 100104. https://doi.org/10.1016/j.aime.2022.100104
27. L. Sandanamsamy, J. Mogan, K. Rajan, W.S.W. Harun, I. Ishak, F.R.M. Romlay, and K. Kadirgama, Effect of Process Parameter on Tensile Properties of FDM Printed PLA, *Mater. Today: Proc.*, 2024, **109**, p 1–6.
28. Y. Yang, Y. Liu, W. Hao, G. Guo, and X. Cheng, Study on the Fracture Toughness of 3D Printed Engineering Plastics, *J. Mater. Eng. Perform.*, 2022, **31**(4), p 2889–2895.
29. M. Moradi, A. Aminzadeh, D. Rahmatabadi, and S.A. Rasouli, Statistical and Experimental Analysis of Process Parameters of 3D Nylon Printed Parts by Fused Deposition Modeling: Response Surface Modeling and Optimization, *J. Mater. Eng. Perform.*, 2021, **30**(7), p 5441–5454.
30. S. Garg, S. Bansal, and Q. Murtaza, Failure Investigation of an Elbow Pipe Used in Sewage Water Treatment Facility, *Mater. Corros.Corros.*, 2024, **75**(9), p 1185–1192. https://doi.org/10.1002/maco.202414336
31. C.K. Yeoh, C.S. Cheah, R. Pushpanathan, C.C. Song, M.A. Tan, and P.L. Teh, Effect of Infill Pattern on Mechanical Properties of 3D Printed PLA and CPLA, *IOP Conf. Ser. Mater. Sci. Eng.*, 2020, **957**(1), p 012064. https://doi.org/10.1088/1757-899X/957/1/012064
32. İ. Böğrekci, P. Demircioğlu, H. Saygın Sucuoğlu, and O. Turhanlar, The Effect of the Infill Type and Density on Hardness of 3d Printed Parts, *Int. J. 3D Print. Technol. Digital Indus.*, 2019, **3**(3), p 212–219
33. M.S. Alsoufi and A.E. Elsayed, How Surface Roughness Performance of Printed Parts Manufactured by Desktop FDM 3D Printer with PLA+ Is Influenced by Measuring Direction, *Am. J. Mech. Eng.*, 2017, **5**(5), p 211–222. https://doi.org/10.12691/ajme-5-5-4
34. V.M. Akhil, S.L. Aravind, R. Kiran, S.P. Sivapirakasam, and S. Mohan, Experimental Investigations on the Effect of Infill Patterns on PLA for Structural Applications, *Mater. Today Proc.*, 2023, **76**, p 636–639. https://doi.org/10.1016/j.matpr.2022.10.292
35. S. Garg, A. Sardar, R. Srivastava, S. Verma, and A.K. Madan, Variation in Tensile Strength of 3D Printed PLA Parts by Varying Infill Density and Infill Pattern, *Saudi J. Eng. Technol.*, 2023, **8**(05), p 103–107.
36. S. Garg and Q. Murtaza, Effect of Filler Paste's Mixing Ratio on the Properties of Al-64430 Dip-Brazed Joints, *Weld. World*, 2024 https://doi.org/10.1007/s40194-024-01772-y
37. B. Aloyaydi, S. Sivasankaran, and A. Mustafa, Investigation of Infill-Patterns on Mechanical Response of 3D Printed Poly-Lactic-Acid, *Polym. Test.. Test.*, 2020, **87**, p 106557.
38. M. Pal and M.G. Edwards, Q-Families of CVD(MPFA) Schemes on General Elements: Numerical Convergence and the Maximum Principle, *Arch. Comput. Methods Eng.*, 2010, **17**(2), p 137–189.
39. S. Ganeshkumar, S. Dharani Kumar, U. Magarajan, S. Rajkumar, B. Arulmurugan, S. Sharma, R.A. Changhe Li, and M.F. Ilyas, Investigation of Tensile Properties of Different Infill Pattern Structures of 3D-Printed PLA Polymers: Analysis and Validation Using Finite Element Analysis in ANSYS, *Materials*, 2022, **15**(15), p 5142. https://doi.org/10.3390/ma15155142
40. N. Maguluri, G. Suresh, and S.R. Guntur, Effect of Printing Parameters on the Hardness of 3D Printed Poly-Lactic Acid Parts Using DOE Approach, *IOP Conf. Ser. Mater. Sci. Eng.*, 2022, **1248**(1), p 012004. https://doi.org/10.1088/1757-899X/1248/1/012004
41. R. Raj Mohan, R. Venkatraman, and S. Raghuraman, Experimental Analysis on Density, Micro-Hardness, Surface Roughness and Processing Time of Acrylonitrile Butadiene Styrene (ABS) through Fused Deposition Modeling (FDM) Using Box Behnken Design (BBD), *Mater. Today Commun.*, 2021, **27**, p 102353. https://doi.org/10.1016/j.mtcomm.2021.102353
42. A. Pulipaka, K.M. Gide, A. Beheshti, and Z.S. Bagheri, Effect of 3D Printing Process Parameters on Surface and Mechanical Properties of FFF-Printed PEEK, *J. Manuf. Process.*, 2023, **85**, p 368–386.
43. A.A. Ansari and M. Kamil, Izod Impact and Hardness Properties of 3D Printed Lightweight CF-Reinforced PLA Composites Using Design of Experiment, *Int. J. Lightweight Mater. Manuf.*, 2022, **5**(3), p 369–383. https://doi.org/10.1016/j.ijlmm.2022.04.006
44. S. Garg and Q. Murtaza, Comparative Analysis of Dip-Brazing and TIG Welding on the Properties of Al-64430 Joints, *J. Adhesion Sci. Technol.*, 2024, **39**(3), p 386–400. https://doi.org/10.1080/01694243.2024.2409317
45. M.L. Dezaki, M.K.A.M. Ariffin, A. Serjouei, A. Zolfagharian, S. Hatami, and M. Bodaghi, Influence of Infill Patterns Generated by Cad and Fdm 3d Printer on Surface Roughness and Tensile Strength Properties, *Appl. Sci. (Switzerland)*, MDPI AG, 2021, **11**(16)
46. P. Patil, D. Singh, S.J. Raykar, and J. Bhamu, Multi-Objective Optimization of Process Parameters of Fused Deposition Modeling (FDM) for Printing Polylactic Acid (PLA) Polymer Components, *Mater. Today Proc.*, 2021, **45**, p 4880–4885. https://doi.org/10.1016/j.matpr.2021.01.353
47. A.I. Portoacă, R.G. Ripeanu, A. Dinită, and M. Tănase, Optimization of 3D Printing Parameters for Enhanced Surface Quality and Wear Resistance, *Polymers*, 2023, **15**(16), p 3419. https://doi.org/10.3390/polym15163419
48. K.E. Aslani, D. Chaidas, J. Kechagias, P. Kyratsis, and K. Salonitis, Quality Performance Evaluation of Thin Walled PLA 3D Printed Parts Using the Taguchi Method and Grey Relational Analysis, *J. Manuf. Mater. Process.*, 2020, **4**(2), p 47. https://doi.org/10.3390/jmmp4020047
49. P. Yadav, A. Sahai, and R.S. Sharma, Strength and Surface Characteristics of FDM-Based 3D Printed PLA Parts for Multiple Infill Design Patterns, *J. Inst. Eng. (India)*, 2021, **102**(1), p 197–207.
50. R.D. Bintara, D.Z. Lubis, and YRAji. Pradana, The Effect of Layer Height on the Surface Roughness in 3D Printed Polylactic Acid (PLA) Using FDM 3D Printing, *IOP Conf. Ser. Mater. Sci. Eng.*, 2021, **1034**(1), p 012096. https://doi.org/10.1088/1757-899X/1034/1/012096
51. E. Provaggi, C. Capelli, B. Rahmani, G. Burriesci, and D.M. Kalaskar, 3D Printing Assisted Finite Element Analysis for Optimising the Manufacturing Parameters of a Lumbar Fusion Cage, *Mater. Des.* 2019, **163**
52. M.C. Dudescu, L. Racz, and F. Popa, Effect of Infill Pattern on Fatigue Characteristics of 3D Printed Polymers, *Mater. Today Proc.*, 2023, **78**, p 263–269.
53. M. Alharbi, I. Kong, and V.I. Patel, Simulation of Uniaxial Stress–Strain Response of 3D-Printed Polylactic Acid by Nonlinear Finite

Element Analysis, *Appl. Adhesion Sci.*, 2020 https://doi.org/10.1186/s40563-020-00128-1
54. Y. Faik, Ş İbrahim Baki, K. Fatih, and U. Levent, The Effects of Different Process Parameters of PLA+ on Tensile Strengths in 3D Printer Produced by Fused Deposition Modeling, *El-Cezeri Fen ve Mühendislik Dergisi*, 2023 https://doi.org/10.31202/ecjse.1179492
55. G.A. Johnson, and J.J. French, Evaluation of Infill Effect on Mechanical Properties of Consumer 3D Printing Materials, *Adv. Technol. Innov.*, 2018, **3**(4), p 179–184.
56. M. Rahmat Derise, and A. Zulkharnain, Effect of Infill Pattern and Density on Tensile Properties of 3D Printed Polylactic Acid Parts via Fused Deposition Modeling (FDM), *Int. J. Mech. Mechatron. Eng.*, 2021, **20**(02), p 54–63.
57. P.K. Mishra, P. Senthil, S. Adarsh, and M.S. Anoop, An Investigation to Study the Combined Effect of Different Infill Pattern and Infill Density on the Impact Strength of 3D Printed Polylactic Acid Parts, *Compos. Commun.*, 2021, **24**
58. M.S. Hussin, S. Hamat, S.A.S. Ali, M.A.A. Fozi, Y.A. Rahim, M.S.I.M. Dawi, and M. Darsin, "Experimental and Finite Element Modeling of Partial Infill Patterns for Thermoplastic Polymer Extrusion 3D Printed Material Using Elasto-Plastic Method," *AIP Conf. Proc.*, 2020
59. F. Aldosari, M.A.A. Khan, M. Asad, and F. Djavanroodi, Finite Element Analysis of PolyLactic Acid (PLA) under Tensile and Compressive Loading, *J. Phys. Conf. Ser.*, 2023, **2468**(1), p 012094.
60. J. Carlsson and P. Isaksson, Dynamic Crack Propagation in Wood Fibre Composites Analysed by High Speed Photography and a Dynamic Phase Field Model, *Int. J. Solids Struct.Struct.*, 2018, **144–145**, p 78–85.
61. I. Fekete, F. Ronkay, and L. Lendvai, Highly Toughened Blends of Poly(Lactic Acid) (PLA) and Natural Rubber (NR) for FDM-Based 3D Printing Applications: The Effect of Composition and Infill Pattern, *Polym Test*, 2021, **99**
62. M.R.M. Aliha, N. Nazemzadeh, S.M.N. Ghoreishi, and S.R. Kafshgar, The Impact of Sterilization, Body Environment Condition and Raster Orientation on Tensile-Shear Cracking of Sub-Sized 3D Printed Specimens, *Theor. Appl. Fracture Mech.*, 2023, **126**, p 103953. https://doi.org/10.1016/j.tafmec.2023.103953
63. D. Bermudez, P.A. Quiñonez, E.J. Vasquez, I.A. Carrete, T.J. Word, and D.A. Roberson, A Comparison of the Physical Properties of Two Commercial 3D Printing PLA Grades, *Virtual Phys. Prototyp.*, 2021, **16**(2), p 178–195.
64. C. Abeykoon, P. Sri-Amphorn, and A. Fernando, Optimization of Fused Deposition Modeling Parameters for Improved PLA and ABS 3D Printed Structures, *Int. J. Lightweight Mater. Manuf.*, 2020, **3**(3), p 284–297.
65. R.K. Upadhyay, A.K. Mishra, and A. Kumar, Mechanical Degradation of 3D Printed PLA in Simulated Marine Environment, *Surf. Interfaces*, 2020, **21**, p 100778. https://doi.org/10.1016/j.surfin.2020.100778
66. Y. Tao, F. Kong, Z. Li, J. Zhang, X. Zhao, Q. Yin, D. Xing, and P. Li, A Review on Voids of 3D Printed Parts by Fused Filament Fabrication, *J. Mater. Res. Technol.*, 2021, **15**, p 4860–4879.
67. D. Rahmatabadi, K. Soltanmohammadi, M. Aberoumand, E. Soleyman, I. Ghasemi, M. Baniassadi, K. Abrinia, M. Bodaghi, and M. Baghani, 4D Printing of Porous PLA-TPU Structures: Effect of Applied Deformation, Loading Mode and Infill Pattern on the Shape Memory Performance, *Phys. Scr.*, 2024, **99**(2), p 025013. https://doi.org/10.1088/1402-4896/ad1957
68. S.A. Tronvoll, T. Welo, and C.W. Elverum, The Effects of Voids on Structural Properties of Fused Deposition Modelled Parts: A Probabilistic Approach, *Int. J. Adv. Manuf. Technol.*, 2018, **97**(9–12), p 3607–3618.
69. E.A. Papon and A. Haque, Tensile Properties, Void Contents, Dispersion and Fracture Behaviour of 3D Printed Carbon Nanofiber Reinforced Composites, *J. Reinforc. Plast. Compos.*, 2018, **37**(6), p 381–395.
70. V. Korkut, F. Darıcık, İ. Aktitiz, and K. Aydın, Failure of Surface Modification 3D Printed Polymer Materials by UV/Ozone Irradiation, *Eng Fail Anal*, 2023, **152**
71. X. Wang, L. Zhao, J.Y.H. Fuh, and H.P. Lee, Effect of Porosity on Mechanical Properties of 3D Printed Polymers: Experiments and Micromechanical Modeling Based on x-Ray Computed Tomography Analysis, *Polymers*, 2019, **11**(7), p 1154. https://doi.org/10.3390/polym11071154

Publisher's Note Springer Nature remains neutral with regard to jurisdictional claims in published maps and institutional affiliations.

Springer Nature or its licensor (e.g. a society or other partner) holds exclusive rights to this article under a publishing agreement with the author(s) or other rightsholder(s); author self-archiving of the accepted manuscript version of this article is solely governed by the terms of such publishing agreement and applicable law.

Journal of Marketing Communications

ISSN: (Print) (Online) Journal homepage: www.tandfonline.com/journals/rjmc20

Micro or Meso: Do influencers influence veganism?

Sakhhi Chhabra, Tahir A. Wani & Vaishali Kaushal

To cite this article: Sakhhi Chhabra, Tahir A. Wani & Vaishali Kaushal (02 Mar 2025): Micro or Meso: Do influencers influence veganism?, Journal of Marketing Communications, DOI: 10.1080/13527266.2025.2470982

To link to this article: https://doi.org/10.1080/13527266.2025.2470982

View supplementary material

Published online: 02 Mar 2025.

Submit your article to this journal

Article views: 18

View related articles

View Crossmark data

Full Terms & Conditions of access and use can be found at
https://www.tandfonline.com/action/journalInformation?journalCode=rjmc20

JOURNAL OF MARKETING COMMUNICATIONS
https://doi.org/10.1080/13527266.2025.2470982

Routledge
Taylor & Francis Group

Check for updates

Micro or Meso: Do influencers influence veganism?

Sakhhi Chhabra[a], Tahir A. Wani[b] and Vaishali Kaushal[c]

[a]XLRI, Delhi-NCR, Haryana, India; [b]National Institute of Technology Srinagar, Hazratbal, Srinagar, Jammu and Kashmir, India; [c]Deputy General Manager, Purple Audacity, Purple Audacity Research and Innovation Private Limited, New Delhi, India

ABSTRACT

The change in the communication landscape and the surging role of influencers motivated us to find how different influencer characteristics affect brand engagement and purchase intention between micro-influencers (<10,000 followers) and meso-influencers (10,000–1,000,000 followers). There is no consensus on the effectiveness of these influencer types in literature. We tested various characteristics in the vegan context to understand if such influencers affect users' intention to adopt vegan products and promote veganism. Using PLS-SEM, we analyzed the data collected from 302 respondents. Furthermore, multigroup analysis was used to test the differences between micro and meso influencers across various paths. Our study suggests that an influencer's physical attractiveness, credibility, and parasocial relationship positively impact brand engagement, enhancing purchase intention towards vegan products. Additionally, we found that brand engagement with micro-influencers leads to purchase intention more effectively than with meso-influencers. This study offers novel insights that can assist in deciding the effectiveness of the type of influencers- Micro vs meso, in creating effective vegan communications and its adoption. Understanding these characteristics would help marketers of vegan brands to make optimal communication decisions. It would facilitate influencers in identifying ways to position themselves better and promote a green future by promoting veganism.

ARTICLE HISTORY
Received 1 October 2024
Accepted 18 February 2025

KEYWORDS
Micro-influencers; Meso-influencers; Vegan; influencer characteristics; brand engagement; sustainable marketing

1. Introduction

Digitization and social media have changed how people communicate, learn, and make purchase decisions. Marketers use multiple touchpoints within social media to engage and convert a customer. The 2020 global lockdown was a catalyst to sway a shift in advertising, especially for product placements, with a 46% increase in social media influencers than celebrity endorsements (Forbes 2021). Social media influencers (SMIs) are digital influencers who have built sizable social networks of followers and influence as opinion leaders (Torres, Augusto, and Matos 2019). The interest in influencer marketing is proliferating as interactions are more content-driven (Lou and Yuan 2019), and product recommendations from influencers drive sales (Mediakix 2019). Owing to the same

CONTACT Sakhhi Chhabra sakhhichhabra@xlri.ac.in XLRI, Delhi-NCR, Haryana, India
Supplemental data for this article can be accessed online at https://doi.org/10.1080/13527266.2025.2470982
© 2025 Informa UK Limited, trading as Taylor & Francis Group

influencer marketing, food and its marketing are not alien to social media influence (Gram et al. 2010).

Influencer marketing is the way companies collaborate with influencers to raise brand recall or recognition and conversion among a specific target group rather than marketing directly to customers (Kim and Kim 2021). With the rising power of influencer marketing within India, it was valued at Rs 12 billion (Statista 2024). It is expected to grow at a CAGR of 25 per cent to reach Rs 105 billion by 2027 (Statista 2024). However, as progressive advertising budgets are allocated to influencer marketing, there is still doubt about their efficacy. This stimulates the need to develop a better understanding of the drivers of influencer marketing success (Hughes, Swaminathan, and Brooks 2019).

Celebrity and macro influencers (over one million followers) have often been earmarked as having the ability to generate awareness from a single post (Li et al. 2024). From giant multinationals with considerable budgets to small brands with limited budgets, they viewed celebrities as the most influential (Lv et al. 2023). Even though Mega & Macro influencers are considered to be experts and rich in cultural capital (Campbell and Farrell 2020; Hernández-Méndez and Baute-Díaz 2024), industry reports have exhibited micro-influencers as more credible and authentic, providing believable content (Audrezet, De Kerviler, and Moulard 2020; Reinikainen et al. 2020). Between these two types of influencers, meso-influencers, aka 'rising stars', have between 10,000–1,000,000 followers.

Prior research has shown that an influencer's likeability, attractiveness, and credibility depend on their followers (De Veirman, Cauberghe, and Hudders 2017; Jin and Phua 2014). Nevertheless, which type of influencer would be more effective in brand engagement is conjectural. The main objective of this study is to compare the influencer characteristics of micro-influencers with less than 10,000 followers and meso-influencers with followers between 10,000–1,000,000 and check their effect on brand engagement and purchase intention. Thus, we aim to find out:

RQ1: How do different influencer characteristics affect brand engagement among micro and meso influencers?

RQ2: How does brand engagement affect purchase intention among micro and meso influencers?

In this research, we shall focus on vegan food as context because of the growing popularity of veganism as a lifestyle (Gheihman 2021). Mega influencers and celebrities have driven this trend by endorsing the environmental and health benefits of the vegan diet (Sharma 2021); however, the role of micro and meso influencers is yet to be tested. Social media has been lately the most convenient platform for activism and creating influence (Vestergren and Uysal 2022), primarily exhibiting a favourable impact on the environment compared to other forms of diet (Chai et al. 2019). Testing the effect of different types of influencers in this context would add a new dimension to sustainable marketing literature (Bryant 2019). The social media platform used for studying this phenomenon is Instagram because of its popularity in influencer marketing (Mediakix 2019), with over two billion people using Instagram at least once a month (Business of Apps 2024). Also, the fact that over 300 million

active users of Instagram are from India and over 70% of users are under 35 years old (Business of Apps 2024) further validates the use of this platform for this research.

Voorveld (2019) asserts that academic research on the effectiveness of SMIs is scant (Ki and Kim 2019; Torres, Augusto, and Matos 2019). Most studies related to the type of SMIs are in the purview of comparison of the efficacy of micro-influencers and celebrities. This leaves a gap for the less explored meso influencers, who can be appealing as brand endorsers since they are rising stars but not established celebrities (Borges-Tiago, Santiago, and Tiago 2023). In this research, we study various characteristics of micro and meso influencers and how they impact brand engagement and purchase intention in the vegan context. The influencer characteristics used in this study have not been combined in the same framework. The study encompasses factors such as physical attractiveness, attitude homophily, influencer credibility, and parasocial relationships as antecedents, bringing a holistic perspective to SMI literature. Earlier studies have tested the effect of various characteristics of influencers with varied outcome variables (Hernández-Méndez and Baute-Díaz 2024; Belanche et al., 2021; Sheng, Lee, and Lan 2023), but these sets of characteristics have not been compared with brand engagement as the outcome variable in a vegan context.

The novel contribution of this study, which distinguishes it from other work, is the comparison of micro and meso influencers together in a vegan context. The literature on food sustainability is limited, which demands more studies in this direction. Methodologically, we have used PLS-SEM to conduct a multigroup analysis and find the significance of the relationship between different variables. This study offers immense benefits to practice. Firstly, the findings can help organizations decide on the type of influencer to use in their marketing communications. Secondly, the firms that deal with vegan products could use the findings of this study to differentiate between micro and meso-influencers and make better marketing decisions. Brand managers of vegan products can benefit by knowing the characteristics required to influence audiences and optimize brand communications. Providing educational content with the right type of influencer will help in the right positioning. Many companies aim to engage consumers with their brand and materialize the association for a better return on investment. Finally, social media influencers could benefit from the results by understanding which characteristics are most significant in engaging followers with brands. This would help them stand out, as compared to others in the market, and establish parasocial relationships. Also, promoting vegan diets can foster change towards a green future and help achieve UN sustainable goals 12 of 'responsible consumption and production' and 13 of 'climate action'.

In the subsequent sections, we present a literature review focusing on constructs used in previous studies to comprehend influencers' characteristics. Then, we conceptualize the model for the research and explain the methodology and data collection process. The fourth section presents the findings by laying down the significant influencer characteristics among micro and meso influencers that affect brand engagement and purchase intention. Section five includes discussions, explaining the novel implications related to the study, and then we conclude with the limitations section and scope for future work.

2. Conceptual background and hypothesis development

As social media influencers have become more popular, many research studies have focused on establishing their success as a marketing tool. Studies categorize influencers by their follower count. The hierarchy starts with micro-influencers, who have fewer than 10,000 followers. Next are meso-influencers, who have between 10,000 and 1,000,000 followers. Finally, macro-influencers, also known as mega-influencers, boast over 1,000,000 followers (Boerman 2020). Campbell and Farrell (2020), in their classification, differentiated between Nano (1,000–10,000 followers) and micro-influencers (10k-100,000). Others have found nano influencers to be part of micro-influencers (Boerman 2020). Similarly, there are influencer classifications that consider Macro influencers with a following of 100k+ and Mega influencers and celebrities as having a following of 1 million+. For this study, we use Boerman's (2020) classification as the base and try to find the difference in characteristics between newcomer micro-influencers with less than 10,000 followers and rising stars meso-influencers with 10,000–1,000,000 followers.

There has been a conjecture in research, with some studies showing the effectiveness of mega-influencers than the micro influencers (De Veirman, Cauberghe, and Hudders 2017; Conde and Casais 2023; Janssen, Schouten, and Croes 2022), while some noticed the inverse impact (Borges-Tiago, Santiago, and Tiago 2023; Kay, Mulcahy, and Parkinson 2020; Park et al. 2021). Handful studies found no differences between influencer types (Aw and Chuah 2021; Boerman 2020; Britt et al. 2020).

The appeal of SMIs contrasts since they have varied traits, skills, and experiences. Owning their visibility online, these endorsers can be reasonably intriguing to brands as they can influence abundant followers at a lower cost than mega-influencers. As influencers gain traction, their followers increase, which may affect many outcomes. The current study uses Cacioppo and Petty (1981) Elaboration Likelihood Model (ELM), which explicitly states that there are two routes of persuasion: the central route, where a person assesses the information provided against how well it supports their values, and the peripheral route, where the person assesses how attractive the communication source is without performing in-depth deliberation. We have specifically chosen influencer's characteristics based on ELM. Influencer credibility and parasocial relationships- part of the central route of persuasion are characterizations of the influencers based on the perceptions of the followers (Masuda, Han, and Lee 2022). Physical attractiveness and attitude homophily, as part of the peripheral route- are qualified as personal attributes that the influencers possess (Masuda, Han, and Lee 2022). An attempt has been made to specifically comprehend how these influencer characteristics differ between micro and meso influencers and affect brand engagement and purchase intention changes.

2.1. Influencer's physical attractiveness

Before social media took the world by storm, advertisers used to cast pretty and handsome celebrities to endorse their products because the audience used to trust their credibility and idealistic beauty (Joseph 1982). The source attractiveness model (McGuire 1985) theorizes that an endorser's attractiveness boosts the success of an endorsed ad because customers form positive stereotypes about attractive people. However, research on social media influencers (SMIs) has found mixed results relating

to physical attractiveness in building trust in influencer-follower relationships. Contrary to conventional wisdom, athlete sex appeal negatively influences brand trust and purchase intention (Frank and Mitsumoto 2023).

The notion that if a communicator is attractive, the audience may be willing to accept the communicator's message (Kahle and Homer 1985) varies in different contexts. In the case of luxury brands (Lee and Watkins 2016) or the beauty and fashion sector (Sokolova and Kefi 2020), physical attractiveness was found to have a substantial effect on forming parasocial relationships and credibility, respectively. Conversely, participants perceived mega-influencers and nano-influencers to possess similar expertise, trustworthiness, and attractiveness in a health communication study (Looi, Kemp, and Song 2023). It is yet to be proven if micro and meso influencers' physical attractiveness affects brand engagement in a vegan context. Thus, we hypothesize:

Hypothesis 1: Physical Attractiveness of (a) micro-influencer and (b) meso influencer is positively associated with follower's brand engagement.

2.2. Attitude homophily

Social media influencers perceived to be similar in beliefs, values, experiences, and lifestyles by the receiver tend to be more effective as they are attitudinally homophilous (Sokolova and Kefi 2020). Shan, Chen, and Lin (2020) stated that a close resemblance between a consumer's ideal self-image and a social media influencer's image leads to effective endorsement outcomes. McCormick (2016) proved that celebrities who are acquainted with their audience are more useful in marketing. The effects of the homophily construct have been found to influence the perceived expertise of vloggers, thereby leading to emotional attachment to them, especially in the beauty industry (Ladhari, Massa, and Skandrani 2020). In an online health behaviour study by Wang et al. (2008), followers were likely to adopt the advice offered by influencers upon finding the online health information stimuli as more homophilous. However, a study of Instagram influencers related to COVID-19-prevention of public service announcements (PSAs) found nano-influencers (<1,000 followers) to have greater homophily than mega-influencers and displayed greater intention to engage in COVID-19 prevention behaviours (Looi, Kemp, and Song 2023). It is speculative if the effect of attitude homophily can be observed on brand engagement between different types of influencers. Thus, the following hypothesis is proposed:

Hypothesis 2: Attitude homophily of (a) micro-influencer and (b) meso influencer is positively associated with followers' brand engagement.

2.3. Influencer credibility

The literature on persuasive communication has demonstrated that to build strong perceptions of their credibility, influencers entail proficiency and trustworthiness amongst their social media audience (Schouten, Janssen, and Verspaget 2020). Research on

endorsement effects has shown that consumers are more likely to positively gauge brands and products endorsed by people perceived as credible (Bergkvist and Zhou 2016; Erdogan 1999). Influencer credibility positively impacts customers' product views, brand attitudes, and purchase intentions (Byun and Ahn 2023; Djafarova and Rushworth 2017; Erkan and Evans 2016; Reichelt, Sievert, and Jacob 2013). Schouten, Janssen, and Verspaget (2020) argue that influencers may be perceived as more credible product endorsers than celebrities as they have established careers by devoting themselves to a specific realm of interest. Influencers are more likely to be perceived as knowledgeable about products and services than traditional celebrities because of their self-acclaimed expertise in their domain of interest (Balog, De Rijke, and Weerkamp 2008; Erz and Heeris Christensen 2018). Djafarova and Rushworth (2017) also echoed that Nontraditional celebrities are progressively regarded as more powerful than traditional celebrities in the online context since they are perceived as more credible and accessible only to a niche group of people.

Akin to the above, Li et al. (2024) and Conde and Casais (2023) mentioned that if consumers are concerned about popularity as the basis of evaluations, then mega- (vs. micro-) influencers could have a positive effect, while the reverse effect could occur if they are involved with authenticity (Park et al. 2021). Nonetheless, in the context of vegan influencers, whether there is a difference between the credibility of micro-influencers and meso influencers is yet to be examined. Thus, we will explore the effect of source credibility on brand engagement in the case of Micro and Meso influencers.

Hypothesis 3: The credibility of (a) micro-influencers and (b) meso influencers is positively associated with followers' brand engagement.

2.4. Parasocial relationship

Parasocial relationships are defined by Horton and Richard Wohl (1956) as the long-lasting bonds consumers obtain with a mediated performer. According to the theory of parasocial interaction (PSI), the appearance of intimacy where the user views the performer as a close conversational friend (Horton and Richard Wohl 1956) is mistaken for a genuine interpersonal relationship (Dibble, Hartmann, and Rosaen 2016). Social media influencers develop PSI by continually sharing details of a person's life and directly interacting with followers (Colliander and Dahlén 2011). These functions create an illusion of intimacy between influencers and followers (Munnukka et al. 2019). Consumers with a high need to belong (NTB) are more likely to form one-sided (parasocial) relationships with celebrities (Boerman and Van Reijmersdal 2020), and bidirectional relations are faux.

A study of young women following celebrities and bloggers on Instagram found that followers can relate to digital personalities more since they seem to have compelling persuasiveness and credibility (Djafarova and Rushworth 2017). Research has indeed found evidence for experiences of PSI with influencers on blogs (Colliander and Erlandsson 2015), YouTube (Folkvord et al. 2019; Lee and Watkins 2016; Munnukka et al. 2019), Facebook (Tsai and Men 2013), and Instagram (Chen 2018). Conversely, a 'real' friendship is more illusory between a blogger and a follower (Labrecque 2014; Lee and Watkins 2016). Aw and Chuah (2021) found that the number of followers hurts the

parasocial relationship. Sheng, Lee, and Lan (2023) found that parasocial relationships with micro-influencers enhance customer engagement, brand preference, and purchase intention. Conversely, a strong parasocial relationship leads to improved following (Conde and Casais 2023). It is yet to be found how the parasocial ties of micro and meso influencers with varying followers affect brand engagement in a vegan context. Thus, the following hypothesis proposes:

Hypothesis 4: Parasocial Relationship of (a) micro-influencer and (b) meso-influencer is positively associated with followers' brand engagement.

2.5. Brand engagement

Businesses are progressively seeking customer involvement and engagement for their brands. Despite substantial practitioner interest, academic inquiry into 'brand engagement' as a marketing outcome variable has been scant (Hollebeek 2011). Especially in the case of influencer marketing as a communication tool, the effectiveness of brand engagement has rarely been captured. It has been stated in the literature that when the message comes from a reference group, the individual uses the brand associated with that message to form their self-concept, establishing a connection or link with it (Escalas and Bettman 2003). Followers of digital opinion leaders influence greater engagement towards the recommended brands by integrating these brands into their self-concept, thus contributing to constructing their identity (Escalas and Bettman 2003; Sprott, Czellar, and Spangenberg 2009).

Marques, Casais, and Camilleri (2021) and Campbell and Farrell (2020) indicated that micro-influencers can establish higher consumer – brand engagement levels. In the case of endorser – brand engagement development, Borges-Tiago, Santiago, and Tiago (2023) found macro-influencers have more engagement than mega-influencers, proving 'less is more'. Macro-influencers proved more effective for those less aligned (Borges-Tiago, Santiago, and Tiago 2023), even though mega-influencers could boost brand credibility and equity for brands with well-established congruence with endorsers. Thus, it is meaningful to research if followers' brand engagement affects purchase intention when different types of influencers are involved. Accordingly, we propose the following hypothesis:

Hypothesis 5: Brand engagement of (a) micro-influencers and (b) meso influencers is positively associated with followers' purchase intention.

2.6. Purchase intention

Over the years, multiple customer equity drivers have been studied in influencer marketing, such as purchase intent, perceived product quality, perceived product design, brand attitude, and brand trust (Frank and Mitsumoto 2023). However, brand engagement's effect on purchase intention has yet to be captured across micro and meso influencers in the vegan context. On Instagram, behavioural intentions are closely linked to actual

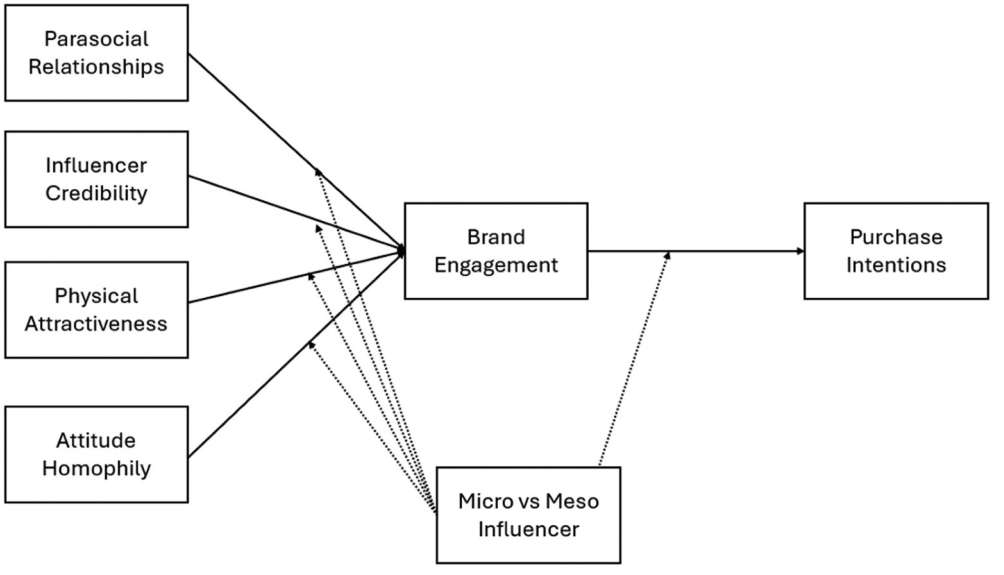

Figure 1. Conceptual Framework.

behaviours (Casaló, Flavián, and Ibáñez-Sánchez 2020). Behavioural intention captures the intent to buy or use the product upon the user's recommendation (Ki and Kim 2019; Thakur, Angriawan, and Summey 2016) or share it with others (Casaló, Flavián, and Ibáñez-Sánchez 2017). Thus, we also measure the interaction effect of all variables put together.

Hypothesis 6: (a) Physical Attractiveness (b)Attitude homophily (c) Credibility (d) Parasocial Relationship (e) Brand engagement has more influence on followers' purchase intention in the case of a micro-influencer than a meso influencer.

The present study examines followers' responses toward influencers promoting a vegan product. Understanding antecedents of brand engagement would aid influencers in building a better bond with their followers. Also, knowing the effect of brand engagement on purchase intention would facilitate the endorsed brands in judging the effectiveness of the type of influencer. The conceptual framework for the study is provided in Figure 1.

3. Methodology

3.1. Instrumentation

Scales for Influencer credibility (Expertise and authenticity) were adopted from Lou and Kim (2019); b) Parasocial relationship from Perse and Rubin (1989); c) Attitude Homophily from Lou and Kim (2019); d) Physical Attractiveness from Duran and Kelly (1988); e) Brand Engagement from Sprott, Czellar, and Spangenberg (2009) and Purchase from Casaló, Flavián, and Ibáñez-Sánchez (2017). A five-point Likert scale

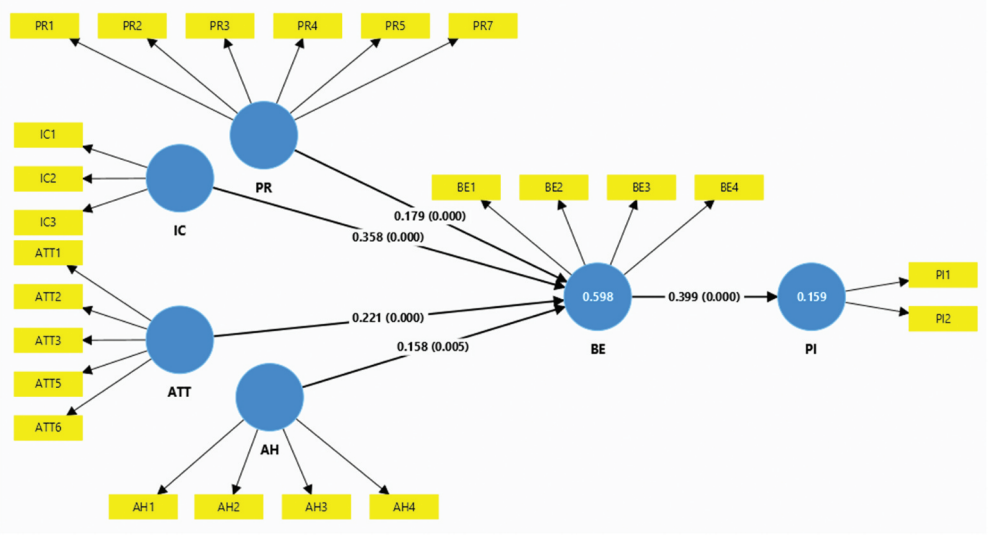

Figure 2. Structural Model (complete Sample).

was used to elicit responses for all the abovementioned constructs (see Table A1-Annexure I for the items). Further, questions on the respondents' demographics and the vegan influencers they follow were designed using nominal scales. A pre-test of the questionnaire was done, wherein 16 participants were invited to provide their feedback. The questionnaire was published online after some linguistic corrections from the feedback received.

3.2. Sampling

A cross-sectional purposive sampling was employed to collect the data online. The survey questionnaire was widely circulated via direct mail and through social media sites like Facebook, Instagram, LinkedIn, and Twitter. Filter questions were asked at the beginning of the questionnaire to elicit responses from only a selected set of people. Only people who use Instagram, follow a vegan influencer and fall in the age group of 15–35 years of age were included. Respondents who answered with a 'No' to any of these questions were prompted to exit the survey. Respondents were asked to provide the name of the 'Vegan' influencer they follow and the influencer's number of followers. Two top influencers from the micro and meso categories were Himani Kaira, Your Vegan Food Explorer & Kuntal A. Joisher and Shweta Dudi, respectively (see Annexure II). We also excluded respondents who were following vegan celebrities with a follower base of more than 1 million since those influencers would be qualified as mega influencers. As many as 1963 people had joined the study over three months of data collection, but only 345 met the criteria of the sample frame. Further, participants were also asked to state their age, gender, education, location, and income. Out of these, 302 were valid after data cleaning. These responses were further divided into two groups: micro and meso. There were

Table 1. Respondent profile.

Demographic	Frequency	Percentage
Age		
15–25	166	54.97%
26–35	136	45.03%
Gender		
Female	183	60.60%
Male	119	39.40%
Education		
Undergraduate	101	33.44%
Postgraduate	201	66.56%
Location		
North India	91	30.13%
South India	64	21.19%
East India	76	25.17%
West India	71	23.51%
Influencer Followed		
Micro-Influencer	168	55.63%
Meso Influencer	134	44.37%

168 respondents following micro-influencers, and the rest of the respondents following meso influencers were 134.

3.3. Respondent profile

The demographic profile of the participants is summarized in Table 1. The sample consisted of a diverse group of individuals. Age-wise, the sample population was fairly distributed.

The cleaned data of 302 respondents was analyzed using structural equation modelling and multigroup analysis. Smart PLS 4 was used as the researchers found PLS-SEM as the ideal tool for data analysis due to its robustness in handling data with smaller samples (Hair et al. 2024) and widespread usage in consumer study research in the last one decade (Sabol et al. 2023). PLS-SEM is a robust methodology for predicting the relationships among multiple variables (Sarstedt, Ringle, and Hair 2014). Also, previous studies in influencer marketing research have used the same technique (Borges-Tiago, Santiago, and Tiago 2023); thus, using PLS-SEM made the comparison easy with such studies.

4. Analysis

4.1. Common method bias

The VIFs (variance inflation factors) were analyzed to look for the common method bias in the data. However, all the values of VIF were well below the threshold of 3.3 (Kock 2017) in the complete sample as well in the data group of micro and meso influencers (see Table A3 in Annexure I), hence establishing the integrity of results and lending confidence to proceed with further data analysis.

4.2. Measurement model

A confirmatory factor analysis was run to assess the overall measurement model in Smart PLS (Henseler, Ringle, and Sarstedt 2015). The results indicated that all the values of Cronbach Alpha, Composite reliability, AVE, VIF, and outer loadings are within the acceptable threshold as suggested by Hair et al. (2019), thus revealing the reliability and validity of the measures (Table A1- Annexure I). Further, the Fornell-Larcker Criterion and HTMT (Henseler, Ringle, and Sarstedt 2015) were used to establish the discriminant validity of the measures (Table A2- Annexure I).

4.3. Structural model

After confirmatory factor analysis, Structural Equation Modelling was performed to test the structural paths of the complete data set and the two data groups (Micro vs Meso). The result of the path coefficient is depicted in Table 2 and Figure 2. The bootstrapping function in SmartPLS was performed to arrive at the results. It is seen that the effect of Physical Attractiveness on brand engagement is significant in overall data ($\beta = 0.221$, $p = 0.00$). It is the same association in both the data samples whether the influencer is a micro vegan influencer ($\beta = 0.190$, $p = 0.00$) or a Meso-Influencer ($\beta = 0.24$, $p = 0.00$). Hence, H1a and H1b are accepted. In the case of Attitude homophily, the results were similar in the overall data group ($\beta = 0.158$, $p = 0.00$) as well as in the case of Micro-Influencer ($\beta = 0.197$, $p = 0.004$) but insignificant for Meso-Influencer ($\beta = 0.107$, $p = 0.243$). Hence, the impact of attitude homophily is positive and significant on brand engagement in the case of micro-influencers, leading to acceptance of H2a but rejection of H2b.

The impact of influencer credibility on brand engagement was significant in all groups, overall group ($\beta = 0.358$, $p = 0.00$) as well as in Micro-Influencer ($\beta = 0.343$, $p = 0.00$) and Meso-Influencer ($\beta = 0.374$, $p = 0.00$) leading to the acceptance of H3a & H3b. Furthermore, the results reveal that the impact of the parasocial relationship on brand engagement is significant in the overall data ($\beta = 0.179$, $p = 0.001$) as well as in the group of respondents following a micro-influencer ($\beta = 0.222$, $p = 0.00$) and Meso-Influencer ($\beta = 0.148$, $p = 0.022$). Hence, H4a and H4b are accepted. Finally, the impact of brand engagement on purchase intention was found to be positive and significant in the overall sample ($\beta = 0.399$, $p = 0.00$) and respondents who followed a Micro-Influencer ($\beta = 0.523$, $p = 0.00$) but was insignificant for those who followed a Meso-Influencer ($\beta = 0.21$, $p = 0.053$). Hence, H5a is accepted; however, H5b is rejected.

Table 2. Structural Model results.

Complete Sample (*N*=302)				Micro-Influencer (*N*=168)			Meso-Influencer (*N*=134)		
Structural Paths	O	T	p value	O	T	p value	O	T	p value
AH➔BE	0.158	2.811	0.005	0.197	2.867	0.004	0.107	1.168	0.243
ATT➔BE	0.221	4.41	0.000	0.190	3.015	0.003	0.24	2.877	0.004
IC ➔BE	0.358	6.258	0.000	0.343	4.314	0.000	0.374	4.361	0.000
PR➔BE	0.179	3.766	0.000	0.222	3.427	0.001	0.148	2.298	0.022
BE➔PI	0.399	6.924	0.000	0.523	7.914	0.000	0.21	1.935	0.053

4.4. Multigroup analysis

Multigroup analysis was run to see if there was a differential impact of the type of influencer on the different relationships in the paths mentioned above. The results are depicted in Table 5. Based on the results, only one Hypothesis, BE➔PI, is accepted (H6e). The rest of the hypotheses are rejected as there was no significant difference between the groups on paths AH ➔BE, ATT➔BE, IC ➔BE, and PR ➔BE. Hence, H6a, H6b, H6c, H6d are rejected.

Hence, the results can be summarised as:

- Significant positive effect observed across all data groups from Physical Attractiveness, Influencer Credibility and parasocial relationship to followers' Brand Engagement
- A significant positive effect was observed in the complete data group and the micro-influencer group from attitude homophily to followers brand Engagement, but not in the meso influencer group.
- Significant positive effect observed in the complete data group and the micro-influencer group from Brand Engagement to purchase intentions, but not in the meso influencer group
- Brand Engagement to purchase intentions was the only path showing a significant difference between Micro and Meso influencers. All other paths exhibited no significant group differences.

5. Discussion

This study focused on understanding if influencer characteristics affect brand engagement and purchase intention among micro and meso influencers in a vegan context. From the various characteristics tested, such as physical attractiveness, attitude homophily, influencer credibility, and parasocial relationship, we found that all characteristics of micro and meso influencers positively impact brand engagement, except for attitude homophily. It does not significantly influence brand engagement in the case of meso influencers.

Regardless of the number of followers, in both the micro and meso influencers, the physical attractiveness of an influencer promoting veganism was positively associated with brand engagement. This is similar to the findings of AlFarraj et al. (2021) and Argyris et al. (2020), which state that an influencer's attractiveness significantly impacts brand engagement. Physical attractiveness significantly impacts brand engagement in the vegan context, as it aligns with the lifestyle values of health, vitality, and ethical consumption that veganism promotes. Attractive influencers are seen as embodying the benefits of veganism, such as improved physical appearance and well-being, which strengthens their message and increases followers' engagement. This connection between appearance and lifestyle creates a visual identity that enhances authenticity, as followers perceive these influencers as trustworthy and aspirational figures. The 'halo effect' further elevates their credibility, making their product endorsements more impactful. Followers may perceive the influencer's attractiveness due to their vegan lifestyle, motivating them to adopt similar habits. Even though the effect of the physical

attractiveness of an influencer is context-driven, attractive influencers who promote veganism reinforce positive associations. Therefore, physical attractiveness in vegan influencers not only captures attention but reinforces positive brand associations and fosters deeper emotional connections with the audience (Bonk and Kubinski 2023).

Although previous literature has demonstrated the positive impact of attitude homophily (AH) on brand engagement (McCormick 2016), our study found that AH leads to brand engagement in the case of micro-influencers but not with meso-influencers. This difference arises because the relatability and the idea of adopting veganism are significantly enhanced with micro-influencers. Further, Micro-influencers, who typically have smaller but highly engaged followings, often share more personal and relatable content about their vegan lifestyle. Micro-influencers often have strong connections with their followers and view them as friends or peers, which can lead to a more engaged and supportive customer base (Sokolova and Kefi 2020). The effectiveness of these endorsements is rooted in the psychological alignment, emotional connection, and aspirational influence that attitude homophily fosters, encouraging followers to adopt and maintain a vegan lifestyle. As the number of followers increases, this effectiveness reduces. Our findings indicate that homophily does not create strong intimacy and trust between meso-influencers and their followers. Meso-influencers often endorse multiple brands and ideas simultaneously, which gives users the impression that their motivations are primarily monetary rather than genuine. Given that veganism is closely tied to people's value systems and beliefs, authenticity is crucial. Therefore, the results show that endorsements from micro-influencers are more effective than those from meso-influencers for vegan products. By collaborating with micro-influencers, brands can foster a sense of community among consumers.

Our research confirms that influencer credibility positively impacts brand engagement, which echoes earlier research (Duh and Thabethe 2021; Sharma, Sahai, and Singh 2022). Vegan consumers are generally well-informed and proactive in their research, and credibility forms a very important part of these consumers (Henchion et al. 2022). Veganism is not just about what you eat; it's also about living a certain lifestyle, adhering to a particular philosophy, and choosing how you want to live. As a lifestyle choice with ethical, environmental, and health implications, veganism relies heavily on trusted voices to spread information and promote plant-based products. Vegan influencers who demonstrate deep knowledge of nutrition, animal welfare, and sustainable living tend to build stronger credibility with their audience. This credibility can translate into higher engagement for vegan brands they promote, as followers are more likely to trust their recommendations for plant-based foods, cruelty-free, or sustainable products.

We found that in both the micro and meso influencer, the parasocial relationship of an influencer promoting veganism was positively associated with brand engagement. Followers are likely to believe endorsements and suggestions from influencers if they see them as real and relevant (Folkvord et al. 2019; Lee and Watkins 2016; Munnukka et al. 2019). Our research validates that influencers and followers have a solid emotional connection; followers view influencers as friends or confidants; therefore, influencers who provide personal narratives, daily schedules, and behind-the-scenes content can promote a sense of authenticity. High degrees of affection and trust characterize these partnerships, and they have the potential to influence brand engagement and loyalty strongly. Influencers can connect emotionally with their followers by sharing details of

Table 3. Multigroup analysis.

Paths	Difference (Micro-Meso)	1-tailed (Micro- Meso) p-value	2-tailed (Micro- Meso) p-value	Hypothesis
AH ➔BE	0.09	.215	.429	Reject
ATT ➔BE	−0.05	.683	.633	Reject
IC ➔BE	−0.032	.602	.796	Reject
PR ➔BE	0.073	.211	.422	Reject
BE ➔PI	0.313	.004	.008	Accept

their vegan experiences, setbacks, and victories. Because of this emotional connection, followers may become more engaged since they are motivated and inspired by the influencer's experiences. Influencers may enhance brand engagement and emotional connection by skillfully narrating veganism's physiological, ethical, and environmental advantages. Vegan consumers often form these relationships by engaging with influencers who share personal stories about their vegan lifestyle, including their ethical motivations, health benefits, and environmental values. These influencers are perceived as friends or confidants, making their product endorsements more genuine and trustworthy. In the Indian context, some influencers have built parasocial relationships by sharing their vegan journeys, offering advice on plant-based nutrition, and advocating for animal rights. Their authentic engagement fosters trust and loyalty, making their followers more likely to adopt vegan products.

Furthermore, previous literature mentions the positive impact of Brand engagement on Purchase intention (Goyal and Verma 2024; Verma 2021). However, in our case, we found that in the case of micro-influencers, brand engagement does lead to purchase intention more than in meso influencers. Table 3 depicts the results of the multigroup analysis, which also explains the difference between the two types of influencers. Micro-influencers often create highly tailored content that directly addresses the interests and concerns of their niche audience. This level of customization enhances the sense of shared attitudes. Furthermore, many micro-influencers maintain closer, more personal and more active interactions with their followers on social media platforms through going live, commenting, direct messaging, and interactive content (polls, Q&As), fostering a sense of community. This can further be leveraged with the help of user-generated content as it leads to increased trust from fellow or prospective customers. Positive reviews and testimonials from customers and influencers can also enhance the perceived value and reliability of the brand, driving purchase intentions.+

5.1. Theoretical implications

Veganism appeals to a niche audience with specific values and interests. With the growing trend of veganism, vegan brands are also growing, and these brands often have strong ethical and environmental values that resonate with consumers independently of influencer endorsements. In this research, we closely study how these influencer characteristics differ between micro and meso influencers and affect brand engagement and purchase intention.

The current study affirms that influencers provide valuable contributions to the literature on influencer marketing, particularly in the context of veganism, an area previously underexplored. The study highlights the significance of influencer characteristics –

credibility, physical attractiveness, and parasocial relationships – in driving brand engagement and purchase intention. This combination of characteristics of influencers in a vegan context has not been studied before. Our study is one of the novel studies where the attitude homophily is not an antecedent to the purchase intention.

Testing and validating the influencer's characteristics based on the ELM model gave a new outlook that followers don't perceive any difference between micro and meso influences for credibility and parasocial relationship, which are part of the central route of persuasion. However, for attitude homophily, which is qualified as a personal attribute, micro and meso influencers are perceived differently. This work gave a new dimension to the use of ELM. Influencers who are looking for brand engagement must work on personal attributes.

Furthermore, this research contributes to the ongoing debate about the relative effectiveness of micro versus meso-influencers. We have specifically concentrated on brand engagement in the context of veganism since it has not been studied as an outcome variable in influencer marketing literature. By demonstrating that brand engagement leads to purchase intention for micro-influencers more than for meso-influencers in the vegan context, the study challenges the assumption that 'bigger is better' in influencer marketing. Our study shares a very clear implication that Brand engagement has more influence on followers' purchase intention in the case of a micro-influencer than a meso-influencer, which means employing micro-influencers will be more effective than employing meso-influencers when we want to push sales of vegan products. By showing that micro-influencers have a stronger effect on purchase intention compared to meso-influencers in the vegan context, this study suggests that smaller, niche influencers can be more effective in certain markets. This extends prior research by emphasizing micro-influencers' effectiveness in promoting ethical, health, and environmental values, which are central to veganism.

5.2. Practical implications:

For vegan brands, the findings suggest strategies to optimise both engagement and conversions. Micro-influencers often have a deep understanding of local cultures and communities; therefore, vegan brands can benefit from this cultural relevance, ensuring their messaging resonates with local authentic, personalised content and strong emotional connections with niche audiences and addresses specific cultural nuances. The study suggests that micro-influencers may offer better returns on investment in terms of driving purchase intentions through brand engagement. Managers should develop tiered influencer strategies, potentially using micro-influencers for targeted engagement and meso-influencers for broader awareness. Therefore, the study highlights broadening the reach as well as optimizing the effectiveness of social media advertising through influencer marketing.

This study has implications for brand managers of vegan products since brands today constantly face difficulties with shifting customer attention, hyper-competition, new media, and changing behaviours, and they are always looking to optimise their brand communication strategy (Batra and Keller 2016). Further, with the increasing number of vegan brands collaborating with influencers on social media platforms, it is crucial to understand consumer decision-making and the success of social media marketing

campaigns. It is important to focus on providing valuable educational content about the benefits of veganism through storytelling and elaborating on the environmental benefits of veganism.

Meso-influencers can be used to disseminate key messages about veganism through compelling, visually produced content and cross-promotional collaborations due to their broader reach. They are ideal for raising brand awareness. Combining both types of influencers can maximise brand visibility and engagement. Marketers should also consider building trust and engagement more effectively than relying on influencers, which can contribute. All these efforts promoting veganism would help achieve the United Nations' sustainable development goal 12 of 'responsible consumption and production' and 13 of 'climate action', ensuring a green future.

5.3. Limitations and scope for future research

India is a country of diverse religions and cultures, and the majority of the religions promote veganism, which could have had an extraneous effect on our results. The authors wish to expand the study to other regions to establish its generalizability across diverse sets of populations. The use of cross-sectional purposive sampling limits the generalizability of the findings to a broader population. Relying on self-reported data from a niche group may introduce selection bias. Additionally, the stringent criteria reduced the final sample size, potentially impacting the robustness of the results. Hence, the authors want to address the use of probability sampling methods in future studies to rule out any author-related biases in the study. There might be other important characteristics of influencers that this study has missed, like social attractiveness, congruence or respect. These characteristics might also significantly impact the purchase intention of followers towards vegan products and need to be further explored. The effect of other types of influencers, such as mega and macro influencers, can be studied with similar sets of variables in future studies. Many other characteristics, like demographics, psychographics, and types, can be integrated into the model to make it more robust and valid. Thus, a triangulation with an exploratory study would further enrich this work.

Disclosure statement

No potential conflict of interest was reported by the author(s).

Notes on contributors

Sakhhi Chhabra is an Asst. Professor for Marketing at XLRI Delhi NCR. She is a Fellow from MDI-Gurgaon in the marketing area and completed her MSc. Marketing from Manchester Business School, UK. She has been teaching core and elective marketing subjects to postgraduate students and executives at various MBA institutes. She has successfully published research papers, case studies, and book chapters in renowned International and National Journals.

Tahir A. Wani is an Assistant Professor of Marketing at the National Institute of Technology Srinagar. His work is focused on subsistence and sustainable marketing. He explores the intricacies of BOP markets, social media, and sustainable consumption.

Vaishali Kaushal is Deputy General Manager at Purple Audacity Research and Innovation Pvt. Ltd., a market research and insights firm. She has a Ph.D. from Delhi Technological University in the customer experience domain. Before this, she holds a double master's degree: a PGDM from the Lal Bahadur Shastri Institute of Management and an M.Sc. (Hons.) in mathematics from Panjab University.

References

AlFarraj, O., A. A. Alalwan, Z. M. Obeidat, A. Baabdullah, R. Aldmour, and S. Al-Haddad. 2021. "Examining the Impact of influencers' Credibility Dimensions: Attractiveness, Trustworthiness and Expertise on the Purchase Intention in the Aesthetic Dermatology Industry." *Review of International Business & Strategy* 31 (3): 355–374. https://doi.org/10.1108/RIBS-07-2020-0089.

Argyris, Y. A., Z. Wang, Y. Kim, and Z. Yin. 2020. "The Effects of Visual Congruence on Increasing consumers' Brand Engagement: An Empirical Investigation of Influencer Marketing on Instagram Using Deep-Learning Algorithms for Automatic Image Classification." *Computers in Human Behavior* 112:106443. https://doi.org/10.1016/j.chb.2020.106443.

Audrezet, A., G. De Kerviler, and J. G. Moulard. 2020. "Authenticity Under Threat: When Social Media Influencers Need to Go Beyond Self-Presentation." *Journal of Business Research* 117:557–569. https://doi.org/10.1016/j.jbusres.2018.07.008.

Aw, E. C. X., and S. H. W. Chuah. 2021. ""Stop the Unattainable Ideal for an Ordinary Me!" Fostering Parasocial Relationships with Social Media Influencers: The Role of Self-Discrepancy." *Journal of Business Research* 132:146–157. https://doi.org/10.1016/j.jbusres.2021.04.025.

Balog, K., M. De Rijke, and W. Weerkamp. 2008. "Bloggers as Experts: Feed Distillation Using Expert Retrieval Models." *SIGIR '08: The 31st Annual International ACM SIGIR Conference Singapore*, Singapore, July 20 - 24, 2008, 753–754. New York, NY: Association for Computing Machinery.

Batra, R., and K. L. Keller. 2016. "Integrating Marketing Communications: New Findings, New Lessons, and New Ideas." *Journal of Marketing* 80 (6): 122–145. https://doi.org/10.1509/jm.15.0419.

Belanche, D., L. V. Casaló, M. Flavián, and S. Ibáñez-Sánchez. 2021. "Building Influencers' Credibility on Instagram: Effects on followers' Attitudes and Behavioral Responses Toward the Influencer." *Journal of Retailing & Consumer Services* 61:102585. https://doi.org/10.1016/j.jretconser.2021.102585.

Bergkvist, L., and K. Q. Zhou. 2016. "Celebrity Endorsements: A Literature Review and Research Agenda." *International Journal of Advertising* 35 (4): 642–663. https://doi.org/10.1080/02650487.2015.1137537.

Boerman, S. C. 2020. "The Effects of the Standardized Instagram Disclosure for Micro-And Meso-Influencers." *Computers in Human Behavior* 103:199–207. https://doi.org/10.1016/j.chb.2019.09.015.

Boerman, S. C., and E. A. Van Reijmersdal. 2020. "Disclosing Influencer Marketing on YouTube to Children: The Moderating Role of Parasocial Relationship." *Frontiers in Psychology* 10:3042. https://doi.org/10.3389/fpsyg.2019.03042.

Bonk, T., and M. S. Kubinski. 2023. "Winning Over Listeners with Podcast Advertising: Exploring the Podcast Audience's Perception of Commercial Messages in Podcasts and the Role of Podcast Hosts."

Borges-Tiago, M. T., J. Santiago, and F. Tiago. 2023. "Mega or Macro Social Media Influencers: Who Endorses Brands Better?" *Journal of Business Research* 157:113606. https://doi.org/10.1016/j.jbusres.2022.113606.

Britt, R. K., J. L. Hayes, B. C. Britt, and H. Park. 2020. "Too Big to Sell? A Computational Analysis of Network and Content Characteristics Among Mega and Micro Beauty and Fashion Social Media Influencers." *Journal of Interactive Advertising* 20 (2): 111–118. https://doi.org/10.1080/15252019.2020.1763873.

Bryant, C. J. 2019. "We can't Keep Meating Like This: Attitudes Towards Vegetarian and Vegan Diets in the United Kingdom." *Sustainability* 11 (23): 6844. https://doi.org/10.3390/su11236844.

Business of apps. 2024. "Instagram Revenue and Usage Statistics." Accessed December 23, 2023. https://www.businessofapps.com/data/instagram-statistics/.

Byun, K. J., and S. J. Ahn. 2023. "A Systematic Review of Virtual Influencers: Similarities and Differences Between Human and Virtual Influencers in Interactive Advertising." *Journal of Interactive Advertising* 23 (4): 293–306. https://doi.org/10.1080/15252019.2023.2236102.

Cacioppo, J. T., and R. E. Petty. 1981. "Electromyograms as Measures of Extent and Affectivity of Information Processing." *The American Psychologist* 36 (5): 441. https://doi.org/10.1037/0003-066X.36.5.441.

Campbell, C., and J. R. Farrell. 2020. "More Than Meets the Eye: The Functional Components Underlying Influencer Marketing." *Business Horizons* 63 (4): 469–479. https://doi.org/10.1016/j.bushor.2020.03.003.

Casaló, L. V., C. Flavián, and S. Ibáñez-Sánchez. 2017. "Antecedents of Consumer Intention to Follow and Recommend an Instagram Account." *Online Information Review* 41 (7): 1046–1063. https://doi.org/10.1108/OIR-09-2016-0253.

Casaló, L. V., C. Flavián, and S. Ibáñez-Sánchez. 2020. "Influencers on Instagram: Antecedents and Consequences of Opinion Leadership." *Journal of Business Research* 117:510–519. https://doi.org/10.1016/j.jbusres.2018.07.005.

Chai, B. C., J. R. Van Der Voort, K. Grofelnik, H. G. Eliasdottir, I. Klöss, and F. J. Perez-Cueto. 2019. "Which Diet Has the Least Environmental Impact on Our Planet? A Systematic Review of Vegan, Vegetarian and Omnivorous Diets." *Sustainability* 11 (15): 4110. https://doi.org/10.3390/su11154110.

Chen, H. 2018. "College-Aged Young consumers' Perceptions of Social Media Marketing: The Story of Instagram." *Journal of Current Issues & Research in Advertising* 39 (1): 22–36. https://doi.org/10.1080/10641734.2017.1372321.

Colliander, J., and M. Dahlén. 2011. "Following the Fashionable Friend: The Power of Social Media: Weighing Publicity Effectiveness of Blogs versus Online Magazines." *Journal of Advertising Research* 51 (1): 313–320. https://doi.org/10.2501/jar-51-1-313-320.

Colliander, J., and S. Erlandsson. 2015. "The Blog and the Bountiful: Exploring the Effects of Disguised Product Placement on Blogs That are Revealed by a Third Party." *Journal of Marketing Communications* 21 (2): 110–124. https://doi.org/10.1080/13527266.2012.730543.

Conde, R., and B. Casais. 2023. "Micro, Macro and Mega-Influencers on Instagram: The Power of Persuasion via the Parasocial Relationship." *Journal of Business Research* 158:113708. https://doi.org/10.1016/j.jbusres.2023.113708.

De Veirman, M., V. Cauberghe, and L. Hudders. 2017. "Marketing Through Instagram Influencers: The Impact of Number of Followers and Product Divergence on Brand Attitude." *International Journal of Advertising* 36 (5): 798–828. https://doi.org/10.1080/02650487.2017.1348035.

Dibble, J. L., T. Hartmann, and S. F. Rosaen. 2016. "Parasocial Interaction and Parasocial Relationship: Conceptual Clarification and a Critical Assessment of Measures." *Human Communication Research* 42 (1): 21–44. https://doi.org/10.1111/hcre.12063.

Djafarova, E., and C. Rushworth. 2017. "Exploring the Credibility of Online Celebrities' Instagram Profiles in Influencing the Purchase Decisions of Young Female Users." *Computers in Human Behavior* 68 (2): 1–7. https://doi.org/10.1016/j.chb.2016.11.009.

Duh, H. I., and T. Thabethe. 2021. "Attributes of Instagram Influencers Impacting Consumer Brand Engagement." *International Journal of Internet Marketing and Advertising* 15 (5/6): 477–497. https://doi.org/10.1504/IJIMA.2021.118261.

Duran, R. L., and L. Kelly. 1988. "The Influence of Communicative Competence on Perceived Task, Social, and Physical Attraction." *Communication Quarterly* 36 (1): 41–49. https://doi.org/10.1080/01463378809369706.

Erdogan, B. Z. 1999. "Celebrity Endorsement: A Literature Review." *Journal of Marketing Management* 15 (4): 291–314. https://doi.org/10.1362/026725799784870379.

Erkan, I., and C. Evans. 2016. "The Influence of eWOM in Social Media on consumers' Purchase Intentions: An Extended Approach to Information Adoption." *Computers in Human Behavior* 61:47–55. https://doi.org/10.1016/j.chb.2016.03.003.

Erz, A., and A. B. Heeris Christensen. 2018. "Transforming Consumers into Brands: Tracing Transformation Processes of the Practice of Blogging." *Journal of Interactive Marketing* 43 (1): 69–82. https://doi.org/10.1016/j.intmar.2017.12.002.

Escalas, J. E., and J. R. Bettman. 2003. "You are What They Eat: The Influence of Reference Groups on Consumers' Connections to Brands." *Journal of Consumer Psychology* 13 (3): 339–348. https://doi.org/10.1207/S15327663JCP1303_14.

Folkvord, F., K. E. Bevelander, E. Rozendaal, and R. Hermans. 2019. "Children's Bonding with Popular YouTube Vloggers and Their Attitudes Toward Brand and Product Endorsements in Vlogs: An Explorative Study." *Young Consumers* 20 (2). https://doi.org/10.1108/YC-12-2018-0896.

Forbes. 2021. "The Importance of Influencer Marketing in the 'New Normal." *Digital Sphere*. https://www.forbes.com/sites/forbesagencycouncil/2021/03/02/the-importance-of-influencer-marketing-in-the-new-normal-digital-sphere/?sh=1377af211448.

Frank, B., and S. Mitsumoto. 2023. "An Extended Source Attractiveness Model: The Advertising Effectiveness of Distinct Athlete Endorser Attractiveness Types and Its Contextual Variation." *European Sport Management Quarterly* 23 (4): 1091–1114. https://doi.org/10.1080/16184742.2021.1963302.

Gheihman, Nina. 2021. "Veganism as a Lifestyle Movement." *Sociology Compass* 15 (5): e12877. https://doi.org/10.1111/soc4.12877.

Goyal, A., and P. Verma. 2024. "The Relationship Between Brand Engagement, Brand Loyalty, Overall Brand Equity and Purchase Intention." *Journal of Strategic Marketing* 32 (1): 65–79. https://doi.org/10.1080/0965254X.2022.2149839.

Gram, M., V. I. de La Ville, A. Le Roux, N. Boireau, and O. Rampnoux. 2010. "Communication on Food, Health and Nutrition: A Cross-Cultural Analysis of the Danonino Brand and Nutri-Tainment." *Journal of Marketing Communications* 16 (1–2): 87–103. https://doi.org/10.1080/13527260903342803.

Hair, J. F., J. J. Risher, M. Sarstedt, and C. M. Ringle. 2019. "When to Use and How to Report the Results of PLS-SEM." *European Business Review* 31 (1): 2–24. https://doi.org/10.1108/EBR-11-2018-0203.

Hair, J. F., M. Sarstedt, C. M. Ringle, P. N. Sharma, and B. D. Liengaard. 2024. "Going Beyond the Untold Facts in PLS–SEM and Moving Forward." *European Journal of Marketing* 58 (13): 81–106.

Henchion, M. M., C. J. De Backer, L. Hudders, and S. O'Reilly. 2022. "Ethical and Sustainable Aspects of Meat Production; Consumer Perceptions and System Credibility." In *Woodhead Publishing Series in Food Science, Technology and Nutrition, New Aspects of Meat Quality*, edited by P. Purslow, 829–851. 2nd ed. Australia: Woodhead Publishing. https://doi.org/10.1016/B978-0-323-85879-3.00001-5.

Henseler, J., C. M. Ringle, and M. Sarstedt. 2015. "A New Criterion for Assessing Discriminant Validity in Variance-Based Structural Equation Modeling." *Journal of the Academy of Marketing Science* 43 (1): 115–135. https://doi.org/10.1007/s11747-014-0403-8.

Hernández-Méndez, J., and N. Baute-Díaz. 2024. "Influencer Marketing in the Promotion of Tourist Destinations: Mega, Macro and Micro-Influencers." *Current Issues in Tourism* 27 (8): 1332–1342. https://doi.org/10.1080/13683500.2023.2214354.

Hollebeek, L. 2011. "Exploring Customer Brand Engagement: Definition and Themes." *Journal of Strategic Marketing* 19 (7): 555–573. https://doi.org/10.1080/0965254X.2011.599493.

Horton, D., and R. Richard Wohl. 1956. "Mass Communication and Parasocial Interaction: Observations on Intimacy at a Distance." *Psychiatry* 19 (3): 215–229. https://doi.org/10.1080/00332747.1956.11023049.

Hughes, C., V. Swaminathan, and G. Brooks. 2019. "Driving Brand Engagement Through Online Social Influencers: An Empirical Investigation of Sponsored Blogging Campaigns." *Journal of Marketing* 83 (5): 78–96. https://doi.org/10.1177/0022242919854374.

Janssen, L., A. P. Schouten, and E. A. Croes. 2022. "Influencer Advertising on Instagram: Product-Influencer Fit and Number of Followers Affect Advertising Outcomes and Influencer Evaluations via Credibility and Identification." *International Journal of Advertising* 41 (1): 101–127. https://doi.org/10.1080/02650487.2021.1994205.

Jin, S. A. A., and J. Phua. 2014. "Following celebrities' Tweets About Brands: The Impact of Twitter-Based Electronic Word-Of-Mouth on consumers' Source Credibility Perception, Buying Intention,

and Social Identification with Celebrities." *Journal of Advertising* 43 (2): 181–195. https://doi.org/10.1080/00913367.2013.827606.

Joseph, W. B. 1982. "The Credibility of Physically Attractive Communicators: A Review." *Journal of Advertising* 11 (3): 15–24. https://doi.org/10.1080/00913367.1982.10672807.

Kahle, L. R., and P. M. Homer. 1985. "Physical Attractiveness of the Celebrity Endorser: A Social Adaptation Perspective." *Journal of Consumer Research* 11 (4): 954–961. https://doi.org/10.1086/209029.

Kay, S., R. Mulcahy, and J. Parkinson. 2020. "When Less is More: The Impact of Macro and Micro Social Media influencers' Disclosure." *Journal of Marketing Management* 36 (3–4): 248–278. https://doi.org/10.1080/0267257X.2020.1718740.

Ki, Chung-Wha 'Chloe'., and Y. K. Kim. 2019. "The Mechanism by which Social Media Influencers Persuade Consumers: The Role of consumers' Desire to Mimic." *Psychology & Marketing* 36 (10): 905–922. https://doi.org/10.1002/mar.21244.

Kim, D. Y., and H. Y. Kim. 2021. "Trust Me, Trust Me Not: A Nuanced View of Influencer Marketing on Social Media." *Journal of Business Research* 134:223–232. https://doi.org/10.1016/j.jbusres.2021.05.024.

Kock, N. 2017. "Common Method Bias: A Full Collinearity Assessment Method for PLS-SEM." In *Partial Least Squares Path Modeling*, edited by H. Latan and R. Noonan, 245–257. Cham: Springer. https://doi.org/10.1007/978-3-319-64069-3_11.

Labrecque, L. I. 2014. "Fostering Consumer–Brand Relationships in Social Media Environments: The Role of Parasocial Interaction." *Journal of Interactive Marketing* 28 (2): 134–148. https://doi.org/10.1016/j.intmar.2013.12.003.

Ladhari, R., E. Massa, and H. Skandrani. 2020. "YouTube vloggers' Popularity and Influence: The Roles of Homophily, Emotional Attachment, and Expertise." *Journal of Retailing & Consumer Services* 54:102027. https://doi.org/10.1016/j.jretconser.2019.102027.

Lee, J. E., and B. Watkins. 2016. "YouTube vloggers' Influence on Consumer Luxury Brand Perceptions and Intentions." *Journal of Business Research* 69 (12): 5753–5760. https://doi.org/10.1016/j.jbusres.2016.04.171.

Li, W., F. Zhao, J. M. Lee, J. Park, F. Septianto, and Y. Seo. 2024. "How Micro-(Vs. Mega-) Influencers Generate Word of Mouth in the Digital Economy Age: The Moderating Role of Mindset." *Journal of Business Research* 171:114387. https://doi.org/10.1016/j.jbusres.2023.114387.

Looi, J., D. Kemp, and Y. W. G. Song. 2023. "Instagram Influencers in Health Communication: Examining the Roles of Influencer Tier and Message Construal in COVID-19-prevention Public Service Announcements." *Journal of Interactive Advertising* 23 (1): 14–32. https://doi.org/10.1080/15252019.2022.2140316.

Lou, C., and H. K. Kim. 2019. "Fancying the New Rich and Famous? Explicating the Roles of Influencer Content, Credibility, and Parental Mediation in adolescents' Parasocial Relationship, Materialism, and Purchase Intentions." *Frontiers in Psychology* 10:2567. https://doi.org/10.3389/fpsyg.2019.02567.

Lou, C., and S. Yuan. 2019. "Influencer Marketing: How Message Value and Credibility Affect Consumer Trust of Branded Content on Social Media." *Journal of Interactive Advertising* 19 (1): 58–73. https://doi.org/10.1080/15252019.2018.1533501.

Lv, J., R. Yang, J. Yu, W. Yao, and Y. Wang. 2023. "Macro-Influencers or Meso-Influencers, How Do Companies Choose?" *Industrial Management & Data Systems* 123 (12): 3018–3037. https://doi.org/10.1108/IMDS-05-2022-0310.

Marques, I. R., B. Casais, and M. A. Camilleri. 2021. "The Effect of Macrocelebrity and Microinfluencer Endorsements on Consumer–Brand Engagement in Instagram." In *Strategic Corporate Communication in the Digital Age*, edited by M. A. Camilleri, 131–143. https://doi.org/10.1108/978-1-80071-264-520211008. Leeds: Emerald Publishing Limited.

Masuda, H., S. H. Han, and J. Lee. 2022. "Impacts of Influencer Attributes on Purchase Intentions in Social Media Influencer Marketing: Mediating Roles of Characterizations." *Technological Forecasting & Social Change* 174:121246. https://doi.org/10.1016/j.techfore.2021.121246.

McCormick, K. 2016. "Celebrity Endorsements: Influence of a Product-Endorser Match on Millennials Attitudes and Purchase Intentions." *Journal of Retailing & Consumer Services* 32:39–45. https://doi.org/10.1016/j.jretconser.2016.05.012.

McGuire, W. J. 1985. "Chapter Attitudes and Attitude Change." In *The Handbook of Social Psychology*, edited by G. Lindzey and E. Aronson, Vol. 2, 233–346. New York: Random House.

Mediakix. 2019. "Influencer Marketing 2019 Industry Benchmarks." Accessed February 9, 2023. bit.ly/3pNFLXs.

Munnukka, J., D. Maity, H. Reinikainen, and V. Luoma-Aho. 2019. ""Thanks for Watching". The Effectiveness of YouTube Vlogendorsements." *The Effectiveness of YouTube Vlogendorsements Computers in Human Behavior* 93:226–234. https://doi.org/10.1016/j.chb.2018.12.014.

Park, J., J. M. Lee, V. Y. Xiong, F. Septianto, and Y. Seo. 2021. "David and Goliath: When and Why Micro-Influencers are More Persuasive Than Mega-Influencers." *Journal of Advertising* 50 (5): 584–602. https://doi.org/10.1080/00913367.2021.1980470.

Perse, E. M., and R. B. Rubin. 1989. "Attribution in Social and Parasocial Relationships." *Communication Research* 16 (1): 59–77. https://doi.org/10.1177/009365089016001003.

Reichelt, J., J. Sievert, and F. Jacob. 2013. "How Credibility Affects eWOM Reading: The Influences of Expertise, Trustworthiness, and Similarity on Utilitarian and Social Functions." *Journal of Marketing Communications*, 20 (1–2): 64–80. https://doi.org/10.1080/13527266.2013.797758.

Reinikainen, H., J. Munnukka, D. Maity, and V. Luoma-Aho. 2020. "'You Really are a Great Big sister'–Parasocial Relationships, Credibility, and the Moderating Role of Audience Comments in Influencer Marketing." *Journal of Marketing Management* 36 (3–4): 279–298. https://doi.org/10.1080/0267257X.2019.1708781.

Sabol, M., J. Hair, G. Cepeda, J. L. Roldán, and A. Y. L. Chong. 2023. "PLS-SEM in Information Systems: Seizing the Opportunity and Marching Ahead Full Speed to Adopt Methodological Updates." *Industrial Management & Data Systems* 123 (12): 2997–3017. https://doi.org/10.1108/IMDS-07-2023-0429.

Sarstedt, M., C. M. Ringle, and J. F. Hair. 2014. "PLS-SEM: Looking Back and Moving Forward." *Long Range Planning* 47 (3): 132–137.

Schouten, A. P., L. Janssen, and M. Verspaget. 2020. "Celebrity Vs. Influencer Endorsements in Advertising: The Role of Identification, Credibility, and Product-Endorser Fit." *International Journal of Advertising* 39 (2): 258–281. https://doi.org/10.1080/02650487.2019.1634898.

Shan, Y., K. J. Chen, and J. S. Lin. 2020. "When Social Media Influencers Endorse Brands: The Effects of Self-Influencer Congruence, Parasocial Identification, and Perceived Endorser Motive." *International Journal of Advertising* 39 (5): 590–610. https://doi.org/10.1080/02650487.2019.1678322.

Sharma, M. 2021. https://theveganreview.com/social-media-influence-on-veganism-instagram-vegan-celebrity-influencers/.

Sharma, M., P. Sahai, and V. K. Singh. 2022. "Engaging Social Media Influencers Credibility on Purchase Behaviour Through Lens of Brand Engagement." *International Journal of Health Sciences* 6 (S2): 11288–11298. https://doi.org/10.53730/ijhs.v6nS2.8030.

Sheng, J., Y. H. Lee, and H. Lan. 2023. "Parasocial Relationships with Micro-Influencers: Do Sponsorship Disclosure and Electronic Word-Of-Mouth Disrupt?" *Internet Research* 34 (3): 849–867. https://doi.org/10.1108/INTR-12-2021-0903.

Sokolova, K., and H. Kefi. 2020. "Instagram and YouTube Bloggers Promote It, Why Should I Buy? How Credibility and Parasocial Interaction Influence Purchase Intentions." *Journal of Retailing & Consumer Services* 53:article 101742. https://doi.org/10.1016/j.jretconser.2019.01.011.

Sprott, D., S. Czellar, and E. Spangenberg. 2009. "The Importance of a General Measure of Brand Engagement on Market Behavior: Development and Validation of a Scale." *Journal of Marketing Research* 46 (1): 92–104. https://doi.org/10.1509/jmkr.46.1.92.

Statista. 2024. "Value of Influencer Marketing Industry in India 2021-2027." Nov 12, 2024. https://www.statista.com/statistics/1294803/india-influencer-marketing-industry-value/.

Thakur, R., A. Angriawan, and J. H. Summey. 2016. "Technological Opinion Leadership: The Role of Personal Innovativeness, Gadget Love, and Technological Innovativeness." *Journal of Business Research* 69 (8): 2764–2773. https://doi.org/10.1016/j.jbusres.2015.11.012.

Torres, P., M. Augusto, and M. Matos. 2019. "Antecedents and Outcomes of Digital Influencer Endorsement: An Exploratory Study." *Psychology & Marketing* 36 (12): 1267–1276.

Tsai, W. H. S., and L. R. Men. 2013. "Motivations and Antecedents of Consumer Engagement with Brand Pages on Social Networking Sites." *Journal of Interactive Advertising* 13 (2): 76–87. https://doi.org/10.1080/15252019.2013.826549.

Verma, P. 2021. "The Effect of Brand Engagement and Brand Love Upon Overall Brand Equity and Purchase Intention: A Moderated–Mediated Model." *Journal of Promotion Management* 27 (1): 103–132. https://doi.org/10.1080/10496491.2020.1809591.

Vestergren, S., and M. S. Uysal. 2022. "Beyond the Choice of What You Put in Your Mouth: A Systematic Mapping Review of Veganism and Vegan Identity." *Frontiers in Psychology* 13:848434. https://doi.org/10.3389/fpsyg.2022.848434.

Voorveld, H. A. 2019. "Brand Communication in Social Media: A Research Agenda." *Journal of Advertising* 48 (1): 14–26. https://doi.org/10.1080/00913367.2019.1588808.

Wang, Z., J. B. Walther, S. Pingree, and R. P. Hawkins. 2008. "Health Information, Credibility, Homophily, and Influence via the Internet: Web Sites versus Discussion Groups." *Health Communication* 23 (4): 358–368. https://doi.org/10.1080/10410230802229738.

Journal of Computational Electronics (2025) 24:66
https://doi.org/10.1007/s10825-025-02301-w

Modelling and simulation of plasma-assisted 2D graphene based solar cells

Shreya Vasu[1] · Shikha Singh[1] · Suresh C. Sharma[1]

Received: 16 July 2024 / Accepted: 23 February 2025
© The Author(s), under exclusive licence to Springer Science+Business Media, LLC, part of Springer Nature 2025

Abstract
A significant photovoltaic material for greater light energy conversion is graphene, mostly due to its exciting features including greater carrier mobility. By substituting a graphene layer for the "hole transport layer" (HTL), a perovskite solar cell's efficiency can be increased. This study demonstrates how growing graphene using the plasma-enhanced chemical vapor deposition (PECVD) technique affects the device efficiency. We use SCAPS-1D to build and simulate a model of ITO/PCBM/$CsPbI_3$/graphene and use $CsPbI_3$ as absorber, PCBM as the electron transport layer (ETL) and graphene as the HTL. The efficiency of solar cell and the plasma parameters are found to be numerically related, and the efficiency of the simulated model and the numerically computed efficiency are compared. Furthermore, it is discovered that increasing the electron and ion density of the graphene sheet causes the device's efficiency to decrease due to an inverse relationship with the Debye length, whereas increasing the electron and ion temperatures causes the device's efficiency to increase due to a linear relationship with the Debye length. This indicates that by adjusting the various plasma parameters at an ideal absorber layer and HTL thickness, the device's efficiency can be increased, improving its performance and practical applications. The obtained results have been verified from the previously done researches based on solar cells.

Keywords Plasma parameters · Graphene-based perovskite solar cells · SCAPS-1D · Plasma-enhanced chemical vapor deposition (PECVD)

1 Introduction

Solar energy is one of the plentiful and durable renewable energy source that is becoming more and more well-liked and pursued in the quest for sustainable, ecologically friendly alternative energy resource as global energy demands increase [1, 2]. The goal of contemporary photovoltaic (PV) research is to build highly efficient devices at low production costs in order to meet future industrial needs. Even though at the moment a lot of research focuses on improving upon the highest performance that can achieved, the photovoltaic characters still remain far below a desirable maximum value [3]. The device efficiency for a perovskite (PVK) solar cell (PeSCs) has increased noticeably from a meager 3.8% to a still-very-low 26.7% [4]. In 2021, Abhishek Raj et al. achieved an efficiency of 18.30% for a $CsGeI_3$-based solar cell [5]. In 2022, Sagar Bhattarai et al. achieved a PCE of 22.16% in a solar cell with $MASnI_3$ as absorber and ZnO and $CuSbS_2$ as carrier transport materials (CTMs) [6]. In 2024, Abhishek Raj et al. achieved PCE = 5.61% with $V_{OC} = 0.91$ V, FF = 55.55% and $J_{SC} = 10.87$ mA/cm^2 for a lead-free doped $Bi_{0.80}La_{0.20}Fe_{1-x}Ti_xO_3$ simulated model [7].

The absorbing layer of perovskite is usually situated between the “hole transport layer” (HTL) and the “electron transport layer” (ETL) in order to establish an effective charge separation. However, recombination of the carriers generated by the sunlight falling on the device which happens at various defect sites at the interfaces, in the ETL/HTL layer, or in the PVK layer obstructs charge collection and transfer. In order to overcome this problem, in 2009, Miyasaka et al. developed organometallic perovskite $CH_3NH_3PbI_3$ in dye-sensitized solar cells (DSSCs) which achieved efficiency of 3.8% [8–11]. Later Park et al.

✉ Suresh C. Sharma
suresh321sharma@gmail.com

Shreya Vasu
shreyavasu219@gmail.com

Shikha Singh
shikhasingh10322@gmail.com

[1] Department of Applied Physics, Delhi Technological University, Delhi 110042, India

Published online: 27 March 2025

adjusted it by to using solid-based hole transport layer (HTL), Spiro-OMeTAD in place of the liquid-based electrolyte in HTL, which led to increase in efficiency up to 9.7% [12].

Due to its favorable band gap, $CsPbI_3$ is regarded as a material that holds great potential for application as the absorber layer in inorganic PeSC [13]. Since its first report in 2015 by Eperon et al. to as reported by Zhao et al. in 2019, the device efficiency for $CsPbI_3$-based PSC has enhanced from 2.9 to 19.03% together with improved stability, indicating its great potential for high-efficiency inorganic PSCs [14, 15]. In 2024, Sagar Bhattarai et al. achieved an efficiency of 17.37% for a $CsPbI_3$-based solar cell with graphene oxide used as HTL and ZnMgO used as ETL [16]. For the charge carrying graphene is anticipated to have a beneficial effect on PeSC construction because of its remarkable features, which includes an elevated room temperature carrier mobility [17] and extremely favorable thermal properties [18], highly transparency [17], high melting point [19]. Yang et al. in 2017 incorporated graphene in TiO_2 dense layer as electron transport layer for cesium-containing perovskite ($Cs_{0.1}MA_{0.9}PbI_3$) and saw that the solar cell efficiency of device improves from 11.2 to 15.4% [20]. When the graphene (Gr) layer is replaced with TiO_2 as the ETL in the PeSC structure, it resulted in $V_{oc} = 0.89$ V, $J_{sc} = 21.73$ mA/cm^2 and PCE = 16.03% as found by Dadashbeik et al. in 2020 [21]. Again in 2020, Ali et al. achieved $V_{oc} = 1.094$ V, $J_{sc} = 21.24$ mA/cm^2, FF = 90.185% and PCE of 20.95% for the simulation device structure based on glass/ITO/graphene/$CH_3NH_3PbI_3$/Spiro-OMeTAD/Au [22].

Graphene is a semimetal without an energy band gap which is required to be used as an electronic transistor; many studies show that different band gap is formed in different situations through which graphene is grown [23–25]. Plasma-enhanced chemical vapor deposition (PECVD) method has a lot of promise for preparing graphene at low temperatures [26, 27]. Band gap engineering by PECVD growth was achieved reporting a band gap of 48 MeV when graphene is grown for 30 min at 950 °C on a sapphire substrate without a catalyst (Changsoo Park et al.) [28]. The perovskite's stability is preserved by decoupling the high-temperature graphene synthesis on a sapphire substrate from the perovskite deposition process via technique transfer. The use of thermally robust $CsPbI_3$ and careful layer sequencing ensures that the absorber remains intact during device fabrication. Using graphene layer in solar cell has improved its efficiency but it can further be modified by growing graphene using PECVD to get better results. In this paper, we simulate a model of an ITO/PCBM/$CsPbI_3$/graphene-based solar cell where graphene is grown using PECVD method in SCAPS-1D software and observe the effect on device efficiency when HTL and absorber thickness is changed. We also develop a numerical model and compare the results with that of the simulated model as well as observe the effect of plasma parameters on the efficiency (Table 1).

Table 1 Parameters and symbols used in the paper [1]

Parameters	Symbols
Efficiency of solar cell	η
Power input	P_{in}
Thickness of graphene layer	t
Fill factor	FF
Short-circuit current density	J_{SC}
Open circuit voltage	V_{OC}
1D donor concentration	N_{1D}
Boltzmann constant	K_B
Oxide permittivity	ε_{ox}
Debye length	λ_D
Electron Debye length	λ_e
Ion Debye length	λ_i
Electron temperature	T_e
Ion temperature	T_i
Electron density	n_e
Ion density	n_i
Conduction band	CB
Valence band	VB
Donor concentration	N_D
Acceptor concentration	N_A
Quantum efficiency	QE_{eff}
Band gap	E_g
Dielectric permittivity	ϵ_r
Electron affinity	χ
Indium tin oxide	ITO
Phenyl-C61-butyric acid methyl ester	PCBM
Metal work function	Φ
Graphene-based perovskite solar cell	GrPrSC
Generation rate of holes	G_n
Generation rate of electrons	G_p
Electronic charge	q
Hole current density	J_p
Electron current density	J_n
Power conversion efficiency	PCE_{eff}
Air mass spectrum	AM
Reverse saturation current	J_o

2 Device simulation and mathematical modelling of ITO, PCBM, $CsPBI_3$, graphene-based perovskite solar cell

2.1 Work 1. Simulation of ITO, PCBM, $CsPbI_3$, graphene-based perovskite solar cell

2.1.1 Solar cell simulation and implementation of graphene layer

A model of ITO/PCBM/CsPbI3/graphene (GrPrSC) is modeled and simulated using the SCAPS-1D. The range of layer thicknesses for sensitivity analysis in a solar cell simulation is selected based on the balance between optical absorption, charge transport efficiency, recombination rates, practical fabrication constraints and thermal/mechanical stability. By iterating through a reasonable set of thicknesses, we have determined the optimal thicknesses that maximize the solar cell's efficiency and performance. Initially, a 0.050 µm-thick layer of ITO serves as the top electrode. PCBM serves as the ETL, measuring 0.010 µm thick, and an HTL layer of plasma-assisted graphene, measuring 0.068 µm thick, is used to collect electrons and holes from the absorber layer. A 0.5 µm-thick layer of $CsPbI_3$ which is a strong absorber in the visible region with an absorption coefficient of 10^5 cm^{-1} ($\alpha = 10^4 - 10^5$ cm^{-1}) is taken into account as the absorber in the PrSC design. Since $CsPbI_3$ is a slightly p-type semiconductor with iodine vacancies, the acceptor density is taken as 1×10^{15} cm^{-3}. Graphene being a semimetal with negligible band gap is heavily doped with donor density 1×10^{19} cm^{-3} and PCBM; a n-type semiconductor has a donor density of 2.93×10^{17} cm^{-3}. Graphene/$CsPbI_3$ interface layers are prone to high defect densities due to lattice mismatching, dangling bonds and imperfections during fabrication. Therefore, a parameter of 1×10^{15} cm^{-2} has been considered to reflect realistic interface defect density. Since interface recombination velocities depend upon defect densities and material quality, electron and hole recombination values ranging from 1×10^5 to 1×10^7 cm/s have been used for front and back electrodes, respectively, in view of the high defect density. In this experiment, thickness of the absorber layer is varied from 0.1 to 1 µm and the graphene layer from 0.001 to 0.01 µm. The results are presented in the results and comments. Au, which has a work function of 5.3 eV, serves as the cathode.

Marc Burgelman created the one-dimensional numerical modelling and simulation program called SCAPS-1D. [29–35]. There are certain one-dimensional equations governing the charge carriers and conduction of semiconductor under the steady state. By resolving those equations, this software facilitates understanding of the basic characteristics of solar cells and pinpoints the key elements influencing their operation.

We know the Poisson's equation to be,

$$\nabla(\varepsilon.\nabla\psi) = -\rho. \tag{1}$$

The equation of continuity for negative charged carriers is given as,

$$\frac{\partial n}{\partial t} = \frac{1}{q}\nabla(J_n) + G_n - R_n. \tag{2}$$

The equation of continuity for positive charged carriers is given as,

$$\frac{\partial p}{\partial t} = \frac{1}{q}\nabla(J_p) + G_p - R_p. \tag{3}$$

During the simulation, the air mass spectrum of AM 1.5 radiation was assumed, keeping a working temperature of 300 K and frequency of 10^6 Hz and the device was operated under illuminated (ON) condition. Figures 1 and 2 show the schematic diagram of the solar cell and the simulated model, respectively.

2.2 Results regarding simulation and discussion

We simulate the ITO/PCBM/$CsPbI_3$/graphene model using the parameters mentioned in Tables 2, 3 and 4, and the results are as follows:

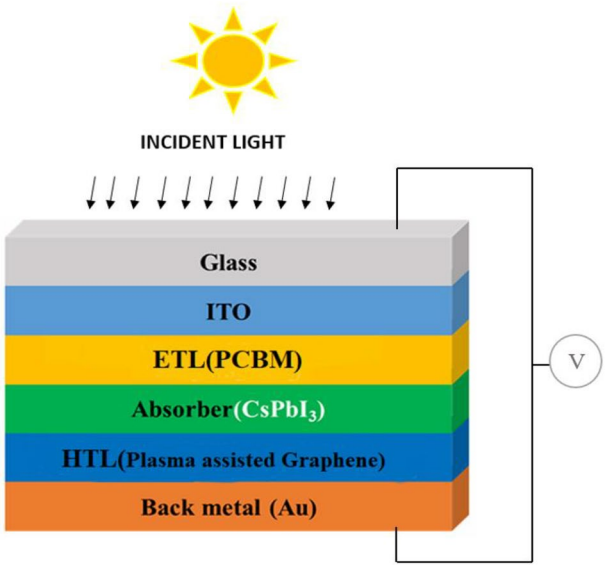

Fig. 1 Schematic diagram of ITO/PCBM/$CsPbI_3$/graphene solar cell

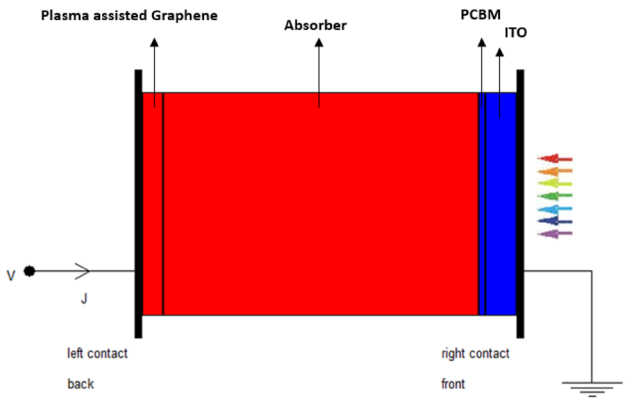

Fig. 2 Simulated structure of the GrPrSC model using SCAPS-1D software

2.2.1 Band gap diagram of the simulated model

Figure 3 demonstrates the GrPrSC model's band gap structure. Different layers of the solar cell are seen in the above figure, which was created using SCAPS-1D software. We can use it to analyze the solar cell's performance.

2.2.2 Examining the quantum efficiency of the simulated model

The quantity known as quantum efficiency Q_{eff} indicates "how many electron hole pairs are produced for every incident photon" [44]. We can determine how much solar energy the device has absorbed overall from the spectra. It provides all detail about the photon, including its transmission, absorption and reflection. Figure 4 depicts the plot of how the quantum efficiency changes when there is a change in the wavelength of the incident light.

Table 4 Parameters used for defect in solar cells [2, 36–43]

S.N	Parameter	Graphene/$CsPbI_3$
1	Type of defect	68.3
2	Capture cross section of electrons (cm^2)	0.098
3	Capture cross section of holes (cm^2)	4.8
4	Energy distribution	10
5	Reference for def. energy level (eV)	3×10^9
6	Energy w.r.t reference	3×10^9
7	Total density (cm^{-3})	1×10^{15}

2.2.3 J-V Characteristics of the solar cell with varying thickness of absorber

The J-V curve is a crucial instrument we use to "evaluate the performance of a solar cell." It offers important insights on the electrical properties of the apparatus. We can also learn about the device's efficiency PCE_{ff} from the J-V curve. When the $CsPbI_3$ layer is 500 nm thick, the J-V curve for the simulated model of GrPrSC is shown in Fig. 5.

Table 2 Simulation parameters of ITO, absorber, ETL and HTL

S.N	Parameter	ITO	Absorber	ETL	HTL
1	Thickness (nm)	500	Variable	50	68.3
2	Band gap (eV)	3.5	1.694	2.0	0.098
3	Electron affinity (eV)	4	3.95	3.9	4.8
4	Layer relative permittivity	9	9	3.9	10
5	CB effective density of states ($1/cm^3$)	2.2×10^{18}	1.1×10^{20}	2.5×10^{21}	3×10^9
6	VB effective density of states ($1/cm^3$)	1.8×10^{19}	8.2×10^{20}	2.5×10^{21}	3×10^9
7	Electron mobility ($cm^2/V.\ s$)	20	25	0.2	10×10^5
8	Hole mobility ($cm^2/V.\ s$)	10	25	0.2	10
9	Shallow uniform acceptor density ($1/cm^3$)	-	1×10^{15}	-	2.328
10	Shallow uniform donor density ($1/cm^3$)	1×10^{21}	-	2.93×10^{17}	1×10^{19}
11	References	[2, 36–38]	[2, 39]	[2, 37–41]	[28, 42]

Table 3 Parameters used for metal contacts [2, 36–43]

S.N	Parameter	Right contact (front)	Left contact (back)
1	Electron surface recombination velocity ($cm.s^{-1}$)	1×10^7	1×10^5
2	Work function of metal used (Au) (eV)	3.8415	5.3
3	Hole surface recombination velocity ($cm.s^{-1}$)	1×10^5	1×10^7

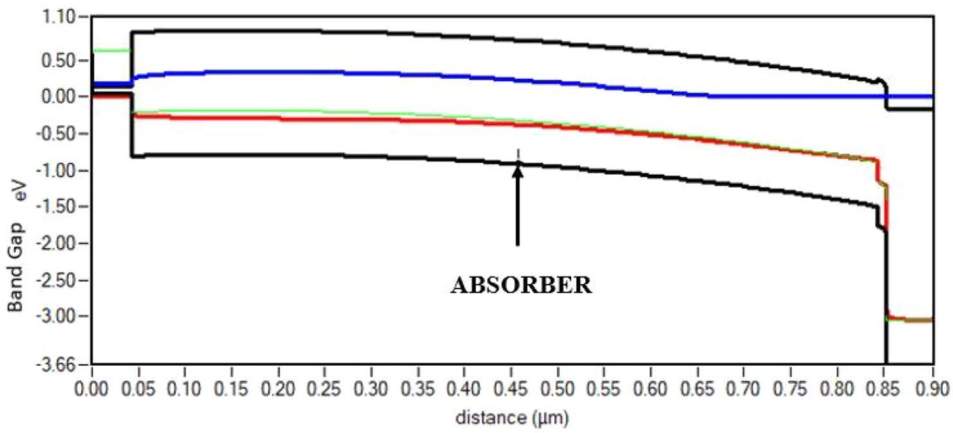

Fig. 3 Band gap diagram of the simulated GrPrSC model

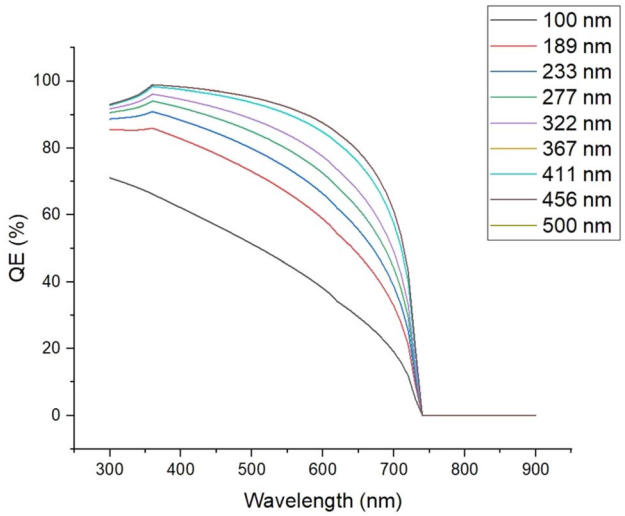

Fig. 4 Plot of change in quantum efficiency for changing wavelength of incident light when the thickness of the absorber layer is varied from 100 to 500 nm

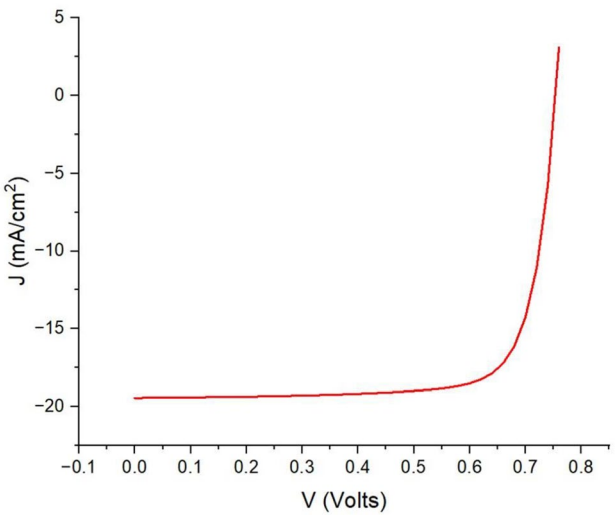

Fig. 5 The J-V curve for the graphene-based solar cell when absorber thickness is 500 nm

As the solar cell is exposed to the sunlight at AM 1.5, the photons falling on the surface of the device trigger the generation of positively and negatively charged carriers called holes and electrons. These electron hole pairs are responsible for the photocurrent that we are able to obtain from the photovoltaic device. The current generated increases if we increase the thickness of the absorber layer. In this research, we have varied the thickness of the absorber layer from 100 to 1000 nm and have observed an increase in the device efficiency. The results are in accordance with the research previously done.

2.2.4 Variation analysis of solar cell parameters with changing absorber thickness simulated in SCAPS-1D software

As observed from Fig. 6, the PCE_{ff} and J_{sc}, respectively, show a steady increase if we increase the absorber ($CsPbI_3$) thickness. This is because of the increase in V_{oc} as observed above in the figure. The curves of efficiency (PCE_{ff}) shoot upward and J_{sc} start to saturate around 800 nm, indicating that any further increment in the thickness of absorber will lead to no changes in the J_{sc} of the simulated GrPrSC device. This is because more incident light gets absorbed leading to a higher current generation and increased device efficiency. However, the light absorption reaches a maximum after a certain thickness and any further increment in the thickness leads to no further changes in the GrPrSC efficiency and the current density. The FF of the simulated devices shows an almost constant trend line, with an incredibly small decrease around 700 nm, as observed from the figure, and V_{oc} shows an increasing trend when we introduce an increment in the absorber ($CsPbI_3$) thickness. From the J-V curve, at 800 nm thick $CsPbI_3$ layer, we obtain a PCE_{ff} of 9.319%, a FF of around 73.30%, J_{sc} around 20.623 mA/cm^2 and V_{oc} near the value 0.616 V.

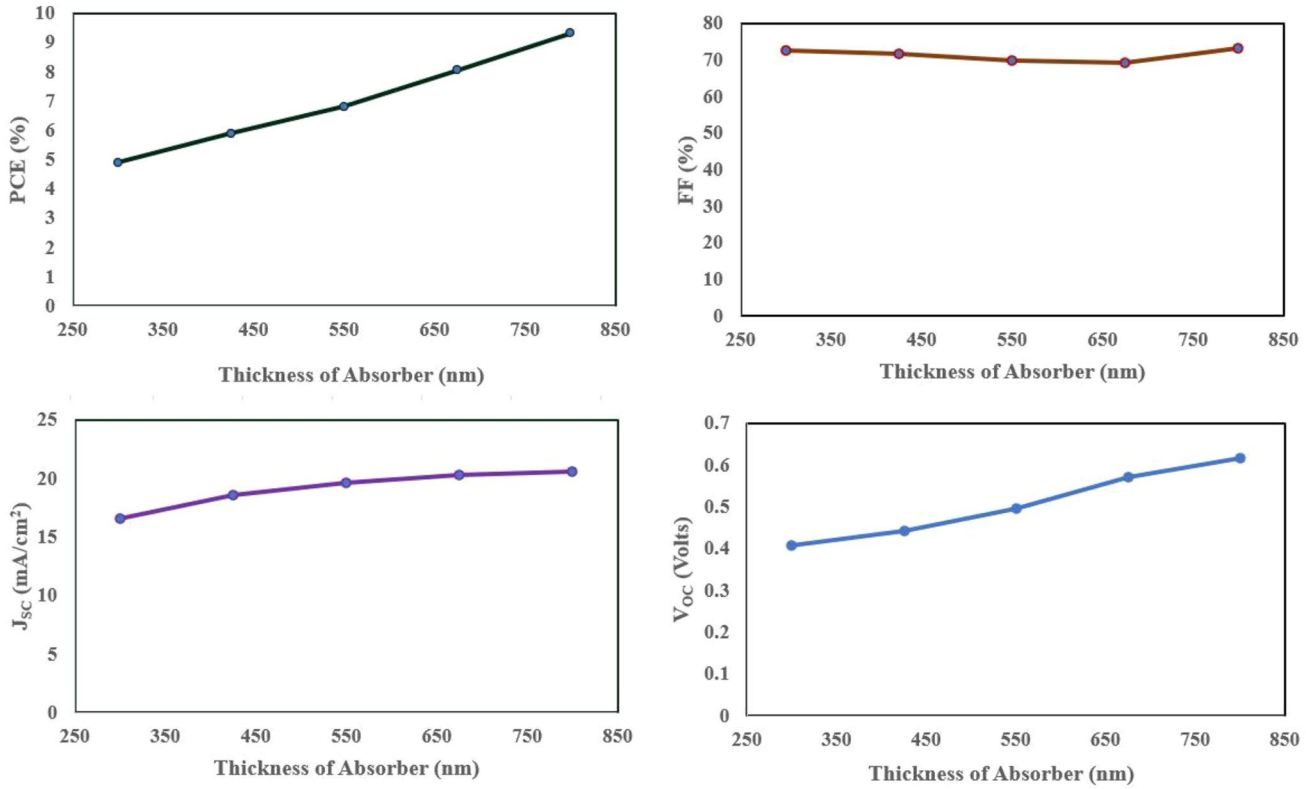

Fig. 6 Plots of the various trends with Jsc, PCEeff, FF, Voc when the absorber thickness changes from 300 nm thick to 800 nm thick

2.2.5 Variation analysis of solar cell parameters with changing HTL thickness simulated in SCAPS-1D software

Figure 7 shows how significant solar cell parameters which describe its working and properties vary graphically with the changing thickness of HTL (plasma-assisted graphene). Not much impact of the HTL replaced by graphene is seen on J_{sc} and shows values ranging from 20.61514 mA/cm^2 leading up to 20.62588 mA/cm^2 where thickness of absorber layer is fixed at 500 nm. Similar trend for FF is observed as shown in the graph. V_{oc} is shown to range from 0.613263 to 0.617753 V. The trends shown in the results are in compliance with the research done previously [45–59].

2.3 Summarized results from SCAPS- 1D simulation

See Tables 5 and 6.

2.4 Work 2. Analytical modelling of ITO, PCBM, $CsPbI_3$, graphene-based solar cell device

In this paper, we establish a numerical relation between the efficiency of a solar cell and plasma parameters. Bechhofer et al. [44] considered an infinitesimally thin 2D semiconductor kept from the dielectric at a distance of $h \to \infty$, along with the electrostatic potential is found to be,

$$V' = \frac{eN_{1D}}{2\pi\epsilon_{ox}} \ln\left(\frac{\lambda_D}{t}\right), \tag{4}$$

The 2D model does not depend upon the dielectric constant of the semiconductor due to our assumption of an infinitesimally thin semiconductor for which the dielectric constant physically does not make sense. Here, N_{1D} is the donor concentration in 1D, t is the thickness of the semiconductor, ϵ_{ox} is the oxide electric permittivity and λ_D is the Debye length of the plasma given by,

$$\frac{1}{{\lambda_D}^2} = \frac{1}{{\lambda_e}^2} + \frac{1}{{\lambda_i}^2} \tag{5}$$

$$\lambda_e = \sqrt{\frac{\epsilon_o K_B T_e}{n_e e^2}}, \lambda_i = \sqrt{\frac{\epsilon_o K_B T_i}{n_i e^2}} \tag{6}$$

and $N_{2D} = N_{1D} \times t_{\text{semiconductor}}$,

where λ_e and λ_i are the electron Debye length and the ion Debye length, respectively. T_e and T_i represent the electron temperature and ion temperature, respectively, and n_e and n_i are electron density and ion density,

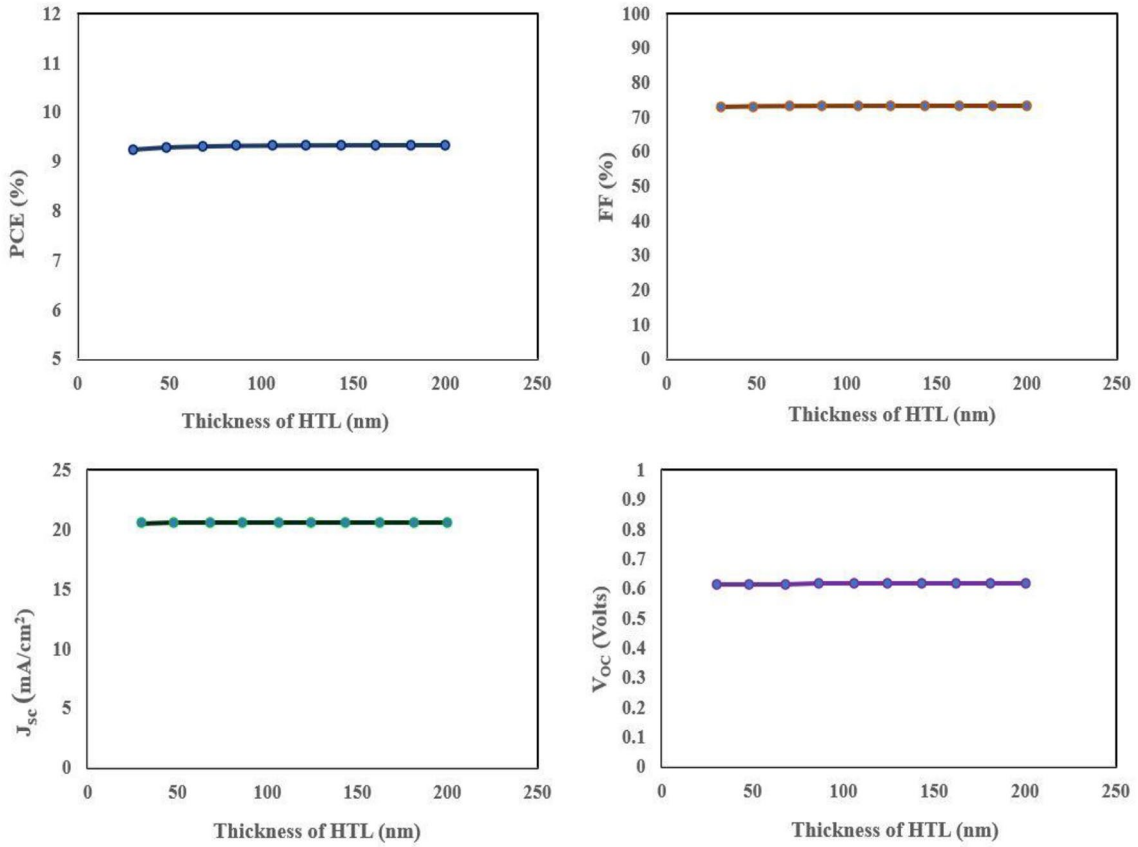

Fig. 7 A constant trend with PCE, J_{sc}, FF, V_{oc} is shown when HTL thickness is changed

Table 5 Variation in solar cell parameters with changing thickness of absorber layer [6]

Thickness of absorber (nm)	V_{OC} (V)	J_{SC} (mA/cm^2)	FF (%)	Efficiency (%)
300	0.408169	16.56865	72.619	4.9111
425	0.442683	18.56369	71.732	5.8948
550	0.495947	19.68441	69.891	6.8231
675	0.572108	20.30594	69.338	8.0552
800	0.616447	20.623	73.301	9.3187

respectively. T is the thermal temperature. We know the expression for the efficiency for a photovoltaic device is,

$$\eta = \left(\frac{FF \times V_{OC} \times J_{SC}}{P_{inc}}\right), \tag{7}$$

where

Table 6 Variation in solar cell parameters with changing thickness of HTL layer [6]

Thickness of HTL (nm)	V_{OC} (V)	J_{SC} (mA/cm^2)	FF (%)	Efficiency (%)
30	0.613263	20.61514	73.061	9.2367
48	0.615308	20.62032	73.224	9.2906
68	0.61636	20.6228	73.295	9.3166
86	0.616939	20.62411	73.331	9.3305
106	0.617279	20.62485	73.349	9.3383
124	0.617476	20.62528	73.3602	9.3429
143	0.617597	20.62555	73.3667	9.3456
162	0.617673	20.62571	73.3706	9.3474
181	0.617721	20.62581	73.373	9.3485
200	0.617753	20.62588	73.3745	9.3492

$$V_{OC} = \frac{K_B T}{e} \ln\left(\frac{J_{SC}}{J_O} + 1\right). \tag{8}$$

and FF is the fill factor, V_{OC} is the open circuit voltage, J_{SC} is the short-circuit current density of the device and J_O is the reverse saturation current. Taking the ratio of Eqs. 4 and 8

then substituting in Eq. 7, we get the expression of efficiency in terms of plasma parameters,

$$\eta = \left(\frac{FF \times J_{SC}}{P_{inc}}\right)\frac{K_B T N_{1D}}{2\pi\epsilon_{ox}V}\ln\left(\frac{\lambda_D}{t}\right)\ln\left(\frac{J_{SC}}{J_O}+1\right). \quad (9)$$

We use this expression to find the variation of efficiency w.r.t thickness of the graphene sheet and the plasma parameters numerically (Table 7).

2.4.1 Comparison between results obtained from simulation of solar cell model in SCAPS–1D and the results calculated numerically

Figure 8 shows a comparison between the variation of efficiency with thickness of graphene obtained through simulation and numerically. The PCE_{ff}, calculated both for the simulated model as well as numerically, shows a slight increase between 30 and 50 nm after which the graph saturates indicating further changes in thickness does not impact the power conversion efficiency (PCE_{ff}). The simulated model yields a result where the PCE_{ff} is 9.316%. FF of the simulated model is 73.295% with 20.629 mA/cm^2 Jsc and Voc being 0.616 V at an optimum thickness of 68.3 nm. The numerical results for the same FF, J_{sc}, V_{oc} and thickness show a PCE_{ff} of 9.668%. A difference of 0.352% in efficiency could arise from more realistic losses assumed during simulation. Discrepancies between simulated and numerically calculated results can be attributed to differences in model assumptions and simplifications. Numerical calculations assume ideal material properties, uniform layers, uniform charge transport, boundary conditions, perfect interfaces, perfect ohmic contacts and ideal temperatures while simulations incorporate realistic losses such as recombination, series resistance, interface defects and non-ideal band gaps. This result is in compliance with the research done by Sagar Bhattarai et al. [6] (Table 8).

Table 7 Summary of results derived from the numerical calculation [44]

Thickness of HTL (nm)	V_{OC} (V)	J_{SC} (mA/cm^2)	FF (%)	Efficiency (%)
30	0.6133	20.61514	73.0606	9.5556
48	0.6153	20.62032	73.2242	9.577567
68	0.6164	20.6228	73.2952	9.668198
86	0.6169	20.62411	73.3307	9.682584
106	0.6173	20.62485	73.349	9.684758
124	0.6175	20.62528	73.3602	9.696722
143	0.6176	20.62555	73.3667	9.699417
162	0.6177	20.62571	73.3706	9.701475
181	0.6177	20.62581	73.373	9.702459
200	0.6178	20.62588	73.3745	9.710422

2.4.2 Analysis of impact of plasma parameters on the solar cell efficiency

Plasma treatment has a significant impact on graphene properties such as doping, defect density, grain size and layer uniformity. Higher plasma power and longer exposure can increase doping and defect density, enhancing interfacial charge transfer but reducing conductivity. Plasma gas composition (e.g., nitrogen or oxygen) influences p-type or n-type doping. Larger grain sizes improve conductivity by reducing grain boundary scattering, while smaller grains

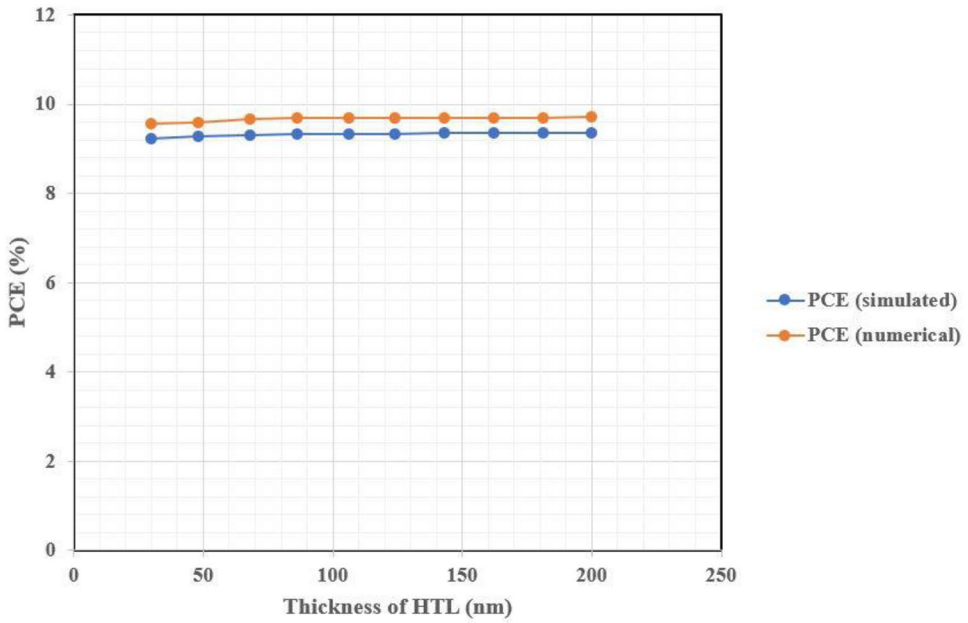

Fig. 8 A comparative plot between the how the graphene thickness (which serves as the HTL) affects the efficiency calculated for the simulated model and calculated numerically

Table 8 Comparison between the results obtained from simulation and numerical modelling [60]

Thickness of HTL (nm)	V_{OC} (V)	J_{SC} (mA/cm^2)	FF (%)	Simulated efficiency (%)	Numerical efficiency (%)	Percentage error (%)
30	0.6133	20.61514	73.0606	9.2367	9.5556	0.318
48	0.6153	20.62032	73.2242	9.2906	9.577567	0.2868
68	0.6164	20.6228	73.2952	9.3166	9.668198	0.3517
86	0.6169	20.62411	73.3307	9.3305	9.682584	0.3521
106	0.6173	20.62485	73.349	9.3383	9.684758	0.3465
124	0.6175	20.62528	73.3602	9.3429	9.696722	0.3538
143	0.6176	20.62555	73.3667	9.3456	9.699417	0.3538
162	0.6177	20.62571	73.3706	9.3474	9.701475	0.3541
181	0.6177	20.62581	73.373	9.3485	9.702459	0.354
200	0.6178	20.62588	73.3745	9.3492	9.710422	0.3612

Table 9 Parameters used for numerical calculation

Parameters	Symbol	Value	References
Electron density	n_e	2.77×10^{17} m^{-3}	[60]
Electron temperature	T_e	2.76 eV	[60]
Ion density	n_i	5×10^{18} m^{-3}	[60]
Ion temperature	T_i	0.2 eV	[60]
Donor concentration	N_{2D}	15×10^{16} m^{-2}	[44]
Oxide dielectric constant	ε_{ox}	3.9 ε_o	[44]

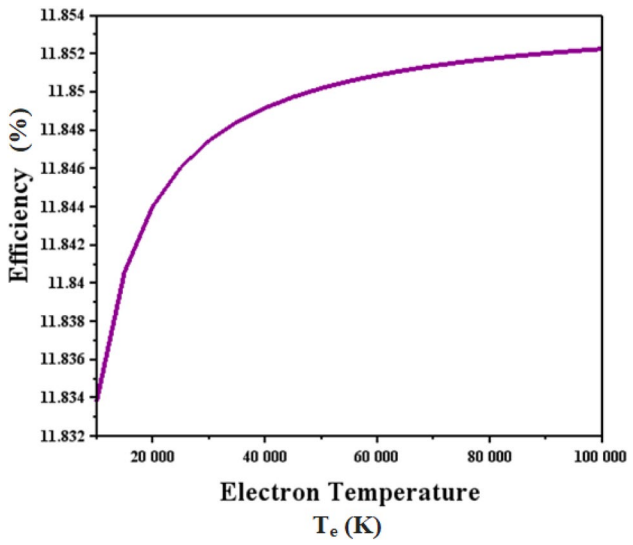

Fig. 9 PCE_{ff} enhances when an increment is introduced in T_e

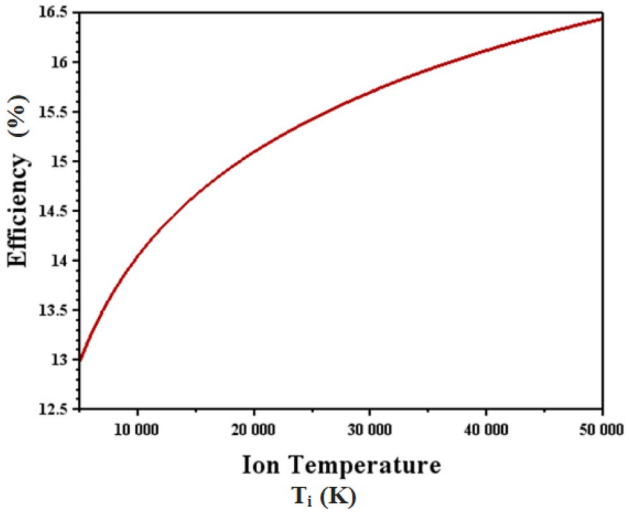

Fig. 10 PCE_{ff} is enhanced when an increment is introduced in T_i

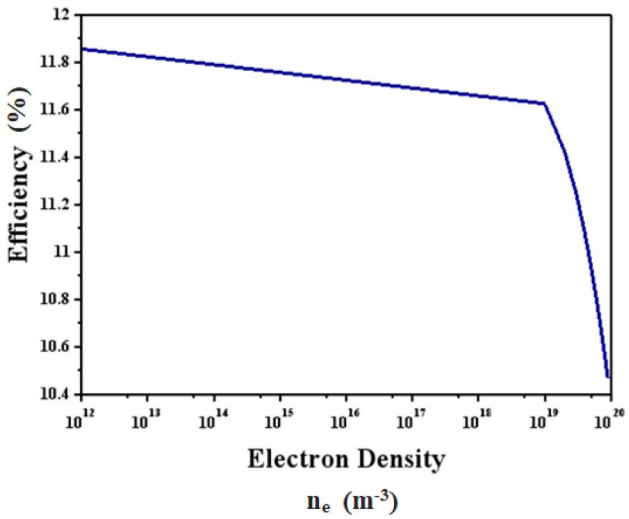

Fig. 11 PCE_{ff} reduces when an increment is introduced in n_e

or defects increase resistance. Uniform plasma treatment ensures consistent layer quality for stable device performance. Optimizing plasma parameters is crucial to balance doping, defects and conductivity, ensuring efficient device operation and performance. We now examine the effect of plasma characteristics on the photovoltaic parameters of

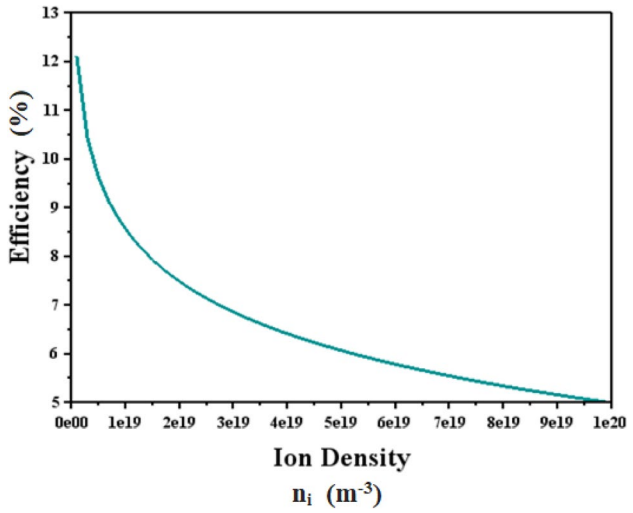

Fig. 12 PCE_{ff} shows an inverse relation with the ion density n_i

the device, specifically efficiency. Table 9 lists the various parameters used in the simulation of the trend lines shown in the graphs below (Figs. 9, 10, 11, 12).

From Figs. 9 and 10, we can observe a direct relationship between T_e and T_i, and the PCE_{ff} of our device. The reason for this change can be attributed to the Debye length λ_D being directly proportional to T_e and T_i and hence has an overall impact upon the results. Hence the graph shows that upon decreasing the T_e and T_i, the PCE_{ff} of the device increases.

Similarly, n_e and n_i are inversely proportional to the Debye length λ_D, leading to an inverse relation with the efficiency resulting in the trends as shown in Figs. 10 and 11.

Figures 9, 10, 11, 12 illustrate the variation trend lines between efficiency of device and plasma parameters (n_e, n_i, T_e, T_i) calculated numerically using the values given in Table 9, at an optimum thickness of 68.3 nm, where FF = 73.295%, Voc = 0.616 V and Jsc = 20.6228 mA/cm^2. Proper plasma conditions are necessary to avoid low recombination rates, low carrier lifetimes and high defect densities. Interface sharpness is also dependent on these plasma conditions. Subpar interface quality can lead to decreased device efficiency. As established during the numerical modelling of the device, the variation of the ratio of t/ λ_D and the resulting 2D Debye screening effect directly impacts the efficiency of the device as shown in Eq. 9. Since the electron density n_e is inversely proportional to the Debye length λ_D, it leads to an inverse relation with the efficiency. Higher density of electrons results in increased collisions and defects. It can also cause rapid growth rates and non-uniformity in the graphene layer. Non-uniformity affects the electrical conductivity of the device and hence affects the device efficiency. On the other hand, the electron temperature is directly proportional to the Debye length λ_D, leading to a direct relation with the efficiency and hence resulting in the trends as shown in Figs. 11 and 12. This could be due to the enhanced reaction kinetics from the increased T_e, leading to formation of higher quality graphene as well as cleaner substrate prior to graphene growth which can help in reducing defects and recombination and improving crystalline quality in the film. Therefore, a balance between the T_e and n_e is necessary to produce high-quality graphene sheets that enhance the efficiency of the GrPrSC. The results are in accordance with previously done research [60–62].

2.5 Summary of the investigation of device efficiency variation with change in plasma parameters

S.N	Parameter	Effect on the solar cell efficiency
1	Electron temperature T_e	Increases with an increase in T_e and λ_D
2	Ion temperature T_i	Increases with an increase in T_i and λ_D
3	Electron density n_e	Decreases with an increases in n_e and λ_D
4	Ion temperature n_i	Decreases with an increase in n_i and λ_D

3 Conclusion

An efficiency of 9.316% is achieved along with an FF = 73.061%, J_{sc} = 20.623 mA/cm^2 and V_{oc} = 0.616 V when a 68 nm thick graphene and 500 nm thick $CsPbI_3$ which here serves as the absorber is taken in a model of ITO/PCBM/$CsPbI_3$/graphene is simulated using SCAPS-1D. Taking the same values from the simulated model and incorporating them in our formula, we deduce the numerical efficiency to be 9.668%. If we increase the electron density, we observe an inverse relation with the efficiency which decreases steadily due to the formation of defects and non-uniformity. Meanwhile upon increasing the electron temperature, the device efficiency also increases, the reason for which can be attributed to increased reaction kinetics, decreased defects and recombination and improved crystalline quality. Therefore, we conclude that manipulation of the PCE of a GrPeSC is possible by changing the $CsPbI_3$ thickness and parameters of the plasma used to grow the graphene sheet.

This study emphasizes the need for sequential fabrication techniques in order to maintain perovskite stability along with high-temperature graphene synthesis, and the optimization of work function for energy alignment with perovskite absorbers. The PECVD technique opens up a plethora of opportunities for the large-scale, efficient and scalable manufacturing of high-quality graphene and improvement in the performance of graphene-based solar cells. Graphene is not easily degradable by atmosphere, and the environmental effect of solar cell manufacturing can be further reduced by developing ecologically benign precursors for graphene production and improving the PECVD process. PECVD is a scalable and industrially viable method. If graphene-HTL integration is optimized, it could reduce PSC fabrication costs. This could pave the way for commercial adoption of graphene-based perovskite solar cells, improving both efficiency and longevity.

Author contributions Shreya Vasu and Shikha Singh had equal contribution in the research, writing of the manuscript and preparation of the data, tables and figures. All authors reviewed the manuscript.

Funding This paper received no funds, grants or other support.

Data availability No datasets were generated or analyzed during the current study.

Declarations

Conflict of interest The authors declare no competing interests.

References

1. Taseen, T.I., Julkarnain, M., Islam, A.Z.M.T.: Design and simulation of nitrogenated holey graphene (C2N) based heterostructure solar cell by SCAPS-1D. Heliyon **10**, e23197 (2024). https://doi.org/10.1016/j.heliyon.2023.e23197
2. Hosenuzzaman, M., Rahim, N.A., Selvaraj, J., Hasanuzzaman, M., Malek, A.B.M.A., Nahar, A.: Global prospects, progress, policies, and environmental impact of solar photovoltaic power generation. Renew. Sustain. Energy Rev. **41**, 284–297 (2015)
3. Khalid Hossain, M., Rubel, M.H.K., Ishraque Toki, G.F., Alam, I., Ferdous Rahman, M., Bencherif, H.: Effect of various electron and hole, transport layers on the performance of CsPbI3-based perovskite solar cells: a numerical investigation in DFT, SCAPS-1D, and wxAMPS frameworks. ACS Omega **7**, 43210–43230 (2022)
4. Shihab Uddin, M., Khalid Hossain, M., Borhan Uddin, M., Toki, G.F.I., Ouladsmane, M., Rubel, M.H.K., Tishkevich, D.I., Sasikumar, P., Haldhar, R., Pandey, R.: An in-depth investigation of the combined optoelectronic and photovoltaic properties of lead-free Cs2 AgBiBr 6 double perovskite solar cells using DFT and SCAPS-1D frameworks. Adv. Electron. Mater. (2024). https://doi.org/10.1002/aelm.202300751
5. Raj, A., Kumar, M., Bherwani, H., Gupta, A., Anshul, A.: Evidence of power conversion efficiency in lead-free $CsGeI_3$ based perovskite solar cell heterostructure via SCAPS simulation. J. Vac. Sci. Technol. B **39**, 012401 (2021). https://doi.org/10.1116/6.0000718
6. Bhattarai, S., Pandey, R., Madan, J., Mhamdi, A., Bouazizi, A., Muchahary, D., Gogoi, D., Sharma, A., Das, T.D.: Investigation of carrier transport materials for performance assessment of lead-free perovskite solar cells. IEEE Trans. Electron Devices **69**(6), 3217–3224 (2022). https://doi.org/10.1109/TED.2022.3165516
7. Raj, A., Sharma, S., VeerSingh, D., Kumar, A., Kumar Chourasia, R., Siqueiros, J.M., Raymond Herrera, O., Anshul, A., Kumar, M.: Photovoltaic energy conversion in multiferroic perovskite absorber-based devices via experiment and theoretical calculations. Physica B B **673**, 415504 (2024). https://doi.org/10.1016/j.physb.2023.415504
8. Saha, N., Brunetti, G., Armenise, M.N., Di Carlo, A., Ciminelli, C.: Modeling highly efficient homojunction perovskite solar cells with graphene-TiO2 nanocomposite as the electron transport layer. IEEE J Photovol **13**(5), 705–710 (2023)
9. Nair, S., Patel, S.B., Gohel, J.V.: Recent trends in efficiency-stability improvement in perovskite solar cells. Mater Today Energy **17**, 100449 (2020). https://doi.org/10.1016/j.mtener.2020.100449
10. Yoo, J.J., Seo, G., Chua, M.R., Park, T.G., Lu, Y., Rotermund, F., Seo, J.: Efficient perovskite solar cells via improved carrier management. Nature **590**(7847), 587–593 (2021). https://doi.org/10.1038/s41586-021-03285-w
11. Kojima, A., Teshima, K., Shirai, Y., Miyasaka, T.: Organometal halide perovskites as visible- light sensitizers for photovoltaic cells. J. Am. Chem. Soc. **131**, 6050–6051 (2009). https://doi.org/10.1021/ja809598r
12. Kim, H.S., Lee, C.R., Im, J.H., Lee, K.B., Moehl, T., Marchioro, A., Moon, S.J., Humphry-Baker, R., Yum, J.H., Moser, J.E., Grätzel, M., Park, N.G.: Lead iodide perovskite sensitized all-solid-state submicron thin film mesoscopic solar cell with efficiency exceeding 9%. Sci. Rep. **2**, 1–7 (2012). https://doi.org/10.1038/srep00591
13. Eperon, G.E., Paterno, G.M., Sutton, R.J., Zampetti, A., Haghighirad, A.A., Cacialli, F., Snaith, H.J.: Inorganic caesium lead iodide perovskite solar cells. J. Mater. Chem. A **3**, 19688–19695 (2015). https://doi.org/10.1039/C5TA06398A
14. Lin, L., Jiang, L., Li, P., Xiong, H., Kang, Z., Fan, B., Qiu, Y.: Simulated development and optimized performance of CsPbI3 based all-inorganic perovskite solar cells. Sol. Energy **198**, 454–460 (2020). https://doi.org/10.1016/j.solener.2020.01.081
15. Bolotin, K.I., Sikes, K.J., Jiang, Z., Klima, M., Fudenberg, G., Hone, J., Kim, P., Stormer, H.L.: Ultrahigh electron mobility in suspended graphene. Solid State Commun. **146**, 351–355 (2008). https://doi.org/10.1016/j.ssc.2008.02.024
16. Bhattarai, S., Khalid Hossain, M., Pandey, R., Madan, J., Samjdar, D.P., Chowdhury, M., Ferdous Rahman, M., Zahid Ansari, M., Albaqami, M.D.: Enhancement of efficiency in $CsSnI_3$ based perovskite solar cell by numerical modelling of graphene oxide as HTL and ZnMgO as ETL. Heliyon **10**, e24107 (2024). https://doi.org/10.1016/j.heliyon.2024.e24107
17. Nair, R.R., Blake, P., Grigoreniko, A.N., Novoselov, K.S., Booth, T.J., Stauber, T., Peres, N.M.R., Geim, A.K.: Fine structure constant defines visual transparency of graphene. Science **320**, 1308 (2008). https://doi.org/10.1126/science.1156965
18. Balandin, A.A., Ghosh, S., Bao, W., Calizo, I., Teweldebrhan, D., Miao, F., Ning Lau, C.: Superior thermal conductivity of single—layer graphene. Nano Lett. **8**, 902–907 (2008). https://doi.org/10.1021/nl0731872
19. Ganz, E., Ganz, A.B., Yang, L.-M., Dornfeld, M.: The initial stages of melting of graphene between 4000 K and 6000 K. Phys. Chem. Chem. Phys. **19**, 3756–3762 (2017). https://doi.org/10.1039/C6CP06940A
20. Yang, P., Zijun, H., Zhao, X., Chen, D., Lin, H., Lai, X., Yang, L.: Cesium-Containing perovskite solar cell based on graphene/

TiO 2 electron transport layer. ChemistrySelect **2**(29), 9433–9437 (2017). https://doi.org/10.1002/slct.201701479
21. Dadashbeik, M., Fathi, D., Eskandari, M.: Design and simulation of perovskite solar cells based on graphene and TiO2/graphene nanocomposite as electron transport layer. Sol. Energy **207**, 917–924 (2020). https://doi.org/10.1016/j.solener.2020.06.102
22 Daraie, A., Fattah, A.: Performance improvement of perovskite heterojunction solar cell using graphene. Opt. Mater. **109**, 110254 (2020). https://doi.org/10.1016/j.optmat.2020.110254
23. Han, M.Y., Zyilmaz, O.B., Zhang, Y., Kim, P.: Energy band-gap engineering of graphene nanoribbons. Phys. Rev. Lett. **98**(20), 206805 (2007)
24. Zhang, Y., Tang, T.T., Girit, C., Hao, Z., Martin, M.C., et al.: Direct observation of a widely tunable bandgap in bilayer graphene. Nature **459**(7248), 820–823 (2009)
25. Guinea, F., Katsnelson, M.I., Geim, A.K.: Energy gaps and a zero-field quantum hall effect in graphene by strain engineering. Nat. Phys. **6**, 30–33 (2010). https://doi.org/10.1038/nphys1420
26 Chen-Hsuan, L., Hao, D., Yeh, N.-C.: A perspective of recent advances in PECVD-grown graphene thin films for scientific research and technological applications. Mater. Chem. Phys. **319**, 129318 (2024). https://doi.org/10.1016/j.matchemphys.2024.129318
27. Li, Na., Zhen, Z., Zhang, R., Zhenhua, Xu., Zheng, Z., He, L.: Nucleation and growth dynamics of graphene grown by radio frequency plasma-enhanced chemical vapor deposition. Sci. Rep. **11**, 6007 (2021). https://doi.org/10.1038/s41598-021-85537-3
28 Park, C.-S., Kim, H.: Variation of band gap in graphene grown by plasma enhanced chemical vapor deposition. Annal. Chem. Sci. Res. **2**(1), 000529 (2020). https://doi.org/10.31031/ACSR.2020.02.000529
29. Burgelman, M., Decock, K., Khelifi, S., Abass, A.: Advanced electrical simulation of thin film solar cells. Thin Solid Films **535**, 296–301 (2013)
30. Decock, K., Zabierowski, P., Burgelman, M.: Modelling metastabilities in chalcopyrite-based thin film solar cells. J. Appl. Phys. **111**, 043703 (2012)
31. Decock, K., Khelifi, S., Burgelman, M.: Modelling multivalent defects in thin film solar cells. Thin Solid Films **519**, 7481–7484 (2011)
32. Burgelman, M., Marlein, J.: Analysis of graded band gap solar cells with SCAPS, In: Proceedings of the 23rd European Photovoltaic Solar Energy Conference, (Valencia, E, September 2008), 2151–2155, WIP, München, (2008)
33. Verschraegen, J., Burgelman, M.: Numerical modeling of intraband tunneling for heterojunction solar cells in SCAPS. Thin Solid Films **515**(15), 6276–6279 (2007)
34. Degrave, S., Burgelman, M., Nollet, P.: Modelling of polycrystalline thin film solar cells: new features in SCAPS version 2.3, In: Proceedings of the 3rd World Conference on Photovoltaic Energy Conversion (Osaka, Japan, May 2003), pp. 487–490, WCPEC-3, Osaka, (2003)
35. Niemegeers, A., Burgelman, M.: Numerical modelling of ac-characteristics of CdTe and CIS solar cells, In: Proceedings of 25nd IEEE Photovol-taic Specialists Conference (Washington D.C., april 1996), pp. 901–904, IEEE, New-York, (1996)
36. Abdelaziz, S., Zekry, A., Shaker, A., Abouelatta, M.: Investigating the performance of formamidinium tin-based perovskite solar cell by SCAPS device simulation. Opt. Mater. **101**, 109738 (2020). https://doi.org/10.1016/j.optmat.2020.109738
37 Anwar, F., Afrin, S., Satter, S.S., RafeeMahbub, S.M.U.: Simulation and performance study of nanowire CdS/CdTe solar cell. Int. J. Renew. Energy Res. (2017). https://doi.org/10.20508/ijrer.v7i2.5688.g7068
38. Moon, M.M.A., Ali, M.H., Rahman, M.F., Kuddus, A., Hossain, J., Ismail, A.B.M.: Investigation of thin-film p -BaSi2/n-CdS heterostructure towards semiconducting silicide based high efficiency solar cell. Phys. Scr. (2020). https://doi.org/10.1016/j.egyr.2021.03.031
39. Jayan, K.D., Sebastian, V., Kurian, J.: Simulation and optimization studies on CsPbI3 based inorganic perovskite solar cells. Sol. Energy **221**, 99–108 (2021). https://doi.org/10.1016/j.solener.2021.04.030
40. Gan, Y., Bi, X., Liu, Y., Qin, B., Li, Q., Jiang, Q., Mo, P.: Numerical investigation energy conversion performance of tin-based perovskite solar cells using cell capacitance simulator. Energies **13**, 5907 (2020). https://doi.org/10.3390/en13225907
41. Singla, A., Pandey, R., Sharma, R., Madan, J., Singh, K., Yadav, V. K., Chaujar, R.: Numerical simulation of CeOx ETL based perovskite solar cell:- an optimization study for high efficiency and stability. In: 2018 IEEE Electron Devices Kolkata Conference (EDKCON); IEEE, (2018) pp. 278−282. https://doi.org/10.1109/EDKCON.2018.8770401
42. Shabat, M. M., Zoppi, G: Simulation on the perovskite-based solar cell with graphene derivative, In: The 8th International Engineering Conference on Renewable Energy & Sustainability, (2023) https://doi.org/10.1109/ieCRES57315.2023.10209480
43. Lakhdar, N., Hima, A.: Electron transport material effect on performance of perovskite solar cells based on CH_3NH_3GeI3. Opt. Mater. **99**, 109517 (2020). https://doi.org/10.1088/1757-899X/1152/1/012033
44. Bechhofer, A.R., Ueda, A., Nipane, A., Tehrani, J.T.: The 2D debye length: an analytical study of weak charge screening in 2D semiconductors. J. Appl. Phys. **129**, 024301 (2021). https://doi.org/10.1063/5.0032541
45. Hossain, M.K., Pervez, M.F., Tayyaba, S., Uddin, M.J., Mortuza, A.A., Mia, M.N.H., Manir, M.S., Karim, M.R., Khan, M.A.: Efficiency enhancement of natural dye sensitized solar cell by optimizing electrode fabrication parameters. Mater. Sci. **35**, 816–823 (2017). https://doi.org/10.1515/msp-2017-008611
46. Son, D.Y., Lee, J.W., Choi, Y., et al.: Self-formed grain boundary healing layer for highly efficient $CH_3NH_3PbI_3$ perovskite solar cells. Nat. Energy **1**, 16081 (2016). https://doi.org/10.1038/nenergy.2016.81
47. Wei, D., et al.: A TiO2 embedded structure for perovskite solar cells with anomalous grain growth and effective electron extraction. J. Mater. Chem. A **5**(4), 1406–1414 (2016). https://doi.org/10.1039/C6TA10418E
48 Saha, N., Brunetti, G., Armenise, M.N., Ciminelli, C.: A strategy to simplify the preparation process of perovskite solar cells by co-deposition of a hole-conductor and a perovskite layer. Adv. Mater. **28**(43), 9648–9654 (2016). https://doi.org/10.1002/adma.201603850
49. Yongzhen, Wu., Yang, X., Chen, W., Yue, Y., Cai, M., Xie, F., Bi, E., Islam, A., Han, L.: Perovskite solar cells with 18.21% efficiency and area over 1 cm^2 fabricated by heterojunction engineering. Nat. Energy **1**(11), 1–7 (2016). https://doi.org/10.1038/nenergy.2016.148
50. Chen, K., Wang, Q., Niu, Z., Chen, J.: Graphene-based materials for flexible energy storage devices. J. Energy Chem. **27**(1), 12–24 (2018). https://doi.org/10.1016/J.JECHEM.2017.08.015
51. Wang, M., Duan, X., Xu, Y., Duan, X.: Functional three-dimensional graphene/polymer composites. ACS Nano **10**(8), 7231–7247 (2016). https://doi.org/10.1021/acsnano.6b03349
52. Sun, P., Wang, K., Zhu, H.: Recent developments in graphene-based membranes: structure, mass-transport mechanism and potential applications. Adv. Mater. **28**(12), 2287–2310 (2016). https://doi.org/10.1002/adma.201502595

53. Huang, H., Chen, W., Chen, S., Wee, A.T.S.: Bottom-up growth of epitaxial graphene on 6H-SiC(0001). ACS Nano **2**(12), 2513–2518 (2008). https://doi.org/10.1021/nn800711v
54. Hirata, M., Gotou, T., Horiuchi, S., Fujiwara, M., Ohba, M.: Thin-film particles of graphite oxide 1: high-yield synthesis and flexibility of the particles. Carbon **42**(14), 2929–2937 (2004). https://doi.org/10.1016/j.carbon.2004.07.003
55. Stankovich, S., et al.: Stable aqueous dispersions of graphitic nanoplatelets via the reduction of exfoliated graphite oxide in the presence of poly(sodium 4-styrenesulfonate). J. Mater. Chem. **16**(2), 155–158 (2006). https://doi.org/10.1039/B512799H
56. Hosen, A., Mian, M.S., AlAhmed, S.R.: Improving the performance of lead-free FASnI3 based perovskite solar cell with Nb2O5 as an electron transport layer. Adv. Theory Simul. (2023). https://doi.org/10.1002/adts.202200652
57. Zhang, T., Li, H., Ban, H., Sun, Q., Shen, Y., Wang, M.: Efficient CsSnI 3 -based inorganic perovskite solar cells based on a mesoscopic metal oxide framework via incorporating a donor element. J. Mater. Chem. A. **8**, 4118–4124 (2020). https://doi.org/10.1039/C9TA11794F
58. Ye, T., Wang, K.K., Hou, Y., Yang, D., Smith, N., Magill, B., Yoon, J., Mudiyanselage, R.R.H.H., Khodaparast, G.A., Wang, K.K., Priya, S.: Ambient-air-stable lead-free CsSnI 3 solar cells with greater than 7.5% efficiency. J. Am. Chem. Soc. **143**, 4319–4328 (2021). https://doi.org/10.1021/jacs.0c13069
59. Xu, X., Wang, J., Cao, D., Zhou, Y., Jiao, Z.: Design of all-inorganic hole-transport-material-free $CsPbI_3$/$CsSnI_3$ heterojunction solar cells by device simulation. Mater. Res. Express **9**, 025509 (2022). https://doi.org/10.1088/2053-1591/ac5778
60. Gupta, N., Gupta, R., Sharma, S.C.: Investigations on the effect of process parameters on the growth of vertically oriented graphene sheet in plasma-enhanced chemical vapour deposition system. Contrib. Plasma Phys. (2021). https://doi.org/10.1002/ctpp.202100069
61. Burgelman, M., Nollet, P., Degrave, S.: Modelling polycrystal-line semiconductor solar cells. Thin Solid Films **361–362**, 527–532 (2000)
62. Khalid Hossain, M., Samajdar, D.P., Das, R.C., Arnab, A.A., Ferdous Rahman, M., Rubel, M.H.K., RasidulIslam, M., Bencherif, H., Pandey, R., Maden, J., Mohammed, M.K.A.: Design and simulation of Cs2BiAgI6 double perovskite solar cells with different electron transport layers for efficiency enhancement. Energy Fuels **37**, 3957–3979 (2023). https://doi.org/10.1021/acs.energyfuels.3c00181

Publisher's Note Springer Nature remains neutral with regard to jurisdictional claims in published maps and institutional affiliations.

Springer Nature or its licensor (e.g. a society or other partner) holds exclusive rights to this article under a publishing agreement with the author(s) or other rightsholder(s); author self-archiving of the accepted manuscript version of this article is solely governed by the terms of such publishing agreement and applicable law.

small science
www.small-science-journal.com

MXene-Integrated Composites for Biomedical Applications: Synthesis, Cancer Diagnosis, and Emerging Frontiers

Aryan Saxena, Akshayat Tyagi, Sushipra Vats, Ishita Gupta, Akhil Gupta, Raminder Kaur, Saurabh Kr Tiwary, Ahmed A. Elzatahry, Maninderjeet Singh,* and Alamgir Karim**

MXenes, a novel class of two-dimensional (2D) transition metal carbides, carbonitrides, and nitrides, have gained significant attention in biomedicine. They are synthesized via two main approaches: top-down etching of MAX (here, M represents an early transition metal, A represents an element belonging to the A-group, and X represents N or C) phase precursors and bottom-up chemical reduction of metal oxides. While the MAX phase method requires high temperatures, influencing morphology and posing safety concerns, alternative non-MAX synthesis routes are emerging. Due to their unique physical and chemical properties, MXene-based composites hold great promise in regenerative medicine, biosensing, and cancer therapy. However, challenges related to their stability, controlled drug release, and biodegradability remain. This review explores advancements in MXene synthesis, emphasizing non-MAX phase fabrication and biomedical applications. Notably, MXene-based composites have shown remarkable potential in cancer treatment, particularly in photothermal and photodynamic therapy. Their mechanisms, advantages, and limitations are discussed, along with future prospects and challenges in clinical translation. The development of MXene composites offers new avenues for innovative cancer therapies, paving the way for improved treatment strategies.

1. Introduction

The introduction of 2D materials has revived the advancement of illness therapy and biomedical research. Compared to single-element graphene, 2D nanomaterials' distinctive properties offer higher performance, flexibility, and compatibility.[1] These qualities were acknowledged after they were awarded the 2010 Nobel Prize.[2] In addition, they differ from other kinds of nanomaterials in properties like physical, chemical, etc., due to their ultrathin thickness and 2D morphological structure.[3] In 2004, Novoselov et al. made a key discovery by utilizing mechanical exfoliation to uncover the distinct transport properties of individual graphene sheets.[4] Due to their extraordinary qualities in building, electrochemistry, and optoelectronics, 2-dimensional materials like graphene are gaining attention in study. This has made it possible for cutting-edge innovations to be made in conventional equipment like sensors,[5] energy converters, and storage appliances.[6] Researchers have realized the possibility of varying the atomic layers in the materials that are layered to generate novel features as a result of their study of 2D materials. Since it was discovered in the year 2011, the transition metal carbide (TMC) and nitride (MXene) have garnered significant recognition because of its unique composition, characterized by a layered structure comprising a nitrogen or carbon layer sandwiched between two transition metal layers.[7] MXene is a potential material for industrial applications such as energy conversion and storage, sensors, optical devices, and environmental usages because of its excellent structural, physical, electrical, and magnetic characteristics.[8] Due to its appealing features, single- and few-layered MXene are the subject of current research rather than multilayered MXene.

A possible solution for biological applications has arisen in the form of MXenes.[9] These compounds have the formula given as $Mn+1AXnTx$ (where n could be from 1 to 3). Here, M stands for transition metals, A represents the main-group elements, X represents nitrogen and/or carbon, T represents surface termination groups, and x stands for the no. of surface functionalities. MAX phases are 3D layered ternary nitrides/carbides, which are the source of these compounds. The selective etching process in

A. Saxena, A. Tyagi, I. Gupta, A. Gupta, R. Kaur
Department of Applied Chemistry
Delhi Technological University
Delhi 110042, India

S. Vats
Department of Chemical and Biomolecular Engineering (Materials Science and Engineering Program)
University of Houston
TX 77204, USA

S. K. Tiwary, A. A. Elzatahry, M. Singh, A. Karim
Department of Chemical and Biomolecular Engineering
University of Houston
TX 77204, USA
E-mail: aelzatah@central.uh.edu; Statesmsmsingh9@central.uh.edu; akarim3@central.uh.edu

The ORCID identification number(s) for the author(s) of this article can be found under https://doi.org/10.1002/smsc.202400492.

© 2025 The Author(s). Small Science published by Wiley-VCH GmbH. This is an open access article under the terms of the Creative Commons Attribution License, which permits use, distribution and reproduction in any medium, provided the original work is properly cited.

DOI: 10.1002/smsc.202400492

MXene production can be influenced by factors like the extent and method of etching, the etching process duration, temperature, etc. Additionally, the specific MAX precursor used helps determine the etching selectivity. The choice of chemical etchant for exfoliation depends on the energy needed for breaking the M—A bond and the specific element being targeted.[10]

The etching process and ambient factors can impact the selective etching procedure, which depends on the kind of MAX precursor employed. The chosen element type and the quantity of energy needed for breaking the M—A bond dictate the chemical etchant for the process of exfoliation (**Figure 1**). Figure 1 illustrates the synthesis methods of MXenes and their biomedical applications, particularly in photodynamic therapy (PDT) and photothermal therapy (PTT). The synthesis is categorized into top-down (e.g., HF etching, bifluoride-based etching, molten salt synthesis) and bottom-up (e.g., chemical vapor deposition (CVD), template methods, and plasma-enhanced pulsed-laser deposition (PEPLD)) approaches. These strategies enable the controlled exfoliation or formation of MXenes with tailored structures and surface terminations, such as O, OH, and F groups, which are essential for their functionalization and stability.

The figure also highlights the application of MXenes in PDT, where reactive oxygen species (ROS) are generated to induce cancer cell apoptosis, and in PTT, where MXenes achieve efficient photothermal conversion under near-infrared (NIR) laser irradiation, leading to targeted tumor ablation. This visual representation emphasizes the critical role of synthesis strategies in enhancing MXene properties for advanced biomedical applications.

This review paper examines the biomedical applications of MXene-based composites with a particular focus on regenerative

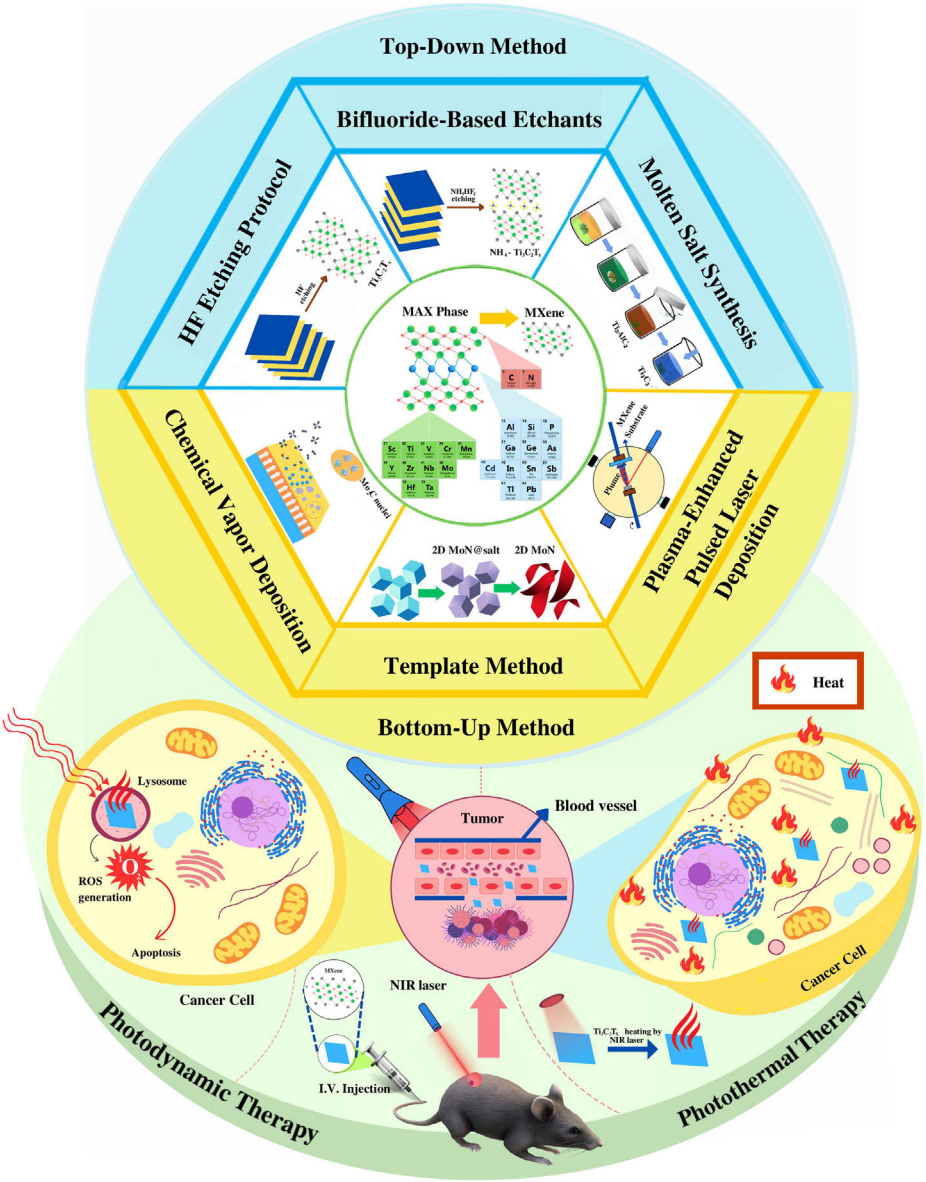

Figure 1. Schematic represents MXene synthesis methods and application in PDT and PTT cancer therapies.

© 2025 The Author(s). Small Science published by Wiley-VCH GmbH

26884046, 0, Downloaded from https://onlinelibrary.wiley.com/doi/10.1002/smsc.202400492 by Delhi Technological University, Wiley Online Library on [05/03/2025]. See the Terms and Conditions (https://onlinelibrary.wiley.com/terms-and-conditions) on Wiley Online Library for rules of use; OA articles are governed by the applicable Creative Commons License

26884046, 0, Downloaded from https://onlinelibrary.wiley.com/doi/10.1002/smsc.202400492 by Delhi Technological University, Wiley Online Library on [05/03/2025]. See the Terms and Conditions (https://onlinelibrary.wiley.com/terms-and-conditions) on Wiley Online Library for rules of use; OA articles are governed by the applicable Creative Commons License

medicine, infection therapy, and cancer treatments. It explores the integration of MXenes with other materials, such as nanosheets (NSs), nanoparticles (NPs), and polymers, and how these combinations influence the physicochemical properties of MXene compounds, including dispersion and photothermal activity. Unlike earlier reviews, which primarily focus on standalone MXene NSs and their general applications in energy storage, sensors, and environmental remediation, this review highlights the transformative potential of MXene-based composites in the biomedical field. By emphasizing composite systems, this review addresses critical challenges like stability, biocompatibility, and biodegradability, often limiting factors for standalone MXenes in physiological environments.

Furthermore, this work bridges the synthesis of MXene composites and their practical biomedical applications. It provides insights into how advanced surface engineering strategies, such as PEGylation and NP functionalization, can overcome issues like aggregation and cytotoxicity. These strategies enhance the applicability of MXene composites in PTT, PDT, and targeted drug delivery. Importantly, this review underscores the synergistic effects achievable with MXene composites, as demonstrated in the combined PTT/PDT systems using MXene-indocyanine green (ICG) hybrids, which exhibit superior therapeutic efficacy compared to individual components.

In addition to therapeutic applications, this review examines the role of MXene-based composites in biosensing and wearable technologies, expanding the scope of their utility in the biomedical domain. This work contrasts with existing literature by addressing the challenges of scalability, stability, and clinical translation. It provides a forward-looking perspective on the future of MXene-based materials in biomedicine. It concludes by outlining the hurdles and opportunities the scientific community must address to develop MXene composites for biological applications further, offering a comprehensive roadmap for future research and practical deployment.

The potential of MXene-integrated composite biomaterials in biomedical applications is examined in this review paper, emphasizing regenerative medicine, infection therapy, and cancer treatments. This article discusses the effects of combining MXenes with other substances, such as NSs, NPs, and polymers, on the physicochemical characteristics of MXene compounds, including dispersion and photothermal activities, in contrast to earlier reviews that concentrated solely on MXene NSs.[11] The article also looks at how these composites might affect the effectiveness of MXene NSs in biomedical usages and their biocompatibility and biodegradability. The article also covers MXene-based wearables and sensor development for biosensing applications. The essay concludes by outlining future directions and difficulties the scientific community must overcome to develop MXene-based materials for biological applications further. This in-depth analysis seeks to provide an invaluable roadmap for future progress in biomedicine, particularly about MXene-based materials.

2. Synthesis and Modification of MXenes of Mxene

2.1. Synthesis of MXene

Recently, wet-chemical etching methods that use hydrofluoric acid or etchants containing or producing hydrofluoric acid have been used to manufacture MXenes.[12–14] The T_x in the formula $Mn+1xnT_x$ represents the surface functions added during this process, such as O, F, or OH. Etching is still essential since mechanical exfoliation cannot produce MXenes in MAX phases because the A and M elements are tightly bound. Almost 20 members have already been generated in the MXene family, and more are anticipated to do so.

The MXene family possesses three different atomic structures, ranging from M_2X to M_3X_2 and M_4X_3, which can be customized to meet specific material requirements.[12,15,16] MXenes possess hydrophilic surfaces.[12] and higher metallic conductivities (around 6000–8000 S cm^{-1}).[17,18] Compared against other two-dimensional (2D) materials like graphene, which makes them appropriate for uses like energy storage devices,[19–22] water desalination,[23] catalysis,[24] electromagnetic interference shielding,[25] and producing transparent, conductive thin films.[17,18,26,27] As a result, MXenes have been attracting immense attention and hold significant potential in various technological fields.

The synthesis process for creating MXenes involves several stages, beginning with the aluminum layer etching from the parent MAX phase. This is followed by exfoliation utilizing a mixture of HF and HCl and the deposition of copper NPs. Once the etching is complete, the material must be washed to eliminate any residual acid and reaction products (salts) present and achieve a safe pH level of around 6. The washing procedure typically involves continuous centrifugation to separate the MXene, which has a multilayered structure, from the acidic solution, allowing for decantation of the acidic supernatant. Afterward, the multilayered flakes can be gathered through filtration with a vacuum and subsequently dried under vacuum conditions once the pH reaches ≈6.[28]

To create MXenes from the MAX phases, layered powders of MAX phases are combined with aq. HF and stirred at room temperature for a specific duration. This selective etching process removes the A layers of the MAX phase, causing the metallic bonds holding the MX layers together to be replaced by weaker surface termination bonds of hydroxyl, fluoride, or oxygen. The resulting mixture was separated from the solid with the help of centrifugation and filtration methods. The deionized water is used to wash the resulting mixture until the solution's pH falls within the 4–6 range, which yields a few-layer (FL) MXene.[29] Its important to note that MXene flakes may crumple when the pH of the MXene solution is lowered, as is the case with $Ti_3C_2T_x$.[30]

While significant progress has been made in synthesizing MXenes and their composites, scalability and reproducibility remain key challenges. Developing greener, cost-effective synthesis methods that avoid hazardous chemicals like HF and bifluorides is essential for industrial adoption. Moreover, innovative strategies such as one-pot synthesis and in situ functionalization could streamline the fabrication of multifunctional MXenes, opening new avenues for biomedical applications.

2.1.1. Top–Down Method of MXene Synthesis

Bulk crystal exfoliation directly through mechanical or chemical means is called the top-down approach. In the synthesis of MXenes, liquid-phase exfoliation is the preferred method

© 2025 The Author(s). Small Science published by Wiley-VCH GmbH

because it tends to produce high-yield and high-efficiency ultrathin nanoscale. Creating nanoscale 2D MXenes from parent MAX-phase ceramics involves two steps. First, multilayer stacked MXenes are delaminated through hydrofluoric acid (HF) etching. Next, the MXenes are disintegrated using either probe sonication breaking or intercalation by organic base molecules to produce a few layers or single-layer MXenes. This method enables the fabrication of various types of MXenes with different morphologies, including size at the nanoscale and thickness at the atomic level (**Table 1**).[31]

HF Etching Protocol: The results obtained from analyzing three different concentrations of HF (30, 10, and 5 wt%) indicate that

Table 1. Procedural steps involved in the fabrication of MXene via top-down synthesis approach.

Method name	Etching	Washing	Drying	References
HF etching ($Ti_3C_2T_x$ using HF)	Ti_3AlC_2 powder (0.5 g) is gradually added to 10 mL of HF solution. The reaction proceeds at 23 °C for 5–24 h, depending on the HF concentration (30, 10, 5 wt%).	Centrifuge the mixture and wash it with deionized water five times. Then, use vacuum-assisted filtration with a PVDF membrane (0.22 µm pore size).	Vacuum dry at 80 °C for 24 h—final samples: 30 F-$Ti_3C_2T_x$, 10 F-$Ti_3C_2T_x$, 5 F-$Ti_3C_2T_x$.	[28]
Bifluoride etching (NH_4HF_2)	Ti_3AlC_2 powder (0.5 g) stirred with 10 mL of 2 M NH_4HF_2 solution at 23 °C for 1 day.	Centrifuge at 3500 rpm and wash with deionized water five times. Filter using a PVDF membrane. Repeat rinsing to remove impurities.	Dry in a vacuum oven at 120 °C for 24 h. Final sample: NH_4-$Ti_3C_2T_x$.	[28]
Cl-terminated $Ti_3C_2T_x$ (molten salt)	Titanium, alumina, and graphite powders mixed with NaCl/KCl salts, shaped into pellets, and heated at 660 °C to form the Ti_3AlC_2 MAX phase.	Dissolve any remaining salts using an ammonium persulfate solution. Wash to remove Cu residues and other contaminants.	Vacuum filtration followed by drying at 80 °C for 12 h.	[189]
MXenes using molten salt synthesis	Ti_3AlC_2 MAX phase etched at 1300 °C. $CuCl_2$ was added after lowering the temperature to 700 °C for $Ti_3C_2T_x$ production.	Wash the product with ammonium persulfate to remove salts and contaminants.	Dry the filtered product in an oven at 80 °C for 12 h.	[189]
HF etching protocol/synthesis of $Ti_3C_2T_x$ using HF as an etchant	Over five minutes, stirring with a Teflon magnetic bar, 0.5 g of Ti_3AlC_2 powder was gradually introduced to 10 mL of etchant. The reaction was then allowed to continue at room temperature (23 °C) for the following durations and concentrations of HF: 5 h for 30 wt%, 18 h for ten wt%, and 24 h for five wt%.	Using centrifugation, each powder was washed five times individually, using a total of 1000 mL of deionized water. (5 min @ 3500 rpm per cycle). $Ti_3C_2T_x$ sediments were vacuum-assisted filtered over a polyvinyl difluoride (PVDF) filter membrane with a 0.22 m pore size before being washed once more with 1000 mL of deionized water (Durapore, Millipore).	MXene particles are vacuum-dried at 80 °C for 24 h. The powders were given 30 F-$Ti_3C_2T_x$,10 F-$Ti_3C_2T_x$, and 5 F-$Ti_3C_2T_x$, respectively, for 30, 10, and 5 wt% HF.	[28]
Synthesis of $Ti_3C_2T_x$ using a fluoride-based etchant, NH_4HF_2	10 mL of 2 M NH_4HF_2 were combined with half a gram of Ti_3AlC_2 powder while continuously stirred. The reaction was then allowed for 1 day at room temperature (23 °C).	The combined produced was centrifuged at a rate of 3500 rpm. After this, they are washed with the deionized water (5 times per 5 min per cycle) following the $Ti_3C_2T_x$ product's passage through a PVDF filter membrane, a 0.22 m pore size, washing was carried out using vacuum-assisted filtration. The filtration system was then used to rinse the product with 1000 mL of deionized water.	The powder was dried in a vacuum oven for 24 h at 120 °C. NH_4-$Ti_3C_2T_x$ is the MXene fabricated by this method.	[28]
Cl-terminated $Ti_3C_2T_x$ and Ti_2CT_x MXenes using molten salt synthesis	Titanium, alumina, and graphite powders are combined with NaCl and KCl salts, shaped into pellets, and heated in a crucible containing a bed of chloride salt at ≈660 °C to produce the Ti_3AlC_2 MAX phase. The molten salt protects the reactants from oxidation by acting as a reactive medium and preventing them from directly touching the air. Etching at 1300 °C for 1-h results in the Ti_3AlC_2 MAX phase. For producing $Ti_3C_2T_x$ MXene, $CuCl_2$ is added to the melted mixture only after lowering the crucible's temperature to 700 °C.	After cooling to room temperature, the samples are rinsed with deionized (DI) water and an ammonium persulfate (APS, (NH4)2S2O8) solution to facilitate the dissolution of any remaining solidified salts and to eliminate the Cu residue from the surface of the MXene particles.	The surface MXene materials formed using this molten salt preparation technique were F-free and Cl-containing. Vacuum filtration is used to collect the finished product, which is then dried for 12 h in an oven at 80 °C.	[189]

© 2025 The Author(s). Small Science published by Wiley-VCH GmbH

26840046, 0, Downloaded from https://onlinelibrary.wiley.com/doi/10.1002/smsc.202400492 by Delhi Technological University, Wiley Online Library on [05/03/2025]. See the Terms and Conditions (https://onlinelibrary.wiley.com/terms-and-conditions) on Wiley Online Library for rules of use; OA articles are governed by the applicable Creative Commons License

eliminating Al could be attained using as little as 5 wt% HF. Additionally, when using a concentration of 30 wt% HF, a 5-h etching period was found to be sufficient. The synthesis of $Ti_3C_2T_x$ can be accomplished using the three different HF concentrations, as depicted in **Figure 2**.

The synthesis of $Ti_3C_2T_x$ MXene involves several steps. First, a Teflon magnetic bar is used to stir 0.5 g of powdered Ti_3AlC_2 into 10 mL of etchant over five minutes. To prevent uncontrolled bubbling from the exothermic reaction, additional Ti_3AlC_2 powder is steadily added. The reaction takes place at ambient temperature, employing distinct HF concentrations and different durations of 5, 18, and 24 h. These durations correspond to HF solutions of 30, 10, and 5 wt%, respectively. These durations are sufficient to achieve exhaustive etching. After etching, the powders are subjected to five wash cycles using 1000 mL of deionized water, each conducted for a brief period at 3500 rpm using centrifugation. The leftover $Ti_3C_2T_x$ sediments are collected by the method of vacuum-assisted filtration over a filter membrane of polyvinyl difluoride (PVDF) with a 0.22 µm filter porosity (Durapore, Millipore) and washed again with 1 L of distilled water before being collected.

MXene particles are vacuum dried at 80 °C for a time period of 24 h. The powders have been given the names 30F-$Ti_3C_2T_x$, 10F-$Ti_3C_2T_x$, and 5F-$Ti_3C_2T_x$, respectively, for 30, 10, and 5 wt% HF. All the three MXene powders have been kept in vacuum condition before being processed or subjected to further examination. As is clear from numerous research and reviews pertaining to MXenes, HF concentrated form has been used frequently as a preferred etchant to extract Al from Ti_3AlC_2 in a selective manner. However, employing diluted etchant with 5 wt% HF is a workaround for not utilizing excessively high HF concentrations. The alternative procedure involves creating etchants with 3–5 wt% HF in situ using fluoride salts like LiF or NH_4HF_2, or hydrogen fluoride.

According to studies on MXenes, concentrated HF has commonly been employed as a favored etchant to extract Al from Ti_3AlC_2 selectively. Therefore, a remedy for not using extremely high HF concentrations is diluted etchant with 5 wt% HF. The alternative procedure involves creating etchants with 3–5 wt% HF in situ using fluoride salts like LiF NH_4HF_2 or hydrogen fluoride.[28]

Bifluoride-Based Etchants: Thin coatings of Ti_3AlC_2[26] have been etched using salts of HF, like NH_4HF_2, at ambient temperature.[32] For a couple of hours, Ti_3AlC_2 powder was etched for 5 days at 60 °C or room temperature.[33] In this article, the delamination methods for MXene powders made with NH_4HF_2 are described along with the method's description (which is covered in more detail later). These are the steps for creating NH_4HF_2 etched $Ti_3C_2T_x$:

In an experiment, 2 M NH_4HF_2 with 10 mL volume was continuously mixed with 0.5 g of Ti_3AlC_2 powder, then left to react at 23 °C for 24 h. The final mixture was centrifuged after that at 3500 rpm, followed by washing five times using deionized water for 5 min per cycle. The $Ti_3C_2T_x$ sample was then filtered using a PVDF membrane filter with a pore size equal to 0.22 µm, and vacuum-assisted filtration was used for washing. The filtered

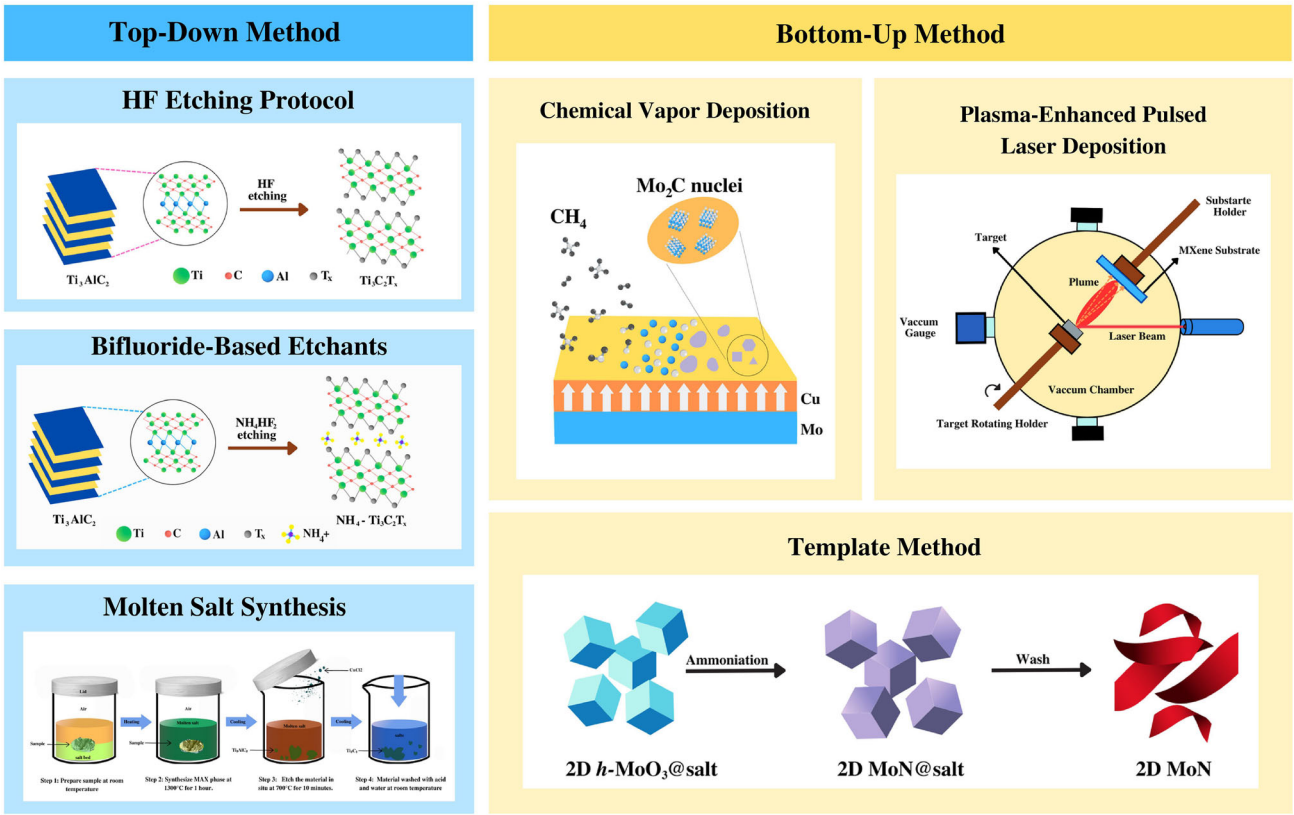

Figure 2. Top-down and bottom-up synthesis methods.

© 2025 The Author(s). Small Science published by Wiley-VCH GmbH

26884046, 0, Downloaded from https://onlinelibrary.wiley.com/doi/10.1002/smsc.202400492 by Delhi Technological University, Wiley Online Library on [05/03/2025]. See the Terms and Conditions (https://onlinelibrary.wiley.com/terms-and-conditions) on Wiley Online Library for rules of use; OA articles are governed by the applicable Creative Commons License

product was further rinsed with 1000 mm of deionized water. A vacuum oven was used at 120 °C for 24 h to dry the powder. The final MXene obtained from this process is known as NH_4-$Ti_3C_2T_x$. This process ensures that the product is free from any impurities and is of high purity, making it suitable for further research and experimentation.

The absence of peaks of Ti_3AlC_2, such as no (002) at 9.5°, in the X-ray diffraction (XRD) pattern tells about the Al selective removal. From 9.5° in the Ti_3AlC_2 predecessors, the basal plane peaks of NH_4-$Ti_3C_2T_x$ are displaced to 8.5° and 7.15°, respectively, corresponding to d-spacings of 10.35 and 12.37. The existence of constrained water molecules and (NH_4^+) ions in between MXene layers contributes to the increased d-spacing after drying.[26,33] In contrast to HF-etched $Ti_3C_2T_x$, NH_4-$Ti_3C_2T_x$ takes more time or vacuum drying at higher temperatures to eliminate the closely packed water molecules from the powder, as depicted in Figure 2.

2.1.2. Molten Salt Synthesis/One-Pot Synthesis Process

Here, the process for synthesizing MXene from elemental precursors using titanium aluminum carbide production, in situ etching, and the method of one molten salt pot is described. The role of molten salts as reaction media is to prevent the reactants from oxidizing throughout the high-temperature fabrication process, hence allowing the production of MXenes in an ambient atmosphere without inert gas protection. This one-pot synthetic approach, which involves a high-temperature etching, takes about 10 min to produce Cl-terminated Ti_2CTx and $Ti_3C_2T_x$ MXenes. This molten salt preparation technique produced MXene without surface F atoms but contained Cl atoms. When tested as an active material in the working electrode of a nonaqueous half-cell, the MXene displayed a fast, reversible Li-ion intercalation reaction.[34]

$Ti_3C_2T_x$ MXene obtained by the one-pot synthesis in an air atmosphere. Here, stoichiometric proportions of graphite, powdered titanium, and alumina are combined using chloride salts (KCL and NaCl), and the mixture is then crushed on a steel die to create a pellet. Finally, the pellet is placed in a crucible and covered with a bed of chloride salt. The crucible is heated in an air atmosphere using a muffle furnace. The KCl and NaCl mixture melts at a temperature of about 660 °C, acting as a reactive medium that prevents the reactants from coming into touch with air directly, preventing oxidation at high temperatures. By etching at 1300 °C for 1 h, the Ti_3AlC_2 MAX phase is created.

Powder XRD studies confirm the successful production of the Ti_3AlC_2 MAX phase at 1300 °C in molten salt. Only when the melts have cooled to 700 °C is $CuCl_2$ introduced to enable the Ti_3AlC_2 MAX phase's in situ etching to create $Ti_3C_2T_x$ MXene. According to a previous study, Ti_3AlC_2 MAX phase etching happens when Cu2+ ions are reduced into Cu and associated Al is oxidized into the vaporous $AlCl_3$ phase, with a boiling point of 181 °C. Once the samples have been cooled to ambient temperature, they undergo a rinsing process using deionized water and a solution containing ammonium persulfate (APS, $(NH_4)2S2O8$). This procedure dissolves the crystallized salts and removes any copper residue from the MXene particle's surface.[34] Vacuum filtration is used to collect the finished product, which is then dried for 12 h in an oven at 80 °C.

2.1.3. Bottom–Up Methods

The bottom-up approach uses tiny organic or inorganic molecules to synthesize MXene. This method has an edge over the top-down method as it facilitates the synthesis in a controlled manner with adequate size and surface terminations.[35] The bottom-up can be applied to prepare MXenes using CVD, atomic layer deposition, and top-down fabrication methods.[26,36–39]

By using direct current magnetron sputtering to deposit Ti, C, and Al elemental targets on an insulating substrate of sapphire, Halim et al. created the Ti_3AlC_2 MAX thin film (**Figure 3**a–c).[26] Once the Al layer was precisely etched, a 1 by 1 cm^2 Ti_3C_2 thin film (19 nm) was created. Around 90% of visible to infrared light was transmitted through the film, which aided in creating monolayer MXene thin films. Moreover, the physical vapor deposition method can make thin films in either the non-MAX phase (Mo_2Ga_2C) or the MAX phase (Mo_2GaC). A straightforward etching approach could also create thin epitaxial Mo_2C films.[40,41]

At a temperature exceeding 1085 °C (shown in Figure 3d–f), a Cu/Mo alloy surface was utilized to create high-quality, 2D ultrathin —Mo_2C material over a large area through CVD, which has been a groundbreaking technique for directly synthesizing MXene-based materials.[36,37] Methane was employed as the carbon source during the CVD process to achieve this.

It was shown that altering the experimental conditions allows one to manipulate the dimensions and thickness of Mo_2C crystals. It was revealed that lateral size and nucleation density rise with increased growth time and temperature, respectively. The same procedure could be employed for creating crystals of Mo in different shapes, like triangles, rectangles, hexagons, nonagons, octagons, and dodecagons.[39] Jia et al. improved this strategy, and by using MoO_2 NSs as templates and Mo sources, ultrathin —Mo_2C NSs were quickly and effectively manufactured.[42]

Contrary to the 2D materials derived from various etchants, MXenes synthesized by CVD contain fewer flaws and no terminations, providing a platform to explore their inherent properties and the effect of the domain boundaries. The bottom-up synthetic techniques should be researched further to fabricate other types of monolayered MXenes with diverse functionalities. Studies relevant to the inherent electrical and optical characteristics of MXenes will benefit from this.[36,43–45]

The top-down approach can produce MXenes in large quantities; however, using HF or LiF/HCl solutions during the synthesis results in flaws and an MXene surface ending with various functional groups.[12] Furthermore, sonication or mechanical vibration causes MXene to shrink and produce more flaws. Studies focused on the inherent characteristics of 2D TMNs and TMCs have been impeded due to mechanical damage and chemical alterations to MXenes. The parent MAX phase with 3D lattice also restricts the species and MXenes structure. Moreover, every MXene created so far has a structure of the M_2X, M_3X_2, or M_4X_3 kind.[12] Furthermore, MX structure MXenes cannot be prepared with this method (such as NbN, NbC, MoN, MoC, etc.).

© 2025 The Author(s). Small Science published by Wiley-VCH GmbH

26884046, 0, Downloaded from https://onlinelibrary.wiley.com/doi/10.1002/smsc.202400492 by Delhi Technological University, Wiley Online Library on [05/03/2025]. See the Terms and Conditions (https://onlinelibrary.wiley.com/terms-and-conditions) on Wiley Online Library for rules of use; OA articles are governed by the applicable Creative Commons License

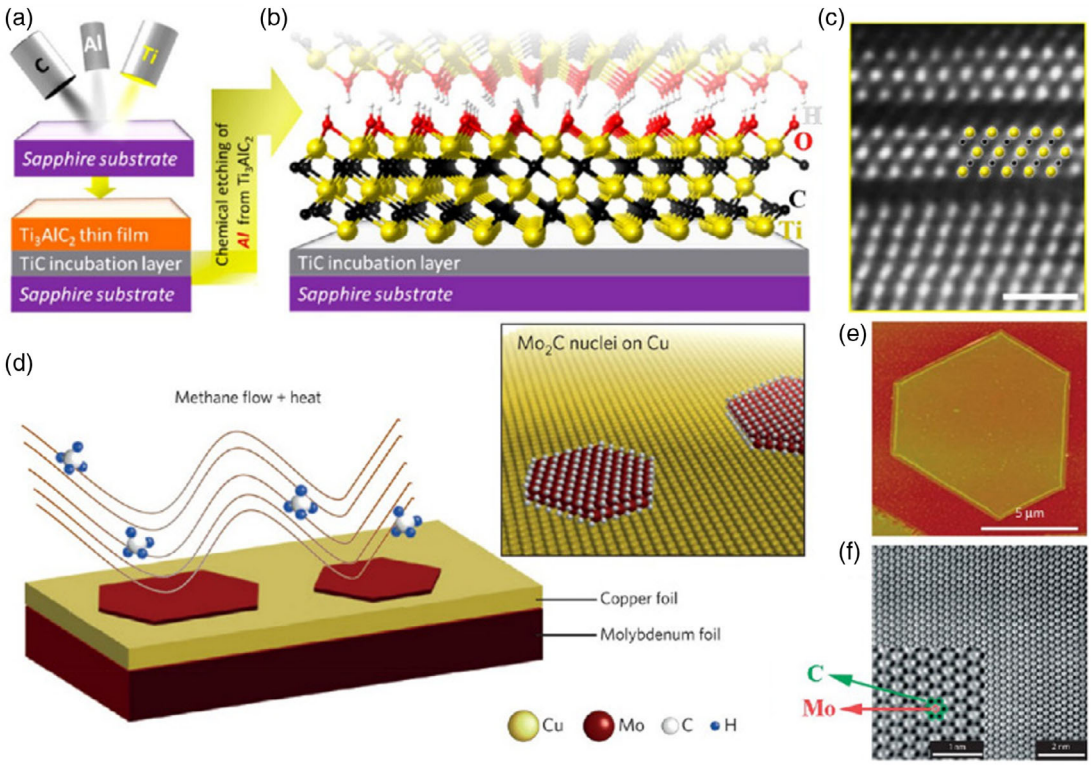

Figure 3. MXenes produced via bottom-up techniques. Nuclear layer formation: a) Ti, Al, and C sputtering on a sapphire substrate are the steps needed to create a Ti_3AlC_2 MAX thin film, b) following selective etching of Al, a schematic of Ti_3C_2Tx, and c) obtained Ti_3C_2Tx's scanning transmission electron microscopy (STEM) image. CVD approach: d) the schematic of the synthesis process of the Mo_2C, e) hexagonal ultrathin Mo_2C crystal AFM image, and f) obtained Mo_2C sheet's STEM image. (Panels (ac): Reprinted with permission.[26] Copyright 2014, ACS. Panel (d): Reprinted with permission.[36] Copyright 2015 Springer Nature. Panels (e,f): Reprinted with permission.[37] Copyright 2015, Springer Nature. Copyright pending).

Using selective area electron diffraction (SAED), it has been discovered that the crystal had an orthorhombic structure (—Mo_2C). Energy-dispersive X-Ray spectroscopy (EDS) maps in **Figure 4**c–e showed that the crystal had a consistent chemical makeup. The lack of flaws in Figure 4f indicates the material's superior crystalline quality. Atomic force microscopy (AFM) measurements were utilized to observe the crystals' slick and spotless surface. Notably, this CVD process can be deployed to create a variety of 2D ultrathin TMC crystals with high quality and various structural variations due to its adaptability.

For instance, by substituting W and Ta foil for Mo foil, respectively, Figure 4h,I illustrates the production of ultrathin 2D hexagonal WC and cubic TaC crystals—the identical procedure examined by Xu et al.[37] It was used by Geng et al.[46] to create 2D Mo_2C crystals. They conducted their research using copper foil with a minimum thickness of 50 m, at a higher temperature of 1100 °C, and different CH_4 concentrations (CH_4 0.1–0.4 sccm, H_2 200 sccm).

The shape of Mo_2C crystals changed depending on the concentration of CH_4 observed by the researchers. At a flow rate of 0.1 cm, the resulting crystals had a fractal shape. However, with an increased methane flow rate, the lattice structure transformed to hexagonal from fractals, as illustrated in Figure 4j. The hexagonal Mo_2C crystal had a more varied crystalline structure than other crystals (as shown in Figure 4k). The most prevalent shapes were rectangular and pentagonal when the methane flow rates were 0.3 and 0.4 cm, respectively. The thickness of the copper foil increased as the thickness of the Mo_2C crystal decreased.

This is because a thicker layer of copper allows more time for Mo to diffuse, leading to a more minor degree of separation on the surface of the liquid copper.

Wang et al.[47] and Xu et al. created a procedure to produce extremely thin TaN using Cu foil/Ta foil as the growth substrate, NH3 as the nitrogen source, and a temperature of 1077 C. This temperature is below the melting point of copper (Cu). This procedure was based on earlier research by Xu et al.[37] Copper foil can keep copper in its solid state during the CVD process. At higher temperatures, Ta atoms in the Cu lattice tended to group rather than be evenly dispersed. Lower temperatures are, therefore, preferred for better control over the formation of these crystals.[47]

Template Method: The template method is a versatile approach for synthesizing 2D TMCs and TMNs using TMOs as precursors. In this method, TMOs are templates that undergo specific chemical reactions, such as carbonization or ammoniation, to produce the desired 2D materials. Xiao et al.[48] demonstrated using the salt-templated method, initially developed for 2D TMO synthesis, to fabricate 2D TMNs. In their study, the salt templates facilitated the formation of uniform, thin layers of TMNs, ensuring better control over the morphology and size of the final material. By

© 2025 The Author(s). Small Science published by Wiley-VCH GmbH

26884046, 0, Downloaded from https://onlinelibrary.wiley.com/doi/10.1002/smsc.202400492 by Delhi Technological University, Wiley Online Library on [05/03/2025]. See the Terms and Conditions (https://onlinelibrary.wiley.com/terms-and-conditions) on Wiley Online Library for rules of use; OA articles are governed by the applicable Creative Commons License

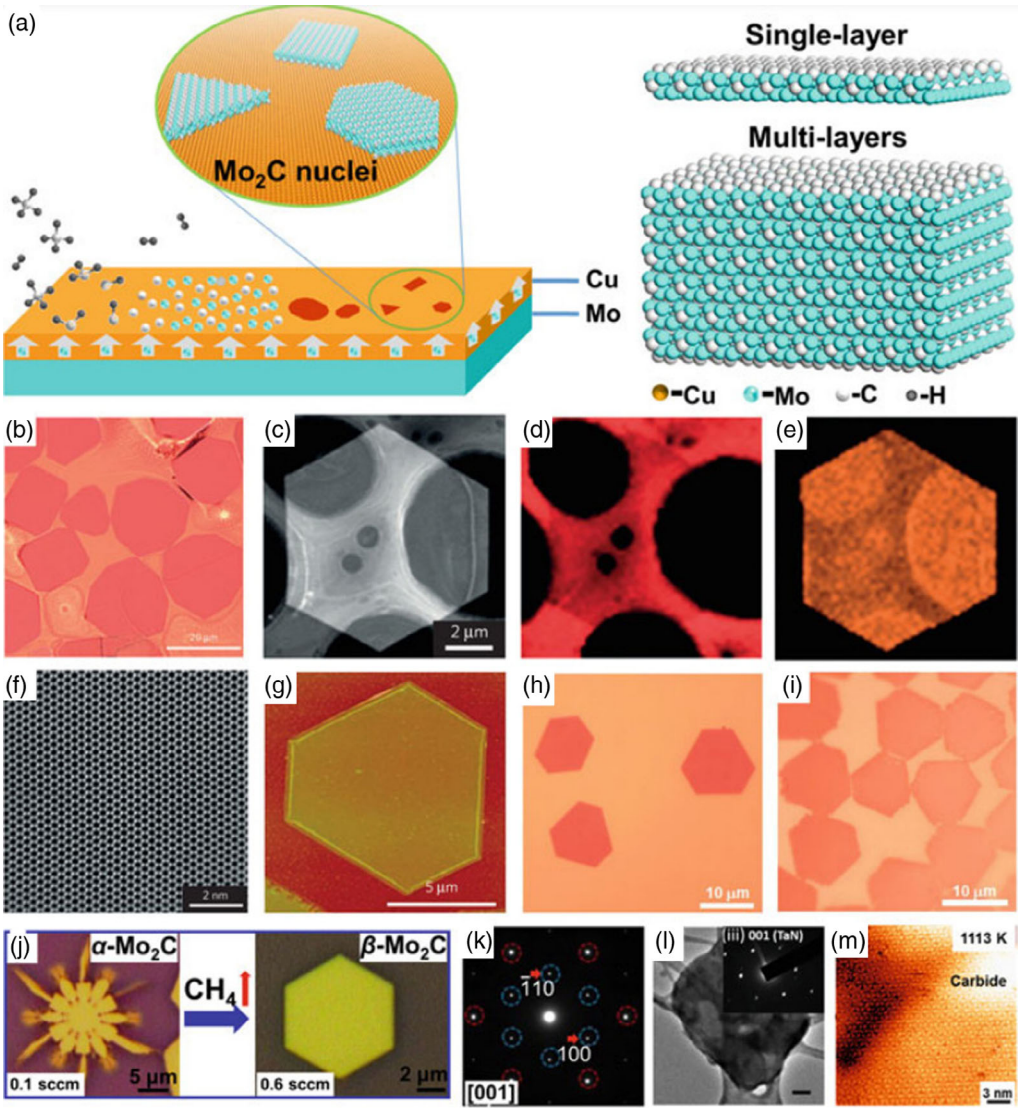

Figure 4. The transition metal nitrides (TMNs) and TMCs 2D thin films were produced using CVD. a) The Schematic diagram shows the formation process and the α-Mo_2C crystals' atomic models with varying thicknesses. b) Ultrathin 2-dimensional α-Mo_2C crystals on the growth substrate are shown in an optical image. c–e) High-angle annular dark-field scanning transmission electron microscopy (HAADF-STEM) image with low-magnification (c) and the C-K (d) and MoK's associated EDS elemental mapping. e) The hexagonal 2-dimensional α-Mo_2C crystal having the lines across through them. f) α-Mo_2C crystal's HAADF-STEM image in c. g) Hexagonal ultrathin 2D α-Mo_2C crystal's AFM image (having a thickness equal to 8.2 nm). h,i) 2-dimensional ultrathin WC (h) and TaC (i) crystals optical images. j) Optical images depicting the structure evolution of the Mo_2C crystal with increment in the flow rate of CH_4 of a fractal Mo_2C crystal and a hexagonal α-Mo_2C crystal getting transferred over SiO_2/Si substrates. k) Hexagonal Mo_2C crystal's SAED pattern. l) 2D TaN crystal transmission electron microscopy (TEM) images at low magnification; the inset displays the SAED pattern. 100 nm wide scale bars are used. m) Periodic "flower-like" ReC superstructure. Reproduced with permission.[37] Springer Nature, panels (b–i) are reprinted. Panels (j) and (k) are adapted from Ref. [46], Institute of Physics. Reproduced with permission.[47] Wiley-VCH, Panel (l) is reprinted with permission,[56] ACS copyright pending, panel (m) is reprinted).

varying the temperature and reaction atmosphere (e.g., introducing carbon or ammonia gas), the composition and structure of the TMNs could be precisely tailored.

Additionally, the template method offers several advantages: 1) Structural control: It enables the synthesizing of well-defined 2D structures with high uniformity and tunable thickness. 2) Scalability: The salt-templated approach can be adapted for large-scale production, making it more feasible for industrial applications. 3) Versatility: This method allows the synthesis of various 2D materials, including carbides, nitrides, and hybrid systems, by carefully selecting the precursor templates and reaction conditions.

Recent advancements have also combined the template method with molten salt synthesis, where molten salts act as both a template and a reactive medium, further improving the synthesis efficiency and material quality—for instance, Jin et al.[49]

© 2025 The Author(s). Small Science published by Wiley-VCH GmbH

26884046, 0, Downloaded from https://onlinelibrary.wiley.com/doi/10.1002/smsc.202400492 by Delhi Technological University, Wiley Online Library on [05/03/2025]. See the Terms and Conditions (https://onlinelibrary.wiley.com/terms-and-conditions) on Wiley Online Library for rules of use; OA articles are governed by the applicable Creative Commons License

Successfully synthesized multilayered and few-layered 2D TMNs and TMCs using molten salts achieve materials with enhanced electronic and catalytic properties—similarly, Xu et al.[50] demonstrated using TMO templates to create hybrid systems for catalysis, energy storage, and biomedical engineering applications. Thus, the template method provides a practical and flexible strategy for fabricating 2D MXene-like materials, expanding their potential applications in diverse fields.

Transition metal oxides (TMOs) are needed for the template approach to fabricate 2D TMCs and TMNs.[42,48,51] The template is carbonized or ammoniated to create the TMOs. Xiao et al. used the salt-templated method of 2D TMO synthesis as previously described[48] and evaluated the manufacture of 2D TMNs using salt templates.

Plasma-Enhanced Pulsed Laser Deposition: **Figure 5**a depicts the image of the aberration-corrected BF-STEM of the ultra-thin Mo_2C crystals. The Mo six rings, which resemble graphene, and the carbon atoms positioned in their center are visible in this photograph.[39] β-phase anticipated structure is the same as α-phase (**Figure 6**b,c). Yet, in β—Mo_2C, the carbon atoms are randomly scattered, whereas in α—Mo_2C, they are orderly grouped in Mo octahedrons. As a result, the strong hexagonal symmetry of the Mo sublattice of α—Mo_2C somewhat gives way to orthorhombic symmetry.

Even though the Mo hexagonal close-packed (HCP) lattice's distortion in —Mo_2C is too tiny for the naked eye to see, reciprocal space can be used to locate it. The contrast in electron diffraction (ED) between the α- and β—Mo_2C is seen in Figure 5d, and it can be observed that in the α-phase, superstructure ED spots are visible.[52] It was inferred that α—Mo_2C can be transformed from β—Mo_2C. During a phase transition, carbon atoms become ordered due to cooling.[53] However, it has been inferred by researchers such as Liu et al.[52] The electron beam irradiation (EBI) could lead to the transition from α to β phase in two-dimensional Mo_2C crystals. In the presence of EBI, the carbon atoms in an ultrathin α—Mo_2C crystal move from a zigzag to a random configuration. In contrast, the distorted HCP configuration is relaxed for Mo atoms to a rigorous configuration. This change from α to β phase can be seen in Figure 6f, where only area I of the crystal has been subjected to a high-dose EBI. The advanced aberration-corrected STEM use in EBI can also provide a way to create lateral junctions of 2-dimensional superconducting α/β Mo_2C having a sharp interface, as well as a platform for investigating vortex physics and the catalytic synergistic effects at the interface between phases—α and β. In addition, Zhang et al.[54] have described how PEPLD can synthesize Mo_2C thin films with an FCC structure.

The Mo atomic planes' interplanar spacing in the three structures is nearly identical. Although the space group of FCC—Mo_2C has been determined to be Fm3m with a lattice parameter of 0.415 nm (Figure 6g), the arrangement of carbon atoms within the structure remains uncertain. Through the use of a metal immiscibility route, 2-dimensional TaC crystals with a rock salt structure were synthesized by Xu et al.[37] and Wang et al.[47] where the latter researchers noted that the crystals' morphology suggested normal growth with a pyramidal morphology (Figure 6h). In CVD-fabricated 2D WC crystals, the tungsten atoms are organized in an AA stacking pattern and form trigonal prismatic structures that can accommodate carbon atoms at their centers (as shown in Figure 6i). This differs from the AB-stacking arrangement of metal atoms observed in α- and β—Mo_2C. Fermions consisting of three components have been recently discovered in WC-structured crystals.[55]

ReC was synthesized on a Re substrate in the study conducted by Qi et al.[56] Although ReC has the same planar structure as WC, the Re and carbon atoms in ReC are arranged in a coplanar 2D structure (Figure 6j). So far, two types of 2-dimensional TMNs, MoN and TaN, have been produced using a bottom-up synthesis methodology. The resulting 2-dimensional MoN crystals, obtained through ammoniation of MoO_3,[48,51] exhibit a hexagonal structure with a space group of P63mc. The molybdenum skeleton has an alternating alignment with slightly misaligned atomic columns. N atoms have been located in interstitial sites in a trigonal prismatic arrangement around the Mo atoms. Nevertheless, the nitrogen nuclear layers perpendicular to the [0001] direction are not situated within the expected coincident trigonal prisms (Figure 6k).

The lattice dimensions of the 2D TaN crystals formed are 0.5196 nm for an as well as b and 0.2911 nm for c, with a space group of P6/mmm (Figure 6l).[47]

According to first-principle calculations, the interstitial carbon atoms of the α—Mo_2C lattice in the octahedrons are somewhat off-center along the *b*-direction. Yet, the same HCP molybdenum atom sublattice is connected to three identical off-center carbon atom arrangements.[39] Topological α—Mo_2C domains may develop if identical carbon atom arrangements exist within the same sublattice of Mo atoms. Liu et al.[39] stated that 2D α—Mo_2C crystals with shapes characterized by three, six, nine, and twelve sides consist of several unique crystalline regions that exhibit domain structure and have delineated linear boundaries. Rectangular and octagonal 2D α—Mo_2C crystals are single crystals.

For instance, the diagonal domains of the α—Mo_2C NS, which is formed of sixfold rotationally symmetric domains, have the identical carbon atom structure as that in Figure 5a. The symmetric arrangement of atomic arrangement of carbon w.r.t the domain boundary has the lowest energy, according to first-principles calculations (Figure 5b). The distorted orientations of the HCP Mo sublattice differ because the asymmetric directions of the carbon atoms in neighboring segments differ. As a result, the domain boundary exhibits a slight shear strain (Figure 5c,d). However, the creation of localized phase-slip events in the boundary causes a considerable impact on the superconductivity.[39]

Mo atoms in —Mo_2C should fundamentally be stacked in the "ABAB" configuration, according to Geng et al.[38] there were two kinds of Mo stacking order, AA and AB, observed at the narrower portion of the hexagonal-shaped β—Mo_2C layer (Figure 5e). They proposed that the presence of different stacking configurations was likely due to partial growth of Mo_2C at the edge and the comparable energy of formation for the two polytypes. Additionally, Geng et al.'s[38] observation of a stacking flaw in the β—Mo_2C NS. Additional Mo atoms can be seen in the middle of the projected Mo six rings, as seen in Figure 5f.

That is, in addition to the "A" and "B" layers, there is a Mo atomic plane of the local "C" layer. Jia et al. have studied that the C-atoms substitution with N-atoms in 2D—Mo_2C resulted in the formation of N-doped —Mo_2C crystals, leading to a

© 2025 The Author(s). Small Science published by Wiley-VCH GmbH

26884046, 0, Downloaded from https://onlinelibrary.wiley.com/doi/10.1002/smsc.202400492 by Delhi Technological University, Wiley Online Library on [05/03/2025]. See the Terms and Conditions (https://onlinelibrary.wiley.com/terms-and-conditions) on Wiley Online Library for rules of use; OA articles are governed by the applicable Creative Commons License

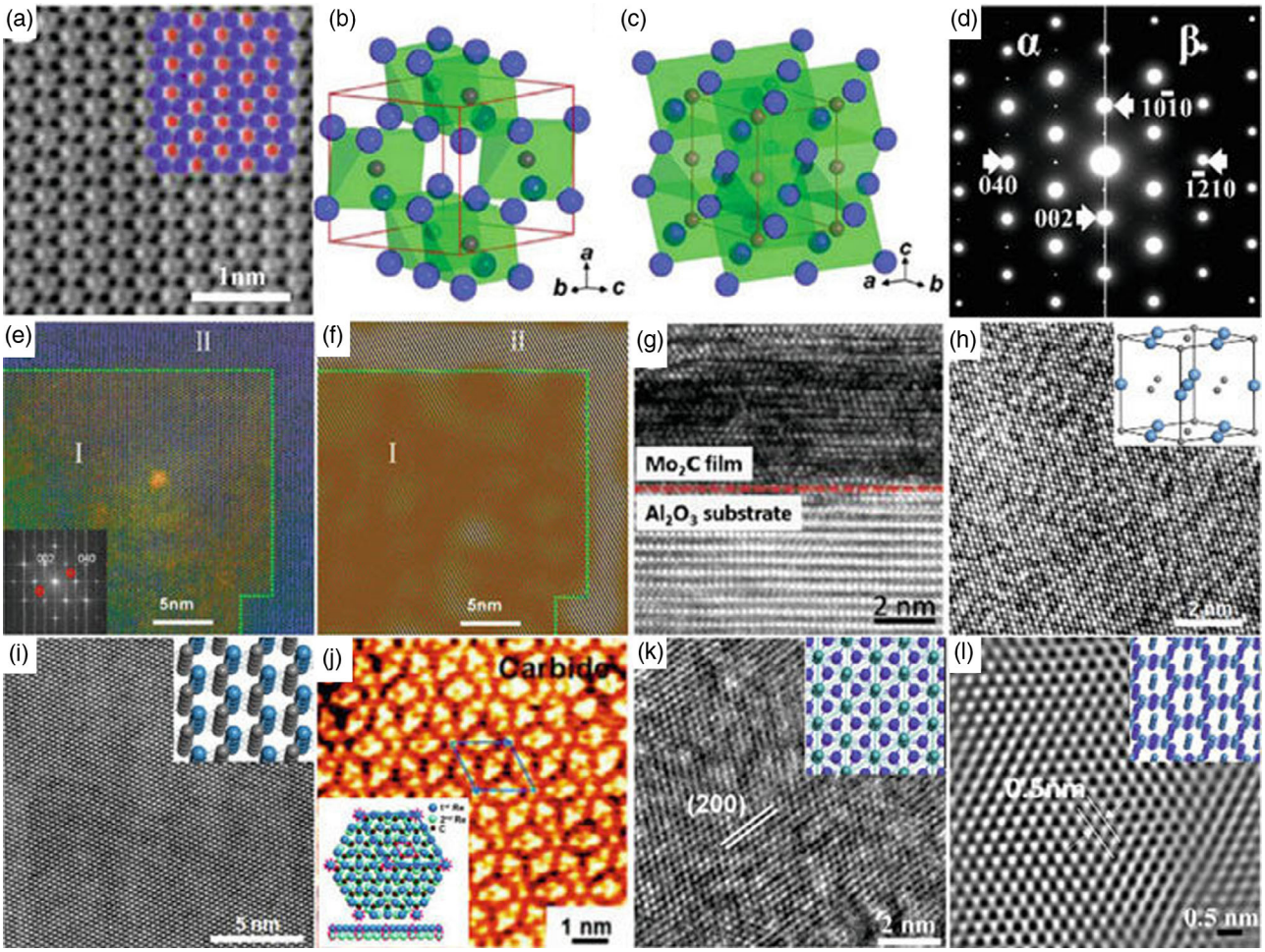

Figure 5. The crystalline nature characterizes the 2D structure of TMNs and TMCs produced using a bottom-up method. a) An ultrathin α-Mo_2C's BF-STEM image crystal viewed from the [100] direction. b,c) Atomic models of the unit cells of α-Mo_2C and β-Mo_2C, respectively. d) ED patterns of ultrathin α-Mo_2C and β-Mo_2C. e,f) The ultrathin Mo_2C crystal is depicted in two forms: through a HAADF-STEM image and its corresponding image obtained from the inverse Fourier transform. g) High-resolution transmission electron microscopy (HRTEM) image of a thin Mo_2C film, face-centered cubic (FCC), and epitaxially grown over a sapphire substrate. h) Image of [111]-oriented HRTEM of a cubic ultrathin TaC crystal, and the inset depicts the TaC unit cell's atomic model. i) Hexagonal ultrathin WC crystal [0001]-oriented HRTEM image and the inset is shown by the WC atomic model. j) ReC's scanning tunneling microscopy (STM) image on a Re substrate is presented, and the of ReC's atomic structure is showcased by the inset, which consists of a single Re and C atom within a rhombic unit cell. k,l) HRTEM images, oriented along the [0001] direction, are shown for hexagonal ultrathin MoN and TaN crystals, respectively. The insets in these images depict the corresponding atomic models. (Reproduced with permission.[39] Copyright 2016, ACS, panel a is reprinted. Reproduced with permission.[52] Copyright 2017, Royal Society of Chemistry, panels (b–f) have been adapted. Reproduced with permission.[54] Copyright 2017, Royal Society of Chemistry, panel (g) is reprinted. Reproduced with permission.[37] Copyright 2015, Springer Nature, the HRTEM images shown in panels (h,i) have been adapted. Reproduced with permission.[56] Copyright 2017, ACS, the STM image in panel (j) is reprinted. Reproduced with permission.[48] Copyright 2017, ACS, the HRTEM image shown in panel (l) has been adapted. Reproduced with permission.[47] Copyright 2017, Wiley-VCH copyright pending, the HRTEM image shown in panel (k) has been adapted).

reduction in the crystal lattice spacing ratio a/b in β—Mo_2C crystals (Figure 5g,h).[57]

2.1.4. MXene Synthesis from Non-MAX Phase

Posttreatment, any remaining In particles which do not undergo the reaction were eliminated by drenching the resulting rock-like substance in concentrated HCl (37%) for a period of 24 h. Afterward, the solution underwent filtration and was subsequently subjected to multiple washes with distilled water through centrifugation until reaching a pH level of around 7. The solution was dried for 20 h at 100 °C in a hot air oven to produce the Mo-In-C non-MAX powder. To convert the parent Mo-In-C into Mo_2CTx, the parent material was carefully etched for 3–5 h in conc. H_3PO_4 (85%, Sigma Aldrich; 500 mg/50 mL). Centrifugation at 4000 rpm was used to repeatedly wash the solution with distilled water until the pH reached about 7. After being ultrasonically exfoliated for 3–5 h, the solution was centrifuged to get the Mo_2CTx powder, which was subsequently dried in a hot air oven.

The prepared MXene exhibited both multilayered and monolayered morphologies, with the difference being attributed to the

© 2025 The Author(s). Small Science published by Wiley-VCH GmbH

26884046, 0, Downloaded from https://onlinelibrary.wiley.com/doi/10.1002/smsc.202400492 by Delhi Technological University, Wiley Online Library on [05/03/2025]. See the Terms and Conditions (https://onlinelibrary.wiley.com/terms-and-conditions) on Wiley Online Library for rules of use; OA articles are governed by the applicable Creative Commons License

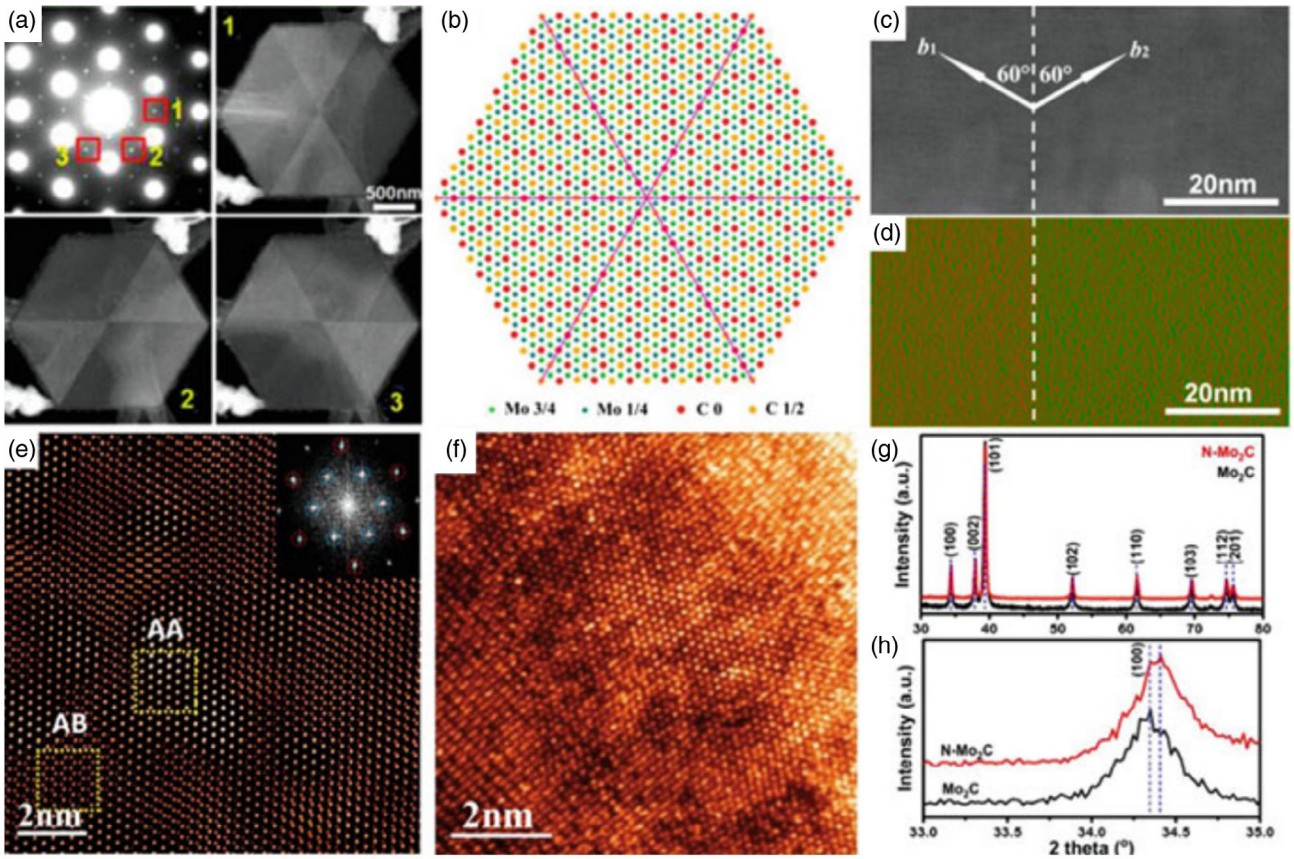

Figure 6. Defect structure of the bottom-up synthesis-produced 2-dimensional TMCs and TMNs. a) Ultrathin α-Mo_2C crystal, ED pattern, and DF-TEM pictures. The DF-TEM pictures denoted by numbers 1–3 have been attained by choosing the ED spots denoted by the yellow numbers 1–3 in the ED pattern, which were selected from the crystal's center. b) Atomic representation of the hexagonal α-Mo_2C crystal demonstrating symmetric carbon distribution concerning domain boundary. c,d) HAADF-STEM picture (c) and the appropriate mapping of shear strain (d) at the incredibly narrow α-Mo_2C domain border. The white dot line indicates the location of the domain boundary. e) An A and AB stacking order is visible in the 2Dβ-Mo_2C crystal in this ADF-STEM image. f) 2D β-Mo_2C crystal stacking error. g) 2D β-Mo_2C and N-doped β-Mo_2C crystal XRD patterns. h) The g local magnified XRD patterns were obtained between 33° and 35°. (Reproduced with permission.[39] Copyright 2016, ACS, panels (a–d) are reprinted with permission.[46] Copyright 2016, Institute of Physics, panel (e) is adapted with permission.[38] Copyright 2017, Wiley-VCH, panel (f) is reprinted with permission.[42] Copyright 2017, ACS copyright pending, panels (g) and (h) are reprinted).

duration of exfoliation. The use of an eco-friendly methodology for the fabrication of single and multilayered Mo_2CTx from non-MAX phases shows promise for electrochemical applications.[58]

Posttreatment, any remaining In particles that did not undergo the reaction were eliminated by drenching the resulting rock-like substance in concentrated HCl (37%) for 24 h. Afterward, the solution underwent filtration and was subjected to multiple washes with distilled water through centrifugation until reaching a pH level of around 7. The solution was dried for 20 h at 100 °C in a hot air oven to produce the Mo-In-C non-MAX powder. To convert the parent Mo-In-C into Mo_2CTx, the parent material was carefully etched for 3–5 h in conc. H_3PO_4 (85%, Sigma Aldrich; 500 mg/50 mL). Centrifugation at 4000 rpm was used to repeatedly wash the solution with distilled water until the pH reached about 7. After being ultrasonically exfoliated for 3–5 h, the solution was centrifuged to get the Mo_2CTx powder, which was subsequently dried in a hot air oven.[58]

2.1.5. Synthesis of MXene-Integrated Composites

The synthesis of MXene-integrated composites is a critical area of research, as these composites often exhibit enhanced multifunctional properties compared to standalone MXenes. MXenes are typically combined with polymers, NPs, or other 2D materials through various synthesis strategies, including physical blending, in situ growth, and chemical crosslinking. These techniques improve the stability and biocompatibility of MXenes and provide tunable properties for biomedical applications such as drug delivery, imaging, and PTT.[59–61]

Physical Blending: MXene NSs are physically mixed with other materials, such as polymers or NPs, to form composites in this

© 2025 The Author(s). Small Science published by Wiley-VCH GmbH

26884046, 0, Downloaded from https://onlinelibrary.wiley.com/doi/10.1002/smsc.202400492 by Delhi Technological University, Wiley Online Library on [05/03/2025]. See the Terms and Conditions (https://onlinelibrary.wiley.com/terms-and-conditions) on Wiley Online Library for rules of use; OA articles are governed by the applicable Creative Commons License

method. Deb and Jain blended Ti_3C_2 MXenes with polyvinyl alcohol (PVA), forming biocompatible and pH-responsive composites demonstrating high photothermal conversion efficiency for tumor-specific therapy.[62] Similarly, He et al. reported that mixing Ti_3C_2 MXenes with hyaluronic acid enhanced their targeting efficiency, enabling drug delivery specifically to tumor sites while improving biocompatibility.[63]

Physical blending with mesoporous silica nanoparticles (MSNs) has also been explored. Wang et al. demonstrated that Ti_3C_2 MXene-MSN composites exhibited pH-sensitive drug release, achieving targeted delivery in acidic tumor microenvironments.[64] Xu et al. developed Ti_2N MSNs for combined PTT and drug delivery, showing improved stability and thermal efficiency.[65]

In Situ Growth: In situ growth involves synthesizing NPs or growing polymer networks directly on the surface of MXene NSs. Deb and Jain successfully grew Fe_3O_4 NPs in situ on Ti_3C_2 MXene surfaces, creating composites with enhanced magnetic resonance imaging (MRI) contrast capabilities and therapeutic potential for photothermal cancer therapy.[62] Similarly, Yang et al. deposited Au NPs on MXene surfaces via in situ reduction, resulting in multifunctional composites for combined catalytic and photothermal applications.[66]

Polymers have also been synthesized in situ. Zhang et al. reported the in situ coating of polydopamine on Ti_3C_2 MXenes, which significantly improved their stability and drug-carrying capacity for targeted delivery applications.[67] Liang et al. developed MXene-gelatin hydrogels via in situ polymerization, demonstrating excellent mechanical properties and wound-healing potential.[68]

Chemical Crosslinking: Chemical crosslinking utilizes covalent bonds or electrostatic interactions to integrate MXenes with other materials. Deb and Jain used catechol-based crosslinking to tune the interlayer spacing of Ti_3C_2 MXenes, enabling controlled drug release for targeted cancer therapy.[62] Similarly, Lu et al. functionalized Ti_3C_2 MXenes with dopamine, enhancing photothermal stability and enabling selective interactions with cancer cells in vitro.[69]

PEGylation is another widely applied crosslinking strategy. Deb and Jain demonstrated that PEG-functionalized Ti_3C_2 MXenes significantly improved biocompatibility and circulation time, making them suitable for imaging-guided cancer therapy.[62] PEGylated Ti_2C MXenes provided excellent photothermal and PDT efficacy, with minimal toxicity in vivo.

Layer-by-Layer Assembly: This technique involves sequential MXenes and complementary materials deposition to form multilayered composites with precisely controlled architectures. Deb and Jain fabricated Ti_3C_2 and graphene oxide (GO) composites using a layer-by-layer assembly approach, achieving enhanced mechanical strength and superior photothermal performance for cancer therapy. A combination of Ti_2C and molybdenum disulfide (MoS_2) in a similar manner, creating composites with tunable optical properties for imaging-guided multimodal therapy.[62]

Additional biomedical applications include antibacterial and drug-release systems. Yang et al. developed MXene/alginate multilayered films for wound healing, demonstrating high antibacterial activity and biocompatibility.[70] Ouyang et al. synthesized MXene-GO multilayer membranes, showing exceptional ion selectivity and stability for controlled drug release applications.[71]

3. Surface Modification and Functionalization

Surface modification of MXenes plays a pivotal role in enhancing their properties for biomedical applications. These modifications typically rely on interactions such as hydrogen bonding, van der Waals forces, electrostatic adsorption, and covalent attachment. For instance, PEGylation stabilizes MXenes by forming electrostatic bonds with negatively charged surfaces, thereby improving colloidal stability and dispersibility in physiological environments. Similarly, covalent modifications, such as catechol functionalization, increase interlayer spacing and enhance drug-loading capabilities, while NP coatings improve surface roughness and photothermal conversion efficiency. These modifications significantly alter MXene properties, including zeta potential, hydrophilicity, and interlayer spacing, which are critical for their applications in biomedical systems. Surface modifications further expand the multifunctionality of MXenes, enabling applications such as imaging, drug delivery, and multimodal therapies. Beyond Ti_3C_2, functionalizing other MXenes, such as Nb_2C with PEG for improved dispersibility and Mo_2C with polyvinyl alcohol (PVA) for pH-responsive behavior, has expanded their applicability.

The reported MXenes often have specific surface terminations, like O, OH, or F, which make their surfaces hydrophilic. Due to the high negative zeta potential (above 40 mV), these MXenes are very stable in water-based colloidal solutions without surfactants.[12,16]

However, ultra-thin MXenes that have undergone delamination are usually unstable in challenging biological environments and do not possess multifunctional properties. This is because they quickly aggregate and deposit in biological environments, similar to many other NPs employed in medical applications.[72,73] As a result, surface engineering is essential to give these nanosystems exceptional stability and size distribution in a physiological environment. Surface engineering can also decorate other functional materials for multiple purposes.

The following two strategies have generally been the main emphasis of MXene surface engineering: the polymer-based surface chemistry method modifies the surface using specific macromolecules or polymers through noncovalent contact. For example, polyvinylpyrrolidone (PVP) molecules were used to adorn the Nb_2C NSs (**Figure 7**a).[74] Soybean phospholipid (SP) was successfully utilized for the Ta_4C_3 NSs surface's modification through electrostatic interactions, while Ti_3C_2 NSs were stabilized in physiological conditions by electrostatically adsorbing PEGylation (Figure 7b,c).[75,76] The other is a surface chemistry based on inorganic NPs, which involves dotting MXenes with multifunctional inorganic NPs to expand the possibilities for their uses. Examples of standard methodologies for combining therapeutic agents with MRI contrast agents (CAs) for simultaneous therapy and imaging include the combination of Ta_4C_3 NSs with Fe_3O_4 NPs (Figure 7d,h) and Ti_3C_2 and MnOx NPs (Figure 7e,i), which gave them the ability to perform simultaneous treatment and imaging capabilities.[77,78] Similarly, combining 2D Ti_3C_2 MXene NSs with polyoxometalates (POMs) based on GdW10 offers a multimodal phototherapy platform with CT and/or MR imaging guidance for transplanted tumors. (Figure 7f,j).[79] Integration of Ti_3C_2 MXene with the MSNs, a traditional therapeutic drug carrier, is the other typical example

© 2025 The Author(s). Small Science published by Wiley-VCH GmbH

26884046, 0, Downloaded from https://onlinelibrary.wiley.com/doi/10.1002/smsc.202400492 by Delhi Technological University, Wiley Online Library on [05/03/2025]. See the Terms and Conditions (https://onlinelibrary.wiley.com/terms-and-conditions) on Wiley Online Library for rules of use; OA articles are governed by the applicable Creative Commons License

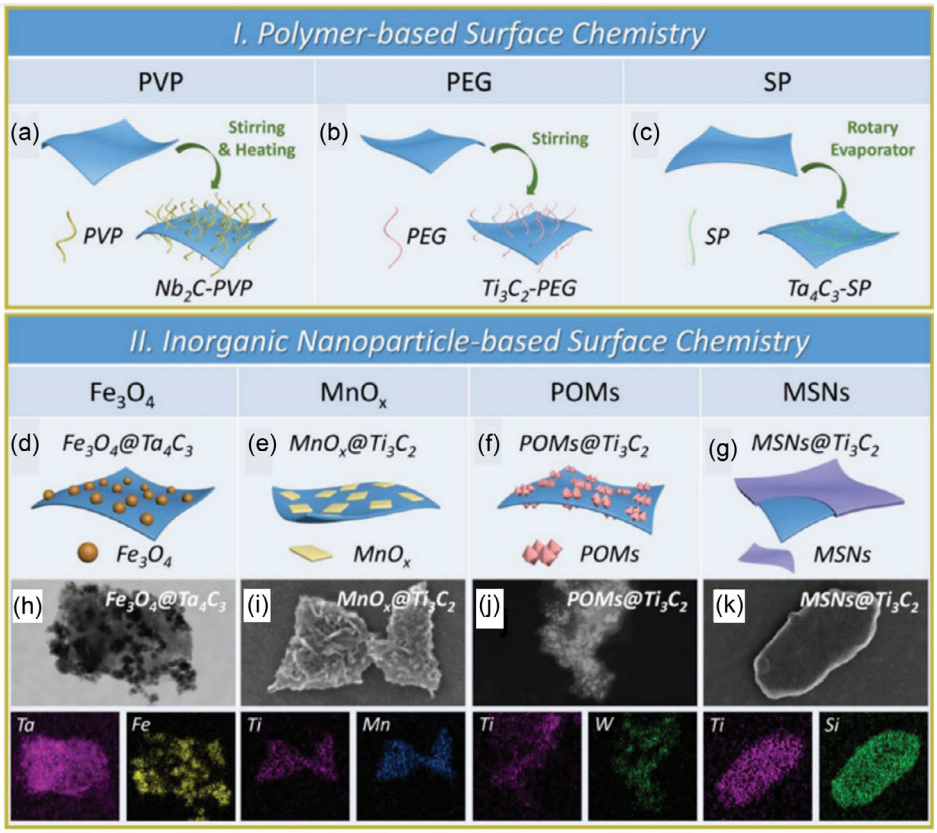

Figure 7. MXenes' surface chemistry for biomedical applications. MXenes' polymer-based surface chemistry is depicted schematically. a) M2X alteration using PVP (for instance, Nb_2C NSs). b) PEGylation of M_3X_2 (e.g., Ti_3C_2 NSs). c) SP modification M_4X_3-based MXenes. MXenes' inorganic NP-based surface chemistry is shown schematically. d) An in situ redox reaction caused superparamagnetic iron oxide (Fe_3O_4) NPs to accumulate on the Ta_4C_3 MXene surface. It has been reproduced with the permission. e) There is a growth of in situ on the Ti_3C_2 surface's small MnOx NSs using a simple redox reaction. f) GdW10-based polyoxometalates (POMs) integration over the Ti_3C_2 MXene's surface via an amide bond. g) Silica (SiO_2) surface nanoporous engineered on the 2-dimensional Ti_3C_2 MXene, which is a sol–gel chemistry-based process. h) Fe_3O_4@Ta_4C_3, i) MnOx@Ti_3C_2, j) POMs@Ti_3C_2, and k) SiO_2@Ti_3C_2 composite MXenes. (Panel (a–d) is reprinted with permission.[77] Copyright 2018, Ivy Spring International Publisher. Reproduced with permission.[78]Copyright 2017, ACS, and panels are adapted with permission.[79] Copyright 2018, Springer, panel (f) is reprinted with permission.[80] Copyright 2018, Wiley-VCH, panel (g) is reprinted with permission.[31] Copyright 2018, Advance Science. Copyright pending; the STEM images and the corresponding element mappings in panels of (h–k) are adapted).

of a drug delivery system (DDS). However, replacing MXene with MSNs can also be a viable option for a DDS. Materials, such as appropriate mesoporous structure with controlled drug loading capacity (DOX), improved biocompatibility/dispersity/hydrophilicity (PEGylation), and the ability to attach RGD molecules to the surface for targeted drug delivery relative to conventional 2D MXenes used for targeted cancer treatment using light therapy (Figure 7g,k).[80] Due to the complexity of their synthesis and integration, these two multifunctionalization techniques are still in their infancy in the graphene/GO family. The development and proliferation of various 2D MXene-based multipurpose NP platforms for healthcare applications are anticipated to be accelerated by the rapid expansion of 2D MXene synthesis and applications.[31]

Future advancements in surface modification techniques will likely focus on tailoring MXene surfaces for precise interactions with biological systems. For example, incorporating bioactive ligands or antibodies could enable highly targeted therapies, while dynamic surface functionalization could allow MXenes to adapt to changing physiological environments. Achieving a balance between hydrophilicity, stability, and multifunctionality will be critical for expanding MXene applications in tissue engineering and wearable biosensors.

3.1. Biodegradability and Biocompatibility

MXenes exhibit remarkable biodegradability and biocompatibility, making them ideal for biomedical applications. For example, Mo_2C-PVA nanoflakes degrade rapidly at pH 9.4 but remain stable in mildly acidic tumor environments (pH 5.4–6.4), ensuring durability for PTT in tumor microenvironments. Comparatively, MXenes degrade faster in basic conditions than GO, which shows slower biodegradation. This pH-responsive degradation behavior of MXenes allows for prolonged therapeutic efficacy in acidic tumor sites while ensuring rapid clearance in everyday physiological environments. High renal and fecal clearance rates and low cytotoxicity have been demonstrated for

© 2025 The Author(s). Small Science published by Wiley-VCH GmbH

26884046, 0, Downloaded from https://onlinelibrary.wiley.com/doi/10.1002/smsc.202400492 by Delhi Technological University, Wiley Online Library on [05/03/2025]. See the Terms and Conditions (https://onlinelibrary.wiley.com/terms-and-conditions) on Wiley Online Library for rules of use; OA articles are governed by the applicable Creative Commons License

surface-functionalized MXenes like Nb_2C-PVP. For example, studies show minimal toxicity in vitro for Ta_4C_3 and Nb_2C MXenes, even at 400 μg mL^{-1} concentrations. In vivo tests confirm excellent biosafety, with no adverse effects observed in significant organs or hematological parameters following MXene administration. These results highlight the potential of MXenes as biocompatible and biodegradable materials for clinical translation.

Ti_2N quantum dots (QDs) were evaluated for their ability to degrade in an aqueous solution, which is otherwise prone to instability due to their nitride-based MXenes, using a concentrated dispersion of Ti_2N QDs (20 ppm) which was constantly shaken on a horizontal shaker with air exposure at 37 °C for different durations of time (such as 0, 2, 4, 6, and 8 days). **Figure 8** indicates that the solution gradually becomes lighter in color over time, suggesting significant degradation of Ti_2N QDs. To examine the mechanism of biodegradation of Ti_2N QDs, Raman analysis was conducted both before and postdegradation, which revealed that hydration and oxidation reactions during biodegradation led to the formation of hydrogen titanium oxide and titanium oxide as the end products. Compared to commonly utilized inorganic PTT agents with low biodegradability, Ti_2N QDs have high biodegradability, making them more appropriate for PTT in medical uses. Ti_2N QDs can maintain suitable structural stability applications like imaging and therapeutic usages during initial circulation. They could be easily eliminated posttreatment from the body, as evidenced by the appropriate excretion rate of Ti_2N QDs from the body. This surface nanopore engineering on Ti_3C_2 MXene combines multiple properties conducive to expanding biomedical engineering using MXene-based nanocomposites (**Table 2**).[81]

Rapid biodegradation of photothermal agents (PTAs) can lead to high in vivo biosafety and reduced long-term toxicity. The

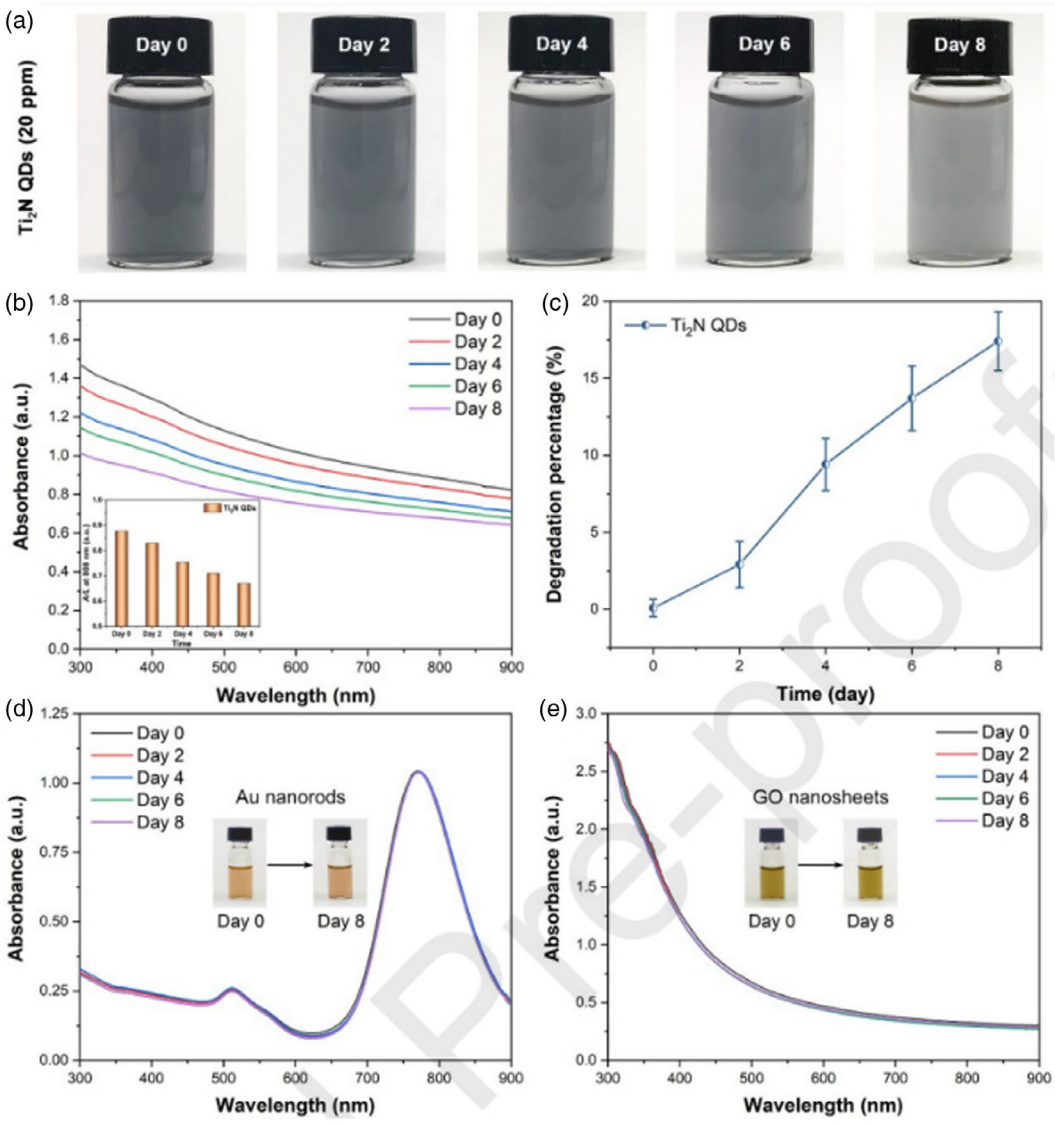

Figure 8. a) Images captured; b) Inset shows the intensity of absorption at 808 nm (A/L) and absorption spectra; c) The percentage of degradation in water of Ti_2N QDs (20 ppm) over a period of 0, 2, 4, 6, and 8 days; d,e) The images (insets) and absorption spectra of degraded gold nanorods and GO NSs in H_2O have been depicted. Reproduced with permission.[81] Copyright 2020, Elsevier copyright pending.

© 2025 The Author(s). Small Science published by Wiley-VCH GmbH

26884046, 0, Downloaded from https://onlinelibrary.wiley.com/doi/10.1002/smsc.202400492 by Delhi Technological University, Wiley Online Library on [05/03/2025]. See the Terms and Conditions (https://onlinelibrary.wiley.com/terms-and-conditions) on Wiley Online Library for rules of use; OA articles are governed by the applicable Creative Commons License

Table 2. Surface modification and functionalization.

MXene/Group crafted onto the surface.	Process deployed	Chemical modifier used	Chemical modification process	Characterization	Effect of surface modification on the product	References
$Ti_3C_2T_x$/ 4-nitrophenyl	Surface-covalent functionalization via diazonium chemistry	4-nitrobenzene-diazonium (4-NBD) tetrafluoroborate salts	$Ti_3C_2T_x$ solution is applied onto SiO_2/Si substrates using spin coating, then treated with 4-NBD/CH_3CN solution in presence of N_2	AFM, TEM	Increase in work function	[190]
$Ti_3C_2T_x$/ Polyethylene glycol PEG6	Esterification reaction	ω-PEG6-COOH (ω is $-NH_2$, $-N_3$, $-CHCH$)	$Ti_3C_2T_x$ is transferred from H_2O to DMF using solvent exchange, and then pristine Ti_3C_2 in DMF is mixed with PEG6-COOH and DMAP.	Four-point probe method, SEM, and TGA	Reduced electrical conductivity; Improved solubility in nonpolar organic solvents	[191]
$Ti_3C_2T_x$/octyl phosphonic acid	Octyl phosphonic acid via hydrogen bonding	Octyl phosphonic acid	MXene NSs are ultrasonicated in xylene solvent, mixed with octyl phosphonic acid, and then ultrasonicated and centrifuged.	TEM, XRD, and X-ray photoelectron Spectroscopy (XPS)	High ON/OFF rate; longer retention time; good ternary yield; better flexibility.	[192]
$Ti_3C_2T_x$/catechols	Dehydrative condensation	Dopamine(DA) and pyrocatechol (PCAT)	A colloidal solution was prepared using the minimally intensive layer delamination method and then subjected to high-speed centrifugation followed by catechol functionalization.	Density functional theory, UV−vis, XRD, Raman and AFM-IR	Increased interlayer spacing; presence of nitrogen on the surface; change in particle morphology and roughness	[193]
W1.33C i-MXene/ Bovine serum albumin (BSA)	BSA as a bioactive macromolecule via H-bonding and/or attractive van der Waals interactions	BSA	BSA solution is blended with NSs; the result is collected via centrifugation, washed with degassed ddH_2O, and the final sediment is redispersed in degassed DI water	STEM and AFM	Biocompatible and pH-responsive; high photothermal-conversion efficiency; rapid degradation; selective accumulation in tumor sites.	[82]
Mo_2C/Polyvinyl alcohol (PVA)	PVA for surface engineering via H-bond and van der Waals interaction	Polyvinyl alcohol (PVA)	Mo_2C-PVA nanoflakes were combined with PVA solution, centrifuged to collect them, and then re-dispersed in Ar-deaerated DI water.	HRTEM, HAADF in STEM and XPS	biocompatibility; faster degradation, high photothermal-conversion efficiency; high dispersity in physiological solutions without agglomeration	[83]
$Ti_3C_2T_x$/Highly Reliable Superhydrophobic Protection	Selective etching with LiF/HCl aqueous solution	Fluoroalkylsilane	$Ti_3C_2T_x$ powder is dispersed in the precursors; colloidal solution is collected after adding ethanol.	SEM, TEM, HAADF-STEM, XPS, and BET	More stable, improved gas sensing performance	[194]

ability of W1.33CBSA NSs to degrade depends on the pH level, with basic conditions causing rapid degradation, while they remain relatively stable under acidic conditions. This suggests that W1.33C-BSA NSs could be more effective in delivering therapeutic results in the tumor microenvironment, which has low pH levels and a hypoxic state. The gauged pH inside 4T1 breast cancer tumors was around 6.0–6.5, indicating that W1.33C-BSA NSs will break slowly in tumors compared to normal tissue. Degradation of W1.33C-BSA NSs in blood is time-dependent and increases with time.

During the initial stage, partial NSs experienced significant surface oxidation, while severe oxidation caused a slight decrease in the planar dimensions of W1.33C-BSA NSs. Ultimately, the complete decomposition of planar dimensions occurred in the final stage. W1.33C-BSA NSs were effectively endocytosed into tumors initially, and surface oxidation occurred in one day. After three days, prolonged incubation led to severe surface oxidation and near-complete disintegration of W1.33C-BSA NSs in planar dimensions, showing high biodegradation. After one hour, the PA signal intensity in muscles was only about 30% of the original. In contrast, 60% of the original PA signals were still detected in the tumor, suggesting slower degradation of W1.33C-BSA NSs in the cancer. High levels of tungsten were found in urine and feces within 48 h after injection, indicating that the NSs were rapidly eliminated through the renal and fecal routes. Therefore, the W1.33C-BSA NSs with high biodegradability can remain in the tumor longer and effectively degrade while exerting therapeutic effects.[82]

It has been revealed that Mo_2CPVA nanoflakes display a degradation effect dependent on pH. There is rapid degradation of Mo_2C-PVA in basic conditions with pH values of 11.4 and 9.4. In contrast, the material has comparatively higher resistance to degradation in a low-pH environment with pH values of 6.4, 5.4, and 3.4. This shows that the therapeutic performance of Mo_2C-PVA nanoflakes, which is coherent with the DLS results, would be more durable in the mildly acidic tumor microenvironment. Notably, in the cell culture medium, the decomposition rate of Mo_2C-PVA nanoflakes was slower than that at pH 7.4 in

© 2025 The Author(s). Small Science published by Wiley-VCH GmbH

26884046, 0, Downloaded from https://onlinelibrary.wiley.com/doi/10.1002/smsc.202400492 by Delhi Technological University, Wiley Online Library on [05/03/2025]. See the Terms and Conditions (https://onlinelibrary.wiley.com/terms-and-conditions) on Wiley Online Library for rules of use; OA articles are governed by the applicable Creative Commons License

phosphate-buffered saline (PBS), owing to the formation of protein corona around nanoflakes, which slowed down the degradation of Mo_2C. Additionally, only a slight change in particle size was observed after 48 h in the nanoflakes of Mo_2C-PVA incorporated in a cell culture medium with 10% FBS.[83]

MXenes that have been evaluated for various biomedical and biological uses are confined to titanium carbide MXene ($Ti_3C_2T_x$, Ti_2CTx), niobium carbide MXene (Nb_2CTx), and tantalum carbide MXene (Ta_4C_3Tx). Owing to the simple fabrication process of $Ti_3C_2T_x$, it is the most extensively assessed MXene among the MXene group. Good absorption of NIR radiation by MXene makes it promising for PTT, theragnostic, and synergistic therapy for cancer treatment. Also, MXenes could be used in filter membranes due to their antimicrobial properties. MXenes were also found to be used as biosensors and in bioimaging after conversion into quantum dots.

So far, the biomedical application of 2D MXenes is still in its initial stage. The research on the cytotoxicity of MXene has been limited thus far despite the spiking interest in varied applications of MXenes. Extensive evaluation of the cytotoxicity and biocompatibility of MXene is indispensable to transforming the small-scale lab experiments of MXenes into biomedical applications on a commercial level.[84]

The effects of vital characteristics of 2D nanomaterials, like dispersibility, solubility, biodegradation, and protracted toxicity, on biomedicine are not known up till now. Recently, to unveil indirectly the detrimental effects of toxicity which can impact human health, an evaluation was carried out on the ecotoxicological potential of nanomaterials based on MXene on aquatic fauna in vivo, using an embryo model of a zebrafish.

The results of neurotoxicity and locomotion studies indicated that neurons present in the zebrafish embryos' spinal cord area treated with $Ti_3C_2T_x$ were comparable to that of the negative control group treated with dimethyl sulfoxide (DMSO), suggesting the highest nontoxic concentration of 50 $\mu g\,mL^{-1}$. These findings, shown in **Figure 9**a, demonstrate that $Ti_3C_2T_x$ MXene does not have any adverse effects on muscle activity or neurons in the zebrafish embryo model, as depicted in Figure 9b,c. Furthermore, the LC50 of $Ti_3C_2T_x$ was found to be greater than 100 $\mu g\,mL^{-1}$, which places it in the "practically nontoxic" group according to the Fish and Wildlife Service's Acute Toxicity Rating Scale. Low cytotoxicity toward cells has been found for both MXenes and associated nanocomposites.

For example, at a concentration value equal to 400 $\mu g\,mL^{-1}$, minimal impact was shown by the Ti_3C_2-SP NSs on the 4T1 cell line viability during a 48 h coincubation period.[85] In Ta_4C_3-SP's vitro toxicity has been evaluated using a standard Cell Counting Kit-8 (CCK-8) assay. It has been observed that the 4T1 cell line survival was not significantly affected by Ta_4C_3-SP, even at high concentrations values equal to 400 $\mu g\,mL^{-1}$ (Figure 9d). Moreover, when Nb_2C-PVP was incubated with breast 4T1 and glioma U87 cancer cells at a concentration value of 200 $\mu g\,mL^{-1}$, it didn't exhibit any noticeable inhibitory effect on either cell line (Figure 9e).[74] Infinitesimal cytotoxicity was observed at 160 $\mu g\,mL^{-1}$ in Mn_xO/Ti_3C_2-SP nanocomposites post 48 h coincubation, implying good biocompatibility of Mn_xO/Ti_3C_2-SP.[78]

Extensive investigations have been carried out in vivo to evaluate the potential biocompatibility and biosafety of surface-modified MXene NSs in mice. For example, on 1, 7, and 28 days, healthy mice were given three doses of MXenes with surface modifications (Nb_2C-PVP dosage of 20 $mg\,kg^{-1}$).[75]

The results demonstrated little variation in mouse behavior across the three treatment groups (exposed to NIR-I, NIR-II, and daylight) as well as the control group. Moreover, there were no fluctuations observed in mouse body weight during the three observation periods. Evaluation of major organs (liver, kidney, heart, spleen, and lung) using hematoxylin and eosin (H&E) staining after a 28-day dietary intervention showed no indications of adverse effects or any signs of acute or chronic pathological damage on comparison of the control group with the treatment groups (Figure 9f). The blood tests, which included hematological indices and biochemical markers, were all within normal limits (Figure 9g,h). Our findings suggest that Nb_2C-PVP is biocompatible for in vivo tumor theragnostic treatment methods. Similar tests were carried out on Ti_3C_2 and Ta_4C_3 MXenes, which had low cytotoxicity and good in vivo biocompatibility.[31]

Long-term studies on the biodegradability and cytotoxicity of MXenes are crucial for their clinical translation. While preliminary studies indicate promising biosafety profiles, understanding the degradation pathways and potential byproducts under physiological conditions will help mitigate concerns regarding long-term toxicity. Leveraging computational tools and machine learning could accelerate the prediction of MXene biocompatibility and optimize their properties for specific biomedical applications.

4. Biomedical Applications of MXenes

MXene-based materials have emerged as a promising class of 2D nanomaterials for biomedical applications due to their unique properties, including high conductivity, tunable surface chemistry, and excellent biocompatibility. Over the past decade, MXenes have transitioned from their initial discovery to multifunctional platforms for imaging, therapy, and diagnostics. **Figure 10** highlights the progress of MXene-based materials in biomedical applications, charting advancements from their discovery in 2011 to present-day innovations. Starting with the HF etching method for Ti_3C_2 synthesis, MXenes have undergone significant development, including surface functionalization, PTT, MRI imaging, and biosensing platforms. Over the years, MXene research has expanded into next-generation technologies such as wearable sensors, aptamer-based diagnostics, and electrochemical point-of-care testing, showcasing their versatility and increasing impact in healthcare. This timeline reflects how MXene discovery has evolved from basic synthesis to multifunctional biomedical applications

4.1. Cancer Diagnosis and Therapy

Surface-engineered MXenes enable multimodal therapies, such as the combination of PTT and PDT. For instance, Ti_3C_2 MXenes modified with ICG function as both PTAs and photosensitizers (PS), achieving simultaneous tumor ablation and ROS generation. Similarly, composites like MXene-Fe_3O_4 and MXene-MnOx integrate therapeutic capabilities with MRI contrast imaging for precise tumor localization and treatment

© 2025 The Author(s). Small Science published by Wiley-VCH GmbH

26884046, 0, Downloaded from https://onlinelibrary.wiley.com/doi/10.1002/smsc.202400492 by Delhi Technological University, Wiley Online Library on [05/03/2025]. See the Terms and Conditions (https://onlinelibrary.wiley.com/terms-and-conditions) on Wiley Online Library for rules of use; OA articles are governed by the applicable Creative Commons License

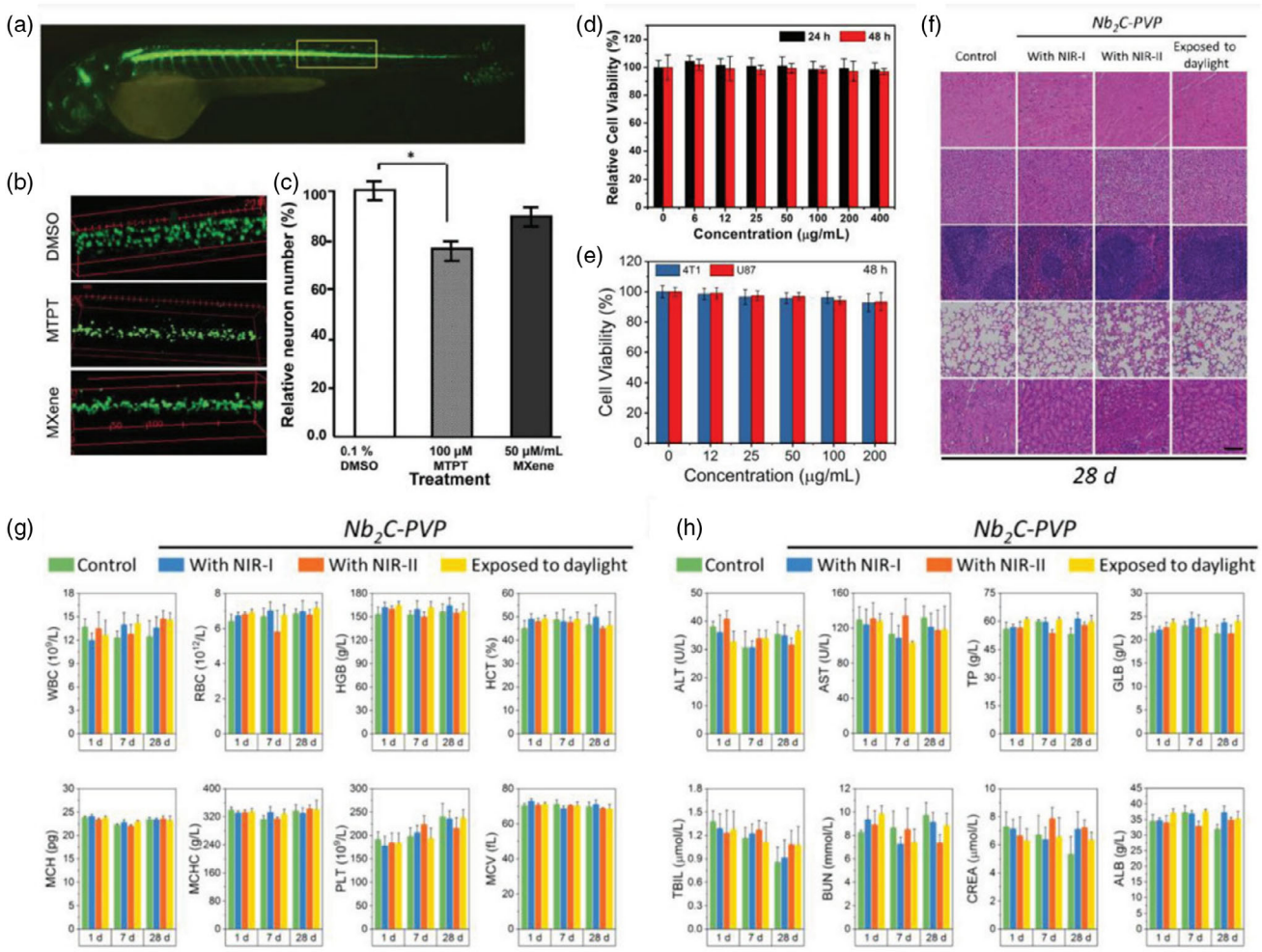

Figure 9. Evaluations of MXenes' biocompatibility, ecotoxicological effects, and biosafety. a) Imaging of an unaltered embryo via confocal laser scanning microscopy. b) Spinal cord near the region of somites 14–17 where different treatments were given to sample embryos. c) The mean number of proportional neurons in untreated embryos (*P 0.05, $n = 14$). Reproduced with permission Copyright 2018, Royal Society of Chemistry. d) The comparative viability of the cell line of 4T1 following incubation with different Ta_4C_3-SP NS concentrations. Reproduced with permission. Copyright 2018, Wiley-VCH. e) The comparative viability of 4T1 as well as U87 cells following exposure to various amounts of Nb_2C-PVP NSs. f) Histological details (H&E stained) were taken from the key organs (spleen, liver, heart, and kidney) of mice treated with Nb_2C-PVP 28 days after injection under various settings (control, exposure to NIR-I, NIR-II, and daylight). Scale bars: 100 μm. g) Hematological parameters and h) the mice's biochemical blood indexes treated with Nb_2C-PVP in 1, 7, and 28 d after injection while subjected to varying treatments (control, exposure to daylight, NIR-I, and NIR-II). Reproduced taking the permission.[74] Copyright 2017, ACS copyright pending.

monitoring. Mo_2C-PVA nanoflakes have demonstrated pH-responsive photothermal performance, making them effective in tumor-specific therapies with minimal off-target effects. These surface modifications improve targeting, stability, and therapeutic efficacy, making MXene-based composites a promising platform for cancer treatment.

Recently, research has shown that MXene exhibits both photothermal and antibacterial properties,[86–88] indicating that MXene could be used as a PTA for fighting bacteria without relying on antibiotics. Furthermore, since MXene belongs to the 2D nanomaterial, it could potentially be able to load drugs similarly to GO. MXene has the potential to serve as a proficient carrier for PS in PDT and a highly effective PTA for PTT. Because of this property, MXene surpasses other nanomaterials in terms of producing a synergistic effect between PDT and PTT. However, for achieving a synergistic effect between PTT and PDT, no research has yet looked into the MXene's potential use as the PTA and the photosensitizer carrier.

Yu and colleagues[89] utilized $Ti_3C_2T_x$ MXene NSs with a size of 454 nm to incorporate ICG and create a hybrid effect of MXene's photothermal effect and ICG's photodynamic effect. In **Figure 11**a, it can be observed that NIR irradiation had no impact on the temperature of water, but it caused a gradual rise in temperature to 44.3 °C of MXene suspension. The temperature of ICG rose quickly within 1–2 min under NIR radiation, but gradually decreased afterward. This behavior of ICG may be attributed to its instability, which has been previously noted in other studies.[90,91] In contrast, ICG-MXene exhibited the

© 2025 The Author(s). Small Science published by Wiley-VCH GmbH

26884046, 0, Downloaded from https://onlinelibrary.wiley.com/doi/10.1002/smsc.202400492 by Delhi Technological University, Wiley Online Library on [05/03/2025]. See the Terms and Conditions (https://onlinelibrary.wiley.com/terms-and-conditions) on Wiley Online Library for rules of use; OA articles are governed by the applicable Creative Commons License

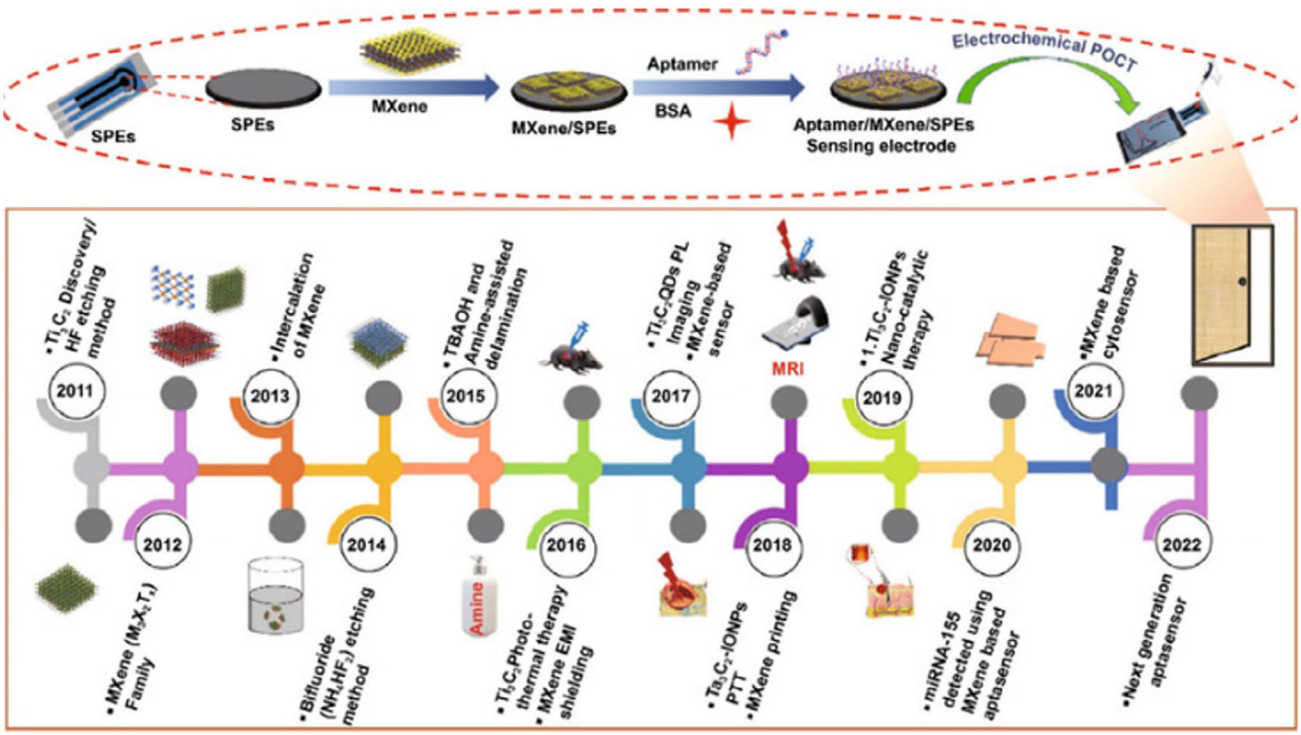

Figure 10. Timeline showcasing the evolution of MXene-based materials from their discovery to advanced biomedical applications, including synthesis, functionalization, PTT, MRI imaging, and biosensing platforms.

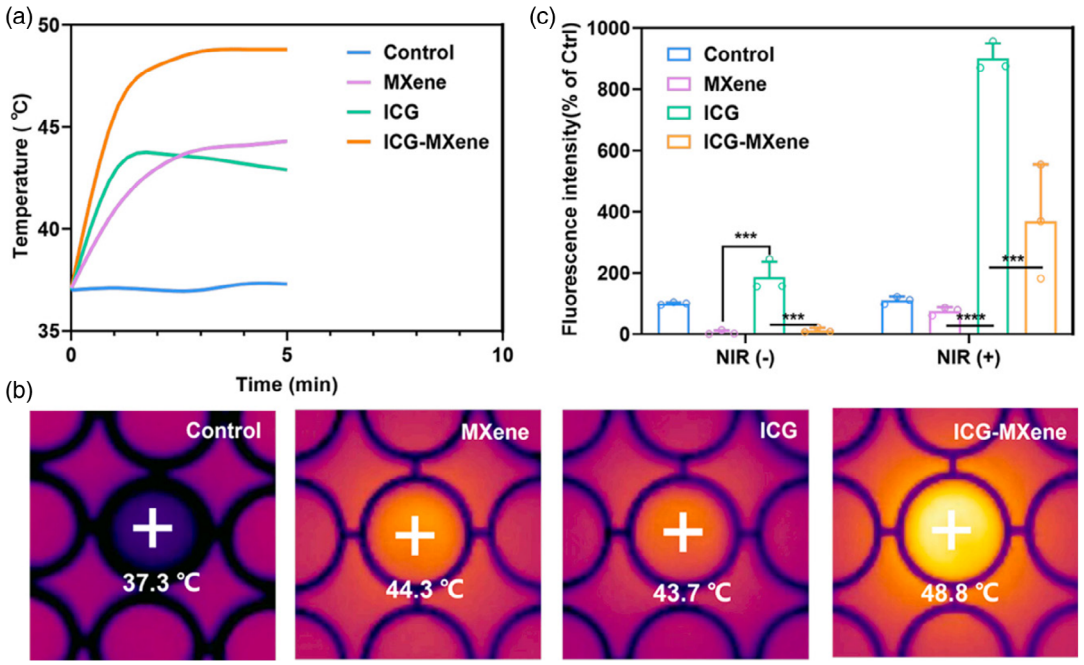

Figure 11. ICG-MXene (5–20 μg mL^{-1}), ICG (5 μg mL^{-1}), and MXene (20 μg mL^{-1}) photodynamic and photothermal effects were evaluated under NIR irradiation (808 nm, 1 W cm^{-2}, 5 min). a) Temperature–time curves illustrate the temperature fluctuations during irradiation. b) Thermal images were captured at the location with the highest temperature. c) The level of ROS was assessed by quantifying the fluorescence intensity of the ROS fluorescent probe DCFH-DA. The data represent the mean ± standard deviation ($n = 3$). Statistical significance was denoted as ***$p < 0.001$ and ****$p < 0.0001$. Reproduced with permission.[89] Copyright 2022, Elsevier copyright pending.

© 2025 The Author(s). Small Science published by Wiley-VCH GmbH

26884046, 0, Downloaded from https://onlinelibrary.wiley.com/doi/10.1002/smsc.202400492 by Delhi Technological University, Wiley Online Library on [05/03/2025]. See the Terms and Conditions (https://onlinelibrary.wiley.com/terms-and-conditions) on Wiley Online Library for rules of use; OA articles are governed by the applicable Creative Commons License

swiftest heating (reaching a temperature of 48 °C in just 2 min) and the greatest temperature level (maintaining it at 48.8 °C for 5 min) as a result of its combination of ICG's ability to heat up quickly and MXene's ability to sustain the heat. The thermal images (shown in Figure 11b) displayed the maximum temperature of each sample. The results indicate that ICG-MXene demonstrates a significantly enhanced photothermal effect in comparison to ICG or MXene alone. To assess the influence of NIR irradiation on the photodynamic effect of water (control), ICG-MXene, ICG, and MXene the level of ROS was quantified using the fluorescent probe DCFH-DA.[92] When NIR was not present, the ROS level was low for all groups as shown in Figure 11c. The results of the antibacterial test indicate that at a low concentration, ICG-MXene has minimal activity against methicillin-resistant Staphylococcus aureus (MRSA) without NIR exposure. However, with only 5 min of NIR irradiation, the combined PTT/PDT effects lead to complete inhibition of MRSA growth.

The versatility of MXenes positions them as promising candidates for emerging biomedical technologies. For instance, MXene-based theragnostic platforms could integrate real-time diagnostic imaging with precise therapeutic delivery, advancing personalized medicine. Moreover, the use of MXenes in regenerative medicine, such as for bone and cartilage repair, and in developing antibacterial coatings for implants and wound dressings, represents exciting frontiers. Collaboration across materials science, biology, and clinical research will be essential to harness the full potential of MXenes in these fields.

4.1.1. PDT

PDT is a medical treatment that includes the systemic administration of a photosensitizer, followed by the targeted irradiation of the affected area. This minimally invasive approach shows potential as a cancer therapy by releasing cytotoxic ROS that can directly destroy local tumor cells. To enhance the effectiveness of PDT, researchers have suggested the use of MXenes as a promising solution. MXenes can help overcome some of the limitations of traditional PS used in PDT, making them a viable option to improve medical technique efficiency. The utilization of PS like Chlorin e6 (Ce6) presents certain challenges due to their poor solubility, vulnerability to photodegradation, low efficiency of delivery, and inability to be absorbed in the most transparent regions of the skin. However, by using two-dimensional nanomaterials (2D NMs), specifically GO, these PS can achieve better water dispersibility while maintaining superior biocompatibility. This provides a solution to the aforementioned issues.

It is essential to develop antibacterial approaches that are not reliant on antibiotics, particularly in the case of infections caused by drug-resistant bacteria. One such approach involves synthesizing ICG-MXene, which combines photothermal and photodynamic effects through a physical mixing process between ICG solution and MXene suspension. Although ICG-MXene at low concentrations does not exhibit significant anti-MRSA activity when NIR is not used, it can entirely inhibit the growth of MRSA when irradiated with NIR for a short duration of 5 min, owing to the synergistic effects of PTT/PDT. ICG-MXene shows promise as a viable nanomaterial for phototherapy against bacteria that are resistant to antibiotics due to its low concentration and the ability to adjust irradiation parameters.

The generation of singlet oxygen ($1O_2$) is because of the energy transfer from photoexcited electrons in Ti_3C_2 to the triplet oxygen ($3O_2$), which is similar to BP and graphene QD's photodynamic behavior.[93,94] Additionally, the localized surface plasmon resonance (LSPR) effect of Ti_3C_2 may contribute to oxygen generation. PDT activated by NIR laser is ideal for deep tissue penetration, and Ti_3C_2 NSs show promise as a new photosensitizer for the effective PDT. However, the energy exchange between oxygen and Ti_3C_2 may be hindered by the polymeric HA shell, resulting in a decrease in oxygen generation after HA capping. Ti_3C_2-DOX NSs, prepared using sequential adsorption technique were loaded with DOX at a high loading capacity. Subsequently, HA was applied as a coating on the NSs to enhance their biocompatibility and target tumor cells that overexpress $CD44^+$.[95,96] The effective incorporation of DOX was verified by examining the UV-vis spectra, revealing a slight shift of the absorption peak of DOX toward longer wavelengths, specifically from 487 to 505 nm (**Figure 12**a).[97]

The hydrodynamic diameters and zeta potentials of Ti_3C_2, Ti_3C_2@DOX, and Ti_3C_2@DOX@HA (also known as Ti_3C_2-DOX) were measured. After loading DOX onto Ti_3C_2, its negative charge was changed to a positive charge of +13.25 mV from −23.18 mV, and then reduced again to a negative charge of −20.71 mV after being capped with HA, which was expected, as shown in Figure 12b.

In the biocompatibility tests of Ti_3C_2 NSs, it was observed that neither unmodified Ti_3C_2 NSs nor Ti_3C_2-DOX caused any significant hemolysis (less than 5%) even when present in a higher conc. of 200 μg mL^{-1}, as illustrated in Figure 12c. To verify the generation of singlet oxygen ($1O_2$), which is the most prominent ROS, 1,3-diphenylisobenzofuran (DPBF) was used as the detector. A decrease in DPBF absorbance demonstrates that the generated 1O2 by Ti_3C_2 NSs was absorbed by DPBF when it gets an exposure to NIR light, as depicted in Figure 12d.

Figure 12e,f shows Ti_3C_2-DOX's stimuli-responsive activity at various pH levels, with or without laser irradiation, or with or without HAase. In neutral environments (such as blood and interstitial fluids in healthy tissues), the HA shell successfully inhibits DOX release. The electrostatic connection in the Ti_3C_2-DOX system is broken by the of Ti_3C_2's laser-induced photothermal effect (heating up to around 50 °C), which results in the release of DOX. This sensitivity to pH points to a better DDS in the acidic tumor environment. Moreover, under the influence of HAase, a significant release of up to 70% of the drug can occur within a span of 48 h at pH 4.5. These results highlight the remarkable responsiveness of Ti_3C_2-DOX to pH, photothermal, and enzyme stimuli, demonstrating its capability for targeted drug release.

Ti_3C_2-DOX exhibits stable properties during storage at 4 °C, with no UV–vis decay or aggregation, suggesting its potential for use as a storable anticancer drug (**Figure 13**a).

In addition, Ti_3C_2-DOX's biocompatibility was considerably increased under biological circumstances after being capped with HA. Without illumination, Figure 13c compares the

© 2025 The Author(s). Small Science published by Wiley-VCH GmbH

26884046, 0, Downloaded from https://onlinelibrary.wiley.com/doi/10.1002/smsc.202400492 by Delhi Technological University, Wiley Online Library on [05/03/2025]. See the Terms and Conditions (https://onlinelibrary.wiley.com/terms-and-conditions) on Wiley Online Library for rules of use; OA articles are governed by the applicable Creative Commons License

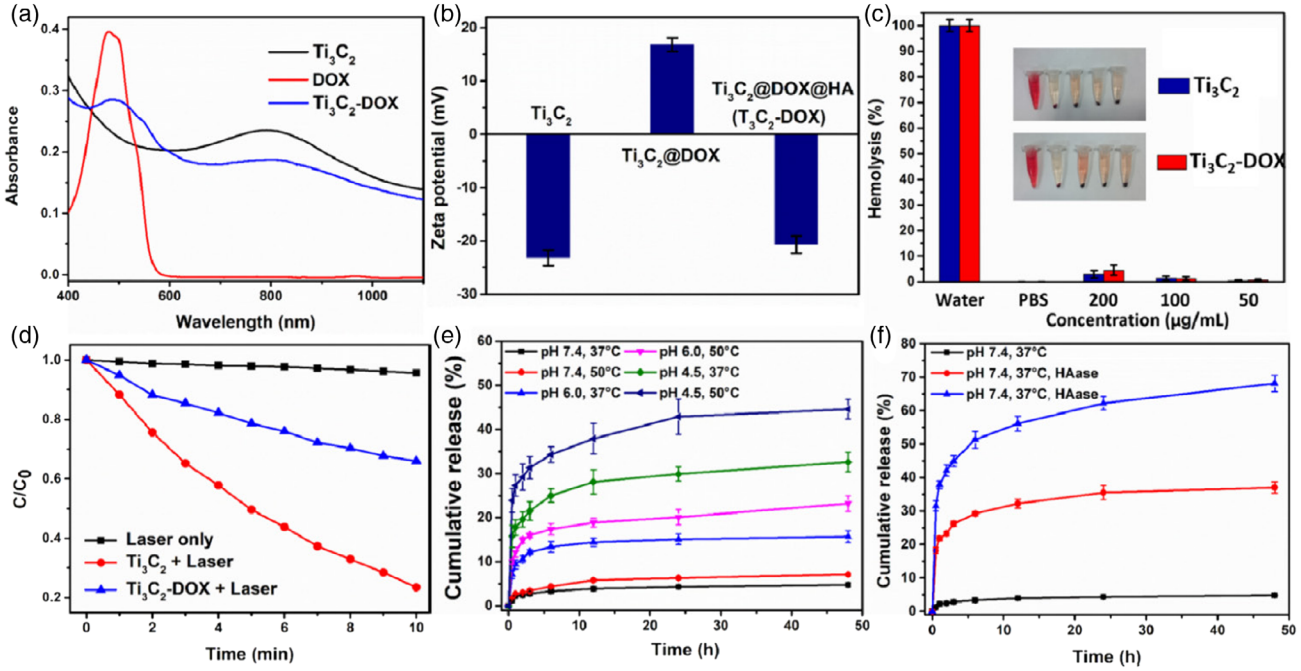

Figure 12. a) Ti_3C_2, DOX, and Ti_3C_2-DOX's UV–vis absorption spectra. b) Ti_3C_2, Ti_3C_2@DOX, and Ti_3C_2@DOX@HA (Ti_3C_2-DOX) zeta potentials. c) Ti_3C_2 and Ti_3C_2-DOX will not both produce hemolysis (less than 5% in the tested range) in the hemolysis experiment at various doses. d) Normalized absorbance of DPBF when exposed to 808 nm light and Ti_3C_2 or $Ti_3C_2Ti_3C_2$-DOX (0.8 W cm^{-2}). e) Drug release profiles at pH 4.5, 6.0, and 7.4 with and without irradiation (808 nm, 0.8 W cm^{-2}). f) Release patterns of drugs that are HAase-responsive at pHs 4.5 and 6.0 both with and without HAase (0.5 mg mL^{-1}). Reproduced with permission.[114] Copyright 2017, ACS copyright pending.

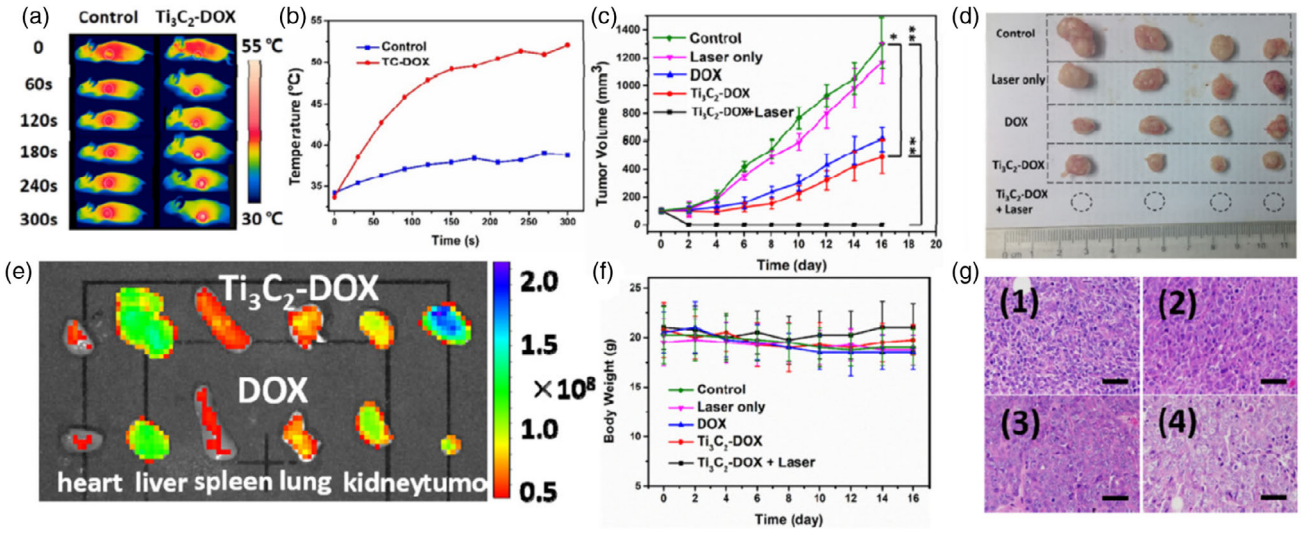

Figure 13. a) Infrared thermal images showing mice 6 hours post-injection of PBS or Ti_3C_2-DOX under varying irradiation durations. b) Temperature variations observed in the tumor region. c) Tumor growth trends ($n = 4$, mean ± SD, $^*P < 0.05$, $^{**}P < 0.01$) recorded throughout the treatment period. d) Digital images of tumors post-treatment. e) Ex vivo fluorescence imaging of tumors and major organs from mice injected with DOX or Ti_3C_2-DOX. f) Body weight fluctuation curves of nude mice over the treatment duration. g) Histological microscopy images of tumors following different treatments: 1) control, 2) laser irradiation alone, 3) DOX, and 4) Ti_3C_2-DOX (after 16 days, scale bar: 50 μm). Reproduced with permission.[114] Copyright 2017, ACS. Copyright pending.

Ti_3C_2-DOX and DOX cytotoxicity at the same dose. Figure 13b,c shows that after exposure to 808 nm laser irradiation (0.8 W cm^{-2}), a considerable increment in cell death has been noticed, demonstrating cancer cells' effective synergistic killing. Figure 13d(i,ii) shows that after laser irradiation, the tumor's temperature rose from 34.0 to 53.1 °C in about 5 min, which

© 2025 The Author(s). Small Science published by Wiley-VCH GmbH

26884046, 0, Downloaded from https://onlinelibrary.wiley.com/doi/10.1002/smsc.202400492 by Delhi Technological University, Wiley Online Library on [05/03/2025]. See the Terms and Conditions (https://onlinelibrary.wiley.com/terms-and-conditions) on Wiley Online Library for rules of use; OA articles are governed by the applicable Creative Commons License

was enough to cause tumor ablation.[98–100] treating with the Ti_3C_2-DOX or free DOX in the absence of laser irradiation only resulted in partial inhibition of tumor growth. However, complete eradication of the tumor without recurrence was achieved through the combined strategy of PDT/PTT/chemotherapy utilizing Ti_3C_2-DOX in the presence of laser irradiation, as depicted in Figure 13d(iii). The developed nanoplatform exhibited better biocompatibility and stimuli-responsive drug release, along with high efficacy in tumor ablation at a low dosage when utilized with a lower power density NIR laser. The specific parameters employed were titanium carbide at a dosage of 2 mg kg^{-1}, DOX loaded at 1.6 mg kg^{-1}, laser wavelength of 808 nm, and a power density of 0.8 W cm^{-2}. MXenes possess properties that render them suitable as PS in PDT, a noninvasive and efficacious approach to cancer treatment. PDT involves generating ROS through photochemical reactions, leading to tumor cell damage. While the majority of research on MXenes has concentrated on their application in PTT, there is growing interest in PDT, frequently in conjunction with PTT. Although the precise mechanism of ROS generation by MXenes is still not fully understood, it is thought that $1O_2$ production may happen as a result of the photo-excited electrons transfer from Ti_3C_2 to triplet oxygen ($3O_2$). Furthermore, ROS generation may be aided by the LSPR effect of MXenes containing transition metals, which is comparable to the capacity of gold NPs to produce ROS when exposed to visible light. The LSPR effect could potentially be improved by the MXene NSs' wide surface area.

Korupalli et al.[101] synthesized a technique to improve the stability of MXene (Ti_3C_2) NSs under oxidative and hydration environments by modifying their surface with sodium ascorbate and dopamine. To generate multifunctional nanosystems having glucose starvation as well as photodynamic therapeutic effects, the modified NSs were then coupled with the glucose oxidase and the photosensitizer Ce6. When subjected to laser energy at 808 and 671 nm, these nanosystems showed outstanding photothermal effects with a conversion efficiency of about 45.1%) and potential for photodynamic treatment (ROS generation). The MXene-based nanosystems were highly effective at killing cancer cells (490%) in the glucose presence and under laser irradiation, thanks to phototherapy and starvation therapy's synergistic effects.[101] The MXenes usage in PDT for cancer treatment has shown promise, but more study is required to fully understand their potential. One of the main concerns is assessing their long-term toxicity to ensure safe clinical use. In vitro and in vivo studies have been conducted to assess their cyto- and biocompatibility. Aside from toxicity, there are other areas where more study is required to fully explore the potential of MXenes for PDT. One of these areas is understanding the mechanisms leading to the ROS generation by these materials, which is essential for effective PDT. Although sufficient studies have been made on using MXenes for cancer treatment, certain aspects require careful consideration. These include potential nontargeted toxicity, selecting the appropriate physical-chemical characteristics before assessing them for cancer therapy, proper characterization, and evaluating their potential biodegradability. In general, more study is required to fully understand the safety profile of these materials before they can be widely used for commercial purposes.

4.1.2. Photoacoustic Imaging (PAI) (in Photothermal)

PAI is a type of biomedical imaging that is gaining popularity nowadays due to its noninvasive and nonionizing nature. This technique involves using a pulsed laser that is directed onto biological tissues, where it is absorbed by light-absorbing domains. This absorption leads to the production of ultrasound waves, known as photoacoustic signals. An ultrasonic transducer receives these signals, which contain information about the tissue's light absorption properties, and uses them to create an image of the tissue's distribution of light absorption. Because PAI is less impacted by light scattering and has a higher spatial resolution than traditional optical imaging, it is better suited for imaging deeper tissues in living things.[102,103] To be an effective contrast agent in PAI, a substance must be able to convert light into heat very efficiently so that it produces a strong signal that contrasts with the PA signal produced by the surrounding tissue. NSs of MXene exhibiting the LSPR effect are considered highly desirable as contrast agents for PAI.[104] Several MXene materials, such as Nb_2CTx,[74] $Ti_3C_2T_x$[78,105] and Ta_4C_3Tx,[106] have been shown to possess excellent photothermal conversion properties.

The impressive photothermal conversion efficiency and excellent biocompatibility of Ta_4C_3Tx-SP distinguish it from other candidates, positioning it as suitable enough for contrast agents in PAI. The photothermal efficacy of a photothermal converter is predominantly governed by two key factors: the photothermal conversion efficiency and the extinction coefficient. The converter's ability to absorb light is indicated by its extinction coefficient, while its performance is indicated by its photothermal conversion efficiency. Ta_4C_3Tx NSs with outstanding NIR photothermal properties were produced by the solvent-assisted exfoliation technique using HF etching and sonification. These NSs, which are extremely thin and two-dimensional in shape, exhibited favorable photothermal characteristics, including a high extinction coefficient, good stability under photothermal conditions, and better photothermal conversion efficiency.[107]

Furthermore, the $Ta_4C_3T_x$ nanoflakes' biocompatibility and physiological stability were greatly improved by surface modification with soybean phospholipids, and tests conducted in vivo and in vitro revealed no discernible toxicity.[106] Lin et al. showed that Nb_2CTx-PVP (polyvinylpyrrolidone), which has potential applications in PAI, exhibited remarkably high photothermal conversion efficiency of 36.4% at NIR-I and 45.65% at NIR-II[108] Furthermore, it demonstrated superior photothermal stability. Given their strong and broad NIR absorption characteristics, metal quantum dots (MQDs) are highly effective as imaging agents for tumor PAI, as well as fluorescence imaging Figure 14c. An MQD was created in 2019 using a fluorine-free technique. The QDs displayed larger and more potent NIR absorption capabilities, with an extinction coefficient of up to 52.8 Lg^{-1} cm^{-1} at 808 nm and a photoconversion efficiency of up to 52.2%, as a result of the variations of AlO anions in significant quantity on their surface (**Figure 14**). Both photothermal treatment (PTT) and PAI on tumors were simultaneously impacted by the produced MXene QDs.[109] Overall, MXene-based PAI is a good potential imaging tool for deep tissue imaging because it has a low tissue attenuation coefficient, which has

© 2025 The Author(s). Small Science published by Wiley-VCH GmbH

26884046, 0, Downloaded from https://onlinelibrary.wiley.com/doi/10.1002/smsc.202400492 by Delhi Technological University, Wiley Online Library on [05/03/2025]. See the Terms and Conditions (https://onlinelibrary.wiley.com/terms-and-conditions) on Wiley Online Library for rules of use; OA articles are governed by the applicable Creative Commons License

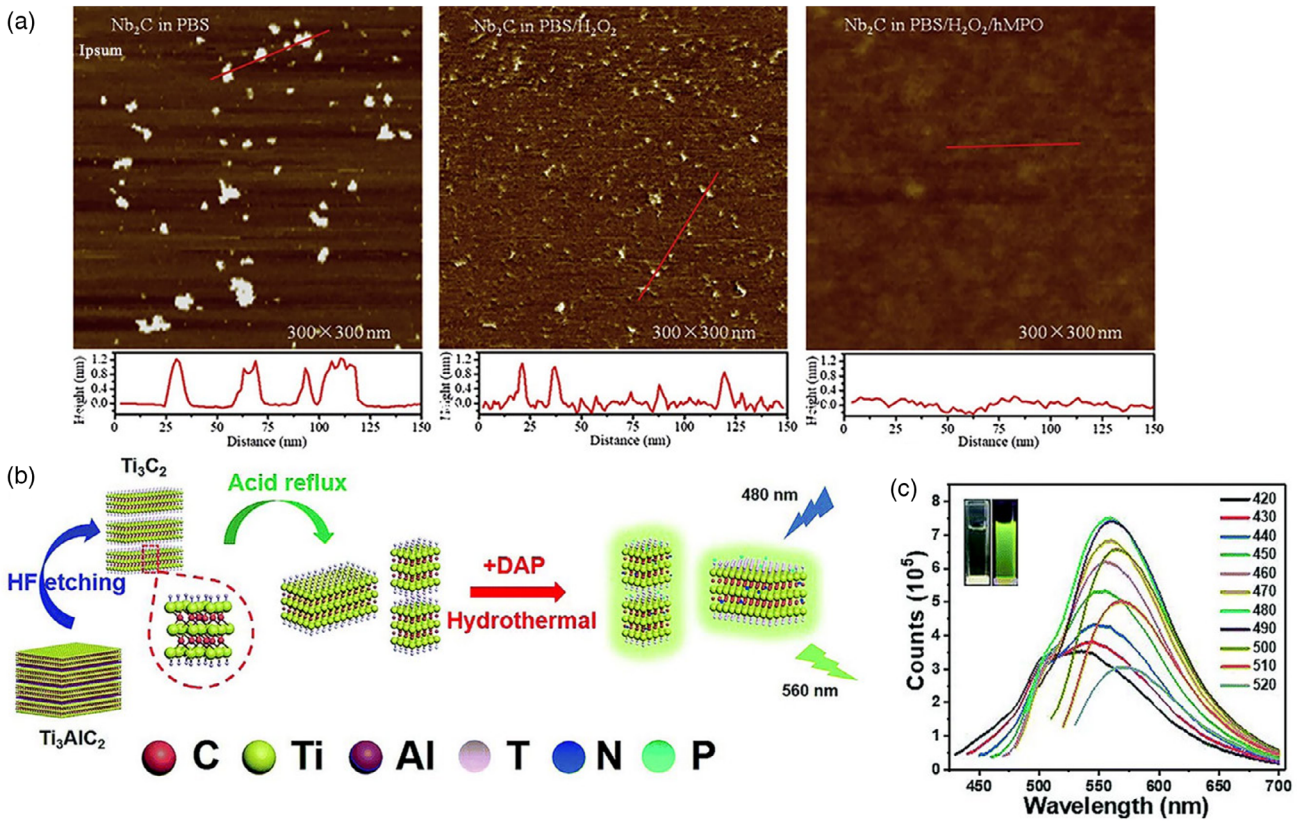

Figure 14. a) AFM pictures of Nb_2CTx QDs subjected to various biodegradation treatments for 24 h, along with their corresponding height distributions. With permission from Reference, this data has been reproduced, which was published by Elsevier in 2020. b) The process for creating N, *P*-MQD in a schematic diagram. c) The spectra that show the emission of fluorescence from *N*, *P*-MQDs, which were created at a temperature of 120 °C, were observed at various wavelengths of excitation. Additionally, a photo taken under UV light with 365 nm wavelength was included in the analysis. Reproduced with permission.[107] Copyright 2023, Journal of Nanobiotechnology. Copyright pending.

the capability of overcoming the limited depth of imaging restrictions of conventional visible light imaging methods.

Drug Delivery Systems: MXenes are ideal for creating gene/DDSs because of their distinctive structure, which lowers drug toxicity, enables targeted drug delivery, and improves the pharmacokinetics of the molecules of the drug. The MXene materials' nanoscale size makes it easier for them to travel through the blood system and build up where the disease is. Furthermore, the MXenes' two-dimensional planar structure provides a sizable specific surface area that enables therapeutic molecules to adhere to the laminar structure's surface. Every year, countless people die from the common disease of cancer, which is becoming a serious threat to the health of humans. By enhancing the cellular uptake of medications and allowing the controlled release of drugs, MXene-based materials have demonstrated promise in the fight against cancer cells.[110–113] MXenes are potentially potent anticancer agents, according to preliminary research. For instance, by sequential surface modification of hyaluronic acid (HA) and doxorubicin (DOX), Chen et al. created a multifunctional Ti_3C_2-based nanoplatform ($Ti_3C_2T_x$-DOX). The surface of $Ti_3C_2T_x$, the tumor-targeted HA's negative charge, and the DOX's positive charge[114] made this possible. Using tetra propylammonium hydroxide (TPAOH) intercalation, $Ti_3C_2T_x$ was created, and after being functionalized with hydroxyl groups, its photothermal effectiveness and light harvesting ability in the NIR region were further enhanced.

The NSs' outer layer was coated with HA to improve biocompatibility and enable active targeting of tumor cells utilizing $CD44^+$ upregulation on the cancer cell membranes.[107] The resulting $Ti_3C_2T_x$-DOX exhibited notable drug loading capacity (up to 84.2%), remarkable biocompatibility, efficient pH-responsiveness, and responsive drug release under NIR laser stimulation, as demonstrated by in vivo and in vitro experiments. Similar to this, large specific surface area SP-modified Ti_3C_2 NSs ($Ti_3C_2T_x$-S_P) can also be stuffed with anticancer drugs (DOX) for effective tumor removal. High drug loading capacity, pH sensitivity, and NIR sensor drug release are all characteristics of this novel drug-delivery nanosystem.[115] However, due to their lack of confined areas for high drug loading, MXenes may encounter difficulties as drug delivery carriers. In a recent study, sol–gel chemistry was used to create surface nanopores on $Ti_3C_2T_x$ to improve drug loading capabilities and broaden MXenes' applications in biomedicine.[80] Employing tetraethylorthosilicate (TEOS) as a precursor and cetanecyltrimethylammonium chloride (CTAC) as a mesoporous guide under alkaline synthesis conditions, a thin mesoporous silica shell layer ($Ti_3C_2T_x$@mMSNs)

© 2025 The Author(s). Small Science published by Wiley-VCH GmbH

26884046, 0, Downloaded from https://onlinelibrary.wiley.com/doi/10.1002/smsc.202400492 by Delhi Technological University, Wiley Online Library on [05/03/2025]. See the Terms and Conditions (https://onlinelibrary.wiley.com/terms-and-conditions) on Wiley Online Library for rules of use; OA articles are governed by the applicable Creative Commons License

was applied to the surface of $Ti_3C_2T_x$ By merging the advantages of both substances as medication transporters—a mesoporous construction that saves space, augmented water-solubility, appropriate surface chemistry, and dispersibility—the interfacial characteristics of $Ti_3C_2T_x$ were improved.

RGD has been covalently bounded to the $Ti_3C_2T_x$@mMSNs modified with PEG to accomplish targeted drug delivery to the tumor site. A uniform pore size of 3.1 nm, a high pore volume of 0.96 $cm^3 g^{-1}$, and a sizable specific surface area of 772 $m^2 g^{-1}$ were all present in the prepared $Ti_3C_2T_x$@mMSNs. These novel composite nanosystems based on MXene have been evaluated in vitro and in vivo, and the results showed that they can effectively eliminate tumors without significant recurrence when used in conjunction with standard cancer treatment modalities involving chemotherapy and localized heat therapy.

In addition, a new material called MBene has been developed for usage in post-MXene applications. Using a chemical etching method that employs microwaves, He et al. was able to successfully synthesize the 2D NS ZBN made of zirconium boride. This material demonstrates exceptional photothermal properties in the NIR spectrum, with a high conversion efficiency equal to 76.8% in the NIRII window at a wavelength of 1060 nm.[107] In addition, the material was surface-modified using borate esterification of hyaluronic acid (HA) to achieve good dispersion, which is important for its use as a platform for multifunctional nanodelivery.

The scientists employed borate esterification to load the chemotherapy drug doxorubicin (DOX) and a nitric oxide (NO) prodrug called Gal-NO onto the ZBN-HA's surface, leading to significant drug loading of ZBN-HA/DOX and ZBN-HA/NO. Through photo-pyrolysis, the ZBN-HA/DOX and ZBN-HA/NO materials underwent deconjugation of HA and aggregation of ZBN. This process facilitated photo-controlled release of the drugs within the tumor and enabled their retention in the tumor site.[116] Overall, due to their small size and flat, two-dimensional structure, MXenes are an excellent material for using as a drug carrier.

4.1.3. PTT

The strong light absorption within the NIR ranges, specifically NIR-I (750–1000 nm) and NIR-II (1000–1350 nm), renders MXenes highly suitable for biological applications and makes them well-suited for applications like PTT and PAI.[117] With very little impact on the viability of normal cells over a wider range measured concentrations wider range, their "light-to-heat" transition capacity is highly effective for the ablation of malignant cells. This may be because of the synergistic photodynamic/photothermal action and the ROS that MXenes cause to form in cancer cells. MXenes are safe for use in nanomedicine because of their photothermal conversion efficiency and high optical absorption, hydrophilicity, and composition of either essential or inert biological components.

MXenes' planar form makes it hard to accomplish high drug molecule loading, and their photothermal efficiency is still somewhat poor. With the potential for combination therapeutic effects, surface modification of MXenes can increase their photothermal stability,[69,111] water solubility,[118–120] and drug-loading capacity, making them suitable photothermal conversing agents and anticancer drug delivery carriers. A fluorine-free technique can be utilized as a substitute for HF etching agents, which may represent significant toxicity hazards in MXene production procedures.

The current advancement in MXene materials for PTT involves the fabrication of $Ta_4C_3T_x$-SP NSs. This enables the dual-mode imaging of live tumors with the help of computed tomography (CT) and photoacoustic (PA) imaging techniques. Nb_2C has an extraordinarily high photothermal conversion efficiency in NIR-I as well as NIR-II regions, in contrast to MQDs, which show a noticeably high photothermal conversion efficiency.[109] Dai et al. used rational design to create Ti_3C_2 material, with the (MnO)x composition fixed to the surface of Ti_3C_2 via a redox reaction.[105] To improve stability, the surface of the (MnO)x/$Ti_3C_2T_x$ was further modified with soy phospholipids (SP). MnOx/$Ti_3C_2T_x$-SP composites were experimentally validated and demonstrated much higher photothermal stability (**Figure 15**). Furthermore, a photothermal conversion efficiency value equal to 22.9% was achieved, which is on par with the conventional Cu_2-xSe carbon nanotubes (22%) and Au nanorods (21%).[105] Because of the strict spatiotemporal management of local heat, PTT has less negative effects than conventional cancer treatment procedures. PTT is commonly heated beyond 50 °C for overcoming heat shock protein-induced thermal resistance, which may cause thermal injury to vital organs near the tumor.[121]

A previous study found that the second biological window in the NIR (NIR-II) range (1000–1350 nm) is more advantageous for deep tissue penetration in comparison with the first biological window (NIR-I) (750–1000 nm).[78] Cao et al. proposed a method that uses tiny fluorescent V_2CTx QDs. It was found out that they possess better photothermal effects in the NIR-II region for cryogenic nuclear-targeted PTT.[122] They also developed a multipurpose thermal therapy platform modified with RGD called V_2CTx-TAT@Ex-RGD. Additionally, Shao et al. found that both nitride-based MXenes and Ti2NTx QDs have particularly higher photothermal conversion efficiencies in first as well as second biological windows of the NIR spectrum (NIR-I showing value of 48.62% at 808 nm; NIR-II showing value of 45.51% at 1064 nm).[81]

Ti_2NTx QDs, besides their high photothermal therapeutic efficacy and strong biocompatibility, have great degrading properties and an efficient excretion rate in vivo, allowing for a seamless elimination from the body (**Figure 16**b). Because of its exceptional photothermal conversion efficiency and NIR absorption properties, MXenes is showing promise as an outstanding agent for deep tissues PTT. Additionally, various surface alterations and alternative plans could enhance the photothermal properties of MXenes and facilitate the efficient eradication of cancer cells Figure 16.

PTT is a therapeutic method which had been proposed and frequently used for the treatment of cancer. The method involves the induction of localized heat in the area of the tumor cells, which results in the elimination of the tumor.

Liu et al. introduced a drug delivery platform using MXene@Au-PEG, incorporating both NIR laser-triggered and pH-responsive drug release mechanisms for effective loading of the chemotherapeutic drug DOX (**Figure 17**c). The $Ti_3C_2T_x$

© 2025 The Author(s). Small Science published by Wiley-VCH GmbH

26884046, 0, Downloaded from https://onlinelibrary.wiley.com/doi/10.1002/smsc.202400492 by Delhi Technological University, Wiley Online Library on [05/03/2025]. See the Terms and Conditions (https://onlinelibrary.wiley.com/terms-and-conditions) on Wiley Online Library for rules of use; OA articles are governed by the applicable Creative Commons License

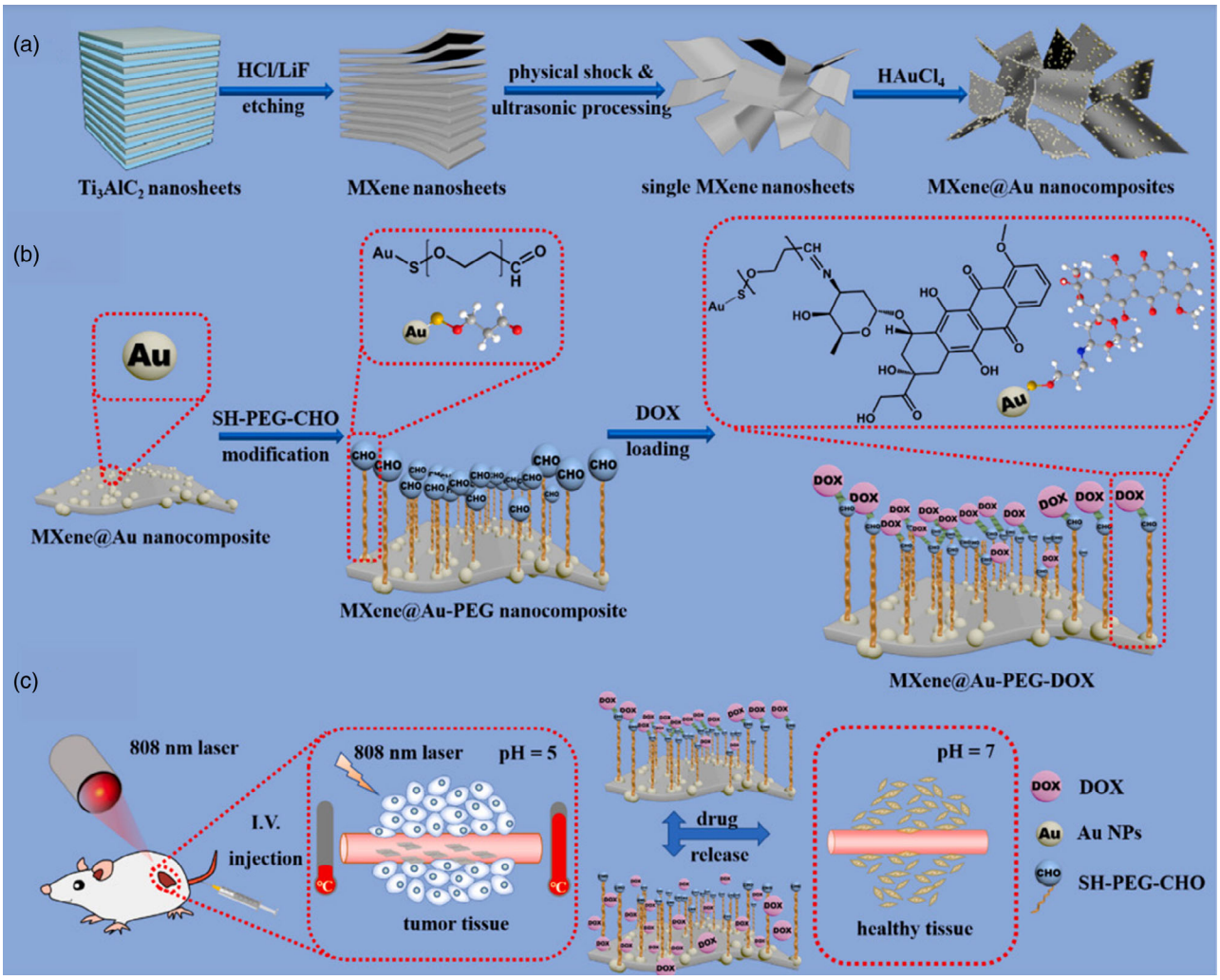

Figure 15. The schematic illustrates the MXene production process and its application in cancer therapy. a) The sequential steps for synthesizing MXene and MXene@Au nanosheets. b) The surface functionalization of MXene@Au with thiol polyethylene glycol aldehyde (SH-PEG-CHO) chains, followed by doxorubicin (DOX) loading. c) A schematic representation of the MXene-based drug delivery system, which is pH-responsive and activated by near-infrared (NIR) laser irradiation for targeted tumor treatment. Reproduced with permission.[78] Copyright 2017, ACS. Copyright pending.

MXene-based DDS was constructed by incorporating Au nanoparticles (Au-NPs) through in situ growth (Figure 17a). For the enhancement of the electrostatic interaction between MXene and Au seeds, the zeta potential of MXene NSs was modified by introducing a positively charged polymer (PAH).[123] This made MXene NSs' surface modification easier. The reduction of $HAuCl_4$ on top of the MXene by the reducing agent HCHO resulted in the formation of Au NPs in situ via seed action.

The surface of MXene@Au was changed using a PEG polymer having —SH and —CHO groups at both ends to improve drug loading capacity as well as biocompatibility and stability in physiological circulation (as shown in Figure 17b). DOX was loaded onto the MXene@Au-PEG drug delivery platform using Schiff base bonds.[124]

The resulting MXene@Au-PEG-DOX system showed drug release modes that were responsive to both pH conditions and NIR laser stimulation. Moreover, the incorporation of Au and PEG into MXene enhanced the DDS's photothermal stability and the nanocomposites biocompatibility as well as facilitated the formation of Schiff base bonds. This improved control over drug release and enabled targeted therapeutic effects.[16] Furthermore, the MXene@Au NSs were capable of generating localized photothermal conversion for tumor thermotherapy under external NIR irradiation. As a result, as shown in Figure 17c, the drug-loaded MXene-based DDS seems promising for efficient combined chemotherapy and PTT.[123]

A co-operative anticancer nanotransporter with magnetic regulating potential and chemo-PTT with dual stimuli-receptive drug release was created using heterostructured titanium carbide-cobalt (Co) nanowires. The drug packing ability of this system was notably high (225.05%), and it demonstrated strong photothermal translation efficiency when illuminated with laser (808 nm) and significant mortality for cancer cells in comparison to chemotherapy or PTT alone.

© 2025 The Author(s). Small Science published by Wiley-VCH GmbH

26884046, 0, Downloaded from https://onlinelibrary.wiley.com/doi/10.1002/smsc.202400492 by Delhi Technological University, Wiley Online Library on [05/03/2025]. See the Terms and Conditions (https://onlinelibrary.wiley.com/terms-and-conditions) on Wiley Online Library for rules of use; OA articles are governed by the applicable Creative Commons License

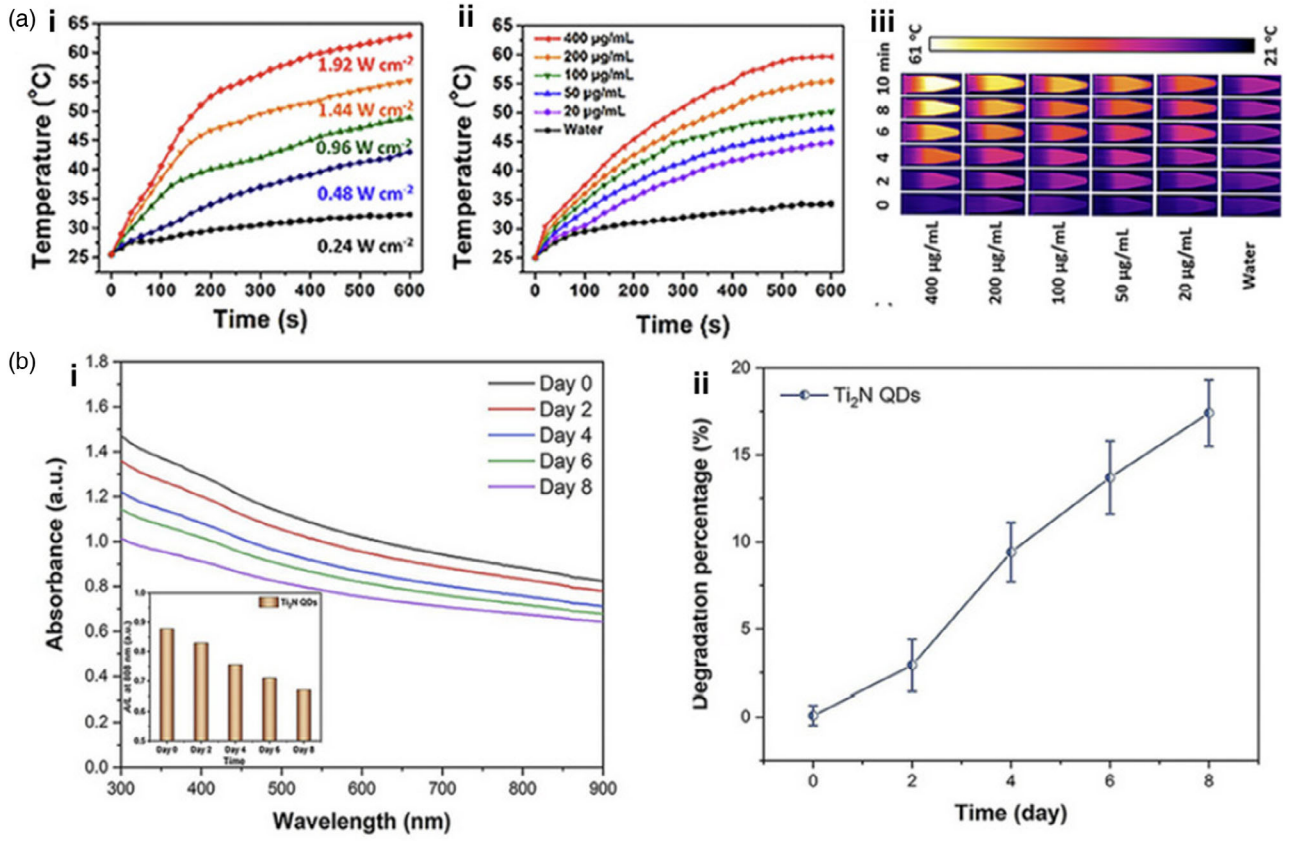

Figure 16. a) V_2CTx-TAT@Ex-RGD (V_2CTx-TAT, 100 g/mL) soln. photothermal heating curves under various power densities of 1064 nanometers (NIR-II) laser irradiation. Under 1064 nm laser illumination at various concentration values with a power density value equal to 0.96 W cm^{-2}, the V_2CTx-TAT@Ex-RGD solution produced photothermal heating curves (ii) and accompanying thermal pictures (iii). ACS 2019, reproduced with permission. b) Ti_2NTx QDs' absorption spectra, including their absorption intensity at 808 nanometers (A/L) and percentage degradation following deterioration in water for a time period of 0, 2, 4, 6, and 8 days. (Panel (a) is reproduced with permission.[122] Copyright 2019, ACS Nano. Panel (b) is reproduced.[107] Copyright 2023, Journal of Nanobiotechnology. Copyright pending.

By employing ultrathin Ti_3C_2-MXene NSs, a detection range from 0.00012000 ng mL^{-1} and a sensitivity of 37.9 A ng^{-1} mL cm^2 $decade^{-1}$ were successfully attained. These biofunctionalized MXenes and MXene-based materials offer promising prospects for the development of highly sensitive biosensors, capable of drug and gene delivery, as well as detecting aptamers, antibodies, cells, DNA, and enzymes. By incorporating GdW10-centered polyoxometalates, surface-engineered and functionalized 2D Ti_3C_2 MXene NSs with excellent biocompatibility were produced, showing promise for treatment of hyperthermia with MR/CT imaging management for xenografts or tumor cells. During the observation phase, tumor tissue was successfully removed with no recurrence. Liu et al. created superparamagnetic 2D Ti_3C_2 MXenes with excellent biocompatibility, displaying high T2 relaxivity of 394.2 mM^{-1} s^{-1} and acceptable contrast-augmented MRI of malignancies, indicating a promising future in medicinal research. In both in vitro and in vivo experiments, they showcased a significant photothermal conversion efficiency of ≈48.6% for the targeted eradication of tumors and cancer cells using photothermal treatment.

Mo_2C MXenes: The study focused on ultrathin 2D molybdenum carbide (Mo_2C) MXenes, which showed strong NIR absorption capabilities, spanning both the 1st and 2nd biological transparency windows. NIR types I and II. To improve biocompatibility and biodegradability even further, the MXenes were treated with poly(vinyl alcohol) (PVA) to form Mo_2C-PVA nanoflakes. The resulting nanoflakes have a broad absorption band that covers the NIR-I as well as NIR-II regions, as well as suitable photothermal-translation proficiency (equal to 43.3% for NIR-II and 24.5% for NIR-I).[42]

Figure 18a depicts a flowchart of the technique used to generate Mo_2C MXene. The bulk ternary layered carbide precursor powders, called as Mo_2Ga_2C, are immersed in an acidic etching solution containing fluoride ions. This technique eliminates the Ga atoms' interlaced layers and dissolves the metallic connections between Ga and Mo in the bulk ceramic structure.[12] The resulting layer-structured greyish Mo_2Ga_2C solid bulk is sinter-processed at 850 °C under vacuum, then immersed in a 12 M HCl solution for removing any excess Ga. (Figure 18b).[83] Field-emission scanning electron microscopy (FESEM) was

© 2025 The Author(s). Small Science published by Wiley-VCH GmbH

26884046, 0, Downloaded from https://onlinelibrary.wiley.com/doi/10.1002/smsc.202400492 by Delhi Technological University, Wiley Online Library on [05/03/2025]. See the Terms and Conditions (https://onlinelibrary.wiley.com/terms-and-conditions) on Wiley Online Library for rules of use; OA articles are governed by the applicable Creative Commons License

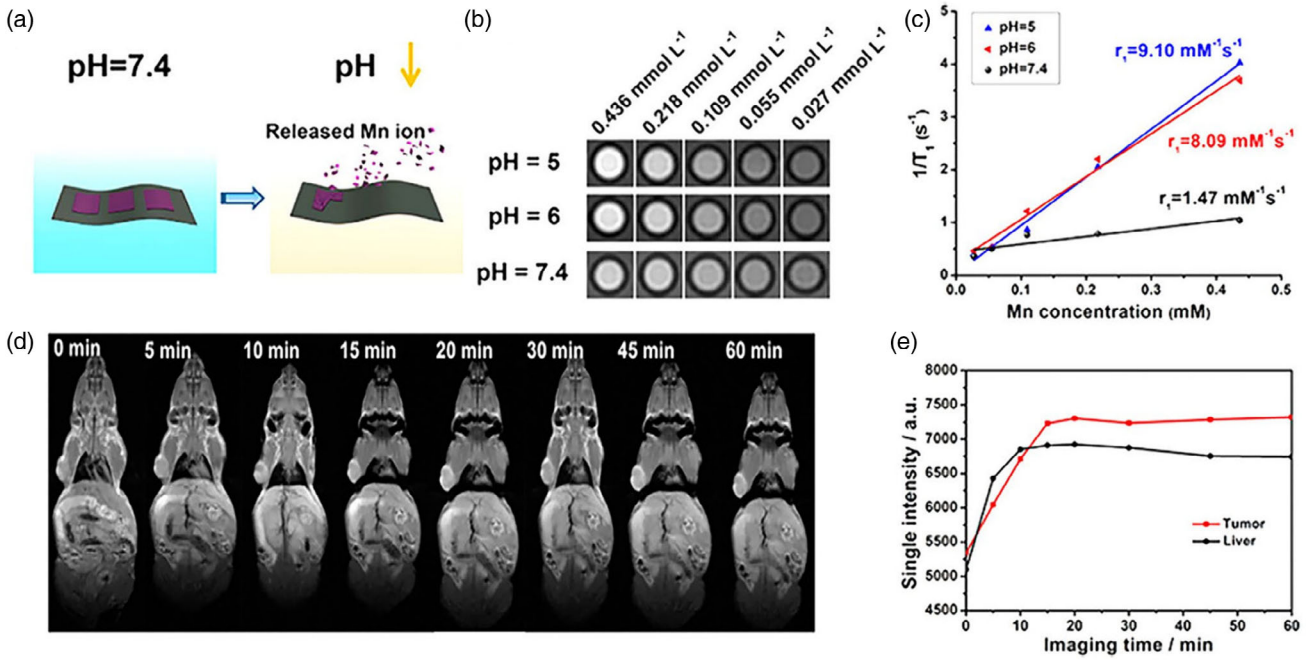

Figure 17. The schematic illustrates the MRI of MnOx/$Ti_3C_2T_x$-SP nanosheets both in vitro and in vivo, highlighting their pH-responsive contrast enhancement. In panel (a), the diagram depicts the breakdown of the MnOx fraction under weakly acidic conditions. Panel (b) presents T1-weighted MRI images of MnOx/$Ti_3C_2T_x$-SP nanosheets after being immersed in buffered solutions with different pH levels for three hours. Panel (c) displays a plot of 1/T1 versus Mn concentration for the nanosheets subjected to these varying pH conditions. In vivo experiments are shown in Panels (d) and (e), where mice were intravenously injected with the MnOx/$Ti_3C_2T_x$-SP nanosheets, capturing the T1-weighted MRI images and signal intensity at different time points. The findings demonstrate that weakly acidic environments facilitate the decomposition of MnOx/$Ti_3C_2T_x$-SP nanosheets, leading to enhanced T1-weighted MRI signals. Furthermore, the in vivo results confirm the nanosheets' excellent biocompatibility and their potential as effective MRI contrast agents for tumor imaging. Reproduced with permission.[123] Copyright 2022, Elsevier. V copyright pending.

employed for preliminary testing of the Mo_2Ga_2C powders. The images obtained showed a typical layered platelet structure with a 136.7 nm thickness (Figure 18c,d). After successful exfoliation in HF solution, the tightly bound layers grew, neatly stacked, and formed a multilayered accordion structure that produced 2D Mo_2C flakes. (Figure 18e–g).

Nb_2C MXenes: Yin et al. have made a composite NS with a 2D core/shell structure for photonic thermos-gaseous therapy. To create the composite NSs, Nb_2C MXene NSs were coated with a mesoporous silica layer using sol–gel chemistry. This coating improved both the biocompatibility and chemical composition, enabling surface modifications and loading of nitric oxide (NO) donors. The resulting Nb_2C-MSNs-SNO composite NSs exhibited high photothermal conversion efficiency in NIR-I (45.65%) as well as NIR-II (36.4%) regions. Additionally, these NSs displayed variable NO release upon thermal shock.[125] They also showed good PA-imaging capabilities, allowing for real-time monitoring of the therapeutic process.[126] In vitro and in vivo tests revealed that these composite NSs have the potential to be a versatile nanomedicine for photonic-triggered thermos-gaseous therapy, providing a promising new cancer therapeutic approach.

TiCN MXenes QDs: MXene QDs were synthesized utilizing a hydrothermal process with TiCN powder as the precursor, which was a straightforward and ecologically friendly procedure. (**Figure 19**a). The MXene QDs showed exceptional fluorescence and water dispersibility, making them suitable for the selective and sensitive detection of ferric ions (Fe^{3+}) and also for potential use in cancer treatment applications. This suggests investigating novel ecologically friendly and sustainable MXene production processes, and also functional modification for sensitive and selective cancer treatments.

Kong et al.[127] synthesized TiCN QDs utilizing TiCN powder as a precursor in an eco-friendly and simple hydrothermal procedure. The process involved combining TiCN powder and deionized water, followed by high-temperature heating, cooling, and centrifugation. The generated TiCN QDs exhibited exceptional fluorescence capabilities as well as good water dispersibility. The fluorescence lifetime of these QDs was 6.33 ns, with an excitation-wavelength-dependent fluorescence characteristic. TiCN QD fluorescence intensity was shown to be pH-dependent, with a maximum intensity at pH 4.0. The TiCN QDs were very sensitive to Fe^{3+} and displayed a gradual decrement in fluorescence intensity at 400 ns as the Fe^{3+} concentration increased. Adding 200 M Fe^{3+} resulted in a 42% reduction in fluorescence quenching.[128] TiCN QDs could be used in biomedical applications, particularly cancer therapy, due to their superior fluorescence features and sensitive ferric ion (Fe^{3+}) detection capabilities.

V_2C MXenes: Cao et al. synthesized an ultrasmall 2-dimensional vanadium carbide quantum dot (V_2C QDs) possessing strong photothermal effects in the NIR window, as well

© 2025 The Author(s). Small Science published by Wiley-VCH GmbH

26884046, 0, Downloaded from https://onlinelibrary.wiley.com/doi/10.1002/smsc.202400492 by Delhi Technological University, Wiley Online Library on [05/03/2025]. See the Terms and Conditions (https://onlinelibrary.wiley.com/terms-and-conditions) on Wiley Online Library for rules of use; OA articles are governed by the applicable Creative Commons License

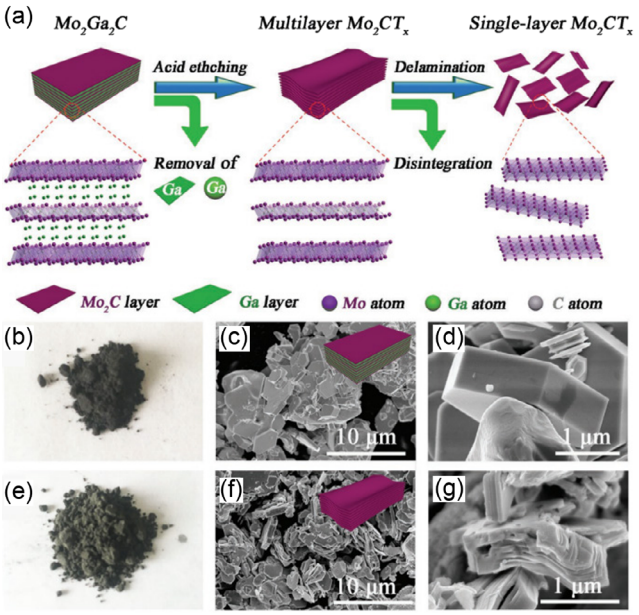

Figure 18. a) Mo_2C MXene preparation and delamination are depicted schematically using a 3-dimensional layer structure (top) and ball-and-stick model (bottom). b) Digital image of the bulk Mo_2Ga_2C ceramic and c,d) FESEM images demonstrating a typical compact layer structure. Mo_2Ga_2C after being treated with a hydrofluoric solution to create multilayer Mo_2C MXenes is shown in the following images: e–g) displaying a structure of exfoliated layers. Reproduced with permission.[83] Copyright 2019, Wiley Online Library. Copyright pending.

as good fluorescence, photoacoustic, and MRI capabilities.[122] A dual-target system for cancer cell membrane and nucleus organelle was developed using small fluorescent V_2C QDs. These QDs were modified with TAT peptides for cell nucleus targeting (V_2C-TAT) and have been encapsulated within endogenous exosomes. Additionally, a cell-targeting Arg-Gly-Asp (RDG) peptide has been incorporated for the construction of the dual-target system (**Table 3**).[129]

When subjected to a 1064 nanometers laser at a value of power density equal to 0.96 W cm2, the V_2C-TAT@Ex-RGD dramatically boosted cell necrosis in vitro. In terms of in vivo cancer treatment, the extended period of blood circulation and the ability to target cancer cells of the V_2CTAT@Ex-effective RGD enabled tumor accumulation, which resulted in appealing antitumor therapeutic efficiency. In vivo, multimodal tumor imaging revealed that the photoacoustic (PA) intensity at the mouse's tumor site treated with V_2C-TAT@Ex-RGD was found to be equal to 2.11 times higher compared to the mouse treated with V2C-PEG-TAT.[122] When compared to the control group, the V_2C-PEG-TAT-treated mouse likewise showed a high PA signal in the tumor site. Under low-temperature conditions, the synthesized V_2C-TAT@Ex-RGD exhibited targeted PTT toward cell nuclei within the NIR-II bio window. These findings suggest a bright prospect for future biomedical applications and novel treatments.[74]

4.2. DDSs

MXenes are ideal for creating gene/DDSs because of their distinctive structure, which lowers drug toxicity, enables targeted

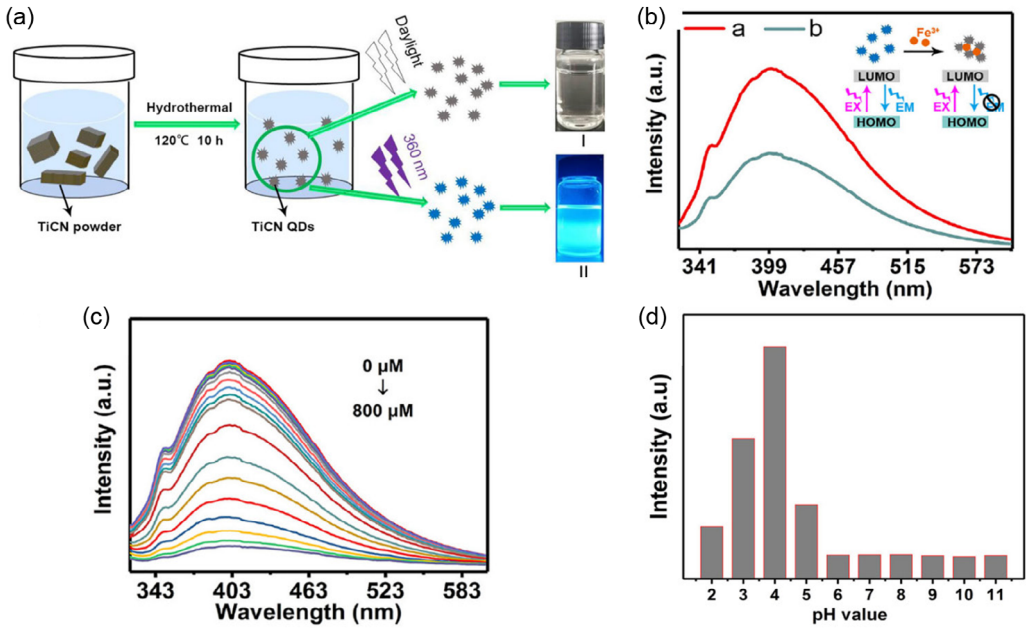

Figure 19. a) A schematic representation of the synthesis of TiCN quantum dots (QDs) with blue fluorescence emission using the hydrothermal method. b) Fluorescence spectra of (a) TiCN QDs and (b) TiCN QDs after the addition of Fe^{3+} at a concentration of 200 μM (The inset illustrates the mechanism of fluorescence quenching of TiCN QDs by Fe^{3+}). c) Fluorescence emission spectra of TiCN QDs in the presence of varying concentrations of Fe^{3+} ions. d) Fluorescence spectra of TiCN QDs at different pH levels. Reproduced with permission.[127] Copyright 2019, Elsevier. Copyright pending.

© 2025 The Author(s). Small Science published by Wiley-VCH GmbH

26840046, 0, Downloaded from https://onlinelibrary.wiley.com/doi/10.1002/smsc.202400492 by Delhi Technological University, Wiley Online Library on [05/03/2025]. See the Terms and Conditions (https://onlinelibrary.wiley.com/terms-and-conditions) on Wiley Online Library for rules of use; OA articles are governed by the applicable Creative Commons License

Table 3. MXenes with diversely appealing cancer treatment and diagnosis potential.

MXenes	Strategy	Advantages	References
Mo_2C	Cancer synergistic phototherapy utilizing the 2 multimodal imaging-guided technique	low tissue toxicity and hematotoxicity; substantial biocompatibility[195]	[195]
Ti_3C_2	photothermal cancer therapy	In vivo/in vitro toxicity not found; There are no evident implanted components that leak into the bloodstream.[85]	[85]
Ti_2C	Photothermal cancer therapy	High biocompatibility, good photothermal conversion efficiency, and high NIR-induced potential for cancer cell death[196]	[196]
Nb_2C	Photo-/chemothermal cancer therapy	Increased photothermal hyperthermia of tumors, improved targeted chemotherapy, and low/noncytotoxicity (at 320 ng mL^{-1}); a respectable photothermal conversion efficiency of 28.6%[197]	[197]
Nb_2C	Photothermal cancer therapy	Higher photothermal conversion efficiency (values equal to 36.4% and 45.65%), noticeable photo thermal stability, exceptional biocompatibility, negligible phototoxicity, and side effects; specialized biodegradability with properties that respond to human myeloperoxidase enzyme[74]	[74]
Ti_3C_2	Photothermal cancer therapy	Significant photothermal conversion efficiency (52.2%); minimal in vivo/in vitro toxicity; excellent biocompatibility; obvious therapeutic use potentials imaging audiovisual[109]	[109]
$MnOx/Ti_3C_2$	MR/PA guided photothermal cancer therapy	Excellent biocompatibility, no toxicity that can be detected, and a good photothermal conversion efficiency (22.9%)[78]	[78]
$MnOx/Ta_4C_3$	Photoacoustic imaging showing the better contrast characteristics; photothermal cancer therapy	Outstanding effectiveness in halting tumor growth; little side effects; absence of notable histological lesions or abnormalities in the major organs; a decent photothermal conversion efficiency of 34.9%[105]	[105]
Ta_4C_3 with surface superparamagnetic iron oxide functionalization composites	Photothermal breast cancer therapy; MRI/CT imaging	Exceptional breast tumor photoablation efficacy, negligible toxicity, great biocompatibility, and great photothermal conversion efficiency (≈32.5%)[77]	[77]
Ta_4C_3	Photothermal cancer therapy	Great biocompatibility, no side effects, and a high rate of photothermal conversion (≈44.7%)[198]	[198]
Ti_3C_2 with GdW10 composites	Photothermal cancer therapy; MRI/CT imaging	Excellent biocompatibility, no observable cell necrosis, and a reasonable photothermal conversion efficiency of about 21.9%[109]	[109]
Ti_3C_2	Chemo-/photothermal cancer therapy	No observable side effects, strong biocompatibility, a significant specificity/selectivity, and an acceptable photothermal conversion efficiency (58.3%).[31]	[31]
V_2C	MR/PA guided photothermal cancer 2 therapy	Decent photothermal conversion efficiency (45.05%), strong tumor-killing potency, excellent biocompatibility, and low temperature[122]	[122]
V_2C	MR/PA guided photothermal cancer 2 therapy	Lower cytotoxicity, effective biodistribution, and high photothermal conversion efficiency (48%)[199]	[199]
Mo_2C	Photothermal cancer therapy	Among its many benefits are its quick biodegradation, higher photothermal conversion efficiency equal to 24.5% for NIR-I and 43.3% for NIR-II, great biocompatibility, minimal toxicity, and effective photothermal tumor eradication.[200]	[200]
Nb_2C	Photothermal cancer therapy	Photothermal conversion efficiency is satisfactory (39.09%); no acute or chronic effects are seen. (in vivo)[125]	[125]
Ti_3C_2 @Au	PA-/CT-guided photothermal cancer 2 therapy	Increased biocompatibility and stability; minimal long-term toxicity;[144]	[144]
Ti_3C_2/doxorubicin hydrochloride@cellulose	Chemophotothermal cancer therapy	Substantial effectiveness for immediate tumor eradication; tailored medication release[201]	[201]

drug delivery, and improves the pharmacokinetics of the molecules of the drug. The MXene materials' nanoscale size makes it easier for them to travel through the blood system and build up where the disease is. Furthermore, the MXenes' two-dimensional planar structure provides a sizable specific surface area that enables therapeutic molecules to adhere to the laminar structure's surface. Every year, countless people die from the common disease of cancer, which is becoming a serious threat to the health of humans. By enhancing the cellular uptake of medications and allowing the controlled release of drugs, MXene-based materials have demonstrated promise in the fight against cancer cells.[110–113] MXenes are potentially potent

© 2025 The Author(s). Small Science published by Wiley-VCH GmbH

26884046, 0, Downloaded from https://onlinelibrary.wiley.com/doi/10.1002/smsc.202400492 by Delhi Technological University, Wiley Online Library on [05/03/2025]. See the Terms and Conditions (https://onlinelibrary.wiley.com/terms-and-conditions) on Wiley Online Library for rules of use; OA articles are governed by the applicable Creative Commons License

anticancer agents, according to preliminary research. For instance, by sequential surface modification of hyaluronic acid (HA) and doxorubicin (DOX), Chen et al. created a multifunctional Ti_3C_2-based nanoplatform ($Ti_3C_2T_x$-DOX). The surface of $Ti_3C_2T_x$, the tumor-targeted HA's negative charge, and the DOX's positive charge[114] made this possible. Using tetrapropylammonium hydroxide (TPAOH) intercalation, $Ti_3C_2T_x$ was created, and after being functionalized with hydroxyl groups, its photothermal effectiveness and light harvesting ability in the NIR region were further enhanced.

The NSs' outer layer was coated with HA to improve biocompatibility and enable active targeting of tumor cells utilizing $CD44^+$ upregulation on the cancer cells membranes.[107] The resulting $Ti_3C_2T_x$-DOX exhibited notable drug loading capacity (up to 84.2%), remarkable biocompatibility, efficient pH-responsiveness, and responsive drug release under NIR laser stimulation, as demonstrated by in vivo and in vitro experiments." Similar to this, large specific surface area SP-modified Ti_3C_2 NSs ($Ti_3C_2T_x$-SP) can also be stuffed with anticancer drugs (DOX) for effective tumor removal. High drug loading capacity, pH sensitivity, and NIR sensor drug release are all characteristics of this novel drug-delivery nanosystem.[115] However, due to their lack of confined areas for high drug loading, MXenes may encounter difficulties as drug delivery carriers. In a recent study, sol–gel chemistry was used to create surface nanopores on $Ti_3C_2T_x$ to improve drug loading capabilities and broaden applications of MXenes in biomedicine.[80] Employing TEOS as a precursor and CTAC as a mesoporous guide under alkaline synthesis conditions, a thin mesoporous silica shell layer ($Ti_3C_2T_x$@mMSNs) was applied to the surface of $Ti_3C_2T_x$ By merging the advantages of both substances as medication transporters—a mesoporous construction that saves space, augmented water-solubility, appropriate surface chemistry, and dispersibility—the interfacial characteristics of $Ti_3C_2T_x$ were improved.

RGD has been covalently bounded to the $Ti_3C_2T_x$@mMSNs modified with PEG to accomplish targeted drug delivery to the tumor site. A uniform pore size of 3.1 nm, a high pore volume of $0.96\ cm^3\ g^{-1}$, and a sizable specific surface area of $772\ m^2\ g^{-1}$ were all present in the prepared $Ti_3C_2T_x$@mMSNs. These novel composite nanosystems based on MXene have been evaluated in vitro and in vivo, and the results showed that they could effectively eliminate tumors without significant recurrence when used in conjunction with standard cancer treatment modalities involving chemotherapy and localized heat therapy.

In addition, a new material called MBene has been developed for usage in post-MXene applications. Using a chemical etching method that employs microwaves, He et al. were able to successfully synthesize the 2D NS ZBN made of zirconium boride. This material demonstrates exceptional photothermal properties in the NIR spectrum, with a high conversion efficiency equal to 76.8% in the NIRII window at a wavelength of 1060 nm.[107] In addition, the material was surface-modified using borate esterification of hyaluronic acid (HA) to achieve good dispersion, which is important for its use as a platform for multifunctional nanodelivery.

The scientists employed borate esterification to load the chemotherapy drug doxorubicin (DOX) and a nitric oxide (NO) prodrug called Gal-NO onto the ZBN-HA's surface, leading to significant drug loading of ZBN-HA/DOX and ZBN-HA/NO. Through photo-pyrolysis, the ZBN-HA/DOX and ZBN-HA/NO materials underwent deconjugation of HA and aggregation of ZBN. This process facilitated the photo-controlled release of the drugs within the tumor and enabled their retention in the tumor site.[116] Overall, due to their small size and flat, two-dimensional structure, MXenes are an excellent material for using as a drug carrier.

4.3. MXene-Integrated Nanocomposites

Dong et al.[111] synthesized a new DDS on the basis of MXene NSs and agarose[130,131] for the controlled anticancer medicine doxorubicin (DOX) release. The MXene or agarose hydrogel loaded with the drug was created by combining MXene NSs[28] and DOX with agarose solution (**Figure 20**a). The MXene@Hydrogel's photothermal heating curves before and after DOX loading were depicted in Figure 20b(i), and the MXene@Hydrogel's maximum temperature after DOX loading remained unaffected at around temperature of 60 °C, which indicates that the drug loading causes no significant impact on the MXene@Hydrogel's photothermal performance. In Figure 20b(ii), the melting behavior of MXene@Hydrogels with various agarose concentrations is depicted. The hydrogels with 0.5% and 1.0% agarose showed noticeable shrinkage, however, the hydrogel with 2.0% agarose did not display any discernible deformation. the MXene@Hydrogel loaded with DOX (20 ppm MXene, 200 ppm DOX) was exposed to NIR irradiation while employing different concentrations of agarose. The results depicted in Figure 20b(iii) indicated that higher agarose concentrations (2.0%) led to delayed and reduced drug release, whereas lower agarose concentrations (0.5%) resulted in rapid drug release. Based on these discoveries, a MXene@Hydrogel formulation consisting of $200\ \mu g\ mL^{-1}$ DOX, 20 ppm MXene, and 1% agarose was chosen for conducting experiments related to drug release. The MXene@Hydrogel loaded with DOX demonstrated a reversible temperature increment and decrement, as depicted in Figure 20b(iv). Significantly, there was rapid release of DOX during the irradiation period (referred to as the 'on' stage), while minimal DOX release occurred in the absence of irradiation (the 'off' stage). This highlights the MXene@Hydrogel's capability to function as a NIR responsive switch. The findings show that intelligent NIR-responsive hydrogels have huge potential for targeted cancer therapy with controlled drug delivery.

A new pH/NIR multiresponsive drug delivery platform on the basis of HAP,[132,133] natural polysaccharide (CS/HA), MXene, and AuNRs[134,135] was created by Wu et al.[136] through the LbL self-assembly technique.[137,138] Natural polyelectrolytes (CS/HA)[135,139] had been alternately coated on the HAP surface[140,141] for minimizing the first burst release[142,143] of HAP. The multilayer microcapsules were subsequently coated with NIR-responsive MXene and AuNRs, resulting in an observable NIR reaction in the HAP-based vehicles.[144,145] Finally, DOX[146] was loaded into the hybrid HAP/CS/HA/MXene/AuNRs microcapsules to test their performance as smart drug carriers. To investigate the in vitro photothermal properties of hybrid microcapsules generated by NIR irradiation, photothermal conversion studies were carried out. The temperature (T) of the suspension containing HAP/CS/HA/MXene/AuNRs rises

© 2025 The Author(s). Small Science published by Wiley-VCH GmbH

26884046, 0, Downloaded from https://onlinelibrary.wiley.com/doi/10.1002/smsc.202400492 by Delhi Technological University, Wiley Online Library on [05/03/2025]. See the Terms and Conditions (https://onlinelibrary.wiley.com/terms-and-conditions) on Wiley Online Library for rules of use; OA articles are governed by the applicable Creative Commons License

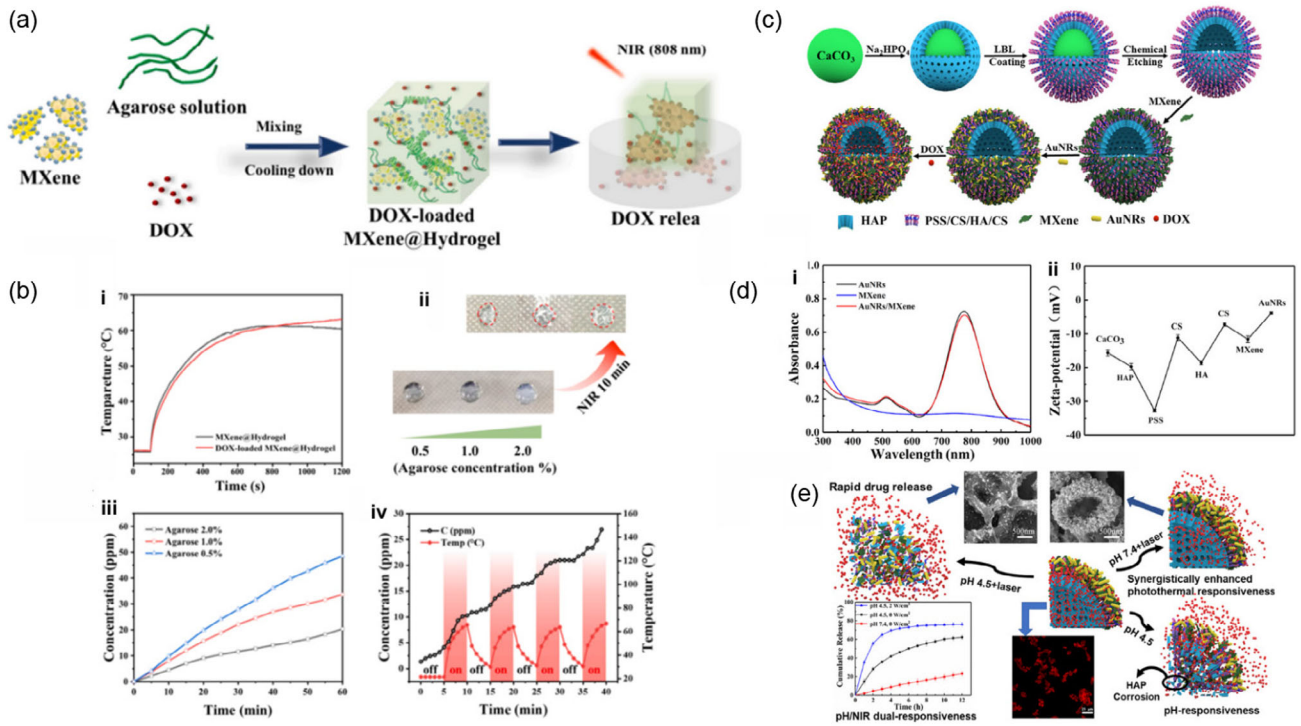

Figure 20. a) Creating a Mxene@Hydrogel loaded with DOX for NIR-controlled drug release using a schematic. b) (i) MXene@Hydrogels photothermal heating curves before and after DOX injection. (ii) The MXene@Hydrogels' melting picture exposed to a 1.5 W cm^2 laser at an 808 nm wavelength and various agarose concentrations. (iii) MXene@Hydrogels' drug release patterns that were DOX-loaded and had various agarose concentrations. (iv) The temperature alteration and release of DOX from DOX-loaded MXene@Hydrogel were assessed throughout four cycles of laser irradiation and subsequent cessation. c) Making CS, HAP, HA, MXene, and AuNRs microcapsules. d) AuNRs, MXene, and the combination of AuNRs and MXene UV–vis–NIR spectra; (i) zeta-potential evolution during HAP/CS/HA/MXene/AuNRs microcapsule preparation; (ii) HAP/CS/HA and HAP/CS/HA/MXene/AuNRs microparticle XRD patterns. e) Schematic representation of the drug release process of HAP/CS/HA/MXene/AuNRs microcapsules in response to pH and NIR. Panels (a,b) are reproduced with permission.[111] Copyright 2021, Elsevier. Panels (c–e) are reproduced with permission.[136] Copyright 2021, Elsevier. Copyright pending.

from 8.5 °C to a value of 38 °C within 60 min as the laser power was elevated from 1.0 W cm^{-2} to a value of 4.0 W cm^{-2}, demonstrating exceptional photothermal responsiveness. At pH value of 4.5, the HAP/CS/HA/MXene/AuNRs microcapsules' cumulative release reached 62.24% within time period of 12 h, whereas at pH 7.4, it was only 23.22%. Furthermore, the temperature increase induced by NIR irradiation enhanced the diffusion of DOX, resulting in an increased release from 23.22% (at 0 W cm^{-2} for 12 h) to 47.05% (at 2 W cm^{-2} for 12 h) at pH value of 7.4.[147]

Wang et al.[148] developed an implantable, NIR light-responsive composite hydrogel device that can release functional proteins on demand[149,150] to modulate receptor-mediated signaling for specific cellular behaviors (**Figure 21**). An agarose hydrogel matrix incorporates Ti_3C_2 MXene and therapeutic proteins in the system. The NIR light energy could be converted into heat by MXene, causing the matrix to go through a reversible phase transition and release the preloaded protein therapeutics. To precisely regulate cellular behaviors and desired cell fates, protein treatments' pattern and release profile may be altered by both internal components, such as agarose concentration, and exterior variables, such as NIR light intensity and irradiation period.

Moreover, this platform offers the potential to deliver diverse protein therapeutics into specific receptor-mediated cell signaling pathways, thereby enhancing tumor eradication and promoting skin wound healing. In contrast to relying on unpredictable disease indicators such as pH value, enzymes, and redox environment, this system relies on precise and controlled external stimuli, like NIR light, for activation. Furthermore, alterations in patient illness indicators have no substantial impact on the system, ensuring therapy efficacy. Because of the depth at which NIR light penetrates tissue, the MXene@hydrogel/protein platform offers more benefits and universality than UV light-responsive hydrogels and can be used to treat deep-tissue cancers in vivo in addition to the therapeutic healing of epidermal wounds. Overall, the work shows that the MXene@hydrogel/protein system has great potential as a smart drug delivery method for precision therapeutics in both cancer therapy and regenerative medicine.

Dai et al.[105] studied the Ta_4C_3-based composite MXene ($MnOx/Ta_4C_3$) for its potential therapeutic and diagnostic uses against cancer.[151,152] The ultrathin 2-dimensional Ti_3C_2 MXene NSs were created using a 2-step exfoliation of bulk Ta_4AlC_3 MAX-phase ceramic[153] utilizing HF etching and TPAOH intercalation. (**Figure 22**a). The —OH groups on the

© 2025 The Author(s). Small Science published by Wiley-VCH GmbH

26884046, 0, Downloaded from https://onlinelibrary.wiley.com/doi/10.1002/smsc.202400492 by Delhi Technological University, Wiley Online Library on [05/03/2025]. See the Terms and Conditions (https://onlinelibrary.wiley.com/terms-and-conditions) on Wiley Online Library for rules of use; OA articles are governed by the applicable Creative Commons License

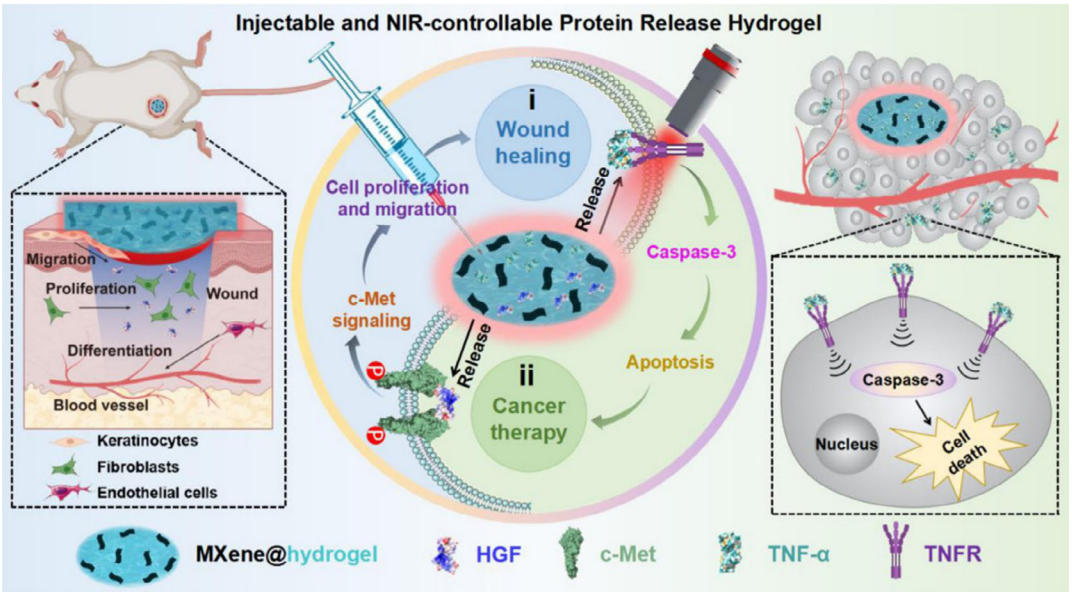

Figure 21. A schematic representation of how the implantable and light protein-releasing system which can be controlled by NIR light works. This technology permits the therapeutic protein's spatiotemporally precise on-demand discharge from an agarose hydrogel coated with Ti_3C_2 MXene. (i) Use a NIR light-controllable MXene@agarose/HGF system to remotely trigger the c-Met-mediated signaling to control cell migration, proliferation, and further increase angiogenesis and wound repair in vivo. (ii) Exogenously eradicate the deep-seated malignancies in a xenograft model by passively inducing receptor-mediated programmed cell death using the MXene@agarose/TNF- system which can be controlled by NIR light. Reproduced with permission.[148] Copyright 2021, Elsevier. Copyright pending.

surface of MXene, have reducing characteristic,[29,154] were discovered to react with $KMnO_4$, which has strong oxidizing characteristics. As a result of the redox process, paramagnetic MnOx species formed embedded on the Ta_4C_3 NSs surface. For enhancing stability, composite NSs surface has been altered with the soybean phospholipid (SP), resulting in the formation of MnOx/Ta_4C_3-SP. Due to tumors' enhanced permeability and retention (EPR), these precisely made composite NSs display a structure-property correlation that is advantageous for cancer theragnostic. For MR imaging of malignancies, the pH-responsive contrast agents are the surface-anchored paramagnetic MnOx components. TEM images revealed a strong bonding between the sheet-like structure of MnOx and the Ta_4C_3 NSs' surface, achieved through a redox interaction between reducing —OH groups and MnO_4-ions (Figure 22b). The CT imaging of tumor-bearing mice demonstrated a notable enhancement in contrast upon MnOx/Ta_4C_3-SP composite NSs' injection, as evidenced by the increase in Hounsfield Unit (HU) value (as depicted in Figure 22c). The researchers took mice's MR images with 4T1 tumors before and after administering MnOx/Ta_4C_3-SP composite NSs (equal to 20 mg kg^{-1}, 100 L) intravenously. They noticed a clear augmentation of the MRI signal in the tumor tissues over the next 60 min following the injection, as well as comparable increases in T1-weighted MR images. (as shown in Figure 22e). Also, to gauge the effect of MnOx/Ta_4C_3–SP composite NSs in the photothermal treatment of tumors in 4T1 breast tumors, mice were split into four groups and given different treatments before being exposed to NIR laser for 10 min. After injecting MnOx/Ta_4C_3SP NSs, the tumors' surface temperature measurement was done utilizing an infrared thermal imaging technique. Within 10 min, the tumor's surface temperature rose to roughly 55 °C, which was sufficient to kill the tumor. The mice's weights were consistently recorded after various treatments (as shown in Figure 22f,g), and it was discovered that mice which have been treated with the MnOx/Ta_4C_3–SP NSs and 808 nm laser radiation had substantially inhibited tumor growth. In contrast, other three groups did not exhibit any significant inhibitory effects on tumor growth. These results indicate that these NSs can be extremely useful for further PTT guiding and monitoring.

Zhang et al.[155] fabricated Ti_3C_2/g-C_3N_4[156–159] nanocomposite films that integrate PTT and oxygen-generating improved PDT in situ. The Al layer was eliminated from 2D Ti_3C_2 NSs using HF aqueous solution,[114,160,161] and the resulting Ti_3C_2 sheets were then intercalated with tetrapropylammonium hydroxide (TPAOH) solution to yield ultrathin Ti_3C_2 NSs. From bulk g-C_3N_4 that was produced using the thermal decomposition process, liquid-phase stripping was utilized to generate few-layer-structured g-C_3N_4 NSs. The electrostatic self-assembly method was used to produce the heterostructured Ti_3C_2/g-C_3N_4 NSs. The Ti_3C_2 incorporation to g-C_3N_4 may vastly improve the material's NIR absorption, which will then enhance the light-activated catalytic action of the resulting nanomaterials to produce higher levels of ROS. Triphenylphosphonium bromide was utilized to further alter Ti_3C_2/g-C_3N_4 (Ti_3C_2/g-C_3N_4-TPP) to produce a mitochondria-targeted and ROS-augmented nanomedicine to work in tandem with PTT to fight cancer. Under NIR irradiation, the hybrid PDT can be realized. Ti_3C_2/g-C_3N_4 NSs could split intrinsic water in type II PDT under low lighting to generate large amounts of oxygen. As a result, energy transfer

© 2025 The Author(s). Small Science published by Wiley-VCH GmbH

26884046, 0, Downloaded from https://onlinelibrary.wiley.com/doi/10.1002/smsc.202400492 by Delhi Technological University, Wiley Online Library on [05/03/2025]. See the Terms and Conditions (https://onlinelibrary.wiley.com/terms-and-conditions) on Wiley Online Library for rules of use; OA articles are governed by the applicable Creative Commons License

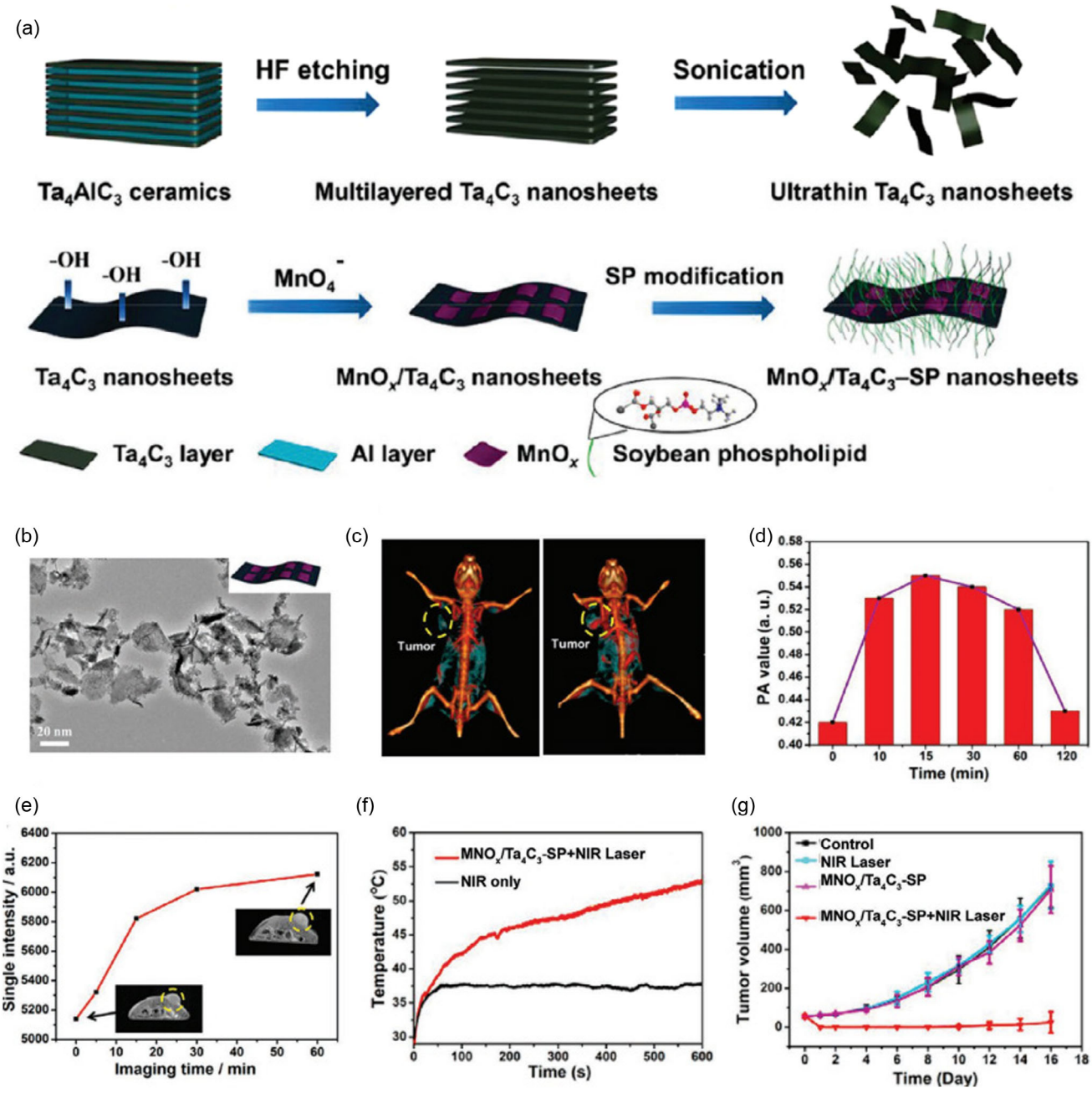

Figure 22. The layout, synthesis, testing, and use of MnOx/Ta_4C_3-SP composite membranes for the photothermal hyperthermia of cancer in vitro and in vivo. a) Schematic representation of the MnOx/Ta_4C_3-SP nanocomposite's fabrication process. b) TEM pictures of NSs made of MnOx/Ta_4C_3. c) Mice in vivo 3D tomography scans taken both prior to and postreceiving MnOx/Ta_4C_3-SP thin sheets intravenously. After receiving the nanocomposites intravenously for extended periods of time, 4T1 tumor-bearing animals showed changes in their d) PA signal values, and e) MRI signal intensity. f) IR thermal raised temperature curves under 808 nanometers laser irradiation at the tumor locations of nude mice implanted with 4T1 breast cancer cells. g) Variations in the relative tumor volume following various administrations. Reproduced with permission.[105] Copyright 2017, ACS. Copyright pending.

from O_2 to 1 O_2 starts the production of cytotoxic 1 O_2. To produce photoactivated holes and electrons, g-C_3N_4's valence band electrons (VB) excited the conduction band (CB) using the type I PDT. Water molecules and the excited holes interacted to form OH species. Furthermore, the Schottky junction between g-C_3N_4 and Ti_3C_2 enables energized electrons from g-C_3N_4 to transfer to Ti_3C_2, resulting in the production of ROS as O_2 is reduced.[162–164]

Ti_3C_2/g-C_3N_4 nanocomposites at different concentrations demonstrated a potent photothermal action under 808 nm laser irradiance. In comparison to unmodified Ti_3C_2 NSs, the Ti_3C_2/g-C_3N_4 nanocomposite exhibited a significant increase in zeta

© 2025 The Author(s). Small Science published by Wiley-VCH GmbH

26884046, 0, Downloaded from https://onlinelibrary.wiley.com/doi/10.1002/smsc.202400492 by Delhi Technological University, Wiley Online Library on [05/03/2025]. See the Terms and Conditions (https://onlinelibrary.wiley.com/terms-and-conditions) on Wiley Online Library for rules of use; OA articles are governed by the applicable Creative Commons License

potential, rising from −4.5 to −22.4 mV during in vitro experiments. Additionally, following surface modification with TPP and PEGNH2, the zeta potential rose more than 2.5 times, from −3.0 to 7.6 mV. With this modification, the nanocomposites gained excellent physiological stability in the crucial in vivo study mediums of PBS (pH value equal to 7.4 at 10 mm), FBS, and DMEM. The Ti_3C_2/g-C_3N_4-TPP nanocomposites demonstrated potent antitumor activity in vivo through the use of multimode PDT and PTT on mice. The Ti_3C_2/g-C_3N_4-TPP-treated group did not exhibit any abnormal blood biochemical indexes, indicating that the composite did not significantly cause renal and hepatic cytotoxicity. Examination of the vital tissues via H&E staining showed no major inflammation or pathological toxicity upon intravenous administration of the NSs after two weeks. These results validated that Ti_3C_2/g-C_3N_4-TPP nanocomposites are biocompatible. The research conducted has expanded the potential uses of g-C_3N_4 in PDT as a means of combating cancer. Additionally, it has contributed significantly to the development of PDT PS that are adaptable and capable of overcoming the limitations associated with tumor hypoxia, which has been made possible through the utilization of photocatalytic nanosystems.

Tao et al.[165] created a self-assembled polymer micelles for simultaneous loading of Combretastatin A-4 (CA4)[166] and Ti_3C_2 to provide combined treatment for tumor cells. (**Figure 23**). In DI water, poly(d,l-lactide) (PDLLA)-PEG-PDLLA[97,167,168] was distributed, and the copolymer spontaneously self-assembled to form poly(d,l-lactide)-poly(ethyleneglycol)-poly(d,l-lactide) (PLEL) micelles. When loading effectiveness was around 99.6%, the hydrophobic drug was then added to the copolymer micelle's hydrophobic core to improve solubility. PLEL micelle structures were present in the solution used to dissolve CA4, and Ti_3C_2 NSs were added to this solution to form the Ti_3C_2/CA4@copolymer micelles. At a laser power value equal to 1 W cm^{-2}, the synthetic micellar hydrogel demonstrated a potential photothermal effectiveness of 41.4%. It could change at body temperature from sol to polymer. The impact of PTT was observed to be significantly affected by the extremely thin MXene structure and the use of thermal therapy. The efficacy of the hydrogel was examined in 4T1 tumor-implanted rodents. After being subjected to 1.0 W cm^{-2} of radiation from a 1064 nm NIR laser, the tumor's temperature rose to 51.3 °C in less than five minutes. Using the Live/Dead staining method (Figure 23), Calcein AM and PI, which have green and red luminescence, respectively, were used to evaluate the ability of Ti_3C_2 NSs to induce hyperthermia. Nearly all of the 4T1 cells were killed when treated with Ti_3C_2 and subjected to 1064 nm irradiance, while the other groups did not show significant levels of cell damage. Free CA4 has been demonstrated to have a rapid clearance rate and an unfavorable dispersion in the ecological environment. However, the hydrogel encapsulation enhanced its absorption by cells.[169,170]

Also, when the fluorescent probe Cy5 was enclosed inside the micelles, the rate of cellular internalization of the micelles gradually increased. Due to augmented retention and prolonged release of the drug, the CA4@copolymermicellar hydrogel had a stronger anticancer action than that of the unbound medication. In contrast to other groups treated, the Ti_3C_2/CA4@PLEL hydrogel + NIR group had higher levels of apoptosis, 5 days after the start of the therapy, based on the analysis of apoptosis/necrosis in 4T1 cancers. CD31 staining was additionally utilized to track angiogenesis. The study revealed that there were fewer vessels in the CA4-treated groups than in the control groups (Figure 23). Ultimately, this study discovered that PTT and interruption of blood supply together had a complementary effect on cancer eradication.

Pan et al.[171] devised biomaterials with various uses for the simultaneous obliteration of bone tumor cells[172] and the bone cell regeneration by assimilating Ti_3C_2 MXenes[74,173,174] into 3D-printed bioactive glass scaffolds (TBGS).[173,175,176] The initial large-scale Ti_3AlC_2 ceramics were subjected to HF etching, and then exfoliated using tetrapropylammonium hydroxide (TPAOH) to produce these 2D ultrathin Ti_3C_2 NSs. BGSs were incorporated with Ti_3C_2 NSs at high initial concentrations to produce a suitable amount for photothermal ablation (**Figure 24**a,b,d). The viability of cells in the laser only, BGS, BGS + laser, and TBGS groups ranged from ≈90 to 100%, exhibiting no noticeable difference compared to the control group

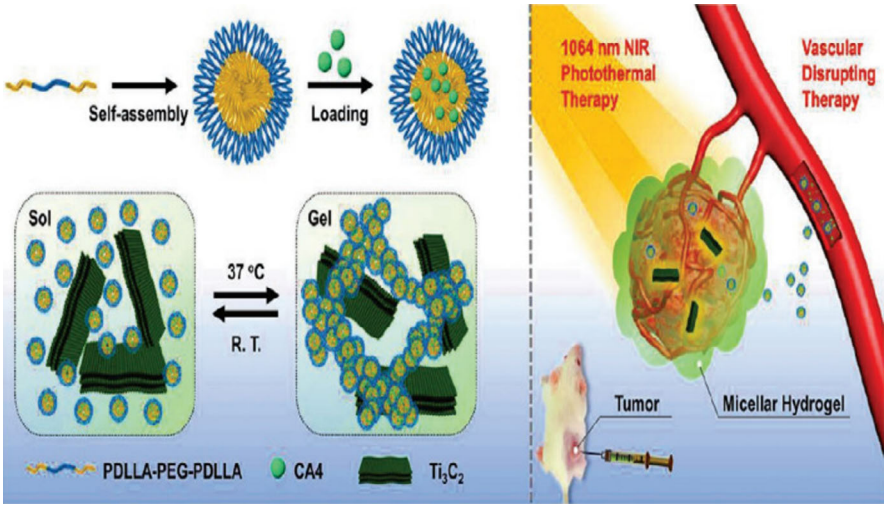

Figure 23. PLEL-based implantable micellar hydrogels containing CA4 and Ti_3C_2 MXene are being developed for PTT and vascular disruption therapy. Reproduced with permission.[171] Copyright 2020, Wiley-VCH. Copyright pending.

© 2025 The Author(s). Small Science published by Wiley-VCH GmbH

26884046, 0, Downloaded from https://onlinelibrary.wiley.com/doi/10.1002/smsc.202400492 by Delhi Technological University, Wiley Online Library on [05/03/2025]. See the Terms and Conditions (https://onlinelibrary.wiley.com/terms-and-conditions) on Wiley Online Library for rules of use; OA articles are governed by the applicable Creative Commons License

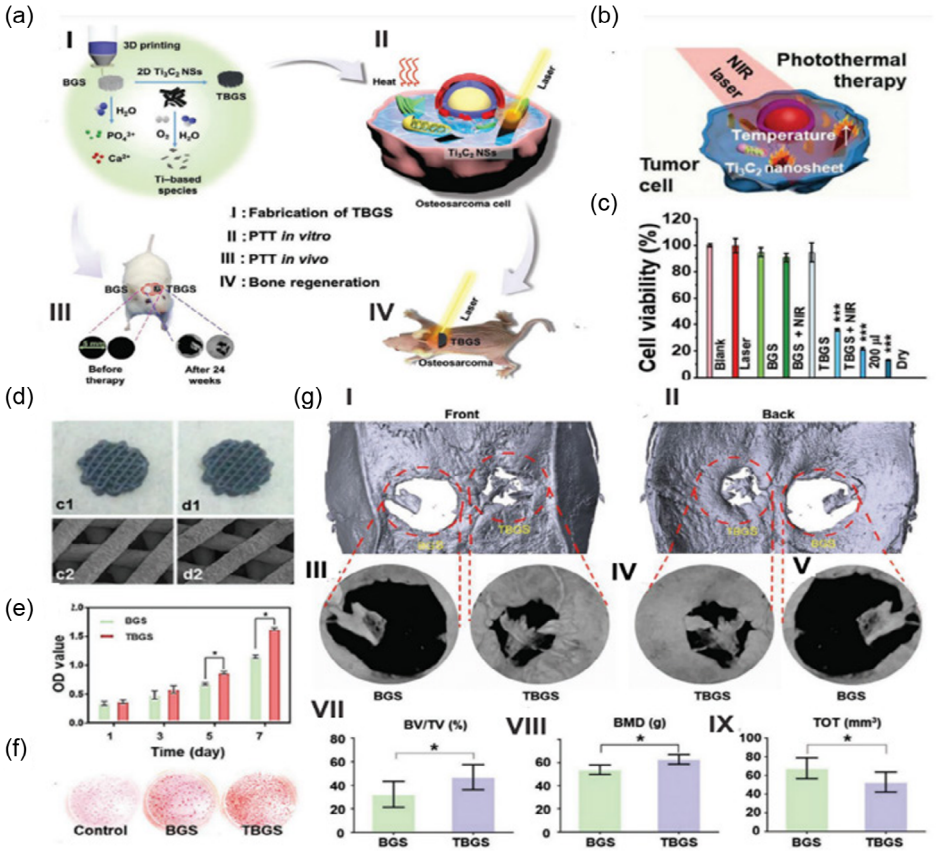

Figure 24. a) Ti_3C_2 MXene-integrated bioactive glass scaffold (TBGS) was designed and created with the intention of destroying bone cancer and regenerating bone tissue. I) The process for making TBGS, which includes 3-dimensional printing a pure bioactive glass scaffold (BGS), integrating Ti_3C_2 MXenes, and degrading those materials on the BGS. By PTT, osteosarcoma cells were eliminated using TBGS in vitro (II) as well as in vivo (III) (III). IV) Bone tissue repair following TBGS and BGS implantation. b) Diagram showing the removal of malignant cells by Ti_3C_2 NSs present on TBGS. c) The relative cell viability of Saos-2 bone tumor cells following therapy under various circumstances. The "200 L" and "Dry" groups refer to the TBGS + NIR group in a dry environment (no DMEM) and 200 L Dulbecco's modified Eagle's medium, respectively. 400 L of DMEM were used for the other groups' experiments. d) Pure BGS (c1, c2) and TBGS pictures captured in photos and SEM scans (d1, d2). Scale bars for images are 3 mm and 500 m, respectively. e) The growth rate of human bone marrow mesenchymal stem cells (hBMSCs) was assessed using the widely used CCK-8 assay, with three replicates performed. f) The deposition of mineralized calcium during osteogenic differentiation has been assessed using Alizarin Red S getting stained at day 21 for the control group, the BGS group, and the TBGS group. The prevalence of red calcium nodules in the TBGS suggests that hBMSCs are capable of becoming osteoblasts in vitro. g) The effectiveness of BGS and TBGS for in vivo osteogenesis. (I,II) 24 weeks after scaffold implantation, 3D-reconstructed circular cranial bone deficiencies. (III-VI) Micro-CT pictures of 5 mm-diameter cranial defect locations at week 24 following surgery. VII) The neonatal osseous tissue volume percentage to the total volume of the defect (BV/TV) (n equals 6). Figures VIII and XI display the measurements of BMD and total porosity (TOT) in newborn osseous tissue, with a sample size of six ($n = 6$). *$p < 0.05$, **$p < 0.01$, ***$p < 0.001$. Reproduced with permission.[171] Copyright 2020, Wiley-VCH. Copyright pending.

(blank) showing the produced TBGSs' outstanding biocompatibility (Figure 24c). Particularly, the cells on BGSs had significantly lesser filopodia than the 2hBMSCs[177] on TBGSs. TBGSs also were more biocompatible and proficient in facilitating cell growth, as quantified by the standard CCK-8 assay (Figure 24e). Alizarin red assay[178] was utilized to evaluate the extracellular matrix mineralization of hBMSCs in the TBGSs, BGSs, and control groups. The findings show the presence of significantly more calcium nodules in the TBGS group, revealing that TBGS augmented the osteogenic capacity of hBMSCs in vitro (in Figure 24f). Moreover, the biodegradation of Ti_3C_2 MXenes into bioactive minerals such as PO_4^{3+} and Ca^{2+} resulted in the formation of Ti-based species, which facilitated the acceleration of new bone formation. After implantation for 24 weeks, microcomputed tomography (micro-CT) analysis of the posterior and anterior aspects of the skull demonstrated that the TBGS exhibited a more effective bone regeneration effect in comparison to the bioactive glass (BGS) without MXenes (Figure 24g(I–VI)).[64] The exceptional osteogenic efficiency of TBGS is highlighted by an elevated level of bone mineral density (BMD) and a greater proportion of newly formed bone cells to volume of the bone defect (BV/TV) in TBGS compared to BGS (Figure 24g (VII-IX)). With the ability to both eradicate tumors and grow new bone cells, these composite scaffolds that

© 2025 The Author(s). Small Science published by Wiley-VCH GmbH

26884046, 0, Downloaded from https://onlinelibrary.wiley.com/doi/10.1002/smsc.202400492 by Delhi Technological University, Wiley Online Library on [05/03/2025]. See the Terms and Conditions (https://onlinelibrary.wiley.com/terms-and-conditions) on Wiley Online Library for rules of use; OA articles are governed by the applicable Creative Commons License

contain Ti_3C_2 MXene have enormous potential to treat bone cancers. Additionally, this broadens the scope of 2-dimensional MXenes' tissue engineering applications in biomedicine.

Lin et al.[74] showcased the remarkable effectiveness of 2-dimensional niobium carbide (Nb_2C) MXene in vivo for the eradication of mouse cancer grafts using photothermal ablation, employing NIR-I as well as NIR-II wavelengths. MXene was produced employing a simple and extensible liquid exfoliation method involving two sequential steps that combines sequential layer separation and insertion processes. To assess the depth of tissue penetration within the NIR-I and NIR-II biowindows, the measurement of laser energy intensity was performed following irradiation of chicken breast muscles. These muscle samples served as models for biological tissues (**Figure 25**a,b). The study assessed the effectiveness of Nb_2C NSs in harnessing deep-tissue photothermal energy within the NIR-I and NIR-II ranges. This

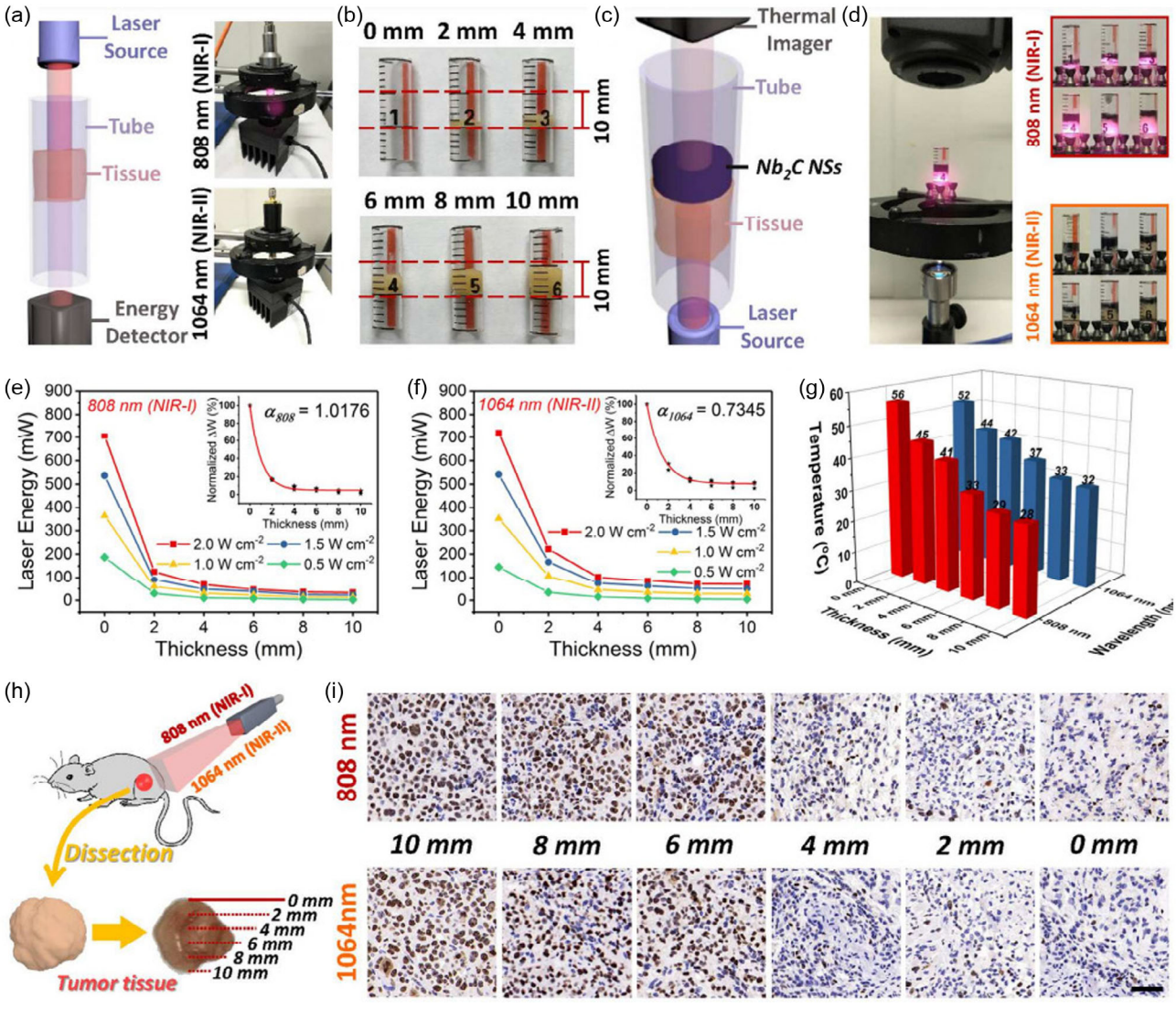

Figure 25. Assessment of In Vitro and In Vivo Tissue Penetration Depth for NIR-I and NIR-II Photothermal Conversion. a) A schematic representation and the experimental setup used to evaluate the tissue penetration capability of NIR lasers at 808 nm and 1064 nm. b) Chicken breast tissues of varying thicknesses (0, 2, 4, 6, 8, and 10 mm) placed in transparent tubes for analysis. c) Schematic illustration and d) corresponding equipment for demonstrating the photothermal conversion of Nb_2C NSs aqueous suspensions upon exposure to tissue-penetrated NIR laser (1.0 W cm^{-2}, 80 μg mL^{-1}). e) Energy intensities of NIR-I (808 nm) laser transmitted through tissues of different thicknesses, with an inset showing normalized penetrated NIR-I energy at varying depths. The attenuation coefficient (α808) for 808 nm NIR-I laser is indicated. f) Energy intensities of NIR-II (1064 nm) laser transmitted through tissues of varying thicknesses, with an inset displaying normalized penetrated NIR-II energy at different depths. The attenuation coefficient (α1064) for 1064 nm NIR-II laser is noted. g) Temperature increase in Nb_2C NSs aqueous suspensions following exposure to tissue-penetrated NIR-I and NIR-II lasers, demonstrating photothermal conversion. h) Schematic representation of in vivo tumor tissue penetration for photothermal conversion using NIR-I and NIR-II. i) Immunofluorescence staining of the Ki-67 antigen to assess cellular proliferation at different depths (0, 2, 4, 6, 8, and 10 mm) within dissected tumor tissues. All images maintain a consistent scale bar of 50 μm. Reproduced with permission.[74] Copyright 2017, ACS. Copyright pending.

© 2025 The Author(s). Small Science published by Wiley-VCH GmbH

26884046, 0, Downloaded from https://onlinelibrary.wiley.com/doi/10.1002/smsc.202400492 by Delhi Technological University, Wiley Online Library on [05/03/2025]. See the Terms and Conditions (https://onlinelibrary.wiley.com/terms-and-conditions) on Wiley Online Library for rules of use; OA articles are governed by the applicable Creative Commons License

evaluation involved exposing chicken breast muscle to laser irradiation (see Figure 25c). An infrared camera was used for recording the infrared thermographs following 5 min of 808 and 1064 nm laser irradiation (at a value of 1 W cm^{-2}) on 100 L of aq. solutions of dispersed Nb_2C NSs (see Figure 25d). When the energy remains of the NIR-I and NIR-II lasers were evaluated after passing via the tissues with varied thickness, the NIR-I laser with a value of 808 nanometers showed a greater absorption propensity than the 1064 nm NIR-II laser. (Figure 25e,f). The calculated attenuation coefficients for the NIR-I and NIR-II fitting curves for 808 and 1064 nm lasers, respectively, are 1.02 and 0.73 (Figure 25e,f, inset). These values show the possibility to efficiently heat the Nb_2C NSs solution without significantly raising the temperature of the cell. The temperature changes observed in different tissue layers when exposed to NIR-I and NIR-II laser radiation tell about the NIR-II laser causing less reduction in photothermal heating in comparison to the NIR-I laser when passed via tissues of similar thickness (Figure 25g).

To establish the optimal depth of tissue penetration for photothermal ablation using NIR-I and NIR-II, mice with 4T1 tumor grafts were exposed to laser irradiation at wavelengths of 808 or 1064 nm. The outcomes of these experiments are illustrated in Figure 25h. Posttreatments, the tumor cells were divided to examine the levels to which the cancerous tissue was growing cells. This showed that a subcutaneous xenograft tumor could be effectively photothermally abated in nude mice at a depth of 4 mm (Figure 25i). Utilizing Nb_2C-PVP NSs for thermal therapy that penetrates deep tissue in biological windows of NIR-I and NIR-II, has a large potential, as shown by the calculation by Bashkatov et al.[179]

Pan et al.[180] created a MXene wherein NaErF4:0.5%Tm@NaLuF4[181,182] NPs had been loaded over the Ti_3C_2 NSs surface for PTT guided by NIR-IIb (1530 nm) and MRI. To create the ultrathin Ti_3C_2 MXene NSs, a 2-step exfoliation procedure was adopted. As a result, nanosized MXene NSs with appropriate planar size and dispersity were produced, in line with the criteria of biomedical research. A conventional solvothermal approach was used to create NaErF4:0.5%Tm@NaLuF4 NPs. The NaErF4:0.5%Tm@NaLuF4 NPs' initial OA ligands were substituted with HCl, which caused the NPs to move from oil to the aqueous phase and, after that, combine with Ti_3C_2 NSs to produce NaErF4@Ti_3C_2 nanocomposites through electrostatic interactions (**Figure 26**A). The in vitro T2-weighted NaErF4@Ti_3C_2's MRI performance at various doses was examined to assess the capacity of NaErF4@Ti_3C_2 to be an efficient MRI contrast agent. As the concentration of NaErF4@Ti_3C_2 composites rises, the pattern, which depicts the strength of the MR signal, becomes darker. These results imply the possibility of NaErF4@Ti_3C_2 nanocomposites serving as effective contrast agents in high-field T2-weighted MRI. When excited by an 808 nm laser, the NIR-IIb signals (1500 nm long pass (LP)) were sufficiently bright for passing through the 3–5 mm deep tissue, enabling high-contrast and high-resolution imaging. The liver and spleen displayed legible light signals within 1 min of injection. The EPR effect led to 1525 nm luminous signals appearing at the tumor location after about 45 min, which indicates that the nanocomposites had begun concentrating in the tumor (Figure 26B). The imaging data was used to usher

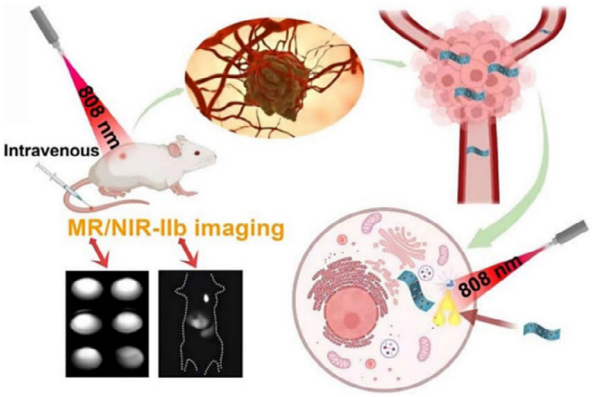

Figure 26. Schematic diagram illustrating the fabrication process of NaErF$_4$@Ti_3C_2 nanocomposites for NIR-II fluorescence imaging-guided PTT in tumor treatment. Reproduced with permission.[180] Copyright 2022, ACS. Copyright pending.

subsequent photothermal treatment. Based on their great photothermal conversion capacity (equal to 43.62% at a value of 808 nm irradiation) and photothermal stability, the proposed composites had been studied more for efficacy with an inhibition ratio equal to 92.9%, which was proven both in vivo and in vitro systematically. Also, there was no detectable nanocomposite toxicity at the administered dose. This research demonstrated the potential of the various MXene-based multifunctional nanomaterials applications in cancer therapy in addition to enhancing their effectiveness.

Figure 27a depicts the scheme developed by Chang et al.[183] which suggests combining Ti_3C_2-MXene-Au nanomedicine with OX40 mAb to create a triad of enzyme dynamic/photothermal/antitumor immune synergistic therapy for TNBC[184] Ti_3C_2-MXene-Au nanocomposites were able to build up at the tumor tissue following biodistribution from IV administration and attained PA/thermal dual-modality imaging in vivo in the interim, owing to the improved retention and permeability effect (EPR) for nanostructures. Laser irradiation would cause localized heating at the tumor tissue for thermal ablation and would expedite the catalysis reaction to yield hydroxyl radicals (·OH), which would cause cancer cell cells to undergo necrosis and apoptosis. Additional administration of OX40 mAb enhanced T cell antitumor immunoreactivity and alleviated tumor cell-mediated immunosuppression. As a result, a safe and dynamic Ti_3C_2-MXene-Au system was developed that facilitates NIR-triggered simultaneous EDT, PTT, and immunotherapy to eliminate cancer cells. Figure 27b displays TEM images revealing a slight bending of Ti_3C_2-MXene Au, characterized by higher electron density, within the cytoplasm. This indicates that Ti_3C_2-MXene Au can easily penetrate and accumulate in tumor cells. By examining 4T1 cells subjected to different treatments, DAMPs expression having CRT, HMGB1, and ATP, which are essential for dendritic cell (DC) maturation and subsequent activation of immunogenic cell death (ICD)-induced antitumor immunity, could be detected.[185–188] In comparison to other groups treated, the Ti_3C_2-MXene-Au + NIR group showed a greater level of HMGB1 discharge from 4T1 cells and stronger fluorescence intensity for CRT. Figure 27c shows that at a conc. of

© 2025 The Author(s). Small Science published by Wiley-VCH GmbH

26884046, 0, Downloaded from https://onlinelibrary.wiley.com/doi/10.1002/smsc.202400492 by Delhi Technological University, Wiley Online Library on [05/03/2025]. See the Terms and Conditions (https://onlinelibrary.wiley.com/terms-and-conditions) on Wiley Online Library for rules of use; OA articles are governed by the applicable Creative Commons License

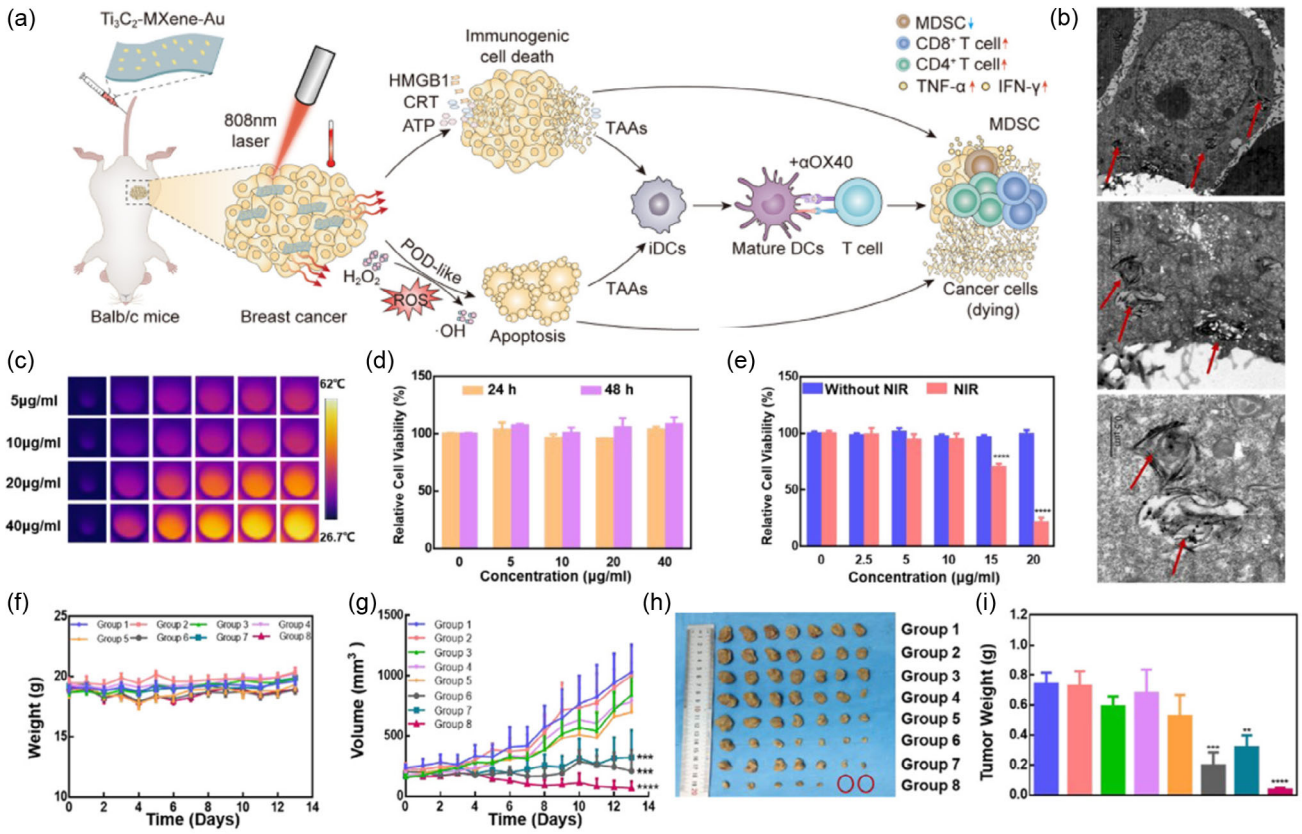

Figure 27. a) Mechanism of the PTT/EDT/immunotherapy triune Ti_3C_2-MXene-Au nanoplatform. b) TEM pictures of a tumor cell containing Ti_3C_2-MXene-Au. c) Ti_3C_2-MXene-Au thermal pictures at different concentrations after laser irradiation. d) The relative viability of MCF10A cells after being exposed to Ti_3C_2-MXene-Au nanocomposites. e) 4T1 cells relative viabilities exposed to laser irradiation and Ti_3C_2-MXene-Au. f, g) Body weights and tumor development in mice which have been implanted with the 4T1 tumor and given various treatments. h) On day 14, representative photographs of tumors in various groups were captured: group 1 – PBS, group 2 – Ti_3C_2-MXene−Au, group 3 – αOX40, group 4 – Ti_3C_2-MXene−Au + αOX40, group 5 – PBS + NIR, group 6 – Ti_3C_2-MXene−Au + NIR, group 7 – αOX40 + NIR, and group 8 – Ti_3C_2-MXene−Au + αOX40 + NIR. i) Measurement of tumor weight was performed on day 14 to quantify the tumor mass. Reproduced with permission from Ref.[183], Copyright 2022, ACS. Copyright pending.

40 μg mL^{-1}, the Ti_3C_2-MXene−Au exhibited a substantial temperature rise from 26.7 to 62 °C when exposed to laser power density equal to 1.5 W cm^{-2} for a time period of 5 min. In contrast, the change in temperature of DI water was ≈5.6 °C, which aligned with the results obtained from the infrared thermal camera measurements. MCF-10 A cells have been given an exposure to the nanocomposites for 24 and 48 h, and no toxicity was observed according to CCK-8 detection, depicted in Figure 27d, indicating that the nanocomposites were safe for use. When irradiated with laser, the Ti_3C_2-MXene−Au nanocomposites exhibited toxicity to 4T1 and MDA-MB-231 cells which was found to be concentration dependent, as depicted in Figure 27e. Anticancer characteristic of combined PTT/EDT treatment was showcased by annihilation of ≈80% of 4T1 cells at 20 μg mL^{-1} concentration. Figure 27f shows infinitesimal variations in the mice weights across all groups. To estimate the therapeutic action, the volume and weight of tumors of every group were measured in Figure 27g,i. Photographs of the pertaining tumor tissues are depicted in Figure 27h.

5. Conclusion

As a result of their distinctive physical and chemical characteristics, MXenes have developed into a new subclass of 2D materials that show promise for application in various biomedical usages. The review study examines the difficulties related to their stability in physiological settings, prolonged drug release, and biodegradability and highlights recent advancements in MXene synthesis using top-down and bottom-up methods. MXene-based composites were studied for their potential in the therapy of cancer, specifically in PDT and PTT. The review paper presents an overview of MXene-based composites for PTT and PDT, such as their mechanism of action, advantages, and limitations. The MXene-based composites development has opened up new opportunities for designing and developing novel therapeutic strategies for cancer treatment. In summary, this article provides insight into MXene's current status in biomedical applications and highlights its potential as a promising material for future biomedical research.

© 2025 The Author(s). Small Science published by Wiley-VCH GmbH

26884046, 0, Downloaded from https://onlinelibrary.wiley.com/doi/10.1002/smsc.202400492 by Delhi Technological University, Wiley Online Library on [05/03/2025]. See the Terms and Conditions (https://onlinelibrary.wiley.com/terms-and-conditions) on Wiley Online Library for rules of use; OA articles are governed by the applicable Creative Commons License

Acknowledgements

The authors acknowledge funding from ACS PRF # 66838-ND7, WELCH # E-2105-20220331, and WELCH # V-E-0003-20230731.

Conflict of Interest

The authors declare no conflict of interest.

Author Contributions

Aryan Saxena: conceptualization (lead); writing—original draft (lead); writing—review & editing (lead). **Akshayat Tyagi**: conceptualization (equal); formal analysis (equal); methodology (equal); writing—original draft (equal); writing—review & editing (equal). **Sushipra Vats**: conceptualization (equal); project administration (equal); validation (lead); writing—review & editing (lead). **Ishita Gupta**: conceptualization (equal); methodology (equal); writing—original draft (equal); writing—review & editing (equal). **Akhil Gupta**: conceptualization (equal); formal analysis (equal); writing—original draft (equal); writing—review & editing (equal). **Raminder Kaur**: project administration (equal); writing—review & editing (equal). **Saurabh Kr Tiwary**: project administration (equal); resources (equal); supervision (equal); writing—review & editing (equal). **Ahmed Elzatahry**: data curation (equal); project administration (equal); supervision (equal); validation (equal); writing—review & editing (supporting). **Maninderjeet Singh**: supervision (supporting); writing—review & editing (supporting). **Alamgir Karim**: supervision (lead); writing—review & editing (lead).

Keywords

2D materials, biodegradability, cancer therapy, drugs, MXene synthesis, photoacoustic imaging photothermal therapy and photodynamic therapy

Received: September 25, 2024
Revised: December 17, 2024
Published online:

[1] K. R. Paton, E. Varrla, C. Backes, R. J. Smith, U. Khan, A. O'Neill, C. Boland, M. Lotya, O. M. Istrate, P. King, T. Higgins, S. Barwich, P. May, P. Puczkarski, I. Ahmed, M. Moebius, H. Pettersson, E. Long, J. Coelho, S. E. O'Brien, E. K. McGuire, B. M. Sanchez, G. S. Duesberg, N. McEvoy, T. J. Pennycook, C. Downing, A. Crossley, V. Nicolosi, J. N. Coleman, *Nat. Mater.* **2014**, *13*, 624.
[2] E. Gerstner, *Nat. Phys.* **2010**, *6*, 836.
[3] H. Zhang, *ACS Nano* **2015**, *9*, 9451.
[4] K. S. Novoselov, A. K. Geim, S. V. Morozov, D. Jiang, Y. Zhang, S. V. Dubonos, I. V. Grigorieva, A. A. Firsov, *Science* **2004**, *306*, 666.
[5] S.-J. Choi, I.-D. Kim, *Electron. Mater. Lett.* **2018**, *14*, 221.
[6] N. K. Chaudhari, H. Jin, B. Kim, D. San Baek, S. H. Joo, K. Lee, *J. Mater. Chem. A* **2017**, *5*, 24564.
[7] M. Naguib, M. Kurtoglu, V. Presser, J. Lu, J. Niu, M. Heon, L. Hultman, Y. Gogotsi, M. W. Barsoum, *Adv. Mater.* **2011**, *23*, 4207.
[8] X. Jiang, A. V. Kuklin, A. Baev, Y. Ge, H. Ågren, H. Zhang, P. N. Prasad, *Phys. Rep.* **2020**, *848*, 1.
[9] L. Feng, Z. Liu, *Nanomedicine* **2011**, *6*, 317.
[10] Z. M. Sun, *Int. Mater. Rev.* **2011**, *56*, 143.
[11] M. Soleymaniha, M.-A. Shahbazi, A. R. Rafieerad, A. Maleki, A. Amiri, *Adv. Healthcare Mater.* **2019**, *8*, 1801137.
[12] B. Anasori, M. R. Lukatskaya, Y. Gogotsi, *Nat. Rev. Mater.* **2017**, *2*, 16098.
[13] Q. Tao, M. Dahlqvist, J. Lu, S. Kota, R. Meshkian, J. Halim, J. Palisaitis, L. Hultman, M. W. Barsoum, P. O. Å. Persson, J. Rosen, *Nat. Commun.* **2017**, *8*, 14949.
[14] J. Zhou, X. Zha, X. Zhou, F. Chen, G. Gao, S. Wang, C. Shen, T. Chen, C. Zhi, P. Eklund, S. Du, J. Xue, W. Shi, Z. Chai, Q. Huang, *ACS Nano* **2017**, *11*, 3841.
[15] T. L. Tan, H. M. Jin, M. B. Sullivan, B. Anasori, Y. Gogotsi, *ACS Nano* **2017**, *11*, 4407.
[16] M. Khazaei, A. Ranjbar, M. Arai, T. Sasaki, S. Yunoki, *J. Mater. Chem. C Mater.* **2017**, *5*, 2488.
[17] A. D. Dillon, M. J. Ghidiu, A. L. Krick, J. Griggs, S. J. May, Y. Gogotsi, M. W. Barsoum, A. T. Fafarman, *Adv. Funct. Mater.* **2016**, *26*, 4162.
[18] X. Sang, Y. Xie, M.-W. Lin, M. Alhabeb, K. L. Van Aken, Y. Gogotsi, P. R. C. Kent, K. Xiao, R. R. Unocic, *ACS Nano* **2016**, *10*, 9193.
[19] M. R. Lukatskaya, O. Mashtalir, C. E. Ren, Y. Dall'Agnese, P. Rozier, P. L. Taberna, M. Naguib, P. Simon, M. W. Barsoum, Y. Gogotsi, *Science* **2013**, *341*, 1502.
[20] M. Ghidiu, M. R. Lukatskaya, M.-Q. Zhao, Y. Gogotsi, M. W. Barsoum, *Nature* **2014**, *516*, 78.
[21] X. Wang, S. Kajiyama, H. Iinuma, E. Hosono, S. Oro, I. Moriguchi, M. Okubo, A. Yamada, *Nat. Commun.* **2015**, *6*, 6544.
[22] X. Liang, A. Garsuch, L. F. Nazar, *Angew. Chem. Int. Ed. Engl.* **2015**, *54*, 3907.
[23] C. E. Ren, K. B. Hatzell, M. Alhabeb, Z. Ling, K. A. Mahmoud, Y. Gogotsi, *J. Phys. Chem. Lett.* **2015**, *6*, 4026.
[24] Z. W. Seh, K. D. Fredrickson, B. Anasori, J. Kibsgaard, A. L. Strickler, M. R. Lukatskaya, Y. Gogotsi, T. F. Jaramillo, A. Vojvodic, *ACS Energy Lett.* **2016**, *1*, 589.
[25] F. Shahzad, M. Alhabeb, C. B. Hatter, B. Anasori, S. Man Hong, C. M. Koo, Y. Gogotsi, *Science* **2016**, *353*, 1137.
[26] J. Halim, M. R. Lukatskaya, K. M. Cook, J. Lu, C. R. Smith, L.-Å. Näslund, S. J. May, L. Hultman, Y. Gogotsi, P. Eklund, M. W. Barsoum, *Chem. Mater.* **2014**, *26*, 2374.
[27] K. Hantanasirisakul, M.-Q. Zhao, P. Urbankowski, J. Halim, B. Anasori, S. Kota, C. Ren, M. Barsoum, Y. Gogotsi, *Adv. Electron. Mater.* **2016**, *2*, 1.
[28] M. Alhabeb, K. Maleski, B. Anasori, P. Lelyukh, L. Clark, S. Sin, Y. Gogotsi, *Chem. Mater.* **2017**, *29*, 7633.
[29] M. Naguib, V. N. Mochalin, M. W. Barsoum, Y. Gogotsi, *Adv. Mater.* **2014**, *26*, 992.
[30] V. Natu, M. Clites, E. Pomerantseva, M. Barsoum, *Mater. Res. Lett.* **2018**, *6*, 230.
[31] H. Lin, Y. Chen, J. Shi, *Adv. Sci.* **2018**, *5*, 1800518.
[32] A. Feng, Y. Yu, Y. Wang, F. Jiang, Y. Yu, L. Mi, L. Song, *Mater. Des.* **2017**, *114*, 161.
[33] L. H. Karlsson, J. Birch, J. Halim, M. W. Barsoum, P. O. Å. Persson, *Nano Lett.* **2015**, *15*, 4955.
[34] Y. Li, H. Shao, Z. Lin, J. Lu, L. Liu, B. Duployer, P. O. Å. Persson, P. Eklund, L. Hultman, M. Li, K. Chen, X.-H. Zha, S. Du, P. Rozier, Z. Chai, E. Raymundo-Piñero, P.-L. Taberna, P. Simon, Q. Huang, *Nat. Mater.* **2020**, *19*, 894.
[35] A. Parihar, A. Singhal, N. Kumar, R. Khan, Mohd. A. Khan, A. K. Srivastava, *Nanomicro Lett.* **2022**, *14*, 100.
[36] Y. Gogotsi, *Nat. Mater.* **2015**, *14*, 1079.
[37] C. Xu, L. Wang, Z. Liu, L. Chen, J. Guo, N. Kang, X.-L. Ma, H.-M. Cheng, W. Ren, *Nat. Mater.* **2015**, *14*, 1135.
[38] D. Geng, X. Zhao, Z. Chen, W. Sun, W. Fu, J. Chen, W. Liu, W. Zhou, K. P. Loh, *Adv. Mater.* **2017**, *29*, 1.
[39] Z. Liu, C. Xu, N. Kang, L. Wang, Y. Jiang, J. Du, Y. Liu, X.-L. Ma, H.-M. Cheng, W. Ren, *Nano Lett.* **2016**, *16*, 4243.

© 2025 The Author(s). Small Science published by Wiley-VCH GmbH

26884046, 0, Downloaded from https://onlinelibrary.wiley.com/doi/10.1002/smsc.202400492 by Delhi Technological University, Wiley Online Library on [05/03/2025]. See the Terms and Conditions (https://onlinelibrary.wiley.com/terms-and-conditions) on Wiley Online Library for rules of use; OA articles are governed by the applicable Creative Commons License

[40] C.-C. Lai, H. Fashandi, J. Lu, J. Palisaitis, P. O. Å. Persson, L. Hultman, P. Eklund, J. Rosen, *Nanoscale* **2017**, *9*, 17681.
[41] C.-C. Lai, R. Meshkian, M. Dahlqvist, J. Lu, L.-Å. Näslund, O. Rivin, E. Caspi, O. Ozeri, L. Hultman, P. Eklund, M. Barsoum, J. Rosén, *Acta Mater.* **2015**, *99*, 157.
[42] J. Jia, T. Xiong, L. Zhao, F. Wang, H. Liu, R. Hu, J. Zhou, W. Zhou, S. Chen, *ACS Nano* **2017**, *11*, 12509.
[43] J. Jeon, Y. Park, S. Choi, J. Lee, S. S. Lim, B. H. Lee, Y. J. Song, J. H. Cho, Y. H. Jang, S. Lee, *ACS Nano* **2018**, *12*, 338.
[44] X. Sang, Y. Xie, D. E. Yilmaz, R. Lotfi, M. Alhabeb, A. Ostadhossein, B. Anasori, W. Sun, X. Li, K. Xiao, P. R. C. Kent, A. C. T. van Duin, Y. Gogotsi, R. R. Unocic, *Nat. Commun.* **2018**, *9*, 2266.
[45] L. Wang, C. Xu, Z. Liu, L. Chen, X. Ma, H.-M. Cheng, W. Ren, N. Kang, *ACS Nano* **2016**, *10*, 4504.
[46] D. Geng, X. Zhao, L. Li, P. Song, B. Tian, W. Liu, J. Chen, D. Shi, M. Lin, W. Zhou, K. P. Loh, *2D Mater.* **2016**, *4*, 011012.
[47] Z. Wang, V. Kochat, P. Pandey, S. Kashyap, S. Chattopadhyay, A. Samanta, S. Sarkar, P. Manimunda, X. Zhang, S. Asif, A. K. Singh, K. Chattopadhyay, C. S. Tiwary, P. M. Ajayan, *Adv. Mater.* **2017**, *29*, 1700364.
[48] X. Xiao, H. Yu, H. Jin, M. Wu, Y. Fang, J. Sun, Z. Hu, T. Li, J. Wu, L. Huang, Y. Gogotsi, J. Zhou, *ACS Nano* **2017**, *11*, 2180.
[49] H. Jin, Q. Gu, B. Chen, C. Tang, Y. Zheng, H. Zhang, M. Jaroniec, S. Z. Qiao, *Chem* **2020**, *6*, 2382.
[50] C. Xu, L. Chen, Z. Liu, H. M. Cheng, W. Ren, in *2D Metal Carbides and Nitrides (MXenes): Structure, Properties and Applications*, Springer Nature **2019**, p. 89.
[51] S. Joshi, Q. Wang, A. Puntambekar, V. Chakrapani, *ACS Energy Lett* **2017**, *2*, 1257.
[52] Z. Liu, Z. Fei, C. Xu, Y. Jiang, X.-L. Ma, H.-M. Cheng, W. Ren, *Nanoscale* **2017**, *9*, 7501.
[53] A. Christensen, E. Andersen, I. Andersen, O. Dahl, M. Nielsen, M. Lehmann, T. Tokii, *Acta Chem. Scand.* **1990**, *44*, 851.
[54] Z. Zhang, F. Zhang, H. Wang, C. Ho Chan, W. Lu, J. Dai, *J. Mater. Chem. C* **2017**, *5*, 10822.
[55] B. Q. Lv, Z.-L. Feng, Q.-N. Xu, X. Gao, J.-Z. Ma, L.-Y. Kong, P. Richard, Y.-B. Huang, V. N. Strocov, C. Fang, H.-M. Weng, Y.-G. Shi, T. Qian, H. Ding, *Nature* **2017**, *546*, 627.
[56] Y. Qi, C. Meng, X. Xu, B. Deng, N. Han, M. Liu, M. Hong, Y. Ning, K. Liu, J. Zhao, Q. Fu, Y. Li, Y. Zhang, Z. Liu, *J. Am. Chem. Soc.* **2017**, *139*, 17574.
[57] C. Xu, L. Chen, Z. Liu, H.-M. Cheng, W. Ren, (Eds.: B. Anasori, Y. Gogotsi), *Bottom-Up Synthesis of 2D Transition Metal Carbides and Nitrides*, Springer International Publishing, Cham **2019**, pp. 89–109.
[58] T. Thomas, S. Pushpan, J. A. Aguilar Martínez, A. Torres Castro, N. Pineda Aguilar, A. Álvarez-Méndez, K. C. Sanal, *Ceram. Int.* **2021**, *47*, 35384.
[59] A. Sarycheva, A. Polemi, Y. Liu, K. Dandekar, B. Anasori, Y. Gogotsi, *Sci. Adv.* **2018**, *4*, 1.
[60] Y. Gogotsi, B. Anasori, *ACS Nano* **2019**, *13*, 8491.
[61] I. C. Lee, Y. C. E. Li, J. L. Thomas, M. H. Lee, H. Y. Lin, *Mater. Horiz.* **2024**, *11*, 876.
[62] V. K. Deb, U. Jain, *Drug Deliv. Transl. Res.* **2024**, *14*, 3009.
[63] Y. Wang, W. Yan, J. Zhang, Z. Li, Y. Guo, *ACS Appl. Nano Mater.* **2024**, *7*, 7345.
[64] J. Wang, Z. Li, Y. Yin, H. Liu, G. Tang, Y. Ma, X. Feng, H. Mei, J. Bi, K. Wang, Z. Chen, *J. Mater. Sci.* **2020**, *55*, 15263.
[65] Q. Xu, C. Chang, X. Wang, C. Li, Y. Chen, Y. Zhang, M. Yin, Y. Li, B. Xiong, B. Lu, *J. Mater. Sci.* **2022**, *57*, 6013.
[66] Z. Yang, L. Yang, Y. Liu, L. Chen, *Molecules* **2024**, *29*, 2383.
[67] W. J. Zhang, S. Li, V. Vijayan, J. S. Lee, S. S. Park, X. Cui, I. Chung, J. Lee, S. K. Ahn, J. R. Kim, I. K. Park, C. S. Ha, *Nanomaterials* **2022**, *12*, 4392.
[68] C. Liang, J. He, Y. Cao, G. Liu, C. Zhang, Z. Qi, C. Fu, Y. Hu, *J. Biol. Eng.* **2023**, *17*, 39.
[69] B. Lu, S. Hu, D. Wu, C. Wu, Z. Zhu, L. Hu, J. Zhang, *J. Mater. Chem. B* **2022**, *10*, 1226.
[70] X. Yang, C. Zhang, D. Deng, Y. Gu, H. Wang, Q. Zhong, *Small* **2022**, *18*, 1.
[71] H. Ouyang, X. Hong, Z. Zhou, P. Xu, H. Tang, Z. Ma, Z. Wang, X. Liao, L. He, *Phys. Chem. Chem. Phys.* **2022**, *24*, 27157.
[72] R. Kurapati, K. Kostarelos, M. Prato, A. Bianco, *Adv. Mater.* **2016**, *28*, 6052.
[73] D. Chimene, D. L. Alge, A. K. Gaharwar, *Adv. Mater.* **2015**, *27*, 7261.
[74] H. Lin, S. Gao, C. Dai, Y. Chen, J. Shi, *J. Am. Chem. Soc.* **2017**, *139*, 16235.
[75] H. Lin, Y. Wang, S. Gao, Y. Chen, J. Shi, *Adv. Mater.* **2018**, *30*, 1703284.
[76] J. Xuan, Z. Wang, Y. Chen, D. Liang, L. Cheng, X. Yang, Z. Liu, R. Ma, T. Sasaki, F. Geng, *Angew. Chem. Int. Ed. Engl.* **2016**, *55*, 14569.
[77] Z. Liu, H. Lin, M. Zhao, C. Dai, S. Zhang, W. Peng, Y. Chen, *Theranostics* **2018**, *8*, 1648.
[78] C. Dai, H. Lin, G. Xu, Z. Liu, R. Wu, Y. Chen, *Chem. Mater.* **2017**, *29*, 8637.
[79] L. Zong, H. Wu, H. Lin, Y. Chen, *Nano Res.* **2018**, *11*, 4149.
[80] Z. Li, H. Zhang, J. Han, Y. Chen, H. Lin, T. Yang, *Adv. Mater.* **2018**, *30*, 1706981.
[81] J. Shao, J. Zhang, C. Jiang, J. Lin, P. Huang, *Chem. Eng. J.* **2020**, *400*, 126009.
[82] B. Zhou, H. Yin, C. Dong, L. Sun, W. Feng, Y. Pu, X. Han, X. Li, D. Du, H. Xu, Y. Chen, *Adv. Sci.* **2021**, *8*, 2101043.
[83] W. Feng, R. Wang, Y. Zhou, L. Ding, X. Gao, B. Zhou, P. Hu, Y. Chen, *Adv. Funct. Mater.* **2019**, *29*, 1901942.
[84] G. P. Lim, C. F. Soon, N. L. Ma, M. Morsin, N. Nayan, M. K. Ahmad, K. S. Tee, *Environ. Res.* **2021**, *201*, 111592.
[85] H. Lin, X. Wang, L. Yu, Y. Chen, J. Shi, *Nano Lett.* **2017**, *17*, 384.
[86] Q. Li, W. Wang, H. Feng, L. Cao, H. Wang, D. Wang, S. Chen, *J. Colloid Interface Sci.* **2021**, *604*, 810.
[87] C. Li, D. Chu, L. Jin, G. Tan, Z. Li, *J. Biomed. Nanotechnol.* **2021**, *17*, 2014.
[88] Y. Gao, Y. Dong, S. Yang, A. Mo, X. Zeng, Q. Chen, Q. Peng, *J. Colloid Interface Sci.* **2022**, *617*, 533.
[89] C. Yu, S. Sui, X. Yu, H. Wenlong, Y. Wu, X. Zeng, Q. Chen, J. Wang, Q. Peng, *Colloids Surf. B Biointerfaces* **2022**, *217*, 112663.
[90] W. Shan, R. Chen, Q. Zhang, J. Zhao, B. Chen, X. Zhou, S. Ye, S. Bi, L. Nie, L. Ren, *Adv. Mater.* **2018**, *30*, e1707567.
[91] M. Zheng, C. Yue, Y. Ma, P. Gong, P. Zhao, C. Zheng, Z. Sheng, P. Zhang, Z. Wang, L. Cai, *ACS Nano* **2013**, *7*, 2056.
[92] C.-K. Su, C.-Y. Chen, P.-J. Tseng, Y.-C. Sun, *Biosens. Bioelectron.* **2015**, *64*, 535.
[93] H. Wang, X. Yang, W. Shao, S. Chen, J. Xie, X. Zhang, J. Wang, Y. Xie, *J. Am. Chem. Soc.* **2015**, *137*, 11376.
[94] J. Ge, M. Lan, B. Zhou, W. Liu, L. Guo, H. Wang, Q. Jia, G. Niu, X. Huang, H. Zhou, X. Meng, P. Wang, C.-S. Lee, W. Zhang, X. Han, *Nat. Commun.* **2014**, *5*, 4596.
[95] J. Wang, J. Liu, Y. Liu, L. Wang, M. Cao, Y. Ji, X. Wu, Y. Xu, B. Bai, Q. Miao, C. Chen, Y. Zhao, *Adv. Mater.* **2016**, *28*, 8950.
[96] M. Culty, H. A. Nguyen, C. B. Underhill, *J. Cell Biol.* **1992**, *116*, 1055.
[97] J. Shao, C. Ruan, H. Xie, Z. Li, H. Wang, P. K. Chu, X.-F. Yu, *Adv. Sci.* **2018**, *5*, 1700848.
[98] J. Xu, F. He, Z. Cheng, R. Lv, Y. Dai, A. Gulzar, B. Liu, H. Bi, D. Yang, S. Gai, P. Yang, J. Lin, *Chem. Mater.* **2017**, *29*, 7615.

© 2025 The Author(s). Small Science published by Wiley-VCH GmbH

26884046, 0, Downloaded from https://onlinelibrary.wiley.com/doi/10.1002/smsc.202400492 by Delhi Technological University, Wiley Online Library on [05/03/2025]. See the Terms and Conditions (https://onlinelibrary.wiley.com/terms-and-conditions) on Wiley Online Library for rules of use; OA articles are governed by the applicable Creative Commons License

[99] R. Lv, P. Yang, F. He, S. Gai, G. Yang, J. Lin, *Chem. Mater.* **2015**, *27*, 483.
[100] R. Lv, P. Yang, F. He, S. Gai, C. Li, Y. Dai, G. Yang, J. Lin, *ACS Nano* **2015**, *9*, 1630.
[101] C. Korupalli, K.-L. You, G. Getachew, A. S. Rasal, W. B. Direrса, M. Zakki Fahmi, J.-Y. Chang, *Pharmaceutics* **2022**, *14*, 304.
[102] W. Rui, C. Tao, X. Liu, *Ultrason. Sonochem.* **2020**, *66*, 105095.
[103] J. Huang, K. Pu, *Angew. Chem. Int. Ed. Engl.* **2020**, *59*, 11717.
[104] C. Coughlan, M. Ibáñez, O. Dobrozhan, A. Singh, A. Cabot, K. M. Ryan, *Chem. Rev.* **2017**, *117*, 5865.
[105] C. Dai, Y. Chen, X. Jing, L. Xiang, D. Yang, H. Lin, Z. Liu, X. Han, R. Wu, *ACS Nano* **2017**, *11*, 12696.
[106] T. Najam, S. S. A. Shah, L. Peng, M. S. Javed, M. Imran, M.-Q. Zhao, *Coord. Chem. Rev.* **2022**, *454*, 214339.
[107] H. Li, R. Fan, B. Zou, J. Yan, Q. Shi, G. Guo, *J. Nanobiotechnol.* **2023**, *21*, 73.
[108] I. S. Raja, M. S. Kang, K. S. Kim, Y. J. Jung, *Cancers* **2020**, *12*, 1657.
[109] X. Yu, X. Cai, H. Cui, S.-W. Lee, X.-F. Yu, B. Liu, *Nanoscale* **2017**, *9*, 17859.
[110] X. Yuan, Y. Zhu, S. Li, Y. Wu, Z. Wang, R. Gao, S. Luo, J. Shen, J. Wu, L. Ge, *J. Nanobiotechnol.* **2022**, *20*, 154.
[111] Y. Dong, S. Li, X. Li, X. Wang, *Int. J. Biol. Macromol.* **2021**, *190*, 693.
[112] Z. Liu, L. Xie, J. Yan, P. Liu, H. Wen, H. Liu, *Aust. J. Chem.* **2021**, *74*, 847.
[113] L. Jin, Y. Ma, R. Wang, S. Zhao, Z. Ren, S. Ma, Y. Shi, B. Hu, Y. Guo, *Mater. Today Adv.* **2022**, *14*, 100224.
[114] G. Liu, J. Zou, Q. Tang, X. Yang, Y. Zhang, Q. Zhang, W. Huang, P. Chen, J. Shao, X. Dong, *ACS Appl. Mater. Interfaces* **2017**, *9*, 40077.
[115] X. Han, J. Huang, H. Lin, Z. Wang, P. Li, Y. Chen, *Adv. Healthcare Mater.* **2018**, *7*, e1701394.
[116] D. Chen, Z. Jin, B. Zhao, Y. Wang, Q. He, *Adv. Mater.* **2021**, *33*, e2008089.
[117] S. Diao, J. L. Blackburn, G. Hong, A. L. Antaris, J. Chang, J. Z. Wu, B. Zhang, K. Cheng, C. J. Kuo, H. Dai, *Angew. Chem. Int. Ed.* **2015**, *54*, 14758.
[118] H. Cho, J. Gao, G. S. Kwon, *J. Control. Release* **2016**, *240*, 191.
[119] R. Omar, Y. L. Bardoogo, E. Corem-Salkmon, B. Mizrahi, *J. Control. Release* **2017**, *257*, 76.
[120] J. Fang, H. Yin, L. Liao, H. Qin, F. Ueda, K. Uemura, K. Eguchi, G. Y. Bharate, H. Maeda, *J. Control. Release* **2016**, *223*, 188.
[121] X. Zhu, W. Feng, J. Chang, Y.-W. Tan, J. Li, M. Chen, Y. Sun, F. Li, *Nat. Commun.* **2016**, *7*, 10437.
[122] Y. Cao, T. Wu, K. Zhang, X. Meng, W. Dai, D. Wang, H. Dong, X. Zhang, *ACS Nano* **2019**, *13*, 1499.
[123] A. Liu, Y. Liu, G. Liu, A. Zhang, Y. Cheng, Y. Li, L. Zhang, L. Wang, H. Zhou, J. Liu, H. Wang, *Chem. Eng. J.* **2022**, *448*, 137691.
[124] J. Y. R. Silva, Y. G. Proenza, L. L. da Luz, S. de Sousa Araújo, M. A. G. Filho, S. A. Junior, T. A. Soares, R. L. Longo, *Mater. Sci. Eng. C* **2019**, *102*, 578.
[125] H. Yin, X. Guan, H. Lin, Y. Pu, Y. Fang, W. Yue, B. Zhou, Q. Wang, Y. Chen, H. Xu, *Adv. Sci.* **2020**, *7*, 1901954.
[126] A. Maleki, M. Ghomi, N. Nikfarjam, M. Akbari, E. Sharifi, M.-A. Shahbazi, M. Kermanian, M. Seyedhamzeh, E. Nazarzadeh Zare, M. Mehrali, O. Moradi, F. Sefat, V. Mattoli, P. Makvandi, Y. Chen, *Adv. Funct. Mater.* **2022**, *32*, 2203430.
[127] W. Kong, Y. Niu, M. Liu, K. Zhang, G. Xu, Y. Wang, X. Wang, J. Li, *Inorg. Chem. Commun.* **2019**, *105*, 151.
[128] R.-M. Kong, L. Ding, Z. Wang, J. You, F. Qu, *Anal. Bioanal. Chem.* **2015**, *407*, 369.
[129] Z. Yu, W. K. Chan, Y. Zhang, T. T. Y. Tan, *Biomaterials* **2021**, *269*, 120459.
[130] M. Khodadadi Yazdi, A. Taghizadeh, M. Taghizadeh, F. J. Stadler, M. Farokhi, F. Mottaghitalab, P. Zarrintaj, J. D. Ramsey, F. Seidi, M. R. Saeb, M. Mozafari, *J. Control. Release* **2020**, *326*, 523.
[131] C. Kim, D. Jeong, S. Kim, Y. Kim, S. Jung, *Carbohydr. Polym.* **2019**, *222*, 115011.
[132] B. Ghiasi, Y. Sefidbakht, S. Mozaffari-Jovin, B. Gharehcheloo, M. Mehrarya, A. Khodadadi, M. Rezaei, S. O. Ranaei Siadat, V. Uskoković, *Drug Dev. Ind. Pharm.* **2020**, *46*, 1035.
[133] W. Lai, C. Chen, X. Ren, I.-S. Lee, G. Jiang, X. Kong, *Mater. Sci. Eng. C* **2016**, *62*, 166.
[134] Z. Zhang, J. Shi, Z. Song, X. Zhu, Y. Zhu, S. Cao, *J. Mater. Sci.* **2018**, *53*, 1810.
[135] S. De Koker, R. Hoogenboom, B. G. De Geest, *Chem. Soc. Rev.* **2012**, *41*, 2867.
[136] Z. Wu, J. Shi, P. Song, J. Li, S. Cao, *Int. J. Biol. Macromol.* **2021**, *183*, 870.
[137] X. Zhu, J. Shi, H. Ma, R. Chen, J. Li, S. Cao, *Mater. Sci. Eng. C* **2019**, *99*, 1236.
[138] L. Yang, J. Shi, X. Zhou, S. Cao, *Int. J. Biol. Macromol.* **2015**, *73*, 1.
[139] M. A. Kalam, *Int. J. Biol. Macromol.* **2016**, *89*, 127.
[140] L. Gu, X. He, Z. Wu, *Mater. Chem. Phys.* **2014**, *148*, 153.
[141] W. Qiao, X. Lan, J. K. H. Tsoi, Z. Chen, R. Y. X. Su, K. W. K. Yeung, J. P. Matinlinna, *RSC Adv.* **2017**, *7*, 44788.
[142] J. Wei, J. Shi, Q. Wu, L. Yang, S. Cao, *J. Mater. Chem. B* **2015**, *3*, 8162.
[143] D. Feng, J. Shi, X. Wang, L. Zhang, S. Cao, *RSC Adv.* **2013**, *3*, 24975.
[144] W. Tang, Z. Dong, R. Zhang, X. Yi, K. Yang, M. Jin, C. Yuan, Z. Xiao, Z. Liu, L. Cheng, *ACS Nano* **2019**, *13*, 284.
[145] H. Xie, P. Li, J. Shao, H. Huang, Y. Chen, Z. Jiang, P. K. Chu, X.-F. Yu, *ACS Sens.* **2019**, *4*, 2303.
[146] M. Cagel, E. Grotz, E. Bernabeu, M. A. Moretton, D. A. Chiappetta, *Drug Discov. Today* **2017**, *22*, 270.
[147] H. Ma, J. Shi, X. Zhu, Z. Zhang, J. Li, S. Cao, *Adv. Compos. Hybrid Mater.* **2019**, *2*, 242.
[148] S. Wang, Z. Zhang, S. Wei, F. He, Z. Li, H.-H. Wang, Y. Huang, Z. Nie, *Acta Biomater.* **2021**, *130*, 138.
[149] D. R. Griffin, A. M. Kasko, *J. Am. Chem. Soc.* **2012**, *134*, 13103.
[150] J. T. Robinson, S. M. Tabakman, Y. Liang, H. Wang, H. Sanchez Casalongue, D. Vinh, H. Dai, *J. Am. Chem. Soc.* **2011**, *133*, 6825.
[151] Y. Jin, Y. Li, X. Ma, Z. Zha, L. Shi, J. Tian, Z. Dai, *Biomaterials* **2014**, *35*, 5795.
[152] M. H. Oh, N. Lee, H. Kim, S. P. Park, Y. Piao, J. Lee, S. W. Jun, W. K. Moon, S. H. Choi, T. Hyeon, *J. Am. Chem. Soc.* **2011**, *133*, 5508.
[153] J. Halim, K. M. Cook, M. Naguib, P. Eklund, Y. Gogotsi, J. Rosen, M. W. Barsoum, *Appl. Surf. Sci.* **2016**, *362*, 406.
[154] M. A. Hope, A. C. Forse, K. J. Griffith, M. R. Lukatskaya, M. Ghidiu, Y. Gogotsi, C. P. Grey, *Phys. Chem. Chem. Phys.* **2016**, *18*, 5099.
[155] Y. Zhang, Y. Cheng, F. Yang, Z. Yuan, W. Wei, H. Lu, H. Dong, X. Zhang, *Nano Today* **2020**, *34*, 100919.
[156] M. Liang, T. Borjigin, Y. Zhang, H. Liu, B. Liu, H. Guo, *ACS Appl. Mater. Interfaces* **2018**, *10*, 34123.
[157] Z. Tong, D. Yang, Z. Li, Y. Nan, F. Ding, Y. Shen, Z. Jiang, *ACS Nano* **2017**, *11*, 1103.
[158] E. Ju, K. Dong, Z. Chen, Z. Liu, C. Liu, Y. Huang, Z. Wang, F. Pu, J. Ren, X. Qu, *Angew. Chem. Int. Ed.* **2016**, *55*, 11467.
[159] X. Zhang, X. Xie, H. Wang, J. Zhang, B. Pan, Y. Xie, *J. Am. Chem. Soc.* **2013**, *135*, 18.
[160] C. Peng, X. Yang, Y. Li, H. Yu, H. Wang, F. Peng, *ACS Appl. Mater. Interfaces* **2016**, *8*, 6051.
[161] Z. Lu, Y. Wei, J. Deng, L. Ding, Z.-K. Li, H. Wang, *ACS Nano* **2019**, *13*, 10535.
[162] T. Su, Z. D. Hood, M. Naguib, L. Bai, S. Luo, C. M. Rouleau, I. N. Ivanov, H. Ji, Z. Qin, Z. Wu, *Nanoscale* **2019**, *11*, 8138.

© 2025 The Author(s). Small Science published by Wiley-VCH GmbH

26884046, 0, Downloaded from https://onlinelibrary.wiley.com/doi/10.1002/smsc.202400492 by Delhi Technological University, Wiley Online Library on [05/03/2025]. See the Terms and Conditions (https://onlinelibrary.wiley.com/terms-and-conditions) on Wiley Online Library for rules of use; OA articles are governed by the applicable Creative Commons License

[163] M. Shao, Y. Shao, J. Chai, Y. Qu, M. Yang, Z. Wang, M. Yang, W. F. Ip, C. T. Kwok, X. Shi, Z. Lu, S. Wang, X. Wang, H. Pan, *J. Mater. Chem. A* **2017**, *5*, 16748.
[164] X. An, W. Wang, J. Wang, H. Duan, J. Shi, X. Yu, *Phys. Chem. Chem. Phys.* **2018**, *20*, 11405.
[165] N. Tao, L. Yandi, Y. Wu, X. Li, J. Li, X. Sun, S. Chen, Y.-N. Liu, *ACS Appl. Bio. Mater.* **2020**, *3*, 4531.
[166] J. H. Gill, K. L. Rockley, C. De Santis, A. K. Mohamed, *Pharmacol. Ther.* **2019**, *202*, 18.
[167] C. Gong, C. Wang, Y. Wang, Q. Wu, D. Zhang, F. Luo, Z. Qian, *Nanoscale* **2012**, *4*, 3095.
[168] K. Shi, B. Xue, Y. Jia, L. Yuan, R. Han, F. Yang, J. Peng, Z. Qian, *Nano Res.* **2019**, *12*, 1389.
[169] T. Liu, D. Zhang, W. Song, Z. Tang, J. Zhu, Z. Ma, X. Wang, X. Chen, T. Tong, *Acta Biomater.* **2017**, *53*, 179.
[170] Y. Wang, T. Yang, X. Wang, W. Dai, J. Wang, X. Zhang, Z. Li, Q. Zhang, *J. Control Release* **2011**, *149*, 299.
[171] S. Pan, J. Yin, L. Yu, C. Zhang, Y. Zhu, Y. Gao, Y. Chen, *Adv. Sci.* **2020**, *7*, 1901511.
[172] M. Kansara, M. W. Teng, M. J. Smyth, D. M. Thomas, *Nat. Rev. Cancer* **2014**, *14*, 722.
[173] L. Moroni, J. R. de Wijn, C. A. van Blitterswijk, *Biomaterials* **2006**, *27*, 974.
[174] M. Naguib, M. Kurtoglu, V. Presser, J. Lu, J. Niu, M. Heon, L. Hultman, Y. Gogotsi, M. W. Barsoum, *Adv. Mater.* **2011**, *23*, 4248.
[175] P. Pei, X. Qi, X. Du, M. Zhu, S. Zhao, Y. Zhu, *J. Mater. Chem. B* **2016**, *4*, 7452.
[176] A.-V. Do, B. Khorsand, S. M. Geary, A. K. Salem, *Adv. Healthcare Mater.* **2015**, *4*, 1742.
[177] P. Aghajanian, S. Mohan, *Bone Res.* **2018**, *6*, 19.
[178] W. L. Smith, C. A. Buck, G. S. Ornay, M. P. Davis, R. P. Martin, S. Z. Gibson, M. G. Girard, *Copeia* **2018**, *106*, 427.
[179] A. Bashkatov, E. Genina, V. Kochubey, V. Tuchin, *J. Phys. D Appl. Phys.* **2005**, *38*, 2543.
[180] J. Pan, M. Zhang, G. Fu, L. Zhang, H. Yu, X. Yan, F. Liu, P. Sun, X. Jia, X. Liu, G. Lu, *ACS Appl. Nano Mater.* **2022**, *5*, 8142.
[181] L. Zhang, X. Li, W. Wang, X. Zhao, X. Yan, C. Wang, H. Bao, Y. Lu, X. Kong, F. Liu, X. Liu, G. Lu, *Nano Res.* **2020**, *13*, 2803.
[182] Q. Chen, X. Xie, B. Huang, L. Liang, S. Han, Z. Yi, Y. Wang, Y. Li, D. Fan, L. Huang, X. Liu, *Angew. Chem. Int. Ed. Engl.* **2017**, *56*, 7605.
[183] X. Chang, Q. Wu, Y. Wu, X. Xi, J. Cao, H. Chu, Q. Liu, Y. Li, W. Wu, X. Fang, F. Chen, *Nano Lett.* **2022**, *22*, 8321.
[184] P. Sharma, *Oncologist* **2016**, *21*, 1050.
[185] B. Yang, J. Gao, Q. Pei, H. Xu, H. Yu, *Adv. Sci.* **2020**, *7*, 2002365.
[186] J. Gao, W.-Q. Wang, Q. Pei, M. S. Lord, H.-J. Yu, *Acta Pharmacol. Sin.* **2020**, *41*, 986.
[187] X. Hu, B. Hou, Z. Xu, M. Saeed, F. Sun, Z. Gao, Y. Lai, T. Zhu, F. Zhang, W. Zhang, H. Yu, *Adv. Sci.* **2020**, *7*, 1903332.
[188] A. Gao, B. Chen, J. Gao, F. Zhou, M. Saeed, B. Hou, Y. Li, H. Yu, *Nano Lett.* **2020**, *20*, 353.
[189] G. Ma, H. Shao, J. Xu, Y. Liu, Q. Huang, P.-L. Taberna, P. Simon, Z. Lin, *Nat. Commun.* **2021**, *12*, 5085.
[190] H. Jing, H. Yeo, B. Lyu, J. Ryou, S. Choi, J.-H. Park, B. H. Lee, Y.-H. Kim, S. Lee, *ACS Nano* **2021**, *15*, 1388.
[191] J. T. Lee, B. C. Wyatt, G. A. Davis Jr., A. N. Masterson, A. L. Pagan, A. Shah, B. Anasori, R. Sardar, *ACS Nano* **2021**, *15*, 19600.
[192] W.-J. Sun, Y.-Y. Zhao, X.-F. Cheng, J.-H. He, J.-M. Lu, *ACS Appl. Mater. Interfaces* **2020**, *12*, 9865.
[193] J. E. Heckler, G. R. Neher, F. Mehmood, D. B. Lioi, R. Pachter, R. Vaia, W. J. Kennedy, D. Nepal, *Langmuir* **2021**, *37*, 5447.
[194] W. Y. Chen, S.-N. Lai, C.-C. Yen, X. Jiang, D. Peroulis, L. A. Stanciu, *ACS Nano* **2020**, *14*, 11490.
[195] Q. Zhang, W. Huang, C. Yang, F. Wang, C. Song, Y. Gao, Y. Qiu, M. Yan, B. Yang, C. Guo, *Biomater. Sci.* **2019**, *7*, 2729.
[196] A. Szuplewska, D. Kulpińska, A. Dybko, A. M. Jastrzębska, T. Wojciechowski, A. Rozmysłowska, M. Chudy, I. Grabowska-Jadach, W. Ziemkowska, Z. Brzózka, A. Olszyna, *Mater. Sci. Eng. C* **2019**, *98*, 874.
[197] X. Han, X. Jing, D. Yang, H. Lin, Z. Wang, H. Ran, P. Li, Y. Chen, *Theranostics* **2018**, *8*, 4491.
[198] Z. Liu, M. Zhao, H. Lin, C. Dai, C. Ren, S. Zhang, W. Peng, Y. Chen, *J. Mater. Chem. B* **2018**, *6*, 3541.
[199] S. Zada, W. Dai, K. Zhang, H. Lu, X. Meng, Y. Zhang, Y. Cheng, F. Yan, P. Fu, X. Zhang, H. Dong, *Angew. Chem.* **2020**, *132*, 6663.
[200] A. Zavabeti, A. Jannat, L. Zhong, A. A. Haidry, Z. Yao, J. Z. Ou, *Nanomicro Lett.* **2020**, *12*, 66.
[201] C. Xing, S. Chen, X. Liang, Q. Liu, M. Qu, Q. Zou, J. Li, H. Tan, L. Liu, D. Fan, H. Zhang, *ACS Appl. Mater. Interfaces* **2018**, *10*, 27631.

Saurabh Kr Tiwary is a Ph.D. candidate in chemical and biomolecular engineering at the University of Houston, having earned his bachelor's degree from Rajiv Gandhi Institute of Petroleum Technology, India, in 2021. As a graduate research assistant, he focuses on polymer nanocomposites, membrane technology for water purification, energy storage, and advanced materials development. His work integrates chemical engineering, materials science, biocompatibility, and nanotechnology to create innovative materials for energy, sustainability, and environmental remediation. Saurabh's research addresses critical global challenges, reflecting his dedication to advancing knowledge and developing solutions in materials science and engineering.

Ahmed Elzatahry, a research professor in the William A. Brookshire Department of Chemical and Biomolecular Engineering at the University of Houston, has over 25 years of expertise in nanomaterials and nanocomposites. His research spans mesoporous and 2D materials, advanced polymer processing, and their applications in energy, catalysis, and biomedicine. Dr. Elzatahry has authored 200+ articles, earning 16,000+ citations, and an h-index of 74. Formerly, he served as Dean at Qatar University, specifically as the Dean of the College of Arts and Sciences and the Dean of Graduate Studies. His work focuses on novel material synthesis and characterization to address complex energy and biomedical challenges.

© 2025 The Author(s). Small Science published by Wiley-VCH GmbH

26884046, 0, Downloaded from https://onlinelibrary.wiley.com/doi/10.1002/smsc.202400492 by Delhi Technological University, Wiley Online Library on [05/03/2025]. See the Terms and Conditions (https://onlinelibrary.wiley.com/terms-and-conditions) on Wiley Online Library for rules of use; OA articles are governed by the applicable Creative Commons License

Maninderjeet Singh, a postdoctoral research scientist at Columbia University, specializes in polymer physics and engineering. He earned his Ph.D. in chemical engineering from the University of Houston in 2023. His research focuses on sustainable polymeric materials for gas separation, CO_2 capture, micro- and nanoplastics, healthcare applications, high-power density energy storage, and electronic devices with expertise in nanotechnology, energy storage, self-assembly, and membrane science. Dr. Singh's interests lie in developing innovative materials for advanced applications and addressing critical challenges facing humankind through answering fundamental questions and by elucidating synthesis–structure–property relationships.

Alamgir Karim, a leading polymer scientist, earned his Ph.D. in physics from Northwestern University in 1992 and completed a postdoctoral fellowship at the University of Minnesota. At NIST, he led the Polymer Blends and Nanomaterials Group. From 2009 to 2017, he served as Goodyear Chair Professor at the University of Akron and Co-Director of the Akron Functional Materials Center. Now a Dow Chair Professor at the University of Houston, Dr. Karim directs the International Consortium for Polymer and Soft Matter. His pioneering research is in polymer nanotechnology, focusing on thin films and interfaces, addresses energy, sustainability, and health challenges.

© 2025 The Author(s). Small Science published by Wiley-VCH GmbH

26884046, 0, Downloaded from https://onlinelibrary.wiley.com/doi/10.1002/smsc.202400492 by Delhi Technological University, Wiley Online Library on [05/03/2025]. See the Terms and Conditions (https://onlinelibrary.wiley.com/terms-and-conditions) on Wiley Online Library for rules of use; OA articles are governed by the applicable Creative Commons License

ECS Journal of Solid State Science and Technology

ACCEPTED MANUSCRIPT

Nanogap Sequestered Dielectric Modulated Gate Engineered Carbon Nanotube Bio-FET based Bio-Sensor

To cite this article before publication: Bhargavi Sharma *et al* 2025 *ECS J. Solid State Sci. Technol.* in press https://doi.org/10.1149/2162-8777/adc2dd

Manuscript version: Accepted Manuscript

Accepted Manuscript is "the version of the article accepted for publication including all changes made as a result of the peer review process, and which may also include the addition to the article by IOP Publishing of a header, an article ID, a cover sheet and/or an 'Accepted Manuscript' watermark, but excluding any other editing, typesetting or other changes made by IOP Publishing and/or its licensors"

This Accepted Manuscript is **© 2025 The Electrochemical Society ("ECS"). Published on behalf of ECS by IOP Publishing Limited. All rights, including for text and data mining, AI training, and similar technologies, are reserved.**.

This article can be copied and redistributed on non commercial subject and institutional repositories.

Although reasonable endeavours have been taken to obtain all necessary permissions from third parties to include their copyrighted content within this article, their full citation and copyright line may not be present in this Accepted Manuscript version. Before using any content from this article, please refer to the Version of Record on IOPscience once published for full citation and copyright details, as permissions will likely be required. All third party content is fully copyright protected, unless specifically stated otherwise in the figure caption in the Version of Record.

View the article online for updates and enhancements.

This content was downloaded from IP address 14.139.251.98 on 01/04/2025 at 05:44

Nanogap Sequestered Dielectric Modulated Gate Engineered Carbon Nanotube Bio-FET based Bio-Sensor

Journal:	*ECS Journal of Solid State Science and Technology*
Manuscript ID	JSS-105573.R1
Manuscript Type:	Research Paper
Date Submitted by the Author:	25-Feb-2025
Complete List of Authors:	Sharma, Bhargavi; Delhi Technological University, Biotechnology; Delhi Technological University, Biotechnology Rewari, Sonam; Delhi Technological University Department of Electronics and Communication, Electronics and Communication Engineering Hasija, Yasha; Delhi Technological University, Biotechnology
Keywords:	FINFET, Nanotubes, Dielectrics

SCHOLARONE™
Manuscripts

Accepted Manuscript

Nanogap Sequestered Dielectric Modulated Gate Engineered Carbon Nanotube Bio-FET based Bio-Sensor

Bhargavi Sharma,[1] Sonam Rewari,[2,z] and Yasha Hasija[1]

[1]Department of Biotechnology, Delhi Technological University, Bawana Road, Delhi-110042, India
[2]Department of Electronics and Communications, Delhi Technological University, Bawana Road, Delhi-110042, India
[z]E-mail: rewarisonam@gmail.com

Abstract

A nanogap sequestered dielectric modulated gate engineered carbon nanotube (GECN) Bio-field-effect transistor (FET)-based bio-sensor suitable for biosensing applications related to breast cancer is proposed. A comprehensive analysis was conducted on the GECN BIO-FET , focusing on different biomolecules namely MCF-10A with relative permittivity as 4.5 is referred as Biomolecule1, Hs578T with relative permittivity as 22 is referred as Biomolecule2 and MDA-MB231 with relative permittivity as 24.5 is referred as Biomolecule3. These biomolecules were inserted in the dielectric and by varying the permittivity of the dielectrics in GECN BIO-FET , the movement of charges in the carbon nanotube-based plasma region is changed, thereby altering I_{ds}, g_m, g_d, SS and other related parameters. Higher sensitivity is achieved in proposed GECN BIO-FET over conventional CN Bio-FET. An analytical (mathematical) model has also been proposed for GECN Bio-FET-based bio-sensor and the analytical/mathematical results are consistent with their counterpart i.e. simulated results.

1. Introduction

Semiconductor MOSFET emanated biosensors are tending owing to their supremacy in terms of miniaturization and sensitivity. However, as silicon nanotubes face scaling challenges, researchers have turned to high-mobility channel alternatives, particularly carbon nanotubes (CNTs). CNTs, defined as graphitic cylindrical or spherical filaments often with conical tips, measure in nanometres in radius and several microns in length. FETs based on CNTs have demonstrated exceptional performance over traditional silicon devices [1] – [6]. For fabrication and study of CNT FETs -PECVD) method is very well established and it has been employed [7] – [10]. Highly dense Carbon Nanotube are also applicable for high frequency application especially single walled owing to their highly sterile nature [11]. Lundstrom et al. [12] further examined CNT FETs for high-frequency applications, noting that the cutoff frequency of CNT Schottky-barrier FETs remains below optimal levels. Li et al. [13] achieved high-performance FETs with PECVD-grown nanotubes, finding that approximately 90% of the CNTs produced were semiconducting. Mitzuni et al. [14] developed CNT FETs with horizontally aligned nanotubes as channels using a grid-inserted PECVD approach, achieving promisable results at shorter channel lengths. Schottky-barrier MOSFET using hafnium for charge plasma generation in undoped silicon, resulting in improved performance [15]. Jo et al. [16] investigated the short length characteristics of transfer properties in FETs using atomic force microscopy, while Manoj et al. [17] investigated an impact of high permittivity on nanoscale Fin FET performance. Tunnel CNT-FET that enables carrier generation through an external bias applied to side contacts has been deeply investigated by Gupta et al. [18]. In another advancement, Brady et al. [19] examined Carbon Nanotube based arrays which are super-efficient in achieving higher I_{ds} densities superior to silicon and gallium arsenide, approaching the quantum conductance limit. Ono et al. [20] created TFTs employing PECVD-grown CNTs, minimizing bundle formation. Wind et al. [21] constructed CNT FETs within a MOSFET framework, with a top-gate design yielding high electrical performance, including a steep subthreshold slope. Shao et al. [22] investigated high-purity semiconducting SWCNTs functionalized to detect SARS-CoV-2 antigens. Yadav and Rewari et. al [23] designed a C-FE-DM-NW FET biosensor for rapid biomolecule detection. Kansal and Sharma [24] studied impact of plasma parameters on CNT FETs elevated-sensitivity. Kansal and Sharma et al. [25], [26] further conducted numerical simulations to assess the performance of dual metal gate CNT FETs for various sensing uses. As the length of the channel decreases in field-effect transistors (FETs), various effects begin to manifest, including impact ionization, drain-induced barrier lowering (DIBL), carrier velocity saturation, gate oxide leakage, hot carrier effects, an increase in subthreshold swing, and higher leakage current. These phenomena are collectively referred to as short-channel effects.

The Triple Metal Gate (TMG) approach utilizes three metal gates with distinct work functions arranged in a manner where $\phi m1 > \phi m2 > \phi m3$. In this configuration, as electrons move from the source to the drain, their velocity decreases compared to a single metal gate (SMG) structure due to the variation in work functions. This reduction in

Accepted Manuscript
For Review Only

velocity helps mitigate the impact ionization effect. Additionally, the use of triple metal gates enhances electrostatic control over the channel. The combination of different work functions aids in optimizing the device's threshold voltage (VTH), thereby reducing the DIBL effect. DIBL occurs when an increase in drain voltage lowers the potential barrier at the source end of the channel, leading to greater leakage current and degraded performance. Furthermore, by strategically selecting the work functions of the metal gates, the subthreshold swing can be optimized, ultimately enhancing the overall performance of the device. Recent breakthroughs in semiconductor technology have significantly contributed to the advancement of field-effect-based biosensors. Innovations in transistor architecture, such as Tunnel Field-Effect Transistors (TFETs), cylindrical channel FETs [27]-[31], and progress in semiconductor material engineering, have enabled enhanced biosensing capabilities. Key developments, including Gate-All-Around (GAA) structures, the incorporation of Germanium (Ge) as a source material, advanced gate engineering techniques, oxide stacking, and graded channel designs, have led to notable improvements in sensitivity and overall performance. These advancements underscore the potential of next-generation transistor technologies in revolutionizing biosensing applications [32]- [37]. However, the large-scale fabrication of Carbon Nanotube FETs remains an ongoing challenge yet to be realized commercially.

In this paper, Nanogap Sequestered Dielectric Modulated Gate Engineered Carbon Nanotube (GECN) Bio-FET based Bio-Sensor has been deeply investigated. Section 2 illustrates the GECN BIO-FET simulation set up along with its structure. Results and discussion part is given in section 3 and the conclusion of our findings is given in Section 4.

2. NANOGAP SEQUESTERED DIELECTRIC MODULATED GATE ENGINEERED CARBON NANOTUBE (GECN) BIO-FET BASED BIO-SENSOR

2.1 GECN BIO-FET DEVICE for Cancer Detection

This study demonstrates the use of a GECN BIO-FET cancer sensor for detecting breast cancer pertaining to its permittivity, driven by recent advances in biosensing technologies and the urgent need for effective diagnostics in the field of oncology. The GECN BIO-FET cancer sensor is thoroughly examined pertaining to its capability to diagnose cancer, with the classification of cancer types primarily determined by the permittivity of the biomarkers, as shown in Table 1 [38], [39].

Table 1. Cancer Cell Type

Permittivity (K)	Cell Type	Healthy/unhealthy
4.5	MCF-10A	Healthy
22	Hs578T	Unhealthy & Cancerous
24.5	MDA-MB-231	Unhealthy & Cancerous

2.2 GECN BIO-FET Simulation Methodology

Figure 1(a) displays a 3D representation of a cylindrical Triple Metal Carbon Nanotube (TMCN) Bio-FET based Cancer Sensor while Figure 1(b) deputizes a 2D GECN BIO-FET based cancer sensor. Center of GECN BIO-FET illustrates plasma-assisted carbon nanotube, surrounded by a layer of silicon oxide, and then by a nanogap cavity. This nanogap cavity is where various cell types of different permittivity are introduced to get detected. The topmost coating of GECN BIO-FET features a triple-metal gate, where the metal type is adjusted by modifying the metal's work function. Additionally, a variety of bio-specimens can serve as biomarkers, which are introduced as specimens in the GECN BIO-FET biosensor's oxide layer situated between the carbon nanotube channel and the triple metal gate. Table II lists the GECN BIO-FET design parameters and simulation methodology on ATLAS Silvaco Device Simulator [40]. The simulation setup for this work has been calibrated using experimental data of DG-CNTFET [41]. A good agreement between the simulated and experimental results for the drain current as a function of gate voltage is shown in Fig. 1(iii).

Accepted Manuscript
For Review Only

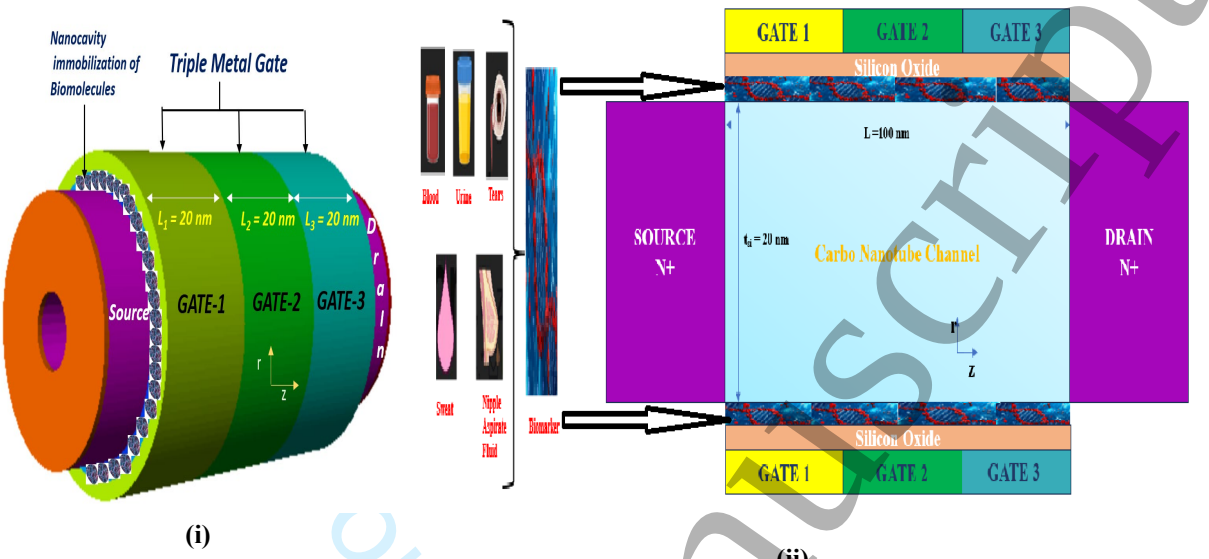

(i) (ii)

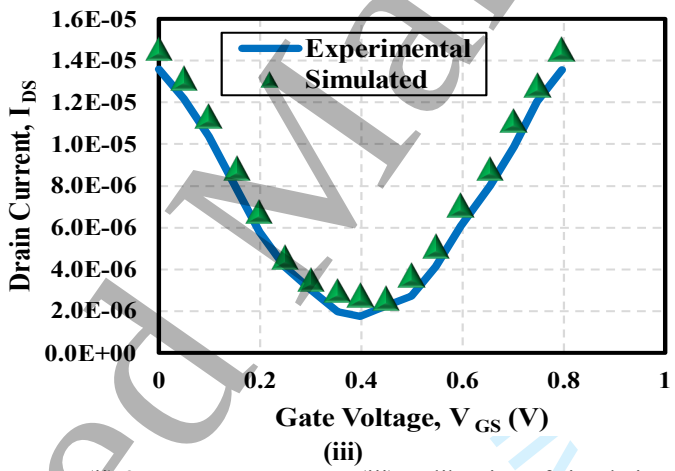

(iii)

Fig1 (i) 3-D GECN BIO-FET (ii) 2-D GECN BIO-FET (iii) Calibration of simulation setup with experimental data [41]

Table II. Device Specification Parameters

Physical Device Parameter	GECN Bio-FET
Channel thickness (t_{ch}) in nm	10
Channel length (L) in µm	3
Source Dimension (L_S) in nm	100
Drain Dimension (L_D) in nm	100
Gate Metal work function (eV)	M_1: 4.2, M_2: 4.0, M_2: 3.68
Oxide thickness (nm)	SiO_2: t_{ox} = 1.0
	HfO_2: t_{ox1} = 2.0
Thickness of Cavity (t_C) in nm	2
Length of cavity (L_C) in nm	100
Physical model	CONMOB
	FLDMOB
	BOLTZMANN
	AUGER
	CVT.

Accepted Manuscript

	SRH
	BGN

The fabrication process for the Nanogap Sequestered Dielectric Modulated Gate Engineered Carbon Nanotube (GECN) Bio-FET starts with the thorough cleaning of a silicon substrate, followed by the deposition of a thin silicon dioxide (SiO_2) layer to serve as an insulator. Carbon nanotubes (CNTs) are then synthesized using catalyst deposition and Plasma-Enhanced Chemical Vapor Deposition (PECVD). During the PECVD process, a hydrocarbon gas such as methane is introduced into a reaction chamber, where a high-frequency electric field generates plasma. This plasma breaks down the gas molecules, allowing carbon atoms to assemble into nanotubes on the catalyst-coated substrate. Plasma-assisted CNT growth offers significant benefits, including enhanced control over structural attributes such as diameter, length, and density. Once CNTs are formed, gate dielectric layers consisting of low-K (SiO_2) and high-K (HfO_2) dielectrics are deposited using techniques such as thermal oxidation, chemical vapor deposition (CVD), and atomic layer deposition (ALD). Nanocavities designed for biomolecule immobilization are created through precise etching, while a dual metal gate structure employing molybdenum (Mo) is fabricated with tailored work functions to optimize gate control. The deposition of metal source and drain contacts follows, alongside the etching of isolation trenches. Biomolecule immobilization is facilitated through functionalization of the nanocavity. To complete the fabrication, a passivation layer is applied, and the device is packaged for subsequent testing and deployment. This comprehensive process ensures high sensitivity and selectivity, making the device highly effective for detecting breast cancer biomarkers.

3. Analytical GECN Bio-FET based Bio-Sensor Model

Subthreshold-Current (I_{sub}) and potential can be mathematically elucidated by applying the solution of II-D Poisson's equation in 3-D cylindrical coordinates. Sharma et. al [32] have explained , II-D Poisson's equation in 3-D cylindrical coordinates can be expressed as:

$$\frac{1}{r}\frac{\partial}{\partial r}\Phi(r,z)+\frac{\partial}{\partial r^2}\Phi(r,z)+\frac{\partial}{\partial z^2}\Phi(r,z)=-\frac{qN_D}{\varepsilon_{si}} \quad \text{(i)}$$

where $\phi(r,z)$ represents the potential distribution across the channel, and N_D is the doping concentration. By utilizing the superposition theorem, the final answer for the potential may be broken down into two parts:

1. Elucidation of I-D V (r, z) is conditioned upon radius (r)
2. Elucidation of II-D U (r, z) is conditioned upon radius (r) and the vertical distance (z).

$$\Phi(r,z)=V(z)+U(r,z) \quad \text{(ii)}$$

Now, equation (i) can be rewritten as a 1-D Poisson equation:

$$\frac{1}{r}\frac{\partial}{\partial r}(V(r))+\frac{\partial 2}{\partial r^2}V(r)=-\frac{qN_D}{\varepsilon_{si}} \quad \text{(iii)}$$

And 2-D Laplace equation as:

$$\frac{1}{r}\frac{\partial}{\partial r}\big(U(r,z)\big)+\frac{\partial 2}{\partial r^2}U(r,z)+\frac{\partial 2}{\partial z^2}U(r,z)=-\frac{qN_D}{\varepsilon_{si}} \quad \text{(iv)}$$

The boundary conditions are of utmost importance while solving 2-D potential problems. These conditions establish precise regulations or limitations at the perimeters or limits of the problem domain.

Boundary conditions for the solution of 2 D potential $\Phi(r,z)$ of the proposed device is given as follows:

(i) $\Phi(t,z)=\Phi_{os}(z)$ (v)

(ii) $\Phi(t-t_{si},z)=\Phi_{is}(z)$ (vi)

(iii) $\frac{\partial}{\partial r}\Phi(r,z)\ (with\ r=teff)=-\delta(Vgs-\Phi_{os}(z))$ (vii)

(iv) $\frac{\partial}{\partial r}\Phi(r,z)\ (with\ r=teff-tsi)=-\delta(Vgs-\Phi_{is}(z))$ (viii)

(v) $\Phi(r,L)=V_{bi}$ (ix)

(vi).$\Phi(r,L)=V_{bi}+V_{ds}$ (x)

$$C_{ox}=\frac{2\varepsilon_{ox}}{(t_m+t_{t_{oxeff}})\,ln(1+\frac{2t_{oxeff}}{(tm+t_{t_{oxeff}})})} \quad \text{(xi)}$$

$\Phi_{os}(z)$ →consistent outer-surface potential, $\Phi_{is}(z)$ →consistent inner-surface potential,

$t_{oxeff}=t_1(SiO_2)+\frac{\varepsilon_{ox}}{\varepsilon_{bio}}t_2(Bio)$ t_1 (SiO_2) is first dielectric layer (SiO_2 Layer) thickness and t_2 (Bio) the biomolecule layer thickness. The dielectric-permittivity of oxide is represented by ε_{ox}, and that of biomolecules by $\varepsilon_{bio.}$

The solution to equation (iii) can be accurately approximated using a parabolic function given below:

Accepted Manuscript For Review Only

$$V(r) = P_0 + P_1 r + P_2 r^2 \quad \text{(xii)}$$

where $P_0 = V_{gseff} - P_1(t + \frac{1}{\Delta}) - P_2(t^2 + \frac{2t}{\Delta})$, $P_1 = -\delta(t_{eff} - \frac{t_{si}}{2})$, $P_2 = \frac{\delta}{2}$, $\delta = \frac{-qN_d}{\varepsilon_{si}}$, $V_{gseff} = V_{gs} - V_{fb} + \frac{qN_f}{C_{ox}}$, $V_{fb} = \phi_m - (\chi_{Si} - q\phi_f)$ → flat band voltage, V_{gs} →applied gate-to-source voltage, N_f → biomolecule charged density, χ_{Si} is electron affinity of Plasma Assisted CNT FET, and ϕ_f is channel fermi-potential. The elucidation of iv is derived as:

$$U(r,z) = \Sigma J_0(\alpha_n r)(M_n \exp(\alpha_n z) + N_n \exp(-\alpha_n z)) \quad \text{(xiii)}$$

with J_0 and J_1 → Bessel functions of order 0 and 1 respectively, M_n and N_n are solved by using boundary conditions (ix) and (x).

α_n is Eigenvalues of: $J_1(\frac{t_{eff}}{\alpha_n}) = \frac{C_{ox}}{\alpha_n \varepsilon_{si}} J_0(\frac{t_{eff}}{\alpha_n})$ (xiv)

II-D cylindrical potential is finally expressed as:

$$\Phi(r,z) = V(r) + \Sigma J_0(\alpha_n r)(M_n \exp(\alpha_n z) + N_n \exp(-\alpha_n z)) \quad \text{(xv)}$$

with $\alpha_n = \frac{1}{\eta_n}$.

I_{sub} is given as:

$$I_{sub} = 2R\pi\mu kT\eta_i \frac{1 - e^{\frac{-qV_{ds}}{kT}}}{\int_0^L \frac{1}{\int_0^{t_{eff}} e^{\frac{q\Phi(r,z)}{kT}} dr} dz}$$

with, Boltzmann's constant, k= 1.38 x 10^{-23}J/K, T=300K, intrinsic-carrier-density, $\eta i = 1.45$,x 10^{10} cm^{-3}electron mobility, μ= 1300 cm^2/Vs.

4. Results and Discussion

GECN BIO-FET cancer sensor is probed in depth for BIOMOLECULE1, Biomolecule2 and Biomolecule3 detection, so as to examine its sensitivity over conventional CN BIO-FET. Fig. 2 embellishes charge concentration along the radial direction in the channel when BIOMOLECULE1, Biomolecule2 and Biomolecule3are inserted in the oxide layer of GECN BIO-FET cancer sensor. It can be easily interpreted from Fig 2 that concentration of charge increases when biomolecules are introduced, moving from a baseline to the presence of BIOMOLECULE1, Biomolecule2, and BIOMOLECULE3 respectively. This shift is linked to changes in permittivity of biomolecules. As the dielectric constant of the immobilized biomolecules rises, radial potential drops owing to stronger coupling between gate and channel. A thorough examination of electrostatics is crucial for accurately characterizing and understanding the electrical properties of an FET-based biosensor. This analysis takes into account variations in the dielectric constant and the charge of biomolecules to ensure optimal sensor performance. Understanding the electrostatic interactions between biomolecules and the FET surface provides key insights into the biosensor's sensitivity and its ability to detect biomolecules with precision. By incorporating electrostatic analysis, the design and functionality of the device can be optimized by evaluating aspects such as material selection, the dimensions and geometry of the sensing region (nano-cavity), and the operating conditions.

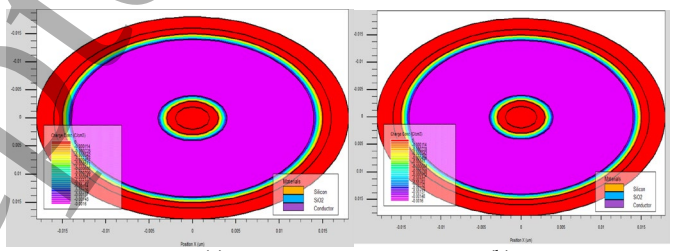

(a) (b)

Accepted Manuscript
For Review Only

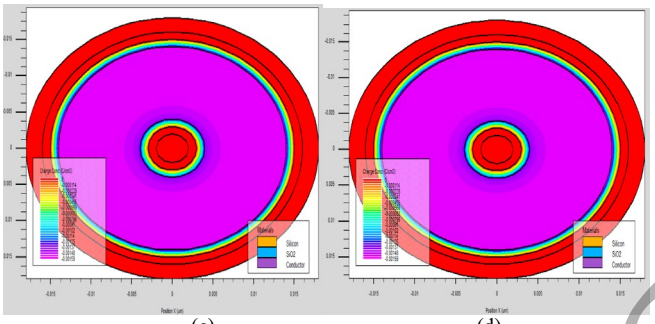

(c) (d)

Fig 2. Charge Concentration for GECN BIO-FET based Biosensor for (a) No Biomolecules (b) BIOMOLECULE1 (c) Biomolecule2 (d) BIOMOLECULE3

Fig. 3. illustrates the conduction current density along the channel when BIOMOLECULE1, Biomolecule2 and the BIOMOLECULE3. The Conduction Current Density increases when biomolecules are introduced, moving from a baseline of BIOMOLECULE1, Biomolecule2, and BIOMOLECULE3 This shift is linked to changes in permittivity of biomolecules. As the dielectric constant of the immobilized biomolecules rises, the oxide capacitance also elevates and hence the conduction current density. The process of securing biomolecules within a nanogap is known as immobilization. This involves various methods to attach biomolecules to the dielectric layer of the FET, enabling them to identify and interact with target analytes. Depending on the specific FET biosensor design and the characteristics of the biomolecules and analytes, different immobilization techniques can be employed, including covalent binding, crosslinking, entrapment, adsorption, and affinity binding. The effectiveness of these methods, combined with careful sensor design and engineering, ensures the precise placement of biomolecules within the nanogap of dielectric-modulated FET biosensors. This, in turn, enhances the device's ability to detect target analytes with high sensitivity and selectivity.

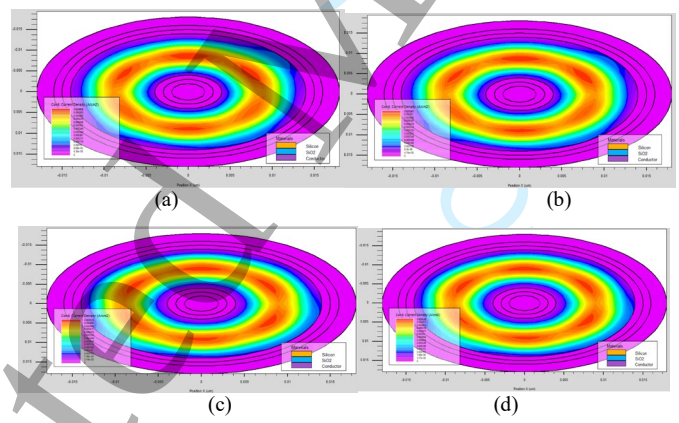

(a) (b)

(c) (d)

Fig 3. Conduction Current Density for GECN BIO-FET cancer sensor (a) No Biomolecules (b) BIOMOLECULE1 (c) Biomolecule2 (d) BIOMOLECULE3

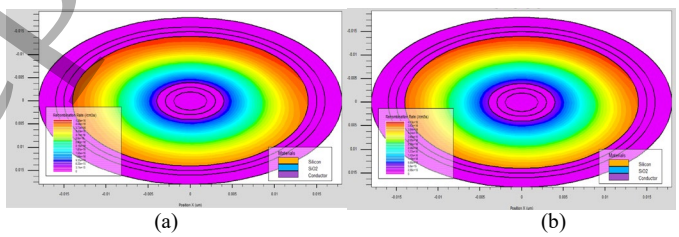

(a) (b)

Accepted Manuscript

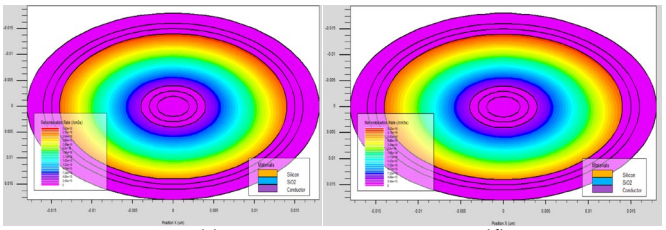

(c) (d)

Fig 4. Recombination Rate for GECN BIO-FET cancer sensor (a) No Biomolecules (b) BIOMOLECULE1 (c) Biomolecule2 (d) BIOMOLECULE3

Fig. 4 illustrates the Recombination Rate along the channel for GECN BIO-FET cancer sensor concerning (a) No Biomolecules (b) BIOMOLECULE1 (c) Biomolecule2 (d) BIOMOLECULE3. The recombination rate declines upon the introduction of biomolecules, shifting from a baseline without biomolecules to conditions with BIOMOLECULE1, Biomolecule2, and BIOMOLECULE3. This shift is linked to changes in permittivity of biomolecules. As the dielectric constant of the immobilized biomolecules rises, radial potential drops owing to stronger coupling between gate and channel.

Fig 5. layouts the contour radial channel potential for GECN BIO-FET cancer sensor (a) No Biomolecules (b) BIOMOLECULE1 (c) Biomolecule2 (d) BIOMOLECULE3. When biomolecules are introduced, the charge concentration rises, transitioning from a state without biomolecules to one with BIOMOLECULE1, Biomolecule2, and BIOMOLECULE3. This shift is linked to changes in permittivity of biomolecules. As the dielectric constant of the immobilized biomolecules rises, radial potential drops owing to stronger coupling between gate and channel..

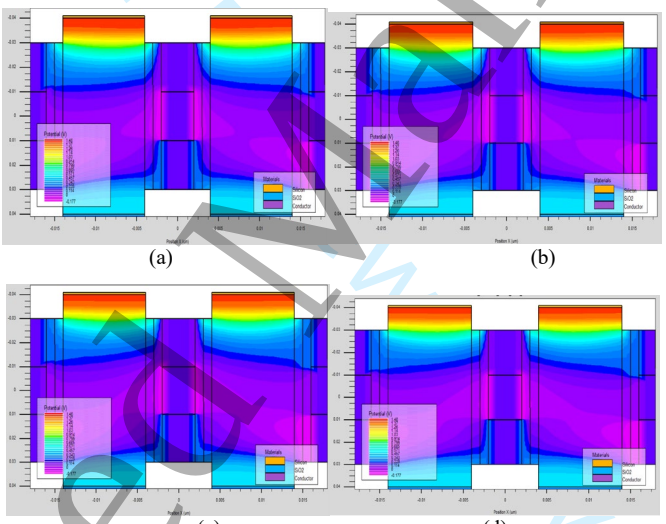

(a) (b)

(c) (d)

Fig 5. Potential Contour plot of GECN BIO-FET cancer sensor (a) No Biomolecules (b) BIOMOLECULE1 (c) Biomolecule2 (d) BIOMOLECULE3

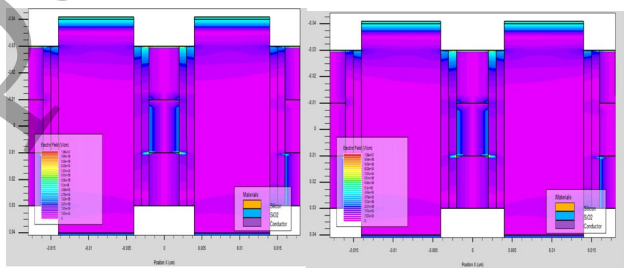

(a) (b)

Accepted Manuscript

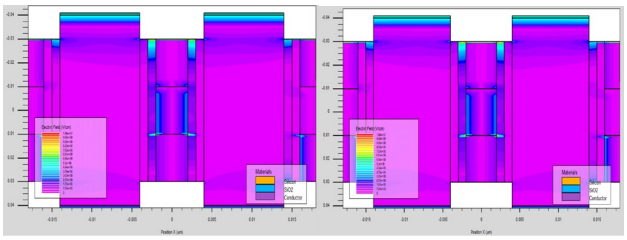

(c) (d)

Fig 6. Electric Field Contour plot of GECN BIO-FET cancer sensor (a) No Biomolecules (b) BIOMOLECULE1 (c) Biomolecule2 (d) BIOMOLECULE3

Fig. 6. illustrates the contour Electric Field plot along the channel for GECN BIO-FET cancer sensor (a) No Biomolecules (b) BIOMOLECULE1 (c) Biomolecule2 (d) BIOMOLECULE3. When biomolecules are introduced, the charge concentration rises, transitioning from a state without biomolecules to one with BIOMOLECULE1, Biomolecule2, and BIOMOLECULE3biomolecules. transitioning from a state without biomolecules to one with BIOMOLECULE1, Biomolecule2, and BIOMOLECULE3. This shift is linked to changes in permittivity of biomolecules. As the dielectric constant of the immobilized biomolecules rises, radial potential drops owing to stronger coupling between gate and channel.

Table 2: Sensitivity Analysis for Different Cancer Biomarker Type

Parameter	Cancer Biomarker Type	GECN BIO-FET biosensor	CN BIO-FET biosensor	% Improvement
S_{idvg}	BIOMOLECULE1	2.20E-6	4.04E-7	444.55%
	Biomolecule2	7.06E-6	1.25E-6	464.8%
	BIOMOLECULE3	1.08E-5	1.78E-6	506.74%
S_{gm}	*BIOMOLECULE1*	3.60E-6	7.30E-7	393.15%
	Biomolecule2	1.27E-5	2.26E-6	461.94%
	BIOMOLECULE3	2.26E-5	3.22E-6	601.86%
S_{idvd}	*BIOMOLECULE1*	3.50E-6	7.30E-7	379%
	Biomolecule2	1.25E-5	2.26E-6	453.09%
	BIOMOLECULE3	1.93E-5	3.22E-6	508.69%
S_{gd}	*BIOMOLECULE1*	4.40E-7	9.00E-8	388.88%
	Biomolecule2	1.54E-6	2.80E-7	450%
	BIOMOLECULE3	1.92E-6	4.80E-7	300%
S_{SS}	*BIOMOLECULE1*	2.50E-2	1.20E-2	108.33%
	Biomolecule2	4.90E-2	2.40E-2	104.16%
	BIOMOLECULE3	5.90E-2	3.60E-2	63.88%

Fig 7. embellishes I_{DS} v/s V_{GS}, showing a clear pattern in which I_{ds} increases without biomolecules to BIOMOLECULE1 and finally to BIOMOLECULE3 for (a) GECN BIO-FET cancer sensor (b) the CN BIO-FET, and (c) the I_D-V_{GS} sensitivity, S_{idvg}. Notably, BIOMOLECULE3 produces maximum I_{ds}, attributed to its higher permittivity compared to other cancer biomarkers. An in-depth study of Figures 7(a) & (b) shows that the GECN BIO-FET exhibits a higher IDS than the CN BIO-FET. This enhancement is due to the triple metal gate structure, which decreases short-channel effects, and boosts the drain current. A biosensor's sensitivity is generally evaluated by measuring the drift in the parameter, which involves various properties, such as threshold voltage or current, which can signify the presence or absence of biomolecules. The biosensor Sensitivity (S_P) can be mathematically defined as the change in concerned parameter without biomolecules ($P_{No\ Biomolecule}$) and with biomolecules present ($P_{With\ Biomolecules}$):

$$SP = P\ (with\ Biomolecules) - P(without\ Biomolecules) \quad \text{(xvi)}$$

For field-effect transistors, the drain current is a key metric. From (1) S_{idvg}, is formulate as [30], [42], [43], [44]:

$$Sidvg = ID\ (with\ Biomolecules) - ID(without\ Biomolecules) \quad \text{(xvii)}$$

By (2), S_{idvg} is computed at different V_{gs}, and the sensitivity results are emulated in Fig. 7(c) and Table 2. It is evident that the GECN BIO-FET shows greater sensitivity for cancer biomarker detection through S_{idvg} compared to CN BIO-FET. This improvement is owing to triple metal gate structure, which minimizes impact ionization effects, reduces short-channel effects, and enhances drain current sensitivity.

Accepted Manuscript
For Review Only

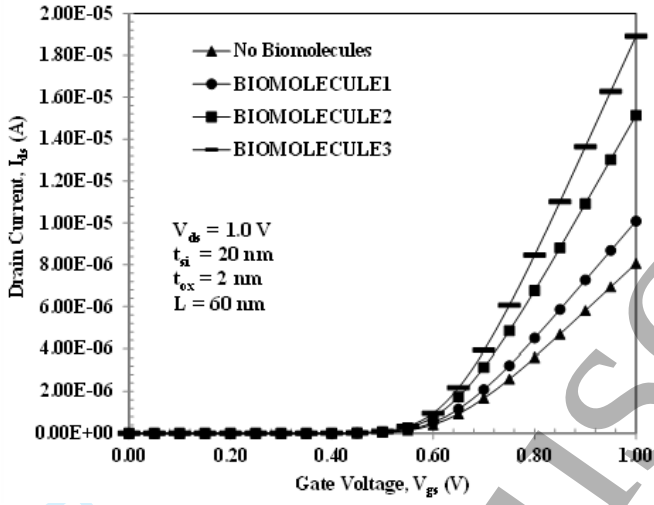

(a)

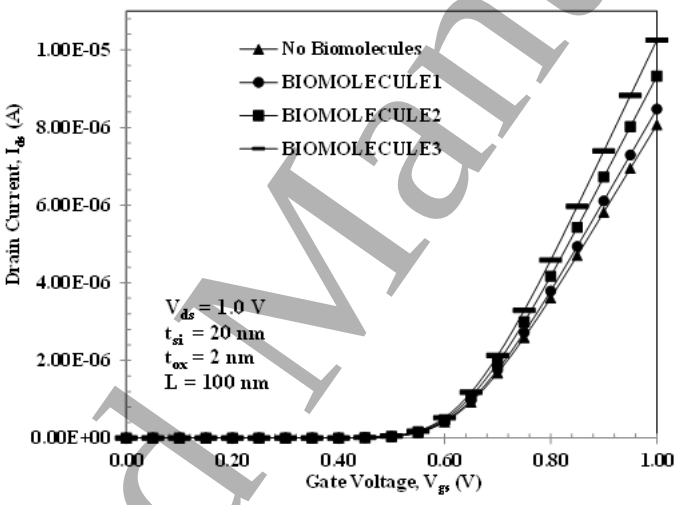

(b)

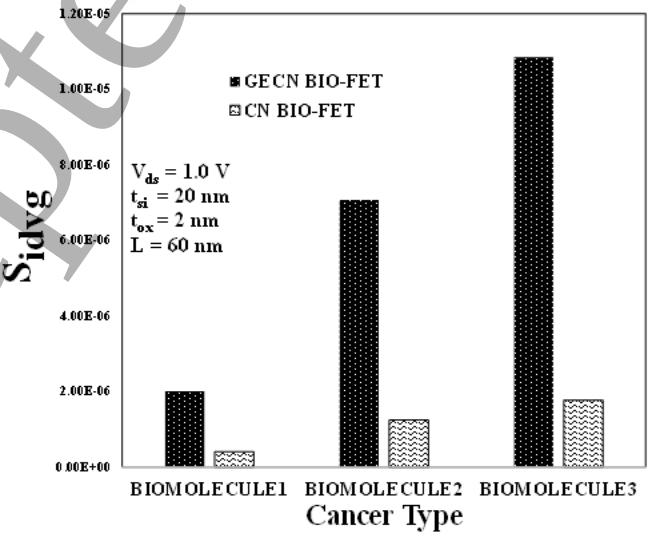

Accepted Manuscript

(c)

Fig 7. I_D-V_{GS} characteristics for different cancer biomarkers of (a) GECN BIO-FET biosensor (b) CN BIO-FET (c) I_D-V_{GS} Sensitivity, S_{idvg}

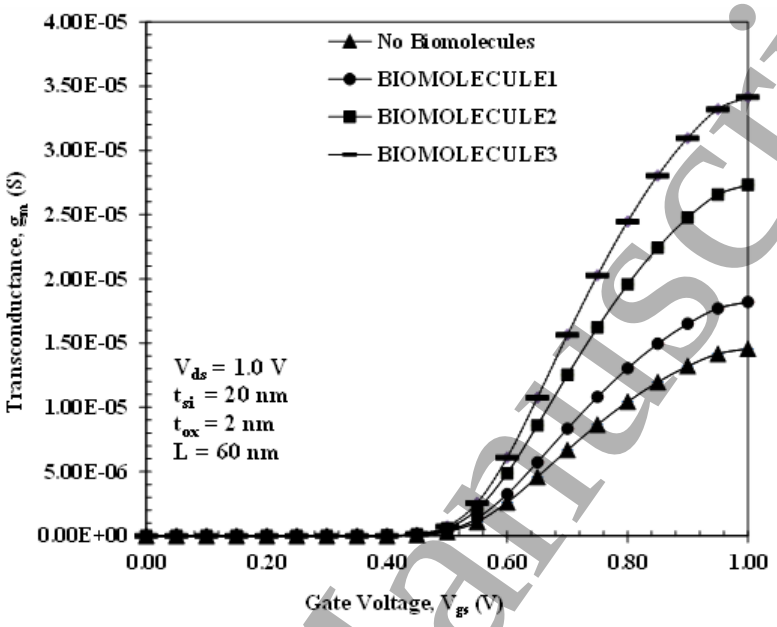

(a)

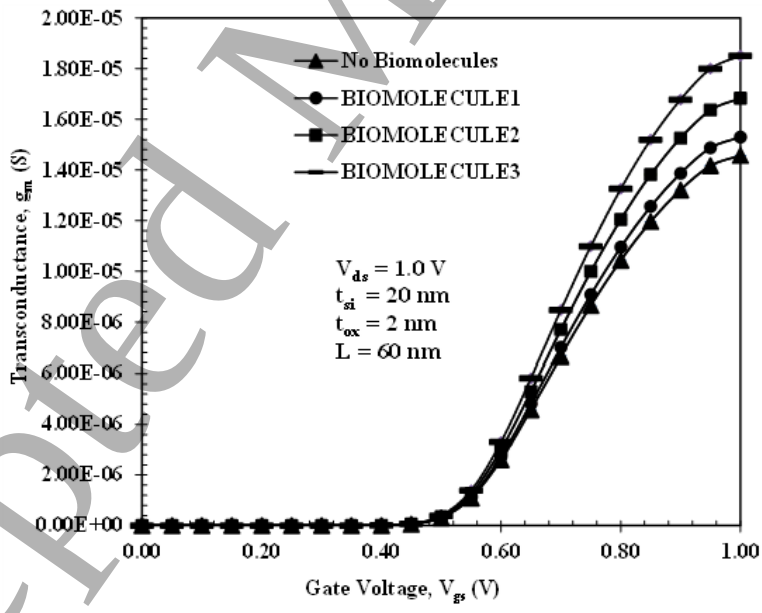

(b)

Accepted Manuscript

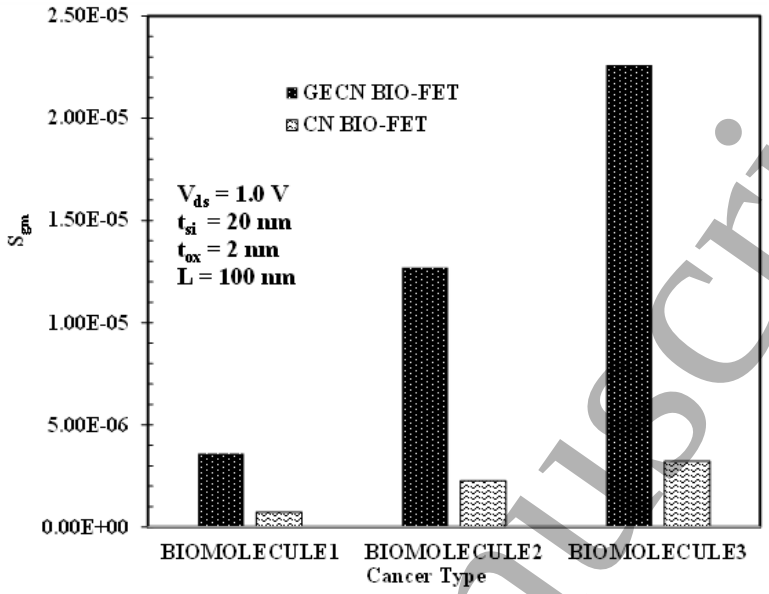

(c)

Fig 8. g_m-V_{GS} characteristics for different cancer biomarkers of (a) GECN BIO-FET biosensor (b) CN BIO-FET (c) I_D-V_{GS} Sensitivity, S_{idvg}

Fig 8. embellishes g_m Vs. V_{GS}, showing a clear pattern in which g_m increases without biomolecules to BIOMOLECULE1 and finally to BIOMOLECULE3 for (a) GECN BIO-FET cancer sensor (b) the CN BIO-FET, and (c) the g_m-V_{GS} sensitivity, S_{gm}. Notably, BIOMOLECULE3 produces maximum g_m, attributed to its higher permittivity compared to other cancer biomarkers. An in-depth study of Figures 8(a) & (b) shows that the GECN BIO-FET exhibits a higher g_m than the CN BIO-FET. This enhancement is due to the triple metal gate structure, which decreases short-channel effects, and consequently boosts the drain current. A biosensor's sensitivity is generally evaluated by measuring the drift in the parameter, which involves various properties, such as threshold voltage or current, which can signify the presence or absence of biomolecules. S_{gm} is computed at different V_{gs}, and the sensitivity results are emulated in Fig. 8 (c) and Table 2. It is evident that the GECN BIO-FET shows greater sensitivity for cancer biomarker detection through S_{gm} compared to CN BIO-FET. This improvement is owing to triple metal gate structure, which minimizes impact ionization effects, reduces short-channel effects, and enhances drain current sensitivity.

Fig 9. embellishes I_{ds} Vs. V_{DS}, showing a clear pattern in which gm increases without biomolecules to BIOMOLECULE1 and finally to BIOMOLECULE3 for (a) GECN BIO-FET cancer sensor (b) the CN BIO-FET, and (c) the I_d-V_{DS} sensitivity, S_{idvd}. Notably, BIOMOLECULE3 produces maximum gm, attributed to its higher permittivity compared to other cancer biomarkers. An in-depth study of Figures 9(a) & (b) shows that the GECN BIO-FET exhibits a higher I_{ds} than the CN BIO-FET. This enhancement is due to the triple metal gate structure, which decreases short-channel effects, and boosts the drain current. A biosensor's sensitivity is generally evaluated by measuring the drift in the parameter, which involves various properties, such as threshold voltage or current, which can signify the presence or absence of biomolecules. S_{idvd} is computed at different Vgs, and the sensitivity results are emulated in Fig. 9 (c) and Table 2. It is evident that the GECN BIO-FET shows greater sensitivity for cancer biomarker detection through S_{idvd} compared to CN BIO-FET. This improvement is owing to triple metal gate structure, which minimizes impact ionization effects, reduces short-channel effects, and enhances drain current sensitivity.

Accepted Manuscript
For Review Only

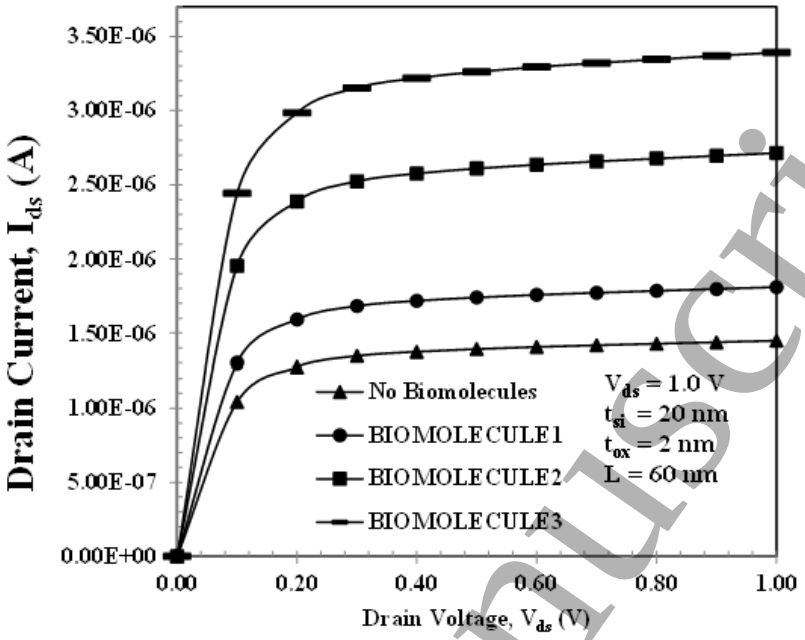

(a)

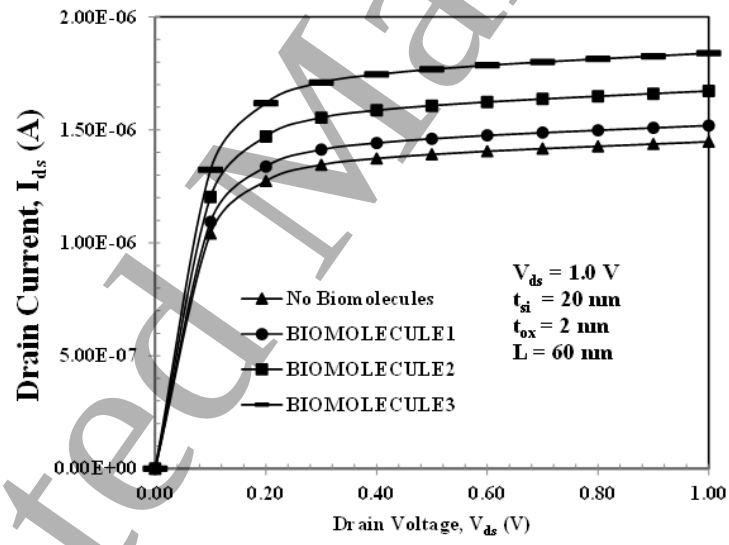

(b)

Accepted Manuscript

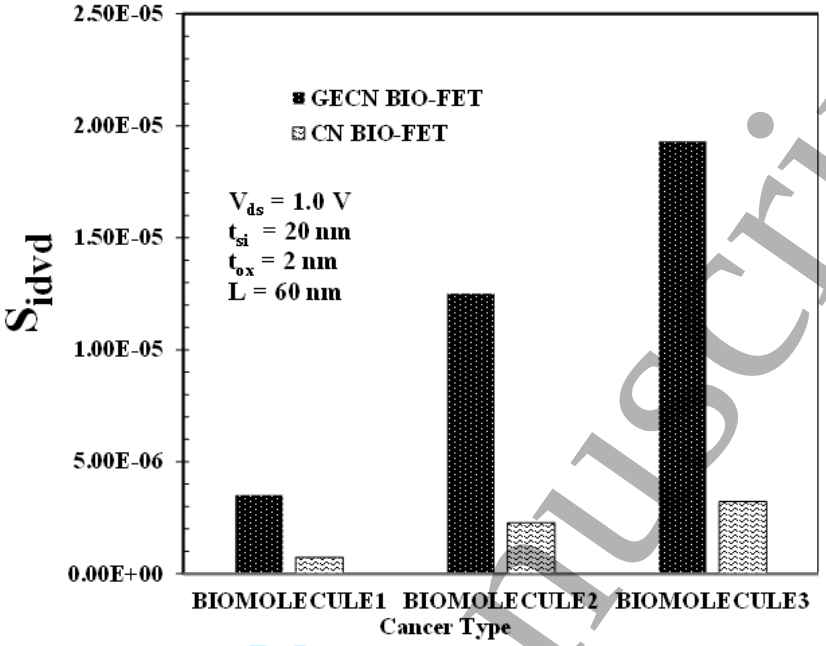

(c)

Fig 9. I_{ds}-V_{DS} characteristics for different cancer biomarkers of (a) GECN BIO-FET biosensor (b) CN BIO-FET (c) I_D-V_{GS} Sensitivity, S_{idvg}

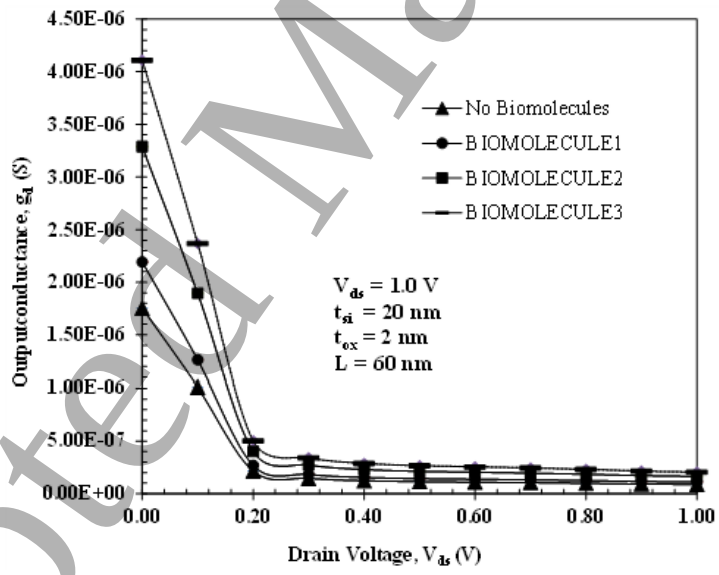

(a)

Accepted Manuscript

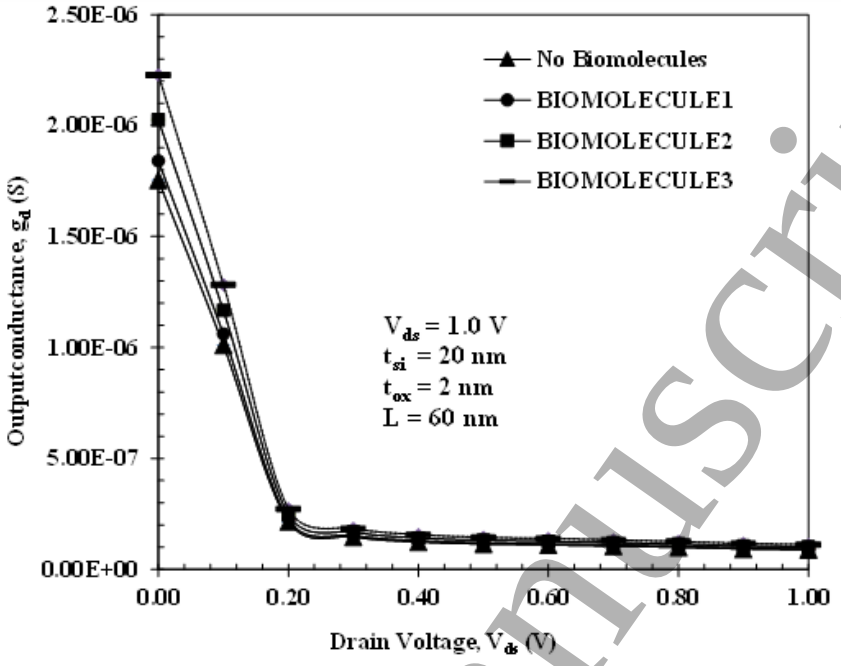

(b)

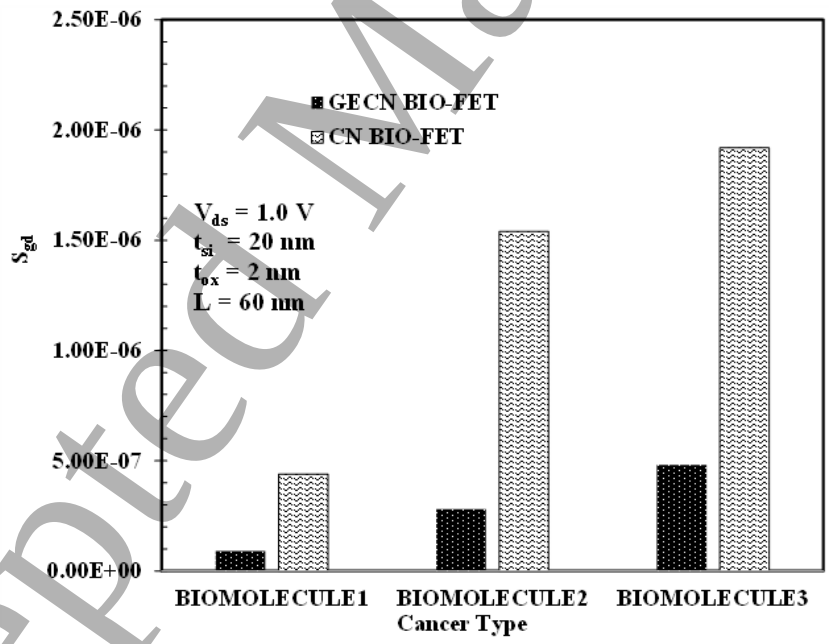

(c)

Fig 10. g_d-V_{DS} characteristics for different cancer biomarkers of (a) GECN BIO-FET biosensor (b) CN BIO-FET (c) g_{ds}-V_{DS} sensitivity, S_{gd}

Fig 10. embellishes g_d Vs. V_{DS}, showing a clear pattern in which g_m increases without biomolecules to BIOMOLECULE1 and finally to BIOMOLECULE3 for (a) GECN BIO-FET cancer sensor (b) the CN BIO-FET, and (c) the g_d-V_{DS} sensitivity, S_{gd}. Notably, BIOMOLECULE3 produces maximum gm, attributed to its higher permittivity compared to other cancer biomarkers. An in-depth study of Figures 10 (a) & (b) shows that the GECN BIO-FET exhibits a higher Ids than the CN BIO-FET. This enhancement is due to the triple metal gate structure, which decreases short-channel effects, and boosts the drain current. A biosensor's sensitivity is generally evaluated by measuring the drift in the parameter, which involves various properties, such as threshold voltage or current, which can signify the presence or absence of biomolecules. S_{gd} is computed at different V^{ds}, and the sensitivity results are emulated in Fig. 10 (c) and

Accepted Manuscript

Table 2. It is evident that the GECN BIO-FET shows greater sensitivity for cancer biomarker detection through S_{gd} compared to CN BIO-FET. This improvement is owing to triple metal gate structure, which minimizes impact ionization effects, reduces short-channel effects, and enhances drain current sensitivity.

Figures 11(a) illustrate the drift in Subthreshold Slope (SS) for different biomolecules for both the devices. The best possible value of SS is 60 mV/decade and it depicts the FET's capacity to switch from completely OFF to completely ON states. The figures indicate that higher permittivity in cancerous cells reduces the Subthreshold Slope. This reduction is associated with a decrease in energy gap, as biomolecules with higher permittivity are used as gate dielectrics, leading to faster switching in the FET device and, consequently, affecting its sensitivity. Figures 11(b) emulates the drift in SS sensitivity, respectively, of the proposed GECN BIO-FET cancer sensor. Subthreshold Sensitivity is measured across various cancer biomarkers, with results in Figure 11(b) and Table 2, showing that the GECN BIO-FET demonstrates improved sensitivity for detecting cancer biomarkers through S_{SS} in comparison to CN BIO-FET. This improvement is also attributed to the triple metal gate structure, which reduces impact ionization effects, minimizes short-channel effects, and enhances drain current sensitivity.

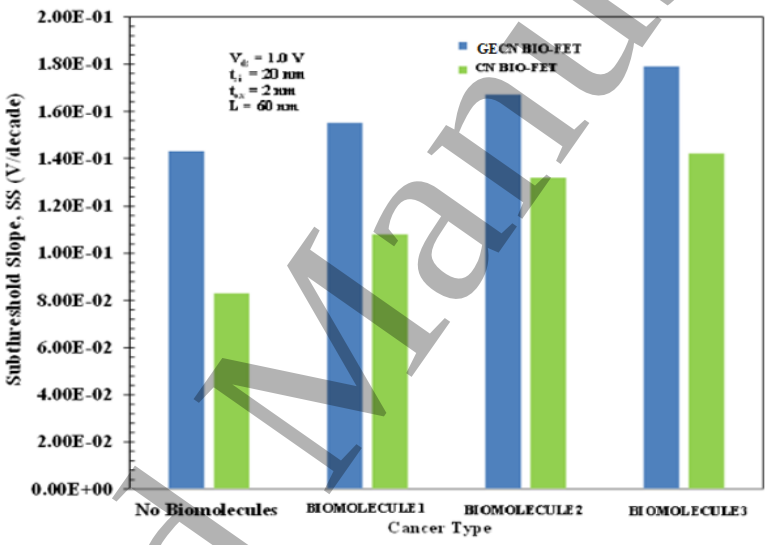

(a)

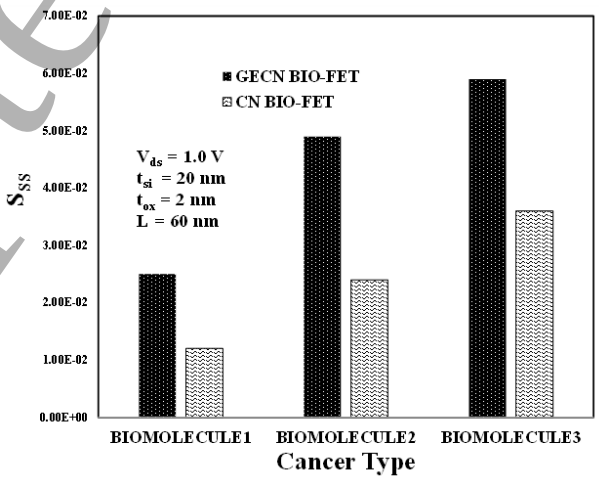

(b)

Fig 11. (a) Subthreshold Slope, SS for different cancer types (b) Subthreshold Slope Sensitivity, S_{SS} for different biosensor

Accepted Manuscript

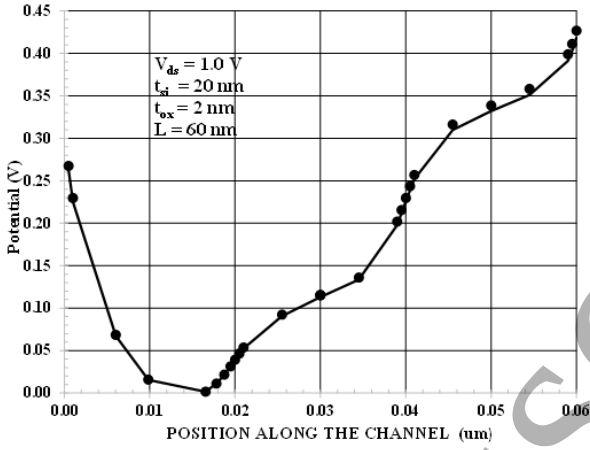

(a)

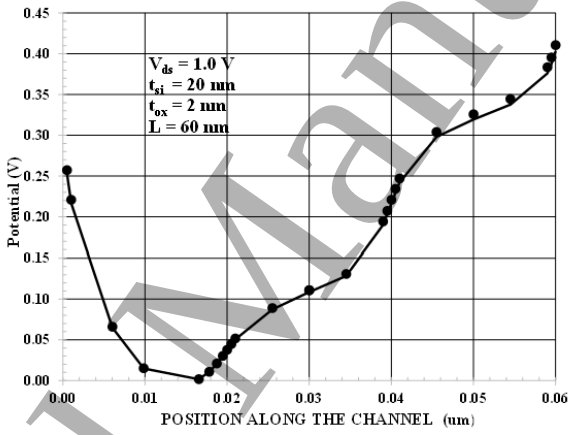

(b)

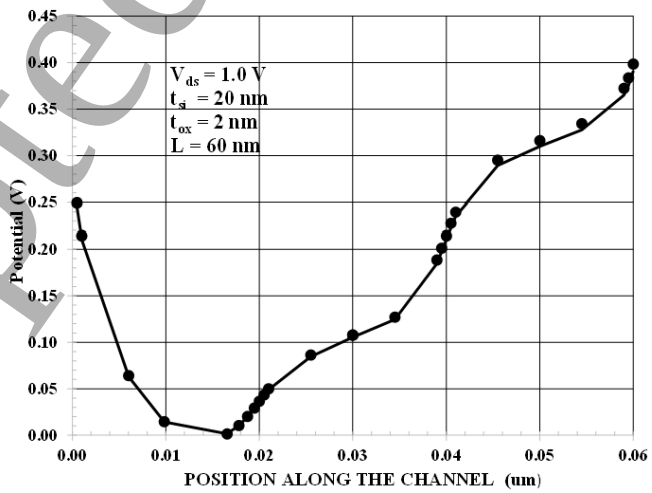

(c)

Fig 12. Analytical and Simulated Results for potential for (a) Biomolecule 1 (b) Biomolecule 2 (c) Biomolecule 3

Accepted Manuscript

Figure 12. Shows Analytical and Simulated Results for potential for (a) Biomolecule 1 (b) Biomolecule 2 (c) Biomolecule 3. Solid marker depicts analytical (mathematical) results and line depicts simulated results. A rise in the potential is detected as shift from Biomolecule 1 to other biomolecules. A drift in permittivity of the biomolecules manifests an analogous drift in oxide capacitance, Cox and thereby altering the potential. It can be interpreted from Fig 12 that analytical/mathematical results are very consistent with their counterpart i.e. simulated results.

Figure 13. Shows Analytical and Simulated Results for Electric Field for (a) Biomolecule 1 (b) Biomolecule 2 (c) Biomolecule 3. Solid marker depicts analytical (mathematical) results and line depicts simulated results. A rise in the potential is detected as shift from Biomolecule 1 to other biomolecules. A drift in permittivity of the biomolecules manifests an analogous drift in oxide capacitance, Cox and thereby altering the potential and as field is a derivative of potential, it also changes. It can be interpreted from Fig 13 that analytical/mathematical results are very consistent with their counterpart i.e. simulated results.

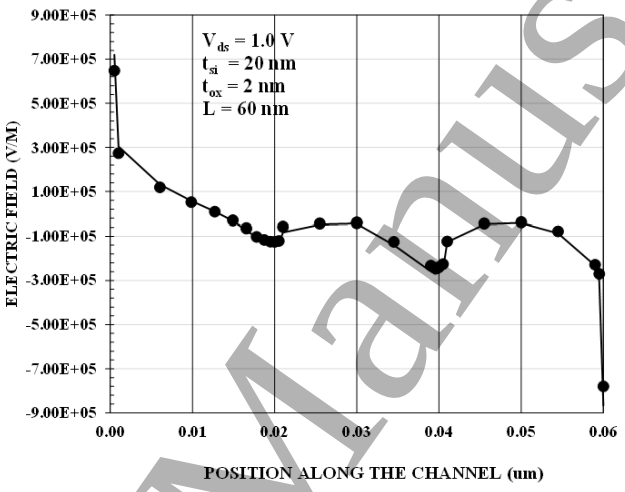

(a)

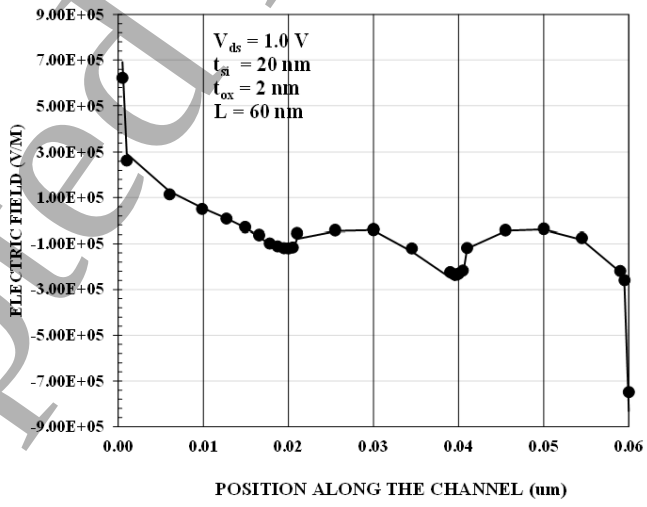

(b)

Accepted Manuscript

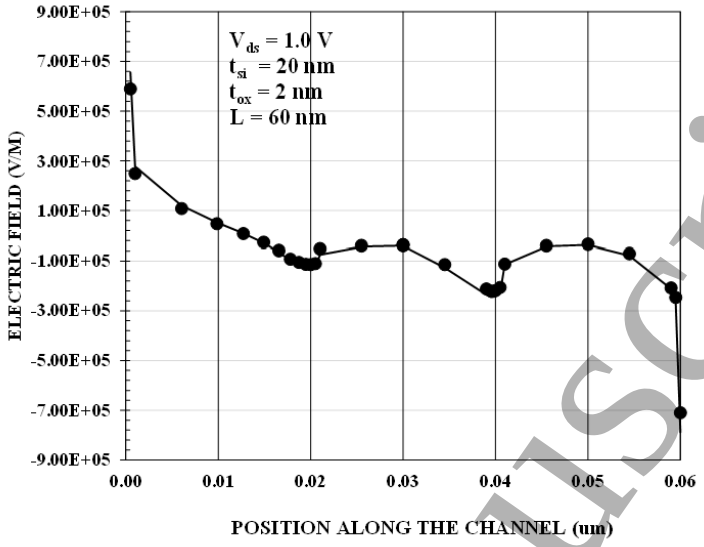

(c)

Fig 13. Analytical and Simulated Results for Electric Field for (a) Biomolecule 1 (b) Biomolecule 2 (c) Biomolecule 3

Figure 14. Shows Analytical and Simulated Results for Drain Current in Subthreshold region, I_{sub} for (a) Biomolecule 1 (b) Biomolecule 2 (c) Biomolecule 3. Solid marker depicts analytical (mathematical) results and line depicts simulated results. A rise in the potential is detected as shift from Biomolecule 1 to other biomolecules. A drift in permittivity of the biomolecules manifests an analogous drift in oxide capacitance, Cox and thereby altering I_{sub}. It can be interpreted from Fig 14. that analytical/mathematical results are in consistent with their counterpart i.e. simulated results.

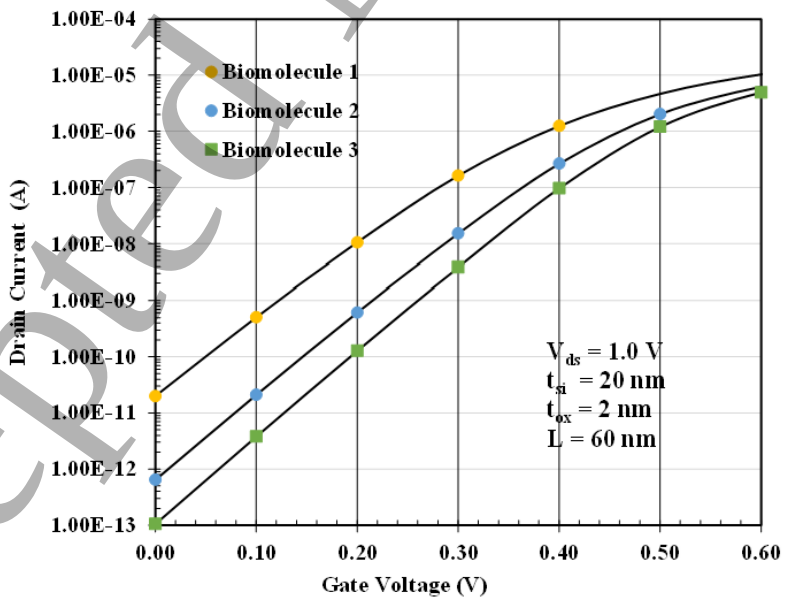

Fig 14. Analytical and Simulated Results for DrainCurrent in Subthreshold region, I_{sub} for (a) Biomolecule 1 (b) Biomolecule 2 (c) Biomolecule 3

Accepted Manuscript
For Review

5. Conclusion

In this manuscript Nanogap Sequestered Dielectric Modulated Gate Engineered Carbon Nanotube (GECN) Bio-FET based Bio-Sensor is proposed in this manuscript suitable for biosensing applications related to breast cancer. A comprehensive analysis was conducted on the GECN BIO-FET, focusing on different biomolecules namely MCF-10A with relative permittivity as 4.5 is referred as Biomolecule1, Hs578T with relative permittivity as 22 is referred as Biomolecule2 and MDA-MB231 with relative permittivity as 24.5 is referred as Biomolecule3. These biomolecules were inserted in the dielectric and by varying the permittivity of the dielectrics in GECN BIO-FET, the movement of charges in the carbon nanotube-based plasma region is changed, thereby altering I_{ds}, g_m, g_d, SS and other related parameters. Higher Sensitivity is achieved in proposed GECN BIO-FET over conventional CN Bio-FET. An analytical (mathematical) Model has also been proposed for GECN Bio-FET based Bio-Sensor and the that analytical/mathematical results are in consistent with their counterpart i.e. simulated results.

REFERENCES

[1]. P. Bergveld, The development and application of FET-based biosensors, Biosensors, Vol.2, no.1, pp 15-33(1986).
[2]. G. Wenga, E. Jacques, A.C. Salaun et al., Step-gate polysilicon nanowires field effect transistor compatible with CMOS technology for label -free DNA biosensor, Biosensors Biolectron., Vol.40, no.1, pp 141-146 (Feb. 2013).
[3]. H.M. Fahad, M.M. Hussain, High-performance silicon nanotube tunneling FET for Ultralow-power logic applications, IEEE Trans. Electron Devices 60(3), 1034(2013).
[4]. C. Qiu, Z. Zhang, M. Xiao, Y. Yang, D. Zhong, L.M. Peng, Scaling carbon nanotube complementary transistors to 5-nm gate length, Science 355(6322), 271(2017).
[5]. I. Santolia, A. Tewari, S.C. Sharma, R. Sharma, Effect of doping on growth and field emission properties of spherical carbon nanotube tip placed over cylindrical surface, Phys. Plasmas 21(6), 063508(2014).
[6]. A. Rochefort, D.R. Salahub, P. Avouri, Effects of finite length on the electron structure of carbon nanotubes, J. Phys. Chem. B 103(4), 641(1999).
[7]. S.C. Sharma, A. Tewari, Effect of plasma parameters on growth and field emission of electrons from cylindrical metallic carbon nanotube surfaces, Phys. Plasmas 18(8), 083503(2011).
[8]. A. Tewari, S.C. Sharma, Theoretical modeling of temperature dependent catalyst-assisted growth of conical carbon nanotube tip by Plasma enhanced chemical vapor deposition process, Phys. Plasmas 22(2), 023505(2015).
[9]. T. Kato, R. Hatakeyama, Growth of single walled carbon nanotube by Plasma CVD J. Nanotechnology Vol. 2010 (2010).
[10]. Y.C. Choi, D.J. Bae, Y.H. Lee, B.S. Lee, G.S. Park, W.B. Choi, J.M. Kim, Growth of carbon nanotubes by microwave plasma enhanced chemical vapor deposition at low temperature, J.Vac. Sci. Technol. A:Vac., Surf., Films 18(4), 1864-1868(2000).
[11]. L. Nougaret, H. Happy, G. Dambrine, V. Derycke, J.P. Bourgoin et al., 80 GHz field effect transistors produced using high purity semiconducting signle-walled carbon nanotubes, Appl. Phys. Lett. 94, 243505(2009).
[12]. J. Guo, S. Hasan, Ali Javey, G. Bosman, M. Lundstrom, Assessment of high-frequency performance potential of carbon nanotube transistors, IEEE Trans. Nanotechnol. 4(6), 715-721(2005).
[13]. Y. Li, David Mann, Marco Rolandi, Woong Kim, Ant Ural et al., Preferential growth of semiconducting single-walled carbon nanotubes by a plasma enhanced CVD Method, Nano Lett. 4(2), 317-321(2004).
[14]. T. Mizutani, Y. Ohno, S. Kishimoto, Electrical properties of carbon nanotube FETs, 2008 International Conference on Advanced Semiconductor Devices and Microsystems, pp 1-8 (2008).
[15]. F. Bashir, S.A. Loan, M. Rafat, A.R.M. Alamoud, S.A. Abbasi, A high performance source engineered charge-plasma based Schottky MOSFET on SOI, IEEE Trans. On Electron Devices 62(10), 3357(2015).
[16]. G. Jo, J. Maeng, Tae-wook Kim, Woong-Ki Hong, Byung-Sang Choi and T. Lee, Channel-length and gate -bias dependence of contact resistance and mobility for In2O3 nanowire field effect transistors, J. Applied Physics 102, 084508(2007).
[17]. C.R. Manoj and V. Ramgopal Rao, IEEE Electron Device Letters Vol. 28, No. 4, 295(2007).
[18]. Ashok Kumar Gupta and Ashish Raman, Performance analysis of electrostatic plasma-based dopingless nanotube TFET, Applied Phys. A 126, 573(2020).
[19]. G.J. Brady, Austin J. Way, Nathaniel S. Safron, Harold T. Evensen, Padma Gopalan, Michael S. Arnold, Quasi-ballistic carbon nanotube array transistors with current density exceeding Si and GaAs, Science Advanced 2, 1 (2016).
[20]. Y. Ono, S. Kishimoto, Y. Ohno and T. Mizutani, Thin Film transistors using PECVD-grown carbon nanotubes, Nanotechnology 21, 205202(2010).
[21]. S. J. Wind, J. Appenzeller, R. Martel, V. Derycke and Ph. Avouris, Vertical scaling of carbon nanotube field effect transistors using top gate electrodes, Appl. Phys. Lett. Vol. 80, No. 20, 3817(2002).
[22]. Wenting Shao, Michael R. Shurin, Sarah E. Wheeler, X. He and A. Star, Rapid detection of SARS-CoV-2 Antigens using high-purity semiconducting single-walled carbon nanotube-based field effect transistors, ACS Applied Materials & Interfaces 13, 10321-10327(2021).
[23]. Shivani Yadav and Sonam Rewari, Trench Gate JAM Dielectric Modulated Nanowire FET (TG-JAM-NWFET) Biosensor, Conf. Proceeding IEEE 2022.
[24]. M. Kansal and S.C. Sharma, Plasma-based nanoarchitectonics for vertically aligned dual-metal carbon nanotube field effect transistor device: Effect of plasma parameters on transistor properties, Appl. Phys. A 128, 28(2022).
[25]. M. Kansal and S.C. Sharma, Performance evaluation & linearity distortion analysis for plasma assisted dual material carbon nanotube field effect transistor with a SiO2-HfO2 stacked gate-oxide structure, Silicon (2022).

Accepted Manuscript
For Review Only

[26]. M. Kansal and S.C. Sharma, Exploration of novel hafnium (HfO2) based plasma-assisted gate all around carbon nanotube FET for high sensing applications, ECS J. of Solid State Science and Technology 11, 101002(2022).

[27]. A. Kaul, S. Rewari, & D. Nand, Macaroni channel-nanowire-field effect transistor (MC-NW-FET) for gate induced drain leakage (GIDL) reduction application. In 2022 IEEE International Conference of Electron Devices Society Kolkata Chapter (EDKCON) (pp. 35-38). IEEE, 2022, November.

[28]. A. Kaul, S. Rewari, & D. Nand, Hetero-dielectric macaroni channel cylindrical gate all around field effect transistor (HD-MC CGAA FET) for reduced gate leakage analog applications. Microsystem Technologies, 30(5), 599-611, 2024.

[29]. A. Kaul, S. Yadav, S. Rewari, & D. Nand, Computational modelling of cylindrical-ferroelectric-dual metal-nanowire field effect transistor (C-FE-DM-NW FET) using landau equation for gate leakage minimization. Micro and Nanostructures, 191, 207851, 2024.

[30] A. Kaul, S. Rewari, & D. Nand , Double Metal Gate Macaroni Nanowire FET (DMGM-NFET) for Improved Performance and Off-State Leakage Reduction. ECS Journal of Solid State Science and Technology, 13(10), 103010, 2024.

[31] Anubha Goel, Sonam Rewari, R.S. Gupta, Performance investigation of neoteric Pt/Pd Junctionless gas tube FET(JL-GT-FET) as a Hydrogen(H_2) gas sensor for industrial applications-analytical model, Micro and Nanostructures, Volume 198, February 2025, 208050.

[32] Amit Das, Sonam Rewari, Binod Kumar Kanaujia, S S Deswal and R S Gupta, Physics based numerical model of a nanoscale dielectric modulated step graded germanium source biotube FET sensor: modelling and simulation, Physica Scripta, Volume 98, Number 11, 2023.

[33] Amit Das, Sonam Rewari, Binod Kumar Kanaujia, S S Deswal and R S Gupta, Analytical modeling and doping optimization for enhanced analog performance in a Ge/Si interfaced nanowire MOSFET, Physica Scripta, Volume 98, Number 7, 2023.

[34] Amit Das, Sonam Rewari, Binod Kumar Kanaujia, S S Deswal and R S Gupta, Analytical investigation of a triple surrounding gate germanium source metal–oxide–semiconductor field-effect transistor with step graded channel for biosensing applications, International Journal of Numerical Modelling: Electronic Networks, Devices and Fields, https://doi.org/10.1002/jnm.3106.

[35] Shivani Yadav, Amit Das and Sonam Rewari, "Dielectric Modulated GANFET Biosensor for Label-Free Detection of DNA and Avian Influenza Virus: Proposal and Modeling" ECS Journal of Solid State Science and Technology, vol. 13, no. 4, p. 047001, 2024, doi: 10.1149/2162-8777/ad3364.

[36] Shivani Yadav and Sonam Rewari, "Nanoscale Trench Gate Engineered JAM Gate-All-Around (TGE-JAM-GAA) Label-Free BioFET for Charged/Neutral Biomolecules Detection," IETE Journal of Research, 70(11), 8263–8277, 2024.

[37] Shivani Yadav and Sonam Rewari, "Dielectric modulated 4 H-SiC source triple metal gate-all-around silicon carbide FET (DM-TMGAA-SiCFET) biosensor for label-free biomolecule detection," Microsystem Technologies (2024). https://doi.org/10.1007/s00542-024-05796-8.

[38] C. Wang *et al.*, "Ultrasensitive, high-throughput and multiple cancer biomarkers simultaneous detection in serum based on graphene oxide quantum dots integrated microfluidic biosensing platform," *Anal. Chim. Acta*, vol. 1178, 2021, doi: 10.1016/j.aca.2021.338791.

[39]. H. D. Sehgal, Y. Pratap, and S. Kabra, "Detection of Breast Cancer Cell-BIOMOLECULE3by Measuring Conductivity of Schottky Source/Drain GaN FinFET," *IEEE Sens. J.*, vol. 22, no. 6, pp. 6108–6115, 2022, doi: 10.1109/JSEN.2022.3148117.

[40]. "ATLAS User's Manual: 3-D Device Simulator, SILVACO International, Version5.14.0.R, 2024.".

[41] X. Yang and K. Mohanram, "Modeling and performance investigation of the double-gate carbon nanotube transistor," *IEEE Electron Device Lett.*, vol. 32, no. 3, pp. 231–233, 2011, doi: 10.1109/LED.2010.2095826.

[42]. A. Das, B. K. Kanaujia, S. S. Deswal, S. Rewari and R. S. Gupta, "Doping induced threshold voltage and ION/IOFF ratio modulation in surrounding gate MOSFET for analog applications," *2022 IEEE International Conference of Electron Devices Society Kolkata Chapter (EDKCON)*, Kolkata, India, 2022, pp. 1-6, doi: 10.1109/EDKCON56221.2022.10032940.

[43] A. Goel, S. Rewari, S. Verma and R. S. Gupta, "Dielectric Modulated Triple Metal Gate All Around MOSFET (TMGAA)for DNA Bio-Molecule Detection," *2018 IEEE Electron Devices Kolkata Conference (EDKCON)*, Kolkata, India, 2018, pp. 337-340, doi: 10.1109/EDKCON.2018.8770406.

[44] Bhargavi Sharma, Shivani Yadav, Sonam Rewari and Yasha Hasija, "DM-CN BIO-FET Biosensor for Breast Cancer Detection: Analytical Model" *ECS J. Solid State Sci. Technol.* **13** 087004**DOI** 10.1149/2162-8777/ad6a88.

Accepted Manuscript
For Review Only

Indian Journal of Chemical Technology
Vol. 32, March 2025, pp. 161-175
DOI: 10.56042/ijct.v32i2.15397

Novel molasses-grafted poly(sodium acrylate) hydrogel: A sustainable solution for water retention and controlled dinotefuran release

Manu Nandal, Vaishali Prashar, Mukul Bansiwal, Ishita Kapoor, Tushar Kansal & Rajinder K. Gupta*

Department of Applied Chemistry, Delhi Technological University, New Delhi, India

*E-mail: rkg67ap@yahoo.com

Received 29 November 2024; accepted 12 February 2025

Sugarcane molasses, a byproduct derived from sucrose manufacturing, is a polyphenolic compound with high sugar content. In this study, a novel molasses-grafted poly(sodium acrylate) hydrogel (M-g-SAH) is synthesized via free radical co-polymerization, using potassium persulfate (KPS) as the initiator and N,N'-Methylenebisacrylamide (MBA) as the crosslinker. M-g-SAH is characterized using Fourier-transform infrared spectroscopy (FTIR), X-ray diffraction (XRD), thermogravimetric analysis (TGA), scanning electron microscopy (SEM) and rheometer. Results demonstrated significant structural, thermal, and morphological changes in M-g-SAH compared to the non-grafted control hydrogel (ctrl). Swelling studies in Milli-Q water revealed that M-g-SAH achieved a maximum swelling index of 225.9 g g^{-1}, with swelling behavior influenced by molasses, KPS, and MBA concentrations. The controlled release of molasses from the M-g-SAH is modelled using Korsmeyer-Peppas, Higuchi, and first-order kinetics. M-g-SAH demonstrated a prolonged release of molasses over 39 h, outperforming the ctrl. According to ANOVA results, the addition of molasses proved to be an effective factor in agricultural trials, as the M-g-SAH hydrogel significantly showed improved water retention and reduced evaporation rate compared to ctrl. Additionally, dinotefuran loading and release studies confirmed M-g-SAH's potential as a pesticide carrier, supporting sustained release applications. These properties make M-g-SAH an eco-friendly and versatile material suitable for agricultural applications.

Keywords: Agriculture, Dinotefuran, Hydrogel, Molasses, Pesticide, Release kinetics

Introduction

Hydrogel forms a 3D network structure comprising polymers crosslinked either chemically or physically. Super absorbent polymers as hydrogels, relative to their own mass, can retain and absorb remarkably enormous amounts of water or aqueous solution[1]. Ideal hydrogels have multiple characteristics; they tend to swell with the liquid and keep their shape intact but increase in volume to reach a physical-chemical equilibrium[2,3]; are non-toxic and inexpensive[4], have high durability, biodegradability[5] and re-wettability. Super absorbent hydrogels have been highly promising in agricultural applications by providing maximum water content and releasing nutrients of choice at the desired rate, thereby increasing crop production by manifolds without negatively impacting the environment[6]. Recent research suggests that incorporating polymer hydrogels into agricultural soil can enhance water efficiency by minimizing water loss and improving soil quality[7, 8]. These hydrogels, known for their water-absorbing properties, significantly enhance soil moisture retention, making them a promising solution for optimizing water utilization in agriculture[9]. Additionally, potassium humate has been found to increase the soil's water-holding capacity while promoting plant growth, improving nutrient uptake, and enhancing yield and fruit quality. A study by Sayed et al., conducted in Egypt during the 2015 and 2016 growing seasons on Egazy olive trees (*Olea europaea* L.), demonstrated these benefits under water stress conditions[10]. Hydrogel-based pesticides function as controlled-release systems, gradually dispensing fertilizers over time. When fertilizers are incorporated into hydrogels, their release rate is significantly slower—approximately half the rate compared to fertilizers dissolved in water alone[11]. In a study by Xianglin et al., a superabsorbent resin modified with sodium humate was developed using inverse suspension polymerization. This resin exhibited excellent water absorption capacity and slow-release characteristics, which were analyzed by monitoring sodium humate release in distilled water[12]. Hydrogels are synthesized from natural polymers, synthetic polymers, and hybrid compositions. Natural polymer hydrogels have gained considerable interest and have undergone examination and evaluation from various perspectives[13].

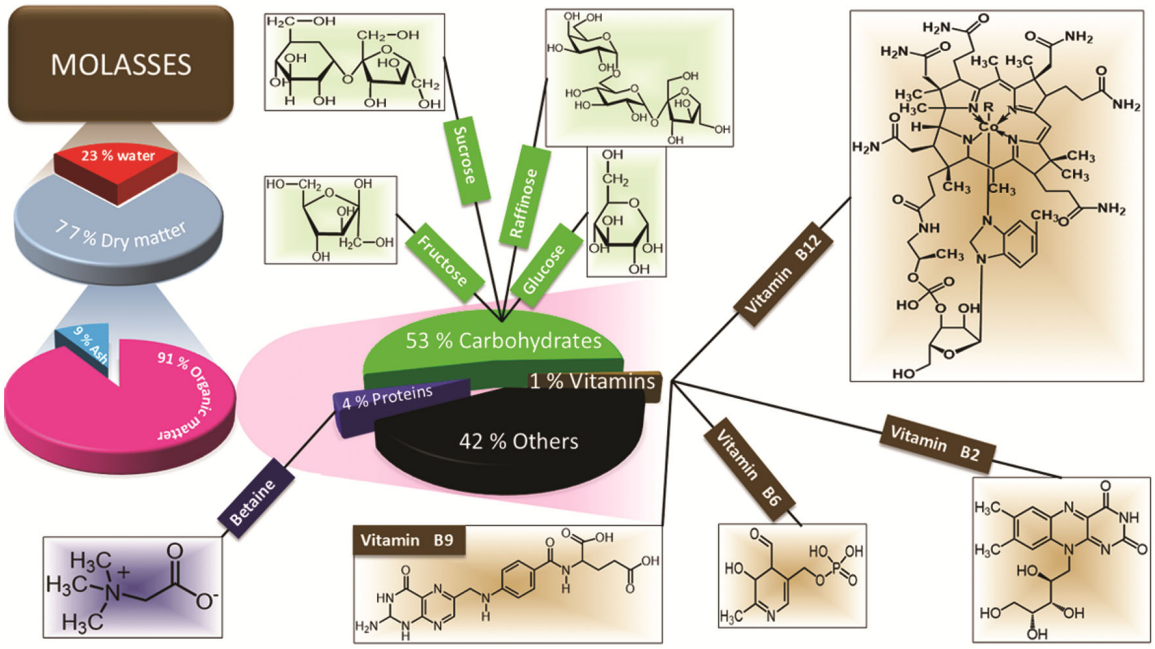

Fig. 1 — Major constituents of cane molasses

Natural biopolymers are commonly employed to prepare "intelligent" hydrogels- ones that show significant changes under the effect of external stimuli. Molasses is a viscous, black-brown effluent obtained in sugar production by repeated crystallization. Sucrose extraction from sugar beets (*Beta vulgaris*) occurs deep in the roots, whereas sugar cane (*Saccharum officinarum*) is derived from the trunk's medullary tissue. The latter comes mainly from South America, Southeast Asia, and the U.S. and is recognized as a high-energy feedstuff owing to its abundance of readily fermentable sugars. Additionally, it contains significant amounts of mineral salts in a bio-accessible form[14]. Fig. 1 shows the chemical composition of cane molasses. It shows that a significant part of molasses is composed of dry matter and serves as a rich source of carbohydrates[15]. Molasses serves as a biodegradable feedstock readily available in adequate amounts to impart antibacterial and antioxidant properties, biodegradable, biocompatible, and nutritional features and no systemic toxicity upon administration[16,17], thereby making it suitable for agriculture and drug delivery. Graft co-polymerization is a well-established and potent method of modifying hydrogels' characteristics, paving the way for adding desired properties and expanding their potential[18]. Hydrogels are typically synthesized by grafting synthetic monomers onto natural polymers. The initiation of radical formation, crucial for polymer growth, is influenced by factors like reaction conditions, solvents, and monomers[19]. Previous studies on molasses have primarily focused on its use as a fermentation feedstock or in the production of biofuels, with limited exploration in polymer chemistry. For instance, Kiselev et al. (2022) investigated the use of sugar beet molasses as a substrate for producing polyhydroxy alkanoates (PHAs) using the bacterium *Cupriavidus necator*. The researchers found that hydrolyzed molasses led to significant biomass and polymer yields, achieving up to 80% polymer yield from bacterial biomass. Similarly, another study explored the use of sugar beet and starch molasses to produce levan, a fructose homopolymer, using *Halomonas sp*. This research showed that pretreated molasses could effectively substitute sucrose, yielding high concentrations of levan. The findings illustrate the versatility of molasses in producing biopolymers, although still within the fermentation context.[20, 21] Another significant study by Fan et al. (2022) integrated sugarcane molasses into lignocellulosic ethanol production, improving fermentation efficiency and increasing ethanol concentrations. The highest ethanol concentration achieved was 94.20 g L^{-1} when molasses was co-fermented with pretreated sugarcane bagasse, showcasing the advantages of using molasses in enhancing biomass resource utilization[22].

Thus, despite its potential, the use of molasses, particularly in hydrogel formation, remains underexplored. This study uses a free radical co-polymerization technique to synthesize and characterize

a novel molasses-grafted poly(sodium acrylate) (M-g-SAH) hydrogel. The incorporation of molasses into the hydrogel is hypothesized to improve its swelling capacity, water retention, and biodegradability, making it particularly suitable for agricultural applications. The structural, thermal, and morphological properties of the M-g-SAH hydrogel are investigated and compared to those of ctrl. The hydrogel's swelling behavior and dinotefuran release kinetics are also examined to evaluate its potential as a water-retention material and a controlled-release system for agrochemicals. The results of this study could provide valuable insights into the development of sustainable hydrogels for use in water management and precision agriculture.

Experimental Section

Materials

Cane Molasses, consisting of concentrated sugarcane juice, iron (1.2%), magnesium (0.4%), and calcium (0.3%),was bought through Amazon from Dhampur Green. Methylenebisacrylamide (MBA) and acrylic acid (A.A.) were obtained from CDH Pvt. Ltd., while potassium persulfate (KPS) was sourced from S.D. Fine Chem Ltd. Sodium hydroxide (NaOH) was procured from Qualikems Fine Chem Pvt. Ltd. All solutions used in the experimental analysis were prepared using Milli-Q (M.Q.) water to ensure purity.

Methods

Synthesis of M-g-SAH

M-g-SAH was synthesized using the free radical co-polymerization technique, with KPS and MBA as the initiator and crosslinker, respectively. At room temperature, the 4.24 g NaOH was added to 7 mL acrylic acid. The reaction mixture containing molasses (0.05 to 0.3g), A.A., NaOH, and KPS (0.25 - 0.56 % of the total monomer) was continuously stirred for 2 h. Subsequently, MBA (0.25 – 0.49 % of the total monomer) was added and stirred at 500 rpm for 2 h. The reaction solution was poured into a test tube and placed in a water bath for 30 min at 60°C. After completion of polymerization, the hydrogel was sliced and soaked in M.Q. water for one day (24 h) to separate unreacted chemicals. Finally, the hydrogel was oven-dried at 70°C until weight stability was achieved[23]. A pictorial representation of the synthesis of M-g-SAH is shown in Fig. 2.

Characterization

In order to facilitate the identification and investigation of the presence of functional groups in the synthesized hydrogels, infrared spectra were acquired using a Perkin Elmer 2000 FT-IR spectrometer with a resolution of 1 cm over a wave number range of 4000 cm^{-1} to 500 cm^{-1}. The PANalytical X'Pert Pro X-Ray Diffractometer was used for X-Ray Diffraction. The surface analysis of the sample was done through SEM, which was carried out on JEOL Japan JSM 6610LV, having two modes, high and low vacuum with electron sources as Tungsten with a voltage range of 1-20 kV and magnification of 1500 and resolution 10 µm. Thermogravimetric Analysis (TGA) was performed using a Perkin Elmer Thermogravimetric Analyzer, TGA 4000, in a nitrogen-controlled atmosphere. The heat was kept constant at 10 °C/min throughout the analysis.

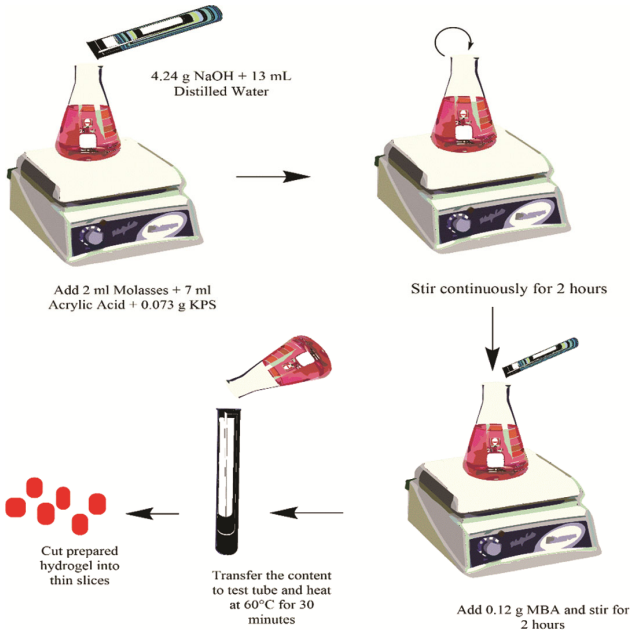

Fig. 2 — Pictorial representation for synthesis of M-g-SAH

Equilibrium Swelling Index

The swelling index of hydrogels, indicative of their water absorption capability, is quantified as the amount of water absorbed. The technique used to evaluate the swelling study of M-g-SAH is well-established and documented in earlier research. The samples under investigation were dried at 50°C until all moisture was eliminated, then weighed and placed in distilled water at room temperature. The samples were weighed at predetermined intervals after being cleaned with filter paper to remove excess water. [24, 25] The swelling index was defined using the Eq. 1.[26]

$$\text{Equilibrium Swelling Index } (gg^{-1}) = \frac{w_s - w_d}{w_d} \quad \ldots(1)$$

Table 1 — Various formulations used in the synthesis of M-g-SAH

Formulation	Molasses (g)	NaOH	KPS (%)	A.A. (mL)	MBA (%)	Equilibrium Swelling index (gg^{-1})	Gel Content (%)
M-g-SAH 1	0.1	8.07	0.25	7.1	0.25	219.73	64.23
M-g-SAH 3	0.1	8.07	0.25	7.1	0.33	183.8	69.62
M-g-SAH 4	0.1	8.07	0.25	7.1	0.41	169.46	73.12
M-g-SAH 2	0.1	8.07	0.25	7.1	0.49	147.28	78.65
M-g-SAH 5	0.1	8.07	0.25	7.1	0.33	184.72	68.21
M-g-SAH 6	0.1	8.07	0.33	7.1	0.33	212.64	64.52
M-g-SAH 7	0.1	8.07	0.41	7.1	0.33	201.33	67.12
M-g-SAH 8	0.1	8.07	0.49	7.1	0.33	189.75	68.34
M-g-SAH 9	0.1	8.07	0.56	7.1	0.33	174.63	71.43
M-g-SAH 10	0.05	8.07	0.25	7.1	0.41	157.56	76.34
M-g-SAH 11	0.1	8.07	0.25	7.1	0.41	163.97	74.63
M-g-SAH 12	0.2	8.07	0.25	7.1	0.41	188.31	69.12
M-g-SAH 13	0.3	8.07	0.25	7.1	0.41	225.9	63.82

where w_s= swollen hydrogel's weight and,w_d= dried hydrogel's weight.

The hydrogel chemical composition, specifically the presence of hydrophilic or hydrophobic groups, also affects their swelling behaviour. The feed composition, including factors such as the changes in concentrations of the crosslinker, initiator, and biopolymer, additionally impacts the swelling ratio. [25]Therefore, the compositions of M-g-SAH varied accordingly, as shown in Table 1.

Gel content determination

The fraction of weight that is insoluble in water is called gel. The soluble fraction of the gel is extracted in boiling water for 24 h with the Soxhlet equipment to determine the gel content. The swollen hydrogels were removed from the apparatus and oven-dried at 50°C. Eq. 2 was used to calculate the gel content of the hydrogel.[27]

$$\text{Gel content (\%)} = \text{SI} = \frac{M_E}{M_I} x100 \quad \ldots(2)$$

M_I is the initial dry weight of hydrogel, and M_E is the final weight of hydrogel after soxhlet extraction.

Measurement of the highest water-retention capacity (W.R.)

This study was conducted on the garden soil of Delhi Technological University, Delhi (28°45'01.9"N 77°07'01.5"E). The moisture content of the soil samples was removed by oven drying for 48 h at 60°C. Then, it was sieved to ensure particle size was less than 30 mesh. The sieved soil samples were then integrated with hydrogel powder up to a concentration of 1% (w/w). The soil-hydrogel mixture was filled into a hollow polypropylene cylindrical tube with a diameter of 5 cm. The bottom of the tube was covered with a nylon cloth, referred to as W_1. A control tube containing soil mixed with non-molasses grafted hydrogel (ctrl) was prepared for comparison. To each tube, 2 mL of M.Q. water was gradually added until it began to seep out from the bottom (W_2). The water addition was repeated every 4 hours to assess the water retention behavior across all samples [28].

Measurement of the Water Evaporation Ratio (WER)

A water evaporation test was conducted for M-g-SAH-treated soil over 55 days. Different sets of hydrogel-treated soil were prepared using oven-dried soil, which had been subjected to drying at 60°C for 48 h. A polypropylene tube was filled with soil, a dried M-g-SAH hydrogel disc, and 50 mL M.Q. water (marked as M_i). The tube, which consisted of ctrl hydrogel, served as a ctrl. The tubes were placed at room temperature and weighed at fixed intervals of 24 h (M_t). WER was determined using Eq. 3.[29]

$$\text{WER} = \frac{(M_i - M_t)}{M_t} x\ 100 \quad \ldots(3)$$

In vitro loading and release of dinotefuran

Dinotefuran was added to the hydrogel by immersing a pre-weighed dry M-g-SAH in dinotefuran solution (2000 ppm) for 24 h. The swollen gels were then withdrawn from the water and oven-dried until a consistent weight was reached.

The dinotefuran released from M-g-SAH was estimated by placing oven-dried, dinotefuran-loaded samples in a beaker containing 100 mL of M. Q water at ambient temperature. Samples for measuring the concentration of released dinotefuran were withdrawn at predetermined intervals while the same volume of M.Q. water was supplemented back to the beaker to maintain a constant volume. The absorbance of the supernatant was measured at 270.5 nm by a UV–

visible spectrophotometer. A standard calibration curve was obtained using Eq. 4 and then applied to determine the concentration of dinotefuran.

$$C\ (ppm) = \frac{A-0.4125}{0.0032} \quad \ldots(4)$$

Where, C represents the dinotefuran concentration in the water sample and A is the UV-visible absorbance of the solution of unknown concentration.

Determination of loading efficiency of dinotefuran

The amount of dinotefuran loaded into the M-g-SAH hydrogel formulations was determined by calculating the difference between the initial dinotefuran and the concentration of free dinotefuran in the corresponding supernatant. This analysis was performed using a UV–Vis spectrophotometer (Shimadzu UV-Spectrophotometer, UV-1800) at a wavelength of 254 nm. Subsequently, a standard curve was utilized to convert the absorbance readings of the samples into dinotefuran concentrations. The loading efficiency (L.E.) of dinotefuran was calculated using Eq.5.[30]

$$LE\ (\%) = \frac{A_{total}-B_{free}}{A_{total}} \text{x } 100 \quad \ldots(5)$$

Where A_{total} is the amount of dinotefuran used to prepare M-g-SAH, and B_{free} is the amount of freely present dinotefuran in the supernatant.

Results and Discussion

Mechanism for the synthesis of M-g-SAH

The KPS initiator generated anionic radicals, which facilitated the formation of phenoxy radicals on molasses. Subsequent reactions of these active radicals with the vinyl groups of sodium acrylate led to the propagation of poly(sodium acrylate) chains. According to Ganguly et al., the divinylic monomer N,N'-methylenebisacrylamide (MBA), incurs interchain covalent crosslinking due to its multifunctional character. Consequently, the poly(sodium acrylate) chains propagated through further cross-linkage until crosslinking occurred between the polymer chains, with MBA as the crosslinker and terminating the process to form M-g-SAH. The electrostatic repulsion between negatively charged carboxylate ions in the poly(sodium acrylate) polymer chains causes network expansion, enhancing the hydrogel's water absorption capacity.

All synthesized hydrogels' swelling behavior and gel content were evaluated in M.Q. water, as summarized in Table 1. Notably, M-g-SAH 13 exhibited the highest swelling capacity among the samples. Due to its superior performance, M-g-SAH 13 was selected for further experimental analysis and detailed studies.

The gel content percentage of hydrogels varied according to the concentration of crosslinker, biopolymer, and initiator. The gel content showed an inverse relation with the swelling of hydrogels, primarily determined by the degree of crosslinking. Increased crosslinking generally leads to a higher gel fraction, which can restrict the mobility of polymer chains. This restriction often results in decreased swelling capacity because the network becomes less flexible, limiting the amount of water absorbed [31]. Gel contents of synthesized hydrogels were found in between 64 - 76 %.

Characterization

FT-IR

The FTIR spectra of the Ctrl and M-g-SAH samples are presented in Fig. 3(a) and 3(b), respectively, as a comparative analysis to elucidate the functional group variations and structural

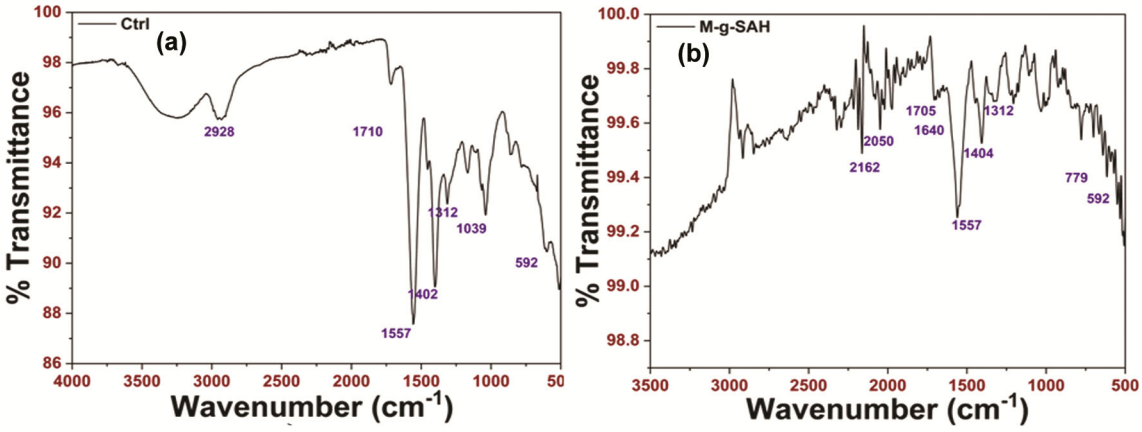

Fig.3 — FTIR spectra of (a) Ctrl and (b) M-g-SAH

characteristics of the materials under investigation. Ctrl has a band around 2928 cm^{-1} owing to the -CH stretching in $-CH_2$ or $-CH_3$ groups. A peak at 1312 cm^{-1} confirms the presence of C-N. The C=O stretching vibration, localized at approximately 1710 cm^{-1}suggests that the carboxylic acid functionalities are present within the matrix[32]. The low-frequency bands around 590 cm^{-1} indicate skeletal vibrations of the polymer backbone.

The significant water content in molasses affects the FT-IR spectrum. The O-H stretching vibrations from water molecules generally show a broad, strong absorption band around 3400 cm^{-1}, and the bending vibrations of water appear near 1640 cm^{-1}. The carboxyl group (-COOH) shows strong stretching vibrations between 1700–1740 cm^{-1}. Phenolic hydroxyl groups also contribute to bands around 3000–3500 cm^{-1} (O-H stretch). Molasses is rich in sugars such as sucrose, glucose, and fructose. These compounds display absorption bands primarily in the 1000–1200 cm^{-1} region, corresponding to C-O stretching vibrations in the carbohydrate structure. The band at 1039 $cm^{-1}$is linked to C-O-C vibrations due to the glycosidic linkages present in carbohydrates of molasses[33]. Peaks between 1620–1650 cm^{-1} may indicate the presence of conjugated or aromatic compounds in molasses.

The presence of two prominent peaks in both ctrl and M-g-SAH at 1557 cm^{-1} and 1402 $cm^{-1}$is associated with the carboxylate anion's vibration[34]. The broad spectrum and a peak at 1312 cm^{-1} and 592 cm^{-1}, respectively, indicate the presence of the C-N and O=C–N groups of MBA[35]. The stretching vibrations associated with C≡C and C≡N bonds exhibit absorption bands typically ranging from 2050~2200 cm^{-1}. In M-g-SAH, the 2162 cm^{-1} and 2050 cm^{-1} peak show weak terminal ≡C-H stretch. A medium to weak intensity level characterizes these bands. The M-g-SAH exhibits new peaks around 2162 cm^{-1} and 2050 cm^{-1}, which are absent in the ctrl. These peaks suggest the successful grafting of molasses onto the hydrogel network, likely introducing new unsaturated bonds or carbonyl groups. The overall similarity in the main COO^- peaks (1557 cm^{-1} and 1404 cm^{-1}) between both spectra confirms that the basic hydrogel structure is retained, while the grafting modifies certain chemical characteristics.

SEM

The SEM images of the Ctrl hydrogel sample and the M-g-SAH sample, both at a magnification of 1500x, are shown in Fig. 4. The ctrl hydrogel surface is even and smooth with some cracks which have been caused by oven drying. On the contrary, the structure of the M-g-SAH sample shows granular, uneven, porous and crosslinked morphology. This significant difference in morphology suggests that the grafting process and incorporation of molasses have dramatically altered the material's structure. The M-g-SAH sample demonstrates much higher porosity compared to the ctrl. The observed properties facilitate the adsorption of more water by molasses-grafted hydrogel in comparison to ctrl hydrogel[36].

XRD

The XRD patterns of the Ctrl and M-g-SAH samples (Fig. 5) are shown in the 2θ range 5°-90°. The M-g-SAH and Ctrl samples exhibited two complex and broad peaks within a specific range, with their peak maxima at 18° and 32°, respectively. The detected maxima in the XRD patterns indicate an amorphous polymer structure, suggesting that the material lacks long-range order and exhibits a disordered arrangement of its constituent polymer chains[25, 37]. The ctrl hydrogel shows a slightly higher

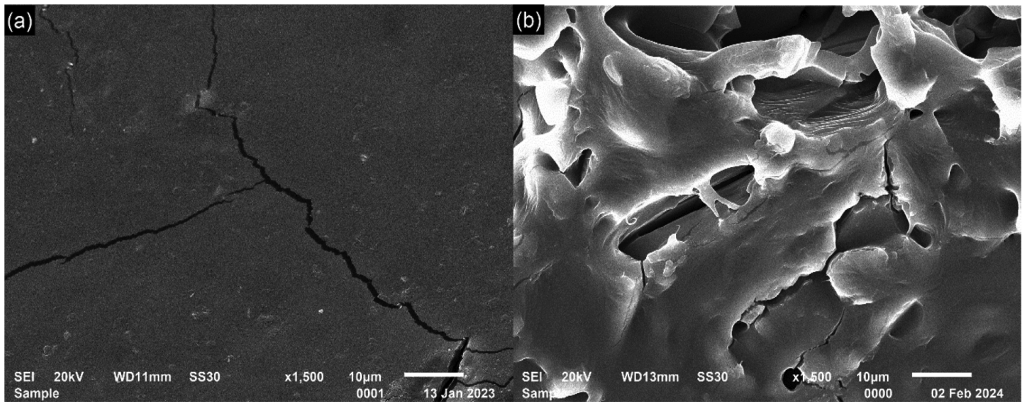

Fig. 4 — SEM images of (a) Ctrl sample and (b) M-g-SAH

intensity and broader peak than the molasses-grafted hydrogel M-g-SAH. The lower intensity of the M-g-SAH sample suggests that incorporating molasses has reduced the overall crystallinity or order within the hydrogel structure, possibly due to the interference of molasses components with polymer chain packing [38]. The absence of new sharp peaks in the M-g-SAH sample indicates that the molasses is well-integrated into the hydrogel structure without forming separate crystalline phases. In conclusion, the XRD results indicate that grafting molasses onto the poly (sodium acrylate) hydrogel has caused changes in the polymer structure, likely reducing its overall crystallinity or order without fundamentally altering its amorphous nature.

TGA and DTA

TGA is a quantitative analysis that assesses the mass variations in hydrogels subjected to heating. This technique helps determine thermal stability, degradation temperatures, and identification of distinct weight loss stages within the hydrogel structure. It also establishes different temperature ranges for different thermal events[39]. Analysis of the thermogram for the M-g-SAH sample, as shown in Fig. 6 (a and b), indicates that both materials show a gradual weight loss as temperature increases. Three distinct weight loss intervals are found within the temperature range of 40-780°C. In the case of M-g-SAH, the initial loss of weight of 24.54% within the temperature range of 40-420°C can be associated with the release of moisture inherently present in the polymeric structure. Subsequently, the temperature interval of 430-580°C is characterized by the onset of sample decomposition, accounting for a weight loss percentage of 23.5%. The third and final stage, incorporating the temperature spectrum of 600-780°C, is linked with the decomposition of the primary polymeric backbone, resulting in a weight loss of 9.55% [40]. The residual mass of M-g-SAH and ctrl were found to be 41.87 and 33.21 %, respectively.

The DTG graph in both samples shows an endothermic event (downward peak) in this range of 0-200°C. However, the ctrl has a sharper, deeper peak around 100°C, indicating a more rapid moisture loss. The M-g-SAH sample shows a broader, shallower peak, suggesting a more gradual moisture loss, possibly due to more vital water binding from the molasses components. Both samples exhibit a prominent endothermic peak centered around 450°C, representing the primary decomposition of the poly sodium acrylate backbone. The maximum degradation was observed at 338°C and 450°C for M-g-SAH and ctrl, respectively.

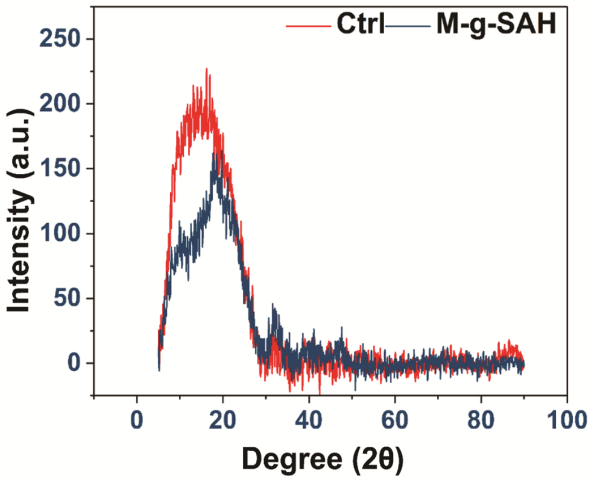

Fig. 5 — XRD plots of Ctrl and M-g-SAH

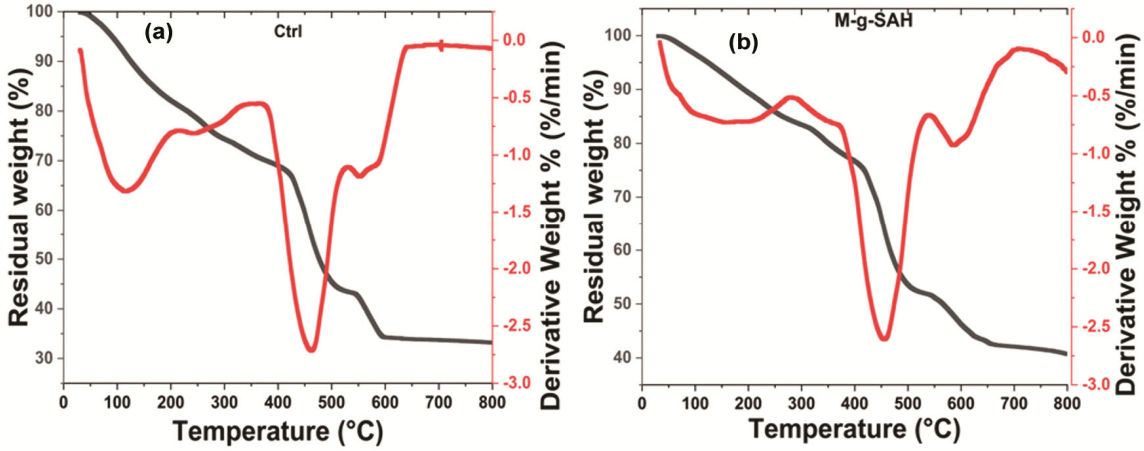

Fig. 6 — TGA and DTA plot of (a) Ctrl and (b) M-g-SAH

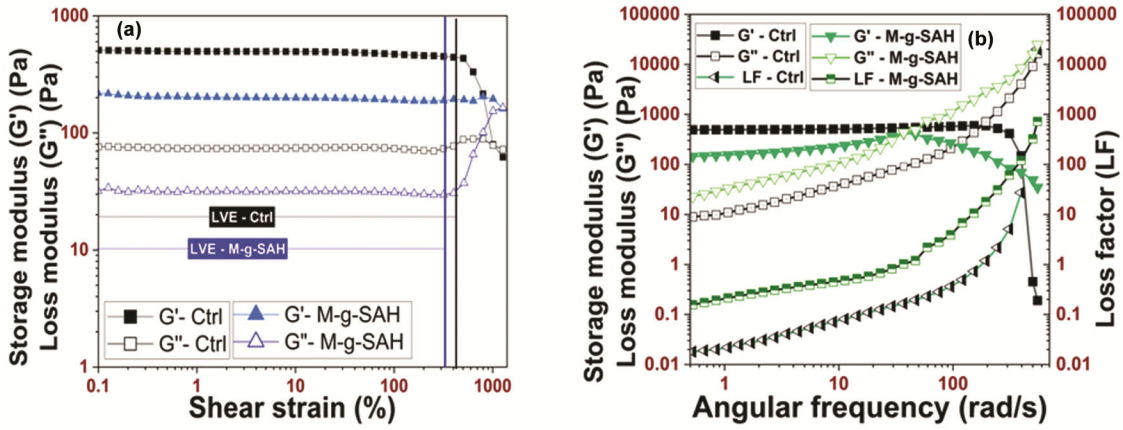

Fig. 7 — Rheological analysis of M-g-SAH and ctrl: (a) amplitude sweep and (b) frequency sweep

Table 2 — Frequency sweep rheological analysis data of M-g-SAH and ctrl hydrogels

Sample	Frequency Region up to cross-over point			Cross-over point	Frequency region after cross-over point		
	Storage modulus G' (Pa)	Loss modulus G" (Pa)	Loss Factor Tan θ	Angular frequency (rad/s)	Storage modulus G' (Pa)	Loss modulus G" (Pa)	Loss Factor Tan θ
M-g-SAH	144.94	22.74	0.156	37	34.62	24876	728.54
Ctrl	491.08	8.89	0.018	194	0.453	9063.7	200081

In conclusion, the molasses-grafted poly(sodium acrylate) hydrogel demonstrates improved thermal stability compared to the non-grafted ctrl, retaining more of its initial weight across the studied temperature range. It suggests that adding molasses to the hydrogel enhances its resistance to thermal decomposition.

Rheology

Rheological studies provide insights into the relationship between the chemical structure of hydrogels and their macroscopic behaviour.[41] The rheological properties of the synthesized hydrogels were compared with ctrl to investigate the effect of molasses in the hydrogels, as shown in Fig. 7(a) and 7(b).

During the amplitude sweep test, the shear stress amplitude was varied at a constant frequency of 10 rad/s. At low strain, both the loss modulus (G") and storage modulus (G') remained stable, indicating that the hydrogel's structure was unaffected. This phase, known as the linear viscoelastic region (LVE), represents the range in which the hydrogel maintains its structural integrity under applied deformation. However, the consistency between G" and G' decreased with a further increase in strain. This deviation from the consistent modulus indicates structure disruption and the LVE region's termination.

Both M-g-SAH and Ctrl show higher storage modulus (G') than loss modulus (G") across most of the strain range, indicating predominantly elastic behaviour. M-g-SAH exhibits lower G' and G" values compared to Ctrl, suggesting it is softer and less rigid. However, M-g-SAH has a broader LVE region, indicating that the grafted hydrogel retains elasticity over a more comprehensive strain range than the ctrl.

During the frequency sweep test, the frequency was varied from 0.1 to 500 rad/s, while the shear strain percentage was maintained constant within the linear viscoelastic (LVE) region. It was observed that at higher frequencies, the loss modulus (G") dominated, whereas, at lower frequencies, the storage modulus (G') was more prominent, indicating a viscoelastic solid behaviour. The parameter Tan θ (dimensionless), representing the ratio of the loss modulus to the storage modulus, typically ranges from 0 to 1 for viscoelastic materials. For purely viscous behaviour, Tan θ approaches infinity, corresponding to a phase angle (θ) of 90°, while for ideal elastic behavior, Tan θ equals 0, corresponding to a phase angle of 0°.[42]

From Table 2, the ctrl has a higher initial G' (491.08 Pa), suggesting a more solid-like structure at lower strains. M-g-SAH has a lower initial G', but the significant increase after the cross-over point suggests a strengthening of the elastic network at higher frequencies. M-g-SAH has a higher loss factor (tan θ) before the cross-over point (0.156), indicating more viscous behavior than the ctrl. Ctrl has a much lower tan θ (0.018) before the cross-over, suggesting it is

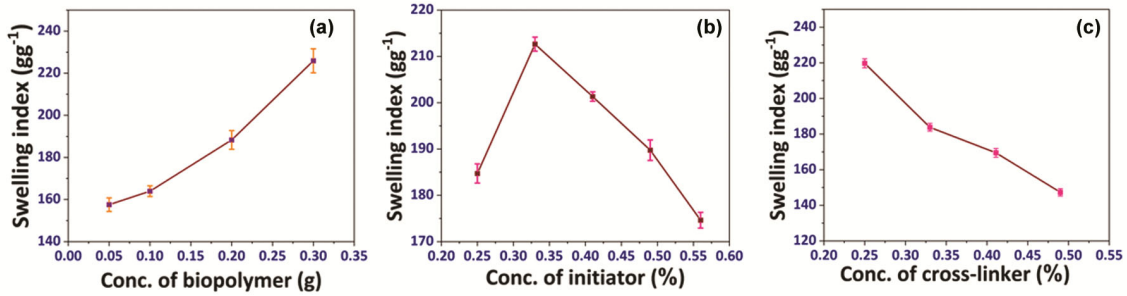

Fig. 8 — Effect of variation of (a) biopolymer (Molasses), (b) initiator (KPS) and (c) crosslinker (MBA) on the swelling index.Error bars represent standard deviation

more elastic even at lower strains. Thus, M-g-SAH hydrogel shows superior performance in terms of elasticity at higher frequencies and more extensive strain ranges, indicating that the molasses grafting enhances the elastic nature of the hydrogel.

Ctrl hydrogel displays more stable solid-like properties in the lower frequency and strain regions but lacks strength at higher frequencies and strains, as indicated by the rapid increase in G" after the cross-over.

Swelling study

a) Influence of Biopolymer on the Degree of Swelling

The concentration of a biopolymer significantly affects the swelling properties of hydrogels. An increment in the concentration of molasses from 0.05 to 0.3g enhances swelling ability from 157.56 to 225.9 $g\,g^{-1}$, shown in Fig. 8(a). The higher concentration of molasses affects crosslinking, resulting in a loose structure[31,43]. Additionally, the diverse hydrophilic groups in molasses offer more opportunities for water molecules to interact, improving the swelling behaviour of hydrogels. These combined effects contribute to the improved swelling behaviour of hydrogels with increased molasses concentration.

b) Influence of Initiator on the Degree of Swelling

The variation of the swelling ability of M-g-SAH hydrogel by changing KPS content is depicted in Fig. 8(b). The swelling ratio is between 184.72 to 174.63 $g\,g^{-1}$ is obtained when KPS content varies from 0.25 to 0.56 %. The higher KPS concentration results in an upsurge in free radical production. An escalation in free radical quantities leads to an accelerated rate of polymerization process. As a result, the polymer chains in the network become more extensive, with a reduction in the average kinetic chain size[23]. This alteration in the network configuration may result in a structure with increased porosity and a higher swelling index. The optimal water absorption occurred at 0.33% of the initiator. Higher initiator concentrations exceeding 0.33% might accelerate reaction velocity, reverting to lowering the hydrogel's network space, which, consequently, may reduce the hydrogel's swelling index.

c) Influence of Crosslinker on the Degree of Swelling

The porous morphology, swelling behaviour, and mechanical integrity of M-g-SAH depend upon the concentration of crosslinking agent (MBA). By adjusting the degree of crosslinking, a molasses-based hydrogel with desired properties can be prepared, providing a versatile platform for designing and customizing pesticide delivery systems. The swelling ratio of the prepared sample decreased from 219.73 to 147.28 g g^{-1} when the amount of crosslinking agent was raised from 0.25 to 0.49 %, as depicted in Fig. 8(c).The cutback observed in water absorption is linked to the generation of a denser structure caused by increased crosslinking, which is associated with a lower water absorption capacity[44]. When the concentration of MBA falls below 0.25%, the graft reaction is ineffective, producing gel-like material with inadequate dimensional stability[28]. MBA enhances crosslinking, decreasing the available free volume within the polymer network, resulting in reduced swelling behaviour of the hydrogel.

Agricultural applications of M-g-SAH

Highest water retention capacity

Water availability in the soil is of utmost importance for better plant growth. Fig. 9 shows the water retention capacity of two hydrogels, M-g-SAH and Ctrl, at different concentrations. Both hydrogels show an increase in water absorption as their concentration increases. The rate of increase is steeper

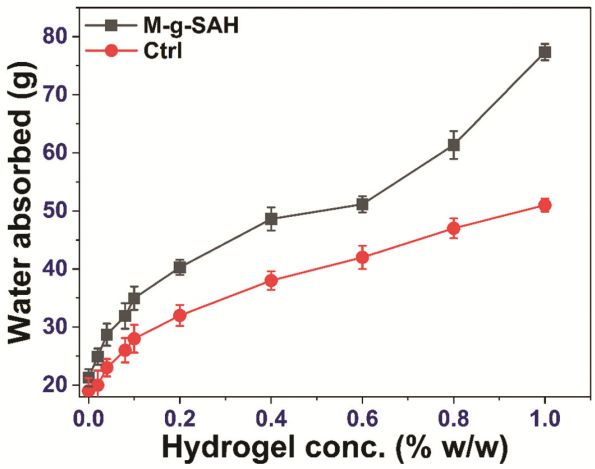

Fig. 9 — Highest water retention capacity of (a) Ctrl and (b) M-g-SAH. Error bars represent standard deviation

at lower concentrations (0-0.2%) and more gradual at higher concentrations. Still, M-g-SAH consistently demonstrated higher water absorption capacity than the ctrl at all concentrations. This superior performance is consistent across all tested concentrations (0-1% wt/wt), with the difference becoming more pronounced at higher concentrations. The improved water retention of M-g-SAH indicates that the molasses grafting process successfully modifies the hydrogel structure, likely increasing its hydrophilicity or creating more water-binding sites. This enhanced water retention property makes M-g-SAH a promising material for applications in agriculture, particularly in water-scarce regions, where it could help to improve soil moisture retention and reduce irrigation requirements.

Water Evaporation Ratio

The water evaporation test, conducted over 55 days, indicates similar trends between the M-g-SAH-treated soil and the ctrl hydrogel-treated soil, as depicted in Fig. 10. The M-g-SAH-treated soil exhibits notably enhanced water retention, characterized by a significantly slower evaporation rate and a more gradual increase in water loss throughout the test period. By the end of the 55 days, the M-g-SAH-treated soil had reached approximately 85% water evaporation. In contrast, the ctrl hydrogel-treated soil showed a steady increase in water evaporation, with around 75% water loss by day 55, likely due to the interaction between water and polymer molecules, along with the macromolecular network hindering evaporation. [29]

Notably, as time progressed, the performance gap between M-g-SAH and the ctrl hydrogel widened,

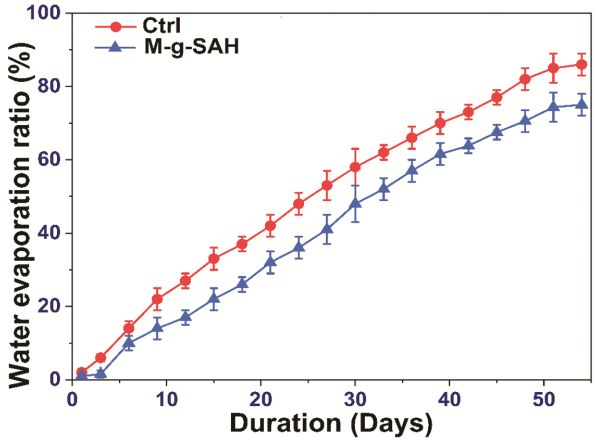

Fig. 10 — Water Evaporation study plots of (a) Ctrl and (b) M-g-SAH. Error bars represent standard deviation

highlighting the superior long-term water retention capabilities of M-g-SAH.

These findings are consistent with swelling study data, where M-g-SAH demonstrated higher swelling capacity than the ctrl hydrogel. The extended duration of water retention after hydrogel application suggests that water can remain in the soil for a longer period, offering plants more time to absorb water. This feature is especially beneficial during extended dry periods or under stress conditions, potentially enhancing plant growth. [45]

The results of the ANOVA (Table 3) revealed a significant difference in water evaporation ratios, water evaporation ratio and amount of dinotefuran released by M-g-SAH and the ctrl hydrogel, as indicated by an observed P-value (F-test) smaller than 0.05. This suggests that the changes observed in the following experiments were not due to random measurement errors but rather to the addition of molasses in hydrogel synthesis.

Dinotefuran Loading Efficiency

An ideal hydrogel used for release application should have good loading efficiency and allow for release over a longer time. The loading efficiency of synthesized dinotefuran-loaded hydrogels M-g-SAH13 and ctrl were found to be 63.52% and 57.44%, respectively.

Release Kinetics of Dinotefuran

The dinotefuran release process from all formulations followed a gradual mechanism. Initially, water penetrates the hydrogel, causing it to swell as it absorbs water. This absorption continues until a dynamic equilibrium is established between the

Table 3 — ANOVA table for conducted experiments

Source	Sum of squares	DF	Mean square	F-Value	P-value
Water Retention Ratio	845.60	3	547.34	110.23	2.67×10^{-3}
Water Evaporation	657.24	3	385.45	97.22	3.78×10^{-2}
Dinotefuran release	256.56	3	220.40	6.45	4.22×10^{-2}

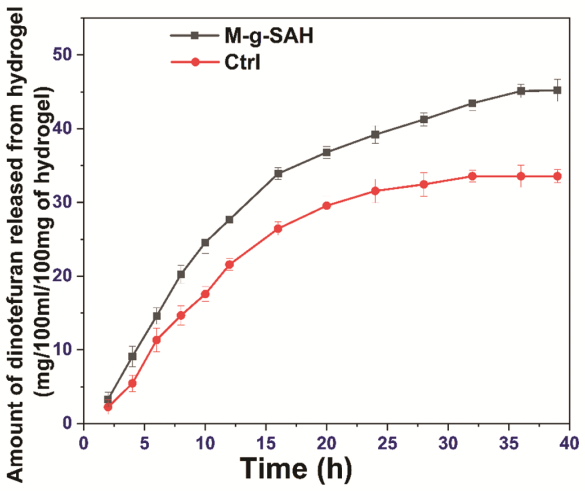

Fig. 11 — Amount of Dinotefuran released from M-g-SAH and Ctrl.Error bars represent standard deviation

hydrogel's free water and the beaker's water. During this phase, the dinotefuran embedded within the hydrogel matrix dissolves and diffuses. The release of dinotefuran into the water occurs due to osmotic pressure differences and the ongoing dynamic exchange of free water between the hydrogel and the environment [29].

The release kinetics of dinotefuran from M-g-SAH and ctrl was observed in M.Q. water. It was found that M-g-SAH and ctrl released dinotefuran for 39 and 32 h, respectively. The amount of dinotefuran released was observed to be 45.2 mg and 33.56 mg for M-g-SAH and Ctrl, as shown in Fig. 11. The disparity in released dinotefuran is attributed to the presence of molasses in the hydrogel.

The Korsmeyer-Peppas model, first order and Higuchi model are employed to describe the release mechanism of dinotefuran from M-g-SAH and ctrl hydrogels (Fig. 12). Korsmeyer Peppas model is described by the Eq. 6.[26]

$$\frac{M_t}{M_\infty} = k_{kP}t^n \qquad ...6$$

Where, M_t represents the concentration at a particular time and M_∞ represents the concentration at the equilibrium point.

This model shows the release behaviour only for the first 60% of the release of the pesticide[46]. The ratio of M_t to M_∞ represents total molasses in fraction released in time 't', while 'k' is a constant related to the polymer structure. The 'n' value indicates the deviation from Fickian behaviour, and it helps characterize the nature of the diffusion process in systems exhibiting non-Fickian or anomalous diffusion. If the value of 'n' is > 0.45, it suggests a diffusion-controlled release mechanism governed by Fickian diffusion. On the other hand, when the value of 'n' lies in the range of 0.45 to 0.89, it indicates a non-Fickian transport mechanism. If the value of 'n 'equals 0.89, it indicates zero-order release (Case II Transport). When the value of 'n' exceeds 0.89, it is classified as super case II transport[26].The coefficient of determination (R^2) value represents the model's accuracy, ranging from 0-1. A value over 0.95 references the model to be accurate.

The Weibull model can be represented using Eq. 7.[26]

$$\{\log(-\ln(1-m)\}=\beta\log(t-Ti)-\log\alpha \qquad ...(7)$$

Where, m is the amount of pesticide dissolved as a function of time t, β=shape parameter, α=scale parameter, Ti=Location parameter/time lag usually zero, t=Time in h. The α-value in the Weibull model shows the time scale or apparent rate constant, while the β value characterizes the shape of the curve. When it comes to polymeric matrices, the exponent β is a marker for the pesticide's method of transport across the matrix. In fractal and Euclidian spaces, Fickian diffusion is linked to β values 0.75; on the other hand, β values in the range 0.75-1 are linked to a combined mechanism (Fick diffusion and swelling-controlled transport). For values of β higher than 1, it is demonstrated that the pesticide transport follows a complex release mechanism [47, 48].

The release kinetics of the pesticide, which followed the first order, can be expressed as Eq. 8.[23]

$$\frac{dC}{dT} = -\,Kc \qquad ...(8)$$

Where K is the first order rate constant expressed in units of time^{-1}.

Eq. 8 can be expressed as $\log C = \log C_0 - Kt/2.303$

where C_0 is the initial concentration of the pesticide, k is the first-order rate constant, and t is the time[49]. The data obtained are plotted as a log

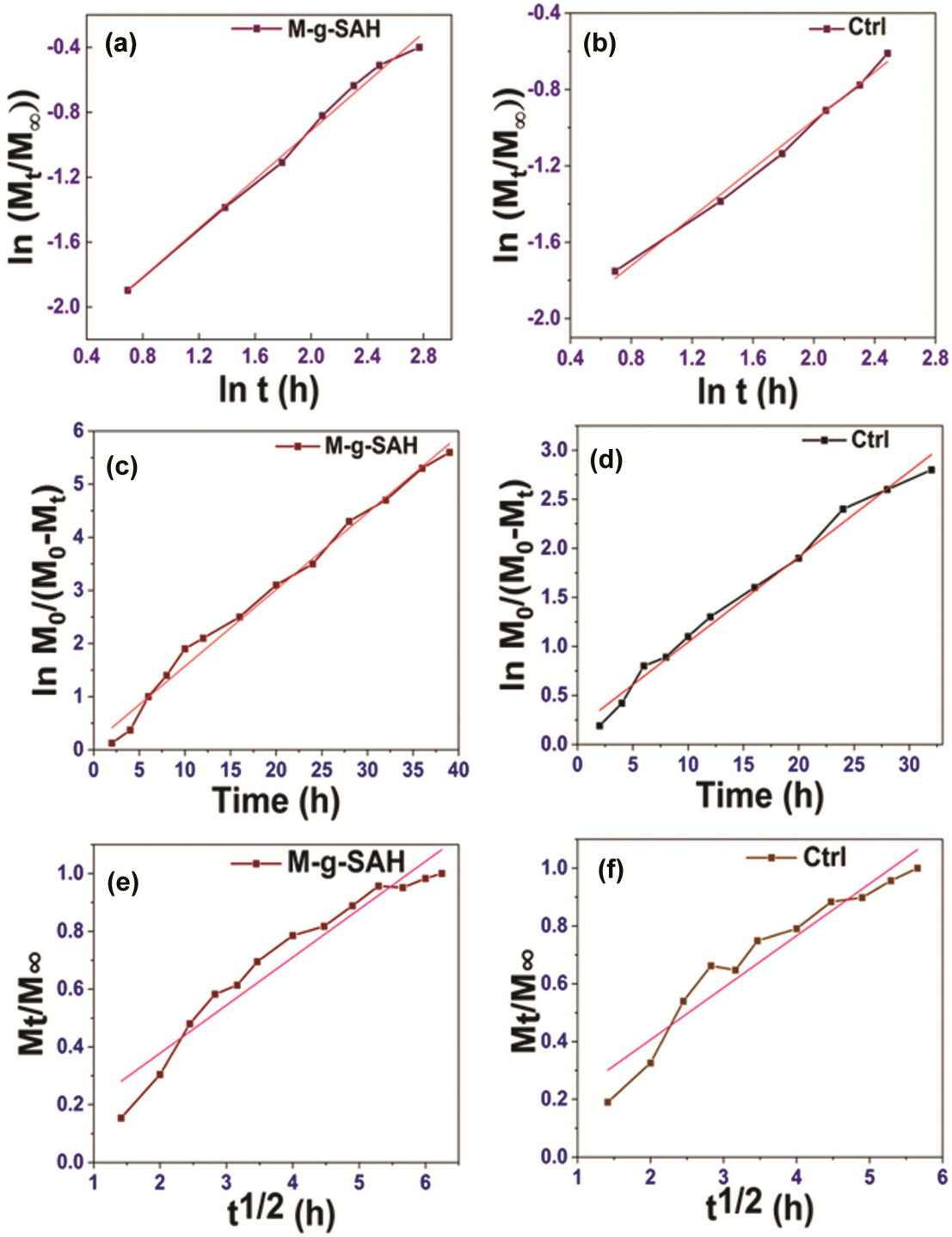

Fig. 12 — Dinotefuran release kinetics using (a) Korsmeyer Peppas Method– M-g-SAH, (b) Korsmeyer Peppas Method- Ctrl, (c) Higuchi model- M-g-SAH (d) Higuchi model- ctrl, (e) First order model- M-g-SAH and (f) First order model- ctrl

cumulative percentage of pesticide remaining vs. time, yielding a straight line with a slope of -K/2.303.

Table 4 shows the R^2 and relevant parameters for the Korsmeyer-Peppas, First Order, and Higuchi model, comparing the M-g-SAH with a Ctrl hydrogel. The 'n' values for both formulations in the Korsmeyer-Peppas Model fall between 0.45 and 0.89 (0.822 for M-g-SAH and 0.764 for ctrl), indicating their anomalous transport (non-Fickian diffusion).

Table 4 — Mathematical models used for the study of release kinetics of dinotefuran

Model	Formulation	R^2	Parameter
Korsmeyer Peppas	M-g-SAH	0.9932	n= 0.822 k=0.468
	Ctrl	0.9956	n= 0.764 k=0.593
First order	M-g-SAH	0.9884	k=0.134
	Ctrl	0.9863	k=0.162
Higuchi	M-g-SAH	0.9387	k=19.452
	Ctrl	0.9278	k=21.614

The higher 'n' value for M-g-SAH suggests a more significant contribution of polymer relaxation/erosion in the release process, possibly due to the molasses grafting. The lower 'k' value for M-g-SAH (0.468 vs 0.593 for Ctrl) indicates a slower initial release rate. The first-order model also demonstrated a good fit for both formulations ($R^2 > 0.98$) but slightly lower than the Korsmeyer-Peppas model. The k value for M-g-SAH (0.134) is lower than the Ctrl (0.162), consistent with the Korsmeyer-Peppas model, indicating a slower release rate for M-g-SAH. The Higuchi Model showed lower R^2 values (0.9387 for M-g-SAH and 0.9278 for Ctrl) than the other models, suggesting that simple diffusion alone does not fully explain the release process. The k value for M-g-SAH (19.452) is lower than the Ctrl (21.614), indicating slower diffusion-controlled release in the modified hydrogel.

Thus, the molasses-grafted hydrogel demonstrates a significantly modified release profile for dinotefuran compared to the ctrl. It exhibits a slower initial release rate and extends the overall release duration from 32 to 39 hours, a 21.9% increase in release time. The combination of slower initial release (lower k values) and longer duration suggests that M-g-SAH provides a more controlled and prolonged release profile.

Conclusion

This study successfully synthesized a molasses-grafted poly(sodium acrylate) hydrogel (M-g-SAH) via free radical co-polymerization, with KPS as the initiator and MBA as the crosslinker. Incorporating molasses, a renewable biopolymer, significantly enhanced the hydrogel's water retention and structural properties. Characterization using FTIR confirmed successful grafting of molasses, while XRD and SEM analyses revealed an amorphous structure and a more porous morphology than the ctrl hydrogel. TGA indicated improved thermal stability, with M-g-SAH retaining 41.87 % of its mass at 800°C, demonstrating superior thermal resistance. The swelling Index of M-g-SAH reached a maximum of 225.9 g g^{-1}. This enhanced swelling behavior was attributed to the higher molasses concentration, which increased the availability of hydrophilic groups. Crosslinker concentrations showed an inverse relationship with swelling, as denser networks restricted water absorption. The hydrogel's gel content ranged from 64% to 76%, reflecting its adjustable crosslinking density. In dinotefuran release studies, M-g-SAH exhibited a sustained release over 39 hours that lasted longer than the ctrl hydrogel (32 h), following non-Fickian diffusion kinetics, as described by Korsmeyer-Peppas and the first-order model. Additionally, dinotefuran loading efficiency was found to be 63.52% which is 10.58% greater than ctrl. In agricultural tests, the hydrogel showed 20% greater water retention than the ctrl, making it highly effective for soil moisture conservation. These results demonstrate that M-g-SAH is an eco-friendly, multifunctional material with great potential for agricultural water management, controlled release systems, and environmental sustainability applications.

Acknowledgements

The authors would like to acknowledge the Institute of Pesticide Formulation and Technology, Gurugram for providing dinotefuran. The authors would also like to thank the Department of Applied Chemistry, Delhi Technological University, Delhi for providing the research facilities.

References

1 Zohuriaan-Mehr MJ, & Kabiri K Superabsorbent polymer materials: A Review, *Iran Polym J*, 17 (2008) 451.

2 Duran S, Şolpan D & Güven O, Synthesis and characterization of acrylamide–acrylic acid hydrogels and adsorption of some textile dyes, *Nucl Instrum Meth Phys Res Sect B Beam Interact with Mater Atoms*, 151 (1999) 196.

3 Kumar J & Purwar R A, Schiff base hydrogel of oxidized okra gum and carboxymethylated chitosan: A biocompatible and biodegradable injectable system for drug delivery in wound care *Colloid Polym Sci*, 302 (2024) 1923.

4 Kumar J & Purwar R, Injectable mesquite gum and carboxymethyl chitosan hydrogel using schiff base crosslinks: a versatile platform for drug delivery in wound care *Macromol Res*, 32 (2024) 1237.

5 Kumar J & Purwar R, Biodegradable, biocompatible, and self-healing, injectable hydrogel based on oxidized Azadirachta indica gum and carboxymethyl chitosan through dynamic imine-linkage for biomedical application, *Iran Polym J*, (2024).

6 Goncalves A A L, Fonseca A C, Fabela I G P, Coelho J F J & Serra A C, Synthesis and characterization of high performance superabsorbent hydrogels using bis[2-(methacryloyloxy)ethyl] phosphate as crosslinker, *Exp Polym Lett*, 10 (2016) 248.

7 Song B, Liang H, Sun R, Peng P, Jiang Y & She D, Hydrogel synthesis based on lignin/sodium alginate and application in agriculture, *Int J Biol Macromol*, 144 (2020) 219.

8 Manu, Kumar D & Gupta R K, Natural polymers-humic acid and lignin based hydrogels: In agriculture, environment and energy storage, *Ind Crops Prod*, 219 (2024) 119029.

9 Prashar V, Nandal M, Gupta R K & Tyagi Y K, Novel Synthesis and application of carboxymethylated cassia fistula -based hydrogel for extended-release of dinotefuran, *ChemSelect*, 9 (2024) e202403421.

10 El-Sayed A E R & Mohamed S, Enhancing olive trees growth and productivity by using hydrogel and potassium humate under rain-fed condition in northern western coastal zone, *Egypt J Desert Res*, 67 (2017) 137.

11 Ghobashy M M The application of natural polymer-based hydrogels for agriculture, *Hydrogels Based Nat Polym*, 12 (2019) 329.

12 Yu X, Wang Z, Liu J, Mei H, Yong D & Li J Preparation, swelling behaviors and fertilizer-release properties of sodium humate modified superabsorbent resin, *Mater Today Commun*, 19 (2019) 124.

13 Peppas N A, Hilt J Z, Khademhosseini A & Langer R Hydrogels in biology and medicine: From molecular principles to bionanotechnology, *Adv Mater*, 18 (2006) 1345.

14 Mordenti A L, Giaretta E, Campidonico L, Parazza P & Formigoni A, A review regarding the use of molasses in animal nutrition, *Animals*, 11 (2021) 115.

15 El-Asri O & Farag M A, The potential of molasses from different dietary sources in industrial applications: A source of functional compounds and health attributes, a comprehensive review, *Food Biosci*, 56 (2023) 103263.

16 Grabek-Lejko D & Tomczyk-Ulanowska K, Phenolic content, anti-oxidant and antibacterial activity of selected natural sweeteners available on the Polish market, *J Environ Sci Heal Part B*, 48 (2013) 1089.

17 Takara K, Ushijima K, Wada K, Iwasaki H & Yamashita M, Phenolic compounds from sugarcane molasses possessing antibacterial activity against cariogenic bacteria, *J Oleo Sci*, 56 (2007) 611.

18 Hu X, Wei W, Qi X, Yu H, Feng L, Li J, Wang S, Zhang J & Dong W, Preparation and characterization of a novel pH-sensitive Salecan-g-poly(acrylic acid) hydrogel for controlled release of doxorubicin, *J Mater Chem B*, 3 (2015) 2685.

19 Tanwar M, Gupta R K & Rani A, Natural gums and their derivatives based hydrogels: In biomedical, environment, agriculture, and food industry, *Crit Rev Biotechnol*, 44 (2024) 275.

20 Küçükaşik F, Kazak H, Güney D, Finore I, Poli A, Yenigün O, Nicolaus B & Öner E T, Molasses as fermentation substrate for levan production by Halomonas sp., *Appl Microbiol Biotechnol*, 89 (2011) 1729.

21 Kucukasik F, Yenigun O & Toksoy O E, Molasses as fermentation substrate for microbial biopolymer production, *New Biotechnol*, 25 (2009) S250.

22 Fan M, Zhang S, Ye G, Zhang H & Xie J, Integrating sugarcane molasses into sequential cellulosic biofuel production based on SSF process of high solid loading, *Biotechnol Biofuels*, 11 (2018) 329.

23 Kumar D M & Gupta R K, Synthesis, characterization and application of Lignosulphonate-g- poly(sodium acrylate) hydrogel, *Indian J Chem Technol*, 30 (2023) 753.

24 Khaleghi M, Ahmadi E, Khodabandeh S M, Aliakbari F & Morshedi D, Temperature-dependent formulation of a hydrogel based on Hyaluronic acid-polydimethylsiloxane for biomedical applications, *Heliyon*, 6 (2020) e03494.

25 Srivastava A, Manu & Gupta R K, Xanthan Gum and lignin grafted chemically Crosslinked hydrogels for dye removal: Synthesis, characterization and isotherms studies, *Polym Sci Ser A*, 65 (2023) 725.

26 Manu, Kumar D & Gupta R K, Novel formulations of humic acid, lignin, and lignite grafted hydrogels for the slow release of thiamethoxam, *ChemistrySelect*, 9 (2024) e202304939.

27 Akalin G O & Pulat M, Controlled release behavior of zinc-loaded carboxymethyl cellulose and carrageenan hydrogels and their effects on wheatgrass growth, *J Polym Res*, 27 (2020) 1.

28 Tanwar M, Gupta R K & Rani A, Carboxymethylated gum tragacanth crosslinked poly(sodium acrylate)hydrogel: Fabrication, characterization, rheology and drug-delivery application, *Indian J Chem Technol*, 30 (2023) 308.

29 Rabat N E, Hashim S & Majid R A, Effect of different monomers on water retention properties of slow release fertilizer hydrogel, *Procedia Eng*, 148 (2016) 201.

30 Dharmalingam K & Anandalakshmi R, Fabrication, characterization and drug loading efficiency of citric acid crosslinked NaCMC-HPMC hydrogel films for wound healing drug delivery applications, *Int J Biol Macromol*, 134 (2019) 815.

31 Finkenstadt V L & Willett J L, Reactive extrusion of starch-polyacrylamide graft copolymers: Effects of monomer/starch ratio and moisture content, *Macromol Chem Phys*, 206 (2005) 1648.

32 Arndt K F, Richter A, Ludwig S, Zimmermann J, Kressler J, Kuckling D & Adler H J, Poly(vinyl alcohol)/poly(acrylic acid) hydrogels: FT-IR spectroscopic characterization of crosslinking reaction and work at transition point, *Acta Polym*, 50 (1999) 383.

33 Eisenberg A, Yokoyama T & Sambalido E, Dehydration kinetics and glass transition of poly(acrylic acid), *J Polym Sci Part A-1 Polym Chem*, 7 (1969) 1717.

34 Yu C, Wang F, Zhang C, Fu S & Lucia L A, The synthesis and absorption dynamics of a lignin-based hydrogel for remediation of cationic dye-contaminated effluent, *React Funct Polym*, 106 (2016) 137.

35 Reddy B V, & Rao G R, Vibrational spectra and modified valence force field for N,N'-methylenebisacrylamide, *Indian J Pure Appl Phys*, 46 (2008) 611.

36 Yadav R, Manu, Aayush & Rani A, Synthesis and characterization of xanthan gum and carboxymethylcellulose sodium salt based ionic crosslinked hydrogels for agricultural application, *Bulg Chem Commun*, 55 (2023) 131.

37 Ahmed I, Mahmood A, Qureshi O S, Sarfraz R M, Ijaz H, Zaman M, Akram M R, Usmani S, Zulcaif & Malook M, Development of tamarind gum/β-CD-co-poly (MAA) hydrogels for pH-driven controlled delivery of capecitabine, *Polym Bull*, 81 (2024) 6173.

38 Khan H, Yerramilli A S , D'Oliveira A, Alford T L, Boffito D C & Patience G S, Experimental methods in chemical engineering: X-ray diffraction spectroscopy - XRD, *Can J Chem Eng*, 98 (2020) 1255.

39 Santos F B, Miranda N T, Schiavon M I R B, Fregolente L V & Wolf Maciel M R, Thermal degradation kinetic of poly(acrylamide-co-sodium acrylate) hydrogel applying isoconversional methods, *J Therm Anal Calorim*, 146 (2021)2503.

40 Manu, Kumar D & Gupta R K, Harnessing lignite-based hydrogel for enhanced uv protection and delivery of dinotefuran in agriculture, *Polym Bull*, Vol (2024).page .

41 Stojkov G, Niyazov Z, Picchioni F & Bose R K, Relationship between structure and rheology of hydrogels for various applications, *Gels*, 7 (2021) 255.

42 Yadav R & Purwar R, Influence of metal oxide nanoparticles on morphological, structural, rheological and conductive properties of mulberry silk fibroin nanocomposite solutions, *Polym Test*, 93 (2021) 106916.

43 Murthy P S K, Mohan Y M, Sreeramulu J & Raju K M, Semi-IPNs of starch and poly(acrylamide-co-sodium methacrylate): Preparation, swelling and diffusion characteristics evaluation, *React Funct Polym*, 66 (2006) 1482.

44 Çaykara T & Turan E, Effect of the amount and type of the crosslinker on the swelling behavior of temperature-sensitive poly(N-tert-butylacrylamide-co-acrylamide) hydrogels, *Colloid Polym Sci*, 284 (2006) 1038.

45 Rajanna G A, Manna S, Singh A, Babu S, Singh V K, Dass A, Chakraborty D, Patanjali N, Chopra I, Banerjee T, Kumar A, Khandelwal A & Parmar B S, Biopolymeric superabsorbent hydrogels enhance crop and water productivity of soybean–wheat system in Indo-Gangetic plains of India, *Sci Rep*, 12 (2022) 11955.

46 Ahmed L, Atif R, Eldeen T S, Yahya I, Omara A & Eltayeb M, Study the using of nanoparticles as drug delivery system based on mathematical models for controlled release, *Int J Latest Technol Eng Manage Appl Sci*, 8 (2019) 52.

47 Ekenna I C & Abali S O, Comparison of the use of kinetic model plots and DD solver software to evaluate the drug release from griseofulvin tablets, *J Drug Deliv Ther*, 12 (2022) 5.

48 Paolino D, Tudose A, Celia C, Di-Marzio L, Cilurzo & Mircioiu C, Mathematical models as tools to predict the release kinetic of fluorescein from lyotropic colloidal liquid crystals, *Materials (Basel)*, 12 (2019) 693.

49 Dash S, Murthy P N, Nath L & Chowdhury P, Kinetic modeling on drug release from controlled drug delivery systems, *Acta Pol Pharm -Drug Res*, 67 (2010) 217.

International Journal of Ambient Energy

ISSN: (Print) (Online) Journal homepage: www.tandfonline.com/journals/taen20

Numerical analysis of various nanofluids in circular and square plate solar collector with spiral and U-bend collector pipe designs

Utkarsh Verma, Shivraj Yadav, Gaurav Kumar & Raj Kumar Singh

To cite this article: Utkarsh Verma, Shivraj Yadav, Gaurav Kumar & Raj Kumar Singh (2025) Numerical analysis of various nanofluids in circular and square plate solar collector with spiral and U-bend collector pipe designs, International Journal of Ambient Energy, 46:1, 2471400, DOI: 10.1080/01430750.2025.2471400

To link to this article: https://doi.org/10.1080/01430750.2025.2471400

Published online: 03 Mar 2025.

Submit your article to this journal

Article views: 10

View related articles

View Crossmark data

Full Terms & Conditions of access and use can be found at
https://www.tandfonline.com/action/journalInformation?journalCode=taen20

INTERNATIONAL JOURNAL OF AMBIENT ENERGY
2025, VOL. 46, NO. 1, 2471400
https://doi.org/10.1080/01430750.2025.2471400

Taylor & Francis
Taylor & Francis Group

Check for updates

Numerical analysis of various nanofluids in circular and square plate solar collector with spiral and U-bend collector pipe designs

Utkarsh Verma, Shivraj Yadav, Gaurav Kumar and Raj Kumar Singh

Department of Mechanical Engineering, Delhi Technological University, New Delhi, India

ABSTRACT

Nanofluids are being used to improve solar collector heat transfer due to rising demand for efficient solar energy systems. Six nanofluids at 2%, 3%, and 4% volumetric concentrations are tested in square and circular flat plate solar collectors with planar spiral and U-bend pipes. ANSYS Fluent 2022 R1 was used for a full Finite Volume Method (FVM) simulation utilizing the SIMPLE k-ϵ turbulence model, with a constant heat flow of 700 W/m⊃2 and variable flow velocities of 0.5, 1, 2, and 4 m.

A 2% concentration of aluminium oxide (Al_2O_3) nanofluid has the maximum heat transfer coefficient, Nusselt number, and thermal performance regardless of collector design. Silver (Ag) nanofluid has exceptional pressure drop at 3% and 4% concentrations. U-bend collectors have a thermal performance ratio of 1.23, compared to spiral collectors' 1.09, showing improved thermal performance with nanofluid concentration. Silicon dioxide (SiO_2) and diamond nanofluids perform poorly in all conditions, suggesting they are unsuitable for solar thermal systems.

Despite their limitations, Al_2O_3 and Ag nanofluids can improve solar collector efficiency, according to this study. The understanding can inform nanofluid solar thermal system development and applications.

ARTICLE HISTORY
Received 11 June 2024
Accepted 18 February 2025

KEYWORDS
Nanofluids; solar energy; solar collector; heat transfer; CFD; thermal efficiency

Nomenclature

C_p	Specific heat capacity (kJ/kgK)
D	Pipe diameter (m)
f	Friction factor
g	Gravity (m/s^2)
h	Convective heat transfer coefficient (W/m^{2}K)
Nu	Nusselt number
Pr	Prandtl number
p	Pressure (Pa)
q''	Heat flux rate per area (W/m^2)
Re	Reynolds number
T	Temperature (K)
T_b	Bulk temperature (K)
T_s	Pipe surface temperature (K)

Abbreviations

CFD	Computational Fluid Dynamics
HTC	Heat Transfer Coefficient

Greek Symbols

α	Thermal diffusivity (m^2/s)
κ	Thermal conductivity (W/mK)
μ	Dynamic viscosity (Ns/m^2)
ρ	Density (kg/m^3)
ϕ	Nanoparticle volume fraction
η	Thermal efficiency of collector

Subscripts

ave	Average value
bf	Base fluid
eff	Effective
m	Mean
h	Hydraulic
nf	Nanofluid
f	Fluid
np	Nanoparticle

1. Introduction

Due to population growth, there has been a sharp rise in demand for energy, which is vital for both technological and economic development. The energy-need is expected to rise by 2.1% annually till 2040. However, the valuable energies, which primarily come from untraditional sources, are limited. Fossil fuels still account for 84% of the world's energy use, despite recent declines brought on by increased use of renewable energy sources (Shaker et al. 2022; Javidan et al. 2022). Conventional energy sources make a significant contribution to greenhouse gas pollution, the main factor in global warming. Renewable sources of energy include hydropower, geothermal, solar, hydroelectric, wind and biomass. Solar energy is regarded as the most abundant of all possible renewable energy sources. The total potential for solar-generated electricity is comparatively high in terms of direct normal irradiance. Solar technology is currently divided into two main categories: (1) Photovoltaic: Sun-

CONTACT Gaurav Kumar gauravkmr716@gmail.com

© 2025 Informa UK Limited, trading as Taylor & Francis Group

light is transformed into electricity using photovoltaic effects. (2) Thermal: Heating and drying are accomplished by utilising solar energy. Especially for domestic and commercial heating uses, flat plate solar collectors are among the most often utilised technology for capturing solar energy. Determining the general viability and performance of solar thermal systems depends much on their efficiency. Combining material qualities, design elements, running circumstances, and the type of heat transfer fluid utilised helps one to ascertain the efficiency of flat plate solar collectors. Improvements in these fields keep improving the performance of flat plate solar collectors, so they become a more practical and efficient way to produce sustainable energy (Shaji 2014; Pandey and Chaurasiya 2017; Struckmann 2008; Bhowmik and Amin 2017; Ho, Yeh, and Wang 2005).

Furthermore, Roohi et al. (2023) investigated and presented is improvement of the PEC parameter by using nanofluid in comparison to base fluid going through a simple tube. The obtained results show that the performance evaluation criterion (PEC) can be improved by 57.3–70.8%, 68.7 ~ 86.4% and 83.4 ~ 105.9% for volume fractions of 1%, 2% and 3%, respectively by means of the CuO/oil nanofluid.

Particularly for heating uses, H.H. Schobert talks on solar plate collectors as a fundamental technique for using solar energy. Using a flat, typically blackened surface that absorbs heat, these devices gather sunlight and then transmit it to a working fluid such as air or water. Because of their simplicity, economy, and efficiency in turning solar radiation into useable thermal energy, Schobert notes their great popularity. Emphasising their part in sustainable energy systems, the book also examines the design issues, materials, and operational factors affecting the performance of solar plate collectors (Schobert 2014). A basic study of flat-plate solar collectors is offered in 1955 H. Hottel and A. Whillier. Considering elements including heat loss, solar insolation, and the temperature of the working fluid, the authors create a technique to assess the efficiency and thermal performance of these collectors. Key ideas like the heat removal factor and collector efficiency factor – which have been indispensable in solar collector design – are introduced here. Establishing ideas still applied in assessing solar collector performance now, this work prepared the stage for next research and development in solar thermal technology (Hottel and Whillier 1955). Hellstrom et al. (2003) investigated flat panel collector performance and optical characteristics. Teflon glazing film and honeycomb boosted the collector's yearly efficiency by 5.6% and 12.1%, respectively. Ho, Yeh, and Wang (2005) study flat plate collectors with double-pass channels and recycling. Traditional solar energy-based heating systems have a collection device, a fluid-circulating heat transfer path, and an energy storage with a heat exchanger. Energy production depends on size, shape, incidence angle, working fluid thermal properties, and collecting device material (Ibrahim et al. 2011; Cruz-Peragon et al. 2012; Rojas et al. 2008; Shih et al. 1995).

The most extensive use of circular cross-section U-bent tubes is in heat exchangers, solar collectors, electronic system cooling, chromatography, and other applications where heat is exchanged (Siah Chehreh Ghadikolaei 2021). Due to enhanced heat transfer rate due to an increase in the heat transfer coefficient, spiral tubes have become desirable for use in these domains. The ability of the spiral tubes to transport heat is affected by these produced secondary flows. The majority of solar applications include raising water temperature for daily domestic use and other objectives. An innovative strategy utilising nanofluids is being used as a passive method not requiring extrinsic energy to increase heat transfer by changing the thermo-physical properties of the working fluid (Gholinia et al. 2021; Siah Chehreh 2021; Sani, Pourfallah, and Gholinia 2022; Karimi et al. 2019). The aim of utilising a nanofluid is to increase the overall fluid thermal conductivity by including foreign particles (Chu et al. 2023; Sheikholeslami et al. 2019; Akbarzadeh et al. 2019; Salavati Meibodi et al. 2015). The conductivity of ethylene glycol and other non-metals was lower than that of metals and their oxides. The compilation of research tackles the improvement in solar collector performance by use of improved thermal analysis methods and nanofluids. Emphasising entropy generation and second law efficiency, researchers have investigated nanofluid turbulent flow in a solar heater with ribbed absorber panels. Using TiO_2 nanofluids in turbulent flow, they examine the heat transfer improvements in parabolic trough solar collectors, therefore showing notable efficiency enhancements. Enhanced turbulent convection is demonstrated by the investigation of Al_2O_3 nanofluid flow in solar flat plate collectors with flat-plate collectors. They experimentally investigated Al_2O_3-H_2O nanofluids and find appreciable efficiency gains. By means of experimental and numerical analyses on Al_2O_3/TiO_2-H_2O nanofluids. Many researchers have verified their favourable effect on the thermal efficiency of flat plate solar collectors (Subramani et al. 2018; Rashidi, Javadi, and Esfahani 2019; Yousefi et al. 2012; Farshad et al. 2019; Tiwari, Ghosh, and Sarkar 2013). Tiwari, Ghosh, and Sarkar (2013) were the first to publish a theoretical study of the effect on a flat plate solar collector, using Al_2O_3/water nanofluid. Collector thermal efficiency was improved by 31.64 percent when Al_2O_3 nanofluid was used in place of regular water. Experimental and statistical research by Farajzadeh, Movahed, and Hosseini (2018) investigated the impact of nanofluids on collector efficiency. They used a mixture of Al_2O_3 and TiO_2 nanofluids diluted in water to a weight of 0.1%wt. Incorporating Al_2O_3/water, TiO_2/water, or both into a system improves thermal efficiency (Gupta et al. 2022; Singh et al. 2021) by 19%, 21% and 26%, respectively. In 2013, Hussein et al. (2013) look at how heat transfer and friction factor in a horizontal tube change with nanofluid volume concentration. The work shows that while raising the friction factor, increasing nanofluid concentration improves heat transmission. Perfect concentrations balance controlled frictional losses with enhanced thermal performance.

Mahanthesh et al. examines the laminar flow and thermal transfer of a magneto-composite nanofluid (C2H6O2-H2O hybrid base liquid combined with MoS2-Ag hybrid nanoparticles) over an isothermal wedge, incorporating the influences of Joule heating and viscous heating (Mahanthesh et al. 2021).

Li et al. examines the thermal performance of a Casson hybrid nanofluid flow within a non-uniform, intricately wavy curved channel, influenced by Hall current and peristaltic motion (Li et al. 2023).

Sun et al. introduces a fractional model for examining the enhancement of heat transfer in a hybrid nanofluid composed of aluminium oxide and titanium oxide nanoparticles dispersed in water and kerosene oil base fluids, influenced by porous media,

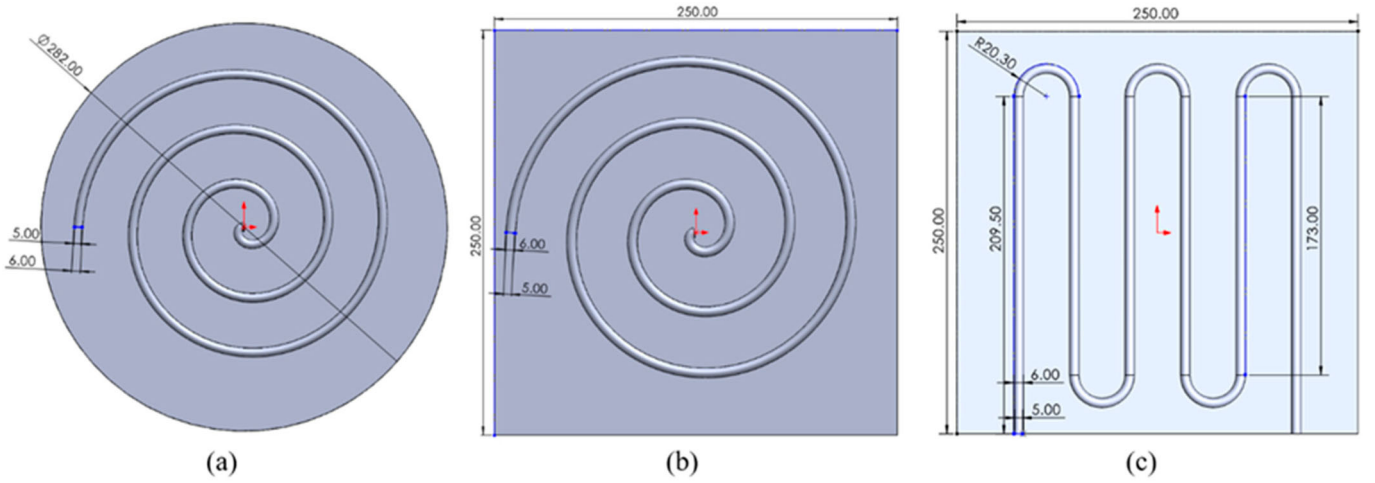

Figure 1. CAD model of the (a) circular plate, (b) square plate spiral and (c) U-bend collectors.

mixed convection, and magnetic forces, under sinusoidal thermal conditions (Sun et al. 2023).

The growing global dependence on renewable energy sources, especially solar energy, makes more effective solar thermal systems imperative. Often employed for their simplicity and economy, flat plate solar collectors can be greatly improved by including nanofluids, which are well-known for their excellent heat transfer characteristics. Still, current studies do not fully grasp how various nanofluids, concentrations, and collector designs affect performance, so more study is needed.

By offering understanding of how to maximise solar collectors utilising nanofluids, this work is essential for developing solar thermal technology. Identifying the most efficient nanofluid-collector combinations helps the research provide workable ideas to improve the cost-effectiveness and efficiency of solar thermal systems, therefore supporting the more general aim of sustainable energy development.

Using sophisticated computer simulations to find ideal combinations, the study intends to examine and compare the thermal performance of six nanofluids at varied concentrations in various solar collector designs.

2. Problem definition

2.1. CAD model and mesh

Flat plate solar collectors are significantly larger than the following used geometries. To reduce simulation efforts for three-dimensional fluid flow in such large collectors, a square and a circular collector plate with an area of 78,125 mm^2 and smaller plate dimensions of 250 × 250 × 1.25 mm^3 (Shaker et al. 2022) and radius 141 mm are used in this study. The pipe is 0.5 mm thick with an outside diameter of 6 mm. The pipe and the plate are made of copper and press welded with a shared thickness of 0.25 mm. Figure 1 depicts the different solar collector designs used in this study: (1) Spiral collector pipe with circular collector plate, (2) Spiral collector pipe with square collector plate, and (3) U-shaped collector pipe with square collector plate. In all the cases the length of collector pipe is 1.36 m. The four layers inflation with a 1.2 growth rate are used along the entire nanofluid to improve mesh accuracy. Simulations are performed after Parametric Analysis to improve mesh accuracy and determine the ideal mesh element size, which is 1 mm. The number elements in the mesh for a 1 mm element size are 1.7001E + 06, 1.4517E + 06 and 1.4468E + 06 for these collectors, respectively.

The following is the flow chart of the research methodology:

CAD Model Development > Mesh Generation > Numerical Set-up > Mesh Sensitivity and Validation > Results Processing.

2.2. Governing equations

A novel mathematical model combines the finite volume method (FVM) and SIMPLE k-ϵ turbulence model to assess nanofluid performance in solar collectors. It innovatively tests six nanofluids at 2%, 3% and 4% concentrations in square and circular geometries with spiral and U-bend pipes. The model provides heat transfer and efficiency insights beyond previous solar thermal system research by addressing different flow velocities and constant heat flux (Figure 2).

A Newtonian, 3-D steady fluid flow is used in this study. The k-ϵ model is used to simulate turbulent flow. As a result of nanofluid secondary flow, it is assumed that the nanofluid concentration is uniform throughout the flow. The thermo-physical system is represented mathematically by the following equations (Zadeh et al. 2021):

$$\text{Conservation of Mass: } \frac{\partial \rho}{\partial t} + \nabla \nabla.(\rho \vec{v}) = S_m \tag{1}$$

$$\text{Conservation of Momentum: } \frac{\partial \rho \vec{v}}{\partial t} + \nabla.(\rho \vec{v}\vec{v}) = -\nabla p + \nabla(\bar{\bar{\tau}}) + \rho \vec{g} + \vec{F} \tag{2}$$

where $\rho, \vec{g}$ are the volumetric forces of gravity and external force, respectively and $\bar{\bar{\tau}}$ is the stress tensor. S_m is the generated mass and $\vec{j}$ is flux penetration of various types.

Equation of Conservation of energy:

$$\text{Conservation of Energy: } \frac{\partial \rho E}{\partial t} + \nabla.(\vec{v}(\rho E + P)) = \nabla \left(k_{e_{ff}} \nabla T - \sum_j h_j \vec{J_j} + (\tau_{e_{ff}}.\vec{v}) \right) + s \tag{3}$$

Here *s* is a generated heat. The following is a definition of the stress tensor:

$$\bar{\bar{\tau}} = \mu\left(\nabla\vec{v} + \nabla\vec{v}^{T} - \frac{2}{3}\nabla.\vec{v}I\right) \tag{4}$$

where I is the tensor on the right-hand side of the equation representing the effect of a change in volume, and is the molecular viscosity. The thermal performance of a numerical model is characterised by:

$$\eta = \left(\frac{Nu}{Nu_0}\right)\left(\frac{f_0}{f}\right)^{\frac{1}{3}} \tag{5}$$

$$\text{Nusselt Number: } Nu = \frac{h_f D_h}{\kappa_f} \tag{6}$$

$$\text{Heat Transfer Coefficient: } h = \frac{q''_{ave}}{T_{s,ave} - T_{b,ave}}$$

$$\textit{Friction Factor}: f = \frac{2D_h\Delta p}{\rho v^2 L} \tag{7}$$

L denotes the tub length, and suffix 0 denotes the clear tube. D_h denotes the flow channel's hydraulic diameter. The average heat transfer coefficient is denoted by the symbol h_m.

In this work the working fluids are six nanofluids, with water serving as the base fluid to give SiO_2-H_2O, Al_2O_3-H_2O, CuO-H_2O, TiO_2-H_2O, Ag-H_2O, and diamond – H_2O containing homogenised suspensions of the respective nanoparticles. To compute the thermo-physical properties of the nanofluids, the succeeding equations are used:

Density:

$$\rho_{nf} = (\phi/100)\rho_{np} + (1 - (\phi/100))\rho_{bf} \tag{8}$$

Heat Capacity:

$$C_{nf} = \frac{(\phi\,/\,100)(\rho C)_{np} + (1 - (\phi\,/\,100))(\rho C)_f}{\rho_{nf}} \tag{9}$$

Thermal Conductivity:

$$\frac{\kappa_{nf}}{\kappa_{bf}} = \frac{\kappa_p + (n-1)\kappa_{bf} - (n-1)\phi(\kappa_{bf} - \kappa_{np})}{\kappa_{np} + (n-1)\kappa_{bf} + \phi(\kappa_{bf} - \kappa_{np})} \tag{10}$$

Viscosity:

$$\mu_{nf} = (1 + 2.5\phi)\mu_{bf} \tag{11}$$

The research assumptions can be taken as

(a) The fluid is Newtonian
(b) The fluid is taken as single continuous phase
(c) The Nano fluid concentration is uniform throughout the flow

The thermo-physical properties of all the nanofluids are calculated based on these equations (Mohammed, Gunnasegaran, and Shuaib 2011) and are listed in Table 1. The thermo-physical properties of the nanoparticle materials and the base fluid are shown in Table 2.

3. Numerical simulation

3.1. Details of set up

ANSYS 2022 R1 Fluent is used to run the numerical simulation in the Finite Volume Method. In every case, the initial temperature of the working fluid is 300 K. The top plate face is constantly exposed to a 700 W/m^2 solar flux. To form homogeneous fluids, volumetric concentration is taken very less. Due to the low nanoparticle concentration, the flow is assumed to be one continuous phase. The sides and bottom of the solar collector are insulated. Kinetic energy, mass, and momentum are discretized using the second-order upwind scheme. The relationship between pressure and velocity is calculated using the SIMPLE technique. The convergence criteria for the residuals of all equations is 10^{-9}. Gradients are found using the Green-Gauss cell-based approach.

3.2. Mesh sensitivity analysis

To discover the optimal mesh condition with the fewest grids while generating equivalent simulation results, a grid independence test is conducted. Parametric optimisation uses a set of parameters and their associated constraints to model the design space. The mesh element size was chosen as an input parameter and adjusted to generate the mesh nodes and mesh elements, as depicted in Figure 3(a). According to the parametric optimisation, for elements smaller than 1 mm, the outlet temperature does not change. As a result, 1 mm is selected as the element size to generate mesh as shown in Figure 1.

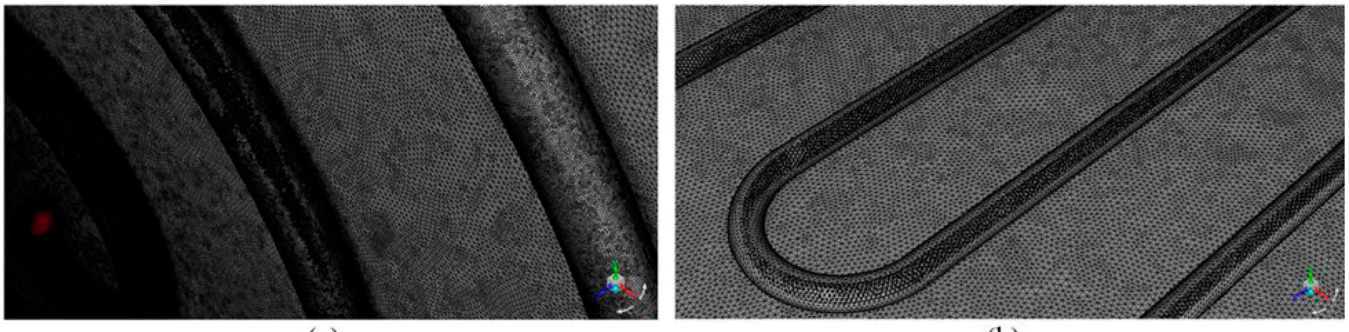

Figure 2. A section of the mesh for (a) spiral collectors, and (b) U-bend collector.

Table 1. Thermophysical properties of nanofluids at 2%, 3% and 4% volumetric concentrations.

Nanofluid (ϕ = 2%)	Nanoparticle	ρ (kg/m^3)	Cp (J/kg K)	κ (W/m K)	α (m^2/s)	**μ(Ns/m^2)**
SiO_2-H_2O	SiO_2	1022.236	4032.25	0.6219	1.508E-7	0.001053
Al_2O_3-H_2O	Al_2O_3	1188.236	3925.47	0.6488	1.391E-7	0.001053
CuO-H_2O	CuO	1108.236	3754.26	0.6472	1.555E-7	0.001053
TiO_2-H_2O	TiO_2	1063.236	3902.53	0.6436	1.957E-7	0.001053
diamond-H_2O	diamond	1048.436	3935.28	0.6504	1.576E-7	0.001053
Ag-H_2O	Ag	1188.236	3484.44	0.6503	1.570E-7	0.001053
1-7 **Nanofluid (ϕ = 3%)**	**Nanoparticle**	**ρ (kg/m^3)**	**Cp (J/kg K)**	**κ (W/m K)**	**α (m^2/s)**	**μ(Ns/m^2)**
1-7 SiO_2-H_2O	SiO_2	1061.20	3859.42	0.6250	1.526E-7	0.001078
Al_2O_3-H_2O	Al_2O_3	1087.35	3807.73	0.6497	1.569E-7	0.001078
CuO-H_2O	CuO	1163.25	3570.74	0.6486	1.561E-7	0.001078
TiO_2-H_2O	TiO_2	1095.75	3775.23	0.6460	1.561E-7	0.001078
diamond-H_2O	diamond	1062.75	3854.35	0.6508	1.588E-7	0.001078
Ag-H_2O	Ag	1283.25	3213.13	0.6508	1.578E-7	0.001078
1-7 **Nanofluid (ϕ = 4%)**	**Nanoparticle**	**ρ (kg/m^3)**	**Cp (J/kg K)**	**κ (W/m K)**	**α (m^2/s)**	**μ(Ns/m^2)**
1-7 SiO_2-H_2O	SiO_2	1046.27	3889.38	0.6290	1.545E-7	0.001103
Al_2O_3-H_2O	Al_2O_3	1117.07	3696.25	0.6624	1.604E-7	0.001103
CuO-H_2O	CuO	1218.27	3403.79	0.6610	1.594E-7	0.001103
TiO_2-H_2O	TiO_2	1128.27	3655.28	0.6573	1.593E-7	0.001103
diamond-H_2O	diamond	1084.27	3753.80	0.6640	1.631E-7	0.001103
Ag-H_2O	Ag	1378.27	2979.23	0.6640	1.617E-7	0.001103

Table 2. Thermophysical properties of nanoparticle materials and base fluid.

Material	ρ (kg/m^3)	Cp (J/kg K)	κ (W/m K)	**μ(Ns/m^2)**
SiO_2	2200	703	1.2	–
Al_2O_3	3970	765	40	–
CuO	6500	535.6	20	–
TiO_2	4250	686.3	8.955	–
diamond	3150	497.27	1000	–
Ag	10500	236	430	–
H_2O	998.2	4182	0.613	0.001003

4. Results and discussion

4.1. Validation

The Dittus-Boelter correlation (Hussein et al. 2013) has been used to validate the results of many similar studies. The Reynolds number in this correlation should be more than 10,000 hence this correlation is invalid for velocities 0.5 and 1 m/s. The Gnielinski correlation (Mohammed, Gunnasegaran, and Shuaib 2011) is another example of a correlation that is able to capture temporary effects. This association requires a Reynolds number of 3000 to 5 × 105. Therefore, velocities of 0.5, 1 and 2 m/s may be accounted for by the Gnielinski correlation, whereas velocities of 2 and 4 m/s can be accounted for by the Dittus-Boelter correlation. All three collector geometries are validated using the mentioned correlations for different Nusselt number values. Nusselt numbers for the turbulent flows were compared to those predicted by the Gnielinski equation, which is represented by the following equations:

$$Nu_G = \frac{(f/8)(Re - 1000)Pr}{1 + 12.7\sqrt{\frac{f}{8}}\left(Pr^{\frac{2}{3}} - 1\right)} \tag{12}$$

$$f = \frac{1}{(0.79 \ln Re - 1.64)^2} \tag{13}$$

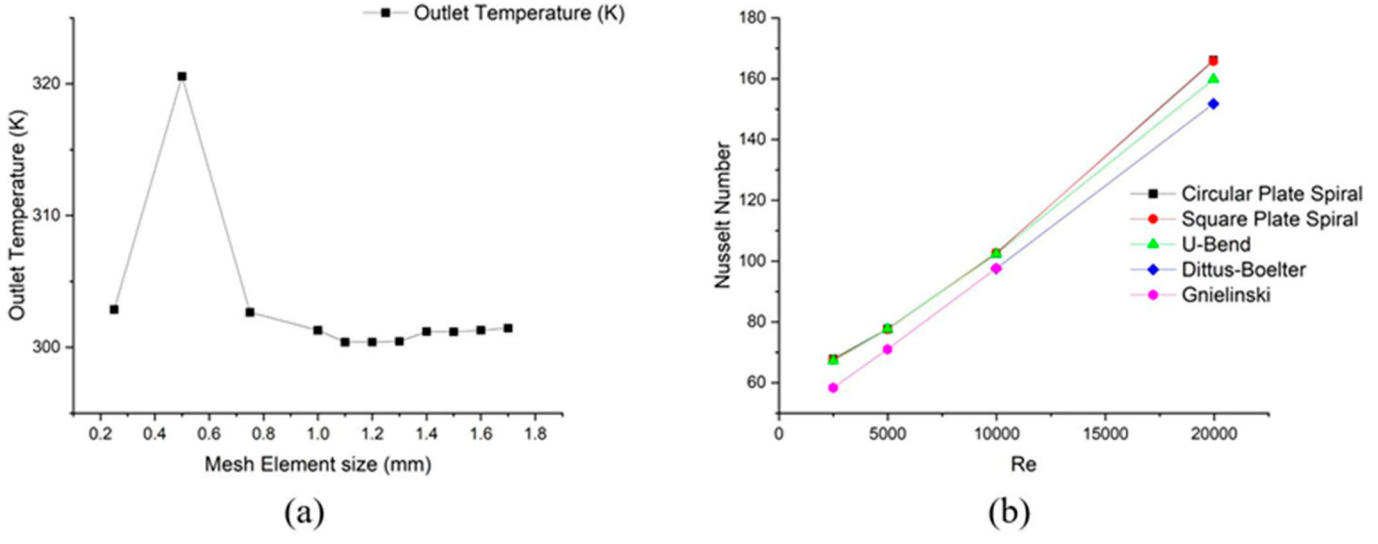

Figure 3. (a) Outlet temperature variation with mesh element size, and (b) Nusselt number comparison in the three collectors with Gnielinski and Dittus-Boelter correlations.

The Dittus-Boelter equation can be used to calculate the Nusselt number by relating the Reynolds number and the Prandtl number.

$$Nu_{DB} = \frac{h_f}{\kappa_f} D_{eff} = 0.023 Re^{0.8} Pr^{0.4} \tag{14}$$

The values of Nu, Nu_G and Nu_{DB} for all six nanofluids are represented in 'Figure 3(a)'. In the mentioned ranges, the Nusselt numbers of all three collectors show only minor variation with the Dittus-Boelter and Gnielinski correlations.

4.2. Water as working fluid

The Nusselt number (Nu) and pressure drop as a function of pipe length for various geometries with water as the working fluid are shown in Figure 3(b). The Nu numbers in spiral collectors are similar to and higher than those in U-bend collectors. This figure also shows that as the Re increases, so does the difference in Nu between spirals and U-bend. This is because of the presence of secondary flows and the greater frequency with which flow directions shift. The pressure drop in the U-bend was found to be significantly higher than in the spiral pipes, especially at high Re (about 22.97% higher). As illustrated in Figure 3(b), the increase in Nu is not as intense hence, at high Re numbers, the U-bend is not recommended.

Temperature changes on the collector surface are illustrated in Figure 4 for the three collector geometries. In this illustration, the flow velocities are 0.5, 1, 2 and 4 m/s. Surface temperature variations of the U-bend and circular plate spiral collectors are less compared to the square plate spiral collector.

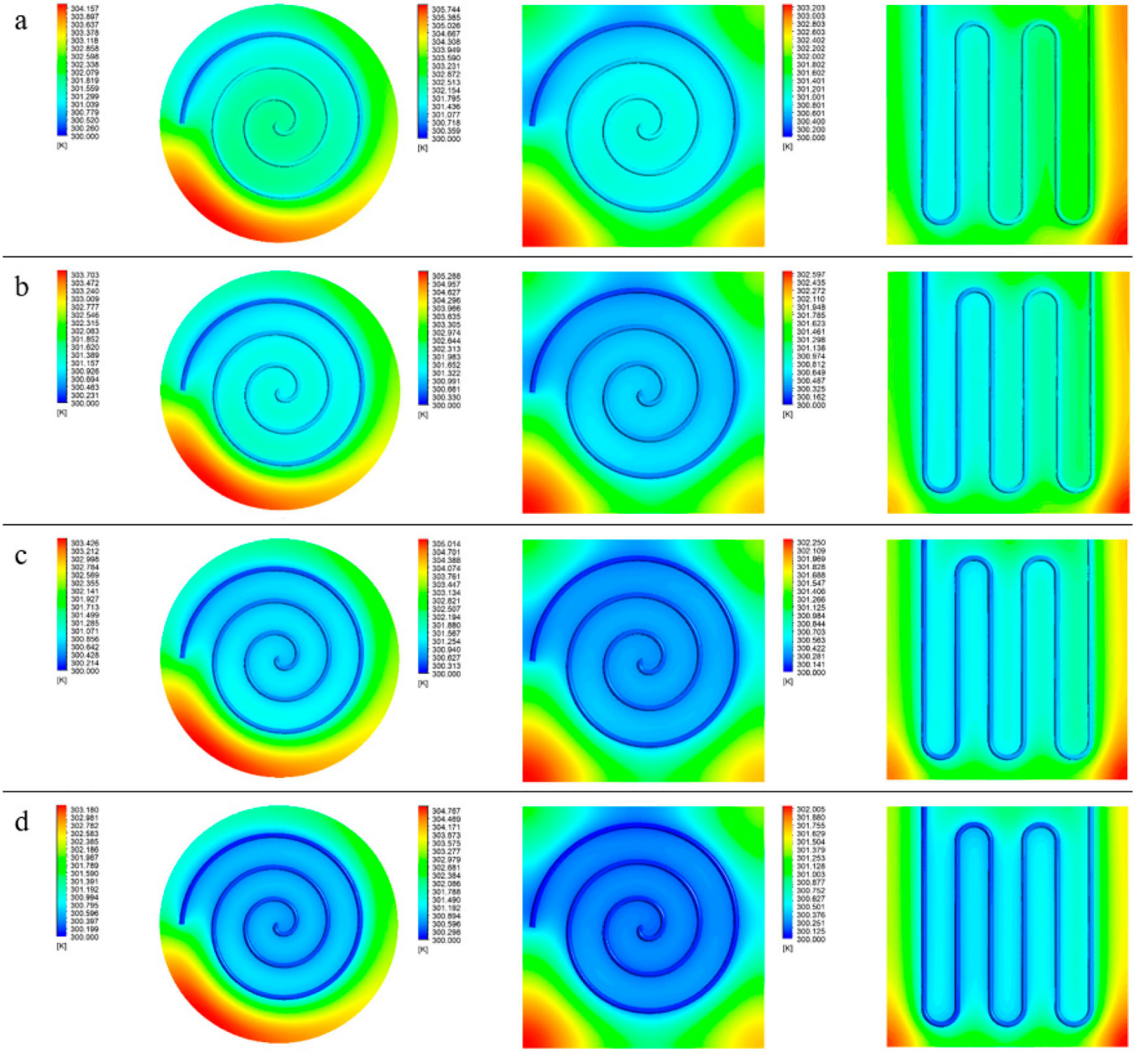

Figure 4. Collector plate temperature variation in the three collectors at a flow velocity of (a) 0.5 m/s, (b) 1 m/s, (c) 2 m/s and (d) 4 m/s.

For v = 0.5 m/s, the maximum surface temperatures of the U-bend and circular plate spiral collectors are 303.20 and 304.15 K, respectively, while the square plate spiral collector has a value of 305.74 K. This is due to the spiral pipe's unique shape. The collector's efficiency suffers because the hot corners of the square plate aren't being used by the spiral pipe.

4.3. Nanofluids ($\phi = 2\%$) as working fluid

In this study, mixtures of six distinct nanoparticles (CuO, Al_2O_3, TiO_2, SiO_2, Ag and diamond) are used. The flow velocity of the nanofluids is varied to record the required results and calculate the heat transfer coefficient (HTC), Nusselt number, pressure drop and thermal performance at with volumetric concentration of 2%. These variations in these factors (at v = 4 m/s) are represented against variation in the volumetric concentration as 2%, 3% and 4%. The calculated results are shown against the variation in Reynolds number, which corresponds to the flow velocities mentioned above. The properties of the nanofluids needed for this work are calculated using equations (8–11) and listed in Table 2. These tables show that when nanoparticles are added to water, properties such as density, thermal conductivity, and viscosity of the resulting nanofluids increase, while the specific heat decreases compared to water. As the change in viscosity is insignificant, the resulting mixtures are assumed to be Newtonian.

4.3.1. Effects on circular plate solar collector

The changes in the heat transfer coefficient against Reynolds number for water and the six nanofluids at $\phi = 2\%$ for the circular plate solar collector is shown in Figure 5(a). This graph shows that by adding nanoparticles, convective HTC increases. The HTC is maximum for Al_2O_3 nanofluid and smallest for SiO_2, with 16.29% and 0.79% higher than water, respectively. The trends of HTC for TiO_2 and diamond are nearly identical, with a 5.35% increase when compared to water. The HTC of Ag and CuO increased by 11.85% and 10.53%, respectively.

The Nusselt number variation against the Re number for water and the six nanofluids at $\phi = 2\%$ for the circular plate solar collector is shown in Figure 5(b) Nu is the ratio of convective

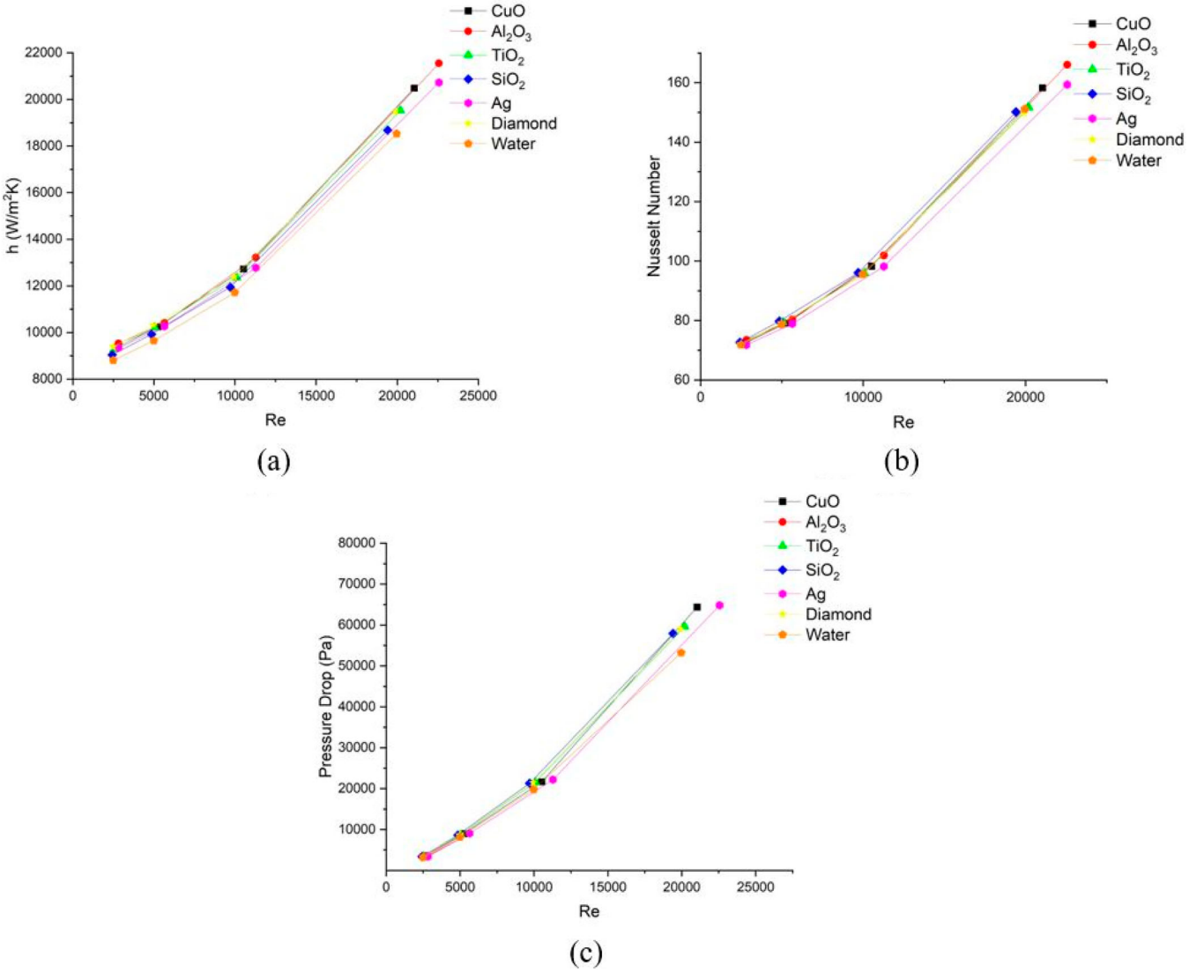

Figure 5. (a) Heat transfer coefficient, (b) Nusselt number and (c) pressure drop variation in the circular plate collector.

to conductive heat transfer at the fluid boundary. This figure shows that Al_2O_3 has the maximum value of Nu, which is 9.87% higher than water, while SiO_2 and diamond have the minimum value of Nu, which is 0.65% lower. This trend is similar to HTC as more heat is transferred from the fluid boundary via convection than conduction, resulting in nanofluids with maximum and minimum HTC having same corresponding Nu values. TiO_2, Ag and CuO have Nu values that are 0.33%, 0.54% and 4.69% higher than water.

Figure 5(c) depicts the pressured drop (Δp) variation with Re for water and the six nanofluids at $\phi = 2\%$ for the circular plate solar collector. According to this figure the increasing Δp trend is nearly identical to the increasing HTC trend. Table 2 can explain this phenomenon according to which, increasing the thermal conductivity of various nanofluids increases density which has a direct effect on pressure drop. Variations in Al_2O_3 and Ag coincide perfectly, having maximum pressure drop as 21.80% higher than water and the minimum pressure drop is in SiO_2, being 8.84% lower. Diamond, TiO_2 and CuO have higher pressure drops of 10.92%, 12.09% and 20.98%, respectively.

4.3.2. *Effects on square plate spiral solar collector*

The variation of HTC against Re number for water and the six nanofluids at $\phi = 2\%$ for the square plate spiral collector is shown in Figure 6(a). Similar to the circular plate collector, the values of HTC increase due to addition of nanoparticles. Al_2O_3 has the maximum value for HTC while SiO_2 has the minimum value, which are 16.31% and 0.78% higher than water. The trends of HTC for TiO_2 and diamond are nearly identical, with a 5.39% increase when compared to water. The HTC of Ag and CuO increased by 11.89% and 7.52%, respectively.

The variation of Nu with Re for water and the six nanofluids at $\phi = 2\%$ for the square plate spiral collector is shown is Figure 6(b). It is very similar to that of circular plate collector with the exception that the value of Nu for CuO has dropped comparatively at 1.83% higher than water. Al_2O_3 has the highest value of Nu which is 9.89% higher than water while SiO_2 and diamond have the minimum Nu which is 0.66% lesser. TiO_2 and Ag have Nu 0.37% and 5.46% higher than water, respectively.

Figure 6(c) depicts the pressured drop variation with Re for water and the six nanofluids at $\phi = 2\%$ for the square plate spiral collector. It is very similar to a circular plate collector, with

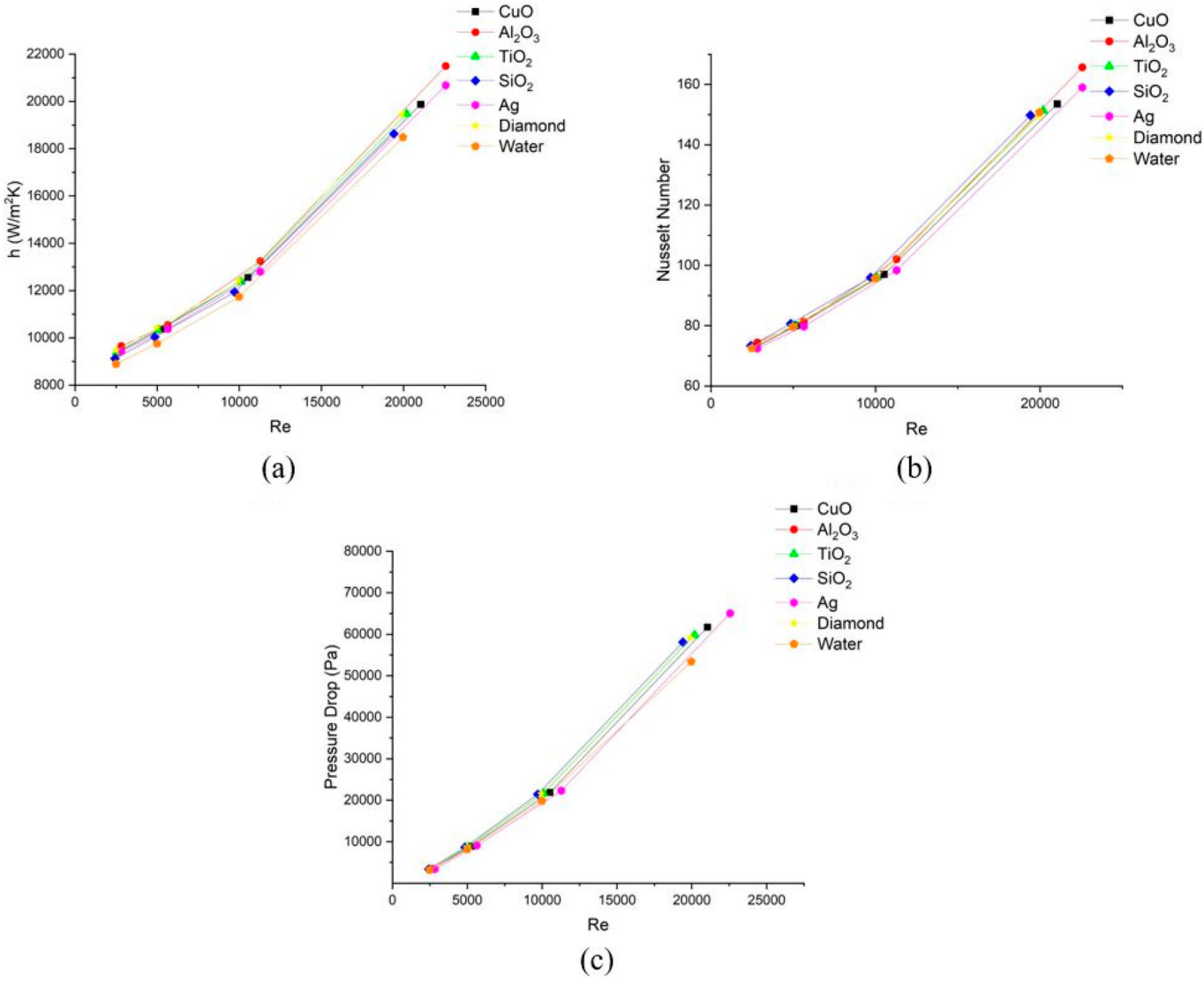

Figure 6. (a) Heat transfer coefficient, (b) Nusselt number and (c) pressure drop variation in the square plate spiral collector.

the exception that CuO comparatively has a lower Δp which is 15.53% higher than water. Al_2O_3 and Ag have the highest pressure drop, which is 21.78% higher than water, while SiO_2 has the lowest pressure drop, which is 8.75% less. The pressure-drop of diamond and TiO_2 is 10.86% and 12.04% higher than that of water, respectively.

4.3.3. Effects on U-bend solar collector

The variation of HTC against Re number for water and the six nanofluids at $\phi = 2\%$ for the U-bend solar collector is shown in Figure 7(a). This trend has a striking similarity with HTC trends of the previous discussed collectors. Al_2O_3 has the maximum value for HTC while SiO_2 has the minimum value, which are 16.58% and 0.73% higher than water. The trends of HTC for TiO_2 and diamond are again nearly identical, with a 5.50% increase when compared to water. The HTC of Ag and CuO increased by 11.93% and 8.27%, respectively.

The variation of Nu with Re for water and the six nanofluids at $\phi = 2\%$ for the U-bend collector is shown is Figure 7(b) and is very similar to that of square plate spiral collector. Al_2O_3 has the highest value of Nu which is 10.15% higher than water while SiO_2 and diamond have the minimum Nu which is 0.71% lesser. TiO_2, CuO and Ag have Nu 0.49%, 2.55% and 5.50% higher than water, respectively.

Figure 7(c) depicts the pressured drop variation with Re for water and the six nanofluids at for the square plate spiral collector which is similar to square plate spiral collector. Al_2O_3 and Ag trends coincide and have the highest Δp, which is 18.60% higher than water, while SiO_2 has the lowest pressure drop, which is 4.02% less. The pressure drops of diamond, TiO_2 and CuO are 6.61%, 8.56% and 12.56% higher than that of water, respectively.

4.3.4. Thermal performance

The thermal properties of all six nanofluids are assessed against Re at $v = 0.5, 1, 2$ and 4 m/s using equations (8–11). As discussed, the nanoparticles increase the HTC of the resulting nanofluids while also increasing the pressure drop. A rise in pressure drop is undesirable and demands the use of a more powerful pump to move the fluid. Hence, achieving the optimal state for using

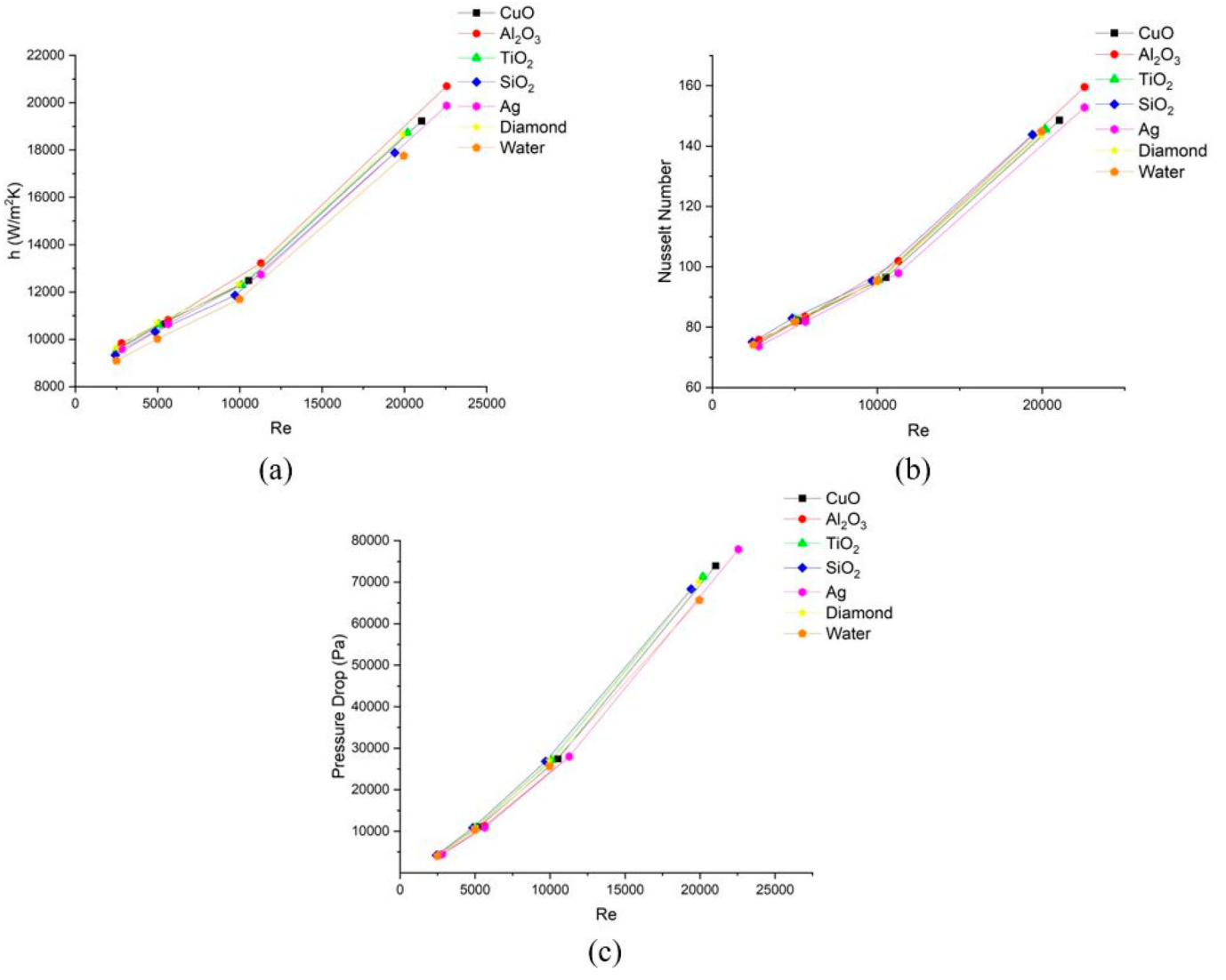

Figure 7. (a) Heat transfer coefficient, (b) Nusselt number and (c) pressure drop variation in the U-bend collector.

nanofluids is critical. Figure 8 shows the thermal performance of nanofluids with varying Re in all three collectors. Thermal performance with $\eta = 1$ is taken as the standard, assuming pure water as the working fluid. Higher thermal performance indicates that the strategy is more economical with increased heat transfer and reduced pressure drop.

Figure 8(a) shows that almost all the nanofluids have a noticeable dip in the values of η at 2 m/s. The thermal performance of TiO_2, SiO_2, diamond and CuO decreases with a rise in Re in circular plate solar collector. Their η nearly identical to water until about Re = 5000, at which point these values fall below 1. CuO has η values close to that of pure. Al_2O_3 provides the highest value of η throughout the range of Re, followed by Ag, and is 8.65% and 4.27% higher than water (at v = 4 m/s), respectively. SiO_2 and diamond have the lowest value η of (at v = 2 m/s), which is about 5% lower than water.

In the case of the square plate spiral solar collector, a zig-zag pattern of η is observed in all nanofluids, as shown in Figure 8(b). As a result, the thermal performance of the nanofluids falls below that of water at v = 4 m/s. SiO_2 and diamond trends almost coincide after 5000 Re, and fall below that of water. For any velocity, Al_2O_3 has the best value of η followed by Ag and CuO among all nanofluids. At v = 2 m/s, Al_2O_3 has a maximum value of η that is 4.7% higher than water. Both SiO_2 and diamond exhibit the lowest value of η (at v = 4 m/s), approximately 3% lower than water. Figure 8 shows that increasing the velocity beyond 2 m/s results in a constant decrease in the thermal performance of all nanofluids.

The thermal performance in the U-bend solar collector vary until 2 m/s after which they increase slightly with variation in Re in all nanofluids, as shown in Figure 8(c). The trends of SiO_2 and diamond almost coincide for the entire range of Re, as do TiO_2 and water. The values η of for these three nanofluids are very close to the corresponding values of water for all flow velocities tested. For any velocity, Al_2O_3, like the previous two collectors, provides the highest value of η followed by Ag and CuO. Al_2O_3 has a maximum value of η that is 10.28% higher than water at v = 2 m/s. Both SiO_2 and diamond have

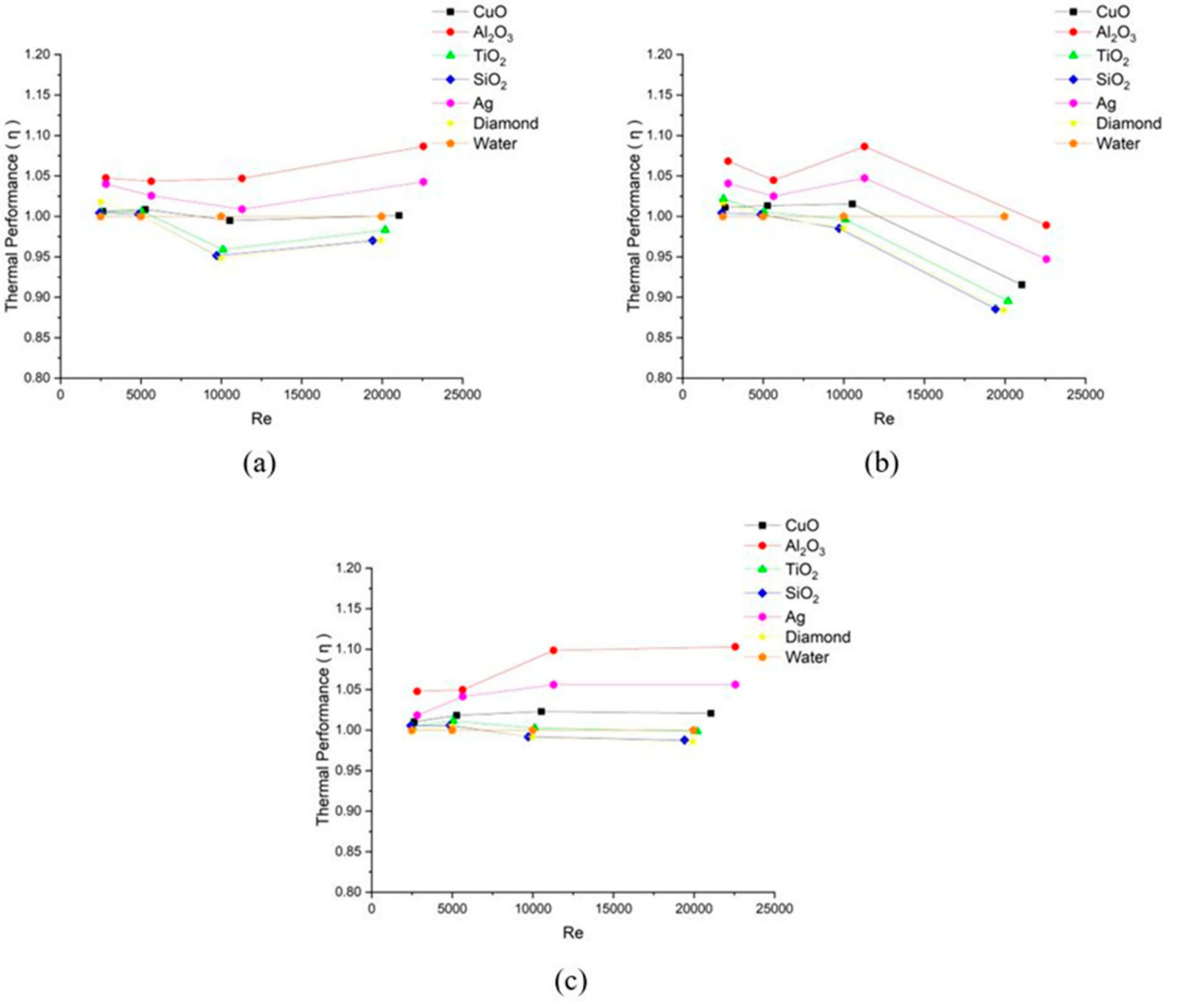

Figure 8. Thermal performance variation in (a) circular plate, (b) square plate spiral and (c) U-bend collectors.

the lowest value of (at v = 4 m/s) which is about 1.4% lower than water.

4.4. Effect of changing nanofluid concentration

Since it was observed that the maximum values of Nu and HTC were observed at v = 4 m/s, the effect of changing the nanofluid concentration to $\phi = 3\%$ and $\phi = 4\%$ are also analysed. Changes in attributes like HTC, outlet temperature and the top surface temperature are recorded and represented as trends against changes in the nanofluid concentrations.

4.4.1. Effects on heat transfer coefficient

Most nanofluids used in this study exhibit a similar trend of decrease in HTC value as their concentration increases from 2% to 4% concentration in the case of the circular plate solar collector as shown in Figure 9(a). Al_2O_3 has a 9.30% drop in HTC from $\phi = 2\%$ to 3%, which nearly coincides with the value of HTC of TiO_2 at $\phi = 3\%$. The HTC values for TiO_2 and diamond are nearly identical at $\phi = 2\%$ and 4%. SiO_2 has the lowest HTC (at $\phi = 4\%$) value, which is 4.10% lower than that of water.

Figure 9(b) shows that, similar to the previous case, the trends of HTC values in most nanofluids is alike, with increase from $\phi = 2\%$ to 4% in the case of square plate spiral solar collector. HTC values for CuO and Ag rise from $\phi = 2\%$ to 4% to have the highest HTC of 21962.24 W/m^{2}K (at $\phi = 4\%$). The decrease in HTC for Al_2O_3 is comparatively large being 8.65%. SiO_2 has the lowest HTC (at $\phi = 4\%$), which is 0.04% less than water.

U-bend solar collector follows a common trend of HTC, which increases from 2% to 4% as shown in Figure 9(c). This is due to the rise in the thermal diffusivity of the nanofluids with increase in ϕ. Al_2O_3 and diamond are exceptions, with a drop at $\phi = 3\%$ and then increase. Ag outperforms all other nanofluids, with an HTC of 22061.74 W/m^{2}K at $\phi = 4\%$. HTC variations in Al_2O_3 and TiO_2 coincide from $\phi = 3\%$ to 4%. SiO_2 has the lowest HTC values.

4.4.2. Effects on Nusselt number

The trends of variation in Nu against volumetric concentration for the respective collectors, as shown in Figure 10, are similar to those of the heat transfer coefficients discussed in the previous section. This is because for any given, the thermal conductivity

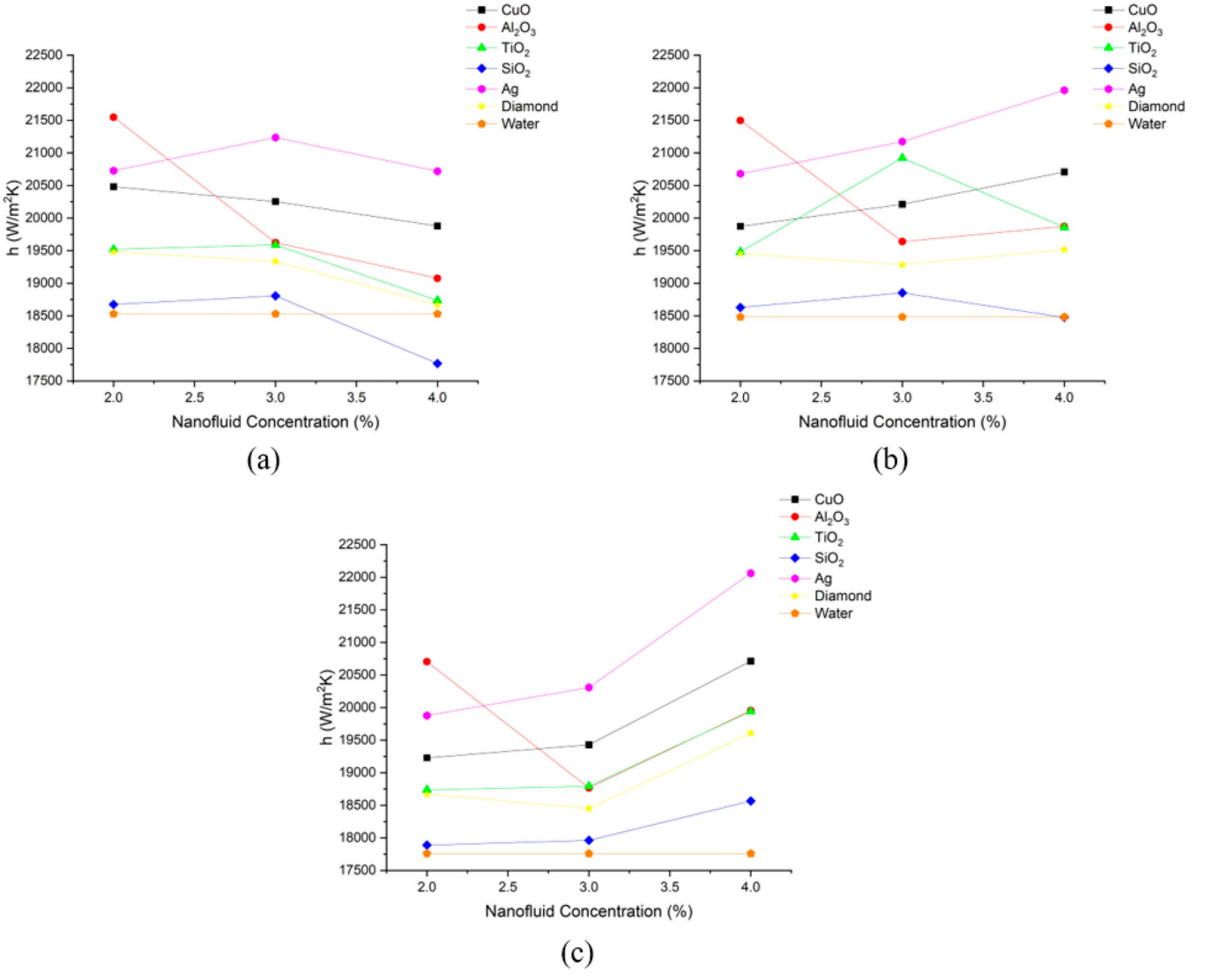

Figure 9. Heat transfer coefficient variation with nanofluid concentration in (a) circular plate, (b) square plate spiral and (c) U-bend collectors.

(κ) values for all nanofluids are quite similar to one another. The values of Nu from equation (6) therefore change as a fraction of h_f. Al_2O_3, TiO_2 and SiO_2 all have values of Nu that are close to water at 3%, with the exception of TiO_2 in square spiral flat plate collector. Nu values for Al_2O_3 in all collectors decrease dramatically at 3% concentration. In the spiral pipe collectors, Al_2O_3 has the highest Nusselt number of about 166 ($\phi = 2\%$), followed by Ag ($\phi = 3\%$ and 4%, respectively), while in U-bend, Ag has the highest Nusselt number ($\phi = 4\%$). SiO_2 has the lowest Nu value in all collectors, at $\phi = 3\%$ for U-bend and 4% for the remaining collectors.

4.4.3. Effects on pressure drop

The continuous curvature of the spiral pipe gives rise to secondary flows which cause pressure loss due to swirling throughout the flow. As a result, as shown in Figure 11, spiral collectors have greater pressure drops than U-bend in which bends account for a smaller portion of the pipe's length compared to the longer straight sections of the pipes. These dampen the effects of secondary flows downstream from the bend. Pressure drops increase with ϕ in spiral pipe collectors, but are more pronounced in circular plate collector. Except for Al_2O_3, all of the nanofluids exhibit a peak in pressure drop values at $\phi = 3\%$ in the U-bend collector with Al_2O_3, TiO_2, SiO_2 and diamond having drop lesser than water at 4%.

At $\phi = 2\%$ and 3%, most nanofluids show similar pressure drop in the spiral collectors, which is much less than the U-bend collector. Also, at 4% the values are almost same in the square plate spiral and U-bend collectors. Ag has the greatest drop in all three collectors, at $\phi = 3\%$ in the U-bend collector and 4% in the spiral pipe collectors. These values are 40.08%, 27.94% and 19.94% higher than of water. SiO_2 has the lowest pressure drop in the circular plate and U-bend collectors, at $\phi = 3\%$ (6.60% higher) and 4% (9.6% lower), respectively, while diamond has the lowest drop (6.79 higher) in the square plate spiral collector.

4.4.4. Effects on thermal performance

Eq. (5) shows that for a particular nanofluid at some velocity in different collectors, values of η can be compared using the ratio $Nu/\Delta p^{1/3}$. Hence, the results of thermal performance for

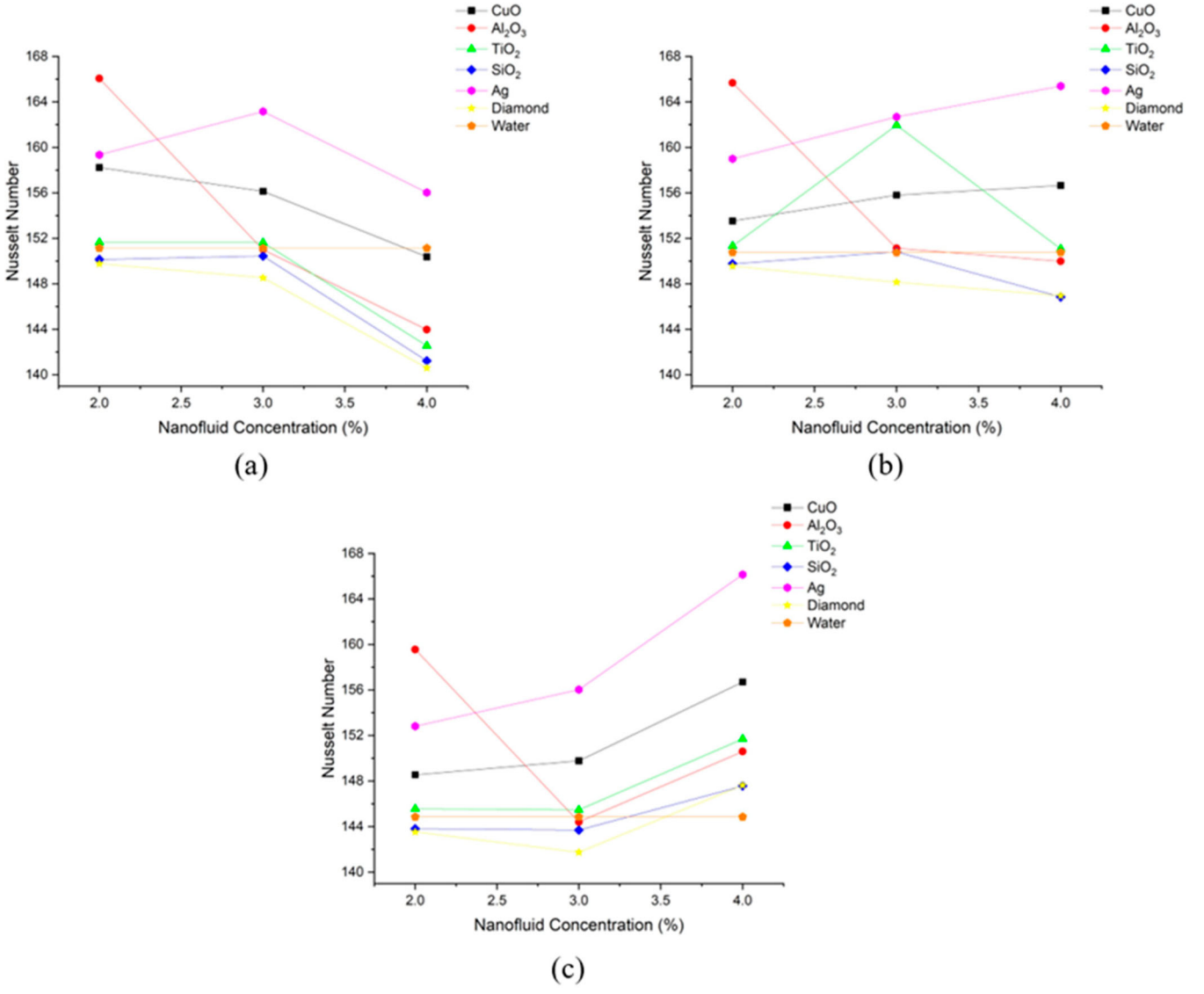

Figure 10. Nusselt number variation with nanofluid concentration in (a) circular plate, (b) square plate spiral and (c) U-bend collectors.

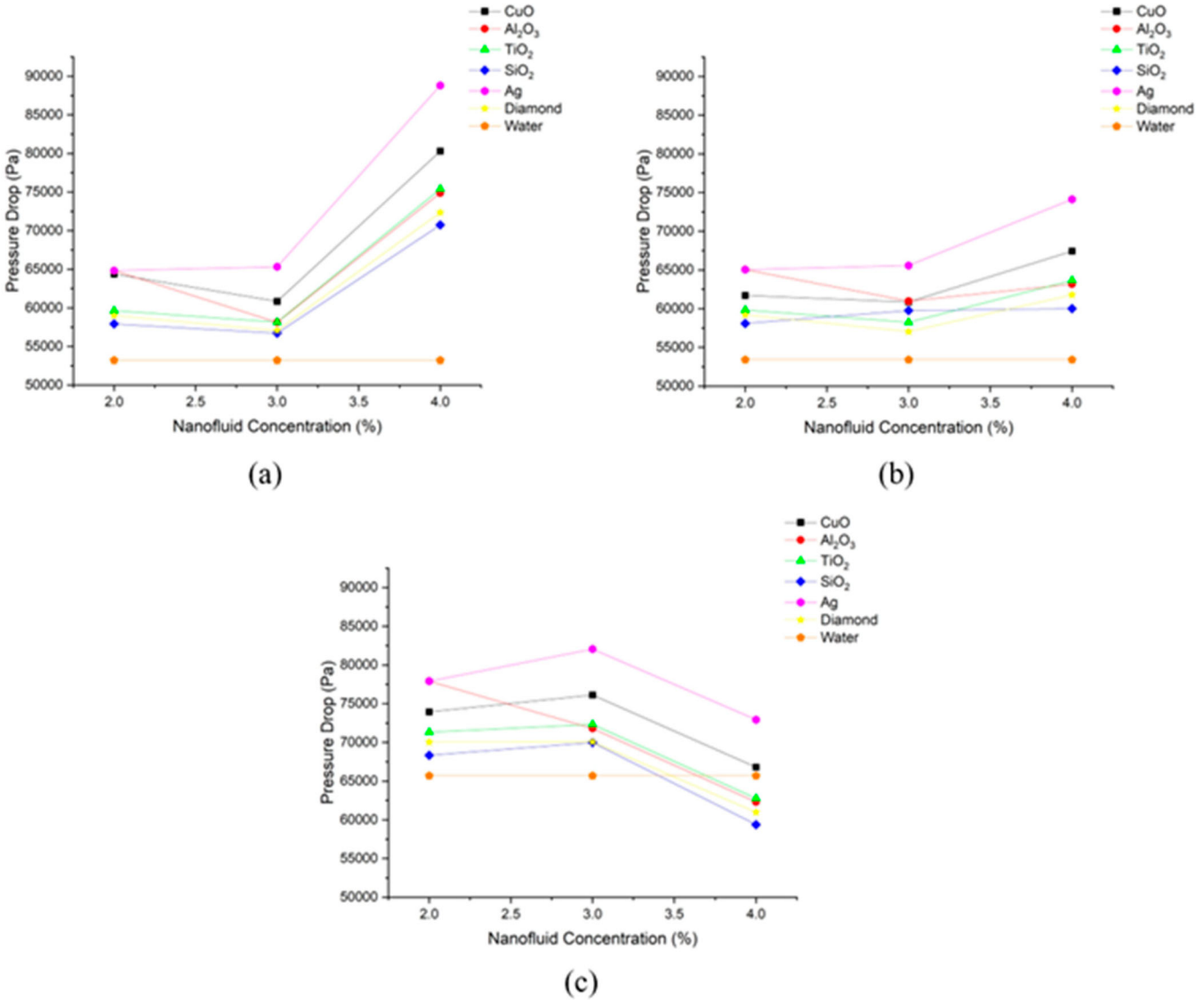

Figure 11. Pressure drop variation with nanofluid concentration in (a) circular plate, (b) square plate spiral and (c) U-bend collectors.

the nanofluids in these collectors can be justified from the trends in previous two sections. These results are shown in Figure 12. Since the pressure drop of nearly all the nanofluids in this range is essentially constant and only slightly increases in the U-bend collector, climbs from $\phi = 2\%$ to 3% in all collectors. In a circular plate collector, when concentration increases from 3% to 4%, the values of Nu decrease and pressure drops increase at the same time. This causes a decrease in, which causes the concentration to drop below that of water at $\phi = 4\%$. Contrasting trends of Nu and pressure drop in U-bend collector cause a rise in η values from 3% to 4% concentration, resulting in η values being higher than water at$\phi = 4\%$. In both of these collectors, thermal performances of Al_2O_3, TiO_2, SiO_2, and diamond at 3% are comparable to those of water. For any concentration in all three collectors, Ag performs best whereas SiO_2 and diamond perform worst at$\phi = 3\%$ and 4%. The highest value of η in spiral collectors is 1.09 (at $\phi = 3\%$) and 1.23 (at $\phi = 4\%$) in the U-bend collector.

5. Conclusions

This study numerically investigates three small-scale solar flat plate collector geometries – a spiral pipe with a circular plate, a spiral pipe with a square plate, and a U-shaped pipe with a square plate – to determine heat transfer coefficient, Nusselt number, pressure drop, and thermal performance.

Working fluids are SiO_2-H_2O, Al_2O_3-H_2O, CuO-H_2O, TiO_2-H_2O, Ag-H_2O and Diamond-H_2O nanofluids in 2%, 3% and 4% volume fractions. The finite volume method solves the governing equations. To investigate pipe Nusselt number fluctuations, numerical simulations are done at flow speeds of 0.5, 1, 2 and 4 m/s. The SIMPLE k-ϵ turbulence model output is validated using Dittus-Boelter and Gnielinski correlations.

At $\phi = 2\%$, Al_2O_3 had the highest HTC and Nusselt number in all three collectors at any velocity. Ag and Al_2O_3 exhibit pressure drops during flow. All nanofluids in all three collectors increase HTC, Nusselt number, and pressure drop over time. As Re grows, circular plate spiral collector thermal performance

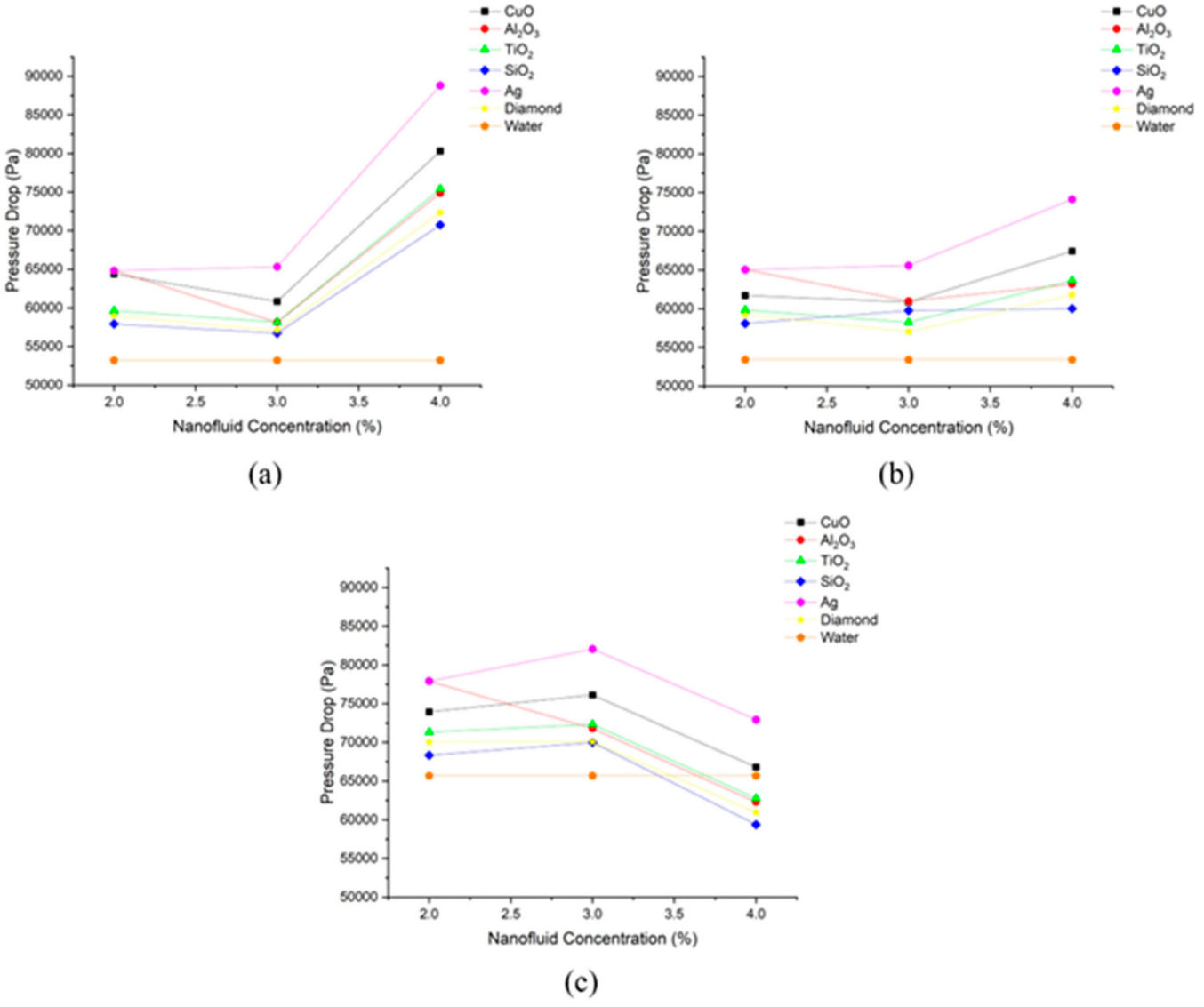

Figure 12. Thermal performance variation with nanofluid concentration in (a) circular plate, (b) square plate spiral and (c) U-bend collectors.

increases but square plate spiral collector thermal performance decreases. Increased Re has little effect on U-bend collector thermal performance. Al_2O_3 outperforms other nanofluids thermally in all three collectors, regardless of flow velocity. Thermal performance is worse for the square plate spiral collector than the other
two.

Ag had the maximum HTC, Nusselt number, and pressure drop at 3% and 4% nanofluid volumetric concentration. At higher concentrations, HTC and Nusselt number increase for all nanofluids while pressure drop decreases in the U-bend collector. At 4% concentration, pressure drop matches the square plate spiral collector. The circular plate spiral collector yields diverse results.

Nanofluid thermal performance declines in circular plate collectors, varies little in square plate spiral collectors ($\phi = 3\%–4\%$), and increases in U-bend collectors. Compared to spiral collectors (at $\phi = 4\%$), these results are significantly higher. Thermal performance peaks at 1.09 in spiral collectors and 1.23 in U-bend collectors.

This work uses optimised nanofluids and collector designs to improve solar thermal system performance. Solar water heating systems for household and industrial use can benefit from higher thermal efficiency. The findings benefit sustainable agriculture by enabling solar-powered desalination and greenhouse heating. The findings can also help develop high-efficiency heat exchangers for industrial process heating and building-integrated solar systems to save urban energy. These applications show the research's adaptability and significance to renewable energy and sustainability.

Future study should experimentally test the numerical findings, examine a broader range of nanofluids, and analyse their performance under changing environmental circumstances. Additionally, exploring long-term stability, optimising collector designs, and conducting energy and exergy assessments would further boost the efficiency and application of nanofluids in solar thermal systems.

Disclosure statement

No potential conflict of interest was reported by the authors.

ORCID

Gaurav Kumar http://orcid.org/0000-0001-5780-0904

References

Akbarzadeh, M., S. Rashidi, N. Karimi, and N. Omar. 2019. "First and Second Laws of Thermodynamics Analysis of Nanofluid Flow Inside a Heat Exchanger Duct with Wavy Walls and a Porous Insert." *Journal of Thermal Analysis and Calorimetry* 135 (1): 177–194. https://doi.org/10.1007/s10973-018-7044-y.

Bhowmik, H., and R. Amin. 2017. "Efficiency Improvement of Flat Plate Solar Collector Using Reflector." *Energy Reports* 3:119–123. https://doi.org/10.1016/j.egyr.2017.08.002.

Chu, Y. M., A. Abbasi, K. Al-Khaled, W. Farooq, S. U. Khan, M. I. Khan, S. M. Eldin, and K. Guedri. 2023. "Mathematical Modeling and Computational Outcomes for the Thermal Oblique Stagnation Point Investigation for non-Uniform Heat Source and Nonlinear Chemical Reactive Flow of Maxwell Nanofluid." *Case Studies in Thermal Engineering* 41: 102626. https://doi.org/10.1016/j.csite.2022.102626.

Cruz-Peragon, F., J. M. Palomar, P. J. Casanova, M. P. Dorado, and F. Manzano-Agugliaro. 2012. "Characterization of Solar Flat Plate Collectors." *Renewable and Sustainable Energy Reviews* 16 (3): 1709–1720. https://doi.org/10.1016/j.rser.2011.11.025

Farajzadeh, E., S. Movahed, and R. Hosseini. 2018. "Experimental and Numerical Investigations on the Effect of Al2O3/TiO2[Sbnd]H2O Nanofluids on Thermal Efficiency of the Flat Plate Solar Collector." *Renewable Energy* 118:122–130. https://doi.org/10.1016/j.renene.2017.10.102.

Farshad, S. A., M. Sheikholeslami, S. H. Hosseini, A. Shafee, and Z. Li. 2019. "Nanofluid Turbulent Forced Convection Through a Solar Flat Plate Collector with Al2O3 Nanoparticles." *Microsystem Technologies* 25 (11): 4237–4247. https://doi.org/10.1007/s00542-019-04430-2.

Gholinia, M., A. A. Ranjbar, M. Javidan, and A. A. Hosseinpour. 2021. "Employing a New Micro-Spray Model and (MWCNTs - SWCNTs) - H2O Nanofluid on Si-IGBT Power Module for Energy Storage: A Numerical Simulation." *Energy Reports* 7:6844–6853. https://doi.org/10.1016/j.egyr.2021.10.047.

Gupta, A. K., B. Gupta, J. Bhalavi, P. Baredar, H. Parmar, and R. Senthil. 2022. "CFD Study on Heat Transfer and Pressure Drop of Nanofluids (SiO2/H2O, Al2O3/H2O, CNTs/H2O) in a Concentric Tube Heat Exchanger." *International Journal of Ambient Energy* 43 (1): 4578–4593. https://doi.org/10.1080/01430750.2021.1913222.

Hellstrom, B., M. Adsten, P. Nostell, B. Karlsson, and E. Wackelgard. 2003. "The Impact of Optical and Thermal Properties on the Performance of Flat Plate Solar Collectors." *Renewable Energy* 28 (3): 331–344. https://doi.org/10.1016/S0960-1481(02)00040-X.

Ho, C. D., H. M. Yeh, and R. C. Wang. 2005. "Heat-Transfer Enhancement in Double-Pass Flat-Plate Solar air Heaters with Recycle." *Energy* 30:2796–2817. https://doi.org/10.1016/j.energy.2005.01.006.

Hottel, H., and A. Whillier. 1955. "Evaluation of Flat-Plate Solar Collector Performance." *Trans. Conf. Use Sol. Energy* 3: OSTI ID 5057828.

Hussein, A. M., K. V. Sharma, R. A. Bakar, and K. Kadirgama. 2013. "The Effect of Nanofluid Volume Concentration on Heat Transfer and Friction Factor Inside a Horizontal Tube." *Journal of Nanomaterials* 2013 (1): 859563. https://doi.org/10.1155/2013/859563.

Ibrahim, A., M. Y. Othman, M. H. Ruslan, S. Mat, and K. Sopian. 2011. "Recent Advances in Flat Plate Photovoltaic/Thermal (PV/T) Solar Collectors." *Renewable and Sustainable Energy Reviews* 15 (1): 352–365. https://doi.org/10.1016/j.rser.2010.09.024

Javidan, M., M. Asgari, M. Gholinia, M. Nozari, A. Asgari, and D. D. Ganji. 2022. "Thermal Energy Storage Inside the Chamber with a Brick Wall Using the Phase Change Process of Paraffinic Materials: A Numerical Simulation." *Theoretical and Applied Mechanics Letters* 12 (3): 100329. https://doi.org/10.1016/j.taml.2022.100329.

Karimi, A., A. A. A. A. Al-Rashed, M. Afrand, O. Mahian, S. Wongwises, and A. Shahsavar. 2019. "The Effects of Tape Insert Material on the Flow and Heat Transfer in a Nanofluid-Based Double Tube Heat Exchanger: Two-Phase Mixture Model." *International Journal of Mechanical Sciences* 156:397–409. https://doi.org/10.1016/j.ijmecsci.2019.04.009.

Li, X., A. Abbasi, K. Al-Khaled, H. Fateh, M. Ameen, S. U. Khan, M. Ijaz Khan, W. Farooq, G. Rasool, and K. Guedri. 2023. "Thermal Performance of Iron Oxide and Copper (Fe3O4, Cu) in Hybrid Nanofluid Flow of Casson Material with Hall Current via Complex Wavy Channel." *Materials Science and Engineering: B* 289: 116250. https://doi.org/10.1016/j.mseb.2022.116250.

Mahanthesh, B., S. A. Shehzad, T. Ambreen, and S. U. Khan. 2021. "Significance of Joule Heating and Viscous Heating on Heat Transport of MoS2–Ag Hybrid Nanofluid Past an Isothermal Wedge." *Journal of Thermal Analysis and Calorimetry* 143 (2): 1221–1229. https://doi.org/10.1007/s10973-020-09578-y.

Mohammed, H. A., P. Gunnasegaran, and N. H. Shuaib. 2011. "The Impact of Various Nanofluid Types on Triangular Microchannels Heat Sink Cooling Performance." *International Communications in Heat and Mass Transfer* 38 (6): 767–773. https://doi.org/10.1016/j.icheatmasstransfer.2011.03.024.

Pandey, K. M., and R. Chaurasiya. 2017. "A Review on Analysis and Development of Solar Flat Plate Collector." *Renewable and Sustainable Energy Reviews* 67:641–650. https://doi.org/10.1016/j.rser.2016.09.078.

Rashidi, S., P. Javadi, and J. A. Esfahani. 2019. "Second Law of Thermodynamics Analysis for Nanofluid Turbulent Flow Inside a Solar Heater with the Ribbed Absorber Plate." *Journal of Thermal Analysis and Calorimetry* 135 (1): 551–563. https://doi.org/10.1007/s10973-018-7164-4.

Rojas, D., J. Beermann, S. A. Klein, and D. T. Reindl. 2008. "Thermal Performance Testing of Flat-Plate Collectors." *Solar Energy* 82 (8): 746–757. https://doi.org/10.1016/j.solener.2008.02.001.

Roohi, R., A. Arya, M. Akbari, and M. J. Amiri. 2023. "Performance Evaluation of an Absorber Tube of a Parabolic Trough Collector Fitted with Helical Screw Tape Inserts Using CuO/Industrial-Oil Nanofluid: A Computational Study." *Sustainability* 15: 10637. https://doi.org/10.3390/su151310637.

Salavati Meibodi, S., A. Kianifar, H. Niazmand, O. Mahian, and S. Wongwises. 2015. "Experimental Investigation on the Thermal Efficiency and Performance Characteristics of a Flat Plate Solar Collector Using SiO2/EG-Water Nanofluids." *International Communications in Heat and Mass Transfer* 65:71–75. https://doi.org/10.1016/j.icheatmasstransfer.2015.02.011.

Sani, F. H., M. Pourfallah, and M. Gholinia. 2022. "The Effect of MoS2–Ag/H2O Hybrid Nanofluid on Improving the Performance of a Solar Collector by Placing Wavy Strips in the Absorber Tube." *Case Studies in Thermal Engineering* 30: 101760. https://doi.org/10.1016/j.csite.2022.101760.

Schobert, H. H. 2014. *Energy and Society*. Boca Raton: CRC Press. https://doi.org/10.1201/b16677.

Shaji, R. 2014. "A Review on India's Renewable Energy Potential." *International Journal of Scientific Engineering and Research* 5: 985–990. http://www.ijser.org.

Shaker, B., M. Gholinia, M. Pourfallah, and D. D. Ganji. 2022. "CFD Analysis of Al2O3-Syltherm oil Nanofluid on Parabolic Trough Solar Collector with a New Flange-Shaped Turbulator Model." *Theoretical and Applied Mechanics Letters* 12 (2): 100323. https://doi.org/10.1016/j.taml.2022.100323.

Sheikholeslami, M., R. ul Haq, A. Shafee, Z. Li, Y. G. Elaraki, and I. Tlili. 2019. "Heat Transfer Simulation of Heat Storage Unit with Nanoparticles and Fins Through a Heat Exchanger." *International Journal of Heat and Mass Transfer* 135:470–478. https://doi.org/10.1016/j.ijheatmasstransfer.2019.02.003.

Shih, T.-H., W. W. Liou, A. Shabbir, Z. Yang, and J. Zhu. 1995. "A New K-ε Eddy Viscosity Model for High Reynolds Number Turbulent Flows." *Computers & Fluids* 24 (3): 227–238. https://doi.org/10.1016/0045-7930(94)00032-T

Siah Chehreh, S. 2021. "An Enviroeconomic Review of the Solar PV Cells Cooling Technology Effect on the CO2 Emission Reduction." *Solar Energy* 216:468–492. https://doi.org/10.1016/j.solener.2021.01.016.

Siah Chehreh Ghadikolaei, S. 2021. "Solar Photovoltaic Cells Performance Improvement by Cooling Technology: An Overall Review." *International Journal of Hydrogen Energy* 46 (18): 10939–10972. https://doi.org/10.1016/j.ijhydene.2020.12.164.

Singh, Y., A. Kumar, R. Maithani, and N. Verma. 2021. "TiO2/H2O Nanofluid Flow and Heat Transfer Analysis in V-Pattern with Combined Protrusion Obstacle Square Channel: Experimental Analysis and CFD Validation." *International Journal of Ambient Energy* 42 (6): 652–671. https://doi.org/10.1080/01430750.2018.1563807.

Struckmann, F. 2008. *Analysis of a Flat-Plate Solar Collector*. Lund: Sweden.

Subramani, J., P. K. Nagarajan, O. Mahian, and R. Sathyamurthy. 2018. "Efficiency and Heat Transfer Improvements in a Parabolic Trough Solar Collector Using TiO2 Nanofluids Under Turbulent Flow Regime." *Renewable Energy* 119:19–31. https://doi.org/10.1016/j.renene.2017.11.079.

Sun, S., M. I. Khan, K. Al-Khaled, A. Raza, S. S. Abdullaev, S. U. Khan, N. Tamam, and S. M. Eldin. 2023. "Prabhakar Fractional Approach for Enhancement of Heat Transfer due to Hybrid Nanomaterial with Sinusoidal Heat Conditions." *Case Studies in Thermal Engineering* 49: 103240. https://doi.org/10.1016/j.csite.2023.103240.

Tiwari, A. K., P. Ghosh, and J. Sarkar. 2013. "Performance Comparison of the Plate Heat Exchanger Using Different Nanofluids." *Experimental Thermal and Fluid Science* 49:141–151. https://doi.org/10.1016/j.expthermflusci.2013.04.012.

Yousefi, T., F. Veysi, E. Shojaeizadeh, and S. Zinadini. 2012. "An Experimental Investigation on the Effect of Al2O3-H2O Nanofluid on the Efficiency of Flat-Plate Solar Collectors." *Renewable Energy* 39 (1): 293–298. https://doi.org/10.1016/j.renene.2011.08.056.

Zadeh, M. N., M. Pourfallah, S. S. Sabet, M. Gholinia, S. Mouloodi, and A. T. Ahangar. 2021. "Performance Assessment and Optimization of a Helical Savonius Wind Turbine by Modifying the Bach's Section." *SN Applied Sciences* 3 (8): 739. https://doi.org/10.1007/s42452-021-04731-0.

J. Inst. Eng. India Ser. A
https://doi.org/10.1007/s40030-025-00884-y

ORIGINAL CONTRIBUTION

Optimizing Wind Load Performance through Shape Modifications and Corner Configurations in High-Rise Buildings: A Computational Fluid Dynamics Study

Sudhanshu Pandey[1] · Nitesh Kumar Thakur[1] · Paras Nath[1] · Deepak Sharma[1] · Ritu Raj[1]

Received: 2 May 2024 / Accepted: 1 March 2025
© The Institution of Engineers (India) 2025

Abstract The rapid evolution of tall buildings has presented challenges that require systematic research and advancements. A major concern for structural designers in tall buildings is the influence of wind loads. Therefore, determining the geometry and corner configuration of a structure is crucial, considering both form and function to effectively address the effects of wind. The aerodynamic performance of a tall structure can experience significant enhancement through the implementation of various shape modifications. Following research conducts a comparative analysis of wind load, distribution of pressure and various coefficients on High Rise buildings with diverse taper ratio and corner configuration for angle of attack of wind between 0° to 90° at an interval of 15°. Computational fluid dynamics through ANSYS CFX employing the Reynolds-Averaged Navier-Stokes k-ε model has been utilized to conduct a numerical analysis, aiming to replicate the flow conditions specified in IS: 875 (Part-III):2015. In each situation we analyze the pressure values, force values, moment values and drag and lift values, as part of the evaluation. To help visualize the changes resulting from the modifications, in construction we present the results visually.

Keywords Shape modification · High-rise building · Aerodynamics coefficients · Flow pattern · Computational fluid dynamics

✉ Deepak Sharma
deepaksharma_2k21phdce02@dtu.ac.in

[1] Civil Engineering Department, Delhi Technological University, Delhi, India

Introduction

Due to the increase in population and less availability of land, high-rise structures are preferred for residential purposes, hotels, hospitals, etc. Structural modifications are done to high-rise structures, e.g., set-back modification, tapering modifications, etc., to make them wind resilient. Such structures are the outcomes of the tenuous balance between robustness, aerodynamic behavior, and the threat of precariousness. High-rise building structures, notably characterized by a diminishing section, have this dominant load affected by the powerful wind. Foremost, it is of high importance to test the aerodynamic performance to guarantee the maximum safety, stability, and efficiency of the structure. Even though the wind tunnel test has been applied worldwide and preserved its meaningfulness, CFD is generally presumed to be more user-friendly. Several standard codes of various countries, like AS/NZS 1170.2 (2011), ASCE/SEI 7-16 (2017), BS 6399-2 (1997), EN 1991-1-4 (2002) and IS 875: Part III (2015) [23–27], are used which provide the guidelines for different cross-section and asymmetrical buildings.

The significance of Computational Fluid Dynamics (CFD) technique facilitates a speedy assessment of wind effects on diverse high-rise building shapes. This method requires the subdivision of the building geometry into tiny elements through meshing. Numerous studies have done which investigated the wind effects on various shapes, such as Bhattacharyya and Dalui's determination of wind pressure on the "E" shape [1], Raj et al. [2] study of wind actions on the "H" shape, He and Song [3] research of wind flow around the TTU building, Sanyal and Dalui [4] observation on rectangular shapes, Paul et al. [5] study on rectangular shapes with horizontal limbs, Paul and Dalui [6] research on the plus shape tall building, Hajra and Dalui [7]

Published online: 26 March 2025

investigation of tall building having octagonal shapes, Raj et al. [8] concentration on high rise building with square models and fish plan shape tall buildings, and Bairagi and Dalui [9] investigation of stepped tall building models. The key outcomes derived from numerical simulations include the notable impact of mesh size on results, the correlation between pressure distribution and building height, observed alterations in velocity on the building model's roof, and the influence of wind exposure on drag force. Notably, a decrement in wind load is predominantly attributed to the corners of shorter edges.

Using boundary layer wind tunnel studies, Nagar et al. [10] investigated the impact of wind forces on square and "H" plan shaped tall structures under both isolated and interfered situations from other comparable tall buildings. The mean of pressure coefficient of wind is calculated for different directions of wind using wind tunnel experiments. Decrease in pressure was found on increasing the angle of attack of wind and that, at full blockage, the suction occurred by the building which is interfering was greater than that occurred by the other interfering conditions. Mallick et al. [11] used ANSYS Fluent to numerically study the wind pressure coefficient on "C" shaped building models. They came to the conclusion that the tall building's pressure distribution was significantly influenced by the structure's geometry, aspect ratios, orientation, and wind incidence angle. Paul and Dalui [12] examined how the wind behaved on various faces of high-rise building with Z-shaped structure for a range of wind directions, from 0° to 150° in increments of 30°. As a result of the integrated effects of both positive and negative pressure on the windward and leeward sides, vortices that are unstable in nature are seen in the wake region when the coefficients of force, coefficients of pressure, and pattern of flow of wind are analyzed for the model. The wind tunnel experiment findings for an irregularly shaped building model with a cross-sectional shape resembling a "L" or "U" shaped were given by Gomes et al. [13] indicated that pressure coefficient varies with the change in shape of building and found that U shaped building performs better than that of the L shaped building in reducing the wind loads from upstream direction. Mukherjee et al. [14] carried out a comprehensive investigation of pressure contours on several faces of a tall structure shaped like a 'Y' due to the interference effect. It has been noted that certain faces showed an unusual change in pressure. The flow pattern surrounding the model was further displayed to aid in the better observation of flow features. Pal et al. [15] experimentally examined the outcomes of a structure which is isolated using wind tunnel testing. Sanyal and Dalui [16] investigated change in aerodynamics coefficients by changing the internal angle between limbs of a Y-shaped tall building for angle of wind attack varying from 0° to 180°.

The previous research showed that modifications in buildings had been carried out to minimize the wind loads but either in tapered form or in corner modification. The combined modifications, i.e., tapered plus corner, had not been investigated much by the researchers and can perform better in minimizing the wind loads. In this present investigation, the emphasis lies in making some major and minor modifications to the structure and then analyzing the effect of wind on modified models. The analysis of modified models is conducted by using Computational Fluid Dynamics (CFD) simulations, making use of ANSYS for numerical simulations in accordance with the guidelines specified in the solver modeling guide in ANSYS CFX. The research centers around a model of High-rise rectangular building of cross-section 60 m × 50 m and height of 120 m, which is our reference model and all the modification are done in this model. In major modification, the faces of building are tapered and the taper ratios of 20V:1H is considered whereas in minor modification corners of building are modified, three corners sharp corner, round corner and cut corner are considered for the taper ratio. The effect of major and minor modification on several aerodynamics coefficients i.e., External pressure coefficient (Cpe), Force coefficients (CF), Moment coefficients (CM), Drag and Lift coefficients (Cd and Cl) depicted using graphs, are compared with the reference model. Most of the previous studies and wind standards of various nations contains the information related to conventional building, they have not mentioned any details about the shape optimization of the building to reduce the wind effects, that's why this is study is carried out.

Structure Under Study

A high-rise building model with a corner arrangement and taper ratio of 20V:1H is cross-examined in the current study using a model with a geometric scale of 1:200. The length and breadth of building are measured as 250 mm and 300 mm, respectively. The structure is 600 mm tall. Building corners are cut, rounded, and sharp. It is assumed that the building models has zero opening. The plan dimensions of the top floor of the tapered building are 240 mm × 190 mm. The actual height of the building is taken as 120 m, and the plan area is 3000 m^2. Figure 1 displays the 3D and plan views of every building used in current study.

a. Model-A: The Rectangular model (Fig. 1a) simple building with cross sectional plan 300 mm × 200 mm and height 600 mm.
b. Model-P: The Rectangular plan model (Fig. 1b) with taper ratio 20V:1H with cross sectional plan 300 mm × 200 mm, height 600 mm and sharp edge corner.

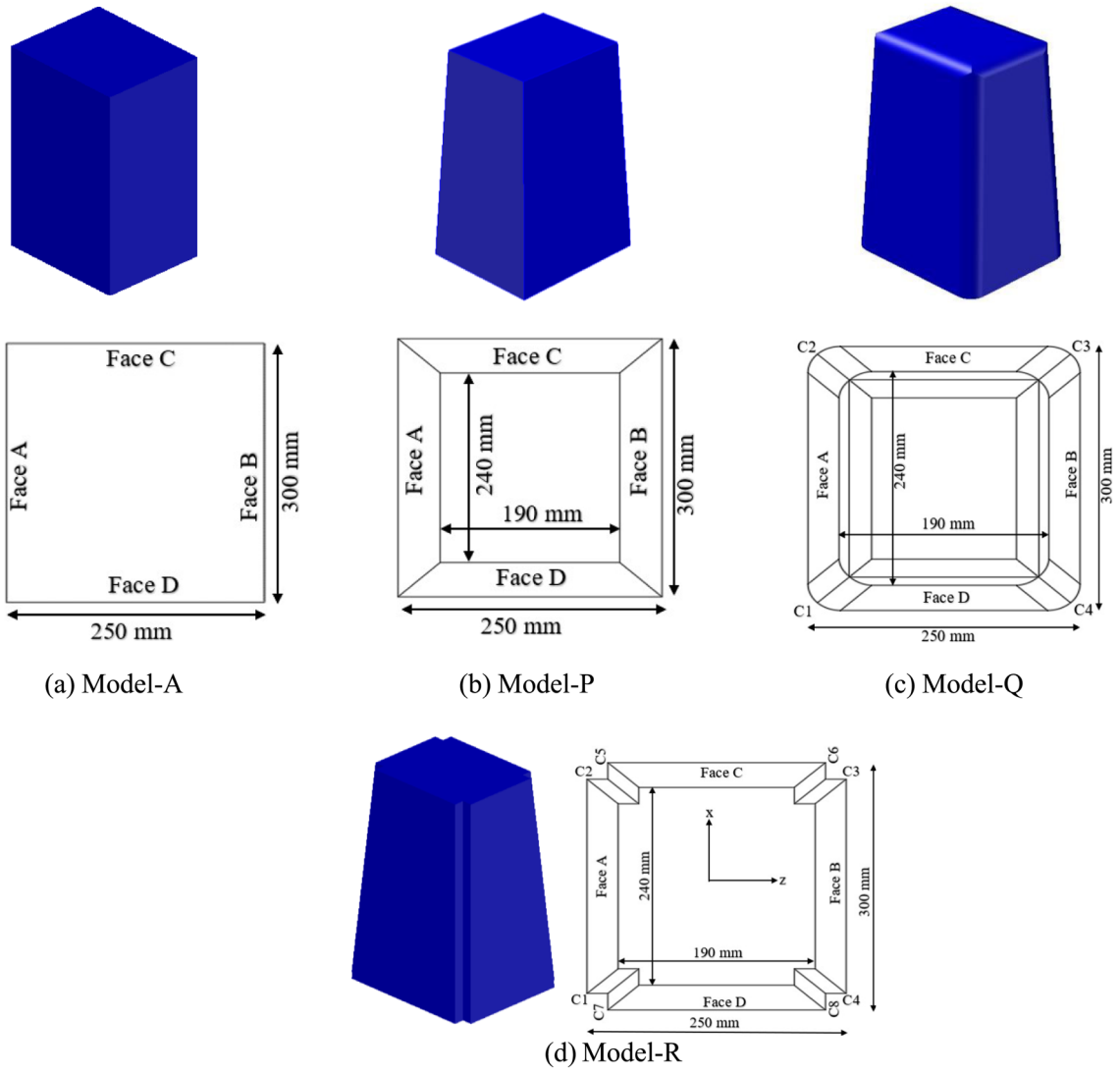

Fig. 1 Cross-sectional and 3D view of all the models

c. Model-Q: The Rectangular plan model (Fig. 1c) with taper ratio 20V:1H with cross sectional plan 300 mm × 200 mm, height 600 mm and round corner.
d. Model-R: The Rectangular plan model (Fig. 1d) with taper ratio 20V:1H with cross sectional plan 300 mm × 200 mm, height 600 mm and cut edge corner.

Verification and Validation

The validation of the numerical method was conducted by inspecting a regular rectangular model, as illustrated in Fig. 1a, for 0° and 90° angle of attack of wind. A 5% tolerance for wind gustiness was included in the assumption of a constant steady-state wind velocity of 10 m/s. In line with IS 875 (Part 3): 2015, a terrain roughness coefficient of 0.147 was used to determine atmospheric boundary layer (ABL) conditions for second category of terrain using the power law equation (Eq. (5)). As seen in Figs. 2 and 3, the pressure coefficients (Cpe) on the Face A, Face B, Face C, Face D of the rectangular model were verified and compared with pertinent codes from various nations. The graphs demonstrate that the numerical approach yielded results within an acceptable range of 20–25% [17].

Numerical Simulation

Because of the unpredictable variations in wind intensity and direction in natural settings, it is challenging to replicate identical wind flow characteristics, particularly in turbulent conditions around bluff bodies, during experimental studies. Computational Fluid Dynamics (CFD) has seen the development of various mathematical models aimed at analyzing

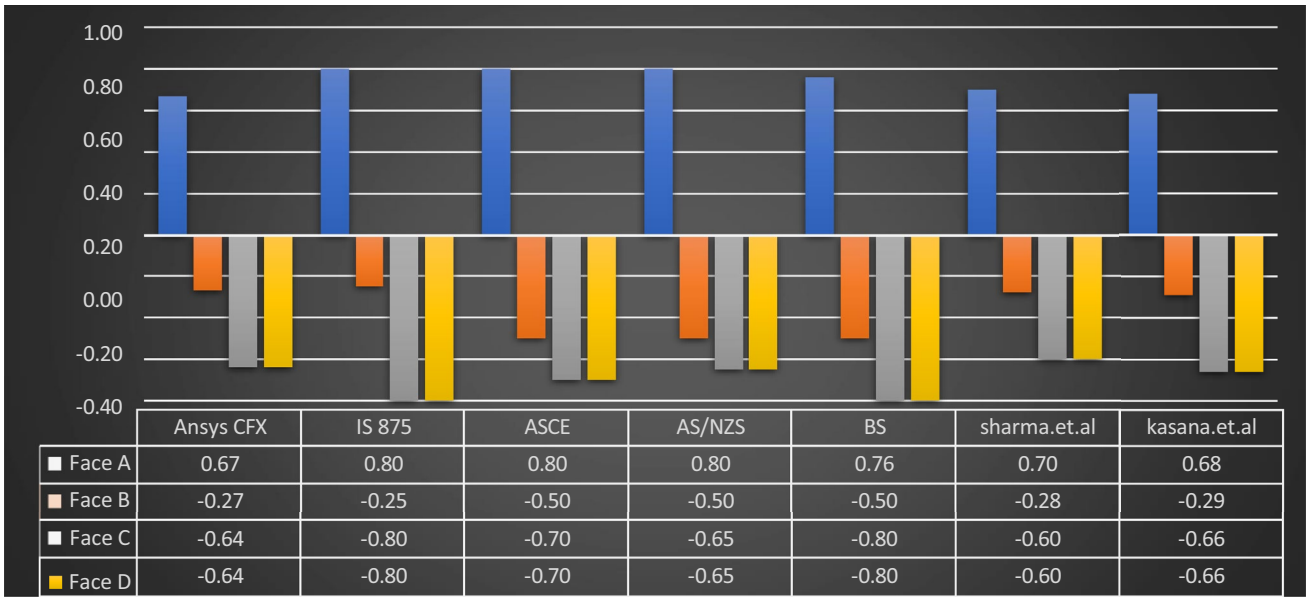

	Ansys CFX	IS 875	ASCE	AS/NZS	BS	sharma.et.al	kasana.et.al
Face A	0.67	0.80	0.80	0.80	0.76	0.70	0.68
Face B	-0.27	-0.25	-0.50	-0.50	-0.50	-0.28	-0.29
Face C	-0.64	-0.80	-0.70	-0.65	-0.80	-0.60	-0.66
Face D	-0.64	-0.80	-0.70	-0.65	-0.80	-0.60	-0.66

Fig. 2 Analysis of area average Cpe on different faces of rectangular building at 0° angle of attack of wind

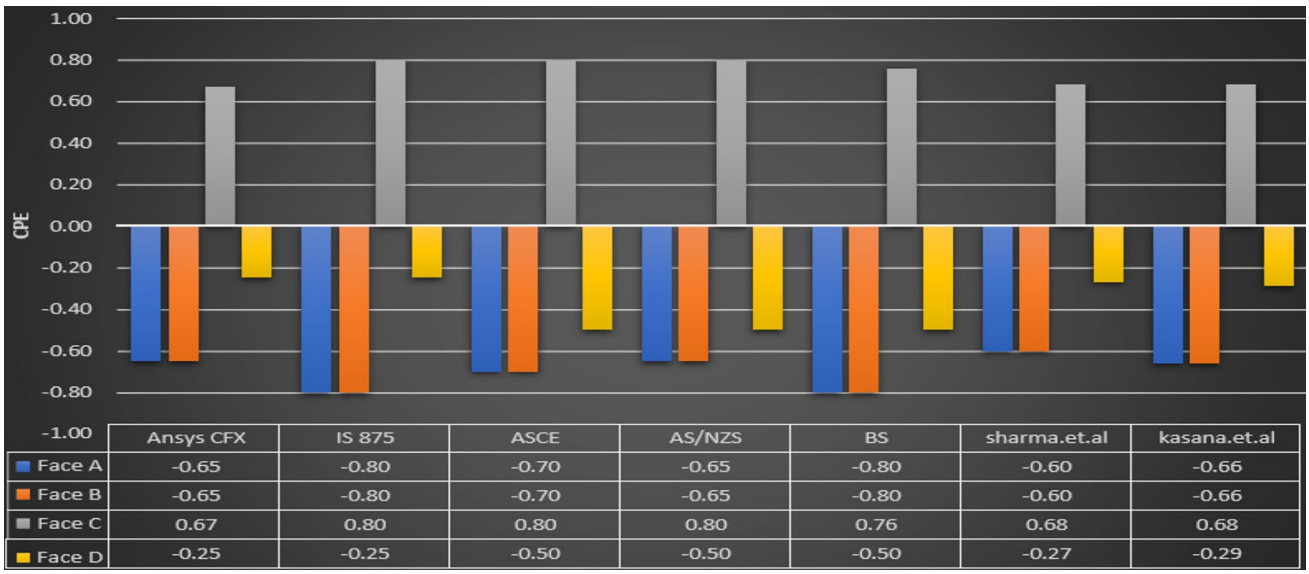

	Ansys CFX	IS 875	ASCE	AS/NZS	BS	sharma.et.al	kasana.et.al
Face A	-0.65	-0.80	-0.70	-0.65	-0.80	-0.60	-0.66
Face B	-0.65	-0.80	-0.70	-0.65	-0.80	-0.60	-0.66
Face C	0.67	0.80	0.80	0.80	0.76	0.68	0.68
Face D	-0.25	-0.25	-0.50	-0.50	-0.50	-0.27	-0.29

Fig. 3 Analysis of area average Cpe on different faces of rectangular building at 90° angle of attack of wind

the pressure and velocity parameters exerted by fluid flow around objects. The foundational equations for describing flow of fluid in the form of partial differential equations, the Navier- Stokes equations of continuity and momentum, are the source of these models. Unfortunately, due to a number of assumptions required to get around unknown variables that cannot be observed during the solution of equations, most of which are regarded unimportant, no model has been able to precisely reflect the genuine flow of wind in nature to this day. The conventional turbulence model of k-epsilon (k-Ɛ) is one model which is frequently used in CFD to study wind flow over blunt bodies.

This model is said to be the simplest as it simply needs boundary and/or beginning conditions and produces better results. It provides a time-averaged steady-state solution for the continuity and momentum equations of the Reynolds Averaged Navier-Stokes (RANS) system. Wind flow is naturally gusty, adding turbulence to the wind's normally constant speed, especially when it comes across obstructions. Little eddies emerge as a result of the frictional shear and buoyancy

produced by these obstructions. Turbulence Kinetic Energy (k) is the energy contained in these eddies. The production of heat and the dissipation of turbulent kinetic energy is due to the frictional shear or viscous force. The process of dissipation is termed as Turbulence Eddy Dissipation (e). The ANSYS software, together with its turbulence model and CFX solver, was used to conduct the current study. Meena et al. [18] (2022a, ANSYS Inc. 2009) defined the equation of K and e in the flow field to solve the continuity equation, momentum equations and transport equations in Ansys CFX (Fig. 4).

Basic Equation

The basic equations that are used in Computational fluid dynamics simulations with k-Ɛ turbulence model are given below. The basis of the fundamental equation which is used to study fluid flow problems are formed by using continuity equation and the Navier-Stokes equations [22].

Navier Stokes Equation:

$$\frac{\partial(\rho u_i)}{\partial t} = -\frac{\partial(\rho u_i u_j)}{\partial x_j} - \frac{\partial P}{\partial x_j} + \frac{\partial}{\partial_{x_j}}\left[\mu\left(\frac{\partial_{u_i}}{\partial_{x_j}} + \frac{\partial_{u_j}}{\partial_{x_i}}\right)\right] + F \tag{1}$$

Continuity Equation:

$$\frac{\partial_\rho}{\partial_t} + \frac{\partial_{\rho_i}}{\partial_{t_i}} = 0 \tag{2}$$

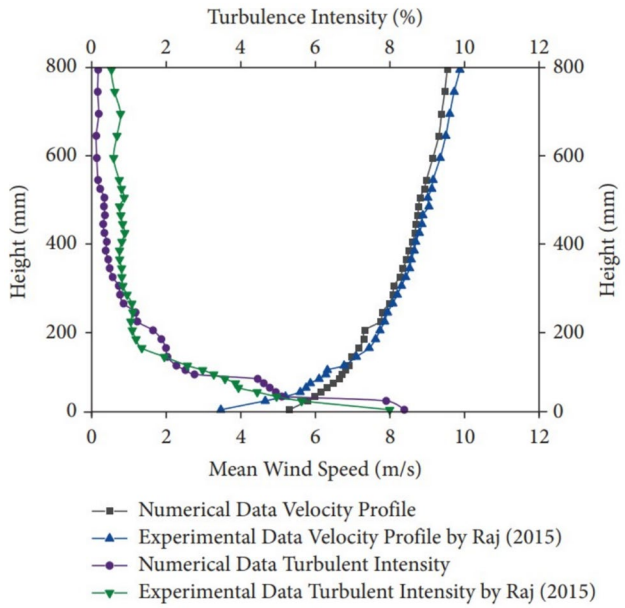

Fig. 4 Velocity profile and turbulence intensity [21]

The transport equations given below describes the turbulence kinetic energy and turbulence dissipation in the traditional k-Ɛ turbulence model.

$$\rho\frac{\partial k}{\partial t} + \rho\overline{u_i}\frac{\partial k}{\partial x_j} = \tau_{ij}\frac{\partial \overline{u_i}}{\partial x_j} - \rho\varepsilon + \frac{\partial}{\partial_{x_j}}\left[\left(\mu + \frac{\mu_t}{\sigma_\varepsilon}\right)\frac{\partial \varepsilon}{\partial x_j}\right] \tag{3}$$

Momentum Equation:

$$\frac{\partial(\rho U_i)}{\partial t} = -\frac{\partial(\rho U_i U_j)}{\partial x_j} - \frac{\partial P}{\partial x_i} + \frac{\partial}{\partial_{x_j}}\left[\mu_{eff}\left(\frac{\partial_{U_i}}{\partial_{x_j}} + \frac{\partial_{U_j}}{\partial_{x_i}}\right)\right] + S_M \tag{4}$$

Mean Velocity Characteristics

The resistance due to friction of objects like naturally occurring plants or man-made buildings on the surface of earth causes the wind speed to gradually decrease as it approaches the surface, reaching the gradient velocity at a given altitude. The region of the Earth's surface where wind speed is not uniform is referred as the atmospheric boundary layer (ABL). In study of wind load for tall buildings, evaluating the change in wind speed along height is essential. Although it is difficult to characterize this variation exactly, several empirical equations have been created to approximate it, as the power law shown in Eq. 5, applied at the inlet of the computational domain. Because of its simplicity, the power law is frequently employed in wind analysis for tall buildings, even though it may not be able to estimate wind velocity inside the first ten meters above Earth. However, at greater altitudes typically above 100 m its wind speed estimate becomes more accurate. The velocity profile obtained by using power-law is shown in Fig. 5. The wind velocity obtained at top of the building is 9.74 m/s.

Power-Law

$$v_z = v_o\left(\frac{z}{z_o}\right)^n \tag{5}$$

where, v_z = Wind's velocity at height Z above ground in longitudinal direction; v_o = Time averaged wind speed (in m/s) = 10 m/s [10]; z_o = Height of wind speed applied = 1 m; n = Terrain roughness constant = 0.147.

Research Methodology

Structured simulation method used in the current investigation is shown in Fig. 6. At first, simulations were run on a rectangle model with certain solver settings, flow parameters, and boundary conditions. After the findings from the rectangle model were confirmed and validated, simulations were run on every model under similar circumstances.

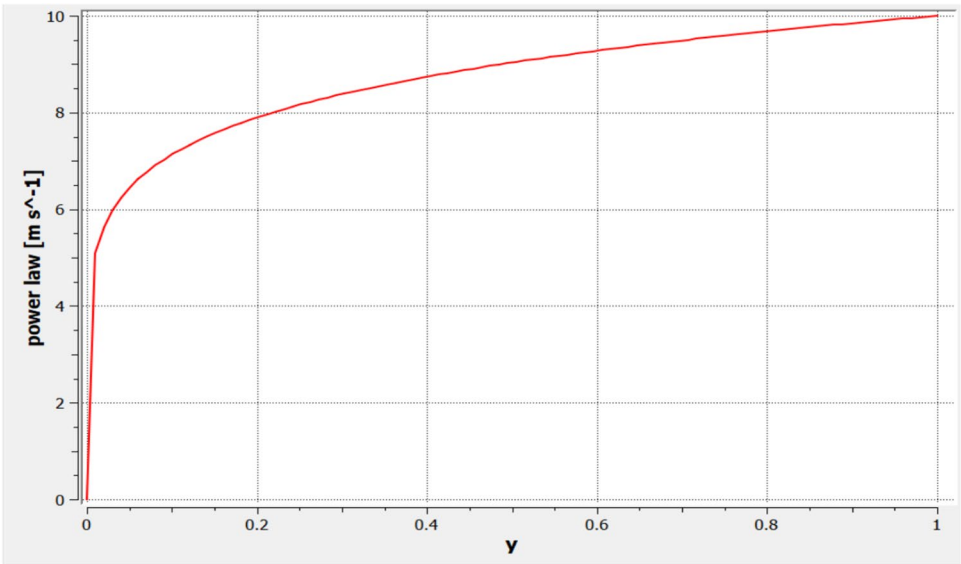

Fig. 5 Graphical representation of power law

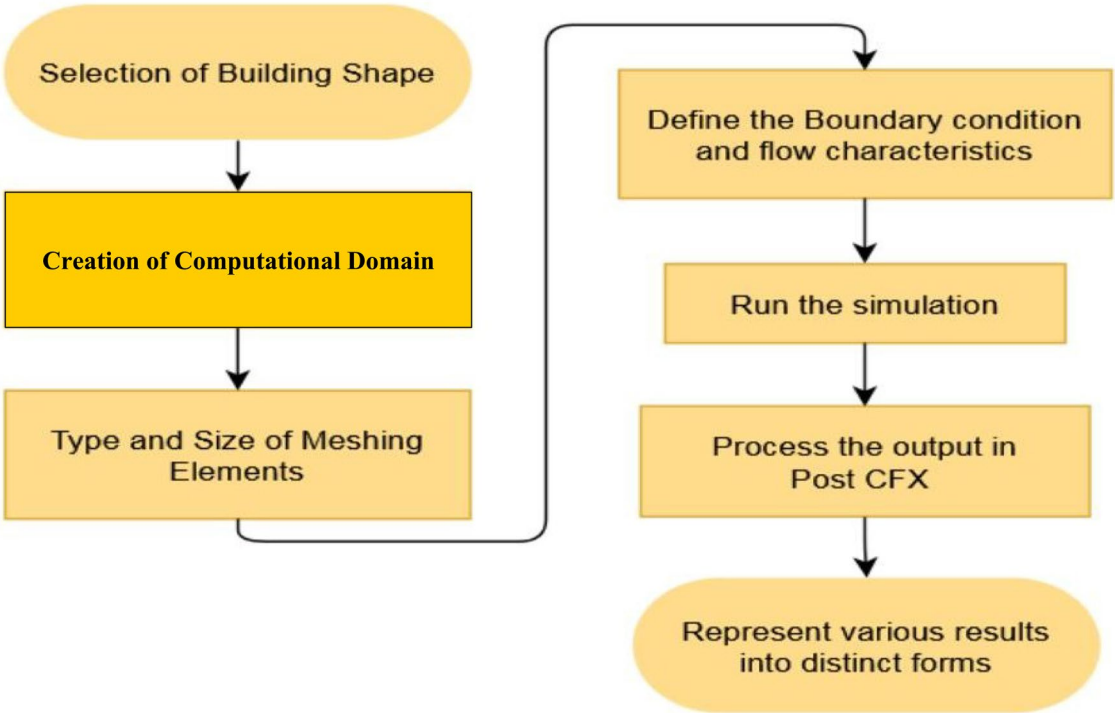

Fig. 6 Structured representation of simulation of model in ANSYS CFX

Computational Domain

Revuz et al. [19] have recommended specific guidelines for designing the computational domain, as well as determining the dimensions and placement of the building model within the computational domain, to closely mimic natural flow conditions. To obtain reliable findings, it is important to make sure that the computational domain closely mimics real-world flow conditions. In order to do this, the computational domain is constructed as a parallelepiped wind tunnel which is virtual in nature, making sure it is big enough to stop wind streams from reflecting back into the model envelope from the borders as shown in Fig. 7, where H is the height of the building.

This guarantees that the blockage ratio stays below 3% and serves to protect the building from any unusual pressure

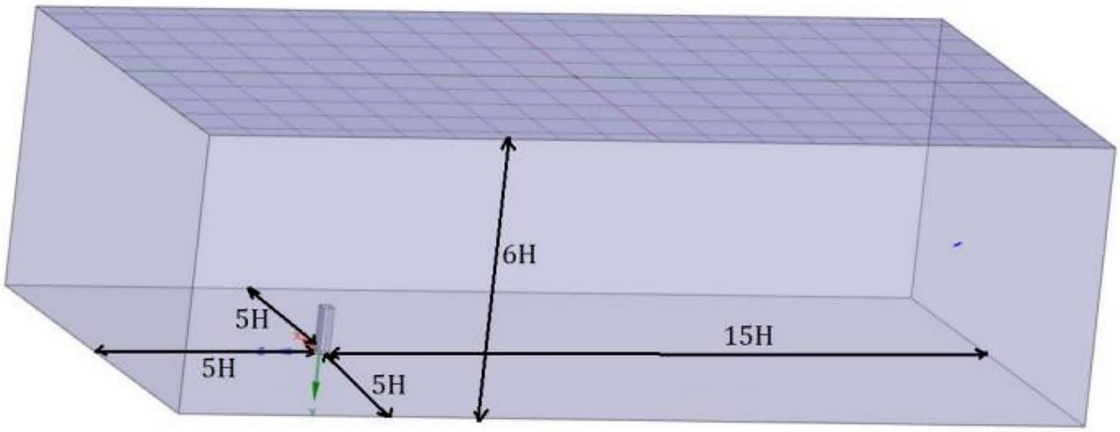

Fig. 7 Dimensions of computational domain

due to wind surrounding its envelope. The size of domain is kept relatively small to prevent the requirement for an overly large computational domain, which would need a higher number of meshing cells. Longer convergence periods for the solution would arise from using more processing power to increase the number of meshing cells. A 120-meter-tall building model with a 3000 square meter plan area is located inside the computational domain of the current investigation, as shown in Fig. 7.

Boundary Conditions

Using the power law, the wind speed was defined at the computational domain's inlet with 5% turbulence intensity in the solver parameters. A relative average static pressure at the outlet is 0 Pa, indicating that there is only atmospheric pressure is acting, and no other force is added to the atmospheric pressure to ensure the continuity and proper flow behavior at the boundary. The top surface of building model and the side walls of computational domain were referred free slip walls, indicating that there is no shear layer formation or boundary layer flow at these surfaces and that these surfaces are frictionless. The velocity of wind in the direction of flow which is parallel to the surface of wall remains limited. However, the ground and walls of the model were designated as no-slip walls, suggesting that boundary layer flow is caused by the friction of the wall surface, which results in zero surface velocity and the formation of a shear layer. The surface roughness of wall was designated smooth.

Computational Grid and Grid sensitivity

The effectiveness of technique of meshing in achieving optimal solutions depends greatly on the way the computational domain and building model surfaces are divided into tiny elements. There are different methods and types of elements that can be used to achieve specific goals. The resolution of the computational grid and model is crucial in determining the final result. Having a larger number of cells typically results in better outcomes, but it also requires more computational resources and time for convergence [20]. For the purpose of accurately mapping physical parameters of flow of wind, such as generation of vortices, separation of flow, and reattachment, a coarser grid resolution was employed for the domain volume. On the other hand, the model's surface geometry was discretized in a more detailed manner, with a specific emphasis on accurately mapping pressure distributions. After trying out various meshing techniques, we selected the one that produced the most accurate validation results. Meshing requires the automatic generation of tetrahedron elements for the computational domain using global settings, while prism elements are applied at walls.

Adjustments were made to the local settings in order to fine-tune the sizing of the face on both the ground and model surfaces. The element size at the base ranged from 0.50 to 0.40 times of domain's size, while the model face sizing varied from 0.25 to 0.2 times of domain's element size. The final cell sizes were determined by optimizing the validation results. The element sizes of mesh were set at 0.44 times of domain's element size for the base and 0.22 times of faces of models. Inflation was implemented to smoothly transition the grid from the domain volume to the model surfaces, resulting in improved outcomes. The meshing of the building and the computational domain is shown in Fig. 8. The resolution resulted in a steady-state solution, with residual RMS errors for mass and momentum convergence ranging between 10^{-4} to 10^{-5} for momentum in all directions and up to 10^{-6} for mass, respectively. The values for momentum in the three directions had domain imbalances of only 0.001%, while for mass, there were no imbalances at all,

Fig. 8 Meshing of models

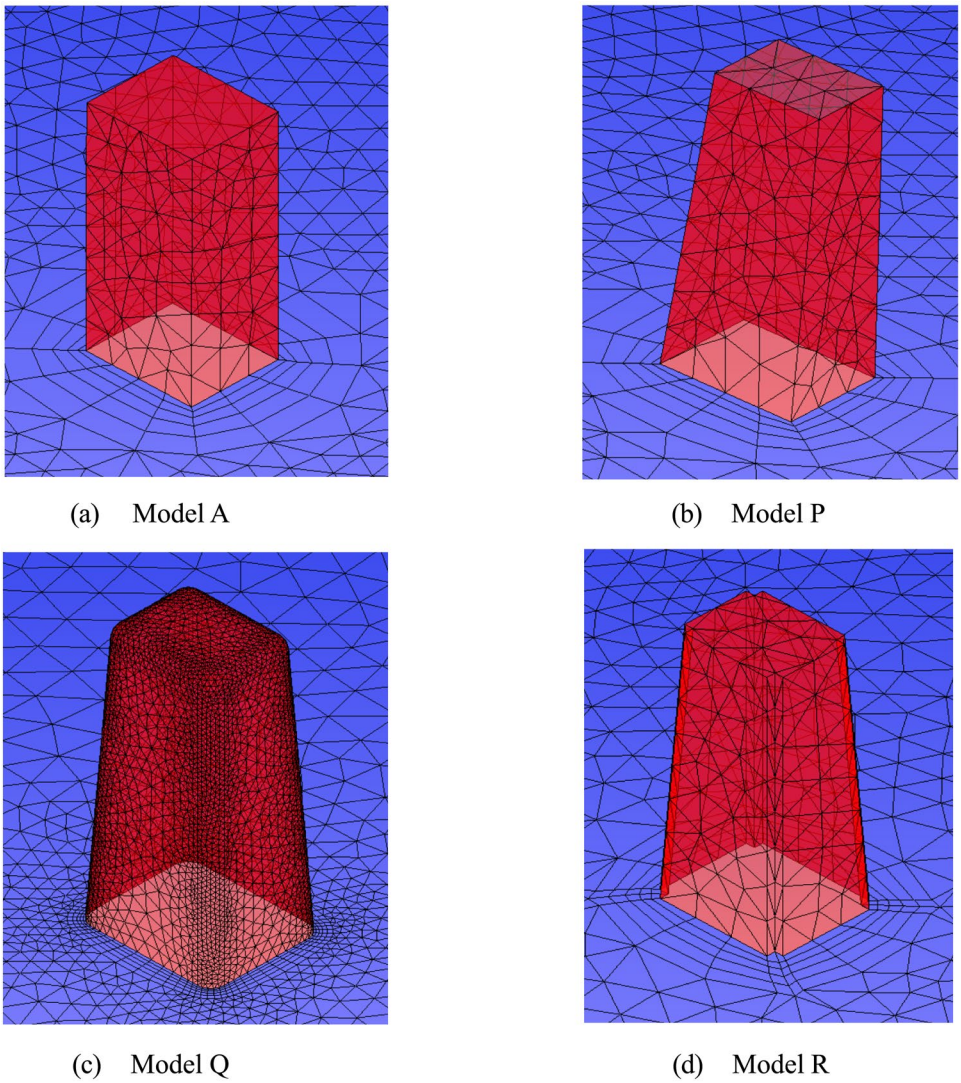

with a perfect 0%. A total of around 1,56,540 nodes were retrieved in the overall domain. There were approximately 9,98,400 discretized elements that were discovered.

Result and discussion

Flow Pattern

Different types of wind characteristics, such as formation of vortex, separation of flow, recirculation, and reattachment, influence the distribution of pressure of wind against high-rise building wall. Figure 9 illustrates the wind flow for Model-A, while Fig. 10 showcases the streamlines for a rectangular model with taper faces and sharp edge corner. Figure 11 shows the horizontal streamlines for Model-Q, while Fig. 12 depicts the wind flow patterns in plan for Model-R. The angle at which wind hits the building influence the size of wake downstream. The largest wake was observed for Model-A when the wind struck at a 30° angle.

The pressure distribution and generation of vortices are determined by the building's geometric configuration. Suction is noticeable on the leeward side of the building relative to the direction of wind, while flow separation leads to increased velocity at the edges. Flow reattachment is more pronounced on the side faces at wind angles of 0° and 15°. Streamline patterns remain consistent regardless of wind speed, primarily dictated by the building's geometry and upstream conditions.

Pressure Coefficients

The coefficient of pressure is a non-dimensional quantity that quantifies the relationship between pressure on a building induced due to wind and the pressure of velocity of the wind at a specific height taken as reference. It depends on

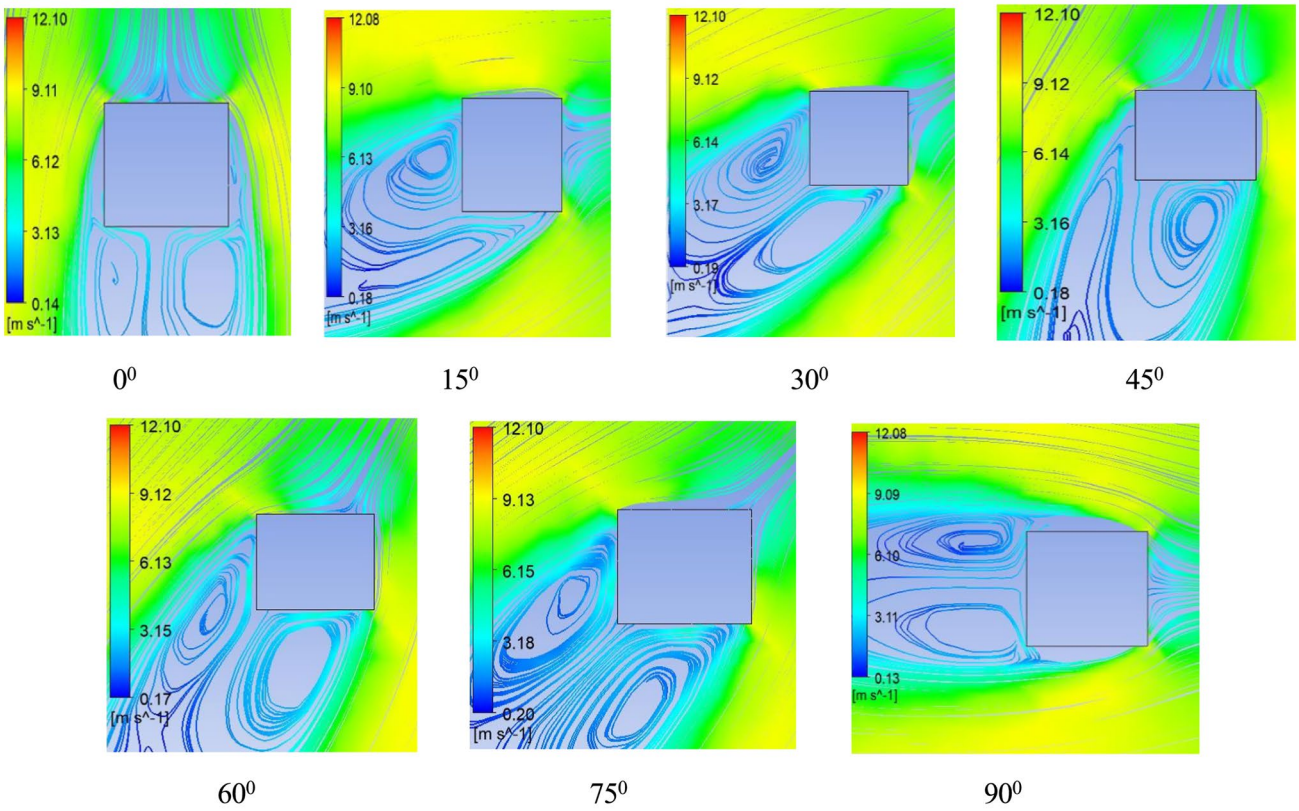

Fig. 9 Flow pattern of model A for all angle of attack of wind

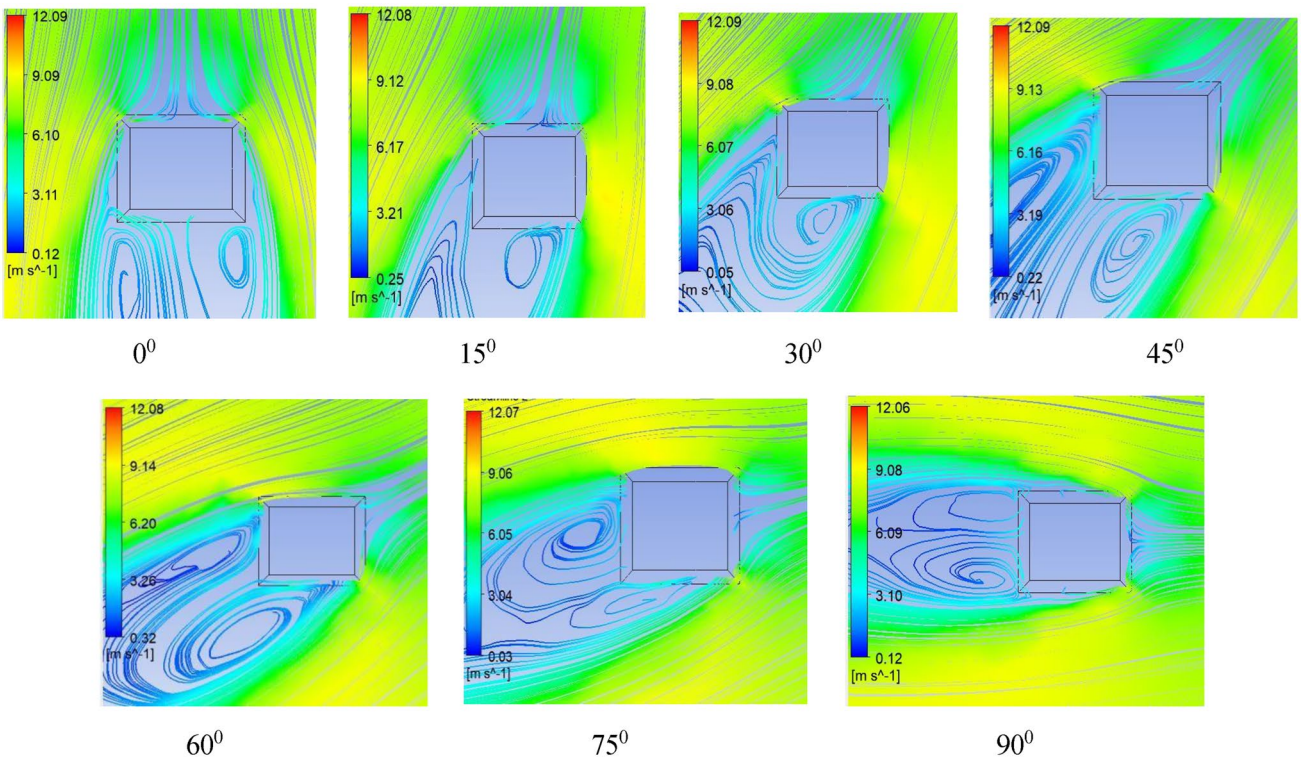

Fig. 10 Flow pattern of model P for all angle of attack of wind

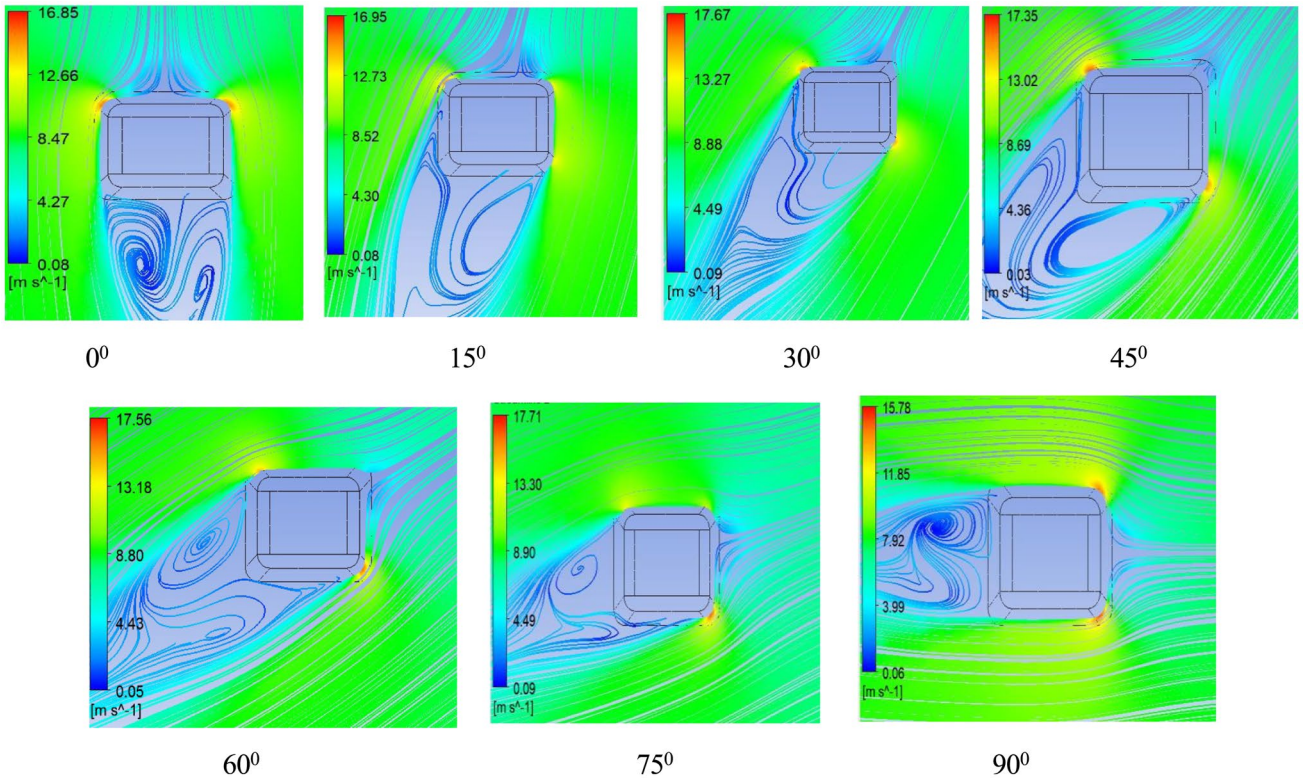

Fig. 11 Flow pattern of model Q for all angle of attack of wind

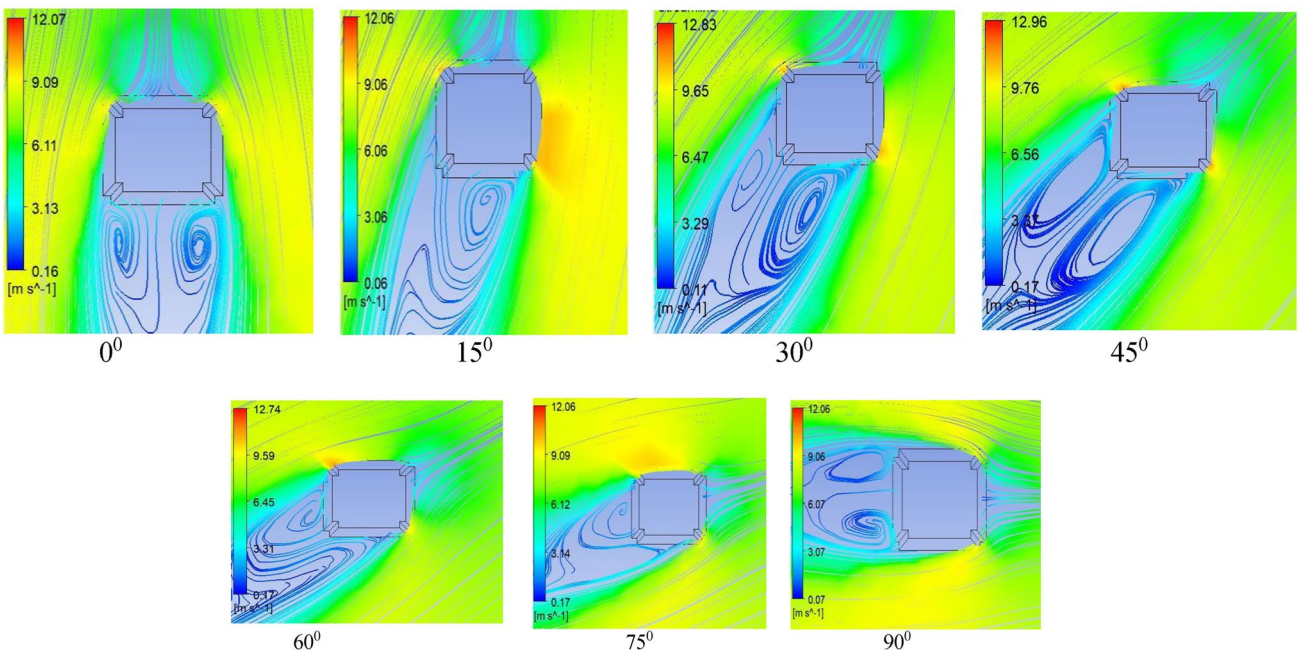

Fig. 12 Flow pattern of model R for all angle of attack of wind

various factors, including the geometry of the building, the angle of attack of wind, and the velocity profile of wind. Figures 13, 14, 15 and 16 shows the average CPe value for

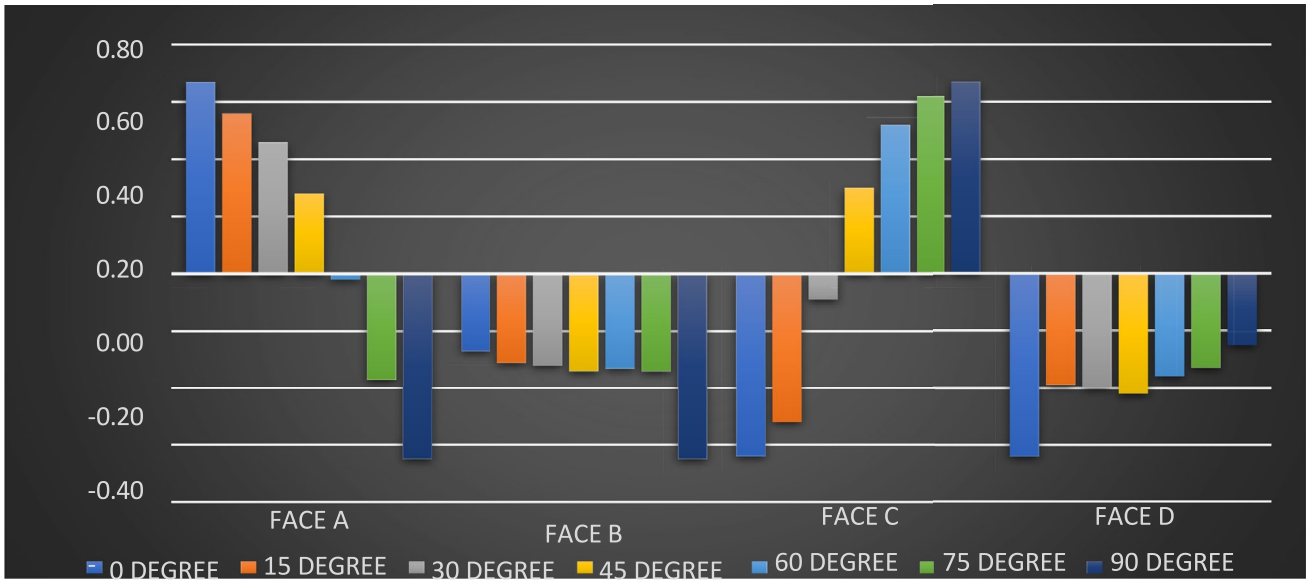

Fig. 13 Variation of area average Cpe on Model A for all wind incidence angles

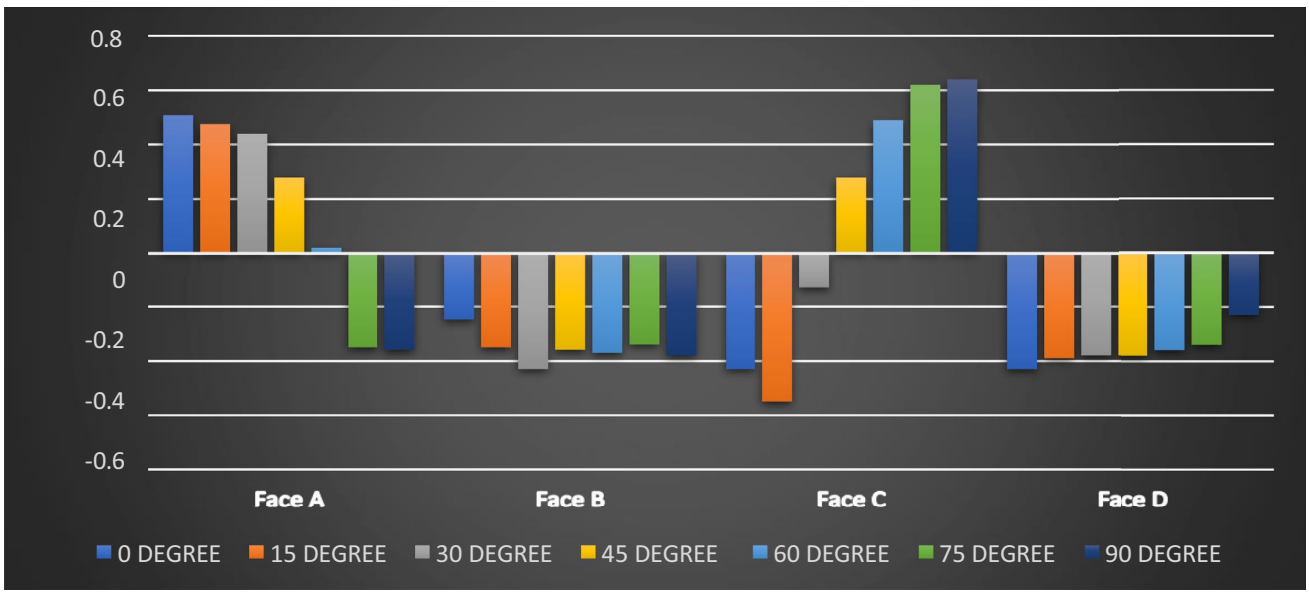

Fig. 14 Variation of area average Cpe on Model P for all wind incidence angles

various models at angle of wind attack ranging from 0° to 90°, with increments of 15°.

In Fig. 13, rectangular Model-A, Face-B and Face-D have experienced suction pressure for all angle of wind attack. Face-A and Face-C experienced maximum pressure at 0° and 90° angle of wind attack, respectively. On Face-A suction was observed at 60°, 75° and 90° angle of wind attack. Face-C observed positive pressure at 45°, 60°, 75° and 90° angle of wind attack. In Model-P, the variation of coefficient of pressure for 0° to 90° wind incidence angle is shown in Fig. 13. Face-B and Face-D have experienced suction for all wind incidence angles. Face-A and Face-C experience max pressure at 90° wind incidence angles. At 75° and 90° angle of wind attack, Face-A is subjected to suction. Face-C experience positive pressure at 45°, 60°, 75° and 90° wind incidence angles.

For Model-Q, tapered model with round corner, Face-B, Face-D, C1, C3 and C4 have experienced suction pressure for all angle of wind attack. Face-A is subjected to positive pressure at 0°, 15°, 30° and 45°. Maximum negative

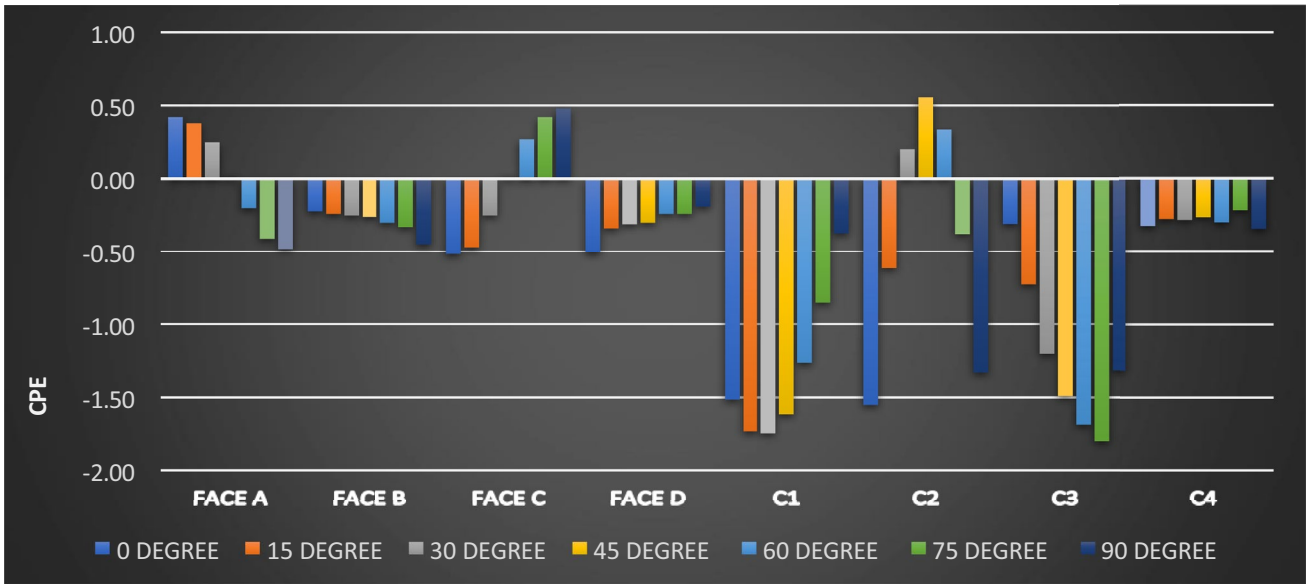

Fig. 15 Variation of area average Cpe on Model Q for all wind incidence angles

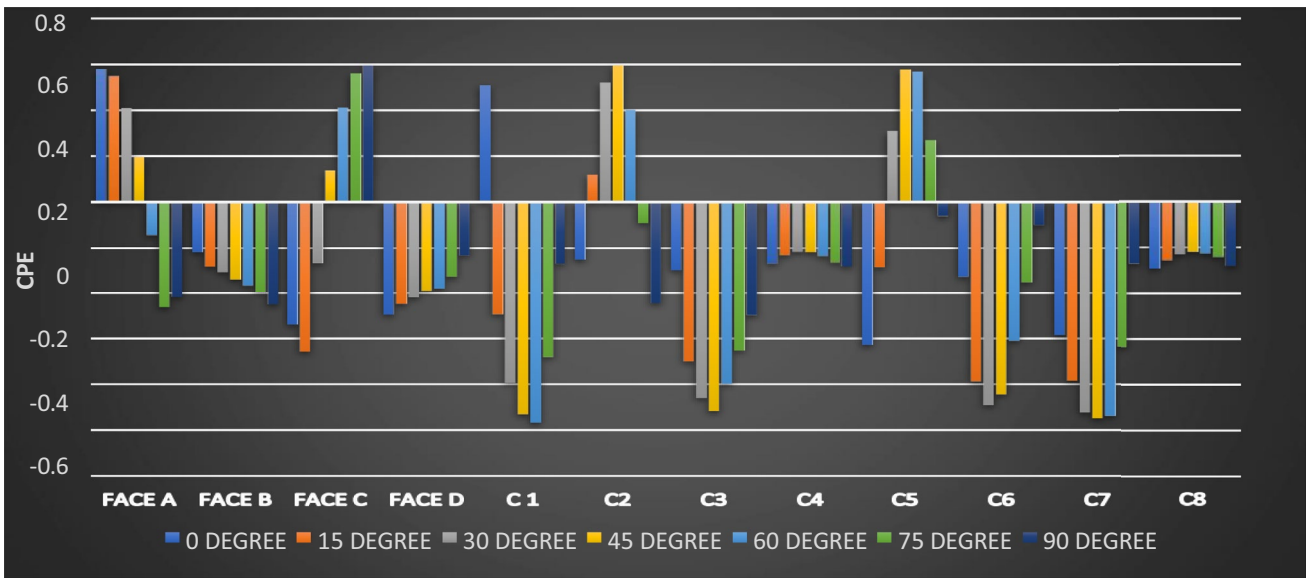

Fig. 16 Variation of area average Cpe on Model R for all wind incidence angles

pressure was observed 0° on Face C and at 75° on C3. At 0°, 15°, 75° and 90° C2 is subjected to negative pressure. For Model-R, tapered model with cut-edge corners, Face-B, Face-D, C3, C4, C6, C7 and C8 have experienced negative wind pressure for all angle of wind attack. Face-A experienced positive pressure at 0°, 15°, 30° and 45° wind incidence angle. At 45°, 60°, 75° and 90° angle of wind attack lift pressure was observed on Face-C. Maximum negative pressure was observed at 60° on C1 and maximum positive pressure was observed at 90° on Face C.

Force Coefficients

The force coefficient (often denoted as CF) is a dimensionless quantity used to quantify the aerodynamic forces experienced by a structure or object due to wind flow. It is commonly used to characterize the pressure distribution and resultant forces acting on surfaces exposed to wind. The formulae of force coefficient is expressed as ratio of the force experienced by the object (such as drag or lift force) to a reference force, which is usually based on the pressure, which is dynamic in nature, of

the approaching wind and the area of surface object. Present research is based upon shape optimization of high rise building using different tapered ratios to reduce the wind effects, so as per the wind standards or previous research, the used equations are the standard equations to predict the nature of wind on the structure, that's why these equations have been applied [22]. The force coefficients in X (C_{FX}) and Z (C_{FZ}) direction are calculated using formula below:

$$C_{FZ} = \frac{\sum F_z}{0.5\rho H L_x V^2} \tag{6}$$

$$C_{FX} = \frac{\sum F_X}{0.5\rho H L_z V^2} \tag{7}$$

$$C_{FR} = \sqrt{{C_{FZ}}^2 + {C_{FX}}^2} \tag{8}$$

where, Fz is the total force (base shear) on the building along the direction of wind, Fx is the total force (base shear) on the building across the direction of wind, Lz is the projected length of the model perpendicular to direction of wind, Lx is the projected length of the model parallel to the direction of wind, ρ is Density of wind taken, H is the height of the building model and V is wind velocity (10 m/s).

The force coefficient in z direction (CFZ) and x direction are calculated using Eqs. 6 and 7 respectively and graphs are plotted which is shown in Fig. 17.

For Model-A, the value of coefficient of force in the z-direction, CFz (irrespective of sign) decreases with an increase in angle of wind attack, and maximum value of CFz was observed at 0° angle of wind attack. The value coefficient of force in the x-direction, CFx (irrespective of sign) decreases from 0° to 15° angle of attack of wind and then increases on increasing the angle of wind attack from 15° to 90° at an interval of 15°. The maximum value of C_{Fx}

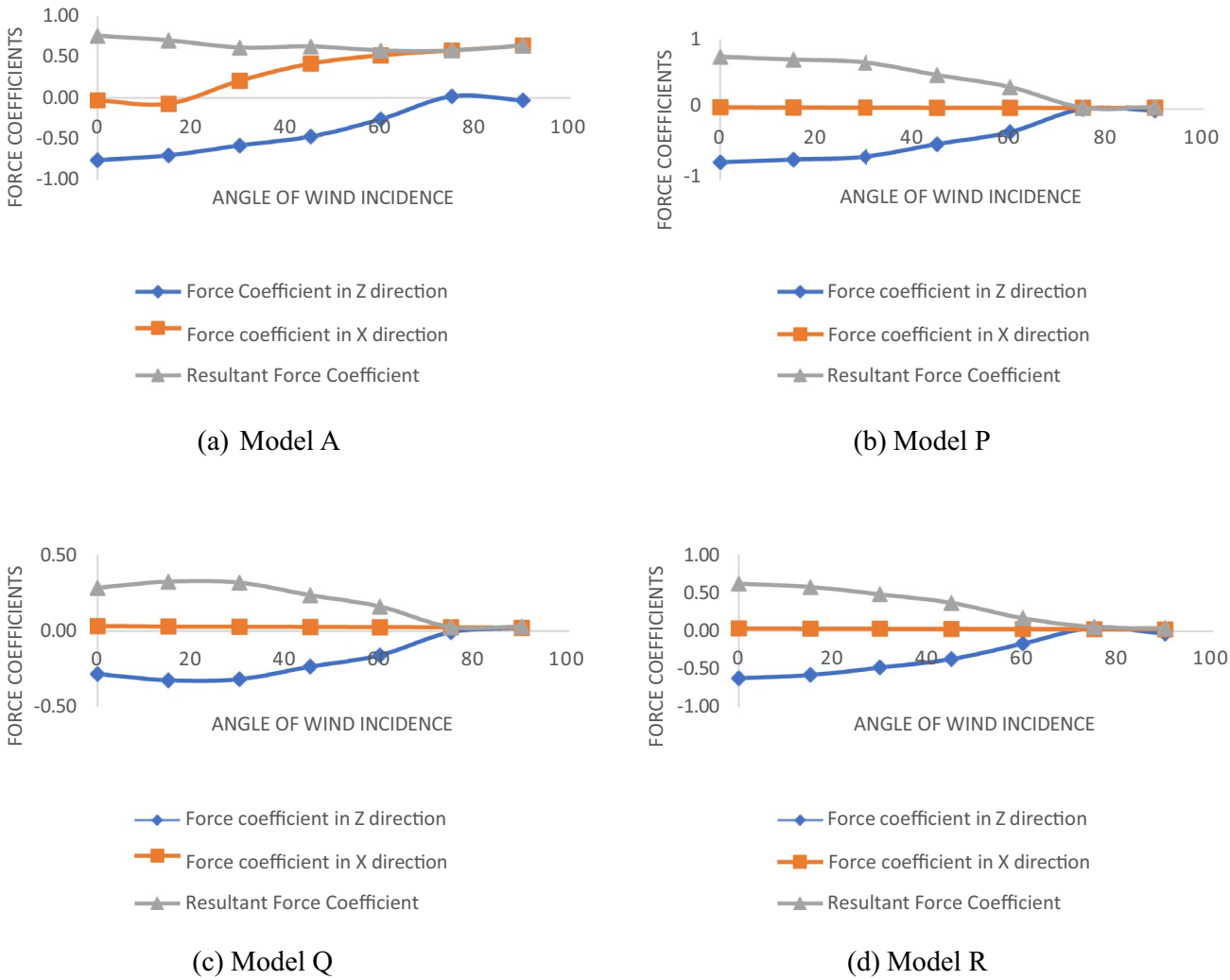

Fig. 17 Variation of Force coefficient for all wind incidence angles

was observed at 900 angle of attack of wind. The resultant force coefficient, C_{Fr} decreases with an increase in angle of wind attack from 0° to 90° at an increment of 150, and maximum value of C_{Fr} was observed at 0° angle of wind attack. For Model-P, the force coefficient in the z-direction, C_{Fz} (irrespective of sign) decreases with an increase in angle of wind attack from 0° to 90° at an interval of 15°, and maximum value of CFz was observed at 0° angle of wind attack. The value of force coefficient in the x-direction, CFx (irrespective of sign) shows no significant change in its value on increasing the angle of wind attack. The resultant force coefficient, C_{Fr} decreases with an increase in angle of wind attack from 0° to 90° at an increment of 15°, and maximum value of C_{Fr} was observed at 0° angle of wind attack.

In Model-Q, the value of CFZ, force coefficient in the z-direction (without considering the sign), is first increases for 15° angle of wind attack from 0° angle of wind attack and then starts decreasing with increase in angle of attack of wind from 15° to 90° with an increment of 15°. The value of force coefficient in x-direction, CFx (irrespective of sign) does not show any valuable change in value when the angle of wind attack increases from 0° to 90° with an increment of 15°. The resultant force coefficient, CFr decreases when the angle of wind attack increases from 0° to 90° with an increment of 15°. The maximum value of resultant force coefficient is experienced at 0° angle of wind attack. In case of Model-R, the value of force coefficient in the z-direction, CFz (irrespective of sign) decreases with an increase in angle of wind attack, and maximum value of CFz was observed at 0° angle of wind attack. The value of coefficient of force in the x-direction, CFx (irrespective of sign) shows no significant change in its value on increasing the angle of attack of wind. The resultant force coefficient, CFr decreases with an increase in angle of wind incidence from 0° to 90° with an increment of 15°, and maximum value of CFr was observed at 0° angle of attack of wind.

Moment Coefficients

The moment coefficient (often denoted as CM) is a dimensionless quantity used to quantify the aerodynamic moments experienced by a structure or object due to wind flow. It is similar in concept to the force coefficient (CF), but instead of representing forces, it represents moments or torques. The moment coefficient is typically expressed as the ratio of the moment experienced by the object about a specific reference point or axis (such as the center of rotation or a fixed point on the object) to a reference moment, which is usually based on the dynamic pressure of the wind which is approaching, the surface area of the object, and a characteristic length. The coefficient of Moment in X (CMX) and Z (CMZ) direction are calculated using formula below:

$$C_{MZ} = \frac{\sum M_z}{0.5\rho H^2 L_Z V^2} \tag{9}$$

$$C_{MX} = \frac{\sum M_X}{0.5\rho H^2 L_X V^2} \tag{10}$$

$$C_{MR} = \sqrt{{C_{MZ}}^2 + {C_{MX}}^2} \tag{11}$$

where, Mz is the total Moment (base moment) in the z-direction, Mx is the total moment (base moment) in the x-direction, Lz is the projected length of the model perpendicular to the direction of wind, Lx is the projected length of the model parallel to the direction of wind, ρ is Density of wind taken, H is the height of the model and V is wind velocity (10 m/s).

The moment coefficient in z direction (CMZ) and x direction are calculated using Eqs. 9 and 10 respectively and graphs are plotted which is shown in Fig. 18.

The coefficient of moment in the x-direction, CMx (irrespective of sign) decreases with an increase in angle of wind attack from 0° to 90° with an increment of 15°. The maximum negative value of CMx was observed at 0° wind incidence angle. The resultant Moment coefficient, CMr decreases with an increase in angle of wind attack from 0° to 90° with an increment of 15°, and maximum value of CMr was observed at 0° angle of win attack. For Model-P, the coefficient of moment in the z-direction, CMz (irrespective of sign) is positive for 0° and 15° wind incidence angle and negative for 30°, 45°, 60°, 75° and 90° wind incidence angle, and maximum negative value of CMz was observed at 90°. The value of moment coefficient in the x-direction, CMx (irrespective of sign) decreases with an increase in angle of wind attack from 0° to 90° with an increment of 15°. The maximum negative value of CMx was observed at 0° angle of wind attack. The resultant Moment coefficient, CMr decreases with an increase in angle of wind attack from 0° to 90° with an increment of 15°, and maximum value of CMr was observed at 0° angle of wind attack.

For Model-Q, the coefficient of moment in the z-direction, CMz (irrespective of sign) is positive for 0° and 15° wind incidence angle and negative for 30°, 45°, 60°, 75° and 90° wind incidence angle, and maximum negative value of CMz was observed at 90°. The coefficient of moment in the x-direction, CMx (irrespective of sign) increases from 0° angle of wind attack to 15° angle of wind attack and then decreases with an increase in angle of wind attack from 15° to 90° with an increment of 15°. The maximum negative value of CMx was observed at 15° angle of wind attack. The resultant Moment coefficient, CMr first increases then decreases with an increase in angle of wind attack from 0° to 90° with an increment of 15°, and maximum value of CMr was observed at 15°

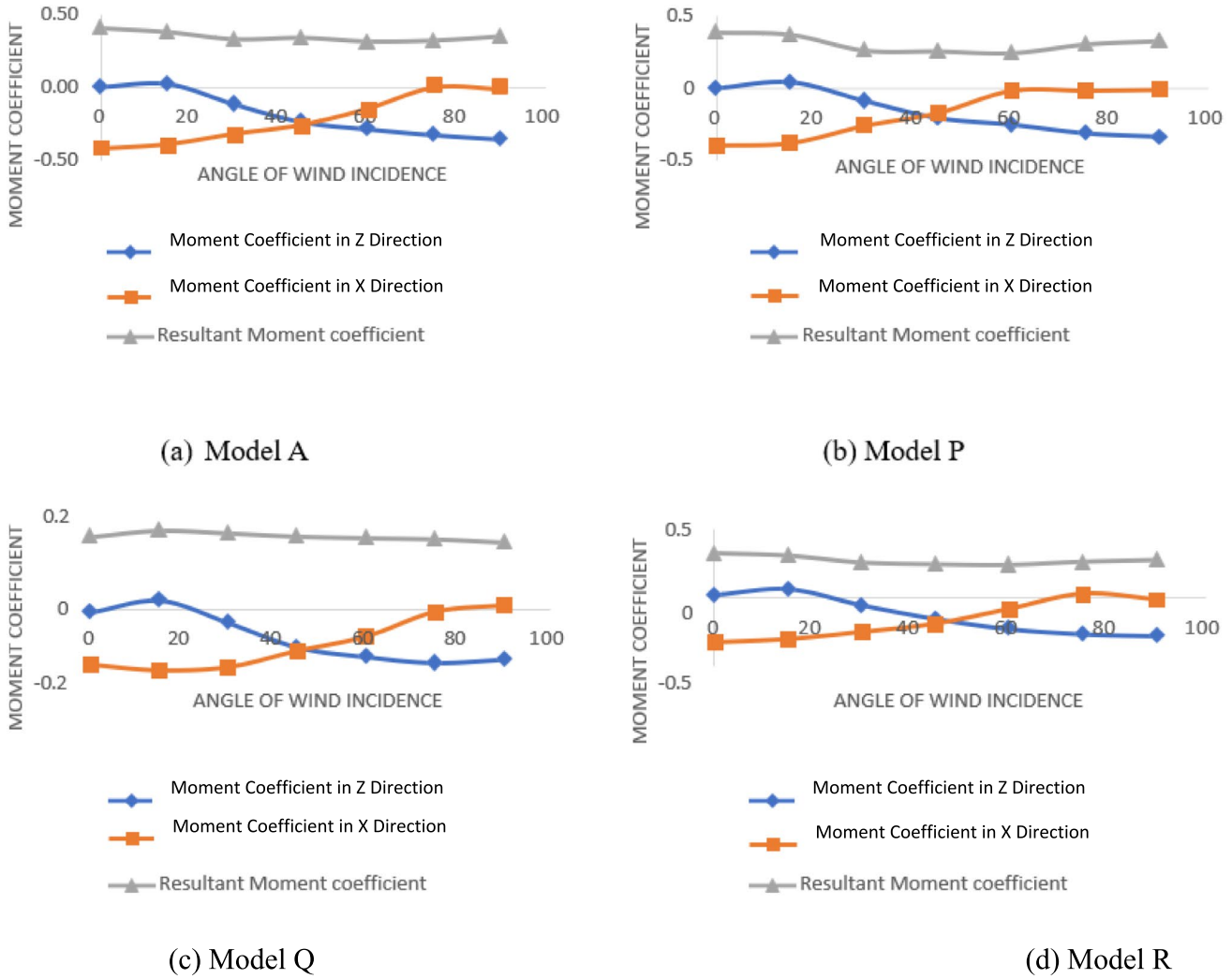

Fig. 18 Variation of Moment coefficient for all wind incidence angles

angle of wind attack. For Model-R, the coefficient of moment in the z-direction, CMz (irrespective of sign) is positive for 0° and 15° angle of wind attack and negative for 30°, 45°, 60°, 75° and 90° angle of wind attack, and maximum negative value of CMz was observed at 90°. The value of moment coefficient in the x-direction, CMx (irrespective of sign) decreases with an increase in angle of wind attack from 0° to 90° with an increment of 15°. The maximum negative value of CMx was observed at 0° angle of wind attack. The resultant Moment coefficient, CMr decreases with an increase in angle of wind attack from 0° to 90° with an increment of 15°, and maximum value of CMr was observed at 0° angle of wind attack.

Coefficient of Drag and Lift

The drag coefficient (Cd) and lift coefficient (Cl) is calculated by using Eqs. 12 and 13. For Model-A, the value of drag coefficient, Cd first decreases with an increase in angle of wind attack from 00 to 450 with an increment of 150 and then increases with an increase in angle of wind attack from 45° to 90° with an increment of 15°. The maximum value of Cd was observed at 0° and 90°. The value of lift coefficient, Cl is negative and positive value of Cl was observed at 15° and 75° respectively. For Model-P, the value of drag coefficient, Cd first decreases with an increase in angle of wind attack from 0° to 45° with an increment of 15° and then increases with an increase in angle of wind attack from 45° to 90° with an increment of 15°. The maximum value of Cd was observed at 0° and 90° angle of wind attack. The value of lift coefficient, Cl is negative at 15°, 30°, 45°, 60° and 90° angle of wind attack and positive for 75° angle of wind attack. Maximum negative and positive value of Cl was observed at 15° and 75° respectively.

In Model-Q, Cd, drag coefficient's value initially increases while increasing the angle of attack of wind from 0° to 45°

with an increment of 15° and after that decreases with increase in angle of wind attack from 45° to 90° with an increment of 15°. Model-Q experienced maximum value of Cd at angle of wind attack 45°. The value of Cl, lift coefficient, is negative at 0°, 15°, 30° and 45° angle of attack of wind and positive at 60°, 75° and 90° angle of attack of wind. Model-Q experience maximum positive value of Cl at 15° angle of wind attack and maximum negative value of Cl at 75° angle of wind attack. In Model-R, Cd, drag coefficient's value initially increases while increasing the angle of attack of wind from 0° to 45° at an interval of 15° and after that decreases with increase in angle of wind attack from 45° to 90° with an increment of 15°. Model-R experienced maximum value of Cd at angle of wind attack 45° and 90°. The value of lift coefficient, Cl is negative at 0°, 15°, 30°, 45° and 90° angle of wind attack and positive for 60° and 75° angle of wind attack. Maximum negative and positive value of Cl was observed at 15° and 75° respectively (Figs. 19 and 20)

$$C_D = \frac{\sum F_{alongwinddirection}}{0.5\rho H^2 L_X V^2} \tag{12}$$

$$C_L = \frac{\sum F_{acrosswinddirection}}{0.5\rho H^2 L_z V^2} \tag{13}$$

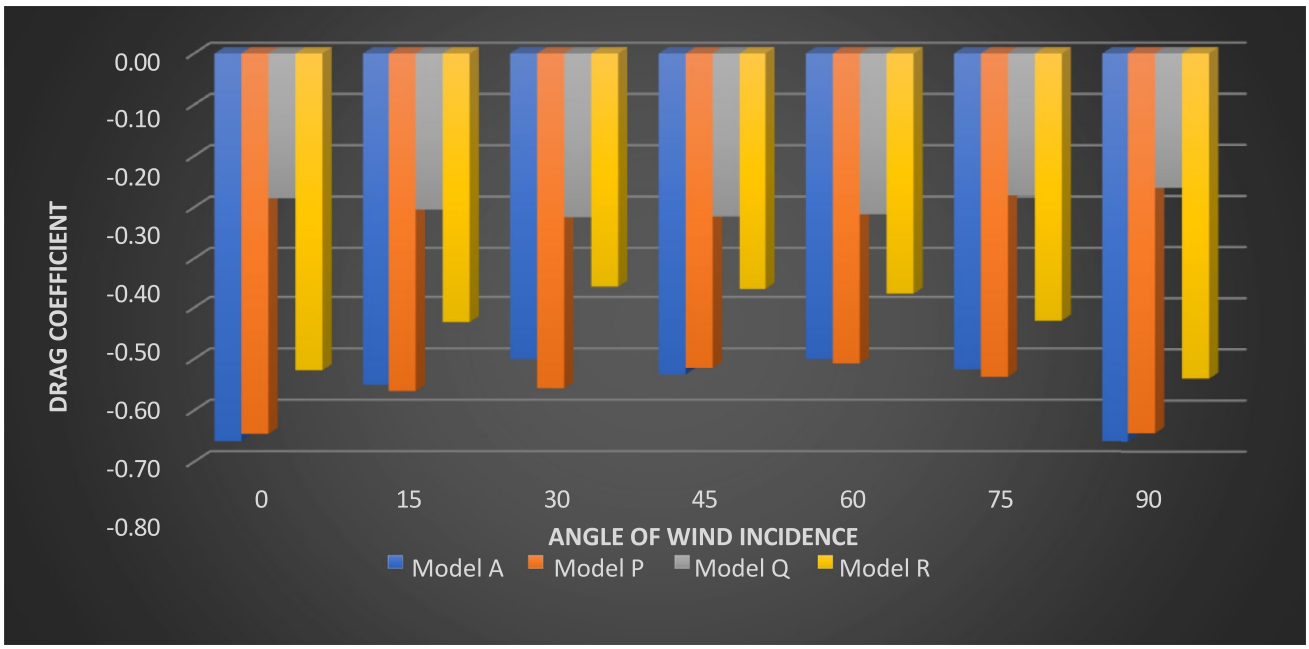

Fig. 19 Variation of drag coefficient of all models for all wind incidence angles

Fig. 20 Variation of lift coefficient of all models for all wind incidence angles

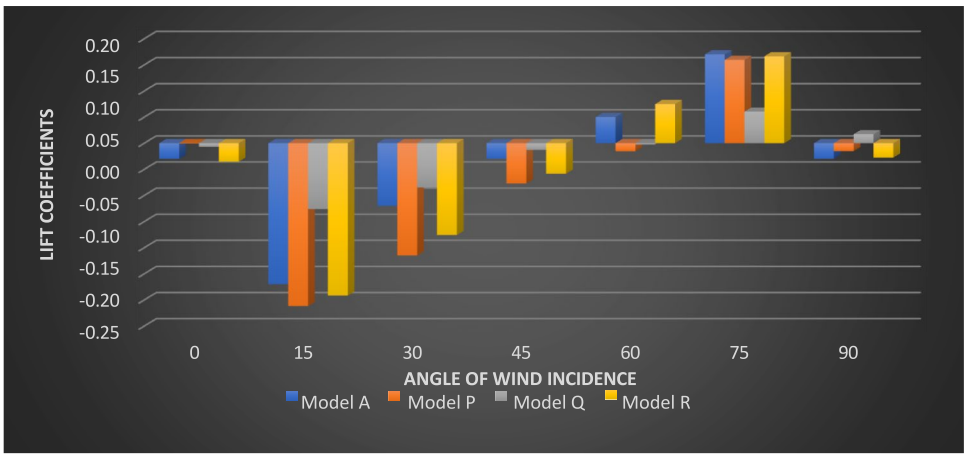

Conclusion

This research examines how taper ratios and different corner configuration affect the wind loads on different plan-shaped tall structures. A numerical simulation is carried out at a length scale of 1: 200 using the ANSYS CFX k-ε turbulence model. For modeling in the numerical simulation, the face average Cp is evaluated and determined to be within a range with several international standards and experimental research. At various angles of wind incidence, streamlines are clearly visible. The following is a summary of the study's noteworthy findings:

1. The important Cpe values on the building's facades are provided by the comparative study of wind analysis that is shown on the tapered model with different corner configurations. It is noticed that on comparing effect of major modification, the Cpe value of Model P i.e., tapered building with sharp edge corner is less than Cpe value of Model A.
2. On comparing the effect of different corners, it was observed that Cpe value of Model Q i.e., Tapered building with round corner configuration is less than Cpe value of Model R i.e., Tapered building with cut corner configuration.
3. The force coefficient in the Z-direction shows decrement in its value on increasing the angle of wind incidence, minimum value of force coefficient in Z-direction was observed for Model Q i.e., Tapered building with round corner configuration.
4. The Coefficient of force in the x-direction is only affected by the taper ratio and is unaffected by corner arrangement, the value of coefficient of force in X-direction is approximately same for Model P, Model Q, Model R.
5. When the angle of wind incidence rises, the Coefficient of moment in the z-direction grows in magnitude, while the Coefficient of moment in the x-direction decreases, the minimum value of moment coefficient in x-direction was observed for Model Q.
6. It can be seen from the graph that each model's drag coefficient graph is roughly mirror-imaged at 45 degrees, while the lift coefficient graph is about anti-symmetric at 45 degrees, and from all the models Model Q gives minimum value for both drag coefficient and lift coefficient.
7. On Comparing all the coefficients of all three models i.e., Model P, Model Q, Model R, the maximum reduction i.e., 43.4% in the aerodynamics effect is seen in Model Q. So, providing tapering in building can reduce the effect of wind and modifying corner can also reduce the aerodynamic effect.

Limitations

The study uses the Reynolds-Averaged Navier-Stokes (RANS) k-ε model, which is a widely accepted method but may not fully capture complex turbulence effects compared to more advanced models like LES (Large Eddy Simulation). The study is based on the boundary conditions prescribed in IS: 875 (Part III):2015. Results might differ under real-world scenarios due to localized climate and environmental factors. Only specific taper ratios and corner configurations are considered. A broader range of geometrical variations may yield insights into additional performance optimizations. The analysis focuses on wind loads and does not account for the material behavior or structural response under dynamic wind conditions.

Future Scope

Incorporate advanced turbulence models such as LES or hybrid RANS-LES approaches to enhance accuracy in predicting complex aerodynamic phenomena. Extend the analysis to account for dynamic wind conditions, such as gusts or fluctuating wind speeds, for better real-world applicability. Complement CFD results with wind tunnel testing or on-site measurements to validate numerical findings. Explore additional geometrical modifications, such as helical designs, recessed corners, and perforated facades, to further enhance aerodynamic performance. Explore the effects of multi-directional and vortex shedding phenomena, particularly for buildings in dense urban environments.

Funding The authors have not disclosed any funding.

Availability of Data All the data utilized for the analysis in this manuscript is available and can be shared upon request.

Declarations

Conflict of interest The authors say they have no competing interests.

Commendations The authors would like to sincerely thank Delhi Technological University, Delhi, India, for giving the research facilities needed to carry out the study.

References

1. B. Bhattacharyya, S.K. Dalui, Investigation of mean wind pressures on 'E' plan shaped tall building. Wind Struct. An Int. J. **26**(2), 99–114 (2018). https://doi.org/10.12989/was.2018.26.2.099

2. R. Raj, T. Rana, T. Anchalia, U. Khola, Numerical study of wind excited action on H Plan-shaped tall building. Int. J. Emerg. Technol. **11**(3), 591–605 (2020), [Online]. Available: https://www.researchtrend.net/ijet/pdf/Numerical Study of Wind Excited Action on H Plan Shaped Tall Building Tushar Rana 2492j8.pdf
3. J. He, C.C.S. Song, A numerical study of wind flow around the TTU building and the roof corner vortex. J. Wind Eng. Ind. Aerodyn. **67–68**, 547–558 (1997). https://doi.org/10.1016/S0167-6105(97)00099-8
4. P. Sanyal, S.K. Dalui, Effects of courtyard and opening on a rectangular plan shaped tall building under wind load. Int. J. Adv. Struct. Eng. **10**(2), 169–188 (2018). https://doi.org/10.1007/s40091-018-0190-4
5. R. Paul, S.K. Dalui, Shape optimization to reduce wind pressure on the surfaces of a rectangular building with horizontal limbs. Period. Polytech. Civ. Eng. **65**(1), 134–149 (2021). https://doi.org/10.3311/PPci.16888
6. R. Paul, S.K. Dalui, Prognosis of wind-tempted mean pressure coefficients of cross-shaped tall buildings using artificial neural network. Period. Polytech. Civ. Eng. **64**(4), 1124–1143 (2020). https://doi.org/10.3311/PPci.16311
7. H. Verma, R.S. Sonparote, Numerical investigation of wind interference effect on twin C-shaped tall buildings. Wind Struct. An Int. J. **37**(6), 425–444 (2023). https://doi.org/10.12989/was.2023.37.6.425
8. S. Pal, R. Raj, S. Anbukumar, Comparative study of wind induced mutual interference effects on square and fish-plan shape tall buildings. Sadhana - Acad. Proc. Eng. Sci. (2021). https://doi.org/10.1007/s12046-021-01592-6
9. A.K. Bairagi, S.K. Dalui, Estimation of wind load on stepped tall building using CFD simulation. Iran. J. Sci. Technol. - Trans. Civ. Eng. **45**(2), 707–727 (2021). https://doi.org/10.1007/s40996-020-00535-1
10. S.K. Nagar, R. Raj, N. Dev, Experimental study of wind-induced pressures on tall buildings of different shapes. Wind Struct. An Int. J. **31**(5), 441–453 (2020). https://doi.org/10.12989/was.2020.31.5.431
11. M. Mallick, A. Mohanta, A. Kumar, V. Raj, Modelling of wind pressure coefficients on C-shaped building models. Model. Simul. Eng. (2018). https://doi.org/10.1155/2018/6524945
12. R. Paul, S.K. Dalui, Wind effects on 'Z' plan-shaped tall building: a case study. Int. J. Adv. Struct. Eng. **8**(3), 319–335 (2016). https://doi.org/10.1007/s40091-016-0134-9
13. B. Bhattacharyya, S.K. Dalui, Experimental and numerical study of wind-pressure distribution on irregular-plan-shaped building. J. Struct. Eng. **146**(7), 1–14 (2020). https://doi.org/10.1061/(asce)st.1943-541x.0002686
14. P.K. Goyal, S. Kumari, S. Singh, R.K. Saroj, R.K. Meena, R. Raj, Numerical study of wind loads on Y plan-shaped tall building using CFD. Civ. Eng. J. **8**(2), 263–277 (2022). https://doi.org/10.28991/CEJ-2022-08-02-06
15. S. Pal, R. Kumar Meena, R. Raj, S. Anbukumar, Wind tunnel study of a fish-plan shape model under different isolated wind incidences. Wind Struct. An Int. J. **33**(5), 353–366 (2021). https://doi.org/10.12989/was.2021.33.5.353
16. P. Sanyal, S.K. Dalui, Effects of internal angle between limbs of 'Y' plan shaped tall building under wind load. J. Build. Eng. **33**, 101843 (2021). https://doi.org/10.1016/j.jobe.2020.101843
17. P. Mendis, T. Ngo, N. Haritos, A. Hira, B. Samali, J. Cheung, Wind loading on tall buildings. Electron. J. Struct. Eng. **7**, 41–54 (2007). https://doi.org/10.56748/ejse.641
18. R.K. Meena, R. Raj, S. Anbukumar, Effect of wind load on irregular shape tall buildings having different corner configuration. Sadhana - Acad. Proc. Eng. Sci. (2022). https://doi.org/10.1007/s12046-022-01895-2
19. J. Revuz, D.M. Hargreaves, J.S. Owen, On the domain size for the steady-state CFD modelling of a tall building. Wind Struct. An Int. J. **15**(4), 313–329 (2012). https://doi.org/10.12989/was.2012.15.4.313
20. J. Franke et al., Recommendations on the use of CFD in wind engineering, COST Action C14 Impact Wind Storm City Life Urban Environ., July 2014 (2004)
21. A. Verma, R.K. Meena, H. Dubey, R. Raj, S. Anbukumar, Wind effect on rectangular and triaxial symmetric tall building having equal area and height. Hindwani - Acad. Proc. Eng. Sci. (2022). https://doi.org/10.1155/2022/4815623
22. A. Kumar, R.K Meena, D. Sharma, R. Raj, Structural parameter of wrench -C shape building using CFD" International journal of construction management
23. IS875 Part 3, 2015. Code of Practice for Design Loads (Other than Earthquake) for Buildings and Structures. Bureau of Indian Standards, New Delhi
24. AS/NZS 1170.2:20112011. "Standard, New Zealand Standard and Australia." Structural Design Actions - Part 2: Wind Actions (AS/NZS 1170.2:2011), Australian/New Zealand Standard
25. ASCE: 7-16(2017). 2017. Minimum Design Loads and Associated Criteria for Buildings and Other Structures. Structural Engineering Institute of the American Society of Civil Engineering, Reston
26. BS 6399-2: 1997 British Standard, Loading for buildings - Part 2: Code of practice for wind loads (1997)
27. EN 1991: E. Standard, Eurocode 1: Actions on structures - Part 1–4: General actions - Wind actions, European Union (2011)

Publisher's Note Springer Nature remains neutral with regard to jurisdictional claims in published maps and institutional affiliations.

Springer Nature or its licensor (e.g. a society or other partner) holds exclusive rights to this article under a publishing agreement with the author(s) or other rightsholder(s); author self-archiving of the accepted manuscript version of this article is solely governed by the terms of such publishing agreement and applicable law.

Journal of Modern Optics

ISSN: (Print) (Online) Journal homepage: www.tandfonline.com/journals/tmop20

Photonic crystal fibres infiltrated with nitrobenzene for low peak power supercontinuum generation in NIR to MIR region

Drishti Singh Tomer & Ajeet Kumar

To cite this article: Drishti Singh Tomer & Ajeet Kumar (14 Mar 2025): Photonic crystal fibres infiltrated with nitrobenzene for low peak power supercontinuum generation in NIR to MIR region, Journal of Modern Optics, DOI: 10.1080/09500340.2025.2478641

To link to this article: https://doi.org/10.1080/09500340.2025.2478641

Published online: 14 Mar 2025.

Submit your article to this journal

Article views: 10

View related articles

View Crossmark data

Full Terms & Conditions of access and use can be found at
https://www.tandfonline.com/action/journalInformation?journalCode=tmop20

JOURNAL OF MODERN OPTICS
https://doi.org/10.1080/09500340.2025.2478641

Taylor & Francis
Taylor & Francis Group

Check for updates

Photonic crystal fibres infiltrated with nitrobenzene for low peak power supercontinuum generation in NIR to MIR region

Drishti Singh Tomer and Ajeet Kumar

Advanced Photonics Simulation Research Lab, Department of Applied Physics, Delhi Technological University, Delhi, India

ABSTRACT

We present a comparative study of silica-based Photonic Crystal Fibres infiltrated with nitrobenzene to generate supercontinuum light with low peak power in the near-infrared to mid-infrared ranges. Using a full vectorial finite element method, we analyzed three designs: symmetrical circular (#C) and asymmetrical elliptical X-polarised (#EX) and Y-polarised (#EY). The circular design showed a dispersion of + 30.211 ps/nm/km, effective mode area of 4.13 μm^2, and nonlinear coefficient of 1962.0 W^{-1} km^{-1}at 1.55 µm. The elliptical designs had dispersions of −10.852 ps/nm/km (#EX) and −8.356 ps/nm/km (#EY), with effective mode areas of 4.55 and 4.60 μm^2, and nonlinear coefficients of 1780.9 and 1761.5 W^{-1} km^{-1}. Using a 10 mm fiber, 50 fs laser pulse, and 650 W pump power, we achieved supercontinuum spectra ranging from 1.3–2.0 µm (#C), 0.9–2.3 µm (#EX), and 1.0–2.4 µm (#EY). These designs are promising for biomedical and sensing applications.

ARTICLE HISTORY
Received 10 November 2024
Accepted 7 March 2025

KEYWORDS
Photonic integrated circuits; supercontinuum generation; nonlinear optics; photonic crystal fibres

1. Introduction

SCG is a complex phenomenon where new frequency in the pulse spectrum is generated by the interaction between various non-linear effects in the fibre, leading to the expansion of a narrow spectrum by several multiples into a continuous broad spectrum. In recent times, SCG has become a focal point of extensive research interest [1–6]. For the first time in 1970, the concept of SCG was introduced [7]. SC is characterized by a continuous broadband spectrum, good coherence and stability. The performance of SCG depends on the pump wavelength, fibre nonlinearity, input pulse energy, fibre length and pulse duration. In addition, important PCF properties such as attenuation, effective mode area, and dispersion also affect the performance of SCG [8]. Preferably, a flat curve with near zero dispersion value, minimum attenuation constant and, an effective mode area are required. These parameters can be controlled by changing the geometrical parameters of the Photonic crystal Fibre (PCF). However, subject to the choice of pump wavelength within the dispersion range, corresponding effects occur in SCG [9]. The performance of the SC is measured by three leading indicators: bandwidth, coherence, and flatness. Nonlinear effects like self-phase modulation (SPM) and optical wave breaking (OWB) contribute to spectral broadening in the all-normal dispersion regime (ANDi). Maintenance of ultrashort pulses without distortion, a consistent and stable power spectral density and a uniform and even temporal profile are a few of the advantages associated with using the ANDi profile of PCFs. The generation of a coherent flat spectrum is made possible by the absence of modulation instability (MI), which is typically detrimental to spectral quality. In this context, the dynamics of solitons play a crucial role by effectively minimizing the impact of noise. These characteristics are advantageous for applications in spectroscopy, metrology, and optical tomography systems including optical coherence tomography (OCT) [10,11]. However, the associated shortcoming with ANDi is the onset of a photo-thermal effect, causing damage to the fibre on the application of high input power.

Conversely, on utilizing anomalous dispersion regime a broad SC spectra can be achieved with low input peak power. SC generation through pumping in the anomalous dispersion regime arises from the combined effects of various soliton dynamics. Key contributing factors include interactions with dispersive waves, the process of soliton splitting, shifts in the soliton's natural frequency,

CONTACT Ajeet Kumar ajeetdph@dtu.ac.in Advanced Photonics Simulation Research Lab, Department of Applied Physics, Delhi Technological University, Delhi 110042, India

© 2025 Informa UK Limited, trading as Taylor & Francis Group

and the influence of stimulated Raman scattering. These mechanisms work together to create the wide spectral broadening that characterizes supercontinuum generation in this regime. However, there is a trade-off between broadening and coherency. So, on broadening, coherency will be compromised. Numerous methodologies have been proposed for the generation of SC in which the high nonlinearities and low dispersion profile hold key roles [12]. A general approach for this is to utilize PCFs made of silica or highly nonlinear soft glasses. Silica can be used for visible to near-infrared (NIR) regions but not for mid-infrared (MIR) due to limited transparency up to 2.5 µm. Another approach that can be used is to utilise tellurite, bismuth-gallate or chalcogenide glasses but they also have compatibility issues with silica for fusion splicing [13]. Such glasses possess a few more limitations like difficulty in the fabrication of complex fibre structures that might require high thermal power which can lead to crystallization, requirement of complex pump systems and limitations in power handling. These glasses may be mechanically weak, may have steep normal dispersion, and have a long ZDW in NIR which can limit the flatness of the dispersion curve and restrict the spectral SCG broadening [14].

Recently, the use of liquid-filled PCFs has drawn much attention as they are capable of overcoming the disadvantages of liquid-filled capillary approach. They are better at improving the flexibility and modal properties of the fibre. It is also feasible to shift the ZDW and resonate it with the pump wavelength of the available laser as well as obtain a flat and ANDi profile in the anticipated spectra [15].

To overcome these shortcomings, recently liquid infiltrated PCFs are designed which have high nonlinear refractive index like CS_2 where $n_2 = 2.2 \times 10^{-18}$ $m^2\,W^{-1}$ at 1032 nm [16], which is quite large in comparison to silica. Some of the recently published work shows where Chemnitz et al., reported on experimental evidence for the dynamics of hybrid solitons, a new type of solitary wave, using a CS_2-filled liquid core optical fibre [17]. Kedenburg et al. demonstrated that the PCF filled with CS_2 is capable of generating a spectral broadening ranging from 1.2 to 2.4 µm [18]. Similarly, Pniewski et al., numerically demonstrated that the PCF filled with toluene can generate a broadband spectrum over 1000 nm [19]. Dai et al., measured a stimulated Raman scattering response around 0.6 µm in a commercially available hollow silica fibre filled with a toluene/chloroform mixture [20] and Van et al., numerically investigated the broadband spectrum of 700 nm in IR wavelength ranges for all-normal dispersion in hollow-core PCFs with toluene [21]. But CS_2 and toluene both are highly toxic. Other organic solvents like nitrobenzene ($C_6H_5NO_2$), tetrachloroethylene (C_2Cl_4), chloroform ($CHCl_3$), benzene (C_6H_6), carbon tetrachloride (CCl_4), and ethanol (C_2H_5OH) etc. are also used which are comparatively less toxic [22]. Vieweg et al., experimentally demonstrated solitonic SC generation over 600 nm bandwidth with PCFs filled with carbon tetrachloride (CCl_4) [23]. In terms of techniques for infiltration, multiple methods have been used depending upon the requirement like photo-polymerization [23], Thermal collapse [24], splicer process or UV adhesive process [25], and Micro channel milling [26].

Structures with multiple hexagonal ring arrangements around the core have been popular [27,28]. However, the spectral bands lack uniform flatness, despite the dispersion curve being nearly zero. Various designs like square, circular, octagonal, pentagonal and spiral structures were used to overcome this limitation [22,29,30]. Circular photonic crystal fibres (PCFs) are particularly well-suited for broadband SCG due to several key features. To begin with, the redshift of the zero-dispersion wavelength (ZDW) significantly boosts the SCG capabilities within MIR range. Moreover, the high symmetry inherent in their design allows for the efficient confinement of electromagnetic energy field within the core. Additionally, a lower dispersion slope in the anomalous dispersion region contributes to reducing noise levels in the SC spectrum. Furthermore, the low group velocity dispersion in the normal dispersion regime enables longer dispersion lengths and promotes greater soliton interactions [31].

In this study, we present a comparative analysis of the effects of nitrobenzene infiltration on SC generation across two different designs. Unlike CS_2 and toluene, nitrobenzene is less toxic. Nitrobenzene has stronger nonlinear optical properties than benzene. The presence of the nitro group in nitrobenzene increases its polarizability, making it more responsive to intense light fields. Utilizing liquids within the air holes offers tunable properties and high nonlinearity, which enhances the bandwidth of SC spectrum with lower pump power and reduced attenuation. One design features a symmetrical structure, while the other incorporates elliptical air holes, introducing birefringence due to asymmetry.

Polarization effects are another essential aspect of the dynamics of SCG in MOFs [32]. The birefringent fibres for SCG have been demonstrated to be quite useful, as it keeps the polarization state preserved along the propagation for all the spectral components. Ortigosa-Blanch et al. have observed that the birefringence can be achieved either by making the PCF design non-symmetrical or by introducing a birefringent material [33]. Elliptical air holes have also been utilized in MOFs to provide an

Table 1. Comparison with previously recognized results of PCFs.

References	#PCF	Pump Wavelength (μm)	Peak power (kW)	Pulse width (fs)	Fibre length	SCG bandwidth (μm)	Dispersion (ps/nm/km)	Nonlinearity ($W^{-1}km^{-1}$)
[50]	Cs_2	1.55	2.0	500	10 cm	1.35–2.11	−114.26	3327
[52]	CCl_4	1.03	62.5	400	20 cm	0.85–1.25	−150	22
[53]	$CHCl_3$,#F_1	1.03	0.83	400	10 cm	0.6–1.26	−7	1290
[53]	$CHCl_3$,#F_2	1.03	4.16	400	10 cm	0.6–1.40	−7.6	440
[54]	$C_6H_5NO_2$, #F_1	1.03	0.83	120	5 cm	1.8–2.8	33.7	–
[54]	$C_6H_5NO_2$, #F_2	1.56	5.55	90	5 cm	0.8–2.1	−2.2	–
[54]	$C_6H_5NO_2$, #F_3	1.56	0.66	90	5 cm	1.3–2.3	–	–
[55]	$C_6H_5NO_2$	1.81	1	50	5 cm	1.3–2.8	–	–
[55]	$C_6H_5NO_2$	1.55	1	50	5 cm	1.3–2.8	–	–
Proposed work	$C_6H_5NO_2$, #C	1.55	0.65	50	10 mm	1.3–2.0	30.211	1962
Proposed work	$C_6H_5NO_2$, #EX	1.55	0.65	50	10 mm	0.9–2.3	−10.852	1780.9
Proposed work	$C_6H_5NO_2$, #EY	1.55	0.65	50	10 mm	1.0–2.4	−8.356	1761.5

increased birefringence effect, as suggested by Steel and Osgood [34].

An SC spectrum ranging from NIR to MIR is generated using a symmetrical graded design at low input pump power. This spectrum extends from 1.3 to 2.0 μm when pumped at a wavelength of 1.55 μm, utilizing a 10 mm long fibre and injecting 50 femtosecond laser pulses at a power of 650 W. In another design using the same pump power, the same fibre length and the same 50fs laser pulse broadening around 0.9–2.3 μm is obtained with X-polarization and broadening around 1.0–2.4 μm is obtained with Y-polarization.

From the perspective of practical implication low input power is crucial. In the case of liquid infiltration in PCFs, they are unstable at high temperatures and high power. They can be easily vaporized if high power is used. The produced SC source can be utilized in a wide range of applications, such as monitoring food quality, biomedical diagnostics, chemical detection & analysis, frequency comb generation, explosive detection, and advanced optical imaging techniques, including OCT. A wide supercontinuum spectrum with low input peak power is presented, in comparison to the lately reported results summarized in Table 1. Moreover, the difficulty of harmonizing SC broadening and preserving coherence has been efficiently resolved.

This paper is organized into five main sections, each addressing a critical aspect of the study. Section one serves as an introduction, providing a brief yet comprehensive overview of the research objectives and the scope of the study. Section two focuses on the design of PCF, outlining the theoretical framework and the design principles employed. In section three, a thorough elucidation of the numerical methodology used in the analysis is provided, detailing the computational techniques and models applied. Section four presents the results obtained from the study, offering an in-depth discussion of their significance and potential implications for the field. Finally, section five concludes the paper, summarizing the key findings and suggesting directions for future research, followed by a comprehensive list of references.

2. PCF geometry

Achieving low loss and a small effective mode area is crucial for the determination of the efficacy of a nonlinear medium for supercontinuum generation. At the same time, dispersion properties are equally important. These factors are largely shaped by the geometry of the fibre. Along with these factors, the material used in the fabrication of PCF should have a high nonlinear refractive index (n_2). The structural view of proposed circular PCF is shown in Figure 1(a,b). This design is symmetrical with circular rings of air holes graded for better confinement of light within the core [35]. The amount of grading (δD) $= d_1 - d_2 = d_2 - d_3 = d_3 - d_4$ has been kept constant at 0.50 μm between two consecutive rings.

Each ring of air holes is designed with a unique diameter: the first ring surrounding the core has a diameter of $d_1 = 2.0$ μm, the second ring $d_2 = 1.5$ μm, the third ring $d_3 = 1.0$ μm and the fourth ring $d_4 = 0.5$ μm. The diameter of the core is constant as $d_{\text{core}} = 1.0$ μm. The first ring contains eight air holes, while the outer rings have a greater number of air holes, creating a symmetrical structure described by $x = r\,cos\,(\theta)\;and\;y = r\,sin\,(\theta)$, where r represents the radial distance from the centre and (θ) varies from 0° to 360°. The pitch (Λ) is defined as the distance between two adjacent air holes, which is set to 1 μm. To eradicate reflections at the boundary, a cylindrical perfectly matched layer (PML) is implemented at the edges of the cladding. The PML is generally 10% to 20% of the whole cladding diameter. Here, it is 1.8 μm. The core is infiltrated with nitrobenzene. Figure 1(c) shows the electric field distribution of the principal mode at pump wavelength.

Similarly, Figure 2(a,b) shows a similar design but with an elliptical first ring around the core. The rest of the design parameters are kept the same. Instead of a circular symmetrical ring of constant diameter

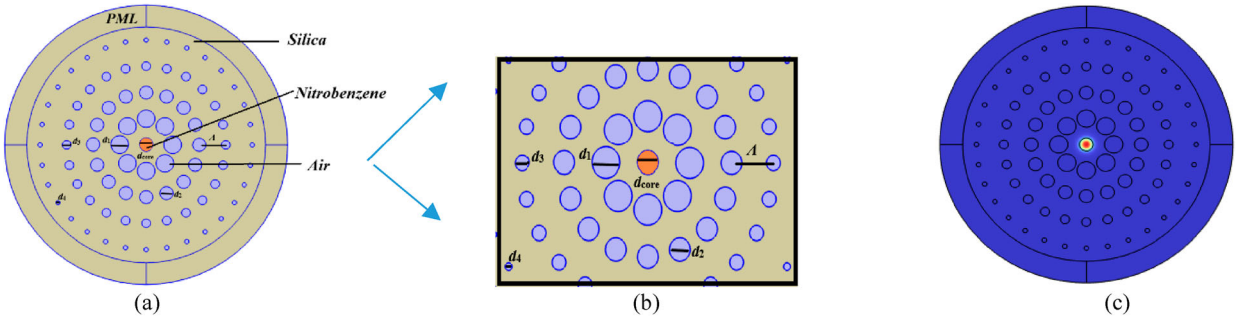

Figure 1. (*a*) Cross-sectional view of the circular PCF (#C), (b) displaying the cladding region for better understanding, and (c) at 1.55 µm the electric field distribution for the fundamental mode within the PCF.

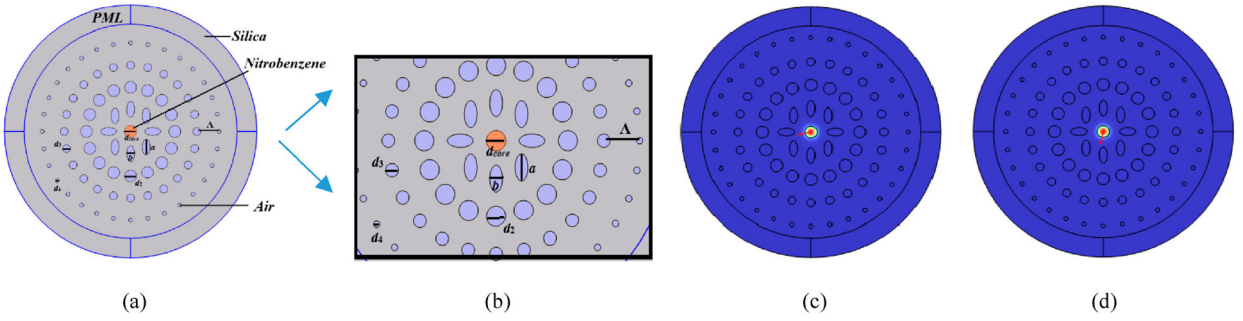

Figure 2. (*a*) Cross-sectional view of the elliptical PCF (#E), (b) displaying the cladding region for better understanding & at 1.55 µm the distribution of electric field for the principal mode along (c) x-direction as (#EX) and (d) y-direction as (#EY).

$d_1 = 2.0\,\mu m$, elliptical air holes are introduced with major axis, $a = 2.0\,\mu m$ and minor axis, $b = 1.0\,\mu m$. Figure 2(c,d) shows the distribution of electric field for the principal mode at pump wavelength along x-direction as (#EX) & along y-direction as (#EY) respectively. Again, the core is infiltrated with nitrobenzene. Both designs are being studied for comparative study.

3. Numerical methodology

3.1. Linear characteristics

After completing the design of PCF, the next step involves calculating the effective mode index (n_{eff}) of the fundamental mode. This calculation is performed using COMSOL Multiphysics software, a powerful simulation tool known for its ability to handle complex geometries. COMSOL employs the finite element method (FEM), a numerical technique that subdivides the computational domain into smaller, simpler parts (finite elements) to solve complex equations governing the behaviour of electromagnetic fields. By applying FEM, the software provides precise results for the effective mode index, which plays a crucial role in characterizing the fibre's optical properties and performance.

The wavelength-dependent refractive index of nitro benzene and silica glass material was calculated by using the Sellmeier Equation (1) given by the relation below

$$n^2(\lambda) = 1 + \sum_{k=1}^{N} \frac{B_k \lambda^2}{\lambda^2 - b_k^2} \tag{1}$$

$B_1 = 1.30628$, $B_2 = 0.00502$, $b_1^2 = 0.02268\,\mu m^2$, $b_2^2 = 0.18487\,\mu m^2$ for nitrobenzene and for silica glass the value of constants are $B_1 = 0.6694226$, $B_2 = 0.4345839$, $B_3 = 0.8716947$, $b_1^2 = 0.0044801\,\mu m^2$, $b_2^2 = 0.013285\,\mu m^2$ and $b_3^2 = 95.341482\,\mu m^2$ with λ as the operating wavelength [36].

Figure 3 shows the variation of refractive index (n) of silica and nitrobenzene with wavelength. For better confinement of light within the core, the refractive index of nitrobenzene must be greater than silica, which is visible from Figure 3.

To calculate the dispersion characteristics of the proposed PCF structures the following correlation has been employed as shown in Equation (2)

$$D(\lambda) = -\frac{\lambda}{c} \frac{\partial^2 Re(n_{eff})}{\partial \lambda^2} \tag{2}$$

In this context, the real part of the effective mode index is indicated as Re (n_{eff}), which describes the portion of the mode index that corresponds to the actual propagation characteristics of the mode within the medium. Additionally, c represents the speed of light in free space, or

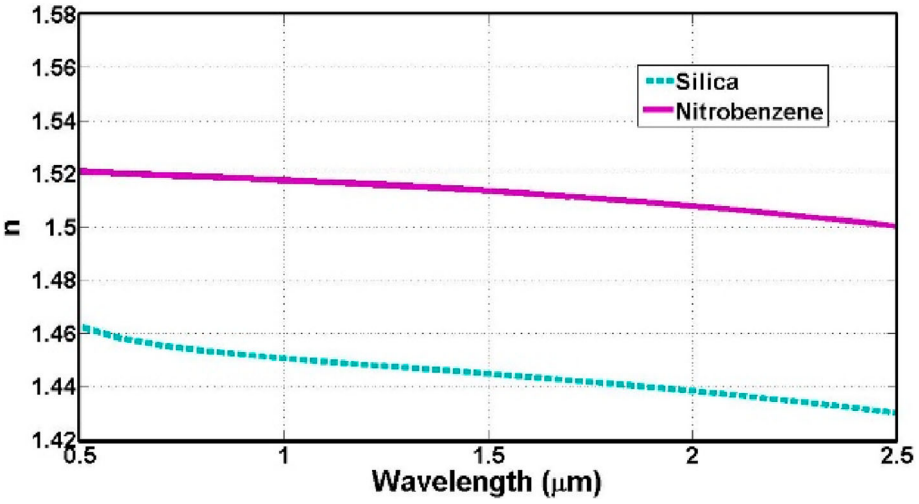

Figure 3. Characteristics of the refractive index (n) of silica and nitrobenzene.

vacuum, which is a fundamental constant used in calculating the propagation properties of light in the absence of any material medium. Using Equation (3), the effective mode area (A_{eff}) of the propagating mode has been calculated [37], and the amplitude of the electric field of the light is represented by E.

$$A_{eff} = \frac{\left(\iint_{-\infty}^{\infty} |E|^2 \mathrm{d}x\,\mathrm{d}y\right)^2}{\left(\iint_{-\infty}^{\infty} |E|^4 \mathrm{d}x\,\mathrm{d}y\right)} \tag{3}$$

3.2. Nonlinear characteristics

For the generation of pump pulses, a tunable hyperbolic secant pulse is used which can be expressed as given in Equation (4)

$$A(0,T) = \sqrt{P_0}\mathrm{sech}\frac{T}{T_0} \tag{4}$$

$A(0,T)$ dictates the shape and amplitude of the pulse over time. P_0 is the maximum peak power of the initial input pulse. T_0 is temporal width calculated as T_{FWHM} divided by 1.7627, where T_{FWHM} is the full-width-half-maxima. Finally, T denotes the time scale aligned with the group velocity (GV) of the pulse. This parameter governs how the pulse propagates through the medium over time, providing insight into the temporal dynamics as the pulse moves forward in the simulation.

The following generalized nonlinear Schrödinger Equation (5) is solved using Split-Step Fourier method to obtain the widening of the spectral range observed in the generated SC within the PCF structure [38]

$$\frac{\partial \tilde{A}'}{\partial z} = i\bar{\gamma}(\omega)exp(-\hat{L}(\omega)z) \mathcal{F}\left\{\bar{A}(z,T)\int_{-\infty}^{\infty} R(T')|\bar{A}(z,T-T')|^2 dT'\right\} \tag{5}$$

where $\tilde{A}'$ is the envelope or the covering of the output pulse, which represents its modulation amplitude or shape and $\bar{A}(z,T)$ represents the envelope at distance z at time t.

The frequency-dependent nonlinear coefficient $\bar{\gamma}(\omega)$ is obtained by using Equation (6), taking into account its dependency on the frequency

$$\bar{\gamma}(\omega) = \frac{n_2 n_0 \omega}{c n_{eff}(\omega) A_{eff}^{1/4}(\omega)} \tag{6}$$

where n_2 corresponds to the nonlinear refractive index of nitrobenzene, which is specifically 2.0×10^{-18} m^2/W at 1550 nm [39]. The refractive index of glass at the specified wavelength is denoted by the symbol n_0, and it serves as a key parameter in calculating n_2, the nonlinear refractive index of the material. In these calculations, where c represents the speed of light in a vacuum. The formulas for determining the modified variables are outlined as follows, incorporating these constants to provide precise values for the refractive properties of the glass at the specific wavelength.

$$\widetilde{A}'(z,\omega) = \tilde{A}(z,\omega)\exp(-\hat{L}(\omega)z) \tag{7}$$

$\tilde{A}(z,\omega)$ is the Fourier transform of $\bar{A}(z,T)$. The linear operator $\hat{L}(\omega)$ is expressed by the following as

$$\hat{L}(w) = i(\beta(\omega) - \beta(\omega_0) - \beta_1(\omega_0)[\omega - \omega_0]) - \frac{\alpha(\omega)}{2} \tag{8}$$

within the PCF design β is the group velocity inverse of pulse covering, where β_1, α and ω_0 represents the propagation constant, the total loss and the reference frequency respectively. The Raman response function$R(t)$ is defined in Equations (9) and (10) as

$$R(t) = (1 - f_R)\delta(T) + f_R\, h_m(t) \tag{9}$$

$$h_m(t) = A_1 e^{(-t/t_{diff})}(1 - e^{(-t/t_{rise,1})}) + A_2 e^{(-t/t_{int})}(1 - e^{(-t/t_{rise,1})}) + A_3 e^{(-t^2/2t_{fast}^2)} \sin(t/t_{rise,2}) \quad (10)$$

where A_1 (1/s) = 0.0288, A_2 (1/s) = 0.0930, A_3 (1/s) = 1.475, t_{diff} (ps) = 31.8, $t_{rise,1}$ (ps) = 0.15, t_{int}(ps) = 0.51, t_{fast} (ps) = 0.08, $t_{rise,2}$ (ps) = 0.10 [39]. For nitrobenzene, the Raman parameter f_R is around 0.87 [36].

4. Results and discussion

In a PCF structure, the broadening of the SC spectrum primarily relies upon the nonlinearity of the material and the dispersion characteristics [40]. The Circular symmetric design is represented as #C, whereas X-polarization of the elliptical design is represented as #EX and Y-polarization of elliptical design is represented as #EY. Figure 4(a) depicts the values of dispersion for design #C with different core size as d_{core} = 1.0, 1.2 and 1.4 µm. The plot shows no major difference in the dispersion values for all chosen d_{core} values. The design is robust. So, d_{core} = 1.0 µm has been preferred as lower area will result into more nonlinearity. Again, in Figure 4(b) for optimization, the pitch (Λ) has been changed as 2.4, 2.8 and 3.2 µm. Λ = 2.4 µm is having no Zero dispersion wavelength (ZDW), Λ = 2.8 µm is having ZDW around 1.2 µm and Λ = 3.2 µm is having ZDW around 1.6 µm. ZDW is the wavelength where the dispersion value exhibited by the waveguide transitions from normal to anomalous dispersion regime i.e. passes zero [41]. It provides an insight to choose a suitable pumping wavelength which will influence SCG process. As if pumped in the anomalous dispersion region, the soliton fission process along with the emission of the dispersive waves is responsible for the broadening in the SC spectrum. On the other end, if pumped in normal dispersion regime SPM will be prevalent phenomenon for broadening. The value of Λ = 3.2 µm is giving more negative dispersion on shorter wavelength side and on longer wavelength side it is having less positive dispersion as compared to other values. It is also giving minimum dispersion value around 1.55 µm. So, for #C, Λ = 3.2 µm has been picked up as pitch. Figure 5(a) shows dispersion profile for different d_{core} (= 1.0, 1.2 and 1.4 µm) for elliptical profile. The dispersion values are distinct for X and Y-polarization. #EX and #EY represents X and Y-polarization of the elliptical design respectively. The pattern is almost similar for all three profiles of different d_{core} values where the difference in dispersion values for X and Y-polarization is becoming prominent at higher wavelengths. Since asymmetrical design leads to birefringence hence this trend is obvious. So, choosing a smaller core diameter of 1 µm will be better since it will lead to greater nonlinearity. Figure 5(b) shows dispersion profile for different values of Λ as 2.4, 2.8 and 3.2 µm for elliptical profile with d_{core} = 1.0 µm. Λ = 2.4 µm is having no ZDW, Λ = 2.8 µm is having ZDW around 1.5 µm and Λ = 3.2 µm is having ZDW around 1.8 µm. Λ = 2.8 µm has been selected as it is giving minimum dispersion value around 1.55 µm.

It is found that changing core diameter has not impacted much to the circular design but it has significantly impacted the dispersion profile in the elliptical geometry on the higher wavelength region. Figure 6(a) shows the variation of birefringence with respect to wavelength. It can be seen that as the value of wavelength increases, the difference in the values of effective mode index between the two states of polarization increases. Birefringence = $|n_x - n_y|$, where n_x & n_y are the x and y components of effective mode index respectively [32]. The value of birefringence at 1.55 µm is 1.3×10^{-3}.

Figure 6(b) shows the variation of effective mode area and nonlinearity (γ) for #C, #EX & #EY. Effective mode area (A_{eff} or EMA) & nonlinearity (γ) holds inverse relation, and this behaviour can be observed when both

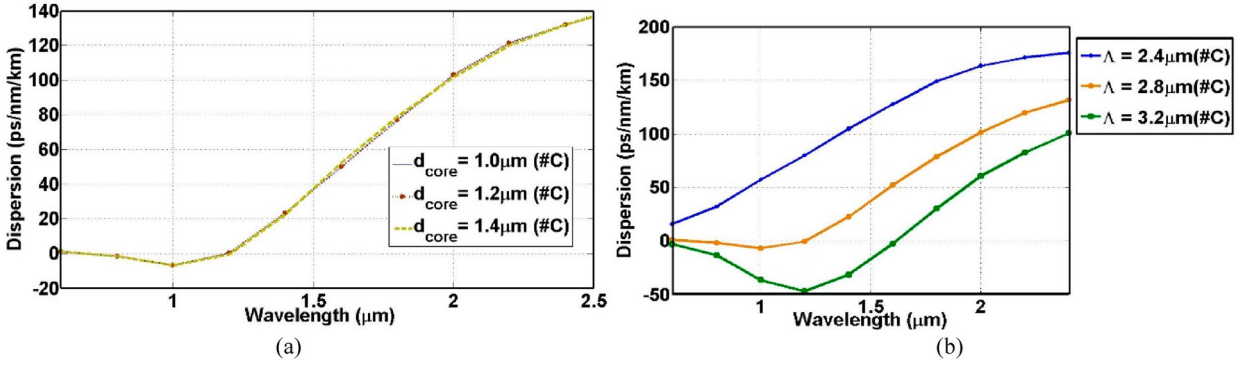

Figure 4. Study of dispersion characteristics of #C with variation of (a) d_{core} and keeping Λ = 3.2 µm as constant, and (b) Λ and keeping d_{core} = 1.0 µm as constant.

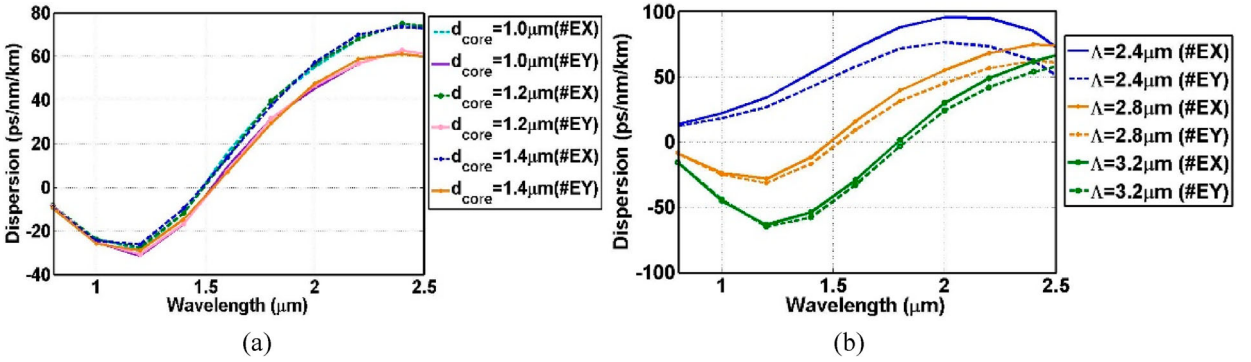

Figure 5. Study of dispersion characteristics of #EX & #EY with variation of (a) d_{core} and keeping $\Lambda = 2.8$ μm as constant, and (b) Λ and keeping $d_{\text{core}} = 1.0$ μm as constant.

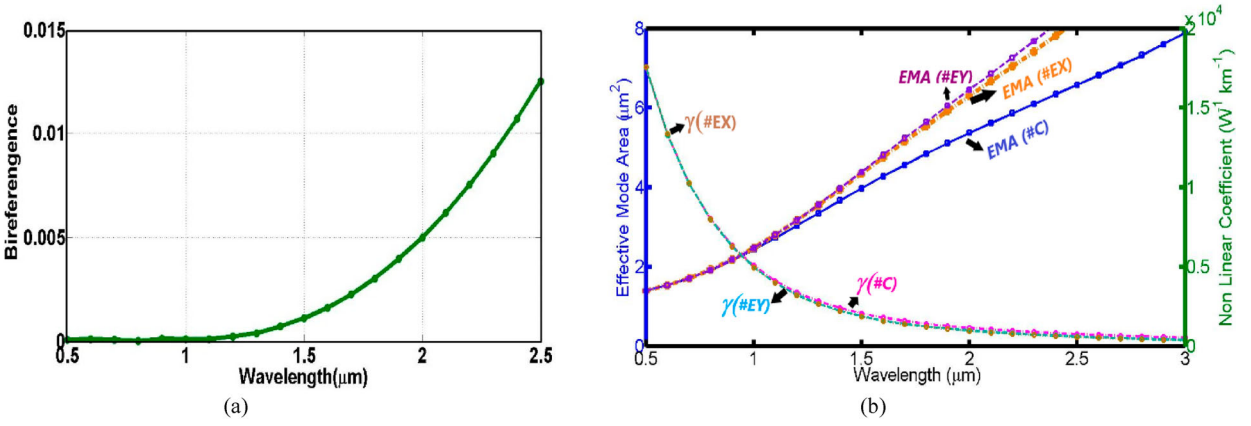

Figure 6. (a) Birefringence for elliptical design and (b) the variation of effective mode area (EMA) and nonlinearity (γ) of #C, #EX & #EY with wavelength.

plotted with respect to the wavelength. The value of A_{eff} at 1.55 μm is 4.13 μm^2 for #C, 4.55 μm^2 for #EX & 4.60 μm^2 for #EY respectively. Similarly, the nonlinear coefficient for #C, #EX & #EY are 1962.0, 1780.9 and 1761.5 W^{-1}Km^{-1} respectively. Our reported dispersion value is less than previous documents works [42–44]. The effective mode area is smaller than other studies with values of 6.67 μm^2 [45] and 7.76 μm^2 [46]. Also, the value of nonlinear coefficient is higher than the results mentioned in other document works [47–49]. In Figure 7(a) a more flat dispersion profile is found for #EX & #EY polarization as compared to #C, which is preferable for obtaining a broad SC spectrum. In Figure 7(b) confinement loss for different designs has been shown. Beyond 2.5 μm the loss is large due to limited transparency of silica.

SCG has been systematically evaluated across a range of parameters, including fibre length, pulse width, and pump power, specifically at a wavelength of 1.55 μm with a repetition rate of 100 MHz and a power level set at −20 dB. The results illustrate that SCG has been successfully observed for different fibre lengths, spanning from 2.5 to 10 mm. This data is presented in Figure 8(a–c), which correspond to samples #C, #EX and #EY respectively. As the fibre length increases, the spectrum undergoes significant broadening. At a fibre length of 2.5 mm, the spectral broadening is minimal, indicating limited extension of the SC. However, the broadest spectral expansion is achieved at a fibre length of 10 mm across all three configurations, #C, #EX and #EY. This length-dependent behaviour highlights the critical role of SPM in expanding the SC as fibre length increases. With further increase in length beyond 10 mm the noise is becoming more prominent and spectrum started to get deteriorate. The coherency is also getting disturbed. The coherence is also evaluated for 650 W pump power, 50 fs pulse width and 10 mm fibre length in Figure 9.

Furthermore, the conducted coherence calculation illustrated in Figure 9 revealed that the spectrum remains coherent throughout the entire SC broadening range: from 1.3 to 2.0 μm for sample #C, from 0.9 μm to 2.3 μm for sample #EX, and from 1.0 μm to 2.4 μm for sample #EY. Beyond 2.5 μm the coherence plot has started to deteriorate as the spectrum shows large noise this is due to the limited transparency window of silica. This coherence assessment is crucial as it demonstrates the stability and quality of the SC spectra across different samples,

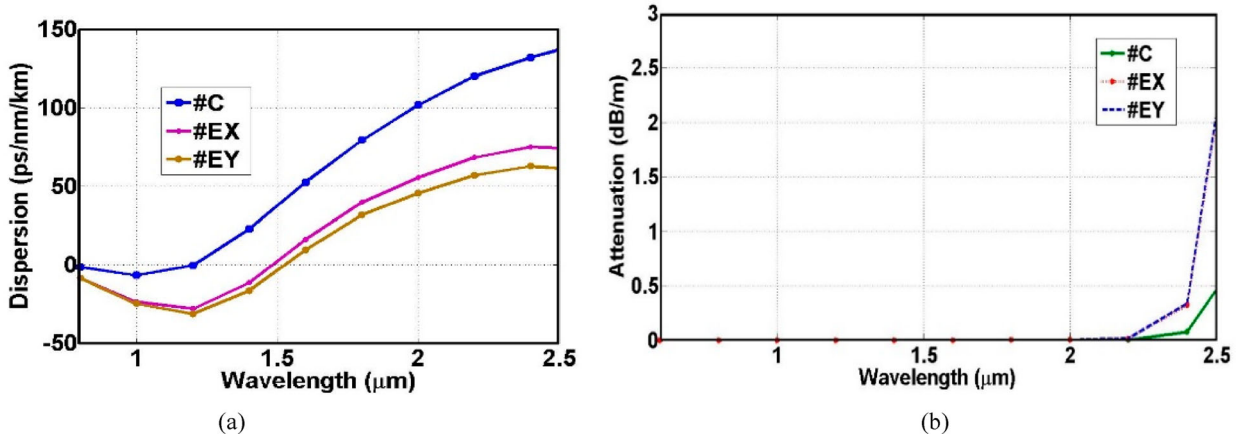

Figure 7. (a) Optimized dispersion characteristics of #C (d_{core} = 1.0 μm, Λ = 3.2 μm) #EX & #EY (d_{core} = 1.0 μm, Λ = 2.8 μm) with wavelength and (b) confinement loss of #C, #EX & #EY.

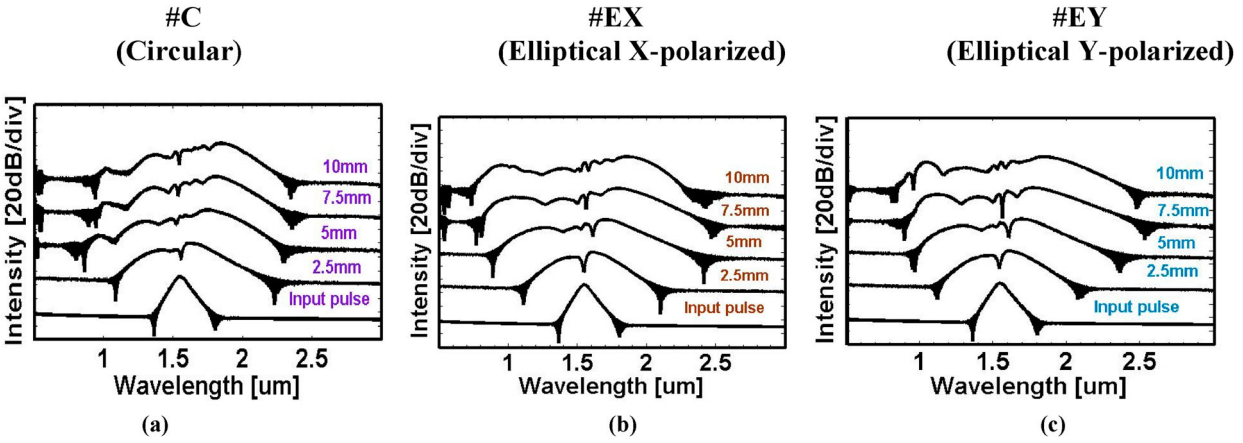

Figure 8. The broadening of SC spectrum at 1.55 μm due to varying fibre lengths of 2.5, 5, 7.5 and 10 mm under conditions of 50 fs and 650 W.

indicating that the generated light maintains a consistent phase relationship within these specified wavelength ranges. The first-order degree of coherence is given by Equation (11) mentioned below.

We have employed one photon per mode noise model which can help in investigating the coherent property of SCG. In this study, the modulus of complex degree of first-order coherence g_{12} is used to calculate the degree of coherence which varies from 0 to 1. Value one signifies a perfectly coherent spectrum, and value zero means no coherence. A value in between 0 and 1 shows moderate coherence behaviour [50].

The electric fields of individual SCG pairs are represented as E_1 (λ, t_1) and E_2 (λ, t_2), where λ represents

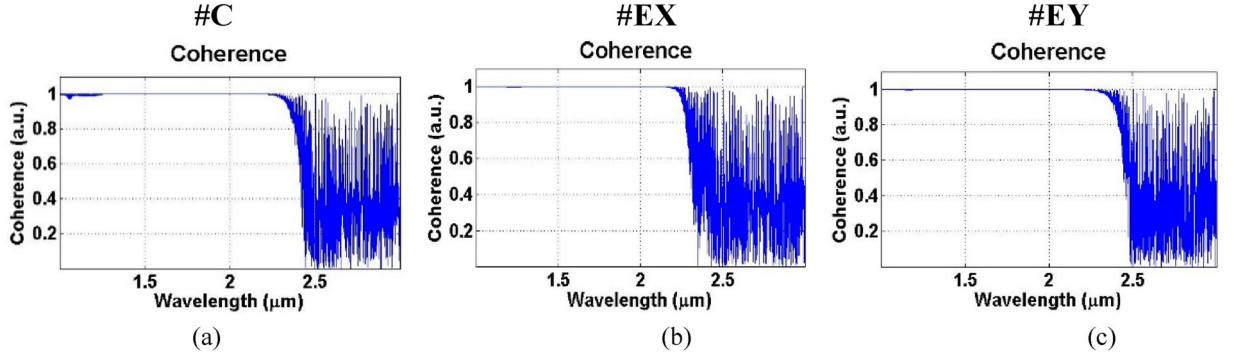

Figure 9. The coherence evolution using 650 W, 50 fs pulse width at 1.55 micron along the fibre length of 10 mm.

the wavelength, and t_1 and t_2 are time variables associated with consecutive SCG spectra. These electric fields correspond to sequential spectra produced by the SCG process, allowing us to examine subtle variations in spectral coherence over time. Angular brackets are used to indicate an average taken across the entire ensemble of pulses, providing a comprehensive measure of the spectral properties. To specifically analyse how coherence depends on wavelength alone, we set the time difference between pulses, $\Delta t = t_1 - t_2$ to zero, effectively isolating wavelength as the primary variable in our coherence assessment.

$$|g_{12}(\lambda(t_1 - t_2)| = \frac{|\langle E_1^*(\lambda, t_1)E_2(\lambda, t_2)\rangle|}{(\langle|E_1(\lambda, t_1)^2|\rangle\langle|E_2(\lambda, t_2)^2|\rangle)^{1/2}} \quad (11)$$

In Figures 10–12 the peak power is changed from 450 to 850 W, with increasing power the spectrum gets shifted towards the Shorter as well as longer wavelength region for #C, #EX, and #EY. The broadening of the SC spectrum appears symmetric, primarily due to nonlinear SPM effects across both smaller and larger wavelength side. At higher peak power, however, the SC spectrum starts to degrade, with a noticeable decrease in coherence as noise increases. This degradation is attributed to absorption occurring in the coating [51]. For #C, #EX & #EY with 450 W the broadening is less and for 850 W noise is large. The maximum & a stable broadening is obtained at 650 W. Subsequently, the effect of increasing pulse widths on the SC has been examined. Figures 13 and 14 illustrate that as the T_{FWHM} rises from 50 fs to 150 fs, the resulting spectra become narrower for configurations #C, #EX, and #EY. It is important to note that shorter pulse durations generally produce broader SC spectra. Consequently, the 50 femtosecond pulses display a more stable spectrum. The maximum spectral broadening at −20 dB for configurations #C, #EX and #EY reaches 1.3 µm to 2.0, 0.9 µm to 2.3 and 1.0 µm to 2.4 µm respectively, with a peak power of 650 W, fibre length of 10 mm and a pulse width of 50 fs.

For 50fs laser pulse at 1.55 µm, β_2 for #C is 3.21×10^{-26} s^2/m, ($T_0 = T_{FWHM}/1.763$), the nonlinear length ($L_{NL} = (\gamma P_0)^{-1}$) and dispersion length ($L_D = (\beta_2/T_0^2)^{-1}$) for proposed PCF are 7.8×10^{-4} m and 2.25×10^{-2} m respectively. The order of soliton $N \approx L_D/L_{NL} \approx 28$ and the fission length of soliton are calculated as $L_{fiss} = L_D/N \approx 0.8$ mm. Similarly, for #EX β_2 is 5.95×10^{-26} s^2/m, $L_{NL} = 8.6 \times 10^{-4}$ m and $L_D = 1.35 \times 10^{-2}$ m respectively. $N \approx 15$ &

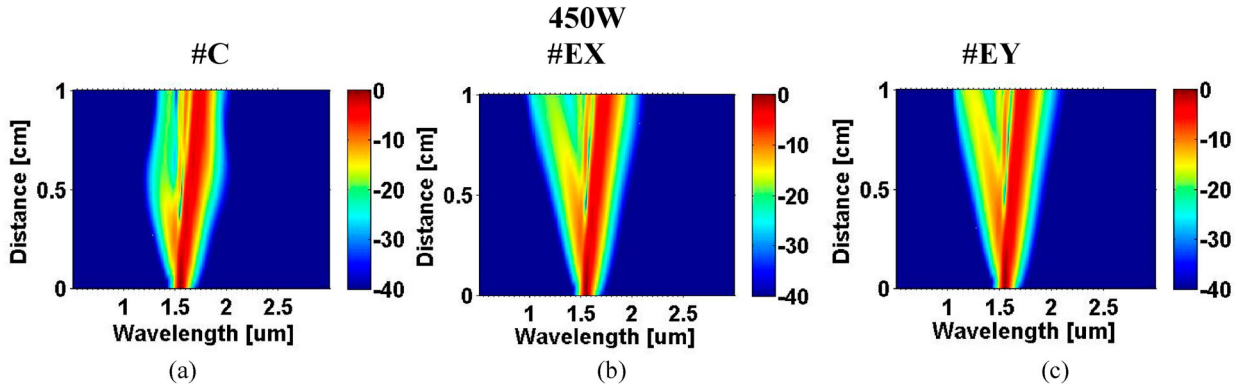

Figure 10. Spectral advancement of SCG at 1.55 µm in (a), (b), and (c) with peak power of 450 W at 50fs & 10 mm.

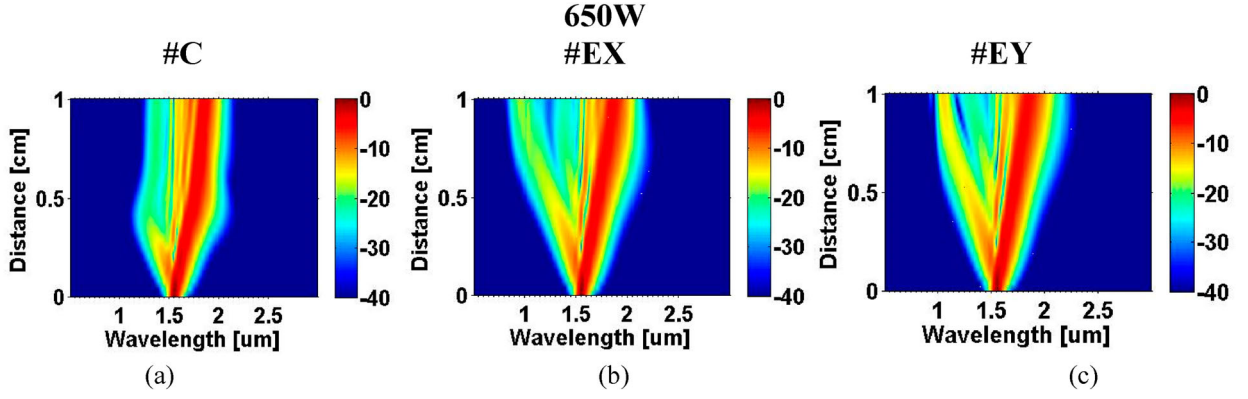

Figure 11. The spectral advancement of SCG at 1.55 µm in (a), (b), and (c) at the length of 10 mm, pulse width 50fs & power 650 W.

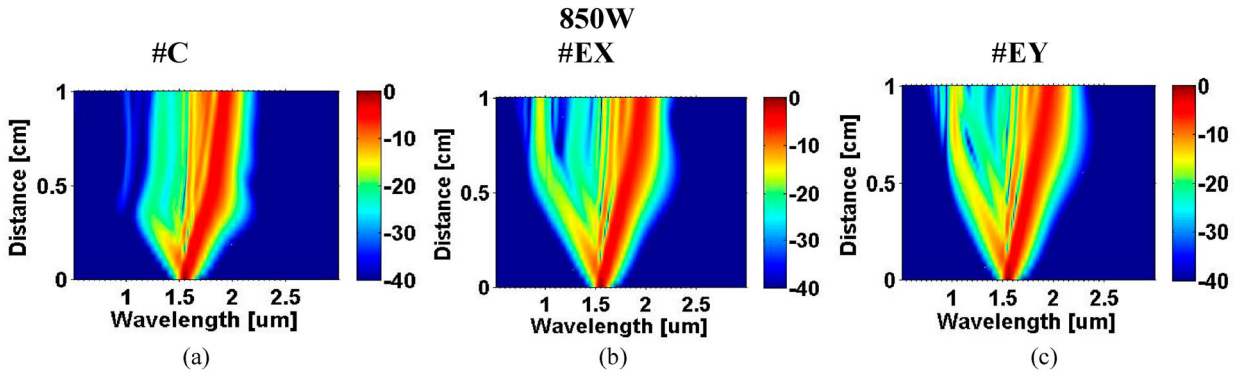

Figure 12. The spectral advancement of SCG at 1.55 µm induced in (a), (b), and (c) with 850 W pump power, pulse width of 50 fs at 10 mm fibre length.

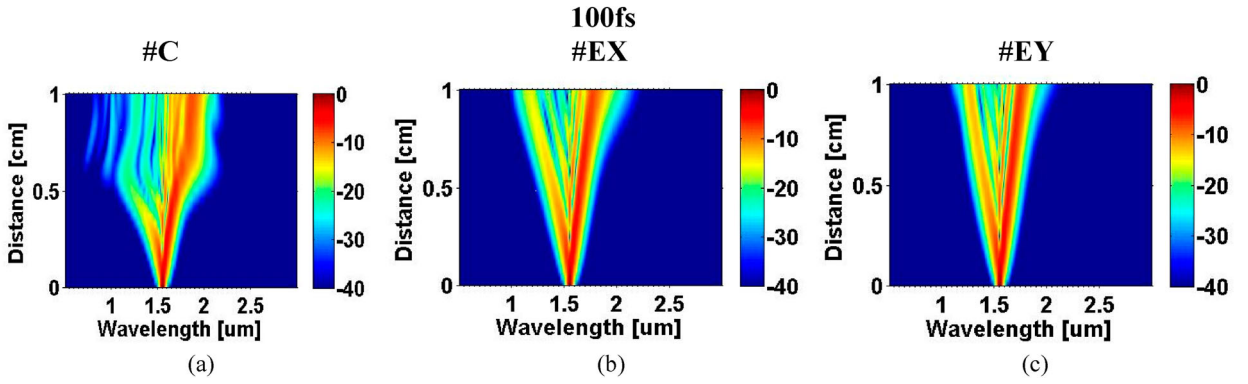

Figure 13. The spectral advancement of SCG at 1.55 µm induced in (a), (b), and (c) with a pulse width of 100 fs at 10 mm fibre length and 650 W pump power.

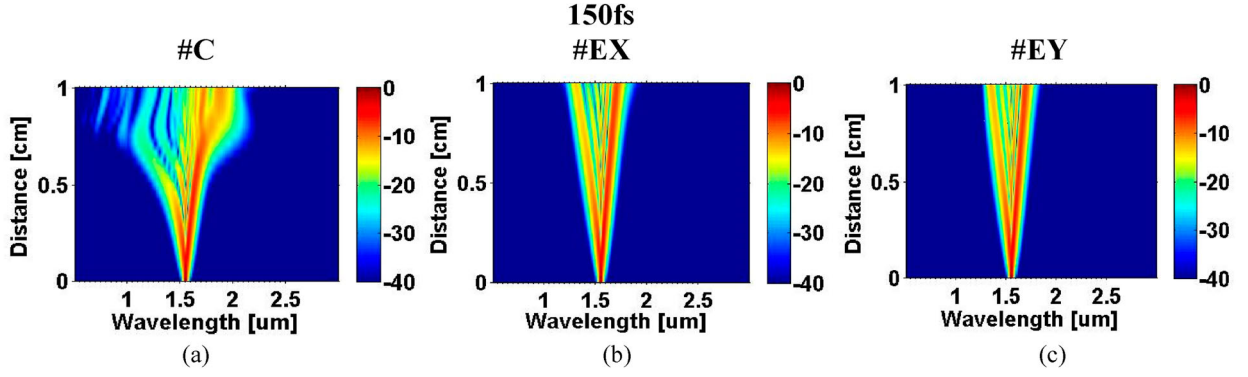

Figure 14. The spectral advancement of SCG at 1.55 µm induced in (a), (b), and (c) pulse width of 150 fs at 10 mm fibre length and 650 W pump power.

$L_{\text{fiss}} = 0.9\,\text{mm}$. For #EY β_2 is 7.12×10^{-26} s^2/m, $L_{\text{NL}} = 8.7 \times 10^{-4}$ m and $L_D = 1.12 \times 10^{-2}$ m respectively. $N \approx 12$ & $L_{\text{fiss}} = 0.93\,\text{mm}$.

To obtain a broader SCG, it is beneficial to have a nonlinear length less than or equal to dispersion length for the proposed fibre. This observation confirms that nonlinear effects play a crucial role in the broadening of the input pulse, while simultaneously preventing excessive broadening due to dispersion before these nonlinear interactions can take place. At the initial stage of pulse propagation, the broadening of the spectrum is primarily influenced by SPM, a nonlinear optical effect where the intensity of the pulse induces changes in its phase. This phase alteration causes a broadening of the pulse's spectral content, leading to the generation of new frequencies. As the pulse continues to propagate and shifts toward longer wavelengths, the broadening becomes dominated by a process known as optical wave

breaking. This phenomenon occurs when the nonlinear effects within the medium become strong enough to significantly modify the intensity profile or shape of the pulse.

On comparing the circular and elliptical design we have found that a broader SC spectra is obtained for elliptical design as compared to circular design when subjected to the same values of fibre length, pump power and pulse width.

Among X &Y polarized states the broadening is more at lower wavelength region in X-polarization whereas for Y-polarization the broadening is more at higher wavelength region.

In summary, the designs we have proposed exhibit a strong potential to achieve a wider and comparable bandwidth for supercontinuum generation while operating at a lower pump power than what has been reported in prior studies. This improvement in performance highlights the efficiency and potential of our approach in enhancing SCG bandwidth without the need for high-power input, as detailed in Table 1. This advancement underscores the effectiveness of our designs in addressing the demands of SCG applications requiring broad spectra at lower energy costs. Also at pump wavelength both the proposed designs have very low attenuation. It can be seen, the SCG in [*52*] has been evaluated at −40 dB with higher peak power. For this fibre, the broadening is more as compared to #C which is evaluated at −20 dB in our case, but still lesser than #EX & #EY at −20 dB. Similarly, the designs mentioned in [*53*–*55*] are using higher peak power at −20 dB but have lesser broadening range than #EX & #EY. The peak power used is very high in the designs mentioned in [*55*–*57*], and the broadening range has also been evaluated at −60 dB & −40 dB respectively. At these dB values both the designs #C & #E have greater broadening. At −40 dB, the SC broadening in our proposed designs is 0.90 µm – 2.3 µm for #C, 0.79 µm – 2.4 µm for #EX and 0.88 µm – 2.46 µm for #EY, respectively.

This study aims to achieve significant spectral broadening at low peak power, offering several advantages for SCG. Operating at reduced peak power minimizes noise levels, improving the quality of measurements and imaging. Additionally, lower peak power typically results in longer pulse durations, which can be advantageous for applications that require prolonged interaction with the sample, including material processing and biomedical imaging [*35*,*57*].

In conclusion, utilizing a lower peak power in SCG leads to the production of more stable and high quality spectra, while also enhancing safety for sensitive samples as it mitigates the risk of damage that can occur from excessive energy exposure.

5. Conclusion

In conclusion, proposed designs exhibit a remarkable ability to achieve both a broader and comparable bandwidth for SCG while operating at a lower pump power of just 0.65 kW. This achievement not only enhances the efficiency of the SCG process but also signifies a significant advancement in the field. Moreover, we have successfully navigated the inherent challenge of balancing the need for spectral broadening with the critical requirement of maintaining coherence. This careful management ensures that the quality and stability of the generated SC light are preserved, paving the way for more practical applications in various fields. This work primarily focuses on a comparative analysis of #C, #EX, and #EY configurations for generating supercontinuum in the near- to mid-infrared range. Results show that an elliptical design produces a broader SC spectrum compared to a circular design, given the same fibre length, pump power, and pulse width. Specifically, a coherent SC spectrum spanning 1.3 to 2.0 µm for #C, 0.9 to 2.3 µm for #EX and 1.0 to 2.4 µm for #EY is achieved with a 10 mm fibre length, 650 W peak power and 50 femtosecond pulse width. Both designs demonstrate low confinement loss at the pump wavelength. Leveraging PCF-based broadband SC light source that covers NIR to MIR spectrum has significant applications in various fields. In practical terms, these technologies facilitate the development of a stable optical frequency comb, which is crucial for high-precision optical coherence tomography (OCT) and spectroscopy. Additionally, they contribute to advancements in biomedical diagnostics, food quality assessment, security, and sensing technologies.

Acknowledgements

Drishti Singh Tomer profoundly recognizes Delhi Technological University, Delhi for providing indispensable support to conduct this work.

Disclosure statement

No potential conflict of interest was reported by the author(s).

Data availability statement

The research mentioned in the article uses no data.

References

[1] Qu Y, Sun W, Cao J, et al. Coherent ultrabroad orbital angular momentum supercontinuum generation in an $AsSe_2$-As_2S_5 microstructured fiber with all-normal dispersion. Opt Commun. **2021**;497:127191. doi:10.1016/j.optcom.2021.127191

[2] Sharma R, Kaur S, Chauhan P, et al. Computational design & analysis of $GeSe_2$-As_2Se_3-PbSe based rib waveguide for

mid-infrared supercontinuum generation. Optik (Stuttg). **2020**;220:165032. doi:10.1016/j.ijleo.2020.165032

[3] Saini TS, Kumar A, Sinha RK. Design and modelling of dispersion-engineered rib waveguide for ultrabroadband mid-infrared supercontinuum generation. J Mod Opt. **2017**;64(2):143–149. doi:10.1080/09500340.2016.1216190

[4] Devika V, Mani Rajan MS, Sharma M. Diamond core PET-PCF for supercontinuum generation using meager power with very low birefringence. Opt Quant Electron. **2022**;54:858. doi:10.1007/s11082-022-04264-9

[5] Devika V, Mani Rajan MS, Thenmozhi H, et al. Flower core photonic crystal fibres for supercontinuum generation with low birefringent structure for biomedical imaging. J Opt. **2023**;52:539–547. doi:10.1007/s12596-022-01002-y

[6] Nair AA, Boopathi CS, Jayaraju M, et al. Numerical investigation and analysis of flattened dispersion for supercontinuum generation at very low power using hexagonal shaped photonic crystal fiber (H-PCF). Optik (Stuttg). **2019**;179:718–725. ISSN 0030-4026. doi:10.1016/j.ijleo.2018.11.021

[7] Alfano RR, Shapiro SL. Emission in the region 4000 to 7000Å via four-photon coupling in glass. Phys Rev Lett. **1970**;24(11):584.

[8] Tomer DS, Kumar A. Design and numerical modeling of chalcogenide parabolic-core waveguide for on-chip supercontinuum generation extending from near-IR region to mid-IR region. Microw Opt Technol Lett. **2024**;66(3):e34105. doi:10.1002/mop.34105

[9] Chauhan P, Kumar A, Kalra Y. A dispersion engineered silica-based photonic crystal fiber for supercontinuum generation in near-infrared wavelength region. Optik (Stuttg). **2019**;187:230–237. doi:10.1016/j.ijleo.2019.03.107

[10] Sylvestre T, Genier E, Ghosh AN, et al. Recent advances in supercontinuum generation in specialty optical fibers. JOSA B. **2021**;38(12):F90–F103. doi:10.1364/JOSAB.439330

[11] Dudley JM, Genty G, Coen S. Supercontinuum generation in photonic crystal fiber. Rev Mod Phys. **2006**;78(4):1135–1184. doi:10.1103/RevModPhys.78.1135

[12] Diouf M, Mandeng LM, Tchawoua C, et al. Numerical investigation of supercontinuum generation through $AsSe_2/As_2S_5$ chalcogenide photonic crystal fibres and rib structures. J Lightwave Technol. **2019**;37(22):5692–5698. doi:10.1109/JLT.2019.2934034

[13] Le H, Hoang V, Nguyen HT, et al. Supercontinuum generation in photonic crystal fibers infiltrated with tetrachloroethylene. Opt Quant Electron. **2021**;53:187. doi:10.1007/s11082-021-02820-3

[14] Heuteu C, Boukar SK, Mandeng LM, et al. Supercontinuum generation of truncated airy pulses in a cubic-quintic $AsSe_2/As_2S_5$ optical waveguide with rib-like structure. J Opt. **2021**;23(9):095503. doi:10.1088/2040-8986/ac0ff4

[15] Van LC, Le Tran BT. Low peak power broadband supercontinuum spectra generated in a square lattice toluene-core photonic crystal fiber with different air hole diameters. Laser Phys. **2023**;33(9):095102. doi:10.1088/1555-6611/ace24d

[16] Kedenburg S, Steinmann A, Hegenbarth R, et al. Nonlinear refractive indices of nonlinear liquids: wavelength dependence and influence of retarded response. Appl Phys B. **2014**;117:803–816. doi:10.1007/s00340-014-5833-y

[17] Chemnitz M, Gebhardt M, Gaida C, et al. Hybrid soliton dynamics in liquid-core fibres. Nat Commun. **2017**;8(1):42. doi:10.1038/s41467-017-00033-5

[18] Kedenburg S, Gissibl T, Steinle T, et al. Towards integration of a liquid-filled fiber capillary for supercontinuum generation in the 1.2–2.4 µm range. Opt Express. **2015**;23(7):8281–8289. doi:10.1364/OE.23.008281

[19] Pniewski J, Stefaniuk T, Van HL, et al. Dispersion engineering in nonlinear soft glass photonic crystal fibers infiltrated with liquids. Appl Opt. **2016**;55(19):5033–5040. doi:10.1364/AO.55.005033

[20] Dai F, Xu Y, Chen X. Enhanced and broadened SRS spectra of toluene mixed with chloroform in liquid-core fiber. Opt Express. **2009**;17(22):19882–19886. doi:10.1364/OE.17.019882

[21] Van LC, Anuszkiewicz A, Ramaniuk A, et al. Supercontinuum generation in photonic crystal fibres with core filled with toluene. J Opt. **2017**;19(12):125604. doi:10.1007/s11082-021-02820-3

[22] Le Tran BT, Van LC. Circular lattice benzene-core PCFs with flat near-zero dispersion for low-power broad-spectrum supercontinuum generation. Phys Scr. **2024**;99(4):045527. doi:10.1088/1402-4896/ad347c

[23] Vieweg M, Gissibl T, Pricking S, et al. Ultrafast nonlinear optofluidics in selectively liquid-filled photonic crystal fibers. Opt Express. **2010**;18(24):25232–25240. doi:10.1364/OE.18.025232

[24] Adnan SA, Abdulwahhab AW, Ismail SN. Fusion splicing: the penalty of increasing the collapse length of the air holes in ESM-12B photonic crystal fibers. Opt Appl. **2016**;46(2):265–275. doi:10.5277/oa160211.

[25] Lin X, Yan H, Ma Y, et al. A construction method of the quasi-monolithic compact interferometer based on UV-adhesive bonding. Rev Sci Instrum. **2023**;94(7):074501. doi:10.1063/5.0155637.

[26] Fürjes P. Controlled focused ion beam milling of composite solid state nanopore arrays for molecule sensing. Micromachines (Basel). **2019**;10(11):774. doi:10.3390/mi10110774

[27] Minh NVT, Van LC, Hong PNT, et al. Supercontinuum generation in a square-lattice photonic crystal fiber using carbon disulfide infiltration. Optik (Stuttg). **2023**;286:171049. doi:10.1016/j.ijleo.2023.171049

[28] Thi TN, Trong DH, Van LC. Comparison of supercontinuum spectral widths in CCl4-core PCF with square and circular lattices in the claddings. Laser Phys. **2023**;33(5):055102. doi:10.1088/1555-6611/acc240

[29] Chaitanya AGN, Saini TS, Kumar A, et al. Ultra broadband mid-IR supercontinuum generation in $Ge_{11.5}$ As_{24} $Se_{64.5}$ based chalcogenide graded-index photonic crystal fiber: design and analysis. Appl Opt. **2016**;55(36):10138–10145. doi:10.1364/ao.55.010138

[30] Saini TS, Baili A, Kumar A, et al. Design and analysis of equiangular spiral photonic crystal fiber for mid-infrared supercontinuum generation. J Mod Opt.

2015;62(19):1570–1576. doi:10.1080/09500340.2015.1051600

[31] Rjeb A, Fathallah H, Chebaane S, et al. Design of novel circular lattice photonic crystal fiber suitable for transporting 48 OAM modes. Optoelectron Lett. **2021**;17:501–506. doi:10.1007/s11801-021-0158-7

[32] Martins ER, Spadoti DH, Romero MA, et al. Theoretical analysis of supercontinuum generation in a highly birefringent D-shaped microstructured optical fiber. Opt Express. **2007**;15(22):14335–14347.

[33] Ortigosa-Blanch A, Knight JC, Wadsworth WJ, et al. Highly birefringent photonic crystal fibers. Opt Lett. **2000**;25(18):1325–1327.

[34] Steel MJ, Osgood RM, Jr. Elliptical-hole photonic crystal fibers. Opt Lett. **2001**;26(4):229–231.

[35] Tomer DS, Kumar A. A graded index hybrid photonic crystal fiber for supercontinuum generation using $AsSe_2$-As_2S_5. J Opt. **2024**: 1–10. doi:10.1007/s12596-024-01954-3

[36] Chu Van L, Nguyen Thi T, Hoang Trong D, et al. Comparison of supercontinuum spectrum generating by hollow core PCFs filled with nitrobenzene with different lattice types. Opt Quantum Electron. **2022**;54(5):300. doi:10.1007/s11082-022-03667-y

[37] Agrawal GP. Nonlinear fiber optics. In: Christiansen PL, Sorensen MP, Scott AC, editors. Nonlinear science at the dawn of the 21st century. Berlin, Heidelberg: Springer; 2000. p. 195–211. doi:10.1007/3-540-46629-0_9

[38] Dudley JM, Taylor JR, editors. Supercontinuum generation in optical fibers. Cambridge: Cambridge University Press; 2010. doi:10.1017/CBO9780511750465

[39] Kedenburg S, Steinmann A, Hegenbarth R, et al. Nonlinear refractive indices of nonlinear liquids: wavelength dependence and influence of retarded response. Appl Phys B. **2014**;117:803–816.

[40] Dudley JM, Genty G, Coen S. Supercontinuum generation in photonic crystal fiber. Rev Mod Phys. **2006**;78(4):1135–1184. doi:10.1103/RevModPhys.78.1135

[41] Garg D, Kumar A. Highly coherent on-chip mid-infrared supercontinuum generation from 1.5 to 25 µm in CdTe-based Rib waveguide. Opt Quant Electron. **2025**;57:96. doi:10.1007/s11082-024-08007-w

[42] Chu Van L, Le Tran BT, Nguyen Thi T, et al. Comparison of supercontinuum generation spectral intensity in benzene-core PCFs with different types of lattices in the claddings. Opt Quant Electron. **2022**;54:840. doi:10.1007/s11082-022-04218-1

[43] Lanh CV, Tran LTB. Low peak power broadband supercontinuum spectra generated in a square lattice toluene-core photonic crystal fiber with different air hole diameters. Laser Phys. **2023**;33:095102.

[44] Lanh CV, Thuy NT, Duc HT, et al. Comparison of supercontinuum spectrum generating by hollow core PCFs filled with nitrobenzene with different lattice types. Opt. Quant. Electron. **2022**;54:300.

[45] Thuy NT, Duc HT, Tran LTB, et al. Optimization of optical properties of toluene-core photonic crystal fibers with circle lattice for supercontinuum generation. J Opt **2022**;51:678.

[46] Lanh CV, Anuszkiewicz A, Ramaniuk A, et al. Supercontinuum generation in photonic crystal fibers with core filled with toluene. J Opt **2017**;19:125604.

[47] Lanh CV, Thuy HV, Van CL, et al. Optimization of optical properties of photonic crystal fibers infiltrated with chloroform for supercontinuum generation. Laser Phys. **2019**;29:075107.

[48] Hieu LV, Thuy HV, Nguyen HT, et al. Supercontinuum generation in photonic crystal fibers infiltrated with tetrachloroethylene. Opt. Quant. Electron. **2021**;53:187.

[49] Hossain MA, Namihira Y, Razzak SA. Supercontinuum generation at 1.55 μm using highly nonlinear photonic crystal fiber for telecommunication and medical applications. . Optical review. **2012**;19:315–319. doi:10.1007/s10043-012-0048-0

[50] Guo Z, Yuan J, Yu C, et al. Highly coherent supercontinuum generation in the normal dispersion liquid-core photonic crystal fiber. Progress In Electromagnetics Research M. **2016**;48:67–76.

[51] Chauhan P, Kumar A, Kalra Y. Numerical exploration of coherent supercontinuum generation in multicomponent GeSe2-As2Se3-PbSe chalcogenide based photonic crystal fiber. Optical Fiber Technology. **2020**;54:102100. doi:10.1016/j.yofte.2019.102100

[52] Hoang VT, Kasztelanic R, Filipkowski A, et al. Supercontinuum generation in an all-normal dispersion large core photonic crystal fiber infiltrated with carbon tetrachloride. Opt Mater Express. **2019**;9(5):2264–2278.

[53] Van Lanh C, Borzycki K, Xuan KD, et al. Optimization of optical properties of photonic crystal fibers infiltrated with chloroform for supercontinuum generation. Laser Phys. **2019**;29(7):075107.

[54] Van LC, Borzycki K, Xuan KD, et al. Supercontinuum generation in photonic crystal fibers infiltrated with nitrobenzene. Laser Phys. **2020**;30(3):035105. doi:10.1007/s12648-023-02830-9

[55] Wen J, Liang B, Qin W, et al. High coherent supercontinuum generation in nitrobenzene liquid-core photonic crystal fiber with elliptical air-hole inner ring. Opt Quantum Electron. **2022**;54(12):817.

[56] Wen J, Liang B, Sun W, et al. Coherence analysis of supercontinuum generation in nitrobenzene liquid-core photonic crystal fiber based on adaptive step-size methods. Opt Quantum Electron. **2024**;56(4):619.

[57] Tomer DS, Kumar A. Ethanol-infiltrated circular photonic crystal fiber for low peak power supercontinuum generation from near-infrared to mid-infrared region. J Opt. **2024**. doi:10.1007/s12596-024-02152-x

Nature Environment and Pollution Technology
An International Quarterly Scientific Journal

p-ISSN: 0972-6268
(Print copies up to 2016)
e-ISSN: 2395-3454

Vol. 24 | No. 1 | Article ID B4182 | 2025

Review Research Paper

https://doi.org/10.46488/NEPT.2025.v24i01.B4182

Open Access Journal

Phytochemistry of *Aloe vera*: A Catalyst for Environment-Friendly Diverse Nanoparticles with Sustained Biomedical Benefits

S. Yadav, A. Khan and J. G. Sharma†
Department of Biotechnology, Delhi Technological University, Delhi-110042, India
†Corresponding author: J. G. Sharma; sharmajaigopal@dce.ac.in

Abbreviation: Nat. Env. & Poll. Technol.
Website: www.neptjournal.com

Received: 08-04-2024
Revised: 15-05-2024
Accepted: 20-05-2024

Key Words:

Aloe barbadensis Miller
Phytochemicals
Phyto-fabrication
Eco-friendly
Nanoparticles
Photocatalyst
Antibiotic-resistant

ABSTRACT

Nanotechnology has become one of the most active fields in the research area and is getting more attention toward nanoparticle synthesis. Green synthesis methods using various plants, fungi, bacteria, and algae were used to synthesize nanoparticles with proper requirements and maintain sterile conditions to get the desired products. *Aloe vera*, a bio-medicinal plant, contains a wide range of phytochemicals such as phenolic, hydroxyl groups, alkaloids, polyols, polysaccharides, etc, which act as reducing and capping agents with high efficiency. This review revealed that aloe vera-derived nanoparticles are safe, stable, cost-effective, and eco-friendly, and they also possess significant applications for drug targeting, disease resistance, tissue engineering, wound healing, anticancer, antibacterial, and cosmetic industries. Synthesized metal nanoparticles are characterized through UV-visible spectroscopy, X-ray diffraction, scanning electron and transmission electron microscopy, photoluminescence, and the Well-diffusion method. It is highly interesting to note that aloe vera-mediated silver and zinc nanoparticles possess high potency against multi-drug resistant pathogens. Here, anticancer, antioxidant, anti-inflammatory, and photocatalytic activity separately showed by aloe vera peel, gel, and leaf, along with possible challenging situations faced during plant extract-based nanoparticle synthesis, are highlighted. Additionally, the introduction of GMOs is subjected to play an important role in advancing green methods. However, more research is required to estimate the dose's safety, degradation, and synergistic mechanism inside the human body for better use of the green method for the treatment of microbial infections.

Citation for the Paper:

Yadav, S., Khan, A. and Sharma, J. G., 2025. Phytochemistry of *Aloe vera*: A catalyst for environment-friendly diverse nanoparticles with sustained biomedical benefits. *Nature Environment and Pollution Technology*, 24(1), B4182. https://doi.org/10.46488/NEPT.2025.v24i01.B4182

Note: From year 2025, the journal uses Article ID instead of page numbers in citation of the published articles.

Copyright: © 2025 by the authors
Licensee: Technoscience Publications
This article is an open access article distributed under the terms and conditions of the Creative Commons Attribution (CC BY) license (https://creativecommons.org/licenses/by/4.0/).

INTRODUCTION

With the reasons for the advances in science and technology research, nanotechnology has become 1 of the most active fields in every research area. They are significantly used in electronic devices and are seeking attention for the synthesis of nanoparticles. Nanoparticles are characterized as of nano or minuscule dimensions as they lie within a range between 1-100 nanometres and possess a large surface-volume ratio and high reactivity with their ideal synthesis route. Nanoparticles display unique properties like magnetic, optical, electrical, chemical, and other various biological properties (Zharov et al. 2005). Top-down & bottom-up approaches synthesize nanoparticles with the involvement of physical and chemical methods for the synthesis of NPs. Chemical synthesis occurs through methods including co-precipitation, sol-gel, hydrothermal, etc. Methods require excessive energy with the release of toxic, carcinogenic by-products (Ying et al. 2022). At present, green chemistry approaches are being used to develop nanoparticles using Phyto-fabrication of plant extracts (precursor) and microbes (Koratala et al. 2023).

An ecologically friendly way to form a stable and novel nanoparticle with the requirement of little energy and chemicals and also eliminating fewer wastes is pointed as "green synthesis". This method is more advantageous as natural sources, nontoxic, and cost-effective (Behravan et al. 2019). Plant extracts, which contain

components like alkaloids, polyphenols, vitamins, and steroids, act as reducing and capping agents and result in the formation of stable metal nanoparticles (Sargazi et al. 2022). Metal NPs produced by plant extracts or green methods are more stable. Phenolic groups in plant extracts have a higher capacity to reduce the metal ions for nanoparticle synthesis in comparison to fungi and bacteria. Plants are getting more attention in synthesizing metal nanoparticles like Cu, Au, Ag, Zn, CO, etc. They exhibit a high composition of biomolecules like proteins, enzymes, flavonoids, and terpenoids. These phytochemicals have great medicinal value and act as reducing and stabilizing agents (Akbar et al. 2020). The extent of metal ions reduction to synthesize specific metal NPs directly depends on the type and concentration of phytoconstituent present in plant extracts (Iravani 2011). With the use of NPs, Antibiotic-resistant bacteria exhibit increased antibacterial activity. The green route reduces the risk of contamination and helps to maintain the cell structure. Plant-mediated nanoparticles have various antimicrobial, anti-inflammatory, drug delivery anticancer, antioxidant, etc properties (Muthu et al. 2021). Its biological production recycles the expensive metals such as gold and silver in the waste stream. With the increment in alkaline conditions, metal ions will get reduced to attain a petite size of the nanoparticle, whereas, with the increment in temperature, there is an increment in the absorption spectra (profound effect), which results in the rapid formation of nanoparticles (Song et al. 2009). Due to the reason of having nano size and the high surface-volume ratio of nanoparticles, they have great application in agricultural fields in the formation of pesticides and fertilizers to resist damage to crops from diseases, drug delivery, and diagnosis in tissue engineering (Altammar 2023). Several different types of nanoparticles varying in size and shape are synthesized with their biological applications. Using biological methods like plant extracts, bacteria, fungi, and other pathogens, green synthesis has emerged as an ideal option over conventional methods for NP synthesis (Behravan et al. 2019).

From ancient times medicinal plants have been seeking more attention in the fields of medicinal drugs and disease treatment. Active components in natural sources play a vital therapeutic role in health benefits. Various plants such as *Medicago sativa, A. indica, Aloe vera, Tamarind, Alfa Alfa, Hydrilla* sp., *Mangifera indica, Cassia fistula, Piper betel,* and many more medicinal plants have been used for metal NP's synthesis. Among various plants, aloe vera is proposed to be chosen for metal nanoparticles due to its cheap, eco-friendly, non-toxic nature and numerous therapeutic properties as anticancer, anti-inflammation, antioxidant, antifungal, etc. *Aloe barbadensis* Miller, commonly called aloe vera, is the oldest plant species with the highest medicinal properties ever known. Aloe vera is one of the most common succulent xerophyte plants of the family *Liliaceae* and is grown in hot and dry climates in India, Japan, and China (Baruah et al. 2016). Aloe plants can grow up to a height of 60-120cm. It can survive as below as 40°C temperature and freezing (Grindlay & Reynolds 1986). This green plant has a high water-storing capacity in leaves to survive in harsh conditions. Aloe leaves are covered with a thick epithelium layer containing colorless, viscous, and bitter gel with parenchymatous cells. Among 420 kinds of *Aloe* species, *Aloe vera* is one of the most effective and active plants with medicinal properties, commercially used (Ahlawat & Khatkar 2011). Several researchers have attempted to identify the active component responsible for the medicinal properties of aloe vera in wound healing in case of burns and inflammation (Rao Kandregula et al. 2015). It contains 200 active components, including enzymes, minerals, polysaccharides, and amino acids, present in different layers or parts of the aloe leaf. Some chemical compounds include anthraquinones, glycoside sterols, lipids, etc. (Gao et al. 2019). These chemical components have different advantages as antiviral, anti-inflammatory, antidiabetic, antioxidative, and anticancer properties. It is widely used in products related to the pharmaceutical, food, and cosmetics industries. Thus, this review provides a detailed analysis of aloe vera-mediated synthesis of nanoparticles (Table 1) through ongoing research related to it with their potential antibacterial, anticancer, and photodegradation applications for a safe future by eco-friendly or green approach.

How is a Flora-Derived Green Synthesis of Metal Nanoparticles Utilized in Comparison to Conventional Methods?

The trend of synthesis of safe, novel, and less harmful nanoparticles is exploited all over. Different methods like physical, chemical, and biosynthesis methods are used for the synthesis of nanoparticles. Despite using physio-chemical methods for producing metal nanoparticles, green synthesis approaches are now exploited in the research sector due to their eco-friendly nature and several clinical and nutraceutical properties. Physical methods for synthesis require high energy and release harmful chemicals and waste products. Chemical methods face many problems, like using toxic and expensive solvents (Kundu et al. 2014) and heating the chemicals at high temp, with low pressure, which leads to increased risk to human health and surroundings (Li et al. 2011). These methods decline the biological applications and desired mass production. To overcome this problem, the global market transitioned towards environment-friendly methods. Different green methods or biological systems are used for nanoparticle synthesis. Biosynthesis methods

are quite safe, Harmless, and novel approaches, including plants and microorganisms for medicinal applications (Rabiee et al. 2020). Microbial systems are cost-effective and nontoxic for the environment, including bacteria, fungi, algae, yeast, etc, for nano-size particles. These work to reduce and stabilize the particular metal nanoparticle (Gericke Mariekie & Pinches Anthony 2006). Among these biological systems, fungi have better quality in production due to low expenses for downstream processing, highly efficient for extracellular enzymes used for large mass production, good metal reduction, and utilization of biomass (Sarkar et al. 2014). It is quite challenging for researchers because of the complexity of toxic metals for the synthesis of nanoscale materials. Microbes-mediated nanoparticles are not completely viable to form the desired product, they require a proper sterile condition and high maintenance. No control for nanoparticle size, structure, and time for microbial screening are some major drawbacks of microbial systems for nanoparticle synthesis (Kundu et al. 2014). Researchers investigated to reveal that plant parts and their extracts are the most ideal and cost-effective, nontoxic method of nanoparticle synthesis with deficient maintenance of requirements in the system. Plant extracts contain numerous active phytocomponents like flavonoids, amino acids, minerals, enzymes, polysaccharides (Gao et al. 2019), polyols, and polyphenols (Ovais et al. 2018). Phytochemicals in plant extracts act as stabilizing agents as compared to microbial systems for nanoparticle synthesis to reduce toxic heavy metals. Any parts like the root, stem, leaf, or flower of a plant containing phytochemicals can be used for synthesizing various nanoparticles like gold, silver, copper, zinc, etc (Iravani 2011). Plant-mediated nanoparticle synthesis is cheap, accelerated, and doesn't require specific conditions and screening of microbial cultures as microbial systems do, and was easily synthesized in a controlled condition at room temperature (Rajakumar et al. 2012) with quite stirring and heating (Acharyulu et al. 2014). This is done by simply mixing the reducing agents present in plant extracts in an aqueous solution of the respective metal of the nanoparticle to be synthesized (Fig. 1). Synthesis of nanomaterial comprises three phases: (a) activation phase; metal ion gets reduced, (b) growth phase; aggregation of small particles to form large nanoparticles via Ostwald ripening, (c) termination phase; concluded the shape of a nanoparticle. The formation of nanoparticles is characterized by a visual change in the color of the solution or by UV-Vis Spectroscopy. Finally, nanoparticles are collected by washing before drying at low temperatures. The capacity of certain metal ions to get reduced depends on the presence and concentration of specific functional groups such as hydroxyl, phenol, aldehyde, ketones, carboxylic acid, and amines, as well as phytochemicals like polyols, polyphenols, and enzymes present in plant extract (Iravani 2011). Plant-mediated synthesis of nanoparticles is stable for getting higher yield, which makes it a highly preferred method over other biosynthesis methods. Plant-extracted nanoparticles have various diagnostic and therapeutic applications in biotechnology. Several nanomaterials synthesized by this method have unique properties. Ex- Gold and silver nanoparticles synthesized by plant extracts have anti-microbial, anticancer, and antiviral properties. Whereas Zinc oxide nanoparticles are efficient for the production of

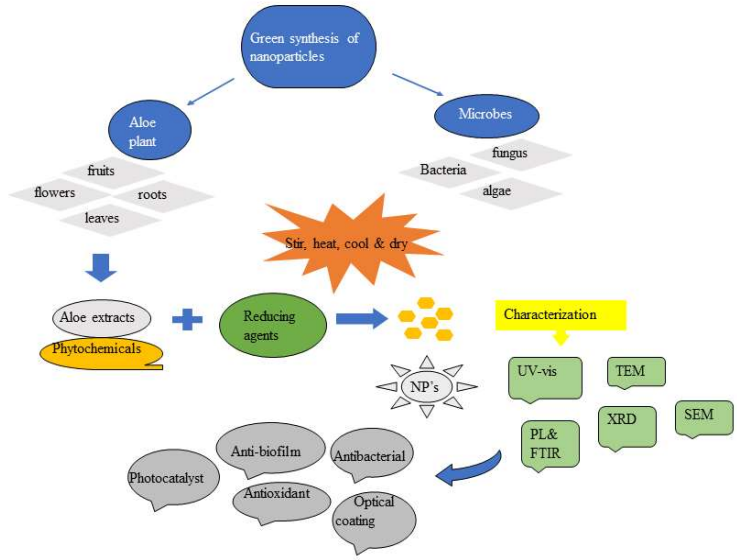

Fig. 1: Plant-facilitated NP synthesis with its biomedical applications.

cosmetic products and for coating purposes (Mittal et al. 2013). Therefore, plant extracts proposed an efficient method for fast, safe, convenient, and stable way of nanoparticle synthesis.

An Overview of the Plant, *Aloe barbadensis* Miller (Aloe vera)

The scientific name of Aloe vera is *Aloe barbadensis* Miller, commonly called 'Gwar path' or simply 'Aloe vera'. It is a green shrub that belongs to the family Liliaceae. It is a xerophytic, succulent plant that grows in dry and hot climates. Triangular leaves of aloe vera are enveloped with a thick epidermis layer and cuticles at the edges. Thick, fleshy leaves contain a bitter and viscous gel with parenchymatous cells. High water-holding capacity makes them able to survive in variable temperatures (Grindlay & Reynolds 1986). It is widely known for its healing and medicinal applications in burns, inflammation, gastric problems, stress, cosmetics, and many more. It contains 200 biologically active aloe components such as proteins, carbohydrates, acemannan, polyphenols, anthraquinones, etc (Talukdar et al. 2023). These secondary metabolites in gel provide anticancer, antidiabetic, antioxidant, antimicrobial, and anti-fungal benefits. Aloe vera consists of three layers. A thick outermost layer or rind produces proteins and carbohydrates. The middle layer contains yellow bitter latex rich in anthraquinones and glycosides (Baruah et al. 2016). The innermost layer contains mainly 98 percent water, and the rest are vitamins, sterols, and glucomannans (Chelu et al. 2023).

It has a unique, fast mechanism to heal damaged tissue by its active secondary metabolites. Mannose-6-phosphate (Hashemi et al. 2015), gibberellin, acemannan (Jettanacheawchankit et al. 2009a), saponin (Baruah et al. 2016), and polysaccharides (Tabandeh et al. 2014) are responsible for repairing damaged tissues. Wound healing is done by activating collagen production to increase blood supply in damaged areas. Also, it induces re-epithelialization by the proliferation of fibroblasts. Some constituents like lupeol (Das et al. 2011), aloe resin Es (Das et al. 2011), bradykinesia, alkaline phosphatase, peroxidase, cinnamic acid (Das et al. 2011), aloin, and aloe emodin, have anti-inflammatory properties. They act by blocking their nitric oxide synthase and cyclooxygenase pathway at the site of infection. Aloe vera extracts have an anticancer effect in lymphoma cells, and murine T-cell lymphoma in a dose-dependent manner was reported. Anthraquinones, emodin, aloin, and acemannan show active anticancer effects by inhibiting tumor growth and promoting apoptosis (Pradhan 2023). Aloe-emodin has antimicrobial properties and inhibits biofilm formation in microbes like *Mycobacterium tuberculosis, Staphylococcus aureus,* and *Enterococcus* (Xiang et al. 2017). By reducing oxidative stress, lowering blood glucose levels, increasing insulin levels, and improving islets in the pancreas, aloe polysaccharides (Kim et al. 2018) and aloe-emodin (Alshatwi & Subash-Babu 2016) act as antidiabetic agents by inhibiting apoptosis and oxidative stress signaling. Aloe vera extracts can improve skin health by promoting collagen formation in fibroblast cells and maintaining skin hydration. Aloe sterols (Misawa et al. 2008), acemannan (Jettanacheawchankitet al. 2009b), aloesin (Wu et al. 2012), and aloin (Jettanacheawchankit et al. 2009b) are active components useful in treating hyperpigmentation, pimples, wrinkles, and other skin-related problems that are yet investigated. Acemannan is the most active phytochemical in reducing oral ulcers, gum diseases like gingivitis and plaque, and neurodegenerative diseases. Processing methods of these compounds can change the concentration of their laxative property. Aloe vera extracts can create toxic effects like kidney issues, allergies, and abdomen pain in some cases if taken in high concentration without prescription. Aloin is mainly responsible for allergy reactions (Fujii 2003). To avoid any toxic effects, a safe dose is necessary for benefits. Aloe extracts are assessed to prevent the generation of ROS and also increase the release of Ca^{2+} ions inside cells to treat neurodegenerative disorders such as Parkinson's, Amyotrophic lateral sclerosis, Alzheimer's, and Huntington's diseases. Researchers found aloe vera wastes to be used as fertilizer, biofuels, drug delivery systems, and in the pharma industry. Evaluating all of the therapeutic properties of this plant, it is a crucial element in green nanoparticle synthesis with various pharmacological effects.

Diverse Forms of Aloe vera-Facilitated Nanoparticles

Aloe vera-derived Ag-nanoparticles: Aloe vera is significantly used for silver nanoparticle synthesis (Ag NPs). Silver nanoparticles gained the most attention for their different properties and applications in various fields of study. Plant extracts containing phytoconstituents are helpful in the reduction of silver ions to form safe, non-toxic, and enhanced therapeutic effects of AV-Ag NPs. Various crucial parameters affecting Ag NP synthesis are pH, the concentration of reducing agent and aloe extracts, and temp. pH can change the size and morphology of NPs (basic pH elevates the synthesis of NPs) (Singh & Dhaliwal 2019). Concentration and reaction time should be optimum for reducing silver ions to form nanoparticles (Devaraj et al. 2013).

Arshad et al. (2022) synthesized AV-Ag NPs against multi-drug resistant pathogens and observed NP synthesis by simply mixing silver nitrate solution and aloe extract solution in 4-6 hrs of incubation at 65°C. Characterization of particles

is done by UV-visible spectroscopy, X-ray diffraction, and scanning electron microscopy, resulting in spherical shape nanoparticles in the range of 30-80nm (Arshad et al. 2022).

Begum et al. (2020) demonstrated the synthesis of AV-Ag NPs to measure antibacterial activity against gram-positive and gram-negative bacteria by disc diffusion method. Synthesis of AV-Ag NPs was carried out by taking a 5:95 ratio of aloe vera extract to silver nitrate solution at optimum pH 8 for a day. Characterization of synthesized NPs by SEM shows spherical particles with a size of 20-24 nm (Begum et al. 2020).

Begum & Mahboob (2019) evaluated the antioxidant properties of aloe extracts and aloe-mediated silver nanoparticles in vitro and in vivo studies. A preliminary identification test was conducted to detect the presence and antioxidant properties of phytochemicals present in the aloe extracts for the synthesis of AV-Ag NPs. AV-Ag NP synthesis was confirmed by UV-vis spectroscopy. A reddish-brown color of the solution was observed due to the excitation of surface plasmon resonance of synthesized silver nanoparticles in the reaction mixture. It resulted in the synthesis of spherical shape AV-Ag NPs with maximum absorption at 400 nm and size in the range of 20 to 24 nm. In Vitro, the antioxidant property was determined by some methods like lipid peroxidation inhibition (LPOI), DPPH, i.e.,1,1-Diphenyl-2-picrylhydrazyl, and reducing power assay based on the concentration of aloe vera extract and AV-Ag NPs. It resulted in high LPOI in aloe vera extract, high DPPH activity, and reduced power activity in AV-Ag NPs. On the other hand, an in vivo study of AV-Ag NPs was performed in rats for 28 days (10 $mg.kg^{-1}$ of body weight). It showed the reno-protective effect by reducing the level of MDA and increasing in level of catalase, SOD, and GSH level. Antioxidant potential and nontoxic effect of AV-Ag NPs based on their conc., size, and exposure period were estimated by this study (Begum & Mahboob 2019).

Nalini & Kay (2020) synthesized spherical AV-Ag NPs, which were 12-40 nm in size measured by SEM and at a temperature of 32°C. They analyzed the antimicrobial properties of these synthesized AV-Ag NPs on cotton fabric against the bacteria E. coli and Staphylococcus aureus. The analysis was carried out in the Well diffusion method and streak plate method to measure the zone of inhibition, with an absorbance at 420 nm, and resulted in bactericidal effects.

Mohamed & El-Masry (2020) prepared AV-Ag NPs with exposure to sunlight to increase the reducing efficiency. NPs were characterized through TEM, FTIS (Fourier transform infrared spectroscopy), and dynamic light scattering. Formation of colloidal spherical AV-Ag NPs, with size in the range of 94 nm, absorption peak noted at 400 nm. The resulting AV-Ag NPs have significantly high antibacterial effects to stop the growth of Gram-positive *Staphylococcus aureus*, Gram-negative *Pseudomonas aeruginosa*, and yeast (*Candida albicans*). Besides, it has high therapeutic or anticancer effects on breast cancer cells (Mohamed & El-Masry 2020).

Vélez et al. (2018) synthesized silver nanoparticles using aqueous and ethanolic extracts of aloe vera as reducing agents. High-resolution TEM was used to identify nanoparticle Sizes and was found to be 2-7 nm by aqueous extracts and 3-14 nm by ethanolic extracts. Researchers reported that even a small concentration of aqueous and ethanolic aloe extracts mediated silver nanoparticles show results for effective removal of harmful mercury detected by atomic absorption spectroscopy and antibacterial activity for mesophilic pathogen *Kocuria variants* (Vélez et al. 2018).

Dinesh et al. (2015) showed that a very low dose of AV-Ag NPs is required to show a mosquitocidal effect against *Anopheles stephensi* and to stop the growth of *Bacillus subtilis* and *Salmonella typhi* in water. They used SEM, XRD, and FTIR techniques for the characterization of synthesized AV-Ag NPs (Dinesh et al. 2015).

Basak et al. (2018) produced spherical aloe-mediated Ag NPs. Evidence of exp. Conclude anticancer activity against MCF-7 and T47D (breast cancer cells) and antimicrobial properties against bacterial species (Basak et al. 2018). In this study, an experiment was performed to compare the antibacterial properties of *Aloe vera, Portulaca oleracea*, and *Cynodon dactylon,* mediated silver nanoparticles through the disc diffusion method, which calculates their MIC (minimum inhibitory concentration) values. Size and shape were determined by technique, SEM, and UV-vis Spectroscopy. They found that aloe vera-mediated NPs exhibit high bactericidal 50µg/mL concentration against various species of bacteria (Abalkhil et al. 2017).

A group of Researchers experimented on 30 male mice weighing between 50 to 70 g. They aim to determine the efficiency of recovering epithelial cells on ulcers due to irradiation. Mice were classified into five groups and exposed to harmful radiation, which resulted in the induction of ulcers in each mouse. After irradiation, the first group received no treatment to function as a control, whereas the Second group was ulcer-induced but no treatment was received for it. The third group was treated with aloe extracts, the fourth group was treated with Ag NPs, and the fifth group was treated with a combination of both, i.e., AV-Ag NPs, respectively. The team identified that AV-Ag NPs treated mice have elevated collagen synthesis due to an increase in IL-10 level when compared to individual AV and Ag NPs. This restoration efficiency of epithelial tissues helps in reducing the adverse

effects of inflammatory reactions and re-epithelialization in case of ulcer formation (El-Batal & Ahmed 2018).

Aloe vera-derived Au-nanoparticles: Gold is effectively being used in the synthesis of nanoparticles due to its high physical, chemical, electric, thermal, and optical properties and exhibits great applications in electronic devices, biomedicines, drug delivery, and sensing devices. Various shapes of gold nanoparticles were synthesized, like spherical, triangles, etc, based on the concentration of aloe extracts used for agglomeration.

Nalini & Kay (2020) synthesized spherical AV-AuNPs (aloe-mediated gold nanoparticles) below 15 nm in size and at a temperature of 34°C measured by SEM after 16 hrs of incubation. They identified the antimicrobial properties of synthesized AV-AuNPs on cotton fabric against E. coli and Staphylococcus aureus. The test was carried out in the Well diffusion method and streak plate method and exhibited an absorbance of 530 nm (Nalini SP & K 2020).

In a study conducted by (Malik et al. 2023) where, they synthesized gold nanoparticles using Aloe vera, *Gymnema sylvestre*, and honey. They aimed to study the toxicity of gold nanoparticles. When chloroauric acid ($HAuCl_4.3H_2O$) was mixed with aloe extracts, it led to a change in color of the mixture from brownish to purple then it was centrifuged at around 150 rpm in a dark room. Characterization of synthesized AuNPs via XRD, UV-vis, FTIR, and SEM. They discovered (AV-AuNPs) of size 30-45 nm, and an absorbance peak was noted at 540 nm. The yield and absorbance of gold NPs directly depend on the elevation of temperature. Furthermore, they examine the cytotoxic effects of AuNPs by conjugating them with anticancer drugs to treat MCF-7 and MDA-MB231 breast cells (Malik et al. 2023).

Chandran et al. (2006) reported the biological synthesis of gold nanotriangles and spherical-shaped silver nanoparticles using aloe vera extracts. When they mixed the chloroauric acid solution and aloe extracts it resulted in a brownish-red color solution after 5 h of incubation. The presence of crystalline gold nanotriangles was detected with size ranges between 50-350 nm and was confirmed by UV- -vis -NIR absorption spectroscopy. It exhibits two absorption bands. TEM analyses that MTP (multiple twinned particles) of varying shapes direct the formation of crystalline gold triangular nanoparticles. Strong NIR absorption is widely used to treat cancer and in optical coating (Chandran et al. 2006).

Aloe vera-derived CuO-nanoparticles: Due to the unique properties of copper oxide nanoparticles, they are highly used in the synthesis of gas sensors and resistant materials. Multiple applications of copper oxide nanoparticles synthesized by varying concentrations of aloe extracts exhibit antibacterial, antifungal, and antifouling activities. From all works of literature, copper has higher antibacterial properties as compared to Ag, Au, and Zn metals.

A study of the synthesis of CuO NPs was carried out by (Narayanan et al. 2023) and his team using aloe extract. 5 g of aloe leaf was mixed with 200 ml of distilled water, heated, cooled, and filtered out. 0.56 g copper acetate monohydrate dissolved in distilled water with magnetic stirring to make a solution. When aloe extract is added to copper sulfate solution, the solution turns out to be green from blue. Brown precipitates of copper oxide particles appeared—characterization of synthesized spherical CuO nanoparticles through UV-vis, FTIR, SEM, and TEM. More than 80 percent of the efficiency of photocatalytic properties of AV-Cu NPs was reported by researchers (Narayanan et al. 2023).

This study aimed to determine the electrocatalyst activity of copper-cobalt oxide-based electrodes on Ni-substrate. In this hydrothermal process, aloe vera extracts are used as surfactants to induce the growth of NPs. Copper & and cobalt oxide-based electrocatalysts exhibit applications in oxygen-evolving processes. In this exp (Sarkar et al. 2023), Ni substrate was prepared by first treating it with acetone, followed by a bath in HCl, distilled water, and ethanol, and drying at the end. On the other side, an aloe vera extract sol. was also prepared by boiling, stirring, and cooling. The reaction was conducted in different mineral mediums (HCl, CA, DEA, NaOH, and H_2NCONH_2) containing an equal ratio of both copper & and cobalt metal oxide on the Ni-substrate. The solution was heated at 130°C, cooled at RT, and dried to separate the catalysts from the Ni substrate. Characterization was successfully carried out by XRD, EDS (energy dispersive spectrum), Field Emission SEM, and testing oxygen evolving performance. This study showed that an acidic mineral medium influences the growth of copper oxide, whereas basic minerals promote the growth of cobalt oxide. Besides this, aloe vera-based metal oxide with urea mineral medium is anticipated to have high electro-catalytic potential on Ni-substrate (Sarkar et al. 2023).

Rehman & Shahid Minhas (2021) experimented by mixing 6 g of copper nitrate solution and aloe extracts at 120°C by stirring for 7 h. Finally, after several hours, black-colored precipitates appeared, confirming 60 nm spherical-shaped CuO NPs. These synthesized nanoparticles are characterized by SEM and XRD. The potency of CuO NPs was discovered to kill MCF-7 cell lines of breast cancer (Rehman & Shahid Minhas 2021).

Researchers successfully synthesize CuO NPs using aloe extracts and copper chloride or copper sulfate as precursors and changing the type and quantity of copper precursor

results in the formation of rod, spherical, and platelet-like shapes of pure copper oxide nanoparticles varying in size from 9-23 nm. Rod and platelet-shaped CuO NPs have high resistance to bacteria due to their increased surface area compared to spherical-shaped particles analyzed by (Tavakoli et al. 2019).

Kumar et al. (2015) studied the synthesis of copper oxide nanoparticles using 5 mL of aloe vera extracts added to 10 mM of copper nitrate. The mixture was heated at 120°C on vigorous magnetic stirring for a day, resulting in a dark red color. Finally, a black ppt of CuO NPs appeared with a size of 22 nm obtained by XRD and TEM techniques. They found efficient antibacterial activity against fish pathogens like *Aeromonas hydrophila, Flavobacterium branchiophilum,* and *Pseudomonas fluorescens,* causing infection in fishes. The bactericidal effects of synthesized nanoparticles were analyzed via the micro-dilution broth technique (Kumar et al. 2015).

Gunalan et al. (2012) reported the synthesis of monodisperse copper oxide nanoparticles by chemical and biological methods. They dissolve copper sulfate and aloe extract solution by continuing magnetic stirring of the mixture. Keeping the mixture under vigorous stirring for 7 hrs at 130°C, a black precipitated solution of copper oxide was observed. After two times centrifugation of the mixture at 3500 rpm, the crushed dry product was collected for its optical property analysis. Maximum particles were observed to be 20 nm, and characterization of CuO NPs was done via UV-vis, photoluminescence, XRD, and SEM (Gunalan et al. 2012).

Aloe vera-derived ZnO-nanoparticles: Zinc oxide has low toxic effects and is under-listed as GRAS (Generally Recognised as Safe) by the US Food and Drug Administration. It has many applications in cosmetics, plastic, paints, pharmacy, and microelectronic devices and is widely used to synthesize efficient nanoparticles against pathogens. At present, further research is going on zinc oxide nanoparticles which are highly used due to their high efficiency as an antimicrobial agent.

To compare inhibitory effects against *Klebsiella pneumonia* isolated from patient samples, Hammood et al. (2022) compared zinc oxide nanoparticles synthesized by aloe vera with chemically synthesized zinc nanoparticles. In this study, 1 mM of ZnO solution was mixed in 10 mL of aloe extracts keeping it for around 30-35 min on a magnetic stirrer, maintaining a neutral pH. The resulting White ZnO nanoparticles underwent centrifugation at 1000 rpm for nearly 10 min before drying and characterization—maximum absorption between 360 to 380 nm depicted by UV-vis spectrum. Scanning electron microscope indicates spherical-shaped Zn nanoparticles of 20 to 40 nm. Other properties of particles were studied via atomic force microscopy, X-ray diffraction, and infrared spectroscopy. This study identified that aloe-mediated zinc nanoparticles exhibit greater inhibition against *K. pneumonia* as compared to commercially prepared zinc nanoparticles (Hammood et al. 2022).

Khatana et al. (2021) synthesized aloe-mediated zinc oxide nanoparticles to examine their antibacterial properties

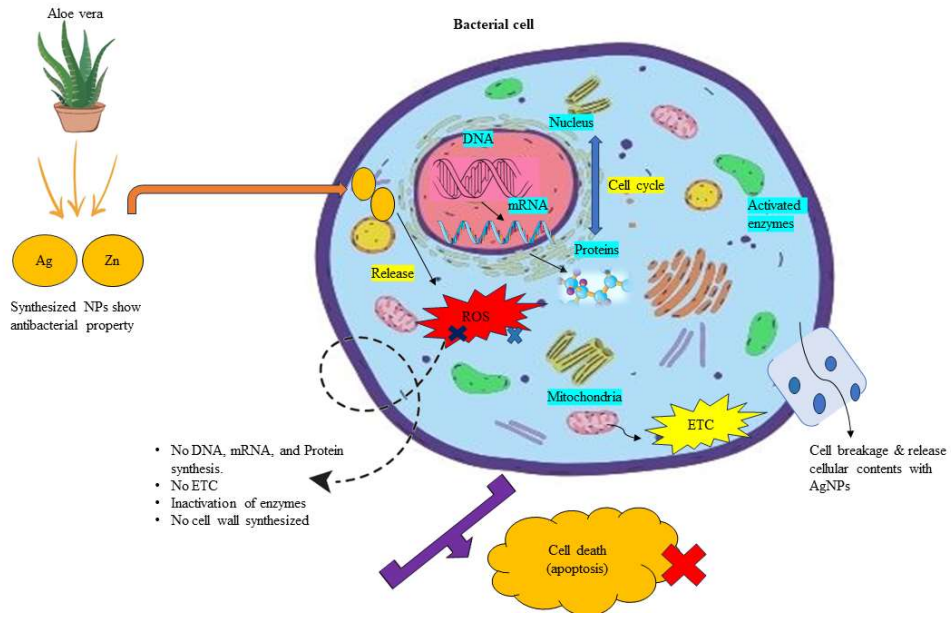

Fig. 2: Role of aloe vera-derived silver and zinc NPs (antibacterial activity).

against different bacterial strains. 100 g of aloe leaves were washed, chopped, and boiled in 100 ml of distilled water and filtered to get a fresh aloe solution. 0.50 g zinc acetate solution was dissolved in freshly prepared aloe extracts solution to 12 pH, and colored zinc oxide nanoparticles were formed. L-ascorbic acid and other components are responsible for ZnO NP synthesis. A flower-like shaped Zn O NP was observed under SEM, showing 0.126 nm of interplanar space. Studied results show high antibacterial efficiency (Fig. 2) against *S. aureus, E. coli,* and *Pseudomonas aeruginosa* (Khatana et al. 2021).

Zinc oxide-nanocomposites (ZnO-BAV, ZnO-WAV, and ZnO-N) were prepared using dried powder of black and white aloe vera and dried powder of Terminalia arjuna nuts by Dar et al. to explore their antibacterial efficiency. At the start of this study, 5 g of dried plant contents of both plants were taken separately in 100 mL of distilled water. Stir each solution at nearly 100 rpm on a hot plate maintaining its temperature at 70°C for 15 min. On the other side, prepare a solution of zinc acetate by adding 2.9 g in 50 ml of distilled water at room temperature for one hour. After preparing both solutions, mix 50 mL of aloe extract in zinc acetate solution and leave at 100 rpm on an orbital shaker for at least 3 hours. After all this procedure researchers centrifuged yellow ZnO nanocomposites settled at the bottom and dried them at 80˚C. Synthesized ZnO-nanocomposites were characterized by UV-visible, SEM, and FTIR techniques, respectively. SEM revealed the morphology of ZnO-BAV (zinc oxide-black Aloe vera) appeared as fibrous-wired of size 27-71 nm, ZnO-WAV (zinc oxide-white aloe vera) as octahedral of size 29-75 nm, and ZnO-N (zinc oxide-nuts) as scattered particles of size 32-83 nm. The disc diffusion method showed a larger zone of inhibition by ZnO-BAV when tested *against E. coli* and *B. stabilis*. ZnO-WAV and Zno-N both showed efficient antimicrobial properties only against E. coli. However, no response showed against *B. stabilis* (Dar et al. 2021).

Sharma et al. (2020) successfully conducted a study on the antimicrobial and photodegradation of dye depending on different sizes and shapes of zinc oxide nanoparticles synthesized. The procedure involved the preparation of zinc acetate dihydrate, Zn $(CH_3CO_2)_2{\cdot}2H_2O$ solution, and aloe leaves were washed, chopped, boiled, and filtered to extract aloe juice. With continued stirring, dropwise addition of aloe extract to different concentrations of 5, 10, and 50 mmol. kg^{-1} of zinc acetate solution at 70°C with pH 11.5. After regular heating for 4 hours, yellow-whitish-colored zinc oxide nanoparticles were synthesized, collected, and dried. UV-visible spectrum analyzes the optical properties of AV-ZnO NPs between 200 to 800 nm with a sharp absorption peak around 370 nm, and the band gap was calculated to be 3.4 eV. SEM, TEM, or EDS (SEM-energy dispersive X-ray spectroscopy) examined the size and shape of ZnO NPs at varying concentrations of Zn $(CH_3CO_2)_2{\cdot}2H_2O$. They obtained hexagonal NPs with a size of 63 nm at 5 $mmol.kg^{-1}$, spherical and hexagonal NPs with a size of 60 to 180 nm at 10 $mmol.kg^{-1}$, and cuboidal or rod-shaped nanoparticles with a size of 40 to 45 nm at 50 $mmol.kg^{-1}$. It has been noticed that 50 mg of the catalytic load is enough for degrading dye for spherical and hexagonal shape nanoparticles. However, there is an increase in degradation efficiency that led to an increase in the concentration of catalytic load for cuboid-shaped zinc oxide nanoparticles. Results also show that synthesized ZnO NPs are effective against pathogens such as *S. aureus, B. subtilis,* and *E. coli* (Sharma et al. 2020).

Aloe peel extract was used by Chaudhary et al. (2019) to synthesize zinc-oxide nanoparticles to depict its efficiency against bacterial and fungal pathogens. Synthesized Zinc oxide nanoparticles were hexagonally confirmed by TEM and with a size range between 50-220 nm UV-vis spectra. Hydroxyl, amine, aromatic, and carbonate groups are responsible for ZnO NP synthesis tested through FTIR. This study results in ZnO NPs having efficient bactericidal and antifungal effects against E. coli and A. niger (Chaudhary et al. 2019). Another similar study on aloe vera peel was performed to form nanovesicles for analyzing active healing mechanisms. Researchers discovered the anti-inflammatory effects of aloe vera peel-mediated nanovesicles (NV's) in macrophages and keratinocytes in case of burn wounds. Synthesized NV's prevent stimulation, contraction, and differentiation of both myofibroblast and fibroblast cells *in vitro* (Ramírez et al. 2024).

Ali et al. (2016) with the help of a simple, safe, and eco-friendly 1-pot biosynthesis method to synthesize Aloe vera functionalized zinc oxide NPs (AV-ZnO NPs) using aloe vera leaf extracts and zinc sulfate. They synthesized these AV-ZnO nanoparticles by heating at 60°C for three hours and with pH-8. It's a simple procedure of synthesis of NPs that doesn't require much temperature, pressure, or any toxic chemical. Characterization of NPs by XRD, SEM, UV-visible spectrum, and SEM-EDX was done to analyze nanoparticles within a range of 13 to 18 nm. The results of this experiment showed that aloe vera functionalized ZnO-NPs (AV-ZnONPs) used as nano antibiotics exhibit great antibacterial and anti-biofilm effects against S. aureus, a gram-positive, and E. coli, a gram-negative bacterium (Ali et al. 2016).

A group of researchers synthesized ZnO nanoparticles by using 60 mL of aloe vera leaf extracts and 5 g of zinc nitrate, a precursor. The mixture was collected in a ceramic crucible and heated at 400°C for two hours in a furnace. The resulting

light-yellow particles were collected, dried, and ground in powder form. ZnO nanoparticles were characterized by a UV-vis spectrum with an absorption peak of 360 nm. SEM and XRD analyze oval zinc oxide nanoparticles with a size range between 70 and 74 nm. It has been found that increasing the concentration of zinc-oxide-nanoparticles resulted in an increment in the growth, hydrogen peroxide, and lipid peroxidation contents of soybean(Hashemi et al. 2016).

Synthesis of ZnO NPs by utilizing precursor (zinc nitrate), cold and hot aloe leaf extracts (biosynthetic process), and sodium hydroxide used for a chemical method to estimate and compare their antibacterial efficiency against various strains of bacteria. Characterization of ZnO-AVH (hot aloe extract), ZnO-AVC (cold aloe extract), and ZnO-C (chemical) through X-RD, SEM, and calculating MIC values. SEM images assessed the morphology of nanoparticles: rod shape of ZnO-AVH &ZnO-AVC and spherical shape: ZnO-C. ZnO-AVC and ZnO-C resulted in small particle size as compared to ZnO-AVH and significantly showed high anti-bacterial effects against strains such as *Bacillus subtilis, Staphylococcus aureus, Pseudomonas aeruginosa,* and *Escherichia coli* (Laxshmi et al. 2012).

In this study, Sangeetha et al. (2011) reported the synthesis of AV-ZnO NPs and compared it to the ZnO-NPs synthesized by chemical method. They examined the morphology and optical properties of both methods. For the chemical method, zinc oxide NPs were produced with the dissolution of zinc nitrate in a sodium hydroxide (NaOH) solution. It formed white precipitates of nanoparticles after ten minutes of centrifugation at 3000 rpm and was dried. On the other hand, side, zinc nitrate was added in different concentrations of aloe leaf and aloe gel solution, and yellow-whitish precipitates appeared in the case of aloe-mediated nanoparticles. They centrifuged it two times at 4500 rpm for 10 to 15 min before drying at 80°C. Characterization of NPs by UV-visible spectra, TEM, and XRD analyze their average size. Aloe leaf (34 nm), aloe gel (35 nm), and approximately 60 nm of average size were analyzed by the chemical process. FTIR predicted the functional group responsible for Zn-NPs formation. Researchers highlighted that aloe-mediated NPs have many applications in the industrial field (Sangeetha et al. 2011).

Aloe vera-derived indium oxide nanoparticles: A semiconductor, indium oxide has a variety of applications in LED (light emitting diodes), solar cells, gas sensors, nanotubes, nanowires, and nanoparticles, etc. indium oxide has the property of great transparency for visible lights and strongly interacts with toxic gas molecules on any surface. Indium oxide nanoparticles are synthesized by chemical methods but they can also be synthesized by green methods by using cost-effective, eco-friendly, non-time-consuming aloe vera extracts.

Synthesis of indium oxide (In_2O_3) nanoparticles was discussed by (Maensiri et al. 2008) using indium acetylacetonate, a precursor, and prepared aloe extracts by boiling. This was prepared by directly dissolving indium acetylacetonate in aloe vera solution by constant stirring and drying at 60°C. calcination of dried indium oxide nanoparticles (In_2O_3 NPs) in box furnaces at different temperatures (400°C, 500°C, and 600°C) for at least two hours. Characterization of calcinated nanoparticles was done through XRD, PL, and TEM. Strong PL was shown by In_2O_3 nanoparticles because of the generation of oxygen vacancy during calcination. TEM discovered cubic In_2O_3 NPs with an average size of 5 to 50 nm depending on calcinated temperature Phokha et al. 2008).

Aloe vera-derived titanium dioxide nanoparticles: Titanium dioxide nanoparticles (TiO_2 NPs) are inflammable, white colored, nontoxic, with surface-reactivity, high thermal stability, and photocatalyst. These are highly used in cosmetic products, drug delivery, implants, and bioimaging. These are considered as effective bactericidal agents against a range of pathogens.

Ahmed et al. (2023) synthesized aloe-mediated titanium dioxide (AV-TiO_2) nanoparticles. They synthesized TiO_2 NPs by simply dissolving titanium isopropoxide (TTIP) as a precursor in a drop-by-drop manner in different concentrations of aloe extract solution (10 mL, 20 mL, and 30 mL) with continued vigorous stirring for two hours. Samples were washed with ethanol and distilled water and dried before their calcination at 450°C. XRD, FTIR, and RAMAN techniques confirmed a small optical band gap and high photocatalytic property of green synthesized spherical TiO_2 when compared to chemically or water-synthesized titanium dioxide nanoparticles. This study showed that aloe vera-mediated titanium dioxide nanoparticles with dose-dependent exhibit high radio-sensitization activity (Ahmed et al. 2023).

Hanafy et al. (2020) focused on the synthesis and characterization of titanium dioxide nanoparticles using aloe vera extract at varied pH (acidic, neutral, and basic) levels. TiO_2NPs involved a procedure, the addition of aloe extract solution drop by drop to titanium tetrachloride ($TiCl_4$) solution at (RT) room temperature. Finally, the mixture was then maintained at three varying pHs with the help of ammonium hydroxide and hydrochloric acid. White suspended nanoparticles were washed and followed by drying at 500°C. Spherical-shaped TiO_2 nanoparticles were characterized through XRD, UV-visible, and TEM. Maximum absorption of TiO_2 NPs under acidic, neutral,

Table 1: A concise summary of parameters for aloe vera-facilitated various nanoparticles.

Type of nanoparticle synthesized	Precursor or reducing agent	Incubation at (temperature)	Morphology and dimensions (in nanoscale)	Estimated property	References
Ag	Silver nitrate soln.	65℃	Spherical 30-80 nm	Antimicrobial	(Arshad et al. 2022)
Ag	Silver nitrate sol.	N/A	Spherical 20-24 nm	Antibacterial	(Begum et al. 2020)
Ag	Silver nitrate sol.	RT	Spherical 20-24 nm	Antioxidant	(Begum & Mahboob 2019)
Ag	Silver nitrate sol.	32℃	Spherical 12-40 nm	Antibacterial	(Nalini & Kay 2020)
Ag	Silver nitrate sol.	Sunlight exposure	Colloidal-spherical 94 nm	Antibacterial, Anticancer	(Mohamed & El-Masry 2020)
Ag	Silver nitrate sol.	57-80℃	2-24 nm	Antibacterial, Elimination of mercury	(Vélez et al. 2018)
Ag	Silver nitrate sol.	N/A	Spherical, cubic 30-57 nm	Mosquitocidal effects	(Dinesh et al. 2015)
Ag	Silver nitrate sol.	N/A	Spherical 10-30 nm	Anticancer	(Basak et al. 2018)
Ag	Silver nitrate and polyvinylpyrrolidone (PVP)	N/A	Spherical 10-17 nm	Anti-inflammatory, Re-epithelialization	(El-Batal & Ahmed 2018)
Au	Chloroauric acid	34℃	Spherical Below 15nm	Antimicrobial	(Nalini & Kay 2020)
Au	Chloroauric acid	30-50℃	Spherical 30-45 nm	Against Cytotoxic effects	(Malik et al. 2023)
Au	Chloroauric acid	N/A	Triangles 50-350 nm	Anticancer, optical coating	(Chandran et al. 2006)
CuO	Copper acetate monohydrate	N/A	Spherical	Photocatalyst	(Narayanan et al. 2023)
CuO	Copper nitrate sol.	120℃	Spherical 60 nm	Anticancer	(Rehman & Shahid Minhas 2021)
CuO	Copper chloride or copper sulfate	N/A	Rod, spherical, platelet. 9-23 nm	Antibacterial	(Tavakoli et al. 2019)
CuO	Copper nitrate sol.	120℃	22 nm	Antibacterial	(Kumar et al. 2015)
CuO	Copper sulfate	130℃	20 nm	Optical property	(Gunalan et al. 2012)
Zn	Zinc oxide	N/A	Spherical 20-40 nm	Antibacterial (Klebsiella pneumonia)	(Hammood et al. 2022)
ZnO	Zinc acetate sol.	N/A	Flower-like 0.126 nm	Antibacterial	(Khatana et al. 2021)
ZnO	Zinc acetate	RT	Fibrous, octahedral 27-75 nm	Antimicrobial	(Dar et al. 2021)
ZnO	Zinc acetate dihydrate	70℃	Hexagonal and spherical 60-180 nm, Cuboid and rod shape 40-45 nm	Antimicrobial Photocatalyst	(Sharma et al. 2020)
ZnO	Zinc sulfate and sodium hydroxide	N/A	Hexagonal 50-220 nm	Antibacterial Antifungal	(Chaudhary et al. 2019)
ZnO	Zinc sulfate	N/A	13-18 nm	Antibacterial Anti-biofilm	(Ali et al. 2016)
In_2O_3	Indium acetylacetonate	400-600℃	Cubic 5-50 nm	Optical property	(Maensiri et al. 2008)

Table Cont....

Type of nanoparticle synthesized	Precursor or reducing agent	Incubation at (temperature)	Morphology and dimensions (in nanoscale)	Estimated property	References
TiO_2	Titanium isopropoxide	450°C	Spherical	Photocatalyst, Radio-sensitizer	(Ahmed et al. 2023)
TiO_2	Titanium tetrachloride	N/A	Spherical 13-22 nm	N/A	(Hanafy et al. 2020)
TiO_2	Titanium oxyhydroxide	N/A	80-90 nm	Photocatalyst	(Nithya et al. 2013)
NiO	Nickel nitrate hexahydrate	300-500°C	Cubic crystals	Antibacterial Antifungal	(Ahmad et al. 2022)
CeO_2	Cerium nitrate hexahydrate	600°C	Spherical 42-50 nm	Antibacterial Antifungal	(Shetty et al. 2022)
CeO_2	Cerium nitrate sol.	N/A	Irregular 13-15 nm	Antibacterial Photocatalyst	(N et al. 2021)
CeO_2	Cerium nitrate hexahydrate	600°C	Spherical, With a diameter of 63.6 nm	Optical property	(Kanneganti et al. 2014)

and basic pH was examined to be 318, 326, and 320 nm, respectively. The average size of TiO_2 NPs was estimated to be 22.86±0.85, 15.83±0.902, and 13.3±0.68 nm. The researchers pointed out that for the formation of small-sized, pure, and crystalline forms of TiO_2, basic pH would be preferred (Hanafy et al. 2020).

The biosynthesis of titanium dioxide NPs was successfully carried out to study and analyze their photocatalytic properties for Rh B dye (Rhodamine B dye). A mixture was prepared by adding titanium oxyhydroxide to aloe vera gel extracts and was stirred for a day. The light green appearance of the solution indicates the synthesis of TiO_2 nanoparticles. Particles were then dried at 120°C. AFM (atomic force microscopy) confirmed the average size of 80 to 90 nm of titanium dioxide nanoparticles. When the photocatalytic efficiency was tested for Rh B dye, it showed that TiO_2 synthesized by aloe vera had high efficiency (41%) of decolorization for dye, whereas chemically synthesized TiO_2 showed less efficiency with 24% (Nithya et al. 2013).

Aloe vera-derived nickel oxide nanoparticles: Nickel oxide nanoparticles possess ideal catalytic, magnetic, biocompatible, antifungal, and antibacterial properties. They are highly used in solar cell batteries, fuel cells, gas sensors, and various biomedical areas.

An experiment was performed by Ahmad et al. (2022) to synthesize nickel oxide nanoparticles using nontoxic, cost-effective, and eco-friendly aloe vera leaves. In this procedure, $Ni(NO_3)2{\cdot}6H_2O$ was added to the aloe vera extract solution and continued stirring on a hot plate for nearly one hour, from 72°C to 80°C. The collected samples of nickel oxide nanoparticles were washed three times with deionized water and then dried at 80°C. After doing this finally, dried particles were collected in a ceramic crucible and kept at 300°C, 400°C, and 500°C for 1-2 h. XRD characterization estimated that pure and stable cubic crystals of NiO are obtained at 500°C, and if temperature exceeds 500°C to 600°C then the crystallinity of NiO NPs declined. The results revealed that NiO NPs annealed at 500°C exhibited high antibacterial activity against both gram-positive and gram-negative strains of pathogens and had less antifungal activity (Ahmad et al. 2022).

Aloe vera-derived cerium oxide nanoparticles: Cerium oxide NPs have a range of applications in nano-pharmacy, solar cells, fuel cells, gas sensors, and other polishing objects. CeO_2 is considered an intelligent photosensitizer, helpful in detecting and targeting cancer.

Shetty et al. (2022) synthesized cerium oxide nanoparticles by "low-temperature combustion process" by mixing 4.3 g of cerium nitrate hexahydrate ($Ce(NO_3)_2\ 6H_2O$) to 9 to 10 ml of aloe vera gel solution acting as fuel. Keep the homogenized solution in a furnace at 600°C, which led to yellow dried particles of CeO_2 nanoparticles. SEM and TEM showed the spherical CeO_2 nanoparticles of size about 42 to 50 nm with crystalline structure depicted through the PXRD (powder X-ray diffraction) technique. The author estimated higher antibacterial properties (MIC-2 to 5 $\mu g.mL^{-1}$) in order of *S. aureus* > *E. aerogenes* > *E. coli* by agar diffusion assay. Whereas antifungal effects (MIC-15 $\mu g.mL^{-1}$) are shown in order of *A flavus* > *A. clavatus* > *A. niger* (Shetty et al. 2022).

Present experimentation analyses the effectiveness of photodegradation and bactericidal properties of CeO_2-NPs. Purushotham et al. (2021) mixed cerium nitrate to aloe gel extract solution on a magnetic stirrer resulting in the synthesis of cerium oxide NPs. PXRD and UV-vis spectroscopy obtained irregular shapes of particles with sizes of about 13 to 15 nm. The increasing order of antibacterial properties was estimated as P. aeruginosa > E. coli > K. pneumonia. Up to 97% degradation of Indigo Carmine was recorded with UV radiation in one hour. 85% to 89% degradation showed with Blue 4 dye in one hour thirty minutes.

Kanneganti et al. (2014) Reported the same as earlier: synthesized cerium oxide nanoparticles by forming a homogenized mixture of cerium nitrate hexahydrate solution and aloe vera gel broth solution. Calcinate particles for two hours to obtain a fine, pure, and dried powder of particles at around 600°C. Resulted particles were characterized through XRD, FTIR, SEM, and TEM analyzers, and the size of cerium oxide NPs was determined as spherical with an average diameter of 63.6 nm through dynamic scattering assay (Kanneganti et al. 2014).

CHALLENGES AND UPCOMING PROSPECTS

Nanotechnology has enormous benefits through nanoparticle synthesis due to the reasons of their targeted drug delivery, reduced toxic effects, high biocompatibility, and safety. Aloe-assisted NPs are modified by conjugation, functionalization, and control of size to enhance their biomedical applications. Here, in this review article, the roles and the various biological benefits of aloe vera-mediated nanoparticles are highlighted. Some challenging situations are faced with plant extracts during dry or hot climates, as there is a reduction in phytochemicals due to the shedding of leaves. This led to low productivity and no control over shape & size. In the future, the demand for products that are aloe-based silver and zinc NPs is expected to elevate. Also, nowadays, Aloe vera-based Ag NPs are highly used for edible product packaging. So, there's a proper need for assessment of the quality, degradation, and other PK (pharmacokinetic) mechanisms inside the human body. Furthermore, the introduction of GMOs for enhancement in proteins, molecules, and other enzymes will be the key future in green synthesis.

CONCLUSIONS

This review article summarizes a quick study of several nanoparticles, such as silver, gold, zinc oxide, copper oxide, indium oxide, titanium dioxide, nickel oxide, and cerium oxide. Production of these metals or metal oxide nanoparticles using *Aloe vera* extract follows a green method. This one-step process is fast, simple, safe, non-hazardous, low-cost, high-yield approach. Synthesized AV-MNPs (Aloe vera mediated metal nanoparticles) concluded with various biomedical properties, including antifungal, antibacterial, anti-inflammatory, anticancer, antidiabetic, and antioxidant. AV-MNPs are characterized by multiple techniques such as UV-visible spectroscopy, scanning and transmission electron microscopy, X-ray diffraction, photoluminescence, and Fourier transform IR spectroscopy. The average size of nanoparticles synthesized varies with the quantity of aloe vera extract used at different temperatures, deduced by cited references. The conclusion from this review highly prefers to use of aloe-mediated nanoparticles, mostly silver and zinc, against bactericidal effects. It also prohibits using too much dose of AV-MNPs as it may cause harmful issues. More research is needed to better understand its safety and clinical use. Besides this, long-time stability, and overcoming barriers to improve the delivery of aloe-mediated NPs to targeted sites must be addressed for further research in this area. There is much research literature available on silver, zinc, and nanoparticles, but insufficient works of literature are available on gold, nickel, cerium, and indium nanoparticles synthesized by the aloe vera plant. So, more focus should be required on less explored aloe-mediated nanoparticles and the reason for their restriction towards using their application must be analyzed. In addition to this, there is also a need to investigate the synergistic potency of aloe vera towards various diseases and other microbial infection treatments.

ACKNOWLEDGEMENT

The authors are very thankful to Delhi Technological University for providing the infrastructure and all facilities.

REFERENCES

Abalkhil, T.A., Alharbi, S.A., Salmen, S.H. and Wainwright, M., 2017. Bactericidal activity of biosynthesized silver nanoparticles against human pathogenic bacteria. *Biotechnology and Biotechnological Equipment*, 31(2), pp.411–417. doi.org/10.1080/13102818.2016.1267594.

Acharyulu, N.P.S., Dubey, R.S., Swaminadham, V., Kollu, P., Kalyani, R.L. and Pammi, S.V.N., 2014. Green synthesis of CuO nanoparticles using *Phyllanthus Amarus* leaf extract and their antibacterial activity against multidrug-resistant bacteria. *IJERT*, 164, pp. 3415-3510

Ahlawat, K.S. and Khatkar, B.S., 2011. Processing, food applications and safety of aloe vera products: a review. *Journal of Food Science and Technology*, *48*, pp.525-533. doi.org/10.1007/s13197-011-0229-z.

Ahmad, B., Khan, M.I., Naeem, M.A., Alhodaib, A., Fatima, M., Amami, M., Al-Abbad, E.A., Kausar, A., et al., 2022. Green synthesis of NiO nanoparticles using *Aloe vera* gel extract and evaluation of antimicrobial activity. *Materials Chemistry and Physics*, 288. doi.org/10.1016/j.matchemphys.2022.126363.

Ahmed, N.K., Abbady, A., Elhassan, Y.A. and Said, A.H., 2023. Green synthesized titanium dioxide nanoparticles from *Aloe vera* extract as a promising candidate for radiosensitization applications. *BioNanoScience*, 13(2), pp.730–743. doi.org/10.1007/s12668-023-01085-2.

Akbar, S., Tauseef, I., Subhan, F., Sultana, N., Khan, I., Ahmed, U. and Haleem, K.S., 2020. doi.org/10.1080/24701556.2019.1711121.

Ali, K., Dwivedi, S., Azam, A., Saquib, Q., Al-Said, M.S., Alkhedhairy, A.A. and Musarrat, J., 2016. *Aloe vera* extract functionalized zinc oxide nanoparticles as nano antibiotics against multi-drug resistant clinical bacterial isolates. *Journal of Colloid and Interface Science*, 472, pp.145–156. doi.org/10.1016/j.jcis.2016.03.021.

Alshatwi, A.A. and Subash-Babu, P., 2016. Aloe-emodin protects RIN-5F (Pancreatic β-cell) cells from glucotoxicity via regulation of pro-inflammatory cytokine and downregulation of Bax and caspase 3. *Biomolecules and Therapeutics*, 24(1), pp.49–56. doi.org/10.4062/biomolther.2015.056.

Altammar, K.A., 2023. A review on nanoparticles: characteristics, synthesis, applications, and challenges. *Frontiers in microbiology*, *14*, p.1155622. doi.org/10.3389/fmicb.2023.1155622.

Arshad, H., Saleem, M., Pasha, U. and Sadaf, S., 2022. Synthesis of *Aloe vera*-conjugated silver nanoparticles for use against multidrug-resistant microorganisms. *Electronic Journal of Biotechnology*, 55, pp.55–64. doi.org/10.1016/j.ejbt.2021.11.003.

Baruah, A., Bordoloi, M. and Baruah, H.P.D., 2016. Aloe vera: A multipurpose industrial crop. *Industrial Crops and Products*, *94*, pp.951-963.

Basak, P., Majumder, R., Jasu, A., Paul, S. and Biswas, S., 2018. Potential therapeutic activity of bio-synthesized silver nanoparticles as anticancer and antimicrobial agent. *IOP Conference Series: Materials Science and Engineering*, 10, p.1202. doi.org/10.1088/1757-899X/410/1/012020.

Begum, Q. and Mahboob, T., 2019. Evaluation of antioxidant activity of biologically synthesized silver nanoparticles using Aloe vera. *Int J Bio l Biotech*, *16*, pp.641-653.

Begum, Q., Kalam, M., Kamal, M. and Mahboob, T., 2020. Biosynthesis, characterization, and antibacterial activity of silver nanoparticles derived from *Aloe barbadensis Miller* leaf extract. *IJB,* 145, p.2383. doi.org/10.30498/IJB.2020.145075.2383.

Behravan, M., Hossein Panahi, A., Naghizadeh, A., Ziaee, M., Mahdavi, R. and Mirzapour, A., 2019. Facile green synthesis of silver nanoparticles using *Berberis vulgaris* leaf and root aqueous extract and its antibacterial activity. *International Journal of Biological Macromolecules*, 124, pp.148–154. doi.org/10.1016/j.ijbiomac.2018.11.101.

Chandran, S.P., Chaudhary, M., Pasricha, R., Ahmad, A. and Sastry, M., 2006. Synthesis of gold nanotriangles and silver nanoparticles using *Aloe vera* plant extract. *Biotechnology Progress*, 22(2), pp.577–583. doi.org/10.1021/bp0501423.

Chaudhary, A., Kumar, N., Kumar, R. and Salar, R.K., 2019. Antimicrobial activity of zinc oxide nanoparticles synthesized from *Aloe vera* peel extract. *SN Applied Sciences*, 1(1), p.144. doi.org/10.1007/s42452-018-0144-2.

Chelu, M., Musuc, A.M., Popa, M. and Calderon Moreno, J., 2023. Aloe vera-based hydrogels for wound healing: Properties and therapeutic effects. *Gels*, *9*(7), p.539. doi.org/10.3390/gels9070539.

Dar, A., Rehman, R., Zaheer, W., Shafique, U. and Anwar, J., 2021. Synthesis and characterization of ZnO-nanocomposites by utilizing *Aloe vera* leaf gel and extract of *Terminalia arjuna* nuts and exploring their antibacterial potency. *Journal of Chemistry*, 20, pp.889-894. doi.org/10.1155/2021/9448894.

Das, S., Mishra, B., Gill, K., Ashraf, M.S., Singh, A.K., Sinha, M., Sharma, S. and Xess, I., 2011. Isolation and characterization of a novel protein with anti-fungal and anti-inflammatory properties from *Aloe vera* leaf gel. *International Journal of Biological Macromolecules*, 48(1), pp.38–43. doi.org/10.1016/j.ijbiomac.2010.09.010.

Gericke, M. and Pinches, A., 2006. Microbial production of gold nanoparticles. *Gold Bulletin*, *39*(1), pp.22-28.

Grindlay, D. and Reynolds, T., 1986. The Aloe vera phenomenon: a review of the properties and modern uses of the leaf parenchyma gel. *Journal of Ethnopharmacology*, *16*(2-3), pp.117-151.

Gunalan, S., Sivaraj, R. and Venckatesh, R., 2012. Aloe barbadensis Miller mediated green synthesis of mono-disperse copper oxide nanoparticles: Optical properties. *Spectrochimica Acta - Part A: Molecular and Biomolecular Spectroscopy*, 97, pp.1140–1144. doi:10.1016/j.saa.2012.07.096.

Hammood, I.A., Nijris, O.N. and Alwan, L.H., 2022. Comparing the effect of zinc oxide nanoparticles biosynthesized by Aloe barbadensis and chemically manufactured on *Klebsiella pneumoniae* isolated from the inflamed middle ear. *International Journal of Health Sciences*, (June, 14), pp.14976–14988. doi:10.53730/ijhs.v6ns2.8964.

Hanafy, M.S., Fadeel, D.A.A., Elywa, M.A. and Kelany, N.A., 2020. Green synthesis and characterization of TiO2 nanoparticles using aloe vera extract at different pH values. *Scientific Journal of King Faisal University*, 21(1), pp.103–110. doi:10.37575/b/sci/2020.

Hashemi, S., Asrar, Z., Pourseyedi, S. and Nadernejad, N., 2016. Plant-mediated synthesis of zinc oxide nanoparticles and their effect on growth, lipid peroxidation, and hydrogen peroxide contents in soybean. *Indian Journal of Plant Physiology*, 21(3), pp.312–317. doi:10.1007/s40502-016-0242-3.

Hashemi, S.A., Madani, S.A. and Abediankenari, S., 2015. The review on properties of Aloe vera in healing of cutaneous wounds. *BioMed Research International*, *2015*(1), p.714216.. doi:10.1155/2015/714216.

Iravani, S., 2011. Green synthesis of metal nanoparticles using plants. *Green Chemistry*, 13(10), pp.2638–2650. doi:10.1039/c1gc15386b.

Jettanacheawchankit, S., Sasithanasate, S., Sangvanich, P., Banlunara, W. and Thunyakitpisal, P., 2009a. Acemannan stimulates gingival fibroblast proliferation; expressions of keratinocyte growth factor-1, vascular endothelial growth factor, and type I collagen; and wound healing. *Journal of Pharmacological Sciences*, 109(4), pp.525–531. doi:10.1254/jphs.08204FP.

Jettanacheawchankit, S., Sasithanasate, S., Sangvanich, P., Banlunara, W. and Thunyakitpisal, P., 2009b. Acemannan stimulates gingival fibroblast proliferation; expressions of keratinocyte growth factor-1, vascular endothelial growth factor, and type I collagen; and wound healing. *Journal of Pharmacological Sciences*, 109(4), pp.525–531. doi:10.1254/jphs.08204FP.

Kanneganti, A., Venkateswara Rao, K., Sai Priya, G., Anil Kumar, K., Venkateswara Rao, K. and Bykkam, S., 2014. Bio-Synthesis of Cerium Oxide Nanoparticles using Aloe Barbadensis Miller Gel. *International Journal of Scientific and Research Publications*, 4(6). Pp.641-652

Khatana, C., Kumar, A., Alruways, M.W., Khan, N., Thakur, N., Kumar, D. and Kumari, A., 2021. Antibacterial potential of zinc oxide nanoparticles synthesized using Aloe vera (L.) Burm.f.: A green approach to combat drug resistance. *Journal of Pure and Applied Microbiology*, 15(4), pp.1907-1914. doi:10.22207/JPAM.15.4.12.

Kim, K., Chung, M.H., Park, S., Cha, J., Baek, J.H., Lee, S.Y. and Choi, S.Y., 2018. ER stress attenuation by Aloe-derived polysaccharides in the protection of pancreatic β-cells from free fatty acid-induced lipotoxicity. *Biochemical and Biophysical Research Communications*, 500(3), pp.797-803. doi:10.1016/j.bbrc.2018.04.162.

Koratala, A., Chandra, N.C., Rabiei, Y., Rezvani, Z. and Neshat, S., 2023. Aloe vera applications and Aloe vera-based nanomaterials. *Journal of Renal Endocrinology*, 9, p.e22063. doi:10.34172/jre.2023.22063.

Kumar, P.P.N.V., Shameem, U., Kollu, P., Kalyani, R.L. and Pammi, S.V.N., 2015. Green synthesis of copper oxide nanoparticles using aloe vera leaf extract and its antibacterial activity against fish bacterial pathogens. *BioNanoScience*, 5(3), pp.135–139. doi:10.1007/s12668-015-0171-z.

Kundu, D., Hazra, C., Chatterjee, A., Chaudhari, A. and Mishra, S., 2014. Extracellular biosynthesis of zinc oxide nanoparticles using *Rhodococcus pyridinivorans* NT2: Multifunctional textile finishing, biosafety evaluation and in vitro drug delivery in colon carcinoma. *Journal of Photochemistry and Photobiology B: Biology*, 140, pp.194–204. doi:10.1016/j.jphotobiol.2014.08.001.

Lakshmi, V., Jeeva, R., Sharath, M.N., Chandraprabha, E., Neelufar, H.A. and Patra, M., 2012. Synthesis, characterization, and evaluation of antimicrobial activity of zinc oxide nanoparticles. *Journal of Biochemical Technology*, 3(5), pp.51–54.

Li, X., Xu, H., Chen, Z.S. and Chen, G., 2011. Biosynthesis of

nanoparticles by microorganisms and their applications. *Journal of nanomaterials*, *2011*(1), p.270974. doi:10.1155/2011/270974.

Maensiri, S., Laokul, P., Klinkaewnarong, J., Phokha, S., Promarak, V. and Seraphin, S., 2008. Indium oxide (In2O3) nanoparticles using Aloe vera plant extract: Synthesis and optical properties. *J Optoelectron Adv Mater*, *10*(3), pp.161-165.

Malik, S., Niazi, M., Khan, M., Rauff, B., Anwar, S., Amin, F. and Hanif, R., 2023. Cytotoxicity study of gold nanoparticle synthesis using aloe vera, honey, and gymnema sylvestre leaf extract. *ACS Omega*, 8(7), pp.6325–6336. doi:10.1021/acsomega.2c06491.

Misawa, E., Tanaka, M., Nomaguchi, K., Yamada, M., Toida, T., Takase, M., Iwatsuki, K. and Kawada, T., 2008. Administration of phytosterols isolated from Aloe vera gel reduces visceral fat mass and improves hyperglycemia in Zucker diabetic fatty (ZDF) rats. *Obesity Research and Clinical Practice*, 2(4), pp.239–245. doi:10.1016/j.orcp.2008.06.002.

Mittal, A.K., Chisti, Y. and Banerjee, U.C., 2013. Synthesis of metallic nanoparticles using plant extracts. *Biotechnology advances*, *31*(2), pp.346-356. doi:10.1016/j.biotechadv.2013.01.003.

Mohamed, N. and El-Masry, H.M., 2020. Aloe Vera gel extract and sunlight-mediated synthesis of silver nanoparticles with highly effective antibacterial and anticancer activity. *Journal of Nanoanalysis*, 7(1), pp.73–82. doi:10.22034/jna.2020.1884807.1176.

Muthu, K., Rini, S., Nagasundari, S.M. and Akilandaeaswari, B., 2021. Photocatalytic reduction and antioxidant potential of green synthesized silver nanoparticles from Catharanthus roseus flower extract. *Inorganic and Nano-Metal Chemistry*, 51(4), pp.579–589. doi:10.1080/24701556.2020.1799404.

Nalini, S.P. and Kay, V., 2020. Green synthesis of silver and gold nanoparticles using aloe vera gel and determining its antimicrobial properties on nanoparticle-impregnated cotton fabric. *Journal of Nanotechnology Research*, 02(03). doi:10.26502/jnr.2688-85210015.

Narayanan, M., Natarajan, R.K., Sekar, D.J.G., Paramasivan, R., Srinivasan, B., Ahmad, Z. and Khan, F.S., 2023. Enriched biological activity of copper oxide nanoparticles derived from Aloe vera extract. *Biomass Conversion and Biorefinery,* 23, p.4589. doi:10.1007/s13399-023-04589-9.

Nithya, A., Rokesh, K. and Jothivenkatachalam, K., 2013. Biosynthesis, characterization and application of titanium dioxide nanoparticles. *Nano Vis*, *3*(3), pp.169-174.

Ovais, M., Khalil, A.T., Islam, N.U., Ahmad, I., Ayaz, M., Saravanan, M., Shinwari, Z.K. and Mukherjee, S., 2018. *Applied Microbiology and Biotechnology,* 18, p.146. doi:10.1007/s00253-018-9146-7.

Pradhan, B., 2023. Phytochemistry, pharmacology, and toxicity of *aloe vera*: a versatile plant with extensive therapeutic potential. *Plant Archives*, 23(2), p.056. doi:10.51470/PLANTARCHIVES.2023.v23.no2.056.

Purushotham, B., Surendra, B.S., TR, S.S. and Prashantha, S.C., 2021. Eco-friendly synthesis of CeO2 NPs using Aloe barbadensis Mill extract: Its biological and photocatalytic activities for industrial dye treatment applications. *Journal of Photochemistry and Photobiology*, *7*, p.100038. doi:10.1016/j.jpap.2021.100038.

Rabiee, N., Bagherzadeh, M., Kiani, M. and Ghadiri, A.M., 2020. *Rosmarinus officinalis* directed palladium nanoparticle synthesis: Investigation of potential antibacterial, antifungal, and Mizoroki-Heck catalytic activities. *Advanced Powder Technology*, 31(4), pp.1402–1411. doi:10.1016/j.apt.2020.01.024.

Rajakumar, G., Rahuman, A.A., Roopan, S.M., Khanna, V.G., Elango, G., Kamaraj, C., Zahir, A.A. and Velayutham, K., 2012. Fungus-mediated biosynthesis and characterization of TiO_2 nanoparticles and their activity against pathogenic bacteria. *Spectrochimica Acta - Part A: Molecular and Biomolecular Spectroscopy*, 91, pp.23–29. doi:10.1016/j.saa.2012.01.011.

Ramírez, O., Pomareda, F., Olivares, B., Huang, Y.L., Zavala, G., Carrasco-Rojas, J., Álvarez, S., Leiva-Sabadini, C., et al., 2024. *Aloe vera* peel-derived nanovesicles display anti-inflammatory properties and prevent myofibroblast differentiation. *Phytomedicine*, 122. doi:10.1016/j.phymed.2023.155108.

Rao Kandregula, G., Ganapathi Rao, K., Ashok, C., Venkateswara Rao, K., Shilpa Chakra, C. and Tambur, P., 2015. Green Synthesis of TiO_2 Nanoparticles Using *Aloe vera* Extract. Available from: https://www.researchgate.net/publication/282502800.

Rehman, A. and Minhas, A.S., 2021. Green Route Synthesis of Copper Oxide Nanoparticles Against MCF-7 Cell Line (Breast Cancer). *NUST Journal of Natural Sciences*, *6*(1).

Sangeetha, G., Rajeshwari, S. and Venckatesh, R., 2011. Green synthesis of zinc oxide nanoparticles by *Aloe barbadensis miller* leaf extract: Structure and optical properties. *Materials Research Bulletin*, 46(12), pp.2560–2566. doi:10.1016/j.materresbull.2011.07.046.

Sargazi, S., Laraib, U., Er, S., Rahdar, A., Hassanisaadi, M., Zafar, M.N., Díez-Pascual, A.M. and Bilal, M., 2022. *Nanomaterials,* 12, pp.1102. doi:10.3390/nano12071102.

Sarkar, D.K., Selvanathan, V., Mottakin, M., Islam, M.A., Almohamadi, H., Alharthi, N.H. and Akhtaruzzaman, M., 2023. Phytochemicals assisted green synthesis of copper oxide/cobalt oxide as an efficient electrocatalyst for oxygen evolution reaction. *International Journal of Hydrogen Energy,* 7, pp.042. doi:10.1016/j.ijhydene.2023.07.042.

Sharma, S., Kumar, K., Thakur, N., Chauhan, S. and Chauhan, M. S. 2020. The effect of shape and size of ZnO nanoparticles on their antimicrobial and photocatalytic activities: A green approach. *Bulletin of Materials Science*, 43(1), pp.1-11. doi.org/10.1007/s12034-019-1986-y.

Shetty, A. N., S., K., Desai, K. K. and Patil, S. C. 2022. Green combustion synthesis of CeO2 nanostructure using Aloe vera (L.) Burm f. leaf gel and their structural, optical, and antimicrobial applications. *BioNanoScience*, 12(3), pp.757-765. doi.org/10.1007/s12668-022-01001-0.

Singh, J.,and Dhaliwal, A. S. 2019. Novel green synthesis and characterization of the antioxidant activity of silver nanoparticles prepared from *Nepeta leucophylla* root extract. *Analytical Letters*, 52(2), pp.213–230. doi.org/10.1080/00032719.2018.1454936.

Song, J. Y., Jang, H. K.,and Kim, B. S. 2009. Biological synthesis of gold nanoparticles using Magnolia kobus and Diopyros kaki leaf extracts. *Process Biochemistry*, 44(10), pp.1133–1138. doi.org/10.1016/j.procbio.2009.06.005.

Tabandeh, M. R., Oryan, A. and Mohammadalipour, A. 2014. Polysaccharides of Aloe vera induce MMP-3 and TIMP-2 gene expression during the skin wound repair of rats. *International Journal of Biological Macromolecules*, 65, pp.424–430. doi.org/10.1016/j.ijbiomac.2014.01.055.

Talukdar, D., Talukdar, P., Luwang, A.D., Sarma, K., Deka, D., Sharma, D. and Das, B. 2023. Phytochemical and nutrient composition of Aloe vera (Aloe barbadensis Miller) in an agro-climatic condition of Mizoram, India. *Asian Journal of Dairy and Food Research*, 17, pp.1-11. doi.org/10.18805/ajdfr.dr-2047.

Tavakoli, S., Kharaziha, M. and Ahmadi, S. 2019. Green synthesis and morphology dependent antibacterial activity of copper oxide nanoparticles. *Journal of Nanostructure*, 9(1), pp.163–171. doi.org/10.22052/JNS.2019.01.018.

Vélez, E., Campillo, G., Morales, G., Hincapié, C., Osorio, J.,and Arnache, O. 2018. Silver nanoparticles obtained by aqueous or ethanolic Aloe vera extracts: an assessment of the antibacterial activity and mercury removal capability. *Journal of Nanomaterials*, 28, pp.1-11. doi.org/10.1155/2018/7215210.

Wu, X., Yin, S., Zhong, J., Ding, W., Wan, J. and Xie, Z. 2012. Mushroom tyrosinase inhibitors from Aloe barbadensis Miller.

Fitoterapia, 83(8), pp.1706-1711. doi.org/10.1016/j.fitote.2012.09.028.

Xiang, H., Cao, F., Ming, D., Zheng, Y., Dong, X., Zhong, X., Mu, D. and Li, B., 2017. Aloe-emodin inhibits Staphylococcus aureus biofilms and extracellular protein production at the initial adhesion stage of biofilm development. *Applied Microbiology and Biotechnology*, 101(17), pp.6671–6681. doi.org/10.1007/s00253-017-8403-5.

Ying, S., Guan, Z., Ofoegbu, P. C., Clubb, P., Rico, C., He, F. and Hong, J. 2022. doi.org/10.1016/j.eti.2022.102336.

Zharov, V.P., Kim, J. W., Curiel, D. T. and Everts, M. 2005. Self-assembling nanoclusters in living systems: application for integrated photothermal nanodiagnostics and nanotherapy. *Nanomedicine: Nanotechnology, Biology, and Medicine*, 1(4), pp.326-345. doi.org/10.1016/j.nano.2005.10.006.

SN Computer Science (2025) 6:270
https://doi.org/10.1007/s42979-025-03808-6

REVIEW ARTICLE

Predictive Analytics of Crime Data in Social Media: A Systematic Review, Incorporating Framework, and Future Investigation Schedule

Monika[1] · **Aruna Bhat**[1]

Received: 28 June 2024 / Accepted: 15 February 2025
© The Author(s), under exclusive licence to Springer Nature Singapore Pte Ltd. 2025

Abstract
Social media is a tool to share ideas, knowledge, and information with a wide group of people. Some people misuse the social networking site for criminal activities. The systematic literature review (SLR) focused on the predictive analysis of crime data in social media. The review is presented on the basis of knowledge of current implications and predictive analysis approaches that have been presented between 2014 and 2024. The SLR includes the analysis and evaluation of large pre-existing technologies to innovate with new information about predictive analysis. Many technologies like machine learning, link analysis, sentimental analysis, and deep learning are discussed in the crime data prediction survey. Also, the types of social media crimes, various methods of social media crime prediction, and the analysis based on tools utilized, assessment measures, and their application domain are devised. Then, the challenges identified based on the review, future scope and the general framework for crime prediction are provided for the design of novel predictive Analysis of crime data by fulfilling the challenges faced by the existing method.

Keywords Crime prediction technique · Link analysis · Machine learning · Sentimental analysis · Data mining

Introduction

Social media is a computer-based platform used for sharing ideas, thoughts, and information by giving instant electronic communication contact [1]. More people of all ages and genders are developing online social media identities to participate in the virtual world. Many have thousands of friends and followers across multiple profiles. At the same time, fake profiles are created to threaten, bully, harass, and stalk people [2]. These are commonly reported crimes on social media. Due to the development of technology in recent years, criminals are modifying intelligent methods to perform crimes. As a result, the number of crimes is increasing and is becoming a major issue in many countries [3–6]. The frequency of crime increases with time [7].

Technology assists people in building an unchallenging lifestyle, which makes a pulse to improve criminals' crime techniques. The internet and the world of associations are the best places to observe crime in addition to the streets [8–10]. It is considered critical to invent and modify methods that aid in intelligent invention and take precautions against these crimes [11, 12]. The criminal acts begin with through-fare crimes and progress to massive dread crimes that, understandably, harm large databases and systems [13]. The crime can be network attacks, hacking, network intrusion, cyber fraud, deceptive information, etc. The invention and research of relevant designs and laws from a massive amount of data appear as a functional instrument for crime prediction [14–16]. There are numerous intelligent technologies for preventing criminal activities, such as examining the criminal's documents and facts and stopping future crimes. Developing an effective crime predictive analysis tool that predicts criminal designs quickly and accurately for future crime pattern detection is a difficult task for researchers.

The tools for crime prediction analysis are recognized as the most important area of analysis that uses data mining methods. Most errors occur when individuals are overworked; computers have been proved to be more efficient and accurate than humans [17–22]. The information from computers is more appropriate and less expensive than appointing and training individuals to collect and analyze

✉ Aruna Bhat
aruna.bhat@dtu.ac.in

Monika
monika.siwaliya@gmail.com

[1] Department of Computer Science & Engineering, Delhi Technological University, New Delhi 110042, Delhi, India

Published online: 11 March 2025

crime data [23]. The technique can assist the investigator without considering experience. The techniques not only assist them in following and resolving crimes but are also used for the analytical prediction of crimes [24]. There are some predictive techniques like data mining approach, ensemble approach, machine learning, deep learning, and clustering that operate on concealed data and can take predictive analysis of updates [25, 26]. The research focuses on obtaining an intuition of the methods for predictive crime data mining [27, 28]. Previously, a survey on predictive analytic techniques was managed with only five techniques that covered a small scope of data mining [29–31].

The systematic review studies on the basis of different technologies that arise to predict the crime data in social media. The prediction technique is done through different methods such as machine learning approach, link analysis, text mining, neural network and sentimental Analysis. These have advantages and disadvantages with respect to the current availability of technologies. The review focused on the techniques and methods for the predictive Analysis of crime data. The research is organized as: Sect. "Systematic review of predictive Analysis of crime data" shows the systematic review of predictive Analysis of crime data, including the research sources and techniques. Sect. "Types of Social media crimes" demonstrates the different types of social media crimes and their comparison. Sect. "Review of Existing Criminal Analysis Techniques" shows the architecture of crime predictive Analysis along with various mechanisms. Sect. "Analysis of Crime Prediction" provides the analysis of the prediction technique based on performance measures and tools utilized. Sect. "Applications" presents the application domain, and Sect. "Challenges" presents the challenges faced by crime data prediction techniques. Sect. "Future scope" demonstrates the future scope of crime data prediction and the general structure of Predictive Analysis of crime data in Sect. "General Structure of Crime Prediction Technique". Finally, the review is concluded in Sect. "Conclusion".

Systematic Review of Predictive Analysis of Crime Data

Crime predictive analytics is a boring procedure for the police or the investigation team to complete that work. The traces left by the criminal is utilized as a clue to recognize the criminal. To create a database related to the particular crimes, a vast procedure is taken before generating the data. There are three steps to finalize the database used for predictive analysis: identification, screening, and eligibility. The conventional methods of criminal data analysis use the uncomplicated process for the processing. There are many techniques for the analysis of the crime and gathering of data based on the information about that crime. The information gathering also acquires more data from the information specified by the resident people. The forecasting is used for finding the crimes by integrating the number of cops into the core areas that are recognized by the system. Figure 1 shows the systematic review of predictive analysis of crime data [32].

Inclusion and exclusion are based on the needs of the review, and the detailed inclusion and exclusion criteria are:

Inclusion Criteria: The research articles for the predictive Analysis of crime data in social media are acquired through various databases using the search terms named keywords such as predictive Analysis, crime data in social media, machine learning, deep learning, and crime prediction. Thus, using a keyword-based search, a total of 4000 articles were gathered for the systematic review of the recently introduced predictive analysis of crime data.

Exclusion Criteria: The research gathered 4000 papers, which were then examined depending on the year of publication, with 1351 articles published before 2014 being removed. Then, 1106 of the selected 2649 articles were deleted since they included a duplicate database. After that, 871 articles were deleted from the 1543 articles that were not related to the predictive analysis of crime data, and the remaining 672 articles were deleted. Finally, 89 articles were chosen based on the title, with 65 articles being approved based on the abstract. Figure 1 shows the systematic review process of predictive crime data.

Risk of Bias: After the exclusion criteria, the risk of bias is evaluated for the remaining research articles related to the predictive analysis of crime data. The risk of bias is evaluated in review-based research to demonstrate transparency and divergence from the proposed predictive Analysis of crime data. The risk of bias is assessed using crime prediction, criminal activity, and crime analysis techniques. All of the chosen publications use one of the three methodologies indicated above, demonstrating the research's transparency without deviation.

Research Screening

It is important that literature review coverage be selected from an appropriate database for the most efficient outcome by increasing the probability of getting the most applicable articles. Figure 2 shows the sources of e-journals utilized for the acquisition of the research articles related to the predictive Analysis. To create this review, huge data sets from e-journals like.

- IEEE Explore (http://ieeexplore.ieee.org)
- ACM Digital Library (www.acm.org/dl)
- Science Direct (www.sciencedirect.com)

Fig. 1 Systematic review of predictive Analysis of crime data

Fig. 2 Research sources

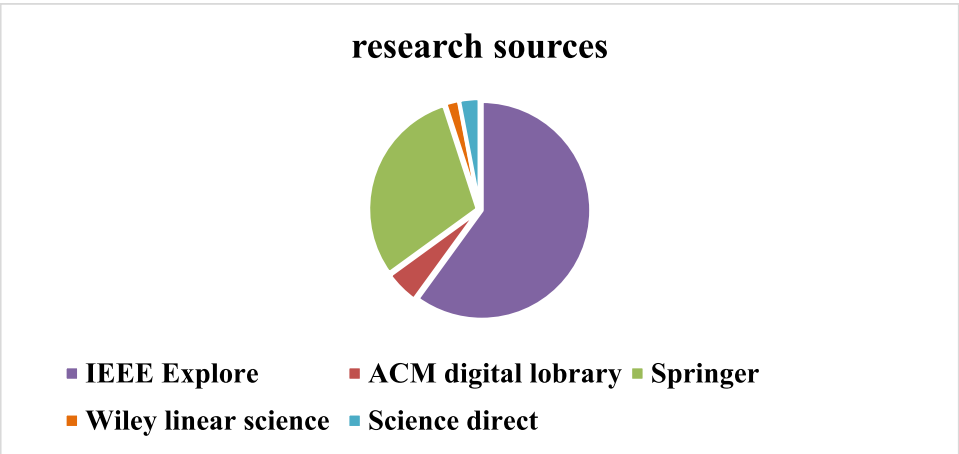

- Springer (www.springerlink.com)
- Wiley Inderscience (http://onlinelibrary.wiley.com)

Research String

Most of the searches include predictive crime analysis,

which contains vast and broad techniques. In the research, most of the extracted content from the journals is utilized. The Table 1 gives the research procedure from different electronic sources.

Types of Social Media Crimes

Social media crimes can encompass a range of illegal activities conducted through or facilitated by social media platforms. Critical crimes are committed on social media platforms such as Twitter, Face book, and Instagram. Social media crime is the most incredible activity on the internet, in which users spend more time on social media than any other work. In this situation, criminals are using their space for their own motives. NW3C reports six crimes: burglary, social engineering and phishing, malware, identity theft, cyber stalking, and cyber casing. In the case of social network burglary, the criminals concentrated on potential targets. Users share their current activities and their personal enjoyment through social media, but criminals follow this information to find an easy way to get the target [33]. Many robberies happen through information related to posts on social media, which provide details that are easy for criminals to access.

Social media phishing involves the manipulation of individuals to gather personal information, often related to financial matters, which is then exploited by criminals for illicit activities. Cybercriminals employ various tactics, such as phishing emails and fraudulent social media profiles, to extract valuable data from unsuspecting users. Despite warnings, some users fall victim to these deceptive schemes, resulting in their devices becoming infected with viruses and malware without their knowledge [34]. Identity theft relies on the unlawful acquisition of personal data to perpetrate criminal activities, while cyber-stalking exploits the victim's distress to gather information. Geo-tagging, a popular feature among social media users, facilitates cyber-casing by revealing location information. Additionally, social media-related crimes extend to credit card fraud, cyber intrusions, data breaches, and disaster fraud, where criminals exploit personal information obtained online for fraudulent purposes [35]. These crimes underscore the importance of vigilance and security measures in safeguarding personal data online.

There are numerous crimes committed through social media, including violent crimes, murder crimes, property crimes, organization-based crimes, gun-related crimes, sexual crimes, and robbery crimes. Table 2 represents the various crimes presented and differentiated on the basis of various law-enforcement agencies [36, 37].

Figure 3 portrays the different social media crimes based on the number of occurrences. Thus, social media is a relatively new form of human communication technology that has grown in recent years.

As a result, effective techniques are required to prevent these forms of social media crimes. The researchers

Table 1 Research procedure from different electronic sources

Sl. no	Electronic resources	Research string
1	ieeexplore.ieee.org	Social media crime data predictive techniques
2	www.acm.org	Predictive Analysis of crime data
3	www.sciencedirect.com	Crime data for predictive Analysis
4	www.springerlink.com	Predictive Analysis of Crime data in social media
5	www.wiley.com	Social media crime and its prediction

Table 2 Social media crimes and law enforcement

S. no	Social media crimes	Local law enforcement
1	State against crimes	Governor, Assaulting president
2	Crime against the public tranquillity	Election percolations
3	Against Religion	Outrage religious assembly
4	Against the property	Robbery, extortion and criminal breach of trust
5	Against Organization	Attempt to cause miscarriage
6	sexual crime	Sexual assault
7	Murder related	Attempt to suicide, kidnapping, abducting and rape
8	Drugs	Drug trafficking
9	Forged Images	Digital impersonation and defamation
10	Profile Pictures	Online impersonation
11	Nudity	Revenge porn

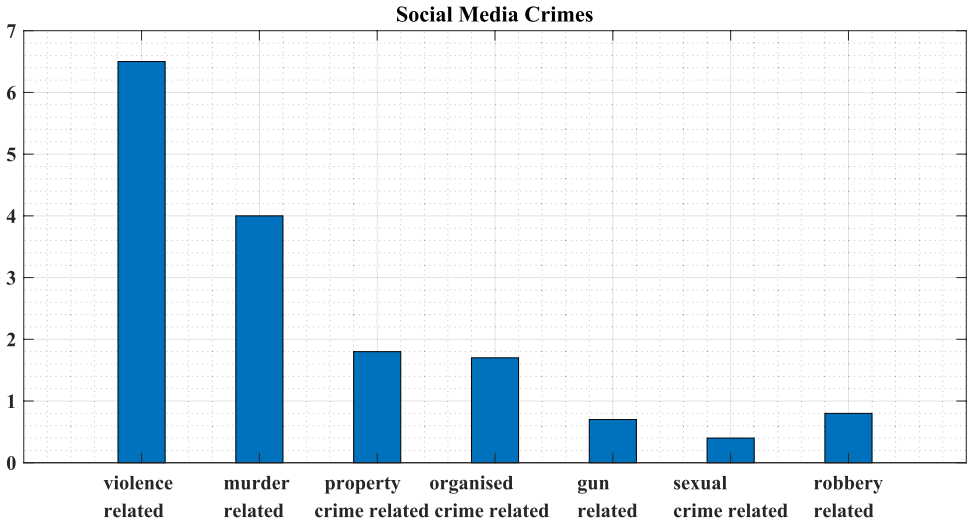

Fig. 3 Different social media crimes

introduced many strategies for crime prediction and Analysis. The review of such methods is used to discover research gaps and build a novel methodology that addresses the issues that the existing methods present.

Review of Existing Criminal Analysis Techniques

The criminal Analysis of the research is categorized into Criminal analysis based on various prediction techniques, Criminal Analysis based on data mining techniques and Criminal Analysis based on sentimental Analysis. Further, the criminal Analysis based on various prediction techniques is divided into five categories: text content and NLP-based technique, crime patterns and evidence-based technique, spatial and geo-location-based technique, prisoner-based technique, and communication-based technique, as illustrated in Fig. 4.

Criminal Analysis Methods for Crime Data Prediction

There are so many predictive criminal analyses derived to forecast social media crimes. Here, the most efficient

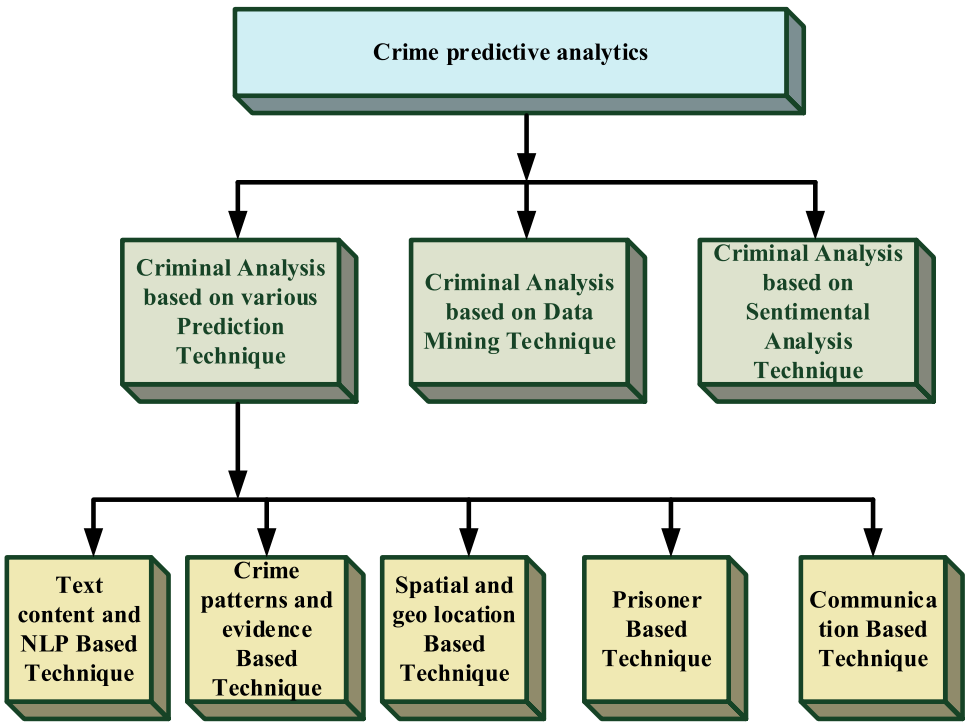

Fig. 4 Types of Criminal Analysis Techniques

existing methods designed to analyze the predicting techniques of crime data are reviewed. They include text content and NLP-based approaches, crime pattern and evidence-based methods, special and geo-location-based methods, prisoner-based predictive Analysis of crime, and communication-based predictive Analysis of crime data.

Liao et al. [33] proposed a crime predictive analysis using Bayesian. The model incorporates data from geographical and victim characteristics, as well as crime properties classified into two categories: private and public. They use a technique known as discrete distance decay to demonstrate a geographical profile, which is considered to be possible in predictive crime. The combination of geographical profile and Bayesian yields highly accurate predictions. While the integration of geographical profiles with Bayesian provides accurate predictions, it might be limited to areas without well-defined geographical patterns. The Bayesian model was computationally intensive while analyzing large datasets, which limits its scalability and real-time applicability.

Joshi A et al. [6] suggested a short-term predictive analysis of crime data with a time horizon of one month, in which they used five different statistical datasets for the prediction. These datasets are then compared with different statistical analysis techniques, and it is concluded that a seasonal pattern exists in crime prediction. General crimes are more prevalent during the summer due to the increased use of social media, and robberies exist due to seasonal pressures with unemployment in the winter. The seasonal patterns may fail to capture complex features of crime dynamics while considering the rapidly changing environments during unusual events.

Chen et al. [38] suggested a short-term crime prediction technique integrated with an autoregressive moving average system, which is used in time-sequence analysis to predict future crimes. The predictive Analysis of crime prediction using the regression analysis method compared three types of crime such as assault, violence, and homicide. These three models give the exact same performance. Over-fitting of the model leads to poor performance while using unknown data, wherein the crime patterns evolve over time.

Dandannavar et al. [39] presented a computational architecture for crime predictive Analysis with a clustering technique. The technique concentrates on the non-availability of non-negative samples in a set of information. The data set is divided into small data sets with the help of k-means clustering, and the labelled classes in the dataset are hotspot classes and non-hotspot classes. They are named with the help of the rate of crime. Clustering-based crime prediction may not capture the entire complexity of crime patterns, whereas crime hotspots evolve over time.

Wang et al. [40] suggested an SVM-based prediction system for the Analysis of crime data. The database used in this model is collected from criminal justice information. A multi-layer neural network is used to train the model. SVM provides performance similar to that of a multi-layer neural network. These two models are integrated with the logistic regression technique to get a highly efficient prediction and better performance. The model was computationally expensive while analyzing large datasets that require complex kernels or hyper-parameters.

Some kinds of cyberbullying have sadly made their way into society and the Internet. It's more important than ever to figure out how to prevent and overcome this problem. They used deep learning techniques to detect cyberbullying incidents automatically. The identification of hostile text was their major responsibility in cyberbullying detection. Fake taxis are dragging down society's safety today, which will have an influence on public transportation's economics. The authors used the candidate selection model and candidate-refined model to construct an intelligent information system to address this issue. To determine the type of crime, analysts must spend a significant amount of time searching for data to determine whether a certain incident falls into a recognized model. If the crime does not fit into any of the existing models, the information must be classified as a new pattern. Once a crime has been identified, it can be prevented, forecasted, and predicted using models.

Text Content and NLP Based Method Criminal Analysis

Text content and NLP are methods used for the predictive analysis of crime data. Sharma M [41] suggested a method that represents a zero-crime community. To analyze doubtful criminal cases, they focused on the importance of data mining and developed a useful tool. Furthermore, an enhanced decision tree algorithm was employed to identify doubtful e-mails pertaining to illegal activity. To create an efficient and fast decision tree in terms of information entropy, an updated ID3 algorithm with an increased characteristic selection technique and an assigned-significant factor, which is clearly formed through a training dataset, presents a new technology with the integration of an updated ID3 classification algorithm and an enhanced feature recognition method for enhanced method accuracy. The ID3 algorithm was efficient for simple decision tree structures. While considering a large dataset with a higher number of features, it might not capture complex features between variables due to its incapability in handling numerous features.

Hamdy et al. [42] proposed a method with respect to people's communication with public networks and the utilization of the internet on mobile devices, such as Google locations and call logs. The work explains a technique for identifying doubtful characters on the basis of social networks and suggests a new technique using social communication with people to assist crime prediction analysis in making efficient and fast decisions. The model was computationally expensive

for large-scale social network analysis when analysed with real-time data streams.

Tam et al. [43] developed an NLP-based crime prediction using the Tweet designed by the hybrid deep learning model. The designed model utilized multi-modal data for predicting the crime using semantic knowledge-based learning. The Analysis depicts the superiority of the model based on assessment measures, and hence, the designed model can predict crime more accurately from the unsupervised learning strategy. The model was limited by the quality and quantity of available tweet data, which may vary significantly across different regions and time periods.

Thus, NLP and text content-based predictive Analysis of crime data may efficiently analyse data for all types of multidimensional and complex data landscapes. Furthermore, it performs a variety of text analysis activities to represent the document for crime prediction. The most difficult aspect of NLP-based criminal prediction is analysing text data, which can have different meanings in different situations.

Crime Patterns and Evidence Based Criminal Analysis Method

In crime pattern and evidence-based predicting approaches, some of the prior methods are detailed in this sub-section. Bogahawatte and Adikari [44] developed a technique that focuses on the use of data mining methods, clustering, and classification for efficient crime investigation and criminal recognition by creating a model called an Intelligent Crime Investigation System (ICSIS) to recognize based on crime scene evidence gathered from the location where the crime occurred. Each crime is carried out in a unique manner or style due to the use of clustering to anticipate the method of crime. The database is trained using a supervised learning method. The technique involves growing a number of agents for predictive analytics of crime. Detecting the criminal's doubt on the basis of Naïve Bayes classifier acquired highly probable suspects from the data set of crime. The reliance on crime scene evidence was limited by the availability and quality of data, which may vary significantly across different cases and jurisdictions.

Agarwal et al. [45] presented a method using the rapid miner tool for forecasting the number of crimes and the expectation of the crime rate using various methods. A K-Means Clustering algorithm is used for the predictive Analysis of the crime. The primary goal of criminal investigation is to extract crime methods, make analytic predictions based on the spatial distribution of current information, and predict crime. The number of clusters (k) that is selected has a substantial influence on the model's accuracy; however, it was difficult to find the ideal value for k.

Kiani et al. [46] suggested a predictive analysis for crime work with respect to the clustering and classification methods. The process includes the collection of crime techniques by crime predictive survey on the information obtained, forecasting of crime on the spatial spread of current information, and crime prediction. They presented a system in which the analytic forecasting through the minimization of outlier recognition operator frame work is done with the Genetic Algorithm. Here, the choice of genetic operators (e.g., crossover, mutation) can significantly impact the performance of the algorithm, and there was no one-size-fits-all approach.

Satyadevan et al. [47] presented a technique to display a greater chance for predictive Analysis of crime events and to imagine crime-concentrated zones. They are not only focused on the events of crime; they concentrate mostly on the factors which affect crime every day. Using Naïve Bayes, Logistic Regression, and SVM classifiers, the categorization of crime patterns and the factors of crime were employed. The technique includes a pattern identification step, which is used to detect the architectural designs in crime by utilizing the Apriori Algorithm. The dependency on a single pattern identification technique may limit the prediction utilizing different types of crime data.

Boukabous et al. [19] designed a crime prediction based on the video evidence using the deep learning model. The designed model identifies complex patterns missed by human surveillance and offers continuous monitoring compared to limited human attention spans. The automated detection of suspicious objects like firearms and weapons using the designed model has the potential for real-time threat alerts to authorities. The model failed to capture the complex features of human behaviour and the potential for deception or camouflage in video footage.

Thus, the prediction of the crime is based on the evidence gathered from the historical information, in which the present information is matched with the previous data that enables the identify the criminal, which is a time-consuming task. Here, the crime prediction is done automatically utilizing the current information and AI techniques based on machine learning and deep learning to forecast the criminal more effectively and in less time.

Spatial and Geo Location Based Criminal Analysis Method

Spatial and geo-location-based methods for the predictive Analysis of crime are detailed in this sub-section. Huang et al. [48] suggested a method based on a variety of techniques for criminal activity forecasting with respect to position-based social network communications. Due to this interactivity, they can gather data by utilizing geographical interactions and gathering data from the people. They conceive a functioning technique in which a sequence of characteristics is grouped from the Foursquare and Gowalla given in the San Francisco Bay zone. The design and events

of crime patterns are followed with respect to the geographical attributes. They are gathered from the map and examined to find the urban areas with greater crime. Using location-based social network documents, the crimes are tracked in urban areas. The distance between two points can be found by the Haversine formula, i.e., the place of crime and venue locations are valued and appear in the Google Maps API and OpenStreetMap. The dependence on location-based social network data was limited by privacy concerns and the availability of comprehensive data sets.

Ristea et al. [49] presented an executed dataset classification to forecast crime groups for various states in the United States of America. A real crime dataset is used in the suggested paper, which was gathered from socio-economic information from the 1990 US Census, law enforcement data from the 1990 US LEMAS survey, and crime data from the 1995 FBI UCR. The method has two different classifications, Naïve Bayesian and Decision Tree, for forecasting the category of crime for various states in the USA. The outcome of the system showed that the Decision Tree technique carried out the Naïve Bayesian method and got an enhanced outcome in forecasting the crime category for the USA. The choice of classification algorithm (Naïve Bayesian or Decision Tree) was suboptimal for certain types of crime data or relationships between variables.

Ioannidis et al. [50] designed a Spatial and regression modelling to investigate associations between these indexes and crime rates. The introduced model demonstrated the potential of using satellite data to analyze crime patterns for residential burglary and street theft. It Identified a link between built-environment density and crime rates in Stockholm, Sweden, by considering neighbourhood type and other social factors. The model was a cost-effective and objective way to analyze large geographic areas. The model was limited by the availability and quality of satellite data, which may vary significantly across different regions and time periods.

Thus, the spatial and geo-location-based predictive Analysis of the crime helps to locate the hotspot of the crime using the spatial and temporal data. In addition, the location for the next crime occurrence can also be employed using spatial and geo-location-based predictive Analysis.

Prisoner Based Predictive Analysis of Criminal Analysis

The prisoner-based technique is used for the predictive Analysis of crime. Sheehy et al. [51] proposed a study that focused on the mentally ill person, in which the person who has a mental illness was detected using their Social Security Number (SSN). Here, for the mentally ill person, the details related to the illness are provided by attaching criminal personal documents and their crime career documents related to social media. Thus, the criminals are divided into "high", "medium" and "low" level groups by considering the illness and crime data. These criminals can be differentiated from others who can cause harm, injury, and damage to their inmates. In addition, the categorization of mental illness into two parts, i.e., "referred" and "not referred," was employed. This is used to assist the guards in recognizing the people who are mentioned for the health check-up. The proposal suggested a result of the inmates who are mentally ill and those who are to be differentiated from the other inmates. The model may be biased towards individuals with a history of criminal activity because it overlooks the individuals with mental illness who have not been involved in crime.

The prisoner-based predictive Analysis employs the criminal behaviour of the mentally ill prisoners that provides treatment for the offender instead of getting incarceration. The information gathered from a single location is utilized for the detection of the mentally ill offender that provides inaccurate results while considering generalized techniques. Thus, the consideration of the data plays a crucial role in crime prediction.

Communication Based Predictive Analysis of Crime

For the predictive Analysis of crime, communication-based techniques are used to find immediate actions. Kamal Taha and Paul D. Yoo et al. [52] presented a forensic investigation technique for finding powerful people who were the cause of a criminal concern. The instant chiefs were recognized as a criminal group. Rectifying these powerful people can cause the robustness of the criminal group. The proposed technique builds on the methodology. They suggested a recent work called SIIMCO, which initially built the plot by showing the criminal group as a network on the basis of information about the crime. The model runs with respect to the generated networks. These networks display criminal organizations or crime documents. The apex indicates each and every criminal, and the link shows the connection link from one criminal to another. They work using some equations that calculate the rate of importance of each apex in the network with respect to all other apexes. Based on this system, they identify the immediate leaders as well as the weighted plot that attaches to the criminals and prepares them for subsequent procedures. Table 3 shows the advantages and disadvantages of the crime analysis based on prediction technique**.**

Crime Data Mining Technique for Predictive Analysis of Crime Data

Entity Extraction

Entity extraction recognizes the text, humans, tables, vehicles, and clothes on the basis of pattern recognition [53],

Table 3 Advantage and disadvantage of each crime based on prediction technique

Technique	Advantage	Disadvantage
Text content and NLP based method criminal analysis	This method leverages natural language processing (NLP) to analyse text content, such as social media posts, emails, or criminal records, providing insights into criminal behaviour and patterns	The accuracy of predictions heavily depends on the quality of the text data and the effectiveness of NLP algorithms. Challenges may arise with unstructured or ambiguous text, leading to inaccuracies in Analysis
Crime patterns and evidence-based criminal analysis method	This method relies on historical crime data and evidence to identify patterns and trends, enabling law enforcement to allocate resources effectively and prevent future crimes	Predictions based solely on past data may overlook emerging or evolving criminal trends. Moreover, biases in historical data may perpetuate inequities in law enforcement practices if not properly addressed
Spatial and geo location based criminal analysis method	Utilizing spatial and geo-location data allows for the identification of crime hotspots and the allocation of resources to high-risk areas	Focusing solely on geographic factors may overlook other important socio-economic and demographic influences on crime
Prisoner based predictive Analysis of criminal Analysis	Analysing data from incarcerated individuals can provide insights into recidivism rates and factors contributing to criminal behaviour	Predictions based on prisoner data may not generalize to the broader population, as factors influencing criminal behaviour vary widely
Communication based predictive Analysis of crime	Analysing communication data, such as phone calls or online interactions, can reveal networks of criminal activity and facilitate early intervention	Privacy concerns and legal constraints may limit access to communication data. Additionally, false positives and misinterpretations of communication patterns can lead to wrongful accusations or infringements on civil liberties

which is the process of collecting selected data from text data. The programmes coded by the hackers were recognized by computer forensics by gathering the same coding for individual groups. The system requires a large number of data sets to produce a better result. Machine learning is the core algorithm utilized in entity extraction and to gather derived patterns. Statistical approaches and rule-based approaches are also used [54] to identify entities using a rule called lexical hand-crafted rules, and for finding the pattern occurrence, statistical-based systems are used [51]. The dependence on pattern recognition was limited by the complexity and diversity of natural language, which makes crime recognition difficult to accurately identify entities in unstructured text data.

Clustering Technique

The clustering technique is used to reduce or increase the likeness in the interclass by gathering information in the class with respect to the properties of data. The method is used in predictive crime analysis to aid in the identification of criminals and the development of a set of plans for detecting crimes [55]. Also, use various measurements for getting distances between objects, like the Euclidean distance, Manhattan distance, and Murkowski distance. In the cluster group, different algorithms are there for making the information into partitions with respect to the demands. The main approaches in clustering techniques are the density-based approach, the constraint-based approach, and the model-based approach for crime prediction. The accuracy of the model is highly dependent on the distance metric and clustering algorithm selection.

Association Rule Mining

Association rule mining is a rule used to find the frequent events in a dataset. In the event of a network attack, association mining rules play an important role. The technique was invented to examine the co-occurrences in the dataset and was also used to find the simultaneous occurrence of the data in a dataset. The association power is calculated on the basis of support, the information set having the applicability of rules, and the number of occurrences of information in transactions that carry different information. The model has struggled to capture the dynamics of evolving crime patterns while considering the rapidly changing environments or unusual events.

Sequential Pattern Mining

It is a technique for identifying network intrusions by determining the sequence of data occurrences in a given period of time. To achieve an efficient result, a large number of

structured datasets are required that were on the structured pattern for performing analysis and recognition. Ayres et al. [56] presented a technique that gives all probabilities of identifying the data transactions as fast as possible, in which a bitmap along with depth-first traversal was utilized. The model was limited by the availability and quality of structured datasets, and it was difficult to identify crime behaviour for certain types of crime data.

Deviation Detection

Deviation detection, otherwise known as outlier detection, examines the information from the dataset for an understandable distinction. For the detection of crime or fraud analysis, deviation detection plays a major role. Aggarwal proposed a technique based on evolution detection with respect to the selection of crossover and mutation techniques, in which a linear method was employed for the recognition of the large information set. They gave the output by a technique called the simulating mechanism [57]. The model has struggled to distinguish between genuine outliers and patterns that were simply unusual but not indicative of malicious activity.

Classification

The technique has a number of sections that have been defined previously. In the classification, the usual features are collected for the prediction of various crimes [58]. A classification scheme was used for forecasting crimes and recognizing the entities involved in crimes with a minimum time. Moreover, predefined training and testing of the data set with a forecasted output of defined accuracy was evaluated. The method focused on finding a group of rules from the given dataset with decision trees, naïve Bayes rules, and SVM [59]. In this, the choice of classification algorithm and feature selection techniques significantly impacts the accuracy of the model.

String Comparator

The string comparator is used to calculate the likeness of the information in a database with respect to the texture fields. Also, it provides deceptive information for the recognition of crime. The comparator output has two stings having a numerical value, and these processes need a high quantity of calculations [60]. The model faced challenges in capturing the complex features of human language and the potential for linguistic ambiguity or deception.

Analysis of Social Networks

The Analysis has a characteristic communication of nodes in the architecture of the social network. It recognizes the criminals by designing a network. These analyses help to analyze the framework of the dataset [61]. Centrality, degree, and density are the important technologies used in social network analysis. The degree is the number of nodes that are attached to other nodes. Centrality represents the node's importance in the framework. Density is the number of edges in a particular area with respect to the total number of edges. Techniques for crime data analysis include feature extraction, clustering analysis, classification process rules, and social network analysis. Table 4 shows the advantages and disadvantages of the crime data mining techniques**.**

Crime Prediction Using Sentimental Analysis

The crime prediction technique employs emotional Analysis, with the acquired dataset representing a collection of tweets from various people in different countries. The system can use this information to analyse and forecast crime. The method of combining crime data with Twitter data for crime forecasting requires a huge volume of data in the database. This data is available on the social networking platform. Geber [62] suggested a prediction model initially related to social media crimes. The system is used to find the pattern of crime with respect to the content of the tweet.

Table 4 Overall Advantage and disadvantages of crime Data mining based crime prediction

Technique	Advantage	Disadvantage
Entity extraction	Due to the Machine learning technique, the technology becomes easier	It needs a high amount of clean data for processing
Clustering	It can identify and recognize outlets by not considering the label data	The price for computing the technique to get effective output is high
Association rule mining	Support all over the technique	Utilized in the most accurate classification rules
Series pattern mining	It has more applications in many fields	It needs a high amount of structured information
Deviation detection	High application in the case of error finding	Hurdle in data dependency
Classification	The utilization of time is minimum	It required a full data set to train the model
String comparator	High accurate with respect to the numerical values	It can't identify the true leader also; the cost of computation is very high

To improve the performance of the system, the model uses convolutional historical data for the forecasting of crime. Also, employ the Dirichlet allocation procedure. It was the first study to analyse Twitter data related to social media crime data using the LDA method to correlate crime data in clusters. The output of these systems gives a worthless and efficient model. To assess the sentiment polarity of tweets, several systems have employed BiLSTM and feed-forward neural networks. Traditional RNNs can only process data in one way, with no consideration given to processing future data. The notion of bidirectional RNN was created to solve this restriction. Different hidden units operate as forward and backward layers in a bi-directional RNN, allowing it to explore the data in both ways. By merging bidirectional RNN with LSTM cells, bidirectional LSTM (Bi-LSTM) was created. In BiLSTM, the output of forward states is not used as an input for backward states and vice versa, preventing gradient explosion. BiLSTM is a variation of LSTM that is more effective than LSTM since it avoids the gradient explosion issue of LSTM. The goal of merging these two methodologies was to make use of BiLSTM and feed-forward neural networks' strengths. The classifier's accuracy for each sentiment class is greater. The findings revealed a link between both the crime patterns anticipated by Tweets and the actual criminal incidences reported. The study's biggest weakness was the lack of geo-tagged tweets, as more than half of Twitter users choose to keep their location hidden for privacy reasons. Using Google's open mapping, the effectiveness of the study was enhanced. The following works are related to sentimental Analysis in crime. The dependence on geo-tagged tweets was limited by privacy concerns and the availability of comprehensive data sets.

Wang et al. [63] proposed a method of crime data predictive Analysis based on real-time tweets from social media to forecast hit-and-run techniques in Virginia. In this case, the system model rejected news portals chosen based on human and collective data backed by those people. Chen et al. [38] introduce a sentimental analysis crime prediction using Twitter data along with the information from the weather data in KDE. It is used for forecasting the position and current time of the criminal. For the purposes of the study, time and weather data are restricted to a subset of data. The model has faced difficulty in capturing the complex interactions between weather conditions and crime patterns that were considered significant aspects for enhancing prediction accuracy.

S. Aghababaei and M. Makrehchi [64] proposed a facility for geo-tagging with the current location of the thief. The method analyses the relationship between the number of people on social media and the tweets generated. They concluded that it was impossible to determine the predictive Analysis without the use of the Twitter database. Like that, A. Almehmadi [51] introduced a systematic analysis of geographic techniques for the prediction of crime data with mobile population tweets. The central demerit of the system was that the studies went on without considering the tweet text data. Instead of that, it only concentrated on the location of the criminal by geo-location data. The used KDE was a geo-location-based method that could not be formed immediately. There were a number of crimes that persisted near the geo-location of the previous crime, and the number of people was different in different areas. The model was computationally expensive for large-scale spatial Analysis, when dealing with high-resolution geo-location data and complex statistical models.

Ristea et al. [65] presented a sentimental analysis of the database as crime-related tweets on the basis of the processing languages and sentimental word net. The model forecasts the crime with respect to the hate tweets, and it has an ability to find the crime subjectivity. It also uses machine learning techniques to improve the performance of sentimental Analysis. Siriaraya et al. [66] suggested a Nave Bayes algorithm-based crime prediction technique. SVM is used for getting the high entropy in the system to find the polarity of the sentimental Analysis. The system was effective, but it neglected the meaning of the tweets collected for the database. The data base collected was real-time tweets from the different countries and regions. The integration of BiLSTM with the feed-forward neural network helps to find the polarity of the tweet generated in the sentimental Analysis. Here, the non-consideration of significant attributes based on sarcasm, irony, or other forms of linguistic ambiguity degrades the performance of the model.

Spatio-temporal feature extraction from the social media data using the large language model (LLM) was designed by [67]. In this, the combined LLM and GNN-based embeddings were employed to predict future values of spatio-temporal variables. LLM-based knowledge representation was employed to generate embeddings for spatio-temporal data, capturing the semantic and contextual information. The designed model acquired an enhanced understanding of implicit spatiotemporal relationships in urban systems. Still, the computational complexity of the model was very high. The prediction of human event modelling using LLM was designed by [68] using extracting reasoning and insights from textual data. The Analysis demonstrates the forecasting accuracy of the model; still, the reliability was considered as the challenging aspect.

Advantages: Sentiment analysis provides insights into public perceptions and attitudes towards crime, criminals, and law enforcement. Analyzing sentiment expressed in news articles, social media posts, and other textual data sources can help law enforcement agencies understand public opinion, which may inform their strategies and decision-making processes. Sentiment analysis can aid criminal investigations by identifying individuals or groups expressing

hostile or threatening sentiments online. Law enforcement agencies can prioritize these cases for further investigation, potentially preventing violent acts or other criminal activities.

Disadvantages: Sentiment analysis algorithms may exhibit biases and inaccuracies, particularly when analyzing subjective or nuanced language. Different individuals may interpret sentiment differently, leading to inconsistencies in the analysis results. Access to comprehensive and diverse data sources is crucial for accurate sentiment analysis. However, obtaining and analyzing large volumes of textual data from various sources can be challenging and time-consuming, limiting the effectiveness of sentiment analysis in criminal Analysis.

Analysis of Crime Prediction

The predictive crime analysis of social media is made based on various techniques, wherein the Analysis based on performance measures, techniques and tools are made in this section.

Analysis Based on Performance Measures

The performance measure is utilized for the evaluation of the techniques used for crime prediction. The metrics and formulas utilized in various techniques are given in Table 5.

Analysis of Crime Data Techniques

The papers used to research the predictive Analysis for crime data are on the basis of different predictive analysis techniques for crime data. Table 6 shows the classification based on different predictive analysis methods like machine learning, deep learning, text mining, and link analysis for getting information about the predictive Analysis of crime data over social networks. Figure 5 shows the graphical representation of the number of research papers required for each technique to research details about the predictive Analysis of crime data.

Analysis Based on Tools

Gathering the correct dataset for the investigation requires more sources for a particular crime. The collection of crime data sources is acquired through police reports, previous files of investigation, intelligent reports, and some open sources of intelligent finding reports. Also, so many tools are required to process the dataset, like HADOOP, CASSANDR, ZOOKEPE, HIVE, and PIG. The comparison table for these processing tools is given in Table 7.

Table 5 Metrics and their formulas

Metric	Formula	Interpretation
Precision [46]	$\frac{TP}{TP+FP}$	Precision measures how many of the predicted crimes were actually correct. A high precision indicates fewer false positives; thus, high precision is preferred
Recall [46]	$\frac{TP}{TP+FN}$	Recall measures how well the model detects actual crime incidents. High recall indicates the correct detection of crimes from most of the actual crimes; thus, high precision is preferred
F-value [46]	$\frac{2}{\left(\frac{1}{P}+\frac{1}{R}\right)}$ Where, P denotes precision and R gives recall	The F1-score balances precision and recall, giving an overall measure of a model's accuracy in detecting crimes while minimizing both false positives and false negatives. It is crucial when there is an uneven class distribution. A high F1-Score indicates a better outcome
Root Mean Square Error [56]	$\sqrt{\frac{1}{N}\sum_{i=1}^{N}\left(PO-PO'\right)^2}$ where, N refers to the total samples, refers to the predicted value PO', refers to the expected value PO	RMSE measures the average magnitude of the prediction error. A lower RMSE indicates more accurate predictions
Mean Absolute Error [56]	$\frac{1}{N}\sum_{i=1}^{N}\left\|PO-PO'\right\|$	MAE measures the average absolute difference between predicted and actual values. A lower MAE indicates the error less predictions

Table 6 Classification based on different predictive Analysis

Technique	Description	Tools	Number of papers research
Machine learning	Recognizing the patterns from the previous experience	Business Miner, Quad stone, AC2, SAS	27
Neural network	Act likethe brain of a human	BrainMaker, 4Thought, Attrasoft, SPSS	12
Text mining	Starts work on confused text	iCrossReader, Perilog, Readware	10
Link analysis	Collecting data form the connection links and Critical link	ATAC, Crime Workbench, NETMAP	9
Sentimental Analysis	Predictive Analysis of crime data using the tweets	SRL, KDE, GloVe model14	7

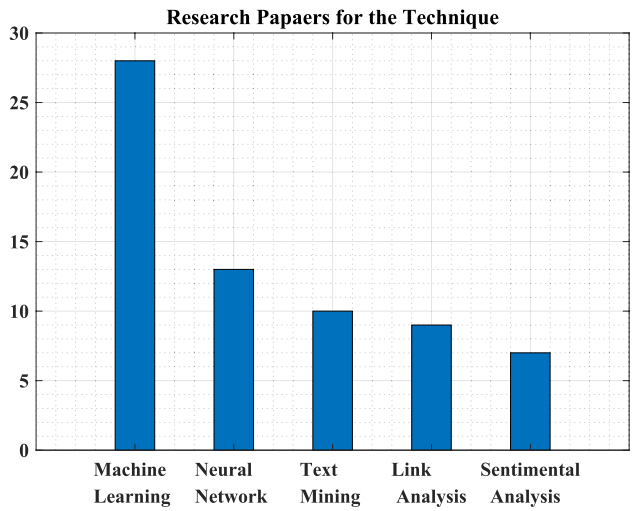

Fig. 5 Number of research papers required for each technique

Applications

The predictive Analysis of crime data has different applications, such as research in marketing section, medical fields, education institutes, banking sectors, etc. [75–77]. The representation of these applications is shown below in Fig. 6.

Marketing research: In the case of the design of selecting objects by a person, the person is used to making a timely arrangement of things that are used for forecasting in marketing diagnosis. This will help to arrange the products, like keeping bread and butter together in a supermarket. So, the technology will reduce the complexity in rearranging the products so they are sufficient in that space.

Medical field: The Analysis of algorithms in the area of the medical field is used to forecast the disease of the patient by examining the symptoms of the disease-affected person. It can help to identify the new symptoms and new diseases that are affecting the patient. So it is possible to forecast the disease with the help of identified symptoms.

Educational institute: To find and understand the student's knowledge and understanding capacities, the Apriori algorithm is used in this case. Rules are utilized to create a

Table 7 classification-based tools used for predictive Analysis of crime data

Tools	Technique	Advantage/ Disadvantage
HADOOP [69, 70]	The open-source techniques of apache foundation with map limit the method. If one system is down at the time of processing the data, then Hadoop duplicates the data in to various systems for processing the information in one of its many systems	The cost of the system is very low due to the utilization of huge number of datasets in commodity hardware
CASSANDR [71]	It has a distributed database for organizing the quantity of information across the system	High tolerance and highly stable system with very less tolerance
ZOOKEPE [72]	It is used to provide the architecture of big data for parallel computation in the prediction of criminal data	The data processing is simple and the transactions are atomized
HIVE [73]	The extraction dataset is done by using the warehousing tool and the data is loaded in files in the Hadoop	For the performance improvement transform the portioned data in tables
PIG [74]	It is used to analyzed large dataset by using this high-level language	Help to transform the unstructured data in to the structured data

Fig. 6 Applications

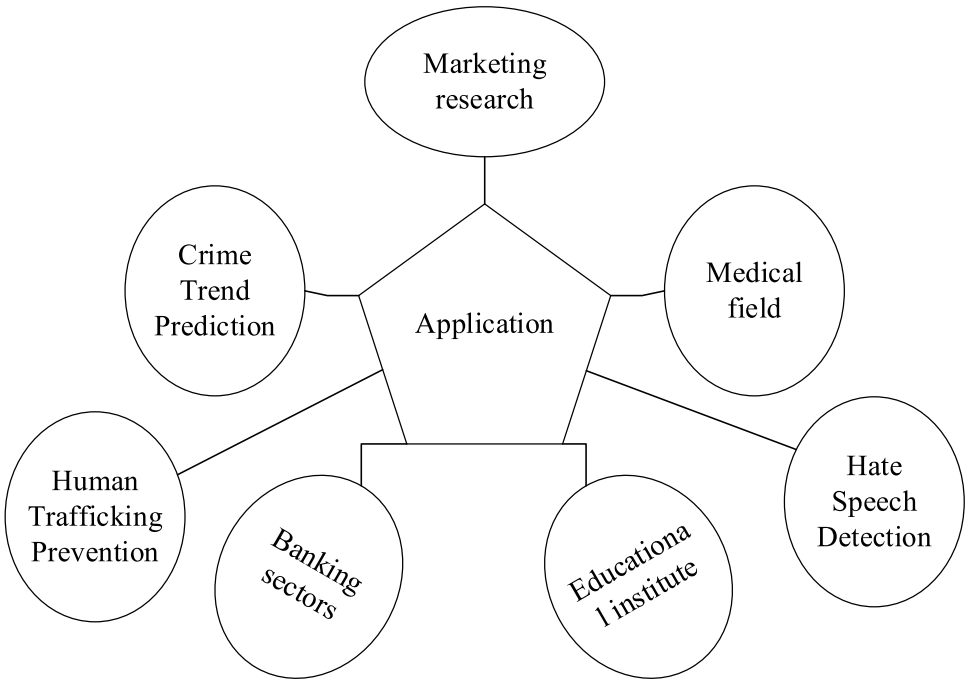

better curriculum for efficient and qualified students. Furthermore, increasing student performance with progressing results is achieved by assessing students' interests in various courses, which helps faculty members understand students' interests and performance in which subject.

Banking sectors: In the banking industry, technology and its algorithms help forecast credit card fraud, marketing and management risks. It is very hard to identify and prevent fraud in these sectors. Therefore, data collected from individuals who utilize bank technologies for their purposes will help identify new activities related to the customer pattern.

Human Trafficking Prevention: Human traffickers often use social media to communicate and recruit victims. Predictive models help detect anomalies in user interactions, patterns, and behaviours. These models have proven useful in identifying potential human trafficking operations by flagging suspicious accounts and activities that align with trafficking indicators.

Hate Speech Detection: Social media platforms with hate speech and cyberbullying incidents. Predictive models trained on Natural Language Processing (NLP) and sentiment analysis are capable of detecting harmful language flagging content before it escalates.

Crime Trend Prediction: Predictive analytics helps in identifying crime patterns by monitoring spikes in illegal activities, such as drug trafficking or violence. Crime forecasting using machine learning techniques has proven beneficial for real-time crime monitoring and prevention.

Some of the real-world applications of the predictive Analysis of social media data are [67, 78–80]:

Deep Learning for Predicting Human Trafficking: Human trafficking is considered a serious and global issue, which is increasing through organized social media platforms. Deep learning models have been used to detect indicators of human trafficking from posts and interactions on social media. Techniques such as Natural Language Processing (NLP) combined with deep learning are employed to analyse the language used in suspicious advertisements or posts.

Social Media Sentiment Analysis for Crime Prediction: Sentiment analysis of social media posts has been successfully used in predicting criminal activity, particularly in monitoring potential outbreaks of violence or protests. Deep learning models, such as Long Short-Term Memory (LSTM) networks, have been used to analyse social media sentiment and forecast crimes such as assaults, riots, or hate crimes.

Using Social Networks for Gang Crime Prediction: Social network analysis with deep learning models has been effective in predicting gang-related criminal activities. By analysing interactions and communications on platforms like Facebook, researchers can predict criminal behaviour among gang members. Deep learning models, such as Graph Neural Networks (GNNs), have been applied to social network data to identify patterns of communication that correspond to criminal planning or gang recruitment.

Twitter Data for Crime Hotspot Detection: In recent years, deep learning models have been applied to Twitter data to predict crime hotspots. Social media data can be used to extract real-time information on public sentiment, social unrest, and specific keywords that indicate potential criminal activity or safety risks. For example, convolutional neural networks (CNNs) and recurrent neural networks (RNNs)

have been employed to analyse geo-tagged tweets to predict areas of high crime risk.

Challenges

The challenges faced by the existing predictive Analysis of crime data that limits the performance of the method are:

- Feature Extraction: Feature extraction is a crucial component that limits the computation overhead and elevates the accuracy of detection. The insignificant attribute selection degrades the performance of the method [49, 81, 82].
- Clustering based prediction: The clustering-based predictive Analysis of the crime data does not work well while utilizing the large data, which leads to the curse of dimensionality. Besides, the data clustering without overlapping and the non-spherical clustering is a challenging task [55, 65].
- Dataset: While using the social data for predictive Analysis of the crime, the location information is not available because some of the social media users hide the location information due to privacy issues. Thus, the predictive Analysis based on the geo-tag base application degrades the performance [2, 83].
- Prediction Accuracy: The prediction accuracy of the method should be higher for the utilization of the application domain. The crime hotspot prediction technique based on the historic information provides inaccurate results. Thus, the crime prediction techniques without considering the current data limit the performance of the model [4, 19, 48].
- Complexity: The system needs to be tested in a portion of space for the working in implementation side. By scaling up the usage of the function, these challengers will gradually reduce and provide the perfect system that can be implemented in the real world. There are many techniques related to these aspects; as the size of the information set will be greater, the processing of data will take more time.
- Legal and Ethical Issues: The social media data often contains personal information, including geo-location, personal opinions, and sensitive content. Using this data for crime prediction can violate privacy laws such as the General Data Protection Regulation (GDPR). The laws demand express user consent, which is frequently hard to get for sizable datasets that are scraped from open or semi-public platforms. Even if the data is publicly available, its use for crime prediction poses ethical concerns about user privacy. People may not expect their social media activity to be used for such purposes, leading to feelings of surveillance or mistrust in the platform [37].

Future Scope

The predictive Analysis of crime data is implemented and forecasted to rectify the present limitations of the current techniques to obtain the maximum result and high performance. Besides, the predictive time needs to be integrated into the crime analysis in future work. The technologies and systems will help to predict and prevent crime and change the law enforcement agencies. With the integration of ML and computer vision, it will learn the pattern of previous crimes and analyze the truth with the help of new surveillance. The ML can learn the pattern of a previous crime and predict similar crimes in the future. Also, the forecasting technique should predict the future of crime without any help from human intervention. In addition, it should create a "crime hotspot" city by examining both the previous and current datasets of crime data. The system needs to predict the crime zone area and time on the social network. Law enforcement keeps these predicted crimes out of the zone. A fully automatic system has the capability to alter the current networking system for security and law enforcement in the future. Thus, a novel framework needs to be developed in the future based on the architecture provided in Fig. 7, to fulfil the challenges presented in the previous section, like more appropriate feature selection technique, better data clustering technique to overcome the curse of dimensionality challenge, utilization of large datasets, higher prediction accuracy, and reduced complexity. The more accurate criminal predictive techniques will be applicable for real-world applications that aid in the prevention of crime through law enforcement agencies.

General Structure of Crime Prediction Technique

Crime predictive analysis uses different techniques based on machine learning and deep learning. The data set created is transmitted to the pre-processing technique on the basis of some conditions. After completing the pre-processing technique, the features are extracted, which is in text format. Then categorization is utilized to create a cluster based on certain demands [49]. The classification is performed in supervised learning mode with the training and test models for recognizing unknown crime information; this technique is termed prediction. This type of architecture can be used for crime prediction analysis in social networks. This methodology makes sure that there is tranquillity and success between the nationals. The crime predictive analysis

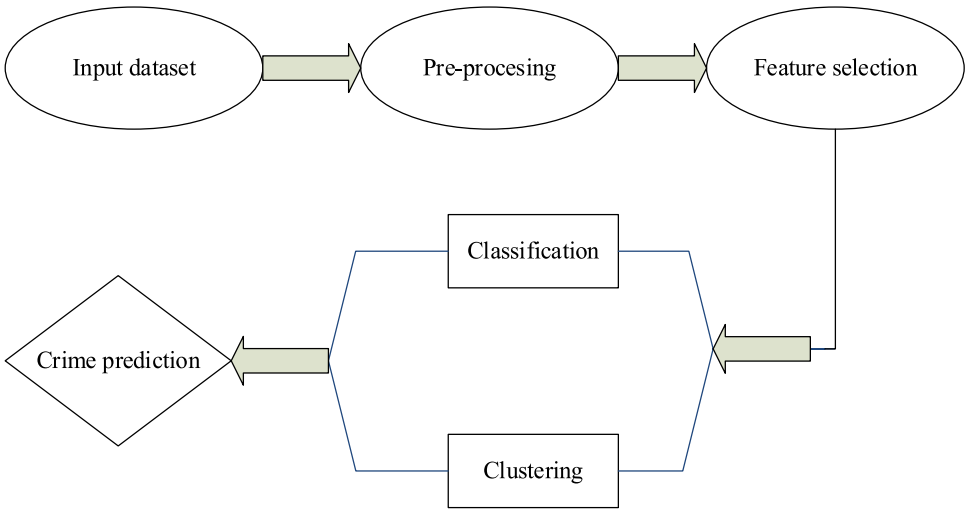

Fig. 7 General crime prediction technique

is carried out through some procedures that are given in Fig. 7. It has a number of states, and each state is utilized in machine learning to forecast the crime clusters on the basis of the crime documents [84]. The data set is created by using the information obtained from the characteristics and behaviour of the criminal.

Conclusion

Growing social media platforms play an important role in social media crimes. In this SLR, the various techniques used to predict crime data in social media are analyzed. Some techniques like link analysis, clustering, machine learning, and sentimental Analysis are used with respect to some rules. This research provided a comparison of different approaches and technologies that are used for the predictive Analysis of crime data in social media with the advantages and disadvantages of each technique. This study is particularly useful for researchers who are exploring the topic of predictive Analysis of crime data on social media. The review investigates the application of each method, including the parameters collected in each method of prediction. Each approach has its own technique for determining the prediction mechanism. These strategies can be used to predict crime while simultaneously presenting a good future.

Funding No funding was received for conducting this study.

Data Availability The manuscript does not have any associated data which was generated.

Declarations

Conflict of interest The authors declare that they have no conflict of interest and have no competing interests to declare that are relevant to the content of this article.

Ethical Approval This article does not contain any studies with human participants or animals performed by any of the authors.

References

1. Shafi I, Din S, Hussain Z, Ashraf I, Choi GS. Adaptable reduced-complexity approach based on state vector machine for identification of criminal activists on social media. IEEE Access. 2021;9:95456–68.
2. Mahajan R, Mansotra V. Correlating crime and social media: using semantic sentiment analysis. Int J Adv Comput Sci Appl. 2021. https://doi.org/10.14569/IJACSA.2021.0120338.
3. Alluri S, Varma MMKS (2021) An ensemble framework to analyze the crimes in social media by using deep learning algorithm
4. Dhomse, K. (2023). Crime prediction and analysis using data mining. Learning, 10(04)
5. Kathole A, Shinde S, Wadhwa L. Integrating MLOps and EEG techniques for enhanced crime detection and prevention. Multidiscip Sci J. 2024;6(1):2024009–2024009.
6. Joshi A, Sabitha AS, Choudhury T (2017) Crime analysis using k-means clustering. In: 2017 International Conference on Computational Intelligence and Networks. IEEE
7. Gupta VK, Shukla SK, Rawat RS. Crime tracking system and people's safety in India using machine learning approaches. Int J Modern Res. 2022;2(1):1–7.
8. Vimala Devi J, Kavitha KS. Adaptive deep Q learning network with reinforcement learning for crime prediction. Evol Intel. 2023;16(2):685–96.
9. Chen P, Kurland J (2018) Time, place, and modus operandi: a simple apriori algorithm experiment for crime pattern detection. IEEE
10. Jain R, Kumar A, Nayyar A, Dewan K, Garg R, Raman S, Ganguly S. Explaining sentiment analysis results on social media texts through visualization. Multimed Tools Appl. 2023;82(15):22613–29.
11. Ferooz F, Hassan MT, Mahmood S, Asim H, Idrees M, Assam M, Mohamed A, Attia EA. Risk and pattern analysis of pakistani crime data using unsupervised learning techniques. Appl Sci. 2022;12(7):3675.
12. Wanchoo K, Desai J (2022) Leveraging big data analytics for predictive policing in India. In ICT Systems and Sustainability (pp 259–269). Springer, Singapore

13. Gorr W, Olligschlaeger A, Thompson Y. Short-term forecasting of crime. Int J Forecast. 2003;19(4):579–94.
14. Jaber M, Sheibani R, Shakeri H (2022) A model for predicting crimes using big data and neural-fuzzy networks. Concurrency and Computation: Practice and Experience, p e6985
15. Prathap BR. Geo-spatial crime density attribution using optimized machine learning algorithms. Int J Inf Technol. 2023;15(2):1167–78.
16. Inbaraj XA, Rao AS (2018) Hybrid clustering algorithms for crime pattern analysis. In: 2018 IEEE International Conference on Current Trends toward Converging Technologies, Coimbatore, India
17. Mandalapu V, Elluri L, Vyas P, Roy N. Crime prediction using machine learning and deep learning: a systematic review and future directions. IEEE Access. 2023. https://doi.org/10.1109/ACCESS.2023.3286344.
18. Ristea A, Al Boni M, Resch B, Gerber MS, Leitner M. Spatial crime distribution and prediction for sporting events using social media. Int J Geograph Inf Sci. 2020;34(9):1708–39.
19. Boukabous M, Azizi M. Image and video-based crime prediction using object detection and deep learning. Bull Electr Eng Inform. 2023;12(3):1630–8.
20. Vo T, Sharma R, Kumar R, Son LH, Pham BT, Tien Bui D, Priyadarshini I, Sarkar M, Le T. Crime rate detection using social media of different crime locations and Twitter part-of-speech tagger with Brown clustering. J Intell Fuzzy Syst. 2020;38(4):4287–99.
21. Prieto Curiel R, Cresci S, Muntean CI, Bishop SR. Crime and its fear in social media. Palgrave Commun. 2020;6(1):1–12.
22. Rajeev H, Chakkaravarty M. Prediction of cybercrime using the Avinashak algorithm. Indian J Artif Intell Neural Netw (IJAINN). 2023;4(1):5–10.
23. Wu J, Abrar SM, Awasthi N, Frias-Martinez E, Frias-Martinez V. Enhancing short-term crime prediction with human mobility flows and deep learning architectures. EPJ Data Sci. 2022;11(1):53.
24. Maimon D, Fukuda A, Hinton S, Babko-Malaya O, Cathey R (2017) On the relevance of social media platforms in predicting the volume and patterns of web defacement attacks. In 2017 IEEE international conference on big data (Big Data), pp 4668–4673. IEEE
25. Dakalbab F, Talib MA, Waraga OA, Nassif AB, Abbas S, Nasir Q. Artificial intelligence and crime prediction: a systematic literature review. Soc Sci Human Open. 2022;6(1): 100342.
26. Aghababaei S, Makrehchi M. Mining Twitter data for crime trend prediction. Intell Data Anal. 2018;22(1):117–41.
27. Boukabous M, Azizi M. Crime prediction using a hybrid sentiment analysis approach based on the bidirectional encoder representations from transformers. Indonesian J Electr Eng Comput Sci. 2022;25(2):1131–9.
28. Keymanesh M, Gurukar S, Boettner B, Browning C, Calder C, Parthasarathy S (2020) Twitter watch: Leveraging social media to monitor and predict collective-efficacy of neighbourhoods. In Complex Networks XI, pp. 197–211. Springer, Cham
29. De S, Kaur M, Behera RK (2022) Crime rate analysis and prediction in delhi using facebook prophet. In Smart Intelligent Computing and Applications, Volume 2 (pp. 419–428). Springer, Singapore
30. Sagala NT (2022) Comparative analysis of grid-based decision tree and support vector machine for crime category prediction. In 2021 International Seminar on Machine Learning, Optimization, and Data Science (ISMODE) (pp 184–188). IEEE
31. Roshankar R, Keyvanpour MR (2023) Spatio-temporal graph neural networks for accurate crime prediction. In 2023 13th International Conference on Computer and Knowledge Engineering (ICCKE) (pp 168–173). IEEE
32. Appleby B, Roskell C, Daly W. What are health professionals' intentions toward using research and products of research in clinical practice? A systematic review and narrative synthesis. Nurs Open. 2016;3(3):125–39.
33. Liao R, Wang X, Li L, Qin Z. A novel serial crime prediction model based on Bayesian learning theory. In: Proceedings of the 2010 IEEE International Conference on Machine Learning and Cybernetics
34. Jenga K, Catal C, Kar G. Machine learning in crime prediction. J Ambient Intell Hum Comput. 2023;14(3):2887–913.
35. Bandekar SR, Vijayalakshmi C. Design and Analysis of machine learning algorithms for the reduction of crime rates in India. Procedia Comput Sci. 2020;172:122–7.
36. Hu C, Yin M, Liu B, Li X, Ye Y. Identifying illicit drug dealers on instagram with large-scale multi-modal data fusion. ACM Trans Intell Syst Technol (TIST). 2021;12(5):1–23.
37. Moore DM. Algorithmic exploitation in social media human trafficking and strategies for regulation. Laws. 2024;13(3):31.
38. Chen X, Cho Y, Jang SY (2015) Crime prediction using twitter and weather, Systems and Information Engineering Design Symposium (SIEDS), IEEE, pp 63–68
39. Dandannavar PS, Mangalwede SR, Kulkarni PM (2018) Social media text-a source for personality prediction. In 2018 International Conference on Computational Techniques, Electronics and Mechanical Systems (CTEMS), pp. 62–65. IEEE
40. Wang P, Mathieu R, Ke J, Cai HJ. Predicting Criminal Recidivism with Support Vector Machine. In: Proceedings of the 2010 IEEE International Conference on Management and Service Science
41. Sharma M (2014) "Z-Crime: a data mining tool for the detection of suspicious criminal activities based on the decision tree, International Conference on Data Mining and Intelligent Computing, pp. 1–6
42. Hamdy E, Adl A, Hassanien AE, Hegazy O, Kim TH (2015) Criminal act detection and identification model, Proceedings of 7th International Conference on Advanced Communication and Networking, pp. 79–83
43. Tam S, ÖzgürTanrıöver Ö (2023) Multi-modal deep learning crime prediction using crime and tweets. IEEE Access
44. Bogahawatte K, Adikari S. Intelligent criminal identification system, Proceedings of 8th IEEE International Conference on Computer Science and Education, pp. 633–638
45. Agarwal J, Nagpal R, Sehgal R. Crime analysis using K-means clustering. Int J Comput Appl. 2013;83(4):1–4.
46. Kiani R, Mahdavi S, Keshavarzi A. Analysis and prediction of crimes by clustering and classification. Int J Adv Res Artif Intell. 2015;4(8):11–7.
47. Sathyadevan S, Devan MS, Gangadharan SS (2014) Crime analysis and prediction using data mining, Proceedings of IEEE 1st International Conference on Networks and Soft Computing, pp. 406–412
48. Huang YY, Li CT, Jeng SK (2015) Mining location-based social networks for criminal activity prediction, Proceedings of 24th IEEE International Conference on Wireless and Optical Communication, pp 185–190
49. Ristea A, Kurland J, Resch B, Leitner M, Langford C. Estimating the spatial distribution of crime events around a football stadium from georeferenced tweets. ISPRS Int J Geo Inf. 2018;7(2):43.
50. Ioannidis I, Haining RP, Ceccato V, Nascetti A (2024) Using remote sensing data to derive built-form indexes to analyze the geography of residential burglary and street thefts. Cartogr Geogr Inf Sci, pp 1–17
51. Almehmadi A (2017) Language usage on twitter predicts crime rates, Security of Information and Networks, pp 307–310
52. Taha K, Yoo PD. SIIMCO: a forensic investigation tool for identifying the influential members of a criminal organization. IEEE Trans Inf Forensics Secur. 2016;11(4):811–22.

53. Hajela G, Chawla M, Rasool A. A clustering based hotspot identification approach for crime prediction. Procedia Comput Sci. 2020;167:1462–70.
54. Kadar C, Maculan R, Feuerriegel S. Public decision support for low population density areas: an imbalance-aware hyper-ensemble for spatio-temporal crime prediction. Decis Support Syst. 2019;119:107–17.
55. Stevens HR, Graham PL, Beggs PJ, Hanigan IC. In cold weather we bark, but in hot weather we bite: patterns in social media anger, aggressive Behavior, and temperature. Environ Behav. 2021;53(7):787–805.
56. Wawrzyniak ZM, Borowik G, Szczechla E, Michalak P, Pytlak R, Cichosz P, Ircha D, Olszewski W, Perkowski E (2018) Relationships between crime and everyday factors. In 2018 IEEE 22nd International Conference on Intelligent Engineering Systems (INES), pp. 000039–000044. IEEE
57. Borowik G, Wawrzyniak ZM, Cichosz P (2018) Time series analysis for crime forecasting. In 2018 26th international conference on systems engineering (ICSEng), pp 1–10. IEEE
58. Soomro TR, Hussain M. Social media-related cybercrimes and techniques for their prevention. Appl Comput Syst. 2019;24(1):9–17.
59. Kadar C, Rosés Brüngger R, Pletikosa I (2017) Measuring ambient population from location-based social networks to describe urban crime. In: International conference on social informatics, pp 521–535. Springer, Cham
60. Kadar C, Pletikosa I. Mining large-scale human mobility data for long-term crime prediction. EPJ Data Sci. 2018;7(1):1–27.
61. Zhao X, Tang J. Crime in urban areas: a data mining perspective. ACM SIGKDD Explor Newsl. 2018;20(1):1–12.
62. Gerber MS. Predicting crime using Twitter and kernel density estimation. Decis Supp Syst. 2014;61(1):115–25.
63. Wang X, Gerber MS, Brown DE (2012) Automatic crime prediction using events extracted from twitter posts, in Social Computing, Behavioral-Cultural Modeling and Prediction. Springer, pp 231–238
64. Aghababaei S, Makrehchi M. Mining social media content for crime predic-tion. IEEE/WIC/ACM Int Conf Web Intell. 2016;13:526–31.
65. Ristea A, Leitner M, Andresen MA (2018) Opinion mining from Twitter and spatial crime distribution for hockey events in Vancouver, AGILE, pp 1–7
66. Siriaraya P, Wang Y, Jatowt A (2019) Witnessing crime through tweets :a crime investiga-tio tool based on social media, In: Internation-al Conference on Advances in Geographic Information Systems, pp 568–571
67. Zhang Q, Ren X, Xia L, Yiu SM, Huang C (2023) Spatio-temporal graph learning with large language model
68. Deng S, de Rijke M, Ning Y (2024). Advances in human event modeling: from graph neural networks to language models. In Proceedings of the 30th ACM SIGKDD Conference on Knowledge Discovery and Data Mining (pp 6459–6469)
69. Wang Y, Su F. Risk assessment for commercial crime and legal protection based on modularity-optimized LM and SCA-optimized CNN. PeerJ Comput Sci. 2023;9: e1683.
70. Raja Raman V (2016) "Big data analytics," Resonance, pp.695–7166
71. Ramesh E, Aggarwal H (2018) Big social data analytics for human behaviour prediction platform: a futuristic approach. Int J 4(2)
72. Gupta G. Introduction to data mining with case studies. PHI Learning Pvt. Ltd.; 2014.
73. Bhuyan HK, Pani SK (2021) Crime predictive model using big data analytics. Intelligent data analytics for terror threat prediction: architectures, methodologies, techniques and applications, pp 57–78
74. Santhiya K, Bhuvaneswari V, Murugesh V. Automated crime tweets classification and geo-location prediction using big data framework. Turk J Comput Math Educ (TURCOMAT). 2021;12(14):2133–52.
75. Alotaibi M, Alotaibi B, Razaque A. A multichannel deep learning framework for cyberbullying detection on social media. Electronics. 2021;2021(10):2664.
76. Azumah SW, Elsayed N, ElSayed Z, Ozer M, La Guardia A (2024) Deep learning approaches for detecting adversarial cyberbullying and hate speech in social networks. arXiv preprint arXiv:2406.17793
77. Pereira-Kohatsu JC, Quijano-Sánchez L, Liberatore F, Camacho-Collados M. Detecting and monitoring hate speech in Twitter. Sensors. 2019;19(21):4654.
78. Taiwo GA, Saraee M, Fatai J. Crime prediction using twitter sentiments and crime data. Informatica. 2024. https://doi.org/10.31449/inf.v48i6.4749.
79. Tekin SF, Kozat SS. Crime prediction with graph neural networks and multivariate normal distributions. SIViP. 2023;17(4):1053–9.
80. Ijiga AC, Olola TM, Enyejo LA, Akpa FA, Olatunde TI, Olajide FI. Advanced surveillance and detection systems using deep learning to combat human trafficking. Magna Scientia Adv Res Rev. 2024;11(1):267–86.
81. Sheehy K et al (2016) Evidence-based analysis of mentally 111 individuals in the criminal justice system, Proceedings of IEEE systems and information engineering design symposium, pp. 250–254
82. Zheng Y. Methodologies for cross-domain data fusion: an overview. IEEE Trans Big Data. 2015;1(1):16–34.
83. Chen P, Yuan H, Shu X. Forecasting Crime Using the ARIMA Model. In: Proceedings of the 5th IEEE international conference on fuzzy systems and knowledge discovery
84. Feng M, Zheng J, Ren J, Hussain A, Li X, Xi Y, Liu Q. Big data analytics and mining for effective visualization and trends forecasting of crime data. IEEE Access. 2019;7:106111–23.

Publisher's Note Springer Nature remains neutral with regard to jurisdictional claims in published maps and institutional affiliations.

Springer Nature or its licensor (e.g. a society or other partner) holds exclusive rights to this article under a publishing agreement with the author(s) or other rightsholder(s); author self-archiving of the accepted manuscript version of this article is solely governed by the terms of such publishing agreement and applicable law.

International Journal of Social Science and Economic Research

ISSN: 2455-8834

Volume:10, Issue:02 "February 2025"

Product Persuasion with Special Emphasis on Electronic Consumer Durables

Laranya Vashist, Chhavi Gupta, Rajveer Arora, Aparna Gopakumar and Ananya Chandra

Birla Vidya Niketan, New Delhi, India

Assisted by-Manya Sharma, student @ Department of design Delhi Technological University, Rohini, Delhi, India.

DOI: 10.46609/IJSSER.2025.v10i02.019 URL: https://doi.org/10.46609/IJSSER.2025.v10i02.019

Received: 2 Feb. 2025 / Accepted: 22 Feb. 2025 / Published: 6 March 2025

Statement of Purpose

This study will examine how product labelling and packaging will shape modern consumer preferences and take the lead over influencer marketing, celebrity endorsements, and sponsored reviews. A survey will be conducted from a range of age and income brackets to explore varied viewpoints regarding the significance of product labelling in relation to future purchase decisions. The responses will examine the importance and necessity of reading product labels before making a purchase.

Participants, who will represent a variety of age groups and socioeconomic backgrounds, will continuously emphasize the instructive power of product labels and packaging in influencing their purchasing decisions.

This insight will challenge conventional marketing strategies and underscore the evolving landscape where consumers will prioritize factual information over influencer endorsements or celebrity affiliations.

By clarifying the changing dynamics of consumer trust and preference, this future research will add important insights to the marketing sector. Businesses and marketers will be urged to reassess their tactics, emphasizing transparency and educational content in an era where customers will increasingly want substance and authenticity in their purchasing experiences as product labelling will emerge as a dominant force in determining consumer decisions.

Based on this base, we will look into how labelling works in electronic consumer durables using few stores as examples such as Croma and Vijay Sales. This will include interviewing salesmen, reading guides and manuals for all kinds of techno devices. In addition, we will generate a

 Copyright © IJSSER 2025, All rights reserved

ISSN: 2455-8834

Volume:10, Issue:02 "February 2025"

transparent, accessible and genuinely enlightening label for everyday products that transcends basic sales strategies to actually educate people about what they are buying.

Introduction

Influencer marketing, celebrity endorsements, and sponsored reviews have a growing impact on customer purchasing choices in the current digital era. When it comes to influencing consumer decision-making, product labelling and packaging continue to play a crucial role. This study intends to investigate how influencers, sponsored reviews, celebrity endorsements, and objective product information along with product packaging affect consumers' purchasing decisions.

Previous studies have indicated that while making a purchasing choice, buyers depend largely on product information. Nonetheless, there might be differences in the efficacy of various information sources. Self-rated knowledge is a significant factor in determining how much a customer relies on product information. Previous studies have demonstrated that self-rated knowledge is a major predictor of comprehension, recall, inference, and evaluation—the four label reading measures.

Product

A product is defined as any good, service, or other valuable item offered for sale in the marketplace. It is designed to meet specific customer requirements or desires, with the primary goal of satisfying these expectations. A product can be either tangible (e.g., gadgets, clothing, or food) or intangible (services, digital products, or experiences).

According to the consumer, a product is anything bought that has the capacity to meet certain demands by providing utility, satisfaction, or advantages. Whether the product is a vehicle, software, or a meal at a restaurant, the main value proposition is how effectively it meets the buyer's demands.

A product's physical shape and functioning are not the only aspects to consider. The notion of a product also includes the extended product, which refers to the additional services or benefits provided to customers after the sale, such as warranties, customer assistance, or even a brand's reputation. This is where the product becomes a component of a bigger experience, providing ongoing value.

Elements of a Product

A product is composed of three key interrelated elements:

- **Packaging:** The manner in which a product is displayed and safeguarded.

 Copyright © IJSSER 2025, All rights reserved

ISSN: 2455-8834

Volume:10, Issue:02 "February 2025"

- **Labelling:** The information placed on a product's packaging that educates consumers about the product.
- **Branding:** It refers to a product's identity, which includes its name, brand, and the promise of value.

These parts are interrelated: labelling is part of packaging, and branding is the consequence of good packaging and labelling, affected by the external market.

Packaging

Packaging is the method and materials used to encapsulate or protect items throughout distribution, storage, sale, and usage. Packaging serves several purposes, including safeguarding the goods, easing transportation, attracting customers, and conveying critical information.

Levels of Packaging:

Primary Packaging: This is the first layer of protection that has direct contact with the product. Its purpose is to protect and preserve the product (for example, a juice bottle or a candy bar wrapper).

Secondary Packaging: This layer combines many main packages for easy handling or distribution (for example, a box holding several toothpaste tubes or a carton containing a dozen soft drink cans).

Transportation Packaging: Packaging used for bulk handling, storage, and transportation of items. It usually uses larger boxes, crates, or pallets and is less concerned with branding or consumer engagement (for example, giant corrugated cardboard boxes).

The significance of packaging:

- Protection: This ensures that the product is not damaged or contaminated.
- Convenience: Easy to handle, store, and transfer.
- Communication: Packaging frequently serves as a "silent salesman" by visually appealing to buyers, conveying crucial information, and separating the product from competition.
- Sustainability: Modern packaging trends favour eco-friendly materials, which reduces the environmental imprint.

Labelling: Objective Product Information

Labelling is the written, printed, or visual information shown on or accompanying a product. Labels are an essential component of packaging since they provide consumers with critical

 Copyright © IJSSER 2025, All rights reserved

ISSN: 2455-8834

Volume:10, Issue:02 "February 2025"

information about the product, its contents, usage directions, safety warnings, and so on. Labelling can also incorporate marketing components such as slogans or brand logos to increase the product's attractiveness.

Labelling is a crucial part of packaging since it provides important product information to consumers. It educates purchasers about the product's contents, quality, and safety, as well as meeting regulatory requirements (such as nutritional information or hazard warnings).

Importance of Labelling-

- **Compliance:** Labelling is crucial for ensuring compliance with legal norms and laws.
- **Informed Decisions:** Labels give vital information to consumers, allowing them to make more educated purchasing decisions.
- **Brand Identity:** A well-designed label may make a product stand out on retail shelves.
- **Trust and Transparency:** Detailed and honest labelling can increase consumer trust, resulting in greater customer loyalty.

Brand

A brand is more than simply a name or a symbol; it embodies the identity, values, and personality of a product or business. It represents consumer perceptions and evolves throughout time via consistent quality, marketing activities, and customer experiences.

Brand Components:

- **Brand Name:** The name under which a product or service is promoted. It should be unique and memorable, making it simple for customers to recognise and remember.
- **Brand mark:** It refers to the visual components (such as logos or symbols) that help recognise a brand. It visually portrays the brand and has the potential to elicit emotions or product connections.

Brand as a product of effective labelling and packaging:

Effective labelling and packaging contribute to a brand's power and attractiveness. Well-designed packaging and accurate, beautiful labelling improve a product's brand image by increasing visibility, perceived quality, and consumer trust. External factors like as competition, market trends, and cultural developments also have an impact on a brand's evolution, defining how it is viewed and valued in the market.

 Copyright © IJSSER 2025, All rights reserved

ISSN: 2455-8834

Volume:10, Issue:02 "February 2025"

Consumers take into account a number of aspects, such as product features, quality, and pricing, while making decisions about purchases. But product branding and packaging and labelling also have a big impact on what they decide to buy. When customers base their judgements on the labelling on product packaging, they take into account the following important factors:

- **Reputation and Brand Name:** When deciding if a product is worthwhile to buy, consumers frequently look to brand names. Reputable and well-established brands are frequently linked to satisfied customers and superior products. Brand names placed prominently on packaging labels can encourage buyers to pick and trust the promoted goods.

- **Ingredients and Nutrition Details:** A lot of customers have certain dietary needs or a preference for particular ingredient kinds. Consumers can make more educated judgments about their dietary preferences when the packaging labels clearly list the components used in the product.

- **Product Claims:** Specific claims, such as "natural," "organic," or "eco-friendly," are frequently made on product package labels. When evaluating a product's quality, safety, and effect on the environment, consumers rely on these statements. The veracity of these assertions has the potential to greatly affect consumers' decision-making processes and affect what they decide to buy.

- **Safety and Warnings:** Any legally mandated safety or warning statements have to be included on product package labels. These advisories advise customers of any hazards connected to the product, such as allergies, safety measures, and expiration dates. Customers depend on these alerts to safeguard their health and the health of their families.

- **Goods Package:** A consumer's choice of goods can also be influenced by the style and appearance of the package. Customers frequently rely on their first opinions on the packaging's aesthetic attractiveness, which may grab their attention and persuade them to think about the product. Bright colours, eye-catching designs, or special features may be used in well-designed packaging to set a product apart from the competition and increase customer appeal.

Impact of Labelling on Consumer Buying Preferences

- **Transparency and Trust:** Putting objective product information in front and centre on product packaging is essential to fostering customer and brand trust. The buyer-seller

 Copyright © IJSSER 2025, All rights reserved

ISSN: 2455-8834

Volume:10, Issue:02 "February 2025"

relationship is strengthened by this openness, which gives unbiased and factual information about the goods. Customers value the assurance that they can depend on the supplied information to make wise choices. However, this transparency must be supported by objective product labelling or package information that is reliable, accurate, and trustworthy.

Tesla: Tesla is renowned for being transparent about the features and technical details of their electric cars. Regarding safety features, performance metrics, and battery range, the manufacturer offers comprehensive information. As more people become interested in electric vehicles, this transparency helps to foster a sense of confidence.

- **Informed Decision Making:** Clear and accurate product labelling enables consumers to make educated purchase decisions based on the product's genuine qualities rather than extraneous influences. Customers can assess a product's suitability for their requirements and preferences when they have access to objective information about its features, advantages, and ingredients. As a result, they are better equipped to make decisions that suit their unique needs and are more satisfied with the things they buy.

- **Consumer Empowerment:** Customers may compare items based on features, advantages, and ingredients with the use of objective information. This gives people the ability to put their beliefs and preferences first.

In addition, consumers are able to evaluate the nutritional worth of various goods and make well-informed decisions regarding their general health because of the presence of nutrition statistics including calories, fat content, and nutritional content. Consumers may evaluate which items fit with their personal values, dietary limitations, or ethical reasons by having access to objective product information. With this degree of empowerment, customers may make decisions that are consistent with their beliefs, which increases their feeling of pleasure and brand loyalty.

Source – Canva

 Copyright © IJSSER 2025, All rights reserved

ISSN: 2455-8834

Volume:10, Issue:02 "February 2025"

Influencers, Celebrity Endorsements, and Paid Reviews

Influencer marketing, celebrity endorsements, and sponsored reviews are important factors in determining the purchasing habits of consumers in the quickly changing world of digital media and consumerism. As corporations recognize the potential of these powerful personalities in grabbing the attention and trust of their target audiences, these methods have become fundamental aspects of marketing efforts.

- **Influencers:** Influencers are people who have built up a sizable social media following, frequently in specialised fields like fitness, fashion, beauty, or lifestyle. Their impact originates from their ability to connect with their audience on a personal level, generating a feeling of genuineness and relatability. Influencers serve as go-betweens for companies and customers by using their internet platforms to promote goods and services. Because the influencers they follow are perceived as peers rather than remote celebrities, consumers are more inclined to believe the suggestions made by these people. The power of influencer marketing resides in its capacity to reach niche markets with a highly engaged audience.

Online Marketing Channels and Types:

1. **Search Engine Optimization (SEO):** By improving a company's position on search engine results pages (SERPs), SEO raises brand awareness and draws in organic traffic.

 Copyright © IJSSER 2025, All rights reserved

ISSN: 2455-8834

Volume:10, Issue:02 "February 2025"

2. **Search Engine Marketing (SEM):** SEM is the practice of purchasing advertisements on search engines such as Google Ads or Bing Advertising.

3. **Social media marketing (SMM):** SMM include content creation and sharing on a range of social media sites, including Twitter, Facebook, and Instagram. It facilitates communication between companies and their target market, increases brand recognition, and increases website traffic. **This kind of marketing includes influencer marketing.**

4. **Email Marketing:** Email marketing involves sending targeted emails to a list of subscribers to promote products or services.

5. **Content Marketing:** Content marketing involves creating and distributing valuable, relevant, and consistent content to attract and retain a clearly defined audience.

6. **Affiliate Marketing:** Affiliate marketing is a performance-based marketing model where businesses reward affiliates for generating leads or sales.

- **Celebrity Endorsements:** For decades, celebrity endorsements have been a cornerstone of traditional marketing, but the development of social media has increased their reach and influence. Celebrities, with their large fan following, are frequently viewed as role models. They may improve brand exposure and credibility by endorsing a product or service. Fans' emotional attachment to celebrities may transfer into consumer loyalty. However, the impact of celebrity endorsements can vary depending on the celebrity's image congruence with the company and the perceived genuineness of the endorsement.

- **Paid Reviews:** Paid reviews entail paying individuals, who are frequently influencers or industry experts, to offer good comments on a product or service. While this method is debatable, it is extensively used as a marketing strategy. Positive ratings, whether organic or purchased, may have a big impact on customer trust and purchase decisions. The legitimacy of reviews, on the other hand, is critical. Consumers are growing more savvy, and finding dishonest or biased reviews may undermine a brand's reputation. Transparency and authentic testimonies are critical to retaining customer trust.

Impact of Social Media Marketing on Consumer Buying Preferences

- **Social Proof:** Influencer and celebrity endorsements can generate a feeling of social proof, impacting customer views and decisions. When customers see their favourite influencers or celebrities promoting a product, they are more likely to feel that the product is of good quality or fits into their desired lifestyle. This social proof has the

 Copyright © IJSSER 2025, All rights reserved

ISSN: 2455-8834

Volume:10, Issue:02 "February 2025"

potential to change customer preferences and boost interest in and consideration of the recommended product.

- **Emotional Appeal:** Celebrities and influencers have the ability to elicit emotions and build aspirational links with things, influencing customer purchasing habits. Influencers and celebrities may develop emotional connections with their audience through carefully crafted content and personal brand image. When these important personalities recommend a product, buyers are more likely to link it with good feelings and ambitions. This emotional appeal has the potential to profoundly affect customer preferences and purchase decisions.

It is not always the case that information on product packaging is correct, as demonstrated in 2015 when lead was detected in Maggi noodles despite no indication on the product label. The testing samples were forwarded to FSSAI labs, which revealed higher-than-allowable levels of lead and the presence of Monosodium Glutamate (MSG), both of which are forbidden in consumable items. However, instances of erroneous product labelling are rare, and laws exist to prevent them.

The Prevention of Food Adulteration Act of 1954 specifies penalties for violators. Depending on the circumstances, the vendor might face 6 months to a year in jail or a fine of 2000 rupees for a first violation. A second violation can result in up to six years in jail and the termination of one's license. Section 320 of the criminal code provides for punishment where contaminated food causes a health danger.

These penalties apply if the item sold does not fulfil consumer standards, has misleading information, contains quality-degrading materials, contains banned preservatives, or fails to satisfy specified quality and purity criteria. As a result, objective product information is widely accepted. However, no laws presently exist to address the issue of producing phoney reviews or misrepresenting items that do not match industry standards. In India, enforcement of these rules is weak, and stricter regulations are required. Many substandard items continue to enter the market with little to no consequence. Regular checks and increased control are required to safeguard consumers and prohibit deceptive tactics, ensuring that only high-quality items are offered.

Case Studies

Dyson:

Dyson is a well-known technology business that is popular for its revolutionary vacuum cleaners, fans, and other household goods. Dyson's marketing approach is centred on emphasizing

 Copyright © IJSSER 2025, All rights reserved

ISSN: 2455-8834

Volume:10, Issue:02 "February 2025"

technology developments and distinctive qualities of its goods. The company emphasizes providing thorough specs, performance indicators, and the underlying technical concepts that distinguish its products.

While Dyson has become well-known for its cutting-edge technology, the company has not relied significantly on celebrity endorsements or influencer relationships to sell its goods. Instead, Dyson's success may be ascribed to the company's dedication to producing high-quality, well-engineered goods that appeal to consumers searching for efficient and dependable home equipment. This example demonstrates that, in some sectors, the power of objective product information may trump the effect of external influencers in influencing customer purchase decisions.

Apple Inc.:

While Apple gives precise specs and features for its goods, such as iPhones and MacBook, the corporation also uses celebrity endorsements and partnerships to carefully utilize external influences. New product launch events frequently involve well-known people from the entertainment world or significant tech professionals. These celebrities help to increase the attractiveness and perception of Apple goods, generating a buzz around the brand.

Despite celebrity endorsements, a large part of Apple's success may be credited to the clear and thorough product information supplied. Apple's product labelling, marketing materials, and user-friendly technical specification presentations all play an important part in influencing consumer decisions. Many buyers rely their purchasing decisions on the perceived quality, usefulness, and design factors highlighted in Apple's product descriptions. Within a famous technological company, this example exemplifies the difficult balance between objective product information and external factors in the customer decision-making process.

Source – Canva

 Copyright © IJSSER 2025, All rights reserved

ISSN: 2455-8834

Volume:10, Issue:02 "February 2025"

Fyre Festival:

Fyre Festival was marketed as an elite and opulent music event, with celebrities and social media influencers playing a key role. Kendall Jenner and Bella Hadid were among the high-profile models and influencers who helped promote the festival on social media, generating a buzz around the event.

When the festival was held in 2017, however, it immediately became clear that the event did not measure up to the grandiose promises made in its marketing campaign. Attendees experienced insufficient housing, terrible amenities, and general turmoil, leading to the festival's final cancellation. The incident became a cautionary tale about the dangers of depending too much on external influences and hype while failing to deliver on the promised product or service.

The example of the Fyre Festival emphasizes the need of maintaining a true and substantial product or service, since external influences alone may not ensure success if they are not backed by a foundation of quality and authenticity.

RXBar:

RXBar, which had previously struggled to gain popularity, had a large increase in sales following an effective packaging change. In 2014, the original package generated $2 million in earnings, but it wasn't until 2017, following a redesign, that the firm saw a startling rise in sales to $160 million. The transition indicates that the new packaging improved visual appeal, articulated a compelling value proposition, strengthened brand identification, and was in line with changing market trends. Notably, displaying nutritional information clearly on the front of the new package implies that objective information is critical in customer decision-making, which contributes to the amazing sales rise witnessed. This instance demonstrates the critical impact packaging plays in shaping consumer perception and creating significant sales increase for a product.

Source- YouTube video (Does Packaging Design Affects Sales?)

 Copyright © IJSSER 2025, All rights reserved

ISSN: 2455-8834

Volume:10, Issue:02 "February 2025"

Conclusion

In conclusion, Consumers' purchase decisions are heavily influenced by the transparency, trust, and empowerment provided by objective product labelling. Objective product information generates a perception of authenticity and dependability in the marketplace by facilitating informed decision-making and emphasizing customer empowerment.

However, it is critical to recognize the powerful effect of celebrities, influencers, and sponsored reviews in moulding consumer choices. Endorsements and compensated reviews provide social evidence, emotional appeal, and perceived legitimacy to consumers, frequently supplementing the function of objective product information.

While businesses frequently use a variety of methods, it is worth noting that the majority of customers base their purchase decisions on product labels. This highlights the need for clear and appealing product information in influencing consumer choices, even when additional tactics such as smart influencer and celebrity collaborations are employed. The prominence of product labelling as a main decision-making element highlights its critical role in catering to varied customer demands and preferences within the complex terrain of today's marketplace.

The study seeks to determine which factor—objective information and labelling, or persuasion through sponsored reviews and celebrity endorsements—has a greater impact on customer purchasing decisions. It compares the influence of both to determine how these aspects balance or dominate in determining customer preferences and purchase behaviour.

Objectives of the Study

1. Examine How Consumer Preferences Are Affected by Product Labelling and Packaging

- Examine if customers give priority to information found on product labels when making decisions about what to buy.
- Examine how reliable consumers believe label information to be in comparison to information from outside sources like influencers, celebrities, and paid reviews.

2. Assess the Influence of External Elements on Consumer Choice

- Evaluate how consumer choices are impacted by influencers, paid reviews, and celebrity endorsements.
- Determine the elements that influence how persuasive external recommendations are to customers.

 Copyright © IJSSER 2025, All rights reserved

ISSN: 2455-8834

Volume:10, Issue:02 "February 2025"

3. Compare and contrast Product Labelling with the Validity and Reliability of External Endorsements

- Assess how reliable consumers believe the information on product labels to be.
- Analyse the validity and reliability of influencer recommendations, paid reviews, and celebrity endorsements in influencing purchasing decisions.

4. Examine Consumer Product Label Knowledge and Understanding

- Examine how much information on product labels is known to consumers.
- Assess whether or not consumers understand the ramifications of the information on labels and whether it influences their choice of products.

5. Evaluate the Effect of Demographic Factors on Consumer Preferences

- Look at how factors like income, gender, and age affect how much importance is given to product labelling.
- Examine the differences in efficacy between external factors and endorsements for various demographic groups.

6. Examine the Psychological Factors Influencing Purchase Behaviour

- Determine the psychological elements that drive consumer behaviour and affect their choices about what to buy.
- Offer insights into the ways that external suggestions and product labelling affect the psychological components of consumer decision-making.

7. Statistical Examination of Survey Information to Confirm Theories

- Employ statistical techniques to examine the information gathered from questionnaires and surveys. Find noteworthy patterns and connections that support or refute the study's theories regarding the connection between product labeling and outside endorsements.

8. Integrate Research Findings with Literature Review Insights

- To contextualize the impact of product labelling and outside endorsements on consumer behaviour, compare the study's findings with literature-based insights.
- Give a thorough explanation of how these variables affect customer preferences.

9. Create a Product Label That Is Transparent, Educational, and Compliant with Laws

 Copyright © IJSSER 2025, All rights reserved

ISSN: 2455-8834

Volume:10, Issue:02 "February 2025"

- Create a label that provides all pertinent information about the product, guaranteeing maximum transparency and safeguarding consumers.
- Promote stricter laws and guidelines for product packaging and labelling to guarantee that customers are given comprehensive, accurate, and clear information about the goods they are buying.

10. Conduct case studies involving consumer complaints about deceptive or incomplete product labels and packaging

- Analyse Case Studies on Consumer Grievances Associated with Product Labelling.
- Find trends in customer complaints and suggest legislative and regulatory measures to improve openness and confidence in product labelling.

11. Examine Labelling methods in Electronic Consumer Durables

- Use certain retailers, like Croma and Vijay Sales, as examples to look at how labelling methods are used in electronic consumer durables.
- Interview sales representatives and go over product manuals to evaluate how comprehensive and clear the labelling is in this industry.

12. Scope for More Research

- Determine which areas need more research, such as how transparent labelling affects consumer trust and brand loyalty over the long run.
- Make recommendations for additional research that can examine how future product labelling and packaging methods may be impacted by regulatory changes, changing customer expectations, and technological improvements.

13. Future Trends:

Propose future trends based on extensive research, providing insightful and data-driven recommendations.

Hypothesis

Harnessing the Informative Influence: Investigating the Dominance of Product Labelling in Shaping Consumer Preferences Over Influencers, Celebrity Endorsements, and Paid Reviews.

This study hypothesizes that product labelling (part of product packaging) holds greater sway in shaping consumer preferences compared to influencers, celebrity endorsements, and paid reviews. The research explores whether consumers prioritize information presented on labels

 Copyright © IJSSER 2025, All rights reserved

ISSN: 2455-8834

Volume:10, Issue:02 "February 2025"

over external influences, suggesting that clear and comprehensive product information and product packaging directly influences purchasing decisions. The assumption is that consumers may find labelled details more credible, potentially making them more influential than external endorsements or reviews.

Furthermore, this research will look into the significance of transparent and easy to comprehend product labelling for electronic consumer durables and how it affects consumer confidence and decision-making in this particular industry.

Because these items are complicated and frequently have a variety of features and technical specs, it is important to have clear labelling to increase consumer confidence and knowledge. We'll look at how well- designed labels can help consumers understand technical language and make rational selections and comparisons.

Significance of the Study

In today's era, where almost every person is surrounded by social media and influencers, consumer behaviour is influenced by a lot of different factors. Social media platforms were originally designed to help people connect with each other; however, these sites have evolved into highly valuable platforms for promoting brands and products through influencers. These platforms have provided consumers with a new way to access product information and have created profitable opportunities for brands and influencers as well.

It is assumed that people are more likely to do something if they perceive it as being a social norm, which means that people are more likely to behave in a certain way if they see that those around them are behaving in the same way. Whenever we are about to purchase anything, we look to our peers to guide us before we form our own opinions and beliefs. However, it is not always the case.

Although nowadays there are a lot of influencers who are seen as trustworthy figures by their followers, it is actually only developing authentic brands that builds consumer trust. Influencers often promote products which may not be entirely reliable, and it is presumed that people would blindly follow them. But that is not entirely true.

Even though people are surrounded by social media and advertisements all the time, they realize the importance of product labelling and packaging and only purchase products if they find them worthy.

Product packaging refers to designing and producing the container or wrapper of a product. There are 3 levels of packaging – primary package (immediate packaging), secondary package

 Copyright © IJSSER 2025, All rights reserved

ISSN: 2455-8834

Volume:10, Issue:02 "February 2025"

(additional layer of protection) and transportation package (packaging necessary for storage, identification and transportation). It plays several roles -

- Protection of product
- Providing information
- Branding & marketing
- Convenience

Product labelling means displaying information about your product on its packaging. Labels protect customers from buying the wrong product. They help in –

- Describing the product and specifying its contents
- Identifying the product or brand
- Grading of products
- Helping promotion of products
- Providing information required by law

Label should be designed and presented in layman terms so that it is easier to understand. Some pre- requisites of a good label are as follows:

- Clarity & simplicity
- Compliance with Laws and Regulations
- Visually Engaging but not Overwhelming
- Durability and Quality
- Honesty and Transparency
- Consistent with Brand Identity
- Sustainability Considerations

It must contain all the correct and pertinent information to ensure that consumers are getting exactly what they're looking for, instead of having to guess. Product labelling should include specific components like-

 Copyright © IJSSER 2025, All rights reserved

ISSN: 2455-8834

Volume:10, Issue:02 "February 2025"

- Product name
- Brand name
- Ingredients
- Net quantity/content
- Manufacturer/distributor information
- Country of origin
- Usage instructions
- Warnings and cautions
- Expiration date
- Nutritional information
- Storage conditions

In India, to protect rights of consumers and to emphasize the need for product labelling and packaging, the Government has enforced numerous laws. These laws act as a measure of protection and self-satisfaction for the customers in terms of quality and quantity. In case the laws are being violated, consumers can seek redressal in district, state or supreme courts, according to the amount of damage incurred. Violation of laws also leads to fines upto Rs.5000 for the producers, and if the offence is repeated, the penalty can be imprisonment upto 5 years. However, in actuality, this is usually not the case. Laws related to product labelling and packaging are not strictly imposed and often violated without any consequences. Moreover, the growing importance of consumer laws under the "Make in India" initiative cannot be overstated. As the manufacturing sector grows, so does the need for strong legal frameworks that protect consumers, ensure product quality, and foster trust in Indian-made products, by aligning with global standards, maintaining transparency, and promoting fair trade practices.

Some of the important laws introduced by the govt. are-

1. Consumer Protection Act, 2019 - This comprehensive law safeguards consumer rights and provides mechanisms for the redressal of complaints regarding defective goods, unfair trade practices, and service deficiencies and ensures that businesses are held accountable for the quality and accuracy of information provided to consumers.

 Copyright © IJSSER 2025, All rights reserved

ISSN: 2455-8834

Volume:10, Issue:02 "February 2025"

2. Legal Metrology Act, 2009 - This law regulates the labelling of products in relation to weights and measures, ensuring transparency and fairness in product labelling and packaging.

3. Food Safety and Standards (Packaging and Labelling) Regulations, 2011 – These regulations ensure that food products are labelled correctly to promote food safety and transparency. Food labels must contain product name, ingredient list, nutritional information, FSSAI license number, expiry date, and vegetarian/non-vegetarian marking.

4. Drugs and Cosmetics Act, 1940 - This law governs the labelling and packaging of pharmaceuticals, drugs, and cosmetics to ensure consumer safety and the authenticity of products. Labels must include **drug composition, usage instructions, batch number, expiry date,** and **manufacturer details.**

Product labelling and packaging is very important in relation to the electronics industry. Great electronics are the culmination of meticulous research, precise engineering, and exhaustive testing. So too are great electronics labels. The labels on electronics teach people how to safely use products. They tell buyers where components were manufactured and what substances they contain. They guarantee authenticity and certify compliance with environmental regulations and quality standards.

Absence of a good label may also cause harm to the users of the product. One such instance is the “Samsung Galaxy Note 7 Battery Explosion Controversy”.

In 2016, **Samsung** launched the **Galaxy Note 7** smartphone, however, within weeks of its release, multiple cases of the phone's **battery overheating** and **exploding** were reported worldwide, including in India. Its packaging and marketing emphasized the phone's advanced technology, including its **battery life and safety features**. However, the labelling failed to disclose potential risks related to the battery's design, which caused **overheating and explosions** in several cases and customers were led to believe the product was entirely safe, with no indication that battery safety could be compromised. This led to several incidents of battery explosions causing injuries and property damages. It also led to huge financial losses for Samsung, and damage to the brand’s reputation.

Hence, good product labelling and packaging is very significant and cannot be compromised.

The phenomenon of social proof also plays a crucial role in influencing consumer behaviour. When consumers observe their favourite influencers using and promoting a product, it creates a sense of trust and validation. This social proof can lead to a Fear of Missing Out (FOMO) effect.

 Copyright © IJSSER 2025, All rights reserved

ISSN: 2455-8834

Volume:10, Issue:02 "February 2025"

Influencers are free to promote any kind of products they want but people must be protected from surreptitious advertising on social media, especially younger users.

Sometimes, people do buy products just to relate with their influencers and to not “miss out”, but most times they buy products based on their understanding.

This study is based on the question: Does influencer marketing actually have a significant impact on consumer´s behaviour and making decisions on purchasing? Our study focusses on the important role of product packaging and labelling, especially in the **electronics industry**.

This is a multifaceted research involving detailed and in-depth study about the topic including a survey as well, where a questionnaire is prepared, asking the respondents questions related to their choices and their thought process prior to purchasing any product.

Literature Review

In the ever-changing environment of customer choices, knowing the variables that impact preferences is critical for both businesses and marketers. This research review investigates the dynamic interaction of product labelling, influencers, celebrity endorsements, and sponsored reviews in changing consumer choices. The key premise of this study is that the informational influence incorporated in product labelling outweighs the impact of other kinds of persuasion.

In a digital age inundated with information, it is critical to identify the variables that genuinely govern customers' decision-making processes. This study attempts to elucidate the present state of knowledge, identify gaps, and lay the groundwork for a more in-depth analysis of the dominance of product labels and packaging in influencing consumer decisions by diving into existing studies in marketing, psychology, and consumer behaviour.

In the article ‘Consumer Psychology Insights and their Use for Operational Book Marketing’ the author provides first insights on how Consumer Psychology could enhance operational book marketing through book design in particular. After highlighting the current German book market and its highly competitive and fast-transforming market situation, the article summarizes recent findings from the field of Consumer Psychology relevant to the book market. The focus lies in the book design which has a large influence on the buyer’s decision making. Three facets of consumer psychological book design (text design, book body and cover design) were the objects of this research and are also a part of product labelling. Research from Consumer Psychology focuses on optimising stimulus design to achieve better information perception, processing and memorization to gain better customer awareness and increase the likelihood of a positive product labelling and buying decision.

 Copyright © IJSSER 2025, All rights reserved

ISSN: 2455-8834

Volume:10, Issue:02 "February 2025"

A study conducted by the Swinburne University of Technology in June 2022 states that brand promotion using celebrities (media, entertainment, and sports stars) and microcelebrities (popular social media users or vloggers) has increased over recent years due to the popularity of social media platforms. The beauty industry has utilised both types of celebrities as influencers to endorse their brands. Despite extensive financial expenditure on using social media influencers by the beauty industry, there is still much to understand about celebrities and micro-celebrities and their effect on consumers' propensity to buy brands based on perceptions formed through celebrity versus micro-celebrity brand endorsements.

Product design has been recognized as an opportunity for differential advantage in the marketplace. The appearance of a product influences consumer product choice in several ways. To assist product development managers in optimising the appearance of products, the present study identified the different ways in which the appearance of a product plays a role in consumer product evaluation and, hence, choice. In addition, the implications for product design of each role are listed, and managerial recommendations for optimising the appearance of products are given. Based on a literature review, six different roles of product appearance for consumers are identified:

(1) communication of aesthetic, (2) symbolic, (3) functional, and (4) ergonomic information; (5) attention drawing; and (6) categorization.

A product's appearance can have aesthetic and symbolic value for consumers, can communicate functional characteristics and give a quality impression (functional value), and can communicate ease of use (ergonomic value). In addition, it can draw attention and influence the ease of categorization of the product. Insight into how appearance characteristics, such as form and colours, may influence consumer choice will increase managers' awareness about how to use product appearance as a marketing tool.

The data analysis by 'Review of International Business and Strategy' revealed an excellent fit for the data and indicated an impact of attractiveness and expertise on online engagement and personal interest. Moreover, a mediating influence was also found for online engagement on the path between influencer credibility and personal interest. This study has the limitation of collecting the data from only three influencers; consequently, collecting data from the followers of more than three influencers would get more generalisable results. Second, considering further, examining the mediating role of other variables such as electronic word-of-mouth (EWOM) and loyalty programs could also provide further insights into the nature of the factors affecting the personal interest. In addition, future studies should examine the differences in using more than one social media platform. The main findings of this study have several managerial implications for marketing management that hint at liking the influencers who are highly trusted owing to

 Copyright © IJSSER 2025, All rights reserved

ISSN: 2455-8834

Volume:10, Issue:02 "February 2025"

their extensive expertise in the area they are marketing rather than only depending on their physical attractiveness. Significantly, a set of managerial implications comes from the current research. Two major areas are the most important; these are the trustworthy issue and the EWOM. Marketers should encourage their customers to openly talk about their experiences as they have an imperative role in liking influencers in a way that improves their personal interest. The second implication is related to social media platform management that marketing managers should resolve any negative EWOM caused and enhance followers' satisfaction levels with the services. The increase in satisfaction positively affects personal interest, and the service makes the influencer role more effective.

A study published in the Journal of Marketing investigates the effect of corporate brand dominance—that is, the visibility of a company's corporate brand in product communications—on the relationship between corporate associations and product evaluations. The results show that corporate brand dominance determines the degree to which associations with the company's corporate ability and corporate social responsibility influence product attitudes, as well as the nature of the moderating effects of fit and involvement.

Another study proposes a domain statement for strategic marketing as a field of study and delineates certain issues fundamental to the field. It also proposes a definition for marketing strategy, the focal organisational strategy construct of the field, and enumerates several foundational premises of marketing strategy. The domain of strategic marketing is viewed as encompassing the study of organisational, inter- organizational and environmental phenomena concerned with the behaviour of organisations in the marketplace in their interactions with consumers, customers, competitors and other external constituencies, in the context of creation, communication and delivery of products that offer value to customers in exchanges with organisations, and the general management responsibilities associated with the boundary spanning role of the marketing function in organisations. At the broadest level, a marketing strategy can be defined as an organisation's integrated pattern of decisions that specify its crucial choices concerning products, markets, marketing activities and marketing resources in the creation, communication and/or delivery of products that offer value to customers in exchanges with the organisation and thereby enables the organisation to achieve specific objectives. Chief among the issues that are fundamental to strategic marketing as a field of study are the questions of how the marketing strategy of a business is influenced by demand-side factors and supply-side factors.

A clear conclusion arises from a review of different research papers and articles that give reasons in favour of product labelling and packaging, as well as opposing positions claiming that influencers, celebrity endorsements, and sponsored reviews are more influential. This literature study demonstrates that product labelling and packaging are becoming more important in

 Copyright © IJSSER 2025, All rights reserved

ISSN: 2455-8834

Volume:10, Issue:02 "February 2025"

moulding customer choices than external factors such as celebrity endorsements or sponsored reviews.

Product labelling includes components like text design, cover design, and aesthetics, all of which play an important part in influencing consumer decisions and leaving an impression. The informational feature, when properly executed, not only increases the product's trustworthiness and credibility but also adds to the development of customer confidence.

Methodology

This study employs a descriptive research design. The methodology consists of several key components: literature reviews, surveys (including both sample and pilot surveys), case studies, interviews, and an analysis of various electronic products' guides and manuals.

Literature Review: To pinpoint important themes and patterns in consumer behaviour, a thorough examination of previous research, industry reports, and scholarly publications will be done.

Survey: To collect quantitative data on preferences, satisfaction, and purchase behaviours, an evenly distributed random sample of consumers within India will be given a standardized questionnaire.

Pilot Survey: To test and improve the questionnaire for reliability and clarity, a small, representative group will be initially surveyed. The improved survey will be shared with the rest of the of the sample after making changes suggested by a small group of people.

Case Studies: In-depth analyses of a few chosen electronic consumer durables of a few brands will be conducted in order to assess their labelling and packaging.

Interviews: To study the impact of labelling and packaging on consumers, salespeople will be interviewed.

Product Labelling and Manuals: To assess how well businesses inform customers about critical product information, an examination of product labels, manuals, and guidelines will be conducted.

Survey Analysis and Results

Survey Design

A set of questionnaires consisting of 9 items will be used as the instrument in this study.

 Copyright © IJSSER 2025, All rights reserved

ISSN: 2455-8834

Volume:10, Issue:02 "February 2025"

The questionnaire begins with the personal information of the respondents i.e. name, gender, age and Income per month / parents' income per month.

- **BLOCK 1:** Q1and Q2 are related to consumer's shopping habits.
- **BLOCK 2:** Q4 and Q5 attempt to delve into the psychological dimensions which can assist in understanding how consumers make purchase decisions.
- **BLOCK 3:** Q6 tells us about the key influences in the decision-making process for purchases.
- **BLOCK 4:** Q3, Q7 and Q8 on how different types of influencers affect preferences, and if influencer-driven consumer preferences are more pronounced in certain industries.
- **BLOCK 5:** Q9 is a subjective question focusing on the quality expectations and industry standards.

Data Sets and Study Area

The survey will be conducted through Google Forms with responses from people of different age and income groups. The form will be circulated through WhatsApp and other social media platforms. People of diverse age groups and social backgrounds will participate in the survey. The survey will be conducted nationally.

The data set includes demographic details such as age, gender and income level. Understanding the composition of the survey participants is crucial for identifying potential patterns in consumer behaviour across different demographic groups.

The participants will be surveyed on their preferences regarding advertisements they see, impact of influencers and social media user experience, marketing, etc.

Pilot Study

A pilot survey will be conducted to check the reliability of the questionnaire. It is a strategy that helps to evaluate or test a questionnaire using a smaller sample size than the planned sample.

Data Collection

The data collected from people of different age groups will be used to arrive at a conclusion. The questionnaire will be sent to the students and teachers of various schools and colleges, employees of various firms and organizations across India.

 Copyright © IJSSER 2025, All rights reserved

ISSN: 2455-8834

Volume:10, Issue:02 "February 2025"

Data Analysis

Statistical tools will be employed to analyse quantitative data in order to get numerical insights. After the responses are sorted and organised into databases, trends and patterns can be systematically investigated. A quantitative summary of the frequency of particular viewpoints among the participant population will be given by descriptive statistics.

Manual analysis will be performed on the qualitative data, carefully reviewing the answers to open-ended questions to look for reoccurring themes and subtle insights.

Respondents' Demographics

The survey held a total number of 413 respondents

GENDER	
MALE	43.8%
FEMALE	55.4%
OTHER	0.7%

SALARY BRACKETS	
LESS THAT Rs.50,000	11.9%
BETWEEN Rs.50,000 AND Rs.1,00,000	24.5%
BETWEEN Rs.1,00,000 AND Rs.3,00,000	34.6%
MORE THAN Rs.3,00,000	29.1%

 Copyright © IJSSER 2025, All rights reserved

ISSN: 2455-8834

Volume:10, Issue:02 "February 2025"

AGE	NO. OF RESPONDENTS
10-20	188
20-30	60
30-40	78
40-50	60
50-60	22
60-70	4
70-80	1

Findings

BLOCK 1:

Q1 and Q2 are related to consumer's shopping habits.

Q1) Before purchasing any product do you like to see/ hear advertisements about it?

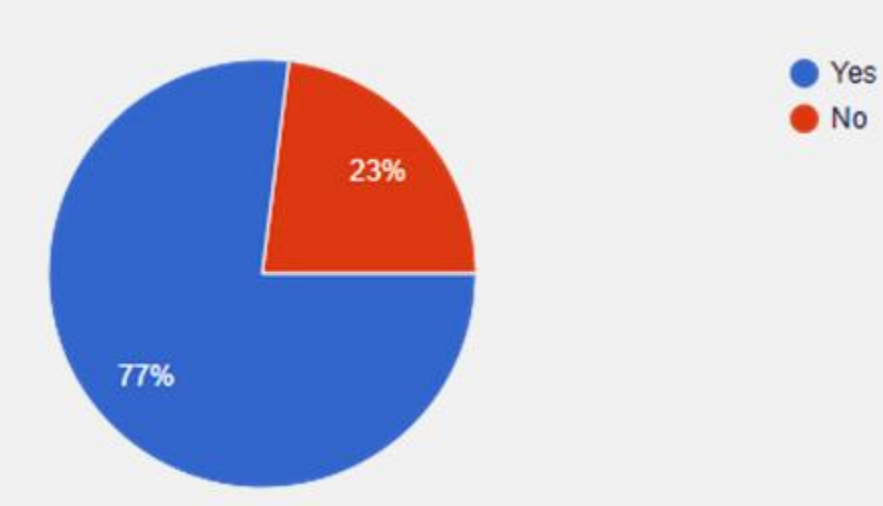

According to the study, 77% of respondents prioritized ads before making a purchase, highlighting the powerful influence of advertising. This suggests that by providing vital information about items, ads play a critical role in increasing consumer awareness and

 Copyright © IJSSER 2025, All rights reserved

ISSN: 2455-8834

Volume:10, Issue:02 "February 2025"

confidence. The remaining 23%, however, represent a growing group of independent-minded consumers who prefer real-world experiences, evaluations, and in-depth research over conventional marketing strategies. This discrepancy reflects a changing consumer environment where transparency and trust are becoming increasingly important.

Advertisers need to adjust by developing campaigns that emphasize sincere and meaningful narrative rather than just promotion. In a time when people are becoming more skeptical of traditional marketing, brands may stay relevant and trustworthy by matching their strategies with the values and interests of their target audience.

Future Trend:

According to the report, a noteworthy trend for the future is the emergence of "authentic advertising", in which companies emphasize openness, narrative, and user-generated material in order to foster trust. Using social proof, influencer endorsements, and interactive experiences will become more and more popular as customers look for real relationships. Additionally, generic messages will be replaced by tailored, data-driven ads that speak to people's beliefs and preferences, maintaining a balance between traditional awareness campaigns and the need for decisions that are meaningful and supported by research.

Q2) Before purchasing any product do you read the product labelling?

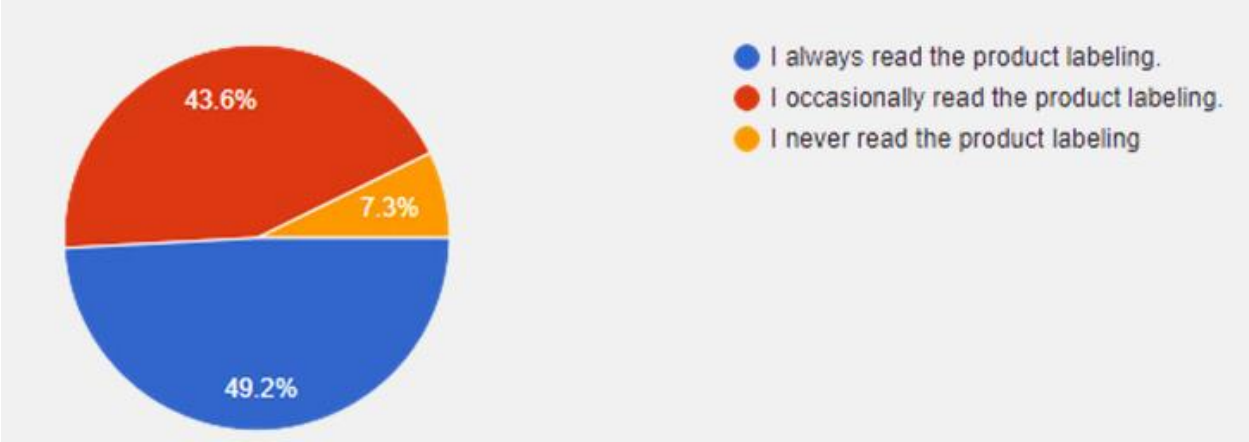

According to the survey, 49.2% of participants routinely read product labels, and 43.8% do so occasionally, indicating a growing consumer preference for transparency. This underlines the significance of clear, accessible labelling in addressing ethical, safety, and health concerns. The 7.3% of people who never read labels may value convenience or have a strong brand loyalty. This behavioural gap points to a dual potential for businesses: simplifying labelling for less involved consumers while simultaneously satisfying knowledgeable people looking for precise,

 Copyright © IJSSER 2025, All rights reserved

ISSN: 2455-8834

Volume:10, Issue:02 "February 2025"

in-depth information. This disparity can be closed and inclusivity ensured by giving priority to sustainable certifications, clear messaging, and label readability.

Future Trend:

There may be a move toward interactive labelling as customers want more clarity. Stronger brand- consumer trust can be developed by using digital tools like QR codes or augmented reality labels to deliver real-time, comprehensive product data, including sourcing, sustainability, and ethical practices.

BLOCK 2:

Q4 and Q5 attempt to delve into the psychological dimensions which can assist in understanding how consumers make purchase decisions

Q4) Have you purchased a product solely based on a recommendation from an influencer or celebrity sponsorship?

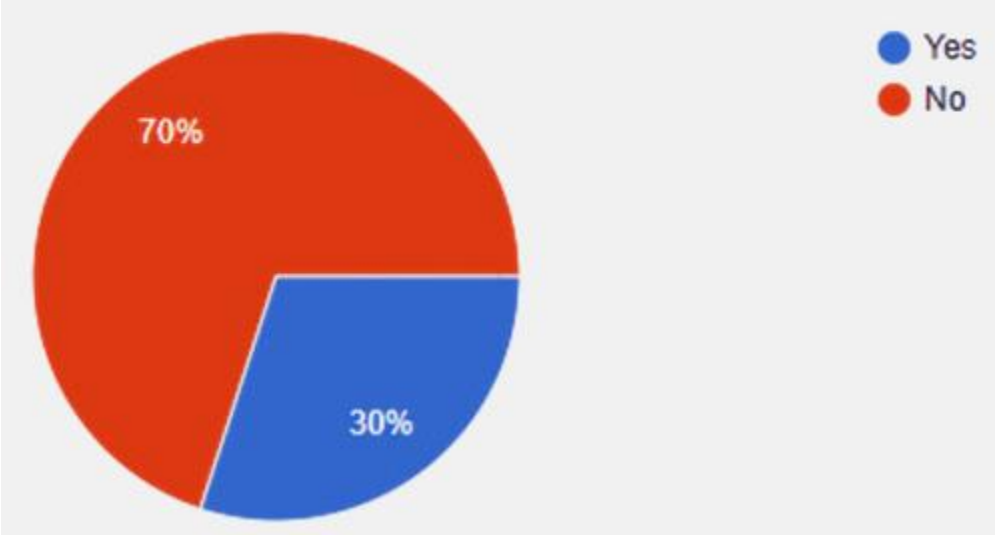

The study found that while 70% of the respondents did not buy a product because of a suggestion from a celebrity or influencer, 30% of them acknowledged doing so. This shows that although a significant percentage of consumers are influenced by influencer marketing, most of them are still discriminating and give consideration to things like product reviews, quality, and individual needs. The frequency of deceptive endorsements and increased attention to sponsored material point to consumers become more astute and discerning. Brands are being pushed to use more genuine and open promotional tactics as a result of a larger trend of growing customer awareness and mistrust about marketing tricks.

 Copyright © IJSSER 2025, All rights reserved

ISSN: 2455-8834

Volume:10, Issue:02 "February 2025"

Future Trend:

Brands may turn to community-driven endorsements or micro-influencers that prioritize relatability and reliability over celebrity status as customers seek authenticity. In the changing landscape of consumer preferences, marketing transparency supported by user testimonials and verifiable claims is probably going to become a defining trend.

Q5) Do you feel pressured to buy certain products because they are popular among your social group or community?

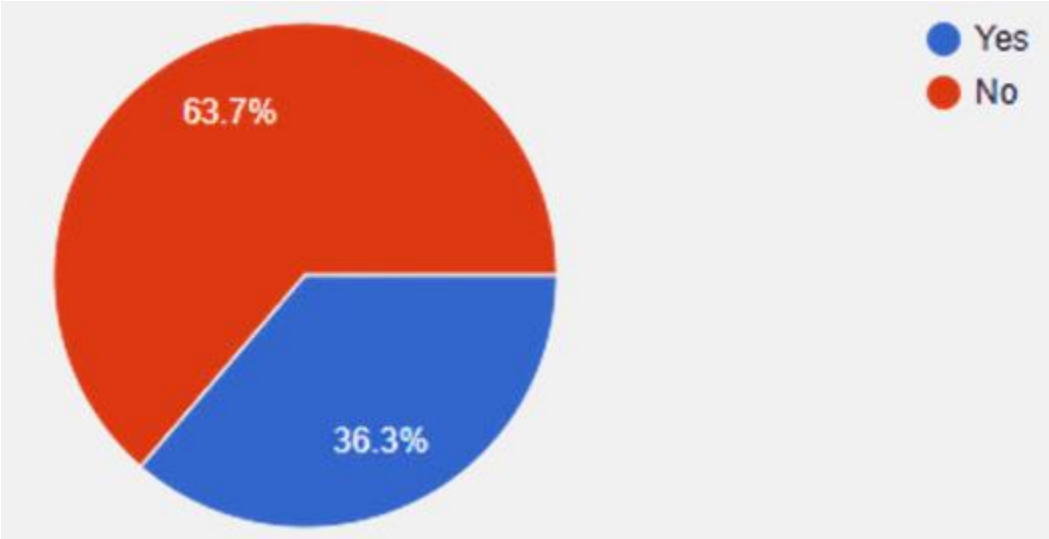

As evidenced by the fact that 36.3% of the respondents acknowledged feeling pressured to purchase goods that are popular in their social circles, peer pressure still has a big influence on consumer behaviour. This suggests that social acceptance and the need to blend in continue to be significant motivators, particularly for younger audiences or people who use social media extensively. The majority—63.7%—reported no such impact, indicating a move toward thoughtful consumption, in which financial awareness, pragmatism, and personal values inform purchases. This gap demonstrates the complex relationship between cultural norms and personal freedom, showing that although society's trends influence some, many people value their own judgment or follow budgetary restrictions over following the crowd.

Future Trend:

Brands may experience a rise in demand for authenticity, transparency, and products that reflect environmental or ethical ideals as mindful consumerism rises. Instead of generic mass trends, consumers are likely to favour individualized recommendations and items that represent their

 Copyright © IJSSER 2025, All rights reserved

ISSN: 2455-8834

Volume:10, Issue:02 "February 2025"

uniqueness. In addition to creating communities that prioritize shared values above popularity, this change may inspire businesses to innovate by providing niche, personalized products.

BLOCK 3:

Q6 is a question which tells us about the key influences in the decision- making process for purchases.

Q6) When considering a purchase, what factors weigh heaviest in your decision-making process?

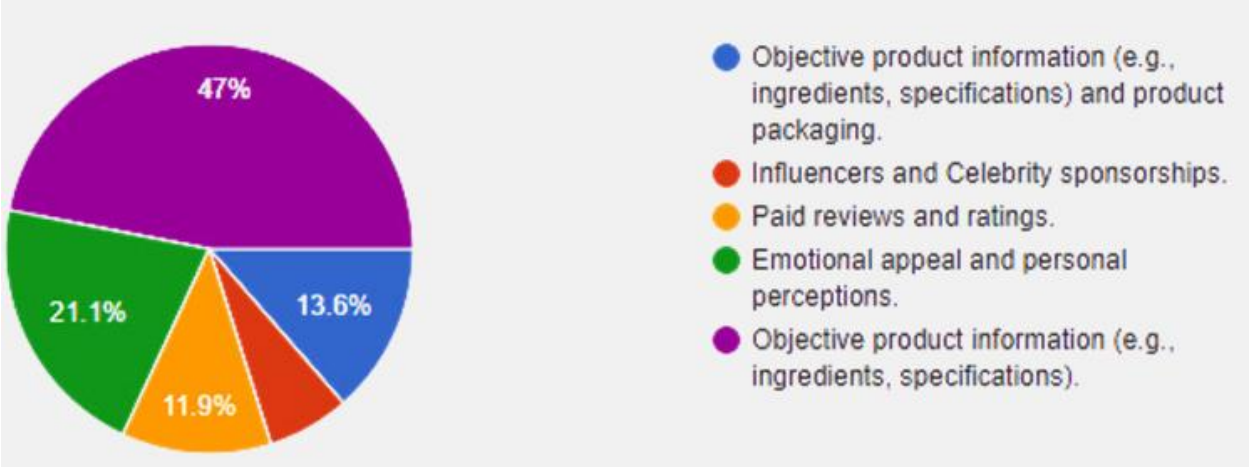

The pie chart shows that 47% of the respondents prioritize objective product information (e.g., ingredients and specifications) and 13.6% also are influenced by product packaging along with labelling in their decision-making process, indicating a clear preference for factual and value-driven factors when making a purchase. Emotional appeal and personal perceptions show the second major factor at 21.1%, showing that while emotional triggers are important, they are secondary to product facts. Influencers and celebrity sponsorships account for only 6.5%, suggesting minimal dependence on endorsements, while paid reviews and ratings are prioritized by 11.9% of respondents. This trend highlights a shift toward transparency and informed decision-making, where consumers place trust in clear and factual product-specific information over external influences like celebrity endorsements or promotional reviews.

Future Trend:

The future purchasing landscape is likely to be shaped by consumers demanding greater transparency and clarity in specific information about products. With more than half (47% + 13.6%) of respondents prioritizing objective product details, buyers are moving towards a preference for factual decision- making over hype or endorsements and advertisements. The relatively low influence of celebrity sponsorships (11.9%) and paid reviews (13.6%) signals a

 Copyright © IJSSER 2025, All rights reserved

ISSN: 2455-8834

Volume:10, Issue:02 "February 2025"

shift away from traditional promotional tactics. Emotional appeal (21.1%) is relevant but will not dominate decisions. Moving forward, businesses will need to focus on providing clear and verifiable product information and inculcating authenticity to resonate with increasingly discerning and value-conscious consumers.

BLOCK 4:

Q3, Q7 and Q8 delve on how different types of influencers affect preferences and if influencer driven consumer preferences are more pronounced in certain industries.

Q3) Do you feel that celebrity recommendations affect your taste and preferences for existing products?

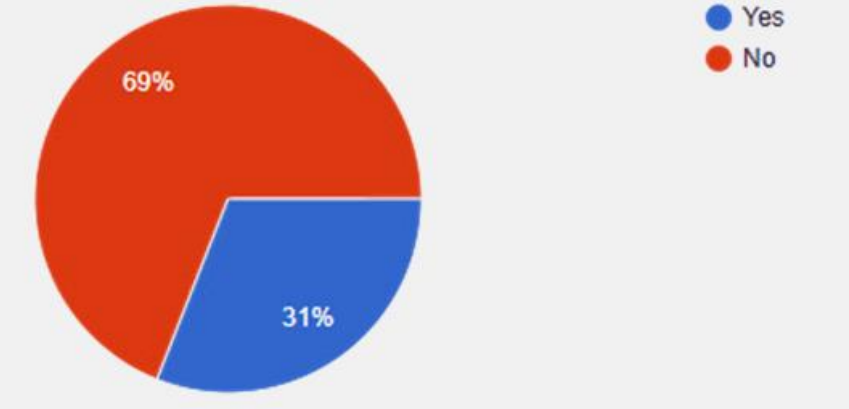

The pie chart reveals that 69% of respondents are not influenced by celebrity recommendations, which indicates a strong preference for independent decision-making based on product value, quality, or personal experience, i.e. respondents' own perception and opinion about the product. In contrast, 31% of respondents still admit to being swayed by celebrity endorsements, showcasing the continued relevance of influencers and celebrity endorsements for a significant minority. This split highlights a dual opportunity for businesses: they can focus on delivering high-quality products to appeal to the majority who value substance while strategically leveraging aspirational branding to engage the 31% who respond positively to such campaigns. Understanding these preferences can help businesses strike a balance between authenticity and influencer-driven marketing to maximise their reach.

Future Trend:

The future trend that can be inferred is that there is a growing consumer preference for independent decision-making based on product quality and personal experiences, rather than relying on celebrity recommendations and influencers. As 69% of respondents currently

 Copyright © IJSSER 2025, All rights reserved

ISSN: 2455-8834

Volume:10, Issue:02 "February 2025"

prioritize substance over influencers influence, this trend may continue to rise with increased detail to product information. However, the 31% influenced by celebrities highlights that influencer marketing will remain relevant, particularly among younger, social media-driven demographics. Moving forward, brands may shift toward micro-influencers and authentic endorsements that align with consumer values, blending trustworthiness with aspirational appeal to cater to both segments.

Q7) To what extent does the information on a product's label influence your trust in products recommended by influencers?

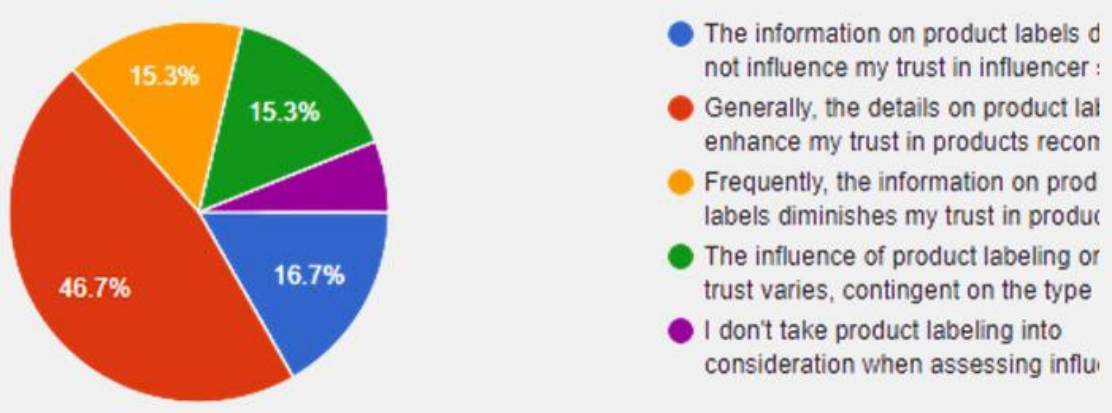

The survey results highlight how product labelling plays a complex role in determining customer trust, especially when it comes to products that influencers recommend. The significance of transparency and trustworthiness is highlighted by the noteworthy 46.7% of participants who link clear labelling to higher confidence. However, 15.3% report feeling less trusted, most likely as a result of differences between the claims made about the product and its actual content. An further 15.3% emphasize the effect of the influencer's image, suggesting that trust depends on both the product and its promoter. It's interesting to note that only 16.7% and 6.1% reject or don't care about labelling, indicating that most consumers consider it to be important. These findings indicate a rising need for influencer credibility, product integrity, and label congruence.

Future Trend:

As awareness grows, companies may use QR codes or AR to create dynamic, interactive labels that guarantee thorough transparency and increase confidence. Collaborations with true niche or micro-influencers who advertise the product according to the specifications mentioned on the labels may also prove to be a crucial tactic in bringing product values into line with audience expectations.

 Copyright © IJSSER 2025, All rights reserved

ISSN: 2455-8834

Volume:10, Issue:02 "February 2025"

Q8) How does the increasing use of influencers to promote products affect your opinions compared to traditional advertisements like TV, newspapers, and pamphlets?

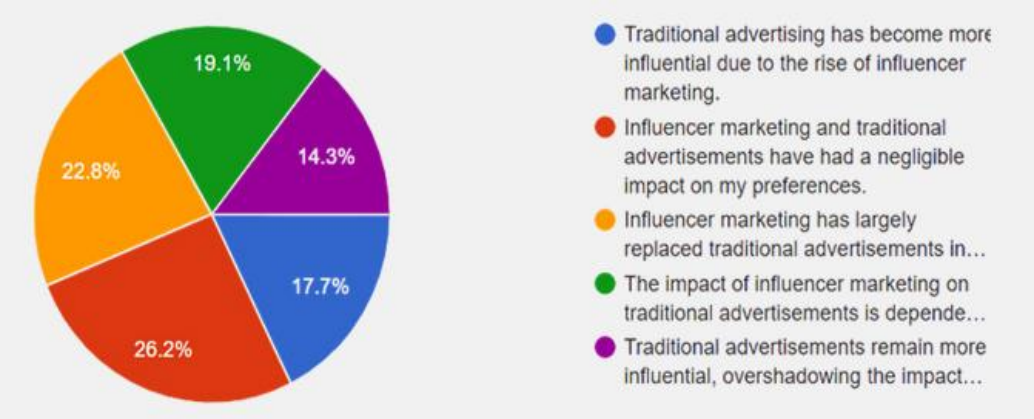

The pie chart highlights a diverse perception of the influence of influencer marketing versus traditional advertisements. The largest portion, 26.2%, suggests that both influencer marketing and traditional advertisements have had negligible impact on consumer preferences, suggesting a group of consumers being unaffected by marketing trends. However, 22.8% feel influencer marketing has largely replaced traditional ads, showcasing its growing prominence. Meanwhile, 19.1% believe influencer impact depends on specific factors, reflecting nuanced views. Traditional advertising is still perceived as influential by 14.3%, while 17.7% believe traditional ads have become more impactful due to the rise of influencer marketing. This data indicates a transitionary phase where influencer marketing is gaining ground and importance but traditional advertisements still hold relevance, with split consumer opinions based on personal experiences and exposure.

Future Trend:

Moving forward, we can expect a blend of both approaches (influencer marketing and traditional ads), with brands using influencer collaborations alongside traditional ads to maximize reach. As consumers become more discerning, authentic and tailored marketing strategies will be essential, with brands leveraging influencers to add credibility and resonance to their campaigns and only providing correct information without missing out on any detail related to the product. The same details or the pros and cons of the product should also be mentioned on the label to enhance consumer's trust.

BLOCK 5:

Q9 is a subjective question focusing on the quality expectations and industry standards.

 Copyright © IJSSER 2025, All rights reserved

ISSN: 2455-8834

Volume:10, Issue:02 "February 2025"

Q9) Did you buy something that a famous personality/influencer/celebrity suggested? Did the product you buy based on the recommendations, met your expectations and was it aligned with industry standards?

Diverse viewpoints surfaced in answer to the subjective question regarding buying things that influencers endorse. Majority of respondents have not bought products based on celebrity endorsements or influencer recommendations, indicating a skeptical and cautious approach to such endorsements. For those who did purchase based on recommendations, say that meeting expectations and alignment with industry standards were crucial for satisfaction. Many respondents wrote that the products bought after influencer's recommendations didn't meet the standards. This reflects a shift towards evidence-based and factual marketing and authenticity, where consumers prioritize independent reviews, product transparency and detailed product information on the labels over celebrity influence.

Hypothesis Proven

The finding results show that Product labelling places a vital role in shaping consumer preferences and choices.

Responses to Question 6 prove our hypothesis. Responses to Question 3 and 7 reaffirm our hypothesis.

Our study confirms that product labelling holds greater sway in shaping consumer preferences compared to influencers, celebrity endorsements, and paid reviews. Findings reveal that consumers overwhelmingly prioritize clear and comprehensive information given on the product labels when making purchasing decisions. This demonstrates that details, such as ingredients, specifications, and certifications, on the labels, are perceived as more credible and trustworthy than external endorsements.

Furthermore, our theory is supported by the understanding that product design and appearance i.e. the packaging also plays a crucial role in consumer decision-making.

The results of Questions 6, 3 and 7 points to the multidimensional nature of product information, providing a thorough grasp of the variables impacting modern customer decisions. This empirical validation strengthens the validity of our findings and adds insightful information to the changing picture of customer preferences in marketing.

Now we'll look at the importance of transparent and easy-to-understand labels that give accurate information for electronic consumer durables.

 Copyright © IJSSER 2025, All rights reserved

ISSN: 2455-8834

Volume:10, Issue:02 "February 2025"

To support our study, we will use a multifaceted method that includes case studies, interviews with salespeople, consumers and technicians, and a careful evaluation of labels, guides, and manuals for a select electronic consumer durables. By analysing real-world instances, we want to demonstrate the influence of unambiguous labelling on customer behaviour and preferences.

Labelling & Electronic Consumer Durables

Introduction

The importance of labelling in electronic consumer items has grown in an era where transparency, safety, and ethical standards are critical to customer confidence. Labels are intended to tell customers about a product's components, safety warnings, and usage instructions, allowing them to make informed purchase decisions. But labels are actually employed as a sales tool, in which exaggeration or incomplete truths are offered in order to attract new consumers. This technique, which emphasises alluring promises with incomplete or incorrect facts, can be damaging, as a half-truth is typically more likely to mislead than an explicit fabrication. This current environment shows substantial gaps in labelling policies and practices, where inconsistent, confusing, or insufficient labelling not only misleads customers but, in some circumstances, poses actual safety hazards.

Consider the example of carmine, which is a captivating pigment, its origins rooted in the vibrant world of cochineal insects. Carmine is a natural red dye derived from the female cochineal insect, notably the Dactylopius coccus species. It is known for its vivid and long-lasting colours. These small insects, native to South America, are dried and crushed to obtain their deep red colour. This pigment, sometimes known as "cochineal extract," "natural red 4", or "E120," is often used to produce a brilliant red colour in candies (e.g., Nerds candies, mentos gum), juices (e.g., dole), and cosmetics (e.g., lipsticks and numerous other cosmetics formulations).

Source: Instagram- theoddanimalspecimens

 Copyright © IJSSER 2025, All rights reserved

ISSN: 2455-8834

Volume:10, Issue:02 "February 2025"

The labelling of Nerds candy is an example of inefficient and conflicting labelling. While the ingredient list indicates the usage of carmine colour—an insect-derived dye—the product is also marketed as vegetarian. This mismatch causes uncertainty for customers looking for clarity on whether the food meets vegetarian dietary criteria, emphasising the need for more accurate and clear labelling processes.

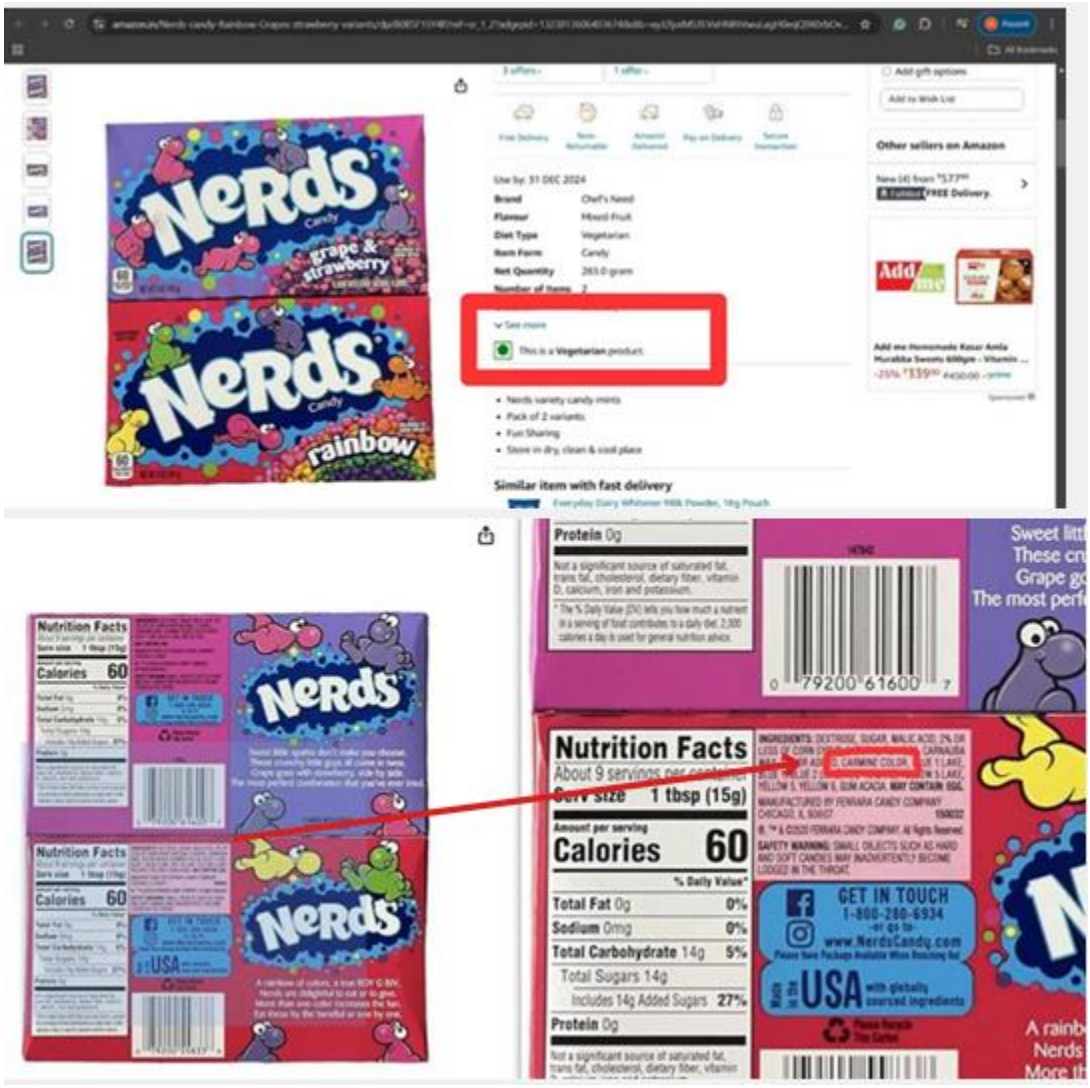

Source: amazon.in

In addition to ingredient labelling, recent events have shown significant loopholes in safety labels for electronic consumer durables. In September 2024, an India Today story reported an alarming incident with Samsung's FE earphones, which burst while being used by a Turkish user, resulting in irreversible hearing loss.

 Copyright © IJSSER 2025, All rights reserved

ISSN: 2455-8834

Volume:10, Issue:02 "February 2025"

Source: India today

The examination of the earphones' packaging and product literature indicated a lack of information concerning the harmful consequences of the materials used in the earbuds, both on the company's official website and famous online shopping platforms like Amazon.

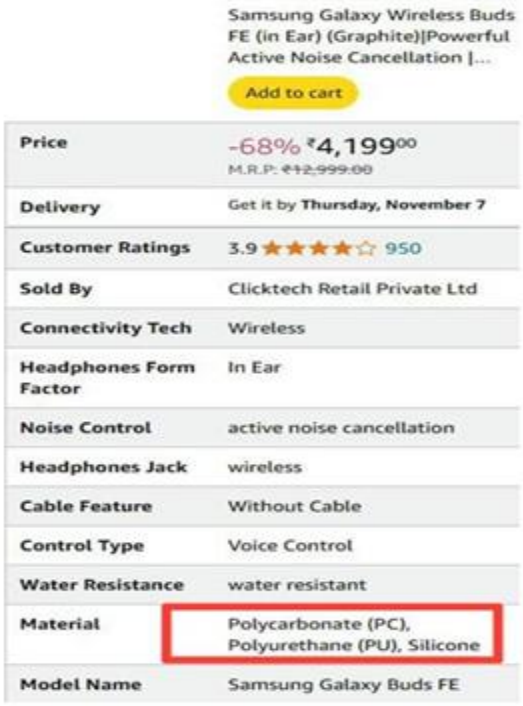

Samsung Galaxy Wireless Buds FE (in Ear) (Graphite)|Powerful Active Noise Cancellation |...

Add to cart

Price	-68% ₹4,199.00 M.R.P: ~~₹12,999.00~~
Delivery	Get it by Thursday, November 7
Customer Ratings	3.9 ★★★★☆ 950
Sold By	Clicktech Retail Private Ltd
Connectivity Tech	Wireless
Headphones Form Factor	In Ear
Noise Control	active noise cancellation
Headphones Jack	wireless
Cable Feature	Without Cable
Control Type	Voice Control
Water Resistance	water resistant
Material	Polycarbonate (PC), Polyurethane (PU), Silicone
Model Name	Samsung Galaxy Buds FE

source: amazon.in

Although the material composition—polycarbonate, polyurethane, and silicone—is indicated on Amazon, possible health dangers associated with these materials, such as the volatile organic compounds (VOCs) and isocyanates emitted by polyurethane, are not mentioned.

 Copyright © IJSSER 2025, All rights reserved

ISSN: 2455-8834

Volume:10, Issue:02 "February 2025"

Source: https://www.protolabs.com/materials/polycarbonate/

This lack of transparency on health hazards associated with materials used in electronics highlights a major issue in labelling, where insufficient safety information fails to safeguard customers and undermines product accountability.

Inefficiencies in the labelling of electronic consumer durables, such as washing machines, smartphones, hair dryers, etc., have an influence on customer trust and market dynamics.

These durable products are substantial investments, with costs ranging from a few hundred to several thousand rupees, so making informed choices is critical. Consumers use labels, product guides, and safety information to determine product quality and suitability for their requirements. When these labels lack clarity, accuracy, or specificity, consumers' belief in the brand suffers, resulting in lower brand loyalty, a poor reputation, and a poor view of the industry. For a country like India, which is expected to become the world's fourth-largest consumer durable market by 2030, ineffective labelling is a barrier to developing a strong local manufacturing base and convincing customers to see Indian-made items as reliable.

Source: indbiz.gov.in

 Copyright © IJSSER 2025, All rights reserved

ISSN: 2455-8834

Volume:10, Issue:02 "February 2025"

India's increased emphasis on local manufacturing, exemplified by programs such as "Make in India," has fuelled ambitions to make the country a major hub for consumer durables. Nonetheless, this expansion necessitates stringent labelling regulations that guarantee consumers are well-informed and confident in their purchases. Indian products have always had a reputation for being of poorer quality, which has hampered their global appeal. By focusing on labelling standards and enhancing trust in them, Indian firms can provide the groundwork for self-sufficiency, improved manufacturing quality, and a strong customer base that values homegrown goods.

We will now fill these gaps by investigating real-life case studies, customer complaints, and interviews to better understand the issues of labelling in electronic consumer durables. This project will use this data to build prototype labels for major items, with an emphasis on washing machines, smartphones, and hair dryers. These labels will highlight clarity, complete safety and material information, and openness to provide customers with the knowledge they need to make safe and educated purchasing decisions.

The analysis will also include recommendations to producers, importers, and retailers on how to implement these better labelling requirements to increase customer trust and market growth. Furthermore, it emphasises the necessity for regulatory authorities to implement stronger labelling laws and undertake frequent assessments in order to maintain high standards. A dedication to clear and accurate labelling methods would not only empower customers but will also position Indian firms as dependable and quality- conscious participants in the global market.

Case Study Analysis

Introduction

A key component of open communication between brands and customers, effective product labelling influences both customer satisfaction and purchase decisions. The examined case studies, however, highlight serious issues in this field, such as inadequate data, subpar design, and an excessive dependence on salespeople for sophisticated consumer durables. These problems run the risk of undermining consumer confidence in brands in addition to preventing them from making well-informed decisions. This study explores the serious flaws in product labelling procedures and emphasizes how they affect customer perception and corporate operations.

Following are the case studies with their analysis

 Copyright © IJSSER 2025, All rights reserved

ISSN: 2455-8834

Volume:10, Issue:02 "February 2025"

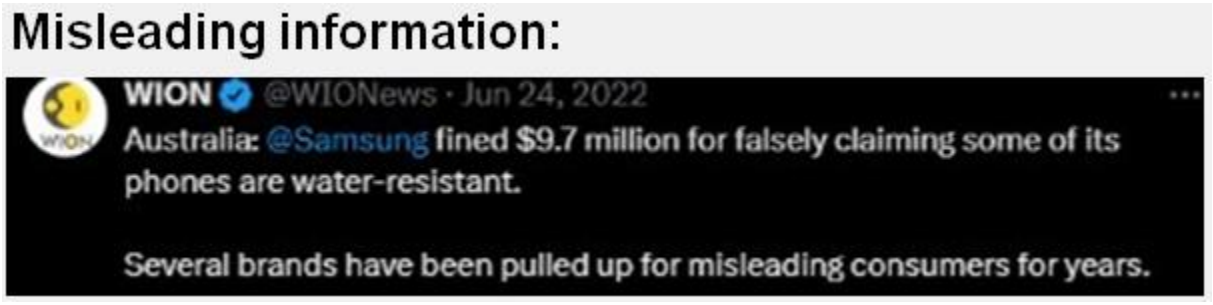

source: X (formerly known as Twitter)) (Samsung smartphone

There is no comprehensive information on the product's warranty or upkeep on the label. If customers feel unprepared for long-term costs, this could be a potential source of their discontent.

Customers may require clarification regarding the product's care and durability, which can be made worse by inaccurate information or ambiguous descriptions. To build trust and make sure that customers are well-informed and ready to make a long-term investment, transparency in these areas is crucial. Businesses can increase customer satisfaction and loyalty by making the label more comprehensive and clearer.

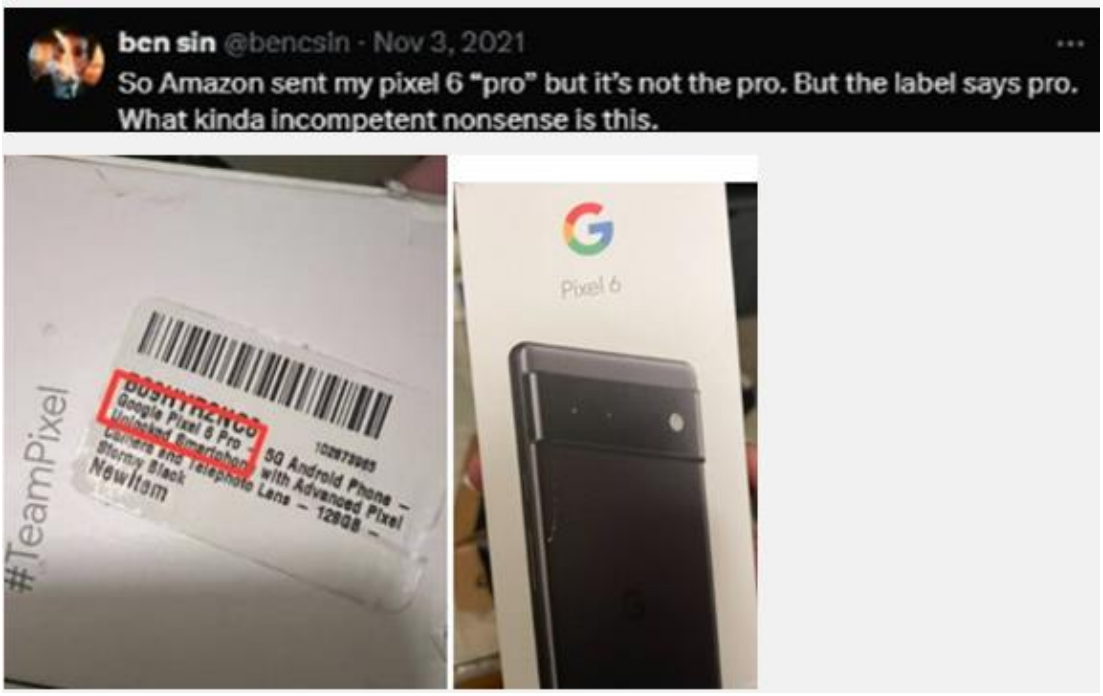

source: X (formerly known as Twitter)) (Google smartphone

 Copyright © IJSSER 2025, All rights reserved

ISSN: 2455-8834

Volume:10, Issue:02 "February 2025"

False labelling occurs when a product is mistakenly identified as a different model, usually one that is more costly than it is. It is challenging to concentrate on important information because of the text's small font and crowded arrangement. Because of the overall disarray in the design, the client may be overloaded with details in a small area. Technical features are attempted to be displayed, but the small text makes it hard for the typical consumer to read quickly.

source: X (formerly known as Twitter)) (Lava smartphone

The lack of important information, such as setup instructions or user safety instructions, could cause confusion when using the product for the first time. Important details that are essential for customers to make an informed choice, such as power consumption or warranty period, are not readily apparent.

Once more, the buyer is duped by giving them inaccurate or insufficient information. In this case, the product only has 4GB of RAM, despite the label stating that it has 12GB. Confusion may result from this, particularly for those buying the product online.

 Copyright © IJSSER 2025, All rights reserved

ISSN: 2455-8834

Volume:10, Issue:02 "February 2025"

source: X (formerly known as Twitter)) (Vivo smartphone

The product's construction quality and materials are not specified, which can be crucial for buyers who are worried about longevity. Additionally, the manufacturing date printed on the label is incorrect, per the post on X (an example of false labelling).

Stricter government regulations and sanctions must be put in place to guarantee that consumers only receive high-quality goods. By taking these steps, a more regulated market may be

 Copyright © IJSSER 2025, All rights reserved

ISSN: 2455-8834

Volume:10, Issue:02 "February 2025"

established, where goods must pass stringent quality checks before being sold to customers and labels accurately describe what they are.

Governments can encourage companies to put quality, product safety, and proper labelling first by enforcing harsher penalties on producers and retailers who disregard these guidelines.

Ambiguous Labelling:

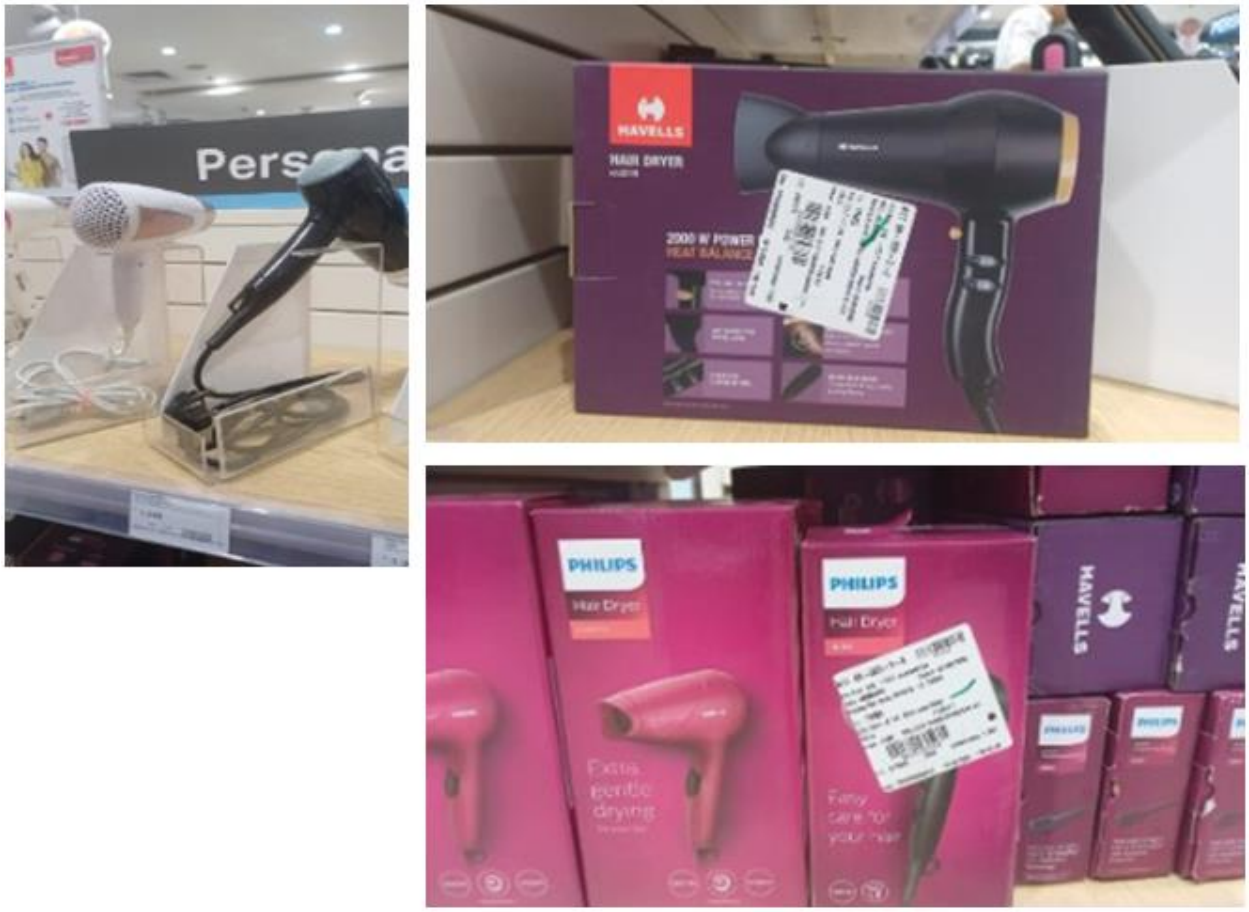

Philips and Havells Hair Dryers

Customer service information and after-sales support are not mentioned, despite the fact that they may be crucial for problems that arise after a purchase.

Customers may believe the product has extra features that aren't there because of the way it is displayed. It's unclear whether the product works with other systems or accessories.

 Copyright © IJSSER 2025, All rights reserved

ISSN: 2455-8834

Volume:10, Issue:02 "February 2025"

Furthermore, crucial details like body type, quality, heat level, and energy consumption are not made explicit. It is essential to give prospective customers this information so they can make an informed choice.

Apple iPhone 13

- It is challenging to discern the most important information from the label (back) because it seems cluttered with too much text.
- Customers may become irate if the label fails to provide enough information about the warranty or after-sales care.
- Customers may be misled about what is included if the product is displayed without all of its expected features or accessories.

 Copyright © IJSSER 2025, All rights reserved

ISSN: 2455-8834

Volume:10, Issue:02 "February 2025"

- All relevant product details, including RAM, storage, screen size, processor, and operating system, should be prominently displayed on product packaging and in stores for items like smartphones.
- Clear information regarding after-sales care and service, including part and repair costs, should also be included.

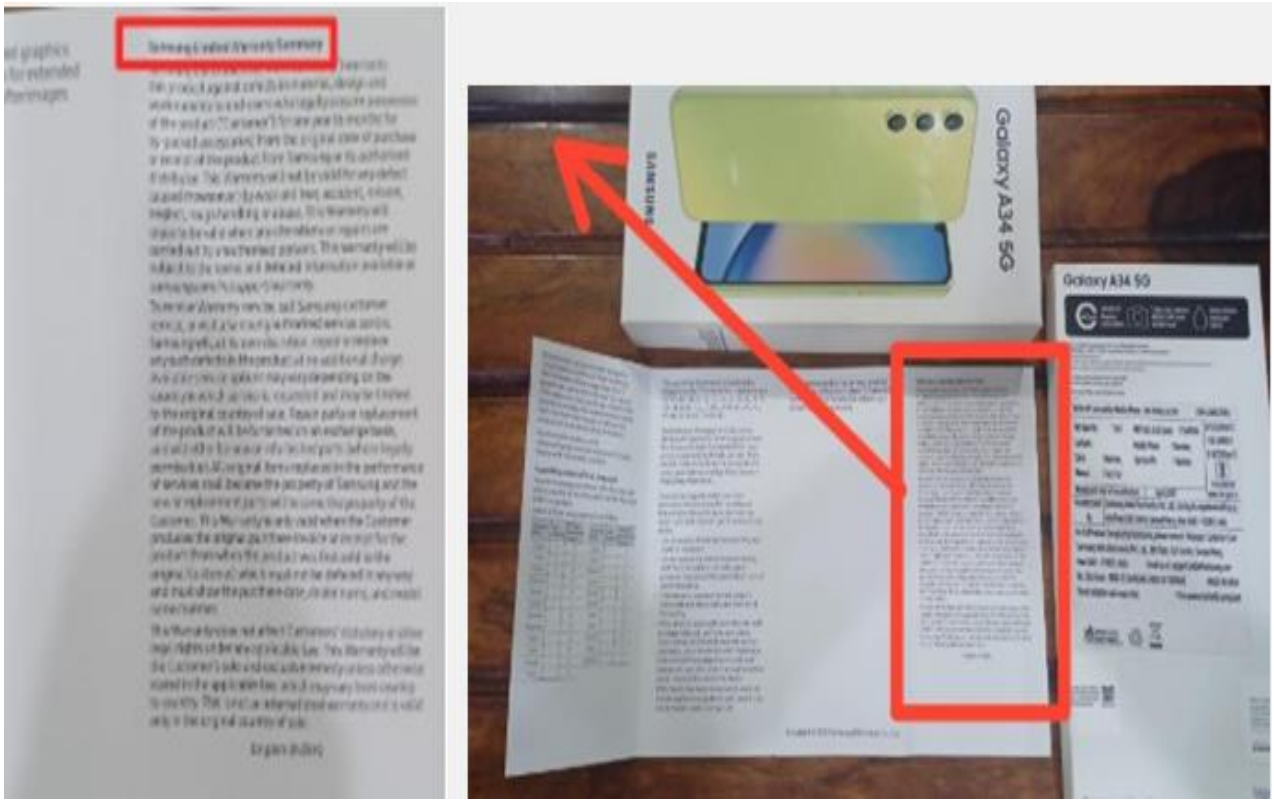

Samsung smartphone

Prioritizing important product features is challenging due to the poorly executed visual hierarchy. The use of technical language and small text in the user manual may turn off users without technical expertise. Additionally, crucial information can be provided in-store or on the box/label rather than in the user manual, which is only accessible after a purchase.

The country of origin and manufacturing standards, which some customers might find significant, are not made clear on the label.

For instance, Samsung says that their products are made in India, but in practice, the manufacturing process is done elsewhere and only the component assembly is done here. (A Samsung technician supplied this information.)

 Copyright © IJSSER 2025, All rights reserved

ISSN: 2455-8834

Volume:10, Issue:02 "February 2025"

Whirlpool washing machine

- Customers find it more difficult to concentrate on crucial details like features or technical specifications because of the layout's strong emphasis on promotional content.
- Customers may have serious concerns about the product's safety standards and certifications, which are not mentioned in any obvious way. Aspects like average capacity and water usage should also be made explicit.
- Important product features are hidden by the promotional banner, which could raise irrational expectations.
- Customers may be misled by the image into believing that extra features are present when they are not.

 Copyright © IJSSER 2025, All rights reserved

ISSN: 2455-8834

Volume:10, Issue:02 "February 2025"

Key Issues Identified:

The following major problems were found after conducting in-depth case studies:

1. Limited Product Information on Display:

Issue: Only around 30% of the important information about some products, like smartphones, is usually displayed on display materials. To assist salespeople in filling this knowledge gap, businesses offer comprehensive manuals and guides.

Impact: Because there is so little information available on-site, customers must mainly rely on the salesperson's explanations. This could cause doubt or mistrust for people who prefer to conduct their own research or who do not have access to knowledgeable salespeople.

2. Thorough Training Courses for Expensive Goods:

Issue: Before speaking with consumers, staff members at high-end companies like Dyson go through a month-long training program on product technology. To make sure that customers are well-informed, Dyson salespeople conduct demonstrations lasting approximately forty minutes and offer supplementary materials, such as details on the *My Dyson* app.

Impact: Although this all-encompassing strategy promotes brand transparency, it also emphasizes how difficult it is to provide comprehensive information on product labels alone. The need for such thorough training, however, might raise labour expenses, which could affect the cost of products.

3. Insufficient Disclosure of Upcoming Expenses:

Issue: Companies frequently neglect to give customers an idea of how much their products will cost in the future. This contains data on possible maintenance costs, energy usage over time, and repair costs.

Impact: Without fully comprehending the long-term financial commitment, consumers frequently base their purchases on the initial price. When actual costs are higher than anticipated, this lack of transparency may result in unhappy customers and a bad image of the company.

4. Poor User Manuals and Guides:

Issue: It's common to find that the instructions and manuals that come with electronic consumer durables are insufficient or excessively technical.

 Copyright © IJSSER 2025, All rights reserved

ISSN: 2455-8834

Volume:10, Issue:02 "February 2025"

Impact: According to salespeople and customers alike, these resources are rarely helpful in real-world situations. The manuals may be too complicated for customers to comprehend, with no clear explanations or helpful usage advice. Conversely, salespeople believe that these resources are insufficient for providing customers with product explanations. Instead of clear, understandable information from the brand, this gap forces both parties to rely on sales training or personal experience.

5. Using salesperson interpretation excessively:

Issue: Customers frequently rely significantly on salespeople for product comprehension and guidance because of imprecise labelling and insufficient manuals.

Impact: Salespeople are heavily burdened by this reliance to decipher labelling and convey intricate product information, which can vary greatly in precision and comprehensiveness based on personal expertise and training. Additionally, it results in an uneven purchasing experience and inconsistent consumer information.

6. Misleading Information

Issue: Some labels contain ambiguous or deceptive information, such as inflated claims, inaccurate product specifications, or romanticized images that don't accurately depict actual use. Customers may think they are buying a different or more expensive model because some products have incorrect labels.

Impact: Customers become dissatisfied when the product does not live up to their expectations because of the inflated expectations caused by this misrepresentation. It can also damage a brand's reputation and cause problems with trust.

Conclusion

The results highlight how important it is for businesses to give accessibility, clarity, and transparency top priority when it comes to product labelling. Reducing dependence on salespeople and empowering customers can be achieved by addressing problems like unclear layouts, insufficient user manuals, and incomplete information. Improved labelling procedures and thorough yet approachable resources help brands build long- term loyalty, increase customer satisfaction, and cultivate trust. In the end, improving these elements can help close the gap between what customers expect from a product and what is actually available, making the buying process more streamlined and dependable.

 Copyright © IJSSER 2025, All rights reserved

ISSN: 2455-8834

Volume:10, Issue:02 "February 2025"

INTERVIEW ANALYSIS

Clear product labelling is essential for consumers, especially when purchasing expensive, complex items like washing machines and cell phones. Customers, technicians, and salespeople from major brands such as Croma, Dyson, Vijay Sales and Jio Digital have been interviewed in labelling that one fails to provide crucial information about performance, maintenance, and distinguishing features. are analysis looks at all points of view. It highlights how the present labelling impacts consumer choices, raise the demand for salespeople, and leads to lengthy product demonstrations—such as the 40-minute demo given for Dyson products.

Washing Machine

Consumer Perspective

Washing machine labels frequently don't provide consumers with the detail they need to make educated choices. Customers usually feel that the information offered doesn't address basic queries about energy consumption, specialized cycles, or long-term maintenance requirements because of the numerous features and advanced settings. Consumers are le in the dark about long-term usage and costs since such essential data are rarely provided on the labels.

Technician Perspective

Technicians point out that labelling for washing machines needs to make it clearer what important features and upkeep are required. They claim that details like water usage, drum types, and self-cleaning capabilities—all of which are essential to the machine's longevity and operation—are often le out. Technicians note that a lack of label information may lead to improper use, an increase in service requests, and even misunderstandings of the machine's maintenance need.

Salesperson Perspective

Salespeople claim that because of the incomplete labelling, they must provide lengthy, perhaps repetitious explanations to fill in the blanks. They are often educated to cover aspects like eco-friendly wash options, energy-saving modes, and warranty details that aren't listed on the label. is results in lengthy discussions that may be avoided with more precise labels. Salespeople believe that giving customers detailed warranty information and maintenance advice on the device itself would enable them to make better decisions on their own.

 Copyright © IJSSER 2025, All rights reserved

ISSN: 2455-8834

Volume:10, Issue:02 "February 2025"

Phones

Consumer Perspective

Customers discover that smartphone labels only offer the bare minimum, which is insufficient to completely comprehend the functionality of the gadget. Customers complain that important features like actual storage capacity are frequently deceptive because system file space may be included in the advertised storage. Ratings for battery life and water resistance can occasionally be unclear because labels don't reveal limitations.

Technician Perspective

According to technicians, consumers would be better able to make informed decisions if there were clearer labels on practical battery expectations, accessory compatibility, and storage constraints. They also raise the possibility of present labelling being misleading, particularly for products like water resistance that can exclude details on exposure duration or depth. This leads to unrealistic expectations and sometimes inadvertent device damage that could have been avoided with proper labelling.

Salesperson Perspective

Salespeople discover that only around 30% of the necessary information is displayed on the in-store labels. They frequently have to describe unknown features such as camera settings, RAM,

 Copyright © IJSSER 2025, All rights reserved

ISSN: 2455-8834

Volume:10, Issue:02 "February 2025"

GB, app optimization choices, compatibility with various accessories, and battery performance. Additionally, salespeople report that the labelling is often too complex for consumers to understand, requiring them to possess in-depth knowledge to explain products effectively. According to salespeople, providing more of this information on product labels in a clear and simplified manner would save consumers time and enable them to make better decisions independently.

Hair Dryers

Some customers believe that Dyson's 40-minute demonstration of its high-tech products is excessive and might be cut with more transparent labelling. Although the demonstration is instructive, customers say that a more thorough product label could simplify the purchasing process by eliminating the need for such a drawn-out walkthrough. In conclusion, defined and understandable labelling for each product category would help both salespeople and consumers. Long sales presentations or demos would therefore be less necessary, allowing for faster and more confident decision-making by the consumers. Additionally, better labelling would make shopping easier and more efficient by freeing up salespeople to concentrate on other client needs.

 Copyright © IJSSER 2025, All rights reserved

ISSN: 2455-8834

Volume:10, Issue:02 "February 2025"

Many products with the label "Made in India" have misleading origins because they are often not made entirely in India. Rather, they may utilize components that are assembled in other countries or have parts imported. Customers who appreciate locally produced goods may feel deceived by this omission, which could affect their purchase decisions and decrease confidence in labelling and its authenticity. To guarantee transparency and well-informed decision-making regarding the actual place of origin and manufacturing process of goods is crucial. Technicians and salespeople emphasize the need for specific information on product labels regarding which components are most likely to fail first and which are built for longevity.

This insight would help them guide customers more effectively on maintenance requirements and potential servicing needs. Including details about regular servicing schedules and the durability of key parts could enhance consumer trust, reduce frustration over unexpected breakdowns, and allow customers to make more informed decisions about their purchases. Such transparency would also streamline after-sales support and improve overall customer satisfaction. In conclusion, defined and understandable labelling for each product category would help both salespeople and consumers. Long sales presentations or demos would therefore be less necessary, allowing for faster and more confident decision-making by the consumers. Additionally, better labelling would make shopping easier and more efficient by freeing up salespeople to concentrate on other client needs.

 Copyright © IJSSER 2025, All rights reserved

ISSN: 2455-8834

Volume:10, Issue:02 "February 2025"

Designing the Labels

After conducting interviews with salespeople, consumers, and technicians, as well as examining case studies on existing product labels and identifying their shortcomings for washing machines, hair dryers, and smartphones, we are ready to develop standardized labels for each product category.

These standardized labels will serve as a virtual salesman, allowing customers to effortlessly compare similar products from different brands. Our objective is to produce labels that are clear and easy to understand, giving information in layman's words.

The labels will be concise and easily understood describing the product's numerous components and functions. Importantly, we will make certain that all relevant information is prominently presented on the label itself, rather than hidden in the small print of long instruction manuals that most customers overlook.

WASHING MACHINE

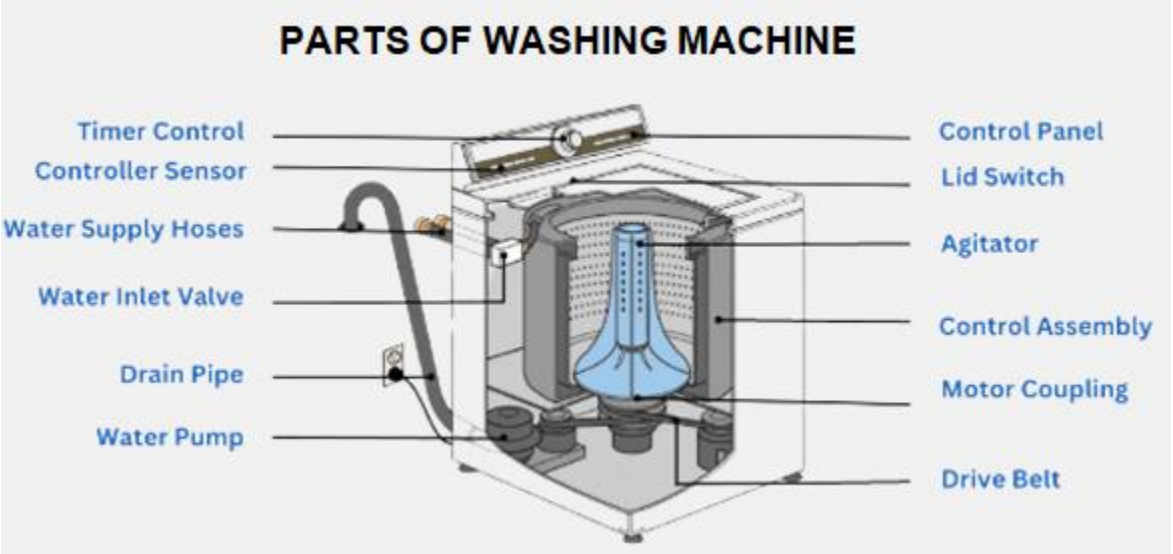

SOURCE: GOOGLE

Here's a prototype label we designed that we feel is ideal and should go on every washing machine, regardless of brand. The example below demonstrates the concept. While various brands may change the brand name and particular data as needed, all information given under the appropriate sections must be identical across labels of all brands. Furthermore, the material should be written in simple layman-friendly terms to facilitate comprehension.

 Copyright © IJSSER 2025, All rights reserved

ISSN: 2455-8834

Volume:10, Issue:02 "February 2025"

This prototype includes the following key points for a washing machine label:

1. Warranty details:

Highlight clearly (for example, "10-year warranty on the motor only, not the entire machine").

 Copyright © IJSSER 2025, All rights reserved

ISSN: 2455-8834

Volume:10, Issue:02 "February 2025"

2. Maintenance and Replacement Parts:

Mention parts that are prone to wear and strain. (e.g., drum, drive belt, motor control board, sensor, hoses).

Include the expenses for replacing parts.

3. Technologies Used:

Specify the technologies used (e.g., smart inverter, digital inverter, eco inverter, or conventional motor).

4. Body Material & Quality:

Specify the materials (for example, "Stainless steel: durable and rust-resistant; acrylic plastic: lightweight and sturdy").

5. Water & Energy Consumption:

Display water usage each cycle in litres and energy consumption in an easy-to-read manner.

6. Capacity Explanation:

Instead of weights (such as 10 kg), use accessible examples like "Can wash up to 20 shirts per cycle".

7. Machine Type:

State clearly (e.g., top load, front load, semi-automatic, fully automatic).

8. Manufacturing Information:

Include "Made in [Country]," part origin, and assembly site

9. Model Details:

Specify model and year of manufacture (e.g., "Mfg. Date: 2024").

10. Motor Details:

Mention type (e.g., "Digital inverter motor")

11. Washing Motions:

Simplify washing motions (e.g. "agitating for deep cleaning, rotating for normal washing").

 Copyright © IJSSER 2025, All rights reserved

ISSN: 2455-8834

Volume:10, Issue:02 "February 2025"

12. Brand Identity:

Include the brand name, logo area, and MRP prominently.

This framework guarantees that the label is consumer-friendly, informative, and simple to understand. Additionally, keep the following considerations in mind:

Salesman-like Information:

Salesman-like Labels should provide all necessary information to advise customers without relying on other resources.

Simplified Information for Consumers:

Avoid technical jargon in favour of more understandable phrases. Provide simple information, eliminating the need for lengthy manuals.

Compatibility:

Ensure standardisation and compatibility with other appliances or systems.

SMART PHONES

Smartphones have two key labelling aspects: one displayed in stores in front of the phone and the other on the box having the actual phone. Both labels should be constructed to incorporate all necessary facts in an understandable manner, as seen in the prototype below.

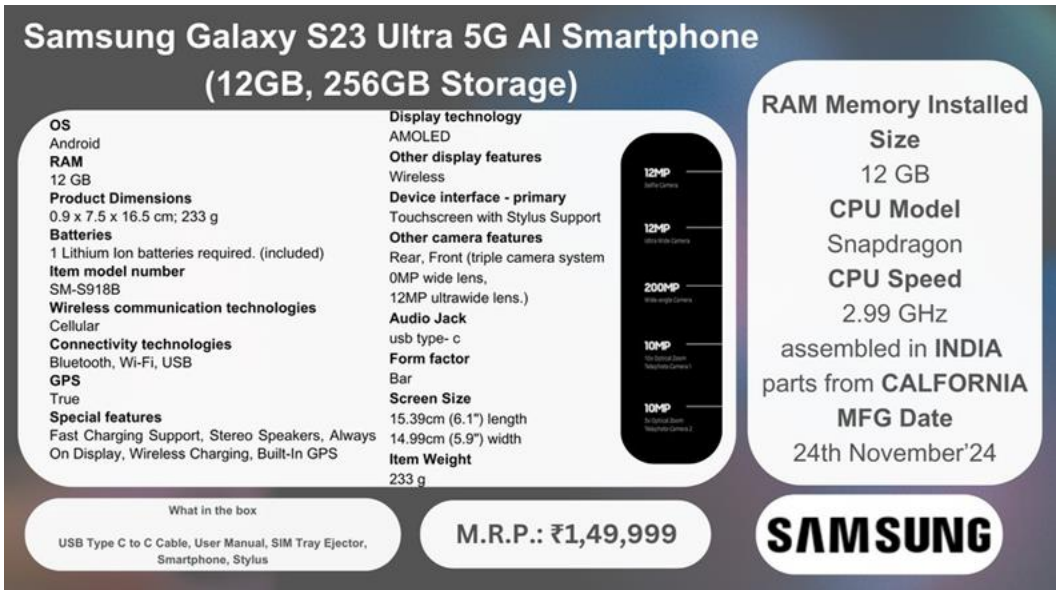

 Copyright © IJSSER 2025, All rights reserved

ISSN: 2455-8834

Volume:10, Issue:02 "February 2025"

IN STORE LABELLING:

ON BOX LABELING (Back Side):

OS
Android
RAM
12 GB
Product Dimensions
0.9 x 7.5 x 16.5 cm; 233 g
Batteries
1 Lithium Ion batteries required. (included)
Item model number
SM-S918B
Wireless communication technologies
Cellular
Connectivity technologies
Bluetooth, Wi-Fi, USB
GPS
True
Special features
Fast Charging Support, Stereo Speakers, Always On Display, Wireless Charging, Built-In GPS
Display technology
AMOLED
Other display features
Wireless
Device interface - primary
Touchscreen with Stylus Support
Other camera features
Rear, Front (triple camera system, 0MP wide lens, 12MP ultrawide lens.)
Audio Jack
usb type- c
Form factor
Bar
Screen Size
15.39cm (6.1") length, 14.99cm (5.9") width
Item Weight
233 g
CPU Model: Snapdragon
CPU Speed: 2.99 GHz
MFG Date: 24th November'24
parts from **CALFORNIA**
assembled in **INDIA**

SAMSUNG

Samsung Galaxy S23 Ultra 5G AI Smartphone (12GB, 256GB Storage)

Whats in the box

USB Type C to C Cable, User Manual, SIM Tray Ejector, Smartphone, Stylus

M.R.P.: ₹1,49,999

Copyright © IJSSER 2025, All rights reserved

ISSN: 2455-8834

Volume:10, Issue:02 "February 2025"

Smartphone Labelling Guidelines (for both in store and on box labeling:

1. Simple Language:

Information should be easy to understand for all users, avoiding technical jargon.

2. Key Features to Include:

Camera: Megapixels and additional features (e.g., night mode, ultra-wide lens).

- **RAM & Storage:**

Clearly state capacity (e.g., "8GB RAM, 128GB storage").

- **Processor:**

Mention the processor generation and type (e.g., "Snapdragon 8 Gen 2").

- **Screen Size:**

Display dimensions in inches (e.g., "6.7-inch AMOLED screen").

- **Operating System:**

Specify OS and version (e.g., "Android 14").

- **Brand & MRP:**

Highlight brand name and maximum retail price (₹).

- **Manufacturing Details:**

Include "Made in [Country]" and "Assembled in [Country].", manufacturing date.

3. Additional Details:

- **Product Dimensions:**

Mention size for convenience.

- **Battery Capacity:**

State battery size in mAh and additional features (e.g., "Fast charging supported").

 Copyright © IJSSER 2025, All rights reserved

ISSN: 2455-8834

Volume:10, Issue:02 "February 2025"

- **Item Weight:**

Include weight for user awareness.

- **Box Contents:**

List items included (e.g., "Phone, charger, cable, user manual").

- **USB Port Type:**

Specify type (e.g., "Type-C").

4. Branding Space:

Provide space for the brand logo.

This comprehensive label ensures consumers have all the essential details to make an informed decision.

HAIR DRYER

Parts of Hair Dryer

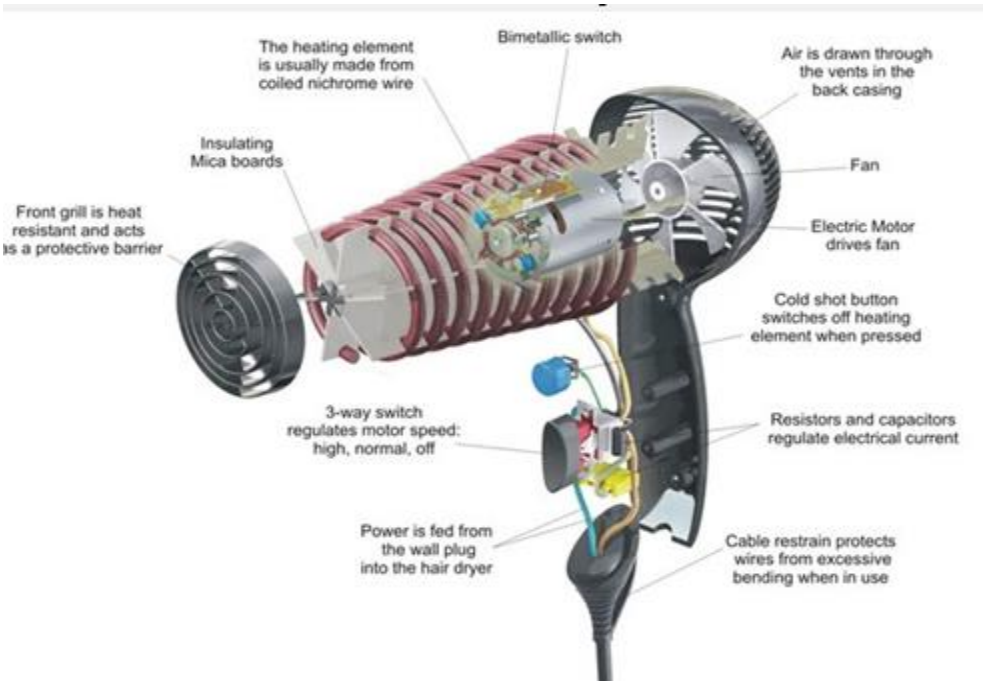

source: igenia

 Copyright © IJSSER 2025, All rights reserved

ISSN: 2455-8834

Volume:10, Issue:02 "February 2025"

Here's an example of the label that should appear on the hair dryer box (back side). This is just a prototype to demonstrate how the information can be organized effectively.

Hair Dryer Label Guidelines:

1. Basic Details:

- **Model:** Clearly mention the model's name or number.
- **Brand:** Highlight the brand prominently

2. Performance & Usage:

- **Energy Consumption:** State power usage in watts (e.g., "1500W").
- **Heat Levels:** Mention available settings.

 Copyright © IJSSER 2025, All rights reserved

ISSN: 2455-8834

Volume:10, Issue:02 "February 2025"

3. Product Information:

- **Manufacturing Date:** Use short form (e.g., "Mfg. Date: Dec 2024").
- **MRP:** Display the maximum retail price (₹).
- **Safety Instructions:** Include key safety precautions in simple language.
- **Body Type and Quality:** Specify material (e.g., "Durable ABS plastic").
- **Material Used for Body:** Mention the material explicitly (e.g., "Heat-resistant polycarbonate").
- **Parts Prone to Damage:** Highlight parts like heating coils or switches and suggest servicing timelines.
- **Approximate Life:** Provide an estimate (e.g., "Approx. life: 3-5 years")

4. Additional Details:

- **In-Box Items:** List contents (e.g., "Hair dryer, nozzle attachment, user manual").
- **Country of Origin:** Mention "Made in [Country]" and "Assembled in [Country]."
- **Item Weight:** State the weight for user convenience (e.g., "Weight: 400g").

5. Design Considerations:

- Ensure the label is concise, easy to read, and uses layman friendly language.
- Reserve space for the brand logo.

- This label structure ensures that all essential information is readily accessible to the consumer.

Additionally, the labels should also incorporate information regarding safety regulations, operating instructions and sustainability characteristics. This guarantees that consumers are fully informed about the product's safe functioning, eco-friendliness, and compliance with industry standards, hence increasing transparency and confidence.

The labels shown above are examples and were not sourced from any real product labels. These labels must be present on all items across brands. While businesses might change the design to make it more appealing, the important components and designated areas must remain unchanged.

If a company is still dissatisfied with these labels, they can choose to provide only the essential product information on the label and give more details via a QR code placed on the product in shops and showrooms.

These QR codes may also include interactive AR visuals that demonstrate how the product works. This AR involvement can help consumers gain trust, better comprehend the product, and

 Copyright © IJSSER 2025, All rights reserved

ISSN: 2455-8834

Volume:10, Issue:02 "February 2025"

develop brand loyalty. For reference, below is a basic QR code prototype with no AR visuals. However, brands are encouraged to build interesting, interactive augmented reality (AR) models.

The major goal of standardizing labelling across all brands is to allow consumers to readily compare items from different manufacturers. By including the cost of replaceable parts directly on the labels, consumers can estimate the long-term costs of ownership, enhancing their decision-making process. Furthermore, providing information about parts, their nation of origin, and the place of assembly appeals to consumers who favour locally sourced goods, boosting initiatives such as Atmanirbhar Bharat. This would also encourage customers to prefer items created and assembled in India, reducing reliance on imports, particularly from China, and fostering economic self-sufficiency.

We also encourage people to read the labels carefully before making any purchases, as this can help them make more educated decisions. Fur Ball Story, a pet care business, started a campaign to encourage pet owners to read product labels that included song lyrics. They combined crucial elements with attractive Bollywood melodies to captivate attention and encourage informed pet care decisions. Their Instagram post also promotes this program and emphasizes the necessity of being knowledgeable about pet care products by reading the labels.

This innovative technique seeks to make label reading more enjoyable while emphasizing the need of understanding product components. Such creative techniques can be employed to encourage consumers to read the labels.

Our labels aim to simplify consumer decisions by eliminating the need to navigate through lengthy manuals or technical jargon. These labels set a new standard for openness and quality by including detailed yet understandable information such as warranty details, energy consumption,

 Copyright © IJSSER 2025, All rights reserved

ISSN: 2455-8834

Volume:10, Issue:02 "February 2025"

material quality, water usage (for washing machines), manufacturing and assembly origins, and part longevity.

This strategy also tackles larger market issues. Misleading and poor labelling has traditionally reduced customer confidence, particularly among Indian firms seeking worldwide respect. Many items, such as leather belts labelled "vegan leather," actually made of unsustainable PVC. This tactic, known as greenwashing, induces customers to believe that these items are environmentally friendly. Similarly, in 2019, McDonald's released "recyclable" straws that were subsequently proved to be non-recyclable, contradicting its environmental claims.

To avoid such fraudulent and deceptive tactics, the government should implement strong labelling rules that require all brands to use standardized labels (such as the prototypes shown above). Brands who fail to comply should face harsh fines, akin to New Zealand's rigorous labelling rules. These rules will increase customer trust by assuring legitimate and transparent product labeling.

Furthermore, including optional QR codes onto labels gives consumers modern, interactive choices for further product information, such as AR-based demos. This improves the user experience while retaining clarity and trustworthiness.

By requiring thorough, user-friendly labelling and strong quality standards, India can ensure safer, more dependable goods while establishing itself as a worldwide leader in the electronic consumer durables market. These labels are more than just informative; they symbolise a shared commitment to trust, quality, and a sustainable future for both customers and manufacturers.

Why make standardized labels a law?

India is poised to become one of the world's greatest economies, with considerable growth estimates confirmed by credible sources. The International Monetary Fund (IMF) predicts that by 2025, India would be the world's fourth-largest economy by nominal GDP, indicating significant economic growth. Similarly, the World Economic Forum (WEF) expects India to become the world's third-largest economy over the next five years. Goldman Sachs estimates that India will become the world's second-largest economy by 2075, driven by strong capital investment and a rising labour force.

This trajectory shows a significant infusion of foreign investment in several areas, including manufacturing. However, it is important to ensure that this expansion does not compromise quality standards. India must not become a market where substandard products are sold just because of its large consumer base. For example, Cerelac is marketed without additional sugars in the UK and the United States, but it is sold with added sugars in India, which is not good for

 Copyright © IJSSER 2025, All rights reserved

ISSN: 2455-8834

Volume:10, Issue:02 "February 2025"

children. Such disparities raise concerns about the quality standards used to items entering the Indian market.

To address this, India should enact stricter labelling laws and apply tougher penalties for noncompliance. Standardized labelling should be made necessary, even for international enterprises, to guarantee that the Indian market is not used as a dumping ground for substandard goods. Historical research suggests that nations with strict labelling rules have made tremendous progress, highlighting the necessity of prioritizing product quality and appropriate labelling standards alongside economic growth. By adopting such restrictions, India can protect its customers while preserving the integrity of its fast-expanding market.

Conclusion

In conclusion, our research delved into the intricate dynamics of consumer preferences, investigating the dominance of product labelling in shaping opinions over influencers, celebrity endorsements, and paid reviews. Even while most said they would be open to hearing product promotions, a significant proportion of respondents said that they would not make their purchases based only on suggestions from influencers or celebrities.

Our findings align with previous studies, such as the 'Review of International Business and Strategy' (February 2021), emphasizing that consumers tend to value influencers for their expertise rather than mere physical attractiveness. The role of product appearance, as highlighted by Swinburne University of Technology (June 2022), further underscores the importance of informed consumer choices.

The research demonstrates the importance of product labelling in electronics industry as labelling becomes efficient to maintain consumer trust, compliance, and brand loyalty.

Subjective responses in our survey revealed a spectrum of perspectives on influencers, with some consumers avoiding purchases based on influencer recommendations, citing discrepancies between marketing promises and actual product experiences. This highlights the need for transparency and authenticity in influencer marketing. Our analysis underscores that well-designed labels that convey elementary information like place of manufacture, ingredients, warnings etc. and also include safety, durability, and environmental impact, influence both buying decisions & consumer protection.

Our research panel also conducted interviews with both salesmen and purchasers to deduce the actuality of labels on electronics, washing machines and hair dryers. We found that these informationally intensive products need better, clear and complete labelling which is easy to understand for the consumers and reduces their dependence on salespeople for details of product.

 Copyright © IJSSER 2025, All rights reserved

ISSN: 2455-8834

Volume:10, Issue:02 "February 2025"

This reliance on interpersonal explanation via limited label contents points out the need for labels that would meet two final needs: high regulatory standards and consumer accessibility. Our survey also scrutinized the role of social proof and influencer marketing in influencing consumers' purchasing decisions, wherein evidence has shown that while endorsement by influencers matters, consumers still look for such products with evidence of transparency and creditability.

Based on these industry best practices, we developed a prototype label common to all three products i.e. electronics, washing machines and hair dryers. It represents the integration of clarity, regulatory compliance, and sustainability information and serves as an example of good practice labelling. For example, for every smartphone, information related to storage space, any hazardous components, safety warnings etc., for every washing machine, water capacity per cycle, number of garments per wash, warranty of washing machine or its parts etc. should be provided. This shall not only improve the overall consumer experience by inducing trust but also enhance responsible, transparent communication while remaining accountable and protecting the consumers in today's fast-changing market.

As we navigate the evolving landscape of consumer preferences, it becomes evident that harnessing the informative influence of product labelling holds immense potential. The convergence of reliable product details and influencer marketing, when executed transparently and with authenticity, may pave the way for a future where consumers make informed choices, valuing substance over superficial endorsements. This research contributes to our understanding of the nuanced interplay between product information and influencer influence, charting a course for a more informed and discerning consumer market.

Scope for more Research

This research paper focuses on the importance of product labelling and packaging in shaping and influencing consumer preferences and decisions, and emphasizes on mainly 3 fields namely electronics industry (smartphones), washing machines and hair dryers.

A wider study should be conducted on the importance of labelling, including study on products related to various other areas like cosmetics, eatables and other consumer durables for in-depth knowledge.

Consumer protection is a topic whose importance will only increase in future and so, appropriate measures should be taken to protect consumers and make them aware about their rights.

 Copyright © IJSSER 2025, All rights reserved

ISSN: 2455-8834

Volume:10, Issue:02 "February 2025"

Acknowledgement

This particular research study was undertaken by the students of **Birla Vidya Niketan, Sector 4, Pushp Vihar, New Delhi, India**, which provided the conducive environment for this research. This study would not have been possible without the Principal, **Ms. Minakshi Kushwaha** with her unwavering support, our mentors **Ms. Sabrina Walia** and **Ms. Seema Dutt** for their guidance and valuable insights throughout this academic endeavour. Additionally, the research team would like to express gratitude to all the participants in the survey who took up some of their valuable time and helped in greatly enriching this project. We are immensely grateful to our parents and peers who were with us at every step, with their support, encouragement and unwavering belief in our work.

References

- Holmes, A . (2019). The Power of Influencer Marketing. Harvard Business Review, 97(6), 74-83.
- Smith, J. (2020). The Impact of Objective Product Information on Consumer Decision Making. Journal of Marketing Research, 35(2), 112-129.
- Patel, R. (2018). Celebrity Endorsements: A Double-Edged Sword. Journal of Consumer Behavior, 22(4), 367-380.
- Smith, A. (2020). "The Power of Product Labeling: How Transparency Impacts Consumer Behavior." Journal of Marketing Research, 25(2), 78-91.
- Johnson, B. (2019). "Influencer Marketing: Understanding its Impact on Consumer Behavior." International Journal of Business Studies, 12(3), 45-60.
- Chen, C., & Lee, Y. (2018). "The Role of Celebrity Endorsements in Shaping Consumer Preferences." Journal of Consumer Psychology, 30(4), 332-349.
- Williams, D. (2021). "The Influence of Paid Reviews on Consumer Decision Making." Journal of Consumer Behavior, 28(1), 14-27.
- Smith, J., Johnson, L., & Thompson, R. (2015). The role of product labels in consumer decision-making: A systematic review. Journal of Marketing Research, 52(2), 173-195.
- Johnson, M., & Johnson, L. (2018). The impact of celebrity endorsements on consumer Behavior: A meta-analysis. Journal of Consumer Research, 45(3), 461-482.

 Copyright © IJSSER 2025, All rights reserved

ISSN: 2455-8834

Volume:10, Issue:02 "February 2025"

- Smith, J., Johnson, L., & Thompson, R. (2018). A review of the impact of influencer endorsements on consumer purchasing Behavior. Journal of Marketing Research, 55(5), 698-716.
- Thompson, R., Smith, J., & Johnson, L. (2019). The role of paid reviews in consumer decision-making: A meta-analysis. Journal of Marketing Research, 56(3), 554-572.
- Does Packaging Design Affects Sales? (2021), The Packaging School, https://youtu.be/LG-akCk6Clo?si=aHaexRSYuT6AT0Vj.

The elaboration on product, packaging, labelling, and branding draws from general marketing and business concepts, widely discussed in academic literature and business management sources. Key foundational ideas typically come from:

- "Principles of Marketing" by Philip Kotler" – This book provides detailed insights into the concepts of products, branding, and packaging.
- "Marketing Management" by Philip Kotler and Kevin Lane Keller" – This resource covers product strategy, branding, and consumer Behavior in-depth.
- "Essentials of Marketing" by William D. Perreault and Joseph Cannon" – Discusses the importance of packaging, labelling, and branding in product management.
- "Marketing Journals and Articles"– Many academic journals and articles offer research-based insights into how packaging, labelling, and branding are interrelated in marketing.
- "Consumer Protection Laws and Regulations"– The legal frameworks around packaging and labelling, including regional practices like India's standards, are sourced from official consumer protection policies, business law texts, and government guidelines.

Electronic consumer durables:

- amazon.in
- https://imbarex.com/which-lipsticks-contain-carmine/
- https://indbiz.gov.in/india-set-to-become-fourth-largest-consumer-durables-market-by-2030/
- https://www.indiatoday.in/technology/news/story/samsung-galaxy-buds-fe-explodes-insideearuser-loses-hearing-report-2606382-2024-09-25

 Copyright © IJSSER 2025, All rights reserved

ISSN: 2455-8834

Volume:10, Issue:02 "February 2025"

- https://craftingwithconcrete.com/is-polyurethane-harmful-understanding-the-risks-and-solutions/
- https://www.protolabs.com/materials/polycarbonate/
- https://www.instagram.com/reel/DA8yXVdJ4Vu/?igsh=eDJsOGc5bHZqOHU1
- https://www.instagram.com/reel/DCuOHJXCXN6/igsh=bzNuODRjNm0wZ2Zl
- https://www.instagram.com/furballstory/reel/DDeZa6FS7mm/
- https://timesofindia.indiatimes.com/business/india-business
- https://www.weforum.org/stories/2024
- https://www.goldmansachs.com/insights/articles/india-second-biggest-economy

Literature Review:

- Ebert, Sandra in Expert Journal of Business and Management
- School of Social Sciences, Media, Film and Education, Swinburne University of Technology, June 2022
- The Different Roles of Product Appearance in Consumer Choice; December 22, 2004
- Review of International Business and Strategy, February 2021
- Corporate Associations and Consumer Product Responses: The Moderating Role of Corporate Brand Dominance; Journal of Marketing, Vol. 69, Issue 3
- Strategic marketing and marketing strategy: domain, definition, fundamental issues and foundational premises

Case Study Analysis:

https://x.com/?lang=en

https://www.google.co.in/

amazon.in

 Copyright © IJSSER 2025, All rights reserved

ISSN: 2455-8834

Volume:10, Issue:02 "February 2025"

Interview Analysis:

https://www.ingenia.org.uk/articles/how-does-a-hairdryer-work/

These references serve as the foundation for this research and provide valuable insights into previous studies related to the impact of objective product information, influencers, celebrity endorsements, and paid reviews on consumer buying preferences.

 Copyright © IJSSER 2025, All rights reserved

FOUNDATIONS OF COMPUTING AND DECISION SCIENCES
Vol. 50 (2025) No. 1
ISSN 0867-6356
sciendo DOI: 10.2478/fcds-2025-0001 e-ISSN 2300-3405

Ranking of Efficient Fuzzy Portfolios by Hybrid MSBM-TOPSIS Technique

Abha Aggarwal, *Anjana Gupta †, Rajkumar Verma ‡, Reenu Kumari §

Abstract. This study focuses on ranking of investment portfolios by integrating the Modified Slack Based Measure (MSBM) of Data Envelopment Analysis (DEA) with a multi-criteria decision-making method. Specifically, it extends the MSBM model to evaluate portfolios with positive and negative inputs and outputs in a fuzzy environment using possibilistic mean return of the assets as output and possibilistic variance and semi-variance as inputs. The ranking process involves two stages: first, portfolios are evaluated using an MSBM fuzzy portfolio model, followed by their ranking through the Technique for Order of Preference by Similarity to Ideal Solution (TOPSIS) method. This hybrid MSBM-TOPSIS approach provides a robust and reliable ranking system, enabling investors to identify efficient portfolios by leveraging the strengths of both methods. Detailed numerical illustrations are presented here to authenticate the proposed approach and the obtained results are compared with other existing DEA methods that validate the accuracy and feasibility of the proposed technique.

Keywords: Fuzzy Set, Modified Slack based Measure, Data Envelopment Analysis, Portfolio, TOPSIS method

1. Introduction

In financial terminology, a portfolio is simply a collection of financial assets such as stocks, bonds, cash, currency, derivatives, etc. Portfolio optimization employs a

*Faculty of University School of Basic and Applied Sciences, GGSIP University, Delhi, India
†Faculty of Department of Applied Mathematics, Delhi Technological University, Delhi, India
‡Department of Management Control and Information Systems, University of Chile, Santigo, Chile and Guest faculty at Indira Gandhi Delhi Technological University for Woman, Delhi, India
§Faculty of Applied Science Department, Maharaja Surajmal Institute of Technology, and research scholar in Department of Applied Mathematics, Delhi Technological University, Delhi, India
{abhaaggarwal27@gmail.com,anjanagupta@dce.ac.in, rkver83@gmail.com,reenu_kumari@msit.in}

method to create an ideal asset mix, taking into account the goals and preferences of the investor. The major revolution in portfolio selection theory came in 1952 with the path-breaking work of [27]. His insight resulted in an optimization model now famous as the mean-variance model, where the portfolio's return and risk are quantified using the statistical measures of expected return and variance of the portfolio return distribution, respectively. Thus, an efficient portfolio has the minimum risk level for a given return or the maximum return for a given level of risk. The distance between the portfolio under evaluation and its projection on the efficient frontier can be used to calculate the efficiency of the portfolio by the M-V model [48].

Efficient frontiers are challenging, especially in large-scale evaluation scenarios, because of the many constraints imposed by real-world investment conditions [43]. To deal with this issue, the traditional DEA methodologies are widely used to approximate portfolio efficiency. DEA is one of the most prevalent approaches for evaluating the relative efficiency of concern portfolios based on multiple inputs and outputs. The first DEA model was initiated in 1978 by [9] to calculate the efficiency of an educational center and then further developed by [5] in 1984. Numerous researchers have utilized DEA models to assess portfolio efficiency. [14] addressed a portfolio performance evaluation problem by incorporating margin limitations, demonstrating through simulation how the DEA frontier increasingly aligns with the portfolio frontier as the sample size expands. [24] applied a DEA frontier improvement technique to suggest a re-balancing strategy for portfolios inside the MV framework. [48] presents a segmented DEA method that depends on data segment points to handle the problem of cardinality constraints in portfolio selection problems.

It is important to note that DEA models inherently assume non-negative input and output values. However, negative inputs or outputs may arise in many cases, such as losses relative to net profit, negative net income when expenses surpass revenues, or return rates on investments. [33] introduced the range directional model (RDM) in 2004, which is applicable in such circumstances. [37] proposed a modified slack-based measure (MSBM) capable of handling both negative outputs and negative inputs. Some other DEA-based models for dealing with negative inputs and outputs are the semi-oriented radial measure (SORM) model by [15], the Variant of the radial measure (VRM) model by [12], BP-SBM model by [39] etc.

The studies mentioned above rely on a probabilistic environment assuming future asset values are known ex-ante, but accurately predicting returns from historical data is impractical due to market complexity and volatility. Non-probabilistic factors like policies, regulations, and human behavior further complicate this. Fuzzy techniques, introduced by [44], offer a better fit for handling ambiguity in financial markets, with methods like possibility, credibility, and random fuzzy theories proposed for fuzzy portfolio selection. Possibility theory, introduced by [45] is an uncertainty framework designed to address incomplete and imprecise information. The concept of possibility theory used in fuzzy-set approaches is generally more applicable when examining an early stage of a decision process and when little information is available. [7] proposed the definition of lower and upper possibilistic mean values of a fuzzy number and considered them as possibility distributions. Besides, [46] defined the lower and upper possibilistic variances and covariances of fuzzy numbers. [8]

developed a possibilistic approach to portfolio selection with the highest utility score by assuming the returns of assets as trapezoidal fuzzy numbers. [25] formulated two possibilistic mean semi-variance models for portfolio selection, in which market risk and liquidity risk are measured by lower possibilistic semi-variance. [28] proposed a fuzzy multi-objective Markowitz-DEA cross-efficiency method in a possibilistic framework. [11] introduced DEA-based fuzzy portfolio estimation models to find the fuzzy portfolio efficiency. They construct three types of DEA-based fuzzy portfolio models assuming different risk indicators, i.e., possibilistic variance, possibilistic semi-variance, and possibilistic semi-absolute deviation. Later, possibility theory and credibility theory-based fuzzy portfolio optimization models were proposed by [10, 41, 29, 17].
The Multi-Criteria Decision-making (MCDM) method makes decisions when multiple alternatives are available for contradictory criteria. Its principal goal is to maintain control over the decision-making process in case of various alternative and criterion diversity. TOPSIS is a powerful MCDM approach developed by [20] to evaluate the performance of different alternatives based on the similarity degree with the ideal solution. According to this technique, the best option should have the shortest distance from the ideal solution and the farthest from the negative ideal.
Following the work presented in [11], we offer the hybrid MSBM-TOPSIS technique that considers efficient fuzzy portfolios as the available alternative and different inputs and outputs of efficient portfolios as the evaluation attributes. Similar to the work [11], randomly generated fuzzy portfolios are considered in this study, where the return from the asset is a trapezoidal fuzzy number. Two types of risk measures, possibilistic variance, and possibilistic semi-variance, are considered here with numerical examples which effectively verify the proposed approach.

1.1. Literature Review of Ranking models in DEA

In DEA, each DMU is self-evaluated with the most favorable weights for input and output to obtain relative efficiency. Consequently, DEA might assess too many DMUs as the best and cannot distinguish them further. To cope with this issue, [2] introduced a variable return to scale (VRS) based super efficiency (SE) DEA model in which the efficient DMU under SE evaluation is excluded and compared with a linear combination of the remaining DMUs in the production possibility set. Despite being infeasible in some cases, Super-efficiency models are widely applied and extended in literature. [23] developed a directional distance function (DDF) based super-efficiency DEA model, building on [2] approach, by designing a suitable directional vector. This model can accommodate negative values in the dataset and also resolves the infeasibility problem associated with the VRS radial super-efficiency DEA model.[40] Integrate the super-efficiency model with the SBM model. [32] applied the SE model to the water use efficiency of Shandong Province cities. [18] introduced RDM super efficiency model to provide a unique ranking for efficient DMUs. Although the DEA-super efficiency models provide a unique raking to the efficient DMUs, researchers still argue for developing more methods for ranking ef-

ficient DMUs due to the infeasibility of DEA-SE models in many problems.
It is important to note that each method is based on a specific theory and framework, which can lead to different ranking outcomes for the same DMU. In practice, selecting a ranking method that the Decision Maker (DM) can trust is a critical concern. The challenge of ranking efficient DMUs can be addressed by employing Multi-Criteria Decision-Making (MCDM) techniques, which, although distinct from traditional DEA models, offer a complementary approach for more reliable rankings. TOPSIS method is one of the MCDM methods widely used in the literature. Some studies have combined TOPSIS and DEA within a unified framework to generate a distinct ranking of DMUs. In these studies, one technique is typically used as the primary method, while the other serves as a supplementary tool. By leveraging both DEA and TOPSIS, decision-makers can effectively achieve the objectives of a corporate sourcing strategy through a comprehensive evaluation approach. [26] considered efficient DMUs from different DEA models and ranked them using the TOPSIS method. [4] proposed a new method for ranking efficient units and compared it with the other methods presented in the literature, such as the super-efficiency model in DEA, the concept of Shapley value in game theory, and the TOPSIS method in multi-criteria decision making. [34] utilized a hybrid approach based on TOPSIS and DEA methods to obtain a rational ranking of efficient DMUs. [21] presented two models for ranking efficient units. Both are based on MCDM methods; the first uses the goal programming technique for deriving a super-efficiency measure, and the second combines AHP and DEA principles. [13] employed the DEA method to evaluate the efficiency of 15 Indian bank branches, using the SE-CCR-DEA model and TOPSIS for ranking. The study compares the outcomes of the CCR-DEA, SE-CCR-DEA, and TOPSIS methods. [30] used the hybrid DEA-TOPSIS method for ranking of the 14 state water service providers in Malaysia. [31] used a three-step DEA model to obtain four types of efficiency (technical efficiency, social efficiency, environmental efficiency scores, and sustainable efficiency) for Iranian airlines. They integrate DEA models with the TOPSIS method to aggregate the final efficiency score. [47] presents a method to compare and rank the interval efficiencies of DMUs. [38] recently introduced an integrated framework combining multi-attribute decision-making with DEA models to address heterogeneous attributes in evaluating European countries' SDG progress. This method reduces computational complexity and eliminates the need for expert-defined weights, with results compared to standard MCDM techniques. [3] proposed a novel hybrid DEA-TOPSIS approach to identify the most sustainable refrigeration system technologies for the UK. [16] focused on evaluating the performance of distance education departments at public universities in Turkey during the 2018–2019 academic year, utilizing both the DEA and TOPSIS methods. The study also aimed to compare and rank the efficient decision-making units based on their efficiency measurements. [6] proposed an integrated interval DEA model that classifies DMUs into three categories—super-efficient, efficient, and inefficient in a single step, accommodating integer and negative data. A detailed review of DEA ranking models has been presented in [1].
From the detailed literature analysis, we conclude that using DEA and TOPSIS is a good idea for handling the problem of robust ranking of DMUs.

1.2. Contributions and Purpose

In this study, we have made an effort to add one more aspect to the DEA application, i.e. ranking of efficient fuzzy portfolios with two risk metrics in the presence of negative input-outputs. The following are the key highlights of the current study.
1. The MSBM model is commonly employed to assess the efficiency of DMUs in the presence of negative data. However, its application in evaluating the efficiency and ranking of portfolios with uncertainty has not been thoroughly explored in the existing literature. This research represents the first attempt to extend the MSBM model within a possibilistic framework, allowing it to address and manage fuzzy variables effectively. By incorporating fuzziness into the model, this study aims to fill the gap in portfolio efficiency analysis and provide a novel approach that enhances decision-making under uncertainty.
2. Based on previous discussions, researchers across different fields generally agree that utilizing DEA and TOPSIS is a valuable approach. Very few studies [19, 22] etc. address full ranking with negative input-output variables, so we combine the MSBM fuzzy portfolio model with TOPSIS to leverage the strengths of both methods.
3. Implementing the MSBM fuzzy portfolio estimation models with TOPSIS for ranking the efficient portfolios is a new application in the field of DEA.
4. We demonstrate the applicability and effectiveness of our methodology using actual data from the Stock Exchange in portfolio construction challenges.

The remainder of the paper is organized in the following manner. Section 2 presents some basic definitions and preliminaries regarding fuzzy numbers and their possibilistic mean, variance, and semi-variance for portfolio selection. Section 3 offers the MSBM fuzzy portfolio estimation model in a possibilistic framework. Section 4 presents the various steps of the TOPSIS method to rank the efficient portfolios. In Section 5, numerical examples are presented to justify the proposed approach. Finally, Section 6 presents the conclusions with some future directions.

2. Preliminaries

In this section, we present the basics of fuzzy sets and fuzzy numbers. Further, the mathematical models of [8], for computing the possibilistic mean, possibilistic variance, and possibilistic semi-variance of a fuzzy number are presented here.

Definition 1 *Let X be a universal set. A fuzzy set $\tilde{A}$ in X is denoted by*

$$\tilde{A} = \{\langle x, \mu_{\tilde{A}}(x)\rangle \mid x \in X\},$$

where $\mu_{\tilde{A}} : X \to [0,1]$ describes the degree of belongings of an element $x \in X$ to the set $\tilde{A}$.

Definition 2 (γ-cut) *Let $\tilde{A}$ be a fuzzy set in X and $\gamma \in (0,1]$. The γ-cut of the fuzzy set $\tilde{A}$ is the crisp set A_γ given by*

$$A_\gamma = \{x \in X : \mu_{\tilde{A}}(x) \geq \gamma\}.$$

Definition 3 *A fuzzy set $\tilde{A}$ in $\mathbb{R}$ is called a fuzzy number if it satisfies the following conditions*

1. *$\tilde{A}$ is normal.*
2. *$\tilde{A}_\gamma$ is a closed interval for every $\gamma \in (0,1]$.*
3. *The support of $\tilde{A}$ is bounded.*

Definition 4 (Trapezoidal fuzzy number (TrFN)) *A fuzzy number $\tilde{A}$ represented by the quadruplet $\tilde{A} = [a, b, \alpha, \beta]$, where $[a, b]$ is the tolerance interval; α and β denote the left and right width of the TrFN- $\tilde{A}$, respectively, is called a trapezoidal fuzzy number if its membership function is given by*

$$\mu_{\tilde{A}}(x) = \begin{cases} 0, & x \le a - \alpha, x \ge b + \beta, \\ \dfrac{x - a + \alpha}{\alpha}, & a - \alpha \le x \le a, \\ 1, & a \le x \le b, \\ \dfrac{b + \beta - x}{\beta}, & b \le x \le b + \beta, \end{cases}$$

Further, the γ-cut of the TrFN $\widetilde{A} = (a, b, \alpha, \beta)$ is the closed interval and given by

$$A^\gamma = [a_1^\gamma, a_2^\gamma] = [(a - (1-\gamma)\alpha,\ b + (1-\gamma)\beta], \quad \gamma \in (0,1].$$

Definition 5 *Let $\tilde{A}$ be a fuzzy number with $A^\gamma = [a_1^\gamma, a_2^\gamma]$, $\gamma \in (0,1]$. The (crisp) possibilistic mean (or expected value) and possibilistic variance of a fuzzy number $\tilde{A}$, denoted by $E(\tilde{A})$ and $Var(\tilde{A})$, is defined as*

$$E(\tilde{A}) = \int_0^1 \gamma \left(a_1^\gamma + a_2^\gamma\right) d\gamma,$$

and

$$Var(\tilde{A}) = \frac{1}{2} \int_0^1 \gamma \left(a_2^\gamma - a_1^\gamma\right)^2 d\gamma.$$

respectively.

It is easy to see that for a TrFN $\tilde{A} = [a, b, \alpha, \beta]$

$$E(\tilde{A}) = \int_0^1 \gamma[a - (1-\gamma)\alpha + b + (1-\gamma)\beta] d\gamma = \frac{(a+b)}{2} + \frac{(\beta - \alpha)}{6},$$

and

$$Var(\tilde{A}) = \left[\frac{(b-a)}{2} + \frac{(\alpha+\beta)}{6}\right]^2 + \frac{(\alpha+\beta)^2}{72}.$$

Further, [36] defined the lower possibilistic semi-variance of a fuzzy number $\tilde{A}$ denoted by $Var^{-}(\tilde{A})$, as

$$Var^{-}(\tilde{A}) = \int_0^1 2\gamma \left(E(\tilde{A}) - a_1^{\gamma}\right)^2 d\gamma.$$

Thus for a TrFN $\tilde{A} = [a, b, \alpha, \beta]$, the lower possibilistic semi-variance is as follows

$$Var^{-}(\tilde{A}) = \left[\frac{(b-a)}{2} + \frac{(\alpha+\beta)}{6}\right]^2 + \frac{(\alpha)^2}{18}.$$

Assume there are n risky assets whose returns are TrFNs represented by $\tilde{r}_i = (a_i, b_i, \alpha_i, \beta_i)$, $i = 1, 2, \ldots, n$ with investment proportion w_i, $i = 1, 2, \ldots, n$, such that $w_i \geq 0$; $\sum_{i=1}^{n} w_i = 1$. Also, there is a fixed linear transaction cost k_i associated with each asset. As a result, the portfolio's probabilistic expected net return, variance, and lower semi-variance, denoted by R, σ^2 and $(\sigma^2)^{-}$ are given by as follows

$$R = E\left(\sum_{i=1}^{n} \tilde{r}_i w_i - \sum_{i=1}^{n} k_i w_i\right) = \sum_{i=1}^{n} \left[\left\{\frac{1}{2}\left(a_i + b_i + \frac{1}{3}\left(\beta_i - \alpha_i\right)\right) w_i\right\} - k_i w_i\right],$$

$$\sigma^2 = Var\left(\sum_{i=1}^{n} \tilde{r}_i w_i\right) = \left[\left(\frac{(b_i - a_i)}{2} + \frac{(\alpha_i + \beta_i)}{6}\right) w_i\right]^2 + \frac{1}{72}\left[\sum_{i=1}^{n} (\alpha_i + \beta_i) w_i\right]^2,$$

and

$$(\sigma^2)^{-} = Var^{-}\left(\sum_{i=1}^{n} \tilde{r}_i w_i\right) = \left[\left(\frac{(b-a)}{2} + \frac{(\alpha+\beta)}{6}\right) w_i\right]^2 + \frac{1}{18}\left[\sum_{i=1}^{n} (\alpha_i w_i)\right]^2,$$

respectively.

2.1. Modified Slack Based Model to handle negative data

To address the issue of negative data in conventional DEA models, [37] introduced a modified slack-based measure (MSBM) model. The MSBM model is modified by [42] for evaluating the performance of production units by taking direction different from [37].

Consider that there are P DMUs to be evaluated, each using m inputs to generate s outputs. Let $x_{tj}, (t = 1, \ldots m)$ represent the t^{th}, input for the j^{th} DMU, and $y_{rj}, (r = 1, \ldots s)$ denote the r^{th} output of the j^{th} DMU. The modified MSBM method is presented as follows:

$$\textbf{(Model I)} \quad \min\ \theta_0 = \frac{1 - \frac{1}{m}\sum_{t=1}^{m} \frac{s_{io}^-}{R_t^-}}{1 + \frac{1}{s}\sum_{r=1}^{s} \frac{s_{ro}^+}{R_r^+}}$$

$$\text{s. t.} \quad \sum_{j=1}^{P} \lambda_j x_{tj} + s_{t0}^- = x_{t0} \quad t = 1, 2, \ldots, m$$

$$\sum_{j=1}^{P} \lambda_j y_{rj} - s_{r0}^+ = y_{r0} \qquad r = 1, 2, \ldots, s$$

$$\sum_{j=1}^{P} \lambda_j = 1 \quad \lambda_j \geq 0, j = 1, 2...P., s_{t0}^-, s_{r0}^+ \geq 0$$

The objective function $\theta_0^\star$ represents the optimal efficiency score of DMU_0. The terms s_{t0}^- $(t = 1, \ldots, m)$ and s_{r0}^+ $(r = 1, \ldots, s)$ represent the t^{th} input excess and r^{th} output shortfall of DMU_0, referred to as slacks. The λ_j $(j = 1, \ldots, P)$ are intensity variables used to link inputs and outputs in a convex combination. Also, R_t^- and R_r^+ are the feasible directions to move and are defined as follows:

$$R_t^- = \max_{j=1,2,\ldots,P} x_{tj} - \min_{j=1,2,\ldots,P} x_{tj}, \quad t = 1, 2, \ldots, m$$

$$R_r^+ = \max_{j=1,2,\ldots,P} y_{rj} - \min_{j=1,2,\ldots,P} y_{rj}, \quad r = 1, 2, \ldots, s$$

In the following section, we present the MSBM fuzzy portfolio estimation models based on [11].

3. MSBM fuzzy portfolio evaluation models in the framework of possibilistic theory

In this section, we present the MSBM fuzzy portfolio estimation model to handle the unpredictability of the variables.

Assume that there are P portfolios to be evaluated. To evaluate a portfolio performance, we consider the risk associated with the portfolio as the input indicator, and the corresponding return as the output indicator. In this study, we assume n risky assets with fuzzy return as $\tilde{r}_i = (a_i, b_i, \alpha_i, \beta_i)$, $i = 1, 2, ..., n$ with investment proportions w_{ij}, $i = 1, 2, ..., n$; $j = 1, 2, \ldots, P$, such that $\sum_{i=1}^{n} w_{ij} = 1$, are considered for constructing j^{th} portfolio which is considered to be a DMU. Suppose k_i is the unit transaction cost

of a unit for the i^{th} risky asset. Then the expected net return, variance, and semi-variance of the j^{th} portfolio denoted by $\overline{R}_j, \sigma_j^2$ and $(\sigma^2)_j^-$ respectively for $(j = 1, 2, \ldots, P)$ are given respectively. To employ the MSBM models for the efficiency evaluation of all portfolios, in our study we consider one input and one output $(m = s = 1)$ criteria as risk and return respectively.

3.1. MSBM fuzzy portfolio evaluation model in possibilistic mean-variance framework

To handle the problem of negative data and to provide a full ranking of all DMUs, [42] suggested a novel MSBM (modified slacks-based model) model. We extend the above-presented model I in the possibilistic mean-variance framework. The mathematical form of the MSBM fuzzy portfolio model with possibilistic variances input (risk) and possibilistic mean as output (return) is given as follows:

$$(\textbf{Model II}) \qquad \min \ \rho_0 = \frac{1 - \dfrac{s_{10}^-}{R_1^-}}{1 + \dfrac{s_{10}^+}{R_2^+}}$$

$$\text{s. t.} \ \sum_{j=1}^{P} \lambda_j \left(\left\{ \sum_{i=1}^{n} \frac{1}{2} \Big[(b_i - a_i) + \frac{\alpha_i + \beta_i}{3} \Big] w_{ij} \right\}^2 + \frac{1}{72} \Big[\sum_{i=1}^{n} (\alpha_i + \beta_i) w_{ij} \Big]^2 \right) + s_{10}^-$$

$$= \left(\left\{ \sum_{i=1}^{n} \frac{1}{2} \Big[(b_i - a_i) + \frac{\alpha_i + \beta_i}{3} \Big] w_{i0} \right\}^2 + \frac{1}{72} \Big[\sum_{i=1}^{n} (\alpha_i + \beta_i) w_{i0} \Big]^2 \right)$$

$$\sum_{j=1}^{P} \lambda_j \left(\sum_{i=1}^{n} \frac{1}{2} \Big[(b_i + a_i) + \frac{\beta_i - \alpha_i}{3} \Big] w_{ij} - \sum_{i=1}^{n} k_i w_{ij} \right) - s_{10}^+$$

$$= \sum_{i=1}^{n} \frac{1}{2} \Big[(b_i + a_i) + \frac{\beta_i - \alpha_i}{3} \Big] w_{i0} - \sum_{i=1}^{n} k_i w_{i0},$$

$$\sum_{j=1}^{P} \lambda_j = 1 \ \ \lambda_j \geq 0 \, , s_{10}^-, \, s_{10}^+ \geq 0, \quad j = 1, 2, \ldots, P$$

Here, R_1^- and R_2^+ can be modified as follows :

$$R_1^- = \max_{j=1,2,\ldots,P}\left(\sum_{i=1}^{n}(\frac{1}{2}[(b_i - a_i) + \frac{\alpha_i + \beta_i}{3}]w_{ij})^2 + \frac{1}{72}[\sum_{i=1}^{n}(\alpha_i + \beta_i)w_{ij}]^2\right)$$
$$- \min_{j=1,2,\ldots,P}\left(\sum_{i=1}^{n}(\frac{1}{2}[(b_i - a_i) + \frac{\alpha_i + \beta_i}{3}]w_{ij})^2 + \frac{1}{72}[\sum_{i=1}^{n}(\alpha_i + \beta_i)w_{ij}]^2\right)$$

$$R_2^+ = \max_{j=1,2,\ldots,P}\left(\sum_{i=1}^{n}\frac{1}{2}[(b_i + a_i) + \frac{\beta_i - \alpha_i}{3}]w_{ij} - \sum_{i=1}^{n}k_i w_{ij}\right)$$
$$- \min_{j=1,2,\ldots,P}\left(\sum_{i=1}^{n}\frac{1}{2}[(b_i + a_i) + \frac{\beta_i - \alpha_i}{3}]w_{ij} - \sum_{i=1}^{n}k_i w_{ij}\right)$$

Let $(\rho^*, \lambda_1^*, \lambda_2^* \ldots, \lambda_P^*)$ be an optimum solution of (Model II). Further, ρ_0^* indicates the optimal efficiency score of the portfolio under evaluation (0^{th}) Here, s_{10}^- and s_{10}^+, respectively denote the excess of input (risk) and shortfall of output(return) of 0^{th} portfolio, and they are identified as slacks.

3.2. MSBM fuzzy portfolio evaluation model in possibilistic mean semi-variance framework

The mathematical form of the MSBM fuzzy portfolio model with possibilistic semi-variance input (risk) and possibilistic mean as output (return) is given as follows:

$$\textbf{(Model III)} \qquad \min\ \eta_0 = \frac{1 - \frac{s_{10}^-}{R_3^-}}{1 + \frac{s_{10}^+}{R_2^+}}$$

$$\text{s. t.}\ \sum_{j=1}^{P}\lambda_j\left(\left\{\sum_{i=1}^{n}\frac{1}{2}\Big[(b_i - a_i) + \frac{\alpha_i + \beta_i}{3}\Big]w_{ij}\right\}^2 + \frac{1}{18}\Big[\sum_{i=1}^{n}(\alpha_i)w_{ij}\Big]^2\right) + s_{10}^-$$

$$= \left(\left\{\sum_{i=1}^{n}\frac{1}{2}\Big[(b_i - a_i) + \frac{\alpha_i + \beta_i}{3}\Big]w_{i0}\right\}^2 + \frac{1}{18}\Big[\sum_{i=1}^{n}(\alpha_i)w_{i0}\Big]^2\right)$$

$$\sum_{j=1}^{P}\lambda_j\left(\sum_{i=1}^{n}\frac{1}{2}\Big[(b_i + a_i) + \frac{\beta_i - \alpha_i}{3}\Big]w_{ij} - \sum_{i=1}^{n}k_i w_{ij}\right) - s_{10}^+$$

$$= \sum_{i=1}^{n} \frac{1}{2}\Big[(b_i + a_i) + \frac{\beta_i - \alpha_i}{3}\Big] w_{i0} - \sum_{i=1}^{n} k_i w_{i0},$$

$$\sum_{j=1}^{P} \lambda_j = 1 \quad \lambda_j \geq 0, \ , s_{10}^{-}, s_{10}^{+} \geq 0, \quad j = 1, 2, \ldots, P$$

Here, R_2^+ is the same as described in the model II and R_3^- is defined as follows:

$$R_3^- = \max_{j=1,2,\ldots,P} \left(\sum_{i=1}^{n} (\frac{1}{2}[(b_i - a_i) + \frac{\alpha_i + \beta_i}{3}] w_{ij})^2 + \frac{1}{18}[\sum_{i=1}^{n} (\alpha_i) w_{ij}]^2 \right)$$
$$- \min_{j=1,2,\ldots,P} \left(\sum_{i=1}^{n} (\frac{1}{2}[(b_i - a_i) + \frac{\alpha_i + \beta_i}{3}] w_{ij})^2 + \frac{1}{18}[\sum_{i=1}^{n} (\alpha_i) w_{ij}]^2 \right)$$

The models mentioned above can determine the efficiency values of all fuzzy portfolios; however, they do not provide a unique ranking of the portfolios. It is important to note that if multiple portfolios are deemed efficient, establishing a complete and unique ranking becomes impossible. Therefore, we apply the TOPSIS method to rank all efficient portfolios and obtain a unique ranking. The TOPSIS method was introduced by [20]. It is a practical method for organizing the available options based on numerous criteria. It outperforms other MCDM methods for solving a wide range of decision-making problems in real-world, due to its simple computational approach and systematic procedure.

4. TOPSIS method to rank the efficient portfolio

TOPSIS is founded on the notion of selecting the best alternative (here DMU) that is as close to the positive ideal solution at the same time being as far away from the negative ideal solution as possible. The best performance values for each portfolio demonstrated by each criterion (here criterion as risk and return) in the decision matrix make up the perfect solution. As a result, we used a negative feature criterion for risk and a positive feature criterion for return.

Let L be the number of efficient portfolios. Suppose we have m inputs and s outputs for each portfolio, let D_1 and D_2 denotes respectively the input and output matrix corresponding to L efficient portfolios. Therefore

$$D_1 = \begin{bmatrix} x_{11} & x_{12} & \ldots & x_{1L} \\ x_{21} & x_{22} & \ldots & x_{2L} \\ \vdots & \vdots & \vdots & \vdots \\ x_{m1} & x_{m2} & \ldots & x_{mL} \end{bmatrix} \qquad D_2 = \begin{bmatrix} y_{11} & y_{12} & \ldots & y_{1L} \\ y_{21} & y_{22} & \ldots & y_{2L} \\ \vdots & \vdots & \vdots & \vdots \\ y_{s1} & y_{s2} & \ldots & y_{sL} \end{bmatrix}$$

Now we have to follow the following steps:
Step 1. Normalization

Calculate the normalized decision matrix corresponding to the cost criterion (m inputs) and benefit criteria (s outputs). Let p_{tl} and q_{rl} ($t = 1, 2, \ldots, m$; $r = 1, 2, \ldots, s$) denotes the normalized value of t^{th} input and r^{th} output of l^{th} DMU respectively and calculated as follows:

$$p_{tl} = \frac{x_{tl}}{\sqrt{\sum_{k=t}^{L} x_{tk}^2}}, \quad \forall t = 1, 2, \ldots, m,\ l = 1, 2, \ldots, L$$

and

$$q_{rl} = \frac{y_{rl}}{\sqrt{\sum_{k=1}^{L} y_{rk}^2}}, \quad \forall r = 1, 2, \ldots, s,\ \ l = 1, 2, \ldots, L.$$

Step 2. Determine the positive ideal and negative-ideal points: Let p_{tw} and q_{tw} denotes respectively be the t^{th} input and r^{th} output of the worst DMU (D_w). Similarly let p_{tb} and q_{rb} denotes respectively be the t^{th} input and r^{th} output of the best DMU (D_b). Then

$$p_{tw} = \max_{1 \le l \le L} p_{tl}, \quad t = 1, 2, \ldots, m,$$

and

$$q_{rw} = \min_{1 \le l \le L} q_{rl}, \quad r = 1, 2, \ldots, s.$$

Similarly

$$p_{tb} = \min_{1 \le l \le L} p_{tl}, \quad t = 1, 2, \ldots, m,$$

and

$$q_{rb} = \max_{1 \le l \le L} q_{rl}, \quad r = 1, 2, \ldots, s.$$

Step 3. Measuring the distance from the ideal and negative ideal points:
Let d_{lw} be the distance between the target DMU l and the worst DMU D_w (best DMU D_b), so

$$d_{lw} = \sqrt{\sum_{t=1}^{m} (p_{tl} - p_{tw})^2 + \sum_{r=1}^{s} (q_{rl} - q_{rw})^2}, \quad l = 1, 2, \ldots, L,$$

and

$$d_{lb} = \sqrt{\sum_{o=1}^{m} (p_{tl} - p_{tb})^2 + \sum_{r=1}^{s} (q_{rl} - q_{rb})^2}, \quad l = 1, 2, \ldots, L.$$

Step 4. Calculate the similarity to the worst condition:
Let s_{lw} be the relative closeness of the target DMU l to the worst DMU D_w.

$$s_{lw} = \frac{d_{lw}}{d_{lw} + d_{lb}}, \quad l = 1, 2, \ldots, L.$$

Here, $0 \le s_{lw} \le 1$, and

$$s_{lw} = \begin{cases} 1, & \text{if and only if the alternative solution has the best condition} \\ 0, & \text{if and only if the alternative solution has the worst condition.} \end{cases}$$

Step 5. Ranking criterion:
Rank the alternatives or portfolios in the descending order of s_{lw}, the alternative with a maximum value of s_{lw} is the best-performing alternative.
The working procedure of the proposed approach has been described in the algorithm 1.

Algorithm 1 Computation Procedure of the proposed method

Input: The Fuzzy returns of Stocks with the different proportions invested in the stocks.
Output: The full ranking of efficient portfolios.
Step 1. Calculate the Efficiency of portfolios by using MSBM fuzzy portfolio models.
Step 2. Rank the portfolios according to the efficiency score.
Step 3. If the no. of efficient portfolio ≥ 1, then apply TOPSIS method.
Step 4. Identification of attributes (Return, Risk) for all the alternatives (efficient portfolios).
Step 5. Form a weighted normalized decision matrix.
Step 6. Calculate the positive and negative ideal points.
Step 7. Evaluate the similarity to the worst condition as the measure of relative closeness s_{lw}.
Step 8. Rank the efficient portfolio in the decreasing order of s_{lw}.

5. Numerical Illustration

To demonstrate the applicability and validity of the proposed method, two numerical examples are presented. In the first example, the possibilistic mean is considered as the output, and the possibilistic variance as the input. In the second example, the possibilistic mean is again used as the output, with the possibilistic semi-variance as the input. All simulations were implemented using MATLAB software.

Example 1
In this example, the returns from risky assets/stocks are provided in Table 1 as trapezoidal fuzzy numbers and are the same as taken by [29] in their study. In the experimental analysis of [29], the historical data of 5 assets from April 2009 to March 2015, in terms of the weekly closing prices are used to simulate the future returns. Furthermore, we create the random sample portfolios using the weights as shown in Table 2. For convenience, we select only those 5 stocks whose returns are negative. We employ Model II to calculate the efficiency and ranking of all randomly generated portfolios. The results are presented in Table 3.

Table 1. The possibility distribution of the return rates and their respective transaction cost of 5 stocks

Stocks	a_i	b_i	α_i	β_i	k_i
S_1	-0.1071	−0.0703	0.0105	0.0541	0.003
S_2	0.0883	0.1057	0.057	0.0772	0.003
S_3	0.0874	0.0948	0.0132	0.0928	0.003
S_4	-0.0907	-0.082	0.0055	0.0336	0.003
S_5	-0.0954	-0.082	0.0093	0.013	0.003

Table 2. The weight of each stock in different randomly generated portfolios

w	1	2	3	4	5	6	7	8	9	10
w_1	0.1875	0.2660	0.2616	0.1956	0.2608	0.1677	0.0637	0.0948	0.3678	0.0891
w_2	0.1566	0.1102	0.2422	0.0962	0.3080	0.2472	0.2610	0.2547	0.2150	0.0561
w_3	0.3301	0.2483	0.1600	0.2975	0.2684	0.2437	0.1899	0.2408	0.0389	0.3180
w_4	0.1585	0.0805	0.2621	0.3064	0.1287	0.1964	0.2413	0.0050	0.2217	0.2013
w_5	0.1673	0.2905	0.0741	0.1043	0.0340	0.1450	0.2442	0.4048	0.1567	0.3355
w_p	11	12	13	14	15	16	17	18	19	20
w_1	0.0099	0.2206	0.3053	0.2608	0.1184	0.1714	0.0244	0.3602	0.0844	0.3571
w_2	0.2762	0.3457	0.2831	0.1016	0.3696	0.0105	0.2256	0.1147	0.0871	0.0746
w_3	0.2373	0.1664	0.0314	0.1039	0.0955	0.1306	0.2335	0.1934	0.2467	0.3654
w_4	0.2792	0.0005	0.1601	0.1654	0.2866	0.3579	0.1711	0.2879	0.2542	0.0149
w_5	0.1974	0.2669	0.2201	0.3684	0.1299	0.3296	0.1253	0.0438	0.3276	0.1879
w_p	21	22	23	24	25	26	27	28	29	30
w_1	0.2904	0.1345	0.0715	0.1815	0.1990	0.0479	0.2311	0.0904	0.2334	0.2311
w_2	01905.	0.0337	0.2241	0.1996	0.2874	0.2777	0.2503	0.0134	0.0418	0.1278
w_3	0.2333	0.3373	0.2388	0.4058	0.0994	0.2683	0.1133	0.2684	0.4218	0.0272
w_4	0.0792	0.2580	0.1773	0.0647	0.1409	0.2410	0.0752	0.2950	0.1474	0.3668
w_5	0.2066	0.2366	0.2884	0.1484	0.2734	0.1651	0.3301	0.3328	0.1556	0.2452

Table 3. The efficiency score and the ranking of portfolios in possibilistic mean-variance framework

portfolio	Return	Risk	Efficiency by model II	ranking by Model II
1	0.0043	0.00052	0.4714	16
2	-0.0198	0.00048	0.4396	18
3	-0.0112	0.00057	0.3138	25
4	-0.0124	0.00045	0.5188	13
5	0.0212	0.00072	0.3558	23
6	0.0048	0.00055	0.4168	19
7	-0.0033	0.00045	0.5696	11
8	0.0040	0.00049	0.5376	12
9	-0.0392	0.00056	0.272	29
10	-0.0174	0.00034	0.672	5
11	0.0085	0.00045	0.6361	7
12	0.0076	0.00065	0.2256	30
13	-0.0286	0.00058	0.2756	28
14	-0.0488	0.00039	0.4689	17
15	-0.0004	0.00055	0.3918	20
16	-0.0605	0.00027	1.0000	1
17	0.0177	0.00031	1.0000	1
18	-0.0280	0.00055	0.3207	2
19	-0.0249	0.00033	0.6474	6
20	-0.0042	0.00060	0.3018	27
21	-0.0078	0.00059	0.3122	26
22	-0.0172	0.00036	0.6346	8
23	-0.0012	0.00044	0.5908	9
24	0.0263	0.00061	1.0000	1
25	-0.0155	0.00053	0.3816	21
26	0.0148	0.00050	0.5745	10
27	-0.0200	0.00052	0.3782	22
28	-0.0343	0.00028	1.0000	1
29	0.0005	0.00049	0.5065	14
30	-0.0577	0.00036	0.4788	15

Table 4. Ranking of efficient portfolios by different methods in possibilistic mean-variance framework

Portfolio	Return	Risk	ranking by Model II	ranking by [42]	ranking by MSBM-TOPSIS method
16	-0.0605	0.00027	1	4	4
17	0.0177	0.00031	1	2	1
24	0.0263	0.00061	1	1	2
28	-0.0343	0.00028	1	3	3

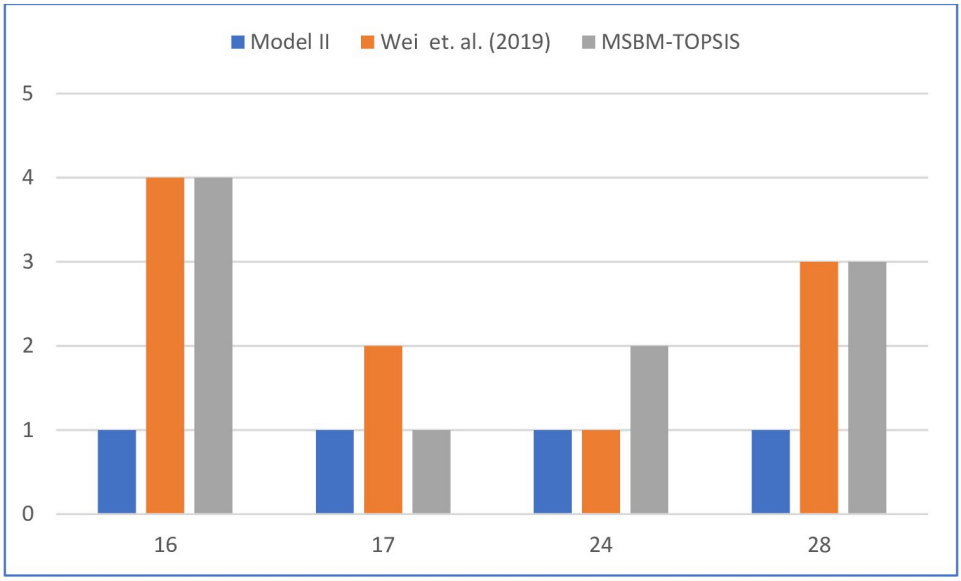

Figure 1. Rankings of efficient portfolios in possibilistic mean-variance framework

Remark 1 *Table 3 shows that the efficiency score of portfolios 16, 17, 24, and 28 is the same, and we cannot distinguish between efficient portfolios further. The MSBM-TOPSIS approach, as stated above, is used to determine the whole ranking. The fourth, fifth, sixth, and seventh column of Table 4 depicts the ranking of efficient portfolios by Model II, by [42], and by the proposed MSBM-TOPSIS method respectively. Figure 1 shows the ranking of efficient portfolios graphically. It should be highlighted that the process described in [42] gives us the whole ranking of all randomly produced portfolios. However, the Super efficiency model of [18] poses an in-feasibility concern. The ranking by the proposed method for Portfolio 16 and Portfolio 28 is the same as obtained by [42]. Compared to the method given by [42], the proposed approach is less calculative and easy to handle.*

If asset return distributions aren't symmetric, using variance as a risk indicator isn't recommended because it initiates to portfolio's projections drastically different from what would be expected in real-life situations. Excessively high and low returns are both regarded as undesirable by variance, which is one of the key disadvantages. Many academics have utilized a variety of techniques to deal with such problems. Risk can be classified using semi-variance as an alternative risk measure. Therefore, a downside risk metric called possibilistic semi-variance is utilized here instead of possibilistic variance as an input parameter. Table 5 shows the ranking, obtained by model III and Table 6 provides the complete ranking of efficient portfolios using different methods.

Table 5. The efficiency score and the ranking of portfolios in possibilistic mean semi-variance framework

Portfolio	Return	Risk	efficiency by Model III	ranking by Model III
1	0.0043	0.00045	0.4694	15
2	-0.0198	0.00043	0.4175	18
3	-0.0112	0.00051	0.2866	25
4	-0.0124	0.00039	0.5195	12
5	0.0212	0.00064	0.3272	23
6	0.0048	0.00049	0.4014	19
7	-0.0033	0.00040	0.5524	11
8	0.0040	0.00044	0.5082	14
9	-0.0392	0.00052	0.2289	28
10	-0.0174	0.00029	0.6719	5
11	0.0085	0.00039	0.6316	8
12	0.0076	0.00060	0.167	30
13	-0.0286	0.00053	0.2242	29
14	-0.0488	0.00036	0.4413	17
15	-0.0004	0.00050	0.353	20
16	-0.0605	0.00025	1.00	1
17	0.0177	0.00027	1.00	1
18	-0.0280	0.00049	0.2996	24
19	-0.0249	0.00029	0.6418	6
20	-0.0042	0.00053	0.2853	26
21	-0.0078	0.00052	0.2826	27
22	-0.0172	0.00031	0.638	7
23	-0.0012	0.00039	0.5777	9
24	0.0263	0.00053	1.00	1
25	-0.0155	0.00048	0.3387	21
26	0.0148	0.00043	0.5724	10
27	-0.0200	0.00047	0.335	22
28	-0.0343	0.00025	1.00	1
29	0.0005	0.00042	0.5146	13
30	-0.0577	0.00033	0.4547	16

Remark 2 *The suggested method's most significant advantage is its feasibility when compared to super-efficiency methods, which are in some situations infeasible.*

Table 6. Ranking of efficient portfolios by in possibilistic mean semi-variance framework

Portfolio	Return	Risk	ranking by Model III	ranking by [42]	ranking by MSBM-TOPSIS method
16	-0.0605	0.00025	1	3	4
17	0.0177	0.00027	1	1	1
24	0.0263	0.00053	1	2	2
28	-0.0343	0.00025	1	4	3

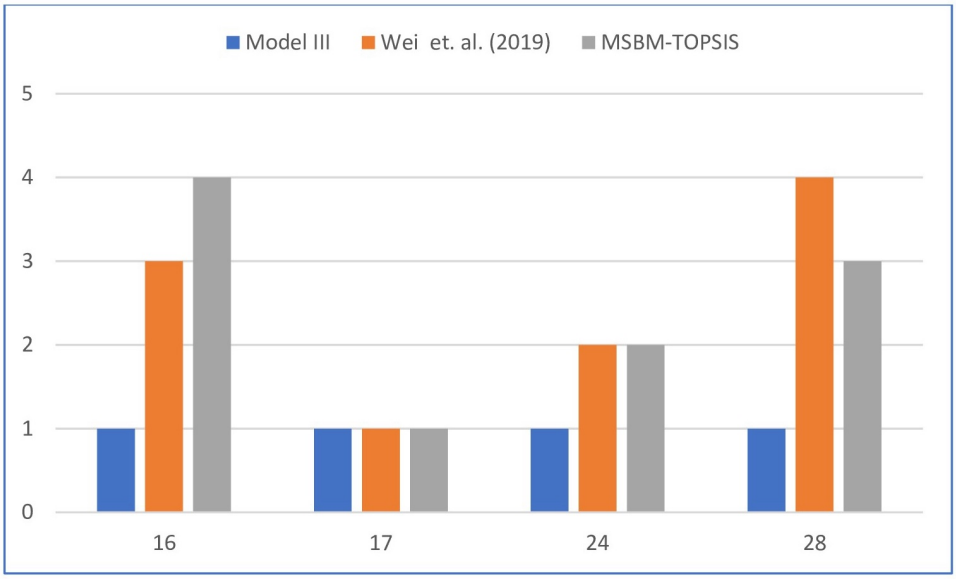

Figure 2. Rankings of efficient portfolios in possibilistic mean semi-variance framework

5.1. Computation Complexity

In this study, we compute the computational complexity by taking into account all logical-mathematical operations, such as addition, subtraction, multiplication, division, exponentiation and square root as described in [35]. The mathematical operations used for creating the return risk are the same for each strategy used in this study. As a result, they weren't considered while determining computational complexity. Suppose we have n efficient portfolio (to be considered as an alternative) and m criteria (return and risk) in the study, then it will take 3nm operations to reach at the weighted normalized matrix, 2(6nm) calculations required to determine the distance between efficient portfolio and the ideal and negative ideal points. nm-n calculations are required for calculating the positive ideal and negative ideal points. Lastly, 2n computations are used to calculate each portfolio's closeness coefficient. As a result, the TOPSIS's computational complexity to determine the full ranking of the efficient fuzzy portfolio in the second stage is determined as follows:

$$T_{n,m} = 3nm + 12nm + nm - n + 2n$$

.
The hybrid MSBM-TOPSIS requires 132 simple operations for the empirical analysis included in this analysis, whereas other DEA models need to solve the mathematical models repeatedly to get the whole ranking for efficient portfolios. Hence, Our method is substantially less intricate than the existing methods, so finding the most effective portfolio will take less time. In contrast to our approach, which uses basic operations to find the best portfolio in the second phase, the super efficiency and modified MSBM method given in[42] often solves at least three models for each portfolio to determine the best portfolio.

6. Conclusion and Future Research Directions

This work investigates the ranking problem of all efficient fuzzy portfolios with positive and negative input-output variables. We know that if a sufficiently large number of portfolios are designated efficient, the DEA's discrimination ability decreases. We extend the MSBM model for handling fuzzy portfolio evaluation problems in the possibilistic mean-variance and possibilistic mean semi-variance framework. By combining the proposed MSBM fuzzy portfolio models with the TOPSIS method, the work has established a hybrid strategy for ranking efficient portfolios in a fuzzy environment. By combining the strengths of MSBM in efficiency evaluation, fuzzy logic in handling uncertainty, and TOPSIS in ranking alternatives, this approach provides a comprehensive tool for investors looking to optimize their portfolios in uncertain market environments.
This approach will be explored in future work to investigate the classification of fuzzy portfolios having input as possibilistic semi-absolute deviation (SAD), possibilistic VaR, and CvaR. In this research, only 1st and 2nd-order moments (mean, variance,

and semi-variance) have been used as output and input. The higher-order moments can be utilized as the input-output values for future work.

Acknowledgment

The authors extend their gratitude to the anonymous reviewers and editors for their valuable comments and suggestions on the earlier draft of this paper.

References

[1] A. Aldamak and S. Zolfaghari. Review of efficiency ranking methods in data envelopment analysis. *Measurement*, 106:161–172, 2017.

[2] P. Andersen and N. C. Petersen. A procedure for ranking efficient units in data envelopment analysis. *Management science*, 39(10):1261–1264, 1993.

[3] B. Arabi, M. Toloo, Z. Yang, P. Zhang, and B. Xu. Sustainable refrigeration technology selection: An innovative dea-topsis hybrid model. *Environmental Science & Policy*, 158:103780, 2024.

[4] S. A. Banihashemi and M. Khalilzadeh. A new approach for ranking efficient DMUs with data envelopment analysis. *World Journal of Engineering*, 17(4):573–583, 2020.

[5] R. D. Banker, A. Charnes, and W. W. Cooper. Some models for estimating technical and scale inefficiencies in data envelopment analysis. *Management science*, 30(9):1078–1092, 1984.

[6] P. Bansal and A. Mehra. Integrated dynamic interval data envelopment analysis in the presence of integer and negative data. *Journal of Industrial and Management Optimization*, 18(2):1339–1363, 2022.

[7] C. Carlsson and R. Fullér. On possibilistic mean value and variance of fuzzy numbers. *Fuzzy Sets and Systems*, 122(2):315–326, 2001.

[8] C. Carlsson, R. Fullér, and P. Majlender. A possibilistic approach to selecting portfolios with highest utility score. *Fuzzy sets and systems*, 131(1):13–21, 2002.

[9] A. Charnes, W. W. Cooper, and E. Rhodes. Measuring the efficiency of decision making units. *European journal of operational research*, 2(6):429–444, 1978.

[10] W. Chen. Artificial bee colony algorithm for constrained possibilistic portfolio optimization problem. *Physica A: Statistical Mechanics and its Applications*, 429: 125–139, 2015.

[11] W. Chen, Y. Gai, and P. Gupta. Efficiency evaluation of fuzzy portfolio in different risk measures via DEA. *Annals of Operations Research*, 269(1):103–127, 2018.

[12] G. Cheng, P. Zervopoulos, and Z. Qian. A variant of radial measure capable of dealing with negative inputs and outputs in data envelopment analysis. *European Journal of Operational Research*, 225(1):100–105, 2013.

[13] A. Chitnis and O. S. Vaidya. Efficiency ranking method using DEA and topsis (erm-dt): case of an indian bank. *Benchmarking: An International Journal*, 2016.

[14] H. Ding, Z. Zhou, H. Xiao, C. Ma, and W. Liu. Performance evaluation of portfolios with margin requirements. *Mathematical Problems in Engineering*, 2014, 2014.

[15] A. Emrouznejad, A. L. Anouze, and E. Thanassoulis. A semi-oriented radial measure for measuring the efficiency of decision making units with negative data, using dea. *European Journal of Operational Research*, 200(1):297–304, 2010.

[16] Y. Ersoy. Performance evaluation in distance education by using data envelopment analysis (dea) and topsis methods. *Arabian Journal for Science and Engineering*, 46(2):1803–1817, 2021.

[17] P. Gupta, M. K. Mehlawat, A. Kumar, S. Yadav, and A. Aggarwal. A credibilistic fuzzy dea approach for portfolio efficiency evaluation and rebalancing toward benchmark portfolios using positive and negative returns. *International Journal of Fuzzy Systems*, 22(3):824–843, 2020.

[18] A. Hadi-Vencheh and A. Esmaeilzadeh. A new super-efficiency model in the presence of negative data. *Journal of the Operational Research Society*, 64(3):396–401, 2013.

[19] A. Hatami-Marbini, J. Pourmahmoud, and E. Babazadeh. A modified super-efficiency in the range directional model. *Computers & Industrial Engineering*, 120:442–449, 2018.

[20] C.-L. Hwang and K. Yoon. Methods for multiple attribute decision making. In *Multiple attribute decision making*, pages 58–191. Springer, 1981.

[21] J. Jablonsky. Multicriteria approaches for ranking of efficient units in DEA models. *Central European Journal of Operations Research*, 20(3):435–449, 2012.

[22] R. Lin. Cross-efficiency evaluation capable of dealing with negative data: A directional distance function based approach. *Journal of the Operational Research Society*, 71(3):505–516, 2020.

[23] R. Lin and Z. Chen. A directional distance based super-efficiency dea model handling negative data. *Journal of the operational Research Society*, 68(11):1312–1322, 2017.

[24] W. Liu, Z. Zhou, D. Liu, and H. Xiao. Estimation of portfolio efficiency via dea. *Omega*, 52:107–118, 2015.

[25] Y. J. Liu and W. G. Zhang. Fuzzy portfolio optimization model under real constraints. *Insurance: Mathematics and Economics*, 53(3):704–711, 2013.

[26] F. H. Lotfi, R. Fallahnejad, and N. Navidi. Ranking efficient units in DEA by using TOPSIS method. *Applied Mathematical Sciences*, 5(17):805–815, 2011.

[27] H. M. Markowitz. *Portfolio selection*. Yale university press, 1968.

[28] Z. Mashayekhi and H. Omrani. An integrated multi-objective markowitz-DEA cross-efficiency model with fuzzy returns for portfolio selection problem. *Applied Soft Computing*, 38:1–9, 2016.

[29] M. K. Mehlawat, P. Gupta, A. Kumar, S. Yadav, and A. Aggarwal. Multiobjective fuzzy portfolio performance evaluation using data envelopment analysis under credibilistic framework. *IEEE Transactions on Fuzzy Systems*, 28(11):2726–2737, 2020.

[30] N. R. Mohd Rashid, B. A. Halim, N. S. Tarmizi, N. F. S. Faizal, and I. Zulkeflee. Efficiency measurement and ranking of malaysian water supply service using hybrid dea-topsis. In *AIP Conference Proceedings*, volume 2905. AIP Publishing, 2024.

[31] H. Omrani, M. Shamsi, and A. Emrouznejad. Evaluating sustainable efficiency of decision-making units considering undesirable outputs: an application to airline using integrated multi-objective dea-topsis. *Environment, Development and Sustainability*, pages 1–32, 2022.

[32] Z. Pan, Y. Wang, Y. Zhou, and Y. Wang. Analysis of the water use efficiency using super-efficiency data envelopment analysis. *Applied Water Science*, 10(6): 1–11, 2020.

[33] M. Portela, E. Thanassoulis, and G. Simpson. A directional distance approach to deal with negative data in DEA: An application to bank branches. *Journal of Operational Research Society*, 55(10):1111–1121, 2004.

[34] S. A. Rakhshan. Efficiency ranking of decision making units in data envelopment analysis by using TOPSIS-DEA method. *Journal of the Operational Research Society*, 68(8):906–918, 2017.

[35] K. Rashidi and K. Cullinane. A comparison of fuzzy dea and fuzzy topsis in sustainable supplier selection: Implications for sourcing strategy. *Expert Systems with Applications*, 121:266–281, 2019.

[36] A. Saeidifar and E. Pasha. The possibilistic moments of fuzzy numbers and their applications. *Journal of computational and applied mathematics*, 223(2):1028–1042, 2009.

[37] J. A. Sharp, W. Meng, and W. Liu. A modified slacks-based measure model for data envelopment analysis with 'natural' negative outputs and inputs. *Journal of the Operational Research Society*, 58(12):1672–1677, 2007.

[38] M. Soltanifar, M. Tavana, F. J. Santos-Arteaga, and H. Sharafi. A hybrid multi-attribute decision-making and data envelopment analysis model with heterogeneous attributes: The case of sustainable development goals. *Environmental Science & Policy*, 147:89–102, 2023.

[39] K. Tone, T.-S. Chang, and C.-H. Wu. Handling negative data in slacks-based measure data envelopment analysis models. *European Journal of Operational Research*, 282(3):926–935, 2020.

[40] T. H. Tran, Y. Mao, P. Nathanail, P.-O. Siebers, and D. Robinson. Integrating slacks-based measure of efficiency and super-efficiency in data envelopment analysis. *Omega*, 85:156–165, 2019.

[41] E. Vercher and J. D. Bermúdez. Portfolio optimization using a credibility mean-absolute semi-deviation model. *Expert Systems with Applications*, 42(20):7121–7131, 2015.

[42] F. Wei, J. Song, C. Jiao, and F. Yang. A modified slacks-based ranking method handling negative data in data envelopment analysis. *Expert Systems*, 36(1): e12329, 2019.

[43] H. Xiao, T. Ren, and T. Ren. Estimation of fuzzy portfolio efficiency via an improved DEA approach. *INFOR: Information Systems and Operational Research*, 58(3):478–510, 2020.

[44] L. A. Zadeh. Fuzzy set theory and its applications. *University of California, California*, 8:338, 1965.

[45] L. A. Zadeh. Fuzzy sets as a basis for a theory of possibility. *Fuzzy sets and systems*, 1(1):3–28, 1978.

[46] W.-G. Zhang and Z.-K. Nie. On possibilistic variance of fuzzy numbers. In *International Workshop on Rough Sets, Fuzzy Sets, Data Mining, and Granular-Soft Computing*, pages 398–402. Springer, 2003.

[47] X.-X. Zhang, W. Liu, X. Wang, W. Zuo, Y.-M. Wang, and L. Sun. Ranking dmus by using interval efficiencies in data envelopment analysis. *Journal of Intelligent & Fuzzy Systems*, (Preprint):1–13, 2024.

[48] Z. Zhou, Q. Jin, H. Xiao, Q. Wu, and W. Liu. Estimation of cardinality constrained portfolio efficiency via segmented dea. *Omega*, 76:28–37, 2018.

Received 03.06.2024, Accepted 21.12.2024

Optical and Quantum Electronics (2025) 57:211
https://doi.org/10.1007/s11082-025-08130-2

Realization of all optical silicon slab waveguide based universal logic gates

Yash Yadav[1] · **Yogita Kalra**[1]

Received: 7 January 2025 / Accepted: 23 February 2025
© The Author(s), under exclusive licence to Springer Science+Business Media, LLC, part of Springer Nature 2025

Abstract
In this paper the design and implementation of SSW based all-optical NAND and NOR logic gates have been proposed. The design leverages the properties of silicon's high refractive index at optical communication wavelengths (1.55 μm), which ensures low critical angles and enhanced optical confinement in slab waveguides. The gates operate on the interference of the input signals. The designed NAND and NOR logic gates have been optimized for performance in both TE and TM modes using FDTD software MEEP. The NAND logic gate exhibits a contrast ratio of 34.79 dB with a modulation depth of 97.11% for TE mode and 38.42 dB with a modulation depth of 97.11% for TM mode. The NOR logic gate exhibits a contrast ratio of 40.91 dB with a modulation depth of 98.34% for TE mode and 38.42 dB with a modulation depth of 98.60% for TM mode. The designed universal logic gates exhibit high-speed performance, with propagation delay times measured in femtoseconds. The proposed gates exhibit higher performance metrics significantly outperforming existing optical logic gate designs.

Keywords Silicon slab waveguide · Optical logic gates · NAND logic gate · NOR logic gate

1 Introduction

Logic gates form the foundation of digital electronics, performing essential operations in all computing devices. As electronics push toward higher speeds and lower power consumption, traditional logic gates using electronic signals are becoming inadequate. In recent years, various methods have been explored for implementing optical logic gates (Kotb et al. 2023a), such as those based on semiconductor optical amplifiers (SOA), four-wave mixing, microring resonators, two-photon absorption (TPA), spatial filtering, and photonic crystals (Kotb et al. 2022; Hou et al. 2016; Wu et al. 2021; Rani et al. 2015; Li et al. 2005; Xu et al. 2007). However, optical logic gates have emerged as promising alternatives to electronic counterparts, driven by the demand for high-speed,

✉ Yogita Kalra
dryogitakalra@dtu.ac.in

[1] Advanced Simulation Lab, TIFAC-CORE in Fiber Optics and Optical Communication, Department of Applied Physics, Delhi Technological University, Delhi, India

energy-efficient computing. Most of the former all-optical realizations face limitations due to power dissipation and high laser intensities. A much simpler implementation of optical switches or logic gate structures, allowing already a high degree of integrability has been theoretically proposed using silicon slab waveguide (SSW).

Research on silicon waveguides has advanced significantly in the fields of optics and communication, particularly within silicon photonics. Silicon waveguides are an attractive choice for guiding light in integrated photonic circuits, benefiting from silicon's high refractive index contrast, which allows for strong light confinement and miniaturization of devices, due to its compatibility with standard CMOS fabrication processes, offering scalability and integration potential for complex photonic circuits (Merlo et al. 2021; Fu et al. 2013) Recent research on SSW based logic operation like (Kotb et al. 2023a; Kita et al. 2020; Wang and Long 2018; Aggarwal et al. 2024) has focused on enhancing waveguide performance by reducing propagation losses and optimizing dispersion characteristics to enable functionalities like wavelength conversion and optical amplification. These advancements hold promise for the development of scalable and cost-effective solutions in next-generation optical networks, driving innovations in data transmission, signal processing, and high-performance computing. The proposed NAND and NOR gates serve as fundamental building blocks for universal logic circuits, and their implementation using all-optical components enables interference between electromagnetic fields from two input waveguides at the waveguide junction. A key advantage of this switching architecture is its high signal contrast between on and off states at the output port, along with the elimination of back-reflections into the input ports. As the interference occurs instantaneously, the switching process in the waveguide junctions is inherently ultrafast, paving the way for low-power, high-speed optical computing systems.

The realization of all optical SSW based universal logic gates operations using linear interference effects in dielectric crossed waveguide structures where photons as carriers of information increase the data-bandwidth drastically. This linear effect provides the possibility to avoid excessive heating of the structures, since only low electromagnetic intensities are needed to drive the switching and logic elements(Qian and Caulfield 2006). The switching property is based on the interference of the signal (Gaussian Source) originating from two input ports and one control port at the waveguide junction. When the incoming signal and the control signal are in phase, they interfere constructively, resulting in a logic output of 1. Conversely, when these signals are out of phase, they interfere destructively, producing a logic output of 0. Due to low field intensities and the potential high degree of integration, linear interference effects appear very promising and will be under consideration in this paper (Caulfield 2004; Zhang et al. 2007).

The proposed design of SSW based NAND and NOR optical logic gates takes advantage of silicon's intrinsic properties, particularly its refractive index (around 3.47) at the widely-used optical communication wavelength of 1.55 μm (Aggarwal et al. 2024). This significantly enhances the optical confinement within the waveguide, ensuring efficient light guidance even at nanoscale dimensions. The critical angle for total internal reflection is reduced due to the strong refractive index contrast between the silicon core and the surrounding cladding, typically air or silicon dioxide. This enables tighter mode confinement, allowing the structure to support both Transverse Electric (TE) and Transverse Magnetic (TM) modes with minimal propagation loss and high efficiency (Vivien and Pavesi 2016). The finite-difference time-domain (FDTD) software MIT Electromagnetic Equation Propagation (MEEP) is used for the simulation, optimization, and realization of NAND and NOR logic gates for both polarizations. The simulation parameters include a resolution with a step size of 20, a perfectly matched layer (PML) as

the boundary condition with an iteration unit of 200.(Oskooi et al. 2010). The simplicity of the SSW design, combined with its high operational speed, positions these logic gates as a promising alternative to more complex optical gate structures, such as those utilizing photonic crystals (Kosmidou and Tsiboukis 2003). This work contributes to the growing body of research in silicon photonics. Further, the fabrication of SSWs is compatible with existing semiconductor manufacturing technologies, including standard CMOS processes, which enhances the practicality of integrating these gates into the next generation of computing architectures (Jindal et al. 2023). The use of fiber optic technology for signal transmission further supports their seamless incorporation into modern photonic systems (Parandin and Karkhanehchi 2017). As optical communication technologies advance, these designs could play a key role in the evolution of scalable, energy-efficient computing architectures, shaping the future of high-speed information processing.

2 Design of NAND and NOR all optical logic gates

The design of Y shaped SSW based NAND and NOR optical logic gates is proposed leveraging the distinct propagation characteristics of TE and TM modes to achieve all-optical logic operations. At the core of the structure there is a Y shaped SSW with two input ports (A and B) and one output port. A Control waveguide has been added to the Y shaped waveguide to create phase difference between the input signals resulting in the constructive or destructive superposition for both polarizations. The phase angle of the input light beam can be varied, as demonstrated by Birr et al. (2015).

To optimize the performance and mode control, air holes are strategically placed within the structure as shown in Fig. 1. To obtain the optimized radius of the air holes the variation of normalized transmission efficiency vs radius of the air hole for TE and TM mode respectively have been obtained as shown in Fig. 2a, b. For TM mode maximum normalized transmission efficiency is obtained at the radius of radius of 0.15 μm at the center (0,0) of the waveguide. For TM mode the optimized radius of air hole is obtained as 0.05 μm at (0,-0.5) from the center of the waveguide. The optimized strategically placed

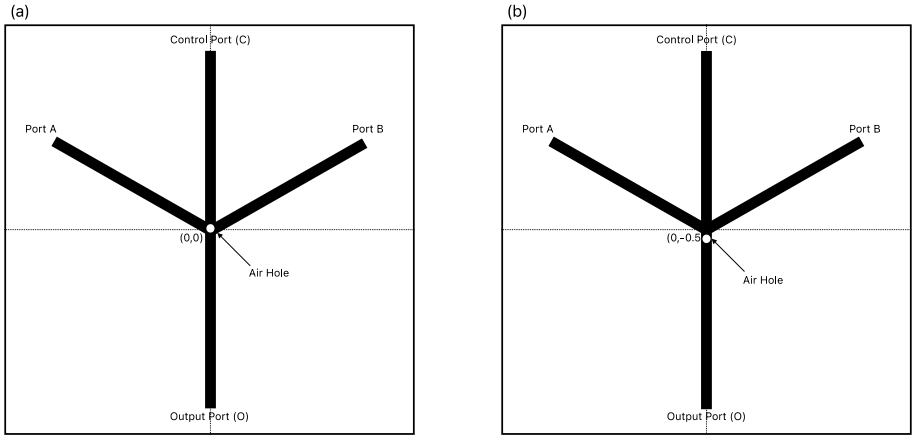

Fig. 1 Schematic representation of basic logic gates created using SSWs for (a) TE mode propagation, and (b) for TM mode propagation

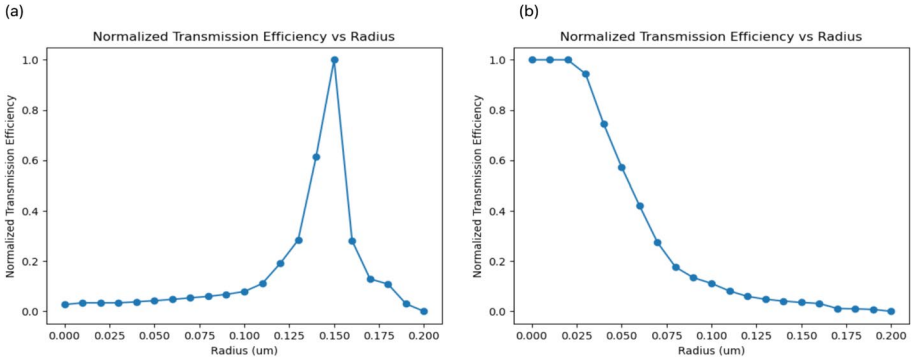

Fig. 2 **a** Variation of transmission efficiency with the radius of the air hole for TE mode of propagation, **b** Variation of transmission efficiency with the radius of the air hole TM mode of propagation

air hole redistributes the input signal coming from the two input waveguides along with the control signal to generate the desired output in the output waveguide.

The designed waveguides are tailored for single-mode operation based on the equation.

$$v_c = \frac{c}{2d\sqrt{n_1^2 - n_2^2}}, \tag{1}$$

where 'd' represents the width of the SSW, with n_1 being the refractive index of silicon at the input light frequency v, n_2 the refractive index of air, and c the speed of light in a vacuum (Aggarwal et al. 2024). To meet the single-mode condition, the input light frequency v must exceed the critical frequencyv_c. As a result, the waveguide widths are set to 0.241 µm for the TE mode and 0.345 µm for the TM mode. These specific dimensions are chosen to ensure efficient confinement of each mode with minimal propagation loss, thereby optimizing the device's overall performance. (Fujisawa and Koshiba 2006).

The performance analysis of the SSW based NAND and NOR logic gates are based on the power loss calculation and truth table data for both the TE and TM modes of propagation (Anagha and Jeyachitra 2022). The losses have evaluated using the following equation:

$$loss = 10log_{10}\left(\frac{P_{out}}{P_{in}}\right), \tag{2}$$

P_{in} and P_{out} represents the input and output powers. This formula helps quantify how much optical power is lost during propagation through the logic gate, and these losses are critical in determining the efficiency of the logic operation (Tresna and Maruyama 2019).

The contrast ratio (CR) is defined according to Eq. (3), presented below(Al-Sabea et al. 2022).

$$CR(dB) = 10ln\left(\frac{P_{out}|ON_{min}}{P_{out}|OFF_{max}}\right) \tag{3}$$

In this expression, $Pout \mid ONmin$ denotes the minimum power for logic level '1' while $Pout \mid OFFmax$ represents the maximum power for logic level '0'.

Similarly, the modulation depth (MD) is characterized by Eq. (4), shown below(Al-Sabea et al. 2022).

$$MD = \left(\frac{T|ON_{max} - T|OFF_{min}}{T|ON_{max}} \right) \times 100\% \tag{4}$$

In this context, $T \mid ONmax$ signifies the maximum transmission value for logic level '1' and $T \mid OFFmin$ corresponds to the minimum transmission for logic level '0'.

The data rate is determined using the Nyquist formula, represented in equation ((5) Hossain et al. 2023).

$$Datarate = 2Blog_2(M) \tag{5}$$

In this expression, $M = 4$ indicates the total number of signal levels (00, 01, 10, and 11), while B denotes the optical bandwidth, which can be calculated using Eq. (6).

$$B = \left(\frac{c}{\lambda^2} \right) \Delta\lambda \tag{6}$$

Here, c represents the speed of light in a vacuum, λ is the operating wavelength, and Δλ refers to the signal's spectral width. In this study, the operating wavelength λ is set to 1.55 µm, and the bandwidth (Δλ) is 10 µm, yielding an optical bandwidth B of 1.25 THz. This results in a data rate of 5 Tb/s(Hossain et al. 2023; Kotb et al. 2023b).

To evaluate the performance of these logic gates, the ratio of output power (P_{out}) to input power (P_{in}) is calculated. If the ratio exceeds 0.5, the output is considered as logic "1"; if it is less than 0.5, the output is regarded as logic "0". For both gates, the majority of the outputs show a significant distinction, with values above 0.5 in true logic cases and below 0.5 in false logic cases. This clear differentiation between output states ensures reliable logic operation with minimal error, making the detection of logic levels straightforward.

3 Realization of all optical NAND and NOR logic gate

3.1 NAND logic gate

The intensity distribution for different input combinations is depicted in Fig. 3 for TE mode and Fig. 4 for TM modes. These figures provide a visual representation of how the

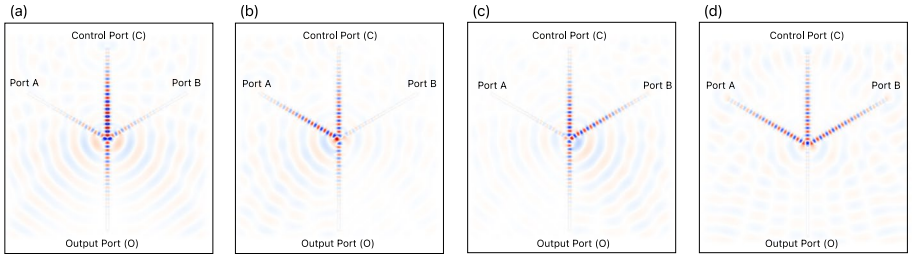

Fig. 3 The intensity distributions representation of the NAND logic gate for TE mode of propagation **a** A = 0, B = 0, C = 1($\phi = 0^o$), O = 1, **b** A = 1, B = 0, C = 1($\phi = 0^o$), O = 1, **c** A = 0, B = 1, C = 1($\phi = 0^o$), O = 1, **d** A = 1, B = 1, C = 1($\phi = 180^o$), O = 0

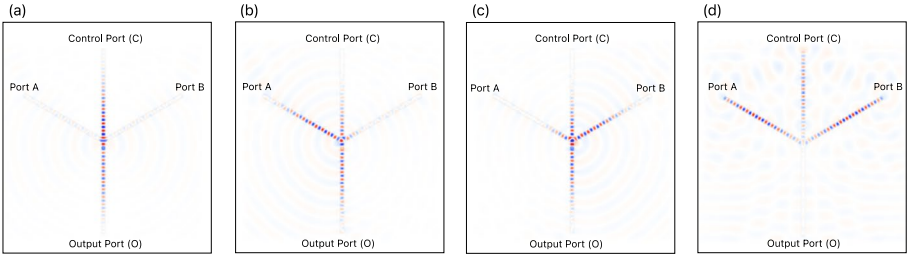

Fig. 4 The intensity distributions representation of the NAND logic gate for TM mode of propagation (a) A = 0, B = 0, C = 1($\phi = 0^o$), O = 1, (b) A = 1, B = 0, C = 1($\phi = 0^o$), O = 1, (c) A = 0, B = 1, C = 1($\phi = 0^o$), O = 1, (d) A = 1, B = 1, C = 1($\phi = 180^o$), O = 0

optical power is distributed within the waveguide for each input state. For both TE and TM mode the intensity is concentrated within the central waveguide when the output is "1", indicating efficient transmission. For the input combination (1,1), the intensity drops significantly, showing that the NAND gate is successfully suppressing the output signal.

Table 1 shows the truth table for NAND logic gate demonstrates the anticipated logic behavior, the output is low (logic "0") only when both inputs are high (logic "1"), and high (logic "1") for all other input combinations. Losses for each input configuration are measured independently for both TE and TM modes. These loss values provide insight into the gate's operational efficiency in each mode, which is essential for assessing its suitability for use in photonic circuits.

3.2 NOR logic gate

The intensity distribution for the NOR gate under various input conditions is shown in Fig. 5 for TE mode and Fig. 6 for TM modes. the intensity is concentrated within the central waveguide for the (0, 0) input, indicating strong signal transmission for the "1" output. For input configurations that yield a "0" output (e.g., 0, 1 or 1, 0), the intensity reduces significantly, demonstrating that the gate successfully blocks the signal in these cases. For the (0, 0) input, the intensity is focused, supporting the "1" output, while for other input configurations, the intensity decreases, yielding higher losses.

Table 2 shows the truth table for NOR logic gate exhibits the anticipated logic behavior, the output is high (logic "1") only when both inputs are low (logic "0"), and low (logic "0") for all other input combinations. Losses for each input combination were measured separately for the TE and TM modes, offering a thorough evaluation of the gate's performance in both modes.

3.3 Analysis of NAND and NOR optical logic gate

Various parameters such as maximum transmission; Contrast ratio and modulation depth for the designed structure have been calculated and summarized in Table 3.

The response time of the proposed structure is depicted by Fig. 7a, indicates that the time required for the output power to increase from 0 to 90% of the average steady-state output power P_{av} for TE mode is ct = 0.17 μm or $t_1 = 0.57$ fs. This response time consists of two components: the transmission delay or delay time ($t_{11} = 0.33$ fs) and the time required for the output power to increase from 0 to 90% or the rise time is determined by the

Table 1 Truth table for the NAND logic gate in TE and TM modes of propagation where normalized output power is in terms of input power P_{in}

Logical operations				TE mode		TM mode	
Input at A	Input at B	Logic output	Input at C (ϕ = Phase difference)	normalized output	Loss (dB)	normalized output	Loss (dB)
0	0	1	1 ($\phi = 0^o$)	0.9026 P_{in}	0.4452	0.8574 P_{in}	2.5386
0	1	1	1 ($\phi = 0^o$)	0.8430 P_{in}	0.7416	0.9965 P_{in}	0.0154
1	0	1	1 ($\phi = 0^o$)	0.8529 P_{in}	0.6913	0.9965 P_{in}	0.0154
1	1	0	1 ($\phi = 180^o$)	0.0260 P_{in}	15.834	0.0184 P_{in}	17.343

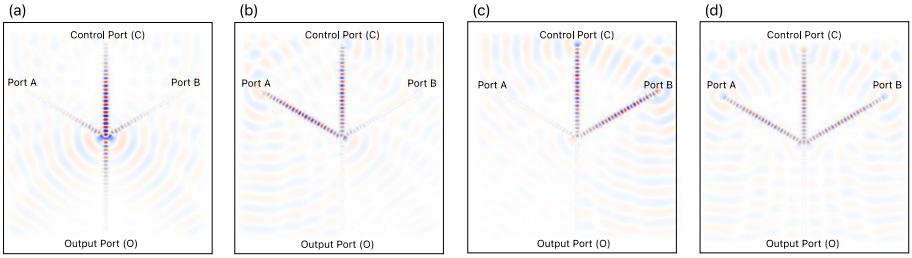

Fig. 5 The intensity distributions representation of the NOR logic gate for the TE mode of propagation **a** A = 0, B = 0, C = 1($\phi = 0^o$), O = 1, **b** A = 1, B = 0, C = 1($\phi = 180^o$), O = 0, **c** A = 0, B = 1, C = 1($\phi = 180^o$), O = 0, **d** A = 1, B = 1, C = 1($\phi = 180^o$), O = 0

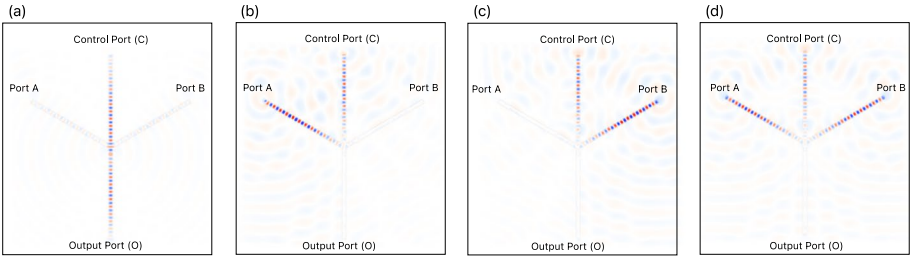

Fig. 6 The intensity distributions representation of the NOR logic gate for TM mode of propagation **a** A = 0, B = 0, C = 1($\phi = 0^o$), O = 1, **b** A = 1, B = 0, C = 1($\phi = 180^o$), O = 0, **c** A = 0, B = 1, C = 1($\phi = 180^o$), O = 0, **d** A = 1, B = 1, C = 1($\phi = 180^o$), O = 0

Table 2 Truth table for the NOR logic gate in TE and TM modes of propagation where normalized output power is in terms of input power P_{in}

Logical operations				TE mode		TM mode	
Input at A	Input at B	Logic output	Input at C (ϕ = Phase difference)	normalized output power	Loss (dB)	normalized output power	Loss (dB)
0	0	1	1 ($\phi = 0^o$)	0.9026 P_{in}	0.4452	0.8574 P_{in}	2.5386
0	1	0	1 ($\phi = 180^o$)	0.0150 P_{in}	18.236	0.0120 P_{in}	19.195
1	0	0	1 ($\phi = 180^o$)	0.0151 P_{in}	18.186	0.0120 P_{in}	19.195
1	1	0	1 ($\phi = 180^o$)	0.0260 P_{in}	15.834	0.0184 P_{in}	17.343

Table 3 Maximum transmission, Threshold transmission, Maximum Contrast ratio and Maximum modulation depth of NAND and NOR gates for TE and TM mode

Logic gate	Polarization	Logic gate (maximum transmission)	Threshold transmission	Maximum contrast ratio	Maximum modulation depth
NAND gate	TE mode	(90.26%)	0.50	34.79 dB	97.11%
NOR gate		(90.26%)		40.91 dB	98.15%
NAND gate	TM mode	(99.65%)	0.50	38.42 dB	98.34%
NOR gate		(85.74%)		38.42 dB	98.60%

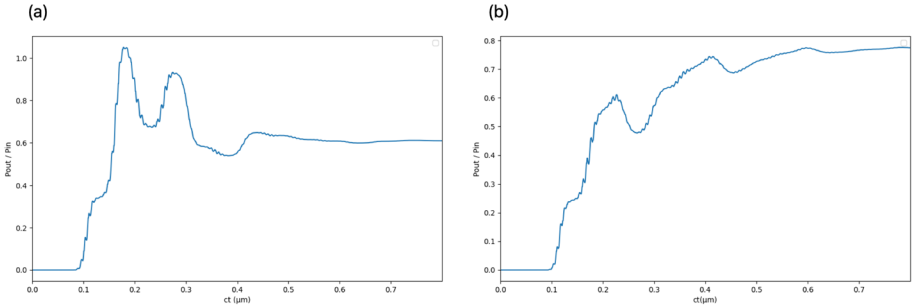

Fig. 7 Response time in terms of time evolution of the output power for all optical logic gate design for **a** TE mode and **b**TM mode

(t_{12} = 0.24 fs).Given that the system operates on linear materials, the fall time from P_{av} to 10% of P_{av} is also approximately (t_{12} = 0.256 fs). Consequently, the logic gate can produce a narrow pulse with a width of $2t_{12}$ = 0.48 fs, then the response time is 0.81 fs. Similarly, Fig. 7b depicts the response time of the proposed structure for TM mode is ct = 0.21 μm or t_1 = 0.70 fs, t_{11} = 0.37 fs, t_{12} = 0.33 fs, $2t_{12}$ = 0.66 fs, then the response time is 1.03 fs. So the Delay time for proposed structure is 0.81 fs and 1.03 fs for TE and TM mode. The proposed all-optical logic gate design operates at very low power levels, making it a promising candidate for use in developing all-optical integrated circuits (Wu et al. 2012). The tolerance study is also done which is a very important aspect from the fabrication point of view by variating the radius of the air hole by ± 5%. It is observed that ~ 3% change is observed in the transmitted intensity for TE mode and the respective ~ 0.8% change is observed in the transmitted intensity for TM mode.

The proposed all optical SSW based universal logic gates are evaluated in comparison with previous works based on key performance criteria, including the number of logic gates achieved, operating wavelengths and contrast ratio, Response time as summarized in Table 4. The data presented in this table demonstrate that our waveguide effectively performs the required logic operations while achieving a significantly higher contrast ratio and operating at the commercially viable wavelength of 1550 nm.

4 Conclusion

This paper presents a comprehensive design and analysis of all-optical universal logic gates based on SSWs, harnessing the superposition of light for effective optical signal processing. The designs have been rigorously tested for a fan-in of 2 and a fan-out of 1, establishing their suitability for fundamental logic operations.

This design, with its compact structure provides low-power solution for all-optical logic gates. The optimized dimensions of the waveguides and the strategic placement of air holes ensure the contrast ratio of NAND logic gate is 15.10 dB with a modulation depth of 97.11% for TE mode and 15.40 dB with a modulation depth of 97.11% for TM mode. Similarly for NOR logic gate the contrast ratio is 16.68 dB with a modulation depth of 98.34% for TE mode and 16.68 dB with a modulation depth of 98.60% for TM mode.

Devices have been developed with extraordinarily small footprints, excellent efficiency, and novel characteristics that can be achieved using the additional degrees of freedom

Table 4 Comparison of proposed work with the previous existing methods

Design and Methods	Logic gates	Wavelength (μm)	Contrast ratio (db)	Response time	References
Optical interferometric metal slot waveguide	NOT, XOR, AND, OR, NOR, NAND, XNOR	632.8	6 to 16	NA	Pan et al. (2013)
Y shaped Photonic crystal waveguides	AND, XOR, OR, NOT, NAND, NOR, XNOR	1.55	5.42 to 9.59	1.024 ps	Rani et al. (2015)
ultra-compact photonic gates	AND, OR, NOT, NAND	1.3	0.5 to 5.79	NA	Neşeli et al. (2022)
1D MIM structures	OR, XOR, NOT, AND, XNOR, NAND, NOR	1.55	15	NA	Bian and Gong (2014)
Ψ- shaped for linear optical logic gates	AND	1.55	6	NA	Kita et al. (2020)
T- shaped defect	NAND, NOR, XNOR, OR	1.55	8.66	NA	Priya et al. (2021)
Z-shaped silicon waveguides	XOR, AND, OR, NOT, NOR, XNOR, NAND	1.55	29 to 33.26	NA	Kotb et al. 2023b)
Dielectric-metal-dielectric design	OR, XOR, NOT, AND, XNOR, NAND, NOR	0.9 to 1.33	5.37 to 22	NA	Al-Musawi et al. (2020)
SSW based universal logic gates	NAND, NOR	1.55	0.95	0.81 fs to 1.03 fs	This work

(Wang et al. 2018; Shen et al. 2014). Due to the availability of 3D FLDW technology and lithographic manufacturing processes (Marshall et al. 2009; Gao et al. 2018; Li et al. 2022), the possibility to anticipate the experimental verification of the proposed waveguide based on the major findings of this simulation. The experimental realization of multiple acousto-optic lattice generators (AOLGs) utilizing various optical waveguides has been extensively reported in recent years, facilitating the advancement of analogous implementations (Kita et al. 2020; Marshall et al. 2009; Gao et al. 2018; Donzella et al. 2015; Fu et al. 2012).

In comparison to traditional electronic logic gates, which exhibit propagation delays of the order of nanoseconds, and photonic crystal (PhC) logic gates with delays in the picosecond range, the proposed SSW based logic gates demonstrate an impressive operational delay in the femtosecond range. This rapid response time enhances their competitiveness for future high-speed optical circuits, paving the way for advancements in optical information processing.

Acknowledgements Authors gratefully acknowledge the initiatives and support from the TIFAC-Centre of Relevance and Excellence in Fiber Optics and Optical Communication at Delhi College of Engineering, now DTU, Delhi, under the Mission REACH program of Technology Vision-2020, Government of India.

Author Contributions All authors contributed equally to the conception design, analysis and writing of the manuscript by Yash Yadav and Yogita Kalra.

Funding The authors declare that no funds, grants, or other support were received during the preparation of this manuscript.

Data Availability No datasets were generated or analysed during the current study.

Declarations

Competing Interests The authors declare no competing interests.

References

Aggarwal, A., Mittal, A., Kalra, Y.: Design of silicon slab waveguides based all-optical logic gates. Microw. Opt. Technol. Lett. (2024). https://doi.org/10.1002/mop.33981

Al-Musawi, H.K., Al-Janabi, A.K., Al-abassi, S.A.W., et al.: Plasmonic logic gates based on dielectric-metal-dielectric design with two optical communication bands. Optik (Stuttg) (2020). https://doi.org/10.1016/j.ijleo.2020.165416

Al-Sabea, Z.S., Ibrahim, A.A., Abdulnabi, S.H.: Plasmonic logic gates at optimum optical communications wavelength. Adv. Electromagn. **11**, 10–21 (2022). https://doi.org/10.7716/aem.v11i4.1894

Anagha, E.G., Jeyachitra, R.K.: Review on all-optical logic gates: design techniques and classifications heading toward high-speed optical integrated circuits. Opt. Eng. (2022). https://doi.org/10.1117/1.OE.61.6.060902

Bian, Y., Gong, Q.: Compact all-optical interferometric logic gates based on one-dimensional metal-insulator-metal structures. Opt. Commun. **313**, 27–35 (2014). https://doi.org/10.1016/j.optcom.2013.09.055

Birr, T., Zywietz, U., Chhantyal, P., et al.: Ultrafast surface plasmon-polariton logic gates and half-adder. Opt. Express **23**, 31755 (2015). https://doi.org/10.1364/OE.23.031755

Caulfield, H.: The logic of optics and the optics of logic. Inf Sci (n y) **162**, 21–33 (2004). https://doi.org/10.1016/j.ins.2003.01.002

Donzella, V., Sherwali, A., Flueckiger, J., et al.: Design and fabrication of SOI micro-ring resonators based on sub-wavelength grating waveguides. Opt. Express **23**, 4791 (2015). https://doi.org/10.1364/OE.23.004791

Fu, Y., Hu, X., Lu, C., et al.: All-optical logic gates based on nanoscale plasmonic slot waveguides. Nano Lett. **12**, 5784–5790 (2012). https://doi.org/10.1021/nl303095s
Fu, Y., Hu, X., Gong, Q.: Silicon photonic crystal all-optical logic gates. Phys. Lett. A **377**, 329–333 (2013). https://doi.org/10.1016/j.physleta.2012.11.034
Fujisawa, T., Koshiba, M.: All-optical logic gates based on nonlinear slot-waveguide couplers. J. Opt. Soc. Am. B **23**, 684 (2006). https://doi.org/10.1364/JOSAB.23.000684
Gao, L., Chen, L., Wei, H., Xu, H.: Correction: Lithographically fabricated gold nanowire waveguides for plasmonic routers and logic gates. Nanoscale **10**, 14771–14771 (2018). https://doi.org/10.1039/C8NR90158A
Hossain, M., Rakshit, J.K., Bhatnagar, A., Chattopadhyay, T.: Silicon microring resonator based all-optical 3-input majority gate and its applications. Optik (Stuttg) **282**, 170891 (2023). https://doi.org/10.1016/j.ijleo.2023.170891
Hou, J., Chen, L., Dong, W., Zhang, X.: 40 Gb/s reconfigurable optical logic gates based on FWM in silicon waveguide. Opt. Express **24**, 2701 (2016). https://doi.org/10.1364/oe.24.002701
Jindal, P., Abou Houran, M., Goyal, D., Choudhary, A.: A review of different techniques used to design photonic crystal-based logic gates. Optik (Stuttg) **280**, 170794 (2023). https://doi.org/10.1016/j.ijleo.2023.170794
Kita, S., Nozaki, K., Takata, K., et al.: Ultrashort low-loss Ψ gates for linear optical logic on Si photonics platform. Commun Phys (2020). https://doi.org/10.1038/s42005-020-0298-2
Kosmidou, E.P., Tsiboukis, T.D.: An FDTD analysis of photonic crystal waveguides comprising third-order nonlinear materials. Opt Quantum Electron **35**, 931–946 (2003). https://doi.org/10.1023/A:1025122517879
Kotb, A., Zoiros, K.E., Li, W.: Silicon-on-silica waveguides-based all-optical logic gates at 1.55 μm. Phys Scr. **98**, 035517 (2023)
Kotb, A., Zoiros, K.E., Hatziefremidis, A., Guo, C.: Optical Logic gates based on Z-shaped silicon waveguides at 155 μm. Micromach (Basel) (2023). https://doi.org/10.3390/mi14061266
Kotb A, Zoiros KE, Li W (2022) 320 Gb/s all-optical logic operations based on two-photon absorption in carrier reservoir semiconductor optical amplifiers. Optik (Stuttg) 265:. https://doi.org/10.1016/j.ijleo.2022.169494
Li, Z., Liu, Y., Zhang, S., et al.: All-optical logic gates using semiconductor optical amplifier assisted by optical filter. Electron. Lett. **41**, 51–52 (2005). https://doi.org/10.1049/el:20053385
Li, M., Li, C., Chen, Y., et al.: On-chip path encoded photonic quantum toffoli gate. Photonics Res **10**, 1533 (2022). https://doi.org/10.1364/PRJ.452539
Marshall, G.D., Politi, A., Matthews, J.C.F., et al.: Laser written waveguide photonic quantum circuits. Opt. Express **17**, 12546 (2009). https://doi.org/10.1364/OE.17.012546
Merlo, J.M., Wu, X., Kempa, K., Naughton, M.J.: All-optical logic gates based on anomalous floquet photonic topological insulator structures. J. Opt. **23**, 065001 (2021). https://doi.org/10.1088/2040-8986/abf8cd
Neşeli, B., Yilmaz, Y.A., Kurt, H., Turduev, M.: Inverse design of ultra-compact photonic gates for all-optical logic operations. J Phys D Appl Phys (2022). https://doi.org/10.1088/1361-6463/ac5660
Oskooi, A.F., Roundy, D., Ibanescu, M., et al.: Meep: a flexible free-software package for electromagnetic simulations by the FDTD method. Comput. Phys. Commun. **181**, 687–702 (2010). https://doi.org/10.1016/j.cpc.2009.11.008
Pan, D., Wei, H., Xu, H.: Optical interferometric logic gates based on metal slot waveguide network realizing whole fundamental logic operations. Opt. Express **21**, 9556 (2013). https://doi.org/10.1364/oe.21.009556
Parandin, F., Karkhanehchi, M.M.: Terahertz all-optical NOR and AND logic gates based on 2D photonic crystals. Superlatt. Microstruct. **101**, 253–260 (2017). https://doi.org/10.1016/j.spmi.2016.11.038
Priya, N.H., Swarnakar, S., Krishna, S.V., Kumar, S.: Design and analysis of a photonic crystal-based all-optical 3-input OR gate for high-speed optical processing. Opt Quant. Electron (2021). https://doi.org/10.1007/s11082-021-03374-0
Qian, L., Caulfield, H.J.: What can we do with a linear optical logic gate? Inf Sci (n y) **176**, 3379–3392 (2006). https://doi.org/10.1016/j.ins.2006.02.001
Rani, P., Kalra, Y., Sinha, R.K.: Design of all optical logic gates in photonic crystal waveguides. Optik (Stuttg) **126**, 950–955 (2015). https://doi.org/10.1016/j.ijleo.2015.03.003
Shen, B., Wang, P., Polson, R., Menon, R.: Integrated metamaterials for efficient and compact free-space-to-waveguide coupling. Opt. Express **22**, 27175 (2014). https://doi.org/10.1364/OE.22.027175
Tresna, W.P., Maruyama, T.: Propagation loss on a SiSlab waveguide simulation revisited. J Phys Appl. **2**(1), 76 (2019)
Vivien, L., Pavesi, L.: Handbook of Silicon Photonics, 1st edn. CRC Press (2016)

Wang, J., Long, Y.: On-chip silicon photonic signaling and processing: a review. Sci. Bull. (Beijing) **63**, 1267–1310 (2018)

Wang, J., Shi, Y., Hughes, T., et al.: Adjoint-based optimization of active nanophotonic devices. Opt. Express **26**, 3236 (2018). https://doi.org/10.1364/OE.26.003236

Wu, C.J., Liu, C.P., Ouyang, Z.: Compact and low-power optical logic NOT gate based on photonic crystal waveguides without optical amplifiers and nonlinear materials. Appl. Opt. **51**, 680 (2012). https://doi.org/10.1364/AO.51.000680

Wu, W., Sun, Q., Wang, G., et al.: Tunable all-optical AND logic gates via four-wave mixing based on graphene-on-silicon slot microring resonators. Opt Laser Technol (2021). https://doi.org/10.1016/j.optlastec.2021.106926

Xu, Q., Lipson, M., Almeida, V.R., et al.: All-optical logic based on silicon micro-ring resonators References and Links. Opt Express (2007). https://doi.org/10.1364/OE.15.000924

Zhang, Y., Zhang, Y., Li, B.: Optical switches and logic gates based on self-collimated beams in two-dimensional photonic crystals. Opt. Express **15**, 9287 (2007). https://doi.org/10.1364/OE.15.009287

Publisher's Note Springer Nature remains neutral with regard to jurisdictional claims in published maps and institutional affiliations.

Springer Nature or its licensor (e.g. a society or other partner) holds exclusive rights to this article under a publishing agreement with the author(s) or other rightsholder(s); author self-archiving of the accepted manuscript version of this article is solely governed by the terms of such publishing agreement and applicable law.

Regional disparities in social support services for vulnerable populations in France: inequalities in access and inclusion

Mansift Kaur and Neha Narula

Abstract

Purpose – *This study aims to examine regional disparities in the distribution of social action facilities for vulnerable populations in France, including disabled individuals, the elderly and those with mental illness. It highlights inequalities in facility availability and their impact on social inclusion, aiming to inform policy measures for equitable resource allocation.*

Design/methodology/approach – *The Theil entropy index to quantify inequality across France's 18 administrative regions using data from the Permanent Database of Facilities (BPE, 2021) has been used in this study.*

Findings – *The findings indicate notable regional disparities. Mayotte exhibits the most equitable access, whereas French Guiana, Île-de-France and Provence-Alpes-Côte d'Azur experience the highest levels of inequality. Brittany and Nouvelle-Aquitaine display moderate disparities. These results underscore the necessity for targeted interventions to enhance access to essential services.*

Originality/value – *This study presents a novel analysis of social action facility disparities in France, offering empirical insights for policymakers and service planners. By highlighting structural gaps, it supports the development of targeted strategies to promote social inclusion and ensure fair service distribution for vulnerable populations.*

Keywords *Regional inequalities in France, Social action facility distribution, Social inclusion, Support for vulnerable populations*

Paper type *Research paper*

Mansift Kaur is based at Delhi Technological University, Delhi, India. Neha Narula is based at Motilal Nehru College Evening, University of Delhi, New Delhi, India.

Introduction

Even though France has a good reputation for its health system, there are significant gaps in the provision of social support services for the more vulnerable groups such as the elderly, persons with disabilities and those suffering from mental health illnesses. The health-care policy purports to provide services to all, but it does not attempt to resolve the unequal provision of services. The health-care structure in France is different from the UK with its National Health Service (NHS), which takes these inequalities of health into consideration, and The Netherlands with its mitigative approach to risk health-based insurance (Bartley, 2001). Also, most people are concerned about the limitations of health services as opposed to the availability of social support services, which is the focus of this study.

In 2019, life expectancy in France was 82.5 years, while healthy life expectancy stood at 72.1 years (World Health Organization, 2024), highlighting the strength of the country's health-care system. However, significant regional disparities remain in social support services such as long-term care, disability assistance and mental health accommodations.

Funding: The authors received no external funding for this research.

Conflict of interest: The authors declare no conflicts of interest relevant to this article.

These inconsistencies contribute to social exclusion and widen inequalities for vulnerable groups.

This study analyzes the distribution of social action facilities in France's regions. Using data from the Permanent Database of Facilities (BPE) 2021, the extended database of facilities developed by the National Institute of Statistics and Economic Studies (INSEE), the research proposes to estimate inequality in the facility distribution using the Theil entropy index. Fair access to social support services is crucial for inclusion. Unequal distribution worsens disparities, especially for vulnerable populations.

Review of literature

To comprehend how social and health-care services are distributed in France, one must think of the broader social factors contributing to such inequalities. The conditions people experience in their life courses – from birth to old age – are crucial in creating social health inequalities. Although chronic illnesses can later influence a person's social position, preexisting redistribution mechanisms are often insufficiently responsive to these overlaid social determinants (Nay *et al.*, 2016). This structural imbalance is even more accentuated within the disability population group, which faces gross socio-economic disadvantages. People with disabilities often have less education, fewer job opportunities, limited financial resources and compromised health outcomes as compared with people with no disabilities. Although individuals with disabilities constitute over one-eighth of the US population, they are seldom included in sociological research on inequality (Shandra, 2018).

The historical evolution of disability in France reveals underlying inequalities that persist today. In its early stages, disability was categorized into separate groups, including war veterans, individuals injured in workplace accidents and children with disabilities. A comprehensive framework of disability based on these categories did not emerge until the late 20th century. This transformation was motivated by the rehabilitation paradigm shift, focusing on daily living needs versus the underlying causes of impairments (Ville and Ravaud, 2007). However, despite this integration, structural obstacles in service delivery persist, leading to regional disparities in access to support systems for disabled individuals.

A similar challenge exists in mental health services. In France, the expenses related to mental illnesses are funded by various entities, including the national health insurance system, county councils and the social welfare system. While these organizations regularly publish reports on mental health spending, variations in their assessment methods pose challenges to achieving a clear and comprehensive view of resource allocation (Laidi *et al.*, 2023). France has traditionally aimed to remove financial barriers to healthcare, emphasizing formal equality in access. This approach has played a key role in reducing risk behaviors linked to social determinants (Nay *et al.*, 2016). However, ensuring financial accessibility does not necessarily result in fair distribution of services, especially in mental health care, where structural deficiencies and workforce shortages persist.

Jacquet *et al.* (2018) showed pronounced socioeconomic inequities in mental health and depression in France, in absolute and relative terms, across a variety of indicators, including education level, income and self-reported financial well-being. One of the world's densest psychiatric care systems has more than 13,000 registered psychiatrists, yet it is in a crisis. Cuts to public health funding, coupled with an anticipated 30% decrease in the number of psychiatrists over the next 20 years, threaten the long-term viability of mental health services (Verdoux, 2007). These challenges are particularly severe in lower-income regions, where mental health services are already limited, exacerbating existing inequalities.

Beyond mental health, disparities in social class also play a crucial role in shaping overall health outcomes. In France, significant health inequalities exist among social classes,

particularly in premature male mortality rates. Those with lower levels of education, income and socio-professional status are more likely to report poor health, with social isolation further exacerbating their conditions. Even when socioeconomic status (SES) is considered, weak social ties remain strongly associated with negative health outcomes (Heritage, 2009). Such findings demonstrate the complicated nature of the relationship between social isolation and health, signifying the need to provide equitable healthcare as well as social support that ensures access at both financial and geographical levels to develop avenues for fostering inclusion into society.

Despite the implementation of public health policies and awareness campaigns, these socioeconomic health disparities remain persistent. This underscores the need for continuous data collection to quantify and monitor inequalities across different health domains (Jacquet *et al.*, 2018). Over the past decade, several national initiatives have aimed to improve mental health services; however, the expected outcomes have yet to materialize (Verdoux, 2007). The persistence of these issues suggests that policy efforts must be more targeted, addressing not only funding but also the structural inefficiencies that hinder equitable facility distribution.

In both education and housing, comparable inequalities arise. Genuine inclusion for students with disabilities goes beyond mere physical presence – it requires a comprehensive strategy that emphasizes their well-being, social integration and academic success (Guillemot *et al.*, 2024). The importance of suitable living conditions is equally critical. Well-designed, well-located housing with appropriate support and technology significantly enhances the well-being, health and community integration of people with disabilities. The transition to individualized apartments fosters independence, personal choice and improved participation, highlighting the necessity of adaptive housing models that cater to evolving needs (Douglas *et al.*, 2022). However, such models remain inconsistently implemented across different regions, further contributing to unequal experiences of social inclusion.

Data and methodology

France's administrative framework consists of three hierarchical levels: communes, departments and regions. Regions are the largest administrative units, and they oversee economic planning, vocational training and educational facilities at the top level. Departments are subdivisions of regions and handle matters relating to health, social services, infrastructure and education. The smallest administrative unit is the commune. It takes care of local governance, public services and economic development.

This study examines the distribution of social action facilities across France's 18 administrative regions – 13 in Metropolitan France and five in the overseas territories – using data from the 2021 BPE, provided by the INSEE. The analysis centers on social action facilities, which include support for the elderly, disabled individuals and those with mental health conditions, rather than direct medical or health-care services.

The study uses the Theil entropy index, a well-established measure of inequality, to quantify regional disparities. A Theil index of zero represents a perfectly equal distribution of social action facilities within that region, whereas higher values indicate greater disparities. By aggregating facility counts at the commune level, region level Theil indices are calculated, offering a clearer understanding of the uneven allocation of social support services across France.

The social action Theil indices assess disparities in the distribution of social action facilities across France's 18 regions, as presented in Table 1. For these facilities, a separate Theil index is computed for each region, capturing intra-regional distribution patterns. Additionally, the overall inequality in social action facility distribution across all regions is quantified using equation (1):

Table 1 Different facilities in social action category in France

Serial No.	*French*	*English translations with definitions*
1	Adultes handicapés: accueil/hébergement	Disabled adults: Accommodation (these include family placement centers, accommodation centers, specialized reception homes (MAS), occupational centers, medicalized reception homes (FAM), experimental establishments for disabled persons and accommodation establishments, medicalized or not for disabled persons)
2	Adultes handicapés: services d'aide	Disabled adults: Support services (these include pre-orientation centers, vocational rehabilitation centers, home care services, services for social life support (SAVS) and adult disabled medical-social support services (SAMSAH). The clientele of this type of equipment evolved as of January 1, 2020)
3	Adultes handicapés: services de soins à domicile	Disabled adults: Home care services (these are activities of support and rehabilitation care: comprehensive home support and care services for disabled persons (SPASAD) and home nursing care services (SSIAD) for disabled persons)
4	Autres établissements pour adultes et familles en difficulté	Other facilities for adults and families in difficulty: These include nomadic parking areas, accommodation centers for migrant workers, youth worker hostels, accommodations for families of patients, non-specialized housing facilities and MAH (hospital reception homes). Completeness is not guaranteed in this type of equipment
5	Centre accueil demandeur d'asile	The reception centers for asylum seekers (CADA) serve as temporary accommodation facilities that provide housing for individuals seeking asylum throughout the entire duration of their refugee status application process. This includes accommodation, administrative support (assistance with the asylum application process), social support (access to healthcare, schooling for children, etc.) and financial assistance. CADA is generally managed by associations or companies
6	Centre provisoire d'hébergement	Provisional accommodation centers (CPH) provide temporary housing for individuals or families granted refugee status by the French Office for the Protection of Refugees and Stateless Persons (OFPRA) or the National Court of Asylum (CNDA). In addition to accommodation, these centers offer socio-professional support services aimed at facilitating initial integration into French society. This includes assistance with accessing rights and entitlements, enrolling children in schools, obtaining medical care and other essential services. Since 2017, there has been an increasing number of these Provisional Accommodation Centers established across France. This information is based on data released on December 4, 2017, by the Ministry of the Interior, which outlined the planned expansion of accommodation facilities for asylum seekers and refugees
7	Chrs: centre d'hébergement et de réinsertion sociale	Social accommodation and reintegration centers (CHRS) are responsible for offering lodging, housing, assistance and social integration services to individuals or families experiencing significant challenges, aiding them in attaining or regaining personal and social independence. These individuals may include victims of violence, individuals struggling with alcoholism and drug addiction or those transitioning from incarceration. There are different types of CHRS today: some are specialized establishments for specific groups (pregnant women, individuals leaving prison, etc.), while others are common law establishments known as "all public" (homeless youth, the severely marginalized, etc.)
8	Enfants handicapés: hébergement	Disabled children: Accommodation (these include medical-educational institutes, medical-pedagogical institutes, medical-professional institutes, specialized kindergartens, rehabilitation institutes, establishments for physically and/or mentally handicapped individuals, visual and/or auditory impaired individuals, specialized family care centers, accommodation centers and experimental establishments for disabled persons)

(*continued*)

Table 1

Serial No.	*French*	*English translations with definitions*
9	Enfants handicapés: services à domicile ou ambulatoires	Disabled children: Home or ambulatory services [these are special education and home care services, medico-psycho-pedagogical centers (CMPP), early medical-social action centers (CAMSP), and university psychological assistance offices (BAPU)]
10	Établissement d'accueil du jeune enfant (eaje)	Early Childhood Reception Facility (EAJE): These are facilities authorized to accommodate, on a non-permanent basis, children under 6 years old and receiving a CAF service allowance: collective or parental daycare centers, daycare centers, kindergartens. These are the facilities as of January 1, 2020, corresponding to establishments funded in 2019 by the CNAF
11	Personnes âgées: hébergement	Elderly persons: Accommodation: These are accommodation establishments for elderly persons: hospices, retirement homes, EHPA, EHPAD, autonomy residences (housing centers requalified as autonomy residences by the ASV law) and temporary accommodation residences. It is possible to find different types of structures at the same address: retirement home, autonomy residence, hospice, residence, etc
12	Personnes âgées: services d'aide	Elderly persons: Support services: These include home help services, medical-social alarm systems, assistance services for elderly persons and persons with Associated Motor Deficiency (DMTA) and meal delivery services at home. The equipment is located at the service headquarters. At the same address, there may be home help services, medical-social alarm services, or any other form of assistance. The clientele of this type of equipment evolved as of January 1, 2020
13	Personnes âgées: soins à domicile	Elderly persons: Home care services: Home care services are available for old people and those with Associated Motor Deficiency (DMTA). The necessary equipment is housed at the service headquarters. As of January 1, 2020, the clientele for these services has evolved
14	Protection de l'enfance – action educative	Child protection – educational action: These include educational action centers (FAE), educational services for the courts (SEAT), educational action centers (CAE) and open-environment educational action services (AEMO). All these facilities are under the guardianship of the judicial administration. The completeness of the equipment is not guaranteed in this category
15	Protection de l'enfance – hébergement	Child protection – accommodation: These include mother–child reception facilities, social nurseries, youth homes, villages and houses for children with social characteristics, socio-educational family placement centers. All these facilities are under the guardianship of the departmental councils
16	Travail protégé	Protected work: These are social establishments for assistance through work (ESAT) and protected workshops

Source(s): Definitions have been taken from Fichier national des établissements sanitaires et sociaux – FINESS and Caisse nationale des allocations familiales – CNAF

$$T_i^{SA} = \sum_{j=1}^{n} \frac{s_{ij}}{\overline{s}_i} \cdot \ln\left(\frac{s_{ij}}{\overline{s}_i}\right) \quad (1)$$

where:

- T_i^{SA} is the Theil index for region i;
- s_{ij} represents the number of facilities for facility type j in region i;
- $\overline{s}_i$ is the mean number of facilities across all facility types in region i; and
- n is the total number of facility types.

Results and discussion

The analysis of Theil indices reveals significant variations in the distribution of social action facilities across French regions as shown in Table 2. A higher Theil index value indicates greater disparity in facility availability, while a lower value suggests more equitable distribution across regional facility types.

The findings indicate that Mayotte demonstrates the most equitable distribution of social action facilities, followed by Corsica, Hauts-de-France, Grand Est, Normandy and Bourgogne-Franche-Comté. These regions exhibit relatively uniform access to various types of social action facilities. Particularly noteworthy is Mayotte's position as the region with the lowest inequality metrics among all French regions.

Several regions display moderate levels of inequality in facility distribution, including Martinique, Centre-Val de Loire, Occitanie, Brittany, Auvergne-Rhône-Alpes, Réunion, Nouvelle-Aquitaine, Réunion, Pays de la Loire and Guadeloupe. While these regions show some variation in facility availability across different facility types, their overall distribution patterns remain relatively balanced, though access disparities persist to some degree.

The most pronounced inequalities are witnessed in Île-de-France, Provence-Alpes-Côte d'Azur and French Guiana. These regions demonstrate substantial disparities in the distribution of social action facilities, with certain facility types being notably more prevalent than others. This pattern indicates significant imbalances in facility accessibility within these regions.

The analysis reveals a complex landscape of facility accessibility, with some regions achieving relatively equitable distribution of each facility type, while others display marked disparities in facility availability across different types.

Our findings are consistent with prior research on disparities in France, particularly within the health sector. In French Guiana, severe social and economic inequalities persist, with 53% of the population living below the French poverty line, youth unemployment at 31% and 66.9% of residents affected by overcrowded housing. Low levels of education and the cost-of-living limit access to essential services, which worsens health and social care inequalities (Osei *et al.*, 2022). Restrictions in funding and a chronic shortage of health workers have

Table 2 Social action Theil indices for different regions of France

Serial No.	*Region*	*Theil index*
1	Auvergne-Rhône-Alpes	0.4012648
2	Bourgogne-Franche-Comté	0.3649068
3	Brittany	0.4289574
4	Centre-Val de Loire	0.4024867
5	Corsica	0.3323889
6	French Guiana	0.5093637
7	Grand Est	0.3351432
8	Guadeloupe	0.4869971
9	Hauts-de-France	0.3325167
10	Île-de-France	0.5669347
11	Martinique	0.3796885
12	Mayotte	0.2364374
13	Normandy	0.3432604
14	Nouvelle-Aquitaine	0.4300255
15	Occitanie	0.4640335
16	Pays de la Loire	0.4824870
17	Provence-Alpes-Côte d'Azur	0.5096508
18	Réunion	0.4789118

Source(s): Authors' own work

resulted in a great public health problem through care renouncement (Van Melle *et al.*, 2019).

Beyond overseas territories, regional inequalities in metropolitan France also reflect economic disparities. The southern region of Provence-Alpes-Côte d'Azur exhibits significant inequality of opportunity, highlighting income disparities across the country (Plassot and Sicsic, 2023). On the other hand, western regions like Nouvelle-Aquitaine, Centre-Val de Loire, Pays de la Loire and Brittany exhibit considerably lower levels of absolute inequality of opportunity compared to other areas of France (Plassot and Sicsic, 2023).

Notably, our findings challenge the assumption that all overseas regions are inherently disadvantaged due to geographic isolation. For instance, La Réunion benefits from the highest average public sector income due to higher wage premiums, while Corsica's income levels closely align with the national average (Govind, 2020). Similarly, our study reveals that social support services are distributed roughly equally in Mayotte and Corsica as compared to several other mainland regions. This is another fact supporting the idea that economic and social policies, not geography, determine equitable services.

Lower inequality is associated with better health-care access and outcomes. In 2015, hospital care data indicated a schizophrenia prevalence rate of 225 per 100,000 individuals. However, the report highlighted notably lower rates in eight regions, including Hauts-de-France, Bourgogne-Franche-Comté, Centre-Val de Loire and Normandy (Larroumets, 2018). Our study shows that these regions have relatively less unequal distribution of social action facilities. Mortality rates also vary significantly across different areas of France. They tend to be lower in affluent metropolitan and suburban areas and considerably higher in economically disadvantaged regions, agricultural and industrial plains and rural areas (Fayet *et al.*, 2020).

Conclusion

Regional disparities in health and social support services in France necessitate a decentralized approach rather than a uniform policy. Considering the diverse inequality gaps among the regions, policies must be designed according to the particular needs within those regions. Decentralization gives more regional autonomy; it allows authorities to apply more specific targeted interventions and improve the resource allocation efficiency. In regions with better-balanced service distribution, resources can be shifted to other vital demands to create support systems that are more effective.

While social support services are crucial in supplementing medical and health-care provisions, ensuring continued investment in health-care services remains imperative. The French government should address health inequalities both procedurally and instrumentally because mere allocation of resources cannot do the job. Achieving meaningful outcomes necessitates a sustained commitment and coordinated action across all levels of decision-making (Bellanger and Jourdain, 2004). To effectively tackle health disparities, policies must enhance data collection, addressing macro-social factors such as income and housing while expanding healthcare access in underserved regions. Providing targeted support for low-income individuals – such as paid sick leave, reintegration programs and financial aid – will help mitigate the broader social determinants of health (Bartley, 2001). By embracing a more region-specific and comprehensive strategy, France can make meaningful progress toward reducing social and health inequalities nationwide.

However, this study has certain limitations. The Theil index gives equal importance to each region, regardless of its geographic size. As a result, differences in index values may partly reflect variations in the average size of regions in France. Furthermore, this

study does not take into account the demand-side perspective, potentially overlooking cases where there is limited demand for a standard social action facility in a particular region. As a result, such facilities may be less concentrated in some regions, leading to an inflated Theil index value and portraying a higher degree of inequality than what actually exists.

References

Bartley, M. (2001), "Health inequalities in France", *International Journal of Epidemiology*, Vol. 30 No. 3, pp. 628-631, doi: 10.1093/ije/30.3.628.

Bellanger, M.M. and Jourdain, A. (2004), "Tackling regional health inequalities in France by resource allocation: a case for complementary instrumental and process-based approaches?", *Applied Health Economics and Health Policy*, Vol. 3 No. 4, pp. 243-250, doi: 10.2165/00148365-200403040-00007.

Douglas, J., Winkler, D., Oliver, S., Liddicoat, S. and D'Cruz, K. (2022), "Moving into new housing designed for people with disability: preliminary evaluation of outcomes", *Disability and Rehabilitation*, Vol. 45 No. 8, pp. 1370-1378, doi: 10.1080/09638288.2022.2060343.

Fayet, Y., Praud, D., Fervers, B., Ray-Coquard, I., Blay, J.Y., Ducimetiere, F., Fagherazzi, G. and Faure, E. (2020), "Beyond the map: evidencing the spatial dimension of health inequalities", *International Journal of Health Geographics*, Vol. 19 No. 1, pp. 1-11, doi: 10.1186/s12942-020-00242-0.

Govind, Y. (2020), "Post-colonial trends of income inequality: evidence from the overseas departments of France", Available at SSRN 4575893.Govind, Yajna, Post-Colonial Trends of Income Inequality: evidence from the Overseas Departments of France, doi: 10.2139/ssrn.4575893.

Guillemot, F., Lacroix, F. and Nocus, I. (2024), "Subjective well-being and social inclusion at school for students with a disability, according to their parents, in France", *Research in Developmental Disabilities*, Vol. 153, p. 104814, doi: 10.1016/j.ridd.2024.104814.

Heritage, Z. (2009), "Inequalities, social ties and health in France", *Public Health*, Vol. 123 No. 1, pp. e29-e34, doi: 10.1016/j.puhe.2008.10.028.

Jacquet, E., Robert, S., Chauvin, P., Menvielle, G., Melchior, M. and Ibanez, G. (2018), "Social inequalities in health and mental health in France. The results of a 2010 population-based survey in Paris metropolitan area", *Plos One*, Vol. 13 No. 9, p. e0203676, doi: 10.1371/journal.pone.0203676.

Laidi, C., Blampain-Segar, L., Godin, O., de Danne, A., Leboyer, M. and Durand-Zaleski, I. (2023), "The cost of mental health: where do we stand in France?", *European Neuropsychopharmacology*, Vol. 69, pp. 87-95, doi: 10.1016/j.euroneuro.2023.02.004.

Larroumets, P.G. (2018), "Schizophrenia: study of epidemiological and economic regional disparities", *Value in Health*, Vol. 21, p. S76, doi: 10.1016/j.jval.2018.07.569.

Nay, O., Béjean, S., Benamouzig, D., Bergeron, H., Castel, P. and Ventelou, B. (2016), "Achieving universal health coverage in France: policy reforms and the challenge of inequalities", *The Lancet*, Vol. 387 No. 10034, pp. 2236-2249, doi: 10.1016/S0140-6736(16)00580-8.

Osei, L., Basurko, C., Nacher, M., Vignier, N. and Elenga, N. (2022), "About the need to address pediatric health inequalities in French Guiana: a scoping review", *Archives de Pédiatrie*, Vol. 29 No. 5, pp. 340-346, doi: 10.1016/j.arcped.2022.03.009.

Plassot, T. and Sicsic, M. (2023), "Mapping inequality of opportunity in France and its regions: a data-driven analysis of income inequality from fiscal administrative data", available at: https://univ-pantheon-assas.hal.science/hal-04273119v1

Shandra, C.L. (2018), "Disability as inequality: social disparities, health disparities, and participation in daily activities", *Social Forces*, Vol. 97 No. 1, pp. 157-192, doi: 10.1093/sf/soy031.

Van Melle, A., Cropet, C., Parriault, M.C., Adriouch, L., Lamaison, H., Sasson, F., Duplan, H., Richard, J.B. and Nacher, M. (2019), "Renouncing care in French Guiana: the national health barometer survey", *BMC Health Services Research*, Vol. 19 No. 1, pp. 1-11, doi: 10.1186/s12913-019-3895-6.

Verdoux, H. (2007), "The current state of adult mental health care in France", *European Archives of Psychiatry and Clinical Neuroscience*, Vol. 257 No. 2, pp. 64-70, doi: 10.1007/s00406-006-0693-z.

Ville, I. and Ravaud, J.-F. (2007), "Introduction French disability studies: differences and similarities", *Scandinavian Journal of Disability Research*, Vol. 9 Nos 3/4, pp. 138-145, doi: 10.1080/15017410701685877.

World Health Organization (2024), "France [country overview", available at: https://data.who.int/countries/250 (accessed 4 April 2024).

Corresponding author

Mansift Kaur can be contacted at: mansift_24phdueco01@dtu.ac.in

For instructions on how to order reprints of this article, please visit our website:
www.emeraldgrouppublishing.com/licensing/reprints.htm
Or contact us for further details: permissions@emeraldinsight.com

International Journal of Current Science Research and Review
ISSN: 2581-8341
Volume 08 Issue 03 March 2025
DOI: 10.47191/ijcsrr/V8-i3-34, Impact Factor: 8.048
IJCSRR @ 2025
www.ijcsrr.org

Secure and Efficient Routing in Fog-Enabled VANETs: A Clustering-Based Approach

Anshu Devi[1], Ramesh Kait[2], Virender Ranga[3]
[1,2]Department of Computer Science & Applications, Kurukshetra University, Haryana
[3]Information Technology Department, Delhi Technological University, Delhi, Haryana

ABSTRACT: Vehicular Ad Hoc Networks (VANETs) play a crucial role in intelligent transportation systems (ITS) by enabling seamless vehicle-to-vehicle (V2V) and vehicle-to-infrastructure (V2I) communication. However, VANETs face significant challenges related to security, routing efficiency, and dynamic load balancing. This paper proposes a novel approach integrating clustering-based routing, fog computing, and authentication mechanisms to enhance network performance. The article proposes a new method for node authentication and redistribution of loads in vehicular ad-hoc networks (VANETs). The proposed method is designed to do better for VANETs in all aspects related to secure node authentication and the efficient load assignment among fog nodes. The approach uses a polynomial-based node authentication protocol and balances the network load dynamically by evaluating two parameters: Network Availability Bandwidth (NAB) and request count. Simulation-based performance evaluation was carried out for comparisons with existing algorithms. Metrics of comparison included throughput, packet delivery ratio (PDR), and latency. The proposed method clearly shows all improvements over existing algorithms. Throughput increased by 8591.86 packets per second; PDR improved to 0.833; latency was cut down to 6.4951 seconds, which makes it a potential candidate for performance enhancement in VANETs.

KEYWORDS: Clustering, Load Balancing, Intelligent Transportation Systems, Vehicular Ad Hoc Networks.

INTRODUCTION

The merging of vehicular ad hoc networks (VANETs) with fog computing has in recent years provided promising solutions for mitigating the hurdles of vehicular communications, especially about security and efficiency. VANETs are a special case of ad hoc mobile wireless network created to support communications between vehicles, roadside infrastructure, and other entities in the transportation ecosystem [1]. These networks are indeed characterized by dynamic topology structures, high mobility, and are real-time demanding making the conventional routing protocols insufficient for vehicular communication purposes [2-3]. In an attempt to solve these challenges, fog computing concept is facilitated into VANETs [4]. Fog computing allows the distribution of computational tasks, storage, and services close to the source of data, i.e., on the edge of the network. This reduces latency, enhances scalability, and enables faster data processing [5-6].

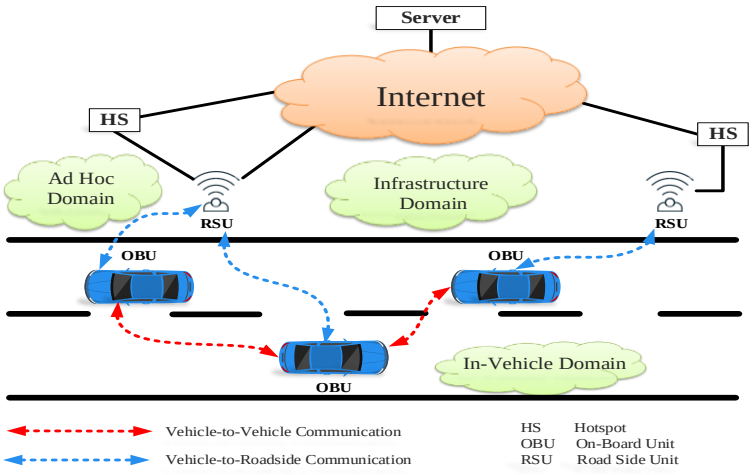

Figure 1. VANET Communication Architecture

International Journal of Current Science Research and Review
ISSN: 2581-8341
Volume 08 Issue 03 March 2025
DOI: 10.47191/ijcsrr/V8-i3-34, Impact Factor: 8.048
IJCSRR @ 2025
www.ijcsrr.org

The synergistic combination of VANETs and fog computing, namely Fog-Enabled VANETs, has immense potential for advancing intelligent transportation systems (ITS), autonomous driving, and real-time traffic management [7,8]. Illustration of the VANET architecture and vehicle communication with cloud is given in Figure 1 [9]. However, secure and efficient routing in Fog-enabled VANETs is a challenging problem [10,11]. The challenges involved include secure transmission of sensitive data between a car and infrastructure, resource allocation, and managing a highly dynamic network condition [12-13]. This has called for a new class of routing strategies which combine the guarantee of secure communication with increased efficiency of the network.

This paper proposes a clustering-based methodology for the routing of secure and efficient transmission of data in Fog-Enabled VANETs. Clustering operates on the principle of keeping vehicles and infrastructure nodes together in clusters, all managed by a cluster head. This clustering structure produces improved data management and bettering use of resources among the components. In addition, a security layer is integrated into the routing process to protect the confidentiality, integrity, and authenticity of data sent through the network.

RELATED WORK

Recent years have witnessed a notable enhancement in the VANETs and fog computing literature with various approaches evidenced to address security, performance, and efficiency. A review of major studies depicting very important results on such challenges related to routing and security in fog-enabled VANETs, especially stressing clustering-based approaches is given in this section. Wang et al. (2015) put forward 2FLIP, the two-factor lightweight privacy-preserving authentication mechanism for VANETs to present a secure and efficient authentication mechanisms. The significance of maintaining privacy while ensuring efficient communication in VANETs was emphasized, most particularly in high mobile environments. 2FLIP provides reduced overhead on normal authentication mechanisms, and thus it can boast of scalability and strong security in resource-constrained vehicular environments [14]. Zhang et al. (2019) provided reliable multiservice delivery in fog-enabled VANETs by the incorporation of mechanisms that handle misbehavior detection and tolerance. In order to detect malicious vehicles that attempted to disrupt the network, this approach used a combination of trust- and reputation-based modularities. By incorporating misbehavior detection with fog-enabled services, this study guaranteed that the network could continue to communicate and deliver data reliably, tagged with the warnings of malicious nodes [15].

In terms of the preservation of privacy, Han et al. (2020) established an anonymous authentication scheme on fog computing for VANETs. This technique allowed for the identity of vehicles to remain confidential but secure at the same time for communication. Not only could the scheme prevent the unauthorized tracking of vehicles, but it also addressed the issues of privacy protection while maintaining a secure and efficient communication framework. This was supplementary work on the broader front to ensure the simultaneous maintenance of privacy and security in VANETs [16]. The empowerment of fog computing in VANETs also exploits this approach to resolve issues of energy and load balancing. Hameed et al. (2021) provided sufficient focus on energy-and performance-aware load balancing in vehicular fog computing, suggesting algorithms to balance the computational load among fog nodes. The method was aimed at minimizing power consumption while improving performance, thus allowing the efficient usage of resources in such a way as to not diminish system performance [17].

In a similar manner, energy-aware load balancing management techniques for fog-based VANETs were researched and proposed by Qun and Arefzadeh (2021). Their hybrid algorithm encompassed some energy-aware strategies to enhance the load distribution and energy consumption in large-scale vehicular networks [18]. Several studies have pointed out various clustering schemes for enhancing performance in VANET. Khudhair et al. (2023) proposed a clustering approach to a VANET that is intended to create clusters within the networks for a better performance. The authors have focuessed on several aspects however stability of network and scalability was enhanced, minimizing the communication overhead [19]. Devi et al. (2022) has employed the machine learning concept for automatic cluster head selection in fog-enabled VANETs. The proposed approach used machine-learning algorithms to dynamically select cluster heads depending on the network situation, vehicle mobility, and energy efficiency. This included better load balancing, leading to improved overall network performance in fog-assisted VANETs, since it operated towards addressing the problem of ensuring reliable and efficient network infrastructure [20].

Ahmed et al. (2024), having contributed AODV-RL with the BHA Attack Defense by enhancing the AODV routing protocol, called for a secure and dependable routing approach of the IoV-Internet of Vehicles-network. Their writing combined the routing protocol with the defense against Black Hole and Gray Hole attacks. The guaranteed improvement of routing efficiency and security

International Journal of Current Science Research and Review
ISSN: 2581-8341
Volume 08 Issue 03 March 2025
DOI: 10.47191/ijcsrr/V8-i3-34, Impact Factor: 8.048
IJCSRR @ 2025
www.ijcsrr.org

was thus assured in the IoV network, which becomes critical considering that in VANETs and fog computing, attacks on the routing paths can jeopardize the system performance severely [21]. In summary, these studies provide a whole view of several forms of systemic processes regarding security and efficiency problems within VANETs when combined with fog computing. They have given rise to extremely pertinent aspects for augmenting the security and efficiency of VANETs such as privacy-preserving authentication, energy efficiency, misbehavior detection, and clustering mechanisms. Clustering methods have gained more importance in enabling improved load balancing, scalability, and overall robustness for VANETs in holistic integrated environments. Using machine learning and hybrid optimization techniques further addressed some of the dynamic and resource-constrained settings of vehicular networks, and it is one of the focus areas for future exploration in this domain.

PROPOSED METHODOLOGY

The proposed methodology focusses on the improvement of the routing performance and security in fog-enabled VANETs based on three methods: clustering-based routing, curve fitting-based authentication, and dynamic load balancing.

A. Clustering based Routing

To minimize routing overhead and enhance network stability, vehicles are grouped into clusters based on their proximity. A Cluster Head (CH) is selected for each cluster to communicating data to the neighboring CHs or fog nodes. The clustering process minimizes communication cost by selecting the CH closest to other vehicles in the cluster and can be formulated mathematically. The clustering process formulated and presented as follows:

$$CH = arg\,min_{\{i \in V\}} \Sigma_{j \in C}\, d(i,j) \quad (1)$$

Where, CH is the selected Cluster Head, V represents the set of vehicles, C is the cluster, and $d(i,j)$ is the Euclidean distance between nodes.

B. Curve Fitting-Based Authentication

The proposed methodology focusses on the improvement of the routing performance and security in fog-enabled VANETs based on three methods: clustering-based routing, curve fitting-based authentication, and dynamic load balancing. Authentication is performed using the following equation:

$$y = a_n x^n + a_{\{n-1\}} x^{\{n-1\}} + \ldots + a_1 x + a_0 \quad (2)$$

Where y represents the expected node behavior, and a_n are coefficients determined through least squares regression.

C. Dynamic Load Balancing

A dual-threshold policy is used for distributing computational tasks to fog nodes. It minimizes the load there by calculating the Neutralized Available Bandwidth (NAB) of all fog nodes, which redistributes load to maintain maximum proper utilization of resources.

$$W_i = \frac{NAB_i}{Req_i} \quad (3)$$

Where, W_i is the weight assigned to node$i$, NAB_i is the neutralized available bandwidth, and Req_i represents the number of requests at the fog node. The algorithmic steps following in the proposed methodology are summarized in Algorithm 1.

International Journal of Current Science Research and Review
ISSN: 2581-8341
Volume 08 Issue 03 March 2025
DOI: 10.47191/ijcsrr/V8-i3-34, Impact Factor: 8.048
IJCSRR @ 2025
www.ijcsrr.org

Algorithm 1 Node Authentication and Load Balancing for VANETs

Require: x (Node identifier or input feature), $coefficients$ (List of polynomial coefficients), $requests$ (List of incoming requests), fog_nodes (Dictionary of nodes with NAB and request count), $upper_threshold$, $lower_threshold$ (Threshold values for load balancing)
Ensure: Updated fog_nodes resource utilization

{Step 1: Authenticate Node}
$y \leftarrow 0$
for $i = 0$ to n **do**
  $y \leftarrow y + coefficients[i] \times x^i$
end for
{Step 2: Load Balancing}
for all $R_j \in requests$ **do**
  $best_node \leftarrow None$
  $best_weight \leftarrow -\infty$
  for all $node \in fog_nodes$ **do**
    $NAB_i \leftarrow fog_nodes[node]['NAB']$
    $Req_i \leftarrow \max(fog_nodes[node]['Requests'], 1)$
    $W_i \leftarrow NAB_i / Req_i$
    if $W_i > best_weight$ **then**
      $best_weight \leftarrow W_i$
      $best_node \leftarrow node$
    end if
  end for
  if $best_weight > upper_threshold$ **then**
    $min_load_node \leftarrow \arg\min(fog_nodes[node]['Requests'])$
    $fog_nodes[best_node]['Requests'] \leftarrow fog_nodes[best_node]['Requests'] - 1$
    $fog_nodes[min_load_node]['Requests'] \leftarrow fog_nodes[min_load_node]['Requests'] + 1$
  else if $best_weight < lower_threshold$ **then**
    $fog_nodes[best_node]['Requests'] \leftarrow fog_nodes[best_node]['Requests'] + 1$
  end if
  for all $node \in fog_nodes$ **do**
    $fog_nodes[node]['Utilization'] \leftarrow fog_nodes[node]['Requests'] / fog_nodes[node]['NAB']$
  end for
end for
return fog_nodes

The algorithm is designed for node authentication and load balancing in VANETs with two components including node authentication and load balancing. In the first step, this algorithm computes polynomial-based authentication for each node given a set of input coefficients and the node identifier to generate a value that guarantees the legitimacy of the node in question. Load balancing is addressed in the next phase by the assessment of each incoming request by which an optimal node is made available to respond to the request. This is done by ordering the nodes based on the NAB and the request count, with advantage given to the node with the least workload imbalance. Should a node receive requests higher than a preconfigured upper threshold, the system will direct the incoming request to a less-loaded node. Conversely, if a node is less loaded (below a lower threshold), the entry load is increased. In the end, resource utilization for every node is recalculated such that resources are fairly distributed. The updated state of the fog nodes with respect to proper load balancing and node availability in their capacity to reply to future requests is then returned by the algorithm.

RESULTS AND ANALYSIS

The effectiveness of the proposed work is evaluated using three performance metrics namely, throughput, packet delivery ratio (PDR), and latency. The comparative analysis involves 300 vehicle nodes and two existing studies namely, Khudhair et al. and Ahmad et al. This serves the purpose of determining how well the proposed algorithm fosters the reliability of the networks, optimizing data transmissions and lowering delays in packet delivery. By virtue of the dynamicity of VANETs, each contributed enhancement towards such metrics impacts the overall efficiency of the network by upholding better communication in real-time traffic contexts. The results

International Journal of Current Science Research and Review
ISSN: 2581-8341
Volume 08 Issue 03 March 2025
DOI: 10.47191/ijcsrr/V8-i3-34, Impact Factor: 8.048
IJCSRR @ 2025
www.ijcsrr.org

provide insights into the scalability and resilience of the proposed methods against other contemporary methods. The three key metrics used for evaluation are as follows:

- Throughput reflects the number of packets that are forwarded successfully per unit time showing the network ability to endure data traffic.
- Packet Delivery Ratio (PDR) is the metric that is used to monitor the ratio of the packets that successfully reached its the destination against the total number of packets that were sent. This reflects the efficiency of the network.
- Latency is another measure that represents the time that the packet takes to reach its destination from the source. This metric is particularly important for real-time applications in VANETs.

The parametric values to reflect the performance of the proposed method, Khudhair et al. [19] and Ahmad et al. [21] is summarized in Table I.

Table I Comparative Analysis

Methods	Throughput (p/s)	PDR	Latency (s)
Proposed	8591.86	0.833	6.4951
Khudhair et al. [19]	7868.00	0.766	7.4943
Ahmad et al. [21]	8218.60	0.778	7.6064

The performance analysis shows that the throughput attained by the proposed cluster-based cooperative approach was 8591.86 p/s, which is superior to 7868.00 p/s Khudhair et al. [19] and 8218.60 p/s by and Ahmad et al. [21]. The elevated throughput reflects the capacity of the topology to group together data transmissions in a way that minimizes overhead by allowing localized traffic within groups, hence reducing contention and repeated transmissions. The complement of this mechanism is fog computing, which processes packets at the edge, reducing burden on the core network and making the transmission more efficient. The increased throughput signifies timely delivering of traffic conditions, warnings, and critical information within an intelligent vehicular network-based traffic transportation system.

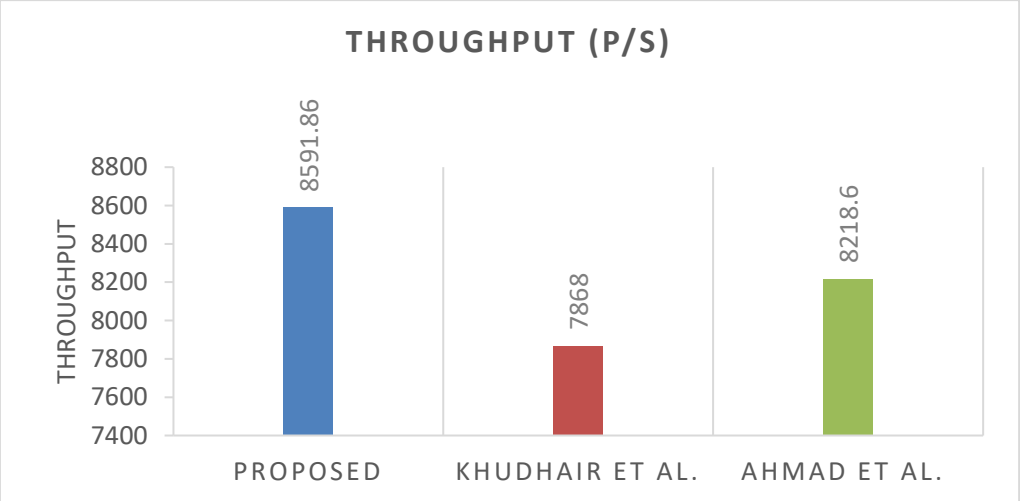

Figure 1 Throughput Comparative Analysis

The packet delivery ratio (PDR) is used to measure the reliability of data transmission in finding a secure and obstruction-free communication within VANET. The PDR attained by the cluster-based cooperative approaches is 0.833 much better than the aforementioned values of 0.766 and 0.778 reported by , Khudhair et al. [19] and Ahmad et al. [21], respectively. PDR increases primarily because of the cluster-based routing algorithm, which reduces the disruptive effects of rapid topology changes on route stability. Also, Fog processing reduces the data packet drop due to efficient in-field transmission and delivery even in dynamic

International Journal of Current Science Research and Review
ISSN: 2581-8341
Volume 08 Issue 03 March 2025
DOI: 10.47191/ijcsrr/V8-i3-34, Impact Factor: 8.048
IJCSRR @ 2025
www.ijcsrr.org

vehicular environments. Higher PDR is thus vital for applications like crash warnings, traffic congestion alerts, and cooperative driving assistance where packet dropping can result in serious implications.

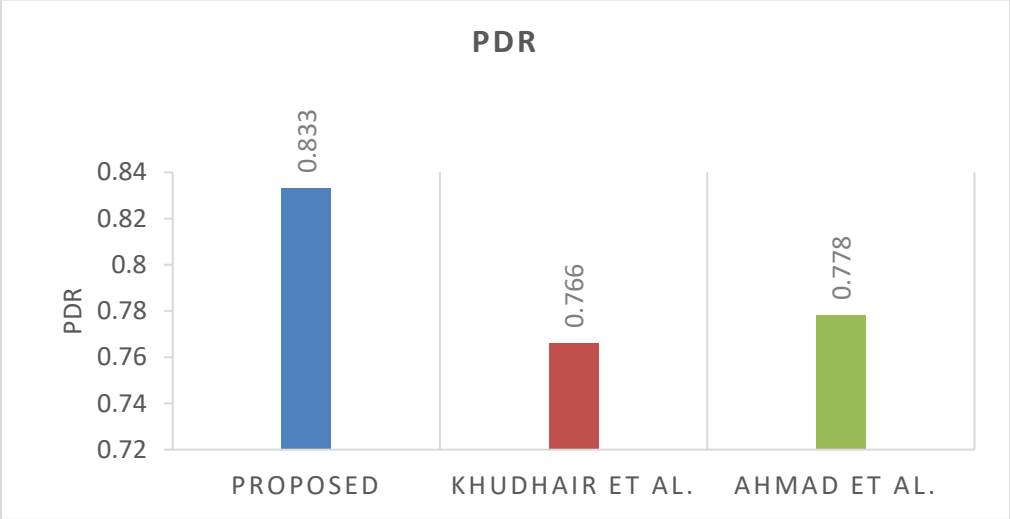

Figure 2 PDR Comparative Analysis

Latency is a key point in VANETs, important for real-time applications wherein timely information exchange is fundamental. The proposed method obtained a latency of 6.4951 seconds, which is very low compared to the measurement of 7.4943 seconds taken , Khudhair et al. [19] and 7.6064 seconds taken for Ahmad et al. [21]. The cause for this lower latency is the use of an efficient hierarchical clustering structure that works to minimize data transmission delays by providing an optimized route for message delivery and minimizing the chances of any broadcast storms. Additionally, fog-enabled computing prevents overwhelming the cloud server during the decision-making process, which further cuts down on decision turn-around time. Thus, the obtained low latency translates to an efficient and timely information delivery mechanism of functionless VANET applications wherein every second is a big deal, such as in accident prevention and emergent vehicle routing.

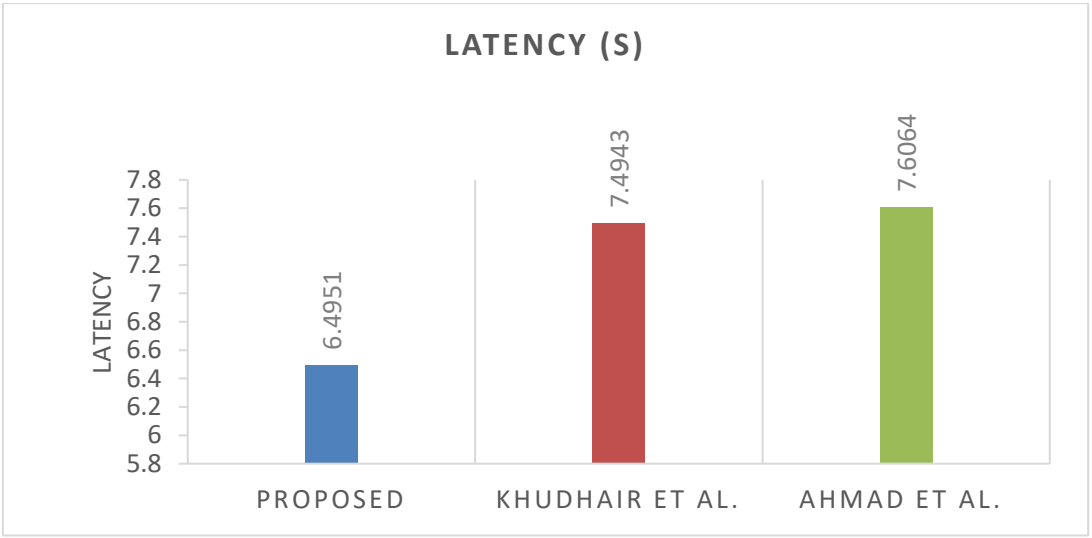

Figure 3 PDR Comparative Analysis

The performance evaluation proved that the clustering-based routing strategy adds a substantial level of safety and efficiency in fog-enabled VANETs. This provides higher throughput; this ensures efficient data handling capacity, the improved PDR guarantees dependable message dissemination, and lower latency favors real-time responsiveness. In addition, this clustering approach provides

International Journal of Current Science Research and Review
ISSN: 2581-8341
Volume 08 Issue 03 March 2025
DOI: 10.47191/ijcsrr/V8-i3-34, Impact Factor: 8.048
IJCSRR @ 2025
www.ijcsrr.org

additional security in that it limits unnecessary data transmission, thus reducing the probability of malicious attacks such as packet drops and data tampering through the non-existence of paths for packet travel. The method combines fog computing to further diminish security threats by providing data authentication and intrusion detection at local fog nodes, thereby reinforcing the network against malicious parties.

Overall, the proposed method provides a good compromise between security and efficiency properties of the system, proving to be a mixture of a scalable and resilient routing protocol for next-generation VANETs. The findings justify the organization onto a clustering-based approach that would increase communication reliabilities capable of improving real-time decision making and safe transmission of data over fog-enabled vehicular networks.

CONCLUSION

The proposed work focusses on authentication and load distribution in VANETs and handles the authentication of nodes with dynamic load balancing supported using NAB and request count. All these permutations ensure the network functions optimally in a secure manner. The simulations proved that it surpasses existing algorithms in terms of throughput, packet delivery ratio (PDR), and latency. If these results are viewed with regards to enhancement, the proposed solution manifests a superior throughput of 8591.86 packets per second PDR of 0.833 and a cut-down latency of 6.4951 seconds. Since any other advancements in this area make this proposition promising correlated to the working field of VANET for real-time applications, it shows an endeavor to enhance the performance of VANETs. Those very results also testifying proving the proposed approach effective in enhancing the job of the networks brings an additional value proposition in the area of VANET optimization. Further areas of work can deal with issues about scalability and integration with other network protocols to enhance more in larger and complex environments.

REFERENCES

1. Karabulut, M. A., Shahen Shah, A. F. M., Ilhan, H., Pathan, A. K., and Atiquzzaman, M., *Ad Hoc Networks*, **150**, 2023, p. 103281.
2. Swetha, K., and Rama Devi, B., *IJITR International Journal of Innovative Technology and Research*, **4**(5), 2016, pp. 4219–4223.
3. Devi, A., Kait, R., and Ranga, V., *Cyber Security and Intelligent Analytics*, 2022, pp. 141–150.
4. Jalali K.A., Z., Mansouri, N., and Khalouie, M., *Computer Science Review*, **48**, 2023, p. 100550.
5. Devi, A., Kait, R., and Ranga, V., *International Journal of Performability Engineering*, **20**(9), 2024, pp. 572–580.
6. Devi, A., Kait, R., and Ranga, V., *Cloud Computing, and Wireless Network Optimization*, 2019, pp. 148–164.
7. Chand, N., Mishra, S., and Kumar, V., *Communications and Network*, **5**(1), 2013, pp. 12–15.
8. Eze, E. C., Zhang, S. J., Liu, E. J., and Eze, J. C., *International Journal of Automation and Computing*, **13**(1), 2016, pp. 1–18.
9. Elias, S. J., Hatim, S. M., Darus, M. Y., Abdullah, S., Jasmis, J., Ahmad, R. B., and Khang, A. W. Y., *Indonesian Journal of Electrical Engineering and Computer Science*, **13**(3), 2019, pp. 1280–1285.
10. Mishra, R., Singh, A., and Kumar, R., *2016 International Conference on Electrical, Electronics, and Optimization Techniques (ICEEOT)*, 2016, pp. 1050–1055.
11. Taheri-abed, S., Eftekhari Moghadam, A. M., and Rezvani, M. H., *Cluster Computing 2023*, **26**(5), 2023, pp. 3113–3144.
12. Sheikh, M. S., and Liang, J., *Wireless Communications and Mobile Computing*, 2019.
13. Devi, A., Kait, R., and Ranga, V., *International Joint Conference on Advances in Computational Intelligence*, 2022, pp. 705–715.
14. Wang, F., Xu, Y., Zhang, H., Zhang, Y., and Zhu, L., *IEEE Transactions on Vehicular Technology*, **65**(2), 2015, pp. 896–911.
15. Zhang, X., Lyu, C., Shi, Z., Li, D., Xiong, N. N., and Chi, C. H., *IEEE Access*, **7**, 2019, pp. 95762–95778.
16. Han, M., Liu, S., Ma, S., and Wan, A., *PLoS One*, **15**(2), 2020, p. e0228319.
17. Hameed, A. R., ul Islam, S., Ahmad, I., and Munir, K., *Sustainable Computing: Informatics and Systems*, **30**, 2021, p. 100454.
18. Qun, R., and Arefzadeh, S. M., *IET Communications*, **15**(13), 2021, pp. 1665–1676.

International Journal of Current Science Research and Review
ISSN: 2581-8341
Volume 08 Issue 03 March 2025
DOI: 10.47191/ijcsrr/V8-i3-34, Impact Factor: 8.048
IJCSRR @ 2025
www.ijcsrr.org

19. Khudhair, H. A., Albu-Salih, A. T., Alsudani, M. Q., and Fakhruldeen, H. F., *Bulletin of Electrical Engineering and Informatics*, **12**(5), 2023, pp. 2978–2985.
20. Devi, A., Kait, R., and Ranga, V., *Communication and Intelligent Systems: Proceedings of ICCIS 2021*, Springer Nature Singapore, 2022, pp. 1169–1179.
21. Ahmad, N., Mohammadani, K., Bashir, A. K., Omar, M., Jones, A., and Hassan, F., *CMES-Computer Modeling in Engineering & Sciences*, **139**(1), 2024, pp. 1–20.

Cite this Article: Devi, A., Kait, R., Ranga, V. (2025). Secure and Efficient Routing in Fog-Enabled VANETs: A Clustering-Based Approach. International Journal of Current Science Research and Review, 8(3), pp. 1304-1311. DOI: https://doi.org/10.47191/ijcsrr/V8-i3-34

SELF-POWERED FLEXIBLE MICRO-SUPERCAPACITOR BASED ON OPTIMIZED LASER INDUCED GRAPHENE ELECTRODES FOR SUSTAINABLE ENERGY HARVESTING AND STORAGE

Faizan T. Beigh[1], Vishal Singh[1], Bharti Singh[2], and Dhiman Mallick[1]
[1]Department of Electrical Engineering, Indian Institute of Technology Delhi, New Delhi, INDIA
[2]Department of Applied Physics, Delhi Technological University, New Delhi, INDIA

2025 IEEE 38th International Conference on Micro Electro Mechanical Systems (MEMS) | 979-8-3315-0889-0/25/$31.00 ©2025 IEEE | DOI: 10.1109/MEMS61431.2025.10917686

ABSTRACT

The present paper reports a single-step fabricated laser induced graphene (LIG) based interdigitated electrodes (IDE) with exceptionally low sheet resistance ($5\Omega sq^{-1}$) for energy storage and harvesting, essential for flexible wearable devices. By optimizing LIG parameters we obtain doping-free fabrication of IDEs for Micro-supercapacitors (MSCs). Unlike conventional designs, the proposed MSCs feature self-charging capabilities using piezoelectric Polyvinylidene fluoride (PVDF) as separator and Polyvinyl Alcohol (PVA)/KOH as gel electrolyte. The LIG based self-powered MSC demonstrates an areal capacitance (C_{Ar}) of ~18mF/cm² at 10mV/s, good cyclability (~85% retention) after 5,000 cycles, a series resistance (R_{SI}) of 150.8Ω, and a charge transfer resistance (R_{CT}) of ~1600 Ω, all achieved through a simple, scalable, and sustainable process.

KEYWORDS

Self-powered, LIG, IDEs, Supercapacitor, Flexible, Wearables, Piezoelectric.

INTRODUCTION

Graphene manifests a wide range of applications due to its exceptional properties of high flexibility, electrical conductivity, mechanical robustness and large effective surface area. It's high effective surface area and superior electrical conductivity makes it ideal materials for fabrication of Micro-supercapacitors (MSCs) [1]. MSCs, offer exceptionally high capacitance per unit volume and are increasingly recognized as reliable energy storage devices [2]. Although graphene has attracted significant attention due to its potential as an electrode material for MSCs, significant scalability issues persist due to cost and infrastructure requirements. In contrast, LIG provides a more cost-effective approach to fabricate graphene-based devices. This method transforms a polyimide (PI) precursor into a graphene-rich, porous carbon network through a photothermal reaction triggered by the interaction between laser irradiation and the polymer substrate [3]. LIG has gained rapid popularity as a highly effective material for electrodes in several flexible and large area electronic applications. However, the capacitance of pristine LIG materials tends to be relatively low. To increase this, base material for LIG i.e. PI, is often modified by doping them with electroactive atoms such as nitrogen, sulfur, or phosphorus or by covering them with electroactive materials such as carbon-based substances, metal oxide, metal phosphates, metal-organic frameworks[4]. However, such modification techniques usually require complicated procedures that increase the cost of fabrication. This work reports a simplified fabrication process through the optimization of LIG parameters such as laser-scan-speed (mm/s), laser-power (%), focal height (h), Dot-per-inch (DPI), and nature of underlying support for the PI substrate. The fine-tuning of laser parameters, results in a highly reproducible dopant-free LIG pattern with an impressively low sheet resistance (R_{sheet}) ~5Ω/sq, I_D/I_G ~ 0.27 and high effective surface area of 127 m²/g. These findings enabled the fabrication of IDE-MSCs shown in Fig. 1(a) with active area of 1.27cm², electrode width (E_w=~6mm) and electrode gap (E_g=~500µm). For achieving full sustainability and flexibility in MSCs, a major limitation is their reliance on external power supplies for operation [5]. This issue is addressed by incorporating a piezoelectric layer of PVDF in between PVA/KOH solid gel electrolyte. Applying mechanical forces induce electric charge using the piezoelectric effect, which can be captured and stored in MSC, allowing the self-powered operation [6].This integration further improves sustainability and mechanical flexibility, making it appropriate for a variety of large area wearable electronics applications.

MATERIALS AND METHODS

Materials and Instrumentation

A 100W CO_2 laser (Fig. 1(b)) was used for laser ablation of PI (100um thickness). PVDF film embedded between the PVA/KOH electrolyte gel acts as the piezoelectrical generator for the self-powdered MSCs. Material characteristics inspection was performed using scanning electron microscope (SEM-model JSM-7800F-Prime-8KV),X-ray-photo electron spectroscopy(XPS), Brunauer-Emmett-Teller (BET) while Raman spectroscopy was employed to identify the functional group and defects within the LIG materials. For measuring the electrical characteristics, a Keithley 4200A-SCS Parameter Analyzer was used. The electrochemical performance of the fabricated device was assessed using a Keithley 2400 Source Meter to obtain the cyclic voltammetry (CV) response.

EXPERIMENTAL SECTION

Preparation of LIG based IDE-MSC

To identify the optimal LIG parameters for fabricating MSC electrodes, a 10x7 matrix of squares (Fig. 1(c)) was patterned on polyimide (PI) using varying laser scan speeds (mm/s) and laser powers (%).While DPI and focus height were kept as reported in our previous work [7]. For uniform heat distribution, the PI was placed on a metallic support. The metal's high thermal conductivity helped transfer heat between the laser and the PI, preventing excessive heat buildup. As shown in Fig. 1(c)(ii), well-formed patterns were only achieved when the laser power exceeded 15%.

Authorized licensed use limited to: DELHI TECHNICAL UNIV. Downloaded on April 01,2025 at 04:49:47 UTC from IEEE Xplore. Restrictions apply.

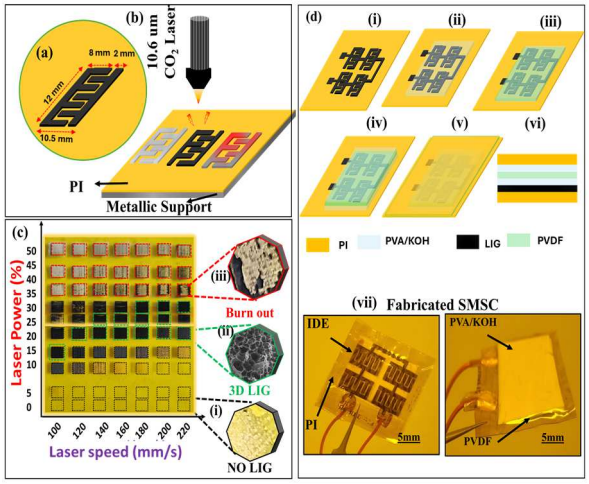

Figure 1: LIG setup for fabrication of IDE MSCs (a) IDE-MSCs fabricated with 1.27 cm² active area, $E_w \approx$ 6 mm, and $E_g \approx$ 500 µm (b) 100W C02 laser with PI apexed to metallic surface for better heat transfer between Laser and PI interface. (c) 10×7 LIG pattern on PI with varying laser speed(mm/s) and laser power (%) with other parameters fixed (DPI=250, focus height =6 mm). (d)(i-v) Fabrication flow of IDE MSC with (vi) side views of each material used for making MSCs. (vii) Top and bottom views of the actual fabricated MSC.

However, when the power exceeded 35%, the PI burned. Similarly, high scan speeds and low power levels produced no significant changes, as confirmed by Fig. 1(c)(i), where no alterations in the PI surface morphology were observed. LIG formation only occurs when the necessary threshold parameters are exceeded. In this work, a laser scan speed of (120-130) mm/s and a laser power of (20-25) % were used to fabricate (IDE-MSCs).

Preparation of PVA/KOH gel Electrolyte

The Fabrication flow of IDE MSCs is shown in Fig.1(d)(i-vii). First, 4 g of KOH was mixed with 40 ml of DI water and heated at temperatures 80°C for 60 min. As soon as the solution started becoming viscous, a mixture of 4 g of KOH and 16 ml DI water was added slowly. Then the prepared sample was drop casted on IDE and on top it PVDF film was placed. Again, PVA/KOH was drop casted on PVDF film to create a sandwiched structure of PVA/KOH-PVDF-PVA/KOH.

Working principle of Self-Powdered MSC (SMSC)

The working principle of fabricated SMSC is based on combination piezoelectrical energy harvesting and electrochemical energy stored, shown in Fig. 3(a). The optimized LIG IDE offers a large surface area ~127m^2/g with lowers sheet ~5/sq. The IDE acts as place for charge storage during charging and its planar design aids in rapid ion transfer leading to fast charging and discharging the MSC. Secondly, the IDE design adds mechanical resistance to bending when compared to bulk design configuration. When the mechanical force is applied, the PVDF film undergoes deformation, and a potential difference is generated across its surface. The harvested kinetic energy drives the ions, primarily K^+ and OH^-

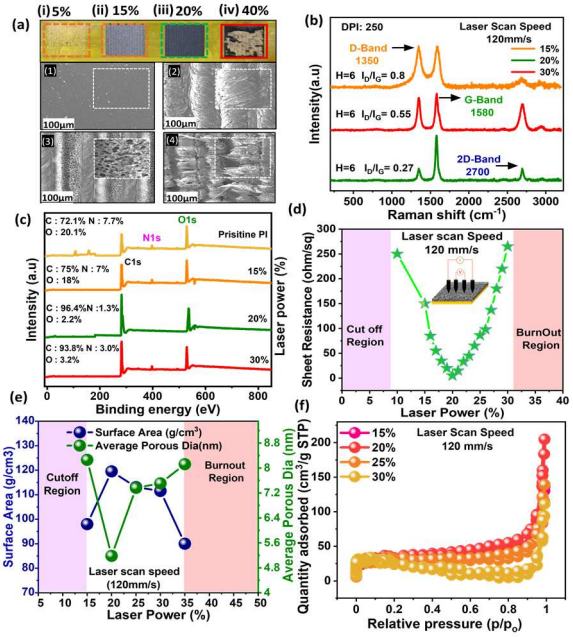

Figure 2:Impact of laser power on LIG quality: (a) (i-v) Optical and (1-4) SEM images of LIG samples at varying laser-power(%) with constant scan speed (120 mm/s) scale bar of 100um (b) PL-Raman analysis of LIG at 15%, 20%, and 30% (laser-power) with fixed (DPI=250) (c) XPS analysis showing LIG composition on PI surface (d) Laser power effect on R_{sheet} of LIG; (e) Effect of laser power (%) on surface area and pore diameter at a fixed laser scan speed (120 mm/s).(f) N_2 adsorption-desorption isotherms for different laser powers (%) at a fixed laser scan speed (120 mm/s).

present in the electric double layer capacitor (EDLC), towards the oppositely charged LIG electrode. Due to optimized LIG parameters, maximum surface area for IDE is achieved without adding additional dopants, thus providing a much cheaper and simpler way to design high performance LIG IDE for SMSCs. This self-powered mechanism allows the MSC to operate without external power source, as the mechanical energy from external stress is directly converted and stored within the MSC. Through continuous mechanical deformation, the PVDF film consistently generates electrical energy, which is stored and can be discharged as needed.

RESULTS AND DISCUSSION

Material Characteristics of LIG IDE

LIG quality was confirmed using SEM-EDX, Raman, XPS and BET analyses, as shown in Fig. 2(a)–(f). The optical images shown in Fig. 2(a)(i–vi) confirm that a darker, smooth pattern was observed at 20% laser power. In contrast, no pattern was observed at 5% laser power, whereas at 40% laser power, the PI surface was completely burnt. These observations were proven correct as the results are correlated to SEM images shown in Fig 2(a)(1-4). From Fig. 2(a)(3), 3D porous LIG can observed. These 3D porous networks provide a high specific surface area for electrolyte ions and thus speed up ion transfer through MSCs. Raman analysis depicted in Fig. 2(b) confirms the degree of graphitization for all the LIG samples with D

Authorized licensed use limited to: DELHI TECHNICAL UNIV. Downloaded on April 01,2025 at 04:49:47 UTC from IEEE Xplore. Restrictions apply.

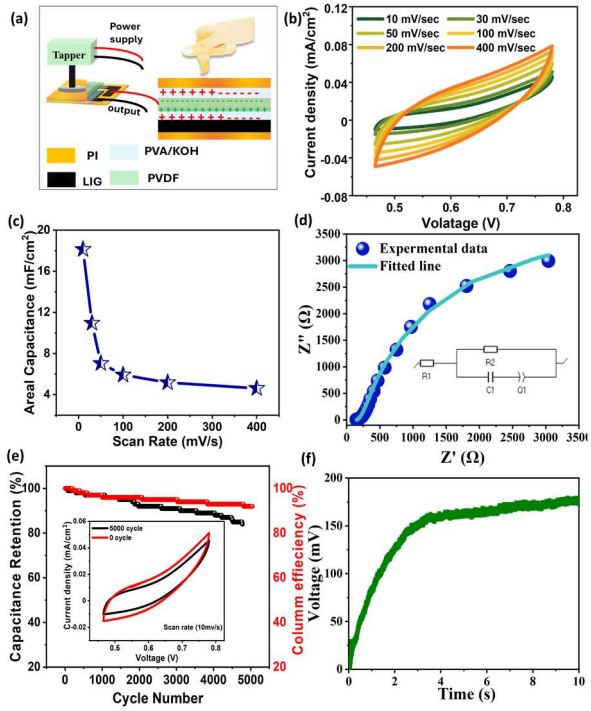

Figure 3: (a) illustrates the working mechanism of fabricated SMSC. (b) Cyclic Voltammetry profile and (c) areal capacitance at varying scan rate, with a maximum capacitance of 18 mF/cm² at 10 mV/s (d) EIS analysis of the single IDE MSC (e) Cyclic stability of a single IDE MSC after 5,000 cycles, retaining 84% capacitance and 96% Coulombic efficiency. (f) Self-charging of the MSC after 10 seconds of finger tapping.

peak, G peak and 2D peak respectively at 1350 cm^{-1}, 1580 cm^{-1}, 2684 cm^{-1}. For laser power (20%) I_D/I_G ~0.27 indicate moderate lattice defects among the other samples [3]. For Higher Laser power (>30%), I_D/I_G increase leading higher defects. Based upon the XPS spectra shown in Fig. 2(c), Pristine PI comprises the elements of Carbon (C1s), Nitrogen (N1s), Oxygen (O1s) with concentrations of 72.1%, 7.7%, 20.1% respectively. For optimized LIG parameters, C1s contents increased to maximum (~96.4%) among other samples. The higher content of C1s improves the conductivity of materials and lowers the sheet resistance of LIG sample [7]. These outcomes were proven with sheet resistance value shown in Fig. 2(d). For laser power of 20%, the overall sheet resistance ~5ohm/sq and for laser power >35%, a sharp increase in sheet resistance was observed. Fig. 2(e–f) presents the BET analysis of LIG samples fabricated at varying laser powers. The optimized LIG sample exhibited the highest surface area (~127 m^2/g) and smallest average pore diameter (~4.8 nm). Thus, the optimized LIG parameters offer a method for fabricating low-resistance, high-quality, high-surface-area, and cost-effective LIG IDE MSCs using a single-step fabrication process, outperforming recent work on LIG [8].

Electrical Characteristics of LIG IDE MSCs

To evaluate the electrochemical performance of the fabricated MSC, cyclic voltammetry (CV), areal capacitance, and capacitance retention were measured under cyc lic bending. Fig. 3(b) depicts CV curves at scan rates ranging from 10 to 400 mV s^{-1}, showing a quasi-rectangular shape that confirms the typical EDLC behavior of the fabricated MSCs. Using CV curves, areal capacitance Fig 3(c) for single MSC were calculated to be 18mFcm^{-2} at 5mVs^{-1} scan rate which is higher than recent reported works on LIG based MSCs [8-9]. Further, electrochemical impedance spectroscopy (EIS), depicted in Fig 3(d), was carried out in range of 0 to 3.5MHz consisting of experimental data and fitted data. Z` represents the equivalent series resistance (R_{SI})~150.8Ω between gel electrolyte and LIG IDE. The inset in Fig. 3(d) illustrates the equivalent circuit diagram. R_{CT} ~1.5 MΩ represents the charge transfer resistance, reflecting the electron transfer resistance at the electrode-electrolyte interface. R_{SI} of ~150.8 Ω corresponds to the series resistance, combining the resistances of the electrode, electrolyte, and interfaces. Both capacitance retention (~85%) and column efficiency (96%) remain high (Fig 3(e)) even after the 5000 cyclic charging and discharging. There is little to no change in CV response initial and finial response that can be clearly observed from inset Fig. 3(e). Such high cyclic stability signifies the use of optimized LIG parameters not only improved the areal capacitance but also helped in improving electrolyte interaction with IDE. To overcome the limitations of conventional MCSs, self-powered behavior of fabricated MSC was shown in Fig. 3(f), where charging up to 180mv with 10s of finger tapping is obtained.

CONCLUSION

This work provides a simple method to fabricate the high performance self-powdered IDE MSC using optimized LIG parameters without need of additional dopants. With optimized laser parameters R_{sheet} ~5Ωsq^{-1}, an I_D/I_G ratio of ~0.27, and a S_{area} ~127m^2/g for IDE MSCs were achieved. These high optimal result for IDE later proven to obtain high cyclic stability for MSCs with impressive C_{Ar} of ~18mF/cm^2 at 10mV/s scan rate. The incorporation of a PVDF film as a piezoelectric layer, combined with a solid PVA/KOH gel electrolyte, allows the self-powered operation of the MSC. The scalability and low-cost fabrication method can pave the way for future flexible, self-powered energy storage devices

ACKNOWLEDGEMENTS

Authors acknowledge I-Hub Foundation for Cobotics Technology Innovation Hub (Grant No: RP04218G), Makerspace, NRF, CRF, IIT Delhi.

REFERENCE

[1] Z. Zhen and H. Zhu, 2018. Structure and properties of graphene. In Graphene (pp. 1-12). Academic Press.

[2] P. R. Bhilkar, “Functionalized Carbon Nanomaterials: Fabrication, Properties, and Applications,” in Materials research foundations, 2023, pp. 72–99.

[3] F. T. Beigh, N. T. Beigh and D. Mallick, "Optimization Strategies for Laser-Induced Graphene on Various Substrates for Flexible Strain Sensing," 2024 IEEE Applied Sensing Conference (APSCON), Goa, India, 2024, pp. 1-4

Authorized licensed use limited to: DELHI TECHNICAL UNIV. Downloaded on April 01,2025 at 04:49:47 UTC from IEEE Xplore. Restrictions apply.

[4] Q. Zhang, F. Zhang, X. Liu, Z. Yue, X. Chen, and Z. Wan, “Doping of Laser-Induced Graphene and Its Applications,” Advanced Materials Technologies, vol. 8, no. 16, Apr. 2023.
[5] T. Liu et al., “High-performance micro supercapacitor assembled by laser-induced graphene electrode and hydrogel electrolyte with excellent interfacial wettability for high capacitance,” Journal of Power Sources, vol. 602, p. 234307, May 2024
[6] N. T. Beigh, F. T. Beigh and D. Mallick, D., 2023. Machine learning assisted hybrid transduction nanocomposite based flexible pressure sensor matrix for human gait analysis. Nano Energy, 116, p.108824.
[7] F. T. Beigh, N. T. Beigh and D. Mallick, 2024, June. High-Performance Flexible Heaters with Optimum Laser Induced Graphene Parameters. In 2024 IEE International Conference on Flexible and Printable Sensors and Systems (FLEPS) (pp. 1-4). IEEE.
[8] A. Ghosh et al., “Enhanced Performance of Laser-Induced Graphene Supercapacitors via Integration with Candle-Soot Nanoparticles,” ACS Applied Materials & Interfaces, vol. 16, pp.40313-40325, July. 2024.
[9] Z. Zhang, M. Song, J. Hao, K. Wu, C. Li, and C. Hu, “Visible light laser-induced graphene from phenolic resin: A new approach for directly writing graphene-based electrochemical devices on various substrates,” Carbon, vol. 127, pp. 287–296, Nov. 2017

CONTACT

*Faizan Tariq Beigh, tel:+91-700-644-0630;
beigh.faizan@gmail.com

Authorized licensed use limited to: DELHI TECHNICAL UNIV. Downloaded on April 01,2025 at 04:49:47 UTC from IEEE Xplore. Restrictions apply.

The current issue and full text archive of this journal is available on Emerald Insight at:
https://www.emerald.com/insight/1934-8835.htm

International Journal of Organizational Analysis

The empirical and managerial landscape of workplace spirituality: a systematic literature review of studies published in ABDC list journals

Nancy Munjal and Geeta Sachdeva
Department of Humanities and Social Sciences, National Institute of Technology, Kurukshetra, India, and

Naval Garg
Delhi Technological University, Delhi, India

Received 27 August 2024
Revised 16 December 2024
28 January 2025
31 January 2025
Accepted 1 February 2025

Abstract

Purpose – The purpose of this paper is to provide a comprehensive understanding of workplace spirituality's (WPS) past, present and future by conducting a systematic literature review over the past 15 years, tracing its emergence in the managerial landscape and identifying the research gaps.

Design/methodology/approach – A PRISMA framework is used to systematically analyse 58 empirical studies categorised according to the ABDC journal quality list and published between 2009 and 2024. Furthermore, this review highlights the key trends, methodological approaches, dimensions explored, geographic distribution, research themes and the existing research gaps. Additionally, the Theory, Context, Characteristics and Methodology framework emphasises critical theoretical perspectives, contextual factors, distinguishing characteristics and methodological approaches that can shape future research in WPS.

Findings – The review revealed the global interest in WPS's positive organisational impacts, supported by rigorous empirical studies and advanced statistical methods. Furthermore, this research highlights a significant gap in exploring WPS antecedents, suggesting a need for future studies to examine the factors contributing to WPS's development and enhancement within organisational settings.

Research limitations/implications – This study focuses on the Scopus database and English-language papers, deliberately excluding other sources such as unpublished work, books and non-empirical articles. Consequently, this study may need to look at some relevant studies.

Originality/value – This study is original in its systematic approach to review the literature on WPS, categorising the empirical articles according to established quality lists and applying the Theory, Context, Characteristics and Methodology framework to identify future research directions. This paper offers a holistic understanding of WPS and provides valuable insights for researchers and practitioners in this evolving field.

Keywords Workplace spirituality, Spiritual organisation, Employee spirituality, Systematic literature review

Paper type Literature review

Declaration of conflicting interests: The authors declare that there is no potential conflict of interest concerning the research, authorship or publication of this article.

Funding: The authors have not received any financial support for the research, authorship and publication of this article.

International Journal of Organizational Analysis
© Emerald Publishing Limited
1934-8835
DOI 10.1108/IJOA-08-2024-4778

1. Introduction

Originating in the 1920s, workplace spirituality (WPS) gained renewed traction in the 1980s, emerging as a prominent megatrend within the business landscape (Marques *et al.*, 2007), and its geographical presence was first observed in the USA (Hicks, 2007). The complexity and varied perspectives on WPS have further fuelled its prominence in human behaviour (Smith and Rayment, 2007); Ahmadi *et al.*, 2014, leading to increased innovation and creativity among personnel (Bantha and Nayak, 2020), increased employee productivity and competitive advantage for organisations (Biswakarma, 2018), a positive psychological environment for workers (Mohammed and Elashram, 2022) and well-being of employees who seek meaning and purpose from their work rather than just materialistic outcomes (Aboobaker, 2022). The paradigm shift in organisational thinking stems from the realisation that focusing solely on financial and operational success is insufficient for sustainable growth (Marques *et al.*, 2007). We live in an era where employees seek more than just financial compensation. Therefore, WPS has gained attention from academicians and practitioners because of its valuable contribution to organisations and society over the past two decades (Mhatre and Mehta, 2022).

There is no universally accepted definition of WPS, and different authors have defined spirituality in diverse ways. Mitroff and Denton (1999) defined WPS as a framework of organisational values, practices and experiences that promote the development of a more profound sense of meaning, purpose and self-transcendence. Further, Krishnakumar and Neck (2002) defined it as creating an environment where organisational members experience a sense of inner well-being, purpose and self-worth in their work, irrespective of the presence or absence of religious belief. Robbins (2003) defined it as "The recognition that people have both a mind and a spirit, seek to find meaning and purpose in their work, and desire to connect with other human beings and be part of a community".

Moreover, over the past two decades, several authors have suggested different dimensions of WPS. Ashmos and Duchon (2000) proposed a conceptual framework of WPS that encompasses three dimensions: "Inner life, sense of community, and meaningful work". Milliman *et al.* (2003) recognised three significant facets of WPS: "meaningful work, sense of community, and alignment with organisational values." Petchsawang and Duchon (2012) suggested "meaningful and purposeful work assignment, sense of community and transcendence" as dimensions of WPS (Pandey *et al.*, 2009) and Garg (2017) proposed Indian spiritual constructs from Hindu mythological books: "swadharma, lokasangraha, sense of Community, authenticity, karma Capital and kritagyata". These dimensions are not mutually exclusive, and different authors may use different terminology or groupings according to the research requirements.

Although there is a substantial body of literature on WPS from the past two decades, systematic review studies in this domain are still scarce. Systematic review is an umbrella term and, thus, can preside over in various ways, that is, systematic literature review, bibliometric review or meta-analytical review. To the best of our knowledge, a few researchers have conducted a systematic literature review (Mhatre and Mehta, 2022; Singh and Singh, 2022; Vasconcelos, 2022) and bibliometric analysis (Munjal and Sachdeva, 2024; Barik and Nayak, 2023; Mohan and Murugan, 2024; Raamkhumar and Swamy, 2023 and Rajni *et al.*, 2022).

Singh and Singh (2022) found that WPS is a complex, multidimensional concept demanding a conclusive definition encompassing personal, psychological and social aspects. While WPS initiatives are linked to positive outcomes, such as increased commitment, engagement and satisfaction, potential negative aspects have also been observed. On the

other hand, Raamkhumar and Swamy (2023) conducted a bibliometric analysis of WPS to bridge the gap between research and practical application in organisations. It identified intellectual structures and emerging themes, laying the groundwork for developing WPS modules for real-time practice. The study highlighted recent trends and thematic evolution in WPS using performance metrics and science mapping techniques. Although, along with these, numerous scholarly efforts have been made to consolidate the literature, still the understanding of WPS has remained incoherent.

Given the extensive body of empirical studies on WPS, the current study will offer an updated and comprehensive overview of the knowledge in this domain. This review intends to conduct a systematic literature review focusing on 58 empirical articles on WPS published between 2009 and 2024. This review sources its articles from the Scopus database, widely recognised as the most extensive data source for various fields (Pranckutė, 2021). From the 1,069 identified articles, only those ranked on the Australian Business Deans Council (ABDC, 2022) journal quality list were selected. Given the focus on WPS from a managerial and business perspective, the ABDC list, specifically tailored to business and management disciplines, offers highly relevant insights for research in these fields. While other lists like, the SJR ranking list, offer a broader scope of journals across various disciplines, its inclusion could have introduced journals less aligned with the business and management perspective. ABDC list helps identify journals that are most likely to publish research that aligns with the interests and needs of the business community (Lac *et al.*, 2008). Furthermore, the ABDC list is widely recognised and used by leading business schools in Australia and many Asian countries to filter out substandard journals (Prabhu and Srivastava, 2023), ensuring that the research published in these journals is high quality and credible. This systematic review of empirical articles identified research gaps and future directions using the Theory, Context, Characteristics and Methodology (TCCM) framework, focusing on theoretical underpinnings, contextual nuances, methodological advancements and practical implications to guide future research in the domain of WPS. Addressing a notable gap in the literature, our research enhances accessibility and clarity by consolidating comprehensive conclusions across reviewed studies.

2. Research methodology

A systematic literature review is an organised, precise, comprehensive and systematic approach that enables researchers to comprehend vast amounts of information by uncovering, evaluating, analysing and synthesising existing data related to a particular research question (Khirfan *et al.*, 2020). This study followed the Preferred Reporting Items for Systematic Reviews and Meta-Analysis (PRISMA) guidelines to ensure transparency and rigour. PRISMA is an evidence-based framework designed to enhance the quality and clarity of systematic reviews by providing detailed recommendations for study selection, data collection and synthesis (Page *et al.*, 2021). By adhering to PRISMA, the study aims to minimise bias, enhance the reliability of findings and contribute valuable insights in the domain of WPS. The PRISMA guidelines outline a comprehensive framework for conducting systematic reviews. This study adhered to the following key guidelines:

- *Search strategy*: A comprehensive and replicable search strategy was designed to identify relevant studies within the Scopus database. The strategy included search terms, Boolean operators and filters, ensuring comprehensive coverage of the research objective.
- *Eligibility criteria*: The study established predefined inclusion and exclusion criteria to ensure consistency and relevance in selecting studies.

- *Study selection process*: The selection process follows a two-stage screening approach. The initial stage involves manually reviewing titles and abstracts, followed by a detailed review of full texts. A PRISMA flow diagram illustrates this process (Figure 1).
- *Data extraction and synthesis*: A standardised data extraction form was used to ensure consistency and minimise errors during the process. The form was designed to capture essential information such as study characteristics (e.g. author, year, country and publication source), methodology (e.g. research design, sample size and data collection methods), key findings and thematic insights. This standardised approach facilitated a structured synthesis of the extracted data, enabling uniform comparison across studies and ensuring reliability in the analysis.
- *Reporting and transparency*: The study follows the PRISMA checklist, ensuring that all required items were reported.

This study developed a review protocol that detailed the steps for a systematic literature review. It includes three stages: the first focuses on finding appropriate data sources and search strategies; the second addresses inclusion criteria; and the third involves data collection and analysis.

2.1 Stage 1. Data sources and search strategies

This study's systematic literature review encompassed a thorough search of articles published from 2009 to 2024, covering 15 years to capture the evolution and trends in WPS research over a significant period, providing a comprehensive understanding. In the initial stage, the authors concentrated on selecting suitable databases for article extraction. Ultimately, the choice was made to use the Scopus database because of its robust features for tracking, analysing and visualising research, making it exceptionally valuable for scholarly investigations (Donthu *et al.*, 2021). Additionally, Scopus is particularly advantageous as it is the most reputed social sciences database that specifically indexes high-quality journals in business and management. Other databases, such as WoS and Pubmed, were not used because they encompass a broader range of disciplines beyond business and management, and the focus of this study is specifically on high-quality business and managerial research.

Further, based on previously published work on WPS and inputs from various authors, keywords like "Workplace spirituality", "Spirituality at work", "Organisational spirituality", "Spiritual Organisation", "Spirituality in the workplace", "Employee spirituality", "spirituality-based organisation" and "Spirit at work" were used. In addition, further refinements, like selection of language, subject, document type, open-access articles, etc., were based on inclusion criteria outlined in detail in the next stage of the review process.

2.2 Stage 2. Inclusion criteria

The following are the inclusion criteria that were used to identify the relevant studies from the Scopus database:

- Inclusion criteria.
- *Criteria 1*: "Journal articles", as these articles undergo a thorough peer review process, ensuring the research is scrutinised by experts, which will further enhance the reliability and credibility (The subject area is business/management/accounting, social sciences, arts and humanities and psychology).

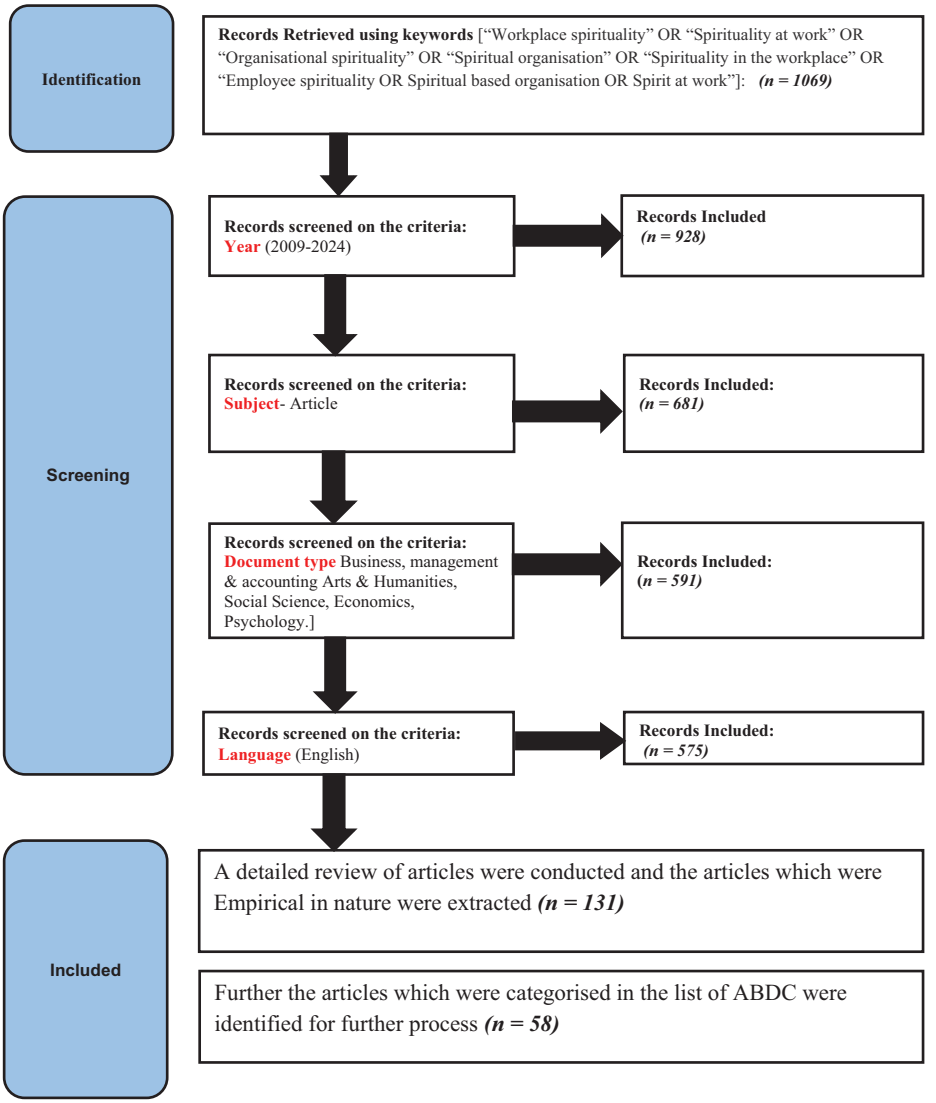

Source: Authors' own work

Figure 1. Data collection approach

- *Criteria 2*: The study is in English, widely used as a primary language for academic and scientific communication.
- *Criteria 3*: The Journal article must be Scopus-indexed, as Scopus is the most comprehensive database for academic journals (Pranckutė, 2021).

- *Criteria 4*: The journal article is empirical to ensure the findings are based on observed and measured phenomena, providing concrete evidence and practical insights that apply to organisational settings.
- *Criteria 5*: The journal article must be listed in the ABDC ranked list, ensuring that the articles are published in reputable and credible journals for their contributions to the field.

2.3 Stage 3. Data collection and analysis

Following the PRISMA guidelines, an initial search was performed in the search section using the query ["Workplace spirituality" OR "Spirituality at work" OR "Organisational spirituality" OR "spiritual organisation" OR "Spirituality in the workplace" OR "employee spirituality" OR "Spiritual based Organisation" OR "Spirit at work"] within the TIT-ABS-KEY section of the advance search section. This search yielded 1,069 articles. By restricting the period to 2009 through June 2024, the articles were reduced to 928. The scope was refined to include only "Article" document types, resulting in 681 documents. The subject areas were then limited to business management, accounting, humanities and social sciences, economics and psychology, bringing the total to 591 articles. Finally, the search was confined to English-language articles, narrowing it down to 575. A detailed review identified 131 relevant empirical studies. Ultimately, applying the criteria that articles must be included in Journals that are listed in the ABDC journal list, 58 documents were selected for review purposes (Figure 1).

3. Findings

This section outlines the findings of the review, highlighting the key insights, patterns and trends identified through a rigorous and systematic literature review process. By narrowing the scope to empirical studies published over the past 15 years (2009–2024), 58 relevant studies were selected (Table 1). These studies provide a comprehensive overview of conclusions drawn from prior research, the variables explored as outcomes, antecedents, mediators or moderators and the methodological approaches used. Together, they offer a synthesised perspective on the current state of knowledge in the field of WPS.

3.1 Research publication trends

Considering the empirical articles published in ABDC Category Journals, the publication trend in the domain of WPS from 2009 to 2024 reveals several key patterns (Figure 2). The trend indicates that between 2009 and 2014, empirical studies on WPS were at the nascent stages of development, and research in this area was beginning. Since 2015, there was a noticeable surge in research activities within this domain. Following the spike in 2015, there was a sharp decline in 2016, dropping back to 1 empirical publication. Since 2017, there has been a substantial increase in publications, although a slight downfall was observed in 2021. However, the publication trend gained good momentum thereafter. Considering the pattern and the rate at which articles have been released up until this point (June 2024), it is safe to assume that the publication this year will surpass those of the previous year.

3.2 Distribution of articles in various categories

The journals in this list are classified into four categories: A*, A, B and C, each reflecting different levels of quality and impact within the academic community. Table 2 lists the 58 articles published in four different category journals from the Scopus database. Of 58

Table 1. Summary of reviewed articles

Author	Category	Sample	Variables	Technique	Conclusion
Pawar (2009)	ABDC-B	156 Employees from Various Organisations	IDV – Aspects of WPS (meaning in work, the community at work, and positive organisational purpose); DV – Aspects of work attitude – (job satisfaction, job involvement, and organisational commitment); Moderating variable – Individual spirituality	Multiple regression	"The study findings strongly supported the anticipated connections between aspects of WPS and work attitudes. Additionally, the findings indicate that individual spirituality may moderately influence the impact of aspects of WPS on work attitude"
Altaf and Awan (2011)	ABDC-A, FT50	76 Employees from Various Organisations	IDV – Work overload; DV – Job satisfaction; Moderating variable – Workplace spirituality	Correlation and regression	"Work overload negatively impacts job satisfaction, highlighting the detrimental effects of excessive work demands on employees' performance. Further WPS plays a crucial role in moderating the relationship between job overload and job satisfaction"
Petchsawang and Duchon (2012)	ABDC-C	250 employees from food and baking companies	IDV – Workplace spirituality; DV – Work performance; Mediating variable – Meditation practice	Multiple regression	"The research discovered that regular meditation practice partially mediates the relationship between WPS and work performance. The inference could be drawn that, the more spiritual the individuals are, the more they practice meditation, leading to improved work performance"
Sprung *et al.* (2012)	ABDC-A	854 participants	IDV – Workplace aggression; DV – Employee outcome; Mediating variable – Workplace spirituality	Hierarchical regression	"The study offers initial indications suggesting that spirituality could affect employees' reactions to workplace dynamics like aggression, suggesting a potential significance of spirituality within work settings. Results indicated that spirituality correlated with favourable results when workplace aggression was absent. However, in the presence of workplace aggression, spiritually inclined employees experienced more adverse outcomes compared to their less spiritual counterparts"

(*continued*)

Table 1. Continued

Author	Category	Sample	Variables	Technique	Conclusion
Nasurdin *et al*. (2013)	ABDC-C	171 academic staff employees from Higher education	IDV – Workplace spirituality; DV – Organisational citizenship behaviour; Moderating variable – Gender	Confirmatory factor analysis, hierarchical regression	"Some dimensions of WPS (meaningful work and alignment of values) contribute positively to certain aspects of organisational citizenship behaviour, partially confirming the hypothesis. However, gender does not significantly affect the relationship between dimensions of WPS and organisational citizenship behaviour, leading to the rejection of the second hypothesis"
Daniel (2015)	ABDC-C	308 students from part-time MBA students	IDV – Workplace spirituality; DV – Stress; Moderating variable – Gender	Structural equational modelling	"Results indicate that engaging in meaningful activities was negatively and significantly correlated with work stress both in Mexico and the USA. However, the hypotheses related to other aspects of WPS i.e., the sense of community and inner life were found to be insignificant in both countries"
Jena and Pradhan (2015)	ABDC-B	208 Manufacturing Public Sector	IDV – Psychological capital; DV – Workplace spirituality; Moderating variable – Emotional intelligence	Multiple regression	"The study establishes a positive relationship between employees' psychological capital and WPS, indicating the significance of these constructs in organisational settings. The results indicate that EI acts as a moderator in enhancing the association between psychological capital and WS, suggesting that individuals with higher emotional intelligence may experience a stronger connection between their psychological resources and spiritual values in the workplace"
van der Walt and Swanepoel (2015)	ABDC-C	412 employees from two organisations in Welkom, South Africa	IDV – Workplace spirituality; DV – Job involvement	Multiple regression	"In South African settings, there exists a positive correlation between WPS and job engagement, underscoring the significance of fostering spiritually oriented work environments. Furthermore, the research underscores the necessity for organisations to tackle employee-centric concerns by integrating spirituality within the workplace, recognising that employees increasingly prioritise factors beyond mere concentration, particularly amidst evolving internal and external dynamics"

(*continued*)

Table 1. Continued

Author	Category	Sample	Variables	Technique	Conclusion
Rahman *et al.* (2015)	ABDC-C	220 non-academic staff members from higher learning institutes	IDV – Trust and workplace spirituality; DV – Knowledge sharing behaviour; Mediating variable: Perceived risk	Structural equational modelling	"The study discovered a significant positive link between WPS and the knowledge-sharing behaviour of non-academic staff. This suggests that employees are more inclined to share knowledge when they view their workplace as fulfilling their spiritual requirements. Additionally, the research explored the role of trust in knowledge sharing. Although the direct relationship between trust and knowledge sharing was not explicitly stated, the study revealed that perceived risk variables partially mediate this connection"
Roof (2015)	ABDC-A, FT50	124 employees working in various institutions	IDV – Individual spirituality; DV – Dimensions of employee engagement (vigour, dedication, absorption)	Multiple regression	"Empirical evidence supports a relationship among individual spirituality and overall employee engagement, including vigor, and dedication. However, there was no observed relationship between individual spirituality and the engagement dimension of absorption. These findings suggest encourage further exploration of the relationship between spirituality and engagement, particularly why absorption is unaffected"
Afsar and Rehman (2015)	ABDC-C	448 employees and 79 managers from 2 knowledge-intensive industries	IDV – Workplace spirituality; DV – Innovative work behaviour; Mediating variable – Person-Organisation fit	Regression and structural equation modelling	"WPS positively impacts employees' innovative work behaviours and their perception of P-O fit. Perceived P-O fit partially mediates the relationship between WPS and innovative work behaviour. Furthermore, both subordinate and supervisor evaluation show that WPS and perceived P-O fit lead to higher levels of innovative work behaviour."
Gatling *et al.* (2016)	ABDC-A	190 Supervisors from US Hospitality Organisation	IDV – Workplace spirituality; DV – Intention to quit; Mediating variable – Organisational commitment	CFA and structural equational modelling	"There is a positive relationship between WPS and organisational commitment (OC). conversely, OC negatively correlates with intention to quit (ITQ). furthermore, OC fully mediates the negative relationship between WPS and ITQ. The study also expands self-determination theory (SDT) by connecting it to WPS, showing how fulfilling psychological needs can impact work attitudes in hospitality supervisors"

(*continued*)

Table 1. Continued

Author	Category	Sample	Variables	Technique	Conclusion
Pawar (2016)	ABDC-B	123 Working Participants	IDV – Workplace spirituality (meaningful work and sense of community); DV – Employee Well-Being (emotional well-being, psychological well-being, social well-being and spiritual well-being)	Exploratory factor analysis and regression	"In this study, a scale for spiritual well-being is developed using Exploratory Factor Analysis. Furthermore, the results state that it provides important empirical evidence that WPS positively relates to emotional, psychological, social, and spiritual well-being, which are the 4 major aspects of Employee well-being. The findings suggest cultivating a trust-oriented and spiritually supportive work environment can enhance knowledge sharing among non-academic staff."
Rahman *et al.* (2016)	ABDC-B	240 non-academic staff from higher learning institutions	IDV – Workplace spirituality and trust; DV – Knowledge sharing behaviour; Mediating variable – Perceived risk	Structural equational modelling	"Research findings indicate a significant positive correlation between WPS and knowledge-sharing behaviour among non-academic staff in private higher learning institutions. Additionally, trust among the staff positively influences knowledge-sharing behaviour, with this effect being mediated by the perception of risk. Thus, the findings suggest that fostering a trust-oriented and spiritually supportive work environment can promote knowledge sharing among non-academic staff"
Afsar and Badir (2017)	ABDC-C	434 employees and 59 Supervisors from top 5 hotels of China	IDV – Workplace spirituality and perceived organisational support; DV – Innovative work behaviour; Mediating variable – Person-Organisation fit	Structural equational modelling	"There is a positive relationship between WPS and innovative work behaviour (IWB), suggesting that spiritual values in the workplace can enhance creativity and innovation. Further, the results also suggest that Person-organisation (P-O) fit mediates the relationship between WPS and IWB, as well as between perceived organisational support (POS) and IWB, indicating that alignment of personal and organisational values is crucial for fostering innovation. Also, perceived organisational support positively affects IWB, showing that when organisations care for their employees' well-being, employees are more inclined to engage in proactive and innovative behaviours"

(*continued*)

Table 1. Continued

Author	Category	Sample	Variables	Technique	Conclusion
Petchsawang and McLean (2017)	ABDC-C	248 employees from such four organisations that offer meditation courses and 315 employees from such four organisations that do not offer any such courses	IDV – Mindfulness meditation; DV – Work engagement; Mediating variable – Workplace spirituality	CFA, Pearson correlation, and structural equational modelling	"This article suggests that WPS fully mediates the relationship of mindfulness meditation and work engagement, suggesting that fostering a spiritual workplace can enhance employee engagement. Further, the authors claim that organisations that support mindfulness meditation may see improved work engagement and performance, emphasising the reciprocal relationship between employer support and employee commitment"
Pawar (2017)	ABDC-B	115 employees from two electric power generation organisations	*Direct effect model:* IDV – Employees Individual Spirituality and Organisational Spirituality DV – Meaning and community at work *Moderating effect model:* IDV – Employees' individual Spirituality; DV – Workplace Spirituality; Moderating variable – Organisational Spirituality	Multiple regression	*Direct effect model:* The study strongly supported the direct effects model, showing that organisational spirituality is more significantly associated with facets of WPS than individual spirituality. *Moderating effect model:* The moderating effect model was not supported, indicating that individual spirituality does not influence WPS through organisational spirituality
Garg (2017)	ABDC-C	418 employees from various industries situated in NCR	IDV – Workplace spirituality DV – Organisational performance; Mediating variable – organisational commitment, employee engagement, work motivation	Structural equational modelling	"The article concludes that WPS significantly greatly impacts organisational performance in India. It highlights that affective and normative commitment, employee engagement, and work motivation partially mediate this relationship. The study suggests that when employees' spiritual needs are fulfilled at work, they show a higher level of commitment, engagement, and motivation, which in turn enhances improved organisational performance. The article also introduces 'Kritagyata' (gratefulness) as a new construct of Indian spiritualism, emphasising its importance in understanding WPS within the Indian cultural framework"

(*continued*)

Table 1. Continued

Author	Category	Sample	Variables	Technique	Conclusion
Jena and Pradhan (2018)	ABDC-A	761 respondents	IDV – Workplace spirituality DV – Employee commitment; Mediating variable – Organisational citizenship behaviour. Moderating variable – Emotional intelligence	CFA and structural equational modelling	"The paper concludes that WPS is a strong indicator of employee commitment (EC) in Indian organisations. It notes that while organisational citizenship behaviour (OCB) and emotional intelligence (EI) do not significantly mediate or moderate the relationship between WPS and EC. Instead, the presence of WPS itself directly impacts the commitment level of employees towards their work and organisation. The study recommends that HR interventions should aim to align personal roles with organisational goals to cultivate a dedicated workforce"
Belwalkar *et al.* (2018)	ABDC-B	613 Banking Employees	IDV – Workplace Spirituality (meaning and purpose in work, recognition of an inner life or spirit) and interconnectedness DV – Organisational citizenship behaviour; Mediating variable – Job Satisfaction	Exploratory factor analysis and regression	"The study found a positive link between WPS components (meaning and purpose, interconnectedness) and OCBs, with job satisfaction as a mediator. The inner life aspect of WPS didn't correlate with OCB as a whole but showed a significant positive relationship with individual OCB components like altruism, civic virtue, courtesy, and sportsmanship, except conscientiousness. Additionally, all the elements of WPS were found to enhance job satisfaction among employees"
Rezapouraghdam *et al.* (2018)	ABDC- A*	380 hotel employees from 5-star hotels	IDV – Workplace spirituality DV – Pro-environmental behaviour (OCBE); Mediating variable – Connectedness to nature. Moderating variable – Environmental awareness	CFA and regression	"The study indicates a positive correlation between WPS and employees' OCBE, implying that a spiritually supportive work environment can boost pro-environmental actions. Additionally, the research identifies connectedness to nature as a mediator in the relationship between WPS and OCBE, suggesting that a strong sense of unity with nature can promote environmental citizenship behaviour"

(*continued*)

Table 1. Continued

Author	Category	Sample	Variables	Technique	Conclusion
Milliman *et al*. (2018)	ABDC- A	292 employees from Hospitality Sector	IDV – Workplace spirituality DV – Employee commitment; intention to stay, service delivery	CFA and structural equational modelling	"WPS has a positive impact on employee engagement and their intention to stay, indicating that a work environment promoting meaningful work, community, and alignment with organisational values can boost employees' commitment and motivation. Conversely, Engagement is closely related to improved service delivery, it doesn't directly influence employees' intention to stay. Additionally, WPS indirectly affects service delivery through employee engagement, highlighting the importance of fostering a spiritually supportive work environment to improve customer service"
Iqbal *et al.* (2019)	ABDC-C	400 SME employees	IDV – Perceived job characteristics DV – Sustainability; Mediating variable – Workplace spirituality	Structural equational modelling	"Perceived job characteristics significantly impact WPS. Which in turn mediates the relationship between perceived job characteristics and environmental sustainability. Moreover, the study emphasises the crucial of SMEs in environmental sustainability, particularly in Pakistan and India. It also suggests that emphasising perceived job characteristics is essential for SMEs to address environmental sustainability challenges in dynamic markets"
Aboobaker *et al.* (2019)	ABDC-B	523 teachers from technical education institutions	IDV – Workplace spirituality DV – Intension to stay; Mediating variable – Well-being at work Moderating variable – Career choice	Structural equational modelling	"WPS significantly improves employee well-being and their desire to remain in the organisation. The relationship between WPS and job outcomes is influenced by a teacher's deliberate career choice. Additionally, there is a positive link between WPS and employee well-being, which subsequently impacts their intention to stay. The study recommends that organisations create a work environment that promotes meaningful work, a sense of community, and alignment with organisational values to enhance employee retention"

(*continued*)

Table 1. Continued

Author	Category	Sample	Variables	Technique	Conclusion
Joelle and Coelho (2017)	ABDC-A		IDV – Workplace spirituality DV – Individual performance; Mediating variable – Workers' attitude	CFA and structural equational modelling	"This study identifies significant findings related to the role of spirituality in the workplace. The introduction of Emotional Balance and Inner Peace (EBIP) as a novel dimension enhances the traditional conceptualisations of spirituality at work. The research highlights that job resourcefulness mediates the relationship between spirituality at work and individual performance, indicating a substantial impact. Additionally, the study finds that spirituality at work positively influences affective commitment, which subsequently affects job resourcefulness and performance"
Bayighomog and Araslı (2019)	ABDC-B	250 full-time frontline employees from 5-star hotels	IDV – Spiritual leadership DV – Customer-oriented boundary-spanning behaviours; Mediating variable – Spiritual well-being	Confirmatory factor analysis	"The study emphasises the critical role of spiritual leadership in enhancing employees' spiritual well-being and fostering behaviours that improve customer engagement. It identifies three essential types of customer-oriented boundary-spanning behaviours: service delivery, internal influence, and external representation, which are vital for linking the organisation with its customers. The research demonstrates that the influence of spiritual leadership on these customer-oriented behaviours is fully mediated by employees' spiritual survival and well-being"
Bhaskar and Mishra (2019)	ABDC-A	332 responses from different business sectors	IDV – Perceived organisational support DV – career satisfaction and turnover intention; Mediating variable and moderating variable – Workplace spirituality	EFA, CFA, hierarchical regression	"The article explores the influence of WPS on career satisfaction (CS) and turnover intentions (TIs), with perceived organisational support (POS) serving as a foundational element. The findings indicate that WPS enhances CS and decreases TIs by strengthening the connection between employees and the organisation through POS. Additionally, WPS, particularly through the dimensions of meaningful work and a sense of community, mediates the relationship between POS and CS. Furthermore, WPS moderates the relationship between POS and TIs, demonstrating that higher levels of WPS are associated with lower tis"

(*continued*)

Table 1. Continued

Author	Category	Sample	Variables	Technique	Conclusion
Rahman *et al*. (2019)	ABDC-B	160 sales executives	IDV – Workplace spirituality DV – Executive sales performance Mediating variable – Employee commitment	CFA and structural equational modelling	"The study examines the impact of WPS and employee commitment on the performance of sales executives in Bangladesh. The findings indicate that WPS leads to greater employee commitment, which subsequently enhances sales performance. Employee commitment serves as a mediating factor between WPS and sales performance, suggesting that while WPS does not directly affect sales performance, it does so indirectly by fostering greater commitment among employees"
Mahipalan and Sheena (2019)	ABDC-C	322 secondary school teachers	IDV – Workplace spirituality DV – Psychological well-being Mediating variable – Subjective stress	Structural equational modelling	"The article explores the connection between WPS, subjective stress, and psychological well-being among secondary school teachers in India. The findings reveal that WPS is positively linked to psychological well-being and inversely related to job stress. Subjective stress significantly mediates the relationship between WPS and psychological well-being, indicating that lower levels of stress amplify the positive effects of WPS on well-being. These results imply that fostering WPS can effectively manage stress and enhance teachers' psychological well-being, which is crucial for their effectiveness in teaching"
Zhang (2020)	ABDC-A, FT50	458 employees from different organisations in China	IDV – Workplace spirituality DV – Unethical pro-organisational behaviour Mediating variable – Job satisfaction	CFA and hierarchical regression	"The article explores the relationship between WPS and unethical pro-organisational behaviour (UPB), emphasising the mediating role of job satisfaction. The study finds that certain aspects of WPS are positively linked to UPB, indicating that employees might engage in unethical actions that benefit their organisation under the influence of WPS. Job satisfaction is identified as a mediator in this relationship, with higher job satisfaction potentially increasing the likelihood of UPB. These findings are particularly pertinent in the Chinese cultural context, where collectivism and strong organisational loyalty may promote UPB"

(*continued*)

Table 1. Continued

Author	Category	Sample	Variables	Technique	Conclusion
Bantha and Nayak (2020)	ABDC-C	340 employees (software engineers and product developers)	IDV – Workplace spirituality DV – Innovative work behaviour Mediating variable – Psychological empowerment	Structural equational modelling	"The study examines the connection between WPS and employees' innovative work behaviour, focusing on the mediating role of psychological empowerment. The findings indicate a positive relationship between WPS and both psychological empowerment and innovative work behaviour. Moreover, psychological empowerment fully mediates the relationship, suggesting that WPS enhances employees' innovative work behaviour mainly through the mechanism of psychological empowerment"
Haldorai *et al.* (2020)	ABDC-A*	641 employees from luxury hotels	IDV – Organisational justice and ethical climate DV – Workplace deviant behaviour and organisational citizenship behaviour Mediating variable – Workplace spirituality	Structural equational modelling	"The study explores how WPS mediates the relationship between ethical climate and organisational justice, and their subsequent effects on workplace deviant behaviour and organisational citizenship behaviour among hotel employees in India. The findings reveal that WPS mediates the connection between organisational justice and organisational citizenship behaviour and the relationship between ethical climate and workplace deviant behaviour. Organisational justice is shown to reduce workplace deviance and enhance organisational citizenship behaviour, while an ethical climate positively affects organisational citizenship behaviour and decreases workplace deviant behaviour"

(*continued*)

Table 1. Continued

Author	Category	Sample	Variables	Technique	Conclusion
Aboobaker *et al.* (2020)	ABDC-C	308 employees from private sector organisations	IDV – Workplace Spirituality (meaningful work, sense of community and alignment with organisational values) DV – Employee loyalty (intention to stay, benefit insensitivity toward alternate employers and word-of-mouth about the organisation)	CFA and regression	"The study explores the relationship between WPS and employee loyalty among millennials in India, concentrating on how factors like meaningful work, a sense of community, and alignment with organisational values influence loyalty. Employee loyalty is assessed through indicators including the intention to remain with the organisation, a lack of sensitivity to benefits offered by other employers, and the propensity to engage in positive word-of-mouth promotion. Targeting millennials, who are notably inclined to frequent job changes, the research highlights the importance for organisations to cultivate a sense of purpose and connection to enhance loyalty within this demographic"
Saadatyar *et al.* (2020)	ABDC-B	550 health-care employees from two international hospital	IDV – Workplace spirituality DV – Competitive advantage Mediating variable – Organisational commitment	CFA and structural equational modelling	"This research concludes that WPS enhances competitive advantage primarily by influencing organisational commitment levels, with a stronger direct relationship observed between WS and competitive advantage. WS impacts all three dimensions of organisational commitment–affective, continuance, and normative—but only affective commitment mediates the relationship between WS and competitive advantage in the hospitals studied. The research confirms that WS helps to develop organisational competitive advantage, highlighting the commitment-related pathways through which WS impacts overall performance"

(*continued*)

Table 1. Continued

Author	Category	Sample	Variables	Technique	Conclusion
Garg (2020)	ABDC-C	194 managers from various insurance industry employees	IDV – Workplace spirituality DV – Organisational performance Mediating variable – Organisational citizenship behaviour	Necessary condition analysis and hierarchical regression	"The study investigates the impact of WPS and organisational citizenship behaviour (OCB) on organisational performance in the Indian insurance sector. WPS, as understood through Indian spiritualism, appears to be essential for improving organisational performance. It includes concepts like swadharma, lokasangraha, authenticity, sense of community, karma capital, and kritagyata. OCB, which includes altruism, courtesy, conscientiousness, civic virtue, and sportsmanship, partially mediates the relationship between WPS and organisational performance"
Otaye-Ebede *et al.* (2020)	ABDC-A, FT50	51 branches from retail organisations	IDV – Workplace spirituality DV – Moral judgment and prosocial motivation Mediating variable – Ethical climate	CFA and structural equational modelling	"To investigate the connections between performance outcomes, ethical climate, and WPS, the paper presents a multilevel model based on social cognitive theory. According to the study, spirituality at work has a positive impact on the ethical atmosphere, which in turn affects moral judgment and prosocial motivation. The relationship between WPS and organisational and individual performance outcomes, like service performance and helpful behaviour, is mediated by the ethical climate. This study adds to our knowledge of how spirituality in the workplace can promote moral behaviour, which benefits both individual and organisational performance"
Saxena *et al.* (2020)	ABDC-B	202 employees from oil and gas industry	IDV – Workplace spirituality DV – Stress	Multiple regression	"With a focus on contrasting offshore and onshore settings, the study examines the relationship between WPS and stress management among workers in the Indian oil and gas industry. The results show a strong inverse relationship between onshore employees' level of stress and WPS. Additionally, the study shows that, in comparison to their onshore counterparts, offshore workers experience higher levels of stress and have fewer opportunities to practice WPS"

(*continued*)

Table 1. Continued

Author	Category	Sample	Variables	Technique	Conclusion
Jeon and Choi (2021)	ABDC-B	383 employees from private organisation in south Korea	IDV – Workplace spirituality DV – Life satisfaction; Mediating variable – Organisational commitment Moderating variable – Religious affiliation	CFA and hierarchical regression	"The study examines the relationship between WPS and life satisfaction, incorporating organisational commitment as a mediating factor and religious affiliation as a moderating variable. The findings indicate that the three subdimensions of WPS–meaning at work, membership, and inner life—are positively correlated with both organisational commitment and life satisfaction. Organisational commitment serves as a mediator, suggesting that higher levels of WPS contribute to greater life satisfaction through enhanced organisational commitment"
Sharma and Singh (2021)	ABDC-C	717 employees from public and private sector	IDV – Workplace spirituality and perceived organisational support; DV – Organisational effectiveness; Moderating variable – Demographic variables	Linear regression	"The study examines the relationship between WPS and organisational effectiveness within the higher education sector in India, focusing on academics. WPS, characterised by a sense of purpose and interconnectedness at work, is shown to foster positive attitudinal traits that enhance organisational effectiveness. This effectiveness is measured holistically, including group functioning, job satisfaction, and goal integration. The research provides empirical evidence demonstrating a positive association between WPS and organisational effectiveness, accounting for a significant portion of the variance. Additionally, the study finds that this relationship is generally consistent across various demographic factors, with gender emerging as the only significant moderator"

(*continued*)

Table 1. Continued

Author	Category	Sample	Variables	Technique	Conclusion
Shrestha and Jena (2021)	ABDC-C	167 employees from 25 different organisations	IDV – Workplace spirituality; DV – Organisational cynicism, CWB, turnover intension; Moderating variable – Psychological capital	CFA and linear regression	"The study examines the influence of WPS and psychological capital (PsyCap) on employee negativity, which encompasses organisational cynicism, counterproductive work behaviour, and turnover intentions. Findings indicate that WPS negatively impacts employee cynicism and turnover intentions, suggesting that fostering a spiritually enriched workplace can enhance employee retention and reduce cynicism. Additionally, PsyCap serves as a moderating factor, buffering the adverse effects of low WPS on turnover intentions, thereby mitigating negative outcomes. However, the study did not establish a direct link between WPS and counterproductive work behaviour, indicating the presence of other mediating factors"
Soliman *et al.* (2021)	ABDC-A	218 higher education lecturers	IDV – Workplace spirituality; DV – Lecturers engagement, lecturers' commitment, lecturers' workforce agility, lecturers trust, lecturer's empowerment	Structural equational modelling	"The study examines the impact of WPS on various attitudes of lecturers in higher education institutions (HEIs) specialising in tourism and hospitality. The findings indicate that WPS positively affects lecturers' engagement, commitment, workforce agility, trust, and empowerment. Utilising a quantitative approach, the data were collected from 218 lecturers in Italy and Portugal and analysed using PLS-SEM. The findings significantly underscore that WPS enhances lecturers' work attitudes and behaviours. This research contributes to the understanding of WPS within the context of tourism and hospitality HEIs, providing valuable insights for management practices and future academic inquiries in tourism management"

(*continued*)

Table 1. Continued

Author	Category	Sample	Variables	Technique	Conclusion
Lata and Chaudhary (2021)	ABDC-A, FT50	Banking industry – 225 IT industry – 220	IDV – Workplace spirituality; DV – Workplace incivility; Moderating variable – Dark triads (Machiavellianism, psychopathy, narcissism)	Regression	"The study investigates the association between WPS and the incivility employees face from supervisors and colleagues. It posits that WPS, encompassing meaningful work, a sense of community, and alignment with organisational values, tends to inversely correlate with experienced incivility. Additionally, the study explores how dark triad personality traits (Machiavellianism, psychopathy, and narcissism) moderate this relationship. The findings suggest that although WPS generally mitigates incivility, the presence of dark triad traits diminishes this effect"
Hunsaker and Ding (2022)	ABDC-B	236 workers in the service and manufacturing sector	IDV – Workplace spirituality DV – Innovative work behaviour; Mediating variable – Employee flourishing Moderating variable – Workplace satisfaction	CFA and hierarchical regression	"This study examines how WPS has a positive effect on employees' innovative work behaviour (IWB). the study identifies employee flourishing as a mediating factor and workplace satisfaction as a moderating factor in this relationship. The authors suggest that organisations should cultivate an environment that promotes WPS to enhance employees' sense of flourishing and satisfaction, thereby boosting innovation. This research addresses existing gaps by elucidating the complex interplay between WPS and employee flourishing in fostering innovative behaviour among Chinese millennials"

(*continued*)

Table 1. Continued

Author	Category	Sample	Variables	Technique	Conclusion
Sarkar *et al.* (2022)	ABDC-C	347 employees across various industries	IDV – Workplace spirituality (meaningfulness, meditative work, collaborative problem-solving, Authenticity, lokasangraha) DV – Psychological capital (hope, optimism, efficacy and resilience)	Multiple regression	"A Cross-sectional Study" demonstrates that WPS significantly predicts employees' Psychological Capital (PsyCap), which encompasses hope, optimism, efficacy, and resilience. Grounded in the broaden-and-build theory, the study analyses data from 347 employees across various industries in India using partial least squares structural equation modelling (PLS-SEM). The findings reveal that WPS fosters positive psychological resources in employees. Consequently, business leaders and organisational development practitioners are encouraged to implement spirituality-based interventions to maximise employees' psychological resources"
Sapra *et al.* (2022)	ABDC-B	101 faculties from private universities in Delhi NCR	IDV – Workplace spirituality DV – Academic performance	Linear regression	"The paper concludes that implementing WPS significantly influences the performance of higher education faculty. It suggests that elements such as compassion, mindfulness, meaningful work, and transcendence contribute to improved academic organisational performance, which is evident in aspects like academic reputation, graduate employability, research output, internationalisation, and community services"
Srivastava and Gupta (2022)	ABDC-A	322 hotel employees from the northern region of India	IDV – Workplace spirituality DV – Well-Being of employees Mediating variable – Workforce agility and organisational identification	Structural equational modelling	"The findings establish a positive link between WPS and employee well-being, with workforce agility and organisational identification as parallel mediators. The COVID-19 pandemic severely affected hospitality sector employees, causing significant uncertainties and economic challenges, that adversely affect their mental health and wellbeing. The study highlights the necessity of supportive organisational practices and systems to promote flexibility, adaptability, and rapid response to disruptions. It suggests that hotels provide mental and emotional support to staff during crises"

(*continued*)

Table 1. Continued

Author	Category	Sample	Variables	Technique	Conclusion
(Jalan and Garg, 2022)	ABDC-C	385 participants from Indian police personnel	IDV – Workplace spirituality DV – Occupational stress	Hierarchical regression	"this study examines the relationship between WPS and occupational stress (OS) among Indian police personnel. The findings indicate that certain dimensions of WPS, namely 'sense of community' and 'alignment with organisational values, 'significantly reduce OS among police officers. Contrary to expectations, the data did not support the hypothesis that meaningful work correlates with lower OS. The study also identifies demographic factors, including age, experience, educational qualifications, rank, and grade, as influential in the levels of OS experienced. Higher level of stress was observed among younger officers, those with greater responsibilities, and those with higher educational qualifications"
Paul and Jena (2022)	ABDC-C	345 teaching professionals employed in higher education institutes	IDV –Workplace spirituality DV – Teachers' professional well-being Mediating variable – Positive psychological capital	Structural equational modelling and regression	"The results of the study show a strong positive relationship between teachers' professional well-being (TPW) and WPS. Additionally, it discovers that this relationship is partially mediated by positive psychological capital (PPC). The Study emphasises how crucial it is to help teachers develop a spiritual sense to better manage work-related stress and enhance their professional well-being. This study addresses a gap in the existing literature by exploring the interconnectedness of WS, TPW, and PPC, specifically within the context of higher education in India"

(*continued*)

Table 1. Continued

Author	Category	Sample	Variables	Technique	Conclusion
Pattanawit and Charoensukmongkol (2022)	ABDC-C	398 agents from 60 brokerage firms	IDV – Workplace spirituality DV – Customer-Oriented Organisational Citizenship Behaviour and job performance Mediating variable – Person job fit	CFA and structural equational modelling	"This study concludes that WPS is positively associated with person-job (P-J) fit among real estate agents. P-J fit partially mediates the relationship between WPS and customer-oriented OCB, and fully mediates the relationship between WPS and Job Performance. Moreover, WPS directly influences customer-oriented OCB but does have a significant direct effect on job performance"
Jena (2022)	ABDC-B	761 responses from various public and private sector organisations	IDV – Workplace spirituality DV – Employee performance; Mediating variable – Organisational citizenship behaviour Moderating variable – Emotional intelligence	CFA and regression	"This study concludes that WPS has a positive impact on employee performance (EP). the research demonstrates that organisational citizenship behaviour (OCB) strengthens the WS-EP relationship, while emotional intelligence (EI) significantly enhances EP and moderates the effect of WS on EP. The findings suggest that recognising and addressing employees' spiritual needs within the workplace can lead to improved performance. Additionally, the study emphasises the critical roles of OCB and EI in this dynamic, highlighting the importance of incorporating spiritual wellness into organisational practices to create a more productive and satisfying work environment"
Srivastava and Madan (2023)	ABDC-B	348 frontline hotel employees	IDV – Ethical leadership DV – Behavioural outcomes Mediating variable – Workplace spirituality	Structural equational modelling	"This study concludes that WPS mediates the relationship between ethical leadership and behavioural outcomes. The study finds that ethical leadership is positively related to organisational citizenship behaviour (OCB) and negatively related to unethical pro-organisational behaviour (UPOB). In the context of the North Indian hotel industry, WPS is shown to enhance OCB and reduce UPOB among employees"

(*continued*)

Table 1. Continued

Author	Category	Sample	Variables	Technique	Conclusion
Saxena and Prasad (2023)	ABDC-C	406 employees from banks	IDV – Workplace spirituality DV – Innovative work behaviours; Moderating variable – Role of sense of God	EFA, CFA, regression	"This paper examines the impact of WPS on innovative work behaviour (IWB) within India's banking sector, emphasising the moderating role of the sense of God (SOG). the study concludes that WPS, as a multi-dimensional construct, significantly influences IWB among bank employees. Specifically, seven dimensions of WPS are identified, and of these, meaningfulness, compassion, gratitude, and authenticity notably enhance IWB. The SOG moderates the relationship between WPS and IWB, indicating that a stronger spiritual connection or sense of God can amplify the positive effects of WPS on IWB."
Jnaneswar and Sulphey (2023a)	ABDC-C	333 Employees from various Organisations	IDV – Workplace spirituality DV – Employee mental well-being Mediating variable – Self-compassion and mindfulness	CFA and structural equational modelling	"This Study concludes that WPS, mindfulness, and self-compassion are crucial determinants of employee mental well-being. Utilising structural equation modelling (SEM) to analyse data from various Indian organisations, the study finds that mindfulness and self-compassion directly influence employees' mental well-being. Furthermore, WPS significantly enhances both mindfulness and self-compassion"
Jayakumar and Vinodkumar (2023)	ABDC-B	617 government male drivers in Kerala	IDV – Personal attributes (age, marital status, work experience, etc.) DV – Job performance Mediating variable – Workplace spirituality (meaningful work, sense of community, mindfulness and compassion)	EFA, CFA, regression	"The study examines the mediating role of WPS among Indian bus drivers and concludes that WS elements—fully mediate the relationship between personal attributes and job performance outcomes. The findings indicate that higher levels of WS are linked to improved job performance and fewer accidents. Additionally, the research shows that WPS levels significantly reduce when working hours surpass legal limits, emphasising the necessity of regulated work hours to maintain high WS and job performance"

(*continued*)

Table 1. Continued

Author	Category	Sample	Variables	Technique	Conclusion
Bantha and Nayak (2021)	ABDC-C	750 software professionals	IDV – Workplace spirituality DV – Employee creativity Mediating variable – Psychological capital	Structural equational modelling	"The study investigates the correlation between WPS and employee creativity, specifically examining the mediating effect of psychological empowerment among Indian software professionals. The results indicate a positive association between a spiritually enriched work environment and enhanced employee creativity. Moreover, psychological empowerment is identified as a partial mediator in this relationship, suggesting that employees who feel psychologically empowered are more likely to exhibit creativity in spiritually supportive workplaces"
Aftab *et al.* (2022)	ABDC-B	268 employees from the IT industry	IDV – Ethical leadership DV – Job satisfaction; Mediating variable – Workplace spirituality Moderating variable – Self-efficacy	Structural equational modelling	"The study explores the impact of ethical leadership (EL) on job satisfaction (JS) and WPS within Pakistan's IT industry. Findings indicate a positive correlation between EL and both WPS and JS. Furthermore, WPS is identified as a partial mediator in the EL-JS relationship, implying that EL fosters JS through the enhancement of WPS. Additionally, self-efficacy (SE) moderates this relationship, suggesting that individuals' confidence in their abilities amplifies the effect of EL on their job satisfaction. The research underscores the significance of ethical leadership in promoting meaningful work and improving job satisfaction in the IT sector"
Garg and Saini (2023)	ABDC-B	516 employees from different supply chain companies	IDV – Workplace spirituality DV – Innovative work behaviours; Moderating variable – Perceived working condition	Hierarchical regression	"The study examines the influence of (WPS) on innovative work behaviour (IWB) within Indian supply chain companies, emphasising the moderating role of perceived working conditions. The findings reveal that the four Indian spirituality constructs of WPS —significantly predict IWB among employees. Additionally, perceived working conditions significantly moderate the WPS-IWB relationship. The research contributes to the broaden-and-build theory and the theory of intangible resources by evidencing the positive impact of WPS on IWB"

(*continued*)

Table 1. Continued

Author	Category	Sample	Variables	Technique	Conclusion
Delle and Segaro (2023)	ABDC-C	351 postgraduation employees who were also working	IDV – Workplace spirituality DV – Entrepreneurial behaviour; Moderating variable – Psychological ownership	CFA and structural equational modelling	"The study investigates the relationship between WPS and entrepreneurial behaviour among employees, with an emphasis on the mediating role of psychological ownership (PO). results indicate a positive association between WPS and entrepreneurial behaviour, suggesting that a spiritually supportive work environment enhances employees' entrepreneurial activities. Psychological ownership is identified as a full mediator in this relationship, signifying that employees who feel a strong sense of ownership over their work are more likely to engage in entrepreneurial behaviours"

Source: Authors' own work

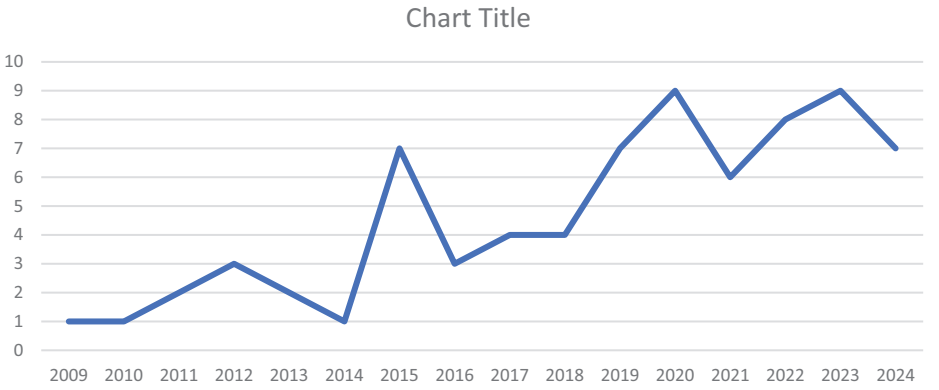

Source: Authors' own work

Figure 2. Recent publication trend

Table 2. Distribution of articles according to the ABDC ranking list

Category	No. of articles
A*	2
A	13
B	19
C	24

Source: Authors' own work

articles, two articles were published in the A* category journals; one of them indicates a positive correlation between WPS and pro-environment work behaviour, implying that a spiritually supportive work environment can boost pro-environmental actions (Rezapouraghdam *et al.*, 2018). Concurrently, the other article indicates how WPS mediates the relationship between ethical climate and organisational justice and their subsequent effects on workplace deviant behaviour and organisational citizenship behaviour among hotel employees in India (Haldorai *et al.*, 2020). Moreover, 13 articles were published in A category Journals, 19 were categorised in the B category journals and 24 were listed in C category journals. Of 58 articles, five articles are published in FT50 journals, offering significant insights into the domain of WPS. FT50 refers to the Financial Times Top 50, a list of 50 business journals considered as the most influential and prestigious in business and management. The findings of these articles are as follows:

Altaf and Awan (2011) found that work overload negatively impacts job satisfaction, highlighting the detrimental effects of excessive work demands on employee performance. Roof (2015) provided empirical evidence supporting a relationship between individual spirituality and overall employee engagement, including vigour and dedication, but found no significant relationship with the engagement dimension of absorption. Zhang (2020) discovered that certain aspects of WPS are positively linked to unethical pro-organisational behaviour, suggesting that employees might engage in unethical actions benefiting their organisation under the influence of WPS. Otaye-Ebede *et al.* (2020) revealed that WPS

positively influences the ethical atmosphere, which affects moral judgment and prosocial motivation. Additionally, Lata and Chaudhary (2021) posit that WPS, encompassing meaningful work, a sense of community and alignment with organisational values, tends to correlate inversely with experienced incivility. These findings contribute to the growing literature on WPS, underscoring the significance of integrating comprehensive strategies to enhance effectiveness and improve overall well-being.

3.3 Allocation of articles in various journals

The 58 articles were published across 34 different journals with their respective publishers. Among these, six articles were published in "*The Journal of Business Ethics*" (featured by Springer); the significant findings include that the WPS, encompassing meaningful work, a sense of community and alignment with organisational values, tends to correlate with experienced incivility inversely. Additionally, this study explores how dark triad personality traits (Machiavellianism, psychopathy and narcissism) moderate the aforementioned relationship (Lata and Chaudhary, 2021). Furthermore, five articles were published in the "*Journal of Management, Spirituality and Religion*" (featured by Ingenta); the empirical evidence demonstrates that there is a positive association between WPS and organisational effectiveness, accounting for a significant portion of the variance (Sharma and Singh, 2021). Moreover, four articles were published in the "*Journal of Organisational Change Management*" (featured by Emerald Insight); essential findings of a study from JOCM indicate that organisational commitment serves as a mediator, suggesting that higher levels of WPS contribute to greater life satisfaction through enhanced organisational commitment (Jeon and Choi, 2021). Of 58 articles, the majority, amounting to 34, were published by Emerald, representing approximately 58.6% of the total articles reviewed. Ingenta and Springer published six articles each, covering about 10.3% each. Sage contributed five articles, accounting for 8.6%, while Elsevier published four articles, making up 6.9% of the total. The remaining three articles, constituting about 5.2%, were published by various other publishers, including AOSIS, Inderscience and Adonis and Abbey. This distribution underscores Emerald's dominant role in publishing these articles, with different publishers contributing to a lesser extent.

3.4 Distribution of articles by country

Table 3 presents the distribution of research contributions across nations categorised into developing, developed and those contributing to multiple categories. Among the developing countries, India notably holds the highest number of contributions with 30, which underscores India's growing presence and impact within the global research landscape in the domain of WPS, reflecting its expanding academic capabilities. Followed by Pakistan with three empirical articles and a single contribution each from Malaysia, China, Thailand, Ethiopia, Iran, Bangladesh, Italy and South Africa. On the other hand, the developed nations category is dominated by the USA with seven contributions, followed by South Korea with two and a single contribution from Australia and Italy each. Moreover, a noteworthy collaboration between neighbouring countries is evident within the data set, exemplified by joint research contributions from nations sharing geographical borders. This comprehensive review also identifies a significant gap in studies focusing on WPS in the African and South American continents. This lack of research highlights the need for more attention and investigation into how WPS impacts employees and organisations in these regions. The collaboration between the USA and Mexico, as well as India and Pakistan, reflects a transcending of geopolitical boundaries in pursuit of common scientific objectives. This demonstrates the capacity of research to serve as a bridge for collaboration, facilitating the

Table 3. Distribution of articles by country

Countries	No. of articles
Developing nations	*(45)*
India	30
Malaysia	2
China	2
Pakistan	2
Turkey	2
Others (including one article each)	6
Developed nations	*(11)*
USA	7
South Korea	2
Others (including one article each)	2
Multiple nations	*(2)*
South Korea	1
India and Pakistan	1

Source: Author's own work

sharing of expertise, resources and insights across borders for the collective advancement of science and innovation.

3.5 Dimensions and scales used by various studies

WPS focuses on integrating an individual's personal beliefs, values and sense of purpose with their work life. Over the past two decades, authors have proposed multiple scales of WPS. It is essential to recognise that these scales, which further constitute the dimensions, are not mutually exclusive, and different researchers may use different terms or categorisations based on the needs of their studies. Table 4 shows how various authors have used and adapted different scales over time to explore the concept of WPS in their research. Most studies have used the scales developed by Ashmos (2000) and Milliman *et al.* (2003). Ashmos and Duchon proposed a conceptual framework in 2000, the WPS domain, that encompasses three dimensions: "inner life, sense of community, and meaningful Work". Milliman *et al.* (2003) recognised three significant facets of WPS: "meaningful work, sense of community, and alignment with organisational values". Petchsawang and Duchon (2012) proposed the dimensions "meaningful and purposeful work assignment, sense of community, and transcendence". Further, Indian Spiritual Constructs proposed from Hindu Mythology books: "swadharma, lokasangraha, sense of community, authenticity, karma capital, and kritagyata". Similarly, various authors have introduced many other dimensions, and different studies have used them according to their purpose, highlighting the evolving nature and diverse perspectives in the field of WPS.

3.6 Statistical techniques

Of the total studies analysed, the predominant techniques used for data analysis included multiple and hierarchical regression, structural equation modelling (SEM) and confirmatory factor analysis (CFA) (Table 1). Multiple regression was used to understand the relationship between several independent variables and a single dependent variable, enabling practitioners to determine the strength and nature of these relationships (Gordon, 1968).

Table 4. Dimensions used by various authors

Adopted/adapted scales	Authors
Ashmos (2000)	Pawar (2009); Nasurdin *et al.* (2013); Daniel (2015); Gatling *et al.* (2016); Afsar and Badir (2017); Pawar (2017); Bhaskar and Mishra (2019); Mahipalan and Sheena (2019); Bantha and Nayak (2021) and Bantha and Nayak (2020)
Milliman *et al.* (2003)	Afsar and Rehman (2015); Pawar (2016); Rezapouraghdam *et al.* (2018); Iqbal *et al.* (2019); Aboobaker *et al.* (2019); Zhang (2020); Aboobaker *et al.* (2020); Saadatyar *et al.* (2020); Lata and Chaudhary (2021); Hunsaker and Ding (2022); Jalan and Garg (2022) and Pattanawit and Charoensukmongkol (2022)
Petchsawang and Duchon (2012)	Petchsawang and Duchon (2012); Rahman *et al.* (2015); Petchsawang and McLean (2017); Sharma and Singh (2021) and Sapra *et al.* (2022)
Pandey (2017) and Pandey and Garg (2020)	Garg (2017); Garg (2020); Saxena *et al.* (2020); Sarkar *et al.* (2022) and Garg and Saini (2023)
Pradhan *et al.* (2017)	Jena and Pradhan (2018), Paul and Jena (2022) and Jena (2022)
Underwood (2011)	Sprung *et al.* (2012) and Roof (2015)
Valasek (2009)	Rahman *et al.* (2016) and Aftab *et al.* (2022)
Maginnis (2001)	Altaf and Awan (2011)
Kolodinsky *et al.* (2004)	Van der Walt and Swanepoel (2015)
Anthony (2009)	Rahman *et al.* (2015)
Miller (2001)	Belwalkar *et al.* (2018)
Rego *et al.* (2007)	Rahman *et al.* (2019)
Beehner and Blackwell (2016)	Soliman *et al.* (2021)
Daaleman (2004)	Jnaneswar and Sulphey (2023a)
Hinkin (1995)	Delle and Segaro (2023)
Multiple scales used	Milliman *et al.* (2018), Joelle and Coelho (2019), Otaye-Ebede *et al.* (2020), Haldorai *et al.* (2020), Shrestha and Jena (2021) and Mahipalan and Sheena (2019)

Source: Authors' own work

Hierarchical regression provided a more nuanced analysis by allowing for the assessment of the incremental value of additional predictors (Petrocelli, 2003). SEM, primarily conducted through Partial Least Squares (PLS) or ANOVA software, enabled the analysis of intricate relationships between observed and latent variables, offering a comprehensive framework for testing theoretical models. Notably, SEM was applied in 26 studies. CFA was instrumental in validating the measurement models, ensuring the validity and reliability of the studied constructs (Brown and Moore, 2012). Specifically, CFA was used in 23 studies. Regression techniques encompassing multiple, linear and hierarchical regression were used in 30 articles.

Furthermore, exploratory factor analysis (EFA) was used in five studies, specifically in the context of developing new measurement scales. This technique is mainly used to validate the scale. It is noteworthy that none of the studies relied solely on descriptive statistics. These advanced analytical techniques collectively contributed to robust and rigorous data analysis, enhancing the credibility and depth of the research findings.

4. Research gaps

Various research gaps emerged from the existing empirical articles (Table 5). One prominent gap is the lack of longitudinal studies, which limits the ability to understand changes over time and establish causality. There is also a need for more qualitative studies to provide deeper insights into complex phenomena that quantitative methods may overlook. Additionally, collecting data from multiple sources can enhance the reliability and comprehensiveness of findings. Cross-cultural studies are necessary for the generalisability of the results. Moreover, using probability sampling methods can improve the representativeness of the samples while investigating more mediators and moderators, which can provide a nuanced understanding of the underlying mechanism. Addressing these gaps can significantly advance empirical research by providing more robust, relevant and applicable findings.

4.1 Lack of longitudinal studies

Most of the reviewed articles primarily use a cross-sectional approach (Jayakumar and Vinodkumar, 2023; Garg and Saini, 2023; Jena, 2022; Haldorai *et al.*, 2020), which involves

Table 5. Research gaps from existing articles

Serial no.	Research gaps	Supporting studies
1.	Lack of longitudinal studies	Jayakumar and Vinodkumar (2023); Garg and Saini (2023); Jena (2022); Haldorai *et al.* (2020); Sharma and Singh (2021); Bantha and Nayak (2021); Aftab *et al.* (2022); Delle and Segaro (2023); Lata and Chaudhary (2021) and Zhang (2020)
2.	Need for qualitative studies	Sarkar *et al.* (2022); Soliman *et al.* (2021); Jeon and Choi (2021); Garg (2020); Garg (2017); Rahman *et al.* (2016) and Roof (2015)
3.	Data should be collected from multiple sources	Garg and Saini (2023); Delle and Segaro (2023); Jnaneswar and Sulphey (2023); Lata and Chaudhary (2021); Garg (2020) and Garg (2017)
4.	Need for more cross-cultural studies	Aftab *et al.* (2022); Garg and Saini (2023); Jnaneswar and Sulphey (2023); Srivastava and Madan (2023); Srivastava and Gupta (2022); Lata and Chaudhary (2021); Haldorai *et al.* (2020) and Afsar and Rehman (2015)
5.	The probability sampling method should be used	Jnaneswar and Sulphey (2023); Hunsaker and Ding (2022); Bayighomog and Araslı (2019) and Rahman *et al.* (2016)
6.	Investigation for more mediators and moderators	Pattanawit and Charoensukmongkol (2022); Srivastava and Gupta (2022); Soliman *et al.* (2021); Shrestha and Jena (2021); Jeon and Choi (2021); Garg (2020); Zhang (2020); Bhaskar and Mishra (2019); Aboobaker *et al.* (2019); Garg (2017); Afsar and Rehman (2015); Rahman *et al.* (2015) and Nasurdin *et al.* (2013)
7.	Larger sample size	Sarkar *et al.* (2022); Shrestha and Jena (2021); Jeon and Choi (2021); Saxena *et al.* (2020); Iqbal *et al.* (2019); Milliman *et al.* (2018); Rezapouraghdam *et al.* (2018); Garg (2017); Afsar and Badir (2017); Rahman *et al.* (2015); Daniel (2015) and Pawar (2009)
8.	Examine the influence of variables with negative connotations	Srivastava and Gupta (2022)

Source: Authors' own work

observing a particular phenomenon at a single point in time. This prevalent use of cross-sectional methods highlights a significant gap, that is, the absence of longitudinal studies. This type of study provides insights into the temporal dynamics of change, allowing researchers to establish cause-and-effect relationships and observe long-term trends and patterns.

4.2 Need for more qualitative studies

As per the observation, the reviewed articles predominantly rely on quantitative methods. This reliance on a quantitative approach highlights the significant gap, that is, the need for more qualitative studies (Sarkar *et al.*, 2022; Soliman *et al.*, 2021; Jeon and Choi, 2021; Garg, 2020; Garg, 2017), which include interviews, focus groups, case studies and participant observations, that can further contribute to a more holistic and nuanced perspective, ultimately leading to effective interventions.

4.3 Data should be collected from multiple sources

Many of the reviewed studies rely on a single-source data collection method (Garg and Saini, 2023; Delle and Segaro, 2023; Jnaneswar and Sulphey, 2023; Lata and Chaudhary, 2021; Garg, 2020), which can introduce biases and limit the comprehensiveness of the findings. Moreover, collecting data from multiple sources will significantly enhance the study's reliability, validity and comprehensiveness.

4.4 Need for more cross-cultural studies

A significant number of the reviewed studies are limited to single cultural contexts, which restricts the generalisability and applicability of the findings across different cultural settings. This highlights the critical gap, which is the need for more cross-cultural studies (Aftab *et al.*, 2022; Garg and Saini, 2023; Jnaneswar and Sulphey, 2023; Srivastava and Madan, 2023; Srivastava and Gupta, 2022; Aftab *et al.*, 2022), essential for identifying universal patterns and cultural-specific differences and providing a nuanced understanding of human phenomena.

4.5 The probability sampling method should be used

Most of the reviewed studies relied on non-probability, limiting the representativeness of the findings. Thus, some of the studies have highlighted the need for the probability sampling method (Jnaneswar and Sulphey, 2023; Hunsaker and Ding, 2022; Bayighomog and Arasli, 2019; Rahman *et al.*, 2016), ensuring the representativeness of the population and enhancing the validity of the research findings.

4.6 Investigation for more mediators and moderators

Previous studies also recommend expanding the investigation to include more mediators and moderators to gain a more comprehensive and nuanced understanding of complex relationships between WPS and various outcomes (Pattanawit and Charoensukmongkol, 2022; Srivastava and Gupta, 2022; Soliman *et al.*, 2021; Shrestha and Jena, 2021; Jeon and Choi, 2021; Garg, 2020; Zhang, 2020).

4.7 Large sample size

Many studies use small sample sizes, limiting the reliability and robustness of their findings. Thus, a larger sample size enhances the statistical power of the study, making it more likely to detect authentic relationships among variables and allow for more accurate and reliable

conclusions (Sarkar *et al.*, 2022; Shrestha and Jena, 2021; Jeon and Choi, 2021; Saxena *et al.*, 2020; Iqbal *et al.*, 2019; Milliman *et al.*, 2018).

4.8 Examine the influence of variables with negative connotations

Many of the reviewed studies tend to overlook or inadequately examine the influence of variables with negative connotations (Srivastava and Gupta, 2022). Understanding these negative connotations is essential for gaining a complete and accurate picture of the factors affecting individuals and communities.

5. Discussion and conclusion

This research examined the existing WPS literature spanning the past 15 years (2009–2024). The present study extensively evaluates the publication trends and provides a comprehensive synthesis of empirical studies within this domain, analysed using the PRISMA framework. This approach ensures a structured and rigorous review process, enhancing the reliability and validity of the findings. The categorisation of studies according to the ABDC quality list of journals underscored the quality and academic rigour of the literature reviewed. The review highlights the pervasive positive impact of WPS on various individual and organisational outcomes. A significant number of studies point to enhancing innovative work behaviour (IWB) (Afsar and Rehman, 2015; Afsar and Badir, 2017; Bantha and Nayak, 2020; Hunsaker and Ding, 2022; Saxena and Prasad, 2023; Garg and Saini, 2023), performance (Petchsawang and Duchon, 2012; Garg, 2017c; Jayakumar and Vinodkumar, 2023; Jena, 2022), organisational commitment (Gatling *et al.*, 2016; Garg, 2017c; Soliman *et al.*, 2021; Jeon and Choi, 2021) and organisational citizenship behaviour (Nasurdin *et al.*, 2013; Haldorai *et al.*, 2020; Jena, 2022). These findings suggest that organisations fostering spirituality in the workplace can expect a more innovative, committed and productive workforce. Further, the common statistical techniques include multiple and hierarchical regression (Pawar, 2009; Petchsawang and Duchon, 2012; Saxena *et al.*, 2020; Sarkar *et al.*, 2022), structural equation modelling (Rahman *et al.*, 2015; Afsar and Badir, 2017; Bantha and Nayak, 2021; Aftab *et al.*, 2022) and factor analysis (Nasurdin *et al.*, 2013; Bayighomog and Araslı, 2019; Zhang, 2020; Jayakumar and Vinodkumar, 2023). The frequent use of these advanced analytical methods indicated a robust approach to explore the complex relationships inherent in WPS research. SEM, in particular, allows for the examination of multiple interrelated variables simultaneously, providing a deeper understanding of the constructs involved. Also, it reveals diverse geographic origins, with significant contributions from developing and developed nations. Among developing nations, countries such as India (30), Malaysia (2), China (2) and others including Pakistan (3), and many others have significantly contributed. Conversely, developed nations like the USA (seven), South Korea (two) and Australia (one) are also prominent, with Italy contributing across both developed and developing categories. This distribution highlights the growing global interest in WPS and indicates a need for more research from neglected regions. High-impact journals such as those from Emerald (34), Ingenta (6), Sage (5), Springer (6) and Elsevier (4) have published most of these studies, highlighting the global interest and academic recognition of WPS research. Moreover, the next section of the study depicts the future avenues for research through the TCCM framework. Furthermore, a burgeoning body of research has delved into various themes of WPS, indicating various antecedents, outcomes, mediators and moderators, highlighting its multifaceted impact on organisational dynamics.

6. Future avenues for research (TCCM framework)

This section suggests future research directions based on the identified gaps in the existing literature. The authors in this study have adopted the TCCM framework (Paul and Rosado-

Serrano, 2019) to structure the literature review more systematically. This framework categorises the studies based on four key components: Theory, Context, Characteristics and Methodology. By using this approach, the theoretical and empirical breadth of the research field is mapped, providing a clearer understanding of the constructs, their interrelationships and the research methods used. This structured organisation enhances the coherence and thoroughness of the review, aligning it with current scholarly practices and contributing to a more comprehensive evaluation of the literature.

6.1 Theory

The review reveals that self-determination theory (SDT), broaden-and-build theory, social exchange theory (SET) and social cognitive theory (SCT) were the most frequently used theories in the domain of WPS.

6.1.1 (A) Self-determination theory. SDT is a macro theory of human motivation developed by Edward L. Deci and Richard M. Ryan. It evolved from research on intrinsic and extrinsic motivation (Deci *et al*., 2017). SDT highlights three crucial psychological needs; competence, autonomy and relatedness – that, when satisfied, promote autonomous motivation, high-quality performance and wellness (Deci and Ryan, 2008). SDT's core principles closely align with the key aspects of WPS, which include inner life, meaningful work and a sense of community (Gatling *et al*., 2016). SDT's emphasis on psychological needs satisfaction can enhance WPS by fostering an environment where employees feel competent, autonomous in their decisions and connected to their peers. It is indicated that when these needs are met, employees exhibit higher levels of job satisfaction, engagement and overall well-being (Gagné and Deci, 2005). Workplace environments that nurture spiritual values and practices can significantly contribute to employees' intrinsic motivation and fulfilment (Fry, 2003; Jurkiewicz and Giacalone, 2004). In the domain of WPS, this theory has been explored by various researchers (Gatling *et al*., 2016; Bantha and Nayak, 2021; Bantha and Nayak, 2020; Saxena and Prasad, 2023; Delle *et al*., 2023). In the context of work attitudes within the hospitality environment, SDT provides a robust framework for understanding the impact of WPS, and by meeting these needs, WPS significantly improves work attitudes, resulting in more engaged, motivated and satisfied employees in the hospitality industry (Gatling *et al*., 2016).

Moreover, SDT argues that an individual is self-motivated and self-determined, which initially enhances the spiritual environment, and when these psychological needs are met, it facilitates IWB through psychological empowerment (Bantha and Nayak, 2021). Furthermore, high levels of WPS enhance feelings of freedom and autonomy, boosting employee engagement and entrepreneurial behaviour. SDT also highlights the mediation role of psychological ownership, explaining how it bridges the relationship between WPS and entrepreneurial behaviour by emphasising the importance of intrinsic motivation and self-determination in this process (Delle and Segaro, 2023).

6.1.2 (B) Broaden-and-build theory. Broaden-and-build theory, introduced by Barbara Fredrickson in 1998, posits that fulfilling employees' spiritual needs, such as a sense of purpose, inner peace and connectedness, is crucial in expanding their perspectives, and employees are more likely to experience positive emotions. In the domain of WPS, this theory has been explored by various researchers (Jnaneswar and Sulphey, 2023; Garg and Saini, 2023; Sarkar *et al*., 2022; Aboobaker *et al*., 2019; Paul and Jena, 2022). The broaden-and-build theory demonstrates the relationship between self-compassion and mental well-being. Positive emotions expand cognition and thinking flexibility, fostering creative problem-solving. Self-compassionate individuals experience fewer negative and more positive emotions, enhancing their mental well-being. Empirical evidence supports that self-compassion's positive emotional

state improves mental health, illustrating the connection between self-compassion, positive emotions and overall mental well-being (Jnaneswar and Sulphey, 2023b). Moreover, the broaden-and-build theory explains the relationship between WPS and IWB by highlighting how positive emotions expand employees' awareness and encourage novel thoughts and actions. This broadened perspective provides social and psychological resources, fostering creativity and innovation. Satisfying employees' spiritual needs further enhances this outlook, promoting IWB. Thus, WPS, through positive emotions and fulfilling spiritual needs, cultivates an environment that boosts innovation and creativity (Garg and Saini, 2023). Furthermore, the broaden-and-build theory also elucidates the relationship between WPS and psychological capital (PsyCap) by highlighting how positive emotions broaden individuals' thought-action repertoires, building enduring resources. Empirical evidence from the study supports this theory in a non-Western context, particularly among Indian employees, demonstrating the significant impact of WPS on PsyCap (Sarkar *et al.*, 2022).

6.1.3 (C) Social exchange theory. SET suggests that individuals engage in social interactions by weighing the potential rewards and costs to maximise benefits and minimise losses. It proposes that the relationship involves mutually dependent, tangible and intangible exchanges between the employee and the employer (Cropanzano and Mitchell, 2005). SET indicates that employees who value the benefits provided by their organisation, such as salary, fringe benefits or even working conditions, are likely to exhibit more positive work attitudes in response (Haar, 2006). Employees might feel obligated to give back to their organisation when they receive personal advantages from the organisation's resources or attributes, whether financial or non-financial (Yee, 2010). Researchers and practitioners (Haldorai *et al.*, 2020; Zhang, 2020; Aboobaker *et al.*, 2020; Shrestha and Jena, 2021) have explored various relationships using this theoretical concept. In a study, SET explains the relationships between organisational justice, ethical climate, WPS and workplace deviant behaviour by suggesting that employees' perceptions of fairness and ethical treatment influence their behaviours. When employees perceive unfair treatment, they develop hostile attitudes, leading to deviant behaviours (Haldorai *et al.*, 2020).

Moreover, another article highlights that this theory suggests the positive interactions and resources provided by the organisation, such as meaningful work, a sense of community and alignment with organisational values, lead to positive employee outcomes. Employees who perceive that their organisation supports their spiritual needs experience higher well-being as a form of reciprocation. Additionally, employees are likelier to stay with an organisation that fulfils their spiritual and emotional needs (Aboobaker *et al.*, 2020).

6.1.4 (D) Social cognitive theory. The SCT, developed by Albert Bandura, explains how personal factors, behaviours and environmental influences interact to shape workplace behaviours (Bandura, 1986). Employees learn by observing colleagues, particularly those deemed successful, which influences their behaviours (Bandura *et al.*, 2001). Self-efficacy, or the belief in one's ability to succeed, is crucial in enhancing motivation and job performance (Bandura and Wessels, 1997). The concept of reciprocal determinism highlights the dynamic interaction between an individual's attitudes, behaviours and work environment. It can be applied to the concept of WPS to understand how spiritual values and practices are learned, adopted and reinforced in an organisational context. Otaye-Ebede, in his study, applies SCT to explore the relationships between WPS, ethical climate and various outcomes. SCT suggests that such internal and external cues shape behaviours like prosocial motivation and moral judgment. Ethical climate, which reflects perceptions of organisational practices with ethical content, is also influenced by WPS. This ethical climate impacts individual outcomes, including prosocial motivation and organisational outcomes, such as

branch-level helping behaviour and service performance, demonstrating how WPS fosters a positive ethical environment and enhances overall performance.

Therefore, many theories could be identified from this comprehensive review. However, only a few have been frequently cited (as discussed above). Consequently, there is a need to integrate some other theories to expand and enrich the theoretical framework of WPS. We recommend using theories like spiritual leadership theory, theory of charismatic leadership, servant leadership theories, spillover theory, person-organisation fit theory, identity theory and psychological well-being theory, which future researchers may now use to explore and understand the dynamics of WPS within various contexts.

6.2 Context

Regarding the context, the authors have analysed the researchers' exploration of various industries, and a comprehensive examination of these empirical articles reveals that 12 of 58 studies, that is, approximately 20% of the total articles have focused on the education sector (Paul and Jena, 2022; Sapra *et al.*, 2022; Soliman *et al.*, 2021; Aboobaker *et al.*, 2019), the significant findings reveals that "the relationship among teachers' professional well-being and WPS is partially mediated by positive psychological capital (PPC). The study emphasises how crucial it is to help teachers develop a spiritual sense to manage work-related stress better and enhance their professional well-being" (Paul and Jena, 2022). Moreover, another study suggests that elements such as compassion, mindfulness, meaningful work and transcendence contribute to improved academic organisational performance, which is evident in aspects like academic reputation, graduate employability, research output, internationalisation and community services. (Sapra *et al.*, 2022). Secondly, nine of the total studies have focused on the hospitality sector (Srivastava and Gupta, 2022; Haldorai *et al.*, 2020; Bayighomog and Araslı, 2019; Milliman *et al.*, 2018; Afsar and Badir, 2017; Gatling *et al.*, 2016). The results posit that the COVID-19 pandemic severely affected hospitality sector employees, causing significant uncertainties and economic challenges, that adversely affect their mental health and well-being. This study highlights the necessity of supportive organisational practices and systems to promote flexibility, adaptability and rapid response to disruptions (Srivastava and Gupta, 2022). Furthermore, seven studies, in total, concentrated on the Banking and Finance Sector (Srivastava and Madan, 2023; Lata and Chaudhary, 2021; Garg, 2020; Belwalkar *et al.*, 2018). As a multidimensional construct, results conclude that WPS significantly influences IWB among banking sector employees (Saxena and Prasad, 2023). Additionally, many studies do not define a specific sector; they have considered multiple organisations across various industries.

Though these studies provide significant insights, future researchers could also investigate spirituality in other sectors like IT, retail, manufacturing and FMCG industries, which are comparatively less explored and are known for their fast-paced, high-pressure and dynamic environments and researching spirituality in these areas can provide valuable insights into how spiritual practices and beliefs may help employees cope with stress, improve job satisfaction, foster a positive work culture, enhance resilience and contribute to better overall performance.

6.3 Characteristics

Given the focus of the articles under review, the authors categorised them into four primary themes. Most articles address theme 1, which pertains to the Outcomes of WPS (n = 36), followed by theme 3, which elaborates on the mediators and moderators explored concerning WPS.

Theme 1: Outcomes of WPS: Of 58 studies reviewed, 46 papers identified an association between WPS and various outcomes. These 46 papers highlighted 36 distinct outcomes influenced by WPS (Table 6). In the contemporary workplace, fostering a sense of purpose and connection among employees can lead to remarkable individual and organisational outcomes. At the individual level, employees exhibit a more positive work attitude (Pawar, 2009), heightened performance (Petchsawang and Duchon, 2012) and deeper job

Table 6. Outcomes of workplace spirituality

Outcomes of workplace spirituality	Articles
Work attitude	Pawar (2009)
Work performance	Petchsawang and Duchon (2012)
Organisational citizenship behaviour	Nasurdin *et al.* (2013) and Haldorai *et al.* (2020)
Stress	Daniel (2015) and Mahipalan and Sheena (2019)
Job involvement	van der Walt and Swanepoel (2015)
Knowledge sharing behaviour	Rahman *et al.* (2015) and Rahman *et al.* (2016)
Employee engagement	Roof (2015)
Innovative work behaviour	Afsar and Rehman (2015); Afsar and Badir (2017); Bantha and Nayak (2020); Hunsaker and Ding (2022), Saxena and Prasad (2023) and Garg and Saini (2023)
Intention to quit	Gatling *et al.* (2016)
Employee wellbeing	Pawar (2016) and Srivastava and Gupta (2022)
Moral judgement	Otaye-Ebede *et al.* (2020)
Employee commitment	Jena and Pradhan (2018) and Milliman *et al.* (2018)
Pro-environmental behaviour	Rezapouraghdam *et al.* (2018)
Intention to stay	Milliman *et al.* (2018)
Individual performance	Joelle and Coelho (2019)
Customer-oriented boundary-spanning behaviour	Bayighomog and Araslı (2019)
Executive sales performance	Rahman *et al.* (2019)
Psychological well-being	Mahipalan and Sheena (2019)
Unethical pro-environmental behaviour	Zhang (2020)
Employee loyalty	Aboobaker *et al.* (2020)
Competitive advantage	Saadatyar *et al.* (2020)
Organisational performance	Garg (2017) and Garg (2020)
Pro social motivation	Otaye-Ebede *et al.* (2020)
Life satisfaction	Jeon and Choi (2021)
Organisational effectiveness	Sharma and Singh (2021)
Organisational cynicism	Shrestha and Jena (2021)
Turnover intention	Shrestha and Jena (2021)
Workforce agility	Soliman *et al.* (2021)
Workplace incivility	Lata and Chaudhary (2021)
Psychological capital	Sarkar *et al.* (2022)
Professional well-being	Paul and Jena (2022)
Employee creativity	Bantha and Nayak (2021)
Employee performance	Jena (2022)
Professional well-being	Paul and Jena (2022)
Employee mental well-being	Jnaneswar and Sulphey (2023)
Entrepreneurial behaviour	Delle and Segaro (2023)

Source: Authors' own work

involvement (van der Walt and Swanepoel, 2015). This sense of engagement fuels creativity and enhances psychological well-being (Mahipalan and Sheena, 2019). Furthermore, with reduced stress (Daniel, 2015), turnover intention (Shrestha and Jena, 2021) and workplace incivility (Lata and Chaudhary, 2021), the work environment becomes healthier and more satisfying. Employees are more inclined to share knowledge and engage in organisational citizenship behaviour (Nasurdin *et al.*, 2013; Haldorai *et al.*, 2020), demonstrating a strong sense of community and responsibility. Their moral judgment and prosocial motivation underscore a commitment to the organisation's values, fostering employee loyalty (Aboobaker *et al.*, 2020) and a stronger intention to stay (Milliman *et al.*, 2018). As a result, employees experience more excellent professional (Paul and Jena, 2022) and mental well-being (Jnaneswar and Sulphey, 2023a). At the organisational level, these individual shifts translate into improved performance (Garg, 2017; Garg, 2020) and competitive advantage (Saadatyar *et al.*, 2020). The organisation benefits from increased productivity and efficiency, gaining a significant edge over competitors. Enhanced knowledge sharing (Rahman *et al.*, 2016) and innovation (Afsar and Badir, 2017) drive organisational success and adaptability, while reduced organisational cynicism (Shrestha and Jena, 2021) and turnover intention (Shrestha and Jena, 2021) reflect a positive cultural shift. Workforce agility (Soliman *et al.*, 2021) improves as employees adapt more changes, supported by a shared sense of purpose. Ultimately, WPS enhances individual fulfilment and propels the organisation towards sustained success and a thriving work environment.

Theme 2: Antecedents of WPS (Table 7): The second theme highlights that, in contrast to the numerous studies on the outcomes of WPS, only two studies have examined the antecedents of WPS (Jena and Pradhan, 2015; Pawar, 2017). Jena and Pradhan, in their study, establish a positive relationship between employees' psychological capital and WPS, indicating the significance of these constructs in organisational settings. Further, Pawar strongly supported the direct effect model, showing that organisational spirituality is more significantly associated with facets of WPS than individual spirituality.

Theme 3: Mediators and moderators of WPS: Variables that significantly impact the relationship between independent and dependent variables can function as mediators or moderators (Baron and Kenny, 1986; Farooq *et al.*, 2024). This theme examines various factors influencing the relationship between WPS and its outcomes (Tables 8 and 9). Mediators are variables that explain how or why WPS leads to specific outcomes, and through this review of empirical studies, it could be discovered that regular meditation practice partially mediates the relationship between WPS and work performance (Petchsawang and Duchon, 2012). Furthermore, organisational commitment fully mediates the negative relationship between WPS and intention to quit (Gatling *et al.*, 2016). On the other hand, moderators are the variables that affect the strength or direction of this relationship. This study explores new variables like dark triad personality traits (Machiavellianism, psychopathy and narcissism) and the role of the sense of God (Lata and Chaudhary, 2021; Saxena and Prasad, 2023) as moderators, which respectively moderate the relationships taking dependent variables as workplace incivility and IWB.

Table 7. Antecedents of workplace spirituality

Antecedents of workplace spirituality	Articles
Psychological capital	Jena and Pradhan (2015)
Organisational and employee individual spirituality	Pawar (2017)

Source: Authors' own work

Table 8. Mediators of workplace spirituality

Mediators of workplace spirituality	Articles
Meditation practice	Petchsawang and Duchon (2012)
Perceived risk	Rahman *et al.* (2016)
Person-organisation fit	Afsar and Rehman (2015); Afsar and Badir (2017) and Pattanawit and Charoensukmongkol (2022)
Organisational commitment	Gatling *et al.* (2016); Garg (2017) and Saadatyar *et al.* (2020)
Employee engagement	Garg (2017)
Work motivation	Garg (2017)
Organisational citizenship behaviour	Jena and Pradhan (2018); Jena (2022) and Garg (2020)
Job satisfaction	Belwalkar *et al.* (2018) and Zhang (2020)
Connectedness to nature	Rezapouraghdam *et al.* (2018)
Worker's attitude	Joelle and Coelho (2019)
Wellbeing at work	Aboobaker *et al.* (2019)
Spiritual well being	Bayighomog and Araslı (2019)
Employee commitment	Rahman *et al.* (2019)
Subjective stress	Mahipalan and Sheena (2019)
Psychological empowerment	Bantha and Nayak (2020)
Ethical climate	Otaye-Ebede *et al.* (2020)
Workforce agility	Srivastava and Gupta (2022)
Organisational identification	Srivastava and Gupta (2022)
Psychological capital	Paul and Jena (2022)
Perceived working condition	Garg and Saini (2023)
Psychological ownership	Delle and Segaro (2023)

Source: Authors' own work

Table 9. Moderators of workplace spirituality

Moderators of workplace spirituality	Articles
Individual spirituality	Pawar (2009)
Gender	Nasurdin *et al.* (2013) and Daniel (2015)
Emotional intelligence	Jena and Pradhan (2015); Jena and Pradhan (2018) and Jena (2022)
Environmental awareness	Rezapouraghdam *et al.* (2018)
Career choice	Aboobaker *et al.* (2019)
Religious affiliation	Jeon and Choi (2021)
Demographic variables	Sharma and Singh (2021)
Psychological capital	Shrestha and Jena (2021)
Dark traits	Lata and Chaudhary (2021)
Role of sense of God	Saxena and Prasad (2023)

Source: Authors' own work

Theme 4: WPS as mediator and moderator: WPS as a mediator and moderator refers to the role of WPS in influencing the relationships between other variables within an organisational context. Six papers examined and revealed WPS as a mediator among various variables (Sprung *et al.*, 2012; Petchsawang and McLean, 2017; Iqbal *et al.*, 2019; Haldorai *et al.*, 2020; Aftab *et al.*, 2022; Jayakumar and Vinodkumar, 2023). An article also analysed WPS as a moderator (Altaf and Awan, 2011), which depicts how WPS influences the strength or direction of the relationship between work overload and job satisfaction where

work overload negatively impacts job satisfaction, highlighting the detrimental effects of excessive work demands on employees' performance. Furthermore, a paper examined WPS as a mediator and a moderator (Bhaskar and Mishra, 2019). This article explores the influence of WPS on career satisfaction and turnover intentions, with perceived organisational support serving as a foundational element. The findings indicate that WPS enhances career satisfaction and decreases turnover intentions by strengthening the connection between employees and the organisation through perceived organisational support.

Therefore, a comprehensive analysis of 58 articles revealed that 46 studies specifically examined the outcomes of WPS, highlighting that researchers' significant interest and focus have been placed on understanding how spiritual elements within the workplace impact different aspects of organisational life. However, very few researchers have investigated WPS's antecedents, indicating a significant gap in the research. Consequently, future researchers should focus on identifying and elaborating on various factors that lead to the development and enhancement of WPS (Jena and Pradhan, 2015; Pawar, 2017; Srivastava and Madan, 2023). Therefore, it is also recommended that future researchers investigate WPS, as an outcome to obtain a deeper comprehension of elements that provide a more detailed view of its role within organisational settings.

6.4 Methodology

Of the total articles reviewed, a significant majority of 56 studies, or approximately 96.6%, were cross-sectional studies. The results indicate a positive association between WPS and entrepreneurial behaviour, suggesting that a spiritually supportive work environment enhances employees' entrepreneurial activities (Delle and Segaro, 2023). Another cross-sectional study demonstrates that WPS significantly predicts employees' psychological capital (PsyCap), which encompasses hope, optimism, efficacy and resilience, grounded in the broaden-and-build theory (Sarkar *et al.*, 2022). On the other hand, only two articles, representing about 3.4%, were longitudinal. Longitudinal study involves collecting data from the same sample at multiple points over an extended period. It provides insights into the temporal dynamics of change, allowing researchers to establish cause-and-effect relationships and observe long-term trends and patterns. This shift would provide more comprehensive insights into the evolution of phenomena over time, thereby enriching the overall understanding and robustness of the research field. The findings posit that WPS positively impacts employees' IWB and perception of P-O fit. Perceived P-O fit partially mediates the relationship between WPS and IWB (Afsar and Rehman, 2015). The overwhelming predominance of cross-sectional studies suggests a prevalent focus on capturing data and observing changes over an extended period. For future researchers, it would be beneficial to increase the number of longitudinal studies (Garg and Saini, 2023; Jnaneswar and Sulphey, 2023; Saxena and Prasad, 2023; Srivastava and Madan, 2023; Lata and Chaudhary, 2021; Bantha and Nayak, 2021; Bhaskar and Mishra, 2019). Secondly, relying on a single source for data collection introduces common method variance, which can distort results and compromise the validity of findings (Lindell and Whitney, 2001). To address this limitation, future researchers could adopt a double-sourcing approach by gathering data from multiple sources (Garg and Saini, 2023; Delle and Segaro, 2023; Jnaneswar and Sulphey, 2023; Lata and Chaudhary, 2021; Garg, 2020; Garg, 2017) which will further lead to reduced biases, enhanced validity and more generalised results. Also, in many studies, the sample size is small, with little or no explanation regarding the sample's adequacy. A small sample can limit the study's statistical power, reducing the ability to detect significant effects and undermining the generalisability of the findings. To address these

issues, future researchers should ensure adequate sample sizes (Sarkar *et al.*, 2022; Shrestha and Jena, 2021; Jeon and Choi, 2021; Saxena *et al.*, 2020; Iqbal *et al.*, 2019; Milliman *et al.*, 2018; Rezapouraghdam *et al.*, 2018; Garg, 2017; Afsar and Badir, 2017; Rahman *et al.*, 2015; Daniel, 2015; Pawar, 2009), by conducting power analyses to determine the minimum number of participants needed to detect expected effects with sufficient power.

Therefore, future researchers should consider using a longitudinal research design to better capture the temporal dynamics of WPS and its effects. Additionally, data should be collected from multiple sources to mitigate common method bias, and the sample size should be significantly large to enhance the generalisability and robustness of the findings.

7. Limitations

The current review was limited to the Scopus database only, which may have excluded some research on WPS from other relevant databases. Another constraint is the exclusion of unpublished articles, books, conference proceedings, dissertations, thesis and non-empirical articles. Additionally, the review was restricted to analyse English-language papers because of other language constraints. As a result, only publications that met the specified inclusion criteria were considered. While this review aimed to select high-quality studies, but because of its rigorous inclusion criteria, some relevant research articles might have remained unnoticed, especially from flagship journals such as the *Journal of Management, Spirituality and Religion* (*JMSR*). Despite these limitations, the studies reviewed are varied, comprehensive and effectively offering a broad representation of published articles.

References

Aboobaker, N. (2022), "Workplace spirituality and employee wellbeing in the hospitality sector: examining the influence of fear of covid-19", *Psychological Studies*, Vol. 67 No. 3, pp. 362-371, doi: 10.1007/s12646-022-00666-7.

Aboobaker, N., Edward, M. and Ka, Z. (2019), "Workplace spirituality, employee wellbeing and intention to stay: a multi-group analysis of teachers' career choice", *International Journal of Educational Management*, Vol. 33 No. 1, pp. 28-44, doi: 10.1108/IJEM-02-2018-0049.

Aboobaker, N., Edward, M. and Ka, Z. (2020), "Workplace spirituality and employee loyalty: an empirical investigation among millennials in India", *Journal of Asia Business Studies*, Vol. 14 No. 2, pp. 211-225, doi: 10.1108/JABS-03-2018-0089.

Afsar, B. and Badir, Y. (2017), "Workplace spirituality, perceived organisational support and innovative work behaviour: the mediating effects of person-organisation fit", *Journal of Workplace Learning*, Vol. 29 No. 2, pp. 95-109, doi: 10.1108/JWL-11-2015-0086.

Afsar, B. and Rehman, M. (2015), "The relationship between workplace spirituality and innovative work behaviour: the mediating role of perceived person-organisation fit", *Journal of Management, Spirituality and Religion*, Vol. 12 No. 4, pp. 329-353, doi: 10.1080/14766086.2015.1060515.

Aftab, J., Sarwar, H., Kiran, A., Qureshi, M.I., Ishaq, M.I., Ambreen, S. and Kayani, A.J. (2022), "Ethical leadership, workplace spirituality, and job satisfaction: moderating role of self-efficacy", *International Journal of Emerging Markets*, Vol. 18 No. 12, doi: 10.1108/IJOEM-07-2021-1121.

Ahmadi, S., Nami, Y. and Barvarz, R. (2014), "The relationship between spirituality in the workplace and organizational citizenship behavior", *Procedia- Social and Behavioral Sciences*, Vol. 114, pp. 262-264, doi: 10.1016/j.sbspro.2013.12.695.

Altaf, A. and Awan, M.A. (2011), "Moderating affect of workplace spirituality on the relationship of job overload and job satisfaction", *Journal of Business Ethics*, Vol. 104 No. 1, pp. 93-99, doi: 10.1007/s10551-011-0891-0.

Anthony, J. V., (2009), "Examining the relationships of spirituality and religiosity to individual productivity in the United States", The dissertation Submitted to Northcentral University, Graduate Faculty of the School of Business and Managementin Partial Fulfillment of the Requirements for the Degree of Doctor of Philosophy, Prescott Valley, Arizona, April 2009.

Ashmos, D. and Duchon, D. (2000), "Ashmos duchton, 2000", *Journal of Management Inquiry*, Vol. 9 No. 2, pp. 134-145, doi: 10.1177/105649260092008.

Bandura, A. (1986), Social foundations of thought and action, *Englewood Cliffs, NJ*, Vol. 2, pp. 23-28.

Bandura, A. and Wessels, S. (1997), "Self-efficacy", *Cambridge: Cambridge University Press*, pp. 4-6.

Bandura, A., Caprara, G.V., Barbaranelli, C., Pastorelli, C. and Regalia, C. (2001), "Sociocognitive self-regulatory mechanisms governing transgressivebehavior", *Journal of Personality and Social Psychology*, Vol. 80 No. 1, pp. 125-135, doi: 10.1037//0022-3514.80.1.125.

Bantha, T. and Nayak, U. (2020), "The relation of workplace spirituality with employees' innovative work behaviour: the mediating role of psychological empowerment", *Journal of Indian Business Research*, Vol. 13 No. 2, pp. 223-235, doi: 10.1108/JIBR-03-2020-0067.

Bantha, T. and Nayak, U. (2021), "The relation of workplace spirituality with employee creativity among Indian software professionals: mediating role of psychological empowerment", *South Asian Journal of Business Studies*, Vol. 12 No. 3, doi: 10.1108/SAJBS-08-2020-0270.

Barik, S. and Nayak, T. (2023), "Workplace spirituality: exploring past, present and future through bibliometric analysis", *Benchmarking: An International Journal*, Vol. 31 No. 9, doi: 10.1108/BIJ-04-2022-0251.

Bayighomog, S.W. and Araslı, H. (2019), "Workplace spirituality–customer engagement nexus: the mediated role of spiritual leadership on customer-oriented boundary–spanning behaviours", *Service Industries Journal*, Vol. 39 Nos 7/8, pp. 637-661, doi: 10.1080/02642069.2019.1570153.

Beehner, C.G. and Blackwell, M.J. (2016), "The impact of workplace spirituality on food service worker turnover intention", *Journal of Management, Spirituality & Religion*, Vol. 13 No. 4, pp. 304-323, doi: 10.1080/14766086.2016.1172251.

Belwalkar, S., Vohra, V. and Pandey, A. (2018), "The relationship between workplace spirituality, job satisfaction and organisational citizenship behaviours – an empirical study", *Social Responsibility Journal*, Vol. 14 No. 2, pp. 410-430, doi: 10.1108/SRJ-05-2016-0096.

Bhaskar, A.U. and Mishra, B. (2019), "Putting workplace spirituality in context: examining its role in enhancing career satisfaction and reducing turnover intentions with perceived organisational support as an antecedent", *Personnel Review*, Vol. 48 No. 7, pp. 1848-1865, doi: 10.1108/PR-08-2018-0305.

Biswakarma, G. (2018), "Impact of workplace spirituality on employee productivity in nepalese hospitality organizations", *Journal of Tourism and Hospitality Education*, Vol. 8, pp. 62-76.

Brown, T.A. and Moore, M.T. (2012), "Confirmatory factor analysis", *Handbook of Structural Equation Modeling*, pp. 361-379.

Cropanzano, R. and Mitchell, M.S. (2005), "Social exchange theory: an interdisciplinary review", *Journal of Management*, Vol. 31 No. 6, pp. 874-900, doi: 10.1177/0149206305279602.

Daaleman, T.P. (2004), "Religion, spirituality, and the practice of medicine", *The Journal of the American Board of Family Practice*, Vol. 17 No. 5, pp. 370-376.

Daniel, J.L. (2015), "Workplace spirituality and stress: evidence from Mexico and US", *Management Research Review*, Vol. 38 No. 1, pp. 29-43, doi: 10.1108/MRR-07-2013-0169.

Deci, E.L., Olafsen, A.H. and Ryan, R.M. (2017), "Self-determination theory in work organizations: the state of a science", *Annual Review of Organizational Psychology and Organizational Behavior*, Vol. 4 No. 1, pp. 19-43.

Deci, E.L. and Ryan, R.M. (2008), "Self-determination theory: a macrotheory of human motivation, development, and health", *Canadian Psychology/Psychologie Canadienne*, Vol. 49 No. 3, pp. 182-185, doi: 10.1037/a0012801.

Delle, M.T. and Segaro, E.L. (2023), "Workplace spirituality and entrepreneurial behaviour among employees in organisations: the role of psychological ownership", *Journal of Enterprising Communities*, doi: 10.1108/JEC-10-2022-0161.

Delle, M.T., Segaro, E.L. and Naldi, L. (2023), "Time will tell: psychological ownership, temporal focus and attitudes toward women as managers in Ethiopia", *International Journal of Organizational Analysis*, Vol. 31 No. 6, pp. 2665-2688, doi: 10.1108/IJOA-10-2021-3017.

Donthu, N., Kumar, S., Mukherjee, D., Pandey, N. and Lim, W.M. (2021), "How to conduct a bibliometric analysis: an overview and guidelines", *Journal of Business Research*, Vol. 133, pp. 285-296, doi: 10.1016/j.jbusres.2021.04.070.

Farooq, F., Mohammad, S.S., Nazir, N.A. and Shah, P.A. (2024), "Happiness at work: a systematic literature review", *International Journal of Organizational Analysis*, Vol. 32 No. 10, doi: 10.1108/IJOA-08-2023-3902.

Fry, L.W. (2003), "Toward a theory of spiritual leadership", *The Leadership Quarterly*, Vol. 14 No. 6, pp. 693-727, doi: 10.1016/j.leaqua.2003.09.001.

Gagné, M. and Deci, E.L. (2005), "Self-determination theory and work motivation", *Journal of Organizational Behavior*, Vol. 26 No. 4, pp. 331-362, doi: 10.1002/job.322.

Garg, N. (2017), "Workplace spirituality and organisational performance in Indian context: mediating effect of organisational commitment, work motivation and employee engagement", *South Asian Journal of Human Resources Management*, Vol. 4 No. 2, pp. 191-211, doi: 10.1177/2322093717736134.

Garg, N. (2020), "Promoting organisational performance in Indian insurance industry: the roles of workplace spirituality and organisational citizenship behaviour", *Global Business Review*, Vol. 21 No. 3, pp. 834-849, doi: 10.1177/0972150918778983.

Garg, N. and Saini, D. (2023), "Workplace spirituality to cultivate innovative work behaviour: the moderating role of perceived working conditions", *International Journal of Sociology and Social Policy*, Vol. 44 Nos 1/2, doi: 10.1108/IJSSP-03-2023-0050.

Gatling, A., Kim, J.S. and Milliman, J. (2016), "The relationship between workplace spirituality and hospitality supervisors' work attitudes: a self-determination theory perspective", *International Journal of Contemporary Hospitality Management*, Vol. 28 No. 3, pp. 471-489, doi: 10.1108/IJCHM-08-2014-0404.

Gordon, R.A. (1968), "Issues in multiple regression", *American Journal of Sociology*, Vol. 73 No. 5, pp. 592-616.

Haar, J.M. (2006), "Challenge and hindrance stressors in new Zealand: exploring social exchange theory outcomes", *The International Journal of Human Resource Management*, Vol. 17 No. 11, pp. 1942-1950, doi: 10.1080/09585190601000147.

Haldorai, K., Kim, W.G., Chang, H.S. and Li, J.J. (2020), "Workplace spirituality as a mediator between ethical climate and workplace deviant behaviour", *International Journal of Hospitality Management*, Vol. 86, doi: 10.1016/j.ijhm.2019.102372.

Hinkin, T.R. (1995), "A review of scale development practices in the study of organizations", *Journal of Management*, Vol. 21 No. 5, pp. 967-988.

Hunsaker, W.D. and Ding, W. (2022), "Workplace spirituality and innovative work behaviour: the role of employee flourishing and workplace satisfaction", *Employee Relations*, Vol. 44 No. 6, doi: 10.1108/ER-01-2021-0032.

Iqbal, Q., Ahmad, N.H. and Ahmad, B. (2019), "Enhancing sustainable performance through job characteristics via workplace spirituality: a study on SMEs", *Journal of Science and Technology Policy Management*, Vol. 12 No. 3, pp. 463-490, doi: 10.1108/JSTPM-02-2018-0022.

Jalan, S. and Garg, N. (2022), "Exploring linkages between workplace spirituality and occupational stress among indian police personnel", *South Asian Journal of Human Resources Management*, Vol. 9 No. 1, pp. 53-78, doi: 10.1177/23220937211059626.

Jayakumar, V. and Vinodkumar, M.N. (2023), "The mediating role of workplace spirituality between personal attributes and job performances of Indian bus drivers", *Journal of Organizational Change Management*, Vol. 36 No. 3, pp. 452-471, doi: 10.1108/JOCM-04-2022-0119.

Jena, L.K. (2022), "Does workplace spirituality lead to raising employee performance? The role of citizenship behaviour and emotional intelligence", *International Journal of Organizational Analysis*, Vol. 30 No. 6, pp. 1309-1334, doi: 10.1108/IJOA-06-2020-2279.

Jena, L.K. and Pradhan, R.K. (2015), "Psychological capital and workplace spirituality: role of emotional intelligence", *International Journal of Work Organisation and Emotion*, Vol. 7 No. 1, pp. 1-15, doi: 10.1504/IJWOE.2015.073119.

Jena, L.K. and Pradhan, S. (2018), "Workplace spirituality and employee commitment", *Journal of Enterprise Information Management*, Vol. 31 No. 3, pp. 380-404, doi: 10.1108/JEIM-10-2017-0144.

Jeon, K.S. and Choi, B.K. (2021), "Workplace spirituality, organisational commitment and life satisfaction: the moderating role of religious affiliation", *Journal of Organizational Change Management*, Vol. 34 No. 5, pp. 1125-1143, doi: 10.1108/JOCM-01-2021-0012.

Jnaneswar, K. and Sulphey, M.M. (2023), "Workplace spirituality, self-compassion and mindfulness as antecedents of employee mental wellbeing", *South Asian Journal of Business Studies*, Vol. 12 No. 2, pp. 269-292, doi: 10.1108/SAJBS-07-2020-0258.

Joelle, M. and Coelho, A.M. (2017), "The impact of spirituality at work on workers' attitudes and individual performance", *The International Journal of Human Resource Management*, Vol. 30 No. 7, pp. 1111-1135.

Jurkiewicz, C.L. and Giacalone, R.A. (2004), "A values framework for measuring the impact of workplace spirituality on organisational performance", *Journal of Business Ethics*, Vol. 49 No. 2, pp. 129-142, doi: 10.1023/B: BUSI.0000015843.22195.b9.

Khirfan, L., Peck, M.L. and Mohtat, N. (2020), "Digging for the truth: a combined method to analyse the literature on stream daylighting", *Sustainable Cities and Society*, Vol. 59, p. 1, doi: 10.1016/j.scs.2020.102225.

Kolodinsky, R.W., Giacalone, R.A. and Jurkiewicz, C.L. (2004), "Exploring personal, organizational and interactive workplace spirituality outcomes", *Paper Presented at the Academy of Management Annual Meeting, New Orleans, LA*, pp. 1-28.

Krishnakumar, S. and Neck, C.P. (2002), "The 'what', 'why' and 'how' of spirituality in the workplace", *Journal of Managerial Psychology*, Vol. 17 No. 3, pp. 153-164, doi: 10.1108/02683940210423060.

Lac, M., Sukunesan, S., Cain, A., Vasa, R. and Mouzakis, K. (2008), "25 Th Australasian conference on information systems".

Lata, M. and Chaudhary, R. (2021), "Workplace spirituality and experienced incivility at work: modeling dark triad as a moderator", *Journal of Business Ethics*, Vol. 174 No. 3, pp. 645-667, doi: 10.1007/s10551-020-04617-y.

Lindell, M.K. and Whitney, D.J. (2001), "Accounting for common method variance in cross-sectional research designs", *Journal of Applied Psychology*, Vol. 86 No. 1, pp. 114-121, doi: 10.1037/0021-9010.86.1.114.

Maginnis, J.B. (2001), "Spiritual well-being of workers: exploring a neglected performance antecedent", *An Application of Technology Management Project*, University of Phoenix.

Mahipalan, M. and Sheena, S. (2019), "Workplace spirituality, psychological well-being and mediating role of subjective stress: a case of secondary school teachers in India", *International Journal of Ethics and Systems*, Vol. 35 No. 4, pp. 725-739, doi: 10.1108/IJOES-10-2018-0144.

Marques, J., Dhiman, S. and King, R. (2007), *Spirituality in the Workplace: What It is, Why It Matters, How to Make It Work for You*, Personhood Press.

Mhatre, G.S. and Mehta, K.N. (2022), "A review of workplace spirituality: identifying present development and future research agenda", *Management Research Review*, Vol. 46 No. 9, doi: 10.1108/MRR-11-2021-0800.

Miller, J.J.P. (2001), "Learning from a spiritual perspective", in *Expanding the Boundaries of Transformative Learning: Essays on Theory and Praxis*, Palgrave Macmillan, New York, pp. 95-102.

Milliman, J., Czaplewski, A.J. and Ferguson, J. (2003), "Workplace spirituality and employee work attitudes: an exploratory empirical assessment", *Journal of Organizational Change Management*, Vol. 16 No. 4, pp. 426-447, doi: 10.1108/09534810310484172.

Milliman, J., Gatling, A. and Kim, J.S. (2018), "The effect of workplace spirituality on hospitality employee engagement, intention to stay, and service delivery", *Journal of Hospitality and Tourism Management*, Vol. 35, pp. 56-65, doi: 10.1016/j.jhtm.2018.03.002.

Mitroff, I.I. and Denton, E.A. (1999), "A study of spirituality in the workplace", *MIT Sloan Management Review*.

Mohammed, S.M. and Elashram, R.E. (2022), "The impact of spiritual leadership on workplace spirituality in the light the covid-19 pandemic in the governmental health sector", *Leadership and Organization Development Journal*, Vol. 43 No. 4, pp. 623-637, doi: 10.1108/LODJ-11-2021-0515.

Mohan, M.G. and Murugan, M. (2024), "Bibliometric analysis and research directions concerning visualisation of workplace spirituality", *Multidisciplinary Reviews*, Vol. 7 No. 3, doi: 10.31893/multirev.2024050.

Munjal, N. and Sachdeva, G. (2024), "Examining the evolution of workplace spirituality: a bibliometric approach", *Journal of Human Values*, p. 9716858241287479, doi: 10.1177/09716858241287479.

Nasurdin, A.M., Nejati, M. and Mei, Y.K. (2013), "Workplace spirituality and organisational citizenship behaviour: exploring gender as a moderator", *South African Journal of Business Management*, Vol. 44 No. 1, pp. 61-74, doi: 10.4102/sajbm.v44i1.148.

Otaye-Ebede, L., Shaffakat, S. and Foster, S. (2020), "A multilevel model examining the relationships between workplace spirituality, ethical climate and outcomes: a social cognitive theory perspective", *Journal of Business Ethics*, Vol. 166 No. 3, pp. 611-626, doi: 10.1007/s10551-019-04133-8.

Page, M.J., McKenzie, J.E., Bossuyt, P.M., Boutron, I., Hoffmann, T.C., Mulrow, C.D., … and Moher, D. (2021), "The PRISMA 2020 statement: an updated guideline for reporting systematic reviews", *BMJ*, doi: 10.1136/bmj.n71.

Pandey, A., Gupta, R.K. and Arora, A.P. (2009), "Spiritual climate of business organizations and its impact on customers' experience", *Journal of Business Ethics*, Vol. 88 No. 2, pp. 313-332, doi: 10.1007/s10551-008-9965-z.

Pattanawit, P. and Charoensukmongkol, P. (2022), "Benefits of workplace spirituality on real estate agents' work outcomes: the mediating role of person-job fit", *Management Research Review*, Vol. 45 No. 11, pp. 1393-1411, doi: 10.1108/MRR-06-2021-0482.

Paul, M. and Jena, L.K. (2022), "Workplace spirituality, teachers' professional well-being and mediating role of positive psychological capital: an empirical validation in the Indian context", *International Journal of Ethics and Systems*, Vol. 38 No. 4, pp. 633-660, doi: 10.1108/IJOES-08-2021-0163.

Pawar, B.S. (2009), "Individual spirituality, workplace spirituality and work attitudes: an empirical test of direct and interaction effects", *Leadership and Organisation Development Journal*, Vol. 30 No. 8, pp. 759-777, doi: 10.1108/01437730911003911.

Pawar, B.S. (2016), "Workplace spirituality and employee well-being: an empirical examination", *Employee Relations*, Vol. 38 No. 6, pp. 975-994, doi: 10.1108/ER-11-2015-0215.

Pawar, B.S. (2017), "The relationship of individual spirituality and organizational spirituality with meaning and community at work", *Leadership & Organization Development Journal*, Vol. 38 No. 7, pp. 986-1003, doi: 10.1108/LODJ-01-2016-0014.

Petchsawang, P. and Duchon, D. (2012), "Workplace spirituality, meditation, and work performance", *Journal of Management, Spirituality and Religion*, Vol. 9 No. 2, pp. 189-208, doi: 10.1080/14766086.2012.688623.

Petchsawang, P. and McLean, G.N. (2017), "Workplace spirituality, mindfulness meditation, and work engagement", *Journal of Management, Spirituality and Religion*, Vol. 14 No. 3, pp. 216-244, doi: 10.1080/14766086.2017.1291360.

Petrocelli, J.V. (2003), "Hierarchical multiple regression in counseling research: common problems and possible remedies", *Measurement and Evaluation in Counseling and Development*, Vol. 36 No. 1, pp. 9-22.

Prabhu, M. and Srivastava, A.K. (2023), "Leadership and supply chain management: a systematic literature review", *Journal of Modelling in Management*, Vol. 18 No. 2, doi: 10.1108/JM2-03-2021-0079.

Pranckutė, R. (2021), "Web of science (WoS) and Scopus: the titans of bibliographic information in today's academic world", *Publications*, Vol. 9 No. 1, doi: 10.3390/publications9010012.

Raamkhumar, M.H. and Swamy, T. (2023), "Workplace spirituality: the game changer of 21st century workplace", *Multidisciplinary Reviews*, Vol. 6 No. 4, pp. 2023042-2023042.

Rahman, M.S., Mat Daud, N., Hassan, H. and Osmangani, A.M. (2016), "Effects of workplace spirituality and trust mediated by perceived risk towards knowledge sharing behaviour", *VINE Journal of Information and Knowledge Management Systems*, Vol. 46 No. 4, pp. 450-468, doi: 10.1108/VJIKMS-06-2015-0033.

Rahman, M.S., Osmangani, A.M., Daud, N.M., Chowdhury, A.H. and Hassan, H. (2015), "Trust and work place spirituality on knowledge sharing behaviour: perspective from non-academic staff of higher learning institutions", *The Learning Organization*, Vol. 22 No. 6, pp. 317-332, doi: 10.1108/TLO-05-2015-0032.

Rahman, M.S., Zaman, M.H., Hossain, M.A., Mannan, M. and Hassan, H. (2019), "Mediating effect of employee's commitment on workplace spirituality and executive'ssales performance", *Journal of Islamic Marketing*, Vol. 10 No. 4, pp. 1057-1073, doi: 10.1108/JIMA-02-2018-0024.

Rajni, Swami, A., Khan, M., Hemrajani, P. and Dhiman, R. (2022), "Mapping the intellectual structure of workplace spirituality through bibliometric analysis", *FIIB Business Review*, doi: 10.1177/23197145221099090.

Rego, A., Pina, E., Cunha, M. and Souto, S. (2007), "Workplace spirituality, commitment, and self-reported individual performance: an empirical study", *Management Research: Journal of the Iberoamerican Academy of Management*, Vol. 5 No. 3, pp. 163-183.

Rezapouraghdam, H., Alipour, H. and Darvishmotevali, M. (2018), "Employee workplace spirituality and pro-environmental behaviour in the hotel industry", *Journal of Sustainable Tourism*, Vol. 26 No. 5, pp. 740-758, doi: 10.1080/09669582.2017.1409229.

Roof, R.A. (2015), "The association of individual spirituality on employee engagement: the spirit at work", *Journal of Business Ethics*, Vol. 130 No. 3, pp. 585-599, doi: 10.1007/s10551-014-2246-0.

Saadatyar, F.S., Poursalimi, M., Al-Tabbaa, O. and Iannotta, M. (2020), "Workplace spirituality as a source for competitive advantage: an empirical study", *International Journal of Organizational Analysis*, Vol. 28 No. 3, pp. 655-676, doi: 10.1108/IJOA-10-2019-1915.

Sapra, J., Khosla, K. and Dungrakoti, G. (2022), "Spirituality at workplace and its impact on academic performance: an empirical study among private higher education faculties of Delhi NCR", *Journal of Organizational Change Management*, Vol. 35 No. 1, pp. 18-37, doi: 10.1108/JOCM-08-2020-0248.

Sarkar, A., Garg, N. and Palo, S. (2022), "Workplace spirituality and psychological capital (PsyCap) of the employees: a cross-sectional study", *Global Business Review*, doi: 10.1177/09721509221111445.

Saxena, A. and Prasad, A. (2023), "Exploring the influence of dimensions of workplace spirituality on innovative work behaviour: role of sense of god", *International Journal of Ethics and Systems*, Vol. 39 No. 2, pp. 183-212, doi: 10.1108/IJOES-12-2021-0220.

Saxena, A., Garg, N., Punia, B.K. and Prasad, A. (2020), "Exploring role of Indian workplace spirituality in stress management: a study of oil and gas industry", *Journal of Organizational Change Management*, Vol. 33 No. 5, pp. 779-803, doi: 10.1108/JOCM-11-2019-0327.

Sharma, N. and Singh, R.K. (2021), "Workplace spirituality and organisational effectiveness: exploration of relationship and moderators", *Journal of Management, Spirituality and Religion*, Vol. 18 No. 1, pp. 15-34, doi: 10.1080/14766086.2020.1829011.

Shrestha, A.K. and Jena, L.K. (2021), "Interactive effects of workplace spirituality and psychological capital on employee negativity", *Management and Labour Studies*, Vol. 46 No. 1, pp. 59-77, doi: 10.1177/0258042X20962994.

Singh, R.K. and Singh, S. (2022), "Spirituality in the workplace: a systematic review", *Management Decision*, Vol. 60 No. 5, pp. 1296-1325, doi: 10.1108/MD-11-2020-1466.

Smith, J.A. and Rayment, J.J. (2007), "The global SMP fitness framework", *Management Decision*, Vol. 45 No. 2, pp. 217-234, doi: 10.1108/00251740710727250.

Soliman, M., Di Virgilio, F., Figueiredo, R. and Sousa, M.J. (2021), "The impact of workplace spirituality on lecturers' attitudes in tourism and hospitality higher education institutions", *Tourism Management Perspectives*, Vol. 38, doi: 10.1016/j.tmp.2021.100826.

Sprung, J.M., Sliter, M.T. and Jex, S.M. (2012), "Spirituality as a moderator of the relationship between workplace aggression and employee outcomes", *Personality and Individual Differences*, Vol. 53 No. 7, pp. 930-934, doi: 10.1016/j.paid.2012.06.011.

Srivastava, S. and Gupta, P. (2022), "Workplace spirituality as panacea for waning well-being during the pandemic crisis: a SDT perspective", *Journal of Hospitality and Tourism Management*, Vol. 50, pp. 375-388, doi: 10.1016/j.jhtm.2021.11.014.

Srivastava, S. and Madan, P. (2023), "Linking ethical leadership and behavioural outcomes through workplace spirituality: a study on Indian hotel industry", *Social Responsibility Journal*, Vol. 19 No. 3, pp. 504-524, doi: 10.1108/SRJ-08-2021-0345.

Underwood, L.G. (2011), "The daily spiritual experience scale: overview and results", *Religions*, Vol. 2 No. 1, pp. 29-50.

Valasek Jr, A.J (2009), *Examining the Relationships of Spirituality and Religiosity to Individual Productivity in the United States*, Northcentral University.

van der Walt, F. and Swanepoel, H. (2015), "The relationship between workplace spirituality and job involvement: a South African study", *African Journal of Business and Economic Research*, Vol. 10 No. 1, pp. 95-116, doi: 10.10520/EJC171069.

Vasconcelos, A.F. (2022), "Organisational spirituality: a literature review and research agenda", *International Journal of Organisational Analysis*, Emerald Group Holdings, doi: 10.1108/IJOA-04-2022-3230.

Yee, L.-L. (2010), "Encouraging extra-role behavior in a channel context: the role of economic-, social-, and justice-based sharedness mechanisms", *Industrial Marketing Management*, Vol. 39 No. 2, pp. 195-201.

Zhang, S. (2020), "Workplace spirituality and unethical pro-organisational behaviour: the mediating effect of job satisfaction", *Journal of Business Ethics*, Vol. 161 No. 3, pp. 687-705, doi: 10.1007/s10551-018-3966-3.

Corresponding author
Naval Garg can be contacted at: naval.garg@dtu.ac.in

For instructions on how to order reprints of this article, please visit our website:
www.emeraldgrouppublishing.com/licensing/reprints.htm
Or contact us for further details: **permissions@emeraldinsight.com**

Nature Environment and Pollution Technology
An International Quarterly Scientific Journal

p-ISSN: 0972-6268
(Print copies up to 2016)
e-ISSN: 2395-3454

Vol. 24 | No. 1 | Article ID B4191 | 2025

Review Research Paper

https://doi.org/10.46488/NEPT.2025.v24i01.B4191

Open Access Journal

The Utility of Synthetic Biology in the Treatment of Industrial Wastewaters

Monica Joshi and Jai Gopal Sharma†
Department of Biotechnology, Delhi Technological University, Delhi-110042, India
†Corresponding author: Jai Gopal Sharma; sharmajaigopal@dce.ac.in

Abbreviation: Nat. Env. & Poll. Technol.
Website: www.neptjournal.com

Received: 23-04-2024
Revised: 24-05-2024
Accepted: 10-06-2024

Key Words:

Water conservation
Groundwater depletion
Aquifers
Industrial wastewater
Sustainable development

Citation for the Paper:

Joshi, M. and Sharma, J.G., 2025. The utility of synthetic biology in the treatment of industrial wastewater. *Nature Environment and Pollution Technology*, 24(1), B4191. https://doi.org/10.46488/NEPT.2025.v24i01.B4191.

Note: From year 2025, the journal uses Article ID instead of page numbers in citation of the published articles.

Copyright: © 2025 by the authors
Licensee: Technoscience Publications
This article is an open access article distributed under the terms and conditions of the Creative Commons Attribution (CC BY) license (https://creativecommons.org/licenses/by/4.0/).

ABSTRACT

Effective treatment of industrial wastewater effluents before discharging them to the soil and water bodies has always been one of the paramount environmental concerns. The pollutants in untreated wastewater effluents have hazardous implications for human health and the ecosystem. Conventional physical and chemical processes of industrial wastewater treatment have many complications and they often fall short in the treatment of new and diverse varieties of pollutants. Several microbial strains in nature have shown their remediation property, but they possess limited efficiency in breaking down pollutants into non-toxic components. Synthetic biology is a perfect amalgam of two fields – biological science and engineering, and it has transformed our ways of understanding the functioning of complex biological systems. Researchers have reported that some engineered microbes can achieve remediation efficiency of up to 100% in specific pollutants such as heavy metals and hydrocarbons. For example, microbes like *Pseudomonas veronii* have been shown to reduce cadmium concentrations by up to 100%, and *Pseudomonas putida* has been shown to reduce phenol concentrations by 92%. Synthetic biology-based biosensors are also being developed for pollution monitoring and control of industrial wastewater. In this review, we discuss these advancements of synthetically engineered microorganisms in the treatment of industrial wastewater.

INTRODUCTION

Industries are the major driving force behind the growth and development of a country, but they also produce toxic effluents that are the leading cause of water and soil pollution (Saxena 2020). Effluents released from the manufacturing processes of petrochemical, textile, electroplating, pharmaceutical, and food industries constitute industrial wastewater (Nasr 2022). This effluent consists of a variety of organic and inorganic matter, dyes, and metal ions (chromium, cadmium, lead, copper, zinc, and nickel) (Nasr 2022). These contaminants cause the degradation of the natural biota of water, air, and soil by changing their physiochemical properties (Saravanan et al. 2023). Furthermore, untreated wastewater discharged into the river can cause several severe diseases like chronic dermatoses and skin cancer, lung infection, and eye irritation (Kesari et al. 2021). Hence, the wastewater discharged from these industries is the prominent cause of toxicity to human health and the environment (Singh et al. 2023). It has been reported that around 3-10 billion gallons of untreated wastewater is released into the environment, and an estimated 80 percent of wastewater is reused globally without any intervention of physical or chemical treatment (Saddique et al. 2023). The rise in the global population will also lead to the global rise of the concertation of discharged industrial wastewater. Untreated industrial wastewater pollutants contain harmful pollutants which, if entered into the water supply, would lead to deterioration of water quality (Jones et al. 2021) or, if entered into the food chain, would lead to severe allergies and other diseases. Hence, effective wastewater treatment processes are needed.

For the treatment of industrial wastewater, many chemical and physical techniques have been in application, like physical sedimentation, physical filtration, ozonation, chemical precipitation, adsorption, and ion exchange (Saravanan et al. 2021). However, they have many limitations, like high costs needed for optimum working and maintenance, low resource recovery from industrial wastewater, and utilization of high energy for the treatment processes to happen (Dutta et al. 2021, Yaashikaa et al. 2022). Biological methods that are utilized for the treatment of industrial wastewater are microbial remediation, aerobic treatment, anaerobic treatment, oxidation ponds, and activated sludge. These methodologies also have many limitations, such as the sludge disposable problem in the case of activated sludge methodology, the need for very large space to be successfully operational in the case of oxidation ponds, high capital cost, and odor nuisance in anaerobic treatment, cost expensive in aerobic treatment (Saravanan et al. 2021). Hence, we need a microbial wastewater system over a traditional wastewater system that would be green, sustainable (Sharma et al. 2023), and highly efficient. It has been long established that the intrinsic degradation property of microbes can be utilized in the degradation of environmental pollutants. This intrinsic property is applied in the bioremediation process where microbes, via their metabolic processes, degrade and convert the pollutants into less toxic substances. Despite this impressive ability of microbes, bioremediation has many limitations, like incomplete breakdown of organic pollutants, low efficiency of microbial remediation, and remediation process only effective for biodegradable contaminants (Jabbar et al. 2022). These limitations of microbial bioremediation processes can be improved by synthetic biology.

Using synthetic biology, we can modify metabolic pathways or/and create new metabolic pathways in new microbial cells that would be able to degrade not only biodegradable pollutants but also synthetic pollutants. The main synthetic pollutants occurring in the environment are pesticides, pharmaceuticals, polycyclic aromatic hydrocarbons (PAHs), phthalates, chlorinated phenol compounds, absorbable organic halides, and inorganic metal ions (Bhatt et al. 2021). Synthetic biology is a field that utilizes the principles of both biology and engineering field to create novel biological systems having modified or new functions. This is achieved by using molecular and computational tools that create the new genetic architecture of a microbe (Jiménez-Díaz et al. 2022). This new genetic architecture consists of a series of new components (gene promoters, transcription factors, enzymes, etc.) that together build new metabolic pathways with end products that could be studied and even re-build (Rylott & Bruce 2020). Hence, in the field of environmental remediation, advances in synthetic biology led to the construction of microorganisms that can scavenge and biodegrade a variety of toxic wastes like aromatic compounds, pesticides, microplastics, greenhouse gases, etc (Thai et al. 2023).

The integration of the field of synthetic biology and remediation (synthetic bioremediation) using microbes for the treatment of industrial wastewater has shown immense advancements in recent times. Many engineered microbial strains have shown their capability to degrade contaminants. Recently, Tomijiro Hara et al., in their experiment, engineered an *E. coli* strain capable of degrading a variant of Polychlorinated biphenyls (organohalide pollutants) in a natural landscape at a level that is sufficient for clean-up of PCB pollution (Hara et al. 2021). Sharma et al. reported that the genetically engineered *Pseudomonas* strain shows an enhanced ability of metal remediation in aquatic and terrestrial ecosystems near the industrial sites of pulp and paper (Sharma et al. 2021). Enzyme engineering within the microorganisms not only speeds up the remediation process but also solves the key limitations of chemical treatments and minimizes over-reliance on them. Additionally, microorganisms, with the help of synthetic biology tools, are created that can function as biological sensors (Aminian-Dehkordi et al. 2023). These biological sensors help in the real-time monitoring of pollutant levels and, hence, are an effective technique for monitoring water quality (Aminian-Dehkordi et al. 2023).

Synthetic biology can also be used to study the microbiota of industrial wastewater treatment plants using tools such as metagenomics, metatranscriptomics, metaproteomics, and metabolomics. These tools can help identify the key genes, enzymes, pathways, and microorganisms involved in pollutant degradation and reveal the relationship between running parameters and the keystone microorganisms (Jiang et al. 2022). In the world of bioremediation, synthetic biology could be used to design biosensors, enzymes with unique activities towards persistent organic xenobiotics, organisms that are resistant to challenging environmental conditions, robust biopolymers, artificial storage organelles for toxic metals, and much more (Rylott & Bruce 2020). Here in this review, we present synthetic biology approaches applied in the treatment of industrial wastewater. We begin with describing important components used in bioengineering including chassis, genetic circuits, transcription factors, and gene editing tools. Then, we move to specific synthetic biology ways for the treatment of industrial wastewater, where we describe strategies like metabolic pathway modifications, enzyme engineering, and synthetic microbial consortia for pollutant degradation. Furthermore, we discuss

biosensors for the detection of pollutants in industrial wastewater. Finally, the role of biofilms in enhancing the efficiency of biodegradation is discussed.

SYNTHETIC BIOLOGY COMPONENTS USED IN BIOENGINEERING

Sometimes, the term engineering biology is used as an alternative to the term synthetic biology (Zhang et al. 2023). The ultimate goal of synthetic biology is to bioengineer microorganisms having specific functionalities (Kim et al. 2016a). This goal is achieved by following the iterative "design-build-test-learn" (DBTL) cycle (Kitano et al. 2023, Garner 2021). In the first stage, the design of a biological system with pre-defined functionalities is created, followed by the build step, where simulations of that system will be conducted (Garner 2021). Assessment of differences between the performances of the simulation and the actual biological system in a real-life situation is conducted (test stage), and new insights are driven from it (learn stage) (Garner 2021).

Chassis

Despite the advancements in microbes-assisted remediation, bioremediation when using native microbes is not able to effectively degrade calcitrant pollutants because of genetic instability in microbes (Yaashikaa et al. 2022) and minor fluctuations in environmental like changes in pH, temperature, etc., could interfere with their ability needed for the degradation of the pollutants (Singh et al. 2021). Synthetic biology can overcome these challenges by building microbial systems as chassis for the bioremediation of these pollutants. In synthetic biology, chassis is referred to as a genetically modified model cell (McCarty & Ledesma-Amaro 2019). In a chassis, computational and molecular tools are used to engineer the genetic circuits and metabolic pathways to express desired results (Kim et al. 2016b). Most commonly, chassis organisms used in synthetic biology are the bacteria *Escherichia coli* and *Bacillus subtilis* and the yeast *Saccharomyces cerevisiae* (Tang et al. 2020, Kim et al. 2016b). These organisms have properties that make them a suitable chassis. These organisms are characterized by fast growth, supported by a wide variety of molecular tools. This led to an easy understanding of synthetic biology circuits and metabolic pathways (Kim et al. 2016b). Chassis can be constructed in two ways: top-down approach and bottom-up approach (Chi et al. 2019).

Genetic Circuits

To get a desired expression from the host cell, it is important to achieve precise control of gene expression, which is achieved by using synthetic genetic circuits. Synthetic genetic circuits are made up of networks of multiple interconnected gene switches that regulate cellular function by controlling the initiation and termination of a target gene expression (Xie & Fussenegger 2018). The synthetic biology field is primarily based on the construction of genetic circuits that could work either independently within cells or together by combining with a cell's biological network (MacDonald & Deans 2016).

Transcription Factor

Transcription is a crucial process as it is the fundamental step in the molecular processes that determine cell behavior and health (MacDonald & Deans 2016). Gene expression in a cell is initiated by the transcription process (Tietze & Lale 2021). The promoter situated upstream region of the gene's coding sequence determines the rate of transcription in a cell (Eisenhut et al. 2024). Therefore, scientists often alter the promoter region to regulate the strength of gene expression (Eisenhut et al. 2024). Hence, the most important regulatory point in a genetic circuit is transcription (Bradley et al. 2016). Scientists are aiming for better control of the genetic circuits by studying transcriptional networks in the cell.

Moreover, they are looking for endogenous trigger systems that turn on genetic circuits. With the help of these endogenous trigger systems, they can fine-tune the genetic circuits to find disease, bio-engineer new cell functions, and program cells with the ability to make independent decisions (MacDonald & Deans 2016). Another aspect of transcriptional regulation that makes it crucial for synthetic biology applications is that transcriptional regulation paves the way for a cell to regulate its enzymatic levels and stoichiometry, thereby preventing harmful metabolite accumulation, underutilized enzymes and the formation of unnecessary macromolecular compounds (Engstrom & Pfleger 2017).

Transcription in cells is regulated by transcription factors that activate or repress promoter activities (Tietze & Lale 2021). Synthetically engineered transcription factors are composed of a binding domain that identifies and then binds to a specific target DNA sequence and an effector domain that can activate or inhibit transcription (Eisenhut et al. 2024). Using in-silico technology, synthetic transcription factors can be created. Synthetic transcription factors for the regulation of gene expression are derived from proteins like zinc fingers (ZFs), transcription activator-like effectors (TALEs), and clustered regularly interspaced short palindromic repeats associated protein (CRISPR-Cas) (Chen et al. 2022). Synthetic zinc fingers are constructed by combining several zinc protein domains, where each zinc finger protein is typically made of 30 amino acids that are organized in a $\beta\beta\alpha$

motif. These engineered zinc fingers can identify 9-18 base pairs of specific DNA sequences, facilitating the targeting of desired sequences within the genome and thereby regulating gene expression (MacDonald & Deans 2016, Dai et al. 2018). On the other hand, TALEs are huge DNA-binding proteins having a size greater than 120 kilodaltons. These proteins have secretion signals on their N-termini end and nuclear localization signals on their C-termini end. The central helical domain region constitutes the bulk of these proteins as it is made of 15.5-19.5 near-perfect repeats of 34 amino acids and is responsible for the majority of DNA sequence-specific binding activity (Engstrom & Pfleger 2017). Recently, CRISPR-based tools have gained immense popularity for metabolism regulation, either independently or as part of a genetic circuit (Lv et al. 2022). CRISPRi (CRISPR-interference), a modification of CRISPR system, is used for sequence-specific transcriptional regulation. CRISPRi is made of two units – Cas9 endonuclease, which is catalytically inactive, and a single guide RNA (sgRNA), which precisely binds to targeted DNA at specific locations in the genome. Inactive Cas9, when targeted to promoter regions, acts as an RNA-guided repressor protein, which stops transcription by blocking polymerase movement through steric hindrance. With the help of this tool, multiple gene regulation can happen simultaneously by changing either the expression of Cas9 or the level of complementarity between the synthetic guide RNA (sgRNA) and the target sequence (Kent & Dixon 2020).

Gene Editing Tools

We can rationally engineer microbial cells at a global (genome) or local (gene) level by precisely modifying DNA sequences with the help of gene editing tools (Rafeeq et al. 2023). It has been shown in many types of research that genetically modified organisms are better at bioremediation processes than native microorganisms across various environments such as soil, groundwater, and activated sludge, exhibiting enhanced capabilities in degrading diverse organic pollutants as they show greater resistance to heavy metals, has greater substrate range, increase enzyme activity, and binding affinity (Haripriyan et al. 2022). The gene editing process involves the use of engineered enzymes (nucleases) that are able to create double-strand breaks in the DNA at desired locations. These double-strand breaks are then repaired by nonhomologous end joining (NHEJ) or homology-directed repair (HDR) (Barreiro & García-Estrada 2022). Key genetic tools employed for this are CRISPR-Cas, ZFN, and TALEN. Among these, CRISPR is the most effective and productive gene editing tool. CRISPR-Cas system has three main types – I, II, and III (Jaiswal et al. 2019). The Cas9 cleavage protein binds to the target sequence that is determined by the RNA guide molecules, which is the sequence after the protospacer adjacent motif (PAM) sequence in the genome. Following this, scientists can delete, correct, or insert genes into the break. Deletion occurs with the aid of non-homologous end-joining (NHEJ), and correction and insertion occur with the aid of homology-directed repair (HDR) (Gao et al. 2020). CRISPR-Cas system can modify the metabolic degradation pathway of specific pollutants in a microorganism by inserting or deleting the genes at multiple regions, thereby enhancing the bioremediation process (Ahmad et al. 2023). In a study, it was found that the biotransformation efficiency in *Bacillus licheniformis* reached a hundred percent after the deletion of the *yvmC* gene by employing the CRISPR-Cas9 technique (Rafeeq et al. 2023). When compared with the CRISPR-Cas system, both ZFN and TALEN cannot modify multiple genomic regions and can randomly bind to DNA sequences, leading to a much higher probability of off-target mutation (Jaiswal et al. 2019). The limitation of CRISPR-Cas is large Cas protein size leads to difficulty in cell delivery, the requirement of more whole genome data, and some chances of off-target mutation (Ranjbar & Malcata 2022). Hence, gene editing tools aim to achieve a better microbial bioremediation process by introducing diverse genes into the microbial cell to target specific pollutants (Hassan & Ganai 2023).

SYNTHETIC BIOLOGY WAYS FOR TREATMENT OF INDUSTRIAL WASTEWATERS

Microbial enzymes are responsible for the breakdown of toxic pollutants. There are four steps in the mechanism of microbial degradation of pollutants: 1. Microorganisms produce surfactants for the emulsion of pollutants; 2. The outer layer of the microorganism then adsorbs emulsified pollutants; 3. The adsorbed pollutant enters from the outer cell film layer to the cell layer via passive or active transport; 4. Upon entering the cell, the pollutant undergoes an enzymatic reaction with the corresponding enzymes to complete its degradation process (Yaashikaa et al. 2022).

In this new era of advancements in multi-omics techniques and genetic engineering, we can now select the most suitable microorganism host for the remediation process. Various tools based on genomic, proteomics, and metabolic data are employed to identify catabolic genes, novel pathways, or proteins involved in the biodegradation process so that we can engineer efficient metabolic degradation pathways for a target pollutant. Additional analysis of transcriptomic data can equip us with important information like cellular responses, post-exposure to toxic pollutants, and their influence on the metabolic state (Jiménez-Díaz et al.

2022). Synthetic biology synthesizes its components (gene promoters, transcription factors, enzymes, etc.) with the help of molecular tools and system biology, that together construct the metabolic degradation pathways with outputs that can be tested, reconstructed, and fine-tuned (Rylott & Bruce 2020).

CONSTRUCTION OF MODIFICATIONS IN METABOLIC DEGRADATION PATHWAYS

A series of general steps can be followed for the construction of modifications in metabolic degradation pathways: 1. Select your target pollutant and determine its physical and chemical properties; 2. Study the existing metabolic pathways in microorganisms that can degrade the target pollutants. Investigate the information of metabolites and enzymes that serve as the building blocks of the degradation pathway; 3. Select a suitable chassis based on multi-omics data analysis. Utilize molecular bio tools to introduce gene-encoding enzymes responsible for pollutant degradation into the chassis; 4. Optimize the synthetic metabolic degradation pathway. This can involve adjustments in the expression level of pathway genes and balancing metabolic flux. The pathway is shown in Fig. 1. For instance, *Pseudomonas sp. The B13* degradation pathway was modified, which led to increased efficiency in the degradation of methyl phenols and methyl benzoates (Ahmad et al. 2023). However, the process of screening the host for suitable enzymes that are capable of acting on the target pollutant is time-consuming. Additionally, conducting multiple biodegradation assays simultaneously in the laboratory poses significant challenges (Adetunji et al. 2023). Thanks to the advancements in computational techniques, in-silico bioremediation methods have emerged to cater to this problem. This in-silico approach relies on various scientific fields, including genomics, computational biology, proteomics, bioinformatics, molecular modeling, molecular dynamics simulation (MDS), and specialized algorithms for pathway prediction. Additionally, this approach also utilizes the dataset from several microbial databases. Furthermore, progress in sequencing technologies and bioinformatic algorithms has helped us in improving the bioremediation efficiency as these advancements led us to the further in-depth analysis of genomic sequences, which helped us in finding the innate metabolic enzymes and pathways for bioremediation (Tran et al. 2021).

The EAWAG Biocatalysis/Biodegradation Database, which contains the EAWAG-BBD pathway prediction system, can be used for the in-silico construction of metabolic degradation pathways. This EAWAG biodegradation database contains comprehensive information on microbial biochemical catalysis reactions that include biodegradation pathways for various chemical compounds and their microbial enzymes. By accessing this database, users can predict the degradation pathway of the target pollutant (Singh et al. 2020). Kelly et al. proposed a mechanism based on computational methods to find a suitable enzyme candidate for the degradation of toxic personal care products present in wastewater that are not effectively eliminated by conventional wastewater treatment. Computational analysis was done to study the biodegradability of the specific pollutant, and a pathway prediction system was utilized to find the metabolic pathways and enzymes that would react with the pollutant. They were successfully able to identify the enzyme with a degradation rate 40 times higher than previously reported rates (Aukema et al. 2017).

In addition to the design of the degradation pathway, the choice of chassis is also very important. For this, several microbial cells have been considered over the years, but none of them satisfies all the desired characteristics that are required in an ideal microbial degrader host. *Pseudomonas Putida,* which is soil bacteria, has emerged as a potential host degrader as it fulfills many criteria for growing and surviving in adverse environmental conditions and the ability to degrade recalcitrant pollutants (Dvořák et al. 2017). With the help of next-generation sequencing and omics data analysis, we can study biochemical catalysis taking place inside the microbial host as well as between the microbial host and the contaminant environment (Yaashikaa et al. 2022). The incorporation of synthetic metabolic pathways into actual producer strain has been

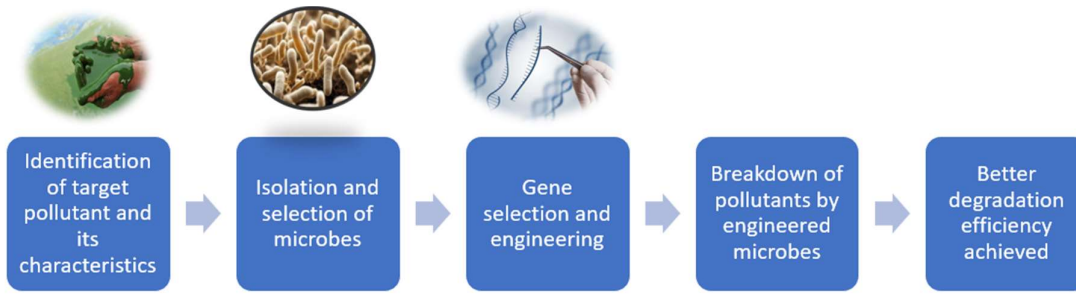

Fig. 1: Workflow of pollutant degradation using synthetic biology.

made easier by the new technological advancements in genetic engineering. DNA assembly tools, such as BioBrick assembly, Gibson assembly, Golden Gate assembly, ligase cycling reaction, single strand assembly, transformation-associated recombination (TAR) cloning, and uracil-specific excision reagent (USER) cloning, are examples. These tools have simplified the assembling process of multicomponent and large-sized gene clusters. DNA assembly tools have enabled the expression of assembled metabolic pathway genes using plasmids. Additionally, we can construct optimized metabolic pathway genes for expression in specific host strains (e.g., codon-optimized) using oligonucleotide and gene synthesis technologies (Choi et al. 2019). By engineering metabolic degradation pathways, we can prevent the production of toxic intermediates (Yaashikaa et al. 2022).

Enzyme Engineering

Over the past few decades, it has been reported that several bacterial species have the ability to produce enzymes. Many of these bacterial enzymes have shown their role in the mitigation or elimination of complex environmental pollutants (Singh et al. 2020). Enzymes are highly efficient biological catalysts, and they can transform toxic compounds into simpler, non-toxic compounds. Thereby, bacteria utilize these enzymes in their metabolic cycle for the effective removal of pollutants from the contaminant sites. Among the major classes of enzymes, oxidoreductases, and hydrolases are the classes that have been most extensively researched for their property of degrading toxic compounds into environmentally safer compounds. This is due to the fact that these enzyme classes possess high catalytic activity and the ability to target wide ranges of substrates, including xenobiotic pollutant compounds (Zhu et al. 2019). Over the past few years, researchers have been working on isolating microbial enzymes to use in biodegradation pathways instead of using the whole organism. This is because enzymes exhibit greater substrate specificity and a higher motility rate owing to their smaller size. However, we are still not able to fully utilize the potential of this technique because of some limitations like lower productivity, activity, and stability of enzymes, as they are very sensitive to the changing environmental factors, and that will have an adverse effect on their activity (Ahmad et al. 2023).

Also, for the enzymatic degradation of complex environmental pollutants like lignin in paper and pulp effluents, pesticides, aromatic hydrocarbons, and plastics, large quantities of enzymes need to be produced. However, these enzymes are produced in insufficient quantities (Aminian-Dehkordi et al. 2023). However, recently, some studies have shown how, by using recombinant DNA technology technique, we can produce large quantities of required enzymes. For example, according to a recent study, recombinant enzyme laccase was produced by various host organisms like bacteria, yeast, and filamentous fungi (Zhu et al. 2019). In another study, it has been shown that the production of recombinant hydrolases, such as lipases, carboxylesterases, and cutinases, has a high potential for pollutant remediation (Zhu et al. 2019). Furthermore, enzyme engineering can modify such properties in enzymes, making them have better catalytic activity and stability than native enzymes (Yang et al. 2021), so that they will be useful for onsite bioremediation of contaminated sites (Bhatt et al. 2021). Enzymatic properties of the rate-limiting enzymes of the important degradation pathways are extensively researched, and from that, important enzymatic data are analyzed (Yang et al. 2021).

The steps involved in enzyme engineering are as follows: 1. Protein engineering; 2. Modification of the enzyme; and 3. Screening of the modified enzyme (Bhatt et al. 2021). Protein engineering can be done in three ways – rational design (site-directed mutagenesis), random methods like random mutagenesis, and directed evolution. Rational design is a useful approach if we already know the structure and mechanism of the target protein. In a recent experiment, a novel fungal polyphenol oxidase was engineered by site-directed mutagenesis to produce different enzyme variants with increased catalytic activity and varying specificities for bioremediation of chlorophenols (Zhu et al. 2019). Another study reported that after the rational modification of the carboxylase enzyme, the biodegradation of a harmful phenol derivative was increased by forty percent, and the stereoselectivity property of that modified enzyme was increased by thirty-nine-fold (Aminian-Dehkordi et al. 2023). On the other hand, the directed evolution approach can yield enzymes having enhanced properties even in the absence of information regarding protein structure or catalytic mechanism (Zhu et al. 2019). For instance, using this approach, ligninolytic enzymes in fungi were modified with properties such as extreme pH resistance (Zhu et al. 2019).

Synthetic Microbial Consortia

Microbial cells rationally engineer their metabolic pathways by using metabolic engineering. The overall efficiency and functioning of these reconstructed pathways depend on various factors, including precursors, cofactor demands, and the optimal expression of pathway enzymes. However, sometimes, these reconstructed metabolic degradation pathways do not function as expected because of a metabolic burden on the microbial cell. To improve this limitation of metabolic burden in a cell, microbial co-cultures have been rationally designed to distribute the metabolic burden of complex and lengthy biosynthetic pathways across

different strains or species, thereby enhancing bio-production performance. This co-cultivation technique can successfully reduce the metabolic stress of engineered microbial cells caused by the overexpression of long and complicated metabolic pathways (Jawed et al. 2019).

When the population of two or more microbial species live together in a symbiotic relationship, this relationship is known as microbial consortia. The microbial consortia can perform complex metabolic processes that would be impossible for a single strain to do. A single strain of a microorganism is not able to produce different varieties of enzymes that are required for the complete degradation of the xenobiotic pollutants found in the environment. It has been observed that naturally occurring microbial consortia can degrade complex compounds but their degradation efficiency is less. They can degrade compounds like plastics, petroleum, antibiotics, azo dyes, and some pollutants found in sewage. We can enhance the degradation efficiency by constructing synthetic microbial consortia by adding new genetic materials and modules (Sharma & Shukla 2020).

The synthetic microbial consortia can be rationally constructed in two ways – top-down approach and bottom-up approach. The top-down approach involves a multi-omics study of microbial communities to understand the workings of the microbial system at the molecular level and then constructing novel communities based on this knowledge. Whereas the bottom-down approach involves rational engineering of microbial consortia based on genetic elements, modules, circuits, and metabolic pathways to obtain microbial consortia with improved efficiency, stability, and controllability. Considering the difficulty in making synthetically engineered cells, the bottom-up approach is mostly used for the construction of synthetic microbial consortia (Jia et al. 2016). Techniques that synthetic biology uses to engineer microbial cells can also be employed in engineering complex functions and behaviors of microorganisms in microbial consortia. This can be achieved by using tools such as intercellular signaling, exogenous inputs, and syntrophic interactions. All these tools, combined, can control factors like population level, task distribution, and spatial arrangements among the microorganisms in the microbial consortia (McCarty & Ledesma-Amaro 2019). In bioremediation, other than improved biodegradation efficiency, consortia also have other advantages like providing support for secondary applications of treated wastewater and the promotion of ecological sustainability (Sharma et al. 2023). In an experiment, the researcher created a consortium by combining the bio-surfactant producer *Rhodococcus erythropolis OSDS1* with petroleum hydrocarbon degraders *Serratia proteamaculans S1BD1, Alcaligenes sp. OPKDS2, Rhizobium sp. PNS1, and Pseudomonas sp. BSS9BS1*. This consortium exhibited higher efficiency and a wider range of capabilities in degrading petroleum hydrocarbons as compared to a single strain (Gao et al. 2020). Leong et al., in their experiment, showed a pollutant removal efficiency of 94% from municipal wastewater using microbial consortia involving microalgae and bacteria (Gao et al. 2020). Despite many advantages of using synthetic microbial consortia, many limitations of this technique are also there. These limitations include a limited understanding of bacteria interaction patterns and mechanisms, difficulty in rational designing efficient and functional microbial communities, and determining the roles played by these communities in different areas (Gao et al. 2020).

Another important point that should be considered when creating synthetic microbial consortia is the appropriate selection of chassis strains. It should be determined whether the chassis strains with efficient catalytic abilities would be compatible to co-exist with other strains. For this, strains with low mutation rates, no production of toxic by-products, and levels of high tolerance should be selected. Additionally, proper division of labor should be followed while dividing long degradation pathways into several strains. While synthetic microbial consortia reduce the metabolic burden on cells, excessive segmentation of metabolic pathways will also lead to confusion and disrupt efficient mass transfer among strains in consortia. Recent studies have reported an increase in the efficiency of degradation of complex compounds by microbial consortia if the strains in consortia are assembled in an orderly spatiotemporal manner. Assembly of spatial-linked microbial consortia can even involve incompatible microbial strains. This has great potential in the bioremediation field (Cao et al. 2022).

SYNTHETIC BIOLOGY APPROACH FOR DETECTION OF POLLUTANTS

The choice of method for removal of pollutants in wastewater is based on the contamination level of pollutants in the wastewater (Razzak et al. 2022). Microbes can act as very capable sensors because of some inherent qualities. Their small size enables them to be a highly sensitive small-scale detector that can sense, integrate, and react dynamically to various environmental factors. Biosensors are defined as genetically engineered microbes or independent biological components that are engineered to sense environmental signals and convert them to detectable output for us. They can also report microbial interactions in complex environments. The biosensor consists of the following modular features: 1. Sensor module – detects specific environmental conditions as input signals; 2. Processing module – calculate the input signals; 3. Output module – generates signals that can be

detected and measured. An important characteristic that a biosensor must possess to effectively study ecological processes is the capability to survive and perform in a contaminant region without getting interfered with by environmental conditions like temperature, hydration, pH, and substrate levels (Del Valle et al. 2021).

Microbial whole-cell biosensors comprise a genetic component that functions as a sensor to detect an analyte or a toxin and a reporter protein that generates a measurable output signal. These microorganisms' genomes or plasmids are genetically incorporated with the genes that are necessary for cellular response to the target analyte or toxin with the reporter protein. CFE biosensors are also known as cell-free transcription/translation systems. As the name suggests, they function independently of cellular processes; they are the isolated genetic circuits in the environment that sense and respond to the changing environmental factors. CFE biosensors have many advantages like no risk of plasmid loss and genetic instability and no need for biocontainment upon deployment. Ethical issues of using living microbes as a sensor can be avoided by using CFE. However, there is a major disadvantage to employing cell-free biosensors; at the industrial level, CFE biosensors have a high cost of production and deployment. Furthermore, with the use of bioinformatics tools, we can identify synthetic pathways to convert indetectable molecules into detectable ligands, constructing modular CFE for a wide variety of applications. Biosensor systems have modular and engineerable genetic components, which makes them highly optimizable and portable systems (Aminian-Dehkordi et al. 2023). Nowadays, we can engineer biosensors that are able to detect multiple environmental contaminants by eliciting a distinct signal for each kind of contaminant. These kinds of biosensors hold more significance in real-life situations as environmental regions are not contaminated by only one type of pollutant. Rather, they are contaminated by a wide variety of pollutants with varying physical and chemical properties (Yaashikaa et al. 2022). Whether a biosensor is suitable or not for a real-life situation is assessed by the following criteria: specificity and sensitivity to the target contaminant, range of its operation in the environment, and dynamic range. Computational tools and machine learning tools have fastened the designing and development of more advanced novel biosensors (Yu et al. 2023).

BIOFILMS IN WASTEWATER TREATMENT

Biofilm is the term coined for aggregated microbial communities that are permanently bound to the outer surface of living or non-living systems present in the environment and are encased by the self-generated layer of extracellular polymeric substance. The following steps take place in the biofilm formation: microbiome bound to the surface of the living or non-living system, synthesis of extracellular polymeric substance (EPS) around the microbiome, microbial communication via signaling, and the transition of the microbiome into planktonic cells (Chattopadhyay et al. 2022). Biofilm formation is dependent on several factors: the optimum presence of nutrients and energy required for their growth, the right environmental parameters in terms of geochemistry, the existence of inhibitors, predator microorganisms that feed on biofilms, and the effect of hydrodynamics on the transport of solutes which leads to mechanical stress on biofilms (Garg et al. 2023). Biofilms can survive harsh environmental conditions like changes in pH, occurrence of toxic chemicals and free radicals, and depletion of nutrients. Biosurfactants present in the EPS layer are involved in the formation of biofilms. These biosurfactants take part in the bioremediation process of environmental pollutants (Chattopadhyay et al. 2022). In a biofilm, pollutants are more bioavailable to the degrading organisms and microorganisms show enhanced potential in degrading pollutants. Microbial metabolism is responsible for this, and enzymes of the metabolic pathway convert environmental pollutants into non-toxic compounds (Muhammad et al. 2020).

CONCLUSIONS

With the global rise in the number of industries in the near future, there will be a tremendous rise in the volume of discharged wastewater from the industries as well. Wastewater contains various untreated harmful toxic wastes, which, when discharged into the water and soil, cause serious harm to the environment and human health. Therefore, finding novel, effective ways for the treatment of wastewater is very important. Herein, we have discussed how synthetic biology can help revolutionize the field of bioremediation of recalcitrant pollutants found in wastewater by designing effective and sustainable biological systems. Now, we can bioengineer novel microorganisms to target specific categories of pollutants and, hence, enhance the efficiency of wastewater treatment processes. Nowadays, more recalcitrant pollutants are identified in industrial wastewater, which cannot be treated by conventional bioremediation practices. Synthetically bioengineered microorganisms can solve this problem.

Moreover, the use of bioengineered microorganisms in different wastewater treatment systems, like activated sludge reactors, makes these systems highly efficient. By integrating synthetic biology techniques and these treatment systems, scientists can improve efficiency and save energy and cost. They can also design specific wastewater treatment

systems to meet the specific needs of different industries. Metabolic pathways for the degradation of target pollutants can be completely re-engineered. However, the task of optimization is difficult. Enzymatic properties can also be remodified. Synthetic biology-based biosensors are used to detect pollutant levels and also study microbial interactions with pollutants in a complex environment. Synthetic microbial consortia surpasses the limitations of the synthetic bacterium in the bioremediation of pollutants. However, many challenges limit the application of synthetic biology in the treatment of industrial wastewater pollutants. Modified microorganisms are still not able to effectively target some pollutants. We are still not able to fully comprehend the interactions between the pollutants and the microorganisms in the environment nor the interactions of the microorganisms with each other in the complex environment. It's taking time for the researchers to identify novel enzymes for bioremediation. We need to apply computational approaches to identify novel enzymes and also make them robust by necessary optimization. Furthermore, transferring synthetic microbes from the lab to the environment also leads to ethical issues. Synthetically designed microbes can disrupt the biosphere by gene transfer to other bacteria. In conclusion, many studies have shown the utility of synthetic biology in the bioremediation of pollutants but still, we need more research studies to address the challenges to harness the full potential of synthetic biology in the treatment of industrial wastewaters.

ACKNOWLEDGMENT

The authors would like to thank Delhi Technological University for providing infrastructure and facilities.

REFERENCES

Adetunji, C.O., Morumda, D., Dauda, W.P., Abraham, P., Glen, E., Abraham, M.P., Ifechukwude, C.N., Adetunji, J.B., Kanmodi, K.K. and Nnyanzi, L.A., 2023. *In silico Approaches to Macromolecular Chemistry*, Elsevier, pp.479–501.. https://doi.org/10.1016/B978-0-323-90995-2.00003-5.

Ahmad, A., Mustafa, G., Rana, A. and Zia, A.R., 2023. Improvements in bioremediation agents and their modified strains in mediating environmental pollution. *Current Microbiology*, 80(6), p.208. https://doi.org/10.1007/s00284-023-03316-x.

Aminian-Dehkordi, J., Rahimi, S., Golzar-Ahmadi, M., Singh, A., Lopez, J., Ledesma-Amaro, R. and Mijakovic, I., 2023. Synthetic biology tools for environmental protection. *Biotechnology Advances*, 68, p.108239. https://doi.org/10.1016/j.biotechadv.2023.108239.

Aukema, K.G., Escalante, D.E., Maltby, M.M., Bera, A.K., Aksan, A. and Wackett, L.P., 2017. Identification of bioremediation potential: carbamazepine and other recalcitrant personal care products. *Environmental Science & Technology*, 51(2), pp.880–888. https://doi.org/10.1021/acs.est.6b04345.

Barreiro, C. and García-Estrada, C., 2022. *New Frontiers and Applications of Synthetic Biology*. Elsevier, pp.45–65. https://doi.org/10.1016/B978-0-12-824469-2.00012-9.

Bhatt, P., Gangola, S., Bhandari, G., Zhang, W., Maithani, D., Mishra, S. and Chen, S., 2021. New insights into the degradation of synthetic pollutants in contaminated environments. *Chemosphere*, 268, p.128827. https://doi.org/10.1016/j.chemosphere.2020.128827.

Bradley, R.W., Buck, M. and Wang, B., 2016. Tools and principles for microbial gene circuit engineering. *Journal of Molecular Biology*, 428(5), pp.862–888. https://doi.org/10.1016/j.jmb.2015.10.004.

Cao, Z., Yan, W., Ding, M. and Yuan, Y., 2022. Construction of microbial consortia for microbial degradation of complex compounds. *Frontiers in Bioengineering and Biotechnology*, 10. https://doi.org/10.3389/fbioe.2022.1051233.

Chattopadhyay, I., J, R.B., Usman, T.M.M. and Varjani, S., 2022. Exploring the role of microbial biofilm for industrial effluents treatment. *Bioengineered*, 13(3), pp.6420–6440. https://doi.org/10.1080/21655979.2022.2044250.

Chen, W.C.W., Gaidukov, L., Lai, Y., Wu, M.-R., Cao, J., Gutbrod, M.J., Choi, G.C.G., Utomo, R.P., Chen, Y.-C., Wroblewska, L., Kellis, M., Zhang, L., Weiss, R. and Lu, T.K., 2022. A synthetic transcription platform for programmable gene expression in mammalian cells. *Nature Communications*, 13(1), p.6167. https://doi.org/10.1038/s41467-022-33287-9.

Chi, H., Wang, X., Shao, Y., Qin, Y., Deng, Z., Wang, L. and Chen, S., 2019. Engineering and modification of microbial chassis for systems and synthetic biology. *Synthetic and Systems Biotechnology*, 4(1), pp.25–33. https://doi.org/10.1016/j.synbio.2018.12.001.

Choi, K.R., Jang, W.D., Yang, D., Cho, J.S., Park, D. and Lee, S.Y., 2019. Systems metabolic engineering strategies: Integrating systems and synthetic biology with metabolic engineering. *Trends in Biotechnology*, 37(8), pp.817–837. https://doi.org/10.1016/j.tibtech.2019.01.003.

Dai, Z., Zhang, S., Yang, Q., Zhang, W., Qian, X., Dong, W., Jiang, M. and Xin, F., 2018. Genetic tool development and systemic regulation in biosynthetic technology. *Biotechnology for Biofuels*, 11(1), p.152. https://doi.org/10.1186/s13068-018-1153-5.

Del Valle, I., Fulk, E.M., Kalvapalle, P., Silberg, J.J., Masiello, C.A. and Stadler, L.B., 2021. Translating new synthetic biology advances for biosensing into the earth and environmental sciences. *Frontiers in Microbiology*, 11, p.373. https://doi.org/10.3389/fmicb.2020.618373.

Dutta, D., Arya, S. and Kumar, S., 2021. Industrial wastewater treatment: Current trends, bottlenecks, and best practices. *Chemosphere*, 285, p.131245. https://doi.org/10.1016/j.chemosphere.2021.131245.

Dvořák, P., Nikel, P.I., Damborský, J. and de Lorenzo, V., 2017. Bioremediation 3.0: Engineering pollutant-removing bacteria in the times of systemic biology. *Biotechnology Advances*, 35(7), pp.845–866. https://doi.org/10.1016/j.biotechadv.2017.08.001.

Eisenhut, P., Marx, N., Borsi, G., Papež, M., Ruggeri, C., Baumann, M. and Borth, N., 2024. Manipulating gene expression levels in mammalian cell factories: An outline of synthetic molecular toolboxes to achieve multiplexed control. *New Biotechnology*, 79, pp.1–19. https://doi.org/10.1016/j.nbt.2023.11.003.

Engstrom, M.D. and Pfleger, B.F., 2017. Transcription control engineering and applications in synthetic biology. *Synthetic and Systems Biotechnology*, 2(3), pp.176–191. https://doi.org/10.1016/j.synbio.2017.09.003.

Gao, B., Sabnis, R., Costantini, T., Jinkerson, R. and Sun, Q., 2020. A peek in the micro-sized world: A review of design principles, engineering tools, and applications of the engineered microbial community. *Biochemical Society Transactions*, 48(2), pp.399–409. https://doi.org/10.1042/BST20190172.

Garg, E., Varma, A. and Smitha, M.S., 2023. *Modern Approaches in Waste Bioremediation*. Springer International Publishing, pp.365–375. https://doi.org/10.1007/978-3-031-24086-7_17.

Garner, K.L., 2021. Principles of synthetic biology. *Essays in Biochemistry*, 65(5), pp.791–811. https://doi.org/10.1042/EBC20200059.

Hara, T., Takatsuka, Y., Nakata, E. and Morii, T., 2021. Augmentation of an engineered bacterial strain potentially improves the cleanup of PCB water pollution. *Microbiology Spectrum*, 9(3). https://doi.org/10.1128/spectrum.01926-21

Haripriyan, U., Gopinath, K.P., Arun, J. and Govarthanan, M., 2022. Bioremediation of organic pollutants: A mini-review on current and critical strategies for wastewater treatment. *Archives of Microbiology*, 204(5), p.286. https://doi.org/10.1007/s00203-022-02907-9

Hassan, S. and Ganai, B.A., 2023. Deciphering the recent trends in pesticide bioremediation using genome editing and multi-omics approaches: A review. *World Journal of Microbiology and Biotechnology*, 39(6), p.151. https://doi.org/10.1007/s11274-023-03603-6

Jabbar, N.M., Alardhi, S.M., Mohammed, A.K., Salih, I.K. and Albayati, T.M., 2022. Challenges in the implementation of bioremediation processes in petroleum-contaminated soils: A review. *Environmental Nanotechnology, Monitoring and Management*, 18, p.694. https://doi.org/10.1016/j.enmm.2022.100694

Jaiswal, S., Singh, D.K. and Shukla, P., 2019. Gene editing and systems biology tools for pesticide bioremediation: A review. *Frontiers in Microbiology*, 10, p.87. https://doi.org/10.3389/fmicb.2019.00087

Jawed, K., Yazdani, S.S. and Koffas, M.A.G., 2019. Advances in the development and application of microbial consortia for metabolic engineering. *Metabolic Engineering Communications*, 9, e00095. https://doi.org/10.1016/j.mec.2019.e00095

Jia, X., Liu, C., Song, H., Ding, M., Du, J., Ma, Q. and Yuan, Y., 2016. Design, analysis, and application of synthetic microbial consortia. *Synthetic and Systems Biotechnology*, 1(2), pp.109–117. https://doi.org/10.1016/j.synbio.2016.02.001

Jiang, S., Tang, J., Rahimi, S., Mijakovic, I. and Wei, Y., 2022. Editorial: Efficient treatment of industrial wastewater with microbiome and synthetic biology. *Frontiers in Environmental Science*, 10, p.292. https://doi.org/10.3389/fenvs.2022.902926

Jiménez-Díaz, V., Pedroza-Rodríguez, A.M., Ramos-Monroy, O. and Castillo-Carvajal, L.C., 2022. Synthetic biology: A new era in hydrocarbon bioremediation. *Processes*, 10(4), p.471. https://doi.org/10.3390/pr10040712

Jones, E.R., van Vliet, M.T.H., Qadir, M. and Bierkens, M.F.P., 2021. Country-level and gridded estimates of wastewater production, collection, treatment, and reuse. *Earth System Science Data*, 13(2), pp.237–254. https://doi.org/10.5194/essd-13-237-2021

Kent, R. and Dixon, N., 2020. Contemporary tools for regulating gene expression in bacteria. *Trends in Biotechnology*, 38(3), pp.316–333. https://doi.org/10.1016/j.tibtech.2019.09.007

Kesari, K.K., Soni, R., Jamal, Q.M.S., Tripathi, P., Lal, J.A., Jha, N.K., Siddiqui, M.H., Kumar, P., Tripathi, V. and Ruokolainen, J., 2021. Wastewater treatment and reuse: A review of its applications and health implications. *Water, Air, and Soil Pollution*, 232(5). https://doi.org/10.1007/s11270-021-05154-8

Kim, J., Salvador, M., Saunders, E., González, J., Avignone-Rossa, C. and Jiménez, J.I., 2016a. Properties of alternative microbial hosts used in synthetic biology: Towards the design of a modular chassis. *Essays in Biochemistry*, 60(4), pp.303–313. https://doi.org/10.1042/EBC20160015

Kim, J., Salvador, M., Saunders, E., González, J., Avignone-Rossa, C. and Jiménez, J.I., 2016b. Properties of alternative microbial hosts used in synthetic biology: Towards the design of a modular chassis. *Essays in Biochemistry*, 60(4), pp.303–313. https://doi.org/10.1042/EBC20160015

Kitano, S., Lin, C., Foo, J.L. and Chang, M.W., 2023. Synthetic biology: Learning the way toward high-precision biological design. *PLOS Biology*, 21(4), e3002116. https://doi.org/10.1371/journal.pbio.3002116

Lv, X., Hueso-Gil, A., Bi, X., Wu, Y., Liu, Y., Liu, L. and Ledesma-Amaro, R., 2022. New synthetic biology tools for metabolic control. *Current Opinion in Biotechnology*, 76, p.102724. https://doi.org/10.1016/j.copbio.2022.102724

MacDonald, I.C. and Deans, T.L., 2016. Tools and applications in synthetic biology. *Advanced Drug Delivery Reviews*, 105, pp.20–34. https://doi.org/10.1016/j.addr.2016.08.008

McCarty, N.S. and Ledesma-Amaro, R., 2019. Synthetic biology tools to engineer microbial communities for biotechnology. *Trends in Biotechnology*, 37(2), pp.181–197. https://doi.org/10.1016/j.tibtech.2018.11.002

Muhammad, M.H., Idris, A.L., Fan, X., Guo, Y., Yu, Y., Jin, X., Qiu, J., Guan, X. and Huang, T., 2020. Beyond risk: Bacterial biofilms and their regulating approaches. *Frontiers in Microbiology*, 11. https://doi.org/10.3389/fmicb.2020.00928

Nasr, M., 2022. Aquatic pollution and wastewater treatment system. In *Algae and Aquatic Macrophytes in Cities: Bioremediation, Biomass, Biofuels, and Bioproducts*, pp.23–37. Elsevier. https://doi.org/10.1016/B978-0-12-824270-4.00006-7

Rafeeq, H., Afsheen, N., Rafique, S., Arshad, A., Intisar, M., Hussain, A., Bilal, M. and Iqbal, H.M.N., 2023. Genetically engineered microorganisms for environmental remediation. *Chemosphere*, 310. https://doi.org/10.1016/j.chemosphere.2022.136751

Ranjbar, S. and Malcata, F.X., 2022. Is genetic engineering a route to enhance microalgae-mediated bioremediation of heavy metal-containing effluents? *Molecules*, 27(5), p.1473. https://doi.org/10.3390/molecules27051473

Razzak, S.A., Faruque, M.O., Alsheikh, Z., Alsheikhmohamad, L., Alkuroud, D., Alfayez, A., Hossain, S.M.Z. and Hossain, M.M., 2022. A comprehensive review on conventional and biological-driven heavy metals removal from industrial wastewater. *Environmental Advances*, 7, p.100168. https://doi.org/10.1016/j.envadv.2022.100168

Rylott, E.L. and Bruce, N.C., 2020. How synthetic biology can help bioremediation. *Current Opinion in Chemical Biology*, 58, pp.86–95. https://doi.org/10.1016/j.cbpa.2020.07.004

Saddique, Z., Imran, M., Javaid, A., Latif, S., Kim, T.H., Janczarek, M., Bilal, M. and Jesionowski, T., 2023. Bio-fabricated bismuth-based materials for removal of emerging environmental contaminants from wastewater. *Environmental Research*, 229, p.115. https://doi.org/10.1016/j.envres.2023.115861

Saravanan, A., Kumar, P.S., Duc, P.A. and Rangasamy, G., 2023. Strategies for microbial bioremediation of environmental pollutants from industrial wastewater: A sustainable approach. *Chemosphere*, 313, p.7323. https://doi.org/10.1016/j.chemosphere.2022.137323

Saravanan, A., Senthil Kumar, P., Jeevanantham, S., Karishma, S., Tajsabreen, B., Yaashikaa, P.R. and Reshma, B., 2021. Effective water/wastewater treatment methodologies for toxic pollutants removal: Processes and applications towards sustainable development. *Chemosphere*, 280, p.595. https://doi.org/10.1016/j.chemosphere.2021.130595

Saxena, G., 2020. *Bioremediation of Industrial Waste for Environmental Safety*. Springer. https://doi.org/10.1007/978-981-13-1891-7

Sharma, B. and Shukla, P., 2020. Designing synthetic microbial communities for effectual bioremediation: A review. *Biocatalysis and Biotransformation*, 38(6), pp.405–414. https://doi.org/10.1080/10242422.2020.1813727

Sharma, M., Agarwal, S., Agarwal Malik, R., Kumar, G., Pal, D.B., Mandal, M., Sarkar, A., Bantun, F., Haque, S., Singh, P., Srivastava, N. and Gupta, V.K., 2023. Recent advances in microbial engineering approaches for wastewater treatment: A review. *Bioengineered*, 14(1), p.2184518. https://doi.org/10.1080/21655979.2023.2184518

Sharma, P., Pandey, A.K., Udayan, A. and Kumar, S., 2021. Role of microbial community and metal-binding proteins in phytoremediation of heavy metals from industrial wastewater. *Bioresource Technology*, 326, p.124750. https://doi.org/10.1016/j.biortech.2021.124750

Singh, A.K., Bilal, M., Iqbal, H.M.N. and Raj, A., 2021. Trends in predictive biodegradation for sustainable mitigation of environmental pollutants: Recent progress and future outlook. *Science of the Total Environment*, 770, p.561. https://doi.org/10.1016/j.scitotenv.2020.144561

Singh, A.K., Chowdhary, P. and Raj, A., 2020. *Microorganisms for Sustainable Environment and Health*. Elsevier, pp. 249–285. https://doi.org/10.1016/B978-0-12-819001-2.00013-9

Singh, B.J., Chakraborty, A. and Sehgal, R., 2023. A systematic review of industrial wastewater management: Evaluating challenges and enablers. *Journal of Environmental Management*, 348, p.119230. https://doi.org/10.1016/j.jenvman.2023.119230

Tang, T.-C., An, B., Huang, Y., Vasikaran, S., Wang, Y., Jiang, X., Lu, T.K. and Zhong, C., 2020. Materials designed by synthetic biology. *Nature Reviews Materials*, 6(4), pp.332–350. https://doi.org/10.1038/s41578-020-00265-w

Thai, T.D., Lim, W. and Na, D., 2023. Synthetic bacteria for the detection and bioremediation of heavy metals. *Frontiers in Bioengineering and Biotechnology*, 11, p. 868. https://doi.org/10.3389/fbioe.2023.1178680

Tietze, L. and Lale, R., 2021. Importance of the 5′ regulatory region to bacterial synthetic biology applications. *Microbial Biotechnology*, 14(6), pp.2291–2315. https://doi.org/10.1111/1751-7915.13868

Tran, K.M., Lee, H.M., Thai, T.D., Shen, J., Eyun, S.-il and Na, D., 2021. Synthetically engineered microbial scavengers for enhanced bioremediation. *Journal of Hazardous Materials*, 419, p.6516. https://doi.org/10.1016/j.jhazmat.2021.126516

Xie, M. and Fussenegger, M., 2018. Designing cell function: assembly of synthetic gene circuits for cell biology applications. *Nature Reviews Molecular Cell Biology*, 19(8), pp.507–525. https://doi.org/10.1038/s41580-018-0024-z

Yaashikaa, P.R., Devi, M.K. and Kumar, P.S., 2022. Engineering microbes for enhancing the degradation of environmental pollutants: A detailed review on synthetic biology. *Environmental Research*, 214, p.86. https://doi.org/10.1016/j.envres.2022.113868

Yang, Y., Zhang, Z.-W., Liu, R.-X., Ju, H.-Y., Bian, X.-K., Zhang, W.-Z., Zhang, C.-B., Yang, T., Guo, B., Xiao, C.-L., Bai, H. and Lu, W.-Y., 2021. Research progress in bioremediation of petroleum pollution. *Environmental Science and Pollution Research*, 28(34), pp.46877–46893. https://doi.org/10.1007/s11356-021-15310-6

Yu, W., Xu, X., Jin, K., Liu, Y., Li, J., Du, G., Lv, X. and Liu, L., 2023. Genetically encoded biosensors for microbial synthetic biology: From conceptual frameworks to practical applications. *Biotechnology Advances*, 62, p.108077. https://doi.org/10.1016/j.biotechadv.2022.108077

Zhang, X.-E., Liu, C., Dai, J., Yuan, Y., Gao, C., Feng, Y., Wu, B., Wei, P., You, C., Wang, X. and Si, T., 2023. Enabling technology and core theory of synthetic biology. *Science China Life Sciences*, 66(8), pp.1742–1785. https://doi.org/10.1007/s11427-022-2214-2

Zhu, B., Chen, Y. and Wei, N., 2019. Engineering Biocatalytic and Biosorptive Materials for Environmental Applications. *Trends in Biotechnology*, 37(6), pp.661–676. https://doi.org/10.1016/j.tibtech.2018.11.005

This article has been accepted for publication in IEEE Journal of Emerging and Selected Topics in Industrial Electronics. This is the author's version which has not been fully edited and content may change prior to final publication. Citation information: DOI 10.1109/JESTIE.2025.3549766

Ultracapacitor Assisted Battery Based HESS for Electric Vehicle Considering Battery Aging

Kuldeep Singh, *Member, IEEE*, Mukhtiar Singh, *Member, IEEE,* Sudarshan K Valluru, *Senior Member, IEEE*

***Abstract*— In this paper, the enhanced performance of a Hybrid Energy Storage System (HESS) comprising Ultracapacitor (UC) and Battery for Electric Vehicle (EV) is achieved by effective use of battery aging information in Energy Management Strategy (EMS). The Model Predictive Control (MPC) algorithm is an efficient EMS that ensures the optimum operation of UC during dynamic operating conditions. The algorithm takes control of UC charging/discharging in such a way that it caters to the high frequency power component of the load while the battery manages the low frequency power component. Further, the EMS explores the impact of a driving cycle on battery life by considering the battery aging effect. During a drive cycle battery experiences charging/discharging phenomenon that depends upon charging rate (C-rate). Here the battery aging model is considered that estimates capacity fade by calculating C-rate for each sampled current for the given drive cycle. The performance of EMS considering battery aging is investigated and shows that battery life is extended if actual capacity fade is estimated. The actual capacity fade at the end of the drive cycle is estimated by variable C-rate rather than presumed constant C-rate. The simulation results obtained shows that performance enhancement is achieved by considering the real C-rate instead of assigning a single C-rate for complete drive cycle which is validated by experimental results.**

***Index Terms*— Ultracapacitor (UC), State of Charge (SoC), Depth of Discharge (DoD), Charging rate (C-rate), Energy Management Strategy (EMS), Electric Vehicle (EV), Indian Drive Cycle (IDC), Bidirectional DC/DC Converter (BDDC), Ampere-hour (Ah), Vehicle to Grid (V2G).**

I. INTRODUCTION

In the present world scenario, the sustainable development is the key area of focus for countries across the globe. With the main aim of reduction in carbon emission, the widespread recognition and interest for electrification of the transportation sector has been developed. The automotive industry is driving itself for better future by introducing hybrid electric vehicle (HEV), Plug –in hybrid electric vehicle (PHEV) and electric vehicle (EV). The performance of EVs mainly depends upon the battery pack used. Majority of the EVs uses Lithium-ion battery (LIB) as the main source due to its relatively high efficiency and long-life. LIBs also play a major role in energy transition now a days since they are used in integration of renewable energy resources. The main concern regarding the use of LIB is that its aging is highly complex electrochemical phenomenon that is characterized by battery capacity loss. There are different causes such as time, high temperature, high cell voltage etc., that leads to aging mechanism such as solid electrolyte interphase layer (SEI), electrolyte decomposition, binder decomposition etc., that starts degradation mode either as loss of lithium inventory, loss of active material or conductivity loss. These all-degradation modes lead to either the capacity fade or power fade over the time [1].

To overcome the drawbacks associated with battery pack, ultracapacitor has been used in hybrid energy storage system (HESS) that complements the battery to improve the performance as it has high power density and long lifecycle [2]. Also, there are studies on DC-DC converter topologies for optimum operation of HESS. The article [3] presents a review on optimization of bidirectional DC–DC converters for hybrid energy storage system from the perspectives of wide bandgap device application, electromagnetic compatibility technology and converter fault diagnosis strategy. In ultracapacitor assisted HESS, battery provides the stable load power whereas UC caters to high frequency power fluctuations. HESS employs battery and ultracapacitor in different configuration such as passive, semi-active and active to power an electric vehicle. To have an optimum sharing of power among battery and UC, a suitable Energy Management Strategy (EMS) is desired. The EMS are classified into offline and online EMS. Offline EMS have been further classified into global optimization based such as dynamic programming (DP) etc., and rule based such as deterministic and fuzzy logic. The online EMS can be categorized into Instantaneous optimization based, Predictive and learning based EMS. Article [4] highlights the prediction-based EMS by using spatial-temporal data-driven full cycle velocity prediction for optimal energy management in battery/supercapacitor based EVs. The article [5] presents a study on online adaptive EMS for the fuel cell hybrid vehicles by using machine learning models to obtain regression learner-based energy management. Authors in [6] have presented a multi-objective grey wolf optimization for sizing of HESS and later uses random forests (RF) method for power distribution based on driving pattern recognition (DPR) by support vector machine (SVM).

The service life of battery-based HESS is critical issue for various types of electric vehicles. There have been serious efforts in past to enhance the performance and to extend the operational life of battery to have better employability in transportation system. Article [7] presents, branch current estimation and correction for parallel connected battery system using dual Back Propagation (BP) neural network so to have safety warning in time when parallel batteries of EVs are

Kuldeep Singh, Mukhtiar Singh and Sudarshan K. Valluru are with the Department of Electrical Engineering, Delhi Technological University, Delhi, 110042, India (corresponding author e-mail: kuldeepsingh@dtu.ac.in).

Authorized licensed use limited to: DELHI TECHNICAL UNIV. Downloaded on March 20,2025 at 04:44:59 UTC from IEEE Xplore. Restrictions apply.
© 2025 IEEE. All rights reserved, including rights for text and data mining and training of artificial intelligence and similar technologies. Personal use is permitted, but republication/redistribution requires IEEE permission. See https://www.ieee.org/publications/rights/index.html for more information.

This article has been accepted for publication in IEEE Journal of Emerging and Selected Topics in Industrial Electronics. This is the author's version which has not been fully edited and content may change prior to final publication. Citation information: DOI 10.1109/JESTIE.2025.3549766

seriously inconsistent. In article [8], [9] and [10], model predictive technique and its modification is being adapted to enhance the performance of HESS in EV and DC Microgrid. The article [11] presents a hierarchical predictive control for electric vehicle with HESS to optimize power demand and energy management simultaneously. The author in [12] and [13] uses equivalent series resistance and prediction-based game-theoretic EMS is utilized to improve the performance. The article [14] presents an advanced battery model for HESS application and [15] highlights vector-controlled power sharing in electric vehicle. The authors in [16] presented a control strategy that minimizes the total cost of system including cost for battery life but lacks real time results as the scenario changes in real world driving conditions. [17] Presents optimal sizing of HESS for different application by considering initial battery cost and 10-years battery replacement cost. The author takes into consideration that the percentage of battery capacity loss is calculated in a very general way by assuming fixed discharging current and C-rate. In article [18], comparison of energy management strategies is done where in battery degradation is discussed for a particular drive cycle but did not consider the varying C-rate. A fixed C-rate for complete cycle renders unrealistic results as battery of an EV do not discharge at constant current throughout a drive cycle. Predicting the number remaining cycle of a battery used in electrified propulsion system has been explored in [19] over varying DoD along with different C-rate. The authors here conducted test on LFP battery by taking 1C, 1/2C and 1/3C charge/discharge current for a cycle. Presuming a constant C-rate for a drive cycle results in inaccurate estimation of capacity loss.

Another scenario that hampers the life cycle of EV battery is its use in vehicle to grid applications (V2G). In [20], the effect of V2G on Lead-acid battery, Nickel-metal hydride battery and Lithium-ion battery is presented. In article [21], highlights the importance of system modelling and optimization for smart management of EV-transportation network-grid integrated system. The top three contender of battery technology for EVs today are, Lead acid battery, Lithium-ion battery, and Nickel-metal hydride battery (NiMH) [22]. Currently the type of battery that is generally used in majority of EVs is Lithium-ion battery (LIB), particularly $LiFePO_4$ (Lithium Iron Phosphate) commonly called as LFP battery. The LFP battery has lower cost and better long-term stability as compared to other LIBs and is extensively used in various transportation applications [19]. The second commonly used LIB technology after LFP is Nickel Manganese Cobalt more generally called as NMC battery. A comparative study on real time verification of EMS has been presented in [23], where NMC battery pack is modelled with life degradation and suggests that including battery aging can slightly improve battery life.

The life of battery is a playing a vital role in adoption of EV throughout the world. In majority of EVs, $LiFePO_4$ battery are preferred over other LIBs. As a matter of fact, the degradation of battery used in EVs is affected by several factors. The major factors that devastate the life of battery the most are, recharging pattern, usage pattern i.e., drive cycle and lastly V2G application. To overcome the stress on battery due to dynamic operation, UC have been employed in HESS to improve the life of battery to some extent. Battery/UC based HESS works in conjunction with each other to improve the performance of system and improves the life of battery. The UC helps in enhancing the performance of EV and increases its life cycle since UC has high number of life cycles and handles larger power density than battery. To have optimum performance, the battery and UC are modelled and its states are estimated to control the power management in HESS. In [24], author presents fractional extended Kalman filter (FEKF) to estimate the state of charge of LIB and UC. In EVs battery aging phenomenon is complex and is modelled by various degradation models [1] and [25]. The dynamic capacity fade model used by [26] is based on original Arrhenius degradation equation is widely used to model the battery aging. The main drawback of the life model used by Wang et al. is that it suits well in rapidly evaluating the capacity loss for a long duration of time. It is not suitable when dynamic changes are occurring and hence the capacity loss expression provided in [26] is differentiated by Petit et al. in [27] to obtain expression of capacity loss that evaluates the infinitesimal variation of capacity due to aging.

The contribution and scope of this article is as follows:

(a) This paper presents, a Model Predictive Control based EMS for battery/UC powered EV. A detailed battery degradation model is used and system performance is analyzed in hardware in loop (HIL) setup.
(b) The control algorithm optimizes the distribution of power among battery and UC and aims to improve system performance while considering the capacity loss during a drive cycle.
(c) The major contribution of the paper is the evaluation of actual battery capacity loss based on variable C-rate, rather than relying on presumed constant C-rate.
(d) Results demonstrate the effectiveness of EMS, which utilizes the battery degradation model for its operation. The overall system performance is improved with prolonged battery life as suggestive from results.

This paper is organized as follows. In section II, system modelling is introduced including battery aging and sizing calculations. The energy management strategy is constructed in section III. Section IV shows the simulation results, comparison and section V presents experimental results. Conclusions are then drawn in section VI.

II. System Description

In literature HESS has been used various topologies. The four possible configurations for battery/UC based HESS are battery semi-active, UC semi-active, parallel, and cascaded topology. As shown in Fig.1, this study employs active topology with two bidirectional DC-DC converters (BDDC) coupled to DC link that feeds an EV motor via a DC/AC inverter. The voltage from two sources is elevated to the DC link and the DC link power is used to feed the motor through an inverter.

The power balance equation for the system then follows as,

$$P_d = \eta_{bat} P_{bat} + \eta_{uc} P_{uc} \quad (1)$$

where, η_{bat} and η_{uc} are the converter efficiency and depends on charge and discharge current and P_{bat} and P_{uc} are battery and

Authorized licensed use limited to: DELHI TECHNICAL UNIV. Downloaded on March 20,2025 at 04:44:59 UTC from IEEE Xplore. Restrictions apply.
© 2025 IEEE. All rights reserved, including rights for text and data mining and training of artificial intelligence and similar technologies. Personal use is permitted, but republication/redistribution requires IEEE permission. See https://www.ieee.org/publications/rights/index.html for more information.

This article has been accepted for publication in IEEE Journal of Emerging and Selected Topics in Industrial Electronics. This is the author's version which has not been fully edited and content may change prior to final publication. Citation information: DOI 10.1109/JESTIE.2025.3549766

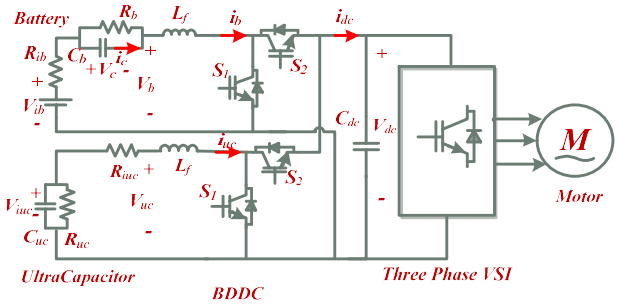

Fig.1. System configuration for battery and ultracapacitor based HESS.

UC power respectively. The power demand of the motor is determined by P_d,

$$P_d = \tau(\omega/\eta) \tag{2}$$

where, $\omega = (v\ G_r)/r_w$, is rotational speed of the motor and η is efficiency. The torque developed at the wheels is computed by knowing resistant force and vehicle speed as,

$$\tau = \left(F_{Total} + M\frac{\mathrm{d}v}{\mathrm{d}t}\right)(r_w / G_r) \tag{3}$$

where, r_w and G_r are the radius of the wheel and gear ratio respectively. The total resistant force (F_{Total}), which is a function of velocity of vehicle (v) and the gradient of the road (θ) is computed using the basic longitudinal dynamics model of vehicle.

$$F_{Total} = A_f \rho\, C_d v^2 + m_v \mu_{rr} g\cos\theta + m_v g\sin\theta \tag{4}$$

where, m_v, g, μ_{rr}, ρ, C_d and A_f are, vehicle's mass, acceleration of gravity, coefficient of rolling resistance, air density, drag coefficient and vehicle's frontal area respectively. The force experienced at the wheels of vehicle is delivered through gearbox. The parameters of the vehicle used for study are tabulated in Table-I.

A. *Battery and Ultracapacitor Modelling*:

To evaluate the HESS system, the battery and ultracapacitor are modelled as first order RC circuit as shown in Fig.1. The battery model consists polarization components RC in parallel configuration, a voltage source in series with internal resistance of the battery.

The cell voltage of battery is given by

$$V_b = V_{ib} - R_{ib} i_b - V_c \tag{5}$$

$$i_c = C_b \frac{\mathrm{d}V_c}{\mathrm{d}t} \tag{6}$$

where, V_b is open terminal voltage of the battery which is a function of SoC, given by

$$SoC = 1/Q_n\left[Q_n - \int C\, R\, \mathrm{i}_b dt\right] \tag{7}$$

Considering the RC circuit model for UC, the cell voltage follows,

$$V_{uc} = V_{iuc} - i_{uc} R_{iuc} \tag{8}$$

$$\frac{\mathrm{d}V_{iuc}}{\mathrm{dt}} = \frac{i_{uc}}{C_{uc}} - \frac{V_{iuc}}{R_{uc} C_{uc}} \tag{9}$$

where, V_{uc} is the output terminal voltage and V_{iuc} is the voltage against the polarization components. The SoC of the UC is computed using

$$SoC = 1/Q_n\left[Q_n SoC_o - \int i_{uc} dt\right] \tag{10}$$

TABLE I
VEHICLE PARAMETERS

PARAMETER	VALUE
Vehicle mass (m_v)	1325 kg
Air density (ρ)	1.29 kg/m^3
Frontal area (A_f)	2.57 m^2
Drag coefficient (C_d)	0.26
Rolling resistance (μ_{rr})	0.0048
Road gradient (θ)	0.175

B. *Battery and Ultracapacitor Sizing*:

The traction battery used in study contains 5 modules of 72 V and 110 Ah. The total voltage of battery pack in HESS is 360 V. The UC pack usually utilizes about 75% of energy stored in the bank by discharges from its rated voltage ($V_{uc\ max}$) to half of its rated voltage ($V_{uc\ min}$) [28]. The energy extracted from UC pack is,

$$E = k\left[\frac{1}{2}C_{eq}V_{uc\,\max}^2 - \frac{1}{2}C_{eq}V_{uc\,\min}^2\right] \tag{11}$$

The energy stored in UC at voltage V_{uc} is given by,

$$E = \frac{1}{2}C_{eq}V_{uc}^2 = \frac{1}{2}\frac{N_P}{N_S}C_{uc}V_{uc}^2 \tag{12}$$

This leads, considering a 10 MJ of energy with regenerative condition for IDC [29], the C_{eq} = 250 F and V_{uc} as 300 V. Referring to the initial voltage of UC pack, N_s = 108 and N_p = 9.

C. *Battery Aging Model*:

The dynamic capacity fade model based on original Arrhenius degradation equation estimates the capacity loss of $LiFePO_4$ battery mainly depends upon C-rate and DoD. The capacity loss is estimated by

$$Q_{loss} = B.\exp\left(\frac{-E_a + \alpha \times C_{rate}}{R \times T}\right)(A_h)^{0.55} \tag{13}$$

Considering cycle number and full cell capacity, A_h is computed as,

$$A_h = n_{cyc} \times DoD \times Ah_{cell} \tag{14}$$

This model estimates the battery capacity loss for a long duration of time but is not suitable when dynamic changes are occurring. Therefore, to evaluate the infinitesimal variation of capacity due to aging, the original expression is differentiated with respect to time to obtain the following expression as,

Authorized licensed use limited to: DELHI TECHNICAL UNIV. Downloaded on March 20,2025 at 04:44:59 UTC from IEEE Xplore. Restrictions apply.
© 2025 IEEE. All rights reserved, including rights for text and data mining and training of artificial intelligence and similar technologies. Personal use is permitted, but republication/redistribution requires IEEE permission. See https://www.ieee.org/publications/rights/index.html for more information.

This article has been accepted for publication in IEEE Journal of Emerging and Selected Topics in Industrial Electronics. This is the author's version which has not been fully edited and content may change prior to final publication. Citation information: DOI 10.1109/JESTIE.2025.3549766

$$\frac{dQ_{loss}}{dt} = \frac{|I|}{3600} z.B.\exp\left(\frac{-E_a + \alpha \times |I|}{R \times T}\right)\left(\frac{Q_{loss}}{B.\exp(\frac{-E_a + \alpha \times |I|}{R \times T})}\right)^{1-\frac{1}{z}} \quad (15)$$

where, Q_{loss} represents battery capacity loss, z is the power factor, R is the gas constant and T is absolute temperature. E_a is the activation energy; B is pre-exponential factor and α is the coefficient for aging acceleration due to current.

III. Energy Management Strategy

To evaluate the performance of the system, the model predictive control (MPC) is used as energy management strategy. The MPC works on the principle of predicting the future output of the system over prediction horizon by using linearized model of system. The control minimizes objective function subjected to constraints and predicts system response with accuracy. In this work, MPC has been used to predict the SoC of UC. The EMS optimizes the objective function to maintain the SoC at desired level and minimizes fluctuations in battery current. The objective function works in a way such that UC must supply sudden large current demand and deliver more power to the load to reduce the stress on battery. The constraints outlying the objective function are lying between maximum and minimum allowable limits of the battery current and SoC of UC. In Matlab/Simulink environment, the MPC is implemented using MPC toolbox. The information related to the system such as manipulated variable, measured and unmeasured outputs and objective function subjected and related constraints are provided in the toolbox. The simplified battery and UC models are considered and a continuous state space model of HESS is developed which is linearized using the MPC toolbox.

The discretized objective function at time k is given by,

$$J = \sum_{j=1}^{P_H} w_1[SoC_{uc}^*(k+j/k) - SoC_{uc}(k+j/k)]^2 + \sum_{j=1}^{C_H} w_2[i_b^*(k+j/k) - i_b(k+j/k)]^2 \quad (16)$$

Subjected to following constraints

$$SoC_{min} \le SoC_{uc}(k+j/k) \le SoC_{max} \quad (17)$$

$$i_{bmin} \le i_b(k+j/k) \le i_{b\max} \quad (18)$$

The positive values of weights w_1 and w_2 determine the dominance of corresponding parts of objective function. So, w_1 should be considered much smaller than w_2 although relatively large value of w_2 increases the likelihood of having a constant battery current, it may result in SoC violation. The weights are carefully chosen considering w_1 smaller than w_2 i.e., $w_1 << w_2$. The discretized model of the system for predicting the SoC of UC has been implemented using zero order hold method and the next state of SoC is computed,

$$SoC_{uc}(t) = SoC_{uc}(t_o) - \int i_{uc}(t)/Q_{nom}\,dt \quad (19)$$

$$\dot{SoC}(t) = -i_{uc}/Q_{nom} \quad (20)$$

$$SoC_{uc}(k+1) = (I + T_s * A)SoC_{uc}(k) + T_s * BI_{mpc}(k) \quad (21)$$

$$\begin{pmatrix} SoC_{uc}(k+1) \\ I_b^*(k+1) \end{pmatrix} = \begin{pmatrix} 1 & 0 \\ 0 & 1 \end{pmatrix}\begin{pmatrix} SoC_{uc}(k) \\ I_b^*(k) \end{pmatrix} + T_s\begin{pmatrix} 0 & \frac{100I_n}{Q_{nom}} \\ 0 & -\frac{1}{\tau} \end{pmatrix}\begin{pmatrix} SoC_{uc}(k) \\ I_b^*(k) \end{pmatrix} + T_s\begin{pmatrix} \frac{-100I_n}{Q_{nom}} \\ \frac{1}{\tau} \end{pmatrix} I_{mpc}(k) \quad (22)$$

$$y(k) = C\begin{pmatrix} SoC_{uc}(k) \\ I_b^*(k) \end{pmatrix} \quad (23)$$

where matrices A, B and C are system matrix and T_s is sampling time of MPC controller. The overall control scheme used is represented as flowchart in Fig.2.

A. EMS Evaluation using Battery Aging

The MPC controller produces reference currents such that the UC provides sudden and large amount of power and battery operates to provide constant power. In objective function, the weight w_2 is given high priority such that battery current fluctuation is minimized therefore the C-rate corresponding to the current is limited for a given drive cycle. Since the battery current during the drive cycle changes as power requirement changes, corresponding C-rate varies over a range. In evaluating the battery capacity loss for a drive cycle, considering a single C-rate for entire drive cycle provides inaccurate results. Therefore, C-rate corresponding to actual battery current is obtained by sampling the battery current for a given drive cycle by using numerical methods. Here Indian Drive Cycle (IDC) [30] is used to evaluate the system, the duration of drive cycle is 108 seconds hence current is sampled at every one second and corresponding C-rate is computed. For estimating the capacity loss, the actual C-rate is used to calculate the pre-exponential factor B given by,

$$B = \exp\left[1.226^{-0.297 \times C_{rate}} + 9.263\right] \quad (24)$$

The pre-exponential factor along with A_h throughput is used to evaluate the actual capacity loss. The A_h throughput is evaluated using,

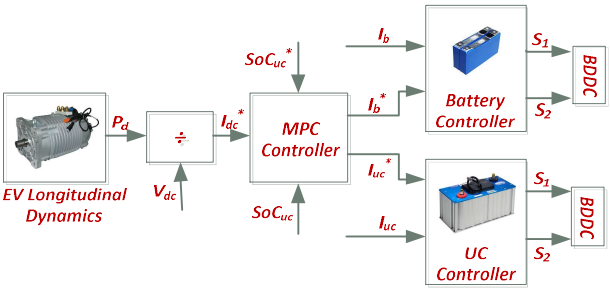

Fig.2. Flowchart for control of HESS

Authorized licensed use limited to: DELHI TECHNICAL UNIV. Downloaded on March 20,2025 at 04:44:59 UTC from IEEE Xplore. Restrictions apply.
© 2025 IEEE. All rights reserved, including rights for text and data mining and training of artificial intelligence and similar technologies. Personal use is permitted, but republication/redistribution requires IEEE permission. See https://www.ieee.org/publications/rights/index.html for more information.

This article has been accepted for publication in IEEE Journal of Emerging and Selected Topics in Industrial Electronics. This is the author's version which has not been fully edited and content may change prior to final publication. Citation information: DOI 10.1109/JESTIE.2025.3549766

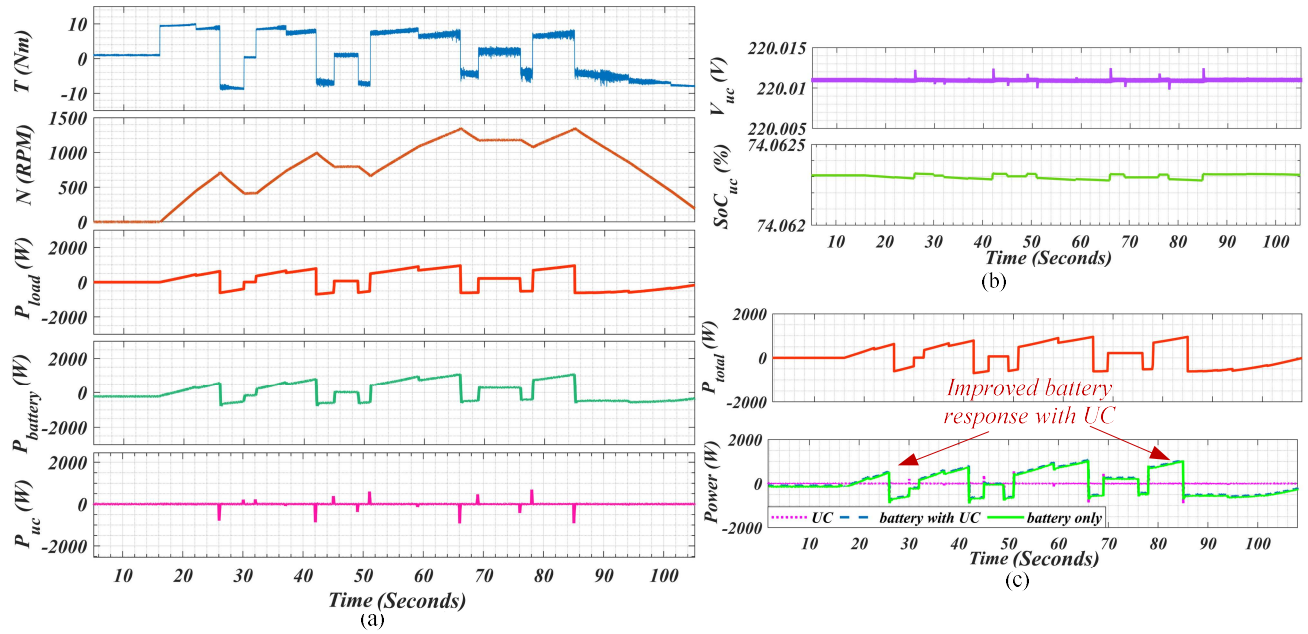

Fig.3. Results for complete drive cycle showing, (a) Torque, speed, load power, battery power, and UC power. (b) Voltage of UC and SoC, (c) Load power, battery power with and without UC.

$$A_h = \frac{1}{3600}\int_0^t |I|dt \tag{25}$$

These two components are used in battery capacity loss expression given in (15) to determine the capacity loss at the end of the drive cycle. The capacity loss obtained by degradation model, helps to determine the remaining capacity of the battery at the end of the drive cycle. This analysis can be extended to evaluate the capacity loss for *n* number of cycles by evaluating capacity fade and updating capacity of battery for next cycle.

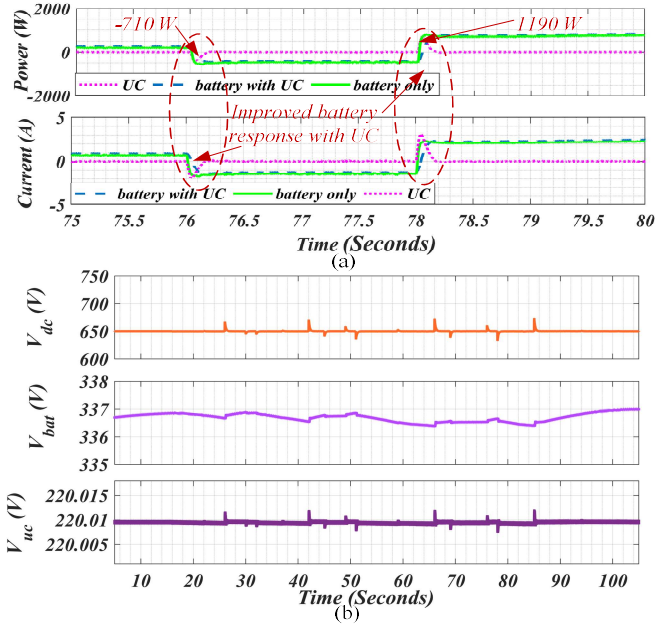

Fig.4. Results showing (a) zoomed view of battery and UC power and current (b) DC bus voltage, battery voltage and UC voltage for complete drive cycle.

IV. Simulation Results

The Matlab/Simulink environment is used to evaluate the performance of HESS and obtain the simulation results for IDC. From the longitudinal modeling of EV, velocity profile, torque requirement and total power demand of EV has been obtained from the drive cycle. The load power requirement is met by battery and UC both and is observed in Fig.3 (a). Because UC has high power density and faster response time, it acts as supportive device at times when there is change in power requirement. The UC is quick to recharge as well during regenerative mode of operation. As is evident from result shown in Fig.3 (a). The voltage and SoC of UC are indicated in Fig. 3 (b), for complete drive cycle and both are maintained at their limits. In Fig. 3 (c), the result shows the load power requirement is met by the battery and UC together. The UC power is seen as spike, and is present at times when there is transition and is supportive in nature to the battery. The result suggests that battery with UC operation is addition of battery only power and UC power. In Fig.4, the dynamics of HESS during acceleration, cruising, and de-acceleration mode is shown. The results present battery and UC power along with current. In case of battery only operation i.e., without UC, battery alone endures the power requirement and suffers more impact which results in faster battery aging.

Whereas in battery with UC operation, it makes wise use of UC to deliver the high frequency component of power thereby relieving the stress on battery. The result shows the peak power supplied by UC is 1190W at 78 sec., and absorbs a peak negative power of 710W at 76 sec., in regenerative mode. The parameters used for HESS system are tabulated in Table–II.

Authorized licensed use limited to: DELHI TECHNICAL UNIV. Downloaded on March 20,2025 at 04:44:59 UTC from IEEE Xplore. Restrictions apply.
© 2025 IEEE. All rights reserved, including rights for text and data mining and training of artificial intelligence and similar technologies. Personal use is permitted, but republication/redistribution requires IEEE permission. See https://www.ieee.org/publications/rights/index.html for more information.

This article has been accepted for publication in IEEE Journal of Emerging and Selected Topics in Industrial Electronics. This is the author's version which has not been fully edited and content may change prior to final publication. Citation information: DOI 10.1109/JESTIE.2025.3549766

TABLE II
PARAMETERS OF HESS

	PARAMETER	VALUE
Battery Bank	Voltage	360 V
	Capacity	110 Ah
	No. of Parallel connection	1
	No. of Series connection	5
UC Bank	Voltage	292 V
	Rated Capacitance	3000 F
	No. of Parallel connection	9
	No. of Series connection	108

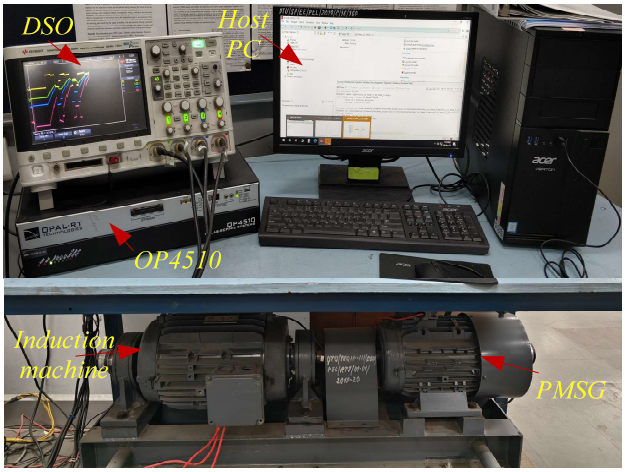

Fig.5. Hardware in loop setup for HESS.

V. EXPERIMENTAL RESULTS

A Hardware-in-Loop (HIL) configuration for the HESS considered has been assessed and verified using real-time simulator OPAL RT (OP4510). HIL setup consisting of real time simulator and a host computer for model creation and simulation management, interfaced with hardware components. An Ethernet cable is used as a connecting link between the host computer and the real-time simulator. The HIL setup shown in Fig.5 is evaluated for performance of the HESS. Various MPC parameters such as sampling time, minimum and maximum limit of constraints, tracking weights and control and prediction horizon used are tabulated in Table-III. For a MPC controller, the performance and computational time are linked to control and prediction horizons respectively. The greater the prediction horizon, greater is the understanding of future values and performance is increased. Conversely, if the control horizon is expanded, it will boost the accuracy of the findings on the pretext of longer computation time as number of optimization variables increases. Therefore, control and prediction horizons always have a tradeoff between each other and decision is taken to consider the values accordingly. The HIL setup utilizes analog to digital card (A/D) and digital to analog card (D/A) inbuilt on simulator for data acquisition and processing. The voltage signals are scaled to the input voltage range of ADC and accordingly the DAC signals are stepped up while connecting to hardware setup.

TABLE III
MPC PARAMETERS

PARAMETER	VALUE
Sampling Time (T_s)	50e-4
Prediction horizon (P_H)	15
Control Horizon (C_H)	10
Constraints (SoC_{uc} & i_b)	20-80%
Weights (w_1 & w_2)	0.1, 0.25

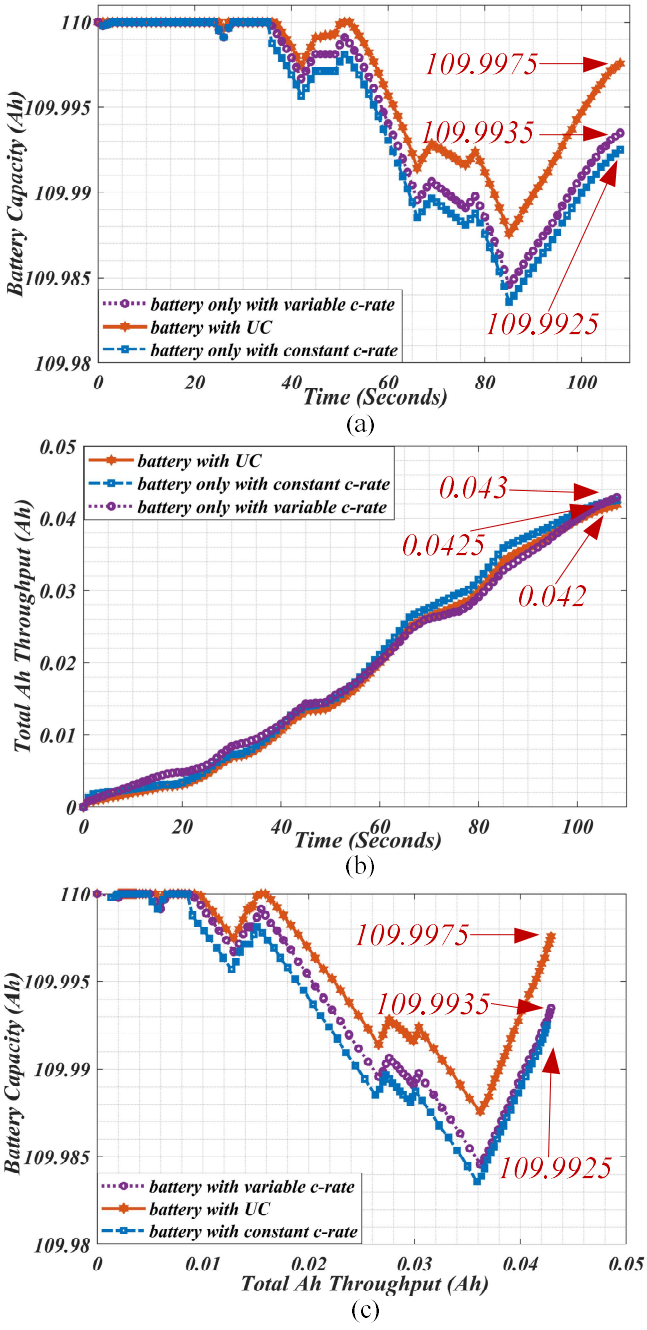

Fig.6. Results showing, (a) Battery capacity (Ah) for complete drive cycle, (b) Total Ah throughput over the complete drive cycle and (c) Battery capacity for total Ah throughput.

Authorized licensed use limited to: DELHI TECHNICAL UNIV. Downloaded on March 20,2025 at 04:44:59 UTC from IEEE Xplore. Restrictions apply.
© 2025 IEEE. All rights reserved, including rights for text and data mining and training of artificial intelligence and similar technologies. Personal use is permitted, but republication/redistribution requires IEEE permission. See https://www.ieee.org/publications/rights/index.html for more information.

This article has been accepted for publication in IEEE Journal of Emerging and Selected Topics in Industrial Electronics. This is the author's version which has not been fully edited and content may change prior to final publication. Citation information: DOI 10.1109/JESTIE.2025.3549766

For evaluating the capacity loss of battery for the selected drive cycle of 108 seconds, experimental data is gathered for current, SoC, DoD and voltage of battery. The data obtained from HIL setup is then sampled for every 1 second by using numerical method and is used to obtain battery capacity (*Ah*) and C-rate.

The C-rate of battery is calculated from sampled current and is grouped together to obtain all the possible values of C-rates for given drive cycle. This helps to obtain accurate results for battery aging as compared to results obtained by presuming a constant C-rate throughout the drive cycle. Therefore C-rate corresponding to actual battery current is eventually used in computing pre-exponential factor *B*. This pre-exponential factor is further used to evaluate the capacity loss during the drive cycle by using battery capacity loss expression.

Fig.6 summarizes results obtained for battery capacity loss under different scenarios. In Fig.6 (a), battery with UC operation has better capacity retention at the end of drive cycle. The results also highlight the comparison between variable C-rate and constant C-rate scenario for battery only operation. It is observed that for battery only operation, battery capacity at the end of driving cycle for variable C-rate is more as compared to constant C-rate. Battery

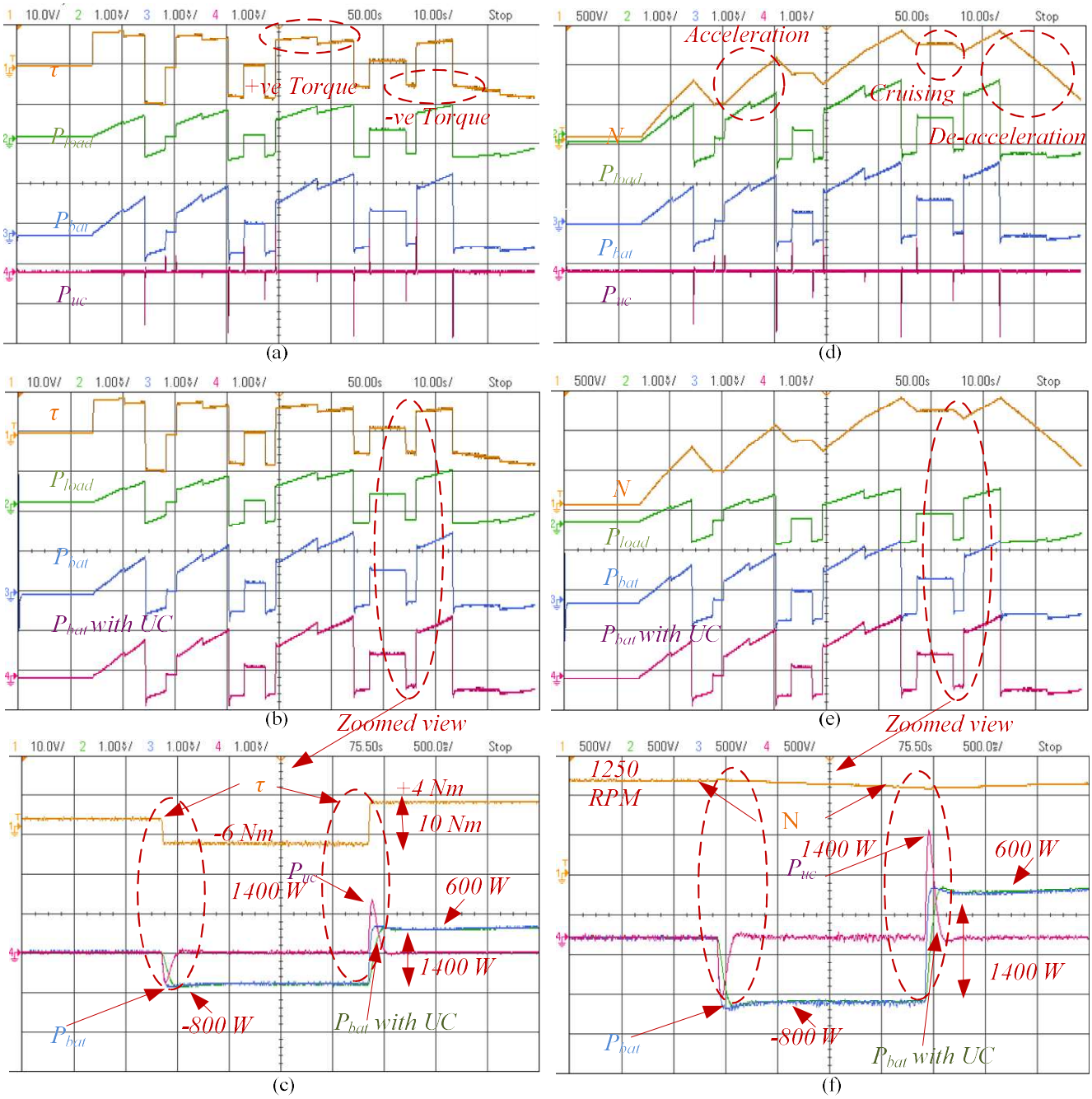

Fig.7. Hardware results for IDC (a) Speed, load power, battery power and UC power (b) torque, load power, battery power with and without UC, (c) zoomed view showing torque, battery power with and without UC and UC power, (d) speed, load power, battery, and UC power, (e) torque, load power, battery power with and without UC along with UC power and (f) zoomed view showing speed, battery power with and without UC along with UC power.

Authorized licensed use limited to: DELHI TECHNICAL UNIV. Downloaded on March 20,2025 at 04:44:59 UTC from IEEE Xplore. Restrictions apply.
© 2025 IEEE. All rights reserved, including rights for text and data mining and training of artificial intelligence and similar technologies. Personal use is permitted, but republication/redistribution requires IEEE permission. See https://www.ieee.org/publications/rights/index.html for more information.

This article has been accepted for publication in IEEE Journal of Emerging and Selected Topics in Industrial Electronics. This is the author's version which has not been fully edited and content may change prior to final publication. Citation information: DOI 10.1109/JESTIE.2025.3549766

with UC has 0.005 *Ah* more than battery only operation for a drive cycle of 108 seconds. In Fig.6 (b), the total ampere hour throughput is obtained from sampled data and is found that there is slight difference in battery with UC and battery only operation. The battery only operation with constant and variable C-rate is almost same but is more than the battery with UC operation which is found to be 0.042 *Ah*. In Fig.6 (c), battery capacity in ampere hour is obtained against the total ampere hour throughput and is observed that at the end of drive cycle battery with UC operation results in better capacity retention than battery alone operation with either constant C-rate or variable C-rate.

Using power balance expression, power required i.e., load power, battery power and UC power are obtained. In Fig.7 (a), the torque, load power, battery power and UC power are shown. The acceleration marks the positive torque, and negative torque is representing de-acceleration of the vehicle. For the complete drive cycle a sequence of positive and negative torque is obtained. It is observed that battery power is following the load power at all the time, UC takes part only when there is sudden change in power demand. This nature of UC is due its high-power density as compared to battery. This makes battery with UC based hybrid system to be more efficient as it helps in relieving the stress on battery due to frequent changing load current. The battery aging is therefore slow downed in the HESS as compared to battery only operation in an EV.

In Fig.7 (b), the torque and corresponding load power are shown, load power demand is met by battery alone for battery only operation and for HESS it is supplied from battery and UC both. It is observed that in battery only operation, battery supplies all the power as required by the motor which creates stress on battery and its degradation occurs at faster rate. In zoomed view shown in Fig.7 (c), result suggests that in HESS, UC power is 1400W and is equal to total change in power demand and this helps in relieving the stress on battery and enhances its life as total ampere hour utilized in HESS is less than in battery only operation.

In Fig.7 (d), the speed profile shows clearly the nature of different modes of operation as acceleration, cruising, and de-acceleration. For entire IDC, a sequence of acceleration, cruising and de-acceleration is observed marked by increasing nature of speed, constant nature of speed and decreasing nature of speed respectively. The associated load power is met by battery and UC both in HESS and is supplied from battery alone in battery only operation. Battery power in HESS and battery only operation is obtained for the different motor speed as shown in Fig.7 (e). A zoomed view shown in Fig.7 (f), presents speed profile, battery only power, battery and UC power in HESS. UC enhances the performance of the system by supplying immediate power requirement by the load and this helps in extending battery life. The UC supports battery by supplying 1400W peak power for corresponding change in load power. From Fig.7 (c) and (f) it is observed that UC supplies power at times when there is sudden change in power demand and absorbs power during regenerative mode. The peak power supplied by UC is 1400W for a 10 Nm change of torque as the load changes from regenerative 800W to degenerative 600W of power. The load power is the sum of battery and UC power in HESS and is equal to battery power in case of battery only operation.

VI. Conclusion

Ultracapacitor assisted battery-based HESS for an EV enhances the lifespan of battery by providing the surge power during sudden power requirement by the load. Model predictive control is used to obtain optimum power split among the two sources. The battery aging is evaluated for battery only operation with constant and variable C-rate. The actual capacity fade at the end of the drive cycle is estimated by variable C-rate rather than presumed constant C-rate. In battery with UC operation i.e., HESS, it is observed that battery aging is slower. Moreover, considering the actual C-rate for evaluating the battery capacity loss provides accurate result as compared to battery aging if evaluated by assuming a constant C-rate. Battery capacity loss is evaluated accurately for given drive cycle in HESS. The advantage of the using actual C-rate versus presumed constant C-rate for drive cycle is clearly supported by the results obtained.

Appendix

Activation energy, E_a = 31,700 J/mol, power factor, z = 0.55 and coefficient for aging acceleration, α = 370.3.

References

[1] W. Vermeer, G. R. Chandra Mouli and P. Bauer, "A Comprehensive Review on the Characteristics and Modeling of Lithium-Ion Battery Aging," *IEEE Transactions on Transportation Electrification*, vol. 8, no. 2, pp. 2205-2232, June 2022.

[2] J. Cao and A. Emadi, "A New Battery/UltraCapacitor Hybrid Energy Storage System for Electric, Hybrid, and Plug-In Hybrid Electric Vehicles," *IEEE Transactions on Power Electronics,* vol. 27, no. 1, pp. 122-132, Jan. 2012.

[3] Jiulong Wang, Bingquan Wang, Lei Zhang, Jianjun Wang, N.I. Shchurov, B.V. Malozyomov, "Review of bidirectional DC–DC converter topologies for hybrid energy storage system of new energy vehicles", *Green Energy and Intelligent Transportation*, vol. 1, issue 2, 2022, doi.org/10.1016/j.geits.2022.100010.

[4] Yue Wu, Zhiwu Huang, Yusheng Zheng, Yongjie Liu, Heng Li, Yunhong Che, Jun Peng, Remus Teodorescu, "Spatial–temporal data-driven full driving cycle prediction for optimal energy management of battery/supercapacitor electric vehicles", *Energy Conversion and Management*, vol. 277, 2023, doi.org/10.1016/j.enconman.2022.116619.

[5] Mince Li, Yujie Wang, Pengli Yu, Zhendong Sun, Zonghai Chen, "Online adaptive energy management strategy for fuel cell hybrid vehicles based on improved cluster and regression learner", *Energy Conversion and Management*, vol. 292,2023, doi.org/10.1016/j.enconman.2023.117388.

[6] M. Li, L. Wang, Y. Wang and Z. Chen, "Sizing Optimization and Energy Management Strategy for Hybrid Energy Storage System Using Multiobjective Optimization and Random Forests," *IEEE Transactions on Power Electronics*, vol. 36, no. 10, pp. 11421-11430, Oct. 2021, doi: 10.1109/TPEL.2021.3070393.

[7] Quanqing Yu, Yukun Liu, Shengwen Long, Xin Jin, Junfu Li, Weixiang Shen, "A branch current estimation and correction method for a parallel connected battery system based on dual BP neural networks", *Green Energy and Intelligent Transportation*, vol. 1, issue 2, 2022, doi.org/10.1016/j.geits.2022.100029.

[8] B. Hredzak, V. G. Agelidis and M. Jang, "A Model Predictive Control System for a Hybrid Battery-Ultracapacitor Power Source," *IEEE Transactions on Power Electronics*, vol. 29, no. 3, pp. 1469-1479, March 2014.

[9] N. -D. Nguyen, C. Yoon and Y. I. Lee, "A Standalone Energy Management System of Battery/Supercapacitor Hybrid Energy Storage System for Electric Vehicles Using Model Predictive Control," *IEEE Transactions on Industrial Electronics*, vol. 70, no. 5, pp. 5104-5114, May 2023.

[10] S. A. Ghorashi Khalil Abadi, S. I. Habibi, T. Khalili and A. Bidram, "A Model Predictive Control Strategy for Performance Improvement of Hybrid Energy Storage Systems in DC Microgrids," *IEEE Access*, vol. 10, pp. 25400-25421, 2022.

Authorized licensed use limited to: DELHI TECHNICAL UNIV. Downloaded on March 20,2025 at 04:44:59 UTC from IEEE Xplore. Restrictions apply.
© 2025 IEEE. All rights reserved, including rights for text and data mining and training of artificial intelligence and similar technologies. Personal use is permitted, but republication/redistribution requires IEEE permission. See https://www.ieee.org/publications/rights/index.html for more information.

This article has been accepted for publication in IEEE Journal of Emerging and Selected Topics in Industrial Electronics. This is the author's version which has not been fully edited and content may change prior to final publication. Citation information: DOI 10.1109/JESTIE.2025.3549766

[11] Yue Wu, Zhiwu Huang, Heath Hofmann, Yongjie Liu, Jiahao Huang, Xiaosong Hu, Jun Peng, Ziyou Song, "Hierarchical predictive control for electric vehicles with hybrid energy storage system under vehicle-following scenarios", *Energy*, vol. 251, 2022, doi.org/10.1016/j.energy.2022.123774.

[12] C. Zhao, H. Yin and C. Ma, "Equivalent Series Resistance-based Real-time Control of Battery-Ultracapacitor Hybrid Energy Storage Systems," *IEEE Transactions on Industrial Electronics*, vol. 67, no. 3, pp. 1999-2008, March 2020, doi: 10.1109/TIE.2019.2901640.

[13] J. Xu, A. Alsabbagh and C. Ma, "Prediction-Based Game-Theoretic Strategy for Energy Management of Hybrid Electric Vehicles," *IEEE Journal of Emerging and Selected Topics in Industrial Electronics*, vol. 3, no. 1, pp. 79-89, Jan. 2022.

[14] T. Mesbahi, P. Bartholomeüs, N. Rizoug, R. Sadoun, F. Khenfri and P. L. Moigne, "Advanced Model of Hybrid Energy Storage System Integrating Lithium-Ion Battery and Supercapacitor for Electric Vehicle Applications," *IEEE Transactions on Industrial Electronics*, vol. 68, no. 5, pp. 3962-3972, May 2021.

[15] R. Shi, S. Semsar and P. W. Lehn, "Single-Stage Hybrid Energy Storage Integration in Electric Vehicles Using Vector Controlled Power Sharing," *IEEE Transactions on Industrial Electronics*, vol. 68, no. 11, pp. 10623-10633, Nov. 2021.

[16] Q. Zhang, F. Ju, S. Zhang, W. Deng, J. Wu and C. Gao, "Power Management for Hybrid Energy Storage System of Electric Vehicles Considering Inaccurate Terrain Information," *IEEE Transactions on Automation Science and Engineering*, vol. 14, no. 2, pp. 608-618, April 2017.

[17] Masoud Masih-Tehrani, Mohammad-Reza Ha'iri-Yazdi, Vahid Esfahanian, Ali Safaei, "Optimum sizing and optimum energy management of a hybrid energy storage system for lithium battery life improvement," *Journal of Power Sources*, vol. 244, pp. 2-10, 2013.

[18] Ziyou Song, Heath Hofmann, Jianqiu Li, Jun Hou, Xuebing Han, Minggao Ouyang, "Energy management strategies comparison for electric vehicles with hybrid energy storage system", *Applied Energy*, vol. 134, pp. 321-331, 2014.

[19] Chen, Li, Yuqi Tong, and Zuomin Dong. 2020. "Li-Ion Battery Performance Degradation Modeling for the Optimal Design and Energy Management of Electrified Propulsion Systems" *Energies* 13, no. 7: 1629.

[20] C. Zhou, K. Qian, M. Allan and W. Zhou, "Modeling of the Cost of EV Battery Wear Due to V2G Application in Power Systems," *IEEE Transactions on Energy Conversion*, vol. 26, no. 4, pp. 1041-1050, Dec. 2011.

[21] Mince Li, Yujie Wang, Pei Peng, Zonghai Chen, "Toward Efficient Smart Management: A Review of Modeling and Optimization Approaches in Electric Vehicle-Transportation Network-Grid Integration", *Green Energy and Intelligent Transportation*, 2024, doi.org/10.1016/j.geits.2024.100181.

[22] E. Chemali, M. Preindl, P. Malysz and A. Emadi, "Electrochemical and Electrostatic Energy Storage and Management Systems for Electric Drive Vehicles: State-of-the-Art Review and Future Trends," *IEEE Journal of Emerging and Selected Topics in Power Electronics*, vol. 4, no. 3, pp. 1117-1134, Sept. 2016.

[23] H. Chen, R. Xiong, C. Lin and W. Shen, "Model predictive control based real-time energy management for hybrid energy storage system," *CSEE Journal of Power and Energy Systems*, vol. 7, no. 4, pp. 862-874, July 2021.

[24] M. Li, L. Wang, Y. Wang, X. Chen and Z. Chen, "A Framework for States Co-Estimation of Hybrid Energy Storage Systems Based on Fractional-Order Theory," *IEEE Journal of Emerging and Selected Topics in Power Electronics*, vol. 11, no. 1, pp. 224-233, Feb. 2023, doi: 10.1109/JESTPE.2021.3135019.

[25] Nils Collath, Benedikt Tepe, Stefan Englberger, Andreas Jossen, Holger Hesse, "Aging aware operation of lithium-ion battery energy storage systems: A review", *Journal of Energy Storage*, vol. 55, part C, 2022, doi.org/10.1016/j.est.2022.105634.

[26] John Wang, Ping Liu, Jocelyn Hicks-Garner, Elena Sherman, Souren Soukiazian, Mark Verbrugge, Harshad Tataria, James Musser, Peter Finamore, "Cycle-life model for graphite-LiFePO4 cells", *Journal of Power Sources*, vol. 196, Issue 8, pp. 3942-3948, 2011.

[27] Martin Petit, Eric Prada, Valérie Sauvant-Moynot, "Development of an empirical aging model for Li-ion batteries and application to assess the impact of Vehicle-to-Grid strategies on battery lifetime", *Applied Energy*, vol. 172, pp. 398-407, 2016.

[28] A. Lahyani, P. Venet, A. Guermazi and A. Troudi, "Battery/Supercapacitors Combination in Uninterruptible Power Supply (UPS)," *IEEE Transactions on Power Electronics*, vol. 28, no. 4, pp. 1509-1522, April 2013, doi: 10.1109/TPEL.2012.2210736.

[29] Vidhya SD, Balaji M. "Modelling, design and control of a light electric vehicle with hybrid energy storage system for Indian driving cycle". *Measurement and Control*, vol. 52, pp. 1420-1433, 2019, doi: 10.1177/0020294019858212.

[30] S. Sharma, A. Goel, R. Suresh, C. S. Lakshmi, R. Mahtta, and S.Sundar. "Assessment of emission test driving cycles in India: A case for improving compliance". pp. 1-23, 2013, doi:10.13140/RG.2.1.1589.4163.

Kuldeep Singh (Member, IEEE) was born in Delhi, India, in 1991. He received the B.Tech. degree in electrical engineering from the Indian Institute of Technology Ropar, India, in 2013 and M.Tech. degree in power systems from Delhi Technological University, New Delhi, India in 2016. He currently working towards his Ph.D. degree with the Department of Electrical Engineering at the Delhi Technological University.

He is currently working as Assistant Professor with the Department of Electrical Engineering, Delhi Technological University, New Delhi, India. Since 2016. His research interests include power electronics, power quality and power systems.

Mukhtiar Singh (Member, IEEE) received the B.Tech. and M.Tech. degree in electrical engineering from the National Institute of Technology, Kurukshetra, India, in 1999 and 2001, respectively, and the Ph.D. degree from the Ecole de Technologie Superieure, University of Quebec, Montreal, QC, Canada, in 2010.

He is currently working as a Professor with the Department of Electrical Engineering, Delhi Technological University, New Delhi, India. He is also in the technical advisory group of leading renewable energy companies. His research interests include power electronics, power quality, renewable energy, and intelligent controllers.

Dr. Singh was a recipient of the IEEE Student Scholarship for one of the best papers in the 34th IEEE Conference on Industrial Electronics, IECON2008, held at Orlando, FL, USA. He is also the winner of the Researchers Merit Scholarship of the University of Quebec for three years consecutively, 2008, 2009, and 2010.

Sudarshan Kumar Babu Valluru (Senior Member, IEEE) received the B.Tech. degree in electrical and electronics engineering from Nagarjuna University in 1995, M.Tech. degree in computer applications in industrial drives from National Institute of Engineering, Mysore in 2000 and Ph.D. from Delhi Technological University, Delhi, India in 2018.

Authorized licensed use limited to: DELHI TECHNICAL UNIV. Downloaded on March 20,2025 at 04:44:59 UTC from IEEE Xplore. Restrictions apply.
© 2025 IEEE. All rights reserved, including rights for text and data mining and training of artificial intelligence and similar technologies. Personal use is permitted, but republication/redistribution requires IEEE permission. See https://www.ieee.org/publications/rights/index.html for more information.

This article has been accepted for publication in IEEE Journal of Emerging and Selected Topics in Industrial Electronics. This is the author's version which has not been fully edited and content may change prior to final publication. Citation information: DOI 10.1109/JESTIE.2025.3549766

He has published more than 45 research papers in various international, national journals and conferences and authored a book on ‘Introduction Neural Networks, Fuzzy Logic, and Genetic Algorithms’ (Jaico publishing house, 2010). Presently he is working as Professor of Electrical Engineering in Delhi Technological University. His area of interests is AI & Bio-Inspired Algorithms, System Chaology, Power Electronics with Electro Mechanical Systems and Electricity Tariffs.

Authorized licensed use limited to: DELHI TECHNICAL UNIV. Downloaded on March 20,2025 at 04:44:59 UTC from IEEE Xplore. Restrictions apply.
© 2025 IEEE. All rights reserved, including rights for text and data mining and training of artificial intelligence and similar technologies. Personal use is permitted, but republication/redistribution requires IEEE permission. See https://www.ieee.org/publications/rights/index.html for more information.

Journal of Engineering Materials and Technology. Received January 13, 2025;
Accepted manuscript posted March 5, 2025. doi: 10.1115/1.4068135
Copyright © 2025 by ASME

Check for updates

Ultrasonic Vibration Assisted Cold Metal Transfer Direct Energy Deposition of Dissimilar SDSS2507-IN718 Alloy parts: Microstructural and Mechanical Characterization

Rajendra Prasad[1*], N. Yuvaraj[1a], Vipin [1b]

Department of Mechanical Engineering, Delhi Technological University

Email Id: rpmeena89@gmail.com, yuvraj@dce.ac.in, vipin@dce.ac.in

Orchid id: https://orcid.org/0009-0000-5387-1406, https://orcid.org/0000-0002-1537-9098, https://orcid.org/0000-0003-4643-7200

Abstract: Cold Metal Transfer (CMT) has emerged as a highly promising method for directly producing or repairing high-performance metal components. Induced fabrication defects, like porosity and heterogeneous microstructures, impact part quality and mechanical performance. Investigating a high-efficiency CMT-based wire arc direct energy deposition method is important for manufacturing high-quality, super duplex stainless steel 2507 (SDSS2507)-Inconel 718 (IN718) parts. Ultrasonic vibration has been used to enhance part performance in melting material solidification procedures. Few studies exist on using ultrasonic vibration in CMT-based wire arc direct energy deposition for dissimilar SDSS2507-IN718 part production. This research proposes the use of ultrasonic vibration (UV) assisted CMT-based wire arc direct energy deposition to manufacture dissimilar SDSS2507-IN718 parts to potentially decrease fabrication faults. Experimental studies are carried out to examine the impact of ultrasonic vibration on the microstructures and mechanical properties of parts manufactured using CMT. The findings demonstrated that the application of ultrasonic vibration improved the microstructure, leading to an average grain size of 4.59 um. Additionally, it effectively fragmented the harmful Laves precipitated phase into small particles that were evenly distributed. Consequently, the yield strength and ultimate tensile strength (UTS) of the fabricated dissimilar SDSS2507-IN718 parts were improved. The microhardness increases from an average of 302 HV to 335 HV, reflecting an 11% gain, at SDSS2507; from 233 HV to 265 HV at the Interface, indicating a 14% increase; and from 249 HV to 270 HV at IN718, demonstrating a 9% enhancement.

Keywords: Direct Energy Deposition, Dissimilar alloy, Ultrasonic vibration, Microstructure analysis, Mechanical Characterization, Cold Metal Transfer

1. Introduction

The joining of dissimilar metal components is of prior importance in several industrial sectors, such as aviation, aerospace, shipbuilding, and automobile manufacturing. The composition of these components typically includes alloys made from steel, magnesium, titanium, and nickel-based superalloys [1]. Obtaining optimal combinations of a variety of metals using conventional joining or welding methods can impose challenges owing to the potential formation of brittle intermetallic compounds (IMCs) during solidification [2]. Reducing the fusion heat input is essential in solid-state bonding to efficiently overcome the primary issue of achieving proper contact between different materials [3]. Steel-nickel alloys are promising for use as structural materials in nuclear energy systems, chemical processing plants, and particularly in gas turbine engines [4]. These alloys are widely valued for their exceptional performance in extreme combustion and chemically hostile circumstances. These materials depicted impressive mechanical characteristics, exceptional resistance to corrosion, strong resistance to deformation at high temperatures, and excellent ability to withstand damage from radiation [5,6]. Inconel 718 is a nickel-iron-chromium superalloy that is highly regarded for its excellent properties. It showed excellent resistance to high temperatures, corrosion, and fatigue while possessing exceptional tensile strength and exhibiting optimal creep behaviour [7]. SDSS2507 demonstrates exceptional performance in difficult environments because of its

Accepted Manuscript Not Copyedited

Downloaded from http://asmedigitalcollection.asme.org/materialstechnology/article-pdf/doi/10.1115/1.4068135/7444918/mats-25-1006.pdf by Delhi Technological University user on 10 March 2025

Journal of Engineering Materials and Technology. Received January 13, 2025;
Accepted manuscript posted March 7, 2025. doi: 10.1115/1.4068185
Copyright © 2025 by ASME

strong resistance to corrosion and impressive mechanical qualities. The high amounts of chromium and nickel and its ferritic-austenitic microstructure are responsible for this [8]. Due to the considerable cost benefit of SDSS2507 compared to the IN718 superalloy, it is more cost-effective to use SDSS2507 for components that operate at lower temperatures. Despite its increased cost, Inconel 718 superalloy remains preferred for parts exposed to higher temperatures. This technique efficiently manages material costs while capitalizing on the unique advantages of each material in their specific working conditions.

Wire-arc directed energy deposition, also called wire-arc additive manufacturing (WAAM), is a cost-effective and highly efficient method for producing large-scale components that are almost complete in shape [9]. The CMT is an advanced version of gas metal arc welding that reduces the amount of heat generated during the metal deposition process. This leads to a reduction in spattering and an improvement in the stability of the arc [10,11]. The CMT uses the filler wire's reciprocal movements in the short-circuiting mode to transport materials. The CMT process is defined by its unique fusion of wire movement and transfer mode [12]. The low heat in CMT WAAM is beneficial for depositing dissimilar alloy additive manufacturing walls, such as steel-nickel, steel-aluminium, and aluminium-nickel, which are commonly used in industrial applications [13].

Several methods, including ultrasonic vibration, electromagnetic field integration, and mechanical stirring, have been employed to reduce fabrication defects by regulating the melting and solidification behaviour of materials in thermal processes such as casting, arc welding, and cladding [14–19]. Ultrasonic vibration is a highly regarded technique among these aiding approaches. It is favoured because it effectively transmits acoustic energy and cavitation and can remarkably control heat and mass transfer [20]. Typically, when a powerful ultrasonic vibration is applied to a liquid, it produces two distinct nonlinear phenomena: acoustic streaming and acoustic cavitation [20,21]. Ultrasonic vibration can reduce the presence of small holes, improve the quality of the grains, and break down the harmful Laves precipitated phase. This leads to enhancements in the tensile strength, modulus, microhardness, and wear resistance of the IN718 parts produced using the ultrasonic vibration-assisted (UV-A) DED method reported by Ning et al. [22]. The latest study on the DED processing of Ti-6Al-4V has provided evidence for the significant impact of UV-induced grain refinement on tensile characteristics [23]. UV improved grain refining and reduced the directional growth of coarse columnar grains. Secondary phases with Mo and Nb easily precipitate in c-Ni grain boundaries. UV-CMT samples had more homogeneous secondary phase distribution due to enhanced grain boundary density by Ma et al. [24]. The latest study [25] found that FGMs without ultrasonic treatment have columnar grains, but ultrasonic treatment refines grains into equiaxed forms, enhancing uniformity and reducing grain size in the case of ultrasonic-assisted double wire arc additive manufacturing (U-DWAAM). Equiaxed grains and reduced crystal size give ultrasonically treated specimens greater tensile strength and lower elongation. Ultrasonic treatment enhances hardness from SS 308L to IN718 by 7%-15% due to microstructural changes, solid solution strengthening, and precipitation enhancement from Ni, Mo, and Nb content.

The majority of research on wire-based additive manufacturing has been on employing ultrasonic vibration-assisted GMAW, CMT, U-DWAAM and laser-based WAAM systems to join various alloys, including steel, aluminium, and nickel. The comprehension of the impact of UV on the microstructural and mechanical characteristics of dissimilar SDSS2507 - IN718 alloy structures produced by CMT WAAM is presently constrained. This study effectively employed ultrasonic aid in the CMT-based WAAM method to manufacture walls of different SDSS2507 and IN718 alloys. This study analyzed the ultrasonic-assisted microstructure and mechanical properties of the interface zone, comparing them to standard conditions.

Accepted Manuscript Not Copyedited

Downloaded from http://asmedigitalcollection.asme.org/materialstechnology/article-pdf/doi/10.1115/1.4068135/7444918/mats-25-1006.pdf by Delhi Technological University user on 10 March 2025

Journal of Engineering Materials and Technology. Received January 13, 2025;
Accepted manuscript posted March 7, 2025. doi:10.1115/1.4068135
Copyright © 2025 by ASME

2. Experimental procedure

2.1 Materials and Methodology

The investigations utilized Inconel 718 and SDSS2507, 1.2 mm filler wire from Advanced PMI Solutions. The substrate plate, 200 mm × 50 mm × 5 mm, was made from stainless steel 304. A CMT-based WAAM method with alternating current produced dissimilar alloy components, IN718 and SDSS2507. In Table 1, we can see the chemical composition of the substrate and filler wire.

Table 1 Chemical composition (Wt %) of the substrate material and filler wire

Chemical Composition %	C	Si	Mn	P	S	Ni	Cr	Al	Mo	Fe	Nb
Stainless steel (304)	0.07	1.03	2.05	0.045	0.030	8.04	17.95	-	-	70.78	-
Super Duplex 2507	0.030	0.80	1.20	0.035	0.020	7	25	-	4	57.82	-
Inconel 718	0.08	0.35	0.45	0.015	0.017	51.05	17.55	0.55	2.9	22.14	4.89

The WAAM system was set up on a Remote (FRC-45 Pro) operated table unit with an ultrasonic vibration unit and a TPS 400i power source to create the samples, as depicted in Fig. 1. The ultrasonic vibration unit generates vibrations during the WAAM process. High-energy ultrasound control systems typically include a transducer, power supply, and ultrasonic horn. Extremely powerful ultrasonic waves are produced by the transducer. The ultrasonic horn was linked to an ultrasonic generating box, functioning at a stable frequency of 30 kHz. The amplitude of ultrasonic vibrations varied between 11 and 99 µm, with a constant value of 60 µm utilized in our experimentation. The input energy and electrical signals are controlled by the power supply. The ultrasonic horn amplifies high-power ultrasound and insulates heat carried through the substrate, preventing transducer damage. The Mechanical and Thermal properties of SDSS2507 and IN718 are shown in Table 2.

Table 2 Mechanical and Thermal Properties of SDSS2507 and IN718

Mechanical Properties	SDSS2507	IN718	Thermal Properties	SDSS2507	IN718
Tensile Strength	800-950 MPa	1,030 MPa	**Melting Point**	1,350–1,450°C	1,330–1,370°C
Yield Strength	550-650 MPa	725 MPa	**Thermal Conductivity**	14 W/m·K at room temperature.	11.4 W/m·K at room temperature
Elongation	25-35% in 50 mm	30-50% in 50 mm	**Thermal Expansion Coefficient**	13.0 µm/m·°C	13.0 µm/m·°C
Hardness	250-350 HV	200-250 HV			

The materials SDSS2507 and IN718 wire are introduced into the central area of an electric arc during the printing process. The meticulous process of depositing the material, line by line and

Accepted Manuscript Not Copyedited

Downloaded from http://asmedigitalcollection.asme.org/materialstechnology/article-pdf/doi/10.1115/1.4068135/7444918/mats-25-1006.pdf by Delhi Technological University user on 10 March 2025

Journal of Engineering Materials and Technology. Received January 13, 2025;
Accepted manuscript posted March 25, 2025. doi: 10.1115/1.4068135
Copyright © 2025 by ASME

layer by layer, resulted in a flawless dissimilar alloy block with or without ultrasonic vibration. This block measures 150mm in length and 100mm in height, consisting of an impressive 60 layers. Table 3 lists optimal process parameters. Due to its compatibility with SDSS2507 and IN718, 99.99% pure argon was used for welding. We chose 15mm nozzle-to-workpiece spacing. The CMT-based WAAM technology applied layers of beads following a cleaning process using acetone. The time interval between layers, known as the interpass dwell duration, was set to 120 seconds. The strain was calculated by utilizing crosshead extension in the tensile test. To compute strain using crosshead extension, we divided the measured crosshead extension (change in length) by the initial gauge length of the specimen under test; the formula is: Strain (ε) = $\Delta L / L_0$, where ΔL represents the change in length (crosshead extension), and L_0 is the starting gauge length of the specimen. Three tensile tests were conducted on the INSTRON 5900R test machine for each condition.

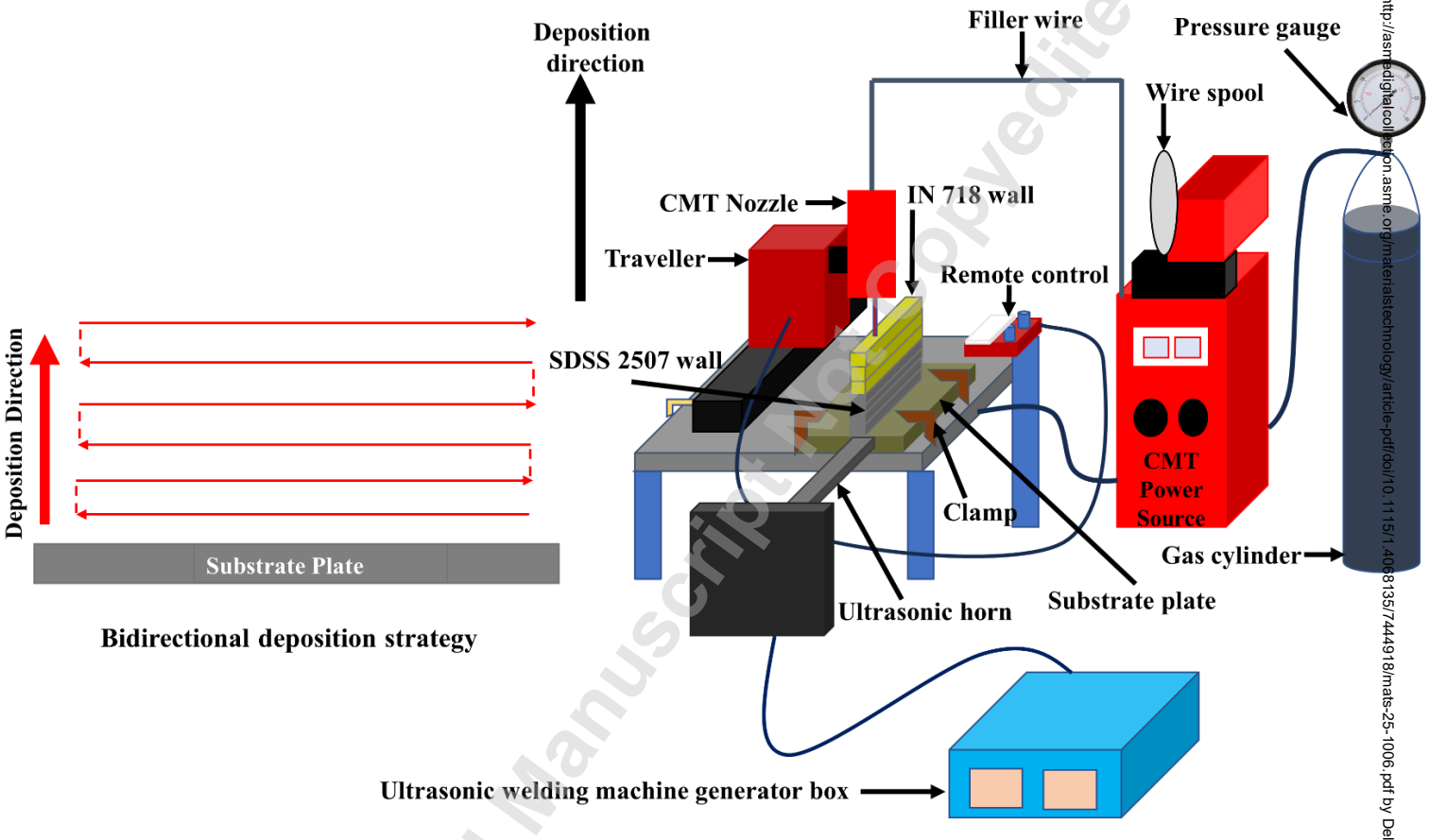

Fig. 1 Schematic CMT WAAM experimental setup with ultrasonic vibration unit for dissimilar alloy using remote-controlled traveller with deposition strategy

2.2 Material characterization

Fig.2(a) shows a schematic diagram of microstructure specimens. Fig.2(b) shows a manufactured WAAM wall of dissimilar SDSS2507-IN718 alloy. Tensile specimens and the dimensions of the tensile representative samples are shown in Fig. 2(c). The samples were meticulously prepared and polished with silicon carbide paper with a range of grit sizes from 300 to 2500 to examine the microstructure. For etching, the IN718 samples were thereafter submerged in a chemical solution that was composed of a mixture of oxalic acid and hydrochloric acid at a ratio of 50:50 [26]. The etching solution for SDSS2507 comprised 80 ml of deionized water, 20 ml of hydrochloric acid, and 0.3g of sodium metabisulfite [27]. Following that, the procedure entailed employing alumina powder on a felt pad for polishing. The detailed microstructures of various alloy samples were analyzed utilizing energy-dispersive spectroscopy (EDS) and scanning electron microscopy (SEM; NOVA NANOSEM

Accepted Manuscript Not Copyedited

Downloaded from http://asmedigitalcollection.asme.org/materialstechnology/article-pdf/doi/10.1115/1.4068135/7444918/mats-25-1006.pdf by Delhi Technological University user on 10 March 2025

Journal of Engineering Materials and Technology. Received January 13, 2025;
Accepted manuscript posted March 7, 2025 doi: 10.1115/1.4068185
Copyright © 2025 by ASME

450). The ImageJ software was utilized to analyze grain size under various processing conditions. The grain size in a certain region was determined by averaging ten measurements.

Table 3 CMT WAAM deposition parameters used in this experiment

WAAM Parameters	Value for SDSS2507	Value for IN718
Current (I)	210	190
Travel speed (mm/s)	6.91	8.94
Gas flow rate (l/min)	25	15
Nozzle tip distance	15	15

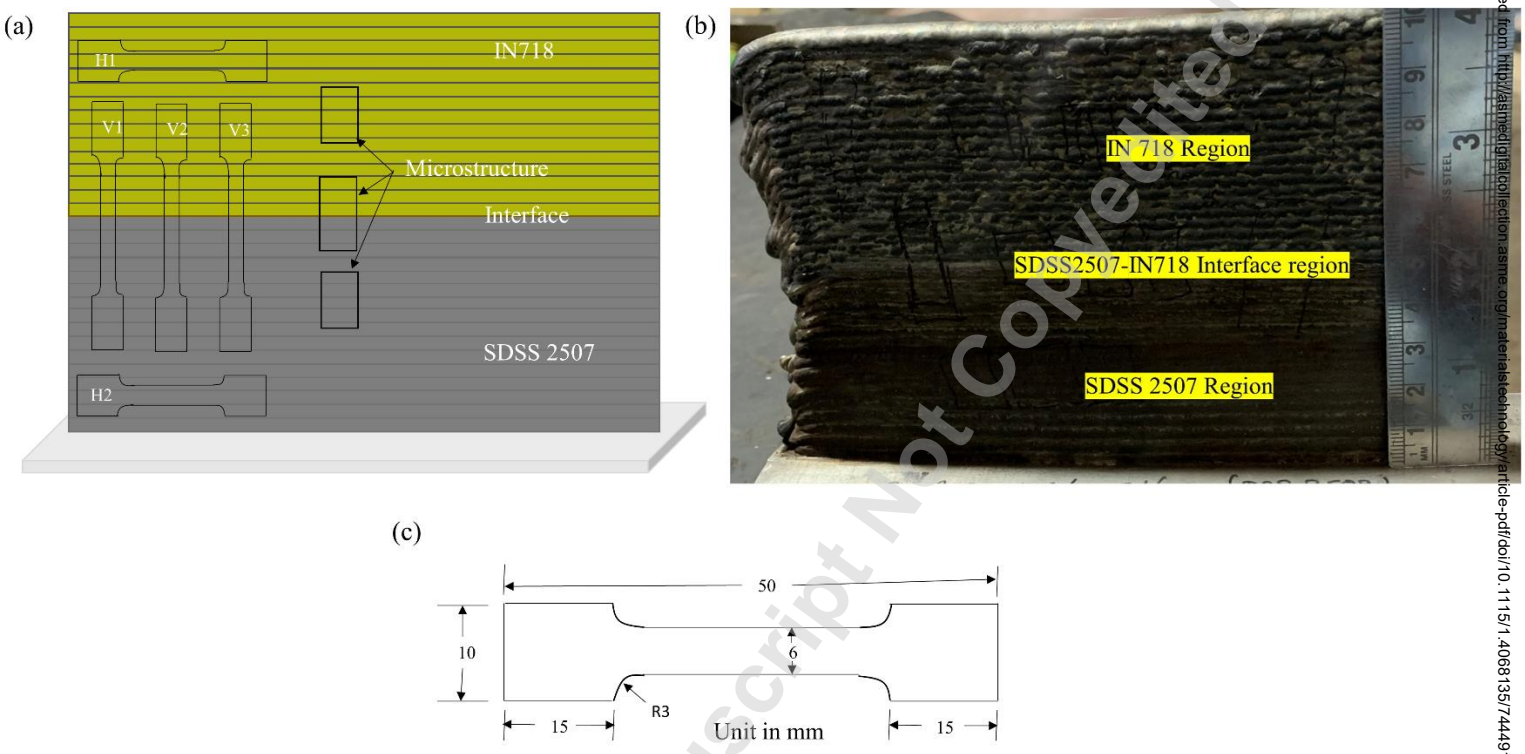

Fig. 2 (a) Schematic diagram of Tensile and Microstructure of Dissimilar alloy (b) Manufactured WAAM wall of Dissimilar SDSS2507-IN718 alloy (c) Tensile specimen dimensions

For the purpose of determining the microhardness of the deposited wall, a Vickers microhardness tester (DURAMIN-40 STRUERS) that was in accordance with ASTM E34 was utilized. A load of 500 gf and a dwell time of ten seconds were utilized to accomplish this. The samples with a shorter grab length were generated using wire electrical discharge machining per the specifications established by ASTM-E8. This was done so that standard tensile testing could be carried out. SiC paper with a grit of 800 was used for polishing the samples to make them smooth and remove any roughness that may have been present. A strain rate of 0.001 s−1 was employed when determining the yield stress. The yield stress was then evaluated with an Instron 5900R mechanical tester, employing a 0.2% proof stress approach for the testing.

3. Result and Discussion

3.1 Grain microstructure

Due to the quick solidification characteristic, the microstructures created from the CMT process differ from those seen in cast or wrought pieces. The microstructural grains of the SDSS2507-IN718 interface, IN718, and SDSS2507 alloy produced by CMT WAAM without

Accepted Manuscript Not Copyedited

Downloaded from http://asmedigitalcollection.asme.org/materialstechnology/article-pdf/doi/10.1115/1.4068135/7444918/mats-25-1006.pdf by Delhi Technological University user on 10 March 2025

Journal of Engineering Materials and Technology. Received January 13, 2025;
Accepted manuscript posted March 3, 2025. doi: 10.1115/1.4068135
Copyright © 2025 by ASME

and with UV are illustrated in Fig. 3. From Fig. 3 (A0, B0, C0), it is evident that the coarse elongated grains were formed when the CMT power was used without UV. The grain size obtained under these circumstances was 6.161 µm, as depicted in Figure 3(b). The locally unidirectional solidification behaviour led to the extended grain growth along the build direction. Under the influence of UV in CMT WAAM, the grains underwent a transition from columnar to equiaxed, as depicted in Fig. 3(A1, B1, C1). This transition resulted in a reduction in grain size to 4.5972 µm.

The grain refinement trend caused by UV can be attributed to two main mechanisms: the breaking up of dendrites due to cavitation and the increased nucleation caused by cavitation [28–30]. When UV is applied to the melting materials, it can rapidly generate cavitation bubbles. Once the bubbles collapsed, the resulting shocks created intense pressure waves that propagated through the acoustic field, potentially causing the fragmentation of elongated dendrite tips. At the same time, convection carried the dendritic tips into the undercooled melt, forming numerous grain nuclei. The ultrasonic cavitation induced a transition from a columnar to an equiaxed form in the molten materials at the elongated dendritic boundary [31], resulting in a significant decrease in the size of the microstructural grains. Transitioning from columnar to equiaxed grains can offer advantages in reducing grain size. Moreover, the attainment of a consistent dispersion of grains was made easier by the standardized temperature pattern created by ultrasonic vibration in particular regions [32].

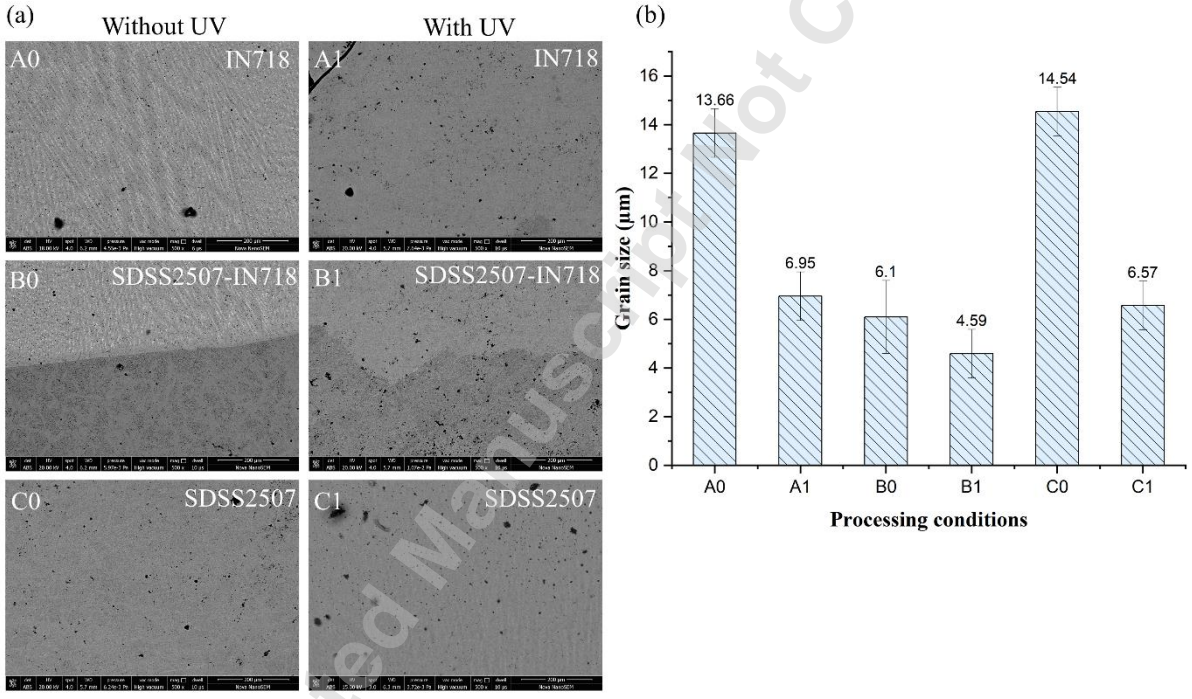

Fig. 3 (a) Microstructural characteristics without and with UV (b) Grain size variation under different processing conditions

3.2 Phase composition analysis

Fig. 4 displays the analysis results of the energy-dispersive X-ray spectroscope for Dissimilar SDSS2507-IN718 parts fabricated using CMT, both with and without the application of UV. It is observed that points 1 and 3 are rich in Ni, Fe, and Cr, while point 2 at the interface zone demonstrates the major variation in Ni, Cr, Fe, Nb and MO.

The white precipitated phase in IN718 point 1 was abundant in Ni, Cr, Nb, and Mo, which were the primary compositional elements of the Laves phase [33]. The Laves phase was a brittle intermetallic compound abundant in Nb and had a typical composition of $(Ni, Cr, Fe)_2$ (Nb, Mo, Ti). Other investigations have also identified the Laves phase in CMT-fabricated IN718

Accepted Manuscript Not Copyedited

Downloaded from http://asmedigitalcollection.asme.org/materialstechnology/article-pdf/doi/10.1115/1.4068135/7444918/mats-25-1006.pdf by Delhi Technological University user on 10 March 2025

Journal of Engineering Materials and Technology. Received January 13, 2025;
Accepted manuscript posted March 03, 2025. doi: 10.1115/1.4068135
Copyright © 2025 by ASME

components [30]. The presence of Nb segregation in the IN718 alloy led to the development of irregularly shaped Laves phase, which was found to have a negative impact on the mechanical properties. This particular phase could potentially enhance crack propagation, reducing the overall strength and ductility of the IN718 alloy. SEM image shows the boundary at position 2. Due to SDSS2507 and IN718's comparable composition, the IF had no defects, and Cr distribution was consistent on both sides. From the EDS region scan, the IF showed no elemental segregation. The IN718 filler wire creates a molten pool on the SDSS2507 layer at the IF. Dissolution of elements was confirmed throughout the IF. The EDS plot shows mixed components and no notable Cr changes.

According to reports, the presence of the Nb element substantially impacts the solidification sequence and the precipitation of strengthening phases in the IN718 alloy [34]. In CMT, the solidification of IN718 starts with a primary liquid reaction, which enriches the interdendritic liquid with elements including Ti, Mo, and Nb. Eventually, the process concludes with a eutectic-type reaction [35]. Because of the limited ability of larger Nb atoms to spread out, it was challenging to dissolve the Laves phase within the matrix of CMT-fabricated parts. However, using UV, the long-bar Laves phase morphology can be broken into smaller particle shapes by delivering high-intensity shock waves. This is illustrated in the SEM images in Fig. 4. By introducing ultrasonic energy, the temperature of the molten pool can be raised, resulting in an increased solubility of Nb in the matrix phase. The results showed UV helped partially dissolve the Laves phase within the matrix. The presence of a small-particle-shaped Laves phase in the matrix contributed to a uniform distribution, resulting in a homogenous phase distribution.

In Fig. 5, the emphasized section indicates the elemental scan area for the compositional characterization of the IF. The elements Nb, Mo, Mn, C, Al, and Si exhibited significant segregation, whereas Ni, Cr, and Fe demonstrated uniform distribution, as illustrated in the elemental mapping.

An EDS scan was performed in the IF region to analyze the elemental composition of the materials, as illustrated in Fig 5. A scan was conducted in the IF area at a distance of 200 µm. The principal elements, namely Fe, Ni, Cr, Mo, and Nb, were documented and are illustrated in Fig. 5 EDS mapping. Fig. 4 illustrates notable fluctuations in the Fe and Ni concentrations at the Interface, attributable to the differing compositional ratios of Ni and Fe in the SDSS2507 and IN718 layers. The differing concentrations of Mn in the two filler wires resulted in a noticeable alteration in the Mn concentration in the transition zone.

Accepted Manuscript Not Copyrighted

Downloaded from http://asmedigitalcollection.asme.org/materialstechnology/article-pdf/doi/10.1115/1.4068135/7444918/mats-25-1006.pdf by Delhi Technological University user on 10 March 2025

Journal of Engineering Materials and Technology. Received January 13, 2025;
Accepted manuscript posted March 7, 2025. doi:10.1115/1.4068135
Copyright © 2025 by ASME

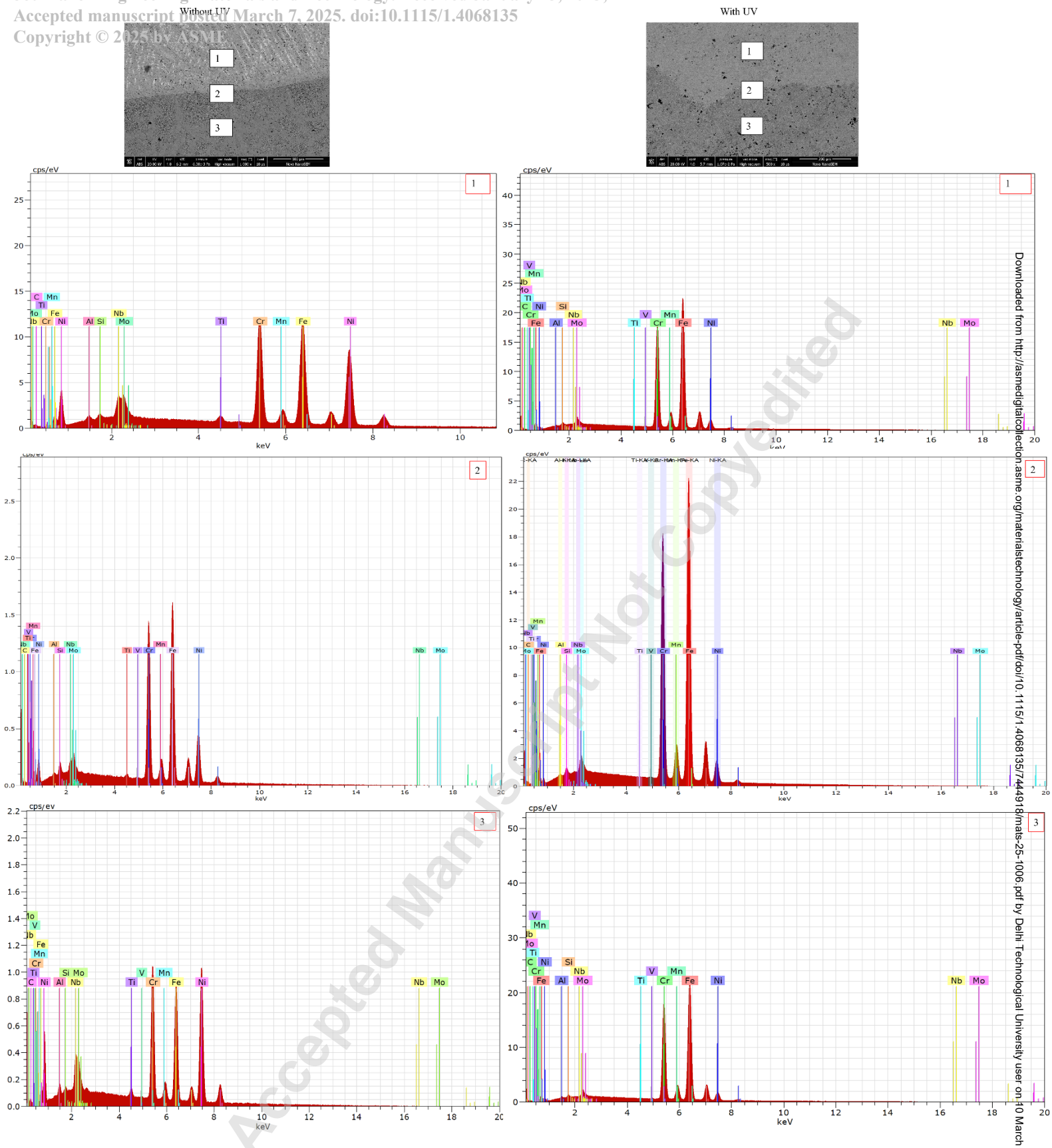

Fig. 4 Energy dispersive X-ray spectroscope analysis results of dissimilar SDSS2507-IN718 parts fabricated by CMT WAAM (a) Without ultrasonic vibrations (b) With ultrasonic vibrations

The minor variation in Cr content is attributed to the dilution of the IN718 layer over the SDSS2507. At the IF, the IN718 filler wire is employed to create a molten pool atop the previously deposited SDSS2507 layer. Consequently, confirmation of element dissolution was

Accepted Manuscript Not Copyedited

Downloaded from http://asmedigitalcollection.asme.org/materialstechnology/article-pdf/doi/10.1115/1.4068135/7444918/mats-25-1006.pdf by Delhi Technological University user on 10 March 2025

Journal of Engineering Materials and Technology. Received January 13, 2025;
Accepted manuscript posted March 7, 2025. doi: 10.1115/1.4068175
Copyright © 2025 by ASME

noted across the IF. The EDS plot reveals that the elements were combined, with no notable variations in the quantity of Cr observed. The existence of the laves phase was confirmed in the IN718 layers. The laves phase is believed to form when certain elements, such as Mo and Nb, segregate during non-equilibrium solidification [36].

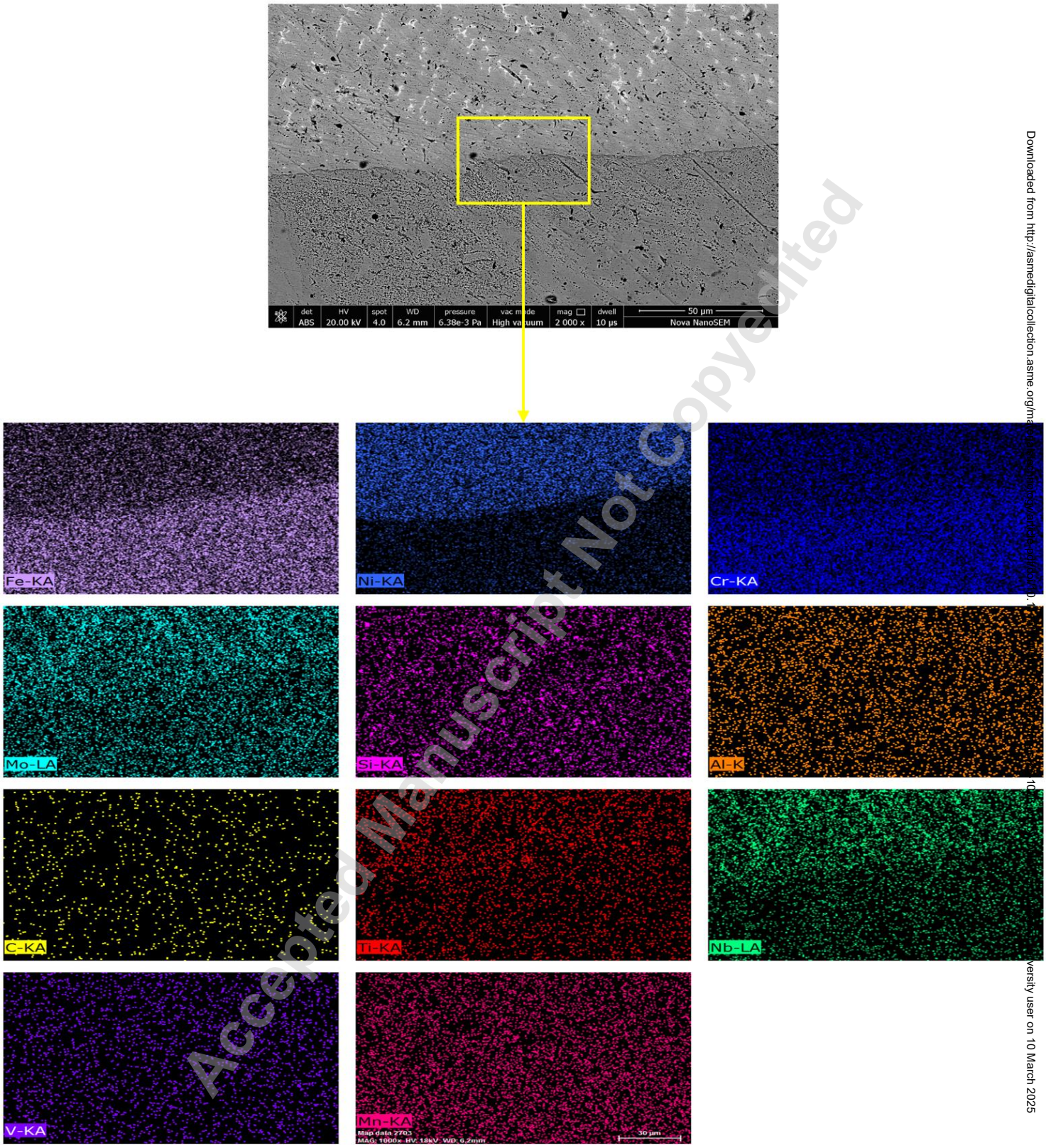

Fig. 5 Dissimilar SDSS2507- IN718 alloy interface region EDS mapping

Accepted Manuscript Not Copyedited

Downloaded from http://asmedigitalcollection.asme.org/materialstechnology/article-pdf/doi/10.1115/1.4068175/7600010/1
10 March 2025
University user on 10 March 2025

Journal of Engineering Materials and Technology. Received January 13, 2025;
Accepted manuscript posted March 7, 2025. doi: 10.1115/1.4068135
Copyright © 2025 by ASME

3.3 Microhardness analysis

Microhardness measurements were performed at three specific places, SDSS2507, SDSS2507-IN718 interface (IF), and IN718, along the building direction, as shown in Fig. 6. The application of UV led to a notable enhancement in microhardness, with a rise from the average value of 302 HV to 335 HV, with an 11% increment, at SDSS2507, 233 HV to 265 HV at Interface with a 14% increment and 249 HV to 270 HV at IN718 with a 9% increment. The findings indicate that ultrasound refinement enhances the microstructure of the thin-wall component, resulting in increased microhardness. Furthermore, the hardness of the material is directly correlated with its microstructure. It is well-established that the microhardness tends to increase as the UTS increases. The link between microhardness and ultimate tensile strength (UTS) suggests that the rise in microhardness is due to the grain refining caused by UV. The reduction in porosity indicated earlier would be advantageous for achieving a more consistent density in the production of parts, hence increasing the quality of the parts with increased microhardness.

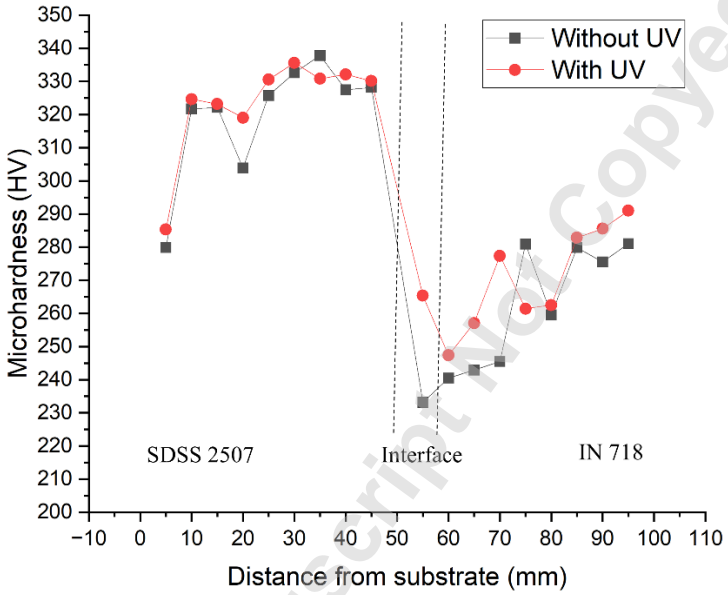

Fig. 6 Microhardness variation of Dissimilar SDSS2507- IN718 parts with or without UV

3.4 Tensile Properties

The stress-strain curve, UTS, yield strength, and ductility of dissimilar SDSS2507-IN718 components made under varying processing circumstances are shown in Fig. 7. The specimens' flow curves were identical with and without UV, but the results were very different. Tensile characteristics were demonstrated as a mean with one standard deviation. The addition of ultrasonic vibration in the CMT WAAM process significantly increased yield strength and UTS. However, it did not have a noticeable impact on ductility when compared to the process without ultrasonic vibration. The increase in yield strength and ultimate tensile strength can be ascribed to the reduction in grain size caused by ultrasonic vibration. Increases in yield strength and decreases in UTS are observed as grain sizes decrease in microstructure. The traditional Hall-Petch equation [37], states that yield strength/UTS is positively correlated with the reciprocal root of grain size, agreed with this tendency. In addition, UV reduced the presence of pores, broke down the Laves phase into smaller fragments, and promoted the even distribution of components. These factors also played a role in increasing yield strength and UTS.

Accepted Manuscript Not Copyedited

Downloaded from http://asmedigitalcollection.asme.org/materialstechnology/article-pdf/doi/10.1115/1.4068135/7444918/mats-25-1006.pdf by Delhi Technological University user on 10 March 2025

Journal of Engineering Materials and Technology. Received January 13, 2025;
Accepted manuscript posted March 7, 2025. doi:10.1115/1.4068135
Copyright © 2025 by ASME

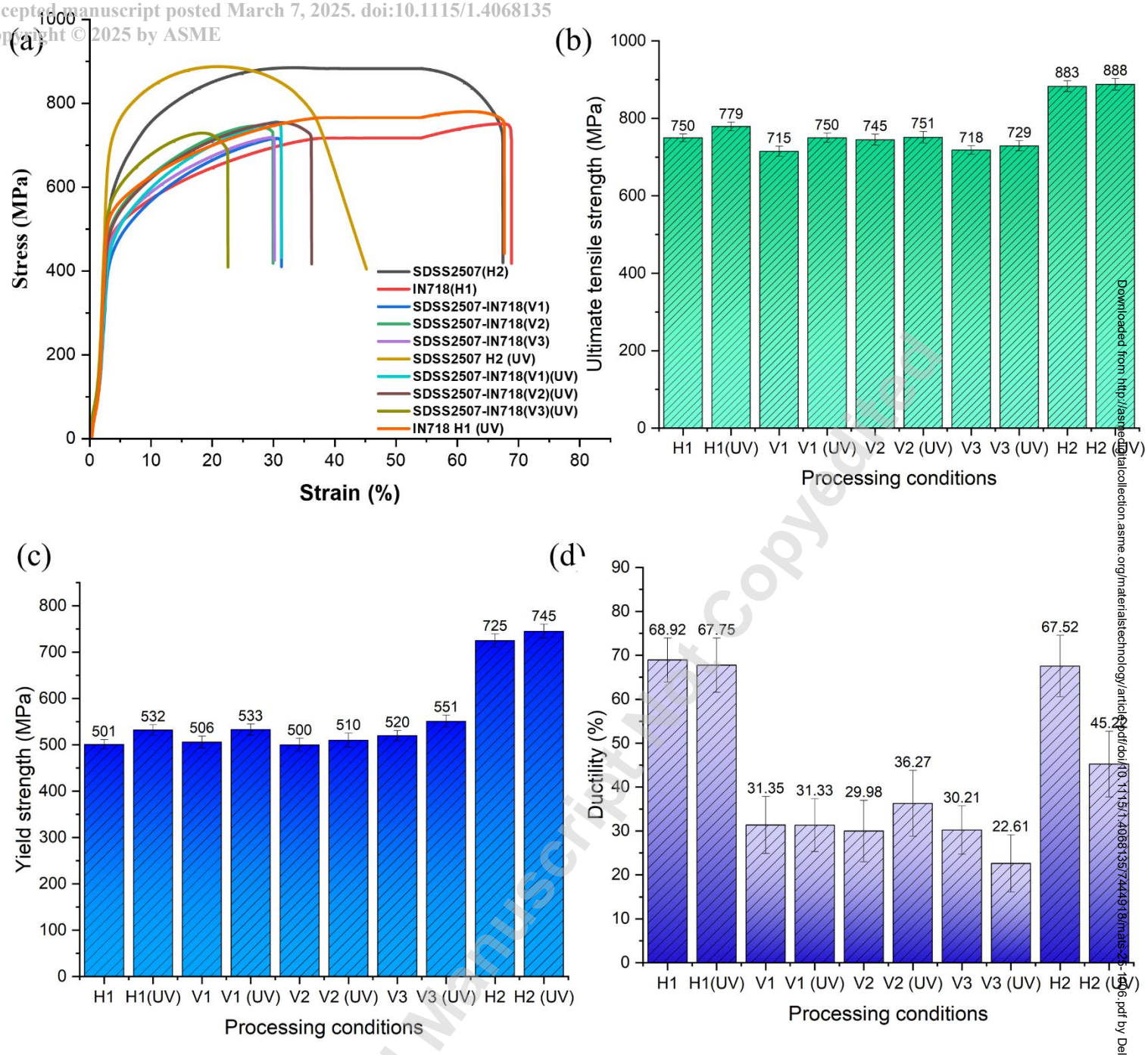

Fig. 7 Comparison of (a) Stress-strain curve, (b) UTS, (c) Yield strength, and (d) Ductility of CMT DED fabricated dissimilar SDSS2507-IN718 parts with or without UV

To better understand how microstructure affects mechanical behaviour, specimens' tensile fracture surface morphology was examined. Fig. 8 displays the distinct tensile fracture surfaces of various specimens, including SDSS2507, the Interface between SDSS2507 and IN718, and IN718, with or without UV. The specimens display equiaxed dimples and transgranular features in both UV and non-UV micrographs, indicating a ductile fracture mode with excellent ductility. Without UV, dimple sizes differed between locations (Fig. 8a, b, c). The breakage of nearby grains caused large and deep dimples, while the fracture of a single grain caused dense and little dimples. Thus, coarse microstructure is linked to big dimples. The microstructure and grain size of the wall component were made smaller and more uniform through the use of ultrasound. This resulted in superior mechanical properties and the presence of more evenly distributed dimples, which were smaller in size and depth (Fig. 8 d, e, f). As a result, the specimens experienced a notable increase in microhardness and strength when subjected to

Accepted Manuscript Not Copyedited

Downloaded from http://asmedigitalcollection.asme.org/materialstechnology/article-pdf/doi/10.1115/1.4068135/7449181/mats-25-1006.pdf by Delhi Technological University user on 10 March 2025

Journal of Engineering Materials and Technology. Received January 13, 2025;
Accepted manuscript posted March 7, 2025. doi: 10.1115/1.4068135
Copyright © 2025 by ASME

ultrasound. However, there was a slight decrease in elongation compared to specimens not treated with ultrasound. The discovery confirms the outcome that the strength of wall components experiences a notable boost while their plasticity sees a slight decline.

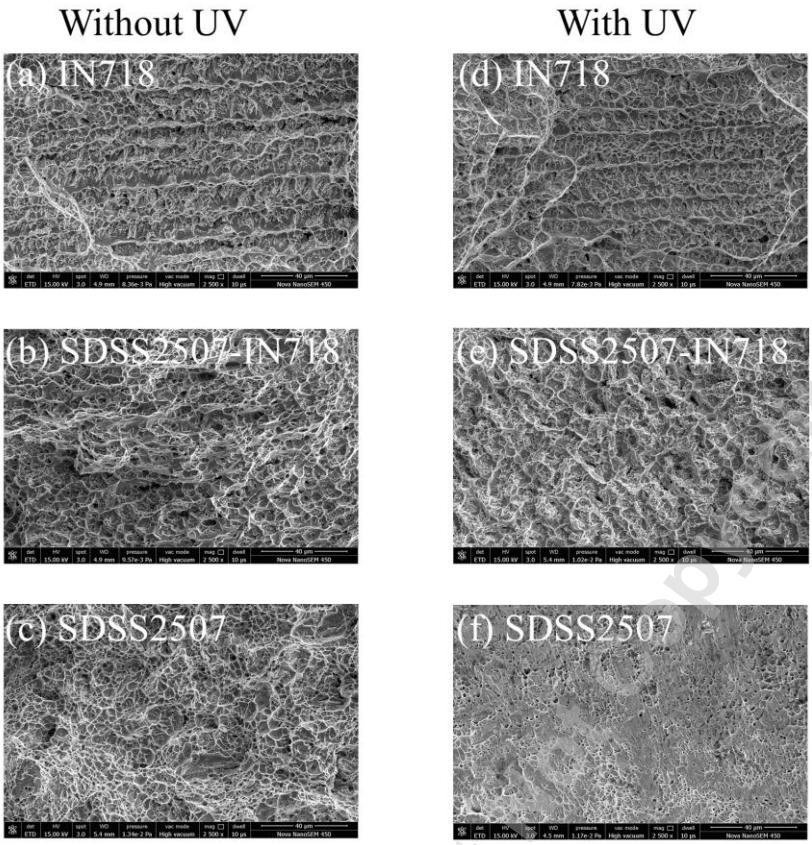

Fig. 8 SEM morphology of fractured surfaces (a, b, c) Without UV (d, e, f) With UV of Tensile specimens

4. Conclusions

The paper demonstrates the successful application of the CMT-WAAM technique to deposit a dual metallic wall consisting of SDSS2507 and IN718, with the aid of ultrasonic vibration. A study was done to examine the effect of ultrasonic vibration on the capacity for formation, microstructure, and mechanical properties. The following conclusion can be made-

- The CMT-WAAM method uses ultrasonic vibration to successfully produce WAAM walls made of dissimilar alloys, such as SDSS2507 and IN718. There were no signs of microstructural defects, including cracks and porosity, in the microstructure.
- The microstructure investigation revealed that deposited welds consisted of dendrites and columnar grains. Utilizing ultrasonic vibration resulted in beneficial outcomes such as reducing the size of grains and inhibiting the preferential growth of large columnar grains.
- The Laves phase, which had a higher Ni concentration in the matrix phase, dissolved more easily with ultrasonic vibration. By employing ultrasonic vibration, the Laves phase morphology, which was characterized by a long bar shape, was uniformly fractured into small sphere-shaped particles. The fundamental reason for this was the extremely high pressure in the acoustic field that was created by ultrasonic vibration.
- The yield strength, UTS, and microhardness of different SDSS2507-IN718 components made with UV-CMT WAAM were significantly enhanced as a result of reduced porosity, refined grains, Laves phase fragmentation, and consistent elemental distribution.

Accepted Manuscript Not Copyrighted

Downloaded from http://asmedigitalcollection.asme.org/materialstechnology/article-pdf/doi/10.1115/1.4068135/7444918/mats-25-1006.pdf by Delhi Technological University user on 10 March 2025

Journal of Engineering Materials and Technology. Received January 13, 2025;
Accepted manuscript posted March 7, 2025. doi:10.1115/1.4068135
Copyright © 2025 by ASME

Author Contribution Statement

Rajendra Prasad: writing – original draft, methodology, investigation, and formal analysis. N. Yuvaraj: writing – review and editing, supervision, and conceptualization. Vipin: Supervision and final approval.

Conflict of Interest

No conflicts of interest have been reported for this manuscript.

References

[1] Marefat, F., Kapil, A., Banaee, S. A., Van Rymenant, P., and Sharma, A., 2023, "Evaluating Shielding Gas-Filler Wire Interaction in Bi-Metallic Wire Arc Additive Manufacturing (WAAM) of Creep Resistant Steel-Stainless Steel for Improved Process Stability and Build Quality," J Manuf Process, **88**, pp. 110–124. https://doi.org/10.1016/J.JMAPRO.2023.01.046.

[2] Soysal, T., Kou, S., Tat, D., and Pasang, T., 2016, "Macrosegregation in Dissimilar-Metal Fusion Welding," Acta Mater, **110**, pp. 149–160. https://doi.org/10.1016/J.ACTAMAT.2016.03.004.

[3] Ahsan, M. R. U., Tanvir, A. N. M., Seo, G. J., Bates, B., Hawkins, W., Lee, C., Liaw, P. K., Noakes, M., Nycz, A., and Kim, D. B., 2020, "Heat-Treatment Effects on a Bimetallic Additively-Manufactured Structure (BAMS) of the Low-Carbon Steel and Austenitic-Stainless Steel," Addit Manuf, **32**, p. 101036. https://doi.org/10.1016/J.ADDMA.2020.101036.

[4] Ahsan, M. R. U., Fan, X., Seo, G. J., Ji, C., Noakes, M., Nycz, A., Liaw, P. K., and Kim, D. B., 2021, "Microstructures and Mechanical Behavior of the Bimetallic Additively-Manufactured Structure (BAMS) of Austenitic Stainless Steel and Inconel 625," J Mater Sci Technol, **74**, pp. 176–188. https://doi.org/10.1016/J.JMST.2020.10.001.

[5] Kim, Y. S., Yun, D., Han, J. H., Ahsan, Md. R. U., Huang, E.-W., Jain, J., Ji, C., Kim, D. B., and Lee, S. Y., 2022, "Bimetallic Additively Manufactured Structure (BAMS) of Inconel 625 and Austenitic Stainless Steel: Effect of Heat-Treatment on Microstructure and Mechanical Properties," The International Journal of Advanced Manufacturing Technology, **121**(11–12), pp. 7539–7549. https://doi.org/10.1007/s00170-022-09723-x.

[6] Ning, F., Jiang, D., Liu, Z., Wang, H., and Cong, W., 2021, "Ultrasonic Frequency Effects on the Melt Pool Formation, Porosity, and Thermal-Dependent Property of Inconel 718 Fabricated by Ultrasonic Vibration-Assisted Directed Energy Deposition," J Manuf Sci Eng, **143**(5). https://doi.org/10.1115/1.4048515.

[7] Ning, F., Hu, Y., Liu, Z., Wang, X., Li, Y., and Cong, W., 2018, "Ultrasonic Vibration-Assisted Laser Engineered Net Shaping of Inconel 718 Parts: Microstructural and Mechanical Characterization," J Manuf Sci Eng, **140**(6). https://doi.org/10.1115/1.4039441.

Accepted Manuscript Not Copyedited

Downloaded from http://asmedigitalcollection.asme.org/materialstechnology/article-pdf/doi/10.1115/1.4068135/7444918/mats-25-1006.pdf by Delhi Technological University user on 10 March 2025

Journal of Engineering Materials and Technology. Received January 13, 2025;
Accepted manuscript posted March 7, 2025. Doi: 10.1115/1.4067555
Copyright © 2025 by ASME

[8] Prathivraj, S., and Gyyaravelu, R., 2024, "Effect of Interpass Temperature on Austenite Ferrite Ratio of Wire Arc Additive Manufactured 2507 Super Duplex Stainless Steel," Mater Lett, **361**, p. 136125. https://doi.org/10.1016/J.MATLET.2024.136125.

[9] Dinovitzer, M., Chen, X., Laliberte, J., Huang, X., and Frei, H., 2019, "Effect of Wire and Arc Additive Manufacturing (WAAM) Process Parameters on Bead Geometry and Microstructure," Addit Manuf, **26**, pp. 138–146. https://doi.org/10.1016/J.ADDMA.2018.12.013.

[10] Prasad, R., Yuvaraj, N., Vipin, and Gopal, A., 2024, "Experimental Investigation of Process Parameters of Cold Metal Transfer Welding-Based Wire Arc Additive Manufacturing of Aluminum 4047 Alloy Using Response Surface Methodology," Welding in the World, **68**(11), pp. 2837–2852. https://doi.org/10.1007/s40194-024-01817-2.

[11] Prasad, R., Yuvaraj, N., and Vipin, 2025, "Wear Characteristics of Dissimilar SDSS 2507–IN 718 Parts Fabricated by Cold Metal Transfer-Based Wire Arc Additive Manufacturing," J Tribol, **147**(10). https://doi.org/10.1115/1.4067555.

[12] Meena, R. P., N, Y., and Vipin, 2024, "A Review on Wire Arc Additive Manufacturing Based on Cold Metal Transfer," Materials and Manufacturing Processes, pp. 1–27. https://doi.org/10.1080/10426914.2024.2323441.

[13] Prasad, R., Yuvaraj, N., and Bajpai, T., 2025, "Experimental Investigation of Process Parameters of Cold Metal Transfer Welding in Vertical Direction Deposition of Stainless-Steel Using Response Surface Methodology," Engineering Research Express, **7**(1), p. 015506. https://doi.org/10.1088/2631-8695/ada223.

[14] Ezatpour, H. R., Sajjadi, S. A., Sabzevar, M. H., and Huang, Y., 2014, "Investigation of Microstructure and Mechanical Properties of Al6061-Nanocomposite Fabricated by Stir Casting," Mater Des, **55**, pp. 921–928. https://doi.org/10.1016/J.MATDES.2013.10.060.

[15] Sun, Q. J., Lin, S. B., Yang, C. L., and Zhao, G. Q., 2009, "Penetration Increase of AISI 304 Using Ultrasonic Assisted Tungsten Inert Gas Welding," Science and Technology of Welding and Joining, **14**(8), pp. 765–767. https://doi.org/10.1179/136217109X12505932584772.

[16] Kore, S. D., Date, P. P., Kulkarni, S. V., Kumar, S., Rani, D., Kulkarni, M. R., Desai, S. V., Rajawat, R. K., Nagesh, K. V., and Chakravarty, D. P., 2011, "Application of Electromagnetic Impact Technique for Welding Copper-to-Stainless Steel Sheets," The International Journal of Advanced Manufacturing Technology, **54**(9–12), pp. 949–955. https://doi.org/10.1007/s00170-010-2981-z.

[17] Kore, S. D., Date, P. P., Kulkarni, S. V., Kumar, S., Rani, D., Kulkarni, M. R., Desai, S. V., Rajawat, R. K., Nagesh, K. V., and Chakravarty, D. P., 2011, "Application of Electromagnetic Impact Technique for Welding Copper-to-Stainless Steel Sheets," The International Journal of Advanced Manufacturing Technology, **54**(9–12), pp. 949–955. https://doi.org/10.1007/s00170-010-2981-z.

[18] Patarić, A., Mihailović, M., and Gulišija, Z., 2012, "Quantitative Metallographic Assessment of the Electromagnetic Casting Influence on the Microstructure of 7075 Al Alloy," J Mater Sci, **47**(2), pp. 793–796. https://doi.org/10.1007/s10853-011-5855-3.

Accepted Manuscript Not Copyedited

Downloaded from http://asmedigitalcollection.asme.org/materialstechnology/article-pdf/doi/10.1115/1.4068135/7444918/mats-25-1006.pdf by Delhi Technological University user on 10 March 2025

Journal of Engineering Materials and Technology. Received January 13, 2025;
Accepted manuscript posted January 30, 2025. doi: 10.1115/1.4068135
Copyright © 2025 by ASME

[19] Cao, G., Konishi, H., and Li, X., 2008, "Mechanical Properties and Microstructure of Mg/SiC Nanocomposites Fabricated by Ultrasonic Cavitation Based Nanomanufacturing," J Manuf Sci Eng, **130**(3). https://doi.org/10.1115/1.2823086.

[20] Abramov, O. V., 1987, "Action of High Intensity Ultrasound on Solidifying Metal," Ultrasonics, **25**(2), pp. 73–82. https://doi.org/10.1016/0041-624X(87)90063-1.

[21] KOMAROV, S. V., KUWABARA, M., and ABRAMOV, O. V., 2005, "High Power Ultrasonics in Pyrometallurgy: Current Status and Recent Development," ISIJ International, **45**(12), pp. 1765–1782. https://doi.org/10.2355/isijinternational.45.1765.

[22] Ning, F., Hu, Y., Liu, Z., Wang, X., Li, Y., and Cong, W., 2018, "Ultrasonic Vibration-Assisted Laser Engineered Net Shaping of Inconel 718 Parts: Microstructural and Mechanical Characterization," J Manuf Sci Eng, **140**(6). https://doi.org/10.1115/1.4039441.

[23] Todaro, C. J., Easton, M. A., Qiu, D., Zhang, D., Bermingham, M. J., Lui, E. W., Brandt, M., StJohn, D. H., and Qian, M., 2020, "Grain Structure Control during Metal 3D Printing by High-Intensity Ultrasound," Nat Commun, **11**(1), p. 142. https://doi.org/10.1038/s41467-019-13874-z.

[24] Ma, Q., Chen, H., Ren, N., Zhang, Y., Hu, L., Meng, W., and Yin, X., 2021, "Effects of Ultrasonic Vibration on Microstructure, Mechanical Properties, and Fracture Mode of Inconel 625 Parts Fabricated by Cold Metal Transfer Arc Additive Manufacturing," J Mater Eng Perform, **30**(9), pp. 6808–6820. https://doi.org/10.1007/s11665-021-06023-5.

[25] Jeong, T. W., Cho, Y. T., Lee, C. M., and Kim, D. H., 2024, "Effects of Ultrasonic Treatment on Mechanical Properties and Microstructure of Stainless Steel 308L and Inconel 718 Functionally Graded Materials Fabricated via Double-Wire Arc Additive Manufacturing," Materials Science and Engineering: A, **896**, p. 146298. https://doi.org/10.1016/J.MSEA.2024.146298.

[26] Meena, R. P., Yuvaraj, N., and Vipin, V., 2024, "Investigations and Optimization of Cold Metal Transfer-Based WAAM Process Parameters for Fabrication of Inconel 718 Samples Using Response Surface Methodology," Arab J Sci Eng. https://doi.org/10.1007/s13369-024-08947-1.

[27] Meena, R. P., Yuvaraj, N., and Vipin, 2024, "Optimization of Process Parameters of Cold Metal Transfer Welding-Based Wire Arc Additive Manufacturing of Super Duplex Stainless Steel Using Response Surface Methodology," Proceedings of the Institution of Mechanical Engineers, Part E: Journal of Process Mechanical Engineering. https://doi.org/10.1177/09544089241230878.

[28] Wang, F., Eskin, D., Mi, J., Connolley, T., Lindsay, J., and Mounib, M., 2016, "A Refining Mechanism of Primary Al3Ti Intermetallic Particles by Ultrasonic Treatment in the Liquid State," Acta Mater, **116**, pp. 354–363. https://doi.org/10.1016/J.ACTAMAT.2016.06.056.

[29] Ruirun, C., Deshuang, Z., Tengfei, M., Hongsheng, D., Yanqing, S., Jingjie, G., and Hengzhi, F., 2017, "Effects of Ultrasonic Vibration on the Microstructure and Mechanical Properties of High Alloying TiAl," Sci Rep, **7**(1), p. 41463. https://doi.org/10.1038/srep41463.

Accepted Manuscript Not Copyedited

Downloaded from http://asmedigitalcollection.asme.org/materialstechnology/article-pdf/doi/10.1115/1.4068135/7444918/mats-25-1006.pdf by Delhi Technological University user on 10 March 2025

Journal of Engineering Materials and Technology. Received January 13, 2025;
Accepted manuscript posted March 7, 2025. doi: 10.1115/1.4068135
Copyright © 2025 by ASME

[30] Jeong, T. W., Cho, Y. T., Lee, C. M., and Kim, D. H., 2024, "Effects of Ultrasonic Treatment on Mechanical Properties and Microstructure of Stainless Steel 308L and Inconel 718 Functionally Graded Materials Fabricated via Double-Wire Arc Additive Manufacturing," Materials Science and Engineering: A, **896**, p. 146298. https://doi.org/10.1016/J.MSEA.2024.146298.

[31] Gäumann, M., Bezençon, C., Canalis, P., and Kurz, W., 2001, "Single-Crystal Laser Deposition of Superalloys: Processing–Microstructure Maps," Acta Mater, **49**(6), pp. 1051–1062. https://doi.org/10.1016/S1359-6454(00)00367-0.

[32] Ning, F., Hu, Y., Liu, Z., Wang, X., Li, Y., and Cong, W., 2018, "Ultrasonic Vibration-Assisted Laser Engineered Net Shaping of Inconel 718 Parts: Microstructural and Mechanical Characterization," J Manuf Sci Eng, **140**(6). https://doi.org/10.1115/1.4039441.

[33] Qi, H., Azer, M., and Ritter, A., 2009, "Studies of Standard Heat Treatment Effects on Microstructure and Mechanical Properties of Laser Net Shape Manufactured INCONEL 718," Metallurgical and Materials Transactions A, **40**(10), pp. 2410–2422. https://doi.org/10.1007/s11661-009-9949-3.

[34] Liu, F., Lin, X., Leng, H., Cao, J., Liu, Q., Huang, C., and Huang, W., 2013, "Microstructural Changes in a Laser Solid Forming Inconel 718 Superalloy Thin Wall in the Deposition Direction," Opt Laser Technol, **45**(1), pp. 330–335. https://doi.org/10.1016/J.OPTLASTEC.2012.06.028.

[35] Wang, Z., Guan, K., Gao, M., Li, X., Chen, X., and Zeng, X., 2012, "The Microstructure and Mechanical Properties of Deposited-IN718 by Selective Laser Melting," J Alloys Compd, **513**, pp. 518–523. https://doi.org/10.1016/J.JALLCOM.2011.10.107.

[36] Haldar, N., Anand, S., Datta, S., and Das, A., 2024, "On Fabrication of Inconel 718 Slab by Wire Arc Additive Manufacturing: Study of Built Microstructure and Mechanical Properties," Arab J Sci Eng, **49**(2), pp. 2045–2063. https://doi.org/10.1007/s13369-023-08095-y.

[37] Hall, E. O., 1951, "The Deformation and Ageing of Mild Steel: III Discussion of Results," Proceedings of the Physical Society. Section B, **64**(9), pp. 747–753. https://doi.org/10.1088/0370-1301/64/9/303.

Accepted Manuscript Not Copyedited

Downloaded from http://asmedigitalcollection.asme.org/materialstechnology/article-pdf/doi/10.1115/1.4068135/7444918/mats-25-1006.pdf by Delhi Technological University user on 10 March 2025

Journal of Physics:
Condensed Matter

PURPOSE-LED PUBLISHING™

PAPER

Unraveling the topological phase in Zintl semiconductors $RbZn_4X_3$ (X = P, As) through band engineering

To cite this article: Ramesh Kumar *et al* 2025 *J. Phys.: Condens. Matter* **37** 185501

View the article online for updates and enhancements.

You may also like

- Mysterious charge ordering on -(BEDT-TTF)$_2$RbZn(SCN)$_4$
Tsuyoshi Takeno, Kei Kobayashi, Yutaka Nishio et al.
- Effects of spin fluctuations, charge fluctuations and lattice distortions on charge orders in - and -type BEDT-TTF salts
Satoshi Miyashita and Kenji Yonemitsu
- An electron paramagnetic resonance study of vanadium centres in $RbZnF_3$ single crystals
H Takeuchi, H Ebisu and M Arakawa

This content was downloaded from IP address 14.139.251.98 on 01/04/2025 at 05:35

IOP Publishing Journal of Physics: Condensed Matter
J. Phys.: Condens. Matter **37** (2025) 185501 (12pp) https://doi.org/10.1088/1361-648X/adc17e

Unraveling the topological phase in Zintl semiconductors $RbZn_4X_3$ (X = P, As) through band engineering

Ramesh Kumar[1], Rajesh Kumar[1], Antik Sihi[2] and Mukhtiyar Singh[1,*]

[1] Computational Quantum Materials Design (CQMD) Lab, Department of Applied Physics, Delhi Technological University, Delhi 110042, India
[2] Department of Physics and Astronomy, West Virginia University, Morgantown, WV 26506, United States of America

E-mail: mukhtiyarsingh@dtu.ac.in and msphysik09@gmail.com

Received 12 November 2024, revised 19 February 2025
Accepted for publication 17 March 2025
Published 31 March 2025

Abstract

We report the topological phase transition (TPT) in compounds of relatively less explored Zintl family $RbZn_4X_3$ (X = P, As) via *first-principles* calculation. These intermetallic compounds have already been experimentally synthesized in a *KCu_4S_3-type* tetragonal structure (P4/mmm) and reported to have a topologically trivial semimetallic nature with a direct band gap. We thoroughly studied the electronic structure, stability of $RbZn_4X_3$ (X = P, As) and demonstrated the TPTs in these materials with external applied pressure and epitaxial strain. The dynamical and mechanical stabilities of these compounds are verified through phonon dispersion and Born stability criteria at ambient and TPT pressure/strain. A topologically non-trivial phase in $RbZn_4P_3$ ($RbZn_4As_3$) is observed at 45 GPa (38 GPa) of hydrostatic pressure and 10% (8%) of epitaxial strain. This non-trivial phase is identified by band inversion between *Zn-s* and *P/As-p_z orbitals* in the bulk band structure of these materials which is further confirmed using the surface density of states and Fermi arc contour in *(001)-plane*. The $\mathbb{Z}_2$ topological invariants (ν_0; $\nu_1\nu_2\nu_3$) for these materials are calculated using the product of parities of all filled bands (Kane and Mele model) and the evolution of Wannier charge centers (Wilson loop method). The change in values of (ν_0; $\nu_1\nu_2\nu_3$) from (*0; 000*) to (*1; 000*), at the particular values of pressure and strain, is another signature of the TPT in these materials.

Supplementary material for this article is available online

Keywords: topological phase transition, topological insulator, Zintl compounds, *first-principles* calculations, surface states, Fermi arc

1. Introduction

The modern era of condensed matter physics and materials research has been significantly shaped by the concepts of topology and symmetry. The topological phase of matter, one of such paradigmatic examples, has two-dimensional gapless surface states with insulating bulk states and is protected by time-reversal symmetry (TRS) as well as crystal symmetries [1–5]. The topological phase occurs when spin-momentum locking of eigenstates takes place at the surfaces of a material in the presence of spin–orbit coupling (SOC). The topological insulators (TIs) [3–5], topological crystalline insulators [6–8], Dirac semimetals [9, 10], Weyl semimetals [11, 12],

* Author to whom any correspondence should be addressed.

© 2025 IOP Publishing Ltd. All rights, including for text and data mining, AI training, and similar technologies, are reserved.

nodal line semimetals [13, 14], $\mathbb{Z}_2$ topological semimetals [15, 16] and triply degenerate node semimetals [17, 18], etc., are a few categories into which topological materials can be divided. These materials display unusual physical properties like topologically protected surface states and possess immense potential to be used in low power high speed electronic and spintronic devices, thermoelectric generators, quantum computing [19–21], etc. A variety of materials, which include binary chalcogenides Bi_2Te_3, Bi_2Se_3, Sb_2Te_3 [3–5]; ternary chalcogenides $TlBiTe_2$, $TlBiSe_2$ [22–24], $PbBi_2Se_4$ [25], $LaBiTe_3$ [26]; honeycomb lattice compounds LiAuSe [27]; half Heusler compounds [28, 29], chalcopyrite compounds [30], etc., are identified with protected topological surface states (TSSs) at ambient conditions. On the other hand, a careful alteration in the strength of SOC can play a vital role in realizing topological phase transition (TPT) in specific materials. The hydrostatic pressure and strain are non-destructive ways of enhancing SOC as the charge neutrality of a material remains intact. The binary and ternary materials like Bi_4Br_4 [31], LaAs [15], YbAs [32], RSb (R = La, Tm, Gd) [16, 33, 34], YX (X = As, Sb, Bi) [35–37] and KNa_2Bi [38], BiTeI [39], Bi_2S_3 [40], BiTeBr [41] have shown non-trivial topological characteristics with hydrostatic pressure, whereas LaSb [42], YBi [37], SnTe [43] transformed into non-trivial topological phase under equilibrium compressive strain.

The Zintl compounds are intermetallic phases in which electropositive cations donate electrons to covalently bonded polyanions [44, 45]. These materials have been widely explored for various fascinating physical properties like superconductivity, magnetoresistance, magnetic ordering, thermoelectricity, and many more [44–48]. Recently, a few studies have discovered a topological phase in these compounds. The ternary Zintl compounds i.e. AIn_2As_2 (A = Ca, Sr, Ba), $Eu_5M_2X_6$ (M = metal, X = pnictide), $Ba_3Cd_2Sb_4$, $Ca_2M_2X_2$ (M = Zn, Cd; X = pnictide), $YbMg_2Bi_2$, $CaMg_2Bi_2$ and BaCaSi have been shown to exhibit topologically non-trivial phase at ambient conditions [49–54]. In other studies, Ba_2X (X = Si, Ge), Sr_2X (X = Pb, Sn) and BaCaX (X = Ge, Sn, Pb) the emergence of topological phase with strain has been demonstrated [49, 55, 56]. In this work, we have studied a relatively less explored class of ternary Zintl pnctide family i.e. XZn_4Pn_3 and XCd_4Pn_3 (X = Na, K, Rb, Cs; Pn = As, P) [44] for their topological aspect. These materials with complex atomic arrangements were synthesized and analyzed for good thermoelectric performance [44, 45, 48]. It was reported that XZn_4Pn_3 and XCd_4Pn_3 compounds adopt a variety of related polymorphic crystal structures [44, 57]. The experimentally grown single crystal of $NaCd_4As_3$ has shown magnetotransport properties, and the structural phase transition in this material leads to the TPT which is attributed to the breaking of mirror symmetry [58]. Under the present unexplored scenario of the topological behavior of this new Zintl family and keeping in mind the recent progress in high-pressure synthesis and TPT in various materials [59–64], we examined the topological phase characteristics of the ternary Zintl compounds $RbZn_4X_3$ (X = P, As) under the influence of hydrostatic pressure and epitaxial strain using *first-principles* calculations. The TPT in $RbZn_4P_3$ and $RbZn_4As_3$ takes place at 45 GPa and 38 GPa of hydrostatic pressure and 10% and 8% of the epitaxial stain, respectively. The existence of TSSs and the Fermi arc in the *(001)-plane* verified the topological non-triviality in these materials. The $\mathbb{Z}_2$ topological invariants have been calculated using the parity analysis as per the Kane and Mele model [65] and the evolution of Wannier charge centers (WCCs) in time-reversal invariant momenta (TRIM) planes.

2. Computational methodology

The *first-principles* calculations based on density functional theory (DFT) [66, 67] were executed using the projector augmented wave (PAW) [68] approach as implemented in the VASP code [69]. The PAW potentials for Rb with 9 valence electrons, i.e. $4s^24p^65s^1$, Zn with 12 valence electrons, i.e. $3d^{10}4s^2$, As with 5 valence electrons, i.e. $4s^24p^3$ and P with 5 valence electrons, i.e. $3s^23p^3$ configuration were employed for the calculations. The Generalized Gradient Approximation (GGA) of Perdew–Burke–Ernzerhof (PBE) [70] followed by modified Becke–Johnson (mBJ) [71] exchange-correlation functionals were used to parameterize the accurate ground state charge density of the materials. The kinetic energy cutoff of $RbZn_4P_3$ and $RbZn_4As_3$ was set to 560 eV and 420 eV, respectively, and the Monkhorst-Pack type k-mesh [72] of $8 \times 8 \times 5$ was used. The effect of SOC was included in self-consistent and post-processing calculations, and the overall energy convergence criteria was set to 10^{-6} eV. The dynamical stability of the material at ambient and elevated pressure and strain conditions was analyzed using the PHONOPY code [73] with a $2 \times 2 \times 2$ supercell. The VASPKIT code [74] was used for the post-processing of the VASP calculations. The $\mathbb{Z}_2$ topological invariants were evaluated using the product of parities at the TRIM points. Wannier90 code [75] was used to obtain maximally localized Wannier functions (MLWFs) and to parameterize a tight-binding (TB) Hamiltonian. The calculated DFT band structure was fitted with the TB-Hamiltonian that was parameterized using the *s-orbital* of Zn and *p-orbital* of P/As atoms. Based on the TB-Hamiltonian interfaced with Wannier90, the surface density of state (SDOS) and Fermi contour were obtained using the Green function approach as implemented in the WannierTools code [76].

3. Result and discussion

3.1. The electronic and topological structure at ambient conditions

The ternary Zintl materials $RbZn_4X_3$ (X = P, As) adopt a centrosymmetric *KCu_4S_3-type* tetragonal structure (P4/mmm) with the polyanionic layers $[Zn_4X_3]^-$ which are charge-balanced by intercalated Rb^+ cations [44, 45]. These polyanionic layers contain tetrahedra ZnX_4 and are stacked along the *c-axis* of the crystal structure. The conventional unit cell

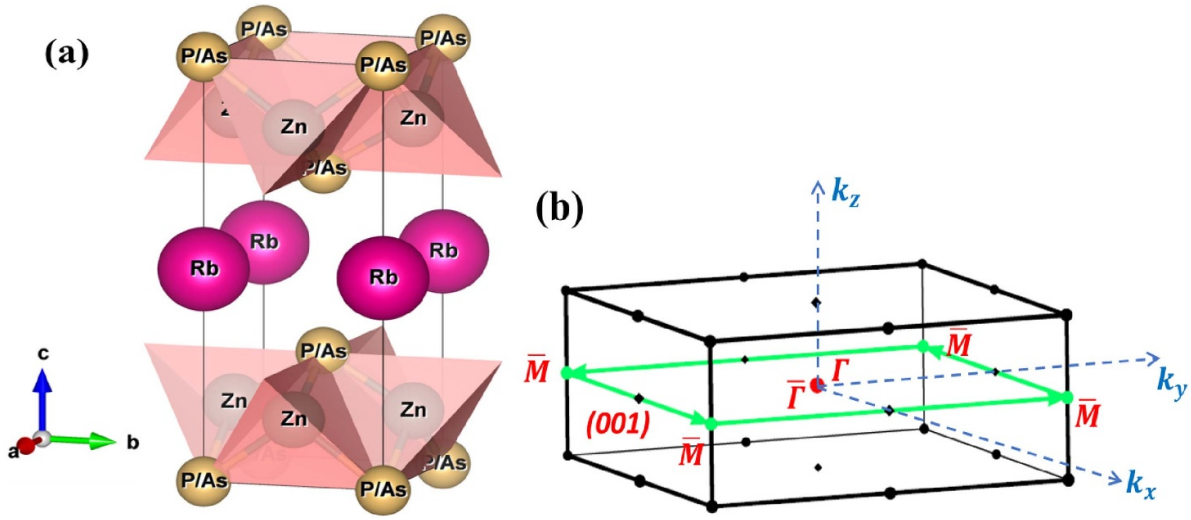

Figure 1. (a) Crystal structure of $RbZn_4X_3$ (X = P, As) (b) The first Brillion zone (BZ) and *(001)-plane* (green) along which surface states are observed.

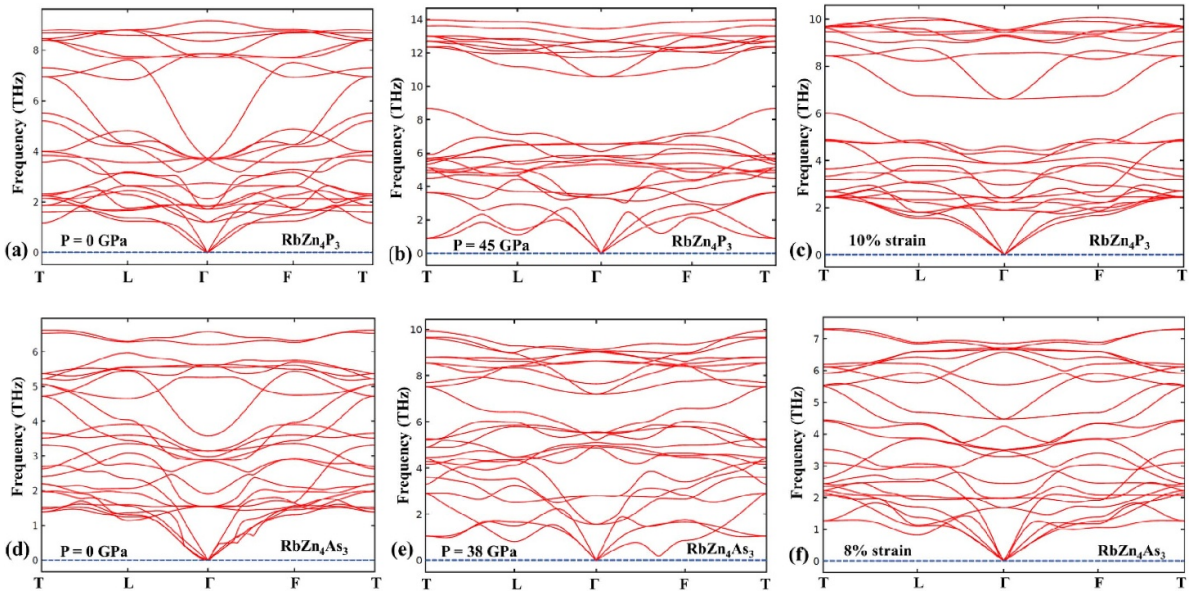

Figure 2. The phonon band structure of (a)–(c) $RbZn_4P_3$ and (d)–(f) $RbZn_4As_3$ hydrostatic pressure and epitaxial strain.

and BZ of the tetragonal $RbZn_4X_3$ are shown in figures 1(a) and (b). The optimized lattice parameters for these materials are in good agreement with the experimental [44] as well as theoretically [48] reported values (table 1). The dynamical stability of these materials has been verified using the phonon dispersion spectrum at ambient and elevated pressure or strain conditions as shown in figure 2. We have also analyzed the mechanical stability of these materials at ambient and elevated pressure/strain where the TPT has been observed. For tetragonal systems, there are six independent elastic constants of stiffness tensor, i.e. C_{11}, C_{12}, C_{13}, C_{33}, C_{44} and C_{66}. The Born stability criteria [77] for the mechanical stability of the tetragonal systems are,

$$C_{11} > |C_{12}|,\ 2C_{13}^2 < C_{33}(C_{11}+C_{12}),\ C_{44} > 0, C_{66} > 0. \quad (1)$$

The calculated values of the C_{ij} under the various hydrostatic pressures and epitaxial strains are shown in table S1 (supplementary information). The elastic constants of stiffness tensors have satisfied equation (1), which has signified the mechanical stability of these materials at ambient and elevated pressure/strain.

The orbital projected electronic band structure of $RbZn_4X_3$ (X = P, As) using GGA-PBE and TB-mBJ functionals without and with SOC are shown in figures 3(a)–(h). The bulk band structure calculations are performed along k-path Γ-*T*-*L*-Γ-*F*-Γ, which contains eight TRIM points of the BZ. It can be seen that the p_x, p_y, p_z-*orbitals* of P/As and the *s-orbital* of Zn are mainly contributing to the ground state eigenfunctions of the material near the Fermi energy. The minima of the conduction band and maxima of the valence band lie at the Γ-*point* and it has the main contribution from the *s-orbital* of

Table 1. The lattice parameters and bulk band gap of semiconductor material $RbZn_4X_3$ (X = P, As).

Materials	Features		Other studies		Present work
			Experimental	Theoretical	
$RbZn_4P_3$	Lattice parameters		$a = b = 4.0593$ Å $c = 10.069$ Å [44]	$a = b = 4.080$ Å $c = 10.230$ Å [48]	$a = b = 4.081$ Å $c = 10.196$ Å
	Band gap E_g	w/o SOC	—	1.02 eV [48]	0.161 eV[a] 1.133 eV[b]
		with SOC	—	—	0.149 eV[a] 1.119 eV[b]
$RbZn_4As_3$	Lattice parameters		$a = b = 4.1714$ Å $c = 10.355$ Å [44]	—	$a = b = 4.200$ Å $c = 10.529$ Å
	Band gap E_g	w/o SOC	—	—	0.000 eV[a] 0.681 eV[b]
		with SOC	—	—	0.000 eV[a] 0.584 eV [b]

[a] GGA-PBE functional; [b] TB-mBJ functional.

Zn. The maxima of the valance band is also at the *Γ-point* and contributed by the p_x, p_y*-orbitals* of P/As, whereas, the p_z*-orbital* of the P/As lies slightly lower than the Fermi energy at ambient conditions, as shown in figures 3(a)–(d), (g) and (h). Figures 3(a)–(d) show the direct band gap in $RbZn_4P_3$ material using the GGA-PBE as well as the TB-mBJ functional, which establishes its topologically trivial semiconducting nature. On the other hand, $RbZn_4As_3$ shows topological band crossing using the GGA-PBE functional (figures 3(e) and (f)), but a direct band gap is observed with the TB-mBJ functional and makes it a topologically trivial semiconductor (figures 3(g) and (h)).

The bandstructure obtained by the GGA-PBE functional predicts lower band gaps as compared to the TB-mBJ functional at ambient conditions as depicted in table 1. It is a common fact that the former underestimates the band gap of semiconducting materials [71]. Our results of the electronic band structure of $RbZn_4P_3$ using TB-mBJ are in good agreement with the previous report [48]. Therefore, we have used this functional for all further electronic and topological properties calculation. $RbZn_4X_3$ (X = P, As) are trivial semiconductors with a direct band gap of 1.133 eV and 0.681 eV, respectively, without SOC. However, the energy band gap of these materials reduced to 1.119 eV and 0.584 eV, respectively, when the effect of SOC is included (table 1). Further, we have constructed the TB Hamiltonian using the Wannier functions to study the *(001)* surface and have observed the absence of Dirac cones in $RbZn_4X_3$ (P, As) systems at ambient pressure as shown in figures 4(a) and (b).

3.2. The effect of hydrostatic pressure and epitaxial strain

To understand the TPT, we have studied the effect of hydrostatic pressure and epitaxial strain on bulk band structures of $RbZn_4X_3$ (P, As). The hydrostatic pressure and epitaxial strain reduce the dimensional confinement of the system, and hence atoms come closer to each other. This in turn reduces the band gap, which vanishes at a particular value of pressure, where TPT takes place. The projected band structures of $RbZn_4X_3$ (P, As) at TPT pressure, i.e. 45 GPa and 38 GPa, respectively, are represented in figures 5(a) and (b). Similarly, the epitaxial strain of 10% and 8% for the $RbZn_4X_3$ (P, As) systems, respectively, have reduced the dimension of the system along the *c-axis* and closed the band gap at the *Γ-point*. The projected band structures of $RbZn_4X_3$ (P, As) at the above epitaxial strains and hence TPT are shown in figures 6(a) and (b).

The hydrostatic pressure and epitaxial strain tune the eigenstates of the system with projections p_x, p_y and p_z*-orbitals* of P/As near the Fermi energy. As the pressure and strain increase, the eigenstate corresponding to the p_z*-orbital* of P/As at *the Γ-point* has shown an upward shift in energy, while the shift in energies of the eigenstates of the p_x and p_y*-orbitals* has a downward direction with respect to the Fermi level. At the TPT, the band inversion takes place between the *Zn-s orbital* and the *P/As-*p_z *orbital* near the Fermi level. The inverted contribution of these orbitals can be observed in the insets of figures 5(a, b) and 6(a, b).

The TB Hamiltonian for $RbZn_4X_3$ (X = P, As) constructed using Wannierization under the hydrostatic pressure and epitaxial strain shows the existence of TSSs along the *(001)-plane* as depicted in figures 5(c, d) and 6(c, d). The corresponding Fermi arcs are also shown in figures 5(e, f) and 6(e, f), which confirms the existence of topological non-trivial states in $RbZn_4P_3$ and $RbZn_4As_3$.

The evolution of the bulk eigenstates of $RbZn_4X_3$ (X = P, As) is given in figures 7(a) and (b). The atomic *p-orbital* of P/As splits into two different energy levels, where p_x- and p_y-*orbitals* are close to the Fermi level rather than the p_z*-orbital*

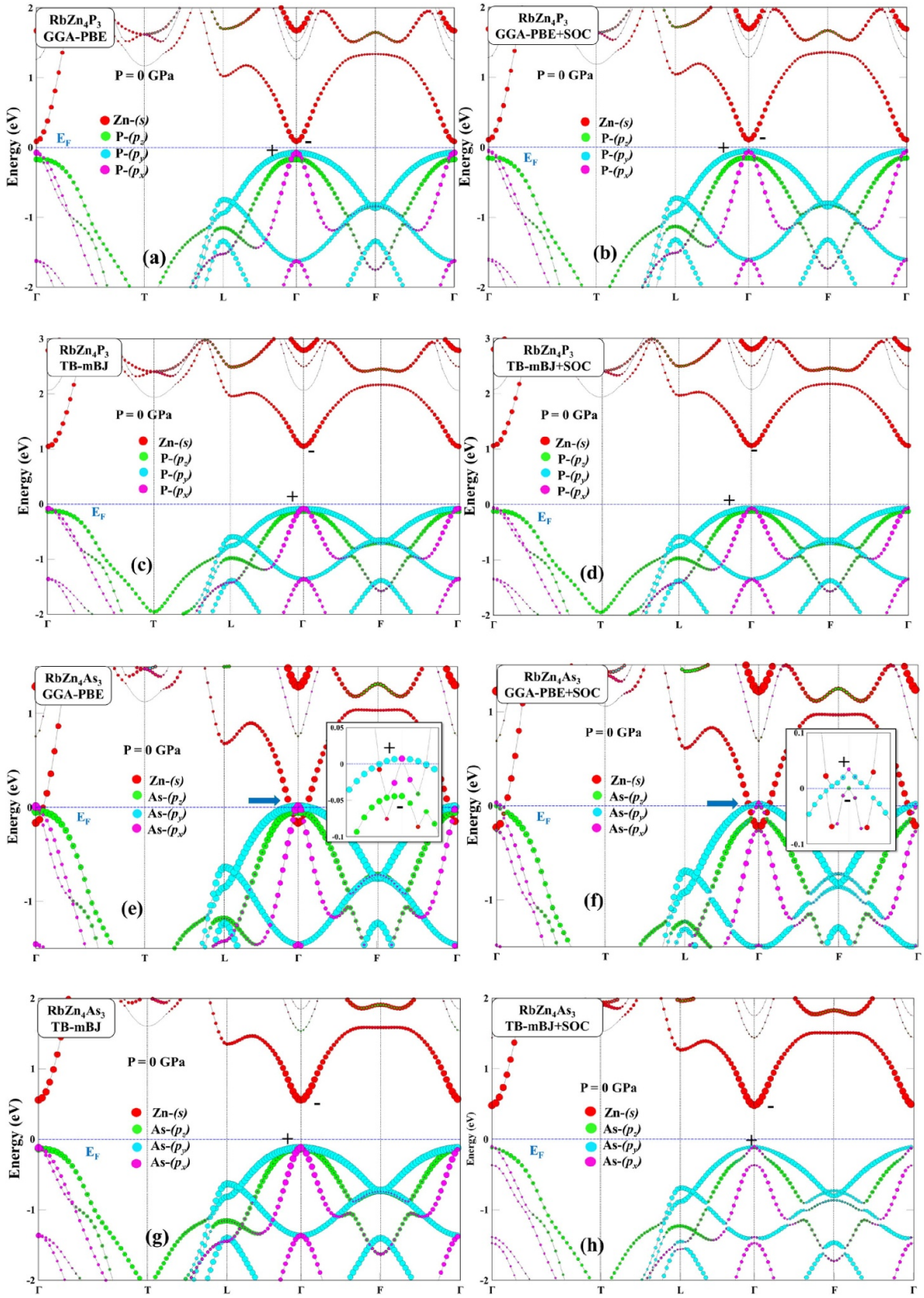

Figure 3. The projected bulk band structure of $RbZn_4X_3$ (P, As) using (a, e) GGA-PBE, (b, f) GGA-PBE + SOC, (c, g) TB-mBJ, (d, h) TB-mBJ + SOC. The Fermi energy (blue dotted line) is set at the 0 eV.

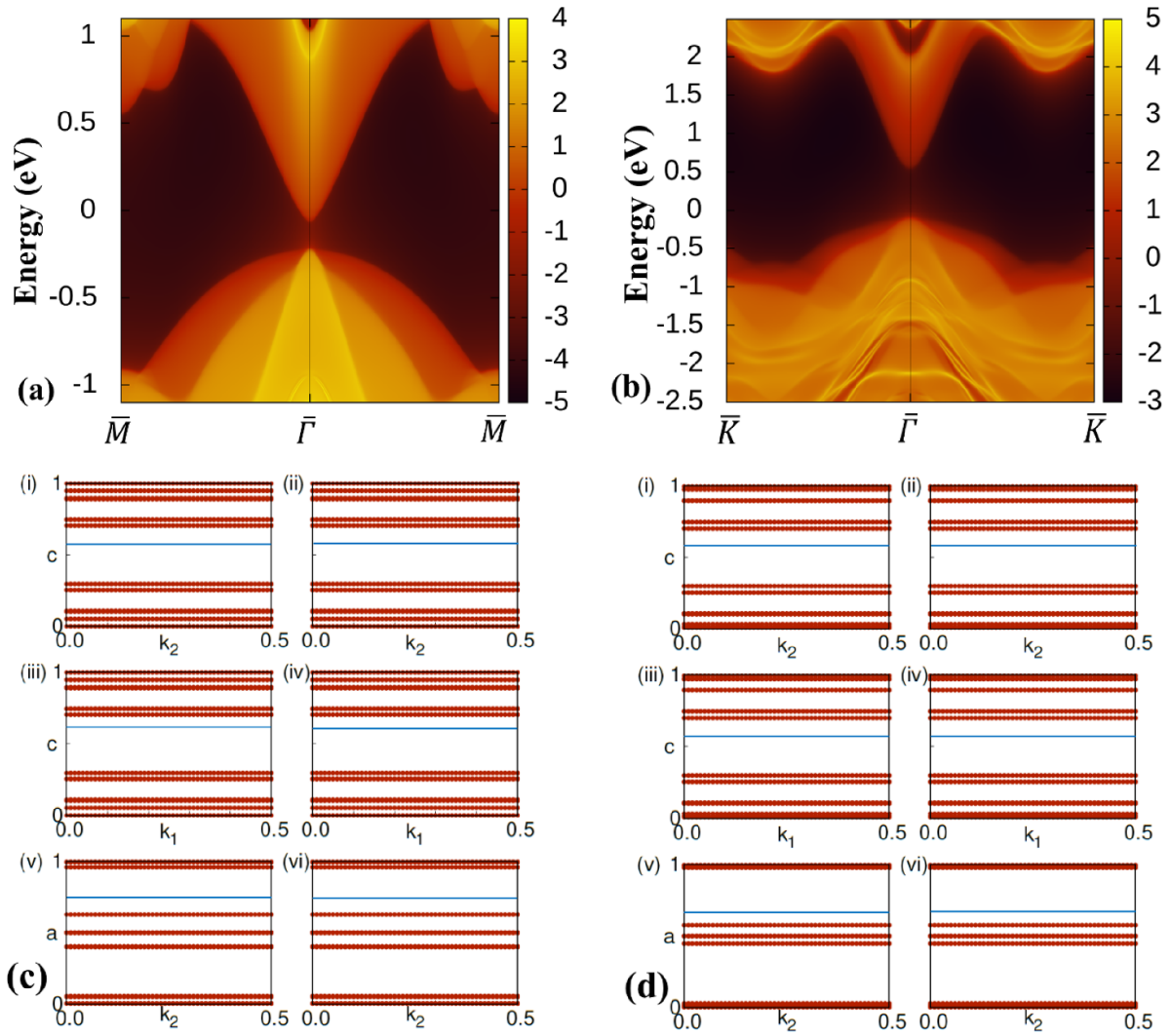

Figure 4. The surface density of state (SDOS) and Wannier charge centers (WCCs) of (a–c) $RbZn_4P_3$ (b–d) $RbZn_4As_3$ materials along the *(001)-plane*, respectively.

but the *s-orbital* holds its non-degenerate nature with the crystal field. The TB-mBJ functional accurately predicted the semiconducting ground state of these materials. Under the effect of applied hydrostatic pressure and epitaxial strain, p_z-*orbital* start moving towards, whereas the p_x- and p_y-*orbitals* of P/As move away from the Fermi level. The *s-orbital* of Zn also moves towards the Fermi level, and at the critical value of the hydrostatic pressure and epitaxial strain, the p_z-*orbital* of the P/As and the *s-orbital* of the Zn show crossing with each other, and band inversion takes place as shown in figures 7(a) and (b). Moreover, we have observed a monotonous decrease in the band gap of $RbZn_4X_3$ (X = P, As) with respect to increasing hydrostatic pressure as shown in figure 7(c). Furthermore, the elevated pressure/strain reduces the lattice dimensions of the unit cell, and hence the eigenstates come closer to each other which increases the overlapping of the orbitals. This increase in overlapping can be deduced in terms of transfer integral or the hopping amplitude. The hopping amplitude values can be extracted from the Wannier Hamiltonian generated via *Zn-s* and *X-*p_z *orbital* projections of the $RbZn_4X_3$ (X = P, As) materials as shown in tables S2–S13 (see supplementary information). The hopping amplitude has been calculated for the spin-up as well as spin-down states at ambient and elevated pressure/strain; however, both spins have nearly the same value of the integral. The diagonal values of the hopping amplitude at ambient pressure (tables S2, S3, S8 and S9) for spin-up as well as spin-down states of $RbZn_4P_3$ and $RbZn_4As_3$ have shown an increment when the hydrostatic pressure (tables S4, S5, S10 and S11) or epitaxial strain (tables S6, S7, S12 and S13) is applied. Moreover, we have calculated the magnitude of the average hopping integral for the *Zn-X* (*X* = *P, As*) as shown in table 2. This has been calculated using the magnitude of the *Zn-X* (*X* = *P, As*) interaction terms which are off-diagonal elements in the Hamiltonian matrix. We can

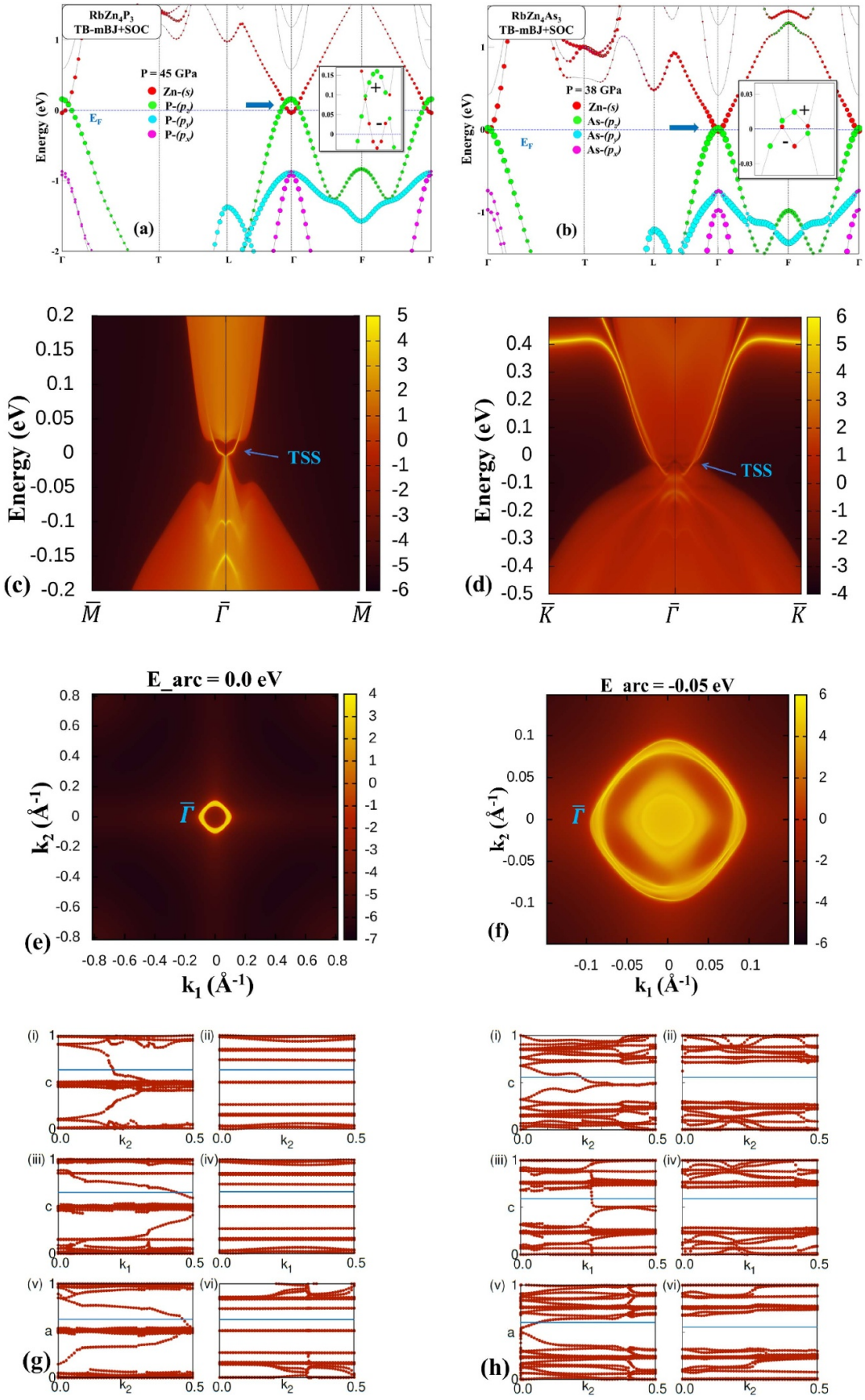

Figure 5. The projected bulk band structure of (a) $RbZn_4P_3$ and (b) $RbZn_4As_3$ at 45 GPa and 38 GPa hydrostatic pressures, respectively. The Fermi energy (blue dotted line) is set at the 0 eV. (c, d) The surface density of states (SDOS), (e, f) corresponding Fermi arc contour and (g, h) Wannier charge centers (WCCs) of $RbZn_4P_3$ and $RbZn_4As_3$, respectively, shows the existence of the topological surface state (TSS).

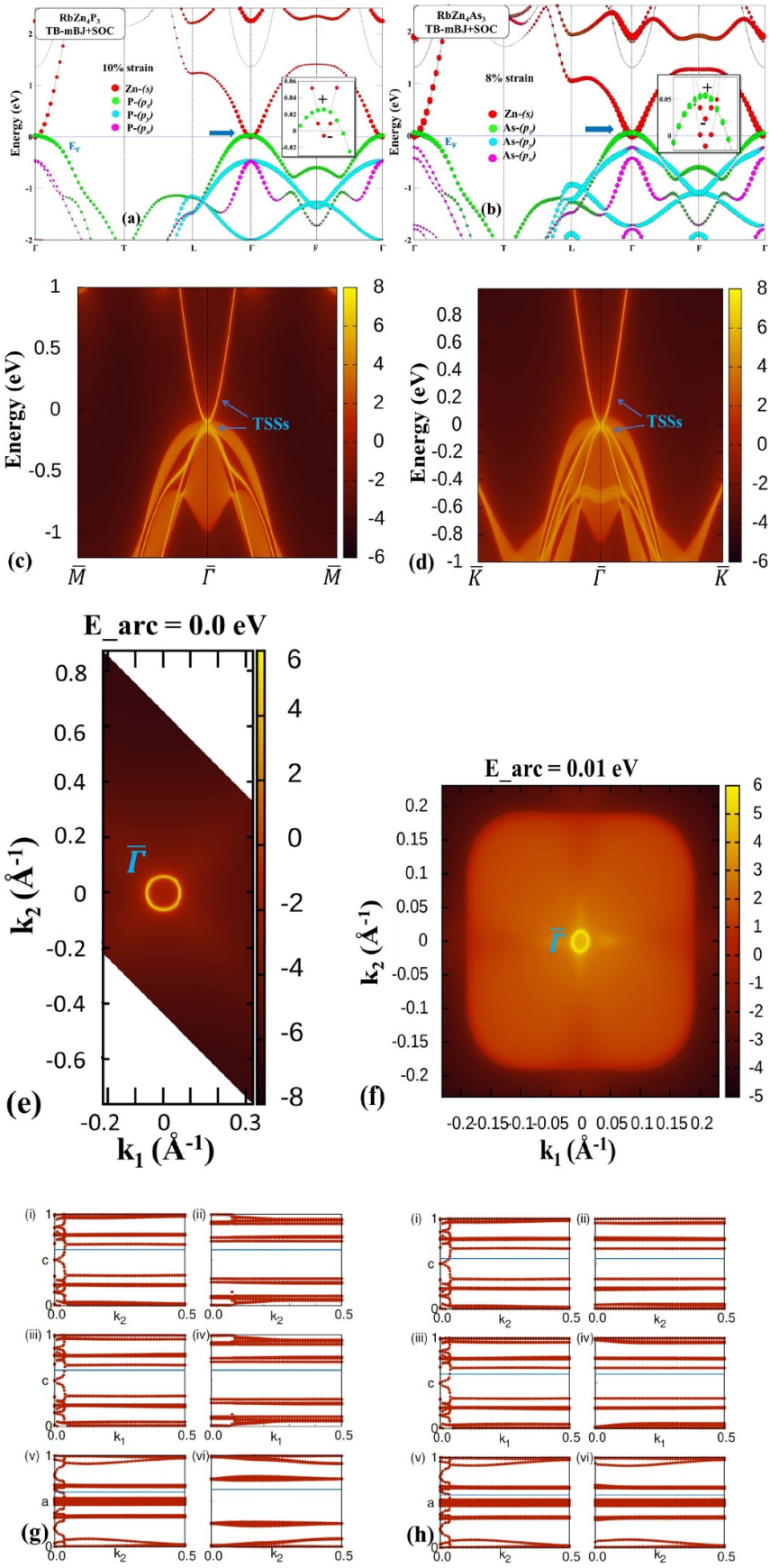

Figure 6. The projected bulk band structure of (a) $RbZn_4P_3$ and (b) $RbZn_4As_3$ at 10% and 8% epitaxial strain, respectively. The Fermi energy (blue dotted line) is set at the 0 eV. (c, d) The surface density of states (SDOS), (e, f) corresponding Fermi arc contour, and (g, h) Wannier charge centers (WCCs) of $RbZn_4P_3$ and $RbZn_4As_3$, respectively, show the existence of the topological surface state (TSSs).

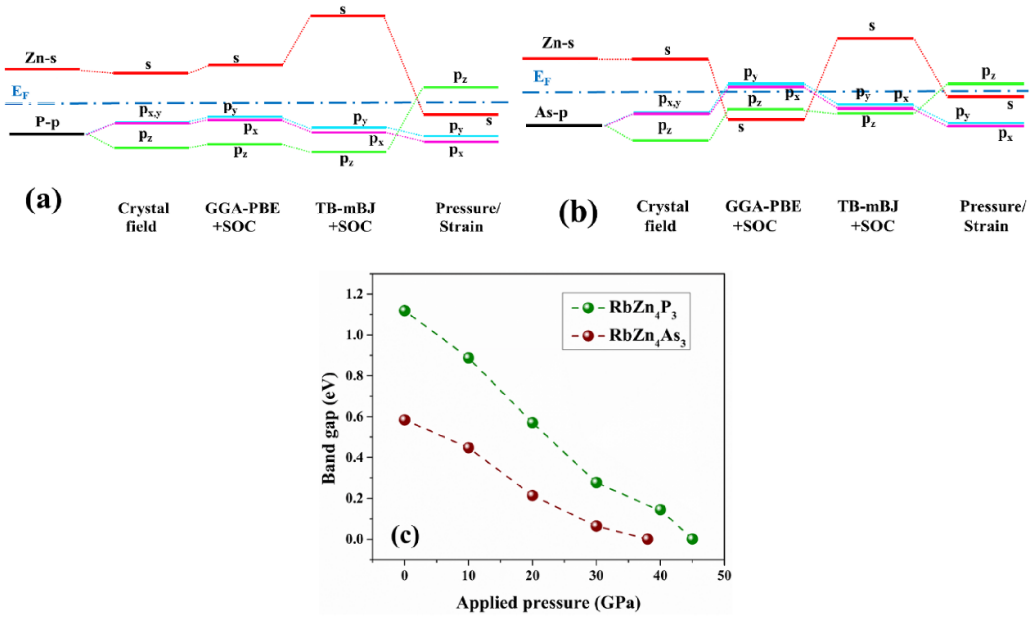

Figure 7. (a, b) The schematic representation for the evolution of bulk energy states of $RbZn_4X_3$ (X = P, As) via—crystal field splitting—GGA-PBE + SOC—TB-mBJ + SOC—hydrostatic pressure and epitaxial strain. (c) The variation of the band gap with applied pressure.

Table 2. The magnitude of the average hopping integral of Zn-P and Zn-As overlapping in $RbZn_4P_3$ and $RbZn_4As_3$ systems with applied hydrostatic pressure and epitaxial strain.

Materials	Pressure/Strain conditions	Magnitude of average hopping integral (up-state) (in eV)	Magnitude of average hopping integral (down-state) (in eV)
$RbZn_4P_3$	Ambient condition	1.2698	1.3112
	Hydrostatic pressure; $P = 45$ GPa	2.0450	1.4601
	10% epitaxial strain	1.8697	2.129
$RbZn_4As_3$	Ambient condition	1.1197	1.3745
	Hydrostatic pressure; $P = 38$ GPa	2.0516	2.0526
	8% epitaxial strain	2.2062	2.2016

observe an increase in the average value of the hopping amplitude under the applied pressure/strain values. The continuous increase in hopping amplitude with an increase in hydrostatic pressure or epitaxial strain has established the increase in overlapping of orbitals.

3.2.1. $\mathbb{Z}_2$ topological invariants. The non-trivial nature of the $RbZn_4X_3$ (X = P, As) with the effect of hydrostatic pressure and epitaxial strain has also been verified with the help of the $\mathbb{Z}_2$ topological invariants. These materials have TRS as well as IS in a tetragonal structure, so, for the calculation of $\mathbb{Z}_2$ topological invariants, the Kane and Mele model [65] can be implemented. According to this model, three-dimensional (3D) materials have eight TRIM points, where the parities of all the filled bands can be used to identify the $\mathbb{Z}_2$ topological invariants with the following equations;

$$(-1)^{\nu_0} = \prod_{n_i=0,1} \delta_{n_1 n_2 n_3} \tag{2}$$

$$(-1)^{\nu_{i=1,2,3}} = \prod_{n_i=1; n_{j\neq i}=0,1} \delta_{n_1 n_2 n_3} \tag{3}$$

where the δ and n_i represent the parities of filled bands and reciprocal lattice vectors. The calculated four $\mathbb{Z}_2$ topological invariants (ν_0; $\nu_1\nu_2\nu_3$) using the product of parities are given in table 3.

The $\mathbb{Z}_2$ topological invariants (ν_0; $\nu_1\nu_2\nu_3$) are (*0; 000*) for both the systems at ambient conditions which established the trivial semiconductor nature of $RbZn_4X_3$ (X = P, As) as observed in bulk band structures (figure 3). Under the applied hydrostatic pressures (45 GPa and 38 GPa) and epitaxial strain

Table 3. The $\mathbb{Z}_2$ topological invariants of $RbZn_4X_3$ (X = P, As) at ambient and applied pressure/strain conditions.

Materials	Pressure/Strain conditions	Number of band inversions	Γ	*3 L*	*3 F*	*T*	$\mathbb{Z}_2$-invariants (ν_0; $\nu_1\nu_2\nu_3$)
$RbZn_4P_3$	Ambient condition	No inversion	+	+	+	+	***(0; 000)***
	Hydrostatic pressure; $P = 45$ GPa	One inversion	−	+	+	+	***(1; 000)***
	10% epitaxial strain	One inversion	−	+	+	+	***(1; 000)***
$RbZn_4As_3$	Ambient condition	No inversion	+	+	+	+	***(0; 000)***
	Hydrostatic pressure; $P = 38$ GPa	One inversion	−	+	+	+	***(1; 000)***
	8% epitaxial strain	One inversion	−	+	+	+	***(1; 000)***

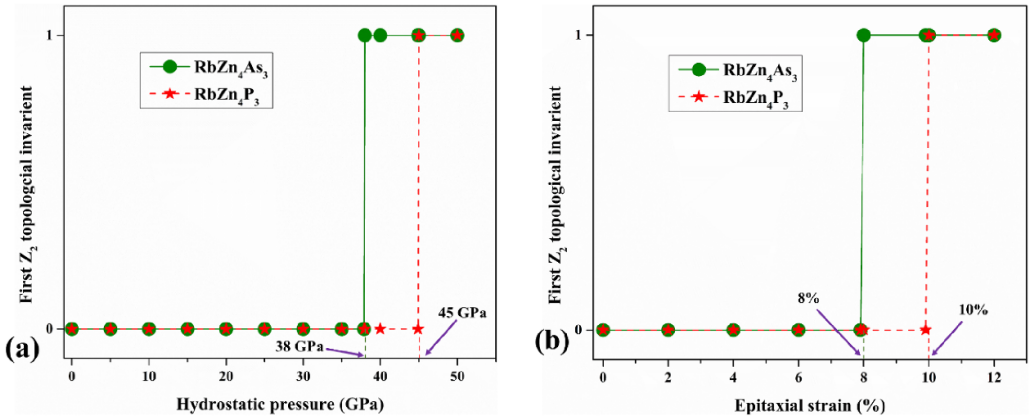

Figure 8. The variation of the first $\mathbb{Z}_2$ topological invariant ν_0 with (a) applied hydrostatic pressure and (b) epitaxial strain.

(10% and 8%), the first $\mathbb{Z}_2$ topological invariant ν_0 switched to 1 and the other three ($\nu_1\nu_2\nu_3$) remains the same for $RbZn_4X_3$ (X = P, As), respectively. The non-zero value of ν_0 established that the materials $RbZn_4X_3$ (X = P, As) are strong TIs at the aforementioned pressure and strain conditions.

Moreover, to determine the $\mathbb{Z}_2$ indices, the evolution of the WCCs in the Wilson loop method [78], along six TRIM planes, i.e. (i) $k_1 = 0.0$; (ii) $k_1 = 0.5$; (iii) $k_2 = 0.0$; (iv) $k_2 = 0.5$; (v) $k_3 = 0.0$; (vi) $k_3 = 0.5$; can also be used. The $\mathbb{Z}_2$ indices for a 3D system can also be calculated using the following equations;

$$\nu_0 = \{z_2\,(k_{i=1,2,3} = 0) + z_2\,(k_{i=1,2,3} = 0.5)\} \bmod 2 \quad (4)$$

$$\nu_{i=1,2,3} = z_2\,(k_i = 0.5)\,. \quad (5)$$

The number of intersections of a random reference line across the k_i-*axis* can be used to calculate the z_2 value in that TRIM plane. It is due to the fact that these systems hold TRS and WCCs that exist along the six different planes which are spanned by TRIM points. The even and the odd number of crossings are, respectively, illustrative of trivial and non-trivial phases with respective $\mathbb{Z}_2$ indices as 0 and 1. At the ambient condition for $RbZn_4X_3$ (X = P, As), there is zero intersection between the reference line and the WCCs in $k_x = 0$, $k_y = 0$, $k_z = 0$ and $k_x = 0.5$, $k_y = 0.5$, $k_z = 0.5$ planes as shown in figures 4(c) and (d), which verifies the trivial nature of the system with $\mathbb{Z}_2$ topological indices (*0; 000*). But, at the particular values of pressure (figures 5(g) and (h)) and epitaxial strain (figures 6(g) and (h)), the bands of WCCs and reference lines show an odd number of intersections in the planes $k_x = 0$, $k_y = 0$, $k_z = 0$, whereas, an even number of intersections are observed for $k_x = 0.5$, $k_y = 0.5$, $k_z = 0.5$ planes. Hence, using equations (4) and (5), the $\mathbb{Z}_2$ topological indices (ν_0; $\nu_1\nu_2\nu_3$) are (*1; 000*). This clearly suggests that the systems $RbZn_4X_3$ (X = P, As) are topologically non-trivial for these particular values of hydrostatic pressure and epitaxial strain.

The variation of the first $\mathbb{Z}_2$ topological invariant (ν_0) with applied pressure and epitaxial strain is represented in figures 8(a) and (b) for $RbZn_4X_3$ (X = P, As). The occurrence of TPT in these Zintl compounds $RbZn_4X_3$ (X = P, As) with hydrostatic pressure and epitaxial strain can be an effective way to obtain the topological phase in suitable material via band engineering.

4. Summary

We have systematically studied TPT in Zintl compounds $RbZn_4X_3$ (X = P, As) with applied hydrostatic pressure and epitaxial strain using DFT and the Green function approach. These materials have been reported, in an experimental study, to exist in the tetragonal phase. Firstly, we have verified the dynamical as well as mechanical stabilities of these materials at ambient and elevated values of hydrostatic pressure and epitaxial strain. We have observed a semiconducting ground state for these materials, via TB-mBJ functional, and the topologically trivial nature at ambient conditions which are in good agreement with available experimental and theoretical studies.

We have incorporated the spin–orbit interaction effect in bulk band structure calculation to observe the inverted contribution of projected orbitals near the Fermi level. Our calculations have predicted the TPT in $RbZn_4P_3$ ($RbZn_4As_3$) with the applied hydrostatic pressure of 45 GPa (38 GPa) and the epitaxial strain of 10% (8%). This TPT has been identified with band inversions between *Zn-s* and *P-*p_z orbitals near the Fermi level. This topologically non-trivial phase has been verified via the SDOSs and Fermi arc contour plotted along the *(001)-plane*. We have also calculated the $\mathbb{Z}_2$ topological indices with the help of the Kane and Mele model as well as the evolution of WCCs at various values of pressure and epitaxial strain to establish the TPTs in these materials.

Data availability statement

All data that support the findings of this study are included within the article (and any supplementary files).

Acknowledgment

All the authors acknowledge the National Supercomputing Mission (NSM) for providing computing resources of 'PARAM Siddhi-AI', under the National PARAM Supercomputing Facility (NPSF), C-DAC, Pune and supported by the Ministry of Electronics and Information Technology (MeitY) and Department of Science and Technology (DST), Government of India. One of the authors (Ramesh Kumar) would like to thank the Council of Scientific and Industrial Research (CSIR), Delhi, for financial support.

Conflict of interest

The authors declare that they have no known competing financial interests or personal relationships that could have appeared to influence the work reported in this paper.

ORCID iDs

Ramesh Kumar https://orcid.org/0000-0002-6916-4973
Antik Sihi https://orcid.org/0000-0001-7862-7370
Mukhtiyar Singh https://orcid.org/0000-0002-2234-7764

References

[1] Hasan M Z and Kane C L 2010 *Rev. Mod. Phys.* **82** 3045
[2] Qi X–L and Zhang S-C 2011 *Rev. Mod. Phys.* **83** 1057
[3] Zhang H, Liu C-X, Qi X-L, Dai X, Fang Z and Zhang S-C 2009 *Nat. Phys.* **5** 438–42
[4] Chen Y *et al* 2009 *Science* **325** 178
[5] Xia Y *et al* 2009 *Nat. Phys.* **5** 398
[6] Fu L 2011 *Phys. Rev. Lett.* **106** 106802
[7] Hsieh T H, Lin H, Liu J, Duan W, Bansil A and Fu L 2012 *Nat. Commun.* **3** 982
[8] Tanaka Y, Ren Z, Sato T, Nakayama K, Souma S, Takahashi T, Segawa K, Ando Y and Sato T 2012 *Nat. Phys.* **8** 800–3
[9] Wang Z, Sun Y, Chen X-Q, Franchini C, Xu G, Weng H, Dai X and Fang Z 2012 *Phys. Rev.* B **85** 195320
[10] Liu Z K *et al* 2014 *Science* **343** 864
[11] Lv B Q *et al* 2015 *Phys. Rev.* X **5** 031013
[12] Xu S-Y *et al* 2015 *Science* **349** 613
[13] Xu Q, Song Z, Nie S, Weng H, Fang Z, Dai X and Dai X 2015 *Phys. Rev.* B **92** 205310
[14] Hu J *et al* 2016 *Phys. Rev. Lett.* **117** 016602
[15] Khalid S, Sabino F P and Janotti A 2018 *Phys. Rev.* B **98** 220102(R)
[16] Guo P J, Yang H C, Liu K and Lu Z Y 2017 *Phys. Rev.* B **96** 081112(R)
[17] Ma J-Z *et al* 2018 *Nat. Phys.* **14** 349
[18] He J B, Chen D, Zhu W L, Zhang S, Zhao L X, Ren Z A and Chen G F 2017 *Phys. Rev.* B **95** 195165
[19] Moore J E 2010 *Nature* **464** 194–8
[20] He M, Sun H and He Q L 2019 *Front. Phys.* **14** 4
[21] Fan Y and Wang K L 2016 *SPIN* **6** 2
[22] Yan B, Liu C-X, Zhang H-J, Yam C-Y, Qi X-L, Frauenheim T and Zhang S-C 2010 *Europhys. Lett.* **90** 37002
[23] Chen Y L *et al* 2010 *Phys. Rev. Lett.* **105** 266401
[24] Lin H, Markiewicz R S, Wray L A, Fu L, Hasan M Z and Bansil A 2010 *Phys. Rev. Lett.* **105** 036404
[25] Jin H, Song J-H, Freeman A J and Kanatzidis M G 2011 *Phys. Rev.* B **83** 041202(R)
[26] Yan B H, Zhang H-J, Liu C-X, Qi X-L, Frauenheim T and Zhang S-C 2010 *Phys. Rev.* B **82** 161108(R)
[27] Zhang H-Z, Chadov S, Muchler L, Yan B, Qi X-L, Kubler J, Zhang S-C and Felser C 2011 *Phys. Rev. Lett.* **106** 156402
[28] Lin H, Wray L A, Xia Y, Xu S, Jia S, Cava R J, Bansil A and Hasan M J 2010 *Nat. Mater.* **9** 546–9
[29] Xiao D, Yao Y Y, Feng W, Wen J, Zhu W, Chen X-Q, Stocks G M and Zhang Z 2010 *Phys. Rev. Lett.* **105** 096404
[30] Feng W, Xiao D, Ding J and Yao Y 2011 *Phys. Rev. Lett.* **106** 016402
[31] Li X *et al* 2019 *PNAS* **116** 17696–700
[32] Singh M, Kumar R and Bibiyan R K 2022 *Eur. Phys. J. Plus* **137** 633
[33] Wadhwa P, Kumar S, Shukla A and Kumar R 2019 *J. Phys.: Condens. Matter* **31** 335401
[34] Nidhi, Kumar R, Bibiyan R K and Singh M 2025 *J. Appl. Phys.* **58** 015304
[35] Kumar R and Singh M 2025 *J. Phys. Chem. Sol.* **196** 112356
[36] Wadhwa P, Kumar R, Kumar S and Shukla A 2020 *Solid State Commun.* **321** 114022
[37] Kumar R and Singh M 2024 *J. Phys.: Condens. Matter* **36** 345601
[38] Sklyadneva I Y, Rusinov I P, Heid R, Bohnen K-P, Echenique P M and Chulkov E V 2016 *Sci. Rep.* **6** 24137
[39] Qi Y *et al* 2017 *Adv. Mater.* **29** 1605965
[40] Yang M, Luo Y Z, Zeng M G, Shen L, Lu Y H, Zhou J, Wang S J, Souf I K and Feng Y P 2017 *Phys. Chem. Chem. Phys.* **19** 29372–80
[41] Ohmura A, Higuchi Y, Ochiai T, Kanou M, Ishikawa F, Nakano S, Nakayama A, Yamada Y and Sasagawa T 2017 *Phys. Rev.* B **95** 25203
[42] Khalid S and Janotti A 2020 *Phys. Rev.* B **102** 035151
[43] Fragkos S *et al* 2019 *Phys. Rev. Mater.* **3** 104201
[44] He H, Tyson C and Bobev S 2011 *Inorg. Chem.* **50** 8375–83
[45] Gvozdetskyi V *et al* 2019 *Chem. Mater.* **31** 8695–707
[46] Dusastre V 2017 *Nat. Mater.* **16** 15
[47] Pakhira S, Heitmann T, Riberolles S X M, Ueland B G, McQueeney R J, Johnston D C and Vaknin D 2021 *Phys. Rev.* B **103** 024408
[48] Sangeeta, Kumar R and Singh M 2022 *J. Mater. Sci.* **57** 10691–701
[49] Wang L-L, Kaminski A, Canfield P C and Johnson D D 2018 *J. Phys. Chem.* C **122** 705–13
[50] Cao W *et al* 2023 *Phys. Rev.* B **108** 224510

[51] Varnava N, Berry T, McQueen T M and Vanderbilt D 2022 *Phys. Rev.* B **105** 235128
[52] Huang J *et al* 2023 *Chin. Phys. Lett.* **40** 047101
[53] Kundu A K, Roy T, Pakhira S, Wu Z-B, Tsujikawa M, Shirai M, Johnston D C, Pasupathy A N and Valla T 2022 *npj Quantum. Mater.* **7** 67
[54] Feng L-Y, Villaos R A B, Maghirang III A B, Huang Z-Q, Hsu C-H, Lin H and Chuang F-C 2022 *Sci. Rep.* **12** 4582
[55] Zhu Z, Li M and Li J 2016 *Phys. Rev.* B **94** 155121
[56] Sun Y, Chen X-Q, Franchini C, Li D, Yunoki S, Li Y and Fang Z 2011 *Phys. Rev.* B **84** 165127
[57] Medina-Gonzalez A M, Yox P, Chen Y, Adamson M A S, Svay M, Smith E A, Schaller R D, Rossini A J and Vela J 2021 *ACS Mater. Au* **1** 130–9
[58] Wang Y-Y *et al* 2020 *Phys. Rev.* B **102** 115122
[59] Kang L, Cao Z—Y and Wang B 2022 *J. Phys. Chem. Lett.* **13** 11521–7
[60] Pei C *et al* 2022 *Cell Rep. Phys. Sci.* **3** 101094
[61] Rajaji V, Arora R, Joseph B, Roychowdhury S, Waghmare U V, Biswas K and Narayana C 2023 *Phys. Rev.* B **107** 205139
[62] Dai G *et al* 2023 *npg Asia Mater.* **15** 52
[63] Chen Y *et al* 2013 *J. Phys. Chem.* C **117** 25677–83
[64] Qi Y *et al* 2018 *npj Quantum. Mater.* **3** 4
[65] Fu L and Kane C L 2007 *Phys. Rev.* B **76** 045302
[66] Hohenberg P and Kohn W 1964 *Phys. Rev.* **136** B864
[67] Kohn W and Sham L J 1965 *Phys. Rev.* **140** A1133
[68] Kresse G and Joubert D 1999 *Phys. Rev.* B **59** 1758
[69] Kresse G and Furthmüller J 1996 *Phys. Rev.* B **54** 11169
[70] Perdew J P, Burke K and Ernzerhof M 1996 *Phys. Rev. Lett.* **77** 3865
[71] Tran F and Blaha P 2009 *Phys. Rev. Lett.* **102** 226401
[72] Monkhorst J H and Pack J D 1976 *Phys. Rev.* B **13** 5188
[73] Togo A and Tanaka I 2015 *Scr. Mater.* **108** 1–5
[74] Wang V, Xu N, Liu J C, Tang G and Geng W T 2021 *Comput. Phys. Commun.* **267** 108033
[75] Marzari N, Mostofi A A, Yates J R, Souza I and Vanderbilt D 2012 *Rev. Mod. Phys.* **84** 1419
[76] Wu Q S, Zhang S N, Song H-F, Troyer M and Soluyanov A A 2018 *Comput. Phys. Commun.* **224** 405–16
[77] Mouhat F and Coudert F-X 2014 *Phys. Rev.* B **90** 224104
[78] Yu R, Qi X L, Bernevig A, Fang Z and Dai X 2011 *Phys. Rev.* B **84** 075119